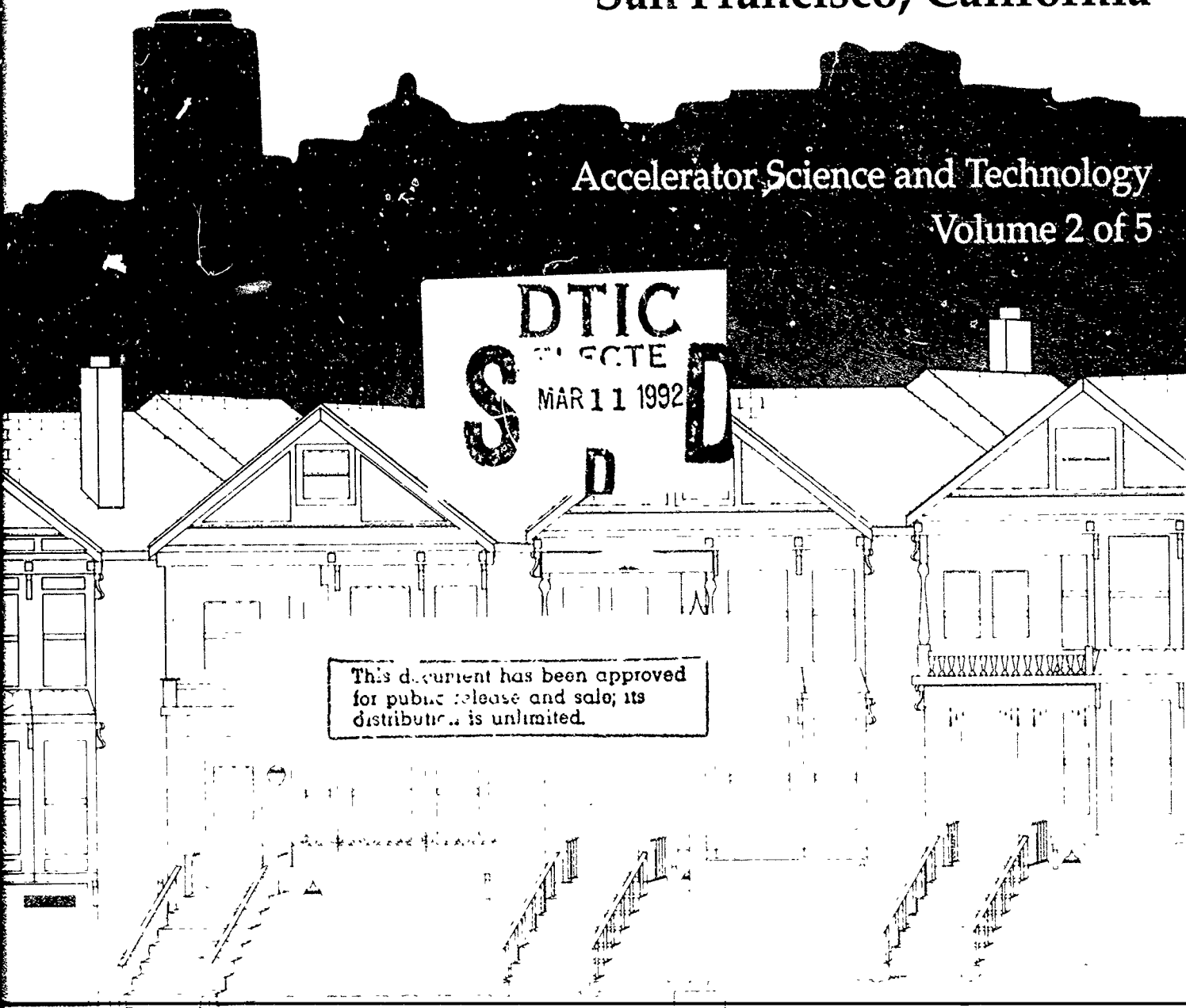
AD-A247 537

91CH3038-7
Conference Record

1991 IEEE Particle Accelerator Conference

May 6–9, 1991
San Francisco, California



Accelerator Science and Technology
Volume 2 of 5

DTIC
ELECTE
MAR 11 1992
S D

This document has been approved for public release and sale; its distribution is unlimited.



Conference Record of the 1991 IEEE Particle Accelerator Conference

DTIC COPY INSPECTED 6

Accesion For
NTIS CRA&I [X]
DTIC TAB [ ]
Unannounced [ ]
Justification .....
By .....
Distribution /
Availability Codes
Dist | Avail and / or Special
A-1 | 21

Accelerator Science and Technology

May 6–9, 1991
San Francisco, California

Volume 2 of 5

IEEE Service Center
445 Hoes Lane
P.O. Box 1331
Piscataway, N.J. 08854-1331
212.00 per set Vol. 1,2,3,4&5
NWW 3/10/92

Organized by
Lawrence Berkeley Laboratory
Stanford Linear Accelerator Center
with Assistance of
Los Alamos National Laboratory

Under the Auspices of
Institute of Electrical and Electronics Engineers—
Nuclear and Plasma Sciences Society

Sponsored by
Department of Energy
Offices of High Energy and Nuclear Physics
Superconducting Super Collider
Basic Energy Sciences
National Science Foundation
Office of Naval Research

92-06078

92 3 09 002

IEEE Catalog Number 91CH3038-7
ISBN 0-7803-0135-8 (Softbound)
ISBN 0-7803-0136-6 (Casebound)
ISBN 0-7803-0137-4 (Microfiche)
Library of Congress Number 88-647453

Additional copies are available from

IEEE Service Center
445 Hoes Lane
P.O. Box 1331
Piscataway, NJ 08854-1331
1-800-678-IEEE

Copyright and Reprint Permission: Abstracting is permitted with credit to the source. Libraries are permitted to photocopy beyond the limit of U.S. copyright law for private use of patrons those articles in this volume that carry a code at the bottom of the first page, provided the per-copy fee indicated in the code is paid through Copyright Clearance Center, 27 Congress Street, Salem, MA 01970. Instructors are permitted to photocopy isolated articles for non-commerical classroom use without fee. For other copying, reprint or republication permission, write to Director, Publishing Services, IEEE, 345 47th Street, New York, NY 10017. All rights reserved. Copyright © 1991 by The Institute of Electrical and Electronics Engineers, Inc.

Cover Artwork by Sylvia MacBride, SLAC
Conference Photos by Tom Nakashima, SLAC

TABLE OF CONTENTS

Volume 1

Conference Organizations ..... Volume 1 v
Comments on the Conference ..... Volume 1 vii
Conference Highlights Photo Section ..... Volume 1 xlv
List of Attendees ..... Volume 5 ix

Opening Plenary Session

Chairman: K. Berkner

Physics and technology challenges of BB factories *(Invited Paper)* — *Michael S. Zisman* 1
Charged particle accelerators for inertial fusion energy *(Invited Paper)* — *Stanley Humphries, Jr.* 6
Physics and technology challenges of ultra low emittance synchrotron light sources *(Invited Paper)* — *S. Krinsky* 11

Accelerator Technology III–Superconducting Components, Magnets

Chairman: P. Mantsch

Superconducting accelerator cavities on a large scale *(Invited Paper)* — *Yuzo Kojima* 16
Microscopic examination of field emission areas in superconducting Nb cavities — *D. Moffat, T. Flynn, L. Hand, J. Kirchgessner, R. Noer, H. Padamsee, D. Rubin, J. Sears, and Q. Shu* 21
Issues confronting vacuum system design for e^+e^- storage rings *(Invited Paper)* — *Nari B. Mistry* 24
APS storage ring vacuum system development — *R. C. Niemann, R. Benaroya, M. Choi, R. J. Dowgat, R. Ferry, G. A. Goeppner, J. D. Gonczy, C. Krieger, J. Howell, R. W. Nielsen, B. Roop, and R. B. Wei* 29
Design of superconducting magnets for the SSC — *R. B. Palmer* 32
Field quality issues in superconducting magnets — *P. Schmüser* 37
A comparison of calculations and measurements of the field harmonics as a function of current in the SSC dipole magnets — *R. C. Gupta, J. G. Cottingham, S. A. Kahn, G. H. Morgan, and P. Wanderer* 42
Analysis of magnetic field measurement results for the AGS booster magnets — *E. Bleser and R. Thern* 45

Low- and Medium-Energy Accelerators and Rings

Chairman: R. Richardson

Some recollections on the story of the cyclotron and comments on higher degrees *(R. R. Wilson Prize Lecture)* — *J Reginald Richardson* 48
Construction and early commissioning results of the AGS booster *(Invited Paper)* — *W. T. Weng, L. Ahrens, R. Damm, and A. J. McNerney* 52
The TRIUMF KAON factory *(Invited Paper)* — *M. K. Craddock* 57
The Superconducting Super Collider low energy booster: A status report — *R. C. York, W. Funk, A. Garren, S. Machida, N. K. Mahale, J. Peterson, F. Pilat, X. Wu, and U. Wienands* 62

Commissioning and first operation of a 500 μA, 30 MeV, H⁻ cyclotron: The TR30 — *B. F. Milton, G. Dutto, P. W. Schmor, H. R. Schneider, R. Dawson, K. L. Erdman, W. Gyles, J. Sample, and Q. Walker* 65
DAΦNE: The Frascati Φ-factory — *G. Vignola* 68
CW racetrack microtrons *(Invited Paper)* — *M. A. D. Wilson* 71
Present status of ion cooler rings *(Invited Paper)* — *Takeshi Katayama* 76

High Energy Accelerators and Colliders

Characteristics of the new Tevatron lattice — *S. Y. Hsueh, D. Finley, N. M. Gelfand, G. Goderre, B. Hendricks, D. Herrup, D. E. Johnson, R. P. Johnson, R. Joshel, K. Koepke, S. Saritepe, and D. Siergiej* 81
PEP-II: An asymmetric *B* factory based on PEP — *A. Hutton and M. S. Zisman* 84
Early operating experience with the new TEVATRON low-β insertion — *D. A. Herrup, C. Ankenbrandt, G. Annala, D. Finley, N. Gelfand, G. Goderre, B. Hendricks, D. E. Johnson, R. P. Johnson, R. Joshel, K. Koepke, S. Pruss, S. Saritepe, and D. Siergiej* 87
Prospects for tunes near the integer at the Fermilab PBAR-P collider — *D. Siergiej, C. Ankenbrandt, D. Finley, G. Goderre, R. P. Johnson, and P. Zhang* 90
Common mode noise on the main Tevatron bus and associated beam emittance growth — *P. Zhang, R. P. Johnson, M. Kuchnir, D. Siergiej, and D. Wolff* 93
Design and multiparticle simulation of the half integer slow extraction system for the main injector — *D. Trbojevic and M. Harrison* 96
Modification of the horizontal dispersion in the Fermilab main ring with additional quadrupoles — *D. Trbojevic, I. Kourbanis, and C. Ankenbrandt* 99
Computation of the TEVATRON luminosity using measured machine parameters — *N. M. Gelfand* 102
Characteristics of the beam during the second Fermilab collider run — *Norman Gelfand* 105
Energy and energy width measurement in the FNAL antiproton accumulator — *M. Church, S. Y. Hsueh, P. A. Rapidis, and S. Werkema* 108
Experimental study of the main ring transition crossing — *Ioanis Kourbanis, Keith Meisner, and King-Yuen Ng* 111
Lattice function perturbations caused by the beam-beam interaction — *D. E. Johnson, N. Gelfand, R. P. Johnson, and S. Saritepe* 114
Evolution of SSC collider design — *M. J. Syphers* 117
Design description of the SSC high energy booster — *D. E. Johnson* 120
The medium energy booster at the SSC laboratory — *Cleon Manz and Rod Gerig* 123
Physics issues of the synchrotron radiation intercept at the Superconducting Super Collider — *Weiren Chou* 126
Planning and development of underground facilities for the SSC — *T. K. Lundin, C. Laughton, D. L. Earsom, and M. J. Syphers* 129
CESR-B, upgrading the CESR facility to B-factory capability — *M. Tigner* 132
A B-factory in the PETRA tunnel — *F. Willeke* 135
Accelerator design of the KEK B-factory — *Shin-ichi Kurokawa, Kotaro Satoh, and Fumihiko Takasaki* 138
Decay rates and average luminosity in a B-factory — *H. Braun, W. Joho, and K. Hübner* 141
Single interaction point operation of CESR — *D. L. Rubin and Louis A. Schick* 144
Observation of transverse polarization in LEP — *J. Badier, A. Blondel, M. Crozon, B. Dehning, L. Knudsen, J.-P. Koutchouk, M. Placidi, and R. Schmidt* 147
The LEP energy upgrade project — *Carlo Wyss* 150
Proton antiproton collisions at a finite crossing angle in the SPS — *K. Cornelis, W. Herr, and M. Meddahi* 153
An optimized e–p insertion for LEP and LHC — *A. Verdier* 156
A transitionless lattice for the Fermilab main injector — *K. Y. Ng, D. Trbojevic, and S. Y. Lee* 159
Examination of the stability of the advanced imaginary γ_t lattice — *K. Y. Ng, D. Trbojevic, and S. Y Lee* 162
A preliminary design of the PS collider — *Y. Mori, M. Yoshii, T. Toyama, I. Sakai, T. Shintomi, T. Suzuki, S. Ninomiya, A. Takagi, H. Sato, S. Hiramatsu, and E. Takasaki* 165

'Siberian Snake' solenoid for the AGS — *L. G. Ratner* 168
The CERN PS complex as part of the LHC injector chain — *R. Cappi, R. Garoby, S. Hancock, M. Martini, N. Rasmussen, T. Risselada, J. P. Riunaud, K. Schindl, H. Schönauer, and E. J. N. Wilson* 171
Mixed ion beams near transition energy — *S. Hancock* 174
Crystal optics of high energy beams — *M. D. Bavizhev, V. M. Biryukov, A. I. Drozhdin, K. P. Myznikov, Y. S. Fedotov, I. A. Yazunin, A. R. Dziba, A. M. Taratin, and S. A. Vorobiev* 177
The BEPC storage ring— *Status and prospects* — *Y. Wu* 180
Status of the Novosibirsk phi-factory project — *L. M. Barkov, S. A. Belomestnykh, V. V. Danilov, N. S. Dikansky, A. N. Filippov, B. I. Grishanov, P. M. Ivanov, I. A. Koop, O. B. Malyshev, S. S. Nagaitsev, I. N. Nesterenko, E. A. Perevedentsev, D. V. Pestrikov, L. M. Schegolev, I. K. Sedlyarov, Y. M. Shatunov, E. A. Simonov, A. N. Skrinsky, I. B. Vasserman, V. G. Vescherevich, P. D. Vobly, and E. I. Zinin* 183
Compensation of the chromatic effects in the Novosibirsk Φ-factory lattice — *V. V. Danilov, A. N. Filippov, P. M. Ivanov, I. A. Koop, and E. A. Perevedentsev* 186
On using bent single crystals for proton extraction from IHEP accelerator — *A. A. Asseev, M. D. Bavizhev, E. A. Ludmirsky, V. A. Maisheev, E. A. Mjae, and Y. S. Fedotov* 189
Bent single crystals to form high energy particle beams — *N. A. Galyaev, V. N. Zapol'sky, V. I. Kotov, S. V. Tsarik, and Y. A. Chesnokov* 192
JINR tau-charm factory design considerations — *V. S. Alexandrov, V. K. Antropov, O. V. Arkhipov, P. F. Beloshitsky, L. V. Bobyleva, D. I. Kaltchev, V. I. Kazacha, N. Y. Kazarinov, A. K. Krasnykh, V. I. Mironov, L. M. Onischenko, E. A. Perelstein, A. N. Sissakian, Y. I. Smirnov, and T. D. Vylov* 195

Beam Dynamics II

Geometrical (Lienard-Wichert) approach in accelerator physics — *S. G. Arutunian and M. R. Mailian* 198
Simulation of a storage ring free electron laser with a mapping algorithm for distribution functions — *V. Ziemann* 201
Particle orbit tracking on a parallel computer: Hypertrack — *B. Cole, G. Bourianoff, F. Pilat, and R. Talman* 204
Lattice parameters database and operational simulation at FNAL and SSCL — *Eric Barr, Steve Peggs, Leo Michelotti, Al Russell, Selcuk Saritepe, C. G. Trahern, and J. Zhou* 207
Effects of errors on the dynamic aperture of the advanced photon source storage ring — *H. Bizek, E. Crosbie, E. Lessner, L. Teng, and J. Wirsbinski* 210
Parasitic crossing at an asymmetric B factory, apiary — *Y. H. Chin* 213
Effect of RF phase noise on the SSC beam — *J. A. Ellison, B. S. Newberger, and H.-J. Shih* 216
Optimizing a nonlinear collimation system for future linear colliders — *N. Merminga, J. Irwin, R. Helm, and R. D. Ruth* 219
Simulation of high energy beam focusing by a plasma — *S. Rajagopalan and P. Chen* 222
Separation criterion and scaling law for long-range beam–beam interactions in the Tevatron — *S. Saritepe* 225
Observation and analysis of time-dependent closed orbit motion in the LAMPF proton storage ring — *R. Hutson, D. Fitzgerald, and R. Macek* 228
Quantum variances for transverse SSC injection dynamics — *T. Garavaglia* 231
Relativistic acceleration and retardation effects on photoemission of intense electron short pulses, in RF-FEL photoinjectors — *J.-M. Dolique and M. Coacolo* 233
Transverse emittance of an intense electron short pulse just emitted by the cathode of a RF-FEL photoinjector: Influence of electrodynamic effects — *J.-M. Dolique and M. Coacolo* 236
Observation of plasma wakefield effects during high-current relativistic electron beam transport — *J. D. Miller, R. F. Schneider, K. T. Nguyen, G. Joyce, D. J. Weidman, J. Goldhar, and H. S. Uhm* 239
Beam dynamics in the spiral line induction accelerator — *S. Slinker, J. Krall, M. Lampe, and G. Joyce* 242
Upgrade of the PHERMEX accelerator — *T.P. Hughes, D. C. Moir, and R. L. Carlson* 245
Experimental studies of emittance growth due to initial mismatch of a space charge dominated beam in a solenoidal focusing channel — *D. Kehne, M. Reiser, and H. Rudd* 248

Simulation studies of emittance growth in RMS mismatched beams — *A. Cucchetti, M. Reiser, and T. Wangler* 251
The incoherent beam–beam effect in linear-on-ring colliders — *C. D. Johnson* 254
Nonlinear dynamics of electrons in alternating-sign toroidal magnetic field — *Y. L. Martirosian and M. L. Petrosian* .. 257
Transport and error sensitivity in a heavy-ion recirculator — *W. M. Sharp, J. J. Barnard, and S. S. Yu* 260
3d and *r, z* particle simulation of beams for heavy ion fusion: The WARP code — *A. Friedman, D. P. Grote, D. A. Callahan, A. B. Langdon, and I. Haber* 263
Canonical particle tracking in undulator fields — *G. Wüstefeld and J. Bahrdt* 266
The spin motion calculation using lie method in collider nonlinear magnetic field — *Y. Eidelman and V. Yakimenko* .. 269
ASAP— *A symbolic algebra package for accelerator design* — *Eva Bozoki, Aharon Friedman, and Ilan Ben-Zvi* 272
Digital computer simulation of three-dimensional ion beam extraction and transport systems — *Jack E. Boers* 275
Digital computer simulation of axisymmetric electron beams and guns of any energy — *Jack E. Boers* 278
Using MOTER to design PILAC — *H. S. Butler, Z. Li, and H. A. Thiessen* 281
ELISE, a code for intensity dependent effects — *Mark Q. Barton* 284
Program DIMAD: Vectorization, links with DA, LIELIB and COSY-∞ — *Roger V. Servranckx* 287
Aperture determination by long term and multiparticle tracking — *G. F. Dell and G. Parzen* 288
A different approach to beam–beam interaction simulation — *Stephen Milton* 291
Chromaticity modelling in the Fermilab main ring — *J. E. Goodwin and S. M. Pruss* 294
Turnplot—A graphical tool for analyzing tracking data — *V. Paxson and L. Schachinger* 297
RAMPRF: A program for synchronous acceleration — *Miguel A. Furman* 300
Application of differential-and-lie algebraic techniques to the orbit dynamics of cyclotrons — *W. G. Davies, S. R. Douglas, G. D. Pusch, and G. E. Lee-Whiting* 303
Recovering phase density distribution from line density — *Joseph M. Kats* 306
DIMAD based interactive simulation of the CEBAF accelerator — *M. H. Bickley, D. R. Douglas, and R. V. Servranckx* . 309
A high-order moment simulation model — *K. T. Tsang, C. Kostas, D. P. Chernin, J. J. Petillo, and A. Mondelli* 312
LEBT modeling with ARGUS — *J. J. Petillo and A. A. Mondelli* 315
Model performance of the new Tevatron Collider lattice — *S. Saritepe and S. Peggs* 318
Conformal FDTD modeling of 3-D wake fields — *T. G. Jurgens and F. A. Harfoush* 321
First polarization calculations in MAD — *Hans Grote* 324
Improvements in MAD in view of LHC design — *F. Christoph Iselin* 327
Space-charge calculation for bunched beams with 3-D ellipsoidal symmetry — *R. W. Garnett and T. P. Wangler* 330
ZLIB: A numerical library for differential algebra and lie algebraic treatment of beam dynamics — *Yiton T. Yan* 333
Applications of ZMAP to the SSC — *A. W. Chao, T. Sen, Y. T. Yan, and E. Forest* 336
Implementation of one-turn maps in SSCTRK using ZLIB — *S. K. Kauffmann, D. M. Ritson, and Y. T. Yan* 339
LIEMAP: A program for extracting a one-turn single exponent lie generator map — *Tanaji Sen, Y. T. Yan, and J. Irwin* . 342
Effect of tune modulation on the dynamic aperture of the SSC lattice — *Tanaji Sen, A. W. Chao, and Y. T. Yan* 345
Closed orbit correction in the SSC — *G. Bourianoff, B. Cole, H Ferede, and F. Pilat* 348
Design characteristics of the Linac–LEB transfer line for the SSC — *R. K. Bhandari, E. Seppi, and S. Penner* 351
The code COSY INFINITY — *M. Berz* 354
Collimator simulation for the TRIUMF KAON factory using DIMAD — *U. Wienands, C. P. Parfitt, and F. W. Jones* . 357
Dynamic aperture and extraction studies for the SSC high energy booster — *S. K. Dutt, A. W. Chao, D. E. Johnson, T. Sen, and Y. T. Yan* 360
Dynamic aperture and performance of the SSC low energy booster lattice — *F. Pilat, G. Bourianoff, B. Cole, R. Talman, and R. York* 363
The extension of the OSCAR2D code to compute azimuthally dependent modes of axially symmetric cavities — *P. Fernandes, G. Sabbi, and R. Parodi* 366
The HIF transport code FOCI — *D. W. Hewett and R. O. Bangerter* 369
Comparison of binning and sorting of magnets in the SSC high energy booster — *Mingyang Li and Shorokou Ohnuma* . 371
The beam dynamics study in a compact synchrotron — *Yunxiang Huang and Shoroku Ohnuma* 374
Compensation of RF transients during injection into the collector ring of the TRIUMF KAON factory — *Shane R. Koscielniak and Tai-Sen Wang* 377

Diffraction radiation by a charge sheet moving past a conducting wedge — *H. Henke* 380
Space charge effects in the SSC low energy booster — *S. Machida, G. Bourianoff, N. K. Mahale, N. Mehta, F. Pilat, R. Talman, and R. C. York* 383
Debunching and capture in the LEB for the SSC — *N. K. Mahale and Miguel A. Furman* 386
Longitudinal matching between the LEB and the MEB for the SSC — *N. K. Mahale and A. Maschke* 389
Constant of motion and dynamic equations for one dimensional autonomous system, and radiation damping — *G. López* . 392
Beam dynamics of multi-tank DTL and CCL designs — *C. C. Paulson, A. M. M. Todd, and S. L. Mendelsohn* 395
Electron density enhancement in a quasi isochronous storage ring — *C. Pellegrini and D. Robin* 398
Simultaneous acceleration of H^+ and H^- in RFQ linacs — *K. R. Crandall* 401
Limiting density distribution for charged particle beams in free space — *James S. O'Connell* 404
Phase space distribution of particles near an isolated difference resonance — *Jicong Shi, Yunxiang Huang, and Shoroku Ohnuma* 407
Transient beam loading reduction during multi-batch coalescing in the Fermilab main ring — *D. Wildman* 410
First turn around strategy for RHIC — *J. Milutinovic and A. G. Ruggiero* 413
Properties of the longitudinal equilibrium distribution in a storage ring — *V. Ziemann* 416
A study of misalignment effects of the ANL-APS electron linac focusing system — *A. Nassiri and G. Mavrogenes* ... 419
Hourglass effects for asymmetric colliders — *Miguel A. Furman* 422
IONSCAN: A program for optimizing charge-state combinations and calculating operating parameters for the Chalk River Superconducting Cyclotron — *Helena Lindqvist* 425
A study for lattice comparison for PLS 2 GeV storage ring — *M. Yoon* 428
Simulation of accelerating structures with large staggered tuning — *K. A. Thompson and J. W. Wang* 431
Tracking with space charge in the Fermilab booster — *S. Stahl and C. Ankenbrandt* 434
Emittance measurement in a magnetic field — *J. K. Boyd* 437
Collective effects in single bunch mode at the photon factory storage ring — *N. Nakamura, S. Sakanaka, K. Haga, M. Izawa, and T. Katsura* 440
Error analyses and modeling for CEBAF beam optical systems: Beam line element specifications and alignment error tolerances — *D. R. Douglas, J. Y. Tang, and R. C. York* 443
The CEBAF beam transport system lattice design — *B. Bowling, D. R. Douglas, L. H. Harwood, J. Kewisch, D. V. Neuffer, J. Y. Tang, and R. C. York* 446
Chromatic correction in the CEBAF beam transport system — *David R. Douglas* 449
Impedance for a multi-cell, multi-block structure — *I. Gjaja, R. Li, and R. L. Gluckstern* 452
Theory of relativistic electron beam bunching by the wakefield effects of a background plasma — *Han S. Uhm* 455
On the impedance due to synchrotron radiation — *S. Heifets and A. Michailichenko* 458
Transverse phase space in the presence of dispersion — *N. Merminga, P. L. Morton, J. T. Seeman, and W. L. Spence* .. 461
Measurements of synchro-betatron coupling by an RF cavity in CESR — *D. Rice, S. Greenwald, Z. Greenwald, and S. Peck* 464
Nearly equal β at CESR — *P. Bagley, M. Billing, S. Krishnagopal, D. Rubin, R. Siemann, and J. Welch* 467
Beam–beam performance as a function of β_0 at CESR — *Louis A. Schick and D. L. Rubin* 470
Tune modulated beam–beam resonances in the Tevatron — *S. Saritepe and S. Peggs* 473
Is beta modulation more or less potent than tune modulation? — *T. Satogata and S. Peggs* 476
Root-mean-square emittance analysis of a multiple beam system — *K. A. Boulais and M. J. Rhee* 479
Coherent beam–beam interaction in DAΦNE — *Kohji Hirata and Eberhard Keil* 482
Longitudinal tune-up of the SSC drift-tube and coupled cavity linac sections — *S. Nath and G. Neuschaefer* 485
A new approach to potential well bunch deformation — *J. Hagel and B. Zotter* 488
A new wake-potential calculation method using orthogonal polynomials — *Tai-Sen F. Wang and Bruno Zotter* 491
Transverse wake field characteristics of the KEK positron generator linac — *Yujiro Ogawa, Tetsuo Shidara, Masaru Takao, and Akira Asami* 494
Longitudinal wake field characteristics of the KEK positron generator linac — *M. Takao, Y. Ogawa, T. Shidara, and A. Asami* 497

Isochronous 180° turns for the SLC positron system — *R. H. Helm, J. E. Clendenin, S. D. Ecklund, A. V. Kulikov, and R. Pitthan* 500
Chromatic correction in the SLC bunch length compressors — *C. E. Adolphsen, P. J. Emma, T. H. Fieguth, and W. L. Spence* 503
Estimation of the longitudinal impedance of the ATF damping ring — *M. Takao, T. Higo, K. Kanazawa, H. Nakayama, J. Urakawa, K. Yokoya, and K. L. F. Bane* 506
Beam pulse shorting phenomena in a rf electron gun — *Y. Huang* 509
Beam emittance and the effects of the RF, space charge and wake fields— *Application to the ATF photoelectron beam* — *Zohreh Parsa* 511
On the low-beta optics for round and flat beams in colliders — *D. Möhl* 514
Synchrotron radiation perturbations in long transport lines — *G. Leleux, P. Nghiem, and A. Tkatchenko* 517
Beam-breakup calculations for the DARHT accelerator — *Paul Allison, Michael J. Burns, George J. Caporaso, and Art G. Cole* 520
Incoherent beam–beam effects for round beams in the Novosibirsk phi-factory project — *N. S. Dikansky, P. M. Ivanov, D. V. Pestrikov, and E. A. Simonov* 523
Longitudinal beam–beam effects for an ultra-high luminosity regime — *V. V. Danilov, P. M. Ivanov, E. A. Perevedentsev, and E. A. Simonov* 526
Compensation of coherent tune shift of betatron oscillation in storage rings — *V. V. Parkhomchuk, A. A. Sery, and V. D. Shiltsev* 529

Applications and New Methods of Acceleration

Applications Chairman: R. W Hamm

Developing a clinical proton accelerator facility: Consortium-assisted technology transfer *(Invited Paper)* — *James M. Slater, Daniel W. Miller, and Jon W. Slater* 532
Progress in light ion fusion *(Invited Paper)* — *D. L. Cook* 537
Overview of X-ray lithography at IBM using a compact storage ring *(Invited Paper)* — *Juan R. Maldonado* 542
Use of a high-current accelerator (CWDD) for neutron radiography — *C. L. Fink, D. L. Smith, and J. W. Meadows* ... 547

New Methods

New Methods Chairman: D. Sutter

The BNL accelerator test facility and experimental program *(Invited Paper)* — *Ilan Ben-Zvi* 550
An update on Argonne's AWA — *M. Rosing, E. Chojnacki, W. Gai, C. Ho, R. Konecny, S. Mtingwa, J Norem, P. Schoessow, and J. Simpson* 555
A new look at inverse Cerenkov acceleration and vacuum laser acceleration — *L. C. Steinhauer, W. D. Kimura, and R. D. Romea* 558
Pulse power driven high power traveling wave tube amplifiers — *J. A. Nation, J. D. Ivers, G. S. Kerslick, L. Schachter, and D. Shiffler* 561
Laser wakefields at UCLA and LLNL — *W. B. Mori, T. Katsouleas, C. B. Darrow, C. E. Clayton, C. Joshi, J. M. Dawson, C. B Decker, K. Marsh, and S. C. Wilks* 564

Linear Accelerators and Pulsed Power Devices

Chairman: B. Jameson

The IH-structure and its capability to accelerate high current beams *(Invited Paper)* — *U. Ratzinger* 567

Design of the SSC linac — *J. Watson, R. Bhandari, C. Chang, Cutler R., L. Funk, G. Leifete, D. Raparia, T. Bhatia, R. Garnett, S. Nath, G. Neuschaefer, and L. Young* 572
Status of PLS 2 GeV linac project — *W. Namkung, M. Cho, I. S. Ko, Y. X. Luo, C. Ryu, S. Won, and T. N. Lee* 575
Beam-dynamics design and performance of the RF deflector in the Los Alamos single-beam funnel experiment — *F. W. Guy, K. F. Johnson, and O. R. Sander* 578
Control of energy sweep and transverse beam motion in induction linacs *(Invited Paper)* — *William C. Turner* 581
Emittance variations in current-amplifying ion induction linacs *(Invited Paper)* — *Thomas J. Fessenden* 586
Fast risetime BLT switches for accelerator applications — *G. Kirkman-Amemiya, N. Reinhardt, M. S. Choi, and M. A. Gundersen* 591

Contents

Accelerator Technology II–RF, Power Supplies, Operations

The SISSI project: An intense secondary ion source using superconducting solenoid lenses — *A. Joubert, E. Baron, C. Grunberg, J. D. Larson, W. Mittig, and F. Ripouteau* 594
Application of carbon fibre composite materials for the collision sections of particle accelerators — *H. Betzold and G. Lippmann* 598
Energy compression system design for the MIT-Bates Accelerator Center — *J. B. Flanz, P. T. Demos, K. D. Jacobs, and A. Zolfaghari* 601
The Brookhaven ATF low-emittance beam line — *X. J. Wang and H. G. Kirk* 604
First-, second-, and third-order achromatic bend systems for free-electron laser applications — *D. P. Rusthoi and E. A. Wadlinger* 607
Commissioning results of the LLUMC beam switchyard and gantry — *M. E. Schulze* 610
SLIA beam line design — *J. J. Petillo, C. Kostas, D. P. Chernin, and A. A. Mondelli* 613
Induction accelerator test module for HIF — *Andris Faltens* 616
Plasma lenses for SLAC final focus test facility — *D. Betz, P. Chen, D. Cline, M. Gundersen, C. Joshi, T. Katsouleas, J. Norem, S. Rajagopalan, J. Rosenzweig, J. J. Su, and R. Williams* 619
Direct observation of plasma wakefield caused by a train of LINAC bunches — *A. Ogata, Y. Yoshida, N. Yugami, Y. Nishida, H. Nakanishi, K. Nakajima, H. Shibata, T. Kozawa, T. Kobayashi, and T. Ueda* 622
The SSC collider beam halo scraper system — *R. Soundranayagam, N. V. Mokhov, M. A. Maslov, and I. A. Yazynin* ... 625
Alignment of the SLC final focus system using beam orbits — *Y. Chao, F. LeDiberder, P. Burchat, W. Kozanecki, and N. Toge* 628
A laser alignment system for low beta quadrupoles — *C. Moore and H. Jostlein* 631
Fiducialization of magnets for the MIT-Bates SHR — *M. Farkhondeh, S. P. Holmberg, W. W. Sapp, and J. D. Zumbro* . 634
Efficiency and frequency stability in a high power microwave gap — *Y. Y. Lau and D. G. Colombant* 637
Fields and trajectories in the magnicon — *Paul Tallerico and Daniel Rees* 640
Proton synchrotron RF cavity mode damper tests — *W. R. Smythe, C. C. Friedrichs, and L. S. Walling* 643
A chopper driven 11.4-GHz traveling-wave RF generator — *G. Westenskow, J. Boyd, T. Houck, D. Rogers, R. Ryne, J. Haimson, and B. Mecklenburg* 646
High-current relativistic klystron amplifier development for microsecond pulse lengths — *M. V. Fazio, B. E Carlsten, R. Faehl, T. J. Kwan, D. G. Rickel, R. M. Stringfield, and P. J. Tallerico* 649
High-power radio-frequency binary pulse-compression experiment at SLAC — *T. L. Lavine, Z. D. Farkas, A Menegat, R. H. Miller, C. Nantista, G. Spalek, and P. B. Wilson* 652
Ferrite tuned cavity as possible source of bunched beam instability — *M. Popovic* 655
Amplification studies of a multi-megawatt two-cavity X-band gyroklystron — *W. Lawson, J. Calame, P. E. Latham, B. Hogan, C. D. Striffler, M. E. Read, V. Specht, W. Main, M. Reiser, and V. L. Granatstein* 658

Overview of the Superconducting Super Collider RF systems — *Jimmy D. Rogers and Jim H. Ferrell* 661
Use of Ferrite-50 to strongly damp higher order modes — *D. Moffat, P. Barnes, J. Kirchgessner, H. Padamsee, D. Rubin, J. Sears, and Q. Shu* 664
Current status of RF system for the SPring-8 — *K. Inoue, T. Nakamura, Y. Kawashima, and M. Hara* 667

Volume 2

Recycling of a LAMPF klystron — *Paul J. Tallerico and Robert L. Cady* 670
A new approach in simulating RF linacs using a general, linear real-time signal processor — *Andrew Young and Stephen P. Jachim* 672
Modeling of a 1700-MHz cluster cavity of planar triodes — *Daniel E. Rees and Carl Friedrichs* 675
Prototype 500 MHz planar RF input window for a B-factory accelerating cavity — *J. Kirchgessner, P. Barnes, R. Gerlack, D. Moffat, H. Padamsee, D. Rubin, and Q. S. Shu* 678
The AGS booster high frequency RF system — *R. T. Sanders, P. Cameron, W. Eng, M. A. Goldman, E. Jablonski, D. Kasha, J. Keane, A. McNerney, M. Meth, M. Plotkin, M. Puglisi, A. Ratti, and R. Spitz* 681
A fast amplitude and phase modulated RF source for AmPS — *F. B. Kroes, E. Heine, and T. G. B. W. Sluijk* 684
Higher order mode damping in a pill box cavity — *F. Voelker, G. Lambertson, and R. Rimmer* 687
RF impedance measurements of the various vacuum chambers for the Advanced Photon Source (APS) — *J. J. Song, J. W. Howell, R. L. Kustom, and J. F. Bridges* 690
Measurements on prototype cavities (352 MHz) for the Advanced Photon Source (APS) — *J. F. Bridges, J. M. Cook, R. L. Kustom, and J. J. H. Song* 693
Calculation of required tuner accuracy and bandwidth with and without fast feedback — *S. R. Koscielniak* 696
Analysis of eddy currents in the walls of the ferrite tuned rf cavity for the TRIUMF Kaon Factory Booster Synchrotron — *I. B. Enchevich, M. J. Barnes, and R. L. Poirier* 699
Power-combining and injection-locking magnetrons for accelerator applications — *Todd A. Treado, Todd A. Hansen, and David J. Jenkins* 702
Performance characteristics of the CEBAF klystron amplifier — *E. W. McCune and R. A. Fickett* 705
Development of 5-cell rf cavity for SPring-8 booster synchrotron — *H. Suzuki, T. Harami, Y. Miyahara, T. Rizawa, S. Satoh, Y. Tanabe, K. Yoshiyuki, T. Nagafuchi, S. Kawazu, and M. Nakano* 707
Status report on the ELETTRA R.F. system — *A. Massarotti, G. D'Auria, A. Fabris, C. Pasotti, C. Rossi, and M. Svandrlik* 710
Component development for X-band above 100 MW — *W. R. Fowkes, R. S. Callin, and M. Studzinski* 713
Comparison of SW and TW non-synchronous accelerating cavities as used in electron beam storage rings — *A. Zolfaghari, P. T. Demos, J. B. Flanz, and K. Jacobs* 716
A high power cross-field amplifier at X-band — *K. Eppley, J. Feinstein, K. Ko, N. Kroll, T. Lee, and E. Nelson* 719
A 2d field solver for periodic structures with special corner elements — *E. Nelson* 722
Gated field-emission cathodes for microwave devices — *P. M. McIntyre, H. P. Demroff, S. M. Elliott, B. Lee, J. D. Legg, Y. Pang, D. L. Parker, M. Popovic, M. D. Stewart, M. H. Weichold, W. Yu, and W. K. Yue* 725
High power X-band coaxial amplifier experiments — *T. J. Davis and J. A. Nation* 728
Studies of an X-band three-cavity gyroklystron with penultimate cavity tuning — *S. Tantawi, W. Main, P. E. Latham, H. Matthews, W. Lawson, C. D. Striffler, and V. L. Granatstein* 731
A second harmonic amplifier for accelerator applications — *P. E. Latham, W. Lawson, C. D. Striffler, and W. Main* ... 734
RF breakdown test of SiO_2 coated copper electrodes — *D. Sun, P. Datte, W. W. MacKay, and F. R. Huson* 736
The AGS booster low frequency RF system — *R. T. Sanders, P. Cameron, W. Eng, M. Goldman, D. Kasha, A. J. McNerney, M. Meth, A. Ratti, and R. Spitz* 739
Bevalac injector final stage RF amplifier upgrades — *D. Howard, J. Calvert, R. Dwinell, J. Lax, A. Lindner, R. Richter, and W. Ridgeway* 742

RF drivers for the Bevalac injector final stage RF amplifiers — *D. Howard, J. Calvert, M. Hui, A. Lindner, N. Kellogg, W. Ridgeway, and K. Woolfe* 745
New design concepts for ferrite-tuned low-energy-booster cavities — *Georg Schaffer* 748
Injection locking of a long-pulse relativistic magnetron — *S. C. Chen, G. Bekefi, and R. J. Temkin* 751
Cyclotron autoresonance maser (CARM) amplifiers for RF accelerator drivers — *W. L. Menninger, B. G. Danly, C. Chen, K. D. Pendergast, R. J. Temkin, D. L. Goodman, and D. L. Birx* 754
Analysis and optimisation of RF power-klystrons by FCI-code — *E.-G. Schweppe, E. Demmel, H. Seifert, S. Isagawa, T. Shintake, and M. Yoshida* 757
Numerical simulation of the SLAC X-100 klystron using RKTW2D — *Robert D. Ryne and Arnold E. Vlieks* 760
250 GHz cold tests for the LLNL CARM experiment — *B. Kulke, M. Caplan, and R. Stever* 763
Test results from the LLNL 250 GHz CARM experiment — *B. Kulke, M. Caplan, D. Bubp, T. Houck, D. Rogers, D. Trimble, R. VanMaren, G. Westenskow, D. B. McDermott, and N. C. Luhmann, Jr.* 766
The linac and booster RF systems for a dedicated injector for SPEAR — *J. N. Weaver, S. Baird, M. Baltay, M. Borland, H.-D. Nuhn, J. Safranek, C. Chavis, L. Emery, R. D. Genin, R. Hettel, H. Morales, J. Sebek, J. Voss, D. Wang, H. Wiedemann, B. Youngman, and R. H. Miller* 769
A high-power free-electron maser for RF acceleration — *F. Hartemann, T. S. Chu, P. Papavaritis, B. G. Danly, R. J. Temkin, G. Faillon, G. Mourier, T. Trémeau, and M. Bres* 772
Fast ferrite tuner for the BNL synchrotron light source — *E. Pivit, S. M. Hanna, and J. Keane* 774
Copper plating the ground test accelerator RFQ — *Henry Mignardot and Joseph Uher* 777
Idle superconducting RF cavities for bunch focusing — *P. Marchand and L. Rivkin* 780
Sliding mode controller for RF cavity tuning loop — *L. K. Mestha and K. S. Yeung* 783
Accelerating cavity development for the Cornell B-factory, CESR-B — *H. Padamsee, P. Barnes, C. Chen, W. Hartung, M. Hiller, J. Kirchgessner, D. Moffat, R. Ringrose, D. Rubin, Y. Samed, D. Saraniti, J. Sears, Q. S. Shu, and M. Tigner* 786
Beam impedance measurements— *Coaxial wire method* — *Giuseppe Di Massa and Maria Rosaria Masullo* 789
A simple analytical estimate of the loss parameter of a large tapered chamber — *James J. Welch* 792
Measurements of high-temperature rf and microwave properties of selected aluminas and ferrites used in accelerators — *R. M. Hutcheon, M. S. de Jong, P. Lucuta, J. E. McGregor, B. H. Smith, and F. P. Adams* 795
100 MW klystron development at SLAC — *A. E. Vlieks, R. S. Callin, G. Caryotakis, K. S. Fant, W. R. Fowkes, T. G. Lee, and E. L. Wright* 798
Computer determination of HOM damping for a prototype JLC accelerator cavity and a prototype B factory cavity — *Norman M. Kroll and Robert Rimmer* 801
SXLS RF cavity and system — *M. Thomas, R. Biscardi, R. D'Alsace, J. Keane, P. Mortazavi, and J. Rose* 804
Low power RF system for the ALS Linac — *C. C. Lo, B. Taylor, and H. Lancaster* 807
Initial operating experience with the auxiliary accelerating cavity for the TRIUMF cyclotron — *R. E. Laxdal, K. Fong, G. H. Mackenzie, V. Pacak, J. B. Pearson, L. Root, and M. Zach* 810
CONDOR simulation of an 11.4-GHz traveling wave output cavity — *Y. Goren and D. Yu* 813
Switchable 10 Hz/1 Hz LEB magnet power supply system — *Cezary Jach* 816
An RF cavity for the B-factory — *R. Rimmer, F. Voelker, G. Lambertson, M. Allen, J. Hodgeson, K. Ko, R. Pendleton, H. Schwarz, and N. Kroll* 819
Survey and alignment of an MLI model 1.2–400 synchrotron light source — *W. J. Pearce* 822
Correlation of beam loss to residual activation in the AGS — *K. A. Brown* 825
The condition of γ-ray emission by electrons interacting with the wall in medium energy electron storage rings — *Y. Gomei and M. Kawai* 828
Gamma ray activation of the Fermilab Pbar target — *C. M. Bhat and J. Marriner* 831
Recent experience with backgrounds at the SLC — *R. Jacobsen, H. Band, T. Barklow, A. Bazarko, K. Brown, D. Burke, D. Coupal, H. DeStaebler, D. Fujino, C. Hearty, S. Hertzbach, J. Jaros, T. Maruyama, T. Tauchi, N. Toge, J. Turk, S. Wagner, and C. Zeitlin* 834
Analysis of uptime efficiency of the SLC as measured by pulse accounting — *D. Bernstein, A. Gromme, D. Ohman, and N. Spencer* 836

First results of proton injection commissioning of the AGS booster synchrotron — *R. K. Reece, L. Ahrens, J. Alessi, E. Bleser, J. M. Brennan, A. Luccio, J. Skelly, A. Soukas, W. van Asselt, W. T. Weng, and R. Witkover* 839
Multi-beamlet injection to the RFQ1 accelerator— *A comparison of ECR and duopigatron proton sources — G. M. Arbique, T. Taylor, M. H. Thrasher, and J. S. C. Wills* 842
Beam transmission and emittance measurements of the RFQ1 accelerator — *G. M. Arbique, B. G. Chidley, W. L. Michel, G. E. McMichael, and J. Y. Sheikh* 845
First two years operational experience with LEP — *R. Bailey, T. Bohl, F. Bordry, H. Burkhardt, K. Cornelis, P. Collier, B. Desforges, A. Faugier, V. Hatton, H. Laeger, J. Miles, J. Poole, G. de Rijk, H. Schmickler, and D. Vandeplassche* 848
Accelerator energy conservation at Fermilab — *James P. Morgan* 851
Designing high energy accelerators under DOE's 'New Culture' for environment and safety: An example, the Fermilab 150 GeV main injector proton synchrotron — *William B. Fowler* 854
Installation of the superconducting magnets in the HERA tunnel — *I. Borchardt, D. Brauer, S. Chermenin, D. Degèle, K. Escherich, H. J. Fiebig, H. Grabe, J. Holz, D. Hubert, R. Kus, M. Leenen, H. Maywald, O. Peters, B. Petersen, K. Pieczora, U. Riemer, Z. Sanok, P. Schmüser, S. Schollmeier, W. Schwarz, G. Tödten, D. Trines, and S. Wolff* 857
Stripping foil losses and space charge blowup in the FNAL booster — *C. Johnstone, D. Bogert, J. Lackey, and R. Tomlin* 860
Fast kicker requirements for the SSC's low and medium energy boosters — *M. Wilson, L. Schneider, D. Anderson, and C. Pappas* 863
A pinger system for the Los Alamos proton storage ring — *T. W. Hardek and H. A. Thiessen* 866
Electrical performance of the injection system kickers at the Saskatchewan Accelerator Laboratory — *C. Figley* 869
PSR switchyard kicker system improvements — *T. W. Hardek* 872
Slow beam extraction experiments at TARN II — *M. Yoshizawa, A. Ando, K. Chida, M. Kanazawa, T. Hattori, H. Muto, A. Noda, K. Noda, M. Tomizawa, and J. Yoshizawa* 875
A triple-isotope injector for accelerator mass spectrometry — *R. J. Schneider, K. F. von Reden, and K. H. Purser* 878
Beam induced heating of ferrite magnets — *W. K. van Asselt and Y. Y. Lee* 881
On-line correction of aberrations in particle spectrographs — *M. Berz, K. Joh, J. A. Nolen, B. M. Sherrill, and A. F. Zeller* 884
The ELETTRA linac to storage ring transfer line — *D. Einfeld and R. Richter* 887
Test and calibration beams at the Superconducting Super Collider — *Frank Stocker, Howard Fenker, and Ron Schailey* . 890
Upgrade of LAMPF's 750-keV, H^+ transport — *J. W. Hurd, A. A. Browman, K. W. Jones, and M. J. Jakobson* 893
User control of the proton beam injection trajectories into the AGS booster — *T. D'Ottavio, A. Kponou, A. Luccio, J. G. Alessi, R. K. Reece, and J. Skelly* 896
Zero-degree injection line for PILAC, the proposed Los Alamos Pion Linac — *Barbara Blind* 899
The APS transfer line from linac to injector synchrotron — *R. K. Koul and E. Crosbie* 902
Dispersion and betatron matching into the linac — *F.-J. Decker, C. E. Adolphsen, W. J. Corbett, P. Emma, I. Hsu, H. Moshammer, J. T. Seeman, and W. L. Spence* 905
Upgrade of the main ring magnet power supply for the KEK 12 GeV proton synchrotron — *H. Sato, T. Sueno, T. Toyama, M. Mikawa, T. Toda, and S. Matsumoto* 908
Correction magnet power supplies for APS machine — *Y. G. Kang* 911
Circuit description of the power systems for pulsed septum magnets at APS — *D. G. McGhee* 914
Design and simulation of high accuracy power supplies for injector synchrotron dipole magnets — *Masoud Fathizadeh* . 917
Power supply system for the TRIUMF KAON factory — *K. W. Reiniger* 920
Problems with tap-changing power supplies — *John Budnick and Robert Forgas* 923
The 10 Hz resonant magnet power supply for the SSRL 3 GeV injector — *R. Hettel, R. Averill, M. Baltay, S. Brennan, C. Harris, M. Horton, C. Jach, J. Sebek, and J. Voss* 926
Magnet power supply as a network object — *S. Cohen and R. Stuewe* 929
Active filter for the DESY III dipole circuit — *W. Bothe* 932
Precision power supply control module — *N. Dobeck, B. Lamora, J. Larkin, M. O'Sullivan, and C. Sharp* 935
Measurements of crowbar performance of the 20 kV 130 A dc power supply of the TRIUMF rf system — *A. K. Mitra* . 938

Transient analysis of the AGS-booster ring dipole and quadrupole magnet system — *W. Zhang, A. V. Soukas, and S. Y. Zhang* 940
Operational results of an improved regulator and trigger system for the 'Fast' Raster Scanning Power Supply system constructed at the Bevalac Biomedical Facility — *G. Stover, J. Halliwell, B. Ludewigt, M. Nyman, and R. Stradtner* 943
Precision current regulation of multipole magnets using commercial SMPS — *Coles Sibley, Oscar Calvo, and Tomás Russ* 946
Principles and theory of resonance power supplies — *A. Sreenivas and G. G. Karady* 949
Control theory: A practical approach — *Mike Anderson and Tom Bertuccio* 952
Theoretical study of H^- stripping with a wiggler magnet — *R. Hutson* 955
The AGS new fast extraction system for the g-2 experiment and RHIC injection — *M. Tanaka and Y. Y. Lee* 958
The Frascati Φ-factory injection system — *R. Boni, S. Kulinski, M. Preger, B. Spataro, M. Vescovi, and G. Vignola* ... 961
Prototype studies of a 1 MHz chopper for the KAON factory — *G. D. Wait, M. J. Barnes, D. Bishop, G. Waters, and C. B. Figley* 964
Results of calculations on the beam deflection due to the 1 MHz chopper for the kaon factory — *M. J. Barnes and G. D. Wait* 967
Construction of a new Tevatron Collider beam abort dump — *B. Hanna and C. Crawford* 970
The SSRL injector kickers — *H.-D. Nuhn, R. Boyce, J. Cerino, and T. Hostetler* 973
Design and performance of the traveling-wave beam chopper for the SSRL injector — *M. Borland, J. N. Weaver, M. Baltay, L. Emery, A. S. Fisher, P. Golceff, R. Hettel, H. Morales, J. Sebek, H. Wiedemann, B. Youngman, R. Anderson, and R. H. Miller* 976
Electrostatic deflector development—At the Chalk River superconducting cyclotron — *V. T. Diamond, G. R. Mitchel, J. Almeida, and H. Schmeing* 979
The proposed injection system for an asymmetric B factory in the PEP tunnel — *E. Bloom, F. Bulos, G. Loew, R. Miller, B. Sukiennicki, T. Mattison, and W. Barletta* 982
HEB to Superconducting Super Collider transfer lines — *F. Wang and R. Schailey* 985
The ELETTRA gun trigger module — *G. Roberto Aiello and Maurizio Bossi* 988
POISSON study of electrostatic septa for the MIT-Bates SHR — *Manouchehr Farkhondeh* 990
The ultra-fast injection kicker for SXLS — *Thomas J. Romano and Richard Heese* 993
SLC kicker magnet limitations — *R. Cassel, A. Donaldson, T. Mattison, G. Bowden, J. Weaver, F. Bulos, and D. Fiander* . 996
The booster-to-AGS beam transfer fast kicker modulators — *W. Zhang, J. Bunicci, W. W. Frey, A. V. Soukas, and S. Y. Zhang* 999
On the design of beam absorbers for the SSC — *Brett Parker* 1002
Thyristor converter simulation and analysis — *S. Y. Zhang* 1005
Applications of the hot isostatic pressing (HIP) for high gradient accelerator structure — *Hiroshi Matsumoto, Mitsuo Akemoto, Hitoshi Hayano, Atsushi Miura, Takashi Naito, and Seishi Takeda* 1008
X-band accelerating structure for Japan linear collider — *T. Higo, M. Takao, K. Kubo, and K. Takata* 1011
Method of longitudinal impedance measurement for accelerator elements in wide frequency region using double Fourier transform — *P. Reinhardt-Nickulin, N. Ilinsky, and S. Bragin* 1014
Prototype of the accelerating resonator for the superconducting sector deuteron cyclotron — *N. V. Vasiliev, A. A. Glazov, E. N. Zaplatin, V. A. Kochkin, and D. L. Novikov* 1017
Design of an accelerating cavity for the Superconducting Super Collider Low-Energy Booster — *C. C. Friedrichs, L. Walling, and B. M. Campbell* 1020
Superconducting niobium sputter-coated copper cavity modules for the LEP energy upgrade — *C. Benvenuti, P. Bernard, D. Bloess, G. Cavallari, E. Chiaveri, E. Haebel, N. Hilleret, J. Tückmantel, and W. Weingarten* 1023
A new main control room for the AGS Complex — *P. F. Ingrassia, R. M. Zaharatos, and O. H. Dyling* 1026
Personnel protection and beam containment systems for the 3 GeV injector — *R. Yotam, J. Cerino, R. Garoutte, R. Hettel, M. Horton, J. Sebek, E. Benson, K. Crook, J. Fitch, N. Ipe, G. Nelson, and H. Smith* 1028
A cooling-water system for the Accelerator Test Facility — *Mitsuo Akemoto, Yutaro Nishinomiya, and Akio Suyama* . 1031

Blumlein-type X-band klystron modulator for Japan Linear Collider — *Tetsuo Shidara, Mitsuo Akemoto, Masato Yoshida, Seishi Takeda, Koji Takata, Iwao Ohshima, and Tsuneharu Teranishi* 1034
High-power input coupler with a cylindrical alumina window — *Mitsuo Akemoto* 1037
X-band klystron modulator for the accelerator test facility — *Mitsuo Akemoto, Tetsuo Shidara, Seishi Takeda, and Junji Urakawa* 1040
Performance test of a 65-MW klystron unit relevant to the microwave source upgrade of the KEK 2.5-GeV linac — *Tetsuo Shidara, Hiroyuki Honma, Katsumi Nakao, Shozo Anami, and Akira Asami* 1043
Superconducting cavity development at Los Alamos National Laboratory — *B. Rusnak, E. R. Gray, R. G. Maggs, D. L. Schrage, A. H. Shapiro, G. Spalek, and P. Wright* 1046
RF pulses with flat output waveform generator in RF power upgrade system — *B. Y. Bogdanovich, A. P. Ignatyev, and V. A. Senyukov* 1048
Tuning and coupling mismatch tolerance in cavities driven by a quadrature hybrid — *Arthur M. Vetter* 1051

Beam Dynamics II

Chairman: R. Gluckstern

On sustaining short, intense bunches in linear and circular accelerators *(Invited Paper)* — *Joseph J. Bisognano* 1054
Acceleration of polarized proton in high energy accelerators *(Invited Paper)* — *S. Y. Lee* 1059
Longitudinal instability in HIF beams *(Invited Paper)* — *Lloyd Smith* 1064
Computer simulation of the coherent beam–beam effect in the LHC — *W. Herr* 1068
The coherent beam–beam interaction — *S. Krishnagopal and R. Siemann* 1071
Effect of non-planar undulators on beam dynamics in ELETTRA — *Lidia Tosi and Ryutaro Nagaoka* 1074
Calculations of the conditions for bunched-beam e-p instability in the Los Alamos Proton Storage Ring (PSR) — *David V. Neuffer* 1077
Measurement of octupole induced decoherence at CESR — *John M. Byrd and David Sagan* 1080

Synchrotron Radiation Sources/FELs

Chairman: H. Winick

New developments on the generation of arbitrary polarized radiation from insertion devices *(Invited Paper)* — *Pascal Elleaume* 1083
Rapidly-modulated variable-polarization crossed-undulator source — *Michael A. Green, Kwang-Je Kim, Walter S. Trzeciak, and P. James Viccaro* 1088
Magnetic field tolerances for insertion devices on third generation synchrotron light sources *(Invited Paper)* — *P. J. Viccaro, R. Savoy, and D. W. Carnegie* 1091
NSLS prototype small-gap undulator (PSGU) — *P. M. Stefan, L. Solomon, S. Krinsky, and G. Rakowsky* 1096
Operation of synchrotron light sources with multiple insertion devices *(Invited Paper)* — *John Galayda and Anne-Marie Fauchet* 1099
Low-emittance in SPEAR — *J. Safranek and H. Wiedemann* 1104
Commissioning of the phase I superconducting X-ray lithography source (SXLS) at BNL — *J. B. Murphy, R. Biscardi, J. Bittner, L. N. Blumberg, E. Bozoki, E. Desmond, H. Halama, R. Heese, H. Hsieh, J. Keane, S. Kramer, R. Nawrocky, T. Romano, J. Rothman, J. Schuchman, M. Thomas, J. M. Wang, J. Krishnaswamy, W. Louie, and R. Rose* 1107
Short wavelength FELs — *Richard L. Sheffield* 1110
Initial operation of the Vanderbilt Free Electron Laser — *Perry A. Tompkins, Foorood Amirmadhi, K. Becker, C. A. Brau, W. D. Andrews, Marcel R. Marc, and J. Kiaie* 1115

Spectrum of coherent sychrotron radiation — *T. Nakazato, M. Oyamada, N. Niimura, S. Urasawa, Y. Shibasaki, R. Kato, S. Niwano, M. Ikezawa, T. Ohsaka, Y. Shibata, K. Ishi, T. Tsutaya, T. Takahashi, H. Mishiro, F. Arai, and Y. Kondo* 1118

Accelerator Technology I—Instrumentation, Control, Feedback

Theoretical studies on the beam position measurement with button-type pickups in APS — *Y. Chung* 1121
A beam position detector for SSC collider rings — *Donald J. Martin* 1124
Beam detector impedance calculation using circuit models — *Donald J. Martin* 1127
Monitoring system to permit accurate alignment of beams at collision in CESR — *J. P. Sikora and R. Littauer* 1130
Development of a wall current beam position monitor for a kaon factory ceramic chamber — *Yan Yin, Bill Rawnsley, George Mackenzie, Dave Pearce, and John Worden* 1133
Measurements and performance of a microstrip beam probe system — *J. D. Gilpatrick, K. F. Johnson, S. Lloyd, D. Martinez, R. Meyer, G. Neuschaefer, J. Power, R. B. Shurter, and F. D. Wells* 1136
Log-ratio circuit for beam position monitoring — *F. D. Wells, J. D. Gilpatrick, R. E. Shafer, and R. B. Shurter* 1139
Capacitive beam position monitors and automatic beam centering in the transfer lines of GANIL — *P. Gudewicz and E. Petit* 1142
Operational amplifier based stretcher for stripline beam position monitors — *W. C. Sellyey and R. W. Kruse* 1145
A beam position monitor for AmPS — *J. Noomen, J. Bijleveld, F. Kroes, T. Sluijk, and H. Verkooijen* 1148
The SSRL injector beam position monitoring systems — *W. Lavender, S. Baird, S. Brennan, M. Borland, R. Hettel, H.-D. Nuhn, R. Ortiz, J. Safranek, J. Sebek, C. Wermelskirchen, and J. Yang* 1151
DELTA beam position monitor — *S. Brinker, R. Heisterhagen, and K. Wille* 1154
Beam position measurement system for SRRC — *G. J. Jan and K. T. Hsu* 1157
The LEP synchrotron light monitors — *C. Bovet, G. Burtin, R. J. Colchester, B. Halvarsson, R. Jung, S. Levitt, and J. M. Vouillot* 1160
A CCD camera probe for a superconducting cyclotron — *F. Marti, R. Blue, J. Kuchar, J. A. Nolen, B. Sherrill, and J. Yurkon* 1163
High-sensitive remote diagnostics of the accelerated particles' beam cross section — *P. Y. Komissarov, V. G. Mikhailov, V. A. Rezvov, A. A. Roschin, V. I. Sclyarenko, and L. I. Judin* 1166
Intensity interferometry and its application to beam diagnostics — *Efim Gluskin* 1169
H^- beam characterization using laser-induced neutralization — *V. W. Yuan, R. Garcia, K. F. Johnson, K. Saadatmand, O. R. Sander, D. Sandoval, and M. Shinas* 1171
Upgrades to the Fermilab flying wire systems — *J. Zagel, A. A. Hahn, G. Jackson, T. Johnson, K. Martin, J. Misek, X. Q. Wang, and W. Ye* 1174
Results from a prototype beam monitor in the Tevatron using synchrotron light — *A. A. Hahn and P. Hurh* 1177
Design and commissioning of flying wires in the Fermilab Accumulator — *X. Q. Wang, T. Groves, A. A. Hahn, G. Jackson, J. Marriner, K. Martin, and J. Misek* 1180
Beam structure and transverse emittance studies of high-energy ion beams — *K. Saadatmand, K. F. Johnson, and J. D. Schneider* 1183
Wire scanners at LEP — *B. Bouchet, C. Bovet, A. Burns, J. Camas, G. Ferioli, C. Fischer, R. Jung, Q. King, K. H. Kissler, J. Koopman, J. Mann, H. Michel, R. Schmidt, and L. Vos* 1186
Design of the AGS Booster Ionization Profile Monitor — *A. N. Stillman, R. E. Thern, R. L. Witkover, and W. H. Van Zwienen* 1189
Beam size measurement at high radiation levels — *Franz-Josef Decker* 1192
Beam emittance measurement technique for PLS-IM-T linac — *Y. X. Luo, W. Namkung, C. Ryu, and I. S. Ko* 1195
A carbon jet beam profile monitor for LEAR — *R. Galiana, D. Manglunki, and C. Mazeline* 1198
Wire scanners for beam size and emittance measurements at the SLC — *M. C. Ross, J. T. Seeman, E. Bong, L. Hendrickson, D. McCormick, and L. Sanchez-Chopitea* 1201

Emittance measurements of FEL accelerators using optical transition radiation methods — *R. B. Fiorito, D. W. Rule, A. H. Lumpkin, R. L. Tokar, D. H. Dowell, W. C. Sellyey, and A. R. Lowrey* 1204
Beam spot size measurement using beamstrahlung signals at the SLC interaction point — *E. Gero, W. Kozanecki, and P. Chen* 1207
Beam diagnostic systems in the IUCF Cooler and cyclotron — *Mark S. Ball, Timothy J. P. Ellison, and Brett J. Hamilton* 1210
The commissioning of the LEP polarimeter — *J. Badier, A. Blondel, M. Crozon, B. Dehning, C. Bovet, P. Castro-Garcia, J. De Vries, G. P. Ferri, M. Glaser, C. Grunhagel, R. Jung, L. Knudsen, F. Lemeilleur, J. Mann, M. Placidi, R. Schmidt, and K. Unser* 1213
AGS booster tune meter kickers — *W. Zhang, J. Bunicci, P. R. Cameron, A. V. Soukas, and W. van Asselt* 1216
Mechanical design of the beam current transformers for the HERA proton ring — *W. Schütte* 1219
Betatron tune measurement system for the HERA proton storage ring — *S. Herb* 1222
Real time spectrum analyzer — *M. Bergher, E. Jules, and A. Louis-Joseph* 1225
A frequency tracking synthesizer for beam diagnostic systems — *D. Peterson and J. Marriner* 1228
The AGS booster beam loss monitor system — *E. R. Beadle, G. W. Bennett, and R. L. Witkover* 1231
A wide band slot-coupled beam sensing electrode for the advanced light source (ALS) — *J. Hinkson and K. Rex* 1234
A real-time longitudinal phase-space measurement technique for H^- beams — *R. C. Connolly and D. P. Sandoval* ... 1237
Fast ion chambers for SLC — *D. McCormick* 1240
Diagnostic instrumentation for the SSRL 3 GeV injector — *J. Sebek, M. Baltay, M. Borland, J. Cerino, L. Emery, R. Hettel, H. Morales, D. Mostowfi, M. Rowen, J. Safranek, J. Voss, J. N. Weaver, H. Wiedemann, Y. Yin, B. Youngman, J.-L. Pellegrin, and V. Smith* 1243
Bunch length measurement using beam spectrum — *Z. Greenwald, D. L. Hartill, R. M. Littauer, S. B. Peck, and D. H. Rice* 1246
Beam diagnostics for the 400 MeV Fermilab linac — *Elliot S. McCrory, Fady Harfoush, G. Jackson, Glenn Lee, and Dennis McConnell* 1249
Tune trackers for the Fermilab Tevatron — *J. Fitzgerald and R. Gonzalez* 1252
Coupled bunch dipole mode measurements of accelerating beam in the Fermilab Booster — *D. McGinnis, J. Marriner, and V. Bharadwaj* 1255
Beam transfer function measurements of accelerating beam in the Fermilab Booster — *D. McGinnis, J. Marriner, and V. Bharadwaj* 1258
Diagnostics for the MLI Model 1.2-400 Synchrotron Light Source — *Dan Y. Wang and Robert Legg* 1261
The design and packaging of the instrumentation electronics for the AGS booster, a generic approach — *G. A. Smith, E. Beadle, V. Castillo, W. Sims, A. Stillman, T. Tallerico, R. L. Witkover, and E. Zitvogel* 1264
Beam current monitoring in the AGS Booster and its transfer lines — *R. L. Witkover, E. Zitvogel, and V. Castillo* 1267
A Faraday Cup with high frequency response for a 200 MeV LINAC proton beam — *M. S. Zucker and J. W. Bittner* . 1270
The tune meter systems at the AGS complex — *W. K. van Asselt, L. A. Ahrens, P. R. Cameron, S. Mandell, G. A. Smith, and W. Zhang* 1273
Betatron tune measurement and control in the PETRA proton ring — *S. Herb* 1276
Prompt diagnostics of the cyclotron dees shift — *N. I. Karpov, Y. M. Krasnikov, I. V. Naumov, S. T. Latushkin, and L. I. Judin* 1279
Instrumentation for SSC test beams — *Howard Fenker, Frank Stocker, and Ron Schailey* 1281
Orbit monitoring in the SLC — *L. Sanchez-Chopitea, P. Emma, and D. Van Olst* 1284
Program for automatic control of beam transfer lines — *S. H. Ananian and R. H. Manukian* 1287
Embedded software for the CEBAF RF control module — *G. Lahti, I. Ashkenazi, C. West, and B. Morgan* 1290
The Tevatron orbit program — *B. Hendricks, R. P. Johnson, R. Joshel, E. Martensson, and D. Siergiej* 1293
Control of the time and energy dependent parameters of the upgraded Tevatron Collider — *D. E. Johnson, G. Goderre, B. Hendricks, R. P. Johnson, and R. Joshel* 1296
Development and application of general purpose data acquisition shell (GPDAS) at Advanced Photon Source — *Youngjoo Chung and Keeman Kim* 1299
UNIX data acquisition system — *I. Kourbanis, S. Peggs, T. Satogata, G. Tsironis, and G. Bourianoff* 1302

Control system user interface for accelerator commissioning and operation — *D. Dobrott, D. Keeley, G. Kolte, Z. Mikic, M. Lee, J. Corbett, S. Howry, and A. King* 1305
Overview of real-time kernels at the Superconducting Super Collider Laboratory — *K. Low, S. Acharya, M. Allen, E. Faught, D. Haenni, and C. Kalbfleisch* 1308
A new man–machine-interface at BESSY — *R. Müller, H.-D. Doll, I. J. Donasch, H. Marxen, and H. Pause* 1311
Alarm handler for the Advanced Photon Source control system — *Martin R. Kraimer, Ben-chin K. Cha, and Mark Anderson* 1314
Correlation plot facility in the SLC control system — *L. Hendrickson, N. Phinney, and L. Sanchez-Chopitea* 1317
Indirect phase locking of RF clock to the beam for BNL booster BPM system — *T. Hayes and A. Zaltsman* 1320
Feed forward rf control system of the Accelerator Test Facility — *Ilan Ben-Zvi, Jialin Xie, and Renshan Zhang* 1323
Progress on bunch lengthening at the NSLS VUV ring — *R. Biscardi, W. Broome, S. Buda, J. Keane, G. Ramirez, J. Wachtel, and J. M. Wang* 1326
Design of a multivariable RF control system using gain-shaping in the frequency domain — *Christopher D. Ziomek, Stephen P. Jachim, and Eckard F. Natter* 1329
Synchronization of a variable frequency source with a fixed frequency source using a sliding-mode controller — *L. K. Mestha and K. S. Yeung* 1332
Phase and amplitude stabilization of short-pulsed, high-power microwave amplifiers — *D. Hopkins, D. Yu, T. Orzechowski, G. Westenskow, and S. Yu* 1335
Measurement of bunch time-structure in KEK PF — *M. Tobiyama, T. Kasuga, T. Obina, T. Takeo, and T. Katsura* ... 1338

Volume 3

Beam diagnostics at the COSY injection beamline — *F. Anton* 1341
Design and testing of the AGS booster BPM detector — *R. Thomas, D. J. Ciardullo, and W. Van Zwienen* 1344
The AGS booster beam position monitor system — *D. J. Ciardullo, A. Abola, E. R. Beadle, G. A. Smith, R. Thomas, W. Van Zwienen, R. Warkentien, and R. L. Witkover* 1347
Contemporary approaches to control system specification and design applied to KAON — *George A. Ludgate, Edwin A. Osberg, and Don A. Dohan* 1350
Rejuvenation of the CPS control system: The first slice — *G. Benincasa, G. Daems, B. Frammery, P. Heymans, F. Perriollat, C. Serre, and C.-H. Sicard* 1353
The UNK control system — *V. N. Alferov, V. L. Brook, A. F. Dunaitsev, S. G. Goloborodko, P. N. Kazakov, V. V. Komarov, A. F. Lukyantsev, M. S. Mikheev, N. N. Trofimov, V. P. Sakharov, E. D. Scherbakov, V. P. Voevodin, S. A. Zelepoukin, and B. Kuiper* 1356
Control system specification for a cyclotron and neutron therapy facility — *Jonathan Jacky, Ruedi Risler, Ira Kalet, Peter Wootton, Alexandra Barke, Stan Brossard, and Ralph Jackson* 1359
The COSY control system, a distributed realtime operating system: First practical experience at the COSY-injector — *M. Stephan, U. Hacker, K. Henn, A. Richert, K. Sobotta, and A. Weinert* 1362
Initial control of the H^- ion source at the Superconducting Super Collider Laboratory — *G. Martinsen, S. Acharya, M. Allen, E. Faught, K. Low, and J. Sage* 1365
PLS linac instrument and control system — *C. Ryu, S. S. Chang, J. H. Kim, M. S. Kim, D. K. Liu, S. Won, and W. Namkung* 1368
Control system for the MLI Model 1.2-400 Synchrotron Light Source — *B. Ng, R. Billing, R. Legg K Luchini, D. Meaney, S. Pugh, and Y. Zhou* 1371
Control system of the superconducting X-ray lithography (SXLS) at Brookhaven — *E. Desmond, J. Galayda, W Louie, B. Martin, and R. Rose* 1374
An inexpensive PC-based ion linac control system — *M. E. Hamm and J. M. Potter* 1377
Control system at the Synchrotron Radiation Research Center — *G. J. Jan* 1380

The SSRL injector control system — *C. Wermelskirchen, S. Brennan, T. Götz, W. Lavender, R. Ortiz, M. Picard, and J. Yang* 1383
Longitudinal damping system for the Fermilab Booster — *I. Haberman and I. Rypshtein* 1386
Design of 4–8 GHz bunched beam stochastic cooling arrays for the Fermilab Tevatron — *D. McGinnis, J. Budlong, G. Jackson, J. Marriner, and D. Poll* 1389
Design of 4–8 GHz stochastic cooling equalizers for the Fermilab Accumulator — *D. McGinnis and J. Marriner* 1392
Bulk acoustic wave (BAW) devices for stochastic cooling notch filters — *Ralph J. Pasquinelli* 1395
Design and operational results of a 'one-turn-delay feedback' for beam loading compensation of the CERN PS ferrite cavities — *F. Blas and R. Garoby* 1398
Improvement of the time structure and reproducibility of the Bevalac spill — *C. M. Celata, M. J. Bennett, D. N. Cowles, B. Feinberg, Robert Frias, M. A. Nyman, G. D. Stover, M. M. Tekawa, and R. Salomons* 1401
Prompt bunch by bunch synchrotron oscillation detection via a fast phase measurement — *D. Briggs, P. Corredoura, J. D. Fox, A. Gioumousis, W. Hosseini, L. Klaisner, J.-L. Pellegrin, K. A. Thompson, and G. Lambertson* 1404
Computer modelling of bunch-by-bunch feedback for the SLAC B-factory design — *D. Briggs, J. D. Fox, W. Hosseini, L. Klaisner, P. Morton, J.-L. Pellegrin, K. A. Thompson, and G. Lambertson* 1407
A longitudinal multibunch feedback system for PEP — *H.-D. Nuhn, Y. Sun, H. Winick, W. Xie, R. Yotam, H. Schwarz, and P. Friedrichs* 1410
Energy feedback system for the SSRL injector linac — *L. Emery* 1413
Design of VAX software for a generalized feedback system — *F. Rouse, S. Castillo, T. Himel, B. Sass, and H. Shoaee* 1416
General, database-driven fast-feedback system for the Stanford Linear Collider — *F. Rouse, S. Allison, S. Castillo, T. Gromme, B. Hall, L. Hendrickson, T. Himel, K. Krauter, B. Sass, and H. Shoaee* 1419
The transverse damper system for RHIC — *J. Xu, J. Claus, E. Raka, A. G. Ruggiero, and T. J. Shea* 1422
The stochastic-cooling system for COSY-Jülich — *P. Brittner, R. Danzglock, H. U. Hacker, R. Maier, U. Pfister, D. Prasuhn, H. Singer, W. Spiess, and H. Stockhorst* 1425
Beam position monitoring in the AGS linac to booster transfer line — *T. J. Shea, J. Brodowski, and R. Witkover* 1428
Design of the AGS Booster Beam Position Monitor electronics — *D. J. Ciardullo, G. A. Smith, and E. R. Beadle* 1431
Modeling in control of the Advanced Light Source — *J. Bengtsson, E. Forest, H. Nishimura, and L. Schachinger* 1434
Accelerator and feedback control simulation using neural networks — *D. Nguyen, M. Lee, R. Sass, and H. Shoaee* ... 1437
Optimal, real-time control–colliders — *J. E. Spencer* 1440
Accelerator simulation and operation via identical operational interfaces — *J. Kewisch, A. Barry, R. Bork, B. Bowling, V. Corker, G. Lahti, K. Nolker, J. Sage, and J. Tang* 1443
The estimation and control of closed orbit in fast cycling synchrotron — *S. H. Ananian, R. H. Manukian, A. R. Matevosian, V. T. Nikogossian, and A. R. Tumanian* 1446
MARCO—Models of accelerators and rings to commission and operate—*L. Catani, G. Di Pirro, C. Milardi, A. Stecchi, L. Trasatti, and M. J. Lee* 1448
Use of digital control theory state space formalism for feedback at SLC — *T. Himel, L. Hendrickson, F. Rouse, and H. Shoaee* 1451
A database for modeling the Brookhaven AGS Booster — *E. H. Auerbach* 1454
A 256 channel digital filter for a data acquisition system — *W. Roberts and B. Aikens* 1455
Proposed data acquisition system for the Fermilab Booster — *V. Bharadwaj, S. Peggs, G. Wu, and C. Saltmarsh* 1458
Arbitrary function generator for APS injector synchrotron correction magnets — *Oscar D. Despe* 1461
Energy feed forward at the SLC — *R. Keith Jobe, Mike J. Brown, Ian Hsu, and Ed Miller* 1464
BPM data acquisition system for the Bates pulse stretcher ring — *O. Calvo, T. Russ, and J. Flanz* 1467
The CEBAF frequency distribution system — *A. Krycuk, J. Fugitt, K. Mahoney, and S. Simrock* 1470
Generalized emittance measurements in a beam transport line — *J. Skelly, C. Gardner, A. Luccio, A. Kponou, and K. Reece* 1473
The control and operation of the programmable wave form generator for the SSRL injector — *S. Brennan, S. Baird, W. Lavender, H.-D. Nuhn, C. Wermelskirchen, and J. Yang* 1476
Triggers and timing system for the SSRL 3 GeV injector — *R. Hettel, D. Mostowfi, R. Ortiz, and J. Sebek* 1478
Main cycle controls for the AGS Booster synchrotron — *B. B. Culwick and S. Yen* 1481

Smart Rack Monitor for the Linac control system — *S. Shtirbu, R. W. Goodwin, E. S. McCrory, and M. F. Shea* 1484
SLC's adaptation of the ALS high performance serial link — *K. Krauter* 1487
Use of Ethernet and TCP/IP socket communications library routines for data acquisition and control in the LEP RF system — *E. Ciapala, P. Collier, and P. Lienard* 1490
Fiber optics in the BNL booster radiation environment — *E. R. Beadle* 1493
I/O subnets for the APS Control System — *N. D. Arnold, G. J. Nawrocki, R. T. Daly, M. R. Kraimer, and W. P. McDowell* 1496
The trajectory control in the SLC Linac — *I. C. Hsu, C. E. Adolphsen, T. M. Himel, and J. T. Seeman* 1499
Machine protection schemes for the SLC — *M. C. Ross* 1502
A programmable beam intensity display system for the Fermilab accelerators — *S. Johnson and D. Capista* 1505
An automated RF control and data acquisition system for testing superconducting RF cavities — *C. Reece, T. Powers, and P. Kushnick* 1508
A new data acquisition and control system for the power amplifier test station — *Mark S. Champion* 1511
Vacuum control system for the MLI Model 1.2-400 Synchrotron Light Source — *S. Pugh and B. Ng* 1514
The new vacuum control system for the SPS — *Detlef Swoboda* 1516
Vacuum and beam diagnostic controls for ORIC beam lines — *B. A. Tatum* 1519
An automated vacuum system — *W. H. Atkins, G. D. Vaughn, and C. Bridgman* 1522
Open loop compensation for the eddy current effect in the APS storage ring vacuum chamber — *Y. Chung, J. Bridges, L. Emery, and G. Decker* 1525
Automatic local beam steering systems for NSLS X-ray storage ring— *Design and implementation* — *O. V. Singh, R. Nawrocky, and J. Flannigan* 1528
Controls and interlocks for a prototype 1 MHz beam chopper — *G. Waters, D. Bishop, M. J. Barnes, and G. D. Wait* . 1531
Beam diagnostics using transition radiation produced by a 100 MeV electron beam — *M. Jablonka, J. Leroy, X. Hanus, J. C. Derost, and L. Wartski* 1534
Intelligent power supply controller — *R. S. Rumrill and D. J. Reinagel* 1537
History data facility in the SLC control system — *Ralph G. Johnson and Gregory R. White* 1540
A beam diagnostic system for ELSA — *M. Schillo, K. H. Althoff, W. v. Drachenfels, T. Goetz, D. Husmann, M. Neckenig, M. Picard, F. J. Schittko, W. Schauerte, and J. Wenzel* 1543
A table driven database and applications generator for accelerator control systems — *Anthony Carter, Coles Sibley, and Tomás Russ* 1546
Grid scans: A transfer map diagnostic — *P. Emma and W. Spence* 1549
Fiber optic communications links for the Main Ring Control System upgrade — *Robert J. Ducar* 1552
The improvement of TRISTAN timing system — *J. Urakawa and T. Kawamoto* 1555
Bunch monitor for an *S*-band electron linear accelerator — *Yuji Otake and Kazuo Nakahara* 1558
C++ objects for beam physics — *Leo Michelotti* 1561
Beam steering using quadrupoles as position monitors — *Jean-Yves Hémery and Thomas Pettersson* 1564
Optical fiber Cherenkov detector for beam current monitoring — *I. V. Pishchulin, N. G. Solov'ev, and O. B. Romashkin* 1567
Electron beam pumped semiconductor laser for particle beam diagnostics — *O. V. Garkusha, I. V. Pishchulin, and O. V. Romashkin* 1570
Method and apparatus for multifunctional nonperturbing diagnostics of H^- beam — *A. S. Artiomov, N. G. Vaganov, A. K. Gevorkov, V. V. Limar, and V. P. Sidorov* 1573
Correlation method of nonperturbing measurements of ion beam energy spectra — *A. S. Artiomov* 1576
Specialized microprocessor modules for the synchrotron automatic control system — *A. G. Agababian, S. H. Ananian, A. A. Kazarian, M. Yu Khoetsian, and A. R. Matevosian* 1579
The pulsers of the damping injection oscillation — *I. N. Ivanov, N. A. Malachov, V. A. Mel'nikov, N. V. Pilyar, A S. Shcheulin, V. V. Akimov, V. B. Ermakov, T. A. Latypov, and G. L. Mamaev* 1582

Beam Dynamics I

Particle amplitude growth due to single or repetitive resonance crossing — *S. R Mane and W. T. Weng* 1585

Construction of high order maps for large proton accelerators — *John Irwin* 1588
Refinement of the Hamilton–Jacobi solution using a second canonical transformation — *W. E. Gabella, R. D. Ruth, and R. L. Warnock* 1591
Tracking studies for the Oxford Instruments Compact Electron Synchrotron — *Chas N. Archie and Jan Uythoven* ... 1594
Suppression of single bunch beam breakup by autophasing — *R. L. Gluckstern, J. B. J. van Zeijts, and F. Neri* 1597
Longitudinal coupling impedance of a thin iris collimator — *R. L. Gluckstern and W. F. Detlefs* 1600
Study of loss factor for slots in the vacuum chamber — *Yong-chul Chae and Lee C. Teng* 1603
Bunched beam longitudinal stability — *R. Baartman* 1606
Reduction of beam breakup growth by bleeding cavities in linear accelerators — *D. G. Colombant and Y. Y. Lau* 1609
Observation of magnetized cooling in the IUCF cooler — *Timothy J. P. Ellison* 1612
Tune splitting in the presence of linear coupling — *G. Parzen* 1615
The WKB approximation and the traveling-wave acceleration cavity — *David C. Carey* 1618
Kick factorization of symplectic maps — *A. J. Dragt, I. M. Gjaja, and G. Rangarajan* 1621
Non-linear resonance studies at the Synchrotron Radiation Center, Stoughton, Wisconsin — *E. Crosbie, J. Bridges, Y. Cho, D. Ciarlette, R. Kustom, Y. Liu, K. Symon, L. Teng, and W. Trzeciak* 1624
Correction of skew-quadrupole errors in RHIC — *G. F. Dell, H. Hahn, S. Y. Lee, G. Parzen, and S. Tepikian* 1627
Invariant metrics for Hamiltonian systems — *Govindan Rangarajan, Alex J. Dragt, and Filippo Neri* 1630
Further dynamic aperture studies on a wiggler-based ultra-low-emittance damping ring lattice — *L. Emery* 1633
Analytic closed orbit analysis for RHIC insertion — *S. Y. Lee and S. Tepikian* 1636
Beam–beam interaction and high order resonances — *S. Tepikian and S. Y. Lee* 1639
Single beam crab dynamics — *T. Chen and D. Rubin* 1642
Emittance growth due to beam motion — *King-Yuen Ng and Jack M. Peterson* 1645
Adiabatic invariance for spatially dependent accelerating structures — *John R. Cary and David L. Bruhwiler* 1648
Particle tracking and map analysis for compact storage rings — *Michael F. Reusch, Etienne Forest, and James B. Murphy* 1651
Symplectic full-turn maps in a Fourier representation — *J. S. Berg and R. L. Warnock* 1654
Comments on the behavior of α_1 in main injector γ_t jump schemes — *S. A. Bogacz and S. Peggs* 1657
A comparison of transition jump schemes for the main injector — *S. Peggs, A. Bogacz, and F. Harfoush* 1660
Normalization of the parameterized Courant–Snyder matrix for symplectic factorization of a parameterized Taylor map — *Yiton T. Yan* 1663
LEP dynamic aperture with asymmetrical RF distribution — *Francesco Ruggiero* 1666
Long-term stability studies for the Large Hadron Collider — *F. Galluccio, Z. Guo, W. Scandale, F. Schmidt, and A. Verdier* 1669
Compensation of linear lattice imperfections in the Large Hadron Collider — *F. Galluccio, Z. Guo, T. Risselada, W. Scandale, and F. Schmidt* 1672
High-luminosity insertion for a B-meson factory — *Bruno Autin* 1675
Diffusive transport enhancement by isolated resonances and distribution tails growth in hadronic beams — *A. Gerasimov* 1678
Evaluation of the synchrotron close orbit — *Yu A. Bashmakov and V. A. Karpov* 1681
Phase trajectory analysis at the nonlinear resonances — *Yu A. Bashmakov* 1684
Emittance calculation using Liouville's theorem for a diagonalized Hamiltonian — *H. Heydari* 1687
Method for calculating strong synchrotron tune modulation of depolarizing resonances in storage rings — *S. R. Mane* 1690
First turn beam correction for the advanced photon source storage ring — *Y. Qian, E. Crosbie, and L. Teng* 1692
Uniform beam distributions using octupoles — *N. Tsoupas, R. Lankshear, C. L. Snead, Jr., T. E. Ward, M. Zucker, and H. A. Enge* 1695
Sensitivity reduction against misalignment of quadrupole and sextupole magnets — *K. Tsumaki, H. Tanaka, and N. Kumagai* 1698
Dynamic aperture of low beta lattices at Tevatron collider — *Vladimir Višnjic* 1701
Adaptive method of closed orbit correction — *Yao Cheng and Chen-Shiung Hsue* 1704
Perturbation treatment of the longitudinal coupling impedance of a toroidal beam tube — *H. Hahn and S. Tepikian* .. 1707

Impact of cross-sectional changes in a beam tube on beam dynamics — *Weiren Chou* 1710
Coupled-bunch instabilities in the APS ring — *L. Emery* 1713
Damping of higher-order modes in a threefold symmetry accelerating structure — *D. Yu and N. Kroll* 1716
Wakefield suppression using beatwave structures — *D. Yu and J. S. Kim* 1719
Measurement of longitudinal impedance for a KAON test pipe model with TSD-calibration method — *Y. Yin, C. Oram, N. Ilinsky, and P. Reinhardt-Nikulin* 1722
Calculation of seed values for longitudinal coupled bunch dipole instability due to uneven bucket population — *S. R. Koscielniak* 1725
Simulation of hollow beams with cancellation of steady state non-linear space-charge — *Shane R. Koscielniak* 1728
Stationary longitudinal phase space distributions with space charge — *R. Baartman* 1731
Characterization and monitoring of transverse beam tails — *J. T. Seeman, F. J. Decker, I. Hsu, and C. Young* 1734
Analysis of resonant longitudinal instability in a heavy ion induction linac — *Edward P. Lee and L. Smith* 1737
An investigation of the source of a low-Q, low-frequency impedance disrupting bunch coalescing in the Fermilab main ring — *P. L. Colestock, J. Griffin, X. Lu, G. Jackson, C. Jensen, and J. Lackey* 1740
A critical survey of stretched-wire impedance measurements at Fermilab — *P. L. Colestock, F. J. Chou, B. Fellenz, M. Foley, F. Harfoush, K. Harkay, G. Jackson, Q. Kerns, D. McConnell, and K. Y. Ng* 1743
Longitudinal instability in the Fermilab accumulator during slow transition crossing — *X. Q. Wang and G. Jackson* .. 1746
Results from longitudinal impedance measurements in the Fermilab Tevatron — *G. Jackson, A. Bogacz, P. J. Chou, P. Colestock, F. Harfoush, X. Lu, K. Y. Ng, W. Pellico, T. Sullivan, and X. Q. Wang* 1749
Measurement of the Fermilab Main Ring longitudinal impedance — *X. Lu and G. Jackson* 1752
Measurement of the resistive wall instability in the Fermilab Main Ring — *G. Jackson* 1755
A test of bunched beam stochastic cooling in the Fermilab Tevatron collider — *G. Jackson, E. Buchanan, J. Budlong, E. Harms, G. Lee, J. Marriner, D. McGinnis, R. Pasquinelli, D. Peterson, D. Poll, D. Rohde, P. Seifrid, and D. Voy* 1758
The self-cooling of charged particle beams in a straight line — *Y. S. Derbenev* 1761
Laser cooling of stored beams in ASTRID — *J. S. Hangst, K. Berg-Sørensen, P. S. Jessen, M. Kristensen, K. Mølmer, J. S. Nielsen, O. Poulsen, J. P. Schiffer, and P. Shi* 1764
Theoretical studies of the ultra slow extraction for the cooler synchrotron COSY-Jülich — *K. Bongardt, D. Dinev, S. Martin, P. F. Meads, H. Meuth, D. Prasuhn, H. Stockhorst, and R. Wagner* 1767
Beam property measurements in the IUCF cooler ring — *M. Ball, D. D. Caussyn, J. Collins, D. DuPlantis, V. Derenchuk, G. East, T. Ellison, D. Friesel, B. Hamilton, B. Jones, S. Y. Lee, M. G. Minty, and T. Sloan* 1770
Intrabeam scattering in the Fermilab antiproton accumulator — *C. M. Bhat and J. Marriner* 1773
Ion clearing by cyclotron resonance shaking — *P. Zhou and J. B. Rosenzweig* 1776
Envelope instability in the Fermilab booster — *P. Zhou, J. B. Rosenzweig, and S. Stahl* 1779
Multibunch instability investigation on a cavity — *E. Karantzoulis* 1782
Beam breakup in recirculating linacs — *B. C. Yunn* 1785
Electromagnetic instability of an intense beam in a quadrupole focusing system — *Cha-Mei Tang and Jonathan Krall* 1788
Instability calculations for the MIT-Bates South Hall Ring — *K. D. Jacobs, P. T. Demos, J. B. Flanz, A. Zolfaghari, J. Wurtele, X. T. Yu, and K. Balewski* 1791
Diagnosis and cure of a transverse instability in the NSLS VUV ring — *J. Rose, R. Biscardi, W. Broome, R. D'Alsace, J. Keane, and J. M. Wang* 1794
Modified octupoles for damping coherent instabilities — *M. Cornacchia, W. J. Corbett, and K. Halbach* 1797
Simulation of longitudinal phase space in the SLC — *Karl L. F. Bane* 1800
Bench measurements of coupling impedance of AGS booster components — *A. Ratti and T. J. Shea* 1803
A feedback for longitudinal instabilities in the SLC damping rings — *Y. Chao, P. Corredoura, T. Limberg, H. Schwarz, and P. Wilson* 1806
Beam breakup with finite bunch length — *C. L. Bohn and J. R. Delayen* 1809
Beam breakup with longitudinal halo — *J. R. Delayen and C. L. Bohn* 1812
Microwave instability at transition—Stability diagram approach — *S. A. Bogacz* 1815
Electron beam injector for longitudinal beam physics experiments — *J. G. Wang, D. X. Wang, and M. Reiser* 1818

Analysis of the longitudinal instability in an induction linac — *J. G. Wang and M. Reiser* 1821
Shielded coherent synchrotron radiation and its possible effect in the next linear collider — *Robert L. Warnock* 1824
Experiments on the beam breakup instability in long-pulse electron beam transport through RF cavity systems — *R. M. Gilgenbach, P. R. Menge, R. A. Bosch, J. J. Choi, H. Ching, and T. A. Spencer* 1827
Studies of coupled-bunch modes in the Fermilab booster — *K. C. Harkay, V. K. Bharadwaj, and P. L. Colestock* 1830
Simulation of multibunch instabilities in the damping ring of JLC — *Kiyoshi Kubo* 1833
Construction of an RF quadrupole magnet for suppressing transverse coupled-bunch instabilities — *Shogo Sakanaka and Toshiyuki Mitsuhashi* 1836
Ion trapping in the CESR B-factory — *David Sagan and Yuri Orlov* 1839
Longitudinal beam response measurements at CESR — *John M. Byrd* 1842
Nonlinear effects in the SLC e^+ transport line — *H. Braun, A. Kulikov, R. Pitthan, and M. Woodley* 1845
Head–tail stability and linear coupling in the Tevatron — *G. P. Goderre, S. Peggs, G. Annala, S. A. Bogacz, D. Herrup, S. Saritepe, T. Sullivan, and T. Williams* 1848
Low loss parameter for new CESR electrostatic separators — *James J. Welch and Zhong Xiong Xu* 1851
Coupled bunch motion in large size rings — *P. L. Morton, R. D. Ruth, and K. A. Thompson* 1854
Simulation and stability of a crab cavity — *Z. Greenwald, S. Greenwald, and D. H. Rice* 1857
Effects of quadrupole wake field on RF focusing in linear colliders — *A. N. Didenko, V. N. Gusarov, and G. A. Kuzmenko* 1860
Realistic modeling of microwave instability effects on the evolution of the beam energy-phase distribution in proton synchrotrons — *J. A. MacLachlan* 1863
Comparison between coasting and bunched beams on optimum stochastic cooling and signal suppression — *J. Wei* .. 1866
Beam life-time with intrabeam scattering and stochastic cooling — *J. Wei and A. G. Ruggiero* 1869
Beta functions in the presence of linear coupling — *G. Parzen* 1872
Dynamic aperture effects due to linear coupling — *G. Parzen* 1875
Brown's transport up to third order aberration by artificial intelligence — *Xia Jiawen, Xie Xi, and Qiao Qingwen* 1878
Resonance seeding of stability boundaries in two and four dimensions — *Leo Michelotti* 1881
Beam dynamics design of an RFQ for the SSC laboratory — *T. S. Bhatia, J. H. Billen, A. Cucchetti, F. W. Guy, G. Neuschaefer, and L. M. Young* 1884
On dynamic aperture — *Zohreh Parsa* 1887
Modelling of space charge effects in the CERN proton synchrotron — *Michel Martini and Oleg Ponomarev* 1890
Observation of space-charge effects in the Los Alamos Proton Storage Ring — *D. Neuffer, D. Fitzgerald, T. Hardek, R. Hutson, R. Macek, M. Plum, H. Thiessen, and T.-S. Wang* 1893
Observations of the PSR transverse instability — *E. Colton, D. Fitzgerald, T. Hardek, R. Macek, M. Plum, H. Thiessen, T. Wang, and D. Neuffer* 1896
Nonlinear dynamics in the booster of the Moscow Kaon Factory — *N. I. Golubeva, A. I. Iliev, and Yu V. Senichev* ... 1899
How to get a separatrix branch with low divergence at a 1/3-integer resonant beam slow extraction — *S. P. Volin* 1902
Racetrack lattices for low-medium-energy synchrotrons — *A. I. Iliev and Yu V. Senichev* 1904
Analytic approach to design of high transition energy lattice with modulated β-function — *A. I. Iliev* 1907

Ion Sources and Injectors

A compact RF driven H^- ion source for linac injection — *J. Patrick Rymer, G. A. Engeman, R. W. Hamm, and J. M. Potter* 1910
The BNL toroidal volume H^- source — *J. G. Alessi and K. Prelec* 1913
Laser diagnostics of H^- formation in a magnetic multicusp ion source — *A. T. Young, P. Chen, W. B. Kunkel, K. N. Leung, C. Y. Li, and G. C. Stutzin* 1916

Optimization of an RF driven H^- ion source — *K. N. Leung, W. F. DiVergilio, C. A. Hauck, W. B. Kunkel, and D. S. McDonald* 1919
IUCF high intensity polarized ion source — *M. Wedekind, R. Brown, J. Collins, V. Derenchuk, D. Dale, D. DuPlantis, T. Ellison, D. Friesel, J. Hicks, D. Jenner, A. Pei, H. Petri, P. Schwandt, and J. Sowinski* 1922
Operational experience with the TRIUMF optically pumped polarized H^- ion source — *P. W. Schmor, L. Buchmann, K. Jayamanna, C. D. P. Levy, M. McDonald, and R. Ruegg* 1925
Operation of the optically pumped polarized H^- ion source at LAMPF — *R. L. York, D. Tupa, D. R. Swenson, and O. B. van Dyck* 1928
Optical pumping of the polarized H^- ion source at LAMPF — *D. R. Swenson, D. Tupa, O. B. van Dyck, and R. L. York* 1931
Installation of the Legnaro ECR ion source — *M. Cavenago, G. Bisoffi, G. Carugno, F. Cervellera, G. Fortuna, M. F. Moisio, V. Palmieri, and K. Rudolph* 1934
Design aspects for a pulsed-mode, high-intensity, heavy negative ion source — *G. D. Alton* 1937
Current density calculation of a high frequency ion source — *H. Heydari* 1940
Review of Mevva ion source performance for accelerator injection — *I. G. Brown, X. Godechot, P. Spädtke, H. Emig, D. M. Rück, and B. H. Wolf* 1943
An antiproton target design for increased beam intensity — *K. Anderson, C. M. Bhat, J. Marriner, and Z. Tang* 1946
Project of complex tandem—RF linear postaccelerator — *O. A. Valdner, V. P. Gass, A. D. Koljaskin, A. N. Pronin, and P. B. Shurupov* 1949
An induction linac injector for scaled experiments — *H. L. Rutkowski, A. Faltens, C. Pike, D. Brodzik, R. M. Johnson, D. Vanecek, and D. W. Hewett* 1952
Testing of a high current DC ESQ accelerator — *J. W. Kwan, G. D. Ackerman, O. A. Anderson, C. F. Chan, W. S. Cooper, G. J. deVries, W. B. Kunkel, L. Soroka, W. F. Steele, and R. P. Wells* 1955
Transport properties of a discrete helical electrostatic quadrupole — *C. R. Meitzler, K. Antes, P. Datte, F. R. Huson, and L. Liu* 1958
Low energy H^- beam transport using an electrostatic quadrupole focusing system — *S. K. Guharay, C. K. Allen, M. Reiser, and V. Yun* 1961
SLC polarized beam source electron optics design — *K. R. Eppley, T. L. Lavine, R. A. Early, W. B. Herrmannsfeldt, R. H. Miller, D. C. Schultz, C. M. Spencer, and A. D. Yeremian* 1964
Observations on field-emission electrons from the Los Alamos FEL photoinjector — *Alex H. Lumpkin* 1967
An RF modulated electron gun pulser for linacs — *Robert Legg and Robert Hartline* 1970
Scaling study of pseudospark produced electron beam — *K. K. Jain, B. N. Ding, and M. J. Rhee* 1972
Low-emittance uniform-density Cs^+ sources for heavy ion fusion accelerator studies — *S. Eylon, E. Henestroza, T. Garvey, R. Johnson, and W. Chupp* 1975
Preliminary design for a thermionic R.F. gun — *G. D'Auria, J. Gonichon, and T. Manfroi* 1978
Applications of diamond films to photocathode electron guns and accelerators — *C. P. Beetz, B. Lincoln, K. Segall, D. Wall, M. Vasas, D. R. Winn, D. Doering, and D. Carroll* 1981
Development of laser optics for the AWA photocathode — *J. Norem and W. Gai* 1984
Flat-beam RF photocathode sources for linear collider applications — *J. B. Rosenzweig* 1987
Electron beam generation from a superemissive cathode — *T.-Y. Hsu, R.-L. Liou, G. Kirkman-Amemiya, and M. A. Gundersen* 1990
Quantum yield measurements of photocathodes illuminated by pulsed ultraviolet laser radiation — *A. T. Young, P. Chen, W. B. Kunkel, K. N. Leung, C. Y. Li, and J. M. Watson* 1993
3D numerical thermal stress analysis of the high power target for the SLC positron source — *Eric M. Reuter and John A. Hodgson* 1996
Mechanical design and development of a high power target system for the SLC positron source — *Eric Reuter, Dean Mansour, Tom Porter, Werner Sax, and Anthony Szumillo* 1999
Channeling crystals for positron production — *Franz-Josef Decker* 2002
SLC positron source pulsed flux concentrator — *A. V. Kulikov, S. D. Ecklund, and E. M. Reuter* 2005
Progress in H^- ion source development at TAC — *J. Culver, K. Antes, F. R. Huson, A. Larsson, C. R. Meitzler, and L. Xiu* 2008

Volume 4

Investigation of an intense H^- ion beam produced by a volume source — *M. Bacal, P. Devynck, C. Michaut, Z. Sledziewski, and F. P. G. Valckx* 2011
Single bunched beam generation using conventional electron gun for JLC injector — *T. Naito, J. Urakawa, M. Akemoto, and H. Akiyama* 2014
Measures to alleviate the back bombardment effect of thermionic RF electron gun — *Y. Huang and J. Xie* 2017
Development of thermionic-cathode RF electron gun at IHEP — *Jialin Xie, Jie Gao, Yongzhang Huang, Renshan Zhang, Hongxiu Liu, and Youzhi Wang* 2020
Characteristics of the H^- /D^- beam extracted from an RF-driven volume source — *G. Gammel, T. Debiak, J. Sredniawski, K. Leung, and D. McDonald* 2023
Design and modeling of a 17 GHz photocathode RF gun — *C. L. Lin, S. C. Chen, J. S. Wurtele, R. Temkin, and B. Danly* 2026
Strain enhanced electron spin polarization observed in photoemission from InGaAs — *T. Maruyama, E. L. Garwin, R. Prepost, G. H. Zapalac, J. S. Smith, and J. D. Walker* 2029
Development of polarized electron sources using AlGaAs–GaAs superlattice and using strained GaAs — *T. Nakanishi, Y. Kurihara, T. Omori, H. Aoyagi, T. Baba, T. Furuya, H. Horinaka, K. Itoga, Y. Kamiya, T. Kato, M. Mizuta, S. Nakamura, T. Saka, Y. Takeuchi, M. Tsubata, and M. Yoshioka* 2032
Magnetic ring for transformation of the heavy ions charge states — *V. P. Kukhtin, Yu P. Servergin, and I. A. Shukeilo* 2035

Linear Colliders

Chairman: C. Pellegrini

Emittance control in linear colliders *(Invited Paper)* — *Ronald D. Ruth* 2037
Application of superconducting RF to linear colliders *(Invited Paper)* — *H. Padamsee* 2042
Accelerator test facility for the JLC project — *Seishi Takeda* 2047
The CERN study of a 2 TeV e^+e^- collider CLIC — *CLIC Study Group* 2052
The final focus test beam project — *David Burke* 2055
The optics of the final focus test beam — *J. Irwin, K. Brown, F. Bulos, D. Burke, R. Helm, G. Roy, R. Ruth, N. Yamamoto, and K. Oide* 2058
High gradient experiments by the ATF — *Seishi Takeda, Mitsuo Akemoto, Hitoshi Hayano, Hiroshi Matsumoto, and Takashi Naito* 2061
Summary of emittance control in the SLC linac — *J. T. Seeman, C. Adolphsen, K. L. F. Bane, P. Emma, F. J. Decker, I. Hsu, T. Limberg, L. Merminga, M. Ross, and W. Spence* 2064
Chromaticity corrections in the SLC final focus system — *N. Toge, K. Brown, D. Burke, R. Jacobsen, P. Krejcik, and V. Ziemann* 2067
An active alignment test facility for the CERN linear collider — *W. Coosemans, I Wilson, and P. Poirier* 2070
Emittance growth in TESLA — *G. A. Krafft, M. Fripp, and J. J. Bisognano* 2073

Ion Sources and Injectors

Chairman: R. Stevens

State of H^- source development *(Invited Paper)* — *K. N. Leung* 2076
H^- temperature measurements by a slit diagnostic technique — *Joseph D. Sherman, H. Vernon Smith, Jr., Carl Geisik, and Paul Allison* 2080
Recent developments in intense polarized hydrogen and deuterium ion sources *(Invited Paper)* — *Thomas B. Clegg* .. 2083

Ion sources for commercial ion implanter applications *(Invited Paper)* — *S. R. Walther, B. O. Pedersen, and C. M. McKenna* 2088
High-current CW RFQ's *(Invited Paper)* — *G. E. McMichael* 2093
SLC positron source—Simulation and performance — *Rainer Pitthan, Hans Braun, J. E. Clendenin, S. D. Ecklund, R. H. Helm, A. V. Kulikov, A. C. Odian, G. X. Pei, M. C. Ross, and M. D. Woodley* 2098
Overall simulation of a positron beam generated by photons from channeled multiGeV electrons — *X. Artru, R. Chehab, A. Jejcic, J. Maillard, and J. Silva* 2101
Electron emission from ferroelectric ceramics — *J. D. Ivers, R. Advani, J. A. Nation, and L. Schachter* 2104
Time-resolved emittance measurements of an excimer-laser-driven metal photocathode — *T. Kauppila, R. Carlson, D. Moir, and R. Ridlon* 2107

Accelerator Technology III—Superconducting Components, Magnets

Magnet design for the DARHT linear induction accelerators — *Michael Burns, Ken Chellis, Cathy Mockler, Tom Tucker, George Velasquez, and Roger Van Maren* 2110
Magnetic data analysis for the ALS lattice magnets — *Roderich Keller* 2113
Magnetic measurements of the XLS magnets — *L. Solomon, J. Galayda, and C. Sylvester* 2116
Magnetic measurements of the 12-pole trim magnets for the 200 MeV compact synchrotron XLS at the National Synchrotron Light Source — *J. Krishnaswamy, Swarn Kalsi, and Hank Hsieh* 2119
Determination of the particle momentum in LEP from precise magnet measurements — *J. Billan, J. P. Gourber, and K. N. Henrichsen* 2122
Measurements of quadrupole magnets for the MIT-bates SHR — *J. D. Zumbro, P. Bonneau, M. Farkhondeh, J. B. Flanz, S. P. Holmberg, T. Russ, W. W. Sapp, and C. Sibley* 2125
Harmonic analysis of Fermilab main ring quadrupoles — *B. C. Brown, P. O. Mazur, J.-F. Ostiguy, S. M. Pruss, and F. Turkot* 2128
Three-dimensional field map of the Fermilab DO detector — *Jean-François Ostiguy and Ryuji Yamada* 2131
Software design for a database driven system for accelerator magnet measurements — *B. C. Brown, M. E. Bleadon, H. D. Glass, R. Glosson, R. W. Hanft, D. J. Harding, P. O. Mazur, J. E. Pachnik, J. W. Sim, K. Trombly-Freytag, and D. G. Walbridge* 2134
Modification of LAMPF's magnet-mapping code for offsets of center coordinates — *J. W. Hurd, S. Gomulka, F. Merrill, and B. L. Weintraub* 2137
A new 3-D integral code for computation of accelerator magnets — *L. R. Turner and L. Kettunen* 2140
The physical way of standardizing magnets — *Franz-Josef Decker* 2143
Septum magnet for electron slow extraction from the Yerevan synchrotron — *A. Z. Babaian, G. B. Bagdasarian, V. T. Nickogosian, A. R. Toumanian, A. G. Zacharian, E. A. Ludmirsky, and J. Rummler* 2146
Observation of a periodic pattern in the persistent-current fields of the superconducting HERA magnets — *H. Brück, D. Gall, J. Krzywinski, R. Meinke, H. Preissner, M. Halemeyer, P. Schmüser, C. Stolzenburg, R. Stiening, R. ter Avest, and L. J. M. van de Klundert* 2149
New final focus system for the SLAC linear collider — *N. Toge, W. W. Ash, H. Band, A. O. Bazarko, Y.-C. Chao, R. Erickson, R. Gray, S. S. Hertzbach, R. R. Kofler, D. Mansour, C. M. Spencer, J. Turk, C. Zeitlin, and V. Ziemann* 2152
Recent improvements in superconducting cable for accelerator dipole magnets — *Ronald M. Scanlan and John M. Royet* 2155
Correction of magnetization sextupole and decapole in a 5 centimeter bore SSC dipole using passive superconductor — *Michael A. Green* 2158
Preliminary study of an integral harmonic analysis magnetic field measurement system for long SSC magnets — *Michael I. Green* 2161

Experiments with all-Kapton insulation and axial prestress in 1.8 m-long SSC R&D magnets — *P. Wanderer, M. Anerella, G. Cottingham, G. Ganetis, M. Garber, A. Ghosh, C. Goodzeit, A. Greene, R. Gupta, J. Herrera, S. Kahn, E. Kelly, A. Meade, G. Morgan, J. Muratore, A. Prodell, P. Radusewicz, M. Rehak, E. Rohrer, W. Sampson, R. Shutt, P. Thompson, and E. Willen* 2164
Construction and results of the 50 mm short R&D dipole magnets — *G. H. Morgan, M. Anerella, J. Cottingham, G. Ganetis, M. Garber, A. Ghosh, C. Goodzeit, A. Greene, R. Gupta, J. Herrera, S. Kahn, E. Kelly, A. Morgillo, J. Muratore, A. Prodell, P. Radusewicz, M. Rehak, E. P. Rohrer, W. Sampson, R. Shutt, P. Thompson, P. Wanderer, and E. Willen* 2167
Magnetic properties of iron yoke laminations for SSC dipole magnets — *S. A. Kahn and G. H. Morgan* 2170
Tests of 1.5 meter model 50mm SSC collider dipoles at Fermilab — *M. Wake, R. Bossert, J. Carson, K. Coulter, S. Delchamps, S. Gourlay, T. S. Jaffery, W. Kinney, W. Koska, M. J. Lamm, J. Strait, R. Sims, and M. Winters* 2173
Mechanical design of the 2D cross-section of the SSC collider dipole magnet — *J. Strait, J. Kerby, R. Bossert, J. Carson, G. Spigo, and J. R. Turner* 2176
Tests of 40 mm SSC dipole model magnets with vertically split yokes — *W. Koska, R. Bossert, K. Coulter, S. Delchamps, S. Gourlay, W. Kinney, T. S. Jaffery, M. J. Lamm, J. Strait, and M. Wake* 2179
Coil end design for the SSC collider dipole magnet — *J. S. Brandt, N. W. Bartlett, R. C. Bossert, J. A. Carson, J. J. Konc, G. C. Lee, and J. M. Cook* 2182
SSC collider dipole magnet end mechanical design — *S. W. Delchamps, R. C. Bossert, J. Carson, K. Ewald, H. Fulton, J. Kerby, W. Koska, J. Strait, M. Wake, and K. K. Leung* 2185
Optimization of the end winding geometry of dipole magnets — *Michael F. Reusch, Don W. Weissenburger, and James C. Nearing* 2188
Bipolar and unipolar tests of 1.5m model SSC collider dipole magnets at Fermilab — *M. J. Lamm, J. P. Ozelis, S. Delchamps, K. J. Coulter, T. S. Jaffery, W. Kinney, W. Koska, J. Strait, M. Wake, D. Fortunato, and D. E. Johnson* 2191
Coil shapes towards pure multipoles in circular regions (a numerical approach) — *V. Thiagarajan* 2194
A software package linking PE2D and ANSYS for SSC magnet design — *Nick Kallas, Chris Haddock, Jay Jayakumar, David Orrell, Greg Snitchler, Giancarlo Spigo, and Jon Turner* 2197
Cooldown stresses on the coldmass of SSC dipole magnets — *B. Aksel and K. Leung* 2200
Divergent quench velocity expression and 4-cm SSC R&D dipole magnets — *G. López* 2203
Mechanical analysis of beam tube assemblies for SSC dipoles during a quench — *S. A. Smith, C. Haddock, R. Jayakumar, J. Turner, and J. Zbasnik* 2206
Hydraulic quench simulations in SSC dipole magnets — *G. Snitchler and B. Aksel* 2209
Quench analysis of the energy deposition in the SSC magnets and radiation shielding of the low-β IR quadrupoles — *G. López* 2212
SSC dipole quench protection heater test results — *C. Haddock, R. Jayakumar, F. Meyer, G. Tool, J. Kuzminski, J. DiMarco, M. Lamm, T. Jaffery, D. Orris, P. Mazur, R. Bossert, and J. Strait* 2215
The SSC collider correction system — *S. R. Stampke, Y. Cai, and J. Skaritka* 2218
Superferric correction magnet test results — *R. Rocha, J. Colvin, F. R. Huson, W. W. MacKay, Y. Miao, S. Pissanetzky, G. Shotzman, and J. Zeigler* 2221
Quench simulation studies of the TAC jelly roll superferric dipole corrector elements for the SSC — *G. López* 2224
Quench performance of superconducting quadrupole magnets for the new Fermilab low beta insertion — *S. A. Gourlay, J. A. Carson, R. Hanft, T. S. Jaffery, K. Koepke, M. J. Lamm, P. M. Mantsch, A. D. McInturff, A. Mokhtarani, D. Orris, and T. Peterson* 2227
Production measurements on the quadrupole correctors for the new low-beta system for the Tevatron collider — *A. Mokhtarani, B. C. Brown, R. Hanft, A. R. Oleck, T. Peterson, and F. Turkot* 2230
Magnetic performance of new Fermilab high gradient quadrupoles — *R. Hanft, B. C. Brown, J. A. Carson, S. A. Gourlay, M. J. Lamm, A. D. McInturff, A. Mokhtarani, and A. Riddiford* 2233
Fabrication and performance of a new high-gradient trim quadrupole for the Fermilab luminosity upgrade — *P. M. Mantsch, J. A. Carson, S. A. Gourlay, M. J. Lamm, and A. W. Riddiford* 2236

RHIC insertion magnets — *R. C. Gupta, J. Cottingham, G. Ganetis, M. Garber, A. Ghosh, A. Greene, H. Hahn, J. Herrera, S. Kahn, E. Kelly, E. Killian, G. Morgan, A. Meade, J. Muratore, A. Prodell, M. Rehak, E. Rohrer, W. Sampson, R. Shutt, P. Thompson, P. Wanderer, and E. Willen* 2239
Iron saturation control in RHIC dipole magnets — *P. A. Thompson, R. C. Gupta, S. A. Kahn, G. H. Morgan, P. J. Wanderer, E. Willen, and H. Hahn* 2242
Revised cross section for RHIC dipole magnets — *P. A. Thompson, R. C. Gupta, S. A. Kahn, G. H. Morgan, P. J. Wanderer, E. Willen, and H. Hahn* 2245
Superconducting magnet program for X-ray lithography source at Brookhaven National Laboratory — *H. Hsieh, R. Blumberg, R. Heese, J. Murphy, S. Pjerov, S. Sharma, E. M. W. Leung, S. Kalsi, and M. F. Reusch* 2248
A dipole magnet model for compact synchrotron light source — *M. Kitamura, H. Yamamoto, H. Tomeoku, and N. Maki* 2251
The superconducting Tritron magnets — *R. Kratz, G. Hinderer, J. Junger, J. Labedzki, and U. Trinks* 2254
Superconducting quadrupole magnet system for TRISTAN mini-beta insertions — *K. Endo, K. Egawa, H. Fukuma, A. Kabe, T. Kubo, S. Kuroda, S. Kurokawa, Y. Morita, Y. Ohsawa, N. Ohuchi, T. Ozaki, R. Sugahara, and K. Tsuchiya* 2257
A design concept for the LHC insertion quadrupoles — *W. Scandale and T. Taylor* 2260
A guideline for design, analysis, and fabrication of vacuum vessels for cryogenic accelerators — *Robert C. Gentzlinger and Kirk E. Christensen* 2263
Instrumentation and control of the AGS booster vacuum system — *J. Gabusi, J. Geller, H. C. Hseuh, P. Rosas, J. Sandburg, B. Shen, P. Stattel, and R. Zapasek* 2266
Pumping mechanisms in sputter-ion pumps low pressure operation — *Kimo M. Welch* 2269
Ceramic beam pipe for the TRIUMF KAON factory synchrotron rings — *T. Hodges, R. Langstaff, C. Oram, M. Featherby, and C. Planner* 2272
Vacuum chamber of the injector synchrotron for the advanced photon source — *R. Benaroya and R. Dortwegt* 2275
Vacuum chamber for the 3 GeV SPEAR injector synchrotron — *H. Morales, N. Hower, U. Cummings, P. Golceff, W. Li, J. Safranek, J. Voss, and H. Wiedemann* 2278
Design considerations for beam tube penetration of a liquid argon collider detector — *Keith Primdahl and Hans Jöstlein* 2281
SLC polarized beam source ultra-high-vacuum design — *T. L. Lavine, J. E. Clendenin, E. L. Garwin, E. W. Hoyt, M. W. Hoyt, R. H. Miller, J. A. Nuttall, D. C. Schultz, and D. Wright* 2284
Photon stimulated desorption of neutral species from aluminum — *T. S. Chou* 2286
Modeling photo-desorption in high current storage rings — *William A. Barletta* 2289
Processing and evaluation of the AGS booster ultra-high vacuum system — *H. C. Hseuh, M. Mapes, P. Schnitzenbaumer, B. Shen, R. Sikora, and P. Stattel* 2292
Calculation of pressure distribution in vacuum systems using a commercial finite element program — *J. Howell, B. Wehrle, and H. Jostlein* 2295
Performance estimation of vacuum system components including crotch and absorber — *T. Nishidono, S. H. Be, H. Daibo, T. Hanasaka, Y. Hirano, S. R. In, Y. Oikawa, H. A. Sakaue, S. Takahashi, S. Yokouchi, and K. Watanabe* 2298
ANL advanced photon source crotch absorber design — *M. Choi, J. D. Gonczy, J. W. Howell, and R. C. Niemann* ... 2301
UHV seal studies for the advanced photon source storage ring vacuum system — *J. D. Gonczy, R. J. Ferry, R. C. Niemann, and B. Roop* 2304
Vacuum design for a superconducting mini-collider — *William A. Barletta and Sergio Monteiro* 2307
Design of the vacuum system for the high energy ring of an asymmetric B-factory based on PEP — *William A. Barletta, Manuel Calderon, Robert Wong, and Theodore Jenkins* 2310
Ion clearing and photoelectron production in the 200 MeV SXLS ring — *H. Halama and Eva Bozoki* 2313
SXLS phase II vacuum system — *J. C. Schuchman, T. S. Chou, H. Halama, H. Hsieh, T. Kim, S. Pjerov, and F. Staicu* 2316
The cryogenic operation of the superconducting magnet system in the HERA proton storage ring: Cool down, steady state operation, quench recovery processes — *G. Horlitz, M. Clausen, H. Lierl, R. Lange, and H. Herzog* 2319
Magnetic permeability of stainless steel for use in acclerator beam transport systems — *Norman Wilson and Paul Bunch* 2322
A closed cycle cryogenic system for testing superconducting RF cavities — *C. Reece, J. Susta, T. Powers, and B. Almeida* 2325
Extraction septum magnet for the SSRL SPEAR injector — *J. Cerino, M. Baltay, R. Boyce, S. Harris, R. Hettel, M. Horton, and K. Zuo* 2328

Operational experience with SLC damping ring kicker magnets — *T. Mattison, R. Cassel, A. Donaldson, G. Gross, and A. Harvey* 2331
Development of epoxy potting for high voltage insulation at SLAC — *G. Gross, R. Cassel, and T. Mattison* 2334
Development and performance of electrostatic deflector insulators for the Chalk River superconducting cyclotron — *C. R. Hoffmann and J. F. Mouris* 2337
A design for a beam halo scraper system for the Tevatron collider — *S. M. Pruss* 2340
Synchrotron radiation masking on asymmetric 6.5 × 4.3-GeV B-factory — *V. E. Blinov, V. A. Lebedev, A. V. Matveev, V. A. Tayursky, and A. A. Zholents* 2342
Engineering design of the PLS 2 GeV storage ring dipole magnet — *E. S. Park, Y. G. Nah, H. S. Han, and Y. M. Koo* 2345
Low-sextupole steering dipoles for the MIT-Bates SHR — *M. Farkhondeh, R. J. Averill, W. W. Sapp, and J. D. Zumbro* 2348
Permanent magnet-based dipole for a small storage ring — *Firas Putris and Wayne Vernon* 2351
Magnet end design: The main injector dipoles — *Jean-François Ostiguy* 2354
Effects of the SRRC second prototype dipole magnet on the SRRC ring — *J. C. Lee* 2357
A radiation-hardened pulsed magnet for the Tevatron-I target station — *P. Hurh, M. Gormley, J. Hangst, S. O'Day, and J. Howell* 2360
Magnets for TRIUMF's KAON factory — *A. J. Otter and P. A. Reeve* 2363
Magnetic devices of the Amsterdam pulse stretcher ring AmPS — *H. Boer Rookhuizen, J. Bijleveld, A. van der Linden, G. Luijckx, R. Maas, and Y. Wu* 2366
The ring magnets for the SSRL SPEAR injector — *M. M. Baltay, J. Cerino, R. Hettel, J. Safranek, J. Voss, H. Wiedemann, and K. Zuo* 2369
The ELETTRA transfer line magnets — *M. Begg, D. Einfeld, and D. Tommassini* 2372
Fabrication and tests of prototype quadrupole magnets for the storage ring of the Advanced Photon Source — *S. H. Kim, K. M. Thompson, E. L. Black, and J. M. Jagger* 2375
A quadrupole magnet for the Fermilab Linac Upgrade — *T. Kroc* 2378
CEBAF cryomodule testing — *Kevin Jordan, Rich Bundy, I. E. Campisi, Ken Crawford, Mike Drury, J. Patrick Kelley, Tim Lee, Jim Marshall, Joe Preble, John Robb, William J. Schneider, Ed Stitts, Ronald M. Sundelin, Henry Whitehead, and Mark Wiseman* 2381
Performance of superconducting cavities for CEBAF — *Peter Kneisel, John Mammosser, Ganapati Rao, Kenji Saito, and Ron Sundelin* 2384
Q degradations in superconducting niobium cavities — *Kenji Saito and Peter Kneisel* 2387
Production of superconducting niobium cavities for CEBAF — *M. Dzenus, K. Iversen, M. Peiniger, and D. Kiehlmann* 2390
First operation of MACSE the Saclay pilot superconducting electron linac — *B. Aune, C. Antoine, B. Bonin, P. Bosland, J. M. Cavedon, S. Chel, C. Chianelli, A. Curtoni, M. Desmons, J. Fagot, J. Gastebois, A. Godin, F. Gougnaud, J. F. Gournay, G. Gourcy, F. Guemas, X. Hanus, C. Henriot, J. Jablonka, J. M. Joly, M. Juillard, E. Klein, F. Koechlin, P. Leconte, A. Mosnier, Phung Ngoc B., M. Promé, H. Safa, T. Tourrette, A. Veyssière, S. Buhler, M. Fouaidy, and T. Junquera* 2393
Superconducting RF activities at Peking University — *Chia-erh Chen, Zui Zhao, Baocheng Zhang, Guangwei Wang, Lifang Wang, and Jinhu Song* 2396
First test of a 1.5 GHz single cell accelerating cavity obtained by magnetron sputtering of niobium — *G. C. Gualco, A. Matrone, S. Rizzo, F. Rosatelli, R. Parodi, P. Fabbricatore, G. Gemme, R. Musenich, and Bi Zhang* 2399
Fabrication techniques and RF properties of niobium thin wall cavities — *M. Sakano, S. Mukoyama, T. Shimano, H. Matsuba, M. Ikeda, T. Fujino, A. Yamamoto, and H. Hirabayashi* 2402
Operational experience with the TRISTAN superconducting RF system — *K. Akai, T. Furuya, E. Kako, K. Kubo, S. Noguchi, and T. Shishido* 2405
Long term performance of the TRISTAN superconducting RF cavities — *E. Kako, K. Akai, T. Furuya, K. Kubo, S. Mitsunobu, H. Nakai, S. Noguchi, T. Shishido, T. Tajima, and T. Takahashi* 2408
High peak power RF processing studies of 3 GHz niobium cavities — *J. Graber, P. Barnes, J. Kirchgessner, D. Moffat, H. Padamsee, D. Rubin, J. Sears, and Q. S. Shu* 2411
Increase in RF surface resistance of niobium as a result of acid treatment — *D. Moffat, P. Barnes, J. Kirchgessner, H. Padamsee, J. Potts, D. Rubin, J. Sears, Q. Shu, and D. Proch* 2414

Test results on 3 GHz structures for a superconducting linear collider — *R. W. Röth, V. G. Kurakin, G. Müller, H. Piel, J. Pouryamout, D. Reschke, H. Padamsee, J. Graber, J. Kirchgessner, D. Moffat, D. Rubin, J. Sears, and Q. S. Shu* 2417
Field emission studies of heat treated and chemically treated superconducting cavities — *H. Padamsee, P. Barnes, J. Kirchgessner, D. Moffat, D. Rubin, J. Sears, and Q. S. Shu* 2420
Crab cavity development for the Cornell B-factory, CESR-B — *H. Padamsee, P. Barnes, C. Chen, J. Kirchgessner, D. Moffat, D. Rubin, Y. Samed, J. Sears, Q. S. Shu, M. Tigner, and D. Zu* 2423
Development and test of an accelerating cavity shape for a superconducting linear collider — *J. Kirchgessner, P. Barnes, M. Hiller, D. Moffat, H. Padamsee, D. Rubin, D. Saraniti, J. Sears, Q. S. Shu, and W. Hartung* 2426
Status of the superconducting cavity program for HERA — *B. Dwersteg, G. Enderlein, W. Körber, A. Matheisen, W.-D. Möller, D. Proch, D. Renken, and J. Sekutowicz* 2429
Investigations on hydrogen contamination of superconducting cavities — *G. Enderlein, W. Körber, A. Matheisen, D. Proch, and F. Schölz* 2432
Transient heat conduction analysis in superconducting cavities — *Xiaoping Cao and D. Proch* 2435
Analysis of the radiofrequency dipole and quadrupole effects in a QW resonator — *A. M. Porcellato, A. Battistella, G. Bisoffi, and M. Cavenago* 2438
Recent developments in high-current superconducting ion linacs — *J. R. Delayen, C. L. Bohn, W. L. Kennedy, C. T. Roche, and L. Sagalovsky* 2441
Status of the SUNY superconducting RFQ — *A. Jain, I. Ben-Zvi, P. Paul, H. Wang, and A. Lombardi* 2444
RF power requirements for a high intensity proton collider— *Part I* — *D. Boussard* 2447
The superconducting cavities for the TRITRON — *P. Schütz, T. Grundey, J. Labedzki, and U. Trinks* 2450
Applied geometric tolerancing in accelerator component design — *Richard E. Lujan and Kirk E. Christensen* 2453
Considerations for design of a micropositioner for cryogenic accelerators — *Stephen C. Lloyd and Robert C. Gentzlinger* 2456
Cryogenic gas disconnect joints used in cryogenic accelerator cold-gas distribution systems — *Norman G. Wilson, Clark Bridgman, and Robert J. Grieggs* 2459
Field measurement of superconducting quadrupole magnets for TRISTAN mini-beta insertions — *K. Egawa, K. Endo, T. Kubo, Y. Morita, Y. Ohsawa, N. Ohuchi, T. Ozaki, R. Sugahara, and K. Tsuchiya* 2462
Design of the magnet for the SPring-8 storage ring — *N. Kumagai, J. Ohnishi, H. Takebe, K. Kumagai, and S. Motonaga* 2465
One-dimensional time-independent conduction states and temperature distribution along a normal zone during a quench — *G. López* 2468
Non similarity solution approximation to the thermal hydraulic quenchback in superconductors — *G. López* 2471
Development of non-ferrous superconducting magnets — *Frank Krienen, Dinesh Loomba, and Wuzheng Meng* 2474
Design considerations and prototype performance of the Fermilab main injector dipole — *D. J. Harding, M. E. Bleadon, B. C. Brown, E. Desavouret, J. D. Garvey, H. D. Glass, F. A. Harfoush, S. D. Holmes, J. C. Humbert, J. M. Jagger, G. R. Kobliska, A. Lipski, P. S. Martin, P. O. Mazur, F. E. Mills, D. F. Orris, J.-F. Ostiguy, S. G. Peggs, J. E. Pachnik, E. E. Schmidt, J. W. Sim, S. C. Snowdon, and D. G. Walbridge* 2477
Time decay measurements of the sextupole component of the magnetic field in a 4-cm aperture, 17-m-long SSC dipole magnet prototype — *A. Devred, J. DiMarco, J. Kuzminski, R. Stiening, J. Tompkins, Y. Yu, H. Zheng, T. Ogitsu, R. Hanft, P. O. Mazur, D. Orris, and T. Peterson* 2480

Beam Dynamics I

Chairman: A. Chao

The impact of persistent current field errors on the stability of the proton beam in the HERA proton ring *(Invited Paper)* — *F. Willeke and F. Zimmermann* 2483
Tuning of final focus system for future linear colliders *(Invited Paper)* — *Katsunobu Oide* 2488
Beam dynamics of cooled heavy ion beams *(Invited Paper)* — *Ingo Hofmann* 2492
Emittance growth in mismatched charged particle beams — *M. Reiser* 2497

Correction of the first order beam transport of the SLC arcs — *N. Walker, T. Barklow, P. Emma, and P. Krejcik* 2500
A new method of correcting the trajectory in linacs — *T. O. Raubenheimer and R. D. Ruth* 2503
Energy change of a depolarizing resonance due to a type-3 Siberian snake — *M. G. Minty, T. J. P. Ellison, J. E. Goodwin, S. Y. Lee, P. V. Pancella, T. Rinckel, M. A. Ross, F. Sperisen, E. J. Stephenson, B. von Przewoski, R. Baiod, Y. S. Derbenev, A. D. Krisch, R. A. Phelps, T. Roser, B. S. van Guilder, B. Vuaridel, E. D. Courant, and L. G. Ratner* 2506
Impedance measurements with strongly cooled beams at LEAR — *J. Bosser, M. Chanel, D. Manglunki, D. Möhl, F. Pedersen, G. Tranquille, D. Vandeplassche, and M. Gurevitch* 2509
Visualization of wake fields in 3-D — *F. A. Harfoush and T. G. Jurgens* 2512

Accelerator Technology I—Instrumentation, Control, Feedback

Chairman: J. Hinkson

RF control system for CEBAF *(Invited Paper)* — *S. Simrock* 2515
Modern computer networks and distributed intelligence in accelerator controls *(Invited Paper)* — *C. Briegel* 2520
Modern operators' consoles for accelerator control at Fermilab — *P. Lucas, K. Cahill, R. Peters, and J. Smedinghoff* . 2523
The advanced photon source control system — *Martin J. Knott, William P. McDowell, Frank R. Lenkszus, Martin R. Kraimer, Ned D. Arnold, Robert T. Daly, Gary R. Gunderson, Ben-Chin K. Cha, and Mark D. Anderson* 2526
Measurement of longitudinal emittance growth using a laser-induced neutralization method — *V. W. Yuan, R. Garcia, K. F. Johnson, K. Saadatmand, O. R. Sander, D. Sandoval, and M. Shinas* 2529
Bunched beam stochastic cooling *(Invited Paper)* — *G. Jackson* 2532
Control of coupled-bunch instabilities in high-current storage rings *(Invited Paper)* — *G. Lambertson* 2537
Real time global orbit feedback system for NSLS X-ray ring — *L. H. Yu, R. Biscardi, J. Bittner, A. M. Fauchet, S. Krinsky, R. J. Nawrocky, J. Rothman, O. V. Singh, and K. M. Yang* 2542
Progress on the development of APS beam position monitoring system — *Glenn Decker and Youngjoo Chung* 2545

Applications and New Methods of Acceleration

RF transfer in the coupled-cavity free-electron laser two-beam accelerator — *Michael A. Makowski* 2548
Beam dynamics and RF evolution in a multistage klystron-like free-electron laser — *Ken Takayama* 2551
Modelling of the transverse mode suppressor for dielectric wake-field accelerator — *Wei Gai and Ching-Hung Ho* .. 2554
Accelerating field step-up transformer in wake-field accelerators — *E. Chojnacki, W. Gai, P. Schoessow, and J. Simpson* 2557
Suitability of tunneling ionization produced plasmas for the plasma beat wave accelerator — *W. P. Leemans, C. E. Clayton, K. A. Marsh, A. Dyson, and C. Joshi* 2560
Vlasov–Maxwell simulations of nonlinear plasma dynamics in the plasma wakefield accelerator — *Jonathan Krall, Glenn Joyce, and Eric Esarey* 2563
High accelerating-gradient accelerator based on magnetic field decay mechanism — *Han S. Uhm* 2566
An active particle accelerator — *T. Goldman* 2569
Design of micrograting structures for laser acceleration of electrons — *Ira S. Lehrman, Michael J. Arida, Richard C. Fernow, and Harold G. Kirk* 2572
An electrostatic accelerator FEL amplifier as a possible microwave power source for linear colliders — *L. R. Elias, D. J. Larson, and I. Boscolo* 2575
Studies of ion acceleration in a one meter laser controlled collective accelerator — *W. W. Destler, J. Rodgers, C. D. Striffler, and R. L. Yao* 2578
Particle trajectories through MIRRORTRON configurations — *D. J. Larson and D. W. Hewett* 2581
Preliminary design of a dedicated proton therapy linac — *R. W. Hamm, K. R. Crandall, and J. M. Potter* 2583
Intensity possibilities for the Loma Linda medical accelerator — *P. E. Young and P. L. Morton* 2586
Heavy ion, recirculating linac, design optimization — *D. W. Hewett and T. F. Godlove* 2589

Physics issues in the design of a recirculating induction accelerator for heavy ion fusion — *J. J. Barnard, M. A. Newton, L. L. Reginato, W. M. Sharp, H. D. Shay, and S. S. Yu* 2592
Engineering systems designs for a recirculating heavy ion induction accelerator — *M. A. Newton, J. J. Barnard, L. L. Reginato, and S. S. Yu* 2595
High-power proton linac for transmuting the long-lived fission products in nuclear waste — *G. P. Lawrence* 2598
Electron accelerator for transmutation of fission products and nuclear fuel cycle actinides — *G. I. Batskikh, B. V. Bekhtev, V. A. Boiko, V. V. Elian, and A. V. Mishchenko* 2601
Radioactive beams with the HHIRF accelerators — *D. K. Olsen, G. D. Alton, C. Baktash, H. K. Carter, D. T. Dowling, J. D. Garrett, D. L. Haynes, C. M. Jones, R. C. Juras, S. N. Lane, I. Y. Lee, M. J. Meigs, G. D. Mills, S. W. Mosko, B. A. Tatum, and K. S. Toth* 2604
Accelerated radioactive beams at TRIUMF — *J. D'Auria, L. Buchmann, J. S. Fraser, and H. Schneider* 2607
Acceleration and mass-separation of radioactive ion beams in an isochronous cyclotron — *G. Berger, T. Daras, M. Loiselet, N. Postiau, and G. Ryckewaert* 2610
Linear resonant accelerators for industrial applications — *O. A. Waldner, V. G. Gass, A. A. Glaskov, V. D. Danilov, B. V. Zverev, A. A. Il'in, A. D. Koljaskin, A. I. Krivonosov, V. N. Leonov, N. R. Lobanov, O. S. Milovanov, A. A. Mishukov, A. N. Pronin, A. A. Revkov, N. P. Sobenin, Y. I. Tlekhas, and P. B. Shurupov* 2613
The test run of the AMS system at Peking University — *Chia-erh Chen, Zhiyu Guo, Shangqing Yan, Min Xiao, Zhengfang Zhang, Fengling Yang, Renxing Li, Jingxiang Yu, Kun Li, Hongtao Liu, Dongxing Jiang, Ruju Zhang, Xiangyang Lu, Bin Li, Weishu Qian, Jinglin Yuan, Zheng Yang, Kexin Liu, and Houzhi Si* 2616
The Ghent State University linear electron accelerator facilities: Status and perspectives — *W. Mondelaers* 2619
EXDEP/CTX—An explosive detection system for screening luggage with high energy X-rays — *Kerry W. Habiger, Jerome R. Clifford, R. Bruce Miller, and William F. McCullough* 2622
CW 100MW microwave power transfer in space — *K. Takayama, S. Hiramatsu, and M. Shiho* 2625
Ion accelerators for space — *R. J. Slobodrian and L. Potvin* 2628
Performance of the CERN plasma lens in laboratory and beam tests at the antiproton source — *R. Kowalewicz, M. Lubrano di Scampamorte, S. Milner, F. Pedersen, H. Riege, J. Christiansen, K. Frank, M. Stetter, R. Tkotz, and E. Boggasch* 2631

Synchrotron Radiation Sources/FELs

Progress with ELETTRA, the synchrotron light source in Trieste — *M. Puglisi and A. Wrulich* 2634
The advanced light source— *Status report* — *Alan Jackson* 2637
The ALS— *A high-brightness XUV synchrotron radiation source* — *A. L. Robinson and A. S. Schlachter* 2640
Aladdin II+ — *Walter S. Trzeciak and Dornis C. Morin* 2643
Status of the SPring-8 project (storage ring) — *M. Hara, H. Kamitsubo, and N. Kumagai* 2646
Status of compact synchrotron light source work at TAC — *C. A. Swenson, F. R. Huson, R. Rocha, and Y. Huang* ... 2649
The DARPA compact superconducting X-ray lithography source features — *Richard Heese, Swarn Kalsi, and Eddie Leung* 2652
The superconducting compact storage ring NIJI-III — *Y. Tsutsui, K. Emura, F. Miura, H. Takada, and T. Tomimasu* . 2655
Calculation of eddy-currents induced in a compact synchrotron superconducting magnet structure during a current ramp — *Swarn Kalsi and Richard Heese* 2658
Orbits, tunes and chromaticities for the BNL SXLS storage ring — *L. N. Blumberg, J. B. Murphy, and S. Sharma* 2661
Lattice properties of the phase I BNL X-ray lithography source obtained from fits to magnetic measurement data — *L. N. Blumberg, J. B. Murphy, and M. F. Reusch* 2664
Beam dynamics of the SRRC 1.3 GeV storage ring — *C. C. Kuo, C. S. Hsue, J. C. Lee, M. H. Wang, and H. P. Chang* 2667
Lattice design of the SRRC 1.3 GeV storage ring — *C. S. Hsue, C. C. Kuo, J. C. Lee, and M. H. Wang* 2670

Volume 5

Magnet lattice of the Pohang Light Source — *J. Choi, T. Lee, K. Nam, and M. Yoon* 2673
Undulator based synchrotron radiation source in the 5–30 eV spectral region — *Xiaohao Zhang, James B. Murphy, and Samuel Krinsky* 2676
Theoretical minimum emittance lattice for an electron storage ring — *S. Y. Lee and L. Teng* 2679
Orbit distortion due to the floor displacement in the light source building under climatic thermal stress — *T. Katsura, Y. Kamiya, and Y. Fujita* 2682
Beam lifetime investigations at BESSY — *L. Schulz, E. Weihreter, and H. Lehr* 2685
The 3 GeV synchrotron injector for SPEAR — *H. Wiedemann, M. Baltay, J. Voss, K. Zuo, C. Chavis, R. Hettel, J. Sebek, H. D. Nuhn, J. Safranek, L. Emery, M. Horton, J. Weaver, J. Haydon, T. Hostetler, R. Ortiz, M. Borland, S. Baird, W. Lavender, P. Kung, J. Mello, W. Li, H. Morales, L. Baritchi, P. Golceff, T. Sanchez, R. Boyce, J. Cerino, D. Mostowfi, D. F. Wang, D. Baritchi, G. Johnson, C. Wermelskirchen, B. Youngman, C. Jach, J. Yang, and R. Yotam* 2688
Commissioning experiences of the ALS booster synchrotron — *Charles H. Kim* 2691
A high energy electron beam facility for industrial research — *S. Okuda, T. Nakanishi, K. Ikegami, S. Nakata, T. Nakagawa, C. Tsukishima, A. Maruyama, H. Tanaka, S. Nakamura, I. Kodera, S. Yamamoto, T. Matsuda, S. Fujimura, H. Itagaki, T. Yamada, and M. Iwamoto* 2694
The booster to storage ring transport line for SRRC — *M. H. Wang, C. C. Kuo, and C. S. Hsue* 2697
Design of beam transfer line and injection system of Pohang Light Source — *In Soo Ko and M. Yoon* 2700
Beam transport to the SXLS ring — *Eva Bozoki* 2703
Design and simulation of fast pulsed kicker/bumper units for the positron accumulator ring at APS — *Ju Wang and Gerald J. Volk* 2706
Magnets with full apertures for extracting synchrotron radiation at the photon factory ring — *Yukinori Kobayashi, Akira Araki, and Yukihide Kamiya* 2709
Status of development of the insertion devices for ELETTRA — *C. Poloni, R. Bracco, B. Diviacco, R. P. Walker, and D. Zangrando* 2712
A wedged pole hybrid type undulator as a synchrotron radiation source — *Shigemi Sasaki, Takeo Takada, Nobuo Matsuki, Shigeki Sasaki, and Hideo Ohno* 2715
Design considerations for a fast modulator in a 'crossed undulator' — *Roland Savoy and Klaus Halbach* 2718
The U5.0 undulator for the ALS — *E. Hoyer, J. Chin, K. Halbach, W. V. Hassenzahl, D. Humphries, B. Kincaid, H. Lancaster, and D. Plate* 2721
Fast excitation variable period wiggler — *A. van Steenbergen, J. Gallardo, T. Romano, and M. Woodle* 2724
Incorporation of a 5 T superconducting wiggler in an MLI synchrotron light source — *Dan Y. Wang, F. C. Younger, and H. Wiedemann* 2727
Ion channel focusing in FEL wigglers — *John Vetrovec* 2730
Performance of rocketdyne phase-optimized pure permanent magnet undulator — *G. Rakowsky, B. Bobbs, J. Brown, P. Kennedy, and G. Swoyer* 2733
Design and test of a model pole for the ALS U5.0 undulator — *W. V. Hassenzahl, E. Hoyer, and R. Savoy* 2736
ALS insertion device block measurement and inspection — *S. Marks, J. Carrieri, C. Cork, W. V. Hassenzahl, E. Hoyer, and D. Plate* 2739
Ion beam probe for measurement of wiggler errors — *John Vetrovec, Bradley Bobbs, and Michael Lampel* 2742
FEL design using the CEBAF linac — *G. R. Neil, J. J. Bisognano, H. F. Dylla, G. A. Krafft, C. W. Leemann, C. K. Sinclair, and B. Yunn* 2745
Coherent X-rays from PEP — *Simon Baird, Heinz-Dieter Nuhn, Roman Tatchyn, Herman Winick, Alan S. Fisher, Juan C. Gallardo, and Claudio Pellegrini* 2748
SATURNUS: The UCLA infrared free-electron laser project — *J. W. Dodd, S. C. Hartman, S. Park, C. Pellegrini, J. B. Rosenzweig, J. A. Smolin, G. Hairapetian, J. Kolonko, W. A. Barletta, D. B. Cline, J. G. Davis, C. J. Joshi, N. C. Luhmann, Jr., S. N. Ivanchenkov, A. S. Khlebnikov, Y. Y. Lachin, and A. A. Varfolomeev* 2751

Performance of the photoinjector accelerator for the Los Alamos free-electron laser — *P. G. O'Shea, S. C. Bender, B E. Carlsten, J. W. Early, D. W. Feldman, R. B. Feldman, W. J. D. Johnson, A. H. Lumpkin, R. L. Sheffield, R. W. Springer, W. E. Stein, and L. M. Young* 2754
CFEL-I: A compact free electron laser — *L. R. Elias, D. R. Anderson, A. L. Centore II, Hua Bei Jiang, I. Kimel, D. J. Larson, M. Tecimer, and Zhong Zhefu* 2757
Design, manufacturing and first measurements of a hybrid permanent magnet undulator for free electron laser — *F. Rosatelli, L. Barbagelata, F. Crenna, M. Grattarola, G. Gualco, A. Matrone, G. B. Ottonello, F. Ciocci, and A. Renieri* 2760
Pulsed undulators for high efficiency FEL oscillators usable in the visible spectrum — *Hubert Leboutet* 2763
Reduction of undulator radiation and FEL small gain due to wiggler errors — *Aharon Friedman* 2766
Heating of the LSS wiggler beam tube due to induced surface current — *W. C. Sellyey and C. G. Parazzoli* 2769
A new possibility of coherent microwave radiation by relativistic particles — *A. N. Didenko* 2775
Effects of construction and alignment errors on the orbit functions of the Advanced Photon Source Storage Ring — *H. Bizek, E. Crosbie, E. Lessner, L. Teng, and J. Wirsbinski* 2778
A low vertical β mode for the LNLS UVX electron storage ring — *Liu Lin and P. Tavares* 2781
Injection into the LNLS UVX electron storage ring — *Liu Lin* 2784
The transport line from MAIRA to the LNLS UVX electron storage ring — *Liu Lin, L. Jahnel, P. Tavares, and R. H. A. Farias* 2787
An active interlock system for the NSLS X-ray ring insertion devices — *R. J. Nawrocky, R. Biscardi, J. Dabrowski, J. Flannigan, S. Ramamoorthy, J. Rothman, J. Smith, I. So, M. Thomas, and G. Decker* 2790
A bypass for synchrotron radiation experiments at the storage ring PETRA II — *W. Brefeld and P. Gürtler* 2793

Low- and Medium-Energy Accelerators and Rings

Beam acceleration in the LBL 88-inch cyclotron with injection from the AECR source — *D. J. Clark, C. M. Lyneis, and Zuqi Xie* 2796
Recent improvements and new possibilities of the GANIL facility — *M. Bajard* 2799
Superconducting booster cyclotron studies at GANIL — *Chabert A., C. Bieth, P. Bricault, M. Duval, J. Fermé, A. Joubert, M. H. Moscatello, F. Ripouteau, and Q. V. Truong* 2802
Developing the Chalk River Superconducting Cyclotron for operation in π-mode — *J. A. Hulbert and X.-H. Zhou* ... 2805
The COSY-Jülich project April 1991 status — *R. Maier, U. Pfister, and J. Range* 2808
ASTRID— *A storage ring for ions and electrons* — *Søren Pape Møller* 2811
Status of the CRYRING project — *K.-G. Rensfelt* 2814
Advanced stacking methods using electron cooling at the TSR Heidelberg — *M. Grieser, D. Habs, R. v. Hahn, C. M. Kleffner, R. Repnow, M. Stampfer, E. Jaeschke, and M. Steck* 2817
The ADRIA project — *A. Dainelli, A. Lombardi, A. Ratti, and A. G. Ruggiero* 2820
The proposal of the accelerator complex of the Moscow kaon factory — *V. V. Balandin, A. G. Chursin, G. A. Dubinsky, S. K. Esin, N. I. Golubeva, A. I. Iliev, L. V. Kravchuk, V. A. Matveev, V. V. Paramonov, A. S. Pashenkov, Y. V. Senichev, E. N. Shaposhnikova, S. P. Volin, V. P. Belov, V. A. Glukhikh, N. D. Mal' ..iy, Y. P. Severgin, M. N. Tarovik, I. A. Shukeilo, G. I. Batskikh, Y. D. Ivanov, Y. S. Ivanov, V. A. Konovalov, K. A. Meshcherov, B. P. Murin, and Y. F. Semunkin* 2823
Application of a new scheme for passing through transition energy to the Fermilab main ring and main injector — *J. A. MacLachlan and J. E. Griffin* 2826
Low momentum compaction lattice study for the SSC low energy booster — *E. D. Courant, A. A. Garren, and U. Wienands* 2829
Operational aspects of electron cooling at the Low Energy Antiproton Ring (LEAR) — *J. Bosser, M. Chanel, R. Ley, D. Möhl, J. C. Ferrier, G. Tranquille, and D. J. Williams* 2832
A combined symmetric and asymmetric B-factory with monochromatization — *A. N. Dubrovin and A. A. Zholents* .. 2835

B-factory optics and beam–beam interaction for millimeter β and locally shortened bunches — *Yuri F. Orlov, Christopher M. O'Neill, James J. Welch, and Robert H. Siemann* 2838
Apiary B Factory lattice design — *M. H. R. Donald and A. A. Garren* 2841
Apiary B-Factory separation scheme — *A. Garren and M. Sullivan* 2844
Feasibility of a φ factory in KEK — *Kohji Hirata and Kazuhito Ohmi* 2847
DAΦNE storage rings — *S. Bartalucci, M. Bassetti, M. E. Biagini, C. Biscari, R. Boni, A. Gallo, S. Guiducci, M. R. Masullo, L. Palumbo, M. Serio, B. Spataro, and G. Vignola* 2850
Conceptual design of a high luminosity 510 MeV collider — *C. Pellegrini, D. Robin, and M. Cornacchia* 2853
A high luminosity superconducting mini collider for phi meson production and particle beam physics — *C. Pellegrini, D. Robin, D. Cline, J. Kolonko, C. Anderson, W. Barletta, A. Chargin, M. Cornacchia, G. Dalbacka, K. Halbach, E. Lueng, F. Kimball, D. Madura, and L. Patterson* 2856
DELTA optics — *D. Schirmer and K. Wille* 2859
Status of DELTA and design of its vacuum system — *Niels Marquardt* 2862
Commissioning the SSRL injector — *S. Baird and J. Safranek* 2865
An isochronous lattice for PEP — *W. J. Corbett, M. H. R. Donald, and A. A. Garren* 2868
Lattice studies for a small storage ring — *Philip Kiefer and Wayne Vernon* 2871
High frequency betatrons — *David R. Winn* 2874
Improvement of 150 MeV racetrack microtron — *T. Hori, M. Sugitani, T. Mitsumoto, and Y. Sasaki* 2877
Measurement and tuning of beam parameters in the heavy ion storage ring ESR — *F. Nolden, S. Baumann, K. Beckert, H. Eickhoff, B. Franczak, B. Franzke, O. Klepper, W. König, U. Schaaf, H. Schulte, P. Spädtke, M. Steck, and J. Struckmeier* 2880
Algorithm for the deflector plates of the 1 MHz chopper for the Kaon Factory — *M. J. Barnes and G. D. Wait* 2883
Conception of the 200 MeV/u booster for the Nuclotron — *I. B. Issinsky and V. A. Mikhailov* 2886
The project of the heavy ion storage rings complex of the JINR at Dubna — *O. N. Malyshev, I. N. Meshkov, R. T. Oganessian, Y. T. Oganessian, V. V. Parkhomchuk, P. Pokorny, A. A. Sery, S. V. Stepantsov, Y. A. Syresin, G. M. Ter-Akopian, and V. A. Timakov* 2888

High-Energy Accelerators and Colliders

Chairman: W. Wallenmeyer

Performance of LEP and future plans *(Invited Paper)* — *Jean-Pierre Koutchouk* 2891
Achieving high luminosity in the Fermilab Tevatron *(Invited Paper)* — *Stephen D. Holmes* 2896
RHIC project *(Invited Paper)* — *Satoshi Ozaki* 2901
The status of HERA *(Invited Paper)* — *B. H. Wiik* 2905
An electron–proton collider in the TeV range — *M. Tigner, B. Wiik, and F. Willeke* 2910
The status and development of the UNK project *(Invited Paper)* — *V. A. Yarba* 2913

Accelerator Technology II, RF, Power Supplies, Operations

Chairman: R. L. Kustom

High frequency cascaded resonant transformer rectifier power supply for neutral beam injection *(Invited Paper)* — *Louis L. Reginato* 2918
Switching power supply regulation of storage ring magnets *(Invited Paper)* — *M. G. Billing* 2923
Multimegawatt RF power sources for linear colliders *(Invited Paper)* — *G. Caryotakis* 2928
The magnicon: A new RF power source for accelerators *(Invited Paper)* — *Oleg A. Nezhevenko* 2933
AC bias operation of the perpendicular biased ferrite tuned cavity for the TRIUMF Kaon Factory Booster Synchrotron — *R. L. Poirier, T. A. Enegren, and I. B. Enchevich* 2943
RF reference generation for the ground test accelerator — *Amy H. Regan and Peter M. Denney* 2946

Alignment issues of the SLC linac accelerating structure — *J. T. Seeman, C. Adolphsen, F. J. Decker, G. Fischer, J. Hodgson, R. Pennacchi, C. Perkins, and M. Pietryka* 2949
Operational history of the SPS collider 1981-1990 — *V. Hatton* 2952
Status of the SLC damping ring kicker systems — *T. Mattison, R. Cassel, A. Donaldson, D. Gough, G. Gross, A. Harvey, D. Hutchinson, and M. Nguyen* 2955

Linear Accelerators and Pulsed Power Devices

Cell design for the DARHT linear induction accelerators — *M. Burns, L. Allison, L. Earley, D. Liska, C. Mockler, J. Ruhe, H. Tucker, and L. Walling* 2958
Transverse impedance measurements of prototype cavities for a dual-axis radiographic hydrotest (DARHT) facility — *L. Walling, Paul Allison, M. Burns, D. J. Liska, D. E. McMurry, and A. H. Shapiro* 2961
A new front-end for the LEP Injector Linac — *Jean-Claude Godot, Louis Rinolfi, Andrea Pisent, and Hans Braun* ... 2964
Photocathode driven linac at UCLA for FEL and plasma wakefield acceleration experiments — *S. Hartman, F. Aghamir, W. Barletta, D. Ciine, J. Dodd, T. Katsouleas, J. Kolonko, S. Park, C. Pellegrini, J. Rosenzweig, J. Smolin, J. Terrien, J. Davis, G. Hairapetian, C. Joshi, N. Luhmann, Jr., and D. McDermott* 2967
Status of the LISA superconducting linac project — *F. Tazzioli, A. Aragona, R. Boni, M. Castellano, G. Di Pirro, S. Faini, M. Ferrario, A. Gallo, S. Kulinski, C. Marchetti, M. Minestrini, P. Patteri, C. Sanelli, M. Serio, A. Stecchi, L. Trasatti, M. Vescovi, L. Catani, S. Tazzari, N. Cavallo, and F. Cevenini* 2970
Status of the ARES R&D program — *R. Boni, M. Castellano, P. Fabbricatore, M. Ferrario, A. Gallo, P. Michelato, M. Minestrini, F. Musenich, C. Pagani, R. Parodi, P. Patteri, L. Serafini, S. Tazzari, and F. Tazzioli* 2973
Preliminary conceptual design for a 510 MeV electron/positron injector for a UCLA ϕ factory — *Glen Dahlbacka, Robert Hartline, William Barletta, and Claudio Pellegrini* 2976
Operating experience with the ALS linac — *F. Selph and D. Massoletti* 2978
Commissioning of the new heavy ion injector at GSI — *N. Angert, L. Dahl, J. Glatz, J. Klabunde, U. Ratzinger, H. Schulte, B. Wolf, H. Deitinghoff, J. Friedrich, H. Klein, and A. Schempp* 2981
Development of a radioactive nuclides accelerator at the Moscow meson factory — *V. A. Andreev, V. A. Bomko, G. N. Vjalov, S. K. Esin, D. V. Gorelov, J. D. Ivanov, A. S. Iljinov, A. A. Kolomiets, V. A. Moiseev, B. P. Murin, P. N. Ostroumov, and A. N. Zelenskiki* 2984
Status of the uranium upgrade of ATLAS — *L. M. Bollinger, P. J. Billquist, J. M. Bogaty, B. E. Clifft, P. Markovich, F. H. Munson, R. C. Pardo, K. W. Shepard, and G. P. Zinkann* 2987
45 MeV linac for the 800 MeV synchrotron radiation light source — *N. Kaneko, M. Y. Yamamoto, O. Azuma, H. Iwata, T. Nakashizu, and Y. Hoshi* 2990
Design studies of SSC coupled cavity linac — *C. R. Chang, R. Bhandari, W. Funk, D. Raparia, and J. Watson* 2993
Tuning of the first 805 MHz side-coupled cavity module for the Fermilab upgrade — *Zubao Qian, Mark Champion, Thomas G. Jurgens, Harold W. Miller, Al[illegible]etti, and René Padilla* 2996
Beam loading in a high current accelerating ga[illegible] — *[illegible] Rhee and B. N. Ding* 2999
An interactive code SUPERLANS for evaluation of RF-cavities and acceleration structures — *D. G. Myakishev and V. P. Yakovlev* 3002
The $3\pi/4$ backward TW structure for the ELETTRA 1.5 GeV electron injector — *P. Girault* 3005
A new electron linac injector design up to 200 MeV — *D. Tronc* 3008
Quadrupole effects in on-axis coupled linacs — *F. P. Adams, R. J. Burton, and J. Ungrin* 3011
Cavity shape and beam dynamics design for a linac for pions — *G. Swain* 3014
Characterization of a ramped gradient DTL: Experiment and theory — *K. F. Johnson, E. A. Wadlinger, O. R. Sander, G. P. Boicourt, G. O. Bolme, C. M. Fortgang, J. D. Gilpatrick, J. Merson, D. P. Sandoval, and V. Yuan* 3017
High order calculation of the multipole content of three dimensional electrostatic geometries — *Martin Berz, William M. Fawley, and Kyoung Hahn* 3020
Measurements on iris-structures with rectangular holes — *M. Kurz, P. Hülsmann, H. Klein, and A. Schempp* 3023
RF tests of a band overlap free DAW accelerating structure — *R. Parodi, A. Stella, and P. Fernandes* 3026

Transient analysis of beam-loaded standing wave accelerator cavities — *Tom Buller* 3029
Three-dimensional space charge and image charge effects in radio-frequency-quadrupole accelerators — *F. W. Guy* . 3032
Acceleration tests of the INS 25.5-MHz split coaxial RFQ — *S. Arai, A. Imanishi, T. Morimoto, S. Shibuya, E. Tojyo, and N. Tokuda* 3035
Numerical simulation of a short RFQ resonator using the MAFIA codes — *H. Wang, I. Ben-Zvi, A. Jain, P. Paul, and A. Lombardi* 3038
Deceleration of antiprotons with a RFQ — *A. Schempp, H. Deitinghoff, A. Firjahn-Andersch, H. Vormann, M. de Saint Simon, J. Y. Hemery, C. Thibault, and F. Botlo-Pilat* 3041
Properties of the GSI HLI-RFQ structure — *J. Friedrich, A. Schempp, H. Deitinghoff, U. Bessler, H. Klein, R. Veith, N. Angert, and J. Klabunde* 3044
New vanes for RFQ1: Fabrication, installation, and tuning — *B. G. Chidley, G. E. McMichael, and T. Tran-Ngoc* 3047
Progress of the 473 MHz four-rod RFQ — *Reza Kazimi, F. R. Huson, and W. W. MacKay* 3050
Development of a variable energy RFQ for cluster acceleration — *A. Schempp, J. Madlung, J. Dehen, H. Deitinghoff, J. Friedrich, A. Kipper, H. O. Moser, G. Hadinger, M. J. Gaillard, R. Genre, and J. Martin* 3053
Least-squares fitting procedure for setting RF phase and amplitude in drift-tube-linac tanks — *F. W. Guy and T. P. Wangler* 3056
Production of tightly focused E-beams with high-current accelerators — *J. W. Poukey, M. G. Mazarakis, C. A. Frost, and J. J. Ramirez* 3059
Longitudinal emittance measurement of the 100 MeV proton beam — *Y. V. Bylinsky, A. V. Feschenko, and P. N. Ostroumov* 3062
The delta-t tuneup procedure for the Fermilab linac upgrade — *Thomas L. Owens and Elliott S. McCrory* 3064
Proton beam acceleration up to 160 MeV at the Moscow meson factory linac — *G. I. Batskich, Y. V. Bylinsky, S. K. Esin, A. P. Fedotov, A. V. Feschenko, Y. D. Ivanov, O. S. Korolev, L. V. Kravchuk, A. I. Kvasha, V. A. Matveev, V. N. Michailov, A. N. Mirzojan, N. P. Murin, P. N. Ostroumov, S. A. Petronevich, B. A. Rubtsov, V. L. Serov, S. I. Scharamentov, N. I. Uksusov, S. Z. Zyarylkapov, and I. A. Sagin* 3067
Drift compression experiments on MBE-4 and related emittance growth phenomena — *S. Eylon, A. Faltens, W. Fawley, T. Garvey, K. Hahn, E. Henestroza, and L. Smith* 3070
Transverse emittance studies of an induction accelerator of heavy ions — *T. Garvey, S. Eylon, T. J. Fessenden, K. Hahn, and E. Henestroza* 3073
Funneling study with a low energy proton beam — *W. Barth and A. Schempp* 3076
LIAM—A linear induction accelerator model — *H. Brand, G. Caporaso, D. Lager, F. Coffield, and F. Chambers* ... 3079
Artificial intelligence techniques for tuning linear induction accelerators — *Darrel L. Lager, Hal R. Brand, William J. Maurer, Fred Coffield, Frank Chambers, and William Turner* 3082
Diagnostics and data analysis for the ETA-II linear induction accelerator — *F. W. Chambers, S. L. Allen, F. J. Deadrick, W. E. Nexsen, A. C. Paul, V. L. Renbarger, and W. C. Turner* 3085
Modeling of switching cores for induction accelerators — *Henry D. Shay, John F. DeFord, and George D. Craig* ... 3088
Modeling magnetic pulse compressors — *Anthony N. Payne* 3091
Measurements of reduced corkscrew motion on the ETA-II linear induction accelerator — *A. L. Allen, H. R. Brand, F. W. Chambers, Y.-J. Chen, F. E. Coffield, F. J. Deadrick, L. V. Griffith, D. L. Lager, W. J. Mauer, W. E. Nexsen, A. C. Paul, S. Sampayan, and W. C. Turner* 3094
Performance characteristics of an induction linac magnetic pulse compression modulator at multi-kilohertz pulse repetition frequencies — *S. Sampayan, F. W. Chambers, F. J. Deadrick, W. A. Niven, C. W. Ollis, A. N. Payne, V. L. Renbarger, E. T. Scharlemann, W. C. Turner, and J. A. Watson* 3097
Degradation of brightness by resonant particle effects — *Y.-J. Chen, G. J. Caporaso, A. G. Cole, A. C. Paul, and W. C. Turner* 3100
Reduction of energy sweep of the ETA-II beam — *W. E. Nexsen, S. L. Allen, F. W. Chambers, R. A. Jong, A. C. Paul, S. E. Sampayan, and W. C. Turner* 3103
ETA-II beam brightness measurement — *A. C. Paul, S. L. Allen, F. W. Chambers, Y.-J. Chen, F. J. Deadrick, and W. C. Turner* 3106

Development of RFQ accelerator for the MMF linac — *V. A. Andreev, S. K. Esin, I. M. Kapchinskij, D. A. Kashinskij, A. M. Kozodaev, A. A. Kolomiets, P. N. Ostroumov, A. M. Raskopin, N. V. Schachrai, and R. M. Vengrov* 3109
High power microwave generation in virtual cathode systems — *A. N. Didenko and V. I. Rashchikov* 3111
Experimental tests of the power supply and prototype cell for the 1.5 MeV SLIA acceleration unit — *P. Corcoran, B. Bowen, V. Bailey, V. Carboni, J. Fockler, B. Chugg, and H. Nishimoto* 3114
Beam breakup considerations in the design of multiple off-axis gaps in an induction accelerator cell for SLIA — *John Edighoffer* 3117
Experimental observations of beam transport in twisted quadrupole fields — *J. P. Lidestri, V. L. Bailey, Jr., J. A. Edighoffer, S. D. Putnam, M. G. Tiefenback, and D. Wake* 3120
Magnet design for SLIA proof-of-concept experiment — *V. Bailey, D. Wake, R. Curry, J. Lidestri, and M. Tiefenback* 3123
Experiments investigating the effects of the accelerating gap voltage pulse on the ion focused (IFR) high current electron recirculators — *M. G. Mazarakis, D. L. Smith, J. W. Poukey, J. S. Wagner, L. F. Bennett, W. R. Olson, B. N. Turman, K. R. Prestwich, and J. Wells* 3126
RADLAC II/SMILE performance with a magnetically insulated voltage adder — *S. L. Shope, M. G. Mazarakis, C. A. Frost, C. E. Crist, J. W. Poukey, K. R. Prestwich, B. N. Turman, K. Struve, and D. Welch* 3129
A novel concept for a lithium lens exciter — *G. G. Karady and H. A. Thiessen* 3132
High-intensity flash X-ray source for HERMES III — *T. W. L. Sanford, J. A. Halbleib, W. H. McAtee, and R. C. Mock* 3135
SLC positron source flux concentrator modulator — *J. de Lamare, A. Kulikov, R. Cassel, and V. Nesterov* 3138
Fast risetime magnetic field coil for electron beam propagation studies — *D. J. Weidman, W. C. Freeman, J. D. Miller, M. J. Rhee, R. F. Schneider, K. T. Nguyen, and R. A. Stark* 3141
Long pulse electron beams — *J. R. Smith, I. R. Shokair, and K. W. Struve* 3144
Kicker pulser charger — *R. Cassel and M. Nguyen* 3147
PSR extraction kicker system improvements — *T. W. Hardek* 3150
Fast thyratron driver — *M. N. Nguyen and R. L. Cassel* 3153
Pulse shape adjustment for the SLC damping ring kickers — *T. Mattison, R. Cassel, A. Donaldson, H. Fischer, and D. Gough* 3156
High voltage pulse cable and connector experience in the kicker systems at SLAC — *K. Harris, M. Artusy, A. Donaldson, and T. Mattison* 3159
Kicker prepulse canceler — *R. L. Cassel and T. S. Mattison* 3162
Kicker thyratron experience from SLC — *A. R. Donaldson, R. L. Cassel, T. S. Mattison, and L. L. Reginato* 3165
The timing and diagnostic systems of the kicker magnet pulsers for the Stanford Linear Collider — *D. E. Gough, R. L. Cassel, A. R. Donaldson, D. P. Hutchinson, and T. S. Mattison* 3168
Fast power supplies for kicker and thin septum magnets in a 1.2 GeV synchrotron radiation source — *B. E. Strickland, G. L. Schofield, B. L. Thomas, W. P. White, B. Ng, and D. Meaney* 3171
Fast TEM kicker with MOSFET solid state driver — *Alfredo Saab, Michael Kogan, and Tomás Russ* 3174
Application of electrostatic undulators for acceleration of intense ion beams — *E. S. Masunov and A. P. Novicov* 3177
The ELETTRA 1.5 GeV electron injector — *D. Tronc, D. T. Tran, C. Bourat, P. Girault, P. Letellier, G. Meyrand, S. Sierra, and A. Massarotti* 3180
Microwave and beam optics design features of a preinjector linac for a synchrotron radiation source — *J. Haimson and B. Mecklenburg* 3183
Electron preinjector for Siberia-2 SR source — *O. A. Nezhevenko, G. N. Ostreiko, B. Z. Persov, S. I. Ruvinsky, G. V. Serdobintsev, E. N. Shaimerdenov, M. A. Tiunov, V. P. Yakovlev, and I. A. Zapryagaev* 3186
Fermilab linac upgrade side coupled cavity temperature control system — *J. Crisp and J. Saiti* 3189
Electron-beam generation, transport, and transverse oscillation experiments using the REX injector — *R. L. Carlson, P. W. Allison, T. J. Kauppila, D. C. Moir, and R. N. Ridlon* 3192
Matching and transport of beams in a continuously twisted quadrupole channel — *M. G. Tiefenback, J. P. Lidestri, V. L. Bailey, Jr., and S. D. Putnam* 3195
PILAC: A pion linac facility for 1-GeV pion physics at LAMPF — *Henry A. Thiessen* 3198
High voltage, high power nested high voltage accelerator — *R. J. Adler and R. J. Richter-Sand* 3201

LELIA: An induction linac developed for FEL application — *P. Eyharts, J. Bardy, P. Anthouard, P. Eyl, and M. Thevenot* 3204
A traveling wave accelerator with HOM outcouplers for FEL's — *R. Miller and M. Lampel* 3276

Linear Colliders

Effect of wakefields on first order transport in the SLC linac — *Chris Adolphsen, Karl L. F. Bane, and John T. Seeman* 3207
Multibunch energy and spectrum control in the SLC high energy linac — *J. T. Seeman, F. J. Decker, R. K. Jobe, and I. Hsu* 3210
Review of tolerances at the Final Focus Test Beam — *F. Bulos, D. Burke, R. Helm, J. Irwin, G. Roy, and N. Yamamoto* 3213
Beam-based alignment and tuning procedures for e^+e^- collider final focus systems — *F. Bulos, D. Burke, R. Helm, J. Irwin, A. Odian, G. Roy, R. Ruth, and N. Yamamoto* 3216
Wakefield measurements of SLAC linac structures at the Argonne AATF — *J. W. Wang, G. A. Loew, J. Simpson, E. Chojnacki, W. Gai, R. Konecny, and P. Schoessow* 3219
Maintaining micron-size beams in collision at the interaction point of the Stanford Linear Collider — *F. Rouse, T. Gromme, W. Kozanecki, and N. Phinney* 3222
Transverse equilibria in linear collider beam-beam collisions — *J. B. Rosenzweig and Pisin Chen* 3225
Progress on the CLIC final focus system — *O. Napoly, P. Sievers, T. Taylor, and B. Zotter* 3228
Optimizing energy spread in the CLIC main linac — *G. Guignard and C. Fischer* 3231
Investigations on beam damping simulations and the associated model of CLIC — *G. Guignard, C. Fischer, and A. Millich* 3234
Microwave quadrupole structures for the CERN linear collider — *W. Schnell and I. Wilson* 3237
Design calculations of the CLIC transfer structure — *Erk Jensen* 3240
Model work on a transfer structure for CLIC — *L. Thorndahl* 3243
Higher order effects in beam-beam deflection — *Yu-Chiu Chao and Pisin Chen* 3246
Beam-beam deflection and beamstrahlung monitor response for tilted elliptic beams — *V. Ziemann* 3249
Simulations on pair creation from beam-beam interaction in linear colliders — *P. Chen, T. Tauchi, and K. Yokoya* ... 3252
Differential luminosity under beamstrahlung — *Pisin Chen* 3255
A practical algorithm for chromaticity correction in linear collider final focus systems — *P. Krejcik* 3258
Linear e^+e^- colliders above 1 TeV (CM) — *Alfred A. Mondelli* 3261
Linac-ring colliders with high disruption parameters— A first test of principle — *J. R. Boyce, S. Jin, J. Kewisch, R. Li, P. K. Kloeppel, B. Niczyporuk, R. Rossmanith, N. Sereno, and R. Whitney* 3264
Misalignment study of NLC bunch compressor — *R. P. Rogers and S. A. Kheifets* 3267
High brightness sources for colliders — *J. E. Spencer* 3270
Investigation of seismic vibrations and relative displacements of linear collider VLEPP elements — *B. A. Baklakov, P. K. Lebedev, V. V. Parkhomchuk, A. A. Sery, A. I. Sleptsov, and V. D. Shiltsev* 3273

Closing Plenary Session

Chairman: J. O'Fallon

CERN plans for the future *(Invited Paper)* — *Carlo Rubbia* 3279

Author Index Follows Pages 699
..... 1340
..... 2010
..... 2672
..... 3283

RECYCLING OF A LAMPF KLYSTRON*

Paul J. Tallerico and Robert L. Cady
Los Alamos National Laboratory
P.O. Box 1663, MS H-827, Los Alamos, NM, 87545

Abstract

This paper describes the modelling, reb...lding, and testing of a modulating-anode klystron having 1.25 MW peak output power,that was originally made for the Los Alamos Meson Physics Facility (LAMPF). All original klystron parameters were retained, with the exception of the center frequency, which was raised from 805 to 850 MHz. Each of the five cavities had to be redesigned to achieve this increase. We describe the rebuilding, which was performed at the LAMPF klystron repair facility, and present experimental characteristics of the rebuilt klystron. The klystron has produced over 1 MW at the new frequency.

I. INTRODUCTION

The klystrons for the Ground Test Accelerator (GTA) have the same specifications as those for LAMPF, with the exception of the center frequency. .A commercial contract was let for the new klystron, but the vendor had several problems with vacuum leaks, cathode emission, and even an open filament. The repeated failures of the prototype were beginning to jeopardize the GTA schedule, so a parallel development effort at Los Alamos was initiated. Since most of the klystron parameters were identical, and the LAMPF klystron rebuild facility [1] still exists, a rebuild of a failed LAMPF klystron was suggested as the most expedient way of obtaining a 1-MW, 850-MHz device.

The one-dimensional klystron code, DMK1, [2] was used to determine that the klystron would operate with about the same efficiency and bandwidth at the new frequency, provided that the five cavities were rebuilt to increase the center frequency of each by 45 MHz. The particular klystron chosen from the accumulation of defective LAMPF klystrons had a broken ion-pump connector, but was thought to be operable in all other aspects.

II. THE REBUILD PROCESS

The rebuild process began with disassembly of the klystron. The parts are shown in Fig. 1. The outside walls of the buncher cavities are stainless steel. A half section of a typical unmodified buncher cavity is shown in Fig. 2. Each buncher cavity also has a side-wall tuner that occupies 90_ in azimuth, and fills the length of the cavity. Using the code SUPERFISH [3], we determined the cylindrical volume that would raise the frequency of each cavity by 45 MHz. A typical cylinder is shown by the dashed lines in Fig 2. The four buncher cavities were cut open near an end, and a stainless steel cylinder was welded to the outer walls of each to raise its frequency. Experimental cylinders were made with the same axial length, but 1.33 times the thickness of

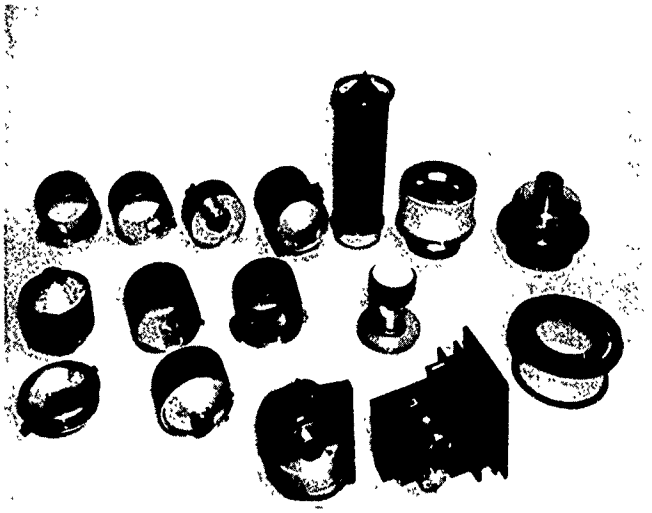


Fig 1. Photograph of the disassembled klystron.

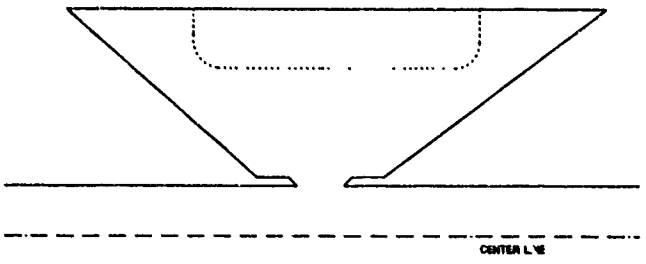


Fig. 2. Drawing of a half of a buncher cavity. Dashed line is new shape to raise the resonant frequency by 45 MHz.

the calculated cylinder, to account for the fact that the experimental parts occupy only 3/4 of the circumference Aluminum cold-test models of the cavities were built to verify the new resonant frequencies. The input cavity presented a new challenge: it requires an input loop as well as a tuner. The space occupied by this loop left less space for the tuning segment, and the gap was increased; in addition the size of the tuning segment was reduced. The input cavity had a downstream gap whose edges had partially melted in an unsymmetrical fashion. We machined the edges down about 2 mm to restore the symmetry. Because the output cavity was copper plated, and could not be welded, this cavity was entirely retuned by increasing the gap length. The output gap was increased by 4.5 mm by machining the gaps. Each cavity was then pressed together and cold-tested to verify the new frequencies, with the tuners adjusted to their central positions. Next the cavities were cleaned and reassembled, using a mandrel to align the parts to the beam axis. All parts

*Work supported and funded by the US Department of Defense, Army Strategic Defense Command, under the auspices of the US Department of Energy.

0-7803-0135-8/91$01.00 ©IEEE

were first cleaned with tricloethelyne, and then soaked in 3 successive 2-hr baths in hot de-ionized water. The water was removed with an ethanol bath, and the parts were baked in an oven with a dry-hydrogen atmosphere. The klystron has an oxide cathode, so the electron gun had to be removed and cleaned, and a new surface was sprayed onto the cathode just before final assembly. After assembly, the klystron was put into an oven, evacuated, and baked for 3 days at 300°C. After the klystron cooled down, the cathode was activated and tested at low voltage. Next the klystron was pinched off, and the water fittings and connectors applied. Tuning mechanisms were attached to allow the cavities to be adjusted as the klystron operates.

III. TEST RESULTS

The completed klystron was operated first in a standard LAMPF modulator [4] and tested to over 1 MW of peak output power at 850 MHz. At this time the cavities were tuned for gain, bandwidth, and efficiency. Next, the klystron was moved to a GTA modulator [5] and more extensive data were taken. The most important data are shown in Fig. 3: where the power output is shown vs the power input for a matched load and for 6 equally-spaced phases of a 1.5:1 VSWR mismatch. The origin of the input power axis was shifted one major division to the right after each curve was taken. This data was taken at 850 MHz, with 82.3 kV cathode voltage and 30 A cathode current. The focus coil current was 17.2 A. The peak body current at saturation was 0.47 A with the matched load, 0.5 A at the first phase of the mismatch, and 0.43 A at the 4th mismatch phase, which is the low-impedance phase. Data on bandwidth and operation at other beam voltages and currents were also taken, but are omitted due to space limitations. The original specification called for 1 ms maximum pulse length and 12% duty factor, but the klystron operated well at 2 ms pulses and at the 2% duty required for GTA

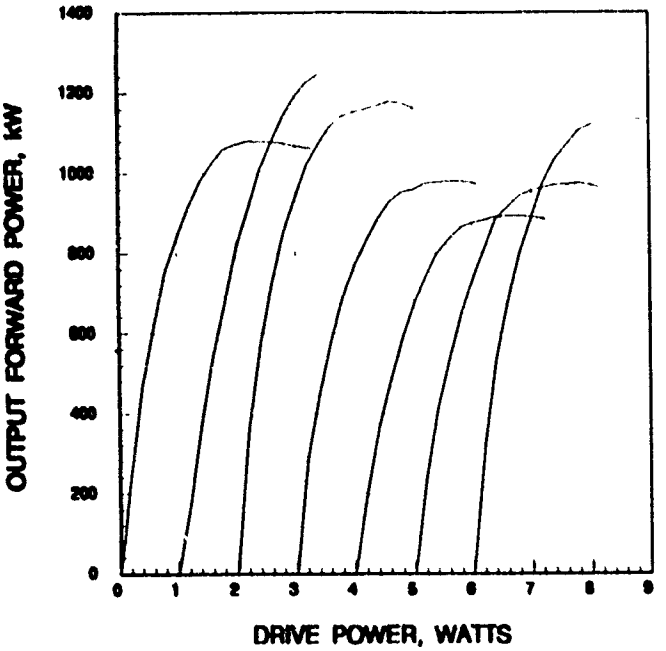


Fig. 3. Output power vs input power for the rebuilt klystron, into a matched load and into 6 phases of a 1.5:1 VSWR mismatch.

ACKNOWLEDGEMENTS

The authors thank Robert Kandarian of LAMPF for his fine mechanical design of the new parts as well as for his expert guidance on the assembly procedures. They also thank Wilfred Romero, Ed Partridge, and Robert Trujillo of the LAMPF klystron repair section, for their excellent craftsmanship in the dismantling, making new parts, testing, and rebuilding the klystron.

REFERENCES

1. P. J. Tallerico, "The LAMPF Klystron Repair Facility," Proton Linear Accelerator Conference, Los Alamos National Laboratory publication LA-5115 (1972), p 427.

2. P. J. Tallerico, "Design Considerations for the High-Power Multicavity Klystron," IEEE Transactions on Electron Devices, p. 374, 1971.

3. M. T. Menzel, H. K. Stokes, "User's Guide for the POISSON/SUPERFISH Group of Codes," Los Alamos Publication LA-UR-87-115, Jan., 1987.

4. P. J. Tallerico, R. L. Cady, J. D. Doss, "Design and Performance of the LAMPF 1.25-MW Klystron Modulator," Proceedings of the 1973 IEEE Modulator Symposium, New York, Sept., 1973.

5. P. J. Tallerico, C. R. Rose, W. North, "Progress on the GTA 850-MHz RF System," Los Alamos Publication LA-CP 90-231, Presented at the NPB Technical Interchange Symposium, San Diego, May, 1990.

A New Approach in Simulating RF Linacs Using a General, Linear Real-Time Signal Processor*

Andrew Young and Stephen P. Jachim
MS-H827, Los Alamos National Laboratory, Los Alamos, NM 87545

Abstract

Strict requirements on the tolerances of the amplitude and phase of the radio frequency (RF) cavity field are necessary to advance the field of accelerator technology. Due to these stringent requirements upon modern accelerators, a new approach of modeling and simulating is essential in developing and understanding their characteristics. This paper describes the implementation of a general, linear model of an RF cavity which is used to develop a real-time signal processor. This device fully emulates the response of an RF cavity upon receiving characteristic parameters (Q_0, ω_0, $\Delta\omega$, R_S, Z_0).

Simulating an RF cavity with a real-time signal processor is beneficial to an accelerator designer because the device allows one to answer fundamental questions on the response of the cavity to a particular stimulus without operating the accelerator. In particular, the complex interactions between the RF power and the control systems, the beam and cavity fields can simply be observed in a real-time domain. The signal processor can also be used upon initialization of the accelerator as a diagnostic device and as a dummy load for determining the closed-loop error of the control system. In essence, the signal processor is capable of providing information that allows an operator to determine whether the control systems and peripheral devices are operating properly without going through the tedious procedure of running the beam through a cavity.

I. INTRODUCTION

Utilizing a baseband complex envelope analogy of an RF cavity system [1-3], a hardware realization (i.e., real-time signal processor) is developed. This processor has the ability to simulate the effect of cavity detuning, beam loading and finite Q. A brief overview of the relevant theory is presented. This paper focuses on the implementation of a theoretical model to create a real-time signal processor and concludes with a direct comparison of the results from the mathematical simulations and the hardware simulations.

II. MATHEMATICAL REALIZATION OF AN RF CAVITY

This section outlines the procedure used to develop a model for an RF cavity which implements the complex envelope isomorphism, initially developed in reference [1]. This approach of modeling a RF cavity deviates from the standard approach of using amplitude and phase analysis by encoding the relevant information into two linear, general low-pass functions: in-phase (I) and quadrature (Q). In essence, the complex envelope analogy reduces a band-pass system into low-pass functions [2].

A single-mode resonant cavity system is composed of four components (see figure 1): an RF source, a transport component, an RF cavity and a beam loading component.

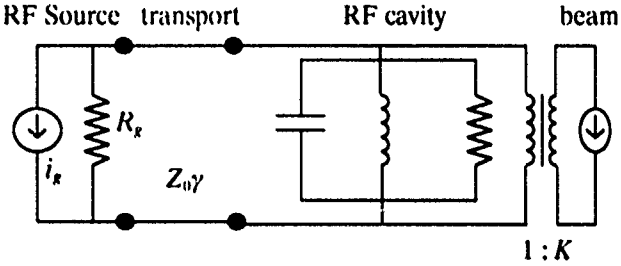


Figure 1. Simplified equivalent circuit of an RF cavity system.

Applying fundamental principles of circuit theory to figure 1, a set of characteristic equations that describe the microwave junctions of the RF cavity system (i.e., forward voltage and reflected voltage) are derived and are graphically illustrated in figure 2. The resonant cavity system block diagram also describes the effects of beam coupling and input coupling. Note that all of the inputs and outputs consist of an in-phase and a quadrature component; hence, the block diagram is more complex than illustrated in figure 2.

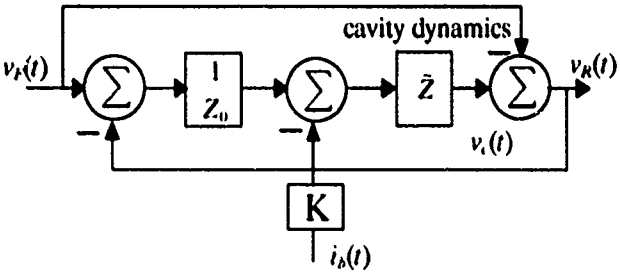
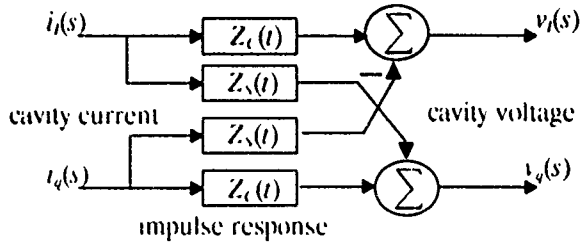


Figure 2. Block diagram of an RF cavity system.

The cavity dynamics are the mathematical realization of the complex convolution integral between a narrow-band RF signal and an RF cavity realized as a bandpass device [3]. From the principles of convolution, a block diagram of cavity dynamics is illustrated in figure 3.



$i_I(t) \equiv$ in-phase component of cavity current
$i_Q(t) \equiv$ quadrature component of cavity current
$v_I(t) \equiv$ in-phase component of cavity voltage
$v_Q(t) \equiv$ quadrature component of cavity voltage

Figure 3. Butterfly realization of the baseband complex envelope model.

*Work supported and funded by the United States Department of Defense, Army Strategic Defense Command under the auspices of the United States Department of Energy

0-7803-0135-8/91$01.00 ©IEEE

The impulse transimpedance response with ω_0 detuned from the drive frequency is defined in equation (1).

$$Z_C(t) = \frac{R_S}{\tau}\left[e^{-\frac{t}{\tau}}\right]\left(\cos\Delta\omega t - \frac{1}{2Q_0}\sin\Delta\omega t\right)$$
$$Z_S(t) = \frac{R_S}{\tau}\left[e^{-\frac{t}{\tau}}\right]\left(\sin\Delta\omega t + \frac{1}{2Q_0}\cos\Delta\omega t\right) \quad (1)$$

where,

$\tau \equiv$ cavity damping time constant (sec)
$R_S \equiv$ cavity shunt resistance (ohms)
$Q_0 \equiv$ cavity unloaded quality factor
$\Delta\omega = \omega_0 - \omega_d \equiv$ cavity detuning frequency (rad/sec)
$\omega_d \equiv$ cavity drive frequency (rad/sec)
$\omega_0 \equiv$ cavity resonant frequency (rad/sec).

The impulse transimpedance response in the Laplace domain is

$$Z_C(s) = \left[\frac{R}{\tau}\right]\left[\frac{s + a_C}{s^2 + b_1 s + b_2}\right]$$
and
$$Z_S(s) = \left[\frac{R}{2\tau Q_0}\right]\left[\frac{s + a_S}{s^2 + b_1 s + b_2}\right] \quad (2)$$

where,

$$a_S = \left(\frac{1}{\tau} + 2\Delta\omega Q_0\right) \qquad b_1 = \left(\frac{2}{\tau}\right)$$
$$a_C = \left(\frac{1}{\tau} - \frac{\Delta\omega}{2Q_0}\right) \qquad b_2 = \left(\frac{1}{\tau^2} + \Delta\omega^2\right).$$

The complex baseband cavity model requires that the input signals are linear, time-invariant equations and the existence of their Laplace transforms. Thus, the model can accurately simulate the effects of cavity detuning and finite Q without being limited to a small signal regime.

III. Design of a Real-Time Signal Processor

A. Implementing the Cavity Model

Implementation of the resonant cavity model is obtained through the use of control theory. Control theory provides a practical realization of the model from a set of equations that describe the response of a system.

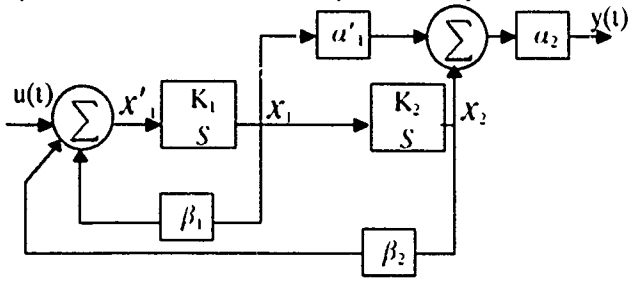


Figure 4. Block diagram of a modified controllable canonical realization.

From basic principles in control theory, equation (2) is realized in a modified controllable canonical form (see figure 4). The transfer function of figure 4 is

$$H(s) = \frac{y(s)}{u(s)} = \frac{a'_1 a_2 K_1 s + a_2 K_1 K_2}{s^2 + \beta_1 K_1 s + \beta_2 K_1 K_2} \quad . \quad (3)$$

The primary reason for using a modified controllable canonical realization is to utilize the zero offset adjustment circuitry which exists with the multiplication circuitry (i.e., α's and β's coefficients). Zero offset adjustment circuitry is needed because of the inherent offset problem associated with transimpedance amplifiers. Another advantage of implementing a modified controllable canonical realization is to increase the bandwidth of the realization by having a gain coefficient (i.e., K_1 and K_2) associated with each integrator (i.e., s^{-1}).

Note that this realization only represents one transfer function (i.e., $Z_C(s)$ or $Z_S(s)$). Thus, four realizations are needed to create the baseband complex envelope model in figure 3. The controllable canonical form provides the foundation for the hardware realization (i.e., the real-time signal processor).

B. Circuit Description of the Real-time Signal Processor

The packaging format for the real-time signal processor utilizes the VXIbus standard [4]. The specific benefits of conforming to the VXIbus architecture include a concise, standardized, modular format with the accessibility of a parallel processing bus, broadband analog bus, precision clocks and integrated power supplies with a cooling system as standard features of the system architecture. The real-time signal processor is limited to a single-wide module illustrated in figure 5.

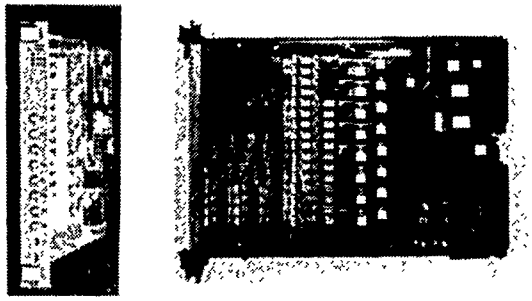


Figure 5. Single-wide real-time signal processor VXI module.

A modular circuit layout minimizes the amount of drafting such that, the VXI processor interface circuitry is created on a separate daughter board with the dimensions of two inches by five inches. The real-time signal processor circuitry is constructed on an eight layer mother board. The layout of the circuitry is in five distinct parts: VXI processor interface, signal conditioning circuitry, digital registers, the multiplying digital to analog circuitry and the analog circuitry. The interface circuitry uses Erasable Programmable Logic Devices (EPLDs) that provide the addressing, timing, data acquisitioning, status and control of the real-time signal processor. Digital multiplication coefficients are down-loaded into separate registers by implementing EPLDs. This allows the ability to remotely control the poles and the zeros of the realization. For example, the data from the output registers

of the EPLDs are the digital inputs for the digital-analog (D/A) multipliers which corresponds to the α and β coefficients shown in figure 4. The analog circuitry consists of the summers (i.e., Σ) and the integrators (i.e., s^{-1}).

IV. Results

In the previous sections, a mathematical realization and a practical realization (i.e., real-time signal processor) of a resonant cavity system were developed. This section illustrates the simulations of both the mathematical realization and the hardware realization in a manner which allows direct comparison of the results.

Numerical simulations of the model were achieved by using a control system software package, MATRIX$_X$. The following results simulate an RF cavity with the following assumptions: $Q = 10k$, $R_s = 50\Omega$, $\omega_d = 425MHz$ and $\omega_0 = 425.04MHz$.

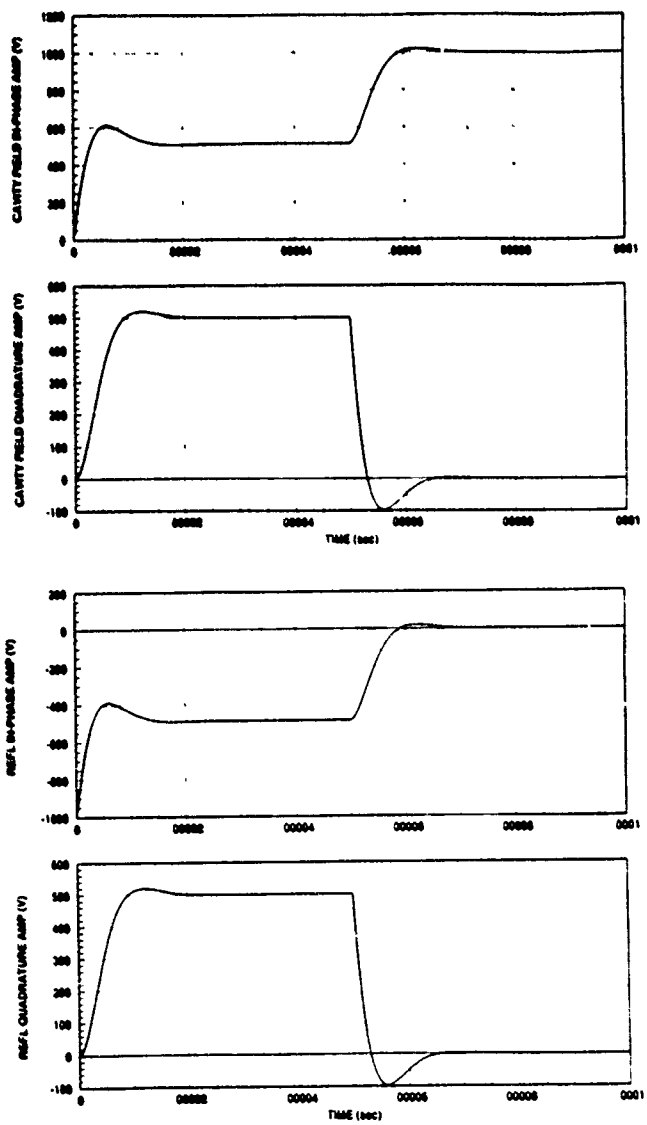
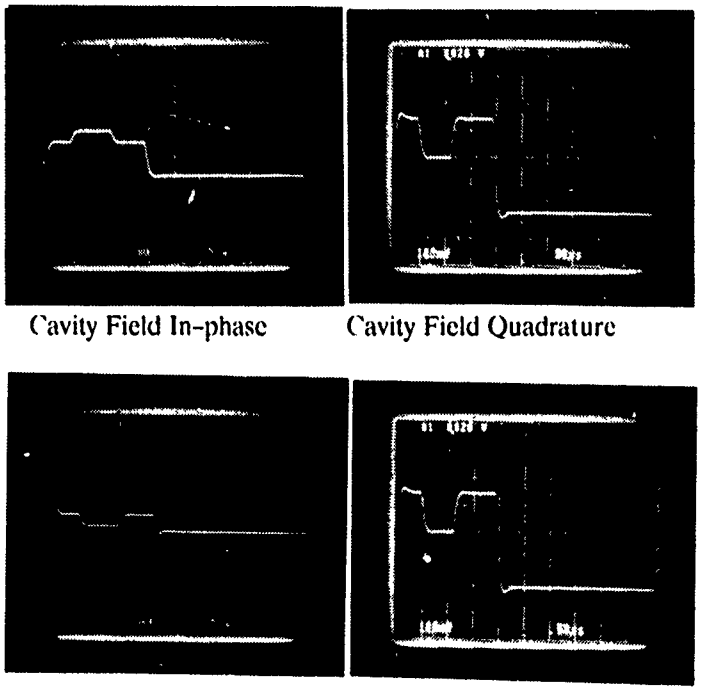


Figure 6. Computer simulations of a cavity operating off resonance with the effects of a beam

The hardware simulations were achieved by loading the appropriate coefficients into the multiplying D/As and simulating the inputs with function generators. The results of the hardware simulations are illustrated in figure 7.



Cavity Field In-phase Cavity Field Quadrature

Refl. Signal In-phase Refl. Signal Quadrature

Figure 7. Hardware simulations of a cavity operating off resonance with the effects of a beam

V. Conclusion

The development of a real-time signal processor to simulate a resonant cavity system which included the effects of beam coupling and input coupling was successful. The results clearly illustrate that there are direct similarities between computer generated responses and hardware generated responses. This accomplishes a primary goal; however, further analysis needs to be proformed that will provide data on the comparison between the response of an actual accelerator and the response of the real-time signal processor.

VI. Acknowledgments

The authors wish to extend their appreciation to B. Cheo, P. Denney, E. Natter, A. Regan and C. Ziomek for their discussions of topics contained in this paper. Also, I. Debaca and S. Scarlott are recognized for their technical support.

VII. References

[1] B. R. Cheo and S. P. Jachim, "Dynamic Interactions Between RF Sources and LINAC Cavities with Beam Loading," to be published in IEEE Trans. Elec. Dev.

[2] S. Haykin, Communication Systems. New York: John Wiley & Sons, 1983, pp. 80-108.

[3] A. Young, "A New Approach in Simulating RF Linacs Using a General, Linear Real-Time Signal Processor," Master's thesis, University of Minnesota.

[4] C. D. Ziomek, "Interfacing RF Control Electronics to the VXIbus for Ground Test Accelerator," Proc. Neutral Particle Beam Tech. Symp., 1990.

Modeling of a 1700-MHz Cluster Cavity of Planar Triodes*

Daniel E. Rees and Carl Friedrichs
Los Alamos National Laboratory

Abstract

In this paper we present the modeling and design of a 1700-MHz cluster-cavity vacuum tube amplifier. We used a three-dimensional, finite-difference code (MAFIA) to characterize the modes that the resonant structure of the amplifier will support. We describe the characteristics of the tube, including performance predictions.

I. INTRODUCTION

As frequency increases into the microwave region, the maximum power output of gridded tubes decreases. Combining several amplifiers is often necessary to achieve medium power (20 - 50 kW). A typical method is to use one or more external combiners; an alternate approach is to use a cluster cavity. In a cluster cavity, a number of gridded tubes are combined in a single resonant structure. As the number of tubes in the cavity increases, the resonant structure must be enlarged; this may cause the circumference to become comparable with multiples of the design wavelength. For this reason higher-order modes must be characterized to determine which is appropriate for amplifier design and to ensure that undesirable modes are avoided. We used a three-dimensional, finite-difference code (MAFIA) to characterize the modes that the structure would support and to modify the cavity design in order to select the desired mode.

II. CLUSTER CAVITY

A. *Mechanical Description*

We will consider the feasibility of a resonant structure that supports a combination of 4 planar triodes without external combiners. Only the output resonator will be described. The input structure will be similar in mechanical design; however, it will be dimensionally different to allow for a different impedance transformation. Figure 1 is a mechanical drawing of the output resonator. It consists of four rectangular waveguide sections, all feeding into a coaxial section. A direct tap to the center conductor of the coaxial section couples power out of the resonator. Four gridded tubes are located approximately a quarter guide wavelength from the end wall of each waveguide section. The end wall is adjustable in position, to allow each tube to be independently loaded. The tubes are operated common grid with a DC anode voltage of approximately 6 kV. An RF contact connects the grid to the bottom surface of the waveguide, and a "sandwich" capacitor isolates the DC bias of the anode and provides a low RF impedance bypass between the anode and the upper surface of the waveguide. The sandwich capacitor is analyzed as a radial mode structure whose radius is adjusted to present an RF short between the bias surface and top wall of the guide.

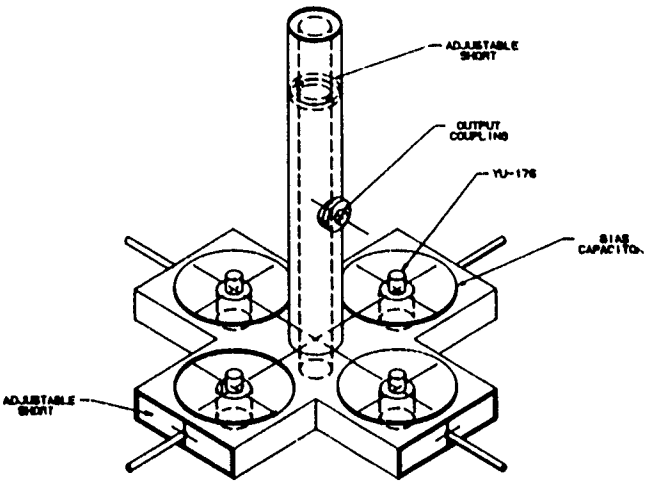


Figure 1. Cluster-cavity output resonator.

Past designs for cluster-cavity amplifiers have attempted to symmetrically populate cylindrical cavities with a number of planar triodes. These designs have experienced difficulties presenting uniform loading to tubes in the cluster and providing independent adjustment to the loading of individual tubes. The design we describe locates the planar triodes in sections of rectangular waveguide with movable end walls that provide each tube with an independent loading adjustment. In addition, the waveguide sections help to increase the resonant frequency of the dipole and quadrapole modes (which cause non uniform loading) with respect to a cylindrical structure of comparable size.

B. *Analysis of Modes in the Cavity Structure*

As illustrated in Figure 1, the output resonator is quite large compared to a wavelength at 1700 MHz (approximately 6.95 inches); for this reason, it is necessary to determine the modes that the resonator will support. The mode selected must be symmetric in each arm of waveguide cross. An axially asymmetric mode at the frequency of operation would result in uneven loading of the planar triodes. If the intersection of adjacent waveguide sections is examined, it is seen that the perimeter of the square containing all points of intersection is more than one wavelength at 1700 MHz; thus, the structure will support axially asymmetric modes. The width of the rectangular waveguide is selected such that only the lowest-order mode (TE10 mode) is supported by the guide. The selected circumference for the coaxial section is less than a wavelength, to ensure that higher-order coaxial modes are

*Work supported and funded by the US Department of Defense, Army Strategic Defense Command, under the auspices of the US Department of Energy.

0-7803-0135-8/91$01.00 ©IEEE

not present; however, the length of the coaxial section is not sufficient to suppress axially asymmetric modes in the waveguide cross.

The composite structure is analyzed using the three-dimensional electromagnetic code MAFIA [1]. MAFIA produces a set of finite-difference equations for the electric and magnetic field vectors of the three-dimensional structure, the solution of which yields the frequency domain solution of Maxwell's equations. The output resonator geometry for the MAFIA simulation is shown in Figure 2. Note, that the structure shown in this figure and in Figures 3 and 4 illustrates the effect of the mesh quantization on the original structure. This is especially apparent in the simulation of circles where MAFIA distorts the circular form. The distortion can be corrected by increasing the number of mesh points (but this requires additional computer time). The quantization level of Figure 2 is considered sufficient for understanding the modes the output resonator will support.

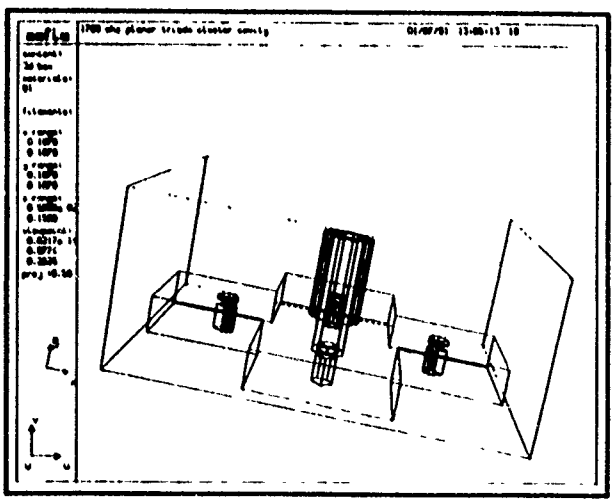


Figure 2. MAFIA plot of output resonator geometry.

Two outputs from the MAFIA simulation are depicted in Figures 3 and 4. These outputs represent the desired mode of operation at 1700 MHz and the nearest axially asymmetric mode at 1807 MHz. The plots lie along a plane dividing the top and bottom of the waveguide cross and illustrate E field vectors in and out of the plot. On the basis of Figures 3 and 4, the output resonator provides axial symmetry at 1700 MHz, which maintains uniform triode loading in each arm of the waveguide section, and the cutoff frequency of the closest asymmetric mode is sufficiently removed from the operating frequency that no design complications arise.

C. Tube Selection and Characteristics

At 1700 MHz, the only gridded tubes available are planar triodes. The tube we selected is the YU-176 EIMAC planar triode, designed for use at up to 2 GHz. This tube requires less than 25 W of heater power and can operate at a DC plate voltage (grid pulsed) of up to 10 kV. For 2-msec pulses at a 10-Hz rate, the cathode can support a DC plate current during the pulse of 2 A. The cluster-cavity amplifier will be operated class AB with the grid grounded and cathode pulsed (equivalent to grid pulsed). By pulsing the cathode voltage, the tubes can be biased class A or class AB during the RF

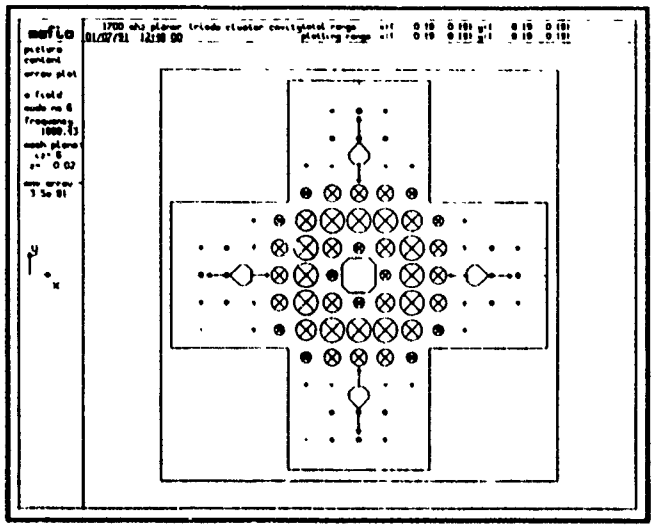


Figure 3. MAFIA electric field plot of desired mode of operation.

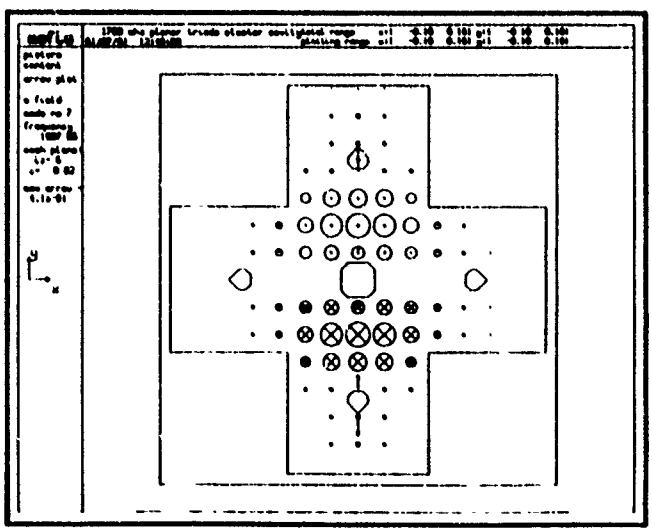


Figure 4. MAFIA plot of closest asymmetric mode.

pulse, and avoid the quiescent current during the interpulse period normally associated with these classes of operation. The operating characteristics for the YU-176 tubes are given in Table 1.

Table 1
YU-176 Operating Characteristics

DC Plate Voltage	8000.0 VOLTS
DC Cathode Bias	60.0 VOLTS
DC Plate Current	2.626 AMPS
DC Grid Current	0.146 AMPS.
DC Cathode Current	2.772 AMPS
Fundamental Peak Plate Current	4.535 AMPS.
2nd Harmonic Peak Plate Current	2.827 AMPS
3rd Harmonic Peak Plate Current	1.079 AMPS.
FundamentalPeak Cathode Current	4.811 AMPS
Peak Plate Swing	3000.0 VOLTS
Output Power	6802.0 WATTS

Table 1
Continued

RF Plate Load	662.0 OHMS
Peak CathodeSwing	80.0 VOLTS
Drive Power	192.4 WATTS
RF Cathode Input Resistance	16.6 OHMS
Plate Dissipation	14531.0 WATTS
Grid Dissipation	2.0 WATTS

These characteristics provide a combined power in excess of 25 kW with an efficiency of approximately 30 percent.

D. Model of Resonant Structure

The resonant structure is modeled as a series of coaxial, radial, and waveguide transmission lines. The position of the coupling point relative to the center of the structure is calculated to provide an impedance transformation from 50 Ω to 662 Ω in the output resonator and 16.6 Ω in the input resonator. The position of the adjustable-length short is calculated to cancel the reactive portion of the impedance at the coupling point. The resulting response of the output resonator is presented in Figure 5.

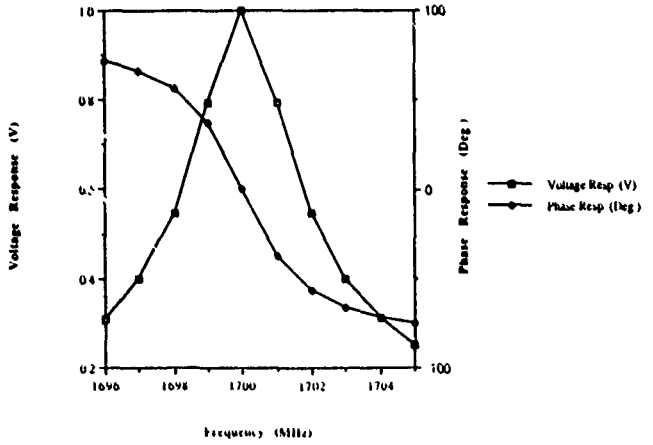


Figure 5. Calculated phase and amplitude response of output resonator.

III. CONCLUSION

A number of planar triodes can be combined in a resonant structure to increase the power level of vacuum tube amplifiers at high frequencies, resulting in a low-cost source of RF for medium-power applications.

IV. REFERENCES

[1] Los Alamos Accelerator Code Group, "MAFIA Users Guide," LA-UR-90-1307, November 14, 1989, Los Alamos National Laboratory.

Prototype 500 MHz Planar RF Input Window for a B-Factory Accelerating Cavity*

J. Kirchgessner, P. Barnes, R. Gerlack †, D. Moffat,
H. Padamsee, D. Rubin, and Q. S. Shu
Cornell University, Laboratory of Nuclear Studies
Ithaca, New York 14853

INTRODUCTION

The Laboratory of Nuclear Studies is proposing an upgrade to the existing CESR electron positron storage ring to make possible the study of CP violation of B meson decays. This "B-Factory", because of the required luminosity and the resultant high beam current, will require very high RF power levels to replace the synchrotron radiation and the HOM (higher order mode) energy losses of the beams.
The proposed design at this time[1][2] would require 16 superconducting cavity structures, each with an RF input power of approximately 400 Kilowatts at 500 MHz.

DESIGN REQUIREMENTS

This power level for a cavity window is rather high by present day standards. Klystrons commonly in use at this time have achieved above this power level using coaxial RF vacuum windows in this frequency range. These windows, in spite of their reliability in Klystrons, have not been shown to be easily adapted to application on accelerating cavities. The reasons for this are as follows; 1) the vacuum in Klystrons is usually better than in accelerating cavities. 2) extreme care is taken with Klystrons to assure that there is very low reflected power back to the Klystron and therefore no standing waves at the window, and 3) in a cavity there may be present HOM power that alters the magnetic and electric fields present at the window, possibly exciting some high frequency resonances associated with the window structure.

In an accelerating cavity and in particular in a superconducting accelerating cavity, with heavy beam loading, the input coupling is usually adjusted to be critical (β=1), that is, with no reflected power at full beam conditions. In the situation of zero beam current the input is overcoupled and therefore, in the case of superconducting structures, essentially all of the input power is reflected. This assumes that the coupling cannot be dynamically adjusted. This condition of high reflected power cannot be avoided because there exists the time before the beam in injected as well as the time after the beam has been lost. In other words, the incident power level can be controlled but the fraction of this power to be reflected will be determined by β which is determined by Q_L of the cavity for fixed coupling. The value of Q_L is determined by the Q_O of the cavity (very high in the case of a superconducting cavity) and the beam loading. In the case of the B-Factory cavity the curve of possible P_r (power reflected) versus P_i (incident power) is shown in figure 1. In this curve, any input power level above 125 Kwatts would maintain the cavity voltage and would be capable of maintaining increasing amounts of accelerated beam currents. The curve assumes that the coupling has been set to β=1 corresponding to input power of 500 Kwatts.

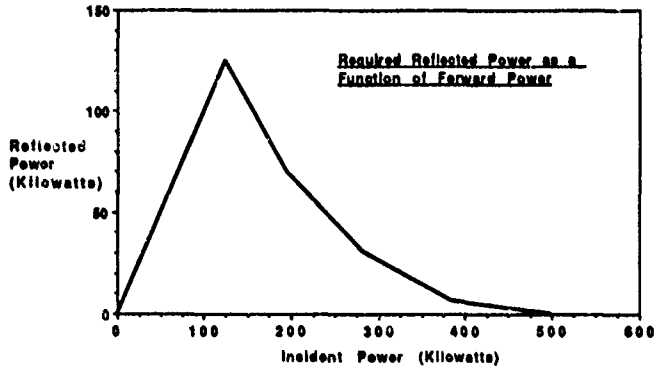


FIGURE 1

The other requirement is that the VSWR of the window be low in order to avoid loss of incident power and to prevent window damage due to heating or arcing because of excessive current or voltage at the required incident power level of 500 Kwatts.

One feature of the requirements is as follows. The reflection of the power from the cavity due to a coupling mismatch ($\beta \neq 1$) comes from a fixed reflection point, probably the coupling iris. This means that the VSWR phase pattern is spatially fixed in the input waveguide. Knowing where the voltage maximums and the current maximums are located along the waveguide, window can be placed at the most advantageous position of phase for its survival.

* Supported by the National Science Foundation, with supplementary support under the U. S.- Japan Agreement.
† GAMMA Microwave, Santa Clara, CA 95054
[1] Cornell Univ. Internal Report, CLNS 91-1050
[2] Cornell Univ. Internal Report, CLNS 90-1039

0-7803-0135-8/91$01.00 ©IEEE

WINDOW DESIGN

Several coaxial windows are in use on superconducting cavities at this frequency up to power levels of 200 Kwatts. To accommodate the higher power levels, it was decided to investigate the feasibility of a planar waveguide vacuum window.

Several qualified commercial manufacturers were requested to propose a design which they felt would meet our requirements and which they could economically produce. Two proposals were satisfactory and the proposal of Gamma Microwave[3] was chosen for development. The window that they designed incorporates the following features;

- •WR1800 Planar Waveguide window.
- •Beryllium Oxide ceramic.
- •All metal parts are copper or Stainless, no Kovar.
- •The Ceramic is brazed directly to Copper.
- •The window has anti multipacting coating.
- •The unit is water cooled.
- •The unit is compatible with vacuum baking.
- •The unit will have low VSWR over sufficient bandwidth.
- •The vacuum side is reduced height WR1800.
- •The window uses 3 small ceramic disks.

A drawing of the window is shown in figure 2. In the process of the detailed electrical design, GAMMA used 1 Mwatt traveling wave as the design objective.

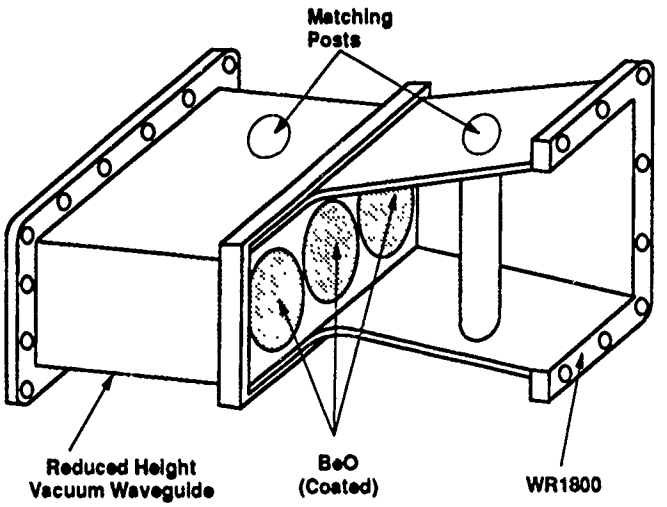


FIGURE 2

The responsibility for high power testing of the window was left to Cornell. While it would have been desirable to have purchased a tested window with guaranteed performance, the cost would have been much higher for two reasons; 1) the manufacturer would have had to purchase and operate a high power transmitter facility and 2) extra contingency would have been placed in the price to cover the risk involved in guaranteed performance.

[3] GAMMA Microwave, Santa Clara,CA 95054

In order to be able to test the window design at full power under vacuum, two windows were required. If two windows were not available, then the high power load would be required to operate in a vacuum (as does the final cavity with beam current).

LOW POWER MEASUREMENTS

Low power measurements were made using a Network Analyzer, a WR1800 full height to half height taper and WR1800 to type N adapters. Measurements were made of VSWR, transmission, and phase shift of each window as a function of frequency. The results are shown in the following graphs; figure 3A - VSWR, figure 3B - power transmission, figure 3C - Phase shift through the window and a taper, and figure 3D - the calculated electrical length of the window, all versus frequency.

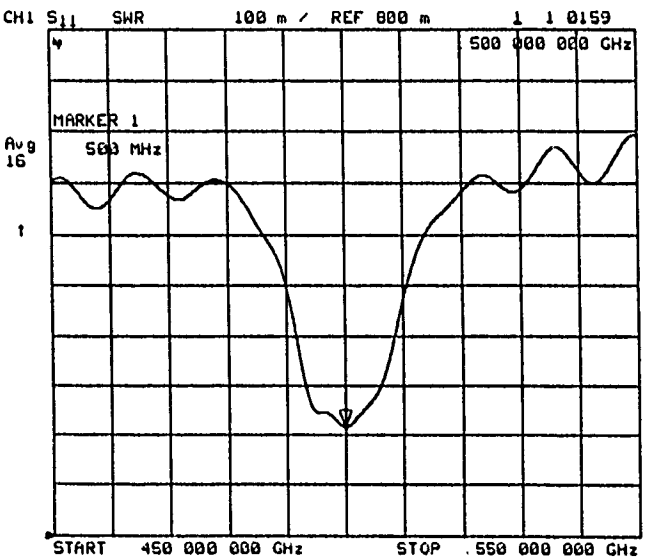


FIGURE 3A

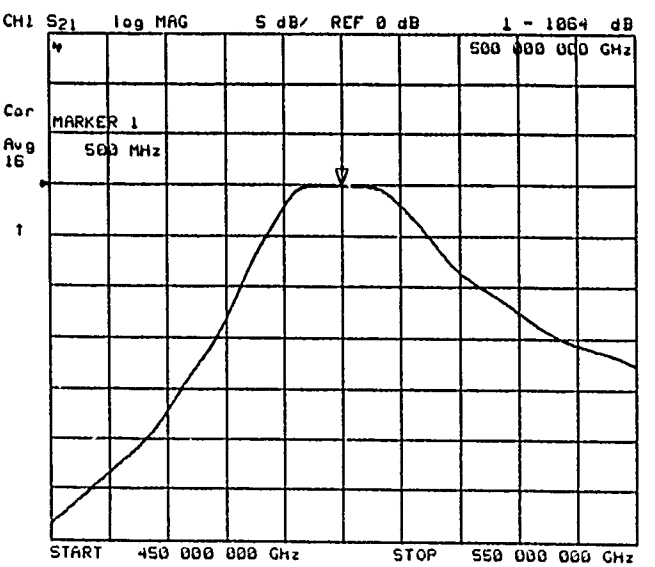


FIGURE 3B

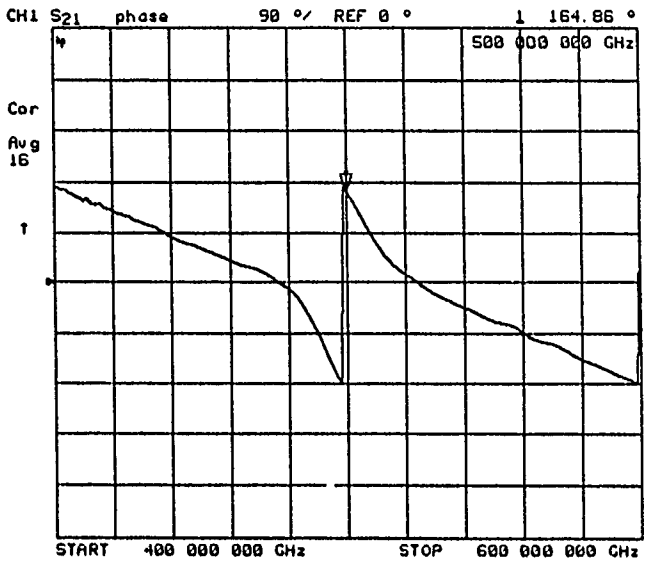


FIGURE 3C

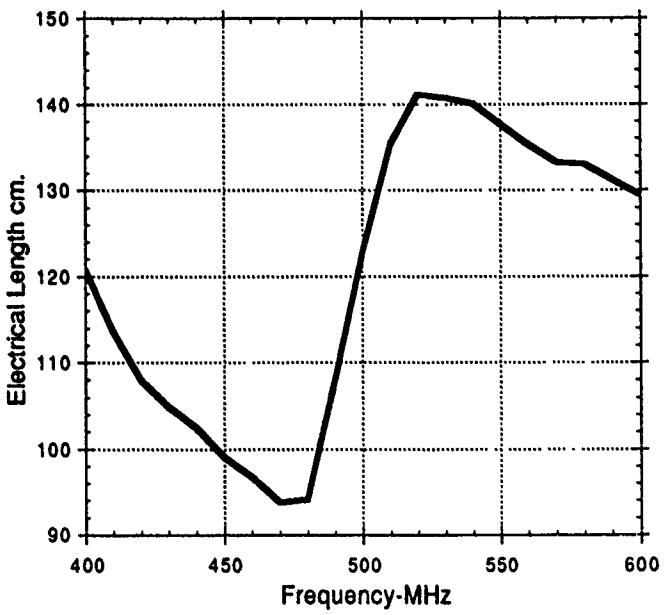


FIGURE 3D

As can be seen the VSWR was less 1:1.05 over ± 5 MHz, there was no measurable transmission loss, and the phase shift was a smooth function of frequency.

HIGH POWER MEASUREMENTS

In order to determine the capability of the windows to operate at the 500 Kwatt power level a series of three tests were planned. The first test is a medium power test with a single window used as part of a resonant waveguide. This test was done primarily because of its simplicity, because it could be done before the second window was delivered, and because the test could be done with a 200 watt amplifier instead of the 500 Kwatt transmitter. The test set up is shown in figure 4.

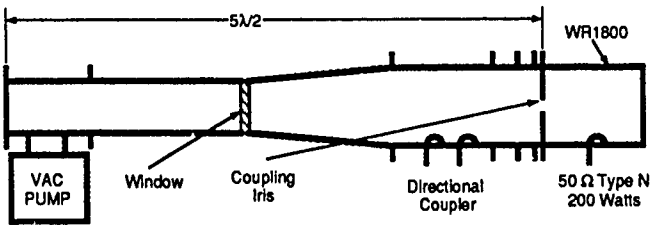


FIGURE 4

With the available 220 watts of input power, the resonant circulating power at the window was 26.8 Kwatts, 13.4 Kwatts in each direction.

The other two high power tests will include both windows and a high power transmitter consisting of a 500 Kwatt Klystron, a high power circulator and a 500 Kwatt high power RF load.. These 500 Kwatt tests have not yet been completed.

The first of these tests, as shown in figure 5, will subject the window to full transmitted power . In this test we will determine the capability of the window to operate at 500 Kwatts transmitted power corresponding to the full beam condition.

The second test, as shown in figure 6, will test the ability of the window to operate at high VSWR. We will be able to vary the phase of the standing wave pattern relative to the ceramic in order to determine the best place to locate the window relative to the cavity. This test will determine the capability of the window to operate at low or zero beam current conditions.

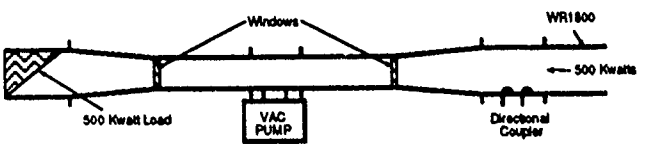


FIGURE 5

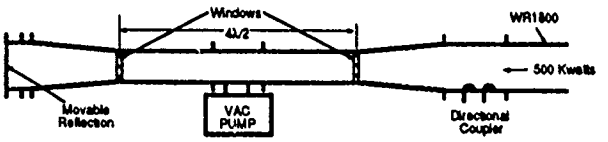


FIGURE 6

RESULTS

The test as described in figure 4 was completed. The circulating power in the resonant waveguide was measured to be 13.4 Kwatts in each direction, or 26.8 Kwatt total. The maximum temperature rise of the window cooling water was less than 3 degrees C. The vacuum base pressure before the test was 6×10^{-9} torr. During the test the maximum measured pressure was 7×10^{-9} torr.

Some temperature rise was observed in the hollow matching posts or tubes on each side of the ceramic. During this test the posts were near a current maximum. For the 500 Kwatt tests, these tubes will be cooled with circulating water.

THE AGS BOOSTER HIGH FREQUENCY RF SYSTEM*

R. T. Sanders, P. Cameron, W. Eng, M. A. Goldman, E. Jablonski, D. Kasha, J. Keane,
A. McNerney, M. Meth, M. Plotkin, M. Puglisi, A. Ratti, R. Spitz

AGS Department, Brookhaven National Laboratory
Upton, NY 11973

Abstract

A high level RF system, including a power amplifier and cavity, has been designed and built for the AGS Booster. It covers a frequency range of 2.4 to 4.2 MHz and will be used to accelerate high intensity protons, low intensity polarized protons and heavy ions, to the 1.5 GeV level. A total accelerating voltage of up to 90 kV will be provided by two cavities, each having two gaps. The internally cross-coupled, pushpull cavities are driven by an adjacently located power amplifier. In order to accommodate beam intensities up to 0.75×10^{13} protons per bunch, a low plate resistance power tetrode is used. The tube anode is magnetically coupled to one of the cavity's two parallel cells. The amplifier is a grounded cathode configuration driven by a remotely located solid-state amplifier. It has been tested in the laboratory at full gap voltage with satisfactory results.

Introduction

The AGS Booster has two RF systems covering a frequency range from 600 kHz to 4.2MHz. The range of the low frequency system is 600 kHz to 2.4 MHz, and will be used for heavy ions. The range of the high frequency system is 2.4 to 4.2 MHz, and will be used to accelerate heavy ions, polarized and nonpolarized protons.

The high frequency system will be required to function with widely different gap voltage ranges, and from essentially no beam loading to proton beam intensities as high as 0.5×10^{13} protons per bunch. However it has been conservatively designed for beam intensities as high as 0.75×10^{13} protons per bunch.

This paper will describe the high frequency system, also known as the Band III system. The low frequency system is discussed in a separate paper, also included in these proceedings.

RF System Configuration and Parameters

The system requirements for high intensity proton beams determine, for the most part, the system configuration and parameters. Table I is a tabulation of requirements for protons, and also two extremes from a light ion to a heavy ion, sulphur to gold respectively.

Table I

	p	S^{+14}	Au^{+33}
RF Amplitude			
injection	45 kV		
ejection	53 kV	< 17 kV	< 17 kV
at max. accel.	90 kV	≤ 17 kV	≤ 17 kV
Harmonic Number	3	3	3
RF Frequency			
injection	2.5 MHz		
ejection	4.11 MHz	3.89 MHz	3.00 MHz
Phase Space Area/A	1.5 eV-s	0.0707 eV-s	0.0707 eV-s
Intensity (per bunch)	0.5×10^{13}	5×10^{9}	1.1×10^{9}
Total Gap Impedance (f_{rf} = 4.1 MHz)	< 24 kΩ	—	—
Acceleration Time	62 ms	≤ 0.7 s	≤ 0.7 s
Peak Beam Power Delivered to Beam	184 kW	1.0 kW	0.4 kW
Maximum $\dot{B}$	9.5 T/s	< 3.5 T/s	< 3.5 T/s
B_{inj}	1.5 T/s	< 0.15 T/s	< 0.15 T/s

To achieve the above requirements, a practical set of parameters were developed. These parameters take into consideration such aspects as beam loading, realizable high voltage designs, limited selection of commercially available electron tubes and high power components, and the limited space available in the Booster tunnel. Furthermore, the shunt impedance will satisfy the Robinson Criterion for open loop operation.[1]

The system parameters are tabulated in Table II.

Table II

Number of RF Cavities	2
Number of Accelerating Gaps	4
Peak RF Voltage per Gap	22.5 kV
Peak RF Power per Cavity (180 kW rms nominal)	264 kW peak
Frequency Range	2.4 to 4.2MHz
Duty Cycle	50% Maximum
Output Impedance	6000 Ohms
Number of Power Amplifiers	2

*Work performed under the auspices of the U.S. Department of Energy.

0-7803-0135-8/91$01.00 ©IEEE

Cavity

The accelerating cavity is pushpull, two gap, and ferrite loaded. It is driven single-ended but is cross coupled to provide for pushpull operation. It is bias tuned to change frequency. It is physically located above and directly coupled to the RF power amplifier. See Figure 1.

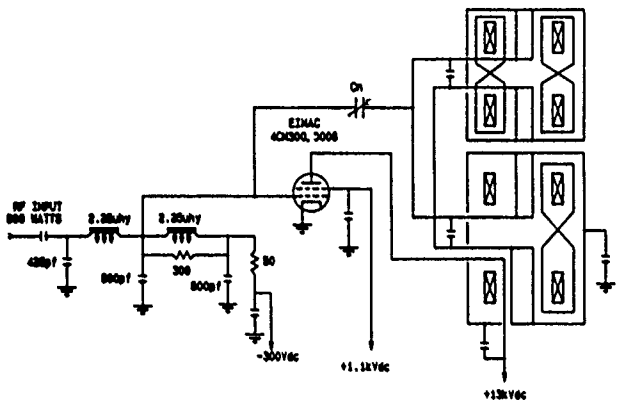


Fig. 1. Schematic Diagram of Band III Power Amplifier and Cavity.

To keep the gap voltage at a reasonable level, and keep the RF flux density, and in turn, ferrite losses manageable, the Band III cavity was designed to have two pushpull cells. The maximum RF voltage per gap is 22.5 kV peak. These cells are connected in parallel. The cavity is coupled to the power amplifier in a single-ended fashion to just one cell. The two ferrite stacks in each cell are cross coupled internally with figure-of-eight windings, essentially causing the cavity to operate as a balanced 1:2 step-up transformer.[2]

The design of the cavity is ultimately determined by the choice of ferrite. The material found best suited to the application is be Philips 4M2. The study of ferrite samples included measurements of permeability, dissipation, instabilities, and other possible anomalies.[5]

The cavity design requires 56 rings total or 14 per stack. Each ring measures 50 cm O.D. by 25 cm I.D. by 2.72 cm thick. With a gap capacitance of 350 pf per gap (chosen for a desired transient response and tuning servo bandwidth), the permeability ranges from 118 with a dc bias of 100 amperes at 2.4 MHz, down to 38.7 with a dc bias of 900 amperes at 4.2 MHz.

The ferrite dissipation is manageable with water cooling provided by copper cooling plates between each ferrite ring. Across the passband the peak dissipation varies from about 0.2 watt/cm^3 statically to 0.325 watt/cm^3 dynamically(ferrite losses are sweep rate dependent), corresponding to total peak power levels of 40 kW to 73 kW, respectively.

The Booster ring will be operated at ultrahigh vacuum and will require that the vacuum chambers, including the cavity, be baked at 200° C. The cavity beam pipes have built-in electric heating elements and thermocouples.

The ferrite stacks are dc biased from a single turn winding. The outer can, beam pipe, and gap connecting busswork form the bias winding. Because the two cavity cells are effectively in series with the dc bias, but in parallel for the RF drive, there is cancellation of RF on the dc bias leads to the cavity. Additional filtering is provided by a bifilar choke inserted into the external bias leads at the cavity.

A Band III power amplifier and cavity is shown installed in the Booster in Figure 2.

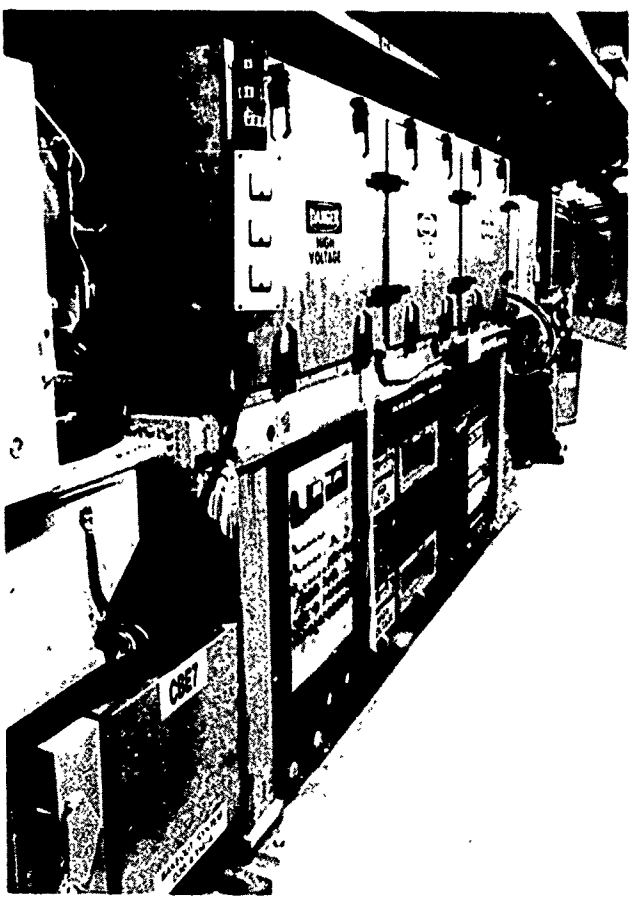


Fig. 2. Band III Power Amplifier and Cavity.

Power Amplifier

The Band III power amplifier design was bounded by a number of constraints. Some of the more important of these include power output requirements, Robinson Stability Criterion, and physical size.[3]

At maximum acceleration, 90 kV peak total accelerating voltage, the total output power required is about 180 kW rms. The amplifier was designed to deliver over 200 kW rms.

Power tube selection and amplifier configuration require careful consideration. Since the shunt impedance is low, the likely tube choice would be triodes. However, it was found that a large power tetrode (the EIMAC 4CM300,000G), could provide an average plate resistance of less than 500 ohms, providing a margin of safety. A grounded cathode tetrode also simplifies the circuit and is able to meet the physical space limitations.

The power tube operates class AB_1. Because of the 1:2 step-up at the cavity, it is necessary for the anode to swing only 11.25 kV. The dc anode voltage is 14.5 kV with a peak plate current of 65 amperes and a short-term average of 24 amperes. The screen voltage is 1.1 kVdc with an average current of about 0.5 amperes. The control grid bias voltage is -300 Vdc and the RF drive voltage is about 280 V peak.

The output circuit of the stage is simplified by bringing the anode voltage lead through the cavity for decoupling as well as RF coupling to the cavity. The need for blocking capacitors and a broadband RF choke are eliminated.

A broadband low pass filter terminated in 50 ohms is used to accommodate a high input capacitance as well as provide a standard impedance for the driver stage. A small amount of neutralization is required and is provided by a neutralizing capacitor coupled from the control grid to the 180° out-of-phase half of the cavity.

The driver stage is a pair of ENI 500 watt solid-state broadband linear amplifiers summed with a high power combiner. These amplifiers are remotely located from the Booster ring to avoid of possible radiation damage.

Cavity Tuning System

Tuning is accomplished by varying the cavity ferrite saturating bias current in response to two signals. The first of these is generated by an open loop program obtained from a function generator which is driven by a frequency-to-voltage converter. The second is the output of a phase detector which compares the phases of the output stage grid and plate voltages. Together they regulate the cavity tuning to within +/-10 degrees of resonance at all gap voltages up to 22.5 kV peak.

The coarse tuning open loop program is used to generate a function that will closely follow the cavity's static tuning curve. Added to this function is a function that is rate sensitive, and roughly corrects for the anomalous response of the ferrite to df/dt.

As the RF drive is swept across the passband from 2.4 to 4.2 MHz, a transistor bank adjusts the bias current from 100 amperes to 900 amperes without beam loading. With beam loading at rated Booster beam intensities, the detuning effect of the quadrature component of the beam current is small. The estimated increase of tuning current at injection is about 22 amperes, and 33 amperes at extraction. The system can deliver up to 1200 amperes.[4]

An important consideration in the servo design is the response to beam induced transients and detuning. Tuning servo frequency response is sensitive to the tuning bias current level. At injection the closed loop bandwidth is estimate to be about 15 kHz. For tuning currents up to 750 amperes the bandwidth is estimated to be 10 kHz. At 900 amperes it is approximately 7 kHz.

Status

The commissioning of two completely tested systems with a proton beam is scheduled for late spring 1991.

Acknowledgements

The authors are very grateful and indebted to an almost endless list of helpful people from Brookhaven and other laboratories for their ideas, suggestions and guidance. Finally, a thank you to Michael Iwantschuk and his technician staff.

References

1. K. W. Robinson, CEA, Report No. CEAL-1010, 1964.
2. M. Meth, A. Ratti, Push-pull Operation of the Cavity, Booster Tech. Note 84, July 1987.
3. M. Meth, A. Ratti, Specifications and Design of the RF Power Amplifier for the Proton Cavity, Booster Tech. Note 92, September 1987.
4. M. Meth, A. Ratti, Beam Loading Analysis of the Booster RF System, Booster Tech. Note 191, April 1991.
5. M.A. Goldman, et al., Proc. IEEE particle Accelerator Conf., Vol. 1, pp.165-167, Chicago, Ill. March 20-23, 1989. Rev.4-22-91.

A FAST AMPLITUDE AND PHASE MODULATED RF SOURCE FOR AmPS

F.B. Kroes, E. Heine, T.G.B.W. Sluijk
NIKHEF-K
P.O.Box 41882, 1009 DB Amsterdam, The Netherlands

Abstract

AmPS (Amsterdam Pulse Stretcher) is a 900 MeV electron stretcher and storage ring. Its installation started early 1991. To compensate for the synchrotron radiation losses and to control the injection and extraction process in the ring a CW RF source will be installed. The source will operate at 2856 MHz. This frequency has been chosen to ensure optimal beam capture of the injected beam from the linac which has a 2856 MHz bunch structure. The RF cavity in the ring is a 40 cm long slow wave structure. It is presently manufactured by Haimson Research Corporation. The filling time of the structure is 22 nsec. During the 3-turn injection and the directly consecutive extraction cycle, fast amplitude and phase modulation will be applied to obtain maximum injection and extraction efficiency. The required RF cavity input power is 30 kW for a ciculating beam of 900 MeV and 200 mA. This power will be delivered by a commercially available 50 kW CW klystron (Thomson). The source will either operate in linear- or saturated mode.

INTRODUCTION

To obtain electron beams with a high duty factor a stretcher ring will be added to the existing Medium Energy Accelerator (MEA). The ring will operate at energies between 250-900 MeV and with circulating currents up to 200 mA (ref.[1])
MEA has been upgraded for this energy range by modifying the modulators and installing new klystrons to obtain higher RF peak power (10MW) during shorter pulsewidth (3.5μs). (ref[2]). The injector is modified to deliver 2.1 μs pulses of 80 mA for the 3-turn injection.
RF related specifications of the stretcher ring:

Energy range	E	[MeV]	300-900
Circulating current	Ib	[mA]	200
Energy spread bucket	δ	[%]	±0.1
Frequency	f	[MHz]	2856
Harmonic number	h		2016
Momentum compaction	α		0.027
Bending radius magnets	ρ	[m]	3.3
Ring circumference	L	[m]	211.618
Circumference period	T	(μs)	0.7

From these numbers the RF parameters which are important for the design of the RF station are calculated.
Table 1 shows the synchrotron radiation loss per turn (Us) with the corresponding synchronous phase angle (ϕs), the total loss (Ut), including the parasitic loss per turn, with the corresponding phase angle (ϕt). Also presented are the required cavity voltage (Vrf) and the cavity input power (Prf) for the 2856 MHz travelling slow wave structure.

Table 1

Beam Energy (MeV)	Us (KeV)	Ut (KeV)	Vrf (kV)	ϕs (degr)	ϕt (degr)	Prf (kW)
300	.2	1.2	26	179.6	177.4	2
500	1.7	2.7	45	177.8	176.7	6
700	6.4	7.4	70	174.7	173.9	15
900	17.6	18.6	105	170.4	169.8	30

The synchrotron tune is approximately 0.03

RF cavity structure

This travelling slow wave structure has a natural phase slip which is optimized for the AmPS case to obtain a nearly synchronous phase orbit for the expected beamloading conditions. (ref.[3])
About 3% of the CW input power will be dissipated as copper losses, the remainder part will be dissipated in the rf load. The rf filltime of the cavity structure is 22 ns which means a very fast response to phase and amplitude changes of the input rf power and beamloading changes. Special care has been taken to damp the HOM (Higher Order Modes) in this structure.

RF injection

During the 3-turn injection at a peakcurrent of 80 mA, the increase of the beamloading in the cavity structure by the three abrupt current steps will result in a change of the desired phase orbit through the structure. Fast phase correction (<50ns) of the field will provide a safeguard against serious beam instabilities associated with this fast injection process.

RF extraction

The rf field in the cavity structure will be used to control the extraction process for maximum extraction efficiency during the time between the successive injections. The objective is a smooth, uniform and complete extracted beam at all energies. Two possible methodes of extraction are foreseen;
- Phase Modulation of the rf field in the cavity structure.
- Amplitude Modulation of the rf field in the cavity structure.

By PM a part of the electrons will be forced out of the stable rf bucket by displacing the bucket in phase bv a fast phase step of the rf field in the cavity structure. This results in positioning of a small fraction of the original trapped electrons outside the bucket. These electrons slowly lose energy and migrate into the extraction zone.
By AM the bucket size will be reduced by decreasing the amplitude of the rf field. Again a part of the original trapped electrons will be positioned outside the stable bucket and slowly lose energy and enter the extraction zone. A mixture of both extraction techniques are possible, simulation calculations for the extraction methodes are started.

0-7803-0135-8/91S01.00 ©IEEE

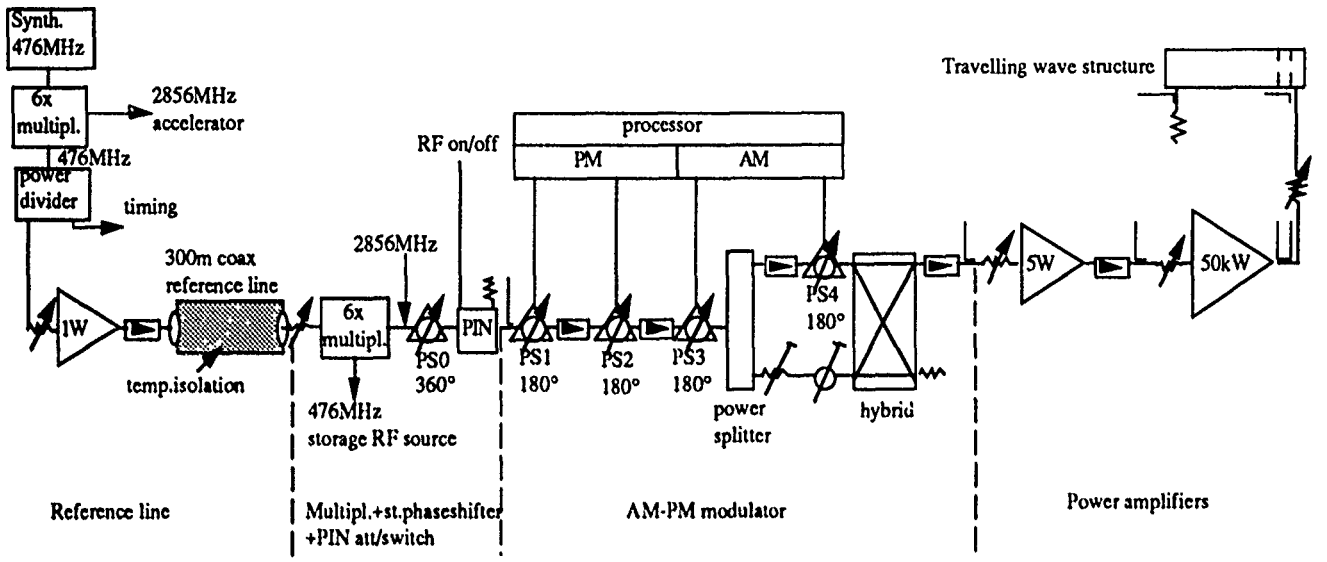


Fig.1 AmPS CW RF source

RF SOURCE DETAILS

In fig.1 The design of the stretcher source is shown. The RF system is divided in 4 parts.

- Reference line
- Multiplier x6, station phase shifter and PIN switch
- AM-PM modulator
- 50 kW power amplifier

General

In the stretcher ring there must be a perfect synchronization between the injected bunches and the rf buckets created in the cavity structure. The past has shown that MEA has a very good longterm stability and delivers high quality beams. To obtain good longterm amplitude- and phase stability in relation to the injected and circulating bunches in the cavity structure much attention is given to the temperature stabilization of the total electrical path length from the 476MHz synthesizer to and including the cavity structure

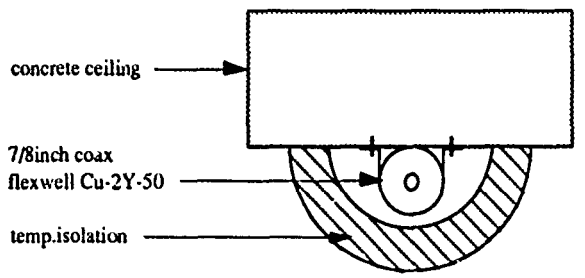


Fig.2 reference line

Reference line

This 7/8 inch phase stabilized coaxial cable (Flexwell Cu-2y-50) has a phase/temperature coëfficient of 8ppm/°C which corresponds to a phase/temp. coëff. of 1.5degr./°C for a 300m length at 476MHz. The attenuation is 2.7dB/100m. After frequency multiplying x6 the phase/temp.coëff. is 9degr./°C at 2856MHz. To obtain a long term stability within 1degr. for this case, the coaxial cable will be mounted to the 1.5m thick concrete ceiling of the accelerator tunnel with thermal isolation around it as is shown in fig.2. Temperature measurements have demonstrated a max. temp change of the concrete ceiling of .1 °C/day.

x 6 multiplier

The multiplier unit is a copy of the one used to generate the 2856MHz accelerator master source signal. The input power is 20mW and the output power is 50mW. It consists of a 476MHz amplifier followed by a passive multiplier/filter unit. The multiplier components are thermostrated for amplitude- and phase stability.(fig.3)

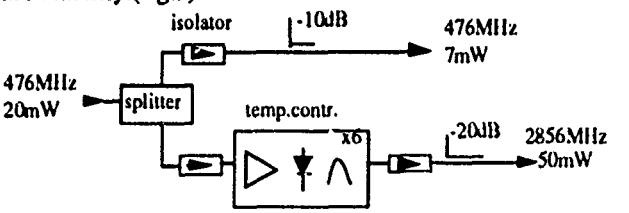


Fig. 3 x6 Multiplier

Station phase shifter and PIN switch

This slow motorized phase-shifter is to control the exact phase relation of the accelerating field in the cavity structure with respect to the bunched beam.

The rf PIN mod./switch has two functions,

1-it will be used as an analog attenuator to control the amplitude of the RF field in the cavity to real zero level during the last part of the extraction cycle ir the case of AM extraction, if the AM control network is not able to come into the few watts power level.

2-it will be used to switch off the RF for safety reasons.

AM and PM modulator

This part consists of four commercially available fast electronic analog phase shifters which are shown in fig. 1 and 4. The Amplitude Modulator consists of phase shifters PS3

and PS4. The voltage behind the hybrid will be modulated by PS4 according to the relation Vcos(ϕ/2) and PS3 will compensate for the ϕ/2 phase shift introduced by PS4. This network introduces AM without phase change over more than 30dB with a resolution of 12 bit. In the case of AM, PS1 and PS2 have constant values.

The Phase Modulator consists, in the first place, of PS1 and PS2. Each Phase shifter has a resolution of 12 bit. Over the 360degr. phase range the insertion loss of both phase shifters together will change about 2dB. The AM part of the circuit will be used for insertion loss compensation. The four phase shifter network introduces PM without amplitude change with 12 bit resolution.

Modulation processor

Pure AM and pure PM are both defined by two, four 4Kx12bit look up tables with corresponds to exact phase shifter settings. Each phase- or amplitude step is defined by 4 phase shifter settings from the two tables. The data for these tables will be obtained by a measurement procedure with a network analyzer. The max. puls rep. rate of the injection will be 400 pps. The max. extraction time is chosen to be 20ms. If we take four 8Kx12bit memories for the phase shifters then we can give a phase- or amplitude step every 2.5 µs, which means every 3 turns. The 2.5 µs is defined by a clock in the processor.

Extraction simulations will define what AM, PM or mixed Modulation curves will be required during the extraction time. The four 8Kx12bit memories will be filled with phase shifter settings according to the calculated extraction modulation curves. The earlier mentioned look up tables act as source tables. A possibility will be built in to change the modulation curves on line to obtain optimized extraction. The memory

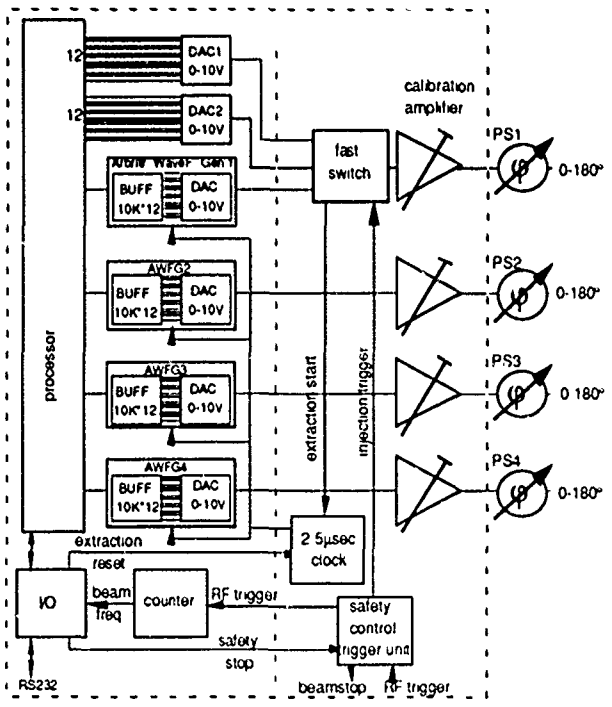


Fig. 4 AM-PM processor

speed is100ns and is fast enough to control the extraction.

During the 3-turn injection, phase correction due to beamloading phase shift will be accomplished by fast switching (20 ns) of the correct voltage levels to PS1.

50kW Power amplifier

The pre-amplifier is a commercially available 37dB, 5W classA linear amplifier used for driving the CW klystron in linear or saturated mode. The bandwidth is more than 100MHz. AM and PM step speed will be limited by the klystron bandwidth (15MHz) only.

The 50kW amplifier tube is the newly developed TH 2110 CW klystron from Thomson. In table 3 the typical specs are given.

Table 3. TH 2110 specifications(typical)

Pout saturated	kW	15	30	50
Beam voltage	kV	17.3	20.8	25.3
Beam current	A	1.9	2.5	3.3
Pdrive sat.	W	4	2	.7
Bandwidth(-1dB)	MHz	5	7	7
Phase sensivity	degr/%V	18	16	14.5
Efficiency	%	45	56	60
Pout(1dB compr.)	kW	6	18	30
Pdrive(1dB compr)	W	.5	.34	0.14

For PM the tube can be used in saturated mode and for AM the tube will be used below the 1dB compression level. For operation at lower levels than specified in the 15kW list and for accurate power control an attenuator is implemented in the RF output of the klystron.

ACKNOWLEDGEMENTS

The work described in this paper is part of the research program of the Nuclear Physics section of the National Institute for Nuclear Physics and High Energy Physics(NIKHEF-K), made possible by financial support from the foundation for Fundamental Research on Matter (FOM) and the Netherlands Organization for Scientific Research (NWO)

REFERENCES

[1] G. Luijckx e.a.,"The Amsterdam Pulse Stretcher project (AmPS),"proc.of the IEEE Part.Acc.Conf., Chicago 1989, March 20-23, pp. 46-48.

[2] F.B. Kroes and E.Heine,"Modification of MEA modulator-klystron units enabling short pulse injection into a pulse-stretcher ring,"proc.of the IEEE Part.Acc.Conf., Chicago 1989, March 20-23, pp. 205-207.

[3] J. Haimson and B. Mecklenburg,"A CW non-synchronous traveling wave structure for a 300MeV Pulse Stretcher ring,"IEEE Part.Acc.Conf., Washington D.C.,March 16-19, pp. 1919-1921.

[4] L.O. Dallin."Time Controlled Monochromatic Extraction from EROS."EPAC 90, Proc. of the 2nd European Part.Acc.Conf., Nice, June 12-16, pp.1260-1262.

HIGHER ORDER MODE DAMPING IN A PILL BOX CAVITY

F. Voelker, G. Lambertson, and R. Rimmer
Lawrence BerkeleyLaboratory
University of California
Berkeley, CA

ABSTRACT

We have substantially damped the higher order modes (HOM's) in a pill box cavity with attached beam pipe, while reducing the Q of the principal mode by less that 10%. This was accomplished by cutting slots in the cavity end wall at a radius at which the magnetic field of the lowest frequency HOM's is large. The slots couple energy from the cavity into waveguides which are below cut off for the principal mode, but which propagate energy at the HOM frequencies. Three slots 120 degrees apart couple HOM energy to three waveguides. We are concerned primarily with accelerating and deflecting modes: i.e. the TM_{mnp} modes of order m=0 and m=1. For the strongest damping, only three m=0 and m=1 modes were detectable. These were the principal TM_{010} mode, the TM_{011} longitudinal mode, and the TM_{110} deflecting mode. In addition the HOM Q's and the reduction of Q for the principal mode were determined by computer calculation. The principal mode Q for an actual rf cavity could not be measured because the bolted joints used in the construction of the cavity were not sufficiently good to support Q's above 6000. The measured Q of the first longitudinal mode was 31 and of the first transverse mode 37. Our maximum damping was limited by how well we could terminated the waveguides, and indeed, the computer calculations for the TM_{011} and TM_{110} modes give values in the range we measured.

I. INTRODUCTION

A large number of modes can be excited in an rf cavity by a bunched beam. Energy at frequencies below the cut off of the beam pipe will be trapped in the cavity, and interact with successive beam bunches. The voltage induced in the cavity at these higher order mode (HOM) frequencies is proportional to the shunt impedance of the mode. Shunt impedance is the product of a geometrical factor (R/Q) and the Q of the cavity; reducing the Q by damping the mode reduces the voltage excited at that frequency.

We are presenting a method to damp the HOM's without excessive damping of the principal mode. This has been demonstrated in a pill box cavity with three slots coupled to waveguides that carry HOM energy to terminating loads.

* Work supported by the Director, Office of Energy Research, Office of High Energy Physics, Advanced Energy Projects Division, U.S. Department of Energy. Contract DE-AC03-76SF00098.

U.S. Government work not protected by U.S. Copyright.

HOM Damping

Imagine a typical rf cavity as a globe with the beam passing through the poles. The magnetic field of the principal mode at the wall is a maximum at the equator, and falls off toward a pole. On the other hand, most of the HOM's have zero H field at the equator, and the H field on the wall is a maximum at some distance away from the equator. The HOM's have broad maximums, and it is feasible to find a position where a slot couples strongly to most of them. The coupling is strongly dependent on the length of the slot, and less on height of the slot. A narrow aspect slot couples adequately, and it perturbs the fundamental mode less than a square aperture. Care must be taken not to place the slots on a zero of one of the HOM's.

The width of the waveguides is greater than the length of the slot, and was chosen to propagate the lowest troublesome HOM, but not the fundamental mode. The evanescent fields of the fundamental mode will reach a short distance into the waveguides, and the terminating loads must be far enough away in the guide to not damp the principal mode. The slots cause additional loss at the fundamental frequency because the wall currents are concentrated at the edges of the slots. Nevertheless, it is possible to have adequate coupling for the HOM's and still lower the fundamental Q less than 10 percent.

Experimental Setup

A pill box cavity with a 38.3 cm diameter and a 25 cm height was available from another mode damping experiment, and it was modified by adding 16.5 cm (inside diameter) beam pipes to each side. See figure 1. The beam pipes were terminated in 20.3 cm long crossed-wedges of 1 cm thick Eccosorb AN-73 material. Three 2.54 cm x 19 cm rectangular waveguides are attached to one end wall at a 14 cm radius and spaced at 120 degree intervals. The waveguides are coupled to the cavity through 2.54 cm x 15.24 cm rectangular slots, and are terminated by lossy elements at the far end. In an r.f. accelerator cavity the TM_{011} longitudinal mode is excited very strongly because it has a large R/Q. Because it is usually lower than the beam pipe cut-off frequency, it is trapped, and also has a high Q. We targeted our slot geometry to couple strongly to this mode, and the damping-waveguide cut-off frequency was chosen to be well below its frequency.

To sense beam coupling to the longitudinal modes, we need an antenna that couples to the E_z fields on the axis of the cavity. On the other hand, we don't want to perturb the fields on the axis with a metal coaxial line. Our solution

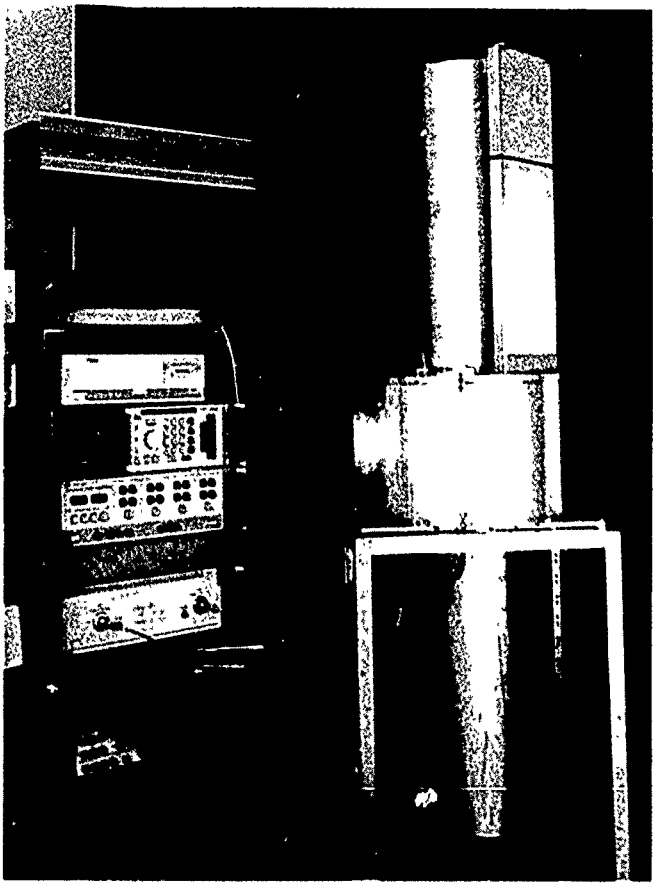


Fig. 1. Pillbox Cavity with One Damping Waveguide (CBB 905-3942)

was to use four 5 mm long electric-probes in the end walls as close to the beam pipe as mechanically feasible. These were spaced 90 degrees apart. Making them alike reduces coupling to modes with m=1, 2, or 3. The signals from these four probes are combined and become one port of the cavity. A similar electric-probe was placed on the opposite end wall and becomes the other port.

The probes are purposefully very short to simplify the Q measurements. The signals from the each pair of adjacent probes were combined in separate 180 degree hybrids. The sum signals from these hybrids are combined in another 180 degree hybrid, and for longitudinal modes the sum output is used as the port to the cavity. To measure transverse modes, i.e. m=1 modes, the difference signal is used as the cavity port. For both cases S_{21} was measured using an HP 8510B Network Analyzer. With the dampers in use, the signals for some modes were very weak, and the readings were enhanced by averaging 128 readings and smoothing the data slightly. We later lengthened the fifth probe to 9 mm to improve the signal-to-noise on some of the readings.

Measured Results

We started our measurements by covering the slots with metal tape to enable us to identify the basic cavity modes, and to allow us to determine the undamped Q's. Modes up to 2 GHz were identified by comparing with calculated frequencies from URMEL code. We also saw some quadrupole and sextupole modes, because the probes were not exactly symmetrical. These should not couple to the beam.

Our initial goal was to damp the HOM's sufficiently to reduce the Q's to less than 100. Our first waveguide terminations consisted of four 18 cm long wedges of Eccosorb material across the 2.54 cm dimension of each guide.

The damping greatly reduced the amplitude of most modes, and it was necessary to average the signals from the weakest signals to reduce the noise background. Even so, many modes disappeared into the noise background completely.

Waveguide Terminations

Preliminary measurements were made with a single waveguide, and a variable length slot. We observed that as the slot length was increased, the TM_{011} mode became smaller in amplitude to a point where it split into two frequencies. Further damping resulted in a greater separation in frequency, but no further reduction in Q.

For the final measurements using three slots, most of the HOM Q's were below 100, but the TM_{011} mode was split in two parts, one with a Q of 50.5 and the other a Q of 105. After some experimentation, we found that the mode splitting was caused by reflection from the waveguide termination. Reflections between the slot and the termination cause the waveguides to act like resonant cavities over-coupled to the main cavity.

The wedges were removed, and terminations made of Eccosorb NZ-51 (.5 cm x 3 cm x 6 cm) tiles inserted into the corner of each waveguide. The character of the split mode was observed as the number of tiles was increased. As tiles were added, the split mode coalesced and a final Q of 31 was reached. With these improvised terminations, the first tiles reached into the evanescent field of the principal mode and lowered its Q. However a longer waveguide with ferrite loading could be designed to give a sufficiently good match and without increasing the principal mode loss.

Calculated Values:

Using the MAFIA code together with a computational method developed by Kroll [1], the shunt impedance and Q of the pillbox cavity was calculated with three damping waveguides. Figure 2 shows the three dimensional model used to calculate these parameters. The cut-off frequency of the damping waveguides is 787 MHz, and the TM_{010} mode at 841 MHz is well damped. There is a TE_{111} mode in the cavity at 708 MHz that is not damped. We expected the symmetry of the probes to reject it, but it was quite visible as an undamped mode. For a typical accelerating rf cavity shape this mode occurs at higher frequency with respect to the fundamental, and it would also to be well damped even though we expect TE modes to couple only weakly to the beam.

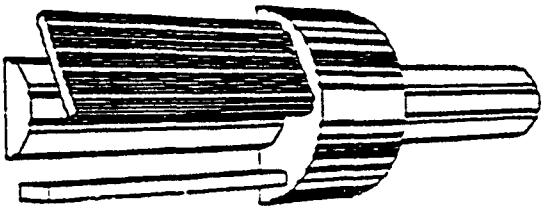


Fig. 2. Three Dimensional Model Used for MAFIA Calculations

The table below summarizes the results of both the calculations and the measurements. The frequencies of the damped modes were perturbed very little by the dampers, and there was no difficulty in identifying them.
Calculated Q values indicated that the principal mode was perturbed a minimal amount; the Q was reduced by only 8 percent. The first longitudinal mode (TM011) and the first transverse mode (TM111) were reduced to Q's of less than 40, and agreed closely with the calculated values. None of the other longitudinal or transverse modes were strong enough to see, but there was one quadrupole mode with a Q of 152. (We don't expect the beam to couple to quadrupole modes.)

	Calculated			Measured	
mode	**freq**	**Q**	**ΔQ**	**freq**	**Q**
TM010	611	33400	-8%	609.5	649*
TM011	840	15-35		836.2	31
TE111	708	39300	-7%	704.2	667*
TM110	907	56		898.8	37
TM111	1021	31		**	**
TE211	957	55		**	**
TM211	–	–	–	1366	152

* Waveguide load sees evanescent field.
** Not visible.

REFERENCES

[1] Conciauro, G. and P. Arcioni, 1990. "A New HOM-free Accelerating Resonator," in Proceedings of the 2nd European Particle Accelerator Conference, Nice., June 12-16, 1990.

[2] Arne F. Jacob, Glen R. Lambertson, Walter Barry, "Higher Order Mode Damping in an ALS Test Cavity," Proceedings of the 2nd European Particle Accelerator Conference, p 928-930, Nice, June 12-16, 1990.

RF IMPEDANCE MEASUREMENTS OF THE VARIOUS VACUUM CHAMBERS FOR THE ADVANCED PHOTON SOURCE (APS)*

J.J.Song, J.W.Howell, R.L.Kustom, and J.F.Bridges
Argonne National Laboratory, Argonne, IL 60439

ABSTRACT

Coupling impedances (Z) for the 7-GeV APS storage ring have been numerically estimated [1]. In order to confirm these calculations, measurements of the coupling impedance of various vacuum components around the main storage ring was done with a synthetic pulse technique. A section of the beam + ante-chamber, a vacuum valve with and without the internal RF screen, and a photon absorber were used as a device under test (DUT) to obtain the preliminary results. The result in the frequency domain (FD) measurement was compared with previous time domain (TD) measurement and with the computer simulation of the APS impedance budget [2]. The Z or k dependance on the pulse length and the thickness of the center wire was examined.

I. INTRODUCTION

The coupling impedance must be kept small so that the desired operating current is achieved. A computational investigation has been carried out to estimate the coupling impedance of a large variety of structures in the APS ring. This was done mainly by W.Chou [2], using the 2D, 3D MAFIA codes and TBCI code. The results are summarized in Table 1 as the APS impedance budget. As seen, the largest longitudinal impedance is contributed by the RF cavities (even though the contribution of the fundamental mode has been subtracted from the calculation) and the transverse impedance is mainly contributed by the transitions between the beam chamber and the insertion device (ID) section. The longitudinal impedance and the transverse impedance are estimated to be 1 Ω and 0.15 MΩ/m, respectively.

The coupling impedance of the APS vacuum chamber components was measured with a coaxial wire method, using a synthetic pulse technique [3]. The measurements were done on a section of the beam- and ante-chamber, and a vacuum valve with and without the internal RF screen. A photon absorber is presently under test. The measurements will assist in the design of the various components of the storage ring, especially the type of the RF screen that will be used near the photon absorber.

---

*Work supported by U.S.Department of Energy, Office of Basic Sciences, under Contract W-31-109-ENG-38.

U.S. Government work not protected by U.S. Copyright.

II. LOSS PARAMETER AND IMPEDANCE

For a given beam bunch with charge, q, the energy loss of the bunch is

$$\Delta E = kq^2 = 2Z_0q^2 \frac{\int I_1(I_1-I_2)\,dt}{(\int I_1\,dt)^2} \quad (eV), \qquad (1)$$

where Z_0 is the characteristic impedance of the coaxial wire, I_1 is the current flowing through the reference chamber, and I_2 is the current flowing through the DUT (see Fig.1). Thus the longitudinal loss parameter can be measured by the integration of the current, which is also a function of the beam bunch length, σ. The coupling impedance, Z, can be derived from the wake potential of a beam bunch,

$$W_b(t) = -\frac{2Z_0\,[I_1-I_2]}{q} \quad (V/pC). \qquad (2)$$

Transforming eq.(2) into the FD gives the longitudinal impedance as;

$$Z(\omega) = 2Z_0 \frac{[I_1(\omega)-I_2(\omega)]}{I_1(\omega)} \quad (\Omega). \qquad (3)$$

III. EXPERIMENTAL SETUP

As depicted in Fig.1, a Network Analyzer (HP8510B) was used to measure the two-port S-parameters of the DUT. The frequency span is varied from 45 MHz to 18 GHz, depending on the appropriate synthetic pulse length, σ. An HP 9000/308 computer was used for data acquisition and the control of the system. The time domain option computes a synthetic pulse via the Fast Inverse-Fourier Transform (FFT) from the FD data. The temperature in the room was 74 ± 2 °F to get a reliable signal from the DUT.

The test system consists of a piece of the APS beam chamber (50 cm long), the DUT (10 cm) and the transition portions (30 cm each). The transition portion is tapered at 10 ° to eliminate multiple reflections due to sharp discontinuities. The parameters in the test system and in the APS storage ring are summarized in Table 2. Three different types of center conductors were used: a 2 mm-brass wire, a 9.5 mm-Cu pipe, and an elliptical 50 Ω-matching Al rod.

In the impedance computation, the use of the transmission coefficient (S_{21}) instead of the reflection coefficient (S_{11}) reduces the error in Z(ω) because the multiple reflections must be considered for the S_{11}:

Table 2. Test system and APS storage ring parameters

Characteristic impedance of the center conductor,	Z_o	= 125, 88, 50 Ω
Sweep frequency,	Δf	= 45 MHz ~18 GHz
Nominal energy,	E	= 7.0 GeV
Revolution Frequency,	f_o	= 271.55 kHz
Beam chamber-cutoff freq.	f_{cut}	= 4.6 GHz
Bunch length, rms	σ_{rms}	= 5.3 mm
Bunch length, FWHM	σ	= 27.5 ps
Number of bunch,	n_b	= 20
Bunch current,	I_b	= 5 mA

$$Z(\omega) = 2Z_o \frac{[S_{21}(\text{ref}) - S_{21}(\text{DUT})]}{S_{21}(\text{ref})} \quad (\Omega). \qquad (4)$$

In order to convert the data into the beam-impedance for a single bunch, the impedance, is normalized:

$$\underline{Z} = \frac{Z(\omega)}{n} \quad (\Omega), \qquad (5)$$

where $n = \omega/2\pi f_o$ and f_o is the revolution frequency of a beam in a storage ring. The total impedance can be obtained by multiplying k by the passage time between bunches in a storage ring, or

$$Z_{tot} = \frac{k}{n_b f_o} \quad (\Omega), \qquad (6)$$

where n_b is the number of bunches in a storage ring.

IV. MEASUREMENTS AND RESULTS

The small section of the beam- and ante-chamber was measured to compare with the previous experiment in the TD [4]. Even though the error of k is as high as 30 % , the resolution is much improved. The TD measurement for the small k-values was repeatable only upto 0.002 V/pC because of the amplitude jitter in the real-time pulse [4]. In the FD measurement, the repeatability error was 6 x 10^{-4} V/pC in the 0-16 GHz span and the k-value was measured to be 2 x 10^{-3} V/pC (see Table 3).

For the large value of the k, There are no significant effects of the size of the center conductor. For the small k, the thickest center piece apparently gives more transmission rate (S_{21}), because it gives the exact 50-Ω matching in the DUT.

The typical result of the longitudinal impedance for the vacuum valve with the RF screen is plotted in Fig.2, using the eqns (4) and (5). Some resonant peaks at 2.3, 5.9, and 9.4 GHz are observed, but the Q values are low ($\leq$ 20) so that the contribution to the overall impedance is small. The cause of these are not specifically known, but several possible candidates are obvious and they will be investigated.

The result transformed into the TD is shown in Fig.3, including the S21 for the valve with no RF screen. The top curve is for the reference chamber, the middle curve is the valve with the RF screen, and the bottom curve is without the RF screen.

Fig.4 shows the relation of k and σ (the bunch length). The bunch length is varied by changing the frequency span over which the data is recorded. The loss parameter (k) is higher for the shorter bunch and much larger for the valve w/o the RF screen. Table 3 summarizes all the loss parameter measurements.

V. CONCLUSION AND NEAR FUTURE PLAN

Several general conclusions can be made:
-The RF-screened valve has a factor of five improvement over a standard valve and the previous TD measurements with the real-time pulse were correct, but had too a low resolution for the small-k.
-Further measurements will be done on the photon absorber, the 352-MHz cavity, the insertion device, the transition section between various size vacuum pipes.
-It is also planed to determine the type of the RF screen on the photon absorber, the experiment on the aperture coupling is under way and the computer simulation was done [5].

VI. ACKNOWLEDGEMENTS

The authors would like to thank Dr.F.Caspers at CERN for stimulating discussions. Also thanks must be given to D.F.Voss, T.Smith, J.Bulmahn, B.Stephenson, and E.Wallace for their technical support.

VII. REFERENCES

[1] L.C.Teng, "Impedance and Current Limitations, DOE Review of APS Project at Argonne Nat'l Lab., March 6-8,1990.

[2] W.Chou, Y.Jin, "Impedance Studies-Part 4: The APS Impedance Budget", ANL-LS-115, 1988; "Impedance and Bunch Lengthening in the APS," in Proc. of the Impedance and Bunch Instability Workshop, (1990)

[3] F.Caspers, "Beam Impedance Measurement By the Wire Method using a Synthetic Pulse Technique," IEEE-Trans. on Nuclear Science, V NS-32, 1914 (1985).

[4] R.L.Kustom, et.al, "RF Impedance Studies of a Beam Chamber and Longitudinally Slot-Coupled Vacuum Pumping Antechamber," IEEE Particle Accelerator Conf., 1304 (1987).

[5] Y.Chae and L.C.Teng, "Study of Loss Factor for Slots in the Vacuum Chamber," in this proceedings.

TABLE 1 APS impedance budget.

Component	Number	Impedance Z/n (Ω)	Zt (MΩ/m)
1. RF Cavity (HOM)	15	0 2	0.02
2. Transition between chamber & ID section	34	0.03	0.06
3. Transition between chamber & rf section	3	0.1	0.003
4. Crotch absorber	160	0.01	0.002
5. Shielded bellows	160	0.04	0 007
6. Shielded transitions	80	0.02	0.003
7. Flange full-penetration weldment	480	0.01	0.008
8. Elliptical tube weldment	80	1E-3	1E-3
9. Shielded end conflat	80	1E-3	1E-3
10. Valve	80	0.01	0.01
11. Beam position monitor	360	0.02	
12. Transition between chamber w. &-w/o ante chamber	120	3E-3	1E-3
13. Resistive wall		0.01	0.01
14. Space charge		1E-5	0.03
15. Others (kickers, bumpers, ion pump ports, etc.)		0.3	
Subtotal		1	0.15
Budget (subtotal X 2)		2Ω	0.3 MΩ/m

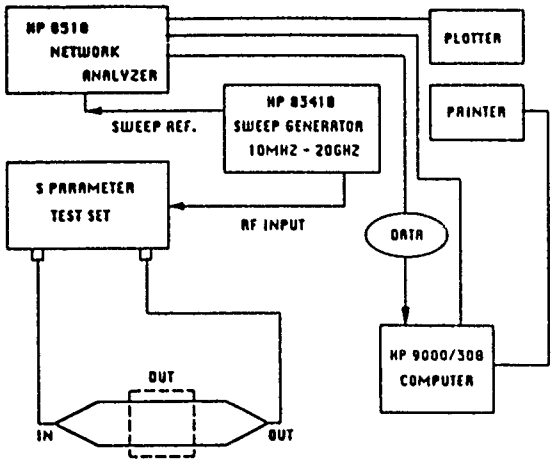


Fig.1 Experimental setup.

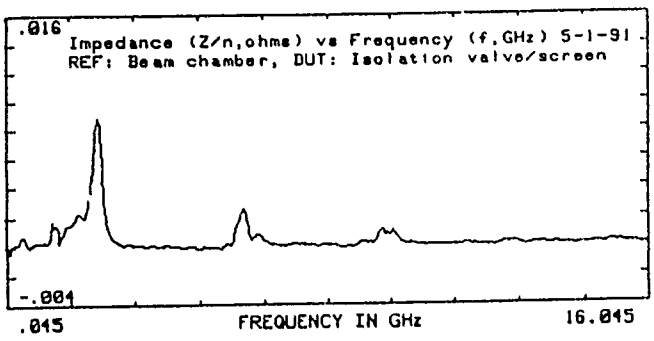


Fig.2 The normalized impedance, $Z(\omega)/n$, of the isolation valve with the RF screen.

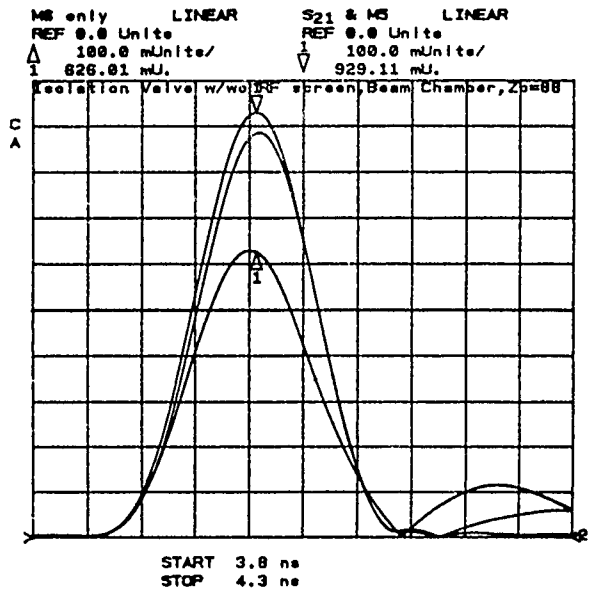


Fig.3 The TD transform of the S21 of DUT: the top curve is the reference chamber, the middle is the RF-screened valve, the bottem is the regular valve.

Frequency (GHz)	0-16	0-10	0-5	2-5
Bunch Length (σ: cm)	1.2	1.8	5.8	9.6
Bunch Length (σ: ps)	37.5	60	192	320
K (Valve w RF)	0.023		0.014	0.008
K (Valve wo RF)	0.123	0.059	0.042	0.039
K (Ante-chamber)	0.002		0.001	
Error in K	6E-04		3E-04	

Table 3. Loss parameters of the various DUTs in frequency spans.

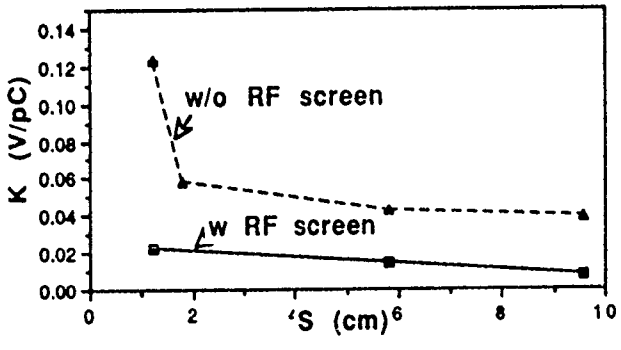


Fig.4 The loss parameter of the isolation valve, k, vs the bunch length, σ.

Measurements on Prototype Cavities (352 MHz) for the Advanced Photon Source (APS) *

J. F. Bridges, J. M. Cook, R. L. Kustom, J. J. H. Song,
Advanced Photon Source
Argonne National Laboratory
Argonne, IL 60439

Abstract

Measurement of the higher order modes of a prototype single-cell 352-MHz cavity for the APS 7-GeV Storage Ring will be presented and discussed. A 352-MHz cylindrical pill-box cavity made of aluminum has been built to test and verify the measurement instruments using the analytically-derived resonant frequencies of both the fundamental and higher-order modes. A cavity made from solid copper was built according to dimensions derived from URMEL program runs. The longitudinal and transverse impedances of the first several higher-order modes have been measured using various shaped metal beads.

I. Introduction

The prototype all-copper cavity for the APS storage ring has been measured for higher-order modes (HOMs) and the data has been categorized by bead-pulling techniques. Those modes which may interfere with beam stability [1] have been damped with low-power devices.

HOM measurements have been previously made on a cylindrical cavity with the E_{010} mode at 351.9 MHz, the accelerating mode for the APS 7-GeV storage ring [4, 5]. This was done to check the instrumentation and to familiarize ourselves with the technique by using a cavity shape that can be analytically solved for higher modes. The accelerating cavity shape is basically spherical with a rounded, slightly reentrant beam pipe (see Figure 1). However the aspect ratio and volume are about the same as in the previously studied cylindrical cavity, therefore the frequency and Q of the modes are also about the same.

II. Method

We used standard bead perturbation techniques [2, 3, 4], primarily with metallic cylinders 25.4mm long by .8mm diameter, to measure the longitudinal E-field for monopole and dipole modes. Such needle-like objects do not significantly perturb the magnetic field or the transverse component of the electric field.

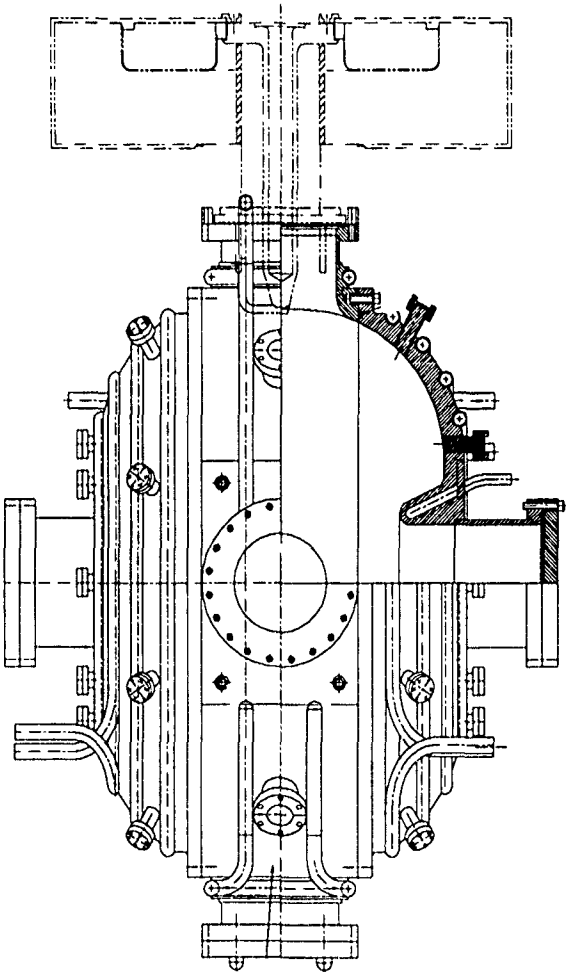


Figure 1

The perturbation of the longitudinal component $\vec{E}_{\|}$ of the electric field is related to the phase shift ϕ of the resonance by

$$-\tan\phi = \frac{Q}{W} 3\Delta V \varepsilon_0 F_1 |\vec{E}_{\|}|^2/2 \qquad (1)$$

(equation (18) on page 8 of [3]) where Q and W are the quality factor of and energy stored in the mode, and ΔV is the volume occupied by a prolate spheroidal perturber of high aspect ratio oriented parallel to $\vec{E}_{\|}$. Then

$$R_{shunt} = \frac{2|\int_0^L (-\tan\phi)^{\frac{1}{2}} e^{i\omega_0 z/c} dz|^2}{3\omega_0 \varepsilon_0 F_1 \Delta V}, \qquad (2)$$

*Work supported by the U. S. Department of Energy, Office of Basic Sciences, under the Contract W-31-109-ENG-38.

U.S. Government work not protected by U.S. Copyright.

is obtained by solving (1) for $\vec{E}_{\|}$ and substituting it into the general equation $R_{shunt} = |V|^2/P$ where $P = \omega_0 W/Q$ is the mean power dissipated and $V = \int_0^L \vec{E}_{\|} e^{i\omega_0 z/c} dz$ is the accumulated voltage difference experienced by a positron during its passage from $z = 0$ to $z = L$.

The form factor F_1 was adjusted by calibration against the analytically known fields and impedances in the right-circular cylindrical cavity, dimensioned so that its resonant frequencies corresponded to those of the prototype cavity.

The analytic value for the R/Q of the fundamental mode in our cylindrical cavity is 209Ω, with no transit time factor. Our measured value was, instead, 319Ω. In agreement with Jacob [3] we attribute the difference to the greater amount of metal contained in a cylindrical needle than in an ellipsoidal one of the same length and width. In the "crudest approximation" (see page 319 of [2]) the frequency shift depends only on the volume of the perturber. The volume ratio between cylinders and spheroids of the same dimensions is 3/2, so we have used that ratio as our calibrating correction factor throughout. The resulting calculations of longitudinal and transverse shunt resistances from measured data agreed closely with the same values calculated by URMEL (see Tables 2 and 3 in [1]).

For dipole modes the longitudinal shunt resistance is zero along the axis of the cavity. By measuring two more longitudinal shunt resistances, off axis but close to and parallel to it, and noncollinear with it, we can get an approximation to the transverse gradient of the longitudinal shunt resistance at the axis. From this, by the Panofsky-Wenzel Theorem, we determine the transverse mode impedance as on page 6 of [3].

III. Data

Data was recorded using an 8510 network analyzer and an HP Vectra computer with our own software. Measurements of the phase deviation of S21 were recorded as the bead was shifted along parallel to the axis of the cavity. Two small loops on the perimeter of the cavity were used as the input and output ports for both the Q and the perturbation measurements. Some data was obtained by driving the cavity through the full-size, high-power loop which was rotated so as to have 50Ω input impedance at the fundamental frequency, 351.9 MHz.

Ten modes were calculated to have impedances that will cause coupled-bunch instabilities near or below the 300 mA positron current which is the design goal of the APS [1]. These modes were measured and are listed in Table 1 along with the impedances calculated using URMEL [1].

Table 1.

Frequency (MHz)	R (Normal MΩ)	Threshold Current (mA)	Damping Ratio (dB)
536.7	1.67	80	23.
588.7	13.6	81	9.
761.1	25.6	43	30.
922.5	0.62	130	-
939.	0.23	340	40.
962.	6.1	180	-
1017.4	2.6	320	13.
1145.1	2.7	80	5.
1210.8	.49	80	-
1509.1	0.36	80	20.

Figure 2 shows the phase shift data for the fundamental mode 351.9 MHz and Figure 3 shows the E_{013} mode at 1210 MHz. These two graphs are typical of all the data, although some modes were noisy and had to be averaged to increase the signal-to-noise ratio.

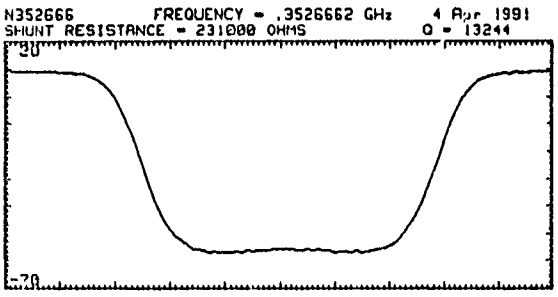


Figure 2

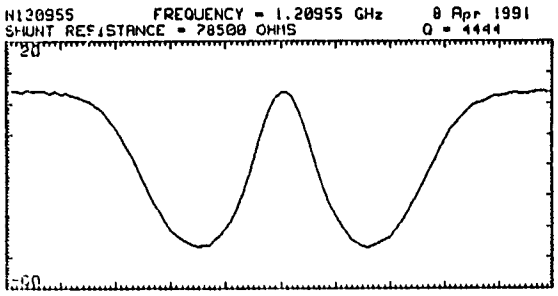


Figure 3

IV. Results

We have measured the modes in Table 1, and significantly damped most of them whose instability thresholds were below 300mA. There are two sets of such modes: those which the magnetic field on the mid-plane coupled to the fundamental drive loop, and those with an E-field perpendicular to the beam at the circumference at the mid plane.

The loop-coupled modes were damped by using a 50Ω resistor on the input port to the loop (see Figure 4) .

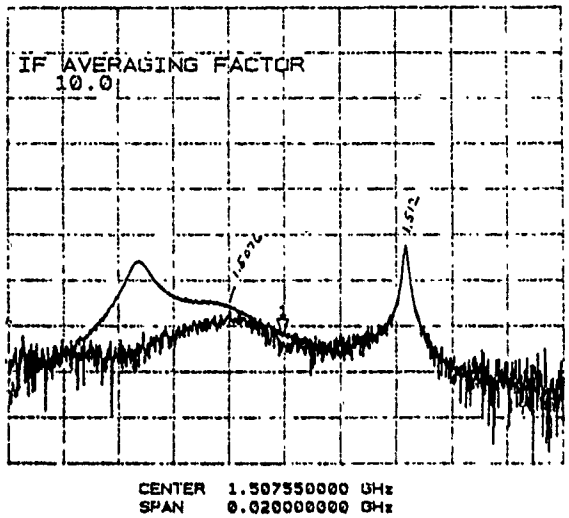


Figure 4

In the final design these modes will be damped by lossy material inserted in the input waveguide near the drive loop. This arrangement will also prevent these frequencies from returning to the splitters, circulator, and eventually the klystron, which are not meant to handle them. Those three modes not damped by the driving loop will be further investigated.

The E-field modes were damped between a factor of 13 and 34 dB using a resistance which was optimized for maximum damping at 940 MHz (see Figure 5).

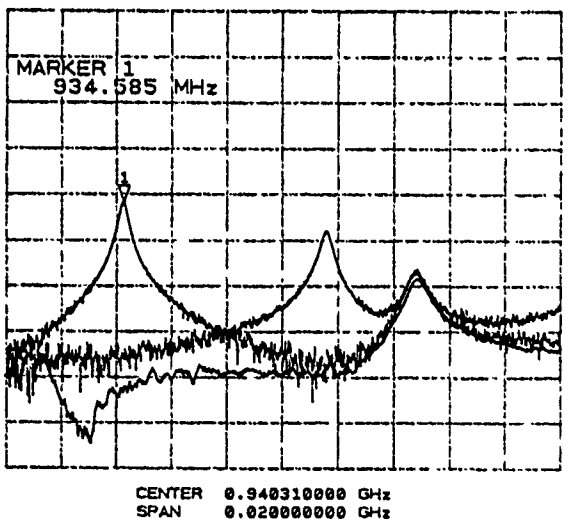


Figure 5

The marker is on the undamped resonance peak. The E-field probes shift the peak about 7MHz higher when inserted into the cavity. Resistively loading the probes damps the resonance about 40dB. (The peak at about 956 MHz is essentially unchanged.)

V. Future Work

We will design and test a magnetically coupled damper for those modes not damped by the drive loop (i.e., 923, 962, and 1211 MHz).

We intend to measure two more sets of HOMs: monopole and dipole modes with instability thresholds between 300 and 600 mA, and a few of the lower quadrupole modes.

We also intend to investigate damper design in more detail, in particular to try to design a damper that will be conjugately matched to the bothersome modes and that will be optimized using the criteria that the damping ratio of each of the modes will raise the instability threshold currents to the same value for all modes. This value might be arbitrary, say 1A, or it might be set at the average of those thresholds between 300 and 600 mA depending on the number in that interval and the ease of damping.

We intend to lengthen the cavity by using shims of copper to learn how the HOMs shift in frequency. Based on this information we may design the cavities to have different shapes in order to spread the HOMs and thereby reduce cavity-bunch instabilities [1].

VI. Acknowledgements

We thank L. Emery and Y. Kang for useful discussions during the writing of this report, and T. Smith, D. Voss, and L. Stephenson for making the measurements on which it is based.

References

[1] L. Emery, "Coupled-Bunch Instabilities in the APS Ring," in *Proceedings of the 1991 Particle Accelerator Conference*, San Francisco, CA, May 1991.

[2] R. F. Harrington, *Time-Harmonic Electromagnetic Fields*, New York: McGraw-Hill Book Company, Inc., 1961.

[3] J. Jacob, *Measurement of the higher order mode impedances of the LEP cavities*, ESRF-RF/88-02, European Synchrotron Radiation Facility, Grenoble, 1988.

[4] R. Kustom, J. Bridges, W. Chou, J. Cook, G. Mavrogenes, and G. Nicholls, "Analysis of RF Modes in the ANL APS Vacuum Chamber Using Computer Simulation, Electron Beam Excitation, and Perturbation Techniques," in *Proceedings of the 1989 IEEE Particle Accelerator Conference*, Chicago, IL, March 1989, pp.1755-1757.

[5] G. Nicholls, J. Bridges, J. Cook, and R. Kustom, "Status Report on the Radio Frequency Accelerating System of the APS at Argonne," in *Proceedings of the 1989 IEEE Particle Accelerator Conference*, Chicago, IL, March 1989, pp.217-219.

Calculation of Required Tuner Accuracy and Bandwidth With and Without Fast Feedback

S.R. Koscielniak
TRIUMF, 4004 Wesbrook Mall, Vancouver, B.C., Canada V6T 2A3

Abstract

An expression for the resonance-controller time constant is given in terms of the allowed tuner error and rate of frequency sweep. A cavity tuner-control with this time-constant guarantees the resonance program is tracked to the desired accuracy. Expressions are given for the permissible tuner frequency error, in terms of the reactive to resistive power ratio, for an accelerating cavity operating with or without fast feedback. An expression is given for the resonance frequency sweep rate for arbitrary drive frequency program and relative beam-loading. The results are applied to the TRIUMF-KAON [1] Accumulator and Booster rings. The constraint imposed on the time constant by accumulation in the former is not severe; a passband of a few hundred hertz is sufficient. However, it is found that in the absence of fast feedback the Booster tuner control must have a passband that extends to 30 kHz. This paper is an abridged version of an unpublished design note [2].

I. Controller Time Constant

We suppose that the cavity resonance frequency is to follow a predetermined program (given by equation 2 below) to within some accuracy $\Delta\omega_0$. In the general case of an arbitrary frequency tuning rate $\dot{\omega}_0(t)$, and varying allowed tuning error $\Delta\omega_0(t)$, the controller time constant required to track the frequency program is:

$$\Delta T \leq \left|\frac{\Delta\omega_0(t)}{d\omega_0/dt}\right|_{\min} . \tag{1}$$

The bandwidth of the tuner control is the inverse of ΔT The value of $\Delta\omega_0(t)$ depends on how much reactive power can be delivered, as shown below.

II. Resonance Program

Let ω_0 = resonance frequency, and ω = drive frequency. Let I_b = beam current component at the radio frequency, and ϕ_b the rf phase of the bunch centre. Let $I_0 = V/R$ be the gap voltage divided by cavity shunt resistance, and Q = cavity quality factor. The resonance frequency program $\omega_0(t)$ is given by:

$$\frac{\omega_0^2 - \omega^2}{\omega\omega_0/Q} = \frac{I_b}{I_0}\cos\phi_b \equiv \tan\Psi_0 . \tag{2}$$

Here Ψ_0 is the tuning angle, and $\tan\Psi_0$ is the beam loading ratio. For brevity, this ratio will be denoted ρ.

III. Allowed Tuning Error

From (2) we may find the relation between incremental changes $\Delta\Psi_0$ and $\Delta\omega_0$:

$$\sec^2\Psi_0\Delta\Psi_0 = \left[\frac{2Q}{\omega} - \frac{\tan\Psi_0}{\omega_0}\right]\Delta\omega_0 . \tag{3}$$

Now from (2) provided $\rho \ll 2Q$

$$\omega_0 \approx \omega\left[1 + \frac{\rho}{2Q} + \frac{1}{2}\left(\frac{\rho}{2Q}\right)^2\right] .$$

$$\text{Hence} \quad \frac{\Delta\omega_0}{\omega_0} \approx \frac{\sec^2\Psi_0}{2Q}\Delta\Psi_0 . \tag{4}$$

Expressions for $\sec^2\Psi_0\Delta\Psi_0$, consistent with accurate generation of the accelerating voltage across the cavity gap, are given in reference [2]. We suppose that the cavity phase and amplitude controls have bandwidth much greater than the cavity tuner and its power supply, so that the generator current exactly compensates the tuning error $\Delta\Psi_0$. Then, as shown in the appendix,

$$\sec^2\Psi_0\Delta\Psi_0 \approx (-)\tan\Delta\phi_g[1 + (I_b/I_0)\sin\phi_b] .$$

Here $\Delta\phi_g$ is the phase difference between the generator current and the gap voltage. $\mathrm{Tan}\Delta\phi_g$ happens to be the ratio of reactive power to resistive power delivered to the cavity. The maximum permissible tuning error occurs when maximum allowable reactive power is delivered by the amplifiers and power tube. Thus

$$\sec^2\Psi_0|\Delta\Psi_0| = (1 + \tan\Psi_0\tan\phi_b)\left[\frac{\text{reactive power}}{\text{resistive power}}\right]_{\max} \tag{5}$$

Combining relations (4) and (5) gives the permissible tuning error :

$$\frac{\Delta\omega_0}{\omega_0} \approx \frac{(1 + \tan\Psi_0\tan\phi_b)}{2Q}\left[\frac{\text{reactive power}}{\text{resistive power}}\right]_{\max} . \tag{6}$$

This is for the case of an rf-cavity in isolation, as treated in the Appendix. If fast feedback [3] around the amplifier is used, then the expression is modified according to the loop gain $H = A_0R$.

$$\frac{\Delta\omega_0}{\omega_0} \approx \frac{(1 + H + \tan\Psi_0\tan\phi_b)}{2Q}\left[\frac{\text{reactive}}{\text{resistive}}\right]_{\max} \tag{7}$$

Since H can be large compared with $\tan\Psi_0\tan\phi_b$, there can be a significant increase in the allowed tuning error

0-7803-0135-8/91$01.00 ©IEEE

This happens, not because feedback alters the time constant of the tuner control, but because feedback makes the gap voltage insensitive to the exact tuning angle.

So far we have assumed that no error is allowed in the cavity voltage. In fact there is only a small gain in the allowed tuner error unless large voltage errors can be tolerated. If the reactive-to-resistive power ratio is unity, and the gap voltage has errors $\Delta\phi_V$ and ΔV, then

$$\sec^2\Psi_0\Delta\Psi_0/\tan\Delta\phi_g \approx$$

$$1 + \frac{I_b}{I_0}\left[\sin\phi_b + (\Delta\phi_V + \Delta V/V_T)(\cos\phi_b - \sin\phi_b)\right] . \quad (8)$$

IV. Resonance Frequency Sweep Rate

Solve relation (2) for ω_0 in terms of $\omega(t)$ and $\rho(t)$. For the case $\rho \ll Q$ we find the approximation $\omega_0 \approx$
$\omega[1 + \rho/2Q]$. Take the time derivative, and neglect terms ρ/Q as insignificant, to give:

$$\dot\omega_0 \approx \dot\omega + \frac{\omega}{2Q}\dot\rho = \omega_\infty\left[\frac{d\beta}{dt} + \frac{\beta}{2Q}\frac{d\rho}{dt}\right] . \quad (9)$$

ω_∞ = drive frequency if $\beta \equiv$ unity; and β is the particle-beam speed divided by the speed of light.

$$\text{Now from (2)} \qquad \frac{1}{\rho}\frac{d\rho}{dt} = \left[\frac{\dot I_b}{I_b} - \tan\phi_b\dot\phi_b - \frac{\dot I_0}{I_0}\right] . \quad (10)$$

Equations (1), (6), (7), (9) and (10) are sufficient to determine the time constant ΔT.

V. KAON Booster

The Booster is a fast-cycling synchrotron with biased sinusoidal magnet excitation. The injection and extraction energies are 0.5 GeV and 3 GeV, respectively. Detailed numerical evaluations would be needed to find the minimum value ΔT_{min} during the acceleration cycle. We will be content with a good estimate, and guess that the ΔT_{min} occurs near mid-cycle. The magnet cycling angular frequency is Ω, assuming single frequency excitation; and the time range is $0 \le \Omega t \le \pi$. We assume all quantities vary in a sinusoidal manner, that is:

$\beta(t) = \check\beta + (1\text{-}\cos\Omega t)(\hat\beta - \check\beta)/2$
$I_b(t) = \check I_b + (1\text{-}\cos\Omega t)(\hat I_b - \check I_b)/2$, and likewise $I_0(t)$.
$\phi_b(t) = (1\text{-}\cos2\Omega t)\dot\phi_b$, so $\dot\phi_b$ = zero at mid-ramp.

We shall denote the value of x at mid-ramp by $\bar x$, an average value by $\langle x\rangle$, and the change from start to finish of ramping by Δx. Substituting the above time variations into equation (9) gives:

$$\dot\omega_0 \approx \omega_\infty\frac{\Omega}{2}\left\{\Delta\beta + \frac{\bar\beta.\tan\bar\Psi_0}{Q}\left[\frac{\Delta I_b}{\langle I_b\rangle} - \frac{\Delta I_0}{\langle I_0\rangle}\right]\right\}$$

For the KAON Booster ring, the change in relativistic β is substantial: $\Delta\beta \sim 0.23$; whereas $(\tan\Psi_0/Q) < 0.006$ so we may drop the second term leaving $\dot\omega_0 \approx \omega_\infty\Delta\beta\Omega/2$. Finally, we may estimate the control time-constant to be $\Delta T =$

$$\frac{\Delta\omega_0}{\dot\omega_0} \approx \frac{(1 + H + \tan\bar\Psi_0\tan\bar\phi_b)}{\bar Q\Omega}\frac{\langle\beta\rangle}{\Delta\beta}\left[\frac{\text{reactive}}{\text{resistive}}\right]_{max} .$$

Substitute values appropriate to the Booster: $\langle\beta\rangle = 0.854$, $\Delta\beta = 0.234$, $H = 65$, $\bar Q = 4000$, $\tan\bar\Psi_0 = 16$, $\tan\bar\phi_b = 1/\sqrt{3}$, and $\Omega = 2\pi \times 50$ Hz. Arguably the power ratio can rise, for short periods, as high as unity. In this case the *time constant* is $\Delta T = 0.2$ milli-second, which means the controller must pass frequencies up to 5 kHz with only -3 dB attenuation.

If the cavity were not equipped with fast feedback around the amplifier, then $H = 0$ and the time constant is significantly smaller : $\Delta T = 30$ micro-second which is equivalent to a 30 kHz passband.

Of course, if less reactive power is allowed than the unity ratio assumed here, then the controller time constant must diminish proportionately.

VI. KAON Accumulator

The Accumulator is a storage ring. Current is accepted from a cyclotron by charge-exchange multi-turn injection for 2×10^4 turns, and transfer is bucket-to-bucket so that the beam never debunches. The synchronous phase angle is zero so that $\tan\phi_b = 0$. Consequently, there is no change in drive frequency ($\dot\omega = 0$) and the resonance frequency program derives entirely from beam-loading. Borrowing from equations (9) and (10) the tuning rate becomes

$$\dot\omega_0 \approx \frac{\omega}{2Q}\dot\rho = \frac{\omega_\infty\beta}{2Q}\frac{I_b}{I_0}\left[\frac{\dot I_b}{I_b} - \frac{\dot I_0}{I_0}\right] . \quad (11)$$

The gap voltage is constant in time and so $\dot I_0 = 0$. In this case, dividing equation (4) by (11) gives :

$$\frac{\Delta\omega_0}{\dot\omega_0} \approx \frac{\sec^2\Psi_0}{(\dot I_b/I_0)}\Delta\Psi_0 .$$

In the Accumulator the beam current follows a linear ramp $I_b(t) = \check I_b + \Delta I_b(t/T_r)$, where T_r is the duration of beam filling. Substituting from equation (9), the controller time constant becomes

$$\Delta T_{min} = \frac{I_0(1 + H)}{\Delta I_b}\left[\frac{\text{reactive power}}{\text{resistive power}}\right] \times T_r .$$

For the Accumulator, values are : $I_0 = 0.34$ A, $\Delta I_b = 2.5$ A, $H = 20$ and $T_r = 20$ ms ; giving $\Delta T_{min} = 58$ ms for unity power ratio. If there is no fast feedback ($H = 0$) the *time constant* becomes 2.7 ms, implying a -3 dB frequency of 370 Hz. This is the minimum recommended value, since one must also consider the need to periodically reset the tuner to the zero beam-load frequency.

VII. Conclusion

The constraints on tuner-control imposed by A ring accumulation are likely much less severe than those deriving from beam-injection transient compensation and periodic tuner resetting.

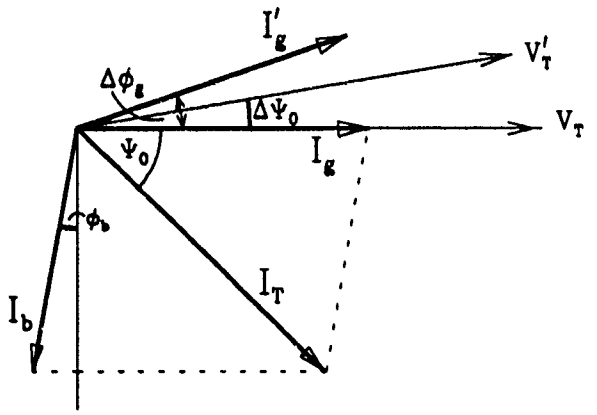
The B ring tuner-control is likely dominated by the substantial change in radio frequency (46-61 MHz), and is probably not feasible without 'fast feedback' around the amplifier.

Appendix: Effect of Tuner Error for Cavity

The conventions used for the phasor diagram follow Pedersen [4]. The cavity-gap voltage (V) lies along the real axis of the complex plane, as does the generator current (I_g), and the beam image-current vector is given by:

$$I_b e^{-j(\phi_b+\pi/2)} = (-)I_b[\sin\phi_o + j\cos\phi_b].$$

All quantities are assumed sinusoidally varying according to $e^{j\omega_c t}$ with ω_c the drive frequency.



A. Steady-State Conditions

The cavity is detuned by an amount $\tan\Psi_0 = 2Q(\omega_0-\omega_c)/\omega_0$. We use the linearized approximation for the cavity impedance: $R\cos\Psi_0 e^{j\Psi_0}$. The total desired voltage is:

$$V_T = I_0 R = \frac{R}{1-j\tan\Psi_0}\left[I_b e^{-j(\phi_b+\pi/2)} + I_g e^{j\phi_g}\right] . \quad (A1)$$

Hence we find the steady-state values I_g and Ψ_0 in terms of I_b and ϕ_b by taking the real parts

$$I_g\cos\phi_g = I_0 + I_b\sin\phi_b \quad (A2)$$

and taking the imaginary parts

$$I_0\tan\Psi_0 = I_b\cos\phi_b - I_g\sin\phi_g . \quad (A3)$$

To minimize the generator current (I_g) we put $\phi_g \equiv 0$.

B. Small Perturbation

Suppose the tuning angle changes by a small amount $\Delta\Psi_0$. To compensate the change ($\Delta V_T e^{j\Delta\phi_V}$) in the total voltage, the I_g vector has to change in magnitude and phase to $I'_g = (I_g + \Delta I_g)e^{j\Delta\phi_g}$ as shown in the phasor diagram. The beam current vector does not move. Let us assume the generator compensation is perfect so that old and new voltages are identical. Hence:

$$R\cos\Psi_0 e^{j\Psi_0}[I_b e^{-j(\phi_b+\pi/2)} + I_g e^{j\phi_g}] =$$

$$R\cos(\Psi_0+\Delta\Psi_0)e^{j(\Psi_0+\Delta\Psi_0)}[I_b e^{-j(\phi_b+\pi/2)}+(I_g+\Delta I_g)e^{j(\phi_g+\Delta\phi_g)}].$$

Set $\phi_g = 0$ and solve for $\Delta\phi_g$ to give $\tan\Delta\phi_g = Y/X$ with

$$\begin{aligned} Y &= [1-\tan\Psi_0\tan\Delta\Psi_0]I_b\cos\phi_b \\ &\quad -[I_b\cos\phi_b + (I_g - I_b\sin\phi_b)\tan\Delta\Psi_0] \\ X &= [1-\tan\Psi_0\tan\Delta\Psi_0]I_b\sin\phi_b \\ &\quad +[(I_g - I_b\sin\phi_b) - I_b\cos\phi_b\tan\Delta\Psi_0] . \end{aligned}$$

Use the steady state conditions to eliminate I_g and $I_b\cos\phi_b$, to give :

$$\tan\Delta\phi_g = \frac{\tan(\Psi_0)-\tan(\Psi_0+\Delta\Psi_0)}{1+(I_b/I_0)\sin\phi_b} .$$

Expand $\tan(\Psi_0+\Delta\Psi) \approx \tan\Psi_0 + \sec^2\Psi_0\Delta\Psi_0$ as a Taylor series. To first order in $\Delta\Psi_0$, we find

$$\tan\Delta\phi_g = \frac{(-)\sec^2\Psi_0}{1+(I_b/I_0)\sin\phi_b}\Delta\Psi_0 . \quad (A4)$$

Note that because $\sec^2\Psi_0$ can be very large (maybe 10^4), $\tan\Delta\phi_g$ can be large even though the tuner error is small $|\Delta\Psi_0| \ll 1$. Consequently, it is correct to retain the tangent term rather than replace with the first order term $\Delta\phi_g$.

C. Significance of $Tan\Delta\phi_g$

Since we have insisted there is no error in the gap-voltage magnitude or phase,
$\frac{1}{2}V(I_g+\Delta I_g)\sin\Delta\phi_g$ is the reactive power, and
$\frac{1}{2}V(I_g+\Delta I_g)\cos\Delta\phi_g$ is the resistive power.
Hence the ratio of reactive to resistive power is simply $\tan\Delta\phi_g$. The sign of $\tan\Delta\phi_g$ indicates that when $\Delta\Psi_0 > 0$ the generator current lags behind the gap voltage, and when $\Delta\Psi_0 < 0$ it leads.

VIII. References

[1] *Kaon Factory Study Accelerator Design Report*; TRIUMF, Vancouver, B.C., 1990.

[2] S.R. Koscielniak: "Calculation of Required Tuner Accuracy and Time Constant"; TRI-DN-90-K126.

[3] D. Boussard: "Control of Cavities with High Beam Loading"; CERN SPS/85-31 (ARF).

[4] F. Pedersen: "Beam Loading Aspects of TRIUMF KAON Factory RF Systems"; TRI-DN-85-15.

Analysis of Eddy Currents in the Walls of the Ferrite Tuned RF Cavity for the TRIUMF Kaon Factory Booster Synchrotron

I. B. Enchevich, Sofia University, Bulgaria,
M. J. Barnes and R. L. Poirier, TRIUMF

Abstract

In the perpendicular biased ferrite tuned cavity of the proposed TRIUMF Kaon Factory Booster Synchrotron, magnetizing flux passes through the cavity walls. If special care is not taken to minimize eddy current loss in the walls, the dissipated power would be excessive and the magnetic fields set up by the eddy currents would disturb the magnetic field being applied. By electrically isolating the cooling structure from the cavity walls and introducing slots in the walls it is possible to bring to an acceptable level both the power loss and the maximal temperatures. Based on the measurements, an analytical model – essentially 3D – was derived and the eddy currents were predicted using the circuit analysis program PSpice. The calculated surface current and power distribution agree with measurements. PSpice can now be used to determine the effect of design changes on the eddy current and power distribution.

I. Introduction

The rf cavity for the TRIUMF Kaon Factory Booster Synchrotron requires a frequency swing of 46 MHz to 61 MHz at a repetition rate of 50 Hz [1]. This will be accomplished using a tuner containing yttrium garnet ferrite where the magnetizing bias field is perpendicular to the rf magnetic field. The ac magnetizing flux passes through the walls of the resonator and special care must be taken to minimize the induced eddy currents [2].

In order to remove the heat resulting from rf and eddy current losses in the cavity walls, and rf losses in the ferrite, the construction of the cavity includes large stainless steel cooling wheels and a cylindrical copper cooling jacket [2]. The power dissipation due to ec losses in the cavity is determined by the relationship between induced emf's, conductivity of materials employed and the geometric configuration.

Previously PE2D has been used to evaluate eddy current loss in the different sections of the cavity [3]. Since electromagnetic software capable of 3D eddy current analysis was not available at TRIUMF PSpice was used to simulate the rf membrane and cooling jacket in 3D. In order to check the quality of the equivalent circuit, 2D simulations were initially performed and compared with the results of measurements. The predictions compared well, and hence a 3D equivalent circuit was simulated. The PSpice software is very flexible: the equivalent circuit is set up such that it is relatively easy to make changes (e.g., changing resistivity and introducing slots).

0-7803-0135-8/91$01.00 ©IEEE

II. Theory & Measurements

The equivalent circuit utilized is based on Faraday's and Kirchoff's laws. The Faraday law of electromagnetic induction, states that a time (t) varying magnetic flux (ϕ) induces an emf (e). In the case of axial symmetry the emf is induced uniformly along the length (ℓ) of any circle whose center lies on the axis. It follows that:

$$e = -\frac{d\phi}{dt} = \oint_0^{2\pi} \overline{E}_r \cdot d\overline{\ell} = E_r \times 2 \times \pi \times r \qquad (1)$$

hence

$$E_r = \frac{e}{2 \times \pi \times r} = -\frac{1}{2 \times \pi \times r} \times \frac{d\phi}{dt} \qquad (2)$$

where E_r represents the azimuthal density of the emf [i.e., the electric field strength] at radius r.

The above was used to obtain a first estimate of the eddy current loss in the walls of the rf resonator for the TRIUMF Kaon Factory Booster cavity [4], and also used to determine the ratings for the power supply for perpendicular biasing of the ferrite in the rf cavity.

For each given radius r the EMF_r is scaled with $EMF_{max} \times r^2/r_{max}^2$. To map experimentally the eddy currents in the ac field, the resonator walls were put in the stripped (without yoke) magnetization coil (Fig. 1).

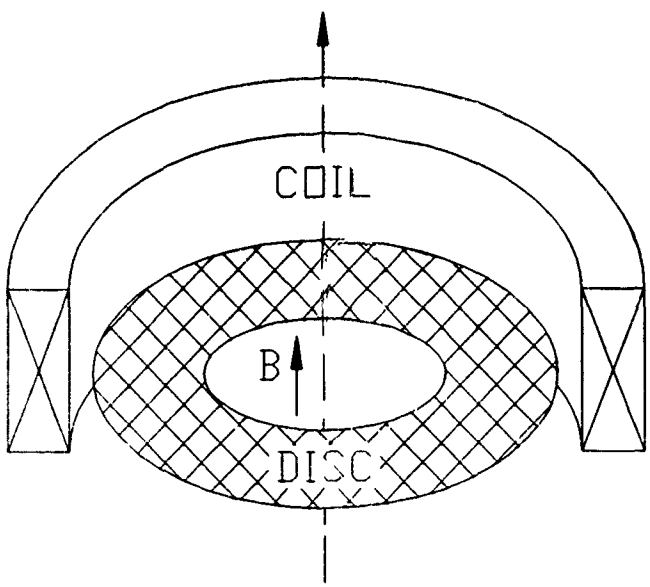


Figure 1 : Experimental set-up for measurement of current and temperature distribution

Measurements of the temperature and currents were taken

at different points for various configurations and conditions. Since the measurement loop included two parts with practically equal and opposite emf, the measured voltage was proportional to the actual surface current (Fig. 2). The temperature was measured using a calibrated thermocouple after the system had reached thermal equilibrium.

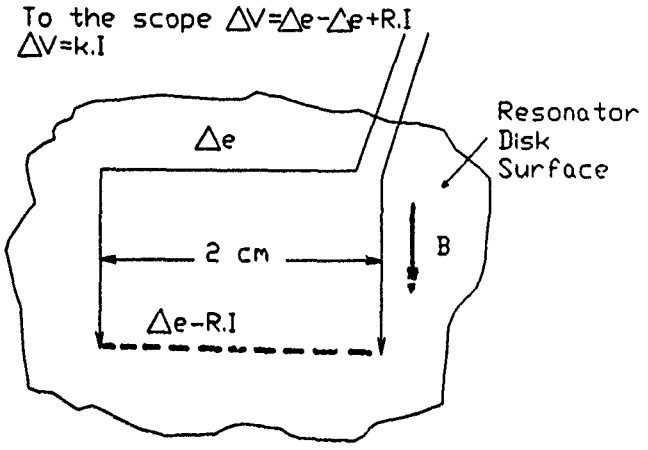


Figure 2: Measurement probe: measured voltage is proportional to surface current.

III. Equivalent Circuit

The equivalent circuit utilized for simulating eddy currents in the walls of the ferrite tuned rf cavity, represents $\frac{1}{8}$ of the disk, i.e. a sector. Each sector is sub-divided into six sub-sectors (Fig. 3). Each of the disk sub-sectors is mathematically modelled using either 2D or 3D "cells". Each cell has its cylindrical coordinates and is characterized by its azimuthal emf and its impedance in the azimuthal, radial and axial direction. The representation of a sub-sector consists of 95 cells; 5 cells for each of 19 rows (Fig. 3). PSpice [6] utilizes nodal analysis methods so it is advantageous to simulate a cell which minimizes the number of circuit nodes [7].

The equivalent circuit utilized neglects reactive components of the cell impedances, reactive coupling between the cells and the effect of skin depth upon effective resistance: this can be justified because of the low frequencies.

Power dissipation within each cell is calculated using the PSpice Analog Behavioral Model (ABM) option [6]. The cells are simulated as subcircuits; a subcircuit call causes the referenced subcircuit to be inserted into the circuit with the given nodes replacing the argument nodes in the subcircuit definition. A row of cells is defined as another subcircuit: a subcircuit representing a sub-sector is constructed from 19 calls of a row subcircuit. The equivalent circuit for a sector is constructed by calling the sub-sector subcircuit six times.

As indicated above, the values of both the azimuthal and radial resistors of a cell, as well as that of the dc voltage source, are dependent upon the geometrical position of the cell and the materials employed. Equations for cell element

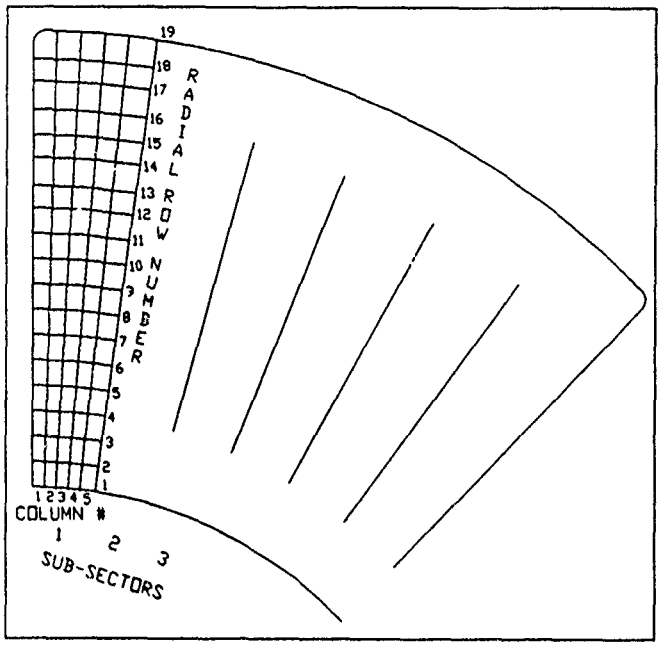


Figure 3: Representation of sector by cells

values are specified, within the equivalent circuit, using function definitions [7].

A. *Boundary Conditions*

The east end of each row of cells in a sub-sector is connected to the west end, of the same row, of an adjacent sub-sector via a resistor, e.g., the east end of row 13 of sub-sector 2 is connected to the west end of row 13 of sub-sector 3 via a resistor. The value of the 'boundary condition' resistors is defined using a Parameter Definition. An open-circuit (i.e., slot) between sub-sectors is simulated by defining the appropriate resistors to have a large value relative to other resistor values in the equivalent circuit. Similarly a high conductivity path between sub-sectors is simulated by defining the appropriate resistors to have a low value relative to other resistor values in the mathematical model.

B. *Analysis*

PSpice version 4.04p was utilized for all the simulations reported. A dc sweep is performed: a fictitious voltage source is swept through one value only, hence the bias point for the circuit is calculated only once. The output file is transferred from a p.c., where the analysis is performed, to a VAX where post processing is performed.

2D modelling of the slotted disk, using a Thevenin equivalent circuit for the cells, requires about 12 MB of memory and 34 hours of CPU time on a 20 MHz 80386 based p c. [7]. As a result of a 16 MB memory limitation with the p.c. used, and in order to simulate the cooling jacket in 3D, it was necessary to significantly reduce the number of circuit nodes, this was achieved by replacing the Thevenin equivalent azimuthal series connected voltage source and resistor by its Norton equivalent The equivalent azimuthal

current is the sum or difference of the current through the current source and parallel resistor [7].

Replacing the Thevenin equivalent by its Norton equivalent circuit resulted in a reduction in circuit memory requirements by a factor of 4.4 and a decrease in CPU time by a factor of 39. The Thevenin and Norton equivalent circuits result in virtually identical predictions for power dissipations and current flow patterns [7].

To simulate the effect of the water cooling jacket upon eddy current loss in the rf membranes, the 18th and 19th rows of each of the six sub-sectors are represented in 3D; this is achieved by modelling 7 layers of 3D cells in axial direction. The inner 17 rows of the sub-sectors are simulated in 2D, and thus their description and element values are unchanged from the 2D equivalent circuit. The values of the cell elements for the 3D analysis are again specified using equations which are coded using function definitions.

IV. Results

Scaling between the calculations and measurements can be carried out by comparing predicted cell current with the corresponding measured voltage drop [7]. Predicted radial current distribution (Fig. 4) and power loss distribution (Fig. 5) agree well with the measured temperature distribution [2,7], though it is difficult to compare them directly. Nevertheless the places where maximal temperatures are measured [2] coincide with the maximum predicted power density. For example, the maximum temperature measured occurs in the same place as the predicted value of maximum power.

V. Conclusion

For low exciting frequency PSpice can be used with confidence to predict the eddy current loss and power dissipation: the predictions should be a worst case as the equivalent circuit simulated neglects both the reactive component of induced emf and the skin depth in the walls.

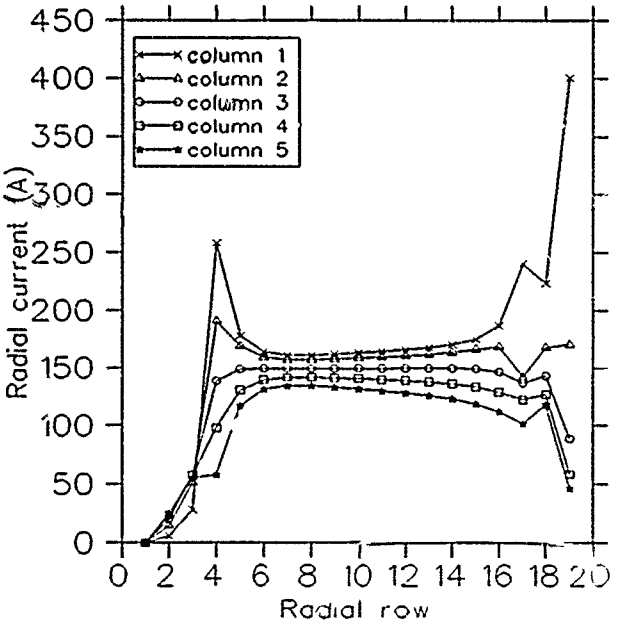


Figure 4: Predicted radial current distribution in sub-sector 1: 3D simulation

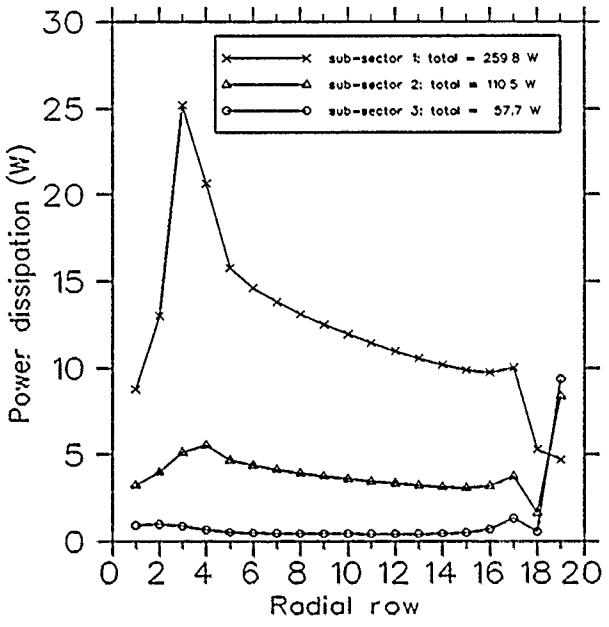


Figure 5. Predicted power loss distribution due to radial, azimuthal and axial currents in sub-sectors 1, 2 & 3: 3D simulation

VI. Acknowledgements

The authors wish to acknowledge stimulating discussions on this subject with Chris Haddock, Peter Harmer's involvement in the modelling, and representatives of MicroSim Corporation for their helpful suggestions regarding this application of PSpice.

VII. References

[1] TRIUMF-KAON Project, *KAON FACTORY STUDY*, Accelerator Design Report, p. 4–23, (1990).

[2] R. L. Poirier, *et al.*, *A Perpendicular AC Biased Ferrite Tuned Cavity for the TRIUMF KAON Factory Booster Synchrotron*, Proceedings of the European Particle Accelerator Conf., Nice, p. 988-990, (1990).

[3] C. Haddock, *et al.*, *Design of an AC Magnetic Biasing Circuit for the KAON Factory Booster RF Cavity*, 11th Intern. Conf. on Magnet Technology, Tsukuba City, Japan, (Sept. 1989).

[4] I. Enchevich, *Reference Design of the Power Supply for Bias of Frequency Modulated RF Cavity with Orthogonal Magnetized Ferrite for the Booster Ring in the TRIUMF KAON Factory* TRI-DN-87, (1987).

[5] L. I. Gutenmacher, *Electrical Models* (in Russian), AS USSR, Moscow (1949).

[6] MicroSim Corporation, *PSpice Version 4.04p, Beta Site Version* released May 1990.

[7] M. J. Barnes, *et al*, *Simulation of Eddy Currents in the Walls of the Ferrite Tuned RF Cavity using PSpice* TRI-DN-K169, (under preparation).

POWER-COMBINING AND INJECTION-LOCKING MAGNETRONS FOR ACCELERATOR APPLICATIONS*

Todd A. Treado, Todd A. Hansen, and David J. Jenkins
Varian Associates
Crossed-Field and Receiver Protector Products
Beverly, MA 01915

ABSTRACT

Single magnetrons are commonly used to drive accelerator cavities, but many applications require multiple sources which can provide phase control operating into multiple cavities. Conventional injection locking techniques provide the means to phase lock magnetrons to within 1° rms phase error but these techniques use circulators. Where weight is a concern or when high power is used, circulators are not feasible or available. We are investigating a number of approaches to achieve phase locking and power combining without the use of circulators. A series of experiments have been undertaken where two magnetrons are injection locked and power combined, first operating into a matched load, second operating into a tunable short, and third operating into X-band cavities.

I. INTRODUCTION

Multiple magnetrons were used to drive high Q linear accelerators prior to the advent of ferrite isolators [1]. It was found that either tuning or some degree of isolation was required to prevent oscillation from starting and remaining in a useless mode [2]. This tuning can be provided by an injected signal within the appropriate locking bandwidth.

In the method described here, an X-band waveguide 3 dB hybrid coupler provides the avenue for both injection locking and power combining of magnetron pairs.

The experimental configuration, shown schematically in Figure 1, has been described previously [3]. The high Q (Q_L = 1600) magnetrons were run in parallel off of the same modulator. The variable phase shifters after the magnetrons were used to optimize the relative phase relationship between the injection locked signals returning to the hybrid. Unfortunately, the phase shifters have a 0.8 dB insertion loss which reduced the system efficiency. The circulator was included to protect the TWT driver against fault conditions. Identical operation was observed with the circulator removed.

The load was connected to port 4 of the hybrid after a variable phase shifter. An E-H tuner was used to provide a load of variable impedance. All components between the magnetrons and the load were WR-90 X-band waveguide components to minimize circuit loss and VSWR.

Phase measurements of the signals incident on the load and reflected from the load were made relative to the output of the driver amplifier chain using two phase bridges.

Two cavity loads were used, each a section of WR-90 waveguide with a tunable short on one end and a quarter-wave transformer on the other. Cavity Q measurements gave the following parameters at 8.96 GHz for the overcoupled cavity: Q_o = 5700, Q_E = 4100, Q_L = 2400, coupling factor = 1.4, and cavity fill time constant = 43 ns. For the critically coupled cavity, Q_L = 2700.

* Supported by Varian IR&D Funds.

0-7803-0135-8/91$01.00 ©IEEE

II. EXPERIMENTAL RESULTS - VARIABLE Z LOAD

The impedance of a cavity changes as the cavity is filled [2]. Therefore, the effect of load impedance upon coupled power phase coherency was investigated by using an E-H tuner to vary the load impedance. The variable phase shifters prior to each magnetron were adjusted for conditions of optimum power combining and maximum isolation into a matched load. With these path lengths set, the E-H tuner was adjusted to provide a purely real impedance, referenced to the output of port 4 of the hybrid. Results of this experiment are shown in Figures 2 and 3. Figure 2 gives the rms phase error for several real load impedances as defined above. The phase error was measured well after the phase lock time and at the same time during each pulse. The rms phase error is a measure of inter-pulse phase coherence. For comparison, a typical klystron has an rms phase error of 0.2°. Figure 3 shows how the phase of the combined signal changes as the load impedance changes.

Unstable operation was observed for normalized load impedances less than unity. It should be noted that a simple change of 90° in the electrical length prior to the load translates the load impedance to a real value in the stable regime.

III. EXPERIMENTAL RESULTS - CAVITY LOADS

Operation of the magnetrons into the cavity loads at long pulse lengths is shown in Figure 4. The forward power (power out of hybrid arm 4 and incident upon the load), the reverse power (power out of hybrid arm 1 and incident upon the driver), and the reflected power (power reflected from the load) are shown at the top of Figure 4 for a 9 us pulse. The phase of the signal incident on the cavity is shown at the bottom. Once the magnetrons have filled the cavity, the phase stays constant within 0.4° for the 9 us pulse. When operated for a pulse length of 18 us, a monotonic 5° phase change was observed across the pulse. This phase change has not yet been explained.

The cavity has been filled when the reflected signal returns to a minimum as the reflected power and the power radiated from the cavity cancel one another. Complete cancellation occurs only for a critically cavity at resonance. For the data shown, the magnetrons were operating 0.5 MHz away from the cavity resonant frequency.

The spike at the beginning of the reverse power pulse correlates with the magnetron phase lock time given in Table 1. During the phase lock time the magnetrons are oscillating incoherently with respect to each other and the hybrid provides no isolation between the driver and the load. Table 1 summarizes the operating conditions for the data of Figure 4. Note that the magnetron phase lock time is greater than the cavity fill time.

IV. CONCLUSIONS

We have demonstrated that injection-locked magnetrons can be used to drive a moderate Q cavity at long pulse without a circulator with excellent phase coherency. The cavity transient impedance does not preclude the magnetrons from filling the cavity, at least when the cavity fill time is less than the magnetron phase lock time.

To more closely model an accelerator application it is still necessary to test the magnetron system without the isolation provided by the variable phase shifters. Beam loading should also be simulated. Presently, we are duplicating the magnetron system at S-band with two 3 MW magnetrons in order to phase lock two low Q, 50-100 MW HPM magnetrons without using a circulator [4].

V. REFERENCES

[1] J.C. Slater, Rev. Mod. Phys. *20*, 473,

(1948).
[2] J.C. Slater, *Microwave Electronics*, Van Nostrand, New York, 1950.
[3] T.A. Treado, et al, "Experimental results of power combining and phase-locking magnetrons for accelerator applications," IEDM Tech. Digest, San Francisco, C.A. Dec. 1990.
[4] T.A. Treado, et al, "Experimental results from the HDL-Varian injection locked, secondary emission, high power magnetron program," IEEE ICOPS Conference Record, Williamsburg, VA, June 1991.

TABLE 1 Operating Conditions for Figure 4

Frequency	= 8.964 GHz
Gain	= 13 dB
Isolation	= 23 dB
Return Loss	= 10 dB
Phase Variation	< 0.5°
Magnetron Q_L	= 1600
Cavity Q_o, Q_E, Q_L	= 5100, 4100, 2400
Magnetron Phase Lock Time	= 400 ns
Cavity Fill Time Constant	= 43 ns

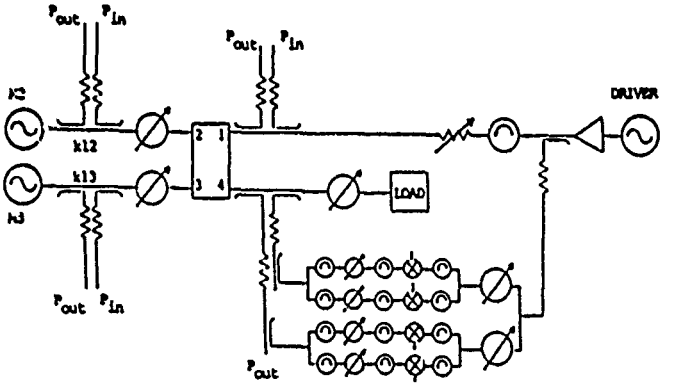


Fig 1 Schematic of Injection Locked, Power Combined Magnetron Experiment.

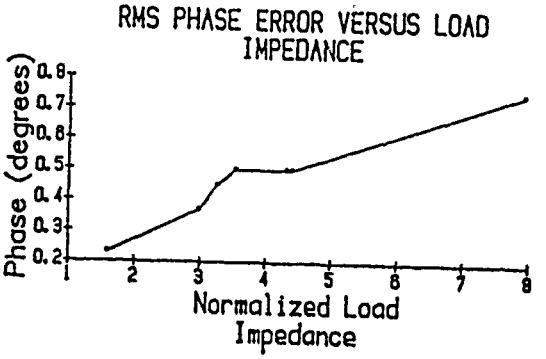


Fig 2 Combined Magnetron RMS Phase Error vs. Normalized Load Impedance.

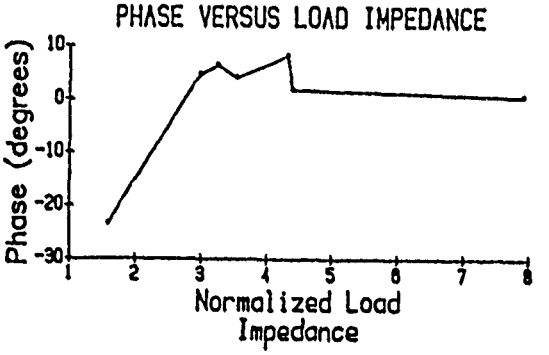


Fig 3 Combined Magnetron Phase vs. Normalized Load Impedance.

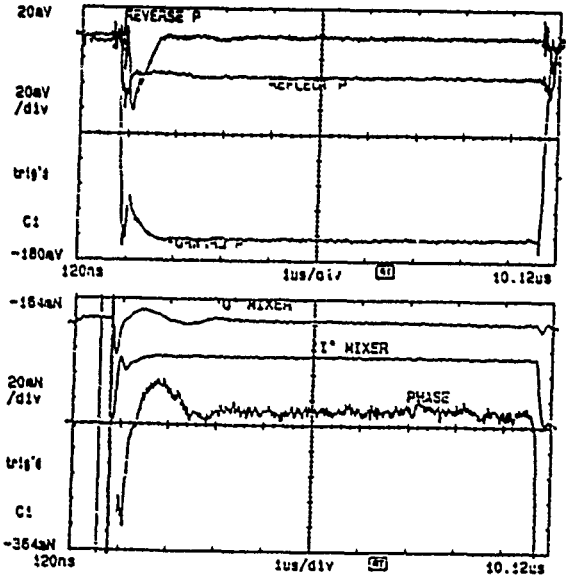


Fig 4 Cavity Filling Experiment, 9 us pulse. Phase (bottom) scale is 0.4° per division.

Performance Characteristics of the CEBAF Klystron Amplifier

E.W. McCune, R.A. Fickett
Varian Associates, Inc.
811 Hansen Way
Palo Alto, CA 94304-1031

Abstract

The Varian VKL-7811W klystron was designed specifically for powering the CEBAF accelerator. The design of this klystron was described in the 1987 Particle Accelerator Conference [1]. Since that time, the design effort was completed, engineering models were evaluated, and quantity production has begun. Klystron production is now proceeding at 13 tubes per month. The tube provides 5 kW CW output power at 1497 MHz and is permanent-magnet focused with a four-cavity interaction circuit. A modulating anode is included to permit power control. This paper reviews the klystron design features, describes the tube development program, and presents the performance characteristics measured on the final design.

I. INTRODUCTION

The design process to develop a klystron amplifier to power the CEBAF accelerator began in 1986 when the requirements became available. The general requirements are listed in Table 1. From the design alternatives considered, a four-cavity permanent-magnet-focused, liquid-cooled design was chosen. Our VKL-7811A klystron had these characteristics and was used as the design starting point. The VKL-7811A had been produced for many years as a 2-kW CW klystron at 1.8 GHz used for satellite communications service. Working from the basic 7811 design, Computer-Aided Design (CAD) techniques were employed to optimize the design for the accelerator application. The results of this effort were described previously [1] and culminated in the VKL-7811W.

Table 1
CEBAF Accelerator Klystron
General Requirements

Frequency	1497 MHz
Power	Up to 5 kW CW Controlled by modulating anode
Bandwidth (–1 dB)	4-8 MHz minimum
Gain	34 dB minimum at 5 kW output power; 2 W maximum drive power
Permanent-magnet-focused	
Water-cooled	

Two prototype models of the VKL-7811W design were fabricated and evaluated to verify the performance characteristics. After satisfactory demonstration of actual performance closely matching the predictions, Varian received an award to proceed with production of 350 units.

0-7803-0135-8/91$01.00 ©IEEE

II. DESIGN FOR MANUFACTURING

Before embarking on the manufacturing effort, the prototype design was completely reevaluated to ensure its suitability for volume production. The overall mechanical design was refined to achieve maximum simplicity and ease of assembly. Individual parts were reviewed to determine allowable variation and acceptable tolerances. Consequently, the final design was optimized for low-cost production while consistently and reproducibly achieving the performance demonstrated by the prototype tubes.

III. THE KLYSTRON DESIGN

The final design selected for production is described in Table 2. A photograph of the klystron is shown in Figure 1. The features developed during the original design effort have been maintained while incorporating enhanced manufacturability. The basic four-cavity-interaction circuit is utilized with cavity loading selected to permit a bandwidth of at least 4.8 MHz to be maintained while the output power is controlled from 5 kW CW down to 1 kW. Power control is achieved by voltage variation on an insulated anode. Beam focusing is provided by a permanent magnet, while cooling is by circulating water.

Table 2
CEBAF Klystron
Design Parameters

Operating Conditions

Beam Voltage	11.6 kV
Beam Current	1.33 A maximum
Anode Voltage	Adjustable from 0 to –7 kV

Design Features

Four-cavity interaction circuit	
Stagger-tuned with resistive loading to achieve a 5-MHz passband	
Electron gun perveance	1.0×10^{-6}
Cathode emission density	0.7 A/cm^2
Cathode material	Type M
Estimated life	over 100,000 hours

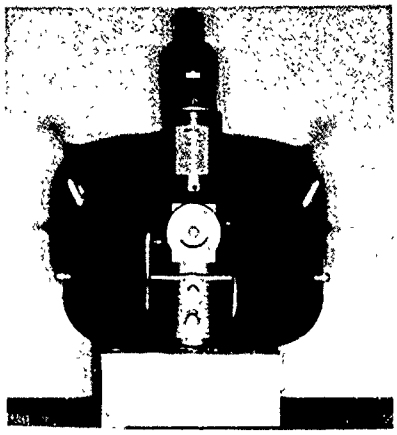


Figure 1. The VKL-7811W Klystron

IV. KLYSTRON PERFORMANCE

Typical performance characteristics are listed in Table 3. Performance was measured for various values of anode voltage. Biasing the anode more negative with respect to ground reduces the beam current and, correspondingly, the rf output power. The bandpass characteristics for several values of anode voltage are shown in Figure 2. For all conditions, the –1 dB passband greatly exceeds the 4.8 MHz requirement.

Table 3
Typical Performance Characteristics

Heater Voltage		6.0	V
Heater Current		6.4	A
Beam Voltage		11.6	kV
Beam Current, Anode at Ground		1.3	A
Output Power		5.1	kW
Drive Power		1.65	W
Bandwidth (–1 dB)		5.5	MHz
Cooling (Water)			
Collector	5 gpm	7	psi
Body	0.5 gpm	2	psi
Connections			
RF Output		1-5/8 rigid coaxial	
RF Input		Type N coaxial	

The power control characteristics of the modulating anode are illustrated in Figure 3. Beam current and power variation with anode voltage are shown.

V. CONCLUSION

The VKL-7811W klystron meets all performance requirements for accelerator driver service. The production status at the end of March 1991 reports delivery of 72 tubes, with production continuing at 13 tubes per month.

VI. REFERENCE

[1] E.W. McCune, "A Klystron Amplifier to Power the CEBAF Accelerator," 1987 IEEE Particle Accelerator Conference, Washington D.C., March 1987.

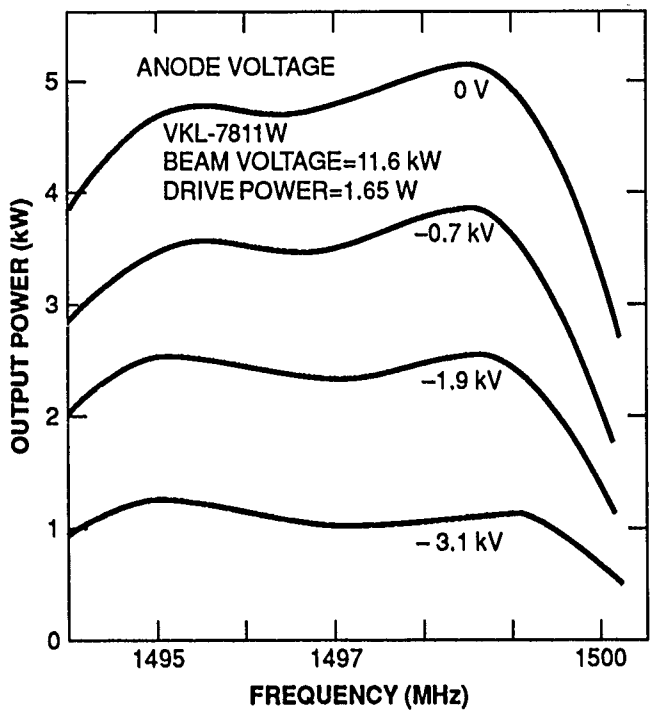


Figure 2. Bandpass Characteristics

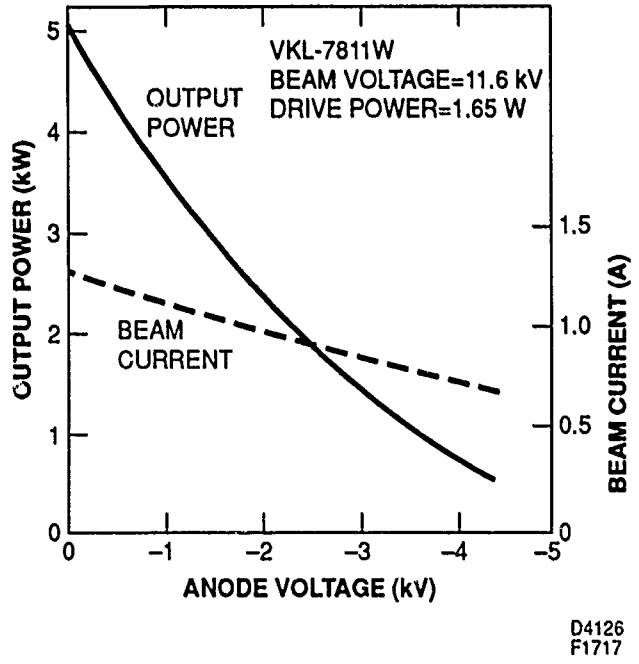


Figure 3. Modulating Anode Control Characteristics

Development of 5-cell RF Cavity for SPring-8 Booster Synchrotron

H. Suzuki, T. Harami and Y. Miyahara
Japan Atomic Energy Research Institute
Tokai-mura, Naka-gun, Ibaraki-ken, Japan

T. Rizawa, S. Satoh, Y. Tanabe, K. Yoshiyuki,
T. Nagafuchi, S. Kawazu and M. Nakano
Toshiba Corporation
1-1-6, Uchisaiwai-cho, Chiyoda-ku, Tokyo, Japan

Abstract

Slot-coupled 5-cell rf cavities are adopted for SPring-8 (Super Photon Ring 8GeV) booster synchrotron. They are operated at 508.58 MHz with 250 kW CW and designed to have 1.7% of coupling coefficient and more than 21 M Ω /m of shunt impedance. A mock-up cavity, made of class-1 oxygen free Cu, has been fabricated for high power tests with a 1 MW klystron. This paper represents the structural features, the thermal analysis, the rf characteristics including higher order modes and the beam instability.

I. INTRODUCTION

The rf system in the synchrotron must provide adequate voltage and power to accelerate electron or positron beam, to compensate for synchrotron radiation losses and also to give overvoltage for a proper beam lifetime. The rf power is mainly dissipated at cavity wall, since the maximum beam current is only about 10 mA. The design requirement for the cavity is to realize a high shunt impedance to reduce the wall losses. So that a multi-cell type cavity that consists of 5 cells was chosen. The synchrotron uses 508.58 MHz rf system, the same frequency that will be used for the storage ring. Two 1-MW KEK-type klystrons will be used in the synchrotron. The rf parameters are listed in Table 1.

Table 1 The rf parameters of the synchrotron

Beam energy (Injection)	1.0	GeV
(Extraction)	8.0	GeV
Magnetic bending radius	29.539	m
rf frequency	508.58	MHz
Harmonic number	672	
Repetition rate	1	Hz
Beam current	10	mA
Radiation loss at 8GeV	12.27	MV/turn
Overvoltage factor	1.48	
Maximum required voltage	18.2	MV
rf voltage at injection	6	MV
Number of cavities	8	
Synchrotron frequency at 8GeV	32.7	kHz
Klystron power	1	MW
Number of klystrons	2	

II. STRUCTURE OF THE CAVITY

A. General Description

The prototype 5-cell slot coupled cavity is shown in Fig. 1. The cavity is designed to operate in the π-mode thus a cell length of 294.74 mm is equal to a half wavelength of the rf frequency. The adjacent cells are inductively coupled each other with four azimuthal slots in a common disk. Nose cones are shaped on disks to make a shunt impedance higher. Diameter of both end cells are slightly larger than that of inner three cells to realize a flat accelerating field distribution called as 'flat-π mode .

The material of the cavity is class-1 oxygen free Cu because of high electrical and thermal conductivity and low outgassing rate. The computer code 'SUPERFISH' was used for designing the cavity. Detailed dimensions were determined experimentally using an aluminum model cavity [1] . The cavity is 1700 mm long. The inner diameter of the cavity is about 430 mm. The bore radius is 40 mm.

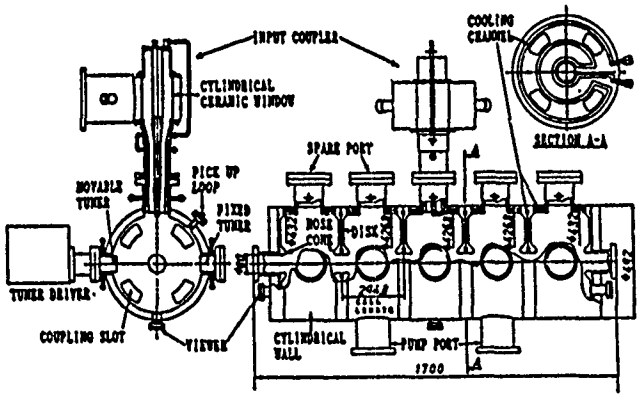


Figure 1. Cross sectional view of the prototype cavity

B. Water cooling channel

Water cooling channels run azimuthally inside the disks and the cylindrical wall. The heat load of 250 kW on the inner surface of the cavity is effectively removed through direct cooling channels. A water flow rate for a whole cavity is 200 l/min.

Each disk consists of two half disks. After machining the cooling channels onto the one side of each half disk as shown in Fig. 1, both of them were bonded by diffusion under high temperature and high

0-7803-0135-8/91$01.00 ©IEEE

mechanical pressure. Cylindrical wall and ports of the cavity were at first sliced into short pieces, in which water cooling channels were made with the above technique. After precise shaping of all disks and the cylindrical walls, they were integrated by means of the diffusion-bonding with thin silver inserts. The use of silver insert can reduce the bonding pressure which does not cause a serious deformation on the cavity.

Figure 2 shows the results of an axisymmetric thermal analysis carried out by using the computer code 'NASTRAN'. A heat load distribution on the inner surface of the cavity was computed by 'SUPERFISH'. Non-axisymmetric structures such as the slots are neglected in these calculations. The power dissipation and water flow rate per cell are 50 kW and 34 l/min, respectively. An inlet temperature of the cooling water was assumed to be 30 °C and temperature rise of the water in the cavity was taken into account.

The maximum temperature of the cavity is 73° C and the maximum frequency shift due to thermal deformation in the diameter of the cavity was estimated to be about -330 kHz at maximum. This is much smaller than tuning range of movable tuners.

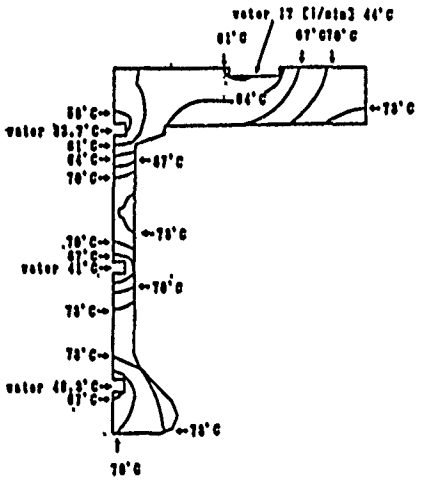


Figure 2. Temperature distribution in a quarter cell of the cavity

C. Tuner

Each cell is equipped with two tuning plungers with diameter of 70 mm. One of them is the fixed tuner which corrects fabrication errors. The other is the movable tuner by which the thermal detuning and the beam loading effect are dynamically compensated during operation. All of the five movable tuners are driven together with an over all stroke of 70 mm.

D. Input Coupler

The waveguide mode of rf power (250kW) is transformed into a coaxial mode through a cylindrical window of 95% alumina ceramic which seals the vacuum of rf cavity. Inner wall of the ceramic window is coated with TiN 6 nm thick to reduce the secondary electron emission. This type of input coupler has been used in TRISTAN of KEK for the APS cavity with the maximum input power of 300 kW [2].

Four spare ports at the top of the cavity are prepared to allow adding higher order mode (HOM) dampers.

III. RF CHARACTERISTICS

A. Accelerating mode

The measured values for accelerating mode are listed in Table 2. Figure 3 shows an electric field distribution of the accelerating flat-π mode along the cavity axis, which was measured by perturbation method. The coupling coefficient K is defined as $K = 2(f0-f\pi) / (f0+f\pi)$ where f0 and $f\pi$ are rf frequency of 0 and π mode. The coupling coefficient of 1.68% seems to be considerably large compared with other slot coupled type cavities [3]. The shunt impedance per unit length is about 23 MΩ/m which satisfies the requirement of the booster synchrotron.

Table 2. rf characteristics of the accelerating mode

rf frequency	508.580	MHz
Unloaded Q (Q0)	29000	
Effective shunt impedance	23	MΩ/m
Coupling coefficient	1.68	
Tuning range of tuners	1.7	MHz

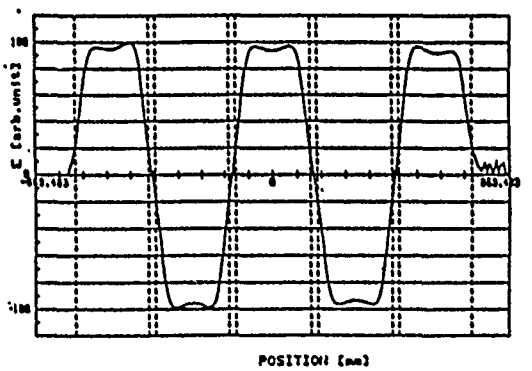


Figure 3. Field distribution of the accelerating mode

B. Higher Order Mode

Four groups of mode TM010, TM011, TM110 and TM111 are important as for beam instability. Therefore these mode in the cavity were identified by perturbation method and their characteristics are shown in Table 3.

As for TM010 mode, R/Q0 values except that of π mode are negligibly small because their transit time factors become nealy zero. TM010 and TM011 modes have longitudinal coupling impedance. TM110

and TM111 modes have transverse one, and each of these modes are split into horizontal and vertical modes because the symmetry of each cell is broken by some ports. The vertical modes of TM110 have smaller Q0 compared with the horizontal mode because their magnetic fields are high and disturbed at the vacuum ports. TM111 modes have no field at the center mirror plane, and the effect of unsymmetry is not strong. Thus their mode separation between horizontal and vertical is not clear.

Table 3 rf characteristics of the HOM

MODE		F0(MHz)	Q0	R/Q0(Ω)	R(MΩ)
TM010	1π/6	816.334	37403	0	0.0
	2π/6	814.134	33008	0	0.0
	3π/6	811.488	35318	0	0.0
	4π/6	809.347	30816	0	0.0
	5π/6	808.180	27689	1163	32.2
TM011	1π/6	720.353	19417	0	0
	2π/6	727.767	17688	57.8	1.02
	3π/6	737.050	21515	163.9	3.53
	4π/6	745.050	24093	57.1	1.38
	5π/6	747.154	23370	38.9	0.913
TM110 (Y)	1π/6	854.642	1816	317.3	0.576
	2π/6	850.481	1618	-----	-----
	3π/6	846.198	5016	418.5	2.44
	4π/6	843.861	5017	1.0	0.005
	5π/6	841.158	5006	87.9	0.317
TM110 (X)	1π/6	859.117	20839	282.3	11.9
	2π/6	855.883	29148	648.6	18.7
	3π/6	849.887	31665	354.6	12.6
	4π/6	846.286	31386	18.6	0.583
	5π/6	844.948	33433	89.8	3.01
TM111	1π/6	998.457	11833	5418	0.24
		998.718	23388	6939	13.1
	2π/6	1007.171	6733	34.7	0.233
		1007.683	15781	1.3	0.115
	3π/6	1010.586	11313	733.6	8.23
		1010.885	19814	690.4	13.7
	4π/6	1031.571	23588	28.8	0.653
		1032.331	23471	15.1	0.339
	5π/6	---------	-----	-----	------
		1038.436	17736	134.8	2.38

----- : Impossible to measure

IV. BEAM INSTABILITY DUE TO THE CAVITY

The beam spends a relatively short time, less than 1 second, in the synchrotron and the maximum current required for the synchrotron is at most 10 mA and 1 mA for multi-bunch and single bunch operation, respectively. However, the beam is injected into the synchrotron at relatively low energy, 1 GeV, and this might enhance beam instability, while the radiation damping time is about 1 sec. As for the higher order modes given in Table 3, numerical estimation of the beam instability at the injection energy was carried out using the computer code ZAP.

At 1 GeV the injected beam has a momentum spread about 1.5% so that the threshold current of the longitudinal microwave instability is quite high. In Fig.4, the rf voltage dependence of the single bunch threshold is shown. The threshold current per bunch is 10.9 mA at an rf voltage of 6 MV. This instability at injection is not expected.

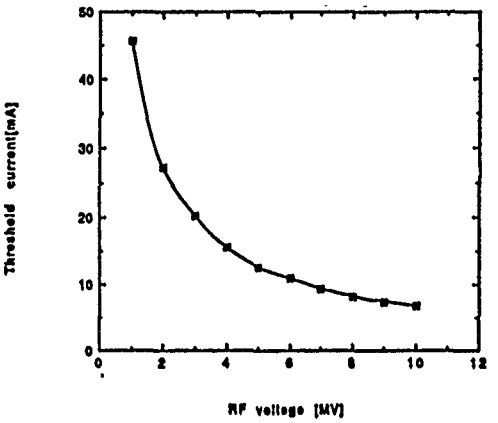


Figure 4. rf voltage dependence of the threshold current of microwave instability at 1 GeV

The growth time of the head tail instability is as short as 10 msec for the single bunch operation. It is necessary to correct the chromaticity in the synchrotron with sextupole magnets.

The growth time of the longitudinal coupled bunch instability predicted by ZAP are in the order of seconds. The instability will be easily suppressed by stronger radiation damping during beam acceleration.

The growth time of the transverse coupled bunch instability predicted are about 10 msec. The instability can be suppressed by a tune spread in the order of 10^{-4}.

V. CONCLUSION

The rf characteristics of the cavity for SPring-8 booster synchrotron were measured. Flat-π mode was realized by adjusting the fixed tuner. The shunt impedance meets the requirement of the booster synchrotron. As a result of the calculation by the ZAP code, some cures might be necessary to suppress transverse coupled bunch instability.

VI. REFERENCES

[1] T. Rizawa et al., "rf Characteristics of 508MHz Slot-coupled Multi-cell Cavity" Ploc. of 2nd European Particle Accelerater Conf., Nice, France, June 1990, pp. 916-918.

[2] T. Higo et al., "rf Cavity for TRISTAN Main Ring", Ploc. of 1987 IEEE Particle Accelerator Conf., Washington D.C., March 1987, pp. 1945-1947.

[3] H. Gerke et al., "Das PETRA-Cavity", DESY PET-77/08, August 1977.

Status Report on the ELETTRA R.F. System.

A. Massarotti
Sincrotrone Trieste and Dipart. di Fisica, Universita' di Trieste
G. D'Auria, A. Fabris, C. Pasotti, C. Rossi, M. Svandrlik
Sincrotrone Trieste, Padriciano 99
34012 Trieste, Italy

Abstract

The results of the R.F. system development are presented. A complete power plant has been tested on a dummy load. The cavity feedthrough has been developed and the progress work on the accelerating cavity is described.

I. INTRODUCTION

ELETTRA is a Synchrotron Light Source under construction in Trieste (Italy) working with beam energies in the range from 1.5 and 2 GeV. It will be constituted of a full energy linac directly injecting the electrons in the storage ring.

Four cavities at 1.5 GeV (six at 2 GeV) operating at 499.654 MHz will be installed in the storage ring [1]. Each one will be fed by a separate independent plant providing up to 60 KW cw RF power (fig. 1).

II. RF POWER SYSTEM STATUS

A. *Power Plant.*

The power amplifier prototype supplied by TVT Cambridge U.K. has been installed in the laboratory. A complete power plant has been assembled using for the measurements at 60 KW a dummy load instead of the cavity. All the prototypes of the components (circulator, 6 1/8" cables, directional couplers, etc) , which are foreseen for the definitive installation in the storage ring, have been tested at full output power with satisfactory results. This power plant will be used as a test facility for the measurement of all the components before their installation in the machine.

B. *RF Cavity.*

The Elettra 500 MHz cavity has a smooth shape, with a radius of 263 mm and an axial length of 302.6 mm. [2]. The measured resonating frequency is 500.1 MHz. The measured Q value is 42000, which with a measured R/Q of 167 Ohm leads to a R_{sh} of 7.0 MΩ. ($R_{sh} = V_{gap}^2/2P$)

The cavity will be tuned by means of a mechanical tuner acting on the length L of the cavity. The prototype structure for the mechanical tuning system has been realized and tested on the cavity for Elettra. The variation of resonant frequency obtained is 8 KHz for one hundredth of mm. of compression or stretching. This is in good agreement with the computer simulation results [2]. Since the maximum frequency shift needed in order to compensate the beam loading is 58 KHz at 1.5 GeV or 82 KHz at 2 GeV, roughly one tenth of mm. of variation in axial length will be sufficient to cover all this range (fig. 2).

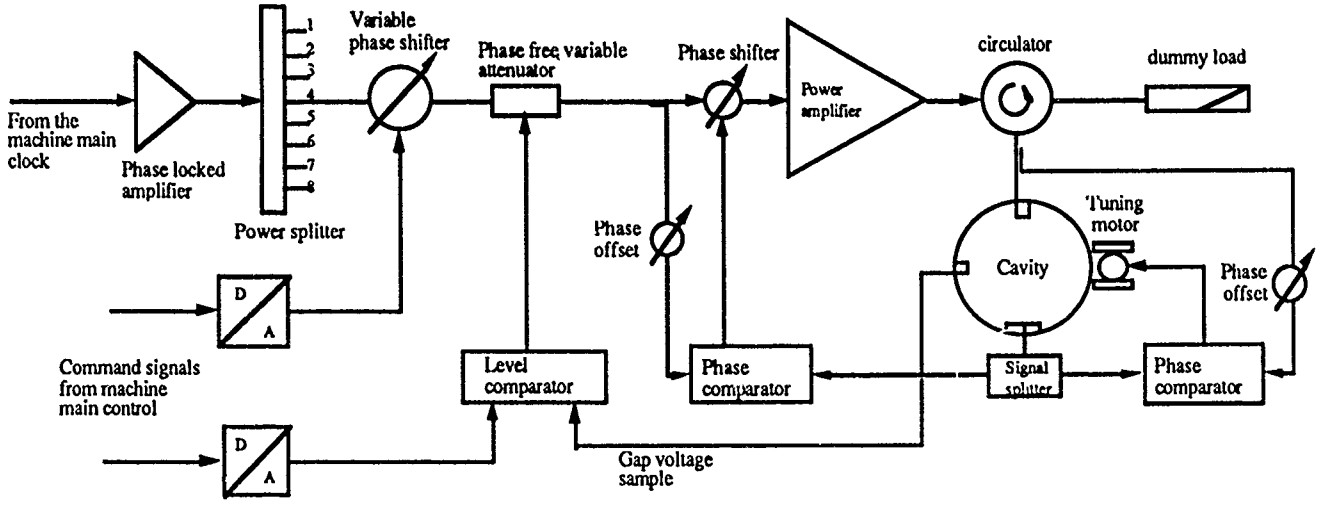


fig.1 Block Diagram of the RF Power Plant.

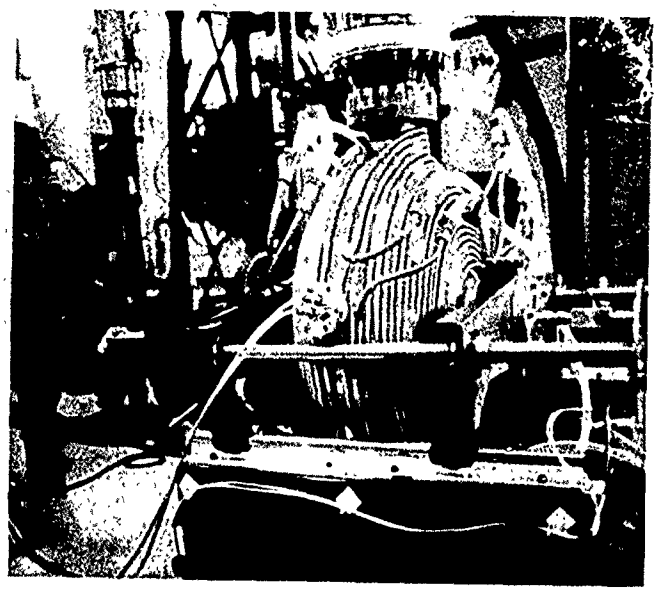


Figure 2. Cavity with mechanical tuning and cooling pipes.

The first prototype of the cavity provided with cooling system has been constructed. In order to carry off up to 36 KW, which is the estimated maximum wasted power in the cavity, the needed waterflow is 180 lit/min. The water input temperature can be varied for tuning purposes between 32 and 52 °C; the temperature difference between input and output is less than 5 °C.

The cavity has been tested in air with the power plant. The input power was raised up to 26 KW (which corresponds to a gap voltage of about 600 KV) without any sparking.

C. Low Level.

The low level control of the cavity will be made of a slow mechanical tuning system and a faster electronic phase loop. An advanced prototype of the first one has been assembled and tested on the Elettra cavity. The satisfying results obtained show that the resonant frequency of the cavity can be kept at ±200 Hz from the operative one. The tuning speed is 200 Hz/sec.

The fast electronic phase control system has been designed and tested on bench, operating on a 500 MHz pill-box cavity, with a response time better than 5 µsec for 1° of phase variation.

The low level distribution system has been designed. The reference signal which is provided by the machine main clock will be first amplified and then splitted in eight independent channels: four of them will be used to drive the RF plants.

III. THE H.O.M. SUPPRESSOR FOR THE ELETTRA R.F. CAVITIES

A. The waveguide suppressor

The beam characteristics of the ELETTRA synchrotron light source [1] require an adequate damping of the H.O.M. spectrum of the RF cavity, despite the open profile chosen for the cavity [2], in order to avoid multibunch instabilities [3]. Therefore the RF cavities should be provided with H.O.M. suppressors. In many other laboratories 'dedicated' devices have been developed, in order to damp some particular dangerous modes [4], [5], as well as broad-band couplers [6]. Anyway, a total damping of the H.O.M. hasn't been yet obtained; and, to prevent instabilities, active feedback systems are foreseen, for example in ALS [6].

The concept of broadband damping, with the final goal of a total suppression of the H.O.M. spectrum has been developed for the Elettra cavities. Our basic idea has been to couple waveguides directly to the cavity, through large coupling apertures. The waveguides have a dominant mode cut-off frequency quite above the resonant frequency of the cavity accelerating mode, but below that of the first H.O.M.; they are terminated on matched terminations. In this way the H.O.M. power excited by the beam can flow through the apertures to the dummy loads, while the accelerating mode power is confined into the resonant cavity.

To evaluate the performance of such a structure we chose a pill-box cavity which has the great advantage of a geometry simpler than the Elettra cavity one. First we studied a scaled prototype in the S-band. Since the results have been encouraging we went on with a 500 MHz prototype, which confirmed these good results [2], [7].

At the conclusion of the preliminary tests with this cavity, the performance of the suppressor has been increased, also with the support of MAFIA simulations, by choosing the most convenient shape and size of the coupling aperture.

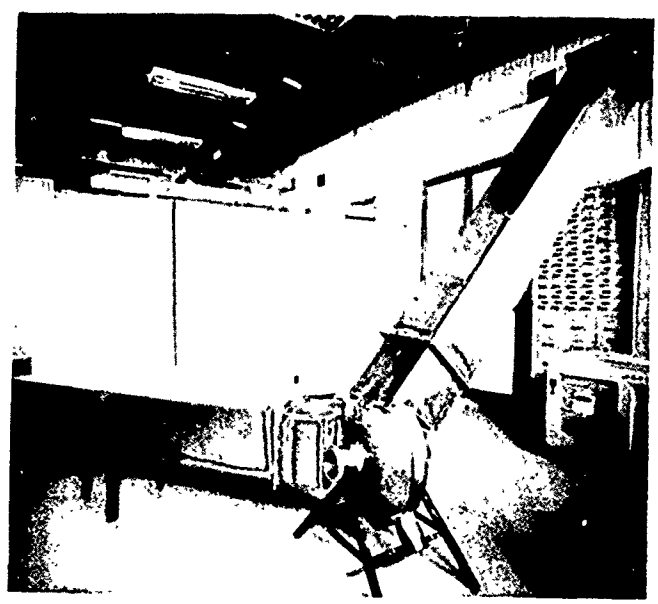


Figure 3. Cavity with prototype of the waveguide suppressor.

Then we studied the problem of the coupling of waveguides to the Elettra cavity. The resulting geometry is rather complex, hence the CPU-time limitations haven't allowed us to perform a complete simulation with MAFIA. Nevertheless, a first coupling geometry, with a coupling

aperture of 75 mm, has been designed with MAFIA. The damping effect was not satisfactory, hence the suppressor has been further developed with a cut and try method in the laboratory, by enlarging the aperture, changing its shape and giving different inclinations to the waveguide. Despite the mechanical difficulties, mainly due to the particular geometry of our cavity, we finally obtained a configuration with satisfying coupling; it is shown in Figure 3. In the cut section the aperture has a square shape with a diagonal size of 230 mm, the inclination angle is 50°.

B. The H.O.M. free structure

Up to this point only one waveguide has been coupled to the cavity. This could be enough for monopole (longitudinal) modes, which have no azimuthal variations and thus have no preferred polarization. But dipole modes, which are responsible for transverse instabilities, have one azimuthal variation and are allowed to have more polarizations in the cavity. Therefore, with only one waveguide, there is still one dipole mode polarization trapped into the cavity, typically with the magnetic field maximum at 90° from the aperture.

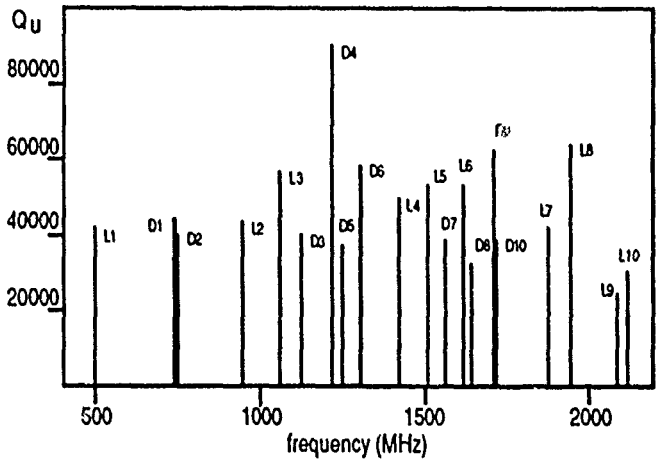


Figure 4a. Undamped cavity modes spectrum.

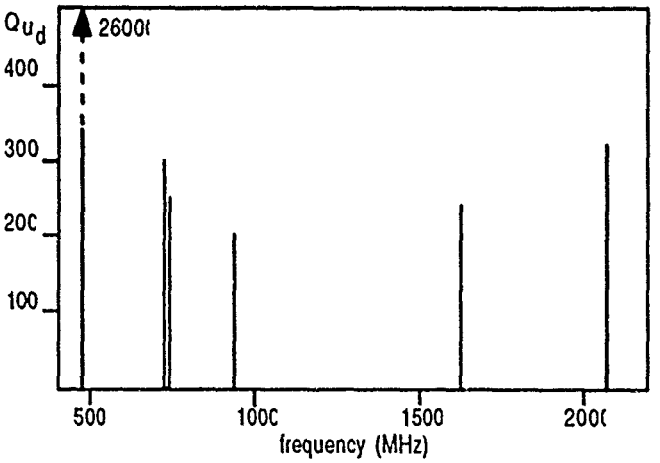


Figure 4b. Damped cavity modes spectrum (scaled by 200).

In order to have a completely H.O.M. free structure it is then straightforward to couple a second waveguide to the cavity, rotated by an angle of 90° from the first one; the coupling aperture should be just the same for the two waveguides.

This final configuration has been tested at our laboratories. Its effectiveness can be easily seen by comparing the damped and undamped mode spectrum in figure 4. Since the Q values of the few resonances measured in the damped cavity are strongly reduced, the scale in figure 4b is enlarged by a factor 200. The resonance around 950 MHz comes out in the new resonating structure and should not be mistaken for the first longitudinal (L2) H.O.M., that seems to be completely damped. Practically all H.O.M. are eliminated, while the fundamental mode is still useful for accelerating purposes ($Q=26000$, $R_{sh}=3.8$ MΩ).

It is to be noted that, coupling two waveguides at 90° to a resonant cavity, we obtain an asymmetrical structure. The accelerating electric field could be consequently distorted. Preliminary calculations show that the distortion can be compensated by locating two cavities close to each other, but rotated by 180° and decoupled through 200 mm long, 50 mm diameter drift tubes. A second solution is to leave the cavities in their present position, but with adequate rotation angles [8].

IV. CONCLUSIONS

The cavity will be tested under vacuum at the design gap voltage before next summer. The cavity tuning system, the phase control system and the RF signal distribution system are either already tested or in advanced design status.

In order to produce a H.O.M. free cavity to be mounted on the Elettra Storage Ring, the engineering of the prototype is now foreseen. Along with this we are studying the behaviour of this suppressor with a pill-box cavity with nose-cones.

REFERENCES

[1] A. Massarotti et al., "RF Power System for the Trieste Synchrotron Light Source ELETTRA", in *Proceedings of the 2nd EUROPEAN PART. ACC. CONF.*, Nice, France, June 1990, pp. 913-915.

[2] A. Massarotti et al., "500 MHz Cavities for the Trieste Synchrotron Light Source ELETTRA", in *Proceedings of the 2nd EUROPEAN PART. ACC. CONF.*, Nice, France, June 1990, pp. 919-921.

[3] E. Karantzoulis and A.Wrulich, "Multibunch Instabilities Investigation for the ELETTRA Cavities", in *Proceedings of the 2nd EUROPEAN PART. ACC. CONF.*, Nice, France, June 1990, pp. 1618-1620.

[4] E.Haebel and Ph.Legendre, "An improved beam tube coupler with enhanced cut-off characteristics, CERN, Geneva, CERN/EF/RF87-1, 1987.

[5] E.Haebel and J. Sekutowicz, "Higher Order Modes coupler Studies at DESY", DESY, Hamburg, FRG, DESY M-86-06, 1986.

[6] A.F.Jacob, G.R.Lambertson, W.Barry, Higher Order Mode damping in an ALS test cavity", in *Proceedings of the 2nd EUROPEAN PART. ACC. CONF.*, Nice, France, June 1990, pp. 928-930.

[7] A.Massarotti and M.Svandrlik, "Proposal for a Broadband H.O.M. Suppressor for the RF Cavity" , Sincrotrone Trieste, Trieste, Italy, ST/M-90/5, 1990.

[8] E.Karantzoulis, Sincrotrone Trieste, Private Communication.

Component Development for X-Band Above 100 MW*

W. R. Fowkes, R. S. Callin, and M. Studzinski
Stanford Linear Accelerator Center, Stanford University, Stanford, CA 94309 USA

I. Introduction

The requirement for some of the components described in this paper began with the Relativistic Klystron program done in collaboration with LLNL and LBL. This effort culminated in a klystron operating at 11.4 GHz delivering 330 MW into a pair of high-gradient accelerating structures [1]. The electron beam for this klystron was formed in a 1 MeV induction linac at a very low duty cycle. The subsequent RF source development work at SLAC for the Next Linear Collider utilized some of these components, and required further and new development of others, to work reliably at higher average power [2].

2. RF Windows

Perhaps the most critical component is the high-power RF window. The first window used at high power was a standard "pillbox" design that is broad-band and requires no additional matching elements, other than that provided by the symmetrically located steps from rectangular to circular waveguide at each end of the circular pillbox. The 27-mm diameter alumina ceramic in the X-band version of this window is very thin physically (about 0.8 mm), and is therefore fragile and difficult to braze. This thin window had several drawbacks. The braze of the metallized edge to the copper sleeve was not always successful. Those that survived the initial brazing operations would sometime fail later, during the crush-seal flange tightening process, or in bake. The performance of the thin-window high-peak power was usually satisfactory for very short RF pulses, but puncturing and fractures occurred above 25 MW at pulse widths in the 100 to 800 nsec range.

A thicker ceramic design, and perhaps one with a larger diameter as well, appeared to be necessary. Half-wave windows are narrow-band by themselves, but can be broad-banded using various techniques [3]. Trapped ghost-mode resonances are always of concern with a thick ceramic. Special care must be taken—by choosing a suitable combination of diameter, thickness, and dielectric constant—so that these trapped resonant frequencies are not located near the operating frequency.

An alumina window with an electrical thickness of 0.43 λ_g' and the same diameter, but lower RF electric field for a given power, as in the thin window described above, was chosen and is shown in Fig. 1. This design uses two symmetrically located inductive elements, in addition to the pillbox transitions, to accomplish the broad band response where the VSWR $\leq$ 1.50 over 10% and $\leq$ 1.10 over 5% bandwidth. The dimensions were chosen primarily to avoid ghost-mode resonances, but the electrical thickness was also chosen based on earlier experience of others in broad-banding thick windows that were not exactly $\lambda_g'/2$. The design optimization was done using a model based on cascading equivalent circuit elements and transmission line sections. The ghost-mode problem is not taken into account in the model, and is determined in a separate calculation.

At this writing we have had no failures of this 3.7-mm thick, 27-mm diameter window; but it is felt that as we push higher in peak power, the surface electric fields stresses at some point will be too great and breakdown will occur. A larger, 47-mm diameter window has been designed that has a frequency response similar to that of the

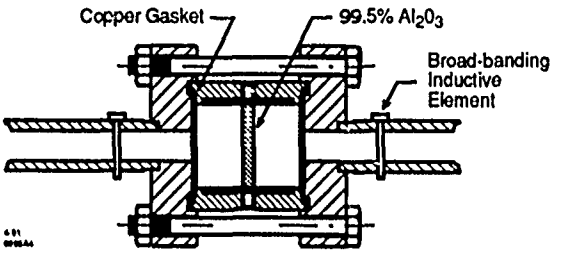


Figure 1. Thick (3.7 mm) pillbox window with broad-banding elements.

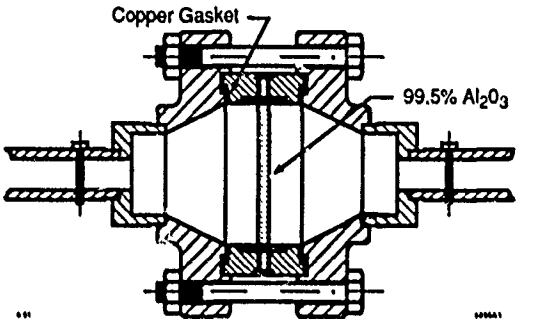


Figure 2. Large diameter ($2a$ = 47 mm) window.

27-mm diameter window. It employs similar broad-banding techniques and uses circular 26° tapered sections to the larger diameter. However, the 47-mm diameter portion of the waveguide can support a total of five modes outside the dielectric, which may cause problems. This latest design, shown in Fig. 2, has not yet been tested.

3. Couplers, Magic Tees, and High-Power Loads

It was felt that cross guide, directional couplers of the Moreno type would be more susceptible to electric field breakdown than some of the sidewall designs. For measuring high-peak power, a broad-band sidewall coupler was designed, using an array of five circular holes, with RF voltage coupling factors based on binomial coefficients. The nominal coupling ratio of this design is 56 dB, and the directivity is typically 35 to 40 dB. The match of the RF windows used on the secondary arms determine the overall directivity. For special applications where a high directivity, broad-band coupler with much tighter coupling is required it was necessary to go to a much longer sidewall design. A 10 dB design uses an array of 31 holes with RF voltage coupling factors, based on Tchebycheff coefficients [4]. This design was used as the input bridge coupler for the Travelling Wave Resonator (TWR) described later.

A conventional magic tee was designed to be used either as a power splitter or power combiner. A single-ended inductive post (2.54 mm diameter, with a spherical end) placed in the throat of the junction provides broad-band matching for the H arm. An inductive post also provides the matching for the E arm, but over a much narrower bandwidth. When used as a power splitter, the unused E arm is usually shorted. The corners in the junction that are exposed to high-RF electric fields have a $\sim$ 1 mm radius. No RF breakdown has been experienced in these devices.

The first high-power load to be put into operation was a 0.75 λ_g' alumina ceramic disk 85 mm in diameter separating a water chamber from the waveguide vacuum. Extra care (unnecessary as it turned out) was taken to avoid overmoding by tapering from 27 to 85 mm in diameter over an electrical distance of about 16 wavelengths. This load worked very well over a very narrow band but had to be retuned to operate at frequencies only 1 or 2% away from the center frequency.

* Work supported by Department of Energy contract DE-AC03-76SF00515.

U.S. Government work not protected by U.S. Copyright.

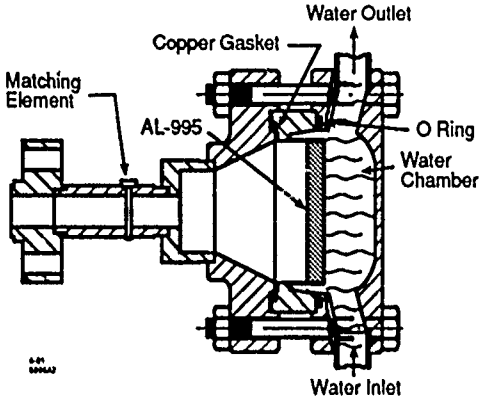


Figure 3. A 50 MW X-band ceramic/water load.

The narrow bandwidth was due to the line length effect between the ceramic/water mismatch (VSWR ~ 3) and corrective matching located some 16 wavelengths away in the WR 90 rectangular waveguide portion to avoid the possibility of mode conversion.

The solution to the narrow bandwidth problem appeared at first to be a long, tapered, lossy metal, water cooled load that required no matching elements. Such a load was designed and built using type 430 stainless steel. The cross-sectional a and b dimensions were tapered through cutoff over approximately 2 meters so that the power lost per unit length and the maximum RF electric field were approximately constant throughout its length. The match over a broad-band of this tapered load was good but it had several drawbacks. The pumping speed of the small cross-section required that several ion pumps be distributed along the length of the load. The original design construction had the four tapered sides welded rather than brazed together. There were likely some unwanted gaps at the corners, possibly trapping contaminants at high current joints, resulting in excessive gassing and some RF breakdown.

Tapering through cutoff has some disadvantages. The RF electric field, constant along most of the load by design, rises at the region near cutoff as the impedance becomes infinite and then imaginary moving through cutoff. If we were to improve on this design we would have the cross-sectional dimensions stop short of cutoff at the tip and still maintain approximately constant dP/dz and maximum electric field along its length. All joints conducting RF current would be brazed rather than welded.

The most promising high-power RF load design appears to be a much more compact version of the quarter wave ceramic/water load. This load is sufficiently broad-band (VSWR ≤ 1.50 over 7% and ≤ 1.10 over 2.6%) and is shown in Fig. 3. A 0.75 λ_g' thick alumina disk, 47 mm in diameter separates water from vacuum in the same manner as the longer, larger, narrow band version described earlier. The ultimate energy/pulse capability is about one third that of the larger, narrow-band version but the very broad-band feature makes it more attractive overall. Two of these loads connected to a power splitter will be used for future 100 MW klystron experiments. A single unit will be used as the dummy load for the Travelling Wave Resonator described later.

4. RF Crush-Seal Flanges and Waveguide Pumpouts

Crush-seal flanges, both rectangular and circular, have been developed to operate at peak power levels in excess of 100 MW. The inner surfaces have been copper plated where RF losses are of great concern, such as in the TWR resonant Loop. These flanges must be mass-spectrometer leak-tight to a helium sensitivity of 2×10^{-10} standard atm cc/sec helium, and must be bakeable to 550°C for time periods exceeding one week. Annealed OFE copper gaskets are used for the sealing media. A unique solution has been applied to avoid diffusion bonding of the copper gaskets to stainless surfaces during bake cycles. The copper gaskets are coated with a ~ 50 Å layer of titanium nitride (TiN) by reactive sputtering. This hard TiN coating does not bond to the stainless surfaces under bakeout, which makes for easy disassembly of the flange after bakeout. These flange designs are similar to earlier seal designs developed at SLAC in the early 1960's by Merdinian. They are relatively insensitive to small imperfections in the copper gasket surfaces, and to edge rollover due to annealing of stainless steel by grazing. The copper gaskets are easily punched from sheet, and are always annealed before use.

A serious problem with X-Band waveguide is its poor vacuum conductance. A meter of waveguide has a conductance of less than 0.7 l/sec. It was necessary to place small ion pumps (2 l/sec) relatively close together—approximately one every 3 meters of waveguide—to maintain pressures low enough to avoid RF breakdown in the waveguide when operating at high-peak power. In order to maximize the pumping speed in this size waveguide, a pumpout was constructed using a 1.5-in OD tubulation, slotted on two sides, so as to envelope a 15-cm section of waveguide containing a total of 264 pumpout holes, each 1.3 mm in diameter . The size of these pumping holes was a tradeoff between adequate RF rejection at 11.4 GHz and pumping speed. The effective net conductance of the entire pumpout structure is about 7 l/sec, and the measured RF loss is equivalent to about 30 cm of WR 90 copper waveguide.

5. High Power Traveling Wave Resonant Ring Utilizing Variable Tuners and Phase Shifter

The RF electric field breakdown limit on conventional X-band components is not usually known. Our experience with high-vacuum waveguide RF seals, RF windows, directional couplers, and ceramic/water loads has been in the relativistic klystron program, where the RF pulse width was only 50 nanoseconds and the pulse repetition rate was 1 or 2 pps. The breakdown limit on most of the components developed thus far had not been reached under those conditions. Traveling Wave Resonators (TWR's) have been used primarily to test RF windows, but also to test other low loss components at power levels higher than RF sources are capable of producing. An S band TWR has been in operation at SLAC since 1962 to test RF windows power levels as high as 200 MW.

A TWR designed to operate at 11.424 GHz has been built to test windows and other components at peak RF power levels in the 100 to 300 MW range. At this writing this TWR is under vacuum and awaiting one of the 100 MW klystrons which will be used as the driving source [5]. The TWR has been thoroughly tested at cold-test power levels, and is shown in Fig. 4. The specifications for this TWR are shown in Table 1.

Operation at a precise frequency may be desired at times. The high-power waveguide resonant loop incorporates a squeeze-type phase shifter that is used to make minor corrections in the TWR resonant frequency because of temperature changes. Gross changes in resonant frequency must be made by replacing a pair of short waveguide spool pieces with another set of a slightly different length, based on calculation. Test pieces of a different electrical length will require a similar change. The squeeze type phase shifter has 16 cm long slots centered in the broadwalls of the copper WR 90 waveguide, with vacuum pumping on both sides of each slot. The slot vacuum chambers are designed with dimensions so that they are anti resonant to unwanted RF coupled through the slots. There is a micrometer control of the cutoff wavelength and resulting phase shift over a range of ±30°, which corresponds to a TWR resonant frequency change of ±6 MHz. All of the waveguide parts in the high power loop portion of the TWR are water cooled, to dissipate heat and for temperature stability. There are no plans at this stage to use a feedback control system for temperature stabilization.

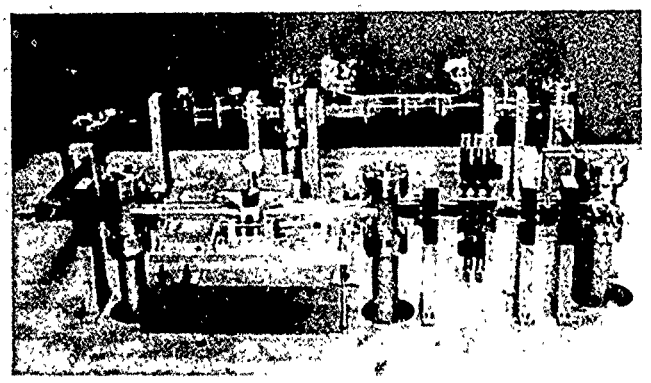


Figure 4. Tunable traveling-wave resonator.

Table 1. TWR Parameters

Expected TWR power	100 to 300 MW
Source power	10 to 30 MW
Resonant loop length	340 cm
Number of wavelengths	106, at 11.424 GHz
Input coupler ratio	10.1 dB
Separation between resonances	71.5 Mhz
Measured cold gain	11.0 dB
One-way loss in loop	0.354 dB
Variable phase-shifter range	±30° (±6 MHz)
Six-element tuner range	$\Gamma \leq 0.05$ any phase
Loaded Q	5500
Voltage time constant	0.153 μsec
Resonance coupling coefficient β	1.23

The extremely critical residual mismatch problem afflicting TWR's is handled by a variable tuner section, with six movable diaphragms in the broadwall. This device will be used to tune out residual mismatches up to an aggregate $|\Gamma|$ of about 0.05 in the resonant loop. Even a small mismatch can cause a serious deterioration in the overall gain of a TWR, as well as cause the buildup of a backward wave, resulting in a much larger mismatch at the input to the TWR as seen by the klystron driver. For example, in this TWR a net voltage reflection coefficient of 0.05 in the ring results in a reduction in power gain of about 40%, and an input reflection coefficient seen by of the klystron of nearly 0.50 (VSWR of 3:1). The resonance curve of the forward wave for the loss and coupling parameters of this TWR becomes double-peaked, for an aggregate residual reflection greater than $|\Gamma| = 0.0428$. Figures 5 and 6 show the theoretical effect that residual mismatches have on the power gain and the input reflection coefficient, as functions of frequency. It is interesting to note that the backward wave resonance does not become double peaked until the loop mismatch exceeds $|\Gamma| = 0.088$, where both it and the input reflection become double-peaked [6].

The maximum-peak power of the TWR will probably be limited by the device under test, which will usually be an RF window. The other critical component in the TWR will be the phase shifter. Should it happen that the breakdown threshold of the phase shifter is lower than that of the device under test, the phase shifter will be replaced by a straight section of waveguide, and the ring kept on resonance by adjusting the frequency of the source driving the klystron.

There are viewports on each bend that are used to observe activity on the window under test, and to help determine if there is any RF breakdown occurring in the phase shifter, tuners, or couplers. The entire ring is made of copper, with stainless steel crush-seal RF flanges that have copper plated RF conducting surfaces. Six ion pumps are distributed around the resonant loop, and another six ion pumps are used on the lower-power waveguide feed lines.

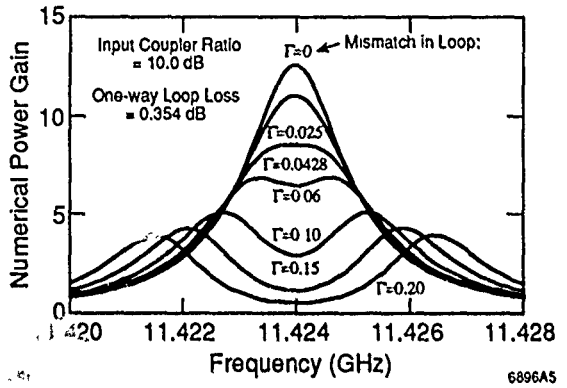


Figure 5. Effect of loop mismatch on TWR gain.

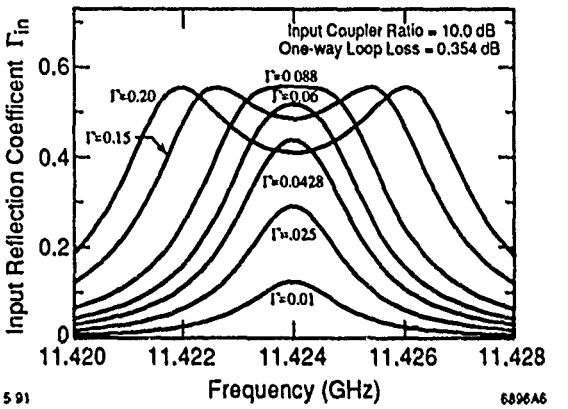


Figure 6. Effect of loop mismatch on input mismatch seen by klystron.

6. Conclusions

At this writing the variable phase shifter and tuners for the TWR and the compact version of the 0.75 wavelength ceramic water load have not been high-power tested. The cold-test measurements on all these devices agree with theory, but their peak-power handling capability remains to be demonstrated. The theoretical design of the 47-mm diameter, thick RF-output window has not yet been satisfactorily confirmed. The 27-mm diameter thick window has performed well, but has not yet been pushed to the high-peak and average power levels, where it is expected to perform reliably. The TWR is expected to be a useful tool to determine the RF breakdown threshold of these—and perhaps other transmission devices that have low loss and short filling times.

References

[1] M. A. Allen et al., "High-Gradient Electron Accelerator Powered by a Relativistic Klystron," Phys. Rev. Lett. 63, pp. 2472–2475, 1989.

[2] W. R. Fowkes et al., "RF Power Generation for Future Linear Colliders," *Proc. 8th Int. Conf. High-Power Particle Beams*, Novosibirsk, USSR, July 1990.

[3] H. J. Shaw and L. M. Winslow, "A Broadband High-Power Vacuum Window for X-band," IRE Trans. on MTT, MTT-6, July 1958.

[4] E. S. Hensperger, "The Design of Multi-hole Coupling Arrays," Microwave Journal, August 1959.

[5] A. E. Vlieks et al., "100 MW Klystron Development at SLAC," SLAC-PUB-5480, May 1991.

[6] W. R. Fowkes and P. B. Wilson, "Application of Traveling Wave Resonators to Superconducting Linear Accelerators," IEEE Trans. Nucl. Sci. NS-18, pp. 173–175, 1971.

COMPARISON OF SW AND TW NON-SYNCHRONOUS ACCELERATING CAVITIES AS USED IN ELECTRON BEAM STORAGE RINGS**

A. Zolfaghari, P.T. Demos, J.B. Flanz, K. Jacobs

Massachusetts Institute of Technology
Bates Linear Accelerator Center
Post Office Box 846
Middleton, Massachusetts 01949

We relate the parameters of detuned standing wave (SW) and non-synchronous beam travelling wave (TW) accelerating cavities of equivalent equilibrium performance when used to compensate for radiation and parasitic energy losses by electrons circulating in a high energy electron storage ring.

The relationship is expressed in terms of the coupling parameter β and cavity tuning angle ψ of the TW accelerator's equivalent SW system. A given TW cavity corresponds to a standing wave system possessing specific settings of β and ψ. This is shown for the constant impedance TW waveguide, for which β and ψ can be expressed as explicit functions of TW cavity length l, attenuation factor l, RF electric field phase velocity V_p, and shunt impedance r. Coupling parameter β depends additionally on SW cavity shunt impedance R.

The basis we have used for formulating the equivalence of the two systems follows Travelling Wave Cavity Non-Synchronous Beam Loading theory developed by G.A. Loew[1] and Standing Wave Circuit Analysis theory as described by P.B. Wilson[2].

1. Cavity Voltage Vectors.

The cavities are considered to be designed so as to achieve storage ring circulation of an electron beam of velocity $\simeq$ c and average current i_o. The beam consists of a sequence of beam bunches separated in time by $T_B=2\pi/\omega$. The beam current has first harmonic component i (frequency ω), which for bunches of narrow phase width approaches the infinitely-narrow bunch width value $i = 2i_o$.

The total acceleration received by the beam electrons when the cavity fields have reached equilibrium is identical in the equivalent cavities. The effects due to the accelerating field generated by the RF power source and the retarding field induced by the harmonic current i are illustrated respectively by the voltage vector V_{RF} and V_B of Figure 1a.

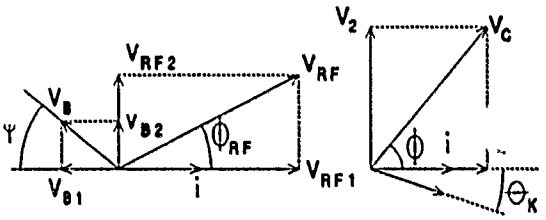


Figure 1a

Figure 1b

In Figures 1a and 1b, the phase of the harmonic current vector i also represents the phase of each beam bunch centroid. Figure 1b shows in addition the phase of a bunch electron which is displaced by θ_K relative to the centroid phase.

Since the accelerated electrons are assumed to be relativistic, their relative phases within each bunch do not change during cavity passage. Their phases relative to the cavity electric fields are on the other hand dependent on the cavity tunes. In the "detuned" TW case we consider, the RF field phase velocity is made less than c, and the electrons gain in phase relative to the accelerating wave during passage. In the detuned SW cavity the electrons shift phase relative to the accelerating wave during passage both because of the difference in cavity and beam frequencies, and because of the transit time effect. In either case the integrated energy change of the electron at θ_K due to the RF electric field is

** Work supported by the U.S. Department of Energy, contract DE-AC02-76ER03069.

0-7803-0135-8/91S01.00 ©IEEE

represented by the projection $V_{RF}Cos(\Phi_{RF}+\theta_K)$, where Φ_{RF} depends on the phase Φ_o relative to the accelerating wave with which the bunch centroid is initially introduced into the cavity.

The effect of the beam-induced cavity field on beam energy is given similarly by the projection $-V_B\cos(\psi-\theta_K)$. The tuning angle ψ is different from zero in the detuned cavities, and has magnitude which depends only on the cavity parameters.

The total energy change V_K of the electron at phase θ_K is given by the projection $V_c\cos(\Phi+\theta_K)$ of the total cavity voltage V_c. In terms of the components V_1 and V_2 of V_c, this is

$$V_K = V_1\cos\theta_K - V_2\sin\theta_K \qquad (1)$$

$$= (V_{RF1}+V_{B1})\cos\theta_K - (V_{RF2}+V_{B2})\sin\theta_K.$$

The detailed dependence of the voltages and phase angles on the TW and SW system parameters provides the connection needed to show the β, ψ equivalence of the two accelerator types. This has been developed using the theories and analyses of references 1 and 2 and is stated without proof in what follows.

2. TW Cavity System

Formulas for V_1 for the constant impedance TW cavity are given in reference 1, which also provides the basis from which V_2 can easily be developed. It is also helpful, in comparing them with their SW cavity counterparts, to write $V_1=V_{RF}+V_{B1}$ and $V_2=V_{RF}+V_{B2}$, thus separating the contributions V_{RF} and V_B due respectively to the RF power source and the electron beam.

Expressed in that way, the components of V_{RF} and V_B are

$$V_{B1} = iV_{B10},\ V_{B2} = iV_{B20}, \qquad (2), (3)$$

$$V_{RF1} = (2IrP_{TW})^{1/2}(C_1\cos\Phi_o + S_1\sin\Phi_o), \qquad (4)$$

$$V_{RF2} = (2IrP_{TW})^{1/2}(C_2\cos\Phi_o + S_2\sin\Phi_o), \qquad (5)$$

Here i is the first harmonic component of the beam current. For sufficiently short bunches the approximation $i=2i_o$ may be used. Shunt impedance r is one-half the "accelerator definition" r_a of shunt impedance usually employed in traveling wave accelerator formulae.

The coefficients in eq's 2 through 5 are;

$$V_{B10} = \alpha r\{\alpha(1-(\delta/I)^2-e^{-Il}[(1-(\delta/I)^2)\cos\delta l - 2(\delta/I)\sin\delta l])-Il\}/I \qquad (6)$$

$$V_{B20} = \alpha r\{\alpha(2(\delta/I)+e^{-Il}[((\delta/I)^2-1)\sin\delta l - 2(\delta/I)\cos\delta l])-\delta l\}/I \qquad (7)$$

$$C1 = +S2 = \alpha(1+e^{-Il}[(\delta/I)\sin\delta l-\cos\delta l])/I \qquad (8)$$

$$C2 = -S1 = \alpha((\delta/I)-e^{-Il}[(\delta/I)\cos\delta l+\sin\delta l])/I \qquad (9)$$

Parameter δ is the slip rate $\omega(V_p - c)/(V_p c)$ of the accelerating wave relative to the accelerated electrons, where ω is the beam RF angular frequency and V_p is the phase velocity of the TW accelerating wave; l is the accelerating length of the cavity; $r = r_a/2$ is the cavity shunt impedance per unit length; I is the cavity attenuation factor per unit length; parameter $\alpha = I^2/(I^2 + \delta^2)$.

P_{TW} and phase angle Φ_o appearing in eq's 4 and 5 are respectively the RF power fed to the TW cavity and the injection phase of the beam harmonic current i and the bunch centroids. When the cavity is used to accelerate a stored beam, P_{TW} and Φ_o are together selected to satisfy conditions which permit its optimum capture and stable circulation. Injection of i at Φ_o corresponds to having the beam bunch centroids at the synchronous phase Φ shown in Figure 1.

Stable circulation requires the centroid energy gain $V_{RF1} + V_{B1}$ to be matched to that of the beam circulation loss energy V_{LSS} of the beam. V_{LSS} is specified once the beam energy and ring magnetic bending radii are given. The required value of Φ_o is thus defined in terms of V_{LSS}, power P_{TW} and V_{B1} via eq's. 2 and 4.

3. Equivalent SW System.

The RF-excited and beam-excited TW cavity voltages V_{RF} and V_B have their exact counterparts in the SW system. In the latter case these are expressed in terms of the quality factor Q_o and tuning angle ψ of the cavity, and the system RF coupling parameter β.

V_{RF}, V_B and i are phase-related as shown in figure 1a. As in the TW cavity, ψ and Φ_{RF} designate the phases of the beam-induced and RF accelerating wave voltages relative to the beam current harmonic.

Development of the SW system theory is described in reference 2, where it is shown that

$$V_{RF} = (8\beta P_{SW}R)^{1/2}\cos\psi/(1+\beta), \quad (10)$$

$$V_B = iR\cos\psi/(1+\beta) \quad (11)$$

$$\simeq 2i_oR\cos\psi/(1+\beta) \quad \text{for narrow bunches,}$$

Where

$R = R_s/2$ = SW cavity effective shunt impedance,

Q_o = cavity quality factor,

$\tan\psi = -2Q_o(f-f_o)/(f_o(1+\beta))$,

f_o = frequency to which the cavity is tuned,

f = accelerated beam bunch and RF power source frequency,

i = accelerated beam first harmonic component,

i_o = beam average current.

4. Equivalent ψ, β Formulae.

Equivalent TW and SW systems are understood to be systems which accelerate identical beams so as to cause the beam electrons to experience the same energy and phase change as they circulate in the ring. For this to occur the RF voltages V_{RF} and V_B and their phases relative to that of the beam current in the two cases should be identical.

It is evident from figure 1 that angles ψ, Φ_{RF} and Φ are related to the components of the TW cavity V_{RF} and V_B through

$$\tan\psi = V_{B20}/V_{B10}, \quad (12)$$

$$\tan\Phi_{RF} = V_{RF2}/V_{RF1}, \quad (13)$$

$$\tan\Phi = (V_{RF2}+V_{B2})/(V_{RF1}+V_{B1}). \quad (14)$$

Also $V_{B1} = -V_B\cos\psi$. Substituting for V_{B1} from eq. 2 and for V_B from eq. 11, β is found to be given by

$$\beta+1 = -2R(\cos^2\psi)/V_{B10} \quad (15)$$

$$= -2R(\cos^2(\arctan(V_{B20}/V_{B10}))/V_{B10}$$

Since V_{B20} and V_{B10} depend only on parameters of the TW cavity (see eq's 6, 7), the equivalent CW system coupling parameter β and cavity tuning angle ψ are thus fixed in terms of those parameters and the shunt impedance of the CW cavity serving as the equivalent.

5. RF Power for equivalent performance.

The SW system power level P_{SW} required to produce equivalent beam handling performance in terms of the corresponding TW cavity power P_{TW} is obtained by using eq's 4 through 9, together with 12 and 13, to express V_{RF} as a function of the TW cavity parameters and power. Substituting for V_{RF} in these terms in eq. 10 yields

$$P_{SW}/P_{TW} = \quad (16)$$

$$IrR(C_1^2+C_2^2)(\cos^2(\arctan(V_{B20}/V_{B10}))/\beta(V_{B10})^2$$

References

[1] G.A. Loew, W.W. Hansen Microwave Lab Report #740, Stanford University, 1960.

[2] P.B. Wilson, High Energy Linacs: Applications to Storage Ring Systems and Linear Colliders, SLAC-Pub-2884, February 1982.

A High Power Cross-Field Amplifier at X-Band*

K. Eppley, J. Feinstein, K. Ko, N. Kroll, T. Lee and E. Nelson
Stanford Linear Accelerator Center, Stanford, CA 94309

Abstract

A high power cross-field amplifier is under development at SLAC with the objective of providing sufficient peak power to feed a section of an X-Band (11.424 GHz) accelerator without the need for pulse compression. The CFA being designed employs a conventional distributed secondary emission cathode but a novel anode structure which consists of an array of vane resonators alternatively coupled to a rectangular waveguide. The waveguide impedance (width) is tapered linearly from input to output so as to provide a constant RF voltage at the vane tips, leading to uniform power generation along the structure. Nominal design for this tube calls for 300 MW output power, 20 dB gain, DC voltage 142 KV, magnetic field 5 KG, anode-cathode gap 3.6 mm and total interaction length of about 60 cm. These specifications have been supported by computer simulations of both the RF slow wave structure as well as the electron space charge wave interaction. We have used ARGUS to model the cold circuit properties and CONDOR to model the electronic power conversion. An efficiency of 60 percent can be expected. We will discuss the details of the design effort.

I. Introduction

The cross-field amplifier (CFA) (Fig. 1) has been considered as a potential RF source to power the Next Linear Collider (NLC). It is a compact, low beam impedance device that can be manufactured at relatively low cost. In many applications, the CFA has been shown to generate very high peak powers at reasonable efficiencies. The NLC, however, calls for power and frequency requirements beyond those of existing tubes. SLAC has undertaken to develop a CFA capable of producing 100MW RF output power with a pulse width of 100 ns at X band without the need for pulse compression. The first experimental tube did not perform up to specifications. We will report here the design effort that went into the second planned CFA, taking into considerations the difficulties encountered in the first tube.

II. Design Considerations

The first design operated at the backward-wave space harmonic with a phase shift of 225 degrees/section and employed a cold platinum cathode. It had suffered from current limitations because of the interference at the cathode by the underlying forward-wave fundamental. At high enough RF fields, this fast-wave component could affect the back-bombarding electrons so as to cut off secondary emission. The new design will synchronize with the backward-wave fundamental with a phase shift of 150 degrees/section and will use a Beryllium oxide cathode which may allow higher peak power since it has a higher secondary yield and lower peak energy. The backward-wave mode is preferred because power can be generated in a shorter distance and the modulation of the reentrant beam is also minimized.

The second CFA will have a waveguide-coupled anode structure[1] (Fig. 2) with an overall lower impedance to increase peak power output at an optimal RF field of 100 kV across the vane tips. Higher RF fields are avoided to reduce problems with current depletion as discussed above, anode heating, and breakdown at the output, as well as to improve power production and phase stability at the input. To maintain this RF level throughout the tube, it is necessary to taper the impedance by making it high at the input end and low at the output end. A linear taper can be achieved by varying the guide width.

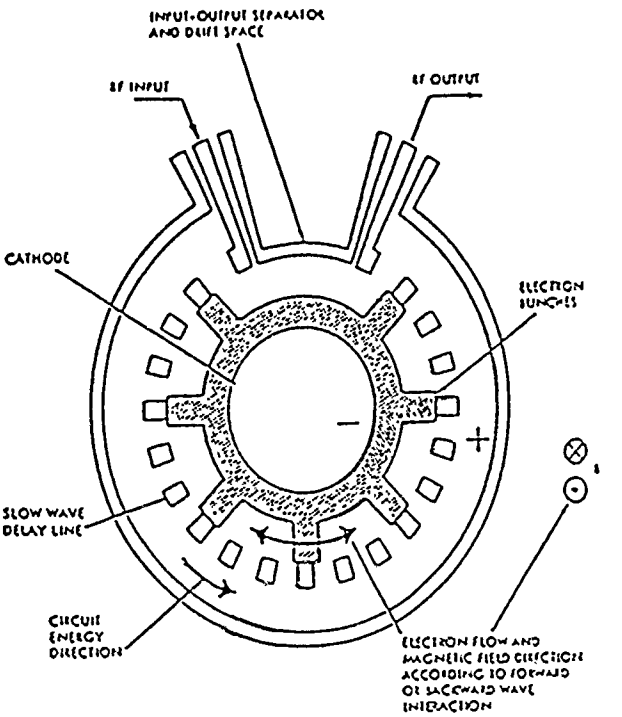


Fig. 1 Schematic of a CFA showing vanes, input, output and sever (drift space with no RF which isolates input and output).

* Work supported by Department of Energy contract DE-AC-0376SF00515

U.S. Government work not protected by U.S. Copyright.

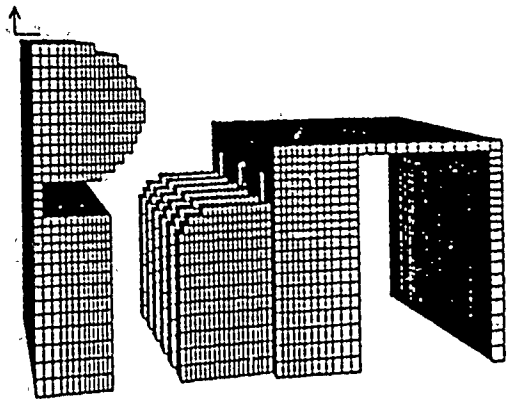


Fig. 2 ARGUS model of the upper half of a CFA section. To the left is the cathode and endhat. To the right is the waveguide coupled anode structure. Three coupling slots can be seen between the resonator and the waveguide.

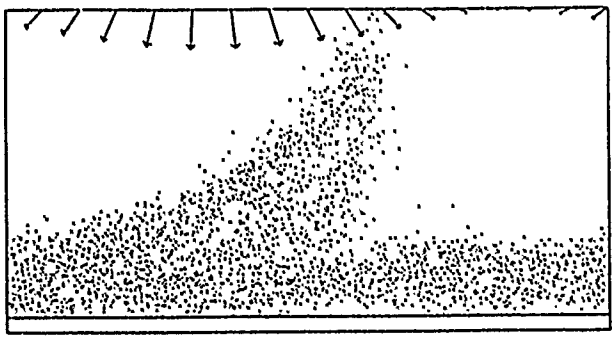


Fig. 3 Simulation of one (slow wave) wavelength of electron distribution showing electron hub and spoke.

III. Design Tools

The waveguide-coupled anode circuit is a 3-D periodic structure that supports both forward and backward waves. We have used the 3-D electromagnetic code ARGUS[2] with quasi-periodic boundary conditions to study the properties of the cold circuit. Dispersion curves and circuit parameters such as impedances can be obtained for the travelling wave modes.

Because CFA's are inherently nonlinear devices accurate modelling of the beam-circuit interaction is essential for design purposes. We have developed a simulation model based on the 2-D PIC code CONDOR[3] to evaluate the performance (e.g. gain and efficiency) of a CFA tube. The calculation of the beam-circuit interaction is similar to that described by Yu, Kooyers and Buneman[4]. The main advance of our model over previous simulations is the realistic tracking of absorption and secondary emission[5]. The simulation region is an integral number of wavelengths long, with periodic boundary conditions and time integration corresponds to progression in space around the tube. Fig. 3 is a time shot of the interaction showing spoke formation from the elctron hub.

IV. Mode Contamination and Competition

Some CFA's have operated successfully with the waveguide-coupled circuit but mode contamination is a concern. Mode purity can be maintained if the circuit is matched. One criteria for the matching is that the voltages across the resonators be equal. This means in effect that the vaned anode structure is unperturbed by the slotted guide so we can treat each separately. We use ARGUS to determine the dimensions of each structure for the appropiate phase shift at 11.424 GHz (150 degrees for the anode and 60 degrees for the slotted guide). The final dimensions for the coupled circuit are obtained by joining the two together and then making the adjustments to correct for any frequency shift.

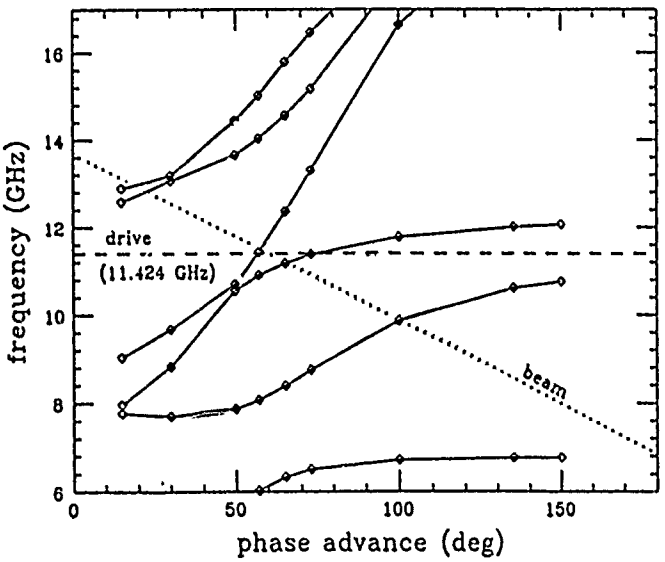


Fig. 4 Dispersion curves for the coupled structure near the input end.

A set of dispersion curves generated by ARGUS for the composite structure near the input end is shown in Fig. 4. An operating point can be identified near the 70 degree phase advance. Also evident is a high frequncy slot mode at a lower phase advance that can interact with the beam and which ARGUS found to have a high impedance. CONDOR simulations including this mode (at low amplitude) and the operating mode showed that the competing mode had enough gain to attain a power level high enough to interfere with the tube operation. A possible remedy being considered is to insert lossy material to selectively damp out this mode.

V. Power Generation and Efficiency

From our CONDOR simulations we have calculated the power generation rate and efficiency versus RF field strength as shown in Figs. 5 and 6. Based on these results, a good operating point has been identified with power generation near 300 MW and total efficiency of over 60 percent. The specifications for this tube are given in the table in section VI.

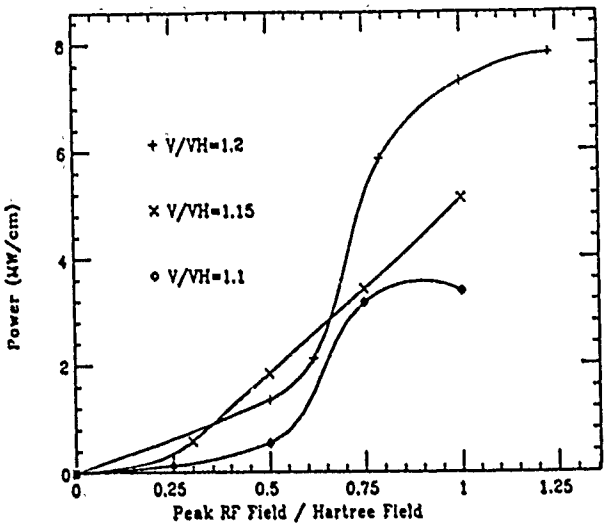


Fig. 5 Power generation rate vs. normalized RF field strength shown for three values of DC voltage/Hartree voltage.

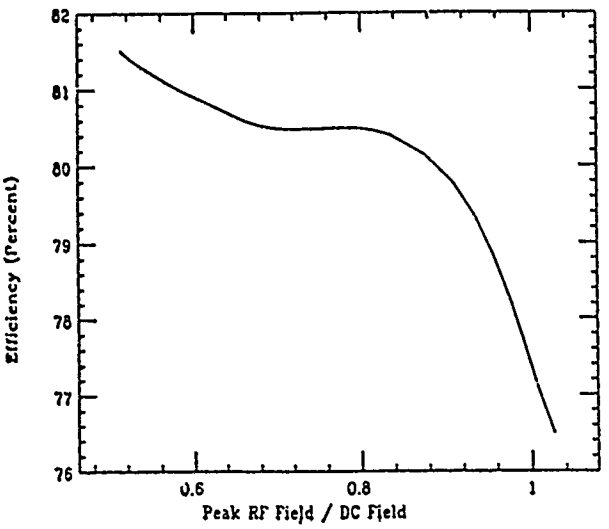


Fig. 6 Efficiency vs. normalized RF field strength.

VI. Table of Tube Specifications

Cathode dimensions: radius = 10.16 cm;
height = 1.65 cm
Anode dimensions: radius = 10.52 cm;
height = 1.65 cm
Anode-Cathode gap = 3.63 mm
Pitch = 2.67 mm
Vane dimensions: height = 1.65 cm,
depth = 4.98 mm
Vane gap width: inner = 1.016 mm; outer = 2.032 cm;
triangular
Waveguide dimensions: height = 1.905 cm;
depth = .762 to 7.62 cm
Slot dimensions: height = 1.905 cm;
depth = 4.57 mm; width = .508 mm
Frequency: 11.424 GHz
Peak Power Output: 300 MW
Power Generation Rate: 6 MW per cm of circumference
RF Pulse Width: 100 ns
Pulse repetition rate: 360 pps
Anode Voltage: 142 kV
Anode Current: 2600 Amp
Peak RF Voltage Across Vanes: 100 kV
Efficiency $\eta_e \cdot \eta_c = .72 \times .9 = 0.65$
Gain: 17 db
RF Drive Power: 6 MW
Emitter: Beryllium Oxide cold cathode
Cathode current density: 41 Amp/cm^2
Number of anode resonators: 225
Average anode dissipation: 40 W/cm^2 at 100 ns
Peak anode dissipation: 1.1 MW/cm^2
Mean anode bombardment energy: 27 kV
Phase shift per resonator: 150 degrees
Phase velocity: 7.31 $\times 10^7$ m/s
Hartree voltage: 118 kV
DC magnetic field: 5 kGauss

VII. References

[1] J. Feinstein and R. Collier, "A Class of Waveguide-Coupled Slow-Wave Structures," *IRE Transactions on Electron Devices*, pp. 9-15, January, 1959.

[2] A. Mondelli, C. Chang, A. Drobot, K. Ko, A. Mankofsky, and J. Petillo, "Application of the ARGUS code to accelerator design calculations," *Proceedings of the 1989 IEEE Particle Accelerator Conference*, Chicago, IL, March 20-23, 1989.

[3] B. Aiminetti, S. Brandon, K. Dyer, J. Moura, and D. Nielsen, Jr., *CONDOR User's Manual*, Livermore Computing Systems Document, Lawrence Livermore National Laboratory, Livermore, California, April, 1988.

[4] S. Yu, G. Kooyers, and O. Buneman, "Time Dependent Computer Analysis of Electron-Wave Interaction in Crossed Fields," *Journal of Applied Physics, 36*, 8, pp. 2550-2559, August, 1963.

[5] K. Eppley, "Numerical Simulation of Cross Field Amplifiers," *Proceedigns of the Conference on Computer Codes and the Linear Accelerator Community*, Los Alamos, N.M., January 22-25, 1990.

A 2d Field Solver for Periodic Structures with Special Corner Elements*

E. Nelson
Stanford Linear Accelerator Center, Stanford, CA 94309

Abstract

A 2d finite element field solver has been written which allows quasi-periodic boundary conditions, making it ideal for calculating travelling waves in periodic structures. Special elements are used at corners for improved accuracy. Comparisons with URMEL[1], URMEL-T[2], SUPERFISH[3] and analytic solutions are made, showing that this code yields better eigenvalues than the URMELs despite the use of a coarser mesh.

I. Introduction

YAP (an acronym for Yet Another Program) is a 2d finite element field solver capable of finding TE and TM modes in planar structures and monopole (TM_0 and TE_0) modes in axisymmetric structures. The structures can include symmetry and periodic boundaries. YAP's algebraic eigenvalue solver uses the inverse power method with an eigenvalue shift, which yields the mode with eigenvalue closest to a specified target eigenvalue. A typical problem uses up to 1000 nodes, consuming about 1 minute of IBM 3091 CPU time.

Readers not interested in the details of the finite element method (section II) or the special corner elements (section IV A) can skip these sections and still understand the rest of the paper.

II. Finite Element Formulation

The finite element formulation follows closely the formulation used by the PRUD-W[4] code. One case is presented here: the TE mode of a planar periodic structure.

Let the field B_z be complex and have an assumed time dependence $e^{-i\omega t}$, and let the interior of the structure be Ω (in the (x,y) plane) with three boundaries: Γ_{metal}, Γ_{right} and Γ_{left}. The latter two boundaries are the right and left boundaries of one cell of the periodic structure, and are connected by the rigid motion $R : \Gamma_{\text{left}} \rightarrow \Gamma_{\text{right}}$. This rigid motion may include rotation as well as translation. The fields in the periodic structure are decomposed into modes with phase advance ϕ, in accordance with Floquet's theorem. The phase advance can be any real number.

A. Strong Formulation

The usual statement of Maxwell's equations is the strong formulation. given the phase advance ϕ, find the eigenvalues ω^2/c^2 and eigenmodes B_z such that

$$\left(\nabla^2 + \frac{\omega^2}{c^2}\right) B_z = 0 \quad \text{in } \Omega, \tag{1a}$$

$$\hat{n} \cdot \nabla B_z = 0 \quad \text{on } \Gamma_{\text{metal}}, \tag{1b}$$

$$B_z(R\vec{x}) = B_z(\vec{x})e^{i\phi} \quad \forall \vec{x} \in \Gamma_{\text{left}}, \tag{1c}$$

$$\hat{n} \cdot \nabla B_z(R\vec{x}) = -\hat{n} \cdot \nabla B_z(\vec{x})e^{i\phi} \quad \forall \vec{x} \in \Gamma_{\text{left}}. \tag{1d}$$

Equations (1c) and (1d) are the quasi-periodic boundary condition.

B. Weak Formulation

An equivalent statement of the problem is the weak formulation: given the phase advance ϕ, find the eigenvalues ω^2/c^2 and eigenmodes $B_z \in \mathcal{V}$ such that $\forall v \in \mathcal{V}$

$$\int_\Omega \nabla v^* \cdot \nabla B_z - \frac{\omega^2}{c^2} v^* B_z \, d\Omega = 0 \tag{2a}$$

where

$$\mathcal{V} = \left\{ v \in H^1(\Omega) : v(R\vec{x}) = v(\vec{x})e^{i\phi} \quad \forall \vec{x} \in \Gamma_{\text{left}} \right\} \tag{2b}$$

and $H^1(\Omega)$ is a complex Hilbert space. The weak formulation is obtained from the strong formulation by multiplying equation (1a) by v^* and integrating by parts.

C. Galerkin and Finite Element Formulations

The Galerkin formulation restricts v and B_z to a finite dimensional subspace $\mathcal{V}^h \subset \mathcal{V}$. This formulation reduces to an algebraic eigenvalue problem which is solved to yield approximate eigenvalues and eigenmodes.

The finite element formulation is the Galerkin formulation with a particular choice of $\mathcal{V}^h$. The domain Ω is partitioned into elements Ω_e, and $\mathcal{V}^h$ is chosen to be a space of functions which are piecewise simple (e.g. linear or quadratic on each element) and continuous. Figure 1(a) is an example of a partition. The choice of $\mathcal{V}^h$ is where YAP and PRUD-W diverge. YAP uses 6-node quadratic lagrange-type triangular elements and special corner elements while PRUD-W uses 8-node curvilinear quadrilateral elements.

In YAP, the fields are quadratic on the master element $\hat{\Omega}$ shown in figure 1(b), where each node represents a separate basis function. These fields are mapped to the actual element Ω_e using a quadratic transformation $T_e : \hat{\Omega} \rightarrow \Omega_e$. This allows the sides of an element to be curved in order to closely follow the boundary of Ω, as seen in elements Ω_1, Ω_3 and Ω_7 of figure 1(a).

* Work supported by Department of Energy contract DE-AC03-76SF00515

U.S. Government work not protected by U.S. Copyright.

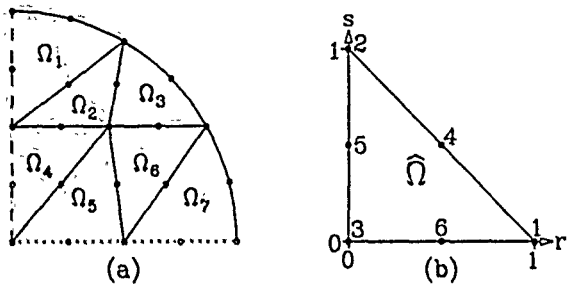


Figure 1. (a) A sphere partitioned into elements. The dotted line is the axis and the dashed line is a symmetry plane. (b) The master element $\widehat{\Omega}$ and its 6 nodes.

III. Analytic Tests

YAP was tested on some analytically solvable structures. Results for two test structures are shown in figure 2. The cutoff TM_{01} mode of a 1 cm length of circular waveguide with 1 cm radius was calculated with YAP and URMEL. The analytic eigenvalue is $\omega^2/c^2 = 5.783185964/\rho^2$, where ρ is the radius of the waveguide. Both programs converged smoothly as the mesh was refined. This allows extrapolation to an infinitely refined mesh, which yields an eigenvalue with significantly reduced error.

The lowest TM_{010} mode of a sphere with 1 cm radius was calculated with YAP, URMEL, URMEL-T and SUPERFISH. The analytic eigenvalue is $\omega^2/c^2 = 7.527929583/r^2$, where r is the radius of the sphere. URMEL and URMEL-T do not converge smoothly as the mesh is refined, making extrapolation difficult. SUPERFISH and YAP converge smoothly.

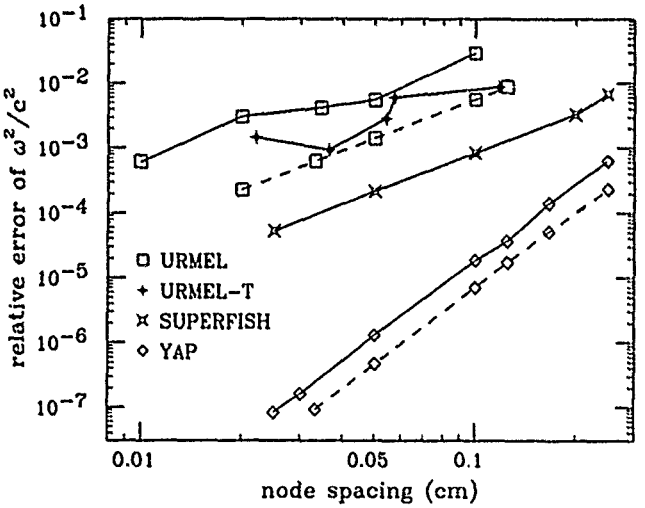


Figure 2. Relative error versus mesh size. The solid lines are tests on a sphere ($r = 1.0$ cm) and the dashed lines are tests on a circular waveguide ($\rho = 1.0$ cm).

The eigenvalues returned by YAP are good, even for coarse meshes. The coarsest sphere test used the mesh of figure 1(a) consisting of only 7 elements and gives an eigenvalue with less than 0.1% error. This is much better than SUPERFISH or the URMELs using a coarse mesh. Also, YAP converges faster as the mesh is refined. For these tests the error dependence on element size, h, is $\mathcal{O}(h^4)$ for YAP, while for SUPERFISH and the URMELs it is $\mathcal{O}(h^2)$. This is the expected behavior, but unfortunately it deteriorates when the structure has sharp corners.

IV. Corners

Consider a sharp corner as shown in figure 3(a). The field w (for example, B_z in a planar TE mode) near the corner has the form

$$w(\rho,\phi) = a_0 + a_1\cos(\pi\phi/\beta)\rho^{\pi/\beta} + a_2\cos(2\pi\phi/\beta)\rho^{2\pi/\beta} + \cdots \tag{3}$$

where ρ is the distance from the corner, β is the corner angle and ϕ is the angle, $0 \le \phi \le \beta$. Some fields may use sin instead of cos and have $a_0 = 0$ in order to satisfy boundary conditions at the metal wall. In either case, the field is not approximated well by the quadratic elements, so a special 7-node corner element[5] is used instead.

A. Details of the Special Corner Element

Figure 3 contains a diagram of the special corner element. Node 3 is the corner node. The basis functions on the master corner element $\widehat{\Omega}$ are:

$$\begin{aligned}
N_1 &= u^\alpha(2^\alpha u^\alpha - 1)(1-v)(1-2v)/(2^\alpha - 1)\\
N_2 &= u^\alpha(2^\alpha u^\alpha - 1)(2v-1)v/(2^\alpha - 1)\\
N_3 &= (1-2^\alpha u^\alpha)(1-u^\alpha)\\
N_4 &= u^\alpha(2^\alpha u^\alpha - 1)4v(1-v)/(2^\alpha - 1)\\
N_5 &= 4^\alpha u^\alpha(1-u^\alpha)v(2v-1)/(2^\alpha - 1)\\
N_6 &= 4^\alpha u^\alpha(1-u^\alpha)(1-v)(1-2v)/(2^\alpha - 1)\\
N_7 &= 4^\alpha u^\alpha(1-u^\alpha)4v(1-v)/(2^\alpha - 1)
\end{aligned} \tag{4}$$

where $\alpha = \pi/\beta$ and

$$\begin{aligned}
u &= r+s & r &= u(1-v)\\
v &= s/(r+s) & s &= uv.
\end{aligned} \tag{5}$$

The transformation $T_e : \widehat{\Omega} \to \Omega_e$ is the standard quadratic one. The global basis functions are continuous provided the elements are properly assembled.

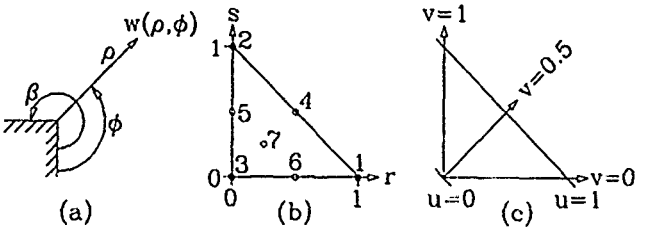


Figure 3. A corner (a), and the nodes (b) and (u,v) coordinates (c) of the master corner element $\widehat{\Omega}$.

B. Tests on a Ridged Waveguide

Figure 4 shows test results of URMEL and YAP on the lowest TE mode of a ridged waveguide. The waveguide dimensions are 1 cm by 0.5 cm with a 0.5 cm by 0.25 cm ridge. Extrapolation to an infinitely refined mesh yields $\omega^2/c^2 = 5.06016\ \mathrm{cm}^{-2}$.

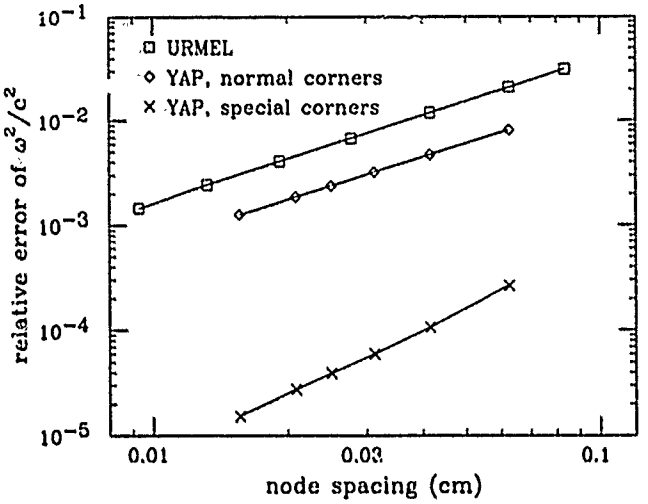


Figure 4. Relative error versus mesh size for a ridged waveguide.

For this structure URMEL and YAP without special corners are similar. The error dependence on the mesh size is $\mathcal{O}(h^{4/3})$ for both programs. This agrees with the theoretical eigenvalue error, $\mathcal{O}(h^{2\pi/\beta})$, where $\beta > \pi$ is the sharpest corner in the structure. Without special corner elements, YAP's error is only a factor of two better than URMEL for a given mesh size.

The special corner elements give YAP significantly improved accuracy and improve the error dependence to $\mathcal{O}(h^2)$, but this is still short of the behavior seen in smooth structures.

V. Quasi-Periodic Boundary Conditions

The quasi-periodic boundary conditions are helpful and sometimes necessary when modelling periodic structures. Only a single period of the structure is modelled, yielding the travelling wave solution for any desired phase advance. If only metal and symmetry boundaries are available, many periods of the structure must be modelled in order to obtain an equivalent standing wave solution for only a few phase advances. Furthermore, only symmetric periodic structures can be modelled this way. No such restriction applies when quasi-periodic boundary conditions are used.

Figure 5 is an example of the use of quasi-periodic boundaries to generate a dispersion curve. Generating the same data using metal and symmetry boundary conditions would require modelling at least six periods and consume more computer time or yield less accurate results. Identifying the phase advance of each mode would also be required.

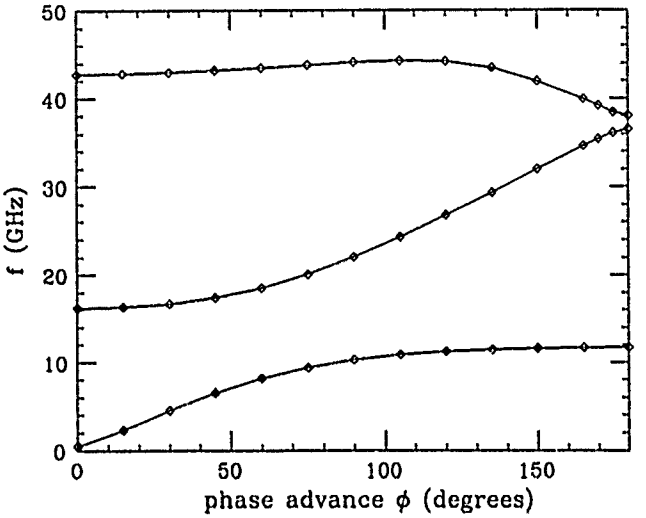


Figure 5. Dispersion curves obtained with quasi-periodic boundaries on a single period of a cross-field amplifier structure.

VI. Conclusion

The finite element method employed by YAP is more accurate than URMEL, URMEL-T and SUPERFISH.

The special corner elements help significantly for structures with sharp corners, but their performance does not match the performance seen with smooth structures. This indicates that the computational effort spent on corner regions is still inadequate compared to other regions where the field is smooth. This can be remedied by either an improved special corner element or a technique like adaptive mesh refinement.

The quasi-periodic boundary condition is an important part of a field solver because it allows asymmetric periodic structures to be modelled and saves time and effort for both the computer and the user.

I would like to thank Juwen Wang for running SUPERFISH tests on a sphere.

VII. References

[1] T. Weiland, Nuclear Instruments and Methods **216**, 329 (1983)

[2] U. Van Rienen and T. Weiland, Particle Accelerators **20**, 239 (1987)

[3] K. Halbach and R. F. Holsinger, Particle Accelerators **7**, 213 (1976)

[4] A. G. Daikovsky, Yu. I. Partugalov and A. D. Ryabov, Particle Accelerators **20**, 23 (1986)

[5] T. J. R. Hughes and J. E. Akin, International Journal for Numerical Methods in Engineering, **15** 733 (1980)

GATED FIELD-EMISSION CATHODES FOR MICROWAVE DEVICES

P. M. McIntyre, H.P. Demroff, S.M. Elliott, B. Lee, J.D. Legg
Y. Pang, D.L. Parker, M. Popovic, M.D. Stewart,
M.H. Weichold, W. Yu, and W.K. Yue
Department of Physics
Department of Electrical Engineering
Texas A&M University
College Station, Texas 77843-4242

Abstract

The Accelerator Research Laboratory at Texas A&M University is developing gated field-emitter cathodes for microwave and millimeter-wave applications. The cathode consists of an array of gated field-emitters which are modulated at microwave frequency to produce a fully modulated electron beam. Field-emitter structures under development include gated knife-edge arrays, reentrant cusps, and porous silicon. All feature extremely high transconductance, low noise, and rugged structure as compared to earlier field-emitter structures.

The Accelerator Research Laboratory (ARL) is developing the gigatron technology [1] for high power mm-wave linac drivers. Gigatron is based on three novel design concepts: a gated field-emitter array to produce an electron beam which is bunched at birth; configuration of the cathode and accelerating region to produce a ribbon beam to eliminate space charge and dispersion limitations; and traveling wave couplers at both the input and output to obtain optimum power transfer even across a wide ribbon beam. The present work focuses on the development of a gated field-emitter array suitable for microwave modulation in a cathode in the gigatron.

Beginning in 1976, C.A. Spindt et al. pioneered the fabrication of gated field-emitter arrays for display applications [2]. Figure 1 shows a typical Spindt tip array. These arrays have been fabricated on center-center spacings as close as 2.5 μm, and have produced electron current densities as high as 1000 A/cm^2 with a gate modulation $\sim$ 100 V. They have been operated for periods of thousands of hours, and exhibit uniform current density over the emitting array. H. Gray et al. has developed designs of tip arrays for vacuum integrated circuits and for microwave power devices [3].

Field Emission at the Cathode Surface

Spindt [2] has analyzed the measured I/V response in terms of the classic Fowler-Nordheim theory:

$$j = aE^2 \exp\left(-b\phi^{3/2}/E\right) \qquad (1)$$

where ϕ (4.5 eV for Mo) is the surface work function, and E is the surface field. In his experiments Spindt has verified Eq. (1) over six decades of cathode current. The experimentally measured quantities are voltage and current; connection to Eq. (1) thus yields a precise measure of the *effective* emitting area at the cathode surface. Spindt shows that the radius of the emitting region thus obtained is only $r_e \sim 2$ Å, a patch a few atoms in diameter. This is to be contrasted to the physical tip radius $\sim$500 Å. Spindt and Herrmannsfeldt [4] have interpreted these results to indicate that emission occurs from atomic-scale surface features which form continuously under application of electric field. These features could be due either to mobile surface contaminants, such as an oxide layer, which produce a local reduction in work function [5], or to whiskers or bumps which protrude from the surface.

Why does emission occur from only one such microregion on each tip surface? The answer lies in an analysis of the space charge associated with the emitted current within the tip-gate region. Suppose a tip geometry such as that of Figure 1, on which emission is occurring from a particular microregion as shown. The emission produces a space charge depression which extends laterally to a distance comparable to the gap g between tip and gate. In the geometry of Figure 1, the most emissive microregion will emit, but its emission will suppress emission from any other microregion on the tip surface. This "natural selection" of one mi-

0-7803-0135-8/91$01.00 ©IEEE

croregion conveys two properties which create potential limits for microwave cathodes. First, the selection is intrinsically unstable: emission can jump from microregion to microregion, producing noise in the microwave emission current. Second, the emission is controlled by the field produced across the tip-base gap g, while the capacitance of the gate/base junction is determined by the gap t between the planar layers of gate and base. The power gain for a microwave cathode scales as $G \sim (t^2/s^2 g)^2$, where s is the mean spacing of emitting microregions. For a tip geometry, $t \sim 1$ μm, $s \sim 2.5$ μm, $g \sim 0.5$ μm, and $G \sim 0.1$. For the ARL stripline and cusp geometries, $t \sim 1$ μm, $s \sim 0.7$ μm, $g \sim 0.1$ μm, and $G \sim 400$ – a thousandfold improvement for microwave modulation.

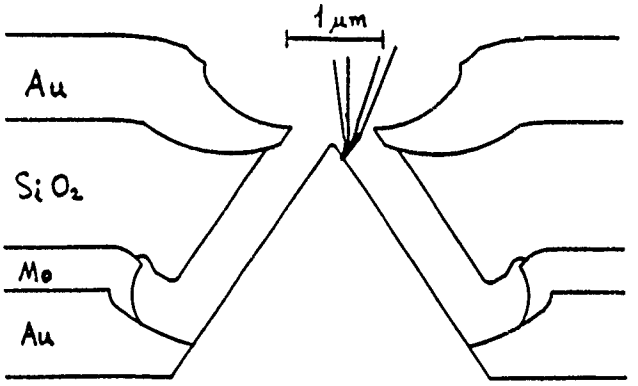


Figure 1. Typical tip geometry for gate field-emitter.

Several challenges confront the development of field-emitter cathodes for microwave and mm-wave devices. First, while the voltage required for modulation is modest, the gate-base junction is very capacitive, and hence exhibits very low impedance at high frequency. Second, recent studies of the physics of the field emission process on a tip [4] show that emission typically occurs from only one microregion, with a size scale as small as ~ 10 Å^2. Third, the input coupler must provide a low-impedance charging path to all tips on an array. ARL and the Institute for Solid State Electronics (ISSE) have developed several approaches to field-emitter arrays which address these challenges: a stripline geometry in which the emitting region is a knife-edge supported on a narrow gap from the gate (Figure 2); an inverted cusp in which the tip is replaced by a thin disc of low-work-function material supported on a cusped column above a metalized base (Figure 3); and a porous silicon cathode in which emitting channels are formed with a typical spacing ~50 Å (Figure 4).

Knife-Edge Emitter Geometry

The knife-edge cathode geometry is shown in Figure 2. The emitting structure is a knife-edge which is formed by etching a thin Mo layer in a multi-laminar deposition of Au-SiO_2-Au-Mo-SiO_2-Au. The gate/base spacing is ~1000 Å, and can be routinely controlled to ±50 Å over an entire wafer. A gate-base voltage of 100 V produces a surface field at the knife-edge of 1.7 GV/m, sufficient to produce 0.3 μA emission current [6] from each microregion. We have established a working dielectric strength of 700 V/μm in the SiO_2 layer.

A second advantage of this design is the enhanced density of emitting microregions. Regions of reduced work function develop along the knife-edge length at a spacing roughly equal to the gap g ~1000 Å between knife-edge and gate —a ten times greater emitter density than tip arrays.

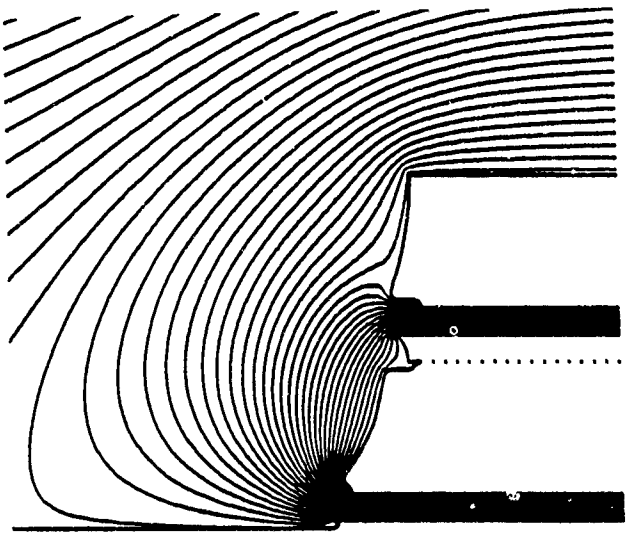


Figure 2. Knife-edge emitter geometry.

Inverted Cusp Cathodes

Figure 3 shows an array of titanium cathodes in which a plasma etch is used to create a thin metal disc supported from a column of small radius. This array was fabricated at ISSE by Legg et al. [7]. A gate layer, formed by a self-aligned deposition of SiO_2 and metal, produces a narrow gap g ~1000 Å between the cathode disc and the annular gate.

The cusp geometry makes it possible to obtain a larger number of emitting microregions on the outer edge of each disc, spaced by a distance ~ g ~1000 Å. This structure is being fabricated with a low-work-function cathode surface (cermet) and low-impedance metalizations on gate and base.

Porous Silicon Emitting Surfaces

Yue et al. [8] have developed a novel material in which a porous layer is grown into a silicon wafer through electrochemical anodization in concentrated hydrofluoric acid. A porous silicon film made by anodizing a heavily doped silicon wafer produces pores perpendicular to the film surface through the whole porous layer with a thickness which can be controlled in the range 0.1- 10 μm. By controlling current density and anodization time, the diameters of pores can be varied from 10 Å to 100 Å with pore density from 10^8 to 10^{11} pores/mm^2. The porous layer is then fully oxidized in a thermal oxide process. At the interface between porous SiO_2 and bulk silicon substrate, an extremely sharp silicon tip is formed beneath each pore.

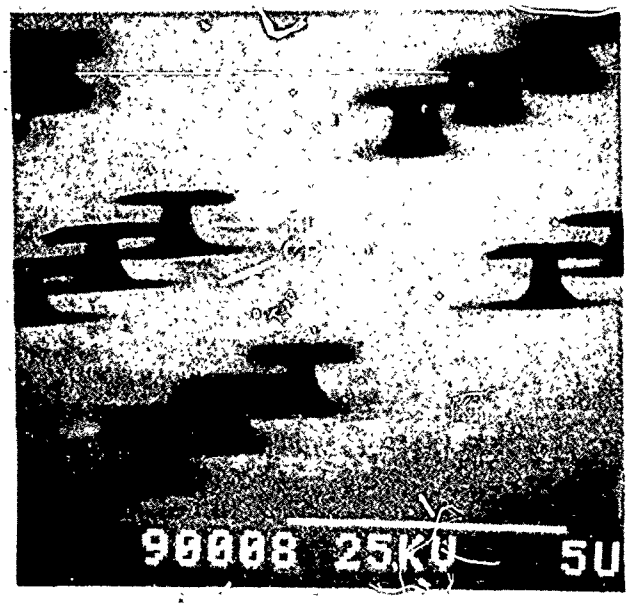


Figure 3. SEM micrograph of inverted cusp cathode array.

During the past year diode arrays of porous silicon have been fabricated at ISSE and the d.c. Fowler-Nordheim response has been measured [3]. The diode employed the above emitters while metal deposited on the surface of the oxidized porous silicon film served as the anode. The turn-on voltage of these diodes was shown to be as low as 3 to 4 volts. An emission current of 25 A/cm^2 can be produced by a 10 V modulation. The I-V characteristic follows the Fowler-Nordheim relation over three decades of current and the I-V relations are stable with temperatures ranging from 25°C up to 250°C. The immense number of independent emitter channels results in an extremely low-noise emission current – a key requirement for mm-wave applications.

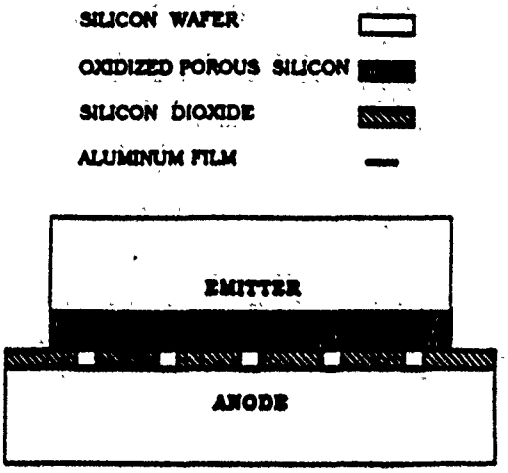


Figure 4. Diode test geometry for porous silicon field-emitter cathode.

We are developing gated microwave cathodes using these three design approaches. During the next year we will evaluate their performance and proceed to microwave testing for power tube cathodes.

This work was supported by contract #DE-FG02-91ER40613, U.S. Department of Energy.

References

[1] P.M. McIntyre *et al.*, IEEE Trans. Plasma Sci. **26**, 2581, 1988.

[2] C.A. Spindt *et al.*, J. Appl. Phys. **47**, 5248 (1976).

[3] D.J. Campisi and H. Gray, Proc. Mat. Res. Soc. Meeting, 1986.

[4] W.B. Herrmannsfeldt *et al.*, "High-resolution simulation of field emission," Third Int'l Conf. on Charged Particle Beams, Toulouse, France (1990).

[5] I. Brodie, Surface Science **70**, 186 (1976).

[6] K. Ken Chin and R.B. Marcus, J. Vac. Sci. Technol. **A8**, 3586 (1990).

[7] J.D. Legg *et al.*, "Fabrication Process for Field Emission Structures," submitted to Vacuum Microelectronics Conference '90.

[8] W.K. Yue *et al.*, "Oxidized Porous Silicon Field Emission Devices," SSEI preprint 1991.

High Power X-Band Coaxial Amplifier Experiments

T.J. Davis and J.A. Nation
Laboratory of Plasma Studies and School of Electrical Engineering
Cornell University, Ithaca, NY 14853

Abstract

Studies are continuing on the development of X-band coaxial microwave amplifiers as a source for next generation linear colliders. Coaxial amplifiers employ an annular electron beam propagating between inner and outer drift tube conductors, a configuration which allows large increases in beam current over standard pencil beam amplifiers. Large average diameter systems may still be used without mode competition since TM mode cutoff frequencies are controlled by the separation between conductors. A number of amplifier configurations are being studied, all primed by a driven initial cavity which resonates around 9 GHz. Simple theory of coaxial systems and particle-in-cell simulations are presented, as well as initial experimental results using a 420 keV, 7-8 kA, 9 cm diameter annular beam.

I. Introduction

Next generation designs of e^+e^- linear colliders have set stringent requirements on the r.f. drive source. In order to achieve the high accelerating gradients (>100 MeV/m) necessary for ~ TeV beam energies, an r.f. driver operating above X-band and 500 MW peak power levels will be needed. Several competing technologies for this source are curren ly being examined, including intensive efforts in relativistic klystrons [1] and gyroklystrons [2]. A developing method is to use binary energy compression [3] to raise the peak power and reduce the pulse length of a lower power tube.

Without the need for pulse compression, an alternative to these hollow tube amplifier configurations is the development of coaxial amplifiers. This geometry uses an annular electron beam propagating between inner and outer drift tube conductors. Previous coaxial high power microwave devices have been built in oscillator configurations [4], and lower frequency (~ 1 GHz) coaxial amplifiers may be capable of ultra-high powers [5].

The coaxial geometry addresses two fundamental limitations of hollow tube devices. First, the use of a large average diameter system reduces the power density (and hence the surface fields) for a given power level, effectively by increasing the cross sectional area of the device. This reduces the possibility of r.f. pulse shortening and field emission in the microwave structures, conditions often seen in highly stressed relativistic klystrons. Second, the coaxial geometry allows for propagation of much higher current beams than conventional pencil beam amplifiers, as a result of increases in both the beam cross sectional area and the limiting current of the system. This increase in beam current, up to a factor of ten in many instances, may enable a higher peak power device at lower beam energies, hence at considerably lower cost. The coaxial configuration does allow TEM as well as higher order TE modes to propagate in the drift regions of the system. Single TM mode interactions may still be designed, since the cutoff frequencies of these modes is controlled only by the separation distance between conductors, not the average diameter. However, control of the TEM and TE modes remains the most difficult problem in design and operation of these amplifiers.

II. Design

The simplest conceptual design for a coaxial amplifier is illustrated in figure 1. An annular electron beam is propagated along the coaxial drift region and is initially modulated by a driven input cavity. The modulated beam is then passed through downstream sections, shown in the figure as a rippled wall slow wave structure (but just as easily other cavities or a mixture of both), to enhance the beam modulation and extract power.

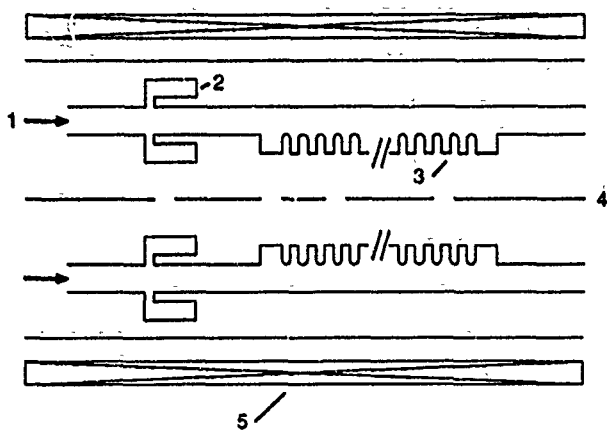


Fig 1. Simple coaxial amplifier. (1) Annular electron beam, (2) driven input cavity, (3) slow wave structure, (4) centerline, (5) field coils.

The input cavity geometry, designed using the SUPERFISII code, oscillates in a 5/2 wavelength mode with a maximal axial electric field at the beam location. $5/2\lambda$ is the approximate bounce length of a TEM wave traveling between inner and outer sections of the cavity This geometry was chosen for its comparatively high Q factors and manufacturing ease relative to other designs

Coaxial slow wave structure designs are straightforward extensions of their hollow tube counterparts Either

0-7803-0135-8/91$01.00 ©IEEE

periodic or Cerenkov structures can be used to create the $v_\phi < c$ condition needed for direct beam interaction. Doubly lined coaxial Cerenkov systems have been studied analytically [6]. Note, however, that a dielectric liner on only the inner or outer conductor may also force a $v_\phi < c$ condition. As an example, the dispersion relation for azimuthally symmetric modes in a coaxial system with a dielectric liner on the inner conductor only is

$$\frac{J_0(k_2 r_{id})Y_0(k_2 r_o) - J_0(k_2 r_o)Y_0(k_2 r_{id})}{J_0(k_1 r_{id})Y_0(k_1 r_i) - J_0(k_1 r_i)Y_0(k_1 r_{id})} = \frac{k_1}{k_2 \epsilon} \frac{J_0'(k_2 r_{id})Y_0(k_2 r_o) - J_0(k_2 r_o)Y_0'(k_2 r_{id})}{J_0'(k_1 r_{id})Y_0(k_1 r_i) - J_0(k_1 r_i)Y_0'(k_1 r_{id})} \quad (1)$$

where $k_1^2 = \omega^2\epsilon/c^2 - \beta^2$ and $k_2^2 = \omega^2/c^2 - \beta^2$ are complex, β is the wavenumber, ϵ is the relative dielectric constant of the liner, and r_i, r_o, and r_{id} are the inner conductor, outer conductor, and dielectric radius respectively. Figure 2 compares dispersion relations for a coaxial system with a periodic inner conductor and with a dielectric lined inner conductor. Both are designed to have forward wave interactions near 9 GHz. Both also exhibit a TEM-like mode down to zero frequency. But due to broad tunability and ease of modeling, design, and manufacturing, dielectric liners will initially be used in the experiments.

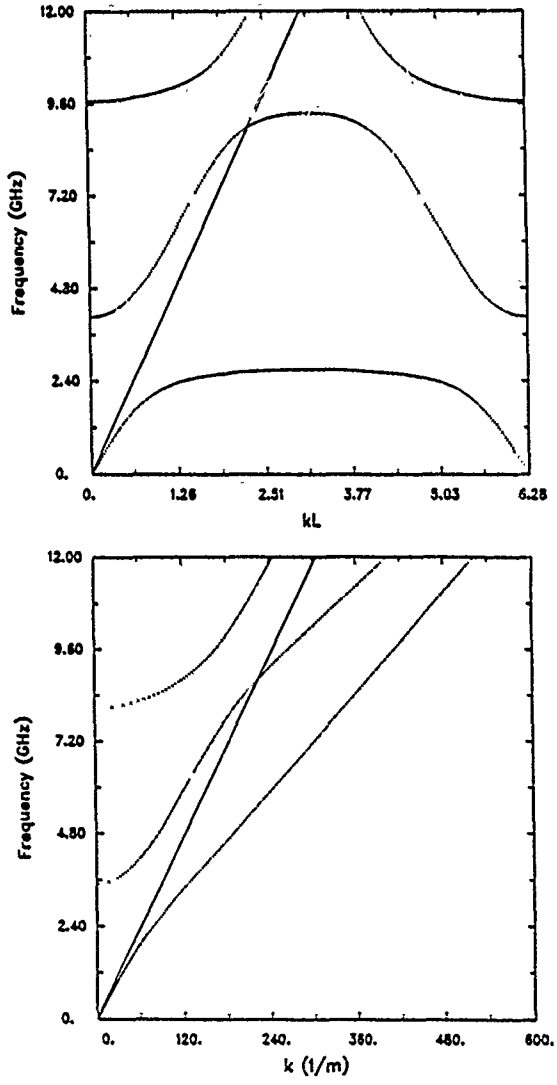


Fig 2 Comparison of dispersion relations for a coaxial system with a periodic inner conductor (above) and a dielectric lined inner conductor (below). Solid lines are beam parameters.

III. Simulations

Various components of these amplifiers have been simulated using the 2 1/2D particle-in-cell code MAGIC. The geometry of the simulation space and beam parameters exactly follow the real experimental quantities. Cavity and structure frequencies are determined by cold tests without particles. The simulation geometry is closed using absorbing boundaries to eliminate any wave reflections at the end of the drift space.

Multiple cavity klystron geometries have been tested and compared to hollow tube relativistic klystron simulations. Unlike the pencil beam case and coaxial klystron simulations reported elsewhere [5], this coaxial system fails to exhibit gain even though substantial modulation can be imposed on the beam. This discrepancy could be due to two factors. First, due to the nature of the time advance algorithm, simulation cavities tend to have low Q factors (<50) and hence maintain very little stored energy relative to actual cavities. Second, and more important, the use of a slightly overmoded cavity (as in the $5/2\lambda$ design) increases the harmonic content of the beam modulation and degrades the efficiency of the output coupling. A better method for system gain is the use of a single mode traveling wave structure.

The dielectric interaction shown previously has recently been simulated using new capabilities in MAGIC. The propagation characteristics of the structure wave match those predicted by the analytic theory. A driven cavity, identical in frequency to the predicted interaction, has been used to impose initial modulation on the beam prior to the dielectric structure. As shown in figure 3, the bunching process started by the cavity is enhanced due to the unstable interaction in the dielectric region.

IV. Experiments

The electron beam in the experiments is generated using a modified ETA module with a 2:1 output ferrite core transformer. The output voltage of this system is 400-500 kV at nominally 40 ohms. A one Tesla solenoidal magnetic field guides the beam down a drift tube of 7.5 cm inner diameter and 9.8 cm outer diameter. Within this drift space no TM mode will propagate.

A number of field emission foilless diode geometries were tested to maximize beam current and optimize beam propagation. Currently, a conical cathode with a graphite knife edge is used to create a uniform beam of 9 cm diameter and 2 mm thickness. The geometry of the diode and equipotential contours is shown in figure 4. This arrangement consistently produces currents of 7-8 kA at

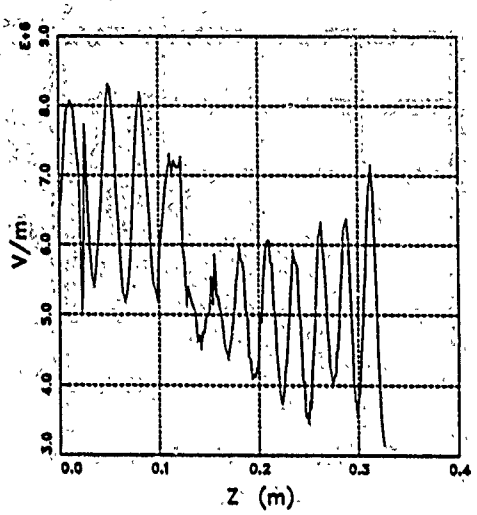


Fig 3. A simulation plot of E_r vs. distance, showing bunching enhancement past the discontinuity where a dielectric liner begins.

420 kV pulse voltages. The conical shape inhibits shank emission, reducing the beam thickness and temperature. Beam propagation and uniformity has been measured using thermal damage paper and is found to be consistent over the meter propagation distance.

Experiments are continuing to characterize the $5/2\lambda$ cavity. The initial coupling arrangement to the cavity was found to excite numerous higher order azimuthal modes and has been changed to a more uniform and higher power cylindrical-coaxial transition. Wires mounted across the cavity aperture have been used to raise cavity Q and isolate resonant peaks, but are too susceptible to beam damage to be used consistently in experiments.

A network analyzer trace of the cavity resonances is shown in figure 5. The dominant resonance is broadband due to coupling of energy out of the cavity aperture. Other peaks correspond to the high order azimuthal modes. Current experiments are attempting to measure the modulation resulting from this cavity using $\dot{B}_\theta$ probes mounted on the drift tube.

V. Conclusions

The choice of a coaxial geometry enables the use of high current, large diameter annular beams, and allows for greater output powers because of reduced surface fields. Since breakdown limits are relaxed, a dielectric lined traveling wave structure is planned to provide a substantial fraction of system gain. Experiments are continuing to characterize the driven input cavity, an essential part of several amplifier configurations.

VI. Acknowledgements

This work was supported by the U. S. Department of Energy, under contract #DE-AC02-80ER10569, and in part by AFOSR and SDIO-IST managed by Harry Diamond Laboratories.

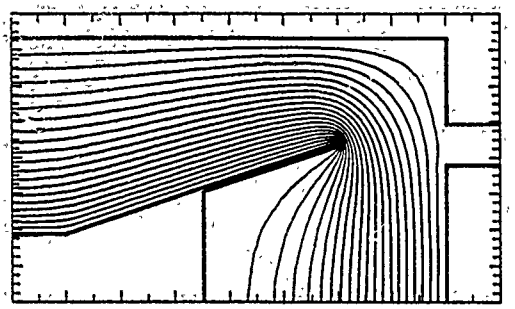


Fig 4. Equipotential contours of annular beam diode.

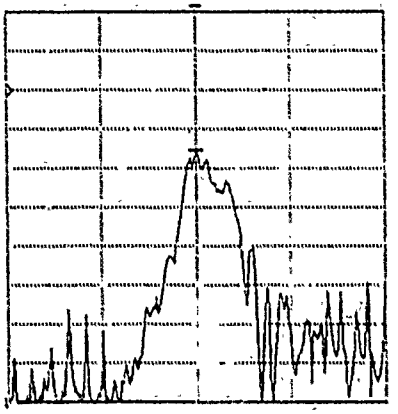


Fig 5. Network analyzer trace of resonances in $5/2\lambda$ cavity.

The MAGIC particle-in-cell code was obtained from Mission Research Corporation through the sponsorship of AFOSR.

VII. References

[1] M.A. Allen et al., "Relativistic Klystrons," in *Proceedings of the 1989 Particle Accelerator Conference*, Chicago, Ill., March 1989, pp. 1123-1127.

[2] K.R. Chu, V. Granatstein, P.E. Latham, W. Lawson, and C.D. Striffler, "A 30-MW Gyroklystron-Amplifier Design for High-Energy Linear Accelerators," IEEE Trans. Plasma Sci., vol. 13, pp. 424-434, December 1985.

[3] Z.D. Farkas, "Binary Peak Power Multiplier and its Application to Linear Accelerator Design," IEEE Trans. Microwave Theory Tech., vol. 34, pp. 1036-1043, October 1986.

[4] John A. Nation, "On the Coupling of an High-Current Relativistic Electron Beam to a Slow Wave Structure," Appl. Phys. Lett. vol. 17, pp. 491-494, December 1970.

[5] J. Krall, M. Friedman, Y.Y. Lau, and V. Serlin, "Simulation Studies of a Klystronlike Amplifier Operating in the 10-100 GW Regime," NRL Memorandum Report 6750, November 1990.

[6] Eusebio P. Garate, Amnon Fisher, and William G. Main, "Coaxial Configuration of the Dielectric Cherenkov Maser," IEEE Trans. Plasma Sci., vol. 18, pp. 831-836, October 1990.

Studies of an X-Band Three-Cavity Gyroklystron with Penultimate Cavity Tuning

S. Tantawi, W. Main, P.E. Latham, H. Matthews, W. Lawson, C.D. Striffler and V.L.Granatstein
Laboratory for Plasma Research and Department of Electrical Engineering
University of Maryland, College Park, Maryland 20742

Abstract

We present experimental results of a 10 GHz TE_{01} mode three-cavity gyroklystron. The beam is produced by a pulse line modulator and magnetron injection gun, which can operate to 433 kV and 225 A with 1 μs flat-top and at a rep rate of 3 Hz. Microwave power is measured by a mode-selective directional coupler and flowing methanol calorimeter. Mode purity is determined by a large anechoic chamber. Initial testing of the first three-cavity circuit has produced a peak power of 23 MW with efficiency of 27% and pulse energy of 36 J. We have a maximum gain of 39 dB at a peak power of 21 MW.

I. INTRODUCTION

The University of Maryland is developing a three-cavity gyroklystron to demonstrate the feasibility of this type of device as an RF source for future TeV linear colliders. To achieve TeV energies, over a thousand phase-locked RF drivers will be required. For this reason it will be important to have RF sources with high gain. To achieve high gain will require a gyroklystron with 3 or more cavities. As a proof of principle our first effort was a two-cavity device which gave encouraging results[1].

A diagram showing the major components of the system appears in Figure 1. The magnetron injection gun (MIG) is designed to give optimum beam quality at 500 kV, 160 A and and α=1.5. At these parameters the velocity spread is 7% [2]. Our modulator produces pulses with flat-top of 1 μs and is currently capable of repetitive operation at 3 Hz up to 433 kV and 225 A. The axial magnetic field is produced by four separate circuits which allow us to vary the magnetic compression to the circuit and also the field profile in the circuit region independently. The circuit is designed for 5.85 kG and the maximum attainable flat field is 6.5 kG.

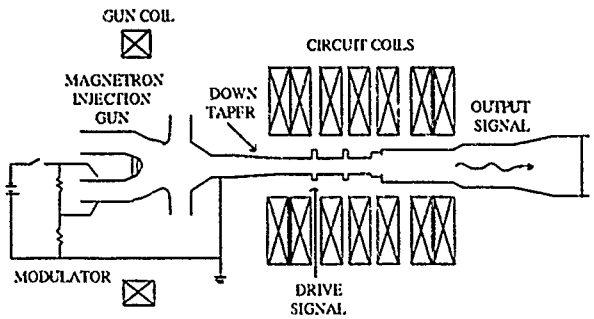


Figure 1. Schematic diagram of gyroklystron system.

Research Supported by the U.S. Department of Energy

0-7803-0135-8/91$01.00 ©IEEE

Figure 2 shows the microwave circuit. Key features of this RF circuit are the remotely tunable buncher cavity and lossy dielectrics. We tune the cavity by simultaneously inserting two metal rods (OD=0.2 in) with rounded ends from opposite sides of the cavity. The tip of the rods can travel from the drift tube radius outward to 5 mm outside the cavity, but most of the 100 MHz tunability occurs while the probes are well into the cavity.

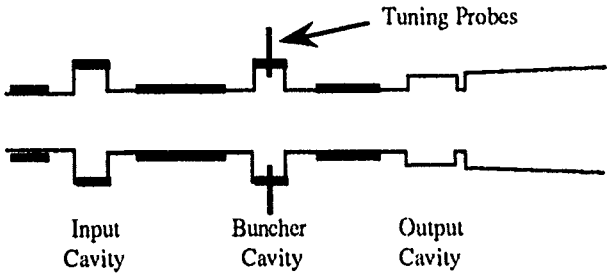


Figure 2. The three-cavity gyroklystron circuit showing the tuning probes and lossy dielectrics. The lossy dielectrics appear as darkened regions in the cavities and drift regions.

In this device the drift regions are not cutoff for all modes and the cavities are over-moded. Due to the Larmor radius of the beam electrons, the drift regions can not be reduced to cutoff all modes without significantly reducing the beam power. To isolate the cavities we loaded the drift regions with lossy dielectric liners, and to prevent parasitic oscillations in the cavities we loaded the radial wall of the cavities with lossy dielectrics (Fig. 2). In the cavities the ε and geometry of the dielectrics were optimized to increase mode selectivity. In the drift regions the dielectrics were optimized to maximize the attenuation of parasitic modes and provide adequate isolation between the cavities[3].

Input power for the gyroklystron was produced by a pulsed magnetron capable of 2 μs pulses of 100 kW. Forward and reverse power were monitored and coupling varied from 30% to 70% depending on the beam parameters.

II. EXPERIMENTAL RESULTS

A. Amplifier operation

This device gives the best power and gain at our highest voltage of 425 kV and current of 212 A. Magnetic field tapering and penultimate tuning are also very important. The best results were achieved with the guide field 33% higher at

the input cavity than at the output cavity and zero penultimate tuning. This case gave 23 MW with efficiency of 27%, gain of 31 dB and total pulse energy of 36 J. Figure 3 shows scope traces of the microwave signal for this case. The best power from a flat field experiment was 12 MW at 5.7 kG and the buncher cavity tuned 16 MHz below the other cavities. Table I summarizes the experimental results for the tapered and flat field cases and Figure 4 shows the magnetic field profile for these cases.

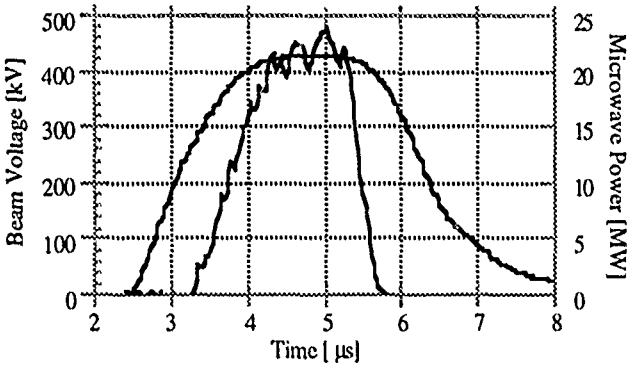


Figure 3. Time dependance of the microwave power and beam voltage.

Bz [kG]	α	Power [MW]	Efficiency %	Gain dB
33% taper	0.66	23	27	31
5.0	0.63	11	13	30
5.7	0.71	12	15	27

Table I. Comparison of results for tapered and flat magnetic field at beam parameters 425 kV and 212 A.

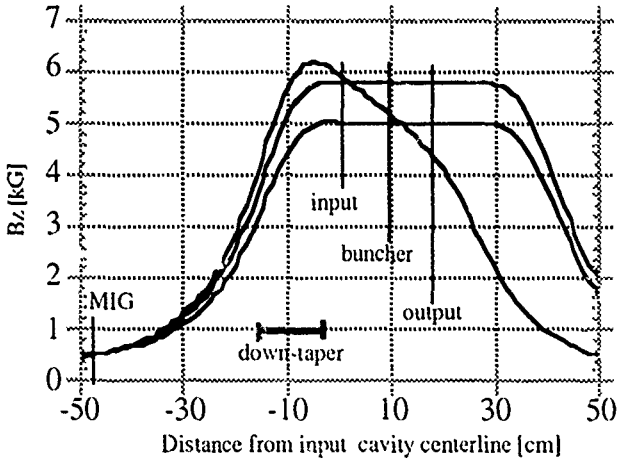


Figure 4. Comparison of magnetic field profiles for flat fields at 5.8 kG and 5.0 kG and a tapered field (B_{in}/B_{out}= 1.33).

The device gives the best gain with the same 33% taper but with the buncher cavity tuned 24 MHz lower than the other cavities. In contrast to standard klystrons which require positive penultimate tuning, the gyroklystron requires negative tuning due to the inverse relation of energy and phase in the electron orbits. Here the gain is 39 dB with peak power of 21 MW and efficiency of 25%. Figure 5 shows the dependance of gain on penultimate tuning for the tapered field described above.

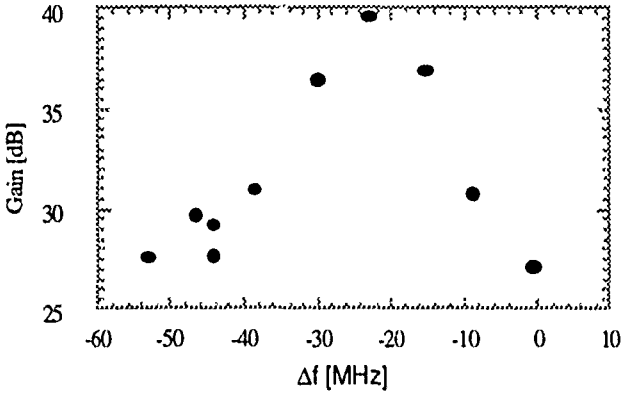


Figure 5. The dependance of gain on penultimate cavity tuning at 420 kV, 212 A and a tapered field (B_{in}/B_{out}= 1.33).

Figures 6 and 7 are contour plots of the measured efficiency and gain vs. beam voltage and current. These plots show that increasing the beam voltage improves the gyroklystron's performance in both power and gain. The dependance on beam current is different. The best output power is achieved slightly below the maximum current and the best gain is achieved at the lowest beam current. These experiments were made with a tapered magnetic field and zero penultimate tuning.

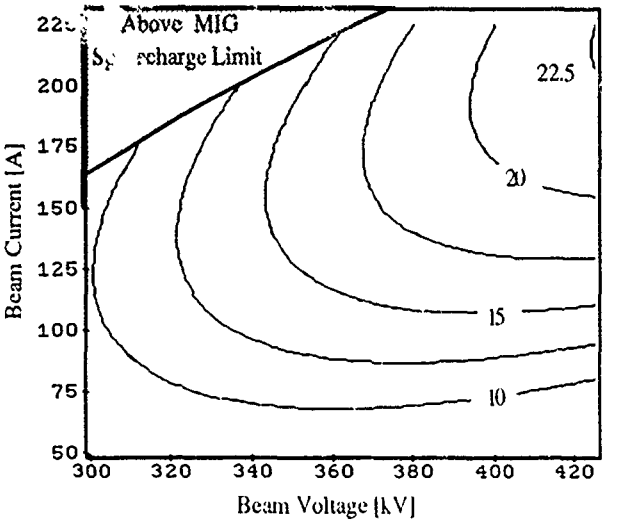


Figure 6. Contour plot of least squares fit to measured Power in megawatts for a tapered magnetic field (B_{in}/B_{out}= 1.33).

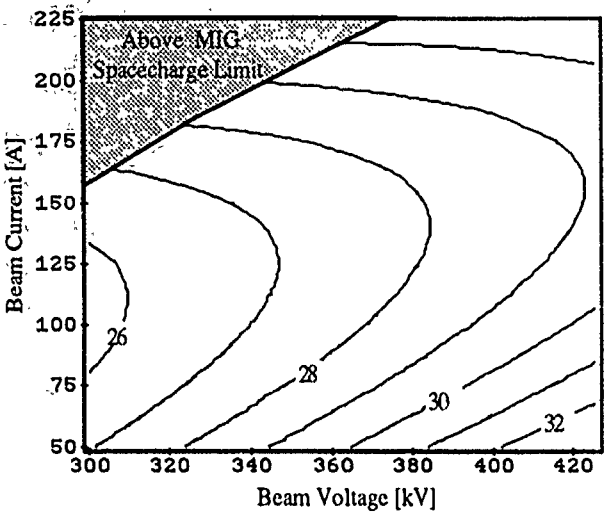


Figure 7. Contour plot of least squares fit to measured gain for a tapered magnetic field (B_{in}/B_{out}= 1.33).

B. Stability

The three factors which limit the power in this tube are the beam voltage limit of 430 kV set by the modulator, a beam instability in the down-taper region (Fig. 1) , and saturation of the output cavity. The modulator is currently being redesigned to allow operation to 500 kV.

The instability in the down-taper region is activated when the beam reaches a certain level of perpendicular momentum ($P_\perp$). If $P_\perp$ is further increased by reducing the magnetic field at the MIG, strong oscillations in the range 6-8 GHz occur in the down-taper region. The onset of these oscillations can be moved to higher $P_\perp$ by increasing the field in the down-taper region (even though this also has the effect of increasing $P_\perp$) or by operation at higher input power. We believe that some of the input power leaks into the down-taper region stabilizing this instability.

Saturation in the output cavity occurs when either $P_\perp$ or the bunching of the beam is increased past a certain point. The beam bunching can be optimized either by reducing the input power, or lowering the gain of the circuit. The gain can be lowered by detuning the buncher cavity or altering the taper in the magnetic field.

The operation and stability of the device is best demonstrated by experimental results at three different magnetic fields: flat field at 5.7 kG, flat field at 5.0 kG and a tapered field (Fig. 4). Comparing the two flat field experiments (Table I), the case at 5.7 kG has a higher field in the down-taper region. This higher field gives better mode suppression, and thus the 5.7 kG case gives the higher α. This is consistent with the slightly higher output power observed in the 5.7 kG case.

The tapered field case is very interesting. Although its α is less than the 5.7 kG flat field case, its output power is almost two times higher (Table I). In addition, flat field experiments with output cavity fields equal to that of the tapered field case give significantly less output power. For this reason we believe that decreasing the guide field across the output cavity region is necessary to achieve high power. In this tapered field case, the field decreases 6% across the output cavity. Because the guide field extends well beyond the end of the microwave circuit, we suspect that a helpful traveling wave interaction may also occur there. This interaction might also benefit from the tapered field. A numerical study to better understand the effects of guide field tapering at the output cavity is now underway.

III. FUTURE WORK

The second three-cavity gyroklystron circuit will be tested in May 91. This circuit will use a more lossy down-taper so that higher α can be achieved. In addition, the quality factor (Q) of the output cavity will be increased from 200 to 350. The first circuit was made with lower Q anticipating operation at 500 kV and α = 1.5. At our current operating parameters an output cavity with a Q of 300 will operate at 50% of the start oscillation current, thus the increased Q should not reduce the stability of the circuit.

IV. REFERENCES

[1] W. Lawson, J. P. Calame, B. Hogan, P.E. Latham, M.E. Read, V.L. Granatstein, M. Reiser, and C. Striffler, "Efficient Operation of a High Power X-Band Gyroklystron," Phys. Rev. Lett. submitted.

[2] W. Lawson, J. Calame, V.L. Granatstein, G.S. Park, C.D. Striffler, and J. Neilson, "The Design of a High Peak Power Relativistic Magnetron Injection Gun," Int. J. Elect. 1986, pp. 969-984.

[3] W. Main, S. Tantawi, P.E. Latham, J. Calame, C.D. Striffler, and V. L. Granatstein, "Design and Tests of a Three-Cavity Gyroklystron," Fifteenth International Conference on Infrared and Millimeter Waves, Conference Digest, 1990, pp. 596-598.

A Second Harmonic Amplifier for Accelerator Applications*

P.E. Latham, W. Lawson, C.D. Striffler, and W. Main
Laboratory for Plasma Research
University of Maryland, College Park, MD 20742

Abstract

The theoretical design of a second harmonic gyroklystron amplifier at a voltage near 500 kV is presented. Because of the relatively high voltage the beam tunnel must be large, so the radiation is not cutoff in the drift tube. To avoid feedback we operate the input cavity at the fundamental, which is cutoff in the drift tube, and design a complex output cavity that emits very little radiation back into the drift tube. The output cavity is described in detail, and the overall gain and efficiency is given.

I. Introduction

For accelerator applications it would be highly desirable to operate a gyroklystron amplifier at the second harmonic, as this would reduce the demands on the magnets. In addition, if subharmonic bunching is used all but the last cavity can operate at the fundamental frequency, allowing a second harmonic device to be easily adapted to an existing fundamental gyroklystron amplifier. The major problem with second harmonic operation at moderate to high voltage, where the Larmor radius is large, is that the radiation may not be cutoff in the drift tube. For instance, the drift sections in the University of Maryland's 500 kV gyroklystron amplifier[1] must be at least 1.5 cm in radius to allow the beam to pass through. At this radius the operating mode, TE_{01}, is cutoff at the fundamental frequency of 10 GHz, but not at the second harmonic. The obvious solution is to operate all but the last cavity at the fundamental frequency and operate the output cavity in the TE_{02} mode at the second harmonic. Then the problem is to make sure that the mode conversion from TE_{02} and TE_{01} is negligible. For multi-megawatt devices the constraints on mode conversion may be so severe that a narrow band filter is needed upstream of the output cavity to keep the radiation from traveling back toward the gun.

In the remainder of this paper we concentrate on the theoretical design of a 20 GHz, second harmonic gyroklystron amplifier consistent with the parameters of the University of Maryland device, which are summarized in Table 1. We will first give the design of the output cavity, then present the nonlinear gain and efficiency.

Table 1: University of Maryland Gyroklystron Parameters.

Beam voltage	425 kV
Beam current	150 A
Pitch angle, $v_{\perp 0}/v_{z_0}$	1
Magnetic field	5.72 kG
Velocity spread	10%

II. Output Cavity Design

Three output cavity designs, in order of increasing complexity, are shown in Figs. 1a–1c. Figure 1a is the simplest: at radii r_1 and r_3 the TE_{02} mode is cutoff, while at radii r_2 and r_4 the TE_{02} mode may propagate. The tapers are designed for low mode conversion to the TE_{01} mode, and either the length of the lip at radius r_3 or the value of r_3 may be adjusted to control the cavity Q. This type of cavity works well at low Q, but at high Q a substantial portion of the output power may be converted to the TE_{01} mode. This is because the outgoing power in the TE_{02} mode is on the order of $1/Q$ of the circulating power, so the amount of mode conversion to the TE_{01} must be significantly less than $1/Q$. For $Q \sim 1000$, which is typical, the mode conversion must be much smaller than -30 dB. Such low mode conversion may not be practical with reasonable length tapers.

This problem can be eliminated by placing a narrow band 20 GHz mode filter upstream of the output cavity, as shown in Fig. 1b. The filter consists of a cavity that has a low Q resonance at 20 GHz, so it won't interact strongly with the beam. Such a cavity will effectively eliminate any power produced in the output cavity from propagating back to the gun.

There is an additional problem with the cavities shown in both Figs. 1a and 1b, the outgoing TE_{02} may be contaminated by the TE_{01} mode. One way to eliminate this is by using the cavity shown in Fig. 1c, in which the radius r_3 is cutoff to the TE_{02} mode. Thus, all the output power is in the TE_{01} mode. The length of the transition between radii r_2 and r_3 may be adjusted to control the amount of mode conversion and thus the cavity Q. With the mode filter in place all the power will be in the forward direction, producing a pure TE_{01} signal.

*Work supported by the U.S. Department of Energy.

0-7803-0135-8/91$01.00 ©IEEE

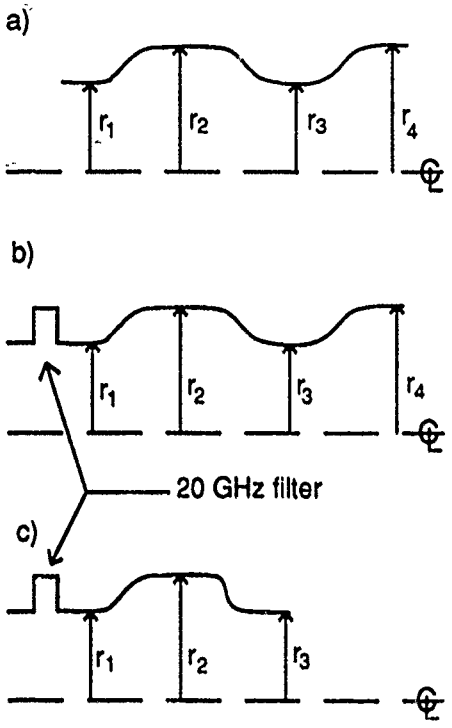


Figure 1: Three output cavity designs in order of increasing complexity.

III. Circuit Design

Our initial design employs two cavities separated by a 1.5 cm radius drift section. The input cavity is 1.7 cm long with a radius of 6.1 cm and a Q of 300. The drift tube is 10 cm in length. For simplicity we chose the output cavity depicted in Fig. 1a. Its dimensions are $r_1 = 1.50$ cm, $r_2 = 1.72$ cm, $r_3 = 1.68$ cm, and $r_4 = 1.80$ cm. At these radii the TE_{01} mode at 10 Ghz is cutoff. All three tapers are 2 cm long, the straight section of the cavity (at radius r_2) is 1.436 cm and the straight section of the lip (at radius r_3) is .330 cm. The resultant Q of the output cavity is 600. With no beam present, analysis of the cold cavity fields indicates that about .3% of the power will propagate back toward the input cavity. This value will probably change when the beam is present.

To calculate the gain and efficiency, we used a nonlinear, partially self-consistent code which computes the steady state amplitude and phase in each cavity[2]. The beam characteristics and applied magnetic field are given in Table 1. For these parameters the efficiency was 22%, corresponding to 15 MW output power. We do not believe that this is an optimized value; there is a large parameter space to search and we have not yet explored all possible combinations of output cavity Q, length and frequency mismatch, and magnetic field. We will continue with our optimization process and report on an improved design at a later date.

The gain of this device was fairly low, only about 16 dB. However, the gain can easily be increased by raising the input cavity Q, tapering the magnetic field or adding an intermediate cavity.

IV. Summary

We have shown that second harmonic operation with bunching at the fundamental frequency is feasible. With a velocity spread of 10%, numerical simulations have achieved an output power of 15 MW (corresponding to an efficiency of 22%) at 20 GHz. We believe that the efficiency will increase significantly as we continue with our optimization. The gain was about 16 dB; this number will also increase with modifications to the input cavity, magnetic field tapering or the addition of an intermediate cavity.

We have also presented a variety of output cavities that can be used to prevent feedback of the output cavity signal into the input cavity and to guarantee that the output will be in a pure mode.

V. References

[1] J.P. Calame, W. Lawson, V.L. Granatstein, P.E. Latham, B. Hogan, C.D. Striffler, M.E. Read, M. Reiser, and W. Main, "Experimental Studies of Stability and Amplification in Four Overmoded, Two Cavity Gyroklystrons Operating at 9.87 GHz," submitted to J. Appl. Phys., February 1991; W. Lawson, J.P. Calame, B. Hogan, P.E. Latham, M.E. Read,V.L. Granatstein, M. Reiser, and C.D. Striffler, "Efficient Operation of a High Power X-Band Gyroklystron," submitted to Phys. Rev. Lett., February 1991.

[2] K.R. Chu, V.L. Granatstein, P.E. Latham, W. Lawson, and C.D. Striffler, "A 30 MW Gyroklystron Amplifier Design for High Energy Linear Accelerators," IEEE Trans. Plasma Sci. **PS-13**, 424 (1985).

RF BREAKDOWN TEST OF SiO_2 COATED COPPER ELECTRODES *

D.Sun, P.Datte, W.W.MacKay and F.R.Huson
Texas Accelerator Center†, 4802 Research Forest Drive,
The Woodlands, TX 77381

Abstract

RF breakdown test results with copper and SiO_2 coated copper are presented. The results show that SiO_2 coating can withstand an rf field as high as 100 MV/m at 471 MHz without sparking and depress the field emission.

Introduction

For high gradient accelerators, rf voltage breakdown is one of the major factors which impose the limits on the maximum field gradient. Since Kilpatrick proposed his semi-empirical criterion for rf breakdown limit in the 1950's [1], several experiments have been conducted to test the rf breakdown limit at various frequencies. But up to now the mechanism of rf breakdown still remains unclear. Different metals were tried to increase the breakdown limit, but there is no substantial increase. The surface coating of rf cavities was proposed to be a possible way to increase the breakdown limit far above the electron multipactoring limit [2][3].

Field emission is another detrimental factor for operation of high gradient accelerators, since it can induce breakdown, consume extra rf power, cause wakefields and possible excitation of unwanted modes of oscillation in the accelerating structures. So the research on how to depress the field emission for high gradient accelerating structures is needed.

In this paper we report our research on the possibility of SiO_2 coating of copper electrodes. Our interest is to investigate what improvement could be made in the depression of the field emission and increase of maximum field gradient by SiO_2 coating.

Experiment Setup

The test setup is shown in Figure 1. A reentrant type resonant cavity is used which consists of two demountable halves and two movable electrodes. The gap and resonant frequency can be changed easily by moving two electrodes. The electrodes are composed of two parts: body and end cap. The end caps to be tested are screwed onto the bodies. A small area of each end plate of the cavity was coated with titanium to depress possible multipactoring. The cavity is partially water cooled.

Two rf probes are mounted at different positions to monitor rf power transmitted into the cavity. Also, the ratio of the two probes' measurements is used to detect other possible modes which may be excited at higher power levels. Seven thermocouples monitor the cavity's temperature at various positions.

An x-ray spectrometer is set up for the measurement of maximum rf field and field emission in the gap. This x-ray spectrometer consists of a NaI detector, a LeCroy 3001 multichannel analyzer, a LeCroy 4608C discriminator, an HP 5314A universal counter and an IBM PC.

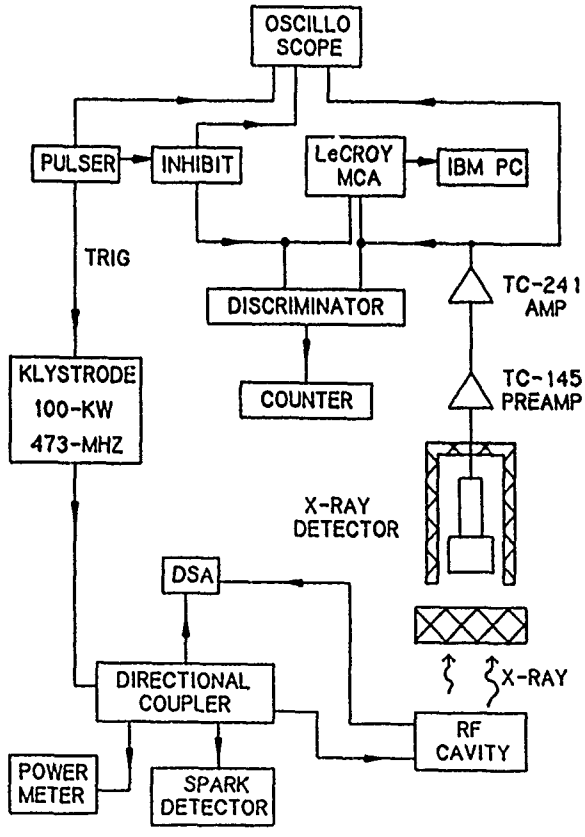


Figure 1. Experiment Setup.

An EIMAC 2KDW60LA klystrode is used as an rf power source providing 8-50 μs long pulses with a repetition rate of 10-100 Hz [4]. The forward and reflected powers are monitored with a calibrated four port directional coupler, a Tektronix 602A digital signal analyzer and an HP 408A power meter. Also the reflected signal is sent to a spark rate counter.

The rf cavity is in a high vacuum chamber which is

*Work supported in part by the SSC

0-7803-0135-8/91$01.00 ©IEEE

pumped by a 500 L/sec turbo pump, a liquid nitrogen cold trap and a mechanical pump. The vacuum feedthrough for the main rf coaxial transmission line is made with a Teflon insulator and a Viton O-ring.

Experimental Procedure

The pure electrode end caps were made of OFHC copper. They were carefully polished to less than 3 μm finish and ultrosonically cleaned. After cleaning, several copper end caps were coated with SiO_2 thin films by electron beam evaporation. The thickness of SiO_2 is 400 nm. The refractive index of SiO_2 is 1.543. Before and after each test the Q and SWR of the cavity and attenuation of rf loops were measured several times with an HP8753B network analyzer. The x-ray spectrometer was calibrated with gamma ray standards (^{133}Ba, ^{57}Co, ^{137}Cs, and ^{22}Na). To compare the field emission, we measured the x-ray intensity at several field levels with both pure copper and SiO_2 coated copper electrodes. The rf frequency was 471 MHz. The rf pulse length was 8 μs, and the repetition rate was 100 Hz. All tests were done after the vacuum chamber was pumped to less than $3x10^{-7}$ torr.

The maximum electric field in the cavity was determined by two methods: pick up loop and x-ray spectrum. The pick up loop method determines the maximum electric field by the expression:

$$E_{max,exp} = E_{max,theo}\left[\frac{Q_{exp}P_{exp}}{Q_{theo}P_{theo}}\right]^{1/2} \qquad (1)$$

where $E_{max,theo}$, Q_{theo} and P_{theo} are the theoretical maximum electric field, Q factor and corresponding dissipated power as calculated by SUPERFISH, and Q_{exp} and P_{exp} are the experimental values.

Since the real field distribution and oscillation modes at high electric field can be different from either those measured at low field level or those calculated by SUPERFISH, it is necessary to employ another method to ensure the accurate determination of the real maximum electric field in the gap. The x-ray measurement is used to determine the maximum energy obtained by the field emitted electrons. The high energy end of the x-ray spectrum (Bremsstrahlung) corresponds to the amplitude of the rf voltage in the gap. The maximum electric field is determined by deviding the voltage amplitude with gap length.

The total intensity of the x-rays can be used to determine the current density of the field emitted electrons by the following expression:

$$I = CjZV^m \qquad (2)$$

where I is the total intensity of the x-ray, C and m are constants, Z is the atomic number of the electrode material, j is the electron current and V is the voltage between electrodes. The x-ray intensity can be determined by the spectrum if the other parameters are fixed.

Experimental Results

1. Breakdown limit

The breakdown started at a field level of 97-100 MV/m with the SiO_2 coated electrodes. This sample was first tested up to 81 MV/m [5]. After the first test, the cavity was opened and the electrode surfaces were visually checked. There was no trace of sparking. Afterward the samples were kept in the ordinary atmosphere for seven months and were tested again. The samples showed good repeatability until the first spark occurred at 97-100 MV/m. After the spark occurred, the signals from x-ray spectrometer were heavily piled up, which indicated a dramatic increase of field emission. After the cavity was opened, there were two small pits seen on the electrode surfaces, similar to those of pure copper electrodes. Except for those two pits, the SiO_2 film remained undamaged. As we previously reported [5], with pure copper electrodes, the sparks started at a electric field of about 60 MV/m. The maximum field of pure copper electrodes can be maintained at a level of 120 MV/m after a long time careful conditioning, but there are a lot of spark traces left on the surfaces after tests.

2. Field emission

Figure 2 shows the x-ray spectrum from SiO_2 coated copper and the pure copper electrodes at an rf field of 42.5 MV/m. The pure copper electrodes had been conditioned and operated at various field levels up to 120 MV/m for a long time. The x-ray spectrum was taken after operations of more than 100 hours. In order to avoid pileup of the x-ray signals, we had to increase the shielding of the x-ray detector with increase of rf field, but at each field level, the same shielding was used for both pure and SiO_2 coated copper electrodes. Table 1 lists the total counts of x-ray signals normalized by the total effective counting time at three different rf field levels. The data shows that the total normalized x-ray counts of the pure copper sample is about 20 times more than that of SiO_2 coated copper.

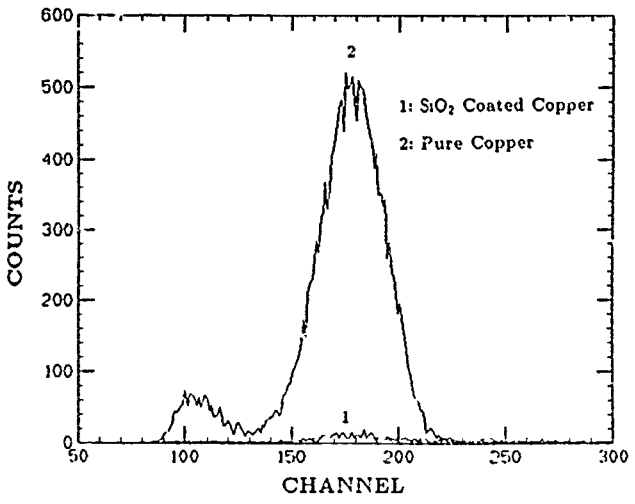


Figure 2. X-ray spectrum at rf field of 42.5 MV/m

TABLE 1
Normalized Total Count

rf field (MV/m)	total counts per second		ratio
	pure Cu	SiO_2 coated Cu	
42.5	2120	104	20.4
67.5	3643	148	24.6
85	4488	86	52.2

Conclusion

1. The above reported results show that the SiO_2 coating can increase the rf breakdown starting level up to 97-100 MV/m. The Kilpatrick limit at 471 MHz is 20 MV/m. This means that SiO_2 coating may provide a method for keeping the electrode surface free of damage during high field gradient operation.

2. The SiO_2 coating can reduce the field emission. Compared with the pure copper electrodes which were used for more than 100 hours, the total normalized counts of the x-ray signals can be decreased up to 20 times. This could improve operation of accelerators at high field gradient by reducing the dark current.

References

† TAC at HARC is a consortium of Rice University, Texas A&M University, the University of Texas, Prairie View A&M University, Sam Houston State University and the Baylor College of Medicine MR Center.

1. W. P. Kilpatrick, "Criterion for Vacuum Sparking Designed to Include Both rf and dc," Review of Scientific Instruments, 28 (10), 824 (1957).

2. W. Peter, "Vacuum Breakdown and Surface Coating of rf Cavities," J. Appl. Phys. 56 (5), 1546 (1984).

3. B. Hoeneisen, Internal Report No.2, Instituto de Fisica Universidad de Guanajuato, 1987.

4. W. W. MacKay, *et al.*, "Operation of a 473MHz Pulsed Klystrode Power Source," Proceedings of the 1990 Linear Accelerator Conference, Albuquerque, New Mexico, September 1990, pp. 186.

5. D. Sun, *et al.*, "Voltage Breakdown Test At 473 MHz," Proceedings of the 1990 Linear Accelerator Conference, Albuquerque, New Mexico, September 1990, pp. 216.

The AGS Booster low frequency RF system*

R.T. Sanders, P. Cameron, W. Eng, M. Goldman, D. Kasha,
A.J. McNerney, M. Meth, A. Ratti, R. Spitz.

AGS Department
Brookhaven National Laboratory
Upton, New York 11973-5000

Abstract

An RF system has been designed to accelerate all the desired species of ions up to Gold, which will be available at β=0.048. The system will run on different harmonic numbers (h). It will start from h = 12 at injection and jump to h = 3 during the cycle. The beam will then be transferred to the high frequency RF system that will bring it to the extraction energy. The low frequency system consists of two single gap cavities that sweep from 0.6 to 2.4 MHz, with gap voltages up to 17 kV. The cavities are loaded with TDK SY7 high permeability ferrite rings. Tuning will be accomplished by changing the permeability of the ferrite with dc bias currents as high as 200 A flowing in two "figure of eight" windings. The cavity will be driven by a 200 kW push-pull tetrode power amplifier, which will be driven by remotely located solid state drivers.

Introduction, system description and parameters

The AGS Booster has two RF systems covering a frequency range from 600 kHz to 4.2 MHz. The low frequency system, also called Band II, operates on a frequency range from 600 kHz to 2.4 MHz and consists of two single-gap cavities, each capable of 17 kV. It will be used in the initial part of the heavy ion acceleration cycle. In this mode the Booster will sweep in less than one second.

The system will run two different harmonic numbers. The ions arriving from the Tandem Van de Graaff will be captured on h=12 from the Band II system and accelerated until the highest frequency available on the Band II cavities is reached. It will then be debunched, while the system is being reset to the starting frequency, recaptured on h=3 and accelerated again.

The final part of the cycle will be done by Band III, which also provides for the acceleration of both polarized and non-polarized protons [1]. The latter is already installed in the Booster tunnel and it is described, together with the "bench" test results, in another paper in these proceedings [2].

	C	Cu	Au	
A	6	63	197	
Z	6	29	79	
Q	6	21	33	
E_{inj}	7.5	2.85	1.06	MeV/u
E_{ext}	966	854	350	MeV/u
β_{inj}	0.12	0.078	0.047	
β_{ext}	0.87	0.85	0.68	
ΔP/P	0.15	0.24	0.40	%
B_{inj}	0.576	0.531	0.645	kG
Bunch Area	<0.05	<0.05	<0.05	eV/u-s
P. total	54	10	3.2	10^9 part
Acc. time	< 620	< 620	< 620	ms

Table 1 - Rf parameters for a few cases of the AGS Booster Heavy Ion cycles.

*Work supported by the U. S. Department of Energy.

0-7803-0135-8/91$01.00 ©IEEE

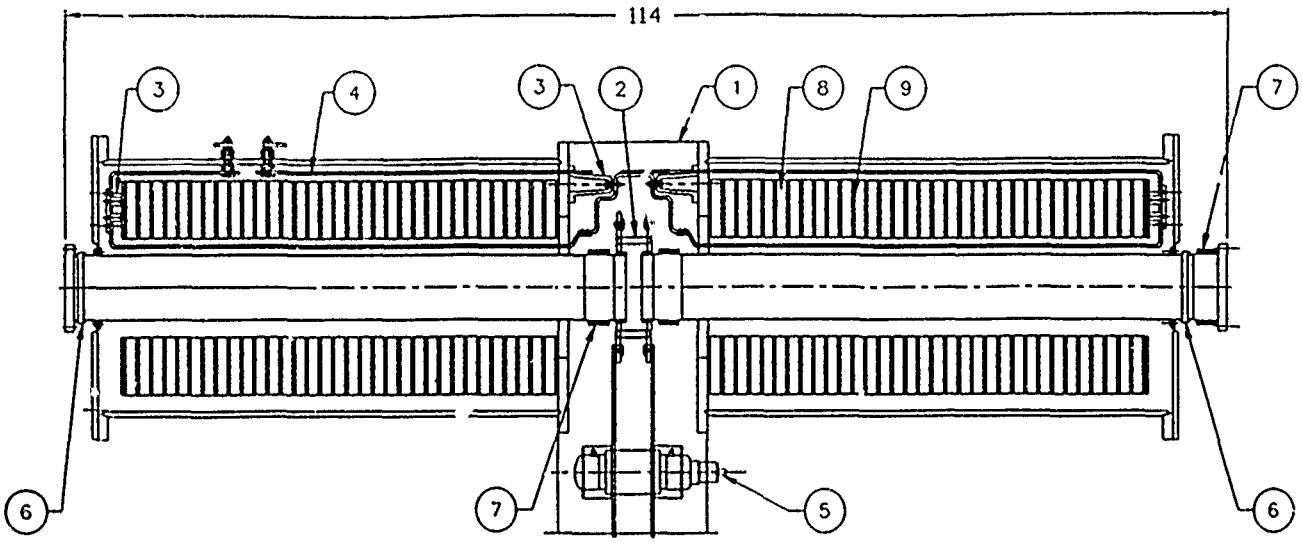


Fig. 1 - The Band II cavity. 1. RF tight enclosure; 2. Ceramic gap insulator; 3. Ceramic bias winding support; 4. DC bias winding; 5. Tuning vacuum capacitor; 6. Ceramic insulator; 7. Bellows; 8. Ferrite; 9. Cooling plate.

The Booster rf parameters are listed in Table 1. The parameters listed for Gold are in the case of the AGS fixed target program. The dB/dt is of the order of 3 T/s, whereas df/dt can be as high as 35 MHz/s. The momentum spread is induced by the rf during the non adiabatic injection. Studies on this scheme are still underway and a final set of parameters will be developed in concurrence with the results of the "bench" tests of the system. Results such as dynamic losses in the cavity, tuning system reset time and maximum tuning range available, are extremely important in choosing the best solution. Table 2 summarizes the high level system configuration.

N. of cavities	2
N. of accelerating gaps	2
Peak rf Voltage/gap	17 kV
Rms rf power/pa.	200 kW
Frequency range	0.6 - 2.4 MHz
Harmonic number	12 - 3
Duty cycle	20 %

Table 2 - Band II rf system parameters.

Cavity design

The Low Frequency RF cavity is a single gap, ferrite loaded resonator. It is not evacuated, since a ceramic gap is sealed on the beampipe. The gap also has a variable tuning capacitor that can adjust the tuning range, if needed.

Following a complete testing and evaluating program [3], the ferrite chosen for this application is the TDK SY7. Each cavity uses 66 rings of this Ni-Zn ferrite, with a relative permeability of 1100. Tuning is accomplished by saturating the ferrite to a relative permeability of 85 with a dc field applied through two buss bars, which cross-couple the two sides of the cavity, guaranteeing the push-pull operation of the system even at very low Q and decoupling the rf from the bias supply [4]. The rf field in the ferrite can be as high as 170 G, with losses up to 300 mW/cc. The rings are therefore sandwiched between water cooled copper plates. The total expected static losses are about 170 kW and due to the relatively long dimensions of each ferrite stack, the stacking order is particularly chosen trying to keep the losses in each of the rings as uniform as possible.

Since the need for ultra high vacuum ($\approx 10^{-11}$ torr) imposes the requirement for the vacuum chamber to be bakeable in the Booster ring at 200° C, the design provides electrical heaters and thermocouples built into and around the beampipe [5]. Insulating blankets are used to protect the ferrite rings from high thermal gradients and stresses. The Band II cavity is shown in Fig. 1.

Power Amplifier

The power amplifier is located in the Booster ring directly below the cavity and it is designed to deliver over 200 kW rms on a 17 kV peak accelerating voltage. It uses two EIMAC Y567B tetrodes capable of plate dissipations up to 150 kW. They are used running class AB_1 in a push-pull configuration, with grounded cathodes. The plate peak current is about 50 A, when the tubes are running at an anode voltage of 12 kV, with the screen grid at 1.1 kV and 3 A of quiescent cathode current.

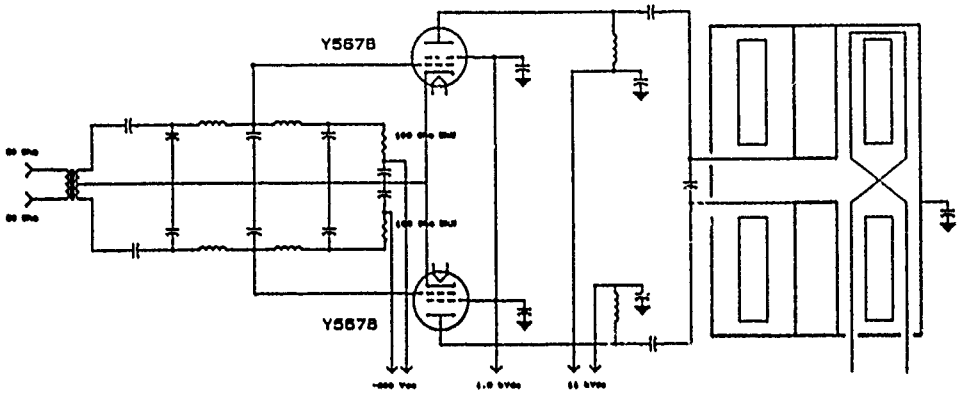


Fig. 2 - The Band II power amplifier

In the case of heavy ions, the power delivered to the beam is negligible compared to the losses in the cavity: all the power is dissipated in the ferrite.

1 kW drive power is delivered by two solid state class A amplifiers into a cross coupling and matching transformer. They are located away from the Booster ring to protect them from radiation damage. The transformer is part of the input filtering network, which is a broadband low-pass filter that includes the tube input capacitance and is terminated into two water cooled 100 Ohms dummy loads. The simplified schematic of the power amplifier and cavity system is shown in Fig. 2. The coupling to the cavity is done via DC blocking capacitors and the B^+ is brought in the amplifier through an RF blocking choke to eliminate the rf voltage affecting the anode power supply

The power amplifier is also equipped with a local control system that allows the amplifier to be operated either from the AGS main control room, the Booster ring or the building where most of the equipment is located. In the last two sites, the system can be run both in manual or automatic mode, which in sequence energizes the filament step-start, the grid, anode and screen supply and eventually tuning supply and rf drivers. The control system includes all of the required safety features and interlocks.

The cavity tuning system is designed to provide up to 200 A into the two turn bias winding. Two signals are used to perform the task: the first is an open loop program obtained from a function generator that uses a frequency-to-voltage converter as its input to create the drive signal from the low level frequency program; the second is a feedback signal coming from the output of a phase detector that compares the rf phases of the plate and grid signals. These signals are used to drive a bank of water cooled power transistors paralleled to provide the required currents.

Status

Commissioning of the Booster is underway at present with proton beams. In this phase the Band II system is not being used. The first cavity is being assembled and assembly of the first amplifier should start soon. Full development of both cavity and amplifier, their testing and installation is scheduled to be completed before the end of the year.

Acknowledgments

The authors are very grateful to all the people who are actively contributing to the design, construction and test of the system. This includes all Booster personnel and management as well as those from other departments or institutions who provided us with ideas, suggestions and encouragements.

References

[1] R. T. Sanders et al., "The AGS Booster high frequency rf system", Proc. European Part. Acc. Conf., Rome, June 1987

[2] R. T. Sanders, et al., "The AGS Booster high frequency rf system" , this proceedings

[3] M. A. Goldman, et al., "Studies of ferrite materials for the AGS Booster synchrotron", Proc. IEEE Particle Accelerator Conf. Vol 1, pp. 165-167, Chicago, Ill., March 1989

[4] U. Bigliani, et al., "The rf accelerating system for the PS Booster", IEEE tr. on Nu. Sc., NS-18, n. 3, p. 233-236, March 1971

[5] H. C. Hseuh, et al., "The ultra high vacuum system for the AGS Booster", Proc. IEEE Particle Accelerator Conf. Vol 1, pp. 574-576, Chicago, Ill., March 1989

BEVALAC INJECTOR FINAL STAGE RF AMPLIFIER UPGRADES

D. Howard, J. Calvert, R. Dwinell, J. Lax, A. Lindner, R. Richter, W. Ridgeway
Lawrence Berkeley Laboratory
University of California, Berkeley, CA 94720

ABSTRACT

With the assistance of the DOE In-house Energy Management Program, the Bevalac injector final stage RF amplifier systems have been successfully upgraded to reduce energy consumption and operating costs. This recently completed project removed the energy-inefficient plate voltage modulator circuits that were used in conjunction with the final stage RF amplifiers. Construction, design, and operating parameters will be described in detail.

INTRODUCTION

The energy saving realized at completion of the project was primarily obtained by eliminating the filament power required for operation of the Hard Tube Modulator system. This saving, coupled with that obtained by removal of the HTM water, air and electronic support systems, accounts for over 30 Kw per hour of operation.

The HTM system was used to key the plate voltage to two tubes, a TH-515 which provides 800 Kw of RF output power and a TH-516 which provides 2.4 MegaWatts. The tubes and their associated amplifier cavities are manufactured by Thomson-CSF and are used as the final RF amplifiers of the T1 and T2 sections of the LINAC portion of the Bevalac Local injector system[1].

First reported in the 1987 Accelerator Conference by J. Alonso et al, the proposal[2] to remove the HTM system was composed of two related but separate project phases. The first required modifying the amplifier structure to remove the ground connection to the final amplifier grid while maintaining a low impedance path for the grid-anode and grid-cathode RF circulating currents. This portion of the project was completed and tested during operation for a year before completing the second stage of the project. The second project provided a fixed source of DC grid bias for the TH-515 and a pulsed grid bias source for the TH-516. The bias voltages appropriately interlock the DC plate voltage supply to the final amplifiers.

GRID ISOLATION

The grid structures of both amplifiers have been modified as shown in Figure 1. The left side of the drawing shows the original structure. As is shown, the grid conductors extend concentrically over the ground cylinder on both the anode and cathode sides of the structure. The grid is insulated from ground on both sides by layers of Kapton. The distance from the anode circuit to the cathode circuit traveling through the structure is 1/4 wave length. Also shown is one of the 8 coaxes that provide a path for the bias voltage and amplifier grid currents. Limited drawing resolution does not show the Multi-Lam compression connectors imbedded in the grid cylinder to receive the coax center conductors.

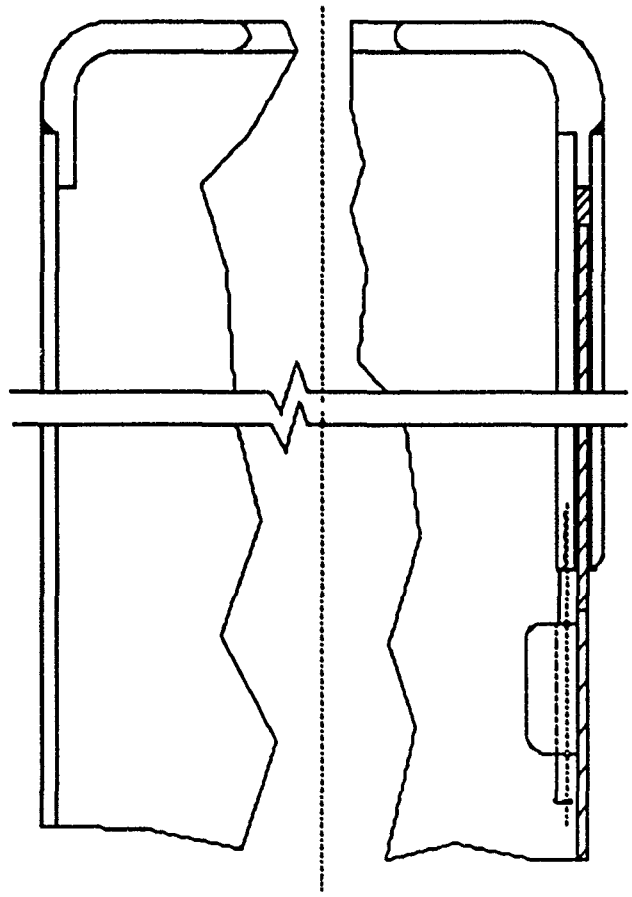


Figure 1.
(Not to scale)

The installation of the grid structure in the amplifier is shown in Figure 2. The distance from the grid cavity shorting plate to the connection point of the eight coaxes is intended to place the coax to grid conductor interface at the minimum point of grid-cathode RF circulating current thereby minimizing the RF voltage generated at the input to each coax.

* This work was supported by the Director, Office of Energy Research, Office of Basic Energy Sciences, Materials Sciences Division of the U.S. Department of Energy, under contract No. DE-AC03-76SF00098.

U.S. Government work not protected by U.S. Copyright.

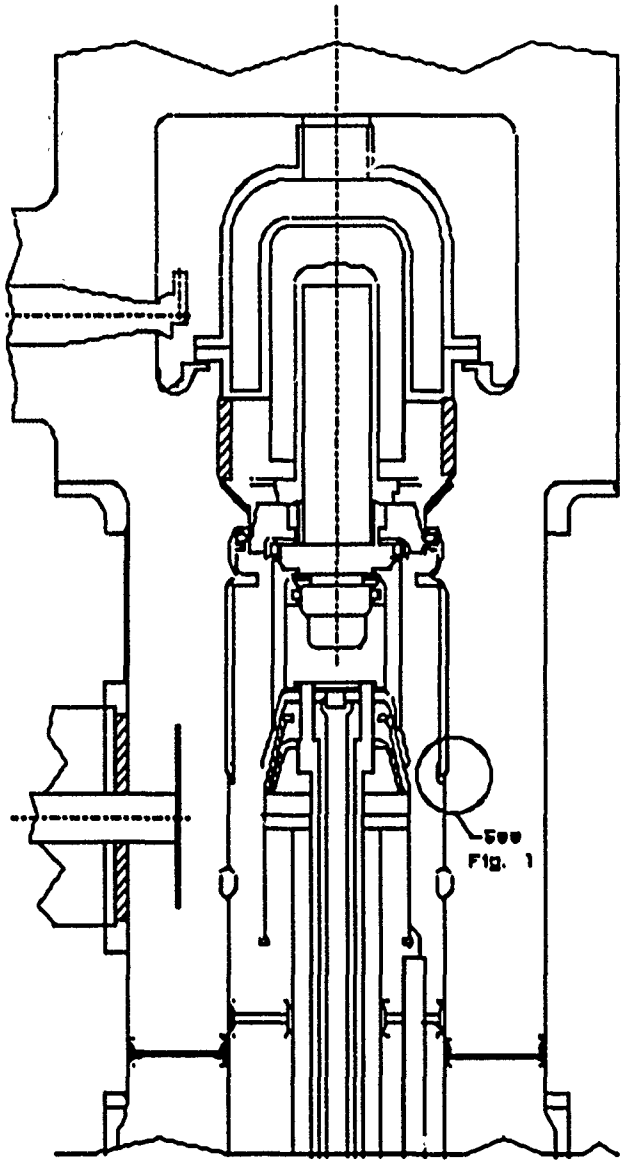


Figure 2.
(Not to scale)

RF DECOUPLING

The RF voltage generated at the inputs of the coaxes is reduced at the output end by employing an open ended, resonant, 1/2 wave length line, constructed to terminate each of the eight coaxes in the center of the resonator and by the use of individual in-line resistors placed in series with each coax. To provide maximum burden to the generated RF, the 10 ohm in-line resistors are placed radially, as close as possible to the minimum impedance point, defined at the center of the Coaxial Terminating Resonator. To reflect minimum impedance to the grid-coax junction, the eight coaxes are a 1/2 wave multiple from the grid to the in-line resistors.

Designed for operation at 200 Mhz, the Coaxial Terminating Resonator is the hub of the RF decoupling system. Shown in Figure 3, mounted on top of the Grid Bias Pulser Chassis, the CTR provides a RF decoupled connection point at its center for interfacing the grid bias voltage from the power supply to the grid. Another RF decoupled center connection point is provided as an input to the grid voltage sensing circuit which is used to interlock the amplifier plate voltage supply.

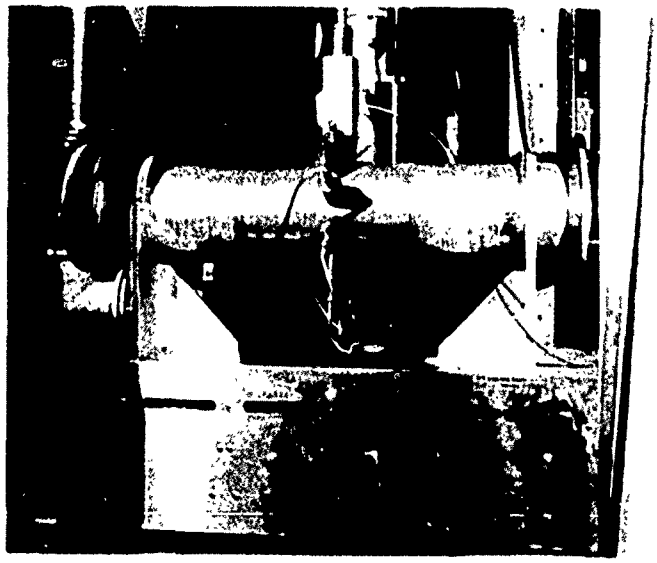


Figure 3.

GRID STRUCTURE TESTS

One grid structure was modified and a CTR was constructed for testing in the T2 system, to determine the integrity of the structure at full RF power. For these tests, the center conductor of the CTR, normally riding at the bias voltage potential, was connected to ground through a resistive network and the HTM left in service. The voltage drop across the network was monitored to determine the operational grid currents and to determine the condition of the isolated grid structure, as absence of output voltage during the On pulse would indicate a shorted grid structure. No abnormalities were observed during these initial tests, and another grid structure and CTR were constructed for installation on the T1 system.

During the first months of operation two failures in the area of the coax to grid interface were experienced. Shown in Figure 1, the clamps that secure the coax outer conductor to the ground structure in this area were modified to increase the center conductor clearance to the grounded clamps. These modified structures continued in service, under all operating conditions, with no further failures for over a year.

BIAS SYSTEMS

The bias system for T1 is a simple full wave bridge power supply. The DC output voltage is adjusted by the input Variac to ensure a cut-off condition for the TH-515 operating near Class B. The bias voltage increases during the pulse as determined by the product of grid current and resistance plus the effect of the grid current charging the power supply output

capacitors. In the pulse Off condition, the capacitors are discharged to the preset bias voltage by bleeder resistors. The value of the bleeder resistance is adequate to discharge any observed or calculated TH-515 grid currents.

The T2 system is more complicated, as the available RF drive is insufficient to overcome the fixed bias. However, the new driver amplifiers[3] under construction at this time are calculated to deliver enough power to operate the T2 system in a fashion similar to T1. At present, to compensate for the inadequate RF drive, the bias voltage is connected to ground through series transistors during the On pulse. The operating grid voltage is determined by the product of grid current and all the grid circuit resistances plus the voltage drop across the series FETs. There are three primary circuit considerations associated with the design of the FET circuits:

* FET Current
* FET Voltage
* Minimizing series circuit resistance

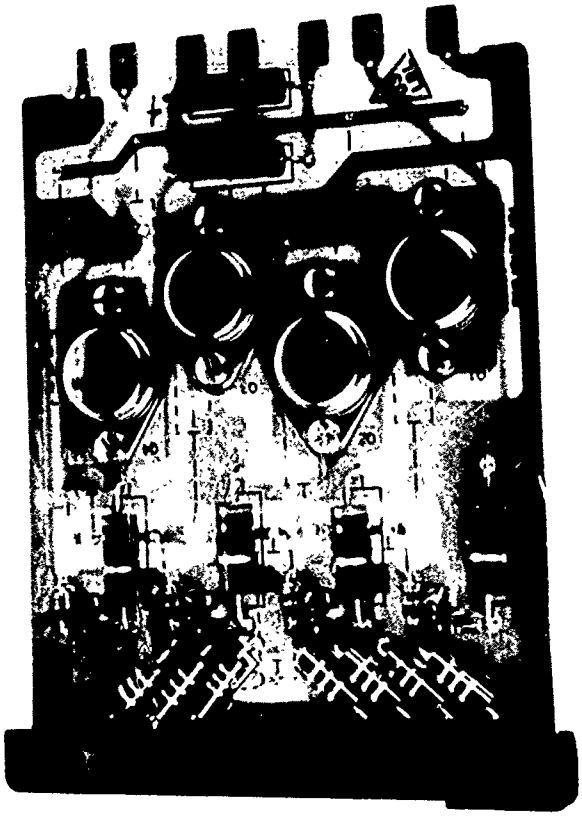


Figure 4.

The FETs are specified by the manufacturer to pass 5 Amps and hold off 1000 Volts. These conditions cannot be simultaneously met for times in excess of 5 usec, consequently fast switch time of the bias voltage is essential. As shown in Figure 4, there are four FETs mounted on each of four identical circuit boards to provide a maximum safe operating current of 80 Amps for the FET circuits. This is a conservative current rating for the calculated and the observed maximum grid currents. Also shown on the board are the 7 parallel resistors that act as a shunt for monitoring the grid currents during operation and 4 LEDs that indicate proper operation of each FET.

Quiescent voltage holding is easily obtained by the 1000 volt FETs; however, excessive transient voltages in the environment of high currents and fast switch times were a major concern. The circuit was modeled in Spice to ensure a fast and critically damped response. The 10 ohm resistors in-line with each coax from the grid going to the CTR are an integral part of the input impedance to the chosen pi filters, which are mounted on the back side of each FET circuit board. The filter output impedance is determined by the FETs and their associated series resistors.

HIGH POWER TESTS

Another 6 Kw per operating hour is saved by reducing the plate supply voltage for the TH-515 and TH-516 by 10 Kv to operate at 30 Kv and by the T1 system efficiency, which was dramatically increased by the addition of fixed bias.

The system did not run long before more breakdowns in the area of the grid to coax interface on the grid structure were observed. The metal clamp rings were replaced with Delrin clamps and the structures have had no further failures. The systems ran undisturbed for about three months when, in the process of on-line testing a spare TH-516, pitting was discovered on the operating tube in the area of the metal to glass seal, near the tube anode. The area was wrapped with Mylar tape. Later inspections revealed no further signs of sparking in the area or through the tape. The HTM system was reinstalled to prevent potential tube damage while a new anode corona shield is being machined. The new shield has not been installed as of this date.

ACKNOWLEDGEMENTS

The authors wish to thank Don Bowman and Noel Kellogg for their continuing support and expert mechanical assistance, Ming Hui for generating the drawings presented in this paper, and Mike Bennett for his assistance in preparing this document.

REFERENCES

1. J. Staples et al, "Initial Operation of the New Bevatron Local Injector", Proc. of the 1985 IEEE Particle Accelerator Conference, May 13-16, Vancouver, BC, Canada
2. J.R. Alonso et al, "Energy Management at the Bevalac.", Proc. of the 1987 IEEE Particle Accelerator Conference, March 16-19, Washington, D.C.
3. D. Howard et al, "RF Drivers For The Bevalac Final Stage Amplifiers", this conference.

RF DRIVERS FOR THE BEVALAC INJECTOR FINAL STAGE RF AMPLIFIERS

D. Howard, J. Calvert, M. Hui, A. Lindner, N. Kellogg, W. Ridgeway, K. Woolfe
Lawrence Berkeley Laboratory
University of California, Berkeley, CA 94720

ABSTRACT

A 200Mhz intermediate power amplifier system, comprised of four separate chassis or cavity amplifiers is being developed as a driver stage for the Bevalac injector final RF amplifiers. These amplifiers are intended to upgrade and replace the present systems with an expected increase in the available RF output power and the system reliability while reducing the associated operating costs. The system construction, design, and initial high power test results will be presented.

INTRODUCTION

The 200 Mhz intermediate power amplifier cart is designed as a self contained, turn-key system to provide amplification from the 10 milliwatt to the 300Kw level in four stages.

The initial stage is a 200 Watt, solid state, RF amplifier with 44 db of gain. The two succeeding stages are cavity amplifiers that incorporate vacuum tubes manufactured by Varian, Power Grid Division. The first of the tube type amplifiers is driven by the 200 W amplifier and contains a 3CPX800A7 triode calculated to output a maximum of 5 Kw. The next stage, driven by the 5 Kw amplifier, contains a 4CW25000B tetrode and is designed to drive the final amplifier. While the 4CW25K stage is calculated to provide a maximum output power of 50 Kw, the drive requirements of the final stage are quite modest by comparison. This feature should provide for conservative operation.

The final stage is designed to operate with either a Varian 4CW100000e or a TH535 manufactured by Thomson-CSF. The final stage gain, using the 4CW100Ke, is calculated to be 13 db at approximately 300 Kw output. Using the Thomson tube, the stage gain is calculated to be slightly greater, however the maximum achievable RF output power is approximately 300 Kw.

All the amplifiers, with their associated electronic supplies, cooling systems, interlocks, and status indicator panels, are installed in a single 6 foot roll-around rack. The rack is constructed of two standard 19 inch double sided racks mounted back to back.

5 KW AMPLIFIER

The 5 Kw amplifier is intended to replace an RCA 7651 amplifier stage. The benefits of this change are simplified cavity construction, reduced bias system requirements, ease of maintenance, and tube replacement cost savings of ~ $800 per tube.

The 3CPX800A7, chosen as the 7651 replacement tube, is an oxide coated cathode, high - mu triode provided by Varian, EIMAC. The initial calculations using 3CPX800A7 tube curves predict 14db gain with 5 Kw of RF output power.

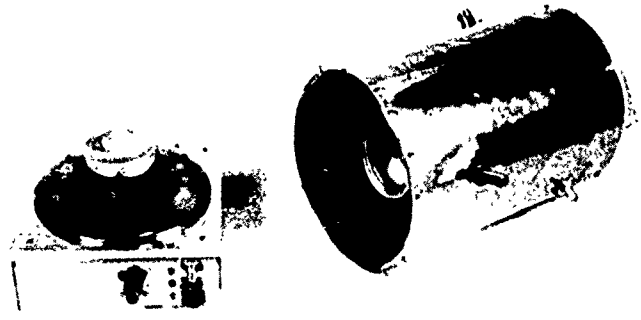


Fig. 1

The 3CPX800A7, the grid circuit enclosure, and the anode circuit resonator are shown in Figure 1. Attached to the coaxial resonator are the anode frequency tuner and the RF output and monitor connectors.

The amplifier is designed to run class B, RF grounded grid and DC grounded cathode. RF grounding of the grid is accomplished by sandwiching the insulated grid plate between ground planes. The grid-cathode RF input circuit is designed to provide adjustment free, wideband operation from 195 Mhz to 205 Mhz, with an input SWR of less than 2:1. The input circuits are "factory tuned" for minimum SWR at 200 Mhz by use of novel tuning devices[1] located within the grid-cathode enclosure. With the exception of the anode connections, all signal, control and power supply voltages are interfaced to or from the amplifier via plugs mounted on the enclosure.

At the design frequency, the tuning devices present positive to negative continuously adjustable input reactances. Each device is shunted by a choke to redistribute the reactance

* This work was supported by the Director, Office of Energy Research, Office of Basic Energy Sciences, Materials Sciences Division of the U.S. Department of Energy, under contract No. DE-AC03-76SF00098.

U.S. Government work not protected by U.S. Copyright.

tuning range and to provide a path for anode return currnet. In circuit, the devices perform as double stub tuners.

HIGH POWER TESTS

The anode cavity resonance was adjusted at each of the operating frequencies listed. The amplifier input impedance was adjusted during full power operation at 198.965 Mhz. No other adjustments were made during the tests.

Frequency	198.9 Mhz	195 Mhz	205 Mhz
Plate Volts	4 Kv	4 Kv	4 Kv
Grid Volts	-27 V	-27 V	-27 V
Plate current	1.7 A	1.8 A	1.2 A
Grid current	28 ma	60 ma	3 ma
Power, DC input	6.8 Kw	7.0 Kw	4.6 Kw
Power, RF input	232 W	257 W	119 W
Power, RF output	4.8 Kw	5.2 Kw	3.0 Kw
Input SWR	1.5:1	1.4:1	1.8:1
Efficiency	70.6 %	73 %	65.5 %
Gain	13.2 db	13.1 db	14.5 db

50KW AMPLIFIER

The 50 Kw amplifier is intended to replace a second RCA 7651 amplifier stage. In addition to most of the previously described benefits, this replacement significantly increases the available RF drive power to the 300 Kw amplifier.

As the Bevalac has many 4CW25000Bs in service, it was chosen as the 7651 replacement tube. This tetrode, employing a thoriated tungsten filament/cathode, has recorded filament life times in excess of 40000 hours. In addition to the the long filament life times, the 4CW25K is a commonly rebuilt tube. These features should dramatically reduce the operating costs of this stage. The initial calculations using 4CW25K tube curves supplied by Varian predict 10db gain with 50 Kw of RF output power.

The 50 Kw amplifier is mounted in the roll around rack on slides to provide easy access for the maintenance or tuning of the components mounted on the amplifier support plate. These components include the 5 Kw amplifier, a 50 ohm dummy load, the 4CW25K plate supply voltage divider, the filament voltage Variacs for the 4CW25K and 3CPX800, and the input impedance tuners for the 50 Kw amplifier. With the exception of the 50 Kw and final stage outputs, all the amplifier input and output connections and the dummy load connection are brought to the front panel, where each stage may be tested, loaded, or configured for normal operation.

The 50 Kw amplifier mechanical layout shown in Figure 2 is not to scale but does approximate the adjustable 3/4 wave resonant anode and half wave resonant grid circuits, the RF output assembly, the anode RF bypassing and the fixed frequency screen-control grid resonator. The resonant frequency of this circuit directly affects the anode to grid circuit isolation. The isolation, measured at -2 db with the grid grounded at the socket, was increased to -47db by terminating the grid as described. The capacity, G1 to G2, is shunted by the reflected impedance of the shorted resonator, which in this case is a line >1/4 <1/2 wave lengths. Refering to the article[2] by Robert Sutherland and William Barkley it can be seen that this is an alternative method to obtain self-neutralization.

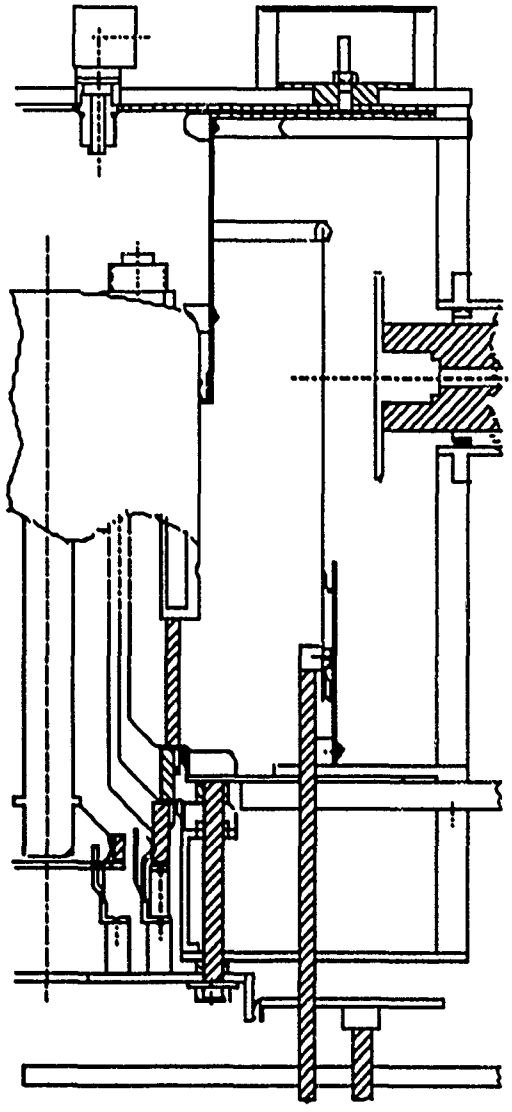


Fig. 2
(Not to scale)

50 KW HIGH POWER TESTS

Frequency	198.9 Mhz	195 Mhz
Plate volts	10 Kv	10 Kv
Screen volts	750 V	750 V
Grid volts	-400 V	-400 V
Plate current	7.4	6.4 A
Screen current	600 ma	480 ma
Grid current	180 ma	Not measured
Power, DC input	74 Kw	64 Kw
Power, RF input	5.0 Kw	4.6 Kw
Power, RF output	53 Kw	44 Kw
Input SWR	1.1:1	1.5:1
Gain	10.2 db	9.8 db
Efficiency	71.5 %	68.8 %

300 KW AMPLIFIER

The final amplifier stage is intended to replace the original RCA 4616 with either a 4CW100Ke or a TH535. Both replacement tubes have thoriated tungsten filament/cathodes and were cheaper than the 4616. The two tubes of different origin were chosen as a hedge against future manufacturing cost increases or lack of availability. The confidence to proceed was given by the success of our European colleagues in testing tubes of different manufacture3 in the same basic structure.

The 4CW100Ke mechanical layout shown in Figure 3 is not to scale but does approximate the 3/4 wave resonant anode and the adjustable half wave resonant grid circuit and the anode frequency tuning slugs.

To date only the 4CW100Ke has been operated at high power. Future operations with the TH535 will require a new flange to interface the tube anode to the bottom plate, removal of the tube socket adapter plate which is installed when using the 4CW100Ke and replacement of two adapters in the grid-cathode circuit.

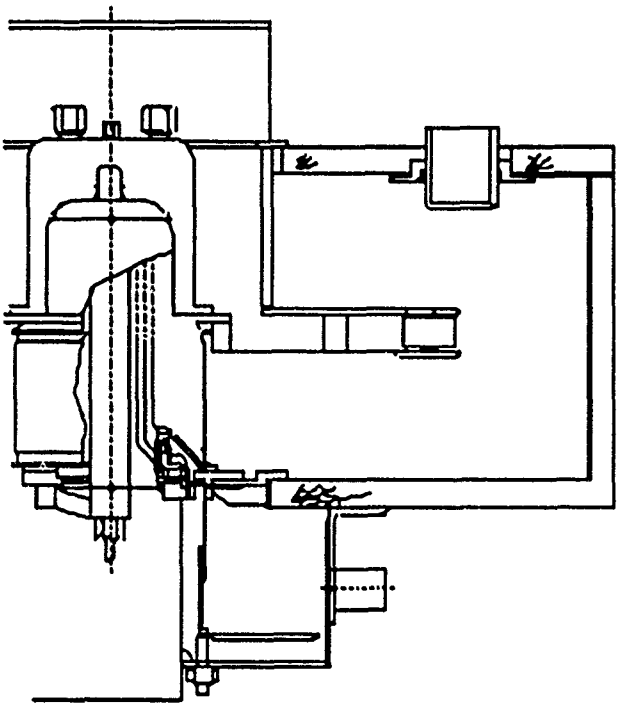


Fig. 3
(Not to scale)

HIGH POWER TESTS

An alternative method of radial line construction for the anode resonator was tried with limited success. A double sided printed circuit board was fabricated as an integral replacement for the capacitively end loaded radial plates shown in Figure 3. The computer generated circuit board layout was sent off-site by modem where the data was transformed to the etched product. Seen as a potentially inexpensive option, the board was successfully operated to 280 Kw output, however the operating pulse width was reduced to less than 1/5 that required. RF generated tracking could be observed between the layers of fiber glass at the outer edge. A new and as yet untested board has been constructed of a solid dielectric in hopes of relieving this problem before incurring the costs of a copper deposited, Teflon board.

The most meaningful high power test was performed when we successfully operated the LINAC RF system with the highest power requirements, using the 300 Kw amplifier with the 4CW100Ke installed. The high power test data documented below were taken with the amplifier loaded by a 50 ohm water load. The data does not reflect any output power limitation associated with the 300 Kw amplifier but rather the drive limitations of the 7651 amplifier. The poor efficiency is caused by the pulsed grid bias system. The addition of the 50 Kw amplifier should eliminate the need for the pulsed bias system and increase the output RF power. As reported4, higher output power from the 300 Kw amplifier may simplify operation of the final amplifier associated with Tank 2 of the LINAC RF system. It is hoped that operation of the 300 Kw amplifier with the higher powered 50 Kw drive system will soon confirm this thought.

Plate volts	18.4 Kv
Screen volts	2.2 Kv
Pulsed grid volts	-340 V
Plate current	29 A
Screen current	1.8 A
Grid current	No reading
Power, DC input	534 Kw
Power, RF input	12.2 Kw
Power, RF output	280 Kw
Input SWR	2.4:1
Gain	13.6 db
Efficiency	52.4 %

ACKNOWLEDGEMENTS

The authors wish to thank Don Bowman, John Lax and Bob Richter for their expert mechanical assistance and support; Marshal Loring and Reid Brandon from Varian for their technical support; all those from Thomson and John Mulroe, from SMA representing Thomson, for providing the TH535, the socket and their technical support; and Mike Bennett for his assistance and support in preparing this paper.

REFERENCES

1. Patent Disclosure submitted.
2. Electronic Design, May 10, 1967
3. Personal Communication with Gerald Hutter , GSI
4 D Howard et al, "Bevalac Injector Final Stage RF Amplifier Upgrades", this conference.

New Design Concepts for Ferrite-Tuned Low-Energy-Booster Cavities

Georg Schaffer
Superconducting Supercollider Laboratory
2550 Beckleymeade Ave., MS 1049, Dallas, TX 75237*

Abstract

The design concepts for ferrite-tuned accelerating cavities discussed in this paper differ from conventional solutions using thick ferrite toroids for frequency tuning. Instead, tuners consisting of an array of ferrite-loaded striplines are investigated. These promise more efficient cooling and higher operational reliability. Layout examples for the SSC-LEB rf system are presented (tuning range 47.5 to 59.8 MHz, repetition frequency 10 Hz).

I. INTRODUCTION

Scenarios of very large proton accelerators and of medium-energy machines for very-high beam intensities usually contain rapid cycling booster synchrotrons in their injector chains in order to save on costly linac energy or to make use of existing circular accelerators of high intensity but limited energy.

The savings on the one side challenge an uppermost performance of the rf acceleration system in the follow-up machine: very high acceleration voltages combined with rapid frequency tuning over a wide frequency range. The rf system of the FNAL booster and its upgrade /1/ is our classical example. 18 ferrite-tuned double-gap cavities produce about 1 MV total rf voltage, tuned in frequency from 30 to 53 MHz, and operating with 15-Hz pulse trains. The 10-GeV Fermilab booster synchrotron is the only one of its kind in operation.

Studies and proposals of accelerators for kaon factories /2-4/ included boosters with a 32 to 11 % frequency swing in the 45 to 60 MHz range and repetition rates between 60 and 25 Hz.

A similar booster (LEB) but for lower intensity and 10 Hz repetition rate is included in the SSC injector scenario /5/.

Tables 1a and 1b contain the main parameters of the rf systems of some of these booster synchrotrons.

II. ORIGIN OF DIFFICULTIES

The cavity reference design for the low-energy boosters of TRIUMF and SSC is the quarter-wave cavity developed at Los Alamos (1984-87). It is shown in Fig. 1.

The use of low-loss microwave ferrites and application of bias fields perpendicular to the magnetic rf fields made it possible to achieve much higher Q-values compared to cavities using NiZn-ferrites (Fermilab-booster). This has stimulated a considerable increase of gap voltages (up to and beyond 100 kV). Magnetic and dielectric losses were seen as limiting factors in the layout of booster (and main ring) rf systems /2,3,5-8/. Mean power densities of about 0.2 W/ccm were considered to be the maximum values for stable operation /2/.

Besides power and cooling limitations, however, another limiting factor has to be taken into account: Partial discharge (corona) between ferrite cores of the tuner /9/. Due to the high dielectric constant of the microwave ferrite (relative epsilon about 14), the electric fieldstrength in small air gaps between ferrite cores is magnified by their relative dielectric constant.

Taking Ed= 25 kV/cm as breakdown field in air, for example, a stack of six ferrite cores with a total height of about 15 cm would begin to show partial discharge beyond a voltage of about 27 kV. The insertion of five layers of beryllia plates for cooling purposes raises this limit to about 39 kV.

Table 1a. Comparison of Various Booster Cavity Data.

Machine	SSC-LEB	TRIUMF-Booster	EHF-Booster	Fermilab-Booster
Energy Range (GeV)	0.6 - 11	0.45 - 3	1.2 - 9	0.2 - 10
Frequency Swing (MHz)	47.5 - 59.8	46.1 - 60.8	50.5 - 56	30.3 - 53.2
Peak Gap Voltage (kV)	88 / 117 normal/extended op.	max. 62.5 / 75 normal/extended op.	2 x 36	2 x 30
DC Beam Current (A)	max. 0.5	2.0 - 2.7	max. 2.55	max. 0.39
Cavity Length (m)	~1.25	~1.23	~3.25	~2.4
RF Input Power / Cavity (kW)	77 / 119	22.5 - 93	100 - 300	100 - 160
Tuning Speed	50 ms (10 Hz)	10 ms (50 Hz)	20 ms (25 Hz)	67 ms (15 Hz)

Table 1b. Total RF Structure Length vs. Machine Circumference.

Number of RF Cavities	8 (single gap)	12 (single gap)	14 (double gap)	18 (double gap)
Total Length, all cavities (m)	~10	~15	~45.5	~43.2
Machine Circumference (m)	540 m	215.7 m	480 m	471 m
Fraction RF, approx. (%)	~1.85	~6.8	~9.5	~9.2

*Operated by the Universities Research Association under contract with the U.S. Department of Energy

U.S. Government work not protected by U.S. Copyright.

The onset of partial discharge may not easily be realized. High reliability in operation can be assured if the cavity is successfully tested with 50 % overvoltage, and if the components withstand a rise in temperature of 65 degree C.

High-power tests with cavities constructed according to /6/ and /8/ have shown that imperfect discharges and insufficient cooling will actually limit the operation of a ferrite-tuned cavity to a low fraction of the design voltage.

In the following, we will concentrate on possible improvements in both voltage holding and average power handling.

III. BENEFITS OF AIRGAPS

The insertion of airgaps between ferrite cores offers two beneficial effects: the breakdown voltage of the ferrite stack rises rapidly with increasing gap height, and the dielectric losses fall dramatically. In fact, they become negligible.

This is illustrated by Fig. 2. For a ferrite stack as shown in Fig. 1, the replacement of 6-mm beryllia disks by airgaps leads to a breakdown voltage of about 102 kV which would solve the voltage problem. Beryllia (or alumina) spacers could be used on the periphery of the ferrite cores where the electric field is low.

IV. AIRCOOLING

For modest average power losses in the ferrite tuner, aircooling may be applied as the most reliable cooling method. With a tuner structure as described above, longitudinal flow of air with strong turbulence around the inner edges of the cores would be most efficient. If we extrapolate experience with aircooled anodes of high-power electron tubes, it appears that average power losses up to about 10 kW.can be handled.

V. NUMBER OF CAVITY UNITS

Since the requirement of reliability overrides other design factors for the SSC low-energy booster, sufficient space for cavities is important. Table 1 shows that the LEB reference design deviates by far from comparable booster designs as to the ratio total rf-structure length to machine circumference.

VI. EDDY CURRENT EFFECTS

The outer conductor of the ferrite tuner will be slotted in order to allow AC components of the bias field to penetrate into the ferrite. It was difficult to develop an adequate solution

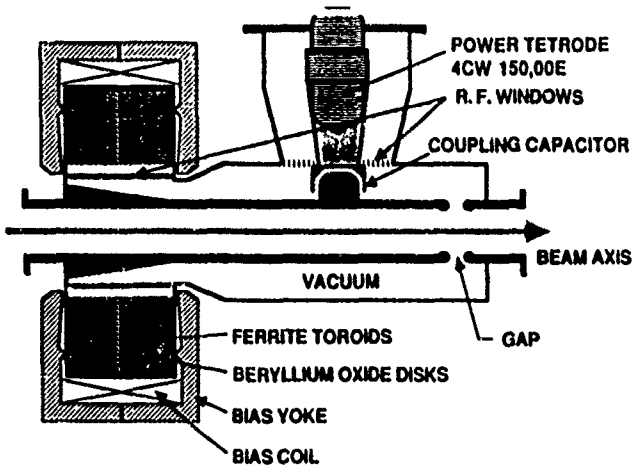


Fig. 1. Ferrite-tuned quarter-wave cavity designed by LANL, chosen as reference design for TRIUMF and SSC.

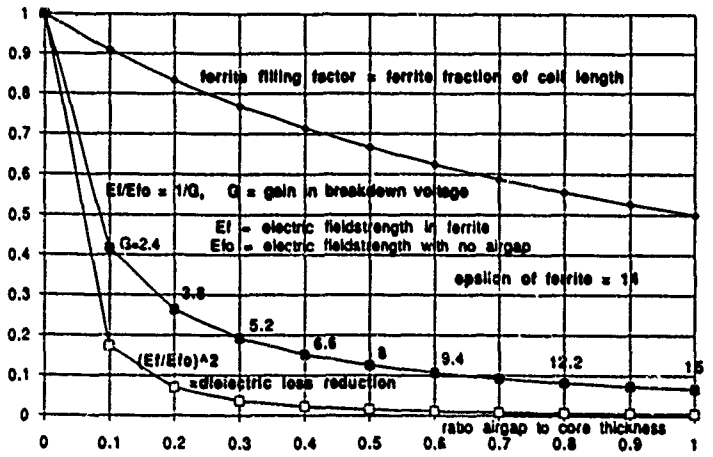


Fig. 2. Effect of airgap: gain in breakdown voltage, and reduction of dielectric ferrite losses.

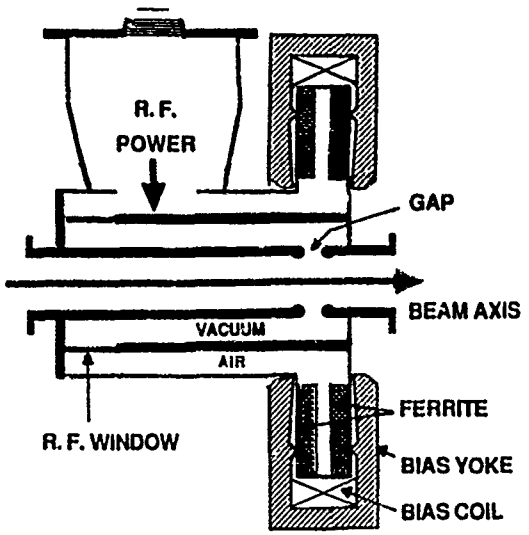


Fig. 3. Folded quarter-wave cavity with pillbox-type tuner

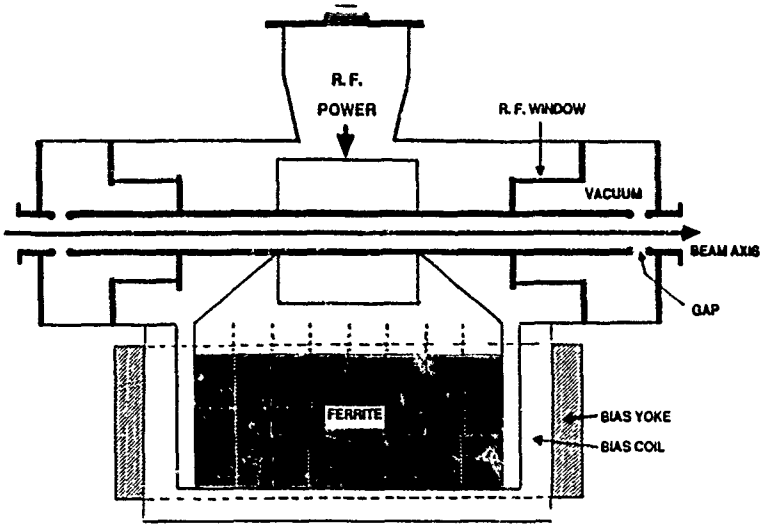


Fig. 4. Drift-tube resonator with lateral stripline tuner.

for the TRIUMF booster (50 Hz) but a satisfying design was found /10/. For the SSC-LEB (10 Hz), eddy current losses play a less important role (reduction by the square of the frequency). However, the penetration of higher harmonics of the bias field still needs attention. Five ms after the beginning of the acceleration cycle, the rate of rf frequency change reaches its maximum of 1 MHz per ms.

VII. FOLDED QUARTER WAVE CAVITY

A more compact cavity design compared to Fig. 1 is shown by Fig. 3. This is a folded quarter wave cavity. It may become attractive for the SSC LEB which requires somewhat less frequency tuning compared to the TRIUMF booster. Note that there will be only one rf window instead of two in Fig. 1.

VIII. HOM DAMPING

It is intended to use the type of HOM damper designed by W. R. Smythe /11/ which can easily be incorporated in any cavity type at the accelerating gap(s).

IX. STRIPLINE TUNERS

The idea of using ferrite-loaded striplines for cavity tuning has been promoted by E. Pivit /12, 13/. Commercial experience exists with a fast ferrite tuner built for the BNL light source /12/. This 20-ohm stripline tuner can handle a maximum dissipated power of 22 kW, max. 505 A and 25.2 kV. The outer conductor of the stripline is of rectangular shape (about 20 cm x 6 cm), the watercooled inner conductor carries ferrite tiles of about 6 mm thickness which are glued onto it with a very thin layer of epoxy resin.

The same technique has been successfully used over several decades in high-power ferrite circulators (in use with e+e- colliders at CERN, DESY and elsewhere for transmission of CW rf power up to 1.1 MW). The cooling capability is of the order of 10 W/ccm. Recent tests with even 20 W/ccm at CERN (324 MHz) did not lead to damages /14/.

Radiation damage tests with thermosetting resins are documented by CERN /15/. Results are shown for absorbed doses up to 100 MGy. It may be concluded that radiation damage will not be a major issue if stripline tuners of the kind described above will be used for booster rf systems.

A double-gap cavity with a broad stripline tuner designed for the possible use in the SSC low-energy booster is sketched in Fig. 4. The width of the inner stripline conductor is 100 cm. The distance between ferrite carriers is 5 cm; the airgap between the 12.5 mm thick ferrite layers is 2.5 cm. The length of the tuner is 40 cm. Tuning from 47.5 to 59.8 MHz requires a permeability tuning from 3.5 to 1.4.

The 4 layers of the tuner have a total surface of 1.6 qm. If 2.5 W/ccm are taken as conservative limit for mean losses we would obtain a value of 40 kW for the tolerable total losses.

With a breakdown fieldstrength of 25 kV/cm in air, the breakdown voltage of this tuner would be around 60 kV.

The voltage stepup ratios from the center of the (150 degree) drift tube to the gaps are 1.6 (47.5 MHz) and 2.3 (59.8 MHz).

The gap voltages of this resonator are limited to about 2 x 50 kV by the cylindrical vacuum windows between inner and outer drift tube conductors. The recommended operational gap voltages are 2 x 35 kV. Thus, 10 cavities would be needed to generate the required 700 kV total rf voltage for the booster.

Stripline-type tuners may also be designed in coaxial or pillbox shape, see for instance Fig. 3 or proposals in /13/.

X. CONCLUSIONS

A variety of options discussed in this report permit substantial improvements on both voltage holding capabilities and tolerable rf power levels of ferrite-tuned cavities for rapid-cycling booster synchrotrons.

XI. ACKNOWLEDGEMENTS

The author has profited from collaboration with colleagues from LANL, TRIUMF, FNAL, and SSCL in various "50-MHz RF Workshops", by contributions from Bosch-ANT, as well as from other Laboratories and Universities. Special thanks should be added to Warren Funk and Jimmy Rogers for valuable comments and support.

XII. REFERENCES

/1/ Q. A. Kerns, et al., "30-53 MHz super cavities for 10 GeV acceleration in the Fermilab booster ring, IEEE Trans. Nucl. Sci. 26 (3), 4111 (1979).

/2/ LANL, "Physics and Plan for a 45 GeV Facility", LA-10720-MS, ch. 7.1, Los Alamos National Laboratory, May 1986.

/3/ TRIUMF, "Kaon Factory Proposal", ch. 4.3.3, Sept.1985, and "Kaon Factory Study", 1990.

/4/ EHF, "Proposal for a European Hadron Facility", ch. 18, May 1987.

/5/ SSC Laboratory, "Site specific conceptual design", ch. 4.2.6, June 1990.

/6/ R. D. Carlini, et al., "The Los Alamos ferrite-tuned cavity", Proc. Internat. Workshop on Hadron Facility Technology, Los Alamos, Feb. 1987.

/7/ H.A. Thiessen, "Wrap-up on ferrite-tuned cavity test at Los Alamos", 50-MHz RF Workshop Duncanville, Oct. 1989.

/8/ G. Swain, "RF design of main ring cavity", and C. Friedrichs, "Testing of main ring cavity", ibidem.

/9/ G. Schaffer, "Comments on the cavity design for the supercollider-low-energy booster (LEB)", SSC-RF Workshop Dallas, April 1990, and LANL Report LA-UR-90-1606, May 1990.

/10/ R. Poirier, et al., A perpendicular AC biased ferrite-tuned cavity for the TRIUMF kaon factory booster synchrotron", 2nd European Particle Accelerator Conference, Nice, June 1990.

/11/ W. R. Smythe, et al., "A versatile cavity mode damper", ibidem.

/12/ E. Pivit, "Fast ferrite tuner for the BNL light source", SSC-RF Workshop, SSC Laboratory, April 1990, and S. Martin, et al., "A stripline design of a fast ferrite tuner (FFT)", 2nd European Particle Accelerator Conference, Nice, June 1990.

/13/ E. Pivit, "Cavity with watercooled ferrite carrier", RF Workshop held at TRIUMF, Vancouver, Oct. 1990.

/14/ E. Pivit, private communication, April 1991.

/15/ H. Schoenbacher and A. Stolarz-Isycka, "Compilation of radiation damage test data, Part II: Thermosetting and thermoplastic resins", CERN 79-08, August 1979, pp 21-129.

Injection locking of a long-pulse relativistic magnetron

S.C. Chen, G. Bekefi, and R.J. Temkin

Massachusetts Institute of Technology
Cambridge, MA 02139

Abstract

We report the injection locking results of a long-pulse (200–400 ns) high power (20–30 MW) relativistic magnetron at 3.3 GHz. Phase-locking with reproducible locked angle is achieved with an injection power ratio as low as 1:200. The locked states are phase stable to within ±3° during the pulse. Phase locking physics is studied and important effects due to frequency pushing are identified. The locking bandwidth and the dependence of final locked phase on injection parameters are measured and are found to agree well with theory.

I. INTRODUCTION

Phase-locking of a high power relativistic magnetron oscillator has been a subject of intensive experimental [1–5] and theoretical research. [6–9] Phase locking through the injection of an external low power reference signal has the following advantages. First, the same phase locking physics applies to all the master-slave pairs and to the whole phase-locked array. No additional complication arises for phase-locking a large number of oscillators. Second, output phase and frequency can be controlled by adjustments made at very low power levels. Third, several high power oscillators can share the same low power driver, which is usually simple and available at low cost.

Injection locking, however, requires high power oscillators with good mode and frequency stability, and with a pulse length longer than the phase-locking time. This paper describes the operation of such a long-pulse relativistic magnetron oscillator system and its injection-locking. Section II describes the apparatus used in the experiment. Section III discusses the general operating characteristics of the free running relativistic magnetron (III.A) and the results of the phase locking experiment (III.B). Section IV summarizes the main results of the phase locking study.

II. APPARATUS

The transformer-based high power modulator produces up to 500 MW, 2 μs pulses with a repetition rate of 5 Hz. [10] The high voltage pulses are delivered through the cathode shank to the magnetron diode. The relativistic magnetron diode is located at the center of the bore of a superconducting magnet capable of generating uniform DC fields up to 22 kG. Microwave output is extracted radially in waveguide through the radial access holes in the superconducting magnet. The experimental parameters are listed in Table I. The magnetron diode (SM2) has a large A-K gap (1.35 cm) to prevent gap-closure and to enhance the power handling capability of the structure. A thick velvet washer (5 mm) is chosen for the phase locking experiment. Thicker cathodes have longer lifetimes and sustain the 2D-mode structure better than thin washers.

III. EXPERIMENTAL RESULT

A. Operating characteristics

Figure 1 shows the time dependence of output microwave and the corresponding magnetron voltage. The microwave duration ranges from 200 to 400 ns. The impedance of the magnetron diode varies slowly with time, and no signs of impedance collapse (on the fast time scale) are observed. Microwaves are generated at the onset of the radial current, which is about 300–400 A Typical peak powers are between 20 and 30 MW. The efficiency, namely the output power normalized to the total electron beam power, is about 16 percent. The efficiency can be improved by reducing the axial current.

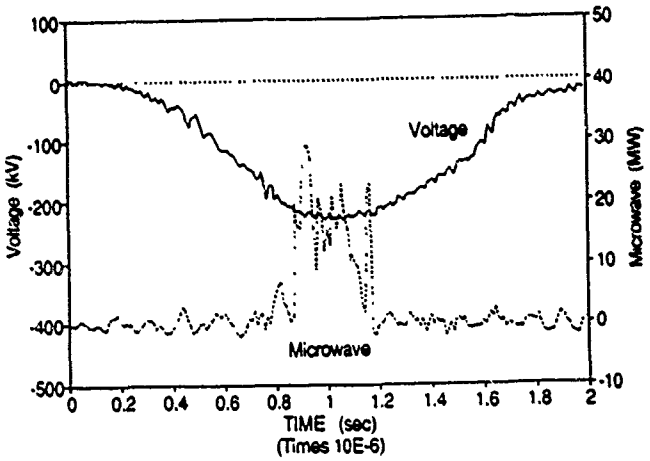


Figure 1 Operating characteristics of a free-running SM-2 magnetron.

B. Phase locking result

The layout of the phase-locking experiment is shown schematically in figure 2. Microwave radiation is extracted from the interaction region through a high power circulator with 20 dB isolation. The power from the tunable 1 MW RF driver is injected through the same circulator into the main oscillator. A 20 dB isolator is placed between the driver and the circulator so that the overall isolation is 40

0-7803-0135-8/91$01.00 ©IEEE

dB. The isolation prevents the driver from being locked by RM's leakage power.

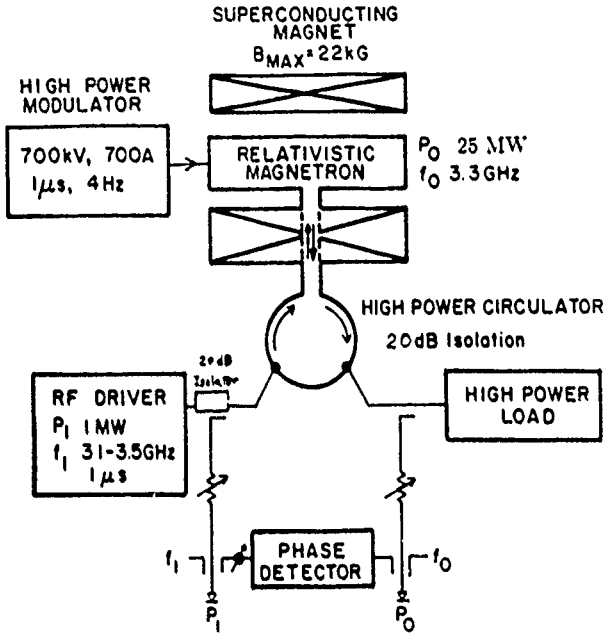


Figure 2 Schematic of the phase-locking experiment.

Clear signs of phase locking are observed. Figure 3 is an example of such a phase-locked shot. The driver signal P_i (middle trace) is monitored before injection into the circulator. The upper trace shows the high power RF from the RM riding on top of a low power injection plateau. The bottom trace in figure 3 shows the evolution of the relative phase. During the absence of the RM signal (for example, in the time interval between 0.9 and 1.1 μs) the phase detector measures the relative phase between the driver signal and its own image – the low power plateau. The result is a relative phase constant in time. We use this as a reference state at 0°. When the RM turns on at 1.15 μs, the relative phase is pulled to a new angle at 12 °. This new phase angle is reproducible from shot to shot and defines a phase locked state which relaxes back to the reference state at 0° when the RM is off. By using a stringent criterion of ±3° to define the phase-locked states, typically the locked duration is between 100 and 300 ns. The shot-to-shot reproducibility of the final locked phase angle is better than ±2°.

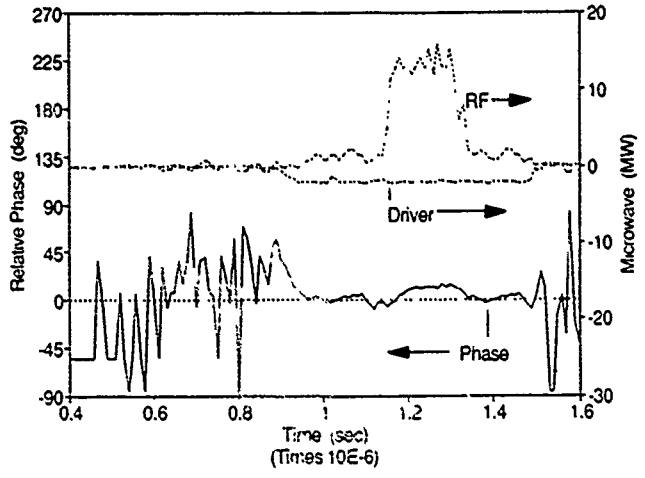


Figure 3 Example of a phase-locked shot.

The results of a large number of experiments involving various injection frequencies (ranging from -10 MHz to 10 MHz) and injection power ratios (ranging from 1:1000 to 1:10) are compiled in figure 4. The solid squares in the figure stand for the cases phase-locked states are identified. The blank squares represent those cases when no phase-locking occurs. A magnetron-specific phase-locking model was developed in reference 6 using the standard equivalent-circuit approach and takes into account the frequency pushing effect. The model predicts a locking-bandwidth wider than that in conventional locking theory

$$\Delta\omega \leq \frac{\omega_0}{2Q \cdot cos\alpha} \cdot \sqrt{\frac{P_i}{P_o}}.$$

In the equation, $\Delta\omega$ is the locking frequency range, ω_0 is the free-running oscillator frequency, α is the frequency pushing parameter,[6] and P_o and P_i are the oscillator output and input power, respectively. The $1/cos\alpha$ factor is the attributed to the frequency pushing effect in RMs.

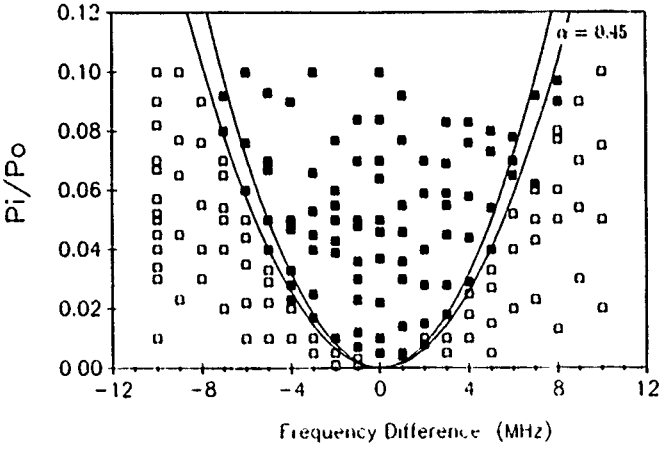


Figure 4 Map of the phase-locking zone.

The two solid curves in figure 4 are the locking zone boundaries predicted by (1) the Adler's condition with frequency pushing effect correction and (2) the Adler's condition alone. The data points are consistent with the theory curve described by the above equation with a pushing parameter α of 0.45.[6]

The magnitude of frequency pushing is also confirmed in an independent measurement of the final phase. In figure 5, the dependence of the final locked-phase on the injection power and frequency is mapped out. The cases for 5 injection frequencies (-4MHz, -2MHz, 0MHz, 2MHz, and 4MHz) are shown for various injection power ratios (1:1000 to 1:10). Again, the data points agree well with the theory with a frequency pushing parameter α of 0.45.

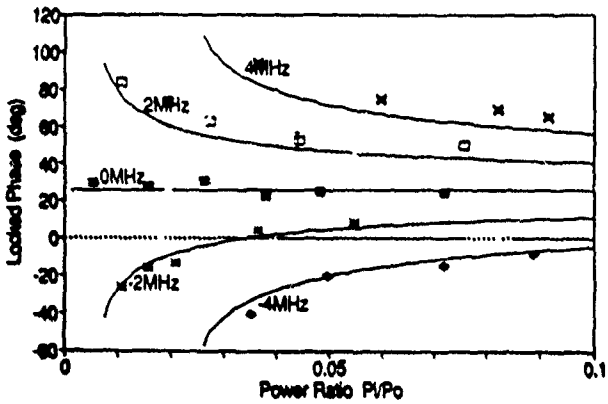


Figure 5 The dependence of the final locked-phase on the injection power and injection frequency difference.

IV. CONCLUSION

We have phase locked an S-band (3.3 GHz) long-pulse high power relativistic magnetron oscillator (400 ns at 25 MW) by external injection (20 kW - 1 MW). A reproducible final phase-locked angle is achieved with an injection power ratio as low as 1:200. The phase stability of the phase-locked states is $\pm 3°$ degrees throughout the 300 ns pulse.

Parametric study of the phase-locked states reveals the importance of frequency pushing effect in phase-locking. The measured locking bandwidth agrees well with the theory which takes into account the frequency pushing effect. The measured dependence of final locked phase on $\Delta\omega$ and P_i/P_o also agrees well with theory.

V. ACKNOWLEDGEMENT

This work was supported by Strategic Defense Initiative Organization, Office of Innovative Science and Technology, and managed by Harry Diamond Laboratories.

VI. REFERENCE

1. S.C. Chen, G. Bekefi, and R.J. Temkin, "Operation of a long-pulse relativistic magnetron in a phase-locking system," H.E. Brandt, Editor, *Proc. SPIE*, vol. 1226, pp. 36-43, 1990.

2. S.C. Chen, G. Bekefi, R. Temkin, and C. de Graff, "Proposed injection locking of a long pulse relativistic magnetron," H.E. Brandt, Editor, *Proc. SPIE*, vol. 1061, pp. 157-160, 1989.

3. S.C. Chen and G. Bekefi, "Relativistic magnetron research," N. Rostoker, Editor, *Proc. SPIE*, vol. 873, pp 18-22, 1988.

4. J. Benford, H.M. Sze, W. Woo, R.R. Smith, and B. Harteneck, "Phase locking of relativistic magnetrons," *Phys. Rev Lett.*, vol. 62, pp. 969-971, 1989.

5. T.A. Treado, R.S. Smith III, C.S. Shaughnessy, and G.E. Thomas, "Temporal study of long-pulse relativistic magnetron operation", *IEEE Trans. on Plasma Science*, vol. 18, pp 594-602, 1990.

6. S.C. Chen "Growth and frequency pushing effects in relativistic magnetron phase-locking", *IEEE Trans. on Plasma Science*, vol. 18, pp 570-576, 1990.

7. G.L. Johnston, S.C. Chen, R.C. Davidson, and G. Bekefi, "Models of driven and mutually-coupled relativistic magnetrons with nonlinear frequency-shift and growth-saturation effects", H.E. Brandt, Editor, *Proc. SPIE*, vol. 1407 (in this volume), 1991.

8. G.L. Johnston, S.C. Chen, R.C. Davidson, and G. Bekefi, "Models of driven relativistic magnetrons with nonlinear frequency-shift and growth-saturation effects", H.E. Brandt, Editor, *Proc. SPIE*, vol. 1226, pp. 108-116, 1990.

9. W. Woo, J. Benford, D., Fittinghoff, B. Harteneck, D. Price, R. Smith, and H. Sze, "Phase locking of high-power microwave oscillators," *J. Appl. Phys.*, vol. 65, pp. 861-866, 1989.

10. W. Mulligan, S.C. Chen, G. Bekefi, B.G. Danly, and R.J. Temkin, "A high-voltage modulator for high-power rf source research", *IEEE Trans. on Elec Dev.*, to be published in April, 1991.

Cyclotron Autoresonance Maser (CARM) Amplifiers for RF Accelerator Drivers

W.L. Menninger, B.G. Danly, C. Chen, K.D. Pendergast, and R.J. Temkin
Plasma Fusion Center
Massachusetts Institute of Technology
Cambridge, Massachusetts 02139

D.L. Goodman, D.L. Birx
Scientific Research Laboratory
Sommerville, Massachusetts

Abstract

Cyclotron autoresonance maser (CARM) amplifiers are under investigation as a possible source of high-power (>100 MW), high-frequency (>10 GHz) microwaves for powering the next generation of linear colliders. A design for a high-power, short pulse, 17.136 GHz CARM amplifier, utilizing a 500 kV linear induction accelerator, is presented.

I. INTRODUCTION

A. Next Generation Collider Requirements

The next generation of TeV e^+e^- linear colliders of reasonable length and cost will require [1,2,3] at least an order-of-magnitude increase in the accelerating gradient above the ~ 10-20 MeV/m that is presently achieved using conventional S-band klystron drivers. In order to obtain these accelerating gradients, the RF peak power and frequency must be increased substantially. The RF peak power breakdown limit is increased by increasing the frequency and decreasing the RF pulse length.

At present, designs for the next generation collider have settled on 17.136 GHz as a reasonable choice for the operating frequency [4,5,6]. The typical peak power that will be required per source is in the 500 MW to 1 GW range, with rf pulse lengths in the neighborhood of 25–50 ns [4,5]. For such a design, accelerating gradients may be on the order of 200 MeV/m.

RF sources capable of fulfilling all of the requirements of these accelerators do not yet exist. Stanford's two mile linear accelerator, SLAC, is powered by S-band klystrons; however, SLAC operates at 2.86 GHz. Because klystrons are very difficult to operate above ~10 GHz, alternative high power RF sources need to be investigated.

B. Promising Sources

Promising sources that may replace the klystron for driving the next generation linear collider are gyroklystrons, free electron lasers (FELs), and Cyclotron Autoresonance Maser (CARM) amplifiers [7,6]. These masers have the potential to operate as high-gain, high-efficiency, high-power amplifiers in the frequency regime applicable to this next generation of colliders.

0-7803-0135-8/91S01.00 ©IEEE

C. Description of a CARM

The CARM is similar to a gyrotron, except that the electromagnetic wave propagates with a phase velocity close to the speed of light. The CARM typically employs relativistic electron beams with pitch angles ($\alpha = v_\perp/v_z$) smaller than that of the gyrotron. However, unlike gyrotrons and free-electron lasers, there are few experimental demonstrations of the CARM [8,9,10].

In design of a high-peak power CARM amplifier, the electron beam energies which result in the most attractive operation are typically in the 0.5 – 2 MeV range. Consequently, beam generation for a high-power CARM amplifier is well suited to two accelerator technologies. Both high-voltage (500 kV – 1 MV) SLAC-type pulse modulators and linear induction accelerators can be used for e-beam generation. For CARM designs based on induction accelerators, the peak beam powers and beam pulse durations result in the generation of rf pulses which are already well suited to the requirements of future colliders. In addition, a unique feature of CARM amplifiers that use a bifilar helical wiggler to spin-up the electron beam is that the wiggler can be designed so that the phase stability of the CARM is substantially enhanced.

We have completed the design study of an induction accelerator driven CARM amplifier with a 500 kV electron beam, and we are currently assembling such a CARM amplifier. This design is attractive for a proof-of-principle CARM amplifier experiment. Results of the design study, as well as final design parameters, are presented in this paper.

II. THEORY

The CARM interaction occurs when electrons undergoing cyclotron motion in an axial magnetic field ($\mathbf{B} = B\hat{z}$) interact with an electromagnetic wave $(\omega, \mathbf{k})$ with wavevector nearly parallel to the axial field $\mathbf{B}$. The resonance condition is then $\omega - k_z v_z = s\Omega_c$, where s is the harmonic number and Ω_c is the relativistic cyclotron frequency defined by $\Omega_c \equiv \Omega_{c0}/\gamma \equiv q_e B/\gamma m_0 c$. The well-known resonance condition for the CARM is thus $\omega = s\Omega_{c0}/\gamma(1 - \beta_z/\beta_{ph})$ where γ and β_z are the electron energy and velocity in the $\hat{z}$ direction. The wave phase velocity is given by $\beta_{ph} \equiv v_{ph}/c = \omega/ck_z$. As is apparent from the resonance condition, the CARM is capable of operation at a large Doppler upshift from the cyclotron frequency (in contrast to the gyrotron). For $\gamma_0^2 \gg 1, \beta_{\perp 0} \approx 1/\gamma_0$, and $\beta_{ph} \approx 1$, there is a γ_0^2 frequency upshift from the relativis-

tic cyclotron frequency Ω_c (or a γ_0 upshift from the nonrelativistic cyclotron frequency, Ω_{c0}). For the numerical results given here, we consider only CARM operation at the fundamental of the cyclotron frequency ($s = 1$).

III. DESIGN

A. Introduction

We have completed the design of a CARM amplifier utilizing a 500 kV linear induction accelerator (LIA) [11]. The CARM amplifier has been designed to run in the TE_{11} mode at 17.136 GHz. A three period bifilar helical wiggler with a wiggle wavelength of 9.21 cm and a field of up to 50 G will be used to spin-up the electron beam. Other parameters from the experiment are listed in Table 1.

Parameter	Design Value
Beam Energy	500 keV
Beam Current, I_b	500 A
Pulse Length	30 ns
Beam Pitch, $\alpha_0 \equiv \beta_{\perp 0}/\beta_{z0}$	0.4
Frequency, $\omega/2\pi$	17.136 GHz
Mode	TE_{11}
Waveguide Radius, r_w	1.3 cm
Phase Velocity, β_{ph}	1.088
Guide Field, B_0	3.06 kG
Detuning, Δ	0.4
Input Power, P_{in}	800 W
Est. Velocity Spread, σ_{pz}/p_z	< 1.6%
Energy Spread, σ_γ/γ	< 1.6%
Efficiency, η, untapered	13.5% ($\sigma_{pz} = 0$) 9.3% ($\sigma_{pz} = 0.02$)
Output Power, P_{sat}	33.6 MW ($\sigma_{pz} = 0$) 23.3 MW ($\sigma_{pz} = 0.02$)
Saturation Length, z_{sat}	0.93 m ($\sigma_{pz} = 0$) 1.01 m ($\sigma_{pz} = 0.02$)
Gain	46.2 dB ($\sigma_{pz} = 0$) 44.6 dB ($\sigma_{pz} = 0.02$)

Table 1: CARM amplifier design parameters.

B. Efficiency Optimization

Figs. 1, 2, and 3 show how the efficiency, the beam pitch, and the saturation length of the CARM amplifier vary with detuning. Different curves in the figures represent different values of coupling and of waveguide radius. The value of $\varepsilon/\varepsilon_c$ indicates how close the interaction is to the theoretical threshold for excitation of an absolute instability, with $\varepsilon/\varepsilon_c = 1$ corresponding to this threshold. For $\varepsilon/\varepsilon_c > 1$, the interaction is further prone to excite an absolute instability. Because of the short pulse length of the induction linac, it is unclear how much of a problem absolute instabilities will pose. The convective instability may still be able to dominate the absolute instability for values of $\varepsilon/\varepsilon_c > 1$. However, the CARM amplifier design is based on operation for values of $\varepsilon/\varepsilon_c$ just below 1. With such a coupling value, it is clear from Fig. 1 that higher detunings yield higher efficiencies, however Fig. 1 does not plot efficiencies for $\Delta > 0.4$ because the efficiency falls off rapidly.

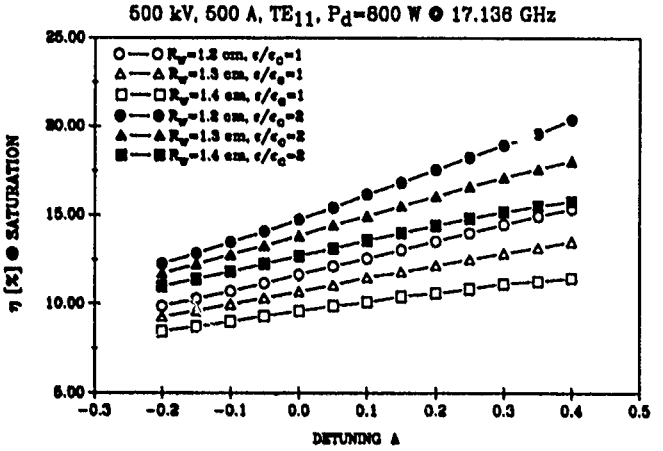


Figure 1: CARM amplifier efficiency.

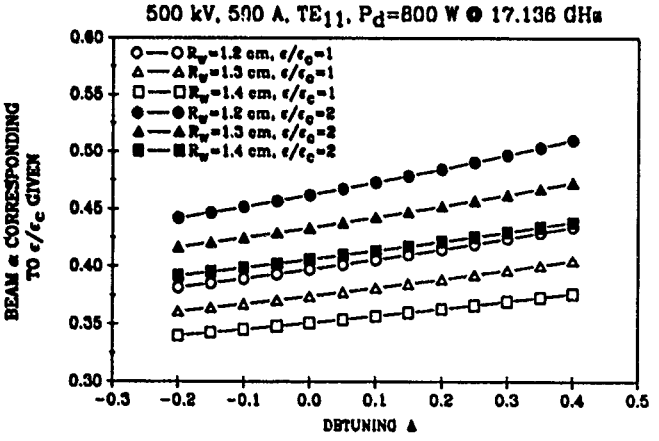


Figure 2: CARM amplifier beam pitch.

C. Phase Stability

We have demonstrated through simulations that a CARM amplifier that utilizes a bifilar helical wiggler to increase the pitch of the electron beam can be optimized to have excellent phase stability. By setting the wiggler guide field and wiggle field to the right values, the correlation between γ_0 and $\beta_{\perp 0}$ runs exactly tangent to the zero phase shift curve for the CARM interaction, as shown in Fig. 4. This dramatically enhances the phase stability of the CARM amplifier. Fig. 5 shows the optimal phase stability results. For the design parameters of Table 1, a phase stability of $\pm 0.8°$ is predicted over a voltage variation of $\pm 1\%$.

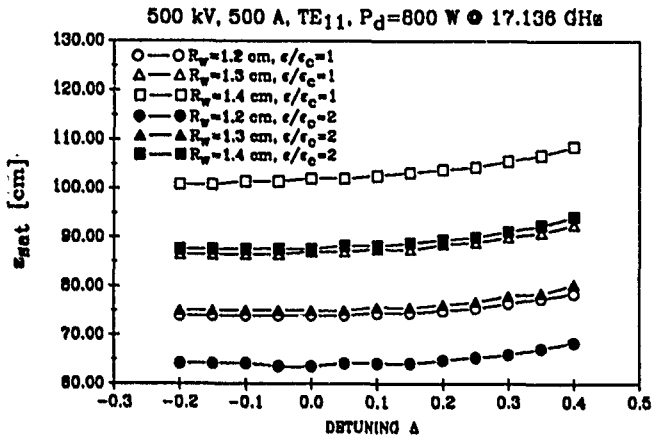


Figure 3: CARM amplifier saturation length.

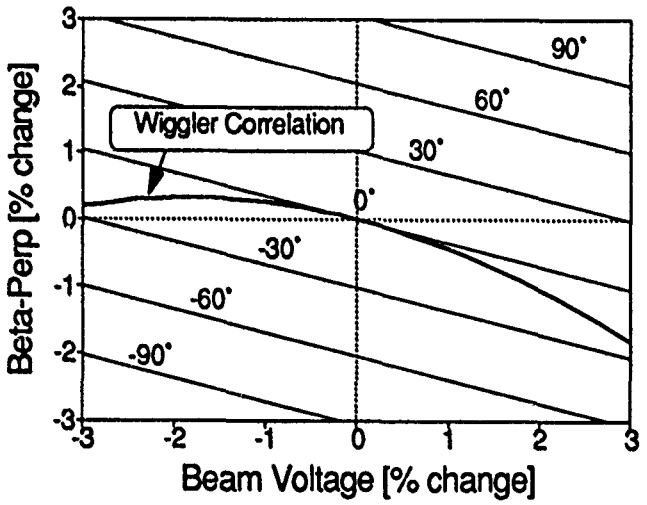


Figure 4: CARM amplifier constant phase curves over beam pitch and beam voltage. The optimal wiggler correlation is superimposed.

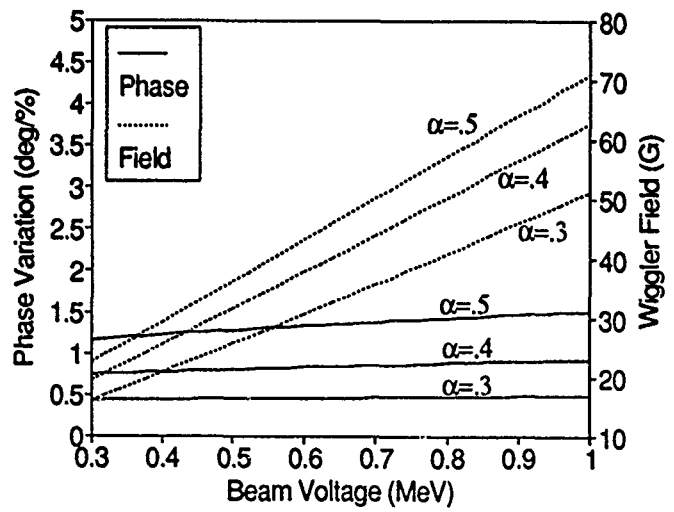


Figure 5: CARM amplifier phase stability over beam voltage for three different values of beam pitch, with wiggler design optimized to maximize phase stability.

IV. Conclusions

The CARM amplifier is a promising source of high frequency radiation for future linear colliders. Interaction efficiencies are predicted to be in the 10-40% range, with higher efficiencies attainable by magnetic field tapering.

References

[1] P. Wilson *IEEE Trans. Nucl. Sci.*, vol. NS-28, p. 2742, 1981.

[2] P. Wilson, "High pulse power rf sources for linear colliders," Tech. Rep. SLAC PUB 3227, SLAC, September 1983.

[3] A. Sessler *Physics Today*, vol. 41, p. 26, 1988.

[4] R. Palmer, "The interdependence of parameters for TeV linear colliders," Tech. Rep. SLAC-PUB-4295, Stanford Linear Accelerator Center, 1987.

[5] . T.G. Lee, private communication, June, 1988.

[6] R. Jong, R. Ryne, G. Westenskow, S. Yu, D. Hopkins, and A. Sessler, "A 17.1 GHz free-electron laser as a microwave source for TeV colliders," *Nucl. Instr. Methods Phys. Res. A*, vol. A296, pp. 776–783, 1990.

[7] B. Danly, J. Wurtele, K. Pendergast, and R. Temkin, "CARM driver for high frequency RF accelerators," in *Proceedings of the 1989 Particle Accelerator Conference*, (F. Bennett and J. Kopta, eds.), pp. 223–225, I.E.E.E., 1989.

[8] I. Botvinnik, V. Bratman, A. Volkov, N. Ginzburg, G. Denisov, B. Kol'chugin, M. Ofitserov, and M. Petelin, "Free electron masers with distributed feedback," *Pis'ms Zh. Eksp. Teor.*, vol. 35, pp. 418–420, 1982.

[9] I. Botvinnik, V. Bratman, A. Volkov, G. Denisov, B. Kol'chugin, and M. Ofitserov, "The cyclotron autoresonance maser operated at a wavelength 2.4 mm," *Pis'ms Zh. Eksp. Teor.*, vol. 8, pp. 1376–1378, 1982.

[10] G. Bekefi, A. DiRienzo, C. Leibovitch, and B. Danly, "A 35 GHz cyclotron autoresonance maser (CARM) amplifier," *Appl. Phys. Lett.*, 1989. To Be Published.

[11] D. Goodman, D. Birx, and B. Danly, "Induction linac driven relativistic klystron and cyclotron autoresonance maser experiments," *Proc. S.P.I.E.*, vol. 1407, 1991. In press.

Analysis and Optimisation of RF Power-Klystrons by FCI-Code

E.-G. Schweppe, E. Demmel and H. Seifert
Philips RHW, Hamburg
and
S. Isagawa, T. Shintake and M. Yoshida
National Laboratory of High Energy Physics, KEK
1-1 Oho, Tsukuba-shi, Ibaraki-ken, 305 Japan

Abstract

FCI-Field Charge Interaction code is a 2 1/2 dimensional particle-in-cell simulation program dedicated to analyse and design high power klystron amplifiers. The code simulates the electron beam motion with cylindrical symmetry, by taking into account the space-charge fields, RF-cavity and external focusing magnetic fields. The cavity voltages and the output power are determined by solving the circuit equations selfconsistently. Simulations of real tubes give better understanding in beam dynamics and lead to improvements in stability and efficiency. Examples of simulations compared with measured data of high power klystrons are presented.

I. Introduction

Since the entrance of digital computers in the 60'th a lot of computer codes for simulation of particle movements forced by static electric and magnetic fields have been developed and presented (SLACTRAY/EGUN, EBQ, INP, DEMEOS, TRACE, etc.). Later on computer codes using disc models have been introduced to calculate the interaction behavior of linear beam tubes (DISK, LPDISK, etc.). But these codes were restricted to small signal simulation, because they did not take into account radial forces of space charge due to bunching effects. The latest developments in computer simulation for particle accelerators lead to particle-in-cell codes where the forces and movement of so called "superparticles" are calculated. With these codes a large signal simulation of high power klystrons is possible today.

II. Calculation

Taking the 6 cavity, 1.1 MW PHILIPS YK1303 klystron as an example the power of the particle-in-cell code FCI developed by T. Shintake at KEK [1] will be demonstrated.

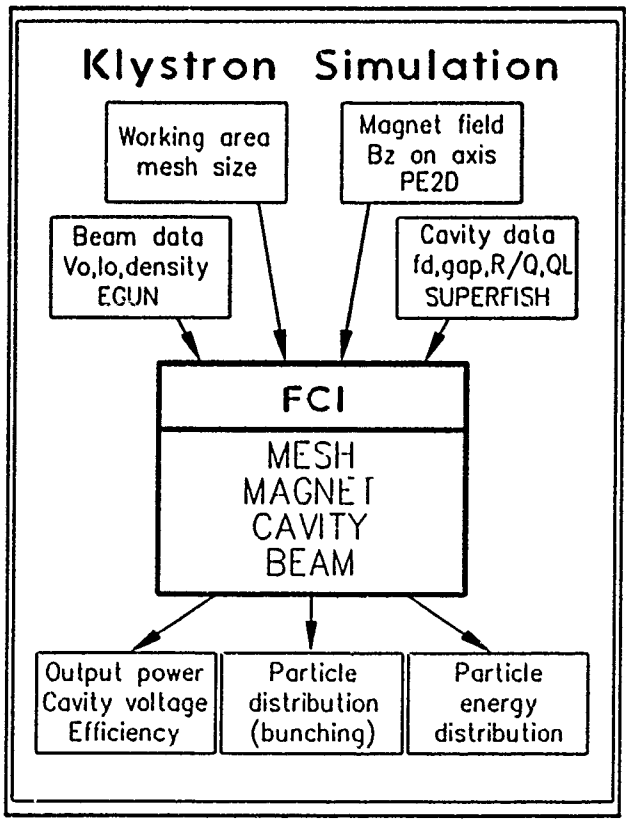


Figure 1. FCI-CODE Input and Output

The code's working area is restricted to the RF-section of a klystron. This area and the mesh size is defind by **MESH** routine. The **MAGNET** routine calculates the two-dimensional focusing field from on-axis mea-

0-7803-0135-8/91$01.00 ©IEEE

sured or calculated (Poisson, PE2D) data. The cavity fields inside the drift-tube regions are determined by **CAVITY** routine from data as f_{drive}, gap position and size, and harmonic number.
From beam voltage and current, beam radius and slope (calculated by EGUN), drive frequency and power, and cavity parameters R/Q, Q_L and f_0 (calculated by Superfish) **BEAM** routine **MODE-1** determine the beam admittances Y_b seen by the cavities. See Fig. 1.

With these Y_b as input parameters **BEAM MODE-2** finally simulates the particle trajectories and calculates all cavity voltages and output power.

III. Results

Fig. 2 shows 4 "snap shots" of beam profile for the YK1303 at P_d = 70W and output power P_o = 1 MW. Time separation is one-quarter RF-cycles. In this presentation the bunching effect can be studied.

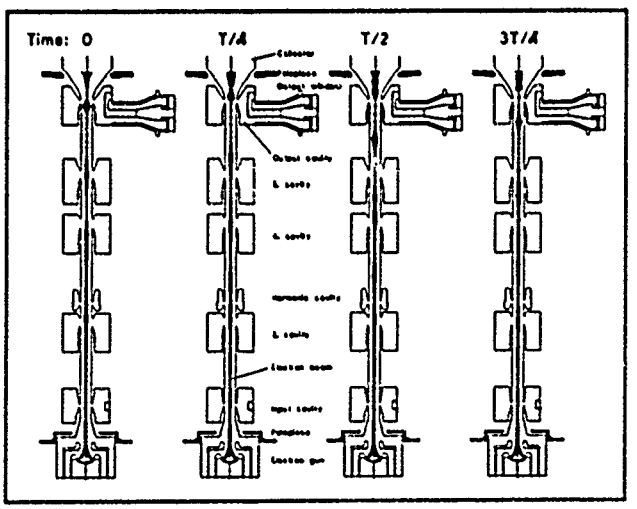


Figure 2. Beam Profile YK1303

Fig. 3 is a result of 7 calculations at varying input power. The gap voltages of 4th and 5th cavity show good linearity, while output power is saturated at a drive power of 70W. The measured data of P_o show good agreement with the simulation.

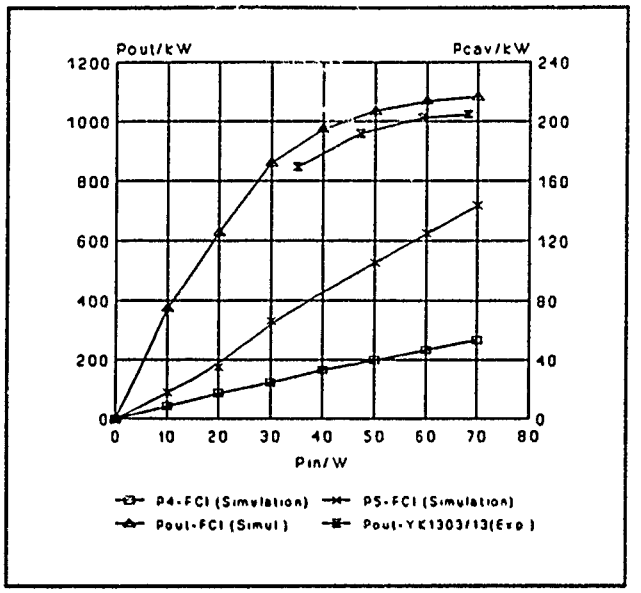


Figure 3. Power Simulation YK1303

The influence of harmonic cavity tuning on output power is shown in Fig. 4. Also in this case the simulated data show good agreement with measured data.

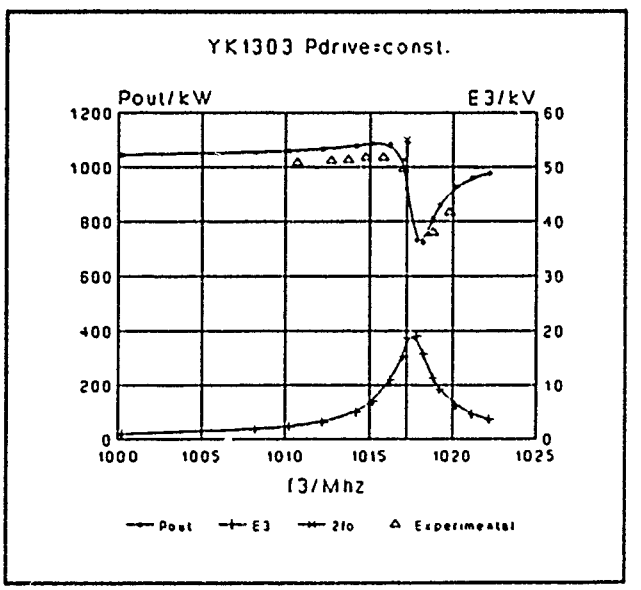


Figure 4. Detuning harmonic cavity

CPU-time for executing CAVITY and BEAM MODE-2 routines takes about 2h on APOLLO 4500 work station.

IV. References

[1] T. Shintake, "High-Power Klystron Simulations using FCI - Field Charge Interaction Code", KEK Report 90-3 May 1990 A/D.

Numerical Simulation of the SLAC X–100 Klystron Using RKTW2D*

Robert D. Ryne
Lawrence Livermore National Laboratory, Livermore, CA 94550

Arnold E. Vlieks
Stanford Linear Accelerator Center, Stanford, CA 94309

Abstract

We have performed numerical simulations of the X–100 klystron being developed at Stanford Linear Accelerator Center. The X–100 is being developed as a possible source for the next generation of linear collider, and will be required to produce ≈100 MW of power for a duration of ≈800 ns. Our simulations were performed using the simulation programs RKTW1D and RKTW2D, developed at Lawrence Livermore National Laboratory. The codes were used to investigate the operation of the klystron over a wide range of operating conditions. We will present comparisons of the simulation results with experimental results.

I. INTRODUCTION

The X-100 klystron, under development at the Stanford Linear Accelerator Center, is being developed as a possible power source for the next generation of linear collider.[1] The X-100 is a 440 keV, 510 amp klystron that operates at 11.4 GHz. It will be required to produce ≈100 MW of power for a duration of ≈800 ns; binary pulse compression will result in a 500 MW, 100 ns rf pulse. So far, the klystron has produced 72 MW of power.

We have performed 1D and 2D simulations of the X-100 with the simulation programs RKTW1D and RKTW2D. Our simulations, based on a simplified model of the output cavity, predict that the klystron will produce 72 MW of power at 440 keV and 450 amps. Below we discuss the structure of the klystron codes and the details of our simulations.

II. KLYSTRON SIMULATION PROGRAMS

RKTW1D and RKTW2D are computer programs that simulate the operation of relativistic klystrons. Both codes are time-dependent, and both assume that the fields in the problem are cylindrically symmetric. RKTW1D is a fast running, 1–dimensional code, while RKTW2D is a slower 2–dimensional code that more accurately models the physical system under consideration. The codes follow a train of RF bunches, one at a time, through a klystron. The codes have the following features:

1. self-consistent beam-cavity interaction
2. self-consistent space charge
3. time-dependent cavity excitation modelled using circuit equations
4. treatment of standing wave (SW) cavities and traveling wave (TW) structures

Prior to executing the klystron codes, one must run SUPERFISH to calculate the eigenmodes of the cavities in the problem.[2] (It is assumed that a single mode is dominant in each of the cavities.) Furthermore, one must run a preprocessor to interpolate the SUPERFISH data onto a uniform rectangular mesh that can be used by the klystron codes. If there are TW structures in the problem, the TW fields are calculated by appropriate superposition of the standing wave SUPERFISH results.

The klystron codes have the ability to read in a particle distribution generated by the electron gun code EGUN.[3] The codes can also read in magnetic field data produced by the magnet design code POISSON.[2]

The basic equations used by the klystron codes are the single particle equations of motion and the circuit equations governing cavity excitation. The single particle equations of motion are the Lorentz force equations using the longitudinal coordinate, z, as the independent variable:

$$\begin{aligned}
\frac{dx}{dz} &= v_x/v_z, \\
\frac{dy}{dz} &= v_y/v_z, \\
\frac{d\psi}{dz} &= \omega/v_z, \\
\frac{dv_x}{dz} &= \frac{q}{\gamma m}\left(\vec{E}+\vec{v}\times\vec{B}\right)_x - \frac{\beta_x}{c}\vec{v}\cdot\vec{E}, \\
\frac{dv_y}{dz} &= \frac{q}{\gamma m}\left(\vec{E}+\vec{v}\times\vec{B}\right)_y - \frac{\beta_y}{c}\vec{v}\cdot\vec{E}, \\
\frac{d\gamma}{dz} &= \frac{q}{mc^2 v_z}\vec{v}\cdot\vec{E},
\end{aligned} \tag{1}$$

where $\psi = \omega t$. (Transverse motion is neglected in the 1–d code.) Beam induced cavity excitation is based on a circuit equation for SW cavities or based on coupled circuit equations for TW structures. Consider the analysis of a TW structure. Assuming a single cavity mode is dominant, let the electric field in the n^{th} cell of the structure be given by

$$\vec{E}_n(\vec{r},t) = f_n\,\vec{\mathcal{E}}_n(\vec{r})\,e^{-i\omega t}, \tag{2}$$

where $\mathcal{E}_n$ denotes an eigenmode with eigenfrequency ω_n. Also, let ω denote the drive frequency of the klystron.

* Work supported by the US Department of Energy contracts W-7405-ENG-48 (LLNL) and DE-AC03-76SF00515 (SLAC)

U.S. Government work not protected by U.S. Copyright.

Then it is possible to show that the excitations f_n are governed by the following coupled equations

$$\ddot{f}_n + \left(\frac{\omega_n}{Q_n} - 2i\omega\right)\dot{f}_n + \left(\omega_n^2 - \omega^2 - \frac{i\omega\omega_n}{Q_n}\right)f_n - (K_n^{n-1}f_{n-1} + K_n^{n+1}f_{n+1}) = \frac{i\omega}{\epsilon_o}\int dV_n \vec{\mathcal{E}}_n^* \cdot \vec{J}_1, \quad (3)$$

where Q_n denotes the quality factor of the n^{th} cell, K_n^{n-1} and K_n^{n+1} denote coupling of the cell n to cell $n-1$ and cell $n+1$, respectively, and $\vec{J}_1$ denotes the RF current associated with the beam. (For a SW cavity, the above set of coupled equations is replaced by a single equation with n=1 and with the coupling constants set equal to zero.)

III. SIMULATION RESULTS

The X-100 klystron consists of an input cavity, three gain cavities, and an output cavity. The klystron operates at 440 keV, 510 amp and at a frequency of 11.4 GHz. The experimental results that we will discuss are based on a double gap, standing wave output cavity. The double gap cavity exhibits lower peak fields than a conventional single gap cavity. However, the double gap cavity does not have cylindrical symmetry, so it cannot be modeled realistically with our klystron codes. Instead, our simulation results are based on a single gap output cavity. Two other important features of our simulation are the following: (1) The beam distribution used by RKTW2D was produced by the electron gun program EGUN; (2) the magnetic field profile used by RKTW2D was produced using POISSON.

Our main results are summarized in Figure 1. Figure 1 shows the klystron output power as a function of beam energy (using a fixed magnetic field profile). The crosses denote experimental results; the dashed line denoted 1d simulation results and the solid line denotes 2d results. At low power, RKTW1D and RKTW2D give nearly identical results, and both are comparable with experimental values. At high power, both codes predict power levels that are greater than or equal to the experimental results, with the 2d code showing better agreement than the 1d code. The main difference between the 2d results and the experimental results is that the 2d results show a peak in output power near 433 kV; however, as we will show below, this is do to current loss in the 440 kV calculation and not do to saturation of the klystron.

The time-dependent nature of our simulations is shown in Figure 2. This figure shows the power output as as a functions of time for the 440 kV case with a 75 W drive. The klystron reaches steady state in less than 20 ns.

Figure 3 shows the RF current as a function of z at 440 kV for three drive powers, 35 W, 50 W and 75 W. The peak rf current with a 75 W drive is 555 amp. A similar plot for the 433 kV case shows that the peak rf current is 615 amp.

Figure 4 shows the DC current as a function of z at 433 kV and 440 kV. In both cases, the EGUN input file has an initial current of 500 amp. RKTW2D predicts that 50 amps of current is spilled at the klystron entrance in the 440 kV case, but only 10 amp is spilled in the 433 kV case. This accounts for why the code predicts more power at 433 kV. The initial beam radius is slightly larger in the 440 kV case. Figure 5 shows the edge radius and the rms radius of the beam for the two cases. The radius of the beam pipe is 4.7 mm.

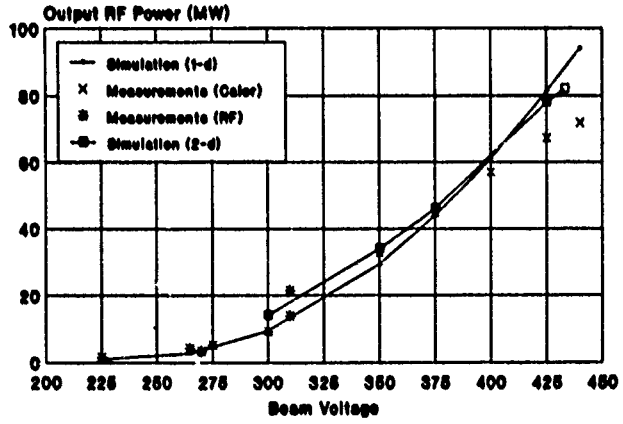


Figure 1 Output power as a function of beam energy: simulation and experiment

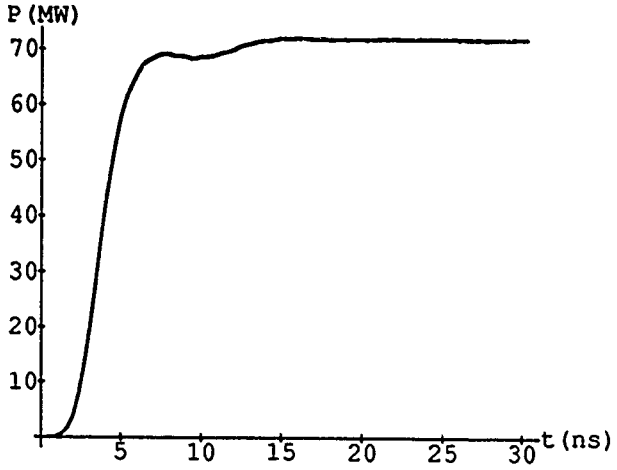


Figure 2 Output power as a function of time (E=440 kV)

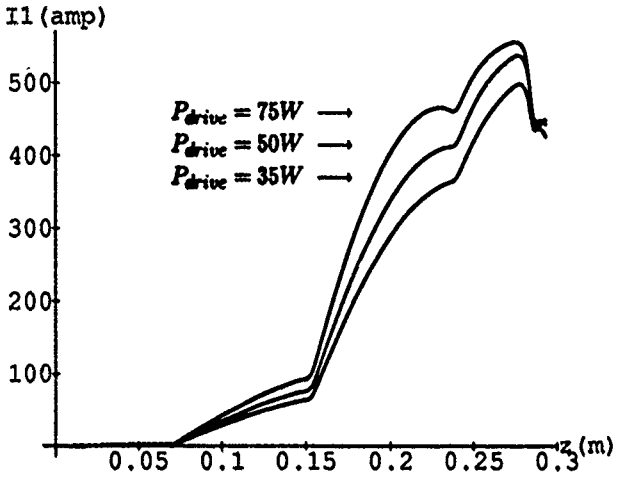


Figure 3 RF current as a function of z (E=440 kV)

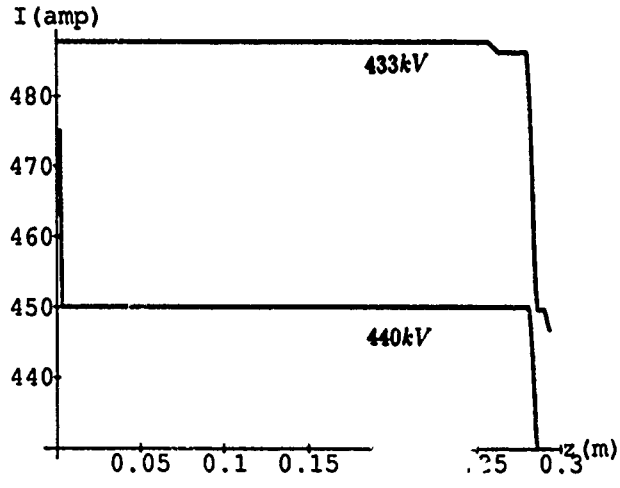


Figure 4 DC current as a function of z

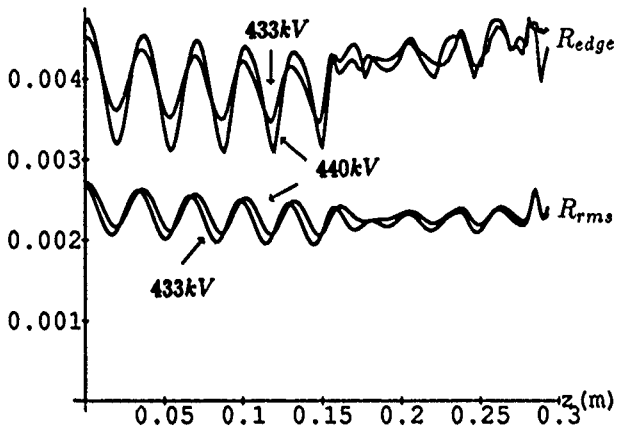


Figure 5 Edge radius and rms radius as a function of z

IV. Summary

We have performed numerical simulations of the X-100 klystron using RKTW1D and RKTW2D. The simulation results are in good agreement with experimental results. The simulation results are sensitive to the initial beam distribution, since the initial beam appears to have a radius approximately equal to the pipe radius. In the future we plan to do simulations of the X-100 with a traveling wave output structure.

V. Acknowledgments

The authors thank E. Wright for performing the EGUN runs that were used to generate the initial beam distributions for the klystron simulations.

VI. References

1. A. E. Vlieks et. al., "100 MW Klystron Development at SLAC," published in this volume.

2.Los Alamos Accelerator Code Group, "Reference Manual for the POISSON/SUPERFISH Group of Codes," LA-UR-87-126 (1987)

3. W. B. Hermannsfeldt, "EGUN — An Electron Optics and Gun Design Program," SLAC Report 331 (October 1988)

250 GHz Cold Tests for the LLNL CARM Experiment*

B. Kulke, M. Caplan, R. Stever
Lawrence Livermore National Laboratory
P. O. Box 808, Livermore, California 94550

Abstract

A cyclotron autoresonant maser (CARM) experiment has been designed and built for operation at 250 GHz, in conjunction with the LLNL ARC induction linac. Beam parameters are 2 MeV, 1 kA, 30 ns. The RF structures tested consist of 7 mm diam, 9-18 cm long Bragg sections. These sections are electroformed, with 50-90 μm deep, sinusoidal ripples spaced at half wavelength intervals. A shallow ripple depth is essential in separating the desired, TE_{11} resonance from neighboring resonances that are excited by mode conversion. We present code results and validating cold test data that illustrate the sensitivity of mode separation to ripple depth. We also present design calculations and calibration data at 250 GHz for a 2 m long, microwave diffraction tank.

I. INTRODUCTION

The LLNL CARM experiment was intended to demonstrate the generation of high-power millimeter waves near 250 GHz, using the 2 MeV, 1 kA, 30 ns beam at the ARC facility as an energy source. The choice of frequency was dictated by the potential application as a high-power source for current drive and disruption control in Alcator-C, an ongoing tokamak experiment. The use of Bragg reflectors in a waveguide environment is well understood[1] although their application at 250 GHz is new, and poses some challenging fabrication problems. The Bragg reflectors can be used either as standalone resonators or as reflective terminations bracketing a smooth-walled resonator section. We used the first configuration for the CARM experiment, in an oscillator-amplifier configuration.[2] The microwave power generated was allowed to radiate into a diffraction tank; the design of this tank is discussed in the latter part of this note.

II. BRAGG SECTION DESIGN AND PERFORMANCE

A cylindrical waveguide can be made into a Bragg section by corrugating sections of wall with sinusoidal ripples that are spaced one-half wavelength apart. Minute reflections from each ripple add up in phase so that by using a large enough number of ripples, an arbitrary amount of reflection of the microwave signal may be achieved, essentially without affecting the waveguide cross section available for, e.g., electron beam passage. Increasing the ripple depth results in greater reflectivity, but also enhances mode conversion and hence must be done with caution. For the CARM experiments, the beam pipe diameter was chosen at 7 mm to allow propagation in the TE_{11} mode at ten times the waveguide cutoff, or 250 GHz. We designed, built, and fully characterized Bragg reflectors with 150 and 300 sinusoidal, 25 μm amplitude ripples. We also built a 300-ripple Bragg section with 45 μm amplitude corrugations, which was used as a standalone resonator in the oscillator-amplifier configuration. This section was not cold tested because we had damaged the necessary diagnostic equipment during earlier beam tests. The ripple period for all sections was 0.6 mm.

The Bragg sections were manufactured at LLNL. The sinusoidal ripple contour was machined into an aluminum plating mandrel to a nominal precision of 100 microinches, using a diamond tool leaving a 16-microinch surface finish. This mandrel was then copper plated and etched away to leave the sinusoidal contour. The Bragg section was then machined to the correct length and the waveguide flanges were attached. For the 45-μm ripple section, the copper plating was made sufficiently massive to allow direct machining of the flanges, thus avoiding the thermal stresses and possible distortion due to soldering.

Analytical expressions for the single-mode reflection coefficients of a Bragg section are available.[1] While these are quite useful for yielding design approximations quickly, they tend to be in error when there is significant Bragg reflection in more than one mode. A more accurate model can be had with a coupled-mode theory and simulation code developed by M. Caplan, which self-consistently considers both forward and reflected wave components of two or more coupled waveguide modes in the presence of wall discontinuities. It turns out that in order to achieve good separation in frequency between the desired, pure TE_{11} reflection region and the adjacent, undesirable TM_{11} region, it is necessary to use a large number of shallow ripples. This is illustrated in Fig. 1, which plots the theoretical, reflected power vs. frequency for a Bragg section with varying ripple number and depth. Figure 2 shows our cold test setup. In order to avoid trapped modes, we coupled the open Bragg section quasioptically to the detector horn, which was placed well into the far-field region. The Bragg section partly reflects the incident TE_{11} power and partly converts it into the TM_{11} mode; however, the latter has a null on axis and is not detected by the receiver, so that the converted power simply registers as more insertion loss. Figure 3 shows the measured insertion loss obtained with a 300 ripple, 25 μm section; the agreement with the theory is seen to be quite good. This result was replicated accurately with two separate, identical Bragg sections, which attests to the accuracy of the machining. Figure 4 shows similar data taken for a shorter section (150 ripples); there is an amplitude disagreement on the order of 10 dB with the theory which is not understood. We also tested the insertion loss of a smooth-pipe section terminated by a short Bragg section at each end, and obtained reasonable agreement with the three resonant peaks predicted from the theory.

*Work performed under the auspices of the U.S. Department of Energy by Lawrence Livermore National Laboratory under contract No. W-7405-ENG-48.

0-7803-0135-8/91$01.00 ©IEEE

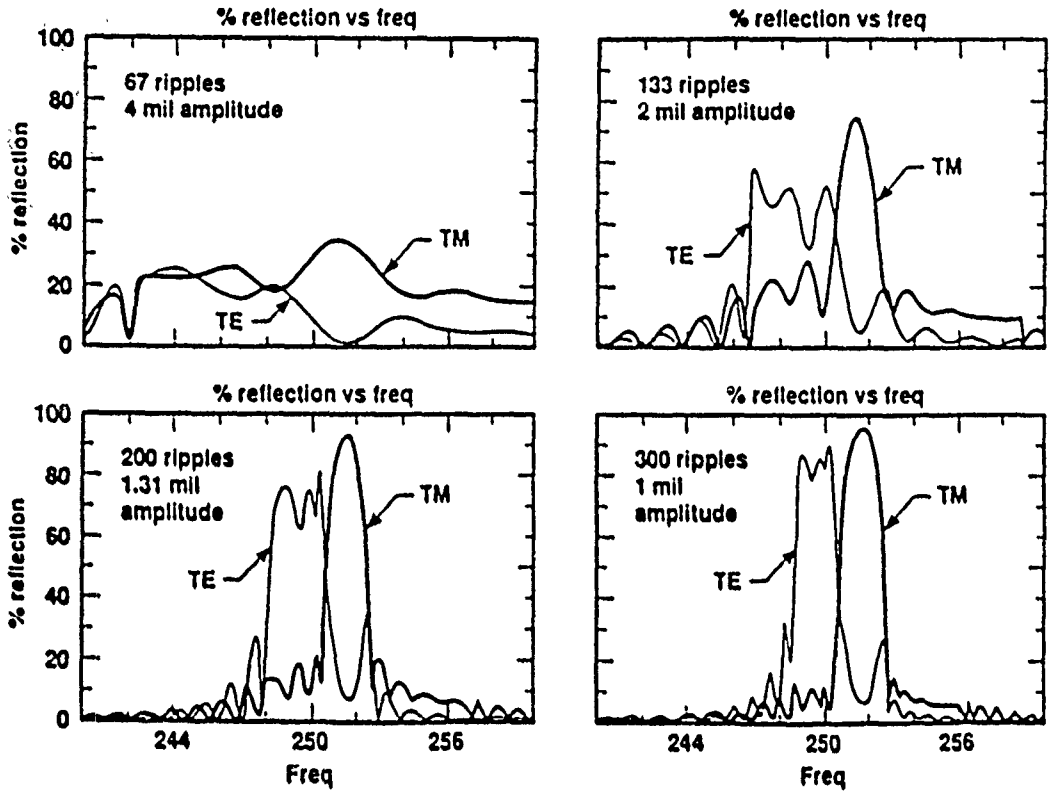


Fig. 1. Two-mode calculation of TE and TM mode reflected power, for different ripple parameters in a 7-mm-diam Bragg section. Good mode separation requires many ripples of small amplitude.

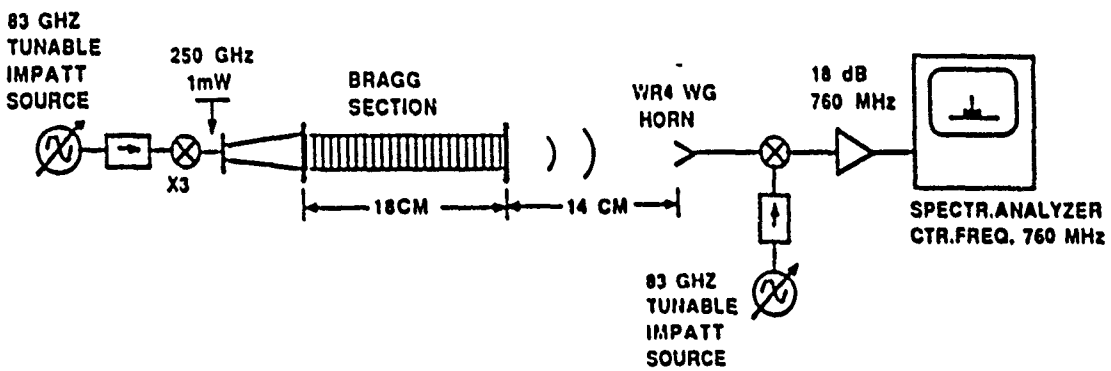


Fig. 2. Apparatus used for insertion loss measurement on Bragg sections. A substitution method was used, with a smooth pipe section as reference. Trapped modes were avoided by leaving the Bragg section open-ended.

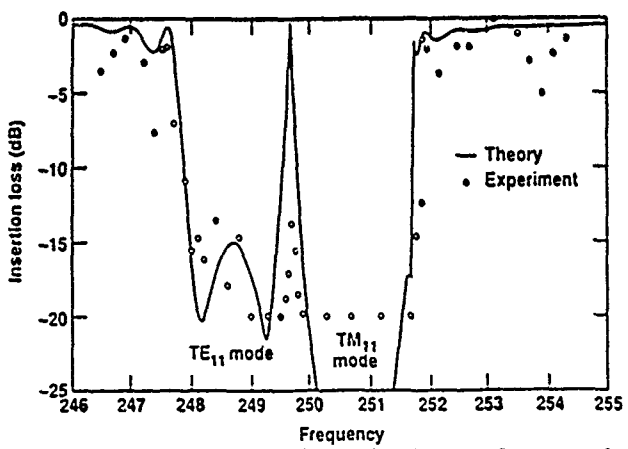


Fig.3. Calculated and measured insertion loss vs. frequency for a 300 ripple, 25 μm amplitude, 7-mm-diam Bragg section.

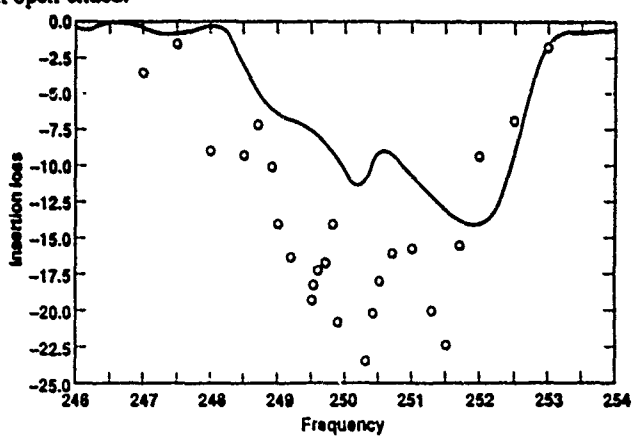


Fig.4. Calculated and measured insertion loss vs. frequency for a 150 ripple, 25 μm amplitude, 7-mm-diam Bragg section.

III. Diffraction Tank Design and Performance

A sketch of the CARM diffraction tank is shown in Fig. 5. Microwave energy is generated in the CARM device collinear with the electron beam; the latter is deflected into the beam dump wall by means of 900 Gauss permanent magnet. The microwave beam is radiated from a 28-mm-diam aperture at the upstream end of the beam dump. The $1/e^2$ contour of the quasioptical beam at 250 GHz will clear the end of the beam-dump; the K_a band signal propagates as in overmoded waveguide. Higher modes may exist and must be taken into account in interpreting the data. The 250 GHz diagnostic consists of two WR4 waveguide stubs, with or without gain horns, at the back flange. A vacuum seal is achieved by means of a thin mica washer and O-ring arrangement, clamped between the WR4 flanges. Both stubs are rotatable to allow a polarization check. Additional attenuation is introduced by a collimating aperture that slides into the tank from one end. K_a band power is monitored by a WR28 waveguide stub that is positioned at the -10 dB point of the main TE_{11} lobe at 25 GHz. An additional, uncalibrated monitoring port is drilled directly into the beam dump wall, and is connected to a standard WR28 waveguide, vacuum window.

Prior to fabrication of the actual diffraction tank, we simulated the configuration on an optical bench, using the same transmitter-receiver combination shown in Fig. 2. Using a simple, free-space transmission model, with standard expressions for antenna gain, we were able to predict the measured, 250 GHz transmission loss within 2-5 dB, even for the case where the collimating aperture was inserted (Figs. 6,7). On the actual tank, the overall attenuation was measured by direct substitution, yielding 32-38 dB at K_a band and 30-36 dB at 246-254 GHz, depending on the collimator aperture. Agreement with the theory was very poor for the off-axis attenuation at K_a band, and within 10 dB at 250 GHz. The greater, measured values at 250 GHz agree more closely with the calculated attenuation for the TE_{12} mode, and this may indicate substantial mode conversion, e.g., at the wall discontinuity near the beginning of the beam dump.

IV. Conclusion

Insertion loss measurements at 250 GHz on two, 300 ripple, 25 μm amplitude, 7 mm diam, Bragg sections gave excellent agreement with the theory. Similar measurements with sections of half that length gave good agreement in terms of the frequency range but yielded an insertion loss that was some 10 dB greater than the model predicted. We believe this may be due to poorer mode separation and stronger mode coupling for the shorter section. Attenuation measurements at 250 GHz made on an optical-bench replica of the CARM diffraction tank gave agreement with modeling predictions within 2-5 dB. Measured loss on the actual tank was 10 dB greater than predicted, probably due to mode conversion at the beam dump discontinuity.

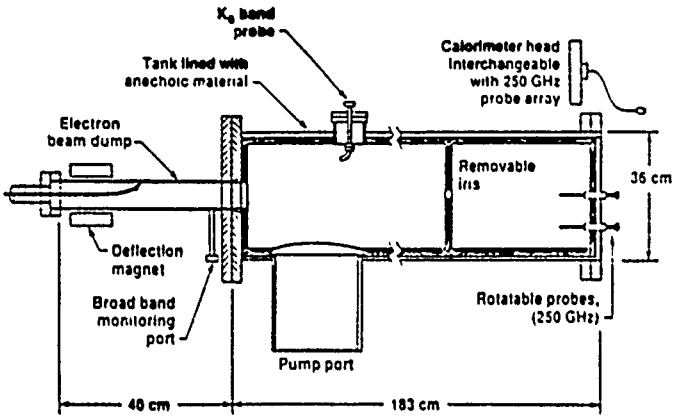


Fig.5. Sketch of CARM microwave diffraction tank.

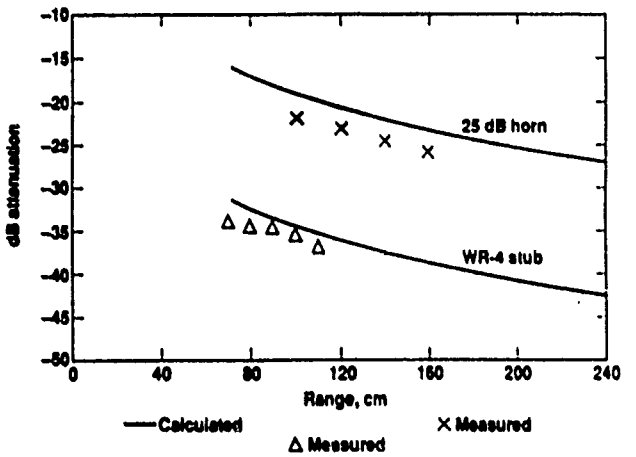


Fig.6. Calculated and measured attenuation vs. range, for simulated diffraction tank geometry, without collimating aperture.

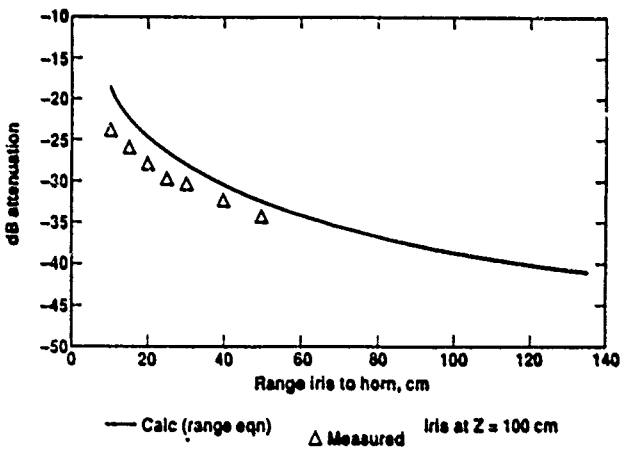


Fig.7. Calculated and measured attenuation vs. range from collimating aperture to receiver, simulated diffraction tank geometry.

V. References

[1] V. L. Bratman, G. G. Denisov, N.S. Ginzburg, and M. I. Petelin, "FEL's with Bragg Reflection Resonators: Cyclotron Autoresonance Masers Versus Ubitrons," *IEEE J. Quantum Electronics QE-19*, p. 282, 1983.

[2] B. Kulke, M. Caplan, D. Bubp, T. Houck, D. Rogers, D. Trimble, R. VanMaren, G. Westenskow, D. B. McDermott, N. C. Luhmann, Jr., and B. Danly, "Test Results from the LLNL 250 GHz CARM Experiment," this Proceedings.

Test Results from the LLNL 250 GHz CARM Experiment*

B. Kulke, M. Caplan, D. Bubp, T. Houck, D. Rogers, D. Trimble,
R. VanMaren, G. Westenskow
Lawrence Livermore National Laboratory

D. B. McDermott, N. C. Luhmann, Jr., UCLA

B. Danly, MIT/PFC

Abstract

We have completed the initial phase of a 250 GHz CARM experiment, driven by the 2 MeV, 1 kA, 30 ns induction linac at the LLNL ARC facility. A non-Brillouin, solid, electron beam is generated from a flux-threaded, thermionic cathode. As the beam traverses a 10 kG plateau produced by a superconducting magnet, ten percent of the beam energy is converted into rotational energy in a bifilar helix wiggler that produces a spiraling, 50 G, transverse magnetic field. The beam is then compressed to a 5 mm diameter as it drifts into a 30 kG plateau. For the present experiment, the CARM interaction region consisted of a single Bragg section resonator, followed by a smooth-bore amplifier section. Using high-pass filters, we have observed broadband output signals estimated to be at the several megawatt level in the range 140 to over 230 GHz. This is consistent with operation as a superradiant amplifier. Simultaneously, we also observed K_a band power levels near 3 MW.

I. INTRODUCTION

The LLNL CARM project has been aimed at developing a high-power source for current drive and disruption control in Alcator-C, an ongoing tokamak experiment, and it is this potential application that dictated the choice of frequency. High-power radar applications also are of interest, although these would generally be at lower frequencies. As high-power drive sources are difficult to find at 250 GHz, the experiment was configured as a self-contained oscillator/amplifier combination. The experiment was fielded at the ARC induction linac facility at LLNL,[1] using a superconducting magnet that was provided by UCLA.

II. APPARATUS

The overall CARM experimental configuration is shown in Fig. 1. A 1.1 kA, 1.2 MeV electron beam is generated from a hot cathode, Pierce gun injector, and is accelerated further through 10 induction cells to a final beam energy near 2 MeV. Beam transport at a nominal, 1-2 cm diameter is achieved through a series of solenoids generating some 500 G on axis. Magnetic flux through the cathode is controlled by a bucking coil. At the 2 MeV level, the beam is focussed into a 12-mm-diam pipe immersed in a 10 kG, axial guide field provided by the superconducting magnet, where a 30-50 G transverse field generated by a bifilar wiggler converts some of the axial into transverse momentum. After leaving the wiggler, the electrons undergo further momentum conversion as the beam drifts into the 25-30 kG, high-field plateau where the RF interaction takes place inside a 7-mm-diam pipe. The RF circuit here consists of a single, 18-cm-long Bragg section followed by a 20 cm long, smooth-walled amplifier section, all positioned inside the 40 cm long, high-field plateau. The Bragg section supports a standing wave, and thus can act as a self-contained cavity oscillator. For a nominal $Q = 5000$, the calculated start-oscillation threshold is 200 A. Calculated cavity fill times are in the 20-30 ns range. The entire RF section is contained inside an aluminum strongback that functions as the vacuum envelope. The configuration shown in Fig. 1 has a pair of Bragg sections bracketing a smooth-walled resonator section; this arrangement was tried initially but was damaged due to beam strike and overheating. Table I summarizes the experimental parameters for the single-Bragg configuration.

The diffraction tank is designed as a calibrated, high-power attenuator. The microwave beam is dissipated in the Eccosorb AN-72 absorptive lining. For the initial experiment, the tank was calibrated only for the TE_{11} mode at 250 GHz (on-axis port positioned at the downstream flange) and 25-40 GHz (waveguide stub located off axis). An auxiliary, uncalibrated, broadband port is attached directly to the beamdump; a small, immersible turning mirror is used to deflect energy from the narrow, 250 GHz beam into this diagnostic. The measured attenuation was 31.5 dB for the calibrated, 250 GHz channel, and 32-38 dB for K_a band. Losses in the overmoded waveguide runs leading from the diffraction tank to the detectors in the control room were calibrated separately. Further details concerning the diffraction tank are contained in a companion paper.[2]

III. RESULTS

The experiment consisted of optimizing the electron beam transmission through the accelerator, wiggler, and RF circuit section, and then maximizing the output power by adjusting the cathode flux, the wiggler current, and the axial field in the high-field region. The electron beam current was monitored at the injector, at the entrance to the wiggler, and at the entrance to the beam dump. Typically, we were able to transmit 700 A out of a total 1100 A emitted from the injector, through the 7-mm-diam RF section.

*Work performed under the auspices of the U.S. Department of Energy by Lawrence Livermore National Laboratory under contract No. W-7405-ENG-48.

0-7803-0135-8/91S01.00 ©IEEE

Microwave power was measured in the control room, using separate detectors for the 250 GHz and the K_a band channels, respectively, with signals carried from the diffraction tank through two separate waveguide runs. The 25-mm-diam aperture placed in front of the receiving horn discriminated against modes with nulls on boresight, i.e., modes other than $TE_{1,n}$. Waveguide sections were used as high-pass filters to bound the signal frequency. During initial runs, we also carried out more precise frequency measurements, using a heterodyne system.

Typically, we observed simultaneous signals near beam pipe cutoff (K_a band), consistent with gyrotron-type operation, and above 140 GHz, over a large range of axial B field and alpha. The broadband, high-frequency signals were consistent with operation as a superradiant CARM amplifier excited by noise. Heterodyning with a subharmonic mixer and a 60-90 GHz, tunable source (BWO) serving as the local oscillator, and using a 173 GHz high-pass filter, we detected high-frequency signals over the full local-oscillator range, suggesting frequency components as high as 270 GHz, although aliasing with a 180 GHz maximum frequency could not be ruled out. For the high-frequency signal, we estimated a peak power of 53 MW, using a Hughes 47328H-3111 diode detector with a calibrated sensitivity valid for 250 GHz. Because of the rapid falloff of detector sensitivity with frequency, however, and assuming the actual signal frequency to be significantly below 250 GHz, this power estimate may be optimistic by an order of magnitude. The power level at K_a band was estimated at 3.5 MW, using a detector calibration valid for 26 GHz. The pulse width in the 250 GHz channel typically had a spiky appearance, although intermittently we also saw pulsewidths of 5-10 ns. The pulsewidth at K_a band generally corresponded to the beam pulsewidth, about 30 ns.

In a subsequent run, having damaged the heterodyne system earlier, we only used high-pass filtering corresponding to cutoff frequencies of 140, 173, and 230 GHz. Sweeping through the magnetic field range 25-55 kG, and velocity ratio $0.2 < \text{alpha} < 0.4$, we observed the strongest signals above 230 GHz with field values near 29 kG. Unlike the lower frequency signals, we were unable to see the 230 GHz filtered signal through the on-axis probe on the diffraction tank. In order to observe these signals, we had to connect the 250 GHz channel to the uncalibrated, broadband port at the side of the beam dump, with the small turning mirror inserted. The relative signal strengths through the different filters, all going into an identical detector, are shown in Fig. 2. The 230 GHz filtered signal amplitude was within an order of magnitude of the lower frequency amplitudes, and hence should have been equally detectable with the on-axis probe.We believe this signal may have had a null on boresight. With the magnetic field at 29 kG but reducing the wiggler field to achieve alpha ~ 0.15, we intermittently observed 60-80 mV amplitudes on the 230 GHz filtered signal. This is an order of magnitude stronger than the other observed signals, and it may indicate excitation of a Bragg section resonance, though not necessarily the TE_{11} mode.

IV. Conclusion

In initial beam runs on a 250 GHz CARM experiment in an oscillator-amplifier configuration, we have observed upshifted signals over a wide frequency range, from 140 to over 230 GHz. We conservatively estimate the power levels to be on the order of several megawatts. Simultaneously we have measured 3.5 MW peak power at K_a band frequencies, corresponding to conventional gyrotron operation. Most of the observed high-frequency signals are consistent with operation as a superradiant amplifier starting from noise. Anomalously strong signals observed intermittently, indicate possible excitation of the single Bragg section resonator.

V. References

[1] M. Caplan, B. Kulke, D. G. Bubp, D. McDermott, and N. C. Luhmann, Jr., "A 250 GHz CARM Oscillator Experiment Driven by an Induction Linac," 12th Int. Free Electron Laser Conf., Paris, France, Sept. 17-21, 1990.

[2] B. Kulke, M. Caplan, and R. Stever, "250 GHz Cold Tests for the LLNL CARM Experiment," this Proceedings.

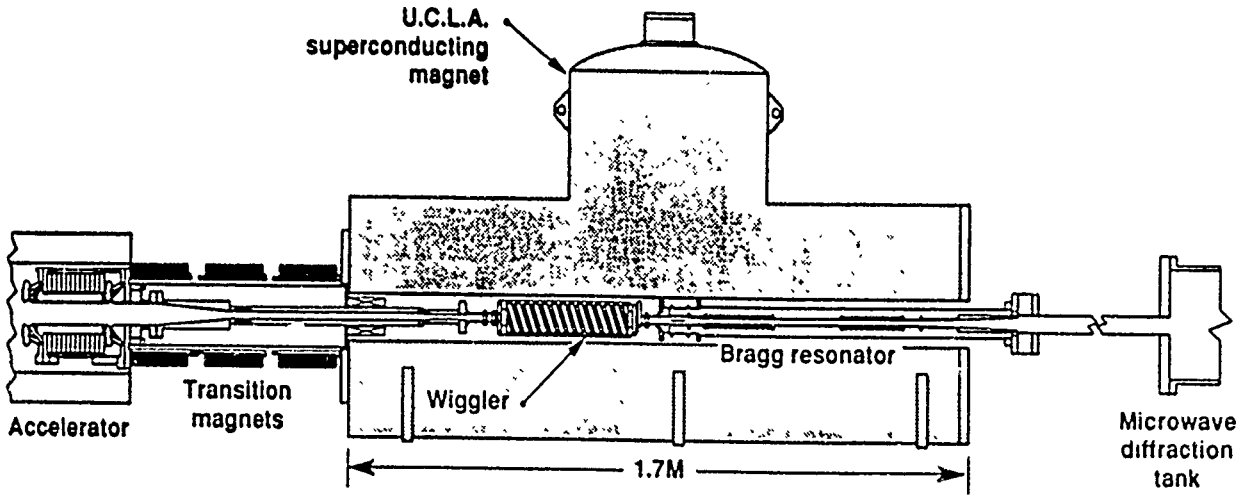


Fig. 1. CARM experimental configuration. In this experiment, only a single Bragg section was used.

Table 1. CARM Experimental Parameters

Electron beam:	
Energy	1.7 - 1.9 MeV
Current	500-600 A
Diameter in RF section (est.)	5 mm
Pulse width in RF section	30 ns
Repetition rate	1 Hz
Wiggler:	
Configuration	bifilar helix, six periods
Pitch/diameter	5.28 cm/5.2 cm
Drive	15 V, 8 A, watercooled
Transverse field on axis	50 G
Axial field in wiggler region	10 kG
RF oscillator section:	
Mode	TE_{11}
Op. frequency/cutoff frequency	250 GHz/25 GHz
Phase velocity/c	1.005
Bragg section length/diameter	18 cm/7 mm
No. of sinusoidal corrugations	300
Corrugation amplitude	45 μm
Theoretical Q	5000
Theoretical alpha (velocity ratio)	0.3
B field on axis	25-30 kG
RF amplifier section:	
Smooth-pipe length/diameter	20 cm/7 mm
B field on axis	25-30 kG

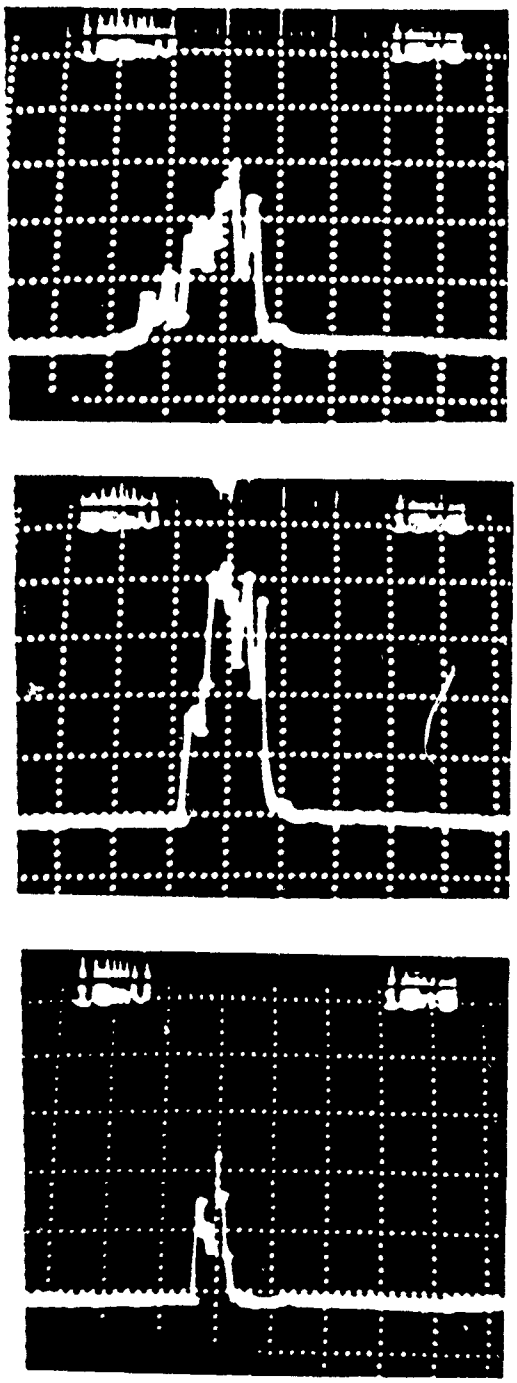


Fig. 2. Signal traces detected at broadband port, using different waveguide highpass filters, and a Hughes 47328H-3111 detector. Time scale is 10 ns/div throughout.
- Top trace, 140 GHz cutoff filter, 100 mV/div.
- Center trace, 173 GHz cutoff filter, 50 mV/div.
- Bottom trace, 230 GHz cutoff filter, 10 mV/div.

The Linac and Booster RF Systems for a Dedicated Injector for SPEAR*

J.N. WEAVER, S. BAIRD, M. BALTAY, M. BORLAND,† H.-D. NUHN, J. SAFRANEK, C. CHAVIS, L. EMERY,† R.D. GENIN, R. HETTEL, H. MORALES, J. SEBEK, J. VOSS, D. WANG,‡ H. WIEDEMANN, B. YOUNGMANN
Stanford Sychrotron Radiation Laboratory, Stanford, California 94309
and
R.H. MILLER
Stanford Linear Accelerator Center, Stanford, California 94309

Abstract

A 120 MeV, 2856 MHz, TW linac, with a microwave gun, alpha magnet, and chopper, has been built at SSRL as a preinjector for and along with a 3 GeV booster synchrotron ring. The resulting injector will be available on demand to fill SPEAR, which is a storage ring now dedicated to synchrotron light production. The linac sections were purchased from China, the XK-5 klystrons were obtained surplus from SLAC, the modulators are a variation on those at SLAC and were built by SSRL, the alpha magnet and chopper were designed and built at SSRL and the microwave gun was designed and built in collaboration with Varian Associates. The RF system for the booster ring is similar to those at SPEAR and PEP and was built by SSRL. Some of the interesting mechanical and electrical details are discussed and the operating characteristics of the linac and ring RF system are highlighted.

I. INTRODUCTION

The Stanford Positron Electron Accelerator Ring (SPEAR) started out in the early 1970s as an electron positron high energy physics facility with two colliding beam interaction regions. In 1974 the ψ-J particle was discovered independently at SLAC's SPEAR and BNL's (Brookhaven National Laboratories) AGS. With the advent of PEP and SLC/SLD at SLAC, the high energy physics effort at SPEAR wound down and since 1989 it has been used solely as a source for synchrotron radiation for SSRL and visiting experimenters. Initially, it was thought that SLC could continue to fill SPEAR on some reasonable schedule, but that has not been possible in practice. So a little over three years ago a major project was begun at SSRL to build a dedicated full energy injector. [1] The new injector consists of: 1) a 2 MeV microwave electron gun 2) a 120 MeV, 9 m long, short pulse, 2856 MHz linac and 3) a 3 GeV, 134 m in circumference, 358.54 MHz synchrotron booster ring, all pulsing at a 10 Hz rate. The day before Thanksgiving of 1990 a 2.34 GeV beam was injected and stored in SPEAR, marking the end of the formal construction and commissioning phases. Remoting of controls, improving the stability, familiarizing operators with the controls and quantifying machine characteristics has been the thrust of recent efforts. In the following sections a description is given of the injector's two separate and different frequency RF systems. Synchronization of the two, non-harmonic (unfortunately) systems is achieved through the linac's chopper. [2] Synchronization of injection into SPEAR is discussed elsewhere. [3]

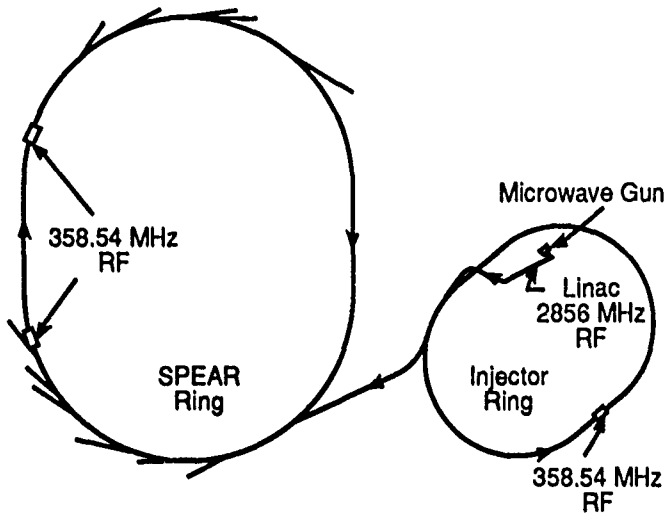


Figure 1. SSRL's Major RF Systems.

II. THE LINAC

The linac, as shown in Fig. 1, injects at a 10 Hz rate, three, 120 MeV bunches, spaced by 350 ps and of $\approx 4 \times 10^8$ electrons each, into the injector booster ring through a series of bend magnets, a pulsed kicker magnet and a septum magnet. A 2 MeV microwave gun puts out less than a 2 μs long string of several thousand bunches. Since each bunch is the result of a portion of a sinesoidal electric field on a thermonic cathode, the energy spread and longitudinal extent of each bunch is considerable. [4]. An alpha magnet with an internal scraper is used to compress the bunches longitudinally and scrape off a large portion of the low energy tail. Before entering the linac a fast rising pulse, traveling upstream on a stripline chopper, sweeps the multibunch beam by a slit. The result is that only approximately three bunches emerge to be accelerated by the linac. The gun-to-linac layout is shown in Fig. 2, and it is described in detail in references [2, 4, 5] and [6]. Figure 3 shows the linac RF circuit schematically and Fig. 4 shows the high power part of the RF circuit isometrically.

Three, SLAC-type, $2\pi/3$ mode, traveling-wave accelerator sections (DLWG's) were purchased from IHEP (Institute of High Energy Physics), Beijing, PRC. The DLWG tuning was checked at SLAC as part of an acceptance test and found to be very good. Furthermore, a high power

* Work supported by Department of Energy contract DE-AC03-76SF00515 and the Office of Basic Energy Sciences, Division of Material Sciences.

† Now at Argonne National Labs, Argonne, IL 60439.

‡ Now at Bates Linac-MIT/LNS, Middleton, MA 01949.

U.S. Government work not protected by U.S. Copyright.

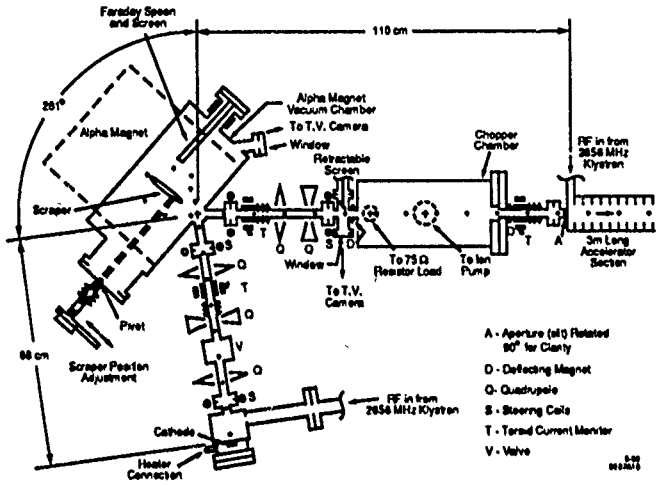


Figure 2. Gun-to-Linac Layout.

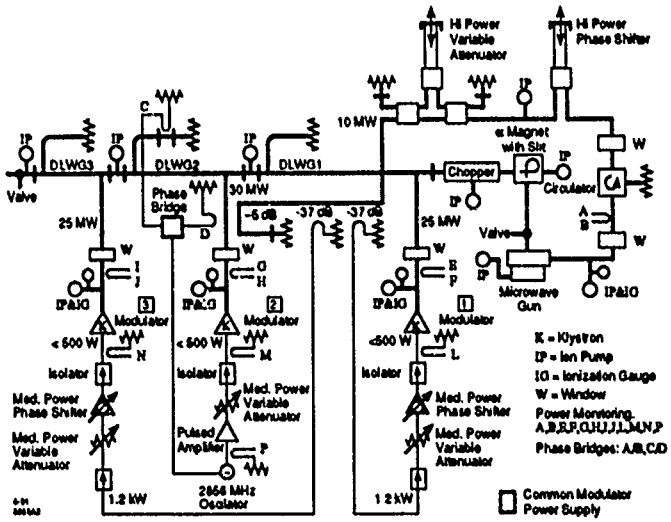


Figure 3. SSRL Injector Linac RF System Schematic.

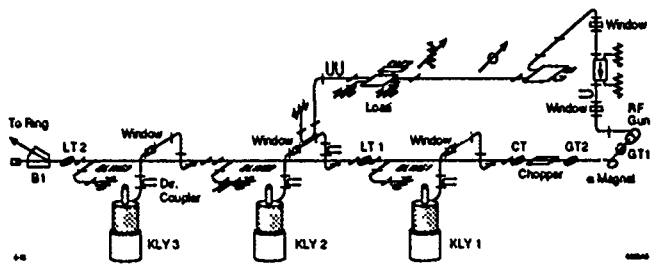


Figure 4. Isometric View of the Linac.

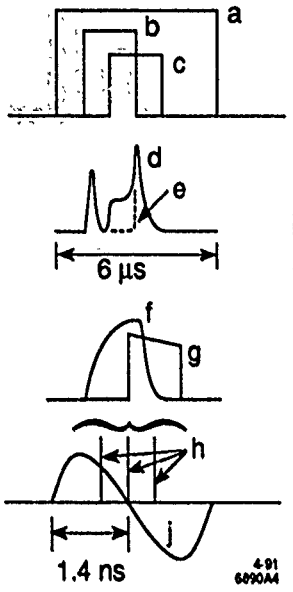
waveguide phase shifter, a high power waveguide attenuator and high power kanthal-coated stainless steel vacuum waveguide loads were purchased from IHEP, which in turn obtained them from domestic PRC industries. External copper cladding and soldered on water lines were added by SSRL to make them water cooled like those at SLAC. A 24 hour, 200°C, nitrogen gas flushing followed by a 72 hour, 200°C, vacuum bake preceded installation on the linac. This SLAC baking receipt greatly reduced the water vapor, et cetera, absorbed in the kanthal and thus considerably lessened the time required for RF processing of the linac. The phase shifter and attenuator operate well now that some mechanical drive mechanism problems have been attended to.

SLAC fabricated vacuum rectangular waveguide networks connect the three surplus SLAC XK-5 klystrons to the linac and the microwave gun. The klystrons are powered by a modified SLAC type modulator, which is fed by a 480 VAC, 3ϕ, variable voltage transformer. Following the transformer is a single, 25 kV dc (maximum) power supply. This supply then feeds in parallel three separate modulators (charging chokes, pulse forming networks and thyratron switches), one at each of the klystrons. Each klystron has a 12:1 step-up pulse transformer in its cathode oil tank. The pulse transformer delivers upwards to 300 kV, which means upwards to 30 MW plus of peak RF power from each klystron. Individual modulators and klystrons may be taken off-line by means of disconnect bars in the high voltage power supply distribution box.

The RF drive circuit, shown in Fig. 3, starts with a 2856 MHz, 5 mW VCO that drives a 1 kW peak, Micon/MPD, RF amplifier. The latter contains of a solid state, 1 W cw preamplifier and three cascaded Eimac 8847A planar triodes that are operated class C for 6 μs at the 10 Hz rate, as shown in Fig. 5a. SLAC-built, medium power (< 2 kW peak), solid-state, variable attenuators [7] are used at the input to each klystron. Microwave Applications Group's, analog, rotary-field, ferrite, phase shifters are used at the inputs to klystrons 1 and 3, which are driven by signals derived from the output of klystron 2, as done at BNL's light source. A motor driven attenuator and phase shifter are installed in the gun's high power input waveguide. In addition, the RF power level out of klystron 3 has been made subject to the beam energy, as monitored by a beam position monitor (BPM) located after the first bend magnet at the end of the linac. The BPM signals are processed and fed through a feedback loop to drive attenuator 3; thus, beam energy fluctuations are damped. The other two klystrons are normally run saturated. When any klystron sees a reflected signal greater than 3 MW (a VSWR of 2:1 at 30 MW), an interlock circuit switches to maximum attenuation to drop the klystron output power. RF processing of the DLWG's and loads is accomplished by varying the appropriate attenuators. By using proper combinations of the three phase shifters, the gun phase can be adjusted relative to the whole linac and each DLWG can be phased separately relative to the gun. Of course, field changes in the alpha magnet produce phase drifts, which can be corrected for, too. The gun resonant frequency is fine tuned by changing its water temperature. By adjusting the gun input RF power and the gun current, by way of the gun filament temperature, beam loading can be optimized as shown in Fig. 5e.

The circulator shown in Fig. 3 and 4 is not a vacuum item, so it is isolated by windows from the otherwise vacuum rectangular waveguide. It is pressurized with dry nitrogen to 30 psig, which is marginal for 3 to 4 MW. Sulphur hexafloride was not used because of possible, irreversible, linac section damage from a catastrophic vacuum failure during operation. It is not clear the circulator is necessary, so its removal is being considered, especially if and when tests of the gun at higher RF power are performed.

The linac vacuum system contains one 8 l/s, one 20 l/s and nine 30 l/s ion pumps and four ionization gauges, as



a) Drive amplifier RF output.
b) Klystron RF output.
c) Accelerator section RF output.
d) Microwave gun reflected RF with the heater off (no beam).
e) Microwave gun reflected RF with beam.
f) Beam envelope out of the gun.
g) Beam chopper pulse.
h) Chopped beam micropulse out of the linac.
j) Ring cw RF expanded to show timing for capture of the linac beam.

Figure 5. Linac and Booster Ring Pulse, RF and Beam Timing.

shown in Fig. 3. A beamline vacuum valve and waveguide window allow isolation of the gun vacuum from the linac when desired and a beamline valve at the end of the linac allows isolation of the linac. The ionization gauges operate interlocks that switch off the RF if the pressure goes too high. The linac has three different temperature water circuits; 1) 25° ± 5°C low conductivity water from the SLAC system for the klystrons, 2) 45° ± 0.1°C water for the DLWG's and 3) 35° to 55°C, adjustable but stable to ± < 1°C, water for the microwave gun, depending upon its operating parameters. The second system is self contained with a pump, a heater, a heat exchanger (the heat is rejected to the SLAC system) and a mixing valve. It supplies 60 gpm at 70 psig. The third system taps off < 2 gpm from the second system and puts it through a heater and/or a heat exchanger to get the desired temperature at the gun, then returns it. Separate temperature sensors for the DLWG's and the gun work through two controllers to regulate the mixing valve and a heater, respectively.

III. Booster Ring RF

As shown in Fig. 1 and 6, a second lower frequency RF system is part of the injector and SPEAR. The booster ring is 160 wavelengths in circumference and SPEAR is 280, so every seventh turn around the booster ring is synchronous with the same bucket in SPEAR on every fourth turn. Three bunches from the linac are let into the booster at the right time, as seen in Fig. 5h and j, by synchronizing the chopper with the booster RF. The booster RF cavity is an early SPEAR cavity refurbished, the 358.54 MHz, 500 kW cw klystron is a PEP type tube tuned for the slightly different (alas!) SPEAR frequency and the control system is a carbon (or Xerox?) copy of PEP's [8] Since the booster ring is more stable if the RF accelerating fields are not so strong during the low energy part of the ramping cycle, the reference for the amplitude feedback circuit is ramped along with the synchrotron, as shown in Fig. 6.

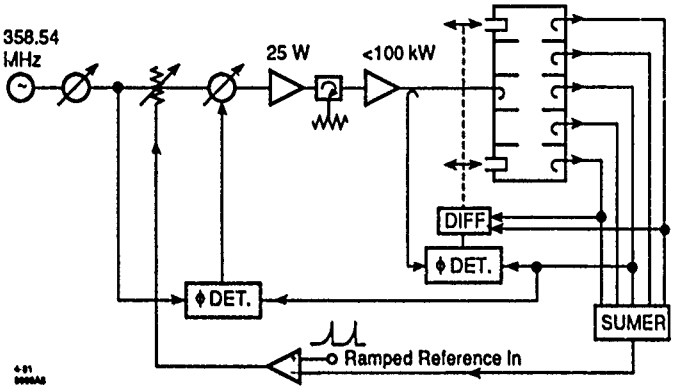


Figure 6. Injector Booster Ring RF Circuit.

IV. Operations

The microwave gun, alpha magnet and chopper came on-line without much difficulty, although numerous hours were spent studying and characterizing the preinjector. The linac high power RF networks RF processed in less than 40 hours initially and now pump down in less than a day, if let up to nitrogen. It takes several days, and a hot nitrogen bake of the RF loads may be required, if the linac is let up to air. The modulators had a few high voltage growing pains, but they have settled down since. The chopper with its permanent magnets is designed to limit excessive beam transmission (potentially 1000 times the design value), but under poor set-up conditions for the GTL (Fig. 2) or unusual failure modes for the chopper (eg., slow rise time) the linac is shut off by average current monitoring circuits. In general the RF circuits for the injector are not required to be ultra stable or critically adjusted. So the broad optimums often encountered for the GTL settings in particular have not been a fundamental limitation.

References

[1] H. Wiedemann et al., "3 GeV Injector Synchrotron for SPEAR," Proc. 1991 PAC, San Francisco, CA.

[2] M. Borland et al., "Design and Performance of the Traveling-Wave Beam Chopper for the SSRL Injector," Proc. 1991 PAC, San Francisco, CA.

[3] R. Hettel et al, "Triggers and Timing System for the SSRL 3 GeV Injector," Proc. 1991 PAC, San Francisco, CA.

[4] M. Borland, PhD thesis, Stanford University, (1991).

[5] M. Borland et al., "Performance of the 2 MeV Microwave Gun for the SSRL 150 MeV Linac," Proc. 1990 Linac Conf., 761-3, Albuquerque, NM.

[6] Tanabe et al., SLAC-PUB-5054, (Aug. 1989).

[7] H. Schwarz, IEEE Trans., NS-32, 1847-51, (Oct 1985).

[8] J.-L. Pellegrin et al., IEEE Trans., NS-28, 2320-2, (Jun 1981).

A High-Power Free-Electron Maser for RF Acceleration

F. Hartemann, T.S. Chu , P. Papavaritis, B.G. Danly, and R.J. Temkin
Plasma Fusion Center
Massachusetts Institute of Technology
Cambridge, Massachusetts 02139

G. Faillon, G. Mourier, T. Trémeau and M. Bres
Thomson Tubes Electroniques
78141 Vélizy, France

1. INTRODUCTION

Free-Electron Lasers (FELs) [1] are coherent sources of high-power electromagnetic radiation. In the microwave part of the spectrum, high efficiencies can be achieved at power levels in the multi-megawatt range. FELs can be operated as amplifiers or as phase-locked oscillators, which makes them suitable candidates for the next generation of drivers for high-frequency RF acceleration [2]. In this paper, results of the design and operation of a single-mode 28 GHz Free-Electron Maser (FEM) oscillator and a 35 GHz high-gain FEM amplifier are presented and discussed. The experiment is driven by a 700 kV, 900 Ω HV modulator, and operates with a pulse length of 1 μs at power levels in the 1-3 MW range. To obtain the 100-500 MW, 10 ns pulses required for RF acceleration at high frequencies (Ka-band), frequency chirping and subsequent pulse compression of the amplified RF signal may be used. For this type of application, phase stability is critical, and a detailed study comparing FEMs and Cyclotron Autoresonance Masers (CARMs) is currently underway at MIT [3]. Higher peak powers and shorter pulse lengths can also be obtained by driving the electron beam with a lower impedance accelerator, such as an induction linac.

2. AMPLIFIER EXPERIMENTS

The overall experimental setup is shown in Fig. 3. The electron beam used in both experiments is produced by a thermionic electron gun which was successfully operated up to 580 kV and 120 A, with a measured perveance of 0.27μperv in excellent agreement with the design value. Beam compression to a radius of 3 mm was achieved with minimal scalloping, in good agreement with adiabatic theory. The design value for the axial energy spread is $\Delta\gamma_{\|}/\gamma_{\|} < 0.2$ %. The spread inferred from experimental data is $\Delta\gamma_{\|}/\gamma_{\|} < 0.5$ %. The beam is then transported through the interaction region by a 2.35 kG axial guide magnetic field generated by a set of 7 water-cooled coils. A permanent magnet helical wiggler with 30 mm period and 500 G amplitude is used to provide the perpendicular momentum of the interacting electrons. To ensure stable high-quality group I helical orbits in the interaction region, the wiggler has a 10-period long linearly tapered introduction.

The very low energy spread and high currents obtained allow operation of both experiments in the Raman regime, as confirmed by our experimental data. At low gain (< 5 dB), and low power (≃ 100 mW), voltage tuning was obtained between 18 GHz and 40 GHz, and absorption tuning of the fast space-charge wave was observed from 18 GHz to 60 GHz. These results are in excellent agreement with what theory predicts for the coupling of the TE_{11} waveguide mode to the slow space-charge wave through the Raman free-electron laser interaction. The experimental FEM voltage tuning curve is shown in Fig. 1. In addition, we achieved very wide instantaneous

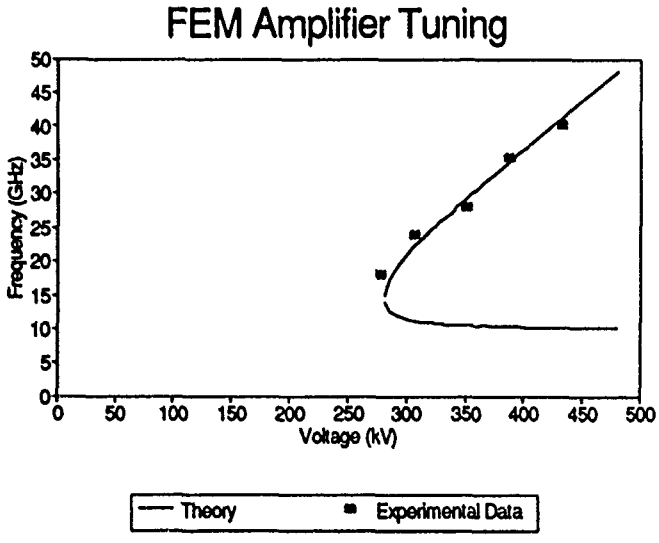


Figure 1: FEM Amplifier Voltage Tuning

bandwidth close to grazing interaction : 18 GHz to 30 GHz. In the high gain amplifier experiments, the input power will be provided by a 40 kW, 35 GHz, 400 ns magnetron and coupled into the system via an SF_6 pressurized waveguide and a linear TE_{11} mode launcher. For diagnostic purposes, the power is coupled out at the end of the interaction region by a dual 50 dB directional coupler with outputs at 90°. Feedback supression is obtained by inserting a 30 dB attenuator after the output coupler. Both the coupler and the load have VSWRs< 1.05 at 35 GHz. Computer simulations show that for a cold electron beam interacting with a TE_{11} electromagnetic mode with an input power of 5 kW at 35 GHz, the FEM saturates at z_{sat} = 80 cm, at a power level of 3 MW, yielding an untapered efficiency of 12 %. For an axial energy spread of $\Delta\gamma_{\|}/\gamma_{\|}$ = 2 % in the wiggler interaction region, the saturated power is predicted to be 2 MW.

3. OSCILLATOR RESULTS

The 28 GHz FEM oscillator experiment will use a step-rippled

0-7803-0135-8/91$01.00 ©IEEE

Bragg resonator cavity optimized with power reflectivities $R_1 = 0.95$ and $R_2 = 0.25$ and an effective length $L^* = 25$ cm, for TE_{11} operation. The system was initially operated as an oscillator without the Bragg cavity and was found to operate in a single axial mode at 30 GHz, with a line width $\Delta f < 10$ MHz, at power levels of 1-2 MW and efficiencies above 10 %. Multimode operation was also observed, with a mode spacing of 55 MHz corresponding to the cavity length. In these experiments, the oscillator spectrum is measured by mixing the RF output with the signal of a local oscillator (LO). The resulting low-frequency beat wave ($|\omega_s - \omega_{LO}|/2\pi < 1.0$ GHz) is then gated for 100 ns and dispersed through a Surface Acoustic Wave (SAW) device. The delay is proportional to the frequency of the beat wave; the dispersion of the SAW device is 100 MHz/μs. For the data shown in Fig. 2, $\omega_{LO} = 29.5$ GHz,

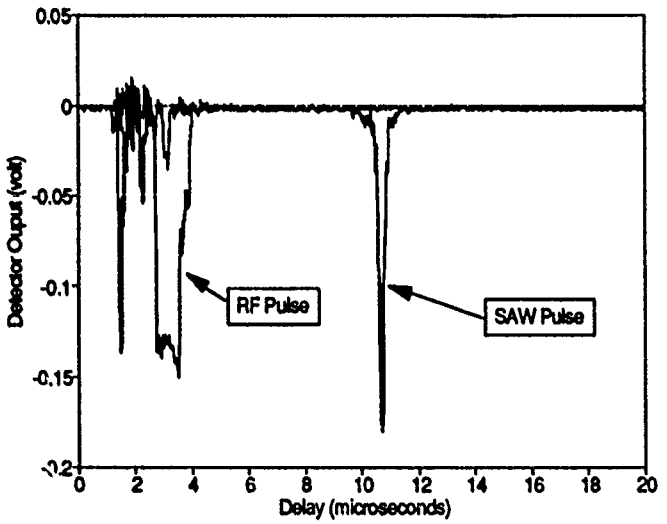


Figure 2: Single-mode Masing at 30 GHz

and we observe a single line at 30 GHz with a linewidth $\Delta\omega_s/2\pi < 10$ MHz. The oscillator can be then be phase-locked to a local oscillator, yielding the required phase control of the RF. However, for the oscillator, the cavity filling time may be relatively long, and the saturated power levels too low to achieve the parameters required for RF acceleration with the electron beam used here. Therefore, the amplifier approach, coupled to a pulse compression scheme, seems more suitable to this type of application.

References

[1] C.W. Roberson and P. Sprangle. A review of free-electron lasers. *Phys. Fluids B*, 1(1):3–42, 1989.

[2] A.M. Sessler. *Physics Today*, 41:26, 1988.

[3] W.L. Menninger, B.G. Danly, C. Chen, K.D. Pendergast, R.J. Temkin, D.L. Goodman, and D.L. Birx. *Cyclotron Autoresonance Maser (CARM) Amplifiers for RF Accelerator Drivers.* IEEE PAC '91, San Francisco, 1991.

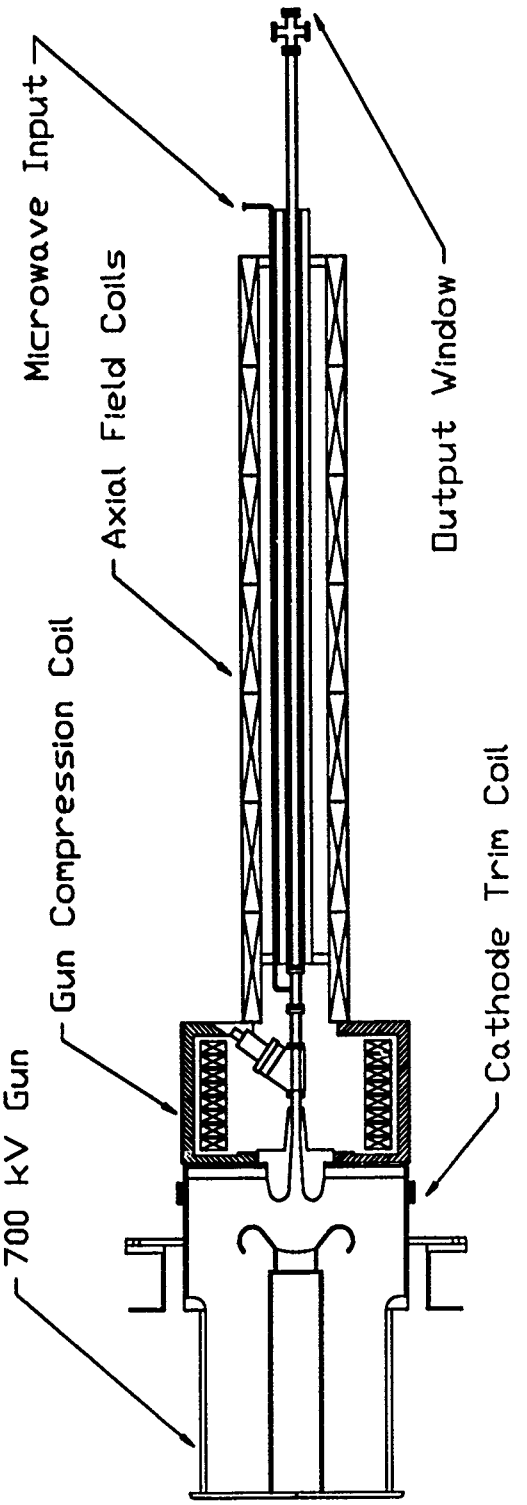


Figure 3: Overall Experimental Setup

FAST FERRITE TUNER FOR THE BNL SYNCHROTRON LIGHT SOURCE*

E. Pivit[1], S.M. Hanna, and J. Keane
National Synchrotron Light Source
Brookhaven National Laboratory
Upton, New York

Abstract

A new type of ferrite tuner has been tested at the BNL. The ferrite tuner uses garnet slabs partially filling a stripline. One of the important features of the tuner is that the ferrite is perpendicularly biased for operation above FMR, thus reducing the magnetic losses. A unique design was adopted to achieve efficient cooling. The principle of operation of the tuner as well as our preliminary results on tuning a 52 MHz cavity are reported. Optimized conditions under which we demonstrated linear tunability of 80 KHz are described. The tuner's losses and its effect on higher-order modes in the cavity are discussed.

I. INTRODUCTION

Tuning of RF cavities in storage rings is needed to maintain accelerating gap voltage under varying beam load conditions. Conventionally, this has been done using motor-driven capacitive posts or inductive loops. Under conditions of fast injection, the need exists for a different type of tuner in which the mechanical movements of the tuning elements are eliminated. In this paper we report on a Fast Ferrite Tuner (FFT) to be used in the VUV storage ring at the National Synchrotron Light Source.

At the NSLS, the VUV-ring is an electron storage ring dedicated to synchrotron radiation in the UV range and is normally operated at 745 MeV. A single 52 MHz accelerating cavity is used to compensate for the 14.7 KW of synchrotron radiation per ampere of stored beam. This RF cavity requires detuning range of 50 KHz to maintain the correct phase relation between the cavity voltage and the beam current. Currently, a combination of a mechanically driven loop tuner and water temperature variation is used to provide the required detuning. Our objective is to replace these techniques by the ferrite tuner, thus eliminating the beam instabilities associated with certain positions of the mechanical tuner.

*Work performed under the auspices of the U.S. Department of Energy.

[1]ANT Nachrichtechnik, GmbH, W. Germany.

II. PRINCIPAL OF OPERATION

A. *Basic Concept*:

A loop-coupled transmission line is used to tune the 52 MHz cavity. The transmission line is partially loaded by ferrite. By changing the bias field, the permeability of the ferrite can be changed. This results in the change in the circulating current in the coupling loop, which in turn changes the magnetic field in the region around the loop. Thus, the ratio of the magnetic to electric stored energy in the cavity is changed with the accompanying change in the cavity's resonant frequency.

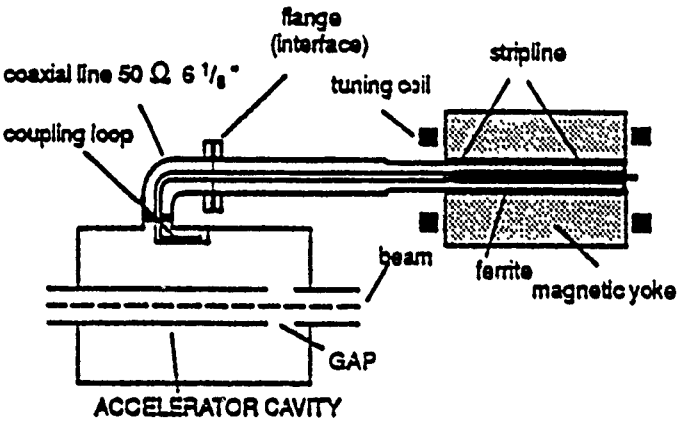


Fig. 1. Configuration for the ferrite tuner and the RF cavity.

B. *Material:*

Recently, the use of substituted yttrium iron garnet (YIG) has been suggested [1,2]. The choice of such microwave ferrite enjoys the important advantage of custom tailoring the saturation magnetization to the specific application and thus minimizing the bias field requirement. The permeability changes as:

$$\mu = 1 + \frac{4\pi M_s}{H} \qquad (1)$$

where $4\pi M_s$ is the saturation magnetization, and H is the dc field inside the ferrite.

0-7803-0135-8/91$01.00 ©IEEE

The garnet is biased above saturation and with the dc magnetic field perpendicular to the rf magnetic field. The ferrite is operated above the gyromagnetic resonance in the region where the dissipative part of the permeability, μ'' is low, thus reducing the magnetic losses.

C. *Circuit Model:*

The ferrite tuner can be modeled as a short-circuited trasmission line whose effective length varies as a function of the bias current, $l(I)$ as shown in Fig. 2.

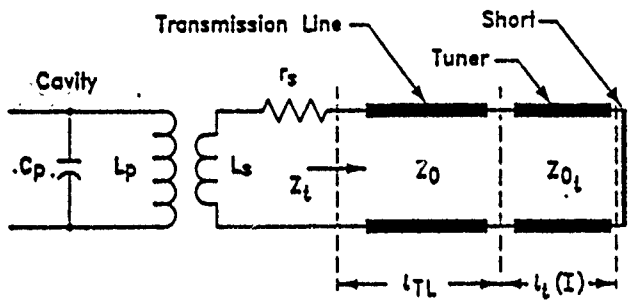


Fig. 2. Transmission line model for the ferrite tuner.

From the tuner equivalent circuit shown in Fig. 3 (a), one can deduce the coupled impedence reflected into the cavity. This is shown in Fig. 3(b).

$$Z_c=\frac{(\omega M)^2}{Z_s+Z_t}=\frac{K_{ps}K_{ps}(\omega L_p)(\omega L_s)}{Z_s+Z_t} \qquad (2)$$

Since the resistive part of Z_s is negligible, then $Z_s = j\omega L_s$.

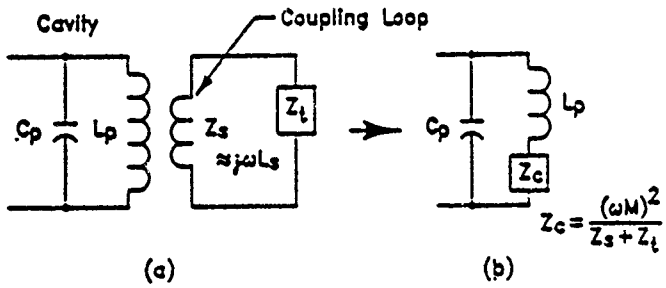


Fig. 3. Equivalent circuits for the tuner and coupling structure.

If we define $K^2 = K_{ps} K_{sp}$, we obtain

$$Z_c=\frac{K^2(\omega L_p)(\omega L_s)}{Z_s+Z_t}=\frac{-K^2Z_pZ_s}{Z_s+Z_t} \qquad (3)$$

The resonance frequency of the cavity is

$$2\pi f = \frac{1}{\sqrt{L_{eff}C_p}} \quad where \quad L_{eff}=L_p\left[1-\frac{K^2}{1+\frac{Z_t}{Z_s}}\right] \qquad (4)$$

If the capacitance is fixed , then we have

$$\frac{\Delta f}{f}=-\frac{1}{2}\frac{\Delta L_{eff}}{L_{eff}} \qquad (5)$$

Maximum change in the cavity frequency will be between open circuit ($L_{eff}=L_p$) and short circuit ($L_{eff}= L_p [1 - K^2]$). Thus the maximum amount of frequency shift is limited by the degree of coupling, K^2. Our experimental results showed clearly this effect.

III. RESULTS OF PRELIMINARY TUNER TESTING

A. *Tunability:*

We have optimized the coupling between the tuner and the cavity as well as the length of the connecting transmission line to obtain the required tunability. A length of ℓ = 56.5" gave a linear tuning characteristics as shown in Fig.4. The cavity's frequency is plotted against the tuner biasing current, I. The maximum frequency shift obtained is 78 KHz, which exceeds the design goal of 50 KHz. The voltage standing-wave ratio (VSWR) at the cavity's driving port varied between VSWR = 1.064 at I = 0 A and VSWR = 1.414 at I = 130 A.

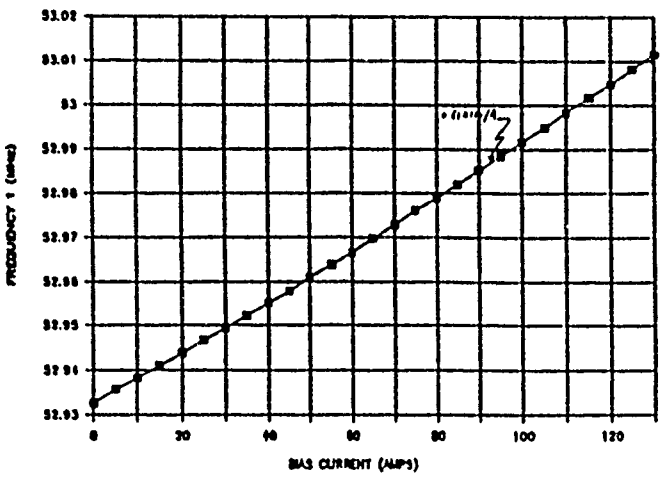


Fig. 4. Tuning characteristics of the FFT.

B. *Variation of Tuner Losses:*

The Q of the tuner system was measured as a function of the bias current. The results of the measurement are shown in Fig. 5. It can be seen from the figure that Q first increases with bias current up to 30 amperes and then decreases. Since we are biasing the ferrite above FMR, then, as we increase the bias field, μ'' becomes smaller resulting in lower magnetic

loss in the ferrite and subsequently higher Q. As for the slight decrease in Q for higher bias currents, we have considered different effects. One possible explaination would be the fact that the tuner effecively becomes a shorter trasmission line as we increase the bias. Thus, for a given voltage at the coupling loop, the electric field in the ferrite increases. This results in the observed increase in losses as manifested by the monotonic decrease in Q.

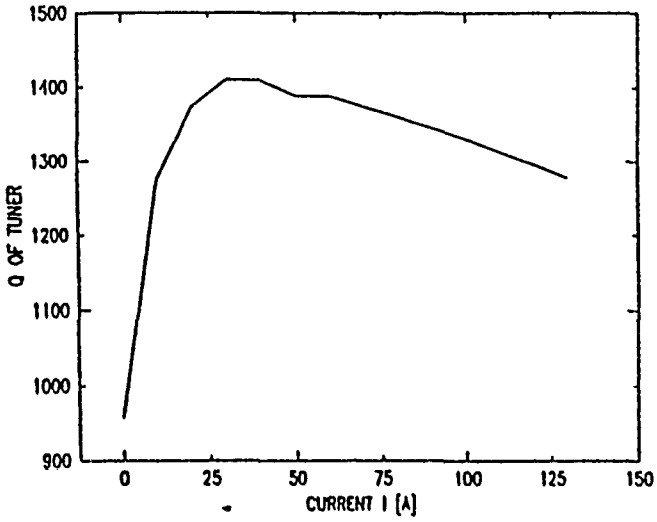


Fig. 5. Variation of the Q of the tuner system.

C. *Effect of Tuner on the Cavity's Higher-Order Modes:*

To investigate the effect of the tuner on the excitation of higher-order modes (HOM's) in the VUV-ring cavity, we have analyzed the HOM's induced by the tuner in a replicate study cavity. Specifically, we probed these modes that resulted in a change of field in the accelerating gap. Detailed results of these gap measurements will be reported in a separate publication. Up to 200 MHz there was no observed change in the cavity's response as shown by comparing Fig. 6 (a and b) to Fig. 7 (a and b).

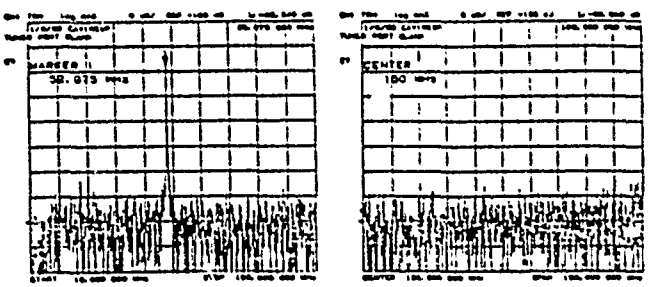


Fig. 6. Cavity response with the tuner port blocked.

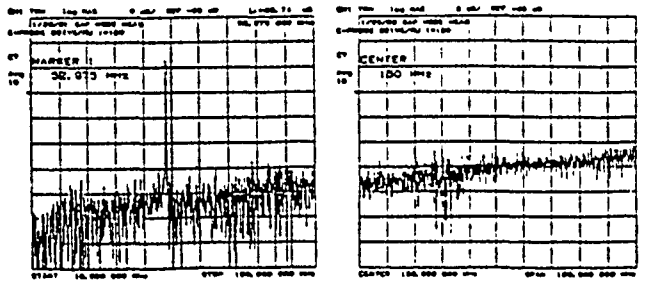


Fig. 7. Cavity response with the tuner coupled to the cavity (I = 130 A).

At higher frequencies, the tuner shifted some of the cavity's HOM's and introduced additional ones. We show in Fig. 8 (a and b) the mode at 272 MHz as an example. Currently, we are studying different approaches to suppress the additional HOM's that are due to the ferrite tuner. This includes the use of a terminated waveguide as a suppressor.

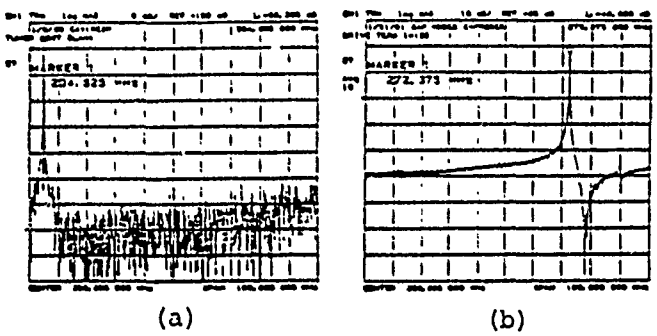


Fig. 8. Shift in one of the cavity's HOM's due to tuner: (a) tuner port blocked, (b) I = 130 A

IV. CONCLUSIONS

From our preliminary tests on the new ferrite tuner, it is clear that we were able to achieve the design goals concerning the tunability required. The low tuner losses, as demonstrated by the measured high tuner's Q, are credited to the normal bias approach which we use and biasing the ferrite above FMR. The design approach adopted also has the advantage of efficient cooling of the garnet slabs in the stripline configuration.

ACKNOWLEDGEMENT

We wish to acknowledge the technical support of R.D'Alsace and W. Broome.

REFERENCES

[1] W. R. Smythe and T. G. Brophy, IEEE Trans. on Nucl. Sci , NS-32, No.5,2951 (1985)

[2] R.M. Hutcheon, Proc. of the IEEE Part Accel Conf., 1543 (1987).

COPPER PLATING THE GROUND TEST ACCELERATOR RFQ

Henry Mignardot and Joseph Uher
University of California, Los Alamos National Laboratory
P.O. Box 1663, MS H821, Los Alamos, NM 87545

Abstract

The copper-plating process for the Ground Test Accelerator (GTA) radio frequency quadrupole (RFQ) vanes required a full development program and tight quality control procedures. The copper plating development program utilized full-size RFQ major and minor vane mockups to develop plating fixturing and to establish the plating parameters necessary to meet the GTA RFQ plating specifications. After several modifications to the fixturing and plating processes, the mockup vanes were copper plated to GTA specifications and the actual GTA RFQ could then be copper plated. This development technique, using full-size mockups for establishing reliable and accurate plating fixtures and proven plating processes, is the key to success for copper-plating any special piece of technical and expensive hardware. This paper discusses the GTA RFQ copper-plating critical issues; the plating-fixture development; the copper-plating processes; RFQ plating specifications as they apply to thickness, uniformity, and adhesion; and the quality assurance procedures.

I. INTRODUCTION

The Ground Test Accelerator (GTA) Radio Frequency Quadrupole (RFQ) was successfully copper plated through a joint effort of the Los Alamos National Laboratory (hereafter refered to as the University of California) and the Industrial Plating Company, Seattle, Washington.

The GTA RFQ is a 50-mA cryogenically cooled rf accelerator with an exit-beam energy of 2.5 MeV. The aluminum core tank design, of eight major vane / minor vane segments, allows for simplified assembly. The core tank is 2.794 m in length. There are two longitudinal sections of approximately 1.397m each and four transverse sections (see Fig. 1). The RFQ vanes were machined by the Mechanical and Electronics Support Division (MEC), at the University of California from thick 2219 T851 aluminum plate. This material was chosen for its high strength, stability during machining, and its excellent weldability [1]. The vane segments are bolted together transversely, with dowel pins between the major and minor vanes to ensure precision section-to-section alignment.

The GTA RFQ was copper plated using the UDYLITE Bright Acid Copper High Speed (UBAC-HS) Bath Process. This paper will focus on the GTA RFQ copper-plating requirements, the plating development program, the final plating results, and quality assurance.

II. GTA RFQ PLATING CRITICAL ISSUES

A critical issue that required special consideration was the handling of the RFQ vanes, because of their delicacy and extreme complexity. Specific handling and shipping instructions had to be devised to ensure that the vanes would not be damaged in any way. For a representation of the RFQ core tank assembly before plating (see Fig. 2).

Other critical issues included determining the technical plating specifications and the finished product plating requirements; and establishing quality assurance procedures to meet final inspection requirements.

The technical plating specifications pertain to the thickness and uniformity of the plating, and were defined on two levels: those for critical and those for noncritical surfaces. The thickness and uniformity specification for the critical

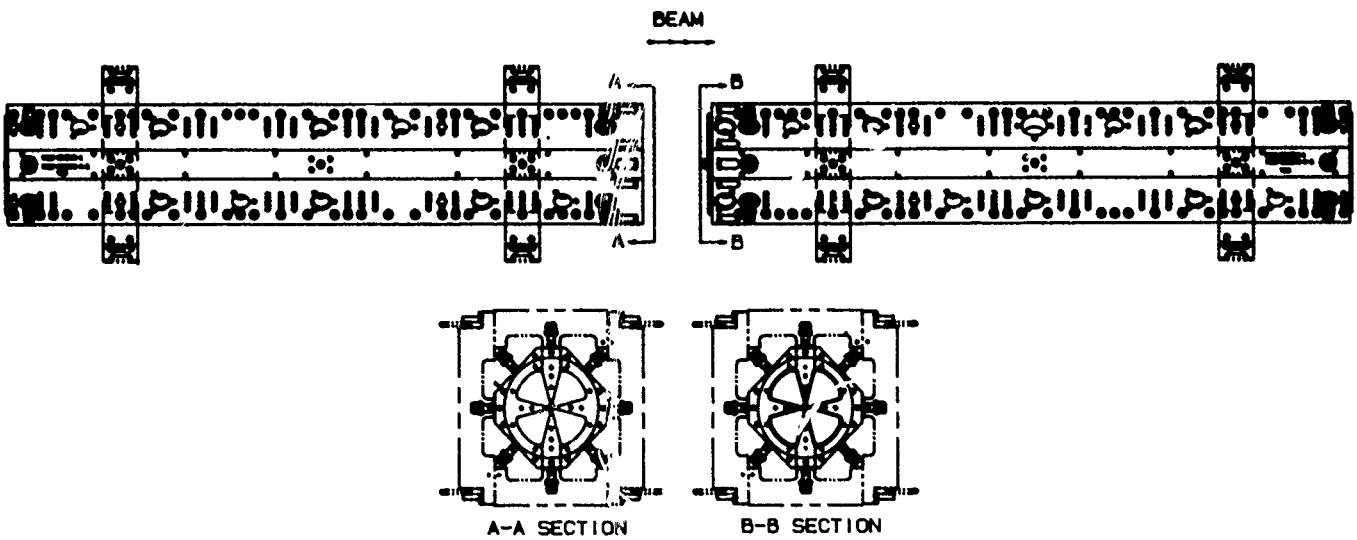


Figure 1. GTA RFQ core tank.

*Work supported and funded by the US Department of Defense, Army Strategic Defense Command, under the auspices of the US Department of Energy.

0-7803-0135-8/91S01.00 ©IEEE

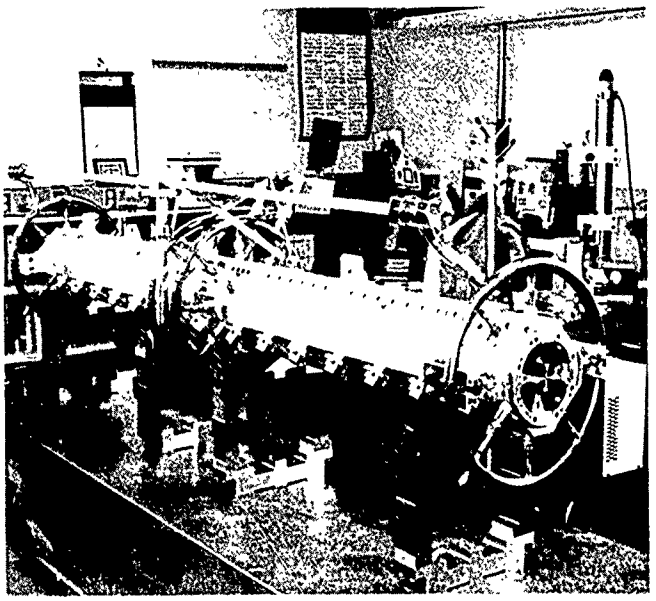


Figure 2. RFQ core tank assembly before plating.

surfaces was 0.001 in. ±0.0003 in., and that for noncritical surfaces was 0.001 in ±0.0005 in. Those surfaces not requiring plating were masked.

The finished product plating requirements were stringent on surface finish thickness and uniformity. The surface finish of the copper plating was specified to be no worse than the substrate finish before plating, which was approximately a 50 μ in. finish. Small nodules, fines, steps, roughness, or other defects on critical vane surfaces potentially arising from the plating processes were specified unacceptable.

Quality Assurance (QA) procedures were established and implemented to assure compliance with the specifications and requirements during copper electroplating and delivery of the components. A major goal of this QA program was to generate and maintain a permanent record of compliance.

III. GTA RFQ PLATING DEVELOPMENT PROGRAM

To ensure that the RFQ copper plating specifications and requirements could be met, we set up a plating development program to qualify a fixture and a process for copper plating the RFQ vanes. Full-size mockups of both the major and minor vanes were copper plated and used to verify compliance with all plating specifications. These mockup vanes were also used as development models to verify correct anode and cathode configurations and placements with respect to the specific vane contours and porthole locations required for plating (see Fig. 3). Next, a plating fixture was developed that combined correct placement of both anode and cathode arrangements, and served as a handling fixture to for transfering the vanes from one bath to another.

Finally, we developed the precise bath parameters and characteristics: plating solution mixtures, bath temperatures, electroplating power settings, and time in baths.

The UDYLITE UBAC 2X Acid Copper Plating Process is a bright acid copper bath for the deposition of a brilliant, ductile copper plate. The outstanding advantages of the deposit are its high brightness, excellent leveling, and exceptional ductility. This deposit has practically the same ductility as a deposit from a pure acid copper solution free from addition

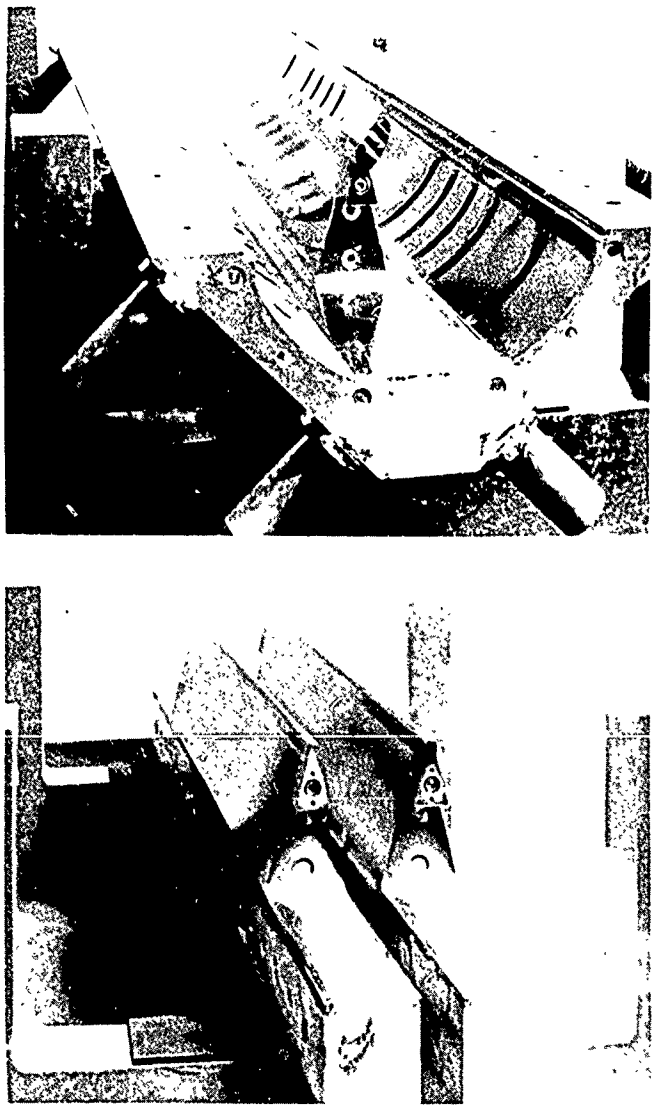


Figure 3. RFQ major and minor vane mockups.

agents. More important, the UBAC 2X Acid Copper Process has the ability to produce this finely leveled and ductile plate continuously in heavy production, because no harmful breakdown products are formed during electrolysis. The excellent leveling is very important, because the specific radio frequency (rf) requirements do not allow polishing and/or buffing of the surface.

Before plating, an anode was placed in the slug tuner port of the major vanes to ensure that the port hole would be uniformly copper plated. The current density settings required to plate the minor vanes were approximately 22 Amp/in at 0.001 in./hr., and for the major vanes, approximately 44 Amp/in. at 0.001 in./hr.

The main steps in the copper plating sequence of the vanes were as follows excluding details such as cleaning, rinsing, and plating preparation:

1. The vanes were cleaned with soap and mild cleanser to get rid of water brake on the surface.
2. The vanes were dipped in an actane solution for preparation and activation of aluminum pores.

3. The vanes were dipped in 50% nitric acid to eliminate foreign contaminants on the aluminum surface.
4. The vanes were given a 10-second zincate dip to increase surface adhesion properties.
5. The vanes were dipped in 50% nitric acid for removal of excess zincate.
6. Again, the vanes were dipped in zincate for approximately 40 seconds.
7. The vanes were dipped into an electrolysis nickel bath until a thickness of approximately 0.0002 in had been deposited.
8. The vanes were put through a copper strike process, again for a thickness of approximately 0.0002 in.
9. The vanes were rinsed with pumice to remove excess copper strike.
10. Next, the vanes were dipped in 10% sulfuric acid to reactivate the copper.
11. Finally, the vanes were put into a bright acid copper dip of approximately 20 minutes for minor vanes, and approximately 40 minutes for the major vanes.

Only after acceptance of the mockup plating to the specified requirements were the actual RFQ vanes copper plated. The actual plating took place immediately after mockup plating acceptance, to ensure correct plating bath parameters and characteristics.

IV. QUALITY ASSURANCE PROCEDURES

The thickness and uniformity of the copper plating on the vanes was measured using two different techniques. Our first measuring technique was the standard one for coating thickness, which uses the BETA backscatter principle. This technique can be used to measure the thickness of any coating having an atomic number sufficiently different from that of the substrate material. The maximum measurable thickness for a given coating is that thickness beyond which the intensity of the backscattered radiation is no longer sensitive to small changes in thickness. This technique can also be used to determine the mass of a coating per unit of area. When calibrated under specified operating conditions, the instrument measures the coating thickness to within an accuracy of 10 percent of its true thickness.

The other measuring technique uses the DEA coordinate measuring machine (CMM) and a master set of dowel pins located in the back of each vane. CMM data from initial, pre-plating inspection of the vanes was stored and later compared with data for the plated vanes. The difference between the two gives an accurate representation of the plating thickness.

The surface finish was inspected using a portable surface profilometer. The surface finish of the plated vanes was specified to be no worse than the substrate finish before plating.

Adhesion of the copper plate to the vane surface was specified as a metallurgical bond with the substrate material. Tests were conducted to verify compliance with this specification using the mockups and component adhesion test coupons. An "X" 1 in. high was scribed on the copper plating on the upper half of each coupon, penetrating the plating to verify that the substrate material was clearly visible. At the points formed by the intersecting lines of the "X", several attempts were made to separate the copper plating from the substrate material by prying and gouging with a sharp pointed instrument. In addition, adhesion was checked by bend tests. Any separation of the copper plating from the substrate material during either type of test would have been cause for rejection of the plated mockups.

V. CONCLUSIONS

The copper plating process described in this paper was shown to be workable and to produce accurate results (see Fig. 4).

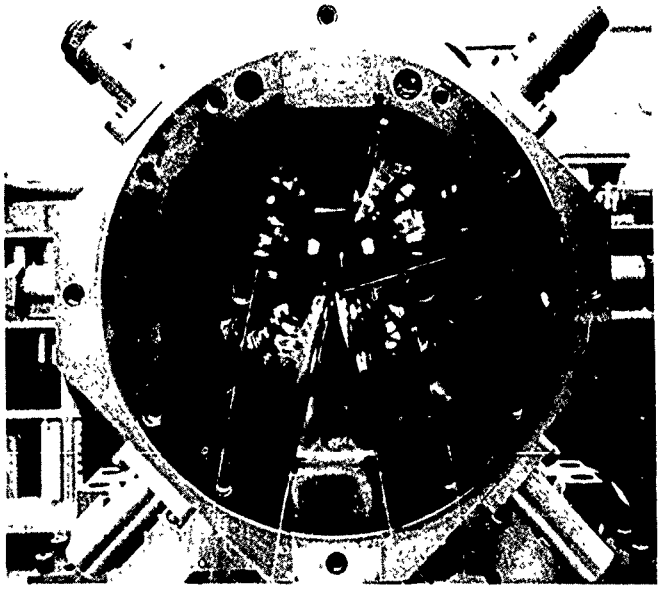


Figure 4. RFQ copper plated.

The plating was well within the tolerance of 0.001 ± 0.0003 in. on the vane tips, and 0.001 ± 0.0005 in. on noncritical surfaces. The uniformity and thickness results are tabulated in Fig. 5.

Minor Vanes:

$\bar{x}$(VD1) = 0.0009 in.	s(VD1) = 0.0003 in.
$\bar{x}$(VU1) = 0.0010 in.	s(VU1) = 0.0002 in.
$\bar{x}$(VU3) = 0.0011 in.	s(VU3) = 0.0001 in.
$\bar{x}$(VD3) = 0.0010 in.	s(VD3) = 0.0002 in.

Major Vanes:

$\bar{x}$(VD4) = 0.0010 in.	s(VD4) = 0.0002 in.
$\bar{x}$(VU4) = 0.0010 in.	s(VU4) = 0.0001 in.
$\bar{x}$(VU2) = 0.0013 in.	s(VU3) = 0.0002 in.
$\bar{x}$(VD2) = 0.0012 in.	s(VD2) = 0.0003 in.

Figure 5. RFQ Plating Results

VI. REFERENCES

[1] Nathan K. Bultman, "Mechanical Fabrication Aspects of the GTA RFQ", *1990 Neutral Particle Beam Technical Symposium*, San Diego, CA (May, 1990).

IDLE SUPERCONDUCTING RF CAVITIES FOR BUNCH FOCUSING

P. Marchand, L. Rivkin
Paul Scherrer Institut, CH-5232 Villigen PSI

I. INTRODUCTION

In the feasibility study for a B-Meson Factory using the CERN ISR tunnel and the LEP injection system (BFI) [1], a combination of normal conducting (n.c.) and superconducting (s.c.) RF cavities has been proposed as an alternative in the context of upgrading the luminosity towards 10^{34} cm^{-2} s^{-1} [2,3]. In such a hybrid n.c./s.c. system, both systems may contribute to the compensation of the beam energy losses as well as to the longitudinal focusing of the bunches. Another possibility is to limit the role of the s.c. system to a pure focusing task by setting its synchronous phase to zero (no acceleration). In this latter scheme, the s.c. cavities might be operated in a completely idle mode (i.e., no external RF source). The RF power required for the compensation of the beam energy losses would be entirely provided by the n.c. system. A proper detuning of the s.c. cavities should permit use of the beam induced voltage as the focusing voltage.

The steady state and dynamic behaviour of a single RF system, in the presence of beam loading, has been already largely treated [4,5,6,7]. Extending the analysis to the more general case of two RF systems coupled through the beam was the subject of a previous note [8]. No major critical issues, as compared to conventional methods, were encountered in the context of the BFI. On the contrary, the partial or complete separation of functions, powering and longitudinal focusing, characteristic of this system, makes it particularly flexible. The main results of this study and examples of applications are presented. The possibility of testing the bunch shortening provided by idle s.c. cavities in an existing storage ring is also discussed.

II. STEADY STATE DESCRIPTION

Only the beam-RF system interactions at the fundamental frequency will be considered. The higher order modes (HOM) of the RF cavities are supposed to be sufficiently damped and are taken into account only as extra beam energy losses. In addition, we will assume short e^- (or e^+) bunches above the transition energy and $T_b/T_f \ll 1$ (T_b : time between bunch passages, T_f : cavity filling time). The fundamental interaction between the beam and an RF system can be then described by the phasor diagram of figure 1.

V, cavity voltage (phase reference)
R, cavity shunt impedance
β, input coupling factor
i_b, fundamental beam current (twice the average value, I_b)
$2i_g$, generator short circuit current[1]
Φ_g, phase of the generator current
Φ_S, synchronous phase
Ψ, cavity detuning angle

$$tg\Psi = \frac{2\,Q\,\delta f}{(1+\beta)\,f_r} \qquad \delta f = h f_0 - f_r$$

Q, cavity quality factor — h, RF harmonic number
f_0, revolution frequency — f_r, cavity resonant frequency

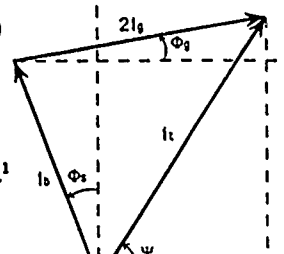


Fig. 1 : Phasor representation of the beam-cavity interaction

[1] value "seen" by the beam (i e , transformed by the coupling circuit)
[2] index 1 and 2 used for the n.c and s c. system, respectively

An equilibrium or steady state condition is defined by

$$\Delta U/e = V\ sin\Phi_S\ ,$$
$$\sigma_s \propto (h\ V\ cos\Phi_S)^{-1/2}\ ;$$

ΔU is the energy loss per turn and σ_s, the RMS bunch length. At a given RF frequency, the specification of ΔU and σ_s leads to a unique solution for both V and Φ_S. The power delivered to the beam is then $P_b = V\ I_b\ sin\Phi_s$ and the cavity dissipation, $P_d = V^2/2R$. The minimum power requirement, $P_g = P_b + P_d$, corresponds to the matched case (no reflection), obtained when the reactive current is compensated by the proper detuning, δf and the coupling factor set such $\beta = 1 + P_b/P_d$.

In the presence of two different RF systems, each of them may be described as before[2] and the steady state definition becomes

$$\Delta U/e = V_1\ sin\Phi_{S1} + V_2\ sin\Phi_{S2}\ ,$$
$$\sigma_s \propto (h_1\ V_1\ cos\Phi_{S1} + h_2\ V_2\ cos\Phi_{S2})^{-1/2}\ .$$

For fixed RF frequencies ($h_1 \leq h_2$), a specified stationary condition can now be obtained from different combinations of both RF system parameters ($V_1, \Phi_{S1}, V_2, \Phi_{S2}$).

In the particular case where the second RF system is idle, the equivalent phasor diagram is reduced to that of figure 2.

$i_{g2} = 0$
$\beta_2 = 0$
$\Phi_{S2} = \Psi_2 - \pi/2$
$V_2 = 2\ R_2\ I_b\ cos\Psi_2$

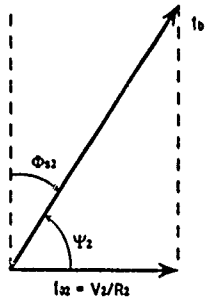


Fig. 2 : Phasor representation for idle cavities

The beam-cavity interaction corresponds to a power lost by the beam, equal to the cavity dissipation:

$$P_{b2} = V_2\ I_b\ sin\Phi_{S2} = -P_{d2} = -V_2^2/2R_2\ .$$

With s.c. cavities and large enough I_b, $\Phi_{S2} \simeq 0$, $\Psi_2 \simeq \pi/2$ ($cos\Psi_2 \simeq 1/tg\Psi_2$) and the induced voltage is then

$$V_2 = (R/Q)_2\ I_b\ f_{r2}\ /\ \delta f_2\ ,\ \text{where}\ \delta f_2 \gg f_{r2}/Q_2\ .$$

A steady state is now defined by

$$\Delta U/e = V_1\ sin\Phi_{S1}\ ,$$
$$\sigma_s \propto (h_1\ V_1\ cos\Phi_{S1} + h_2\ V_2)^{-1/2}$$

and can be obtained from different operating points within the range $0 < \Phi_{S1} \leq \pi/2$. Thus, σ_s is adjustable, without other interference, by simply varying δf_2 and, for a specified σ_s, there is still a degree of freedom available.

The power requirement is minimum if the n.c. system is matched and $V_1 = \Delta U/e$ (or $\Phi_{S1} = \pi/2$). This corresponds to a complete separation of functions: powering by the n.c. system ($P_b = V_1 I_b$), focusing by the s.c. one ($\sigma_s \propto V_2^{-1/2}$).

The preceding situations are generally met for e^- or e^+ in storage regime ($\sigma_s \ll c/f_{r2}$, $I_b = I_{bmax}$). Now it happens that, during the accumulation, one passes through different operating states while I_b varies from zero to I_{bmax}, in successive steps ΔI_b. The value of δf_2, which can then be freely set, determines the increasing rate of V_2 versus I_b. It has to remain larger than a few s.c. cavity bandwiths and such that the resonance does not approach too closely the next beam spectrum line (typically, $\delta f_2 < f_0/2$). At low I_b, as long as $V_2 \ll V_1$, a proper

0-7803-0135-8/91S01.00 ©IEEE

trapping of the injected bunches necessitates $V_1 > \Delta U/e$. This constraint may determine the operating point. It is also possible to make use of the power reserve existing at low beam loading for varying V_1 during the accumulation.
The stability of the system in presence of perturbations, the subject of the next section, is another important consideration.

III. DYNAMIC BEHAVIOUR

A. Stability criterion

In the presence of a single RF system, the stability condition is defined by the well known Robinson criterion [5] which, in our notations, can be expressed as:

$$0 < sin2\Psi < 2\ cos\Phi_S\ /\ Y\ ,\quad \text{where}\ \ Y = i_b/i_0\ .$$

We found in ref. 8 that, extended to the more general case of a double RF system, the upper stability limit, becomes:

$$sin2\Psi_1 < \frac{2\ cos\Phi_{S1}}{Y_1} + \frac{h_2 V_2}{h_1 V_1 Y_1}\ (2\ cos\Phi_{S2} - Y_2\ sin2\Psi_2)\ . \quad (1)$$

If the second RF system is idle, the second term of the right hand side in (1) cancels ($\Phi_{S2} = \Psi_2 - \pi/2$, $Y_2 = 1/cos\Psi_2$) and we once again obtain the classical Robinson limit for the first RF system, as if it was alone:

$$sin2\Psi_1 < 2\ cos\Phi_{S1}\ /\ Y_1\ . \quad (2)$$

This result states that the stability condition for the hybrid n.c./idle s.c system is met as soon as the Robinson criterion is fulfilled for the n.c system; in particular, (2) will be automatically satisfied if the n.c cavities operate in the matched case at maximum beam current and $0 < \Phi_{S1} < \pi/2$.

B. Stability margin and transient effects

In practice, a sufficient safety margin is necessary to cope with departures from the ideal conditions previously assumed. Generally, for e^- or e^+ in a normal storage regime (constant or slowly variable i_b), the parameters can be precisely set by means of "slow" amplitude and tuning servo controls. The main source of perturbation then results from the accumulation, when I_b increases from zero to I_{bmax} in successive injections, ΔI_b. The sudden changes of beam loading temporarily destroy the steady state equilibrium and induce transient oscillations of the RF voltage. Emittance blow up or even beam losses may occur if the safety margin is not sufficient.
According to our preceding results, the stability region increases when the operating point moves away from the condition $\Phi_{S1} = \pi/2$. The presence of "fast" compensation (phase loop, feedforward, RF feedback, external coupling of the two systems) would significantly modify the situation.
The transient effects directly produced in the n.c. system should be negligible compared to the s.c. one. If the latter could be considered individually, as a "free oscillator", the frequency of the transient oscillations would be δf_2, its damping rate, T_{f2} (natural s.c. cavity filling time), and its amplitude, expressed in terms of instantaneous power [8],

$$\Delta \dot{P}_2 = \Delta V_2\ I_b\ ,\ \text{with}\ \ \Delta V_2 = (R/Q)_2\ \Delta I_b\ f_{r2}\ /\ \delta f_2\ . \quad (3)$$

However, the s.c. system cannot be treated independently since it is coupled to the n.c. system through the beam. A correct analysis requires considering the global system response (in particular, its slowest damping rate) which depends on the steady state operating conditions of both systems. Equation (3) should nevertheless give a good idea of the real maximum transient amplitude, conversely, as we will see in a following example, the damping time may be much shorter than T_{f2}.
Due to the high degree of freedom available with this system, a general analytic approach is quite complex. In the next section, we estimate the effects for particular applications.

IV. EXAMPLES OF APPLICATIONS

The n.c/idle s.c. system provides an economical way of generating very high RF voltage, with additional degree of freedom available, due to the separation of longitudinal focusing and energy loss compensation functions.
This seems to be particularly well suited for the needs of flavor factories (Tau-charm, B-meson) where short bunches together with high design current are required.
Achieving very short bunches and high peak currents is also important in synchrotron light sources, storage ring drivers for short wavelength FELs as well as in the damping rings for future linear colliders. With very short bunches, we enter a regime where the effective impedance seen by the beam decreases with bunch length, resulting in the increase of the threshold peak current for the turbulent bunch lengthening instability. Such dependence of the threshold on bunch length has been observed experimentally (e.g. SPEAR, LEP) [9,10]. In LEP, the threshold current is ten times higher than what one would expect in the long bunch regime.
Two examples of possible applications are described in the following section.

A. B-meson factory

We now consider the use of a n.c./idle s.c. system in the high energy ring of the $L = 10^{34}\ cm^{-2}\ s^{-1}$ BFI proposed in ref. [1]. The main design parameters of the ring and characteristics of the RF system [2,3] are listed below.

- **ring parameters :**
  E = 8 GeV, ΔU = 6 MeV , mom. comp. fact. = 0.005
  I_b = 1.12 A , n_{bunch} = 320 , σ_s = 4.8 mm
- **n.c. RF parameters :**
  $Q_1 \simeq 50000$, $(R/Q)_1 = 73\ \Omega$/cav , $n_{cav1} = 32$
  8 MW of installed RF power
- **s.c. RF parameters :**
  $Q_2 \simeq 10^9$, $(R/Q)_2 = 40\ \Omega$/cav , $n_{cav2} = 40$
  120 MV of total voltage

The number of cavities is adjusted for practical values of the accelerating gradient, input coupler power, HOM and fundamental dissipation. Instability thresholds have also been taken into account. The frequency of both systems is 500 MHz. Higher harmonic s.c. cavities would lead to an intolerable reduction of the longitudinal acceptance during the accumulation.
The following table presents a set of typical operating conditions for the n.c. system.

Φ_{S1} [°]	V_1 [MV]	P_{d1} [kW]	P^{RF}_{total} [MW]	β_1	δf_1 [kHz]
25.	14.4	920.	7.7	8.4	80.
35.	10.6	500.	7.3	14.6	97.
45.	8.6	330.	7.1	21.6	103.
55.	7.4	240.	7.0	27.8	97.

In all cases, a matched condition at full beam current is assumed. The 8 MW available power, allows operation at Φ_{S1} as low as 25° which corresponds to a quite comfortable stability margin. With less power, it is still possible to achieve an efficient capture of the 8 cm injected bunches, by varying V_1 during the accumulation.
For a total filling time of a few minutes and injection pulses around 3 mA, the transients directly produced in the n.c. cavities should be negligible. However, those induced by the idle s.c. system must be considered more carefully. An estimate of their maximum effects is given below, for $\Phi_{S1} \simeq 30°$ and different values of δf_2.

δf_2 [kHz]	ΔV_2 [kV]	$\Delta \hat{P}_2$ [kW]	$\Delta \hat{P}_2/P_1$ [%]	$\Delta\Phi_{S1}$ [°]	τ [ms]
8.2	320.	350.	5.0	1.7	5.2
25.	100.	115.	1.7	0.6	0.4
50.	50.	60.	0.9	0.3	1.7
150.	17.	20.	0.3	0.1	100.

ΔV_2 and $\Delta \hat{P}_2$ are defined in (3); $\Delta\Phi_{S1}$ is the equivalent phase variation in the n.c. system and τ, the slowest damping rate obtained by solution of the characteristic equation [8]. The first line corresponds to the value of δf_2 required for $\sigma_s \simeq 5$ mm ($V_2 = 110$ MV) in the storage regime; $\tau \simeq 5$ ms. In the next line, δf_2 is set for minimum damping time ($\tau \simeq 400\mu$s). This is not necessarily the optimum condition: the two last examples show higher τ, but lower amplitude. In the search for the best compromise, amplitude, damping rate and eigenfrequency values must be simultaneously taken into account.

The above results seem quite compatible with the expected safety margin. Thus, the n.c. system could be equipped with only conventional "slow" amplitude and tuning controls; for the s.c. cavities, a servo mechanism controlling their voltage, via the action of a tuner, would be sufficient. If it were necessary, "fast" compensation methods could be added.

B. Synchrotron light source

In the context of a parameter study for a possible future Swiss Light Source (SLS) we have considered the use of idle s.c. cavities to obtain bunches as short as $\sigma_s = 1$ mm .

Operated at 1.5 GeV, a 200 m long ring with momentum compaction factor around 0.002 and using a 500 MHz RF system (1 MV voltage), would produce 6 mm long bunches.

Introducing idle s.c. cavities that would provide 30 MV induced voltage, would shorten the bunch to 1 mm. Due to the expected slow filling rate of the ring, the problem of injection transients should not be critical. Both 500 MHz and 1.5 GHz were considered, and while the higher harmonic system results in some saving of space needed for the cavities, the HOM problem may become more serious.

It should be possible, by careful design, to build a ring with broad band impedance $Z/n < 1\Omega$. For short bunches, the effective impedance seen by the beam could be much smaller, resulting in higher achievable peak currents. However, some theoretical considerations [11] suggest that the lowest limit of the effective impedance is the so-called "free space" impedance, which in our case would be around 0.2 Ω. If this were confirmed, the impedance constraints on the vacuum chamber and RF cavities could be relaxed by the use of short bunches.

A test of the effective impedance scaling with bunch length, down to this limit, should be possible in the proposed experiment at EPA ring which is described below.

V. TEST ON AN EXISTING MACHINE

Electron Positron Accumulator (EPA) is a part of the LEP preinjector complex. Operated at 500 MeV, the 126 m long ring provides eight e^- or e^+ bunches with σ_s from 20 to 40 cm. Up to 40 KV is produced with a single 19 MHz cavity.

A higher harmonic n.c. RF cavity (the convenient choices could be 114 MHz PS, 200 MHz SPS or 350 MHz LEP) with a voltage around 1 MV would shorten the bunch to about 1 cm.

An idle 500 MHz s.c. cavity, prototype of a single cell cavity considered in the designs for the B-factory, could provide an additional 3 MV induced voltage that would shorten the bunch further to a few millimeters. Such a cavity would be equipped with an efficient HOM damping system assuring the multibunch stability control. During normal operations, it could be tuned very far from the resonance, lowering the induced voltage to value much less than the main RF voltage.

The broad band impedance in EPA, dominated by the contribution from the kicker magnets, is about 16 - 20 Ω. The added RF cavities will not increase the overall impedance by much. Conversely, with the 1 cm long bunches, the effective impedance should be approximately twenty times smaller than the low frequency limit quoted above.

Already with 1 mA, the induced 3 MV in the idle s.c. cavity, will make the bunch 4 mm long and reduce the effective impedance below the "free space" impedance estimate for EPA. In these conditions, we expect a ratio coherent-to-incoherent synchrotron radiation of about two and it should grow linearly with current. Thus, a test at EPA would provide plenty of signal to check the calculations that take into account the shielding effects of the vacuum chamber [12].

Bunch shortening provided by idle cavities could be preliminarily tested in the CERN SPS: on the one hand, by idling a part of the existing 200 MHz n.c. cavities, in the 300 mA proton beam, on the other hand, by combining this system with the two installed 350 MHz s.c cavities, in the e^- beam. In the first case, the idle n.c. cavities are less sensitive to transient effects; in the second case, the voltage induced in the idle s.c. cavities by the available e^- current of 0.5 mA will remain low compared to the accelerating voltage. However, these experiments should bring much information concerning the practical operation of such a system.

VI. CONCLUSION

A hybrid n.c./idle s.c system is particularly well suited for the needs of $e^-(e^+)$ storage rings or colliders where short bunches together with intense beam are required. The study of its application for two possible future machines, the B-meson factory in the CERN ISR and the Swiss Light Source, did not point out any further difficulties as compared to conventional systems. On the contrary, the additional degree of freedom available, due to the separation of functions, powering and longitudinal focusing of the beam, makes it very flexible.

We propose testing the principle with the existing equipment and the available beams of the CERN SPS as well as in a further experiment at CERN EPA, with a prototype of a 500 MHz s.c. cavity considered in the designs for the B-meson factory.

In addition, the EPA test would permit to study the scaling of the effective ring impedance with bunch length, down to the "free space" limit and to experimentally check the coherent radiation level over a large range of bunch length.

If this system were confirmed to be operational, it could be attractive for a wide domain of other applications.

References

[1] CERN 90-02 or PSI PR-90-08 (March 1990).
[2] P. Marchand, PSI TM-12-90-01 (January 1990).
[3] P. Marchand, Proc. 2nd EPAC, p.1088, Nice (June 1990).
[4] P.B. Wilson, 9th Conf. on High En. Acc., Stanford (1974)
[5] K.W. Robinson, CEAL-1010 (1964).
[6] F. Pedersen, IEEE Tr. Nucl. Sci NS-22, p.1906 (1975)
[7] D. Boussard, CERN SPS/86-10 ARF (May 1986).
[8] P. Marchand, PSI TM-12-90-09 (October 1990)
[9] A. Chao, J. Gareyte, SLAC PEP-224 (December 1976)
[10] D. Brandt et al, Proc. 2nd EPAC, p.240, Nice (June 1990)
[11] S. Chattopadhyay, Editor, Part. Acc. 25, 2-4 (1990)
[12] R. Warnock, KEK report 90-21 (February 1991)

Sliding Mode Controller for RF Cavity Tuning Loop

L.K. Mestha
Superconducting Super Collider Laboratory*, Dallas, Texas 75237

K.S. Yeung
University of Texas, Arlington, Texas 76019

Abstract

Ferrite tuned cavities must operate under a wide range of accelerating frequencies. The tuning is done by modulating the current in the coil surrounding the ferrite. Feedback controllers are used to improve the tuning condition by sensing the phase error. The design of controllers currently in use is based on classical frequency domain techniques. Classical controllers in this application are sensitive to variations in the tuning system parameters. Also, these controllers generally fail to provide correct transient response when there is beam in the cavity, since the beam loading changes the transfer function of the system. We have designed a robust and adaptive controller based on sliding mode techniques for a cavity tuning system on the ISIS synchrotron. The techniques are extendable to other systems.

I. INTRODUCTION

The analogue tuning loop used on ISIS RF systems (Figure 1) was unable to provide the required accuracy. Hence a digital feedforward controller based on inverse transfer characteristic of the type shown in Reference 1 was used. The application of such a digital loop has also been proposed for TRIUMF cavities[2]. Stability of such a feedback loop is ensured by exact pole-zero cancellation, which is difficult to achieve in practice. Also the stability cannot be guaranteed at all operating conditions for all the tuning systems due to variations in system characteristics. Ideally, a stand-alone, self-correcting, intelligent feedback controller would be well-suited for the system. Such controllers can be designed in classical frequency domain or with the recently invented, more powerful time-domain approach such as adaptive or variable structure controllers. The advent of new techniques would allow us to include variation in tuning system conditions due to beam loading, since the beam effects on the cavity can be regarded as external disturbance.

The design of the time-domain controllers such as self-tuning or model reference adaptive controllers is not only complex, but the hardware implementation turns out to be more cumbersome. A controller based on variable structure principle such as the sliding mode has all the good features of the adaptive controllers, and the algorithm is not difficult to implement. The controller we have discussed needs information about the description of the transfer function model in terms of time, t, in linear state space form with variables $\{\underline{A}, \underline{b}, \underline{C}, D\}$ as system matrices, $u_i(t)$ the control signal, $y(t)$ the output signal, and $\underline{x}(t)$ the state variable matrix as follows:

$$\begin{aligned} \dot{\underline{x}}(t) &= \underline{A}\underline{x}(t) + \underline{b}u_i(t) \\ y(t) &= \underline{C}\underline{x}(t) + Du_i(t)\,. \end{aligned} \tag{1}$$

However, it is not very difficult to obtain system matrices once the frequency response characteristic is measured. Several techniques are shown in Reference 3. Since the controller is inherently insensitive to disturbance and to parameter variation – unlike the classical PID, phase lag, phase lead and state feedback – we expect to achieve good performance when the beam is injected in the machine. At the end of this paper a schematic layout of an analogue implementation is shown which can be interfaced to Figure 1 to the output of the function generator.

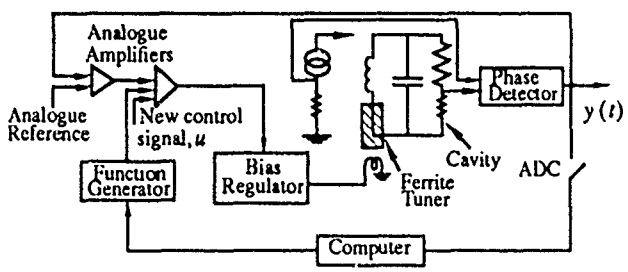


Figure 1. RF system representing cavity tuning loops.

II. SYSTEM MODEL

The cavity tuning model shown in Reference 3 for Figure 1 was obtained in z-domain and was of the 7th order. It was then converted to continuous time-domain state-space form of the type shown in Equation 1 by using a sampling period of 10μs which was used at the time of measurement. Since we observed some pole-zero cancellation in the 7th order model of the system, we used the standard model order reduction routines of Reference 4 by looking at the weightage on the Gramian vectors. Finally, we arrived at a 3rd order state space model. To check the validity of the 3rd order model a step response of the 7th order discrete domain transfer function model was compared with the reduced 3rd order continuous domain state space model. The agreement was found to be very good. Hence the controller with a reduced 3rd order model was designed.

III. SLIDING-MODE CONTROLLER DESIGN

The system Equation 1 can be rewritten with the individual elements and is shown in Equations 2 and 3 below.

$$\begin{bmatrix} \dot{x}_1 \\ \dot{x}_2 \\ \dot{x}_3 \end{bmatrix} = \begin{bmatrix} a_{11} & a_{12} & a_{13} \\ a_{21} & a_{22} & a_{23} \\ a_{31} & a_{32} & a_{33} \end{bmatrix} \begin{bmatrix} x_1 \\ x_2 \\ x_3 \end{bmatrix} + \begin{bmatrix} b_1 \\ b_2 \\ b_3 \end{bmatrix} u_i(t) \tag{2}$$

*Operated by Universities Research Association, Inc.,
U.S. Department of Energy, Under Contract No. DE-AC02-89ER40486.

U.S. Government work not protected by U.S. Copyright.

$$y(t) = \begin{bmatrix} c_1 & c_2 & c_3 \end{bmatrix} \begin{bmatrix} x_1 \\ x_2 \\ x_3 \end{bmatrix} + Du_i \qquad (3)$$

The variables x_1, x_2 and x_3 are time varying functions called internal states of the system. In our cavity tuning problem they can be estimated. A brief discussion of this is given later. These estimated states are used in the controller to obtain the control signal. The control signal u_i can be assumed to have two inputs, u and Δu_d, where u is the signal generated by the controller and Δu_d the input disturbance:

$$u_i(t) = u(t) + \Delta u_d(t) \; . \qquad (4)$$

Using the estimated states a time dependent sliding variable S is defined as follows:

$$S = \begin{bmatrix} g_1 & g_2 & g_3 \end{bmatrix} \begin{bmatrix} x_1 \\ x_2 \\ x_3 \end{bmatrix} = g^T \underline{x} \; . \qquad (5)$$

The components g_1, g_2 and g_3 of the matrix g^T are assumed to be known at this stage. However, later in this paper we discuss briefly a method to calculate them. To design a stable feedback loop we need to choose a suitable, positive definite Lyapunov function. In this particular case we can use the function as

$$V(t) = \frac{1}{2} S^2 \; . \qquad (6)$$

For global stability the Lyapunov function, V, must be positive definite, and its first derivative, $\dot{V}$, must be less than zero. In other words,

$$S\dot{S} < 0 \; , \qquad (7)$$

where $\dot{S}$ is the time-derivative of Equation 5 and is given by

$$\begin{aligned} \dot{S} &= g^T \{ \underline{A}\underline{x} + \underline{b}(u + \Delta u_d) \} \\ &= g^T \begin{bmatrix} \underline{a}_1 & \underline{a}_2 & \underline{a}_3 \end{bmatrix} \underline{x} + g^T \underline{b} (u + \Delta u_d) \\ &= \begin{bmatrix} \alpha_1 & \alpha_2 & \alpha_3 \end{bmatrix} \begin{bmatrix} x_1 \\ x_2 \\ x_3 \end{bmatrix} + \beta (u + \Delta u_d) \; , \end{aligned} \qquad (8)$$

with

$$\underline{a}_1 = \begin{bmatrix} a_{11} \\ a_{21} \\ a_{31} \end{bmatrix}, \quad \underline{a}_2 = \begin{bmatrix} a_{12} \\ a_{22} \\ a_{32} \end{bmatrix}, \quad \underline{a}_3 = \begin{bmatrix} a_{13} \\ a_{23} \\ a_{33} \end{bmatrix}, \quad \begin{aligned} \alpha_i &= g^T \underline{a}_i \\ i &= 1, 2, 3 \\ \beta &= g^T \underline{b} \; . \end{aligned} \qquad (9)$$

We can split the parameters, α_1, α_2, α_3, and β into the nominal parameters, α_1°, α_2°, α_3°, and β° and unknown parameters, $\Delta\alpha_1$, $\Delta\alpha_2$, $\Delta\alpha_3$, and $\Delta\beta$ as follows:

$$\begin{aligned} \alpha_i &= \alpha_i^\circ + \Delta\alpha_i \quad \Big| \quad i = 1, 2, 3 \\ \beta &= \beta^\circ + \Delta\beta \; . \end{aligned} \qquad (10)$$

The nominal parameters were calculated using the measured system matrices $\{\underline{A}, \underline{b}\}$ and the matrix g^T of the controller The unknown parameters are associated with the amount of system uncertainties excluding the disturbance signal. Also, let the control law, u, calculated by the controller, be divided into two parts: the continuous part, u_c, and the switching part, u_s. The continuous part will hold the tuning phase error zero under ideal plant conditions; at the same time the switching part will drive the phase error zero whenever there is uncertainty. Thus

$$u = u_c + u_s \; . \qquad (11)$$

The control signals u_c and u_s are designed such that the Lyapunov stability condition dictated by Equation 7 is satisfied under the normal operating conditions. Also the control signals must not exceed the upper limits set by the bias regulator. Since u_c is used as the control function for the continuous part, we can group all the nominal parameters as follows:

$$u_c = -\frac{1}{\beta^\circ} \sum_{i=1}^{3} \alpha_i^\circ x_i \; . \qquad (12)$$

Substituting Equations 10, 11 and 12 into Equation 8 and rearranging, we obtain

$$\dot{S} = \beta u_s + \beta \Delta u_d + \sum_{i=1}^{3} \left(\Delta\alpha_i - \frac{\Delta\beta}{\beta^\circ} \alpha_i^\circ \right) x_i \; . \qquad (13)$$

The switching part of the control signal, u_s, is arranged with gains to overcome the uncertainties as follows:

$$u_s = -[k_1|x_1| + k_2|x_2| + k_3|x_3| + k_0] \, \mathrm{sgn} S \; . \qquad (14)$$

The function $\mathrm{sgn}S$ in Equation 14 is the *signum* function which has a value either +1 or -1 when $S \geq 0$ and $S < 0$, respectively. The constants, k_0, k_1, k_2, k_3 are selected such that Equation 7 is always satisfied. Clearly, with the following conditions on the gains, we can keep the loop stable if

$$\begin{aligned} k_i &> sup \left| \frac{1}{\beta} \left(\Delta\alpha_i - \frac{\Delta\beta}{\beta^\circ} \alpha_i^\circ \right) \right| \quad i = 1, 2, 3 \\ k_0 &> |\Delta u_d| \; . \end{aligned} \qquad (15)$$

The abbreviation *"sup"* used in Equation 15 is pronounced as *"supremum"* to represent the maximum value of the function. If the system parameters $\{\underline{A}, \underline{b}\}$ were accurately measured and if the variation due to temperature or other unknown effects is ignored, then the gains k_1, k_2 and k_3 can be set to zero. Whereas the gain k_0 is still required to handle the input disturbance, Δu_d, when the beam is turned on. The choice of these gains gives different weightings to the cost of control. Precise values can be set by actually working on the system. Also, when the feedback gains, $k_0 \rightarrow k_3$, are zero in Equation 14, then u_s is zero. Under this condition the control signal is $u = u_c$, obtained by solving Equation 12, which appears like a linear state feedback controller. Since this type of controller may give oscillatory control signal, a saturation function could be defined in place of $\mathrm{sgn}S$. It is defined with a constant δ such that $\mathrm{sgn}S = 1$ for $S > \delta$, $\mathrm{sgn}S = -1$ for $S < -\delta$, and $\mathrm{sgn}S = S/\delta$ for $\delta \geq S \geq -\delta$.

IV. ESTIMATION OF THE STATES

From the previous section we noted that the required control signal, u, can be generated by solving Equations 5, 11, 12, and 14. We can do this provided the internal states, x_1, x_2 and x_3 are known. In our problem they must be estimated. The state estimator is known as the "observer". We use the output signal, $y(t)$, and the input signal, $u_i(t)$, and obtain a standard Luenberger observer. A simple design technique is discussed by

Kailath[5]. Hence, we simply quote the equation below:

$$\dot{\hat{x}} = \underline{A}\hat{x} + \underline{b}u_i + \underline{m}[y - \underline{C}\hat{x}] - \underline{m}Du_i \qquad (16)$$

Where, $\hat{x}$ is the estimated state vector used to calculate the sliding variable, S, and $\underline{m}$ is the feedback gain vector. This gain vector is obtained from the system parameters, $\{\underline{A}, \underline{C}\}$, and an arbitrary set of eigenvalues[5]. As a rule of thumb, the eigenvalues of the observer are chosen such that the observer states converge to actual values almost 10 times faster than the controller eigenvalues corresponding to g_1, g_2 , and g_3. For designing the observer we have assumed that the input signal, $u_i(t)$, is measurable, meaning the disturbance signal, Δu_d, is accessible. In other words, Equation 16 will not estimate the states accurately when the beam comes on and hence may give problems, especially when the eigenvalues are chosen close to the controller. Further work is underway to overcome the observer defects.

For overall stability the eigenvalues of the observer and controller must be negative. The g matrix for the controller is selected by trial and error method or by using eigenvalue assignment technique shown in Reference 6. In both cases the equivalent closed loop system, described by

$$\dot{x} = [\underline{A} - \underline{b}(g^T\underline{b})^{-1}g^T\underline{A}]x, \qquad (17)$$

must have negative eigenvalues for stability. Equation 17 is obtained by substituting the condition[7] $\dot{S} \equiv 0$ in Equation 8 and using the resulting expression for the equivalent control signal, u_i, in Equation 1. When $\dot{S} \equiv 0$ one of the eigenvalues of Equation 17 is zero[6]. Hence, for our system we specify only two eigenvalues, λ_1 and λ_2, and ignore the third. The g matrix is then obtained from the following equation:

$$g^T = q^T\alpha(\underline{A}), \qquad (18)$$

where the function $\alpha(\underline{A}) = (\underline{A} - \lambda_1)(\underline{A} - \lambda_2)$, and the matrix, q^T is equal to the last row of the inverse of the controllability matrix of the system (Equation 1), and the symbol T is used to signify the tranpose of the matrix.

V. IMPLEMENTATION AND SIMULATION

The feedback loop can be implemented, as always, in two ways, using analogue or digital circuits. A schematic layout for analogue implementation is shown in Figure 2. The controller implementation would require a multiplexer to determine the sign change in the sliding variable. For digital implementation, a DSP chip, TMS320C30, from Texas Instruments with a 32-bit floating point multiplication and accumulation time of 60ns can compute the control signal in under 5μs, in real time.

We have simulated the loop performance with the controller at 5μs sampling rate in Figure 3, with a step disturbance signal of $\Delta u_d = +0.1$ V between 5 ms and 10 ms. Various parameters are shown in Figure 3. A saturation function with $\delta = 1 \times 10^{-6}$ is used in place of sgn$S$. Clearly the output transients are controlled under less than 0.4°. At this stage it is recalled that the switching part of the control signal must not be made zero; otherwise the output of the system will become unbounded. This is because one of the eigenvalues of Equation 17 is close to zero. Also, the controllability matrix of the system is observed to be very close to singularity. Hence all the feedback parameters must be carefully chosen.

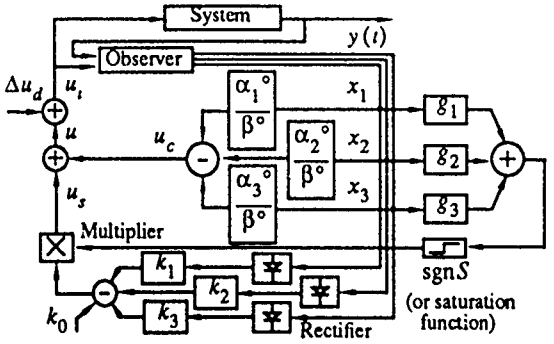
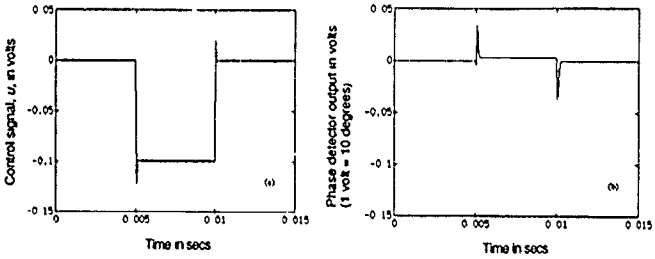


Figure 2. Analogue implementation of the sliding mode controller



$$\lambda_{Observer} = [-25\ -50\ -75] \times 10^4$$

$$\lambda_{Controller} = [-25\ -250\ 0] \times 10^3 \qquad g = \begin{bmatrix} 5.61223 \\ 19.90693 \\ -1.02001 \end{bmatrix} \times 10^{-3}$$

$$k_0 = 0.11, k_1 = 200, k_2 = 100, k_3 = 200$$

Figure 3. (a) Control signal, u , and (b) the phase error signal, y, under a step disturbance, $\Delta u_d = 0.1$ V.

VI. CONCLUSIONS

We have shown a modern control technique to design a robust feedback controller such as the "sliding-mode" starting from an experimental "Bode diagram" of the system. We retain all the simplicity of the state feedback controller and add robustness to handle variation in tuning errors due to beam loading or other uncertainties on the system. Although the controller is robust, a non-robust state estimator may give problems unless the eigenvalues are carefully selected.

VII. ACKNOWLEDGEMENTS

Authors wish to thank C.M. Kwan from U.T. Arlington for his contribution to the simulation.

VIII. REFERENCES

[1] L.K. Mestha, "Digital Feedback Control for Radial Beam Position", RAL Report No. RAL-84-031, April 1984.

[2] S.T. Craig et al., "RF Field Control for Kaon Factory Booster Cavities", Chalk River Lab., AECL-10312, Nov. 1990.

[3] L.K. Mestha et al., "Application of System Identification Techniques to an RF Cavity Tuning Loop", European Particle Accelerator Conference, Nice, June 12-16, 1990.

[4] MATLAB User's Guide, The Math Works Inc., USA, 1989.

[5] T. Kailath, *Linear Systems*, Prentice Hall, Inc, 1980.

[6] K.S. Yeung et al., "An Eigenvalue Assignment Scheme for the State Feedback and The Sliding Mode Feedback of Multivariable System", *IEEE Trans on Automatic Control* (Under Review).

[7] U.Itkis, *Control Systems of Variable Structure*, John Wiley & sons, New York, 1976.

Accelerating Cavity Development for the Cornell B-Factory, CESR-B*

H. Padamsee, P. Barnes C. Chen, W. Hartung, M. Hiller[1], J. Kirchgessner, D. Moffat, R. Ringrose, D. Rubin, Y. Samed, D. Saraniti, J. Sears, Q. S. Shu and M. Tigner

Laboratory of Nuclear Studies, Cornell University.

ABSTRACT

To achieve luminosities of 30-100 times CESR, 1-2 amps of current must be stored. A CESR B-factory [1] parameter list calls for 50 MV for two rings, to be supplied by 16 cells operating at 10 MV/m gradient. With a new cell shape, the impedances of the dangerous higher order modes (HOM) are drastically reduced. All HOMs modes propogate out of the cavity via the beam pipe, which is specially shaped. This allows HOM power couplers to be placed completely outside the cryostat. A ferrite absorber on the beam pipe lowers all Qs to ~100, which is sufficient to avoid multi-bunch instabilities without feedback systems. A waveguide input coupler on the beam-pipe provides Qext as low as $5x10^4$, with a C- slot shaped iris that has a negligible effect on the cavity loss parameter.

THE CASE FOR SUPERCONDUCTING RF CAVITIES

To achieve the desired currents in a B-factory, it will be essential to lower the impedance of the ring. RF cavities are a chief source of impedance. The advantage of using SRF is that higher gradients are possible than with room temperature RF, allowing a substantial reduction in the number of cells and their corresponding impedance. There is a substantial savings in capital cost from the smaller RF intallation which need only provide the beam power, the cavity dissipation being negligible. Corresponding savings in operating cost are realized. A quantitative comparison between a normal conducting RF system for a machine such as CESR-B and the SRF system envisioned is presented in Table 1.

Here we consider the use of single cell copper cavities with the same cell design as the superconducting cells, to properly compare the impedances presented. A maximum operating gradient of 1 MV/m for copper cavities is assumed, based on the need to keep the overall cell dissipation below 100 Kwatts/cell (10 watts/cm^2). NC cavities presently used in storage rings dissipate between 15-60 kWatts/cell [2]. The comparison shows that the SRF version has 10 times fewer cells (impedance), a 13 Mwatt RF power installation savings, and a 22 Mwatt wall plug power saving. The 2 Kwatt refrigerator needed in the SRF version would absorb < 1/4 of transmitter capital cost savings, and consume < 1 Mwatt of wall plug power. Today superconducting structures for storage rings TRISTAN, HERA AND LEP reach average gradients over 10 MV/m in acceptance tests. Recently a 5-cell, 500 MHz cavity reached 16 MV/m accelerating gradient[3].

Table 1 : Comparison between a normal conducting and superconducting RF system for the CESR-B factory

	LER	HER
Voltage (MV)	12	35
Beam Power (MW)	1.5	4.5
Normal Conducting		
Gradient (MV/m)	1	1
No. of cells	40	117
Cavity dissipation (MW)	3.4	9.8
Superconducting		
No. of cells	4	12
Gradient (MV/m)	10	10
Cavity dissipation (watts) ($Q = 1x10^9$)	408	1224

While this experience shows that the desired gradient of 10 MV/m is feasible, the maximum beam current stored has been less than 100 mA. Our design concept faces the challenges to advance the capability of SRF cavities to handle amps of current. A new cell shape has been chosen to reduce the impedances of higher order modes and to faciliate power extraction and damping. New fundamental power couplers are considered to increase the input power capability from the present-day maximum of 100 kwatt to at least 400 kwatts. New higher mode couplers are considered to increase the power handling capability from 100 watts to 10 kWatts. To avoid multi-bunch instabilities in face of the tight bunch spacing of 10 nanosecs, higher modes need to be heavily damped to Qs < 100.

CELL SHAPE.

Fig. 1 compares the new cell shape with the normal conducting cell shape presently used in CESR, and with the superconducting cavity shape that will be used for LEP-II. A major advance provided by the new shape is that the impedance of the most dangerous HOMs have been reduced by factors much lareger than the drop in fundamental R/Q. It should be noted that this shape is significantly more open than the existing superconducting cavity shapes.

*Supported by the National Science Foundation with Supplementary Support from the US-Japan Collaboration.

[1]Babcock and Wilcox, Lynchburg, Va.

0-7803-0135-8/91$01.00 ©IEEE

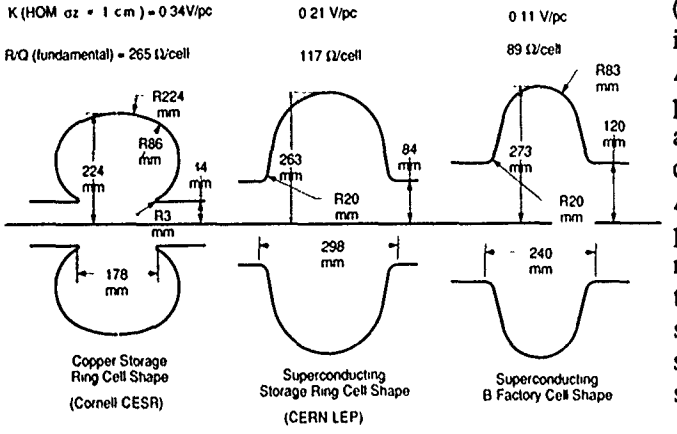


Fig. 1 Comparsion of storage ring cell shapes

Table 2 lists the properties of the fundamental mode as computed by SUPERFISH.

Table 2 : Properties of the fundamental mode.

Frequency	500	Mhz
R/Q	89	Ohms/cell
k(fund.)	0.07	V/pC
Emax/Eacc	2.5	
Hmax/Eacc	52	Oe/MV/m
Dissipation	102	Watts/cell

(Q =1x10^9, Eacc= 3 MV/cell)

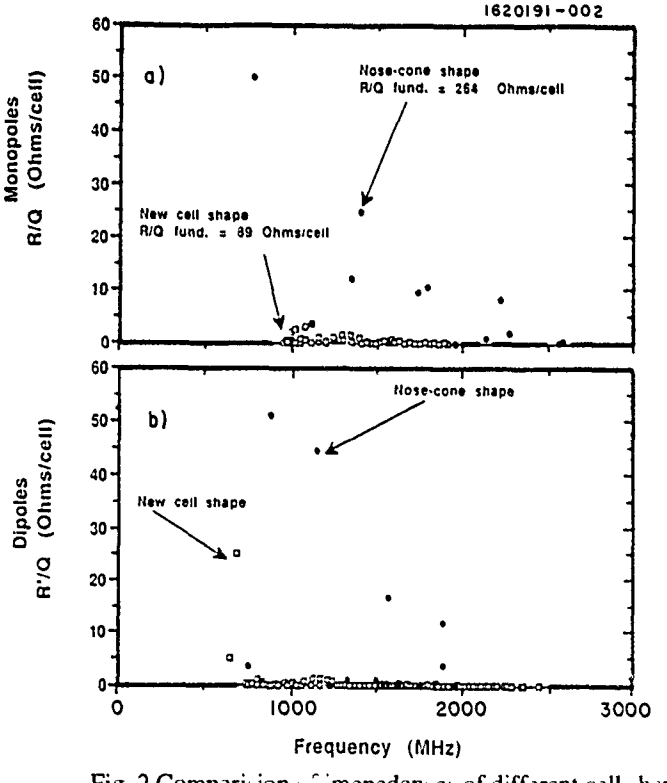


Fig. 2 Comparision of impedances of different cell shapes

Fig. 2 compares the R/Qs of CESR NC cell shape with the proposed CESR-B cell shape. For longitudinal HOMs (a), and all but two transverse modes (b), the highest impedance has been reduced by more than a factor of 10. Another major advance is that all longitudinal HOMs propagate out of the cavity via a round beam pipe. This allows all HOM coupling devices to be placed outside the cryostat, greatly simplifying power extraction and damping. All but the two lowest frequency transverse HOMs also propagate out the beam pipe. To extract the two "trapped" modes, we propose, following a new idea of Kageyama[4], to use a fluted beam pipe of cross-section similar to that shown in Fig. 3. Both calculations and model measurements show that the rectangular waveguides formed by the flutes serve to guide out the troublesome transverse modes.

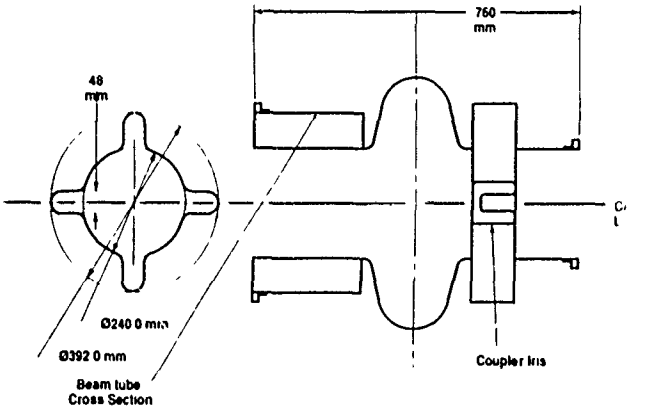


Fig. 3 Fluted beam pipe and input coupler geometries

FUNDAMENTAL COUPLER AND WINDOW

In comparison to a coaxial coupler, a waveguide has low power densities and needs only outer wall cooling, The overall size and static heat load is reduced by using a half-height guide. A design of the coupling iris between the cavity and the waveguide has been developed (see Fig. 3) Bench tests on a 3000 MHz copper model show QL as low as 5x10^4. A progress report on the window is given in another paper [5]. A 500 MHz prototype Nb cavity/coupler and high power window have been ordered from industry.

HIGHER MODES

Calculated Q values < 70 were found for a representative set of highest R/Q (max 3.5 Ω/cell) longitudinal modes. For this, a 15 cm absorptive band with RF surface resistance 10^4 times copper is placed on the beam pipe. A promising absorbing material, called Ferrite-50, possessing the desired properties has been found. A complete discussion of its properties and mode damping success is presented in another paper [6]. A factor of 6 smaller scale copper cavity model (3 GHz fundamental frequency) was equipped with Ferrite-50 beam tube sections.

Strong damping (Q < 100) was observed for all discernable modes (longitudinal and transverse). Fig. 4 shows typical results. Calculations using the program ZAP show that this degree of damping will be sufficient to avoid multi- bunch beam instabilities without the use of a longitudinal feedback system.

Calculated Q expected from a beam pipe absorber for the transverse propagating modes were < 75. The two trapped modes have quite high impedances (Fig. 2b). A model 3 GHz cavity was equipped with a fluted beam tube at one end, and the Q of the trapped modes was found to be lowered to <200. ZAP calculations show that some transverse feedback will still be required mainly to deal with the resistive wall instability from the impedance of the vacuum chamber, aggravated by the ferrite sections.

At 1 cm bunch length, with HOM loss factor of 0.1 V/pC, the power loss will be 0.8 Kwatts/cell and 4.3 kWatts/cell for the high and low energy rings. In the resonant case, 1.5 kWatts is expected for the worst mode. The image current wall losses are estimated to be < 1 kwatt per section.

Figure 5 shows the cavity and cryostat with input coupler, and higher mode absorber concepts.

REFERENCES

[1] M. Tigner, this conference
[2] D. Rubin, AIP Conf. Proc. 214, Ed. A.M. Sessler, 235 (1990)
[3] Y. Kojima, this conference.
[4] Kageyama, KEK B-Factory Workshop, Oct. 1990
[5] J. Kirchgessner, et al, this conference.
[6] D. Moffat et al, this conference.

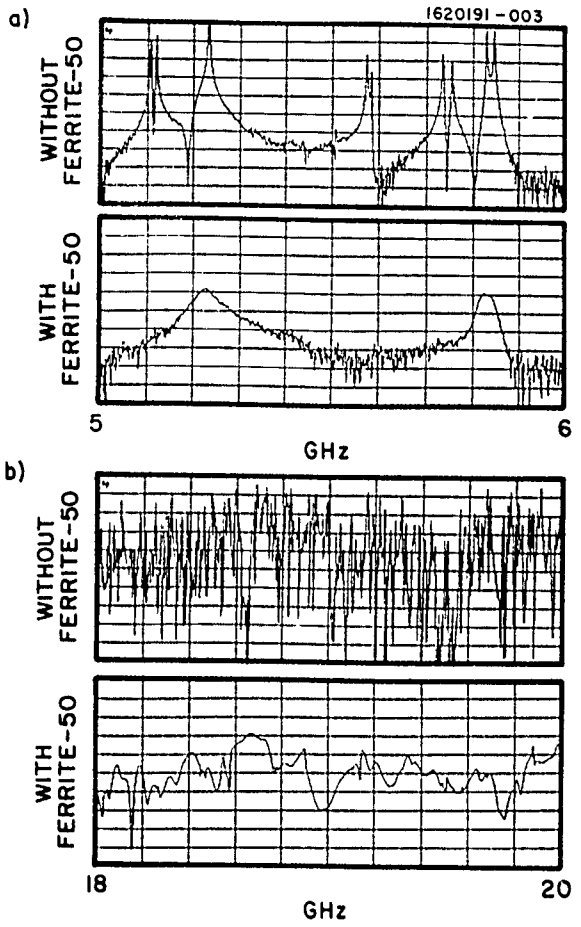


Fig. 4 Damping of higher order modes measured

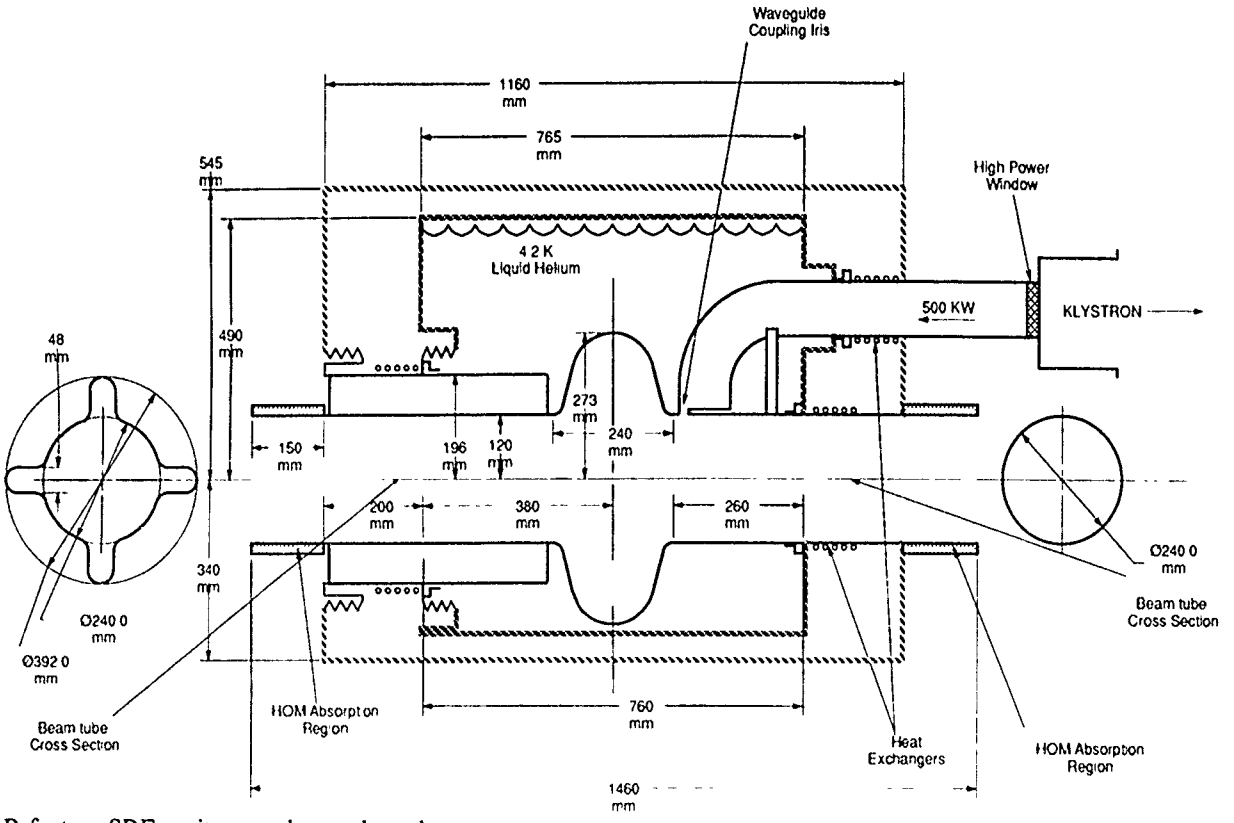


Fig. 5 B-factory SRF cavity, couplers and window concept

Beam impedance measurements.Coaxial Wire Method.

Giuseppe Di Massa*, Maria Rosaria Masullo
Istituto Nazionale di Fisica Nucleare - sez. di Napoli
Mostra d'Oltremare, Pad. 20 - 80125 Napoli, Italy.
* Dip. Elettrico Univ. della Calabria - 87036 Rende (CS), Italy.

Abstract

The measurement of coupling impedance of accelerator vacuum chamber components by wire method using a synthetic pulse technique is presented. A standard instrumentation, like a Network Analyzer able to work in the microwave region, is used in order to perform measurements in frequency domain. An off-line Fast Fourier Transform can be used to treat the data. A suitable time-frequency de-embedding technique is proposed. Experimental results are presented.

I. INTRODUCTION

A Φ Factory machine, DAΦNE [1], has been proposed at the National Lab. of INFN of Frascati - Italy- (a general talk is presented elsewhere at this conference). The goal of this accelerator is to reach a luminosity of 10^{32} cm^{-2} sec^{-1} at 510 MeV. To achieve this requirement high currents, short bunch lengths, long lifetimes and high stable beam are required. All these requirements are strictly related to the design of the whole machine and they can be affected by intrabeam scattering, μ-wave instabilities, coupled bunch instabilities, whose thresholds are linked to the vacuum chamber geometry, to RF cavity properties depending on the interaction of the bunch with the surrounding structure (coupling). A problem of great importance is the controlling of the machine impedance to be kept at a low value(under 5Ω). This means that all the accelerator components like kickers, bellows, etc. that can give a big contribution to the total impedance, have to be carefully designer and tested before the installation. From this the necessity of a laboratory method to measure impedance follows, it has to be used as a feedback on the design of the machine elements.

We propose to use the coaxial wire method [2] instead of the frequency perturbation one [3], because of the low quality factor (Q) linked to the low impedance to be measured in our components. The used technique transforms the Device Under Test [DUT] in a coaxial line by putting in a central wire in order to measure the transmission through the line.

The method was proposed by Sands and Rees [2] to measure the energy loss of a stored beam to a cavity. The basic idea is that a short current pulse, travelling on a thin wire can simulate a particle bunch and if they have the same time shape then the energy lost in both cases is the same. Some examples of bench measurements of energy loss and machine component impedance are reported in [4,5,6].

We performed our measurements in frequency domain where the current technology allows obtaining higher precisions. The transmission through the DUT can be affected by discontinuities met by the pulse along the wire.

In order to minimize the presence of unwanted reflections matching sections are used to maintain as much as possible a constant impedance value till the DUT.The data analysis is than carried in the time domain where is possible to identify the unwanted reflections and to eliminate them by filtering. The new signal is then transformed again in the frequency domain through a Fourier Transform. It has to be mentioned that the goodness of this filtering, called time gating, and de-embendding the main pulse is linked to the right geometry of the matching section and spacers. The presence of spacers is needed in order to separate the main pulse from the others and to "cut" the signal in the time domain without taking away important informations.

II. IMPEDANCE CALCULATION

A current pulse $\mathbf{i_1(t)}$ is fed into a cylindrical coaxial structure (reference pipe) with characteristic impedance $\mathbf{Z_L}$ (Fig.1a). The energy contained in the pulse is given by

$$U_1 = \int_{-\infty}^{+\infty} Z_L \, i_1^2(t)\, dt \qquad (1)$$

The same pulse is fed into the structure with the testing object that replaces a part of the coaxial line (Fig. 1b). Assuming that the pulse is only slightly modified by the testing object, i.e. $\mathbf{i_2(t)=i_1(t) + \Delta t}$, the energy contained in the pulse so perturbed can be written as:

$$U_2 = \int_{-\infty}^{+\infty} Z_L \, i_1^2(t)\, dt + \int_{-\infty}^{+\infty} 2\, Z_L \, i_1(t)\, \Delta t \, dt \qquad (2)$$

where it is assumed (small perturbations)

$$| \Delta i(t) | << | i(t) | \qquad (2a)$$

Comparing the energy lost by the pulse, $\mathbf{U = U_1 - U_2}$, with the expression of the energy loss of a bunch of particles

$$U = q \int_{-\infty}^{+\infty} W_b \, I(t)\, dt \qquad (3)$$

it can be derived that the signal difference $\Delta i(t)$ times $(-2\, Z_L/q)$ is equal to the wake potential $\mathbf{W_b\,(t)}$ of a bunch of particles with the same shape

$$W_b(t) = -2\,\frac{Z_L}{q}\,\Delta i(t) \qquad (4)$$

0-7803-0135-8/91S01.00 ©IEEE

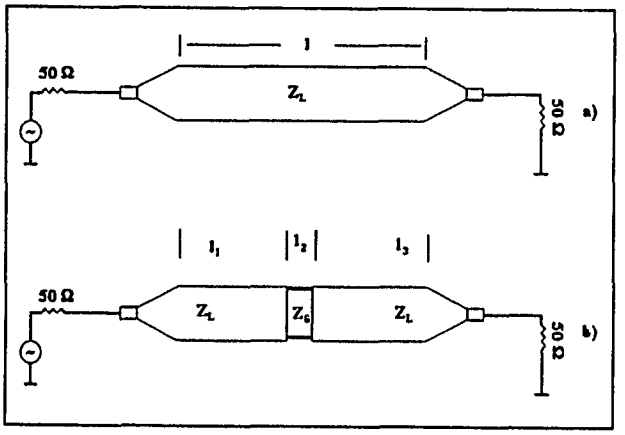


Figure 1- Schematic diagram of experimental set-up: a) reference pipe; b) test structure.

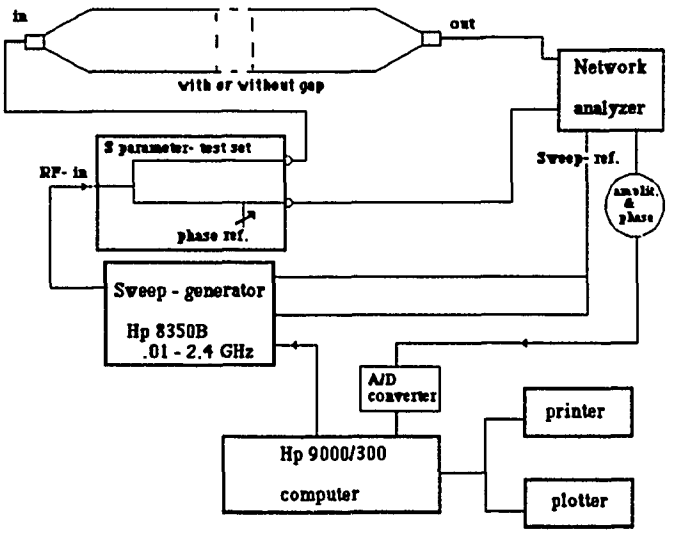


Figure 2 - The layout of the set-up used for the measurement.

Transforming eq. (4) into the frequency domain yields

$$Z(\omega)\, I_1(\omega) = -2\, Z_L\, [I_1(\omega) - I_2(\omega)] \qquad (5)$$

The eq. (5) suggests to perform the measurement directly in frequency domain (Fig. 1) measuring the scattering parameter $S_{12}(w)$, that gives the transmission coefficient. According to eq. (5) the longitudinal coupling impedance is given by:

$$Z(\omega) = 2\, Z_L \frac{S_{12} - S_{12}^{ref}}{S_{12}^{ref}} \qquad (6)$$

where S_{12} and S_{12}^{ref} stand for the structure with the discontinuity and for the reference pipe respectively.

It has to be pointed out that the use of small perturbation approximation (eq. 2a) is better satisfied the thinner is the central wire (Z_L increases), but to keep $\Delta i(t)$ at a measurable value the wire cannot be reduced too much. A good compromise needs [2,7].

III. EXPERIMENTAL RESULTS.

A first measurement was performed on a 10 mm gap in a copper beam pipe. Two little metallic strips are used to assure the electric continuity between the two pipe pieces. The total length, tube plus gap, is 477.6 mm, with a diameter of 69 mm. Two matching cones, 500 mm long, are used in order to slowly adapt the 69 mm diameter pipe to an N connector. A .95 mm wire is stretched in the center of the tube. A line with the same dimensions, put between the two cones, is used as reference pipe.

The layout of the set-up used for the measurement is reported in Fig. 2. For the data acquisition and for the control of the Sweep oscillator we've used an Hp 9000/300 computer connected to a measurement system (Network Analyzer (N.A.), Sweep oscillator , etc.) trough an Hp-IP bus. The signals (Amplitude and Phase) from the N.A. are sent to a A/D convert and read from the computer for the subsequent analysis. Transmission measurements are performed in the frequency domain over some range of frequency values. An inverse Fourier Transform is performed on the frequency-domain data. A train of pulses is then observed in the time-domain trace. These pulses are due to multiple reflections from mismatches in the matching section and at the test device. Then the first pulse is isolated by gating (is kept) and is Fourier-transformed to yield a frequency response with the beating caused by multiple reflection removed.

In fig. 3 the amplitude of the transmission coefficient, S_{12}^{ref}, for the reference pipe (solid line) is compared to the transmission coefficient, S_{12}, of the gap discontinuity (dashed line). The phase of the signals are dropped due to lack of space. In fig. 4 and 5 the time domain transforms of the detected signals are reported, they clearly show multiple reflections due to mismatches in the feeding structure. In fig. 6 the frequency domain transmission coefficients S_{12} and S_{12}^{ref} obtained after a time domain gating of 4 nsec around the main pulse, are reported. Finally, in fig. 7, according to (6) and using the gated signals, the real and imaginary parts of coupling impedance $Z(\omega)$ are depicted. Instead of using spacers, when the structure assumes too big dimensions, a numerical expansion technique, like Chirp-z, can be used. Another possibility is to use a more sophisticated technique of de-embedding [8]. The two mentioned techniques are particularly useful when the impedance of large object have to be measured. Experimental verifications of these techniques are in progress.

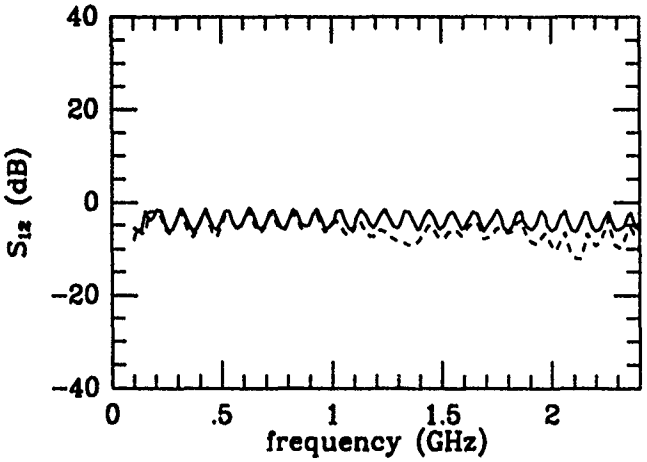


Figure 3 Transmission coefficient. Reference pipe (solid) gap-discontinuity (dashed)

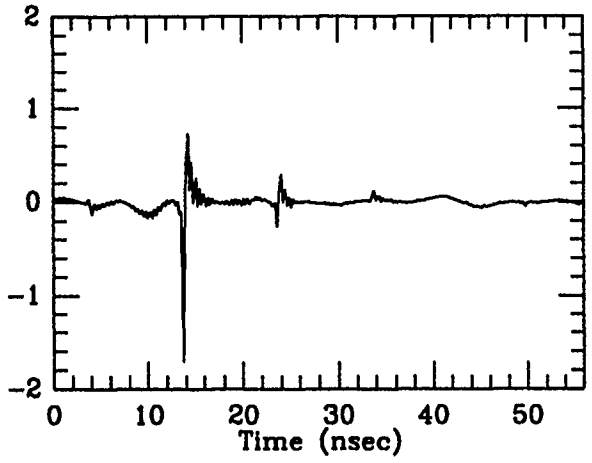


Fig. 4 Time domain transform relevant to reference pipe.

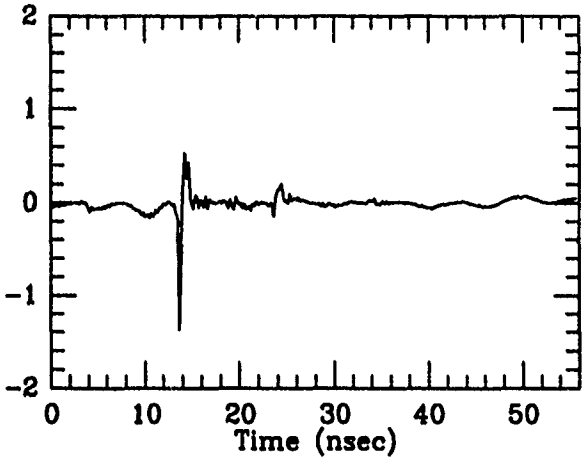


Fig. 5 Time domain transform relevant to gap discontinuity

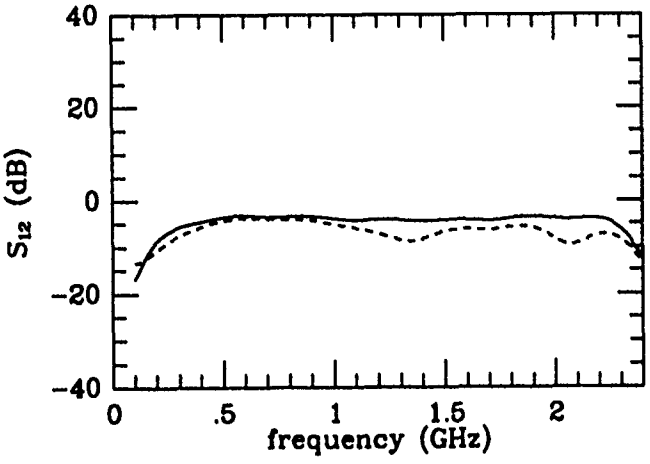


Figure 6 Transmission coefficient after time domain gating Reference pipe (solid), gap-discontinuity (dashed).

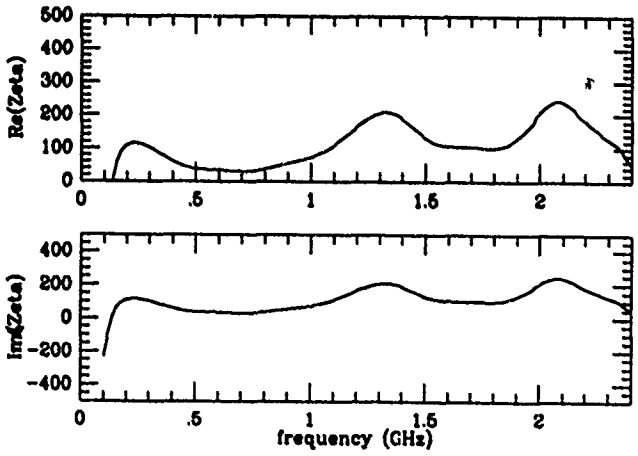


Figure 7 Longitudinal impedance for the gap discontinuity

V. REFERENCES

[1] *PROPOSAL FOR A Φ-FACTORY*, LNF-90/031(R),Frascati, Italy, 1990.

[2] M. Sands, J. Rees: "A bench measurement of the energy loss of a stored beam to a cavity", PEP-95, 1974.

[3] L.C. Maier, J.C. Slater, "Field strength measurements in resonant cavities", Journal of Applied Physics, Vol. 23, pp.68, 1952.

[4] F. Caspers: "Beam impedance measurement by wire method using a synthetic pulse technique ", IEEE Trans. Nucl. Science, vol. NS_32, pp. 1914, 1985.

[5] L.S. Walling, D.E. McMurry, D.V. Neuffer, H.A. Thiessen, "Transmission-line impedance measurements for an advanced hadron facility", Nuclear Instruments and Methods in P.R., A281, pp. 433-447, 1989.

[6] G. Di Massa, M.R. Masullo, "Beam impedance measurements using a synthetic pulse technique", in EPAC European Particle Accelerator Conference, Nice, France,June 1990.

[7] H. Hahn, F. Pedersen: " On coaxial wire measurements of the longitudinal coupling impedance", BNL-50870, Brookhaven, USA, 1974.

[8] G. Gronau, I. Wolff, "A simple broad-band device de-embedding method using an automatic network analyzer with time domain option", IEEE Tran. on Microwave Theory and Tec., Vol. 37, pp. 479-483, March 1989.

A Simple Analytic Estimate of the Loss Parameter of a Large Tapered Chamber *

James J. Welch, Laboratory of Nuclear Studies, Cornell University, Ithaca, NY 14853

Abstract

When bunch lengths are much smaller than the dimensions of the structure of interest, it is often either impossible or excessively time consuming to obtain estimates of the loss parameter by numerical methods. Furthermore, numerical results are not generally scalable to other bunch lengths, chamber angles or sizes. In the case of a cylindrical chamber very large compared with the bunch length, and tapers on each end, an estimate for the loss parameter may be made by first making some assumptions about the distribution of electromagnetic fields, and then calculating the electromagnetic energy left behind when the bunch leaves the chamber. The result is an analytic formula for the loss parameter, with no free or empirical parameters, that agrees well with TBCI calculations of a 20° tapered chamber. Besides its intuitive appeal, this formula is especially useful in providing design assistance as to the best taper angle, diameter, and chamber lengths.

Electromagnetic Field Model

It is well known that for $\gamma >> 1$ in free space or in a uniform beam tube, the electromagnetic field of a short bunch of electrons is greatly compressed, so that it is almost entirely perpendicular to the direction of motion. The energy stored in the electromagnetic field traveling with the bunch is likewise confined to a thin pancake whose thickness is approximately the bunch length. If we allow the cross section of the beam tube to have a sudden change, the pancake can deform, generate reflections or even thicken, but it must do so within the constraints imposed by the finite speed of light, i.e. causality.

The general vacuum chamber geometry considered here is shown in figure 1. Under certain conditions, the loss parameter is independent of the outer radius R and may be calculated as if the taper continued indefinitely. For a highly relativistic uniform bunch of length Δl, if the path length **ABC** is greater than L by at least Δl, then the perturbation of the electromagnetic fields at **A** cannot reflect off the outer wall at **B** and catch up with the back of the bunch at **C**, where the bunch leaves the chamber. This is only approximately true for a gaussian bunch. Once the bunch re-enters the beam pipe, it is difficult for reflections of the electromagnetic pancake to catch up to the back of the bunch because the group velocity in the beam pipe is substantially less than c, and the walls of the beam pipe have nonzero resistivity. So any energy left in the chamber after the bunch leaves cannot effectively interact with the bunch charge and will be 'lost'. From the geometry in figure 1, it can be seen that the energy lost is approximately independent of the outer radius R if

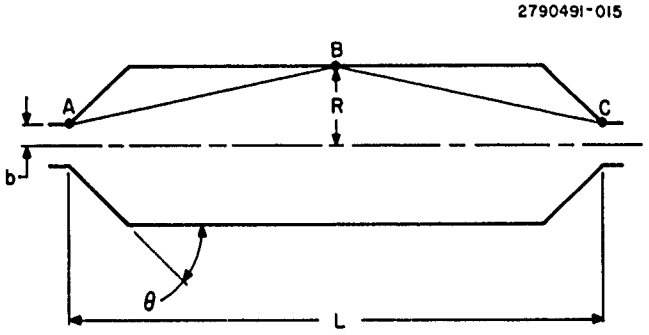


Figure 1: A cylindrically symmetric chamber with tapered ends is shown in this figure. Points **A** and **B** are the beginning and end of the chamber. Point **B** is the point where a signal from **A** could reflect and reach **C** in the minimum time.

$$\sqrt{2(R-b)^2 + L^2} - L > \sigma \qquad (1)$$

Bench measurements showing this effect does indeed occur can be found in [1].

When a short uniformly charged bunch of length Δl and charge ΔQ first enters the taper, we can expect on physical grounds, that the electromagnetic field will look like that shown in figure 2. The shape of the leading edge of the shell is determined by causality. It is a constant distance from point **A** in the section shown in figure 2. For radial coordinate r less than b, the field lines are straight; essentially the same as when the bunch was in the beam pipe. Causality would allow the trailing edge to be further behind the leading edge than Δl shown in the figure. This thickening of the shell could come about from perturbed fields generated at different azimuthal points but at the same longitudinal position as point **A** in figure 2. The effect would be most pronounced for $L \lesssim b^2/\sigma$ and stronger

*Work supported by the National Science Foundation

0-7803-0135-8/91$01.00 ©IEEE

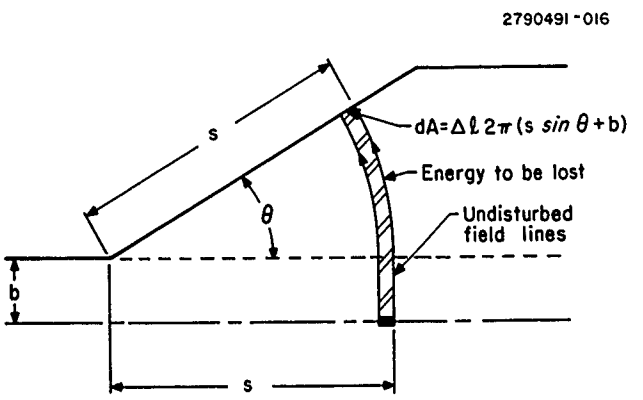


Figure 2: A highly relativistic uniformly distributed bunch of electrons will generate a thin shell of intense electromagnetic field in a shape approximately as shown in this figure.

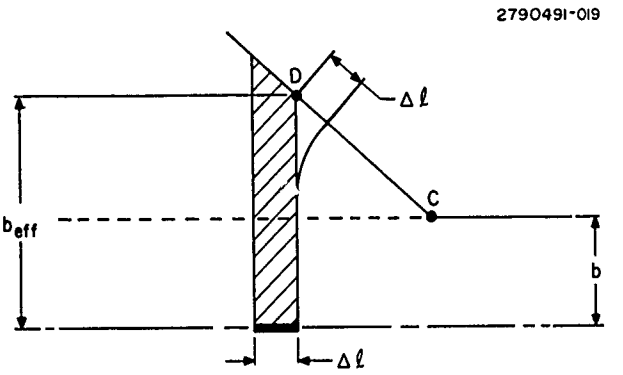


Figure 3: The effective exit radius of the beampipe b_{eff} is defined in this figure as the radius for which a signal from point **D** could catch up with the back of the bunch at point **C**.

for steeper taper angles. We will neglect this effect. By neglecting it, we will overestimate the strength of the electric field in the shell as well as the energy loss.

We will further assume that reflections from the entrance taper, traveling in the opposite direction of the bunch, are not significant. They are not appreciably seen in TBCI calculations, and in principle, could be removed by smoothing the discontinuity at point **A**. If there are no reflections, there should be no field behind the segment of charge.

By applying Gauss's law to the surface bounded by the 'wavefronts' associated with the front and back of the bunch and the outer annular segment of length Δl located at angle θ we have for $r \geq b$,

$$E = \frac{2\Delta Q}{\Delta l(s\sin\theta + b)} \tag{2}$$

The magnetic field can be computed in exactly the same manner using Ampere's law. The total electromagnetic energy in the field volume $r \geq b$ is,

$$\Delta U = \frac{2}{8\pi}\int_0^{\theta} E^2 dV = \frac{2(\Delta Q)^2}{\Delta l}\int_0^{\theta} \frac{d\theta}{(s\sin\theta + b)} \tag{3}$$

A factor of two was included to take into account the magnetic field contribution. The integral can be evaluated for two separate cases, $s > b$ and $s < b$. We are mainly interested in $s > b$ where,

$$\Delta U = \frac{(\Delta Q)^2}{\Delta s}\frac{2s}{\sqrt{s^2 - b^2}}\ln\left(\frac{(s + \sqrt{s^2 - b^2})\tan\theta/2 + b}{(s - \sqrt{s^2 - b^2})\tan\theta/2 + b}\right) \tag{4}$$

A simpler formula can be obtained by making slightly different assumptions about the shape of the electric field lines. When s is large compared with the beam pipe radius b, the 'wavefront' approximately resembles a pure spherical shell with radius s centered on the chamber axis, extending to angle θ. The energy stored in fields for $r > b$ when the particle is at position $s = L$, is calculated by integrating the energy from a minimum angle θ_0, where

$$\theta_0 = \tan^{-1}(b/L) \tag{5}$$

to the taper angle θ. The result of this integration for uniformly charged bunches is,

$$U = \frac{2Q^2}{\Delta l}\ln\left[\frac{\tan(\theta/2)}{\tan(\theta_0/2)}\right] \tag{6}$$

Equation 4 reduces to equation 6 when $b/L << 1$.

Formulae for the Loss Parameter

Notice the field energy stored in the volume $r > b$ grows with increasing s. We will assume that when the beam reaches the far end of the chamber, the field is reestablished in the beam pipe and no further energy is lost. That is, when the bunch position is at $s = L$, the energy in the electromagnetic field for $r \geq b$ is 'scraped off' and can never again interact with the bunch. This assumption is similar to one made by Dôme [3] that for $r < b$ the fields of a point charge in the cavity are the same as they were when the charge was in the beampipe. An analogous argument was made by V.E. Balakin and A.V. Novokhatsky [2] for energy lost by a structure consisting of a sudden reduction in pipe diameter.

Of course, an assumption of pure scraping for $r < b$ precludes diffraction of fields at the exit end of the chamber which would tend not to scrape off so much field energy. Diffraction effects at the exit of the chamber occur if reflections of the front of the pulse from the exit taper (point **D** in figure 3) can reach the beampipe opening before the back of the bunch. A shallow taper will tend to capture much more of the electromagnetic energy. If we replace Δl in figure 3 with σ, then the effective exit radius for gaussian bunches may be defined as,

$$b_{eff} \equiv b + \sigma\cot\theta/2 \tag{7}$$

Taking the formulae for the energy loss of a short uniform bunch, equations 4 and 6, and assuming no thickening of the electromagnetic pulse, we can average over a gaussian longitudinal distribution to arrive at an expression for the energy loss for a gaussian bunch.

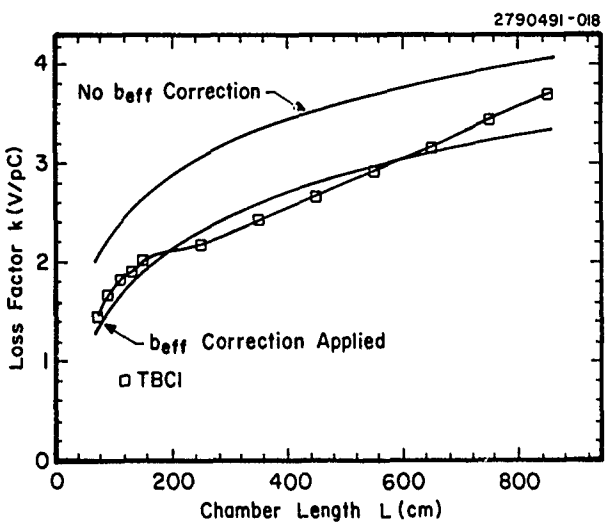


Figure 4: TBCI calculations for a 20 degree tapered chamber with beam pipe radius of 2.5 *cm* are plotted with the equation 6, with and without the modification due to diffraction applied.

Let the charge per unit length be λ and substitute λ for $\Delta Q/\Delta l$ into either equation 4 or 6. The expressions for the energy lost can then be written in the form,

$$dU = \lambda^2 f(L,\theta,b)ds \tag{8}$$

where *ds* is an infinitesimal length of charge. For gaussian bunches,

$$\lambda = \frac{Q}{\sqrt{2\pi}\sigma} e^{-s^2/2\sigma^2} \tag{9}$$

Integrating dU yields,

$$U = \frac{1}{2\sqrt{\pi}} \frac{Q^2}{\sigma} f(l,\theta,b) \tag{10}$$

The loss parameter is defined as $k = U_{loss}/Q^2$ where Q is the total bunch charge and U is the total bunch energy loss. Applying this form to equation 6 yields for a gaussian bunch,

$$k = \frac{1}{\sigma\sqrt{\pi}} \ln\left[\frac{\tan(\theta/2)}{\tan(\theta_0/2)}\right] \tag{11}$$

where all variables are assumed to be written in CGS units. In more commonly used units:

$$k\ [V/pC] = \frac{0.508}{\sigma\ [cm]} \ln\left[\frac{\tan(\theta/2)}{\tan(\theta_0/2)}\right] \tag{12}$$

Comparison with other Estimates

A comparison between TBCI calculations [5] and the analytic formula, equation 6, for 20° tapers is shown in figure 4. With no diffractive correction applied, i.e., $\theta_0 = \tan^{-1}(b/L)$, equation 6 consistently gives a higher estimate of the loss factor, particularly for shorter chamber lengths. Rather surprising is the fact that the difference between equation 6 and the TBCI results is more or less constant with respect to chamber length, indicating the corresponding difference in energy loss occurs only when the bunch enters or leaves the chamber. Figure 4 also shows that, even though for most of the range of chamber lengths calculated, the 'catch up' condition (equation 1) is not obtained, the effects of the reflections are small. When a diffractive correction $\theta_0 = \tan^{-1}(b_{eff}/L)$ is applied, there is constant reduction of the loss of approximately the right magnitude to account for the discrepancy between the TBCI data and the formula.

The other comparison I will make is with an analytic formula derived for 90 degree tapers by Heifets [4]. That is,

$$k = \frac{1}{\sigma\sqrt{\pi}} \ln\frac{\sigma L}{b^2} \tag{13}$$

subject to the restriction $L >> b^2/\sigma$. When $\theta = 90°$ is put into equation 6 and $L >> b$ the difference in k between and equation 6 and equation 13 approaches

$$\frac{1}{\sigma\sqrt{\pi}} \ln\frac{2b}{\sigma} \tag{14}$$

This difference is significant compared with the total loss factor unless $L/b >> b/\sigma$, but this is exactly the limitation given to equation 13.

References

[1] J.N. Weaver, P.B. Wilson, and J.B. Styles, *Bench Measurements of Loss Impedance for PEP Beam Line Components*, SLAC-PUB-2284, March 1979,

[2] V.E. Balakin and A.V. Novokhatsky, Proc. of the 12th Intern. Conf. on High Energy Accel. Fermilab, August 11-16, 1983, p117

[3] G. Dôme, *Wake Potentials of a Relativsitic Point Charge Crossing a Beam-Pipe: An Analytical Approximation* IEEE Trans. Nucl. Sci., vol. NS-32, No. 5, October 1985

[4] S. A. Heifets, *Diffractive model of the high-frequency impedance*, Phys. Rev. D, Vol. 40, No. 9, p 3097, Nov. 1989

[5] The TBCI calculations were performed by C. Chen, and will soon be appearing in a CLNS publication available from Newman Laboratory of Nuclear Science, Cornell University.

Measurements of High-Temperature RF and Microwave Properties of Selected Aluminas and Ferrites Used in Accelerators

R.M. Hutcheon, M.S. de Jong, P. Lucuta,
J.E. McGregor, B.H. Smith and F.P. Adams
AECL Research
Chalk River Laboratories, Stn. 111
Chalk River, Ontario, Canada, K0J 1J0

Abstract

Modern accelerator design practice includes the use of alumina rf and microwave windows and high-quality ferrites in applications with ever-increasing requirements on power handling ability. Modeling studies of such designs are of increasing economic importance, but frequently are hindered by a lack of measured values of the ceramic loss factors. AECL has developed a system to measure the complex permittivity of small samples over a frequency range from 50 to 2450 MHz and up to 1000°C in temperature. Samples of rf window materials from several suppliers have been studied, with a view to relating the dielectric loss factor to the microscopic material properties. As well, the temperature dependence of the dielectric and magnetic loss factors of a few relevant ferrites were measured at selected frequencies.

I. INTRODUCTION

The challenge in modern accelerator design is to satisfy the increasing demands on performance and/or output without incurring the cost penalty usually associated with brute force techniques. New materials and new technologies are the main tools one uses, but to use them successfully requires increasingly sophisticated knowledge of their properties and interplay with each other. Metal oxide ceramics have a long history of use in accelerator systems, but improvements in their properties and development of new ceramics have opened up new design possibilities.

The 50 MHz cavities designed and constructed at Chalk River Laboratories [1] for the PETRA and HERA accelerator ring use high-quality ceramics in three separate applications to achieve the design requirements at reduced cost:

(1) A large alumina insulator spans the PETRA cavity accelerating gap, so that high vacuum is maintained in the beam line while the bulk of the cavity can operate in air. A cw rf voltage of 100 kV is maintained across a 200 mm gap using a 340 mm long, 155 mm diameter, 7 mm wall high-density alumina cylinder.

(2) A perpendicular-biased ferrite frequency shifting system allows electronic slewing of the cavity by 0.5 MHz (1%) at an average cavity input power of 6 kW. Use of the low loss TransTech G510 ferrite reduced the tuner average power dissipation up to 1000 W (0.5 W/cm^3 of ferrite), while simple interleaving of the ferrite rings with high thermal conductivity, hot isostatic press (HIP) sintered, beryllia rings provided adequate cooling.

(3) Unbiased ferrite with a specially chosen rf loss-versus-frequency characteristic was used in a simple higher order mode damping system.

Usually, the principles behind the use of these ceramics are well understood, but an engineered optimum design requires detailed knowledge of the rf properties, which often is not available. For example, two alumina insulator materials were tried in the PETRA cavity from different sources. Both had adequately low dielectric loss at room temperature, but in one material losses increased much more rapidly with temperature, and resulted in a marginal design, given the available cooling.

Studies have been initiated to measure the dielectric and magnetic properties of ceramics used in accelerator engineering design and to attempt to understand the mechanisms behind the rf loss processes in these materials.

II. A SYSTEM FOR MEASURING RF PROPERTIES USING THE CAVITY PERTURBATION METHOD

The Chalk River measurement system uses the traditional cavity perturbation technique, where a sample is introduced into either the electric or magnetic field region of a cavity and the change in frequency and quality factor, Q, are related to the permittivity and permeability of the sample. A small cylindrical sample, mounted in a thin-walled fused quartz tube, is heated to high temperature and rapidly inserted into a cooled rf cavity. As the sample cools, a Hewlett-Packard 8753 network analyzer, controlled via IEEE 488 interface by a personal computer, determines the resonant frequency and Q approximately every half second and accumulates the numbers in a file for later analysis. The data analysis assumes the validity of the general formalism of resonant cavity perturbation theory, but the absolute calibration relies on measurements at room temperature of known materials, on a detailed understanding of the full complex cavity perturbation theory formulation [2], and on comparisons with computer simulations using the fully complex version of SUPERFISH, which includes loss in materials.

Under the assumptions listed below, the exact resonant cavity frequency shift formula may be reduced to the following form

0-7803-0135-8/91$01.00 ©IEEE

Wesgo or Kyocera aluminas. All the loss tangent values at 1000°C were at least an order of magnitude larger than that measured for a high-purity, single-crystal sapphire calibration sample, demonstrating that impurity and/or grain boundary effects are still the determining factor in this temperature range.

IV. LOW-LOSS FERRITES FOR PERPENDICULAR BIAS APPLICATIONS

The ferrites recently proposed for electronic frequency slewing of high-power cavities are used in the perpendicular bias mode (magnetic bias field perpendicular to the rf magnetic field) to reduce magnetic losses. Trans Tech aluminum substituted YIG ferrites, G810 and G510, have been used in this mode because both their magnetic and dielectric losses are low. However, the increased amount of ferrite required to obtain a large frequency swing [3] means that the ferrite extends into regions of higher electric field, and more accurate estimates of the dielectric loss (and heating) are required.

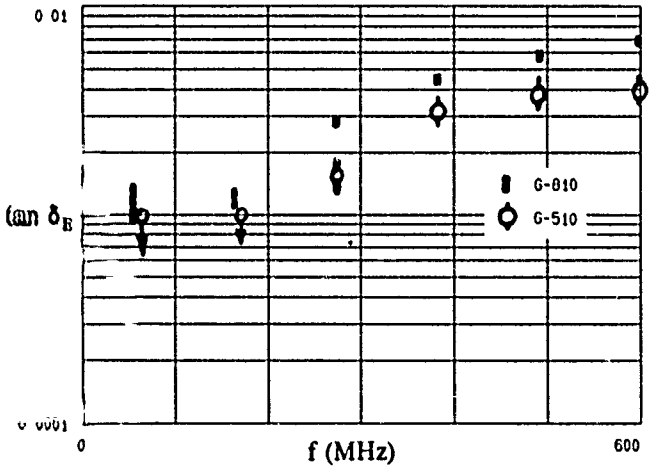


Figure 3. Measured room temperature (22°C) dielectric loss tangent of unbiased G810 and G510.

The dielectric constants of Trans Tech G510 and G810 were measured without magnetic bias (Figure 3). The presence of magnetic bias is thought to have no influence on the dielectric properties. A careful room temperature (22°C) measurement on unbiased G810 at 54.5 MHz gave $\epsilon_r' = 14.2 \pm 5\%$ and $\epsilon_r'' = 0.014 \pm 30\%$, for $\tan \delta_E = 1.0 * 10^{-3} \pm 30\%$. The G510 values were $\epsilon_r' = 13.3 \pm 5\%$ and $\epsilon_r'' \leq 0.012$, for $\tan \delta_E \leq 0.9 * 10^{-3}$. These values suggest a dielectric loss power dissipation of the order of 0.15 W/cm³ in a 1 kV/cm, 50 MHz internal rf field. The value of ϵ_r' is constant over the frequency range in Figure 3, while the increase of the loss tangent with frequency clearly rules out electron conduction as the loss mechanism.

V. A HIGH-LOSS FERRITE FOR RF ABSORPTION APPLICATIONS

Ferrites have been used as rf absorbers in high-power tube resonators to suppress spurious resonances and higher order mode excitation. Recently, they have been used as a broadband absorber of all TE and TM modes above cutoff in a waveguide mode damper coupled to rf cavities in high-current storage rings. The ferrite must have a large loss factor for both electric and magnetic fields so that all mode distributions are attenuated.

Trans Tech F50 is specified to have excellent high-vacuum properties, a nominal Curie temperature of 390°C, and a nominal room temperature electrical resistivity of 25 ohm-cm. The permittivity and "scalar" permeability [2] were measured at 2.42 GHz under zero magnetic bias field (Figure 4). The lack of a defined bias field direction means that the measured value is an average over the presumably random orientations of the individual domain field directions. The phenomenon of the "effective" scalar rf permeability being less than unity over a region just below the Curie point is common to many ferrites in this frequency range.

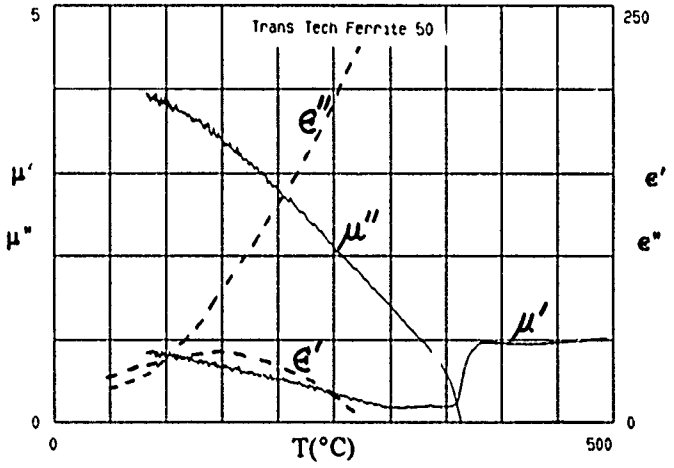


Figure 4. Measured permittivity and scalar permeability of Trans Tech F50 ferrite at 2.4 GHz.

Under the assumption that the dielectric loss is caused purely by free electron conduction, the room temperature value of ϵ_r'' may be used to deduce an effective resistivity for this sample of 37 ohm-cm.

V. REFERENCES

[1] L.W. Funk et al., "52 MHz RF Systems for PETRA II and HERA Proton Synchrotrons", Particle Accelerators, 29, pp. 71-76 (1990).

[2] R.M. Hutcheon et al., "A Technique for Rapid Scoping Measurements of RF Properties up to 1000°C", Electromagnetic Energy Reviews, 2, 46 (1989).

[3] R.L. Poirier, T.A. Engren, C. Haddock, "A Perpendicular AC Biased Ferrite Tuned Cavity for the TRIUMF Kaon Factory Booster Synchrotron", Proceedings of the 2nd European Particle Accelerator Conference, 1, 988 (1990).

$$\frac{\Delta f}{f} + j\cdot\Delta\left(\frac{1}{2Q}\right) \approx - \frac{\chi_e}{\left(1+\chi_e F_{sh}\right)}\cdot\frac{V_s}{V_c}\cdot A \qquad (1)$$

where χ_e is the complex relative susceptibility (dimensionless), F_{sh} is a sample shape factor (real, dimensionless), V_s and V_c are the sample and cavity volumes, respectively, and A is a dimensionless real constant depending only on the shape of the cavity and the shape of the unperturbed fields. The assumptions are:

(a) The sample is located in a region of uniform field.

(b) The sample shape is an ellipsoid of rotation.

(c) The stored energy in the sample is small compared to that stored in the rest of the cavity.

It may be shown that relation (1) applies to non-ellipsoidal shapes when empirical values of A and F_{sh} are used. This approximation has been checked with full complex numerical calculations and found to be accurate to ± 3% for sample length to diameter ratios down to 3.5:1.

III. LOW-LOSS ALUMINAS FOR RF AND MICROWAVE APPLICATIONS

Initial studies of loss mechanisms were done on samples from four ceramics that had been purchased and used as rf and microwave windows (Table 1). All are high-purity aluminas and have low dielectric loss tangent (tan δ = ε"/ε') at room temperature. Structural studies were done both of fracture surfaces and of polished and thermally etched faces. As well, energy dispersive X-ray analysis (EDX) was used to give an indication of the type and amount of impurities (assumed to be sintering aids). The dielectric constants were measured (Figure 1) using 12 mm long, 3.5 mm diameter specimens that had been diamond-core drilled, cleaned and held in air at 1000°C for 2 hours in high-purity alumina boats.

Table 1

Measured Properties of Four RF Window Materials

Specimen	Additives	Grain Size	Pores	Cryst.Str.	tan δ
Wesgo AL-995	< 0.5%	Aver. 25μm Range 5-60	S 1-3 μm	α -	≤ 1x10⁻⁴ 25°C 2x10⁻⁴ 300 C 50x10⁻⁴ 1000°C
Degussit AL23	< 0.5%	Aver. 30μm Range 3-80	S. 1-3 μm	α -	≤ 1x10⁻⁴ 25 C 3x10⁻⁴ 300 C 17x10⁻⁴ 1000°C
Kyocera	< 0.5%	Aver. 40μm Range8-120	4 μm .5-30	α -	≤ 1x10⁻⁴ 25°C 3x10⁻⁴ 300°C 56x10⁻⁴ 1000°C
Coors AD 995	1< Ca < 2% 0.5< Mg < 1%	Aver. 15μm Range 5-40	S. 1-3 μm	95%α - spinel	≤ 1x10⁻⁴ 25°C 11x10⁻⁴ 300°C 37x10⁻⁴ 1000°C

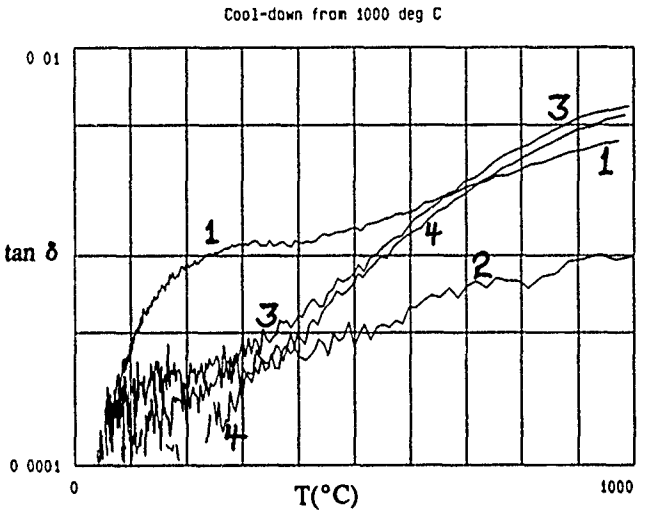


Figure 1. Measured loss tangent at 2.4 GHz for (1) Coors AD-995, (2) Degussit AL-23, (3) Kyocera, (4) Wesgo AL-995.

The Coors loss tangent temperature dependence is clearly different from the others (Figure 1), rising steeply above room temperature and peaking (or leveling) around 300°C. The same temperature dependence occurs at lower frequencies (Figure 2) and will lead to thermal runaway above specific high rf power levels. The frequency dependence (Figure 2) clearly demonstrates that electron conductivity, which would give $\epsilon'' \propto f^{1}$, is not the loss mechanism. The spinel structure, evident in the Coors EDX spectrum, is the only clear difference between the materials, and will be studied as a possible mechanism of low-temperature loss in aluminas.

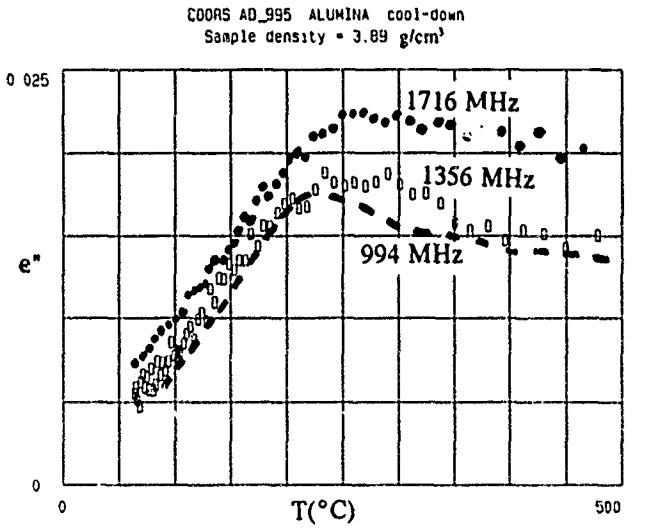


Figure 2. Measured absorptive part of the permittivity for Coors AD-995.

The high-temperature loss tangent appears unrelated to the previously mentioned low-temperature loss, for at 1000°C the Coors material has a lower tan δ value than either the

100 MW KLYSTRON DEVELOPMENT AT SLAC*

A.E.VLIEKS, R.S.CALLIN, G. CARYOTAKIS, K.S. FANT,
W.R. FOWKES, T.G. LEE, E.L. WRIGHT

Stanford Linear Accelerator Center, Stanford, CA 94309

Abstract

A klystron designed to operate at 11.4 GHz and 440 kV is presently SLAC's strongest RF power source candidate for the Next Linear Collider. It is expected to provide 100 MW of RF power with a pulse width of 1 microsecond. Many of the conventional tube technologies are being pushed to their limits. High electron beam power densities, RF electric gradients in cavity gaps and stresses on the ceramic RF output windows are among the most severe problems to be dealt with. This paper describes progress in the development of this device including results from single and double gap output cavities and various styles of RF output windows.

I. INTRODUCTION

RF power sources are under development at SLAC in order to satisfy the power requirements of a next generation linear collider. For peak accelerating fields of 50 MV/m a power requirement of 60 MW/m will be required in the current minimum design. To satisfy this requirement efforts are underway to develop a 100 MW klystron at 11.424 GHz. The design parameters for this klystron are shown in Table 1.

Table 1.
SLAC XC Klystron Design Parameters

Operating frequency	11.424 GHz
Peak Output Power	100 MW
RF Pulse Width	100-1000 ns
Pulse Repetition Rate	120 pps
RF pulse risetime	$\leq$ 10 ns
Beam Voltage	440 kV
Beam Current	511 A
Efficiency	45%
Saturation Gain	55 dB
Focussing Field	kG
Beam Areal Compression	90:1
Max. Surface Grad. in Gun (at F.E.)	308 kV/cm
Maximum Surface Grad. in Output Gap (for single-gap Cavity)	1.33 MV/cm
Maximum Surface Grad. in Output Gap (for 2-gap Cavity)	774 kV/cm
Average cathode current density	9 A/cm^2
Total length	$\approx$ 1.5 m

We have currently designed and built three versions of a 100 MW klystron (called XC1, XC2 and XC3) to test various alternatives to RF windows, output cavities and beam optics. In addition, a series of diode tests were performed to test the breakdown limitations in cathode/anode designs[1] and beam transmission.

In addition to developing a klystron for a future collider, this program has a second purpose. This is to develop a power source to test accelerator structures and other devices. Thus far we have used these klystron prototypes to test a Binary Pulse Compressor[2] (BPC), to serve as a driver for a Crossed-field Amplifier(CFA) and (in the near future) to drive a high power Resonant Ring[3].

II. INITIAL TESTS

The first test performed on this klystron design was a beam diode test. It consisted of an electron gun identical to the one designed for a 100 MW klystron, a drift section with the same length as the klystron, and the solenoid magnet designed for the klystron. The drift section was divided into several thermally isolated parts which were equipped with thermistors to measure beam interception. The purpose of the test was to verify the beam perveance, cathode/anode voltage standoff capability and beam quality which had been determined by the electron trajectory simulation code EGUN[4] and the magnet code POISSON[5]. Results verified that the perveance was at the design value of 1.75 μ perv. and that the beam interception was $\approx$ 2%. In addition, no difficulties with cathode/anode breakdown were found. A later experiment[1], with a specially coated focus electrode, indicated that a standoff capability of 360 kV/cm for 5 μs pulses and (in excess of) 400 kV/cm for 1 μs pulses could be expected.

III. KLYSTRON: GENERAL DESCRIPTION

All three klystrons have been designed to operate at 440 kV with a perveance of 1.75 μ perv. The thermionic cathode has a diameter of 8.9 cm and a beam loading of $\approx$ 9 A./cm^2. The areal compression ratio of the beam is 190:1, which is a value somewhat larger than usual for a klystron. To accomplish this compression, the beam is first compressed electrostatically by a factor of $\approx$ 40 and then further compressed magnetically in a slow, adiabatic manner. This latter compression is performed in a long tapered drift tube section (30 cm) between the gun and input cavity. Magnetic focussing is accomplished with a 6 kG. solenoid magnet and a separate trim coil wound directly on the klystron body upstream of the input cavity. Results from EGUN[6] indicated that this trim coil might improve beam quality. The solenoid magnet field is controlled by six independent sets of coils (including bucking coil) to shape the field to the design value. In the third klystron (XC3) the field was modified by removing the trim coil and shaping the field with a smaller diameter steel gun pole piece.

* Work supported by Department of Energy contract DE-AC03-76SF00515.

0-7803-0135-8/91S01.00 ©IEEE

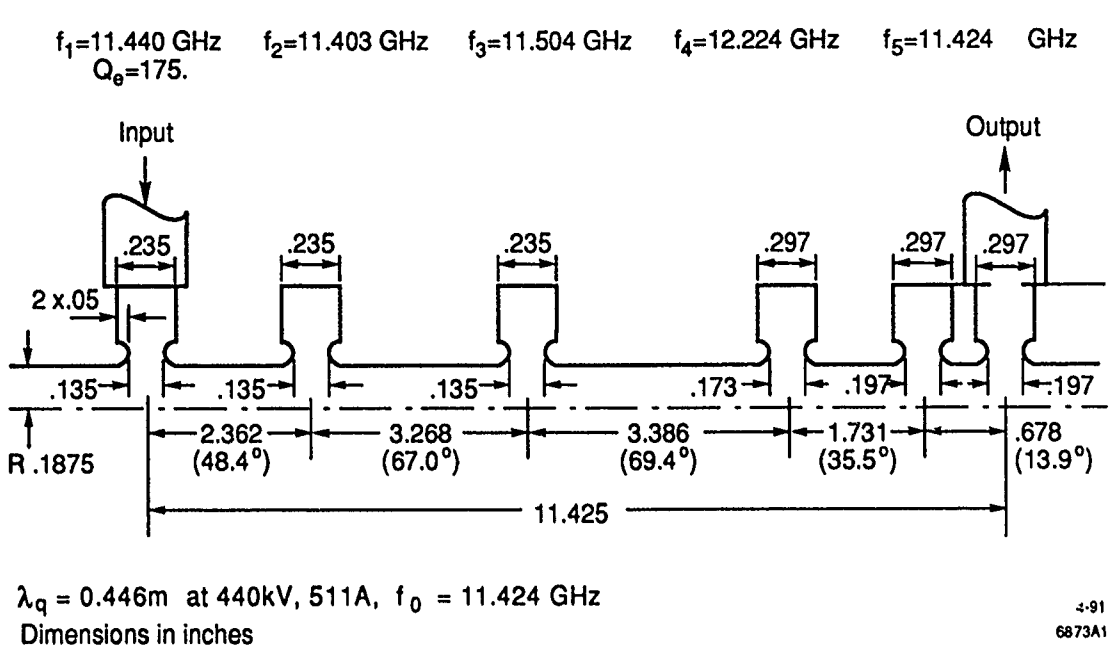


Figure 1. XC2 Klystron, Double-Gap Output Cavity Design Values.

The importance of the bucking coil is also diminished in this design.

The RF section consists of an input cavity, two gain cavities, a penultimate cavity and an output cavity. (See Fig. 1). Details of the different output cavities are described below.

The number of waveguides leaving the output cavity is different for the three klystrons but in all designs two output windows are used. For XC1, two waveguides leave the output cavity directly while XC2 and XC3 use a single waveguide. In this latter design, the power is then divided by a 3 dB splitter into two separate waveguides. Two different window designs have been used and are described below.

Pumping of the klystrons is accomplished by means of 2 l/s vac-ion pumps mounted on the input and output waveguides. Typical klystron pressures are $1\text{-}5 \times 10^{-9}$ Torr. as read by the pump currents.

IV. XC1

XC1 was the first X-band klystron tested in this program at SLAC. It was a five cavity klystron with a single gap output cavity. Thin (.79 mm) RF windows were used because of simplicity and the need for wide bandwidth. (The klystron was to be used in CFA experiments).

The peak power attained with XC1 was 65 MW. This was only attained at narrow pulse widths however (30 40 ns). At wider pulse widths RF breakdown limited the peak power attainable although RF conditioning did improve the RF breakdown threshold somewhat. Results of peak power generated at threshold both initially and after $\approx$ 250 hours of operation are shown in Fig. 2. As is seen in the figure, the peak fields in the output cavity for a 1 μs pulse were only 600 kV/cm which is much less than the 1330 kV/cm expected at 100 MW.

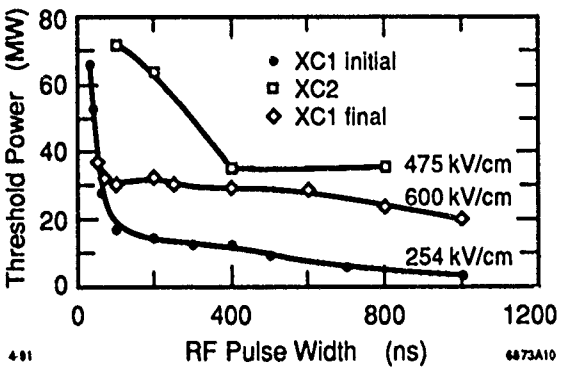


Figure 2. Measured Power Units as a function of pulse width for XC1 & XC2.

After studying the performance of the klystron, it was used as a driver for CFA experiments and BPC tests. Unfortunately during the latter tests, the windows were damaged which terminated further testing. Evaluation of the klystron indicated that significant beam erosion and RF breakdown had occurred in the output cavity. In addition, damage was observed at the other cavities and at the entrance to the drift tube.

V. XC2

Because of the problem of RF breakdown in XC1 it was decided to change the output cavity design to a dual-gap cavity. This would have the effect of reducing the peak cavity fields by $\approx$ 60%. In addition, some small changes were made to the RF circuit to improve its performance.

Other changes in this tube included the addition of beam diagnostics. The copper klystron body was thermally isolated into five sections by thin (.3 cm) stainless steel plates. Five thermistors were installed into the body within 2 mm of the drift tube radius at key locations. The

most important of these were the two located at the rear end of the penultimate and output cavities. In addition, the collector was electrically isolated from the tube body to permit direct measurement of transmitted beam current.

Initial tests indicated improvements in peak power to 72 MW for pulse widths of 100 ns. Figure 3 shows the klystron performance as a function of beam voltage. The highest power levels were measured calorimetrically at pulse widths ranging from 100 to 200 ns at a pulse repetition rate of 180 pps. At the highest beam voltage, calorimetric power measurements were compared to RF measurements (crystal diode detector) under identical conditions and found to give equivalent results. As can be seen in Fig. 2, peak power levels of 35 MW were measured for pulse widths of up to 800 ns. These power limits were more the result of the experimental requirements at the time rather than a firm breakdown limitation. For the most part, this klystron was used to supply power to the BPC experiment which required $\approx$ 35 MW RF power at a pulse width of 800 ns. At the conclusion of BPC testing it was found that both RF windows were broken. This necesitated a pause in experimentation until these windows could be replaced. During repair, it was found that beam erosion due to interception had taken place in the output section of the klystron. It was unclear whether or not any RF breakdown had also taken place.

At the time of this writing, the windows of XC2 have been replaced with a more robust "thick" design and the tube is again operational. Improvements to beam optics is expected due to improved alignment procedures and tighter tolerances of the solenoid magnet to the klystron.

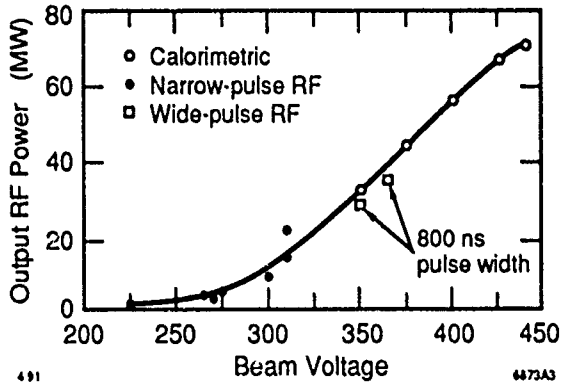


Figure 3. XC2 Output Power.

VI. XC3

This klystron was designed with the same modifications as the current XC2. The only difference was in the magnetic field profile near the cathode which was improved to reduce the beam fill factor and subsequent interception at the end of the magnetic compression stage.

During initial testing the beam intercepted the drift tube in the output cavity region causing melting. This resulted in the development of a 13 8 GHz. oscillation in the output cavity. This oscillation was present even in the absence of RF drive power. Its intensity was somewhat controllable by "squeezing" the beam with the solenoid magnet. The oscillation caused excessive heating in the output cavity, probably by disrupting the beam, and also outgassing in the windows. (The windows are opaque to this higher frequency mode). After disassembling the klystron, extensive damage was discovered in the septum and downstream gap of the output cavity. This cavity is currently being replaced and the tube will be in operation in the near future.

VII. Summary

Three X-band klystrons have been designed and tested as part of development of an RF source for a future Linear Collider. At this time 72 MW RF power has been generated with a pulse width of 100 ns and 35 MW has been generated at 800 ns.

In order to improve the current design significantly, the problems of beam interception and RF breakup must be overcome. Beam interception is a particularly difficult problem because the high current density of the beam can cause intrapulse melting for almost any level of body interception. To alleviate this problem, future klystron modifications will include improved beam optics, a larger output cavity radius, and beam collimators near the input and output cavity positions to limit the size of the beam and remove any beam halo. These modifications will also reduce the likelihood of RF breakdown if the latter was caused by gassiness caused by localized heating and melting. Modifications to the output cavity design are also underway in the form of lower field designs. These include a 3-gap output cavity and a multiple-gap traveling wave output cavity.

Further work in RF window design is also underway. In addition to the new "thick" ($.43\lambda_g'$), currently in test, a larger diameter (4.6 cm) design is being developed.

References

[1] "High Gradient Electron Guns." K.S. Fant et al., SLAC-PUB-5325 (August 1990).

[2] "High power Radio-Frequency Binary Pulse Compression Experiment at SLAC" T.L. Lavine et al. SLAC-PUB-5451 (May 1991).

[3] "RF Component Development for X-Band above 100 MW," W.R.Fowkes, R.S. Callin and M. Studzinski, SLAC-PUB-5545, (May 1991).

[4] "EGUN: An Electron Optics and Gun Design Program." W.B. Herrmannsfeldt, SLAC-PUB-0331 (October 1988).

[5] "Reference Manual for the POISSON/SUPERFISH Group of Codes." Los Alamos National Laboratory, LA-UR-87-126 (January, 1987).

[6] "Design of a 100MW X-Band Klystron," K. Eppley, SLAC-PUB-4900 (February 1989).

COMPUTER DETERMINATION OF HOM DAMPING for a PROTOTYPE JLC ACCELERATOR CAVITY and a PROTOTYPE B FACTORY CAVITY*

Norman M. Kroll†
University of California,San Diego,
Department of Physics- 0319 La Jolla, CA 92093-0319
and
Stanford Linear Accelerator Center, Stanford University, Stanford, CA. 94309

Robert Rimmer#
Lawrence Berkeley Laboratory,
UCB, Berkeley, CA. 94720

Abstract

In this paper we describe the determination of the properties of the above referenced cavities with particular emphasis on the damping of the higher order modes (HOM). Because mode frequency spectra were determined for a large number of shorted waveguide lengths, rather complete analyses are possible. Phase frequency plots have proved to be an invaluable aid in sorting out overlapping resonances and separating cavity resonances from waveguide resonances Algorithms for the determination of the parameters of several resonances simultaneously have been developed. Determinations of Q from multiresonance analyses are compared to those from single resonance analyses, and the changes are typically found to be small.

I. INTRODUCTION

The damping of higher order modes in accelerator cavities has been a subject of extensive study for many years. The primary technique employed has been to couple the energy out through wave guides to be terminated in matched loads. Computer programs such as MAFIA (as in this paper) have been extensively employed to assist in the design of such structures. To obtain values of the Q_{ext} and the shifted resonant frequencies due to the wave guide loading, it has been necessary to develop special analysis techniques to be applied to the results obtained from a program such as MAFIA. The methods of Kroll-Yu[1] (KY) and Kroll-Lin[2] (KL, or KYL when referring to them collectively) are examples of such techniques and will be employed for the two problems which we discuss in this paper. The thrust of KYL was aimed towards minimizing the number of computer runs needed. The two examples discussed here are, however, considerably more complex than those discussed in those papers, and the rather large number used here have permitted a more complete overall analysis of the mode spectrum. Also, since we are still acquiring experience with these methods, the larger "data sample" is very useful for providing validation.

A problem which we have experienced in applying KYL has been the separation of waveguide resonances from cavity resonances. One deals here with the spectrum of a lossless coupled cavity waveguide system, and any run at a particular waveguide length will produce a series of resonances, some cavity associated, some waveguide associated, and some, when the two occur at neighboring frequencies, strongly coupled. When the waveguide coupling is not too strong, these cases can be readily distinguished by inspection of field plots. Current interest, however, centers about the strongly coupled case where this method has not always been convincing. We have found phase-frequency plots to be of great assistance in sorting out this problem.

The phase of a given computer determined mode at a particular waveguide length is given by

$$\varphi = 2\pi L/\lambda_g$$

As the length is varied each mode traces out a section of a phase-frequency curve. As pointed out by KY each such section is displaced by a multiple of π from a single universal curve that applies to all of the modes. The designation "phase-frequency plot" is intended to refer to that single universal curve. An example is provided by Fig. 1. It is based on data reported by Higo et. al at the LINAC 90 conference[3]. We were provided with a list of the lowest seven modes arising from MAFIA runs at twelve different waveguide lengths. The quantity $n\pi$ was subtracted from the phase of the n'th mode at each length and the entire set of 84 points plotted. As is apparent from Fig. 1, the points do indeed trace out a smooth curve. The high density of points in the low frequency portion of the curve results from the high degree of overlap which results from the $n\pi$ shifts. The smallness of the scatter is an indication of the high quality of the computer output. The cavity resonances are associated with the steeper portions of the curve, and as we shall discuss later, the low frequency portion is indicative of overlapping resonances. The presence of these overlapping resonances has been the motivation for the development of multiresonance fitting procedures. Both single mode propagation and a unique symmetry relation between the fields in the two outputs has been assumed in the above discussion. These were assured by the boundary conditions applied in the MAFIA calculations.

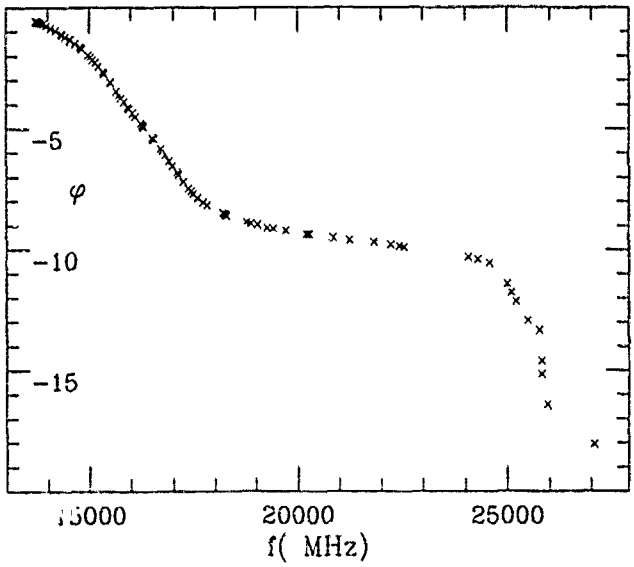


Fig. 1 Phase frequency plot for JLC prototype cavity.

2. THE JLC CAVITY

The KYL methods are based upon the following representation of the phase-frequency relation:

$$\varphi(\omega) = \sum_i \arctan\left(\frac{v_i}{\omega - u_i}\right) - \chi(\omega)$$

$$\chi(\omega) = \chi_0 + \omega\chi'$$

For each mode, u/2v is the Q value and u the resonant frequency. The branches of the arctangents are to be chosen so as to obtain a smooth curve. The function χ is intended to represent the effect of resonances not taken into account explicitly. If one ignores χ, it is apparent that as the frequency passes through a resonance the phase decreases by π. If all resonances occurring within a given

*Works supported by Department of Energy contracts AS03-89ER40527†, AC03-76SF00515‡, and AC03-76SF00098#.

0-7803-0135-8/91$01.00 ©IEEE

frequency interval are recognized and included explicitly in eq. (1), then χ may be presumed to be due to resonances outside the interval and therefore to vary by substantially less then π over the same interval. Thus we do not consider a "feature" in the phase-frequency plot to correspond to a resonance unless a phase change of π is involved, and strongly overlapping resonances produce phase changes which are multiples of π.

Applying these considerations to Fig. 1, we conclude that the region below 18000 MHz contains three overlapping resonances, the region 18000-24000 MHz is resonance free, and the region 24000-26000 MHz contains two resonances. The isolated point above 26000 suggests an additional resonance, but because of inadequate supporting information we ignore it in our analysis. We determined resonance parameters for the three low frequency and two high frequency parameters separately. To obtain parameters for the low frequency resonances we chose eight more or less evenly spaced data points between 15340 and 18236 MHz, and determined the six resonance parameters and two χ parameters so that the theoretical curve passed through the eight selected points. The results of this procedure are shown in Fig. 2. The resultant fit is seen to be excellent, and the theoretical curve fits the data accurately until the high frequency resonances are approached. Attempts to fit the data with only two resonances failed and showed clearly that the

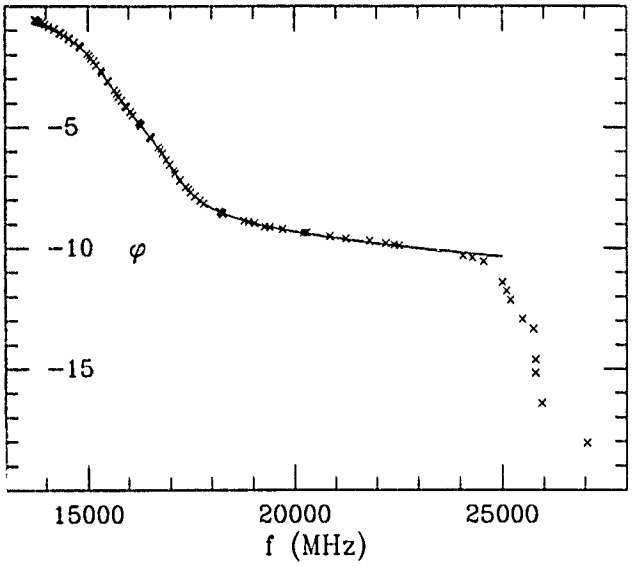


Fig. 2 Three resonance eight point fit for the low frequency resonances.

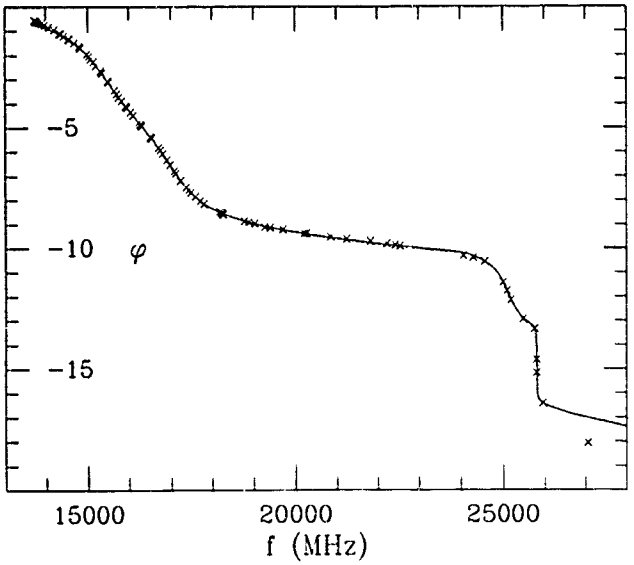


Fig 3 Composite plot of the low frequency fit of Fig 2 with a two resonance six point fit to the high frequency resonances The break point is at 24100 MHz

phase span in the resonance region combined with the slope of the resonance free region is inconsistent with the assumption that only two resonances are involved. For the high frequency resonances we selected six points in the range 25006 to 25956 MHz and determined four resonance parameters and two χ parameters so that the theoretical curve passed through the six selected points. A composite curve containing both fits is shown in Fig. 3. The break between the two representations occurs at ~ 24100 MHz where the two curves cross. Frequencies and Q values that yielded Fig. 3 are shown in Table I. The figures in parentheses are those obtained from single resonance four parameter fits carried out with data points selected from the neighborhood of the resonance as determined by visual inspection of Fig. 1. Mode 2 is not discernible in this way and attempts to find it with the four point method after its position had been determined were not successful. Nevertheless the results show that the four point method can give quite reliable results even in the presence of severe overlap. It appears that the free slope parameter does a quite effective job of taking account of the effect of omitted resonances on the Q values.

Table I. Frequencies and Q's for the JLC Cavity

Mode Number	Frequency (MHz)	Q
1	15375 (15552)	10.9 (12.0)
2	16077	7.1
3	17048 (16927)	14.8 (13.5)
4	25121 (25138)	43.1 (42.0)
5	25814 (25814)	~1000 (~1000)

We have not identified the modes because we have not seen the associated field plots. Fig. 1 of ref. 3 plus the symmetry imposed in the MAFIA calculations suggest TM_{110}-π for mode 1 and TE_{111}-0 for mode 2 or 3. We suspect that the other of these two modes is associated with the radial slot in the disk.

3. THE PROTOTYPE B FACTORY CAVITY

The cavity referred to in the heading above consists of a pill box with three waveguides mounted symmetrically on one end, emerging perpendicular to the end, and with the wide dimension perpendicular to the radius. In addition it includes a cylindrical section of smaller radius intended to represent the beam pipe, symmetrically disposed on the two ends and terminated with a short. A computer simulation of half the cavity is shown in Fig. 4. It is a *B* factory prototype only in the context of a study of higher order mode damping.

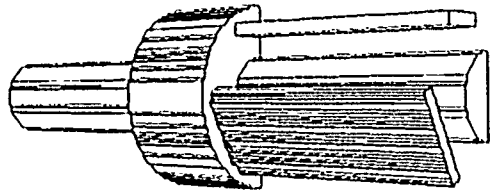


Fig. 4 MAFIA simulation of the prototype B factory cavity used for the MAFIA computations.

Because the cavity is symmetric under 120^0 rotation about the beam axis, its modes can be characterized by an $m=-1$, $m=0$, or $m=1$ symmetry index corresponding to the lowest fourier component in the azimuthal fourier expansion of the fields. The $m=+-1$ modes are degenerate, but because only half the cavity is modeled only a single linear combination of this pair appears. Thus we can analyze the $m=0$ and $m=1$ modes separately.

MAFIA calculations were carried out for 14 different lengths of waveguide, beginning with zero. The results of the calculation are summarized in Fig 5. Connecting lines have been drawn which preserve the mode order of $m=1$ and $m=0$ modes separately. Identification was based upon the fact that fields at the end of the waveguide should be equal for the $m=0$ case and in the ratio -1 to 2 for the $m=1$ case (the -1 refers to the amplitude in the full width waveguide). Because the computer mesh does not accurately reflect

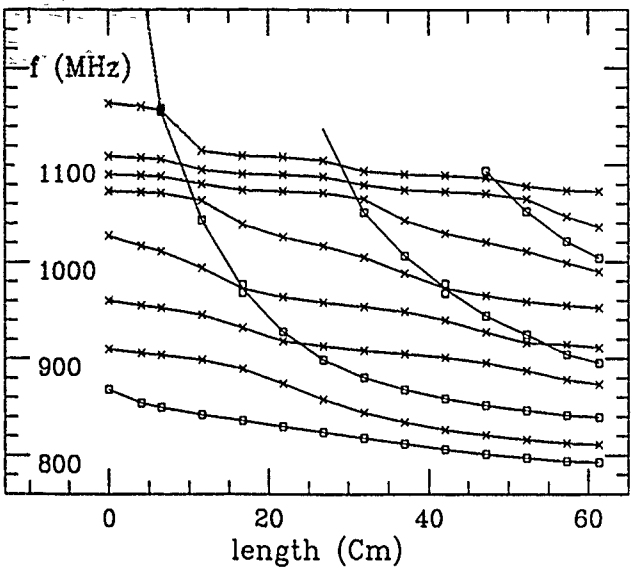


Fig. 5 MAFIA computed mode spectra of the Prototype B factory cavity shown as a function of the length of the shorted waveguides. Connecting lines join points belonging to the same symmetry class. m=0 square points. m=1 x points.

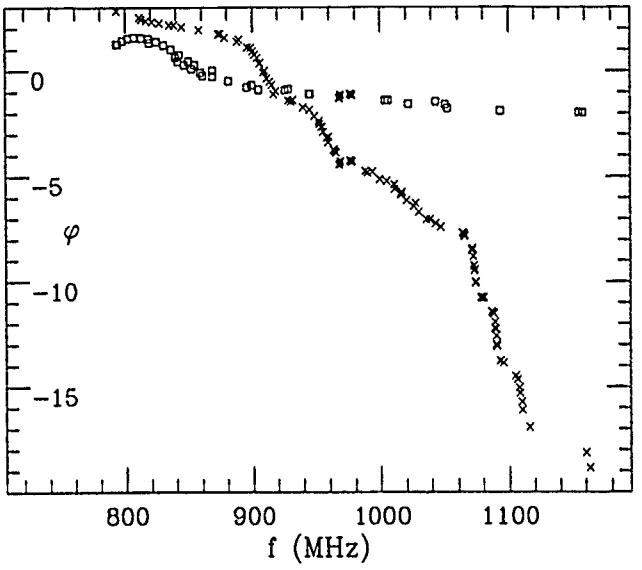


Fig. 6 Phase-frequency plot for the prototype B factory cavity. m=0 square points. m=1 x points. ambiguous (plotted twice) star points.

the symmetry of the physical structure, these relations are satisfied only approximately, and large deviation occurs at the crossing points. The $n\,\pi$ displacement procedure is applied to the *m=0* and *m=1* sequences separately, and the phase-frequency curves illustrated in Fig. 6 emerge. The squares mark *m=0* and the x's *m=1*. The four "star" points are from the crossing regions and have ambiguous symmetry. Both points appear on each curve. These points were avoided in carrying out frequency-Q determinations. The figure also contains points from a calculation carried out at length 61.29cm with a magnetic boundary condition imposed at the waveguide ends. These fall on the universal curves if their phase is displaced by an extra $\pi/2$.

The *m=0* curve exhibits a maximum at the low frequency end instead of the usual monotonic decrease. This is due to a mode trapping phenomenon which has plagued the application of waveguide damping. The mode involved here is the TM_{011}. It has a frequency of 868.36 MHz for the closed cavity, well above the waveguide cutoff of 786.86. As the waveguides emerge from the cavity end and lengthen, the frequency of the mode is pulled down and eventually falls below the guide cutoff frequency. When this happens the phase-frequency plot is guaranteed to exhibit a maximum as a function of frequency. (The reality of this phenomenon has been confirmed with an analytically solvable model.) The mode did not actually fall below cutoff at the largest length (61.29cm). However, the appearance of the maximum is considered to be the indication that it will eventually do so. Replacing the electric boundary condition with a magnetic one at the waveguide end has an effect similar to increasing the length, and such a calculation was performed to see whether it would exhibit an extra trapped mode. Indeed such a mode was found at 773.87 MHz, which we take to be a confirmation of the above. Apart from the trapped mode, the *m=0* curve shows only one resonance, a detrapped and low Q counterpart of the trapped TM_{011} mode. The determination of the resonance parameters of this mode is degraded by the fact that the KY phase-frequency formula does not include the trapping phenomenon, so that the Q determination appears to be uncertain up to a factor two or so.

The *m=1* phase-frequency curve is of the expected form and clearly shows the seven lowest waveguide damped *m=1* modes. Four parameter single resonance fits have been carried out using both the KY and, where adequate data was available, the KL method. The phase-frequency plot identifies appropriate regions for the selection of data points for fitting and enables one to avoid the study of waveguide resonances. The two methods are found to be in excellent agreement except for the low Q TM_{011} mode. As mentioned before, we consider this to be due to the fact that the phase-frequency formula does not include the trapping phenomenon. These results are summarized in Table II. The waveguide loaded frequencies F_L for the trapped modes are taken directly from the MAFIA results.

Table II. Frequencies and Q's for the Prototype B Factory Cavity

Mode type	F_0 (MHz)	F_L(KY) (MHz)	F_L(KL) (MHz)	Q(KY)	Q(KL)
TM_{010}	617.17	610.94		trapped	
TE_{111}	711.61	708.00		trapped	
TM_{011}	868.36	<773.87		trapped	
TM_{011}		841-842	840-845	15-17	24-35
TM_{110}	909.58	906.7	906.7	55	56
TE_{210}	959.92	956.9	956.6	56	55
TM_{111}	1027.22	1021.3	1021.4	32	31
TM_{112}	1073.44	1073.0	1073.7	338	336
TM_{113}	1090.53	1090.0	1090.0	401	411
TM_{114}	1109.39	1108.6	1107.5	300	318
unknown (m=1)	1163.15	1162.0		333	

The TM_{11n} modes above 1070 MHz are associated with the sudden opening of the beam pipe to propagation in the TE_{11} waveguide mode (cutoff at 1064 MHz). The bulk of the stored energy as well as the extra nodes are in the beam pipe for all three. An experimental investigation of this cavity has been carried out by Voelker et al[4]. Absorbers were placed in the beam pipe so that agreement with computed Q's of the "beam pipe" modes is not expected. Otherwise reasonable agreement was obtained.

We thank T. Higo and M. Takao for providing as with the MAFIA generated data for the JLC cavity, and X-T. Lin for assistance with the graphics.

REFERENCES

1. N Kroll and D. YU, Part. Acc. 34 p. 231 (1990)
2. N. Kroll and X Lin, Proc. 1990 Linac Conf. Albuquerque, NM, June 10-14 (1990) p. 238
3 T. Higo, M. Takao, M Suetake, K. Kubo, and K. Takata, Proc. 1990 Linac Conf. Albuquerque, NM, June 10-14 (1990) p. 147. We undertook the analysis of this cavity at the request of T. Higo.
4. F. Voelker, G. Lambertson, and R. Rimmer; IEEE Part. Acc. Conf., San Francisco, CA. May 6-9 (1991) Abs. HRA22.

SXLS RF Cavity and System*

M. Thomas, R. Biscardi, R. D'Alsace, J. Keane, P. Mortazavi
National Synchrotron Light Source
Brookhaven National Laboratory
Upton, New York 11973

J. Rose
Grumman Aerospace Corporation
Bethpage, New York 11714

Abstract

The design of a 700 MeV superconducting compact electron storage ring for applied X-Ray lithography is in its final stage. This succeeds a 200 MeV warm dipole model constructed and now in operation at BNL. RF cavities and systems in both machines will be discussed. This paper will present cavity design parameters, construction, and the kind of mode suppression as well as the type of tuner and input window to provide 300 KV of accelerating voltage at 211.54 MHz. A 65KW, RF power source will be described.

I. INTRODUCTION

Recent interest in synchrotron radiation as a source of X-rays for lithography from large electron storage rings has stimulated the design of rings of a more compact size. The 51 meter circumference VUV ring, and the 170 meter X-ray ring at the National Synchrotron Light Source (NSLS), are two examples of the larger storage rings. These are machines emitting radiation from conventional magnets based on well established engineering technology.

The design and construction of an 8.5 meter circumference Superconducting X-Ray Lithography Source (SXLS) at the NSLS at Brookhaven was funded by DARPA in 1988, in which machine building technology will be transferred to two companies in U.S. industry, the Grumman Aerospace Corp. and General Dynamics.

Phase I of the project, a 200 MeV, conventional magnet machine was completed in the fall of 1990 and has been in operation since then for low energy injection studies and machine diagnostics. A low level, 10KW RF cavity[1] and system are used that will be upgraded to a 65KW system for the Phase II, 700 MeV, superconducting machine. The Phase II cavity is designed and will be described below. Some construction details and operation of the Phase I cavity and system will also be discussed.

Phase II Cavity Structural Design

The overall space available, both axially and radially, has remained unchanged compared with the Phase I cavity, but with the higher input power required, the cavity had to be designed in such a way to have sufficient surface cooling for manageable heat removal and still maintain adequate capacitance across the gap. The final design, shown in Fig. 1, consists of three main sections joined together with two circumferential electron beam welds. The number of mechanical joints was kept to a minimum in order not to compromise the vacuum integrity and Q of the cavity.

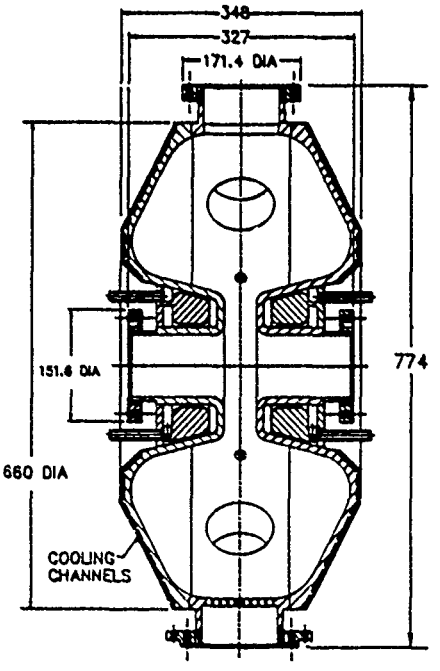


Fig. 1

For a maximum of 300 KV gap voltage, the total dissipated power was calculated to be 27.5 KW which is distributed on the inside surfaces of the cavity. For adequate cooling and maintaining high Q, Oxygen Free High Conductivity (OFHC) copper was selected as the base

*Work performed under the auspices of the U.S. Department of Energy under contract DE-AC02-76CH00016 and funded by DoD/DARPA.

U.S. Government work not protected by U.S. Copyright.

material. A series of rectangular grooves are machined over 75% of the external surfaces, and subsequently copper plated into channels by an electroforming process.

The finite element program, ANSYS, was used to optimize the cooling channel configuration on the structure. An axisymetric finite element analysis was carried out to determine the temperature rise and the thermal plus pressure deformation. A water flow rate of 20 GPM is distributed through several parallel channels to maintain water velocity of 10 Ft/sec, which yielded a convective film coefficient of 1.4 Watts/Cm^2°C. A maximum heat load of 27.5 KW results in a temperature gradient causing a deformation, mainly across the drift tube, by 0.16 mm. This inward displacement reduces the final resonant frequency by 200 KHz which is adjusted for in the fabrication. The complete cavity assembly with peripheral equipment installed is shown in Fig. 2.

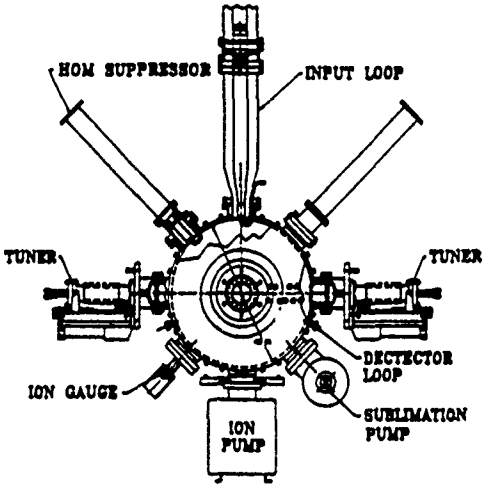


Fig. 2

A commercial heat/cool refrigerating pumping system capable of maintaining a set temperature to within ±1°C, provides the necessary flow rate during operation.

The vacuum window for the drive loop, due to power restrictions, will be a standard 6 inch coax type used in other cavities at the NSLS. Since the port openings in the cavity are smaller, a half-wavelength tapered section will be installed between the cavity and the window.

A ferrite frequency tuner has been ordered to use in the resonator to compensate for reactive detuning. A 53 MHz tuner of similar design is currently being tested at this facility.

Multipactoring and RF Conditioning

After cleaning, assembly, and vacuum leak checking, the XLS Phase I Cavity was baked for 48 hours at 150° C and upon cooling, RF power was applied to condition the inner surfaces.

The XLS cavity had multipactoring levels in regions of 1W, 15W, 600W, 1200W, 1700W, 2400W, 6000W and 9000W that were difficult to condition out. It was decided to coat the cavity with titanium nitride using a method developed at SLAC[2] and successfully used in other cavities at the NSLS.

Varian 'Ti-Balls' were placed into the cavity in various positions to uniformly distribute a 100-200 angstrom coating of titanium/titanium nitride upon the inner surfaces. The vessel was evacuated to 10^{-7} Torr and dry Nitrogen gas leaked in to a pressure of $2\text{-}4\text{x}10^{-5}$ T. The Ti-Balls are heated for a specific time followed by a 2 hour nitrogen soak for more nitride conversion, before removal.

After this process, the cavity was RF conditioned and only the 1W multipactoring level remained. It should be noted that the vessel was cycled several times to dry nitrogen and to air, and after evacuation each time, the surfaces remained conditioned. The SXLS Phase Two Cavity will be prepared in the same fashion.

Higher Order Mode Suppression

Phase I cavity high order modes were damped using four damping antennae and two shorted loops. The damping antennae couple power out to 50 ohm water cooled loads. The cavity is a quarter wave T.E.M. resonator, capacitively loaded with a removable drift tube.

Mode damping was accomplished by first measuring the cavity spectra as a reference. Field plots from both URMEL and SUPERFISH were studied for high E field patterns of the undesirable modes. Model probes loaded with 50 ohm terminators were placed in available ports to penetrate regions

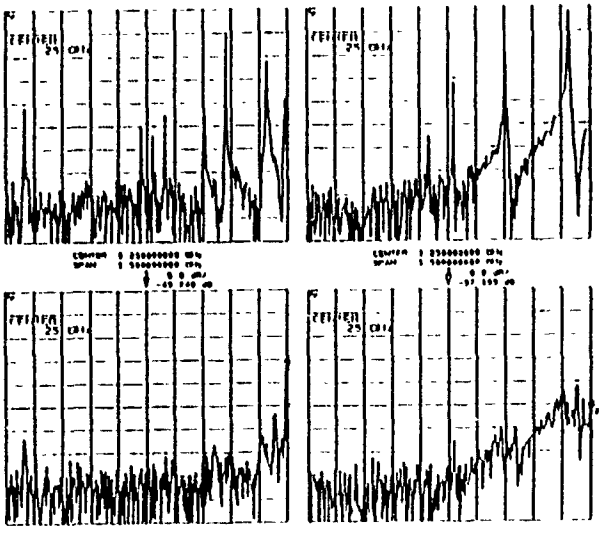


Fig. 3

of high field density. The length of each probe was adjusted for maximum mode attenuation. Care was taken to avoid coupling to the fundamental. A dipole mode at 600Mhz was damped with two shorted loops installed at ports located 90° apart. The adjustable shorts were positioned for maximum damping and then locked into place. The results of damping the dipole and monopole modes are shown in Fig. 3.

For the Phase II Cavity, a broadband mode damper was developed using a wave guide as a high pass filter. The waveguide design chosen is a capacitively "T" loaded wave guide which reduces the waveguide dimensions to be compatible with the cavity port dimensions. The cutoff frequency of 300 MHz presents good isolation of the fundamental and a reasonable guide wavelength for an overall broadband termination. Fig. 4a shows the SUPERFISH field plot of the waveguide at cutoff.

Several terminations were tried on the waveguide: simple resistors in parallel across the gap, and two different taper lengths of ferrite loaded rubber. A 'discrete' slotted line was developed by drilling probe holes along the length of the waveguide and measuring the standing wave. The 8 inch taper was chosen (see Fig. 4c) as a result of these measurements. It is believed that the increase in VSWR at 2518 MHz is a result of a higher order mode propagating in the waveguide, with a cutoff frequency of 2426 MHz, which is not properly terminated. The final design will include absorber material placed to attenuate this mode.

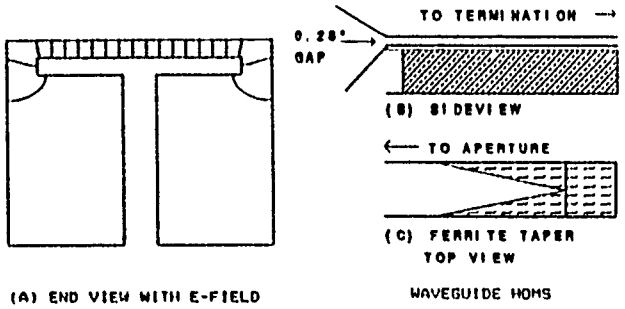


Fig. 4

The coupling was arrived at empirically, by optimizing the attenuation of monopole modes with a single waveguide. Aperture coupling was the most successful and was optimized by extending the top and bottom surfaces of the waveguide gap into the cavity then tapering them to intercept more field, much like a parallel plate tapered horn, as shown in Fig. 4b.

Two aperture coupled waveguides were installed orthogonally to each other and tested on a low power test cavity. The results are shown in Table I. In the final design, the rubber-based ferrite absorber will be replaced with a vacuum compatible ferrite material.

RF System and Control

A single 65 KW, 211.54 MHz RF power amplifier system is required to supply power to the cavity field gradient and for beam loading. The system will have amplitude and phase control as well as 1 MHz of resonator tuning to compensate for the reactive loading of 0.5 amps of beam current.

All setpoints and monitors will be computer controlled through a CAMAC interface chassis driven by HP workstations[3]. Two custom boards will contain the phase, amplitude and tuner controllers.

MONOPOLES		DIPOLES	
FREQUENCY (MHz)	Attenuation (dB)	FREQUENCY (MHz)	Attenuation (dB)
214	0.18	620	7.5
785	17	855	5
1044	17	1144	16
1452	13	1575	12.5
1494	10.5	1917	0
1757	12.5	1369	11
2022	12.5	*1494*	6.5
		1875	12.5 - 15
2256	7 to 11	2118	17.5
2501	.5	2315	8.5 - 11
2594	1.5	2452	5
2833	.5		
2959	6		

Both waveguides were terminated with an 8 inch ferrite taper and aperture coupled using "duckbill" extensions of approximately 2.5 X 3.5 inches. The flange extension was angled at 30 to 45 degrees, T-ext at 45 degrees.

Table I

A 4KW, solid-state amplifier drives power into the final stage powered by a water-cooled Eimac 4CW100,000E tetrode, fitted into a custom resonator. The complete system is being manufactured by the QEI Corporation, Williamstown, N.J. as per NSLS specifications.

Conclusions

The Phase I facility has operated with circulating beam in excess of 1 ampere at 200 MeV, and consistently runs with currents of 600 mA. Injection studies are also being done at 80 MeV and at 120 MeV. The Phase II cavity and RF power assembly should be ready for assembly and test in about one year.

Acknowledgements

The authors would like to thank Werner Pirkl for suggesting the T-loaded waveguide structure for use as a HOMS and Wayne Broome for his valuable contributions in its development. Special thanks go to Jeff Aspenleiter, Scott Buda and Gloria Ramirez for their excellent technical support.

References

[1] P. Mortazavi, S. Sharma, J. Keane and M. Thomas, "Mechanical Design of SXLS Radio-Frequency Cavity", Proc. of the 1989 IEEE Part. Acc. Conf.

[2] E.W. Hoyt and W. P. Schulz, "Titanium Nitride Coating of Aluminum Multipactoring Accelerating Structures, Stanford Linear Accelerator Center", SLAC-TN-75-3.

[3] E. Desmond (BNL), J. Galayda (ANL), and W. Louie, B. Martin, R. Rose (Grumman Aerospace Corp.), "Control System of the Superconducting X-Ray Lithography Source at Brookhaven".

Low Power RF System For The ALS Linac

C.C. Lo, R. Taylor, and H. Lancaster

Accelerator and Fusion Research Division, Lawrence Berkeley Laboratory
University of California, Berkeley, CA 94720

Abstract

The Linear Accelerator (Linac) in the Advanced Light Source (ALS) is designed to provide either single or multiple bunchers of 50 MeV electrons for the booster synchrotron. Three cavities are used in the Linac for electron bunching. The two subharmonic bunching cavities operate at 124.914 MHz and 499.654 MHz respectively. The S Band buncher operates at 2.997924 GHz. The low level RF system includes a master signal source, RF burst generators, signal phase control, timing trigger generators and a water temperature control system. The design and performance of the system will be described.

I. Introduction

The Linear Accelerator of the ALS is used to provide single or multiple bunches of 50 MeV electrons for the booster synchrotron. Figure 1 shows the major components of the ALS Linac. The electron gun serves as the source of the electrons. A series of up to 19 micro electron bunches or a single macroelectron bunch is initiated by pulsing the cathode or gating the grid of the electron gun, respectively. The cathode of the gun is being pulsed by 124.914 MHz pulses which are derived from the 499.654 MHz Master Oscillator. The electron bunches exiting the gun and entering the 124.914 MHz buncher[1] has a width of 2.5 ns. The first buncher compresses the 2.5 ns bunch to a width of 800 ps. The 499.654 MHz buncher[1] further compresses the electron bunch to a width of 200 ps. After the 7th gap of the S Band buncher[2] the electron bunch attains a width of 20 ps. Input/Output ports have been provided for in all subsystems for the ALS Intelligent Local Controller (ILC) in the ALS Control System[3] to take control of most of the functions when required. Local controls on all functions are provided.

II. System Design and Operation

The 499.654 MHz master oscillator[4] is composed of two individual oscillators. One is a temperature compensated crystal oscillator (TCXO) and the other is a oven controlled/voltage controlled crystal oscillator (OC/VCXO). The OC/VCXO provides a signal tunable through a range of +/- 100 Khz via the local control or through the ILC to facilitate various physics investigators. Nine signal distribution amplifiers each producing 1 W are used to distribute the master oscillator signal to wherever it is needed.

A 6X multiplier converts the master oscillator signal to 2997.924 MHz for the S-Band RF system whereas a divider converts the master signal to 124.914 MHz for the first

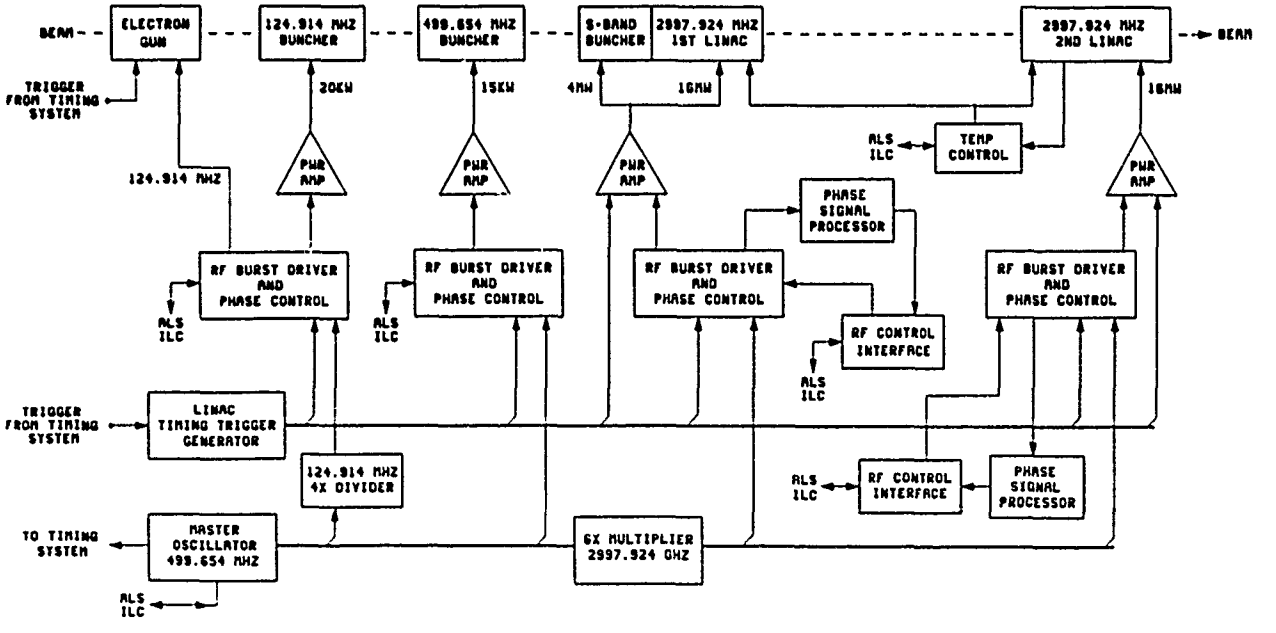


Figure 1. Block Diagram of the ALS Linac RF System

U.S. Government work not protected by U.S. Copyright.

subharmonic buncher RF system as well as for the Gun pulsing and the ALS Timing System.

The Linac RF system operates in the pulse mode. The pulsing frequency is 10 pulses per second. Only one of these pulses interacts with electron bunches, the other 9 pulses are used for calibration and tuning purposes. Three RF burst generators are used to drive two subharmonic bunchers, the S-Band buncher and two Linac guides. Phase adjustments and phase loops have been implemented in the designs to insure proper bunching and compensating for detuning due to various factors. The two subharmonic bunchers are pulsed on for 20 μS whereas the S-Band buncher and the two Linac guides are pulsed on for 1.5 μS.

The Linac operates at a temperature of 40 degree C. The water temperature is precisely controlled to within 1 degree by a Water Temperature Controller which compares the sensor signal with a stabilized voltage reference. The bipolar error signal is processed by two polarized amplifiers; one for heating and one for cooling. The error signal is also available to the ILC. The ALS Linac only requires heating, therefore the cooling part of the device is not used. The heating control output range is 0 to +10 V which is the input requirement of the SCR heater supply. The temperature can be set either locally or via the ILC.

In the two subharmonic buncher systems, the outputs from the RF burst generators drive the high power amplifiers which follow, producing 20 KW and 15 KW for the 124.914 MHz and the 499.654 MHz systems respectively. Due to the low Q design of the buncher cavities, a phase control loop is probably not necessary and has not been implemented at this time.

In the S-Band system, the output of the 6X multiplier drives the SLAC solid state amplifier[5]. The RF gate is set at 8 μS. The first 5-6 μS allows the phase of the output signal to stabilize before the Klystron amplifier is pulsed on. A fast response phase shifter is built into the SLAC solid state amplifier to perform internal phase stabilization[5]. The same phase shifter is also used for beam loading compensation[6] in the ALS.

It is important to keep the phase relationship between the RF signal and the electron bunch(es) at a proper constant for maximum bunching effect. Besides the manual or ILC adjustable phase shifters, provision for a phase servo loop has been set up to minimize the phase change from pulse to pulse. Figure 2 shows the functional block diagram of the Signal Processor. The phase error signal is derived from the SLAC Phase and Amplitude Detector[7]. At the moment when all signal phases have stabilized within the 1.5 μS S-Band RF burst, a sample of the phase error is taken, digitized and converted to a dc error voltage of the opposite sign. The voltage is fed back to the loop phase shifter and correct the phase for the next RF pulse. Since the transfer function of the phase and control voltage is not perfectly linear, the effectiveness of this concept still needs to be evaluated. The sampling of the phase error signal is only taken when there is no electron bunch to interact with the RF pulse. Output of the phase error signal and input for the phase correction to and from the ILC have been provided for possible future computer control of the phase loop.

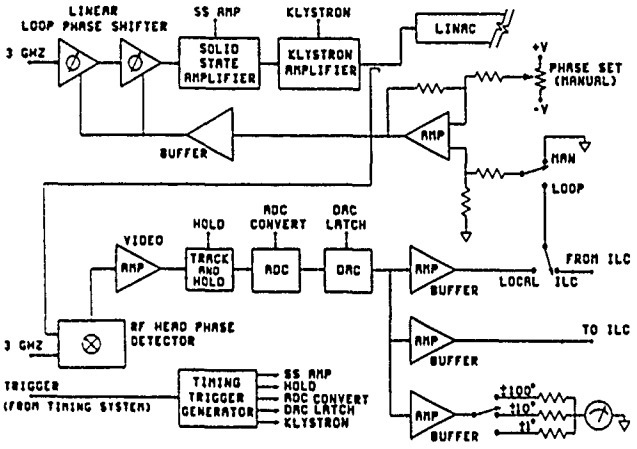


Figure 2. Block Diagram of the Phase Servo Signal Processor

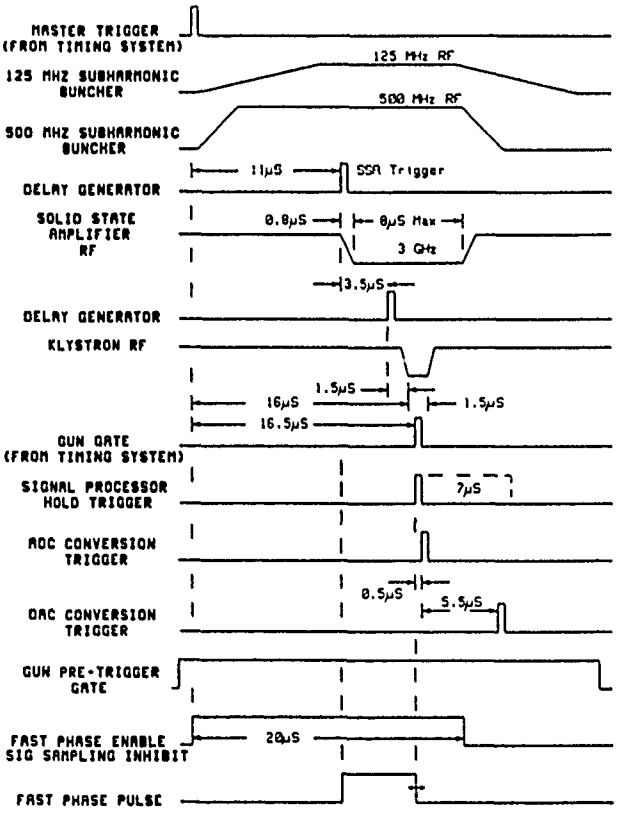


Figure 3. Timing Diagram of the ALS Low Power RF System

III. Timing Operation of the System

Figure 3 shows the timing operation of the Linac RF system. The sequence starts with a master trigger pulse, which either comes from the synchronized trigger generator in the Linac test phase or from the ALS Timing System in final operation. The master trigger pulse is then distributed via the Master Trigger Fan Out Module. The output trigger pulses are used to trigger the 125 MHz and 500 MHz buncher driver with each RF gate lasting 20 μS. Another trigger pulse is used to initiate the 11 μS delay

trigger for the S-Band solid state amplifier, which is gated on for 8 μS. The Solid State Amplifier has an inherent delay and takes a total of 0.8 μS for the RF to reach flat top. It takes another 4.7 μS for the signal phase to stabilize; a total of 5.5 μS to reach the phase stabilized region.

The solid state amplifier trigger starts two other delay triggers; one is the Klystron trigger which has a delay of 3.5 μS and the other one is the signal processing hold trigger, which has a 5.5 μS delay. From the time the Klystron amplifier is triggered to mid way of the flat top portion of the Klystron RF pulse, it takes 2 μS. Therefore at the flat top portion of the Klystron RF gate, the Solid State Amplifier is also in the phase stabilized region. At this time, 16.5 μS after the Master trigger, the Gun pulse arrives at the Linac. Also at this time when there is no Gun pulse, that is 9 out of 10 pulses, the signal processing hold trigger is initiated to sample the phase error of the system. 500 nS after the signal processing hold trigger, the ADC start convert trigger is started and 5.5 μS after that, the DAC convert trigger is initiated. The output of the Signal Processing Module is a dc signal whose level corresponds to the phase error of the S-Band system. A dc signal with the opposite sign is send to the loop phase shifter correcting the phase for the next RF pulse. The accuracy of the correction depends on the linearity of the transfer function of the phase and control voltage of the phase shifter.

A Gun pre-trigger signal from the Timing System is present whenever a gun pulse is expected. This pre-trigger pulse is used to start a 20 μS gate which inhibits the sampling of the phase error whenever beam loading is expected. This 20 μS gate also enables a Fast Phase Pulse which is necessary to compensate for the beam loading effect on the accelerator RF. The timing, the width, and the amplitude of the Fast Phase Pulse are adjusted to obtain the best results in beam loading compensation. This signal is sent to the fast phase shifter in the front end of the solid State Amplifier to change the phase of the RF signal to perform this task.

IV. Conclusions

The design and operation of the low power RF system for ALS Linac have been presented. A total of more than 30 pieces of electronics components have been fabricated to build the system. In the S-Band system, the phase shifters, the phase and amplitude detector and the solid state amplifier are built by SLAC. The Linac produced the first beam in February 1991 in the trial run. A 50 MeV beam was obtained as monitored by a Faraday Cup at end of the Linac in March 1991. The low power RF system electronics components, however, have been running since November of 1990 without any problem. Operating experience still have to be acquired to evaluate the effectiveness of the phase loop servo in the S-Band system.

V. Acknowledgment

The authors express their thanks to A. Geyer for his efforts in coordinating the fabrication of most of the electronics components in the system described.

*This work was supported by the Director, Office of Energy Research, Office of Basic Energy Sciences, Materials Sciences Division of the U.S. Department of Energy, under Contract No. DE-AC03-76SF00098

VI. Reference

1. C.C. Lo, B. Taylor, H. Lancaster, and J. Guigli, "Advanced Light Source Linac Subharmonic Buncher Cavities;" Proceedings of 1989 IEEE PAC, Vol.1, pp. 956-958. LBL-25975.
2. B. Taylor, H. Lancaster, and H. Hoag, "Engineering Design of the Injector Linac for the Advanced Light Source;" Presented at the 1988 Linear Accelerator Conference, Williamsburg, VA, October 2–7, 1988, LBL-26025.
3. S. Magyary, et al., "Advanced Light Sourc Control System;" Proceedings of 1989 IEEE PAC, Vol. 1, pp. 74–78, LBL-28412.
4. C.C. Lo, B. Taylor and K. Baptiste, "Advanced Light Source Master Oscillator;" Proceedings of 1989 IEEE PAC, Vol. 1, pp. 118-120, LBL-25974.
4. J.G. Judkins, J.E. Clendenin and H.D. Schwarz, A Solid State High Power Amplifier For Driving The SLC Injector Klystron, Proceedings of 1985 IEEE PAC. SLAC-PUB-3610, March 1985.
5. J.G. Judkins, J.E. Clendenin, and H.D. Schwarz, "A Solid State High Power Amplifier for Driving teh SLC Injector Klystron;" Proceedings of 1985 IEEE PAC, SLAC-PUB-3610, (March 1985).
6. F. Selph, "Compensation of Beam Loading in the ALS Injector LInac;" Presented at the 1988 Linear Accelerator Conference, Williamsburg, VA, October 2–7, 1988, LBL-25630.
7. J.D. Fox and H.D. Schwarz, "Phase and Amplitude Detector System for the Stanford Linear Accelerator;" Proceedings of 1983 IEEE PAC, SLAC-PUB-3071, March 1983.

Initial Operating Experience with the Auxiliary Accelerating Cavity for the TRIUMF Cyclotron

R.E. Laxdal, K. Fong, G.H. Mackenzie, V. Pacak, J.B. Pearson, L. Root, M. Zach
TRIUMF, 4004 Wesbrook Mall, Vancouver, B.C., Canada V6T 2A3

Abstract

A 92 MHz auxiliary accelerating cavity has been installed in the TRIUMF cyclotron. It operates at the fourth harmonic of the dee frequency with a planned peak voltage of 150 kV. At full power it will almost double the present energy gain per turn in the 400-500 MeV range, reducing by 25% the stripping loss of the H^- beam. Low current beam tests have been conducted at voltages of up to 90 kV and a maximum voltage of 145 kV has been attained. The cavity has also been used to flattop the integrated energy gain per turn. A description of the cavity design and a summary of the operating experience is given.

I. Introduction

The 500 MeV TRIUMF cyclotron routinely accelerates 150 μA of H^- ions. Electromagnetic stripping, rising rapidly from 400 MeV, is responsible for ~1/2 of the total particle losses and ~2/3 of the total activation of the cyclotron. The use of additional accelerating cavities was suggested as early as 1983 [1], primarily to aid in improving the extraction efficiency for H^- extraction for injection into a KAON Factory [2]. However, even after another method of improving extraction efficiency was chosen [3], the increased energy gain per turn and consequent reduction in the number of turns, hence losses, in the outer radial region were sufficient motivation to design, manufacture and install one cavity.

The cavity operates at the fourth harmonic (92.24 MHz) of the main rf frequency and consists of a trapezoid of dimension $\lambda/4$ radially and $\beta\lambda/2$ azimuthally, so that the orbiting ion receives two acceleration impulses on each passage (Fig. 1). The peak accelerating voltage rises sinusoidally with radius, covering the energy range from 370-520 MeV. The maximum energy gain per turn will increase from the present 320 keV to 620 keV.

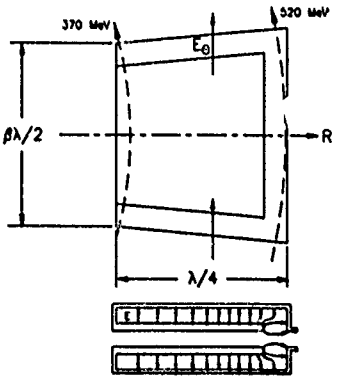


Figure 1: Schematic view of the cavity.

II. Cavity and Amplifier Design

The cavity has been described elsewhere [4]. Briefly, it consists of two halves (Fig. 2), placed above and below the beam plane, separated by 64 mm and mounted independently from the vacuum chamber floor and lid to minimize activation. All conducting walls defining the rf boundaries are made from 1.6 mm thick OFHC Cu sheets with most seams TIG welded, and then brazed together. The cantilevered hot arm is exceptionally stiff (~220 N/mm) to minimize tip vibrations (2.7 μm p-p @ 20 Hz). Cooling circuits were designed to limit the temperature rise from the skin losses (up to 8.5 W/cm^2) to below 25°C. Coarse frequency adjustment is done on assembly by shimming the hot arm to ground arm distance. Fine tuning is provided by a water cooled, hinged flap, built into each ground arm, actuated through a zero backlash linkage system. Each cavity half can be remotely installed in ~20 min.

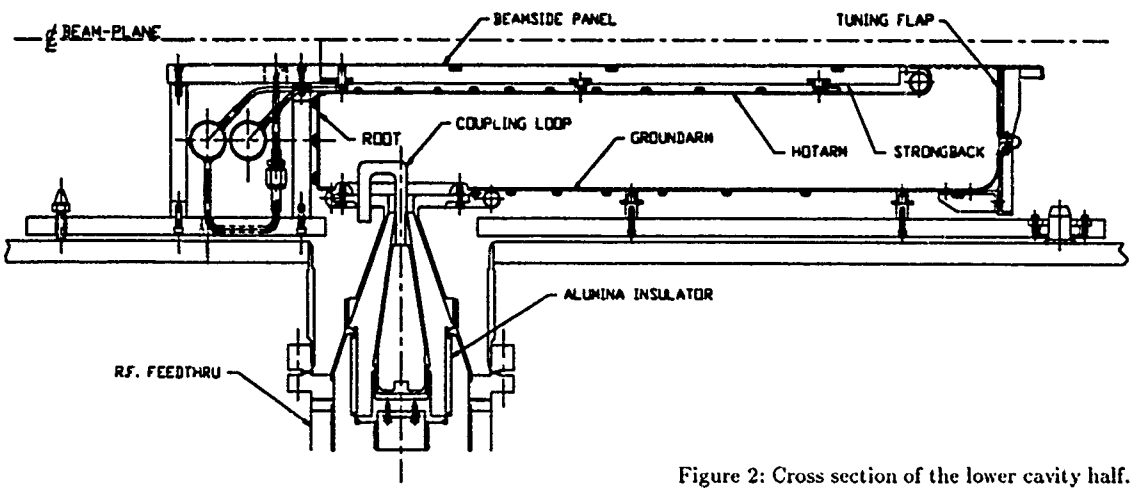


Figure 2: Cross section of the lower cavity half.

0-7803-0135-8/91$01.00 ©IEEE

The water cooled coupling loop is connected to a 6 inch transmission line of adjustable length via a smooth transition section. A single tetrode power amplifier can deliver 160 kW, well in excess of the power required (~120 kW) for a voltage of 150 kV and a 200 μA beam.

III. Low Level RF and Control System

A block diagram of the control system is shown in Fig. 3. The cavity voltage, sampled by a capacitive probe, is demodulated by a temperature-compensated diode detector, and feedback regulated by a Proportional-Integral-Derivation (PID) controller, resulting in a stability of better than 0.5%. The phase is regulated to better than 1° by a 40 dB dynamic range phase detector and another PID controller. The gain and frequency parameters of the PID controllers are programmable through a dedicated microprocessor embedded in a VME crate. This enables the feedback parameters to be changed in response to eventual gain variations. The microprocessor also handles automatic power-up sequencing, system status monitoring, and local display/control, and in addition, communicates with the cyclotron central control system through ethernet.

The 92 MHz rf for the cavity is generated from a phase-locked loop (PLL) referenced to the 23 MHz signal from the cyclotron dee gap. The PLL output signal is four times the frequency of the input reference, with a phase noise level less than −60 dBc at 10 kHz from the carrier. This output is split into two parts: one is used as the phase reference; the other is amplitude and phase modulated before it is used to drive the power amplifier chain. A digital frequency-hold/pull-in circuit enables the PLL to hold its frequency indefinitely when the reference signal is absent. This allows the cavity to maintain thermal equilibrium even when the cyclotron rf is turned off. If the reference signal returns at a frequency different from the previous setting, the capture process in the PLL is deliberately slowed down to enable the tuning mechanism in the cavity to follow the frequency drift until the error is less than 10 kHz. The phase loop is then closed, and the output frequency locked to the reference.

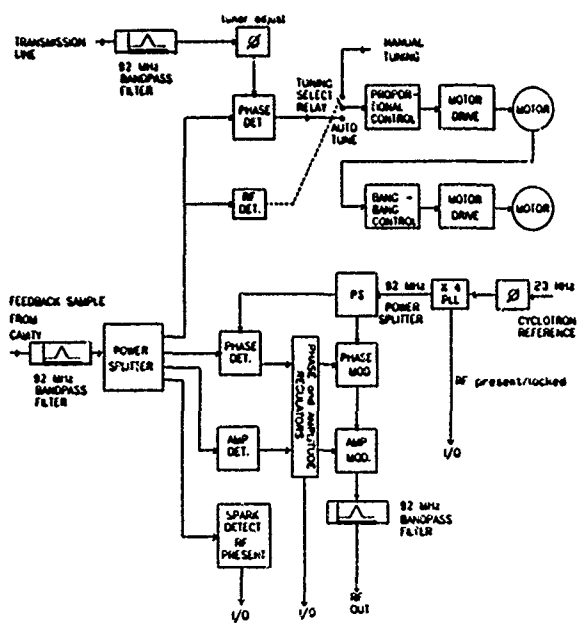


Figure 3: A block diagram of the control system.

The signal for the cavity tuning flaps comes from an independent servo loop which compares the phase difference between the rf field at the cavity accelerating gap and at the coupling loop, and activates a pair of flap drives to maintain the phase difference at 90°. The servo loop is disabled by an additional circuit when the cavity voltage is below the multipactoring level.

IV. Commissioning

The cavity was pre-commissioned outside the cyclotron in an auxiliary vacuum vessel. Signal level measurements using an HP network analyzer and on-line modelling using a computer code, NODE [5], provided significant time saving in the pre-commissioning phase.

Installation of prototypes in the cyclotron and initial high power testing can only be done during the scheduled shutdowns that occur twice a year. The cavity was installed in April 1990, and a voltage of 100 kV was achieved in several hours. Pressure excursions in the cyclotron, probably due to rf heating, stopped the first commissioning phase at this point.

In the second commissioning session in October 1990, 145 kV was achieved, but later a failure in the high voltage vacuum feedthrough caused a premature curtailment of the test. During the repair of the feedthrough it was also noted that rf energy, leaking out of the cavity, had damaged a beam diagnostic probe a few metres away.

In subsequent tests the control system was successfully commissioned. In the latest shutdown in April 1991, top-bottom telescopic shorting contacts were added to the cavity outside the 520 MeV beam orbit, to help reduce the rf leakage. Further commissioning will commence immediately after this conference and it is expected that the design voltage will be achieved at this time.

V. Beam Tests

The first tests with beam were done during the initial commissioning. The beam induced voltage in the cavity, while tuned to the resonant frequency but not energized, was 10 kV with 100 μA circulating. Detuning the cavity by 200 kHz reduced the induced voltage to 3% of the above value. The cavity was then energized to 90 kV and a series of measurements were taken with circulating currents of low intensity. In Fig. 4 time-of-flight (TOF) measurements of the beam through the cyclotron are summarized and compared with results from computer simulations. The measurements show that, even at 90 kV, reductions of ~20 μsec or ~100 turns are possible, depending on the isochronism and beam phase width, and at 150 kV a reduction of 140 turns is expected. This would reduce the activation from electro-magnetic stripping by ~35%.

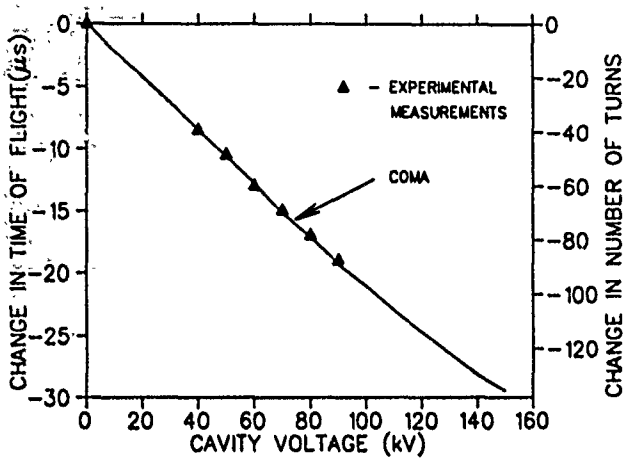


Figure 4: The reduction in the measured time-of-flight (TOF) of the beam through the cyclotron to 500 MeV for various cavity voltages is compared to the results of a computer simulation using the matrix code COMA [6]. The reduction in number of turns is also shown. (Without the cavity the beam makes ~400 turns in the cavity region.)

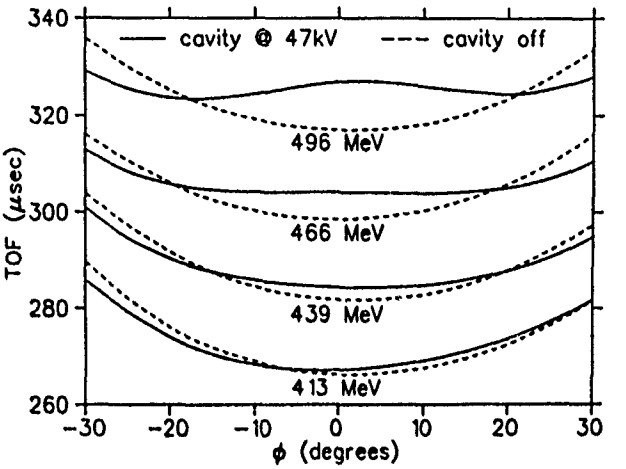


Figure 6: Measured then smoothed TOF curves for four different energies as a function of initial phase for *cavity off* (dashed curve) and *cavity on* at 47 kV (solid curve). The cavity was phased to give the best flattop at 466 MeV.

Lower voltages were used to investigate the use of the cavity in flattopping the energy gain per turn. In an isochronous cyclotron the TOF is dependent on the energy gain per turn and the degree to which the magnetic field is isochronous. The time-variation of the fundamental accelerating field is responsible for a cosine-like phase dependence in the energy gain per turn, and hence the TOF is also affected. This variation in the TOF with phase can be reduced substantially, producing a flattopping effect, by adding a higher harmonic cavity opposed to the fundamental. The higher the harmonic number of the cavity, the narrower would be the resultant flattop. The cavity voltage determines the number of turns through the cavity necessary to reach the optimum flattop condition.

For the test the initial beam phase width (23 MHz) was reduced from the nominal 30° used for high current operation, to 5° by inserting radial slits in the centre region. The position of the phase-band with respect to the accelerating field was then altered by scanning the rf frequency, and the TOF was recorded. In Fig. 5 the measured TOF values to 500 MeV are plotted as a function of initial phase for various cavity voltages. At 36 kV an optimal flattop occurs over a phase range of ~30°. The slightly asymmetric result at 48 kV shows the effect of the cavity field being slightly out of phase with respect to the fundamental, prior to optimization.

The cavity was then powered to 47 kV and phased to give the optimum TOF flattop at an energy of 466 MeV. At this setting the TOFs to various other energies were also recorded (Fig. 6). *Cavity on* results are compared with the corresponding *cavity off* data. The figure shows how the cumulative effects of the opposing cavity field produce optimal flattopping at only one energy. The variations in the phase of the minimum TOF are due to radial variations in the cyclotron isochronism.

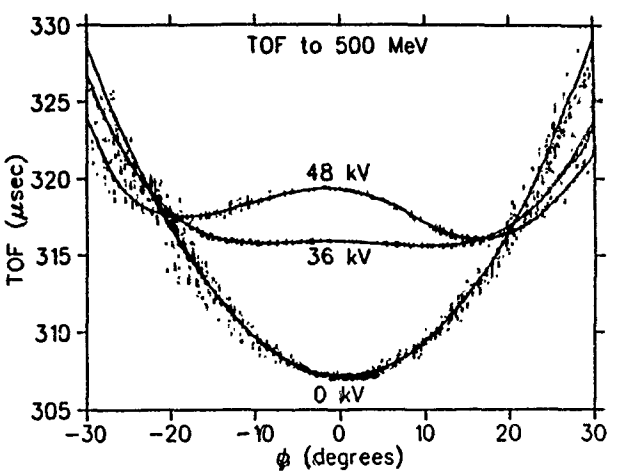


Figure 5: Measured TOF values to 500 MeV as a function of the initial phase for three different cavity settings, 0 kV, 36 kV and 48 kV, with the cavity phased to oppose the fundamental. Smooth curves are plotted through the experimental data points.

VI. References

[1] J.R. Richardson, TRIUMF report TRI-DN-83-42, 1983.

[2] M.K.Craddock, "The TRIUMF KAON Factory", these proceedings.

[3] R.E. Laxdal, *et al.*, IEEE Trans. Nucl. Sci. NS-32 No.5, p. 2453, 1985.

[4] M. Zach, *et al.*, *Proc. European Part. Accel. Conf.*, p. 973, Nice, 1990.

[5] K. Fong, TRIUMF report TRI-DN-89-33, 1989.

[6] C. Kost and G. Mackenzie, IEEE Trans. Nucl. Sci. NS-22 No.3, p. 1922, 1975.

CONDOR SIMULATION OF AN 11.4-GHZ TRAVELING WAVE OUTPUT CAVITY*

Y. Goren† And D. Yu
DULY Consultants, Rancho Palos Verdes, CA 90732

Abstract

The CONDOR code is used to simulate the cold test and the beam-induced microwave amplification of an 11.4-GHz, six-cell, disk-loaded, traveling wave cavity. Cold test simulation results are in agreement with a modified Slater's theory. Power extraction at the output port is calculated by launching a train of Gaussian electron bunches through the structure. Results are consistent with recent relativistic klystron experiments using a similar TW output cavity. It is further shown that, depending on operating beam parameters, the power extraction efficiency can be maximized by modification of various cells in the TW structure.

INTRODUCTION

Recently there has been a resurgent interest in the traveling wave (TW) amplifier as an output power extractor for high-power klystrons. One reason is that the peak electric fields at the gaps are lower for multiple cavities, thereby mitigating the possibility of breakdown and other anomalous beam loading at the output gap of high-power devices. Recent experiments by a SLAC/LLNL/LBL collaboration[1] generated over 300 MW of microwave power using an 11.4-GHz traveling wave amplifier driven by relativistic electron bunches from an induction linac. The experimental work was aimed to investigate the relativistic klystron concept as a high power microwave source for future high gradient accelerators. A six-cell, traveling wave (TW), $2\pi/3$ disk-loaded structure[2] was used as a power extractor. With this output cavity a threefold power enhancement over a standing wave cavity used in previous experiments was observed without any pulse shortening. The TW structure was able to achieve power levels of about 300 MW with a beam of 1.3 MeV of kinetic energy and 600 A of current.

This paper reports on an effort to numerically simulate the cold test and the beam-induced high power microwave amplification of TW ouput cavities using the CONDOR program. The CONDOR code is a self-consistent, 2-1/2 dimensional electromagnetic and particle time-domain simulation code. It has the capability of utilizing external ports for driving or extracting electromagnetic radiation from an rf structure. Results of the simulations are compared with theories and experiments.

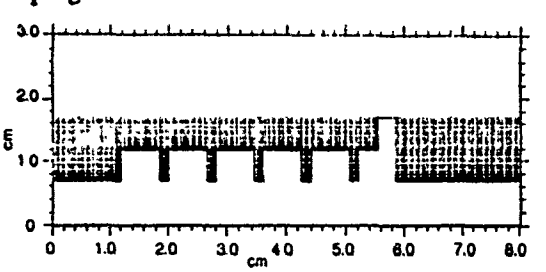


Fig. 1 Six-cell TW structure model

CONDOR SIMULATION

A six-cell TW cavity described in Figure 1 is used as the basic structure for simulation. The cavity diameter is 2.5 cm and the iris diameter is 1.5 cm. The disk thickness is 0.15 cm. The total cavity length is 4.65 cm. These dimensions are close, though not exactly the same as the cavity in references 1 and 2. They are conveniently chosen for this study so that the boundaries of the cells coincide with the mesh lines in a model of moderate size. An axisymmetric output port is opened in the last cell to extract rf power from the structure. The aperture of the output port is critically coupled to the last cell. This is done by launching an 11.4-GHz rf wave through the structure, and adjusting the output aperture dimensions until reflections into the last cell are eliminated. Using this cold test simulation technique, we study the axial electric field behavior along the cavity. Figure 2 is a 'snapshot' of the E_z field at steady state. The average wavelength is 2.91 cm, leading to an average phase velocity of 1.11c. The coupling of the cavity to the external port results in a tapering of the rf phase velocity from about 0.97c at the first cavity to about 1.24c at the output port. No attempt was made to optimize the phase velocities to synchronize with the electron velocity for maximum power extraction.

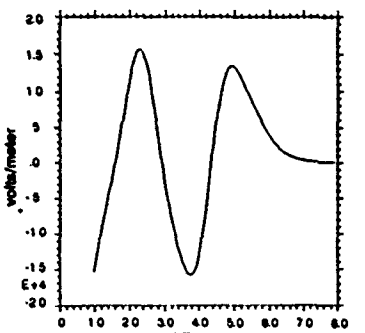


Fig. 2 Axial electric field at 6.5 nanoseconds

An important parameter which characterize any TW structure is the interaction impedance defined by $Z \equiv E_z^2/(K^2P)$, where K is the wavenumber and P is the power flow through the structure. The interaction impedance vs. axial length is plotted in Figure 3. It is seen that the

0-7803-0135-8/91$01.00 ©IEEE

impedance of the first cell is about 1/6 of the adjacent cells, implying a relatively low contribution of this cell to the overall power. The impedance of the last cell is expected to be low as the electric fields decay towards the output port (see Figure 2).

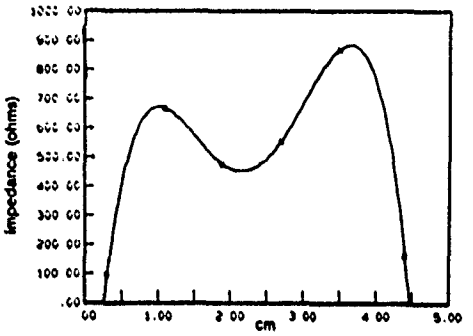


Fig. 3 Interaction impedance for 6-cell TW cavity

Introduction of beam loading into the rf structure is done by launching a fully bunched Gaussian beam with temporal width of 0.125T, where T is the rf period. The beam assumes a Maxwellian energy distribution of one percent around 1.2 MeV of kinetic energy. Figure 4 describes the electromagnetic spectrum of the output power for the case of 300 A of rf current. A second harmonic signal of 8 dB below fundamental (and a third harmonic) is observed. These harmonics reflect the spectral contents of the Gaussian bunches used in the simulation. The

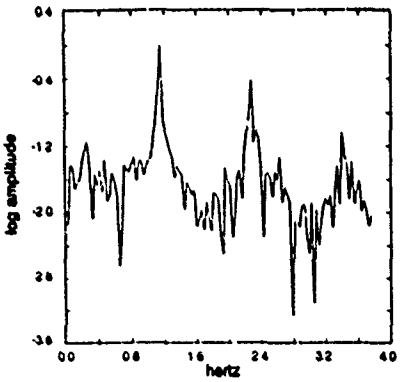


Fig. 4 Fourier components of output power

instantaneous power flow through the output port for a 1.2-MeV, 300-A driving beam is shown in Figure 5. After four nanoseconds of power overshooting, a steady state is

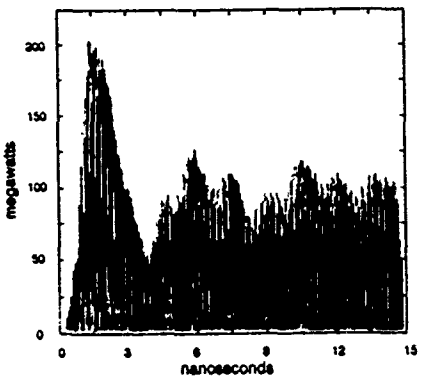


Fig. 5 Output power for a 6-cell cavity

established with an average power of 52.8 MW. Low frequency modulation of the rf power is observed throughout the entire pulse. Filtering or suppressing this modulation is required for stable phase operation. Figure 6 shows the output power vs. beam current. At low currents, the power increases quadratically. At higher currents, it varies linearly before tapering toward saturation. A peak power of 296 MW is achieved for an rf current of 700 A, with a saturated efficiency of 33%. The maximum electric field on the cavity surfaces under this operating condition does not exceed 1.2 MV/cm. Thus even without optimizing the TW structure, the CONDOR simulation is consistent with the experimental results of ref. 1.

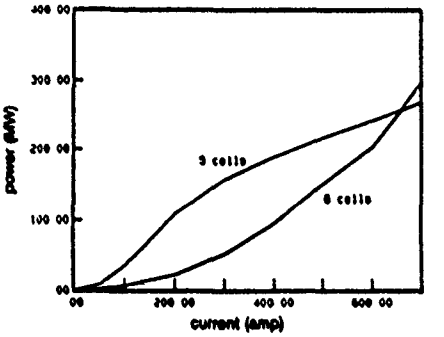


Fig. 6 Comparison of 5- and 6-cell cavity output power

By modifying various cells in the TW structure, the overall efficiency can be optimized for a given electron beam. For a 300-A, 1.2-MeV beam we have found that by applying high rf absorption to the first two cavities the efficiency increased from 14.8% to 16%. A substantial increase in efficiency is found in this case by reducing the cavity length from 4.65 cm to 4.0 cm while eliminating the first cell, leaving the structure with five cells. A peak rf power of 172 MW is obtained for a 1.2-MeV, 300-A beam with this configuration. The power further increases somewhat with a small increase in the volume of the first cell. Finally we maximize the rf efficiency to about 43%, or 156 MW of power, for the geometry given in Figure 7. As shown in Figure 6, the efficiency is beam dependent and slowly decreases from 43% at 300 A to 32% at 700 A.

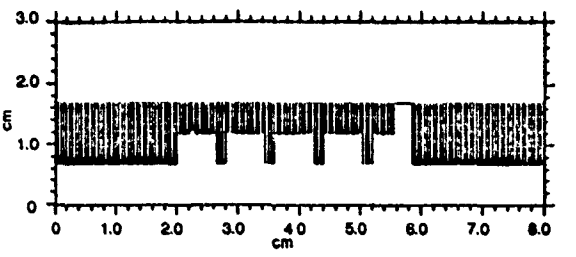


Fig. 7 Five-cell TW structure model

DISCUSSIONS

It is interesting to note that the numerical results for cold test in the last section agree well with J.C. Slater's theory, but not with J.R. Pierce's analysis of TW periodically loaded waveguide. The cold test phase velocity predicted

by Pierce for an infinite periodic structure with our six-cell geometry is 0.37c, compared with 0.97c to 1.24c variation obtained by the CONDOR code. Moreover the TW interaction impedance predicted by Pierce is about 8 ohms for this geometry, compared with the variation between 100 ohm to 900 ohm seen in Figure 3. The discrepancy is likely attributed to negligence in treating field distortion around the irises in Pierce's theory. Cold test numerical results, on the other hand, match quite well with the theory of periodic structures developed by J.C. Slater. A phase velocity of 1.14c is predicted for an infinitely long TW structure with about 600 ohms of interaction impedance.

Slater's approach can also be adopted for a finite-length structure as we show below. In this approach, a single cell is viewed as a two port (or four terminal) rf structure in which the iris is treated as a lump susceptance. Using Slater's notation the transverse electric and magnetic fields are related by:

$$I_n = iV_nY_0\,[\cot(kL)-b_0] - iV_{n+1}Y_0\csc(kL)$$

$$I_{n+1} = iV_nY_0\csc(kL) - iV_{n+1}Y_0\cot(kL)$$

where k is the wavenumber and L the length of a single cell, Y_0 is the waveguide admittance, $-ib_0Y_0$ is the iris susceptance, I_n and V_n are respectively the transverse magnetic and electric field for the nth cell. Eliminating I_n from two successive cells gives the relation among V_n:

$$V_{n+2} - V_{n+1}A + V_n = 0$$

For an infinitely long periodic structure one can substitute $V=V_0\exp(igL)$ to obtain an expression for the wavenumber:

$$\cos(gL) = \cos(kL) - \frac{b_0}{2}\sin(kL)$$

with the phase velocity given by $v_p = \omega/g$. For a finite length structure, the above equation for V_n becomes a matrix equation to which we have to apply appropriate boundary conditions at the ends of the structure. As an example we outline a design procedure for a six-cell cavity. Requiring zero transverse electric field on the l.h.s. of the cavity and a given reflection coefficient ρ on the r.h.s., we obtain a 4x4 matrix whose eigenvalues are given by the solutions of the secular equation:

$$(A^2-1)+(A_f-A)A(A^2-2) = 0$$

$$A_f = iZ[\sin(kL_6) + iZ\cos(kL_6)]^{-1}$$

where $Z=(1+\rho)/(1-\rho)$, and L_6 is the effective length of the last cell. We obtain immediately a particular solution for V_n, i.e. $V_1=0$, $V_2=1$, $V_3=A$, $V_4=A^2-1$, $V_5=A(A^2-2)$, and $V_6=A_fA(A^2-2)$. Starting with a closed cavity ($\rho=-1$), we can solve the secular equation analytically to give four modes which have, respectively, $\pi/6$, $\pi/3$, $\pi/2$ and $2\pi/3$ phase shift per cell. The cell dispersion relation is given by:

$$A = 2\cos(kL) - b_0\sin(kL)$$

$$\textit{where} \qquad A = \pm\sqrt{\frac{3}{2}\pm\frac{\sqrt{5}}{2}}, \qquad k = \sqrt{\left(\frac{\omega}{c}\right)^2 - \left(\frac{2.405}{R_w}\right)^2}$$

for the propagating mode in the cell. R_w is the cavity radius. Given the operation frequency f and the beam energy the length of each cell is determined by the requirement of synchronizing the electron velocity with the phase velocity (v_p). For example, $L=v_p/3f$ for $2\pi/3$ mode, and $L=v_p/4f$ for $\pi/2$ mode. The wall radius is determined for a given iris susceptance. The iris susceptance can be calculated using the SUPERFISH code ($b_0=0.99$ in our CONDOR runs). Next, changing the reflection coefficient ρ from -1 to 0 will allow for output power flow. For a given value of ρ, an eigenvalue k (now complex) is obtained from the secular equation for the mode of interest. To keep the cavity on resonance, the wall radius, R_w, can be obtained from the real part of k. Finally, the waveguide-loaded Q of the TW cavity is determined by the imaginary part of k. A further extension of the modified Slater method to include beam loading for a finite length structure is being considered.

SUMMARY

We have presented numerical simulation results for a TW output cavity using the CONDOR code. The results are consistent with data from recent relativistic klystron experiments. It is shown that the simulation technique can be a useful tool to complement other TW cavity design methods. A simple design procedure has been outlined to determine the dimensions of the TW cavity.

ACKNOWLEDGEMENTS

We thank S.T. Brandon and R. Ryne of LLNL, and P. D. Coleman of SSC Laboratory for helpful discussions.

*Work supported by DOE SBIR grant DE-FG03-90ER81080

†Now at the SSC Laboratory

[1] G. Westenskow, et. al. UCRL-JC-103784, Proc. of 1990 Linear Accelerator Conference, Albuquerque, NM, September 10-14 (1990) p. 192.

[2] J. Haimson, B. Mecklenburg, Proc. of 1990 Linac Conf. (1990) p. 244.

[3] J.R. Pierce, "Traveling-Wave Tubes", D. Van Nostrand Company Inc.

[4] J.C. Slater, "Microwave Electronics", Dover (1950)

Switchable 10 Hz/1 Hz LEB Magnet Power Supply System

Cezary Jach
Superconducting Super Collider Laboratory*
Accelerator Division
2550 Beckleymeade Avenue
Dallas, Texas 75237

Abstract

The Low Energy Booster (LEB) is a rapid cycling synchrotron to be built at the Superconducting Super Collider Laboratory in the Injector Complex. The Low Energy Booster will be ready for operation by late 1995.

The LEB is used to accelerate protons from an injection momentum of 1.2 GeV/c to an extraction momentum of 12 GeV/c. The machine is a separated function design with dipole and quadrupole magnets driven by a single power supply system. Tracking errors between dipoles and quadrupoles are corrected by separate quadrupole magnets powered from independent power supplies.

The dipoles and quadrupoles are excited with a 10 Hz biased sine wave or 1 Hz linear ramp. Change of operating mode from 10 Hz to 1 Hz takes no more than 2 hours.

This paper describes the present design of the ring magnet power supply system.

I. INTRODUCTION

In the 10 Hz operating mode dipole and quadrupole magnets are excited with a biased sinusoidal current of the form:

$$i(t) = I_{dc} - I_{ac}\sin(2\pi ft) \qquad (1)$$

In the 1 Hz operating mode the magnets are energized with a piece-wise linear current having approximately 0.3 second linear rise, 0.3 second linear fall, 0.1 second flat bottom, 0.1 second flat top. Remaining 0.2 second is reserved for connecting the linear segments via parabolas.

Both modes of operation require the power supply system to produce a peak current of 3750 Amperes. The regulation requirement for both modes is 100 ppm of full scale.

II. MAGNETS

The ring magnet power supply system energizes 138 main magnets in the booster, 48 dipoles and 90 quadrupoles. There is 1 type of dipole and 5 types of quadrupoles (5 different lengths). The magnet excitation coils are copper conductors with a cooling hole in the center. Magnet parameters are listed in Table 1.

Table 1. LEB Magnet Parameters

Number of dipoles	48
Peak current	3750 A
Peak field	1.3 T
Dipole inductance	4.8 mH
Dipole dc resistance	4.2 mΩ
Dipole ac resistance at 10 Hz	7.3 mΩ
Number of quadrupoles	90
Quadrupole peak current	3750 A
Quadrupole peak pole tip field	0.8 T
Quadrupole mean length	0.6 m
Quadrupole mean inductance	0.3 mH
Quadrupole mean dc resistance	1.5 mΩ
Quadrupole mean ac resistance at 10 Hz	2.3 mΩ

Figure 1 shows the power supply network. The two modes of operation are provided by this network.

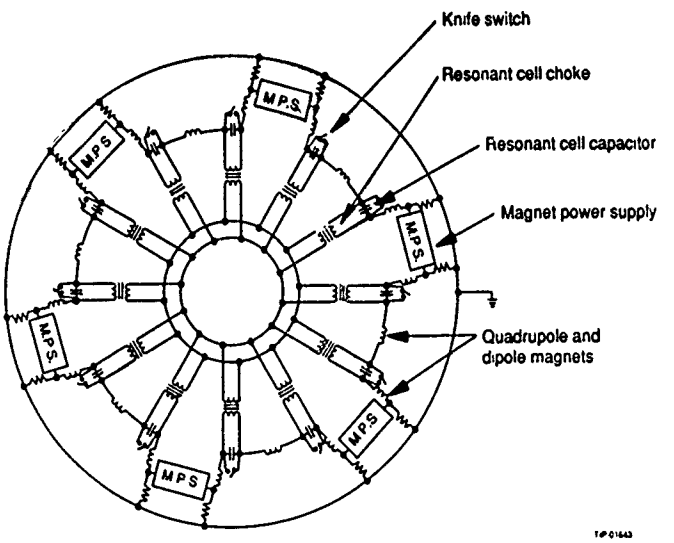


Figure 1. LEB Magnet Power Supply Network

*Operated by the Universities Research Association, Inc., for the U.S. Department of Energy under Contract No. DE-AC02-89ER40486

U.S. Government work not protected by U.S. Copyright.

III. 1 Hz Mode of Operation

In the 1 Hz mode, the knife switches are closed. Figure 2 shows the magnet current waveform.

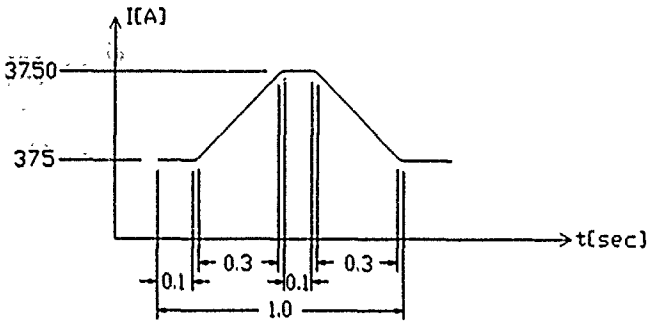


Figure 2. Magnet current waveform, 1 Hz mode of operation.

The power supply parameters for 1 Hz mode are listed in Table 2.

Table 2. Power Supply Parameters, 1 Hz Mode

Magnet load dc resistance	340 mΩ
Magnet load inductance	260 mH
Maximum output current	3750 A
Minimum ramp/reset time	0.3 sec
Maximum dI/dt	11.25 kA/sec
Maximum voltage required	4230 V
Number of distributed power supplies	6
Power supply peak voltage	700 V
Power supply peak current	3750 A
Power supply rms current	2270 V
Maximum operating voltage to ground	350 V
Current regulation	100 ppm of full scale

IV. 10 Hz Mode of Operation

In the 10 Hz mode, the knife switches are open. The power supply system is required to produce current of the form (1). Figure 3 shows the magnet current waveform.

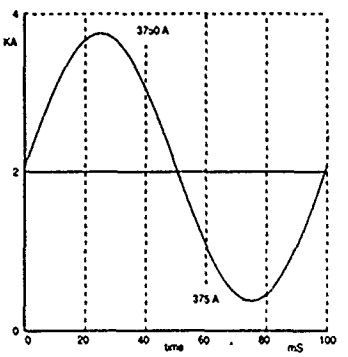


Figure 3. Magnet current waveform required for 10 Hz.

To avoid drawing a large reactive power from the ac source, it is necessary to use a circuit which is resonant at 10 Hz and in addition provides a path for the dc bias current. These requirements are satisfied by the distributed resonant circuit shown in Figure 1. The power supply specifications for 10 Hz mode are listed in Table 3.

Table 3. Power Supply Parameters, 10 Hz Mode.

Total magnet inductance	260 mH
Number of resonant cells	12
Resonant choke inductance	35 mH
Number of chokes	12
Resonant capacitor capacitance	18.8 mF
Number of capacitor banks	12
Single cell parameters	
Resonant cell magnet load dc resistance	28.3 mΩ
Resonant cell choke dc resistance	15.0 mΩ
Resonant cell dc resistance	43.3 mΩ
Maximum magnet dc current, I_{dc}	1875 A
Dc voltage required	81 V
Resonant cell magnet load ac resistance	42.5 mΩ
Resonant cell choke ac resistance	22.5 mΩ
Resonant cell capacitor ac resistance	2.8 mΩ
Resonant cell magnet impedance	0.043 + j1.38 [Ω]
Resonant cell choke impedance	0.073 + j2.20 [Ω]
Resonant cell capacitor impedance	0.003 - j0.85 [Ω]
Resonant cell impedance	0.079 + j0.00 [Ω]
Peak magnet ac current, I_{ac}	1875 A
Ac voltage required	148 V
Total ring parameters	
Number of distributed power supplies	6
Power supply peak voltage	460 V
Power supply peak current	3750 A
Power supply rms current	2300 A
Total ring ac losses	1660 kW
Total ring dc losses	1830 kW
Total magnet stored energy	1850 kJ
Total choke stored energy	1950 kJ
Total capacitor stored energy	855 kJ
Total ring Q	32.4
Maximum operating peak voltage to ground	1420 V

V. Power Supplies

Six power supplies (M.P.S. in Figure 1) are used to energize the magnets in both the 1 Hz and 10 Hz modes. Figure 4 shows the basic power supply circuitry.

Two extended delta-wye transformers with three-phase full wave thyristor bridges operate off a 12.47 kV input line. The extended delta-wye transformer was chosen in order to achieve 6-phase, 12-pulse rectification and at the same time keep the impedance of both rectifier bridges matched. Bypass thyristors across the input of a passive filter provide a path for magnet discharge current. The passive filter is a second order damped low-pass filter. Its resonant frequency is approximately 100 Hz. The phase shift of the filter at 10 Hz is only -2°. The distortion of the filter output voltage has no noticeable effect on the magnet current because of the high Q of the 10 Hz resonant network. For 1 Hz operation, the output voltage is corrected in a fast voltage feedback circuit.

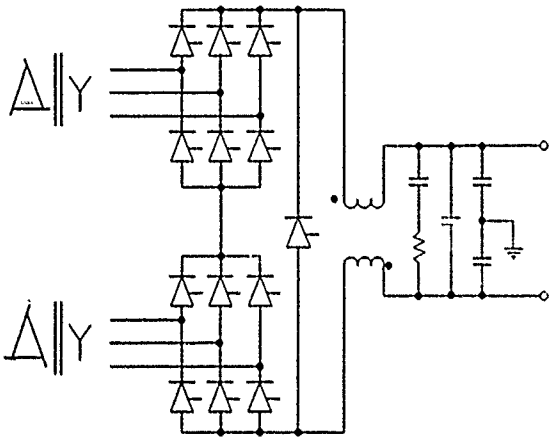


Figure 4. LEB power supply diagram.

VI. Power Supply Regulators

Two separate regulators are used to regulate the power supply voltage and current in two modes of operation.

The magnet current shown in Figure 2 and 3 must be repeated within 100 ppm of full scale. For the magnet current of Figure 3, the regulation is accomplished by a regulator which consists of a fast acting voltage loop controlled by the sum of two current loops. The voltage loop provides fast correction for line transients. Two components of magnet current, I_{ac} and I_{dc}, have their individual feedback loops. A precision zero-flux transductor is used to measure the magnet current. The two components are extracted from the transductor signal and compared with the two references. The current error signals are summed and used as the reference for the voltage feedback loop. The current loops' lagging corner frequencies are matched by adjusting the time constant of the feedback circuits around their error amplifiers. The current feedback loop open loop bandwidth is approximately 0.1 Hz.

For the magnet current of Figure 2 regulation is accomplished by a regulator which consists of two nested loops; a fast acting voltage loop for rejecting line transients and a slower current loop. The same precision zero-flux transductor is used to measure magnet current. The current feedback loop has an open loop bandwidth of approximately 40 Hz. It provides correction for the magnet load pole (0.2 Hz) and has a dc gain of approximately 80 dB.

VII. Harmonic/Power Factor Correction

In order to achieve a power factor of 0.9 at the point of common coupling with the 12.47 kV distribution and total harmonic distortion of 5%, a harmonic filter is planned.

The filter is rated at 16 MVA and consists of a high pass stage, a band pass stage and a power factor stage. The high pass stage is tuned to 1300 Hz and the band pass stage is tuned to 720 Hz. The filter reactance at 60 Hz is capacitive and produces a capacitive reactive power of 11.1 Mvar needed for power factor correction. Figure 5 shows the arrangement of the major components of the harmonic filter.

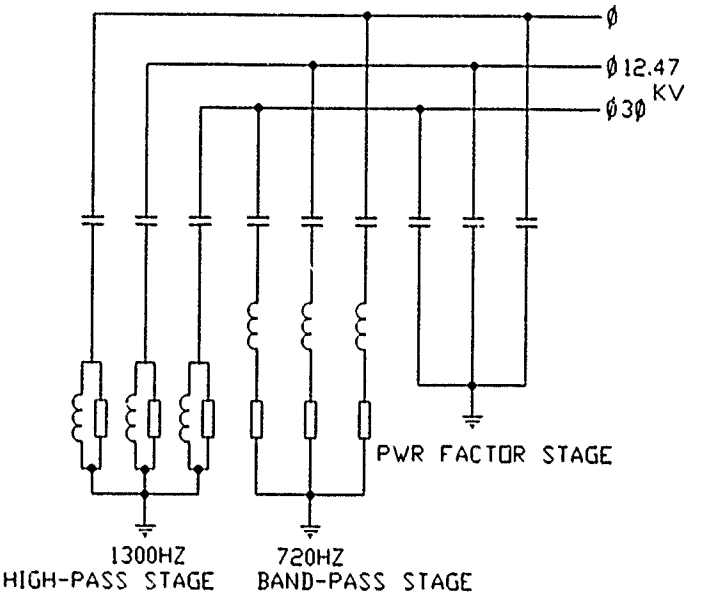


Figure 5. Harmonic filter diagram

VII. References

R. Hettel, R. Averill, M. Baltay, S. Brennan, C. Harris, M. Horton, C. Jach, J. Sebek, J. Voss, "The 10 Hz Resonant Magnet Power Supply System for the SSRL 3 GeV Injector", *IEEE* Press, Proceedings of this conference.

K.W. Reiniger, "Power Supply System for the TRIUMF KEON Factory", Proceedings of this conference.

W. Bothe, P. Pillat, "Magnet Excitation Circuit for DESY II" *IEEE Transactions on Nuclear Science*, Vol. NS-32, No. 5, October 1985.

J. Ryk, "Gradient Magnet Power Supply for the Fermilab 8 GeV Proton Synchrotron", FERMILAB-PUB-74/85.

C.W. Brown, K.E. Owen, "Stabilization of the Magnet Power Supplies for the NINA Synchrotron", Proceedings of the International Conference on Magnet Technology, Oxford, 1967.

An RF Cavity for the B-Factory*

R. Rimmer, F. Voelker, G. Lambertson, LBL,#
M. Allen, J. Hodgeson, K. Ko, R. Pendleton, H. Schwarz, SLAC‡,
N. Kroll, UCSD†/SLAC

Abstract

The paper describes the proposed design for the 476 MHz accelerating cavity for the SLAC/LBL/LLNL B-Factory. This machine will require a high power throughput to the beam because of the large synchrotron radiation losses, and very low impedances for the higher order modes because of th high current proposed. Use of conventional construction in copper means that careful consideration has to be paid to the problem of cooling. The need for a high shunt impedance for the accelerating mode dictated the use of a re-entrant shape. This maximized the impedance of the fundamental mode with respect to the troublesome longitudinal and deflecting higher order modes, when compared to open or "bell shaped" designs. A specialized damping scheme was employed to reduce the higher order mode impedances while sacrificing as little of the fundamental mode power as possible. This was required to suppress the growth of coupled bunch beam instabilities and minimize the workload of the feedback system needed to control them. A window design capable of handling the high power was also required.

I. INTRODUCTION

The B-Factory RF system is required to meet the demands of a high luminosity, and therefore high current, while operating in a reliable manner befitting the "factory" philosophy of the project [1]. Choices of the parameters of the RF cavity are intended to be conservative and reasonable extrapolations from existing technology. The chosen frequency of 476MHz is a subharmonic of the SLAC linac frequency, to allow for stable injection. Commercial 1MW Klystron designs can be made to work at this frequency The very large beam currents, 1.48A in the High Energy Ring (HER) and 2.14A in the Low Energy Ring (LER), require up to 10MW and 5MW respectively to replace the energy lost to synchrotron radiation, cavity wall heating, and other effects. The need for short bunches (σ_l =1cm), requires a voltage of 18.5MV for the HER, 9.5MV for the LER. Unfortunately the number of cavities over which the power can be distributed must be kept to a minimum because, with such large currents, the impedances of higher order modes (HOMs) will cause very large longitudinal and transverse coupled-bunch instablility growth rates. Even so it is necessary to provide damping of these modes in the cavities and an active bunch-by-bunch feedback system in each ring to control this. Since most of the power goes into the beam, the saving in RF power from using superconducting cavities would not be large, and has to be weighed against the increased complexity associated with the cryogenic system. Also the technology for coupling such large drive and HOM power to and from a superconducting cavity is not yet mature. For these reasons and because expertise in the project team is primarily with room temperature structures, conventional copper construction was preferred. Single cell cavities of a re-entrant design were chosen to maximize the shunt impedance of the fundamental mode with respect to HOMs. It was decided to limit power to 500kW in each cavity (and window), of which up to 150kW is dissipated in the walls, yielding 20 cavities in the HER and 10 in the LER. This gives a gap voltage in the cavities of less than 1MV and an average field of about 4.3MV/m. The high wall dissipation requires careful attention to be paid to the cooling system, especially around structures such as the damping waveguides, which may have localized concentrations of current

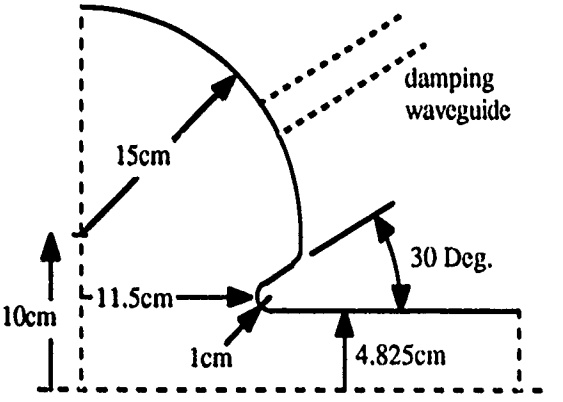


Fig.1: Basic B-Factory cavity shape

II. CHOICES FOR CAVITY PARAMETERS

Cavity designs and commercial 1MW CW klystrons are available at around 350MHz and 500MHz. PEP, LEP and APS use 350MHz, while Daresbury (SRS), KEK and ALS operate at 500MHz. A frequency in the higher region was chosen because less overvoltage is required in the cavity to achieve the short bunch length and more bunches can be circulated.

The type and shape of the cavities is determined by the need to maximize the fundamental mode shunt impedance with respect to HOMs. This is best achieved with a re-entrant or "nose-cone" shape. With conventional copper construction, an open or bell shape, as often used in superconducting cavities, does not work as well in this respect. The shape chosen (fig.1)

* Work supported by the Director, Office of Energy Research, Office of High Energy Physics, Advanced Energy Projects Division of the U.S. Department of Energy.
# Lawrence Berkeley Lab.,DOE contract DE-AC03-76SF00098
‡ Stanford Linear Accelerator Center, DE-AC03-76SF00515
† U.C.San Diego, DOE contract DE-AC03-89ER80726

0-7803-0135-8/91$01.00 ©IEEE

is similar to those used in the SRS, KEK and ALS, with a beam pipe internal radius of 4.825cm, (coming from the internal dimensions of a standard sized 10cm OD pipe used for the vacuum chamber in the RF straight). Analysis of the basic shape was done using the 2D URMEL code [2] Single cells were chosen to keep the number of HOMs to a minimum, in multi-cell structures the coupling between cells results in more modes.

URMEL calculates the transit time corrected shunt impedance R_s ($=V^2/2P$) for the basic shape to be about 5.3MΩ with a Q of 45,000 and R/Q of 116Ω. In a real cavity this impedance is degraded by the addition of ports and damping waveguides and by the effect of wall temperature on the conductivity of the copper. Experience with other designs suggests about 10% will be lost with the addition of the tuner, drive and other ports. Using MAFIA [3] and ARGUS [4] to study the 3D shape shows a loss of 10% or less in the fundamental mode R_s and Q when the damping waveguides are added (R/Q stays about the same). Based on extrapolation from existing cavities and thermal studies using ANSYS [5], loss of efficiency due to surface temperature rise may be as high as 14% with 150kW dissipated in the cavity. Thus a practical shunt impedance of 3.5MΩ with a Q of about 30,000 should be achievable, (table 1).

To get the required match at the nominal operating currents requires a coupling factor β of about 3.7. Loop and aperture couplers were considered, the loop has the advantage that the coupling factor can be adjusted by rotating it, but it must be well cooled because of the very high surface current densities. An aperture has the advantages of simplicity and lower surface currents but may need a larger opening in the cavity and requires a sliding short circuit in the waveguide to adjust the match which may be a problem because of limited space in the tunnel. A loop is favored because of the compactness and adjustability and because of the experience of the SLAC team with this type of coupler.

Either type of coupler requires the use of a vacuum window at some point. Existing designs using a ceramic window in the aperture or as part of the loop structure are not well suited to such high power levels. It was decided to locate the window well away from the harmful cavity standing wave fields, which may evanesce some distance into the waveguide, using a simple waveguide window. Designs are being developed commercially for 500kW CW operation. The location of the window in these designs requires that part of the waveguide be evacuated which may increase conditioning time. Anti-multipactor coatings will be applied to the windows and may be used on other surfaces if any problems are encountered with excessive multipactor during conditioning.

Active tuning of the cavities is proposed to be done by motorized plungers of the type used in PEP. These have carbon brushes to prevent HOM power from getting into the bellows. An interesting alternative is to distort the cavity slightly by external pressure to change its frequency. This has the advantage that no hole needs to be cut in the cavity wall. Both of these methods will be investigated in more detail.

Table 1: RF Parameters for the high and low energy rings.

Parameter	HER	LER
RF frequency (MHz)	476	
Beam current (A)	1.48	2.14
Number of cavities	20	10
Shunt Impedance R_s* (MΩ)	3.5	
Gap Voltage (MV)	0.93	0.94
Accelerating gradient (MV/m)	4.2	4.3
Wall loss/cavity (kW)	122	130
Coupling factor without beam (β)	3.7	3.8
Unloaded Q of cavity	30000	

* $R_s = V^2/2P$

The high beam currents have the potential for very high coupled-bunch instability growth rates, requiring special attention to be paid to the HOM impedances of the cavities. Existing damping techniques using externally applied tuned couplers have not proved effective enough to meet the B-Factory requirements, and reduce the growth rates to a level where an economically feasible feedback system could take control. For this application damping waveguides were included in the design of the cavity right from the start. These waveguides are designed to propagate at the HOM frequencies and are positioned to couple most strongly to the most troublesome modes while avoiding the field nulls of all the other modes (so that no modes, however innocuous, remain trapped). The waveguides are below cutoff at the fundamental mode frequency and result in only a small perturbation of the accelerating field. The effect of the size, shape and location of the damping waveguides has been studied experimentally on a simple pillbox cavity [6] and calculated using MAFIA and ARGUS, for the pillbox case and realistic B-Factory cavity shapes. Neither MAFIA nor ARGUS is currently capable of solving the complex eigenvalue problem created by lossy materials in the damping waveguides so the method of Kroll and Yu [7,8] was used to calculate the mode frequencies and Q's of the loaded structures. Three waveguides are used, spaced 120 degrees apart around the cavity azimuth so that all HOMs up to sextupole (m=3), and many higer orders, can be damped. This maintains symmetry, avoiding introducing low order (m=1,2) multipole components into the fundamental mode .

Experiments on the pillbox cavity showed that strong damping of HOMs can be achieved, and the measured Q's agreed well with those calculated by MAFIA/Kroll-Yu. Initially it was intended to get the Q's down to below 100 for the worst modes, on the pillbox this was achieved with only a 8% (calculated) loss in fundamental mode. Loaded Q for the longitudinal (m=0) TM011 mode was calculated to be between 15 and 35, measured to be 31. The dipole (m=1) TM110 mode was calculated to have a Q of 55, measured to be 37.

The first attempt to calculate the damping of the B-Factory cavity used a model having three rectangular waveguides with a cut-off frequency of about 600MHz. These waveguides were too broad to join directly to the cavity wall so an iris was used. Results for this geometry show strong

damping of the worst HOMs, with a Q of about 30 for the TM011 mode, with about 12% loss of the fundamental mode Q (table 2). It may be possible to reduce this degradation of the fundamental mode by smoothing out the sharp corners in the iris. In an attempt to dispense with the iris altogether a scheme was developed using smooth ridged waveguides which can be made small enough to open directly into the cavity. Using this scheme the Q of the TM011 mode is reduced to less than 26 (possibly as low as 12 - there is some uncertainty due to the limited number of data points used in the Kroll-Yu method), while the fundamental mode Q is lowered by only 7%. The ridged waveguides have a slightly larger area, which may account for the stronger damping, while the smoothing of the corners and the lack of iris could explain the reduced perturbation of the fundamental mode. Other HOMs are reduced to Q's in the range 30-50, except for the TM020 which was accidentally missed by the placement of the ridged waveguide. (When the waveguide shape was changed the effective center of the waveguide moved slightly, onto a null of the TM020 magnetic field).

Table 2: Damping of prototype cavity by waveguides.

	No Waveguides			Rect wg+iris		Ridged wg	
mode	freq (MHz)	Q_0	RT^2 (MΩ)	Freq (MHz)	Q_L	Freq (MHz)	Q_L
TM010	480	40003	4.71	475	35248	473	37344
TM011	750	33270	1.35	745	30	738	12-26
TM020	993	38700	0.009 Trans.* (MΩ/m)	997	>1000	992	>5600
TE 111	685	54844	0.191	680	~65	678	30-47
TM110	794	57762	18.3	795	~73	793	31-64
TM111	1068	51836	33.2	1040	>50	1038	>49

* $R/k(r)^2$ (where r is the beam pipe radius=0.04825m)

Work is continuing on the optimization of the shape and position of the damping waveguides to get the lowest Q's for the most significant modes and to check all the higher order modes to make sure none are missed. Additional damping may be achieved by using higher order mode filters in the drive waveguide as there will be significant transmission through the power coupler for many HOMs. As a last resort any single mode which still has a significant impedance may be tackled by a tuned antenna inserted through a service port.

The high power dissipation and multiple apertures in the B-Factory cavity require careful attention to the problem of cooling. It is proposed to use a construction similar to that of the Daresbury and ALS cavities where the cooling water is channeled between two shells forming the inner and outer surfaces of the cavity. Particular care must be taken to ensure adequate cooling of the nose-cones and the damping waveguide apertures. The surface power dissipation is available from the numerical codes and this information can be transferred to a finite element program to perform thermal and, ultimately, stress analyses of the proposed designs. Early investigation suggested there might be strong local heating in the nose-cone region and around the rectangular waveguide iris. Current work is taking account of these results and the present design iteration is including a wider nose-cone angle (30 degrees) which allows easier access for the cooling water, and will feature a smoothed iris or rounded ridged waveguide.

Field enhancement on the small radius of the cavity nose-cone, as calculated by URMEL, leads to local surface electric fields about 5.9 times the average accelerating field in the cavity. At about 25MV/m this is comparable to the Kilpatrick number at this frequency, 20.9MV/m, so sparking should not be a problem after conditioning.

III. DEVELOPMENT PROGRAM

The current design effort is targeted on optimization of the RF performance of the cavity shape and the damping scheme, while keeping in mind the problems of cooling and mechanical construction. The first test of the design will be the construction of a low power test model to measure the effectiveness of the damping scheme and confirm the calculated mode spectrum. An automatic bead-puller is being constructed to allow detailed investigation of the HOM impedances. This model may also be used to test the RF control loops, using a low power amplifier instead of the klystron. At the same time programs will be under way to evaluate high power window and coupler designs, leading ultimately to their verification in a high power test stand at SLAC. Any lessons learned from the low power tests will be included in the next design iteration of the cavity which will concentrate on the engineering of a high power prototype.

IV. REFERENCES

[1] "An Asymmetric B-Factory based on PEP," Conceptual Design Report, LBL PUB-5303, SLAC 372

[2] U. Laustroer, U. van Rienen, T. Weiland, "URMEL and URMEL-T Userguide," DESY M-87-03, Feb 1987.

[3] "Reports at the 1986 Stanford Linac Conference., Stanford, USA, June 2-6 1986," DESY M-86-07, June 86

[4] A.Mondelli, et.al. "Application of the ARGUS Code to Accelerator Design Calculations," Proc. 1989 PAC, Chicago IL, March 20th-23rd, 1989.

[5] From Swanson Analysis Systems Inc., Johnson Road, P.O.Box 65, Houston, PA, 15342-0065.

[6] F. Voelker, G. Lambertson, R. Rimmer, "Higher Order Mode Damping in a Pill Box Cavity," Proc. 1991 PAC, San Francisco, May 6-9th. 1991. LBL-30625, BECON-92

[7] N. Kroll, D. Yu, "Computer Determination of the External Q and Resonant Frequency of Waveguide Loaded Cavities," SLAC-PUB-5171.

[8] N. Kroll, R. Rimmer, "Computer Determination of HOM Damping for a prototype JLC Accelerator Cavity and a prototype B-Factory Cavity," Proc. 1991 PAC, San Francisco, May 6th-9th. 1991.

Survey and Alignment of an MLI Model 1.2-400 Synchrotron Light Source

W J. Pearce
Maxwell Laboratories, Inc., Brobeck Division
4905 Central Avenue
Richmond, California 94804

Abstract

A cost effective technique was developed for the timely alignment of the magnets, support stands, and diagnostic equipment using readily available instrumentation. The procedure includes use of a commercially available theodolite coordinate measurement system for alignment of the dipole magnets, and optical tooling techniques for smoothing out errors in the position of the quadrupoles to sub-millimeter tolerances. The monument network, fiducialization of magnets and supports, and special tooling are discussed.

I. Introduction

The survey and alignment of an MLI Model 1.2-400 synchrotron light source is underway. This is a 1.2 GeV Chasman-Green lattice with an average radius of 17.6 meters and circumference of 55.2 meters. The primary ring magnets to be aligned are eight dipoles, twenty quadrupoles, and sixteen sextupoles. Twenty magnets in the transport line are also to be aligned.

Commercially available and cost effective instrumentation is used. The magnet supports incorporate screw adjustments for six degrees of freedom. Special fixtures were necessary for some of the magnets.

II. Monument Reference System

The monument network consists of fourteen primary monuments, twelve in the ring and two in the linac tunnel, as shown in figure 1. A central monument was not used because of interference with the building structure.

The monuments are very precise 3.5 inch diameter steel spheres that hold optical targets at the geometric center of the sphere; the target remains at the center regardless of the angular position of the sphere. The spheres rest in stainless steel cups epoxied into the concrete floor, and fitted with a protective cover when a sphere is not installed. These primary monuments each have x, y, and z coordinates in the global coordinate system.

Additional secondary monuments of the brass plug type with scribe marks are used as required in the ring and especially in the transport line to simplify optical tooling setups.

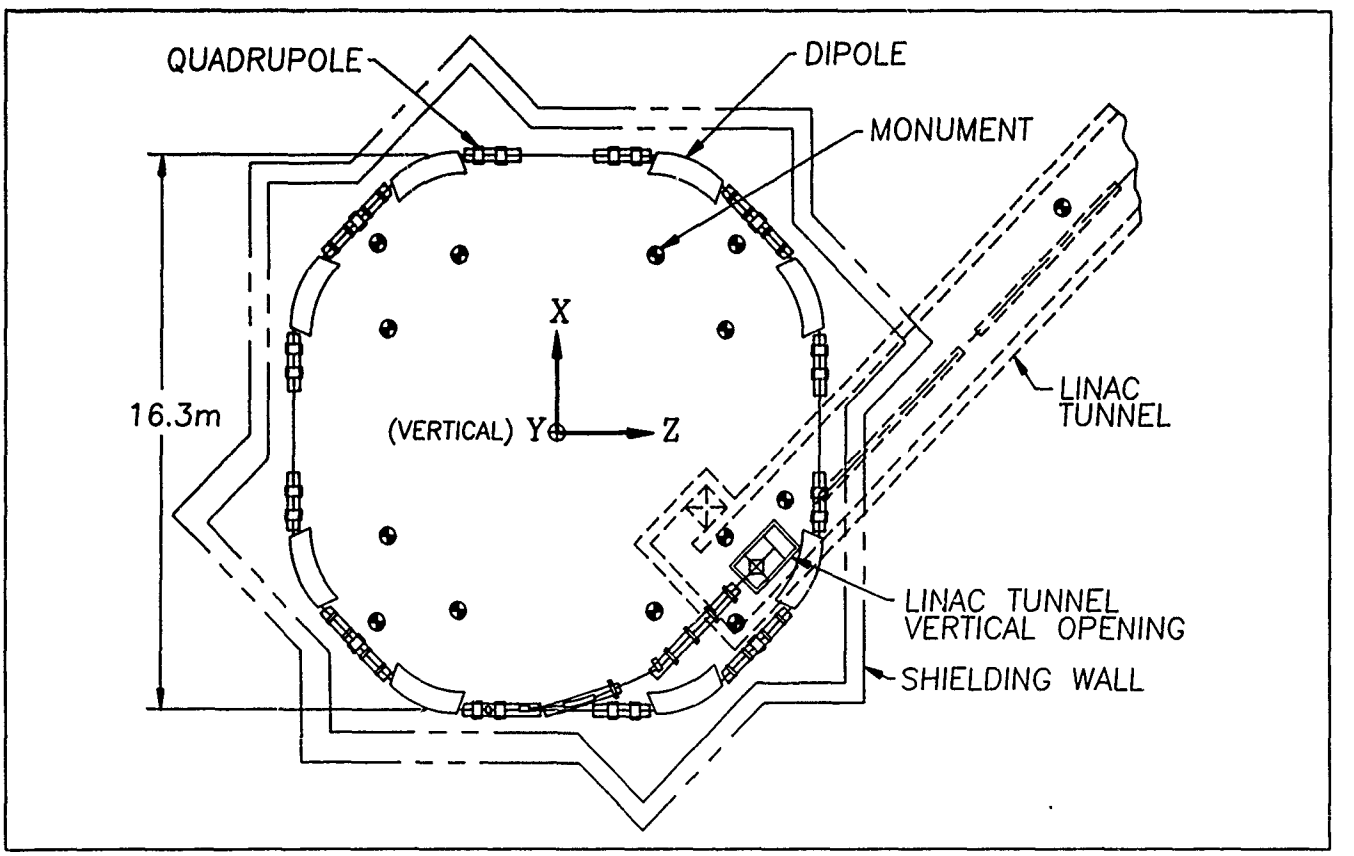


Figure 1. Monument network.

0-7803-0135-8/91$01.00 ©IEEE

III. Tolerances

The tolerance definition is based on a Gaussian distribution and the values below represent one standard deviation (1 σ). The dipole tolerances are relative to the primary monument network; the quadrupole tolerances are relative to the neighboring dipoles. The largest acceptable tolerance for any single item is twice the 1 σ value.

The tolerances must include the total of all the errors generated: the error from magnetic center to pole tip, the lamination edge feature with respect to the pole tip, the survey target to lamination edge feature repeatability, the survey error, and the alignment tolerance.

Table 1. Tolerances of ring magnets

	DIPOLES	QUADRUPOLES
x	0.60 mm	0.30 mm
y	0.60 mm	0.30 mm
z	0.60 mm	0.50 mm
pitch	1.0 mrad	1.0 mrad
yaw	1.0 mrad	1.0 mrad
roll	0.34 mrad	0.80 mrad

IV. Instrumentation and Data Reduction

The alignment of the ring magnets is performed in a two-tier hierarchy. First, the dipoles are aligned relative to the primary monument network, and then the girders with quadrupoles and sextupoles are aligned relative to the dipoles. The linac and transport line are aligned with respect to the primary monument network.

For preliminary placement of all the magnet supports, and for final alignment of the dipole magnets relative to the geodetic coordinate system, an industrial measurement system (IMS) is used. A typical IMS system has at least two electronic theodolites which can measure vertical and horizontal angles to 0.5 arc seconds. The theodolites enter digitized angular data into a minicomputer for conversion into x, y, and z coordinates.

Leveling of magnets and stands is accomplished with the use of a precision optical level, accurate to 0.025 mm at distances up to 20 meters.

Alignment of the quadrupoles and sextupoles relative to the neighboring dipoles, as well as alignment of some magnets on the transport line, is accomplished with an optical tooling setup that measures offsets (see figure 2). The optical tooling scales are fitted with interchangeable feet that have either a round end for use against the laminations directly, or a conical seat for use with tooling balls.

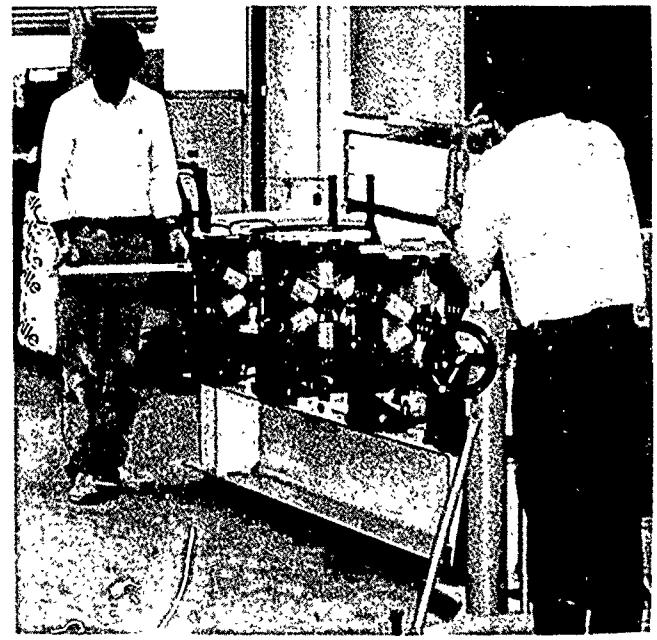


Figure 2. Optical tooling setup for measuring offsets.

V. Fiducialization of Magnets

The magnetic axis determines the path of the particles through the magnetic field. The magnetic axis is virtual, and needs to be related to physical fiducials on the outside of the magnet. In this application, the mechanical axis of the magnet is sufficiently collinear with its magnetic axis to allow individual pedigrees for each magnet to be avoided. Since all laminations for any one magnet are stamped from a single die set, all outside edges and features stamped into the laminations carry a high dimensional accuracy with respect to the pole tips. The relative position of the mechanical center to features such as notches and edges on the outside edges of the laminations can be readily determined. These features are used to locate fixtures which incorporate fiducials, and the position of the fiducials relative to the mechanical axis is known within a certain tolerance.

For example, at each end of each dipole, on the magnet midplane, is a welded tab with a precision 0.250 inch diameter hole (see figure 3). The relationship between this hole and the

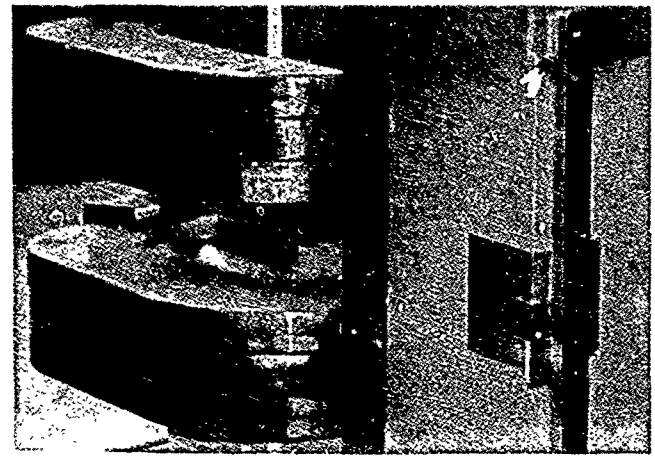


Figure 3. Fiducial on the dipole midplane.

mechanical center of the magnet is known to be within ±0.15 mm in the x-z plane. The holes will accept either theodolite targets or tooling balls, and are sufficient to align the dipoles in x, z, and yaw. The tabs were located with a large aluminum tooling plate which keyed to the magnet in a reproducible and determinate fashion. The magnetic measurements were also referenced to this plate, so that if it becomes necessary to pedigree the magnets later, there is a known mechanical relationship between the magnetic measurements and the fiducial positions.

The magnets are aligned in roll with bridge fixtures containing 20 arc second bubble levels. The fixtures rest on the unpainted surfaces on top of the magnets (see figure 4).

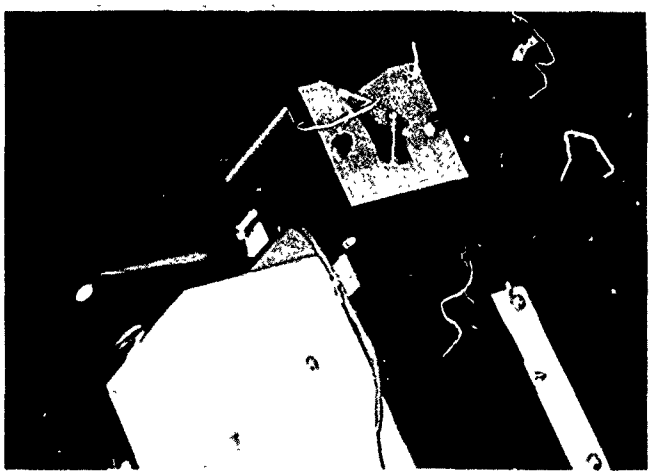


Figure 4. Bridge fixture on quadrupole magnet, showing 20 arc sec bubble level.

VI. Magnet Supports and Adjustments

Each ring dipole stand has three adjustable legs. The leg adjustments are used together for aligning all six degrees of freedom. The horizontal screws allow adjustment in x, z, and yaw, and the vertical threaded rod and nut allow adjustment in y, roll, and pitch.

The quadrupole and sextupole stands have similar adjustments for adjusting the entire straight-section girder (see figure 5). The individual magnets on each shared girder also have provisions for adjustment, using jackscrews for all six degrees of freedom.

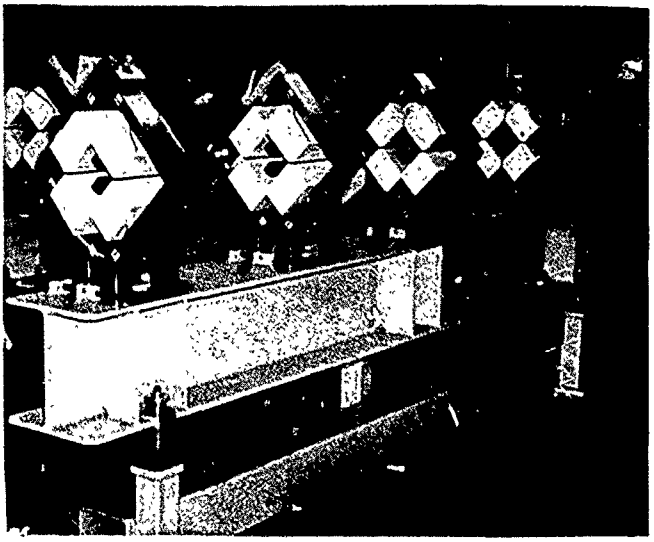


Figure 5. Adjustable legs on multipole magnet girders.

VII. Alignment Procedure

The dipoles are leveled and set at the correct height by using the roll fixtures and an optical level, with adjustments being made on the three large vertical nuts on the support base. A 10 ton hydraulic jack is necessary to partially relieve the load on the adjusting screw for vertical adjustments on the dipoles.

The IMS is used to determine the x-z coordinates of the dipole fiducials; these are compared with the ideal values, and corrections to the x-z coordinates are computed. The magnet is then fitted with dial gauges to measure motion in the x-z plane, and moved the calculated amount with the horizontal push screws.

Each of the quadrupole and quadrupole/sextupole straight section girders (complete with magnets and vacuum chambers) is installed as one assembly on the support base, with the adjustment system set midrange. Leveling is performed first with a roll fixture and the optical precision level for pitch and y. Next, z is set with an inside micrometer. Finally, x and yaw are set with an optical tooling setup between adjacent dipoles. A reference plane is set up by using a jig transit bucked into the fiducials the ends of the dipoles. Measuring horizontal offsets to this plane allows setting x and yaw.

A final survey is then made on all magnets to ensure that they are within the tolerances specified.

CORRELATION OF BEAM LOSS TO RESIDUAL ACTIVATION IN THE AGS*

K. A. BROWN
BROOKHAVEN NATIONAL LABORATORY
UPTON, NEW YORK 11973

ABSTRACT and INTRODUCTION

Studies of beam loss and activation at the AGS have provided a better understanding of measurements of beam loss and how they may be used to predict activation. Studies have been done in which first order correlations have been made between measured beam losses on the distributed ionization chamber system in the AGS and the health physics recorded residual activation. These studies have provided important insight into the ionization chamber system, its limitations, and its usefulness in the prediction of activation based on monitored beam loss.

In recent years the AGS has run high intensity protons primarily for rare kaon decay experiments. In this mode of running the AGS typically accelerates beam from an injection momentum of 0.644 GeV/c up to a slow extracted beam (SEB) momentum of 24.2 GeV/c. The beam intensities are on the order of 4.5×10^{13} protons per AGS cycle at injection to as high as 1.9×10^{13} protons per AGS cycle at extraction. Residual activation varies around the AGS ring from the order of 5 mR/hour to levels of the order at 5 R/hour. The highest levels occur around the AGS beam catcher and the extraction equipment.

COMPARING BEAM LOSS TO ACTIVATION

The dose rate from activation induced by high energy particles interacting with a material such that a large number of isotopes are produced can be expressed by [1,2]

$$D = k\,\xi\,ln\,(1 + T/t), \qquad (1)$$

Where ξ is the number of high energy particles per interaction and k is a constant for any set of irradiation, target and geometrical conditions. The time T is the amount of time the material was bombarded with high energy particles (the irradiation time) and the time t is the time elapsed after the bombardment stopped (the cool-down time). There are two basic assumptions behind this relationship. The first is that a sufficiently large number of different isotopes are produced by spallation reactions such that the half-life distribution among isotopes can be approximated by a continuous function. The second assumption is that since activity is not measured until after over 15 minutes of cool-down has lapsed and before a period of two years has elapsed, reasonable limits can be placed on this continuous function to enable a relatively simple expression to be derived [3,4,5].

There are 120 ionization chamber monitors distributed around the AGS ring, one every 3° of the accelerator circumference. Each monitor is located on the underside of the main magnet girders along the outside of the ring. Each subtends two main magnets, these monitors were sampled at regular intervals while the AGS was running for its' physics program. At the end of the run a total of N measurements had been made of beam distributions around the ring. A single measurement is called r (ϕ, ϵ, n), where ϕ is the position (every 3°), ϵ corresponds to beam energy, and n represents one of N samples. Since the effect of a beam loss ξ_n decreases at some rate R_n, where ξ_n corresponds to a measurement made at a time t_n, then the weighted average beam loss distribution at the end of the physics run will be;

$$\langle r\,(\phi,\epsilon)\rangle = \frac{\sum_n r\,(\phi,\epsilon,n)\cdot Rn}{\sum_n Rn} \qquad (2)$$

By taking Rn as

$$R = \ln\left(1 + \frac{t_w}{t_f - t_n}\right), \qquad (3)$$

where t_w is the amount of time for beam loses (i.e.; beam is accelerated for ~ ½ sec so t_w is taken as 0.5 sec), and t_f is the time at which the run ended, then the measured beam loss is now weighted to the decay rate of the induced activation.

The absolute amount of beam lost is measured using beam current transformers. These also were sampled at regular intervals for the duration of the physics run. The weighted average beam loss at an energy ϵ for the entire run is then

$$\langle \xi(\epsilon)\rangle = \frac{\sum_n \xi(\epsilon,n)\cdot Rn}{\sum_n Rn} \qquad (4)$$

The measured beam loss distribution around the AGS is

* Work performed under the auspices of the U.S.Dept. of Energy.

0-7803-0135-8/91$01.00 ©IEEE

$$\langle \xi(\phi,\epsilon) \rangle = \langle \xi(\epsilon) \rangle \cdot \frac{\langle r(\phi,\epsilon) \rangle}{\sum_{\phi} \langle r(\phi,\epsilon) \rangle} \qquad (5)$$

The background activation and the background activation decay rate were measured before the physics run began. The activation added during the physics run was then calculated from the activation measured just after the physics run ended. So at a particular location ϕ the added activation due to beam lost during the physics run is

$$D(\phi) = \sum_{i=\epsilon} k(i) \cdot \langle \xi(\phi,i) \rangle \cdot R \qquad (6)$$

where $R = ln(1 + T/t)$; (7)

Since the amount of material between a point of a beam loss and the point of which scattered particles interact with the ionization chamber is not a constant, the value of k will vary with the changing thickness of material around the ring. This is because the variations in the amount of target material/absorber will cause variations in the measured loss in the ionization chambers. Since there is a distinct periodicity in the location of elements in the AGS then these variations in k should show up systematically around the AGS. In order to try to normalize out these geometrical variations the above relationship is altered slightly. So,

$$D(\phi) = \sum_{i=\epsilon} \frac{k(i)}{g(\phi,i)} \cdot \langle \xi(\phi,i) \rangle \cdot R \qquad (8)$$

In the AGS $\langle \xi(\epsilon) \rangle$ occurs only at three particular times in the accelerator cycle. This simplifies the above sum to just three terms and this reduces the problem to n equations with 3n/12 + 3 unknowns. If $g(\phi)$ is not independent of energy then there are n/12 + 3 unknowns. For 120 monitors we can have as many as 33 unknowns (the periodicity of the AGS lattice is 12).

Data and Results

The results presented in this report represent the combination of data taken during two SEB physics runs at the AGS. When necessary, I distinguished between these two runs by labeling them RUN1 and RUN2, respectively.

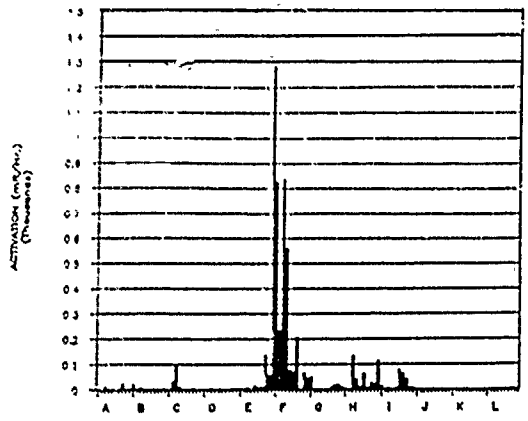
Figure 1 is an example of the activation added during RUN2. The uncertainty in these estimates is about ± 50%.

The weighted average beam loses are given in Table 1 below.

Table 1 Values of $\langle \xi(\epsilon) \rangle$

	Irrad.T (Hours)	Cool t (Hours)	Inject. (200 MeV-1 GeV per hour)	Trans. (8 GeV) per hour	Ext. (24 GeV)
RUN1	455	5.75	1.9×10^{16}	8.3×10^{14}	3.4×10^{14}
RUN2	1000	46.0	2.8×10^{16}	1.2×10^{15}	6.0×10^{14}

Figure 1 Estimated Added Activation RUN2



AGS Superperiods

The uncertainty in these values varies but are of the order of ± 10 - 25%. An example of the weighted average beam loss distributions at transition energies and at extraction energies are shown in Figures 3 and 4. These are also from RUN2. Uncertainties in these values also vary but are on the order of ± 100%.

Values for k/g were calculated using equation (8). As can be seen in Figures 1, 2 and 3 beam losses tend to be concentrated in certain areas. This greatly reduces the number of usable measurements. Figures 4 and 5 show the resulting values of k/g for transition energy losses and extraction energy losses versus other positions in a superperiod. (The exact location is given as a label for the data point, i.e., L10, G.4, etc.) In both figures it can be seen that values of k/g for the upstream half of a superperiod (first 10 magnets) are consistently greater than values for the downstream half. This is actually quite easily explained. In the AGS, for every superperiod, the first 10 main magnets have their backlegs facing toward the outside of the ring while the last 10 main magnets have their backlegs facing towards the inside. Since loss monitors are located only on the outside the difference becomes obvious.

Since there is more material between the point of a loss and the point at which the scattered flux intersects an ionization chamber in the upstream half of a superperiod, then the expected signal from the chamber would be smaller, thus making ξ smaller and giving a larger value for k/g. So at least two values of g can be determined for each energy. In Table 2 the values for k/g, k, and g are presented.

Figure 2 Wt. Av. Loss Distributions
RUN2 Transition Losses

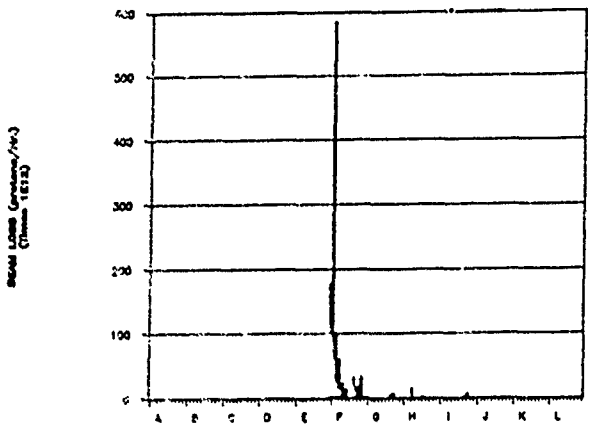


Figure 3 Wt. Av. Loss Distribution
RUN2 Extraction Losses

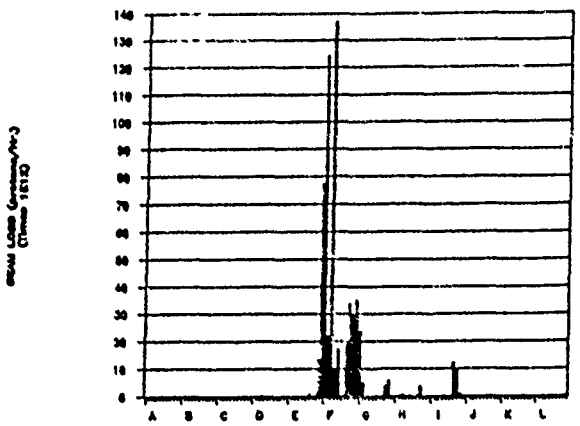


Figure 4 Value of k/g vs. Position
Transition Energy

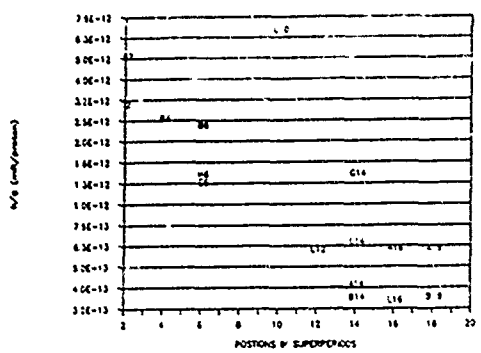
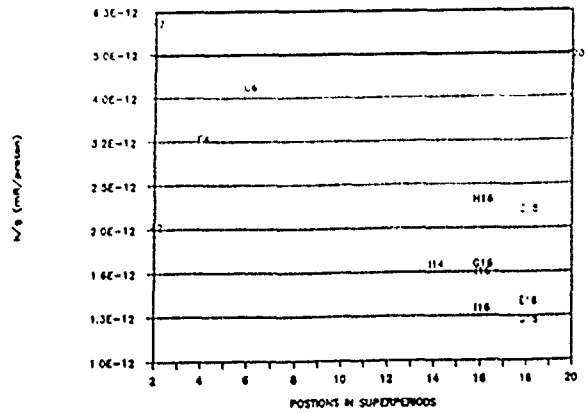


Table 2 Average Values of k/g, k and g

	US k/g	DS k/g	k	US_g	DS_g
Injection		5.8×10^{-15}			
(± Stand Dev.)		±170%			
Transition	3.2×10^{-12}	6.0×10^{-13}	1.9×10^{-12}	0.59	±2
(± Stand.Dev.)	± 56%	± 52%	± 51%	± 0.4	±0.5
Extraction	4.5×10^{-12}	1.6×10^{-12}	3.1×10^{-12}	0.69	1.9
(± Stand.Dev.)	± 24%	± 22%	± 21%	±0.2	±0.5

{Units for k/g and *k* are mR/hour/proton/hour}

Figure 5 Extraction Energy



CONCLUSION

An understanding of the AGS ionization chamber system has been greatly improved. At high energies there appears to be at least a factor of 2 difference in response between monitors in the upstream and downstream halves of a super-period. At lower energies this factor appears to get even larger. By measuring the absolute amount of loss in the different locations around the AGS it is possible to predict within ± 50% the maximum amount of activity induced in those areas.

Acknowledgements

I would like to thank G. Bennett, J.W. Glenn, M. Tanaka, S. Musolino and P. Golon for their comments and assistance. P. Carolan assisted in creating some of the computer software needed for these studies. I would like to thank the AGS MCR operators and HP technicians for their assistance in the data collection.

REFERENCES

1. An Approximate Relation for the Prediction of the Dose Rate from Radioactivity Induced in High Energy Particle Accelerators, A .H. Sullivan, Health Physics, Vol. 12, (August 1972) pp.253-255.
2. Induced Radioactivity and its Relation to Beam Losses in the CERN 26 GeV Proton Synchrotron, A.H Sullivan, Nuclear Instruments and Methods in Physics Research A257, (1987) pp.185-188
3. Induced Radioactivity, Marseel Barbier, CERN, 12969
4. Accelerated Health Physics, H. Wade Patterson and Ralph H. Thomas, LBL, U. of Colo., Berkeley, 1973.
5. Beam Loss and Induced Activation in the AGS, K A Brown, BNL AGS/AD/Tech. Note #337 (internal note), April 1990
6. 1987 Particle Accelerator Conference, K Brown and M Tanaka, Studies of Induced Radioactivity at the AGS (BNL No 39325)
7. Lessons for Kaon Factories from the CERN PS, Y Baconnier, Intern Workshop on Hadron Facilities Tech , Santa Fe , February, 1987

The Condition of γ-ray Emission by Electrons Interacting with the Wall in Medium Energy Electron Storage Rings

Y. Gomei, M. Kawai
Toshiba Corp., ULSI Research Center
1, Komukai Toshiba-cho, Saiwai-ku, Kawasaki 210, Japan

Abstract

The condition of γ-ray emission is reported on medium energy electron storage rings. The electrons interact with the wall during injection and after being scattered by residual gas molecules or by mutual Coulomb interaction while circulating in the ring. It is shown that the location where heavy interaction occurs can be determined from the injection condition and the design condition of the electron orbit. The angle, by which the electrons impinge on the wall, is usually about 1° or less to the surface. The γ-ray emitted to the side of building walls in this case can be effectively shielded by the material located along the beam ducts. An important point is that, in shallow impinge of electrons, convergent γ- ray emission occurs in the back scattering direction of electrons. By installing additional shielding materials for this convergent emission, the thickness of building shielding walls can be effectively alleviated.

I. INTRODUCTION

Synchrotron radiation emitted from medium energy electron storage rings is a candidate to be used for lithography to produce future large scale integrated circuits. Since the machine is to be used in the industrial community, the cost effectiveness becomes an important issue. This is also the case for the building structure to shield γ-ray and the accompanied neutrons. This paper analyses the process, in which the electrons interact with the wall, and tries to propose an effective way to shield γ-ray.

It is well-known that the γ-ray is convergently emitted in the direction of electron path way and that the accompanied neutron emission, in contrast, is rather isotropic. It has been shown that the γ-ray is self-shielded by the target and its emission tends to be isotropic when electrons collide on the target in grazing incidences [1]. This is considered to be a key to effectively reduce the thickness of the building shielding wall. This paper is organized as follows. In Sec. 2, electron-wall interaction in beam ducts is analyzed, showing that the electrons impinge on the wall in very shallow angles and that the location, where severe interaction occurs, can well be identified depending on magnet lattice structures and on electron scattering mechanisms. Sec. 3 describes the γ-ray emission for far grazing incidence of electrons. Sec. 4 discusses how to put additional shielding materials to alleviate the thickness of building shielding walls, which is followed by conclusions in Sec. 5.

II. ELECTRON-WALL INTERACTION

In usual multi-turn injection, the electron orbit is rather slowly retrieved to the original position to try to keep the injected amount highest. The electrons inevitably interact with the inflector wall in this method [2]. The incident angle (measured from the wall surface) in this case is given by [3]

$$x_i' = A_i \gamma_{xi}, \quad (1)$$

$$A_i = (x_{inj} - x_o)^2/\beta_{xi}, \quad (2)$$

$$\gamma_{xi} = (1+\alpha^2_{xi})/\beta_{xi}, \quad (3)$$

$$\alpha_{xi} = -\beta'_{xi}/2, \quad (4)$$

where the subscript i denotes the inflector location, x_{inj} is the horizontal displacement of the injection point, x_o is the retrieving orbit center, and β_x is the horizontal betatron function. Suppose $x_{inj} = 0.045$ m, $x_o = 0$ to make the value of x'_i maximum, $\beta_{xi} = 5$ m, and $\beta'_{xi} = 4$, the x'_i obtained is 0.02 rad (1.1°). It should be pointed out that during injection the electrons interact with the wall mainly at the inflector location, once the closed orbit distortion is corrected.

Initial large orbit oscillation of injected beams is reduced by radiation damping. The electrons, thereafter, impinge on the wall surface only when they receive large scattering either by interaction with residual gas molecules or by mutual Coulomb interaction. First, in elastic scattering with residual gas molecules, the betatron oscillation itself is increased. Since the duct size is usually smaller in the vertical direction, the interaction occurs when the vertical oscillation, given by the following equation, is beyond the wall position.

$$y = \theta_s^2 \beta_y \beta_{ys}, \quad (5)$$

where θ_s is the scattering angle, β_y is the vertical betatron function at the interaction point, and β_{ys} is the one where the scattering takes place. After averaging with respect to the elastic scattering throughout the ring, the value of θ_s, which is necessary for electrons to hit the wall, is given by

$$\theta_{sw} = A_y / \beta_y \beta_y \quad (6)$$

where A_y is the duct half height, and β_y is the value averaged along the beam orbit. According to the equation of Moeller scattering [4], the dependency of the total cross-section in elastic scattering is given as

0-7803-0135-8/91$01.00 ©IEEE

$$\sigma_c \propto 1/\theta^2_{sw} \propto \beta_y\beta_y/A^2, \qquad (7)$$

showing that the probability of electron–wall interaction in this case is almost linear to the value of β_y in each position. After analyzing the beam trajectory in phase space, the following incident angle is obtained as the most typical value.

$$y'_w = \alpha_y\sqrt{\varepsilon_y/\beta_y}, \qquad (8)$$

$$\alpha_y = -\beta'_y/2, \qquad (9)$$

$$\varepsilon_y = A_y^2/\beta_y. \qquad (10)$$

Taking A_y = 2 cm, β_y = 8 m, and β'_y = 7 as an example, the value of y'_w is 0.0087 rad (0.52°). General trends are that the larger θ_{sw} which is of smaller probability, gives the larger y'_w because the electron–wall interaction occurs in the smaller β_y.

The other way of interaction with residual gas molecules is Bremstrahlung radiation induced by nuclear atoms and direct interaction with the molecule orbital electrons. In these two processes as well as in mutual Coulomb interaction, the electrons loose the energy beyond the aperture of rf acceleration. After circulating numerous times in the ring, they reach the energy in which the electron orbit displacement is beyond the wall position. It is evident that the electron–wall interaction of this kind occurs near the place where the momentum dispersion function η is maximum. The typical incident angle in this case is given by

$$x'_w \sim \eta'_w A_x/\eta_{max}, \qquad (11)$$

where A_x is the horizontal duct half size, and the subscript w means the typical position near the maximum η. Taking A_x = 5 cm, η'_w = 1.5, and η_{max} = 4 m as an example, the value of x'_w is 0.019 (1.1°).

The numerical examples stated in this section are what we think most probable for each case. These values may be increased mainly depending on the magnet lattice structures. We would further state that this increase is within a factor of 2 in the kind of the machines related to this study.

III. γ–RAY EMISSION

Electromagnetic interaction process between electrons and wall materials for very shallow incidence of electrons was simulated by using the Monte Carlo computer code EGS4 written by Nelson et al. [5]. Fig. 1 shows the angular dependence of the γ–ray emission for the electron energy of 1 GeV and the incident angle Ψ_i of 1°. To show the dependence, the angle Ψ_e was counted in the direction in which the γ–ray goes through the target. Since the target is the duct wall in real cases, this direction is hereafter called a wall side. When the target thickness d is 2 mm, the line–of–sight electron path length, d/sin Ψ_i, is 11.4 cm. This indicates that the incident electrons still have an energy of several 10 MeV when they come out of the wall. The γ–ray emission, therefore, has a peak in the direction of incident electrons. When the d is

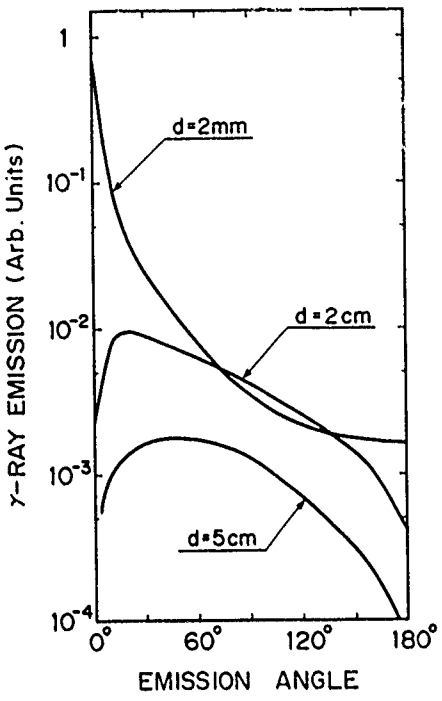


Fig. 1 Angular dependence of the γ–ray emission for the electron energy of 1 GeV, the incident angle of 1°, and different target thicknesses (d). The emission is the mean value inside the emission angle.

increased to 2 cm, the incident electrons are completely stopped in the forward direction. The γ–ray produced near the entrance region is effectively shielded, which results in disappearance of the convergent emission. The scattered electrons, by the way, yield slightly higher γ–ray emission near Ψ_e = 90°, compared with the case for d = 2 mm. By increasing the d to 5 cm, the γ–ray emission becomes much less than the d = 2 mm case throughout the emission angle.

The convergent γ–ray emission always exists in the electron backscattering direction, which is hereafter called a vacuum side. Fig. 2 compares the angular dependence of the γ–ray emission of the vacuum side in d = 5 cm with the one of the wall side in d = 2 mm. The electron energy and the incident angle are the same as for Fig. 1. The γ–ray emission of the vacuum side is observable over Ψ_e = 1° in the figure. It has a peak near Ψ_e = 2.5°, the maximum value of which is about a forth of the emission in d = 2 mm and $\Psi_e \sim 0°$. Although the vacuum side emission becomes slightly larger than the wall side one for d = 2 mm over Ψ_e = 10°, these two curves behave quite similarly in the region Ψ_e > 2.5°, indicating that the shielding effect for the released γ–ray is accidently comparable between these two cases.

IV. DISCUSSION

It was shown that the place, where electron impinge on the wall is highly localized, is injection sections and near the position with η_{max}. The scheme of local shielding for the latter is shown in Fig. 3. It is common in separated function lattices that the η_{max} is located in quadrapole magnets. To shield the wall side emission, additional shielding material is installed

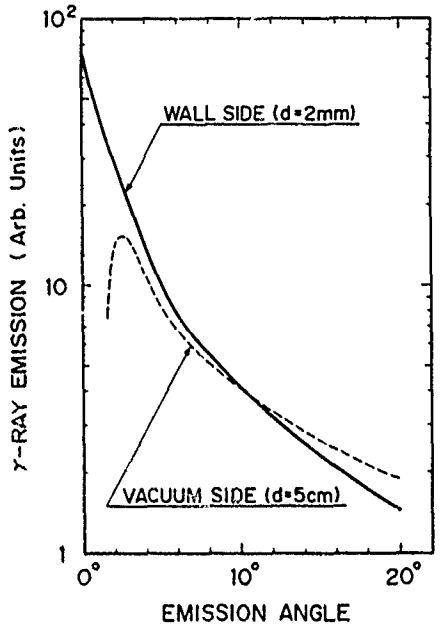


Fig. 2 Angular dependence of the γ-ray emission for the wall side in d=2 mm and for the vacuum side in d=5 cm.

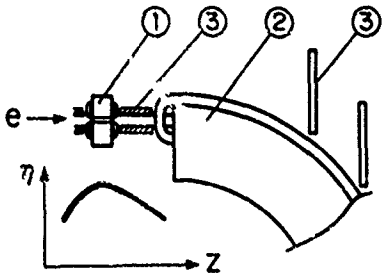


Fig. 3 Arrangement of local shielding for straight sections: 1 quadrapole magnet; 2 bending magnet and 3 shielding material.

along the beam duct. Special care was taken for the vacuum side emission, since the convergently emitted γ-ray can reach bending sections and go through the gap of magnet iron cores. Additional shielding blocks are installed in front of the straight section, the detailed arrangement of which should be determined depending on the neighboring hardware structures. As for the γ-ray emission from the injection sections, thin inflector walls give highly convergent emission which is something like the wall side emission for d = 2 mm plus the vacuum side emission. Local shielding should properly be designed considering these angular dependences.

The γ-ray emission in the bending sections is mainly attributed to the electrons elastically scattered by residual gas molecules. As was described in Sec. 2, the electron impinge in this case is in vertical direction. The γ-ray emitted on the wall side is therefore shielded by the magnet iron core. The important matter again is the vacuum side emission which can go through the iron core gap. The point, which is different from the case in the straight sections, is that the electron-wall interaction is distributed depending on the β_y value and that the γ-ray emission direction is correspondingly distributed, as is shown in Fig. 4. If one calculates the γ-ray absorption at any point near the bending magnet, the following equation may be

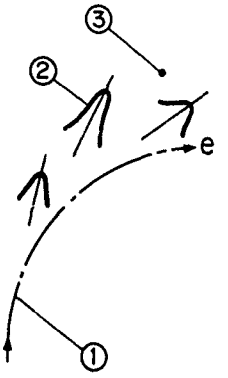


Fig. 4 γ-ray emission from bending sections: 1 electron orbit; 2 emitted γ-ray; and 3 estimation point.

applied for an order of estimation.

$$I_{ab} = I_c f_c f_v f_b f_i , \qquad (12)$$

where I_c is the reference value which is, in this case, the emission at $\Psi_e \sim 0°$ in d = 2 mm in Fig. 1, f_c denotes the fraction of all the stored electrons which impinges on the wall after elastic scattering with residual gas molecules, f_v is the mean ratio of the vacuum side emission with the reference emission, f_b is the fraction of the elastically scattered electrons whose γ-ray emission has a chance to project any estimation point near the bending magnet, and f_i denotes the averaging factor by integration with respect to projecting directions and lengths. Although the exact value of each f should be determined by detailed simulation analysis, we would suggest to use the following to draw a crude image: f_c = 1/3; f_v = 1/2; f_b = 1/8; and f_i = 1/10. These conditions give $I_{ab} = I_c/480$, indicating that almost no additional shielding is necessary for the related γ-ray emission.

V. CONCLUSIONS

The condition of γ-ray emission was studied on medium energy electron storage rings. It was shown that the location where heavy electron-wall interaction occurs can well be identified and that electron impinge takes place in shallow angles. Effective ways to shield the convergently emitted γ-ray were proposed on the basis of the angular dependences of the emission. It should be pointed out that the convergent emission is mainly attributed to electron-wall interaction in straight sections and that the emission from bending sections themselves is more or less divergent.

REFERENCES

[1] H. Dinter, T. Tesch, Nucl. Instr. Meth. 143 (1977) 349.
[2] K. Nakayama, Y. Gomei, Proc. 1st European Particle Accelerator Conf., Rome, 1988 (World Scientific) P.537
[3] S. Krinsky, M.L. Perlman, R.E. Watson, in Handbook on Synchrotron Radiation, Vol. 1, edited by E.E. Koch (North-Holland, 1983) P.65.
[4] H. Bruck, Accelerateurs Circulaires de Particules (Presses Universitaires de France, Paris, 1966).
[5] W.R. Nelson, H. Hirayama, D.W.D. Rogers, Stanford Linear Accelerator Center, SLAC Report 265 (1985).

Gamma Ray Activation of the Fermilab Pbar Target

C.M. Bhat and J. Marriner
Fermi National Accelerator Laboratory *
P.O. Box 500, Batavia, Illinois 60510

Abstract

A model for calculating induced radioactivity by a pulsed primary high energy beam has been developed. This model is consistent with the formalism for continuous beam by Barbier[1]. The method predicts the radioactivity of one of the earlier Fermilab antiproton production targets quite well.

I. INTRODUCTION

A quantitative understanding of the induced radioactivity in the parts of a high energy particle accelerator and particle detectors has been a topic of interest for a long time. A theory of induced radioactivity by a continuous beam of high energy particles on a thick target has been developed [1]. But the particle beams from a high energy synchrotron are pulsed, sometimes with pulse repetition rate of several seconds. For example, the proton beam used to produce pbars at Fermilab has pulse length of 1.6μ sec and a pulse separation of about 2.0 sec. In this report a model of residual gamma ray activity of a target which is exposed to pulsed beams is developed. An expression to be used in any such calculations is derived and applied to predict the activity of the Fermilab pbar source.

II. CALCULATION OF GAMMA-RAY ACTIVATION

When a high energy particle interacts with a nucleus it may be elastically scattered. knock out some nuclei or create some new high energy particles. The energetic secondary particles also induce nuclear reactions. This gives rise to nuclear and electromagnetic showers. Each nuclear reaction center is called a star. If the resulting nuclei are unstable, they will de-excite by boiling off neutrons, gamma rays, beta rays or by emitting internal conversion electrons. Each decay process will be characterised by its individual decay constant. A previous study[2] in the energy range from 3GeV to 30GeV on the formation cross sections for various radioactive nuclei in a copper target indicated no energy dependence. Based on similar observations on many target materials the cross-section for formation of any radioactive nucleus produced in the interaction of high energy particle has been parameterised [1]. However a more precise calculation might need additional experimental data on decay constants and formation cross sections in order to take into account the effect of every individual product.

Total gamma ray radiation dose rate D of a target in (R/hr), which is bombarded by high energy particle beam is,

$$D = -A\sum_j \frac{dN_j}{dt_c}\sum_k E_k(j)$$

$$= N_o A\sum_j \sigma_j \lambda_j \frac{1-e^{-\lambda_j t_I}}{1-e^{-\lambda_j t_p}} e^{-\lambda_j t_c}\sum_k \omega(E_{kj})E_k(j)$$

$$\int_V \frac{e^{-\mu(E_{jk})X(x,y,z)}\rho_s(x,y,z)}{4\pi(X+d)^2}dV \qquad (1)$$

where A is a constant to express results in terms of (R/hr). $\sum_j \frac{dN_j}{dt_c}$ is the activity of the source (a derivation of an expression for the pulsed primary beam is given in Appendix A). t_c, $E_\gamma(k)$, σ_j and λ_j are respectively the cooling time (sec), energy of gamma ray (MeV), the formation cross section of j (in mb/sr), radioactive decay constant for j (in sec^{-1}) N_o is the number of primary beam particles per pulse. t_p is the pulse repetition time (sec). $\mu(E_{jk})$ is the attenuation coefficient of the gamma ray in the target material(cm^{-1}). ρ_s is the star density of nuclear interactions (cc^{-1}). t_I is the total time (sec) that target has been irradiated with the primary beam. The constant A [3] is given by,

A = 1.297E-11/gm if X and d are in meters

A = 6.0E-10/gm if X and d are in ft

if the activity, $\sum_j \frac{dN_j}{dt_c}$ is given in units of Curies. Because of the spatial dependence of the star density in the target and geometry of the target, it is difficult to

0-7803-0135-8/91$01.00 ©IEEE

evaluate the integral in Eq. 1. However, one can incorporate these aspects into a Monte-Carlo code and estimate the dose rate exactly.

We have made calculations for pbar target used in the 1988-89 collider run. Predictions have been compared with the available data. In all of the calculations the star densities have been generated by Monte-Carlo calculations using MARS10 [4] which uses a hadron nucleus interaction model. Further we assume that the source of radiation is situated at the center of the target. Thus in our model all gamma-rays undergo attenuation by the same amount of target material irrespective of the star location. This assumption is reasonable one for a cylindrically symmetric target with

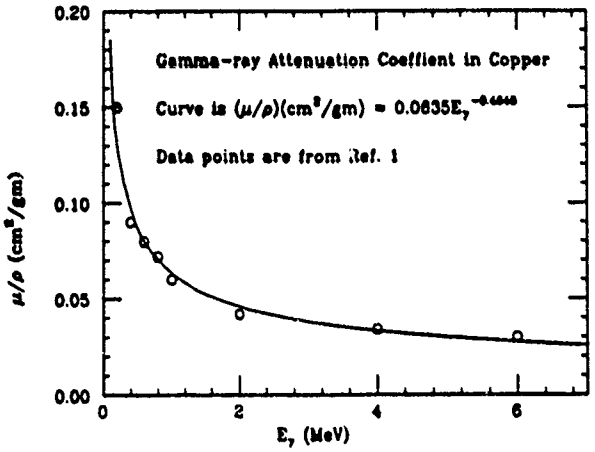


Figure 1. Gamma ray attenuation Coefficient in Copper. The curve represents a logarithmic fit to the data.

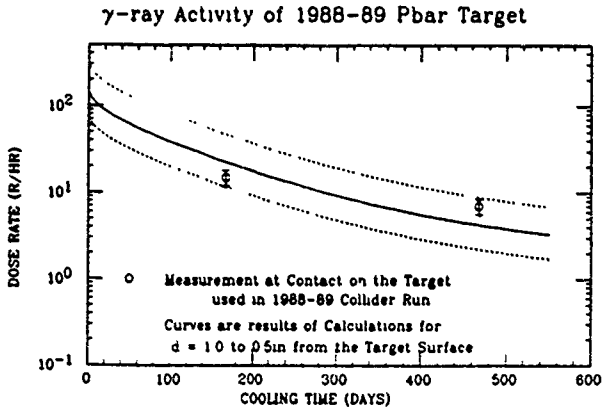


Figure 2. A comparison between predicted and measured radioactivity dose rate as a function of cooling time for one of the Fermilab pbar target

the beam along the axis and for a target with its dimension much smaller than the distance between the detector and the target surface. The gamma-ray attenuation coefficient, μ, can be obtained by a logarithmic fit to the data[1], which is shown in Fig. 1. About forty radioactive nuclei (with life time $\tau \geq 5$ min) have been taken into account in our calculations. Fig. 2 gives a comparison of the prediction and the measured value. The target was used for of 392 days with total of 292 days of irradiation and with an average N_o = 1.0E+12 p/pulse-sec. We calculated the number of stars in the target at about 4 per 120GeV proton. The calculated residual radioactivity is in good agreement with the data. However, several uncertainties exist in the method of measurement to get these data points. The radiation detectors used to measure target activities are known to have about 20% instrumental uncertainty in their measured values. Other large source of uncertainty could arise from the estimation of the distances between target to the detector. Also one has to notice that the beam axis in these targets were along a chord of a cylindrical rotating target with axis of rotation perpendicular to beam axis. Under these circumstances it is incorrect to assume the source of the gamma radiation is at the center of the target. Therefore only the data points labeled " dose rate at contact" have been used to compare with the predictions. Better data are essential to make better comparisons.

III. SUMMARY

A theory of induced radioactivity has been developed for pulsed primary high energy beam. The theory is consistent with the formalism for continuous beam by Barbier. Attempt has been made to compare predictions with the available data from targets used in the previous collider runs at Fermilab and a reasonable agreement is achieved.

REFERENCES

* Operated by the Universities Research Association, Inc., under contracts with U.S. Department of Energy.

1. M. Barbier, Induced Radioactivity, North-Holland Publishing Company (1969).

2. J. Hudis et al, Phys. Rev. Vol. 129 (1962) 434.

3. L. Coulson et al, 'Radiation Guide Fermilab Fifth Edition 1988.

4. N.V. Mokhov, MARS10 Manual, Fermilab, FN-509 (1989).

Appendix A

INDUCED RADIOACTIVITY BY A PULSED HIGH ENERGY BEAM

Let N_o be the number of incident particles per pulse and let the time intervals between two successive pulses be t_p. As a result of interaction between the beam and the target many radioactive nuclei are formed. Let σ_j be the cross section for formation of the radioactive nucleus 'j'. The radioactive nuclei may be formed in their ground state or in any of their excited states. But the excited nuclei decay to their ground state very rapidly (with a characteristic life time of the order of few nsec or psec) resulting in a burst of gamma rays within a few microseconds of the beam interactions. The unstable nuclei in their ground state or in a meta-stable state undergo spontaneous radioactive decay. The number of radioactive nuclei of the type 'j' formed in an elemental volume dV = dxdyds at the end of the interaction of the first beam pulse is given by,

$$(dN_j)_1 = N_o dS \sigma_j \tag{1}$$

where dS = ρ_s(x,y,s)dV is the number of stars in the volume dV. By the end of the second pulse the number of radioactive nuclei 'j' left is,

$$(dN_j)_2 = N_o dS \sigma_j (1 + e^{-\lambda_j t_p}) \tag{2}$$

where λ_j is the radioactive decay constants. Similarly extending this for n pulses the total number of radioactive nuclei left not decayed are

$$(dN_j)_n = N_o dS \sigma_j (1 + e^{-\lambda_j t_p} + e^{-2\lambda_j t_p} + \ldots\ldots + e^{-(n-1)\lambda_j t_p})$$

$$(dN_j)_n = N_o dS \sigma_j \frac{1 - e^{-\lambda_j n t_p}}{1 - e^{-\lambda_j t_p}} \tag{3}$$

Let us assume that the irradiation is stopped after time $t_I = n_I t_p$ and target is let to cool for time t_c. The the number of radioactive nuclei left are

$$(dN_j) = N_o dS \sigma_j \frac{1 - e^{-\lambda_j t_I}}{1 - e^{-\lambda_j t_p}} e^{-\lambda_j t_c} \tag{4}$$

The long term radioactivity comprises essentially that arising from gamma decays alone. To calculate the residual radioactivity we have to take into account the total number of gamma rays (including annihilation of antiparticles into gamma rays) from each nucleus, $\omega(E_{kj})$, with gamma ray energy E_k. Finally these newly emitted gamma rays at (x,y,z) in the target will be self attenuated by the target material. Let $\mu(E_{jk})$ be the attenuation coefficient of the gamma rays. Let X(x,y,z) be the thickness of the target material through which a gamma ray travels before it is being detected by a detector at a distance d from the target. Then

$$dN_j = N_o \sigma_j \frac{1 - e^{-\lambda_j t_I}}{1 - e^{-\lambda_j t_p}} e^{-\lambda_j t_c}$$

$$\sum_k \omega(E_{kj}) \frac{e^{-\mu(E_{jk}) X(s,y,z)} \rho_s(x,y,z)}{4\pi(X+d)^2} dV \tag{5}$$

The instantaneous gamma decay rate of this isotope is obtained by differentiating Eq. 5 with respect to t_c.

$$-\frac{dN_j}{dt_c} = N_o \sigma_j \lambda_j \frac{1 - e^{-\lambda_j t_I}}{1 - e^{-\lambda_j t_p}} e^{-\lambda_j t_c}$$

$$\sum_k \omega(E_{kj}) \frac{e^{-\mu(E_{jk}) X(s,y,z)} \rho_s(x,y,z)}{4\pi(X+d)^2} dV \tag{7}$$

Thus the total gamma-ray activity of the target will be the sum of activities of all gamma rays coming from different types of radioactive nuclei and the star densities integrated over entire target volume. Then we will get

$$-\sum_j \frac{dN_j}{dt_c} = N_o \sum_j \sigma_j \lambda_j \frac{1 - e^{-\lambda_j t_I}}{1 - e^{-\lambda_j t_p}} e^{-\lambda_j t_c}$$

$$\sum_k \omega(E_{kj}) \int_V \frac{e^{-\mu(E_{jk}) X(s,y,z)} \rho_s(x,y,z)}{4\pi(X+d)^2} dV \tag{8}$$

The above equation could be tested for a continuous beam. In Eq. 3 we find that for a continuous beam N_o has to be replaced by $N_o \delta t$ and set the limit δt to zero. Then

$$dN_j = N_o \sigma_j \frac{(1 - e^{-\lambda_j t})}{\lambda_j}$$

which is identical to one in Ref. 1. This confirms the consistency of the formalism for pulsed primary beams.

Recent Experience with Backgrounds at the SLC

R. JACOBSEN, H. BAND, T. BARKLOW, A. BAZARKO, K. BROWN, D. BURKE, D. COUPAL, H. DeSTAEBLER, D. FUJINO, C. HEARTY, S. HERTZBACH, J. JAROS, T. MARUYAMA, T. TAUCHI, N. TOGE, J. TURK, S. WAGNER, C. ZEITLIN

Stanford Linear Accelerator Center

Stanford University, Stanford CA 94309

Abstract

During the 1990 SLC/Mark II runs, machine backgrounds visible in the new vertex detectors were studied. These detectors had active elements at radii from 3 to 17 cm and were subjected to backgrounds unique to linear colliders. We describe recent progress in identifying sources and developing control techniques.

I. Introduction

During the original Mark II run at the Stanford Linear Collider (SLC) in the summer of 1989, the most significant background was from synchrotron radiation generated while focusing the beams to a collision. Studies at that time[1] found that the source was non-Gaussian tails on the beams, and that the backgrounds could be controlled to some extent using collimation and careful manipulation of the beam optics.

The SLC was shut down in the Fall of 1989 for various upgrades, including improvements to the collimation systems. An additional four set of collimators, a total of 16 jaws, where installed at the end of the linac. The collimators in the Beam Switch Yard (BSY) and Final Focus System (FFS) were repositioned to allow more flexibility in operation.

Also during this time two new vertex detectors were installed in the Mark II.[2] The inner one is the Silicon Strip Vertex Detector[3] (SSVD) which has 18,000 silicon strips at about 3 cm radius. Outside it is the Drift Chamber Vertex Detector[4] (DCVD) which contains 34 layers of sense wires from 5 to 17 cm radius. Together these chambers provide unprecedented tracking accuracy for a collider detector. As part of their installation, the Mark II internal masking's hermeticity was improved by adding more material in every accessible gap and the masks were realigned.

Work supported by Department of Energy contract DE-AC03-76SF00515.

U.S. Government work not protected by U.S. Copyright.

II. Operation

The SLC made a short engineering run during January 1990, followed by a longer run for physics during the summer of 1990. From the start, synchrotron background in the main Mark II tracking chamber was significantly reduced from the prior years run. Occupancies, which had been typically 15% to 20% during the previous year, were now below 5%. The improvement is attributed to the additional collimators at the end of the linac, which made it possible to do both primary and secondary collimation in a region with zero nominal dispersion. The additional masking material, including the material of the vertex detectors, also contributed.

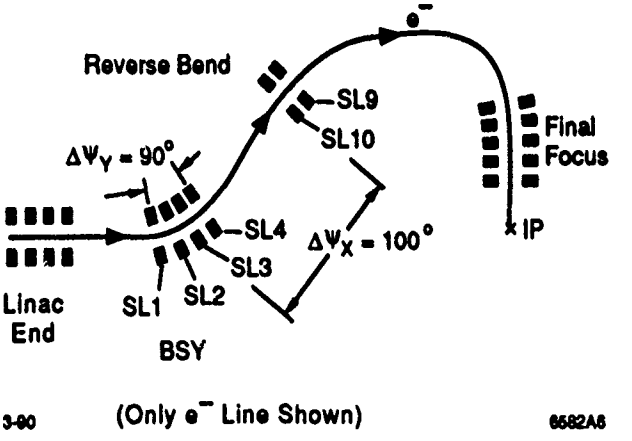


Figure 1 The general layout of SLC collimation. Thirty-two movable collimator jaws are located at the end of the linac, 16 in each side of the Beam Switch Yard and Arcs, and 19 in each side of the Final Focus System.

Unfortunately, backgrounds in the new vertex detectors were larger than expected. Figure 2 shows a typical event. The noticable features are the curved tracks, which are charged particles with transverse momenta up to about 10 MeV/c, and the dark areas which are thought to be curled-up electron tracks from soft photon conversions. This background was strongly biased toward low radius and very rarely extended beyond the DCVD.

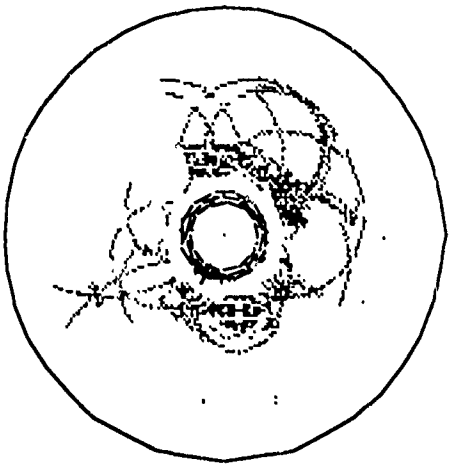


Figure 2 Backgrounds in a typical Mark II event. The outer circle represents the DCVD outer wall at 17 cm radius. The 36 line segments near the center are the individual silicon modules of the SSVD. The DCVD sensitive area is in between. Approximately 15% of the DCVD time bins have been fired. Each hit is drawn twice due to the ambiguous drift direction. The spots outside the circle are hits found in the Mark II main tracking chamber - it's occupancy is negligible.

The SSVD's occupancy was in the range of 2% to 10%, while the DCVD occupancy averaged 15% with some periods much higher. The SSVD has a much finer granularity than the DCVD, which combines with insensitivity to low energy photons to reduce the effect of these backgrounds. The DCVD tracking information could be used up to occupancies of approximately 40%.

The near-photographic information from the DCVD made it possible to study the origin of the background tracks, although no Z (along the beam axis) information was available. It appears that the tracks are coming from energetic showers in the masks near the Mark II. Simulations indicate that of order 1 beam particle hitting masks inside the detector, 50 particles hitting the beampipe inside the final triplet magnets, or 1,000 on the inner 100 microns of the mask at the entrance to the final triplet would reproduce the background density.

The optics and collimation should make it impossible for any of these regions to be hit directly by beam particles, and studies indicate that the source is most likely edge scattering from upstream collimators. Unfortunately, these collimators are needed to remove large beam tails created by various non-linear processes in the linac and transfer lines. It becomes an operational problem to balance the various good and bad effects of collimation.

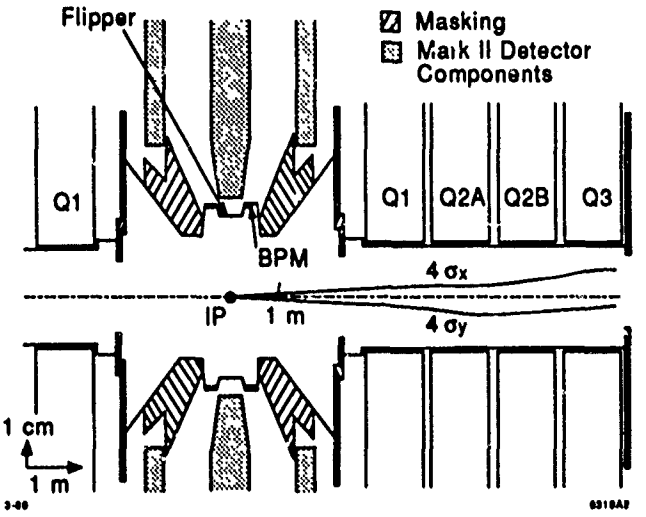


Figure 3 Masking and beam line components near the Mark II detector. Particle trajectories are shown for four times the nominal angle at the IP in both X and Y.

III. Prospects

The Mark II has now been replaced on the SLC beam line by the Stanford Large Detectors (SLD). SLD has newly designed masking, no vertex drift chamber, a main drift chamber with significantly less material and different final triplets. All of these are expected to reduce it's sensitivity to machine backgrounds. Additionally, work proceeds on controlling the SLC emittance and beam profile. An engineering run is planned for this summer to investigate the effects of these changes.

IV. Acknowledgments

We would like to thank the SLC operations and maintenance staff whose tireless attention to the machine made these observations possible.

V. References

[1] R. Jacobsen et al., "Detector Background Conditions at Linear Colliders", *5th International Conference on Instrumentation for Colliding Beam Physics*, Novosibirsk, USSR March 1990, pp. 455-461

[2] G. Abrams et al., "The MARK II Detector for the SLC", Nucl. Instrum. Methods, vol A281 pp. 55-80 1989

[3] R. Jacobsen et al., "The Silicon Strip Detector at the Mark-II", *5th International Conference on Instrumentation for Colliding Beam Physics*, Novosibirsk, USSR March 1990, pp. 120 - 128

[4] J. Jaros et al., "Calibration and Performance of the MARK-II Drift Chamber Vertex Detector", *5th International Conference on Instrumentation for Colliding Beam Physics*, Novosibirsk, USSR March 1990, pp. 11 - 23

Analysis of Uptime Efficiency of the SLC as Measured by Pulse Accounting

P. Krejcik, D. Bernstein, A. Gromme, D. Ohman, N. Spencer
Stanford Linear Accelerator Center
Stanford University, Stanford, California 94305

Abstract

The repetition frequency of a linear collider can deviate substantially from nominal design values as a result of lost pulses. Pulses are typically lost as a result of a veto imposed by the many Machine Protection Systems. A system has been installed at the SLC to use the existing beam position monitor hardware to count every beam pulse that passes by each of the strategic locations. Also counted are the signals from various beam dumpers, as well as trigger signals generated by the MPS. Representative data of SLC running are shown that have been used to determine how to improve running efficiency.

INTRODUCTION

The goal is to quantify the efficiency and reliability of the accelerator performance in terms of the beam delivered by the individual systems. Identifying the contributions to loss in overall efficiency should help in determining which subsystems warrant the most effort to improve performance. The ultimate measure of accelerator performance is the useable luminosity delivered to the detector. However, this is determined by a complex mix of many parameters such as beam current, repetition rate, beam size and background levels in the detector. In order to provide an unambiguous measure of hardware reliability for delivering beams the Beam Pulse Accounting (BPA) system only takes note of the number of delivered beam pulses that pass a predetermined intensity threshold.

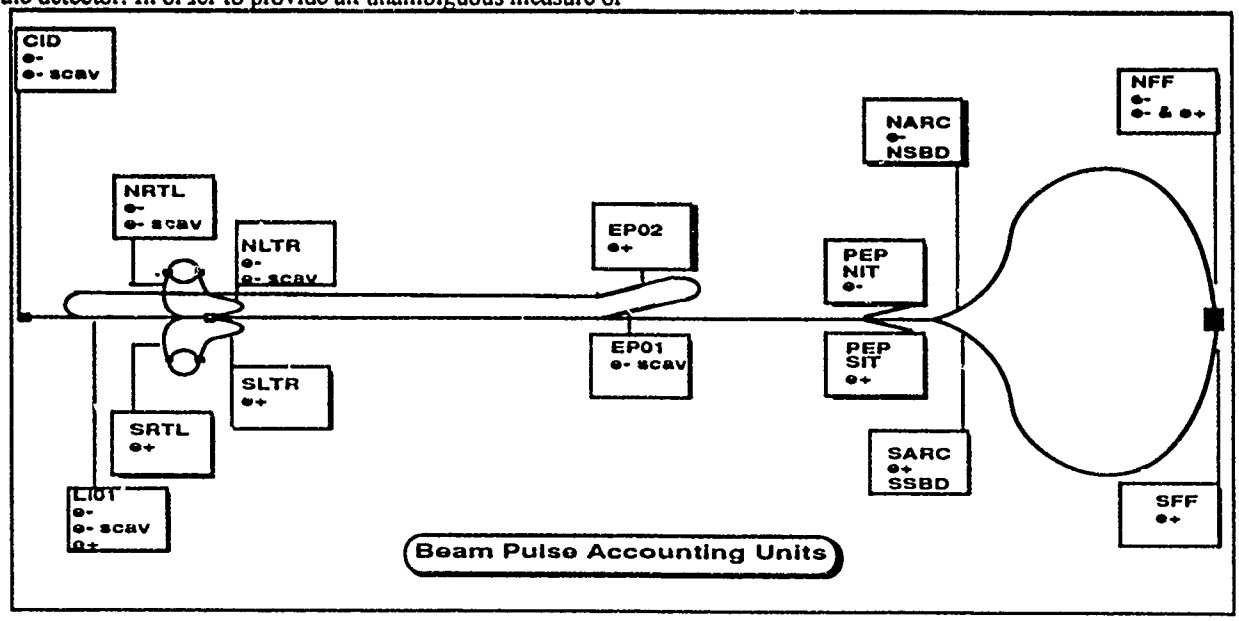
The system uses the existing beamline monitoring devices (BPMs) and adds on top of them a new system for counting and storing the number of beam pulses. This counting system had to satisfy a number of requirements:

1. The intensity threshold above which a beam pulse is counted is remotely programmable.

2. The dynamic range of the threshold setting is capable of handling a wide range of beam intensities encountered in the accelerator - from high currents in the injector to low currents for PEP injection.

3. The counting distinguishes between the different types of beam pulses - electrons, positrons and positron production bunches that can be present, as well as different beam modes for SLC and PEP running.

4. Since much information can also be gained from counting the number of times a pulser fires to veto a beam, provision is also made on each unit to count the signal from an auxiliary input. In the final focus the inputs are used to do coincidence counting of e- and e+ together with detector livetime signals.



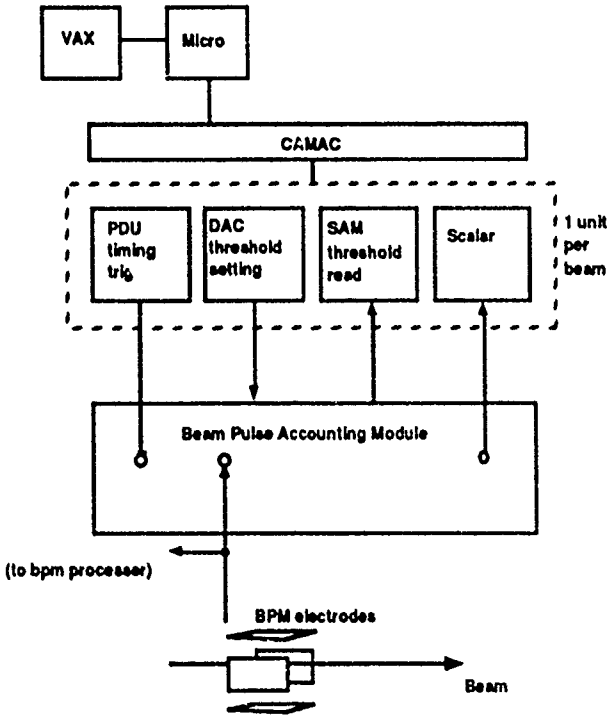
Work supported by the Department of Energy, Contract DE-AC03-76SF00515

0-7803-0135-8/91$01.00 ©IEEE

To assess the performance of individual accelerator systems the pulse accounting units are placed at strategic locations representing interfaces between systems. These locations are shown in fig. 1.

SYSTEM HARDWARE

A block diagram of the main components of the beam pulse accounting system is shown in fig.2.



Schematic of the Beam Pulse Accounting System

Figure 2

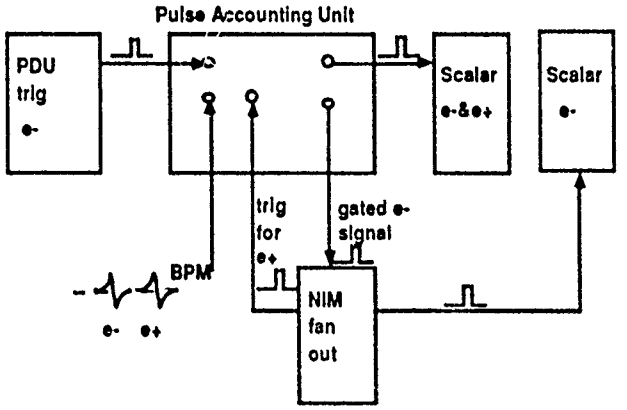
The voltage pulse from an existing BPM is split before going to a BPM processor. The signal is summed and passes through a comparator whose level is set remotely via an input signal from a digital-analog converter (DAC) module which is also read back from an output going to a signal aquisition module (SAM) module. The DAC/SAM combination appears as an AMPLifier device in the control software allowing it to be TRIMmed and monitored. The purpose of this threshold level is to allow counting only of pulses above a certain intensity level. Typically this level is set to be just above the noise level of the bpm signal, but it can be programmed to reject pulses below some other threshold value.

The Beam Pulse Accounting unit has a second input channel for a trigger signal supplied from a pulse delay unit (PDU) module. The gating of the beam pulse signal can thus be controlled with the standard TIMING software in the control system. The reason for gating the beam pulse signal is to distinguish between the different SLC bunches. In linac Sector 1, for example, an electron bunch, a positron bunch and a scavenger electron bunch are all present and separated by about 60 ns.

The gated signal is shaped and its output sent to a scalar module. The scalar is then read and cleared periodically by the control system.

A third input is also supplied on the beam pulse accounting unit to gate and count some arbitrary logic pulse signal to provide auxiliary information such as the occurrence of kicker pulses which would veto the beam.

The bpm input, PDU input, DAC input, SAM output, auxiliary input and scalar outputs together constitute one channel of the Beam Pulse Accounting module. Three of these channels are built into each module so that the unit is capable of counting all three beam signals from one bpm.



Beam Pulse Coincidence Setup

Figure 3

A special configuration of this unit is used in the final focus, shown in fig. 3, to make the unit also act as a coincidence counter for e- and e+. The output pulse going to the scalar to count e- is also used as trigger signal to gate the e+ signal which arrives approximately 30 ns later at the bpm.

PROCESS SOFTWARE

The on-line control system software performs four categories of tasks which are accessed from a touch panel for the SLC Control Program (SCP) software.

1. Setting up of the pulse accounting unit using the AMPL and TRIG features and reading the scalar using the SCLR feature. Several button macros make us of the correlation plot software to scan the AMPL and TRIG values to optimally set them.

2. A batch process is executed on the VAX which reads and clears all the scalars every 6 minutes. From this the average rate, expressed as pulses per second, is saved together with the integrated counts for each of the beams at each of the bpms. The integrated counts are recorded per hourly interval, per 8 hour shift, per day and per week.

3 The HISTory Buffer (HSTB) software archives each of these values and allows them to be individually plotted over a chosen time interval going back as far as one week. After one week the HSTB further condenses them to archive them for

longer term records. Fig. 4 shows a typical history plot of beam rate over 6 minute intervals as well as a plot showing the integrated counts per hour.

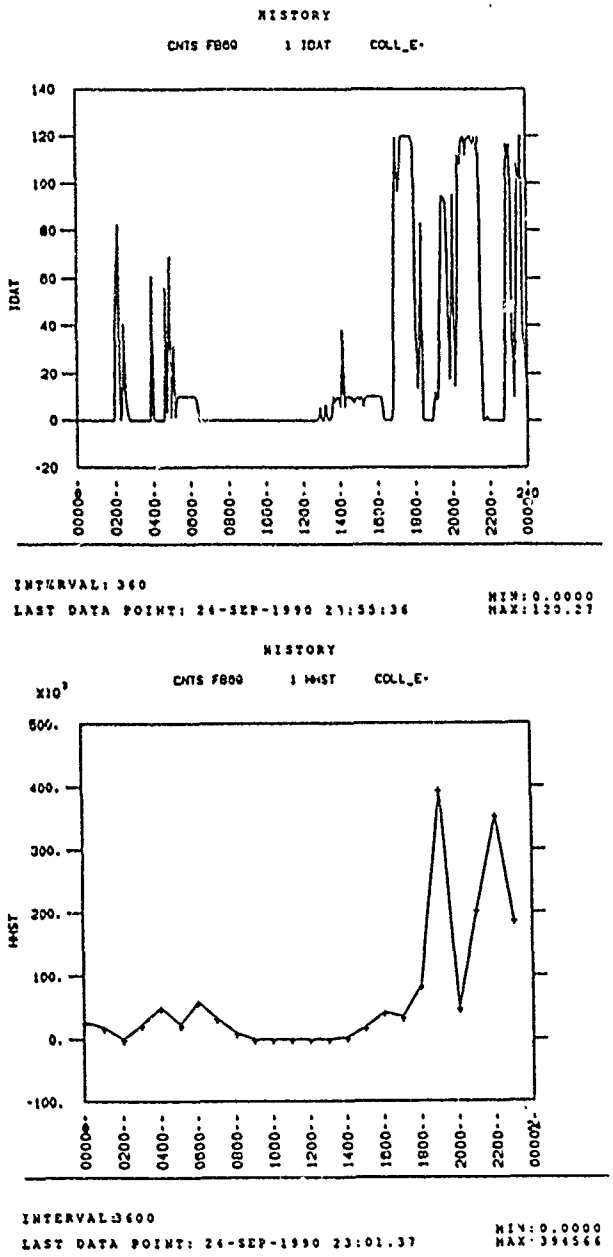


Figure 4 . Online history buffer data showing the recorded beam repition rate in pps (top) for e- reaching the IP, and the same data binned into integrated hourly counts (bottom).

4. Separate from the beam pulse acquisition software are a set of so-called pseudo scalars that count the number of pulses sent out by the Master Pattern Generator (MPG) to the timing system. This enables the number of beam pulses that should be transported in the machine to be compared to the number measured at the bpms. The MPG also has several inputs from the Machine Protection System that cause the machine either rate limit or switch off entirely. The number of beam pulses on which this occurs can also be counted thereby giving information on the frequency of trips from various causes around the machine. The data from the pseudo scalars is processed by the history buffering routines in exactly the same way as the beam pulse data.

MEASURING SLC PERFORMANCE

The on-line history plot software provides an immediate check on the running of the machine. It also provides basic statistics on the performance of the machine, such as the fraction of up-time. Further analysis can be done by exporting the data offline into spreadsheet type programs. This allows more useful comparisons to be made between the various machine subsystems and thus highlight the relative contributions to the pulses failing to make it to the detector at the interaction region (IP).

The example chosen in fig.5 shows the throughput of the collision electron bunches from electron gun (CID), through the North Linac To Ring (NLTR) beamline, the North Ring To Linac (NRTL), the North Arc (NARC), the North Final Focus (NFF) and the coincidence with positrons at the IP. The data is binned into 8 hour shifts during a 3 day period of machine physics. Also shown is the frequency of trips, or rate limiting, due to insertion of the damping ring complex FARCs, the Operator rate limit button and the scavenger lectron bunch extraction line MPS trips.

ACKNOWLEDGEMENTS

The authors gratefully acknowledge the advice of K. Jobe and the assistance of M. Harms, R. Humphrey, M. Ortega and D. van Olst in completing this project.

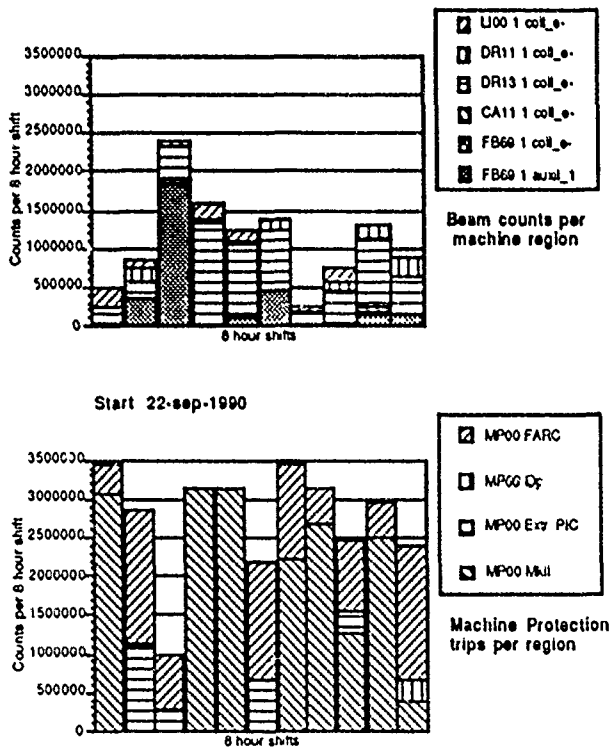


Figure 5. An example of how Beam Pulse Accounting data can be binned and different machine regions compared. The complementary data showing which part of the machine vetoed the beam pulses is shown in the lower half.

FIRST RESULTS OF PROTON INJECTION COMMISSIONING OF THE AGS BOOSTER SYNCHROTRON*

R.K. Reece, L. Ahrens, J. Alessi, E. Bleser,
J.M. Brennan, A. Luccio, J. Skelly, A. Soukas,
W. van Asselt, W.T. Weng, R. Witkover

AGS Department, Brookhaven National Laboratory
Associated Universities, Inc., Upton, NY 11973 USA

Summary

Beam performance for the injection phase of proton beam commissioning of the AGS Booster synchrotron will be presented. The beam from the 200 MeV Linac is transported through a new beam line into the Booster. This Linac-to Booster (LTB) beam line includes a 126° bend and brings the injected beam onto the Booster injection orbit through the backleg of a main ring dipole magnet. Transfer of beam from the Linac to the Booster, spiralling beam and closing the orbit in the Booster ring are discussed. Injection and transport through one sector of the ring has been accomplished.

Review of Booster Facilities

The transfer of beam to the Booster synchrotron from the Linac includes a transport beam line of 114 feet in length. This LTB beam line is made up of three sections (Fig. 1). Section 1 runs from the deflection point in the Linac High Energy Beam Transport (HEBT) beam line (that transports beam to the AGS) to the 126° bend region. Section 2 is the 126° bend region from DH2 to DH5. Section 3 runs from the exit of DH5 into the Booster through the backleg iron of the C5 main ring dipole.

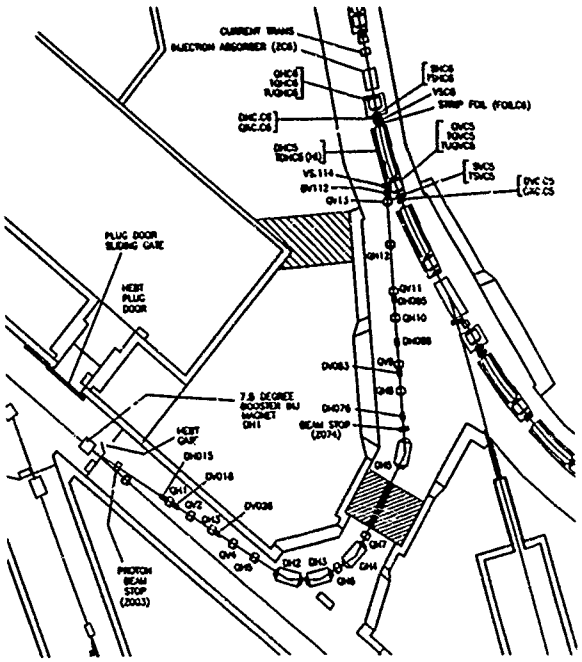


Fig. 1. LTB beam line and injection region.

The LTB section 2 is an achromatic bend region that spans the transition shielding between the HEBT area and the Booster ring enclosure. The 126° bend is created with four identical dipoles powered in series and has two quadrupoles. Section 1 contains five quadrupoles and Section 3 contains six quadrupoles to permit the beam to be optically matched at the entrance to the bend region and into the Booster ring respectively.

The Booster ring[1] has a FODO lattice with missing main dipole magnets to allow for injection/extraction magnets, RF cavities and other insertions. There are forty-eight half-cells with 24 quadrupoles in each plane. The main dipoles and quadrupoles are powered in series. The main quadrupoles have additional primary and secondary windings for tune and stopband correction respectively. There are also correction dipole magnet assemblies at each main quadrupole magnet for orbit correction and local orbit bumps in both planes.

Instrumentation

Detailed descriptions of the beam instrumentation developed for use in the Booster facility can be found elsewhere in these proceedings. However, an overview of their application is included.

Linac-To-Booster (LTB) Instrumentation

There are two beam current transformers, one at each end near the HEBT beam line and near the Booster ring.[2]

The beam position measurement in this line is done by using seven resonant stripline beam position monitors, each providing both horizontal and vertical information. [3] In each monitor, the four plate sum signal provides in addition an approximate beam current measurement.

Beam profile information in LTB is obtained using two insertable multiwire profile monitors. The data provided by these monitors in conjunction with a sequence

*Work performed under the auspices of the U.S. Department of Energy.

0-7803-0135-8/91$01.00 ©IEEE

of programmed changes in specific LTB quadrupole magnets settings, can yield for the user an emittance and Twiss parameter measurement[4] for a specified location in the beam line.

Beam loss information[5] along the beam line is given by eight coaxial loss monitor cables distributed in a contiguous manner throughout LTB. This loss monitor system is a nearly generic module in the overall loss monitor system for the Booster facility.

Booster Ring Instrumentation

The first instrumentation element the incoming proton beam intercepts in the Booster ring after being stripped to H^+ in a carbon foil is one of 46 split plate Pick Up Electrodes (PUE's).[6] These PUE's each measure beam centroid position in one plane and are located immediately prior to each quadrupole magnet that focuses the beam in the plane of measurement. There are 24 in the vertical plane and 22 in the horizontal; one horizontal PUE is missing at the extraction point and one missing at the Internal Beam Dump because of the horizontally oversized vacuum chambers at these locations.

Just past the immediate proton injection point is located a current transformer assembly that has incorporated in it two transformers. The Injection Transformer has a time constant capable of monitoring the injected beam pulse from the Linac of 150 to 250 μs and the other Circulating Beam Transformer with an appropriate time constant to monitor the remainder of the acceleration cycle, ($\approx$ 60 ms for protons).

The current transformers and the PUE's respond to both stripped and unstripped beams (with the appropriate sign reversal). Remote control of the stripping foil position (in/out) allowed a very valuable switching between these conditions.

Preparation for Commissioning

Before any part of the Booster facility could be commissioned with beam and in addition to the installation and testing activities, each phase of commissioning had to be prepared and thoroughly reviewed. In particular, all new beam areas are considered from the point of view of the creation of new radiation sources. As part of the process there had to be included an outline for conducting the beam tests and the area(s) reviewed beforehand to identify the locations where a credible accelerator fault could produce a local beam loss with the resulting prompt radiation. These beam fault conditions then had to be created and the studies conducted as part of the commissioning procedure. The results are then reviewed before continuing with the next phase of commissioning. Also, the personnel necessary to participate in each aspect of commissioning were trained prior to carrying out the tests with beam.

Commissioning with Beam

Commissioning of the Booster facility has been done in phases as each separable area of the accelerator is completed. The phases were identified as 200 MeV beam transport through the first two sections of the LTB beam line, transport through all of LTB and to the Booster injection region, transport through one sextant of the Booster, spiralling beam, accelerating beam and finally extracting beam from the Booster. Final stages of Booster ring equipment installation prohibited the spiralling of beam in the Booster and as of this writing, the beam has been transported through the injection beam line and around one sextant of the ring. The ability to transport beam to this point has been invaluable in providing the first beam control and measurement information from the available diagnostics.

In order to match the beam optics at the entrance to the LTB beam line, the HEBT emittance and Twiss parameters were determined at the LTB injection point using a Least Squares fit to HEBT profile data. The range of movement in any of the Twiss parameters at this point is constrained by the fact that both the AGS and the Brookhaven Linac Isotope Production (BLIP) facility are serviced by the HEBT beam line. However, the range over which these incoming beam parameters may be varied was sufficient to define the input trajectory and optical conditions and transfer the beam into the LTB beam line. Control of the LTB optics and trajectory to the Booster ring was then straightforward using magnet calibration data.

At the exit of LTB section 2, a temporary carbon beamstop was installed to allow the transport of low intensity beam through LTB sections 1 and 2 so that beam tests could proceed with the beam aborted safely in one location and not create residual radiation in areas where the installation effort continued. This was very important in the early stages of testing the instrumentation, data acquisition and methods of controlling beam parameters, (trajectories and optics).

Beam position measurements from the stripline BPM's in the LTB beam line reproduced to better than 0.5mm. The data from the BPM's was then acquired and used in a user friendly trajectory correction program to determine and implement the necessary changes in correction dipoles to minimize orbit errors in the beam line. The details of this program and associated algorithms can be found elsewhere in these proceedings.[7]

The beam loss monitor system proved to be sensitive to beam loss of less than 1×10^{10} protons per pulse at a given location. The output of the loss monitor system is coupled with the Fast Beam Interrupt (FBI) system used to provide a rapid inhibit ($\approx$ 15μs) of the injected Linac beam if integrated beam loss exceeds an assigned limit.

With the commissioning of the AGS Booster as an accelerator, new aspects of the controls system for the AGS facility have also been undergoing a commissioning process. Included in this is the first use of a timing system environment that is centered around the ability to operate each accelerator (Linac, Booster and AGS) for multiple users in a Pulse to Pulse Modulated (PPM) manner. This tool has been used at the PS at CERN for many years to increase the available access to the beam in individual accelerators within the facility. Each software utility developed now has the capability to acquire data for any or all separate users of the beam. One of the new software tools that has proven to be very useful in providing the user with real-time machine data (as a function of PPM beam user) is the General Purpose Monitor (GPM).[8] In this program, the user is able to acquire and display data from any defined collection of devices as a function of time. It is also "user friendly" in that the association of devices of interest is trivially modified (even amid the standard commissioning chaos) for immediate display. This has been used extensively for radiation monitoring.

When the proton injection area of the Booster ring was available to accept beam, one sextant of the main ring buss (dipoles and quadrupoles in series) was powered by an independent DC power supply so as to assure that the beam could not be carried beyond a well defined location in the ring. Beam was then transported through section 3 of the LTB beam line and injected into the Booster ring at the C5 location.

There was some concern over the beam trajectory through the C5 main dipole magnet. The incoming H^- beam from the LTB line initially traverses a field free region of the C5 magnet but as it crosses (at an angle of approximately 11° to the tangent of the magnet) between the C5 magnet coils, the field increases quickly to the central dipole field of the magnet. This effect was studied extensively by mapping the field and model tracking of particles through this magnet. Since the net dipole effect on the incoming H^- must bring the beam to a nominal x,x' as determined by the injection orbit at this location, it was essential to know this trajectory precisely. Position measurements at the first PUE in the Booster ring (C6 quadrupole) are within estimated error of the position of the model Booster injection orbit. Angle information at the injection foil will determine whether the injected beam will have the appropriate trajectory to merge with the equilibrium orbit of the Booster ring. Model studies have shown that if this is not the case, a small translation of the downstream LTB beam line elements will be necessary and sufficient to correct any misalignment.

Future Commissioning

Installation and preliminary testing of the Booster ring equipment will be completed by the end of May. Since one of the two proton RF cavities is presently ready to be used with beam, beam spiralling and acceleration should be achieved by mid-June. The extraction equipment will be fully tested and available for beam tests also by this date. Since the AGS is running for the High Energy Physics (HEP) program, access to the AGS ring for equipment installation and testing of the Booster To AGS (BTA) transfer beam line is restricted. In order that the extraction process can be tested, another temporary beamstop has been installed a few meters into the BTA line.

All of the commissioning efforts have been and will continue to be done at a relatively low beam intensity until the machine is well understood. Higher intensity studies will follow early in FY'92.

Acknowledgements

These first commissioning achievements represent the results from the long efforts of a large community of dedicated people at BNL. In particular, we wish to recognize the mechanical and electrical engineering support by J. Brodowski and I. Marneris, respectively; the AGS Main Control Room operations personnel who helped smooth the edges at each commissioning step; Controls Group participation by D. Barton, W. Buxton, T. Clifford, B. Culwick, R. Enriquez-Leder, and V. Wong played an essential role. Finally, the wise counsel of several colleagues, especially D. Beavis, J.W. Glenn, Y.Y. Lee, D. Lowenstein, and L. Ratner helped to make the commissioning a more coherent process.

References

1. AGS Booster Design Manual (Rev. 1, Oct., 1988).
2. R.L. Witkover, private communication.
3. T. Shea, Beam Position Monitoring in the AGS Linac-to-Booster Transfer Line, this proceedings.
4. J. Skelly, Generalized Emittance Measurements in a Beam Transport Line, this proceedings.
5. E. Beadle, The AGS Booster Beam Loss Monitor System, this proceedings.
6. D. Ciardullo, The AGS Booster Beam Position Monitor System, this proceedings.
7. T. D'Ottavio, User Control of the Proton Beam Injection Trajectories in the AGS Booster Synchrotron, this proceedings.
8. J.T. Morris, private communication.

MULTI-BEAMLET INJECTION TO THE RFQ1 ACCELERATOR - A COMPARISON OF ECR AND DUOPIGATRON PROTON SOURCES

G.M. Arbique, T. Taylor, M.H. Thrasher and J.S.C. Wills
AECL Research, Chalk River Laboratories
Chalk River, Ontario, Canada K0J 1J0

Abstract

A 2.45 GHz electron cyclotron resonance (ECR) ion source, recently developed at Chalk River, was installed on the RFQ1 facility for comparison with the duoPIGatron source used previously. The proton fraction of the ECR ion source is 80 to 85 percent, much higher than the 30 to 35 percent of the duoPIGatron. Measurements of the beam transmission through the RFQ, as well as the emittance of the extracted and the accelerated beams, are reported. Four-aperture extraction columns were used on both sources.

I. INTRODUCTION

The original ion source for the RFQ1 cw proton accelerator [1] was a three-aperture duoPIGatron. Although the RFQ1 duoPIGatron [2] generates 320 mA/cm^2 at matched perveance, the proton fraction is low. A current density, as high as 450 mA/cm^2, is achievable with the source, but the required extraction gap, at matched perveance, is too small for reliable operation. In fact, the RFQ1 design current could only be achieved by increasing the number of extraction apertures to four [3]. In addition, the lifetime of the source is reduced by the periodic failure of the cathode, the efficiency of conversion of hydrogen gas to protons is very low and an extensive system of power supplies at high voltage is required.

A high-current low-emittance electron-cyclotron resonance (ECR) ion source with an exceptionally high proton fraction [4] has been developed as an alternative source for RFQ1. The source, shown in Figure 1, is driven by 2.45 GHz microwaves introduced to the plasma chamber via a dielectric window. The axial magnetic field, to satisfy the electron-cyclotron resonance condition and confine the plasma, is supplied by two solenoids. The duoPIGatron source extraction geometry is used, but with a larger extraction gap to lower the matched proton current to that required for the the RFQ.

This paper compares the performance of the duoPIGatron and the ECR proton sources. Measurements were made on the beams from the two sources immediately after extraction, following mass separation and after acceleration in the RFQ1 accelerator.

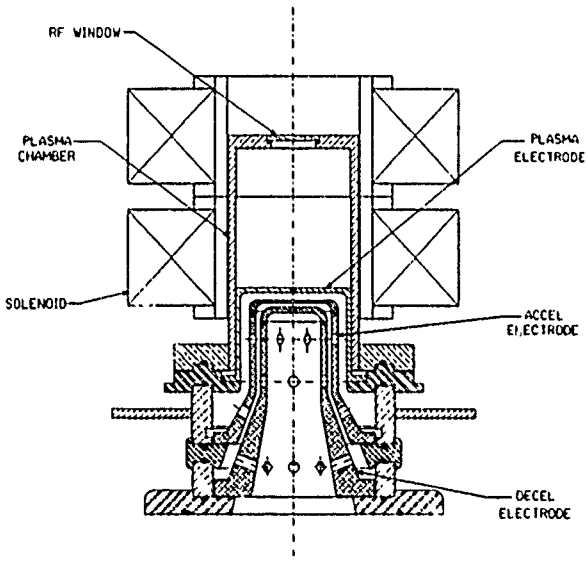


Figure 1. ECR proton source.

II. EXTRACTION FROM ION SOURCES

The duoPIGatron with a 0.64 cm acceleration gap and four 0.50 cm diameter extraction apertures, equally spaced on a 0.53 cm radius, generated a "matched" (i.e., minimum divergence) beam of hydrogen ions, for an extraction voltage of 50 kV, at a total beam current of about 250 mA. The proton fraction was typically 30 to 35 percent, resulting in an extracted proton current of between 75 and 90 mA. Some beam was lost in the low-energy beam transport line so that the required 90 mA could be supplied to the RFQ only by operating the source at higher than match current. On the other hand, the proton fraction of the ECR ion source is between 80 and 85 percent so that, even with the acceleration gap almost doubled to 1.2 cm, a proton current of 95 to 100 mA can be generated with a total matched current of only 120 mA.

0-7803-0135-8/91$01.00 ©IEEE

The normalized rms emittance of the unseparated beam from both the ECR and the duoPIGatron ion sources, measured on an ion source test stand, is less than 0.05 π-cm-mrad. In both cases, the emittance of the individual beamlets is typically 0.008 π-cm-mrad and the corresponding rms divergence is 12 mrad. However, the overall beam divergences are different because the individual duoPIGatron beamlets diverge from the beam centroid by about 10 mrad, while the beamlets from the ECR ion source are parallel. The cause for the misalignment of the duoPIGatron beamlets is under investigation.

The replacement of the duoPIGatron with the ECR ion source reduces the gas load on the injector vacuum system by about a factor of five. The ECR ion source operates stably with a hydrogen mass flow of no more than 5 std. cm^3/min, whereas the duoPIGatron usually operates at 25 std. cm^3/min.

The duoPIGatron, a mature design, is a reliable source and operates stably, without drift, over long periods; lifetime is limited by the oxide-coated cathode to about 200 h. The ECR ion source, which is still in early development, has at present a similar lifetime, limited here by dielectrics in the microwave window and plasma chamber liners. The microwave window is slowly degraded by electrons backstreaming from the extraction column, and the plasma chamber liners, introduced to enhance the proton fraction [4], are subject to contamination as well as catastrophic failure. These two factors may also contribute to drift and instability seen in the extracted beam from the ECR. Retuning the microwave line invariably restores the beam, and installation of a circulator improved stability. Nonetheless, the ECR source operated for over one-hundred hours before it was disassembled for repair of a dielectric liner.

III. INJECTION TO RFQ1

The 50 keV RFQ1 low-energy beam transport system (LEBT) is shown in Figure 2. The LEBT includes a 60° dipole magnet to separate molecular ions from the beam and solenoids after the ion source and at the entrance to the RFQ that match the beam to the acceptance of the RFQ. The beam is set up on a plunging beam stop (PBS) in the injector exit line, which is then raised to inject beam into the RFQ. Apertures in the LEBT, at the first solenoid and in the exit line, limit the size of the transported beam.

The current measured by non-intercepting beam-current monitors, at the exits from the injector and the RFQ, as well as the current on a beam-size-limiting aperture at the PBS, after the exit monitor, are shown as a function of the current from both the duoPIGatron and the ECR ion source in Figure 3. The solenoid fields were optimized for maximum accelerated current at each point.

The ECR ion source delivers a higher proton current than the duoPIGatron at less than half of the total source current. However, like the duoPIGatron, the ECR source can only achieve the 75 mA design current through the RFQ when it is operated at higher than matched perveance. Beam losses with

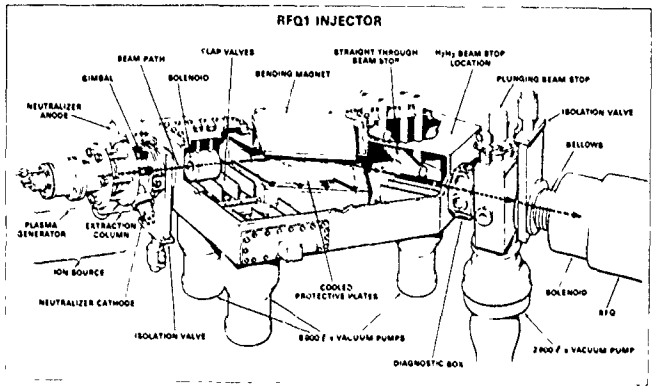


Figure 2. RFQ1 injector.

the ECR source are less at the start of the LEBT, but are excessive at the PBS aperture. At matched perveance, the RFQ transmission appears to be about 75% with the ECR ion source, slightly lower than the 80% achieved with the duoPIGatron The output emittance of the RFQ, measured in the horizontal plane of the injector dipole, was 0.04 π-cm-mrad for a matched ECR beam, the same as for matched duoPIGatron injection [3]. RFQ output emittance trends are similar for the two ion sources.

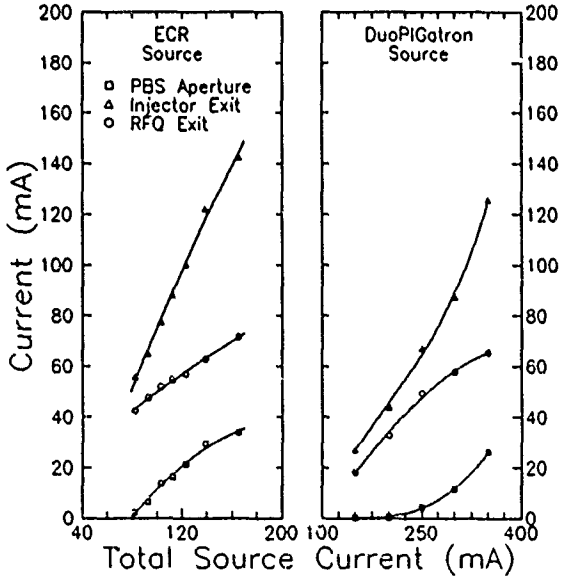


Figure 3. Injection and RFQ output currents for ECR and duoPIGatron ion sources.

The differences in the beam transport to the RFQ may be related to the variation in the beamlet-to-beamlet divergence of the two ion sources. The LEBT was designed so that a multi-beamlet beam with space charge would pass through a "gentle" waist between the solenoids. Calculations with the

beam transport code TRANSOPTR [5] indicate a waist further downstream when beamlets diverge from the ion source. Parallel beamlet extraction results in a larger beam envelope at the PBS aperture. The increased beam loss on the PBS aperture at higher beam currents, with both ion sources, is also consistent with space-charge blow-up. This is probably the dominant effect, as losses at the PBS are similar for the two ion sources for given injector exit proton currents. Apertures in the injector exit line have yet to be optimized for ECR source operation (un-monitored beam losses in the exit line may be responsible for the lower RFQ transmission with the ECR source).

IV. DISCUSSION

The 75 mA design RFQ1 current was achieved with the ECR source. The ECR ion source consistently gives at least double the proton fraction of the duoPIGatron and, in almost every other respect, performs at least as well as the duoPIGatron. Reliability deficiencies will be addressed by a second-generation ECR ion source presently being fabricated.

The full potential of the high-current low-emittance ECR ion source has yet to be realized. The high-proton fraction opens up the possibility of direct injection, without mass separation, into the RFQ. The lower gas consumption reduces the injector pumping requirements. Proton current densities of up to 315 mA/cm^2 have already been demonstrated on a test stand so that the emittance may be dramatically reduced with beam current extraction from a single-aperture. The ECR source solenoids can be isolated from the plasma chamber, eliminating the need for dc power supplies at high voltage. A simple dc waveguide break already allows the microwave power supply to be at ground.

V. ACKNOWLEDGEMENTS

The authors thank E.C. Douglas for hours spent on design of the ECR source; the efforts of D.G. Hewitt in machining the source assembly and of L.F. Birney in installing the source on RFQ1 are also greatly appreciated. During the experiments the RFQ was operated by A.D. Davidson and J.Y. Sheikh; B.H. Smith and W.L. Michel provided diagnostics support.

VI. REFERENCES

[1] G.M. Arbique et al., "CW Operation and Initial Beam Experiments with the RFQ1 Accelerator", 1988 Linear Accelerator Conf. Proc., CEBAF, Newport News, VA, 91, 1988.

[2] M.R. Shubaly and M.S. de Jong, "High Current DC Ion Beams", IEEE Trans. on Nuclear Science, Vol. NS-30, No. 2, 1983 April.

[3] G.M. Arbique et al., "Beam Transmission and Emittance Measurements on the RFQ1 Accelerator", these conference proceedings.

[4] T. Taylor and J.S.C. Wills, "A High Current Low Emittance ECR Proton Ion Source", to be published.

[5] E.A. Heighway and M.S. de Jong, "TRANSOPTR - A Beam Transport Design Code with Space Charge, Automatic Internal Optimization and General Constraints", AECL Report, AECL-6975(Rev. A), 1984 June.

BEAM TRANSMISSION AND EMITTANCE MEASUREMENTS ON THE RFQ1 ACCELERATOR*

G.M. Arbique, B.G. Chidley, W.L. Michel,
G.E. McMichael and J.Y. Sheikh
AECL Research, Chalk River Laboratories
Chalk River, Ontario, Canada K0J 1J0

Abstract

RFQ1 is an accelerator project to develop high-proton current cw RFQ's suitable for scientific and industrial applications such as neutron sources, nuclear waste transmutation and fissile fuel breeding. The accelerator, which comprises a 50 keV dc injector and a 0.6 MeV cw radiofrequency quadrupole accelerator, is a test bed for a wide range of high-power RFQ experiments. The structure was designed to accelerate 75 mA of protons and has achieved the full design current. Measurements are reported on the output beam transmission and emittance for four-beamlet proton beam injection from a duoPIGatron ion source.

I. INTRODUCTION

The RFQ1 [1] project is a research program for the development of high-current cw radio-frequency quadrupole (RFQ) proton accelerators. The injector is designed to provide a matched 50 keV multi-beamlet dc proton current, variable up to 90 mA, to the RFQ. The RFQ is a 100% duty factor radiofrequency quadrupole, designed to accelerate 75 mA of protons to a final energy of 600 keV.

Since commissioning, in mid-1988 [2], the major design targets have been achieved on the RFQ1 facility, and the experimental program with the duoPIGatron source has been completed. Recent experiments were concerned with emittance and beam transmission measurements to characterize the RFQ output beam under a variety of operating conditions. A final set of experiments, using an ECR source on the injector, are reported elsewhere in these proceedings [3].

The RFQ1 vanes are being replaced to increase output energy to 1.25 MeV. To avoid confusion the 600 keV output accelerator will, in future, be referred to as RFQ1-600 and the new version as RFQ1-1250.

II. DESCRIPTION

Figure 1 shows an artist's representation of the injector and RFQ subsystems.

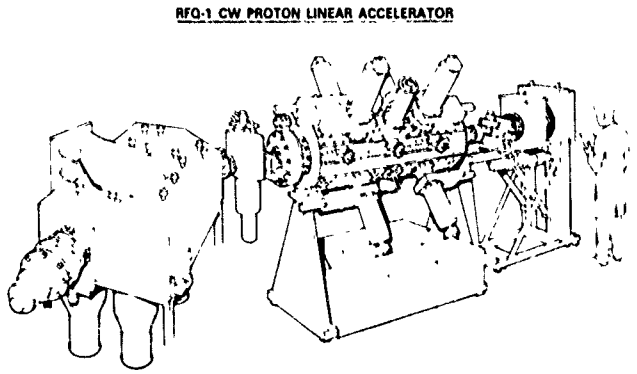


Figure 1 RFQ1 accelerator components and layout.

The major components of the injector are an ion source and low-energy beam transport system (LEBT). For the purposes of this paper the ion source is a duoPIGatron [4], providing high currents with modest proton fractions (30%-35%). The LEBT includes a 60° dipole magnet to separate the unwanted molecular species from the beam. Solenoids, after the source and at the RFQ entrance, match the ion source beam to the RFQ acceptance. A plunging beam stop (PBS) at the exit of the injector is used for beam set-up, and is raised to inject beam to the RFQ.

The accelerator is a cw four-vane type RFQ, resonant at 267 MHz. The mean bore radius is 4.13 mm. At the design peak electric fields of 1.5 Kilpatrick [5] (24.7 MV/m) the intervane voltage is 78 kV.

III. BEAM TRANSMISSION

The PARMTEQ [6] code predicts 85% transmission (75 mA output current) for a 90 mA 0.05 π-cm-mrad emit-

*This work was partially supported by Los Alamos National Laboratory under contract No. 9-X5D-7842D-1.

0-7803-0135-8/91$01.00 ©IEEE

tance input beam. At injection currents less than 50 mA (i.e., lower space-charge) transmissions in excess of 90% are predicted. Attempts to achieve the design 75 mA RFQ output current with a three-aperture source on the RFQ1 injector were unsuccessful, because the source could not supply enough current [7]. With the installation of a higher-current four-aperture duoPIGatron, with 15% higher emittance, the 75 mA RFQ design current was achieved.

The best match of the injector LEBT beam to the RFQ acceptance is achieved when the source is operated at matched perveance. For a multi-aperture source, matched perveance is defined as the output current which yields the minimum beamlet-divergence (and hence minimum emittance). As a practical means of varying the injector current, the source is often operated off-match by varying the source plasma density. Apertures in the injector, at the injector solenoid and in the vicinity of the PBS, limit the size of the beam.

Figure 2 shows injector and RFQ output currents as a function of source current. Non-intercepting beam-current monitors measure the exit currents, and the PBS aperture, downstream of the injector exit monitor, is isolated from ground to measure intercepted current. At 250 mA the source is matched, and transmission is optimized at 80% with 50 mA accelerated current. When operating the source "over-matched", proton current in excess of the design 90 mA could be transported to the RFQ, and accelerated current approached a plateau of about 70 mA. RFQ transmission for four-beamlet injection is lower than with the three-beamlet source, due to the higher source emittance and increased PBS aperture diameter [7]. The high beam loss on the PBS aperture at high-current, is consistent with space-charge induced beam blow-up and is another factor limiting injected current to the RFQ. Beam loss mechanisms will be more fully investigated with emittance measurements on the injector output beam.

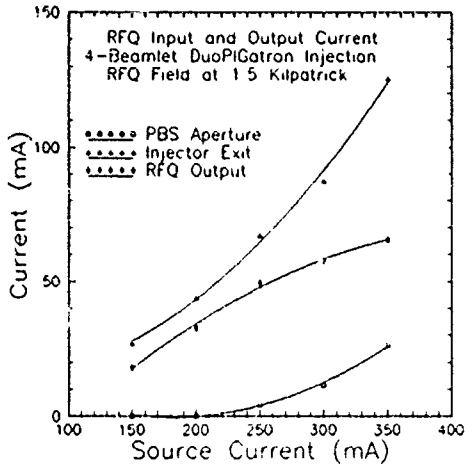


Figure 2. Injector and RFQ output currents.

Injector current may be varied, without increasing source emittance, by maintaining matched perveance while mixing argon with the source hydrogen gas feed [1]. When injected current is reduced using this method transmission increases. At one-half nominal injection current, transmission is 90%, in excellent agreement with PARMTEQ predictions.

Transmission, at high-current, could be raised by increasing the vane-tip field above the design level, but field levels in RFQ1-600 were limited due to an rf overheating problem at the ends of the vane-seal-gaskets. Nonetheless, by operating 10% above the design field level and by running source beam in excess of 350 mA, the design 75 mA current was accelerated through the RFQ, with transmission of 75% (with the more efficient ECR source [3] an accelerated current of 79 mA was achieved).

IV. RFQ Output Emittance

An Emittance Measurement Unit (EMU) is used to measure the output beam emittance of the RFQ. The output beam is intercepted by a moveable water-cooled beam-stop fitted with a 5 cm long copper slit. The slit transmits a narrow portion of the beam to a Faraday cup behind a second movable slit. Slit arrangements are available for either the X,X' or Y,Y' measurements.

Figure 3 shows a typical X,X' measurement (i.e., measured in the horizontal plane of the injector 60° bend magnet) for matched beam injection at the design field. Here the emittance is 0.04 π-cm-mrad (normalized rms). The original four-beamlet distribution is no longer evident after acceleration through the RFQ. Under the same measurement conditions the Y,Y' emittance was nearly 20% larger.

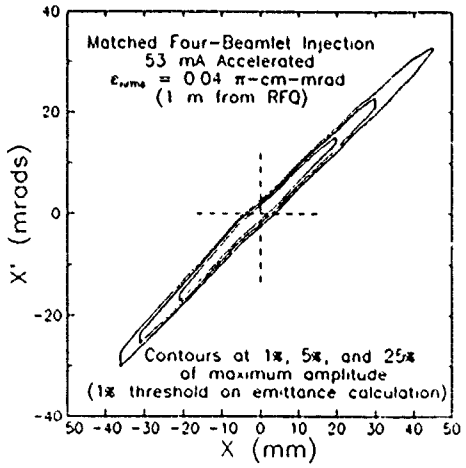


Figure 3. RFQ output emittance for four-beamlet injection.

The four-beamlet output emittance is in close agreement with the value measured for three-beamlet transmission and is less than the estimated injector emittance (based on measurements on an ion source test stand). Increasing the PBS aperture diameter and operation with the higher emittance four-aperture source had no measurable effect on the RFQ output emittance. This agrees with PARMTEQ calculations, which indicate that the RFQ acts as an emittance scraper due to beam spill at higher currents.

That the RFQ acceptance space is filled is further shown by the change in emittance when the RFQ current is varied by running the source off-match. Above 50 mA the emittance remains constant, while it increases at lower currents. The larger RFQ output beam emittance is due to reduced space-charge defocusing, also a larger emittance input beam may arise from operating the source off-match. When the injector proton current was reduced at matched perveance, by adding argon gas, the RFQ output emittance remained constant.

Reducing RFQ field also results in increased output beam emittance. At matched current injection, operation of the RFQ at 80% of the design field results in an emittance increase of about 35%, a similar decrease in transmission also occurs. The emittance increase is explained by the reduced longitudinal acceptance, which results in growth of lower-energy beam components [6]. There was no measurable change in emittance when fields were increased to 110% of design. A similar effect occurs when input beam energy is reduced. Injection at 45 kV (5 kV below design) resulted in 65% transmission (for a best match 45 mA injection beam) and a 30% emittance increase.

V. Dipole Field Tilt Measurements

The motor-driven RFQ1 tuners [8] have been used to introduce dipole field perturbations during beam operation. Tuners are situated in opposite quadrants and by inserting one and retracting the other, rf power (and hence field levels) in these quadrants can be perturbed in equal and opposite directions (adjacent quadrant fields are unperturbed). Dipole perturbations were also induced by radial movements of one vane. This raises fields in the shifted-vane quadrants and lowers fields, by an equal measure, in the quadrants opposite.

For matched four-beamlet injection, beam transmission was unaffected when quadrant fields differed by less than 8%. A measurement with a field difference of 14% showed a transmission decrease of 10%. Over the range of field imbalances investigated no change in output emittance was found. These measurement results are in good agreement with PARMTEQ predictions.

VI. Summary

The experimental program on RFQ1-600 has been completed and the major design goals have been achieved. The RFQ proved to be a robust and reliable machine capable of operating up to the 1.6 Kilpatrick field level. A high tolerance to cw beam spill (> 30 mA) in the structure facilitated the measurement of beam parameters over a range of "off-optimum" operating conditions.

Measured transmission and emittance were in agreement with PARMTEQ code predictions over a wide range of operating conditions.

VII. Acknowledgements

The authors are indebted to the efforts of numerous persons involved in the RFQ1 project. In particular: L.F. Birney, A.D. Davidson, and M.H. Thrasher, who operate and maintain the accelerator and systems; and A.B. Hood and B.H. Smith, for electronics support.

VIII. References

[1] G.M. Arbique et al., "Commissioning of the RFQ1 Injector", Proc. IEEE Particle Accelerator Conference, Washington D.C., 1558, 1987.

[2] G.M. Arbique et al., "CW Operation and Initial Beam Experiments with the RFQ1 Accelerator", 1988 Linear Accelerator Conf. Proc., CEBAF, Newport News, VA, 91, 1988.

[3] G.M. Arbique, T. Taylor, M.H. Thrasher and J.S.C. Wills, "Multi-Beamlet Injection to the RFQ1 Accelerator - A Comparison of ECR and DuoPlGatron Proton Sources", these conference proceedings.

[4] M.R. Shubaly and M.S. de Jong, "High Current DC Ion Beams", IEEE Trans. Nucl. Sci. NS 30, No. 2, (1983).

[5] W.D. Kilpatrick, "Criterion for Vacuum Sparking Designed to Include both RF and DC", Rev. Sci. Instr., Vol 28, No. 10, Oct 1957.

[6] K.R. Crandall and T.P. Wagner, "PARMTEQ - A Beam Dynamics Code for the RFQ Linear Accelerator", Proc. Workshop on Linear Accelerator and Beam Optics Codes, San Diego, CA, Jan 19-21, 1988, AIP Conf. Proc. No. 177,22.

[7] G.M. Arbique et al., "Beam Performance and Measurements on the RFQ1 Accelerator", Proc. 1990 Linear Accelerator Conference, Albuquerque, NM, 677, 1990.

[8] T. Tran-Ngoc et al., "Components for CW RFQ's", Proc. 1990 Linear Accelerator Conference, Albuquerque, NM, 48, 1990

First Two Years Operational Experience with LEP

R. Bailey, T. Bohl, F. Bordry, H. Burkhardt, K. Cornelis, P. Collier, B. Desforges, A. Faugier, V. Hatton, H. Laeger, J. Miles, J. Poole, G. de Rijk, H. Schmickler, D. Vandeplassche
CERN, 1211 Geneva 23, Switzerland

Abstract

On July 14, 1989 a beam of positrons was injected into LEP from the SPS and completed the first full turn. One month later all 4 experiments, ALEPH, DELPHI, OPAL and L3 detected their first Z^0 particles.

From September to December 1989, the machine was operated in a mixed mode of machine studies and operation for physics. At the end of this period a total of over 1.7 inverse picobarns of integrated luminosity had been recorded per experiment, resulting in a total of more than 70,000 Z^0s detected.

At the request of the physicists, the energy of each fill was varied, half the number of fills were at the Z^0s peak, i.e. a centre-of-mass energy of 91.25 GeV, the rest at ± 3, ± 2, ± 1 GeV around the peak energy.

During 1990, LEP was operated in the same way as in 1989. From March to July 1990, 12.1 inverse picobarns and three quarters of a million Z^0s were produced.

Physics fills of 6 hours duration in 1989 were increased to 10-12 hours in 1990 as the lifetimes of the beams increased with the steadily improved vacuum in the ring.

This paper summarizes the experience over the first two years of LEP operation giving typical and peak performance figures.

I. THE FILLING PROCESS

The first part of the SPS supercycle is dedicated to injection, acceleration and extraction of protons from 14 to 450 GeV.

Four bunches of positrons at 3.5 GeV are then injected and accelerated to 20 GeV before being ejected and transferred to LEP. Four more bunches of positrons follow 1.2 seconds later followed by two cycles of four electron bunches. Intensities of about 8 x 10^9 particles per bunch are typical. In special machine-study sessions a single bunch current of 0.75 mA (approximately 4 x 10^{11} particles) has been accumulated, with a total of 2.8 mA in the four bunches. The design intensity is 0.75 mA in each of the four electron and positron bunches.

Under optimum conditions the leptons are injected into LEP and accumulated at a rate of 0.3 mA per minute. The average total intensity of electrons and positrons accumulated at 20 GeV in 1989 was 2.2 mA; there was little increase from September to December, 1989. In 1990, after optimizing the length of the bunch coming from the injectors from 2.5 to 3.0 ns, and a change of working point from Qh = 71.375, Qv = 77.290 to Qh = 71.280, Qv = 77.190, there was a steady increase in accumulated current to an average overall fill of 3.1 mA, with a maximum of 4.2 mA.

Beam is accumulated at 20 GeV in the machine with low beta insertions, ß* of 21 cm, provided by the superconducting quadrupoles in those regions in the four experimental points.

Ramping the beam to physics energies from 20 to 45.625 GeV is reached in 7 minutes at present although this can be reduced to less than 1 minute if required.

Squeezing of the beams at collision energies in the four interaction regions is applied after correction of tunes and closed orbit. The squeeze in the vertical plane from 21 cm to 7 or 5 cm takes about 2 minutes; this is followed by further tune and orbit corrections.

II. MACHINE PERFORMANCE FOR PHYSICS

With averages of 3.5 mA total beam accumulated at 20 GeV, 3.0 mA are typically seen in the experiments after the ramp and squeezing process at 45 GeV with modest background levels. Steady reproducible operation for the four experiments has been possible with these levels of intensity. Peak and mean performance figures for 1989 and 1990 are given in Table 1.

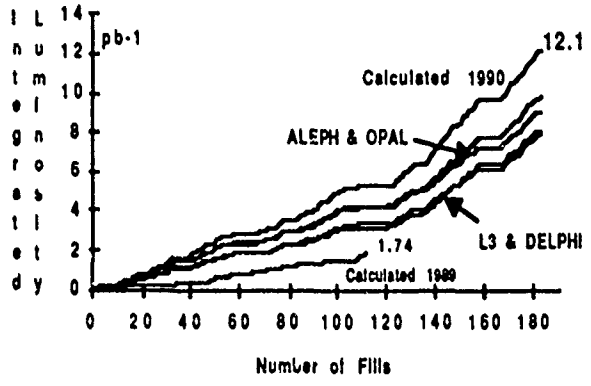


Figure 1. Integrated luminosity for 1989 and 1990.

The integrated luminosities for 1989 and 1990 are plotted in Figure 1 together with the integrated luminosities, for 1990, measured by the four experiments. At currents in excess of 3 mA at peak energies, there is an appreciable beam-beam effect which leads to increased beam size and corresponding reduction in luminosity seen by the experiments compared to that expected from scaling with intensity.

Attempts to run for physics at vertical beta* lower than 7 cm in 1989 were stopped due to non-reproducibility of results; in some experiments, there was no measurable improvement in the luminosity at the lower values. Operation at 4.3 cm was much more critical than at 7 cm. In 1990 good reproducible operating conditions were achieved with a ß* of 5 cm.

0-7803-0135-8/91S01.00 ©IEEE

In common with the experiences reported from other electron machines [1], good vertical orbit control is essential to achieve satisfactory accumulation at the injection energy and high luminosities at top energy. Furthermore, a well-corrected vertical orbit in the RF straights helps to reduce the risk of synchro-betatron resonances. As is well known [2], the effect of coupling together with the influence of the vertical closed orbit on residual vertical dispersion, have a strong impact on vertical emittance. The notion of "Golden Orbits", which provide short-term reference points for good operation, was invoked in 1990 with some success. Empirical application of symmetric and asymmetric vertical closed orbit bumps around the even interaction points (thereby including the superconducting insertion quads, beta ~ 400 m) was also used operationally with success. These bumps modified the dispersion and also had the effect of improving the background conditions for the physics experiments.

Since the beginning of 1990 continuous measurements of the tunes during critical phases of machine operation like energy ramping or beta squeezing are possible. This is either done in the FFT mode of the Q-measurement system or in PLL mode. On the first case the tunes are derived from the peaks of the spectral distribution of the beam movement or in the second case, by reading the frequency of the beam exciter, which by means of a phase lock condition maintains steady beam oscillations at the resonance of the beams.

These measurements were successfully used to correct the current variations during energy ramping to maintain the tunes constant within $\Delta q \leq 0.02$.

A further improvement in tune stability was the contruction of a closed loop digital tune digital tune regulator, which based on the continuous tune measurements computer correction signals for the main quadrupole PCs and maintained the tunes constant within $\Delta q \leq 0.005$.

The different luminosities seen by the four experiments were extensively studied. In the last month of operation in 1990, optimization of the currents in the low-beta insertion superconducting quadrupoles resulted in an improved uniformity and an overall increase for given intensities. One source of the difference was traced to a misalignment of the quadrupoles in the cryostat.

III. INTERRUPTIONS TO NORMAL OPERATION

An average of 36% of the scheduled time for physics operation was spent data taking in 1989 and 43% in 1990.

In 1989 and 1990, 35% and 33% respectively of all fills were lost due to equipment faults. A number of these occurred when a power converter tripped off due to cooling problems, or the mains voltage dipped. Concerning the RF system, the largest such system in the world, trips in one or more of the RF units was a feature of LEP operation in 1990.

During the period of commissioning of the many LEP systems efficiency was reduced in 1989 by the second type, as is usual with a new and complex machine. Improved understanding of the operation and faster recovery from equipment failures resulted in shorter turn-around times in 1990.

Table 1
LEP performance during physics operations in 1989 and 1990

		1989		1990		Design
		Best	Average	Best	Average	
Total current accumulated 20 GeV	mA	2.85	2.20	4.20	3.10	6
Beta at the experiments (V)	cm	7	7	4.30	7 and 5	7
Current in collisions 45 GeV	mA	2.64	1.66	3.60	2.50	6
Calculated initial luminosity	10^{30}	4.25	1.59	11.00	5.10	16
Calculated integrated luminosity	pb^{-1}		1.74		12.10	
Filling time	h:min	0:50	7:35	1:20	6:57	
Coast duration	h:min	12:45	5:00	22:35	7:30	
Total coast time/scheduled	%		36		43	
Total number of coasts			97		143	
Percentage of coasts lost	%		35		33	

pb^{-1} = Inverse picobarns. Calculation based on intensities, emittance.

Due to the high degree of computerization, software problems and inefficiencies caused significant delays between coasts in 1989. There has been considerable improvement in 1990 but much has still to be done.

All CERN machines are affected by critical days, i.e, days during which the electricity supply company, under the contract terms, can request the shedding of load for a period of 18 hours per day, for 22 days spread randomly over the 5 months from November to March. Six days of operation were lost in 1989 and five in 1990. Thunderstorms in the region result in interruptions due to voltage dips on the 50 km overhead 400 kV line from the power station to CERN.

The injector chain contributed little to the down time although vacuum leaks in the RF cavities in both the SPS and PS were a source of concern; the leaks were on the damping loop bellows which took the cavity off-tune during the passage of the high intensity protons. This was less of a problem in 1990.

Analysis of seven weeks of LEP fills in 1990 is shown in Table 2. The times for filling, ramping and squeezing for 60 fills are indicated compared to the shortest turn-around time so far recorded in 1990, fill number 235. Short-term interruptions randomly spread over all the LEP systems and non-reproducible accumulation conditions resulted in a doubling in the filling time. Fill times of about one hour are expected in 1991.

IV. JOINT LEP AND SPS OPERATIONS

A decision was taken early in the LEP project by the LEP management board that LEP should be operated from the SPS control building by the Group responsible for SPS operations. Combined operations of SPS and LEP has proved very successful.

During the commissioning phase the Operations Group worked with the equipment specialists and machine physicists, and by September 1989 the Group was in full operation control for physics running and contributed to the machine studies.

While the commissioning of LEP was being done, the SPS continued a full programme of fixed target proton physics, operated from the same building but from a room separate from LEP operations. In 1990, during the yearly two months maintenance stop, the SPS control room was modified and LEP operation consoles installed; the operation of the two machines is now successfully and efficiently done from the same room by a crew of four. There has been no measurable reduction in the efficiency of operation of the SPS during operation of LEP.

The primary services for LEP operation were also supervised from the SPS-LEP operations building during this period. These services include electricity, water, ventilation, cryogenics, vacuum, controls, radiation surveillance, fire alarms, and others. This function has been incorporated in the CERN-wide primary services supervision from the start of 1991.

V. ACKNOWLEDGEMENTS

The operation of the LEP machine demands the close collaboration between the operation teams, the equipment groups, the machine physicists and the experimental physicists for whom the machines run. The success of the operation of LEP reflects the success of these close collaborations and those with the engineers and physicists of the CPS and SPS complexes.

The authors would like to thank all the members of the Operation Groups, both CPS, SPS, and LEP for their support in this venture.

VI. REFERENCES

[1] Y. Funakoshi et al., "Luminosity tuning in Tristan main ring", 2nd European Particle Accelerator Conference, Nice, France, June 1990, vol. 27, pp. 59-64.

[2] T.O. Raubenheimer and R.D. Ruth, "Analytic estimates of coupling in damping rings", SLAC PUB 4914, March 1989

Table 2
Analysis of seven weeks of LEP fills in 1990

	Down Time	Recovery	Accumulation	Ramp	Squeeze	Total fill	Physics	Total Cycle
Average	1:31	0:31	2:11	0:28	0:27	5:09	7:52	13:01
r.m.s.	2:18	0:45	1:55	0:14	0:18	3:28	5:04	6:12
Minimum	0:00	0:00	0:30	0:05	0:07	1:20	0:12	-
Maximum	10:00	4:10	11:15	1:10	1:40	16:50	22:35	34:00
Shortest fill time	0:30	0:00	0:30	0:05	0:15	1:20	9:02	10:22

All times in hours:minutes

Accelerator Energy Conservation at Fermilab

James P. Morgan
Fermi National Accelerator Laboratory*
P.O. Box 500
Batavia, IL 60510

Abstract

The Fermilab Accelerator Division has adopted an energy conservation plan in an attempt to reduce power levels during extended periods of beam downtime. The plan was implemented for the first time during the 1990 Fixed Target program. In this paper I will describe how accelerator power levels are reduced, and attempt to assess the impact of the plan on accelerator operations and energy consumption.

1 Introduction

The Fermi National Accelerator Laboratory is a large consumer of electrical power, using about as much as a moderate sized town. During periods of High Energy Physics (H.E.P.), the accelerators and related support equipment consume more than half of the site-wide power. There are periods of time when component failure causes a disruption in the Physics program. It is possible to conserve energy during these periods of beam downtime without adversely affecting machine dependability.

Although the Accelerator Operations group strives to provide steady beam during Physics runs, there are inevitably periods when the beam is interrupted by equipment failures. In the past, the main power supplies for the various accelerators would continue to run, despite the fact that there was no beam to accelerate. The 1990 Fixed Target run had the highest reliability of the Tevatron era, but still had over 1,000 hours of downtime. During past Physics runs, there were often unneeded Main Ring Cycles occuring that are now removed. The Accelerator Operations group began to informally investigate the possibility of reducing power levels during periods of beam downtime in 1987. Initial results were encouraging, but a formal plan was not created until the Department of Energy offered incentives for energy reduction ideas. During the Fixed Target program in 1990, the first formal accelerator energy conservation plan was put into effect.

*Operated by the Universities Research Association, Inc. for the U. S. Department of Energy

0-7803-0135-8/91$01.00 ©IEEE

2 Modes of Operation

2.1 Fixed Target

During Fixed Target operation, the particle beam actually travels through a series of five accelerators before being delivered to the experimental areas. A failure of any one of these machines will prevent beam from being available to the experimenters. The journey begins in the Preaccelerator, where H- ions are accelerated to 750 keV. The ions continue through the Linac, and exit with a kinetic energy of 200 MeV. The first circular accelerator is the Booster, which cycles at 15 Hz and has an extraction energy of 8 GeV. During injection into the Booster, the electrons are stripped from the Hydride ions, leaving protons. The 8 GeV protons are transported to the Main Ring, which was originally the final accelerator. It now serves as an injector for the Tevatron and it takes 3 seconds to accelerate beam to the Tevatron injection energy. The Tevatron accepts 150 GeV protons from the Main Ring and accelerates them to 800 GeV. The Tevatron cycle repeats every 57 seconds. The particles are resonantly extracted to the experimental areas through a system of transport lines and splitting stations known as the Switchyard.

2.2 Colliding Beams

Unlike Fixed Target operation, where the particle beam is extracted from the Tevatron, proton and antiproton beams are stored for long periods of time in the Tevatron during Colliding Beams. The"stores" may last for more than a day barring equipment failure. While data is being taken at the experimental facilities, the other accelerators are used to provide beam for antiproton production. The particle beam follows the same path through the Preaccelerator, Linac, Booster and Main Ring, though the final energy for "Pbar stacking" is 120 GeV. The 120 Gev protons are extracted from the Main Ring and strike a Copper target. Among the resultant secondaries are antiprotons of approximately 8 Gev which are directed to a Debuncher ring for reduction of momentum spread and emittance, then to the Accumulator ring for storage. When a new store is initiated, antiprotons are extracted from the Accumulator, then accelerated in the Main Ring

	Fixed Target	*Collider*	*Shut down*
Linac	2.0	2.0	1.2
Booster	2.5	2.5	0.8
Main Ring	3.5	5.0	0
Tevatron	3.0	1.5	0
Cryogenics	11.5	10.5	1.0
Swyd./8-Gev.	1.7	0.9	0.3
Util./Misc.	10.3	12.1	6.7
Accel. Total	34.5	34.5	10.0
Exper. Areas	17.0	6.5	3.5
Other	3.5	4.0	3.0
Site Total	55.0	45.0	16.5

Table 1: Typical Monthly Average Power Levels (MW)

before transfer to the Tevatron. The Tevatron accelerates the counter-rotating beams of protons and antiprotons to 900 Gev.

3 Site Power Consumption

Site-wide power consumption increases substantially during H.E.P. periods (see Table 1). In addition to the power used by the magnet power supplies and utilities, there is also considerable power use by the cryogenic system and experimental areas. A long list of smaller power supplies and support equipment also is energized during running periods. Site power useage is higher during Fixed Target Physics, but the difference is primarily due to increased power consumption in the experimental areas. Although Tevatron power use is lower in Collider mode, this is offset by an increase in Main Ring power. Linac and Booster power levels are the same in both modes of operation. During Fixed Target, the Switchyard transport lines are energized to deliver beam to the experimental areas. The Switchyard is not powered during Collider operation.

4 Description of Plan

The current energy conservation plan initiates the reduction of accelerator power levels in a way that won't delay the return of beam when the downtime ends. Also, during normal operation, the number of accelerator cycles is monitored, and any extraneous cycles are removed. This combination of trimming unneeded power use, and reducing power consumption during component failures is the nucleus of the plan. It is critical that power levels be reduced in an uncomplicated way and that the accelerators return to their normal mode of operation quickly.

After careful consideration, it was decided that the benefits from reducing Linac power was more than offset by potential difficulties. Potential power savings would be small, and reduction would not be able to be performed quickly or dependably. Similarly, it was decided that Booster power levels would be only reduced during lengthy periods of beam downtime. The main power supply for the Booster is the Gradient Magnet Power Supply (G.M.P.S.). Although there is a power reduction of about 1 MW when G.M.P.S. is turned off, there is a small loss in transmission efficiency due to thermal effects when the supply is first powered up. This problem can be mitigated by powering up GMPS a few minutes before the down period is expected to end.

The Main Ring and Tevatron provide the best opportunities for conserving accelerator energy at Fermilab. For periods of downtime anticipated to be less than an hour, the duty cycle of the Main Ring is reduced substantially. In this way magnet temperatures do not drop drastically, and power supplies and the R.F. continue to be periodically exercised. For periods of downtime anticipated to last a number of hours, the Main Ring ramp is turned off totally. The Tevatron is normally held at the "reset energy" of 90 Gev during down periods. Running at this low energy, and D.C., the power supply output and cryogenic demands are very small. Both rings can be brought back to the normal running mode in a minute or two. By reducing the Main Ring ramps and placing the Tevatron into a low energy store, power levels for the two machines are typically reduced from about 6.5 MW to 1 MW. In addition, there is savings from the reduced demand on the refrigeration system.

During Fixed Target operation, the Switchyard is used to transport beam to the experimental areas. During the Tevatron cycle, the majority of the Switchyard magnets are ramped up, and held at high field during the extraction process, which takes about 20 seconds. It is possible to prevent the magnets from ramping by withholding the ramp trigger. An automated system was developed that temporarily disables the trigger on cycles when no beam is present in the Main Ring and Tevatron. The Experimental Areas are also provided with a trigger at the same time to reduce power levels in their beamlines. When the Switchyard does not ramp, the power consumption is reduced by 1.2 MW.

5 Operational Experience

Results from the 1990 Fixed Target run have been very encouraging. After a short period of experimentation early in the Physics run, the mechanics of reducing power were worked out in such a way that machine reliability was not adversely affected. Because of the concern about cycling power supplies, energy levels were normally reduced by decreasing duty cycles.

To reduce Main Ring power, the number of ramps was reduced to two 120 GeV ramps every 57 second cycle. The operational configuration of ramps could quickly be returned when needed. This also reduced the amount of thermal changes that the magnets experienced. Typically, temperatures changed by small amounts, and returned to their previous levels within a few minutes of restoring

	Sitewide	*Accelerator*	*Exp. Areas*
1987 Collider	45.6	34.7	7.6
1987-88 Fixed Target	55.0 *53.1*	34.4 *32.5*	17.3
1988-89 Collider	44.5	34.0	6.2
1990 Fixed Target	55.0 *51.4*	34.8 *31.4*	16.9

Table 2: Average Power Levels (MW) *Pbar subtracted*

	Fixed Target 1987-88	*Fixed Target 1990*
H.E.P.	2,872	3,205
Studies	619	344
"Up" Time	3,491	3,549
Failure	2,047	1,225
Start-Up	181	98
Total	5,719	4,872

Table 3: Machine Reliability (Hours)

the normal ramp configuration. The Tevatron was put into a low energy D.C. mode to reduce power. To avoid problems with remnant field changes, the Tevatron was normally ramped a few times before beam was injected. Often the Main Ring and Tevatron could be returned to their operational state shortly before the downtime ended. Switchyard energy reduction was automated, and required minimal operator intervention. The only difficulty observed was that the Switchyard showed small beam position changes after the magnets had not been powered for approximately an hour or more.

6 Power Saved

At first glance, a look at the raw power data from the past two Fixed Target runs is somewhat discouraging. Average power levels for the Site were approximately the same. The accelerator related energy use showed a small increase, and the Experimental Areas showed a small decrease (see table 2). However, there were several notable differences between the two Fixed Target programs that mask the success of the energy conservation program. The large decrease in component failure during the most recent run is the most significant difference. During Tevatron magnet changes, the accelerators and beamlines are turned off for up to 5 days. The numerous magnet replacements caused the average site power for the run to be artificially low. Also, there was an experiment added to the Antiproton (Pbar) source for the 1990 program. This required power for the Pbar rings, as well as additional Main Ring cycles used to accumulate antiprotons. Table 2 reflects the net site and Accelerator power levels for the two runs when Pbar power levels are disregarded.

The 1990 Fixed Target run saw a dramatic reduction in downtime over the previous run (see table 3). A large percentage of the downtime that occured during the 1987-88 Fixed Target run was due to Tevatron magnet failures. A program of magnet maintenance and repair between the two runs drastically reduced the number of failures. This (happily) resulted in fewer opportunities to conserve power then expected.

It is relatively easy to account for the differences in power use due to the Pbar experiment. The Pbar power levels were calculated for both running periods and subtracted from the accelerator total. Records exist which indicated approximately how many Main Ring cycles were required for Pbar production. After the data has been corrected in this way, a reduction in accelerator power use is apparent.

It is more difficult to normalize the power data to the dependability of the accelerators. It is clear that the average power for the 1987-88 Fixed Target run would have been significantly higher if it wasn't for the large amount of downtime. Using data from Table 2, the accelerators were engaged in H.E.P. or studies 61% of the time in the 1987-88 run, and 73% of the time in the 1990 run. Two methods were used in an attempt estimate the energy saved. In the first, monthly data was compared from the two runs that had approximately the same amount of downtime. This involved taking the best months from the 1987-88 run and comparing them to the worst months from the 1990 run. The second involved extrapolating data from the 1987-88 run to match the 1990 run. Although both methods are imperfect and highly subjective, they both arrived at an energy reduction of about 3 MW for accelerator related power. The Switchyard contribution was a 7% reduction in ramps, which amounts to only .1 MW. This would suggest that experimental areas beamlines realized an average power reduction of up to .7 MW (they use 8-10 MW when running). When integrated over the entire 29 week Fixed Target run, this would amount to 14,600 MW-Hr saved by the accelerator division, and 3,400 MW-Hr by the Experimental Areas.

7 Conclusion

The Accelerator Division conservation program was success during the most recent Physics run. A substantial amount of energy was saved with minimal impact on machine reliability. Future efforts will be directed towards automating energy reduction.

References

[1] *Fermilab Accelerator Statistics*

[2] *Fermilab Master Sub-Station Monthly Energy Report*

[3] James P. Morgan. *An Energy Conservation Proposal*

Designing High Energy Accelerators Under DOE's "New Culture" for Environment and Safety: An Example, the Fermilab 150 GeV Main Injector Proton Synchrotron

William B. Fowler
Fermi National Accelerator Laboratory*
Batavia, Illinois 60510

Abstract

Fermilab has initiated a design for a new Main Injector (150 GeV proton synchrotron) to take the place of the current Main Ring accelerator. "New Culture" environmental and safety questions are having to be addressed. The paper will detail the necessary steps that have to be taken in order to obtain the permits which control the start of construction. Obviously these depend on site-specific circumstances, however some steps are universally applicable. In the example, floodplains and wetlands are affected and therefore the National Environmental Policy Act (NEPA) compliance is a significant issue. The important feature is to reduce the relevant regulations to a concise set of easily understandable requirements. The effort required and the associated time line will be presented so that other new accelerator proposals can benefit from the experience gained from this example.

I. INTRODUCTION

The U.S. Department of Energy (DOE) proposes to construct and operate the "Fermilab Main Injector" (FMI) accelerator, which would be a 150 GeV proton synchrotron, at the Fermi National Accelerator Laboratory (Fermilab) in Batavia, Illinois. The paper VGR 2 Achieving High Luminosity in the Fermilab Tevatron given by S.D.Holmes, describes the details of the design. Since always at the forefront in environmental issues is the "no action alternative," it seems appropriate to repeat the justification for the project.

The high energy physics program at Fermilab investigates the structure of matter using the collision of particles to create new matter. These collisions take place in the Tevatron tunnel and in the fixed target experimental areas. The FMI would provide particles for injection into the Tevatron, and for delivery to the existing fixed target experimental areas during collider operations. The FMI would permit simultaneous operation of Fermilab's collider and fixed target programs, thereby making possible an increase in Fermilab's physics output. In order for Fermilab to maintain a vital long-range colliding-beam physics program, it is necessary that the luminosity increase significantly each year so that higher energy constituent collisions can be explored. The cumulative integrated luminosity should roughly double every year in order that new physics can be explored.

In October 1989, the Director of the Office of Energy Research of the DOE asked HEPAP to offer guidance with regard to "the relative importance and appropriate balance. (a) between operations and major upgrades at a given laboratory, and (b) among the proposed major upgrades and new facilities at the various laboratories." In April 1990 HEPAP issued the report (Report of the HEPAP Sub-panel on the U.S.High Energy Physics Research Program for the 1990's). HEPAP unanimously endorsed this report at a meeting on April 23 and 24, 1990. The report says "The Sub-panel (1) strongly recommends the immediate commencement and speedy completion of construction of the Tevatron Main Injector at Fermilab... (2) The Sub-panel assigns highest priority to the first of its recommendations. The increased luminosity provided by the Tevatron Main Injector will place Fermilab in an excellent position to discover the top quark. The necessary technology for this project is firmly in hand, and a carefully considered and reliable design exists." On the basis of this recommendation, the FMI was included in the President's FY92 budget submitted to Congress on February 4, 1991.

The Fermilab's Tevatron is presently running with a peak luminosity of 2×10^{30}. Fermilab's primary design goal is to increase the luminosity at the collider detectors by at least a factor of 30. Another goal is to increase the intensity of protons for fixed target operation by a factor of 3. Increasing the luminosity is intimately related to increasing the number of antiprotons available. Measures are currently being taken to increase the antiproton production rate by a factor of about 3. However, following implementation of these improvements, the 20-year-old Main Ring accelerator will remain the primary bottleneck restricting further production rate improvements. All of the accelerators that are involved in the production of antiprotons have significantly larger apertures than the Main Ring; therefore, the Main Ring is the bottleneck in antiproton production. The FMI would remove this bottleneck, since it replaces the old Main Ring in all of its functions, and its aperture would be matched to the other accelerators thereby assuring the achievement of a luminosity of 5×10^{31}.

II. DOE NEPA INITIATIVE

Sensitivity to Environmental issues increased significantly with the appointment of Admiral James Watkins (Ret.) as Secretary of Energy by President Bush. In June 1989, Adm. Watkins (Ret) announced a ten-point initiative intended to strengthen environmental protection, safety and waste-management activities in the U.S.Department of Energy. In February 1990, SEN-15 was issued which clarified the NEPA (National Environmental Policy Act signed into law by President Nixon on New Years Day 1970) initiative and spelled out implementation procedures. NEPA requires review of all activities which may significantly impact the environment. This includes threatened or endangered species or critical habitats, floodplains and wetlands, and sole source aquifers. When a new construction project or a modification involves any activities with potential for environmental impact, it requires a NEPA review.

*Operated by Universities Research Association under contract to the U.S.Department of Energy

0-7803-0135-8/91S01.00 ©IEEE

In his February notice, Watkins reiterated how, in forming his initiatives, "I found that many of the Department's activities under NEPA had been carried out in a decentralized, non-uniform and self-defeating manner. I also state my intention to become personally involved in NEPA decision making and to ensure that NEPA actions are more closely coordinated with the governors of the states which host DOE facilities..."

"Indeed," Watkins continued, "mission goals are best served by early and adequate NEPA planning, which avoids the delays that often follow 11th-hour consideration of NEPA requirements, the resulting failure to comply fully with those requirements and, ultimately, the necessity to cure NEPA-related deficiencies before an important project may proceed. If the Department is to err in its judgment as to the extent of NEPA review required of new projects, it should err on the side of full disclosure and complete assessment of environmental impact."

III. PERMITS

Various federal environmental statutes impose environmental protection and compliance requirements that have to be adhered to. In addition there are state and local regulations that are equally important. Many of these came about as a result of NEPA, which besides setting forth a national policy for the environment, established the Council on Environmental Quality (CEQ). The CEQ issued Regulations for Implementing the Procedural Provisions of NEPA. These rules are found in the Code of Federal Regulations (40 CFR Parts 1500-1508). This is where the methodology of Environmental Impact Statements (EIS) with the final action of a Record of Decision (ROD) was established. Also, the simpler process of an Environmental Assessment followed by a Finding of No Significant Impact (FONSI) or a determination that an EIS is required was outlined.

Federal statutes that may apply to construction and operation of accelerator projects include the Clean Water Act, the Clean Air Act, the Safe Drinking Water Act, the Solid Waste Disposal Act, the National Historic Preservation Act, the Endangered Species Act, and the Farmland Protection Policy Act.

CLEAN WATER ACT - This Act makes it illegal to discharge any pollutant into any body of water, i.e. lakes, streams, wetlands, potholes, mud flats, intermittent streams, and wet meadows without a National Pollutant Discharge Elimination System (NPDES) permit. Under a new addition this will require a NPDES permit for storm water discharges by October 1991. Under Section 404 the U.S.Corps of Engineers (COE) issues permits for the filling of wetlands. The COE does not issue 404 permits unless it has received a 401 water quality permit from the state EPA. Executive orders 11988 and 11990 concern floodplain management and protection of wetlands. DOE will take action to avoid, to the extent possible, adverse impacts associated with the destruction of wetlands and the occupancy and modification of floodplains and wetlands. When this is not possible a mitigation plan will be implemented to compensate for the action.

CLEAN AIR ACT - This Act has provisions for the Attainment and Maintenance of National Air Quality Standards (NAAQS), Prevention of Significant Deterioration (PDS), and New Source Performance Standards (NSPS), which are mostly applicable to such things as dust from construction activities. Perhaps the item of significant concern for particle accelerators is the provision for the National Emission Standards for Hazardous Air Pollutants (NESHAPS).

For FMI operations, radiation doses have been calculated for normal operation losses within the operating envelope. This includes accelerator beam intensity, number of hours of operation per year, and various configurations of the experimental program. The calculations also take into account the use of the beam abort dump and above normal losses.

FMI radionuclide emissions to the atmosphere are anticipated to be 1,100 Curies/yr, and in compliance with the U.S. EPAs NESHAP (40 CFR 61 Sub-parts A and H). The off-site dose rate from Fermilab after the FMI becomes operational is estimated as 0.33 mrem/yr, well below the NESHAP standard of 10 mrem/yr. With FMI operations maximized, total yearly off-site dose from Fermilab is estimated as 1 mrem/yr.

NATIONAL HISTORIC PRESERVATION ACT - This Act requires that any project that is under consideration must take into account sites, buildings and structures that are eligible for inclusion in the National Register. DOE must afford the Advisory Council on Historic Preservation a reasonable opportunity to comment with regard to such undertaking.

ENDANGERED SPECIES ACT - This Act requires consultation with the U.S.Fish and Wildlife Service before undertaking any action to insure that the action is not likely to jeopardize the continued existence of any endangered species or threatened species, or result in the destruction or adverse modification of the critical habitats of such species. Accordingly, it was judged prudent to investigate whether there are any threatened or endangered species that might be affected by the proposed FMI construction. Fermilab; therefore, contracted with consultants in birds, plants, insects, amphibians, fish and mammals to conduct field surveys in the area that would be impacted by the construction.

Suitable habitat and the presence or absence of the listed species were recorded. The consultants' reports are cited in the FMI Environmental Assessment Report.

IV. CHRONOLOGY AND COST

As has been emphasized in the above it is important to start the NEPA process as early as possible; however, it is obvious that the design has to have progressed sufficiently that enough information is available that environmental studies are feasible. In the case of the FMI, this point was reached in the fall of 1989.

The FMI would be a 150 GeV accelerator with a circumference of about one-half that of the existing Main Ring. The FMI would be situated tangent to the Tevatron at the F0 straight section[1] in the southwest corner of the

[1]The Main Ring and Tevatron accelerators are designed with six straight sections, where the beam travels a short distance in a straight line, alternating with six arc sections where it follows the path of a circle with a radius of one kilometer. These 150-m long straight sections are labeled A0, B0, ..F0, and are spaced equally around the ring.

Fermilab site. The FMI would be constructed using newly designed (iron and copper) dipole magnets.

The proposed FMI, whose location is shown in Figure 1, must serve a number of purposes. It must function as a bi-directional injector into the Tevatron. This means it must be near and approximately tangent to the Tevatron. Secondly, it must receive 8 GeV protons from the Booster and 8 GeV antiprotons from the Antiproton Source. It must also provide 120 GeV protons to the antiproton target. Finally, the FMI must provide a 120 GeV beam to the present Fermilab fixed target facility hardware.

The principal housing of the FMI would utilize below grade enclosures. The FMI ring enclosure would be an oval-shaped, below grade structure, approximately 10,900' long, with a 10' wide by 8' high cross section. The floor of the enclosure would be level and at an elevation of 713'6" above sea level, 18' to 33' below existing grade. Earth shielding berms over the FMI enclosure would provide the required 21' of earth equivalent shielding.

The FMI ring enclosure would be constructed on a reinforced concrete cast-in-place (CIP) base slab. Approximately 9,900' of the ring would be built with precast concrete inverted "U" sections that would be welded to the CIP base slab. The remaining parts would be CIP.

Beginning in April 1990, $200,000 of Illinois Challenge Grant funds became available to conduct environmental studies and preliminary design. The first activity was to prepare the application for the joint permit for filling of the wetlands and the modification of the floodplain of Indian Creek. The application was submitted in September 1990.

In parallel, an Environmental Assessment (EA) was prepared which required several drafts. The submission to the environmental part of DOE occurred on April 1991. It is anticipated that if the EA is acceptable and a FONSI is sustained, then the start of construction will be October 1991 or as soon as construction funds become available. Illinois provided an additional grant of $2,000,000 in the spring of 1991 of which $500,000 was specified for environmental efforts.

Using the above plan the funds expended for the environmental effort for the FMI is estimated to be $1,400,000, since Fermilab has matched the funds of the State of Illinois as required by the terms of the Grant.

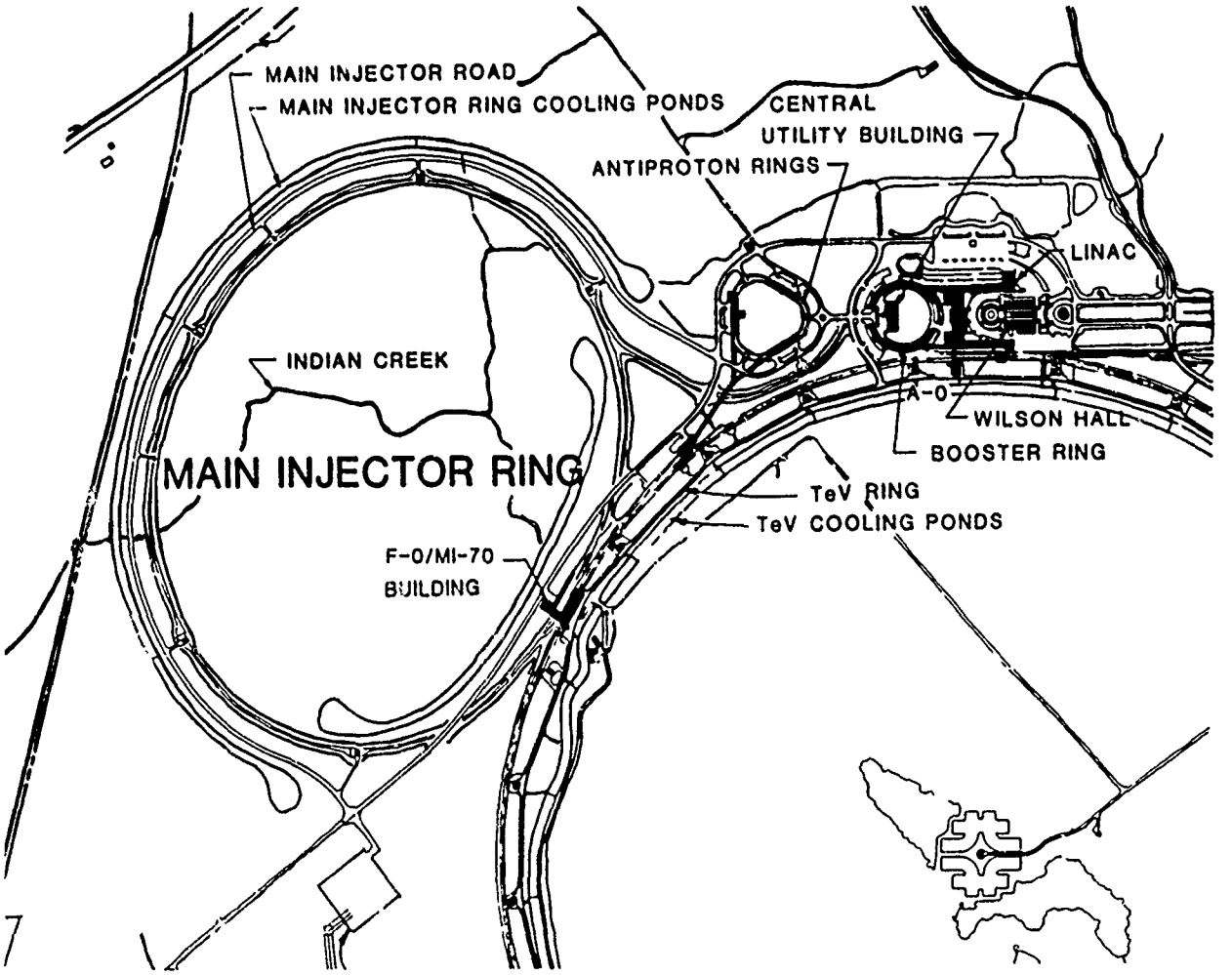


Figure 1. Fermilab Main Injector location. Indian Creek crosses the ring at several points. Approximately 100 acres of wetland is adjacent to the creek. The area of wetland that would be permanently filled has been reduced to six acres by minimizing the width of the construction at the affected areas.

INSTALLATION OF THE SUPERCONDUCTING MAGNETS IN THE HERA TUNNEL

I. Borchardt, D. Brauer, S. Chermenin, D. Degèle, K. Escherich, H.J. Fiebig, H. Grabe, J. Holz, D. Hubert, R. Kus, M. Leenen, H. Maywald, O. Peters, B. Petersen, K. Pieczora, U. Riemer, Z. Sanok, P. Schmüser, S. Schollmeier, W. Schwarz, G. Tödten, D. Trines, S. Wolff
Deutsches Elektronen-Synchrotron DESY, 2000 Hamburg 52, Notkestraße 85 - Germany

Abstract

The arcs of the proton storage ring of HERA are equipped with superconducting magnets. Installation, manpower involved, and experience gained are described.

I. INTRODUCTION

The collider facility HERA in Hamburg consists of two storage rings of 6.3 km length, a 30 GeV electron ring and a 820 GeV proton ring. The assembly of the rings was completed in October 1990. The arcs of the proton ring with a total length of 5.5 km are equipped with superconducting magnets [1] which are arranged in a regular FODO cell structure consisting of two quadrupoles and four dipoles. The cryostats of the dipoles and the quadrupoles have a length of 9.7 m and 4 m respectively. There are 422 dipoles and 224 quadrupoles in the ring including some special magnets. In addition there are about 1500 superconducting correction elements.

All magnets were subjected to an extensive acceptance test comprising checks on mechanical accuracy, alignment, and proper cable connections. In the magnet test facility [2] all magnets were cooled down to 4.7 K to measure the magnetic fields [3], determine the quench performance and test for leaks. The results from the mechanical and magnetic measurements were used to define the position of the magnets for an optimal performance of the machine [11]. For the same reason the dipoles from the two manufacturers were put into separate octants of the machine, as their magnetic properties were slightly different. In the middle and at both ends of a quadrant cryogenic boxes [9] are installed supplying the helium cooling of the magnet strings.

II. THE SEQUENCE OF INSTALLATION

After the cryogenic test and a final quality control the magnets were transported to HERA halls West or East for storage, which was made necessary by the selection procedure.

A special designed installation vehicle [4] with a hydraulic lift system was used to bring the magnets to their preselected position and put them onto their support (see Fig. 1). With the vehicle one could fit a magnet between two already installed magnets with an accuracy of a few mm.

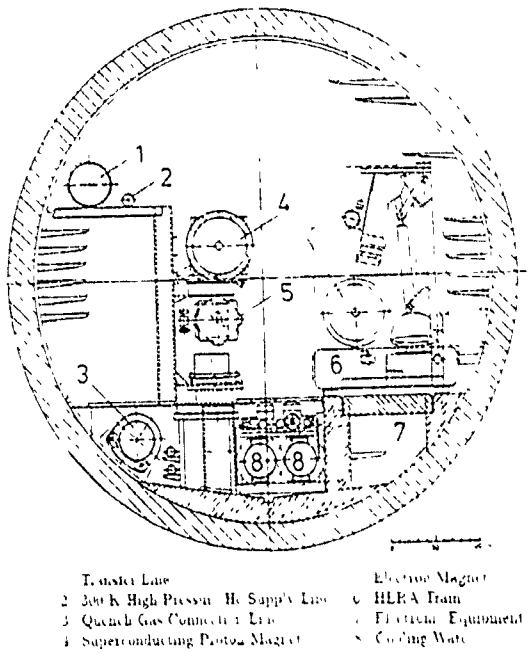


Fig. 1 Schematic Cross Section of the Tunnel

The installation started in most octants at the far end of the tunnel section with respect to the hall, where the magnets were stored. Thus the activities following the placing of the magnets were not affected by the passage of the vehicle.

Once the magnets rested on their supports, the fixtures which attached the inner magnet vessel rigidly to the outer vacuum vessel during transport were removed. Later on the suspension points were covered with superinsulation and the access flanges were closed.

When a string of at least 6 dipoles and 4 quadrupoles was mounted, the magnets were aligned and fixed in position [6]. Immediately after the alignment the beamtubes were flanged together and plastic bags were put around the flange connections and the neighbouring bellows (see Fig. 2) in preparation of the helium leak test [5] which was performed once all the magnets of an octant were installed.

The superconducting cables for the main dipoles and quadrupoles as well as the 20 superconducting wires for the correction coils are guided within the single phase helium tube of the magnet string. First the main superconductors of adjacent magnets were soldered using a special soldering tool with rf heating and then insulated by

0-7803-0135-8/91$01.00 ©IEEE

Kapton foils. The cables for the correction coils are held in grooves on an epoxy fibreglass cylinder surrounding the main conductors (see Fig. 2).

Considerable effort was spent on the quality control of the solder connections. After a first manual check, which effectively eliminated wiring errors, a magnet string of 120 m length was tested by a computerized system. A current was fed into each of the 20 bus wires consecutively and the voltages at every interconnection were compared to the expected values. In addition high voltage checks were made.

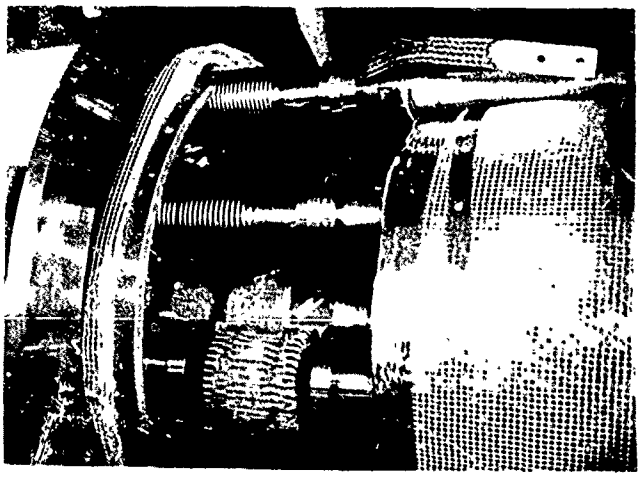


Fig. 2 Interface Between Magnets

After the electrical check welding sleeves (see Fig. 2) were slid over the flanges and the welding was done with a special machine. The tubes for the two phase helium and the shield line were connected in a similar way.

The bellows in the helium lines were secured by support shells to prevent buckling at the maximum pressure of 20 bar. After wrapping superinsulation around the tubes, the heat shield in the interface region was closed and insulated. Finally the sliding joints of the vacuum vessels were moved over the interface and fastened with screws (see Fig. 3).

Whenever a section between two quadrupoles was finished this way, the vacuum vessel was evacuated and tested for external leaks [7], [8]. (The quadrupoles contain vacuum barriers).

In parallel to the work described so far the safety valves (Kautzky valves [9]) for the single and two phase helium lines were mounted and connected to the quench gas return tube (see Fig. 1).

When an octant was installed and the insulating vacuum established, the helium lines of the magnets were pressurized one after the other

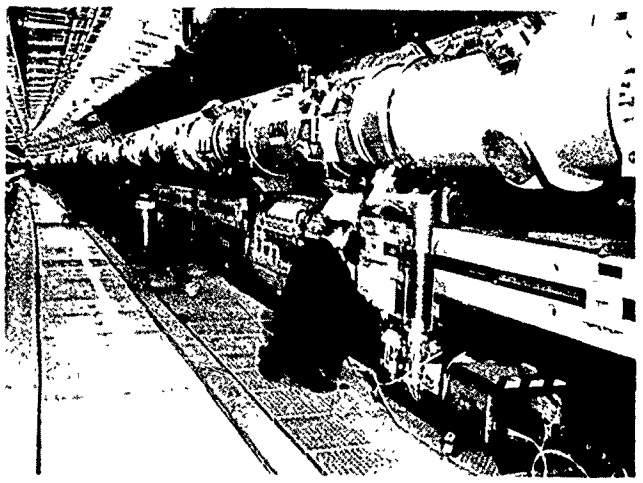


Fig. 3 Completely Installed String of Magnets

and an integral leak test was performed. For this purpose pump stations equipped with helium analysers were installed every 50 m [8], [10].

Towards the end of the arcs the magnet spacing deviates from the regular structure and magnets are spaced at larger distances. These drift spaces are bridged by special cryostats, which contain the beam pipe, the helium lines and the superconducting cables. The installation of these 28 cold straight sections was similar to that of the magnets.

III. MANPOWER AND INSTALLATION SPEED

Fig. 4 shows the progress of installation for a few key activities. The low speed of the installation in the beginning is partly due to the lack of experience of the people involved. In addition, the delivery of magnets from the various manufacturers had not yet reached the full rate.

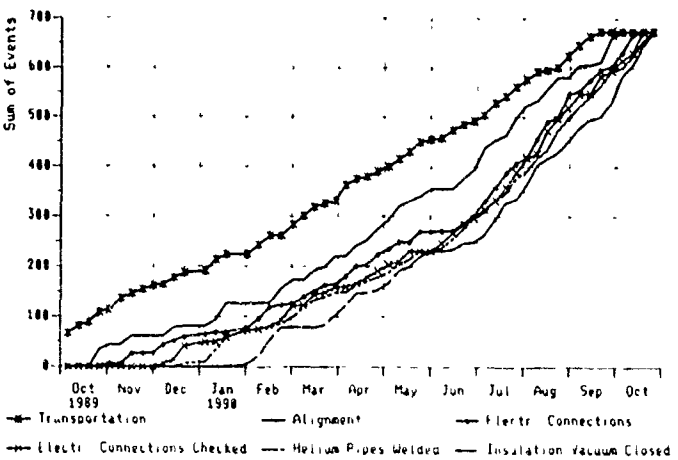


Fig. 4 Progress of Installation

Another restriction was caused by the selection procedure of the magnets.

A group of people was assigned to each task of the installation. The number of people working on the various tasks are given in Table 1, split into engineers and craftsmen. In the last few months of installation the number of people was increased to speed up the installation and to meet the planned completion date.

Task	Initial Phase		End Phase	
	Scientists Engineers	Technicians Craftsmen	Scientists Engineers	Technicians Craftsmen
Planning and Control	1	2	1	2
Transport	1	9	1	9
Alignment	2	3	2	3
Transport Securities		2		4
Electrical Connections	1	5	1	7
Electrical Checks	1	2	1	3
Welding		2		3
Insulation		7		9
Vacuum	2	6	4	12-14
Total	8	38	10	52-54

Table I Manpower

IV. EXPERIENCES

The installation and the following cryogenic and electrical test of the first octant revealed a few deficiencies of the design and the fabrication, which could, however, be fixed without major problems. The fact that the magnet string performed essentially as expected, for example that the welding joints between the magnets were leak-tight or that powering the magnets caused no problems, encouraged the installation crew and gave confidence in the techniques, which were applied during the installation.

During the installation of the first octant there was some interference between the different task groups, which reduced the efficiency. Later on, as the activities became more separated in the tunnel, the installation speed increased and gradully approached the design value of 15 magnet interfaces per week.

Each task group noted the completion of their work on a form attached to each magnet, thus informing the next group. It also allowed a simple control of the status and an analysis of the progress of installation.

The storage of magnets, which was made necessary by the selection procedure and the distribution of dipoles from the two manufacturers into separate octants posed a slight problem for some time. The available area in the halls was not sufficient, so that magnets had to be stored in the tunnel before they could be brought to their proper position. This complicated the logistics but did not introduce a noticeable delay of the installation.

In addition to the installation reported here there were people working for example on the cryogenics, on the various controls of cryogenics, magnets, monitors, and vacuum systems and on the installation of machine components in the straight sections. The coordination of all these activities without delaying the time schedule was only possible by shifting some activities to night hours. For instance most of the cabling in the tunnel was done at night.

To shorten the time, which was lost to cover the substantial distances between the halls and the actual working section in the tunnel, bicycles were supplied. Lighter equipment and tools were transported in light trailers. For heavy equipment the transport vehicle was used.

Delays caused by missing equipment or unforeseen difficulties were compensated by overtime work, contract manpower, and rearrangements of the installation schedule.

V. REFERENCES

[1] S. Wolff, Superconducting Magnets for HERA, 13th Int. Conf. on High Energy Part. Acc., Novosibirsk 1986, Vol. 2, p. 29
H. Kaiser, Design of Superconducting Dipole for HERA, 13th Int. Conf. on High Energy Part Acc., Novosibirsk, 1986, Vol. 2, p. 49

[2] R. Meinke, Methods for Production Measurements of Superconducting Magnets, DESY, HERA 90/06

[3] R. Barton et al., Performance of the Superconducting Magnets for the HERA Accelerator, DESY HERA 89/20

[4] Design and construction by K. Sinram and G. Wöbke

[5] D. Brauer et al., The Cold Bore Beam Pipe Vacuum System of HERA, to be published

[6] W. Schwarz, Hochgenaue dreidimensionale Punktbestimmung zur Justierung von Teilchenbeschleunigern, Zeitschrift fur Vermessungswesen, 115, 7/8, p. 333

[7] D. Hubert et al., Internal Report in German, HERA PVAK No. 82

[8] M. Bohnert et al., The Insulation Vacuum Systems of the HERA Proton Storage Ring, to be published

[9] H.R. Barton et al., The Refrigeration System for the Superconducting Proton Ring of the Electron Proton Collider HERA, Adv. Cryo. Eng. Vol. 31, 1986, p. 634

[10] D. Hubert et al., Internal Report in German, HERA PVAK No. 84

[11] F. Willeke, Internal Communication, unpublished

Stripping Foil Losses and Space Charge Blowup in the FNAL Booster

C. Johnstone, D. Bogert, J. Lackey, R. Tomlin
Fermi National Accelerator Laboratory, P.O. Box 500, Batavia, Illinois 60510*

Abstract

An automated profile measuring system using single wire scanners has been implemented in the Fermilab Booster Synchrotron which allows the beam profile to be measured on a turn-by-turn basis. More than 30 profiles after injection can be accumulated before the wire degrades the beam significantly. As the Fermilab Booster utilizes a multiturn injection scheme, foil losses can be studied by comparing 1- and 2-turn injection and varying the number of passes a low-intensity beam makes through the foil. By using the low-intensity results, foil losses can be eliminated from high-intensity, multiturn injection data, thereby alllowing a quantitative look at space-charge blowup. The results obtained for foil losses and space-charge blow-up in the Fermilab Booster are presented here.

Introduction

In a circular accelerator, a single wire proves to be an effective diagnostic tool from which profiles of the circulating beam can be extracted on a turn-by-turn basis. The profile is obtained by reading the current on the wire at selected time intervals within the beam cycle and then advancing the wire to different positions and recording the same information on subsequent beam pulses. For thin wires the losses on a turn-by-turn basis are small and readily calculable. For wire thicknesses of a few mils, effective beam profiles can be generated for up to 60 turns before wire distortions significantly alter the beam characteristics. A more serious limitation than wire losses on the data analysis has been found to be the pulse-to-pulse stability of the beam.

A second application of these wires has allowed a view into the internal properties of a beam pulse. If the time interval at which the wire readout occurs is set to a fraction of the total timespan of a beam pulse, individual profiles can be generated which represent a particular time in the beam pulse. In this way intensity and position variations within a beam pulse can be studied.

Experimental Results

Four vertically mounted and four horizontally mounted tungsten wires, all 5 mils thick, are positioned about the Booster Synchrotron. A stepping motor capable of stepping the wire in submillimeter increments is used to control the wire position. Two of these wires were used to make extensive horizontal profile measurements in the Booster. One of them, WINFH, is positioned a centimeter upstream of the H^- stripping foil. It intersects both the injected H^- beam and the closed orbit proton beam. The second one used was just downstream of the last ORBUMP magnet. Four pulsed magnets called ORBUMPs (used to bump the closed orbit) perform injection in the Booster. Because the ORBUMPS move the beam across the injection aperture, the wire just upstream of the stripping foil has the added advantage that it does not intercept the beam continuously until the beam reaches its closed-orbit position (see Figure 1).

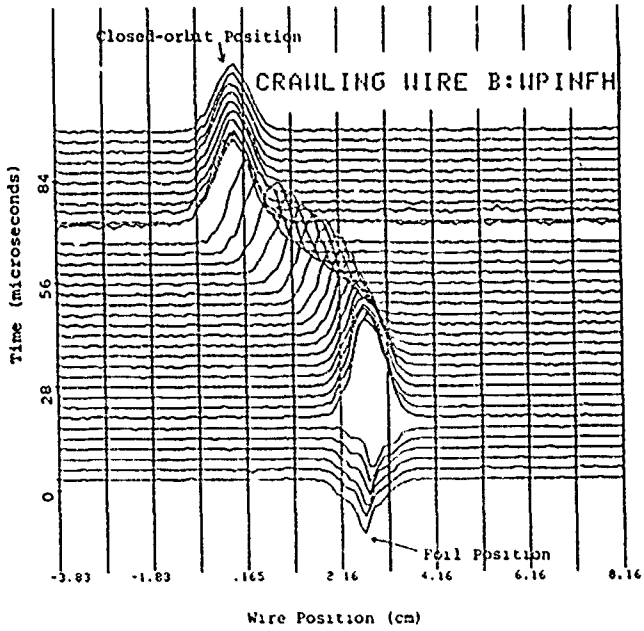


Figure 1. *Turn-by-turn wire profiles generated in the Fermilab Booster Synchrotron at injection. The negative profiles are the incoming H^- beam which eventually strips and moves off the foil into the closed-orbit position.*

For the measurements, the wire was stepped in 1 mm steps across 121 positions for a total of 12 cm across the Booster Synchrotron beam aperture. Since the rotational period of the beam in the Booster is 2.8μsec at the injected energy of 200 MeV, this is the frequency at which the wire was read out in order to obtain turn-by-turn injection profiles. The raw wire data is sent through a 1 MHz filter and amplified before being input to a fast digitizing Gould scope. The Gould scope is read out through a GPIB interface and into Fermilab's main accelerator controls system by frontend PDPs. The PDPs then transfer the data into a filesharing utility on a VAX. Because of the limited resources on the PDP frontends, only 36 time ticks of data can be conveniently stored at one wire position, so only 36 profiles are generated per run. For long term data storage

*Operated by the Universities Research Association under contract with the U. S. Department of Energy

0-7803-0135-8/91$01.00 ©IEEE

and ease of analysis the data are compressed into binary ZEBRA [1] data structures.

A series of measurements were taken for low-intensity operation which include 1/2-turn, 1-turn, 2-turn, and 3-turn injection, and high-intensity which included 4-turn, 5-turn, and 6-turn injection using both wires. This corresponded to intensities of 2.5E11 protons for 1/2 turn up to about 2E12 protons for 6 turns in the Booster. To extract foil effects, only one turn's worth of beam is injected into the Booster so that at this intensity space charge is not a problem (5E11 protons extended over the 474-meter circumference of the Booster). In all cases the ORBUMP timing was changed to vary the number of passes the beam made through the foil to isolate foil losses.

In a second application of the wires, internal profiles of a beam pulse were measured in the beamline which transfers extracted beam from the Linac and prepares it for injection into the Booster. The specific vertical wire used, WS2H, was located at the entrance to the injection septum where it intercepts both the H^- beam in the transfer line and the closed-orbit proton beam circulating in the Booster (see Figure 2). Except for timing, the other details of the readout are the same as detailed above. Data were taken on 1/2-turn, 1-turn, and 6-turn injection which correspond to 1.4, 2.8, and 16.8 microsecond long beam pulses, respectively. Data were read out every .07 microseconds to give 20 and 40 internal horizontal profiles on the 1/2-turn and 1-turn data, and every .56 microseconds to give 30 internal horizontal profiles on the 6-turn data.

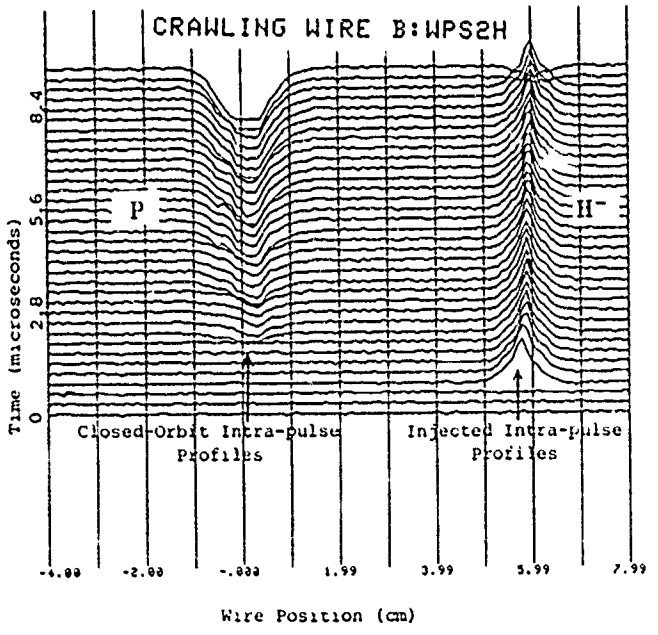


Figure 2. *Intra-pulse wire profiles generated at the injection septum for 6-turn, 16.8 μsec long injection. The profiles were inverted for purposes of data analysis.*

Data Analysis

The stored ZEBRA files were read, analyzed, and histogrammed using a software physics analysis package, PAW [2]. The raw profiles were fit with a Gaussian which proved to be an excellent description of the data giving a χ^2 of less than 1 for the majority of the fits. From each of the Gaussian fits, a central peak position, an overall normalization, a standard deviation, and a constant background were found. The average beam position was found to be consistent to 1-1.5 mm which indicates both stability in overall beam conditions and the effectiveness of this method of measuring beam profiles. Since beam intensity is proportional to the total area under a measured profile, the overall normalization multiplied by the standard deviation was used to describe the relative beam intensity of each profile (ignoring the constant factor of 4π in the integral of the area). The beam intensity when derived in this fashion typically exhibits fluctuations of around 10% between runs. This variation appears to be due to both the accuracy of the fit and real fluctuations in injected intensity.

Foil Loss Results

Foil losses were determined using the WINFH wire because the first profiles captured of the beam as it moves off the foil do not entail losses from wire scattering (see Figure 1). To measure foil losses, the time of the ORBUMP cutoff was extended by 33 μsecwhich had the effect of causing the beam to make an additional 12 passes through the foil (2.8 μsec per turn at 200 MeV). In practice, foil losses proved difficult to determine because they are about .5% per pass through the Booster's 200 $\mu gm/cm^2$ stripping foil for 200-MeV H^- beam. Foil scattering was finally measured using 1-turn injection at a time when the pulse-to-pulse intensity stability was 3%. Data were taken with the ORBUMP timing alternated between the runs to compensate for any long term drifts. Foil losses were found to account for a 6% degradation in beam intensity with a standard deviation of 2% for the 12 additional passes made through the foil. This implies .5% scattering loss per turn through the foil with a σ of .17%.

Injection Loss Results

A more interesting result to come out of the foil loss and space charge studies was a measure of the losses suffered at injection presumably due to a mismatch between the transfer line and the Booster. These injection losses were over by the third turn injected beam took around the Booster (Figure 4). Unfortunately over ten turn's worth of data were unanalyzable due to the field changing in the ORBUMP magnets as they shut off. The wires were so close to these magnets a current was induced by the decaying magnetic field wiping out an intensity determination for this interval. Hence the blank spot in the figure. Future data will be taken with wires well away from any stray fields.

Injection losses measured off the wires were around 10% per turn in the first 2 turns (after correcting for wire losses). The effect of wire scattering on the beam was estimated using an exponential with a varying exponent. Well away from injection the beam losses are strictly due to wire scattering, and the exponential factor used to describe the drop in intensity as a function of turn number is readily pulled out of the data. The variation of the second term in the exponent with respect to turn number corresponded to an approximate linear widening of the beam profile due to wire scattering (the equation used to calculate the profile width was extracted from profile data

extending over 35 turns). Wire losses are inversely dependent on profile width so that the factor which describes broadening appears as a denominator in the exponent.

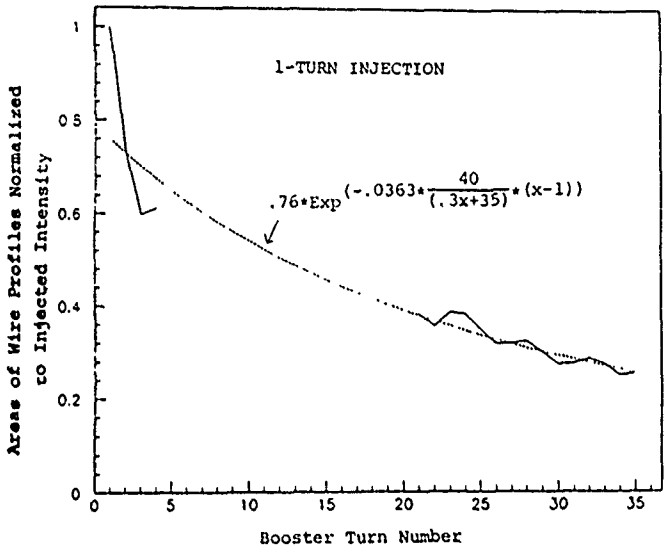


Figure 3. *Intensity as a function of turn number in the Booster. The exponential wire losses plotted (- - -) are described by the equation shown. The variable x in the equation is the turn number.*

Space-Charge Results

A possible hint of a space charge blowup was evidenced in the 5-turn data where after 9 turns, or 4 turns after injection is complete, another dip in beam intensity is observed (Figure 4). This dip is not observed in the 1-,2-,and 3-turn data. A toroid located in the injection region also shows a decrease in beam intensity about 4 turns after injection for 6-turn injection However, given the problems with the wires near the ORBUMPs, we plan on taking these same data using a different wire.

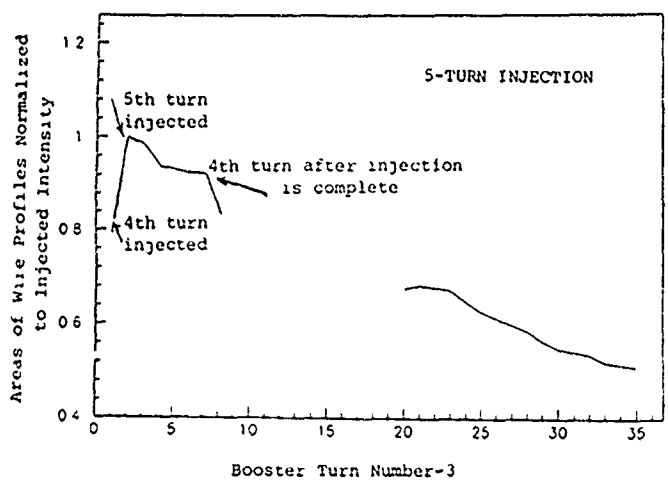


Figure 4. *Beam intensity as a function of Booster turn number.*

Intra-pulse Studies

The original plan when intra-pulse studies were initiated was primarily to study the effects of the transfer-line debuncher on beam pulses. In Figure 2, raw 6-turn profile data is displayed for the septum wire, WS2H. One can observe both the inverted positive H^- profile to the right and the well-separated negative closed-orbit profile on the left (also inverted) on this wire. Based on the Gaussian fits to these data, the entire position history of the beam pulse as a function of time can be displayed (Figure 5). Half of the central peak movement of the 6-turn pulse occurs in the first 2.8 *μsec* or the first turn around the Booster with a slower drift following. More dramatic position changes can be accomplished by changing the debuncher settings as also shown in Figure 5, yet the internal position structure remains the same. Presumably the jumps in overall peak position are due to energy changes in the beam as a result of the debuncher. One- and also half-turn data also show 2 mm internal position changes from beginning to end.

From the position movements, an approximate spread in energy can be calculated if the entire shift is attributed to changes in the beam energy. Using TRANSPORT, a 300-keV difference in energy produced a .2 mm spread at the injection septum for this line. This is in good agreement with a BPM measurement [3] which gives a $\delta p/p$ of 250 keV.

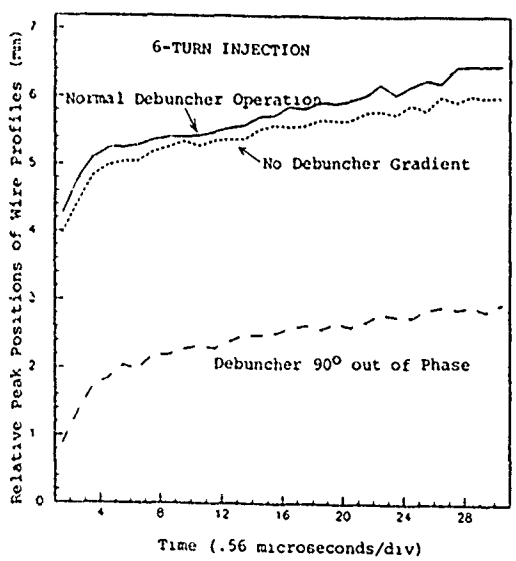


Figure 5. *Central peak position plotted versus time within a 16.8 μsec or 6-turn injected H^- beam pulse for different debuncher settings.*

References

[1] R. Brun, O. Couet, C. Vandoni, P. Zanarini, *"Physics Analysis Workstation," CERN Computer Center Program Library, Long Writeup, Q121, Oct. 1989.*

[2] R. Brun, J. Zoll, *"ZEBRA-Data Structure Management System," CERN Computer Center Program Library, Q100, 1989.*

[3] E. McCrory, *private communication, Jan. 1990.*

Fast Kicker Requirements for t SSC's Low and Medium Energy Boosters

M. Wilson, L. Schneider, D. Anderson, C. Pappas
Superconducting Supercollider Laboratory†
Accelerator Division
2550 Beckleymeade Avenue
Dallas, Texas 75237

Abstract

Requirements for the transfer kickers that move beam from the Low-Energy Booster (LEB) to the Medium-Energy Booster (MEB) are being established. Magnetic field intensity, pulse shapes, and available space for the kicker magnets within the ring beamlines are known to a level that allows preliminary design to begin on these systems. This fast kicker system, which must transfer the entire 12 GeV/c LEB batch to the MEB, is required to produce 150-200 G fields that rise in 60-80 ns, with a pulsewidth of 1.9 μs. The present MEB filling scenario requires this kicker system to operate in a 6-7 shot burst mode at repetition rates as fast as 10 Hz.

I. REQUIREMENTS

The 570 m LEB, when completely filled, holds 114 proton bunches spaced 5.0 m apart (21 ns at the injection energy of 600 MeV/c). After acceleration to the top-end energy of 12 GeV/c , the revolution period is reduced to approximately 1.9 μs (16.7 ns/bunch spacing). One filling scenario for the collider, shown in Figure 1, requires that the MEB be filled with six LEB batches, each containing 109 proton bunches, with a three-bunch gap between LEB batches. Three such MEB fills, with 25-bunch (400ns) gaps between, completely fill the High Energy Booster (HEB) while leaving an appropriate abort gap of 1.7 μs (103 bunches). Eight full HEB cycles would then fill each collider ring.

Filling the MEB with 109-bunch trains implies that five of the original bunches must be removed during the transfer. In order to reduce the radiation levels at the MEB injection point and not overly constrain the MEB injection kicker risetime, four bunches are lost at the LEB ejection point and the fifth is lost at the MEB injection point. This allows the risetime of the LEB ejection kicker magnet to be up to 80 ns (five 16.7 ns bunch spacings, minus one bunch width of 3.3 ns). Packing the LEB batches in the MEB requires the risetime of the MEB injection kicker to be less than 63 ns (four bunch spacings minus one bunch width). The pulsewidth of both the LEB ejection and the MEB injection kickers must be at least the full LEB revolution time of 1.9 μs. To control overall beam emittance growth, the magnetic field amplitude must vary over the entire pulsewidth by less than ±1.0 percent, and shot-to-shot variations must also be kept to this level.

The vertical ejection scheme for the LEB includes a four-magnet local orbit bump, a kicker magnet system, and two ejection septum magnets. In order to produce the required downstream deflection, the ejection kicker magnet must produce an integrated field of 600-750 G-m. Approximately 6.5m of space has been allocated in the LEB ring for the kicker magnets. The internal dimensions of the vacuum chamber at the kicker magnet location are dictated by the size of the 600 MeV/c injected beam, and has been set at 6.5 cm wide by 8.0 cm high. The 'good-field' region, defined as the area in which the magnetic field varies by less than 0.5 percent, must be 2.0 cm wide by 5.0 cm high.

For MEB injection, the required total magnetic field is approximately 480 G-m, with at least 6.0 m available for kicker magnet hardware in the beamline. The magnet aperture is presently set at 10.0 cm wide by 5.0 cm high, with the 'good-field' region approximately the same as that in the LEB ejection kicker. Injection into the MEB is in the horizontal direction.

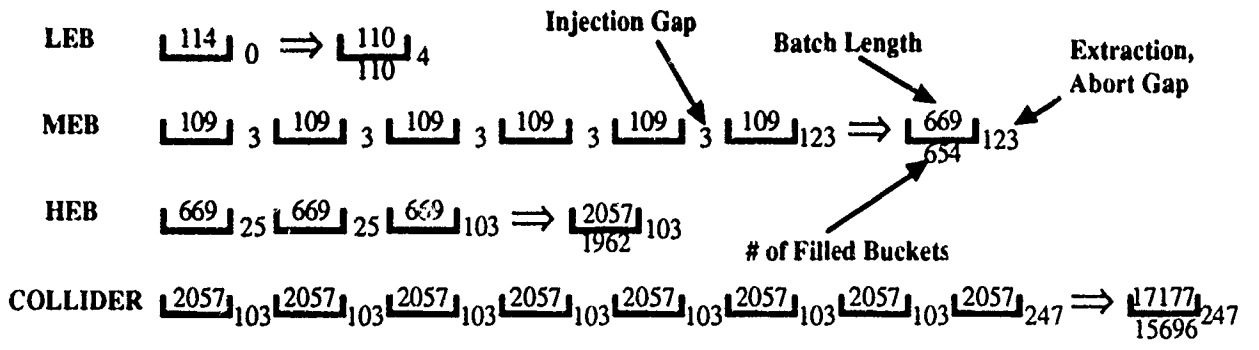


Figure 1. Collider Ring Filling Scenario. Batch Lengths and Gaps are Represented in Number of Beam Buckets, with Each Bucket Equal to 5.0 m of Ring Circumference, or 16.68 ns in Time at Relativistic Energies.

†Operated by the Universities Research Association, Inc., for the U. S. Department of Energy under Contract No. DE-AC02-89ER40486.

U.S. Government work not protected by U.S. Copyright.

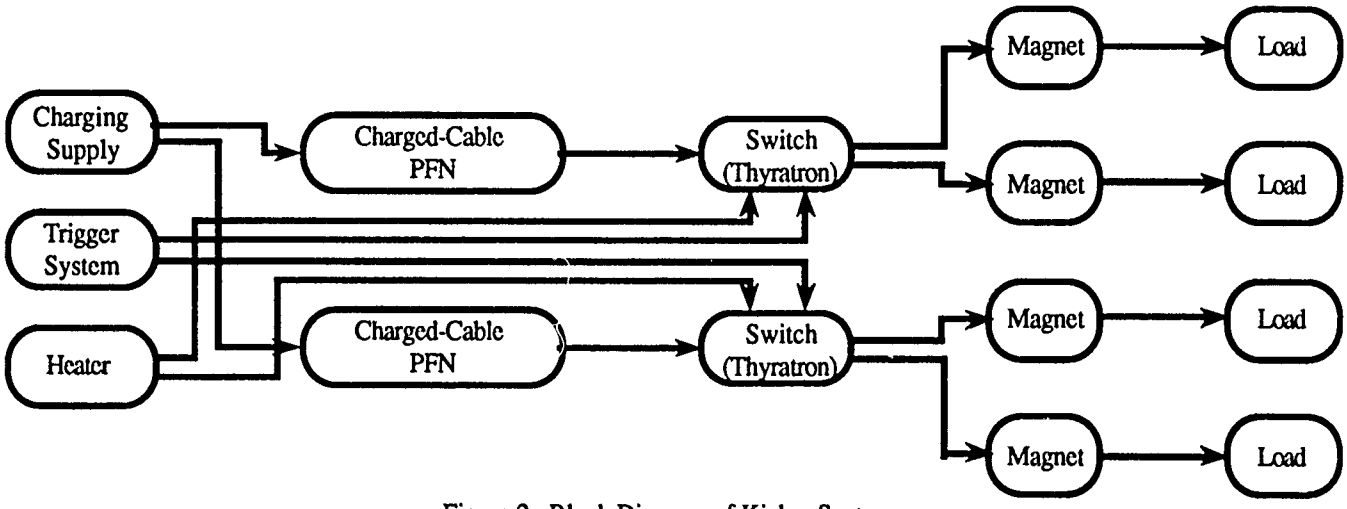


Figure 2. Block Diagram of Kicker Systems

II. LEB Ejection Kicker System Design

All of the SSC ejection and injection kicker systems consist of, as a minimum, (a) a charging system, (b) a triggering system, (c) a pulse-forming network (PFN), (d) a triggered switch, (e) a pulsed magnet, and (f) a terminating load. Such a system is shown in Figure 2. The short pulsewidth of the LEB ejection kicker allows the use of charged cable as the pulseforming network. Standard RG-220 50 Ω cable is the preliminary choice, as it has proven reliability in kickers and other high-voltage pulsed and DC systems[1]. The output voltage pulse from the charged cable is half the charge voltage and twice the electrical length of the cable. For the LEB ejection and MEB injection kickers, 190 m cables will be required. Other system parameters are driven by the magnet requirements presented above.

The available length for the LEB ejection kickers cannot be filled entirely with magnets. Terminations, flanges, bellows, and vacuum hardware combine to limit the total space for actual magnetic material to 4.8 m. This implies a maximum field magnitude over the length of the magnet of 156 G.

Figure 3 is a cross-sectional view of a possible LEB ejection kicker magnet. The magnet aperture (gap x pole width) is 7.5 by 9.0 cm, which includes a one centimeter allowance in each dimension for the beampipe wall and tolerance build-up. For a C-magnet, with μ_r=40, w=9 cm, g=7.5 cm, c (the ferrite pathlength)=30 cm, and t (ferrite thickness)=4 cm, the inductance is

$$L = \mu_0 w/(g+wc/t\mu_r) = 1.23\ \mu h/m, \qquad (1)$$

and the current necessary to deliver the required B is

$$I = B\,(g+wc/t\mu_r)/\mu_0 = 1140\ A. \qquad (2)$$

Assuming the maximum voltage that can be delivered is 30 kV (implying maximum charge and switch voltages of 60 kV), the maximum modulator source impedance is 26 Ω. Two parallel RG-220 cables, with an equivalent impedance of 25 Ω, results in the electrical length of the magnet equaling

$$v^{-1} = \sqrt{LC} = L/Z_0 = 1.23\ \mu h/25\Omega = 50\ ns/m. \qquad (3)$$

To meet the risetime requirements, it is expected that the magnet lengths will be less than 0.5 m, so that no more than 25 ns of the equivalent magnetic field risetime is due to the transit time of the magnet.

In order to match the magnet to the input cable impedance, the capacitance of the busbar to ground must be

$$C = L/Z_o^2 = 2.0\ nF/m \qquad (4)$$

The capacitance of the busbar to the outer case is approximately 0.2 nF/m, so additional capacitance must be added. As is shown in Figure 3, this might be accomplished by using the ceramic beampipe as a stripline capacitor, with the inside of the pipe nearest the busbar coated with conductor and grounded at one end. If 3 mm thick busbars are used, this conducting strip must be approximately 6 cm wide, which fits well within the 6.5 cm inner dimension of the beampipe. The remaining inside walls of the beampipe will be coated with high-resistivity material to provide a path for static charge bleed-off, while allowing fast magnetic field penetration.

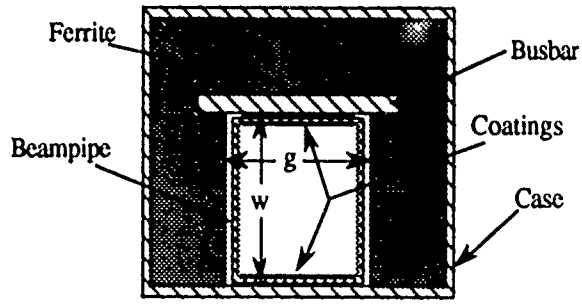


Figure 3. Cross-Section of Possible LEB Injection Kicker Magnet.

Thyratrons are expected to be the switch choice for the fast kicker systems. Assuming four cables are switched by each thyratron (at a voltage of 60 kV) and the current risetime is approximately 30 ns, the switch dI/dt is 4.6 kA/30 ns = 1.5 x 10^{11} A/s. This value is within the range of existing thyratrons such as the EEV CX1725.[2]

III. MEB INJECTION KICKER SYSTEM DESIGN

Figure 4 depicts a possible cross-section for the MEB injection kicker magnets. Using the above formulas, with a polewidth of 11 cm and a gap of 6 cm, the inductance of the busbar will be 1.72 μh/m. Assuming that 4.8 of the available 6.0 m will be magnetic material implies a magnetic field within the magnet of 100 G. The current required to generate this magnetic field is approximately 640 A. Selecting 50 Ω as the impedance for the busbar results in cable and switch voltage of 64 kV and busbar voltage of 32 kV. The capacitance of the busbar to ground must be 690 pF/m to match the 50 Ω input impedance. Approximately one-quarter of this capacitance exists between the busbar and the grounded magnet case; the remainder can be easily obtained using the conductive coating design described above.

The inverse velocity of the magnet will be 1720 nh/50Ω = 34 ns/m. By splitting the 4.8 m magnet length into eight 0.6 m magnets, 20 ns transit times are obtained. Two modulators, each consisting of a single thyratron and four RG-220 cables, are required to drive the entire system of eight magnets. The total current of 2.6 kA is required to rise in approximately 20 ns, for an average dI/dt of 1.3×10^{11} A/s. This current rate of rise is also within the range of existing thyratrons.

IV. SUMMARY

Requirements for the LEB-to-MEB transfer kicker systems are determined, in large part, by the chosen collider filling scenario. For the presented filling scheme, the LEB ejection kickers must generate 100-150 G magnetic fields in less than 80 ns with pulse flatness of better than 1.0 percent over the pulsewidth of 1.9 μs. The system to generate the required

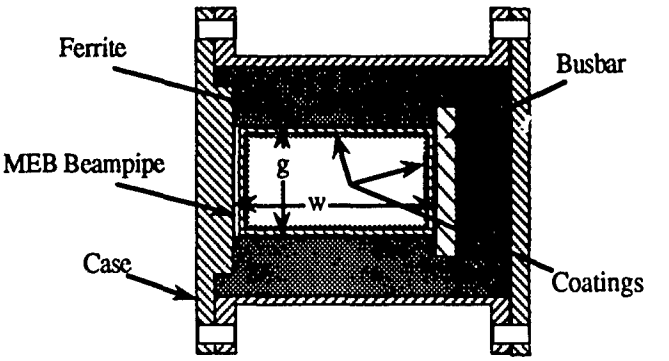


Figure 4. Cross-Section of Possible MEB Injection Kicker Magnet

fields is envisioned as a set of eight or more ferrite magnets, each less than 0.5 m in length, driven by at least four thyratron-switched charged cable modulators. The MEB injection kickers must generate approximately 100 G fields in less than 65 ns with similar pulse flatness and shot-to-shot repeatibility. This system has been scoped as a set of eight 0.6 m magnets driven by two modulators that are identical to those used to drive the LEB ejection system.

V. REFERENCES

[1] C. Crawford, J. Dinkel, J. Lackey private communication, February, 1991.

[2] H. Menown, C. A. Pirrie, "Advanced Thyratrons as Switches for the Nineties," 17th Mower Mod. Symp, 86CH2262-4, Seattle, WA, 1986.

A PINGER SYSTEM FOR THE LOS ALAMOS PROTON STORAGE RING

T. W. Hardek and H. A. Thiessen
Los Alamos National Laboratory, Los Alamos, New Mexico 87545

Abstract

Developers at the Proton Storage Ring have long desired a modulator and electrode combination capable of kicking the 800-MeV proton beam enough to conduct tune measurements with full intensity beams. At present this has been accomplished by reducing the voltage on one extraction kicker modulator and turning the other off. This method requires that all of the accumulated beam be lost on the walls of the vacuum chamber. In addition to tune measurements a more recent desire is to sweep out beam that may have leaked into the area between bunches. A four-meter electrode has been designed and constructed for this purpose. The design is flexible in that the electrode may be split in the center and rotated in order to provide vertical and horizontal electrodes each 2 meters long. In addition two solid-state pulse modulators that can provide 10kV in burst mode at up to 700 KHz have been purchased. This hardware and its intended use are described.

1 Introduction

The Los Alamos Proton Storage Ring (PSR) accumulates 800-MeV beam from the LAMPF linear accelerator and compresses macropulses up to 1 msec in length into intense 250 nsec pulses which drive a spallation neutron source. In the past only low-intensity tune measurements were routinely made. To provide tune data at any time throughout the accumulation cycle a pinger system has been developed. In addition to tune data the system described here can provide a series of kicks synchronized with the revolution frequency and timed to sweep beam from the area between bunches. It is believed that electrons trapped by the proton beam are causing an instability [1]. By sweeping beam out from the region between bunches we should be able to verify this theory.

0-7803-0135-8/91S01.00 ©IEEE

2 Pinger Uses

Tune Measurements

The most obvious use for our pinger is to kick the beam and observe the resulting betatron motion. From this oscillation one calculates the tune and can measure tune as a function of time into cycle or as a function of beam intensity. We plan to use the pinger in conjunction with wide-bandwidth beam-position-sensing electrodes and very high-speed digitizers to provide a spectral display of beam motion. With a total applied voltage of 20 kV we can provide a 1.1 mrad kick. Folded into the PSR lattice this would provide a maximum deflection of about 11 mm.

Beam Sweeping

A not so obvious use for the pinger is Beam Sweeping. The design of our storage ring allows some beam to leak out of the bunches. This leaves small amounts of beam filling the space between bunches and allows electrons to be trapped. As long as the space between bunches is clean the electrons will hit the beam pipe walls and not be trapped. A small amount of beam leaked into the space between bunches traps the electrons and may cause an instability. We plan to sweep any beam that leaks into the space between bunches out of the ring with the pinger system. We will produce a string of deflecting pulses synchronized to the revolution frequency and kick the beam on every 4th turn. One would prefer every turn but the revolution frequency is 2.8 MHz and the pulsers can only run at 700 KHz.

A preliminary test of beam sweeping was performed during the later part of our 1990 run cycle. Fig. 1 is a comparison of longitudinal beam distribution in the PSR with the sweeping pulse chain on (A) and off (B). During this experiment the minimum available sweeping pulse was 150 nsec while the space between bunches was only 100 nsec. We actually kicked some of the bunch; thus we had more beam loss than anticipated. We did make the beam stable by sweeping beam from between the bunches but we were

not able to discern whether this was due to an intensity decrease or from cleaning out the area between bunches.

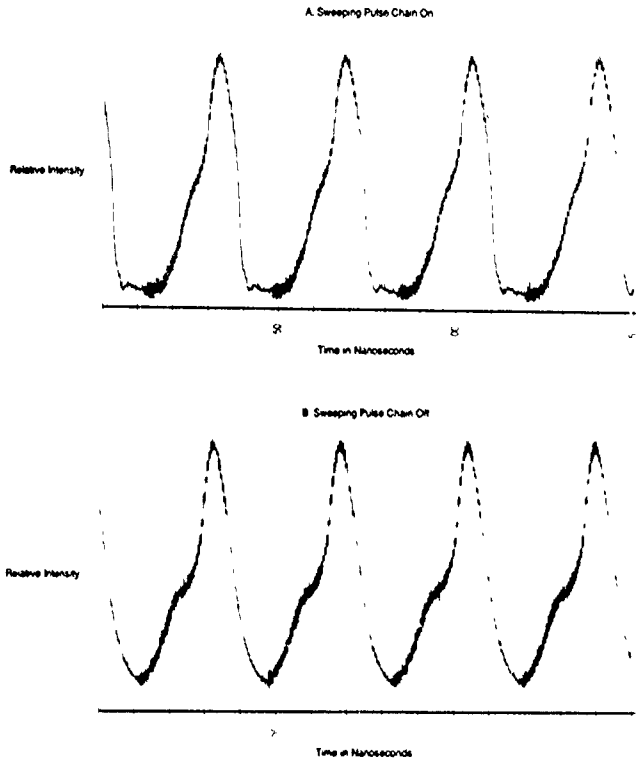


Figure 1: Comparison of longitudinal beam distribution in PSR with the sweeping pulse chain on (A) and off (B).

Beam Shaking

It is also possible to shake electrons out of the proton beam. The technique is utilized to remove trapped ions at Cornell, CERN, and FNAL [2]. We would use the pinger electrode for this purpose by powering it from a broadband RF amplifier. In our case we would drive the electrode in the 50 to 100 MHz range.

Clearing Fields

Another way to remove unwanted electrons is to install clearing electrodes. We have already completed experiments operating our extraction kicker electrodes at several kV with little or no effect. The kicker electrodes are 4 meters in length and there are two sets. The pinger electrode will give us another 4-meter electrode to energize and it is located in a different part of the ring.

3 Electrodes

Our pinger electrodes are configured as a balanced 100-ohm transmission line. We drive the electrodes from two separate sources of opposing polarity such that each pulser looks into a 50-ohm terminated line. Each electrode is back-terminated in 50 ohms through cables long enough to prevent any reflections from arriving back at the electrodes during the flat top portion of the pulse. Terminating resistors are simple carborundum resistors 2 inches in diameter, 12 inches long supplied with integral corona ring end caps. The resistors are immersed in oil and cooled by immersing a water-cooled coil of copper tubing into the oil.

Fig. 2 gives the end view of our pinger electrode showing the Macor support insulators, corona rings that shield the triple junction where the stainless steel end piece contacts the Macor insulator, and the adjusting hardware at the rear of the insulator. The drawing shows the electrodes in their horizontal deflecting orientation, but we will actually install the electrodes in their vertical deflection orientation with the electrodes at the top and bottom. The ears at the

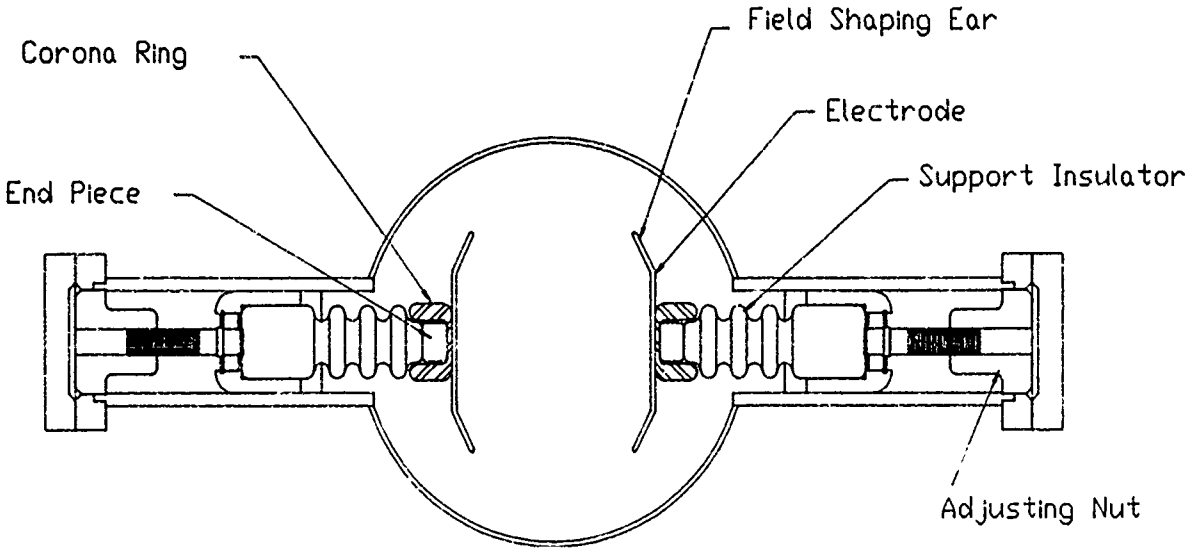


Figure 2: End view of pinger electrode.

edges of the plates were adjusted for best field uniformity [3]. In this design the field is uniform to one percent over an area of 9 cm horizontally (± 4.5 cm) 4 cm vertically (± 2.0 cm) and uniform to 6 percent out to ± 3 cm vertically. We have split the housing and the electrodes at the center to allow for their use as independent vertical and horizontal electrodes of half their present 4-meter length. The support insulator design was borrowed from the PSR Extraction Kicker electrodes to save design time and minimize the number of spare parts required.

We have set 4 inches as the minimum allowable aperture anywhere within the PSR beam pipe. The pinger electrodes are set to this 4-inch spacing to maximize the available kick.

Power is supplied to the electrodes through-off-the-shelf vacuum feedthroughs that present a fairly uniform 50-ohm impedance. The long ports on the housings were included to allow the eventual replacement of the lower-voltage stock feedthroughs with the higher-voltage feedthroughs used in our extraction kickers.

4 Pulse Modulators

We supply pulses at the downstream end of each electrode thus taking advantage of both the magnetic and the electric fields. We pulse one electrode with a positive 10-kV pulse and the other electrode with a negative pulse. Since they are produced by separate units that drive a balanced line it is desirable to have the pulses well matched and to have them arrive at the electrode at the same time. In our application we are not very sensitive to pertubations on the top of the pulse that mismatches would cause, but still wish to minimize these pertubations. We do not yet have enough experience with these units to know how well matched the pulsers will remain over time.

Table I gives the specifications for the pulse modulators we are using. The modulators are commercial products and are all solid-state. The unique feature of these units is that they can produce a string of pulses at up to 700-kHz repetition rate. Our units have been modified to allow up to a millisecond long burst of 700-kHz 90-nsec-long pulses.

Table I: Pulse Modulator Electrical Specifications

Minimum Output Voltage	1kV
Maximum Output Voltage	10kV
Maximum Output Current	200 Amperes
Minimum Pulse Width	90 nsec
Maximum Pulse Width	270 nsec
Rise Time	40 nsec
Fall Time	40 nsec
Pulse Recurrence Frequency	50 Hz
	700 KHz Burst

5 Acknowledgements

The authors wish to thank Woodson Bowman of AT-3 for assembling the hardware, the Mechanical section of MP-5 for installing the electrode and for providing machining assistance, and Linda Walling and her team for completing beam coupling impedance measurements. Pulse modulators were provided by Directed Energy, Inc.

References

[1] D. Neuffer et al., contributed paper, 1991 Particle Accelerator Conference, San Francisco, California.

[2] J. Marriner, D. Mohl, Y. Orlov, A. Poncet, S. Van der Meer, "Experiments and Practice in Beam Shaking," Particle Accelerators, **30**, 13 (1990).

[3] J. F. Power, B. Blind, A. J. Jason, "The Los Alamos Proton Storage Ring Fast-Extraction Kicker System," IEEE Transactions on Nuclear Science, NS-32, Number 5, Particle Accelerator Conference, 1985, Page 3021.

Electrical Performance of the Injection System Kickers at the Saskatchewan Accelerator Laboratory *

C. Figley
Saskatchewan Accelerator Laboratory
University of Saskatchewan
Saskatoon, Saskatchewan, Canada S7N 0W0

Abstract

This paper describes the results of upgrading the electrostatic kicker system at the Saskatchewan Accelerator Laboratory (SAL). The second of two kickers required for multi-turn injection into the Pulse Stretcher Ring (PSR) has been commissioned. Previously, with only one kicker, the injected beam duration was limited to slightly less than one pass around the circumference of the PSR. Multi-turn operation (up to three turns) enforced stringent field quality constraints and required a significant improvement in the electrical performance of the original kicker. After long-term operational experience the original modulator was upgraded and used as a model for the new assembly. The tandem kickers have successfully demonstrated multi-turn injection. Salient results of these investigations are presented.

I. INTRODUCTION

The Saskatchewan Accelerator Laboratory has recently commissioned the second of two kickers required for multi-turn injection into the Pulse Stretcher Ring (PSR). This injection process allowed the insertion of a one microsecond beam pulse into a 360 nanosecond long ring. In a previous paper, [1] the basic modulator design was discussed along with a brief summary of the early experience with the unit. Early investigations of factors such as average power, peak current, component stress, field quality, etc., and the engineering concerns of maintenance, reliability and lifetime led to the design of the original electrostatic deflector and compatible modulator.

The deflector plates shown in Figure 1 are 12 cm x 40 cm each and are separated by 3 cm within the vacuum tank. The kicker modulator is capable of producing field strengths of up to 26 kV/cm on the deflector assembly. This is accomplished by driving one plate positive and the other negative for a maximum differential of 80 kV. Normal operating repetition rates are up to 360 Hz. Pulses are generated by a slow charging circuit and a fast, high current shunt circuit. This modulator is characterized by its small size, low power (the main high voltage power supplies deliver only a few hundred watts) and simple layout. These features translate into an inexpensive and reliable system. A simplified schematic of the newest version of the modulator is shown in Figure 2.

The kicker operates by first charging the deflector plates using two identical triode circuits. These triodes are triggered

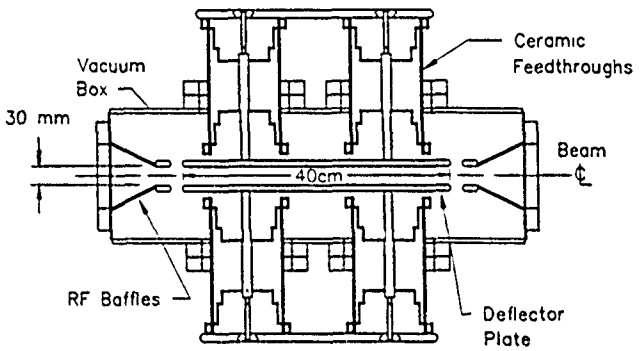


Figure 1. Deflector plate mechanical assembly.

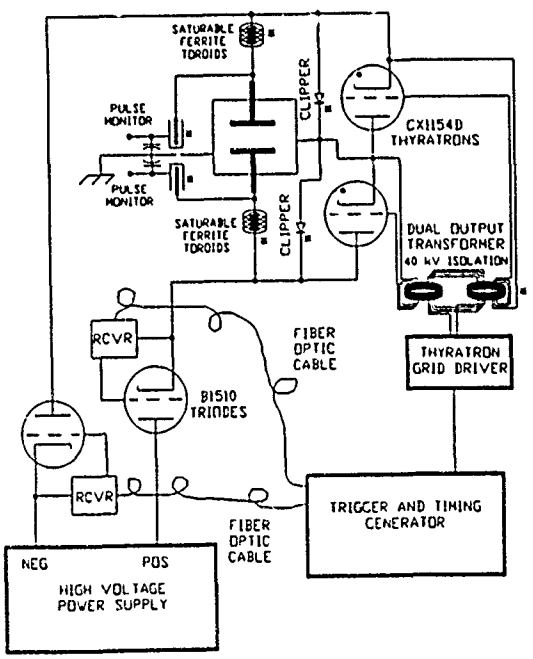


Figure 2. Simplified schematic of the kicker modulator. Filament and support circuits are deleted for clarity. Recent modifications are indicated by a *.

prior to the beam arrival. The pulse voltage is allowed to settle for approximately 100 μs to stabilize the "flat top" portion of the field pulse. The long charge time is not critical since there is no beam in the ring just prior to injection. After the deflector is fully charged, the triodes are disabled, fixing the plate voltages. The beam is then injected into the PSR and the thyratrons trig-

* This work was support by the Canadian National Science and Engineering Research Council (NSERC)

0-7803-0135-8/91S01.00 ©IEEE

gered so that as the tail end of the beam pulse passes into the kicker, the field begins to collapse. Ideally, the pulse should fall instantaneously to zero and remain there for the entire interpulse period. A typical field waveform produced by the kicker is shown in Figure 3. The field falltime is typically 20 ns.

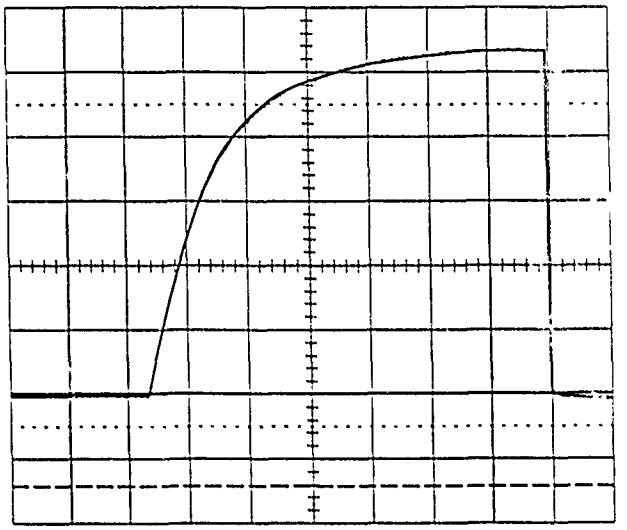


Figure 3. Typical field pulse showing charge period. Horizontal scale 20 μs/div, vertical amplitude of peak is 50 kV corresponding to 16.7 kV/cm deflector field.

After 18,000 hours of operation and occasional maintenance, several problem areas were identified. Before assembling the second kicker, the first modulator was modified to improve the performance, reliability, and remote adjustment features. These changes were as follows:

- Inexpensive high voltage pulse monitors with fast risetimes to aid diagnostics and tuning were developed.
- Improved the thyratron driver unit to provide matched triggers to each thyratron.
- Added saturable ferrite cores in strategic locations to limit trigger pulse coupling into the main deflectors and to sharpen the falltime of the pulse.
- Added clipper diodes to the thyratrons and to the extreme ends of the power supply circuits to limit reflection and undershoot of the pulses.
- Added grounding harnesses to "noisy" portions of the circuit and improved the enclosure to limit radiated interference.
- Converted the triode filament supplies to DC operation to stabilize tube gains.
- Improved triode and thyratron air cooling for better drift and jitter performance.

While using a single kicker, the injected beam was limited to slightly less than one turn around the PSR to allow for the finite falltime of the field. The second kicker allowed multiturn injection by providing a kick to the head end of the beam pulse already circulating inside the PSR before it passed through the first kicker field on its second and third orbits. The result of this compensatory kick was to overlap the beam circulating in the PSR.

When using two kickers, the match between the two deflecting wave forms is critical. The technique depends on "exactly" correcting the kick of the first deflector with the second. The quality of the "exact" match determines the quality of the resultant stored beam.

II. UPGRADE RESULTS

The second kicker, which is an electrical twin of the upgraded original, was mounted downstream of the previous unit (with respect to the injected beam trajectory). The second modulator and its connections to the deflector assembly were mechanically copied as far as possible to provide the best match of stray circuit elements and in turn match the resulting pulses in time, amplitude and contour. The undershoot portion of the field was reduced as much as possible to achieve the best overall performance for both single and multi-turn injection. This allowed cleaner single kicker operation and, with a smaller error kick to contend with, simplified matching the two kicker response.

A pre- and post-fine tuning comparison of the original kicker pulse edge is shown in Figure 4. In Figure 5 the trailing edge of the improved pulse is expanded to show more detail. The dramatic effects appear in the collapsing portion of the pulse. As can be seen from the undershoot of the waveform in

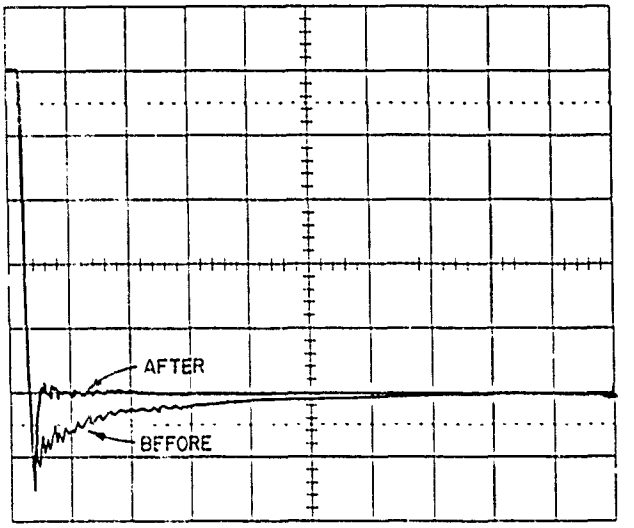


Figure 4. Typical field pulse before and after the upgrade. Peak amplitude is 16.7 kV/cm, horizontal scale 0.5 μs/div.

the earlier version, an undesirable kick was applied to the beam. Several sets of saturable ferrite inductors and clipper diodes were connected in various configurations in an attempt to "clean up" the basic waveform. The result was a significantly improved pulse, with the tail and undershoot portion of the field waveform reduced in amplitude and in time. This equated to a reduction of the erroneous beam deflection to about two percent of the previous value with no serious degradation of the 20 ns falltime. The ferrites also eliminated a small amount of trigger pulse coupling through the thyratron grids to the deflector plates. Previously, this caused a minor disturbance of the flat top

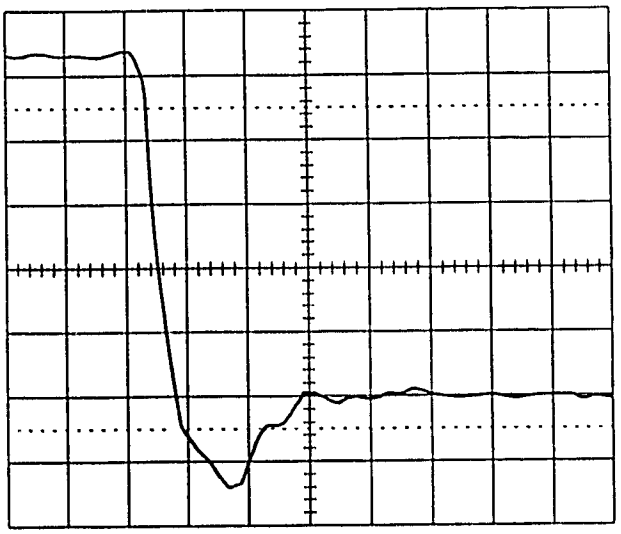


Figure 5. Typical field pulse after the upgrade. Trailing edge expanded to show region of scale 50 ns/div.

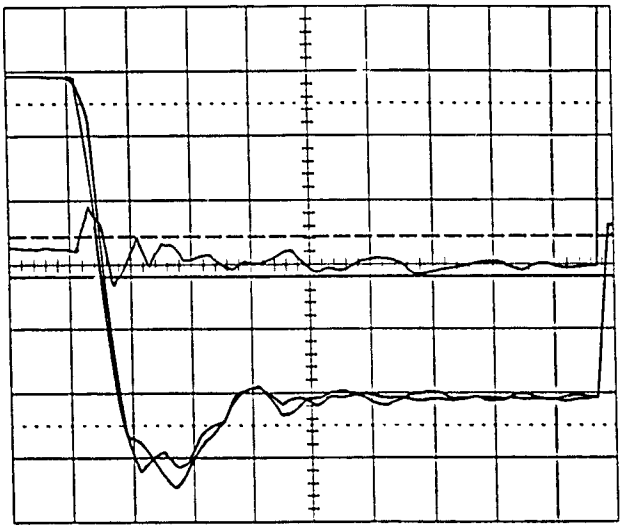


Figure 6. Comparison of the two different kickers. Field pulses aligned in time and matched in peak amplitude. Smaller amplitude central trace is the difference between the two fields (see note in text).

of the main deflector pulse for several hundred nanoseconds just before the field collapsed.

An improved driver system was incorporated to allow precision trimming of the firing times of the two thyratrons. A special high voltage isolating pulse transformer was developed. This transformer had a loosely coupled primary and a dual core, one for each secondary winding. While essentially two transformers in series, this design was adopted since the primary current was inherently the same around both cores. This geometry helped compensate for the differences caused by stray capacitance and leakage in a two transformer series layout which normally shunt away some of the current. The separated core structure had the best success ensuring that the trigger driven into each thyratron grid were closely matched in time and amplitude. This timing must be tightly controlled to achieve the highest possible collapse rates and reduce the ripple and overshoot on the electric field pulse. The driver allowed a single primary trigger pulse to drive both thyratrons while maintaining a relative timing adjustment range of approximately 50 ns. This was sufficient to compensate for short-term thyratron drift.

As a demonstration of the ability of this new layout to meet the matching requirements, a measurement was made of each kicker field and then the resultant waveforms were subtracted to yield the mismatch (or erroneous) field seen by the circulating beam (see Figure 6). This differential field translates into undesirable beam deflections. The four high voltage probes used to measure the relative voltages on the plates were matched to 2% in gain and had risetimes of 18 to 25 ns. Even without correcting the waveforms for probe variations, it appears that a field of only a few percent of peak exists for two to three hundred nanoseconds following the discharge. It should be noted that the first few cycles of the differential waveform are strongly affected by the alignment of the two falling edges of the main fields, emphasizing the need for accurate timing and identical shapes. Improvements can be made to this measurement by compensating for the individual probe responses.

III. CONCLUSION

The recent results of the kicker upgrade at SAL have been encouraging. The improved performance of the tandem kicker system in terms of pulse quality and ease of modulator adjustment should be adequate for the next series of PSR developments. Additionally, work continues on eliminating the residual undershoot remaining on the pulses. Future investigations will focus on correcting the high voltage probe differences, developing an automatic firing time drift compensator and linking the two kickers with a high level microprocessor controller. This should allow optimization of the relative timings between the two kickers and thus minimize beam disturbances.

IV. REFERENCES

[1] Curtis B. Figley, "A HIGH SPEED ELECTROSTATIC KICKER FOR THE PULSE STRETCHER RING AT SASKATCHEWAN ACCELERATOR LABORATORY," Nuclear Instruments and Methods in Physics Research, A273, pp. 59-62, 1988.

PSR SWITCHYARD KICKER SYSTEM IMPROVEMENTS

T. W. Hardek
Los Alamos National Laboratory, Mail Stop H852, Los Alamos, New Mexico 87545

Abstract

A switchyard kicker system which allows time sharing of beam between the Los Alamos WNR/LANSCE complex and other LAMPF users was redesigned as part of the Proton Storage Ring addition. The system consists of two pulsers providing 1750-ampere, 1-msec pulses to a pair of 1 meter long ferrite magnets. The system was designed to operate at 24-Hz maximum repetition rate. In 1986 a modification was made to the equipment to allow operation at 40 Hz. While the system operated reliably this way some difficulties were observed. A desire on the part of the users to operate the system at 60 Hz coupled with a major system failure led to design changes to load resistors, drive cables, charging system, and cooling system. These changes are described along with an analysis of the difficulties encountered with the original hardware.

1 Introduction

A pair of ferrite magnets, each one meter in length and having an aperature of 9.65 cm by 5.25 cm, are used to switch beam between the WNR/LANSCE complex and other LAMPF experimenters. The magnets are pulsed to 1750 amperes for 1 msec with a nominal risetime of 40 μsec. A pair of modulators utilizing 22-section pulse-forming networks (PFN) provide the current pulse. Fig. 1 is a block diagram showing the modulator configuration [1].

The original specification called for a maximum repetition frequency of 24 Hz, but a desire to send more beam to the WNR/LANSCE users raised the rate to 40 Hz [2]. The PFN is resonantly charged, then an SCR switches current to the magnet. To speed up the charging time the charge inductor was decreased from 16 mhy to 5 mhy and the discharge resistor was removed. It was also necessary to add blowers to the ducts carying the drive cables to keep these cables from overheating.

Attempts to push the repetition rate to 60 Hz resulted in the marginal failure of a charging system SCR and the loss

0-7803-0135-8/91S01.00 ©IEEE

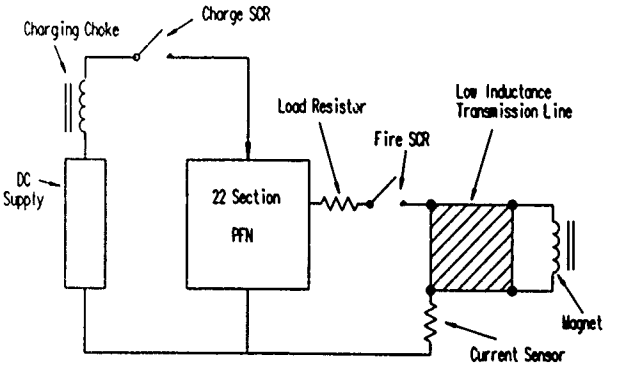


Figure 1: Modulator Block Diagram

of a load resistor. Of course the marginal SCR would heal itself before we could find it, so the replacement of the load resistor was the only corrective action taken. We replaced the load resistor many times before we finally were able to find the faulty SCR and replace it. As an interim solution a high-current fast-acting fuse was inserted in the DC feed line to the charging system and at least this saved the load resistor. We also designed a replacement load resistor that could handle the entire DC power-supply capacity.

Having experienced trouble running at 60 Hz we did a thorough study of the modulators, which resulted in fairly major system modifications. Our study showed that the drive cables were very marginal at 60 Hz, cooling for charging SCRs was inadequate, and the charging chokes saturated and overheated. We have replaced the charging chokes and drive cables, redesigned the load resistor, reinstalled the discharge resistor and completely reworked the cooling system.

2 Charging System

Fig. 2 is a simplified drawing of the charging system. Charging is initiated by firing S1 and terminated by firing S2. When S2 is fired, the load resistance (0.1 ohm) and a discharge resistor (1 ohm) are shunted across the charging inductor. For 24-Hz operation the L/R discharge time would be 15 msec. When the system was modified for 40 Hz operation the charging inductor was reduced to 5 mhy

(the inductor had a 5-mhy tap) and the discharge resistor was jumpered out. For 40-Hz operation the discharge time actually increased to 50 msec, forcing the inductor to carry a high DC current. This is the source of the core saturation. Our solution was to replace the charging inductor with one that can handle the DC component and to insert a small discharge resistor. The present circuit utilizes a 0.5-ohm discharge resistor and a 5-mhy charging inductor for a discharge time constant of 10 msec.

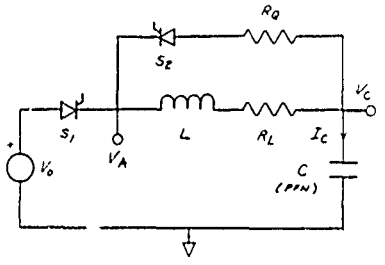


Figure 2: Simplified Charging System Diagram

Fig. 3 is a photograph showing the discharge resistor. It consists of a series of 0.04-inch-wall 3/8-inch-diameter stainless steel tubes. With 5 GPM of water flow each segment can dissipate 5kW. The tubes are bent back on themselves to minimize inductance leaving about 1.6 μhy per element; however, in this application low inductance is not important.

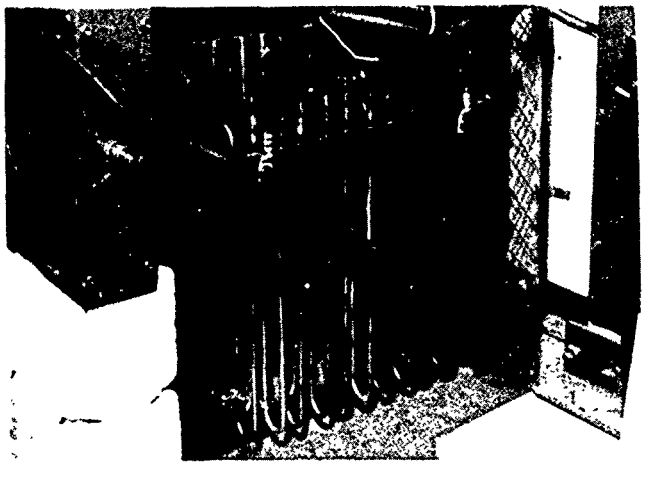


Figure 3: Discharge Resistor

Fig. 4 shows the charging inductors. Nominal inductance is 5 mhy with tap points every 0.5 mhy down to 2 mhy. The core is sized to cary 500 amperes maximum DC with a clipped sinusoidal AC component of 200 amperes peak-to-peak covering 14 msec of a 16.6-msec period (60-Hz repitition rate).

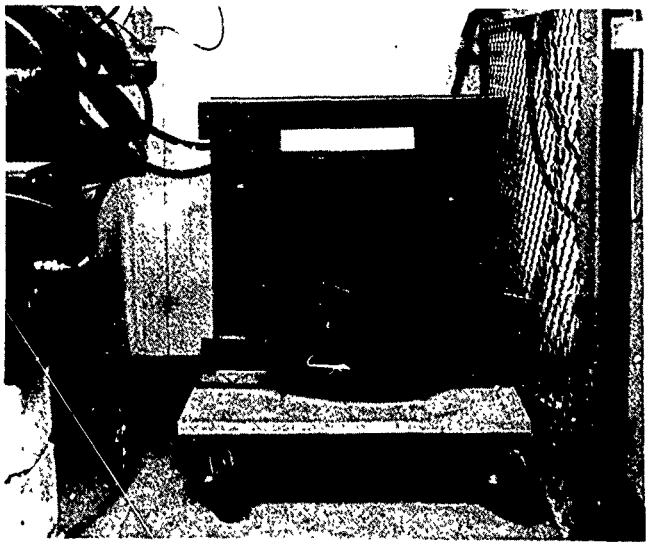


Figure 4: Charging Inductors

3 Transmission Lines

The switchyard kicker pulse modulators are located in a remote location out of the radiation area where the magnets reside. Eighty feet of power transmission line connects the modulators to their magnets. The single-turn ferrite kicker magnets appear electrically as a 3 uhy inductance with about 1 milliohm of series resistance. The magnets are pulsed to 1750 amperes with a rise time of about 40 μsec. In order to achieve this rate of rise with reasonable voltages the power transmission lines must have as low inductance as possible. One does not want to drop all the voltage in the transmission lines. A multi-layer parallel-strip line cable was developed to meet this low inductance requirement. The original design called for a line formed from 20 strips of 12-mil copper sheet and electrically connected with each strip alternating in polarity [3]. This results in 20 transmission lines effectively connected in parallel to provide a composite line with a high frequency characteristic impedance of 0.07 ohms and an inductance of 0.28 nhy per meter. In practice this line was reconfigured to appear electrically as 6 parallel transmission lines for a characteristic impedance of 0.23 ohms and an inductance of 0.9 μhy per meter.

The line was assembled from 1.9-inch-wide copper strips with a plastic insulating jacket bonded to both sides. Individual strips were then taped together and an outer braided jacket was slid over. An external layer of rubber tape was placed over the braid. With this geometry it is important to keep the individual conductors as close together as possible and many layers of tape were needed to accomplish this. 450 watts is dissipated in this cable at the 24 Hz pulse rate. Thermal conductivity of the various layers of tape is quite poor but is adequate for operation at 24 Hz. To operate at 40 Hz, blowers were installed at

the opening of the ducts the cables are fed through. The cable was very marginal at 60 Hz even with the blowers.

To provide operation at 60 Hz we have replaced the original transmission lines with a modified design. Fig. 5 shows the construction of our new lines. The individually insulated single conductors have been replaced with pairs of conductors with a dielectric layer bonded between them and an insulating layer bonded over the outside surfaces. Since the individual lines are complete in themselves there is no real need to insure close spacing. We covered our lines with a woven plastic mesh which is quite open, allowing good heat transfer to the cooling air. In addition to removing the thermal barrier we increased the thickness of the copper strips to 16 thousands of an inch and increased their width to 2.75 inches. Our 80-foot lines have a characteristic impedance of 0.06 ohms, a DC resistance of 3.7 milliohms, an inductance of 7.7 nhy and a capacitance of 2.2 mfd.

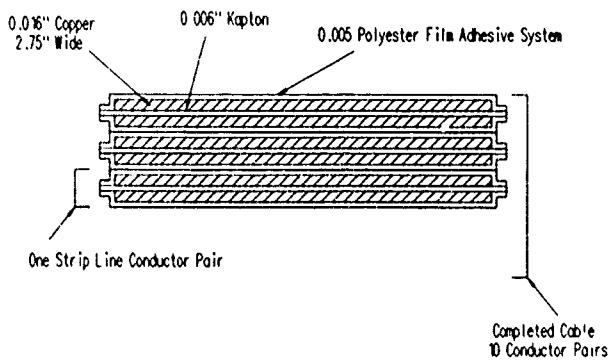


Figure 5: Low-Inductance Transmission Line

4 Load Resistor

During our early attempts to operate the system at 60 Hz we encountered difficulty with a charging SCR (see Fig. 2). When this SCR shorted, 4kj, the entire stored energy of our DC charging supplies, was sent through our load resistor. The original load resistor design consisted of a meandering strip of manginin placed in a water jacket such that the water would flow across the resistor material. This load-resistor design exhibited quite low inductance and easily dissipated the normal 400j of energy. We have replaced this load resistor with 120 inches of stainless steel tubing bent back on itself to reduce its inductance to about 0.3 μhy. Fig. 6 is a photograph of this load resistor. With 5 gpm of cooling water flow we can dissipate 5000 watts with only a 10-degree maximum temperature rise.

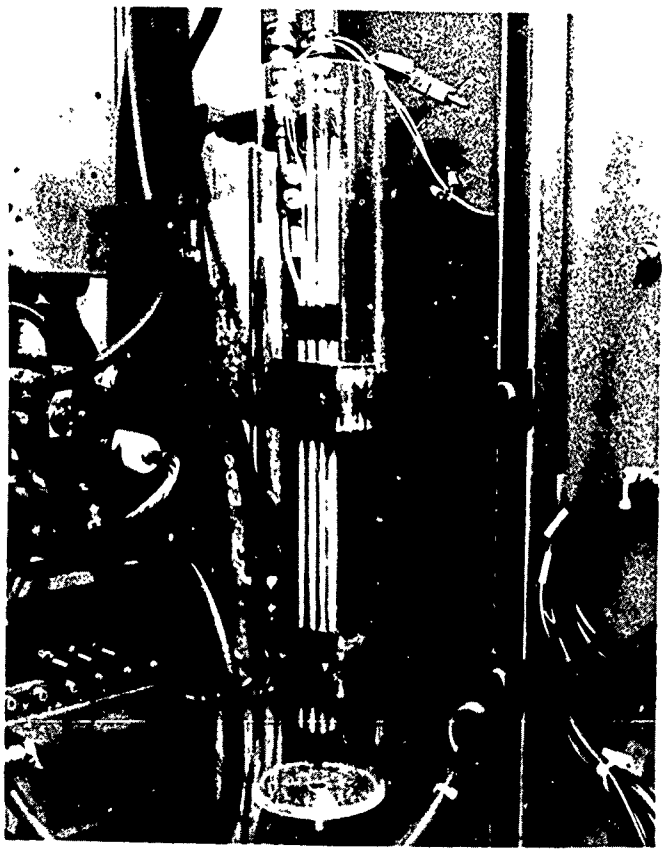


Figure 6: Load Resistor

5 Acknowledgements

The author wishes to thank C. Hansen for his major contribution to our cable design and charging choke specifications, the MP-5 Mechanical section for constructing our load and charging resistors, and D. Shadel and the technicians of the MP-5 Pulsed Power section for installing the hardware.

References

[1] R. A. Hardekopf, E. F. Higgins, J. S. Lunsford, "Ferrite Kicker Magnet for the LAMPF Switchyard Upgrade," IEEE Transactions on Nuclear Science, Volume NS-32, Number 5, Particle Accelerator Conference, 1985, Page 3634.

[2] J. Power, "Switchyard Kicker 40-Hz Upgrade," AT-3 Technical Note 135, 1986.

[3] B. R. Sandburg, "Investigation of Transmission Lines for PSR Magnets and Cavity Tuners," PSR Technical Note 103, 1982.

SLOW BEAM EXTRACTION EXPERIMENTS AT TARN II

M. Yoshizawa, +A. Ando, K. Chida, *M. Kanazawa, &T. Hattori, H. Muto,
$A. Noda, *K. Noda, M. Tomizawa, J. Yoshizawa and A. Mizobuchi
Institute for Nuclear Study, University of Tokyo
Tanashi-city, Tokyo 188, Japan

Abstract

Beam test of a slow extraction system has been performed at the injection energy (10 MeV/u) for α particles in order to study the feasibility of the system. Beam spill time of 0.7 second has been achieved for 3 x 10^5 extracted particles although the effect of the current ripple in the magnet power supplies are observed.

I. INTRODUCTION

In order to respond to the increasing needs for biomedical research utilizing ion beams with intermediate energies(several hundreds MeV/u), a slow beam extraction system has been designed and constructed at TARN II. The system consists of an electrostatic septum(ESS), a magnetic septum(SM), a sextupole magnet(SX) and three bump coils attached to the ordinary lattice dipole magnets as shown in Fig. 1. The horizontal betatron tune is shifted from 1.70 to 1.6666···by decreasing the field gradients of radially focusing quadrupole magnets after acceleration. In Table 1, designed hardware equipments for the slow extraction system are listed up. All the equipments have been studied off-line beforehand and then are installed into the ring. In the present paper, their typical characteristics are briefly described together with the recent results of the beam test.

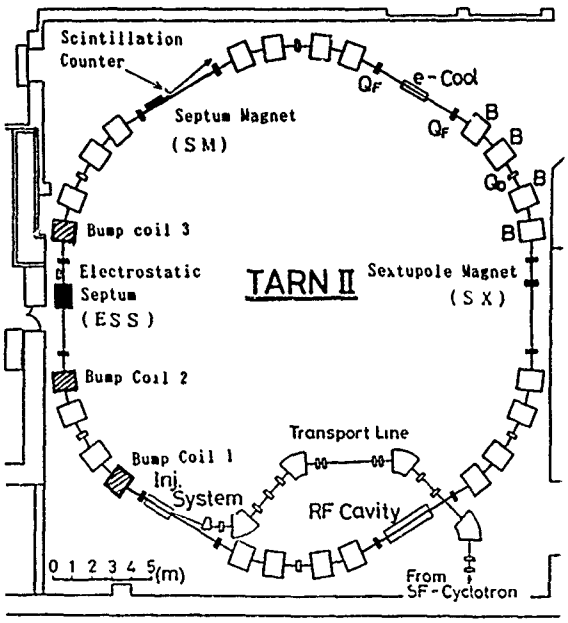


Fig. 1 Layout of the slow extraction system of TARN II.

+Research Center for Nuclear Physics, Osaka University
*National Institute of Radiological Sciences
&Tokyo Institute of Technology
$Present Address: Institute for Chemical Research, Kyoto University

0-7803-0135-8/91$01.00 ©IEEE

II. HARDWARE EQUIPMENTS

A. Electrostatic Septum (ESS)

In order to reduce the beam loss, the first septum is an electrostatic type with a septum wires made of Re-W alloy 90 μm in diameter stretched with spacing and tensions of 1.25 mm and 600 g, respectively. The negative high voltage is applied to an electrode made of titanium opposing to the septum wires with the earth potential. Up to now, already a high voltage more than 90 kV has been safely applied for the gap of 10 mm whereas the designed value is 85 kV for the highest energy. With evacuation utilizing a tarbo-molecular pump and a Cryogenic pump with pumping speeds of 200 *l*/sec and 1600 *l*/sec,respectively, the final end of the vacuum pressure at the chamber of the electrostatic septum has reached 1 x 10^{-10} Torr after a baking process.

Table 1

Hardware Equipments for Slow Beam Extraction

Sextupole Magnet	B"L, Bρ = 0.3015 1/m² (DC mode)
Electrostatic Septum	E = 70~85 kV/cm, L = 1.0 m, Deflection Angle = 5.8 mrad, Septum Thickness = 0.15 mm
Septum Magnet	B = 5 kG, L = 1.0 m, Deflection Angle = 85.2 mrad, Septum Thickness = 9 mm
Bump Coil 1	Deflection Angle = 5.4 mrad
〃 2	〃 =-7.1 mrad
〃 3	〃 = 7.1 mrad

B. Septum Magnet (SM)

In order to suppress degassing rate, the second septum is made of solid iron block instead of laminated plates although it assumes DC operation. The septum thickness allowable for the present case is 9 mm and the current density in the septum coil amounts to 78 A/mm^2 for the highest excitation of 5kG. It is found that the temperature rise of the septum coil in the air is below 30°C for the maximum excitation current of 2500 A and is well in a range of practical use. As the insurating materials for return and septum coils, ceramic coating and sheets of Kapton are used, respectively, large degassing rate is anticipated. However, the end pressure of 2.2 x 10^{-10} Torr has been attained at the septum magnet chamber by evacuation with a turbo-molecular pump of pumping speed of 400 *l*/sec.

C. Sextupole Magnet (SX)

As an exciter of the resonance, a sextupole magnet made of soft iron block is utilized at the position shown in Fig. 1. The needed strength of the sextupole for extraction is S (=B"L/Bρ) =0.3015 1/m^2 (Table 1). The beam life time was measured for various strength of the sextupole as shown in Fig. 2. If we assume the injection and maximum extraction energy of 10 MeV/u and 350 MeV/u, respectively, the ratio of the magnetic rigidity between injection and maximum energies amounts to 6.4 times and if the sextupole magnet is DC operated its strength, S, at the injection energy amounts to 1.9 1/m^2, which is found to lead to a short beam life as shown in Fig. 2. So the sextupole magnet is changed to be ramped during acceleration time of TARN II as long as about 4 sec.

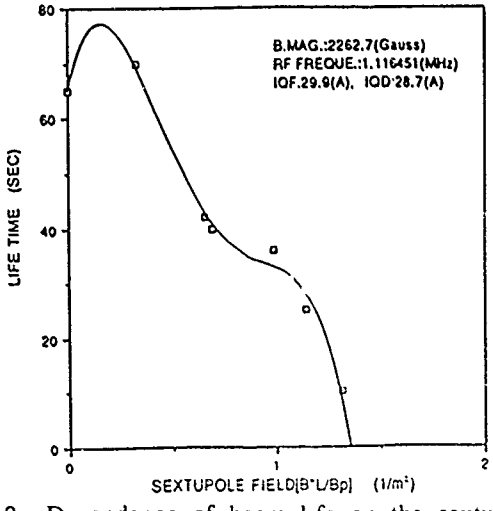


Fig. 2 Dependence of beam life on the sextupole strength.

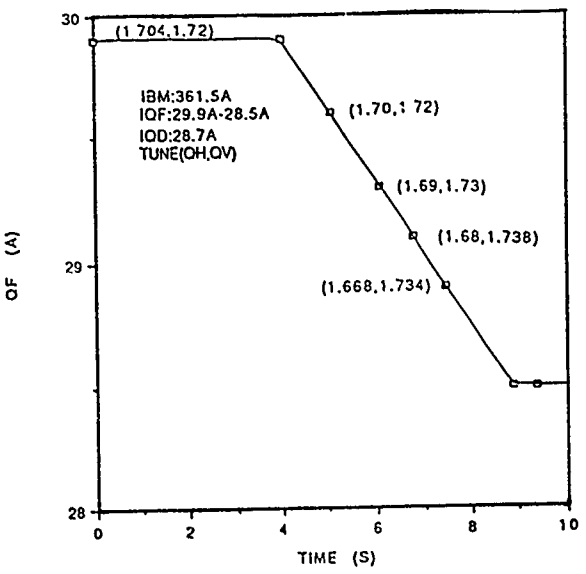


Fig. 3(a) Ramping pattern of radially focusing quadrupole magnets.

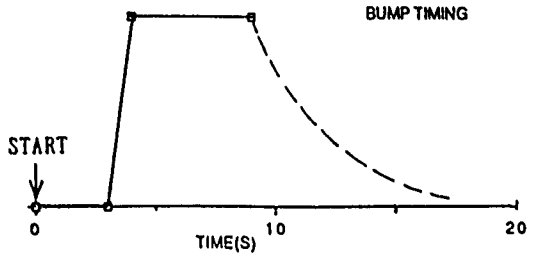


Fig. 3(b) Ramping pattern of bump coils.

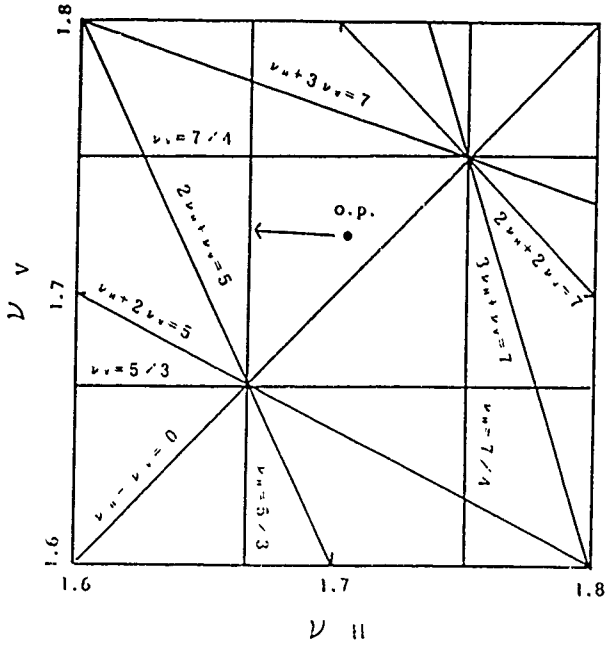


Fig. 4 Working line in the tune diagram during the beam test.

III. PROCEDURE OF BEAM EXPERIMENTS

As the preliminary test of the slow extraction system, the α beam is extracted at the injection energy(10 MeV/u). The field gradient of the radially focusing quadrupole magnets are reduced after beam injection and RF capture as shown in Fig. 3(a). In the process, the operating point in the tune diagram is shifted as shown in Fig. 4. In order to make the beam aperture to be minimum at the entrance of the electrostatic septum, three bump coils are excited by the timing as shown in Fig. 3(b). The intensity of the circulating beam in the ring decreases corressponding to the timing when the signals at the scintillation counter set at the exit of the septum magnet are observed (Fig. 5). The output signals from the photo-multiplier is processed through the electronics system as shown in Fig. 6 to observe the time structure of the extracted beam. As is shown in Fig. 7, the duration of the extracted beam of the intensity of 3×10^5 is about 0.7 second although the beam intensity is modulated from 100% to 0% by 50 Hz due to the presence of large current ripple of the power supplies of the magnets in the lattice. The results presented here are very preliminary ones and further study is needed to improve the beam spill and emittance of the extracted beam and so on.

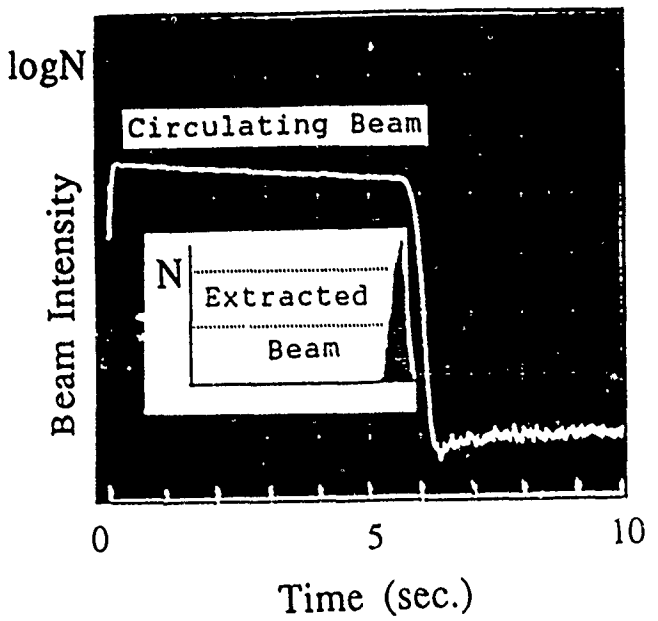


Fig. 5. Time variation of intensities of the circulating and extracted beam.

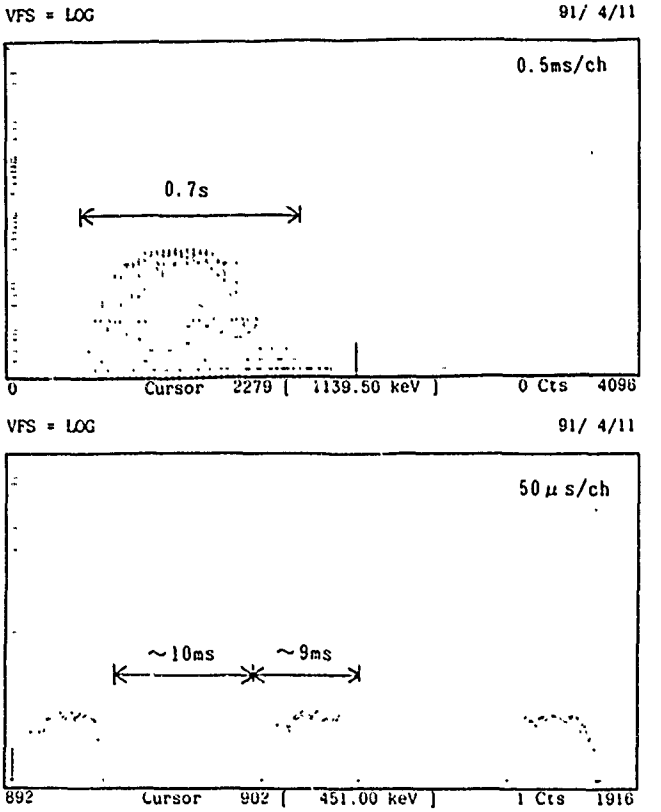
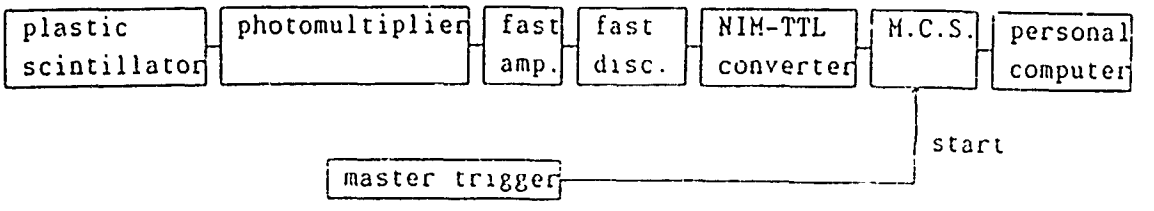


Fig. 7 Time structure of the extracted beam.



(M.C.S.: multi-channel scaling module)

Fig. 6 Block diagram of the electronics system used for detection of the extracted beam.

IV. REFERENCES

[1] A. Noda et al., "Slow Beam Extraction System of TARN II", Proc. of the 2nd European Particle Accelerator Conference, pp. 1263-1265, Nice, France, 1990.

[2] M. Yoshizawa et al., "DC Septum Magnet for TARN II", Proc. of the 6th Symp. on Accelerator Science and Technology, pp.175-177, Tokyo, Japan, 1987.

[3] A. Noda et al., "DC Septum Magnet for Beam Extraction", Proc. of the 1989 Particle Accelerator Conference, pp. 363-365, Chicago, U.S.A., 1989.

A TRIPLE-ISOTOPE INJECTOR FOR ACCELERATOR MASS SPECTROMETRY

R. J. Schneider and K. F. von Reden
Woods Hole Oceanographic Institution
Woods Hole, Massachusetts 02543
K. H. Purser
US-AMS Corporation
Topsfield, Massachusetts 01983

Abstract

Performance of the newly installed 40 keV negative ion injector for the three isotopes (masses 12,13 and 14) of natural carbon is discussed. A cesium sputter ion source and an achromatic arrangement of four dipole magnets with two electric slot lenses is being used, to achieve minimal aberrations for the injected beam into a tandem.

I. INTRODUCTION

As part of the new AMS system built for the National Ocean Sciences AMS Facility [1] at Woods Hole Oceanographic Institution (Woods Hole, MA) by US-AMS Corporation [2] (Topsfield, MA), an injector for simultaneous acceleration of the three natural isotopes of carbon was designed. The extremely low abundance of carbon-14 compared to carbon-13 (times 10^{10}) and carbon-12 (times 10^{12}) makes ratio mass spectrometry difficult. Sequential measurements are subject to differences in beam-loading as well as the usual short-term tandem accelerator instabilities. The frequently used electrostatic "bouncer" has limited efficiency. Since the carbon-13/12 ratio is stable, and varies only slightly from sample to sample, simultaneous acceleration of all three isotopes with online measurement of the 13/12 ratio makes a useful diagnostic indicator of fractionation effects and other systematic problems.

II. PHYSICAL DESCRIPTION

A. Ion Source

The cesium sputter ion source was based on work by Middleton [2] and is similar in principle to that built by Genus Corporation for Lawrence Livermore National Laboratory. It has an hemispherical ionizer, through the center of which the negative ion beam is extracted. Cesium vapor is stabilized by regulating the temperature of both the reservoir and the transfer tube closely. The cesium ions are accelerated through about 8 kV from the ionizer to the target. The graphite sputter targets (containing the samples for analysis) are pressed into 2 mm diameter holes in aluminum cartridges. A carousel holds 59 of these targets. The target changer is operated by DC servomotors on the high voltage deck. The sputtered negative ions emerge through the hole in the ionizer and pass through a 32 kV extraction gap, so that the total energy is 40 keV. The acceptance half-angle is 22 milliradians, limited by an aperture plate at the exit of the source. A cylindrical einzel lens brings the beam to an object point for the recombinator. There is an insertable Faraday cup to measure source output.

B. Recombinator

This arrangement of magnetic and electrostatic elements was optimized by the Toronto group (It is sometimes referred to as a Brown achromat)[3]. Although not the first application of a recombinator to AMS, this one is simple to set up and align, because of the separated functions of the vertically focussing electric slot lenses and horizontally focussing dipole magnets. The tilt of the horizontal focal plane with respect to the plane of symmetry, due to second order aberrations, is partially corrected by concave exit faces of the magnet poles. As a result, the emerging isotopes should diverge by no more than 3.7 milliradians, which is within the acceptance of the accelerator. The four 45° magnets which make up the spectrometer have 260 mm bending radii for

This work is supported by National Science Foundation Grant OCE-8802509
0-7803-0135-8/91$01.00 ©IEEE

mass 13, 50 mm apertures and normal entrance and exit angles. The two slot lenses operate at 20 kV and cause a vertical cross-over at the center of the system. They also incorporate vertical steerers. The horizontal separation of the three parallel beams in the mirror plane of the recombinator is 19 mm. An aperture plate at this location removes mass 15 (NH^-) and higher masses. There are no defining apertures for mass 12, 13 and 14. A chopper wheel was introduced at this location to attenuate the mass 12 beam by a factor of 85, which makes it approximately equal in intensity to the mass 13 beam. Faraday cups are inserted to measure the mass 12 in the mirror plane, and at the entrance lens to the accelerator. Insertable flags can block the mass 13 and 14 beams for testing purposes.

III. PERFORMANCE

A good vacuum in the ion source is necessary for low backgrounds. We use a 400 L/s turbopump which keeps the pressure below 2 x 10-6 Torr. In addition, a 150 L/s turbo is located at the center of the recombinator. A fully loaded target wheel takes at least an hour to outgas. At the exit of the source, total currents of nearly a milliampere are seen. At the center of the recombinator, we typically obtain 40 to 50 microamperes of analyzed mass 12 beam (before attenuation) from our graphite targets, which contain 2 mg of carbon; these beams persist for several hours. (Beams as high as 200 microamperes are possible, with suitable target material.) The beam spots at the center of the recombinator are 3 mm diameter, so the mass resolution is about 15%. At the exit of the recombinator, the beam which is injected into the accelerator contains 35% mass 12 (^{12}C), and 65% mass 13 (^{12}CH, ^{13}C) with a trace of mass 14 ($^{12}CH_2$, ^{13}CH and ^{14}C). The total current at this point is about 2 microamperes. The beam diameter is less than 3mm. Use of the chopper wheel as an attenuator for the ^{12}C beam does not affect the stability of the measured carbon 13/12 ratio, which can be measured to one part in a thousand. With no attenuator, the transmission of a ^{13}C beam switched through the three separate trajectories of the injector showed equal transmission. The first injector has been operational with the rest of the AMS system at Woods Hole since early 1991.

A second injector leg is now under construction, and is expected to be operational in mid-1991. Figure 1 shows the complete dual leg injector. A switching magnet is used to select the injector.

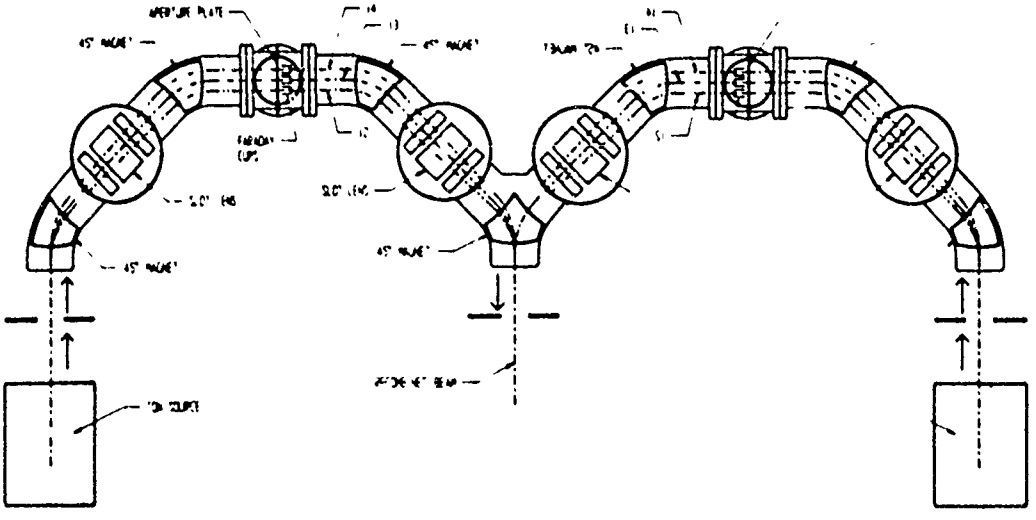


Figure 1. The dual-leg injector, with two recombinators, two ion sources and a switching magnet. The two ion sources are separated by 3.5 meters.

IV. REFERENCES

[1] G.A. Jones, A.P. McNichol, K.F. von Reden and R.J. Schneider, "The National Ocean Sciences AMS Facility at Woods Hole Oceanographic Institution," Nuclear Instruments and Methods in Physics Research, vol.. B52, pp. 278-284, 1990.

[2] K.H. Purser, T.H. Smick and R.K. Purser, "A Precision 14C Accelerator Mass Spectrometer," Nuclear Instruments and Methods in Physics Research, vol.. B52, pp. 263-268, 1990.

[3] A.E. Litherland and L.R. Kilius, "A Recombinator for Radiocarbon Accelerator Mass Spectrometry," Nuclear Instruments and Methods in Physics Research, vol.. B52, pp. 375-377, 1990.

This work is supported by National Science Foundation Grant OCE-8802509

BEAM INDUCED HEATING OF FERRITE MAGNETS*

W.K. van Asselt and Y.Y. Lee
AGS Department, Brookhaven National Laboratory
Upton, NY 11973

ABSTRACT

Alerted by impedance measurements of ferrite kicker magnets[1] and by apparent beam induced pressure increase in the neighborhood of window frame kicker magnets, bench measurements of magnet heating have been done. They confirmed the necessity of interrupting the ferrite yoke. Another method, which can be applied for existing magnets, will be described.

OBSERVATIONS AND MEASUREMENTS

Figure 1 shows a vacuum scan in the AGS at the A-10 straight section, where window frame kicker magnets are located. The scan was taken during a high intensity running period and includes a scheduled maintenance shutdown. The horizontal line indicates the period without circulating beam. At the beginning of that shutdown, it was seen that the vacuum decreases by an order of magnitude and that it increases again when the AGS resumed running. Measurements of beam impedance of ferrite magnets[1] led to the assumption that the ferrite is outgassing due to beam induced heating.

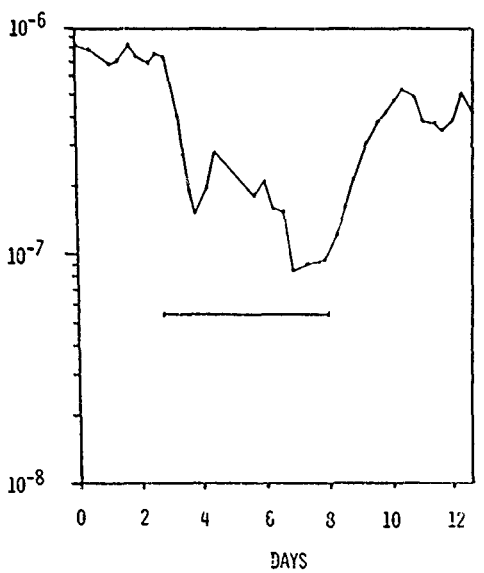


Figure 1. Vacuum scan at A-10 straight section in the AGS ring

To investigate this phenomena further, a bench measurement was set up in which an rf power amplifier (ENI A-500) was used to simulate the beam. Ferrite bricks (C2050), similar to the ones in the kicker magnets, were stacked to form a one-foot long window frame magnet with 8" x 5" outside and 6" x 3" inside dimensions and the power amplifier was connected via a copper rod through the magnet into a dummy load. The transmitted current was monitored with a current transformer. The temperature of the ferrite bricks was measured with thermocouples. Figure 2 shows the temperature of the ferrite as a function of time after the power amplifier was turned on for two different frequencies. The starting temperatures are slightly different, reflecting that the curves were obtained on different days. The heating of the ferrite is seen to increase strongly with frequency. Especially the behavior at the higher frequency explains the observed pressure rise in the vicinity of the kicker magnet in the AGS, since Fourier analysis of the circulating beam shows that all harmonics of the rf frequency show up in the spectra.

The measurements have been repeated for the case in which the ferrite yoke has been interrupted by a 1 mm

*Work performed under the auspices of the U.S. Department of Energy.

0-7803-0135-8/91$01.00 ©IEEE

copper sheet as a diamagnetic barrier in the magnetic path. Even with a current of 3.5 A at 12 MHz through the magnet for many hours, no temperature change of the ferrite has been observed.

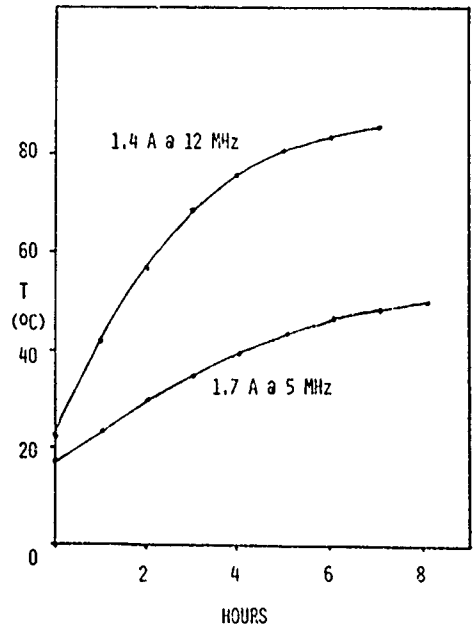


Figure 2. Temperature of ferrite as a function of time at two rf frequencies.

Another way to prevent flux being coupled into the ferrite is to wrap a shorted coil around the ferrite yoke. Such a coil will generate a current such that the next flux remains zero to fulfill the boundary condition, that there cannot be any voltage drop across the short circuit. Actually due to the finite resistance of such a coil, some residual flux may flow. With R the resistance of the coil and L the inductance of the magnet, it can be shown that with a current $I \times \sin(\omega t)$ in the primary winding, the induced current in the coil is within the limit $\omega L \gg R$:

$$I \times [R/\omega L \cos(\omega t) + \sin(\omega t)].$$

For the magnets under investigation, the contribution to the flux due to this effect is negligible.

With a current of 3.5 A at 12 MHz, the experiment was repeated. A temperature increase of 4°C was observed after a period of 8 hours. Apparently some flux leaks around the short circuit. Nevertheless, since the test showed so much improvement and since a shorted coil can be installed so easily on the existing magnets, it was decided to install shorted coils in the symmetry plane of the kicker magnets in the AGS during the summer shutdown of 1989. Figure 3 shows a vacuum scan similar to Figure 1 during the high intensity run following the installation of the shorted coils on the kicker magnets. It is seen that there is still interaction between the beam and the vacuum, but it should be noted that the operating pressure in the AGS improved by an order of magnitude, thereby significantly increasing the sensitivity for outgassing.

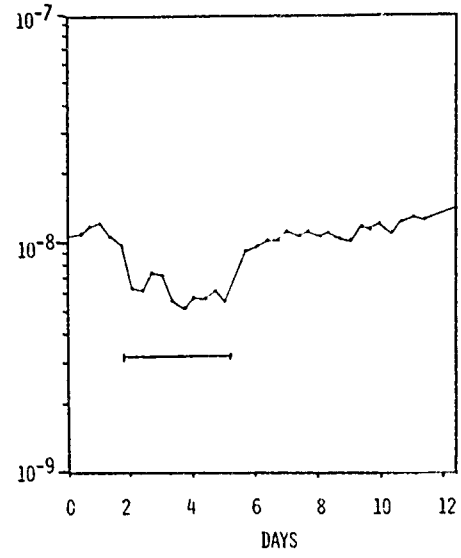


Figure 3. Vacuum scan during high intensity running after installation of shorted turns.

The ferrite (CMD5005), which has been selected for all the fast kicker magnets for the AGS Booster, has good vacuum properties and a high permeability. A sample of the ferrite was

obtained and tested in a similar way. Figure 4 gives the temperature measurement for a current of 1 A at three different frequencies. It is seen that in all three cases, the surface temperature of the ferrite rises to above 120°C, which is so close to the Curie temperature of the ferrite that the magnetic properties of the ferrite will have changed drastically. Although the dimensions of the sample were different, 4" x 4" outside and 2" x 2" inside, the higher permeability leads to an increased sensitivity for induced heating.

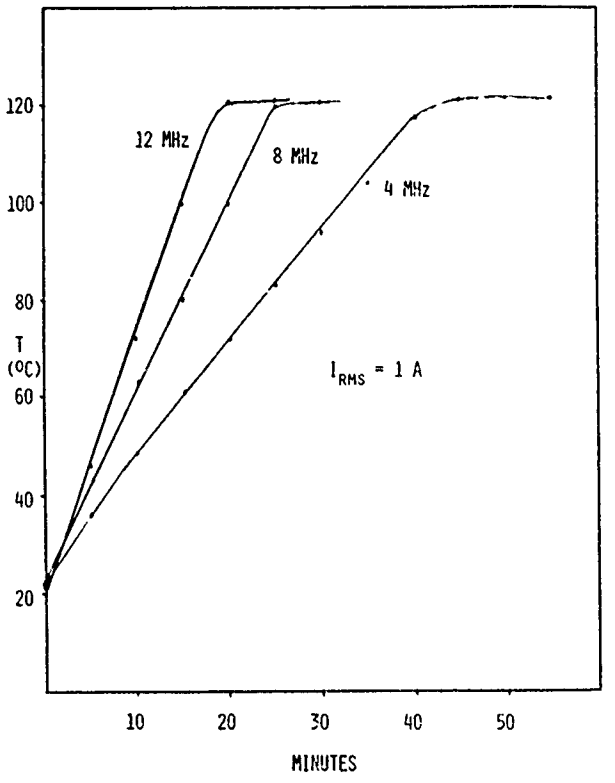


Figure 4. Temperature measurement for a current of 1 A at three different rf frequencies.

With the sample CMD5005 ferrite, the tests with the copper interruption and the shorted coil have been done. With the copper interruption, no temperature rise has been detected with a current of 2 A at 8 MHz during a period of many hours. Under the same conditions, a temperature rise of 1-2 degrees was measured at the end of a 5-hour period for the case of a shorted coil.

CONCLUSIONS

To reduce the impedance to the beam, a diamagnetic barrier in window frame ferrite magnets has proven to be very effective and it is shown that it is necessary for two other reasons; namely, for maintaining the quality of the vacuum and for preserving the magnetic properties of the ferrite.

Equipping window frame magnets with a shorted coil, which can be executed rather easily on existing magnets, has been shown to serve the same purpose, although not as effectively as the diamagnetic barrier.

REFERENCE

[1] F. Voelker, G. Lambertson, Proc. 1989 PAC, p. 851.

On-line Correction of Aberrations in Particle Spectrographs

M. Berz, K. Joh, J. A. Nolen
Department of Physics and Astronomy and
National Superconducting Cyclotron Laboratory,

B. M. Sherrill and A. F. Zeller
National Superconducting Cyclotron Laboratory,
Michigan State University, East Lansing, Mi 48824

Abstract

A new method is presented that allows the reconstruction of trajectories and the on-line correction of residual aberrations that limit the resolution of particle spectrographs. Using a computed or fitted high order transfer map that describes the uncorrected aberrations of the spectrograph under consideration, it is possible to determine a pseudo transfer map that allows the computation of the corrected data of interest as well as the reconstructed trajectories in terms of position measurements in two planes near the focal plane.

The technique is only limited by the accuracy of the position measurements and the accuracy of the transfer map. In practice the method can be expressed as an inversion of a pseudo transfer map and implemented in the differential algebraic framework. The method will be used to correct residual high aberrations in the S800 spectrograph which is under construction at the National Superconducting Cyclotron Laboratory at Michigan State University.

1 Introduction

Efficient modern high-resolution mass spectrographs usually offer rather large phase space acceptances. One such spectrograph is the S800 currently under construction at Michigan State University's National Superconducting Cyclotron Laboratory [1, 2]. Such large acceptance high resolution spectrographs usually require a careful consideration and correction of aberrations. But because of the large phase space acceptance, effects of rather high orders contribute. This makes the correction process often considerably more difficult and complex, and sometimes even prevents a complete correction of aberrations in the conventional sense.

It is often possible to circumvent or at least alleviate these problems by using additional information about the particles. In particular, one often measures not only their final position but also their final angle by means of a second detector. With this additional information it is to some degree possible to retroactively construct the whole trajectory of the particle. This information can be used both for the numerical correction of the quantities of interest, but it also reveals additional properties like the initial angle, which is of course of interest in the study of many nuclear processes.

In the past such trajectory reconstruction techniques were quite involved, often requiring extensive ray tracing and the storage of large arrays of ray data and extensive interpolation. In this paper, we present a rather direct and efficient method based on differential algebraic (DA) techniques.

In recent years we have shown that maps of particle optical systems can be computed to much higher orders than previously possible using DA methods [3, 4, 5, 6]. Furthermore, the techniques also allow the accurate treatment of very complicated fields that can be treated only approximately otherwise. In our particular case, these include the fringe fields of the large aperture magnets required for such particle spectrographs. So for the first time there is now the possibility to really compute all the aberrations that comprise a modern high resolution spectrograph without having to rely on tedious ray tracing.

On the practical side this requires high order codes for the computation of highly accurate maps for realistic fields. The new code COSY INFINITY [7, 8, 9, 10] allows such computations in a very powerful language environment. It also has extensive and general optimization capabilities, supports interactive graphics and provides ample power for customized problems, and it provides all the necessary tools for efficient trajectory reconstruction.

In the next section, we will discuss an important algorithm for this task, the inversion of transfer maps. Section 3 outlines the use of map inversion techniques for the purposes of trajectory reconstruction. Section 4 provides an outlook for the practical application in connection with the S800 spectrograph.

2 Inversion of Transfer Maps

At the core of the operations that follow is the need to invert transfer maps in their DA representation. Though at first glance this appears like a very difficult problem, we will see that indeed there is a rather elegant and closed

*Supported in Part by the U S. National Science Foundation, Grant Number PHY 89-13815
0-7803-0135-8/91$01.00 ©IEEE

algorithm to perform this task.

We begin by splitting the map A_n into its linear and nonlinear parts:

$$A_n = A_{1n} + A_{2n}. \tag{1}$$

Furthermore, we write the sought for inverse as M_n.

$$A^{-1n} = M_n \tag{2}$$

Composing the functions, we obtain

$$\begin{aligned} (A_1 + A_{2n}) \circ M_n &= E_n \Rightarrow \\ A_1 \circ M_n &= E_n - A_{2n} \circ M_n \Rightarrow \\ M_n &= A_1^{-1} \circ (E_n - A_{2n} \circ M_{n-1}). \end{aligned} \tag{3}$$

Here "o" stands for the composition of maps. In the last step use has been made of the fact that knowing M_{n-1} allows us to compute $A_{2n} \circ M_n$. The necessary computation of A_1^{-1} is a linear matrix inversion.

Equation (3) can now be used in a recursive manner to compute the M_i order by order.

3 Trajectory Reconstruction

The result of the computation of the transfer map of the system allows us to relate final quantities to initial quantities and parameters. In our case, the relevant quantities are the positions in x and y directions as well as the measures of slopes p_x/p_0, p_y/p_0 and the energy of the particles under consideration. Usually the initial x, which is determined by the target thickness or a subsequent slit, is kept small to provide a minimal entrance width. So the final positions and slopes are primarily determined by the energy, and to higher orders also by the initial y position and the initial slopes.

In the full transfer map we now set x_i to zero and consider the following submap:

$$\begin{pmatrix} x_f \\ a_f \\ y_f \\ b_f \end{pmatrix} = \mathcal{S} \begin{pmatrix} a_i \\ y_i \\ b_i \\ d \end{pmatrix} \tag{4}$$

This map relates the quantities which can be measured in the two planes to the quantities of interest. The map $\mathcal{S}$ is not a regular transfer map, and in particular its linear part does not have to be a priori invertible. In a well designed particle spectrograph, the linear part has the following form:

$$\begin{pmatrix} x_f \\ a_f \\ y_f \\ b_f \end{pmatrix} = \begin{pmatrix} 0 & 0 & 0 & * \\ * & 0 & 0 & * \\ 0 & * & * & 0 \\ 0 & * & * & 0 \end{pmatrix} \cdot \begin{pmatrix} a_i \\ y_i \\ b_i \\ d_i \end{pmatrix} \tag{5}$$

where a star denotes an entry that is not zero. Since the system is imaging, clearly (x,a) vanishes, and all the other

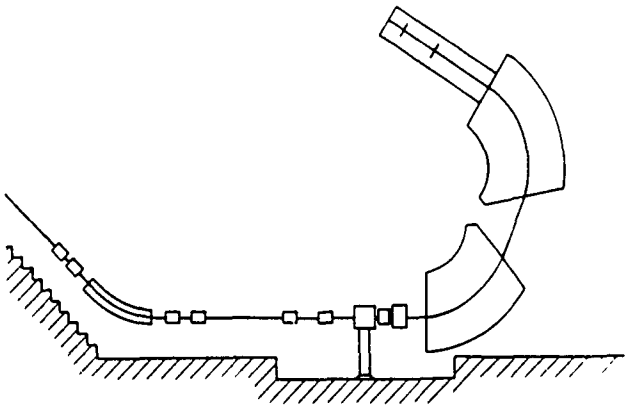


Figure 1: The vertical layout of the S800 spectrograph

zero terms vanish because of midplane symmetry. (x,d) is maximized in spectrograph design, and (a,a) cannot vanish in an imaging system because of symplecticity. In fact, to reduce the effect of the finite size entrance slit, (x,x) is minimized within the constraints, and so (a,a) = 1/(x,x) is also maximized.

Because of symplecticity, (y,y)(b,b)-(y,b)(b,y) = 1, and so we obtain for the total determinant of S:

$$|\mathrm{S}| = (x,d) \cdot (a,a) \neq 0, \tag{6}$$

besides being nonzero, the size of the determinant is also a good measure of the quality of the spectrograph: the larger the better.

So certainly the linear matrix is invertible, and according to the last section, this entails that the whole nonlinear map $\mathcal{S}$ is invertible to arbitrary order, and thus it is possible to compute the initial quantities of interest to arbitrary order.

A closer inspection of the algorithm shows that in each iteration, the result is multiplied by the inverse of the linear matrix S. Since the determinant of this inverse is the inverse of the original determinant and is thus quite small, this entails that the originally large terms in the nonlinear part of the original map are more and more suppressed. So clearly even with trajectory construction, the original investment in the quality of the spectrograph, which is determined by its dispersion and its x demagnification, directly influences the quality of the trajectory reconstruction.

4 The Correction of Aberrations in Spectrographs

The proposed superconducting magnetic spectrograph, the S800 [1] shown in fig. 1, for the National Superconducting Cyclotron Laboratory will allow the study of heavy ion reactions with magnetic rigidities of up to 1.2 GeV/c. It will have an energy resolution of one part in 10000 with a

Table 1: The S800 Spectrograph

Drift	l = 60 cm
Quad	l = 40 cm, G_{max} = 21 T/m , d = .01 m
Drift	l = 20 cm
Quad	l = 40 cm, G_{max} = 6.8 T/m, d = .02 m
Drift	l = 50 cm
Dipole	r = 2.6667 m, $B_{max} = 1.5T$, ϕ = 75 deg, ϵ_1 = 0 deg, ϵ_2 = 30 deg
Drift	l = 140 cm
Dipole	r = 2.6667 m, B_{max} = 1.5T, ϕ = 75 deg, ϵ_1 = 30 deg, ϵ_2 = 0 deg
Drift	l = 257.5 cm

large solid angle of about 20 msr and an energy acceptance of about 10 percent.

The spectrograph will be used in connection with the new K1200 Superconducting Cyclotron for beams of protons up to Uranium with energies of 2 to 200 MeV/u. It will provide unique opportunities for research in various areas, including the study of giant resonances, charge exchange, direct reaction studies and fundamental investigations of nuclear structure [11].

The S800 consists of two superconducting quadrupoles and two 75 degree dipoles with y-focusing edge angles. Table 1 lists the parameters of the system. The settings of the quadrupoles shown here correspond to particles of 193.04 MeV, mass 100 and charge 50. Standard optics notation is used.

After a careful measurement of the crucial fringe fields of the dipoles, we will be using COSY to determine the high order properties of the map of the spectrograph. The computation of the map $\mathcal{S}$ from the resulting transfer map can be performed directly within the COSY environment, and so can the inversion of the map $\mathcal{S}$. Altogether, a correction map $\mathcal{S}$ is found, the nonlinearity of which is determined by the nonlinearity of the original map and the quality in the spectrograph measured by (x,d)/(x,x). It is anticipated that the correction map can be used for an on line determination of the relevant data without having to store the raw two plane position measurements.

In closing we would like to note that the method can also be employed for spectrographs for which no sufficient field measurements are known. To this end, one has to perform experimental ray tracing and fit the resulting data with a polynomial type transfer map. Also in this case, the inversion can be done in the map picture resulting in a rather compact representation of the data necessary for correction.

References

[1] J. Nolen, A.F. Zeller, B. Sherrill, J. C. DeKamp, and J. Yurkon. A proposal for construction of the S800 spectrograph. Technical Report MSUCL-694, National Superconducting Cyclotron Laboratory, 1989.

[2] L. H. Harwood A. F. Zeller, J A. Nolen and E. Kashy. The MSU 1.2 GeV/c spectrograph. In *Workshop on High Resolution, Large Acceptance Spectrometers, ANL/PHY-81-2.* Argonne National Laboratory, 1982.

[3] M. Berz. Arbitrary order description of arbitrary particle optical systems. *Nuclear Instruments and Methods*, A298:426, 1990.

[4] M. Berz. Differential Algebraic description of beam dynamics to very high orders. *Particle Accelerators*, 24:109, 1989.

[5] M. Berz. Differential Algebraic treatment of beam dynamics to very high orders including applications to spacecharge. *AIP Conference Proceedings*, 177 275, 1988.

[6] M. Berz. Differential Algebraic description and analysis of trajectories in vacuum electronic devices including spacecharge effects. *IEEE Transactions on Electron Devices*, 35-11:2002, 1988.

[7] M. Berz. COSY INFINITY Version 3 reference manual. Technical Report MSUCL-751, National Superconducting Cyclotron Laboratory, Michigan State University, East Lansing, MI 48824, 1990.

[8] M. Berz. Computational aspects of design and simulation: COSY INFINITY. *Nuclear Instruments and Methods*, A298:473, 1990.

[9] M. Berz. COSY INFINITY, an arbitrary order general purpose optics code. *Computer Codes and the Linear Accelerator Community*, Los Alamos LA-11857-C.137, 1990.

[10] M. Berz. COSY INFINITY. In *Proceedings 1991 Particle Accelerator Conference*, San Francisco, CA, 1991.

[11] N. Anantaraman and B. Sherrill, Editors. Proceedings of the international conference on heavy ion research with magnetic spectrographs. Technical Report MSUCL-685, National Superconducting Cyclotron Laboratory, 1989.

THE ELETTRA LINAC TO STORAGE RING TRANSFER LINE

D. Einfeld*) and R. Richter**)

*)Fachhochschule Ostfriesland, Constantiaplatz 4, 2970 Emden, FRG
**)Sincrotrone Trieste, Padriciano 99, 34012 Trieste, Italy

ABSTRACT

The injection system for the ELETTRA storage ring is a full energy linac. It will be located underground outside the storage ring so as not to interfere with the experimental area. It will be constructed and operated in two stages: 1.5 GeV (for initial user operation) and 2 GeV (for final operation) with the option of conversion for positrons in a later stage. To obtain a small beam size as well as to implement many of identical elements, the transfer line exist of 4 achromatic arcs, three in the horizontal and one in the vertical direction. The matching between the achromatic arcs is performed with triplet- and FODO-systems. The longest transfer line (1.5 GeV) with a length of 103m needs 30 quadrupoles, 7 bending magnets and 34 steerer magnets. The largest beam size obtained throughout the transfer line is +/- 12 mm for electrons and +/- 17 mm for positrons. To get 95% of particles (2 GeV-positrons) through the transfer line and considering misalignment errors, the aperture of the magnetic elements has to be +/- 25 mm.

I. INTRODUCTION

The injection systems commonly used for second and third generation synchrotron light sources consist of a preaccelerator and a booster synchrotron. At Sincrotrone Trieste, a full energy linac (2 GeV) is now adapted, instead of the previous linac-booster injection system [1], in order to use the linac not only for injection but also for other purposes [1]. The first design of the transfer line [2],[3] was accomplished without any knowledge about the magnets steerers and monitors. Now all these parts are designed and the final structure of the whole transfer line is fixed.

The emittance for the electron beam from the linac is e (1.5 GeV, 80%) = 0.136 pi*mm*mrad and the energy spread is dp/p (1.5 GeV,68%) = 0.735% [4]. This means that the cross section of the beam in the transfer line is mainly given by the energy spread, hence, the deflection of the beam at the different points of the transfer line has to be performed with achromatic arcs. This has to be underlined if a conversation to positrons takes place, because the emittance and the energy spread increase to e (1.5 GeV, 80%) = 2.6 pi*mm*mrad and dp/p (1.5 GeV, 95%) = 1.95 % [5].

According to the design requirements [2],[3], the structure of the transfer line (see figure 1) consists of 4 parts:

1) the linac section between the end of the linac and the point A, where a horizontal deflection of 2p has to be taken to bend the beam to the inner side of the storage ring from which the injection takes place.

2) the horizontal section between the points A and B, with a horizontal deflection angle p at point B to deflect the beam to the storage ring direction.

3) the vertical section between the points B and C where the vertical deflection at the points V and W with a deflection angle p and -p is performed in order to translate the beam to the level and the neighbourhood of the storage ring

4) the injection section between point C and injection point I with a deflection angle p at point C.

II. MAGNETIC STRUCTURE OF TRANSFER LINE

The magnetic structures at points A and B are given by the requirement of an achromatic arc, which consists of two bending magnets (angle p) with a quadrupole in between. For the matching of the beta-functions, 4 quadrupoles are needed between the achromatic arc at point A and the 2 GeV-linac . In order to get small physical dimensions of the magnets, it was choosen to have a high magnetic induction (1.5 T) within the bending magnet and a maximum gradient of 22 T/m within the quadrupole.

The distance between the points A and B in the horizontal section is roughly 40 m. With the conditions at the end and the beginning of the arcs, one has to perform between both points a 1:1 image because in the vertical and horizontal direction the same beta functions exist. The matching can be done with a triplet-, doublet- or FODO-structure [2]. The FODO-structure has the advantage of having the smallest number of quadrupoles, the lowest gradients and the fact that both quadrupoles are identical. The matching to the adjacent achromatic arcs at points A and B can be done with two quadrupoles of opposite sign but with the same excitation. Consequently, for powering the quadrupoles between the points A and B, only two power supplies are needed. To get a higher degree of flexibility three have been taken.
To bridge the space of roughly 33 meters between the 1.5 GeV linac and the achromatic arc at point A in the linac-section, the same FODO-structure is used as in the horizontal one. Hence, identical cells can be used at each side of point A. This means that most of the quadrupoles will have the same excitation and only two power supplies are necessary to power them. This should be very helpful during commissioning.

The vertical section has the task to translate the beam height to the storage ring level. An achromatic arc for this purpose is built up of two magnets, with a deflection angle p each, one to bring the beam up, the other to bend the beam to the storage ring level. In such a structure, one needs at least two quadrupoles between the bending magnets to obtain an achromatic arc [4]. For matching reasons and in order to get a good flexibility, a quadrupole in the middle of the arc has to be added. This quadrupole affects only the beta functions but not the dispersion function.

To decrease the contribution of the energy spread to the beam size, the dispersion function has to be as small as possible. On the other hand, for matching reasons, the beta functions in the vertical and horizontal plane should not exceed 25 m/rad at the ends of the arcs and the difference between both should be as large as possible. These requirements can only be met by using five quadrupoles within the vertical section. These 5 quadrupoles are powered by three power supplies because of the symmetry about the midplane.

To make a dispersion free injection, an achromatic arc between the last bending magnet (point C) and the injection point I has to be build up, too. For the long distance between the bending

0-7803-0135-8/91$01.00 ©IEEE

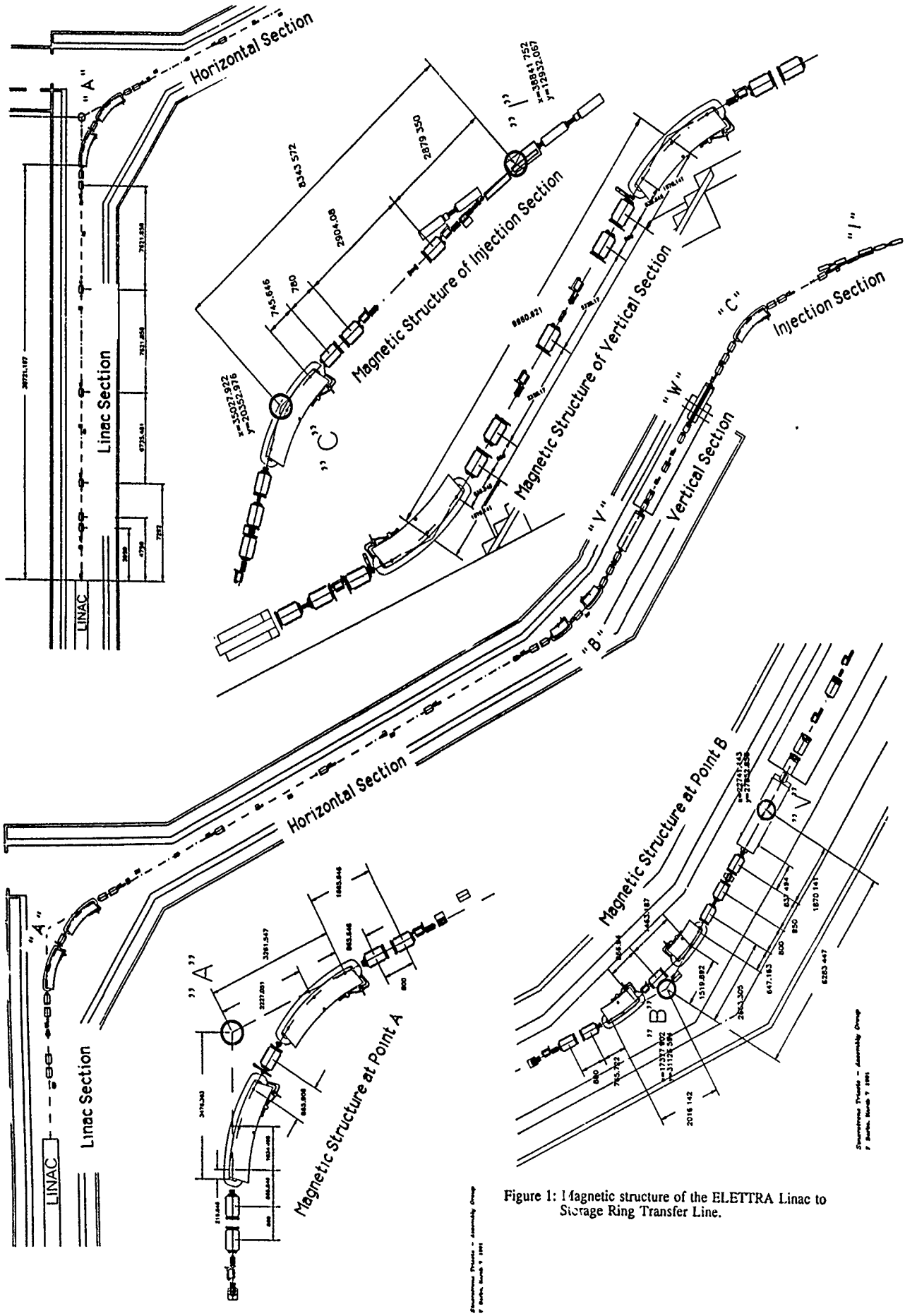


Figure 1: Magnetic structure of the ELETTRA Linac to Storage Ring Transfer Line.

magnet at point C and the injection septum, three quadrupoles are needed. At the end of the transfer line, a matching of the beta functions has to be performed to the values of the storage ring at the injection point. In order to get a smaller bump of the kickers, it might be worthwhile making a matching to bx = 4 m [1]. Furthermore, the injection efficiency is also a function of the injected beam size and, therefore, the injection section of the transfer line must have a high degree of flexibility. Thus, it should be possible to match the phase space of the injected beam in the x- and y-direction to beta values between 2 m/rad and 10 m/rad. To get this high flexibility, one needs at least three quads between the vertical section and the bending magnet at point C and three more quadrupoles between C and injection point I.

The structure of the transfer line is given in figure 1. Considering together all the bending magnets, a total deflection of 180 degree could be performed and with 30 quadrupoles the transfer line has twice as many quadrupoles as in the designed booster synchrotron [1].

III. LATTICE FUNCTIONS AND BEAM SIZES

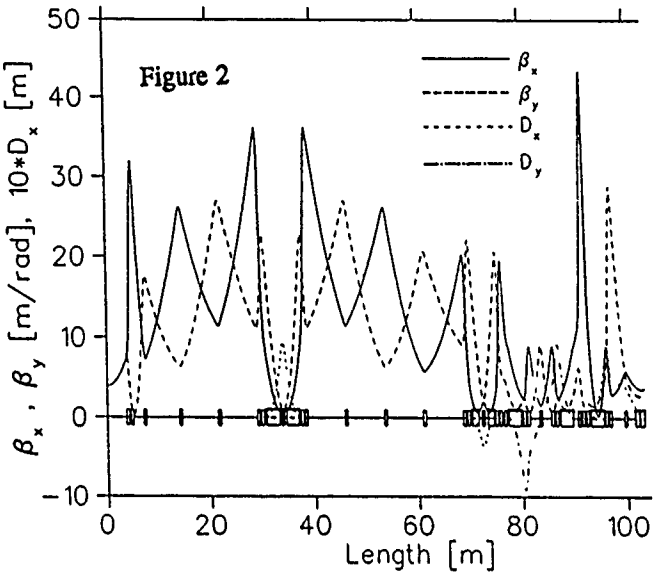
The lattice functions of the whole "ELETTRA Linac to Storage Ring Transfer Line" are given in figure 2. The beam sizes for a 1.5 GeV electron and positron beam (95 % of particles) are given in figure 3 and 4. The largest beta functions in the transfer line are 35 to 45 m/rad; these are relatively small values for a transfer line and, therefore, gradient errors in the quads don't affect the beam sizes very much. The dispersion functions rise in the arc at points A and C as well as in the vertical section to values of 0.8 m.
These large values, in combination with the energy spread, lead to the prominent peaks of the beam envelopes in the transfer line: in the middle of the achromatic arc at point A, in the vertical section at the positions of the quadrupoles and in the injection section at the position of the quadrupole again. According to the particles, there exist beam sizes of 13 to 19 mm at these points. In the other parts of the transfer line, the beam sizes are roughly 2 mm (electrons) and 7-10 mm (positrons). In accordance with these values, an elliptical aperture (20mm * 30mm) at the dispersion region was chosen and a round aperture of 20 mm in the dispersion free regions. With these apertures, and taking into account misalignement errors, it should be possible to get an overall efficiency of 95% within the transfer line.

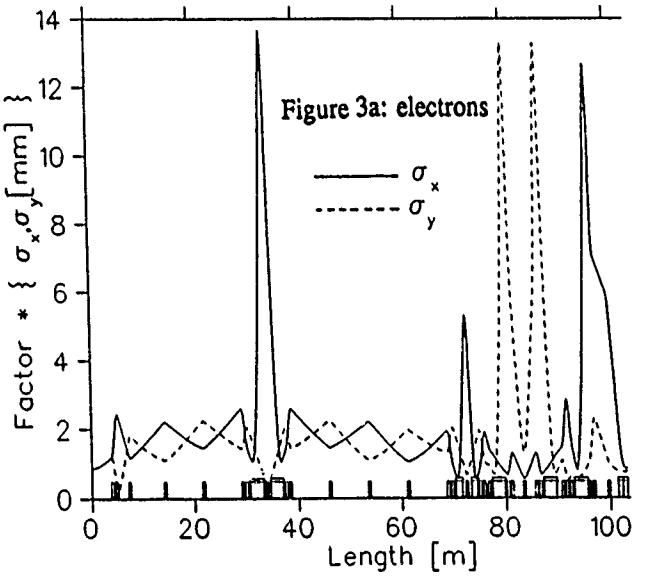
[1] ELETTRA Conceptional Design Report, April 1989
[2] D.Einfeld, 'The Transfer Line from 1.5 GeV Linac to Storage Ring', Sincrotrone Trieste Report: ST/M-90/1
[3] D.Einfeld and F.Iazzourene, 'The ELETTRA Linac to Storage Ring Transfer Line', EPAC 90, Proceedings of the 2nd EUROPEAN PARTICLE ACCELERATOR CONFERENCE, Nice, France, June 1990, pp 1294-1297
[4] G.D.Aurio and A.Massarotti, Private Communication
[5] ESRF Foundation Phase Report, Grenoble, France, 1987
[6] D.Tronc, Private Communication

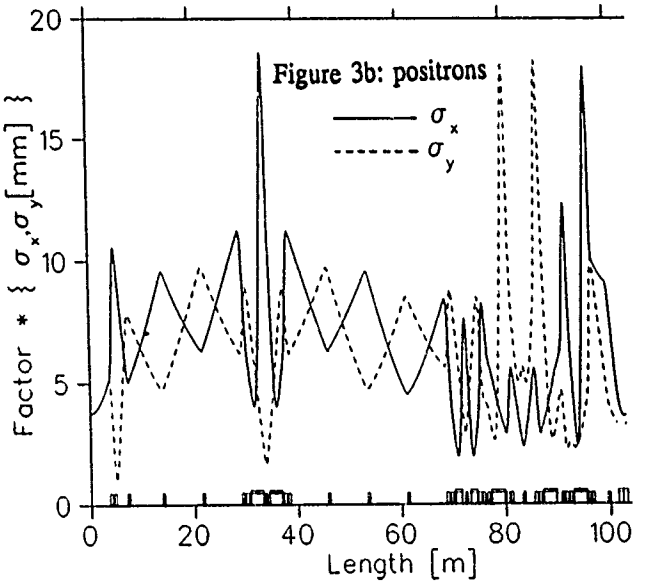
Figure 1: Magnetic structure of the ELETTRA Linac to Storage Ring Transfer Line.

Figure 2: Lattice functions within the ELETTRA Linac to Storage Ring Transfer Line.

Figure 3: Beam sizes within the ELETTRA Linac to Storage Ring Transfer Line for a 1.5 GeV beam and including 95% of particles (3a: electrons, 3b: positrons).







Test and Calibration Beams at the Superconducting Super Collider

Frank Stocker, Howard Fenker, and Ron Schailey
Superconducting Super Collider Laboratory*
2550 Beckleymeade Avenue
Dallas, Texas 75237

Abstract

Development and operation of the research detectors at the Super Collider will require extensive testing and calibration. This will be done by exposing the detector elements to controlled sources of particles similar to those which will be encountered when the experiments are tak..ig data. The SSC Lab is designing a test beam facility to meet the needs of the proposed experiments using beam extracted from one or more of the booster accelerators in the SSC complex. In this report we describe the beam requirements and the transport, targeting, and civil systems needed to provide them.

I. INTRODUCTION

Development and operation of the research detectors at the Super Collider will require extensive testing and on site calibration possibilities over a wide energy range. Todays precision measurments of jets as well as single particles dictates calibration from as low as 1 GeV/c^2 up to the highest possible energies. Such a dynamic range can not be covered by a single test beam. The arrangement of the Medium Energy Booster (MEB) and the High Energy Booster (HEB) of the accelerator complex of the SSC provides a possibility to extract two primary beams of 200 GeV/c and 2 TeV, respectively, and to bring them to a common switchyard as shown in Fig. 1. For financial reasons the 2 TeV beam will be constructed later since it requires an approximately 8000' tunnel to bring it to the location of the MEB closer to the surface, not to speak of the many additional benders and quadrupoles. For the same reason we would build only three of the six forseen 200 GeV beams in a first phase, see Fig. 2. Here we present a study of a possible minimal switchyard for three 200 GeV test beams which has the potential of accomodating a future 2 TeV beam. This layout deviates from earlier scenarios as e.g. described in [1,2]. This design however gives us a measure of our flexibility in test beam

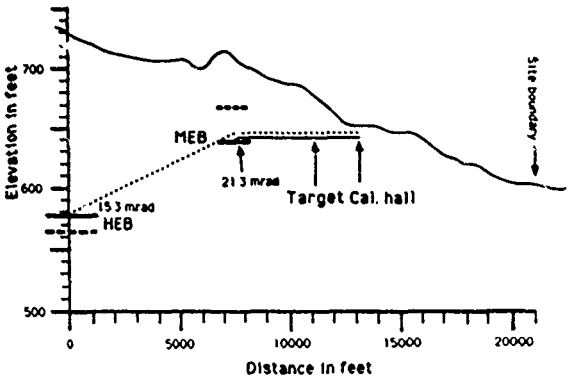


Fig. 1 Elevation View

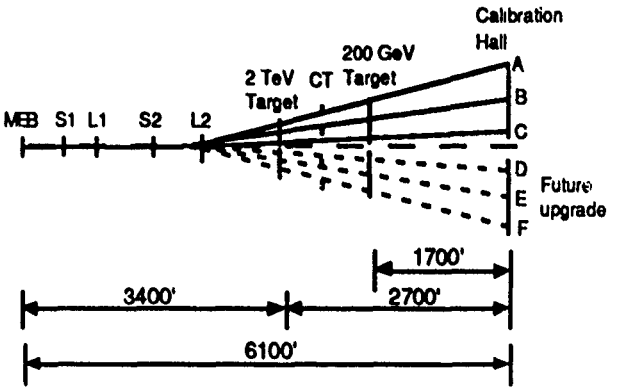


Fig. 2 Test Beam Footprint

geometry. The footprint is so that it may be "duplicated" across the indicated (dashed) symmetry line in Fig. 2 resulting in a total of six 200 GeV beams ond two 2 TeV beams. Dropping one of the planned three 2 TeV beams as in [1,2] reduces the lateral dimensions of the calibration hall and results in major savings of civil construction costs. The 2 TeV beams would lie on top of the middle 200 GeV secondary beams providing the bigger separation of the test stations to cope with the wider muon cone. The presented footprint and layout is only one of several studied scenarios based on the accelerator layout known at that time. The actual layout will emerge as soon as the accelerator elevations and locations will be frozen.

II. LAYOUT

Early in the design it became apparent that the main cost driver is real estate. We therefore tried to minimize the required footage of beamline rather than the number of components like benders and septa. The presented

*Operated by Universities Research Association under contract with the U.S. Department of Energy.

0-7803-0135-8/91$01.00 ©IEEE

switchyard is, however, not the shortest possible one for 200 GeV, but the shortest one which allows for a 2 TeV upgrade. A detailed analysis of the civil construction requirements however dictated a stretch of the primary beamline in order to put the calibration hall as well as the target hall at locations minimizing the large excavations. This layout also optimizes the part of the switchyard which can be constructed by cut and cover rather than by expensive tunneling.

The muon shielding requires a certain minimal distance of the calibration hall from the target. CASIM [3] simulations indicate 1700' for the 200 GeV beam and 2700' for the 2 TeV beam in order to have a maximum muon flux of 150 kHz/m^2 as requested by the experimental community. The target hall however represents an important cost driver and we studied a possible scenario with a common target hall (dubbed "CT" in Fig. 2). This represents a compromise between particle yield at low energy and increased muon background for the 2 TeV running.

The above mentioned muon background also drives the distance between the individual calibation bays in the calibration hall. For 200 GeV this distance becomes smaller than what is required by purely mechanical and practical requirements (approx. 30'). The dimensions of the calibration hall have a great influence on the overall costs. We therefore decided to restrict the number of 2 TeV beams to a maximum of two, one at "B" and "E" (see Fig. 2) respectively (The muon cone for 2 TeV is much wider).

Care was taken during the design of the footprint to group as many beam elements as possible in order to minimize the number of magnet enclosures and to shorten cable runs.

Potential fire hazard and serviceability of the power supplies requires them to be located above ground, rather than in the tunnel. To distribute the power, as well as cooling water to the magnets, a number of utility shafts of 5' diameter is foreseen along the tunnel.

The split ratio is adjusted by physically moving the septa bank through the beam. The ratio is given by the relative amount of beam that lies to either side of the wires. The septa run at 45 kV/cm, some 90% of their maximum field, to allow trouble free operation. Care has to be taken in the design of the beam optics so that the beam is wide at the location of the septa. This prevents damaging of the wires, reduces scattering and facilitates the adjustment of the splitting ratio.

The beam transport is done with quadrupole doublets. Twelve quads are needed to transport the 3 beams and take care of constraints like magnet apertures and beam size at the septa. No quads are placed downstream of the splitting station. This would refocus the beam and therefore cancel the (small) separation.

Fig. 3 shows the beam envelope.

III. SECONDARY BEAMS

A wide band beam approach has been chosen. Such a beam at Fermilab [4] has an excellent electron yield as well as a high hadron flux.

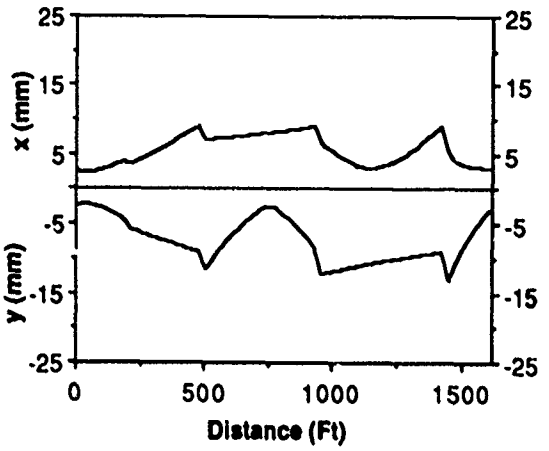


Fig 3 Switchyard Beam Envelope for 200 GeV/c Beam (3 Sigma)

A triplet system a[illegible]s a flux gathering system 150' downstream of the target. It provides a point to parallel imaging. The same enclosure contains the first dipole of the double [illegible]eg system which provides muon shielding from the production target. A bend angle of 6 mr allows for reasonable real [illegible]e and and for good momentum measurement.

Exactly halfway between the target and the calibration hall are the next two magnets of the dogleg structure. The momentum bite and beam intensity may be varied with a variable aperture collimator sitting in the same enclosure.

An enclosure in front of the calibration hall contains the last dog leg magnet and a triplet focusing the beam on the experimental target.

The beam is never momentum dispersed when it passes through a triplet and has, therefore, a large acceptance of about 6 μsr%.

All of the secondary vacuum pipe between the enclosures is direct buried stainless steel pipe of 16" diameter.

IV. YIELDS AND BACKGROUND

Particle yields were determined using parametrizations of Atherton et al. [6] and taking into account the beamline efficiency by using DECAY TURTLE [5]. Fig. 4 shows expected pion rates for 1E11 incident protons assuming a 1

interaction length Be target. The required rates are easily reached for most of the momenta except for the lowest ones where decay in the secondary beam line introduces a cutoff.Below 3 GeV/c, it is difficult to achieve rates of 100 Hz.

The muon contamination of the pion beam is in the order of 2-3 % over most of the momentum range.

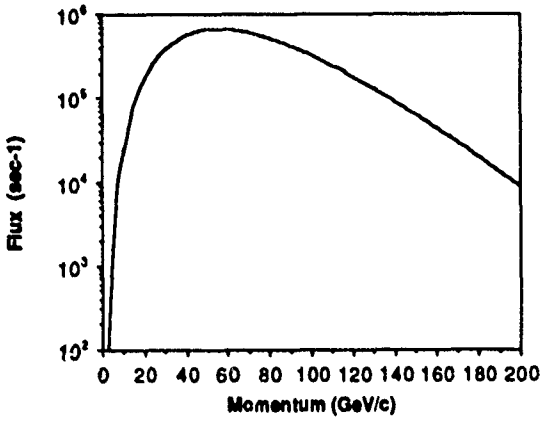


Fig. 4 Pion Rate as a Function of Secondary Momentum, assuming 10^{11} Primary Protons/sec

Electron yields, see Fig. 5, fall sharply for higher momenta. For a primary momentum of 200 GeV/c the rate drops below 100Hz above 150 GeV/c. Should the primary momentum be reduced to eg. 180 GeV/c the rate at 150 GeV would drop to a couple of Hz. This shows the importance of preserving the possibility of ramping the primary beam to 200 GeV/c.

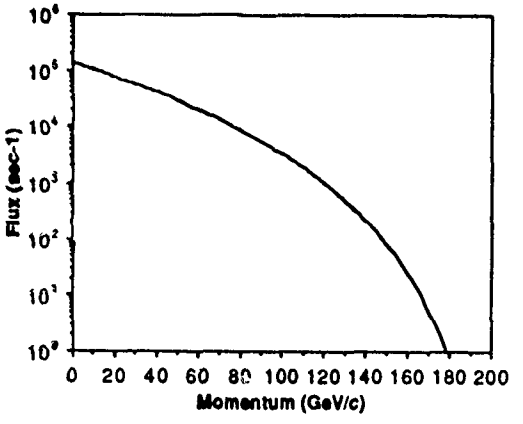


Fig. 5 Electron Rate for 200 GeV/c Protons assuming 10^{11} Primary Protons/sec

The muon background (see Fig. 6) was simulated using CASIM. For the 200 GeV beam the shielding is sufficient to yield approximately 10^4 Hz/m^2. For the 2 TeV beam with a common target hall the shortened secondary beamline results in a flux of over 150 kHz/m^2. The results shown are for the sweeping plane which explains the dip in the curves.

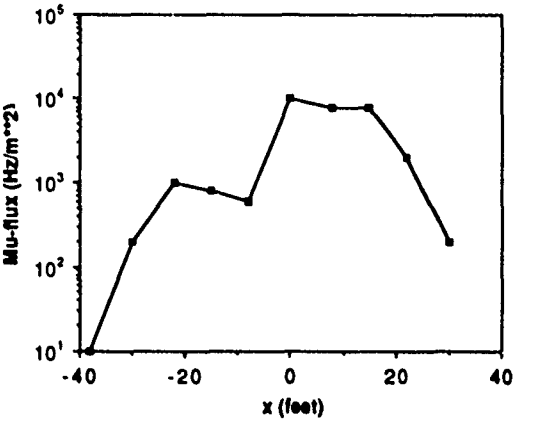


Fig. 6 Muon Flux Density at 1600' from the Target for 10^{11} Protons/sec

We would like to thank R. Stefanski, A. Malensek, J. Bensinger and G. Kalbfleisch for many helpful discussions and J. Bull for providing shielding calculations as well as R. Hoffman for civil construction analysis.

V. REFERENCES

[1] A. Autin et al. , *Calibration Beams at the SSC*, SSC Note SSC-230, 1989.

[2] *Site-Specific Conceptual Design* (SCDR), J. R. Sanford and D. M. Matthews, editors. SSC Report SSCL-SR-1056, 1990.

[3] A. Van Ginneken and M. Awschalom, *High Energy Particle Interactions in Large Targets*. Fermilab Report FN-272, 1975.

[4] J. Butler et al., *Design for a New Wide-Band Neutral Beam for the Tevatron*, Fermilab Report TM-963, April 1980.

[5] K. L. Brown et al., DECAY TURTLE, *A Computer Program for Simulating Charged Particle Beam Transport Systems, Including Decay Calculations*, SLAC Publ. SLAC-246, March 1982.

[6] H. W. Atherton et al., *Precise Measurements of Particle Production by 400 GeV/c Protons on Beryllium Targets*, CERN Note CERN 80-07, 1980.

Upgrade of LAMPF's 750-keV, H^+ Transport

J. W. Hurd, A. A. Browman, K. W. Jones
Los Alamos National Laboratory
Los Alamos, NM 87545

M. J. Jakobson
University of Montana
Missoula, MT 59812

Abstract

The results of the upgrade to the 750-keV H^+ transport at LAMPF are reported. The transport takes the beam from the exit of the 750-kV column to the entrance of the 201-MHz drift tube linac. Components of the transport are used to bunch the beam, to match the beam to the linac, and to adjust the peak current of the beam. The transport is a critical section of LAMPF's accelerator system; a properly tuned and stable beam significantly reduces high-energy losses in the accelerator. The transport was upgraded to decrease the emittance growth of the beam, to facilitate tuning, and to eliminate the time-dependent transients associated with space-charge neutralization of the beam. The new transport was installed and used for beam operations in 1990. The upgrade design goals were successfully achieved. The unnormalized emittance for 95% of the beam was measured at 0.8 π cm-mrad compared with 1.2 π cm-mrad in the previous transport.

I. Introduction

At LAMPF there are three 750-keV transports, one for each of the three types of beams, H^+, H^-, and P^- (polarized protons). These beams are transported from the sources and 750-kV acceleration columns, bunched, merged into one beam line, and matched into the 201-MHz side-coupled linac. This paper describes the successful upgrade of the H^+ transport.

Approximately 30 mA (peak) of H^+ beam from a duo-plasmatron ion source and 750-kV CW is injected into the transport. About 5 mA of H_2^+ and other contaminants are also present. The peak current injected into the linac is adjusted with jaws to be between 14 and 24 mA. In the first rf module, 70% of the beam is captured in the longitudinal bucket and better than 99.9% of the captured beam is accelerated through the rest of the linac to 800 MeV. A good transport tune is needed to achieve the high transmission which is necessary to limit the activation of the linac.

Several features of the transport design help to limit the growth of transverse tails and subsequent beam losses. Design requirements include magnets with small higher-order field harmonics, a transport tune for uniform beam size, and a good match to the linac. Also, the beam size needs to be kept constant in time throughout the 1 millisecond beam pulse, otherwise there will be an effective emittance growth. The new transport addresses these considerations.

II. Details of New Transport

Design Methods

The upgraded transport design is based on measurements of the beam in the previous H^+ transport and the recent upgrade of the 750-keV H^- transport [1]. The transverse phase space distribution of the beam was measured at three locations along the transport using a slit and multi-wire harp. Given this input beam, the match to the linac at the output of the transport, and intermediate constraints on the beam, all the necessary information was available to design the new transport.

The code TRACE was used for first-order modeling of the new transport. The integrating code SCHAR [3,4] was then used to model the beam to all orders for selected cases. The SCHAR studies showed that quadrupoles introduced fewer aberrations than solenoids in the first section of transport, and therefore quadrupoles were used. SCHAR also showed that unacceptably large transverse tails would not be introduced by the new transport.

One point of uncertainty in the design model was space-charge neutralization. Space-charge neutralization is believed to occur in regions of the LAMPF transport and it is suspected to be the cause of observed time-dependent behavior of the beam [5]. The problem is that the degree of neutralization and the region of the transport that is neutralized are not well known. Moreover, it is not clear how measurements of the beam affect neutralization. To overcome these uncertainties, the transport was designed to tune beams with space charge between the two extremes of completely neutralized and unneutralized beam.

Work supported by USDOE Office of Energy Research

0-7803-0135-8/91$01.00 ©IEEE

Transport Configuration

The basic layout of the new transport is shown in Fig. 1. There are three beam diagnostic measurement stations: TAEM1 after the 750-kV column, TAME2 after the pre-buncher, and TDEM1 at the end of the transport before injection into the linac. There are two bends, an 81-degree bend and a 9-degree bend. The 81-degree bend has large dispersion but the energy spread is small, on the order of 500 eV. The energy spread becomes large, on the order of several keV, after the pre-buncher, but the following bend is small, only 9 degrees.

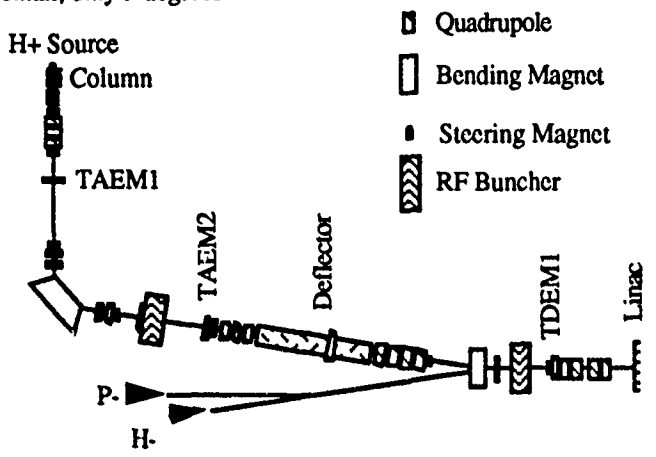


Fig. 1. Basic layout of the new H^+ transport. Also shown are inputs representing the two negative beams, H^- and P^-. The devices labeled with "EM" are slit and multi-wire harp beam diagnostic devices (e.g., TAEM1).

The quadrupoles are configured for the tune shown in Fig. 2. The tune attempts to minimize the peak-to-valley ratio of the beam radius. The previous transport tune had a very small waist in the region of TAEM1 that led to an emittance growth by a factor of about 1.5.

An important feature is the deflector, located near the center of the transport. The deflector is used to control beam injection into the linac. Jaws and apertures upstream of the deflector are used to set the beam current and eliminate unwanted tails.

III. ADVANTAGES OF THE NEW TRANSPORT

Reduced Emittance

The new transport provides a brighter beam with fewer tails so beam losses at higher energies are easier to control and higher peak-current beams can be run. Several factors contribute to the increased brightness. One improvement is the redesigned 750-kV column and the new quadrupole triplet at the exit of the column. The beam out of the previous 750-kV column was large and divergent. The large beam at the exit of the column was focused in the previous transport to a very small waist that resulted in large tails and emittance growth for the space-charge dominated beam. The design of the new transport addresses this problem by shortening the 750-kV accelerating column and by using a set of short, strong field quadrupoles that fit as close by to the exit of the column as possible.

In the previous transport, the beam was turned on into the linac at the same time the source was turned on. Not only was a source turn-on transient observed, but the beam tune in the transport took about 100 μs to stabilize as neutralization occurred in the upstream section of the transport; some linac losses were associated with these transients. The time-dependent transient problem was solved by turning the source on first and allowing the beam to stabilize in the transport, and then turning the beam on into the linac with the deflector [6].

Nonlinear forces due to higher-order fields in transport magnets lead to tails and effective emittance growth. The quadrupole magnets were designed to keep the higher-order harmonics small in the region of the beam. Efforts were made to keep the harmonic amplitudes in the quadrupoles below 0.1% for the n=3, 4, and 5 harmonics, below 0.3% for the n=6 harmonic, and below 0.6% for the n=8 and higher harmonics.

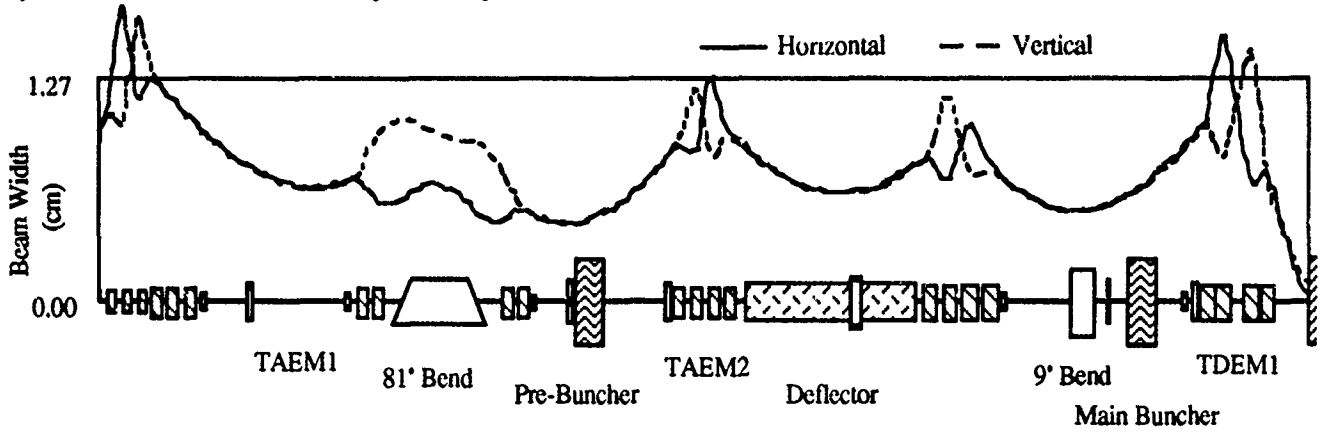


Fig. 2. The horizontal and vertical extent for 95% of the beam is shown for the new transport. Critical facets of the tune are the 0.45-cm waist at the pre-buncher, the relatively small peak-to-valley ratio of the beam envelope though the transport, and the match of the beam to the linac at the end of the transport.

These amplitudes are expressed as a percent of the quadrupole amplitude at a radius of 2.5 cm. For the newly designed, short, strong-field quadrupoles, pole faces were shaped to reduce the n=6 term to 0.7% at 2.5 cm radius.

The present beam has fewer tails and smaller emittance when compared with the previous transport. With the previous transport, the unnormalized transverse emittance of 95% of the beam was approximately 1.2 π cm-mrad. The beam from the new transport has an emittance of 0.8 π cm-mrad and the time-averaged emittance was further reduced by eliminating the time-dependent turn-on transient. The general tune of the linac and the beam losses have qualitatively improved with this improved beam.

Transport Operation

The new design was intended to make the transport easier to tune. This was accomplished by providing an additional slit and multi-wire diagnostic monitor at the front of the transport, by carefully measuring the relation between current and field for all quadrupoles, by using quadruplet assemblies in place of triplets, and ensuring that there were "orthogonal" pairs of steering magnets for steering angle and position at each diagnostic station. The new slit and multi-wired diagnostic station is much closer to the first set of quadrupoles; this makes tuning these elements simpler. Using a quadruplet simplifies the matching problem with four variables (the quadrupole fields) for the four conditions (matching the transverse Twiss parameters). In order to minimize the correction steering needed, pairs of steering magnets were placed such that the steering at a diagnostic station was as independent as possible in position-angle space. This also makes the steering problem easier to solve. Even with orthogonal steering, precise alignment is important in the transport. Steering is only used for small corrections.

Another detail of tuning at LAMPF is the interactive use of the code TRACE. For this model to be usable, it is important to use accurate first-order approximations. These approximations are based on magnet measurements. Quadrupoles were measured with rotating coils [7] and bending magnets were mapped with Hall-probe scans [8].

Once a tune is established for a particular source and current into the accelerator it must be reliably maintained. Typically this can be done by maintaining bending-magnet currents to 0.01%, quadrupole currents to 0.1%, and steering magnet currents to 1%. After a power failure, it is necessary to return the magnetic fields to within these tolerances. This was accomplished in the new transport by the addition of a multiplexed NMR system for the bending magnets and by development of a cycling procedure for the quadrupoles.

IV. FUTURE ENHANCEMENTS

Though the new H^+ transport has been run and is operating well, additional work remains to be done. The transport alignment work is being completed. The last set of quadrupoles common to all three transports has been measured. Measurements indicated much higher than expected components of n=3 at 0.4% of the quadrupole amplitude and n=6 at 3.0% of the quadrupole amplitude at 2.5 cm radius. Tracking studies indicated that these harmonics lead to significant aberrations. New quadrupoles of the standard design are being installed. Other work consists of studies to reduce column arc-downs in the 750-kV column.

Another component in the design stage is an intensity modulator. Beam duty factor could be increased to the H^+ users if an intensity modulator were added to the transport. This device would change the peak intensity in 10-20 μs with minimal change to the beam tune or steering. The physics design for this device is complete and is undergoing engineering review.

V. CONCLUSION

The design goals of the new H^+ transport have been met. The emittance and tails of the beam are reduced. The transport is easier to tune and is more reliable to operate. Standardization has made the transport easier to operate. The troublesome time-dependence has been eliminated by turning the beam on with a deflector downstream of the region where the beam is neutralized.

Further improvements will be achieved by replacement of older style quadrupoles, by alignment of the transport, and possibly by further redesign of the 750-kV column. Higher duty factor could be delivered to the experimenters by installing an intensity modulator, the design of which is currently under review.

VI. REFERENCES

[1] H. S. Butler, A. A. Browman, D. C. Hagerman, and M. J. Jakobson, "New 750 keV H^- Beam Transport Line for LAMPF," IEEE Transactions on Nuclear Science, vol. NS-32, pp. 3086-3088, October 1985.

[2] K. R. Crandall, "TRACE: An Interactive Beam-Transport Program," Los Alamos National Laboratory, LA-5332, UC-28, October 1973.

[3] R. J. Hayden and M. J. Jakobson, "The Space Charge Computer Program SCHAR," IEEE Transactions on Nuclear Science, vol. NS-30, pp. 2540-2542, August 1983.

[4] R. J. Hayden and M. J. Jakobson, "Macrofilament Simulation of High Current Beam Transport," IEEE Transactions on Nuclear Science, vol. NS-32, pp. 2519-2521, October 1985.

[5] J. Hurd and A. Browman, "Transverse Phase Space Time Dependence of LAMPF's High Intensity H^+ Beam," IEEE Transactions on Nuclear Science, vol. NS-28, pp. 2658-2659, June 1981.

[6] J. Hurd, "Solution to the Transverse Phase Space Time Dependence Problem with LAMPF's High Intensity H^+ Beam," IEEE Transactions on Nuclear Science, vol. NS-30, pp. 2487-2488, August 1983.

[7] G. E. Fischer, "Iron Dominated Magnets," in *AIP Conference Proceedings 153, Physics of Particle Accelerators*, New York, 1987, pp.1122-1227.

[8] J. W. Hurd, "Measurement and Resulting First and Second Order Approximations for a 9 Degree Bending Magnet in LAMPF's 750-keV Transport," IEEE Transactions on Nuclear Science, vol. NS-32, pp. 3086-3088, October 1985.

USER CONTROL OF THE PROTON BEAM INJECTION TRAJECTORIES INTO THE AGS BOOSTER

T. D'Ottavio, A. Kponou, A. Luccio, J.G. Alessi, R.K. Reece, J. Skelly
AGS Department, Brookhaven National Laboratory
Upton, NY 11973

INTRODUCTION

The 1.5 GeV(proton) Booster Synchrotron nearing completion at the AGS will get its 200 MeV beam from the linac, via a 34.9 m long linac-to-Booster transport line, LTB. LTB branches off from the existing linac-to-AGS transport line, HEBT, approximately 18.4 m downstream from the linac. A schematic layout of LTB is shown in the bottom part of Fig. 1. The four dipoles, DH2 through DH5, which are identical and are operated in series, provide a 126° bend in the line.

We have employed three strategies for implementing control of the trajectory, namely: (1) a global correction (2) a local correction (3) a zeroing correction. These, as well as their implementation, will be discussed. Operating experience obtained from early commissioning runs will be given.

The hardware used to implement the correction schemes are the beam position monitors, BPMxxx, orbit correctors, DHxxx and DVxxx, and multiwire profile monitors, MWxxx. The quads are QHxxx and QVxxx.

THEORY

Global Orbit Correction

The objective of this scheme is to minimize, in a least squares sense, the displacements from the design trajectory at the position monitors. The beam positions at the monitors are read, and the additional kicks needed at the orbit correctors to give a least squares correction of the trajectory are found. The mathematical treatment[1] is summarized here:

Let x_i(x or y), i = 1,..., m be the displacement at the ith BPM before correction and $T_{ij}\theta_j$ be the displacement of the trajectory at the same BPM due to a kick, θ_j, by corrector j, j = 1,..., n.

$$T_{ij} = \begin{cases} \sqrt{\beta_i\beta_j}\sin(\phi_i - \phi_j), & s_i \geq s_j \\ 0, & s_i \leq s_j \end{cases} \quad (1)$$

where s is distance along the line, β a Twiss function and ϕ the phase advance. Defining a norm

$$S = \Sigma_i\Sigma_j (X_i + T_{ij}\theta_j)^2 \quad (2)$$

then the kicks, θ_j, which minimize the orbit displacements are found by solving the system of equations:

$$\partial S/\partial \theta_j = 0 \quad (3)$$

with the help of the Householder transformation.[2]

This correction may be done on any section of the line, provided it has enough correctors and monitors.

Local Orbit Correction

The purpose of this correction scheme is to find the condition for the beam to pass through the center of a quad, making use of the fact that such a beam suffers no deviation. The scheme requires a corrector upstream of the quad, and a position monitor downstream. We obtain the beam positions for the normal excitation current of the quad, and for two other currents, one higher and one lower. The slope of the curve drawn through these points, in a graph of position versus quad current, measures the deviation due to the quad. Changing the current in the corrector by a small amount and repeating the measurements give data for a second line on the graph. From the corrector current change and the change in slopes of the curves, the current needed to give a line of zero slope (no deviation) is found.

Zeroing

Sometimes, it is desirable to have the beam parallel and on axis at the end of the line segment which has been globally corrected. The zeroing algorithm provides a way to do this. After the global correction has been executed, the last two position monitors in the line segment are read, and the additional kicks in two correctors upstream of them, necessary to bring the beam on axis, are calculated. Zeroing can be used even if the global correction was not executed.

If x_{m-1} and x_md are the orbit displacements at the (m-1)th and mth BPM's, the kicks, θ_{n-1} and θ_n, in the last two correctors are given by:

$$\theta = -T^{-1}\bar{X} \quad (4)$$

* Work performed under the auspices of the U.S. Department of Energy.

0-7803-0135-8/91$01.00 ©IEEE

where T is the response matrix defined in Eq. (1). With small variations, the zeroing algorithm also allows one to bring the beam to a given non-zero displacement and angle at a chosen point along the line.

The data required in Eq. (1) are obtained from MAD[3] for a run with the MAD model of LTB. MAD must be rerun whenever the tune of the quads in the line is changed.

SIMULATION

The first and third correction schemes were extensively tested in simulations on the Apollo Domain network used to control the Booster and its beam transfer lines. Distorted orbits were generated by small random misalignments of all the magnets in the line.

IMPLEMENTATION

Hardware/Software Environment

The LTB Steering software is currently being used on a Hewlett Packard/Apollo 4500 workstation running the Apollo Domain operating system. The software was developed using the C++ programming language and uses the Apollo Dialogue graphical user interface (GUI). User interaction is through a GUI library developed in-house.

Setpoint selection and data transmission from magnets and instrumentation occurs through a hierarchical communications pathway. A Device (a magnet, for example) transmits its data (its current and status) to a Controller, which also collects data from many other Devices. The Controller is periodically scanned for its data by a Station. The Station acts as a final collector of data from its set of Controllers before data are sent across a local area network (LAN) to a Host. The Host takes the data off the LAN and sends it to its clients (the application software). A schematic representation of the basic architecture is shown in Fig. 3.

Program Flow

On entering the LTB Steering program, the user selects a correction method (global or local), a plane (horizontal or vertical) and a section or set of sections within the LTB line where the program will be focused. Initial magnet settings can be set through menu items within the program or through a companion instrumentation program. The user can also ask for the collection of data from one or both multiwire profile monitors in the LTB line, as well as from the seven BPMs. The centroids of the profiles are then used as additional position measurements within the correction algorithms.

Global

To run the global correction algorithm, the user first chooses the menu item which collects the necessary data. This includes the current set of corrector values and positions. In addition, the computer checks quad settings and, if changed, reruns MAD and computes a new response matrix, T_{ij} above. Once the algorithm is run, the program displays both the current corrector and position values and the corresponding values predicted by the global algorithm. The user then has the option of sending these predicted corrector settings to the magnets after which a new set of corrector and position measurements are obtained and displayed. The final display shows position and corrector setting plots using old, predicted and new values. The user can undo these new corrector settings through a menu option.

Local

To begin the local correction algorithm the user selects a corrector, a quadrupole, and a position monitor. The user can then change the corrector and quadrupole step sizes, if desired, from their default values. Selecting the menu item to run the local correction algorithm then causes the computer to vary the quadrupole and corrector by their respective step sizes while collecting a new position measurement after each change. The results are plotted on the screen, and the slopes of the two curves are used to determine the corrector setting which would cause a similar dataset to have a zero slope. If the user chooses to use the newly calculated corrector setting, new position measurements for the entire line are collected and displayed. As with the global implementation, the user can rollback to the original corrector setting.

CONCLUSIONS

The steering algorithms applied to our earlier tests of the proton injection line into the Booster proved flexible and useful to allow for a clear transport of the beam along the line. Figures 1 and 2 show the results of the global and local orbit correction in the LTB line. The experience will be important to implement similar methods for correcting the orbits in the Booster Synchrotron Ring and in the other transfer lines.

REFERENCES

1. F.Z. Khiari and A.U. Luccio, private communication.
2. A SLATEC routine. See also, W.H. Press et al., Numerical Recipes, Cambridge University Press, 1988, pp. 59.
3. F.C. Iselin and J. Niederer, the MAD Program, Version 7.2, CERN/LEP-TH/88-38.

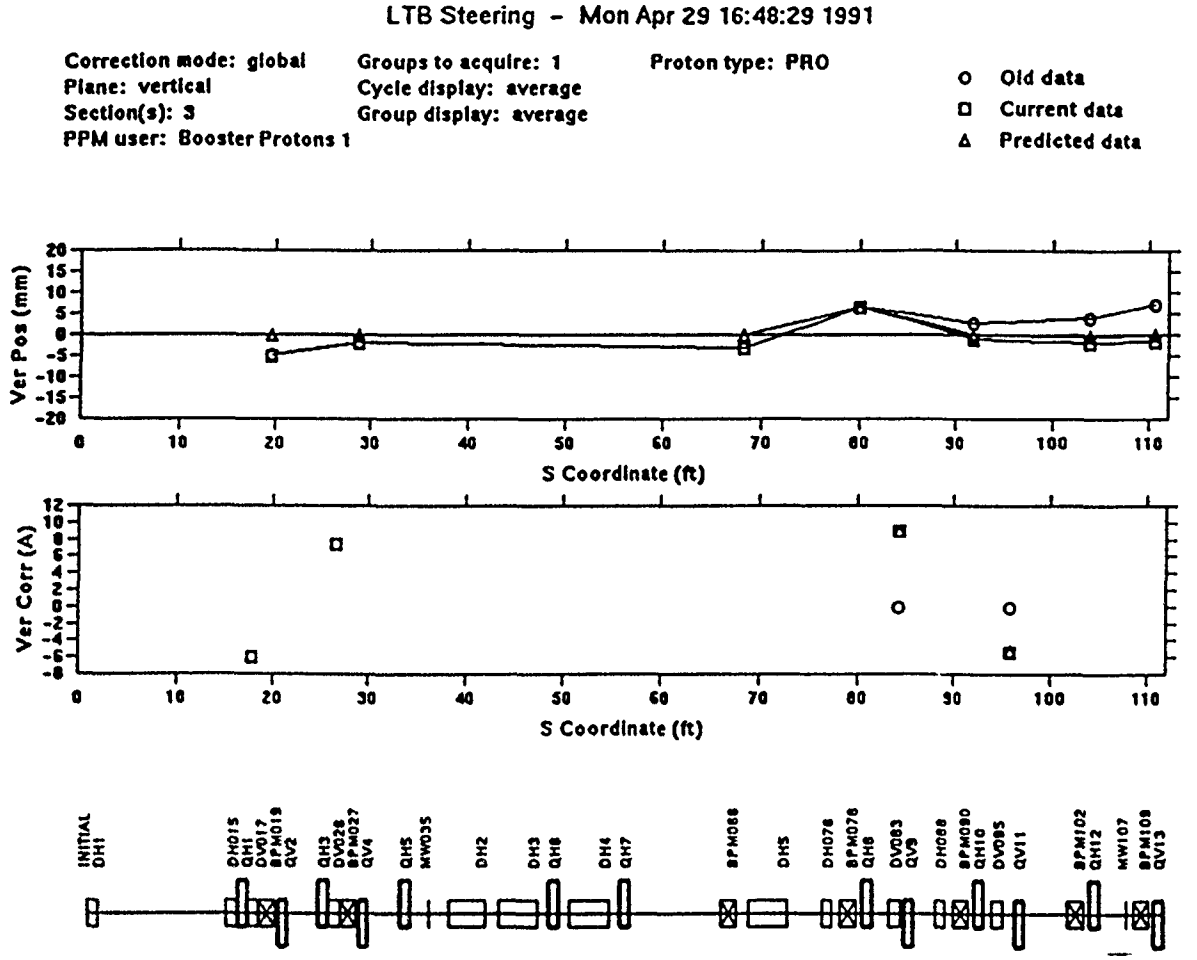


Fig. 1. Global steering algorithm in the LTB-vertical plane.

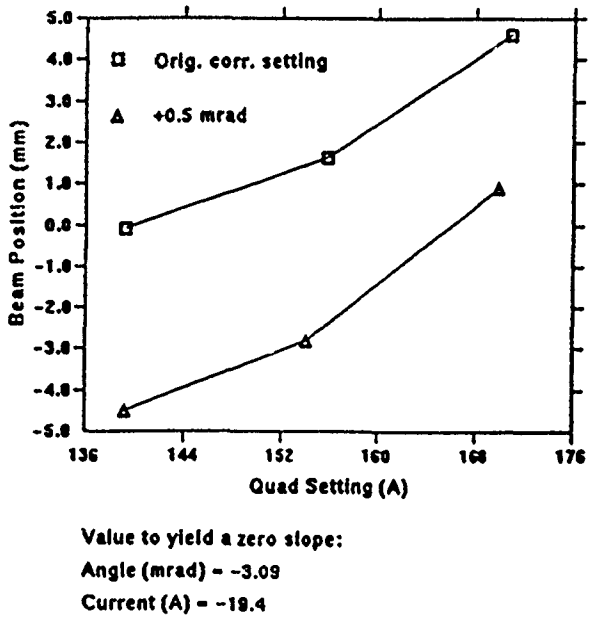


Fig. 2. Local steering algorithm in the LTB.

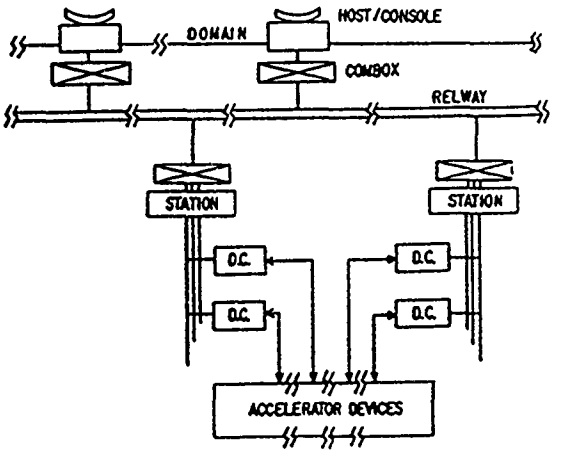


Fig. 3. Hardware/software environment.

Zero-Degree Injection Line for PILAC, the Proposed Los Alamos Pion Linac*

Barbara Blind
AT-3, MS H811
Los Alamos National Laboratory
Los Alamos, NM 87545

Abstract

In this paper, an optimized injection line for PILAC [1], the proposed Los Alamos Pion Linac, is presented. With the other optimized components (pion source, accelerator, and high-resolution beamline and spectrometer), the system is capable of delivering 10^9 920-MeV pions per second to the target.

I. INTRODUCTION

The injection line transports beam from the pion source to the accelerator. The requirements for this line are discussed and its properties are described. Issues concerning the linear transport are touched upon, but the emphasis is on the tuning process for the nonlinear elements used for aberration correction. The beam-optics code MARYLIE [2] was used for all nonlinear optimizations and to evaluate the performance of the line. The line was optimized for 380-MeV pions (peak of pion production) but, in accordance with specifications, can transport pions of up to 530 MeV.

II. REQUIREMENTS

A. Geometry

The line must be as short as possible. After 20 m, half of the 380-MeV pions will have decayed. There must be sufficiently long drifts to place radiation shielding for the magnetic elements. Pion production is peaked in the forward direction, favoring a zero-degree injection system. Consequently, the line must feature a bend to subsequently separate pions from protons.

B. Matching

The line must provide a transverse and longitudinal match between source and accelerator. Transversely, the small-size, high-divergence beam from the pion source (in TRANSPORT [3] notation described by $x = 0.45$ cm, $x' = 50$ mrad, $r_{12} = 0$, $y = 0.45$ cm, $y' = 50$ mrad, $r_{34} = 0$) must be matched to the accelerator acceptance ($x = 3.845$ cm, $x' = 6.479$ mrad, $r_{12} = -0.429$, $y = 5.631$ cm, $y' = 6.924$ mrad, $r_{34} = -0.817$). Longitudinally, an upright beam covering ± 45 psec and ± 16 MeV at the pion source ($s = 1.3$ cm, $\delta p/p_o = 3.32\%$) is accepted by the accelerator, provided the beam correlation is that which would be seen after traversal of an 11-m drift.

*Work supported by Los Alamos National Laboratory Institutional Supporting Research, under the auspices of the US Department of Energy.

0-7803-0135-8/91$01.00 ©IEEE

C. Aberration Correction

The line must have a layout conducive to placement of nonlinear elements. Because both the transverse emittance and the momentum bite of the beam transported by the line are large (22.5 π-cm-mrad and $\pm 3.32\%$, respectively), the beam will be severely degraded by both chromatic and geometric aberrations unless sextupoles and octupoles are added to cancel the most detrimental of these aberrations.

III. PROPERTIES

The injection line has a length of 20.083 m and consists of a matching section followed by a 90° bend (Fig. 1).

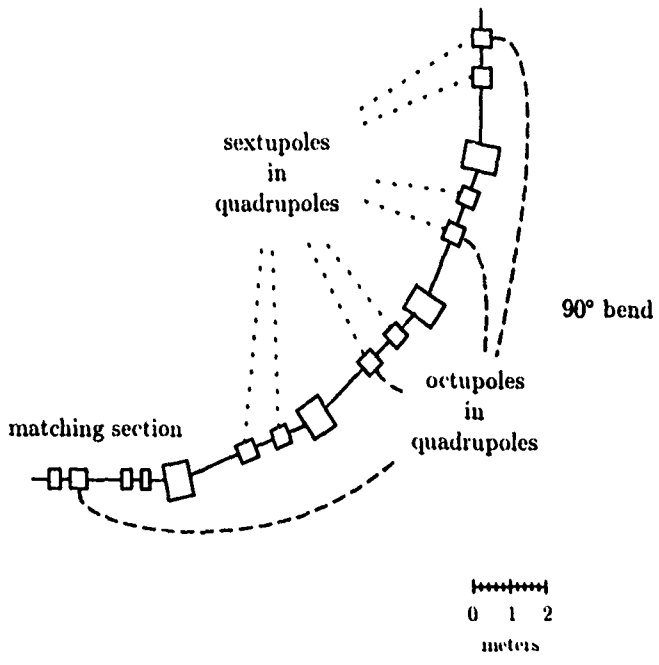


Figure 1. Layout of the PILAC zero-degree injection line.

The four-quadrupole matching section provides the proper transverse match between pion source and accelerator in the tightest possible configuration. The first doublet consists of two strong focusing elements. It represents a compromise between compactness of design (component spacing and dimensions) and pole-tip field strength. Strong focusing as close as possible to the pion source minimizes both chromatic and geometric aberrations. However, a 0.5-m drift between the pion source and the first quadrupole is needed for radiation shielding.

The 90° bend has the component layout and first-order focus of a second-order achromat [4]; its transverse transfer

matrix is the unit matrix. Because the accelerator input beam transports well through the bend, it is possible to perform the transverse matching entirely upstream of the bend. The beam size in the bend is largely governed by dispersion. An FD lattice has a noticeably smaller dispersion than a DF lattice of the same geometry. For FD lattices, varying the dipole edge angles has an insignificant effect. Consequently, parallel-pole-face dipoles were assumed. A bend angle per dipole of 22.5° results in an equivalent drift for the line of 11.06 m for 380-MeV pions (5.10 m for 530-MeV pions). There is a 1.5-m drift between dipoles and F-quadrupoles to accomplish the separation of pions from protons.

The line features four sextupole pairs and four octupoles to correct the most detrimental chromatic and geometric aberrations. For compactness, the nonlinear elements are placed inside the quadrupoles.

IV. TUNING OF SEXTUPOLES

Sextupoles in the dispersive section of the injection line influence second-order chromatic aberrations. Tuning of these sextupoles to produce a second-order achromat is compared with the tuning of the PILAC injection line, which produces a line with output-beam Twiss parameters $(\beta_x, \alpha_x, \beta_y, \alpha_y)$ that do not linearly depend on momentum. In either case, pairs of sextupoles are placed such that the second-order geometric aberrations caused by individual sextupoles are cancelled. However, cross-coupling of the sextupole pairs generates residual third- and higher-order aberrations.

A. Second-Order Achromat

A second-order achromat consists of four identical cells with 90° phase advance per cell, each containing bending and focusing elements. This automatically leads to a first-order achromat with $R_{16} = 0$ and $R_{26} = 0$. Two families of sextupoles, tuned so that the horizontal and vertical chromaticities are zero, cause all second-order chromatic transfer-matrix elements to vanish except R_{566}, the quadratic dependence of longitudinal position on momentum. The resulting bend is called a second-order achromat.

The matched beam of the bend, when sent through the bend with sextupole families turned off, has output-beam Twiss parameters that do not linearly depend on momentum. However, there are other transverse and longitudinal chromatic aberrations, manifesting themselves, for instance, in the nonzero chromaticities. Beams other than the matched beam have a linear dependence of the output-beam Twiss parameters on momentum, which gets zeroed with the two sextupole families, whose settings are beam independent.

B. Twiss-Parameter-Corrected Injection Line

When a matching section precedes the just-mentioned second-order achromat, the output beam exhibits the chromatic aberrations caused by the quadrupoles in the matching section. One continues to have $R_{166} = R_{266} = 0$ and $R_{516} = R_{526} = 0$, but all other previously zero second-order chromatic transfer-matrix elements are nonzero.

For an output beam intended to match to the transverse acceptance of an accelerator, the quantities that should not exhibit aberrations are the Twiss parameters. Using MARYLIE, the linear dependence of the Twiss parameters on momentum was zeroed for the line using four pairs of sextupoles. The procedure does not work for a line in which the matched beam of the bend goes through the bend.

V. TUNING OF OCTUPOLES

Once the sextupoles are properly tuned, octupoles can be used to correct some of the third-order aberrations. Octupoles in the dispersionless sections of the injection line are used to influence third-order geometric aberrations, and octupoles in the dispersive section to influence third-order chromatic aberrations.

Because there are many nonzero third-order geometric transfer-matrix elements, an informed selection must be made. For a line accomplishing a true point-to-parallel focus, there are three Lie polynomials that, when zeroed, eliminate all third-order geometric aberrations distorting the output beam. The injection-line focus is approximately a point-to-parallel focus. There are only two independent octupole positions in the dispersionless sections of the injection line (as deduced from very large settings when using three octupoles to zero all three Lie polynomials). The third-order geometric aberrations of the injection line are caused mostly by quadrupole fringe fields, which are treated in MARYLIE in hard-edge approximation. The second quadrupole in the matching section, in which the beam is large vertically, is a major contributor to these aberrations. Thus, two octupoles were used to zero those two Lie polynomials that cause aberrations in the vertical phase space.

Two octupoles in the dispersive section of the injection line were used to zero two Lie polynomials that significantly contribute to the dependence of the horizontal particle coordinates on the cube of the momentum.

VI. EVALUATION

To evaluate the design, a beam was transported through the injection line using MARYLIE. An input beam in MARYLIE coordinates was generated. These coordinates are $Z_1 = x$, $Z_2 = p_x/p_o \approx x'$, $Z_3 = y$, $Z_4 = p_y/p_o \approx y'$, $Z_5 = s/\beta$, and, for $\delta p/p_o \ll 1$, $Z_6 \approx -\beta\delta p/p_o$, where p_x and p_y are particle momenta, p_o is the design momentum, and $\beta = v/c$. MARYLIE uses MKSA units. Allowed input-beam coordinates lie inside two-dimensional ellipses in Z_1Z_2 and Z_3Z_4 phase space (specified above) and inside a rectangle with $-0.0135 \leq Z_5 \leq 0.0135$ and $-0.032 \leq Z_6 \leq 0.032$ in Z_5Z_6 phase space. Probabilities were determined assuming a Gaussian distribution in Z_1 and Z_3 (like the pion-producing proton beam, with $Z_1 = 0.0045$ or $Z_3 = 0.0045$ corresponding to 2σ) and a uniform distribution in Z_2, Z_4, Z_5, and Z_6. A pion was

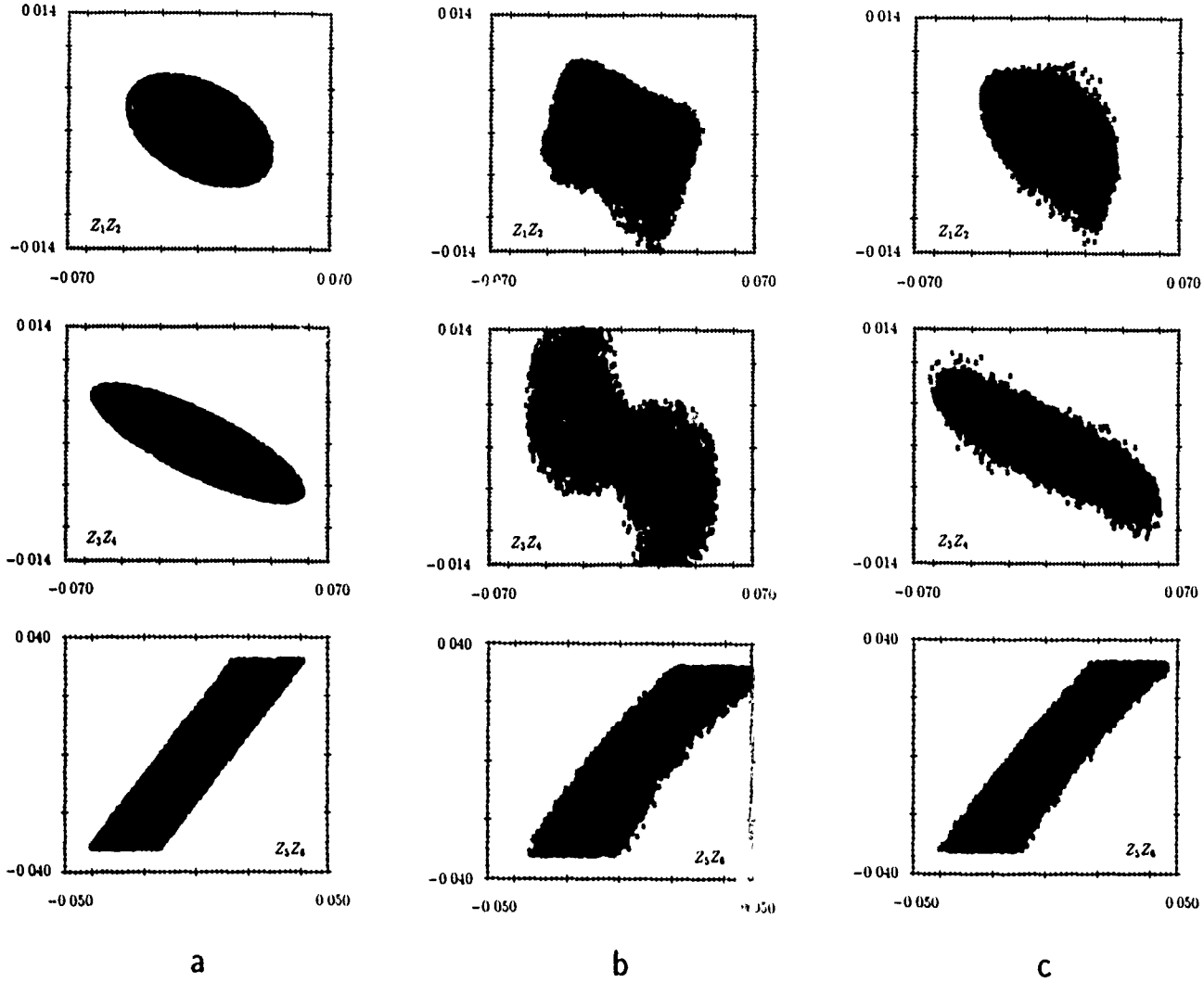


Figure 2. Transverse and longitudinal phase-space projections of the output beam for the injection line (a) in linear approximation, (b) without nonlinear elements, and (c) with nonlinear elements.

considered captured if its output-beam coordinates lie inside the two-dimensional ellipses defining the transverse acceptance of the accelerator. The longitudinal output-beam coordinates of the pion were not taken into consideration.

For the injection line as described, 82.2% of the pions lie in the transverse acceptance of the accelerator. Only 56.5% of the pions are captured when the nonlinear beamline elements are turned off. Pion decay is not folded into these numbers. Figure 2 shows the Z_1Z_2, Z_3Z_4, and Z_5Z_6 phase-space projections of the output beam for the injection line (a) in linear approximation, (b) without nonlinear elements, and (c) with nonlinear elements. In (b), the butterfly shape characteristic of chromatic aberrations is clearly visible horizontally but is masked vertically by the strong third-order geometric aberrations from quadrupole fringe fields.

VII. ACKNOWLEDGMENTS

The author thanks Karl Brown, especially for pointing out the need for strong focusing close to the pion source, and Filippo Neri for deriving the expressions for the momentum dependence of the output-beam Twiss parameters, for modifying MARYLIE to allow optimizing these quantities, and for participating in countless discussions about MARYLIE and Lie algebra.

VIII. REFERENCES

[1] H. A. Thiessen, "PILAC. A Pion Linac Facility for 1-GeV Pion Physics at LAMPF," this conference.

[2] A. J. Dragt, L. M. Healy, F. Neri, R. D. Ryne, D. R. Douglas, and E. Forest, "MARYLIE 3.0 - A Program for Nonlinear Analysis of Accelerator and Beamline Lattices," *IEEE Trans. Nucl. Sci.* 32(5), 2311 (1985).

[3] K. L. Brown, D. C. Carey, Ch. Iselin, and F. Rothacker, "TRANSPORT, a Computer Program for Designing Charged Particle Beam Transport System," SLAC-91 (1973 rev), NAL-91, and CERN 80-04.

[4] K. L. Brown and R. V. Servranckx, "First- and Second-Order Charged Particle Optics," SLAC-PUB-3381 (July 1984).

The APS Transfer Line from Linac to Injector Synchrotron*

R. K. Koul and E. Crosbie
Argonne National Laboratory
Advanced Photon Source
9700 South Cass Avenue
Argonne, IL 60439

Abstract

The design of the APS transfer line from linac to injector synchrotron has been completed. The details of this transfer line are given below.

This paper describes the low-energy-transfer-line designed for the APS. The low energy transfer line constitutes two transport lines. One of these lines runs from linac to the positron accumulator ring, also called "PAR", and is 23.7138 m long. The second part of the low energy transport line runs from the "PAR" to the injector synchrotron and is about 30.919 m long. The above length includes two quadrupoles, a bend magnet and a septum magnet in the injector synchrotron (see Fig. 1 and Table 2).

The positron bunches of emittance $\epsilon_N = 6.6$ mm-mrad arriving at the end of the linac at 450 MeV have twiss parameters as given by Nassiri [1].

$$\alpha_x = 1.6808,\ \beta_x = 7.2161,\ \alpha_y = -1.77586,\ \beta_y = 6.6888 \quad (1)$$

The transfer line (see also Yoon and Crosbie [2]) from linac to "PAR" is made up of ten quadrupoles and one bending magnet B4 (see Fig. 1). The bending magnet bends the beam by 0.2 radians towards the septum magnet in the "PAR". The five quadrupoles in the region between the bend magnet and the septum magnet in the "PAR" give a phase shift of 2π radians, in order to get dispersion free bunch at the end of the septum magnet. The twiss parameters at the end of the linac given above are matched with the twiss parameters and the dispersion functions at the end of the septum magnet, in the "PAR" lattice structure. These parameters at the end of the "PAR" septum are given by

$$\alpha_x = -0.94910,\ \beta_x = 2.1261,\ \alpha_y = -0.02429,$$
$$\beta_y = 8.2401,\ \eta_x = 0.0,\ \eta'_x = 0.0 \quad (2)$$

The matching procedure was carried out using computer code "COMFORT". The distance (2.9 m) between the last quadrupole and the septum magnet in the "PAR" is fixed because of the considerations of the available space in that region. The layout of this region of the transfer line is shown in Fig. 1.

Details of the magnet dimensions and their strengths are given in Table 1. The order of the magnets is the order in which they appear in the transfer line as one traverses from the linac to "PAR". The β functions in the horizontal and the vertical plane along with the dispersion function, η, in the horizontal plane are shown in Fig. 2. The maximum β_y is approximately 20 m and occurs at the quadrupole before the bend magnet. The maximum value of the β_x is about 16 m.

In addition to the above elements, the linac to "PAR" part of the low energy transfer line contains eight steering magnets and seven beam position monitors. Of the eight steering magnets four are for steering in the horizontal plane and the remaining four are to be used for steering in the vertical plane. Similarly, out of the seven beam position monitors three are to be used for diagnostics in the horizontal plane and the remaining four for diagnostics in the vertical plane. The relative positions of these steering magnets are also given in Fig. 1. The calculations for the strength and the dimension of these steering magnets was carried out using a computer code locally developed for this purpose. However the code was tested for the calculation of twiss parameters against the "COMFORT" run.

The second part of the low energy transport line carries the positron bunches from the "PAR" septum to the injector synchrotron. Again the energy of the positron bunches is about 450 MeV. This section is made up of two bend magnets (B1 , B2), and eleven quadrupoles joining the "PAR" septum magnet "B3" on the one end and the injector synchrotron septum magnet on the other end. The bend magnet B2 bends the bunch, coming from the "PAR" septum magnet (bend angle of -0.2 radians) through an angle of 0.2 radians. The section between the bend magnet B2 and the septum magnet B3 is the same as the section between the bend magnet B4 and the septum magnet B3. It produces a dispersion free beam in the region between B2 and B1. The next section between bending magnet B2 and the bending magnet B1 has four quadrupoles which can be used as tuning quadrupoles for tuning on to four twiss parameters in the vertical and horizontal direction. The bend magnet B1 bends the beam at an angle of approximately -0.1859 radians towards the injector synchrotron septum. There are two quadrupoles in the section between the bend magnet B1 and the injector synchrotron septum, which are arranged such that the bunches entering the injector synchrotron are dispersion free at the end of the dipole magnet B (see Table 2). The detailed layout can be seen in Fig. 1, and the relative positions, the dimensions and the strengths of the magnets are given in Table 2. The maximum value of the β function from B2 to the injector synchrotron septum is about 26 m. In

*Work supported by U S Department of Energy, Office of Basic Energy Sciences under Contract No. W-31 109-ENG 38.

0-7803-0135-8/91$01.00 ©IEEE

designing the transfer line from the "PAR" to the injector synchrotron, some part of the injector synchrotron is included. The twiss parameters given by the injector synchrotron lattice at the beginning of the drift O1 (see Table 2) are matched with the twiss parameters given at the beginning of the "PAR" septum magnet given above (sign of the α function must be reversed) through the transfer line. Again, the computer code "COMFORT" was used for matching purposes. The twiss parameters at the position O1 are given below. The sign of the α function corresponds to the motion from "PAR" to the injector synchrotron.

$$\alpha_x = 0.4620,\ \beta_x = 2.1724,\ \alpha_y = -2.5084,\ \beta_y = 15.6557 \quad (3)$$

The detailed form of the β_x, β_y and the η_x is given in Fig. 3. In addition to the above components this part of the transfer line contains six steering magnets and seven beam position monitors. Of the six steering magnets, three are used for steering in the horizontal direction and the remaining three in the vertical direction. Similarly, of the seven beam position monitors four are to be used for monitoring the horizontal position and the remaining three for monitoring the vertical position. The maximum $B\ell$ = 0.012 T.m for these steering magnets. These calculations were also carried out using the locally developed code. The details of their positions and other parameters are given in the Table 2.

Table 1
LTOP Parameters

(150 MeV. $B\rho$ = 1.303 T-meter, -Positive K_1 means horizontal defocussing.)
Input Twiss Parameters α_x = 1.6808, β_x = 7.2161, α_y = −1.7336, β_y = 6.6888
Output Twiss Parameters α_x = −0.0919, β_x = 2.1261 α_y = −0.0213 β_y = 8.2101

Element	Length	β or Magnet Strength $K_1 = B\ell/B\rho[m]^{-2}$ $\rho_0[m]$	Theta1	Theta2
DRIFT O1	1.21			
Steering,	0.15	0.15		
DRIFT O1	0.1			
QUAD Q1	0.3	1.32181181		
DRIFT O2	2.75			
QUAD Q2	0.3	-0.75140313		
DRIFT O3	0.1			
Steering,	0.15	0.15		
DRIFT O3	2.65			
QUAD Q3	0.3	1.221 9368		
DRIFT O1	2.01			
BPM,				
DRIFT O1	0.1			
QUAD Q4	0.3	1.22257231		
DRIFT O2	0.1			
Steering,	0.15	0.15		
DRIFT O4	1.7965			
BPM,				
DRIFT O4	0.1			
QUAD Q5	0.3	-1.35660365		
DRIFT O5	0.1			
Steering,	0.15	0.15		
DRIFT O5	0.15			
SEPTUM B2	0.1	0.2	0.1	0.1
DRIFT O2	0.66			
BPM,				
DRIFT O2	0.1			
QUAD Q6	0.2	1.1366.613		
DRIFT O6	0.1			
Steering,	0.15	0.15		
DRIFT O6	0.15			
BPM,				
DRIFT O6	0.1			
QUAD Q10	0.3	1.47 .4221		
DRIFT O6	0.1			
Steering,	0.15	0.15		
DRIFT O6	0.75			
BPM,				
DRIFT O6	0.1			
QUAD Q11	0.3	1.2211		
DRIFT O6	0.1			
Steering,	0.15	0.15		
DRIFT O6	0.75			
BPM,				
DRIFT O6	0.1			
QUAD Q12	0.3	1.61 .4611		
DRIFT O3	0.1			
Steering,	0.15	0.15		
DRIFT O6	0.15			
QUAD Q13	0.3	1.4172 .68		
DRIFT O4	0.2			
BPM,				
DRIFT O4	2.0 7.47			
SEPTUM B3	0.1	0.2	0.1	0.1

REFERENCES

[1] Ali Nassiri, Private communication.

[2] M. Yoon and E. Crosbie, APS note LS-119 (1988).

Table 2
PTOB Paramenters

(150 MeV $B\rho$ = 1.303 T-meter -Positive K_1 means horizontal defocussing.)
Input Twiss Parameters α_x = 1.6808, β_x = 7.2161 α_y = −1.7386, β_y = 6.6888
Output Twiss Parameters α_x = −0.0919, β_x = 2.1261 α_y = −0.0213 β_y = 8.2101

Element	Length	β or Magnet Strength $K_1 = B\ell/B\rho[m]^{-2}$ $\rho_0[m]$	Theta1	Theta2
SEPTUM B3	0.1	-0.2	0.0	0.2
DRIFT O11	2.9065796672			
QUAD Q13	0.3	0.318237169		
DRIFT O13	0.9			
BPM,				
DRIFT O13	0.1			
QUAD Q12	0.3	3.61736031		
DRIFT O12	0.1			
Steering,	0.05	0.21		
DRIFT O12	0.75			
BPM,				
DRIFT O12	0.1			
QUAD Q11	0.3	10.2311		
DRIFT O11	0.1			
Steering,	0.05	0.07		
DRIFT O11	0.75			
BPM,				
DRIFT O11	0.1			
QUAD Q10	0.3	1.87910321		
DRIFT O10	0.1			
Steering,	0.05	0.133		
DRIFT O10	0.75			
BPM,				
DRIFT O10	0.1			
QUAD Q9	0.3	1.13681613		
DRIFT O9	0.1			
Steering,	0.05	0.13		
DRIFT O9	0.75			
SEPTUM B2	0.1	0.2	0.1	0.1
DRIFT 3E	0.50			
BPM,				
DRIFT 3E	0.1			
QUAD Q8	0.3	-2.32101116		
DRIFT 3D	0.60			
QUAD Q7	0.3	2.33313632		
DRIFT 3C	0.87279613			
Steering,	0.05	0.13		
DRIFT 3A	0.1			
QUAD Q6	0.3	-2.31912369		
DRIFT 3B	0.5			
BPM,				
DRIFT 3B	0.10			
QUAD Q5	0.3	2.71335332		
DRIFT 3A	0.1			
Steering,	0.05	0.13		
DRIFT 3A	0.15			
SEPTUM B1	0.1	-0.16336022	0.0293011	0.0293011
DRIFT O1	1.7391501176			
BPM,				
DRIFT O1	0.1			
QUAD Q1	0.30	1.32786361		
DRIFT O6	0.9			
QUAD Q3	0.30	0.87701161		
DRIFT O5	0.9			
	(Inside Booster)	(Inside Booster)		
SEPTUM SEP	0.5	0.26731	0.13377	0.13377
DRIFT O1	1.55			
QUAD Q2	0.30	0.635272		
DRIFT O3	0.3115			
SEPTUM B	3.077	-0.09239676	0.01619989	0.01619989
DRIFT O2	0.3115			
QUAD Q1	0.30	0.710363		
DRIFT O1	1.1			

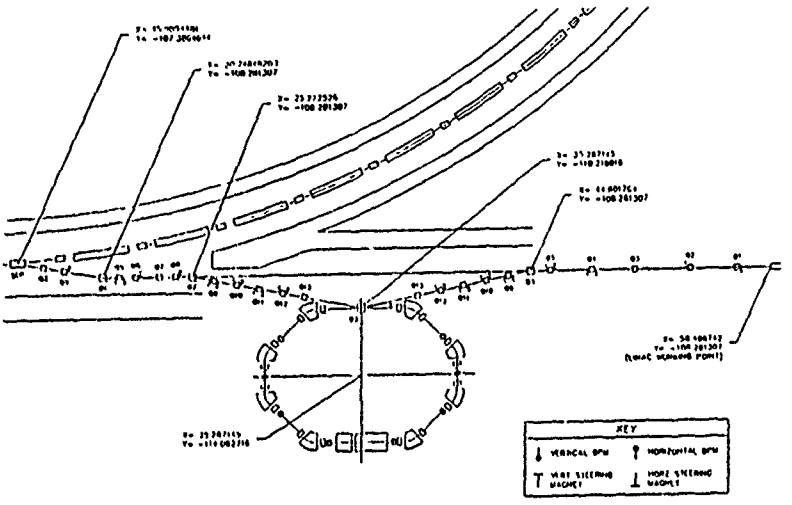


Figure 1. Low Energy Transport Line

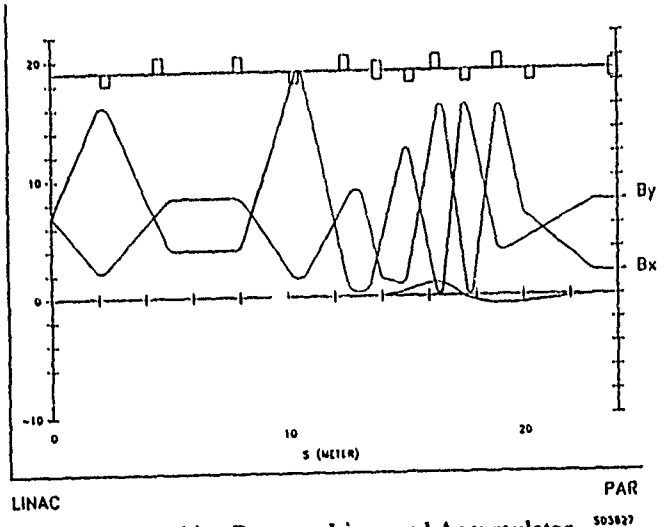


Figure 2. Matching Between Linac and Accumulator

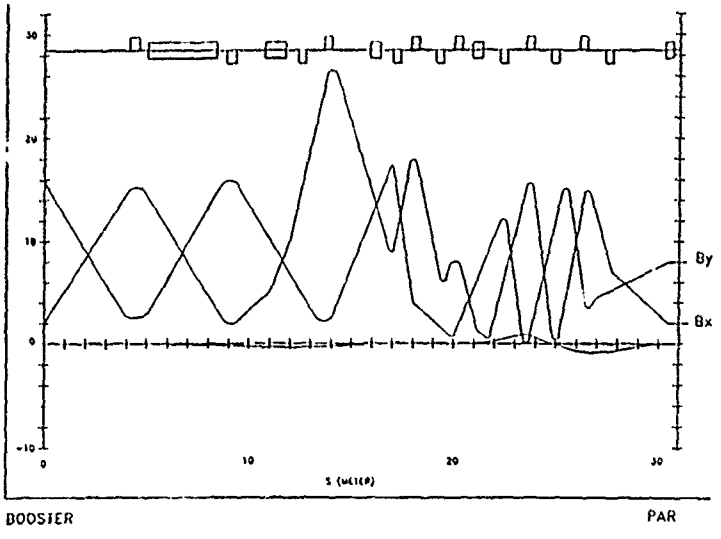


Figure 3. Booster - PAR (PTOB)

Dispersion and Betatron Matching into the Linac

F.-J. Decker, C. Adolphsen, W.J. Corbett, P. Emma,
I. Hsu, H. Moshammer, J.T. Seeman, W.L. Spence,

Stanford Linear Accelerator Center, Stanford, California 94309*

Abstract

In high energy linear colliders, the low emittance beam from a damping ring has to be preserved all the way to the linac, in the linac and to the interaction point. In particular, the Ring-To-Linac (RTL) section of the SLAC Linear Collider (SLC) should provide an exact betatron and dispersion match from the damping ring to the linac. A beam with a non-zero dispersion shows up immediately as an increased emittance, while with a betatron mismatch the beam filaments in the linac. Experimental tests and tuning procedures have shown that the linearized beta matching algorithms are insufficient if the actual transport line has some unknown errors not included in the model. Also, adjusting quadrupole strengths steers the beam if it is offset in the quadrupole magnets. These and other effects have lead to a lengthy tuning process, which in the end improves the matching, but is not optimal. Different ideas will be discussed which should improve this matching procedure and make it a more reliable, faster and simpler process.

1 Theoretical Considerations

A mismatch in betatron functions of the beam (α, β) and the lattice ($\tilde{\alpha}$, $\tilde{\beta}$) and a non-zero dispersion (η or $\eta' \neq 0$) at the beginning of the linac enlarges the effective emittance (ϵ_{eff}). A dispersion η causes different beam positions for different energies $\Delta x = \eta \Delta E/E$. This effect can be estimated by the following example. For an energy spread $\frac{\sigma_E}{E} = \delta \approx 1\%$, a dispersion of $\eta = 10\,\mathrm{mm}$ will lead to an emittance growth of roughly 10% (at a beam size of $\sigma = \sqrt{\epsilon\beta} = 316\,\mu\mathrm{m}$):

$$\epsilon_{eff}\beta = \sigma^2 = \epsilon\beta + \eta^2\delta^2 = (0.1 + 0.01)\,\mathrm{mm}^2, \qquad (1)$$

if there is a similar disturbance in the angular component with η'. Otherwise the full expression has to be recognized:

$$\epsilon_{eff} = \epsilon\sqrt{1 + [\eta^2 + (\beta\eta' + \alpha\eta)^2] < \delta^2 > /(\epsilon\beta)}, \qquad (2)$$

which corresponds to a bigger (and additionally mismatched [1]) ellipse in phase space.

A betatron mismatch has no immediate effect on the emittance, but will increase the emittance by the filamentation of the phase space ellipse induced by an energy spread. This magnification due to the betatron mismatch is given by:

$$\beta_{mag} = \frac{1}{2}\left(\frac{\tilde{\beta}}{\beta} + \frac{\beta}{\tilde{\beta}}\right) + \frac{1}{2}\left(\alpha\sqrt{\frac{\tilde{\beta}}{\beta}} - \tilde{\alpha}\sqrt{\frac{\beta}{\tilde{\beta}}}\right)^2 . \qquad (3)$$

e.g.: $\alpha = \tilde{\alpha} = 0$

$(\beta - \tilde{\beta})/\tilde{\beta}$	$\beta_{mag} - 1$
0.5	0.08
1.0	0.25
2.0	0.67
4.0	1.60
$n > 10$	$\approx n/2$

Fig. 1 shows the beam in real space for β, η-mismatch and also higher order contributions. Besides the theoretical considerations, the observed practical problems during the actual minimization process will be described.

2 Dispersion Match

Although the dispersion adjustment should be performed only after the betatron match is done, it will be described first.

2.1 Measurement

There are two different techniques to determine the influence of the dispersion term:

1. The emittance, determind by wire scanners (or screens), is compared for the two cases: a) with the normal 1% energy spread (compressor in RTL is on) and b) with no energy spread (compressor off).

2. By changing the phase and amplitude of the compressor to provide an acceleration, no acceleration or deceleration, it will lead to an offset Δx at the BPMs (beam position monitors), if dispersion term are present.

Additionally, a skewness in the beam distribution measured by a wire (screen) indicates higher order energy dependencies (T_{166} [4]), which can be determined by the BPM-data: For lower and higher energies Δx has the same sign.

*Work supported by the Department of Energy contract DE-AC03-76SF00515.

0 7803-0135-8/91$01.00 ©IEEE

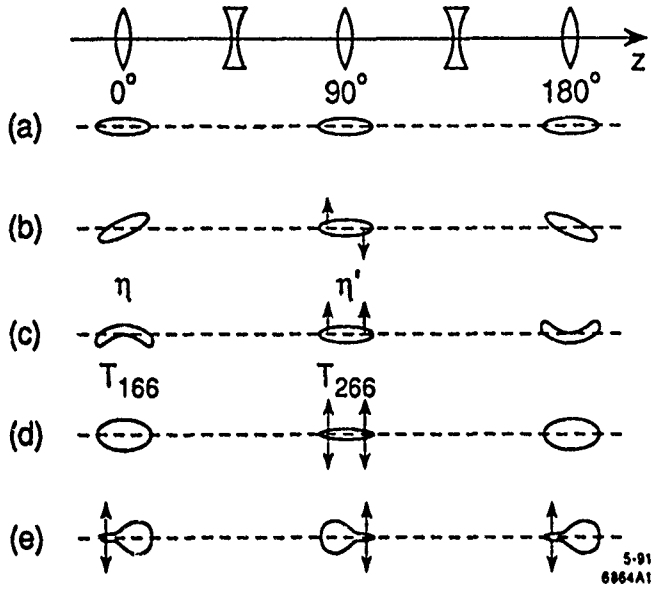


Figure 1: Beam Mismatches.

The beam response in x,z-space is shown for different mismatches. The beam has a longitudinal energy correlation introduced by a compressor and follows a 90° per cell lattice (arrows indicate additional x'): a) Matched beam, b) dispersion in space ($\eta = R_{16}$) and angle ($\eta' = R_{26}$), c) higher order dispersion (or dispersive chromaticity): T_{166}, T_{266}, d) betatron mismatch ($\beta \approx 4\beta$), e) (betatron-) chromaticity is different focusing for different energies and resultant betatron match within the beam for not fully compressed bunches.

2.2 Correction

A combination of quadrupoles (η, η'-knobs) is changed, which should not influence the betatron match. Depending on the measurement techniques either the overall effect is decreased by minimizing the emittance or spot sizes, or the actual dispersion and higher orders are measured and can be compensated by a right amount of the η, η'-knobs and sextupole adjustments. Here some of the main techniques and their advantages are discussed:

1. The emittance is minimized and checked with wires at the beginning (or end) of the linac: The precise measurement leads to a more direct minimization of the important quantity, a residual dispersion may compensate rf-kicks and wakefields.

2. The two-dimensional spots on two screens are minimized by finding two good settings per screen $(\eta, \eta') = (\eta_1, 0)$ and $(0, \eta_1')$ and set to common solution: It is a quick method, but not necessarily the most accurate one.

3. Calculate and/or iterate BPM-data: The dispersion alone is minimized, residuals from rf-kick or wakefields remain. This method gives quantitative results for dispersion and also for higher orders.

For the higher order in dispersion, e.g. the betatron chromaticity, two methods have to be combined: At different energies, set by the compressor, the betatron matching (see below) is measured with the wires.

3 Betatron Match

The twiss parameters α and β of the beam have to be measured and compared to the design $\tilde{\alpha}$, $\tilde{\beta}$.

3.1 Measurement

The measurement is done by either a quadrupole scan or by multiple wire measurements. For the first method, the beam size on a screen or wire is recorded for different quadrupole settings. The second method needs at least three wires (screens), which measure the beam size at different phase advances giving α, β and ϵ (emittance) of the beam [2, 3]. From the mismatch of the beam with respect to the design the beta-magnification β_{mag} (see eq. 3) is calculated.

3.2 Correction

With the known lattice, α and β of the beam can be tracked back to the beginning of the RTL and the corresponding beta-knobs changed by the appropriate amount. Most often the knobs are empirically tuned to minimize β_{mag}.

3.3 Difficulties with Betatron Adjustment

A variety of problems, such as measurement inaccuracies, magnetic hysteresis and RTL focusing errors, makes the minimization of β_{mag} below a value of 1.2 difficult. Some problems, their origin and their effects are summarized below:

1. Measurement error: Wire vibrations, photo multiplier saturation, bad timing of the gate (or nonlinearities of screens) may cause a wrong matching minimum.

2. Hysteresis in magnets: β_x, β_y knobs become nonorthogonal, especially if quadrupole trims have different signs in respect to common power supply.

3. Lattice: (i) Nearly degenerated matching knobs using only four quads require big changes, which steer the beam. (ii) Nonlinear knobs. (iii) Vertical focusing depends on steering through sextupoles.

4. Changing only one quad: Then less change is necessary. The measured hysteresis gap is $\approx 1\,\%$, while a $0.6\,\%$ change gives already $\beta_{mag} = 2$ (see Fig. 2).

5. Not stable over days: With a different steering near the nonlinear septum or a vertical steering, the adjustment changes.

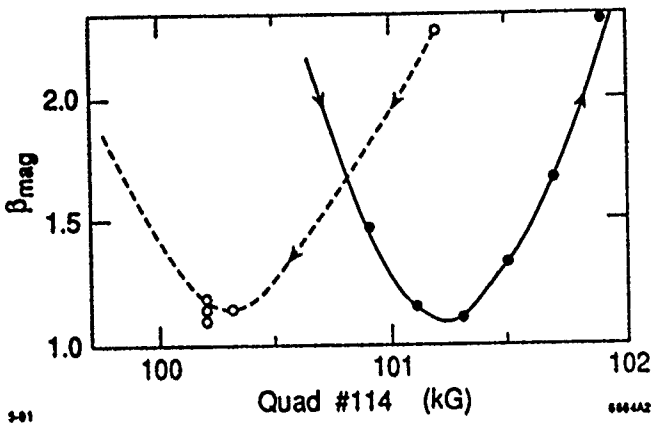


Figure 2: Betatron Match Sensitivity.

Here one of the "matching" quadrupoles (number 114) in the RTL is changed by a few percent. For a 0.4 % change of the magnetic field the betatron magnification (corresponding to an emittance growth after filamentation) is 1.5. The difference going up or down the hysteresis loop (see arrows) is about 1 % in field strength, which makes it difficult to adjust combinations of magnets.

4 Precise Adjustment

It should be mentioned that a coarse adjustment is achieved quite quickly and keeps the emittance blow-up below 30–50 % of the $1.6 \cdot 10^{-5}$ m rad normalized damping ring emittance. A precise adjustment can also be obtained, but usually only in one plane (x or y).

4.1 Adjustment Procedures

Over the years several betatron matching "knobs" have been generated using four matching quadrupoles. They are configured to change orthogonally one component of β_x, α_x, β_y, α_y or more precisely, they control the cosine-like, $\tilde{\beta}/\beta$, and sine-like, $\tilde{\alpha} - \alpha\tilde{\beta}/\beta$, components of a beta-beat.

Historically the first set of knobs failed, since the power supply of one quad couldn't regulate well at the desired low amount. Then a second set was made using a small trim power supply for that quad. The difficulty with these knobs is that small misalignments of the strong matching quads cause a big steering of the beam. A third set uses only one matching quad and three pairs of quads in the dispersive region of the RTL. They require only small changes (less steering), but they have quite a large cross-talk between the x and y plane.

A different technique uses the four matching quads but with dynamic knobs. This means the measured response of the knobs is used to calculate the desired coefficients for the four quads. A potential problem is the hysteresis of the magnets. Another method tries to avoid the hysteresis by calculating the desired change and trimming the magnets to these values after standardization. This requires quite a long time, steers the beam and seems to have a poor convergence.

The simplest way is taking only the most sensitive quad for the desired change and taking care of the normal standardization direction on the hysteresis loop. This is not totally orthogonal and therefore insufficient for a complete betatron match.

4.2 New Ideas

A number of ideas have been generated during discussions, but haven't been tried yet. One is to use more than four quads and minimize the sum of changes to get the desired effect. This would be less degenerat, so less quad changes and therefore less steering will occur. Also the x–y cross-talk might be less, but no hysteresis of the magnets are considered. To avoid hysteresis knobs may be used which always have the quads going in the standardization direction (or against for resetting). A variation might be a knob which brings a quadrupole current (if tweaked against hysteresis) far beyond the required value and then back following the standardization direction (quasi-standardized). Also a different standardization method [5] might be considered, which is insensitive against tweaks around an optimal setting. Together with dynamic knobs, a fast procedure has to be found, since drifts of 20-30 % in emittance over a few days have been observed.

5 Conclusion

Dispersion and betatron matching into the SLC-linac can reduce the emittance growth below about 30 %. For a further reduction, different procedures are needed, which deal with the problems of hysteresis in the magnets, measurement errors, sensitivity of the lattice and long-term stability.

References

[1] N.Merminga, P.L.Morton, J.T.Seeman, W.L.Spence, *Transverse Phase Space in the Presence of Dispersion*, PAC, San Francisco, May 1991.

[2] M.C. Ross, N. Phinney, G. Quickfall, H. Shoaee, J.C. Sheppard, *Automated Emittance Measurement in the SLC*, SLAC-Pub-4278 or PAC, Washington, D.C., March 1987.

[3] M.C. Ross, J.T. Seeman, E. Bong, L. Hendickson, D. McCormick, L. Sanchez, *Wire Scanners for Beam Size and Emittance Measurement at SLC*, PAC, San Francisco, May 1991.

[4] C. Adolphsen, P.J. Emma, T.H. Fieguth, W.L. Spence, *Chromatic Correction in the SLC Bunch Length Compressor*, PAC, San Francisco, May 1991.

[5] F.J. Decker, *The Physical Way of Standardizing Magnets*, PAC, San Francisco, May 1991.

Upgrade of the Main Ring Magnet Power Supply for the KEK 12GeV Proton Synchrotron

H.SATO, T.SUENO, T.TOYAMA, M.MIKAWA and T.TODA
National Laboratory for High Energy Physics, 1-1, Oho, Tsukuba-shi, 305, Japan

and S.MATSUMOTO
Dokkyo University School of Medicine, Mibu-machi, Tochigi, 321-02, Japan.

Introduction

In order to use the slow extracted beam of the PS more effectively, the period of slow extraction has been extended. In this paper, upgrade of the main ring magnet power supply will be described. The main power supply consists of thyrister rectifiers, DC filters, reactive power compensators, AC harmonic filters and control systems. To increase the current capacity during flat top, the rectifiers and transformers were improved. AC network and DC filters were remained as it is, since the acceleration and deceleration times were not varied. Analog control devices and the computer control soft ware have also been improved to realize a 2 sec flat top with a 4 sec repetition rate compared with the former 0.6sec flat top with a 2.5 sec repetition rate.

The magnet power system

The magnet power system consists of magnet power supply (23.6MVA), reactive power compensator systems (20 MVar lag for fundamental) and harmonic filter banks (20 MVar lead). The ring magnet power system has three separated magnet power supplies, one is for the bending magnets and the other two are for the horizontally and vertically focusing quadrupole magnets. The quadrupole magnet currents must be tracked separately to the bending magnet currents for precise tuning of betatron oscillation to perform the optimum beam acceleration.

Desired exciting currents of these magnets are fed by output voltages of power thyristor converters controlled by ignition angles. They are given by analog phase shifters which compare with the reference and the pattern voltages through negative feedback of two loops by a minor automatic voltage regulator (AVR) and by the main automatic current regulator (ACR). These patterns are output to the converters through DAC every 600 Hz synchronized on the six phase ac line by the control computer system.[1] The computer rewrites the control voltage pattern in accordance with measured deviations from the reference current by a repetitive control algorithm.[2] The load parameters of the main magnets and the typical current patterns of the bending magnet are shown in Table 1 and Fig.1, respectively.

In order to suppress the ac line voltage flicker induced by the pulsed lag reactive power of magnet power supply converters, reactive power compensator of thyristor controlled reactor has been equipped of total power of 20MVar.[3] These lag powers are compensated by lead power of the four banks of resonance type harmonic filters [4] (4MVA for third, 4MVA for fifth, 3MVA for seventh and 9MVA for high pass).

The logical ripple components over 300Hz are reduced well by the passive low pass [5] and the dynamic filters.[6] Fig.2 shows a Schematic diagram of the main ring power supply system.

Table 1.The load parameters of the main magnets.

	B Magnets	Q Magnets
Resistance	0.75Ω	0.32Ω
Inductance (at Inj.)	1.1H	0.12H
Time Constant	1.5sec	0.38sec
Injection Current	200A	110A
Flat Top Current	2850A	1600A
Acceleration Time	790msec	
L (dI/dt)	3400V	210V
R x I (at Flat Top)	2100V	510V

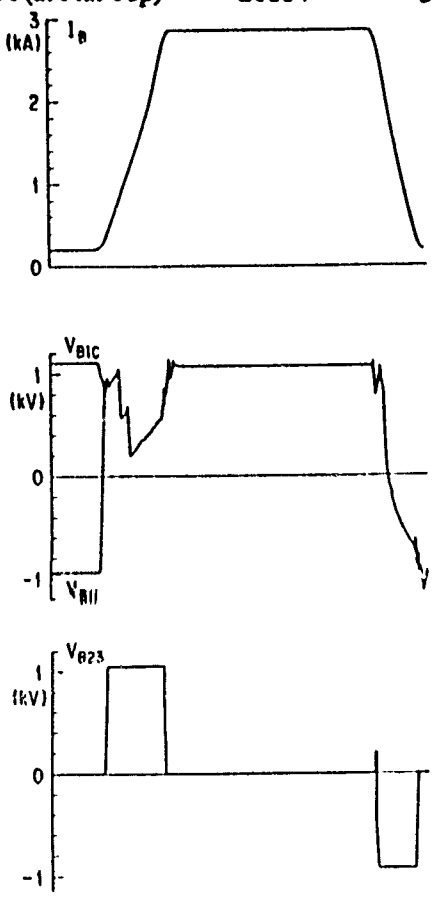


Fig.1 Typical Current and Voltage Patterns of the Bending Magnet at 12 GeV Operation.
Up to bottom; Current, Converter and Inverter Voltage, B23 Converter Voltage.

0-7803-0135-8/91$01.00 ©IEEE

Upgrade of the current capacity

The bending magnets power supply has consisted of six twelve-pulse rectifiers and controlled by six groups of voltage patterns. Each bridge of the B1 group is fired by a converter-inverter operation in order to reduce the direct current ripple component during injection period and further to reduce the ac line flicker.[7] These patterns are also optimized for reactive power and for voltage ripples to be minimized by controlling by-pass thyristors of four group B23 converters. These voltage patterns are also shown in Fig.1.

To increase the current capacity of the B1 group rectifier, B0 is connected in parallel with B1 via interphase reactors and controlled by the same voltage pattern as B1. The transformer banks are connected with 15degree difference resulting in a 24-pulse rectifier. Each bridge of them is also fired by a converter-inverter operation. An allowable current deviation in the interphase reactors between B0 and B1 is designed to be 15%, then the feedback control system as shown in Fig.3 is used to decrease the imbalance current between transformers.

To increase the current capacity of the B23 converters during the by-pass period, new thyristor switches are connected in parallel with the former by-pass thyristor.

Each of the quadrupole magnet power supplies have been controlled by group of the pattern and have been fed by two power transformers.

Control System

Fig. 4 gives a schematic block diagram of the hybrid control system.. The analog system covers the ACR and AVR loop as a real-time negative feed back control to thyristor switching. The control voltage is a sum of the pattern signals AVR and ACR. By a 16-bit DAC, the pattern voltages and current are given for every 12-pulsed thyristor group at the 600 Hz control clock synchronized to the ac-line voltage.

The control computer system consists of the main cpu system HIDIC-V90/25 and input and output controllers HISEC-04M.[8] These control computer systems and operation terminal in the accelerator central control room of are connected by a local area network.

The bending magnet power supply is controlled by six voltage patterns for thyristor converter groups and by the current pattern for the ACR. The quadrupole magnet power supplies also work by the reference voltage to the thyristor group and by the current pattern. These patterns are fed through 16-bit DAC sets by the output controller H-04M.

The input controller as the detector system H-04M logs magnet currents from DCCT and voltages through the sets of 16-bit ADCs at every 600Hz control clock cycle.

For extension of the flat top period, memory and hard disc capacity was increased and reproduce an application soft ware. If the operation will be performed with the long flat top pattern, the control clock is synchronized with 300Hz to save the memory.

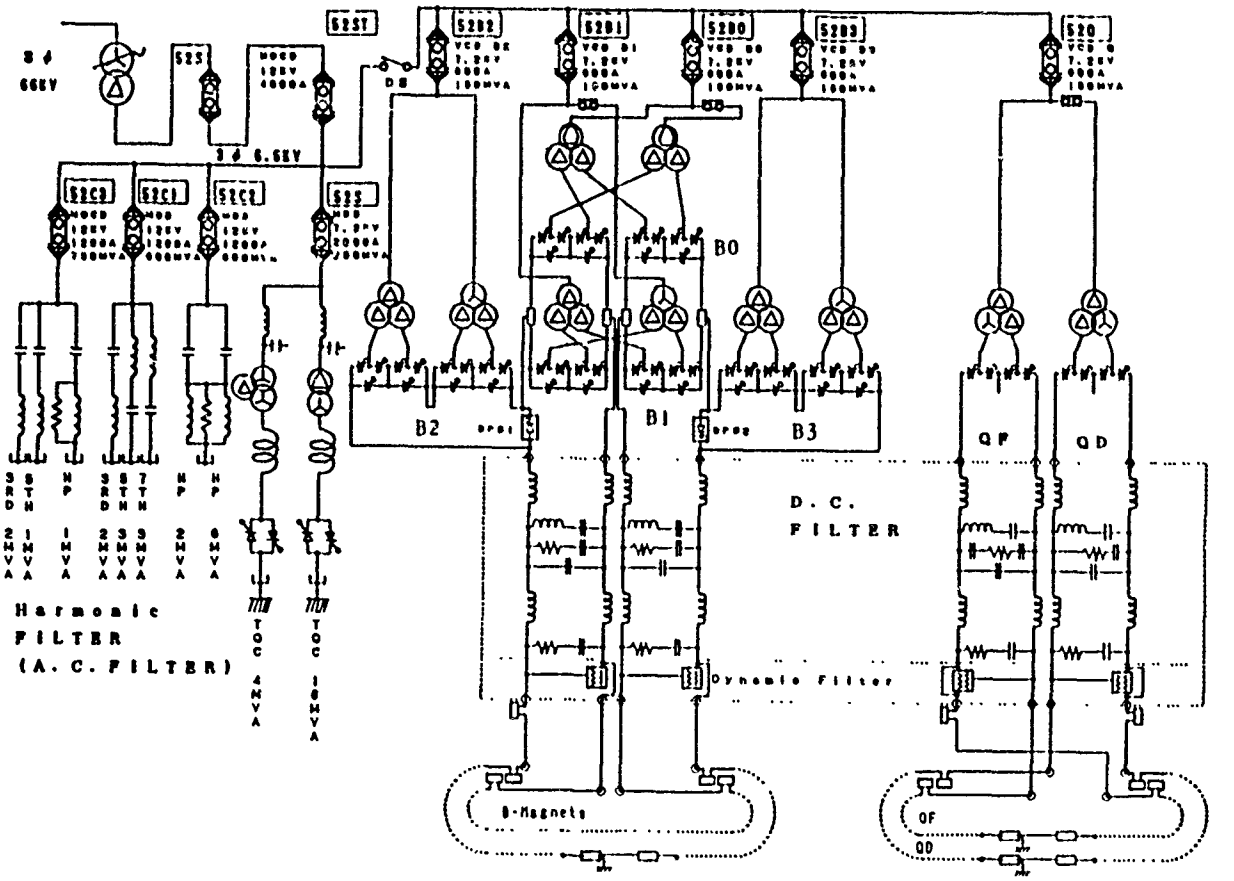


Fig.2 Schematic Diagram of the KEK 12GeV PS Main Ring Power Supply

Results

The magnet power system of the KEK 12 GeV PS was upgraded to expand the flat top. The current capacity of bending magnets power supply has increased. The analogue and computer control system have been also reconstructed. Eight twelve-pulse rectifiers for the bending magnets are still controlled by six groups of voltage patterns. The hybrid control system with the analog ACR and AVR loop as real-time negative feed back control and the repetitive current and voltage control have been performed.

Acknowledgments

The authors would like to express their sincere thanks Prof. Michio Nakano (Tokyo Inst. Tech.) for his discussions and much advice on the control system. They also express their thanks to Prof. M. Kihara, who is the director of PS division, for his advice and support. They are much indebted to many colleagues of the PS division for their discussions and collaborations.

References

[1] T.Sueno, M.Toda, S.Matsumoto and K.Mikawa, "Software Systems of the Main Ring Magnet Power Supply for the 12 GeV PS," Proceedings of the 6th Symp. on Acc. and Tech., 1987, Tokyo, Japan, pp.155.

[2] S.Matsumoto, T.Sueno, K.Mikawa and N.Kumagai, "Control of the Main Ring Magnet Power Supply for the 12 GeV PS," Proceedings of the 6th Symp. on Acc. and Tech., 1987, Tokyo, Japan, pp.158.

[3] S.Matsumoto, H.Baba, H.Sato, T.Sueno and K.Mikawa, "Improved Control System of the Thyristor Flicker SuppressorFor the KEK 12GeV PS," IEEE Transactions on Nuclear Science, NS30(1983)2932

[4] T.Shintomi, M.Masuda and S.Matsumoto,"Harmonic Current AC Filters at a Large Accelerator," Particle Acc8(1978)87

[5] H.Sato,"Passive Low Pass Filter for the Large Power Device," KEK Internal ASN-277(1987) in Japanese

[6] H.Baba, H.Sato, S.Matsumoto, T.Kubo, K.KItagawa, K.Asaji and A.Kabe,"Improved Dynamic Filters for the Main Ring Magnet Power Supply of the KEK 12 GeV PS," IEEE Transactions on Nuclear Science, NS28(1981)3068

[7] T.Shintomi and M.Masuda,"The Converter-Inverter Operation of the Power Supply for the KEK Proton Synchrotron," KEK-74-2.

[8] S.Matsumoto, T.Sueno, K.MIkawa, M.Toda and H.Baba, "New Multi-Microprocessor Control System of the Main Ring Magnet Power Supply for the KEK 12 GeV PS," Proceedings of the 1987 IEEE Particle Accelerator Conference, 1987, Washington D.C., pp.689.

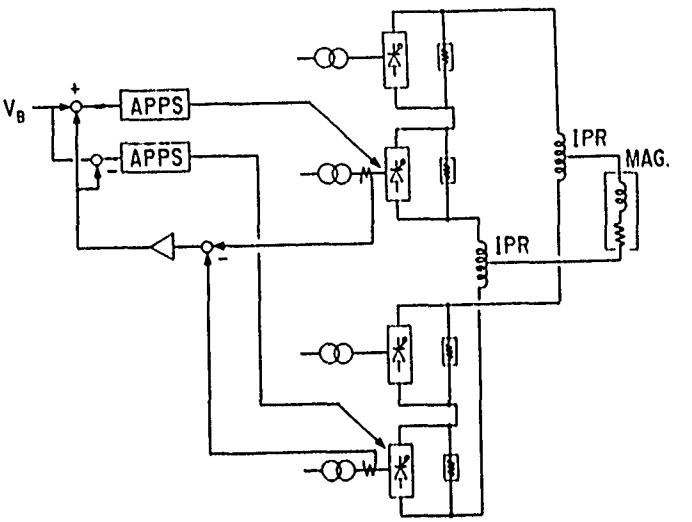


Fig.3 Feedback control of the primary transformer current deviation.

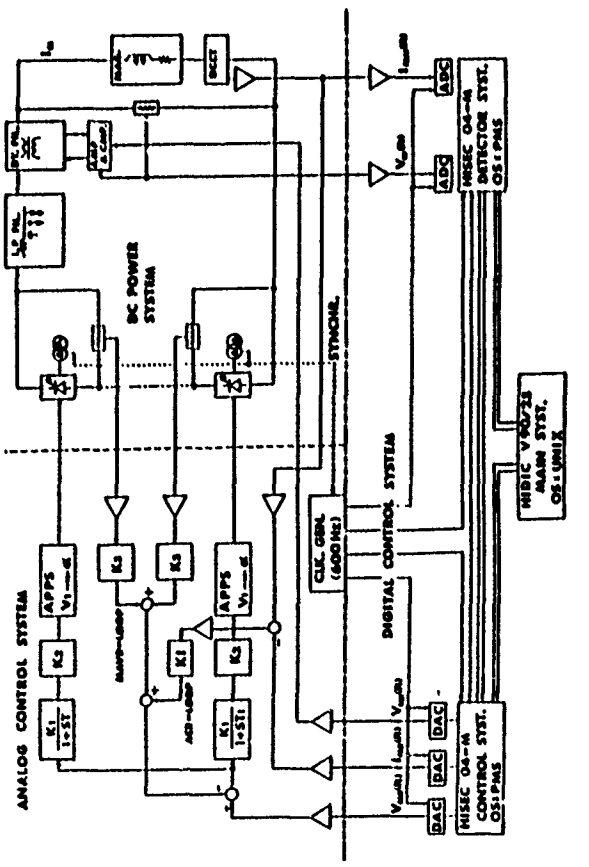


Fig.4 Schematic Block Diagram of the Hybrid Control System.

Correction Magnet Power Supplies for APS Machine*

Y. G. Kang
Argonne National Laboratory
9700 S. Cass Avenue
Argonne, IL 60439

Abstract

The Advanced Photon Source machine requires a number of correction magnets; five kinds for the storage ring, two for the injector synchrotron, and two for the positron accumulator ring. Three types of bipolar power supply will be used for all the correction magnets. This paper describes the design aspects and considerations for correction magnet power supplies for the APS machine.

I. INTRODUCTION

A number of correction magnets are required for the APS machine to correct the beam. There are five kinds of correction magnets for the storage ring, two for the injector synchrotron, and two for the positron accumulator ring (PAR). Table 1 shows a summary of the correction magnet power supplies (CMPSs) for the APS machine. For the storage ring, the displacement of the quadrupole magnets due to the low frequency vibration below 25 Hz has the most significant effect on the stability of the positron closed orbit. The primary external source of the low frequency vibration is the ground motion of approximately 20 μm amplitude, with frequency components concentrated below 10 Hz. These low frequency vibrations can be corrected by using the correction magnets, whose field strengths are controlled individually through the feedback loop comprising the beam position monitoring system.

A total of eighty correction magnets are distributed around the injector synchrotron ring. These magnets provide the field changes required for the beam orbit correction during the acceleration period at the rate of 2 Hz. Since the exact field correction required at each correction magnet location will not be known until a beam is actually accelerated, an arbitrary function generator (AFG) [1] is required to produce a correction field.

The correction field required could be either positive or negative. Thus for all the correction magnets, bipolar power supplies (BPSs) are required to produce both polarities of correction fields. Three different types of BPS are used for all the correction magnets. Type I BPSs cover all the correction magnets for the storage ring, except for the trim dipoles. The maximum output current of the Type I BPS is 140 Adc. A Type II BPS powers a trim dipole, and its maximum output is 60 Adc. The injector synchrotron and PAR correction magnets are powered from Type III BPSs, whose maximum output current is 25 Adc.

II. CIRCUIT CONFIGURATION

Figure 1 shows the simplified circuit configuration of a bipolar power supply. The topology is a full-bridge dc-to-dc converter. The switching frequency is 20 kHz synchronized with the main clock. The regulation is achieved by

Table 1: Summary of correction magnet power supplies for the APS machine.

					Rating			$\Delta I/I_{max}$				
	Correction Magnets	No. of Units	L [H]	R [Ω]	I [A]	V [V]	P [kW]	Tracking Error	Ripple Current	Stability	Reproducibility	Ref. Res. [bit]
Storage Ring	V.Corr. Sextupole	280	0.086	0.187	113	21.13	2.39	5×10^{-4}	1×10^{-3}	3×10^{-4}	6×10^{-4}	13
	H. Corr. Dipole	240	0.0122	0.1275	90	11.48	1.03	7×10^{-4}	"	"	"	"
	Skew Quadrupole	20	0.0122	0.1275	90	11.48	1.03	"	"	"	"	"
	H. & V. Corr.: H.	78	0.003	0.095	134	12.73	1.71	"	"	"	"	"
	H. & V. Corr.: V.	78	0.004	0.133	116	15.43	1.79	"	"	"	"	"
	Trim Dipole Coil	80	0.016	0.234	54	12.64	0.68	"	"	"	"	"
Injector Synch.	H. & V. Corr.: H.	40	0.47	1.378	21	28.94	0.61	4×10^{-3}	"	"	"	12
	" : V.	40	0.106	2.422	17	41.17	0.70	"	"	"	"	"
PAR	H. & V. Corr.	20	0.229	2.87	19	3.61	0.07	4×10^{-4}	"	"	"	"
	Trim Dipole	8	0.04	0.19	13	37.31	0.49	"	"	"	"	"

* Work supported by U.S. Department of Energy, Office of Basic Energy Sciences under Contract No. W-31-109-ENG-38.
U.S. Government work not protected by U.S. Copyright.

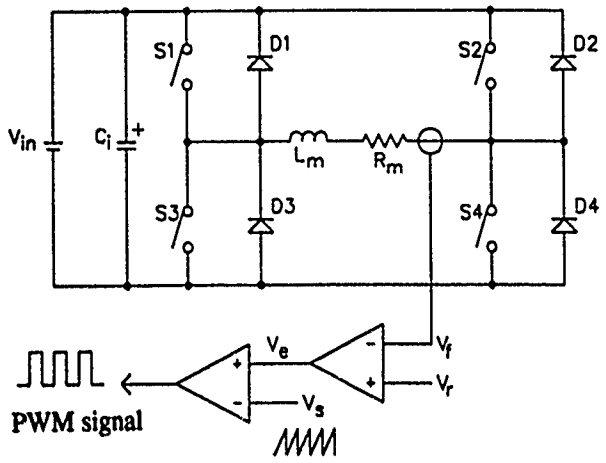


Fig. 1: Simplified circuit of a bipolar power supply.

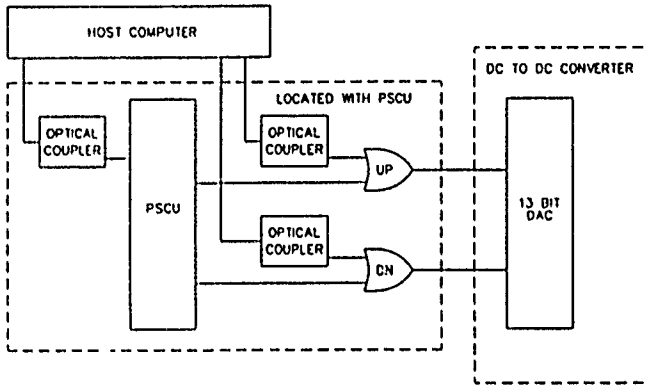


Fig. 2: Simplified block diagram of a control scheme.

controlling the pulse width. Power MOSFETs are considered for the switching devices due to their excellent switching characteristics and easier drive requirement. Another advantage of using power MOSFET is that the new generation of power MOSFETs allows us to utilize their inherent body diodes for the anti-parallel diodes of the switches. L_m and R_m represent the inductance and resistance of a correction magnet. For positive magnet current, switches S1 and S4 are closed. Only the upper switch S1 is controlled according to the pulse width modulation (PWM) signal, while the bottom switch S4 remains closed. When S1 is opened, the magnet current decays through the still closed switch S4 and diode D3. However, double gating, which controls both S1 and S4 simultaneously, may be required to keep di/dt constant around zero. For negative current, switches S2 and S3 and diode D4 are used in a similar fashion. In order to regulate the magnet current, the magnet current information is fed back to an error amplifier input via a current measuring device as the feed back signal, V_f, and is compared with the reference voltage, V_r, provided by a digital-to-analog converter (DAC). The current measuring device considered is either a shunt resistor or a zero-flux current transductor (CT). Since the current loop has slow response to the input voltage variation due to the large time constant of a correction magnet, the voltage-feedforward technique, which varies the ramp slope, is used in the regulator circuit for constant volt-second operation to the input variation. The unregulated dc input bus voltage, V_{in}, is provided by a separate ac/dc rectifier.

III. CONTROL

A. Control for storage ring CMPSs

Figure 2 shows the simplified block diagram of a control scheme of correction magnet power supplies for the storage ring. PSCU is the power supply control unit which contains the intelligence that interfaces directly to each power supply hardware for control, monitoring, and communicating to the host computer. One PSCU can control as many as eight correction magnet power supplies.

It was planned to use a 13-bit DAC for the reference signal generation, however it may be necessary to use a higher-resolution-bit DAC . The host computer provides a current value to the PSCU, and it sends out a pulse train to the DAC to set the dc-to-dc converter's output current. This current is the average (bias) correction current, and the current setting is done with an open loop. The host computer can then modulate the correction magnet's current by counting the DAC up and down for the dynamic correction. This dynamic correction is done with a closed feedback loop. The control computer will sense the correction magnet's field, and manipulate it to compensate for the attenuation and phase delay due to the eddy current effect of the vacuum chamber [2].

Figure 3 shows the simplified regulator circuit to generate gating signals. The reference signal, V_r, from a DAC is 0 to +5V for the positive magnet current and 0 to -5V for the negative current. A polarity signal, which determines a set of switches to be controlled, is derived from the reference signal by using a comparator. If it is a positive value, then a high signal is obtained. Similarly if it is a negative value, a low signal is obtained. The feedback signal, V_f, is provided from a current measuring device. Assuming a higher-resolution-bit DAC is required for a storage ring correction magnet, a zero-

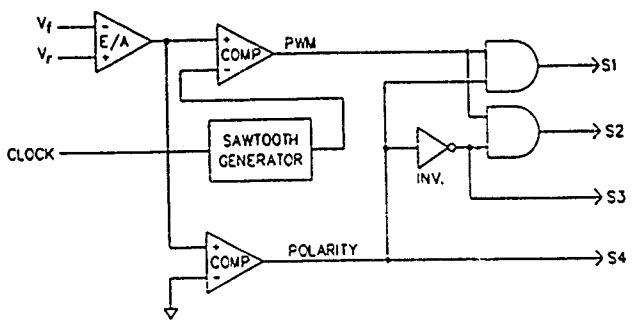


Fig. 3: A simplified regulator circuit.

flux CT provides +10V (-10V) for maximum positive (negative) current. This +/- 10V signal is reduced by half to match with the reference signal, V_r. The output of the error amplifier, V_e, is compared with a saw tooth signal, V_s, at a comparator, generating a pulse train. This PWM signal is combined with the polarity signal using an AND gate to determine which switch S1 or S2 is to be controlled. The maximum duty cycle could be 100%, however, in general, it is 50% at minimum input voltage and full load current for dc correction current, leaving the remaining 50% for the dynamic correction.

B. Control for injector synchrotron and PAR CMPSs

Basically the same control circuit as in the storage ring CMPS apply to the injector synchrotron and PAR CMPSs. The differences will be described in this subsection. For the reference signal, a 12-bit DAC is used, and a shunt resistor is used for the current measuring device, developing about 0.2V across the shunt at full magnet current. Thus, this signal needs to be amplified and isolated prior to the error amplifier input terminal.

As explained in the Introduction, an AFG is used to generate the reference correction signal, V_r, for injector synchrotron CMPSs. The AFG is located in the PSCU, and its design is based on scanning out encoded data from a semiconductor memory, a first-in-first-out (FIFO) device. The AFG input data consists of a maximum of 20 correction values randomly spaced within the injector synchrotron acceleration window (250 ms). Additional points between these values are then linearly interpolated to create a uniformly spaced 1000 data-point function stored in the FIFO. Each point is scanned out in synchronism with the acceleration cycle, and used to clock an up/down counter driving the DAC. Since the function data is first stored before use, its effect is a feedforward (open loop) correction. The optimum function for each correction magnet is determined via an iterative process based on the beam position during machine tune-up.

Since PAR correction magnets do not require any dynamic correction, only dc bias level information is received from the host computer. Therefore the same power supply as for injector synchrotron, (i.e. Type III BPS), is used, except that the PSCU does not include an AFG.

IV. DRIVE

Although the drive requirements for power MOSFETs are relatively simple compared with the equivalent bipolar transistors, some considerations are needed for high-current power MOSFETs. The input capacitances of high-current power MOSFETs are quite large, for example it is approximately 20 nF for a 200-A MOSFET. This is perhaps an order of magnitude higher than the typical TO-3 or TO-220 power MOSFET, and it has a definite impact on the driver design. Moreover, when high currents are switched at high speed, the parasitic circuit inductances in a practical circuit become significant. At drain currents greater than 50A, a di/dt on the order of 5 A/ns is readily achievable. At this speed, parasitic circuit inductances become first-order determinants of performance for 200-A MOSFETs. As drain current is increased, di/dt increases also. Consequently, the higher di/dt causes a larger voltage to develop across the parasitic circuit inductance. At turn-off, this voltage positively biases the gate, and hence increases crossover time. If the voltage developed across the parasitic circuit inductances is countered by a negative gate bias, the crossover time is decreased [3]. Therefore, for storage ring CMPSs, Type I and II BPSs, a negative gate bias of -5 V is applied to the switch S1 (S2) during OFF time. But for Type III BPSs only a positive gate signal from an IC MOSFET driver is applied to the switch since the magnet current is about 20A range.

V. PROTECTION

A. Input capacitor protection

When both switches S1 and S4 (or S2 and S3) are opened due to any undesired failure, the energy stored in the magnet has to be dumped into the input capacitor via the anti-parallel diodes D2 and D3 (or D1 and D4). In this case, the input capacitor voltage will exceed its voltage rating (100 V for example). Therefore, the input capacitor must be protected from exceeding its voltage rating.

The idea to limit the input voltage is as follows. Whenever the power supplies need to be shut down due to any fault condition, we need to make sure that the upper switch S1 (or S2) is opened first , and the bottom switch S4 (or S3) is opened some time later to allow the magnet current to decay through the normal freewheeling path and not through the input capacitor.

B. Monitoring and interlocks

In order to protect the power supply system, the monitoring circuitry monitors some important parameters, such as magnet current, input bus voltage, temperatures of switches, cooling water temperature and pressure, and bias supply condition. If any fault condition is detected, a shut down signal is generated to disable the gating signals.

VI. References

[1] O. D. Despe, "Arbitrary Function Generator for APS Injector Synchrotron Correction Magnets," ANL Light-Source Note, LSN-158, November 1990.

[2] W. Praeg, "Frequency Response of Storage Ring Magnets, Eddy Current Shielding of Vacuum Chamber," ANL Light-Source Note, LSN-45, December 1985.

[3] W. Schultz, " Multichip Power MOSFETs Beat Bipolars at High Current Switching," Electronic Design, pp. 223- 232, June 1984.

Circuit Description of the Power Systems for Pulsed Septum Magnets at APS *

D. G. McGhee
Argonne National Laboratory
9700 S. Cass Avenue
Argonne, IL 60439-4814

ABSTRACT

This paper describes the design and simulation of power circuits for the 4 Advanced Photon Source (APS) pulsed septum magnets which will be transformer type or transformer coupled to their switching circuits. Three are for synchrotron injection, extraction and Storage Ring injection, operating at a 2 Hz pulse rate; one is for the Positron Accumulator Ring (PAR) operating at a 60 Hz pulse rate for both injection and extraction. The septum current pulse is approximately a half-sine-wave with a base width of approximately 1/3 ms and a peak current, repeatable within ± 0.05%, in the transformer primary between 3.5 kA and 4.7 kA. The septum magnets have a primary inductance between 16 μH and 23 μH. Circuit design considerations of the switching, logic and simulations are presented.

I. INTRODUCTION

The transformer septum magnets must be pulsed at a 60 Hz rate to inject beam from a 450 MeV positron linac into the PAR and extract beam. Of the 60 pulses per second, the first 24 are used for injection, 25 through 29 are not used and 30 is used for extraction.

The other 3 septum magnets will be operated at a repetition-rate of 2 Hz. Two of the magnets are identical transformer type septum magnets which operate at the same values. These are the synchrotron extraction and the storage ring injection magnets with a primary inductance of 23 μH and resistance of 6.3 mΩ, and must be pulsed at 2 Hz to extract beam from the synchrotron and inject beam into the storage ring at 7.7 GeV. The third septum magnet is used to inject electrons into the synchrotron at 650 MeV or positrons at 450 MeV, and is also a transformer septum magnet, with a primary inductance of 21 μH, a resistance of 6.7 mΩ, and must be pulsed at 2 Hz.

The power supplies are designed to produce pulses of approximately a half-sine-wave having a base width of about 1/3 ms and peak currents repeatable within ±0.05% and adjustable from 470 A to 4.7 kA. A few ms after the forward current pulse, the magnet steel is reset by a half-sine pulse of reverse polarity. Use of a transformer design minimizes the cost of the capacitors used for energy storage.

During injection and extraction from the PAR and the synchrotron, as well as injection into the storage ring, the septum magnets must be pulsed. The combined rise and fall time of the pulse should be ≤ 1/3 ms with a flat-top time of >1 μs. These requirements can be met with a capacitor discharge circuit that is resonant with the septum magnet at a frequency of approximately 1500 Hz. The peak currents in the transformer primaries range from 3800 A to 4227 A and ranges from 11400 A to 16888 A in the secondaries.

These requirements can be met with a half sine-wave pulse. This is accomplished by discharging the energy stored in capacitor bank C_2 into the magnet as illustrated in Figs. 1a and 1b. On triggering the forward thyristor S_3, the energy stored in C_2 between pulses is discharged into the magnet circuit. S_3 turns off at the end of the first half-cycle of the damped oscillation. C_2 is then left with a smaller charge of opposite polarity until reverse thyristor S_4 is triggered and the second half-cycle takes place with current flowing in the opposite direction. The difference between the initial and the final charges is furnished by the charging supply between septum pulses.

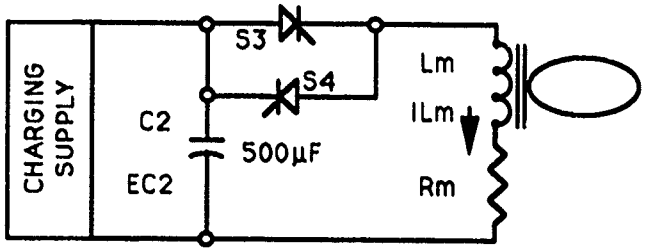


Fig. 1a. Magnet pulse switching circuit

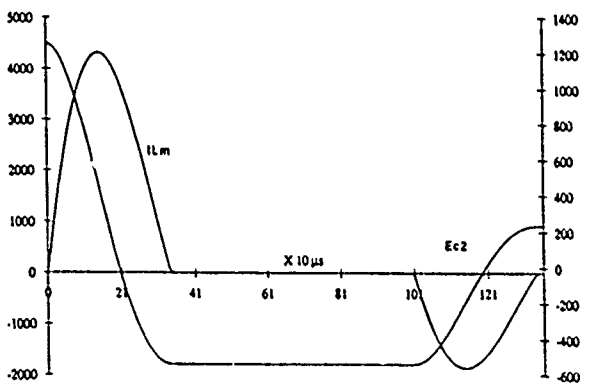


Fig. 1b. Magnet current and voltage waveforms

II. SWITCHING CIRCUITS

Circuit Equations

The switching circuits for these 4 septum magnets operate the same.[1] When capacitor C_2 of Fig. 1a is discharged into the load, an oscillatory current will result, provided the total resistance in the circuit is sufficiently low.

* Work supported by the U. S. Department of Energy, Office of Basic Energy Sciences, under Contract No. W-31-109-ENG-38.

U.S. Government work not protected by U.S. Copyright.

The resonant frequency of the circuit is:

$$fr = \beta/2\pi, \qquad [s^{-1}] \quad (1)$$

where $\beta = ((1/L_mC_2)-(R_m^2/4L_m^2))^{0.5}$, $[s^{-1}]$

C_2 = capacitor bank [F]
L_m = total circuit inductance [H]
R_m = total circuit resistance. [Ω]

The current at any time is:

$$i = (E/\beta L_m)\, e^{-at} \sin \beta t, \qquad [A] \quad (2)$$

where t = time after discharge starts, [s]

$$a = R_m/2\, L_m. \qquad [s^{-1}]$$

The required voltage on C_2 for the different peak operating currents is:

$$E_{c2} = i\beta L_m/e^{-at} \sin \beta t. \qquad [V] \quad (3)$$

The time where the current reaches its first peak is:

$$tp = 1/\beta \tan^{-1} \beta/a. \qquad [s] \quad (4)$$

The first current peak does not occur at precisely the first quarter period of the discharge cycle, but at a time before. The term $\tan^{-1} \beta/a$ describes the phase angle at which the peak current occurs.

In this application, R_m is made appreciably less than the value for critical damping. With $1/L_mC_2 > R_m^2/4L_m^2$, we can write $\beta \approx 1/(L_mC_2)^{0.5}$.

III. CONTROLLED CHARGING-CHOKE CIRCUIT

Fig. 2 shows the controlled charging-choke circuit and the capacitor discharge circuit of Fig. 1a combined. Discharge capacitor C_2 is charged and recharged to make up the circuit losses incurred by pulsing the magnet. These losses are made up from an unregulated dc power supply powered from a 3-phase line, for the PAR septum power supply. A commercial 1kW regulated dc power supply PS1 and capacitor bank C_f is used for the other 3 septum power supplies. PS1 has constant voltage and constant current mode of operation with automatic crossover. This allows the direct connection to C_f, as PS1 will operate in the constant current mode until crossover occurs at the output voltage setpoint. Capacitor bank C_f allows the losses to be made up at a fixed time before the next pulse of the main switching circuit. The controlled charging circuit is comprised of L_2, C_2, S_1 and S_2. Gating on of S_1 starts the charging of C_2 from the dc power supply. At time 0 the supply voltage Ea begins to drive an essentially sinusoidal current through the charging circuit.

$$E = iR_2 + L_2(di/dt) + (1/C_2)\int_0^{t1} i_{c2}\, dt \qquad [V] \quad (5)$$

At time t_1, the current is at its peak and $L_2\, di/dt = 0$,

$$E = iR_2 + (1/C_2)\int_0^{t1} i_{c2}\, dt. \qquad [V] \quad (6)$$

Between t_1 and t_2 the decaying charging current generates a voltage L_2 (di/dt) which aids the supply voltage to charge capacitor C_2 to a voltage larger than Ea. In the case where R is 0, this voltage will be, at time t_2,

$$e_{c2} = E + L\,(di/dt) = 2E. \qquad [V] \quad (7)$$

By providing a thyristor across the charging choke as shown in Fig. 2, the charging cycle can be terminated at any instant between times t_1 and t_2. A fraction of capacitor voltage e_{c2} is compared with a reference voltage. When the capacitor voltage is ≥ to the supply voltage at time t_r, a pulse can be generated which turns on S_2. With S_2 conducting, driving voltage L_2 (di/dt) is removed from the circuit and capacitor voltage e_{c2} is larger than the power supply voltage Ea, thyristor S_1 is back-biased and charging current i_{c2} stops. The current i_{L2} flowing in choke L_2 at time t_r will decay with a time constant L_2/R_2, where R_2 is the resistance of the choke and thyristor S_2 circuit. Thyristor S_2 remains on until S_1 is gated on starting the charge cycle again or until the choke

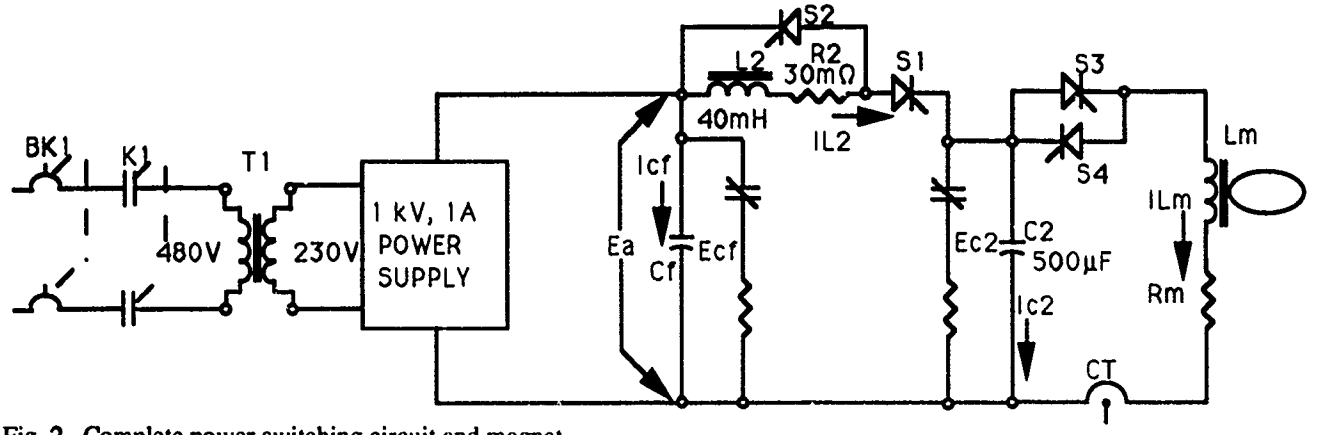


Fig. 2. Complete power switching circuit and magnet

current decays to 0. The current i_{L2} flowing in the choke when S_2 is turned off will aid in charging capacitor C_2 (the energy $0.5\,L_2\,i_{L2}^2$ is returned to the circuit). This makes the circuit very efficient.

It should be noted that the Q of the discharge circuit in Fig. 1a must be <5 for this charging circuit to operate properly. As the Q increases, current flowing in choke L_2 will decrease. This decreases the operating range of the charging circuit.

Pulsing the Magnet Without Resetting the Core

Heat losses in the magnet can be cut as much as 1/3 by not gating S_4, but the magnet core will not be reset. This mode of operation allows the dc power supply and filter to operate at a lower voltage. Also, the circuit Q could be increased, thus increasing the operating efficiency. Fig. 3 shows the change in charging time for the first 6 charge cycles of capacitor C2 with S4 gated, and Fig. 4 shows the first 9 charge cycles without S4 gated. It should be noted the first charge cycle is the longest in both cases, and the second is next longest without S4 gated and the shortest with S4 gated. Steady-state requires between 6 and 20 pulses, depending on the circuit Q.

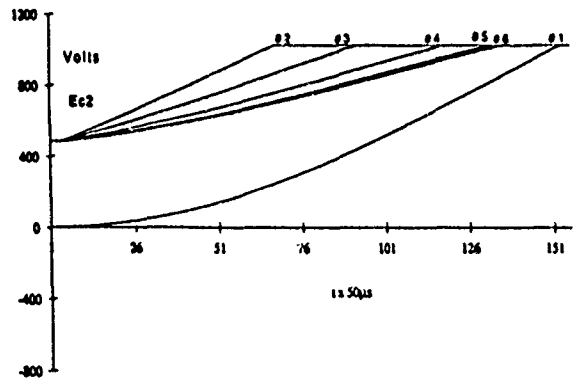


Fig. 3. Charging of C2 with S4 gated

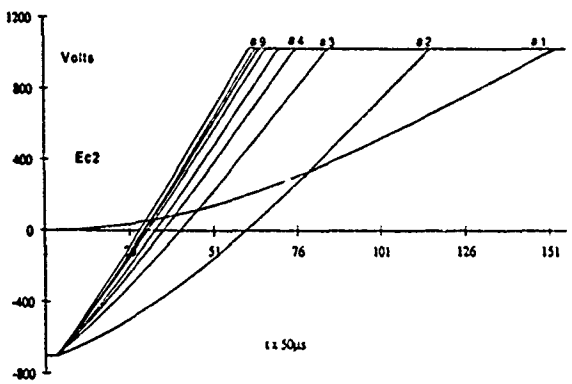


Fig. 4. Charging of C2 without S4 gated

VI. SIMULATION RESULTS

All 4 of the septum magnet and power supply circuits were simulated with a piecewise simulation program.[2] Typical waveforms for the pulsed septum magnets operating at 2 Hz are shown in Figs. 5a, 5b and 5c. The simulated waveforms have a varied time axis so that they show in detail what happens during the charge and discharge of C_2.

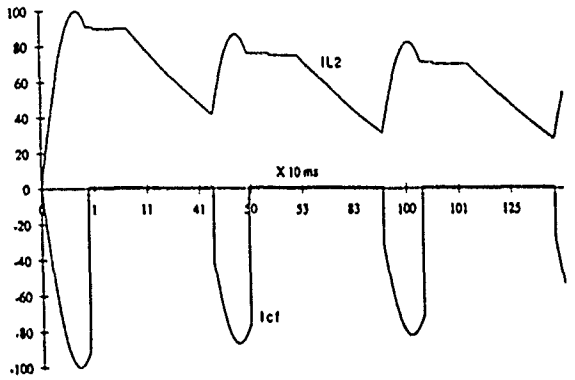


Fig. 5a. Simulation of current in inductor IL2, capacitor Cf

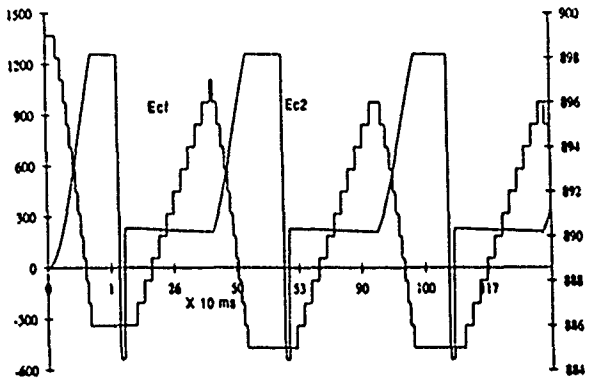


Fig. 5b. Simulation of voltages across capacitors Cf and C2

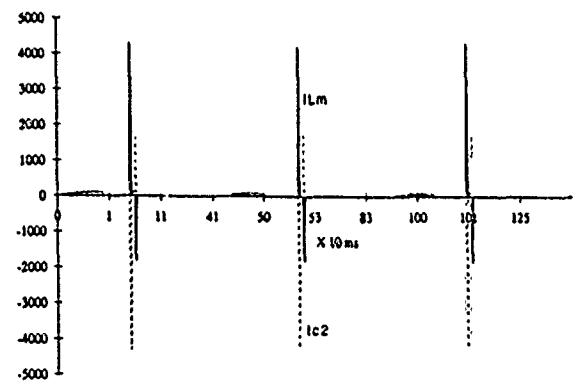


Fig. 5c. Simulation of current in inductor ILm and capacitor Cf

V. REFERENCES

1. D. G. McGhee, "Pulsed Power Supply for PAR Injection/Extraction Septum Magnet," ANL Light-Source Note, LS-159, September 23, 1990.
2. D. E. Piccone, I. L. Somos, and W. H. Tobin, "Piecewise Simulation (PS) Computation Method for Computing Transient Phenomena," *IEEE-IAS Annual Meeting*, September 1975, pp. 326--331.

Design and Simulation of High Accuracy Power Supplies for Injector Synchrotron Dipole Magnets*

Masoud Fathizadeh
Argonne National Laboratory
9700 South Cass Avenue
Argonne, IL 60439

Abstract

The ring magnet of the injector synchrotron consists of 68 dipole magnets. These magnets are connected in series and are energized from two feed points 180° apart by two identical 12-phase power supplies. The current in the magnet will be raised linearly to about 1 kA level, and after a small transition period (1 ms to 10 ms typical) the current will be reduced to below the injection level of 60 A. The repetition time for the current waveform is 500 ms. A relatively fast voltage loop along with a high gain current loop are utilized to control the current in the magnet with the required accuracy. Only one regulator circuit is used to control the firing pulses of the two sets of identical 12-phase power supplies. Pspice software was used to design and simulate the power supply performance under ramping and investigate the effect of current changes on the utility voltage and input power factor. A current ripple of $\pm 2 \times 10^{-4}$ and tracking error of $\pm 5 \times 10^{-4}$ was needed.

I. INTRODUCTION

Each power supply consists of four phase controlled half-wave wye group converters. Each of the two half-wave converters are connected through an interphase transformer to obtain a 120° conduction. The input voltage for these two half-wave converters are 60° apart. In order to obtain the high voltage needed for the load, two of the full-wave converters are connected in series. The power supply is equipped with a passive L-C-R filter to reduce the ripple content of the output current. The large size of the filter is reduced by adding anti-parallel thyristors to the output of the power supply. At low current level these thyristors are turned on until the current reaches the flat -top then the firing pulses of these thyristors are removed and the power supply is pulsed for full conduction. The output of the power supply will back bias the thyristors and force them to commutate. The power supply output will be ramped. During acceleration the power supply will operate as a rectifier and inject current into the magnet while, during reset the power supply operates in inversion and bucks the voltage across the magnet. To regulate the current in the magnet a high precision, low drift, zero flux current transductor is used. This transductor senses the magnet current and then provides the controlling signal through the regulator for the firing pulses of the thyristors in the converters. A 15 bit Digital to Analog Converter (DAC) is programmed by the control computer for the required current shape. The DAC provides the reference for the current regulator. Fast correction for the line transients is provided by a relatively fast response voltage loop controlled by the high gain, slow response current loop. Only one regulator circuit is used for two power supplies. This regulator controls the firing pulses for two sets of identical 12-phase thyristor power supplies. These pulses are transmitted via optical links. Figure 1 shows the block diagram for power supplies connected to magnet load.

II. BASIC REQUIREMENT

The voltage, current and regulation requirements for synchrotron dipole magnets are given below [1]:

Injection Current [A]	61
Extraction Current [A]	1044
Injection Voltage [V]	42, 1140
Extraction Voltage [V]	724, 1822
Reset Voltage [V]	-373, -1055

Regulation ($\Delta I/I_{max}$)

Reproducibility	$\pm 1 \times 10^{-4}$
Current Ripple	$\pm 2 \times 10^{-4}$
Tracking Error	$\pm 5 \times 10^{-4}$

III. DESIGN AND RESULTS

A. *Filter Design*

A filter with the cut-off frequency of 720 Hz was designed to eliminate the fundamental and higher harmonics of the current in the power supply. The transfer function of the filter is given in the following [2]:

$$\frac{e_o}{e_i} = \frac{sT_2 + 1}{s^3 T_2 L_1 C_1 + s^2(T_1 T_2 + L_1 C_1 + L_1 C_2) + s(T_1 + T_2 + T_3) + 1} \quad (1)$$

where $T_1 = R_1 C_1$, $T_2 = R_2 C_2$, $T_3 = R_1 C_2$, $L_1 = 10$ mH, $C_1 = 14.25\ \mu$F, $C_2 = 142.5\ \mu$F and $R_2 = 16.8\ \Omega$.

* Work supported by U.S. Department of Energy, Office of Basic Energy Sciences under Contract No. W-31-109-ENG-38.

U.S. Government work not protected by U.S. Copyright.

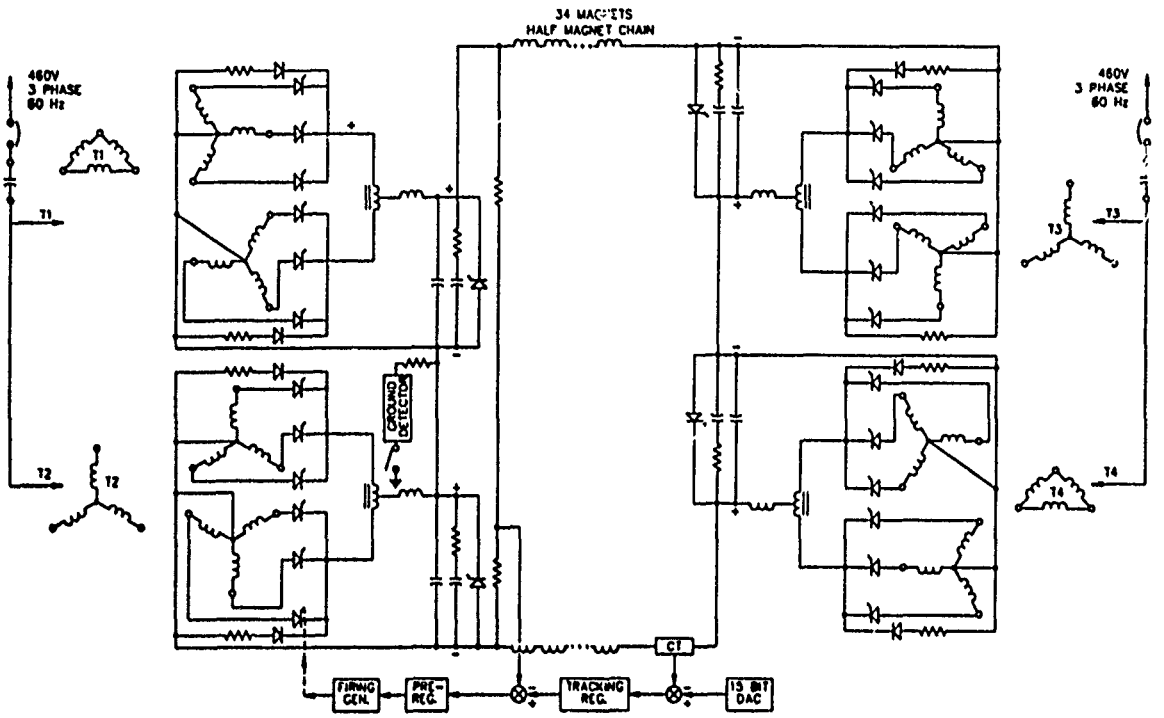


Figure 1. Block diagram for synchrotron dipole power supplies connected to magnets

B. *Regulator Design*

In order to track the current reference with the desired accuracy, a controller with very high gain is needed. A proportional plus integral (PI) controller can provide such a high gain. Both current and voltage loops utilize PI controllers. The voltage loop time response is set to correct for 720 Hz ripple produced before the main filter. However, the time constant of the current loop is set equal to the magnet time constant to obtain a proper control.

The pspice software was used to simulate the behavior of the synchrotron dipole power supplies. In our studies the following assumptions were made:

a) The impedance of the AC source connected to the power supply was assumed to be 5% . This information was needed to study the voltage drop at the transformer terminals.

b) 20% imbalance of AC source voltage was considered to evaluate the effect of interphase transformers.

Our study consists of three parts as follows:

1) The rated input voltage was applied to the power supply and the current in the magnet was ramped 60 A to 1044 A. Ripple content, linearity of current and controller tracking capability was then evaluated.

2) The effect of harmonics current injected from the power supply to the utility line was investigated.

3) Input kVA and power factor for the power supply at different load level were computed.

Part-1: The results which were obtained from the simulation of the power supply indicated that the controller can track the current reference within the specified limit. Figure 2 represents the tracking capability of the controller. For current level between 5% to 100% of rating current the difference between reference and actual magnet current is always less than 0.005%. The obtained value of the current error confirms the specified tracking capability of the controller.

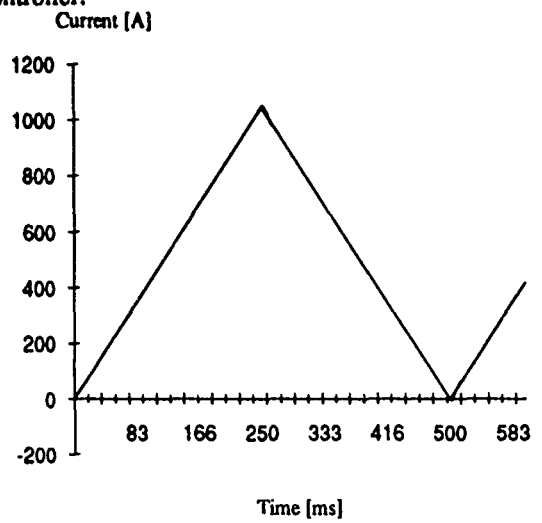


Figure 2. Typical synchrotron magnet current waveform

Part-2: The harmonic contents of the input current can be calculated by the following equation [3]:

$$i_a = \frac{6}{N\pi} I_d \left[\cos\omega t - \frac{1}{11}\cos 11\omega t + \frac{1}{13}\cos 13\omega t \ldots \right] \qquad (2)$$

where I_d is the dc current in the magnet, N is the transformer turn ratio and i_a is the ac input line current. The above equation indicates that the line current has harmonics of the order h = 12k±1, where k is an integer with values k = 1,2,....

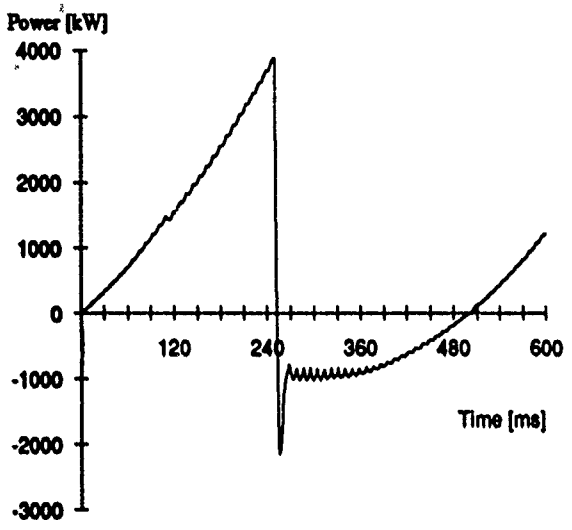


Figure 3. Input power variation during rectification and inversion

The harmonic currents injected into the utility line by the power supply can be eliminated by addition of a filter to the input of the power supply. However, the filter design must take account of the ac system impedance at harmonic frequencies in order to provide adequate filtering and to avoid certain resonance conditions. The system impedance depends on the system configuration, loads, generation pattern, and transmission line in service. Therefore, any change in the system configuration will require the modification of the filter. However, the harmonic contents of the current have a minimal effect on a stiff system. Transmission lines with low impedance and large substation transformer can provide a stiff system.

Part-3 The calculated rating of each power supply is 930 kVA. The power supply power factor for different output current values are calculated and plotted in Fig. 4. The effect of ac line voltage change on the output dc current was also examined. The line voltage was gradually reduced from 100% to 95% rating within 150 ms and then was boosted to its rated value. Figure 5 shows the line voltage change along with output dc current. It can be noticed that the fast response of the voltage loop can correct for the input ac line changes.

IV. CONCLUSION

A twelve-pulse phase controlled power supply was designed and simulated. i) It was concluded that due to the large amount of inductance in the load, a small amount of filtering was required to suppress the ripple contents of the output current. ii) Proportional plus integral controller for both current and voltage loop was required. iii) The power supply injects harmonics of the order of h = 12k±1 into the utility line. A stiff system with reasonably large substation transformer was recommended to correct this effect.

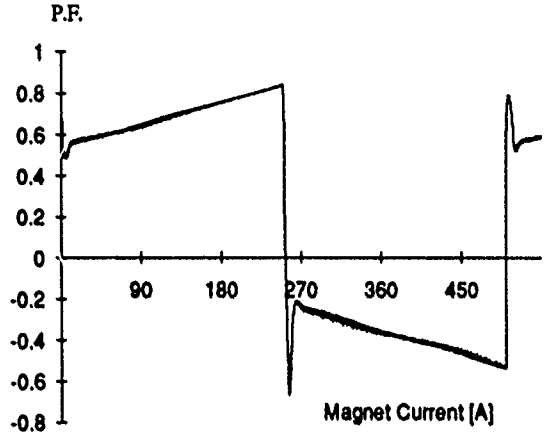


Figure 4. Power factor variation of power supply during rectification and inversion.

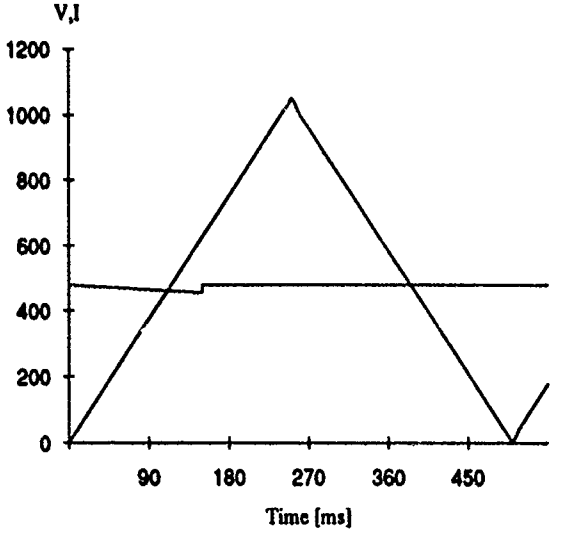


Figure 5. Effect of line voltage change on output dc current.

V. REFERENCES

[1] Advanced Photon Source Design Handbook Vol. II Dec. 1989

[2] W.F. Preag, "A high-current low pass filter for magnet power supplies," IEEE Trans. Industrial Electronics and Control Instrumentation, Vol. IECI-17, No. 1, pp. 16-22, Feb. 1970.

[3] N. Mohan, T.M. Underland, and W.P. Robbinson, *Power Electronics Convertors, Application and Design*, New York: John Wiley & Sons, Inc. 1987.

Power Supply System for the TRIUMF KAON Factory

K.W. Reiniger
TRIUMF, 4004 Wesbrook Mall, Vancouver, B.C., Canada V6T 2A3

Abstract

The TRIUMF KAON Factory consists of 5 rings, 3 of which are dc powered and 2 synchrotrons running at 50 Hz and 10 Hz, respectively. This paper deals with the power supply system envisaged for the accelerator ac well as the experimental results obtained using dc-biased single and dual frequency resonant magnet excitation for the booster and driver synchrotrons.

I. Dc Rings

A, C & E ring dipoles and quadrupoles are designed for 1000 A, with 0.001% current regulation required for E ring dipoles. This regulation requirement almost precludes the use of SCR supplies. Our study showed that large switching supplies were feasible and economically competitive with active filtered 12 or 24 pulse SCR equipment. Power supply ratings of 450 Vdc, 1000 A, current regulated to 0.001%, meet requirements for most of the dc magnet strings. One unit powers all A ring dipoles. With series voltage sources, power is provided to the C and E ring dipoles. The same unit is used for quadrupoles. A full power prototype was built which met design criteria.

II. Acceleration Rings

Booster and Driver ring magnets require dc biased ac excitation with repetition rates of 50 Hz and 10 Hz respectively. Typical current waveforms are shown in Fig. 1.

To minimize ac line disturbances, resonant magnet excitation was selected as proposed by J.A. Fox [1]. D ring dual frequency operation is as proposed by Praeg [2] . The 3 to 1 rise to fall ratio results from switching out of 8/9 of the resonant capacitance during the reset period. This mode of operation was verified using NINA magnets in our magnet test stand.

Dc bias is provided by a 12 pulse SCR unit delivering 650 Vdc @ 3000 A acting in series with a number of voltage sources. Dc bias is inserted in a modified resonant cell where the bias supply is not subject to the alternating current component. Ac makeup power flows through the bypass capacitor which is in parallel with the supply An 80 Vdc 3000 A supply was used as the bias supply in the magnet test stand.

A. *Ac Makeup Power*

Ac makeup power which serves to excite and control the resonant response, is coupled via primary windings on the dc bypass chokes. Booster makeup power may be

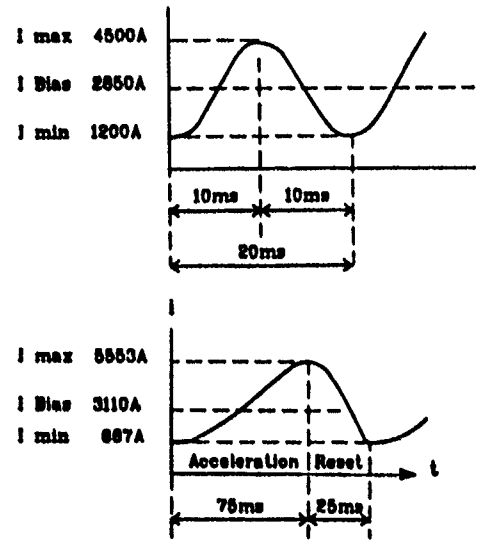


Figure 1: a) Booster dipole current cycle (50 Hz). b) Driver dipole current cycle (10 Hz).

sinusoidal. The Driver, however, which has dual frequency components, requires distributed pulse forming networks which provide a power makeup pulse during the acceleration interval. This method was verified experimentally on the magnet for both Booster and Driver applications.

B. *Dc Bypass Chokes*

Various competing designs were developed and yet need to be refined for the final configuration.

C. *Quadrupoles*

F and D quadrupole resonant networks are slaved to the dipole circuit. Straight section quadrupoles, sextupoles and COD magnets are driven by programmable supplies.

D *Control*

All magnet power supplies have their own controllers which communicate to the central control system via coaxial cable. The controller contains digital, analog and ADC circuitry required for either local or remote operation of the power supply. These units are based on existing G-64 format controllers currently in use at CERN.

III Experimental Work

A test facility was set up to investigate resonant circuit parameters at intermediate and full operating power levels.

Preliminary tests were carried out using NINA magnets to investigate dual frequency resonance as it would apply to the Driver ring Tests were conducted at 50 Hz nominal

0-7803-0135-8/91$01.00 ©IEEE

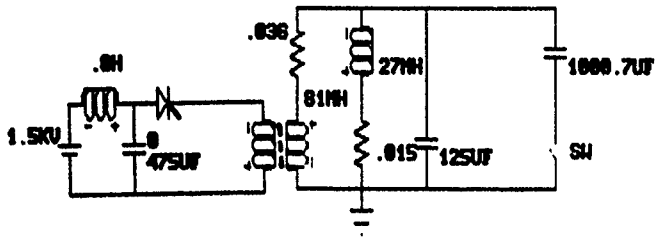


Figure 2: Dual frequency test circuit.

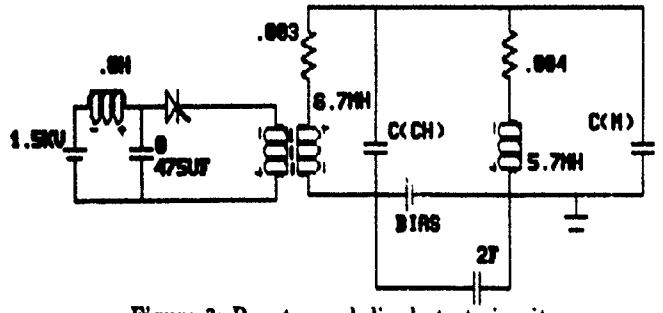


Figure 3: Booster and dipole test circuit.

repetition rates with 33.3 Hz rise and 100 Hz fall components. The results of this investigation were a first step in choosing appropriate parameters for the full system design as they would apply to the Booster and Driver synchrotrons [3–6]. Test circuit shown in Fig. 2.

A Booster dipole prototype was constructed and the test facility was reconfigured to excite the magnet to full operating level at 50 Hz with dc bias, for magnet measurement purposes (Fig. 3). Various tests were carried out at 50 and 33 Hz to establish circuit performance. The results of these tests with regards to the shift in the natural resonant frequency as a function of excitation and the implications on ac makeup power requirements help to define system requirements as well as giving a good basis for the development of the various control loops [6].

IV. Test Results

The following graph (Fig. 4) presents results obtained while maintaining a constant voltage from the high voltage ac makeup supply with a starting magnet current of 500 A rms. The frequency of the makeup pulse was then varied from optimum to see the resulting changes in power requirement from the source. This test simulates a change of natural resonant frequency from the nominal operating point. Plotted are source current, peak pulse current, and magnet rms current vs. frequency.

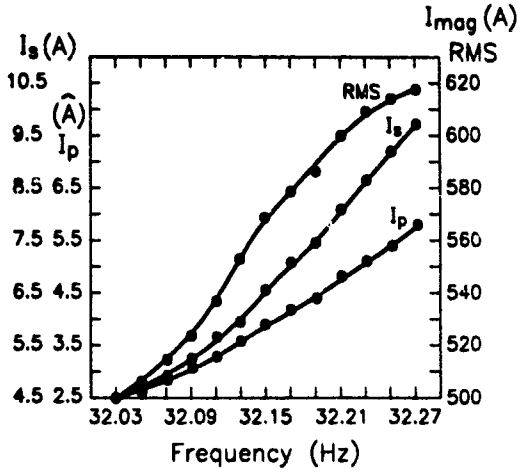


Figure 4: Ac makeup source current, pulse peak current and rms magnet current as a function of driving frequency with v_{source} constant.

Figure 5 shows the variation of the system natural resonant frequency as a function of ac excitation and dc bias level variation (32 Hz case).

Figure 6 shows the variation of ac makeup power as a function rms magnet current and dc bias level (32 Hz case). The frequency characteristics are as presented in Fig. 5.

Figure 7 shows the variation of the system natural resonant frequency as a function of ac excitation and dc bias level variation (50 Hz case).

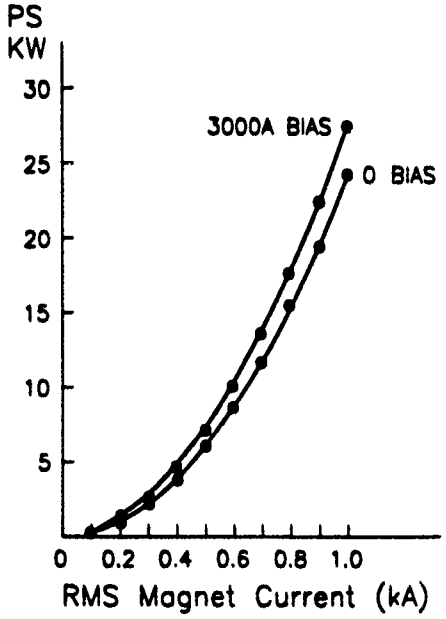


Figure 5: Ac makeup power as a function of excitation (32 Hz case).

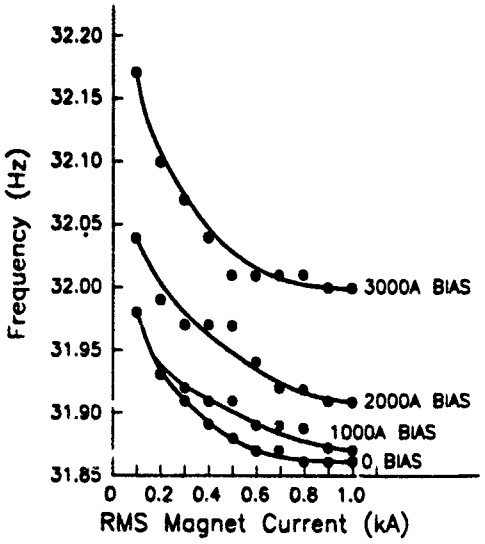


Figure 6: Shift in natural resonant frequency as a function of excitation (32 Hz case).

Figure 8 shows the variation of ac makeup power as a function rms magnet current and dc bias level (50 Hz case). The frequency characteristics are as presented in Fig. 7.

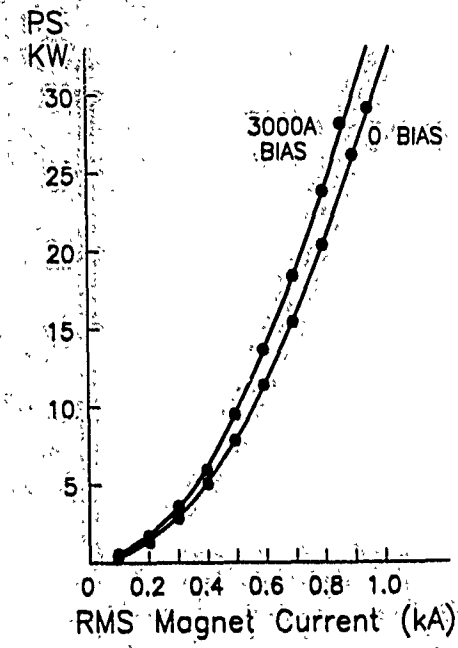


Figure 7: Ac makeup power as a function of excitation (50 Hz case).

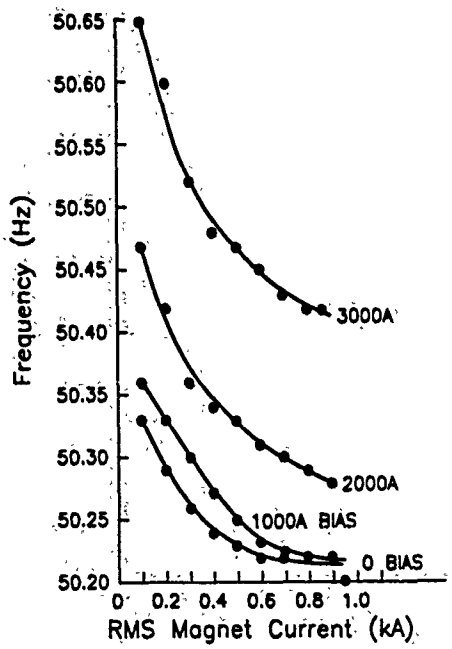


Figure 8: Shift in natural resonant frequency as a function of excitation. 50 hz case.

V. Conclusions

To obtain stable system operation, it is advantageous to excite the resonant circuit slightly off the natural resonant frequency, which will drift as a function of temperature and other parameters. This results in a fixed operating frequency. The power required from the ac energy makeup varies depending on the difference between the operating point and the natural resonant frequency. System detuning from optimum can be monitored by observing the variations in power delivered by the ac makeup supply. Dynamic tuning correction by the adjustment of the resonant capacitance, allows the system to operate at optimum power efficiency. These adjustments should be relatively infrequent and are only necessary when the normal dynamic operating range is exceeded.

Components for the ac power makeup portion of the driven slaved quadrupole resonant system must be overrated by some factor of 30 to 50% from nominal to allow for sufficient dynamic operating range to track the dipoles, as well as to have sufficient capacity to deal with natural resonant frequency shifts.

Test results show that due to the high Q of the circuits, a relatively small mismatch effectively doubles the current requirement from the power supply feeding the pulse forming network. This implies that the nominal rating of the supply must be significantly higher than required for optimum tune. The average current rating of the pulse forming network charging inductor must be conservative. The mismatch also results in significantly higher peak currents through the PFN switch and discharge inductor which must be appropriately rated. The discharge inductor must stay out of saturation since its inductance directly effects the width of the power makeup pulse which should stay constant, otherwise the result will be system instability.

VI. References

[1] J.A. Fox, "Resonant Magnet Network and Power Supply for the 4 Gev Electron Synchrotron NINA", Proc. IEE, 112, 1107 (1965).

[2] W.F. Praeg, "Dual Frequency Ring Magnet Power Supply with Flat Bottom", IEEE Trans. Nucl. Sci. NS-30, 4 (1983).

[3] K.W. Reiniger and G. Heritier "Experimental Results of High Power Dual Frequency Resonant Magnet Excitation at TRIUMF", TRI-PP-88-46, May 1988.

[4] K.W. Reiniger "The Generation of a Reference Design for TRIUMF Kaon Factory Booster Magnet Excitation", Proc. IEEE 89CH2669-0 (1989)

[5] TRIUMF KAON Factory Report, 1985.

[6] KAON Factory Study, 1990.

Problems With Tap-Changing Power Supplies

John Budnick
Robert Forgas
Indiana University Cyclotron Facility
2401 Milo B. Sampson Lane
Bloomington, IN 47408

Abstract

To meet conflicting requirements for low ripple, high stability, wide bandwidth, high efficiency, and low radiated EMI, a synchrotron dipole power supply was built with an SCR tap-switched primary isolation transformer and linear bipolar transistor passbank. Numerous operational problems encountered after delivery and installation have necessitated a major overhaul of many of the supply's systems to meet full accelerator design goals. Particular emphasis is paid to the technique for switching taps on-the-fly for reliable operation.

I. INTRODUCTION

In October of 1983 the Indiana University Cyclotron Facility began construction of a 500 MeV electron cooled storage and acceleration ring. The ring is hexagonal in shape with six sets of dipoles. The dipoles placed a number of conflicting requirements on the power supply required to drive them:

1.) Low current ripple (5 mA @ 1650A)
2.) High DC current stability during fill and flattop (<10 PPM)
3.) Only moderate time constant of dipoles available for filtering voltage ripple (2.2 sec)
4.) Fast cycling (2-4 sec ramp from 45 to 500 MeV)
5.) "Reasonable" efficiency
6.) Restriction on the use of phase controlled SCRs due to close proximity of experimental equipment to power supplies (and consequent coupling of line noise into sensitive detector and beam monitoring sensors)

Dipole requirements were for 1650A and a peak load voltage of 185V at 500 MeV, 1 Tm/sec.

While a normal type of supply for this application would usually be an SCR phase controlled supply with damped LC filter and probably invert-to-the-line mode of operation, requirements 1.), 3.), 6.), and possibly 4.) would seem to work against such a topology. Consequently, a specification was written favoring the use of a linear bipolar transistor passbank and tap changed primary isolation transformer tapped for 70% (overwound), 100%, and 130% secondary output voltage that would be connected to the 600VAC line by back-to-back SCR pairs. A vendor was selected and the supply built, tested, and installed in the facility. A block diagram of the supply appears as Fig.1.

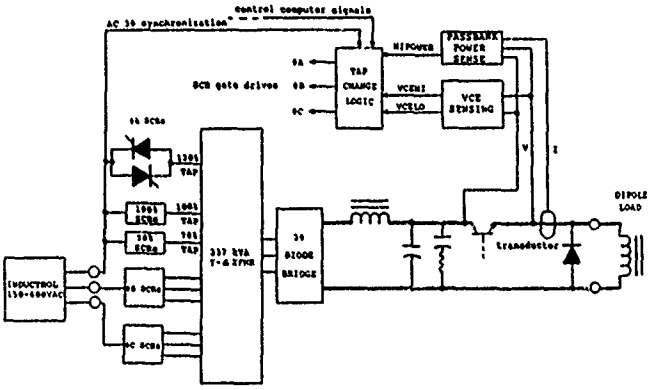


Figure 1. Tap-changing supply block diagram

Numerous problems were encountered in the first two years while the Cooler ring was being shaken down and commissioned. After inordinate expenditure of limited manpower resources in trying to keep the system operational and the fact that the supply could not reliably ramp beyond 287 MeV the decision was made in late 1989 to overhaul the entire tap-change scheme. The following sections recount progress in overcoming limitations of the supply and appear in rough chronological order; typically only one upgrade at a time was installed due to the tight running schedule.

Work supported by the U.S. National Science Foundation under grant NSF PHY 87-14406

0-7803-0135-8/91$01.00 ©IEEE

II. PASSBANK OVERPOWER PROTECTION

During the acceleration portion of an operating cycle the supply normally requires 130% (tap3) selection to provide inductive forcing voltage (Ldi/dt) to the load. As the ramp begins to round off and head into flattop the load voltage drops rapidly; excess voltage from being on tap3 is now forced across the passbank until the supply can fully complete a downshift to 100% (tap2), initiated by either VCEHI or HIPOWER (Fig.1) in conjunction with the external computer command allowing it to start the downshift. Timing here becomes quite critical as the passbank DC dissipation limit is only 70 kW and passbank power levels can easily exceed 100 kW while waiting to downshift.

To overcome these deficiencies a passbank power monitor board was constructed to closely model the second-breakdown portion of the D60T passbank power transistors. Computed power is determined by multiplying collector current and passbank voltage. This is then fed to an RC network to do a first-order approximation of the transistor hot-spot temperature. This signal then feeds a comparator that shuts off drive to the tap-change SCRs in the event of overpower. Raw DC collapses within 10 msec and the passbank power stress is relieved. To backup this primary overpower system two slower overpower interlocks from the existing systems function to drop out the main contactor. While previous overpower events had destroyed transistors by the dozens we have now completed two years of running with no further transistor failures.

III. TAP CHANGE SCHEME

Originally the supply was intended to initiate tap changes based on both internal status signals (VCEHI, VCELO, and HIPOWER) and external control computer signals (to prevent tap changing while not ramping). Operationally there were territorial disputes from this combined hardware/software tap change scheme. The upgrade called for only internally triggered switching to be used. Also, to make use of only internal trigger signals a series of tests determined that tap changes would have to execute in less than 50 msec in order to avoid overpower trips.

Because the existing tap change scheme did not directly sense SCR status, occasionally blown SCR fuses would result from multiply energized taps, causing several hours of downtime to replace. In the upgraded tap change logic, SCR ON/OFF sense would be determined by either SCR anode current sensing or SCR anode-cathode voltage sensing. Pros and cons for the two approaches are shown in Table 1:

Table 1
SCR ON/OFF sensing

Method	Pro	Con
Current sensing	*low cost, simple	*poor signal-to-noise ratio *not inherently failsafe
Voltage sensing	*good signal-to-noise ratio over many decades of SCR current *failsafe	*complex

The degree of "failsafeness" refers to whether the system would allow a tap change in the event of typical component failures; bad CTs, broken connectors and so on would give a "no current, OFF" status allowing a new tap to be loaded while an existing tap was still energized. Similar failures with voltage sensing (bad PTs, broken connectors, etc.) would give a "no voltage, ON" status and inhibit new tap loads; at worst a phase imbalance interlock would occur as opposed to SCR fuse failures. A block diagram of the tap change technique appears as Fig. 2. Because we were not interested in precise values of SCR anode-cathode voltages (anything over 15 volts was considered OFF) a series of inexpensive 50VA 600/120V machine tool control transformers were used as SCR potential transformers.

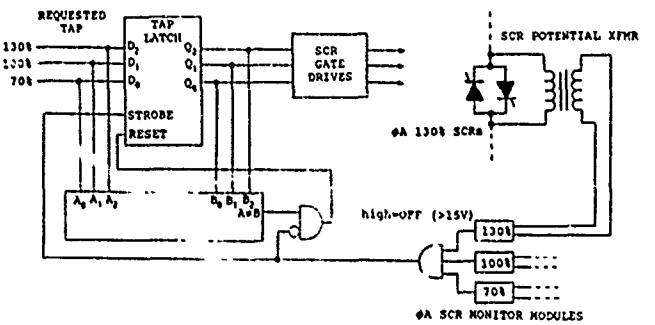


Figure 2. Tap change technique (phase A)

Results after 8 months of running have validated the usefulness of the technique. No further SCR fuse failures have occurred while ramping to record energies for the ring (485 MeV) in numerous runs. As expected, tap changes are fast (10msec) and are clean step changes up and down. Because of the immediate success of the technique, further side effects of the tap-changing approach became apparent above the former 287 MeV supply limit.

IV. SUPPLY RESPONSE TO UNREGULATED DC STEP CHANGES

Filter Damping

Ringing of the input filter on tap changes leads to small undershoots in the unregulated DC. For lower energy ramps (< 287 MeV) these could be tolerated by setting the AC input voltage slightly high by using the inductrol in Fig. 1. For higher energy ramps, power constraints rule out this technique and as a consequence transient saturation of the passbank occurs, leading to output glitches. Simply increasing the filter damping was not an option as ripple (which was already considered high) would increase with increasing filter damping.

After modeling the input filter in SPICE and exploring several impractical non-linear filter damping resistor options (e.g., PTC thermistor arrays) a two-state variable damping filter modification was decided upon; this is shown in Fig. 3.

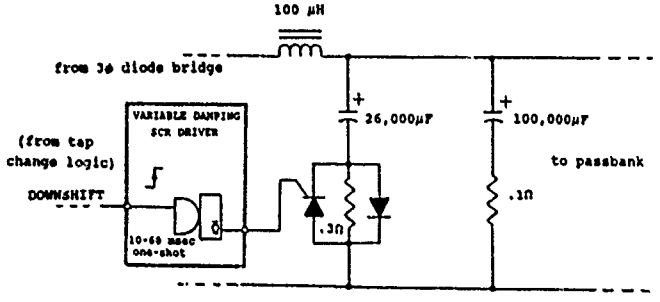


Figure 3. Filter variable damping

During normal operation the SCR around the damping resistor is ON and, in conjunction with the anti-parallel diode, provides a short-circuit for capacitor ripple currents. When a downshift occurs the SCR gate drive is turned off momentarily (10-60 msec), the SCR commutates and the normal large reverse ring current out of the filter is reduced greatly due to the sudden "appearance" of the .3 ohm resistor. Damping is such that no undershoot now appears; the supply does not lose regulation and normal steady-state ripple is unchanged.

Passbank Oscillations

The final roadblock to 500 MeV operation proved to be troublesome passbank internal oscillations. Due to the high f_t of the D60T transistors, the sudden rise in passbank voltage when going into magnet reset (current drops from 1600A to 250A) causes a shock-induced oscillation of the passbank at several kilohertz. This was eliminated (after numerous false starts) by using a distributed capacitive bypassing of the collector to minus bus scheme.

V. TAP OSCILLATION DETECTION; FORBIDDEN RAMPS

An anticipated result of using only internal signals to control tap changing is that in certain instances it may not be possible to find a stable operating point (given a desired ramp rate, flattop, and inductrol setting) where passbank voltage is sufficient but passbank power is not excessive. In these instances of "forbidden ramps" the supply will enter a steady-state oscillation mode trying to switch rapidly between taps to satisfy both conditions; damage to magnetic components, filter capacitors, and switchgear could result if this continued.

To prevent damage a tap oscillation detector looks at the 100% tap (since any oscillations must involve this middle tap) and shuts down the supply if more than a minimum number of tap changes occurs in an adjustable timeout period (typically 1 sec). This circuit has also proved useful in preventing damage from high-order dropped bits in the DAC. The resulting sawtooth waveform from the DAC would normally cause a rapidly tap-changing supply situation and consequent supply damage. A block diagram of this circuit is shown in Fig.4.

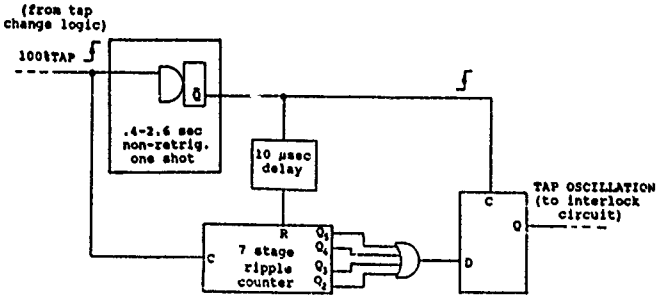


Figure 4. Tap oscillation detector

VI. SUMMARY

With sufficient justification it is possible to produce reliable tap-switched power supplies to meet multi-kilowatt load requirements. The justification (given the supply complexity) is rather limited to special combinations of requirements in cases demanding:

- *high bandwidth for small ramp following errors
- *moderate time constant loads where the load itself provides insufficient ripple current attenuation so that an active filter is necessary
- *need exists to minimize line noise, equipment size, energy costs
- *high DC current stability with minimum AC ripple

The 10 Hz Resonant Magnet Power Supply for the SSRL 3 GeV Injector*

R. Hettel, R. Averill†, M. Baltay, S. Brennan, C. Harris†,
M. Horton, C. Jach‡, J. Sebek, J. Voss
Stanford Synchrotron Radiation Laboratory, Stanford, CA 94309-0210

Abstract

The booster synchrotron for the recently commissioned SSRL Injector facility employs a 10 Hz resonant magnet power supply system to accelerate an electron beam from 120 MeV to 3 GeV. The booster dipole and quadrupole magnets are connected in series within a system of 17 distributed resonant cells driven by a pulsing network. Tracking power supplies driving the trim coils of the two quadrupole families are used to stabilize betatron tunes during energy ramping.

I. INTRODUCTION

A 10 Hz resonant magnet power supply system, or White Circuit [1], was chosen over a directly driven 2 Hz system for powering the SSRL Injector booster synchrotron in order to isolate the reactive power load of the cycling magnets from the AC mains distribution system at SLAC and SSRL. We viewed the White Circuit as being more simple, reliable, and better suited to our engineering expertise than other possible isolating systems such as mechanical flywheels, motor generators, and superconducting energy storage devices.

II. SYSTEM DESIGN CONSIDERATIONS

Four major design specifications were required to establish the basic White Circuit network: 1) the operating frequency; 2) the method of powering the quadrupoles; 3) the number of resonant cells and their configuration; and 4) the DC and AC power supply configuration.

A. Operating Frequency

The 10 Hz operating frequency was selected because 1) it would allow the use of 0.06" steel laminations for the booster magnet cores, costing significantly less than the more commonly used 0.025" laminations [2]; 2) it would permit the use of a thin (0.3 mm) stainless steel vacuum chamber; and 3) 10 Hz could be readily phase-locked to the line frequency, thus facilitating the stabilization of power supply noises at harmonics of 60 Hz. Also less beam intensity per/cycle would be needed to achieve a given SPEAR fill rate than for the 2 Hz system. Operating frequencies of 12 Hz and 15 Hz were considered, but they would cause more losses in the magnet cores.

B. Quadrupole Power

By connecting the quadrupole magnets in series with the dipoles in the White Circuit, we eliminated the need for a separate and carefully matched resonant power system for each of the two quadrupole families. On the other hand, this solution compelled us to implement quadrupole trim circuits so that betatron tunes could be stabilized during acceleration. Each trim circuit required a voltage-bucking transformer (or choke) of size and cost comparable to that for the inductor that would have been needed for an independent resonant circuit. The main advantage of this system was one of control and ease of matching the current waveforms in all magnets.

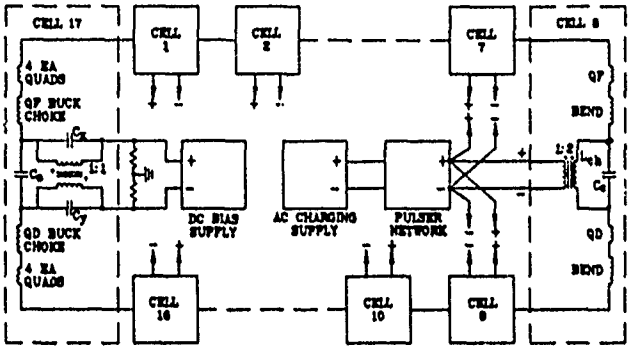


Figure 1. 17 cell White Circuit for the SSRL Booster

C. Resonant Cell Configuration

A distributed multiple cell White Circuit design was chosen 1) to solve an equipment space problem by distributing the energy-storing chokes and capacitor banks under the booster magnet girders; 2) to avoid the difficulty of engineering and fabricating a single massive choke that would weigh close to 50 tons; and 3) to limit the induced AC voltage level in the system.

To simplify coil insulation design and to enable us to use readily available semiconductor components, we decided to limit the peak AC + DC voltage difference between any system component and ground to 2 kV or less. This implied that no more than two dipoles and some number of less inductive quadrupoles should be included in a cell. Since the lattice had 32 dipoles, 16 cells were needed for them. A 17th cell was required for the two quadrupole bucking chokes and 8 of the 40 quadrupoles that were not in the dipole cells.

D. Power Supply Configuration

A final major design decision was to separate the sources of DC and AC power for the White Circuit and to drive the 10 Hz current oscillation through transformer windings on the cell chokes. We were wary of using a combined AC and DC supply system connected in series with the magnets because 1) we anticipated difficulties in injection at low energy due to magnet current disturbances, possibly including the transmission line or standing wave modes [3], driven by high frequency noise and ripple in

* Work supported by Department of Energy, Office of Basic Energy Sciences, Division of Material Sciences.
† Consultants to SSRL. R. Averill now at MIT Bates Lab.
‡ Presently at the SSC, Waxahachie, Texas.

0-7803-0135-8/91$01.00 ©IEEE

the voltage sourced by the series-connected rectifier supplies; and 2) it would not be possible to operate the circuit in an underbiased mode unless the supply were capable of inversion, a capability that would be accompanied by higher voltage ripple.

We further reduced the level of current disturbances at injection by implementing a pulsed AC power system as opposed to one that would continuously drive the 10 Hz oscillation. A pulsing network [4] was designed to generate a 17 msec current pulse to the cell chokes while the magnet current was decreasing and no beam was in the machine. Transient current disturbances caused by the pulse would damp out before new beam was injected and the accelerating current waveform would be noise-free.

III. WHITE CIRCUIT IMPLEMENTATION

A. Network Configuration

Figure 1 depicts the 17 cell White Circuit design for the SSRL separated function booster lattice. The 17th cell is configured to permit insertion of the DC bias current from a voltage-regulated DC power supply; a split coil configuration of the cell choke enables it to be used as part of the balanced 10 Hz blocking filter for the supply. The 10 Hz circuit resonance is driven by coupling the output power from the 10 Hz pulser through transformer windings on the 16 standard cell chokes. Component and system specifications for 3 GeV operation are summarized in Table I.

The 16 cell chokes are connected to the pulser with equal length cables in a star configuration; this configuration ensures the equalization of impedances between pulser and cells and between any two cells. Equalization of pulser-cell impedances is necessary for the uniform and nonreactive distribution of power to the circuit. Cell-cell equalization maximizes the even distribution of circulating currents between cells when one becomes mistuned and thus helps equalize the otherwise imbalanced cell voltages. The 17th cell is not pulsed in order to avoid driving the pulse current through the DC bias supply.

The values for cell capacitance and choke inductance were determined by minimizing the estimated total cost for capacitors and chokes assuming a that the cost per joule for capacitors would be a little more than twice that for chokes. The actual cost ratio turned out to be ~2.2.

Table I. 10 Hz White Circuit Parameters at 3 GeV

COMPONENT	QTY	VALUE		RATING	DC/AC PS kW
Dipole	32	21.1	mH	630 Apk/380 ARMS	2.4/2.9
QF	20	1.0	mH	" / "	.46/.43
QD	20	0.8	mH	" / "	.40/.36
Buck Choke	2	20.0	mH	" / "	3.9/5.0
Cell Choke	17	80.0	m	500 Apk/345 ARMS	7.8/4 1
Cell Cap	16	8.9	m	640 VRMS	0/0 5
Cell 17 C_p	1	5.3	mF	2 kV pk	0/1 0
Cell 17 C_{17}	1 ea	6.3	mF	320 VRMS	0/0.2
Charge Choke	1	250	mH	273 Apk/210 ARMS	0/5 0
Pulse Choke	1	2.0	mH	4 kApk/1.2 kARMS	0/10
Pulse Cap	1	14 2	mF	2 kV pk	0/2

DC Bias PS:	735	VDC @ 320 ADC	DC Pwr: 235 kW
AC Charging PS:	1020	VDC @ 273 Apk/210 ARMS	AC Pwr: 215 kW
Circuit Q:	28		

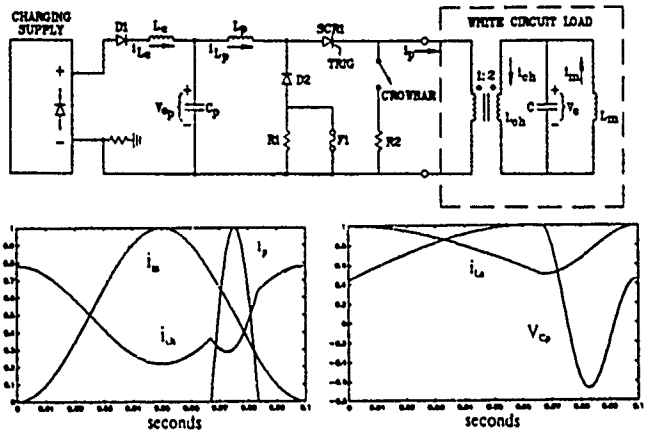


Figure 2. Pulser network and circuit waveforms

A bucking choke is needed for each quadrupole family in order to cancel the voltage induced on the trim coil circuit by the main coil circuit and vice versa. The primary windings of this choke are connected in series with the quadrupole trim windings, while the secondary windings are connected antiphase in series with the main coils. The mutual inductance of the bucking choke must match the sum of mutual inductances of the quadrupole main/trim coil transformers for proper operation.

B. Pulser Network

The 10 Hz pulsed power system is shown in figure 2. It consists of a capacitor bank C_p that is resonantly charged from a DC voltage regulated power supply through a charging choke L_c and discharged through a pulse choke L_p when SCR1 is triggered. The resonant discharge frequency is 30 Hz; current conducts through SCR1 during the first half cycle of this oscillation, providing ~17 msec wide current pulse to the parallel-connected choke primary windings. When the current pulse falls to 0 A, SCR1 stops conducting and the voltage across C_p is negative. This voltage drives a 30 Hz negative current half cycle through L_p via F1 and D2 that partially recharges C_p to a positive voltage. Full recharging of C_p is completed by current from the charging supply through L_c. In the event of a circuit fault where SCR1 latches on or otherwise conducts during the wrong phase of the 10 Hz cycle, F1 will blow and R1 will serve to limit the current in diode D2 and SCR1 to a nondestructive level for those semiconductor devices.

The resonant frequency of the recharging circuit is ~2.5 Hz so that the capacitor voltage has not quite reached an oscillation maximum when the 10 Hz trigger is applied. This ensures a continuous non-zero charging current and reduces the transient current loading on the power supply.

C. Chokes

The dimensional envelope of the cell choke was determined by the available space under the magnet girders in the booster tunnel. The core and air gap configuration was designed using the POISSON magnet modeling program to maintain a constant inductance to within ±0.5% over its full range of current energization for up to 3.5 GeV operation. The core design, shown in figure 3, has the advantage that it was relatively easy to fabricate and was readily tunable so that the same core design could be

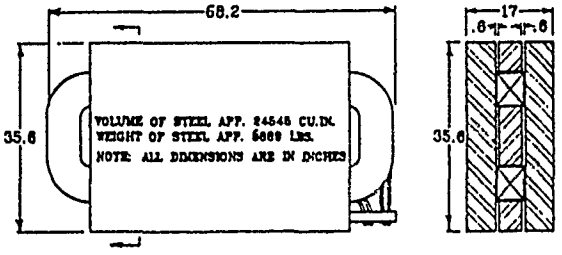


Figure 3. White Circuit cell choke

used for both the charging and bucking chokes by adjusting the gap height. It has the disadvantage that stray fields leak from the air gaps in the side legs and disturb CRT displays and some other types of sensitive instrumentation.

As was done for the 10 Hz magnets, the cell, charging, and bucking choke cores were fabricated using 0.06" 1005 steel laminations [2]. The resulting AC power dissipation in the circuit was approximately twice what it would have been if 0.025" electrical steel laminations had been used.

The 30 Hz pulse choke has 0.025" core laminations stamped from the same die used for the booster dipole laminations. It too has air gaps in the side legs, but only at the center parting plane of the upper and lower core halves. The middle and side end poles are tapered in an approximate Rogowski contour to reduce heating and magnetic forces that tend splay the end laminations.

D. Capacitors

Each cell capacitor bank is configured from a set of six 5700 μF capacitor groups together with one trimmer group. Three parallel-connected groups are connected in series with the other three parallel-connected groups; the trimmer group is connected in parallel with this total assembly and adjusted to form the 8900 μF nominal capacitance needed for 10 Hz operation. The groups can be rearranged in a 2-parallel, 3-series pattern for 15 Hz operation.

Each 5700 μF group is comprised of 60 each 95 μF capacitor units connected in parallel and mounted on a tray that, together with the five other similar trays and one trimmer tray, slides into a cabinet that fits under a booster magnet girder.

The trimmer tray consists of binary-weighted groups of capacitor units that can be switched in and out to tune the resonant cell. The trimming resolution is 0.6% of the total cell capacitance, permitting a frequency tuning resolution of 0.3%.

The cell 17 capacitor banks C_x, C_y and C_o, and the pulser capacitor bank C_p are also configured using capacitor trays, but in these cases they are all connected in parallel. The cell 17 capacitor banks each have trimmer trays with trimming resolutions similar to that for the cell banks. The individual capacitor units for C_o and C_p are rated for peak voltages of 2.2 kV and 2.7 kV respectively, adequate for both 10 Hz and 15 Hz operation.

All capacitor units are fabricated using metallized polypropylene and consequently have a low temperature coefficient that limits the thermal drift in resonant frequency to less than 0.4% over a 25°C range.

E. Power Supplies

Two 480 kW voltage regulated power supplies are used to power the White Circuit. Both are 12-pulse SCR controlled supplies rated for 1200 VDC, 400 A service with 480 VAC mains input. The DC Bias supply has a 7 Hz L-C low pass output filter to reduce the output ripple voltage Hz to less than 1 V pk-pk. This ripple specification ensures that magnet bias current ripple will be 0.1% or less of the 25 A injection current. The Charging supply does not require the output filter since L_c and C_p in the pulser network perfrom this function. The effects of harmonic voltage ripple are further reduced by phase-locking the 10 Hz circuit trigger, and thus the magnet current oscillation, to 60 Hz [5].

The injection current is stabilized to the 0.1% level, well within the 0.5% energy acceptance of the booster, by deriving the linac trigger timing from a biasable peaking strip installed in a booster dipole [5]. The peaking strip generates a timing pulse when the injection magnetic field threshold is reached, relieving the regulation requirement for the power supplies that would otherwise be on the order of 0.01% of their output currents. Instead the supplies are regulated to the order of 0.1% so that the extraction current and beam energy will be stable to that level.

The quadrupole tracking supplies are configured using pulse width modulated bipolar servo amplifiers powered from a common 300 V bulk supply. Each amplifier can be programmed to source up to 60 A peak current, 10% of the 3 GeV main coil energization, and has a bandwidth of ~300 Hz. The regulation requirement is again on the order of 0.1% to meet injection stability needs.

IV. Operational Experience

The White Circuit has been proven to be a reliable and relatively simple system to operate during its several months of 2.35 GeV operation. Most of the commissioning effort was devoted to repairing coil and core vibration problems in some of the magnets and chokes and to improving the high power operation of the power supplies. Since then, end laminations on some of the choke cores have come loose and occasionally a capacitor fuse must be replaced. 3 GeV operation is scheduled for 1992.

The magnet current waveform during the ramp is observed to be free of harmonic contamination. This coupled with the injection current stability obtained with the peaking strip and the tune stability achieved with the quadrupole tracking system contributed greatly to the success of the White Circuit in meeting the Injector facility goals.

V. References

[1] M.G White, *et al., A 3 BeV High Intensity Protron Synchrotron*, proceedings of CERN Symposium, June, 1956.

[2] M. Baltay, *et al., The Ring Magnets for the SSRL SPEAR Injector*. In these proceedings, 1991.

[3] A.G. Ruggiero, *Analysis of the Booster Power Supply Loop*, FNAL technical note TM-612-0323, Sept. 1975.

[4] H.H. Woodson, *Dynamic Operation of the AC Magnet Power System*, CEA technical note CEA-74, Aug. 1959.

[5] R. Hettel, *et al., Triggers and Timing System for the SSRL 3 GeV Injector*. In these proceedings, 1991.

Magnet Power Supply as a Network Object

S. Cohen and R. Stuewe
Los Alamos National Laboratory
Los Alamos, NM USA 87545

Abstract

Magnet power supplies with embedded microprocessor controls are being installed in the beam-lines of the linear accelerator and proton storage ring at LAMPF. Using an RS422 link they communicate with the accelerator control system through a terminal server connected to the site-wide DECnet backbone. Each supply is, for all intents and purposes, a network object. The controller has a command set of over seventy-five three-character ASCII control and read-back instructions. Strategies for choosing the appropriate control protocol and the process of integrating these devices into a large accelerator control system will be presented.

I. INTRODUCTION

Magnet power supplies with embedded microprocessor controls are being installed at the Clinton P. Anderson Meson Physics Facility (LAMPF). The LAMPF Control System (LCS)[1] interface for the supplies must be designed so that all existing applications that need to access power supply control channels remain unchanged. Control information to the units can originate from three sources; the front panel of the supply, a remote panel which can be mounted thousands of feet from the supply and an RS-422 ASCII uplink. Connection to the accelerator control system is through the uplink. Power supply control protocol consists of seventy-five ASCII commands. Only a handful of these instructions need be known to the LCS for routine adjustments and control. The remainder are intended for power supply set-up and troubleshooting.

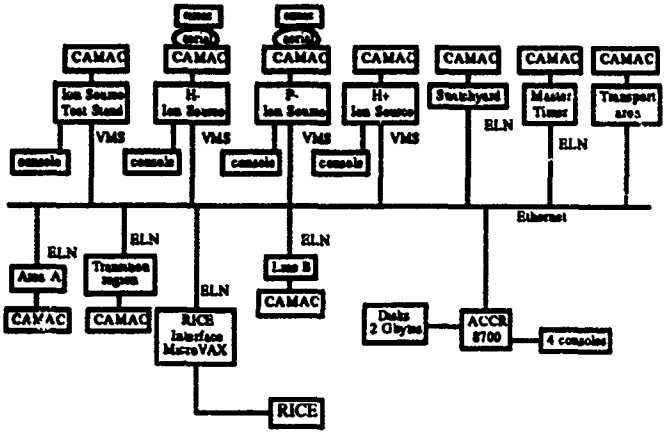


Figure 1. The topology of the LAMPF control system.

These supplies are more appropriately termed magnet controllers. They appear to the LCS as an integrated current source and electromagnet combination. In fact, key interlocks from the magnet themselves are attached to and monitored by the supply. For example, a water over-temperature trip from the magnet will cause the supply to ramp off with no intervention from the accelerator control system. Some supplies that we are installing provide a current of 1000 Amperes at 500 Volts into a one Henry inductive load. Regulation is one part in 10^4. Power supply control is significantly more complex than just "on" and "off."

II. RS-422 INTERFACE TO THE LAMPF CONTROL SYSTEM

In the past we have interfaced serial communication devices to the LCS using either a CAMAC serial communications module or a connection to terminal server. We chose the latter for this latest serial device.

Asynchronous serial communications using CAMAC is a compromise, at best. Using CAMAC modules for serial communication involves another layer of in-house software that must be developed. Serial communications modules of different types cannot, in general, be interchanged without software modifications. If the location of the supply requires a CAMAC crate to be located some distance from its control computer then a serial highway needs to be used to extend the CAMAC bus. This adds another data bus that must be maintained.

Terminal server protocol is already integrated into the LCS computers' VMS or VAXELN operating system[2]; no additional drivers or other special interface software need be written. Terminal servers can be attached anywhere along the existing control system's ethernet backbone that runs the linear accelerator's half-mile length. Our experience using the terminal servers has shown that they are reliable and are straightforward to program.

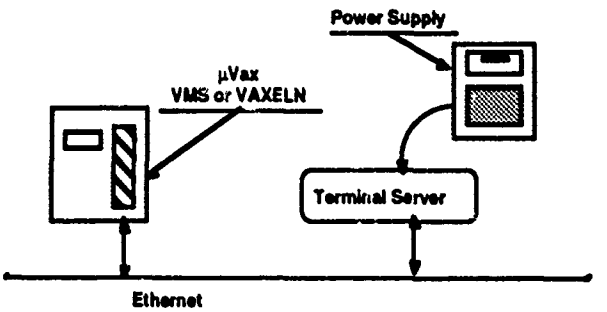


Figure 2. Power supply as a network object.

Work supported by the US Department of Energy

0-7803-0135-8/91$01.00 ©IEEE

III. EMBEDDED CONTROLLER SOFTWARE DEVELOPMENT

The software for the embedded controller was designed and written by the power supply vendor[3] using our detailed specifications. Our contract required delivery of a software emulation of the power supply for our testing and evaluation months before the first prototype power supply was to arrive on-site. We were able to provide feedback to the vendor early in the development cycle. The emulator runs on an MS-DOS computer and uplink communication is provided through its serial communications port. A number of modifications and additions were prompted by our experimentation.

The emulator PC is connected to a terminal server. Diagnostic codes, running on a networked LCS computer, simulate the command environment in which the actual supplies will exist. The supply controller is required to respond to commands at a rate of no less than 10 Hz.

The supply's command repertoire was expanded and modified as result of our experimentation with the emulator. Control commands for setting limit points and a new response mode are examples of items that were added.

A. Limit Points

Current and voltage limit point commands were added to supplement the power supply's trip point instructions. The limit point settings should prevent excessive overcurrent and overvoltage shutdowns that result from mistakes in entering new set point values. The device will not attempt to seek a set point that exceeds its limit point. If a set point request exceeds the limit point, the supply will remain in its present state and reply with an error code. In contrast, if the power supply's output voltage or current exceeds its trip point it will ramp off.

B. Verification modes

There are a number of reply formats to which the controller can be set. The supply has four response modes, Complete Verification (CVN)[4], Complete Verification Off (CVF), Short Verification (SVN) and Numeric Verification (NVN). In every case except CVF, an end of line, <EOL>, character or characters are appended to the controller's reply[5]. A terse two-digit-number response is ideal for computer control, but not particularly convenient for the human technician doing troubleshooting. The variety of response modes allow one to obtain a good match between the user and the supply controller.

Examples of the response formats to an ON command, after an interlock fault is detected, is illustrated in Table 1.

Table 1

Comparison of power supply response formats. The response is to an "ON" command after an interlock has tripped.

Verification Mode	Controller response
CVN:	ON Ok Error Bad State <EOL>
CVF:	*nothing*
SVN:	Error 06<EOL>
NVN:	06<EOL>

The NVN mode, most natural for computer-to-power-supply communication, was added a as a direct result of our emulator testing. Note that the CVF mode, the original mode supplied by the vendor for external computer control, provides no response to any command that it understands. There are obvious problems with using this mode for computer control.

IV. ACCELERATOR CONTROL SYSTEM INTERFACE

The existing control system provides a hook into which we were able to attach these new intelligent supplies the *pseudo device*. The pseudo device mechanism is actually a generic interface to the LCS run-time database[6,7]. The job of the *pseudo device* software is to allow database access calls used by all of the existing control system applications to access and control any piece of hardware without knowing its operating details. The *pseudo device* must take care of all details, including any differences in the operational model of the target device and the LCS.

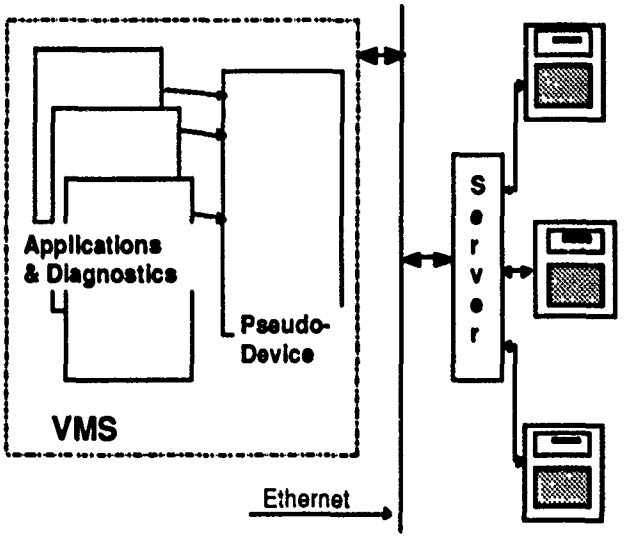


Figure 3. The pseudo device interface.

For historical reasons, analog control in the LCS is assumed to be incremental. That is any command value requested is assumed to be an increment to be added to the present setting of the device. This puts it clearly at odds with our new supplies' set point control philosophy. *Pseudo device* software must compensate for this. All analog data received from the supply is coded as a set of ASCII characters. It must be parsed and converted to REAL*4 format before being sent to the control system.

Each terminal server connection requires its own VMS I/O queue. The *pseudo device* acts as a terminal server port manager and maintain dialogs with multiple supplies. It decides what threshold of inactivity will trigger a port disconnect. Each queue uses some of the precious VAX CPU cycles.

Diagnostic programs will be able to access all of the power supply command set through a special diagnostic pass-through channel for each supply. Commands, not just those

known by the run-time database, will be accessible though a simple terminal interface for remote troubleshooting.

V. POWER SUPPLY INITIALIZATION

Each supply's operational parameters must be protected from unauthorized modification, i.e. values such as the trip point settings, interlock fault parameters and ground current trip points. Commands that effect sensitive parameters will be accepted only if the supply is placed in the password-protected super-user mode. The controller reverts to the normal user mode after a time-out period has been exceeded. There are additional set-up values such as the definitions of the twenty-four interlock faults. Initially these need to be entered interactively by a human user. Once this is done the entire set of values can be downloaded to the control system computer. In the future the power supply can be reconfigured by uploading the stored block of values to the controller. The block is protected by a checksum so that file "spoilage" can be detected. The block-load command is not a super-user command, but the checksum scheme prevents tampering with the file. We have not addressed the issues of version management of the magnet block files. A workable scheme to keep track of hundreds or thousands of these parameter files must be devised.

VI. CONCLUSIONS

We feel that the additional time and effort that is being spent now on a generic power supply interface will be well worth it. The requirement for the vendor to supply an emulator for a new device early in the design cycle proved invaluable. In addition to revealing unforeseen flaws in the original controller design, it allowed us to confidently start work on the LCS control interface before any hardware existed. We are planning to put the supplies in service during the 1992 LAMPF run cycle.

VII. REFERENCES

[1] S.C. Schaller and E.A. Bjorklund, "Distributed Data Access in the LAMPF Control System", Particle Accelerator Conference, Washington, DC USA (1987)

[2] Digital Equipment Corporation LAT protocol

[3] Alpha Scientific Electronics, Inc., Hayward, CA 94545

[4] For a full description of the controller and its command set see:
R.S. Rumrill and D.J. Reinagel, "Intelligent Power Supply Controller", in this conference proceedings.

[5] The following characters can be selected as an end of line character sequence: LF (ASCII 10), CR (ASCII 13), CR and LF or LF and CR.

[6] S.C. Schaller and P.A Rose "Data Acquisition Software for the LAMPF Control System", Particle Accelerator Conference, Santa Fe, NM USA (1983)

[7] S.C. Schaller, J.K. Corley and P.A Rose, "Optimizing Data Access in the LAMPF Control System", IEEE Trans. Nuclear Science., NS-32, 5, (1985)

Active Filter for the DESY III Dipole Circuit

W. Bothe
DESY, Notkestr. 85, 2000 Hamburg 52, Germany

Abstract

The DESY III dipole circuit is now operated in a ramp mode cycle with 3.6 s repetition rate. Excitation is done by a 12-pulse thyristor converter, followed by a passive filter. The existing current control could be improved by addition of an active filter. The use of a more efficient passive filter reduces the size of the active filter and does not deteriorate the dynamic behaviour. The design of the control loops and the results of the simulation are presented.

Introduction

The ramping time of the DESY III proton synchrotron dipole magnets was determined to be about 1.5 s. With that and the time constant of the dipole circuit an excitation power of more than twice the I^2R-value or a total of 2.7 MW is necessary. A conventional 2-quadrant thyristor converter/inverter for 12-pulse operation is used as a main power supply, symmetrically controlled during the whole 3.6 s cycle time but operated in a gated freewheeling mode during the 100 % flat top and the 4.1 % injection flat bottom phases. In addition to this filtering of the output voltage, especially of its 600 Hz component, is needed. During the first stage a simple critical damped low-pass filter was provided to get a good dynamical behaviour. Later improvements of the synchrotron operation showed the necessity of a lower harmonics content. This can be attained by addition of an active filter, thus also improving the dynamical behaviour of the automatic control system. Figure 1 shows the equivalent circuit diagram.

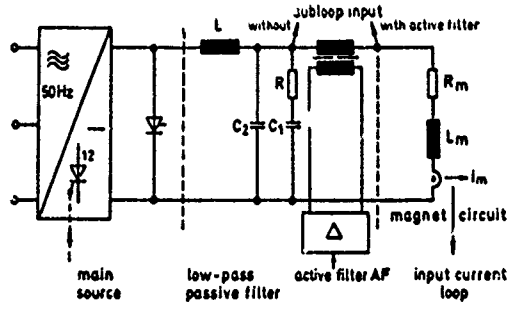


Fig.1: DESY III dipole excitation - Basic circuit diagram

System structure and equivalent block diagrams

Figure 2a represents the circuit containing all the elements of the multi-loop feedback system. The transfer functions of the single structure elements are listed below ($s = j\omega s^{-1}$).

F_{S1}: 2nd order rational approximation for the dead time T_t of the DC source. $T_t = 0.83$ ms. F_{S2}: Passive filter PF (series reactor without losses)

$$F_{S2} = \frac{1 + 2d \cdot s/\omega_0}{1 + 2d \cdot s/\omega_0 + (1+m)s^2/\omega_0^2 + 2md \cdot s^3/\omega_0^3} \quad (1)$$

$$m = \frac{C_2}{C_1}; d = \frac{R}{2\omega_0 L}; \omega_0^2 = \frac{1}{LC_1} \text{ (see Fig.1)}$$

F_{S3}: magnet circuit; 1st order delay network; $T_m = 1.7\ s$
$V_0 = \frac{U_G}{I_{mn}R_m}$ U_G: voltage of the DC source
I_{mn}: nominal rated magnet current

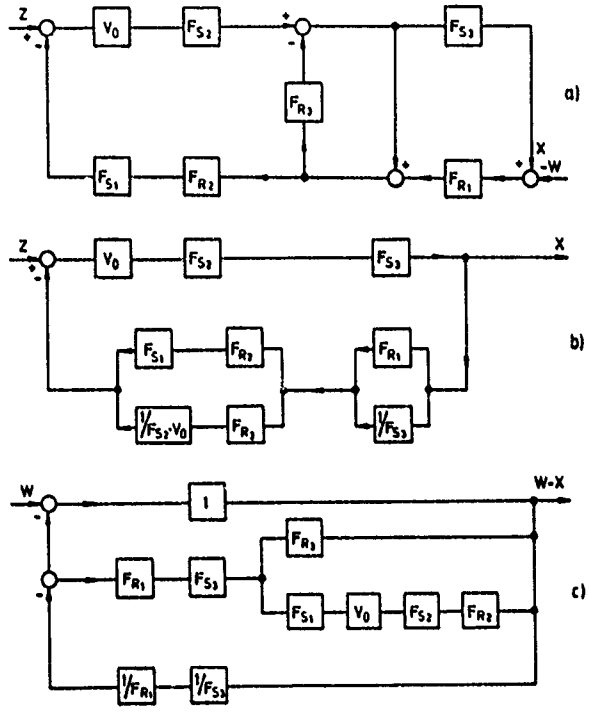


Fig.2: Multiloop control system -Block diagrams (see text)

F_{R1}: magnet current regulator

$$F_{R1} = \frac{V_I \cdot (1 + sT_m)}{sT_m} \qquad PI - characteristic \quad (2)$$

$$F_{R1} = \frac{V_I \cdot (1 + sT_m)(1 + sT_2)}{s^2 T_m T_2} \qquad PI^2 - characteristic \quad (3)$$

F_{R2}: voltage regulator; $F_{R2} = F_{R21} \cdot F_c$

$$F_{R21} = \frac{V_{II} \cdot (1 + sT_2)}{sT_2} \qquad PI - characteristic \quad (4)$$

F_C: compensating element ("phase shifter")

$$F_C = \frac{1 + sT_3}{1 + sT_4} \cdot \frac{1 + sT_3}{(1 + sT_5)(1 + sT_6)} \quad (5)$$

0-7803-0135-8/91$01.00 ©IEEE

F_{R3}: active filter AF

$$F_{R3} = V_{III}\frac{T_7 \cdot T_8 \cdot s^2}{(1+sT_7)(1+sT_8)(1+sT_9)^2} \qquad (6)$$

$T_7 = 10\,ms$; $T_8 = 4.6\,ms$; $T_9 = 0.32\,ms$; $V_{III} = 8$

The representation of Fig. 2a requires that no or only negligible reaction occurs between structure elements opposite to the arrow direction. Figure 2b shows the monoloop block diagram which is equivalent to Fig. 2a for the effect of the most important disturbance variable ΔU_{line} and also for the open-loop response. The use of line diagram Fig. 2c leads to the simulation of the normalized following error. The simulations were carried out with the aid of the Hewlett Packard "Linsys" method.

Dynamic characteristics

The layout of the elements of the automatic control system was done with the aim to get a minimum tracking error. For that, the following measures were taken into account:
- high gain of the current loop at the expense of the subloop gain. In the case of the AF circuit a compromise must be found because the size of the AF depends on the reciprocal of the subloop gain;
- compensating networks F_C in case of the structure with only PF to enlarge the open-loop bandwidth. Having a suitable layout, F_C acts mainly as phase shifter with little influence on the magnitude. See also Ref. [1];
- double integration in the current path. In this case, the voltage subloop may not have an integral element to ensure the stability of the whole system.

The following error was analyzed for the first transition period of the magnet current between the DC injection level and the beginning of the linear ramp. Its duration is 0,1 s and during this time the control input w obeys to the equation

$$w = a \cdot t^3 + b \cdot t^4 \qquad (7)$$

a and b have to be determined such that at the end of the transition period $\dot{w}$ is equal to the ramp gradient and $\ddot{w} = 0$.

Circuits with passive filter only

We compare the circuits having 2 different low-pass passive LC-filters

a)
critical damped; $\omega_0 = 2\pi \cdot 37\,s^{-1}$
according to the a.m. transfer function F_{S3}: $d = 1$; $m = 0$
Damping of the 600 Hz component: 18 dB

b)
third order; $\omega_0 = 2\pi \cdot 26\,s^{-1}$; $m = 0.1$; $d = 0.4$
Damping of the 600 Hz voltage component: 35 dB

a)
current loop: PI-characteristic: $V_I = 1500$
voltage loop: PI-characteristic: $V_{II} = 2$; $T_2 = 0.05\,s$
$T_3 = 3\,ms$; $T_4 = 15\,ms$; $T_5 = T_6 = 0.2\,ms$

b)
current loop: PI-characteristic: $V_I = 900$
voltage loop: PI-characteristic: $V_{II} = 2$; $T_2 = 0.005\,s$
$T_3 = 6\,ms$; $T_4 = 3\,ms$; $T_5 = T_6 = 0.4\,ms$

Figure 3 shows the open-loop responses for these two cases with the following parameters of the feedback amplifiers:

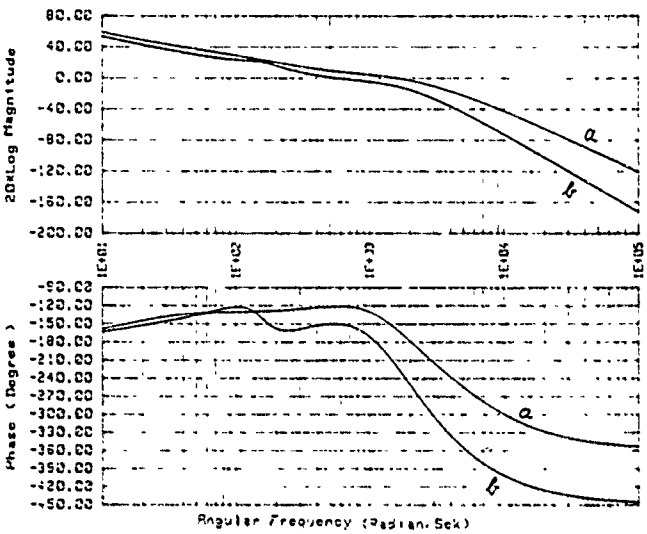


Fig.3: Circuit with passive filter only - Open loop frequency responses (see text)

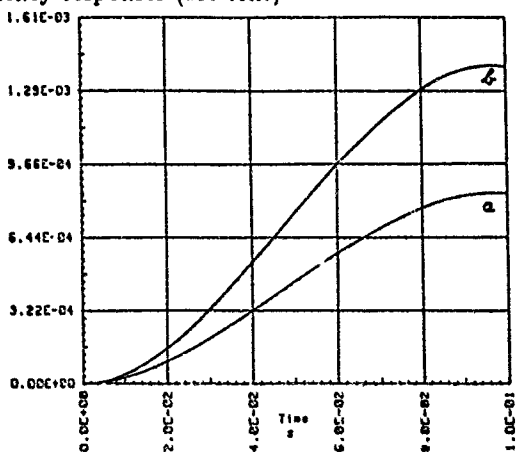


Fig. 4: Circuit with PF only - Tracking error (see text)

In Fig. 4 the tracking error of the magnet current, related to the nominal rated current is represented with a maximum at the end of the transition period due to the single integration of the current loop. This value is kept during the ramp phase.

Circuits with passive and active filters

The active filter has a transfer function as described above. The other system parameters are

passive filter: third order; $\omega_0 = 2\pi \cdot 27.5\,s^{-1}$; $m = 0.1$; $d = 1$
current loop: V_I = 1000; 2000; 4000; PI or PI^2 characteristic
voltage loop: V_{II} = 3.74; PI or P-characteristic; T_2 = 15 ms

Figure 5 shows the frequency responses of the active filter

(b) and the open voltage loop (a) and Fig. 6 the open-loop Bode Diagrams for the whole system.

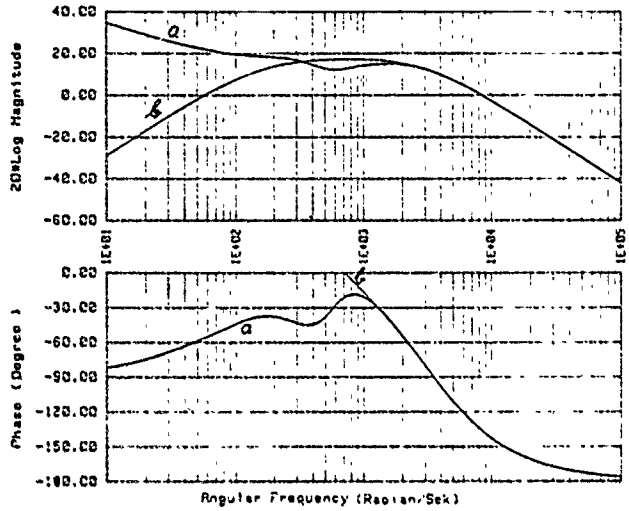


Fig.5: Circuit with passive and active filter – Bode Diagrams of the open voltage loop (a) and the AF (b)

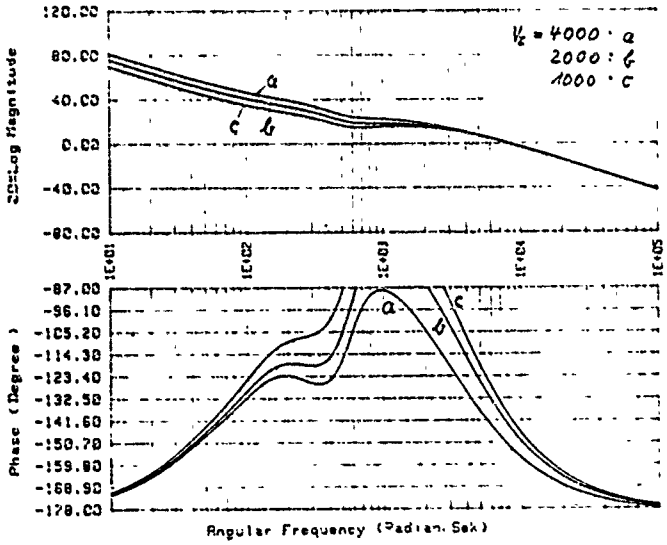


Fig.6: Circuit with passive filter and active filter – Bode Diagrams of the whole open-loop system

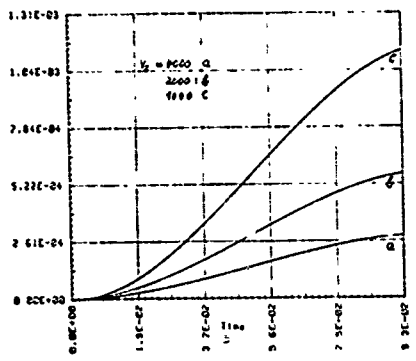


Fig.7: Circuit with passive and active filter – Tracking error for mono-integrating current loop

For these no conspicuous difference was found for the two different current loop characteristics.

Figure 7 and 8 are graphics of the tracking error for the two different current loop modes. In the continuation in time of Fig. 8, the following error decays to zero during the linear ramp. Figure 9 shows the frequency response: magnet current to passive filter output with (b) and without (a) AF thus showing the damping of the 600 Hz component.

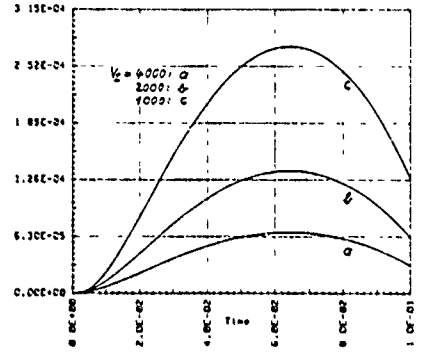


Fig.8: Circuit with passive and active filter – Tracking error for dual-integrating current loop

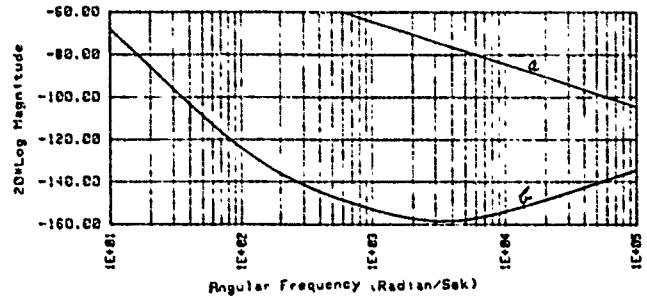


Fig.9. Harmonics attenuation without (a) and with (b) active filter. (see text)

Results

The graphs of the following error show a strong dependence on the current loop gain, which may be enlarged considerably by the use of an active filter. A more effective passive filter ensures that the remaining amount of harmonics voltage to be absorbed by the active filter remains small. – The input of the voltage subloop after the AF has nearly no harmonics content – 115 dB for 600 Hz or 0.7 mV – and therefore offers much better conditions than in usual installations with PF only. In the optimum case of Fig. 8, the maximum of the tracking error of the magnet current related to its actual value is $1.3 \cdot 10^{-3}$. Compensation by introduction of the second derivative of the reference value as described in [1] would minimize this value during the transition period strongly. The remaining tracking error at the start of the linear ramp can not be compensated by this methods but its value, related to the actual magnet current value, is only 4×10^{-4} and decays rapidly.

References

1. W. BOTHE, *"Magnet circuits for DELTA"* Proceedings of the 2nd EPAC (1990), pp. 1212 - 1214

Precision Power Supply Control Module*

N. Dobeck, B. Lamora, J. Larkin, M. O'Sullivan, C. Sharp
Continuous Electron Beam Accelerator Facility
12000 Jefferson Avenue
Newport News, VA. 23606

ABSTRACT

A temperature stabilized, digital input circuit module using surface mount technology has been developed for use as the precision control element in a 10 A bipolar trim magnet regulator. Regulators using this module have shown stability of 20 ppm over 8 hours. This circuit module combines the functions of a current measuring shunt, serial DAC, precision voltage reference, high gain error amplifier and readback buffer amplifier. Loop gain and compensation are done externally to the module. The module can be used in high current power supplies by replacing the internally derived current signal with the output signal from an external high current shunt or transductor.

INTRODUCTION

The power supplies which provide currents to approximately 1900 focussing and steering magnets in the CEBAF recirculating electron accelerator will periodically be adjusted based on measurements from numerous beam monitors located around the accelerator. Initially, power supplies with 1000 ppm combined drift and ripple performance were considered adequate to drive these magnets. This level of performance was achievable using readily available devices and well understood analog techniques without need for stringent temperature control measures.

Further analysis of beam dynamics indicated that power supplies with 100 ppm ripple performance were needed. This level of performance required that an entirely different approach be taken for the low level power supply control circuitry.

The key component was the current sensor which provides a feedback signal to the error amplifier. Even a good shunt resistor, such as one made of manganin, has a temperature coefficient of about 15 ppm/°C. Resistance drift over 24 hours due to expected ambient temperature change alone would more than use up the entire error budget. A zero-flux transductor was considered for the current sensing device but was rejected because the size and cost were too high for this application. Hall effect devices were rejected because of temperature stability and noise considerations.

The only feasible choice turned out to be a shunt resistor tightly coupled to a thermally regulated substrate which isolates the shunt from ambient temperature fluctuations and minimizes the effect of self-heating. The first effort in this direction combined a manganin shunt resistor and a preamplifier which were both mounted on a temperature regulated aluminum block. This isothermal block was mounted on a backplane and the high level feedback signal from the preamplifier was routed to the power supply printed circuit board through a backplane mounted connector.

It then became clear that it is very desirable to combine all temperature sensitive devices on the same isothermal block and mount the "core controller" block right on the power supply printed circuit board. This approach gives very good thermal performance as well as minimizing the amount of EMI which can be coupled into the low level regulation circuitry. Because the monitoring and control of each power supply module was being done with an on-board microprocessor and signal convertors, it was possible to closely connect the core controller to the necessary signal processing circuitry. Figure 1 shows a simplified schematic of the entire regulator.

DETAILED DESCRIPTION

Since beam variables, as measured by the beam monitors, are the controlled parameters, the magnet power supplies need not have particularly high absolute accuracy. A requirement of 0.1% FS (full scale), absolute accuracy was established based on interchangeability and diagnostic considerations. More important than accuracy are resetability and stability. Based on extensive modeling of CEBAF beam dynamics, minimum targets of 14 bit monotonicity and 100 ppm total envelope of uncertainty (drift plus peak-to-peak noise and ripple) per eight hour shift were chosen. The two major error components, noise and temperature induced drift, were tentatively budgeted at 34 ppm, peak-to-peak, and 2.5 ppm/°C respectively.

The stability of a high precision, current regulated power supply is usually limited by the quality of the current sensor used as the feedback device. The two most common high precision current sensors are zero flux magnetic transductors and resistive shunts. Zero flux transductors were rejected because of cost and size considerations. Initial investigation and experiments with conventional resistive shunts indicated that the temperature coefficient of resistivity and thermoelectric effects were unacceptably high.

To achieve the necessary noise and drift goals for the CEBAF power supplies, a new packaging and circuit architecture were developed by Highland Technology, Inc. A "core" power supply controller (patent applied for) was designed which combines a precision current shunt, preamplifier, serial DAC, voltage reference, error amplifier and support electronics into a single, temperature stabilized

*Supported by D.O.E. contract #DE-AC05-84ER40150

0-7803-0135-8/91$01.00 ©IEEE

assembly. A simplified schematic of the core controller is shown in Figure 2, and its physical layout is shown in Figure 3. The controller is fabricated on a solid aluminum block to which are bonded a planar current shunt, a surface mount circuit board, a temperature sensor and a heating element. The shunt preamplifier, DAC, error amplifier, associated voltage regulators and the temperature control loop components are mounted on the circuit board so that all components are very tightly coupled thermally to the temperature controlled aluminum baseplate. The magnet load current, which may be as much as 10 A, is connected to the controller through two of the metallic mounting standoffs. Low level signals pass through a small 12 pin connector. A 16 bit serial input DAC was chosen to minimize data connections and their associated thermal leakage paths. The feedback compensation elements of the error amplifier were not included on the controller assembly to allow external control of power supply control loop dynamics.

Integration of all sensitive components into a temperature regulated assembly provides substantial reduction of temperature coefficient and thermoelectric error sources. Such effects are reduced by the effective "stiffness" of the thermal control loop (ambient temperature change divided by assembly temperature change) which is about a factor of 100. It is interesting to compare this current controller design to a typical "ovenized" electronics package which might be used for something like a crystal oscillator which does not dissipate much heat. In the case of the current controller, the heat from the resistive current shunt is a major error source to the temperature control loop of the isothermal block and can potentially cause severe temperature gradients within the assembly. Unlike the case of the crystal oven, the current controller design requires much lower thermal resistances between all components and must be packaged to allow a predictable heat leak to the ambient environment so that shunt power dissipation cannot push the temperature control loop out of regulation.

The final current controller design operates at 68°C and dissipates about 5 W under normal operation. The shunt element is punched from sheet manganin and contributes about 0.7 W at full scale output current of 10 A. The controller package is plugged onto the main power supply card and is held in place with four screws. The core controller assembly is covered with a phenolic potting shell giving an overall size of 3×3×0.75 inches.

CONTROL LOOP DYNAMICS

The accelerator focus and steering magnets vary in inductance from 40 mH to about 1 H with typical resistances in the 2 ohm range. It was desired to configure the control loop dynamics to allow a single power regulator card design to drive any magnet while simultaneously providing high stability margins and minimum noise levels. Current regulation is achieved by the overall type 1 (integrating) feedback loop with the RC network and the magnet L/R time constant dominating closed loop dynamics. The output amplifier and power booster stages employ two additional inner feedback loops to insure that the output stage performs as a very stiff, wideband voltage amplifier with good local power supply ripple rejection. The use of local output stage feedback allows the overall current control loop to be optimized on loop stability and noise bandwidth considerations without concern for power supply noise or output stage drifts. The RC compensation was chosen to provide integration at low frequencies, leveling off to a flat loop gain of 1500 at about 0.3 Hz with the magnet's effective L/R time constant providing the final 6 db/octave rolloff. The resulting current regulator has excellent phase margin for all required magnet loads. The output impedance of the regulator makes a smooth transition from a high value (corresponding to a constant current mode) at low frequencies to a low value (corresponding to a constant voltage mode) at high frequencies. This restricts loop noise bandwidth and allows the magnet L/R time constant to participate in attenuating high frequency noise and ripple.

PERFORMANCE

Because the controller is meant to be part of a high gain feedback loop, as well as requiring a serial data input link, it is difficult to test it as an isolated device. Instead, all but the simplest testing was done with the device installed in a fully functional power supply module.

Key power supply performance parameters are DC current stability, power line harmonic rejection, low frequency noise and resetability. High frequency noise is of less concern because of the filtering effect provided by the L/R time constant of the magnets.

DC current stability, low frequency noise and resetability were measured using a precision transductor and an $8\frac{1}{2}$ digit DVM. The particular DVM used had automatic sampling, storage and analysis capability which allowed substantially more data acquisition and analysis to be done than is normally the case with a DVM. A temperature coefficient of about 2 ppm/°C was calculated based on tests run over several days.

Resetability was measured at +/- 2 A, +/- 4 A, +/- 6 A, +/- 8 A. The test method used sent a current command to the power supply, read the zero flux transductor output with the DVM and then sent a command of the opposite polarity to the power supply. This cycle was repeated numerous times and the data used to plot resetability histograms which showed a spread of less than 5 ppm.

Current ripple was measured by using a FFT (Fast Fourier Transform) analyzer to generate the frequency spectrum seen at the output of the transductor electronics. To generate a worst case estimate, the harmonic components were directly added to derive the current ripple The FFT spectra are additionally useful because of information gained by knowing what line frequency harmonics are present although a time domain trace of the current ripple would be very useful because it would be a much

easier method of checking if the power supply was meeting ripple specifications. Currently work is underway to set up instrumentation capable of furnishing a time domain trace of current ripple. Figure 4 shows a typical output frequency spectrum.

The temperature coefficient is less than 2 ppm/°C with a worst case peak-to-peak current noise envelope of about 50 ppm of magnet FS current. Some small nonlinearities and thermal effects are observed, probably caused by thermally induced stresses and residual thermal gradients. These effects are in the 10 ppm range and of no consequence. Some of the regulators have shown a worst case 60 Hz ripple of about 40 ppm which is thought to be largely due to stray magnetic field pickup due to positioning in the relay rack.

The power supply drift over a 24 hour period with a 28°C ambient temperature swing is in the 50 ppm range.

In addition to the development and evaluation testing of the design itself, each core controller is extensively tested at the factory as well as passing through an acceptance test at CEBAF.

EXTENDED USE

Although the controller was primarily developed for use in relatively small corrector and focussing magnet power supplies, it will find widespread use at CEBAF as the key element in a standard control module which will include all low level circuitry necessary for any size of power supply. For use with high current power supplies it will be necessary to disconnect the internal shunt preamplifier output and introduce an external high level feedback signal from a transductor or high power shunt.

The present controller unit will give 100 ppm performance over a fairly wide ambient temperature swing while 10 ppm drift performance is possible by enclosing the entire low level regulator module in a temperature controlled environment and using a transductor with a suitably low temperature coefficient.

SUMMARY

A temperature regulated core controller has been developed for use in a 10 A, bipolar corrector power supply which gives better than 100 ppm performance over a wide ambient temperature range. The controller combines a precision shunt, preamplifier, serial DAC, voltage reference and error amplifier in a compact, printed circuit board mountable package. Use of the controller can be extended to any size power supply by using an externally generated feedback signal rather than relying on the internal shunt and preamplifier.

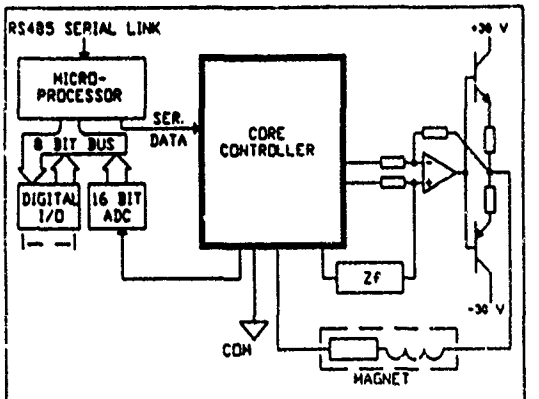
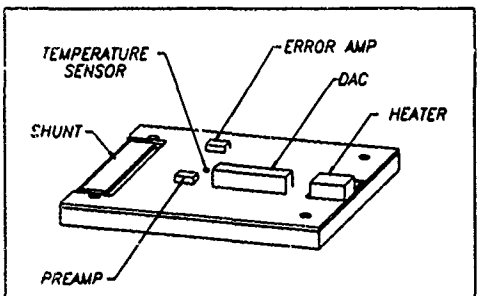


FIG. 1 - CURRENT REGULATOR DIAGRAM



CONTROLLER PHYSICAL LAYOUT
FIGURE 3

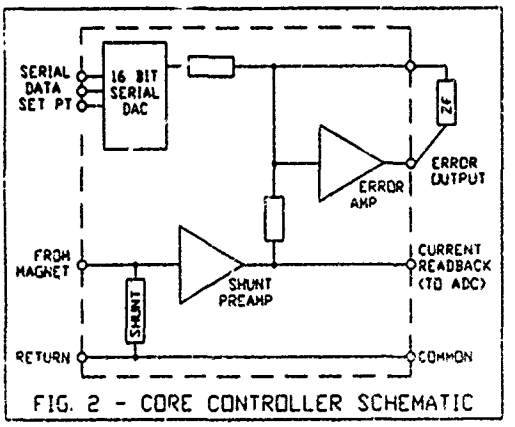


FIG. 2 - CORE CONTROLLER SCHEMATIC

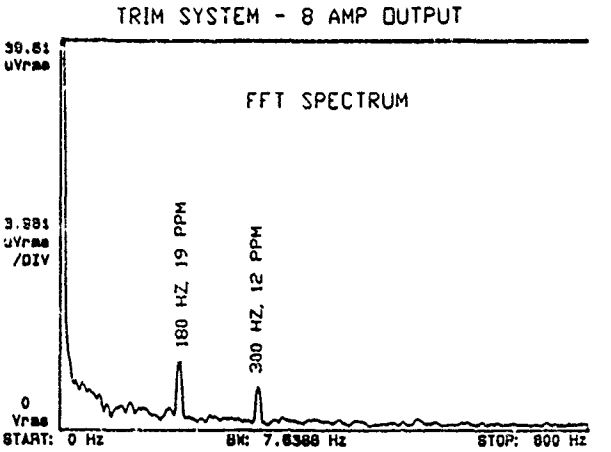


FIG. 4

Measurements of Crowbar Performance of the 20 kV 130 A dc Power Supply of the TRIUMF rf System

A.K. Mitra
TRIUMF, 4004 Wesbrook Mall, Vancouver, B.C., Canada V6T 2A3

Abstract

The TRIUMF rf system operates at a fixed frequency of 23.06 MHz with a power capability of 1800 kW. The dc plate power for the four push-pull power amplifiers is provided by a single dc power supply at 20 kV, 130 A and the amplifiers are protected by a single ignitron crowbar circuit. In the case of voltage breakdown outside the tube, the triggering of the crowbar circuit relies on the voltage developed across a low resistance shunt in the return path of the common dc power supply. Frequent failure of the crowbar ignitrons, following an external dc voltage breakdown, led to the investigation of the crowbar performance. Current transformers have been installed in the common B^+ line to the power amplifiers and the anode circuit of the ignitron crowbar in order to measure amplitude, duration and time delay of various dc currents under fault conditions. Similar current transformers were installed in the individual anode circuits of the power amplifiers to provide protection to the complete system in case of an external dc voltage breakdown. The results of these measurements and recommended solutions for operations are reported.

I. Introduction

The eight power amplifiers which constitute the main rf system of the TRIUMF cyclotron [1,2] are protected by a single ignitron crowbar circuit. The purpose of the crowbar is to provide a fast short circuit on the output of the 20 kV dc power supply to direct the stored energy in the filter capacitors away from the fault should any of the eight amplifiers arc internally or high voltage breakdowns occur in the circuitry outside the tubes. The firing signal for the crowbar circuit is obtained from voltage developed across a series resistance in the cathode circuit of each amplifier and a low resistance shunt in the return path of the power supply. The ignitron crowbar is thus triggered by any of the nine signals or combination of them. Frequent crowbar firing and failure of some of the ignitrons led to this investigation of crowbar performance.

Four current transformers using low μ NiZn ferrite of 8" o.d. and 5" i.d. and a single layer winding of 8 turns, have been placed at appropriate locations in the dc power supply for measurement of fault currents and evaluation of the crowbar performance. The units are enclosed in shielded boxes and have been tested at 45 kV without any breakdown. Two more transformers are planned to be installed in the near future.

II. System Description

The basic schematic of the 20 kV dc power supply is shown in Figure 1 where PA1 to PA4 are the four push-pull power amplifiers. The sensing resistors in the cathode circuit of PA1–PA4 and the dc shunt 50 mV/150 A have been used to sense and trigger the ignitron crowbar. The current transformers CT1 to CT4 are the recently installed components in the dc power supply. Two commercially available Pearson 301X transformers have also been mounted next to CT1 and CT2 for calibration and initial measurements.

The current transformer CT1 senses ignitron current only when it fires. CT2 measures the dc operating current (approx. 80 A) when rf is switched on/off and also responds to the instantaneous short circuit currents should any of the anode supply lines to the power amplifiers short. Hence, the output of CT2 can be used to trigger the ignitron crowbar under the above fault condition. Current transformers CT3 and CT4 are to be used only for monitoring the fault condition of the power amplifiers although they can be utilised to trigger the crowbar if needed.

III. Calibration and Measurement

The current transformers have been calibrated against the Pearson which has a sensitivity of 0.01 V/A with 1 MΩ termination. Figure 2 shows the voltage outputs of the Pearson and CT1 when rf drive is switched off. The measured sensitivity of the current transformer is 0.023 V/A.

Short circuit current measurements from the dc shunt and the Pearson transformer (location CT1) are shown in Figures 3 and 4 respectively. The test was carried out by firing the ignitron from the crowbar logic circuit. The voltage developed across the shunt gives a short circuit current of 3960 A whereas the Pearson output leads to a short circuit current of 2200 A. The higher current from the shunt measurement is due to the presence of rf noise. A PSPICE simulation of the power supply circuit with a single phase star-delta configuration and full wave rectifiers, yields a peak short circuit current of 3000 A.

The total charge/minute for the ignitron computed from

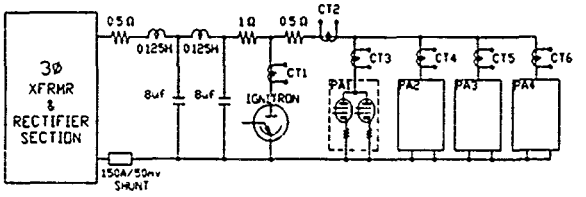


Figure 1 Schematic drawing of the dc power supply.

0-7803-0135-8/91$01.00 ©IEEE

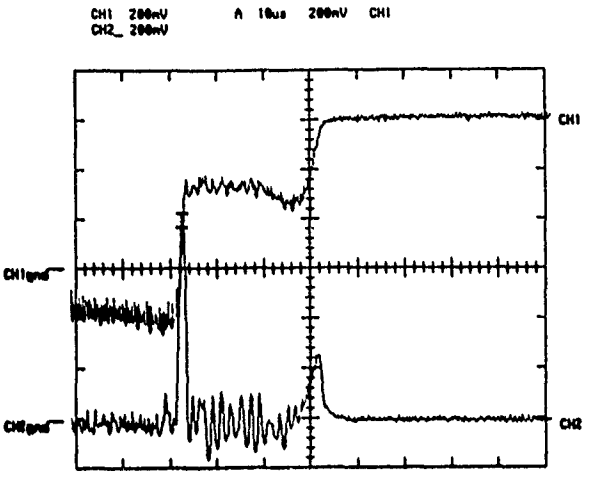


Figure 2. On-line calibration of current transformer. Ch1 - Pearson output. Ch2 - CT1 output.

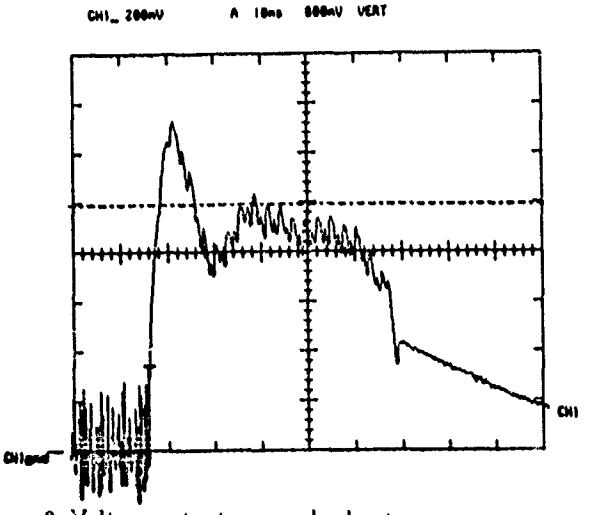


Figure 3. Voltage output across dc shunt.

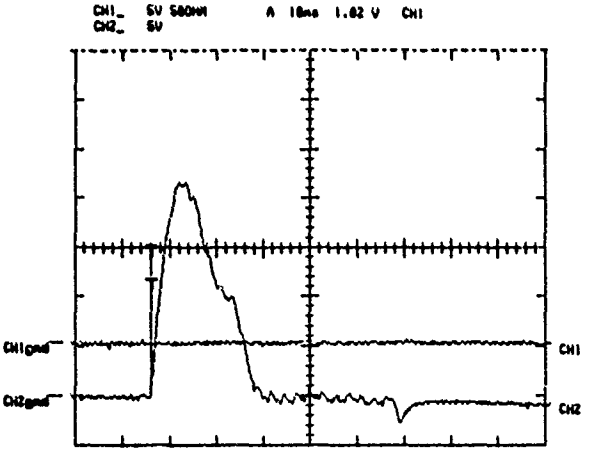


Figure 4. Voltage output from the Pearson transformer.

the above current measurement is 1.1 Coulomb and the duration of the ignitron current is 53 msec (~3 1/2 cycle).

IV. Summary of Measurements

The following results can be summarised from the measurements:

1. The peak instantaneous anode current through the ignitron is 2200 A
2. The duration of ignitron anode current is 53 msec.
3. The main circuit breaker is opening in 3 1/2 cycles.
4. The total charge/minute is 1.1 Coulombs for the ignitron.
5. The delay between fault and ignitron firing is 1.4 μsec.

V. Discussion

In the present configuration of the crowbar circuit, reflected power due to momentary sparks in the resonator system, arcs in the power combiners, and spurious rf noise etc. cause the ignitron to fire falsely when it is sufficient to switch off the rf drive without switching off the dc power supply. Output from the current transformers, which are rf shielded, can be employed to trigger the crowbar circuit only when the instantaneous dc current exceeds a certain pre-set value.In this way, with fewer ignitron firings, longer life of ignitrons can be achieved. It is rather easy to stay within the maximum voltage or current rating of a particular ignitron, however, exceeding one key factor, i.e. the current energy transfer per minute in Coulombs, has an adverse effect on the life of the ignitron tube due to anode heating. Exceeding the current pulse duration also gives rise to side-wall erosion, causing further reduction of tube life.

VI. Future Scope

It is evident that a reliable crowbar firing scheme has to be developed employing current transformers as outlined in this paper. Fiber optic links can be incorporated between the output of the transformers and crowbar firing circuit to enable implementation of these transformers in the existing protection circuit of the complete system. Voltages developed across resistive shunts can be filtered adequately with RLC networks but can still be utilised in the crowbar firing circuit with slower response time.

VII. Acknowledgements

The author wishes to thank Mr. R. Worsham for his encouragement for carrying out this work and Mr. R. L. Poirier for constant help and discussion.

VIII. References

[1] K.L. Erdman *et al.*, "TRIUMF Amplifier and Resonator System", Proc. *6th Int. Cyclotron Conf.*, AIPCP #9 (AIP, 1972) p. 451.

[2] R.H.M. Grummer, R.L. Poirier and M. Zach, "TRIUMF RF System - Initial Operating Problems and Their Solutions", Proc *7th Int. Conf on Cyclotrons and their Applications* (Birkhauser, 1975), p. 167-170.

[3] A.K Mitra and P.J. Tallerico, "Spark Gap Crowbar for High Voltage Power Supply", IEEE Trans. Nucl. Sci , NS-30, No.4, p. 2862, 1983.

TRANSIENT ANALYSIS OF THE AGS-BOOSTER RING DIPOLE AND QUADRUPOLE MAGNET SYSTEM[1]

W. Zhang, A.V. Soukas, and S.Y. Zhang

AGS Department, Brookhaven National Laboratory, Upton, NY 11973

ABSTRACT

A case study has been conducted for the quantitative analysis of the transmission line effects in the Brookhaven AGS Booster ring dipole and quadrupole magnet string. The Booster is a rapid cycling synchrotron (7.5 *Hz*) which is excited by multiphase rectifier power supplies. A computer model and a simulation program are developed to study the transient current response of the magnet string due to an applied step voltage. To damp out the staircase noise caused by wave reflection during the current ramp, external resistors will be added in parallel with each half dipole magnet and each quadrupole magnet. The system model and simulation values are based on the actual magnet parameters, the magnet power supply bus system, and the proposed current ramping rate. The system simulation approach can be applied to a larger system as well, and will be briefly discussed.

INTRODUCTION

In the AGS Booster main ring, there are 36 dipoles, 24 horizontal and 24 vertical focusing quadrupoles. The main coils of these magnets are connected in series and powered by multiphase rectifier power supplies. The requirements for the AGS Booster ring power supplies are quite varied. They must act as accurate low voltage supplies for beam injection; they must ramp rapidly up and down, in two distinctly different modes, for beam acceleration and cycle recovery; and also be capable of flat top operation for a period greater than two seconds for accumulation of polarized proton beams. It is known that magnet strings will behave like a varying impedance transmission lines, due to their distributed inductances and capacitances. This leads to the concern of pulse reflection noise problem during fast current ramping. The circuit models of the dipole and quadrupole magnets are shown in Figure 1. In these models, L_D, R_D, C_D are the dipole magnet inductance, resistance, or capacitance, respectively. And, L_Q, R_Q, C_Q are defined similarly for the quadrupole magnet. The parameters used in the simulation are summarized in table 1.

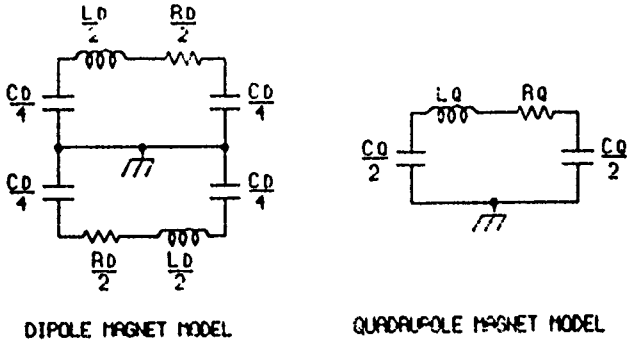


Figure 1. The dipole and quadrupole magnet models.

Table 1. Magnet Parameters

Magnet	Dipole	Quadrupole
Inductance	3.2 mh	0.35 mh
Resistance	1.5 mohm	0.9 mohm
Capacitance	10 nf	2 nf

A simplified schematic of magnet bus connection and power station arrangement is shown in Figure 2.

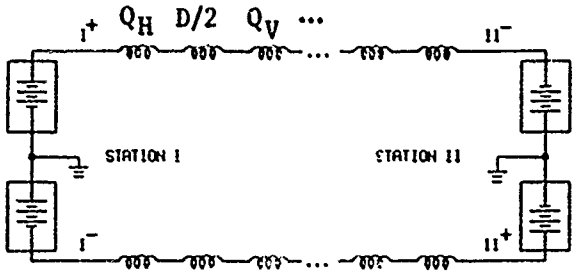


Figure 2. Simplified schematic of the AGS-Booster ring magnet power supply system.

[1] Work performed under the auspices of the U.S. Department of Energy.

0-7803-0135-8/91$01.00 ©IEEE

This arrangement virtually splits the circuit into two identical strings. One is from I^+ to II^-, and another is from II^+ to I^-. There are 12 identical sections in each string, a total of 24 sections in the ring. Figure 3 shows a typical section consisting of 2 quadrupole magnets and 3 top or bottom halves of dipole magnets. The computer simulations are based on the circuit model of one entire string powered by two supplies, one at each end, with the same voltage amplitude but opposite polarities.

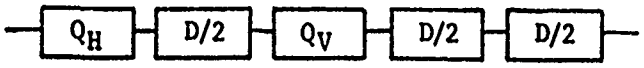


Figure 3. A typical section of the magnet string.

SIMULATION RESULTS

The transient current response due to an applied voltage step is the main interest in this study. In the AGS Booster operation, the magnet current must ramp up linearly from 600 *amperes* to 2500 *amperes* in 60 *ms*. This requires a voltage step about +/−1068 *volts* at each end.

Each magnet string is a balanced circuit about the center. Therefore, the center point is a virtual short of the transmission line, when the magnet string is powered by a pair of power supplies with equal amplitude and reversed polarity. The wave reflection time is twice the half way delay time of the transmission line. The initial magnitude of the staircase noise is about U/Z, where U is the voltage step, and Z is the average impedance of the transmission line.

To damp out the noise, first we added an external resistor in parallel with each half dipole magnet. As one might expect, the result shows that the smaller the external resistance, the faster the noise damping rate. However, the current sharing between the external resistor and the dipole magnet results in a current difference between the dipole and quadrupole magnets. For better tracking of the quadrupole and dipole fields in the Booster ring, it is necessary to put an external damping resistor in parallel with each quadrupole magnet as well as across the dipole magnet.

The damping resistor used with each half of the dipole magnet is 300 Ω, as suggested by M. Meth in [4], and a 50 Ω resistor is used for each quadrupole magnet. Figure 4 shows 6 current curves of quadrupole and dipole magnets located at the first, middle, and last section of the magnet string, for the first 2 *ms* after the excitation. Figure 5 (a) shows the absolute current difference, as a percentage, between quadrupole magnets and the design value, and (b) of the dipole magnets. It can be seen that the current differences reduce to below 0.01% in 600 μs. The average absolute current difference of dipole and quadrupole magnets to the design value is shown in Figure 6, where it decreases to less than 0.01% in about 200 μs. It may be noticed that this scheme now contains a high impedance resistive bypass with the main magnet string. Therefore, the nonlinearity of current ramping caused by parallel and series resistance should be taken into account. Figure 7 shows the dipole and quadrupole magnet current differences to the design value in percent. The peak difference is about 0.76%. A cure of this problem is to apply small trimming steps during current ramping, and current tracking to the command will not be a problem. Compared to the initial step, each trimming step must be fine enough, so that the reflection noise will not become noticeable.

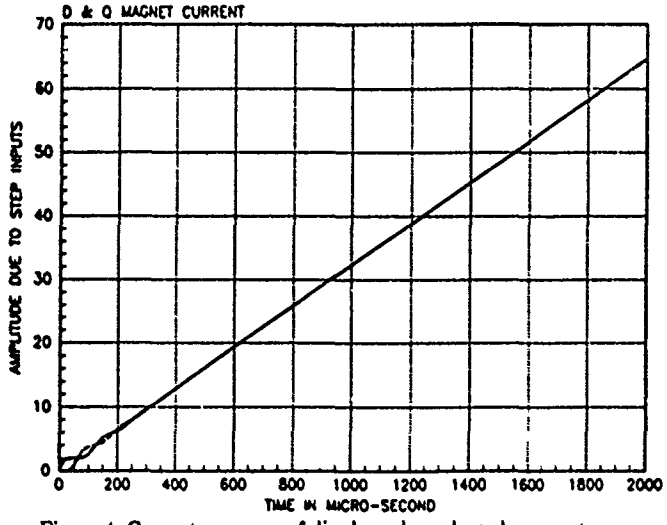


Figure 4. Current response of dipole and quadrupole magnets.

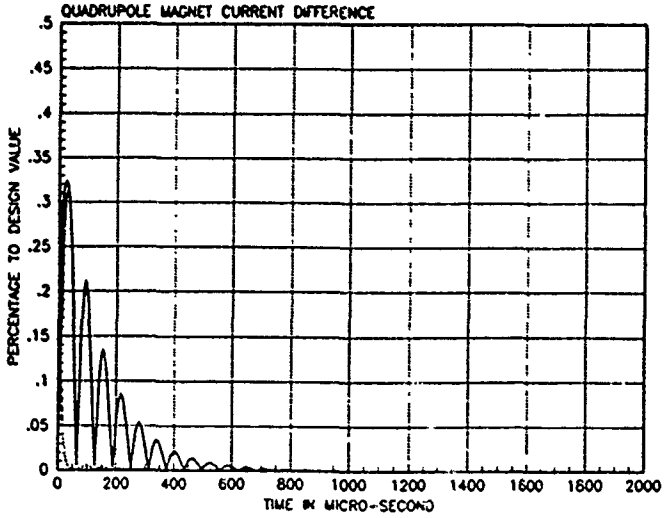


Figure 5 (a). The absolute current difference between quadrupole magnets.

SIMULATION APPROACH

The circuit model of the AGS Booster ring magnet string is a high order ladder network. For an N section L-C ladder network, the network matrix size is usually $2N \times 2N$, which can easily go beyond the capability of the electronic simulation programs. To simulate the Booster ring magnet string, we formulate the network in state space form. The voltage across the capacitor and the current through the inductor are chosen as the state variables. Since most high order ladder network have all the distinctive eigenvalues, the simulation can be obtained by using an eigen-system analysis approach. Applying a similarity transformation to the state equation, the output can be converted to a summation of the exponential functions. In this simulation, time step iteration is not involved. The simulation accuracy depends on the circuit model and eigen-parameter computation. This method turns out to be effective and of better simulation accuracy. However, it is restricted that the network must be a linear system. This is an extension of the method we used to simulate our fast kicker systems. Some detailed information is given in reference [5]. The circuit is simulated in $MATRIX_X$[2]. We developed our own user code. Expanding the stack size of the program, this method can be applied to a larger system.

ACKNOWLEDGEMENT

The authors wish to thank Mr. Roger Katz and Mr. Richard Casella for their support in using the Apollo system, also Dr. M. Meth for useful discussions about the problem.

REFERENCES

[1] "Booster Design Manual," AGS Booster Project, Brookhaven National Laboratory, 1988.

[2] O. Calvo and G. Tool, "Analysis of Transmission Line Effects in the SSC Magnet System," Proc., 1987 PAC.

[3] O. Calvo, et al., "Magnet Current Regulation in the SSC," Proc., 1987 PAC.

[4] M. Meth, "Magnet Wave Propagation," AD Booster tech. note #136, BNL, 1989.

[5] W. Zhang, et al., "A PFN and Transmission Line Simulation Method for Energy Discharge Systems," IEEE Conf. Rec., 19th PMS, 1990.

[2] $MATRIX_X$ is a trademark of Integrated Systems Inc., Santa Clara, CA 95054.

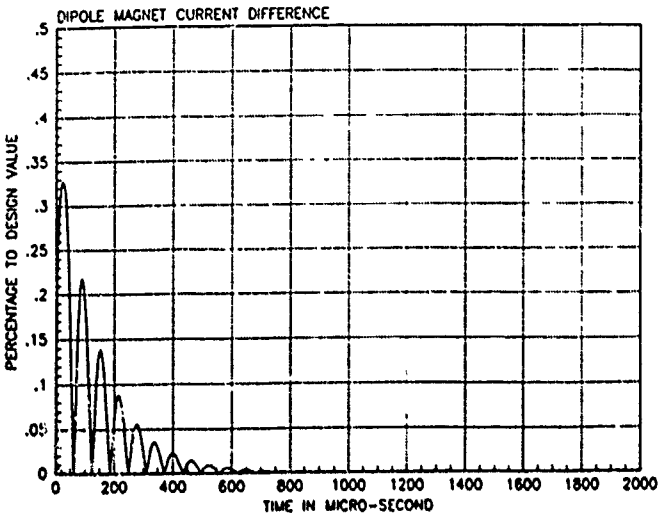


Figure 5 (b). The absolute current difference between dipole magnets.

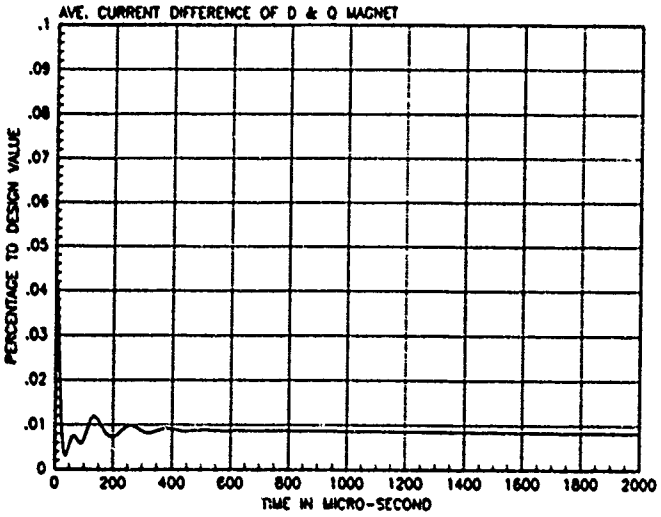


Figure 6. The average absolute current difference of quadrupole and dipole magnets.

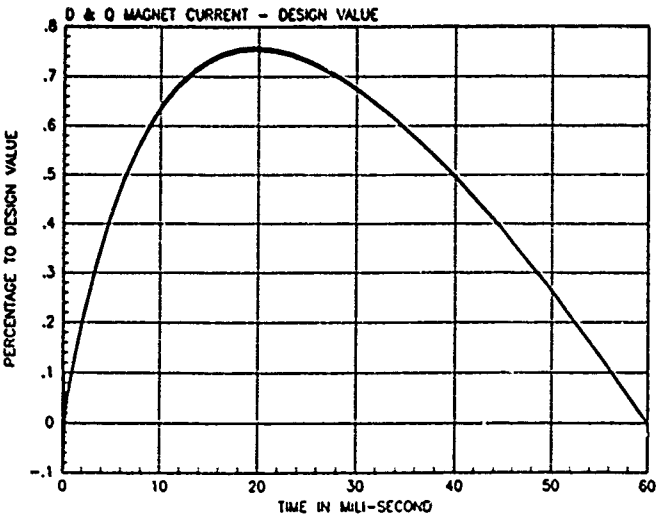


Figure 7. Current difference to the design value.

Operational results of an improved regulator and trigger system for the "Fast" Raster Scanning Power Supply System constructed at the Bevalac Biomedical Facility*

G. Stover, J. Halliwell, B. Ludewigt, M. Nyman, R. Stradtner
Lawrence Berkeley Laboratory,
University of California, Berkeley Calif. 94720

Abstract

A new and improved regulator and trigger control system has been installed in the "Fast" Raster Scanning Power Supply [1]*. The beam scanning system was developed to achieve a more precise and efficient dose delivery method for radiotherapy treatments [2]. This article discusses design considerations, measured results, and provides further elaboration of subsystem feedback and control functions that had not been discussed in the previous paper [1,5].

I. INTRODUCTION

The Raster Scanner that is presently being commissioned at the Bevalac Biomedical Facility is an important new beam delivery technique for performing radiotherapy with charged particle beams. A tightly focused light ion beam is deflected in a raster scanning fashion with the purpose of conforming the dose distribution to the treatment volume [2,3,4,5]. This requires very well regulated power supplies for tightly controlling the beam spot movement and achieving the desired dose distribution.

Initial system testing of the power supply revealed several component and system reliability problems in the "Fast" scanner section. The following paper offers a condensed discussion of the nature of these problems and their subsequent resolution.

II. REVIEW OF "FAST" SYSTEM

As shown in fig. 1 the fast scanner system is powered by a single unipolar SCR controlled power supply that applies a bipolar forcing voltage to the magnet via a synchronized bridge network of silicon controlled rectifiers (SCR) switches and a single gate turn-on thyristor (GTO) power connecting switch [6]. A current-regulated feedback loop precisely controls the the magnet field during both the charging and discharging cycles. The power regulating actuator (426 amps @ 220 volts max) is a grounded source MOSFET transistor assembly (16 heat sinks with 25 devices per heat sink) that is mounted in the return leg of the SCR bridge network. During the discharge cycle a majority of the stored energy of the magnetic field is dissipated in the diode resistor (energy dump) network and the remainder in the actuator. High power back-to-back zener diodes connected across the magnet provide over voltage protection and act as a freewheeling voltage clamp to extinguish the residual magnet current. The latter process necessarily occurs at very low currents and is required before the bridge switches can reverse the magnet polarity. This transition is defined as the "zero current crossover region" of the scanning cycle.

III. PROBLEMS ENCOUNTERED AND SOLUTIONS DEVISED

A. Operational problems:

Throughout the construction of this project all the standard methods of noise suppression and decoupling were carefully employed to suppress extraneous cross talk and undesirable feedback paths. However, recurrent system and component failures during the power testing phases revealed valuable information for further system improvements.

Noise induced failures demonstrated several inherent weaknesses in the GTO commutation circuits and the need to expand and improve the fault detection and alarm circuitry. Unexpected delays in the switching confirmation circuitry (B dot trigger circuit) resulted in unnecessary perturbations in the zero current crossover region and suggested a need for better triggering alternatives. The current dependent transconductance of the FET actuators at very low currents contributed to feedback loop stability problems. The nature and scope and of these problems suggested a systematic improvement of the regulator/trigger control scheme.

B. The basic triggering philosophy:

The there are several underlining principles implemented in the regulator/trigger chassis that make control of the switching network unusually precise and immune to misfire. First, the sequence for the triggering of the SCR and GTO switches is divided into four logical "states". These are; the charging cycle (GTO is "on" with one set of SCRs conducting) and the magnet current polarity is forward (1) or reversed (2) and the discharging cycle (GTO is "off" with with one set of SCRs conducting) and the magnet is discharging (freewheeling) down from the forward (3) or reverse (4) polarity condition toward the zero current crossover region. Secondly, the process of switching between states is verified. Each "state" command that sets a desired firing sequence for the GTO and Bridge switches is quickly compared against selected magnet parameters that are continually monitored within the system.

* This investigation was supported by the U.S. Department of Energy Contract No. DEAC0376SF00098 and in part by the National Institute of Health under Grant No. CA49562.
U.S. Government work not protected by U.S. Copyright.

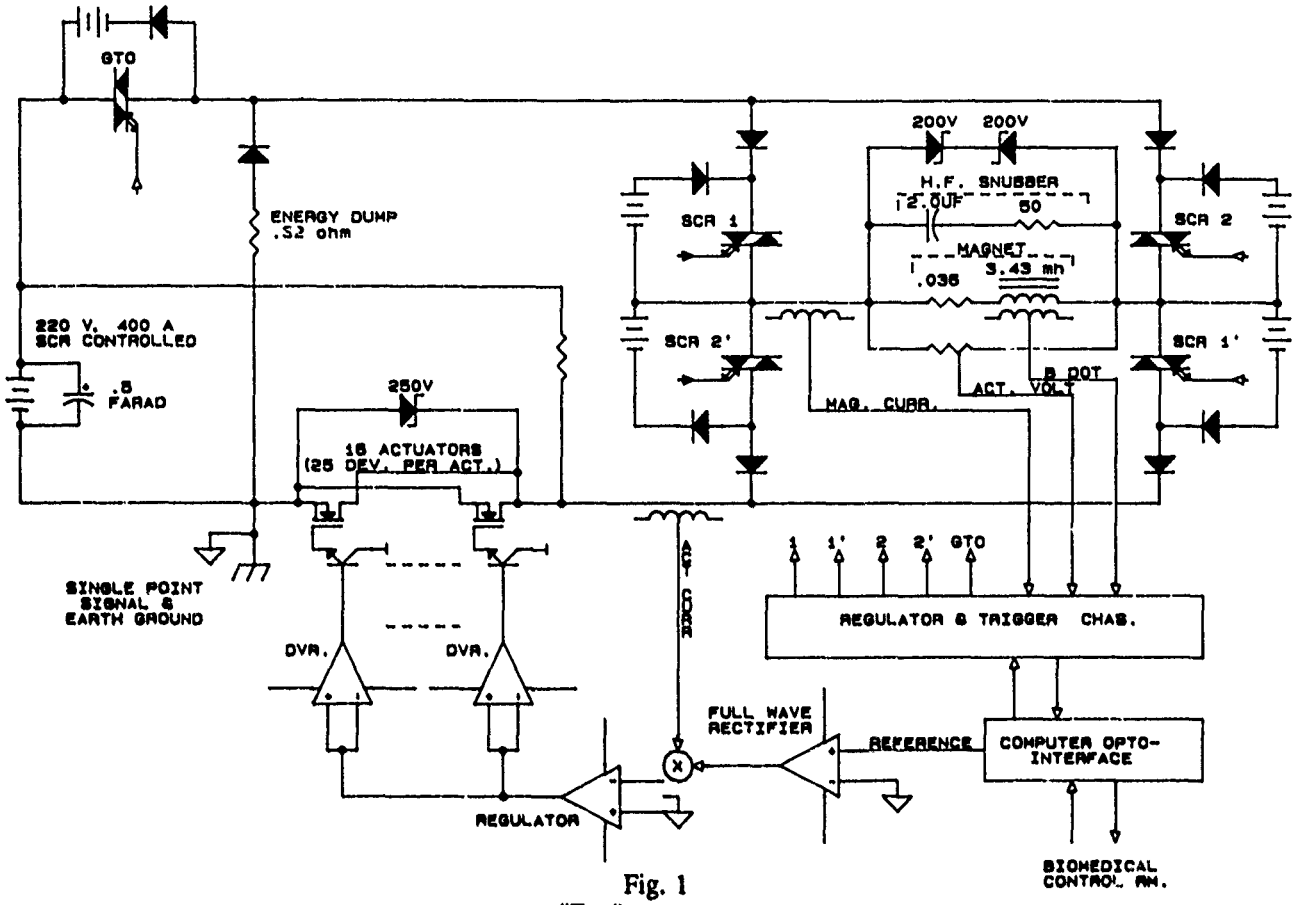


Fig. 1
"Fast" scan system

These four separate and unique "states" in conjunction with the verification function eliminate any possibility of the firing logic loosing track of the scanning process. A "short through" condition were two SCRs on the same side of the magnet fire simultaneously will also be avoided. If the chosen switch state is incorrect the system can shut down in a well defined and protected manner.

An example of the "state" and verify operation is illustrated during the zero current crossover region. As the magnet current (trace #1 of fig. 2) approaches its polarity switching region (< 4.0 amps.) the conducting SCRs are commutated off. To aid the SCR commutation the regulator feedback loop is also momentarily opened and the series actuators driven into the nonconduction. As seen in trace #2 the magnet bucking voltage rapidly rises to its zener clamp level (app. 325 volts) forcing the remaining magnet current to decay rapidly to zero. When the magnet voltage has collapsed to a preset threshold, the actuator is then driven to an optimal bias level to initiate a smooth transition to the next state. At the point where the locus of the controlling reference signals a polarity reversal the alternate SCRs are turned on and the feedback loop is closed. The resulting controller scheme is very flexible and provides full four quadrant scanning with triangular or any selection of variable slope waveforms.

C. New Regulator/trigger hardware layout:

The regulator/trigger system is divided into two chassis. All analog monitor, feedback, and control signals are fed to and from the regulator chassis. Reference control and feedback regulator circuits are contained within the chassis. The magnet parameters (zero cross region, B dot, reference locus, current and voltage) and the fast alarms are detected in the regulator chassis and digitally transmitted to the trigger chassis.

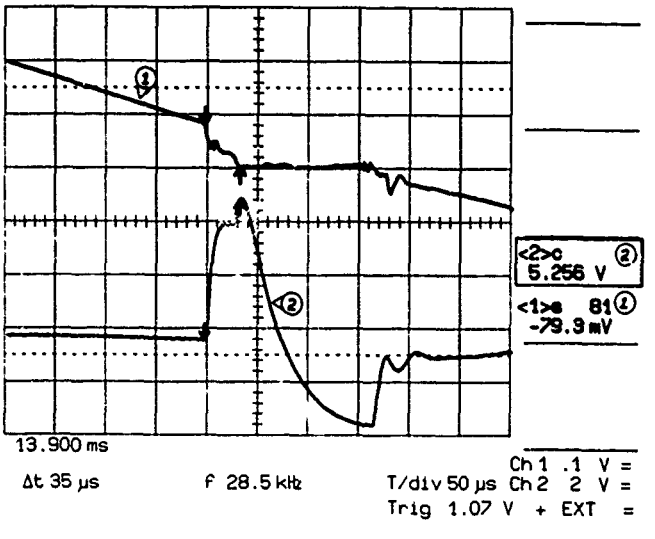


Fig. 2
Magnet current (#1- 5A/div.) vs Magnet voltage (#2 - 100 V/V)

The trigger chassis accepts commands from the beam delivery control system and provides the control logic for the

state controller and the servo/fault detection circuitry the chassis generates the proper "states" that are translated into trigger signals for the bridge SCRs and GTO during the scanning cycle. At any zero current crossover region or during any serious fault condition the trigger chassis opens the regulator feedback loop and drives the actuator and magnet by a predefined current level.

To protect the system from catastrophic failures a more extensive set of fast alarms was installed in the regulator chassis. In conjunction with open loop control function of the trigger chassis the magnet can be ramped down in a very predictable manner at any power level. The fast alarms are supplemented by delayed alarms that allow the completion of a scan cycle if a few actuator transistors have failed during the cycle.

The noise layout for the regulator chassis needed to be very rigorous. To minimize cross talk all analog and digital signals were separately routed by the careful placement of the subsystem functions. All sensitive analog signals are interconnected via twisted pair wire and received by laser trimmed precision differential amplifiers [7].

Both chassis were designed to promote ease of testing and debugging. Among the number of available options is a simulation mode. All the necessary magnet parameters that are required for normal operation are simulated and fed back into the chassis to completely recreate the pulse sequence for the SCR and GTO switches.

D. Other Hardware modifications:

All the power switches in the original "fast" scanner system were Toshiba GTOs. During the power testing phase a number of gate drive units and GTOs failed. The expense (~$1000.00 per device) and long delivery time (>20 weeks) posed a serious bottleneck for efficient repair times. Consequently we decided to replace bridge GTOs with off-the-shelf SCRs. As shown in Fig. 1 isolated trigger, commutation, (effective at < 5.0 amps.), and bias current holding circuits were added to each SCR to make their operation compatible with the GTOs they replaced. The GTO power switch was retained for it's superior high current commutation ability(> 600 amps.).

To protect the actuators from the induced magnet voltage when the power GTO switches off, a power zener string of about 250 volts was connected across the actuator assembly. A bias resistor connected from the main power supply to the drain of the actuators provides a bias current to prevent the actuators from saturating during the zero current crossover region. Finally, in an attempt to eliminate the last of the obvious ground loops and adhere to the single point ground philosophy all control and monitor signals to and from the scanner system and the Biomedical control room were optically isolated.

IV. RESULTS

The oscilloscope photograph in Fig. 3 shows the transductor magnet current for both systems. The upper trace illustrates the zig-zag pattern of the fast system magnet current sweeping from a range of +/- 220 amps. The slope is approximately 34 amps./ ms. or 68 % of the maximum value. The lower waveform is the derivative of the magnetic field and is obtained from a B dot coil mounted in the "fast" magnet gap. Over most of the sweep the B dot variation is < +/- 2.0%. The large deviations observed during the zero crossing region can be tolerated in the clinical application since their excursions last less than 1.0 ms. Gross deviations in B dot occur for about 2 ms as the GTO switch is turned off and the magnet begins to freewheel down towards zero current. This problem will be corrected. The raster scanning beam delivery system is now being commissioned and its clinical use will start in the near future.

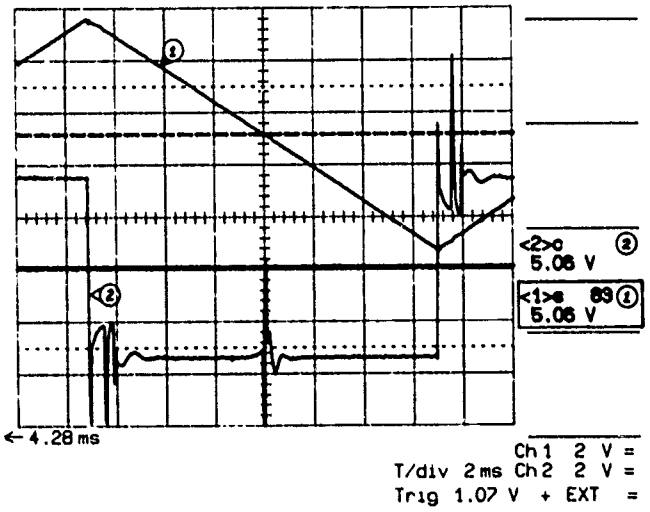


Fig. 3
Magnet current (#1- 100A/div.) vs B dot voltage (#2) full scan

V. REFERENCES

[1] G. Stover, M. Nyman, J. Halliwell, R. Dwinell. "Operational results for the Raster Scanning Power Supply System constructed at the Bevalac Biomedical Facility". Presented at the 1989 IEEE Particle Accelerator Conference, Chicago, IL, March 20-23, 1989, LBL-25931. Published in IEEE Proceedings, pages 1890-92.

[2] T. R. Renner, W. T. Chu, B. A. Ludewigt, J. Halliwell, M. A. Nyman, R. P. Singh, R. Stradtner, "Preliminary Results for a Raster Scanning Beam Delivery System", Proceedings of the 1989 IEEE Particle Accelerator Conference, Chicago, IL., p. 669, Vol 1, March 1989.

[3] W. T. Chu, T. R. Renner, and B. A. Ludewigt, "Dynamic Beam Delivery for Three-Dimensional Conformal Therapy," Proceedings of the EULIMA Workshop on the Potential Value of Light Ion Beam Therapy, eds. P. Chauvel and A. Wambersie, November 3-5, 1988, Nice, France, EUR 12165 EN, pp. 295-328 (1989).

[4] J. E. Milburn, J. T. Tanabe, T. R. Renner, and W. T. Chu, "Raster Scanning for Relativistic Heavy Ions," Proceedings of the 1987 IEEE Particle Accelerator Conference, Accelerator Engineering and Technology, Washington, D. C., March 16-19, 1987, Vol. 3: 2000-2002 (1987).

[5] G. Stover, M. Nyman, J. Halliwell, I. Lutz, and R. Dwinell. "A Raster Scanning Power Supply System for Controlling Relativistic Heavy Ion Beams at The Bevalac Biomedical Facility". Presented at the 1987 IEEE Particle Accelerator Conference, Washington, DC, March 16-19, 1987, LBL-22200. Published in IEEE Proceedings, pages 1410-12.

[6 Manufactured by Toshiba semiconductor

[7] 1NA105 precision unity gain manufactured by Burr Brown.

PRECISION CURRENT REGULATION OF MULTIPOLE MAGNETS USING COMMERCIAL SMPS

Coles Sibley, Oscar Calvo and Tomás Russ
Massachusetts Institute of Technology
Bates Linear Accelerator Center
PO Box 846, Middleton Ma, 01949

ABSTRACT

The South Hall Ring (SHR) under construction at the MIT-Bates Linear Accelerator Center will provide a high duty factor electron beam and internal target capability for nuclear research. For proper operation of the pulse stretcher ring, a large number of highly stable power supplies are required. Most of these supplies will be powering multipole magnets at currents ranging from 10 A. to 155A. with the output power between 1.2 and 11.5 KW. The high stability specifications of these supplies, better than 25 PPM of the 1.1 GEV current value, including temperature drift and ripple, normally suggests the purchase of custom manufactured supplies. However, due to the costs of custom supplies, we tested the feasibility of upgrading commercial supplies with an external controller to improve the current regulation from a typical value of 200 PPM to better than 25 PPM.

Several upgrade configurations were tested. The results of those tests are discussed as well as some data on the final design.

I. INTRODUCTION

The South Hall Ring project under construction at Bates Linear Accelerator Center will require over 80 power supplies for the multipole elements. Some of the quadrupoles and sextupoles will be run in series to cut down on the number of supplies. Their stability, including ripple, noise and drift, must be better than 25 PPM over a temperature span of 10°C. Usually this type of power supply is custom made and costs from 2 to 3 times more than an "off the shelf" supply of similar output power. Due to the cost considerations we opted to test several supplies, both linear and switching, with an external upgrade to improve the stability specifications to better than 25 PPM. After testing several configurations, we settled on a design which uses two control loops, a voltage loop which is inside the supply to reduce the ripple to acceptable levels and an external control loop which regulates the current loop and keeps the drift within tolerances. This approach has been tested and regulates the supplies within the tight stability specifications required for the successful operation of the South Hall Ring.

II. DESIGN APPROACH

It is easily shown that the components which affect the stability drift performance are the shunt, analog reference, and the error amplifier. We opted to place these components on an external controller board with low drift devices. Once this is done, the greatest effect on the ripple and noise specifications are given by the gain of the feedback loop and good shielding and grounding practices. In the first configuration that was tested, our error amplifier output was "ORed" with the supply's voltage and current regulation loop. The shunt was placed directly in series with the internal shunt, within the output capacitor circuit, thus seeing a "fast" current being shorted through the capacitor and a "slow" current from the load. The loop transfer curves are shown in figure 1.

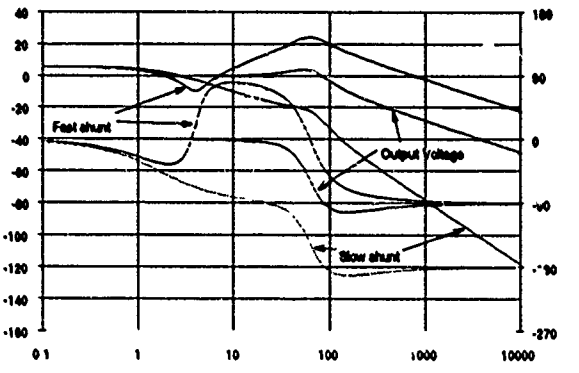


Figure 1. Spice model of a Bode plot for the shunt currents and output voltage

In this case an integrator with a simple zero-pole pair compensates for the load and filter. The required rejection at the line frequencies was easy to obtain. The problem with this configuration is that the leakage current through the capacitor changes with temperature, so we would see drifts in the output current due to room temperature changes. We then moved the shunt outside the capacitor so it would be regulating only on the load current. This solves the drift problem, but the resulting

0-7803-0135-8/91$01.00 ©IEEE

current transform has an additional pole, thus increasing the complexity of the feedback loop. In this configuration it is hard to get enough rejection of the line ripple. The final setup was to use the original voltage loop, with minor adjustments in the feedback to reject the line noise. The output of our regulation loop is then used as the reference into the voltage loop. This gives us a fast inner loop which compensates for line ripple and noise, and a slow outer loop for control of the current stability.

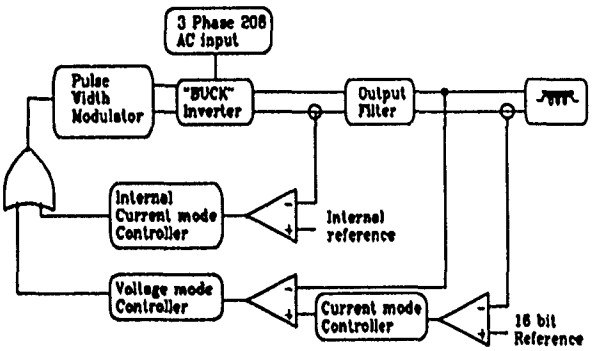


Figure 2. Block diagram of power supply control loops.

III. System Overview

The power supply consists of three separate systems: the commercial power supply, the analog board and the digital board. The power supplies are manufactured by Electronic Measurements, Inc. in Neptune NJ. They are powered in the constant voltage mode, using the error signal from the analog board as the voltage reference. The current control mode acts as a local current limit.

The Bates analog board [1] contains the DAC, three ADC's, the shunt amplifier, the error amplifier, and the interface to the digital board. The analog board is galvanically isolated from the digital board. The shunt has a flow switch used as a power supply interlock in the digital board. Control signals, the DAC setting and the three ADC signals are run serially through optocouplers for isolation. Power coming from the digital board goes through dc to dc converters for isolation.

The digital board contains a Bitbus interface for remote control, the serial interface between the analog board and the digital board, the status from the power supply, the control logic for the power supply DC on/off, power supply interlock resetting, and the magnet interlocks. There is a microcontroller (8044) which takes care of the communications and timing. Ramping and cycling procedures are handled by the microcontroller.

IV. Power Supply Configuration

The EMS "DCS" series power supplies are switching mode power converters with output power ranging from 600 watts to over 10 Kilowatts. The power supplies overall regulation is about 0.1 %.

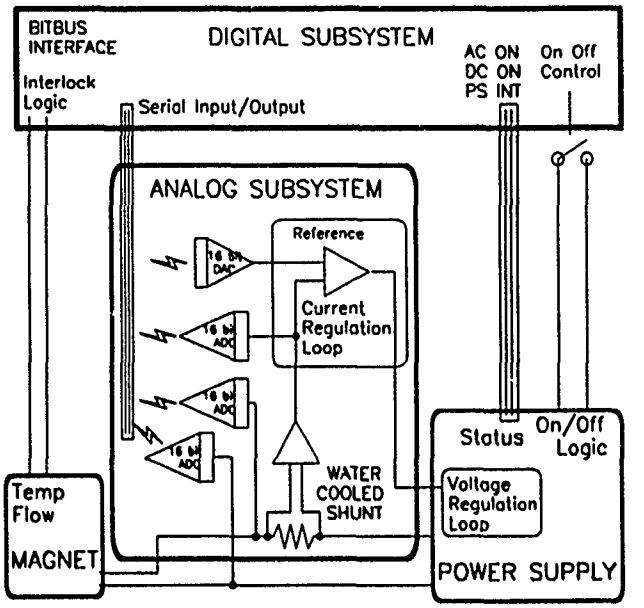


Figure 3. Block diagram of the power supply system.

The basic hardware configuration is the same for both the voltage and current modes of operation. A reference signal is compared with a sample of either the voltage or current, and the difference is amplified through an error amplifier. Both error amplifiers have an integrator and a zero-pole configuration. The feedback is designed to be stable when powering a wide range of loads. The output of the voltage error amplifier is then ORed with the output of the current error amplifier and a shutdown circuit such that any one can shut down the PWM but only one will regulate at a time, depending on the load resistance. The PWM drives a full bridge configured as a buck converter. For the 5 and 10 KW supplies, two or four bridges are run in parallel to double or quadruple the current capacity.

V. Controller Configuration

In order to meet the stability specifications, an external shunt and a stable reference are added to the system. The voltage reference is a Thalor precision 5v reference with a temperature coefficient of better than .6PPM/°C and line regulation specifications of better than 2PPM. / V. The DAC is 16 bits and has a long term drift of less than 1PPM/°C and offset of better than .5PPM/°C. The shunts are Zeranin shunts with a tolerance of .1 percent. The temperature coefficient is 3 PPM over a temperature range of 0 to 60 °C. They are water cooled with an input water temperature of 30° ± 1°C and can dissipate up to 200 watts. The shunt signal goes through a common mode filter to kill any switching frequency noise with a cutoff frequency of about 600Hz and is then amplified by an instrumentation amplifier (an LT1101) with a fixed gain of 10, then amplified again (Av~1.2) to have an output of 10 volts at the supplies full output current. The second amplifier has the necessary offset and gain adjustment for calibration purposes. This signal is routed to the front

panel for monitoring, and also to a voltage divider whose output goes to the error amplifier and to a 16 bit ADC. This circuit is shown in Fig. 4. The output of the error amplifier goes into the voltage channel reference input of the power supply. The shield of this cable is where the common of the supply is tied to the common of our analog circuit. All shields coming in to the analog board are tied at the same place on the ground plane of the analog board to eliminate any ground loops.

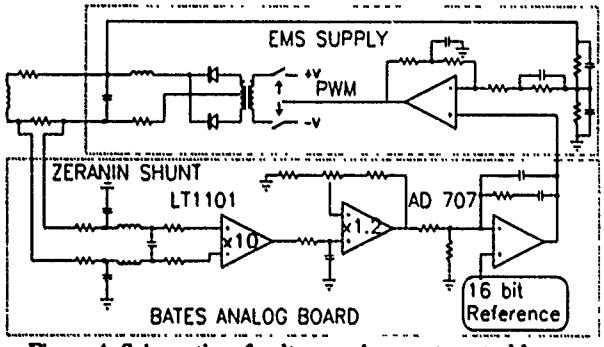


Figure 4. Schematic of voltage and current control loops

VI. VOLTAGE LOOP

The stability specification of 25 PPM includes all ripple and noise. The worst case for ripple is at 60 Hz with a single quadrupole as the load. After calculating the maximum ripple from each supply and comparing that with the maximum current ripple allowable, we find that each supply's voltage feedback loop has to be modified slightly. Table 1 shows the minimum amount of gain boost required for each supply to bring the ripple and noise specifications into tolerance. From this table, we see that if we boost the voltage loop gain by 10 to 20 dB, we will more than cover all the cases for the ripple specifications. Fig. 5 shows the measured loop response, with a quadrupole as the load, for the EMS loop and the modified voltage loop. The supply used in this example was an EMS 60-80. Figure 4 shows the modified voltage feedback circuit. In this case, the addition of an integrator in the voltage feedback loop would have been beneficial. This can be implemented with just a change of values in the original EMS design.

Amps	155	110	80	60	60	52	40	40	10
Volts	70	95	70	80	40	48	120	30	125
DB's	1.6	2.7	4.2	3.2	7.7	7.7	.74	12.4	3.7

Table 1

With the voltage loop closed at a bandwidth of between 5 and 10Khz, the loop has enough rejection at the line frequency for the stability specifications. The current loop now can be closed at a low enough frequency so the extra pole introduced by the load is above the bandwidth of the circuit and does not affect the current loop stability. Figure 6 shows the current loop response with the voltage loop closed. From this chart it is clear that we will not have any problems with stability as long as we close the loop under 100 Hz.

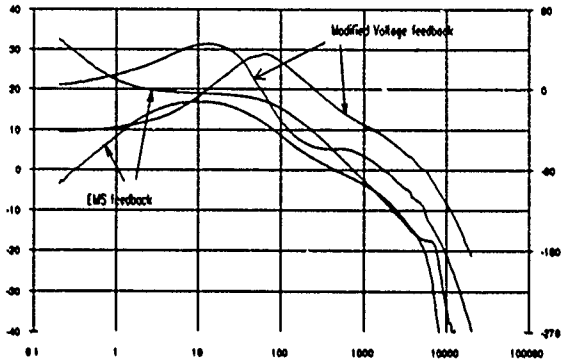


Figure 5. Bode plot comparing the modifies voltage feedback loop with the original feedback loop.

At approximately 360 Hz there is a resonant circuit due to a mismatch in the input common mode filter. Below this frequency the gain drops rapidly due to the shunt filtering.

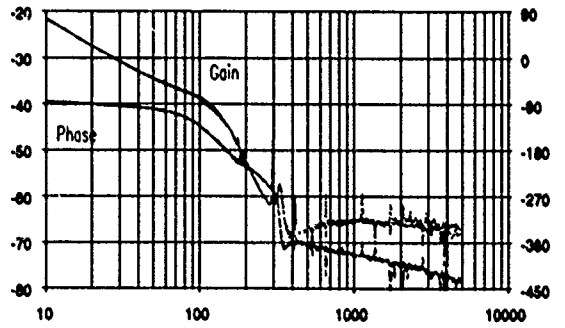


Figure 6. Current loop with voltage loop closed.

VII. CONCLUSION

The design discussed has been shown to comply with the high stability specifications for the multipole power supplies in the South Hall Ring project. We have ordered 81 power supplies for the quadrupole and sextupole magnets which will utilize this upgrade. The supplies will be upgraded and tested by EMS with deliveries expected in August 1991.

References

1. T. Russ, C. Sibley, "A distributed Power Supply Controller using the Bitbus Interface", Nuclear Instruments and Methods in Physics Research, A293, 1990
2. O. Calvo, C. Sibley, T. Russ , "High Stability Switching Mode Power Converters for Magnetic Loads.Proceedings of the 1990 Linear Accelerator Conference . p493
3. Instruction Manual for EMS Power Supply EMS 80-60, Electronic Measurements, Neptune, NJ

PRINCIPLES AND THEORY OF RESONANCE POWER SUPPLIES

A. Sreenivas G.G. Karady
Department of Electrical Engineering
Arizona State University, Tempe, AZ

Abstract

The resonance power supply is widely used and proved to be an efficient method to supply accelerator magnets. The literature describes several power supply circuits but no comprehensive theory of operation is presented. This paper presents a mathematical method which describes the operation of the resonance power supply and it can be used for accurate design of components.

1. INTRODUCTION

The resonance power supply is being used for accelerator magnet excitation in the last two decades.The first application was in the Princeton Pennsylvania Accelerator [1]. In 1978 Praeg and McGhee [2] reported the utilization of series resonant network to generate biased sine wave excitation current for the Argonne National Laboratory Synchrotron. Subsequently Praeg and colleagues presented several papers discussing the dual frequency resonance power supply with flat top and flat bottom [3,4]. Karady et al [5,6] presented a design method for a 10 kA, 10 kV resonance power supply in which they proposed component realization and system optimization. In the literature transient simulation techniques (SPICE, MICROCAP etc.) are used to analyze the operation of resonance power supplies. These techniques simulate the operation correctly but do not describe the phenomena. A mathematical analysis is required to obtain better understanding of the system operation.

The resonance power supply operation consists of distinct periods and each period represents a state of the system. The cyclic operation of the power supply can be described by the transition from one state to the other. Each period can be described by a set of state equations. The state space method simplifies the computation and provides insight into the physical phenomena.

The purpose of this paper is to apply the state space method for the analyses of resonant power supply operation.

2. METHOD OF ANALYSIS

a. System definition

The resonance power supply circuit diagram and the required current wave shape are shown in Figure 1. It can be seen that the system operation is divided into four states: injection, acceleration, flat top and reset.

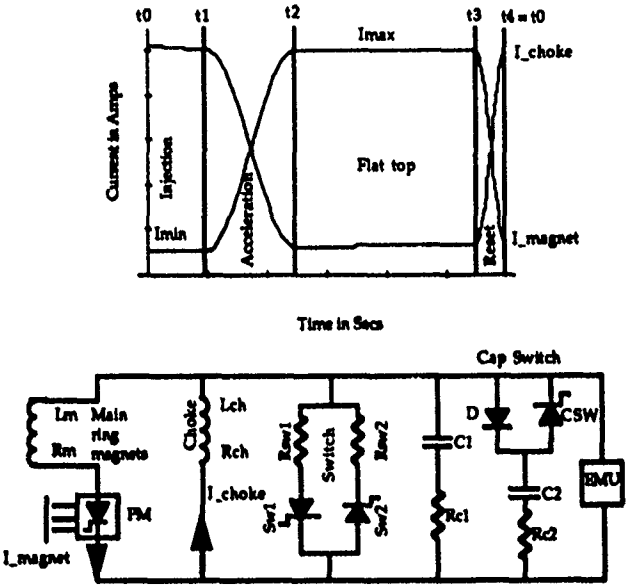


Figure 1. Required Current shape and Circuit diagram.

b. Concept of the analysis

The circuit diagram for each state was identified and the state space equations were derived. In steady state sequential operation the states follow each other. Therefore the initial conditions for a state are the final conditions of the previous state. This procedure results in a set of simultaneous differential equations. The solution of these equations using the state space method describes the system operation. The state equations were also solved using the Laplace Transform method. The solutions obtained by the state space method were verified by the Laplace Transform method using the MATHEMATICA package for computation.

c. List of symbols

Lm, Rm Magnet inductance and resistance respectively.
Lch, Rch Choke inductance and resistance respectively.
C1, Rc1 Capacitor Bank 1 and bus bar resistance respectively.
C2, Rc2 Capacitor Bank 2 and bus bar resistance respectively.

3. OPERATION ANALYSIS

a. Injection

The system equivalent circuit for the injection period is shown in Figure 2.

0-7803-0135-8/91$01.00 ©IEEE

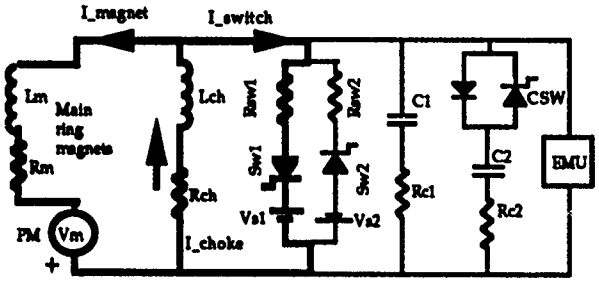


Figure 2. Current path during injection period

The state space equations for this circuit are :

$$\frac{\partial i_{ch}}{\partial t} = -\alpha\, i_{ch} - \frac{(V_{s1} + i_m R_{SW1})}{L_{ch}} \quad 1$$

$$V_m = i_m R - V_{s1} - i_{ch} R_{SW1} \quad 2$$

where,

$$\alpha = \frac{(R_{ch} + R_{sw1})}{L_{ch}}, \quad R = R_{ch} + R_{sw1} \quad 3$$

The solution of these equations results in the equation,

$$i_{ch}(t) = i_{cho}\, e^{-\alpha t} + \left(\frac{I_{mo} R_{sw1}}{R} - \frac{V_{s1}}{R}\right)(1 - e^{-\alpha t}) \quad 4$$

The equations 1 and 2 in state space form are,

$$\begin{bmatrix} i_{ch}(t) \\ \frac{di_{ch}}{dt} \\ i_m(t) \\ \frac{di_m}{dt} \end{bmatrix} = \begin{bmatrix} a1 & 0 & a2 & 0 \\ b1 & 0 & b2 & 0 \\ 0 & 0 & 1 & 0 \\ 0 & 0 & 0 & 0 \end{bmatrix} \begin{bmatrix} Icho \\ i_{ch}(t0) \\ Imo \\ i_m(t0) \end{bmatrix} + \begin{bmatrix} a3 \\ b3 \\ 0 \\ 0 \end{bmatrix} \quad 5$$

The final value of the choke and magnet current for the injection period are the initial values for the acceleration period.

b. Acceleration

The acceleration period starts with the opening of the GTO switch SW1 and the closing of the capacitor bank switch CSW. The switches insert the capacitor banks in the circuit. The current paths are shown in Figure 3.

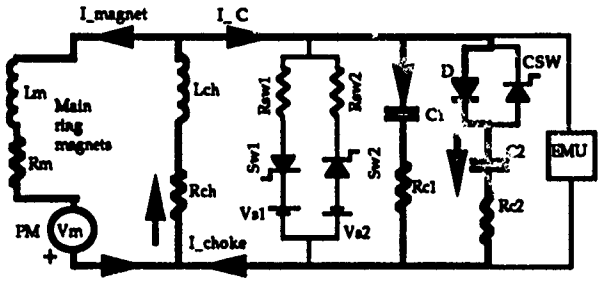


Figure 3. Current path during acceleration.

The differential equations representing the accelerating period are given by,

$$\frac{\partial^2 i_{ch}}{\partial t^2} = -a\,\frac{\partial i_{ch}}{\partial t} - \frac{i_{ch}}{CL_{ch}} + \frac{1}{L_{ch}}\left(R_c \frac{\partial i_m}{\partial t} + \frac{i_m}{C}\right) \quad 6$$

$$\frac{\partial^2 i_m}{\partial t^2} = -b\,\frac{\partial i_m}{\partial t} - \frac{i_m}{CL_m} + \frac{1}{L_m}\left(R_c \frac{\partial i_{ch}}{\partial t} + \frac{i_{ch}}{C}\right) \quad 7$$

where,

$$a = \frac{R_c + R_{ch}}{L_{ch}}, \quad b = \frac{R_c + R_m}{L_m} \quad 8$$

The solution of the circuit equations is obtained from the state representation,

$$\begin{bmatrix} \dot{x1} \\ \dot{x2} \\ \dot{x3} \\ \dot{x4} \end{bmatrix} = \begin{bmatrix} 0 & 1 & 0 & 0 \\ a1 & a2 & a3 & a4 \\ 0 & 0 & 0 & 1 \\ b1 & b2 & b3 & b4 \end{bmatrix} \begin{bmatrix} x1 \\ x2 \\ x3 \\ x4 \end{bmatrix} \quad 9$$

The final values obtained from equation 9, are used as initial values for the next state.

c. Flat Top

The flat top state is initiated by the closing of SW2, which short circuits the capacitor bank. The current path is similar to that shown in Figure 2, except that, the current direction is reversed and SW2 is operating instead of SW1. The state space equations for this period are similar to that of the injection period.

The final values of the flat top period are used as initial values for the next state.

d. Reset

The reset period is initiated by the opening of SW2, which inserts the capacitor bank in the circuit. The current path is

similar to that shown in Figure 3, but now only capacitor bank C1 is in the circuit.

The state space equations are similar to the equations obtained for the acceleration period.

The final values obtained are used as initial values for the next injection state of the next cycle.

4. SOLUTION STRATEGY

The input data required for the solution of the state space equations are : a) The starting time and ending time for each state, b) The system parameters(resistance, inductance, capacitance values), c) The constraints on the magnet current. For example the magnet current has to be kept constant during the flat top and the maximum and minimum values of the magnet current for any cycle are fixed.

The analysis uses two variables Icho and Imo which are the initial choke and magnet currents. The state space representation of different periods in terms of these variables are formulated. The system behavior is studied with respect to variations in Icho and Imo and other parameters.

5. LOSS ANALYSIS

The application of the developed method is demonstrated by the calculation of energy losses in a resonant power supply system described in detail by Karady et al [5]. The analysis starts with computation of voltage required in series with the magnet during injection and flat top periods. These voltages are highly regulated ramps to keep the magnet current constant. The state space equations were solved using the described method using the MATRIXX Math Program.

Typical results are shown in Figure 4, which presents the capacitor bank current during the acceleration and reset period. Figure 5 shows the load on the system as a function of time. It can be seen that the majority of the losses occur during the flat top period. Also the calculation indicates that the current at the end of the reset is less than the initial current required for the injection period. Therefore the system requires additional energy injection.

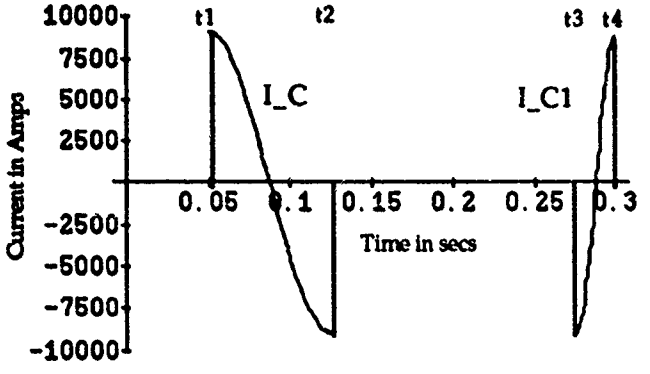


Figure 4. Capacitor bank current in Acceleration and Reset.

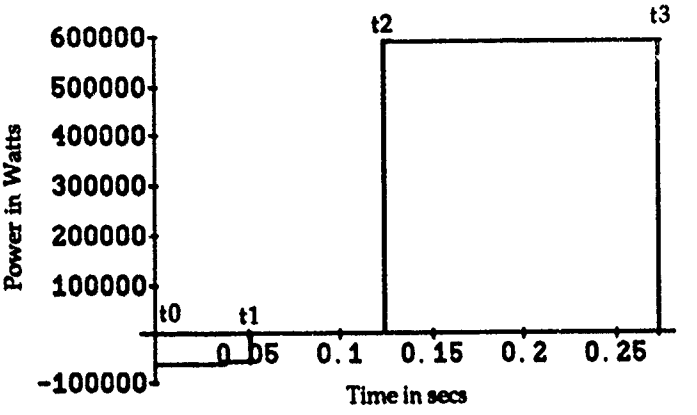


Figure 5. Load on the system as a function of time.

6. CONCLUSION

The results of the presented analysis can be summarized in the following points;

1. This paper introduces the state space method for the analysis of resonant power supply operation.
2. The state space method reduces simultaneous differential equations to a set of linear equation, which reduces computational complexity.
3. This method can be used an an effective design tool for physical realization of resonance power supplies.
4. The advantages of the method were demonstrated using a practical example.

7. REFERENCES

[1] S. Waaben, "Princeton pennsylvania Accelerator," Nuclear Instruments and Methods, Vol 9, pp. 78-86, 1960.

[2] W.F. Praeg and D. McGhee, "Ring Magnet Power Supply for a 500 MeV Synchreotron," IAS Annual Meeting, Conference Record, pp.1118-1124, 1978.

[3] W.F. Praeg, "Dual Frequency Ring Magnet Power Supply with Flat Bottom," IEEE Transaction on Nuclear Science, Vol NS-30, pp.2873-2875, 1983.

[4] W.F. Praeg, "A Multi-Functional Ring Magnet Power Supply for Rapid Cycling Synchrotrons," IEEE Transaction on Nuclear Science, Vol NS-30, pp.3749-3751, 1985.

[5] G. Karady, H.A. Thiessen and E.J. Schneider, "Resonant Power Supplies for a Rapid Cycling Accelerator," IEEE Transactions on Nuclear Science, Vol 35, pp.1092-1098, 1988

[6] G. Karady, H.A. Thiessen, "Optimization of the Resonant Power Supply Circuit," Particle Accelerator Conference, Vol 3, pp.1916-1918, 1989.

Control Theory: A Practical Approach

Mike Anderson & Tom Bertuccio
Indiana University Cyclotron Facility
Bloomington, Indiana 47405

Abstract

Stability and frequency response enhancements can be made to custom manufactured and off-the-shelf power supplies. Combined power converter and magnet loads that result in poor transient response and marginal loop stability due to inadequate phase margin can be corrected with a systematic approach utilizing lead compensation techniques. Using a Venable Systems 350 Frequency Response Analyzer two actual case studies are documented demonstrating a practical approach to stabilizing and enhancing a power supply's performance. A description of the system and conventions are followed by a description of two power supplies with specific deficiencies. The first case study involves a power supply without a dominant pole output capacitor. The next case study involves a power supply driving a highly damped resonant load. The paper in concluded a by a discussion of measurements pitfalls.

I. INTRODUCTION

This paper will outline two case studies where the frequency response of laboratory grade precision power supplies were enhanced. The techniques used are simple, practical ways to compensate feedback loops. The approach consists of first measuring the frequency response of a system. Second, selecting a desired frequency response (i.e. crossover frequency and phase margin). Third, designing and implementing an error amplifier and/or other compensating amplifiers that fulfill the specifications. And, finally verifying the results by measurement.

Trial and error schemes so often used by power supply vendors proved to be inadequate especially when the favored approach is to employ a large capacitor across the output. The IUCF Cooler Ring having been designed with a highly interactive power supply network required the removal of all output capacitors which necessitated the complete redesign of all control loops. Some 50 channels were involved and simple "seat of the pants' tinkering clearly would not suffice. A device was needed to measure the frequency response (under closed-loop conditions) to allow quick, reliable measurements of loop characteristics over a range of operating conditions, and synthesis methods to properly match the dynamics of all elements of the network.

Past practices at this facility did not have the capability to execute the above approach until the rental and finally purchase of a Venable Model 350 Frequency Response Analysis System (VFRAS). However due to the need for precision ramping of power supplies under adverse condition (i.e. removal of output capacitors), a practical approach was developed to enhance the operation of dozens of power supply channels.

Additionally, efforts have been directed toward successfully modeling measured data. However, to date we have achieved only limited success, although in the near future we expect to complete accurate models.

II. DISCUSSION

A. Test Equipment

The VFRAS consists of a personal computer, software, and a three channel commercial frequency response analyzer.

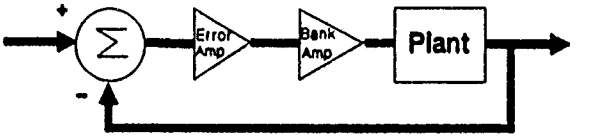


Figure 1 - *System Block Diagram.*

Figure 1 shows a general block diagram of the power supplies that are to be discussed. Measurements are accomplished by inserting a 100 ohm resistor within the loop. An excitation signal creates a perturbance which can be measured around the loop. Transfer functions for different blocks within the loop and the loop itself are represented in Bode diagram format. Furthermore, closed loop plots can be made by exciting the reference input and measuring the output over the input.

Additionally, the VFRAS will design an error amplifier for loops with an undesirable response. There are three error amplifier lead compensation design options which are determined by phase requirements. The first is a simple integrator. The second has a pole at the origin and a zero followed by a pole. The last option is used when phase boost requirements are greater than 90°, and consists of a pole at the origin, two zeros at the same frequency followed by two poles at the same frequency.[1,2]

B. General Block Diagram

As illustrated in Figure 1, there are three main blocks within the control loop, the plant, the bank drive amplifier (BDA), and the error amplifier. The plant is a combination of transistor pass bank, magnet load and feedback transducer. The BDA and the error amplifier can be modified to achieve the desired response. In addition, each block has been modeled using Spice which were later compared to measured data. However, only limited success has been achieved with the plant model.

The pass bank is arranged in a darlington configuration (i.e. 1 transistor driving 9 transistors driving 95 transistors). This system was modeled using Spice and circuit analysis

0-7803-0135-8/91$01.00 ©IEEE

techniques. This system consists primarily of a single pole caused by the inductive load. A hybrid pi model was used to model the transistor bank. The driver transistors and the bank transistors can be modeled to a composite transistor representing the entire pass bank[3]. The feedback transducer in the first case is a water cooled shunt and in the second case is transductor.

The BDA feeds the plant and consists of a common emitter amplifier driving a common collector amplifier which in turn drives the plant. A 'thumbnail' derivation proved to be quite accurate and was later verified by Spice. This system is characterized by a constant gain and a zero followed by a pole. This provides phase boost and gain to the feedfoward loop. The results were later used to adjust the frequency response.

The error amplifier is a chopper stabilized inverting operational amplifier whose feedback network is chosen via K factor analysis to the desired loop crossover frequency and phase margin.

C. First Case Study

This power supply furnishes current to coils in several quadrapole magnets and was specified to be ramped. However due to transformer coupling of loads with other supplies the output capacitors had to be removed. This upset the system dramatically and resulted in a 200 amp oscillator. The frequency response without the output capacitor is shown in figures 2 and 3.

To stabilize the supply a large capacitor was inserted across the error amplifier, this enabled the frequency response of the different system blocks to be measured. The ability to view an accurate frequency response of a system greatly enhances an engineers ability to effectively design a compensator. Without measured data the system characteristics can only be modeled by analysis which is cumbersome, time consuming, and does not accurately account for parasitic and variable parameter effects. Data over several decades takes only a matter minutes and is accurate when proper measurement techniques are observed.

To compensate the loop at a suitable crossover frequency the VFRAS was used to design an error amplifier. However, the desired response could not be achieved. This was due to a desired phase boost of the error amplifier to be greater than 90°. When a phase boost greater than 90° is desired, the VFRAS creates an error amplifier with a pole at the origin and two zeros located at the same frequency followed by two poles. The slope of the error amplifier is +1 at crossover (the zeros create a slope of +1 and the phase boost). If the loop has a slope of only -1 at the desired crossover frequency, the loop will not crossover until after the crossover frequency and when the phase boost has diminished. Therefore, the option of using phase boost greater than 90° is limited to modulators with a slope of -2 at the crossover frequency, which in turn will provide the loop with a crossover slope of -1.

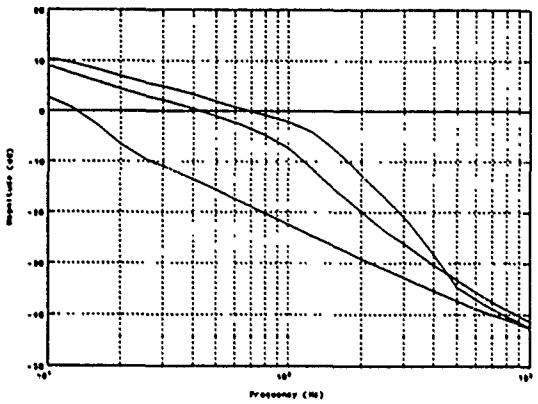


Figure 2 - *Magnitude plot of the plant plus the modified bank drive amplifier at different operating points.*

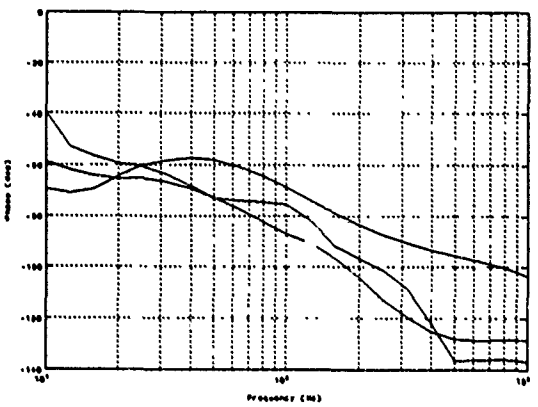


Figure 3 - *Phase plot of the plant plus the modified bank drive amplifier at different operating points.*

To overcome the above setback, the characteristics of the BDA amplifier were capitalized. According to the equation for the BDA the pole and zero can be modified by changing a few feedback components. By using an 'R-C box' and the circuit derivation we were able to predict and monitor the response while modifications were being made. Our objective was to create enough phase boost at a particular band of frequencies to allow the use of an error amplifier which needed a phase boost less than 90^0. This was accomplished and the resulting loop plot is shown in Figures 4 and 5.

The crossover frequency of the loop is a function of the current and V_{ce}. Therefore, a family of plots are taken for the plant at different operating conditions and a median value is chosen for crossover taking care that the phase margin does not become too small at high frequencies.

Given all system parameters such as load inductance, transistor parameters, etc. generally speaking the above, might have been accomplished. However, the power supply in this case drives a fraction of the coils per magnet to which it is connected. Also connected to these same magnets are other power supplies which in turn are connected to other magnets. It was the transformer coupling effect from this arrangement that prompted the removal of the output capacitors from the power supplies.

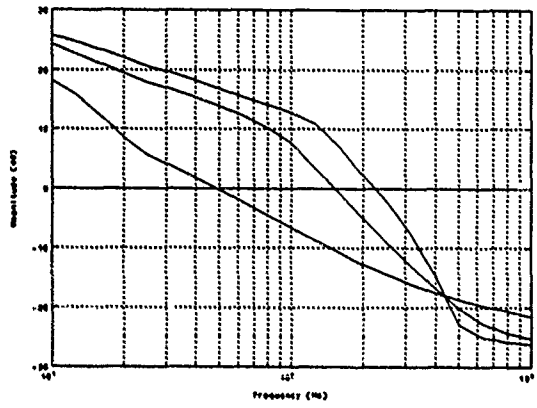


Figure 4 - *Loop magnitude plot at different operating points.*

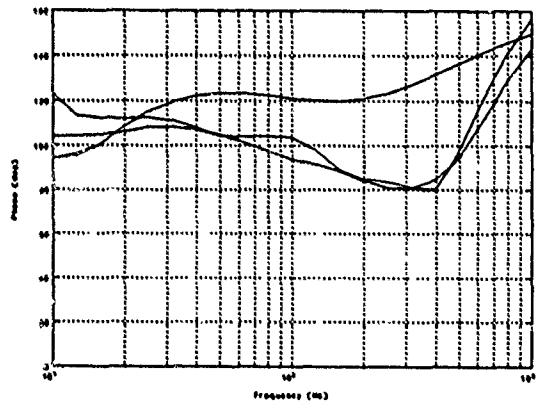


Figure 5 - *Loop phase plot at different operating points.*

Measured data attributes two poles to the plant. However, when the coupling effect of the other magnet coils are ignored, circuit analysis suggests only one pole. Indeed, it would have rather difficult to model the effect of the transformer coupled loads. Without the measured data the above results probably would not have been possible, namely due to the nature of the load.

Furthermore, the variable dynamic response characteristics due to varying operating conditions is involved. The transistor gain, as well as other transistor characteristics vary at different operating points (in this case over five transistor stages). In addition, this supply has no preregulator thus, the V_{ce} changes as a function of operating current, which in turn compounds the variation in transistor gain. All theses characteristics change as the temperature of the system varies.

D. Second Case Study

This study involves a the main Cooler Ring dipole magnet power supply. The load consisted of twelve dipole magnets whose combined inductances 160mH paralleled by a series network of 3 ohms and 20 millifarads. Due to ringing, the output capacitors were modified to a damping network. The added 3 ohm resister to the original 20 millifarad output capacitor (to damp the load) modification resulted in a marginally stable loop.

This supply has a significantly different current capability compared to the first case study. The darlington configuration in this case has one transistor driving 10 transistors driving 66 transistors driving 676 transistors. In addition, the transistors used in the first case were Westinghouse 164-08, and this supply uses Westinghouse D60T transistors.

The approach to achieving a desirable response was similar to case study one. Initially there were several unsuccessful attempts at crossing over the loop at a particular frequency. However, by modifying the BDA and then modifying the error amplifier a desirable frequency response was realized.

E. Pitfalls

Erroneous measurements can occur for several reasons. When using closed-loop measurement techniques circuit impedances should be considered[4,5]. For our application we found, when making measurements at relatively high frequencies (i.e. > +5kHz), the excitation signal should be injected prior to the error amplifier. For measurements of relatively low frequencies the signal should be injected after the operational amplifier. However these are relative to specific operating systems. Ground loops should be avoided by supplying power to the measurement device (VFRAS) via an isolation transformer; and injection transformers should also be used to isolate the excitation signal. In addition loads shorted to ground may result in erroneous measurements.

III. CONCLUSIONS

Specialized laboratory grade power supplies can be modified to meet specific needs of a user. Frequency response measurement device is an invaluable tool for control loop system design. In addition the VFRAS was able to measure the transfer functions of subsystems (i.e. amplifier or plant). The user also has the capability to verify and compare theoretical designs to practical measured data. This approach of measuring a system response gives practical and useful concrete information in a matter of minutes. Furthermore, the package provides in most cases a simple solution to control loop stability problems.

IV. REFERENCES

[1] Dean Venable, "K-Factor Simplifiers Linear Amplifier Design", PCIM, vol. 13, Oct. 1987.

[2] Dean Venable, "The K-Factor: A New Mathematical Tool for Stability Analysis and Synthesis," Powercon 10 Proceedings, Power Concepts Inc, March 22-24, 1983.

[3] P.R. Gray and R.G. Meyer, *Analysis and Design of Analog Integrated Circuits*, New York: John Wiley & Sons, 1977, pp

[4] "Venable System Reference Manual Model 350 System", Torrance, Ca.: Venable Industries, 1986.

[5] D.J. Caldwell, "Minimize Loading Errors in Loop-Gain Measurements," EDN, vol 35, pp.165-170, May 1990.

Theoretical Study of H⁻ Stripping with a Wiggler Magnet

R. Hutson

Medium Energy Physics Division, Los Alamos National Lab, Los Alamos, NM 87545

Abstract

The first step for injecting protons into the LAMPF Proton Storage Ring (PSR) at LANL is to strip a beam of 800-MeV H⁻ ions to H^0 with a 1.8-T dipole magnet. Because of the finite lifetime of energetic H⁻ ions in the magnetic field, their trajectories bend before stripping causing the angular spread of the beam, and therefore its emittance, to grow during the stripping process. In the case of the PSR, the horizontal beam emittance grows by a factor of roughly three during injection. As a consequence, beam losses in the ring are significantly greater than they would be if there were not emittance growth. A speculative technique is proposed in which the beam divergence growth and resulting emittance growth is reduced by stripping the H⁻ in a wiggler magnet whose transverse field alternates in direction as a function of position along the beam axis. The wiggler field configuration is adjusted so that the angular beam spread introduced during passage through one unidirectional-field increment of path is relatively small and so that 99.99% of the beam is stripped after passing through the whole magnet. With careful field design the net added angular beam spread is reduced because the incremental angular spreads are painted back and forth over the same small range. In the hypothetical case described, the calculated emittance growth and beam loss increase are significantly smaller than those calculated for a conventional stripper magnet.

I. INTRODUCTION

The PSR, shown in Figure 1, is filled with protons in a two-stage process. First 800-MeV H⁻ ions in the injection line are stripped to H^0 with a 1.8–Tesla dipole stripper magnet; the H^0 are then stripped to H^+ by passing through a 200-$\mu g/cm^2$ carbon foil in the ring itself. After the ring is filled, the stored protons are extracted and transported to the neutron production target at the Los Alamos Neutron Scattering Center (LANSCE).

The H⁻ stripping process has an unwanted side effect in that it leads indirectly to unwanted losses of beam circulating in the PSR; the beam is lost through collisions of protons in the tails of the stored beam with limiting apertures in the ring. The resulting activation of ring components makes ring maintenance more difficult. How does the H⁻ stripping process lead to this problem? H⁻ stripping in a magnetic field is a probabilistic process described by a field-dependent ion lifetime; therefore, ions travel a finite distance before being stripped. Because the stripper magnet field is vertically pointing, the trajectory of an H⁻ will be deflected through some angle in the horizontal plane before being stripped. Since the stripping per unit path length is probabilistic, the angles through which a collection of H ions are deflected before being stripped will cover a range. Figure 2 illustrates this. This additional angular spread added to the inherent divergence of the incoming H⁻ beam causes the horizontal-plane emittance of the H^0 beam to be larger than that of the

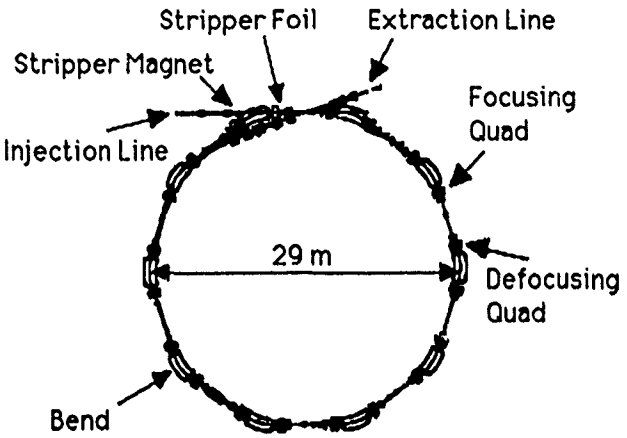


Figure 1. Layout of the LANL Proton Storage Ring.

original H⁻ beam. If this emittance growth were reduced, the stored-beam size, which increases as the emittance of the injected H^0 increases, would be made smaller, and beam losses, which increase with beam size, would be reduced.

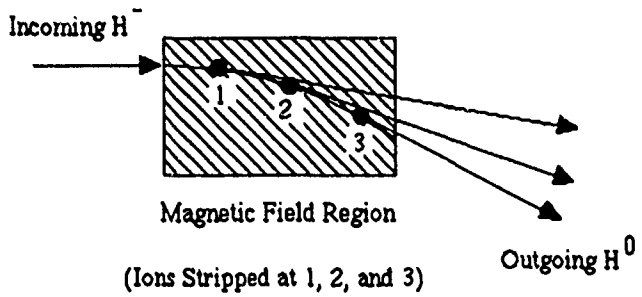


Figure 2. Illustration of H^0 Angular Spread Resulting from Spread of H⁻ Lifetimes in Magnetic Field Region.

In the next section, a speculative scheme is proposed to reduce the emittance growth during H⁻ stripping by the use of a magnet whose field transverse to the beam direction alternates in direction as a function of distance along the beam. This type of magnet is commonly referred to as a wiggler magnet in synchrotron-light-source or free-electron-laser systems. In section III, theory relevant to H⁻ stripping and emittance growth is discussed, while section IV contains results of divergence growth calculations based on the theoretical formulas. Calculated PSR beam losses derived from results of the divergence growth estimates are discussed

0-7803-0135-8/91$01.00 ©IEEE

in section V. In the last section practical considerations regarding wiggler magnet construction are mentioned briefly.

II. REDUCTION OF BEAM DIVERGENCE GROWTH WITH A WIGGLER-MAGNET STRIPPER

In the present PSR stripper magnet the incoming H^- ions see a field that rises rapidly from zero to 1.8 Tesla. Special effort was made to design the magnet so that this rate of rise was as large as possible [1] since, for this case in which all the beam is stripped to H_0 in the fringe field region, the faster the field rises the smaller is the divergence added to the beam because of H^- trajectory deflection before the ion is stripped.

The proposal that divergence growth could be reduced by stripping with a wiggler magnet hinges on the idea that, instead of stripping all the beam as rapidly as possible, as is done with the present PSR stripper magnet, stripping could be spread out over a cascaded series of relatively weak field segments, in any one of which only a fraction of the beam would be stripped, and for any one of which a relatively small range of divergence angles would be introduced. If the fields in successive segments alternate in direction, the divergence angles caused by successive segments would paint back and forth over the same small range so that the net divergence added to the completely stripped beam would be relatively small. This is shown schematically in Figure 3.

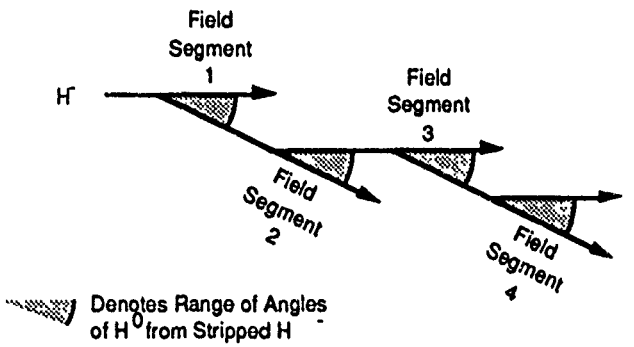


Figure 3. Illustration of the Range of Deflection Angles Contributed by Each of Four Field Segments in a Wiggler-Magnet H^- Stripper (The contributions from all segments overlap the same range of angles).

From this figure it is evident that here would be an increase in transverse beam size and a resulting emittance increase. However, in the case of stripping of the H^- beam for injection into the PSR, this effect is small compared to the effect of divergence growth.

III. THEORY

A. H^- Lifetime and Stripping Rate

If $\tau(z)$ is the H^- ion rest-frame lifetime for stripping to H^0 in a field of B(z) Tesla, where z is the H^- position along the beam direction, then the fraction of the original number of number of ions stripped per unit path length travelled can be expressed [1] as

$$\frac{df}{dz} = -\frac{f(z)}{\beta\gamma c\tau(z)} \ m^{-1} \qquad (1)$$

where β and γ, the relativistic β and γ, are 0.841 and 1.848 respectively for 800-MeV H^- ions, and c is the speed of light. The rest-frame lifetime has been expressed by Scherk [2] as

$$\tau(z) = \left[\frac{A_1}{E(z)}\right] \exp\left[\frac{A_2}{E(z)}\right] \quad \text{sec} \qquad (2)$$

where $A_1 = 2.47\times10^{-6}$ V-s/m, $A_2 = 4.49\times10^{9}$ V/m, and E(z), the ion rest-frame transverse electric field, is given by

$$E(z) = \beta\gamma cB(z) \ V/m \qquad (3).$$

B. Angular Divergence Added by H^- Stripping

For a vertically pointing field, the net horizontal-plane angular deflection of an H^- trajectory after it has travelled from z=0 outside the field region to a point z inside the field can be written as

$$\theta(z) = \int_0^z \frac{B(\xi)}{4.866} d\xi \qquad (4)$$

where 4.866 is the beam stiffness (in Tesla-m) of 800-MeV H^- ions, and B is in Tesla.

The quantity of interest at this point is the distribution, at z, of deflection angles for the ensemble of H^0s arising from those H^- ions that have been stripped. If N_0 is defined as the number of H^- ions entering the stripper magnet field, then the deflection distribution can be expressed as

$$\frac{dN}{d\theta} = -N_0 \frac{df}{dz} \times \frac{dz}{d\theta} = -N_0 \frac{df}{dz} \times \frac{1}{\frac{d\theta}{dz}} \qquad (5)$$

where $\frac{df}{dz}$ is given by equation (1), and $\frac{d\theta}{dz}$ is obtained by differentiating in equation (4). For the PSR stripper magnet all the beam is stripped in the rapidly rising field at the entrance to the magnet gap. The distribution of deflection angles, $N(\theta)$, is gaussian-like and can be characterized by an rms width, θ_{rms}.

B. Beam Emittance Growth

The emittance, ε, of the H^- beam at the entrance to the stripper magnet can be expressed as $\varepsilon_{in} = \pi\sqrt{\det \sigma_{in}}$ [3] with the sigma matrix being defined as

$$\sigma_{in} = \begin{bmatrix} \sigma_{11} & \sigma_{12} \\ \sigma_{21} & \sigma_{22} \end{bmatrix} \qquad (6).$$

$\sqrt{\sigma_{11}}$ and $\sqrt{\sigma_{22}}$ are the rms spatial and angular widths in the horizontal plane, and the off-diagonal elements $\sigma_{21} = \sigma_{21}$

describe the orientation of the beam ellipse in x-θ phase space.

If the rms angular spread of the deflection angles caused by the stripper magnet field is written as θ_{rms}, then the only change in the sigma matrix for the H^0 beam exiting the magnet is in the σ_{22} element. The new element, σ_{22}, is

$$\sigma_{22} = \sigma_{22} + \theta_{rms}^2 \qquad (7).$$

For a typical PSR injection line tune, this increase in σ_{22} results in an emittance growth of approximately a factor of three.

IV. CALCULATED DIVERGENCE GROWTH

A. *Present PSR Stripper Magnet*

By substituting known or hypothesized magnetic field distributions into the appropriate expressions in section III, one can then use equation (5) to calculate the distribution of deflection angles of H^0's exiting from a stripper magnet. Such simulations have been done for configurations similar to the PSR stripper magnet and the results agree well with measurements [1]. For the present PSR stripper magnet the predicted rms spread introduced into the beam is 0.37 mrad.

B. *Proposed Wiggler-Magnet Stripper*

In order to illustrate the validity of the wiggler-magnet stripper concept, angular divergence calculations were done for a hypothetical magnet whose field direction alternates through ten cycles of a sine-wave function with cycle length of 1.5 cm, and whose maximum field strength is 1.26 T. With this choice of cycle length and maximum field strength, integration of equation (1) over the full magnet length (twenty half cycles) shows that 99.99% of the incoming H^- will be stripped. This high stripping efficiency is essential because any unstripped H^- beam is lost in such a way that it contributes to the very beam losses that the use of a wiggler-magnet stripper is meant to reduce.

The angular spread introduced into the beam by a single half-cycle of the magnet described above is described by equation (5), and is calculated to have an rms width of only 0.18 mrad. As was pointed out earlier, since the angular spread from alternate segments of the magnet paint back and forth across each other, the rms spread for one segment applies to the total stripped beam at the end of the magnet. The calculated rms spread of 0.18 mrad is a roughly 50% reduction below the 0.37 mrad rms spread calculated for the present PSR stripper.

V. BEAM-LOSS CALCULATIONS

If the stripper-added beam divergence and the resulting emittance growth were reduced by use of the wiggler-magnet stripper described above, how much would ring beam losses be reduced? To answer this question, a Monte Carlo program was written to simulate beam losses on the limiting apertures in the PSR. One input to the program is the emittance of the injected beam, i.e., the emittance of the H^0 beam as it exits the stripper magnet. Calculations of beam loss rates for the PSR using the present stripper magnet are within about 20% of the measured values. This result indicates that the Monte Carlo program model used is reasonably accurate. The calculated loss rate with wiggler-magnet stripping is only 45% of the rate calculated for the present stripper magnet. This is a significant reduction; it indicates that, in the absence of other limiting factors, the circulating beam current in the PSR could be doubled without increasing losses above those now observed.

VI. LIMITATIONS OF MAGNET TECHNOLOGY

Until now nothing has been said about the possibility of building a wiggler magnet that would meet the specifications of cycle length and field strength needed in order for it to function as an effective stripper magnet. A brief review of current wiggler magnet technology was done, and the conclusion reached was that, with present state-of-the-art technology, it is probably not feasible to build a magnet with specifications that match those of the hypothetical magnet described in section IV. But, verification of this conclusion would require a systematic study of a range of designs involving consideration of stripping efficiency and divergence growth for different numbers of field cycles, different cycle lengths, and different maximum field strengths.

Permanent magnet wigglers are limited to relatively low field strengths (typically less than a kilogauss) with a resulting low H^- stripping efficiency, and are also subject to radiation damage in the high-energy proton and neutron environment near the PSR stripper location. A difficulty with electromagnet construction is in attaining the relatively high maximum field values needed while at the same time spacing the individual magnet segments closely enough together to make cycle lengths near one or two centimeters.

In spite of these limitations on field strength and cycle length, specifications attainable with present technology seem close enough to encourage further study.

VII. REFERENCES

[1] A. Jason, D. Hudgings, O. van Dyck, "Neutralization of H^- Beams by Magnetic Stripping," IEEE Trans. Nucl. Sci., vol. NS-28, June 1981, pp. 2704–2706.

[2] L. Scherk, "An Improved Value for the Electron Affinity of the Negative Hydrogen Ion," Can. J. Phys., vol. 57, p. 558, 1979.

[3] K. Brown, "Beam Envelope Matching for Beam Guidance Systems", Nucl. Instr. Meth., vol. 187, pp. 51–65, 1981.

The AGS New Fast Extraction System for the g-2 Experiment and RHIC Injection*

M. TANAKA and Y.Y. LEE
Brookhaven National Laboratory
Upton, NY11973

Abstract

The AGS requires a new fast extraction beam (NewFEB) system for the muon g-2 experiment and the Relativistic Heavy Ion Collider (RHIC). The proposed NewFEB system will consist of a new fast multi-pulsing kicker placed at straight section G10 and an ejector septum magnet at H10,together with local orbit bumps generated by powering backleg windings on the AGS main magnets. The new system is capable of performing single bunch multiple extraction as often as every 8 ms up to 12 times per AGS cycle, in addition to the standard single turn fast extraction. The conceptual design of the NewFEB sysytem will be discussed.

I. Introduction

Since the present fast extraction beam (FEB) and single bunch extraction (SBE) systems[1] are no longer available for the post-Booster era, the NewFEB system will serve as the AGS extraction system not just for the muon g-2 experiment[2] but also for RHIC[3] and any future neutrino physics program. The AGS Booster, nearly completed, should soon be able to increase the proton intensity in the AGS by a factor 4 and to allow the AGS to accelerate heavy ions (HI) beyond Si^{28} up to Au^{197}.

For the g-2 experiment, which is now constructing a 14 m diameter superferric muon storage ring (μ-SR) with B=1.5 T in order to improve the previous measurement of the anomalous magnetic moment (a_μ) by a factor of 20, NewFEB must meet the following requirements: (1) extract proton bunch beam up to full energy and intensity to the new V-target through the existing U-line for 3.1 GeV/c pion production, (2) perform single bunch multiple extraction (SBME) at $\sim$ 8 ms intervals up to 12 times per AGS cycle. The remaining bunches, if any, have to be debunched and go though the slow extraction beam (SEB) channel.

With the NewFEB system the AGS will also serve as an injector for the RHIC, which is now under construction. The circumference of the RHIC ring is 19/4 times larger than the AGS and its harmonic number at injection is 342 compared to 12 of the AGS. The present RHIC design assumes that the AGS can accelerate a variable number of bunches per pulse and the FEB/SBE system can be used as the extraction system for RHIC injection. The exact AGS operation mode for RHIC injection has not yet been fixed: (1) one may transfer all bunches (*e.g.*, 12/11 for protons, 3 for HI) to RHIC in a single turn (FEB, box-car stacking), or (2) one may transfer individual bunches one by one into the waiting rf buckets in RHIC (SBME). RHIC two rings will be filled with 57 bunches one after another in two minutes every $\sim$ 10 hours.

The schematic layout of the AGS-RHIC complex is shown in figure 1.

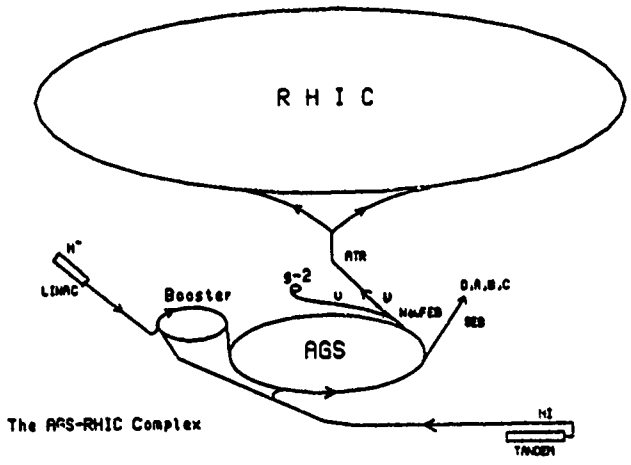


Fig. 1. Schematic layout of the AGS-RHIC complex.

II. Design of the NewFEB

A. Machine and Beam Parameters

For design purposes, we may assume that (1) p=29 GeV/c, (2) the 95% normalized emittance of the high intensity beam is $\epsilon_h^n(95) = \epsilon_v^n = 50\pi$ mm-mrad, (3) the maximum momentum spread allowed is $dp/p = \pm 2 \times 10^{-3}$. The current AGS machine parameters are summarized as follows:

*Work performed under the auspices of the U.S. Department of Energy

0-7803-0135-8/91$01.00 ©IEEE

Table 1. AGS Parameters

Circumference	C=2πR=807.075	[m]
Curvature	ρ=85.17	[m]
Revolution Time	t_{rev}=2.692	[μs]
Tune	Q_h=Q_v=~ 8.7	
Beta Functions	$\beta_{h,v}^{max,(min)}$=22.5 (10.5)	[m]
Dispersion Function	D_x^{max}=2.20	[m]
No. of Bunches	N_b=12,(3 for HI)	
Full Bunch Length	t_b=35±5	[ns]
Gap bet. Bunches	t_s=224(peak-to-peak)	[ns]
Typical Intensity	$1.6 \cdot 10^{13}$	[ppp]
	$3.0 \cdot 10^{8}$	[*Si*/p]
Typical AGS Cycle	2.0(FEB),3.4(SEB)	[s]
Typical Energy	24.5,28.5(p)	[GeV]
	14.5(*O*,*Si*)	[GeV/N]
Emittance	$\epsilon_{h,v}^n$=35π	[μm-rad]
Momentum Spread	dp/p=0.12	[%]

For RHIC injection, the expected values of ϵ^n, dp/p and t_b for both protons and HI are substantially lower than the current values since the Booster can deliver more intensity than that assumed for the RHIC design parameters[3]. At 10-foot straight section (G10,H10), β_h and β_v are rapidly changing as well as D_x while at 5-foot s.s. $\beta_h \cong \beta_{max}$, $\beta_v \cong \beta_{min}$ and $D_x \cong D_{max}$:

location	β_h (m)	β_v (m)	D_x (m)
10-ft s.s.	19.9 to 12.0	12.0 to 19.9	2.09 to 1.63
5-ft s.s.	22.1	10.5	2.17

Figure 2 shows the wall monitor display of the bunch structure in the AGS after the third bunch is extracted for the SBE operation.

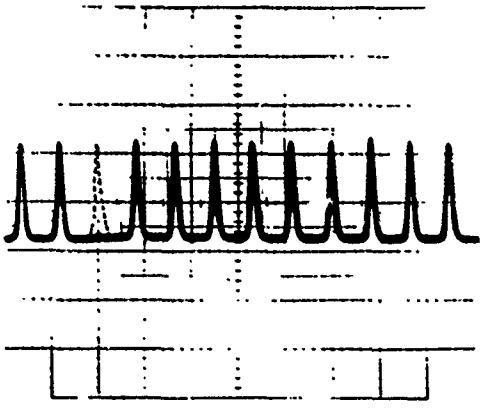


Fig. 2. Display of the bunch structure in the AGS

B. Fast Kicker

The full horizontal beam width, is usually defined by $w_f = 2\sqrt{\epsilon_n \beta_h/\pi + (D_x dp/p)^2}$, assuming that the dp/p distribution is symmetric, and the transverse and longitudinal emittances are uncorrelated, where $\epsilon_h = \epsilon_h^n \cdot (m/p)$. Hence, at p=29 GeV/c, using the 99% emittance we have w_f(H10)=16.4 mm. Assuming that we need 2 mm separation at both sides of the septum of the ejctor magnet (SMH10), and ~ 10 mm septum thickness, then the required separation of the circulating beam and the beam kicked by the fast kicker at G10 (FKG10) is δx=30.4 mm. The FKG10 must deflect the beam by

$$\vartheta(G10) = \delta x(H10)/\sqrt{\beta_h(G10)\beta_h(H10)}\sin(\delta\mu)$$

=-2.00 mrad where $\delta\mu$ is the betatron phase advance from FKG10 to SMH10, and which corresponds to $\int Bdl = B_0 \cdot l_{eff} = -0.19$ T-m.

We consider a C-type ferrite magnet with a limited aperture, w(idth)=38.5 mm and g(ap)=17 mm, to minimize the required voltage on pulsing the FKG10. Choosing l_{eff}=2.0 m, we find the magnetic field is B_0=0.95 T, the magnet current, $I = B_0 \cdot g/\mu_0$=1.29 kA and the corresponding total magnet inductance, $L_{mag} = \mu_0 \cdot l_{eff}/g$=5.69 μH.

In order to achieve clean bunch-to-bunch extraction, the kicker fall time must be as rapid as the rise time. The total duration is T_0=t_{rise}+t_{flat}+t_{fall}=160+40+180=380 ns and the pulse waveform is essentially half sine. The recharge time must be a few ms. The minimum pulse voltage to perform the full field in t_{rise}=160 ns is V=L_{mag}dI/dt=$B_0 \cdot l_{eff} \cdot w/t_{rise}$=45 kV. Since we have to add the additional stray inductance and it is also desirable to keep $V \leq$~ 30 kV, the magnet will be subdivided into several shorter modules and powered in parallel. If the pulser is to be mounted outside the ring due to the high radiation environment, it will have to be a *matched* pulse forming network (PFN). The magnet is loaded with capacitance so it behaves like a transmission line of the correct impedance. The PFN storage voltage will be twice the maximum pulsing voltage and it has to be oil insulated.

C. Ejector Magnet

A new out-of-vacuum ejector septum magnet (SMH10) has been built for standard FEB operation and its magnetic properties have been intensively analyzed. However, for NewFEB operation the ejector magnet has to stay a DC mode over 100 ms, the septum thickness must be increased from the current value of 2.3 mm to ~ 10 mm. If the magnet is water-cooled, ~ 5 mm thickness might be sufficient.

D. Orbit Bump

Local orbit deformations are needed to move the circulating beam into the aperture of the fast kicker and also to bring the beam adjacent to the septum of the ejector. These bumps are generated by powering backleg windings on selected AGS main magnets so arranged that the tune shifts and stopbands at Q_h=8.5 are minimized. We first consider two standard 3/2 λ horizontal bumps, one (BLWG10) for FKG10 and another (BLWH10) for SMH10. With this configuration, a tracking study shows that the available space for the kicked beam is rather marginal

around G17. So we make modifications to create a hybrid (2λ) bump (BLWGH), eliminating some backleg windings and doubling kicks at some.

In figure 3 , we show a schematic layout of the NewFEB extraction components (BLWGH, FKG10, SMH10) and the particle trajectories with and without FKG10 and SMH10 on.

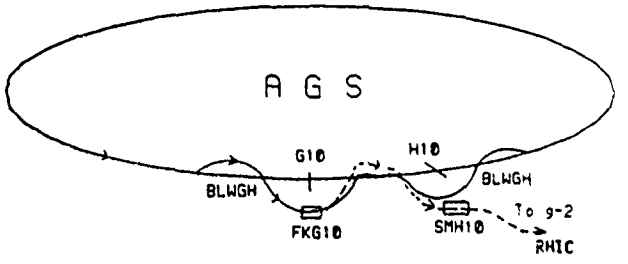


Fig. 3. Schematic layout of the NewFEB components.

II. Simulation

To find out the extracted beam parameters at the middle of straight section H13, *i.e.*, the entrance of the U-line, a simulation was performed with a simple model of the AGS, using the accelerator modeling program MAD which includes quadrupolar and sextupolar components of the main combined function magnets and the NewFEB extraction components. First, we run MAD to obtain the desire orbit at FKG10 and at SMH10, making fine adjustments of BLWGH. Then, the particle with initial conditions (x, x') at the beginning of s.s.G10 is traced through the lattice and receives an appropriate kick (1.6 mrad) at FKG10 and an additional kick (20 mard) at SMH10 up to the middle of s.s.H13, where the beam should be about $\sim$ 43 cm away from the central orbit, free from the fringing field of the ring magnets. The simulation results on the extracted beam parameters at s.s.H13 are summarized as follows:

x = 43.8 cm	x'=63.8 mrad		
α_x=-5.75	β_h=46.4 m	α_y= 0.83	β_v= 3.6 m
D_x=1.24 m	D'_x=0.19		

Due to its high intensity operation for the g-2 experiment, it is important that the NewFEB system can achieve a high extraction efficiency ($\geq$99%). On the other hand, for RHIC injection, stability and reproducibility of the extracted bunched beam parameters are crucial since any change (pulse-to-pulse, cycle-to-cycle) of the extracted beam parameters will directly influence RHIC performance.

III. Summary and Plan

The basic conceptual design is made on the NewFEB system at the AGS, which is capable of performing SBME for the g-2 experiment and RHIC injection. It is expected that detailed engineering design work will start soon since the μ-SR and RHIC are scheduled to be completed in 1994 and in 1997, respectively. Further simulation studies of the NewFEB extraction and beam transfer from the AGS to RHIC (ATR) will be needed to specify tolerances of the NewFEB system components as well as the overall required AGS capability as the injector for RHIC.

Acknowledgements

We would like to thank many members of the AGS Department, especially the Extraction Group for their helpful discussions and suggestions received during our conceptual design work on the NewFEB system. M.T. is also very grateful for the advice and help given by D. Fiander at CERN on the pulser.

References

[1] W.T. Weng, *The AGS New Fast Extraction System and the Single Bunch Extraction Test*, IEEE NS-30, No. 4 (1983)

[2] Experiment 821, *A New Precision Measurements of the Muon g-2 Value at the level of 0.35 ppm.*

[3] BNL-52195, *Conceptual Design of Relativistic Heavy Ion Collider*, May 1989.

The Frascati Φ-Factory Injection System

R. Boni, S. Kulinski, M. Preger, B. Spataro, M. Vescovi, G. Vignola
INFN, Laboratori Nazionali di Frascati, C.P.13, 00044 Frascati (Roma), Italy

Abstract

The injection system, for the Frascati Φ–factory DAΦNE [1], is designed to store ≈10^{13} positrons and electrons in the two main rings in an overall injection time at startup of ≈10 minutes. The system will consist of a high current electron Linac (E≈250 MeV), a low current high energy electron-positron section (E>510 MeV) and a compact damping ring in order, to avoid injection saturation, to increase longitudinal acceptance and to decouple the design of the main rings from injection requirements. The two Linac sections will provide ≈0.3 nC of positrons within ±1% energy spread in 10 ns pulses for injection at 50 Hz into a single 76 MHz bucket of the damping ring. Extraction of the high quality damped bunch from the accumulator will take place at 1 Hz, filling one main ring bucket at a time. The Linac design foresees 3 m long 2π/3 TW constant gradient accelerating sections with SLED systems in order to increase the energy gain. The magnetic structure of the damping ring is designed to be accommodated in a 12x12 m^2 hall, and it is made of four quasi-achromatic bending sections and four long straights to accommodate injection and extraction pulsed elements and the RF system.

I. INTRODUCTION

DAΦNE, the Frascati Φ-factory project, is a high luminosity (>10^{32} $cm^{-2}s^{-1}$) storage ring running at a centre of mass energy of 1020 MeV. To achieve such a high luminosity, a large number of electron and positron bunches (120) circulate in two separate rings, colliding at a small angle in the horizontal plane. The total number of particles in each ring exceeds 10^{13}, thus setting challenging requirements on the design of the positron injection system. Since the operating time structure of the bunch configuration will be chosen upon the results of machine commissioning, single bunch injection has been recommended, so that the use of a small full energy storage ring which serves as an accumulator between a positron/electron Linac and the main ring seems to be the only possible solution to store the whole charge in the required injection time of ≈10 minutes. To mantain a high average luminosity, topping-up will be performed when the stored current drops below a given level, so that full injection will be necessary only at machine start-up.

Particles accelerated from the Linac will be injected at 50 Hz into the accumulator, extracted at 1 Hz and injected into the main rings, filling one bucket at a time. In order to reach the design positron current, 360 pulses will be transferred from the accumulator to the main ring. In the case of electrons, due to the larger current from the Linac, injection rate is foreseen to be much faster.

0-7803-0135-8/91$01.00 ©IEEE

Table 1 shows the efficiencies assumed to estimate the required current from the Linac injection section.

Table 1
Injection, transport and extraction efficiencies

Transport from Linac gun to converter	0.4
Electron-positron conversion @ 250 MeV	0.008
Transport from converter to accumulator	0.9
Injection into accumulator	0.5
Extraction from the accumulator	0.9
Transport and injection into main ring	0.8

With these assumptions the positron charge per pulse delivered by the Linac is 0.3 nC, while the electron charge from the gun is 95 nC.

II. THE LINAC

The schematic layout of the DAΦNE Linac is shown in Fig.1. The main Linac components are: thermionic gun, prebuncher and buncher at the Linac frequency f = 3GHz, high current TW electron Linac with output energy ≥ 250 MeV, electron-positron converter, positron capture section, low current e^-e^+ TW Linac with energy ≥ 510 MeV, magnetic focusing elements.

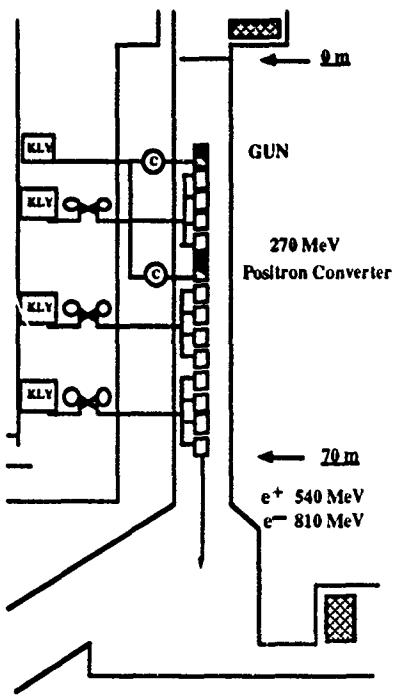


Figure 1. Layout of the Linac.

The gun, dimensioned for the maximum positron peak current, will be used for both operating modes. The main gun parameters are listed in Table 2.

Table 2
Main gun parameters

Type	Pierce, triode
Cathode radius	R_k = 40 mm
Cathode diameter	D_k = (25+30)mm
Anode potential	Ua = 100 kV
Current	Ig = 10 A
Emittance(invariant)/π	$\varepsilon_n = 1 \times 10^{-4}$ m·rad
Macrobunch length	t_b = 10 ns
Repetition rate	f_r = 50 Hz

The bunching system will consist of a TM010 single cell cavity prebuncher and a 10+20 MeV buncher with few graded β cells. The buncher length will be about 1+1.5 m. The purpose of the system is to bunch the 'continuous' electron current emitted by the gun in a train of micropulses which corresponds to less than 15 degrees of the period of the Linac radiofrequency, and to accelerate the electrons to relativistic velocities before injecting them into the constant phase velocity (v=c) accelerating structure of the Linac.

According to the analysis presented in [2] we propose the use of $2\pi/3$ travelling wave (TW) constant gradient (CG) accelerating structures together with a SLED type pulse compression system. The advantages of such a structure in comparison with others, i.e. $\pi/2$ TW or $2\pi/3$ TW constant impedance (CI), are described in [3]. In our case their best features are: lower sensitivity to frequency deviations, lower beam loading derivative and lower sensitivity to beam breakup in comparison with CI structures. It is also important that such structures have been successfully tested in large size accelerators like SLAC, DESY and LEP.

We have optimized the optimum section length, the field gradient and the minimum klystron number for the following parameters: quality factor Q = 15,000; beam pulse duration t_b=10ns; klystron output power P=45 MW; RF pulse duration t_k=4.5 μs; storage cavity (for pulse compression) quality factor $Q_c=10^5$; effective electron energy at the converter Ec > 250 MeV; output positron current i^+>30ma (at 510 MeV in ±1%).

The Linac will be installed into the 70 m long existing tunnel of the ADONE Linac. Assuming a Linac filling factor of 0.7, the total length of the accelerating sections should be around 50 m corresponding to a field gradient of about 20 MV/m. Our analysis shows that the optimum section length is 3 m. Some possible configurations for the DAΦNE Linac, based on the 3 m long sections are given in Table 3.

All the configurations presented in Table 3 fulfil the above mentioned requirements. Additional informations, like reliability and costs are then necessary to support the final choice. From this point of view the solutions with lower gradient (i.e. 21 MV/m) are preferable since:

- most of the existing large electron Linacs operate below 20 MV/m.
- the existing tunnel in the LNF area allows the installation of about 50 m of active Linac which means a possible total energy of 1000 MeV with an accelerating gradient of 20 MV/m.
- as shown in Table 3 we estimate that a 20 MV/m Linac is cheaper than a 30 MV/m one.

Table 3
Possible DAΦNE Linac Configurations

N° sections	14+2*	12+2*	10+2*
E(MV/m)	21	21	30
i^+ (ma)	50	36	50
W_c (MeV)	390	270	380
W_t (MeV)	930	810	940
N° klystr. **	4(4)	3(4)+1(2)	5(2)+1(2)
cost. (relat.)	1.05	1.	1.13

* 20 MeV Bunchers
** The number of sections per klystron in brackets.

The main components of the positron source are: the converter, the magnetic focusing and the high gradient capture accelerating section. The converter will be made of high Z materials such as Ta or Au, resistant to thermal and mechanical stresses. The average power of an electron beam passing through the converter will be about 1.2 kW, the power dissipated in the converter being about 16% (ie. ~ 200 W) of the total beam power. Considering the good performances of the ADONE converter [4,5], which can dissipate about 10 kW, we intend to adopt a similar solution for DAΦNE. Since the electron energy on the converter will be more than twice that of ADONE Linac, also the thickness of the target should be larger (e.g. ≈ 2 radiation lengths).

The electrons will be focused by a quadrupole triplet to form a spot with a diameter smaller than 1 mm, the positrons will be confined by a very intense tapered magnetic field of the order of 5+6 Tesla generated by a flux concentrator [6]. Further optimization of the capture efficiency can be obtained by adding after the flux concentrator a short very high gradient accelerating capture section with the proper phase [7].

III. THE ACCUMULATOR

The use of an accumulator between the Linac and the main rings has the following major advantages:

- it avoids injection saturation due to the large number of injection pulses (≈1.6×10^4) by subdividing them into 45 pulses into the accumulator times 360 pulses into the main rings;
- it provides a larger longitudinal acceptance, since the RF frequency of the accumulator can be much lower than the main ring one;
- it decouples the design of the main rings from injection requirements, since the emittance and energy spread of the damped beam from the accumulator are much smaller than those of the beam coming directly from a Linac.

The length of the accumulator has been chosen as 1/3 of the main ring circumference, to easily synchronize injection of any desired bucket of DAΦNE. For the same reason, the RF frequency of the accumulator cavity is exactly 5 times lower than the main ring one.

Fig. 2 shows the layout of the positron/electron accumulator with the schematic of the transport channels from the Linac and to the main rings. Positrons will be injected into the accumulator from the left channel and extracted from the right one, while electrons will follow the opposite path. A symmetric set of four kickers will provide the necessary orbit distortion for injection and extraction of both electrons and positrons.

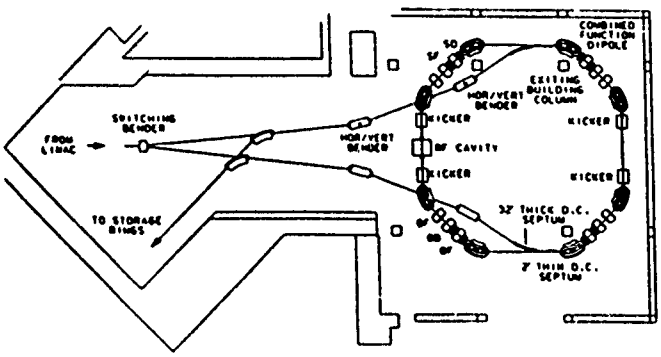


Figure 2. The Accumulator Layout.

The accumulator lattice, derived from the storage ring ACO in Orsay [8], has a fourfold symmetric periodicity, and has been chosen to optimize injection performance. The optical functions of one fourth of the ring are shown in Fig. 3.

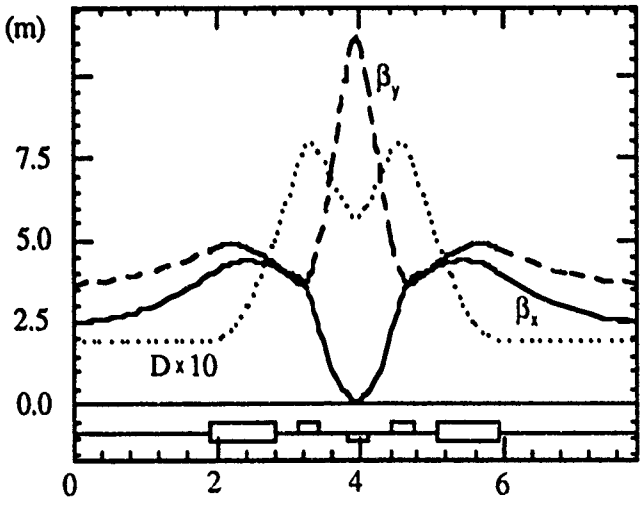


Figure 3. Optical Functions of one fourth of the Ring.

Four low-dispersion 3.6 m long straight sections provide enough space for the kickers, the injection septa and the RF cavity. Each bending section includes two 45° magnets with field index n=0.5 to ensure the best damping partition, a quadrupole triplet to tune the horizontal phase difference between the kickers and the septa and a couple of sextupoles to correct the chromaticity in both the horizontal and the vertical plane.

The gradient bending magnets will be H-shaped with a bending radius of 1.1 m, corresponding to a centre field of 1.55 T, with a minimum gap of 5 cm. The quadrupoles are designed to a magnetic length of 34 cm, with a maximum gradient of 8.3 T/m and a bore radius of 5 cm. The sextupoles have a magnetic length of 10 cm, with a maximum gradient of 80 T/m^2. Four kickers are used simultaneously for injection of electrons and positrons from the Linac. This arrangement has been chosen to exactly cancel the perturbation of the already stored beam at each injection pulse. Only two of them provide the necessary kick to extract the beam from the accumulator. The required kicker pulse length is ≈100 nsec and the maximum strength is 67 G·m for injection and 110 G·m for extraction. Table 4 gives a parameter list for the accumulator.

Table 4
Parameters of the accumulator

Energy (GeV)	0.51
Circumference (m)	31.52
Straight section length (m)	3.67
Horizontal betatron wavenumber	2.89
Vertical betatron wavenumber	1.13
Dispersion at Straight Section Centre (SSC) (m)	0.13
Horizontal β at SSC (m)	2.51
Vertical β at SSC (m)	3.87
Maximum dispersion (m)	0.81
Maximum horizontal β (m)	4.24
Maximum vertical β (m)	10.40
Horizontal betatron damping time (msec)	19.71
Vertical betatron damping time (msec)	19.71
Synchrotron damping time (msec)	9.86
Momentum compaction	0.059
Emittance (mm·mrad)	0.27
r.m.s. energy spread (%)	0.042
Horizontal r.m.s. beam size at SSC (mm,no coupling)	0.82
Vertical r.m.s. beam size at SSC (mm,full coupling)	0.72
Horizontal chromaticity (sextupoles off)	-4.13
Vertical chromaticity (sextupoles off)	-4.10
RF frequency (MHz)	76.09
RF voltage (MV)	0.1
Harmonic number	8
RF energy acceptance (%)	±1.55
r.m.s. bunch length (cm, radiation only)	2.86

IV. REFERENCES

[1] G. Vignola et al., "DAΦNE, the Frascati Φ-Factory Project", these proceedings.

[2] S.Kulinski, R.Boni, B.Spataro, M.Vescovi, G.Vignola, "The Linear Accelerator for DAΦNE Injection System", DAΦNE Tech. Note, LC-1, Febr. 1991.

[3] R.B. Neal, "The Stanford Two Mile Accelerator", W.A. Benjamin Inc. N.Y. 1968.

[4] R.Andreani and A.Cattoni, "Positron Converter for the Frascati Linear Accelerator", Nucl. Instr. Meth., Vol.129, pp.365-371, 1975.

[5] R.Boni, S.Guiducci, M.Vescovi, "A New System for Positron Focusing at the Frascati Linac", LNF - 81/6 (R), 1981.

[6] D. Sherden, "Tapered Solenoid for SPC Positron Source", SLC Design Book, MEMO CN-22.1980.

[7] B. Aune and R.H. Miller, "New Method for Positron Production at SLAC", SLAC PUB. 2393 Sept. 1979.

[8] P.Marin et al., "Status Report on the Orsay Electron Positron Storage Ring", VI Int Conf. on H E.A Cambridge 1967

Prototype Studies of a 1 MHz Chopper for the KAON Factory

G. D. WAIT, M. J. BARNES, D. BISHOP, G. WATERS
TRIUMF, 4004 Wesbrook Mall, Vancouver, B.C., Canada V6T 2A3
C. B. FIGLEY
SAL, Saskatoon, Saskatchewan. Canada

Abstract

A 1.025 MHz ($\simeq 10^6$ discrete pulses/s) beam chopper is required for the injection line into the Accumulator ring of the KAON Factory at TRIUMF [1]. The beam chopper will create 108 ns gaps in the 1 GeV/c H^- beam to allow enough time for the magnetic field to be established in the kicker magnets in each of the 5 rings. The required deflection of 1 mrad can be achieved with a set of plates 5 cm apart in which the product of voltage difference and plate length is 37.7 kV·m. The "kick" must have a rise and fall time of less than 39 ns and a flat top of 49 ns and 92 ns on alternate pulses. A novel design concept for a 1 MHz chopper has been developed involving an energy storage system where the electric pulses are stored in a large diameter (10 cm) low loss coaxial cable. Measurements on the performance of a high voltage prototype are presented. Results are encouraging and show that this novel design can be implemented successfully for the KAON Factory.

I. Introduction

The TRIUMF cyclotron will be used as an injector for the KAON Factory synchrotron. The H^- beam pulse period is 43.5 ns, and allowing for jitter the effective beam burst width will be about 4.5 ns so that the effective gap between beam bursts will be about 39 ns [1]. The chopper rate will be 1.025 MHz with a 100% macro-duty factor with alternate pulse widths of 49 ns and 92 ns, as shown in Figure 1, so that 2 and 3 bunches will be removed alternately at approximately 1 μsec intervals. Similar device at other laboratories operate at either low repetition rates in the 100 Hz range [2,3] or for example at a 0.25% macro-duty factor and 10 MHz [4]. The deflected beam bunches will impinge on a stripper foil and be further separated

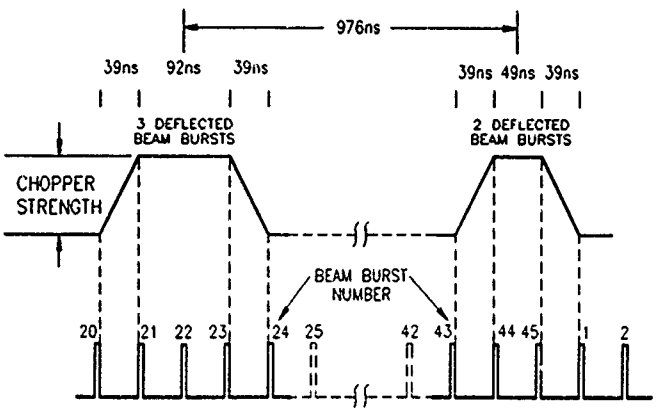


Figure 1: Pulse pattern of prototype 1 MHz chopper.

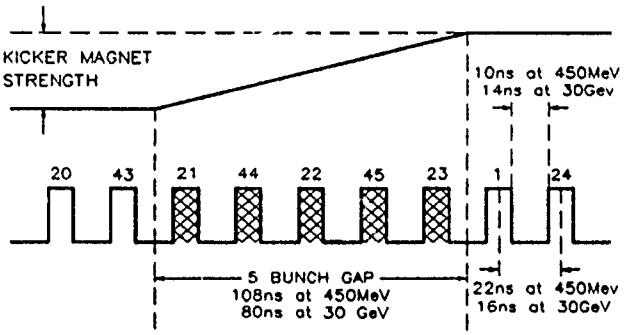


Figure 2: Beam burst pattern in the Kaon Factory rings.

from the undeflected H^- beam by a downstream dipole magnet and directed to a 10 μamp beam dump. The accumulator ring will store H^- pulses in sets of 45, interleaved into two groups as shown in Figure 2 and the gap between most pulses will be reduced to 10 ns. The resultant gap for the kickers will be 108 ns in the accumulator ring with 5 consecutive bunches missing.

The rise and fall time of the driving voltage pulse ($\tau_{v(r)}$), between a% and b%, and the propagation time (τ_{beam}) of the H^- beam through the center fed deflector plates must satisfy [9]:

$$\tau_{v(r)}^{x} + (M \times \tau_{beam})^{x} \leq (39\ ns)^{x} \qquad (1)$$

Where x is a power function and depends on the shape of the rising edge but is constant for fixed M ($= \frac{b-a}{100}$). If the pulse shape is trapezoidal then x $\simeq$ 1.6 (2.1) for a 5% $\rightarrow$ 95% (10% $\rightarrow$ 90%) risetime [9]. If the deflector plates are 4 m long and the kick rise time is defined from 10% $\rightarrow$ 90%, then from equation (1) the rise time of the electrical pulse must be less than 38 ns.

II. Chopper Design Concept

The original design concept has been described elsewhere [5,7,8] but has been modified somewhat and the present system will be outlined here. Electrical pulses will be stored in a very low loss coaxial cable that has a one way propagation time of approximately 1 μs. This will permit the storage of two pulses of different widths that are 1 μs apart.

A. *Original Design Concept*

In the original design there were two tetrodes mounted at one end of a storage cable. The far end of the storage cable was connected to the center of a set of open circuit deflector plates which are configured as a 100 Ω stripline

0-7803-0135-8/91$01.00 ©IEEE

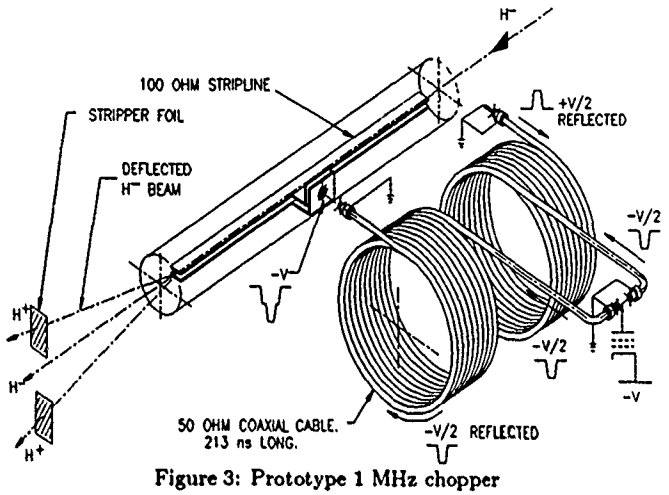


Figure 3: Prototype 1 MHz chopper

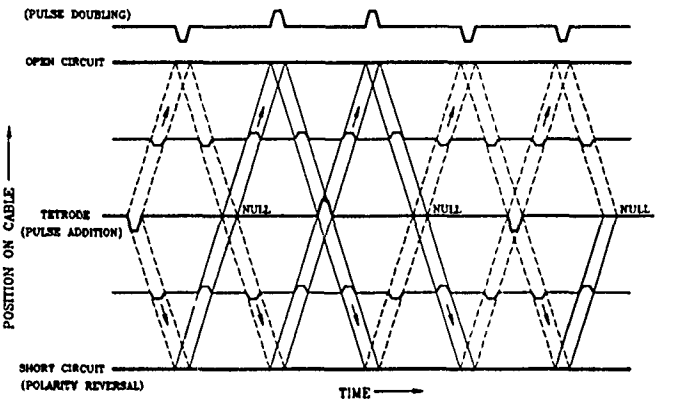


Figure 5: Lattice diagram of the 1 MHz chopper pulse pattern.

to match the impedance of the 50 Ω storage cable. The charger tetrode was used to reshape the leading edge of the stored pulse and the clipper tetrode was used to reshape the trailing edge of the pulse. The cable was connected to the charger tetrode at the cathode and to the clipper tetrode at the anode. The main disadvantage of this circuit was that the stray capacitance of the tetrode with the cathode connection was too high. The total stray capacitance in the prototype was about 1000 pF and it was not possible to achieve the required rise time. The best achieved rise and fall time of a 7 kV positive pulse was 65 ns and 90 ns respectively when both tetrodes were connected.

B. Present Design Concept

The schematic for the present version of the KAON Factory chopper is shown in Figure 3. There is only one CY1172 [6] tetrode which is anode connected to the center of the storage cable. The total stray capacitance is about 240 pF. One end of the center fed cable is short circuited at the far end and the other end is open circuited. The cable is mounted to the tetrode in such a way that the inductance of the connection and the stray capacitance of the tetrode appears as a segment of lumped element 50 Ω transmission line. The inductance of the anode connection is shown in figure 4.

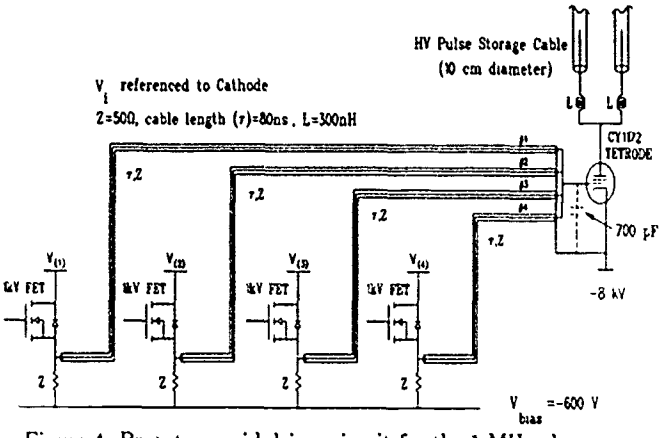


Figure 4. Prototype grid driver circuit for the 1 MHz chopper.

Figure 4 shows the output stage of the control grid driver circuit. The pulse pattern on each of the four parallel grid drivers was controlled through four fiber optic links from a pulse sequencer [11]. The pulse widths and amplitudes of each of the four fet pulsers could be controlled independently. The pulse sequencer permits operation with various burst lengths at macro-duty factors up to 100%.

Figure 5 shows the ideal pulse pattern at the center and at the open circuit end of the pulse storage cable. Each alternate reflection from the ends of the cable causes a null at the center of the cable. When the pulse at the center of the storage cable is negative the tetrode is turned on to restore the leading edge (charge). When the pulse at the center of the storage cable is positive the tetrode is turned on to restore the trailing edge (clip). The duration and the amplitude of the clipper pulse must be controlled very precisely to avoid overshoot or undershoot. The amplitude of the charge pulse is not so critical but the timing of this pulse relative to the storage cable length must be precisely controlled.

III. Prototype Tests

The prototype tests were carried out at about 2.3 MHz since the total available length of 10 cm diameter storage was 426 ns. The prototype deflector plates have not been connected to the system for any of the tests to date. If there were no stray capacitance or inductance then the pulse period at the end of the open circuit cable would be 426 ns. However the presence of stray inductance and capacitance introduces a delay. At a 3% macro-duty factor and a high voltage of 8 kV, the pulse period was varied until the fall time of the negative pulse was minimized. The best fall time occurred at a period of 436 ns (2.29 MHz). The free running period of pulses when the tetrode is turned off is 440 ns. Thus there is an effective phase shift of 4 ns every pulse period, between a driven edge of a pulse and the interpulse ripple. This turns out to be a significant advantage in eliminating the interpulse garbage. The interpulse garbage delays in phase for a few hundred pulses until it becomes absorbed into a high voltage pulse.

The pulse patterns shown in Figure 6 were measured 200 μs after the first pulse at a 3 % macro-duty factor

The solid (dashed) curves show the data for a wide (narrow) pulse pattern at the grid, anode and the open circuit end of the cable. The width of the anode pulse is determined by the relative delay of the grid clipper pulse. The amplitude of the pulses is about 7 kV and it can be seen that the null between the anode pulses is very clean. Table 1 shows a summary of the rise and fall times of the 4 measured voltage pulses at the open circuit end of the cable for the wide pulse pattern sequence shown in Figure 6. The deflection rise and fall times were calculated [9] for a set of 4 m deflector plates using the measured pulse patterns. The phase jitter shown in Table 1 relative to the first positive pulse and the ramp times must fit into the 39 ns gap between beam bursts.

Tests were also carried out at a 50% macro-duty factor and the pulse patterns were the same but the voltage levels were lower due to limitations in the power supplies. The power dissipation in the 150 kW tetrode was only about 7 kW at a 50% duty factor but the power dissipation in the grid pulser prevented operation above this rate. However the pulse repetition rate of 2.29 MHz is more than double the rate required for the final version so we were able to achieve 1.14×10^6 pulses/s at about 6.5 kV continuously.

Table 1.
Rise and fall times of wide pulses

Location of Pulse Edge	Voltage rise, fall (ns) 10%→90%	Deflection rise, fall (ns) 10%→90%	Phase Jitter $\Delta\phi$ (ns) ±50%→±50%
1st pos			
Leading	14.7	18.2	0.0
Trailing	43.3	43.6	0.0
2nd pos			
Leading	31	31.4	+6.2
Trailing	34.1	36.3	−6.8
1st neg			
Leading	27.6	27.5	+9.5
Trailing	34.6	36.7	−6.7
2nd neg			
Leading	16.2	19.4	−2.1
Trailing	38.5	39.9	+0.2

IV. Conclusions

The results show that the prototype chopper can achieve operation at 1 MHz continuously for 6.5 kV pulses and that we are very close to meeting the rise and fall time specification of 39 ns. Modifications are presently underway to further reduce the stray capacitance and inductance associated with the tetrode connection to reduce the ramp times and the phase jitter. The high voltage power supply is being replaced so that the chopper operate at 12 kV. The grid pulser is being improved so that we can achieve operation at 2.3 MHz continuously for the prototype tests.

V References

[1] TRIUMF KAON FACTORY STUDY, Accelerator Design Report, May 1990.

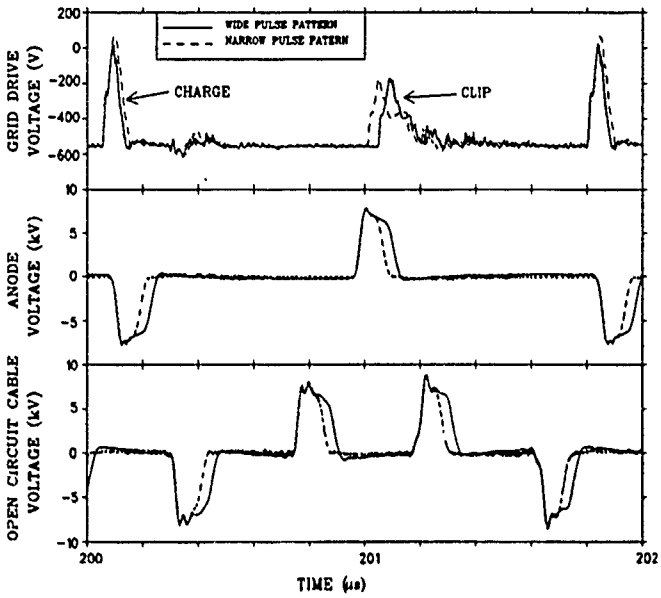


Figure 6: Measured pulse patterns on the grid, anode and end of the open circuit cable

[2] J. F. Power, B. Blind, A. J. Jason, "A Los Alamos Proton Storage Ring Fast-Extraction Kicker System",IEEE Trans. on Nucl. Sci. vol., no 5, p. 3021, 1985

[3] C. B. Figley," A High Speed Electrostatic Kicker for the Pulse Stretcher Ring at Saskatchewan Accelerator Laboratory",Nucl. Instr. and Meth, vol. A273, 1988. 59-62

[4] G. J. Krausse, "A 10 MHz High Voltage Modulator with Pulse-Width and Repetition-Rate Agility",IEEE Pulsed Power Conference, Arlington, VA, June 1985.

[5] M. J. Barnes, D. C. Fiander, C. B. Figley, V. Rödel, G. D Wait, G. Waters. "A 1 MHz Beam Chopper for the KAON Factory", (Proceedings of European Particle Accelerator Conference, June 1990).

[6] English Electric Valve Co. Ltd., Chelmsford, Essex, UK.

[7] C. B. Figley, G. D. Wait, M. J. Barnes, "A 1 MHz Chopper for Injection into the TRIUMF KAON Factory", Proceedings of Power Modulator Symposium, San Diego, June 1990.

[8] G. D. Wait, M. J. Barnes, C. B. Figley,"Prototype Studies of a 1 MHz Beam Chopper for the KAON Factory", Proceedings of USSR Particle Accelerator Conference, Moscow, Oct 1990.

[9] Barnes M. J., Wait G. D., "Results of Calculations on the Beam Deflection due to the 1 MHz Chopper for the KAON Factory" Proceedings this Conference.

[10] Barnes M. J., Wait G. D., "Algorithm for the Deflector Plates of the 1 MHz Chopper for the KAON Factory" Proceedings this Conference.

[11] Waters G., D. Bishop, Barnes M. J., Wait G. D. "Controls and Interlocks for a Prototype 1MHz Beam Chopper" Proceedings this Conference.

Results of Calculations on the Beam Deflection due to the 1 MHz Chopper for the Kaon Factory

M. J. Barnes, G. D. Wait
TRIUMF, 4004 Wesbrook Mall, Vancouver, B.C., Canada V6T 2A3

Abstract

Deflection of 1 GeV/c H^- beam bunches to be eliminated by the 1 MHz chopper, for the proposed Kaon factory at TRIUMF, will be provided by an electric field between a set of deflector plates [1,2]. Deflection rise time is a function of beam transit time through the deflector plates and the rise time of the stored voltage pulse. This paper presents the results of time-domain mathematical simulations to assess the relationship between the above quantities: the results of these simulations allow an accurate determination of the required rise-time of the stored voltage pulse. The representation of the deflector plates is modified so that linear displacement of the beam, as well as angular deflection, may be assessed. Simulations have also been performed to assess the attenuating effect of the deflector plates upon both angular deflection and linear displacement of the H^- beam caused by voltage ripple. A measured voltage pulse is simulated as driving the deflector plates, and beam deflection is predicted.

I. Introduction

Angular deflection rise [fall] time is a function of the beam transit time through the deflector plates and the rise [fall] time of the stored voltage pulse [3,4]. The relationship between total angular deflection rise [fall] time ($t_{\Theta_t(r/f)[a\%\rightarrow b\%]}$), between $a\%$ and $b\%$, the rise [fall] time of a trapezoidal driving voltage ($t_{v(r/f)[a\%\rightarrow b\%]}$), between $a\%$ and $b\%$, and the transit time of the beam through the deflector plates (τ_{beam}) is assumed to be of the form:

$$t^x_{\Theta_t(r/f)[a\%\rightarrow b\%]} = t^x_{v(r/f)[a\%\rightarrow b\%]} + (M \times \tau_{beam})^x \qquad (1)$$

Where:
x is a power function relating the variables;
M is a multiplier for the beam transit time through the deflector plates: the value of M is related to the definition of the rise-time $\left[M = \frac{b-a}{100}\right]$.

The results of mathematical simulations are used to determine the dependence of the power function (x) upon the rise [fall] time of the driving voltage waveform and the physical length (ℓ) of the deflector plates [4].

A beam particle can exit the deflector plates with a trajectory parallel to the horizontal ($\Theta_t = 0°$) but linearly displaced from the centre-line of the plates [4]. Thus in order to track beam particles through the deflector plates it is necessary to calculate both angular deflection and linear displacement of the particles. Hence the mathematical model of the deflector plates [5] has been modified such that linear displacement of beam particles is also predicted.

As a result of parasitic inductance and capacitance associated with the 1 MHz chopper there may be voltage ripple on the storage cable [6]. The deflector plates can act to attenuate the effect of the ripple [4,7]. Simulations have been performed to assess the attenuating effect of the deflector plates as a function of the frequency of the ripple and the physical length of the plates.

II. Calculation of Power Function 'x'

If a voltage pulse with zero rise-time is applied to centre-fed deflector plates the total angular deflection (Θ_t) experienced by a particle exiting the plates will increase linearly from zero, at a time τ_m after application of the ideal pulse, to its idealized flat-top value (Θ_{ti}), at a time $\tau_m + \tau_{beam}$ after application of the pulse [4,5] where:

$$\tau_{beam} = \frac{\ell}{\beta c} \qquad (2)$$

In the ideal case the total angular deflection increases from 0 % to 100 % of Θ_{ti} in time τ_{beam}. However, if the limits of interest of angular deflection are 5 % and 95 % of Θ_{ti} then, in the ideal case, the 90 % angular deflection excursion occurs in a time interval (Δt) given by:

$$\Delta t = M \times \tau_{beam} \qquad (3)$$

where $M = 0{\cdot}9$.

Previous mathematical simulations of the 1 MHz chopper assumed that the value of x is unity [2,3,6]: thus the permitted voltage rise [fall] time ($t_{pv(r/f)}$) was calculated from:

$$t_{pv(r/f)[a\%\rightarrow b\%]} = t_{\Theta_t(r/f)[a\%\rightarrow b\%]} - M \times \tau_{beam} \qquad (4)$$

where $t_{\Theta_t(r/f)[a\%\rightarrow b\%]} = 39$ ns [8,9]. However the general form of equation 4 is:

$$t_{pv(r/f)[a\%\rightarrow b\%]} = \left(t^x_{\Theta_t(r/f)[a\%\rightarrow b\%]} - (\tau_{beam} \times M)^x\right)^{\frac{1}{x}} \qquad (5)$$

Time domain PSpice simulations have been carried out to evaluate x. An 80 section representation of the deflector plates [4,5] was utilized to assess the dependence of the power function (x) [see equation 1] upon the beam transit-time multiplier (M) for 5 different conditions.

- $\ell = 4$ m ($\tau_{beam} = 18{\cdot}06$ ns), $t_{v(r)[0\%\rightarrow 100\%]} = 20$ ns;
- $\ell = 3{\cdot}78$ m ($\tau_{beam} = 17{\cdot}1$ ns), $t_{v(r)[0\%\rightarrow 100\%]} = 20$ ns,
- $\ell = 2$ m ($\tau_{beam} = 9{\cdot}03$ ns), $t_{v(r)[0\%\rightarrow 100\%]} = 20$ ns,
- $\ell = 4$ m ($\tau_{beam} = 18\ 06$ ns), $t_{v(r)[0\%\rightarrow 100\%]} = 36$ ns,
- $\ell = 3{\cdot}78$ m ($\tau_{beam} = 17\ 1$ ns), $t_{v(r)[0\%\rightarrow 100\%]} = 6\ 67$ ns

The dependence of 'x' upon 'M' is shown in fig 1 for each of the last 4 simulations: the value of x for

0-7803-0135-8/91$01.00 ©IEEE

$t_{v(r)[0\%\rightarrow 100\%]}$ = 20 ns, is almost identical for the cases where $\ell = 3{\cdot}78$ m and $\ell = 4$ m. The value of the power function increases with reducing beam transit-time multiplier. If the total angular deflection rise [fall] time is defined as 5 % to 95 % (M=0·9) then the power function lies in the range 1·6 to 1·7 (fig. 1). For x=1·6 (M=0·9), and 4 m deflector plates (τ_{beam}=18·06 ns) $\Rightarrow t_{pv(r/f)[5\%\rightarrow 95\%]}$=32·6 ns (c.f. $t_{pv(r/f)[5\%\rightarrow 95\%]}$=22·7 ns if x is assumed to be 1·0).

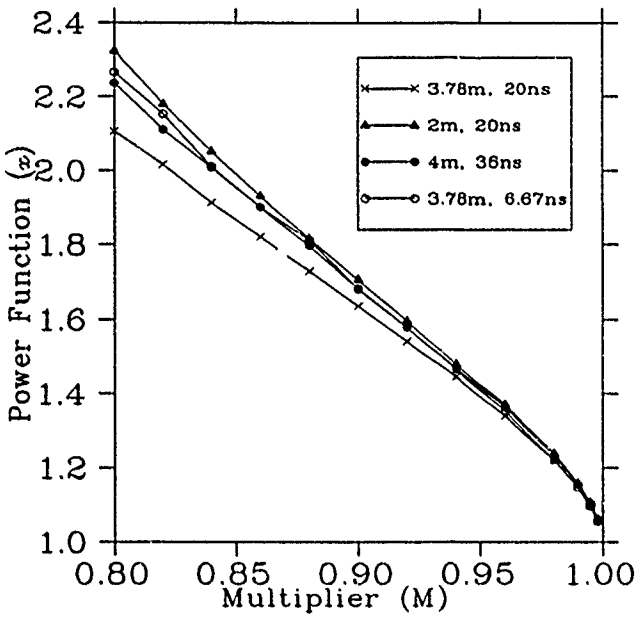


Figure 1: Power function (x) versus beam transit time multiplier (M)

III. Modified Representation of Plates

A. *Improved Precision*

Equations given elsewhere [10,11] for the electric and magnetic components of angular deflection sum the incremental deflections ($\Delta\Theta_{en(tn)}$ and $\Delta\Theta_{mn(tn)}$, respectively), at N+1 circuit nodes in the mathematical model of the deflector plates, while giving each of the incremental deflections an equal weighting function. However $\Delta\Theta_{en(tn)}$ and $\Delta\Theta_{mn(tn)}$ represent the incremental deflections, over a length $\Delta\ell$ of the deflector plates, assuming that instantaneous node voltage ($V_{n(tn)}$) and instantaneous branch current ($I_{n(tn)}$) are constant over length $\Delta\ell$ (version 1·0 of deflector plate mathematical model). But $\Delta\Theta_{en(tn)}$ and $\Delta\Theta_{mn(tn)}$ at the ends of the plates should ideally be calculated assuming that $V_{n(tn)}$ and $I_{n(tn)}$ are constant over a length $\frac{\Delta\ell}{2}$: version 1·1 of the mathematical model of the deflector plates simulates the ends of the plates accordingly. Details of the revised mathematical model can be found elsewhere [4].

A draw back of the modified mathematical model of the deflector plates is the increased CPU time required. the ceiling compute step which PSpice uses is proportional to the delay of the shortest transmission line represented. The shortest delay is reduced by a factor of $\frac{\beta}{0\,25}$, thus the CPU time and segment size required all increase significantly [4].

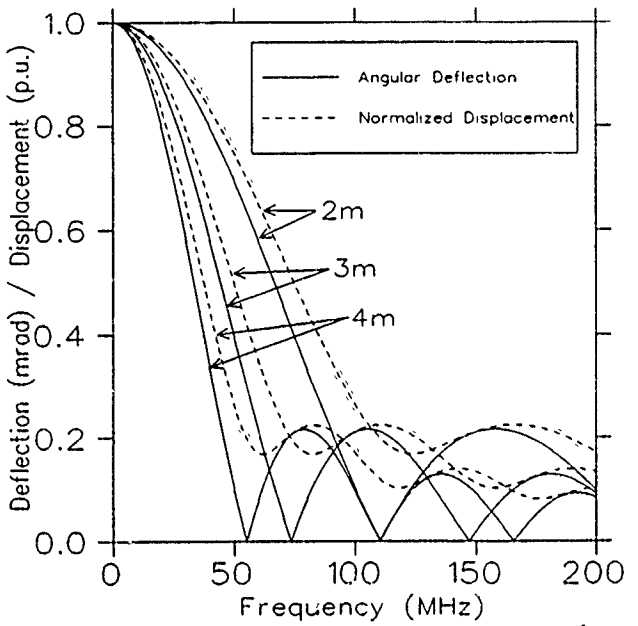


Figure 2: Dependence of linear displacement, normalized to $\frac{\ell}{2}$, and total angular deflection upon frequency and plate length

B. *Linear Displacement of Beam*

The idealized linear displacement ($dy_{i(e)}$) of a beam particle, at the exit to the deflector plates, is given by [4]:

$$dy_{i(e)} = \Theta_{ti} \times \frac{\ell}{2} \qquad (6)$$

However a beam particle which exits the deflector plates with a trajectory parallel to the horizontal ($\Theta_t = 0°$) may be displaced from the centre line of the deflector plates [4]. Thus in order to determine the linear displacement of a particle at the exit of the deflector plates (dy_e), and a distance ℓ_{ds} down-stream of the exit, the PSpice equivalent circuit of the deflector plates has been modified: details of the revised model are given elsewhere [4].

The modified representation of the plates is used for the remainder of the simulations reported in this paper.

IV. Effect of Deflector Plates Upon Ripple

As a result of parasitic inductance and capacitance associated with the 1 MHz chopper there may be voltage ripple on the storage cable [6]: the deflector plates can act to attenuate the effects of the ripple. A frequency domain analysis of a 40 section representation of the deflector plates has been performed using version 1 05p of PSpice [12]. the results of these simulations are shown in fig. 2. For the 1 MHz chopper any significant voltage ripple is likely to be in the frequency band up to 50 MHz [6] Thus, in general, the longer the deflector plates the less is the effect of a given frequency voltage ripple upon the angular deflection and normalized linear displacement of the beam (fig. 2). For a given product of deflector plate length and frequency (e.g. 4 m plates and 25 MHz ripple, or 2 m plates and 50 MHz ripple) the angular deflection of the beam is a constant. similarly the normalized linear displacement of the beam, at the exit of the plates, is also

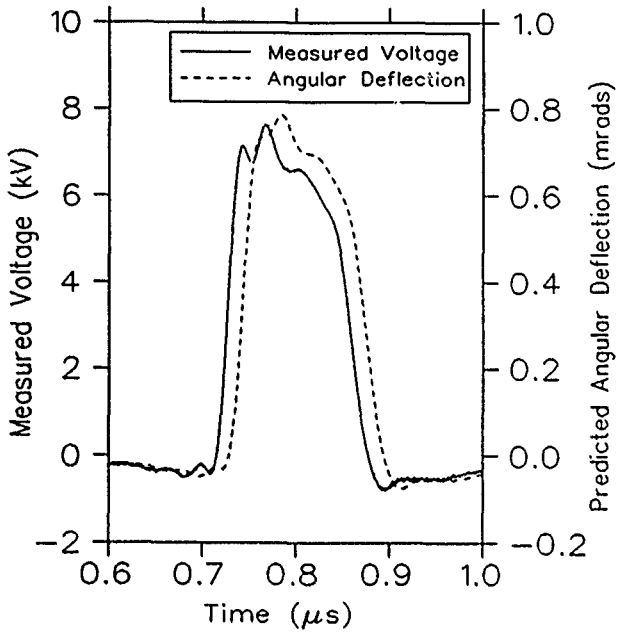


Figure 3: Measured voltage waveform and predicted total angular deflection

a constant. Thus 20 MHz voltage ripple applied to 5 m deflector plates, or the same magnitude of 33·3 MHz ripple applied to 3 m plates have the same effect upon the beam.

Version 4·05p of Probe [12] was utilized to output tables of frequency versus magnitude (in dB) and phase (in degrees) for total angular deflection and linear displacement, at the exit of the plates, for a 40 section representation of 4 m plates. These tables are used as data for the frequency response extension of the controlled sources, of the Analog Behavioral Model option, for Pspice simulations: the frequency response tables are the total angular deflection and linear displacement transfer functions for the deflector plates.

A time domain simulation was then performed using the frequency response tables (1 MHz → 2000 MHz) for the deflector plates, and a piece-wise linear (PWL) approximation of a representative driving voltage was simulated [7]. The predicted angular deflection and linear displacement are virtually identical to those predicted when a discrete element representation of the plates is used: however the CPU time for the transient analysis is reduced to 6 % of that required for the discrete component representation [7].

Fig. 3 shows a plot of measured voltage for the prototype 1 MHz chopper [9]: the digitized waveform was stored on a p.c. and subsequently used as time-voltage corner points for a PWL independent voltage source in a PSpice simulation. The PWL source is used as input to the frequency response table representations of 4 m deflector plates. The predicted angular deflection is also shown in fig. 3. The rise-time of the measured voltage shown in fig. 3 is 17.7 ns (5 % → 95 %): the predicted rise-time for the angular deflection (21.7 ns) is less than that which would be calculated using equation 5, with x=1·6. The deflector plates reduce the effect of the pre-pulse and 'flat-top' ripple upon the angular deflection (fig. 3).

V. Conclusion

Two quantities are used to relate beam transit time through the deflector plates (and hence the physical length of the plates), the rise [fall] time of a trapezoidal driving voltage and the rise-time of the total angular deflection: a power function and a multiplier for the beam transit time. For angular deflection rise-time defined between 5 % and 95 % the power function x has a value of approximately 1·6 for a trapezoidal driving voltage: however 1·6 is a conservative 'rule-of thumb' for determining required rise [fall] time for stored voltage pulses.

A frequency domain analysis of the mathematical model of the deflector plates shows that, for a given product of frequency and plate length, the effect of voltage ripple upon the beam is a constant. In addition, for voltage ripple in the frequency band up to 50 MHz, the longer the plates the less is the effect of a given frequency ripple upon the beam.

VI. References

[1] G. D. Wait., M. J. Barnes, C. B. Figley. "A 1MHz Beam Chopper for the Kaon Factory". TRI-DN-89-K70.

[2] M. J. Barnes, D. C. Fiander, C. B. Figley, V. Rödel, G. D. Wait, G. Waters. "A 1 MHz Beam Chopper for the Kaon Factory", (Proceedings of European Particle Accelerator Conference, June 1990).

[3] D. C. Fiander, G. D. Wait, M. J. Barnes. "Advantages of Center Feeding the Deflector Plates for the 1MHz Chopper System". TRI-DN-89-K45.

[4] M. J. Barnes, G. D. Wait. "Simulation of Deflector Plates and Assessment of Rise-Times for the 1 MHz Chopper". TRI-DN-90-K149.

[5] M. J. Barnes, G. D. Wait. "Algorithm for the Deflector Plates of the 1 MHz Chopper for the Kaon Factory". Proceedings of this Conference.

[6] M. J. Barnes, G. D. Wait, D. C. Fiander. "PSpice Simulation of the 1 MHz Chopper, Including a CY1172 Tetrode Model". TRI-DN-90-K123.

[7] M. J. Barnes, G. D. Wait "Interaction of Stray capacitance, Storage Cable Delay, and Deflector Plate Length for the 1 MHz Chopper". TRI-DN-90-K148.

[8] TRIUMF KAON FACTORY STUDY, Accelerator Design Report, May 1990.

[9] G. D. Wait, M. J. Barnes, D. Bishop, G. Waters, C. B. Figley. "Prototype Studies of a 1 MHz Chopper for the Kaon Factory", Proceedings of this Conference.

[10] M. J. Barnes, G. D Wait, D. C. Fiander "Mathematica Modelling of the 1MHz Beam Chopper for the Kaon Factory", (Proceedings of European Particle Accelerator Conference, June 1990).

[11] M. J. Barnes, G. D. Wait, D. C. Fiander. "Influence of Stray Capacitance and Delay of Storage Line upon the Performance of the 1MHz Chopper".TRI-DN-89-K76.

[12] MicroSim Corporation, PSpice version 4·05p, Beta site version released December 1990.

Construction of a New Tevatron Collider Beam Abort Dump

B. Hanna,C. Crawford
Fermi National Accelerator Laboratory *
P.O. Box 500, Batavia, Illinois 60510

Abstract

As part of the Collider upgrade a new abort system is to be installed in the Tevatron at A0. It consists of two sets of fast kickers and two 90% full aperture graphite beam dumps. This system will abort both protons and antiprotons. Details of the beam dump design and construction are presented.

Introduction

During past Collider runs beam was aborted at the long straight section C0. Protons were aborted using the already existing external beam dump[1] while antiprotons were aborted via kicker magnets at C17 and an internal "block" located at the downstream end of the C0 long straight section. For the upcoming Collider run new abort systems will be installed at A0 long straight for both protons and antiprotons. There are three compelling reasons for doing this: 1) the space in the C17 warm section is to be used exclusively for Separators , 2) the abort kicker power supplies used two stage thyratron tubes which were susceptible to prefires and 3) 36 x 36 bunch operation requires the kickers to be as close to one another as possible.

The new system to be installed consists of 10 steel cored kickers, 5 at each end of the straight section, 2 internal beam absorbers and 2 sets of beam position monitors one set in front of each absorber. The kickers are each 88.06" long while each absorber is 188" long. Before a Collider run can begin all devices in A0 used for Fixed Target extraction must be removed. The abort system will be mounted on moveable plates and rolled in after the extraction devices are moved out.

Design Parameters

The requirements of the abort system are detailed in Reference [2]. All the calculations were based on the following intensities:

150 GeV Intensity = 4.4E12 protons
1 TeV Intensity = 2.6E12 protons
1 TeV Intensity = 2.6E12 antiprotons

As for the number of aborts; it was assumed that during the setup time, when the energy is 150 GeV that the abort would be fired once every 2 minutes for up to 4 hours; that protons would be aborted 6 times a day at 1 TeV and that antiprotons would be aborted 2 times a day at 1 TeV.

Given the above intensities the abort must be designed such that it contains most of the beam energy. Excess energy escaping the abort material would be deposited in superconducting magnets and could result in quenching the magnet. Approximately 1mJ/gram deposited in a superconducting coil will result in a quench[1,2]. In addition the material must be able to withstand both the instantaneous thermal shock and the steady state temperature. Consideration must also be given to the levels of residual radioactive activity as well as to the radiation levels outside the tunnel enclosure. Since this is an internal beam dump it must be compatible with the tevatron beam tube vacuum requirements and consideration must be given to accident conditions, ie what if the aborted beam goes through the beam pipe in the absorber?

The design chosen for the absorber mimics the already existing TeV abort dump[1]. Figures 1 and 2 show a cross section and the longitudinal view of the absorber. Specifically

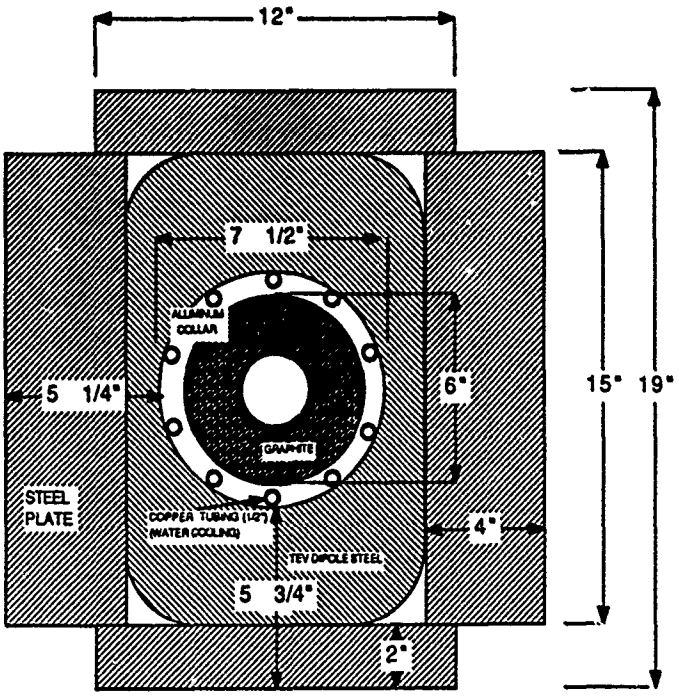


Figure 1. Cross section of the Absorber. From reference[2].

there is 350 cm of graphite followed by 75 cm of aluminum and finally 25 cm of steel. All the absorber material is in the

---

* Operated by Universities Research Association, Inc. under contract with the U.S. Department of Energy.

0-7803-0135-8/91$01.00 ©IEEE

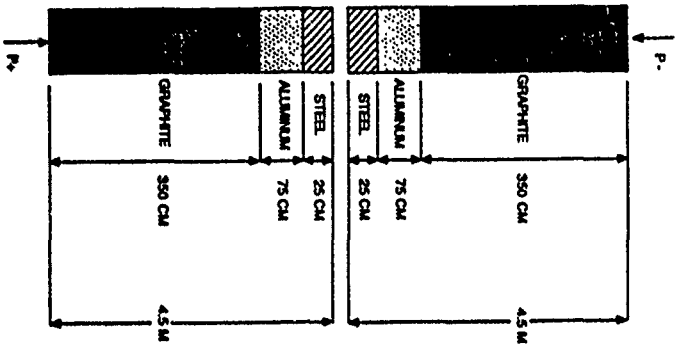


Figure 2. Longitudinal structure of the Absorber. From Ref[2].

form of 1" disks; this laminated approach minimizes the chances of damage due to instantaneous thermal effects. Using the MARS10 Monte Carlo program for this design it was determined that less than .002mJ/gram of energy would be deposited in the coils of the downstream superconducting devices at 1Tev and 5.3E12 particles[2]. Under these same beam intensity and energy conditions the maximum energy deposited in the graphite was determined to be 678 Joules/gram[2]. This leads to a instantaneous temperature rise of 350 degrees C ,well within the limits of the graphite . To estimate the steady state temperature the following 1 hour cycle was used: 30 150 GeV pulses 2 minutes apart and one 1 TeV pulse. Given this cycle the time averaged energy deposited is 162 watts/meter at the hottest longitudinal location. From this the maximum steady state temperature is found to be 116 degrees C in the graphite where the beam hits[2]. The calculations assumed no water cooling. A test was done with a short module having the same cross section as the actual absorber. A heating rod was placed where the beam would go and was powered using a transformer such that 162 watts/meter of power was dissipated in the rod. Thermocouples were placed in the graphite (1.75 cm from the heater), in the Aluminum Collar(in the middle of the collar) and at several locations on the iron yoke around the collar. As was the case for the calculations there was no water cooling. Figure 3 shows the calculations and measurements.

In order to calculate the induced radioactivity on the surface of the assembly a MARS10 calculation was done. The results indicated that the levels would be less than 100mR at contact 24 hours after beam was turned off.

Design

The absorber consists of 6 parts: the Aluminum collar, the disks, the beam tube, the end pieces, radiation shielding and temperature instrumentation.

The Aluminum collar is the vessel that contains the graphite, aluminum and steel disks and acts as a heat sink to the disks (and is water cooled). The end pieces mount directly on the collar making a vacuum tight seal so that the disks, especially the graphite , can have a rough vacuum pulled on it. The vacuum is maintained via a rotary pump. There are two

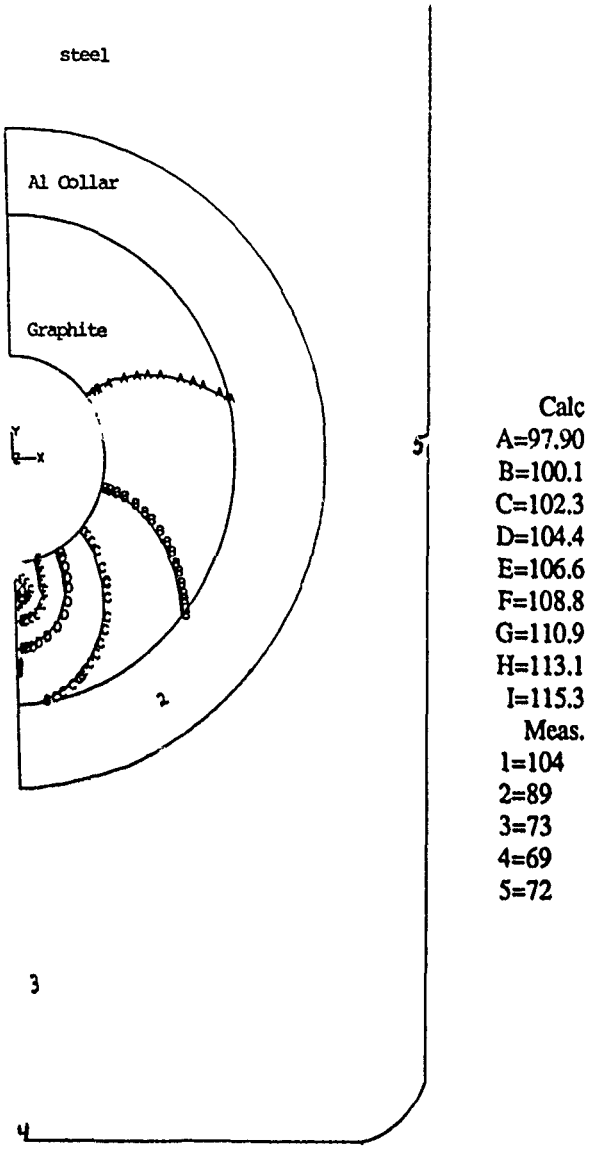


Figure 3. Calculated and measured temperature distribution for the steady state case. All temperatures in degrees C. From Ref[2].

reasons for keeping the disks in vacuum; first this will minimize the loss of graphite due to oxidation which occurs at elevated temperatures and second by removing the atmospheric pressure the forces on the beam tube are eliminated so that if the beam hit the beam pipe the resulting heating up of the beam pipe would not damage it. For water cooling eight 1/2" grooves are cut in the collar and these are fitted with aluminum tubes which connect to the LCW system. The inside surface is machined to a tolerance of 1/64". The collar is 180" long, has an OD of 7.47" and an ID of 5.56" It is made from 6061-T6 aluminum.

The three types of disks all share a common design: they are 1" thick, have a 2.5" diameter hole in the center for the beam pipe and are 5.35" in diameter. These disks are not circular but have the flat top. This area is used to mount a spring loaded brass bullet which provides a downward force, of magnitude 2 pounds, on the disk to increase the contact

between the disk and the collar. This provides for better heat transfer to the Aluminum collar.

The beam tube is made of 6061-T6 aluminum and is .049" thick. The reason for such a thin beam pipe is due to the above mentioned accident condition of the beam hitting the beam pipe. Under worse possible conditions it is predicted that the maximum temperature this beam pipe could reach would be 311 degrees C. This is well below the melting point and, since there is no atmospheric pressure, the beam tube will suffer no deformation (although calculations show that even with atmospheric pressure deformation would not occur until over 400 degrees C[4]). Vacuum in the beam tube should be better than 1E-9 Torr.

The end pieces are used to make the seal for the rough vacuum in the absorber. A vacuum of 1E-3 Torr would be quite adequate. O-Rings made of ethylene-propylene (for radiation resistance) are used. Each end piece is composed of three parts: an Aluminum to Stainless transition piece, a face plate and an O-ring collar. The aluminum side of the transition piece is welded onto the aluminum beam pipe. The upstream transition piece also has a "window" machined out of it for the beam to go through; the beam only sees 1 mil of aluminum. The window itself is .75" wide and extends in a circular path 15 degrees to either side of the center. While the beam tube is 2.5" in diameter this end of the absorber is 4.5" in diameter in order to accommodate both circulating and aborted beam. The face plate bolts directly to the Aluminum collar and contains an O-ring which seals to the collar face. The O-ring collar bolts to the face plate and has one O-ring which seals around the beam pipe.

The radiation shielding is composed of two parts. First the absorber is placed in a shortened Tevatron dipole iron yoke. Secondly this assembly is surrounded by steel plates; 4" thick plates on the sides and 2" plates on top and bottom. The net result is that there will be 5.25" of steel on the sides and 5.75" of steel on the top and bottom.

In order to insure that the absorber is performing as expected temperature readbacks have been included. To monitor the temperature a set of four K type thermo-couples will be placed at various points along the absorber. There were two criteria for placement: first they should be placed on the bottom near shower maxima and second there must be some way to get the thermocouple in contact with the aluminum collar. Since the absorber is encased in a TeV magnet iron yoke we can take advantage of the "smart bolt" holes already in the iron, and, by carefully specifying where to cut the iron, appropriate holes are made available. To mount the thermocouples, modified TeV "smart bolts" will be used and the thermocouple will be spring loaded to improve thermal contact. Readbacks can be monitored in the Control Room via a system identical to that used for existing equipment. In addition thermostats will be placed in additional "smart bolt" holes. Their purpose will be to inhibit any beam injection if the temperature goes above 90 degrees C.

Construction Problems

The construction of three absorbers (two for use and 1 spare) proceeded smoothly taking 2 months total to build all of them. Only two problems arose during this time. The first was welding the upstream transition piece to the thin walled aluminum beam tube. This transition piece is rather large (7/8" wide) and thus massive compared to the wall of the beam tube. Indeed at first we experienced a great deal of trouble making this aluminum to aluminum joint vacuum tight. Two changes made the most improvements: 1) a design change to include a 1/8" weld relief with a curvature of 1/32" and 2) cleaning all surfaces and welding rods with a solution (Weld-O) containing hydroflouric acid immediately before welding. We also clamped a heat sink around the beam tube. After these changes no further welding problems occurred.

The second problem concerned the alignment of the disks when inserted into the aluminum collar. Since it is desirable to have the best possible thermal contact to the collar as near to where the beam is as possible it is important that the force exerted by the springs exert a downward force. If a disk was rotated then there would be a sideways force as well and the location of best thermal contact would be rotated away from where the beam would go. In order to keep all the disks in the same upright orientation we used a single thin strip of aluminum (1/2" wide by 1/16" thick) that ran the length of the aluminum collar as a guide. The brass bullets that sit on top of the springs would follow this strip thus keeping all the disks upright. The strips were held in place via counter sunk screws on the inside of the collar. Tension was maintained on the strip during installation to minimize bowing when inserting the disks. Rotation in the other direction is prevented by the disks themselves; the length of the flat part of the disk from the spring to either edge is 1/2" so the strip is close to touching one of the edges.

Acknowledgements

We would like to thank Warren Classert for his efforts in the construction of the Absorbers and to Merril Albertus and Paul Feyerhausen for their help in moving, storage and leak checking these devices. We also wish to acknowledge Mike Harrison and Nikolai Mokhov for their help in the design of this device.

References

[1] J.Kidd , et al., "A High Intensity Beam Dump for the Tevatron Beam Abort System," IEEE Transactions on Nuclear Science , Vol NS- 28, pp 2774-2776,June 1981.

[2] C.Crawford., "The A0 Abort System for the Tevatron Upgrade", TM-1564,Fermilab Internal Memo ,March 1989.

[3] C.Crawford., "TEV Abort Upgrade Design Note; Absorber Beam Tube", Fermilab Internal Memo, November 1988 .

The SSRL Injector Kickers*

H.-D. Nuhn, R. Boyce, J. Cerino, T. Hostetler
Stanford Synchrotron Radiation Laboratory, P.O. Box 4349, Bin 69, Stanford, CA 94309-0210

Abstract

The kicker units for injection and ejection at the new *SSRL* Injector Synchrotron are built from two kicker modules driven by compact in-air delay line thyratron pulsers. The kickers have an aperture of 25 mm×60 mm. The injection kicker is 60 cm long (30 cm each module) and bends the 150 MeV electron beam by 42 mrad during injection. The extraction kicker module is 120 cm long (60 cm each module) and bends the 3 GeV beam by 4 mrad for extraction. The pulsers produce current pulses in the order of 900 A with a fall time of 200 nsec for injection, a rise time of 260 nsec for extraction and a pulse length (rise plus flat top time) of 400 nsec.

I. Introduction

SSRL, the Stanford Synchrotron Radiation Laboratory successfully commissioned a new injector for the SPEAR electron storage ring in Summer and Fall of 1990[1].

SPEAR originally built as an electron-positron storage ring for high energy physics collider experiments by *SLAC*, has been used during the last 15 years parasitically as well as in dedicated operation for synchrotron radiation experiments. SPEAR was handed over to *SSRL* in October 1990 after the high energy physics program was terminated.

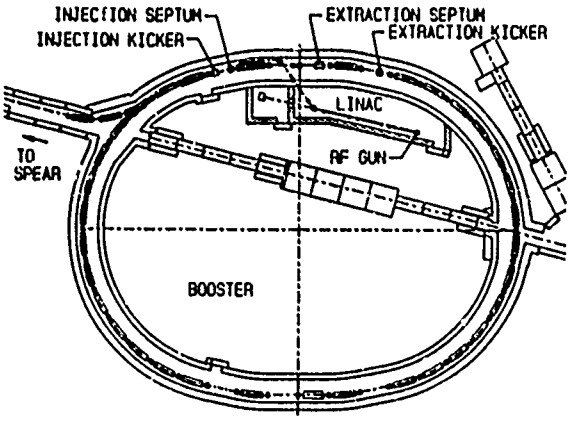


Figure 1
Booster Ring and Kicker Positions

The new injector includes a 2 MeV thermionic RF gun, a 150 MeV electron linac and a 3 GeV booster synchrotron with a 445 nsec revolution time. The main magnets (Dipoles and Quadrupoles) are operated in a White circuit configuration at a 10 Hz repetition rate [2].

Injection as well as ejection is done by a combination of a single kicker unit and a septum magnet, because the booster is designed to accelerate either a single bunch or bunch trains of a length of up to half the circumference of the booster. In the single bunch mode the bunch will be created by filling 3 or more linac bunches into one booster bucket in one shot.

Fig. 1 gives a rough layout of the site and shows the location of the injection and ejection kickers.

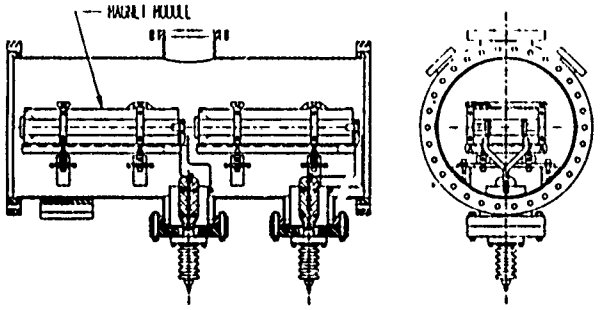


Figure 2
Schematic of the Injection Kicker

The injection kicker has to change the path of a train of three or more S-band bunches (2.856 GHz), that are singled out by a chopper from the bunch train out the gun [3], by 42 mrad at 150 MeV.

The ejection kicker has to bend one 3 GeV bunch by about 4 mrad.

The triggers for the kickers are prepared, based on a biased peaking strip in a booster magnet, by a timing and trigger system that provides phase coupling to the White circuit as well as to the phase of the selected SPEAR RF bucket [4].

Tab. 1 lists the basic parameters of a kicker module.

Table 1
Parameters of a Kicker Magnet

Length (Inj.)	300	mm
Length (Ej.)	600	mm
Gap Height	25	mm
Gap Width	60	mm
Conductor Thickness	60	mm
Required Kick Angle (Inj.)	42	mrad
Required Kick Angle (Ej.)	4	mrad

II. Magnets

The injection and ejection kicker modules each are made of two submodules (kicker magnets). Each kicker magnet is made from ferrite blocks, that form an H-frame around a copper winding. The assembly is held in place by an aluminum support structure and located in stainless steel vacuum tanks. Fig. 2 shows the layout of a ferrite magnet.

*Work supported by the Department of Energy, Office of Basic Energy Sciences, Division of Material Sciences.

0-7803-0135-8/91$01 00 ©IEEE

The ejection kicker magnets have double the length of the injection kicker magnets but are of the same design. The ferrite blocks are of CMD5005 material (from CERAMIC MAGNETICS), which is a high μ NiZn ferrite.

III. PULSE GENERATOR

A. Circuit Description

Each submodule of each kicker (injection as well as ejection) is pulsed independently from a 'Delay Line Pulser' as shown in fig. 3. The two submodules, forming one kicker, are triggered simultaneously and they are charged from the same HV power supply. The Pulse Forming Network (PFN) and a peaking capacitor is charged by the HV DC power supply, capable of up to 30 kV, via a 470 kΩ charging resistor. The PFN is made of two 50 Ω coaxial cables

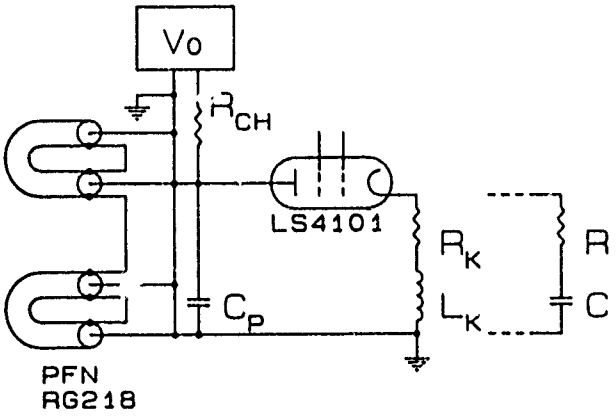


Figure 3
Circuit Diagram of the Injection Kicker Pulse Generator

with the center conductors and the shields, respectively, of the four ends connected to each other. Each PFN cable is 80 m in length to produce a 400 nsec lasting current pulse. The kicker pulse is initiated by a trigger to the EG&G #LS-4101 Hydrogen Thyratron. Most of the PFN charge is absorbed by the 12.5 Ω load resistor that is in series to the kicker magnet. Part of the pulse is reflected back into the PFN. The current I_K through the kicker and the load resistor is described by

$$\frac{d^2I_K}{dt^2} + 2\beta\frac{dI_K}{dt} + \omega_0^2 I_K = \frac{2V_+}{L_K C_P Z_0}$$

with $\beta = \frac{1}{2}[\frac{R_K}{L_K} + \frac{1}{Z_0 C_P}]$ and $\omega_0^2 = \frac{1}{L_K C_P}[1 + \frac{R_K}{Z_0}]$. The forward voltage V_+ is either half the charging voltage V_0 during the rise time and the pulse top duration or, during fall time, the voltage that had been reflected during the rise time of the pulse. We are operating with a load resistor impedance R_K, that matches the PFN characteristic impedance, Z_0, i.e. $R_K = Z_0$. The capacitance of the peaking capacitor can be expressed as $C_P = L_K/(R_K^2 f)$. For critical damping one gets a value for the factor f of 5.82. To achieve the smallest variation in current at the top of the pulse one needs to work slightly above critical damping, i.e. a smaller value of f. The risetime, for an increase in amplitude from 0-95%, approximately $3/\beta$ is then given by $\tau = 6L_K/(R_K[1+f])$.

This circuit provides a rapid rise time and a fairly fast fall time. The fall time is longer than the risetime because it is driven by the reflected pulse that is decaying toward zero volts. The fall time could be be shorted by removing the load resistor R_L as done by Gabor et al. [5]. The decay of the pulse amplitude is then driven by the reflected voltage going toward $-V_0$. The pulse is shut off by the thyratron when the current is going to become negative. With such a circuit modification rise and fall time would be approximately equal. With critical damping the risetime would be about 60 % larger than that in the unmodified circuit (f = 4.0) Disadvantages of that circuit are high negative voltage amplitudes in the PFN cables as well as high reversed voltages across the thyratron tube, possibly lowering the life time of these components.

Fig. 3 also shows an option to put an RC combination across the kicker magnet and the load resistor. This helps to filter higher frequency components from the kicker pulse and to lower reverse voltages across the thyratron. It causes a deterioration of the current pulse, though. Tab. 2 lists the basic parameters of a pulse generator. The ejection parameters are refer to the circuit with the RC compensation included.

Table 2
Parameters of the Pulse Generator

Repetition Rate	10	Hz
Injection		
PFN Voltage 150 MeV	20.9	kV
Flat-Top Top Current	836	A
Rise Time (5% to 95%)	120	nsec
Flat-Top Duration	260	nsec
Fall-Time (95% to 5%)	200	nsec
Ejection		
PFN Voltage 3.0 GeV	20.1	kV
Flat-Top Top Current	804	A
Rise Time (5% to 95%)	260	nsec
Flat-Top Duration	190	nsec
Fall-Time (95% to 5%)	300	nsec

B. Thyratron Auxiliary Supplies

The cathode as well as the anode of the thyratron are at a potential difference of $V_0/2$ against ground for the duration of the kicker pulse. The auxiliary voltages and control signals have to be supplied while keeping the anode and grid potentials separated from ground potential. In this case all signals required to operate the thyratron (i.e. cathode heater current, reservoir heater current, grid bias and trigger voltages as well as auxiliary grid voltage)

are generated by a commercial device from IMPULSE ENGINEERING INC. operating at ground potential. The potential separation during the duration of the pulse is done by magnetization of a ring ferrite in the following way: The cables required for the transmission of the auxiliary voltages as well as diagnostic cables from the thyratron to ground potential are shielded with a metal grid hose, carrying the return current, and are coiled around a ferrite ring with cross section A in N windings. The assembly is designed that the integrated voltage drop across the coil during the kicker pulse increases the magnetic flux density in the ferrite rings from negative to positive saturation: $\int V dt = NA \int dB = NA(B_{END} - B_{START})$. Thus posing a large resistance to the pulse current. [6]. The ferrite is biased with a negative magnetic field to achieve the largest effect and potted to improve its high voltage capability.

IV. PERFORMANCE

A prototype of the injection kicker pulser has been intensively tested and optimized in 1989. Work was done in particular to optimize the shielding of the RF noise and to improve the high voltage capability of the compact pulser enclosure. Fig. 4 gives the form of the current pulse as sensed

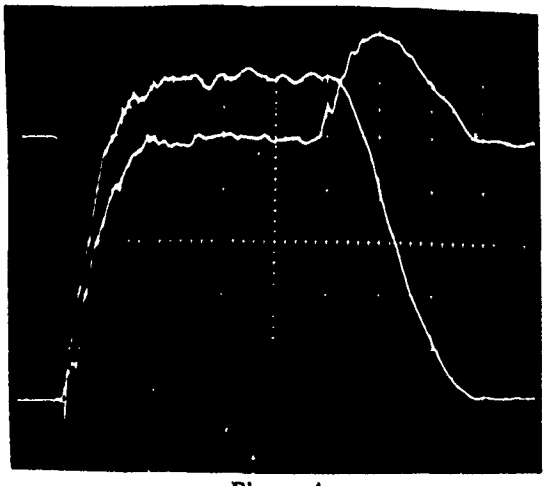


Figure 4
Current and $d\phi/dt$ Pulse of the Injection Kicker

with a current transformer. The scale is 100 nsec/div and 100 A/div for the horizontal and vertical axis, respectively. The pulse height of 600 A corresponds to about 15 kV PFN voltage. The pulse has been produced by 100 m long PFN cables. The separation of the cathode voltage from ground works very well. The injection kicker has routinely been operated since the beginning of the booster commissioning in July 1990. Routine operation of the ejection kicker started in October 1990. The performance of the kickers is very satisfying. The injection efficiency into the booster often exceeds 80 to 90 %. With optimal settings of the booster correctors the intensity doesn't drop significantly in the first revolution. This indicates that kicks caused by the reflected pulse current are small enough to keep the injected beam within the vacuum aperture. The electromagnetic noise generated by the kickers during the pulse reduces the sensitivity of the transport line beam position monitors that are located closely to the kickers. Fig. 4 also shows the $d\phi/dt$ signal measured with a one loop coil in the gap of the kicker magnet. Fig. 5 shows the gap field vs. time (i.e. the integrated $d\phi/dt$, normalized to the coil area).

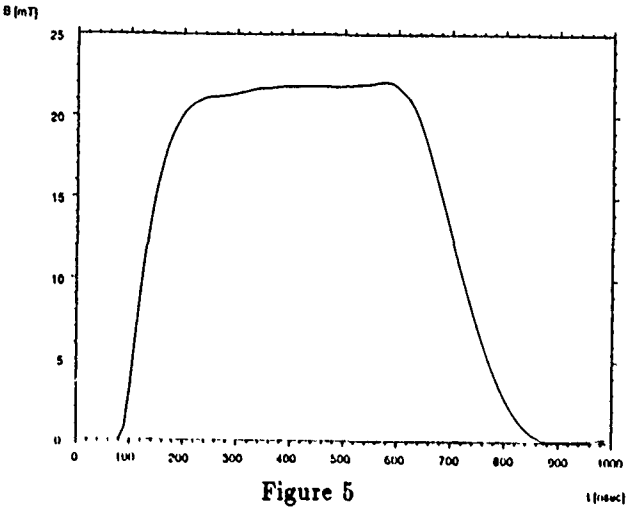


Figure 5
Magnetic Field Measurement in the Gap of the Injection Kicker

V. ACKNOWLEDGEMENTS

A study by A. Fisher [7] comparing different kicker-magnet circuits aided the design of the pulse generator. We wish to thank R. Cassel from *SLAC* for his consulting aid during the design and development phase of the pulse generator and may of the *SSRL* staff members for their support.

VI. REFERENCES

[1] J. Safranek and S. Baird, "Commissioning the SSRL Injector." In these proceedings, 1991.

[2] R. Hettel, R. Averill, M. Baltay, S. Brennan, C. Harris, M. Horton, C. Jach, J. Sebek, and J. Voss, "The 10 Hz Resonant Magnet Power Supply System for the SSRL 3 GeV Injector." In these proceedings, 1991.

[3] M. Borland, J. Weaver, M. Baltay, L. Emery, R. Hettel, H. Morales, J. Sebek, B. Youngman, R. Anderson, A. Fisher, and R. Miller, "Design and Performance of the Traveling-Wave Beam Chopper for the SSRL Injector." In these proceedings, 1991.

[4] R. Hettel, D. Mostowfi, R. Ortiz, and J. Sebek, "Triggers and Timing System for the SSRL 3 GeV Injector." In these proceedings, 1991.

[5] G. Gabor and F. Voelker, "Kicker Magnets for the Advanced Light Source," in *Proceedings of the 1989 Particle Accelerator Conference, Chicago*, March 1989. IEEE Catalog Number 89CH2669-0.

[6] R. Cassel, "private communication," 1989.

[7] A. Fisher, "Comparison of Kicker-Magnet Circuits," ACD-Note 71, SSRL, 1989.

Design and Performance of the Traveling-Wave Beam Chopper for the SSRL Injector*

M. BORLAND,† J.N. WEAVER, M. BALTAY, L. EMERY,† A.S. FISHER,‡ P. GOLCEFF
R. Hettel, H. Morales, J. Sebek, H. Wiedemann, B. Youngman§
Stanford Synchrotron Radiation Laboratory, Stanford, CA 94309
R. ANDERSON
American Control Engineering, 7636 Miramar Road, Suite 1200, San Diego, CA 92126
R.H. MILLER
Stanford Linear Accelerator Center, Stanford, CA 94309

Abstract

A pulsed, split-parallel plate chopper has been designed, built, and installed as part of the preinjector of the SSRL Injector. Its function is to allow into the linear accelerator three consecutive S-band bunches from the long bunch train provided by a RF gun. A permanent magnet deflector (PMD) at the chopper entrance deflects the beam into an absorber when the chopper pulse is off. The beam is swept across a pair of slits at the beam output end when a 7 kV, 10-ns rise-time pulse passes in the opposite direction through the 75 Ω stripline formed by the deflecting plates. Bunches exiting the slits have their trajectories corrected by another PMD, and enter the linac. Beam tests demonstrate that the chopper functions as expected.

I. INTRODUCTION

The SSRL Injector[1,2] is unusual in that it uses a microwave or RF electron gun[3] rather than a conventional DC gun. Details of the gun and the gun-to-linac transport are reported elsewhere[4,5,6]. For the present, we simply review some of the main features.

The RF gun was designed in collaboration between SSRL, Varian Associates, and AET associates, and consists of a thermionic cathode mounted in the first half-cell of a $1\frac{1}{2}$ cell side-coupled, velocity-of-light standing wave cavity. Because the cathode is thermionic, a beam is produced as long as RF is supplied to the gun (after the cavity fields have built up sufficiently). The average beam momentum is typically 2 MeV/c.

The RF frequency of the gun is 2856 MHz, while that of the booster accelerating cavity is 358.54 MHz. Three to five RF gun bunches can be captured in any RF bucket of the booster. One potential operating mode is to fill many consecutive booster buckets with three gun bunches each. These bunches would then be accelerated together in the booster and injected into SPEAR in a train, filling the same number of consecutive buckets in the storage ring. Such an approach is more complicated than filling a single booster bucket with three bunches. In addition, if one fills only one booster bucket, one can obtain arbitrary filling patterns in SPEAR by filling different booster RF buckets on different booster cycles. Hence, it was decided to design a chopper that would fill only a single booster RF bucket per booster cycle.

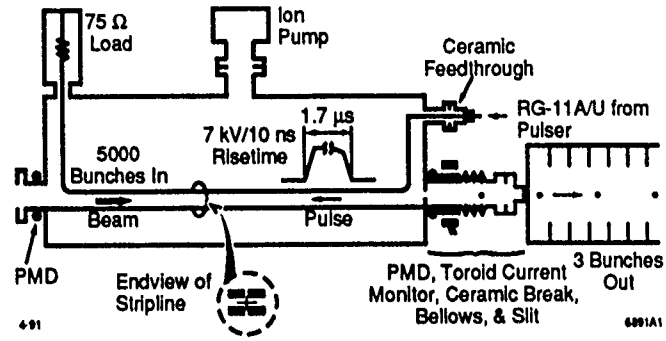


Figure 1. Side view of the chopper.

Following the gun is the gun-to-linac (GTL) transport line, which consists of five quadrupoles, steering magnets, an alpha-magnet[6,7], diagnositic instrumentation, and the chopper. A diagram of the GTL appears in another paper in these preceedings (see Fig. 1 of [2]). The combined optics of the quadrupoles and alpha-magnet is required to produce sufficiently small vertical beam sizes at the end of the chopper for proper chopper operation, while simultaneously fitting the transverse phase space for both the horizontal (x) and vertical (y) planes into the acceptance of the first linear accelerator section.

II. PRINCIPLE OF OPERATION

The RF pulse is $\approx 2\,\mu$s long and the gun charging time constant is $\approx 0.3\,\mu$s, so that the gun emits ≈ 5000 bunches per RF pulse. Since only about three of these bunches are to be used, the beam hits an absorber until it is time to kick the beam into the linac. As seen in Fig. 1, the chopper incorporates two permanent-magnet deflectors (PMDs), one before and one after the pulsed portion of the chopper. The pulsed element in the chopper is a split parallel plate transmission line enclosed in a evacuated cylindrical pipe. The deflection caused by the first PMD results in the beam hitting the water-cooled, copper, downstream endwall of the chopper tank. It can easily be seen that the Lorentz forces on a relativistic beam, due to transverse electric and magnetic fields of a TEM wave, cancel if the wave and beam travel in the same direction and add if in opposite directions. Therefore, when the chopper is pulsed at the desired time, the steep, nearly linear, rising edge of a pulsed TEM

*Work supported by the Department of Energy contract DE-AC03-76SF00515, and the Office of Basic Energy Sciences, Division of Material Sciences.

†Now at Argonne National Laboratory, Argonne, IL 60439

‡Now at Brookhaven National Laboratory, Upton, NY 11973

§Now at Stanford Linear Accelerator Center, Stanford, CA 94309

0-7803-0135-8/91$01.00 ©IEEE

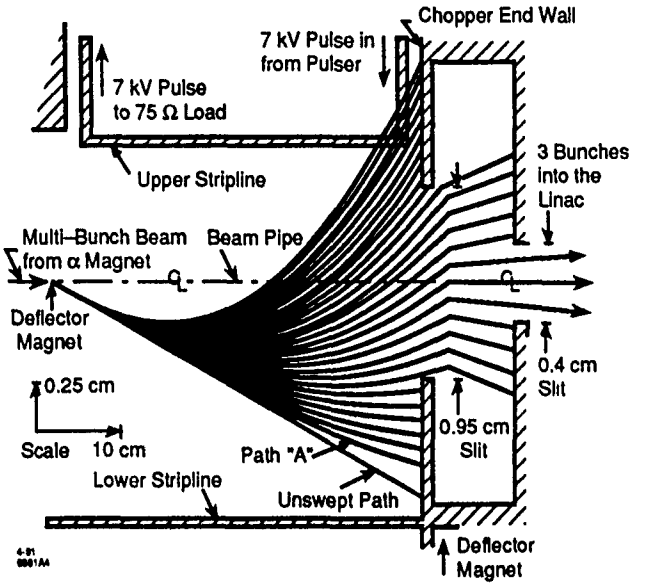


Figure 2. Beam bunch trajectories through the chopper. Path "A" is $\approx$ 1.3 ns into the pulse, when the pulse has filled the stripline. Subsequent paths are 350 ps apart until the 7 kV pulse peak is reached after $\approx$ a 10 ns risetime.

wave is launched upstream on the stripline-like structure and causes the beam to be swept across an opening in the absorber. The choice of a 40 cm long, 75 Ω stripline allowed the pulser voltage, its rise time, which is less for a larger impedance, and the alpha magnet to linac distance to be kept reasonable. Those bunches that pass through the 9.5 mm opening in the absorber are deflected by the second PMD so that they are traveling with nearly zero slope, but still continue to diverge slightly. Further filtration of these bunches occurs at the 4 mm slit just before the first linac cell. The vertical, angular divergence of the bunches is partially taken care of by longitudinal acceleration and quadrupole focussing in the linac, all of which, when taken together, determine the acceptance of the linac. Furthermore, it can be shown that the vertical separation, x, of the bunches at the output end of the plates is given approximately (with a few fudge factors and constants left out here and there) by $x \alpha V_0 l^2(1+\beta)/(g f_0 t_r p_z)$, where V_0 is the peak voltage of the pulse, l is the plate length, β is the normalized relativistic velocity of the beam and comes from the magnetic field contribution, g is the plate gap spacing, f_0 is the microwave frequency that determines the bunch spacing, t_r is the pulse's linear risetime from 0 to V_0 and p_z is the longitudinal momentum of the beam These points are illustrated in Fig. 2.

Experimental confirmation that the chopper works as planned has been obtained by viewing the beam on a phosphorescent screen at the end of the linear accelerator. With appropriate adjustment of the optics, the bunches can be dispersed vertically on the screen, rather than focussed as usual. Depending on conditions such as the beam energy from the gun and tuning of the GTL optics, three to five dominant bunches are seen, as shown in Fig. 4, with several very low intensity bunches before and after. This is

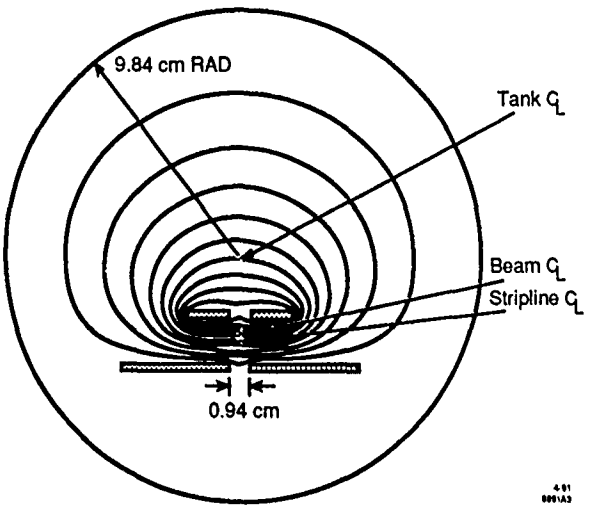


Figure 3. Cross section of the chopper tank showing the parted stripline and the electric field equipotential lines. Note that the field is less in the midplane than between the plates. The plates are split in order to lessen interception by the vertically sweeped beam. The lower plate is grounded at each end. The beam centerline (before and after the chopper and its deflection magnets), is 3.18 cm below the tank centerline. The stripline centerline is 3.43 cm below the tank centerline and the stripline plate spacing is 1.84 cm.

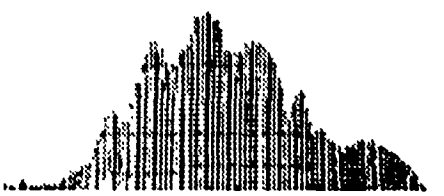


Figure 4. Three plus bunches at the end of the linac as the chopper culls them from the output the microwave gun.

in good qualitative agreement with simulations done using the tracking program **elegant**[8].

III. Design of the Stripline and Tank

An electrostatic analog and the program **estat** were used, instead of such a standard code as **Poisson**[9], to solve Laplace's equation in two dimensions for a TEM mode on the stripline in the chopper tank. Time domain reflectometry was used to verify that the impedance of the finished stripline in the task is indeed 75 Ω. Figure 3 shows a cross-sectional view of the chopper tank and plates, along with equipotential lines for the electric field.

The upper plate is bent upwards by 90° at each end, continuing the transmission line with the end-walls of the chopper serving as the ground plane. This continues until just before the plate joins to the feedthroughs, so that impedance mismatches are avoided The feedthrough on the upstream end of the chopper tank is terminated by a column of resistors with a total resistance of 75 Ω.

The column consists of eight in-serie groups of six, 56 Ω, 2 W, carbon resistors in parallel, roughly forming a cylin-

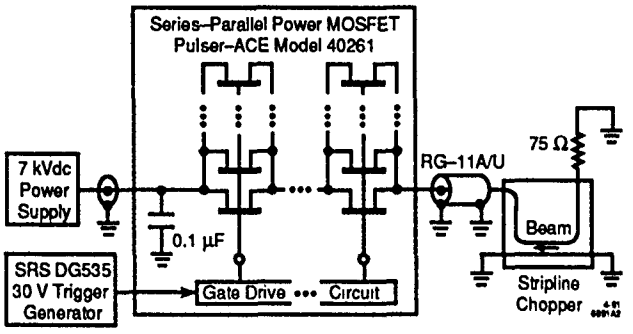


Figure 5. Simplified circuit of the pulser, stripline chopper and 75 Ω Load

der or tube. Around this column is a hollow aluminum cylinder that is grounded to the chopper tank at the bottom, and connected at the top by a metal disk to the end of the resistive column. The inside diameter of the aluminum cylinder and the diameter of the resistive column are such as to form a coaxial transmission line with an impedance of roughly 75 Ω. A small resistor inserted near ground in the resistive column provides a 1:1000 signal that can be viewed on an oscilloscope.

IV. Design of the MOSFET Pulser

The pulser was designed and built by American Control Engineering. It consists, as shown in Fig. 5, of a 0 to 7 kV variable voltage power supply, a high voltage storage capacitor and a fast MOSFET switch. The latter is the heart of the pulser and consists of a gate driver circuit and ten paralleled strings of twenty power MOSFET packages in series. The switch is used to generate a fast risetime (10 ns), short (1.7 μs), capacitive-discharge pulse that passes through the 75 Ω chopper tank to its 75 Ω load.

The MOSFET's fast and relatively clean on and off power switching capability is the result of significate advances in technology since its introduction in 1975. Basically, a power MOSFET uses VLSI technology to get up to $3 \times 10^5/\text{cm}^2$ selfblocking, field-effect transistors on a die with a gate, a source and a drain connection to the outside of a typical TO-220 package. If a voltage is applied between the gate and the source, the drain to source resistance drops dramatically. When this voltage is removed, the resistance increases equally quickly, typically in $\approx$ 2 to 4 ns at the chip level, since there is no storage time due to minority carriers as in conventional bipolar transistors. The turn-on speed is affected by the gate to source capacitance as well as by the smaller drain to gate capacitance. The latter is multiplied by an effect akin to the Miller effect; thus, for fast turn-on the gate drive source impedance must be low. As always with fast and especially high power switching circuits considerable care must be taken in the detailed circuit design and packaging. For this pulser proprietary topology plus carefully selected and matched components provide for uniform current sharing among the individual parallel MOSFET devices, both during turn-on and turn-off as well as during the switching process. Spurious oscillations of the MOSFET devices are eliminated by a combination of series gate resistances and Q spoiling ferrite beads surrounding each of the gate connection leads.

Voltage grading of the series connected stages is required in order to ensure that the voltage rating of each of the individual stages is not exceeded when the switch is off. This grading is provided by high speed zener diodes that are connected in parallel with the MOSFET devices. These diodes also absorb the energy that has been stored in the switch assembly inductance during the turn-on time and is released during the turn-off process. The design is such that one or two failed stages will not generally cause unsatisfactory operation of the switch stack, provided that the diminished voltage rating is not exceeded.

Typical individual power MOSFET devices can operate at 50 to 1000 V and switch 1 to 100 A in 5 to 10 ns at megahertz rates with 0.01 to 1.5 Ω turned-on resistances. They are very rugged and reliable and can be seriesed and paralleled as was done in this case. This unit has operated reliably and well for nearly a year in spite of some customer supplied cable connection arcing problems.

References

[1] H. Wiedemann, et al., "3 GeV Injector Synchrotron for SPEAR," Proc. 1991 PAC, San Francisco, CA.

[2] J.N. Weaver, *et al.*, "The Linac and Booster RF System for a Dedicated Injector for SPEAR," Proc. 1991 PAC, San Francisco, CA.

[3] S.P. Kapitza, V.N. Melekhin, *The Microtron*, Harwood Academic Publishers, London, 1978, pp. 7-11.

[4] E. Tanabe, *et al.*, SLAC-PUB-5054, (Aug. 1989).

[5] M. Borland, *et. al*, in *Proceedings of the Linear Accelerator Conference*, (Sept. 1990).

[6] M. Borland, *A High-Brightness Thermionic Microwave Electron Gun*, Stanford University Ph.D. Thesis, (1991).

[7] H.A. Enge, *Rev. Sci. Inst.*, 34(4), (1963).

[8] M. Borland, "`elegant`: A Matrix/Integrating Code for Third-Order Tracking," SSRL ACD-Note, to be published.

[9] K. Halbach, "A Program for the Inversion of System Analysis and Its Application to the Design of Magnets," in *Proceedings of the* 2nd *Conference on Magnet Technology*, Oxford, (1967).

ELECTROSTATIC DEFLECTOR DEVELOPMENT AT THE CHALK RIVER SUPERCONDUCTING CYCLOTRON

W.T. Diamond, G.R. Mitchel, J. Almeida and H. Schmeing
Atomic Energy of Canada Limited, Research Company
Chalk River Laboratories
Chalk River, Ontario, Canada K0J 1J0

Abstract

An electrostatic deflector is used to extract heavy-ion beams from the Chalk River superconducting cyclotron. Deflector voltages up to 100 kV across a 7 mm gap (143 kV/cm) are needed to extract the full range of beams that the cyclotron is designed to accelerate. This goal remains a challenge, but substantial progress has been made over the past year. Voltages over 90 kV have been reliably maintained over a 7.5 mm gap with a magnetic field of 3 T. Voltages of 74 kV have been used with a reduced gap of 4.75 mm (corresponding to a field greater than 150 kV/cm) to extract beams with magnetic fields up to 4.25 T. Major progress was achieved when we introduced a water-cooled, negative high-voltage electrode, and changed the sparking plates and the thin septum from molybdenum to stainless steel. Efforts are continuing to attain a field of at least 143 kV/cm over a gap of at least 6 mm width.

INTRODUCTION

The electrostatic deflector is the first extraction element in the Chalk River superconducting cyclotron. The deflector is mounted in a dee and the high voltage is fed down the center of the dee stem. Two insulators, mounted above the midplane, support the high-voltage electrode. Details of insulator design are given in another paper at this conference[1]. The design goal for the deflector was 100 kV over a gap of 7 mm, corresponding to an electric field of 143 kV/cm. The cyclotron operates over a range of magnetic fields from 2.5 to 5 T, and at r.f. frequencies from 30 to 60 MHz. Residual radiofrequency fields can heat the deflector to temperatures above 200 °C. These harsh operating conditions have made it very challenging to reach the design goal. However, electric fields of up to 155 kV/cm over a reduced gap of 4.75 mm have been attained. The smaller gap reduces the extraction efficency by up to 30 %, depending on the ion beam. However, we have reliably extracted carbon at 50 MeV/amu and iodine at 19 MeV/amu, beams near the upper limit of the mass-energy diagram of the Chalk River superconducting cyclotron.

DEFLECTOR GEOMETRY

The deflector geometry has been described in detail[2,3] previously. Two important changes have been made since then. Overheating was identified[3] as a serious problem. We consequently water-cooled as many grounded parts of the deflector as reasonably attainable, including the lower septum support and the insulator housing. However, experiments on a test stand[3] showed that cathode heating was the most important issue. Subsequently we designed a new water-cooled high-voltage electrode. Figure 1 shows the details. The high voltage is provided by a cable (A) fed down the upper dee stem[1], inside a 13 mm diameter copper tube. High-purity (about 16 MΩ-cm) water is circulated between the high-voltage cable and a thin teflon tube (B), and returned between the teflon tube and the copper tube. The high-voltage cable is terminated with a stainless-steel hemisphere (C). A 2 cm water column provides a 30 MΩ series resistor between the high-voltage electrode and the cable. The teflon tube is inserted from the top of the cyclotron and mated with a tapered end fitting (D) that is part of the high-voltage electrode. The water passes through four small holes in this fitting into a 3.2 mm I.D. copper tube (E) that provides the feed water to the the high-voltage electrode (F). The copper tube joins the stainless-steel body of the deflector electrode in a friction fitting. The return flow is from the upper water channel (G) into the 11 mm I.D. stainless-steel tube (H) that forms the outer part of the coaxial water feed. This tube is welded to the high-voltage electrode (I) and to the threaded fitting (J).

The water channels in the high-voltage electrode were machined into the stainless-steel electrode body, and a 1 mm plate was welded over it. The electrode was then machined on top and bottom to produce the basic outer profile (7.9 mm radius) and rolled to the radius that matches the extraction radius of the cyclotron. The connections to the water-cooled support were machined after the rolling process to avoid distortion.

The feed insulator (K) is made from machinable ceramic (Macor) or alumina. A teflon lining (L) is epoxied inside the ceramic insulator[1], and a smoothly

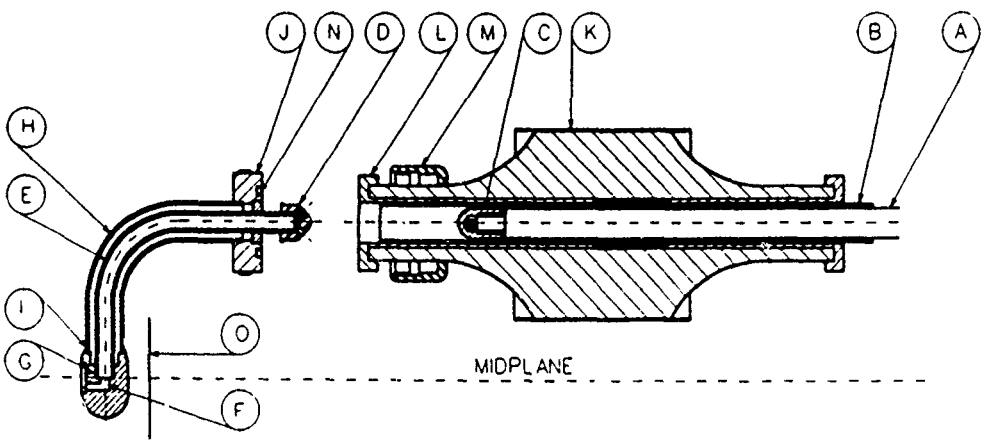


Figure 1. Cross-sectional view of the high-voltage electrode (a) and the high-voltage feed insulator (b). Details are explained in the text.

0-7803-0135-8/91$01.00 ©IEEE

contoured stainless-steel fitting (M) is captured by a flange on the teflon before the epoxy joint is made. We mount the insulator inside the upper dee and install the high-voltage electrode by making the connection between (J) and (L) with the fitting (M), through removeable access ports in the bottom of the upper dee. An o-ring (N) makes the water-to-vacuum seal. Details of the septum (O) mounting have been given in previous papers[2,3].

A second important change has evolved as a result of our efforts in testing materials for high-voltage properties[3]. Tests using molybdenum sheet as an anode showed severe degradation in voltage standoff after a spark at high electric fields. Small flakes of molybdenum were identified on the cathode after these tests. These flakes likely become new electron-emission sites. Stainless steel performed much better in the same series of tests and has been used for both the sparking plates and the septum for the last 6 months.

DEFLECTOR PERFORMANCE

A previous paper[3] describes the electrical circuit of the deflector, including details of the water column that provides about 30 MΩ series resistance at the high-voltage electrode. A linear voltage-current relationship is observed at low electric fields. This is a measure of the total series resistance, from a fixed surge resistor of 31 MΩ on top of the cyclotron, the water column of about 30 MΩ and the returning water annulus, which typically has a resistance of about 750 MΩ. At high electric field, the leakage current, believed to be from Field Emitted Electrons (FEE), increases more than linearly. The FEE current is observed to increase exponentially with the electric field and it heats the anode surface locally where it hits. At some level, a discharge will occur accross the gap. Such a spark can either reduce the FEE current if it conditions the emitting site, produce no measureable change, or it can severly degrade the high-voltage performance of the gap. The strong magnetic field of the superconducting cyclotron directs the electrons vertically to the sparking plates above and below the high-voltage electrode and focuses them to much smaller spots than electrostatic focusing alone would do. As an example, 70 keV electrons have a gyroradius of only 0.18 mm at a magnetic field of 5 T. This can, in principle, increase the damage from a spark and the rate of evaporation of anode material that is produced at the impact point of the FEE current on the anode. However, our results have shown that magnetic effects are less severe than thermal effects. Most efforts to improve the performance of the deflector have aimed at reducing the FEE current by reducing the peak electric field through careful shaping of the high-voltage electrode, by cooling the cathode surface to reduce thermal enhancement effects[3] and by proper choice of anode material. If the electron emitting sites are located in the vicinity of an insulator, surface charging may occur and metal evaporation from the hot spot on the anode may coat the insulator leading to insulator failure. The insulators on the Chalk River superconducting cyclotron are well shielded[1] and have not suffered particularly from these effects. The deflector has been operated continuously for periods of more than a week with FEE currents as high as 250 microamps. However, recently, these FEE currents have typically been kept at less than about 60 microamps.

Figure 2 shows the measured FEE current as a function of the average deflector field. Four sets of data are shown representing the best performance at the dates given. All data, except those marked March/91, were obtained with the magnet at about 3 T and the r.f. switched off. The March/91 data were obtained with a magnetic field of 4.25 T and the r.f. operating at high power at 58 MHz. The Nov./89 and March/90 data were obtained with a 6.5 mm gap, the Dec./90 data used a 5.5 mm gap and the March /91 data were obtained with a 4.75 mm gap. Some of the improvement has been from this gap reduction. Typically, the maximum voltage that a gap can hold increases only as the square root of the gap width. As the gap is increased, the maximum field will therefore be smaller. Throughout the cyclotron commissioning, we have sought to find a good compromise in the gap width between reasonable beam transmission and the maximum deflector field. A gap of 5 to 6 mm appears to be an acceptable compromise for many beams. We believe that the leakage current originated only from cathodic emmission, and that insulators have not been a limiting factor in our system.

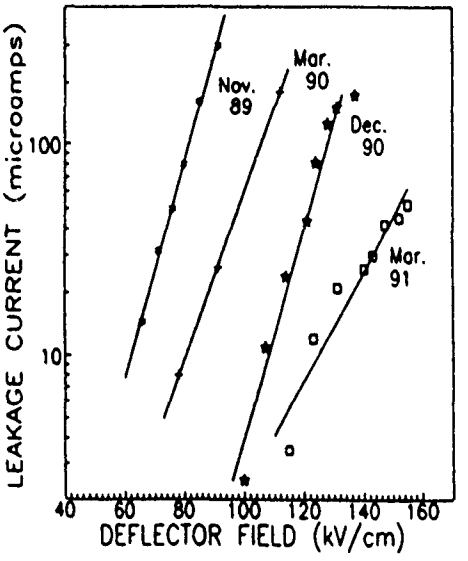


Figure 2. Lowest deflector leakage current as a function of the electric field at several dates during the last 16 months.

The data for Nov./89 and March/90 were described in some detail previously[3]. The high-voltage electrode was then made from solid stainless steel. The increase in the maximum sustainable deflector field that could be obtained at those dates is believed to be mostly from profile changes on the ends of the high-voltage electrode, to reduce the peak electric field, and from changes in the conditioning procedures. Calculations show that the peak electric field is 20 % above the average field for a 6 mm radius at the top and bottom of the electrode. The ends of the electrode have a compound radius involving both the top-to-bottom and side-to-side profiles. The most visible areas of spark damage are generally at the two ends of the electrode. When an attempt was made to use the deflector (March/90 data) to extract a carbon beam at 45 MeV/amu, r.f. heating and beam loading (estimated to be between 10 and 15 watts) increased the leakage current. This lead to a reduction of the maximum useable deflector field by 10 to 15 %.

Many ideas were tested during 1990. An important test-stand result confirmed that sparks between a stainless-steel cathode and a molybdenum-plate anode (the same material in use for sparking plates) transfer small (10 to 50 microns width) flakes of molybdenum to the cathode. Enhanced FEE currents from these flakes reduce the voltage-standoff capability of the gap by nearly 40 %. Molybdenum

flakes could not be conditioned away. An experiment in the test stand was repeated three times, in which the same molybdenum anode and stainless-steel cathode were tested to successively higher electric fields until a severe spark lead to a deterioration of the maximum sustainable electric field by about 40 %. In each case, opening the test chamber and cleaning the cathode surface with alcohol, restored the performance. No other cathode or anode change was attempted at this time. These experiments led us to change the septum and sparking plates from molybdenum to stainless steel. This change produced noticeable improvements, with the best result being 90 kV over a 6.5 mm gap. However, r.f. heating lead to a deterioriation in performance back to the previous level.

Attempts were then made to reduce the cathode heating. The first attempt was to use a high-voltage electrode made from solid copper instead of stainless steel. Although test-stand results at that time showed that copper was much poorer than stainless steel for high-voltage standoff, it has much higher thermal and electrical conductivity, which makes it less suseptible to r.f. heating. A solid copper high-voltage electrode with copper hangers was tested. The results are shown on Figure 2, marked Dec./90. To achieve this result, the copper electrode required considerable conditioning (several days of operation at high voltage) with no magnetic field, followed by operation at a magnetic field of about 3 T and then with high-power r.f. present. This electrode was used to extract carbon at 50 MeV/amu, a beam that represented a major milestone for the cyclotron's commissioning because it meets one of the machine's design goals.

The water-cooled high-voltage electrode, described in the first part of this paper, was built and tested as the next development step. Its first operation exceeded the performance of the copper electrode, and it was used to extract ion beams of carbon at 45 MeV/amu as well as chlorine at 35 MeV/amu in an 8-day experiment. After a careful cleanup of the entire deflector and some conditioning, the results shown for March/91 were obtained. This deflector improved with use and helped us to extract iodine at 19 MeV/amu at a gradient of about 150 kV/cm, with a gap of 4.75 mm. It has also been tested to 95 kV with a 7.5 mm gap with no magnetic field present and to 94 kV with a magnetic field of 3 T.

TEST STAND RESULTS

The program to improve the deflector has had considerable guidance from results obtained from a test stand. This test stand was described in detail and some results were reported[3] previuosly. All recent tests point towards the importance of the choice of anode material for peak high-voltage performance. Table 1 shows the results of tests on three materials.

Table 1. Breakdown voltage (kV) for combinations of copper, stainless-steel and titanium electrodes. The gap was 2.5 mm.

Cathode Material	Anode Material		
	Copper	Stainless Steel	Titanium
Copper	64	92	98
Stainless Steel	74	96	110
Titanium	72	88	110

The tests were made with 19 mm diameter cyclindrical electrodes, with a 2.5 mm gap. All of the electrodes were machined and polished with (wet) 600 grade silicon-carbide paper. The cathode was connected to a low-capacitance power supply with a 2 m long cable. No series resistance was used for these tests and the cable capacitance was about 500 pf. The voltage was raised in 2 kV increments from about 40 kV until a breakdown occurred that produced irreversible damage. Typically, a number of sparks occur as the voltage approaches the breakdown voltage. These sparks can either condition the gap and reduce the leakage current or produce no obvious changes. The breakdown voltage is determined by a spark that typically trips the power supply off. When the voltage is re-applied, continuous sparking will occur at 15 to 20 % lower voltage, an indication of irreversible damage. Good reproducility (about 5 %) has been obtained in tests of some of the combinations.

Table 1 shows the important role of the anode material for a gap of 2.5 mm. The field-emitted electrons originate from the cathode and interact with the anode. The surface properties of the anode (such as adsorbed gas) then play an important role in the breakdown process.

Efforts are underway to apply these results to the deflector. In the present deflector design, the back side of the high-voltage electrode and regions above the hangers that support the high-voltage electrode are copper. Attempts will be made to cover as much of these areas as practical with titanium and to replace the septum and sparking plates with titanium to see if further improvements can be made. A second water-cooled high-voltage electrode will also be fabricated from titanium.

SUMMARY

Improvements incorporated into the deflector of the Chalk River superconducting cyclotron have allowed us to extract ion beams up to 50 MeV/amu, the design goal of the accelerator. Deflector fields exceeding the design goal of 143 kV/cm have been achieved and maintained over a reduced gap of 4.75 mm with some loss in beam intensity. A deflector field of 94 kV across a 7.5 mm gap has recently been achieved both with and without magnetic field, but without r.f. We shall continue to improve this system with the aim of achieving a deflector field of about 150 kV/cm at a gap of at least 6 mm.

ACKNOWLEDGEMENTS

The authors would like to acknowledge the valuable technical help of N. Bray, R.E. Milks, J.F. Mouris, D.R. Proulx and R.R. Tremblay.

REFERENCES

[1] C.R. Hoffmann and J.F. Mouris, these proceedings

[2] C.R. Hoffmann and C.B. Bigham, Proceedings of the 1987 IEEE Particle Accelerator Conference, Washington D.C., (1987) p. 1567.

[3] W.T. Diamond, C.R. Hoffmann, G.R. Mitchel and H. Schmeing, XIV International Symposium on Discharges and Electrical Insulation in Vacuum, Santa Fe, New Mexico, Sept. 17-20, (1990) p. 630.

THE PROPOSED INJECTION SYSTEM FOR AN ASYMMETRIC B FACTORY IN THE PEP TUNNEL

E. Bloom, F. Bulos, G. Loew, R. Miller, B. Sukiennicki, T. Mattison*
Stanford Linear Accelerator Center
Stanford University, Stanford, CA 94309
and
W. Barletta†
Lawrence Livermore National Laboratory
Livermore, CA 94551

I. ABSTRACT AND INTRODUCTION

The proposed asymmetric energy B Factory to be built in the PEP tunnel at SLAC will require a highly effective and profuse source of low emittance electron and positron bunches. The B Factory will consist of two rings of equal size, a 9 GeV electron ring and a 3.1 GeV positron ring, each with 1658 bunches with total circulating currents of 1.5 and 2.1 amperes respectively. As the luminosity lifetime of the collider is expected to be about two hours, the injector should be capable of filling the rings in a small fraction of an hour. It turns out that with some simple modifications, the SLC linac with its damping rings and positron source is ideally suited to fulfill this function effectively. The overall injection system is described below.

II. SYSTEM SPECIFICATIONS AND DESCRIPTION

The specifications and required parameters of the injection system are shown in Table I. It is seen that each of the 1658 stored bunches will require about 5 x 10^{10} particles. In the topping-off filling mode (80→100%), assuming that each bucket receives about 5 single bunches from the injector with 50% filling efficiency, the linac will have to provide single bunches of $4x10^9$ particles/bunch as compared to 2-5 x 10^{10} particles/bunch in the regular SLC mode. This should be very easy. In the full filling mode, the first 80% of each bucket will be filled, also with 5 linac bunches, but at the rate of $2x10^{10}$ particles/bunch, and the remaining 20% at the topping-off rate as above. Assuming that both rings are filled by alternate linac pulses, each at a 60 pps rate, it is easily seen that the filling operations will take on the order of 3 and 6 minutes respectively.

A schematic of the SLC injection system is shown in Fig. 1. The injector will consist of the first 19 sectors of the linac, the two damping rings and the positron source. The 3.1 GeV positrons will be extracted at the end of Sector 3 through a DC chicane which will let the electrons continue on, either to the end of Sector 7 for extraction at 9 GeV via a slowly pulsed magnet, or to Sector 19 at about 30 GeV for positron production. The remaining 11 sectors of the linac may be

TABLE I

B FACTORY INJECTION SPECIFICATIONS AND PARAMETERS

Beam Energy:	
High-energy ring (HER) (e^-) [GeV]	9 [range: 8-10]
Low-energy ring (LER) (e^+) [GeV]	3.1 [range: 2.8-4]
Beam current:	
HER ring [A/$10^{10}e^-$]	1.48/6777
LER ring [A/$10^{10}e^+$)	2.14/9799
Particles per bunch:	
HER ring[$10^{10}e^-$]	4.1
LER ring [$10^{10}e^+$]	5.9
Linac repetition rate [pps]	60/120
Linac current [10^{10} $e^{\pm}$ per pulse]**	0.4-2
Invariant linac emittance [m-rad]	$5x10^{-5}$
Filling times:	
Topping-off (80-100%) [min]	3
Full Filling (0-100%) [min]	6
Magnet standardization time [min]	15
Ring circumference [m]	2199.318
Revolution period [μs]	7.336
Revolution frequency [kHz]	136.311
Bunch frequency [MHz]	476/2 = 238
Time between bunches [ns]	4.20
Harmonic number	3492
Number of bunches (leaving 5% gap)	1746 - 5% = 1658
Horizontal damping time.	
HER [ms]	38
LER with wigglers [ms]	36
LER without wigglers [ms]	150
Geometric beam emittance [nm-rad]:	
HER horizontal/vertical	48/1.9
LER horizontal/vertical	96/3.8

**Assuming 50% filling efficiency

*Work supported by Department of Energy, contract DE-AC03-76SF-00515.
†Work supported by Department of Energy, contract W-7405 ENG-48
U.S. Government work not protected by U.S. Copyright.

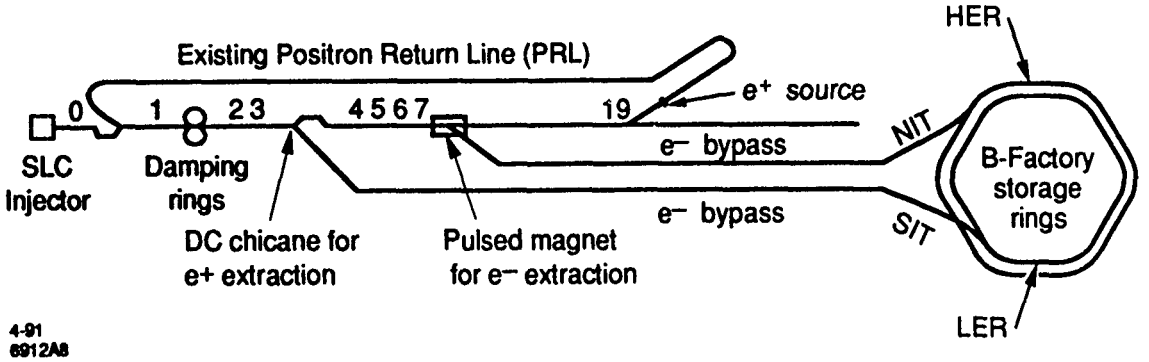


Fig.1. Schematic of the B Factory $e^{\pm}$ injection system, based on use of the SLC linac with bypass lines. The numbers along the linac indicate the location (not to scale) of each sector. Each of the 30 sectors is 100 m long.

turned off. Once extracted, the respective bunches of electrons and positrons will be transmitted through two separate bypass lines to the existing NIT and SIT lines presently used to fill PEP from the end of the linac. The NIT and SIT lines are well instrumented and will not be described in this paper. The advantages of the system proposed here are numerous: a) it preserves all other High Energy Physics opportunities at SLAC; b) the bunches leave the linac at the desired energy, thereby eliminating the need for backphasing and minimizing wakefields in unnecessary accelerator structures; c) by alternating e^+ and e^- pulses at 60 pps, only one bunch will be stored at a time in each damping ring; d) no additional fast kickers (often unreliable) will be needed; e) between filling times, it will be possible to "park" e^+ and e^- bunches at a low rate in NIT and SIT Faraday cups to optimize readiness for filling on demand; f) finally, by selecting a ring RF frequency of 476 MHz, i.e., 1/6 of the linac RF frequency of 2856 MHz, synchronization will be greatly simplified.

The bypass lines will consist of 10 cm-diameter aluminum pipe (for adequate pumping speed) with 2.5 cm-diameter constrictions every 50m where a FODO array of quadrupoles and beam position monitors will be located. These apertures will be fully adequate since the low-emittance beams will have σ_r's of less than 1.5 mm. A cross-section of the linac housing with the overhead-suspended quadrupoles showing the respective tilts of the extraction planes is given in Fig. 2. The existing positron return line (PRL) is shown for reference in the upper right-hand corner. Table II gives a list of the components in the bypass lines. The matching quadrupoles are part of 360 degree-phase advance achromatic bends joining the linac to the bypass lines, and these to NIT and SIT.

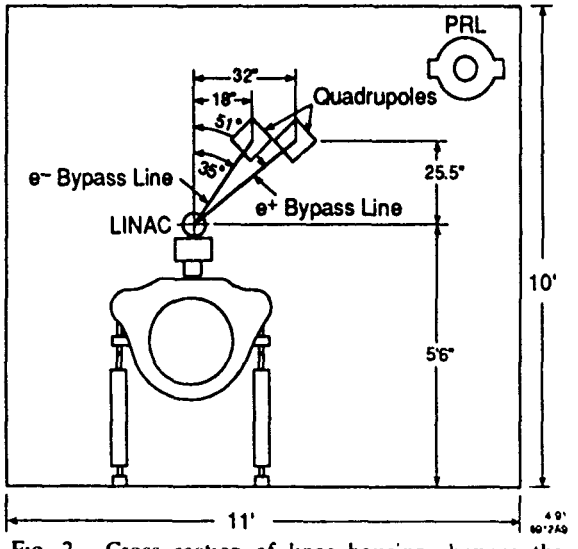


Fig. 2 Cross section of linac housing showing the location of the electron and positron FODO array quadrupoles. Note the tilts of the extraction planes

TABLE II
LINAC BYPASS LINE COMPONENTS AND SPECIFICATIONS

	POSITRON LINE	ELECTRON LINE
Length (km)	~2.6	~2.2
Energy (GeV)	2.8-4	8-10
No of quadrupoles		
Matching	24	24
FODO array	52	44
Steering correctors	64	56
Beam position monitors	64	56
	(64 readouts)	(56 readouts)
Profile monitors	2	2
Pumps (120L/s)	29	23
Vacuum roughing connections	29	23
Fast valves	1	1
Isolation valves	14	13

III. INJECTION INTO THE HER AND LER

In contrast to the single PEP ring, for which the injection lines come down vertically into the plane of the ring and are tangent to the inside, the HER and LER injection lines will be brought down on the outside of the two rings - into the plane of the HER at IR-10 and into the plane of the LER at IR-8. The proposed method of injection is very similar to the one used in PEP. It assumes β_x = 80 m and β_y = 20 m in 40-m-long injection regions. Horizontal injection occurs as shown in Fig. 3. The closed orbit of the stored beam is temporarily distorted by means of four DC bump magnets and three kickers Details of the horizontal phase space (x,x') for the stored and injected beam are shown at three sequential points in time following the turn-on of the DC bump magnets. (i) stored beam is moved by 0.5 cm to DC bumped position, $10\sigma_x$ away from the inner edge of the 3-mm septum; (ii) stored beam is within 6 σ_x of the septum inner edge, incoming beam from the linac is tangent to the stored-beam

orbit and within 2 σ_i of the outer septum edge; (iii) approximately four turns later, the stored beam is back to its DC bumped orbit: the incoming beam is inside the ring within $2\sigma_x$ of the inner septum edge, ready to damp and merge with the stored beam. It is assumed that the injected beam has a β_x of 30 m.

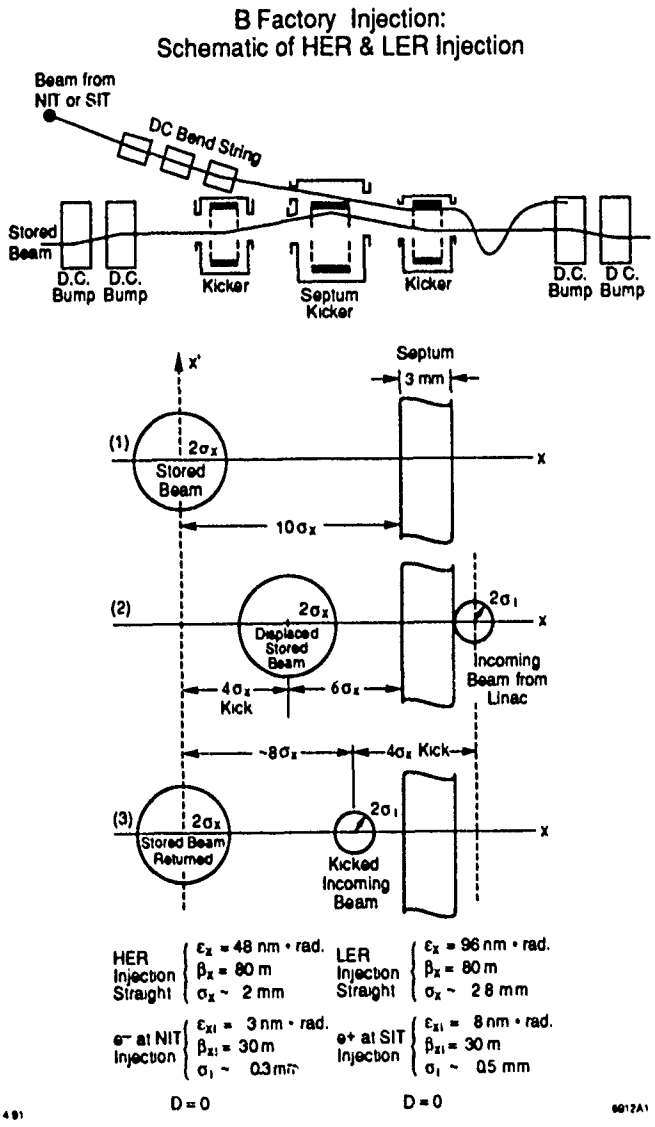
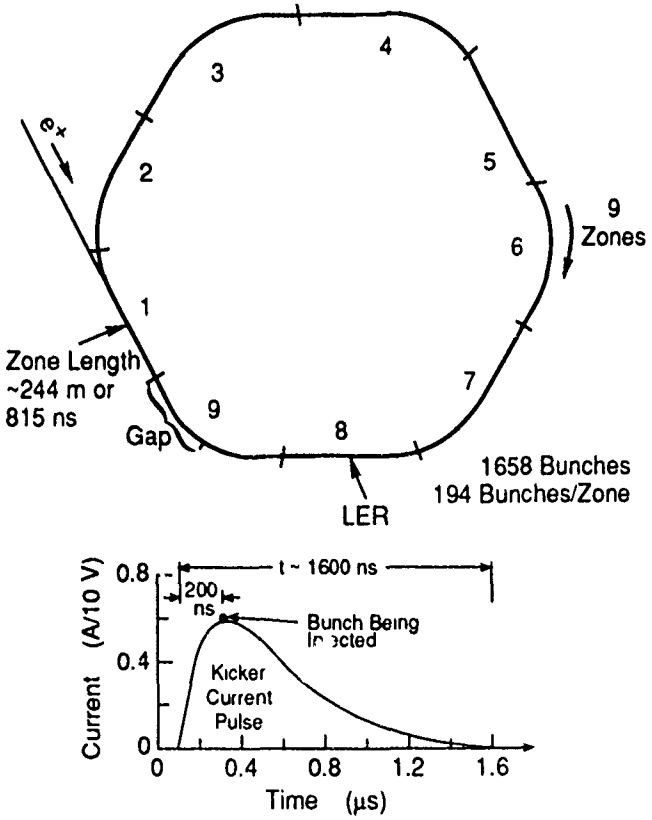


Fig. 3 Schematic of Injection Kicker System, and horizontal transverse phase space (x,x') of stored and incoming beams during three successive steps of the injection process (HER and LER). The diameters of the stored and incoming beams are not drawn to scale.

For injection purposes, each ring is divided into nine rotating "zones" of equal length as shown in Fig. 4. A zone has a length of about 244 m (or 815 ns) and contains 194 bunches. One of these zones in each ring will remain about half empty to leave a gap for ion control. We describe here the process for filling the LER at a 60Hz rate; the HER is filled in a similar way. The transverse damping time for the HER is 38 ms and for the LER 36 ms. If the damping contribution of the wigglers in the LER is ignored, a worst-case situation in terms of injection, then the LER has a damping time of 150 ms. The beginning of each zone is determined by the time onset of the kicker current pulses. All three kicker pulsers are identical, consisting of critically damped RLC circuits that rise and fall to practically zero within less than 1500 ns. The first bucket to be filled in zone n is located roughly 200 ns after the beginning of the kicker pulse so as to ride on the flat top where sensitivity to time jitter is minimized. Since the rise time of the pulse is much shorter than the fall time, bunches recently stored in zone n - 1 are unaffected. Bunches in zone n + 1 (at least 815 ns later) are kicked slightly, but since they have been in the ring for the longest time, their orbits are almost fully damped, and, to the extent that the kickers are matched, these bumps are closed. Thus, single buckets in zones 1 through 9 are filled in succession, after which, 9 times 1/60th of a second, or 150 ms later (that is, one damping time in the LER in the absence of wigglers), the next adjacent buckets (4.2 ns later) in each zone are filled, and so on. With this method, damping in the LER, even without wigglers, is adequate. The entire filling sequence will be computer controlled and automated for both rings.



Zone Filling Sequence: 1,2,3,4,5,6,7,8,9 (partially), 1.etc. . .

Fig 4 Azimuthal zone filling sequence for the LER, showing nine zones. The kicker pulse shown (equal for all kickers) was computed by assuming charged, critically damped RLC circuits [R = 2 (L/C) $^{1/2}$] in which the current reaches its maximum at t = 2 L/R after a thyratron is fired and allows the circuit to be discharged

HEB to Superconducting Super Collider Transfer Lines

F. Wang and R. Schailey
Superconducting Super Collider Laboratory*
2550 Beckleymeade Avenue
Dallas TX 75237

Abstract

We present here an optics design for a beam transport system which will be used to inject 2 TeV proton beam from the High Energy Booster into the Superconducting Super Collider. The main design issues are the use of conventional magnets for constructing this high energy beamline and maintenance of small beam transverse emittance during the transfer process. Effects of various errors have been investigated in detail, then tolerances for errors are given. With the design criterion and beam position correction scheme proposed, proton beam transverse emittance dilution is expected to be less than five percent.

I. Introduction

The HEB is the last synchrotron of the three injector synchrotrons in cascade of the injection systems for the two Superconducting Super Colliders. The devices that eject proton beam from the HEB for injection both clockwise and counterclockwise into the bottom and top colliders are located within the west long straight section of the HEB. The collider injections take place in the west utility straight sections which are located directly under the HEB west long straight section. The elevation separation between the lower collider and the HEB is 14m which is determined by a radiation shielding requirement. In SSCL Site-Specific Conceptual Design[1], the two beam lines joining HEB and colliders include warm septum magnets, pulse kicker magnets at both ends of the lines, superconducting major vertical bending magnets, and quadrupoles.

To eliminate troubles of transfer line superconducting magnet quenches, this design makes use of warm magnets only. The total length of each of these lines, determined by geometric boundaries, is about 631m. The use of low field conventional bends requires additional effort to find an optical structure to accomplish matching of optical parameters, while keeping reasonable β and dispersion function amplitudes through the line.

Another main issue of this transfer system design is to preserve the small proton beam transverse emittance during ejection, transfer, and injection which is important for obtaining high collider luminosity. Effects of magnet misalignment and various field errors to emittance dilution have been investigated to determine tolerances for errors and magnet design criterion. A beam position correction system is also proposed to reduce dilution effects due to beam centroid displacement at injection region.

II. Beam Optics and General Layout

The layout of the ejection, beamlines, and injection devices is shown in Fig.1. The HEB ejection kickers and the Collider injection kickers provide horizontal shifting of the beam orbit. The beamline magnets bend beam vertically only.

Each of these two beamlines consists of two quasi achromatic bending sections with inverse deflecting direction. The short straight section between them provides the flexibility of optical parameter adjustments. The two lines are similar, with the exception of 0.2m difference of middle straight section length, and slightly different operating fields to accommodate different elevation levels of the two colliders. Similarity of design is important in maintaining ease of operation.

The upper limits of bending field and quadrupole field gradient adopted here are 1.81T and 30T/m, respectively, for 4cm full aperture magnet design. About 50% of beam line length is occupied by bending magnets. The requirements to leave space for crossing of one line with top collider, as well as the crossing of two lines push part of the bending magnets further away from both ends of the beamline. Both the low bending field and space requirements demand the increasing of total bending angle while leaving less space and more difficulty to accomplish phase space and dispersion matching and keeping amplitudes of β and dispersion function small. The optical functions of the beamline are shown in Fig.2. The maximum β function

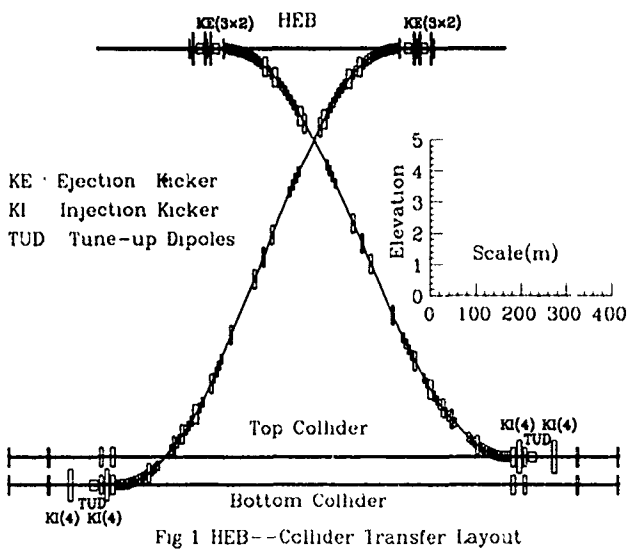


Fig 1 HEB--Collider Transfer Layout

*Operated by Universities Research Association under contract with the U.S. Department of Energy

0-7803-0135-8/91$01.00 ©IEEE

amplitude is 425m, and dispersion is compressed to less than 2m everywhere.

III. Effects of Magnet Misalignment and Field Errors

There are two major concerns caused by various errors for this transfer system: aperture requirement, and beam transverse emittance dilution. Since high bending field and quadrupole gradient have to be used, small magnet aperture is desired. The 2 TeV proton beam has a very small transverse emittance: $4.7\times10^{-10}\pi$ m rad. Beam dimensions have little influence on aperture consideration. Tolerances of systematic magnet alignment and magnet field errors are set to allow beam to pass the beamline without position corrections. The more critical tolerances come from the requirement to preserve beam transverse emittance. Small position and angular errors to the ideal collider closed orbit will cause large emittance dilution if they are not precisely corrected. Statistical bending field errors and quadrupole gradient errors are responsible for position mismatching and optical parameters mismatching which will inevitably lead to emittance dilution. Dilution effects due to centroid displacement, mismatching of β, and dispersion functions at injection in a circulating accelerator are well described by M. J. Syphers[2]. For injection position mismatching one has:

$$F_x \sim \frac{\sigma^2}{\sigma_0^2} = 1 + \frac{1}{2}\left[\frac{\Delta X_{eq}}{\sigma_0}\right]^2 \qquad (1)$$

where

$$\Delta X_{eq} = \sqrt{(\Delta X)^2 + [\beta\Delta X' + \alpha\Delta X]^2}$$

The dilution factor is defined as the ratio of phase space areas containing 95% of the beam particles, after and before dilution occurs. Since the transverse beam rms size σ_0 is about 0.2-0.3mm, ΔXeq from Eqt. (1), should be less than 0.1 mm if dilution less than 5% is required.

A program code is developed for a quick and effective evaluation of all the relevant quantities at injection point caused by various errors of the beam transport system. The program can perform a fixed error calculation as well as multi-trial simulations with normally distributed random errors of a given standard deviation for all magnet misalignment, field, gradient errors, and initial beam conditions. One can then decide what tolerances for errors should be set, and what kind of position correction scheme should be used to reduce the aperture requirement and preserve beam emittance.

Table 1. sums up the resulting error tolerances from analysis and simulation[3], which is required for either free pass of 30mm beamline aperture without position corrections, or emittance dilution of less than 5%.

Table 1. Tolerances for various errors

Error Type	Tolerances	Required as
Q Trans. shift	0.2 mm	Aperture
B Rot. about Z	1.0 mrad	"
ΔB/B(systematic)	0.001	"
Q gradient	0.002	Emittance
ΔB/B (regulation)	5×10^{-5}	"
Kickers ΔB/B	0.003	"

In addition to these error tolerances, a beam position correction system must be included to provide precise matching of the injected beam trajectory to collider closed orbit.

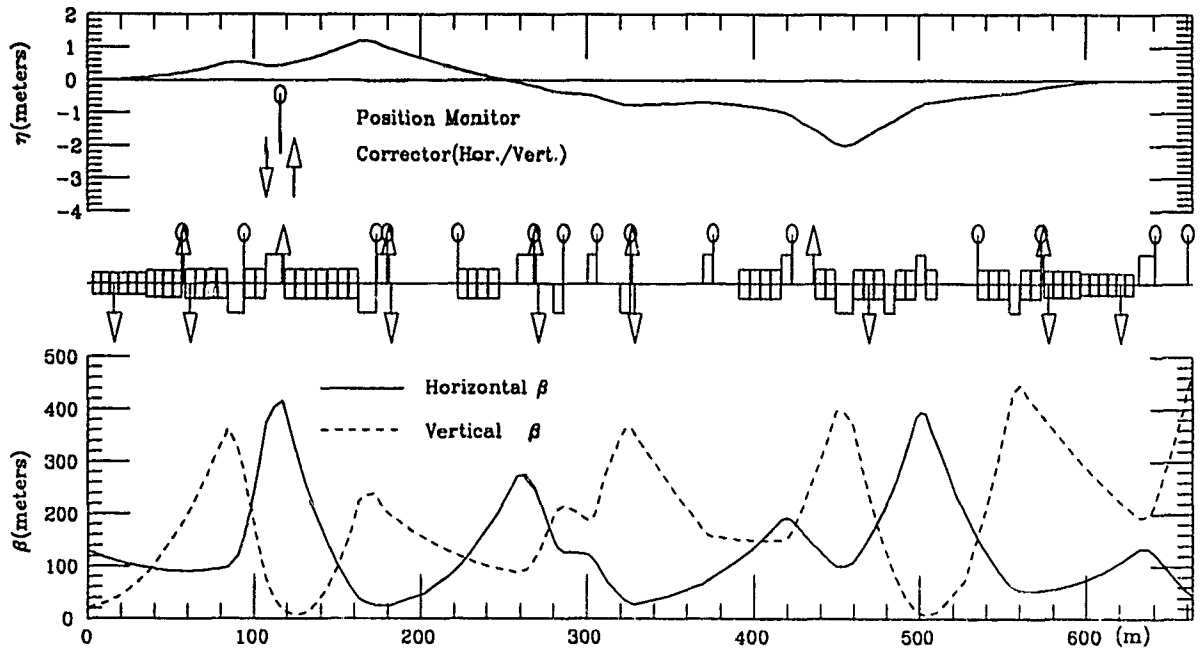


Fig.2 Beam Line Amplitude, Dispersion Functions and Position Correction Scheme

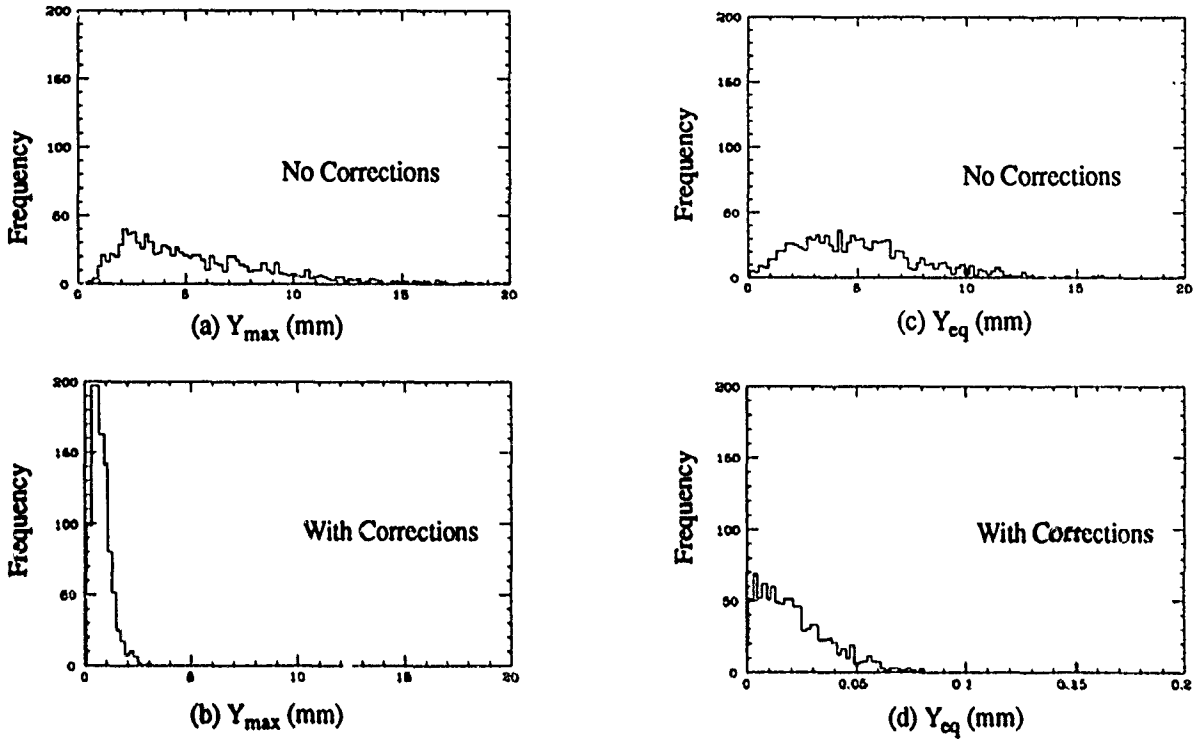


Fig.3 Distributions of maximum displacement and Y_{eq} before & after corrections, for 1000 trials with errors listed in Tab.1 (aperture), and [illegible] rms Δy=0.8 mm, $\Delta y'$=12 μrad

IV. Beam Position Correction Scheme

A proposed beam position correction scheme is shown in Fig.2. The correction scheme has two stages: in most of the line, each corrector takes care of the position errors read from the monitors between itself and the next corrector. The quantity $\Sigma(X_i+\Delta X_i)^2$ is minimized to obtain needed corrector strength. Here X_i is the position error before correction and ΔX_i is the displacement produced by the corrector at the ith position monitor. At the end of beam line there are two pairs of correctors, one for each transverse direction. Position errors are read from two monitors which are located in a utility straight section of the collider. The correction is then applied to both position and angular deviation of beam centroid to collider closed orbit. The strength of these two correctors are obtained by minimizing the quantity $\Sigma (X_i+\Delta X_{1i}+\Delta X_{2i})^2$.

Since the required emittance dilution is small, the two monitors located in the straight section between collider quadrupole QU3 and QU4 require a position resolution of 10 μm. Another pair of monitors located downstream of kickers will provide horizontal position errors for kicker amplitude fine adjustment. All the correctors, except kickers, are out of colliders; therefore, beamline position corrections will not interfere with circulating beam.

A number of simulations of correction process have been made in order to find a scheme which makes use of fewer correctors, lower correcting strengths and desired correction results.

Fig.3 depicts the correction results for 1000 trials simulation in vertical direction. The maximum vertical beam centroid displacement along the beamline, Y_{max}, is less than 2.[illegible]m after corrections and the quantity Y_{eq} in Eqt. (1), is less than 0.07mm at end of beamline, which corresponds to a dilution factor of 1.03.

V. Conclusion

The use of conventional magnets to construct the beam transfer lines between the two superconducting proton machines with the imposed geometry is viable. Beam transverse emittance dilution will also be under control with proper error tolerances set and a precise position correction scheme.

Authors would like to express their appreciation to Drs. D. Johnson, E. Seppi, and M. J. Syphers for their support and instructive discussions.

VI. References

[1] *Site-Specific Conceptual Design*, SSCL-SR-1056, p.119 1990.

[2] M. J. Syphers, *Injection Mismatch and Phase Space Dilution*, FN-458, 1987.

[3] F. Wang and R. Schailey, *Design Issues for the HEB-Collider Transport System*, SSCL ADOD- 017B, 1991.

The ELETTRA Gun Trigger Module

G. Roberto Aiello*, Maurizio Bossi
Sincrotrone Trieste
Padriciano 99, 34012 Trieste, Italy

Abstract

The ELETTRA injector is a full energy Linac. The Linac and the pulsed magnets need to be synchronized with the beam in the storage ring in order to fill it with the proper bunch pattern. Most of the triggers for the timing system are generated by a module which is named Gun Trigger module. The gun is triggered in synchronism with a reference bucket of the storage ring. It can be programmed with a delay between 2 and 864 ns, a range which covers one revolution period of the storage ring, so any arbitrary bucket of the ring can be filled. The module generates also the gun trigger for working in FEL mode, which needs a repetition from 30 to 50 ns in a 10 µs window. The jitter of all these triggers is less than 50 ps. The Gun Trigger module is developed in VMEbus standard, using TTL and ECL technology. It is remotely programmable through the ELETTRA control system. The general architecture of the ELETTRA timing system is also described in the paper.

I. INTRODUCTION

The timing system generates pulses with fixed and variable delay, required to trigger the injection and the beam diagnostics [1]. The Linac and the pulsed magnets need to be synchronized with the beam in the storage ring in order to fill it with the proper bunch pattern. The Linac works at 10, 5, 2 or 1 Hz. The trigger which gives the injection rate is the Line Trigger (LT); it is derived by dividing the 50 Hz line frequency. The timing system must allow different modes of operation: Single Bunch, Multi-Bunch, and FEL. In Single Bunch mode only one bucket of the storage ring must be filled; in Multi Bunch mode the buckets of the storage ring must be uniformly filled; in FEL mode a trigger repetition from 30 ns to 50 ns must fire the gun of the Linac.

The jitter of the gun trigger must be smaller than 200 ps in order to fill only the selected buckets. The pulsed magnets have to be synchronized 500 µs in advance because of their risetime. Their jitter must be smaller than 3 ns [2]. The most critical part of the timing system described below is the Gun Trigger module. Semicustom ECL integrated circuits from Siemens are used: 16 bits programmable counters which can work up to 750 MHz. This choice has been allowed to realize all the trigger generators in only one VMEbus board, reducing the space, the complexity and the power consumption with respect to other solutions.

II. TIMING SYSTEM ARCHITECTURE

Most of the synchronization problems come from the Single Bunch working mode. The gun needs to be synchronized to the bucket to fill in the storage ring at a 10 Hz injection rate.

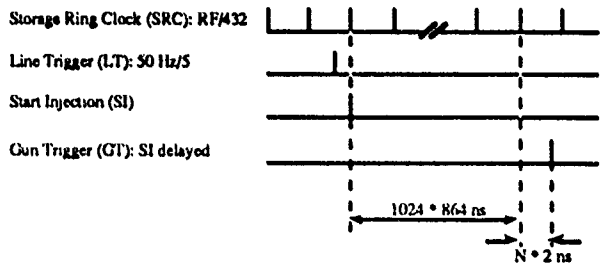


Figure 1. Injection Timing: the Gun Trigger is delayed by 884.7 µs (1024*864 ns) from SI. One more adjustable delay in 2 ns step is used to fill any bucket of the storage ring. Other triggers can be derived from SI in order to provide any pretrigger required.

In order to realize this timing, the Gun Trigger Module generates the following triggers [figure 1]:

- Storage Ring Clock [SRC]: Synchronized to the reference bucket of the storage ring, it is obtained by dividing the radio frequency [RF] by the harmonic number of the storage ring (432); its frequency is 499.654 MHz / 432 = 1.157 MHz.
- Start Injection [SI]:It is synchronized to SRC and its period is that of the Line Trigger; 10 Hz phased with the line frequency.
- Gun Trigger [GT]: It is delayed by 884.7 µs (1024 * 864 ns) from SI. An additional programmable delay in 2 ns steps is used for synchronizing that to the required bucket of the storage ring.

* Now at the Superconducting Super Collider Laboratory, 2550 Beckleymeade Ave., MS 1046, Dallas, TX 75237

0-7803-0135-8/91$01.00 ©IEEE

The modulator and pulsed magnets triggers are generated by delaying SI. A 4 ns step programmable delay module is used for this purpose.

III. DESCRIPTION OF THE MODULE

The Gun Trigger Module contains the SRC, GT and SI generators [figure 2]. The SRC generator is a 16-bit programmable counter always enabled. The whole programming range gives frequencies from 33.3 MHz down to 7.6 KHz, but it is used here to obtain 1.157 MHz. The SI Generator is a 10-bit counter and SRC is its clock. It starts counting at the arrival of the 10 Hz Line Trigger and its first pulse is SI. When it finishes counting, it generates its ripple carry [EN_GT]: this trigger occurs 884.7 µs (1024 x 864 ns) after SI.

The GT generator is also a 16-bit programmable counter. EN_GT enables the counting. This delay can be programmed from 10 ns to 131 µs, but only delays from 864 ns to 1728 ns (864 ns + 864 ns) are used: it allows synchronization of GT to each bucket of the storage ring. All the generators are remote controlled from the VMEbus.

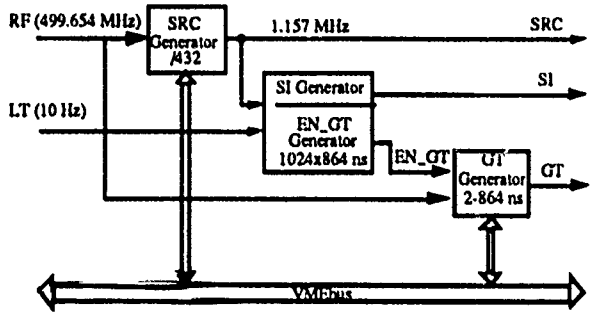


Figure 2. Logic block diagram. SI is the first SRC count after LT. EN_GT is the ripple carry after 1024 SRC counts and enables the GT counter.

Two Gun Trigger Module must be used. The first one will generate the triggers shown in figure 1. The second one will generate the triggers for the FEL mode: a repetition from 30 to 50 ns will be used instead of GT. This repetition is realized using the SRC generator of the second board.

The board is a four layer VMEbus compatible board: one ground plane, one power plane and two signal planes. It is developed in ECL technology except for the VMEbus interface which uses TTL technology.

The 50 Ohm input has a probe to test the input radi o frequency signal. A 100114 line receiver drives the input signal to the 500 MHz counters through a 50 Ohm microstrip line. The input circuit accepts amplitude from -10 dBm to 10 dBm. The output signals are at the NIM standard (-14 to -18 mA on 50 Ohm).

The SI and EN_GT generators are implemented with two ECL PALs (Programmable Array Logic): 1016RD8 from National Semiconductor. The clock is SRC. The Enable is the 10 Hz trigger, the Reset is GT. The 10 Hz trigger starts the counting and GT resets the counter. SI is generated at the first SRC pulse after the Enable, EN_GT at the last count.

The same IC is used for both the SRC Generator and for the GT Generator: the SH100CK1133, a semi-custom chip from Siemens. It is a 16 bit programmable counter which can work up to 750 MHz. This choice reduces the complexity of the board [figure 3], the power consumption, and the space respect to other solutions.

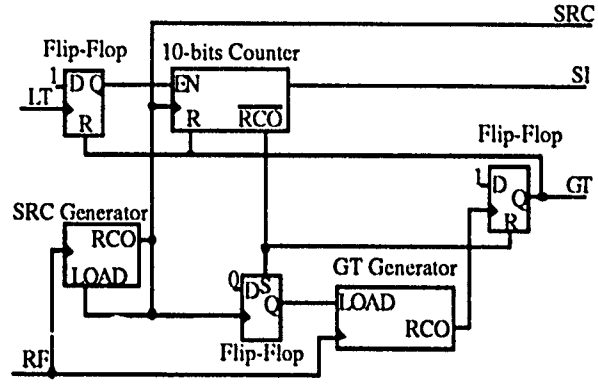


Figure 3. Schematics of the logic which realizes the timing. Only six chips are used.

The -5.2 V for powering the ECL devices comes from an external power supply through a connector on the front panel to give full VMEbus compatibility. The ECL logic levels and the -2 V level for the signal pulldowns are derived from the -5.2 V. The total power consumption is about 4 A on the -5.2 V and 2 A on the +5 V.

IV. CONCLUSIONS

The Gun Trigger module allows to delay the pulse which fires the gun up to 864 ns in 2 ns steps with respect to the Storage Ring Clock, a signal synchronized to a reference bucket of the storage ring. The jitter measured from these triggers is less than 50 ps.

Three Gun Trigger Module boards have been built. Their characteristics satisfy the initial requirements. Two of these boards will be used for the ELETTRA timing system.

V. REFERENCES

[1] G.R. Aiello and A. Carniel, "Timing System Project", Sincrotrone Trieste ST/M-89/11, July 1989.

[2] D. Tommasini, "Determination and Design of Septa Magnets for ELETTRA", Sincrotrone Trieste ST/M-TN-90/16, August 1990.

POISSON Study of Electrostatic Septa for the MIT–Bates SHR*

Manouchehr Farkhondeh,
Massachusetts Institute of Technology
Bates Linear Accelerator Center
Middleton, MA 01949.

Abstract

The POISSON group of computer codes [1] was used to study the details of field distributions of electrostatic septa for use with the MIT–Bates South Hall Ring (SHR). Studies were made to minimise field penetration and field gradients near the foil strips while satisfying the technical constraints. In addition, effects of upstream guard foils and an additional electrode opposite these foils on the field shapes were studied in great detail. The guard foils will shadow the main foils from the direct beam, and the electrode will prevent the secondary low–energy electrons from the guard foils from reaching the anode. Our optimal configuration of foils and electrodes as well as the electric field shapes are presented.

1 Introduction

The SHR under construction at the MIT–Bates Linear Accelerator Center will be a high intensity pulse stretcher facility with high quality cw electron beams of up to 1.0 GEV, operating in both storage and extraction modes. The ring lattice will consist of over 200 electromagnets distributed over a ring circumference of 190 m. A description of SHR is given in ref. [2]. As any other pulse stretcher rings with extraction capabilities, SHR requires two electrostatic septa near the injection and extraction regions for providing the required deflection to the circulating electron beam during the injection and extraction periods. After the short injection period, these septa should have no effect on the circulating beam. A 40 mA 1.6 μsec wide electron pulse which raps around the ring twice, by its nature, makes the requirements on the septa very demanding. The septa must have two distinct field regions: (a) a field-free region for circulating beams, and (b) a high transverse field region for injected and extracted beams with a field strength of 50 KV/cm. The purpose of these studies have included finding an optimum design in which the field penetration to the region (a) is minimum while maximizing the field uniformity in region (b).

These septa will have an active length of about 150cm formed by a row of thin foil strips at ground potential and positioned 2 cm from the solid anode at 100KV. The foils are mounted on a long semicircular carrier at ground potential with foils stretched vertically along its diameter. Figure 1 shows the basic components of the septa. Our POISSON calculations included 5 mm wide foil strips and a range o spacing from 0.3mm to 1.mm.

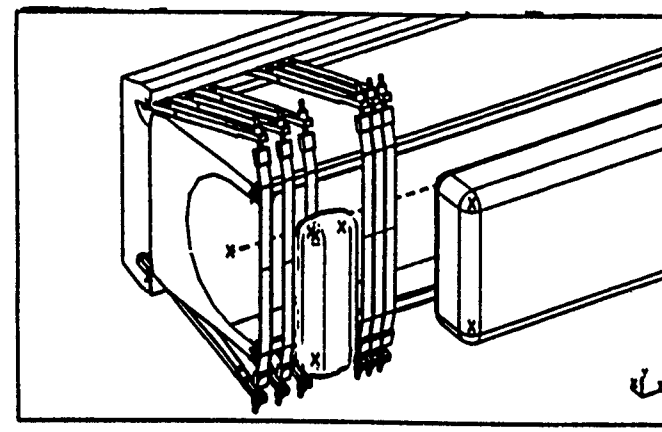


Figure 1: schematic view of the electrostatic septa.

Because of optics considerations and because a few μA of beam will strike the extraction septum under normal operation, the design seeks to minimise thermionic, field and secondary emission as well as thermal distortions of the foils. To accomplish this, guard foils have been added upstream of the main foils to protect them from the direct beam. The guard foils will shadow the main foils from the direct beam and an additional electrode opposite these foils will confine the secondary low energy electrons from reaching the anode, thus reducing the current drawn on the power supply. POISSON has been instrumental in finding the negative potential for the guard electrode which will optimize this confinement while maintaining good field uniformity.

*Work supported.in part by DOE contractDE-AC02-76ER03069.
0-7803-0135-8/91$01.00 ©IEEE

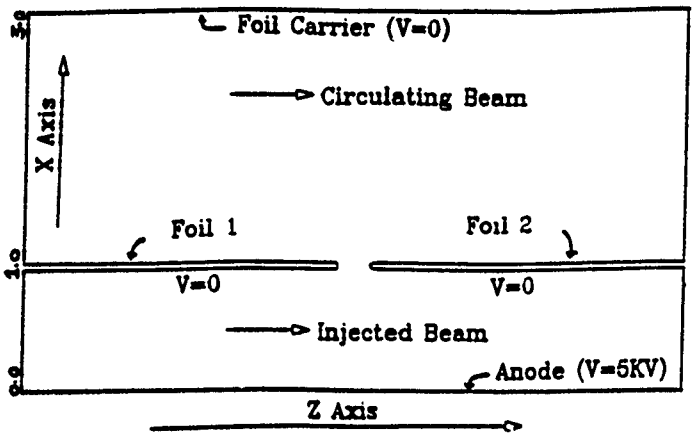


Figure 2: Schematic of POISSON input geometry for the "uniform" field region of septa.

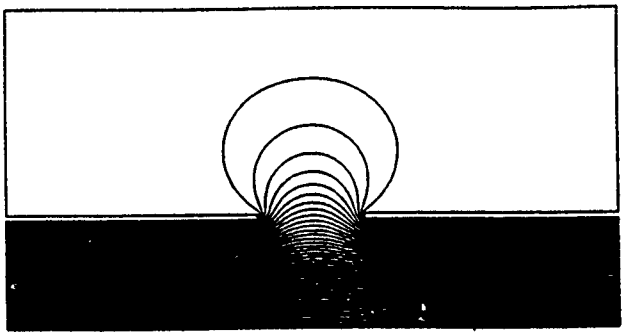


Figure 3: Equipotential lines for the "uniform" field region of the septa

2 Programming Considerations

A full scale POISSON layout of these septa would require a mesh size of less than 50μm (foil thickness) spanned over several centimeters; this makes the number of mesh points extremely large, exceeding the program's normal limits. Instead, one lays out only that portion of the geometry which is relevant to the question under study. For instance, when studying the field near the foils, we used a mesh size of 20μm and limited the overall area under study. When studying the field in the entrance region over several centimeters along the beam, a coarser mesh size has been used as well as an artificial foil thickness of 0.2mm. For the former case, we placed an anode at a distance of 1.0 mm from the wire to provide the 50 KV/cm field gradient. The results presented in this report are for foil spacings of 0.3 mm and edge radius of 0.025 mm.

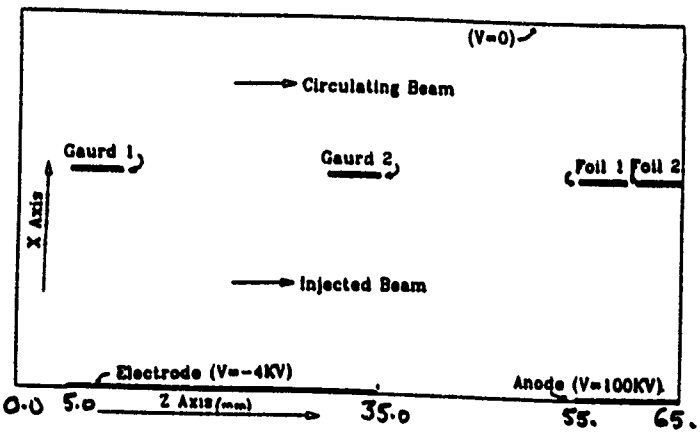


Figure 4: Schematics of POISSON input geometry for the entrance region with guard foils and additional electrode.

3 Uniform Field Region

To study field penetration, we examined a segment of the uniform region of septa away from the entrance and exit areas. The layout is shown in Figure 2. To limit the total number of mesh units and to set correct boundary conditions, we have used a 5 KV anode located at a distance of 1mm from the foils and required that the equipotential lines be normal to the surfaces of the anode and the ground plates at opposite ends of the gap. Figure 3 show the equipotential lines in a unit cell. The transverse field E_X integrated along the beam direction is used to define the effective field:

$$LE_{eff} = \int_{Z=0}^{Z=5.3(mm)} E_X(X,Z) \cdot dZ \qquad (1)$$

The integral here includes one half of two adjacent foils and the gap in between. This quantity has a variation of the order of 2×10^{-5} for $0.05 \leq X \leq 0.9$ mm which is well within the specified tolerance for the septa.

4 Entrance Region

We have also studied the effects of guard foils together with an additional electrode at ground or negative potential located in the plane of the anode and 20mm upstream as shown in Figure 4. The electrode at some negative potential will reverse the direction of the electric field near the guard foils so that the low energy electrons produced by the beam hitting the guard foils would not find a path to the anode. Several configurations were studied with POISSON and the results follow. The layout includes the entrance region 65 mm upstream of the first main foil, the

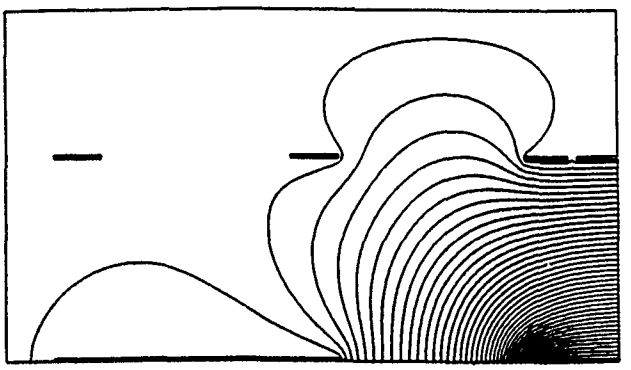


Figure 5: Equipotential lines for the entrance region of the septa with electrode at -4.0KV

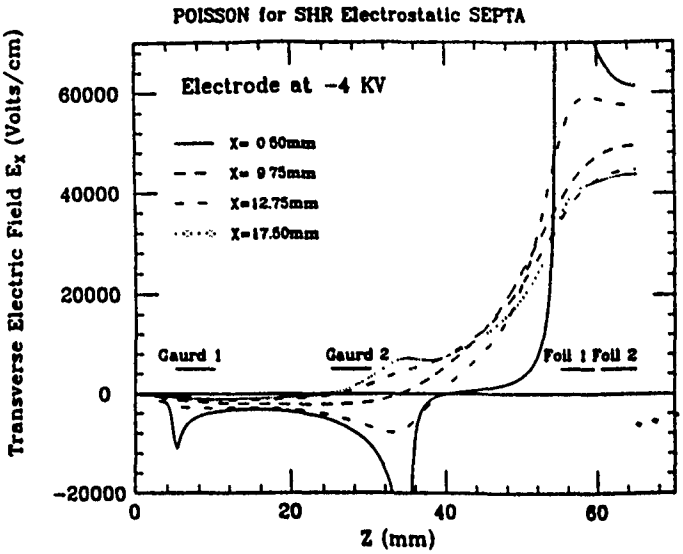


Figure 6: Transverse electric field of the entrance region of the septum for a range of X values, with anode at X=0.25 and foils at X=20 mm.

anode at 20 mm distance and a ground plane at 10 mm on the circulating beam side. We have studied this case for a range of electrode potentials from 0 to −4 KV. The equipotential lines for the case of −4KV are shown in Figure 5. The transverse electric field as a function of Z is shown in Figure 6 for a range of transverse positions X in the gap. The following observations can be made from these results:

- The additional electrode at V=0 reduces the electric field in the vicinity of the first guard foil, but the field still remains positive.
- For V=−1.0KV the electric field in the entrance region is negative in the lower half of the gap ($0 \leq X \leq 10.$) and is slightly positive in the upper half of the gap near the guard foils; this voltage is insufficient for confinement of the low energy electrons.
- For V=−4.0KV the electric field remains negative for all transverse distances across the gap near the first guard foil and becomes positive after the second guard foil.
- The integrated transverse field over the 65mm entrance region shows a variation across the gap which increases with increasing electrode voltage. The variation is about 1.% for V=0 V, and about 6.5% for V=−4 KV, still acceptable since the entrance effective field is less than 2 percent of the total effective field of the septum.
- At V=−4KV the sign and magnitudes of the longitudinal electric field (E_Z) helps to further confine the low energy electrons (longitudinally) to the entrance region.

5 Conclusions

For our configuration the following conclusions can be made:

1. In the "uniform" field region, the relative variation of the effective field as a function of transverse distance across the gap is better than 1×10^{-4}.
2. An addition of an electrode at negative voltage opposite the guard foils lowers the electric field near the guard foils but increases the effective field variation across the gap to about 1×10^{-3}. With the electrode at V=−4 KV both components of the electric field provide confinements of low energy electrons to the entrance region and away from the anode. While higher negative voltage increases the confinement, it also adds to the overall non-uniformity of the field.

References

[1] POISSON/SUPERFISH Group of Codes, Los Alamos Accelerator Code Group, LA-UR-87-115.

[2] J.B. Flanz et al., Proceedings of the 1989 IEEE Particle Accelerator Conference, March 20-23, 1989, p.34.

THE ULTRA-FAST INJECTION KICKER FOR SXLS*

Thomas J. Romano and Richard Heese
National Synchrotron Light Source
Brookhaven National Laboratory
Upton, New York

Abstract

The single bump injection scheme for the SXLS (Superconducting X-Ray Lithography Source) compact synchrotron required very stringent rise and fall time of no more than 15 nsec and a flat-top of 50-60 nsec. These parameters were achieved in a magnetic device of 75 cm length with a maximum field of 75 gauss. The construction and switching techniques along with the associated components will be described. Results of magnetic field measurements and measurements of the effect of the kicker on the injected beam will be presented. The device is presently working in the room-temperature magnet prototype of the SXLS ring and will be used as injection bump for the final superconducting compact synchrotron.

I. INTRODUCTION

The development of X-Ray lithography by the semiconductor industry will require a large flux of X-Rays at 10 Å wavelength from as small a source as possible. To achieve this goal, Brookhaven National Laboratory, with funding provided by DoD/DARPA is constructing a Superconducting X-Ray Lithography Source (SXLS), namely an 8.5 m circumference synchrotron that will be able to supply the required flux of X-Rays at 10 Å for a semiconductor production facility.[1-3] Because of space limitations on this compact machine, a single bump injection system was developed, requiring a fast kicker with a rise and fall time of 10-20 ns and a flat-top of 50 ns, which gives two horizontal kicks to the stored beam and one kick to the injected beam. The angular deflection of > 8 mrads for this device at an injection energy of 200 MeV, plus the limited space available for the magnet itself and the energy storage and trigger systems set the parameters of .75 m magnet length with a field strength of 7.5 x 10^{-3} T. Figure 1 shows the location of the kicker in the plan view of the warm prototype ring. It is located in the straight section opposite the injection septum and extends through the quadrupole-sextupole-quadupole triplet.

*Work performed under the auspices of the U.S. Department of Energy and funded by the Department of Defense.

0-7803-0135-8/91$01.00 ©IEEE

Currents in excess of 1,200 mA have been stored in this compact synchrotron.

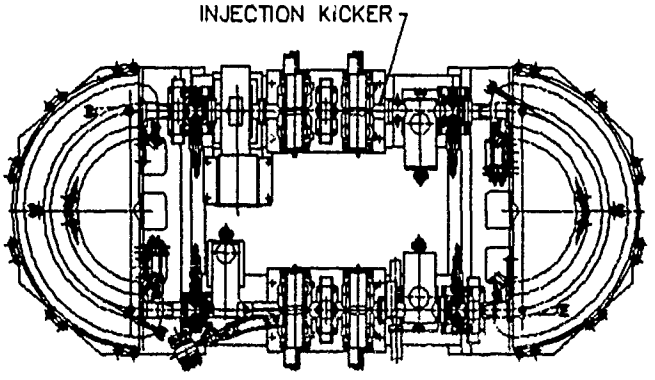


Fig. 1.

II. MAGNET CONSTRUCTION

The magnet is a single turn split cylinder, concentric with the stainless steel vacuum pipe, and is water-cooled. The water-cooling is not necessary from a power dissipation point of view; but the entire straight section will be used in the superconducting dipole version of this machine, where enough synchrotron radiation will strike the outer plate to cause a severe heating problem. Figure 2 shows a cut-away schematic view of the device.

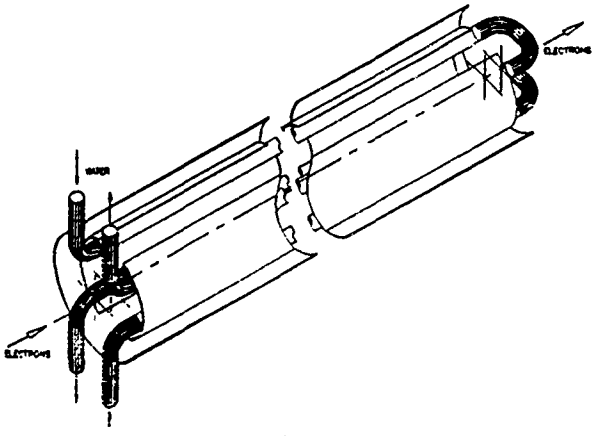
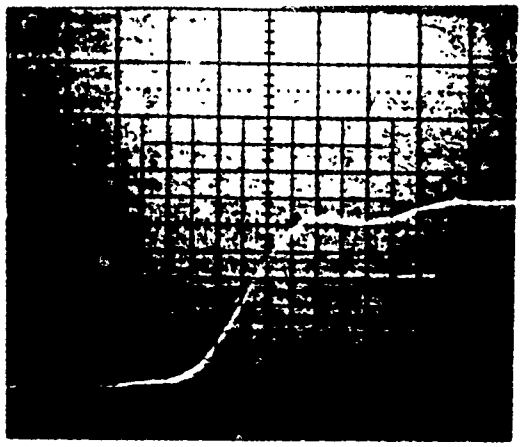


Fig. 2.

The magnet design is a result of several compromises. The angle subtended by the copper conductors are ± 30° from the horizontal instead of the expected ± 60°. This is to increase the field strength at the center of the magnet at the expense of field homogeneity. The large sextupole component of the field is offset somewhat by the overhang caused by the cooling pipes and by the image currents generated in the vacuum chamber walls. The spacing from the chamber walls was optimized to provide enough field versus providing sufficient horizontal aperture for the circulating electron beam. The 2-D magnet configuration was verified with POISSON.

III. MAGNET DRIVE SYSTEM

The switch tube selected for this circuit was the English Electric Valve Type CX1588, a hydrogen-filled ceramic thyratron. It was the only tube that proved capable of driving this device. It consistently exceeded its advertised current rate of rise (125 kA/μsec) and has exceedingly low timing jitter (~ 200 ps). Since we are operating the tube in the crowbar mode, it easily handles the 2000 Amperes at an energy storage voltage of 20,000 volts. Jitter and drift are major concerns; the filaments and reservoir are powered by regulated DC power supplies. To further increase stable operation, the tube is supplied with a 1500 V trigger pulse having a rate of rise of 65 V/ns (see Fig. 3).



10 ns/cm 500 V/cm
Fig. 3.

To achieve the rapid rise-time, the trigger circuit, consists of 20 Unitrode type GA301 SCR's in a series string. The circuit was adapted from the Unitrode Applications Handbook.[4]

To avoid introducing additional inductance, the thyratron and its energy storage capacitors were mounted coaxially in a copper cylinder directly connected to the beam pipe at the feedthrough location. Reverse current blocking diodes are mounted as close to the magnet as possible, and all connections are made with low-inductance copper strips. Needless to say, the placement of components is extremely critical and a considerable effort was expended to obtain the optimum magnet performance. The entire assembly of trigger and charging circuits was shielded to the maximum possible RFI specifications to avoid interference with the single turn beam position determination system.

IV. MAGNET PERFORMANCE

It proved extremely difficult to measure the fields produced at the pulse widths required by the design. Therefore, a much larger capacitance was connected to the magnet, resulting in a longer pulse length, thus enabling the calibration of the magnet to be determined with a known pick-up coil. The table below shows the field in gauss produced at three different pulse lengths and at three different currents:

	0.6 μsec	1.4 μsec	2.0 μsec
500 A	24.4	25.7	24.8
1000 A	48.6	52.0	49.6
1500 A	74.2	75.2	74.8

The calibration of the magnet is thus set at .05 gauss/A. This agreed with the estimates made with POISSON.

Current measurements during operation is made with a permanently mounted current transformer in the discharge path. Since this transformer will detect all currents through the diodes and magnet capacity to ground, it does not display the true current wave shape and is not used as such. It is only used as a peak current detector to verify the correct operation of the kicker.

The true performance of the kicker was determined by its effect on the injected electron beam in the SXLS synchrotron, by moving the time of firing of the kicker relative to the incoming electron bunch, and measuring resulting displacement on a fluorescent flag downstream of the magnet. Figure 4 shows the result of these measurements.

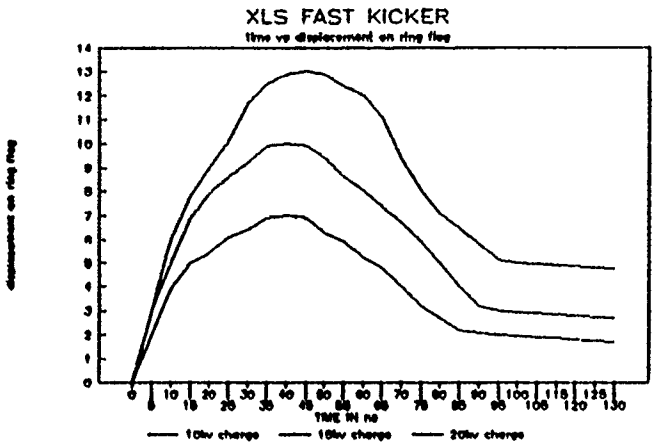


Fig. 4.

The kicker achieves 80% of its maximum value after 15 ns, has a "flat-top" of about 35 ns, and falls to 25% of its peak value in another 20 ns. The long, low-field tail, decaying in several hundred ns is probably flux "captured" in the beam pipe, and decays as the eddy currents decay. These small kicks do not harm the beam or the injected pulse. From a machine physics point of view, it is beneficial to have a slightly larger kick of the stored beam the second time; we normally operate that the first kick to the stored beam occurs at the 25 ns point, the second kick to the stored beam, and the first kick to the injected bunch then occurs at the 52 ns point. The third kick at $\approx$ 80 ns is not detrimental to the circulating beam.

V. CONCLUSIONS

A very difficult magnet needed to be developed to assure the successful performance of the compact synchrotron. This has been achieved, the maximum current injected into the SXLS machine has been in excess of 1200 mA, with injection rates of up to 10 mA per "shot", at a repetition rate of 0.67 Hz.

ACKNOWLEDGEMENTS

The authors would like to thank the NSLS mechanical group for the construction of the final device, and J. Krishnaswamy for helping with the magnetic measurements.

REFERENCES

1. J.B. Murphy, et al., this Proc. (1991).
2. R. Heese, S. Kalsi, E. Leung, this Proc. (1991).
3. J.B. Murphy, et al., Proc. 2nd European Particle Accelerator Conference, p.1828 (1990).
4. Unitrode Applications Handbook, Unitrode Corp., Lexington, MA 02173 (1987-88).

SLC KICKER MAGNET LIMITATIONS *

R. Cassel, A. Donaldson, T. Mattison
G. Bowden, J. Weaver, F. Bulos
Stanford Linear Accelerator Center,
Stanford, California 94309

and D. Fiander
CERN

Abstract

The SLC Damping Ring kicker magnets requires a fast magnetic field rise time of 58 nsec, a peak field of 800 gauss, a pulse amplitude stability of 0.01 %, and a reasonable operational lifetime. The original Kicker magnets designed by SLAC and at FERMI were not able to fulfil the SLC kicker requirements. Extensive studies were conducted to determine the limitation in the magnets, response of the ferrite in kicker magnet, and the modifications needed to improve the kicker magnet performance. The paper details the SLAC and FERMI kicker magnets limitation of performance.

Background

The SLAC, SLC damping rings not only require a fast kicker magnet rise time (58 nsec), wide pulse (100 nsec) a large kick (320 gauss-meters), and regulation requirements (0.01%) but the space allocated in the damping rings for the kickers was to short (46 cm) for a conservative kicker magnet design. The resulting high magnetic field of 800 Gauss requires the use of a ferrite loaded kicker magnet. With these restrictive parameters the magnet limitation become the performance driver in the kicker system. With the inherent jitter the thyratron used in the kicker systems (approximately +- 200 psec) the slope (dB/dt) of the kicker field at extraction time must be less than 0.05% /nsec compared to the peak dB/dt of approximately 3% /nsec to achieve the 58 nsec rise time.

Basic Physics of ferrite kickers

From basic physic principal it is clear to the first order that to proved the required magnetic kick, the energy required is proportional to the square of the magnetic kick amplitude, linear with the cross sectional area of the kicker field and inversely proportional to the length of the magnet.
Joules = $(\text{gauss-m})^2$*(area)/(length)
Therefore the shorter the magnet the more joules are required and with a fixed rise time, the more power is required. The minimum voltage needed on the kicker magnet however is related to the magnetic kick, the effective width of the gap and inversely to the rise time. Volts = (gauss-meters)* (effective width)/(rise time). What this first order equations infer is that the minimum voltage on a kicker magnet is independent of the length of the magnet or more important independent of any attempts that are made to change the impedances by adjusting the capacitance of the magnet or pulser. For the SLC case the absolute minimum voltage independent of the design is 20 kv with a minimum energy of approximately 1 joule. The only effective parameter to reduce the voltage needed on the magnet is to reduce the effective width of the gap. The minimum voltage or joules is fixed by these simple concepts. The actual values can be much larger depending on the design.

Magnet types.

The original SLAC kicker magnet was a slab ferrite construction using the ferrite as an isolator and attempting to use the ferrite capacitance to produce a transmission line magnet. Figure 1 It was not understood that this construction in fact dose not produce a transmission type magnet but a magnet that looks electrically like a lumped inductor. The reason for the lumped inductor effect is because the fields in the ferrite can travel lengthwise down the magnet which produces a field at the end of the magnet delayed only by the speed of light from the front of the magnet independent of the amount of capacitance.

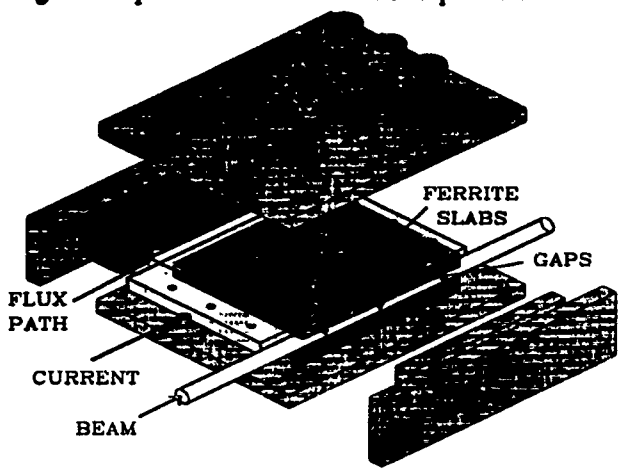


Figure 1
Slab SLAC Kicker Magnet

* Work performed under U.S. Department of Energy Contract DE-AC03-76SF00515

0-7803-0135-8/91$01.00 ©IEEE

The effect can clearly be seen by observing the delay of a pulse propagating in the magnet by probing the field along the magnet. Figure 2

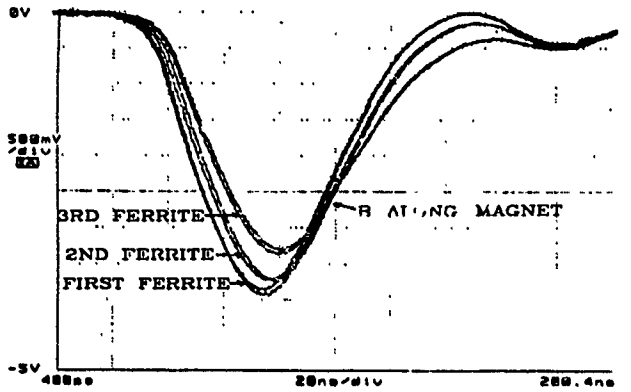


Figure 2
Three Ferrite Slab SLAC Kicker

A true propogation delay only occurs when there is a break in the ferrite. The effect on the magnetic field waveform of a lumped inductor magnet is to have the integral of the field rise with a exponential time constant determined by the effective magnet inductance divided by two time the line impedance. (t = L/2*Z) The exponential response means that without voltage pulsed wave shaping the magnetic field integral will take at least 4 time constants or approximately 80 nsec to be flat enough to meet the 0.01% stability requirement. This exponential behaver means that the SLAC magnet field waveform cannot be made flat enough to meet the specifications for the SLC electron damping ring. To produce a true transmission or delay line kicker magnet, the magnet must be divided into isolated section so that the magnetic field cannot propagate along the magnet without being delayed by the capacitance in the magnet. Figure 3

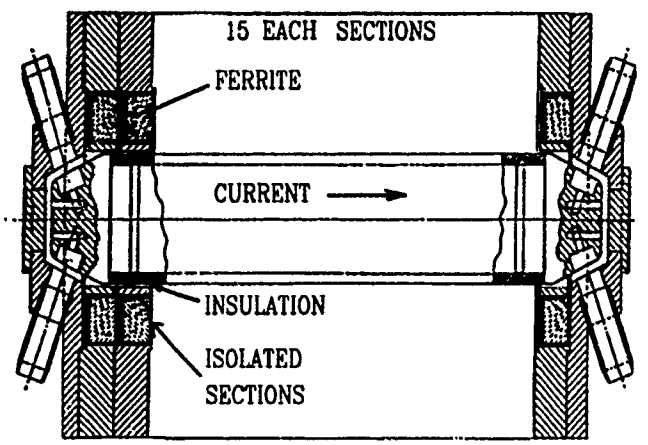


Figure 3
FERMI magnet design

The kicker magnet made by FERMI lab for SLC was of this type of construction and as expected it exhibits the propagation delay of transmission type magnet. Figure 4

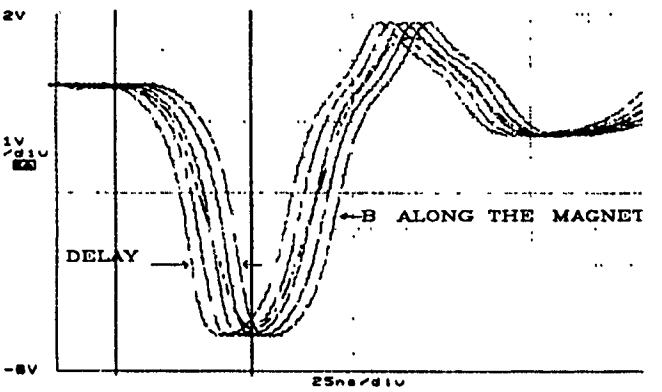


Figure 4
15 section FERMI Kicker

A transmission line is characterized by it impedance and delay. $Z^2 = L/C$ and $T^2 = L*C$ which infers that $T*Z=L$ For the FERMI magnet Z = 17 ohms and T > 30 nsec. Although the magnet transit time is short enough to meet the SLC requirements the magnet is not matched to the pulser cables which is 12.5 ohms. This results in a reflection from the load end which causes a rise in current at the end of the pulse producing an unacceptable dB/dt at the beginning of the pulse during extraction. (Figure 5)

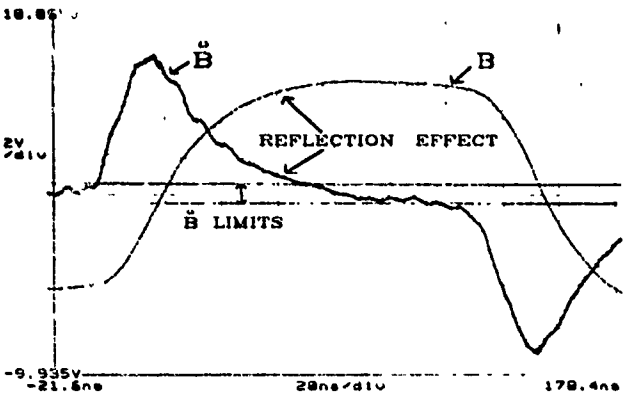


Figure 5
FERMI Mismatched Impedance

Both present kicker magnets SLAC and FERMI types produce an unacceptable dB/dt characteristic due to there inherent design deficiencies.

Ferrite material

In both the SLAC magnet and FERMI magnet the chose of ferrites and ferrite path length were not optimal. In the SLAC magnet the ferrite was chosen to have a high permeability, however the ferrite path length was made long in the believe that the additional capacitance would make the magnet a transmission line magnet. The combination of

high permeability and long path length results in a unacceptably high stored energy. The FERMI magnet use a low permeability thinking that the low permeability would be stable and help to match the impedance of the magnet to the pulser. In reality the change in permeability verse field strength was very large and that combined with the long ferrite path length selected to produce a large enough capacitance resulted in the magnet having to much stored energy and to high characteristic impedance. The high impedance causes an increase in field at the end of the pulse due to a reflection from the load cables. The ferrite material and path length chosen did not proved the performance required.
The preferred ferrite design would be to have a high permeability ferrite and a short path length to maximize the fields and at the same time minimize impedance changes due to changes in permeability.

There was considerable concern that the frequency response losses or dispersion in the ferrite was causing the problems with magnet shape. Simulation were made and tests performed to establish these effects. Although dispersion is evident in all the ferrites when the rise time is made fast enough, the dispersion effects and frequency response are secondary to impedance mismatch and lumped inductor effects.
There has been no indication that the ferrites losses or frequency response is effecting the pulse shape substantially and that if the impedance is corrected the magnetic response will not be adequate.

Stray Fields

Another effect which was overlooked is stray magnetic fields. Stray fields in the FERMI magnet are much larger then expected. The result is a larger stored energy in the magnet and therefor a longer transit time than expected. Field plots of the FERMI kicker magnet revealed that field penetrated the gaps in the structure and increases the transit time by as much as 20%. (Figure 6) Unfortunately very little can be done to eliminate these fields since they are inherent in the design mechanical design.

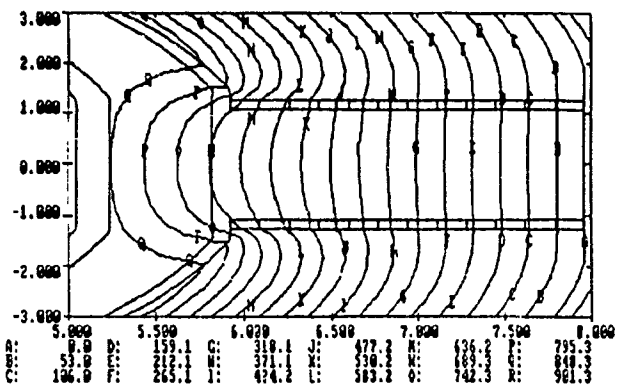


Figure 6
Stray Fields in FERMI Kicker

Field compression

The stored energy or the transit time of the magnet can be reduced by a small amount without changing the central magnetic field by reducing the effective width of the field. This was accomplished by what we call a flux gasket. The gap magnetic fields are restricted by a small amount at the top and bottom of the gap by use of a conductor. With the short pulses of the kicker a conductor can shields and shapes the magnetic field. The results of the flux gasket is to reduce the stored energy by a small amount which decreases the transit time of the magnet. (Figure 7)

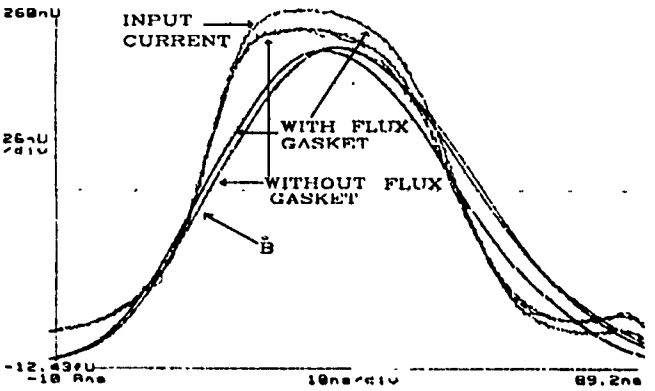


Figure 7
Flux Gasket Delay Change

Conclusion

The SLC kicker magnetic pulse shape problems are in essence design problems of not including what constitutes a transmission type magnet, under estimating the effect of changes in permeability of the ferrite, and not appreciating the amount of stray inductance in the magnet. The short magnet length compounded the problems by requiring more current and thereby a lower magnet impedance. With this accumulated design knowledge we have been able to designed a new magnet which takes into account all of these shortcomings producing a magnet which is match to the pulser and a transmission type magnet.

To every complex problem there is an answer that is simple, neat and Wrong.

References

[1] F. Bulos, et al., "Some Fast Beam Kicker Magnet Systems at SLAC", Proceedings of the 1987 IEEE Particle Accelerator Conference, p. 1884.

[2] T. Mattison, et al., "Operational Experience with SLC Damping Ring Kickers", elsewhere in these Proceedings.

[3] T. Mattison, et al., "Status of the SLC Damping Ring Kickers Systems", elsewhere in these Proceedings.

THE BOOSTER-TO-AGS BEAM TRANSFER FAST KICKER MODULATORS[1]

W. Zhang, J. Bunicci, W.W. Frey, A.V. Soukas, and S.Y. Zhang

AGS Department, Brookhaven National Laboratory, Upton, NY 11973

ABSTRACT

This work describes modulator developments for the Brookhaven Booster extraction and the AGS injection fast kickers. The modulators are projected for both proton and heavy ion operation. The equivalent load inductance is about 2.1 to 2.3 μH for each modulator. The PFN voltage is required to be below 40 kV for operation in air. The rise time of the pulse for proton beam transfer is 120 ns up to 97% of full current (1000 A), and for heavy ion beam transfer, the requirement is 160 ns up to 98% of full current (1615 A). During the fourth batch transfer of the proton beam from the Booster to AGS, the pulse fall time of the AGS injection fast kicker has to be very fast (< 140 ns), so that it does not appreciably deflect the first batch of injected protons that is circulating in the AGS. To achieve the design specifications, an extensive development effort has been pursued, including distributed parameter estimation and measurement, computer aided analysis and design, pulse shaping and tail-biting circuit test, proto-type construction, etc. The test results will be presented.

INTRODUCTION

The Brookhaven AGS Booster will serve as a multifunction synchrotron injector for the AGS, capable of accelerating protons from 200 Mev, the Linac operating energy, to 1.5 Gev, at a maximum repetition rate of 7.5 Hz (4 pulses/AGS pulse). The Booster is also capable of accelerating heavy ions to a magnetic rigidity equal to 17.52 $Tesla-meters$, at < 1 Hz repetition rate (1 pulse/AGS pulse). Beam transfer from the Booster to the AGS will be bucket to bucket. There are three RF accelerating buckets in the Booster, and twelve in the AGS. During each pulse of proton beam transfer, three Booster proton bunches will be transferred to three of the twelve AGS buckets.

The AGS injection and Booster extraction kickers are the complementary system to each other. Centrally-fed picture frame lumped inductance ferrite magnets are used for both kickers. The kicker parameters are listed in Table 1 and 2. The Booster magnet must be capable of being baked up to temperatures of 250 $^{\circ}C$, since the Booster operating vacuum is in the 10^{-11} $Torr$ range.

Table 1 - AGS INJECTION KICKER PARAMETERS

	Proton	Heavy Ion
Rigidity	7.51 $T-m$	11 $T-m$
Strength	3 $mrad$	3 $mrad$
Rise time	120 ns (*to* 97%)	160 ns (*to* 98%)
Pulse length	600 ns	1000 ns
Fall time	140 ns	$<$2300 ns
Pulse overshoot	3%	2%
Flat top ripple	$<$3%	$<$2%
PFN voltage	30 kV	42 kV
Peak current	1006 A	1473 A

Table 2 - BOOSTER EXTRACTION KICKER PARAMETERS

	Proton	Heavy Ion
Rigidity	7.51 $T-m$	11 $T-m$
Strength	5 $mrad$	3.8 $mrad$
Rise time	120 ns (*to* 97%)	160 ns (*to* 98%)
Pulse length	$>$600 ns	$>$1000 ns
Pulse overshoot	3%	2%
Flat top ripple	$<$3%	$<$2%
PFN voltage	30 kV	40 kV
Peak current	1000 A	1615 A

The AGS injection kicker consists of three lumped magnet sections with equal inductance, which will be driven by three identical pulsers. The Booster extraction kicker has a similar arrangement of four identical subsystems The load and loop stray inductance is about 2.1 μH for each AGS injection subsystem and 2.35 μH for each Booster extraction subsystem.

[1] Work performed under the auspices of the US Department of Energy

0-7803-0135-8/91$01.00 ©IEEE

SYSTEM DESCRIPTION

The modulators are basically E-type pulse forming networks with equal capacitance and equal inductance for each section. The PFN voltage is required to be about 40 kV or below for operation in air To meet the different kicker current and rise time requirements of proton and heavy ion operation, a terminating resistor is switched to match and mismatch the pulse forming network impedance.

The pulse front edge sharpening is accomplished by using two R-C compensation networks. The $R_a - C_a$ in parallel with the first PFN capacitor is an energy compensation network. It provides additional energy needed to build up the current in the load magnet during the later portion of the pulse rise period. The proper selection of R_a will give a fast rising front edge current with an acceptable overshoot or even without an overshoot.

A sink network $R_b - C_b$ is used in parallel with the matching resistor. The capacitance C_b together with the magnet inductance constitute a resonant network that reduces the resistance to the energy discharging of the PFN front edge capacitor during the pulse rising period. The damping resistor R_b is used to avoid possible oscillation in the $L-C$ network, and its value should be much smaller than that of the impedance matching resistor. During the flat top of the pulse, both C_a and C_b hold at a constant voltage, therefore the pulse flat top is not affected. Figure 1 (a) shows the current waveform of the proto-module of the Booster extraction kicker, and (b) the magnetic field waveform of the proto-magnet. The Booster extraction kicker modulators have been constructed, and are presently in the installation process.

In addition to the fast rise time and low ripple flat top, the pulse fall time of the AGS injection kicker has to be less than 140 ns, for proton injection. A test pulser, based on a circuit improved from a schematic

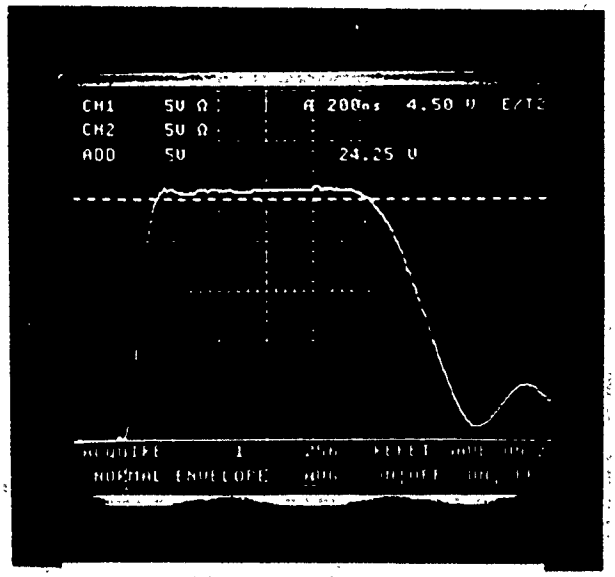


Figure 1 (a). Current puise waveform.

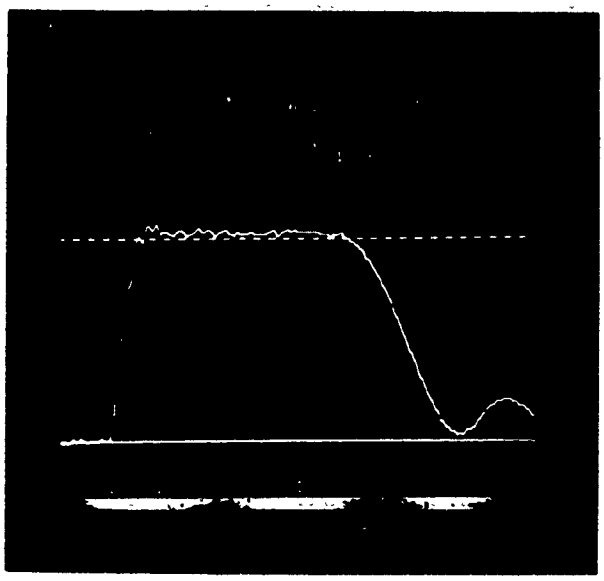


Figure 1 (b). Magnetic field waveform.

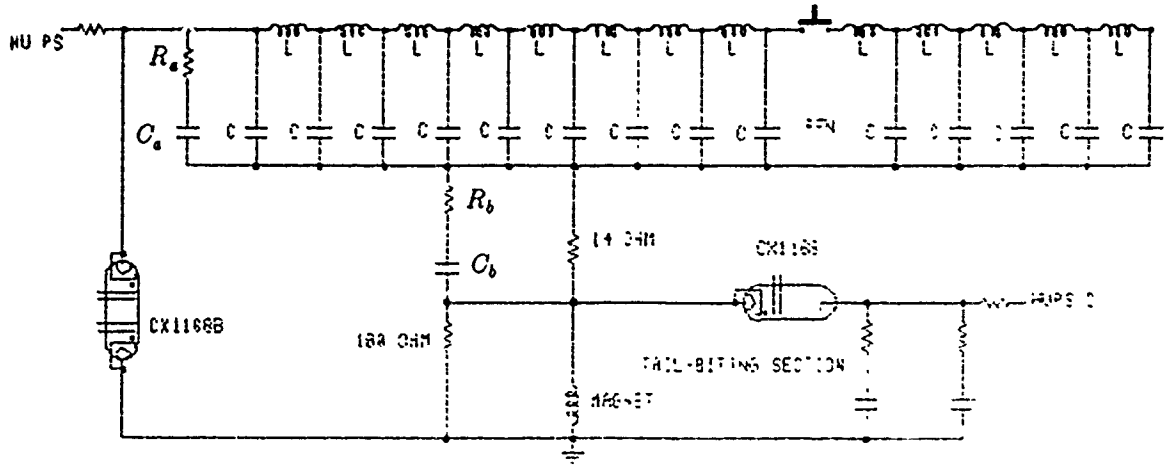


Figure 3. AGS injection fast kicker modulator

in [2], has been simulated, constructed and tested. The EEV CX-1154 thyratrons were used as the main switch and tail-bitting switch. This test unit has been powered up to 25 kV, and about 900 A including the tail-bitting function. Figure 2 shows a typical current pulse fall time obtained in this test unit. The construction unit will use two gap thyratrons to increase voltage hold-off capability. Figure 3 is the schematic diagram of the AGS injection fast kicker modulator.

The three modules of the AGS injection fast kicker are being built. Figure 4 shows a current waveform from one of the modules with fast fall time. However, the unit was tested only up to 500 A, due to noise problems. Since the modulators will be mounted inside the AGS ring, limited space makes it very difficult for package design. The width of each modulator is only 1 foot. The present package design eliminated all thyratron shieldings, which may result in lowering the noise immunity of the floating deck structure of the tail-bitting thyratron. Other factors such as grounding design and trigger scheme may also contribute to the noise problems. Some design changes including an auxiliary trigger circuit of the tail-bitting thyratron, grounding, packaging, and the possible interchange of circuit locations of the main and tail-bitting sections are being considered. Testing will resume soon after the Booster installation is completed.

Computer aided design and analysis have been used heavily for the modulator development. The pulse distortion due to distributed capacitance and inductance has been investigated by computer simulation and actual test. The test results and simulations have been agreed very well. Some results are included in references [3, 5] MICRO-CAP (I,II,III) and $MATRIX_X$ are used for computer simulation[2].

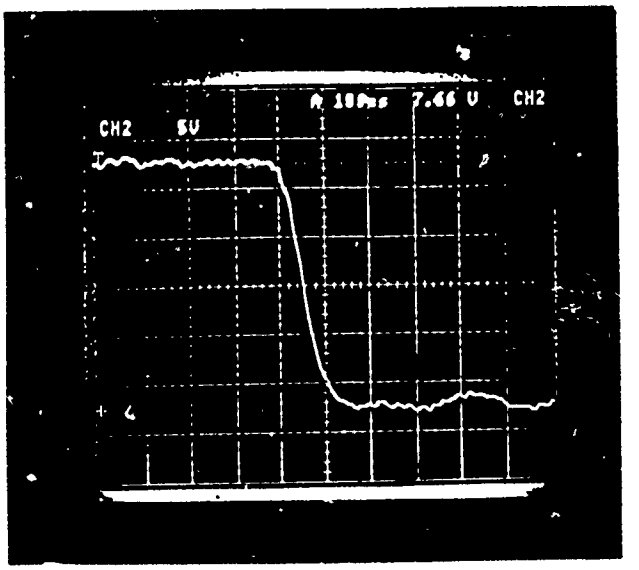


Figure 2. Current pulse falling edge with tail-bitting.

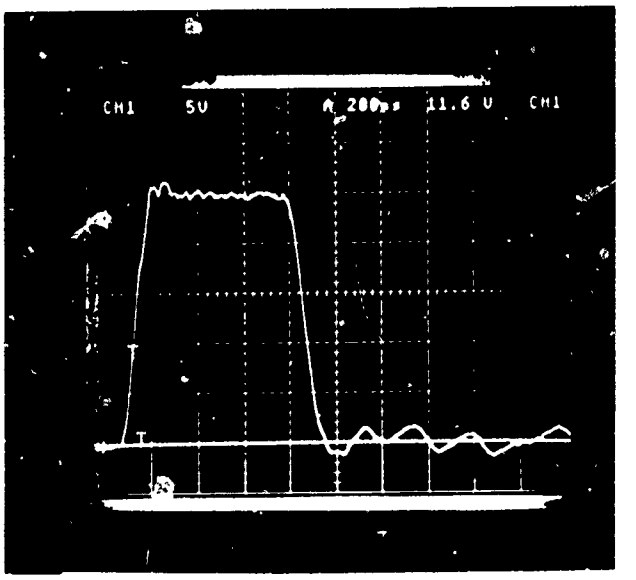


Figure 4. Current pulse waveform with tail-bitting

REFERENCES

[1] "Booster Design Manual," AGS Booster Project, Brookhaven National Laboratory, 1988.

[2] J. Pachner, Jr., "A Pulsed Ferrite Inflector for the Emittance Measuring Device of the Chalk River High Current Facility," Proc., 1973 PAC.

[3] W. Zhang, et al., "Test Fast Kicker Pulser," Proc., 7th IEEE PPC, 1989.

[4] W. Zhang, et al., "Test Modulator of AGS Injection Fast Kicker," IEEE Conf. Rec., 19th PMS, 1990.

[5] W. Zhang, et al., "Report on the Test and Measurement of the Fast Kicker System," AD Booster tech. note #133, BNL, 1989.

[2] MICRO-CAP is a product of Spectrum Software, Inc., Sunnyvale, CA 94086 $MATRIX_X$ is a trademark of Integrated Systems Inc., Santa Clara, CA 95054

On the Design of Beam Absorbers for the SSC

Brett Parker

Accelerator Design and Operation Division
Superconducting Super Collider Laboratory*
2550 Beckleymeade Avenue
Dallas, TX 75237, USA

Abstract

The 20 TeV beam absorbers for the Superconducting Super Collider (SSC) present a formidable design challenge. Protons from the SSC will have: 20 times the energy, be 20 times harder to bend, and be distributed with a natural transvers-size $\sqrt{20}$ times smaller than from all previous accelerators. This paper concentrates on the thermo-physical demands made on a beam backstop in terminating 20 TeV protons. In particular radiation-shielding, logic, control, and beam diagnostic requirements will not be discussed[1]. We will report on Monte Carlo simulations, made using the MARS10 code of N. Mokhov[2], which provides a basis for evaluating beam spreading and painting scenarios. The merits of various standard painting schemes are then discussed. Finally we present some new options for spreading the beam spot which are currently under investigation.

1. INTRODUCTION

The SSC parameters relevant to the design of beam absorbers are shown in Table 1. Note that the product of the energy per proton and the number of protons per beam gives a circulating energy of 420 megajoules for each collider ring. This kinetic energy is roughly equivalent to the amount dissipated in an 850 car freeway chain-reaction accident; obviously this much energy must be absorbed in a controlled, safe and reliable way.

Table 1.
SSC Parameters Relevant to Beam Absorber Design

Proton Energy	2-20 TeV
Design Luminosity	10^{33}
Circumference	87.12 km
Revolution Time	290 μs
Abort Gap	3 μs
Fractional Momentum Spread	$\sim 6 \times 10^{-5}$
Bunch Length	5-6 cm
Bunch Spacing	5 m
Number of Bunches Per Ring	17,424
Protons Per Bunch	$3/4 \times 10^{10}$
Protons Per Ring	1.3×10^{14}

The beam-abort system is specified to be fast-acting and capable of single-turn (~300 μs) extraction of the entire beam from a ring within three turns of the generation of an abort signal[1]. Fast kicker magnets will dispatch the beam through the field-free region of a string of Lambertson-style septum magnets, down a separate ~2 km long channel and ' .. multi-layer beam backstop. The central backstop-core will consist of graphite 10 m in extent and 2 m in diameter. Surrounding the graphite will be additional radiation-shielding and monitoring devices. Graphite will be used for the core-region both to diminish the long-term production of residual radioactivity and to maximize design-robustness (by longitudinally spreading the shower energy-deposition).

2. METHODOLOGY

The high-energy cascade showers resulting from 20 TeV protons are simulated using the MARS series of computer code of N. Mokhov[2]. The current version, MARS12, runs efficiently under VMS™, DOS and UNIX™ operating systems on several different computers. The MARS code reproduces existing inclusive particle-spectra from Tevatron energies through thermal-neutron capture[3,4]. A comparison, shown in Figure 1, made between MARS and the codes FLUKA87[5] and CASIM[6] exhibits good agreement[4].

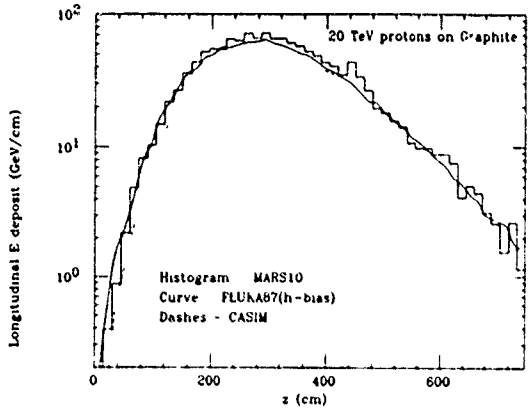


Fig. 1. The longitudinal energy deposition (GeV/cm) for 20 TeV protons incident on graphite calculated using MARS10 (histogram), FLUKA87 (curve) and CASIM (dash)[4].

Recent calculations, made with a new GHEISHA/GEANT version, are also in agreement with MARS results[7]. Since the physics of shower-cascades scales as $\log(s)$, (s = total energy squared) our predictions for energy-deposition in the beam backstop should be reliable; this is in contrast to the situation for processes, which are much more sensitive to details of exclusive reaction channels, such as muon-production at the SSC interaction points.

*Operated by Universities Research Association, Inc., for the U.S. Department of Energy under Contract No. DE-AC0289ER40486.

U.S. Government work not protected by U.S. Copyright.

We present results for the instantaneous temperature rise, derived from a material's thermo-physical properties (i.e. enthalpy reserve = heat needed to raise material's temperature) under the premise that the energy is deposited everywhere at the same instant in time. Such an approximation is suitable for the short, 290 μs, beam spill time and facilitates the interpretation of beam heating in terms of temperature cracking or melting limits.

3. RESULTS

For the core of the beam backstop, it is desirable to choose a material with a high cracking/melting temperature and low density (to spread the shower longitudinally as much as possible); for these reasons, graphite is a natural choice. Carbon's low atomic number, also helps to reduce the amount of long-term induced radioactivity due to spallation fragments. A reference plot of $\Delta T(r,z)$, the radially-symetric temperature distribution, due to a round-Gaussian (σ=10cm) beam profile incident along the axis of a graphite core, is shown in Figure 2. for 1.3×10^{14} protons ($=10^{33}$ luminosity).

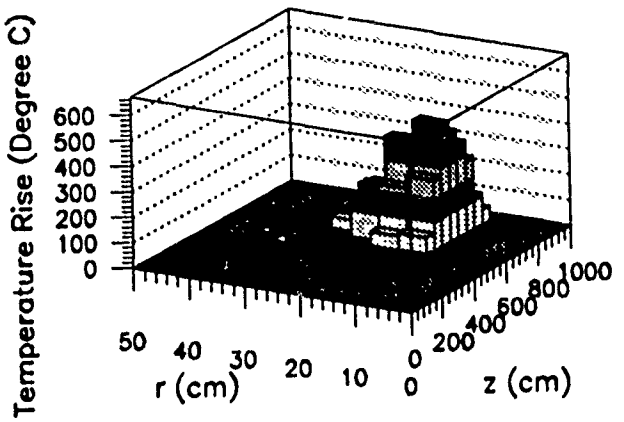


Fig. 2. Radially-symetric temperature rise calculated for 1.3×10^{14} protons incident on graphite for a round-Gaussian beam profile and 20 TeV. The heating-maximum, 670° C, occurs on axis at 250—300 cm longitudinal distance.

Along the z-axis, where the beam is most intense, the temperature profile follows the longitudinal energy deposition curve shown in Figure 1 and away from the axis the temperature rise is modulated by the assumed Gaussian beam profile. For this and subsequent comparisons, in each case, we have made simulations for 17k incident protons which yields few percent statistical errors at the shower maximum. Note that as the hadronic (and electromagnetic) shower starts, there is a rapid rise in the rate of energy deposition followed by a maximum that is reached about 3 m (or 7 interaction lengths) spanning a length of 3 m.

For a fixed beam intensity, the variation of the maximum instantaneous-heating with beam size is shown in Figure 3. Since a material's specific heat varies with temperature, the integration of its specific heat curve, its enthalpy reserve, will not be a linear function of temperature change for large changes. The con olution, for graphite, between its enthalpy reserve and a σ^2 variation of beam size gives an approximate $\sigma^{-4/3}$ scaling. A relevant design limit (ΔT = 2300° for graphite) known as the fracture limit is indicated on Figure 3.

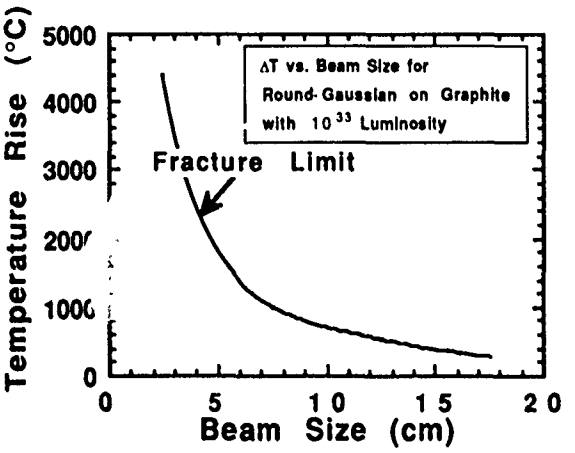


Fig. 3. Temperature rise as a function of beam σ for 1.3×10^{14} protons incident on graphite at 20 TeV .

This limit, which is lower that graphite's melting point, comes from thermal shock considerations[8]. It is prudent to maintain an operating margin that reflects systematic uncertainties in the simulation and so as not to preclude future luminosity (via beam current) upgrades.

A 10 cm beam spot, obtained from magnetic quadrupole-focusing, satisfies the above; however, a prohibitive amount of defocusing strength is required because of the SSC (~.1 mm) beam size and momentum. An extension is to defocus asymmetrically in one dimension (horizontal) and sweep the beam spot with a slow kicker magnet in the other transvers dimension (vertical). Unfortunately, the presence of too large a magnification in any plane drives a need for unacceptably large abort line apertures. One is soon led to consider beam painting schemes. In Figure 4 we show a beam profile that corresponds to the baseline CDR[1] "spiral kicker" scheme. For the CDR approach one uses two set of orthoginal, fast damped-magnetic kickers, along with limited magnification, to move the beam spot on the backstop face. Note that the damping causes beam pileup on the inner face of the spiral which sets an inner limit for painting. Also if the phase relationship of between the orthoginal kickers of 90° is not maintained, an oval beam spot (as shown in Figure 5) results.

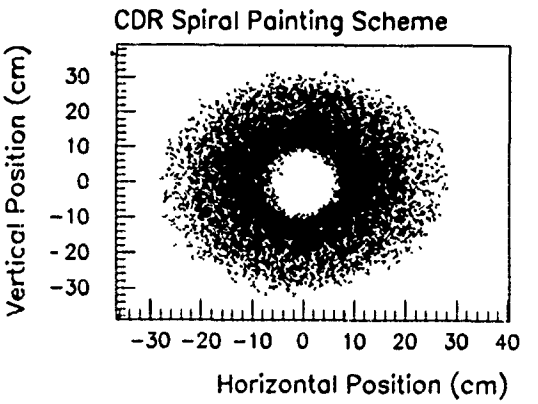


Fig. 4. Nominal beam profile for CDR spiral painting scheme.

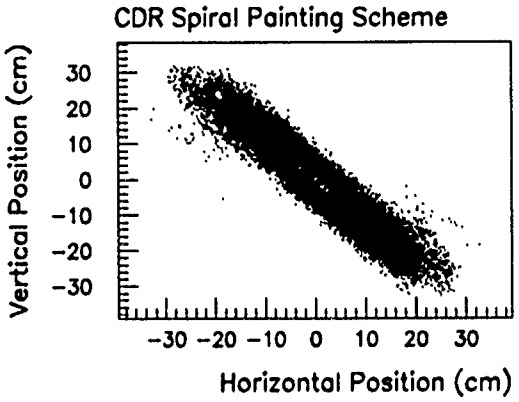


Fig. 5. CDR spiral painting with phase slippage.

A raster-pattern (shown in Figure 6) can be created via a combination of fast and slow kickers. Such a painting scheme with less needed fast-kicker strength and vastly reduced sensitivity to phase errors, is expected to be more reliable than the CDR spiral plan; however, there is some beam pile up near the outer edges of the raster pattern.

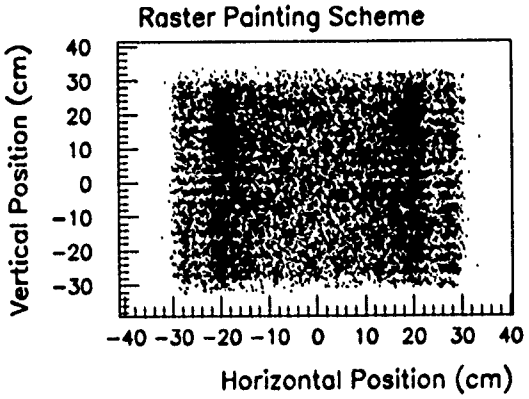


Fig. 6. Beam profile for raster painting scheme.

Attempts have been made to mitigate this edge concentration by the addition of nonlinear (sextupole, octupole etc.) magnetic elements to the abort channel in a manner similar to that suggested by B. Blind[9]. The addition of nonlinearities, while helpful in spreading (or folding) the pattern edges, reintroduces some sensitivity to initial beam position offsets at the beginning of the abort channel. The addition of a short sextupole would be beneficial if it is found convenient to have moderate kicker damping (~20% over the 300 μs spill). A properly placed sextupole could be used to "square up" the resulting trapazoidal-shape raster pattern (Figure not shown).

It has been suggested to place a series of thin targets well upstream of the beam backstop to further spread the beam; however, simulations show that a few radiation lengths of material will add little, about a μradian, to the beam divergence at 20 TeV. Such a plan would place an intense radiation source undesirably close to the collider tunnel.

4. FUTURE PROSPECTS & CONCLUSIONS

At present a raster-scan based technique is the most promising and budget-friendly approach. Future detailed design work calculations will revisit: shielding and radiation requirements, muon vectors etc. Also work is underway to investigate the feasibility of using unconventional components to eliminate either the kicker magnets or the conventional quadrupoles.

Preliminary studies using the code TBCI[10] suggest it might be possible to use the beam's wake-field to excite transverse-deflection modes of a passive beam-tube insert. We are examining candidates in terms of enhancing wake-field effects. If a suitable, simple and inexpensive structure is found, one could imagine repeating said structure many (10^3—10^4) times near the beginning of the abort channel. With sufficient repetition and enough bunches participating (a modest faction of 17,000), a useful increase of beam emittance may be possible. Such a passive "beam-spoiler" has the advantage of being fail safe. Also the magnitude of the effect would automatically track increases in beam current for upgrades.

For the conventional quadrupole magnets, which must be powered continuously, one might consider using a plasma lens[11] or pulsed quadrupole[12]. Some of the very effects that limit the applicability of these devices (beam-plasma scattering and nonlinear aberrations) would be beneficial in this case. The tradeoff for such devices would be betwe reduced power consumption vs. an increased system complexity. Maybe the ultimate (pie in the sky) beam-spoiler could use a self-excited plasma inside a self-excited cavity; who knows.

References

[1] "SSC Conceptual Design Report," SSC-SR-2020, March 1986; Task Force Report, J. D. Jackson, Editor, "SSC Environmental Radiation Shielding," SSC-SR-1026, July 1987; "SSC Site-Specific Conceptual Design," SSCL-SR-1056, July 1990.

[2] N. Mokhov, "The MARS10 Code System," Fermilab FN-509, 1989.

[3] N. Mokhov, Sov. J. Part. Nucl., Vol. 18(5), pp. 408-426, 1987.

[4] N. Mokhov , in "Radiation Levels in the SSC Interaction Regions," SSC-SR-1033, pp 303-311, 1988.

[5] P. Aarnio *et al.*, CERN TIS-RP/190, 1987.

[6] A. Van Ginneken, Fermilab FN-272, 1975.

[7] N. Mokhov and Igor Azhgirey, Institute for High Energy Physics, Protvino, USSR, Private Comm.

[8] J. Kidd *et al.*, IEEE Transactions on Nuclear Science, Vol. NS-28, No. 3, June 1981.

[9] B. Blind, "Generation of a Rectangular Beam Distribution for Irradiation of the Accelerator Production of Tritium Target," Los Alamos preprint LA-UR-90-2759, 1990.

[10] Th. Weiland, computer code TBCI, DESY, 2000 Hamburg 52, Notkestr. 85, Germany, copyright 1986.

[11] G. Le Dallic *et al.*, "First Test Results from the New CERN Plasma Lens," preprint; J. Cristiansen *et al.*, CERN Report, CERN/PS/84-10, 1984.

[12] M. Modena, P. Sievers, CERN/AT-MA/90-22, 1990.

Thyristor Converter Simulation and Analysis

S. Y. Zhang

AGS Department, Brookhaven National Laboratory
Upton, NY 11973

Abstract- In this paper we present a simulation on thyristor converters. The simulation features nonlinearity, non-uniform firing, and the commutations. Several applications such as a current regulation, a converter frequency characteristics analysis, and a power line disturbance analysis will be presented.

I. Introduction

A thyristor converter is often modeled as a zero-order hold, a first order or second order Pade approximations, or a time delay. The applications of these models are restrictive according to the circumstances. First of all, the thyristor converter is a device that is in nature controlled by firings. Therefore the converter is a nonuniformly sampling element. Secondly, the sampled bridge sine waveforms produce different small signal gains according to the firing angles and the converter voltage output levels In the third, other phenomena such as commutations sometimes change the converter phase and gain characteristics dramatically.

To a large class of thyristor converter applications we may eventually need a simulation that helps in the analysis as well as in the system design.

In this paper we present a simulation programmed in a high level language MATLAB. The MATLAB is basically designed for linear system analysis and signal processing. The simulation package consists of two aspects. One aspect represents the nonlinearities of the converter caused by the bridge waveforms, thyristor firings, and commutations, and another aspect contains the linear system analysis and signal processing.

We also present in this paper with some applications such as a current regulation analysis, an analysis of the converter frequency characteristics, and an analysis of the power line disturbance effect for a thyristor converter magnet driver.

Work performed under the auspices of the U.S Department of Energy

0-7803-0135-8/91$01.00 ©IEEE

II. Simulation

In the thyristor converter simulation, we adopt the ramp comparator firing principle. The simulations are based on a 3 phase AC power supply system, and the fundamental parameters for the converter simulation can be listed as the follows. 1). Number of pulse. 2). Amplitude and phase of the bridge sine waveform for each phase or each pulse. 3). Simulation steps and times. 4). Fundamental bridge waveform frequency. 5). Firing range. 6). Ramp slope. 7). Ramp position. 8). Input signal.

With a setting of all these parameters, we can have a fundamental simulation that does not include any commutation, distortion, and voltage or current regulations. Since the commutation affects the system power factor, the voltage ripple, and causes additional phase delay in the regulation loops, it is important in the thyristor power conversion system analysis. Taking advantage of the computing, we use prevalent conditions in the simulation to determine the commutation. For example, at each step we update the load current by using the linear system analysis commands and then use it along with the bridge voltage waveform to calculate the commutation. Thus, possible errors generated from the converter output current and voltage estimations can be eliminated.

The parameters that are necessary in the converter simulation with commutations are the follows. 9). Load transfer function. 10). Bridge line inductances. Also possible the circuit resistances and the thyristor voltage drops.

Very often a converter is controlled by either a voltage or a current regulation loop. To simulate a high order dynamic system that includes nonlinear components is a hard task. For a thyristor converter, however, there exists a simple solution. It is interesting to notice that after firing the converter voltage is simply determined by the bridge sine waveform until the next firing This provides considerable convenience in the converter regulation simulation. Taking the advantage, the simulation is in fact executed periodically alike an open loop calculation that saves significant computations and therefore gives rise to a

possibility to realize the simulation.

The parameters necessary for the regulated converter simulation are therefore the follows. 11). The transfer function of the voltage senser and the filter. 12). The transfer function of the regulator.

With all these parameters defined, in Fig.1 we show the simulation for a 24 pulse converter that is controlled by a voltage feedback loop and is driving a magnet. Fig.1a is with a low loop gain, and Fig.1b shows the result with high loop gain.

III. Current Regulation

We simulate a 12 pulse converter current regulation system under certain conditions. In this simulation, using popular models to the thyristor converter such as the first order phase delay and the second Pade approximations to the time delay with the statistical sampling time gives rise to untrue stability margin and oscillation frequency.

In fact, the models used to analyze the system should be modified according to the operation conditions that include the number of pulse, the converter voltage output, the bridge voltage, and the commutations. In this simulation, for example, the results are quite different if we include the effect of the commutations. In Fig.2 we show the two converter current waveforms with the same conditions except the latter is with a current commutation, that helps to stabilize the system. We may conclude that in a system analysis which utilizes models the converter simulation can be used to modify a model and then use it to verify the design.

IV. Frequency Characteristics

It is often of interest to know the thyristor converter frequency response characteristics. These properties include the phase delay and gain variation to signals with different frequencies, i.e. the Bode plot; the phase delay and gain variation to signals with the same frequency but different phases; and the gain variation at different converter voltage output levels. With digital Fourier transform, the simulation provides a possibility for a thorough study of these issues.

Due to the limited data available in the simulation, the analysis technique is different from the real time test. The following problems deserve attentions in the frequency domain analysis.

The error introduced in the digital Fourier transform usually belongs to the picket-fence effect, the aliasing and the leakage. Letting the sampling time be very small compared with the interested signal frequencies and enlarging the sampling data number can easily solve all the problem. Unfortunately both implies to increase the number of the data, and that is a difficult object in simulation. It is therefore necessary to find a solution that will suit the conditions in the simulation and yield only tolerable errors. First, we should define a number of simulation steps that is suitable for FFT package. Secondly, we should define a sampling period that along with the sampling data number gives rise to a frequency resolution that matches the input signals. This will greatly reduce the error caused by the picket-fence effect and the leakage. Third, of course, the useful signals in the analysis should be placed close to the origin of the frequency range of the Fourier analysis in order to avoid possible aliasing.

V. Power Line Disturbance Simulation

A thyristor converter directly powered from the power line is sensitive to the variations from the power grid and the local power stations. Due to the limited converter sampling frequency the disturbances may affect the load current immediately and then the disturbance is corrected gradually by regulations. A test for the effect of such a disturbance is difficult, while a simulation becomes a straightforward means in the analysis.

To reject the power line disturbances, a voltage regulation loop becomes necessary. We show an example for a sophisticated converter system that is proposed for the Brookhaven AGS Booster Accelerator main magnet. The system consists of 6 stations, each station is a 1000V 24 pulse converter. In the operation, the stations turn on subsequently, and when the magnet current reaches the peak the converters turn to energy invert. The magnet current repeatability requirement is very critical to the particle beam extraction and therefore the power line disturbance should be eliminated to the minimum. In Fig.3, we show the simulated converter voltage output waveform. In Fig.4, we show the magnet current error ratio due to a 1 percent step power line disturbance that occurred at 8ms from the beginning of the cycle, that present a 0.12 percent repeatability for the disturbance. We may conclude that some other technique is necessary in order to further improve the magnet current repeatability that is required to be under 0.1 percent.

References

[1] E. A. Parrish and E. S. McVey, "A theoretical model for single-phase silican controlled rectifier systems," *IEEE Trans. Automat. Contr.*, vol AC-12, pp 577-579, 1967.

[2] L. R. Rabiner and C. M Rader, "Digital Signal Processing," IEEE Press, New York, 1972

[3] Rohrmayer, "Operation of Accelerators directly off the utility systems," *IEEE Trans. Nucl. Sci*, vol NS-11, 1967.

[4] D Wolff, H Pfeffer, C. Briegel and J Dinkel, "Improving regulation in the Fermilab main ring magnet power supply system," *IEEE Trans. Nucl Sci*, vol NS-28, pp 3088-3090, 1981

Figure Captions

Fig. 1a Converter Voltage Waveform with Low Loop Gain

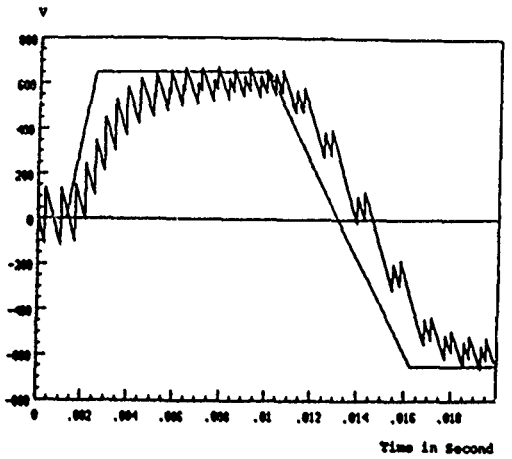


Fig. 1b Converter Voltage Waveform with High Loop gain

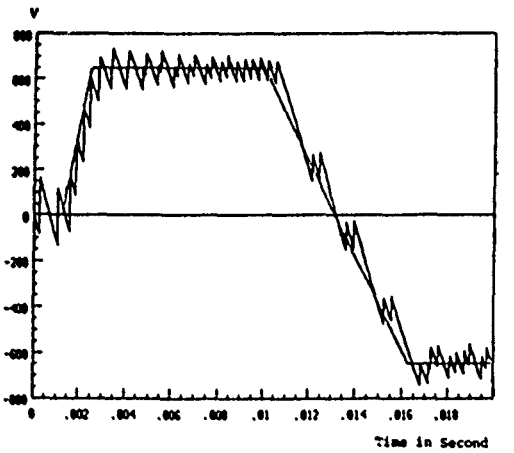


Fig. 2a Current Regulation, without Commutation. From Top to Bottom, Gain is from Low to High.

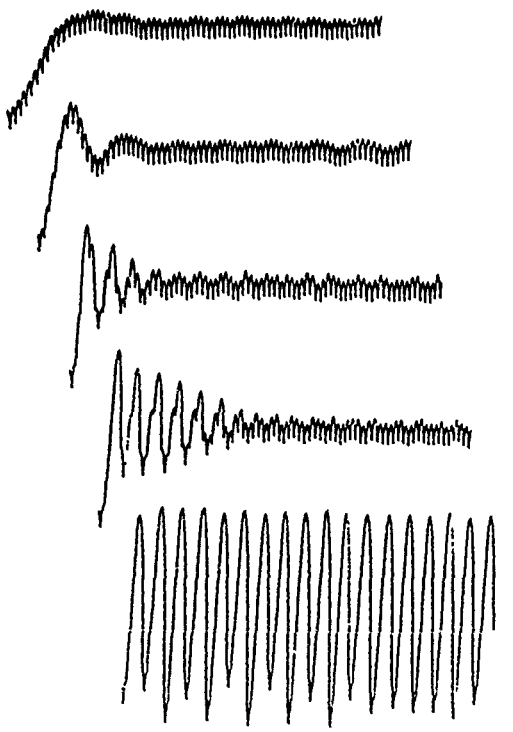


Fig. 2b Current Regulation, with Commutation. From Top to Bottom, Gain is from Low to High.

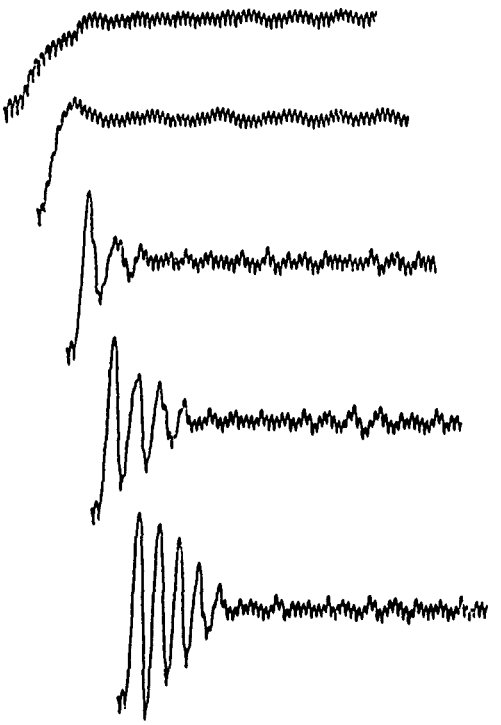


Fig. 3 AGS Booster Main Magnet Voltage Waveform

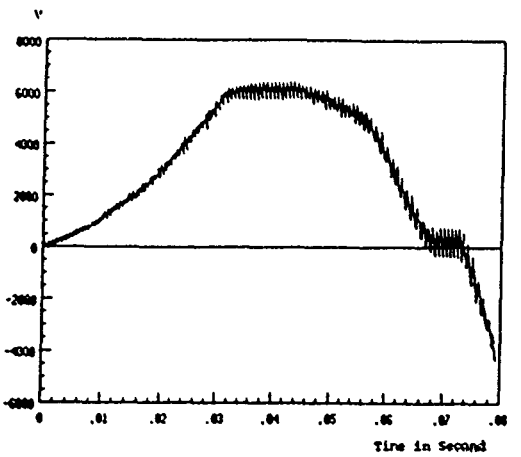
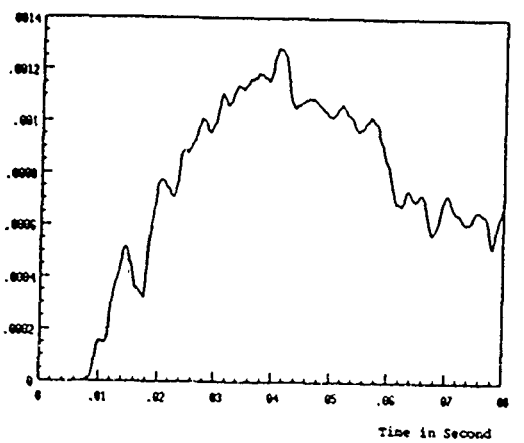


Fig. 4 Current Error Ratio due to Power Line Disturbance



Applications of the Hot Isostatic Pressing (HIP) for High Gradient Accelerator Structure

Hiroshi Matsumoto, Mitsuo Akemoto, Hitoshi Hayano, *Atsushi Miura, Takashi Naito, and Seishi Takeda
KEK, National Laboratory for High Energy Physics
Oho 1-1, Tsukuba-shi, Ibaraki-ken 305, Japan

*The Graduate University for Advance Studies
KEK, National Laboratory for High Energy Physics
Oho 1-1, Tsukuba-shi, Ibaraki-ken 305, Japan

Abstract

In order to reduce the dark current from disk edges in the traveling wave accelerator structure at field gradient up to 80 MV/m, a new type of disk was proposed which consisted of a part of Titanium around the beam hole area and a part of OFHC outer ward. These two parts are joined by a hot isostatic pressing (HIP) technique. HIP makes diffusion bonding at temperatures ranging from 700 to 850 °C at an isostatic Ar gas pressure of 1,200 kgf/cm^2 in a pressure vessel. All samples showed the vacuum leak rate of less than 10^{-9} Torr•l/sec and tear strength of about 6.4 kgf/mm^2 in the reaction zone between two metals.

I. INTRODUCTION

The accelerating gradient of the Japan Linear Collider(JLC) is 100 MV/m for the X-band main linac and 50 MV/m for the S-band injector and the pre-accelerator. We have already achieved the acceleration of the electron beam of 0.9 A and pulse width of 0.2 µsec by the traveling wave 0.6 m long structure at the gradient of 85 MV/m with 1µsec RF pulse duration at 50 Hz [1]. At this gradient, however, the dark current is very large from disk edges and breakdown occurs frequently, while at 70 MV/m, beam acceleration is made fairly stably. It seems feasible to operate the accelerating structure at this gradient for the practical use after a reasonable processing period. In this sense, the operation of 50 MV/m at S-band is quite promising.

Experimental studies on the upper limit of the electric field strength in conventional disk loaded structures and single cavities have been reported from several laboratories [2][3]. From these studies, there found many factors to be discussed concerning RF breakdown phenomenon with dark current such as surface finish, micro dusts, electron multiplications and vacuum conditions, etc. However, the fundamental mechanism of the RF breakdown is not yet clear. As is appeared in references [4] and [5], the electron multiplications at disk edges is a main reason to limit the accelerating gradient and the other factors such as surface cleanness, surface finish and vacuum conditions were not serious problems [6]. In order to reduce the dark current and increase the upper limit of RF breakdown, we designed a new disk which was consisted of two metals, OFHC and Titanium(Ti-6Al-4V). As the secondary electron emission coefficients of Titanium is less than unity, the beam hole of a disk is designed to be made of Titanium. We applied diffusion bonding by hot isostatic pressing to join Titanium to OFHC. We made the coaxial columnar blocks with OFHC(outer) and Titanium(inner) by this technique. This paper describes the preliminary results of characteristics of HIP diffusion bonded OFHC-Titanium metals.

II. EXPERIMENTAL PROCEDURES

A. Hot Isostatic Pressing

Hot isostatic pressing(HIP) is a thermomechanical process for materials that makes use of applied gas pressure in order to achieve high density and diffusion bonding in the treated material. HIP subjects generally a material to pressures as high as 2,000 kgf/cm^2 and temperatures up to 2,000 °C in a pressure vessel. The source of the heat is a furnace within the pressure vessel, holding temperatures well below the melting point of the material being processed. This method can be used for a wide range of materials such as metals, ceramics and composites.

B. Materials Characteristics

HIP was applied to diffusion bonding of OFHC cylinders and Titanium bars. The chemical compositions of the samples are listed in Table 1. The composition of the OFHC is very high quality type and the Titanium corresponds to the Japanese Industrial Standards(JIS) type.

Table 1
Chemical composition of OFHC cylinders

MATERIAL	CHEMICAL COMPOSITION (%)									
	PB	ZN	Bi	CD	HG	O	P	S	SE	TE
OFHC	5	<1	<1	<1	<1	3	2	8	<1	<1
	CHEMICAL COMPOSITION (%)									
	H	O	N	Fe	C	Al	V			
Ti-6Al-4V	*88	0.18	0.017	0.23	0.019	6.34	4.13			

* ppm (x10^{-6})

C. Fabrication Methods

Samples of OFHC cylinders and Titanium bars were machined from each columnar block. The surface finish(RMS)

0-7803-0135-8/91$01.00 ©IEEE

of the inner wall of OFHC is less than 0.5 μm and the one of Titanium bar is less than 0.2 μm. Dimensions of these samples are listed in Table 2.

Table 2
Dimensions of samples

	OFHC	Ti-6Al-4V
DIAMETER OUTER	ø 110 ± 0.1mm	ø 40 -0.05/-0.0mm
INNER	ø 40 +0.05/+0.0mm	
LENGTH	110 ± 0.1 mm	110 ± 0.1 mm
SURFACE FINISH (RMS)	< 0.5 μm INNER WALL	< 0.2 μm OUTER WALL

These metals were cleaned by acetone and then Titanium bar was set inside of OFHC cylinder. The sample was placed into a completely leak-tight soft iron capsule. These capsules were pumped down at less than 10^{-3} Torr and then sealed-off.

The results at three different temperatures, 700 °C, 750 °C and 800 °C were obtained in a HIP cycle in a pressure vessel. An isostatic pressure was held at 1,200 kgf/cm^2 by pure Ar gas for 2 hours. Above parameters for HIP-cycle (temperature, pressure and holding time) are based on metallurgical and economical considerations. A schematic view of the HIP-cycle is shown in Figure 1.

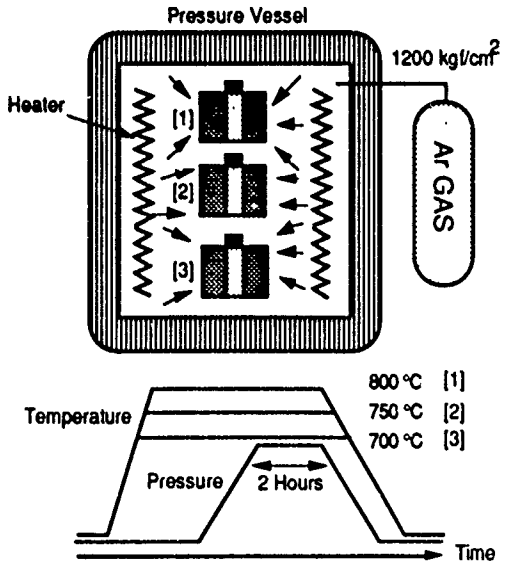


Figure 1.HIP diffusion bonding process.

III. EXPERIMENTAL RESULTS

A. Micro structures

The quality of HIP was studied with metallographical measurements (optical microscope and scanning electron microscope) and mechanical tests. At three different HIP temperatures(700 °C, 750 °C and 800 °C) with an isostatic pressure of 1,200 kgf/cm^2 for 2 hours, all samples became fine micro-strucutre and well homogeneous. In this experiment at these three different temperatures the grain growth of whole OFHC and Titanium was not observed. The micro-structures of a HIP sample and a forged OFHC are shown in Figure 2. The forged OFHC is generally involves large number of micro-pores of a size of a few μm at grain boundary. Figure 2 shows that the micro-pores disappeared in HIP processed OFHC. Moreover, HIP processed OFHC is much more homogeneous than forged OFHC. Titanium is free from porosity even in forged material.

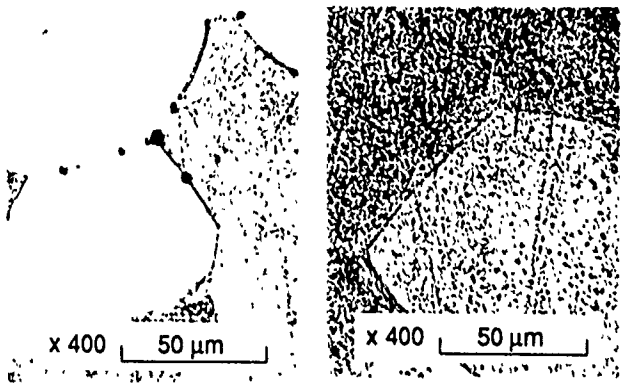


Figure 2. An optical micrograph showing forged OFHC(left) and HIP-OFHC(right) at temperature of 800 °C and the isostatic pressure of 1,200 kgf/cm^2 for 2 hours.

B. Reaction Zone

The width of HIP reaction zone in three samples were ranging from 7.3 μm to 20 μm corresponding to applied HIP temperatures. These reaction zone were etched and measured by an scanning electron microscope as shown in Figure 3.

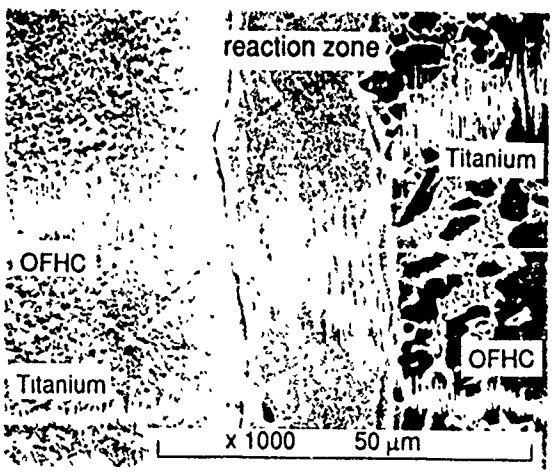


Figure 3. Scanning electron micrograph of HIP processed OFHC-Titanium sample.

Figure 3 shows the reaction zone between two materials which indicates that quality is high and porosities and impurities are not seen. The x-ray analysis of reaction zone in Figure 3 shows the contents of OFHC and Titanium in the reaction zone.

C. Mechanical Properties

The quality of HIP was studied with mechanical tests and metallographical measurements. The tear strength was measured using a plates with a thickness of 2 mm which were JIS standard tear test specimens as shown in Figure 4. Five specimens were machined from each sample. The reaction zone is in the middle of the gauge length.

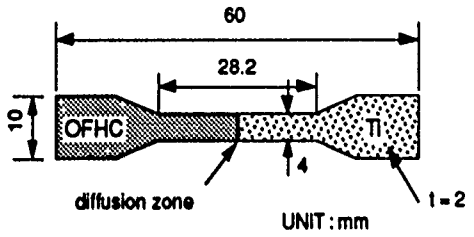


Figure 4. JIS standard tear test specimen. Viewing from top.

We obtained the tear strength of 6.4 kgf/mm^2 in average for the three different HIP temperatures. The minimum value of strength was 4.9 kgf/mm^2. Figure 5 shows the tear strength of all the specimens, which does not depend on HIP temperature. All of the test specimens were fractured at inside of reaction zone where the concentrations of OFHC and Titanium were equal.

The vacuum leak rate of the reaction zone is well blow 10^{-9} Torr•l/sec.

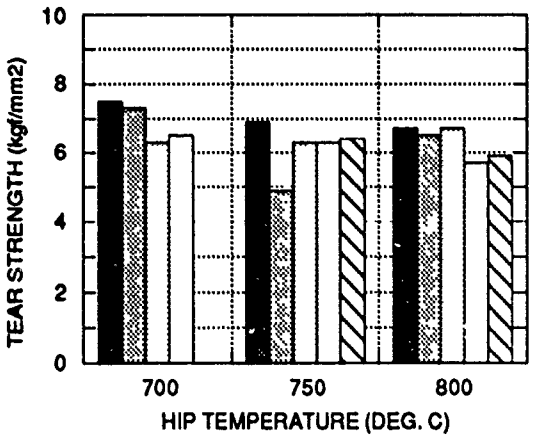


Figure 5. Tear strength by JIS standard test.

IV. DESIGN OF DISK STRUCTURE

A. Calculation of Q

The new disk structure is designed for conventional disk loaded structure which is consisted of HIP bonded OFHC and Titanium metals. The calculated results of Q value by the use of MAFIA coed was 12,000 for the $2\pi/3$ mode It is about 14 % lower than the normal cavity which is made of only with OFHC. The dimensions and drawing of the cavity are shown in Figure 6.

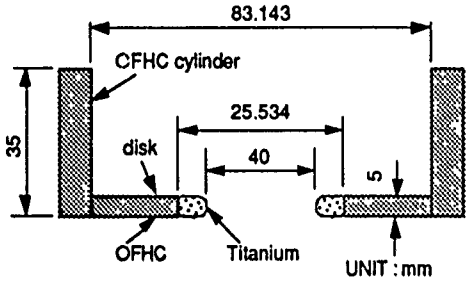


Figure 6. Titanium bonded disk structure.

V. SUMMARY

HIP diffusion bond of OFHC and Titanium was successfully made at temperatures ranging from 700 °C to 800 °C and the pressure of 1,200 kgf/cm^2 for 2 hours. The micro-pores in the OFHC are disappeared with HIP processing. Quality of the reaction zone is high and it is free from porosities and impurities. The minimum tear strength of reaction zone is 4.9 kgf/mm^2. The vacuum leak late of reaction zone is less than 10^{-9} Torr•l/sec. The calculated Q-value of Titanium bonded disk was 12,000. These results indicate that the Titanium bonded disk can be applied to high gradient accelerator structures.

VI. ACKNOWLEDGMENTS

HIP was performed by NKK corporation. Also the analysis of samples was performed by the joint work of KEK and NKK corporation. The authors wish to thank to the group of NKK corporation led by Mr. Hoshiaki Terao for their many fruitful discussions.

VII. REFERENCES

[1] H. Matsumoto et al., "High Gradient of the S-band Electron Linac", Linear Accelerator Conference, pp. 629-631, September 1990.

[2] G. A. Loew and J. W. Wang, "RF Breakdown and Field Emission", SLAC-PUB-4845, January 1989.

[3] E. Tanabe, "Breakdown in High-Gradient Accelerator Cavities, IEEE Trans. NS-30, No. 4, pp 3551, 1983.

[4] S. Takeda et al., "High Gradient Experiment by Accelerator Test Facility for Japan Liner Collider", Linear Accelerator Conference, pp.144-146, September 1990.

[5] S. Takeda et al., "High Gradient Experiments by ATF", Particle Accelerator Conference, May 1991.

[6] J. W. Wang, "Some Problems on RF Breakdown in Room Temperature, A Possible Criterion", SLAC/AP-51, April 1986.

X-band Accelerating Structure for Japan Linear Collider

T. Higo, M. Takao, K. Kubo and K. Takata
KEK, National Laboratory for High Energy Physics
Oho 1-1, Tsukuba-shi, Ibaraki-ken 305, Japan

Abstract

Candidates of the accelerating structure for realizing an operation in a multi-bunch mode in a linear collider were described. The external Q value of the TM110-π mode in a damped structure with slotted disk is very sensitive to the geometry. It was found impossible to reduce the Q value less than 100 for a structure with a beam hole radius of a=3.75mm, while it can be as low as 12 for the structure with a small beam hole of a=3mm. Furthermore, calculation for one of such a structure showed the reduction of the Q value of the accelerating mode 20 percent and that of R/Q 10 percent. As a candidate of damped structure whose Q value of the TM110 mode is insensitive to the geometry change, a so called crossed waveguide type was examined next. Only the TE111 type mode was found below 40GHz and no other mode was observed, indicating this structure a good candidate. An example of a so called detuned structure showed good damping within the following bunches.

INTRODUCTION

In order to obtain a high luminosity in a linear collider, the emittance of each bunch should be maintained small to make the spot size at interaction point small enough. The luminosity can still be increased if we can operate the linac in a multi-bunch mode. In the Japan linear collider (JLC), ten bunches, each contains 10^{10} particles and spaced Tb=1.4ns apart with each other, are accelerated in an RF pulse using structures with a/λ of 0.14[1]. The energy of each bunch should reside in the acceptance of final focus in the presence of fundamental beam loading and also the long range longitudinal wake fields of higher modes. On the other hand, the transverse emittance of each bunch should also be preserved in the presence of long range dipole wake fields. In this paper, we discuss some possible cures against these multi-bunch effects in the linac focused on transverse case.

The simplest way of cure against the long range wake field is to damp the excited field in the structure before the arrival of the following bunch. This can be achieved in a so called damped structure. Two types of structures are discussed in the next section. Another type of cure is considered in the following section, where the excited wake field can be cancelled out by carefully tuning frequencies of all cells. This structure, so called detuned structure, is primitively described.

DAMPED STRUCTURE

Typical long range wake fields to be considered in the accelerating structure for JLC main linac are summarized in Table 1 together with the target values Q(Target) for each mode[2].

Table 1 Relevant long range wake fields.

Mode	Freq.	Wake	Q (Target)
Longitudinal	(GHz)	($\times 10^{15}$ V/C/m)	
TM010	11	0.5	
TM020&011	26	0.05	
TM021	36	0.09	270
Transverse	(GHz)	($\times 10^{17}$V/C/m^2)	
TM110	16	1.1	15
TM111	26	0.18	38
TM121	36	0.12	61

A. *Slotted-disk type*

To achieve the target Q value especially for TM110 mode, we investigated two-cell structure (DS-1) with a slotted disk at the middle of two cells[2]. Two waveguides are attached to the slots so that the TM110-π mode can be damped out through these waveguides. In this configuration, resonant frequencies were calculated using the code MAFIA[3] by varying the shorting position in the damping waveguides. The obtained tuning curves were analyzed by the authors [2,4] and by N. Kroll[5] and listed in Table 2. The results indicate that the structure which suffices the criterion of the Q value is possible at least in this two-cell cavity.

Table 2. Analysis of damped structure DS-1.

	This author		N. Kroll	
	f(GHz)	Q	f(GHz)	Q
TM110	15	15-25	15.4	11
slot mode ?			16.1	7
TM111	17	25-30	17.0	15

In order to damp the wake field in both polarizations, which is needed in actual linac structure, the other damping ports perpendicular to the previous ones should be equipped[6]. An example is shown schematically in Figure 1, where the direction of the damping ports at one disk is perpendicular to that at the next.

The obtained external Q values of the TM110-π mode for these structures are listed in the columns of DS-2 and DS-3 in Table 3. The parameters W, H1 and H2 were varied to obtain as low Q value as possible. As shown in the table, the Q value is very sensitive to the structure, especially to the beam hole aperture. In the same table are listed the parameters of the two-cell cavity DS-1 of Table 1 and KEK-B scaled to 11.4GHz from the design of KEK-B factory [7]. These examples indicate a good damping for the structure with a small beam hole. The damping mechanism of this structure is not well understood but it seems that the low Q value of TM110-π is difficult to realize in the structure with a large beam hole. The beam hole

0-7803-0135-8/91$01.00 ©IEEE

radius of JLC accelerating structure is larger than 3.7mm and it seems difficult to apply this type of structure.

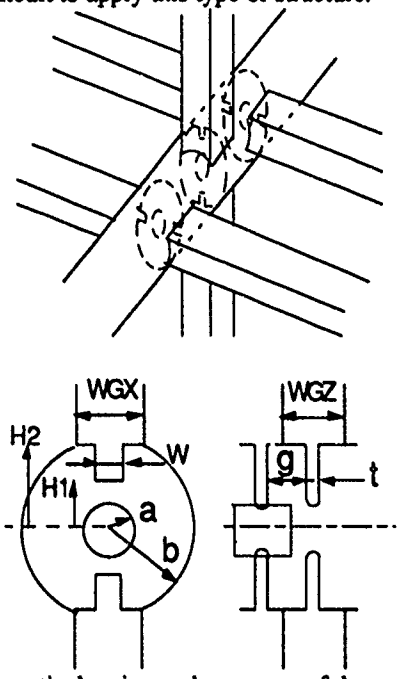


Fig. 1. Schematic drawing and geometry of damped structure DS-2 and DS-3.

Table 3. Parameters of various damped structures with slots in the disk. (units in mm)

Param.	KEK-B*	DS-1**	DS-2	DS-3
a	2.23	3.6	3.75	3.0
b	8.28	10.6	9.0	9.0
t	2.23	2.0	2.0	2.0
nose	1.78	no	no	no
g	12.01	6.75	6.75	6.75
W	4.45	5.0	4.0	3.0
H1	3.55	5.5	5.5	4.75
H2	6.54	9.0	7.5	9.5
WGX	10.24	11.1	10	10
WGZ	9.35	11.1	14	14
cells	2	2	periodic	periodic
Qex (TM110π)	30	15-25	420	12

* four damping ports connected to the slots in a disk.
** only two ports and slots in the same plane.

Table 4. Parameters of accelerating mode.

param.	NDLS	DS-2
a (mm)	3.75	3.75
b (mm)	10.6	9.0
f (GHz)	11.4	11.3
Q	7000	5870
R/Q (Ω/cell)	42	38
vg/c	0.023	-0.004

Parameters of the accelerating mode in $2\pi/3$ mode are also calculated by MAFIA for normal disk loaded structure (NDLS) and a damped structure (DS-2). The results are listed in Table 4[4]. The accelerating mode passband of DS-2 was found slightly backward because of a strong magnetic coupling through damping port and wide slot in the disk. This characteristic enables us to tune the group velocity of the accelerating mode without changing the beam hole aperture. The reduction of the Q value and the R/Q are calculated to be about 10 and 20 percent, respectively. This pushes the peak power for the structure very high necessary to obtain a given accelerating gradient.

B. *Crossed waveguide type*

The damping of higher modes in the structure of crossed waveguide type[8] is thought to be insensitive to the geometry change. In order to make all higher modes damped, a structure shown in Fig. 2 was examined. Each cell of the structure has 8 damping ports of 2mm×11mm in cross section extended to four directions and divided into two groups by a septum of its thickness 2mm at the middle of the cell. The septum has a hole of radius 8mm which determines a cell radius. The thickness of the disk is 2mm and the beam hole radius is 3.5mm.

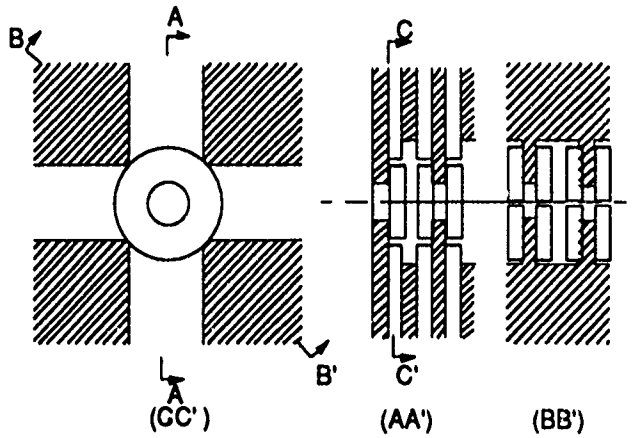


Fig. 2. Geometry of crossed waveguide type damped structure.

In Fig. 3 are shown the tuning curves obtained for a structure with these boundary conditions where such modes as TM110, TM111 and TM011-like ones can exist. The results were plotted as (ϕ,freq) diagram as suggested by N. Kroll[5]. According to Slater's formula[9], the parameters are related as

$$\frac{\phi}{\pi} = \frac{2}{\lambda g}\, d \cdot n = \frac{1}{\pi} \operatorname{Arctan} \sum_a \frac{\frac{1}{Qa}}{\frac{\omega}{\omega a} - \frac{\omega a}{\omega}}$$

where d is the position of the shorting plane, n the numbering of the branch, Q_a and ω_a the Q value and the angular frequency of a mode a. Here, the origin of the parameter d is set at the center of the structure. In this calculation, the shorting plane of the waveguide were varied in only one direction (X direction). The parameter ϕ changes by π if one passes a resonance. All the steep changes of ϕ in the figures of TM110 and TM111 show the resonances composed of TE20 waveguide mode trapped in the waveguide of Y direction except the resonance at 25GHz in the figure of TM111. As the field pattern of this mode is similar to that of TE111 mode in the cell,we guess its R/Q value small. In addition, the Q value of this mode is as small as 36 obtained from the fitting of the tuning curve. From these consideration, the dangerous modes such as TM110 and TM111 are well damped in this type of damped structure. On the other hand, the steep resonances below 30GHz in the figure TM011 are attributed to

the resonances in the waveguide of Y direction in TE10 waveguide mode. As the frequency of TM011 mode in normal disk loaded structure is about 26GHz[2] and the perturbation added from normal disk-loaded structure to this type of damped structure usually pushes the resonance frequency low, we conclude again that the TM011 mode is also well damped in this type of structure. As a final check, we should check the tuning curves by varying the shorting plane of all waveguides at once.

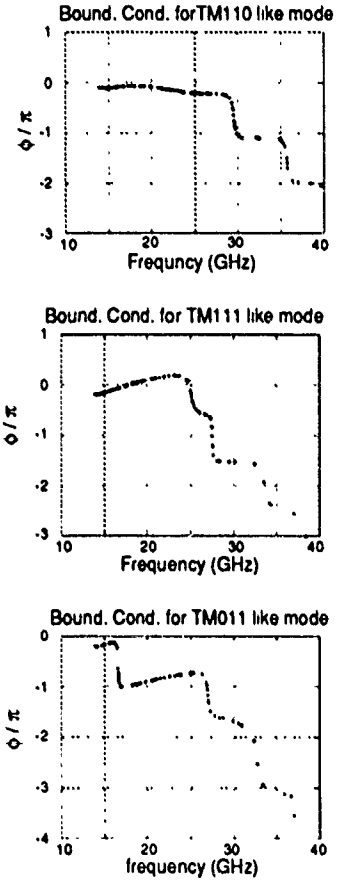


Fig. 3 Tuning curve of damped structure of crossed wageguide type.

DETUNED STRUCTURE

The wake field of TM110 mode should be reduced by two order of magnitude at the next bunch if we assume the same amount of damping criterion cited in the previous section. Simplest way to reduce the wake field at the following bunch is to tune a higher mode frequency to make a zero crossing at the following bunches, but it is difficult to realize this cancellation for more than a mode at once. Another extreme [10] is to cancel out the wake field of each cell by varying the frequencies of the higher mode from cell to cell along a certain length of linac well shorter than the betatron wavelength.

To obtain a good damping at the next bunch and beyond that to the last bunch, a distribution similar to gaussian is desirable. An example of such a distribution is described as

$$P(f) = \frac{T}{4}\left\{2\ S(df) + S(df - \frac{1}{T}) + S(df + \frac{1}{T})\right\}$$

for $|\ df\ | < \frac{\delta f}{2}$, where $df \equiv f - f0$ and $S(x) \equiv \frac{Sin(\pi Tx)}{\pi Tx}$.

In Fig. 4 is shown the wake field excited by a bunch and integrated within 321 cells with frequencies distributed in the above formulus with T=2.4ns and $\delta f/f = 0.104$.

As the broad minimum at the next bunch (1.4ns) is mainly determined by $\delta f/f$, it can be controlled easily. The wake field after second bunch is well below 10^{-2}.

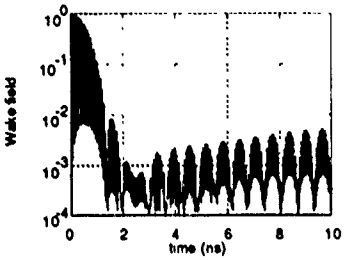


Fig. 4 Wake field integrated along 321 cells with $\delta f/f = 0.104$ and T=2.4ns.

In the above estimation, we neglect those effects such as a finite coupling between cells, the successive excitation of wake field from cell to cell, different values of R/Q among cells and the fabrication error of each cell frequency. These effects should be carefully taken into account. Moreover, an actual geometry which provides us ten percent frequency distribution should be found. We should also estimate the effect of other higher modes.

SUMMARY

Some possible candidates of the structure for JLC which cures the effects due to the long range wake fields were examined. The damped structure with slots in the disk was found too sensitive to apply to the actual structure for JLC. A damped structure of crossed waveguide type was found good as for the characteristics of the higher modes. A detuned structure with its frequency distributed similar to a truncated gaussian shows a good cancellation of a higher mode.

REFERENCES

[1] K. Yokoya, Proc. First Workshop of Japan Linear Collider, 1989, Tsukuba.

[2] T. Higo et al., Proc. Linear Accelerator Conference, Alburquerque, 1990.

[3] K. Klatt et al., Proc. of the 1986 Linear Accelerator Conf., SLAC-Report-303,1986, p276-278.

[4] M. Takao, to be published.

[5] N. Kroll, private communication.

[6] T. Higo, Proc. Second Workshop of Japan Linear Collider, 1990, Tsukuba.

[7] M. Suetake et al., "Accelerator Design of KEK B-Factory",KEK Report 90-24, 1991, p85.

[8] H. Deruyter et al., SLAC-PUB-5263, 1990.

[9] J. C. Slater, "Microwave Electronics", Van Nostrand, 1950

[10] H. Deruyter et al., SLAC-PUB-5322, 1990.

METHOD OF LONGITUDINAL IMPEDANCE MEASUREMENT FOR ACCELERATOR ELEMENTS IN WIDE FREQUENCY REGION USING DOUBLE FOURIER TRANSFORM

P. Reinhardt-Nickulin, N. Ilinsky, S. Bragin
Institute for Nuclear Research
of the Academy of Sciences of the USSR
Moscow, USSR

I. INTRODUCTION

Estimation of impedance for accelerator vacuum pipe usually is performed by coaxial line technique. Well known method developed last years based on this technique is the method of synthetic pulse [1]. In this method frequency dependences of transmission coefficients S_{21} of wave skattering matrix for test or reference beam pipe segments are represented by means of inverse Fourier transform to time domain. It's permit to observe besides of main transmitted pulse many reflected pulses caused by mismatchs at matching sections consisting of adapters, cable junctions and other elements which are needed for measurement set-up. For removing these reflections the time filtering and space separation of reflected pulses are used.Two additional metal segments of waveguide must be embedded in scheme of measurements, which are located at both sides of measured element and permit to eliminate reflected pulses from main pulse in some time interval τ.

Time filtering provides only first pulse transmission from time representation of S_{21}. Total transmission coefficient after using of time gating for system, consisting of matching sections, additional waveguides and measured waveguide, is

$$S_{21tot} = S_1 \cdot S_2 \cdot S_{21} \cdot e^{j(\Theta_1+\Theta_2)} \qquad (1)$$

where S_1, S_2 - transmission coefficients of matching sections, $e^{j(\Theta_1+\Theta_2)}$ - transmission coefficient of additional sections - spacers, S_{21} - transmission coefficient of test or reference element. This method may be used for frequencies above 45 MHz. However, if it's necessary to measure the impedance at low frequency, the length of additional sections becomes too large in accordance with [2], and bench installation becomes inconvenient. That is why for measuring S_{21} in frequency region including low frequencies, it's necessary, as it's done usually, preliminary to calibrate measuring set-up together with matching sections. Calibration may be executed in different ways. One of these methods is TSD-method [2,3], permitting to determine coefficients S_1 and S_2 in frequency domain, and then to carry out series of measurements, from which using known S_1 and S_2 and by some calculations, one can determine coefficient of interest S_{21} , and then - impedance. However, from our point of view TSD-procedure is large and inconvenient too, because it uses many calibration standards, and consequently it takes many mechanical operations Besides that TSD-method resulting functions have considerable noise. These disadvantages excite the wish to modify the method of synthetic pulse. Below it is considered the method of double Fourier transform, which allows to measure the impedance of distributed discontinuity for both low and high frequencies Also, it is considered main causes of errors and the results of measurements are given.

II. SCHEME AND ALGORITHM OF MEASUREMENTS

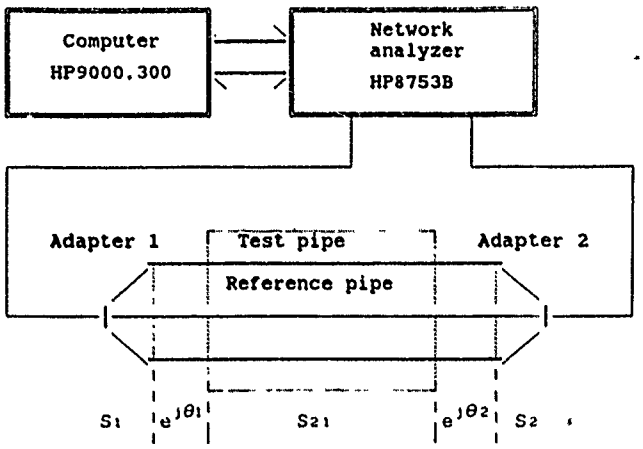


Fig.1. Measurement set-up.

Measurement set-up (Fig.1) consists of network analyzer HP 8753B controlled by computer, and experimental part. Network analyzer contains double vector voltmeter, generator-synthesizer of harmonic signal and receiver for measurement of S-parameters. Experimental part of set-up being connected to inputs 1 and 2 of S-parameters receiver consists of reference metal waveguide of the same cross-section and length as the test waveguide has; adapters 1 and 2 tapering from cross-section of test or reference pipe to cross-section of connecting cables with 50 Ohm characteristic impedance. These cables feed the signals to inputs 1 and 2 of analyzer. The 10 dB attenuators are placed before inputs 1 and 2 Attenuators are needed for improving the accuracy. Besides that the set-up can include additional segments of coaxial line -spacers with the length of $c\tau/2$ (c - the speed of light) for separation of reflections in time interval τ. Choicing the central conductor which forms coaxial line from reference or test waveguide, it's necessary to try to achieve the same characteristic impedance as the connecting cables have. The requirement for choicing the central conductors of adapters is the same. In this case the reflections are minimized. Simplified algorithm of measurements is shown on Fig.2. The process of measurements consists of following stages. 1) Choicing of initial values of parameters (limits of frequency region, the value of signals, number of measurements in series for procedure of averaging etc.). 2) Calibration, this is measuring and storaging total transmission coefficient $S_{21tot\,ref}$ by calibration line made of reference waveguide 3) Measurement of test object transmission coefficient $S_{21tot\,tst}$ in frequency domain 4) Inverse Fourier transform of $S_{21tot\,tst}$ 5) Fixing of

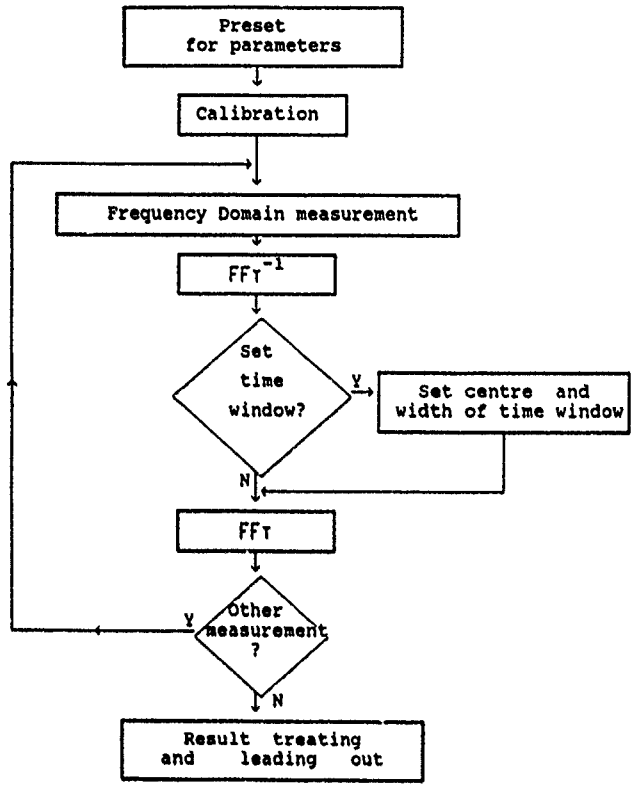


Fig.2. Simplified Flow Diagram for Measurement Procedure.

time gates, this is fixing of gates centre and width. 6) Fourier transform of the part of $S_{21tot\ tst}$ time representation,which cuts out by means of time gates.7) Treating and leading out the results of measurements.

The main difference between this method and one proposed in [1] is preliminary calibration measurement of $S_{21tot\ ref}$ on reference calibration line, which is stored in analyzer and automatically effects on consequent measurement of $S_{21tot\ tst}$. In method of synthetic pulse descripted in details in [2] following procedures are made separately: measuring of $S_{21tot\ ref}$ and $S_{21tot\ tst}$, inverse Fourier transforms, time gating of parts of transmission coefficients and Fourier transforms. As the result of these operations we get the ratio of transformed functions:

$$\frac{S_{21tot\ tst}}{S_{21tot\ ref}} = \frac{S_1 \cdot S_2 \cdot S_{21tst}}{S_1 \cdot S_2 \cdot S_{21ref}} = \frac{S_{21tst}}{S_{21ref}} , \qquad (2)$$

from which it's simple to find active and reactive parts of impedances. In our case ratio $S_{21tot\ tst}/S_{21tot\ ref}$ is got at once after measuring $S_{21tot\ tst}$, because preliminary calibration measurement of $S_{21tot\ ref}$ is stored in analyzer HP 8753B, and it means, that any consequent measurement is normalized by value $S_{21tot\ ref}$. Inverse Fourier transform is made at once from ratio of these frequency functions, i.e.

$$\phi(t) = \Phi^{-1}\left(\frac{S_1(f) \cdot S_2(f) \cdot S_{21tst}(f)}{S_1(f) \cdot S_2(f) \cdot S_{21ref}(f)}\right) \qquad (3)$$

In accordance with [2] general expression for transmission coefficient taking into account the reflections equals

$$S_{21tot} = \frac{S_1 S_2 \cdot e^{j(\Theta_1+\Theta_2)}}{\left(1 - e^{j2(\Theta_1+\Theta_2)} S_{21tst} S_{12tst} \Gamma_{2f} \Gamma_{1r}\right)} \times$$

$$\times \frac{S_{21tst}}{\left(1 - e^{j2\Theta_1} \Gamma_{tst} \Gamma_{1r}\right)\left(1 - e^{j2\Theta_2} \Gamma_{2f} \Gamma_{tst}\right)} \qquad (4)$$

where $\Gamma_{tst}, \Gamma_{1r}, \Gamma_{2f}$ - corresponding coefficients of reflections at junctions between spacer and test object, adapter 1 and first spacer, second spacer and adapter 2. If matching between parts is good enough, then coefficients of reflection are small, and it means, that products of coefficients are small all the more. So we can write

$$S_{21tot} \approx S_1 \cdot S_2 \cdot S_{21tst} \cdot e^{j(\Theta_1+\Theta_2)} \cdot (1+X)(1+Y)(1+Z) , \qquad (5)$$

where X, Y, Z - second members of differences in brackets from S_{21tot} denominator. S_{21tot} can be represented as the sum, which contains the members with products of reflection coefficients and the member $S_1 \cdot S_2 \cdot S_{21tst} \cdot exp(j(\Theta_1 + \Theta_2))$. The same speculations may be applied to system, containing reference coaxial line. Thus, time representation of ratio $S_{21tot\ tst}/S_{21tot\ ref}$ approximately equals

$$\phi(t) \approx \Phi^{-1}\left(\frac{S_{21tst}}{S_{21ref}}\right) + \Phi^{-1}\left(\frac{\mathcal{F}(S_{21tst}, S_{12tst}, \Gamma_{tst}, \Gamma_{1r}, \Gamma_{2f})}{\mathcal{F}(S_{21ref}, S_{12ref}, \Gamma_{ref}, \Gamma_{1r}, \Gamma_{2f})}\right) \qquad (6)$$

The first member represents the normalized transmission coefficient needful for getting impedances of distributed discontinuity, and second member represents the functions of reflections. If now to pick out part of $\phi(t)$ by means of time gating in some time interval τ (τ is such, that during τ only normalized forward pulse passes), then we get

$$\phi(t) = \Phi^{-1}\left(\frac{S_{21tst}}{S_{21ref}}\right) \qquad (7)$$

Fourier transform of this function gives us the ratio being searched:

$$\frac{S_{21tst}}{S_{21ref}} \approx \left(1 - \frac{R}{2Z_c}\right) \cdot exp\left(-j\frac{X}{2Z_c}\right) , \qquad (8)$$

where R and X - active and reactive parts of searched distributed impedance [1], Z_c - characteristic impedance of reference coaxial line. It's simple to notice from above speculations, that the result must be depended on width of time gates τ. Indeed, if the gates are too wide,then reflection signals distort resulting functions. And if the gates are too small, then the results are distorted due to cut-off of low frequencies. To avoid this disadvantage in [2] the authors make conclusion about necessity of very long spacers. However, from our point of view spacers must not be so long to become inconvenient, but estimating measurements may be carried out for determination of distributed excessive impedance. Indeed, if spacer has the length $\approx$ 60 cm, then time separation between forward and reflected signals is $\approx$ 4 ns. Therefore if we should take the gates width a little smaller than 4 ns, then the transmission coefficient would become smaller too in frequency region $< (1/\tau)$, and consequently the impedance would become larger in this region. However, if the result impedance would be smaller than allowable value, then this result would

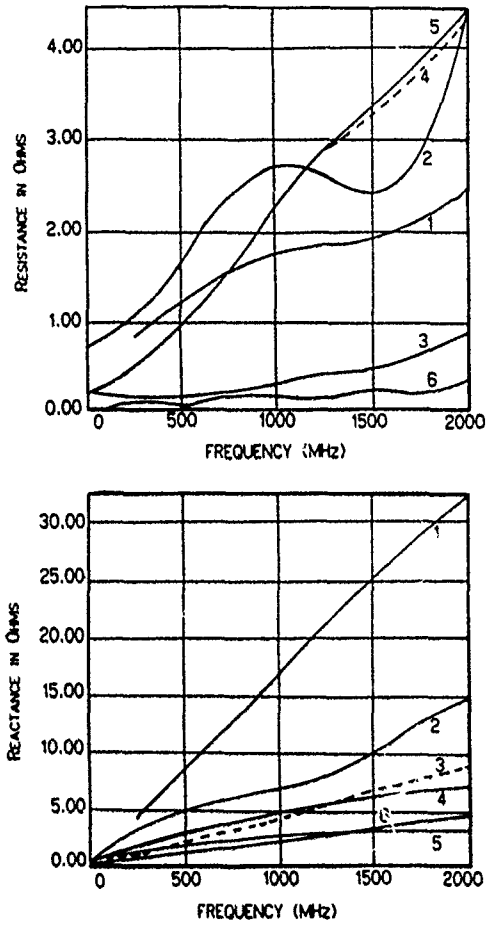


Fig.3. Comparison of measurement results.

be overestimation and might be used. Decreasing of τ must not be too large, because it can cause considerable increasing of measured impedance value at low frequencies and decreases im, ce at high frequencies. As shown in [1], S_{21} dependences, w i have been got at different τ, must not be sharply different one from another. That is the indicator of correctly choosen τ. Besides, it should be noticed, that in measurements of distributed discontinuity spacers aren't necessary if the length l of test object is large enough, because in this case reflected signals appear after time period $\tau = 2l/c$, and it is impossible to avoid the reflections in adapters as with spacers as without it.

III. RESULTS OF MEASUREMENTS

Frequency dependences of active and reactive parts of impedance which have been got for model element - beam position monitor - are shown on Fig.3 (curves 1) Frequency range for synthetic pulse measurement was from 0 3 MHz to 3000 MHz Model element with the length of 70 cm has rectangular form and consists of fiberglass plates. On the inner surfaces of this plates $\approx$ 4 mm wide copper foil strips are pasted, leaving small intervals of $\approx$ 1 mm between them. There is $\approx$ 25 mm wide not filled interval on the inner surface in the centre of each plate. Copper foil strips are pasted in this intervals on the outer sides. To the cuts, which are made in outer strips five 10 Ohm resistors are soldered. This resistors are electrically shorted to each other on both sides of cuts, i.e. their total resistance equals to 2.0 Ohm for each plate. For comparison on Fig 3 the measurement results from [4] are shown for following cases. similar monitor with slightly different cross-section (curves 2); chamber with the same size and cross-section, where all foil strips are uninterrupted and are placed on inner sides (curves 3); chamber, which four centre foil strips on the inner sides are cut and their ends are led out through dielectric and this ends are either electrically shorted (curves 4) or the resistors are soldered between this ends (curves 5); SAIC chamber [2] with strips of silver paste on two sides and with two full foiled sides (curves 6). From comparison of curves for active and reactive impedance parts it's simple to notice that monitors having not screened dielectric inside vacuum chamber have considerably larger impedance, than monitors, which have all copper stripes inside chamber. Minimal active impedance, as it should be, have the chamber with uninterrupted strips of silver paste, placed on inner sides. From behaviour of the curves at lowest frequencies we can conclude, that impedance does increase at low frequencies. However, if particle circulation frequency in synchrotron is $\omega_0 \approx 250kHz$, and we are interested in active impedance at frequency $\omega \approx 1MHz$, then impedance per harmonic $Z/n = Z/(\omega/\omega_0)$ <0.05 Ohm. This value is comparable with width of measurement "noise way". And consequently for 50 monitors installed on ring noise error is less than $\approx$ 0.1 Ohm, and full monitor's impedance for full ring < (2.5 ± 0.1) Ohm. It's simple to see, that at frequencies above 1 MHz impedance per harmonic becomes still less.

IV. CONCLUSIONS

Method of double Fourier transform is the development of synthetic pulse method [1] and differents from it in following points: 1) application of simple calibration in algorithm; 2) extension of measurement region to low frequencies; 3) simplification of measurement algorithm. The results, which have been got, show that at correctly choosen τ longitudinal impedance of distributed discontinuity may be estimated with good accuracy in full frequency region of interest without spacers.

V. ACKNOWLEDGEMENTS

This work was carried out at Canadian national centre TRIUMF, and authors are glad to thank Cris Oram, who organized and coordinated this work, and Yan Yin for great and all-round help.

VI. REFERENCES

[1] F. Caspers,"Beam Impedance Measurement by the Wire Method Using a Synthetic Pulse Technique,"IEEE Trans. on Nucl. Sci., Vol. NS-32, No.5, October 1985, p.1914.

[2] L. S. Walling, D. E. McMurry, D. V. Neuffer and H. A. Thiessen,"Transmission-Line Impedance Measurements for an Advanced Hadron Facility,"Proceedings of Advanced Hadron Facility Accelerator Design Workshop (February 22-27, 1988), LA-11432-C, Conference, UC-414, January 1989, p.381.

[3] Y Yin, C Oram, N. Ilinsky, P Reinhardt-Nikulin,"Measurement of Longitudinal Impedance for a KAON Factory Test Pipe Model with the TSD-Calibration Method," This conference.

[4] Y. Yin,"A Wall Current Beam Position Monitor Built on a Ceramic Chamber," TRI-DN-90-K144, July 1990

PROTOTYPE OF THE ACCELERATING RESONATOR FOR THE SUPERCONDUCTING SECTOR DEUTERON CYCLOTRON

N.V.Vasiliev, A.A.Glazov, E.N.Zaplatin, V.A.Kochkin, D.L.Novikov
Joint Institute for Nuclear Research, Dubna, USSR

Summary

A fullscale prototype of the accelerating cavity for the superconducting deuteron sector cyclotron at the energy 100 MeV is described.

The fundamental frequency and the distribution of the radiofrequency voltage along the accelerating gap were calculated by the RFC3D programme for calculating of 3-dimensional components of the electromagnetic field. The rf measurements proved the validity of the calculations with the accuracy better than 5% for the cavity fundamental frequency and 10% for the voltage.

Introduction

The structural features of the DC-1 sector cyclotron [1] required a halfwavelength resonator with a Δ-electrode as an accelerating element. The Table lists the main parameters of the RF system of DC-1 [2].

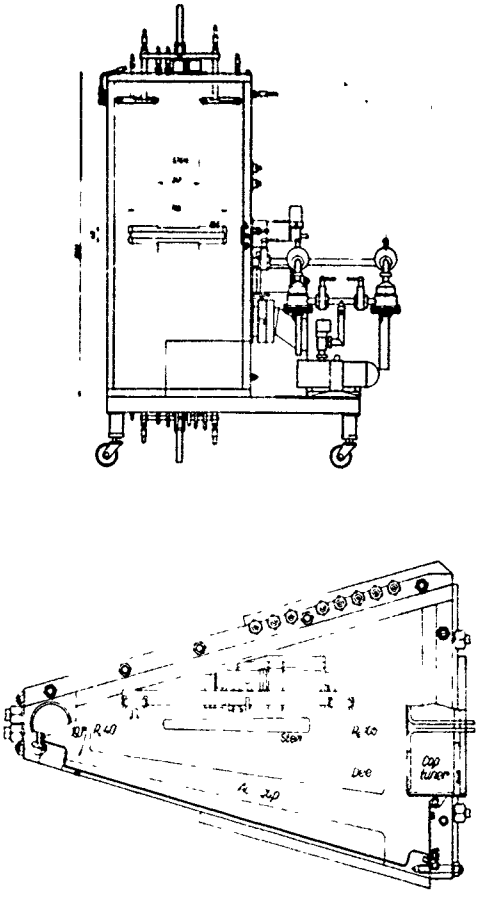


Fig. 1. The general view and median cross section of the resonator.

Table

Number of cavities	2
RF frequency	74.25 MHz
Harmonic number	6
Mean injection radius	40 cm
Mean extraction radius	115 cm
Accelerating voltage	300 kV
Azimuth dimension of resonator	30°
Losses in one resonator	40 kW

The main structural features

The resonator is a right-angle prism about 2 m high, its base being a trapezium with equal sides. The general view and median cross section of the resonator are shown in Fig. 1.

The resonator walls are made of aluminiumalloy with copper cladding inside. The space for the resonator in the cyclotron is 30° and is limited by two neighbouring magnet sectors. The side walls of the resonator are as thin as possible to keep the necessary internal volume. It is the magnet cryostat walls that are of the supposed to carry atmospheric load. The gaps between the side walls of the resonator and the cryostats are pumped down to rough vacuum. Other resonator walls are 50 mm thick and withstand the atmospheric load.

To tune the resonator and to achieve the necessary behaviour of the variation of the accelerating voltage in the acceleration zone, there are movable panels and a trimmer capacitor that changes the capacitance between the outer end of the Δ-electrode and the resonator wall. The contacts of the panels are made of copper foil 0.3 mm thick pressed to the walls by sending air under pressure into a rubber hose placed in a slot under the contact tabs. The hose is a vacuum tube with the inner hole 4 mm diameter and walls 4 mm thick. The design pressure is up 14 atm. The necessary pressure was determined in a direct experiment. The natural frequency of the resonator changes within 100 kHz as a function of the pressure in the contact opening system. The minimal working pressure is 10 atmospheres and the quality factor is 10000.

The copper cladding is cooled by water under pressure running in soldered on copper tubes. The water reaches the panels and the trimmer capacitor through guide rods.

The resonator is supposed to be evacuated by two electric discharge pumps. To prevent oil fumes from penetrating in the initial vacuum system, adsorption traps will be used.

Measurements of resonator characteristics

The main resonator characteristics measured at a low power level are the quality, the range of tuning with the trimmer capacitor, the accelerating voltage distribution along the accelerating edge.

Fig. 2 shows the resonance frequency plotted as a function of the gap between the short-circuiting panels of the resonator. The theoretical and experimental values are given. The discrepancy is 5%.

0-7803-0135-8/91$01.00 ©IEEE

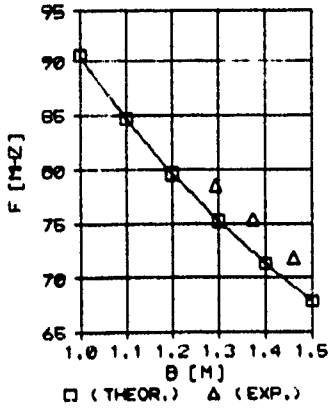


Fig. 2. Resonance frequency vs cavity height.

The calculation was performed by means of the programme RFC3D [3] for calculation of 3-dimentional components of an electromagnetic field. Fig. 3 shows the possible range of resonator frequency tuning with the trimmer capacitor for the maximum and minimum gap between the resonator tuning panels.

Measuring of the accelerating voltage is the most labour-consuming process and required special equipment and measuring devices. To solve this and similar problems, a multipurpose measuring complex has been developed on the basis of the personal computer. The perturbation method was used for measurement [4]. The perturbing body was a copper ball 6 mm in diameter fixed to a capron thread. Since the ion trajectories in the Δ-electrode are close to a straight line perpendicular to the axis line of the electrode, radii were measured from this axis, and the systems that guided the movement of the thread with the ball were parallel to this axis.

In measurements we registered the output analogue signal from the phase voltmeter, which was proportional to the variation of the RF field phase in the resonator caused by the perturbing body: $\Delta\varphi \sim E$ (E is the value of the electric field at the perturbation point), and the voltage from the multiturn potentiometer connected to the motor that moved the ball. The preliminary software processing of the characteristics consisted in removal of the experimental errors (temporal thermal instability of instruments and the resonator itself, deviation from the zero level). Then the dependence of the accelerating voltage on the radius U(R) was calculated. In Fig. 4 one can see this dependence compared with the calculated one.

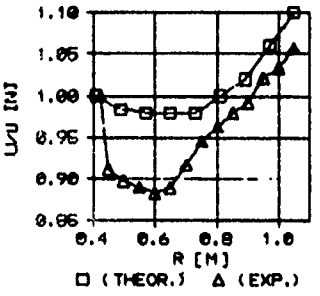


Fig. 4. Accelerating voltage vs radius.

The non-compensated capacitive coupling was used for excitation of the resonator. Since there was coupling capacitance (C_c), the frequency tuning of the resonator should be slightly shifted from its own resonance toward the capacitance region. Considering the equivalent resonator coupling system circuit, we can obtain in this case that $C_c = [\, 2\pi f(Z_{in}R_{sh})^{1/2}\,]^{-1}$, where Z_{in} is the input resistance of the coupling system, R_{sh} is the shunt resistance of the resonator, f is the frequency. The resonator has such parameters that they allow $Z_{in} = Z_{0f}$ (Z_{0f} is the wave resistance of the feeder). The coupling system design allows stepless variation of the coupling capacitance for fine matching tuning. Retuning goes on without violating the vacuum. The impedance and the input phase of this coupling system are shown in Fig. 5.

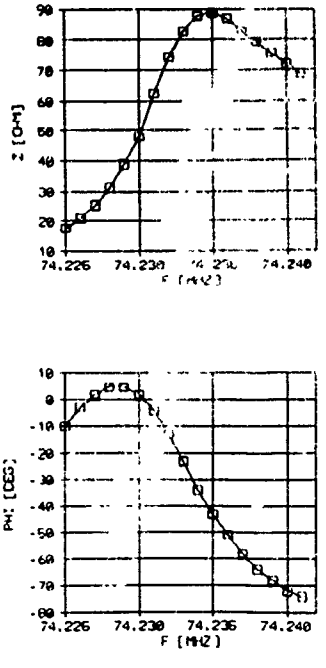


Fig. 5. Impedance and input phase of coupling system.

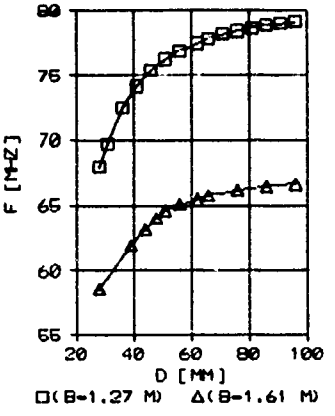


Fig. 3. Resonance frequency vs trimmer capacitor gap for max and min cavity height.

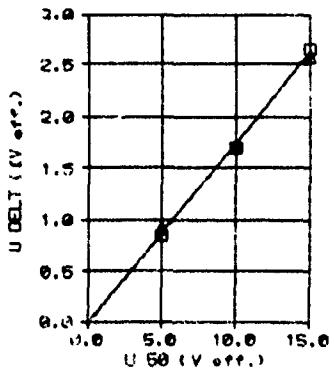


Fig. 6. Accelerating voltage vs coupling system input voltage.

Fig. 6 shows the dependence of the voltage at the accelerating Δ-electrode in the region of the injection radius U_{Δ} on the input voltage of the matched ($Z_{in} = R_{in} = 50$ Ohm) coupling system U_{50}. The dependence was measured with the help of the calibrated measuring loop. Using the obtained result one can find out that the power of the Δ-resonator will be about 40 kW at the accelerating voltage $U_{delt} = 300$ kV.

A 100 kW self-excited oscillator with the intrinsic feedback has been developed for experimental excitation of the resonator. Coaxial circuits and flat film capacitors are used here. The initial excitation of the resonator performed according to this scheme in the air allowed 10 kV at the Δ-electrode. This oscillator is planned to be used in a pulsed mode of operation.

References

1. A.A.Glazov et al. JINR, R9-81-734, Dubna, 1981.
2. A.T.Vasilenko et al. JINR, R9-90-176, Dubna, 1990.
3. A.N.Bespalov et al. Proc.of the 10th All-Union Conference on Accelerators, JINR, D9-87-105, Dubna, 1987, v. 2, p. 257.
4. L.B.Mullet. AERE G/R 883, Harweli, 1957.

Design of an Accelerating Cavity for the Superconducting Super Collider Low-Energy Booster

C. C. Friedrichs and L. Walling
Los Alamos National Laboratory

B. M. Campbell
Superconducting Super Collider Laboratory

Abstract

This paper presents the history and current status of the design of the accelerator cavity to be incorporated into the Low-Energy Booster (LEB) of the Superconducting Super Collider (SSC). The LEB is a proton synchrotron, 540 meters in circumference, and having 108 buckets around the ring. Acceleration programs, each 50 msec long, take place at a rate of 10 per second. The beta change of the particles from injection to extraction is from 0.8 to 0.997. Since the rf excitation frequency must track beta, the rf frequency must shift from 47.5 to 60 MHz over the 50-msec acceleration program. The cavity will use ferrite in a perpendicular control bias mode to effect the required tuning.

I. INTRODUCTION

Development of perpendicularly biased, ferrite-tuned cavities for use in proton synchrotrons was ongoing at Los Alamos from 1984 through October 1990, when the project moved to SSC. During the tenure at Los Alamos, two different cavities using perpendicular control bias were designed, fabricated, and tested. The first cavity was designed to achieve a 20% tuning range; after testing was completed at Los Alamos, it was delivered to the Tri Universities Meson Facility (TRIUMF) at Vancouver, B. C., for further evaluation. The second cavity was designed for use in a higher-energy synchrotron, and could be tuned over a 4% frequency range. After completion of the test program at Los Alamos, this cavity was delivered to SSC for incorporation into their ferrite-tuned cavity test stand. High-power operation of these cavities demonstrated that ferrite permeability changes of 1.4 to 3.5 are easily obtainable, and very high magnetic and electric Qs can be realized even under high-power conditions. Both cavity designs were successful, but both demonstrated a strong need for improvement in the ferrite-cooling technique. This paper presents a basic cavity design similar to that of the first Los Alamos cavity, but incorporating a substantially improved ferrite-cooling concept. The cavity and amplifier are tunable over the required range 47.5 to 60 MHz. The circuit Q will be approximately 5000, and the average shunt impedance over the band will be approximately 160 kΩ. The cavity has an overall length is approximately 1.1 meters. It is designed for reliable operation with a gap voltage of 120 kV.

Work supported and funded by U. S. Department of Energy.

0-7803-0135-8/91$01.00 ©IEEE

II. Booster Cavity Design

A. Design Concept

The major design issues for a ferrite-tuned cavity are as follows: How is the cavity excited ? How is the ferrite biased ? How is the ferrite cooled ? The correct answer to all three for a high-reliability design is believed to be "As simply as possible". With that dictum in mind, the present design has evolved. A simplified drawing of the proposed cavity is shown in Fig. 1.

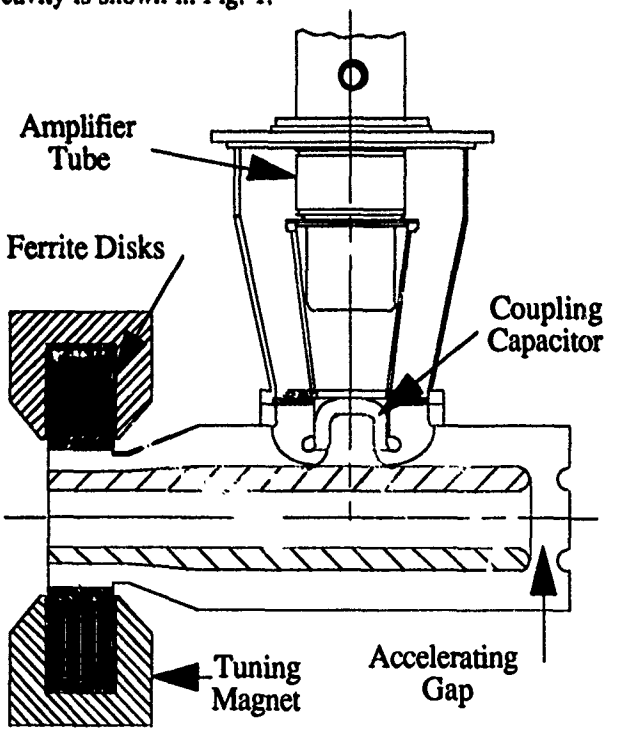


Fig. 1. The Proposed LEB Cavity

The proposed design uses a quarter-wave coaxial resonator with the accelerating gap at the high-voltage end and the ferrite at the high-current end. The excitation amplifier, which uses a 4CW150,000E tetrode, is incorporated directly into the cavity structure, with the cavity serving as its output network. A coupling capacitor is used to match the amplifier to the cavity impedance at the coupling point.

The ferrite tuner is configured such that rf wave propagation in the ferrite-filled region is in the radial rather

than the azimuthal direction. This radial-mode tuner permits the design of a simple bias magnet with uniform bias fields throughout the ferrite. This design does give rise to appreciable tuning fields on the beam axis; however, if the cavities are positioned in back-to-back pairs with opposite polarity tuning fields, field variations of up to 15 % between the pairs can be tolerated without upsetting the properties of the beam.

The ferrite is constructed from toroid disks approximately 2.5 cm thick. The disks will be about 14 cm inside radius by 30 cm outside radius and the disk separation will be between 0.3 and 0.5 cm. The separations provide channels for the cooling fluid. These channels are vertical, which allows the cooling fluid to flow in the direction of natural convection .

B. Ferrite Loss Characteristics

If one operates the ferrites in a mode such that the control bias H field is parallel to the rf H field[1] , then the permeability seen by the rf wave is the slope of the B-H curve at the operating point. If, however, one operates the ferrites in a mode such that the control bias H field is perpendicular to the rf H field , then the permeability seen by the rf wave is the ratio of B to H, where both are total values of the control fields. The significance of this is that in the perpendicular bias mode, substantial changes in rf permeability may be effected with the material in total saturation. The rf magnetic loss is related to the area within their hysteresis loops, and this area is essentially zero when the material is in saturation. Magnetic Qs substantially greater than 10^4 have been realized in the test cavities under high-power conditions.

The nickel-doped yttrium-iron-garnet ferrites that have been tested also exhibit very low dielectric loss. The electric Qs of these materials seem to be between 1000 and 5000 in the 50-MHz region.

C. Analysis Methods

It is impossible or at least extremely difficult, to construct a complete model from which all aspects of performance may be predicted. The design engineering goal is of course to create approximate models good enough to provide valid predictions over the realm for which the model was created. The LEB cavity is a fairly complex system, and numerous types of models have been created in an attempt to predict its operational behavior. The performance of the amplifier tube is analyzed by assuming sinusoidal input and output voltages, ignoring transit time, and Fourier-analyzing the current wave forms. The 2D code "Superfish" is valid for examining the cavity structure without its amplifier arm, but its most important contribution is in checking the transmission line model[2]. The transmission line model of the complete rf structure yields excellent predictions of voltages, currents, impedances, resonance, Q, and losses associated with the fundamental frequency, but its usefulness does not extend to higher frequencies. The 2D code "Poisson" accurately predicts the static conditions of the biasing circuit, and it is very useful for the basic design of the tuning magnet; but it does not treat the eddy current problem associated with the actual cycling bias conditions. A good 3D code for this problem has not yet been located. The 3D code "MAFIA"[3] has been used effectively for examining both higher order modes (HOMs) and field asymmetries in the gap induced by the amplifier arm of the cavity.

The ferrite cooling is analyzed using a 3D finite element model of a 45° ferrite segment. Boundary conditions of both free and forced fluid convection were analyzed. The ferrite will fracture at a tensile stress of 39 MPa., and its curie temperature is 200°C. The analysis predicts that tensile stress failure would occur well before the curie temperature was reached. This method of analysis will be used to determine the required velocity of forced convection after remaining tests are completed and a cooling fluid selection has been made.

D. Higher Order Mode Dampers

All rf cavities have an infinite number of HOMs, each of which present to the beam a complex impedance near the mode frequency. These modes interact with the beam, resulting in instabilities that produce either longitudinal or transverse defocussing and beam loss. Two HOM dampers have been proposed for the LEB cavity. Prototypes of each have been built and tested at low power on the second Los Alamos cavity.

One damper[4] consists of an annular 250 MHz cavity located close to and in series with the acceleration gap. The damper cavity is loaded by four shunt resistors, resulting in a Q of about 1.3. The cavity is designed such that it damps the HOMs much more strongly than the fundamental. The test results for this damper on the second Los Alamos cavity indicate that a similar design tailored for the SSC LEB cavity will satisfactorily damp all longitudinal HOMs up to 1 GHz. The normal cavity losses (ferrite and wall losses) at frequencies above 1 GHz are sufficiently high that external mode damping is not required. This damper is simple and is easily adapted to any cavity which has the accelerating gap located on one end. A potential drawback to this damper is that the ratio of first HOM to fundamental mode damping is not inherently large, and excessive fundamental damping may be required in order to quench the first HOM.

The other damper consists of an external transmission line. One end is attached to a capacitive ring enclosing the cavity center conductor near the gap, and the other end is connected to the cavity center conductor near the shorted end of the cavity. The transmission line is shunted by a 50-ohm resistor near the gap. The length of the transmission line is adjusted until the voltage across the resistor is zero. This mode damper works on the assumption that when this condition is met for one mode, namely the accelerating mode, it is not met for HOMs and their power is dissipated in the resistor. This coupler experiences very high circulating currents at the fundamental frequencies, and care must be taken to maintain the structure as a high Q (low loss) circuit. An effective damper of this type with adequate coupling capacitance should result in no more than 10% damping at the tuned frequency; however since the damper is a very high-Q circuit there would be large damping over parts of the 12.5 MHz LEB tuning range. Another problem with this type of coupler is that it can miss modes. Computer modeling predicted and measurements verified this possibility in the tests on the Los

Alamos cavity for a mode at 300 MHz. Preliminary computer modeling does not predict missed modes in the quarter-wave LEB cavity.

E. Cooling Fluids

Several cooling fluids are under consideration for use in the cavity tuner. The first is a Fluorinert ™ [1] liquid, FC-77 ™. This liquid has a dielectric constant of 1.86, an electric Q $>10^4$, a voltage breakdown of 223 kV/cm, and a boiling point of 97° C. It is the cooling fluid of choice pending SSC environmental and safety approval. The second fluid being considered is water. In spite of its high dielectric constant of 78 and Q <200 it is possible to shape the cooling courses such that high fields are never present in the water. This consideration is necessary to keep its own heat dissipation from becoming objectionably high. The third fluid under consideration is air. Its cooling efficiency is much lower than the liquids, consequently very high air velocities would be required The maximum expected voltage gradients in the air will be about 15 kV/cm. and the inception of corona or even arcing will occur at 25 kV/cm. Air operation would be at 60% of breakdown, while the liquids would both be operated below 10% of breakdown. If the ferrite losses prove to be on the low end of their expected range forced air cooling could become an attractive choice.

III. Test Tuner

A new ferrite test tuner has been designed and is being fabricated to replace the tuner on the second Los Alamos cavity. This tuner is designed to operate with either water or Fluorinert ™ as the cooling fluid. The purpose of the test tuner is to learn as much as possible about the use of both liquids in the presence of high level rf fields. Both the ferrites and the cooling courses in the test tuner will be instrumented with fiber optic temperature probes. Since calorimetric data accuracy with direct liquid cooling will be much greater than in previous tuners, it will be possible to substantially improve the ferrite loss calculations, in particular those calculations which predict the electric Q. The data will also be useful in verifying the finite element thermal calculations. After the tests are completed the metallic tuner parts will be microscopically examined for corrosion from the water.

IV. Conclusion

Since the proposed LEB Cavity is based on a design which incorporates many proven concepts, the probability of achieving a system which operates reliably at the full design voltage seems to be very high. Throughout the design process there has been a conscious attempt to cover the areas of uncertainty with workable contingencies. After the most recent test tuner has been fully evaluated, the LEB cavity design will be finalized, and a full working prototype will be fabricated and tested. The fall back position for this design is that if it doesn't work reliably at full design voltage, it will very probably work reliably at some reduced voltage, and additional cavities would be required to provide 700 kV per turn. There is enough room in the LEB design to accommodate twice the planned number of cavities.

V. Acknowledgments

The LEB Cavity design effort is the culmination of a seven year project, and over these years many people have made substantial contributions. Arch Thiessen, George Spalek, and Rod Smythe are recognized for their assistance, guidance and inspiration. The excellent technicians who all made creative contributions are Mark Doub, Dave Guenther, and Dave Keffeler. George Swain and Bob Kandarian are recognized for their excellent work in producing the design of the second Los Alamos Cavity. Finally Jimmy Rogers and various members of his RF Group are recognized for their assistance, guidance and motivation since the project moved to SSC.

VI. References

1. W.R. Smythe, T.G. Brophy, R.D. Carlini, C.C. Friedrichs, D.L. Grisham, G. Spalek, and L.C. Wilkerson, "RF Cavities with Transversely Biased Ferrite Tuning," *IEEE Trans. Nucl. Sci.* 32 (5), (1985), #2951.

2. C.C. Friedrichs, "Analytic Evaluation of the LAMPF II Booster Cavity Design," *IEEE Trans. Nucl. Sci.* 32 (5), (1985), #2843.

3. M.J. Browman, R.K. Cooper, C.C. Friedrichs, "Testing Urmel-3D by Modeling a Ferrite Tuned RF Cavity," Proceedings of the 1987 IEEE Particle Accelerator Conference, Washington, D.C., (March 1987), pp1898-1900.

4. W.R. Smythe, C.C. Friedrichs, and L.S. Walling, "Proton Synchrotron RF Cavity Mode Damper Tests," 1991 Particle Accelerator Conference, San Francisco, CA (May 1991).

[1] Product of 3M Company.

Superconducting Niobium Sputter-coated Copper Cavity Modules for the LEP Energy Upgrade

C. Benvenuti, P. Bernard, D. Bloess, G. Cavallari, E. Chiaveri, E. Haebel,
N. Hilleret, J. Tückmantel and W. Weingarten
CERN — European Organization for Nuclear Research
CH–1211 Geneva 23 (Switzerland)

Abstract

Experience from the construction, assembly, and tests of two superconducting (s.c.) cavity modules for LEP are given. Each module consists of four individual four-cell 352 MHz Nb sputter-coated Cu cavities equipped with an RF power coupler, higher-order-mode (HOM) dampers and frequency tuner, housed in a single cryostat. The demountable HOM dampers of a new type designed for sputter-coated cavities allow Q_{ext} of 9000 for the HOMs with the largest (R/Q). Q values are higher (4.5 to $11 \cdot 10^9$) than those for similar Nb sheet cavities up to the maximum accelerating fields obtained (6 to 9.5 MV/m). The field limitation is electron loading and never thermal breakdown. Results on vertical tests of individual cavities are reported (Q value, maximum accelerating fields, residual resistance). They are complemented by results on horizontal tests of individual cavities, and on the fully equipped klystron-driven four-cavity module.

I. INTRODUCTION

The first s.c. cavity module for the LEP energy upgrade [1] to centre of mass energies of 200 GeV "LEP 200" has been installed in the first shutdown of LEP in winter 1990 [2]. This module consists of four individual four-cell cavities mounted in one common cryostat. The cavities are made of "cavity grade" Nb sheet. However, for reasons of higher thermal conductivity and reduction of material costs an alternative solution has been pursued at CERN from the beginning: thin Nb films deposited on a Cu cavity body as substrate [3] (Nb/Cu cavities). This technology has been mastered, and in addition offers inherent advantages not anticipated. Thermal breakdown (quench) from tiny normal conducting defects is absent thanks to the large thermal conductivity of the OFHC–Cu used (400 to 500 W/(mK)). Shielding against static magnetic fields of the same order of magnitude as the earth's magnetic field is unnecessary [4], significantly alleviating the task to obtain high Q values in an accelerator environment. A twin module of two Nb/Cu cavities [5] has successfully been operated in the SPS accelerator. What remains to be shown is the feasibility of an industrial production of such cavities. Therefore, CERN has launched a series production of a small number of Nb/Cu cavities in house. Eight of them have been assembled into two modules to complement the first one from Nb sheet. One is already installed in LEP, the second one is due for installation in a short summer shutdown, raising the total installed s.c. RF voltage up to the designed 102 MV.

II. FABRICATION AND SURFACE PROCESSING

The beam tubes are rolled, longitudinally electron beam (EB) welded, ball extruded to give way to the power and HOM coupler holes. The cavity half cells are produced by lathe spinning. The beam tubes as well as the half cells are degreased, ground, if necessary, electropolished (40 μm, phosphoric acid, n-butanol), and rinsed with water. Conflat type flanges are brazed to the coupler and beam tube ports. All parts are joined by EB welding. The whole cavity is degreased, filled with sulfamic acid, chemically polished (20 μm, sulfamic acid, n-butanol, hydrogen peroxide, and ammonium citrate), rinsed with sulfamic acid, water, and alcohol, and dried under clean laminar air flow. The magnetron cathode is mounted in a class 100 clean room. This is what we call a standard process. The sputtering is performed by stepwise powering different electromagnets inside the cathode. Other details can be found elsewhere [6]. The magnetron is removed in the clean room, the cavity equipped with RF input and pick-up antennas, closed, and rinsed with ultrapure water (18 MΩ cm) from a moving PVC tube. The resistivities of the inlet and outlet water are recorded. Presently, we also monitor the TOC (total organic carbon), particle content (> .1 μm), and at regular intervals the bacteria content of the water plant. After drying by pumping, the cavity is vented with filtered (.2 μm pore size) dry nitrogen gas, mounted on the cover of the vertical cryostat, evacuated and cooled down for the RF tests (table 1).

Table 1
RF tests on Nb/Cu LEP type cavities (only the last coating is listed)

Cavity #	Coating #	Treatment	$Q(E_a \approx 0)$ [10^9]	E_a max [MV/m]	# Hot spots[a]
45	4	SV	7.5	4.6	0
46	3	SCV	7.0	5.4	0
		WRV	7.1	6.7	
		H	4.9	5.5	
47	2	SCV	12.	8.1	1
		H	7.0	2.8	
		H	8.5	6.1	
48	3	SCV	8.5	6.8	0
		V(b)	8.0	6.5	
49	3	SCV	10.	9.4	3
		H	6.4	7.1	
50	3	SCV	9.0	5.2	0
51	1	SV	8.0	7.7	5
		H	4.5	5.3	
		MH	4.6	6.1	
52	1	SV	8.1	9.7	0
		H	5.3	5.4	
53	2	SV	9.0	8.3	1
		H	5.9	8.0	
54	1	SV	10.	8.3	
		H	5.2	6.5	
55	1	SV	7.5	7.1	
		H	5.5	7.4	
56	2	S(c)V	9.0	1.5	0
		WRV	9.0	6.9	
57	1	SV	8.5	5.8	0
		H	2.7	5.1	
		H	2.8	5.3	
		MH	2.8	5.3	
		V	3.2	3.7	
		WR(d)V	8.5	6.4	
		(c)H	8.0	7.6	

Legend: S = standard treatment, C = chemical polishing of Cu instead of electropolishing, R = rinsing, W = water, H = horizontal test, V = vertical test without welded He tank, M = magnetic compensation coils mounted, (a) = "hot spot" is explained in the text, (b) = with He tank mounted, (c) = no WR, (d) = desinfected W.

0-7803-0135-8/91$01.00 ©IEEE

III. THE RF TESTS

A. *The tests of the individual cavities in a vertical cryostat*

The vertical test consists of the determination of the Q value vs accelerating gradient E_a at 4.2 K (fig. 1), RF and He processing (conditioning the cavity in a low partial pressure of He gas), if necessary, to eliminate electron loading and lowering the temperature by pumping on the He bath to determine the residual surface resistance R_{res}, the BCS surface resistance R_{BCS}, and performing temperature mapping [7].

Whenever the cavity has given unsatisfactory results, for instance stepwise Q decrease and/or persistent electron loading from defects of the Nb layer [3], the cavity is warmed up for repair which consists of removing the blister or stripping the Nb layer and recoating the cavity. The maximum accelerating gradient of an individual cavity is 9.7 MV/m (table 1), the maximum Q value (4.2 K) at 6 MV/m $4.8 \cdot 10^9$, the average Q value (4.2 K) at 6 MV/m $4.0 \cdot 10^9$.

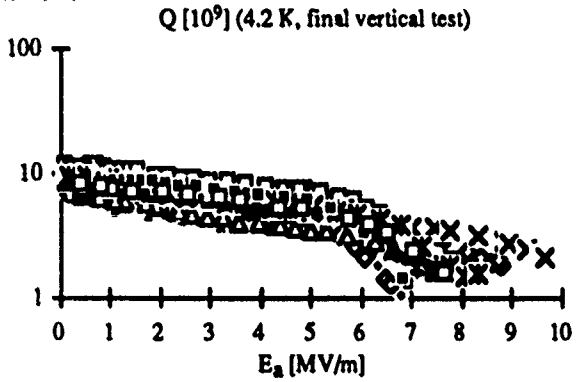


Fig. 1 Q value vs accelerating field for LEP type Nb/Cu cavities.

In order to study the long-term stability of the coating we have stored a cavity for two years under dry filtered N_2 gas. The RF performance was unchanged. A 500 MHz monocell cavity, when stored under laboratory air for one year, showed a slight decrease of Q. It has been much more pronounced after a bakeout at 200°C (factor 2 lower).

B. *The tests of the individual cavities in a horizontal cryostat*

When the vertical tests give satisfactory results, the He tank is welded around the cavity. It is again rinsed with ultrapure water, equipped with the final pick-up antennas, other fittings, and the tuners [8], assembled in the horizontal accelerator cryostat, evacuated to a pressure in the lower 10^{-7} mbar range, and cooled down to 4.5 K. Again, the Q value vs accelerating gradient E_a is determined.

In about half the cases, the results of the vertical and horizontal tests coincide within the measurement error (10%). In the other cases a decrease of the Q value to up to a factor of 2 has been encountered. One such cavity (# 57 in table 1) was remeasured vertically (same result as horizontally), rerinsed with ultrapure water from our clean water plant which before has been subject to disinfection from bacteria (< 10 colonies per 100 ml water). The Q went up to the one obtained before the degradation. The cavity was assembled for the horizontal test (no water rinsing) and the $Q(E_a)$ curve remained essentially the same as in the previous vertical test.

C. *Tests on the static magnetic field dependence*

The results of tests under different static magnetic fields confirm what has been observed in several previous tests. Up to twice the earth's magnetic field, no changes in Q value are seen.

We also have applied larger static magnetic fields B_0 (up to 5.1 mT) perpendicular to the equatorial surface by mounting a coil of .45 m diameter 8 cm off the equator of one cell. After cool down we have determined $Q(E_a)$ in a convenient parametrization as, for instance, $Q(E_a) = Q_0 \exp(-\alpha E_a)$ [4], and have taken temperature maps (tables 2 and 3). From the absolute calibration of the resistors [9] we analyze the supplementary residual surface resistance. When the cavity is exposed to a static magnetic field of 5.1 mT, strong electron multipacting is observed.

Table 2
Parametrized Q curve ($Q(E_a) = Q_0 \exp(-\alpha E_a)$) at 4.2 K for different local static magnetic fields

B_0[mT]	Q_0	α [m/(MV)]	Q (6MV/m)
0	9.5	.141	4.1
2.5	8.9	.158	< .7
4.1	7.8	.197	< .52
5.1	8.0	.268	< .36
The relative error of Q_0 and α is 10%, [Q] = 10^9, [Ea] = MV/m.			

Table 3
Increase of local residual surface resistance at 3 K by static magnetic field of 2.5 mT

E_a [MV/m]	R_s^{local} [nΩ]
4.1	73 ± 30
5.3	178 ± 83
6.3	231 ± 56

D. *Test of the complete cryomodule and operation in LEP*

After the test of the individual cavities in their horizontal accelerator cryostat each cavity is equipped with two HOM couplers and a power coupler [8] (cryo-unit). Four cryo-units are joined together in a clean area into the common accelerator cryostat of 12 m length (cryomodule). Its total length is determined by the width of the access pits of LEP. The cryomodule is of modular construction. It has the maximum length that can pass through the LEP access pits. For the test in the laboratory with a 1 MW klystron, the average accelerating gradient has been 5 MV/m, in LEP, 3.7 MV/m, somewhat lower than the design value (5 MV/m). This is mainly due to an instability of the RF voltage of one individual cavity, being investigated right now. The total RF voltage from 2 cryomodules in LEP is 50 MV.

For the HOM couplers we have chosen a demountable geometry. The tubular coupling port needs a s.c. surface which is always sputter deposited with the cavity. The fundamental mode current is shunted away at the front end of the coupler, where all surfaces are s.c., such that no current flows across the joint [10]. In addition, this HOM coupler interacts electrically and magnetically, which improves the damping of the TE_{111} dipole modes at 460 MHz. The overall damping supplied is relatively high, Q_{ext} being 9000 for the TM_{011} mode with the largest (R/Q) value, 55 Ω. This coupler has sufficient damping to cope with 16 bunches in LEP.

IV. DISCUSSION

There are features which do not vary significantly between different cavities. The BCS surface resistance is constant (fig. 2), $\langle Q_{BCS}(4.2\ K)\rangle = (1.1 \pm .1) \cdot 10^{10}$. The lowest residual resistance is < 2 nΩ. We did not observe a quench due to excess heating at a

defect. There are 7 coatings with no "hot spots" (table 1), defined as a peak on the temperature map exceeding 100 mK (500 mW at 2.5 K). Conditioning the cavity to cure against electron multipacting at $E_a \approx 5$ MV/m [11] is short (minutes). Whenever we have tested the Q value under the influence of static magnetic field up to about two times the earth's magnetic field, the result was null. Led by this encouraging experience, the cryomodule is operated in LEP, the performance of the cavities to be produced by industry has been specified as $Q_0 \geq 4 \cdot 10^9$ at $E_a = 6$ MV/m and 4.5 K.

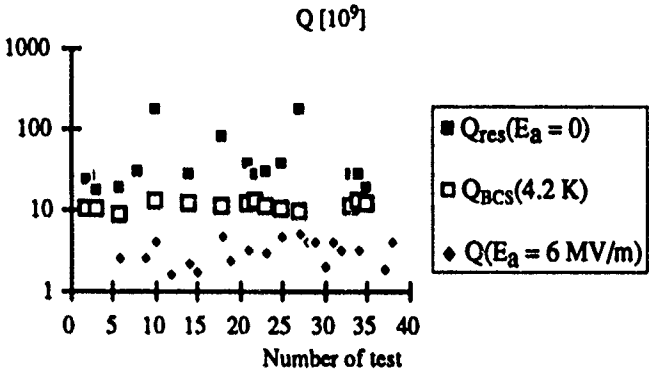


Fig. 2 Q values vs test number for all RF tests performed.

There are other features, however, which differ from one cavity to the other. For example, the number of hot spots varies between 0 and 5. There are cavities (about one half), the Q value and accelerating field of which are lower in the horizontal test than in the preceding vertical test. The residual Q value, $\langle Q_{res} \rangle = 5 \cdot 10^{10}$, and the Q value at 6 MV/m, $\langle Q(6MV/m) \rangle = 3 \cdot 10^9$, show a scatter (fig. 2). High resistivity of the drain water (> 10 MΩcm) is not a sufficient condition to guarantee short He processing (several hours) (fig. 3). But it is a necessary condition to avoid exceedingly long He processing times (> 25 h).

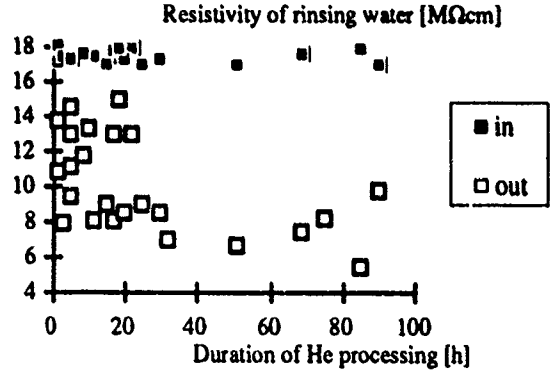


Fig. 3 Long duration of He processing is correlated with a low resistivity of the drain water (not correlated with the inlet water).

These observations indicate that the parameter set for cavity processing is not yet sufficient. In this respect our report gives the status on how to improve cavity performance and is not yet a final one.

We feel that the water quality is important, and we will not exclude the possibility that the assembly might have caused some problems (after displacing the cavity from the horizontal to the vertical test set-up, the electron loading increased). There is a correlation of the drain water resistivity and the time needed for "He-processing", which is applied to reduce electron loading by field emission. This is consistent with the results on Nb sheet cavities at KEK [12]. After having controlled the clean water parameters (TOC < 50 ppb, bacteria content < 10 colonies per 100 ml, resistivity > 17.5 MΩcm) and, if necessary, purged the clean water plant, the Q value has been high and the maximum accelerating field has been obtained rapidly without long conditioning. After a contamination we have been able to reestablish the performance of a cavity with clean water rinsing only (# 57 in table 1).

The insensitivity of the Nb/Cu cavities against small enough static magnetic fields is confirmed but does not survive up to fields of 3 mT and larger, which are in the order of stray fields of s.c. magnets (future LHC). When the cavity is exposed to a uniform static magnetic field the losses are certainly more than 4 times larger than the experimentally observed losses from the coil (which locally generates the same field). From that the upper bound of the Q value indicated in table 2 is derived.

V. CONCLUSION

The first cryomodule of four 352 MHz Nb-coated Cu four-cell cavities is being operated in LEP. The average gradient is 5.0 MV/m in the laboratory and 3.7 MV/m in LEP. The maximum accelerating field of an individual cavity is 9.7 MV/m. With 2 s.c. modules 50 MV has been obtained in LEP.

Acknowledgements

We thank E. Picasso for initiating and continuously pushing the project. Colleagues from machining, cleaning, chemical, heat treatment , electron beam welding, brazing and cryogenic facilities, have contributed to the success of the project. We thank them all for their untiring enthusiasm. The collaboration with the AT-Cryogenics and the SL-RF groups was indispensible and is gratefully acknowledged.

REFERENCES

[1] C. Wyss, this conference.

[2] C. Arnaud et al., proc. 2nd Europ. Part. Acc. Conf., Nice, eds P. Marin and P. Mandrillon (1990) 152.

[3] C. Benvenuti et al., Appl. Phys. Lett. 45 (1984) 583; C. Benvenuti et al., IEEE Trans. Mag. MAG-21 (1985) 153.

[4] G. Arnolds-Mayer and W. Weingarten, IEEE Trans. Mag. MAG-23 (1987) 1620.

[5] C. Benvenuti et al., proc. 2nd Europ. Part. Acc. Conf., Nice eds P. Marin and P. Mandrillon (1990) 1079.

[6] C. Benvenuti et al., proc. 3rd Workshop on RF Superconductivity, Argonne, Ill., USA, ed. K.W. Shepard, ANL-PHY-88-1 (1987) 445.

[7] P. Bernard et al., Nucl. Instr. and Meth. 190 (1981) 257.

[8] G. Cavallari et al., proc. 3rd Workshop on RF Superconductivity, Argonne, Ill., USA, ed. K.W. Shepard, ANL-PHY-88-1 (1987) 565.

[9] R. Romijn et al., IEEE Trans. Mag. MAG-19 (1983) 1318.

[10] E. Haebel et al., in preparation.

[11] W. Weingarten, proc. 2nd Workshop on RF Superconductivity, CERN, Geneva, Switzerland, ed. H. Lengeler (1984) 551.

[12] K. Saito et al., proc. 4th Workshop on RF Superconductivity, KEK, Tsukuba, Japan, ed. Y. Kojima (1989) 635.

A NEW MAIN CONTROL ROOM for the AGS COMPLEX*

P. F. INGRASSIA, R. M. ZAHARATOS and O. H. DYLING**

BROOKHAVEN NATIONAL LABORATORY
UPTON, NEW YORK 11973

INTRODUCTION

A new Main Control Room (MCR) has been built to control the accelerators of the AGS Complex. A new physical environment was produced to better control light, sound, temperature, and traffic. New control consoles were built around the work-stations that make up the distributed control system. Equipment placement within consoles and console placement within the room reflect attention to the "human factors" needs of the operator.

MASTER PLAN

The Master Plan called for a doubling of MCR floor space to 1600 sq.ft, a new lab for the accelerator operators, new office space, an MCR conference room, a relocated kitchen, and a small room for use as a distribution point for control wire and signal cable. Modification of the facility began in 1987. In order to minimize the impact on the Physics program work was carried out during subsequent summer AGS shutdowns and was completed in 1989. Further, the plan would correct many of the problems found in the 26 year old MCR: insufficient number of control stations, inadequate and poor control over lighting, inadequate heating and ventilation, high ambient noise levels, and years of accumulated control and signal wire.

Five control consoles were built and installed to increase the number of machine physicists, operators, and development personnel that could be supported simultaneously. The consoles were all designed and implemented as general purpose consoles so that a user would be able to control any facet of the accelerator operation from any of the control consoles. The consoles were arrayed in circular fashion, see Figure 1, in order to better allow the operations staff to be aware of who the users of the controls were at any time.

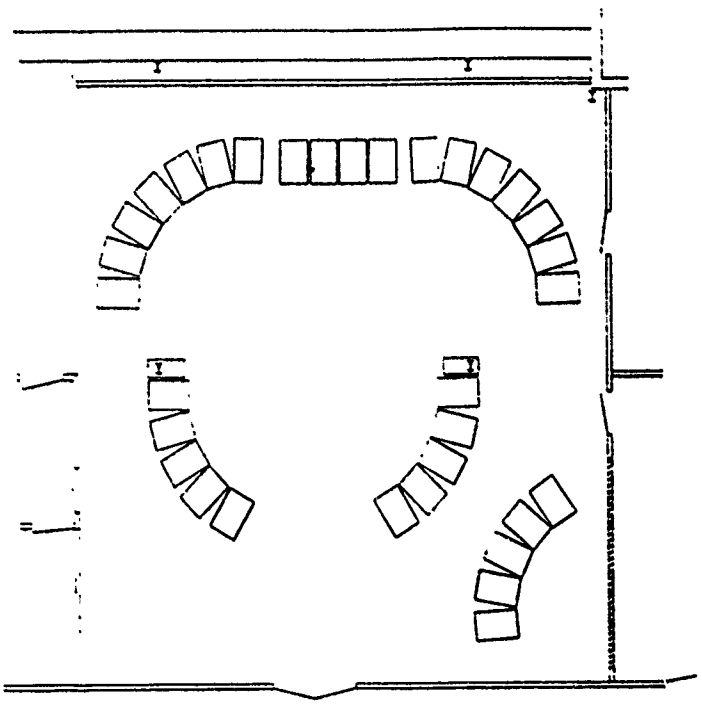


Figure 1

Lighting for the new MCR is provided by four independent concentric rings of fluorescent lighting fixtures. The outermost ring is a "wall wash" designed to provide sufficient ambient lighting for most tasks in the room and yet minimize glare on the work-station screens. The innermost rings consist of two foot by two foot fixtures that make use of anti-glare diffuses. Each console is also provided with locally controlled task lighting in the form of two incandescent spotlights aimed at the console work area.

Two air conditioning zones are provided for cooling and ventilation. The volume above the dropped ceiling is used as a supply plenum in order to provide air with reduced

*Worked performed under the auspices of the U. S. Dept. of Energy

**Plant Engineering Department, Brookhaven National Laboratory

0-7803-0135-8/91$01.00 ©IEEE

foot supply diffuses are regularly interspersed amongst the lighting fixtures. The air return is a room long duct located along the MCR north wall and it is an integral part of the forty foot long storage closet.

Ambient noise is controlled by a fabric covered acoustic wall tile and by acoustic ceiling tiles. Particularly noisy equipment was removed from the MCR entirely.

Hundreds of pounds of cable and wire were removed from the MCR. Cable distribution is accomplished by pathways under a new raised computer floor. A "terminal room annex", adjacent to the north west wall of the MCR, is the source for all signal and control wire as opposed to the holes in the ceiling that previously directly fed the consoles. Signal distribution, in the terminal room annex, is done on a per console basis and one has the ability to cross-connect signal wires between any consoles simply by installing jumper cables at this master matrix.

THE CONSOLES

Each general purpose console, see Figure 2, is made up of a core of five racks, four of which contain identical components, placed in the same location at each control station. The fifth rack contains special equipment, for example high speed oscilloscopes and each rack houses a laser printer. The heart of each control station is a 19" color monitor driven by an Apollo 4500 processor and 15" color monitor driven by an Apollo 3000 processor. The former work-station is used to run multiple graphics displays while the latter runs just two programs; one for equipment control and the other to provide switching for the analog and video signal multi-plexers [1] and oscilloscope triggers.

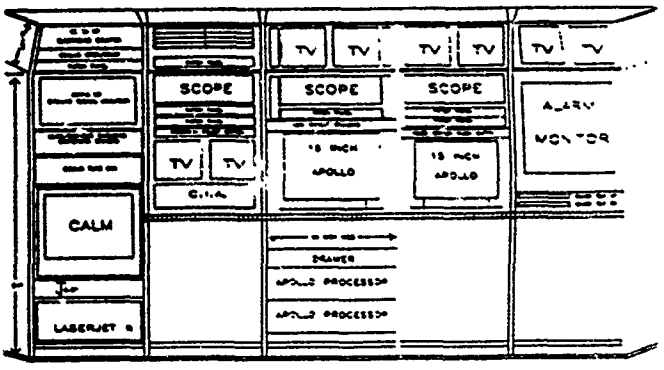


Figure 2

Each console supports three, four channel oscilloscopes of varying speed and capability. Eight, 9" video monitors at each console can be connected to any of 64 input videos. Each console can also reserve the input to a central video copier for hard-copy records of any video input. An alarm screen is also provided at each station.

Communications hardware was also addressed. A commercially available digital phone system, was installed to incorporate public address, two radio channels, four interphone channels, and normal telephone functions. Two such units are placed at each console.

Each console is ideally suited to support two operators. Equipment is arrayed such that the most frequently used functions are located at the center of the console. Less frequently used systems are placed at the extremes. The console wraps around the operator in two planes so that minimal head movement is required to see any of the displays.

CONCLUSION

After a year of use and some fine tuning the users are, in general, pleased with the results. The project is the result of the hard work and dedication of the MCR operations staff and a host of others in the AGS Department. Special recognition goes to Dr. Th. Sluyters and Mr. J. Griffoli whose vision and support made the new MCR possible.

REFERENCE

1. T. D'Ottavio, et al., "Programs for Control of an Analogue-Signal Switching Network", Nuclear Instruments and Methods in Physics Research, 1990, North-Holland.

Personnel Protection and Beam Containment Systems for the 3 GeV Injector*

R. Yotam, J. Cerino, R. Garoutte, R. Hettel,
M. Horton, J. Sebek
Stanford Synchrotron Radiation Laboratory, P.O. Box 4349, Bin 69, Stanford, CA 94309-0210
E. Benson, K. Crook, J. Fitch, N. Ipe,
G. Nelson, H. Smith
Stanford Linear Accelerator Center, Stanford University, Stanford, CA 94309-0210

Abstract

The 3 GeV Injector is the electron beam source for the SPEAR Storage Ring, and its personnel safety system was designed to protect personnel from both radiation exposure and electrical hazards. The Personnel Protection System (PPS) was designed and implemented with complete redundancy and is a relay based interlock system completely independent from the machine protection system. A comprehensive monitoring of the system status, and control of the Injector PPS from the SPEAR Control Room via the control computer is a feature. The Beam Containment System (BCS) is based on beam current measurements along the Linac and on Beam Shut Off Ion Chambers (BSOIC) installed outside the Linac, at several locations around the Booster, and around the SPEAR storage ring. An outline of the design criteria is presented with more detailed description of the philosophy of the PPS logic and the BCS.

I. Introduction

A Personnel Protection System can be considered to have two main parts, an access control system and a radiation alarm system.

The access control system is intended to prevent unauthorized or accidental entry into radiation areas. Elements of this system include physical barriers, beam stoppers, signs, closed circuit TV, flashing lights, audible warning devices including the associated interlock system, and a body of administrative procedures that define conditions where entry is safe. The radiation alarm system can include radiation sensors which monitor radiation field directly, or indirect methods like the use of beam current detectors.

The Injector is divided into two independent Personnel Protection Systems, one for the Linac vault and Diagnostics room and the second for the Booster ring and transport line. The SPEAR storage ring is controlled by and independent PPS.

The LTB (Linac-To-Booster) beam stoppers separate the Booster from the Linac and are controlled from the Booster PPS Control Panel. The BTS (Booster-To-SPEAR) beam stoppers separate the SPEAR storage ring from the Booster and are controlled from the SPEAR PPS Control Panel.

The Linac, the Booster, and the SPEAR Storage Ring are operated as independent systems. Linac studies can be carried out by switching the Linac beam into the Diagnostics room while permitting entry to the Booster, and Booster studies can be carried out by inserting the BTS stoppers, which allows entry to SPEAR. The various modes of operation are summarized in table 1.

Table 1
The Linac, Booster, and SPEAR Storage Ring modes of operation.

Linac	BOOSTER	SPEAR
Operates	Operates	Operates
Operates	Operates	Does not operate
Operates	Doesn't Operate	Operates
Operates	Doesn't Operate	Doesn't Operate
Doesn't Operate	Operates	Operates
Doesn't Operate	Operates	Doesn't Operate
Doesn't Operate	Doesn't Operate	Operates
Doesn't Operate	Doesn't Operate	Doesn't Operate

II. Philosophy

The Injector PPS provides the operational flexibility required for the various modes of operation yet is sufficiently interlocked so that reliance on administrative procedures is minimized. The aim of the PPS is to protect people and not the machine, therefore the system is fully independent and distinct from the machine control system. The main design rules for the PPS [1] are: (1) The using of components with high degree of reliability (2) Designing fail-safe circuits (3) Building duplicate circuits or redundant components in critical applications where the single failure of a circuit or device could lead to a hazard.

III. System Design [2]

A. Access Interlocks

The Linac vault and Diagnostics room Access Interlock is designed to provide the following Security Levels:

Permitted Access — Unrestricted entry to the Linac vault and the Diagnostics room. The Linac RF and the electrical hazards are OFF.

No Access — The Linac vault and Diagnostics room are searched and secured. Linac may be turned ON.

*Work supported by the Department of Energy, Office of Basic Energy Sciences, Division of Material Sciences.

0-7803-0135-8/91$01.00 ©IEEE

The Booster Access Interlock is designed to provide the following Security Levels:

Permitted Access — Unrestricted entry to the Booster area. Beam OFF, LTB stoppers and Booster RF are IN/OFF, electrical hazards are OFF.

Controlled Access — Entry under control of the Booster operator; requires a key release and logging of entries. Beam OFF, LTB stoppers and Booster RF are IN/OFF, electrical hazards are OFF.

Restricted Access — Booster has been searched and secured. Beam OFF, LTB stoppers and Booster RF are IN/OFF, electrical hazards may be energised.

Restricted Access Safety Key (RASK) — Booster has been searched and secured. Beam OFF, LTB stoppers and Booster RF are IN/OFF, electrical hazards may be energised. The RASK mode provides a mechanism for a Hazard Test Team to enter the Booster and test electrical hazards.

No Access — The Booster has been searched and secured. LTB stoppers may be opened and Booster RF may be turned ON, electrical hazards and beam may be turned ON.

The transfer of the Booster access mode is always done in a sequence:

$$PA \Rightarrow CA \Rightarrow RA \Rightarrow NA$$
$$PA \Leftarrow CA \Leftarrow RA \Leftarrow NA$$

Table 2
Access/Stopper Requirements.

Requires that / Access to	SPEAR Ring Stoppers	BTS Stoppers	Booster Stoppers	Additional Requirements
SPEAR Ring	IN	IN	N/A	SPEAR RF and Electrical Hazards OFF
BTS Transport Line	IN	IN	IN	
Booster Ring	N/R	N/R	IN	Booster Electrical Hazards OFF
Linac/Diag. Rooms	N/A	N/A	N/R	Linac RF and Elec. Hazards OFF

—N/A = not applicable, N/R = not required—

The access to the SPEAR or Booster ring requires that the appropriate stoppers be "IN". The Access/Stopper status are given in table 2.

Table 3
PPS Violation and Response.

RESPONSE / PPS VIOLATION	SPEAR RING STOPPERS	BTS STOPPERS	BOOSTER STOPPERS	LINAC	SPEAR INJECTION SEPTUM MAGNET PS	HUTCH STOPPERS	ADDITIONAL RESPONSE
SPEAR RING	IN	IN	IN IF BTS STOPPERS ARE NOT IN	OFF IF LTB OR BTS STOPPERS ARE NOT IN	N/A	N/A	DUMP SPEAR ELECTRICAL AND RF HAZARDS
BTS	IN	IN	IN	OFF IF LTB OR BTS STOPPERS ARE NOT IN	N/A	N/A	DUMP BOOSTER ELECTRICAL AND RF HAZARDS
BOOSTER RING	N/R	N/A	IN	OFF IF LTB STOPPERS ARE NOT IN	N/A	N/A	DUMP BOOSTER ELECTRICAL AND RF HAZARDS
LINAC AND DIAGNOSTICS ROOMS	N/R	N/R	IN IF LTB STOPPERS ARE NOT IN	OFF	N/A	N/A	
SYNCHROTRON BEAM LINE HUTCH	IN	IN	IN IF BTS STOPPERS ARE NOT IN	N/R	N/A	IN	

–N/A = not applicable, N/R = not required–

B. Rules and Functional Description

1. All doors have provisions for opening mechanically in emergency situations.
2. Emergency Off units are installed in the Linac vault and Diagnostics room, and in the Booster ring.
3. Opening the gates for entrance to the Booster or exit from inside while the Booster is in the Controlled Access, is supervised by an Operator. A solenoid release mechanism is used.
4. In Restricted Access only the electrical hazards may be energised. The Booster RF power system is interlocked Off during this access mode.
5. When the Booster is in Restricted Access or No Access, NO gate is allowed to open under any circumstances except emergencies. Any time a gate is opened a Security Fault results.
6. Opening any interlocked gate or door when not allowed, or actuating an Emergency Off button or Emergency Entry/Exit, in the Linac vault and Diagnostics room, after they have been searched and secured results in a Security Fault and terminates the secured state. The Linac vault and Diagnostics room must be re-searched and re-secured. The response to a PPS violation in the Linac vault or Diagnostics room is shown in table 3.
7. Opening any interlocked gate or door when not allowed, or actuating an Emergency Off button or Emergency Entry/Exit, after the Booster has been searched and secured results in a Security Fault and terminates the secured state. The Booster must be re-searched and re-secured. The Booster must be re-searched and re-secured. The response to a PPS violation in the Booster is shown in table 3.

The response to PPS violations in the SPEAR ring [3], the Booster-To-SPEAR transport line and in a synchrotron beam line hutch is also shown in table 3.

C. The RASK Mode

The personnel protection system is designed to protect personnel from both radiation exposure and electrical hazards. As such, the Access Interlock prevents the operation of electrical hazards while personnel are in the ring. The RASK mode provides a mechanism for a test team to enter the Booster and test electrical hazards. RASK is the acronym for Restricted Access Safety Key. When in the RASK mode: (1) The Booster can not be transferred to No Access (2) The keybanks at the entry points to the Booster cannot release additional keys. (3) The keyswitches on each Emergency Off unit are active, and the Safety Key can switch ON the Hazard Enable Permissive. (4) The emergency off units in the Booster provide a local shut-off of the all electrical hazards in case of an emergency.

D. Operation of the Booster PPS from SPEAR Control Room

The PPS is interfaced to the control computer through isolated digital input and output modules known as IDIMs and IDOMs respectively. The IDIMs and IDOMs are CAMAC based modules. For each hardware PPS status lamp and control button there is an equivalent digital signal interfaced through IDIM and IDOM modules. This facilitates the construction of the computer status monitoring and control system menu which is designed to look very similar to the actual PPS panel, and to minimize any potential source of confusion about the differences in operation between the two. Operating the Booster PPS by computer has the same effect as pushing the physical buttons on the PPS control panel. The PPS logic is in control of the system and will not respond to erroneous remote commands unless the correct conditions exist. One additional feature of the computer interface is that the digital control functions are interlocked with a hardware enable button located in the SPEAR Control Room which must be pushed for any computer control commands to have effect. This is to prevent accidental commands sent to the Booster PPS by the computer user at the SPEAR Control Room.

E. Beam Containment

The Beam Containment System (BCS) [4] is based on beam current measurements along the Linac, on monitoring the chopper high voltage pulse, and on Beam Shut Off Ion Chambers (BSOIC). The Beam Containment Interlock for the Injector is designed to remove power from the three Linac sections that accelerate particles from ≈2.5 MeV to ≈150 MeV by interrupting trigger signals to the Linac modulators and to the RF amplifier that provides the s-band drive signal to the Linac klystrons if: (1) The number of accelerated particles in the Linac pulse exceeds a preset limit. (2) The high voltage pulse applied to the chopper is too high, allowing more than a few s-band bunches to enter the Linac. (3) An excessive radiation level is detected by any one BSOIC connected to the interlock. Redundancy in the beam current measurement is provided by measuring the current at two locations using two toroids and two Average Current Monitors (ACM). The output signal from each toroid is amplified and integrated. If the integrated current exceeds a preset value, a system fault is generated. The BSOIC's are installed in the following locations: one BSOIC inside the Booster ring shielding adjacent to the LTB line, (the fault channel of this BSOIC is automatically bypassed when the Booster is in No Access); two BSOIC's outside the Linac room; five BSOIC's outside the Booster ring and the Booster-To-SPEAR transport line, and twelve BSOIC's around the SPEAR ring. All BSOIC's are adjusted to produce an alarm signal if the radiation level exceeds 10 mrem/hr, and produce a trip if the radiation level exceeds 50 mrem/hr. All BSOIC's faults are latched and are individually resetable locally with Interface Chassis reset buttons, or the can be reset collectively via the Injector computer.

IV. Glossary

LTB stoppers:	Two mechanical stoppers and one dipole magnet
Booster stoppers:	LTB stoopers and the Booster RF
BTS stoppers:	One mechanical stopper, BTS dipole magnets, and Ejection Septum manget

V. References

[1] SLAC, "Health Physics Manual of Good Practices for Accelerator Facilities," April 1984. SLAC Report - 327.

[2] R. Yotam, R. Hettel, and J. Cerino, "Design Proposal for the SSRL Injector Project Booster Personnel Protection System," August 1990. SSRL Engineering Note 169.

[3] H. Smith and R. Yotam, "Design Proposal to Rebuild the SPEAR Personnel Protection," January 1991. SSRL Engineering Note 170.

[4] R. Hettel, "SSRL Injector Beam Containment Interlock," May 1991. SSRL Engineering Note.

A COOLING-WATER SYSTEM FOR THE ACCELERATOR TEST FACILITY

Mitsuo Akemoto
KEK, National Laboratory for High Energy Physics
Oho 1-1, Tsukuba, Ibaraki 305, Japan

and

Yutaro Nishinomiya* and Akio Suyama
Taiyo Valve Mfg. Co., Ltd.
Ohta-ku, Tokyo 143, Japan

Abstract[1]

A cooling-water system for the Accelerator Test Facility of Japan Linear Collider has been constructed and operated successfully. The input temperature of the cooling-water supplied to the subharmonic bunchers, prebunchers and accelerating structures is required to hold at 36.5 ± 0.1 °C in order to insure the electrical phase stability. The temperature control for this system employs a three-way valve, a tank and line heaters. The design, specifications and results of performance tests of the system are described.

I. INTRODUCTION

A TeV electron-positron linear collider JLC (Japan Linear Collider) has been proposed in KEK. In order to realize the JLC, there are many technical problems to be solved. In order to solve the technical problems and develop the linear collider technologies, the Accelerator Test Facility (ATF) has been built [1]. In the ATF in Phase-I, we have constructed the injection system consisting of a 240 keV electron gun, subhermonic bunchers (SHB), prebunchers and a short regular section which is 0.6 m long of a 2856 MHz, $2\pi/3$ mode, constant-gradient structure [2]. A cooling-water system has to be developed in order to realize the stable operation of the ATF. A cooling-water system for the ATF is classified into two types as a dummy load cooling-water system and a 0.1 °C control cooling-water system. The former supplies the cooling-water to the dummy load of the accelerating structure, helmholtz coils and so on, which are not necessary for high precision temperature control. The latter supplies the cooling-water to the SHBs, prebunchers and accelerating structures, which are necessary to control the temperature of the cooling-water with an accuracy of ± 0.1 °C in order to insure the electrical phase stability. In this paper, the design, specifications and results of performance tests of the 0.1 °C control cooling-water system are described.

II. DESIGN AND SPECIFICATIONS

The temperature control of the accelerating structure is necessary to maintain electrical phase stability. In the ATF, we use the 0.6 m accelerating structure which is $2\pi/3$ traveling wave constant gradient type with 17-cells. The phase shift caused by the deviation of the temperature of this accelerating structure is about 7 °/°C. Therefore, the stability of water temperature must be < ± 0.1 °C.

The input temperature of the cooling-water in the accelerating structure is usually around 30 °C. The cooling-water system for this input temperature needs a refrigerator since maximum atmospheric temperature is more than 30 °C in summer. If the input temperature is set at more than 35 °C, we can adapt a simple cooling-water system using a heater and cooling tower. Thus, the input temperature was set at 36.5 °C to employ a cooling-water system controlling water temperature only by heaters. The control system with the heater is easy and adaptable for high precision temperature control. Thus, the temperature of the cooling-water supplied to the injector must be held at 36.5 ± 0.1 °C. Design and operating parameters for this system are shown in Table 1.

Table 1
Design parameters of the 0.1 °C control cooling-water system

Component	Flow(l/min.)	Heat load(kW)
SHB(119 MHz)	5	0.027
SHB(238 MHz)	5	0.027
SHB(476 MHz)	5	0.027
Prebuncher I	10	0.1
Prebuncher II	10	0.1
Buncher	15	0.5
0.6 m accelerating structure	20	7.2
Accelerating structure*	20x3	7.2x3
Total	130	29.581

(* Three accelerating structures will be installed in future.)

III. SYSTEM DESCRIPTION

A. Equipment

A flow diagram of the system is shown in Fig. 1. It consists of three loops as follows; the primary, the secondary and the accelerator cooling-water loop. Two heat exchangers HEX1

*Present address: Nichias Corporation, Tokyo 105, Japan.

0-7803-0135-8/91$01.00 ©IEEE

and HEX2 are used to separate the primary cooling-water from the radioactive water of the injector.

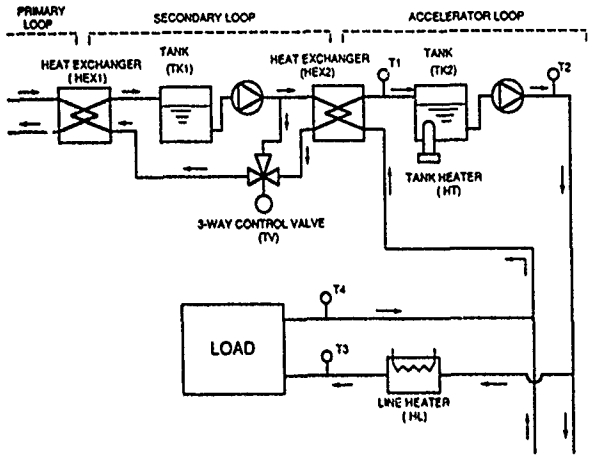


Fig. 1. Flow diagram of the 0.1 °C control cooling-water system

As a primary loop, we uses the laboratory cooling-water system which consists of a closed-loop and a cooling tower having a 0.44 MW rating at 30 °C and a flow of 850 l/min, and is automatically operated at the setting value of 30 °C.

The secondary cooling-water loop consists of a pump, a storage tank (TK1), two heat exchangers HEX1 and HEX2, and the three-way valve. It is connected to the primary and the accelerator cooling-water loop through the HEX1 and HEX2, which have a rated capacity of 59 kW. The three-way valve is used to control the temperature of cooling-water of self-loop. The pump has a rated delivery of 200 l/min. and a discharged pressure of ~ 2 kg/cm^2.

The accelerator cooling-water loop consists of a storage tank (TK2) with a heater, a pump and line heaters. It is used to provide the cooling-water to accelerator components such as the SHBs, prebunchers and accelerating structures. The tank TK2 has a 5 kw heater (HT) to control its water temperature, and a pump to keep the water temperature uniformly. The capacity of the tank TK2 and the capability of the heater HT were determined experimentally. The circulating pump has a rated delivery of 150 l/min. and a discharged pressure of ~ 3 kg/cm^2. The line heater is set just before each load and controlled with an accuracy of ± 0.1 °C. The heater capability for the 0.6 m accelerating structure is 2kW. All pipes are made from the stainless steel SUS 304. Table 2 shows specifications of the system. The storage tanks, pumps and heat exchangers are housed in the same equipment.

B.Temperature monitor and control

In order to monitor the water temperature and control the three-way valve, the tank heater and line heaters, we use four thermistor sensors T1, T2, T3 and T4, which have an accuracy of ± 0.01 °C. The sensors are located as shown in Fig. 1. The procedure of the temperature control in this system consists of three steps such as the three-way valve control, the tank heater control and the line heater control. Firstly, the three-way valve is controlled at the setting value of 36.0 °C by the feedback control using the thermistor sensor T1. Secondary, the heater set in the tank TK2 is controlled at the setting value of 36.3 °C by the feedback control using the thermistor sensor T2. Finally, the line heater for each load is controlled at the setting value of 36.5 °C by the feedback control using the thermistor sensor T3. All controls for the three-way valve and heaters are carried out by using PID control.

The distance between the cooling-water equipment and line heater is about 20 m and the system is distributed in wide range. In order to operate this system, we adapt the intensive control and monitoring system. It is also necessary for the easiness of both a maintenance and a operation. The controls console is located near the cooling-water equipment and has the control panel which contains all the necessary controls, meters, and interlock displays to operate this system.

Table 2
Specifications of the 0.1 °C control cooling-water system

(1)Primary cooling-water loop	
Pipe diameter	$2\frac{1}{2}$ B(JIS* 65 A)
Water flow	200 l/min.
Input temperature	33 °C (max.)
Heat Exchanger capability (HEX1)	59 kW
(2)Secondary cooling-water loop	
Pipe diameter	$2\frac{1}{2}$ B(JIS 65 A)
Capacity of storage tank (TK1)	300 l
Heat Exchanger capability (HEX2)	59 kW
(3)Accelerator cooling-water loop	
Pipe diameter	$1\frac{1}{2}$ B(JIS 40 A)
Capacity of storage tank (TK2)	300 l
Tank heater (HT)	5 kW
Line heater (HL)	0.5 ~ 2 kW
Accuracy of thermistor sensor	± 0.01 °C
Total heat load	29.581 kW

*JIS : Japanese Industrial Standards

IV. PERFORMANCE TESTS

Prior to the practical use of the ATF cooling-water system, we performed tests by feeding the RF power to the 0.6 m accelerating structure. The procedure of the test is as follows: After adjusting the PID control, the RF power of 100 MW, 800 ns width and 50 pps is switched on and off after 20 minuets. During 30 minuets, we monitored the temperatures at T2, T3 and T4.

Figure 2 shows the temperatures at T2, T3 and T4 as a function of time. It shows that the input temperature (T3) of the cooling-water is sufficiently controlled with an accuracy of ± 0.1 °C.

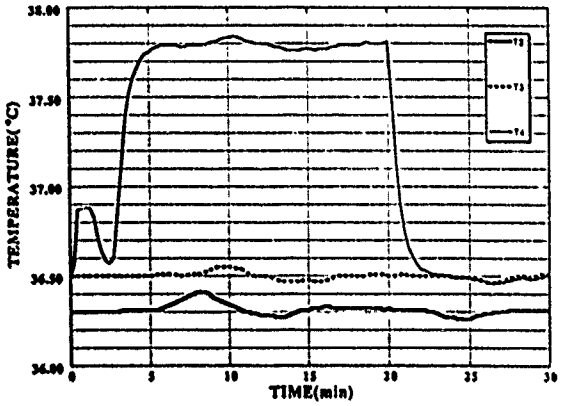


Fig. 2 Temperature at T2,T3 and T4 as a function of time. The first peak at T4 is due to RF-OFF for the interlock.

Next, we tested the system under the condition that the capacity of the storage tank TK2 was 100, 200 and 300 litters because it was one of the most important parameters in this system. Figure 3 shows the temperature at T3 as a function of time for the tank TK2 of 100, 200 and 300 litters. It shows that the temperature control becomes difficult as decreasing the capacity of the TK2 but the accuracy of ± 0.1 °C is obtainable for the capacity of the TK2 of more than 200 litters.

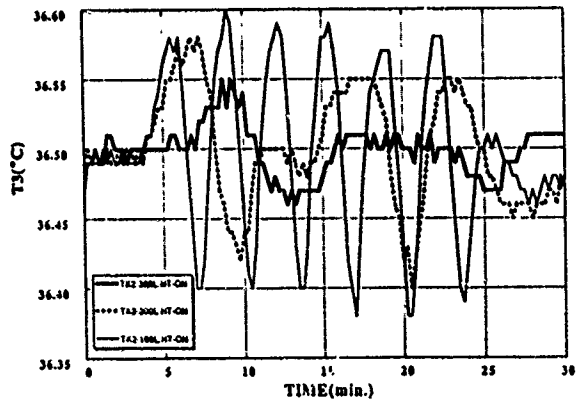


Fig. 3 Temperature at T3 as a function of time for the storage tank TK2 of 100, 200 and 300 litters.

Finally, we performed the test mentioned above under the condition that the heater of the TK2 was off. Figure 3 shows the temperature at T3 as a function of time. It shows that if the capacity of the TK2 is more than 300 litters, the temperature control with an accuracy of ± 0.1 °C is possible even in the case that the heater of the TK2 is off.

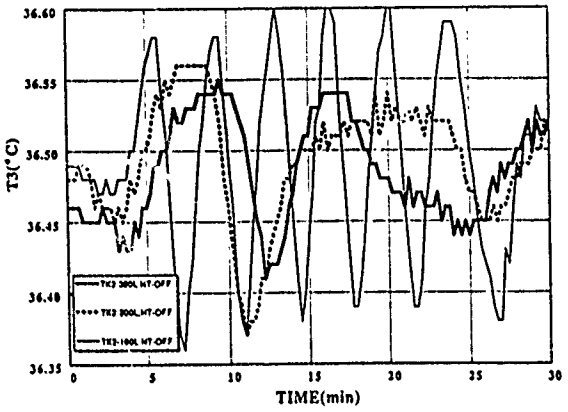


Fig. 4 Temperature at T3 as a function of time for the storage tank TK2 of 100, 200 and 300 litters. The heater of TK2 is off.

V. SUMMARY

The construction of the water-cooling system for the ATF has been completed and operated successfully. The high precision temperature control of 36.5 ± 0.1 °C was performed by using the three-way valve, the tank heater and the line heater without any serious problem.

VI. ACKNOWLEDGEMENTS

We would like to express our thanks to Professors K. Takata and S. Takeda for their encouragement. We also thank to Mr. H. Matsumoto for his helpful advice and to other members of JLC R&D group for their kind supports.

VII. REFERENCES

[1] S. Takeda, "Accelerator Test Facility for the JLC," contributed paper to this conference.

[2] H. Matsumoto et al., "High-gradient of the S-band Electron Linac," Proc. of the 1990 Linear Accelerator Conference, Albuquerque, 629-631,September 1990.

Blumlein-type X-band Klystron Modulator for Japan Linear Collider

Tetsuo Shidara, Mitsuo Akemoto, Masato Yoshida, Seishi Takeda and Koji Takata
KEK, National Laboratory for High Energy Physics
1-1 Oho, Tsukuba-shi, Ibaraki-ken, 305 Japan
Iwao Ohshima and Tsuneharu Teranishi
Heavy Apparatus Engineering Laboratory, Toshiba Corp.
2-1 Ukishima-cho, Kawasaki-ku, Kawasaki-shi, Kanagawa-ken, 210 Japan

Abstract

A Blumlein-type X-band klystron modulator using magnetic-pulse-compression (MPC) techniques was designed and constructed relevant to the future Japan Linear Collider (JLC) project. This modulator has been designed to produce pulses that are 200-ns wide, 600-kV peak voltage, 1200-A peak current and a short rise time of ~ 70 ns with a repetition rate exceeding 200 Hz. To realize a compact modulator, a spiral structure was adopted to conductors of the triaxial Blumlein. Special care was taken regarding the location of the magnetic switch and the charging reactor in order to eliminate any undesirable voltage during the charging process. Details concerning this X-band klystron modulator and its preliminary performance are described.

I. INTRODUCTION

An e^+e^- linear collider in the TeV region (JLC project) has been proposed as a post-TRISTAN project [1,2]. Considering the relation which governs the design of a linear collider, an accelerating gradient of the order of at least 100 MV/m is required for the facility to be of reasonable scale. Achieving this high gradient requires a high-power microwave source with a peak output power of ~ 150 MW/m at a frequency of 11.4 GHz [2]. The development of high-power X-band klystrons using conventional technology was started for this purpose [3]. A 30-MW model of this X-band klystron was high-voltage conditioned using one of the modulators prepared for the KEK test accelerator facility (TAF) which was established in 1987 to pursue R&D technology for future linear colliders [4]. Although processing with 2-μs and 2-Hz pulses was successful [3], the development of an X-band klystron modulator using MPC techniques [5] was initiated in order to supply very short pulses (~ 200 ns), since the required pulse flat-top is of the order of 100 ns [2].

Two types of modulator designs using MPC techniques are considered because of their very short rise-time capability and high reliability; they consist of only passive components, such as saturable inductors, capacitors and Blumlein. One is a semi-conventional-type modulator which comprises a pulse-forming network (PFN), a pulse transformer and magnetic switches (see Fig. 1). A detailed description is given in ref. [6]. The other is a Blumlein-type modulator (see Fig. 2). Since the impedance of the Blumlein is half that of the klystron load, this type modulator seems to have some advantage in realizing a very short rise time which is generally very difficult for a high-impedance load.

This paper describes the Blumlein-type X-band klystron modulator and its preliminary performance tests.

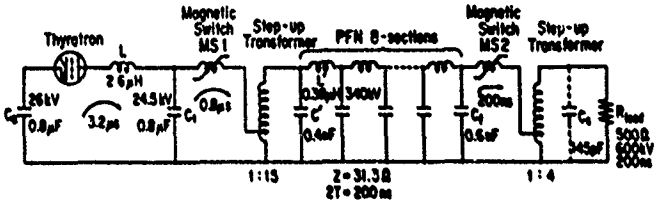


Figure 1. Simplified diagram of the X-band klystron modulator using a PFN, pulse transformer and magnetic switches.

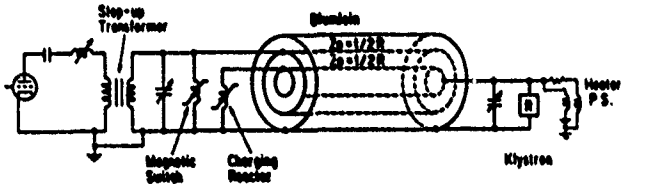


Figure 2. Simplified diagram of the Blumlein-type modulator.

II. BLUMLEIN TYPE X-BAND KLYSTRON MODULATOR

A. Modulator Specifications

The specifications of the X-band klystron modulator are listed in Table 1.

Table 1
Specifications of the X-band klystron modulator

Output pulse voltage range	400 ~ 600 kV
Output pulse current (Max.)	1200 A
Output impedance	500 Ω
Rise time	less than 100 ns
Pulse length (flat-top)	longer than 100 ns
Pulse amplitude drift	less than 1 %
Jitter	less than 5 ns
Pulse repetition rate	200 pps

The output impedance of the modulator is strongly dependent on the microperveance of the klystron. Although the impedance of the prototype X-band klystron is of the order of several kΩ, the impedance of the modulator was designed to be 500 Ω for the following reasons: 1) Since we are in the very first R&D stage of using the X-band klystron, we must consider the lowest probable value of the klystron regarding impedance in order to prepare for any change in its design.

0-7803-0135-8/91$01.00 ©IEEE

2) In order to reduce the construction costs of the future linear collider, simultaneous power feeding to several klystrons from a single modulator is inevitable, which results in a relatively low impedance. 3) For an efficient production of pulses with a very short pulse flat-top (~ 200 ns) a lower impedance is preferable, since a rather high impedance (several kΩ) results in a longer rise time (more than 500 ns) due to the estimated stray capacitance around the output circuit and klystron socket (~ 150 pF).

The limits to pulse amplitude drift and pulse height deviation are determined from the requirement of acceptable phase modulation of the microwave source (~ 5°). A relativistic beam voltage of 600 kV lessens the requirements on the pulse-top flatness and amplitude stability, since the velocity of electron beams in the X-band klystron is not so sensitive to changes in the beam voltage within this relativistic voltage range.

B. Blumlein-type Modulator

Although the Blumlein-type modulator may seem to be very simple (see Fig. 2), careful attention has been paid to the design, especially to the location of the magnetic switch and the charging reactor as well as to the triaxial Blumlein.

Figure 3 shows the simulated output waveforms for two different locations of the magnetic switch and the charging (bypass) reactor. Since we don't want any undesirable voltage during the charging process, the location of the magnetic switch and the charging reactor is very important in order to eliminate it.

Figure 4 shows a cut-away view of the triaxial Blumlein. In order to realize a compact, high-impedance Blumlein, a spiral structure was adopted for the inner conductors. The number of windings for these spiral conductors was designed so as to cancel their resultant magnetic flux in order to make sure of its Blumlein action. The final design parameters of the Blumlein are as follows: The central conductor is a 30-turn spiral conductor with a diameter of 290 mm. The middle

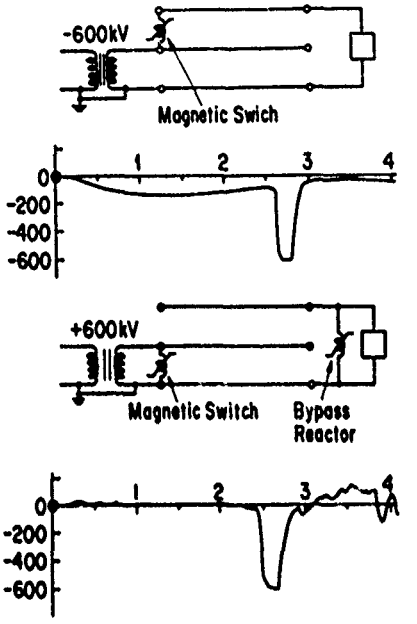


Figure 3. Blumlein-type modulators with two different locations of the magnetic switch and their simulated output waveforms.

conductor is also a spiral conductor with 22 turns and 400 mm in diameter. The outer-most conductor is an aluminum cylinder with an inner diameter of 550 mm. The total length of this Blumlein is 1 m.

III. PERFORMANCE TEST

A. Preliminary Test

Before proceeding to tests at a full voltage of 600 kV, a preliminary test was performed at ~ 200 kV in order to

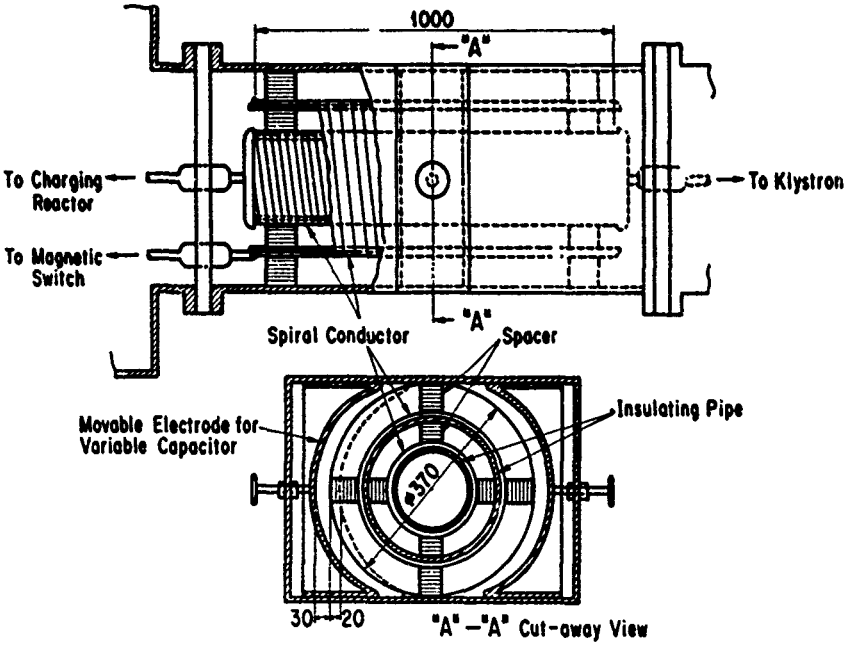


Figure 4. Cut-away view of the triaxial Blumlein.

confirm the above-mentioned design. Figures 5 and 6 show the input- and output-side voltage waveforms of the Blumlein, respectively. The input pulse with a 1.1 μs pulse width and a 210 kV peak voltage has been successfully compressed down to 260 ns with a peak voltage of 178 kV. An expanded output voltage waveform is shown in Fig. 7. Although a pulse flat-top length of 155 ns is sufficient for our use, a pulse rise time of 138 ns is rather longer than we expected. The main cause of this relatively long rise time is the stray capacitance of the magnetic switch. We must, therefore, reduce this stray capacitance in order to realize a very short rise time.

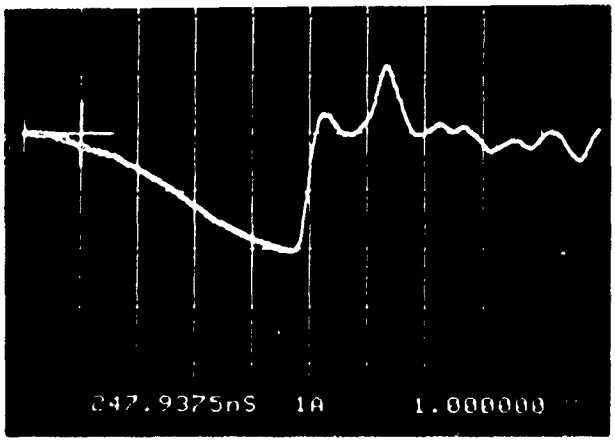


Figure 5. Input voltage waveform of the triaxial Blumlein. (vert. 100 kV/div., hor. 200 ns/div.)

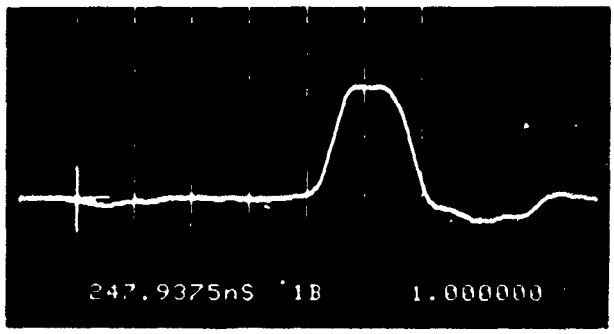


Figure 6. Output voltage waveform of a triaxial Blumlein. (vert. 100 kV/div., hor. 200 ns/div.)

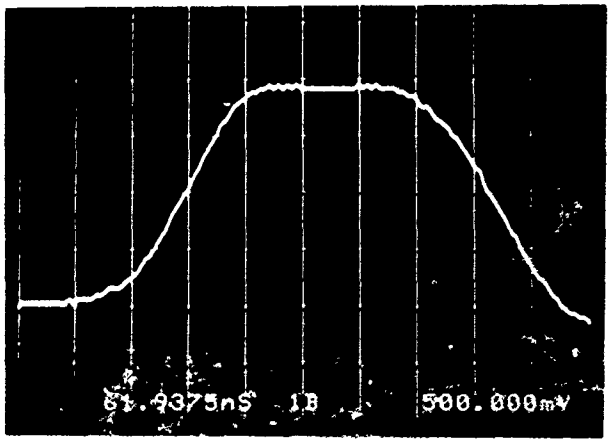


Figure 7. Expanded output voltage waveform of the triaxial Blumlein (vert. 50 kV/div., hor. 50 ns/div.)

B. Full Voltage Test

Since the preliminary tests of the Blumlein-type modulator have been very hopeful, we are now proceeding to carry out tests at full voltage (~ 600 kV). Figure 8 shows the locations of individual components in the 600-kV compatible Blumlein-type modulator. Although the core material of the magnetic switch and the charging reactor in the preliminary test is Co amorphous, we are planning to use Fe amorphous cores because of a high ΔB capability which enables us to reduce the size of the magnetic switch as well as the charging inductor. A full-voltage test of this modulator will start soon.

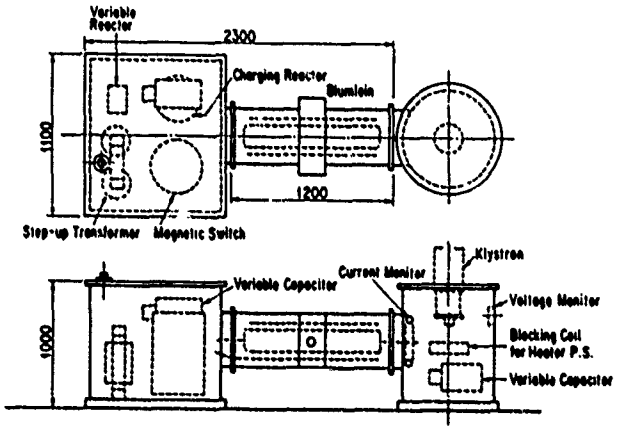


Figure 8. Location of individual components in the 600-kV compatible Blumlein-type modulator.

IV. ACKNOWLEDGEMENT

The authors wish to express their gratitude for the encouragement and financial support received from Director General, Prof. H. Sugawara as well as Directors, Profs. Y. Kimura and S. Iwata. They also wish to express their thanks to FEL R&D group members (especially Profs. S. Hiramatsu and J. Kishiro) and X-band klystron R&D group members for the fruitful discussions.

V. REFERENCES

[1] K. Takata and Y. Kimura, "TRISTAN and High Energy Accelerator Plans at KEK", Particle Accelerators, 26, pp.87-, 1990.

[2] S. Takeda, "Japan Linear Collider (JLC)", Particle Accelerators, 30, pp.143-, 1990.

[3] H. Mizuno et al., "X-band Klystron Diode Test for Japan Linear Collider (JLC)", Particle Accelerators, 30 pp.167-, 1990.

[4] S. Takeda et al., "Electron Linac of Test Accelerator Facility for Linear Collider", Particle Accelerators, 30, pp.153-, 1990.

[5] D. L. Birx et al., "Technology of Magnetically Driven Accelerators", IEEE Trans. Nucle. Sci., 32, pp.2743, 1985.

[6] T. Shidara et al., "R&D on an X-band Klystron Modulator for Japan Linear Collider", KEK preprint 90-74, August 1990.

HIGH-POWER INPUT COUPLER WITH A CYLINDRICAL ALUMINA WINDOW

Mitsuo Akemoto
KEK, National Laboratory for High Energy Physics
Oho 1-1, Tsukuba, Ibaraki 305, Japan

Abstract

A high-power rf-input coupler has been installed in the TRISTAN alternating periodic structure (APS) cavity operating at 508 MHz. It has a cylindrical alumina window coated with TiN of 60 Å thickness and feeds the power of 225 kW (CW) to the cavity. In an early stage of development, the multipactoring discharge of the window was a primary problem. After the coating, the window discharge was not observed. The total number of 112 couplers has been installed in the TRISTAN ring and successfully operated for about 17,000 hours since spring of 1985. The most serious trouble with the operation was a failure of the loop. This problem was discovered after about 5,000 hours of operation. We have performed improvements of the coupler including the loop.

I. INTRODUCTION

In the TRISTAN accumulation ring (AR) and main ring (MR), alternating periodic structure (APS) cavities [1] operating at 508 MHz are used for the acceleration of the e^+e^- beams. The RF power of 1 MW generated by a CW klystron is fed to four APS cavities through a waveguide system with a 10 % power loss. A total number of 112 input couplers is needed during operation. We have developed a high power input coupler with a cylindrical ceramic window, whose typical operation power is 225 kW [2]. The couplers have been installed and operated since spring of 1985. In this paper, the structure, high power characteristics and long term performance of the couplers are described.

II. STRUCTURE

A. General description

The APS cavity has a coupler port on vertically up or down side of one of the accelerating cells. The coupler is required to transform the waveguide to the coaxial mode and to feed the power to the cavity through the magnetic coupling of the accelerating mode.

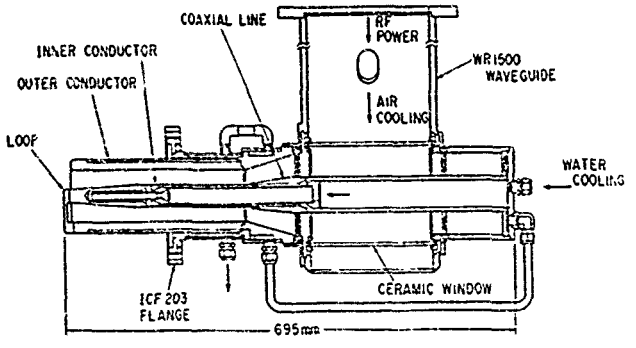


Fig. 1 A cross section of the input coupler.

A cavity coupling factor is set to ß=1.3 to compensate for beam-loading during operation. The coupler was designed to stand the maximum operational input power of 250 kW. A simple structure was chosen to be suitable for mass-production. A cross section of the input coupler is shown in Fig. 1.

It consists of a coaxial line with a loop antenna, a cylindrical alumina RF window and a rectangular waveguide. Dimensions of the coupler were adjusted to obtain a good matching by the studies using a cold model.

B. Coaxial line

The coaxial line is of 50 Ω and terminated by the loop. It is made of OFHC copper because of its low resistive loss, low out gas and good thermal conductivity, except for the ICF-203 rotatable vacuum flange and the body jacket which are made of stainless steel. The parts are assembled by silver-brazing in hydrogen furnace.

The loop is formed by a short bar bridging inner and outer conductors. The bar is connected to the conductors with copper-plated stainless-steel bolts. The loop is separated from transition part by more than $\lambda/2$ to prevent undesirable interference between them. The coupling is adjusted by rotating the direction of the loop to vary the effective coupling area for the magnetic field. Both inner and outer conductors are cooled by water flow of 6 l/min.

When a coupler is mounted to a coupler port of the cavity, the gap between the outer surface of the coupler and the inner surface of the port forms a coaxial line. Its length is set to about $\lambda/2$ from the cavity surface to have a choke property at 508 MHz for the coaxial TEM mode. The accelerating mode still penetrates into this coaxial line in the form of the TE_{11} mode that may give rise to undesirable two side multipactoring. Thus, the coaxial gap is carefully chosen to be 1.0 mm to suppress the multipactoring.

C. RF Window

A cylindrical RF window made of 95 % alumina ceramics (152 mm in diameter, 193 mm long, 5 mm thick) is used for vacuum seal. It is located at the position where the waveguide mode is transformed to the coaxial one. It is welded to the outer conductors of the coaxial line with a Tig method. The dielectric or resistive heating of the ceramic window is directly cooled by forced air. The vacuum side of the ceramics is coated with TiN of 60 Å thickness to prevent the multipactoring discharge that gives rise to the excessive local heating of the ceramic window. The effect of the coating is detailed in the next section. The coating is performed by dc reactive sputtering with Ti target in the N_2 and Ar mixture gas of 10^{-2} Torr.

D. Waveguide

The WR1500 waveguide is made of the 6063-TS aluminum. It is equipped with two nozzles to blow RF window by air

0-7803-0135-8/91$01.00 ©IEEE

flow of ~ 1.0 m^3/min from the blower. The air is drawn out through 60 little holes in the shorting plane.

III. HIGH POWER CHARACTERISTICS

Prior to the final mounting on the APS cavity of the TRISTAN ring, the couplers were conditioned up to 300 kW measuring their high power characteristics. The surface temperature distribution of the RF window was monitored from the RF input side by an infrared thermometer 6T61(NEC SAN-EI). From a view port of the cavity just below the coupler, the vacuum side of the coupler was watched by a color TV camera to observe a glow discharge phenomenon if it happened. The cavity was evacuated by a turbo molecular pump of 300 l/sec. The cavity vacuum was monitored by a cold cathod gauge and its value was used to control the conditioning process. The RF power was slowly increased by keeping the pressure below 5×10^{-6} Torr.

Figure 2 shows a typical example of the surface temperature distribution of the ceramic window at input power of 150 kW.

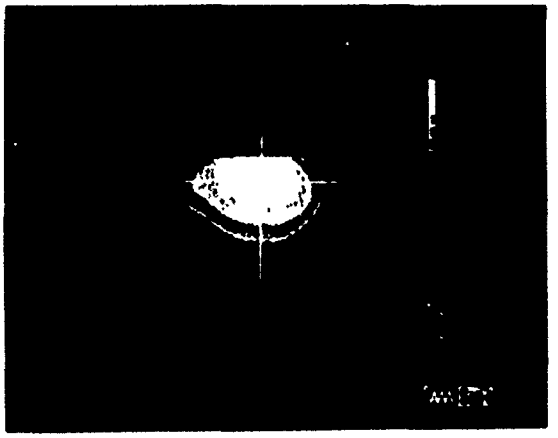


Fig. 2 Temperature distribution of the ceramic surface.

In this example, the coupler is mounted to the up side of the cavity; the loop is on the down side, while the shorting plane of the coaxial line is on the up side. One of the most characteristic features of the temperature distribution is that a hot spot appears around the center and up side of the ceramic cylinder, where the electric fields of both the waveguide mode and coaxial mode become the maximum. The temperature rise ΔT at the hottest spot of the ceramics was measured as a function of the input power. Three examples are shown in Fig. 3.

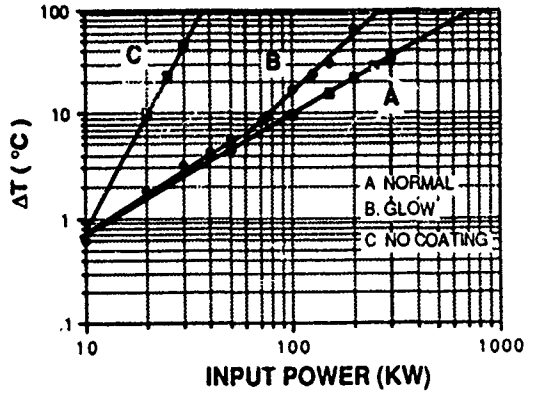


Fig. 3 Temperature rise of the ceramics versus input power.

Performance of the ceramic window could be characterized by the value of a parameter n defined by $\Delta T \sim P^n$, where P is input power. If the value of n is between 1 and 1.4 (shown as the example A in Fig. 3), the performance is normal revealing no glow discharge in the TV monitor mentioned above.

In an early stage of development, the multipactoring discharge of the window was a primary problem. The hottest spot of the ceramics showed nonlinear temperature rise of n=3.7 (shown as the example C in Fig. 3) with the purple glow discharge. If the input power was further increased, the ceramics cracked by local thermal stress in some cases. This nonlinear temperature rise in the local spot was due to a one-sided multipactoring on the ceramic surface, which was also observed in the output window of the high power klystron [3]. To suppress the secondary electron emission, the inner surface of the ceramics was coated with a 60 Å TiN layer. After the coating, the temperature rise was remarkably reduced and the window glow was not observed.

IV. PERFORMANCES

One hundred and four couplers were used with mean input power of about 200 kW in the MR [4]. Fifty seven percent of them were continuously operated without any troubles. Until January of 1991, the operation time of couplers amounted to about 14,000 to 17,000 hours. Table 1 shows the summary of the failed couplers during the last four years.

Table 1
Summary of the failed couplers

Failure mode	Number of couplers	Percentage
Loop failure	14	54%
Grow discharge	9	35%
Window failure	2	8%
Others	1	3%
Total	26	100%

The failures are mainly classified into three categories as follows.

A. Loop failure[5]

The loop is fixed by three plate-type SUS bolts copper-plated by 10 μm thick. The heads of the bolts were melted in 14 couplers. The loop was also bent in some couplers. This trouble is not initial failure but begins to occur at more than 5,000 hour operation and increases thereafter. The loop is not directly cooled and has the resistive loss of about 30 W at input power of 200 kW. It is also noted that the couplers are operated under hard heat cycle during the beam energy ramping. Thus, the loop should be welded or brazed to the inner and outer conductors to solve this problem.

B. Glow discharge

Blue or purple glow was observed in the coaxial line and window. The example B of Fig. 3 shows a typical example of the ceramic temperature rise with glow discharge. There was a critical level at around 60 kW and a nonlinear window heating and blue or purple discharge were observed above this level.

This indicates that the coating effect against multipactoring was diminished.

C. Window failure[6]

Figure 4 shows an example of the window which is cracked because of local thermal stress. It is seen from the RF input side. The center of the cracking occurs around location of the maximum E-field. This window cracking seems to be caused by the multipactoring discharge.

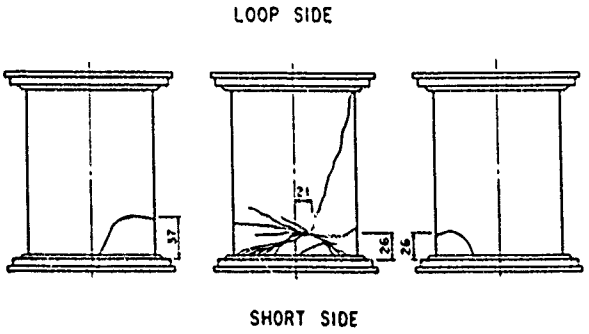


Fig. 4. An example of the window cracked because of local thermal stress.

V. IMPROVEMENTS

In order to obtain the high reliability, we have performed the improvements of the coupler. Also the interlock for the window heating is scheduled.

A. Loop brazing

In order to solve the loop problem, the loop was brazed to the inner and outer conductors in hydrogen or vacuum furnace. The new structure connecting between the inner and outer conductors by a Tig method at the short side of the coaxial line was adapted to protect the TiN coating of the ceramic window from the high temperature of the furnace. Figure 5 shows the structure of the improved coaxial line at the short side. This new type coupler has been installed in the MR and operated for about 3,000 hours without any serious problem. All the old couplers will be replaced by this new type ones.

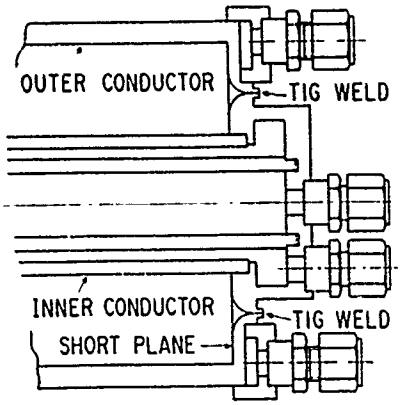


Fig. 5. Structure of the short side coaxial line improved.

B. TiN coating in the coaxial line

There are higher order multipactoring modes in the coaxial line. In order to prevent these multipactoring discharges which work as a trigger of the grow discharge, the vacuum sides of both the inner and outer conductors were coated with TiN of 200 Å and 60 Å thickness respectively.

C. Interlock for the window heating

As the window heating is rapidly advanced if the multipactoring discharge occurs, it is need to switch off the RF input power before cracking the window. The interlock system checking directly the temperature of the window surface is effective. An spot-type infrared thermometer considering its low cost will be used.

VI. CONCLUSIONS

The total of 112 couplers has been installed in the MR and AR and successfully operated for about 17,000 hours without any serious trouble except the loop problem. This problem has been solved by brazing the loop.

VII. ACKNOWLEDGEMENTS

I would like to thank to Profs. Y. Kimura and K. Takata for their encouragement. I would like to thank to Prof. Y. Yamazaki for the design and construction of this coupler in the early stage. I also wish to thank members of TRISTAN RF cavity group for their support and useful discussions.

VIII. REFERENCES

[1] T. Higo et al.,"RF cavity for TRISTAN main ring," Proc. 1987 Particle Acc. Conf. (Washington D. C, USA, 1987), KEK Preprint 87-4 (1987).
[2] M. Akemoto et al.,"High power input coupler for the TRISTAN APS cavity," Proc. 7th Symp. Accelerator and Technology, (Osaka, Japan, 1989).
[3] S. Isagawa et al., "Development of High Power CW Klystrons for TRISTAN," Proc. 1987 Particle Acc. Conf. (Washington D. C, USA, 1987), KEK Preprint 87-7 (1987).
[4] M. Ono et al.,"Operation of High Power RF source in the source in the TRISTAN MR," Proc. 6th Symp. Accelerator Science and Science and Technology, (Tokyo, Japan, 1987), KEK Preprint 87-98.
[5] M. Akemoto,TRISTAN memo, No. 126, 1989.
[6] M. Akemoto,TRISTAN memo, No. 227, 1989.

X-BAND KLYSTRON MODULATOR FOR THE ACCELERATOR TEST FACILITY

Mitsuo Akemoto, Tetsuo Shidara, Seishi Takeda and Junji Urakawa
KEK, National Laboratory for High Energy Physics
Oho 1-1, Tsukuba, Ibaraki 305, Japan

Abstract

An X-band Klystron Modulator has been designed and constructed to drive two kinds of prototype X-band pulsed klystrons: (1) 30 MW klystron (XB-50K) requiring a 450 kV beam voltage with a 0.5 μs flat top and (2) 120 MW klystron (XB-72K) requiring a 550 kV beam voltage with a 0.5 μs flat top. The modulator generates 2.0 μs pulses with 37 kV voltage and 7300 A peak current for the operation of the XB-72K. It is a conventional line-type modulator with a 6 section pulse forming network (PFN) which is resonantly charged and discharged by a thyratron switch at up to 200 pps. In order to reduce the size of the modulator, a special low inductance capacitors using a film coated thin Al-electrodes of 300 Å thickness has been developed for the PFN. Its output pulse voltage is stepped up to 15 times by a pulse transformer. The design, specifications and results of performance tests of the modulator are described in this paper.

I. INTRODUCTION

A TeV electron-positron linear collider JLC (Japan Linear Collider) has several technical problems to be solved. A high-power rf source is one of the most important issues. In order to realize 100 MV/m accelerating gradient, the developments of X-band 100 MW-class klystron and its modulator are required. At the same time, more than 4,000 klystrons are necessary for JLC. Therefore, it is crucial to develop klystron modulators considering in the following items: (1) small size, (2) low cost, (3) high reliability, (4) mass production and (5) high efficiency.

As a first step of the development of 100 MW class klystron at X-band, a 30 MW klystron named XB-50K was designed and fabricated [1]. 11 MW RF power of 70 ns pulse width was achieved at the repetition rates of 2 pps but an RF window ceramic was fatally damaged. RF power test using new RF window will be carried out in May 1991. Also a 120 MW klystron named XB-72K has been designed and will be fabricated in July 1991. In order to operate above two kinds of prototype klystrons, we have designed and constructed a line-type modulator using a pulse forming network (PFN) and a pulse transformer in the Accelerator Test Facility (ATF) [2] for the JLC. The development of an X-band modulator using magnetic-pulse-compression techniques was simultaneously started to produce pulses that were 200 ns wide, 600 kV, 1200 A peak current and a short rise time of ~90 ns [3].

II. DESIGN AND MODULATOR SPECIFICATIONS

Table 1 shows the specifications of the prototype X-band klystrons. The modulators for these klystrons are required to generate a high-voltage of 550 kV and a short RF pulse width of 400 ns, so that its rise time has to be as short as possible considering the power efficiency.

Table 1
Specifications of X-band klystron

Klystron	XB-50K	XB-72K
Peak power output	30 MW	120 MW
RF pulse width	400 ns	400 ns
Operating frequency	11.424 GHz	11.424 GHz
Peak beam voltage	450 kV	550 kV
Peak beam current	172 A	490 A
Peak beam power	77 MW	270 MW
Klystron impedance	2616 Ω	1122 Ω
Power gain	59 dB	53-56 dB
Efficiency	41 %	45 %
Microperveance	0.57	1.2

The line-type modulator was chosen because of its high efficiency, relatively low cost and high reliability that had been proved at SLAC so far. The level of the main high-voltage in the modulator was mainly limited by the ratings of the available switch tubes. The thyratron ITT F-169 (rating: 100 kV) was chosen. In order to obtain a shorter rise time, it was necessary to keep the turns ratio of the pulse transformer as low as possible. In the present case, a pulse transformer with a turns ratio of 1 : 15 was used to step up to the voltage necessary for the klystron. As a consequence, the modulator is required to generate pulses with 37 kV in peak. This peak voltage demands about 72 kV maximum on the PFN which gives a sufficient margin to 100 kV thyratron. For a small size of the modulator, a thyristor unit for regulating ac line voltage, a water cooling for the charging unit and an inverse-clipping shunt circuit, and a PFN capacitors using a film coated thin Al-electrodes were employed. The cabinets of the dc power supply and klystron modulator was separately used, considering that other large dc power supply with common-bus will be used to many modulators in future [4]. Specifications of the modulator are listed in Table 2. The details are described in the following sections.

Table 2
Specifications of the modulator

Operation mode	XB-50K	XB-72K
Peak power output	77 MW	269 MW
Average power output	39 kW	97 kW
Output pulse voltage	30 kV	37 kV
Output pulse current	2581 A	7342 A
Output impedance	11.6 Ω	5.0 Ω
Pulse flat top	0.5 μs	0.5 μs
Rise time	< 0.5 μs	< 0.5 μs
Pulse height deviation from flatness	1.0 % (p-p)	1.0 % (p-p)
Pulse repetition rate	200 pps	200 pps
Transformer ratio	1:15	1:15

III. HIGH VOLTAGE DC POWER SUPPLY

0-7803-0135-8/91$01.00 ©IEEE

A simplified diagram of the dc power supply is shown in Fig. 1.

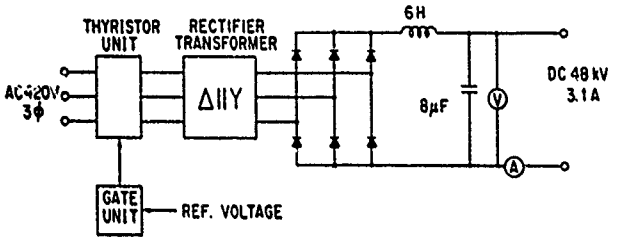


Fig. 1. A simplified diagram of the dc power supply

The line input is 420 V ac, three-phase and 50 Hz. A thyristor unit is used to regulate the ac line voltage in a range of 0 ~ 98 %. This unit is also used to disconnect the line within a few ms, when the interlock of over-current or over-voltage of the dc power supply and klystron modulator is worked. The output voltage of the thyristor unit is controlled with an accuracy of ± 0.5% by a feedback loop to the output voltage of dc power supply. The stepped-up ac is rectified to dc in 3-phase full wave scheme. The LC filter decreases the voltage ripple and determines the voltage drop due to the pulse load. A capacitance of 6 μF makes this drop 2.0 % for the operation of XB-72K klystron. The specifications of the dc power supply are listed in Table 3. The rectifier transformer, rectifier and choke are housed in the same oil tank.

Table 3
Specifications of the dc power supply

dc output voltage	48 kV
dc average output current	3.1 A
Ripple at full load	< 1.0%

IV. KLYSTRON MODULATOR

The klystron modulator is composed of a charging unit with a de-Qing circuit and a discharging unit with the PFN, a trigger circuit, a thyratron and an inverse-clipping shunt circuit as shown in Fig. 2.

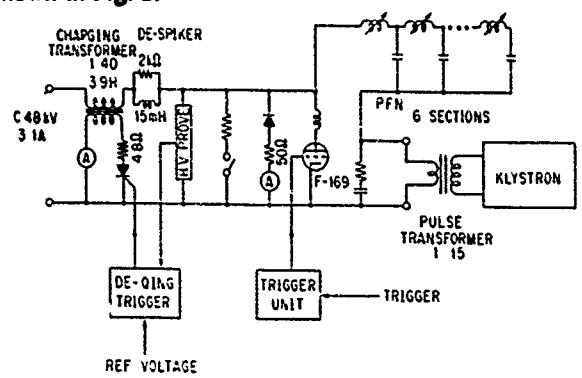


Fig. 2. A simplified diagram of the modulator

The PFN capacitors are resonantly charged through a charging transformer. The inductance of the charging transformer was determined by the resonant charging frequency and total capacitance of the PFN. The repetition rate is 200 pps and charging time is chosen to be 2.5 ms (half of the maximum repetition time). The de-Qing circuit in the secondary of the charging transformer regulates the voltage applied to the PFN. A step down ratio of 40:1 was chosen to employ a silicon-controlled rectifier (SCR) switch. A simple series connection of the resistor and the SCR switch was adopted. The regulation of the de-Qing circuit is chosen to be 5 %.

For the operation of two kinds of klystron, two kinds of the PFN unit consisting of 6 sections with fixed capacitors and tunable inductors are used in order to exchange the PFN unit easily. The specifications of the PFN unit are listed in Table 4.

Table 4
Specifications of the PFN unit

PFN unit	XB-50K unit	XB-72K unit
Output impedance	11.6 Ω	5.0 Ω
Operating voltage	70 kV	90 kV
Pulse width	2.5 μs	1.8 μs
Number of sections	6	6
Residual inductance	150 nH	150 nH
Total capacitor	98 nF	164 nF
Total inductance	4.98 μH	16.2 μH

Since the inductance of the PFN coil, especially for XB-72K, is small, it is necessary to minimize the residual inductance of the capacitor. The residual inductance of each section has to be less than 150 nH. For this purpose, a special capacitor was developed. The details will be described in the following section. Tunable inductors are mounted on the capacitor's high voltage bushing stub. Fine adjustment is made by varying the insertion depth of an aluminum cylinder in the coil.

V. PFN CAPACITOR

A PFN capacitor is one of the most important parts in the line-type modulator. Especially, a small size of the capacitor should be developed as the charging voltage of the PFN and repetition rate become higher. The elements of the high-voltage capacitor usually consist of sheets of a condenser paper and film as a dielectric material, and aluminium foil as an electrode. In order to obtain a higher energy density and low inductance of the capacitor, we adopt the new type element as shown in Fig. 5 [5]. It is composed of two polypropylene films coated with thin Al-electrodes (300 Å) which form a series of microscopic capacitor. Therefore, it makes possible to achieve a higher energy density and to fabricate the capacitor of self healing type. A unit capacitor for XB-50K and XB-72K consists of 23 and 17 elements in series, respectively. At each section of the PFN, two parallel oil-immersed capacitors in a same metal box are used to reduce their residual inductances. As the results, the residual inductance of each section was less than about 135 nH and the volume of the capacitor became about 60 % of the usual capacitor.

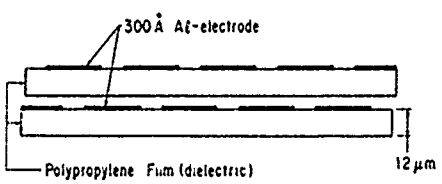


Fig. 3. Structure of the PFN capacitor

VI. CONTROL AND MONITOR

The control system of the modulator is schematically shown in Fig. 4. This system makes it possible to control the dc power supply and the klystron modulator in local operation and/or remote operation mode.

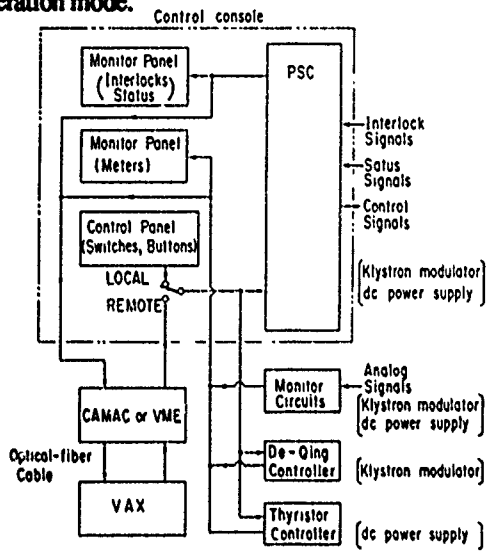


Fig. 4. Block diagram of the modulator control system.

In case of the local mode, the modulator can be manually controlled with the control console. It is located near the modulator and has the control panel which contains all the necessary controls, meters, and interlock displays to operate the modulator. The controls of the thyristor unit and de-Qing, and monitors of analog signals must be made with fast speed. They are therefore directly carried out by the hardware. A programmable sequence controller (PSC) is mainly used to control the on/off switches of devices and the display of the interlock status and on/off status and so on, since it acts with a high reliability but its working speed is slow. The remote control and data collection are performed by the PSC and hardware. They are connected to the ATF control system [6] consisting of CAMAC and a microVAX which are connected to the KEK network. The control system using VME will be also tested for the design of the future control system.

VII. PERFORMANCE TESTS

Prior to the practical use of the modulator for klystrons, it was tested by feeding the output power to a dummy load in

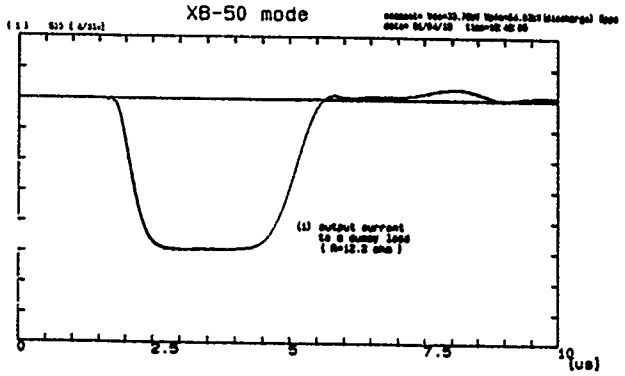


Fig. 5. Output pulse current (peak ~ 2480 A) at dummy load (H: 1 kA/div., V: 500 ns/div)

which a ceramic resistor is used. After adjusting the PFN inductances, waveforms of the output pulse for XB-50K and XB-75K were monitored by a current transformer and a capacitive divider. Figure 5 shows the current of the output pulse for XB-50K provided on conditions that output voltage of the dc power supply is 33.8 kV, the charging voltage of the PFN is 64 kV, the output pulse voltage is 30.3 kV, the repetition rate is 5 pps and the dummy load is 12.2 Ω. The output pulse was a rise time(0-90%) of 530 ns, 1.43 μs flat top with ± 0.5 % and 3.0 μs width. Figure 6 shows the current of the output pulse for XB-72K provided on conditions that PFN is 5 sections, the output pulse voltage is 38 kV, the repetition rate is 5 pps and the dummy load is 5.2 Ω. The output pulse was a rise time(0-90%) of 380 ns, 0.6 μs flat top with ± 0.5 % and 1.9 μs width.

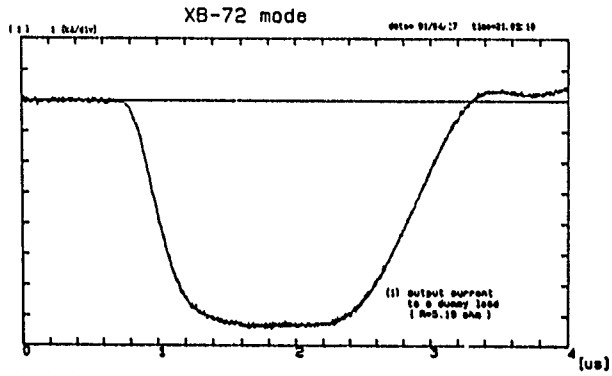


Fig.6. Output pulse current (peak ~ 7300 A) at dummy load (H: 1 kA/div., V: 200 ns/div)

VIII. SUMMARY

In order to operate a 30 MW or 120 MW prototype X-band klystron, we have designed and constructed a line-type modulator using a PFN and a pulse transformer. In the test operation of the modulator using a dummy load, 3.0 μs wide pulses with 30 kV voltage and 2480 A current for XB-50K mode, 1.9 μs wide pulses with 38 kV voltage and 7300 A current for XB-75K mode were successfully generated.

IX. ACKNOWLEDGEMENTS

We wish to express our thanks to Professors Y. Kimura and K. Takata for their encouragement. We also thank to Messrs. A. Tokuchi and H. Yoshimoto for the fabrication of the klystron modulator.

X. REFERENCES

[1] H. Mizuno et al., "X-band klystron for Japan Linear Collider," Proc. of the 1990 Linear Accelerator Conference, Albuquerque, 168-170(1990).
[2] S. Takeda, "Accelerator Test Facility for the JLC," contributed paper to this conference.
[3] T. Shidara et al., "Blumlein-type X-band klystron for Japan Linear Collider," contributed paper to this conference.
[4] M. Akemoto et al.,"Klystron modulators with HV common-bus for the JLC," Proc. of the 1990 Linear Accelerator Conference, Albuquerque, 171-173(1990).
[5] M. Hasebe (Nichicon Co.), private communication.
[6] H. Hayano et al., "Control system of ATF," Proc. of the 1990 Linear Accelerator Conference, Albuquerque, 468-490(1990).

Performance Test of a 65-MW Klystron Unit Relevant to the Microwave Source Upgrade of the KEK 2.5-GeV Linac

Tetsuo Shidara, Hiroyuki Honma, Katsumi Nakao, Shozo Anami and Akira Asami
KEK, National Laboratory for High Energy Physics
1-1 Oho, Tsukuba-shi, Ibaraki-ken, 305 Japan

Abstract

There is a plan to upgrade the KEK 2.5-GeV linac regarding its microwave source, which is relevant to both the asymmetric B-factory two-ring collider project and 3-GeV operation of the Photon Factory (PF) storage ring. The required increase in the injection linac energy from the present 2.5 to 4.25 GeV (3 GeV for PF) necessitates the replacement of the existing 30-MW klystrons with new 65-MW units. Since a total modification of the klystron modulator would cost too much, the output voltage and average power of the modulator have remained unchanged. Consequently, an increase in the klystron beam voltage could only be obtained by increasing the pulse transformer step-up ratio from the present 1:12 to 1:15. A new test station using a 65-MW klystron was established in order to confirm a stable operation of the modified unit. An output power of 58 MW with a 1μs duration was successfully generated in a preliminary test.

I. INTRODUCTION

As phase-III of the TRISTAN project, an asymmetric B-factory two-ring collider is being considered [1]. The required beam energy and design luminosity are 8×3.5 GeV^2 and 1×10^{34} /cm^2/sec from physics experiments. The two existing injectors for the TRISTAN main ring, the KEK 2.5-GeV linac [2] and the accumulation ring (AR), are also to be used for the injectors of the new B-factory rings. Since the required injection energy of positron and electron beams for the B-factory are 3.5 and 2.5 GeV, respectively, the energy of the linac should be increased from the present 2.5 to 3.5 GeV.

An energy upgrade of the linac is also required from the PF storage ring. The increase of the ring operation energy from the present 2.5 to 3.0 GeV would provide hard X-ray users with a great number of advantages: a photon flux in the 20 ~ 40 keV region, which is difficult to produce by the usual type X-ray source, except for a synchrotron radiation source, becomes brighter by more than 10 times.

In order to meet the demands (see Table 1) from both the B-factory project and PF 3-GeV operation, a study group of the linac upgrade was organized in June of 1989 and has put forward several linac upgrade designs [3]. Since the injection energy and charge accumulation rate for the PF 3-GeV operation are not severe, compared with those for the B-factory project, we mainly considered the requirements regarding the B-factory project.

The following plans were tentatively adopted: I) In order to increase the positron intensity (1) positron beams with pulse widths longer than 50 ns are accelerated; (2) the location of the positron production target is to be moved from the present 250-MeV down to the 750-MeV point of the linac, since the positron production efficiency is proportional to the injection energy of the primary electron beams, and (3) the positron capture efficiency is improved by enlarging the acceptance of the positron focusing system. II) In order to increase the energy of the linac to 4.25 GeV (750-MeV primary electron beams + 3.5-GeV positron beams) an upgrade of the microwave source is planned by replacing the present 30-MW klystrons with 65-MW high power klystrons. The resultant accelerating gradient is 14.4 MV/m (see Fig. 1), which is sufficient for a linac with a total accelerating structure length of 300 m.

This paper describes the upgrading of the microwave source as well as performance tests of a test station which was established in order to confirm the feasibility of this upgrade.

Table 1
Present status of the linac and requirements from the B-factory project and PF 3-GeV operation.

	percent			B-factory		PF 3-GeV
	for AR		for PF	for AR		for PF
	e^- 2ns	e^+ 2ns	e^+ 40ns	e^-	e^+	e^+
Energy (GeV)	2.5	2.5	2.5	2.5	3.5	3.0
Charge accumulation rate ($\times 10^{-8}$ C/min)	22.5	1.5	12	30 (75)	25 (75)	25
Pulse width (ns)	1	1	40	50	50	50
Peak current (mA)	150	10	2	2 (5)	1.6 (5)	1.6
Pulse repetition rate (pps)	25	25	25	50	50	50
Energy spread (%)	0.5	0.5	~1	~1	~1	~1

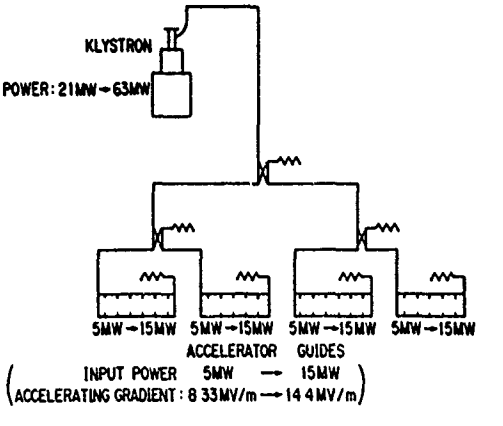


Figure 1. Upgrade scheme of the power feed system to an acceleration unit.

0-7803-0135-8/91$01.00 ©IEEE

II. MICROWAVE SOURCE UPGRADE

A. *Klystron*

Although, klystron E-3712 of Toshiba Corp. has successfully produced a power output of 100 MW [4], we are planning to introduce 65-MW klystrons (e.g. SLAC 5045-type klystron [5]) because of the large reservoir of practical experience from the SLC operation. Table 2 shows the specifications of the original and upgraded klystrons.

Table 2
Comparison of the original and upgraded klystron specifications

	Original	Upgraded
Model designation	Mitsubishi PV-3030	unspecified
PF peak output power (MW)	30	65
Beam voltage (kV)	270	350
RF pulse width (μs)	3.5	2.2
Repetition rates (pps)	50	50
RF gain (dB)	51	50
Micro-perveance	2	2
Efficiency (%)	40	45

B. *Klystron Modulator*

A doubling of the klystron output power requires a modification of the klystron modulator system. In order to reduce costs of the modulator modification, the output voltage and average power of the upgraded modulator have remained unchanged. An 80-kV increase in the klystron beam voltage is compensated by increasing the pulse transformer step-up ratio from the present 1:12 to 1:15. Accordingly, our new modulator is required to generate pulses with a 23.5-kV peak voltage, 6150-A peak current and 145-MW peak power. Since the output impedance of the pulse-forming network (PFN) has been reduced from the original 6.0 to 3.6 Ω, the pulse width has also been reduced from 3.5 to 2.2 μs. A significant increase in the PFN discharge current is compensated for by using two PFN capacitors in parallel. Figure 2 shows a simplified diagram of the upgraded modulator. Specifications of both the original [6] and upgraded modulators are also shown in Table 3.

Table 3
Comparison of the original and upgraded modulator specifications

	Original	Upgraded
Maximum peak power (MW)	84	145
Maximum average power (kW)	14.7	14.7
Transformer step-up ratio	1:12	1:15
Output pulse voltage (kV)	23.5	23.5
Output pulse current (A)	3600	6150
PFN impedance (Ω)	6.0	3.6
PFN total capacitance (μF)	0.3	0.3
Pulse width (μs)	3.5	2.2
Rise time (μs)	0.7	0.8
Fall time (μs)	1.2	1.5
Pulse repetition rate (pps)	50	50
Maximum pulse height deviation from flatness (%)	0.3 (peak to peak)	0.5
Maximum pulse amplitude drift (%/hour)	0.3	0.5
Thyratron anode voltage (kV)	47	47

III. PERFORMANCE TESTS AT TEST STATION

A. *Test Station*

In order to confirm the above-mentioned modifications, a test station using a 5045-type klystron was established. This klystron has been delivered from SLAC under the US-Japan collaboration program. Figure 3 shows the new test station of a 5045 klystron and tank assemblies. The PFN unit of a 30-MW klystron test station has changed to a new design which meets the demands from the 5045-type klystron. Since we only have one klystron test station and we must prepare at least one 30-MW klystron unit per month for our linac operation, the 5045-type klystron was set 15 m apart from the modulator in order not to interfere too much with tests of the usual 30-MW klystron unit. The 5045-type klystron unit was connected with the modified klystron modulator using 12 coaxial cables (each cable is 50 Ω and 20 mm in diameter) in parallel in order to ensure impedance matching.

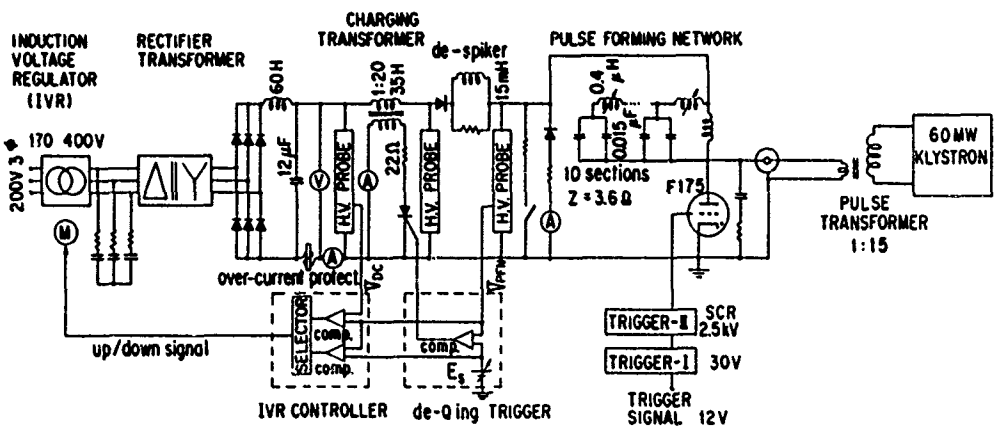


Figure 2. Simplified diagram of the upgraded modulator.

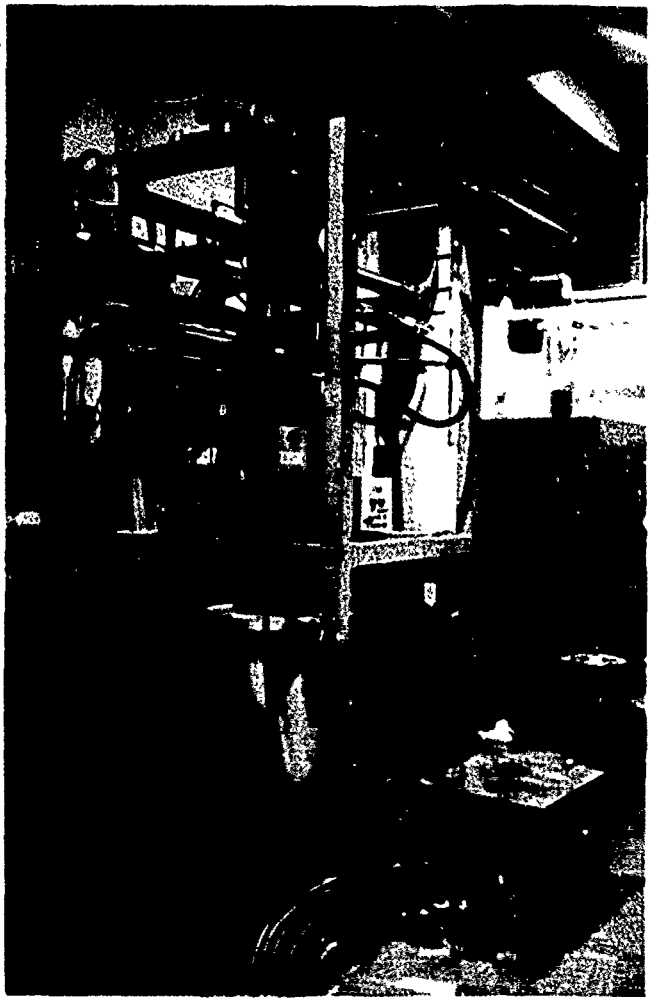


Figure 3. 5045 klystron and tank assemblies set at a new test station.

B. Performance Tests

High-power tests of this test station were performed. Figure 4 shows the beam current and power output versus the beam voltage of the 5045 klystron unit. An output power of 58 MW with a 1 μs duration was successfully generated at a 345-kV peak voltage and 380-A peak current. Figure 5 shows the output pulse voltage (peak 345 kV) and power output (peak 58 MW) waveforms. The rather long pulse rise time may be caused by the use of 15 m long coaxial cables. We are now planning to install at least one 65-MW klystron unit in our 2.5-GeV linac klystron gallery in order to confirm the long-term stability of this unit as well as the modified klystron modulator.

IV. ACKNOWLEDGEMENTS

The authors would like to express their thanks to Profs. K. Takata and S. Takeda for the delivery of a 5045 klystron. They would also like to express their gratitude to the B-factory working group members for their valuable discussions. They would like to acknowledge valuable information received from Drs. M. Allen and A. Vlieks concerning the operation status of the 5045 klystrons at SLC.

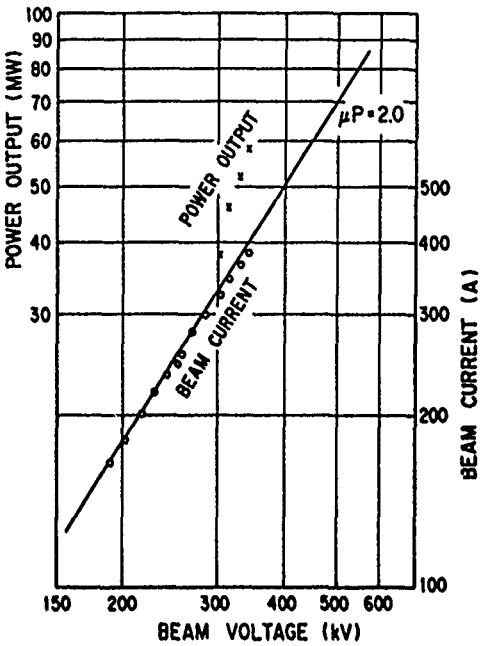


Figure 4. Beam current and power output versus the beam voltage.

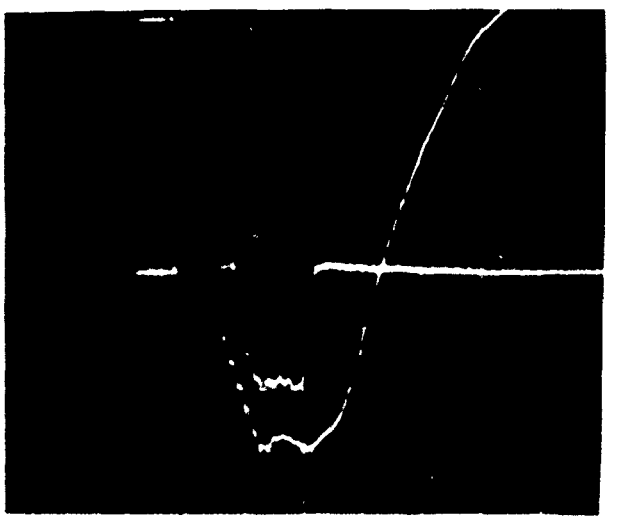


Figure 6. Output pulse voltage (upper; vert. 50 kV/div., hor. 1 μs/div.) and power output waveforms (lower; vert. 10 mV/div.)

V. REFERENCES

[1] ed. by H. Ozaki and Y. Yoshimura, "Feasibility Study for an Asymmetric B-factory at KEK", KEK-Report-90-7, June 1990.

[2] J. Tanaka, "Construction of the Photon Factory 2.5 GeV Injector Linac", Nucle. Instr. Meth., 177, pp.101, 1980.

[3] A. Asami et al., "Linac Upgrade", *Proc, of the Workshop on Asymmetric B Factory at KEK*, KEK-Report-89-17, pp.252, 1989.

[4] H. Yonezawa et al., "Development of a 100 MW S-band Pulse Klystron", Particle Accelerators, 30, pp.219-224, 1990.

[5] T. G. Lee et al., "A 50-megawatt Klystron for the Stanford Linear Collider", SLAC-PUB-3214.

[6] T. Shidara et al., "Klystron Modulator for the KEK 2.5 GeV Linac", Nucle. Instr. Meth., A279, pp.423, 1989.

SUPERCONDUCTING CAVITY DEVELOPMENT AT LOS ALAMOS NATIONAL LABORATORY*

B.Rusnak, E.R.Gray, R.G. Maggs, D.L.Schrage, A.H.Shapiro, G.Spalek, P.Wright
Los Alamos National Laboratory, Los Alamos, NM 87545

Abstract

A capability to design, fabricate, and test superconducting cavities has been established at Los Alamos Natinal Laboratory. Chemically treated single-cell niobium cavities are being tested at high fields (805 MHz and 3 GHz). Because the accelerating gradients achieved in these cavities are usually limited by field emission, conditions affecting field emission and cavity loss are being investigated by making changes in the established cavity-processing sequence. This paper discusses one of those changes and results.

Introduction

Single-cell, 3 GHz cavities are being tested to refine cavity processing and assembling procedures. These cavities are high-RRR niobium, spheroidal in shape, and use indium seals between the beam tubes and stainless steel flanges. Part of the testing program is the development of a distribution of cavity performance as measured by peak electric field in the cavity. The results of measurements made over more than a year are summarized in Fig. 1. Certain of these results indicated a cavity contamination problem, especially after high-field operation. Addressing this problem led us to make a change in the chemical polishing procedure.

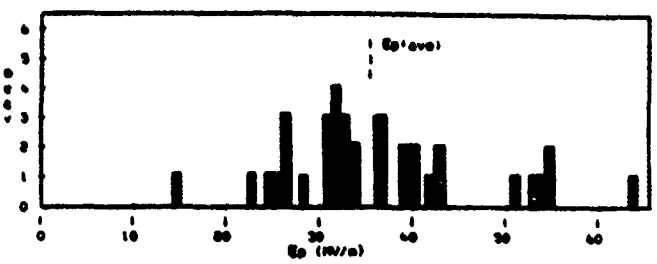


Fig. 1. Distribution of 3 GHz cavity tests related to the maximum peak electric field achieved. ▨ = runs with modified chemistry, ■ = standard 1,1,1 chemistry. For the cavity geometry, $E_{peak}/E_{accel} = 3.64$. Cavity $Q_0 = 4\text{-}10 \times 10^9$ at 1.8 K. Total of 36 runs on 9 cavities.

*Work supported by Los Alamos National Laboratory Institutional Supporting Research, under the auspices of the United States Department of Energy.

Observations

Figure 1 shows that the average peak electric field achieved is 35 MV/m, which corresponds to an average accelerating gradient of 9.7 MV/m. It also shows that one out of five cavity runs resulted in a fairly low peak electric field, around 26 MV/m. Usually, this occurred after a cavity had first run at a higher field level. Attempts to improve performance by rinsing the cavity with water and methanol proved futile. In addition, the majority of cavities that fell in the 26 MV/m cluster also showed a bump at 3.4 K in their $1/Q_0$ vs T_c/T plots. A typical example of such a plot is shown in Fig. 2.

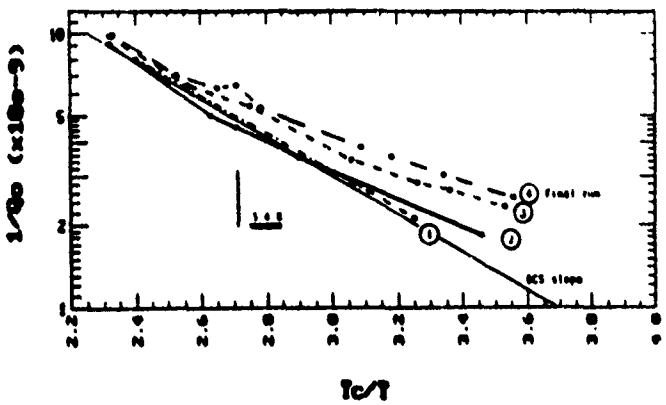


Fig. 2. Plot showing non-BCS behavior around 3.4 K in Final Run 4

Because indium is a superconducting metal, and T_c of indium is 3.4 K, we speculated that the bump in the $1/Q_0$ curve had something to do with indium contamination. The presence of the bump could be explained by the fact that indium is a normal conducting contaminant above 3.4 K (which would cause the $1/Q_0$ curve to approach a constant value above this temperature) and that at 3.4 K, when the indium becomes superconducting, the loss caused by the contaminant becomes negligible and the overall cavity behavior returns to conformance with BCS theory.

Further, the roll-off of the cavity Q_0 at 26 MV/m appeared qualitatively more precipitous than a roll-off due to field emission. A 26 MV/m peak electric field gives a peak magnetic field level in the cavity of 303 Gauss. For indium at 1.8 K, H_c is 211 Gauss. Assuming indium contamination was not uniform in the cavity, it seemed plausible that the cavity magnetic field was driving the indium normal, leading to a lower cavity Q_0.

0-7803-0135-8/91$01.00 ©IEEE

Test Results

Because this roll-off behavior at 26 MV/m was not necessarily removed by a 2-minute dip in 1,1,1 hydrofluoric, nitric, and phosphoric acids, we conducted to a qualitative study of the dissolution rates of niobium and indium in different acids. We found that in the 1,1,1 acid mixture, niobium dissolved more quickly than did indium. This means that a 2 minute polish in 1,1,1 could leave indium on the cavity surface, if the acid could not completely dissolve the niobium underneath to release it. The tests also showed that pure nitric acid would readily dissolve indium, but had no effect on niobium. Further research indicated that pure nitric acid would not hydrogen-impregnate the niobium and thereby degrade the Q_0.

Figure 3 shows the results of three high field tests run on one cavity. The first test was the initial one run after fabrication and after the removal of 57 microns with a 1,1,1 acid mixture. The second test was done after another 18 microns had been removed witn 1,1,1. This run exhibited a 25 MV/m roll-off, indicating that something had contaminated the cavity; either the 18 micron polish did not remove the contamination from the first run or it occurred after the polishing step. For the third test, the cavity was dipped only in pure concentrated nitric acid for 10 minutes, then rinsed. In this run, the cavity achieved the same peak electric field as in the initial run, but at a lower Q_0. This test suggested that whereas a moderate (2 minute) 1,1,1 polish would not remove indium contamination, a pretreatment with pure nitric acid would.

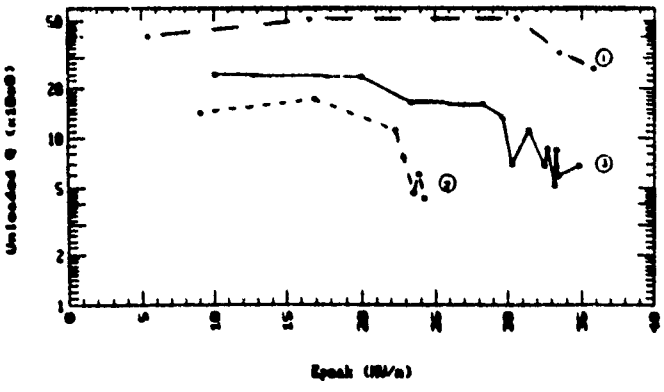


Fig. 3. Comparison of tests after different acid treatments
1 - 57 um removed with 1,1,1 initial run
2 - 18 um removed with 1,1,1, second run
3 - 10 minutes in conc nitric acid only, third run

We consequently changed our chemical polishing procedure from one using only the 1,1,1 mixture to one that incorporates a 10 minute pretreatment in pure concentrated nitric acid before the cavity is polished in 1,1,1 The intent is to remove any indium, or other foreign metal contaminant, from the niobium surface before the 1,1,1 niobium polish.

Though more data is needed, the five cavity tests done so far, using the new procedure, have not shown the symptoms postulated to be due to indium contamination. The cavities also had higher than average fields see (Fig. 1).

Discussion

Indium contamination may be a significant problem with the Los Alamos 3 GHz cavity design, because the width of the indium sealing flange on the cavity is 0.188 inches and the indium wire used is 0.020-0.030 inch. This makes it likely that indium will protrude into the cavity, potentially causing contamination . Using a wider flange may mitigate the problem, or make it less frequent, but as long as indium is used as the flange sealing material, the cavity interior will always be exposed to it to some degree.

Summary

Contamination of superconducting cavities is always a problem. In this instance, the observed behavior of poorly performing cavities indicated that indium contamination may be responsible. The standard chemical polishing treatment was modified to include a 10 minute pretreatment with pure concentrated nitric acid before the standard 2 minute dip in 1,1,1. Preliminary results from five cavity tests indicate that this modification may decrease the number of cavity tests that fall in the lower lobe of the performance distribution.

Acknowledgements

The authors would like to thank Randy Edwards for his assistance with the chemical polishing of the cavities and the testing of materials in various acids. His expertise was very helpful

RF Pulses with Flat Output Waveform Generator in RF Power Upgrade System

B.Yu.Bogdanovich, A.P.Ignatyev and V.A.Senyukov

Moscow Engineering Pysics Institute,

Moscow, 115409, USSR

Abstract

The paper contains theoretical and experimental research results of electron linac with RF power upgrade system as an RF source. Application of this systems gives a possibility to increase the accelerated beam energy without RF source (generator or amplifire) power increasing. Cavities are used for RF energy storage in this system as well as in SLED one. In difference with this system usage of amplitude-phase modulation of generator wave allows to form a flat topped RF pulse of accelerated wave. In this case a beam energy increasing can be achieved without beam energy spread widen.

INTRODUCTION

A serios problem of accelerated beam energy spread widen arises when designing an electron linac with RF power upgrade system as a power source.

Some evident advantages are inherent to RF power upgrade systems with cavities as an energy storage elements. But its have an essential fault aslo. When using such a system for electron linac feeding a considerable changing of RF wave amplitude at accelerating structure input results in accelerated beam energy spread widing. This changing is conditioned by a cavity emitted wave damping at a stored energy use period. One possible way to overcome this fault is discussed in work [1]. Here in order tocompensate an energy spread widing one should accomplish a beam current modulation within a beam pulse duration. However this method have a limited usage, in particular, it can not be used for negligible current loading cases.

Another way of this problem solving is suggested in this paper. A flat output waveform RF pulses are formed by this linac RF power feeding system with RF energy compression. Such a pulses at accelerating structure input are formed by means of amplitude-phase modulation of the RF power generator (or amplifire) wave. Here it must be pointed out that such a way of RF power pulses shaping is available only for energy upgrade systems in which an output wave is formed by a generator wave and emitted from a storage cavity one combining [1-4].

THEORY

It is an exponential law the emitted from a storage cavity wave amplitude during an output RF pulse is decreasing according to. So the generator wave amplitude should increase in time during RF pulse in order to compensate the emitted wave decreasing. The resulted output wave amplitude will be constant within some time interval if the generator wave amplitude increasing law is choosed in a proper way. Time interval duration, where output wave amplitude is constant, depends on different system parameters and, in particular, on the wave amplitude value at the accelerated structure input which is needed. The pulse flat top end moment corresponds to that one when a generator output RF power comes to its maximum value because this value is limited and the output RF wave amplitude couldn't increase more.

Electron linac with such a system as an RF source is shown in fig.1. The main elements of this linac are as following: an initial RF generator 1 (here and after number of element corresponds to its position in fig.1); output RF power amplifire (klystron) 2; highspeed phaseshifter 3; two storage cavities 4 connected to the accelerating structure by a 3-dB coupler 5; cavities coupling change elements 6; auxiliary RF amplifire 7; shaped pulse generator 8 and accelerating structure 9.

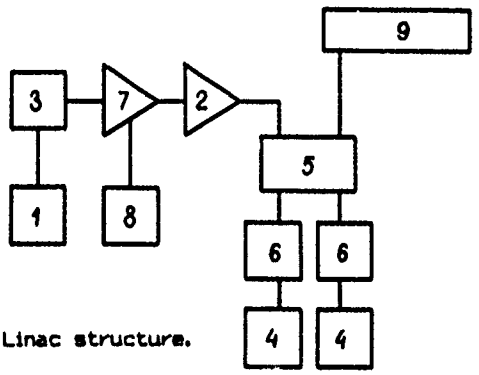


Fig.1. Linac structure.

The linac RF system work can be illustrated with the help of time diograms shown in fig.2. RF energy accumulation at cavities 4 takes place during the first and the best part of a generator RF pulse duration (time interval from 0 to t_0). In this period in order to store a maximum possible amount of field energy the cavities coupling is established to proper value by means of elements 6. By the way it can be pointed out that this elements presence is not necessary. Cavities coupling value increasing (by means of elements 6) and generator wave phase inverse are accomplished at the same moment t_0. This results in stored energy discharge from the

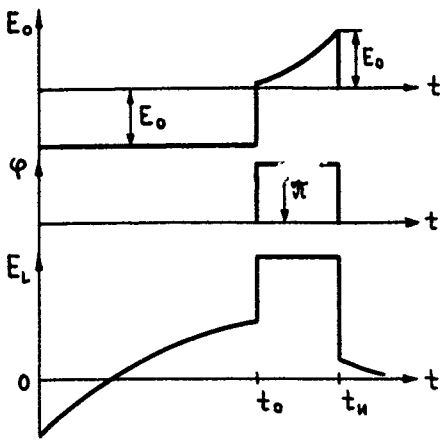


Fig.2. Linac operating time diograms.

0-7803-0135-8/91$01.00 ©IEEE

cavities. The discharging period duration equals to the rest part of generator RF pulse one (time interval from t_o to t_u). Amplitude modulation of the amplifire 2 output wave takes place within this period. It's accomplished by the amplifire exited wave modulation as well as it is for the phase modulation. Auxiliary amplifier 7 with shaped pulse generator 8 and a highspeed phaseshifter 3 are used for this combined amplitude-phase modulation. As a result a flat top output waveform RF pulse is formed at an accelerating structure input. In order the pulse top to be a really flat the amplifire 2 output wave amplitude must be changing in accodance with a cirtain law.

To define this law one could consider an equation for cavity emitted wave amplitude E_e [2]:

$$T_c \frac{dE_e}{dt} + E_e = -\alpha E_o \qquad (1)$$

where E_o -amplifire output wave amplitude; $\alpha = 2\beta/(1+\beta)$; ; $T_c = Q_o/\pi f_o(1+\beta)$- cavity time constant; β - cavity coupling factor; Q_o and f_o - cavity unloaded Q - factor and frequency, respectively.

Considering the amplifire wave E_o to be constant within time interval $(0, t_o)$ and output wave $E_L = E_o(t) + E_e(t)$ to be constant within time interval (t_o, t_u) the solution of equation (1) could be represented as following:

$$E_o(t) = \begin{cases} -E_o, & 0 \le t < t_o \\ -\left\{\frac{1}{\alpha_2 - 1} E_L + \left[\frac{2\sqrt{\beta_1\beta_2}}{1+\beta_1} E_o\left(1 - e^{-t_o/T_{c1}}\right) - \right.\right. & \\ \left.\left. - \frac{\alpha_2}{\alpha_2 - 1} E_L\right] e^{\frac{\alpha_2 - 1}{T_{c2}}(t - t_o)}\right\}, & t_o \le t \le t_u \end{cases} \qquad (2)$$

where $\alpha_2 = 2\beta_2/(1+\beta_2)$; $T_{c1} = Q_o/\pi f_o(1+\beta_1)$; $T_{c2} = Q_o/\pi f_o(1+\beta_2)$; β_1 and β_2 - cavity coupling factor within energy storage time period $(0, t_o)$ and stored energy using period (t_o, t_u), respectively.

This case an output wave amplitude E_L for corresponding time intervals is:

$$E_L(t) = \begin{cases} -\alpha_1 E_o e^{-t/T_{c1}} + (\alpha_1 - 1)E_o, & 0 < t < t_o \\ E_L, & t_o \le t \le t_u \\ (E_L - E_o) e^{-(t - t_o)/T_{c2}}, & t > t_u \end{cases}$$

where $\alpha_1 = 2\beta_1/(1+\beta_1)$.

The analisis of equation (2) shows that a power upgrade factor $K_p = (E_L/E_o)^2$ for certain output RF pulse duration $\Delta t = t_u - t_o$ reaches its maximum value for quite concrete cavity coupling factors β_1 and β_2. Curves of power upgrade factor dependens against cavity coupling factors values are shown in fig.3. The curves are given for alternating coupling ($\beta_1 \neq \beta_2$) and constant coupling ($\beta_1 = \beta_2 = \beta$) systems bouth. Coupling factors β_1 and β_2 are equal to its optium values.

EXPERIMENTS

A 30 MeV electron linac was used for experimental investigations of this RF energy compression system. The main parameters of this linac are the following: accelerated beam energy 10-30 MeV; beam current 0-300 mA; amplifire output power 20 MW; RF pulse duration 2.5 μS ; accelerated structure length 4.4 m; loading factor $a/\lambda = 0.14$.

A cylindrical cavities with quality factor $Q_o = 90 \cdot 10^3$ and coupling factor $\beta = 10$ are used as an energy storage elements in experimental unit. It

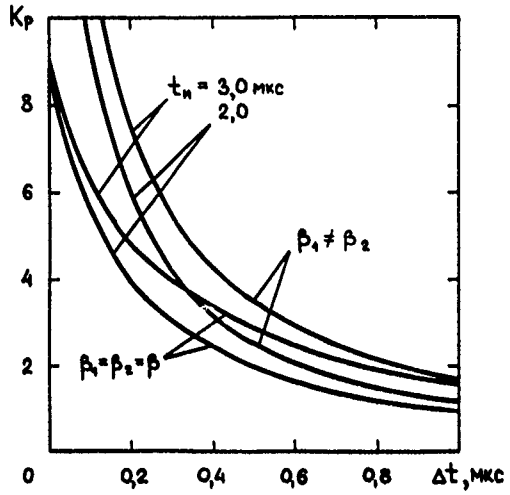


Fig.3. Curves of upgrade factor K_p v.s. pulse duration Δt for optimum value of coupling factors β_1 , β_2 and β .

is a constant coupling system. Complicated amplitude-phase modulation was carried out with the help of highspeed phaseshifter based on semiconducter elements (phase modulation) and an auxiliary amplifire based on a traveling wave tube controlled by a shaped pulse generator (amplitude modulation).

Experimentally measured values of power upgrade factor K_p v.s. output pulse duration Δt are given at fig.4. The same dependens but calculated for the same values of Q_o and β are shown here also.

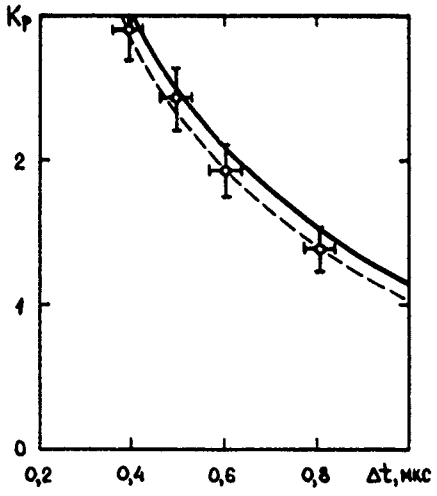


Fig.4. Measured (– – –) and calculatid (———) values of K_p for cavity with $Q_o = 90 \cdot 10^3$ and $\beta = 10$.

Experiments accomplished to investigate a linac beam energy spread behaviour when using an amplitude-phase modulation of an RF generator wave show that a beam energy spread (at a half-height level) for output puls duration from 0.4 to 1.0 μS in this case is about 4-5 times narrow that it is for SLED system (i.e. without amplitude modulation) [3]. Here it makes 2-3 %. A typical beam energy spectra obtained by a magnetic analyser are given in fig.5. For the same operating parameters of the linac a beam energy spectra for SLED system use are given also.

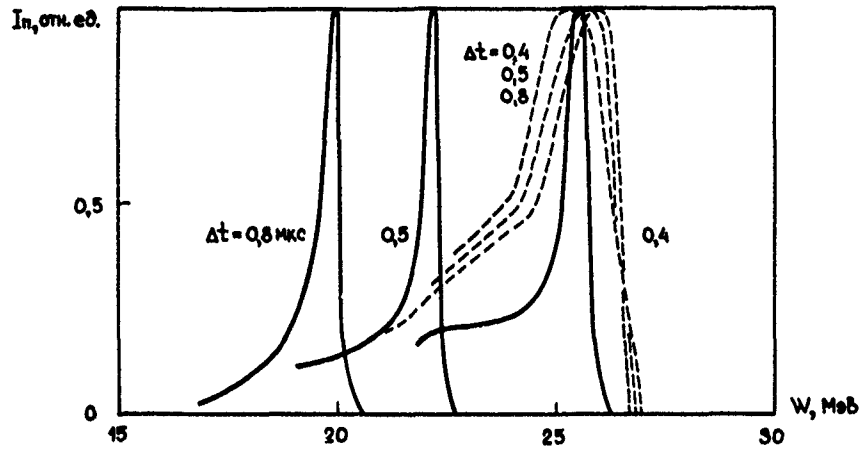


Fig.5. Accelerated beam energy spectra for RF energy compression system with (———) and without (— — —) amplitude-phase modulation.

As a result one may point out that a linac accelerated beam increase without energy spread widen can be achieved by using an RF energy compression system with cavities as an energy storage elements and amplitude-phase modulation of a generator beam for linac RF feeding. A beam energy spread in this case would be at least not wider then it's for initial linac configuration (without any compression system). It allows to make an energy compression system with storage cavities application field much wider.

References.

[1]. Z.D.Farkas, H.A.Hogg, G.A.Loew, A.R.Wilmunder. 'Microwave developments at SLAC', IEEE Trans. on Nuclear sciece, Vol.NS-24, N3, pp.1827-1829, March 1977.

[2]. Z.D.Farkas,H.A.Hogg,G.A.Loew, P.B.Wilson.'SLED: A Method of Doubling SLAC's Energy', in Proc.of 9th Int. Conf. on High Energy Accelerators, Stanford, California, March 1974, pp.576-583.

[3]. B.Yu.Bogdanovitch, V.A.Senyukov, A.V.Shalnov, 'Linеynіy uscoritel elektronov s nacopleniem energii v systeme VCh pitaniya',preprint MEPhI 039-88, Moskva, 1988.

[4]. Z.D.Farkas,'RF Energy Compressor',IEEE MEE-S. International Microwave Symposium Digest, May 1980, pp.84-86.

Tuning and Coupling Mismatch Tolerance in Cavities Driven by a Quadrature Hybrid[1]

Arthur M. Vetter
Boeing Defense and Space Group
P.O. Box 3999
Seattle, Washington 98124

Abstract

If cavities having identical complex reflection coefficients are driven by a quadrature hybrid, all of the reflected power appears at the terminated port of the hybrid. Mismatch of tuning angle or coupling coefficient results in voltage standing wave ratio greater than unity in the hybrid input port. In this paper, allowed mismatch is related to the allowed standing wave ratio.

I. INTRODUCTION

An attractively simple and economical drive concept for accelerator cavities employs quadrature hybrids to drive cavities in pairs (Fig. 1). This protects the klystron from reflected power from the cavities during ordinary (non-fault) operation, so long as their complex reflection coefficients and beam loading are equal, without recourse to high power circulators. assuming a perfectly balanced split and correctly matched phase lengths in the drive legs to the two cavities, the voltage standing wave ratio (VSWR) seen by the klystron will be entirely due to differences in the tuning, coupling, and beam loading of the two cavities. Here, we set out to find the allowable mismatches in tuning and coupling for a given maximum VSWR, assuming no beam present.

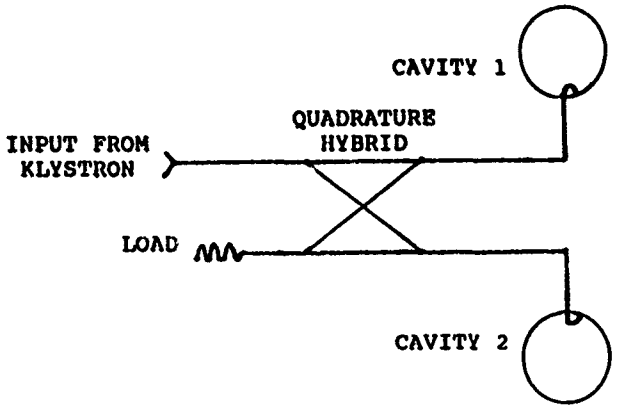


Figure 1. Cavity drive circuit schematic.

[1]Work supported by USASDC under contract number DASG60-90-C-0106

II. BACKGROUND: Q CIRCLE, REFLECTED VOLTAGE AND TUNING ANGLE

As drive frequency is swept upward through resonance, the complex reflection coefficient of a cavity moves along a circle tangent to the unit circle at the left side of the Smith chart [1]. This circle is called the Q circle, presumably because it contains information from which the loaded, unloaded, and external Q's of the cavity can be calculated. Figure 2 shows a schematic representation of a Q circle, defining various angles, phasors, etc. used herein.

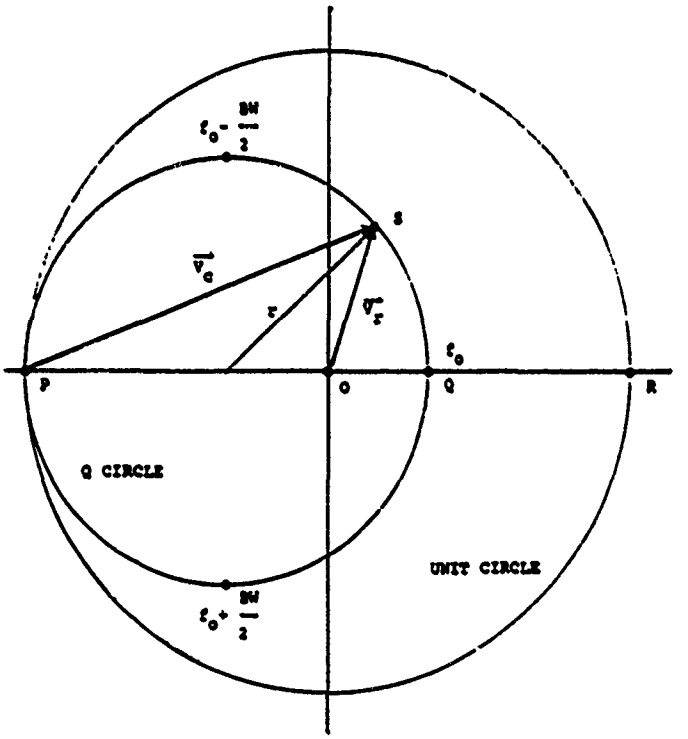


Figure 2. Voltage phasors for a cavity resonant at f_0, having a bandwidth BW. Point S moves clockwise around the Q circle as f increases.

Note in particular that the reflected voltage phasor V_r is the complex sum of the voltage V_c from inside the cavity and the negative unit phasor representing the reflection from the coupling aperture itself:

$$V_r = V_c - 1 \cdot \qquad (1)$$

0-7803-0135-8/91$01.00 ©IEEE

In order to optimize efficiency at full beam current, accelerating cavities are made to be overcoupled when no beam is present; for such cavities, the standing wave ratio on resonance equals the coupling coefficient β. In Fig. 2, the forward voltage phasor is a vector of unit length (i.e., the length PO) from left to right. The standing wave ratio σ (on resonance) is obviously the ratio of the length PQ to the length QR.

$$\beta = \sigma = \frac{\overline{PQ}}{\overline{QR}} = \frac{2r}{2 - 2r} \quad . \tag{2}$$

This can be inverted to obtain the Q circle radius in terms of the coupling coefficient.

$$r = \frac{\beta}{1 + \beta} \quad . \tag{3}$$

The angle ψ between the real axis and phasor V_C is called the tuning angle, and is given in terms of the difference between resonant frequency f_0 and drive frequency f by

$$\tan\psi = \frac{2(f_0 - f)}{\text{Bandwidth}} = \frac{2Q_L(f_0 - f)}{f} \quad , \tag{4}$$

where Q_L is the loaded Q of the cavity. The tuning angle is therefore a measure of the resonant frequency error.

Reflected Voltage Phasor

In Fig. 2, V_C is readily seen to be given by

$$V_C = r + re^{i2\psi} \quad . \tag{5}$$

Thus, Eqns. (1), (3), and (5) can be combined to give the reflected voltage phasor:

$$V_r = \frac{\beta e^{i2\psi} - 1}{\beta + 1} \quad . \tag{6}$$

Reflected Phasors at the Hybrid Input Port

Assuming an ideal quadrature hybrid, each of the two cavity feed waveguides will have a forward voltage amplitude reduced by $1/\sqrt{2}$ from the forward voltage in the hybrid input. Each of the reflections from the cavities produces a reverse wave at the input and load ports which is reduced by another factor of $1/\sqrt{2}$, so that the overall normalization factor for reflections in the input port is 1/2. Furthermore, the reflection from the second cavity, as seen in the hybrid input port, undergoes a phase shift of 180^0 which is equivalent to a sign change. Thus, normalized to the forward wave in the feed guide from the klystron to the hybrid, the reverse voltage phasor due to the cavity pair is

$$V_{rh} = \frac{V_{r1} - V_{r2}}{2} = \frac{\beta_1 e^{i2\psi_1} - 1}{2(\beta_1 + 1)} - \frac{\beta_2 e^{i2\psi_2} - 1}{2(\beta_2 + 1)} \quad , \tag{7}$$

where subscripts 1 and 2 refer to cavities 1 and 2.

III. CASE I: TUNING MISMATCH WITH EQUAL COUPLING

At this point we make the assumption that the cavity coupling coefficients are practically equal. The modulus of the reflected phasor can be shown to be given by

$$|V_{rh}| = \frac{\beta \sin(\delta\psi)}{\beta + 1} \quad , \tag{8}$$

where

$$\delta\psi = |\psi_1 - \psi_2| \quad .$$

Relation to Input Standing Wave Ratio

The standing wave ratio in the hybrid input is

$$\sigma_h = \frac{1 + |V_{rh}|}{1 - |V_{rh}|} = \frac{1 + \beta\left[1 + \sin(\delta\psi)\right]}{1 + \beta\left[1 - \sin(\delta\psi)\right]} \quad . \tag{9}$$

With $[\beta]$ as a parameter, Eqn. (9) is plotted over the range from 1 to 1.6 (covering the range of typical allowable klystron load mismatches) in Fig. 3.

Equation (9) may be inverted to find the allowed tuning angle difference for cavities of a given coupling:

$$\delta\psi = \sin^{-1}\left[\frac{1 + \beta}{\beta}\,\frac{\sigma_h - 1}{\sigma_h + 1}\right] \quad . \tag{10}$$

IV. CASE II: COUPLING MISMATCH WITH EQUAL TUNING

We now assume the cavities have equal tuning angles ψ, but different coupling coefficients. Equation (7) reduces to

$$V_{rh} = \frac{e^{j2\psi}+1}{2}\left[\frac{1}{\beta_2+1} - \frac{1}{\beta_1+1}\right] . \qquad (11)$$

The modulus of this phasor is maximized for cavities resonant at the driving frequency ($\psi = 0$), for which case

$$V_{rh} = \frac{1}{\beta_2+1} - \frac{1}{\beta_1+1} . \qquad (12)$$

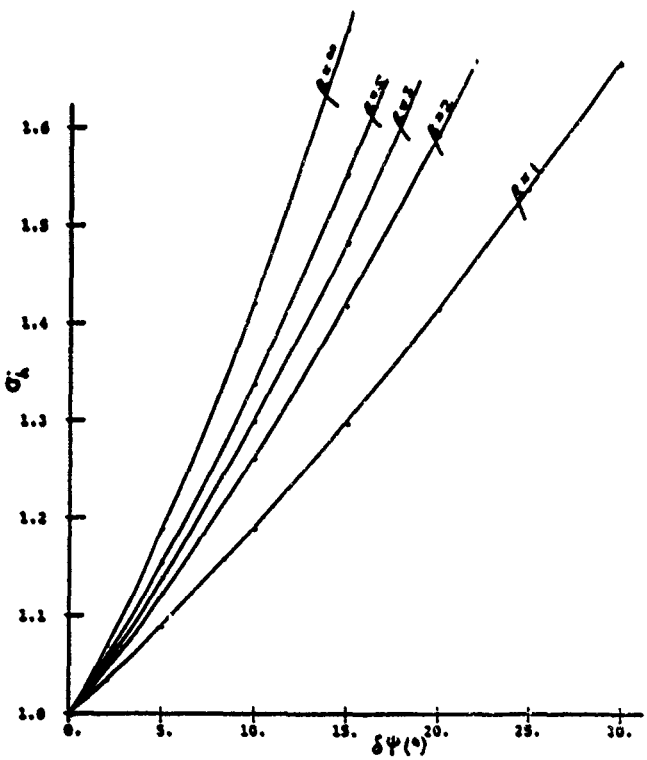


Figure 3. Standing wave ratio at hybrid input plotted against tuning angle difference for various coupling coefficients.

If we define coupling mismatch $\delta\beta$ as the difference between coupling coefficients,

$$\delta\beta = \beta_2 - \beta_1 ,$$

then the reflected voltage phasor modulus can be expressed in terms of this difference:

$$V_{rh} = \frac{-\delta\beta}{(\beta_1+1)^2 + \delta\beta(\beta_1+1)} . \qquad (13)$$

This result can be used to find the coupling mismatch corresponding to a specified standing wave ratio. If $\beta_2 > \beta_1$, then

$$\delta\beta_+ = \frac{(\sigma_h - 1)(\beta_1+1)^2}{2 - \beta_1(\sigma_h - 1)} ; \qquad (14a)$$

if $\beta_2 < \beta_1$, then

$$\delta\beta_- = \frac{(\sigma_h - 1)(\beta_1+1)^2}{\beta_1 - \sigma_h(\beta_1+2)} . \qquad (14b)$$

V. REFERENCE

[1] E. L. Ginzton, Microwave Measurements, New York: McGraw-Hill, 1957 ch 10.

On Sustaining Short, Intense Bunches in Linear and Circular Accelerators*

Joseph J. Bisognano
Continuous Electron Beam Accelerator Facility
12000 Jefferson Avenue
Newport News, VA. 23606

ABSTRACT

The ability of existing analytical and numerical tools to predict beam performance at the short bunch lengths and high peak currents characteristic of contemporary accelerator designs is discussed. Recent advances in calculating the high frequency behavior of impedance and in describing bunched-beam collective dynamics are highlighted. A critical review is presented of outstanding problems that must be addressed before a thorough description of short, intense bunches is obtained.

INTRODUCTION

Performance optimisation for linear and circular colliders, FEL drivers, damping rings, and synchrotron light sources often yields configurations with short bunches of high phase space density. For example, sub-centimeter interaction point β^*s are needed in high luminosity collider designs, and the variation of β over the scale β^* in turn demands sub-centimeter interaction lengths and, therefore, sub-centimeter bunch lengths. Chromatic effects can further constrain these highly charged, short bunches to low momentum spread. Similar demands are made on free electron laser drivers where high peak current at low momentum spread is necessary to achieve appreciable gain. Bunches must be longer than the slip distance $N\lambda$ (where N is the number of periods of the wiggler and λ is the wavelength of the radiation), and longer bunches offer better frequency definition (narrower bandwidth). However, for fixed peak current the advantages of reduced total bunch charge, rf phase length, and wakefields make short bunches attractive, and at IR wavelengths and below typical scenarios again involve centimeter and sub-centimeter bunches.

For a relativistic bunch of length $\ell = c\tau$, the width of the frequency spectrum $\Delta\omega$ of the wall currents due to either the gross charge distribution or perturbations will be of order $1/\tau$. A diffractive model of the coupling (machine impedance) of beam-induced fields to vacuum chamber discontinuities suggests a rolloff at frequencies above c/a, where a is the beam pipe radius. The sub-centimeter bunches discussed above are typically transported in multi-centimeter radius beam pipes, and, consequently, the beam coupling varies strongly over the frequency widths of possible collective modes and the rolloff region is sampled.

To fully understand this short bunch regime, which is more typical of electron than proton accelerators, two principal questions must be addressed. First, what is the frequency dependence of the machine impedance at frequencies well above the beam pipe cutoff (or alternatively, the time dependence of the wakefields at distances small compared to the beam pipe radius). Secondly, what is the correct description of collective phenomena for finite length bunches with strongly frequency dependent coupling. During the past few years there has been substantial progress in answering the first question, with various analytic approximations and numerical models yielding consistent conclusions on the scaling laws for high frequency machine impedances. The results have been more mixed with respect to the latter question, with reasonable success in explaining transverse instabilities in storage rings and curing emittance degradation in linacs, but only qualitative agreement with observed longitudinal, single-bunch instabilities in storage rings.

In September 1990 the Fourth Advanced ICFA Beam Dynamics Workshop focused on collective effects in short bunches, and the results presented at that meeting by a number of researchers strongly informs this present review. The proceedings of the workshop was published as a KEK Report[1] and, in addition to the individual papers, it provides overview notes and extensive references which are recommended.

IMPEDANCE BEYOND CUTOFF

In the last few years significant progress has been made in clarifying the asymptotic behavior of impedance in the ultrarelativistic limit $v = c$. First, a variety of approximate approaches[2] have consistently shown that the real (resistive) and imaginary (reactive) parts of the longitudinal impedance Z of an isolated cavity vary as $\omega^{-1/2}$ for high enough frequencies , $\omega \gg c/a$. For an infinitely periodic structure, on the other hand, the resistive impedance is found to rolloff asymptotically as $\omega^{-3/2}$ and the reactive, as ω^{-1}, consistent with causality. A relatively simple description of the transition between the two regimes is given by Gluckstern[3] in terms of the complex admittance per cell $NY_N(k) = N/Z_N(k)$ for $k = \omega/c$ and N cells:

$$NZ_0Y_N(k) \cong Z_0Y_1(k) + \alpha\sqrt{N-1}\,\arctan\left(\frac{\alpha}{2\sqrt{N}}\right) \quad (1)$$

where

$$\alpha = \frac{(1+j)a\sqrt{\pi k}}{\sqrt{L}} \quad (2)$$

and where $Z_0Y_1(k)$ is the averaged admittance for a single cell

$$Z_0Y_1(k) = \frac{(1+j)a\sqrt{\pi k}}{\sqrt{g}} \quad (3)$$

*Supported by D.O.E. contract #DE-AC05-84ER40150

0-7803-0135-8/91$01.00 ©IEEE

The cell gap is g and the intercell spacing is L. For $N \to \infty$

$$NZ_0Y_N(k) \to \frac{(1+j)\pi a\sqrt{\pi k}}{\sqrt{g}} + \frac{j\pi ka^2}{L} \qquad (4)$$

and $\omega^{-3/2}$ dependence is obtained for the resistive part of the impedance if the second term is large compared to the first; *i.e.*, $ka^2 \gg L^2/g$. The derivation demands that $ka^2 \gg L$. It would appear that for large spacing L the impedance returns to a sum of single cavities values. If, however N is held fixed and the limit $k \to \infty$ is taken

$$NZ_0Y_N(k) \to \frac{(1+j)\pi a\sqrt{\pi k}}{\sqrt{g}}\left[1 + \frac{\sqrt{g(N-1)}}{2\sqrt{L}}\right] \qquad (5)$$

Note that for $N \gg L/g$ the impedance per cavity is reduced by a factor $1/\sqrt{N}$.

The analogous longitudinal couplings for dipole and higher modes, which are excited by offset beams, have been found to exhibit (up to constants) the same behavior. Neither wall resistivity nor beam pipe curvature has been included in the analyses to date, and it must be pointed out that all of the results have involved some level of approximation. Iterative methods or smoothing may not be convergent, and truncation of matrices and finite mesh size may introduce spurious behavior, but the fact remains that a broad range of approximate methods agree on the basic asymptotic frequency behavior of impedance. A rigorous result for some closed geometry with beam pipe, unfortunately, has yet to be achieved.

Experimentally, the clearest evidence of $\omega^{-1/2}$ behavior comes from reinterpretation of an ISR experiment by Hoffmann, Risselada, and Zotter.[4] It is argued that parasitic losses are due to single protons individually interacting with the machine impedance. The interaction frequency is determined by the width of the field lines at the wall, $\Delta\omega \sim c\gamma/a$. For high energies (31.4 GeV) frequencies over 60 GHz are sampled. Measurements of energy loss at three different energies (3.6 GeV, 15.4 GeV and 31.4 GeV) are consistent with the $\omega^{-1/2}$ behavior of isolated cells.

LOSS FACTORS AND WAKE POTENTIALS

The longitudinal and transverse wake potentials (W_ℓ and W_t, respectively) are the effective Green functions for beam self-interaction in a quasistatic limit. They are Fourier conjugate to the impedance functions. The associated loss factors, k_ℓ and k_t, are averages of the respective wake potentials over a given particle distribution, and are, in particular, functions of the rms bunch length σ. For $\omega^{-1/2}$ behavior, we have

$$k_\ell \propto \sigma^{-1/2} \qquad (6)$$
$$k_t \propto \sigma^{1/2} \qquad (7)$$
$$W_\ell \propto \tau^{-1/2} \qquad (8)$$
$$W_t \propto \tau^{1/2} \qquad (9)$$
$$k_\ell \propto \sigma^{0} \qquad (10)$$
$$k_t \propto \sigma^{1} \qquad (11)$$
$$W_\ell \propto \tau^{0} \qquad (12)$$
$$W_t \propto \tau^{1} \qquad (13)$$

where τ is the distance behind the exciting charge, and τ and σ are assumed small.

As is clear from equations (6-13), extrapolations of measurements performed with relatively long bunches and of numerical models at the limits of computer capacity depend on which asymptotic regime is applicable. Consider for example, the choice of bunch length in a linear collider. If $\omega^{-1/2}$ behavior is realized, then exceedingly short bunches would appear unattractive since energy losses and bunch-induced energy spreads (of order $2k_\ell Q$) would be exacerbated while transverse wakes would only be modestly reduced. It is also noted that $\tau^{-1/2}$ small time behavior for W_ℓ yields somewhat more curvature energy spread than does a constant longitudinal wake. If $\omega^{-3/2}$ behavior is obtained, the transverse wakes would be strongly reduced with short bunch length with little impact on energy loss and energy spread. Although pulsed, room temperature linacs such as SLAC appear to be safely in the latter regime, the wide spacing L of standing wave superconducting cavities in superconducting linacs may not satisfy the condition $a^2/\sigma \sim ka^2 \gg L^2/g$ for equation (4) to yield $\omega^{-3/2}$ rolloff.

BEAM DYNAMICS OF LINACS AND STORAGE RINGS

For the relatively short time a bunch is in a relativistic linac, the longitudinal motion is essentially frozen. Longitudinal electric fields can change the energy of beam particles, but since there is no slip associated with energy offset, current modulations are not induced. Thus, the principal longitudinal concerns are energy spreads induced by the gross charge distribution. Transversely, there can be amplification from the head to tail of the bunch since transverse wakes can induce betatron oscillations which can in turn excite further wakes. This is described by[5]

$$\frac{d}{ds}\left(\gamma(s)\frac{d}{ds}x(z,s)\right) + \left(\frac{2\pi}{\lambda(s)}\right)^2\gamma(s)x(z,s) = r_0\int_z^\infty dz'\rho(z')W_t(z'-z)x(z',s) \qquad (14)$$

The emittance degradation is dominated by the the transient amplification of the largest perturbations, element alignment and jitter, which are of relatively low frequency compared to typical bunch lengths. In this regime, where the perturbation $x_0(z,s)$ is independent of z along the bunch, an energy variation from head to tail can cancel the wake force through chromatic variation of the focusing strength. This, of course, is the principle of BNS damping or autophasing which has been successfully applied to SLAC. Note that this effect scales with $\Delta\gamma$, not $\frac{\Delta\gamma}{\gamma}$,[6] for fixed betatron wavelength, and is therefore more effective at high energies.

In any case, the frozen longitudinal motion and short linac propagation time allows for effective numerical simulation with the beam bunch divided into slices which can be successively updated for ultra relativistic wakes. Together with the better estimates as described above of the short time or high frequency behavior of beam coupling, the necessary fundamental numerical modeling tools are well in hand. The situation for storage ring bunches remains more clouded in spite of considerable work. The fundamental difference is clearly the importance of longitudinal motion in the dynamics of storage ring bunches. Synchrotron motion is an important ingredient, but the principal physics is in the fact that perturbations in energy can lead to current variation which can in turn excite wakefields. An additional feature is the need to address long term stability rather than transient growth.

MODE COUPLING ANALYSIS

Internal bunch instabilities, both transverse and longitudinal, have provided a fundamental limitation in the design of short-pulse-length synchrotron light sources, high-phase-space-density damping rings, and single pass FEL drivers. Although several formalisms have been developed to describe this class of beam instability, they share a common structure. The starting point is typically the linearised Vlasov equation,

$$\frac{\partial f}{\partial t} + \dot{x}\frac{\partial f}{\partial x} + \dot{p}_{ext}\frac{\partial f}{\partial p} + \frac{\partial f_0}{\partial p}G[f] = 0 \qquad (15)$$

where x and p are appropriate generalised coordinates, $\dot{p}_{ext}$ is the external focusing, and $G[f]$ is some linear functional acting on the distribution f. For a coasting beam f_0 is independent of x, and Fourier analysis yields a simple algebraic equation. For a bunched beam, however, f_0 is no longer independent of x, and Fourier analysis yields a convolution integral.

Typically, a set of basis states (possibly degenerate) is chosen with the higher states corresponding roughly to shorter wavelength internal ripples. For each mode there is an associated eigenfrequency $m\omega_s$, a multiple of the synchrotron frequency. The impedance and beam current generate an additional interaction between the states which is expressed as a perturbing matrix generated by expectation values of impedance in the space of the eigenstates. In general reactive impedance can couple a basis element to itself and generates diagonal frequency shifts as its leading term. Resistive impedance provides the primary coupling between neighboring states. In this manner, the integral equation implicit in the Vlasov equation for a finite length beam is converted into an infinite dimensional matrix equation.

Determination of the threshold current for longitudinal and transverse instability ostensibly requires solution of an infinite dimensional matrix problem. In practice, the matrix is truncated and numerically diagonalized. Instability can evolve in a number distinct ways. First, modes (which at zero current are spaced by the synchrotron frequency) can be shifted as a function of current by the diagonal elements of the perturbation matrix. Modes of the right class can couple when their frequencies match, and can yield instability if there exists a nonzero off-diagonal resistive coupling. For transverse instabilities in storage rings this picture appears to give a reasonable description of experiment, with the lowest m=0 mode shifted until it collides with the m = -1 mode. The spectrum of the m=0 mode primarily samples the better known, lower portions of the impedance spectrum. Spectral shifts and stability enhancement from chromaticity are also observed and are in reasonable agreement with theory.[7] Predictions based on higher modes are more problematic.

For longitudinal dynamics the lowest $m = \pm 1$ mode ($m = 0$ corresponds to the unperturbed distribution) significantly samples impedance in the rolloff region for short bunches where the reactive impedance is changing sign and there is a strong resistive component. Whether bunch lengthening or shortening is predicted is particularly sensitive to assumptions about the impedance spectrum. Calculation of mode shifts is less certain and, in fact, the onset of instability is not typically associated with mode shifts.[8] A second method for generating instability in a matrix theory is for the off diagonal resistive elements to become comparable in size to the unperturbed mode spacing. For coupling of two neighboring modes, shifts in frequency would be expected, but this may not be the case when many modes are involved. The success of the infinite matrix approach for the transverse mode coupling instability depends very strongly on the *very finite* dimensionality ($m = 0$ to $m = -1$) of the underlying physics. Experience with the longitudinal instability suggests that its solution may not be so well behaved, and results have not been significantly more predictive than simple "massaged" scaling laws.

OPERATOR EQUATIONS AND INFINITE MATRICES

Successful conversion of an integro-differential equation and its associated eigenvalue problem into a truncated infinite matrix equation depends on both the boundedness of the operators and the basis set chosen for the expansion. Typically, one is provided with necessary conditions for convergence of the approximation scheme, but a particular operator may, in fact, submit to the approximation even if it does not satisfy such a condition. Such *luck* requires experimental confirmation. It will be argued heuristically in this and the following section that the matrix techniques used to describe longitudinal bunch instabilities do not satisfy some of the simplest necessary conditions for convergence. This is particularly the case for impedances which asymptotically scale as $\omega^{-1/2}$.

Intuition from finite dimensional matrices to infinite dimensional operators is clearest for a subset of bounded operators called *completely continuous*. Such operators map bounded sequences of vectors to convergent sequences of vectors;[9] in other words, the matrix elements M_{mn} fall off rapidly with m and n. For example, the identity op-

erator is bounded, but not completely continuous. Simple differentiation corresponds to multiplication by harmonic number (or matrix index) n in a Fourier series decomposition, and is neither bounded nor completely continuous. For completely continuous operators, one can be rather cavalier in the choice of basis set.

For operators whose elements either grow, tend to constants, or decrease too slowly (*e.g.*, inverse square root) with index, infinite matrix decompositions are not generally well behaved except for carefully selected basis sets.[10] These basis sets should share, for example, boundary values or boundary behavior with the underlying problem. Other choices of basis can lead to misleading results.

Consider, for example, the Legendre equation

$$\frac{d}{dx}(1-x^2)\frac{df}{dx} = -\omega^2 f \tag{16}$$

which describes space charge waves on a cold, parabolic bunch in the approximation of the electric field being proportional to the derivative of the longitudinal charge distribution. As a simple test of matrix truncation, this system was analysed using a simple Fourier series in sines and cosines. The infinite matrix generated was truncated and numerically solved. Diagonalisation produced good values ($\sim n(n+1)$) for the lowest even eigenvalues at a reasonably small matrix dimension, but the lowest odd eigenvalues had failed to converge even for a 180 by 180 matrix. The symmetry and nodes of the eigenfunctions, however, were suggestive of Legendre polynomials. Apparently the zero boundary condition of the sine functions has introduced convergence problems in the expansions of the Legendre polynomials, which are nonzero at the bunch ends. The Legendre operator has one other feature of note – it has positive expectation values, and it is this fact which allows the infinite matrix problem to work with carefully chosen basis sets. The Legendre model above represents a finite bunch with a sharp, but physically interesting interaction, and may exhibit more singular behavior than smoother distributions and interactions.

The question, then, with respect to the bunched beam problem is whether the underlying infinite matrix is either 1) completely continuous and susceptible to an arbitrary basis expansion or 2) well-behaved, but requiring a carefully matched basis set, or 3) pathological.

SINGULARITY OF LONGITUDINAL EQUATIONS

For frequency shifts Ω large compared to the synchrotron frequency, the matrix equation for longitudinal bunch motion takes a particularly simple form, which is sufficient to illustrate the issue. Following Wang,[11] we expect an infinite dimensional equation for high harmonic number of the form

$$\rho_m = \sum_{n=-\infty}^{\infty} T_{mn}\rho_n \tag{17}$$

where

$$T_{mn} = \frac{IZ(n)}{n}\lambda_{m-n}H(\frac{\Omega}{\sqrt{mn}}) \tag{18}$$

$$H(\frac{\Omega}{\sqrt{mn}}) \propto \int_{-\infty}^{\infty} d\omega \frac{g'(\omega)}{\frac{\Omega}{\sqrt{mn}} - \omega} \tag{19}$$

and I is the average current, $Z(n)$ is the impedance at harmonic n, and λ_n is the Fourier coefficient of the unperturbed charge distribution. Note that for $\Omega/\sqrt{mn}$ large compared to the width of the revolution frequency distribution g, $H \propto mn$. This implies, for example, that although the diagonal elements T_{nn} will scale as $Z(n)/n$ for small frequency shifts, for sufficiently large shifts the scaling can be as strong as $nZ(n)$. Consider now, the two asymptotic forms of impedance described earlier. In the infinite periodic limit, the leading behavior will be a reactive $1/n$ for $Z(n)$. In the limit $\Omega \to \infty$ T_{nn} remains bounded, but does not rolloff. This situation is marginal for convergence of arbitrary series expansions. For the isolated cavity, both the reactive and resistive impedance falls as $1/\sqrt{n}$, and for large shifts T_{nn} tends to a $\sqrt{n}$ behavior. Since this $\omega^{-1/2}$ scaling, as discussed earlier, is most likely for storage rings, this estimate suggests that special care must be taken in choosing basis sets. The large resistive term, in fact, may prevent the process from converging at all at large values of current. Typically, convergence becomes problematic when the self-adjoint (in this case, the reactive part) is not dominant.

It should be noted that for finite γ, the impedance is sharply rolled-off at frequencies greater that $\gamma c/a$, and the matrix is indeed finite but exceedingly large in dimension. Also, for fixed Ω, T_{mn} does finally rolloff at sufficiently large index, say n_Ω. However, n_Ω increases with increasing Ω. The primary lesson to be drawn from from the discussion is that matrix truncation can be misleading, and that physical solutions, at a minimum, may require matrices of a dimension considerably larger than first expected.

OTHER APPROACHES

The lack of startling quantitative success for truncated matrix methods may be due to numerical difficulties. On the other hand, it may be the case that some important physics is missing from the model, and there has been some activity with this perspective. Clearly, the first concern would be that the impedance function itself is not well estimated. It seems to be the case, however, that fitting to magnitude and shape leads to internal inconsistency, for example, between threshold current and parasitic losses.[12] Oide and Yokoya[13] argue quite legitimately that the impact of potential well distortion of the underperturbed distribution must be included, and have produced a Vlasov matrix analysis (using a new set of basis states) which indicates that threshold behavior can be dramatically altered by inclusion of potential well distortion in a self-consistent manner. Agreement appears good between this theory and simulation for some specific impedance shapes. Of particular note is that a strong capacitive component enhances thresholds by shortening the

bunch and preventing deterioration of the incoherent synchrotron frequency. A thermodynamic approach to turbulent bunch lengthening has been proposed by Meller.[14] The free energy of numerically-obtained, time-dependent distributions is compared to the conventional stationary Maxwell distribution for impedances with a resistive component. It is found that above a threshold current a time-dependent solution has a lower free energy and is therefore the preferred state for the beam. This transition is interpreted as the threshold for turbulent bunch lengthening. Comparison to SPEAR observations and simulation are promising. Hirata[15] also finds time dependent solutions, but for localised structures, and demonstrates that they can be the preferred state of the beam. More effort, both analytic and numerical, should be focused on such nonperturbative methods. Finally, many computer simulations[8] have been implemented and the general features of bunch lengthening with momentum growth have been observed. At least qualitative agreement with experiment is found. From the arguments in previous sections, some care may be necessary to model the isolated cavity with $\omega^{-1/2}$ asymptotic behavior.

SYNCHROTRON RADIATION IMPEDANCE

For small storage rings there may be another important source of coherent interaction of the beam with its environment – the synchrotron radiation process. Synchrotron radiation in bends and wigglers is suppressed at frequencies below a cutoff value many times the TM mode cutoff. For a chamber consisting of two infinite parallel plates, for example, separated by $2h$, the synchrotron radiation power takes on free space values only for frequencies ω satisfying[16]

$$\omega \gtrsim \frac{c}{\rho}\left(\frac{\rho}{h}\right)^{3/2} \tag{20}$$

where ρ is the bending radius. If this power loss is interpreted as an effective resistance, in the spirit of machine impedances, the peak value of

$$\frac{Z}{n} \simeq 300\frac{h}{R}\text{ohms} \tag{21}$$

where R is the average radius of the machine.

Taken at face value, this impedance could be the limiting component for small machines. Consider a compact synchrotron light source with $\rho = 1$ meter, $R = 2$ meters, and vacuum chamber half height of 1 centimeter. Then a maximum value of Z/n of 1.5 ohms is obtained at a frequency $\omega = (2\pi)50$ GHs. For short bunches where the impedance from vacuum chamber discontinuities is rolling off, the synchrotron impedance could be dominant. However, the synchrotron-radiation-induced coherent interaction may be of a different character. Wavelengths are now of the order of the transverse beam dimensions, the interaction occurs over an extended region (bending magnets and wigglers), and synchrobetatron coupling is inherent in the process. Much work has been done on the electromagnetics of synchrotron radiation,[17],[18] primarily in analysis of the resonance structure of a toroidal beam pipe. The beam dynamics has received only rudimentary attention. With the commissioning of small, clean compact synchrotron light sources, some experiments may be possible.

CONCLUSIONS

There has been much analytic progress in understanding the high frequency behavior of accelerator impedance. Analysis of beam dynamics has been successful for low-order transverse mode coupling, but there is no cogent analysis of longitudinal turbulent bunch lengthening. For single-cavity impedances, the interaction may be too singular to be well treated by a small-dimensioned matrix approach, and more global treatments may hold the best promise for prediction. Computer simulations have been exceedingly successful in modeling linac beam dynamics, where both the finite duration of beam propagation and frozen longitudinal motion with causal wakes ease calculations. For storage rings, it remains that the compute-efficient codes necessary for simulating many turns require compromises in electromagnetic modeling which limit quantitative agreement with experiment. Finally, the effects of coherent synchrotron radiation on beam stability remains an open question that could soon be addressed experimentally in compact synchrotron light sources.

REFERENCES

[1] K. Hirata and T. Susuki, ed., KEK Report 90-21, February 1991.

[2] S. Chattopadyhay, ed., *Particle Accelerators*, Special Issue: *Impedance Beyond Cutoff*, various articles, 25, 2-4, 1990.

[3] R. Gluckstern, *Proceedings of the Particle Accelerator Conference*, Chicago, Illinois, p. 1157, March 1989.

[4] A. Hoffmann, T. Risselada, and B. Zotter, KEK Report 90-21, p. 138, February 1991.

[5] A. Chao, B. Richter, and C.-Y. Yao, *Nucl. Instrum. Meth.*, 178, 1980.

[6] S. Heifets (private communication).

[7] M.-P. Level, KEK Report 90-21, p. 101, February 1991.

[8] B. Zotter, KEK Report 90-21, p. 1, February 1991.

[9] F. Riesz and B. Sz.-Nagy, *Functional Analysis*, Ungar, New York, 1965.

[10] S. G. Mikhlin and K. L. Smolitskiy, *Approximate Methods for Solution of Differential and Integral Equations*, American Elsevier Publishing, New York, 1967.

[11] J. M. Wang, in *Physics of Particle Accelerators*, AIP Proceedings 153, p. 697, AIP, New York, 1987.

[12] T. Susuki, Y. Chin, and K. Satoh, *Particle Accelerators*, 13, p. 179, 1983.

[13] K. Oide and K. Yokoya, KEK Preprint 90-10, 1990.

[14] R. Meller, *Proceedings of Particle Accelerator Conference*, p. 1155, Washington, D. C., 1987.

[15] K. Hirata, KEK Report 90-21, p. 73, February 1991.

[16] A. Faltens and L.J. Laslett, in *1975 Isabelle Summer Study*, BNL-20550, 1975.

[17] R. L. Warnock and P. Morton, *Particle Accelerators*, 25, 2-4, p. 113, 1990.

[18] K-Y. Ng, *Particle Accelerators*, 25, 2-4, p. 153, 1990.

Acceleration of Polarized Proton in High Energy Accelerators

S.Y. Lee†
Department of Physics, Indiana University, Bloomington, IN 47405

ABSTRACT

In low to medium energy accelerators, betatron tune jumps and vertical orbit harmonic correction methods have been used to overcome the intrinsic and imperfection resonances. At high energy accelerators, snakes are needed to preserve polarisation. We analyze the effects of snake resonances, snake imperfections, and overlapping resonances on spin depolarisation. We discuss also results of recent snake experiments at the IUCF Cooler Ring. The snake can overcome various kinds of spin depolarisation resonances. These experiments pointed out further that partial snake can be used to cure the imperfection resonances in low to medium energy accelerators.

1. Introduction

The ability to accelerate of polarised protons to high energies is important for polarised proton collision experiments. During the acceleration process, polarised protons encounter thousands of spin depolarisation resonances. These resonances arise mainly from the the horisontal fields in focusing quadrupoles. The horisontal fields rotate the spin away from the vertical axis. If the kicks are correlated each turn, then the resonance condition arises. There are two types of spin depolarisation resonances[1]: intrinsic resonance at $K = kP \pm \nu_y$ and imperfection resonance at $K = k$, where k is an integer and P is the superperiodicity of the accelerator. K is the resonance tune obtained from Fourier analysing quadrupole kicks around the accelerator. The resonance width or strength, ϵ, is defined as the corresponding Fourier amplitude.

In circular accelerators, the spin vector precesses around the vertical axis with a frequency of $G\gamma$ per turn[2], where G=(g-2)/2=1.792846 is the anomalous g-factor of the proton. The spin tune, ν_s, of the polarised proton is therefore $\nu_s = G\gamma$. When the spin tune equals the resonance tune, successive kicks add up coherently to give rise to depolarisation. Fig. 1 shows resonance strength as a function of the energy for various accelerators. Observe that the intrinsic resonance strength is of the order of $|\epsilon| \lesssim 0.5$ for RHIC and $|\epsilon| \lesssim 5$ for the SSC.

We shall review the effect of snake resonances, and the effect of overlapping resonances and snake imperfections. The paper is organized as follows: Section 2 discusses the spin equation of motion. Section 3 deals with the spin motion in the presence of snakes. Section 4 reviews snake design. A conclusion is given in Section 5.

2. Spin Equation of Motion

The spin equation of motion for a moving particle in a static magnetic field is given by[3]

$$\frac{d\vec{S}}{dt} = \frac{e}{\gamma m}\vec{S} \times [(1+G\gamma)\vec{B}_\perp + (1+G)\vec{B}_\parallel]. \qquad (2.1)$$

where $\vec{B}_\perp$ and $\vec{B}_\parallel$ are the transverse and longitudinal components of the magnetic fields respectively. G is the anomalous gyromagnetic g-factor and γmc^2 is the energy of the moving particle. Let us use the coordinate system of the reference orbit, where $\hat{x}, \hat{s}, \hat{z}$ are unit vectors corresponding to radial outward, longitudinal, and transverse vertical respectively. Eq.(2.1) can then be transformed to,[1]

$$d\vec{S}/d\theta = \vec{S} \times \vec{F}, \qquad (2.2)$$

with $d\theta = ds/\rho$, where s is the longitudinal path length and ρ is the radius of curvature. The vector $\vec{F} = F_1\hat{x} + F_2\hat{s} + F_3\hat{z}$, can be expressed in term of particle coordinate as, $F_1 = -\rho z''(1+G\gamma)$, $F_2 = (1+G\gamma)z' - \rho(1+G)(\frac{z}{\rho})'$, $F_3 = -(1+G\gamma)$. Defining a 2-component spinor, Ψ, with $S_i \equiv < \Psi|\sigma_i|\Psi >$, Eq.(2.2) becomes,

$$d\Psi/d\theta = -\frac{i}{2}(G\gamma\sigma_3 - F_1\sigma_1 - F_2\sigma_2)\Psi = -\frac{i}{2}H\Psi\ . \qquad (2.3)$$

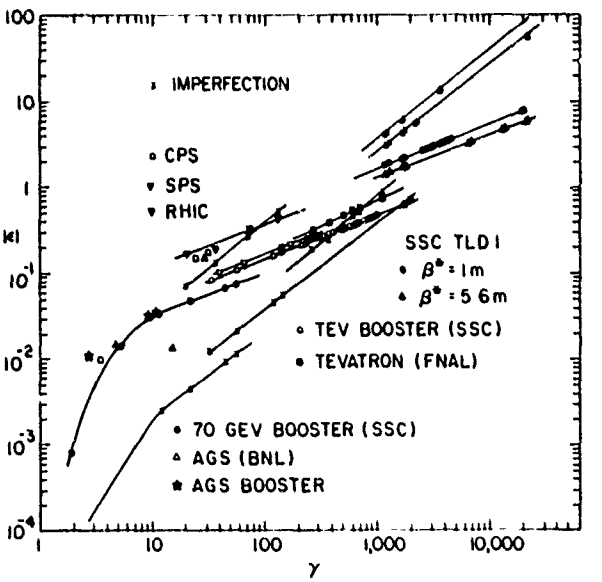


Fig.1 Compilation of intrinsic and imperfection resonance strengths for accelerators in the world. Note the scaling law of $\epsilon_{int} \sim \sqrt{\gamma}$ and $\epsilon_{imp} \sim \gamma$. The rms quadrupole misalignment assumed is ± 0.1 mm. The normalized emittance is $10\pi\mu$m-rad.

The off-diagonal matrix element of H, $\xi(\theta) \equiv F_1 - iF_2$, characterizes the spin depolarization kick by coupling the up and down components of the spinor wave function. Given the repetitive nature of circular accelerators, $\xi(\theta)$ can be Fourier analyzed as $\xi(\theta) = \sum \epsilon_j e^{iK_j\theta}$, where the Fourier amplitude, ϵ_j, is resonance strength and the resonance tune, K_j, is given by $K_j = k \cdot P \pm m\nu_y$ for intrinsic resonances and $K_j = k$ for imperfection resonances. Intrinsic resonances arise from the vertical betatron motion of particle, and imperfection resonances arise from

0-7803-0135-8/91$01.00 ©IEEE

the vertical closed orbit distortion. In a real accelerator, synchrotron and transverse betatron motions may also be coupled. The resonance condition becomes more generally $K_j = k \cdot P \pm m\nu_y \pm n\nu_x \pm l\nu_{syn}$, where k, l, m, and n are integers and ν_{syn} is the synchrotron tune.

For a single resonance, i.e. $\xi(\theta) = \epsilon \cdot e^{iK\theta}$, the spinor wave function for constant $G\gamma$ can be found easily[3], i.e. $\Psi(\theta_f) = t(\theta_f, \theta_i)\Psi(\theta_i)$ with

$t(\theta_f, \theta_i) = e^{-\frac{i}{2}K\theta_f\sigma_3} e^{\frac{i}{2}[\epsilon_R\sigma_1 - \epsilon_I\sigma_2](\theta_f - \theta_i)} e^{\frac{i}{2}K\theta_i\sigma_3}$.

Here $t(\theta_f, \theta_i)$ is the spin transfer matrix, whose components are given by, $t_{11}(\theta_f, \theta_i) = ae^{i[c - K(\theta_f - \theta_i)/2]}$, and $t_{12}(\theta_f, \theta_i) = ibe^{-i[d + K(\theta_f + \theta_i)/2]}$, with $t_{21} = -t_{12}^*$, $t_{22} = t_{11}^*$ and $b = \frac{|\epsilon|}{\lambda}\sin[\lambda(\theta_f - \theta_i)/2] = (1 - a^2)^{1/2}$, $c = \arctan[\frac{\delta}{\lambda}\tan(\lambda(\theta_f - \theta_i)/2)]$, $d = \arg(\epsilon^*)$, $\lambda = (\delta^2 + |\epsilon|^2)^{1/2}$, and $\delta = K - G\gamma$. The off-diagonal matrix elements t_{12}, t_{21} are the depolarisation driving terms, where the parameter b oscillates with an amplitude $|\epsilon|/\lambda$. When snakes are inserted into accelerator, the sine factor in the parameter b remains small until the next snake, which rotates the spin by 180^0 around a horisontal axis. The depolarisation driving terms can thus be arranged to cancel each other.

3. Spin Motion in accelerator with Snakes

A snake is a local spin rotator[4], which rotates the particle spin by π radians about a horisontal axis without perturbing the particle orbits outside snake region. A partial snake differs only in the amount of spin rotation angle, e.g. a 10% snake rotates spin by 0.1π radians. Thus a snake is characterised by the amount of spin rotation angle, ϕ, and the snake axis angle, ϕ_s, with respect to $\hat{x}$ (radial outward direction).

The spinor wave function at a snake will be transformed locally according to

$$\Psi(\theta^+) = e^{i\frac{\phi}{2}\hat{n}_s\cdot\vec{\sigma}}\Psi(\theta^-) = S(\phi_s)\Psi(\theta^-),$$

where $\hat{n}_s = (\cos\phi_s, \sin\phi_s, 0)$ denotes the snake axis with respect to horisontal outward direction $\hat{x}$, and $\phi = \pi$ is spin rotation angle. $\theta^{\pm}$ depicts asimuthal orbit rotation angles just before and after snake.

Let us assume that there are N_s snakes with snake axes, $(\phi_1, \phi_2, \cdots, \phi_N)$ distributed in the accelerator. Let $\theta_{i,i+1}$ be the asimuthal orbit rotation angle between the i-th, and (i+1)-th snakes. The distribution of snakes should satisfy the following conditions

$$\sum_{k=odd}^{N_s}\theta_{k,k+1} = \sum_{k=even}^{N_s}\theta_{k,k+1} = \pi\,, \qquad (3.1a)$$

$$\nu_s = \frac{1}{\pi}\sum_{k=1}^{N_s}(-1)^k\phi_k = j + \frac{1}{2} \quad j = integer\,. \qquad (3.1b)$$

Eq.(3.1a) ensures that spin tune, ν_s, is independent of particle energy. Eq.(3.1b) can be used to set the spin tune to a most favorable number in avoiding snake resonances, which will be discussed in the following section. As an example, in an accelerator with two snakes, $N_s = 2$, the snakes should be separated by an orbital angle of π and the snake axes of these two snakes should be orthogonal to each other in order to maintain a spin tune of 1/2. For accelerators with a large number of snakes, there are many ways to organize snakes to obtain proper snake superperiodicity and proper spin tune.

Let us consider an accelerator with $N/2$ pairs of (ϕ_2, ϕ_1) snakes. The spin transfer matrix after passing through a pair of (ϕ_2, ϕ_1) snakes is given by,

$$\tau(\theta_0 + \frac{4\pi}{N}, \theta_0) = S(\phi_2)t(\theta_0 + \frac{4\pi}{N}, \theta_0 + \frac{2\pi}{N})S(\phi_1)t(\theta_0 + \frac{2\pi}{N}, \theta_0)$$

The components of spin transfer matrix are given by,

$$\tau_{11}(\theta_0 + \frac{4\pi}{N}, \theta_0) = -e^{-i(\phi_2 - \phi_1)}(1 - 2b^2e^{i\Phi}\cos\Phi), \quad (3.2a)$$

$$\tau_{12}(\theta_0 + \frac{4\pi}{N}, \theta_0) = -2iabe^{-i(c - 2K\pi/N_s + \phi_2)}\cos\Phi. \quad (3.2b)$$

with $\tau_{21} = -\tau_{12}^*$; $\tau_{22} = \tau_{11}^*$ and where $\Phi = K\theta_0 + 2K\pi/N_s + d - \phi_1$, and the parameters, a, b, c, and d are given by $b = \frac{|\epsilon|}{\lambda}\sin\frac{\pi\lambda}{N_s} = (1 - a^2)^{1/2}$; $\lambda = (\delta^2 + |\epsilon|^2)^{1/2}$; $\delta = K - G\gamma$; $c = \arctan[\frac{\delta}{\lambda}\tan\frac{\pi\lambda}{N_s}]$; and $d = \arg(\epsilon^*)$.

The spin motion in accelerator can then be obtained iteratively by using the spin tracking equation through pairs of snakes:

$$T(\theta_{n+1}) = \tau(\theta_{n+1}, \theta_n)T(\theta_n)\,, \qquad (3.3)$$

where $\theta_{n+1} = \theta_n + 4\pi/N_s$. Eq.(3.3) can be solved using a power series expansion in the strength parameter b^2; i.e.

$$T_{11} = T_{11}^{(0)} + T_{11}^{(1)} + T_{11}^{(2)} + \cdots, \qquad (3.3a)$$

$$T_{12} = T_{12}^{(1)} + T_{12}^{(2)} + T_{12}^{(3)} + \cdots, \qquad (3.3b)$$

where $T_{11}^{(i)} = O(b^{2i})$ and $T_{12}^{(i)} = O(ab^{2i-1})$. A set of hierarchy equations to solve Eq.(3.3) iteratively can be obtained. By solving the spin tracking equation, one can find the spin tune and snake resonance condition. The final polarisation is obtained from the expectation value of σ_3 in spinor wave function ,i.e.

$$< S >= |T_{11}|^2 - |T_{12}|^2 = 1 - 2|T_{12}|^2$$

where the unitarity condition, $|T_{11}|^2 + |T_{12}|^2 = 1$, has been used.

3.1 Snake resonances

Without lose of generality, we shall first discuss an accelerator with two snakes (ϕ_2, ϕ_1), located at an orbital angle of π from each other. The one turn map(OTM)) is given by

$$\tau_{11}(\theta_0 + 2\pi, \theta_0) = -e^{-i\pi\nu_s}(1 - 2b^2e^{i\Phi}\cos\Phi)\,, \quad (3.4a)$$

$$\tau_{12}(\theta_0 + 2\pi, \theta_0) = -2iabe^{-i(c - K\pi + \phi_2)}\cos\Phi\,, \quad (3.4b)$$

where $\pi\nu_s = \phi_2 - \phi_1$ and $\Phi = K\theta_0 + K\pi + d - \phi_1$ is the characteristic phase of the orbital motion. The perturbed spin tune, Q_s, given by the trace of OTM, is $\cos\pi Q_s = b^2\sin(2\Phi)$ with $\nu_s = 1/2$. The parameter b is 1 when $|\epsilon| = N_s/2$. Thus during acceleration through a resonance with strength $|\epsilon| \approx N_s/2$, the perturbed spin tune, Q_s, will range over a whole integer unit and will cross the intrinsic

resonance comdition many times. Therefore polarization can not be preserved. When the maximum of $|Q_s - \frac{1}{2}|$ equals the deviation of the vertical betatron tune from half integer, the resonance condition recurs. The maximum tolerable resonance strength is thus given by

$$< \epsilon_c >= \frac{\arcsin(|\cos \pi K|^{1/2})}{\pi} N_s \,. \qquad (3.5)$$

Eq.(3.5) indicates that the tolerable critical resonance strength will be larger when the betatron tune is nearer to an integer. Numerical simulations agree well with the prediction of Eq.(3.5). The spin motion in the accelerator can then be obtained iteratively from the spin tracking equation, Eq.(3.3). To first order, we obtain easily

$$T_{12}^{(1)}(\theta_{n+1}) = iab(-1)^n e^{-i(\epsilon - K\pi + \phi_2)} \{ e^{i(\Phi + nK\pi)} \zeta_{n+1}(K + \nu_s) + e^{-i(\Phi + nK\pi)} \zeta_{n+1}(K - \nu_s) \} \qquad (3.6)$$

where $\zeta_n(q)$ is the enhancement function and is given by,

$$\zeta_n(q) = \frac{\sin nq\pi}{\sin q\pi}. \qquad (3.7)$$

At $q = integer$, we find that $\zeta_n(q) \to n$. This means that the off-diagonal kicks add up coherently on each turn through snake pairs. This condition is indeed a nominal resonance condition, since the spin tune equals a spin resonance position of $\pm K$. However since the betatron tunes of accelerator are not half integers, the condition $K \pm \nu_s = integer$ will never occur. Avoiding snake resonances, polarization will fall within the envelope of

$$\ll S \gg = 1 - 2|T_{12}|^2 = 1 - 8a^2b^2.$$

A few important observations can be drawn here:

1. $T_{12}^{(1)}(\theta_{n=even}) \cong 0$ at an imperfection resonance, $K = integer$. This means that imperfection kicks cancel each other every two turns around the accelerator. Thus snakes cure most effectively imperfection resonances. At $2nK = integer, K \neq 1/2$, a similar cancellation of $T_{12}^{(1)}(\theta_m)$ occurs at $m = 2n\ turns$ around accelerator.

2. The envelope function $\ll S \gg$ has many nodal points, where the depolarisation driving term vanishes, i.e. $b = 0$ or 1. These nodal points corresponds to the spin matching condition[3,5], where $G\gamma = K \pm \sqrt{(integer \cdot N_s)^2 - |\epsilon|^2}$. Thus these nodal locations are separated approximately by N_s units of $G\gamma$. These nodal points play an essential role in spin restoration during the passage through a depolarisation resonance.

Based on the linear response theory of Eq.(3.6), we expect that snakes will not work at a betatron tune equal to a half integer. Fig. 2 shows the polarization vs. the fractional part of the vertical betatron tune. A surprisingly many depolarization resonances appear at a betatron tune of rational numbers, e.g. 1/6, 5/6, 1/10, 3/10, etc.. To understand these resonances, we have to study the spin tracking equation beyond linear order in b. These higher order snake resonances can also be studied by solving spin hierarchy equations[3]. In general, the snake resonance condition is given by, $m\nu_s + nK =$ integer, with $m, n =$ odd integers.

Since the betatron tunes of colliders, such as RHIC, SPS, Tevatron, and SSC, have to avoid low order betatron resonances for a long term orbital stability, snake resonances do not impose further constraints to the operational condition of the colliders. The resulting tolerable resonance strength[3] agrees well with the critical resonance strength of Eq.(3.5). One can generalize the discussion to multi-snake accelerators, in which the snake resonance condition is modified by the snake superperiodicity P_s. At higher snake superperiodicities, there are fewer snake resonances, yet the resonance width is increased. The basic physics remains however unchanged.

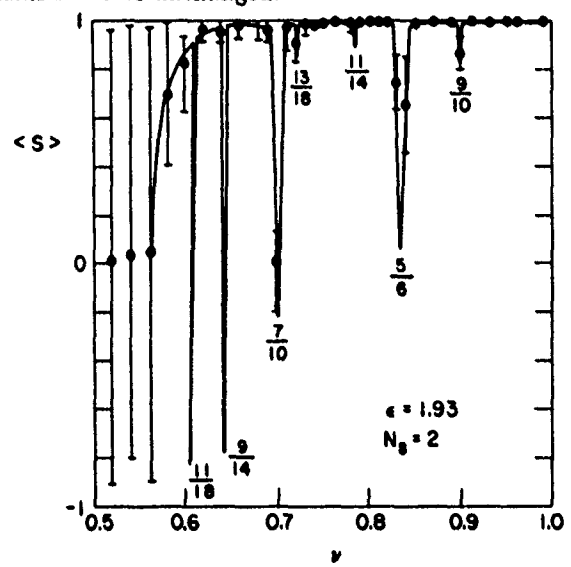


Fig.2 Beam polarisation after passage through a single spin resonance is shown as a function of the fractional part of spin resonance tune. Higher order snake resonances are seen clearly.

3.2 Overlapping Resonances

The spin resonance tune and resonance strength are intrinsic properties of the lattice design as well as the beam emittance. Important intrinsic resonances are normally well separated and can be treated as isolated resonances. However intrinsic and imperfection resonances may overlap. Section 3.1 showed that imperfection kicks cancel each other every two turns around accelerator. When an intrinsic resonance is present, the self cancellation mechanism of depolarisation kicks disappears. Spin becomes susceptible to depolarization kicks.

Fig. 3 shows tolerable resonance strengths of overlapping imperfection and intrinsic resonances. When the strength of an intrinsic resonance, $|\epsilon_{int}|$, is very small, the tolerable imperfection resonance strength, $|\epsilon_{imp}|$, becomes very large due to the self cancellation mechanism of Section 3.1. However, when $|\epsilon_{int}|$ is slightly increased, tolerable $|\epsilon_{imp}|$ decreases drastically until about $|\epsilon_{imp}|/\frac{N_s}{2} \leq 0.3$, where the imperfection resonance strength plays a minor role in depolarization process. Tolerable intrinsic resonance strength can then be increased until about $|\epsilon_{int}|/\frac{N_s}{2} \leq 0.4$. The tolerable imperfection strength will be $|\epsilon_{imp}|/\frac{N_s}{2} \leq 0.3$. For the SSC and RHIC, we expect

$|\epsilon_{imp}|/\frac{N_s}{2} \leq 0.05$ with 0.3 mm rms closed orbit distortion[3]. Beyond this intrinsic resonance strength, the perturbed spin tune plays a decisive role in determining the tolerable intrinsic and imperfection resonance strengths until the critical resonance strength, $< \epsilon_c >$, is reached. The relationship between tolerable intrinsic and imperfection resonances is also valid for an accelerator with multi-snakes. A pleateau for a limiting imperfection resonance is clearly seen on Fig. 3, which indicates the sensitivity of spin to imperfection errors when an intrinsic resonance is present nearby. The sensitivity is clearly due to the disappearence of the self cancellation mechanism. To achieve a higher tolerance to imperfection resonances, we can set a limit on the tolerable intrinsic resonance strength as $|\epsilon_{int}|/\frac{N_s}{2} \leq 0.4$, or $N_s \geq 5|\epsilon_{int}|$.

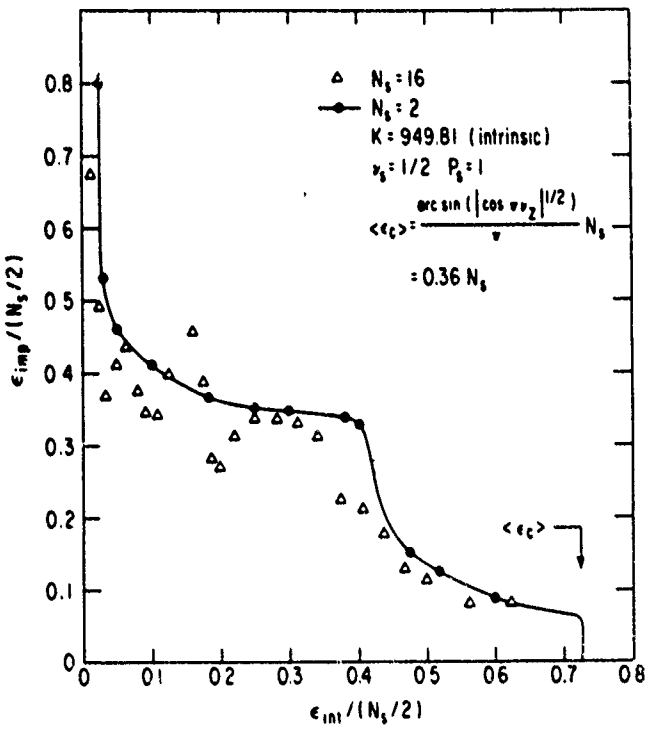


Fig.3 Correlation between tolerable intrinsic and imperfection resonance strengths for $N_s = 2$ and $N_s = 16$. See Section 3.2 for further discussion.

3.3 Snake Imperfections

When the spin rotation angle, ϕ, of Eq.(3.1) deviates from π by $\Delta\phi = \pi - \phi$, the spin transfer matrix of snake becomes,

$$S(\phi_s) = e^{-i\frac{\Delta\phi}{4}\hat{n}_s\cdot\vec{\sigma}} e^{i\frac{\phi}{2}\hat{n}_s\cdot\vec{\sigma}} e^{-i\frac{\Delta\phi}{4}\hat{n}_s\cdot\vec{\sigma}}. \qquad (3.8)$$

Thus the spin rotation angle error is equivalent to an imperfection spin resonance, with $\epsilon^{eq}_{imp} = \frac{\Delta\phi}{\pi}$. The corresponding spin tune then becomes energy dependent. To leading order, we obtain

$$\cos\pi\nu_s = \frac{N_s}{2}\cos(2G\gamma\pi/N_s)\sin^2(\frac{\Delta\phi}{2}), \qquad (3.9)$$

where the linear dependence of Eq.(3.9) on N_s is due to the assumption that each snake has an identical systematic error in the spin rotation angle. In reality, the snake rotation angle may deviate from π randomly, so the resulting spin tune modulation will not increase linearly with the number of snakes. Tracking calculation shows that the characteristic behavior is similar to that of Fig. 3.

Besides the error in ϕ, the snake axis angle, ϕ_s may also deviate from the ideal situation. The resulting spin tune is again energy independent (Eq.(3.1b)). The snake resonance condition determines the tolerable snake axis angle[3].

3.4 Snake Experiments

Recently, Krisch et al.[6] have carried out successfully a series of experiments in the IUCF Cooler Ring to test snake concept. Using a single solenoid snake, polarized protons have been accelerated through imperfection and intrinsic resonances without losing polarization The experiments also discovered synchrotron spin resonance in a proton storage ring. Synchrotron spin resonances have played important roles in electron storage rings, but have never before been found in the proton storage ring. Snakes cure synchrotron spin resonance as well. Along with experimental tests with full snakes, the partial snake concept of Roser[7] has also been studied extensively. Indeed partial snakes can be used in low to medium energy machines for correcting imperfection resonances. An interesting question involves the evolution of spin tune when snake is adiabatically turned on. Numerical tracking calculations have been performed to study the problem. A new series of experiments using a solenoid rf kicker[6] have been approved at the Cooler Ring to study more complex problems, such as overlapping resonances, spin tune, etc.

4. Snake Design

Since the invention of the snake idea by Derbenev and Kondratenko, the design of snake and/or spin rotator has become an interesting task. There are many varieties of snake designs[6,8]. For low to medium energy accelerators, Helical type snakes[8] seems to offer advantages in obtaining smaller transverse orbit displacements. At higher energies, snake design is flexibile.

The essential feature of the Steffen snake is the symmetric arrangement of vertical bending magnets and antisymmetric horizontal bending magnets. These features can be preserved in the following modified snake configuration

$$S_m = (-H,\ -V,\ mH,\ 2V,\ -mH,\ -V,\ H),$$

where $m = 2$ corresponds to the Steffen's snake. The number m is determined by geometry, i.e.

$$(m-1)\left(d + \tfrac{1}{2}(m-1)\ell_x + \ell_y + \ell_g\right) = \ell_x + \ell_y + 2\,\ell_g\ .$$

The spin rotation angle, ϕ, and snake axis angle, ϕ_s, are given by

$$\cos\frac{\phi}{2} = \cos^2\psi_y + \cos m\psi_x \sin^2\psi_y \qquad (4.1)$$

$$\cos\phi_s = \frac{-\sin\frac{m\psi_x}{2}\cos\psi_y}{\sqrt{\cos^2\frac{m\psi_x}{2} \quad \sin^2\frac{m\psi_x}{2}\cos^2\psi_y}} \qquad (4.2)$$

Note that $m\psi_x$ and ψ_y are the relevant variables in determining ϕ and ϕ_s. For a partial snake, we have $\phi < \pi$.

When ψ_x, ψ_y are small, one obtain then $\phi \approx 2m\psi_x\psi_y$ and $\phi_s \approx \frac{\pi}{2} + \frac{m\psi_x}{2}$. Fig. 4 shows ψ_x, ψ_y relationship of Eq. (4.1) and ϕ_s vs. ψ_y for $m = 2$. When $\phi_s = 0$, or π, the snake axis is along the radial $\hat{x}$ axis. The compact snake configuration saves about 15% of total length. Besides, total $\int Bd\ell$ and the horizontal orbit displacement, D_x, are also reduced.

By adjusting the parameter m, we can obtain a proper distance $2d$ between two halves of a snake. The orbit displacements at middle of two halves of a snake can be corrected by a orbit shifter of $(-V', V')$ at both ends of a snake. However when the distance $2d$ becomes large, we will have m≃1. Obviously, the total length and the radial orbital displacement of a snake increases as well. Such a split snake configuration is not practical for an insertion detector area. It can be used in accelerators with two adjacent straight sections separated by a quadrupole. Such a snake configuration eases design criteria of low energy ($\leq$ 30 GeV) accelerators.

To fit a collider interaction region (IR) into the space between the split snake, the snake configuration can be modified[8] to obtain split snake with $m = 2$. The advantage of the split snake configuration is that the spin in the mid section of a snake will be in the horizontal plane. Such a snake therefore serves a dual purpose of being a snake and a spin rotator for helicity state experiments. For a spin up particle passing through a half snake, the spin orientation becomes $S_x = -\sin m\psi_x \sin\psi_y$; $S_y = \sin^2 \frac{m\psi_x}{2} \sin 2\psi_y$; $S_z = 0$. Such a scheme can save the need of four spin rotators in a polarised proton experiment.

5. Conclusion

The current understanding of polarised proton acceleration in the high energy accelerator has been reviewed. With proper closed orbit correction, the overlapping resonance between the intrinsic and imperfection resonances can be controlled. The number of snakes needed is found to be proportional to the intrinsic resonance strength, i.e. $N_s \approx 5|\epsilon_{int}|$. The snake imperfection is more important with a large number of snakes. We also discuss the snake design issues. A split snake configuration can serve as a snake and as a spin rotator for the helicity state experiments.

† On leave of absence from Accelerator Development Department, Brookhaven National Laboratory, Upton, NY 11973.

References

1. E.D. Courant and R. Ruth, BNL report, BNL-51270 (1980).

2. L.H. Thomas, Phil Mag. 3, 1 (1927). V.Bargmann, L. Michel, and V.L. Telegdi, Phys. Rev. Lett. 2, 435 (1959).

3. S.Y. Lee and S. Tepikian, Phys. Rev. Lett. 56, 1635 (1986). S.Tepikian, Ph. D. Thesis, S.U.N.Y. Stony Brook, (1986); S.Y. Lee, AIP 187, p. 1105 (1988); S.Y. Lee and E.D, Courant, Phys. Rev. D41, 292 (1990); S.Y. Lee, Proc. of Penn. State Workshop on polarized colliders, AIP conf. proceedings, to be published (1991).

4. Ya.S. Derbenev, and A.M. Kondratenko, Sov. Phys. Doklady, 20, 562 (1976); Ya.S. Derbenev et al., Particle Accelerators, 8, 115 (1978).

5. K. Steffen, Particle Accelerator 24, 45 (1989).

6. A.D. Krisch et al., Phys. Rev. Lett. 63, 1137(1989); A.D. Krisch, in the Proc. of Spin Workshop, Protvino, USSR(1989); J.E. Goodwin et al., Phys. Rev. Lett. 64,2779(1990); J.E. Goodwin, Ph.D. Thesis, Indiana University, (1990); M. G. Minty, Ph. D. Thesis, Indiana University (1991); M.G. Minty et al., these proceedings.

7. T. Roser, AIP Conf. Proc. No. 187, p. 1442 (1988).

8. K. Steffen, DESY Report 83-124(1983); D.G. underwood, Nucl. Inst. and Methods, 173, 351 (1980); E.D. Courant, p. 1085 in Ref. 1(1988); U. Wienands, Proc. of 1st European Part. Acc. Conf., Rome, p. 905, (1988); S.Y. Lee, "Snakes and Spin Rotators", BNL 52248 /UC-414 (1990); Nucl. Inst. Method, to be published (1991).

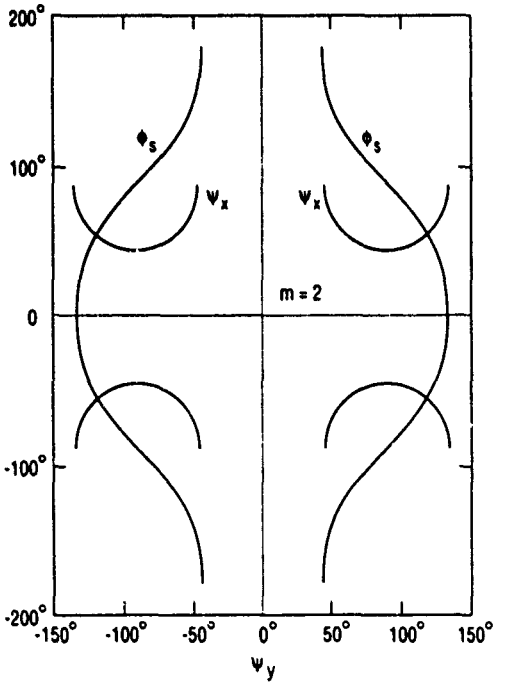


Fig.4 Relation between ψ_x and ψ_y is shown for the Steffen snake configuration. The corresponding snake axis angle is also given.

Longitudinal Instability in HIF Beams*

Lloyd Smith

Lawrence Berkeley Laboratory,
University of California
Berkeley, California 94720

ABSTRACT

In contrast to an electron induction accelerator, in which the particle velocity is virtually constant, the resistive and inductive components of accelerating module impedances can cause instability for an intense non-relativistic heavy ion beam accelerated in a similar structure. Since focusing requirements at the fusion pellet imply a momentum spread $\lesssim 3\times10^{-4}$ at the end of the accelerator, it is essential to understand and suppress this instability. There is also an economic issue involved for this application; selection of parameters to control the instability must not unduly affect the efficiency and cost of the accelerator. This paper will present the results of analytic and computational work on module impedances, growth rates and feed back (forward) systems.

1. INTRODUCTION

Inertial Confinement Fusion is based on the concept of creating a condition of very high density and temperature in a fuel pellet a few millimeters in size for a few nano-seconds. The material is not confined by external forces; the finite reaction time is due to the inertia of the fuel as it flies apart. For this process to work, an energy of several megajoules must be deposited in a thin surface layer in a few nano-seconds-an instantaneous power requirement of several hundred terawatts. The candidates for delivering the energy are lasers, which can deliver the required power but are as yet deficient in total energy and desired repetition rates of a few per second, and particle accelerators, which can deliver the required energy at a good repetition rate but as yet not at the required power level. Because the stopping distance is set by the required thickness of the surface layer, the choices in particle beams range from millions of amperes of light ions at several MeV kinetic energy to thousand of amperes of heavy ions at several GeV kinetic energy. At the heavy ion end of the scale the candidates are a set of R-F linacs plus accumulation and storage rings to reach the required level of joules and watts, and a linear induction accelerator, which is capable of accelerating kiloamperes of beam and would deliver the required energy and power in a single shot. The subject of this paper is a longitudinal instability which is certain to occur in an induction linac and is currently considered to be a major question as to the feasibility of the induction linac option.

Work supported by the Office of Energy Research, Office of Basic Energy Sciences, U.S. Department of Energy. Contract DE-AC03-76SF00098.

U.S. Government work not protected by U.S. Copyright.

II. THE PROBLEM

The instability in question is a close relative of the well-known microwave instability in circular accelerators but with distinctive features in this unfamiliar parameter range. That it should occur in a linear accelerator is due to the fact the ions are non-relativistic all the way (10 GeV at mass 200 → 50 MeV/nucleon → $\beta = 0.3$) and regenerative bunching can occur at an unpleasant rate in a kilo-ampere beam subjected to the impedance of the accelerating modules themselves.

Figure 1 shows a typical module as presently conceived. The module is energized through the transmission line entering at the upper left; the characteristic impedance of this line is seen as a resistance by the beam. Analytic estimates, more or less corroborated by model measurements, indicate that in the frequency range of greatest concern, about five to fifty megahertz, the impedance is well represented by a parallel R-C circuit–the line impedance in parallel with the capacity of the narrow gap below the end of the feed line. At about 100 MHz, there are modes involving the space above the magnetic material to the right of the transmission line which can be represented by a parallel R,L,C circuit. Unfortunately, the Q of this mode depends on R-F properties of the magnetic

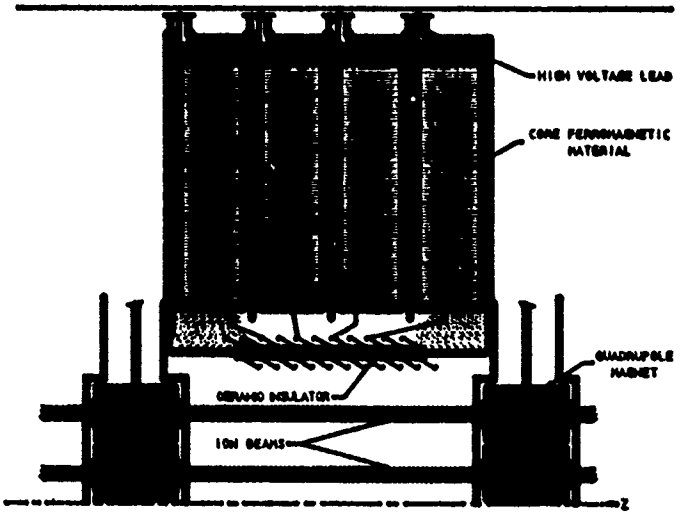


Fig. 1. Typical set of accelerating modules. The voltage is applied through the leads at the top and appears across an insulated gap below the leads. The insulating material can be seen projecting into the space below the magnetic material.

material, probably Metglas, which are not known at this time. Finally, there are many modes at much higher frequency associated with the pill-box like region surrounding the beam, but those are thought to be unimportant. In fact, PIC simulations indicate that even the 100 MHz mode is only marginally important.

The low frequency impedance is, however, quite important and here arises a conflict with the over-all performance and cost. To ease the instability, the line impedance should be as low as possible and the gap capacity as high as possible to shunt the R-F image currents away from the resistance. These desires are diametrically opposed to the demand for high efficiency and low cost. Maximum efficiency requires that the line impedance be equal to the module voltage divided by beam current to minimize reflected power. Also, the characteristic time $\tau = RC$ should be short compared to the beam passage time of 100-500 ns. in order to establish the required voltage without undue strain–i.e., the capacity should be low. As will be seen in the next section, best performance and cost lead to a predicted e-folding distance of about 100 meters in an accelerator five to ten kilometers long. In order to bring the theoretical problem into a range of control by momentum spread (less than ~3×10^{-4} because of chromatic effects in focusing on the fuel pellet) and/or feed-forward (see later section) we contemplate reducing line impedance by a factor of three (25% efficiency loss) and increasing the RC time by a factor of three (cost unknown).

III. THEORY

Instead of working with the Vlasov equation, it is simpler to work with the linearized fluid equations with zero pressure (no momentum spread), keeping in mind that the criterion for stabilization by a momentum spread is the same as for the microwave unstability of a coasting beam. Furthermore, the situation is formally similar to the transverse beam break-up instability without an external focusing force and will be analyzed in a similar fashion. The fluid equations are:

$$\frac{\partial}{\partial t}\frac{I}{v} + \frac{\partial I}{\partial z} = 0 \qquad \text{continuity equation} \qquad (1)$$

$$\frac{\partial v}{\partial t} + v_0\frac{\partial v}{\partial z} = \frac{eE}{m} - \frac{eg}{4\pi\varepsilon_0 mN}\frac{\partial}{\partial z}\frac{I}{v} \qquad \text{Force equation} \qquad (2)$$

$$\frac{\partial E}{\partial t} + \frac{E}{\tau} = -\frac{1}{C}(I-I_0) \qquad \text{Circuit equation} \qquad (3)$$

where I is current, v is velocity, and I_0 and v_0 are the unperturbed values.* C is the capacity, averaged in z, in Farad-meters of the low-frequency equivalent circuit, R is the smoothed resistance in ohms/meter, τ=RC, and N is the number of beamlets simultaneously accelerated.

The second term in (2) is the space charge force per beamlet since the beamlets are isolated transversely by closely spaced conducting sheets inserted in the beam region of Fig. 1. It has the effect of producing space charge waves running forward and backward along the beamlets. As the accelerator was first conceived, there was to be a single beam (N=1) and stability seemed to be insured by the mechanism that backward moving waves growing amplitude would reflect from the back end of the bunch and damp out as they moved forward. In the present concept there would be a dozen or more separate beamlets. The space charge force is then negligible compared to the induced module force in the low frequency range and will be omitted hereafter.

If time is replaced by $t - z/v_0$, the time after the head of the bunch passes a particular point along the accelerator, the equations become:

$$v_0\frac{\partial}{\partial z}\frac{\delta I}{I_0} = \frac{\partial}{\partial t}\left(\frac{\delta v}{v_0}\right) \qquad (1')$$

$$\frac{\partial}{\partial z}\frac{\delta v}{v_0} = \varepsilon \qquad (2')$$

$$\frac{\partial \varepsilon}{\partial t} + \frac{\varepsilon}{\tau} = -K^2 v_0\frac{\delta I}{I_0} \qquad (3')$$

where $\varepsilon = \frac{e\delta E}{mv_0^2}$ and $K^2 = \frac{eI_0}{mv_0^3 C} = \frac{eI_0R}{mv_0^3\tau}$

The most likely way for a perturbation to be launched is by a voltage error on a module at (say) z=0. The initial conditions for the set of equations are then:

$$\frac{\delta v}{v_0}(0,t) = f(t)$$

$$\frac{\delta I}{I_0}(0,t) = 0 \qquad (4)$$

$$\varepsilon(0,t) = \varepsilon(\infty,0) = 0$$

Using a Laplace transform in z:

$$\tilde{y}(k) = \int_0^\infty dz e^{-kz} y(z) \ , \qquad (5)$$

the equations lead to

$$\hat{\varepsilon} = -\frac{K^2}{k^2+K^2}\int_0^t dt' \frac{d}{dt'} f(t')\exp\left[-\frac{k^2}{k^2+K^2}\frac{t-t'}{\tau}\right] \qquad (6)$$

* This analysis neglects acceleration; the qualitative features are not seriously affected by this omission.

If the initial velocity perturbation is $\frac{\delta v}{v_0} = \Delta e^{i\omega t}$, the integral in (6) is easily done and the Laplace transform can be inverted analytically or by a numerical integration around the poles. The analytic result is:

$$\mathcal{E} = -\frac{K\Delta e^{-t/\tau}}{1+i\omega\tau}\left\{\sum_{n=0}^{\infty}\frac{(Kz)^{n+1}j_n(Kz)}{n!^2}\left(\frac{t}{2\tau}\right)^n + i\omega\tau\sum_{n=0}^{\infty}\frac{1}{n!}\left(\frac{t}{\tau}\right)^n\sum_{k=0}^{n}\frac{(Kz)^{k+1}j_k(Kz)}{2^k k!}(1+i\omega\tau)^{n-k}\right\} \quad (7)$$

where $j_n(Kz)$ is the n^{th} order spherical Bessel function.

Figure 2 shows two examples of the corresponding $\frac{\delta v}{v_0}$ as a function of Kz and t/τ. The most violent growth occurs for $\omega\tau = \frac{1}{\sqrt{3}}$ but becomes relatively benign for higher frequencies; the case, $\omega\tau=3$, is also shown for comparison.

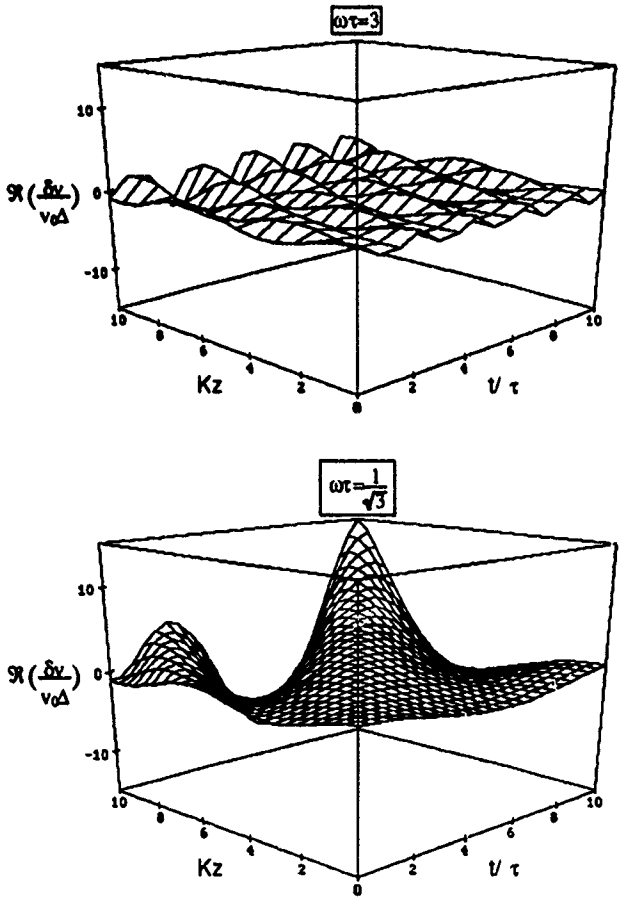


Fig. 2. $\frac{\delta v}{v_0\Delta}$ as a function of Kz and t/τ for $\omega\tau = 3$(top) and $\frac{1}{\sqrt{3}}$ (bottom). Kz = 10 corresponds typically to a distance of one to three kilometers.

Equation (7) is not very revealing of essential features, which can be seen better by setting $\frac{df}{dt} = \delta(t)$ in equation (6) and using a saddle point analysis.[1].

The inversion integral becomes:

$$\mathcal{E}(z,t) = -\frac{K^2}{2\pi i}\int\frac{dk}{k^2+K^2}\exp\left[kz - \frac{k^2}{k^2+K^2}\frac{t}{\tau}\right] \quad (8)$$

The method of steepest descents consists in finding the stationary points of the quantity in the exponent by setting its derivative equal to zero and then integrating across these saddle points to approximate the contour integral. Our interest, however, is only in the real part of the exponential at the saddle points; that is, the real parts of the solutions to the equation:

$$\frac{d}{du}\left[uKz - \frac{u^2}{u^2+1}\frac{t}{\tau}\right] = Kz - \frac{2u}{(u^2+1)^2}\frac{t}{\tau} = 0 \quad (9)$$

The roots of the quartic depend on the ratio $\frac{t}{\tau Kz}$. A case of particular interest [1] is when $\frac{t}{\tau} < \frac{8}{3\sqrt{3}}Kz$. The real part of the exponent is then given by:

$$Kz\left\{u-\Delta + \frac{2u\Delta^2}{\Delta^2+16\mu^4\left[1+\mu^2-2\mu\sqrt{1+\mu^2}\right]}\right\} \quad (10)$$

where $\Delta = t/\tau Kz$ and μ is defined by $\Delta = 4\mu^2\sqrt{1+\mu^2}$. The bracket is a maximum at $\Delta = \frac{3}{4\sqrt{2}}$, where (10) becomes $\frac{Kz}{2\sqrt{2}}$. That e-folding rate is the same as the worst case $\omega\tau = \frac{1}{\sqrt{3}}$ shown in Fig. 2. The point of maximum growth should move backward along the bunch at $\frac{t}{\tau} = \frac{3}{4\sqrt{3}}Kz$, in rough agreement with Fig. 2.

Numerical Values

For $\omega\tau = \frac{1}{\sqrt{3}}$, the frequency is $f = \frac{1}{2\pi\sqrt{3}\tau} = \frac{1}{2\pi\sqrt{3}\,t_p}\frac{t_p}{\tau}$,

where t_p is the pulse duration. For the desirable value, $\frac{t_p}{\tau} \sim 20$, f = 4-20 MHz for t_p = 500-100 n.s. and f = 1-7 MHz for τ increased by a factor of three. These frequencies are well in the range of the R-C model. The growth rate is $\frac{K}{2\sqrt{2}} = \sqrt{\frac{eI_oR}{16W\ell_p}\frac{t_p}{\tau}}$, where W is the kinetic energy and $\ell_p \sim$ 10 meters, is the bunch length. If the module feed line is matched, eI_oR = 1 MeV/meter, the intended acceleration rate.

Then for W = 1 GeV and $\frac{t_p}{\tau} = 20$, $\frac{K}{2\sqrt{2}} \sim (100 \text{ meters})^{-1}$. If R is reduced by a factor of three and τ increased by a factor of three, $\frac{K}{2\sqrt{2}} \sim (300 \text{ meters})^{-1}$.

Feed Forward

Since the ions are non-relativistic ($\beta < 0.3$), the possibility arises of observing some aspect of the unstable growth at one point along the accelerator and preparing a down stream module to apply a correction. Probably the easiest thing to observe is the perturbed electric field, which would appear as an error in module voltage as a function of time during bunch passage. The negative of this error could be applied to the bunch a hundred meters or less down stream. To see how this would work, replace eqn. (2') by:

$$\frac{\partial}{\partial z}\frac{\delta v}{v_0} = \mathcal{E}(z) - \mathcal{E}(z-\ell) \sim \ell \frac{\partial \mathcal{E}}{\partial z} \qquad (2'')$$

where ℓ is the feed-forward distance.

A simple dispersion analysis of (1'), (2") and (3') leads to a damping factor, $\exp\left[-\frac{\omega^7\tau^7}{1+\omega^2\tau^2}K^2\ell z\right]$, which is indicative but misleading in that the apparent advantage of making ℓ large is due to the Taylor expansion approximation in (2"). Figure 3 shows the results of a simulation in which the perturbation grows from noise and in the right hand plot is fed forward at a distance of 100 meters. Much remains to be studied about this scheme, but it looks promising.

IV. CONCLUSION

This instability can be overcome by manipulating R and C of the modules, but at the price of reduced efficiency and increased cost. We shall continue to look for a compromise by involving a feed-forward system and a tolerable momentum spread. We have to rely heavily on theoretical analysis for now since there is no possibility of realistic experimental study without an accelerator capable of handling some hundreds of amperes. A group at the University of Maryland is planning a model experiment using low-energy electrons [2], from which we hope to gain considerable information.

V. REFERENCES

[1] For more details, see E.P. Lee and L. Smith, "Asymptotic Analysis of the Longitudinal Instability of a Heavy Ion Induction Linac," Proc. 1990 Linac Conf. p. 716-718, September 1990. See also E.P. Lee and L. Smith, "Analysis of Resonant Longitudinal Instability in a Heavy Ion Induction Linac," paper LRA62, this conference.

[2] J.G. Wang et al., "Resistive Wall Instability Experiment at the University of Maryland," paper LTP17, this conference.

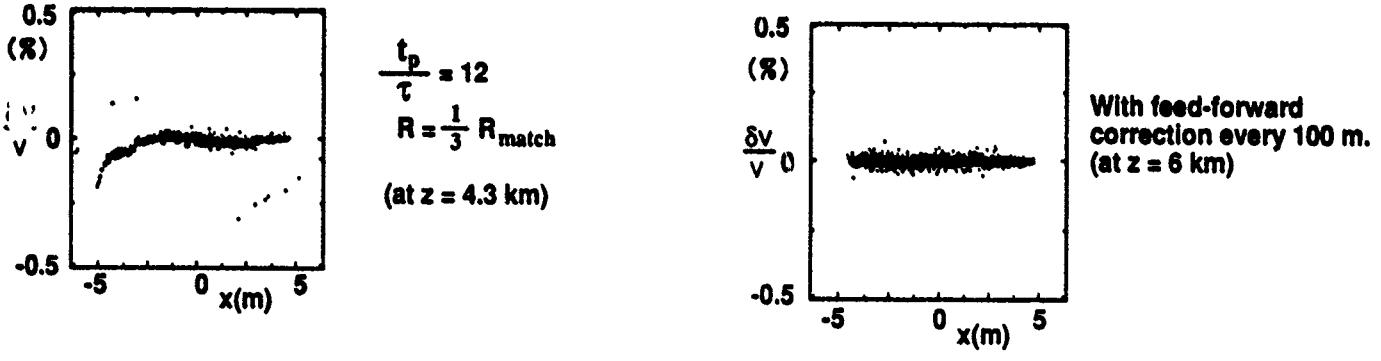


Fig. 3. Phase space plots with and without feed-forward correction. External impedance is assumed to be represented by parallel R and C.

Computer simulation of the coherent beam-beam effect in the LHC

W. Herr, CERN-SL CH-1211 Geneva 23

Abstract

For the Large Hadron Collider in the LEP tunnel (LHC) a non-zero crossing angle is foreseen to avoid multiple collisions outside the interaction point. The two beams can however suffer from long range beam-beam interactions during the time they are in one common vacuum chamber. These long range interactions can excite coherent beam-beam modes and due to the finite separation they are in general non-linear leading to possible coherent resonances of higher order. A computer simulation has been developped and was used to investigate this coherent beam-beam effect. Possible constraints on the LHC parameters are investigated and discussed.

1 Introduction

The LHC is designed to reach very high luminosities above $10^{34} cm^{-2} s^{-1}$ [1] and to achieve this a very large number of closely spaced bunches (4725) is foreseen. Normally, the two beams are separated into two beam pipes except in the interaction regions where they share a vacuum chamber. To avoid that all those bunches collide, a crossing angle of 200 μrad if foreseen. However, long range beam-beam effects cannot be avoided between the incoming and outgoing bunches and it was shown [2] that these long range forces constrain the choice of parameters for the crossing angle and the β^* functions at the interaction point. In this paper the coherent effect of long range interactions will be examined. The excitation of coherent bunch oscillations induced by the beam-beam effect is well known and studied extensively [3, 4] for the case of head-on collisions where the coherent motion is excited by a small transverse displacement of the colliding bunches. For the LHC these coherent oscillations can be excited by long range collisions since they are dipolar kicks and one can expect the excitation of coherent rigid dipole oscillations, i.e. small deviations from the nominal orbit. Their stability is investigated with a simulation program.

2 LHC parameters

Parasitic long range collisions in interaction region

The bunch spacing of 15 ns corresponds to a bunch distance of 4.5m and for the LHC geometry one calculates a total number of 19 parasitic collisions on each side of the collision point. The actual kicks received from opposing bunches are relatively small but since their effect is cumulated over many collisions, the total kick can become very significant [2]. Because a given bunch "collides" with many other bunches in every interaction region, a coupling of all bunches and a large number of coherent modes can be expected. To ensure a stable system, the motion of all these modes with different frequencies must be stable independently.

Beam separation in interaction region

The normalised emittance of the LHC beams is $\epsilon = 3.75$ μm ($\epsilon = \sigma^2\gamma/\beta$) and with a β^* value of 0.5 m this results in a beam size of about 15 μm. The separation between the two orbits d(s) increases linearly with the distance from the interaction point and the normalised separation $d_{sep} = d(s)/\sigma(s)$ is constant between the interaction region and the first quadrupole and can be written as $d_{sep} = \alpha\beta^*/\sigma^*$ with α the full crossing angle and β^* and σ^*, the betatron function and beam size at the interaction point (see e.g. [2]). For the nominal LHC parameters this gives a separation of about 6.5 σ for all long range collisions.

3 Simulation model

Phase space variables and particle transport

The variables used for the simulation are the transverse coordinate and angle of a bunch with respect to the design orbit (x,x'). The bunches are considered as rigid objects in this simulation since only the coherent dipole oscillation is considered. A complete simulation with more than 4000 bunches is unrealistic since the computer time required for the simulation would be too large. The maximum number of bunches in the simulation was 256 per beam. For the particle transport a linear, uncoupled machine is assumed. All the interaction regions are considered identical in the simulation, i.e. same length and same β^*. Details about the simulation can be found in [6].

Beam-beam interaction

For a given bunch the distance from its design orbit can be written as x_1, the distance of the opposing bunch to its design orbit as x_2 and the distance of the two design orbits is d(s). The distance between the two bunches is then given as $\delta x = x_2 - x_1 + d$. The beam-beam interaction between the two bunches is approximated by rigid dipole kicks of the form:

$$f(r) = \frac{8\pi\xi\sigma^2 x_{x,z}}{r\beta}\left(1 - e^{\frac{r^2}{2\sigma^2}}\right)$$

where: $r = \sqrt{x^2 + z^2}$, σ is the transverse beam size and ξ is the linear beam-beam tune shift.

The transverse kick δx' is computed as $\delta x' = f(x_2 - x_1 + d(s)) - f(d(s))$. The term f(d(s)) has to be subtracted since it is an orbit kick caused by the beam-beam interaction and has to be compensated by other means. In this study we are only interested in oscillations of bunches around the orbit.

The separation for the nominal LHC parameters is about 6.5 σ and a linearised beam-beam force as it is usually used to study coherent beam-beam effects from head-on collisions is not sufficient since it would suppress all resonances of orders higher than two and result in too optimistic limits for the stability (for details see [6]). In order to make the model realistic for a smaller number of bunches, several parasitic collisions have been accumulated into a single kick for the test bunch. The phase advance between the long range collisions on one side of the interaction region is small and such a cumulation is justified but the total effect is overestimated since the bunches normally collide with different phases.

Simulation strategy

The program has been written for two dimensions, but the stability was only studied in the horizontal plane where the

0-7803-0135-8/91$01.00 ©IEEE

two beams cross at an angle. The initial orbit displacements of all bunches were chosen as random numbers in the range of $\pm 0.1\sigma$. The results have been shown to be not very sensitive to the initial displacement. For the results presented in the next section only the long range forces are considered.

The program follows all bunches of both beams and keeps track of the phase space variables. An unstable situation is assumed whenever a bunch exceeds a certain limit on the displacement, in most cases a limit of twice the initial deviation from the design orbit is enough and the detection of instability is relatively insensitive to the actual choice of this value. For this detection, the number of turns tracked in each case is in the order of 250 - 1000, but in some cases up to 16000 turns have been tracked to study the possible dependence of the number of turns on the onset of unstable motion. Should the motion remain stable, i.e. bound, then the linear beam-beam tune shift ξ is increased in small steps to find the maximum value where the motion remains stable. To find stability diagrams in the (Q,ξ)-plane, the initial Q-values of the machine are scanned.

4 Results

Equally spaced interaction regions

Although equally spaced interaction regions with a limited number of bunches are not a good model for the LHC, such a scheme is treated for completeness and to compare with the results obtained for clustered interaction regions and many bunches.

Spectrum and stability A simulation has been performed to investigate the stability of a scheme with four bunches and equally spaced interaction regions, in this particular example with 4 collision points, i.e. every second collision is omitted. Fig.1 shows a Fourier spectrum of a bunch where the beam-beam tune shift used was ξ = -0.0034, i.e. the nominal LHC tune shift, the separation was 6.5 σ and 19 long range collisions were cumulated on each side in every interaction region. The horizontal tune was Q_h = 71.28. Three peaks in

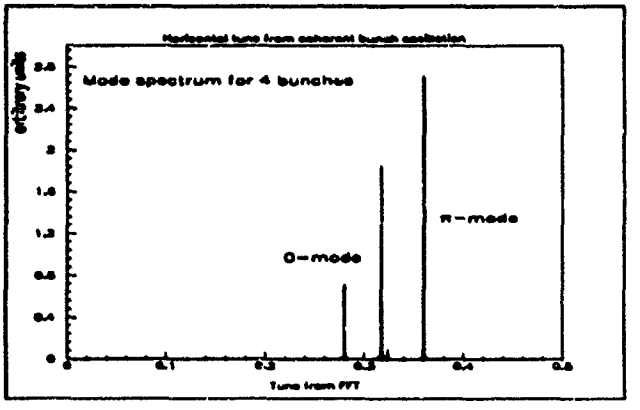


Figure 1: Mode spectrum for four bunches and equally spaced interaction regions

the spectrum can be seen: the peak at the lowest frequency corresponds to the so-called 0-mode without a frequency shift where the bunches move together and which is always stable. The mode where the bunches move maximally out of phase is the so-called π-mode which experiences the maximum frequency shift. This mode can become unstable. Between the 0-mode and the π-mode are the multi-bunch modes and in this very simple case of equally spaced and equal bunches these modes are degenerated into a single mode. The symmetry of the system is the reason for this degeneracy and breaking the symmetry by using two non equidistant interaction points or different phase advances between the interaction points the other modes become visible [5]. The instability is usually presented in the form of a (Q,ξ)-diagram where for every value of the tune Q the tune shift ξ is plotted where instability occurs, i.e. at values of ξ for which the π-mode (or any other mode) is shifted onto a resonance which can be driven by the force. The stability diagram in the (Q,ξ)-plane is shown in Fig.2. Two re-

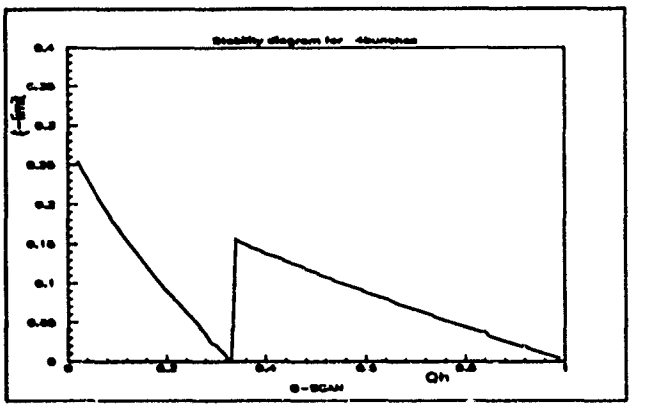


Figure 2: Stability diagram for four bunches and equally spaced interaction regions

gions are visible where the bunch motion becomes unstable: the regions for tune values just below the integer and around the third order resonance. The resonances at 1/2 and 2/3 are suppressed by the symmetry of the system. The stability plot for a single interaction region would show these resonances. For a linearised beam-beam force the third order resonance disappears. Non-linear resonances of orders higher than three have not been seen in the simulations.

Frequency shift An important quantity is the frequency shift of the π-mode since it determines the frequency span of the coherent beam-beam modes. From simulations with simple configurations it can be shown that this shift is only dependent on the total number of long range collisions, the linear beam-beam tune shift ξ, the number of interaction points and the normalised separation. This frequency shift is independent of the total number of bunches as long as the above parameters are kept constant, i.e. for smaller number of bunches the long range kicks are accumulated into a single kick. This allows a simple extrapolation of the frequency span to the nominal LHC parameters.

Clustered interaction regions

In the SSC and the LHC the interaction points are clustered (SSC) or not equally distributed around the ring (LHC), i.e. with different phase advance. In addition, the long range collisions are clustered around the interaction regions since normally the two beams are separated elsewhere.

Frequency shift Assuming three identical interaction regions with a phase advance of Q/2, Q/4 and Q/4 between the collisions, a separation of 6 5 σ and 19 long range collisons on both sides of the collision point, a frequency shift of the π-mode of about 11 ξ is found, i.e. with the current tune values of

Q_x=71.28 and Q_z=70.31 this results in a shift to 71.317 of the horizontal π-mode. The coherent tune shift from the head-on collision at the interaction point however has a opposite sign and partially compensates the long range tune shift. The total shift is therefore $\approx 7.5\ \xi$. It can therefore be extrapolated that a linear tune shift of more than 0.0075 is necessary to get unstable motion. For a linearised beam-beam force a linear beam-beam tune shift as large as ξ=-0.02 would be needed since only first and second order resonances would be excited.

Clustered long range interactions with many bunches To investigate the effect of many long range interactions clustered around the collision points, a larger number of bunches has been simulated (up to 256 per beam) and the long range collisons have been localised around the interaction points. Because a given bunch collides with many other bunches, all bunches couple together and a very large number of multi-bunch beam-beam modes can be observed. In Fig.3

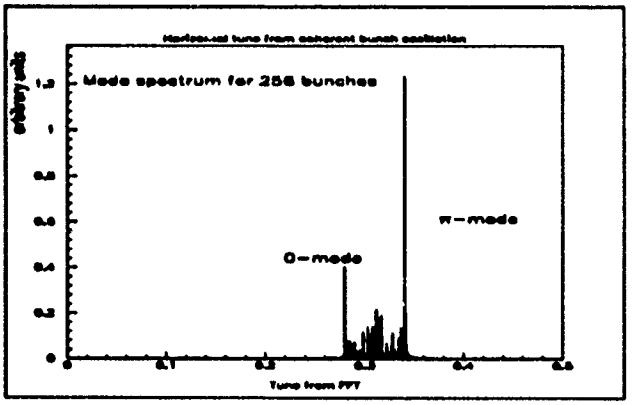


Figure 3: Mode spectrum for clustered long range collisions

the spectrum is shown for 256 bunches and one interaction point with eight clustered long range collisons. A large number of beam-beam modes can be seen between the 0-mode and the π-mode. For the limit of a very large number of bunches the spectrum will become a continuum of modes and the entire tune region up to the π-mode is potentially unstable if a low order resonance is in this region. The stability diagram for the above conditions is shown in Fig.4. The resonances of

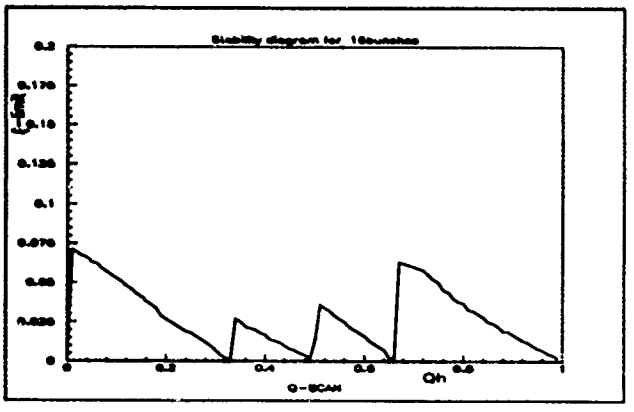


Figure 4: Stability diagram for clustered long range collisions

orders one, two and three are clearly visible. No resonances are suppressed since the symmetry is broken. The widths of the individual resonances are decreasing very fast with the number of parasitic collisions: the long range collisions all occur at different phases between the bunches and a decoherence effect is observed. For larger number of collisions (≥ 6) the linear beam-beam tune shift in the input has to be adjusted with a precision of $\approx 10^{-5}$ to get unstable motion. The limit of instability in Fig.4 had to be carefully searched since with a too coarse scan of ξ the instability could be missed and only the first and second order resonance would be seen. A scan with the required granularity in ξ would not be feasible since the computer time required would be enormous. A method was therefore implemented in the simulation program to find the stability limit for the required resonance by adjusting the π-mode on to the required frequency. Higher order resonances were also studied using this method, but have not been identified, at least not with the number of turns studied (up to 16000 turns). With the nominal LHC parameters, i.e. almost 40 long range kicks per interaction region, a strong decoherence can be expected and the excitation of resonances with orders higher than two will be weak or non-existing.

Dependence on separation The separation determines not only the total frequency shift of the π-mode and therefore the frequency span of the beam-beam modes, but also the non-linearity of the beam-beam potential. For the working point of Q_h = 71.28 a separation of more than 5 σ is necessary in order to remain stable [6]. For the nominal separation of 6.5 σ the motion is stable for $\xi \leq 0.0075$.

5 Conclusion

The coherent dipole oscillations induced by long range beam-beam interactions for the LHC have been investigated and the results can be summarised as follows:

- Coherent dipole oscillations can be excited by long range collisions.
- The separation of several sigma causes the excitation of non-linear coherent resonances of low (3rd) order.
- Clustered interaction regions increase the number of beam-beam modes which can potentially become unstable The frequency space between the 0-mode and the π-mode should be free from low order resonances.
- For the LHC parameters a linear tune shift of $\xi = 0.0075$ per interaction is necessary for unstable motion.
- However, strong decoherence from long range collisions and other damping mechanisms will make it unlikely that the coherent beam-beam effect is a limitation for the LHC with the current working point.

References

[1] *Design Study of the Large Hadron Collider (LHC).* CERN/AC/DI/FA/90-06 DRAFT (1991)

[2] W. Herr; CERN/SL/90-06 (AP) and LHC Note 119.

[3] A. Piwinski; Proc. 8th Int. Conf. High Energy Accel. CERN (1971) 357.

[4] A. Chao and E. Keil; CERN/ISR-TH/79-31 (1979).

[5] E. Keil; LEP Note 226 (1980).

[6] W. Herr; *Coherent dipole oscillations due to long range beam-beam interactions in the LHC.* LHC Note (1991).

The Coherent Beam-Beam Interaction

S. Krishnagopal (*)
Lawrence Berkeley Laboratory,
Berkeley, CA 94720

R.Siemann (**)
Stanford Linear Accelerator Center,
Stanford, CA 94309

Abstract

We present the results of a new beam-beam simulation program that allows for a self-consistent calculation of the electromagnetic fields of the beams by treating general (non-Gaussian) beam-distributions. We find that a new class of coherent instabilities, appearing at certain operating points, dominate the dynamics.

I. INTRODUCTION

One of the factors limiting the performance of e^+e^- storage ring colliders is the beam-beam interaction. There has been much speculation on the role of coherent (or collective) beam-beam effects as a mechanism for limiting the tune-shift, but no consensus has been reached on this issue[1]. Centroid (or dipole) motion, where the centroids of the two beams oscillate relative to each other, is routinely observed in operating storage rings, but there is no evidence that it affects luminosity. Centroid motion is easily detected and could be removed with feedback.

The potential for performance limitations comes from effects that distort the beam shape. Such effects have been analyzed with two different types of models. In the first, of Furman *et al.*[2] and of Hirata[3], nonlinear maps for the colliding beam system are developed in the moments. In earlier work Hirata uses a nonlinear beam-beam kick calculated from a Gaussian beam, which is not consistent with the assumption that the beams remain Gaussian. He finds flip-flop solutions, where both beams maintain unequal sizes. Later attempts at including higher moments were in substantial agreement with the Gaussian calculation. Furman *et al.* maintain self-consistency at the cost of a simplified, linear model of the beam-beam force. They find that equal-size higher-period solutions coexist, and are responsible for performance limitations.

In the second type of model, of Chao and Ruth[4] and of Dikansky and Pestrikov[5], the phase space distributions of the two beams influence each other and modes develop in phase space. The stability of these modes is analyzed with the linearized Vlasov equation, assuming small perturbations from equilibrium. While these calculations indicate the potential importance of coherent beam-beam effects, there are open questions about the approximations used in the calculations, Landau and radiation damping, and the relative importance compared to other effects.

Strong-strong computer simulations are an important tool in the study of the coherent beam-beam interaction. In the usual 'Gaussian simulations' the positions and rms sizes of the beams are first calculated from the coordinates of the test-particles just before the collision. They are then used in an expression for the beam-beam force that assumes the particle distribution to be Gaussian[6]. Unfortunately, this procedure does not allow for a self-consistent calculation of the fields; it restricts the fields directly and the distributions implicitly.

The simulation program discussed in this paper calculates the fields from the coordinates of the test-particles, and does not impose any restrictions on the beam-distributions or the beam-profiles. We find new coherent instabilities that, at certain operating points, dominate the dynamics.

II. FIELD CALCULATION

We worked with beams that were nominally round, *i.e.* the β^*'s and nominal emittances were equal in the two transverse dimensions. The beams were not restricted to remain round[7], but the field calculation is most efficient when the transverse sizes are comparable.

The electromagnetic fields of a bunch are calculated by Lorentz transforming to its rest frame and then solving Poisson's equation. Test particles are cast onto a circular mesh with radial step size Δr and azimuthal bin size $\Delta\phi$. The array that results, $N(r,\phi)$, must be smoothed, otherwise the simulation results are affected by statistical fluctuations due to the finite number of test particles. The average charge is treated first. It is smoothed by least-squares fitting using Forsythe's method[8], and the radial electric field it produces is calculated using Gauss' Law. The azimuthal variation of $N(r,\phi)$ is treated by Fourier analysing $N(r,\phi)$ and checking each Fourier coefficient for consistency with zero. Statistically significant coefficients are fitted and smoothed with Forsythe's method, and the Green's function for Poisson's equation in polar coordinates[9] is used to calculate the potential and the electric field.

U.S. Government work not protected by U.S. Copyright.

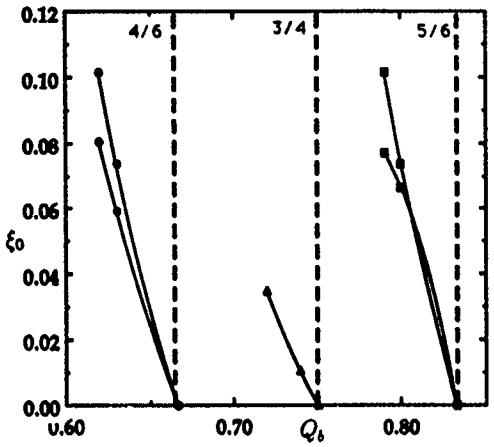


Figure 1: Onset and offset ξ_0 for the various coherent resonances, as a function of Q_b. At the nominal tune of the resonance it is assumed that the resonance 'tube' vanishes. The lines are drawn by interpolating from the calculated data points down to the zero-ξ_0 point.

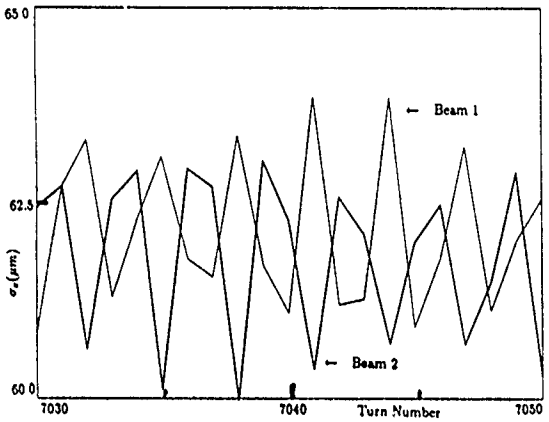


Figure 2: Horizontal beam-size variation over 20 turns. $Q_b = 0.79$, $\xi_0 = 0.08$.

This algorithm was checked for sensitivity to the details of the mesh – the sizes of Δr and $\Delta\phi$ – and was found to be insensitive to them. On the other hand, the number of test particles and the smoothing provided by the least squares fitting were important. Without smoothing, statistical fluctuations dominated for any reasonable number of test particles. With smoothing, results were found to be insensitive to the number of test particles when that number exceeded 5,000; in this work we used 10,000 test particles.

III. SIMULATION RESULTS

Our results show that the coherent behaviour is sensitive to the radiation damping. In this work we concentrated on low-order resonances, up to sixth order, and on damping decrements of $\delta = 1 \times 10^{-3}$ and $\delta = 1 \times 10^{-4}$, corresponding to betatron damping times of 2,000 and 20,000 turns, respectively. Synchrotron motion was not included, and the beams were forced to collide head-on by a 'feedback' system that set the centroids of the beams to zero after each turn. The horizontal and vertical tunes were kept equal (= Q_b, say), and Q_b was restricted to the region $0.5 < Q_b < 1.0$. Results are presented only for the x-dimension; the y-dimension behaved analogously.

A *Tune-Shift Scans*

Figure 1 presents the results of scans over the nominal tune-shift ξ_0, performed at different tunes, in order to determine the tune-shift region over which coherent motion broke out. The data-points in the figure correspond the lowest and highest ξ_0's at which coherent motion was seen, at that particular tune.

For the fourth-order ($\frac{3}{4}$) resonance there seems to be no upper limit to the coherent motion, at least to the maximum ξ_0 of 0.14 investigated. A study of the beam-size variation indicates that the behaviour is period-2 and anti-correlated between the two beams; *i.e.* when one beam is tightly focussed, the other is blown-up. This is consistent with the results of Furman et al.[2] which show a strong fourth-order resonance. This is not a new feature of these simulations; the same behaviour is seen even in Gaussian simulations.

Two sixth-order resonances, the $\frac{4}{6}$ and the $\frac{5}{6}$, were identified and traced out in tune. In contrast to the $\frac{3}{4}$ resonance, they were found to have a *finite* width in ξ_0. This is consistent with the predictions of the second class of models discussed above[4, 5]. The oscillations in the beam-sizes were found to be period-3 and anti-correlated (Fig. 2).

Just below $Q_b = 0.667$ both third ($\frac{2}{3}$) and sixth($\frac{4}{6}$) order resonances could play a role in the dynamics. On the other hand below $Q_b = 0.833$ only the sixth order ($\frac{5}{6}$) resonance is possible. However, the similarity of the coherent dynamics in these two regions (Fig. 1) suggests that the third-order resonance does *not* contribute below $Q_b = 0.667$. More generally one may surmise that odd order coherent resonances do not occur at all. This agrees with the predictions of the second class of models[4, 5], and is significant from the practical point of view.

B *Gaussian vs General Simulations*

To show that the sixth-order resonances are a new feature of these simulations, we performed a set of comparison runs with a Gaussian simulation. For the $\frac{5}{6}$ resonance, at a tune of $Q_b = 0.80$, the region over which coherent motion was seen was scanned using a Gaussian simulation.

The results are presented in Fig. 3 in terms of the beam-size and its variation as a function of ξ_0 for both, the general and the Gaussian simulations. For the former, with 10,000 test particles, the statistical fluctuation in the beam-size is less than a micron. For the latter, with 1,000 particles, it is just over a micron. Larger size-variations are indicative of coherent motion.

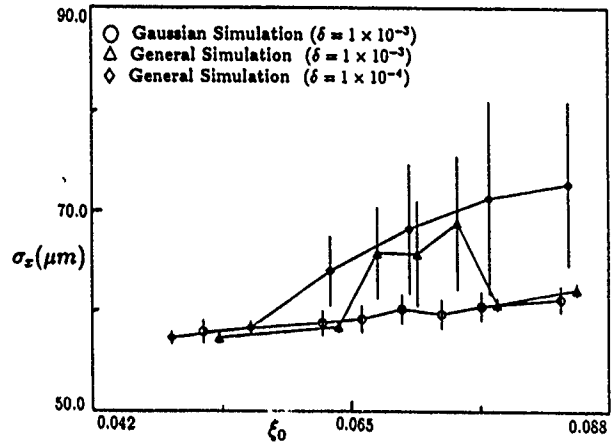


Figure 3: Horizontal beam-size as a function of ξ_0 at $Q_b = 0.80$, for three different cases.

From the figure one sees that for the sixth-order resonance coherent oscillations are present *only* in the more general simulation; they are absent in the Gaussian simulation.

IV. DISCUSSION

The last observation above suggests that it is critical to use general field calculations in the study of nonlinear coherent resonances. The reason is that this allows for a *self-consistent* calculation of the electromagnetic fields from the positions of the test particles. It results in higher-order fixed-point coherent motion.

It should be noted that centroid motion has been removed in these simulations, allowing us to concentrate on quadrupolar coherent oscillations. This is also reasonable from the experimental point of view, because such motion could be removed using feedback systems. If it is allowed to remain, we find that the beam-size variations persist, although they are reduced in magnitude. There is now a large degree of centroid motion between the beams. Thus both centroid and shape oscillations take place, and the situation is complex.

As mentioned earlier, the coherent behaviour is sensitive to the damping decrement δ. With lesser damping the width of the resonance becomes considerably larger, as can be seen from Fig. 3. Further, this could potentially result in higher-order resonances entering the picture; some preliminary results with $\delta = 1 \times 10^{-4}$ indicate that this is indeed the case. Thus, in machines with low radiation damping these coherent coherent resonances could play an important role.

It should be emphasized that the signature of these coherent resonances is a swift, turn-to-turn, variation in the beam-sizes. Since existing detectors are not sensitive to such rapid variations, these resonances could not, hitherto, have been detected.

V. FUTURE WORK AND CONCLUSIONS

Much work remains to be done, and is in progress. Resonance structure with lower damping is being investigated. The impact of removing feedback has to be studied. Sensitivity to initial conditions, consequences of asymmetric parameters between the two beams, and methods of handling flat beams; all these avenues can be explored.

We conclude by observing that a self-consistent calculation of the electromagnetic fields is essential in a study of the coherent beam-beam interaction. It leads to a new class of higher-period coherent instabilities that dominate the dynamics at certain operating points.

This research was conducted using the Cornell National Supercomputing Facility, a resource of the Center for Theory and Simulation in Science and Engineering at Cornell University, which is funded in part by the National Science Foundation, New York State and the IBM Corporation. Early work on this topic was performed at the Laboratory of Nuclear Studies, Cornell University which is supported in part by the National Science Foundation.

(*) Work supported by the Department of Energy, contract DE-AC03-76SF00098.

(**) Work supported by the Department of Energy, contract DE-AC03-76SF00515.

VI. REFERENCES

[1] Working group summaries in the Proceedings of the *Third Advanced ICFA Beam Dynamics Workshop on Beam-Beam Effects in Circular Colliders*, (Novosibirsk: Inst. of Nucl. Phys., 1989), edited by I.Koop and G.Tumaikin.

[2] M.A.Furman, K.Y.Ng and A.W.Chao, SSC-174, (SSCL,1988).

[3] K.Hirata, Phys.Rev.Lett. **58**, 25 (1987); **58**, 1798 (E) (1987); Phys. Rev. **D37**, 1307 (1988); AIP Conf. Proc. **214**, 175 (1990).

[4] A.W.Chao and R.D.Ruth, Part. Accel. **16**, 201 (1985).

[5] N.S.Dikansky and D.V.Pestrikov, Part. Accel. **12**, 27 (1982).

[6] M.Bassetti and G.A.Erskine, CERN-ISR-TH/80-06, (1980).

[7] Earlier work with this restriction is contained in: S.Krishnagopal, Ph.D. Dissertation, Cornell University (1991). There too, the same resonances occur.

[8] L.G. Kelly, *Handbook of Numerical Methods and Applications* (Reading, Mass: Addison-Wesley, 1967), p. 68.

[9] P.M. Morse and H. Feshbach, *Methods of Theoretical Physics* (New York: McGraw-Hill, 1953), p. 1188.

Effect of Non-planar Undulators on Beam Dynamics in ELETTRA

Lidia Tosi and Ryutaro Nagaoka
Sincrotrone Trieste, Padriciano 99, 34012 Trieste, Italy

Abstract

There is a strong interest in the installation of devices that will generate circularly polarized radiation in ELETTRA. However, the impact of such undulators on beam dynamics has been found to be more serious with respect to conventional planar devices, since further strong non-linearities are introduced in both horizontal and vertical planes. An investigation of the consequences of these effects on beam dynamics has been carried out for different types of devices. Various pratical means to compensate their effects, including local optics modifications, are attempted.

I. INTRODUCTION

ELETTRA[1], under construction at Trieste (Italy), is a 1.5-2.0 GeV third generation light source which at full operation will accomodate up to 11 insertion devices. Recently there has been also an increasing interest in the installation of a circularly polarized light source. However, previous studies[2] on the dynamic apertures in presence of helical insertion devices have shown an unacceptable reduction in the maximum stable amplitudes due to the additional non-linearities which these structures introduce in both the horizontal and the vertical planes with respect to the usual plane devices. In fact, the transverse and longitudinal components of the magnetic field in a general helical structure may be written as [3]:

$$\begin{aligned} B_x &= B_o\frac{k_x}{k_y}\,sh(k_x x)sh(k_y y)\cos(kz) + B_o'\,ch(k_x' x)ch(k_y' y)\sin(kz) \\ B_y &= B_o\,ch(k_x x)ch(k_y y)\cos(kz) + B_o'\frac{k_y'}{k_x'}\,sh(k_x' x)sh(k_y' y)\sin(kz) \quad (1) \\ B_z &= -B_o\frac{k}{k_y}\,ch(k_x x)sh(k_y y)\sin(kz) + B_o'\frac{k}{k_x'}\,sh(k_x' x)ch(k_y' y)\cos(kz) \end{aligned}$$

where k_x, k_y, k_x', k_y' must satisfy the two divergence conditions $k_x^2+k_y^2=k^2$ and $k_x'^2+k_y'^2=k^2$ with $k=2\pi/\lambda_o$, λ_o being the insertion device period length. Thus, the field may be looked upon as the superposition of the field **B** generated by a conventional horizontal plane device, whose non-linearities in the transverse planes scale as $(1/\rho k)^2(k_x)^m(k_y)^n$ [4], and of a field **B'** generated by a vertical plane device, which will introduce additional linear and non-linear forces scaling as $(1/\rho' k)^2(k_x')^n(k_y')^m$ [12,3], with ρ and ρ' the bending radii in the fields B_o and B_o' and with m, n = 0, 2,... Considering the exchanging roles that k_y and k_x' play in the two fields and the fact that usually for a plane horizontal device by construction $k_y \equiv k$, all the non-linearities which were present in the vertical plane for the latter are now also present in the horizontal plane, whose maximum stable amplitude for ELETTRA will mostly suffer because of the larger beta value of 8.2 m at the device location against 2.6 m for the vertical one.

A further cause for the strong reduction in the horizontal plane may be searched also in the fact that, whereas for the plane device described by the **B** field a particle injected with zero vertical amplitude will always remain in the horizontal plane, the **B'** field generates a finite vertical amplitude. The lifting of the particle off the horizontal plane will eventually in addition activate non-linearities coming from the strong sextupoles and from the **B** field.

Thus, it is important to be able to minimize the difficulties that a circularly light source may cause to machine operation, by a scanning through the design parameters of different proposals[5], which include a crossed undulator[6], a crossed scheme[7], an asymmetric wiggler[8] and an elliptical wiggler[9], whose most significant dynamic apertures are presented in the following section. An optimal dynamic aperture, which garantees a sufficient safety margin for the dynamic aperture requirements for Touschek and beam-gas scattering and for the injection process[10], has been found for the elliptical multipole wiggler.

In the last section, an enlargening of the maximum horizontal stable amplitude is attempted by lowering the beta value at the device location. Such a modification is found to be quite helpful, especially when no sextupoles are included. However, the inclusion of the latter presents a whole series of problems typically encountered when designing a lattice.

II. DYNAMIC APERTURES

In order to define the design parameters of the helical device whose dynamic aperture would garantee some safety margin for the aperture requirements and to understand the influence of the parameters on the dynamics, investigations on the dynamic behaviour of several possibilities have been carried out. In all the computations, the original tunes have been re-installed by a global compensation, leaving a residual beta beat whose maximum was found to be less than 3% for all cases. After doing the chromaticity correction, four particles with different initial conditions were tracked over 250 turns with the computer code RACETRACK [11,12].

Since the non-linearities introduced by **B'** scale as $1/\rho'^2$, investigations on the influence of the value for B_o' were done for a crossed undulator[6] whose parameters at 2 GeV were taken to be B_o = 0.35 T, λ_o = 0.06 m and N_p = 75. Lowering B_o' from 0.35 T to 0.15 T brought an improvement up to 21 mm in the horizontal and 16 mm in the vertical maximum stable amplitudes against the original values of about 10 mm.

A second series of investigations were made for the crossed scheme[7], in which the light is generated by placing in the same straight section a horizontal plane device U1 with a field **B** followed by a vertical plane device U2 generating a field **B'**.

0-7803-0135-8/91$01.00 ©IEEE

The two devices were chosen to have at 2 GeV the same maximum on axis fields of 0.39 T, $\lambda_o = 0.066$ m and $N_p = 24$. The transverse propagation constants of U1 were maintained constant with $k_y = k$, introducing non-linearities in the vertical plane. The ones for U2 were instead varied in such a way as to realize linearly a horizontally defocussing device with $k_x' = i\ 123\ m^{-1}$, a horizontal drift with $k_x' = 0$, an equally focussing device in both planes with $k_x' = k_y'$ and a vertical drift with $k_x' = k$. As shown in the resulting dynamic apertures in figure 1, there is a strong reduction in both planes for the case in which U2 is horizontally defocussing, since the ratio of the transverse and longitudinal propagation constants is large. All the other cases present different reductions due to the intrinsic non-linearities of the two devices and due to the coupling effects of U2. They may be explained by considering the following equations of motion for U2:

$$x'' = -\frac{1}{2\rho'^2k^2}\left(k_x'^2x+\frac{k_x'^4}{6}x^3+\frac{k_x'^2k_y'^2}{2}xy^2\right)-\frac{\sin(ks)}{\rho'}\left(k_y'^2xy+\frac{k_y'^4}{6}xy^3+\right.$$
$$\left.+\frac{k_x'^2k_y'^2}{6}x^3y\right)+y'\frac{\cos(ks)}{\rho'}k\left(x+\frac{k_x'^2}{6}x^3+\frac{k_y'^2}{2}xy^2\right) \qquad (2)$$
$$y'' = -\frac{1}{2\rho'^2k^2}\left(k_y'^2y+\frac{k_y'^4}{6}y^3+\frac{k_x'^2k_y'^2}{2}x^2y\right)-\frac{\sin(ks)}{\rho'}\left(\frac{k_y'^2}{2}y^2+\frac{k_x'^2}{2}x^2+\right.$$
$$\left.+\frac{k_y'^4}{24}y^4+\frac{k_x'^4}{24}x^4+\frac{k_x'^2k_y'^2}{4}x^2y^2\right)-x'\frac{\cos(ks)}{\rho'}k\left(x+\frac{k_x'^2}{6}x^3+\frac{k_y'^2}{2}xy^2\right)$$

For $k_x' = 0$, U2 introduces practically the same non-linear terms in the vertical plane as U1. The two combined together may explain the large reduction in the maximum vertical amplitude and because of the lifting of particles off the horizontal plane by U2, they contribute with the sextupoles to the reduction of the horizontal one. For the case $k_x' = k$, the above terms do not exist in U2, leading to an enlargement of the maximum vertical amplitude. However, analogous terms exist in the horizontal equations, whose maximum amplitude will suffer mostly. The best compromise seems to be the case in which $k_x' = k_y'$, where even though the equations of motion are the most complex, the strengths of the non-linearities are smaller with respect to the previous cases. Of course the whole mechanism of the dynamics is much more complex, depending on the system and on the combined effects of the sextupoles and the device.

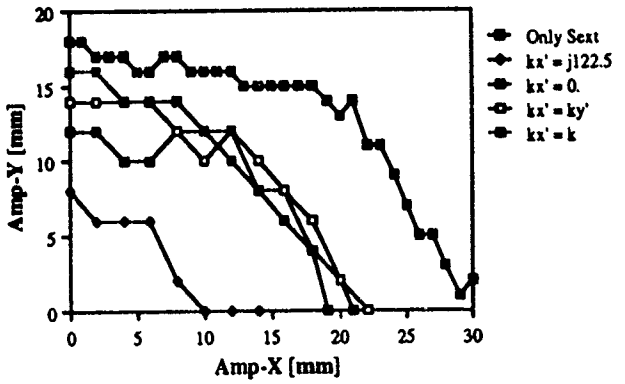


Figure 1. Dynamic aperture for the crossed scheme varying the design parameters of U2

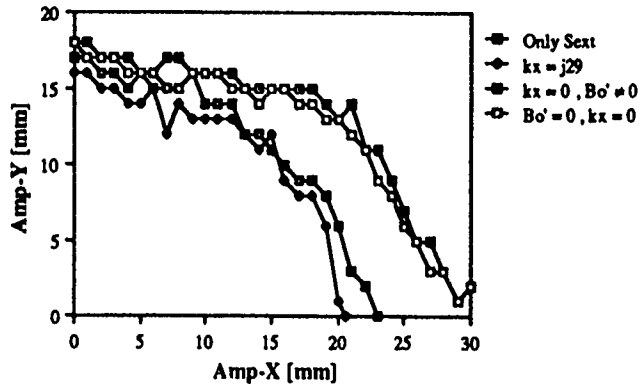


Figure 2. Dynamic aperture for the elliptical multipole wiggler

Investigations have been also carried out for an asymmetric wiggler[8], which is a horizontal plane device whose vertical and longitudinal field components may be written as a sum of harmonics. The dynamic aperture for the device chosen to have at 1.5 GeV an equivalent linear effect corresponding to a maximum on axis field of 0.35 T, $\lambda_o = 0.24$ m and $N_p = 20$ showed no significant reduction with respect to the one with sextupoles alone. In fact, this device presents a small value of k, important for small non-linearities, it produces a small linear distorsion and most important of all it is a plane horizontal device with no B' field.

From the above results, it has become quite evident that the required device must be searched for in the class of helical structures which present low values for all the propagation constants, a small value for B_o' and an adequate value for B_o. While the first two conditions contribute in containing the non-linear and coupling effects, the third must assure a small linear distorsion around the ring in order to not excite additional resonances due to the optical symmetry break. The device was chosen to be an elliptical multipole wiggler[9,13] with $B_o = 0.33$ T, $B_o' = 0.054$ T, $\lambda_o = 0.2$ m and $N_p = 20$ at 1.5 GeV. Since this device allows the switching of the polarization of the light by inverting only the B' field, the matching to the original tunes has been done only for B. Various sets of transverse propagation constants have been scanned in order to find an optimal dynamic aperture and the two most significant corresponding to $k_x = i\ 29\ m^{-1}$, $k_x' = 34.8\ m^{-1}$ and $k_x = 0$, $k_x' = k$ are reproduced in figure 2. In order to give an idea to what extent the presence of B' may limit the horizontal aperture, the dynamic aperture produced by the device when the above field is zero in the case $k_x = 0$ is shown. Since the non-coupling non-linearities introduced by B' are effectively small, it is reasonable to deduce that the small coupling ones combined with the sextupoles and the B field is the main cause of the reduction. Since the elliptical device with $k_x = 0$ seems to garantee some safety margin for the fulfilment of all the necessary aperture requirements, this device may be the most suitable as a circularly polarized light source for ELETTRA.

III. OPTICS MODIFICATIONS

Since ELETTRA presents a large horizontal beta value of 8.2 m against 2.6 m of the vertical, in this section an attempt of containing the non-linear effects in the horizontal plane by lowering the horizontal beta is presented. However, since this operation accomplished at only one straight section renders the sextupole optimization difficult, the optics have been modified in such a way as to pass from a 12-fold symmetry to a 6-fold one. Each superperiod is composed of two of the original ones, in which there is a high beta straight section followed by a low beta one, as shown up to the symmetry point in figure 3. In order to localize as much as possible the modifications, the optical functions before the quadrupole triplet in the low beta section have been fixed to the original values. By the introduction of an additional quadrupole family, the betas were simultaneously lowered and the alfas set to zero at the symmetry point. The quadrupole triplet in the high beta section was then used to globally re-adjust the fractional parts of the tunes to appropriate values. While the horizontal beta is reduced to 1.60 m in the low beta section leading to an increase in the tune of unity, the vertical one remained almost the same. Associated with this change, a sextupole optimization was carried out and the best configuration was found to be just the original harmonic sextupoles powered differently in the two sections. However, a reduction of about 30% in the horizontal dynamic aperture with respect to the original lattice occurs, due to the increase in the number of harmonics influencing the motion noticed in the analysis in single resonance approximation[14].

In order to see the effectiveness of lowering the horizontal beta value, the crossed undulator of the previous section with $B_0' = 0.35$ T was introduced without sextupoles in the ring. The maximum horizontal stable amplitude was found to be 60 mm against 20 mm in the original lattice. Subsequent trackings with sextupoles showed a large sensitivity to the location of the working point, due to the combined effect of the device and of the deterioration of the sextupole distribution compared to the former. The best dynamic aperture, shown in figure 4, was found by shifting slightly the vertical tune.

On this occasion, also a new proposed tracking routine for plane horizontal devices[15] has been extended to non-planar devices.

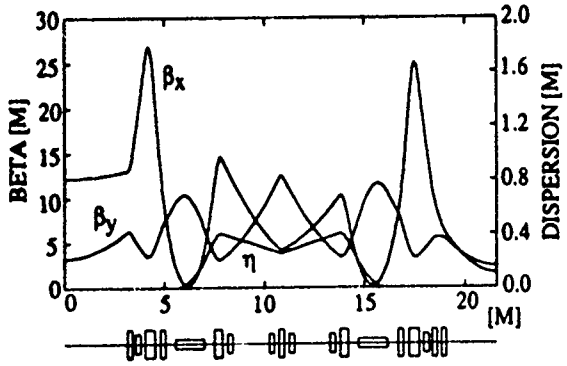


Figure 3. Modified optics

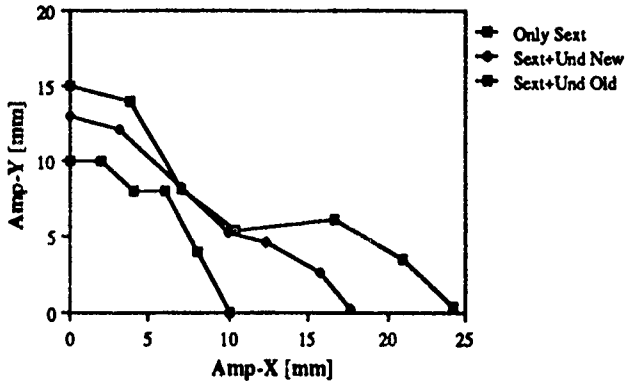


Figure 4. Comparison of the dynamic apertures for the crossed undulator in the original lattice and in the modified one.

IV. CONCLUSIONS

The presence of a helical insertion device in ELETTRA may deteriorate critically the dynamic aperture, due to the introduction of additional non-linearities in both planes. Thus, the request from the users of having a circularly polarized light source has required the necessity of finding a device which fulfills all the aperture requirements. After investigating the beam performance for various possibilities, an elliptical multipole wiggler has been found to be the most suitable. Furthermore, the lowering of the horizontal beta to suppress the non-linearities in this plane has shown to be useful for the crossed undulator, even when the presence of sextupoles may hinder the effectiveness because of the optical symmetry break.

Acknowledgements

The authors wish to thank dr. R.P. Walker and dr. A. Wrulich for many useful discussions and suggestions.

V. REFERENCES

[1] A. Wrulich, "Status of the ELETTRA Project, the Synchrotron Light Source in Trieste", this conference
[2] L. Tosi, R. Nagaoka, "Effects of Helical Undulators on Beam Dynamics", EPAC 1990
[3] R.P.Walker, Sincrotrone Trieste Tech. Note ST/M-TN-89/39
[4] L. Smith, ESG Tech. Note, ESG TECH. NOTE-24.
[5] R.P. Walker, Private Communication.
[6] H. Onuki, Nucl. Instr. Meth., A246 (1986) 94.
[7] K.J. Kim, Nucl. Instr. Meth. 219 (1984) 425
[8] J. Goulon et al., Nucl. Instr. Meth. A254 (1987) 192.
[9] S. Yamamoto, Phys. Rev. Lett. 62 (1989) 2672.
[10] ELETTRA Conceptual Design.
[11] A. Wrulich, "RACETRACK".
[12] R. Nagaoka, L. Tosi, Sincrotrone Int. Report, ST/M-90/6.
[13] B. Diviacco et al., "Status of Development of Insertion Devices for ELETTRA", this Conference.
[14] R. Nagaoka, Sincrotrone Int. Report, ST/M-91/3
[15] J. Bahrdt, G. Wustefeld, Technischer Bericht, BESSY TB Nr. 158, Okt. 1990

Calculations of the Conditions for Bunched-Beam e-p Instability in the Los Alamos Proton Storage Ring (PSR)*

David V. Neuffer
Continuous Electron Beam Accelerator Facility
12000 Jefferson Avenue
Newport News, VA. 23606

ABSTRACT

Recent observations are consistent with the possibility of an "e-p" instability in the PSR, with both bunched and unbunched beam. This instability requires stable trapping of electrons within the space charge potential of the protons and such trapping is not expected with bunched beam at PSR parameters. However, it is shown that electron trapping can occur if some of the beam leaks into the interbunch gap. Such leakage is observationally associated with the instability. Also it is shown that the leakage is consistent with the expected longitudinal dynamics within the PSR. Implications for improving PSR stability are discussed.

INTRODUCTION

Recent observations[1] support the hypothesis that the fast transverse instability observed in the PSR[2] is an electron-proton (e-p) instability, in which stray electrons are trapped within the space-charge of the circulating protons and unstable coupled transverse oscillations of the trapped electrons and protons develop. The instability requires a source of free electrons, stable trapping of electrons within the proton beam, and the exponential development of coherent coupled oscillations.

The oscillations can be described using a simplified linearised model[3],[4],[5] in which the proton beam and trapped electrons have uniform density within an elliptical cross section (a × b). Longitudinal variation is also ignored and the proton and electron densities are:

$$\rho_p = \frac{N}{(L \cdot \pi ab)}, \rho_e = \eta_e \rho_p \qquad (1)$$

where N is the total number of protons, L is the bunch length ($= 2\pi R$ for unbunched beam), and η_e is the neutralisation factor. The equations of coupled vertical motions are:

$$\ddot{y}_p + (Q^2 + Q_p^2)\Omega^2 y_p = Q_p^2 \Omega^2 \bar{y}_e$$
$$\ddot{y}_e + Q_e^2 \Omega^2 y_e = Q_e^2 \Omega^2 \bar{y}_p$$

where

$$Q_e^2\Omega^2 = \frac{4N r_e c^2 (1-\eta_e)}{b(a+b)L}, \; Q_p^2\Omega^2 = \frac{4\eta_e N r_p c^2}{b(a+b)\gamma L} \qquad (2)$$

are the electromagnetic oscillation frequencies of the electrons and protons and Q is the PSR vertical tune. The equations describe dipole-mode oscillations coupled by the centers of charge $\bar{y}_p$, $\bar{y}_e$. Assuming harmonic motion obtains the dispersion relation:

$$(Q_e^2 - x^2)(Q^2 + Q_p^2 - (n-x)^2) = Q_e^2 Q_p^2 \qquad (3)$$

where n is the spatial harmonic of proton oscillation and $x = \omega/\Omega$ is the oscillation frequency in units of revolution frequency ($\Omega = v_p/R$). At PSR parameters, we obtain $Q_e \approx 40 (\approx 100$ MHz). The relation can have complex solutions (instability) with $x \approx Q_e \approx n - Q$; thus the unstable oscillations occur at lower betatron sidebands near 100 MHz. Growth rates (from Im $x\Omega$) of the sidebands can be quite fast; Im $x\Omega \approx 0.1 - 0.01\ \mu s^{-1}$ is readily obtained. The instability requires a minimal value of $Q_p (Q_p > 0.1$ or $\eta_e > 0.01)$, implying a relatively small neutralisation is required. The PSR unstable oscillation frequencies and growth rates, and their dependences on beam size and density are in general agreement with the e-p model.

CONDITIONS FOR ELECTRON TRAPPING IN THE PSR

A key difference between the PSR and the simplified model is that the beam density in the PSR varies longitudinally by large factors, particularly with bunched beam. Stable trapping must be maintained with these variations. The trapping potential in the high intensity PSR beam is quite strong, and electrons should remain trapped within a continuous (debunched) beam. However, with bunched beam, a beam free interbunch non-trapping gap of 100 ns (25 m) passes through the electrons every PSR turn (360 ns). In that gap, even low-energy electrons will be detrapped, hitting the walls with high probability. (10–100 eV electrons travel 20–60 cm.)

The detrapping conditions can be quantified by representing the beam passage as a focussing transport section and the gap as a drift. The full transport is a product matrix:

$$M = \begin{bmatrix} 1 & L_1 \\ 0 & 1 \end{bmatrix} \begin{bmatrix} \cos(k_e L_2) & \frac{1}{k_e}\sin(k_e L_2) \\ -k_e \sin(k_e L_2) & \cos(k_e L_2) \end{bmatrix} \qquad (4)$$

where $k_e = Q_e/R$ and L_2 and L_1 are the bunch and gap lengths. For stable trapping the magnitude of the trace of M must be ≤ 2. At PSR parameters the beam strongly overfocusses the electrons ($Q_e \gg 1$), and the total transport is almost always unstable. Equation 4 assumes a constant beam density; the density within the bunch can be modified to more realistic forms (*i.e.*, parabolic) and the

*Supported by D.O.E. contract #DE-AC05-84ER40150

0-7803-0135-8/91$01.00 ©IEEE

transport recalculated (see reference [6]). At PSR parameters, the same pattern of general instability is obtained, provided that the gap (L_1) is beam-free. Therefore e-p instability should not occur in the PSR with bunched beam if a beam-free gap is maintained.

A different pattern is obtained if the gap does not remain beam-free, but significant amounts of beam leak into the gap. For that case we can approximate the beam density as a sum of a continuous sinusoidal distribution plus a constant background ϵ, similar to profiles observed in the PSR at onset of instability (!):

$$\rho(z) = \frac{N}{2\pi R}[(1+\cos(z/R)) + \epsilon] \tag{5}$$

At PSR parameters, stability conditions (Abs (Tr M) $\leq$ 2) are obtained for almost all conditions (see Figure 1), provided $\epsilon > 0$. The overall stability situation is facilitated by the relatively large distance scale in the PSR bunch; the transitions from high to low density beam are "adiabatic".

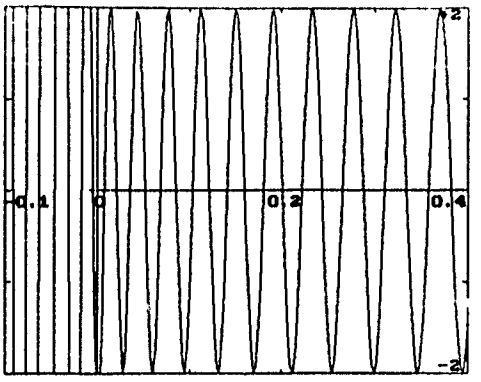


Figure 1. Tr[M] (ϵ) for $N = 2.25 \times 10^{13}$. Stability (electron trapping) is obtained for almost all $\epsilon > 0$.

The calculations demonstrate that electron trapping, and hence e-p instability, can occur if the interbunch gap has filled in with low-density beam. Observationally, instability can occur if the gap has indeed filled in, to some extent, and does not occur if the gap is maintained.

CONDITIONS FOR BUNCH LEAKAGE

Observations in the PSR show leakage of beam from the confining rf bucket when instability occurs. The critical question is whether such leakage may occur within the expected longitudinal dynamics, and in this section results of simulation explorations of this dynamics are reported.

The dominant longitudinal forces are expected to be due to the rf buncher and longitudinal space charge. The PSR has a low-frequency first-harmonic (2.8MHz, h=1) rf system with relatively low voltage ($V_{rf} \approx 10kV$). As a high-intensity machine at relatively low energy (800 MeV), it also has strong space charge forces. In a simple 1-D model the longitudinal space charge debunching force is:

$$F_z = -\frac{eg}{\gamma^2 4\pi\epsilon_0}\frac{d\lambda}{dz} \tag{6}$$

where λ is the beam line density, $\gamma = E/m_pc^2$, and $g = 1 + 2ln(r/b)$ with b and r the beam and pipe radii. With these forces the equations of longitudinal motion are:

$$\frac{d\phi}{dn} = -\frac{2\pi h\eta}{\beta^2}\frac{\Delta E}{E} \tag{7}$$

$$\frac{d}{dn}\left(\frac{\Delta E}{E}\right) = \frac{eV_{rf}}{E}(\sin(h\phi) - \sin(h\phi_s)) - \frac{egR}{2\gamma^2\epsilon_0 E}\frac{d\lambda(z)}{dz} \tag{8}$$

The phase ϕ and relative energy ($\Delta E/E$) have been chosen as dependent variables and turn number (n) is the independent variable. $\eta = (1/\gamma^2 - 1/\gamma_T^2)$ is the frequency slip factor. In the PSR the rf harmonic $h = 1$, and $\Phi_s \approx 0$ (no acceleration).

In addition, beam particles have energy losses of $\sim$ 500 eV per turn, with energy spread, from passing through the stripping foil. Energy losses from impedance couplings may also occur. Transverse variations and transverse-longitudinal couplings may also be important. However, these effects were ignored in initial simulations.

Injection into the PSR is not phase-space matched. The revolution period is 360 ns. The injected (200 MHz) beam is chopped into micropulses within that period centered about 0 with a width of $\sim$ 250 ns, so that no beam is injected near the unstable phase; the interbunch gap is initially beam-free. The beam is injected with small energy spread, but over the injection time the beam rotates to fill most of the rf bucket, with substantial variations in bunch shape and densities. Injection continues for $\sim$ 360 to 720 μs (2000 turns).

In the simulations, the entire beam ($> 10^{13}$ protons) is represented by $\sim$ 6000 macroparticles. The time step used is one turn; an rf kick plus single-turn transport represents the single-particle dynamics. The space charge is proportional to $d\lambda/dz$. λ, the density, is found by splitting the circumference into 64 or 128 bins and finding the macroparticle density within the bins. The derivative $d\lambda/dz$ is found from the difference $(\lambda_{i+1} - \lambda_{i-1})$ of the density of adjacent bins. The method has inaccuracies from the coarseness of the binning and from the macroparticle statistics and the simplified 1-D force representations. The injection procedure is simulated by adding more macroparticles over the injection time, with new particles injected randomly in phase within the injection width and randomly within a small energy spread. A typical run would include 1200 turns of injection followed by 1000 turns of storage. Beam leakage is observed by particle motion outside the confining bucket and into the interbunch gap. The simulations were performed on an IBM PC, which provides instantaneous turn-around and immediate color graphics display of the motion.

Results for a typical case are shown in Figures 2A-2D. The tracking clearly shows beam leakage into the gap. Initial injection places beam in a square wave pulse with small $\Delta E/E$ (Figure 2A). After $\frac{1}{4}$ synchrotron oscillation (600 turns), the rf bunch rotation has introduced a large

$\Delta E/E$ and a large beam density concentration near the center, with large space charge forces (Figure 2B). The space charge force pushes the beam at the edges of the bunch outside the bucket (Figure 2C), some beam spreads into the gap (2D).

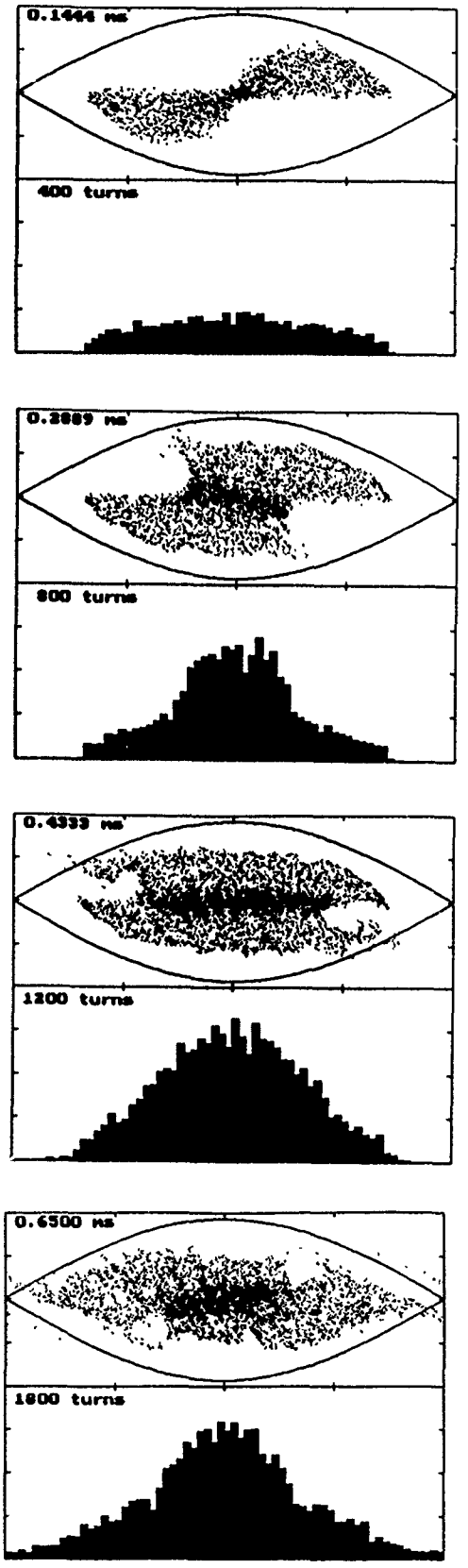


Figure 2A-D Simulation of bunch leakage in the PSR. ($N = 4 \times 10^{13}$, $g = 4$, $V_{rf} = 10kV$)

Injected intensity can be varied to find a leakage threshold. For $N > 3.0 \times 10^{13}$ large leakage occurs, while for $N \leq 1.5 \times 10^{13}$ no leakage occurs and intermediate values show small bunch leakage. Reducing rf voltage reduces the leakage threshold; at $V_{rf} = 6kV$ the threshold is reduced to $1.0 - 1.5 \times 10^{13}$.

In bunched beam simulations, leakage does not occur until after $\sim \frac{1}{2}$ synchrotron oscillation (1200 turns at $V_{rf} = 10kV$), which allows time for the space charge force to develop. With unbunched beam, simple drift fills the gap and this requires much less time. The same bunched-beam time delay is seen in PSR instability observations.

The simulation conditions for bunch leakage are in good agreement with observed PSR conditions for instability. The combination of rf bunching (weak), longitudinal space charge (large), and injection mismatch (large) is sufficient to explain the existence of bunch leakage at high intensities in the PSR.

The calculations show that e-p instability should not occur unless beam leaks into the interbunch gap, and that such leakage can occur within the PSR longitudinal motion. Manipulation of PSR parameters ($V_{rf}(t), \Phi_s$, injection width) to minimize leakage has improved stability and permitted higher intensities in PSR operations, and further optimizations (*i.e.*, with larger V_{rf} or a multiharmonic "barrier-bucket" system) are possible.

We thank E. Colton, R. Macek, H. Schoenauer, H. Thiessen, T. S. Wang, and P. Channell for helpful discussions.

REFERENCES

[1] E. Colton *et al.*, these proceedings (1991 PAC).

[2] D. Neuffer *et al.*, Particle Accelerators 23, 133 (1988).

[3] D. G. Koshkarev and P. R. Zenkevich, Particle Accelerators 3, 1 (1972).

[4] L. J. Laslett, A. M. Sessler and D. Mohl, Nucl. Inst. and Methods 121, 517 (1974).

[5] E. Keil and B. Zotter, CERN/ISR-TH/71-58 (1971).

[6] H. Schoenauer, Proc. *1973 Particle Accelerator Conference*, IEEE Trans. on Nucl. Sci. NS-20, 866(1973).

MEASUREMENT OF OCTUPOLE INDUCED DECOHERENCE AT CESR*

John M. Byrd and David Sagan
Laboratory of Nuclear Studies, Cornell University, Ithaca, NY 14853

Abstract

The Landau damping of the transverse oscillations of a relativeistic bunch can be enhanced by creating an amplitude-dependent betatron tune spread in the bunch. This tune spread can be created by introducing octupole magnets into the lattice. In order to further our understanding of this mechanism we have conducted experiments in CESR where the tune spread of the beam has been measured via measurements of the damping of the centroid motion of the beam after the beam has been kicked. The turn-by-turn transient response of the transverse motion to excitation by injection kickers is measured as a function of octupole current and excitation amplitude. The experimental data is shown to be in good agreement with particle tracking results and the theory of octupole induced decoherence.

Introduction

Unusual transverse impedance effects have been observed in the Cornell storage ring CESR for some time [1,2]. As part of an ongoing effort to understand these effects we have undertaken a study of the betatron tune spread of the bunch due to an octupole component in the accelerator lattice. An intra-bunch tune spread can enhance Landau damping and thus help prevent or delay the onset of instabilities. The ability to directly measure this tune spread is therefore an important aspect in our understanding of beam instabilities.

The octupole induced tune spread can be measured by observing the transient response of the centroid of a kicked beam. The tune spread damps the centroid motion through the dephasing of the individual particles of the bunch. If the beam has a gaussian distribution then analytic formulas can be used to relate the decoherence to the octupole moment. In order to verify the analytic calculations, particle tracking was done using TEAPOT [5] The CESR lattice, including the octupoles, was tracked using a single particle at various amplitudes so that the amplitude dependence of the tune could be determined.

Theory

The theory of the decoherence of a kicked beam has been developed by Meller et al. [3]. For the analysis the amplitude dependent tune $\nu(a_x)$ is assumed to be of the form

$$\nu(a_x) = \nu_0 - \mu a_x^2 , \tag{1}$$

where ν_0 is the frequency at zero oscillation amplitude, and a_x is the amplitude of oscillation normalized to the horizontal betatron beam size $\sigma_{x\beta} \equiv \sqrt{\epsilon_x \beta_x}$. If one assumes that the transverse distribution of the beam is Gaussian then the motion of the centroid of the beam

$$\langle x \rangle = \bar{a}_x \sigma_{x\beta} \sin(\bar{\phi}) \tag{2}$$

after it has been kicked can be calculated analytically. The centroid amplitude $\bar{a}_x$ and phase $\bar{\phi}$ is given by

$$\bar{a}_x = \frac{Z}{1+\theta^2} \exp\left[\frac{-Z^2}{2}\frac{\theta^2}{1+\theta^2}\right] , \tag{3}$$

$$\bar{\phi} = 2\pi\nu_0 N - \frac{Z^2}{2}\frac{\theta^2}{1+\theta^2} - 2\tan^{-1}\theta , \tag{4}$$

where $Z = \beta_x \Delta x'/\sigma_{x\beta}$ is the normalized kick amplitude, N is the turn number and θ is given by

$$\theta = 4\pi\mu N . \tag{5}$$

Considering only octupoles and sextupoles the equation for the tune shift coefficient μ, up to second order, is given by [4]

$$\mu = \frac{3\epsilon_x}{16\pi}\sum_i B_{3,i}\beta_{x,i}^2 + \frac{\epsilon_x}{8\pi}\sum_{jk} B_{2,j}B_{2,k}(\beta_{x,j}\beta_{x,k})^{3/2} \cdot \left\{\frac{\cos\phi_{jk}\sin\phi_0}{1-\cos\phi_0} + \frac{\cos\phi_{jk}\cos 2\phi_{jk}\sin\phi_0}{2(\cos 2\phi_0 - \cos\phi_0)} + \frac{\sin\phi_{jk}\sin 2\phi_{jk}\sin 2\phi_0}{2(\cos 2\phi_0 - \cos\phi_0)}\right\} \tag{6}$$

where ϵ_x is the emittance, $\phi_0 \equiv 2\pi\nu_0$, ϕ_{jk} is the phase advance between the j^{th} and k^{th} sextupoles, and B_2 and B_3 are the strengths of the sextupole and octupole magnets respectively with the kick $\Delta x'$ due to a magnet being given by

$$\Delta x' = B_m x^m \tag{7}$$

*Work supported by the National Science Foundation

0-7803-0135-8/91$01.00 ©IEEE

Experiment

The experimental data used in this report was obtained using a single bunch of positrons with a bunch current of 1/4 mA. In order to ensure that impedance effects (*e.g.* head-tail damping) were negligible the centroid motion with 1/4 mA positrons was compared to the centroid motion using 1/8 mA of positrons. No significant differences were detected. Data obtained using 1/2 mA of positrons showed deviations from the low current data at times greater than ~2000 turns.

Superimposed upon the octupole induced decoherence is the periodic decoherence/recoherence of the centroid motion due to chromaticity of the ring and energy spread of the beam [3]. For typical CESR energy spread, chromaticity and synchrotron tune (~0.05) this effect can be ignored.

Measurements were made by kicking the beam horizontally with a single-turn injection kicker and recording the turn-by-turn coherent transverse motion with a LeCroy Transient Digitizer. Transverse beam motion was detected by a set of capacitive beam buttons configured to be sensitive to horizontal motion. The beam signal pulses were processed using a standard diode pulse stretcher.

It was found both from experimental observation and from particle tracking that for a typical sextupole distribution the centroid decoherence was independent of sextupole strength. The data was thus analyzed using only the first term in Eq. (6). The transient response for three kick amplitudes over the full range of the octupole magnet strength was measured using three equally powered octupoles in the CESR ring. Care was taken to insure that the beam was centered in each of the octupole magnets to avoid steering the beam while changing the octupole strengths. Magnetic measurements of the octupoles gave a value of $B_3 = 2.62/m^3/1000$ current units for each octupole. The average value of the β_x fuction at each octupole was 25 m. The absolute displacement of the bunch centroid was calibrated by simultaneously varying the beam energy and measuring the displacement at the pickup buttons.

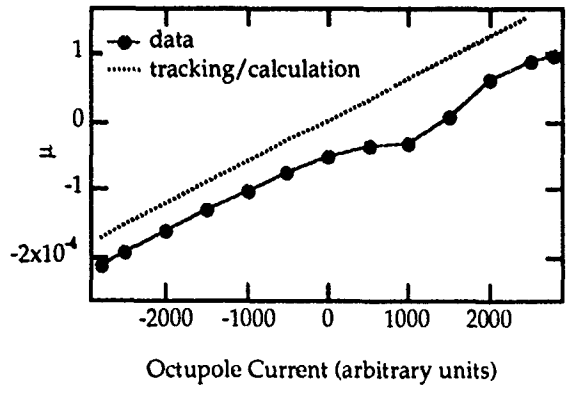


Figure 1: Decoherence parameter μ vs. octupole Current

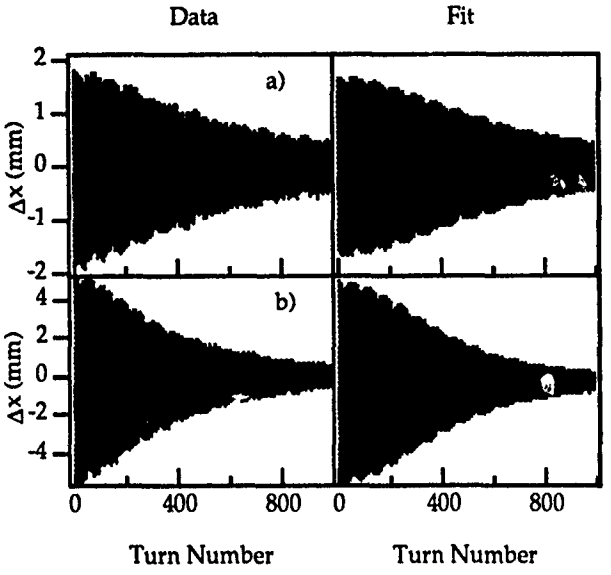


Figure 2: Centroid dependence on kick amplitude,
a) I_{oct} = -1000 current units, Z = 0.75,
b) I_{oct} = -1000 current units, Z = 2.2

Results

The functional form of the centroid motion given in Eqs. (3) and (4) was fit to the measured response using the first 1000 turns of data. Values for the kick amplitude and μ were obtained from the fit. Since the fit period was short compared to the radiation decay time of ~11,000 turns the effect of radiation damping upon the fit could be ignored.

Figure 1 shows the dependence of the decoherence parameter μ as a function of octupole current. The experimental data points were obtained using the observed decoherence and Eqs. (3) and (4). The fitting procedure gives the least accurate results for very small values of μ. Higher order effects may be responsible for the decoherence at this level. The dashed line in the figure shows the expected values of μ based upon Eq. (6) and the measured dependence of B_3 upon octupole current. The results of particle tracking, where the amplitude dependence of the tune was fitted to Eq. (1), gave identical results to the calculated values. In both the calculation and the simulation the calculated value used for the horizontal emittance was $\epsilon_x = 2.04 \times 10^{-7}$m-rad. We interpret the offset between the points and the line as due to a 'natural' octupole moment of the ring. This residual tune shift coefficient μ_0 is probably due to imperfections of the magnets of the ring and for this experiment had a value of $\mu_0 = -0.6 \times 10^{-4}$.

Example decoherence curves are shown in figures 2 and 3. Figure 2 shows the effect of changing the kick amplitude. In figure 2a the measured tune shift coefficient and kick amplitude are $\mu = 1.02 \times 10^{-4}$ and $Z = 0.75$ respectively. In figure 2b the kick amplitude has been increased to $Z = 2.2$ The increase in the kick amplitude between the two

Experiment

The experimental data used in this report was obtained using a single bunch of positrons with a bunch current of 1/4 mA. In order to ensure that impedance effects (*e.g.* head-tail damping) were negligible the centroid motion with 1/4 mA positrons was compared to the centroid motion using 1/8 mA of positrons. No significant differences were detected. Data obtained using 1/2 mA of positrons showed deviations from the low current data at times greater than ~2000 turns.

Superimposed upon the octupole induced decoherence is the periodic decoherence/recoherence of the centroid motion due to chromaticity of the ring and energy spread of the beam [3]. For typical CESR energy spread, chromaticity and synchrotron tune (~0.05) this effect can be ignored.

Measurements were made by kicking the beam horizontally with a single-turn injection kicker and recording the turn-by-turn coherent transverse motion with a LeCroy Transient Digitizer. Transverse beam motion was detected by a set of capacitive beam buttons configured to be sensitive to horizontal motion. The beam signal pulses were processed using a standard diode pulse stretcher.

It was found both from experimental observation and from particle tracking that for a typical sextupole distribution the centroid decoherence was independent of sextupole strength. The data was thus analyzed using only the first term in Eq. (6). The transient response for three kick amplitudes over the full range of the octupole magnet strength was measured using three equally powered octupoles in the CESR ring. Care was taken to insure that the beam was centered in each of the octupole magnets to avoid steering the beam while changing the octupole strengths. Magnetic measurements of the octupoles gave a value of $B_3 = 2.62/m^3/1000$ current units for each octupole. The average value of the β_x fuction at each octupole was 25 m. The absolute displacement of the bunch centroid was calibrated by simultaneously varying the beam energy and measuring the displacement at the pickup buttons.

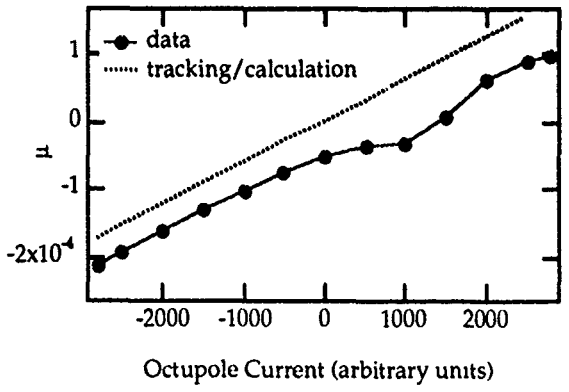


Figure 1: Decoherence parameter μ vs octupole Current

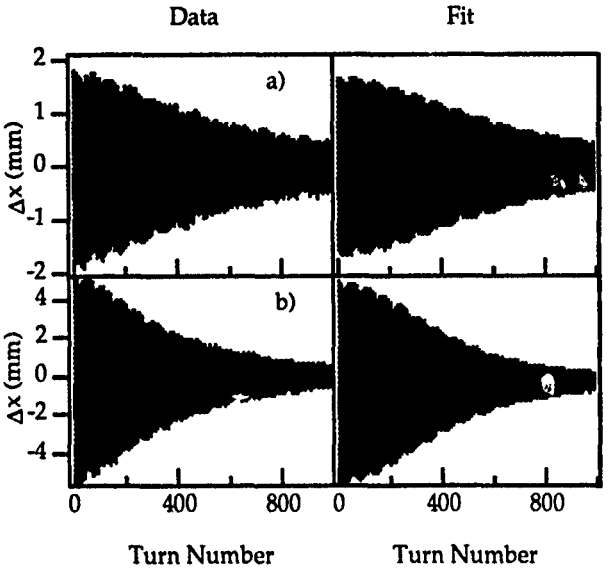


Figure 2: Centroid dependence on kick amplitude,
a) I_{oct} = -1000 current units, Z = 0.75,
b) I_{oct} = -1000 current units, Z = 2.2

Results

The functional form of the centroid motion given in Eqs. (3) and (4) was fit to the measured response using the first 1000 turns of data. Values for the kick amplitude and μ were obtained from the fit. Since the fit period was short compared to the radiation decay time of ~11,000 turns the effect of radiation damping upon the fit could be ignored.

Figure 1 shows the dependence of the decoherence parameter μ as a function of octupole current. The experimental data points were obtained using the observed decoherence and Eqs. (3) and (4). The fitting procedure gives the least accurate results for very small values of μ. Higher order effects may be responsible for the decoherence at this level. The dashed line in the figure shows the expected values of μ based upon Eq. (6) and the measured dependence of B_3 upon octupole current. The results of particle tracking, where the amplitude dependence of the tune was fitted to Eq. (1), gave identical results to the calculated values. In both the calculation and the simulation the calculated value used for the horizontal emittance was $\epsilon_x = 2.04 \times 10^{-7}$m-rad. We interpret the offset between the points and the line as due to a 'natural' octupole moment of the ring. This residual tune shift coefficient μ_0 is probably due to imperfections of the magnets of the ring and for this experiment had a value of $\mu_0 = -0.6 \times 10^{-4}$.

Example decoherence curves are shown in figures 2 and 3. Figure 2 shows the effect of changing the kick amplitude. In figure 2a the measured tune shift coefficient and kick amplitude are $\mu = 1.02 \times 10^{-4}$ and $Z = 0.75$ respectively. In figure 2b the kick amplitude has been increased to $Z = 2.2$. The increase in the kick amplitude between the two

New Developments on the Generation of Arbitrary Polarized Radiation from Insertion Devices

Pascal ELLEAUME
European Synchrotron Radiation Facility
BP 220, F-38043 Grenoble
France

Abstract

The complete description of the polarization of a beam of radiation is described in terms of the total energy and three polarization rates. The polarization characteristics from conventional undulators and wigglers is recalled. A presentation is made of some new Insertion Devices that were proposed and/or built to generate circular polarization and more generally to improve the control of polarization. They are the asymmetric and elliptical wigglers and the helical and crossed undulators.

I. INTRODUCTION

The polarization of the synchrotron radiation is essentially linear with electric field in the horizontal plane of the electron or positron orbital motion. The availability of free straight sections on existing storage rings and the construction of new synchrotron sources that will accommodate a large number of Insertion Devices (ID) has motivated a world wide effort to design and build new exotic IDs capable of generating an arbitrary state of polarization. Of particular interest is the circular polarization. Applications extend from natural or magnetic dichroism, spin polarized photoemission, magnetic scattering... This paper reviews the recent advance in that direction. Previous review papers on this subject can also be consulted[1][2]. In section 2, I briefly summarize the Stokes Decomposition of the polarization of the electromagnetic radiation and define the notations. Section 3 (4) is a description of the main wigglers (undulators) that have been proposed and/or used for the generation of circular polarization. The Illustrations given throughout this paper will be illustrated with the future ESRF electron/positron beam of 6 GeV, 100 mA and horizontal (vertical) emittance of 7 E-9 m (7 E-10 m).

II. GENERALITIES ON THE POLARIZATION

Each electron of the beam generates a wave of electromagnetic field. This wave nearly becomes a planewave by passing through a monochromator. Its polarization state is a pure state which means that it is entirely described by two complex amplitudes (one for the horizontal and vertical plane). The polarization state typically depends on the observer and electron positions and velocities. In practical situations, the radiation beam is generated by an ensemble of electrons each having its own position and angle. Furthermore, the radiation beam is integrated over some area and angle by a detector. As a result, the description of the polarization by means of the two complex amplitudes becomes unsufficient. One must deal with a statistical sum of pure states. The most suitable method to deal with such cases is the density matrix formalism. The density matrix describing the polarization state is a 2*2 hermitian matrix[3] . In the following I shall prefer the Stokes-Poincare representation. It is largely sufficient to make a zoological classification of the various polarizations of radiation, however this may be not as practical as the density matrix if one wants to treat the transformation of the polarization through any scattering or polarization sensitive absorption. Other formalisms exist such as the Jones Matrices. Of course all these representations are equivalent and one can find four independent energy like quantities that completely define the polarization. In the Stokes representation, they are the total intensity I (integrated over the slit aperture) and three polarization rates: $\rho_1 = (I_x - I_z) / I$, $\rho_2 = (I_{45} - I_{135}) / I$, $\rho_3 = (I_r - I_l) / I$. I_x (I_z) is the energy linearly polarized in the horizontal (vertical) plane, I_{45} (I_{135}) is the energy linearly polarized at 45 (135) degrees with the horizontal and vertical directions, I_r (I_l) is the energy circularly polarized with right (left) orientation. Note the following equalities: $I=I_x + I_z = I_{45} + I_{135} = I_r + I_l$. Each of the three polarization rates defined above is a dimensionless quantity between -1 and 1. A pure state of polarization is such that the sum of the square of the three rates is exactly equal to 1. This is trivially verified if all 6 partial intensities I_x, I_z, I_{45}, I_{135}, I_r, I_l are zero except for one. The proof can be extended to the most general pure elliptical state of polarization by decomposing the intensity over the complex amplitudes[4] . The statistical averaging of the different polarization present in a beam is made by summing separately each contribution to the 6 partial intensities described above. As a result of some convexity property one easily show that the sum of the square of the three polarization rates is less than 1 becoming equal to zero for completely depolarized radiation. In the following I shall define the amount of depolarization by introducing the rate of unpolarized radiation ρ_0 such that in any condition:

$$1 = \rho_0^2 + \rho_1^2 + \rho_2^2 + \rho_3^2$$

0-7803-0135-8/91$01.00 ©IEEE

ρ_0 is a dimensionless quantity between 0 and 1. If ρ_0 =0 (1), the radiation is fully polarized (depolarized). In the most general case all four polarization rates depend on the electron beam (energy, sizes, angular spreads, position and angle), the magnetic field of the ID, the photon energy and the detector (aperture, position.). Fully polarized radiation can only be obtained from a filament monoenergetic electron beam and with a point detector.

III. WIGGLERS

The polarization of the radiation generated by a typical N periods wiggler is described by simply summing every 6 partial intensities over each 2N source points. Conventional wigglers generate a radiation essentially horizontally linearly polarized in the plane of the orbit which gradually becomes depolarized as the observer moves away from the orbit plane. Note the difference with bending magnet radiation which becomes completely circularly polarized off axis. The depolarization originates from the statistical average of purely left (originating from a source point of positive field) and purely right (originating from a source point of negative field) radiation with equal probability. In any direction of observation, ρ_2 and ρ_3 are equal to zero. On axis ρ_1 dominates unless the electron beam emittance is extremely large in which case ρ_0 dominates. Two modifications have been used to restore the circular polarization. They are the asymmetric[5] [6] and Elliptical[7] [8] wigglers.

A. Asymmetric Wiggler

The asymmetric wiggler is made of a non sinusoidal magnetic field. Figure 1. presents one possible magnetic design.

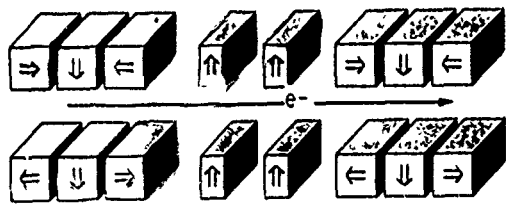


Figure 1. Schematic of an asymmetric wiggler

In an asymmetric wiggler, the two source points per period seen by an observer do not present the same absolute value (as for a conventional wiggler). Ideally the field corresponding to one of the source points is large while the field on the second source point is small and of the opposite sign. The polarization is most easily analyzed by mean of a vertical field vs. horizontal angle diagram such as the one shown in Figure 2. The intersection of any vertical line (corresponding to some direction of observation) with the closed curve generally defines two points the vertical coordinate of which is the magnetic field of the source points. In fact the curve is closed N times on itself defining a total of 2N source points. In some very special cases 4,6... source points per period can be seen.

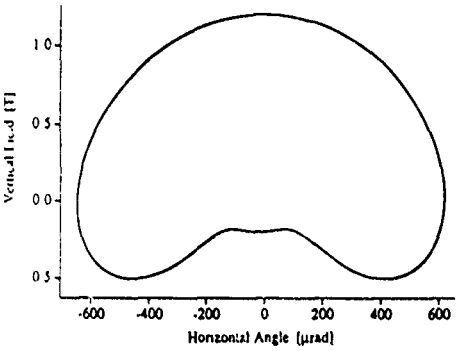


Figure 2. Field vs. Angle Diagram of an asymmetric wiggler

As can be anticipated from Figure 2. , the circular polarization rate depends not only on the vertical angle of observation but also on the photon energy and horizontal angle of observation.

B. Elliptical Wiggler

The elliptical wiggler can be understood as a conventional vertical field wiggler to which a small horizontal field of identical periodicity has been added in such a way that the electron trajectory is a flat ellipse.

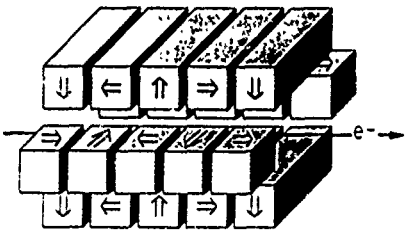


Figure 3. Schematic of an Elliptical Wiggler

The radiation generated on the axis is the sum of the one generated by a positive and negative field but seen from below and above (respectively) the orbit plane. As a result they both present the same circular orientation and they do not cancel out as for a conventional wiggler.

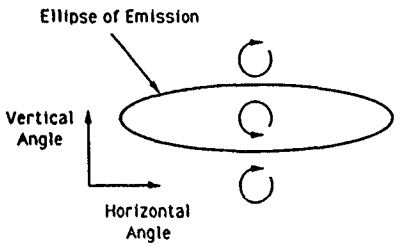


Figure 4. Angular diagram of the emission from an elliptical wiggler. The radiation emitted inside (outside) the ellipse is elliptical right (left)

The choice between asymmetric and elliptical wigglers is largely dictated by engineering complexity. The asymmetric wiggler is much simpler to build and does not require any special vacuum chamber even though potentially less efficient than the elliptical wiggler.

IV. UNDULATORS

A. Linear Undulator

The radiation generated by a single electron over each period of motion typically interferes, resulting in an enhancement of the emission at some particular photon energy. This phenomenon is predominant in undulators while difficult to observe on a wiggler (except for a filament electron beam and a point detector). The transition between undulators and wigglers is usually determined by the deflection cofficient $K = 0.934\ B[T]\ \lambda_0[cm]$. B is the peak sinusoidal vertical field. λ_0 is the spatial period. Undulators (wigglers) typically correspond to $K < (>) 2$ to 3. As for a wiggler, the radiation from an undulator is essentially horizontally linearly polarized on axis. Off axis the polarisation is still linear but inclined with respect to the horizontal plane[9]. In any direction of observation $\rho_3 = 0$. The highest brightness from an undulator is typically obtained by selecting the part of the radiation emitted around the main central axis. Figure 1. presents the flux and polarization rates on the fundamental peak of a conventionnal linear undulator (length 1.6m, period 30 mm K = 0.67) seen through a 1*1 mm slit placed 30m away from the source. The ESRF electron beam has been used : Energy = 6 GeV, Current= 100mA, horizontal (vertical) Emittance = 7 E-9 m (7 E-10 m), horizontal (vertical) beta function = 27 m (11 m).

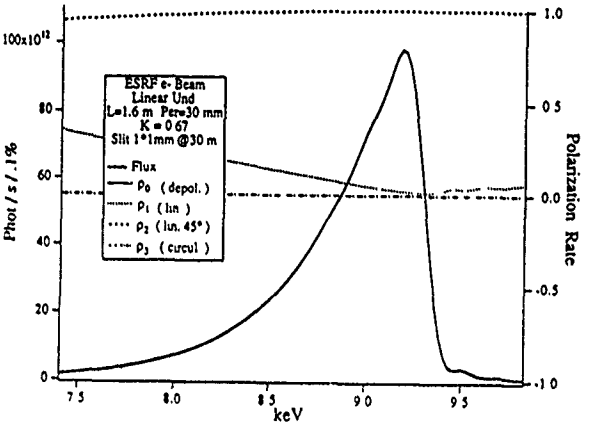


Figure 5. Flux and polarization rate on the fundamental peak from a linear undulator from [10]

Note the very small amount of depolarization which is typical of undulator radiation generated by small emittance electron beams. Various schemes have been proposed and used to generate other polarization states on the central axis, they are described below.

B. Helical Undulator

The most obvious method to restore the circular polarization of the radiation issued from an undulator is to use a helical or elliptical magnetic field geometry. From a technological point of view, a large variety of technical solution exist[11][12][13][14]. For small values of the undulator deflection parameter K, the ellipticity of the radiation is nearly identical to the helicity of the magnetic field. In other words, the electric field of the radiation is nearly proportional to the magnetic field components. Figure 6. presents the flux and polarization rates on the fundamental peak from a helical undulator. The electron beam, slit, undulator length and period are identical to those of Figure 5. . The peak helical field is 0.17 in order to keep the same fundamental energy.

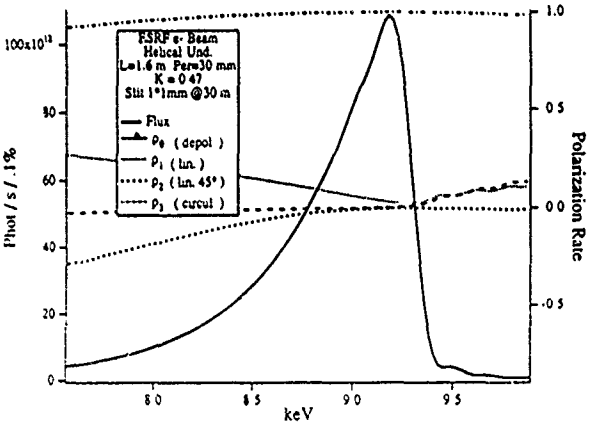


Figure 6. Flux and polarization rate on the fundamental from a helical undulator from [10]

Helical undulators have already been used a few times for FEL applications but very seldom as synchrotron radiation source[15]. Possible reasons are the more complicated magnet technology and the incompatibility of ultra-high vacuum with a circular vacuum chamber to which the field geometry is particularly suited.

C. Crossed Undulator

An other interesting approach to restore the circular polarization is to use a crossed undulator[16][17]. " is an arrangement of two undulators placed successively on the electron beam but rotated by 90 degrees around the beam axis (see Figure 7.).

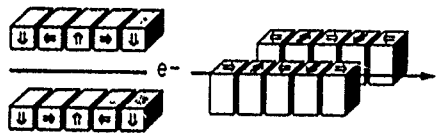


Figure 7. Schematic of a Crossed Undulator

Understanding of the polarization characteristics is not a trivial matter. One way to understand it is to analyze in the time domain the radiation wave generated by a single electron as it crosses the full device. It is made of two successive N periods sinewaves with orthogonal orientation. The spectrum of such a quasi periodic wave presents the usual undulator harmonic peaks, but also an oscillation of the polarization characteristics along the spectrum. Figure 8. presents the flux and polarization rates on the fundamental peak from a crossed undulator. The electron beam, slit, total undulator length and period are identical to those of Figure 5. . Each undulator segment is 0.8 m long.

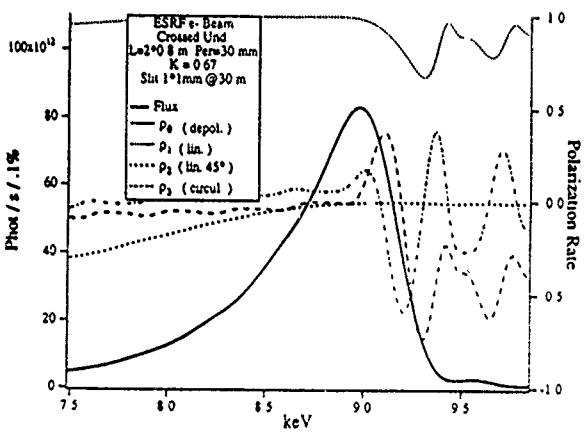


Figure 8. Flux and polarization rate on the fundamental from a crossed undulator from [10]

The high sensitivity of the polarization to the photon energy and angle of observation results in a significant depolarization. This effect has been analyzed in detail for a crossed undulator emitting around 9 keV at ESRF[10] . Even with the low emittance beam of the ESRF, the majority of the radiation generated on each peak of the spectrum is depolarized. Elliptical polarization can be observed only on the high energy side of the peak. One faces a trade-off between flux and circular polarization rate (60% rate for 50% of the peak flux in Figure 8.). Higher polarization rates could be observed by closing the slit but again at the cost of the flux. The phenomenon decreases with electron energy, beam emittance and slit aperture. Experiments looking for circular polarization from a crossed undulator will require extensive alignment and care. The prime advantage of the crossed undulator is its potential rapid switching of polarization orientation (left to right) which can be accomplished by a short electromagnet three pole section (dispersive section) placed between the two undulators.

V. FLIPPING OF THE POLARIZATION

Experiments that make use of the circular polarization very often require a switching mechanism of the orientation from left to right. This operation can be done by playing with some optical element in the beamline or by directly operating on the magnetic field of the ID. The modification of the magnetic field should always be considered as a last alternative since it is very likely to result in a disturbance of the electron beam closed orbit that is detrimental to the large number of other users of such a facility. The higher the electron energy, the lower the perturbation.

Polarization switching can be done with a permanent magnet asymmetric wiggler by periodically inclining the trajectory vertically by mean of a two or four magnets bump placed on each side of the device. In an elliptical wiggler or in a helical undulator, the phasing between the horizontal and the vertical magnetic field flip the polarization. This can be accomplished by a longitudinal displacement of some permanent magnet assembly (a few seconds) or by using an electromagnet (a few hundredths of a second). As we have seen above, the crossed undulator offers a very elegant method for flipping the polarization by means of a dispersive section. If a high photon energy is envisaged, an electromagnet undulator are inefficient and permanent magnets must be used. In that case, an interesting scheme can be used to switch the helicity of the field by separating the magnet responsible for the vertical and horizontal component of the magnetic field on two different jaws (see Figure 9.). Such a device can accommodate a conventional flat vacuum chamber.

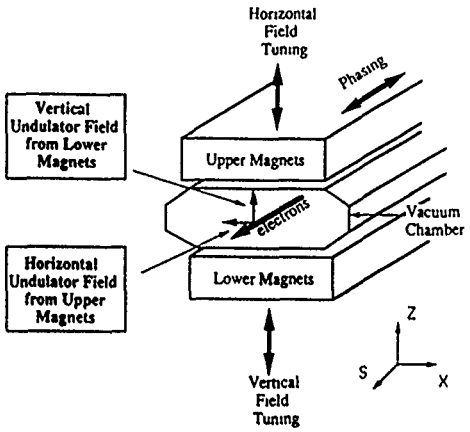


Figure 9.

A helical undulator is presently being built at ESRF based on this concept[18] .

VI. CONCLUSION

New wigglers have been successfully tested in the past years that were built in order to generate circular polarization. New undulator schemes presently under construction are expected to be tested in the coming years. The large world-wide effort to build synchrotron radiation sources will undoubtedly result in an improvement of the ID technology in all aspects and especially the control of the polarization which is a new important demand from the user community.

VII. REFERENCES

[1] P. Elleaume, Rev Sci Instruments, 60 (7), July 1989.
[2] K.J. Kim, Conference on Advanced X-Ray/EUV Sources, Sna Diego, CA, July 11-13,1990.
[3] V. Fano, Rev. Mod. Phys. 29, 74 (1957).
[4] Born and Wolf, Principle of Optics, Pergamon Press (Oxford 1987).
[5] J. Goulon, P. Elleaume, D. Raoux, Nucl. Instr. Meth. A254, 192, 1987.
[6] J. Pfluger, G. Heintze, Nucl. Instr. and Meth. A289 (1990) 300-306
[7] S. Yamamoto, H. Kitamura, Japanese J. of Appl. Physics 26, L1613, 1987.
[8] S. Yamamoto et al., Phys Rev. Lett. 62, 2672, 1989
[9] H. Kitamura, Nucl. Instr. and Methods 177 (1980) 235-238.
[10] X Marechal, P Elleaume, ESRF report SR-ID/91-47.
[11] K. Halbach, Proc. of the SPIE Int. Conf. on Insertion Devices, Vol 582, p68 (1985).
[12] H. Onuki, Nucl. Instr. Meth., A246, 94, 1986.
[13] P. Elleaume, Nucl. Instr. and Meth. A291 (1990) 371-377.
[14] B. Diviacco, R.P. Walker, Nucl. Instr. and Meth. A292, 517, 1990.
[15] E.S. Gluskin et al., Preprint 83-163, Institute of Nuclear Physics, Novosibirsk, USSR.
[16] M. Moissev, M. Nikitin, F. Fedorov, Sov. Phys. J. 21, 332, 1978.
[17] K.J. Kim, Nucl. Instr. Meth. 219, 425, 1984.
[18] P. Elleaume, J. Chavanne, ESRF report SR-ID/91-44.

Rapidly-Modulated Variable-Polarization Crossed-Undulator Source

Michael A. Green[1], Kwang-Je Kim[2], Walter S. Trzeciak[1], and P. James Viccaro[3]

1) Synchrotron Radiation Center (SRC), University of Wisconsin, 3731 Schneider Dr., Stoughton, WI 53589

(Supported by: Div. of Materials Research, National Science Foundation, under Grant DMR-88-21625)

2) Exploratory Studies Group, Lawrence Berkeley Laboratory (LBL), One Cyclotron Road, Berkeley, CA 94720

(Supported by: U.S. Department of Energy, BES-Materials Sciences, under Contract DE-AC03-76SF00098)

3) Advanced Photon Source (APS), Argonne National Laboratory (ANL), 9700 South Cass Ave., Argonne, IL 60439

(Supported by: U.S. Department of Energy, BES-Materials Sciences, under Contract W-31-109-ENG-38)

Abstract

Continuing the growth of insertion devices as synchrotron radiation sources, the needs of research teams in many disciplines now mandate the construction of rapidly-modulated variable-polarization crossed-undulators for polarization sensitive experiments. Such a source is being proposed for the Aladdin storage ring at SRC to provide arbitrary polarization, modulated at 10 Hz, with first harmonic tunable from 8-40 eV. An outline for an entire system's design is presented, including diagnostics, initial-phase beamline, and controls. This facility will immediately benefit the scientific community and impact implementation of similar devices at third-generation facilities like ALS (Advanced Light Source, LBL), and APS.

I. Introduction

As a result of increased demand from the scientific community, several wiggler and undulator sources have been proposed which will increase the flux of circularly polarized x-rays [1]. Except for the crossed-undulator [2,3], all other possibilities employ inherently slow mechanical motion to vary the polarization. Because it uses an electromagnetic modulator, the crossed-undulator offers rapid, variable-waveform modulation between selected polarization states [3].

More than just the source, an entire system is being designed. Also included are: the diagnostics for characterizing the radiation; an initial-phase beamline for research at 8-40 eV; and the requisite computer control and coordination of the source, beamline, and storage ring operation.

Implementation of the crossed-undulator at SRC is being supported by researchers from chemistry, life sciences, materials science, and physics. Additionally, it will be an important precursor of similar devices at third-generation synchrotrons as the ALS and APS where such sources will extend variable-polarization capability to higher photon energies.

II. Conceptual Design

The crossed-undulator design uses two planar undulator sections, each producing linearly polarized radiation, rotated with respect to one another by 90° about their common longitudinal axis, and variably-phased along the same axis, as illustrated in Fig. 1. Specifically, in the present case, the undulators have been oriented at ±45° on either side of the vertical plane through the longitudinal axis. This orientation: maximizes the vacuum chamber's horizontal aperture; produces "erect" linear polarizations which can be interchanged by rapid modulation; and is inherently symmetrical.

A. Discussion Concerning the Radiation

The phasing between the radiations from the two undulators is determined by the differential flight times of electrons and photons travelling between them. Simplistically assuming spacially harmonic fields, and given

γ = electron energy
$\lambda_{u,m}$ = undulator & modulator periods, respectively
$B_{u,m}$ = undulator & modulator magnetic fields, respectively
B_m = $B_m^{dc} + B_m^{ac}\sin\omega t$, sum of the bias & modulated parts
$K_{u,m}$ = undulator & modulator deflection parameters
= $93.4 \times B_{u,m}(T)\lambda_{u,m}(m)$
λ = $\lambda_u(1+\frac{1}{2}K_u^2)/2\gamma^2$, undulator radiation wavelength
z = longitudinal spacing between the undulators
z_m = (effective) longitudinal length of the modulator
= λ_m

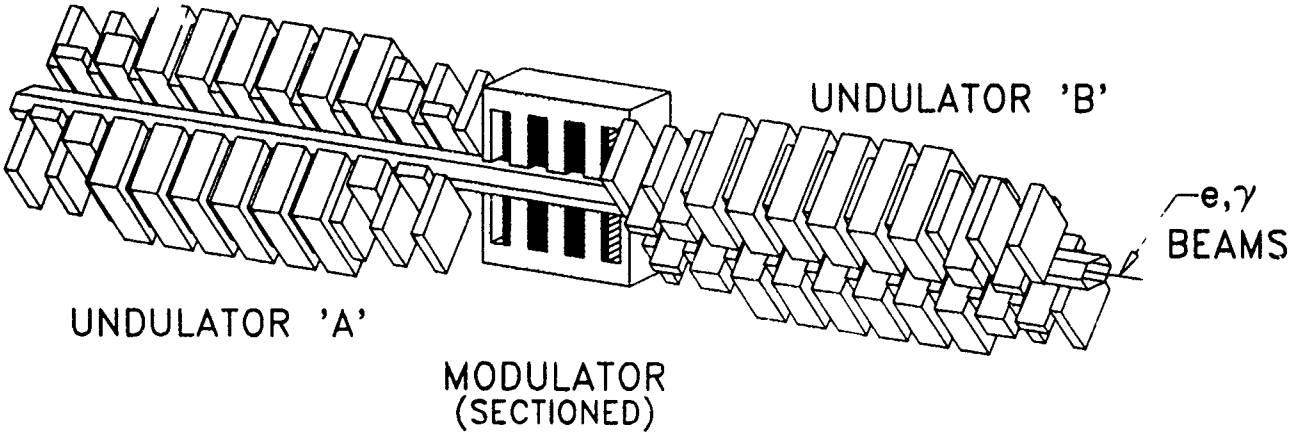


Figure 1. Conceptual illustration of the crossed-undulator source.

0-7803-0135-8/91$01.00 ©IEEE

the phasing, expressed in units of τ (= λ/c), becomes:

$$f = \frac{2z + z_m K_m^2}{2\lambda_u(1+\frac{1}{2}K_u^2)} - \frac{2z + 93.4^2 z_m^3 (B_m^{dc} + B_m^{ac}\sin\omega t)^2}{2\lambda_u(1+\frac{1}{2}K_u^2)} \cdot \quad (1)$$

Thus, for a given wavelength, λ, phasing can be varied both by changing the mechanical spacing between the undulators (z), and the excitation of the modulator (B_{dc} and B_{ac}).

When observed through a monochromator, the combined radiation is generally elliptically polarized. By varying the phasing the polarization of the combined radiation can be adjusted arbitrarily. In particular, it can be modulated between left and right circular polarizations (f = respective odd multiples of $\frac{1}{4}$) or between vertical (f = 1,2,3,...) and horizontal (f = $\frac{1}{2}, \frac{3}{2}, \frac{5}{2}$,...) linear polarizations.

The operation of the crossed-undulator is based on the interference effect, and requires a low-emittance electron beam for satisfactory performance for short wavelength radiation. Because of this, the upper limit will be about 100 eV on Aladdin. The spectral range can be extended to several hundred eV and higher with third-generation synchrotron radiation facilities, such as the ALS and APS.

B. Specifications

Table 1 summarizes requirements from the users of the crossed-undulator and for unimpaired operation of the Aladdin storage ring for all users.

Table 1: Functional Requirements

For Crossed-Undulator Users		
Spectral Range	8-40	eV
Total Phase Shift (ac+dc)	≤ 360	deg
Phase Modulation (ac)		
Rate	10	Hz
Amplitude	≥ 180	deg
For All Storage Ring Users		
Physical/Dynamic Aperture	No Reduction of:	
Injection (100 MeV)	Stored Current	
Full Energy (800 MeV)	Lifetime	
Vertical Beam Stability	Whole Ring, 800 MeV:	
Positioning	10	μm
Size	1.5	%

1. Undulator

Both sections will have independently adjustable gaps, and separate end-correctors and end-clamps. Table 2 shows other specifications generated by the requirements in Table 1. See §II.C.3 for further discussion concerning ring operation.

The undulator spacing, z, must accommodate the modulator and any diagnostics or steering elements for control of the electron beam. Although z must be kept to a minimum to maximize the radiation's degree of polarization, some variation of z will be incorporated. Both undulators, together, can be horizontally retracted from over the vacuum chamber, so as not to adversely affect low-energy injection into the ring.

Table 2: Preliminary Undulator Specifications

Magnetic Structure	Hybrid [4]	
Number of Periods, N	5/section	
Period Length, λ_u	10	cm
Geometry		
Orientations	±45	deg
Position @ Injection	Retracted	
Operating Ranges, Respectively		
Magnetic Gap, g	5 → 9	cm
Magnetic Field	0.38 → 0.11	T
K Value	3.5 → 1	
Photon Energy, 1st Harmonic	8.3 → 40	eV
Multipole Error Limits		
Dipole	8.54×10^{-6}	T·m
Quadrupole	0.04	T
Sextupole	0.3	T/m
Octupole	0.3	T/m^2
Maximum Gap for Retraction	16-19	cm
Vacuum Chamber Cross Section		
Horizontal	7	cm
Vertical	3	cm

2. Modulator

The main requirements for phase shift, frequency, and stability appear in Table 1. Details on this critical component can be found in a companion paper of these Proceedings [5].

C. Performance

By design, the undulators and modulator, will have negligible impact on storage ring operation. Thus, present operational ring parameters can be used for detailed calculations of the properties of the radiation.

1. Aladdin Operation

The ring routinely operates at 800 MeV with initial beam current of about 200 mA. Alternate operation also permits 1000 MeV at 80 mA, primarily for x-ray lithography.

Currently, there are several projects underway for the further improvement of the storage ring. These are primarily directed toward the continuing upgrade in user-oriented features such as the increased utility of Aladdin's long straight sections for insertion devices [6].

2. Polarization and Flux vs. Energy

Using present Aladdin parameters, crossed-undulator performances are as shown in Figs. 2 and 3 for several aperture sizes. For simplification the calculations use a Gaussian aperture-function of rms value $\sigma_\theta = \frac{1}{2}\sqrt{(\lambda/L)}$, where L = undulator length. Notes: the efficiency of the optical system is not accounted for in Fig. 3; also, the improvement programs mentioned above can only improve expected performance.

3. Interaction of Undulator and Storage Ring

Tables 1 and 2 summarized the principal requirements/specifications for undulator operation to non-adversely affect ring operation (for all users). The physical apertures are from

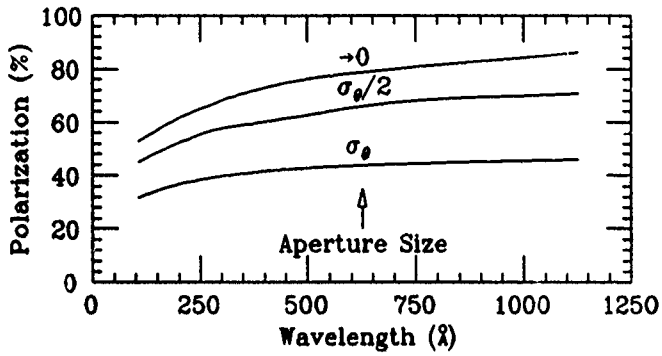


Figure 2: Degree of circular polarization versus wavelength.

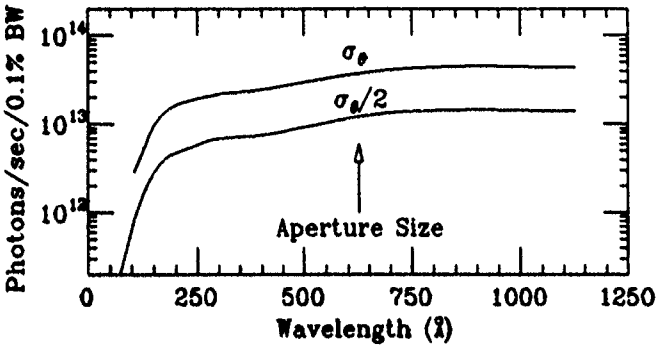


Figure 3: Photon flux versus wavelength.

scraper measurements made during injection, ramping, and full-energy operation. A stable (position and size) circulating beam gives rise to the limits specified on dipole and quadrupole field errors.

At (low energy) injection, acceptable dynamic aperture is easily achieved by simply retracting the undulators from over the beam/vacuum chamber. At full energy, linear lattice calculations on stability with SYNCH, and dynamic aperture calculations with PATRICIA, have been performed resulting in the higher (sextupole and octupole) multipole errors shown. Presently, extensive studies are underway to specify all tolerances including skew multipoles and misalignments.

III. System's Overview

The proposed system will result in a comprehensive facility for the production and utilization of variably-polarized radiation. Briefly, other aspects of the effort are as follows.

Undulator Radiation Diagnostics [7] Two different instruments are proposed to completely characterize the radiation between 10 and 40 eV. The first will measure the spatial dependence of the spectral flux, thus determining the phase-space volume of the radiation. The second is a polarimeter, with triple-reflector analyzer and quarter-wave devices.

Beamline Implementation [8] Taking advantage of the source collimation ($\Sigma_{x',y'} \leq 450$ μrad), distance (20 m), low power, and stability, the beamline is basically of the Wadsworth type [9], featuring: no entrance slit, no prefocusing optics, and a normal-incidence Pruett-Lien 1-m monochromator. These conditions result in a nearly stigmatic image at the exit slit which could be immediately useful.

Storage Ring Adaptations Onsite installation involves the design, construction, and installation of: the common undulator/modulator support structure; vacuum chamber section with localized pumping, clearing electrodes, and beam position monitors; and shielding of concrete and lead.

Control System Distinct functions of the control system include: undulator operation (independent gap control, retraction); modulator excitation (amplitude, waveform, frequency); longitudinal position (phase) control of one of the undulators; local orbit correction; local orbit steering; beamline control of beam energy, polarization, and position/angle. Given this complexity and that it must be transparent to other users of the ring pose a major challenge to the implementation of the control system.

Acknowledgements

Other contributors during the design phase have been: Efim Gluskin and Roland Savoy, APS; Klaus Halbach, Malcolm Howells, Egon Hoyer, and Brian Kincaid, LBL; and Dave Huber, Charles Pruett, and Ednor Rowe, SRC. We especially note the considerable efforts of Marshall Onellion (Dept. of Physics, Univ. of Wisconsin - Madison), Patricia Snyder (Dept. of Chemistry, Florida Atlantic Univ.), Marcos Maestre (Cell and Molecular Biology Div., LBL), and Peter Dowben (Dept. of Physics, Syracuse Univ.) in assimilating supporting materials from the user community.

IV. References

[1] Kwang-Je Kim, "A Survey of Synchrotron Radiation Devices Producing Circular or Variable Polarization," Proc. SPIE Conf. on Advanced X-Ray/EUV Sources, San Diego, CA (July 1990).

[2] M.B. Moiseev, M.M. Nikitin, and N.I. Fedosov, "Change in the Kind of Polarization of Undulator Radiation, Sov. Phys. J., 21, 332 (1978).

[3] Kwang-Je Kim, "A Synchrotron Radiation Source with Arbitrarily Adjustable Elliptical Polarization", Nucl. Instr. and Meth., 219, 425 (1984).

[4] K. Halbach, "Permanent Magnet Undulators", J. Physique, 44, C1-211 (1983).

[5] Roland Savoy and Klaus Halbach, "Design Considerations for a Fast Modulator in a Crossed-Undulator", these Proceedings.

[6] Walter S. Trzeciak and Dornis C. Morin, "Aladdin II", these Proceedings.

[7] Efim Gluskin, ANL/APS, private communication.

[8] Charles Pruett, SRC, private communication.

[9] J.A.R. Samson, *Techniques of Vacuum Ultraviolet Spectroscopy*, John Wiley & Sons, New York (1967), p. 9.

Magnetic Field Tolerances for Insertion Devices on Third Generation Synchrotron Light Sources*

P. J. Viccaro, R Savoy, and D. W. Carnegie
Advanced Photon Source, Argonne National Laboratory
Argonne IL 60439

Abstract

The nearly four orders of magnitude increase in brightness expected for insertion device (ID) x-ray sources on the next generation low-emittance synchrotron facilities will have a tremendous impact on many areas of research. However, in order to deliver the expected performance, the IDs will need to satisfy stringent magnetic and mechanical requirements. Errors in real devices affect both the spectral performance and storage ring. For example, one source of random magnetic field errors relating to the peak field in the device has a direct effect on the peak spectral brightness of undulator harmonics. Other errors result in with the higher moment fields (sextupole, quadrupole, etc.) in the device which can effect the performance of the low-emittance storage ring. Both effects are discussed in terms of the next generation synchrotron facilities.

1. INTRODUCTION

The next generation of low-emittance high-brilliance for synchrotron facilities such as the 7-GeV Advanced Photon Source (APS), 1-2 GeV Advanced Light Source (ALS), the European Synchrotron Radiation Source (ESRF), and SPring 8 (Japan), etc., will have insertion device undulator and wiggler x-ray sources with unique spectral properties. These properties will open new possibilities for scientific research in essentially every area of science and technology. Existing and new techniques utilizing the full potential of these sources, such as their enhanced spectral coherence, unique polarization properties, and high spectral brilliance, will permit experiments not possible with existing sources.

The enhanced performance predicted for ideal undulator sources on the low-emittance rings over that on present synchrotron sources is, in most cases, remarkable, and a considerable amount of effort has been spent over the past years to understand the spectral properties of these devices. During this time, it has become clear that the performance of actual devices will depend not only on the quality of the low emittance particle beam, but also on the achievable magnetic and mechanical tolerances. In addition, the error fields for real devices may introduce deleterious effects on the storage ring and, as a consequence, indirectly affect the undulator spectral performance.

In general, the magnetic field quality or tolerance for actual devices is determined by the storage ring requirements and the acceptable spectral performance. In the following, a summary of these tolerance requirements for typical planar permanent magnet undulator IDs on the new third generation synchrotron facility storage rings is presented. In addition, some recent results for APS prototype undulators are discussed.

The major emphasis of this article is to identify the sources of magnetic field errors in real IDs and to describe the effects of these errors on the spectral performance of the device and on the storage ring.

2. CHARACTERISTICS OF IDEAL PLANAR IDs

A. Baseline Spectral Properties

Both undulators and wigglers are composed of magnet arrays in a planar geometry that set up a spatially oscillating magnetic field along the length of the device [1,2]. These arrays can either be made up of permanent magnets, with or without high-permeability steel poles such as vanadium permendur, or electromagnets. For the new low emittance storage rings with ring energies between 1 and 8 GeV, the majority of IDs have periods less than 20 cm in order to achieve the required spectral energies. This is the optimum range for permanent magnet structures. In almost all cases, rare-earth-transition metal magnets, especially Nd-Fe-B, are used because of their enhanced field strength. The magnetic structures of a pure permanent magnet (PPM) and a hybrid device with vanadium permendur poles are compared in Fig. 1. In both cases, the vertical component of the magnetic field along the z-direction of the ID varies periodically with a period λ_0. For the PPM ID, the field variation along the centerline of the midplane is nearly sinusoidal. For the hybrid structure, the field has higher harmonics determined by the detailed structure of the pole and magnet array.

The slope angle for the sinusoidal field is $\theta = K/\gamma$, where $\gamma = 1957\ E_r$, and E_r is the ring energy in GeV, and K is the deflection parameter given by $K = 0.934\lambda_0(cm)B_0(T)$, where B_0 is the peak magnetic field. In the undulator regime, defined by $K \sim 1$, interference effects occur within the synchrotron radiative opening angle, $\psi = 1/\gamma$, which cause spatial and frequency bunching of the radiation. This gives rise to the typical undulator spectrum consisting of narrow bands of radiation called harmonics.

In general, the spatial distribution of the radiation is complex [3]. Near a harmonic energy, however, it consists of a central radiation cone combined with structure off-axis. For a single particle, the radiative source size and divergence of the central radiation cone of the nth harmonic depend on the wavelength, λ_n, and the length, L, of the undulator, and are given by:

$$\sigma'_r = (\lambda_n/L)^{1/2} \quad \text{and} \quad \sigma_r = (1/4\pi)(\lambda_n L)^{1/2},$$

respectively.

In both ID structures, the spectral properties depend on the trajectory of the particle beam through the device which in turn depens on the magnetic field and the magnetic period of the device.

* Work supported by the U. S. Department of Energy, BES-Materials Sciences under Contract WC-31-109-ENG-38
U.S. Government work not protected by U.S. Copyright.

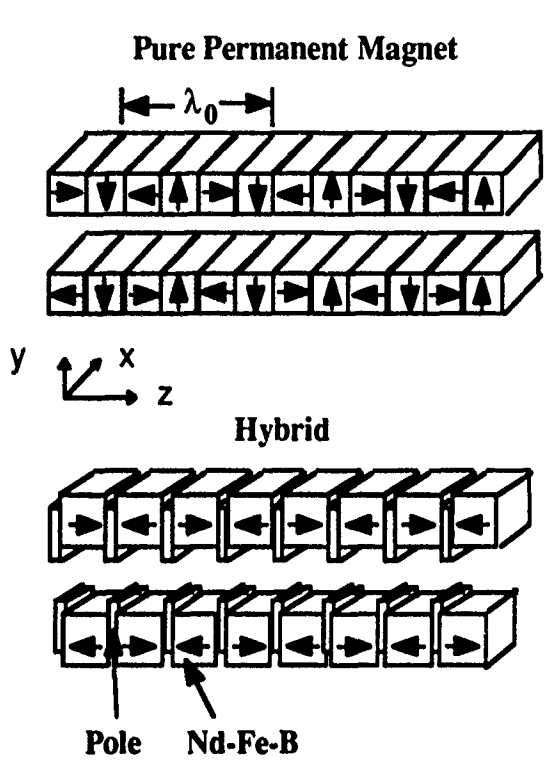


Fig. 1. A pure permanent magnet structure with four magnetic blocks per period compared to a structure with steel poles with approximately the same period.

The spatial and angular distribution of the stored particle beam determined by the emittance will affect the undulator spectral properties most severely. The particle beam distributions are approximately Gaussian and given in terms of the beta functions, β_x and β_y, at the undulator location in the lattice and the storage ring emittance, ε_x and ε_y. For the i=x,y directions, the particle beam size, σ_i, and divergence, σ'_i, are given by:

$$\sigma_i = (\varepsilon_i\beta_i)^{1/2} \quad \text{and} \quad \sigma'_i=(\varepsilon_i/\beta_i)^{1/2}.$$

The effective radiative source size, Σ_i, and divergence, Σ'_i, in the i=x and i=y directions is given approximately by the convolution of the natural single particle source parameters and the particle beam parameters, and

$$\Sigma_i=((\sigma_i)^2+(\sigma_r)^2)^{1/2} \quad \text{and}$$
$$\Sigma'_i=((\sigma'_i)^2+(\sigma'_r)^2)^{1/2}.$$

For third generation storage rings, natural emittances, ε, on the order of of ~1 nm rad will be achieved. Assuming a coupling of ~ 10% between the vertical (y) and horizontal (x) emittances, the magnitude of σ'_y and σ_y are on the order of ~ 5-10 μrad and 50-100 μm, respectively. This is to be compared to the natural radiative opening angle and size of the undulator photon beam, which depends on the x-ray wavelength of the harmonic chosen. For soft x-ray devices with harmonics in the range of 100-1000 Å, the natural undulator source divergence dominates. In the harder x-ray region, the source emittance effect becomes important near 1 Å radiation.

The energy of a given undulator harmonic, n, is given approximately by:

$$E_n(\text{keV})= 0.949\, nE_r^2(\text{GeV})/((1+K^2/2+\gamma^2\psi^2).\lambda_0(\text{cm}))$$

The natural energy band width is given by $\Delta E/E=1/(nN)$, where N is the number of magnetic periods in the device. The bandwidth, ΔE, corresponds to an angular divergence, $\psi\sim\sigma'_r$. This natural energy band width is increased by particle beam parameters such as the emittance and energy spread. For a given storage ring, the baseline energy width will require numerical calculations that take into account the actual angular acceptance and the particle beam emittance. For perturbations that are not much larger than the natural undulator angular width σ'_r, the contributions to the energy spread, $\Delta E/E$, of the harmonics from the particle beam divergence is given approximately by:

$$\Delta_i=(\sigma'_i\gamma)^2/(2(1+K^2/2))$$

where i=x,y. The energy spread of the particle beam will also contribute to the energy width of a harmonic.

The on-axis spectral brilliance, BL0 (sometimes referred to as brightness), in photons/(s 0.1%BW mm^2mrad^2) is defined as:

$$BL0=F/(4\pi\Sigma_x\Sigma'_x\Sigma_y\Sigma'_y)$$

where F is the total flux at a given photon energy in a fixed band width (BW).

These intrinsic spectral properties of undulator radiation including emittance define the baseline performance of ideal devices for different storage ring conditions. This baseline is a convenient one from which to discuss the effects of magnetic field errors on the performance of real devices. One of the effects of particle beam emittance is to complicate the mathematical description of the effects of field errors of real devices on the spectral properties. For some types of errors such as phase errors discussed later, the spectral properties dcan be described approximately by a Gaussian convolution of the error field distribution with emittance. For steering errors, it is not clear whether this approximation can adequately describe the combined effects of error fields and emittance and numerical calulations using the actual magnetic field may be required.

B. Effect on Storage Ring

From the point of view of the storage ring, a perfect undulator with infinite width and plane poles will show some degree of vertical focusing of the particle beam [4]. This focusing is associated with the variation of the magnetic field from the device centerline in the midplane to the pole face and the transverse component of the particle trajectory. For a field with a sinusoidal dependence along the length of the undulator, this focusing is equivalent to a quadrupole component of the magnetic field and results in a tune shift of the storage ring. It is the smallest possible perturbation achievable with a device. The quadrupole component depends approximately on the square of the ratio of the peak field to the ring energy and is

more important for high field devices in low energy storage rings. Non-linear octupole-like terms are also present. The sextupole term vanishes over one period.

There is no net steering given by $\int B \cdot dz$ in one period length of a perfect ID because of the periodic variation of the field. A net steering will occur for configurations of poles in which the net number of periods is a half integer. No net particle beam offset occurs through the device except in this case.

3. PERFORMANCE OF REAL UNDULATOR DEVICES

A. Sources of Magnetic Field Errors

As mentioned, the spectral properties of a given ID on a particular storage ring depend exclusively on the trajectory of the particle beam through the device. For planar devices, which is the focus of this article, the magnetic field is determined by the array of magnetic elements. The field variation along the length of the device for the hybrid structure can have odd harmonics of the field higher than the sinusoidal dipole term. The magnitude of these harmonics can usually be kept below 10% of the main sinusoidal field by appropriate choice of the pole dimensions. Optimization is required since the peak field also depends on the pole thickness. As mentioned, the variation of the magnetic field along the z-direction for a PPM ID is nearly sinusoidal.

For undulators, the presence of higher field harmonics affect the relative intensity and position of the energy harmonics of the device. For wigglers, they will modify the spatial distribution of the photons. These effects cannot really be considered as associated with magnetic field errors since the degree of purity of the fundamental can be controlled in most cases.

Real errors in the magnetic field of both PPM and hybrid IDs arise from several sources. One is the mechanical construction tolerances achieved in the fabrication of the device. These errors involve placement tolerances of pole pieces and magnets, as well as dimensional tolerances on the assembly or backing beams. A second source of field errors is orientation errors and block to block variations of the net magnetic moment of the permanent magnet blocks used in the construction of the device. Finally, the magnetic block can have inhomogeneities in the moment distribution that can be different for different blocks. All of these factors will give rise to magnetic field errors that have both a random and a systematic component. They introduce both particle beam steering, trajectory distortions, and focusing effects in both the vertical and horizontal directions. As a result, they affect the spectral properties of the undulators and the performance of the storage ring

These sources of errors should be distinguished from size effects in real undulators. In general, one predicts the magnetic arrays assuming IDs with infinite width so that the fields are two dimensional. Finite width effects for real devices can be estimated from either experimental results [5] or model calculations (6). In general, the width of a given ID requires optimization in order to maintain magnetic field quality and roll-off in the horizontal (x) direction. This roll-off for an error-free device, results in horizontal focusing as was the case for the vertical focusing as well as other non-linear terms. The width of the magnet and pole array can be readily controlled in order to achieve the price-performance criteria required.

Of the real error sources mentioned, the block properties are the most crucial in determining the final ID performance. In the initial stages of permanent magnet ID development, pure permanent magnet arrays were used to achieve the required field. In this case, the magnetic system is nearly a linear medium since the permeability of the magnet is approximately equal to 1. As a result, the quality of the resultant magnetic field depends directly on the quality of the blocks used in constructing the magnetic array. This means that, ultimately, the field quality depends on the materials properties of the magnets. In principle, this requires very tight fabrication tolerances on the magnetic properties of the blocks and careful sorting [2].

The hybrid structure, on the other hand, offers the advantage that, in principle, the magnetic field is achieved by exciting a steel pole such as vanadium permendur by permanent magnet blocks. The maximum flux in the steel pole should be kept below the saturation level and consequently the magnetic properties depend less on the detailed material properties of either the block or the pole. In addition, a certain amount of error cancelation is expected since the same magnet block excites poles of opposite sign. In actual fact, as will be discussed, the magnetic field errors and performance in both high quality PPM and hybrid structures devices required for the next generation IDs depend to some extent on the permanent magnet block properties in similar ways.

Presently, the fabrication of the Nd-Fe-B blocks that are used in the production of high quality, high field IDs involves a three step process consisting of orientation, pressing, and sintering of fine powder. Isostatic pressing of the magnet in the applied field produces the best performance and most uniform magnets. It also has the highest production cost. In addition, the dimensional tolerance and direction of the moment are more difficult to control because of the lack of a well-defined datum surface.

The bulk magnet properties depend on the average direction of the net moment and the uniformity of the magnetic moment distribution through the block. A perfect set of blocks will all have the same magnitude of the net moment and all the same orientation relative to some specified direction. For real blocks, orientation and magnitude errors in the magnetic moment occur. In the case of a hybrid magnetic structure, orientation errors can give rise to excitation errors in the pole adjoining the magnet since only the perpendicular component of the moment from the block's surface is important. The orientation can also cause a non-zero component of the field on the bottom face of the magnet that can affect the midplane field and zero crossing. In the PPM structure, they contribute directly to the field errors of the device. Errors such as these require careful measurement of the block moment and orientation with a Helmholtz coil arrangement, for example. Once measured, the data can be used in a sorting algorithm to properly select and distribute the errors over the body of the ID.

Block errors much more difficult to measure are associated with non-uniformities in the moment distribution. For the hybrid structure, they are suppressed away from the midplane. They are detrimental, however, on or near the surface of the block facing the particle beam near the zero crossing of the field, since they add net steering of the particle

beam and contribute in a random way to the field error of the device.

An additional factor for the Nd-Fe-B magnets is the temperature behavior of the magnetic moment. Because of their lower magnetic transition temperature, the magnets have a larger temperature coefficient than the cobalt-based alloys. Representative data for the temperature variation of a typical Nd-Fe-B magnet used in the construction of IDs shows a relative variation of the magnetic moment of the block of approximately 12 parts in 10^4 per °C. For the undulator, this translates into a systematic variation in the K-value and, hence, the harmonic energy. The harmonic energy variation of the undulator with respect to the magnetic field corresponds to:

$$\Delta E/E=-(K^2/(1+K^2/2))\Delta B/B.$$

For a K-value of 1, the temperature variation in B results in approximately the same magnitude shift in the harmonic energy. This should be compared with the width of the harmonic, which depends primarily on the number of periods, the harmonic, the emittance of the storage ring, and the limiting apertures of the experiment. For a hundred-period device, the variation in the energy caused by a 1 °C change in temperature corresponds to approximately 1/10 of the natural bandpass ($\Delta E/E$) for the 3rd harmonic with no emittance.

For the wiggler, the temperature variation in the moment will result in the same magnitude shift in the critical energy of the device.

B. Effect on Spectral Properties

In a perfect ID with infinite width, the magnetic field can be completely described in terms of a unique peak field and magnetic period. The errors mentioned above introduce both systematic and random variation in the field. In the simplest picture, the field is assumed to be described by a peak field B_0 plus an error field ΔB_i, which depends on the pole considered. As an approximation, the error fields are assumed random with a Gaussian distribution.

Kincaid [7] did the pioneering work of predicting the effect of random non-correlated errors on the spectral properties of undulators. There are two effects resulting from field errors distributed in the device. The first is that the net steering of the particle beam through the device will not be zero. Each pole will contribute steering due to the error field of $\int\Delta B_i dz$. An example of the steering introduced by a 1% difference in a peak field at a given pole is shown in Fig. 2 As can be seen, the error field will cause a kick in the particles trajectory angle and result in a displacement.

Such displacements are detrimental if the magnitude of the kick angle is larger than the intrinsic divergence of the undulator given in Section 2. For the case of a zero-emittance particle beam, this can be shown [8] to result in an allowable integrated dipole field error of $< 1704/N^{1/2}$G-cm. This, in effect, is equivalent to maintaining steering kink to within the natural divergence cone of the undulator.

With emittance, the kick will depend on the divergence of a given particle in the beam and, as a result, an analytical convolution of the beam emittance effects and fields causing steering is not possible. Full numerical calculations are required.

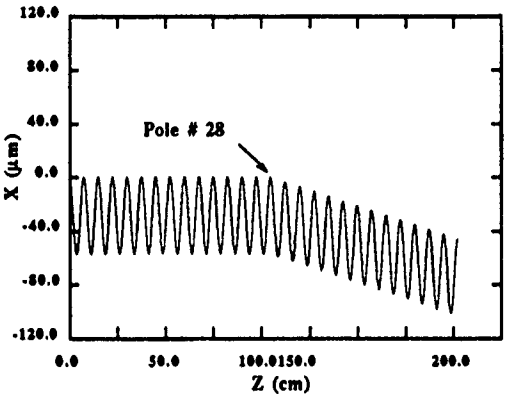


Fig. 2 Steering caused by an 1 % increase in a pole for a hybrid structure with a peak field of 0.46 T and period of 7.5 cm.

The error field, ΔB_i, also contributes to a phase error associated with the difference in the time the particle spends in each pole region. This phase error exists whether steering is present or not and introduces statistical fluctuations in the photon pulse trains and, for the undulator, results in a loss of intensity and broadening of the harmonic. For small steering errors (<0.5%), the phase errors can be convoluted with the emittance to obtain the combined effect. In general, however, calculations for the specific error field distribution are required if the performance is to be predicted accurately. Numerical calculations [9] have shown that the degradation not only depends on the error field but also on the detailed distribution. In any case, random field errors will be less than 0.5% in most cases for the new storage rings [10]. Table 1 shows typical values achieved for an APS prototype undulator installed on the VUV ring at the National Synchrotron Light Source. Also shown are field requirements expected for the undulators at the APS. Similar results have been obtained for a 3.3 cm period prototype undulator.

Table 1. Measured parameters of the APS prototype undulator at a minimum magnet gap of 34 mm.

	Measured (NSLS)	APS
Period	7.5	-
Number of Periods	27.5	-
Minimum Gap (mm)	34.0	10
Peak Field (kG)	4.60	-
(ΔB/B)rms (%)	0.22	0.3
Gap Resolution (μm)	4	2.5
Transverse Rolloff (%) in ±1cm	0.1	0.1
Steering Error (G-cm)	13	<100
Integrated Quadrupole (G)	7	<40
Skew Quadrupole (G) <	10	<20
Integrated Sextupole (G/cm)	60*	<100

Both the steering and phase errors effects are the result of field errors, which depend on several parameters. First, they

depend on the mechanical tolerances of the pole and magnet placement and pole shape. Variations in the effective gap between poles, for example, can result in variations in the magnetic field. The mechanical tolerances on pole and magnet placement and dimensions are between 20 and 100 μm for third generation IDs [11,12]. Field errors are also associated with magnet block properties. Upper limits on moment distributions and orientation errors are on the order of 1% and 1 degree. These values, combined with the required remanent field, B_r, and the third quadrant behavior of the coercive force, H_c, are stringent specifications for the Nd-Fe-B magnet blocks. Limits on the inhomogeneities are under investigation and attempts to measure surface fields are in progress [13].

C. Effect of Errors on Storage Ring

As mentioned, a perfect ID with a finite width will show both horizontal and vertical focusing of the particle beam. In general, the y-component of the field, B_y, can be given as a series expansion:

$$B_y(x,y=0,z)=B_y(x=0,y=0,z)(1+Qx+Sx^2+...)$$

where Q is the quadrupole and S, the sextupole component. The full quadrupole field involves both x and y as well as a skew component with principle axes rotated by 45°. The skew quadrupole mixes x and y and results in a larger coupling constant and, hence, vertical emittance. The sextupole component involves terms like x^2-y^2 and xy. In a real device, the multipoles result from errors in the magnetic structure. The quadrupole, for example, is the result of pole canting errors. For a hybrid device, the B_x component is suppressed at the pole surface resulting, in principle, in a reduced skew quadrupole.

Of interest to the performance of the storage ring is the integrated multipoles over the length of the ID within some specified good field region of the device. The acceptable values depend on the sensibility of the storage ring to the ID, and its ability to correct the effects of the higher moments. Since many IDs will be installed on the new rings, the combined perturbation to the lattice must be considered.

Measurement of the integrated multipoles by scanning point probes or rotating coils are difficult and require in many cases, a precision slightly beyond the state of the art. Measurements of these moments using the storage ring for the APS 7.5 cm prototype undulator are in progress. For an earlier APS prototype device with a 3.3 cm period and 2 m length installed on the Cornell High Energy Storage Ring operating in a special low-emittance mode, the moments determined by the storage ring measurements were consistent with magnetic field measurements. Correlations of this type are necessary if reliable predictions concerning the performances of IDs on the new storage rings are required.

For the case of the APS, the values of the integrated moments are given assuming 34 devices on the storage ring. The values are within the correction capabilities of the magnets within the lattice. Only the sextupole component is significantly different with a value of 0.5 T/m compared to 1 T/m for the APS.

The origin of the higher moments for real devices is still under intense scrutiny. Both the sextupole and skew quadrupoles require further evaluation for the hybrid structure where suppression of the moments should occur. This is most likely the result of the detailed spatial distribution of the error field near the surface of the magnets.

A new three dimensional model that treat these effects has recently been developed [13]. If successful, the model will permit the prediction of higher moments and error fields from localized perturbations in the magnet block.

4. ACKNOWLEDGEMENTS

Stimulating discussions with K. Halbach are greatly appreciated, as are interactions with J. Galayda, W. Hassenzahl, B. Kincaid, and K. Robinson.

5. REFERENCES

1. K. Halbach, J. Appl. Phys. 57,3605(1985)
2. K. Halbach Nucl. Instr. Meth. Phys, Res., A246,77(1986)
3. K.-J. Kim, Characteristics of Synchrotron Radiation, in Lawrence Berkeley Laboratory Publication, X-ray Data Booklet,PUB-490, 1985
4. A. Ropert, High Brilliance Lattices and the Effects of Insertion Devices, in Proceedings CERN Accelerator School, Synchrotron Radiation and Free Electron Lasers, Ed. by S. Turner, Geneva, 1990
5. K. Halbach E Hoyer, S. Marks, D. Plate, and D. Shuman, IEEE Trans. Nucl. Sci., NS32,3640(1985)
6. K. Halbach, Private Communication
7. B. Kincaid, J. Opt. Soc. Am. B2,1294(1985)
8. J. M. Slater, Proc. 1987 IEEE Part. Acc. Conf., 479(1987)
9. R. Diviacco and R. P. Walker, Proc. IEEE 1989 Part. Acc. Conf., 159(1989)
10. E. E. Alp and P. J. Viccaro, Nucl. Instr. Meth. Phys Res. A200,1099(1989)
11. E. Hoyer, J. Chin, K. Halbach, W. Hassenzahl, D. Humphries, B. Kincaid, H. Lancaster, D. Plate, and R. Savoy, Nucl. Inst. Meth. Phys. Res., A291,383(1990)
12. U5.0 Undulator Conceptual Design Report, Lawrence Berkeley Laboratory Publication, PUB-5256
13. K. Halbach, Private Communication

NSLS Prototype Small-Gap Undulator (PSGU)*

P.M. Stefan, L. Solomon and S. Krinsky
Brookhaven National Laboratory
National Synchrotron Light Source, Bldg. 725D
Upton, New York 11973

G. Rakowsky
Rockwell International, Rocketdyne Division
Canoga Park, California 91303

Abstract

The NSLS Prototype Small-Gap Undulator (PSGU) will serve as a tool to study lifetime degradation and the onset of beam instabilities as the beam duct aperture is decreased. The device will consist of a variable-gap vacuum vessel and a permanent magnet undulator, with independent magnet-gap control. The vacuum vessel design attempts to minimize both residual gas pressures and beam impedances. The undulator will be 320 mm long and utilizes a pure-permanent-magnet structure with 6 blocks per 16 mm period. For a nominal operating aperture of 4 mm, PSGU will produce a peak brightness in the fundamental and third harmonic of 7×10^{16} and 1×10^{16} photons$\cdot$sec$^{-1}\cdot$mrad$^{-2}\cdot$mm$^{-2}\cdot$(0.1% BW)$^{-1}$ at photon energies of 2.5 keV and 7.5 keV, respectively.

I. INTRODUCTION

For storage rings used to produce synchrotron radiation, an important constraint on the operation of insertion devices is the minimum allowed magnet gap. A typical insertion device, wiggler or undulator, consists of a periodic magnetic structure, built surrounding the vacuum duct in which the stored beam circulates. The minimum magnet gap restricts the inner aperture of the vacuum duct. If this aperture is decreased, the performance of the storage ring may be degraded through a reduction of beam lifetime, or through the onset of beam instabilities, which may arise from the transverse coupling impedance. Beam lifetime depends on the beam duct physical aperture and on the residual gas pressure in the beam duct. If the limiting physical aperture in the storage ring is located in the insertion device, elastic scattering of beam particles on residual gas nuclei anywhere in the ring can result in particle loss at the insertion device. In addition, the residual gas pressure inside the insertion device influences other lifetime-determining mechanisms, such as bremsstrahlung on nuclei, scattering on electrons, and ion trapping. Photon-stimulated desorption and thermal desorption of gas molecules from the beam duct walls are promoted by synchrotron radiation. Thermal desorption is also promoted by component heating through longitudinal coupling impedances. The residual gas pressure inside the insertion device from these sources generally increases as the aperture is decreased, since a small aperture decreases the pumping conductance of the duct.

On the other hand, the performance of insertion devices is enhanced by decreasing the minimum magnet gap. The peak on-axis magnetic field is increased. For a tunable undulator, the tuning range is extended. Also for undulators, since the ratio of the gap to the undulator period exponentially influences the radiated output power, a reduced magnet gap permits a reduction of undulator period, to produce higher photon energies.

The NSLS Prototype Small-Gap Undulator (PSGU) will serve as a tool to study some of the effects which degrade storage ring performance as the beam duct aperture is decreased. It consists of a variable-gap vacuum vessel and a permanent-magnet, small-period undulator with independent magnet gap control. In the following sections, the design concept of the vacuum vessel, and some details related to it, will be presented, followed by a description of the permanent-magnet undulator, its design parameters, and anticipated performance.

II. VARIABLE - GAP VACUUM CHAMBER

A. Design Concept

The PSGU vacuum chamber concept is illustrated in Fig. 1, and borrows heavily from the design of the LBL/SSRL 54-Pole Wiggler [1]. The figure presents a cross section as seen along the stored-beam direction. Deep wells extend toward the beam from top and bottom wire-sealed flanges. Top and bottom bellows permit the distance between the wells to be increased and decreased by actuators tied between the flanges, outside the chamber. The bottoms of the wells, nearest the stored beam, are thinned, and the magnet beam arrays for the undulator are inserted into the wells, against the thinned sections. The outer vacuum wall, between the bellows, remains fixed in position, and contains ports for pumps, gauges, etc.

This concept holds a number of important features for a study of aperture effects, beyond the ability to vary the

*Work performed under Contract No. DE-AC02-76CH00016 with the U.S. Department of Energy.

0-7803-0135-8/91$01.00 ©IEEE

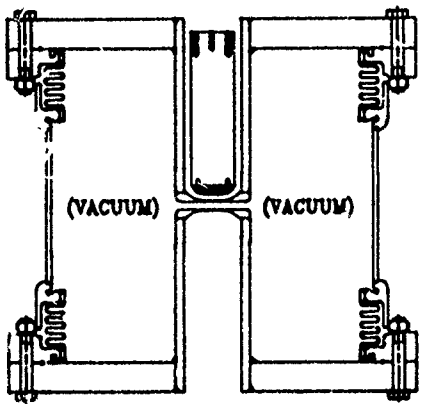


Figure 1. PSGU vacuum chamber concept.

aperture directly. Storage ring injection may require a larger aperture than that used for stored-beam operations, and this requirement is easily accommodated. A low residual gas pressure inside the device is important, as mentioned in the previous section. This implies provision for effective pumping of the minimum-aperture region, and for thorough bake out and conditioning of the vacuum vessel *in-situ*. The present concept permits removal of temperature-sensitive components, i.e., the permanent-magnet undulator, and the precision drive mechanisms, for *in-situ* bake-out of the vessel. In addition, a combination of pumping methods can be utilized to reduce the gas pressure in the minimum-aperture region.

B. Design Details

Figure 2 illustrates the layout of the X13 insertion straight of the NSLS X-Ray Ring, a 2.5 GeV electron storage ring designed for synchrotron radiation production. PSGU will occupy the center of the straight, while downstream, the NSLS Mini-Undulator [2] will be installed. Upstream, an insertable, water-cooled photon absorber will be used to block synchrotron radiation coming from the upstream bend magnet. When inserted to within 15 mm of the beam duct center, 110 W of radiation is absorbed. The shadow of the absorber then extends through PSGU and the Mini-Undulator, and finally ends beyond the downstream sector valve. This will help reduce the residual gas pressure due to photon-stimulated and thermal desorption in the straight. Electron beam position monitors are installed at the upstream and downstream ends of the straight, as well as in the upstream and downstream ends of the PSGU minimum-aperture region. Downstream of the straight section, out on the experimental floor, the X13 beamline, operated by the NSLS Beamline R&D Group, is equipped with photon beam position monitors and other diagnostics, and ties into a closed-loop feedback system for electron beam position stabilization.

The NSLS X-Ray Ring insertion straights are low β straights, with $\beta_x^* = 1.7$ m, $\beta_y^* = 0.35$ m at the straight center. The limiting vertical aperture in the ring is the standard extruded aluminum beam duct at $\beta_y$max, i.e., 42 mm at a β function of 27.5 m. The minimum-aperture region in PSGU extends $\pm$ 200 mm of the straight center, which implies a small-gap limit of 5.5 mm, without reducing the vertical acceptance. The PSGU vacuum chamber is designed to open to a 20 mm aperture and to close essentially to zero. Our nominal design goal is operation at an aperture of 4 mm, although the practical limit will be found experimentally.

As mentioned in the Introduction, transverse and longitudinal coupling impedances contribute to beam instabilities and component heating, respectively. The worst-case resistive-wall power deposition is estimated at 3 W for a 2 mm aperture. This results in an acceptable maximum temperature rise of about 5°C. Instabilities may be significant above 100 mA stored beam current for the same 2 mm aperture, but at the nominal 4 mm value, the beam should be stable to 250 mA, the maximum current presently anticipated. Transitions in and out of the minimum-aperture region are also important for the impedances they can generate. Reduction of impedances requires a smooth continuous conductive path for beam image currents throughout the straight section. We plan to use flexible metal sheets to make the transitions between the minimum-aperture region and the regions upstream and downstream. In addition, a program to experimentally measure longitudinal and transverse coupling impedances of proposed designs, using the methods reported by Walling et al. [3], is presently underway.

III. PSGU MAGNET

The parameters for the PSGU magnet are summarized in Table 1. It uses the high-performance 6-block-per-period version of the Halbach pure-permanent-magnet (PPM) design as developed by Rocketdyne [4]. This design makes possible

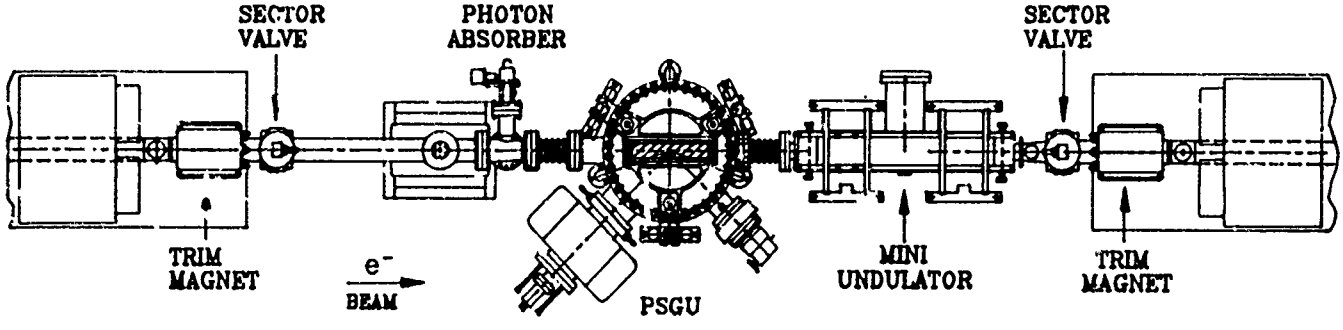


Figure 2. Layout of X13 insertion straight section.

Table 1
PSGU Magnet Parameters

Construction	*6-Block PPM*
Period, λ_u	*16mm*
Length, L	*320mm*
Magnet Gap Range, g	*18 mm - 4 mm*
Deflection Parameter Range, K	*0.1 - 1.5*
Peak On-Axis Field	*64 mT - 1.0 T*
Magnet Alloy	*NdFeB*
Remanence, Br	*1.2 T*
@ Nominal Gap	
Chamber Aperture	*4.0 mm*
Magnet Gap	*6.0 mm*
Peak On-Axis Field	*0.68 T*
Deflection Parameter, K	*1.0*

peak field values comparable to the Halbach hybrid design [5], but retains the benefits of an "iron-free" design, namely the applicability of superposition. Figure 3 presents a schematic view of the construction. To minimize field errors, several stages of characterization, followed by simulated annealing, are performed. Individual blocks are first characterized and sorted into triplet modules of equal strength. For PSGU, the blocks in a triplet are bonded together and post-machined to precise dimensions. The triplets are then characterized and ordered to simultaneously minimize normal and skew multipole errors and optimize performance. Finally, the partially-assembled magnet beams are mapped and end blocks selected to minimize beam steering and displacement.

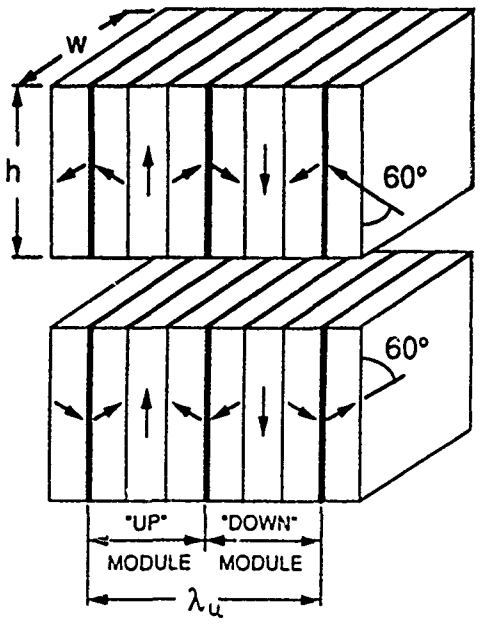


Figure 3. 6-block PPM construction.

The anticipated performance of PSGU at the nominal magnet gap of 6 mm is summarized in Table 2, for the fundamental and 3rd harmonic. These values include the emittance of the NSLS X-Ray Ring. The photon energy of the fundamental was chosen to be the sulfur K absorption edge, in anticipation of possible interest in S microscopy or near-edge spectroscopy. In terms of flux and brightness at this energy, PSGU will provide at least comparable performance to the best existing sources.

Table 2
*PSGU Magnet Performance**

@ Nominal Gap, g = 6.0 mm		
	Harmonic	
	Fundamental	3rd
λ_{out}	4.9Å	1.6Å
$h\nu_{out}$	2.5keV	7.5keV
Peak Brightness†	$7x10^{16}$	$1x10^{16}$
Central Cone Flux‡	$4x10^{14}$	$7x10^{13}$
Total Radiated Power	150 W	
Tuning Range		
Gap Range, g	18 mm - 4 mm	
λ_{out}	3.3Å-6.9Å	1.1Å-2.3Å
$h\nu_{out}$	3.8keV-1.8keV	11.3keV-5.4 keV

*NSLS X-Ray Ring, E=2.53 GeV, I=250 mA.
†Photons•sec^{-1}•mrad^{-2}•mm^{-2}•(0.1% BW)$^{-1}$.
‡Photons•sec^{-1}•(0.1% BW)$^{-1}$.

IV. REFERENCES

[1] E. Hoyer, et al., "The Beam Line VI Rec-Steel Hybrid Wiggler for SSRL," IEEE Transactions on Nuclear Science, Vol. NS-30, pp. 3118-3120, August 1983.

[2] H. Rarback, et al., "The Performance of the NSLS Mini-Undulator," Nuclear Instruments and Methods in Physics Research, Vol. A266, pp. 96-105, 1988.

[3] L.S. Walling, et al., "Transmission Line Impedance Measurements for an Advanced Hadron Facility," Nuclear Instruments and Methods in Physics Research, Vol. A281, pp. 433-448, 1989.

[4] G. Rakowsky, et al., "High-Performance Pure Permanent-Magnet Undulators," Nuclear Instruments and Methods in Physics Research, Vol. A296, pp. 597-602, 1990.

[5] K. Halbach, "Permanent Magnet Undulators," Journal de Physique, Vol. 44, pp. C1-211-C1-216, February 1983.

Operation of Synchrotron Light Sources with Multiple Insertion Devices*

John Galayda
Argonne National Laboratory
Advanced Photon Source
Argonne, IL

Anne-Marie Fauchet
National Synchrotron Light Source
Brookhaven National Laboratory
Upton, NY

Abstract

The stability requirements of the next generation of synchrotron radiation facilities have been achieved on insertion device beamlines of existing rings. However, one insertion device (ID) affects the stored beam and hence the performance of all the other beamlines. Since the effects of the undulators are cumulative, higher levels of performance are required of the accelerator in order to meet and exceed present day standards in rings with many undulators.

This paper will report experience to date in the areas mentioned above at several multi-undulator facilities and efforts to address these problems at facilities in the planning and construction phase. Section II will treat orbit control and feedback. Section III will describe work on linear and nonlinear effects of ideal undulators in accelerators. Section IV will mention undulator imperfections and the demands they make on the accelerator control system.

I. ORBIT CONTROL: FEEDBACK

Orbit stability requirements must be consistent with the emittance of the ring to satisfy all users' needs regardless of differences in beamline designs. For this reason, the motions of the stored beam must be limited to 10% of the rms beamsize and 10% of the rms opening angle at the source point. This corresponds to a 0.5% change in the X-Ray flux through an entrance slit of width equal to twice the rms beam size. Table 1 shows the beam stability requirements at APS and the NSLS X-Ray Ring. The vertical emittances are based on 10% coupling. At APS, the listed vertical motions could be induced by a 1-2 micron displacement of a single quadrupole in the ring or by a changing magnetic field with integrated strength 0.2 gauss·meter. Despite the larger emittance of the NSLS X-Ray Ring, the beam position requirements and the tolerance on quadrupole motions and stray fields are comparable to APS. This is because the beta functions in the ID straight section are much smaller than at APS and the 2.5 GeV NSLS electron beam is less rigid. Feedback orbit control will be essential to achieving the necessary stability.

Table 1
Orbit Control Requirements at APS and NSLS X-Ray Ring

	ϵ_x	δX	$\delta X'$	ϵ_y	δY	$\delta Y'$
APS	8 nm	30 μm	2 μrad	0.8 nm	9 μm	0.9 μrad
X-Ray Ring	100 nm	37 μm	27 μrad	10 nm	6 μm	17 μrad

Local feedback orbit control systems are in widespread use at synchrotron radiation facilities. The SPEAR ring has 9 local feedback loops installed, servicing 4 ID beamlines. The NSLS X-Ray ring has 10 local loops in use during normal operations.

The performance of a single feedback loop is limited by the sensitivity of the detector, the gain (determined by the loop stability), and the voltage and current available to the steering magnets. When more "local" loops are implemented on a storage ring, deviations from locality of the bumps in one loop result in an interaction with all the other loops in the ring. The interaction can reduce the efficacy of the loops. If the coupling between loops is strong enough, the system of loops could become unstable.

Figure 1 shows a diagram of a feedback loop that controls the amplitude of a local orbit bump so as to null the output of a single beam position monitor. It is configured to reduce the beam motion X observed on the detector by powering a bump that subtracts a quantity x from X. The beam position monitor has an output V proportional to x+X :

$$\text{BPM output} \quad V = X+x$$

but x is produced by a "local" bump whose amplitude is proportional to V:

$$\text{Feedback bump} \quad x = -G * V$$

so that

$$(X+x) = X/(G+1)$$

The ambient beam noise X is reduced by a factor (G+1).

We can generalize this treatment to an array of N "almost independent" feedback loops. The i'th loop has a single beam position monitor. Its output voltage V_i is

*Work supported by U.S. Department of Energy, Office of Basic Energy Sciences under Contract No. W-31-109-ENG-38.

U.S. Government work not protected by U.S. Copyright.

intended to create a beam motion xi that is detected only by the very same (i'th) monitor. There is a practical limit to how local a bump can be, however. The i'th BPM still sees only the motion at its own observation point:

$$V_i = X_i + x_i$$

But now the applied correction xi gets contributions from all the other feedback loops:

$$x_i = -\sum_{j=1}^{N} G_{ij} V_j$$

Closing the loops results in an orbit correction described by the matrix equation:

$$X + x = (G + 1)^{-1} * X$$

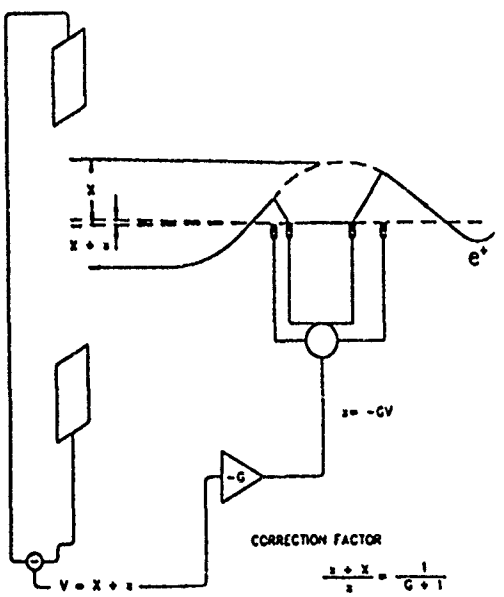


Figure 1. Schematic of local feedback loop - V is the detector output.

In order to have a stable system of N feedback loops, the matrix (G+1) must have a nonzero determinant. We can establish a somewhat stringent condition sufficient for stability by writing

$$(G+1) = g \begin{bmatrix} A_{11} & b_{12} & b_{13} & \cdots & b_{1N} \\ b_{21} & A_{22} & b_{23} & \cdots & b_{2N} \\ \vdots & & & & \\ b_{N1} & b_{N2} & b_{N3} & \cdots & A_{NN} \end{bmatrix}$$

where the A's are all of order one and the b's are all smaller because they represent the deviations from perfect locality of the feedback correction bumps. The determinant of a matrix M may be written as the sum

$$|M| = \sum_{\text{permutations}} (-1)^P M_{1j_1} M_{2j_2} \cdots M_{Nj_N}$$

where p is even if the sequence $j_1, j_2, j_3, \ldots j_N$ is formed from 1, 2, 3,.,N by an even number of permutations and odd if an odd number of permutations is required. The determinant has one term equal to

$$A_{11} \cdot A_{22} \cdot A_{33} \cdot \ldots \cdot A_{NN}$$

and many of terms proportional to products of the A's and b's. If we say that all the Ajj's are proportional to a scaling parameter A and all the bij's are proportional to another scaling parameter b, we can show that the terms of the sum can be grouped by powers of A and b and we can place an upper limit on how many terms of a given order appear in the sum. We may choose the smallest of the Ajj's to be A and the largest of the bij's to be b and we can make the worst-case assumption that all the terms of order $A^{(N-m)}$ have sign opposite to the A^N term.

How many terms in the sum are proportional to $A^{(N-m)} \cdot b^m$? There are [N!/((N-m)!m!)] ways to choose the (N-m) A's from the set of N A's available to us. Then we must choose m b's so that they share no row or column with either the A's or the b's we have already chosen. We can overestimate the number of ways to choose the b's. Once we have selected the N-m rows that will donate their A's to a given term in the sum, we must choose m off-diagonal matrix elements from the m · m submatrix constructed by eliminating all rows and columns which have donated their A's. This m · m matrix still contains one A-term and (m-1) b-terms in each row. We overestimate the number of ways we can choose the remaining b's as (m-1)! since we must choose the b's so that none share the same row or column in the m · m submatrix. The result is that the sum of all terms of order less than A^N in the determinant is less than

$$\det |G+1| \geq \prod_{j=1}^{N} A_{jj} - A^N \sum_{m=2}^{N} \left(\frac{b}{A}\right)^m \frac{N!\,(m-1)!}{(N-m)!\,m!}$$

Again we make an overestimate:

$$\frac{N!}{(N-m)!} \leq N^m$$

The determinant is bounded by

$$\det |G+1| \geq \prod_{j=1}^{N} A_{jj} - A^N \sum_{m=2}^{N} \left(\frac{Nb}{A}\right)^m \cdot \frac{1}{m}$$

If the sum is less than 1, the determinant cannot be zero. Since b measures the deviation of the bump from perfect locality, we conclude that a ring like APS with up to 78 local feedback loops in each plane must have bumps local to about 1% precision just to guarantee stability of the system. The locality condition must be maintained over the working frequency range of the feedback systems, demanding great precision in the matching of frequency response of different steering magnets.

Even if the system of loops is stable, the correction factor may be larger than intended and even greater than one. C. J. Bocchetta and A. Wrulich [1] have studied the

correction factor of stable systems of coupled loops by estimating the worst-case correction factor. They do this by finding the largest eigenvalue for the correction matrix $(1+G)^{-1}$. They investigate some specific error arrangements and prove that, in the case that all the error terms bij are equal, the stability of the correction requires b < 1/N. They go on to investigate transient responses of the system of loops. Their model assumes an iterative correction scheme that samples the beam position. In the worst case, stability required a sampling rate at least twelve times the highest frequency noise to be corrected.

Since the stability margin of a multiloop system is increased as the the number of loops is reduced, global harmonic systems are attractive alternates or supplements to a large number of local feedback loops [2]. Superposition of global and local feedback loops at the NSLS X-Ray Ring showed that global loops and enhance the performance of local loops.

NSLS global feedback systems use analog electronics to process and filter the orbit error signals into analog command voltages to the steering magnets. APS and other machines under construction will utilize digital signal processing and transmission to implement global and local feedback loops. In this case the orbit correction algorithm can emulate local feedback loops, global harmonic feedback, or any other algorithm that proves successful as an orbit correction applications program. This approach requires, however, that the minimum increment in steering magnet current must steer the beam through an angle that is small compared to the stability criterion, i.e., less than one microradian. Furthermore, the correction commands must be obeyed in a time that is short compared to the required response time of the feedback loops, otherwise the digital feedback system will cause transients in orbit motion that exceed the error to be corrected. Fortunately the necessary digital signal processing hardware and high speed communication links are already commercially available. Indeed, the KEK Photon Factory [3] already has a digital global feedback system that consists of an orbit correction application program running continuously in its control computer. The effective bandwidth is a small fraction of a Hertz, but the system is nonetheless a valuable part of PF operations.

II. LINEAR AND NONLINEAR BEAM OPTICAL EFFECTS IN UNDULATORS

The field of an ideal planar undulator has the form

$$B_y = B_0 \cos(k z) \cosh(k y)$$

$$B_z = -B_0 \sin(k z) \sinh(k y)$$

where z is the nominal direction along the beam path and y is vertical. The period of the undulator λ determines k

$$k = 2\pi/\lambda$$

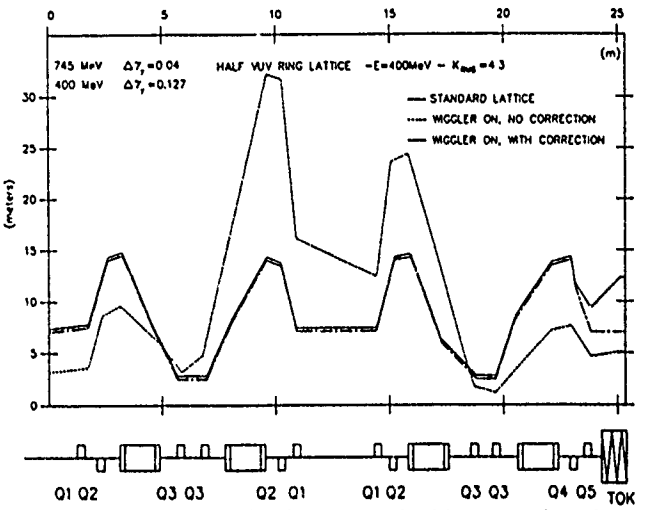


Figure 2. Effect of U13 TOK on vertical betatron functions of the NSLS VUV ring, before and after local correction.

An ideal planar ID would cause absolutely no deflection of the particle beam in the vertical or horizontal direction, and this would be true no matter what the horizontal position or angle of the beam as it enters the device. Even in an ideal ID, however, there is a vertical focussing term. Each pole of the ID causes fringe field focussing, as does any bending magnet.

The vertical focussing of the beam, when averaged over a period of the undulator, is given by [4]

$$y'' + \sinh(2ky)/(4k\,\rho^2) = 0$$

expanding the hyperbolic sine gives

$$y'' + y/(2\,\rho^2) + k^2\,y^3/(3\,\rho^2) = 0$$

The linear focussing term has no dependence on the undulator period while the cubic force term increases with the inverse square of the period, for a fixed field. Table 2 lists some insertion devices installed in the NSLS facility as well as devices planned for ALS, APS and ESRF. The table includes computed values for the vertical linear and nonlinear focussing terms $1/(2\,\rho^2)$ and $(k^2)/(3\,\rho^2)$, weighted by the average values of the vertical beta functions; $<\beta_y>$ for the linear focussing and $<\beta_y^2>$ for the cubic force.

The detrimental effects of the ID on the particle optics may be resolved into two mechanisms. First, the linear focussing breaks the symmetry of the lattice and consequently the symmetry of the beta functions and phase advances. This effect may be compensated to various levels of precision by adjusting the quadrupoles in the ring. The simplest correction is to scale all the quadrupole currents to restore the betatron tunes. By using only the quadrupoles nearest the ID, the distortion of the betatron functions can be localized within the superperiod that contains the ID. This action will generally cause an error in betatron tune which can be corrected with a global adjustment involving almost all the quadrupoles. This "alpha-matching" technique is

Table 2

	ESRF	ALS		NSLS X-Ray Ring			NSLS VUV RING		APS	
	Undulator	U3.65	U20.0	X1	X17	X25	U5 APS	U13 TOK	Undulator A	Wiggler A
Bo (Tesla)	0.45	0.61	1.1	0.35	5.0	1.1	.46	.65	0.86	1.0
λ (cm)	4.4	3.65	20.0	8	17.4	12	7.5	10.	3.1	15
L (m)	1.6	4.9	4.6	3	0.6	1.7	2.1	2.2	2.5	1.5
$\Delta \nu_y$	.0005	.007	.02	.0005	.004	.001	.016	.034	.0113	.0011
A*	675	8484	820	154	18	35	5163	6065	4650	160

*$A = 4\pi^2 \langle B^2_y \rangle L/(3\rho^2\lambda^2)$ (m^{-1})

exemplified in Figure 2, which shows the uncorrected and corrected betatron functions of the NSLS VUV ring with the U13 TOK undulator installed.

Third-generation synchrotron radiation facilities are much less tolerant of asymmetries in phase advance than are other rings. This is true whether the asymmetry is caused by the vertical focussing of undulators or closed orbit errors in the sextupoles. A reasonable dynamic aperture can be achieved in such rings only by careful placement of the very strong chromaticity-correction sextupoles, or else by partially cancelling the effect of the chromaticity-correction sextupoles with additional families of harmonic-correction sextupoles. In principle, the linear focussing effects of the ID could be compensated perfectly. One simply needs enough flexibility in adjusting the neighboring quadrupoles to keep the transfer matrices between sextupoles independent of the ID strength. In practice, other lattice imperfections may mask the potential improvement of a "perfect" linear compensation.

The lowest-order nonlinear focussing force of an undulator has a cubic dependence on y so one can expect stopbands around $4\nu_y$ = integer.

The effects of undulators on ALS has been studied by Jackson, et al. [5]. They compared schemes for correcting the linear focussing and concluded that one may use the defocussing quads nearest the ID to correct the vertical tunes. The horizontal tune correction may then be distributed globally over almost all the horizontal focussing quads. They find that the linear and nonlinear focussing properties of the IDs reduce the dynamic aperture by similar amounts, and that the effect of the IDs is also comparable to the effect of magnet imperfections. Although the undulators reduce the vertical dynamic aperture significantly, it remains larger than the physical aperture.

Tosi and Nagaoka have investigated the effect of helical undulators and variable-polarization IDs in Elettra [6]. IDs that produce circularly polarized radiation generally act like optical elements with both vertical and horizontal focussing.

Undulators planned for ESRF [7] have fields and periods consistent with the 20 mm vertical aperture of the ID straight section. The ESRF ring energy is threefold that of ALS and its undulators have longer period lengths. Hence one expects and finds smaller changes in dynamic aperture than those seen in ALS and Elettra. Like ESRF, linear focussing effects of undulators are very small in APS. Studies of nonlinear effects of undulators are not yet complete.

Evidence of the effect of IDs on particle optics and dynamic aperture have been measured and reported by Brunelle for Super ACO [8] and by Kuske and Bahrdt at BESSY [4]. In both rings, the effect of the cubic force on dynamic aperture was investigated by measuring the beam lifetime as a function of tune with the sextupole magnets turned off. Lifetime reductions in reasonable agreement with results of computer simulations of the dynamic aperture were obtained in both cases.

Detailed studies of the effects of the Phase II insertion devices of the NSLS X-Ray ring at 2.5 GeV are yet to be completed. However, their linear and cubic force terms are expected to have little effect because the vertical β function is only 0.35 meters in the ID straight section. Studies involving beam optical effects of the IDs will be done at 0.75 GeV, the injection energy of the X-Ray ring.

III. UNDULATOR IMPERFECTIONS

The imperfections of a state-of-the art ID should be too small to significantly affect dynamic aperture of a typical synchrotron radiation ring. However even minor field errors can disturb the orbit and linear coupling if the strengths of the undulators are changed during operations. Steering errors caused by gap changes in IDs must be compensated by feedback and by steering magnets that are programmed to change as a function of ID strength.

If the need for orbit stability is driven by the need for highly stable flux into the acceptance of the photon beamlines, then it must also be necessary to have a high level of stability in the skew quadrupole fields as the IDs change gap. If we demand 0.5% stability in photon flux through a 2σ slit that limits the beam vertically, this implies that the vertical emittance must be stable to 2%. The linear coupling must therefore be held constant to 2% of its value, for APS the nominal 10% coupling must remain in the range 9.8%.

10.2% to fulfill this criterion. The undesirable consequences of a beam size change caused by magnetic imperfections in an ID, at SRC in Stoughton, Wisconsin, were reported by Trzeciak, et al. [9]. Ironically the increased coupling caused by changing the gap of the ID improved the beam lifetime by increasing the volume of the bunch and thereby reducing the Touschek loss rate.

The tolerance on the change in linear coupling can be converted to a magnetic field tolerance for APS; the skew quadrupole of an undulator must change less than 65 gauss as the gap changes. Measurement techniques with the necessary sensitivity have been developed and applied, for example, to the NSLS Phase II IDs [10]. Such magnet measurements demonstrate that this specification has been exceeded by the APS undulator in the U5 beamline at NSLS, which has a total (normal + skew) quadrupole integral of 10 gauss [11].

Conceptually simple ingredients are necessary if synchrotron radiation users are to be permitted to change ID strength at will. The problem is not trivial as evidenced by the fact that, at NSLS, SPEAR, SRC, Super ACO and Daresbury SRS, ID strengths are not changed routinely during operations for many users, although gap changes are permitted at SRS. SPEAR and SRC intend to implement independent gap changes on certain devices in these rings in the near future.

While the beam stability can be affected by quite small imperfections in IDs, the most important effects are fortunately linear so that the effects of individual IDs and their corrections should satisfy superposition. This means that, if the accelerator controls system is configured to accommodate it, a matrix can be defined that specifies the vector of necessary changes in all accelerator parameters in terms of the vector of all ID strengths. The necessary changes can then be implemented automatically by the controls system as the users change gaps of the IDs.

SSRL beamlines 5,6 and 10 are configured so that steering corrections are automatically updated to track changes in magnet strength. After further studies, users will be allowed to change strength of the undulator at beamline 5. For the present, undulator strengths at SSRL are changed during operations only after all users have been notified.

Alladin has implemented automatic gap-dependent compensation of orbit errors so that no motions larger than 20 microns (vertical) or 50 microns (horizontal) are caused by changing the undulator gap. The change in vertical beam size that is coupled to gap changes must be corrected automatically before unannounced gap changes will be allowed.

NSLS allows changes of the X1 soft X-Ray undulator strength during operations. The X1 users call the control room to request a change and the ring operators make the change after notifying all users.

Only at the KEK Photon Factory are unannounced gap changes routinely performed in operations. Each of five IDs has a prescribed range over which it may be changed without disturbing orbit stability.

The problems to be solved in operating synchrotron radiation rings with many IDs have been and continue to be studied at facilities presently in operation. With sufficient care and attention to detail, any problems caused by steering errors and linear focussing properties in the undulators can be corrected by feedback or by commanding the necessary steering and quadrupole adjustments in coordination with ID strength changes. Nonlinear focussing effects may reduce the beam lifetime, but this can be an acceptable price to pay for the use of short-period undulators.

IV. ACKNOWLEDGEMENTS

The authors thank D. M. Dykes, M. A. Green, R. O. Hettel, T. Katsura and M. P. Level for information on operating procedures of synchrotron radiation rings.

[1] C. J. Bochetta and A. Wrulich, "Local Feedback Systems Coupled by Transfer Function Errors," Sincrotrone Trieste ST/M-90/7 (September 1990).

[2] L. H. Yu, R. Biscardi, J. Bittner, A. M. Fauchet, S. Krinsky, R. Nawrocky, J. Rothman, O. Singh, K. M. Yang, "Real Time Closed Orbit Feedback System for NSLS X-Ray Ring," these proceedings.

[3] T. Katsura, Y. Kamiya, K. Haga, T. Mitsuhashi, N. Nakamura, M. Katoh and I. Abe, "Beam Position Stabilization at the Photon Factory," Rev. Sci. Inst. 60 (7), pp. 1507-1512 (1989).

[4] P. Kuske, J. Bahrdt, "Influence of the BESSY Undulators on Beam Dynamics," EPAC 90 - Proceedings of the 2nd European Particle Accelerator Conference, Gif-Sur-Yvette, Editions Frontieres, pp. 1417-1419 (1990).

[5] A. Jackson, E. Forest, H. Nishimura, and M. S. Zisman, "The Effects of Insertion Devices on Beam Dynamics in the ALS," Proceedings of the 1989 IEEE Particle Accelerator Conference, IEEE Service Center, Piscataway, NJ 08854, pp. 1752-1754 (1989).

[6] L. Tosi and R. Nagaoka, Effects of Helical Undulators on Beam Dynamics," EPAC 90 - Proceedings of the 2nd European Particle Accelerator Conference, Gif-Sur-Yvette, Editions Frontieres, pp. 1423-1425 (1990).

[7] G. Mulhaupt, "Status of the ESRF," ibid. pp.65-69.

[8] P. Brunelle, "Beam Dynamics with Many Undulators on Super-ACO," ibid. pp 1411-1413.

[9] W. S. Trzeciak, R. W. C. Hansen, M. A. Green, M. Bissen and David Eisert, "Implementation of Undulator Scanning at Aladdin," Nuc. Inst. Meth. A291 (1990) pp. 413-418.

[10] L. Solomon, G. Decker, J. Galayda, "Magnetic Measurements of Permanent Magnet Insertion Devices at the BNL-NSLS," Proceedings of the 1989 IEEE Particle Accelerator Conference, IEEE Service Center Piscataway, NJ 08854, pp. 387-389.

[11] P. J. Viccaro, "Magnetic Field Tolerances for Insertion Devices on 3rd Generation Synchrotron Light Sources," these proceedings.

Low-Emittance in SPEAR*

J. Safranek and H. Wiedemann
Stanford Synchrotron Radiation Laboratory, P.O. Box 4349, Bin 99, Stanford, CA 94309-0210

Abstract

This paper describes the characteristics of a low-emittance configuration and it's implementation in SPEAR at the Stanford Synchrotron Radiation Laboratory (SSRL) to increase the photon beam brightness. The new lattice has an emittance of 129 πnm*rad at 3 GeV compared to the present emittance of 510 πnm*rad.

I. Introduction

The storage ring SPEAR is now fully dedicated to the production of synchrotron radiation at SSRL. Efforts have been made and continue to optimize SPEAR as a synchrotron radiation source including the construction of a dedicated full energy injector[1]. First beam from this injector was injected into SPEAR in November 1990. To further optimize the photon beam quality at SPEAR, studies have been conducted to maximize the photon beam brightness by reducing the particle beam emittance. Low emittance configurations have been proposed previously for SPEAR[2] [3][4], but injection into such configurations was not possible in a reproducible way because of limitations in the injection components. As part of the injector project a third kicker was installed in SPEAR to accommodate beam injection into a new low emittance configuration[5], a configuration designed with the constraint that no significant hardware changes were necessary for its implementation. The emittance in the new low emittance (LE) lattice is reduced by nearly a factor of 4 compared to the presently used high energy physics (HEP) optics.

II. Lattice Design

A. Linear Optics

The main criteria for designing the linear optics of the LE lattice was to maximize the photon brightness from undulators given by:[6]

$$\mathcal{B} = \frac{\mathcal{F}}{(2\pi)^2 \Sigma_x \Sigma_{x'} \Sigma_y \Sigma_{y'}}$$

where $\mathcal{F}$ is the integrated flux and

$$\Sigma_u = \sqrt{\sigma_u^2 + \frac{\lambda L}{8\pi^2}} \qquad \Sigma_{u'} = \sqrt{\sigma_{u'}^2 + \frac{\lambda}{2L}}$$

where u is either x or y; σ_x, $\sigma_{x'}$, σ_y, and $\sigma_{y'}$ are electron beam dimensions; λ is the photon wavelength; and L is the length of the undulator. For maximum brightness we require the dispersion to vanish in the undulator, $\eta_x = \eta_x' = 0$, the betatron functions to be

$$\beta_x \approx \beta_y \approx \frac{L}{2\pi}$$

and the beam emittances ϵ_x and ϵ_y to be minimized. For the layout of magnets in SPEAR, it is impossible to satisfy the first criterion exactly but we were able to reduce

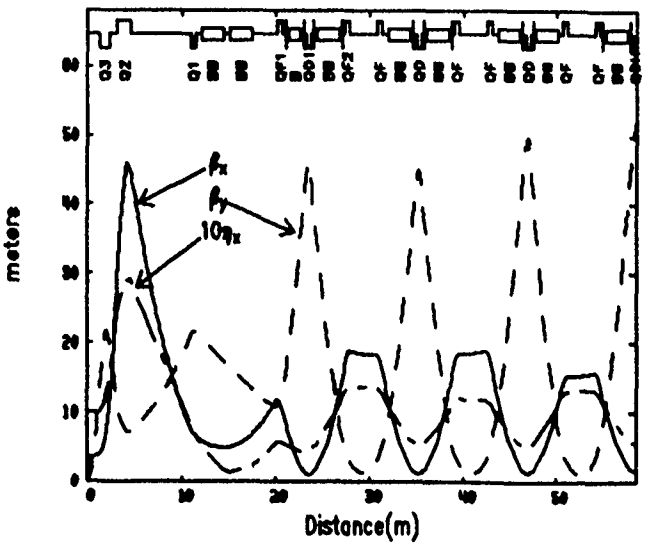


Figure 1
Linear optics of the LE lattice.

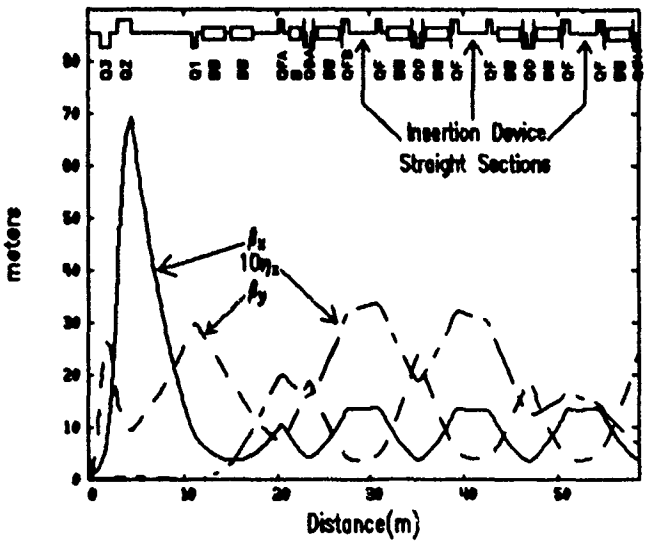


Figure 2
Linear optics of the HEP lattice.

the dispersion in the insertion straights by up to a factor of three (see figs. 1 and 2). The second criteria, the constraint on β_x and β_y gives a much broader maximum with respect to β_x than with respect to β_y. This can be attributed to the fact that the magnitude of the vertical electron emittance, ϵ_y, is closer than ϵ_x to the diffraction limited photon beam emittance from a single electron, $\lambda/4\pi$. For the LE lattice β_y is 1.1 meters in the insertions, which is very close to the optimum value. This small β_y also has the advantage of allowing smaller undulator gaps without reducing the beam lifetime, and it reduces the perturbation

*Work supported by the Department of Energy, Office of Basic Energy Sciences, Division of Material Sciences.

0-7803-0135-8/91$01.00 ©IEEE

of the electron optics from wiggler and undulator vertical focusing and nonlinearities.

Minimization of the horizontal emittance is achieved by minimizing the integral of $\gamma_x\eta_x^2 + 2\alpha_x\eta_x\eta_x' + \beta_x\eta_x'^2$ in the bending magnets. In the arcs, where most of the bend magnets are located, there are only two independently powered quadrupole magnet strings, QD and QF. The emittance is rather insensitive to the strength of the QD's but varies significantly as a function of the strength of QF as shown in fig.3. We note that the LE lattice emittance is very close to the minimum possible emittance for SPEAR. Table 1 compares the emittance with that of other machines of comparable energy.[7] The emittance in the LE lattice is smaller than in other operating synchrotron radiation sources, but is still much larger than in new sources under construction. To achieve such low beam emittances in SPEAR the magnet lattice must be significantly modified. Such modifications are possible without perturbing the location of existing photon beam lines and insertion devices[8] resulting in a beam emittance of 28.5πnm*rad

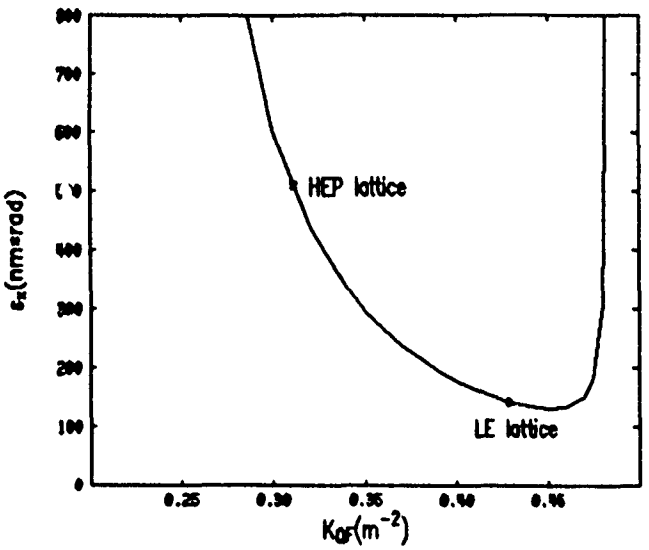


Figure 3
Horizontal emittance vs QF strength with QD strength held constant.

Table 1
Comparison of beam emittances at 3 GeV.

Lattice	ϵ_x @3GeV (πnm*rad)	Status	Design Energy
Beijing	270	Running	2.8GeV
SRS2	243	Running	2.0
Photon Fact.	185	Running	2.5
NSLS X-Ray	152	Running	2.5
SPEAR LE	**129**	Commissioning	**3.0**
Pohang	30	Construction	2.0
Trieste	16	Construction	2.0
ALS	14	Construction	1.5

B. Dynamic Aperture

The LE lattice requires strong quadrupoles with associated large natural chromaticities (see Table 2) requiring strong sextupoles. With careful choice of tunes and some reconfiguring of the sextupole distribution in SPEAR, the dynamic aperture could be preserved to assure beam stability (see fig.4). Tracking studies with PATPET[9] show that this dynamic aperture remains large for off-energy particles and when tracking with magnet strength and alignment errors. Table 2 gives a summary of the properties of the LE lattice. Two previously proposed low emittance SPEAR lattices, the high-beta low-emittance (HBLE) lattice[3] and Blumberg's lattice[4], are included for comparison. The large physical and dynamic apertures in the LE lattice provides for easier injection.

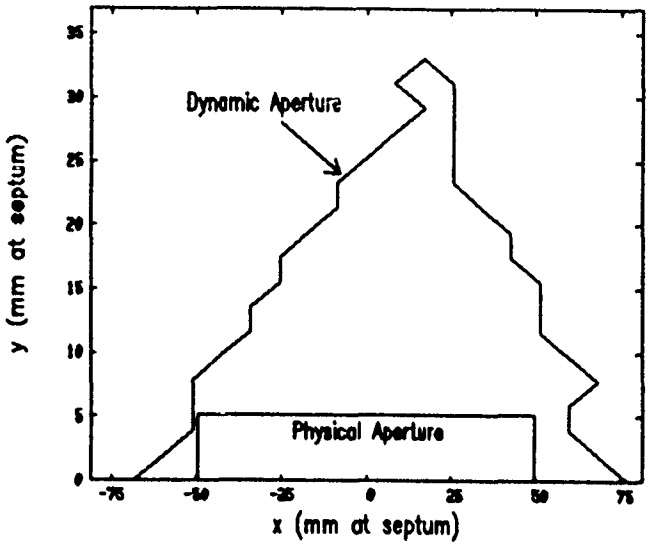


Figure 4
LE lattice dynamic aperture.

Table 2
Comparison of lattice parameters. The emittances are for 3 GeV electrons. The apertures are given in millimeters at the septum, and the dynamic apertures are for 400-turn tracking and with $\xi_x = \xi_y = 3$.

Lattice	LE	HEP	HBLE	Blumberg
ϵ_x(πnm*rad)	129	511	141	142
β_y(m) @ ID's	1.1	3.8	2.8	2.2
η_x(m) @ ID's	1.3	2.7	1.2	1.3
Dyn. Aper.(mm)	72	130	51	27
Phys. Aper.(mm)	50	35	19	35
ξ_x	-12.2	-11.2	-8.8	-11.9
ξ_y	-21.3	-11.2	-9.6	-15.6
ν_x	6.87	5.27	6.25	6.27
ν_y	6.8	5.14	5.19	6.16

C. Lifetimes and Current Limitations

Calculations indicate that bremsstrahlung, Coulomb scattering, Touschek, and quantum lifetimes will all be at

least 18 hours in the LE lattice for single bunch currents below 15 mA. From ZAP[10] calculations we conclude that the single bunch current will be limited by reduction of the longitudinal quantum lifetime from turbulent bunch lengthening. For an rf-voltage of 2.5 MV at 3 GeV, the quantum lifetime will be reduced to 5 hours for a single bunch current of approximately 28 mA.

III. Injection Scheme

Injection into the HEP lattice uses two kickers separated by π in horizontal phase advance. In the LE lattice the phase advance between these two kickers is much larger than π, so a third kicker is needed to produce a local orbit bump for injection. A location was found for this third kicker with the same aperture and strength requirements as for the other kickers. This made it possible to move one of the now obsolete positron injection kickers to this new location to inject electrons. Fig.5 shows the injection scheme. A static bump using the trims on the

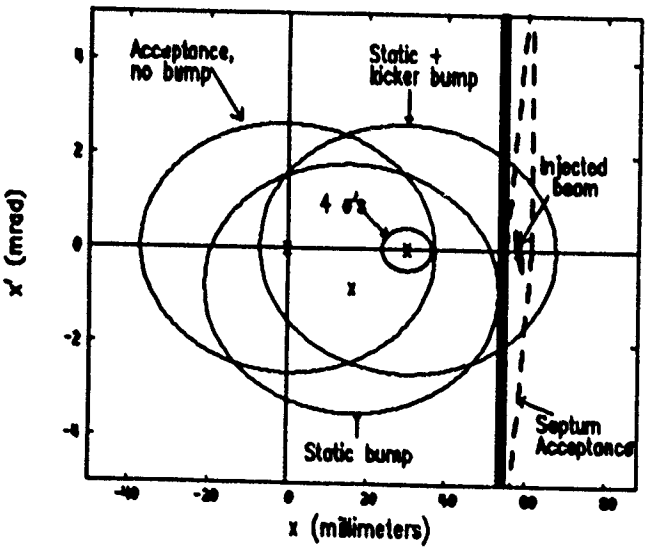


Figure 5
Injection scheme

two bend magnets on either side of the septum corrects the slope of the kicker bump and moves the stored beam acceptance close to the edge of the septum. The pulsed kicker bump the moves the SPEAR acceptance over the septum to accept the injected beam. This figure shows that the cross-section of the septum acceptance and the stored beam acceptance is much larger than the injected beam size, so there is ample room for steering errors of the injected beam. It also shows that the four-sigma ellipse of the stored beam is far from the septum. Scraping four sigma's of the stored beam on the septum is about the point where as much stored beam is lost as injected beam is accumulated. The significant distance of the stored beam from the septum allows for orbit errors and safe margin for reliable injection into this lattice.

IV. Commissioning Results

The first attempt to inject into the LE lattice was made during a 24- hour period on April 23, 1991. Single electron pulses from the SPEAR injector were stored in the lattice with lifetimes on the order of hours, although beam accumulation was not achieved yet. A preliminary measurement of the emittance of the stored electron beam was made by digitizing the signal from a video camera aimed at the synchrotron light monitor (SLM) (see fig.6). The

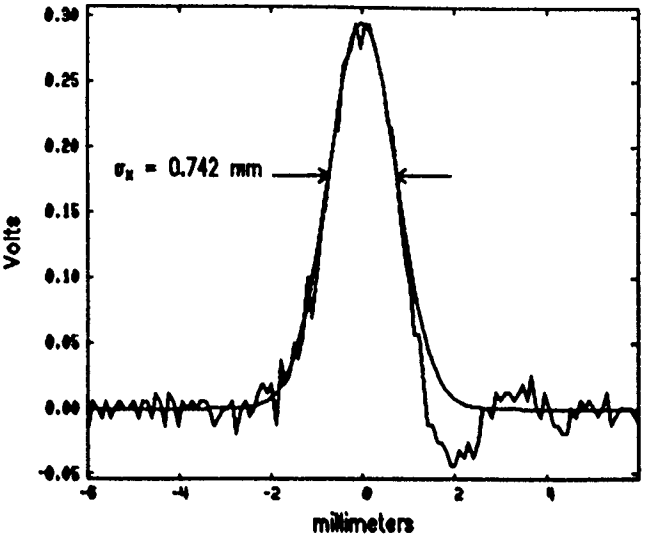


Figure 6
Emittance measurement of 83πnm*rad at 2.27 GeV in the LE SPEAR lattice.

horizontal betatron function at the SLM is β_x = 6.63 m, and correcting for the theoretical beam energy spread we derive from fig.6 an emittance of 83 πnm*rad at 2.27 GeV compared with a predicted emittance of 76 πnm*rad.

V. Acknowledgements

We greatly appreciate the support from the injector group, the SPEAR operators, S. Baird, M. Borland, R. Boyce, J. Cerino, M. Donald, L. Emery, H.D. Nuhn, and J. Sebek.

VI. References

[1] H. Wiedemann, "3 GeV Injector Synchrotron for Spear." At this Conference.
[2] A. Garren, M. Lee, P. Morton, "SPEAR Lattice Modifications to Increase Synchrotron Light Brightness." SPEAR Int.Note #193, April 1976.
[3] R. Liu, "A High-Beta Low-Emittance Configuration for SPEAR," SSRL-ACD 44, SSRL, February 1987.
[4] L.N. Blumberg et. al., "A Low Emittance Configuration for SPEAR," in *IEEE Part.Acc.Conf.*, May 1985.
[5] J. Safranek, "Low Emittance SPEAR: A Lattice and Injection Scheme," SSRL/ACD 77, SSRL, June 1989.
[6] K. J. Kim, "Brightness, Coherence and Propagation Characteristics of Synchrotron Radiation," LBL-PUB 20181, LBL, 1985.
[7] J. Murphy, "Synchrotron light source data book, version 2," BNL 42333, BNL/NSLS, 1990.
[8] H. Wiedemann, "High Brightness Lattice for SPEAR," SSRL-ACD 84, SSRL, September 1988.
[9] L. Emery, H. Wiedemann and J. Safranek SSRL-ACD 36, SSRL, June 1988
[10] M S Zisman, S. Chattopadhyay, and J.J. Bisognano, "ZAP User's Guide," LBL 21270, LBL, Dec. 1986.

Commissioning of the Phase I Superconducting X-Ray Lithography Source (SXLS) at BNL*

J.B. Murphy, R. Biscardi, J. Bittner, L.N. Blumberg, E. Bozoki, E. Desmond, H. Halama, R. Heese, H. Hsieh, J. Keane, S. Kramer, R. Nawrocky, T. Romano, J. Rothman, J. Schuchman, M. Thomas, J.M. Wang
National Synchrotron Light Source, Brookhaven National Laboratory, Upton, NY 11973

J. Krishnaswamy, W. Louie, R. Rose
Grumman Aerospace Corporation, Bethpage NY

Abstract

The goal of the SXLS Project at BNL is to design and construct a compact storage ring as a soft x-ray source for proximity printing x-ray lithography.[1] The final ring will operate at an energy of 700 MeV and it will make use of superconducting dipoles, B_0 = 3.87 Tesla and ρ = 60 centimeters, as a source of λ_c = 10 angstrom x-rays. The project is proceeding in two phases: in Phase I low field iron dipoles (B = 1.1 Tesla) are being used to study the ring at energies of 200 MeV and below; in Phase II the low field dipoles will be replaced with superconducting dipoles. The Phase I storage ring was commissioned during the fall of 1990 and the design current of 500 ma has been exceeded. A report on the performance of the Phase I ring is presented.

1. Storage Ring Lattice

To make the ring as compact as possible (C = 8.5 m), a two superperiod gradient FODO lattice incorporating two 180° combined function dipole magnets was adopted.[2] Since the basic lattice is a "one knob" design with only horizontally focusing quadrupoles and the defocusing sextupole designed into the poleface of the dipole, two sets of poleface windings were installed on the dipoles. One winding has quadrupole symmetry to permit variation of the vertical tune and the other has dipole/sextupole symmetry to provide for tuning of the vertical chromaticity. The quadrupoles are mounted on stepping motors and can be translated by ±3 mm both horizontally and vertically to provide closed orbit correction and there are also four sets of air core dipole orbit correctors. Four 12-pole magnets are also included to provide additional tuning capability.

The basic design parameters of the Phase I SXLS ring are listed in Table 1 and the Twiss parameters are shown in Figure 1.

Table 1: SXLS Phase I Design Parameters

Energy, E [MeV]	200
Circumference, C [m]	8.503
Dipole Magnet Type	EM
Dipole Field, B_0 [T]	1.1
Bending Radius, ρ [m]	.6037
Superperiods, N_s	2
Critical Wavelength, λ_c [A]	423
Horizontal Betatron Tune, ν_x	1.415
Vertical Betatron Tune, ν_y	.415
Energy Loss Per Turn, U_0 [KeV]	.234
Uncorrected Chromaticity, ξ_x,ξ_y	-.49, -1.32
Momentum Compaction, α	.32
Natural Emittance, ε_0 [m-rad]	5.92×10^{-8}

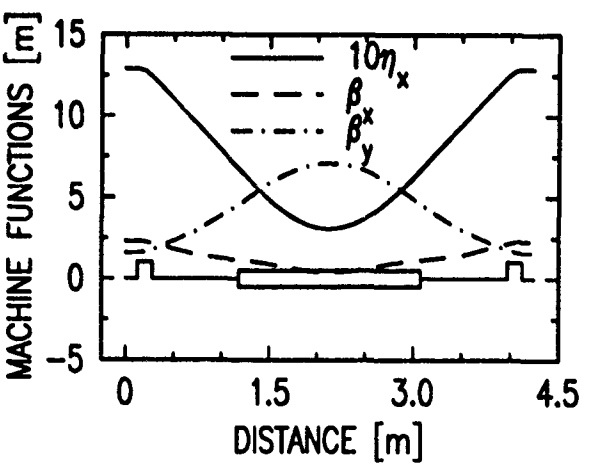


Figure 1: SXLS Optical Functions

2. Commissioning Results

The assembly of the Phase I ring was completed in late August 1990. The existing 80 MeV linac and booster ring at the NSLS serve as the injector for SXLS. A single bunch from the booster (52 MHz bucket) is injected into a 211 MHz bucket in the SXLS ring providing for 1 to 6 bunch operation. The injection system operates at 0.7 Hz. Injection rates of 2-5 ma per pulse are typical although rates of 7-10 ma per shot have been achieved quite frequently at 200 MeV operation. The novel injection scheme involves the use of a single fast kicker magnet[3], with a rise and fall time of 10 ns and a flat top of 50 ns, that gives two horizontal kicks to the stored beam and one kick to the injected beam.

* work performed under the auspices of the U.S. Department of Energy and funded by the U.S. Department of Defense

0-7803-0135-8/91$01.00 ©IEEE

The initial commissioning of the ring was done at 200 MeV. The first turn in the ring was recorded on September 14, 1990. Stored beam was obtained one month later. By mid December 1990 the design current of 500 ma in six bunches was achieved. A maximum stored current in excess of one ampere in six bunches was accumulated with 200 MeV injection (2/91).

At present (5/91) stored currents of 600 ma in six bunches and 200 ma in one bunch are routinely obtained at an injection energy of 200 MeV. For 160 MeV injection we can routinely store 500 ma in six bunches. We have also succeeded in storing 220 ma at an 80 MeV injection energy. With our present injection system, which is optimized for 750 MeV operation of the NSLS rings, it is difficult to fully explore energies below 160 MeV as there is little damping in the booster ring at these energies. Bypassing the booster and injecting the ring directly from the linac at energies of 80 and 120 MeV will be tried in the near future.

The horizontal closed orbit as measured on the PUEs is corrected to $x_{max} < 2$ mm using the air core trims and an outward displacement of the quadrupoles; the maximum vertical orbit deviation is $y_{max} < 0.75$ mm and this is the uncorrected orbit. The betatron tunes in the machine are nominally set at $\nu_x = 1.438$ and $\nu_y = 0.415$. The machine will store beam over a wide range of tunes; the operating point is chosen to maximize the injection efficiency. The chromaticities of the ring have been measured to be $\xi_x = +2$ & $\xi_y = +2$.

Instabilities are observed in the machine but a detailed analysis has not been performed so far. For large stored currents transverse motions of the beam can be observed on the synchrotron light monitor. There are strong synchrotron sidebands evident on the rotation and tune lines indicative of coupled bunch motion. At present we are not using any active feedback systems to stabilize the beam.

3. Vacuum System & Lifetime

The vacuum chamber straight sections are fabricated from stainless steel type 304L and the dipole chambers from INCONEL 625. An in-situ bakeout system is incorporated in the ring and has been used twice: once before commissioning started and again in Nov. 1990 after replacing a faulty vacuum window.

Vacuum pressures are monitored by ion gauges located just outside the entrance and exit of the dipole magnets. In the absence of beam the average pressure read by ion gauges is $P_{ave} \leq 1\times10^{-10}$ torr. Figures 2 & 3 display the average vacuum pressures versus current and beam current versus time respectively for several ring energies in six bunch operation. The stored beam lifetime can be obtained from Figure 3. For the data shown here it takes roughly 10-40 minutes for the current to decrease by 50%, with the longer lifetimes actually occurring at lower energies. An exact prediction of the lifetime at low energy is complicated by ion trapping, intrabeam scattering and anomalous bunch lengthening.

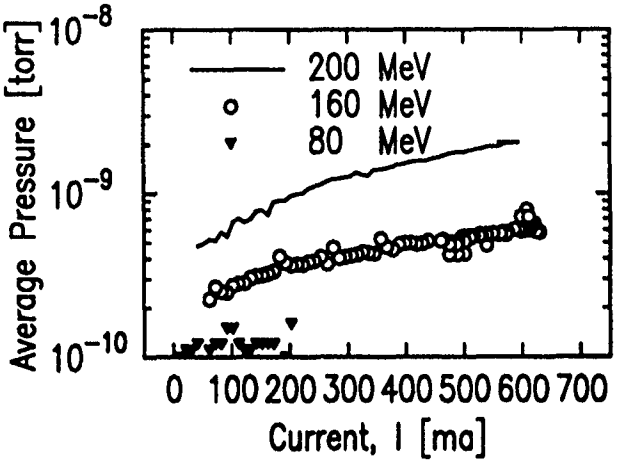


Figure 2: Pressure vs. Current [6 Bunches]

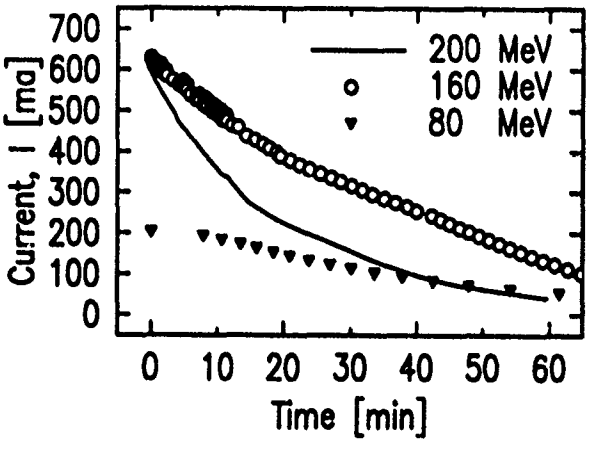


Figure 3: Current vs. Time [6 Bunches]

Major clean-up of the vacuum chamber was done by the stored beam as shown in Figure 4. About 20 amp-hrs at 200 MeV are required to finally condition the chamber during which time the ring pressure decreased by more than two orders of magnitude. To determine the recovery time from a vacuum accident a venting of the ring is planned in the near future.

4. Clearing Electrodes[4]

The vacuum chamber in the ring is equipped with fourteen clearing electrodes, five in each dipole magnet and two in each straight section. The electrodes are metal strips of approximately 20 cm in length located on the bottom of the chamber. They are terminated in their characteristic impedance by 50 Ω lossy cables and are capable of handling 5 KV.

In six bunch operation the clearing electrodes are necessary to reach stored currents in excess of 300 ma. Voltages in the range of 200-700 volts applied to six of the electrodes provides adequate clearing although powering only a single electrode enhances the achievable stored current. Ion clearing currents of 3 nanoamperes/100 ma

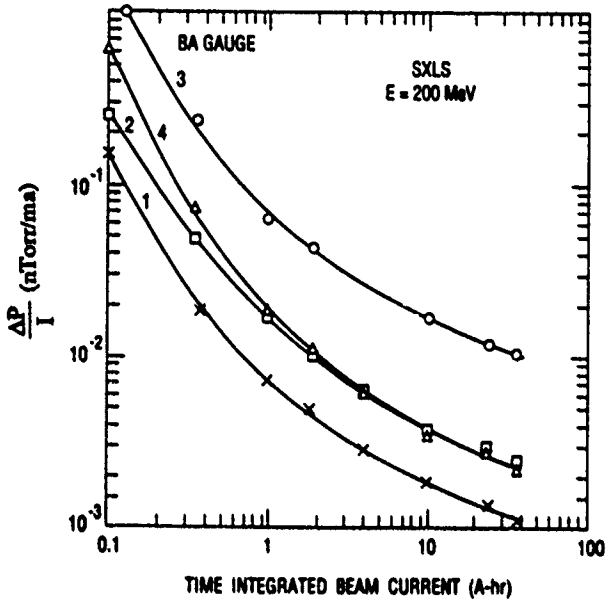


Figure 4: Normalized Pressure Change vs. Beam Dose

have been measured at ring energies of 100 MeV. Preliminary results on the effects of ions on the betatron tunes and the beam size are reported in reference [4].

5. RF System

The 211 MHz RF system is a single gap, capacitively loaded accelerating cavity driven in the TM01 mode and capable of producing a peak gap voltage of 50 kV. Figure 5 displays the measured synchrotron tune as a function of the RF voltage for 200 MeV operation. Gap voltages of 45 KV have produced the best injection rates. Transient beam loading from injecting up to 10 ma per shot has not been a problem. Throughout the commissioning the cavity has been the largest measurable source of outgassing.

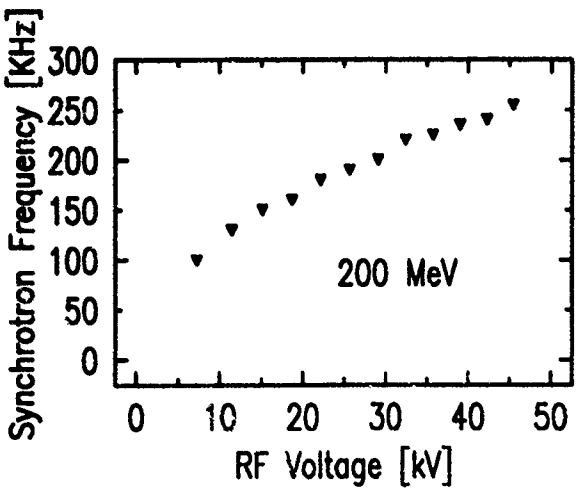


Figure 5: Measured Synchrotron Tune vs V_{RF}

6. Diagnostics

There are four fluorescent flags in the ring for establishing the injection orbit. Pick-up electrodes (PUE) have been built into the vacuum chamber to provide beam position information at six points around the ring. There is a set of four horizontal and vertical PUEs at each end of the two straight sections and a set of two PUEs (hor.) in each dipole. Beam positions in a single turn around the ring are determined by processing the PUE signals with hybrid networks and a Giga-sample/sec digitizing oscilloscope (LeCroy 7200). With stored beam the closed orbit is measured at a 5 Hz rate with dedicated beam position monitors. In addition to the PUEs, two sets of stripline electrodes have been provided, one for "kicking" the beam and the other for monitoring.

Beam current is determined by peak-detecting a rotation harmonic in a PUE sum signal. Transverse dimensions of the electron beam are measured by imaging the beam with a telescope on a CCD TV camera using the synchrotron light coming out of one of the dipole ports. During normal operations, the beam image is continuously displayed on a video monitor and can also be stored to disk with a frame grabber for further processing. Tune measurements are made using a 500 MHz network analyzer (HP 4195A), a wideband RF power amplifier and the striplines. Electronics for damping longitudinal beam instabilities is in the process of being commissioned.

7. Closing Remarks

The successful commissioning of the Phase I storage ring lays a solid foundation on which to build the Phase II superconducting dipole based ring. Ion clearing electrodes have been essential to storing large currents (I > 300 ma) in the ring. Studies will continue on the Phase I ring over the next year to enhance our understanding of the machine and to continue to lower the injection energy.

8. Acknowledgements

The SXLS group gratefully acknowledges the contribution of the NSLS operators, technicians & staff to the commissioning of the machine.

9. References

[1.] J.B. Murphy, et. al., Proc. 2nd EPAC, p. 1828 (1990).

[2.] J.B. Murphy & G. Vignola, editors, "SXLS Design Book", unpublished BNL report (1989).

[3.] R. Heese & T. Romano, this proc. (1991).

[4.] H. Halama & E. Bozoki, this proc. (1991).

Short Wavelength FELs*

Richard L. Sheffield
Los Alamos National Laboratory
Los Alamos, NM 87545

Abstract

The generation of coherent ultraviolet and shorter wavelength light is presently limited to synchrotron sources. The recent progress in the development of brighter electron beams enables the use of much lower energy electron rf linacs to reach short-wavelengths than previously considered possible. This paper will summarize the present results obtained with synchrotron sources, review proposed short-wavelength FEL designs and then present a new design which is capable of over an order of magnitude higher power in the extreme ultraviolet.

I. Introduction

Optical radiation below 200 nm has many potential uses [1]. The class of uses generally fall into two categories: basic research in such areas as biological processes, solid state physics, chemical processes, snapshots of temporially unstable targets, and photolithography for semiconductor processing. Biological studies include UV damage of DNA, Raman spectroscopy, and time resolved fluorescence spectroscopy. Solid state physics research covers ultra-high resolution photoemission from interfaces and surfaces, detectors, optics, and nonlinear harmonic generation. Chemical research include dynamics of highly excited states, gas-phase photochemistry, and surface photochemistry.

Advanced lithographic technologies require feature sizes of less than 0.25 microns [2]. Optical projection lithography is currently used with mecury lamps or excimer lasers and is the process of choice for semiconductor processing. Projection lithography below 0.25 microns was not thought to be possible because of the high power levels (10 to 100 watts) in the 10 to 100 nm wavelength band which is required for adequate wafer throughput. Consequently, large research sums have been spent on alternate technologies (such as x-ray transmission using proximity masks).

Electron synchrotrons can generate radiation from less than 0.1 nm to greater than 100 nm. Even though synchrotrons can produce a wide range of wavelengths, the output power in a narrow bandwidth is limited (Fig. 1) relative to that attainable by free-electron lasers (FELs). More of the above mentioned research applications require higher power levels than synchrotron sources either for increasing the signal to noise ratio or for multiphoton processes. Photolithography requires several orders increase in average power over synchrotrons. The increased power requirements have driven research into the use of free-electron lasers for the generation of short wavelength light.

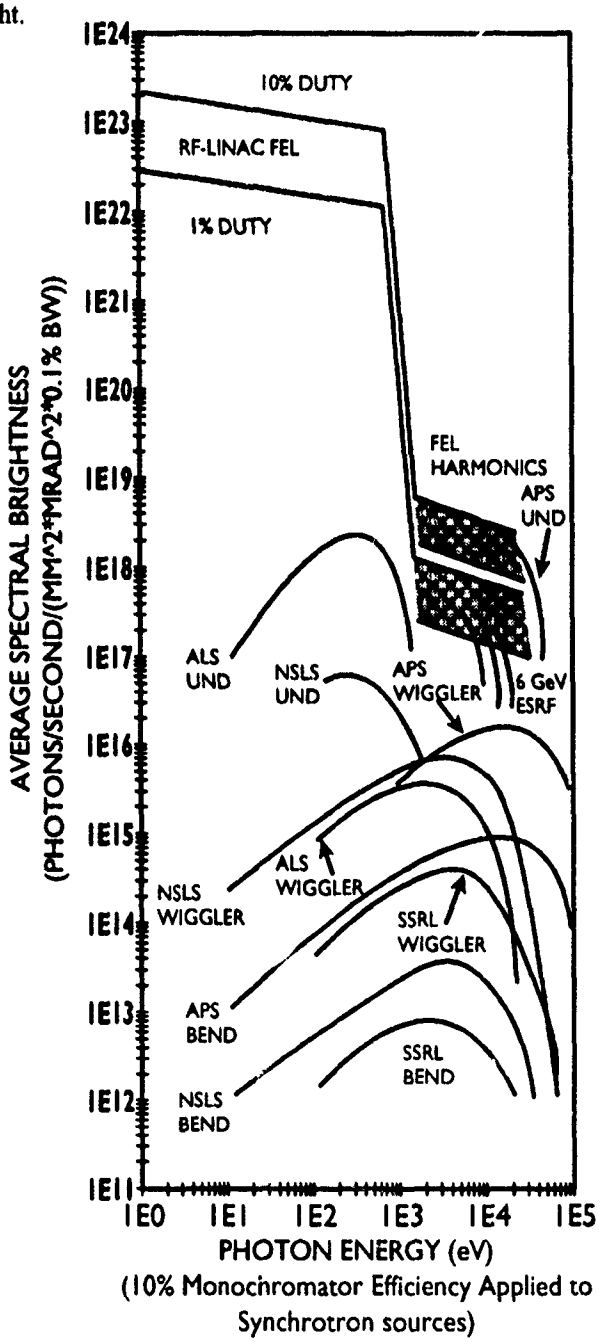


Figure 1. Time-average spectral brightness (delivered on target). Sources are: Stanford Synchrotron Radiation Lab (SSRL), National Synchrotron Light Source (NSLS) at BNL, Advanced Photon Source (APS) at Argonne, Advanced Light Source (ALS) at LBL, and European Synchrotron Radiation Facility (ESRF) at Grenoble.

*Work supported by Los Alamos National Laboratory Institutional Supporting Research, under the auspices of the United States Department of Energy.

0-7803-0135-8/91$01.00 ©IEEE

II. Free-Electron Lasers

A free-electron laser (FEL) converts electron beam energy into a highly collimated, high-power beam of light by stimulated emission. An FEL produces an laser beam of good optical quality and narrow bandwidth and is tunable over a wide wavelength range. A schematic of an rf linac based FEL in an oscillator configuration is shown in Fig. 2. The essential components of an FEL are the electron accelerator and a transversely-oscillating magnetic field (called a wiggler or undulator depending on the magnitude of the on-axis magnetic field). The magnetic field initially causes the electron beam to oscillate, thereby generating spontaneous optical radiation. Later in the process, the magnetic field couples the electron beam motion to the optical field which has built up in the optical resonator for an FEL oscillator or the amplifier wiggler for an FEL amplifier. This motion forces the electrons to do work against the optical field, further increasing the energy in the optical radiation. The performance of the FEL depends to a large degree on the brightness of the electron beam and the wiggler design. Because of recent improvements in the design of electron sources [3]-[4], FELs can now operate in the extreme ultraviolet and soft x-ray regime at relatively low energies (<1 GeV). Since the wavelength of the radiation from the FEL is proportional to the wiggler period, significant research effort is being directed to the design of shorter-period wiggler fields [5]-[7].

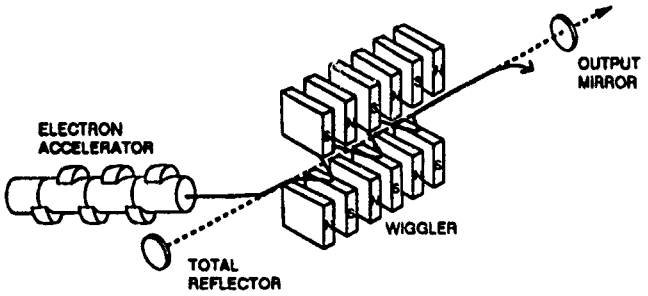


Figure 2. Basic components of a rf linac FEL.

Short-wavelength free-electron lasers fall into two categories: rf linac based and storage ring based. I will briefly describe representative FEL designs for both of the categories.

III. RF Linac FELS

The rf linac category can be divided into two approaches based on the type of FEL optical system used. The two approaches are an optical resonator and a single pass amplifier. In an optical resonator, the light recirculates in a resonator so that the optical power can build up to very high levels, increasing the electron beam to light extraction efficiency. However, mirrors have very low reflectivity in the sub-100 nm region and thus the optical gain must be very high to overcome resonator losses. In an amplifier, the light is single pass and so there are no resonator losses, but the wiggler must be very long (approximately twice as long as in an oscillator) to allow the light to build up to high power levels.

Brian Newnam of Los Alamos National Laboratory has proposed an extreme ultraviolet (XUV) FEL operating down to 1 nm [8]. A system schematic is shown in Fig. 3. The system consists of a single linac driving seven different oscillators, each oscillator producing a different wavelength. Over certain wavelength regions, normal incidence optics have sufficient reflectivity to be used as resonator mirrors [8]. From 60 to 100 nm, polished chemically-vapor-deposited (CVD) silicon carbide exhibits 40 to 50% reflectance at normal incidence. From 80 to 100 nm, unoxidized aluminum films go from 40% to greater than 90% reflectivity. From 10 to 20 nm, Mo and Si multilayer reflectors have between 40 to 50% reflectivity. At the present time, normal incidence optics do not exist for the wavelengths between 20 to 60 nm and below 10 nm. To provide

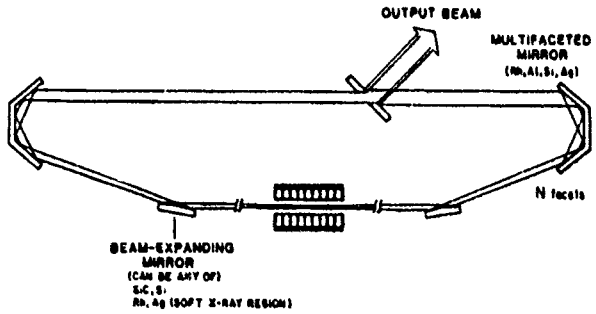


Figure 4. Multifaceted, all-metal mirror grazing-incidence ring resonator. The light from the wiggler first reflects from hyperboloidal mirrors which causes the beam to diverge to reduce thermal distortion of the multifaceted mirrors.

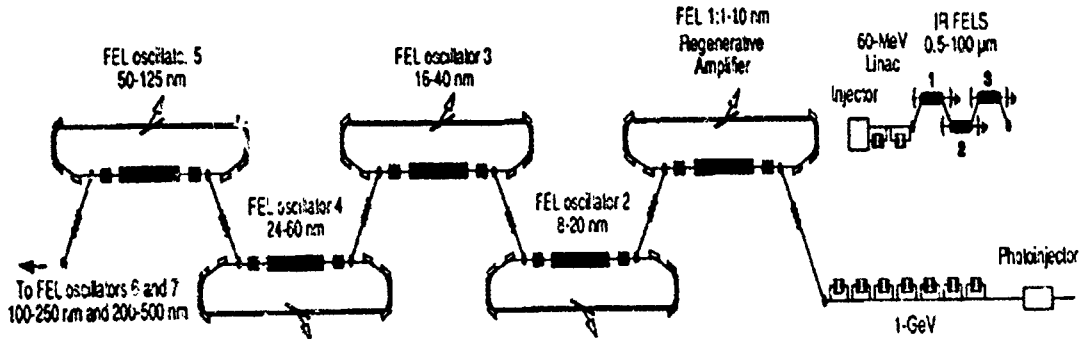


Figure 3. Proposed Los Alamos XUV FEL National User Facility.

mirrors for the remaining wavelengths and to reduce beam-induced thermal distortion of the mirror surfaces, Newnam has proposed a ring resonator with multifaceted mirrors [9], schematically shown in Fig. 4. This mirror system uses the increase in reflectance (greater than 95% per surface at these wavelengths), enabled by total external reflection. The machine parameters are: maximum beam energy of 1 GeV, peak currents of 300 to 400 A, normalized 90% emittance (the 90% emittance = 4 ξ the rms emittance) of <30 π mm-mrad, and a 0.1% energy spread. The wiggler is 5 m long for 50 nm and 12 m long for 4 nm with a wiggler period of 1.6 cm.

The other rf linac designs operate in an FEL amplifier configuration. Two representative designs, one from Brookhaven National Laboratory (BNL) and the other from University of California at Los Angeles (UCLA), follow.

BNL has proposed a Ultraviolet Free-Electron Laser User Facility [10] to be used in conjunction with the National Synchrotron Light Source (NSLS). This FEL operates as an injection-locked amplifier with the seed radiation produced by a conventional tunable laser. A schematic of the system is shown in Fig. 5. The major system features are a photoinjector electron source, a superconducting recirculating linac, and two FEL amplifier beamlines. The repetition rate for the electron pulses from the accelerator is 1 kHz. Each amplifier beamline operates at 0.55 kHz and the output optical pulses from the amplifiers have an adjustable relative timing with respect to each other. The output optical pulses from each amplifier will be split between two experimental stations by rotating mirrors. The machine offers low energy spread (0.1%) and short pulse durations (possibly down to 200 fs). The machine parameters are: 250 MeV final energy, peak current of 300 A, normalized 90% emittance of 32 π mm-mrad, and an energy spread of 0.1%. The wiggler is composed of a short (2.5 m) subharmonic wiggler with 3.5 cm period and a longer (11 m) main wiggler with a 2.2 cm period. The main wiggler has a 4.5 m section which has a 1.2% taper. Research is also presently being conducted on a superconducting wiggler with a 8.8 mm period. At 100 nm, the calculated average power is 1 watt.

At UCLA, an x-ray linear light source (LLS) has been proposed [6]. In this design, very high accelerator gradients (near 200 MeV/m) are used to reduce the overall machine length. To attain the very high gradients, a high frequency (10-30 GHz) accelerator structure is driven by a relativistic klystron, under development by LLNL/LBL/SLAC [11]. A schematic of the relativistic klystron and its induction linac driver is shown in Fig. 6. The FEL designs are based on self-amplified spontaneous-emission (SASE).

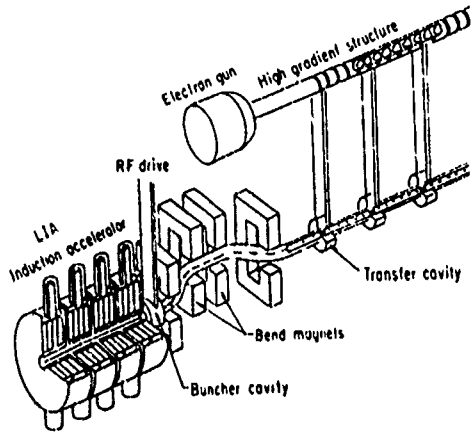


Figure 6. Relativistic klystron driver for UCLA XUV machine.

IV. Storage rings

Another technique for producing short wavelength light is to use storage rings with long straight sections for an FEL oscillator. Proposals have been made by Stanford University [12] (work on this proposal is proceeding at Duke University) and University of Dortmund [13].

The Stanford design is based on a 1 GeV storage ring. A schematic of the machine is shown in Fig. 7. In the long straight section is space for a 27 m long undulator. A 1 GeV linac will inject electrons into the ring at full energy. Alternately, positrons will be injected to increase the lifetime of the stored

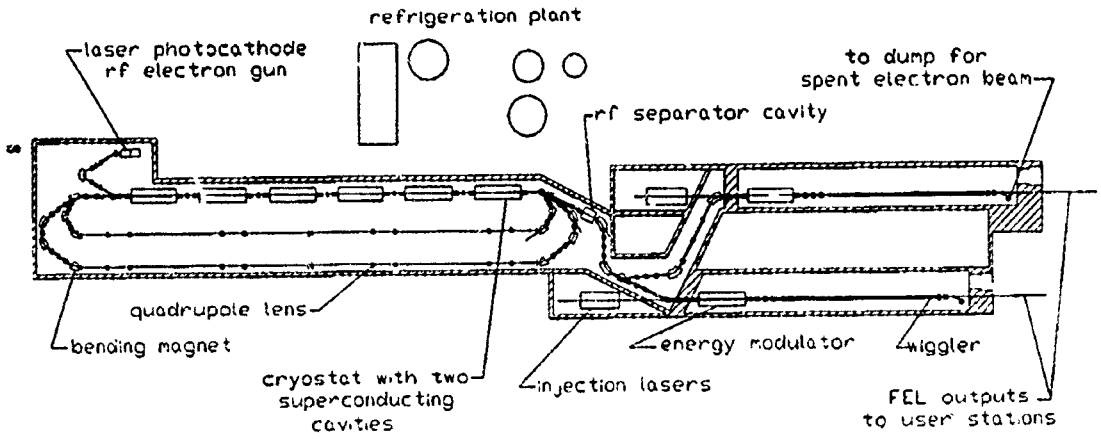


Figure 5. Proposed BNL UV FEL.

beam. In an FEL, electrons gain an energy spread as the electrons interact with the optical field. In storage rings, the induced energy spread is then damped by synchrotron radiation losses with an ~10 ms time constant. The peak current in this design is 270 A with a 90% normalized emittance of 170 π mm-mrad. The machine is designed to produce optical radiation from greater than 100 nm to less than 30 nm.

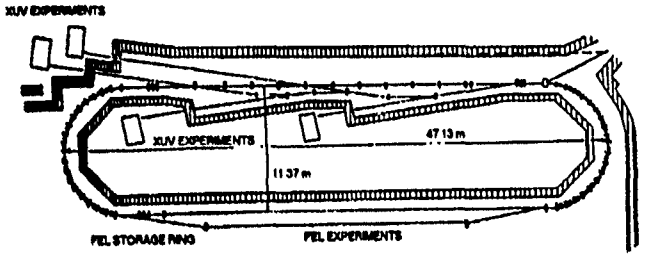


Figure 7. Schematic of Stanford University's 1 GeV storage ring.

The storage ring at the University of Dortmund is called DELTA. The ring has a maximum energy capability of 1.5 GeV. A schematic of the machine is shown is Fig. 8. The DELTA lattice was optimized for FEL operation. Two straight sections approximately 20 m long with zero dispersion and with nearly constant beta functions are available for insertion devices. The ring has a low 90% normalized emittance of 40 π mm-mrad at 1 GeV, short damping time (~ 0.2 s), high peak currents (180 A), and long beam lifetime. The machine is designed to produce optical radiation from 400 nm to 25 nm.

V. Compact Short-Wavelength FEL

A study at Los Alamos National Laboratory was started to determine if a (relatively) small, less costly XUV FEL is now possible using the advances in FEL system components in the last several years. In particular, significant developments have occurred in high-brightness electron linacs [14] and short-

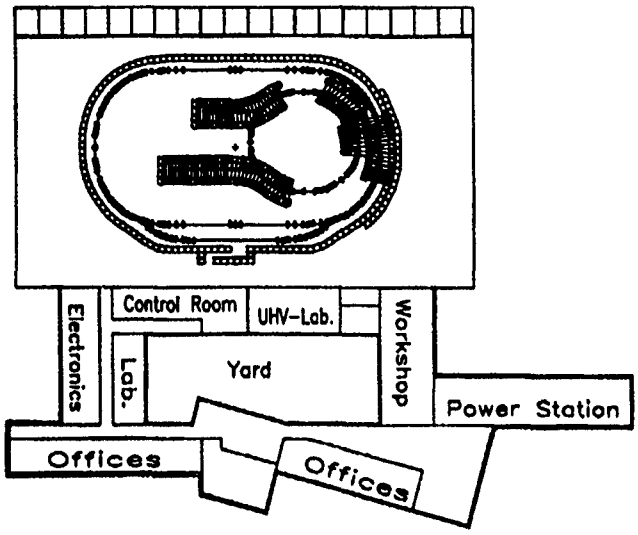


Figure 8. Layout of the Dortmund storage ring, showing the linac, the full-energy booster and the main storage ring.

wavelength wigglers [15]. This study is directed at providing a machine for photolithographic processing applications. The design follows from the Advanced Free-Electron Laser Initiative (AFELI) at Los Alamos National Laboratory.

The AFELI program goals are to build an Advanced FEL (AFEL) using a high-brightness electron beam and a microwiggler, while minimizing size and cost. A schematic of the AFEL is shown in Fig. 9. Extensive linac design calculations have been made using a modified version of PARMELA. This version of PARMELA directly incorporates files from POISSON, MAFIA, and SUPERFISH [16] to accurately describe the field distributions in the accelerator. The electron beam parameters are: 20 MeV final energy, 200 to 300 A peak for 10 ps, and a 90% normalized emittance of less than 15 π mm-mrad. Only those electrons in the middle 75% of the pulse in time contribute to the FEL interaction (the temporal wings do not interact). The

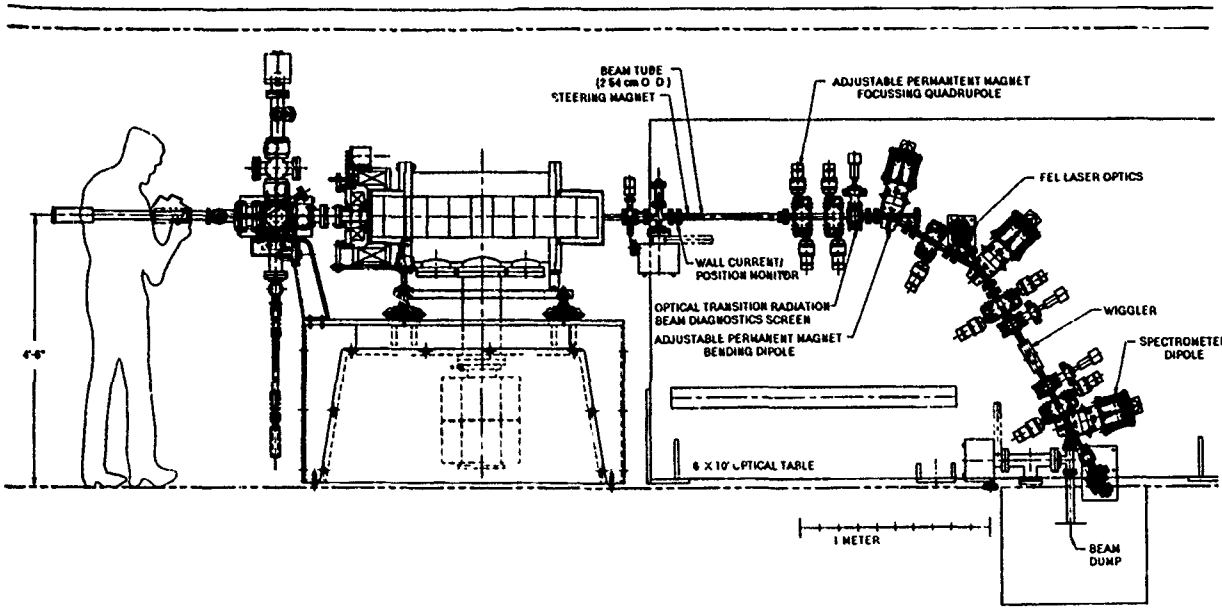


Figure 9. Schematic of the AFEL experiment, showing linac, beamline, and FEL resonator.

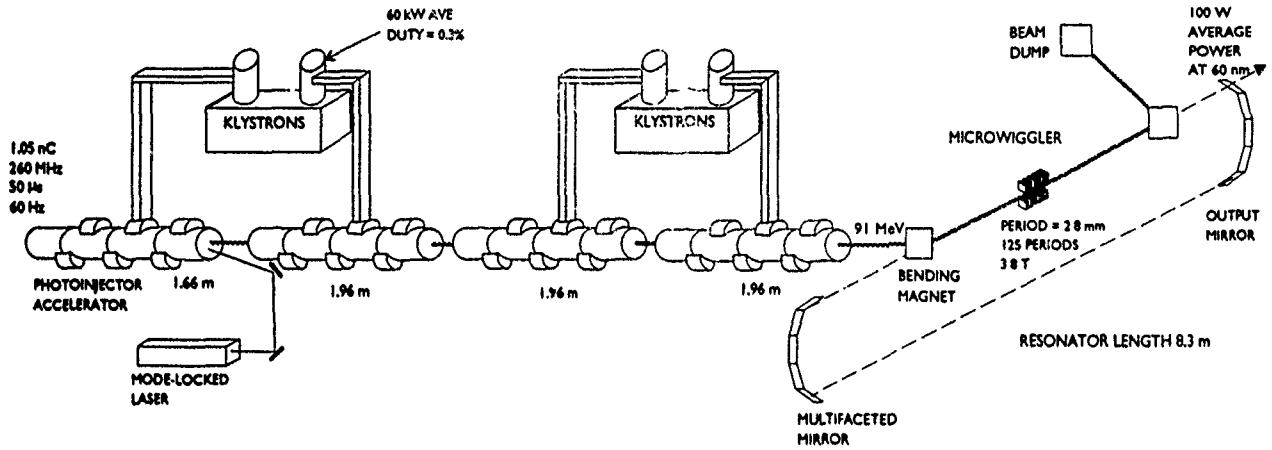


Figure 10. Schematic of a XUV FEL based on the AFEL system design.

emittance of just the middle 75% of the pulse is less than 8 π mm-mrad. The accelerator is 1.2 m long giving a true gradient of 18 MV/m. The calculated gain (with the FEL code FELEX) for the 3rd harmonic of a 3 mm period pulsed wire wiggler is greater than 50% at 390 nm. Accelerator operation is scheduled to begin in the first half of 1992.

Based on the AFEL system, an XUV FEL was designed [17]. The XUV FEL schematic is shown in Fig. 10. The base line design for a 60 nm machine is: 91 MeV final energy, 1 nC micropulse charge, 0.13 A average current, and 160 A peak current. The accelerator is driven by four Thomson CSF 2022E 20-MW 1300-MHz klystrons operated at 60 Hz with a 0.3% duty factor. The overall accelerator length is 8 m. The pulsed wire wiggler has a period of 2.6 mm and is 35 cm long. The optical resonator uses multifaceted reflector optics and is approximately 8 m long. The calculated output power is 100 W at 60 nm.

VI. REFERENCES

[1] Numerous workshops have been held on XUV applications. For detailed information consult the following: *Los Alamos Workshop on Applications of Free-Electron Lasers*, Deacon, D. A. G. and De Angelis, A., eds., Nucl. Instr. and Methods in Phys. Res., A239, pp.371-443; *Los Alamos Workshop on Appplications of Coherent Extreme-Ultraviolet Radiation*, Newnam, B. E., ed., LANL report DRP/DEW-FEL-86:19, 1986; *Report from the NSLS Workshop*, E. D. Johnson and J. B. Hastings, Eds., BNL report 45499,1990.

[2] B. E. Newnam, "Development of Free-Electron Lasers for XUV Projection Lithography," *SPIE Conf. on Free Electron Lasers and Appl.*, **1227**, 1990.

[3] J. S. Fraser and R. L. Sheffield., "High-Brightness Injectors for RF-Driven Free-Electron Lasers," *J. Quantum Electron.*, **QE-23**, pp. 1489-1496, 1987.

[4] K. Batchelor, H. Kirk J. Sheehan, M. Woodle, and K. McDonald, *Proc. Europ. Part. Accel. Conf.*, Rome, Italy, 1988.

[5] R. L. Sheffield, J. H. Booske, B. Danely, K. Halbach, B. Jackson, J. Slater, A. Toor, P. Walstrom, and R. W. Warren, "Workshop Results on Small-Period Wiggler Designs," LANL Report LA-UR-89-2851, 1989.

[6] D. R. Cline, "Development of a Compact X-ray Linear Light Source and FEL at UCLA," *Proc. of the 11th Int. Free Electron Conf.*, Nucl. Instr. and Methods, **A296**, pp. 814-821, 1990.

[7] K. Batchelor, I. Ben-zvi, R. Fernow, J. Gallardo, H. Kirk, C. Pellegrini, and A. Van Steenbergen, "A Microwiggler Free-Electron Laser at the Brookhaven Accelerator Test Facility," Nucl. Instr. and Methods in Phys. Res., A296, pp. 239-243, 1990.

[8] B. E. Newnam, "Free-Electron Laser sources of Extreme-Ultraviolet Radiation and their Vacuum Requirements," *Proc. of the 2nd Int. Conf. on Vacuum Design of Advanced Synchrotron Light Sources*, AIP Conf. Proc., November 13-15, 1990.

[9] B. E. Newman, "Multifacet Metal Mirror Design for Soft X-Ray and Extreme-Ultraviolet Free-Electron Laser Resonators," *Laser Induced Damage in Optical Materials 1985*, H. E. Bennett, A. H. Guenther, D. Milam, and B. E. Newnam, Eds., NBS Spec. Publ. 746, pp. 261-269, 1988.

[10] Brookhaven National Laboratory, draft internal report "UV FEL 2".

[11] A. M. Sessler et. al., Phys. Rev. Lett. **58**, pp. 2439, 1987; W. Allen et al., *Proc. Eur. Particle Accelerator Conf.*, 1988.

[12] H. Wiedemann, Int. Conf. Insertion Devices for Synchrotron Sources, Proc. SPIE **582**, pp. 156-162, 1986; J. E. La Sala, D. A. G. Deacon, and J. M. J. Madey, "Performance of an XUV FEL Oscillator on the Stanford Storage Ring,", Nucl. Instr. and Methods in Phys. Res., **A239**, pp. 262-273, 1986.

[13] N. Marquardt, *Proc. 1989 Part Accel Conf.*, 2, pp 780-782, 1989; D. Nolle, F. Brinker, M. Negrazus, D. Schmitz, and K. Wille, "DELTA, A New Storage-Ring-FEL Facility at the University of Dortmund," Nucl. Instr. and Methods in Phys. Res. **A296**, pp. 263-269, 1990

[14] R. L. Sheffield, "Photocathode RF Guns," *Physics of Particle Accelerators*, AIP Conf. Proc. 184, Vol. 2, pp. 1500-1531, 1989.

[15] R. W. Warren, D. W. Feldman, and D. Preston "High-Field Pulsed Microwigglers," Nucl. Instr. and Methods in Phys. Rev. Res. , to be publ., 1990.

[16] For further information on these codes, see *Computer Codes for Particle Accelerator Design and Analysis A Compendium*, H. S. Deaven and K. C. D. Chan, eds., publ. by Los Alamos Accelerator Code Group, Report LA-UR-90-1766, 1990.

[17] Private communication with Richard Cooper, Los Alamos National Laboratory.

Initial Operation of the Vanderbilt Free Electron Laser *

Perry A. Tompkins, Foorood Amirmadhi, K. Becker, C. A. Brau, W. D. Andrews,
Dept. of Physics and Astronomy, Vanderbilt University, Nashville TN 37235

Marcel R. Marc
5038 Bell Estos Dr., San Jose CA 95124
and
J. Kiaie
517 Hillside Blvd., S. San Fransisco CA 94080

Since their inception in the mid 1970's Free Electron Lasers (FELs) have proven to be unique light sources. For many applications, the problems caused by the complexity of the FEL is greatly outweighed by its flexibility as a research tool. In 1987 Vanderbilt University committed itself to the development of a user-intensive FEL research facility. This facility will be available to Vanderbilt and other institutions to conduct research in Biomedicine and Materials Science. This FEL incorporates a 45 MeV traveling-wave linac with a 2.3 cm period, Halbach-type, permanent magnet wiggler. In the initial configuration this system will selectively lase within the range of 2-8 μm. It will operate with a 0.05% duty factor and with an average power of ~6W. The FEL assembly was completed during the winter of 1990-91. Testing and operation of the FEL were subsequently initiated. The initial operation and performance of the FEL are reported at this time. It is expected that the laboratory will become available for research by users during summer 1991.

1. Introduction

As in more conventional lasers, FELs create coherent, monochromatic, light by stimulated emission amplification[1]. The interaction of an electron beam with specialized magnetic fields replaces the conventional laser medium. Due to the tunability of magnetic field strength and electron-beam energy, the FEL is continuously tunable over wide ranges of the spectrum. The available field strengths and electron-beam characteristics allow FELs to operate in unlased parts of the spectrum and avails to very large beam powers. By combining this tunability with operation on the harmonics it has been possible to tune several FELs over more than an order of magnitude in wavelength[2]. This distinguishes them as the most broadly tunable laser available.

Vanderbilt has successfully operated its new FEL at several frequencies. Spectral data, power measurements and operational stability are discussed in this paper.

2. The FEL System

The Vanderbilt University FEL was built and installed by Sierra Laser Systems. This laser is a compact, predominantly infrared, FEL. It is similar to the Stanford University Mark III FEL[3]. The FEL is controlled by three local STD bus, IBM-type computers located in the klystron equipment racks. These computers communicate via Arcnet with the operator interface computer located in the control room or in one of the experimental laboratories. The operator computer is a SUN Microsystems 386i workstation. The computer control software was partially supplied by Sierra in cooperation with researchers at Vanderbilt.

The electron beam is produced by an rf travelling-wave electron linac operating at 2.856 GHz. This beam is created in an rf-extracted electron gun with a LaB6 cathode[4]. The ~1 MeV beam is then transported through an alpha magnet that compresses the pulse temporally and clips the energy tails[5]. After the alpha magnet, the beam is transported to the entrance of the accelerator. The maximum energy of the rf linac is ~45 MeV. The electron beam parameters are displayed in Table 1.

The wiggler is a 2.3 cm period, Halbach type, hybrid design, using permanent magnets with steel pole pieces. The wiggler parameters are shown in Table 1. There are 208 SmCo permanent magnets used in the wiggler.

Table 1 also shows the expected laser performance. Tuning of the electron energy and the wiggler field strength will allow lasing from 2 to 8 μm. To lase below 2 μm the laser cavity length will be moved to the proper length to facilitate lasing on the third harmonic of the fundamental. More extensive modifications discussed later in this paper will allow lasing

Table 1. Operation Parameters of the Vanderbilt University Free-Electron Laser.

Accelerator:	
Maximum electron energy (MeV)	45
Micropulse peak current (A)	20-40
Macropulse average current (mA)	100-200
Energy spread (%)	0.5
Horizontal Normalised emittance ($\pi mm \cdot mrad$)	4
Vertical Normalized emittance ($\pi mm \cdot mrad$)	10
Wiggler:	
Type	Hybrid
Length (cm)	120
Wiggler Period (cm)	2.3
Number of magnets	208
Type of magnet	SmCo
Magnet energy product (kJ/m^3)	180 - 210
Maximum rms wiggler field (T)	0.47
Laser:	
Wavelength (μm)	1 - 8
Micropulse peak power (MW)	0.5 - 2
Micropulse duration (ps)	0.5 - 3
Micropulse energy (μJ)	1 - 4
Micropulse repetition rate (GHz)	2.856
Macropulse average power (kW)	5 - 25
Macropulse duration (μs)	0.5 - 8
Macropulse energy (mJ)	1 - 200
Macropulse repetition rate (Hz)	0 - 60
Overall average power (W)	0 - 6

* Work supported by the Office of Naval Research under contract N00014-87-C-0146

0-7803-0135-8/91$01.00 ©IEEE

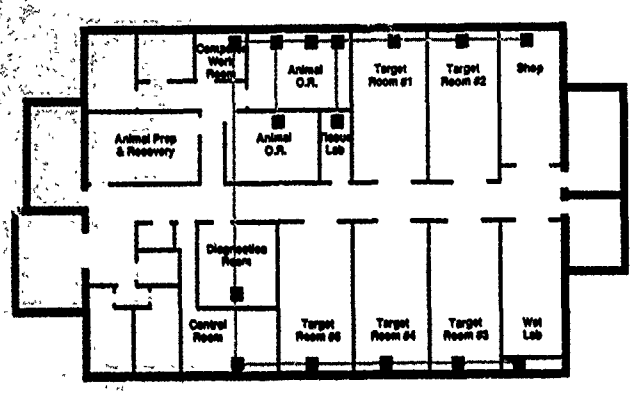


Figure 1. Plan view of the laboratory level of the Vanderbilt University FEL facility.

in different regimes of the spectrum.

The laser is housed in the second basement or vault of the Vanderbilt FEL center. This building is in immediate proximity with the Medical School, Engineering School and the Physics, Chemistry and Biology Departments. The laser light is brought up to the first basement and distributed to the laboratories via an optical beam delivery system(figure 1.) The laboratory level includes a beam-diagnostic room, control room, five laser target rooms, a medical suite and support rooms. The medical suite includes two operating rooms, locker rooms, a computer work room and an animal care facility. Initially, one operating room will be equipped with an articulated arm beam delivery system to manipulate the laser during surgery.

3. The Applications Program

The FEL center at Vanderbilt University is intended to be a national resource for bio-medical and materials science research. Presently six schools and departments at Vanderbilt are collaborating in a broad-based research program. In the future, the program will expand to include users worldwide.

The core applications are characterized by close relationships between experiments. There is also a large degree of collaboration between the scientists on various projects. The experiments on materials science concentrate on the interaction of the FEL light with optical materials, crystals, mammalian tissue, and adsorbates on surfaces. In biophysics, there will be experiments on the vibrational spectroscopy of biopolymers such as DNA, and the effect of crosslinking of RNA on the synthesis of proteins in cells. Molecular biology experiments will explore the dynamics and function of different components of cell membranes. Surgery and medical imaging will be the initial focus of the medical applications portion of the program.

The center also will support a broad group of external users. Research proposals will be accepted in medical research, biology and materials science. Presently several well known scientists have expressed interest in coming to Vanderbilt to do research.

4. Initial Results

The electron and optical-beam parameters of the initial operation of the Vanderbilt FEL program are shown in Table 2. We have observed laser operation at 2.5 μm and at 4.4 μm. The maximum power observed at the second wavelength was 11 kW during the macropulse. The electron energy measurement was obtained by simple dipole deflection from a calibrated steering coil. The current was measured by a beamline current toroid. The optical power of the laser pulse was determined using a calibrated pyroelectric energy meter. The wavelength and spectrum data were obtained using

Table 2: Operation Parameters of Initial Vanderbilt FEL Lasing.

Initial Lasing:	
Electron beam energy (MeV)	42±7
Electron beam pulse length (μs)	~6
Accelerator repetition rate (Hz)	5.4
Electron peak current (mA)	180
Lasing wavelength (μm)	2.53
Laser pulse duration (μs)	~2
Laser energy per pulse (mJ)	15
Corresponding peak power (kW)	8
Most recent data:	
Electron beam energy (MeV)	42±7
Electron beam pulse length (μs)	~6
Accelerator repetition rate (Hz)	10.1
Electron peak current (mA)	190
Lasing wavelength (μm)	4.4
Laser pulse duration (μs)	~2
Laser energy per pulse (mJ)	22
Corresponding peak power (kW)	11

a McPherson 0.3 m monochromator and a gold-doped germanium detector.

Figure 2a shows the most recent spectrum of the laser at 4.4 μm. The shoulder on the low wavelength side of the peak was not understood initially. By taking an expanded spectrum, figure 2b, it was determined that the laser was lasing at two different frequencies. By setting the monochrometer at each peak, and looking at the laser intensity during the macropulse, it was determined that the laser was initially lasing at the longer wavelength, shutting off, and re-starting at the shorter wavelength. It is believed that this behavior is due to a slewing of the energy during the macropulse. This slewing could be easily caused by self-heating of the cathode, thus changing the energy of the electrons into the alpha magnet. The path of the electrons would also change and thus the phase between the gun and the accelerator would be affected. Figure 3 shows the laser intensity during the macropulse when the [illegible] was slightly reduced. This shows the laser cycling on and off three times.

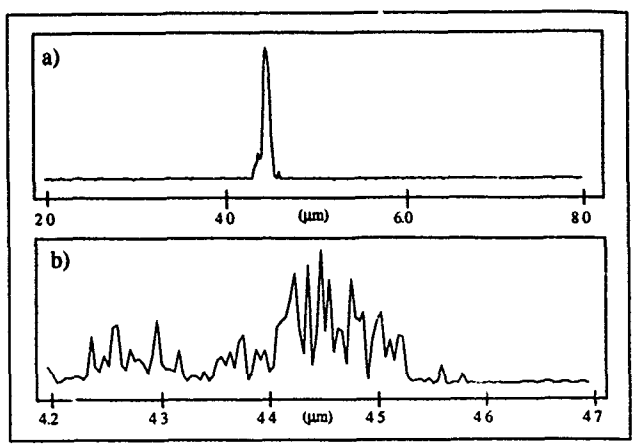


Figure 2. Initial spectrum of the laser operation a) shows the spectrum from 2.0 to 8.0 μm b) shows expansion of a) from 4.2 to 4.7 μm. This spectrum shows lasing at two different frequencies

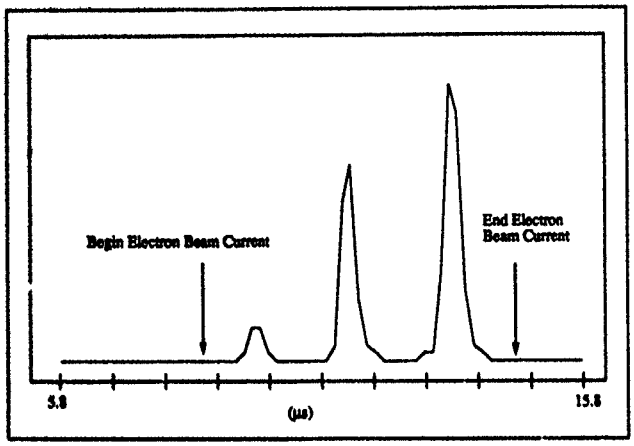


Figure 3. Laser intensity during macropulse. Begining and ending of electron beam current are labeled. The three peaks show the laser cycling on and off during the macropulse.

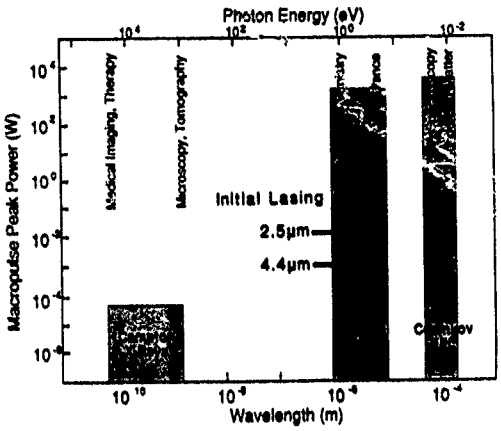


Figure 4. Available power versus available wavelength for the Vanderbilt free electron laser center. This plot includes the machine upgrades that are presently funded.

5. Present Expansions

Bringing the laser to design performance is the main thrust of the Vanderbilt FEL team at this time. Work has also begun on many improvements to the basic laser system to broaden the functionality of the center.

In order to reach the longer wavelengths in the far infrared, a Cerenkov resonator will be built and installed on the beamline after the wiggler. This will allow lasing in the wavelength region from 50 to 200 μm. A Cerenkov FEL operates by interacting an electron beam with a travelling electromagnetic wave. The phase of the e-m wave is synchronised to the electron velocity by use of a dielectric-loaded waveguide[6]. The micropulse peak power is predicted to be of the order of 10MW.

Using an alternate electron beam line that will start after the wiggler, the electron beam can be directed toward a secondary beam chase that leads to the laboratory level. By transporting the laser light to collide with the electron beam, intense, monochromatic, yet incoherent, X-rays can be created with Compton backscattering[7]. After the interaction, the electrons are returned to the beam line just before the beam dump. These X-rays are important for a variety of applications including microscopy, medical imaging and therapy. The X-ray facility will initially operate at wavelengths from 3nm (40 eV) to 0.06 nm (20 keV.) Figure 4 shows the available power versus the available spectrum for the Vanderbilt FEL center.

Incorporation of laser-irradiated cathodes will be another important modification to the present gun configuration. This will include laser heated cathodes and photoelectric cathodes. This improvement will allow greater control over the FEL pulse structure and will increase the beam brightness and therefore FEL gain. Other improvements will facilitate shorter macropulses, shorter wavelengths and shorter micropulses.

6. Conclusions

The Vanderbilt University free electron laser facility has begun operation. While the initial data are sparse the operation of the machine is improving. Further analysis of the energy slewing is presently being accomplished. Other than excessive delays due to parallel debugging of the computer system and the FEL, the project has progressed nominally. This summer, the facility will be made available to the initial users This center is expected to become a national resource for research in biomedical and materials science research With the facility upgrades that are planned, this FEL center will offer a powerful array of wavelengths, pulse structures and beam powers for a myriad of experiments

8. Acknowledgements

The authors wish to express their gratitude to many who have assisted in the initial startup of the Vanderbilt free-electron laser project. The assistance from John Madey, Steve Benson and Eric Szarmes of Duke University was critical to achieve lasing. The technicians at Vanderbilt, Scott Degenhardt and Rick Grant and those at Sierra Laser were instrumental in completing this project. We would like to recognise the outstanding efforts of Mike Cox in the construction and assembly of the system. Greatly appreciated was the assistance from Vanderbilt's "CAMPS" group for obtaining the spectra. We would also like to express our gratitude to Terry King at Vanderbilt and Mark Wilson of NIST for their assistance in this project. Finally we would like to thank Roger Fenner and Danny Anglin of the Vanderbilt University radiation safety office for their extensive support during the commissioning of the machine.

7. References

[1] C. A. Brau, *Free-Electron Lasers*, Academic Press, Boston, 11 (1990).

[2] B. E. Newnam, *et al.*, IEEE J. Quant. Electron. **QE-21**, 867 (1985).

[3] S. Benson, *et al.*, J. Laser Applications 1 (July), 49 (1989).

[4] G. A. Westenskow and J. M. J. Madey, Laser and Particle Beams **2 pt. 2** 223 (1984).

[5] Harald A. Enge, Rev. of Sci. Ins. **34 no. 4** (April) 385 (1963).

[6] J. E Walsh and J. B. Murphy, J. Quant. Electron. **QE-18**, 1259 (1982).

[7] J. Gea-Banacloche, *et al.*, IEEE J. Quant. Electron. **QE-23** (Sept) 1158 (1987).

Spectrum of Coherent Synchrotron Radiation

T. Nakazato, M. Oyamada, N. Niimura, S. Urasawa, Y. Shibasaki, R. Kato and S. Niwano,
Laboratory of Nuclear Science, Tohoku University
Mikamine, Taihaku-ku Sendai, 982, JAPAN
M. Ikezawa, T. Ohsaka, Y. Shibata, K. Ishi, T. Tsutaya, T. Takahashi, H. Mishiro and F. Arai,
Research Institute for Scientific Measurements, Tohoku University
Katahira Aoba-ku Sendai 980, JAPAN
and Y. Kondo
Department of Applied Physics, Faculty of Technology, Tohoku University,
Aramaki Aoba-ku, Sendai 980, JAPAN

Abstract

A spectrum of coherent synchrotron radiation were measured at wavelengths from 0.16 to 3.5 mm. A bunch shape was estimated by the Fourier analysis for this spectrum. This result agrees with that of simulation for the bunching process in the injector of the accelerator. The interferential effects between radiation which were emitted by the successive bunches were observed by an interferometer. It was shown that every radiation had the same phase when it was emitted by a bunch.

I. Introduction

In 1989 the coherence effects in SR were observed for the first time from short bunches accelerated by an electron linac[1]. It had a continuous spectrum and its intensity was more than 10^6 times as strong as that of ordinary SR at $\lambda = 0.33 \sim 2.0$ mm. This enhancement factor was almost as same order as N, the number of electrons in a bunch. The radiation intensity was proportional to square of the beam current or N^2. Radiation was mainly polarized in the orbital plane. The spectrum of coherent SR was dominated by the bunch length of the electron beam as expected by the theory[2, 3].

We will present the measured spectrum and discuss about the relation between the bunch shape and the spectrum. The interferential effects among radiation from different bunches were observed by an interferometer to show a direct evidence of coherent SR.

II. Experimental Method

The experiment was carried out using the Tohoku 300 MeV Linac whose accelerating frequency was 2856 MHz. In this experiment the electrons were accelerated up to an energy of 150 MeV. A duration of the bunch train, or burst width, was 2 μsec and its repetition rate was 300 pulses/sec. The bunch length was designed to be 1.2 mm (4° in RF phase) at the end of the first accelerating structure, where the beam energy was 10 MeV. Accelerated electrons were led to an experimental room through a beam transport, where the bunch length would be stretched to about 1.7 mm (6°). The number of electrons in a bunch was about 3.6×10^8 at an average beam current of 1 μA. The transverse beam size was about 2×2 mm^2 and the beam energy spread was 0.2 %.

The field strength of a bending magnet which was used to generate SR was 0.206 T and a bending radius was 2.44 m at the light emitting point of the electron orbit. The layout of the experimental setup is given in Ref.[1, 2, 3].

Emitted SR was collected by a spherical mirror with the acceptance angle of 70 mrad and was led to a far-infrared spectrometer of Czerny-Turner type through a crystal quartz window. Five echelette gratings were prepared to obtain a precise spectrum of coherent SR in the wavelength region from 0.1 mm to 4.0 mm. The resolution ($d\lambda/\lambda$) of the spectrometer was about 0.01 at $\lambda \sim 1$ mm. The intensity of SR was detected by a LHe-cooled silicon bolometer. The absolute sensitivity of the measuring system was calibrated by a blackbody radiator, which was a graphite cavity of 1500 K. Details of the spectrometer and the calibration method are given in Ref.[4].

An interference experiment was carried out to clarify the emission mechanism of coherent SR. An interferogram of pulsed SR from the successive bunches was measured by a polarizing interferometer[5]. The schematic layout of the interferometer is shown in Figure 1. Radiation which was emitted by a bunch was delayed by ΔL, the optical path difference between two arms, and interfered with another radiation which was emitted by the next bunch. The distance between the successive bunches L_B was 104.97 mm, which corresponded to the wavelength of the accelerating RF. As the variable range of ΔL was from -9 to 110 mm, it covered the bunch distance L_B. (For details of the interferometer see Ref.[6])

III. Experimental Results

As is shown in Figure 2, the complete SR spectrum was obtained in the wavelength region of 0.16 $\sim$ 3.5 mm. Radiation intensity is normalized for a bunch of $N = 1\times10^6$, which corresponds to an average beam current of 0.28 μA. The spectrum is continuous in these wavelengths and shows a broad peak at $\lambda \sim 1.5$ mm. The intensity decreases rapidly for $\lambda \leq 0.5$ mm. The enhancement factor

0-7803-0135-8/91$01.00 ©IEEE

at $\lambda = 1$ mm is obtained to be 0.92×10^6, which is almost as same value as N.

According to the classical electromagnetic theory, the intensity of coherent SR $I_{coh}(\omega)$ is given by

$$I_{coh}(\omega) = I_{incoh}(\omega)\{1 + (N-1)F(\omega)\} \quad (1)$$

$$F(\omega) = \left| \int e^{j\omega \mathbf{n}\cdot\mathbf{r}/c} S(\mathbf{r}) d\mathbf{r} \right|^2 \quad (2)$$

where $S(\mathbf{r})$ is the density distribution of electrons in a bunch, $\mathbf{n}$ a unit vector toward the observing point and $F(\omega)$ a bunch form factor defined by the Fourier transform of $S(\mathbf{r})$. Assuming that the bunch shape $S(\mathbf{r})$ is an even function of $\mathbf{r}$, we can estimate the bunch shape by using the Fourier transform from the observed SR spectrum. Estimated bunch shape is shown in Figure 3(a). The bunch shape resembles a Gaussian function with a sharp peak. The longitudinal bunch length is about 0.25 mm at full width of a half maximum, which is much shorter than the bunch length of 1.7 mm estimated from the characteristics of the linac.

In order to examine a possibility of the sharp structure of the electron distribution in the bunch, the bunching process was simulated by tracking the longitudinal motion of the electrons. The calculation was carried out according to the formulae in Ref. [7, 8]

The bunch shape depends strongly on the relative phase of the RF supplied to the prebuncher, buncher and the first accelerating structure. One of the result of this simulation is shown in Figure 3(b). The main body of the bunch is 1.3 mm in longitudinal length and it has three spikes, which are about 0.1 mm. This result is not an exact but similar shape as our experimental condition, and is consistent with the result of Figure 3(a). The effects of the beam loading and the space charge are not taken into account in the above simulation. To consider these effects, a rough calculation was done by the one-dimensional disk model[9]. The beam intensity was so small that the results was almost same as Figure 3(b).

The observed interferogram by the interferometer is shown in Figure 4. It is clear that the interference modulation at around ΔL=0 mm is repeated at around $\Delta L = L_B$=105 mm. The first modulation at around ΔL=0 mm shows the interference of SR from a bunch with itself, and the second one at around ΔL = 105 mm corresponds to the mutual interference with radiation from the next neighbor bunch. These two interference modulation patterns are congruous with each other within the accuracy of the experiment, i.e. the first radiation emitted by a bunch has the same amplitude and phase as the second one by the next bunch. This is a direct evidence that observed radiation is coherent.

IV. Conclusion

Two additional important results were obtained by the recent experiments.

1) The bunch length which is calculated by Fourier analysis of the radiation spectrum is consistent with the simulated result of the bunching process in the injector of the linac.

2)The coherent property of radiation was directly observed by the interferometer.

V. Acknowledgments

We thank Mr. T. Tsutaya and the staff in the Laboratory of Nuclear Science for their technical support and assistance, Dr. M. Takahashi for his technical guidance on the blackbody radiation source and Prof. I. Sato in KEK for his offering the program code of the one-dimensional disk model. This work was supported in part by a Grant-in-Aid for General Scientific Research and for Encouragement of Young Scientists of Ministry of Education, Science and Culture.

References

[1] T. Nakazato, M. Oyamada, N. Niimura, S. Urasawa, O. Konno, A. Kagaya, R. Kato, T. Kamiyama, Y. Torizuka, T. Nanba, Y. Kondo, Y. Shibata, K. Ishi, T. Ohsaka and M. Ikezawa, Phys. Rev. Lett. **63**, (1989) 1245.

[2] T. Nakazato, M. Oyamada, N. Niimura, S. Urasawa, R. Kato, Y. Shibata, K. Ishi, T. Ohsaka, T. Takahashi, H. Mishiro, M. Ikezawa, Y. Kondo, T. Nanba and Y. Torizuka, Particle Accelerators, **33**, (1990) 141.

[3] Y. Shibata, K. Ishi, T. Ohsaka, H. Mishiro, T. Takahashi, M. Ikezawa, Y. Kondo, T. Nakazato, M. Oyamada, N. Niimura, S. Urasawa, R. Kato and Y. Torizuka, Nucl. Instrum. & Methods **A301** (1991) 161.

[4] K. Ishi, Y. Shibata, T. Takahashi, H. Mishiro, T. Ohsaka, M. Ikezawa, Y. Kondo, T. Nakazato, S. Urasawa, N. Niimura, R. Kato, to be published in Phys. Rev. **A**.

[5] D. H. Martin and E. Puplett, Infrared Phys. **10**, (1969) 105.

[6] Y. Shibata, T. Takahashi, K. Ishi, F. Arai, H. Mishiro, T. Ohsaka, M. Ikezawa, Y. Kondo, S. Urasawa, T. Nakazato, R. Kato, S. Niwano and M. Oyamada, to be published in Phys. Rev. Lett.

[7] R. H. Miller, in *The Stanford Two-Mile Accelerator*, edited by R. B. Neal (W. A. Benjamin, New York, 1968)

[8] R. H. Helm, R. Miller, P. Brunet and X. Buffet, in *Linear Accelerators*, edited by P. M. Lapostolle and A. L. Septier (North-Holland, Amsterdam, 1970).

[9] S. Takeda, K. Tsumori, N. Kimura, T. Yamamoto, T. Hori, T. Sawai, J. Ohkuma, S. Takamuku, T. Okada, K. Hayashi and M. Kawanishi, IEEE Trans. Nucl. Sci. NS-32, No.5, (1985) 3219.

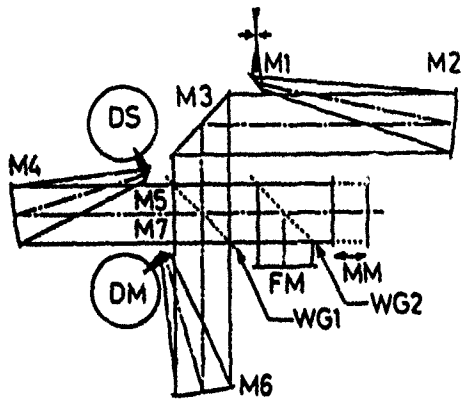


Figure 1. Interferometer to measure the interference effect between the bunches. M1, M3, M5 and M7: plane mirrors, M2, M4 and M6: collimators, WG1 and WG2: wire grids, FM and MM: fixed and moving mirrors, DS and DM: LHe-cooled silicon bolometer for detecting the signal and monitoring.

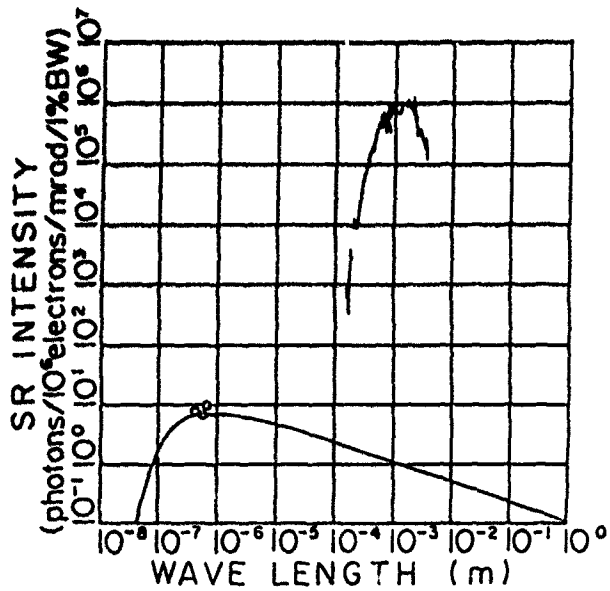


Figure 2. An observed spectrum of coherent SR. The intensity is normalized for a bunch of 1×10^6 electrons. A curve at the bottom is the calculate intensity for incoherent SR. Three circles are the measured intensity of visible SR to confirm the absolute value of this experiment.

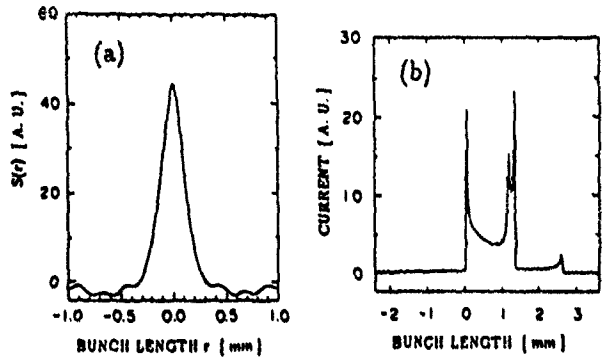


Figure 3. Longitudinal bunch shape obtained (a) from SR spectrum and (b) by the simulation of the bunching process.

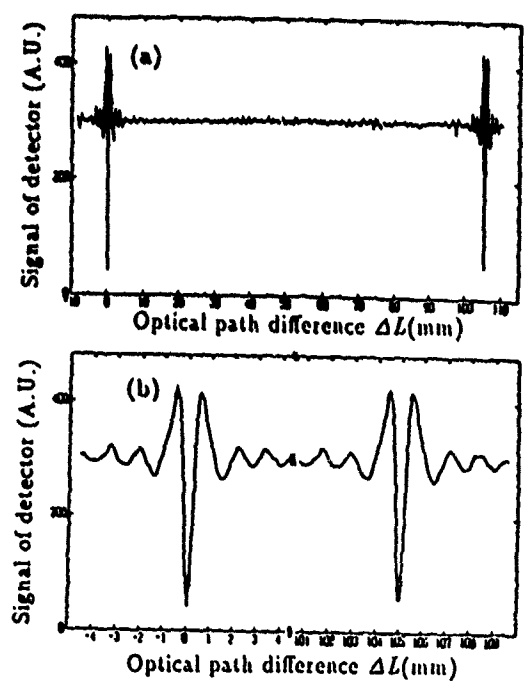


Figure 4. Interferogram of coherent SR.
(a) Full picture.
(b) Enlarged detail at around $\Delta L = 0$ and 105 mm.

Theoretical Studies on the Beam Position Measurement with Button-type Pickups in APS*

Y. Chung
Argonne National Laboratory
9700 S. Cass Ave., Argonne, IL 60439

Abstract

The response of electrostatic button-type pickups for the measurement of the transverse position of charged particle beams was investigated and analytical formulae were obtained for the signal as a function of time t and the coordinates of the beam and the electrodes. The study was done for beam pipes of circular and elliptic cross sections, for rectangular and non-rectangular electrodes, and for several cases of longitudinal beam profiles. The numerical results show good agreement with the analytical results, except that the presence of the photon beam channel and the antechamber causes finite offset (~20 μm) of the electrical center in the horizontal direction. Time domain analysis indicates that the error in the measurement of the beam position using circular electrodes as compared to rectangular ones was found to be less than 100 μm per 1 cm of beam excursion from the center of the beam pipe for the case of APS storage ring vacuum chamber.

I. INTRODUCTION

For capacitive pickup devices[1-3], the position of the charged beam is measured through the difference between the electric potentials which develop on the electrodes. For highly relativistic beams, the image charge has the same longitudinal distribution as the beam, due to the Lorentz contraction of the longitudinal component of the electric field.

In this article, we will analyze the response of the button electrodes in both the frequency and the time domains as a function of the transverse position of the beam, taking into account the finite size of the electrodes. The analytical model assumes a simple elliptic geometry for the beam chamber. The results are compared with those obtained numerically for the actual APS beam chamber, and they will be shown to agree quite well. This justifies the use of the analytical model rather than the time-consuming numerical methods to find the optimal position and size of the electrodes and to analyze how the shape of the electrodes affect the beam position measurement.

II. MONITOR RESPONSE

Consider an infinitely narrow beam moving along the longitudinal direction with the constant velocity V. Following the procedure by Cupérus[4], instead of solving the full electromagnetic problem directly in the lab frame (unprimed), we will transform to the reference frame (primed) where the beam is at rest, obtain the field and then transform back to the lab frame. The electric field **E** in the lab frame is then, using the Lorentz transformation,

$$E_{\parallel} = E'_{\parallel}, \qquad \text{and} \qquad E_{\perp} = \gamma E'_{\perp}, \tag{1}$$

where $\gamma = (1 - V^2/c^2)^{-1/2}$. Thus, the problem is reduced to that of an electrostatic case with linearly distributed charges.[5]

We will first concentrate on the frequency domain, and then discuss the solution in the time domain. Decomposing the electric potential $\Phi'(x, t)$ into Fourier components, we write

$$\Phi'(x, t) = \int dk\, e^{ik\,(z - Vt)}\, \Phi'(x_{\perp}, k), \tag{2}$$

where the linear dispersion relation $\omega = kV$ was assumed. The integration variable k extends from $-\infty$ to $+\infty$. Then the induced current I_p can be expressed as

$$I_p(k) = i\gamma\varepsilon_0 kV \int dS\, e^{ik(z - z_1)}\, \frac{\partial \Phi'(x_{\perp}, k)}{\partial n}. \tag{3}$$

The integration is done over the area of the electrode surface, and z_1 is the z-coordinate of a reference point, e.g., the center of the electrode z_p. **n** is the direction normal to the electrode surface. If the electrode is connected by a coaxial line of characteristic impedance Z_0 and if the capacitance between the electrode and the beam chamber is C_p, then the overall impedance $Z_p(k)$ for the electrode will be

$$Z_p(k) = \left(\frac{1}{Z_0} - ikVC_p\right)^{-1}. \tag{4}$$

If there is frequency filtering represented by F(k), the measured voltage $V_p(k)$ will be

$$V_p(k) = Z_p(k)\, I_p(k)\, F(k). \tag{5}$$

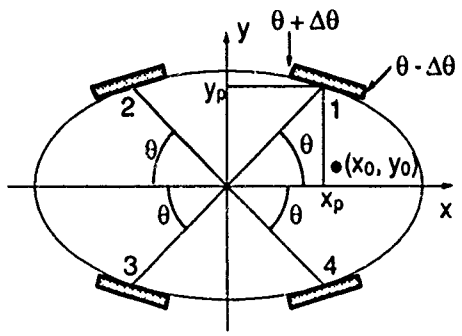


Fig. 1: Geometry of the beam chamber and the pickup electrodes.

*Work supported by the U.S. Department of Energy, Office of Basic Energy Sciences, under Contract No. W-31-109-ENG-38.

U.S. Government work not protected by U.S. Copyright.

From Eqs. (3) and (5), it suffices to solve the Poisson equation for the 2-D static potential $\Phi'(x_\perp, k)$ to obtain the electrode response V_p. The equation is analytically solvable if the beam chamber geometry is somewhat simplified. In this work, elliptic coordinates will be used to approximate the APS beam chamber. We will consider highly relativistic beams only. The current I_b carried by the beam is represented by

$$I_b(k) = \frac{Q_b V D(k)}{2\pi}, \qquad D(0) = 1. \tag{6}$$

Q_b is the total charge in a single bunch and D(k) is the Fourier transform of the longitudinal charge distribution $\rho(z)$.

Assuming a rectangular electrode flush with the interior surface, the electrode current $I_p(k)$ can be expressed as

$$I_p(k) = -i\frac{2\Delta\theta}{\pi} I_b(k) \sin k\Delta z \; G(\mu_0, \theta_0), \tag{7}$$

where

$$G(\mu_0, \theta_0) = 1 + 2\sum_{m=1}^{\infty} \frac{\sin m\Delta\theta}{m\Delta\theta} G_m(\mu_0, \theta_0), \tag{8}$$

and

$$G_m(\mu_0, \theta_0) = \frac{\cosh m\mu_0}{\cosh m\mu_p} \cos m\theta_0 \cos m\theta_p + \frac{\sinh m\mu_0}{\sinh m\mu_p} \sin m\theta_0 \sin m\theta_p. \tag{9}$$

Here, $\Delta\theta$ and Δz are half the angular and the longitudinal sizes of the rectangular electrode. The subscripts 0 and p denote the bunch and the electrode, respectively. From Eqs. (5) and (7), the coupling impedance $Z_c(k)$ can be obtained:

$$Z_c(k) = \frac{V_p(k)}{I_b(k)} = -i\frac{2\Delta\theta}{\pi} \sin k\Delta z \; G(\mu_0, \theta_0) \; Z_p(k) \; F(k). \tag{10}$$

In the time domain, we find from Eq. (5) that $V_p(t)$ is separated into the time-dependent and the position-dependent factors for rectangular electrodes as

$$V_p(t) = T(t) \; P(x_{\perp 0}), \tag{11}$$

where

$$T(t) = \frac{Q_b \Delta\theta}{\pi^2 C_p} \int dk \, \frac{e^{ik(z_1 - Vt)}}{k + i\kappa} \sin k\Delta z \; D(k) \; F(k), \qquad \left(\kappa = \frac{1}{Z_0 V C_p}\right) \tag{12}$$

and

$$P(x_{\perp 0}) = P_0(x_{\perp 0}) + \sum_{m=1}^{\infty} \frac{\sin m\Delta\theta}{m\Delta\theta} P_m(x_{\perp 0}). \tag{13}$$

For the elliptic case,

$$P_m(x_{\perp 0}) = \frac{2}{1 + \delta_{m0}} G_m(\mu_0, \theta_0). \tag{14}$$

Once the longitudinal charge distribution $\rho(z)$ and the filtering function F(k) are known, it is straightforward to calculate the electrode response $V_p(t)$. For certain cases of $\rho(z)$, it is possible to evaluate $V_p(t)$ analytically using the residue theorem of complex variables. In the discussion below, we will use the following parameters: C_p = 6 pF, Δz = 0.5 cm, σ = 1 cm, Q_b = 3.5 nC / mA (single bunch), x_p = 1.38 cm. Figure 2 shows the electrode signal $V_p(t)$ without frequency filtering. If the electrodes are not rectangular, the results are similar but a bit more complicated. One notable difference is that $V_p(t)$ for non-rectangular electrodes is not separable as in Eq. (11).

III. BEAM POSITION MEASUREMENT

As shown in Fig. 1, four button-type pickups will be installed for each unit. The quantities Δ_x, Δ_y and Σ are defined as follows.

$$\begin{aligned} \Delta_x &= V_{p1} + V_{p4} - V_{p2} - V_{p3}, \\ \Delta_y &= V_{p1} + V_{p2} - V_{p3} - V_{p4}, \\ \Sigma &= V_{p1} + V_{p2} + V_{p3} + V_{p4}. \end{aligned} \tag{15}$$

The horizontal and the vertical positions of the beam are then determined from

$$X_0 = \frac{\Delta_x}{\Sigma} \approx S_x x_0 + R_x, \text{ and } Y_0 = \frac{\Delta_y}{\Sigma} \approx S_y y_0 + R_y. \tag{16}$$

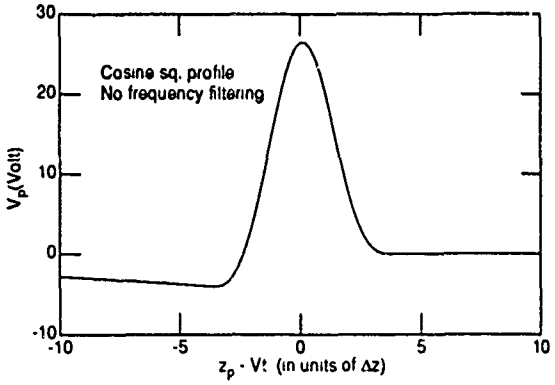


Fig. 2: The electrode signal V_p as a function of time t without frequency filtering. z_p is the electrode center coordinate and Δz is half the longitudinal size.

	Analytical result	Numerical result	
y_0 (cm)	S_x (cm^{-1})	S_x (cm^{-1})	R_x
0.0	0.569	0.565	-0.0011
0.2	0.580	0.576	-0.0011
0.4	0.616	0.610	-0.0011
0.6	0.676	0.667	-0.0010
0.8	0.763	0.747	-0.0010
1.0	0.877	0.850	-0.0009
1.2	1.017	0.974	-0.0008
1.4	1.178	1.113	-0.0008

Table 1: Comparison between the analytical and the numerical results for the x direction. The offset R_x for the analytical case is zero.

The linear approximation is valid only when x_0 and y_0 are small. S_x and S_y are the sensitivity functions and R_x and R_y are the offset errors. Figure 3 shows X_0 as a function of the beam position x_0 for several cases of y_0, and Fig. 4 shows the contour plotting of both X_0 and Y_0. Table 1 lists the sensitivity function S_x obtained analytically for the elliptic beam chamber and numerically for the actual APS beam chamber. The two results agree quite well. The finite offset error R_x is due to broken symmetry in the x-direction due to the presence of the photon beam channel and the antechamber. The optimal position of the electrodes which gives the same sensitivity in both x and y directions was found to be x_p = 1.32 cm. However, this was shifted to x_p = 1.38 cm due to the mechanical constraint of the mounting flanges.

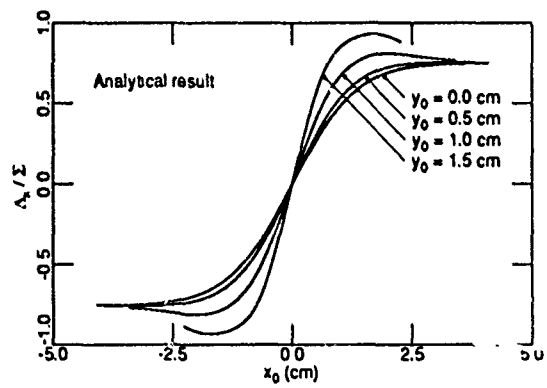


Fig. 3: The ratio Δ_X/Σ as a function of the beam position x_0 for several cases of y_0.

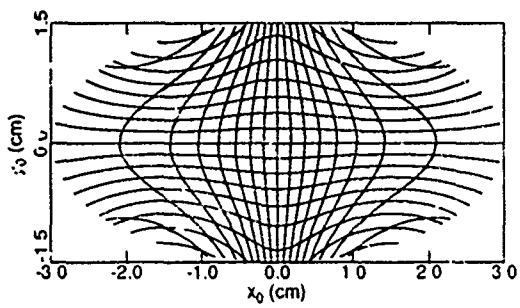


Fig. 4: The contour plotting for $X_0 = \Delta_X/\Sigma$ and $Y_0 = \Delta_Y/\Sigma$ for the elliptic beam chamber.

If the electrodes are not rectangular, X_0 and Y_0 are time-dependent, and the result of measurement will depend on the timing of data acquisition. This error due to the timing jitter will be larger for wide-band detection than for narrow-band detection at low frequency, say, a few hundred MHz. The measurement error can be expressed as

$$\delta x_0 = - \frac{\delta S_x(t)}{S_x(t)} x_0. \qquad (17)$$

$S_x(t)$ is the sensitivity as a function of time. Using hexagonal electrodes in place of circular ones to facilitate analytic integration over the electrode surface, typical error is found to be less than 100 μm per 1 cm of beam excursion from the beam chamber center. It is to be noted that it will diverge to infinity when Σ crosses zero while Δ_x does not. If the timing jitter is small (less than 10 ps) or if a narrow band detection scheme at a few hundred MHz is used, this error will be reduced to a negligible level (less than 10 μm / cm).

IV. CONCLUSION

The characteristic of the BPM system for the APS storage ring was studied analytically and numerically, and the results agree very well. This suggests that the presence of the photon beam BPM system. Using the analytical model, the optimal position of the electrodes was determined such that the sensitivity is as close as possible in x and y directions taking into account other mechanical constraints. A possible source of error in the measurement of the beam position using non-rectangular electrodes was analyzed. The error was found to be typically of the order of 100 μm per 1 cm of beam excursion from the center of the beam chamber and can be reduced significantly by employing proper timing schemes and signal processing.

V. REFERENCES

[1] T. Ring, "Beam Position Monitors for the High Brightness Lattice," Daresbury Laboratory Report, DL/SCI/TM41A, 1985

[2] J. Hinkson, J. Johnson, and I. Ko, "Advanced Light Source (ALS) Beam Position Monitor," *Proceedings of 1989 IEEE Particle Accelerator Conference*, 1507, 1989

[3] J.-C. Denard, A. Carniel, R. Aiello, and T. Monaci, "Beam Position Monitoring System for Elettra," *Proceedings of 1990 European Particle Accelerator Conference*, 726, 1990

[4] J. H. Cupérus, "Monitoring of particle beams at high frequencies," Nucl. Instr. and Meth. **145**, 219, 1977.

[5] J. Borer and C. Bovet, "Computer Response of Four Pick-up Buttons in an Elliptical Vacuum Chamber," LEP Note 461, 1983, and references therein

A Beam Position Detector for SSC Collider Rings

Donald J. Martin
SSC Laboratory*
2550 Beckleymeade Avenue
Dallas, Texas 75237

Abstract

A short-circuited stripline position detector which would operate in flowing liquid helium has been prototyped for the Supercollider main rings. Each sensing device, at 968 locations in each ring, consists of four 15 cm long, 50 Ω strip transmission lines. To maximize signal-to-noise ratio and reduce orthogonal sensitivity, each electrode subtends 70 degrees of the 37 mm aperture. Electrical to mechanical centers are proposed to be maintained within 0.15 mm radius by accurate tooling, so individual calibration would not be required. A radiation resistant, impedance matched vacuum feedthrough which is integral to the output signal cable is being considered. Because of the large quantity of detectors and inherent difficulty of replacement, reliability and manufacturability received the greatest concern during the design.

I. Introduction

A Collider position detector design was needed early in the SSC project, since the detector resides within the cryogenic helium and vacuum environment of the spool piece. The detector design therefore preceded the existence of a comprehensive Beam Position Monitor (BPM) plan. Nonetheless, an early detector design proved useful in several ways. The design addressed space allocation for position detectors, mechanical tolerances of the BPM relative to the magnetic correction elements, and a host of cryogenic issues, such as heat leak, thermal expansion, and thermally induced changes in material properties. The design and fabrication of the devices also tested the entirely new procurement, drafting, and mechanical design departments within the laboratory. SSCL competitively bid the task of fabricating two detectors, and the component parts for two more. The shell and electrodes were fabricated by a precision machine shop in the Dallas, Tx. area. The feedthrough cable assembly, itself the subject of intense investigation, was made by a specialty cable house and installed at detector assembly. The result of this early design work is shown in Figure 1.

The BPM system must provide accurate position and coarse intensity signals under the various operating conditions of the Collider: during machine commissioning, at Collider design intensity, in fault diagnosis, and during specialized accelerator studies. The system may also be called upon to help protect superconducting magnets by reflexively sending abort signals if the closed orbit at any detector exceeds a preset limit. The detectors will be located at the sextupole end of each magnet correction package, every 90 m half-cell length. Each sensing device measures both horizontal and vertical position. Strips short-circuited at one end may be used since directionality is not required in the Collider, and this measure also saves cost, reduces heat leak, and improves reliability.

*SSC operated by the Universities Research Association Inc., for U.S. Department of Energy under Contract DE-AC02-89ER40486.

U.S. Government work not protected by U.S. Copyright.

II. Detector Design

Beam current in the machines is characterized by individual bunches, nominally 14 cm FWHM and separated by 5 m intervals. The stripline area must be sufficient to produce at least -40 dbm signal power at the Collider commissioning levels of 2×10^8 protons per bunch (ppb). This is about the minimum signal power required by AM/PM or log ratio processing.

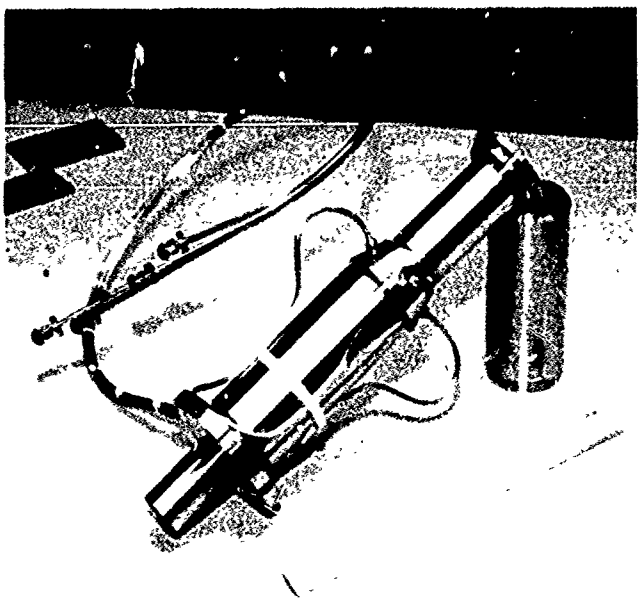


Figure 1. Collider Beam Position Detector

As the desirable properties of stripline monitors are well known, standard design equations from various sources are available [1]. The 5 m bunch spacing suggests strips of 15 cm length and a characteristic impedance in the 50 Ω to 75 Ω range. So that the electrodes will not be aperture defining elements, and to maintain the selected impedance, the beam tube bulges out around them. See Figure 2. The electrodes are also recessed 2 mm outside the aperture so that synchrotron radiation cannot strike them. (Synchrotron radiation impacts the detector design by its ability to produce noise in the electronics). Both the body of the detector and the strip are gradually tapered, up to the point where the coaxial pin and strip connect, to improve the electrical transition between the two geometries The final geometry of the connection is expected to be determined empirically using TDR The downstream end of the detector will be rigidly attached to the sextupole support plate, although the method is not resolved. In the present design, each detector is located by two 0.25 in diameter pins on the cold mass end

plate. One pin is diamond shaped so that a bit of clocking on the round pin is possible. Three machine bolts tighten the detector flange to the spool piece plate. The flanges may then be tack welded together to fix the transverse alignment indefinitely. Advantages to this method are that the distortion of a heavy vacuum sealing weld are avoided, disassembly for repair is easy, and the bolt arrangement allows easy installation on a test stand. The detector is designed with a tailpiece section of beam pipe, which will be robot welded to the beam tube during spool manufacturing. This weld is readily inspectable before the detector assembly is butted against the cold mass end plate.

III. Materials

Ionizing radiation will be present in the Collider and other circular accelerators, with the position detectors duly exposed. Estimates of energy deposition in devices close to the beam pipe have been made by several authors [2,3,4]. Radiation exposure results from beam scattering on residual gas, beam scraping on the beam tube, and catastrophic beam loss. The lifetime radiation dose of beam detectors in the Collider arcs will probably fall in the range 30 to 300 Mrads. A small number of detectors near the Interaction Regions may see doses up to 30 Grads. This radiation restricts the choice of materials that might be used in the detector. Some organic dielectrics, used in high frequency work, must be excluded from consideration as mechanical support materials. Materials that possess radiation hardness, low outgassing rate, maintain dimensions over life, have good RF properties, such as low loss and reasonable permittivity, are few. Ceramics are cautiously being considered in the 4K design, as brittleness and dielectric constant are of concern. A ceramic ring on the stripline upstream end is part of the present design, making the strip about 9% longer electrically, and causing an impedance bump. Detector mechanical pieces are taken from the 300 series of austenitic Stainless steels, which are frequently used in cryogenic engineering for their strength and corrosion resistance. However, some of these metals tend to be unstable at low temperatures, undergoing thermal or stress - induced martensitic transformation, leading to loss of ductility This effect is of greatest concern in the vacuum feedthroughs. There is some evidence that this transformation caused insidious failures in the cryogenic feedthroughs used in the Fermilab Tevatron [5]. Among the Stainless steels, types 310 or 316LN are a good choice for cryogenic applications.

IV. Vacuum Feedthroughs

Each position detector requires four vacuum feedthroughs, so 7,744 are required by the two Collider rings. Because of the great quantity of feedthroughs, and the inherent difficulty of replacement, these components must be very reliable. A detector MTBF of about 10^9 hours keeps the downtime of the Collider to one week of every five years operation, from BPM failures alone. Detector failure is defined as that failure that prevents machine operation. It could result from a helium to beam vacuum leak, a stripline electrode collapsing into the beam aperture, or other unforeseen mode. In this early design, the feedthrough and signal cable to the outside of the cryostat are an integral assembly. The feedthrough is not the usual demountable connector, such as SMA. This is done because the outer body of the detector is exposed to LHe, so a leaking feedthrough would allow LHe into the beam tube. If a connector like SMA were used, it would need to be sealed by a metal sheath, making the connector pair all but inaccessible. Therefore, the connector is eliminated in favor of an all - welded stainless steel assembly. A 0.142 in. diameter solid jacketed cable is commercially available. At the 4K end of the cable, a seal separates beam vacuum from the cable dielectric. This seal will be of the brazed ceramic - to - metal type. If the ceramic develops small cracks, the cable dielectric would be exposed to beam vacuum, but not helium. For a while, the failure would likely be transparent to operation. The 25 cm of cable closest to the beam detector is at 4K. The dielectric would outgas into beam vacuum, but slowly, since most gases trapped there would be solidified. The room temperature end of the cable is hermetically sealed using glass or ceramic. This is done for redundancy, and to keep moisture from entering the cable dielectric. Silica in a finely powdered state is proposed for the cable dielectric, which is highly radiation resistant and largely inert. The silica is vacuum baked at 800°C during cable fabrication, so it is unlikely that significant outgassing through a cracked ceramic would occur. If either cable seal fails, a potential risk to the cable is

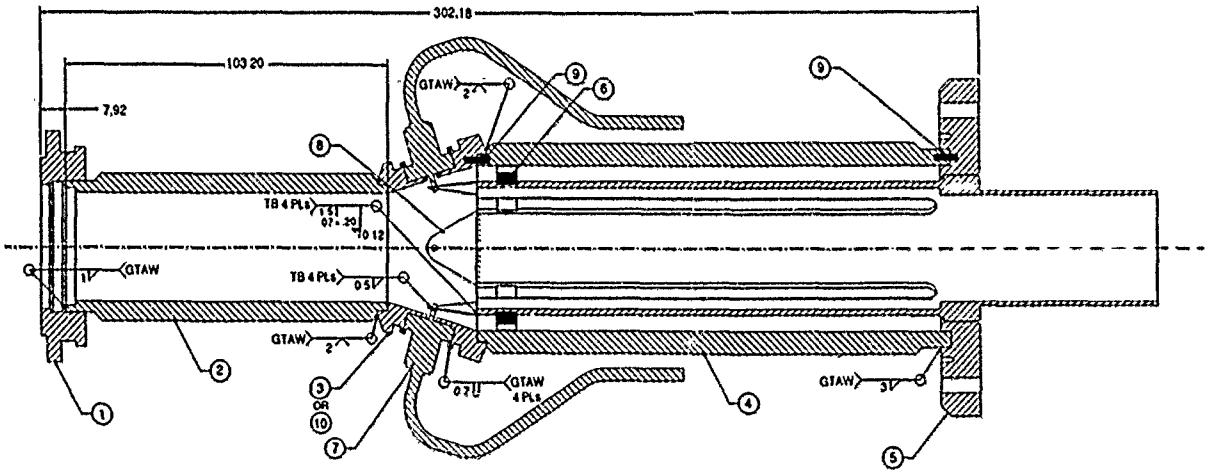


Figure 2. Collider Beam Position Detector Assembly Drawing

absorption of water, as powdered silica is slightly hygroscopic.

Isolation between cryostat guard vacuum and air is maintained through an SMA jack-to-SMA jack coaxial feedthrough. This is done to avoid having the signal cable terminate into the tunnel environment, so that were the end damaged, the entire detector assembly would not have to be replaced. Because the detector is at the end of the cryostat, it is susceptible to handling damage, particularly the signal cables. An option being considered is a sheath covering the four cable bundle, and forming an extra shield against LHe exposure. In this scheme, the signal cables do not seal LHe, so a wider range of coaxial cable types may be considered.

V. Reliability

How often will vacuum feedthroughs fail catastrophically, causing seven to ten day shutdowns of the Collider? A feedthrough may be more likely to fail because an adjacent one failed and the two had to be warmed to room temperature to make the repair. Failure rate may depend upon the number of temperature cycles each feedthrough experiences. It can easily be shown that the average number of lifetime thermal cycles for vacuum feedthroughs is not expected to exceed about 40, making worst case estimates. This suggests a methodology for accelerated life testing of this component.

VI. Conclusion

A prototype Collider ring position detector was designed and fabricated. To date, the device has neither been mechanically inspected or electrically tested. However, a number of design difficulties were uncovered by the exercise. Stress relief of the feedthrough to prevent loading caused by differential expansion was not adequate. The semi - rigid cables, though rugged, may pose an installation problem within the spool piece, since they lack flexibility. Schemes for locating the vacuum feedthroughs outside the liquid helium are being considered, and alternate radiation resistant materials are being investigated for the cable dielectric. An improved set of prototypes are now being designed for use in ASST, the Accelerator Systems String Test, scheduled for late 1992.

VII. Acknowledgment

The author gratefully acknowledges the many useful suggestions provided by R. E. Shafer, which concerned the theoretical and practical design of stripline detectors. The author thanks Richard Talman for valuable discussions on the synchrotron radiation issue. Useful suggestions on mechanical implementation were given by Dan Hutton, Leon Jemes, Jim Hahn, and Charles King. All fabrication drawings were created by Charles King.

VIII. References

[1] R. E. Shafer, R. C. Webber, T. H. Nicol, "Fermilab Energy Doubler Beam Position Detector", IEEE Transactions on Nuclear Science, Vol. NS-28, No.3, June 1981.

[2] I. S. Baishev et al, "Beam Loss And Radiation Effects In The SSC Lattice Elements", Institute For High Energy Physics, USSR, 7/28/90.

[3] T. A. Gabriel, "Preliminary Simulation of the Neutron Flux Levels in the Fermilab Tunnel and Proposed SSC Tunnel", SSC - 110, 8/20/87.

[4] Gilchriese (editor), "Radiation Effects at the SSC", SSC - SR - 1035, 6/88.

[5] R. E. Shafer, personal communication to author.

Beam Detector Impedance Calculation Using Circuit Models

Donald J. Martin
SSC Laboratory*
2550 Beckleymeade Avenue
Dallas, Texas 75237

Abstract

Expressions for the transfer impedance and longitudinal impedance of arbitrarily terminated stripline detectors are developed using a circuit model. Attenuation effects and distributed element effects are considered without requiring a field solution. A rectangular button is treated as a center-tapped transmission line.

Introduction

The Supercollider facility requires position measurement at some 2400 locations, in six different accelerators, beginning at the 35 keV ion source and as beam progresses to the 20 Tev Collider rings. Given that SSC is a green site, that measurement requirements, impedance budgets, signal power, and mechanical envelopes are being determined and vary with each machine, a study of detector responses appeared useful. In the circular machines the bunch interval is 5 m and FWHM bunch width is 14 cm. The short wavelength content of the bunch current is weak. To couple sufficiently at 60 MHz, a reasonable electrode area is required. A properly designed stripline detector can be long enough to produce strong signals while exhibiting a tolerable beam impedance. This discussion concerns the frequency domain analysis of strip transmission lines, arbitrarily terminated, and in one case, center terminated. This familiar beam detector geometry [1,2] is shown in Figure 1.

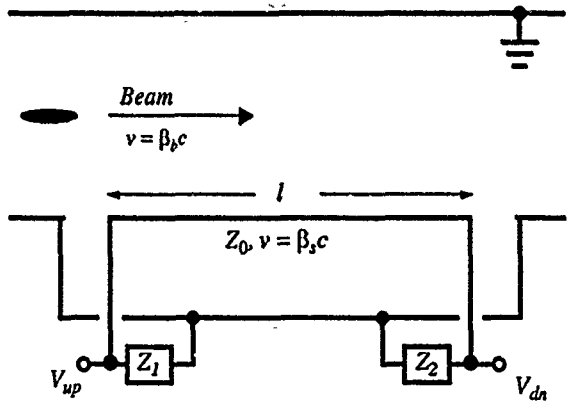


Figure 1. Longitudinal view of stripline beam detector

A stripline may be considered as a section of transmission line of length l which is exposed to the beam's electromagnetic fields. Transverse physical dimensions determine the impedance Z_0. The strip is terminated in an impedance Z_1 at its upstream end, and an impedance Z_2 downstream. The analysis does not restrict Z_1 or Z_2 to be purely real. Signals between the strip and ground conductor travel at the velocity $\beta_s c$. The beam velocity through the detector is $\beta_b c$, where c is the velocity of light in vacuum. The fraction of the total beam current induced on the electrode is g. This analysis considers detectors having only one electrode. Transverse impedances are not calculated.

TEM Circuit Model

Relativistic charged particle beams impose quasi-TEM fields in the metallic structures that enclose them. These fields couple to the stripline, and by a hand-waving argument and application of Lorentz reciprocity [3], the coupling occurs at the ends of the strip. This simplification, and taking the beam as a current source as shown in Figure 2, allows construction of an equivalent circuit. The sources are in phasor form, with the downstream source delayed by the beam flight time $l/\beta_b c$. Since the model contains lumped and distributed elements, it is useful to replace the line by a lumped element T-network [4] of admittances Y_A and Y_B, which is equivalent when $Y_A = Y_0(\coth\gamma_s l + \operatorname{csch}\gamma_s l)^{-1}$ and $Y_B = -Y_0 \sinh\gamma_s l$. The propagation constant for signals on the electrode is given by $\gamma_s = \alpha + i[\omega/(\beta_s c)]$, in which α is the loss term. Converting Z_1 and Z_2 to admittances, the circuit may then be solved using node equations.

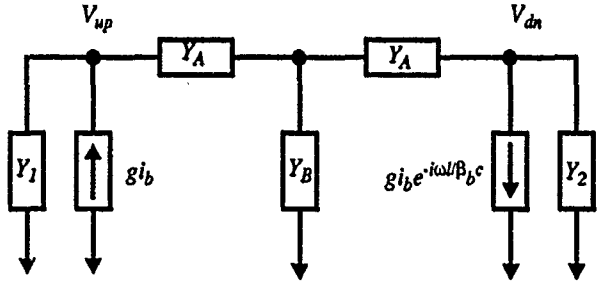


Figure 2. Equivalent circuit for stripline beam detector.

Using $V_{up} = i_b Z_{up}$ and $V_{dn} = i_b Z_{dn}$, the complex transfer impedances expressed by Eqns. 1 and 3 give the relationships between the beam current and the terminal voltages across the loads, Z_1 and

$$Z_{up}(\omega) = g\frac{Z_0}{2}(1+\Gamma_1)\frac{1-(1+\Gamma_2)e^{-\gamma_s l}e^{-\gamma_b l}+\Gamma_2 e^{-2\gamma_s l}}{1-\Gamma_1\Gamma_2 e^{-2\gamma_s l}} \quad (1)$$

Z_2, respectively. By symmetry, $\gamma_b \equiv 0 + i[\omega/(\beta_b c)]$ may be defined as the beam propagation constant. The reflection coefficients

$$\Gamma_1 = \frac{Z_1 - Z_0}{Z_1 + Z_0} \quad \text{and} \quad \Gamma_2 = \frac{Z_2 - Z_0}{Z_2 + Z_0} \quad (2)$$

*SSC operated by the Universities Research Association Inc., for U.S. Department of Energy under Contract DE-AC02-89ER40486.

U.S. Government work not protected by U.S. Copyright.

$$Z_{dn}(\omega) = g\frac{Z_0}{2}(1+\Gamma_2)\frac{(1+\Gamma_1 e^{-2\gamma_s l})e^{-\gamma_b l} - (1+\Gamma_1)e^{-\gamma_s l}}{1-\Gamma_1\Gamma_2 e^{-2\gamma_s l}} \quad (3)$$

are defined in the standard way. Note that it is possible to include loss effects on the electrode simply by using the hyperbolic functions in Y_A and Y_B.

Longitudinal Impedance

An important parameter for stripline sensors is the impedance the strip presents to the beam. In as much as the detector removes real power from the passing beam, that impedance cannot be zero. The impedance $Z_{\parallel}$ is calculated from the transfer impedances by evaluating the ratio of terminal voltages at the upstream and downstream ports, divided by beam current. The transit time phase lag of the bunch at the downstream port must be considered.

$$Z_{\parallel} = \frac{i_b Z_{up}}{i_b} - \frac{i_b Z_{dn}}{i_b e^{-\gamma_b l}} = Z_{up} - Z_{dn} e^{\gamma_b l} \quad (4)$$

Evaluating Eqn. 4 for a lossless ($\alpha = 0$) electrode, and allowing $\beta_b = \beta_s$ gives

$$Z_{\parallel}(\omega) = g^2\frac{Z_0}{2}\frac{(\Gamma_1\Gamma_2 + 2\Gamma_1 + 1)(1 - e^{-i2\theta_b})}{1-\Gamma_1\Gamma_2 e^{-i2\theta_b}} \quad (5)$$

$$\text{where } \theta_b = \frac{\omega l}{\beta_b c} \text{ and later } \theta_s = \frac{\omega l}{\beta_s c}. \quad (6)$$

The factor g^2 appears because only the fraction g of the image current sees the potential $i_b Z_{\parallel}$ at the discontinuities [5]. When $\Gamma_1 = 0$, Eqn. 5 reduces to the well known expression derived by Shafer [6].

Center-Tapped Stripline

A strip identical to the previous case might be loaded, not at each end, but at its center with a resistance Z_L. The calculation proceeds considering two equal transmission lines, each of length $l/2$, and writing the admittance matrix. The transfer impedance magnitude is given by Eqn. 7.

$$|Z_T(\omega)| = \frac{g2Z_L \sin\frac{\theta_b}{2}}{\sqrt{\cos^2\frac{\theta_s}{2} + \left(\frac{2Z_L}{Z_0}\right)^2 \sin^2\frac{\theta_s}{2}}} \quad (7)$$

The longitudinal impedance, when $\theta_s = \theta_b$ and $Z_L = Z_0$, is given by Eqn. 8.

$$Z_{\parallel}(\omega) = 4g^2 Z_0 \frac{2\sin^2\theta_b + i(1+\cos\theta_b)\sin\theta_b}{4\sin^2\theta_b + (1+\cos\theta_b)^2} \quad (8)$$

The quantity $i_b|Z_T(\omega)|$ is plotted against the response of a matched stripline detector using $Z_0 = 50\,\Omega$, $g = .125$, $\beta_s = \beta_b = 1$, $i_b = .192$ A, $l = 15$ cm. See Figure 3. The button's response peaks at twice the frequency of the stripline, but encloses more $\omega H(\omega)$ area. This "rectangular button" detector exhibits weak resonances whenever $\theta_s \neq \theta_b$, and stronger resonances whenever $Z_L \neq Z_0$, as would a stripline with the wrong upstream termination. Considering the resonances, the low signal obtained from a small button, and possibly more difficult mechanical implementation of a large button, use of button detectors is not foreseen at SSC.

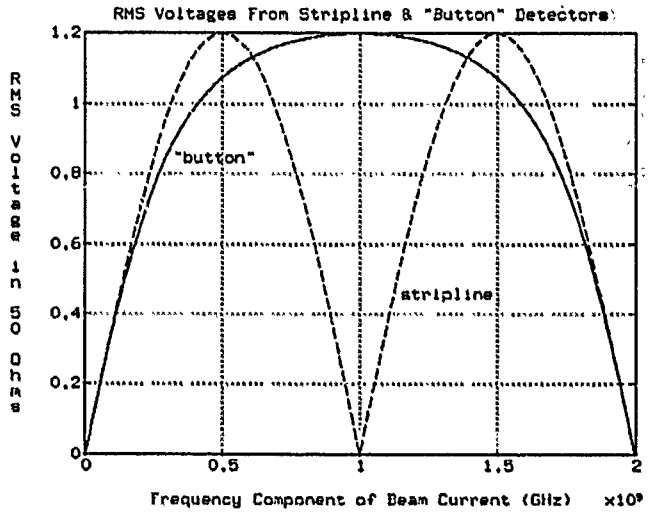


Figure 3. Frequency Response of Button and Stripline

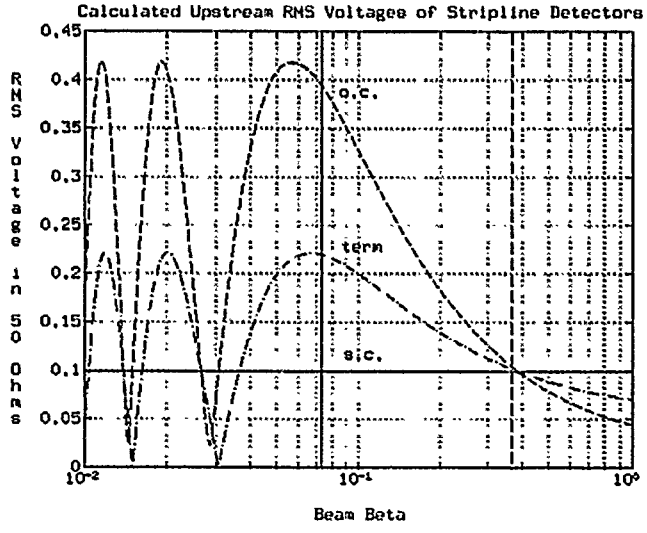


Figure 4. Stripline Response vs. Beam Velocity (β_b)

Open, Shorted, and Terminated Stripline

It is useful to consider the special real values for Γ_2, i.e. values of the downstream resistance Z_2. The cases of interest are the terminated, $\Gamma_2 = 0$, short - circuited, $\Gamma_2 = -1$, and open - circuited, $\Gamma_2 = +1$ loads. The equations describing the frequency responses of

Table 1. Frequency Response Characteristics of Stripline Beam Detectors

	Matched Line $\Gamma_2 = 0$	Open Circuit Line $\Gamma_2 = +1$	Short Circuit Line $\Gamma_2 = -1$
$\lvert Z_{up}\rvert$ $\beta_s \neq \beta_b$	$g2(Z_1 \mid Z_0)\left\lvert\sin\frac{1}{2}(\theta_s+\theta_b)\right\rvert$	$gZ_1\left[\frac{\cos^2\theta_s - 2\cos\theta_s\cos\theta_b + 1}{\xi^2\sin^2\theta_s + \cos^2\theta_s}\right]^{1/2}$	$gZ_0\frac{\lvert\sin\theta_s\rvert}{\sqrt{\xi^{-2}\sin^2\theta_s + \cos^2\theta_s}}$
$\lvert Z_{up}\rvert$ $\beta_s = \beta_b$	$g2(Z_1 \mid Z_0)\lvert\sin\theta_b\rvert$	$gZ_1\frac{\lvert\sin\theta_b\rvert}{\sqrt{\xi^2\sin^2\theta_b + \cos^2\theta_b}}$	$gZ_0\frac{\lvert\sin\theta_s\rvert}{\sqrt{\xi^{-2}\sin^2\theta_s + \cos^2\theta_s}}$
$\lvert Z_{dn}\rvert$ $\beta_s = \beta_b$	$gZ_0\Gamma_1\lvert\sin\theta_b\rvert$	$g(Z_1 - Z_0)\frac{\lvert\sin\theta_b\rvert}{\sqrt{\xi^2\sin^2\theta_b + \cos^2\theta_b}}$	0
$\angle Z_{up}$ $\beta_s = \beta_b$	$\frac{\pi}{2} - \theta_b$	$\tan^{-1}(\xi^{-1}\cot\theta_b)$	$\tan^{-1}(\xi\cot\theta_b)$
$\Delta\omega_{3dB}$ $\beta_s = \beta_b$	ω_0	$\frac{4}{\pi}\omega_0\tan^{-1}\xi$	$\frac{4}{\pi}\omega_0\tan^{-1}\xi^{-1}$
$\left\lvert\frac{V_{up}^{\Rightarrow}}{V_{up}^{\Leftarrow}}\right\rvert$	$\left\lvert\frac{\sin\frac{1}{2}(\theta_s+\theta_b)}{\sin\frac{1}{2}(\theta_s-\theta_b)}\right\rvert$	1	1

$\theta_s \equiv \frac{\omega l}{\beta_s c}$ $\quad \theta_b \equiv \frac{\omega l}{\beta_b c}$ $\quad \xi \equiv \frac{Z_1}{Z_0}$ $\quad \omega_0 \equiv \frac{\beta c \pi}{2l}$ $\quad \Gamma_1 = \frac{Z_1 - Z_0}{Z_1 + Z_0}$ $\quad \Gamma_2 = \frac{Z_2 - Z_0}{Z_2 + Z_0}$

these cases are summarized in Table 1. The peak response of all detectors occurs at $f_0 = \omega_0/(2\pi) = (\beta_b c)/(4l)$ if $\beta_s = \beta_b$. According to the model, the detector response recurs indefinitely in ω. In practice, a bandwidth limitation of the transition pieces between the strip and terminations, as well as propagation of the TE_{11} mode, reduces the detector bandwidth to a few cycles of the sine function.

When $\Gamma_1 = 0$, the three cases converge, the response being independent of Γ_2. The directivity of each detector is the ratio of the upstream voltage $V_{up}^{\Rightarrow}$ obtained when beam travels from port 1 to 2, to the voltage obtained at the upstream port with beam traveling from 2 to 1, $V_{up}^{\Leftarrow}$. Only the downstream terminated detector exhibits directivity, which depends upon the beam and signal propagation constants, and hence is frequency sensitive. When $0 < |\Gamma_2| < 1$, a detector having partial directivity is obtained.

Figure 4 shows the equations in row 1 of Table 1 applied to the SSC Linac. The frequency response as a function of beam velocity, using the values $\beta_s = .386$ (alumina loading), $Z_0 = Z_1 = 50\,\Omega$, $g = .125$, $i_b = .025$ A, $l = 2$ cm, and $f = 428$ MHz, is plotted. Fig. 4 demonstrates the large signal produced by an open - circuited pickup when excited by a non - relativistic beam.

References

[1] Q. A. Kerns, D. B. Large, "Analysis Of A Traveling-Wave Beam Electrode", LRL, UCRL-11551, July 7, 1964.

[2] R. E. Shafer, R. C. Webber, T. H. Nicol, "Fermilab Energy Doubler Beam Position Detector", IEEE Transactions on Nuclear Science, Vol. NS-28, No.3, June 1981.

[3] G. R. Lambertson, "Physics of Particle Accelerators", editors M. Month and M. Dienes, AIP 153, Vol. 1, 1987.

[4] R. E. Collin, "Foundations For Microwave Engineering", McGraw - Hill, pg.198. See problem 4.9.

[5] K. Y. Ng, "Stripline Monitors as Transmission Lines", Fermi National Accelerator Laboratory, Note FN - 534, Feb. 1990.

[6] Ref. [2], Eqn. 5.

Monitoring System to Permit Accurate Alignment of Beams at Collision in CESR*

J.P. Sikora and R. Littauer
Wilson Laboratory
Cornell University
Ithaca, NY 14853 USA

Abstract

Colliding beams in a storage ring should be aligned, in position and angle, to within a small fraction of the beam dimensions. Errors may be corrected by the use of appropriate steering elements (in CESR, electrostatic separators). In view of the small beam size, measurement of the misalignment needs to be highly accurate. In the system used at CESR, the orbits of e^+ and e^- are measured simultaneously, to reduce the effect of small orbit fluctuations with time. In addition, the signals are processed in an automatic gain control (AGC) system which extracts the e^-/e^+ pulse height ratio, with the e^+ pulses being brought to a fixed level. When the beams are coincident, the e^-/e^+ pulse height ratios will be identical on all four buttons of the beam position monitor (BPM). The AGC technique reduces the errors produced if the orbit is not well centered between the pickup buttons.

Introduction

The closed orbits of counterrotating beams in a shared magnetic guide field will coincide, provided that the beams have everywhere the same energy. Perfectly aligned head-on collisions—required to maximize luminosity and reduce beam-beam blowup—might thus be thought to occur automatically. However, residual beam-beam misalignment at the interaction point (IP) can arise from orbit effects due to the rf acceleration system [1]. More importantly, in a ring (such as CESR) which incorporates electrostatic deflectors, or in a collider using two separate guide fields, beam alignment at collision needs to be enforced by deliberate adjustment, using appropriate differential steering elements.

The problem lies in the *measurement* of the alignment error. In principle it would suffice to use the luminosity itself as an indicator; in practice, statistics make this process slow and the many parameters which affect luminosity are not distinguished. A sensitive measurement of orbit alignment at the IP is thus desirable. The system used at CESR is separate from the general orbit-monitoring equipment because a much higher accuracy is required, albeit only in a small section of the ring and only as regards the relative orbits for e^+ and e^-.

Available Sensors

Relative position and angle information is needed for the two beams at the IP. However, the BPMs are at some distance from this point and orbit reconstruction is thus needed. The corresponding trajectories are shown in figure 1, in each case scaled to represent a misalignment which is a small fraction of the natural beam size: at the IP the initial displacement or angle is set equal to 0.1σ, an error of this order being considered at the threshold of significance. Typical values of σ are $\sigma_x \approx 420\mu m$ and $\sigma_y \approx 5.6\mu m$ in displacement, and $\sigma_{x'} \approx 410\mu rad$ and $\sigma_{y'} \approx 310\mu rad$ in angle. The permissible error is much smaller for vertical than for horizontal orbit separation, due of course to the much smaller vertical beam emittance ($\epsilon_y \approx 0.01\epsilon_x$ with $\epsilon_x \approx 1.8 \times 10^{-7} m$).

A single pair of monitors has been used, placed symmetrically on either side of the IP at BPM3 E/W. Our choice optimizes the signal produced by a vertical orbit difference Δy, which is the most difficult to detect; moreover, BPM3 happens to be preferable for practical reasons. Different pairs could be used to maximize the observable orbit error for different parameters ($\Delta x, \Delta y, \Delta x', \Delta y'$), but if the instrumentation can in fact resolve Δy adequately, it should also be sufficient for the other errors.

Energy Difference

Measuring projected trajectories and inferring the beam alignment at the IP is subject to error unless the two beam energies are equal, which is true only if the rf acceleration is effectively symmetrical about the IP. For significant time periods CESR has operated with only a single rf cavity; this gave rise to a fractional $e^+ - e^-$ energy difference at the IP of $\delta \approx 2 \times 10^{-1}$. Under normal conditions—two symmetrically placed cavities—a (much smaller) residual unbalance can still be present.

A nonzero δ falsifies the reconstruction of the relative $e^+ - e^-$ orbits only if the trajectories suffer deflections be-

*Supported by a grant from the National Science Foundation

0-7803-0135-8/91$01.00 ©IEEE

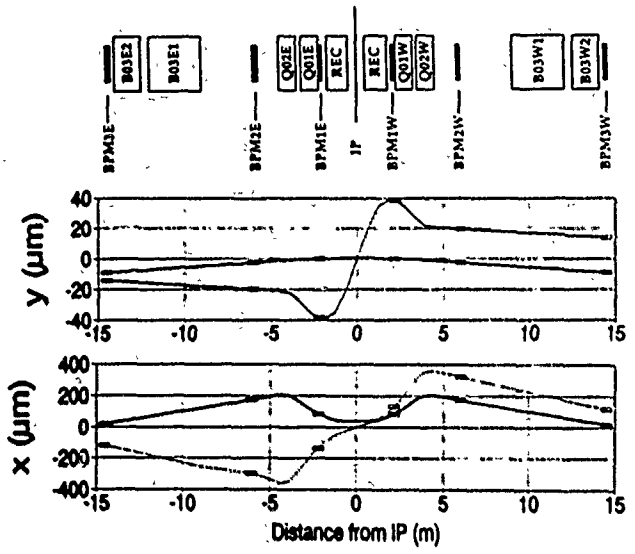


Figure 1: Trajectories with misalignment errors of 0.1σ in displacement and angle. The error values used are: $\Delta x = 42\mu m$, $\Delta y = 0.56\mu m$, $\Delta x' = 41\mu rad$, $\Delta y' = 31\mu rad$.

tween the IP and the BPM in use. As seen from fig.1, two weak guide-field bends at $B03E/W$ (about $20mrad$ each) intervene just before BPM3. For the worst-case $\delta \approx 2 \times 10^{-4}$ they separate two perfectly aligned e^+ and e^- trajectories by $22\mu m$ horizontally at BPM3. This approaches the level of our permissible error, but a correction can be made if ever CESR is operated with only a single rf cavity. Beyond BPM3, however, there are much stronger dipoles and all further BPMs are eliminated from consideration.

Trajectory deflection occurs also if the orbit is not centered in the quadrupoles or the experimental solenoid. Passing a quadrupole of focal length f with an offset x_0 from its magnetic center is equivalent to a dipole deflection of x_0/f. The effects of such deflections have been tracked, in both planes, for all lenses; and offsets of the order of $1mm$ produce at most $4\mu m$ of trajectory separation, again for the single-cavity extreme. In practice such errors should be negligible.

Signal Processing

From fig.1 the required detection sensitivity can be read for relative-orbit measurements at BPM3; the resolution should be within $20\mu m$ horizontally and $10\mu m$ vertically. Despite the unfavorable location of BPM3 for detecting horizontal errors, the vertical requirement is still the more stringent. Given the signal amplitudes at the four buttons (b1 ... b4), the x and y coordinates of the bunch centroid are found from the usual difference/sum algorithm; e.g., $x = X_0(b_2 - b_1 + b_4 - b_3)/(b_2 + b_1 + b_4 + b_3)$, and similarly for y. With the geometric scale factors, X_0 and Y_0, of order $25mm$, the individual button signals must be measured with fractional uncertainties below 4×10^{-4}. Brief ($< 200ps$), bipolar signals are not easily measured with this accuracy.

CESR button signals are usually monitored by diode peak rectification; we have found this to yield the best signal-to-noise ratio. With e^+ and e^- beams simultaneously present, their respective signals could be separated by time gating. However, such gates require very stable synchronization. We prefer, instead, to separate the signals by their *polarity*. To this end, the pulses must first be shaped so as to exhibit a marked asymmetry; then the undershoot from one polarity will not interfere with pulses of opposite sign, provided the e^+ and e^- bunch charges are not too different. This shaping is done by a length (about $100ns$) of lossy cable (RG174/U).

The rectifier outputs are passed through low-pass filters and measured by 16-bit dual-slope integrating digitizers which average over about 0.3 s. These digitizers are synchronized so that the e^+ and e^- readings apply to the same time period; any common orbit fluctuation, due for example to drifts in magnetic steering elements, is thus eliminated.

It would be unrealistic to require precise centering of the orbits within the BPMs; but it is only necessary that the relative $e^+ - e^-$ error vanish, i.e., that the orbits for the two species be off-center by the same amount. The pulses from the four buttons are thus not necessarily equal; however, the four e^- signals should fall into the same pattern as the four e^+ signals. To detect this equality of pattern with high precision, an AGC loop (fig.2) is closed around the processor. By controlling an electronic attenuator, this loop brings each e^+ output, in turn, to a standard reference level, thus making all four e^+ outputs equal. The e^- signals, passing through the same attenuator, will then also all deliver equal outputs, provided they were originally in the same pattern as the e^+ pulses.

In this system, the peak rectifiers serve only to detect equality of signal levels; their actual (nonlinear) transfer function is irrelevant. By the same token, any incidental attenuation which may be introduced by the coaxial relay applies equally to e^- and e^+ and is thus eliminated from consideration. Evidently, the electronic attenuator now becomes the critical element: its treatment of e^- and e^+ pulses must be even-handed. This requires not only insensitivity to pulse polarity and time sequence, but also similar attenuation at the (possibly different) absolute levels for the two species of signals. Though bench measurements can quantify attenuator performance in these respects, ultimately the most sensitive test is to operate the system under various conditions and observe what errors, if any, are produced.

Results

Two diagnostic tests were performed: (1) The relative-orbit readings were taken with a fixed attenuator (-12dB)

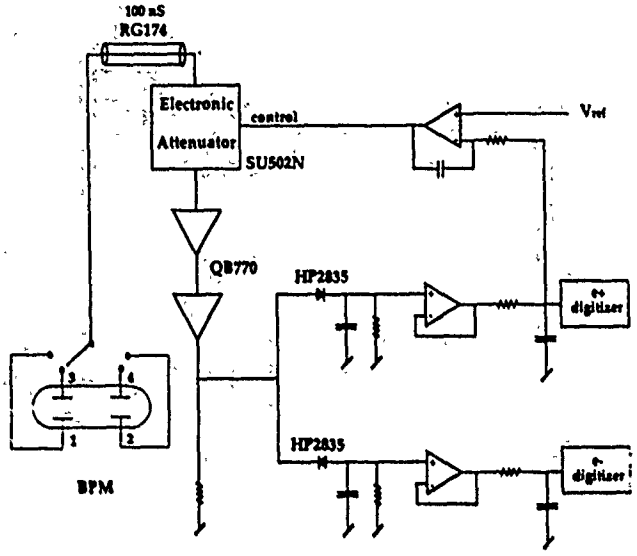


Figure 2: Schematic diagram of the AGC circuit

inserted into the signal path, thus forcing the electronic attenuator into a different region of operation. (2) By the use of an inverting transformer, the roles of e^+ and e^- channels were exchanged, thus also reversing the time sequence of the AGC-stabilised and the companion pulse. These perturbations produced variations in the indicated relative orbit at BPM32, taking into account the resulting sign change, of at most $+/-10\mu m$.

In CESR luminosity runs, the relative-orbit measuring system has been used, in conjunction with horizontal and vertical electrostatic separators, to bring the beams into precise alignment at collision. Maximum luminosity occurs with zero displacement error at the IP, within a few μm. However, the machine appears to prefer a vertical *angular* misalignment (fig.3), with the angle seeming to depend on beam current. Work is proceeding to detemine whether this indication is an instrumentation error or whether it corresponds to some physical effect in the ring.

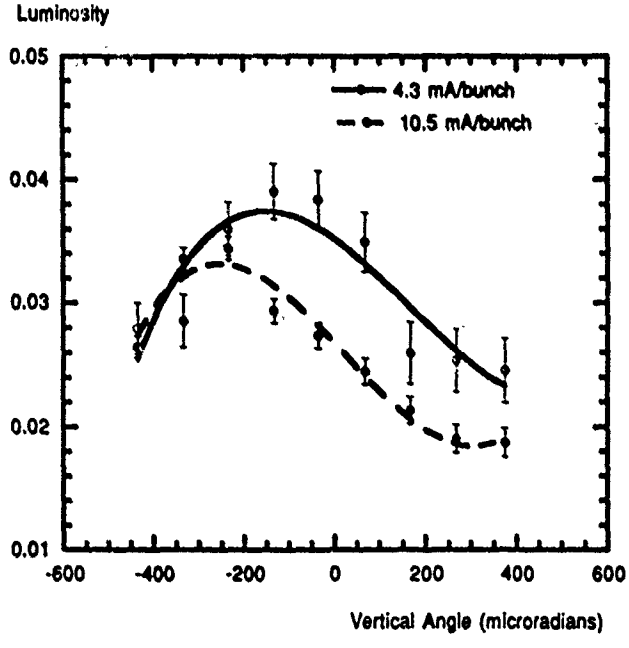


Figure 3: Plot of luminosity vs. relative vertical angle at two different beam currents

References

[1] R. Littauer,"Orbit and Tune Effects of RF Conditions", CBN88-4, CESR internal report.

Development of a Wall Current Beam Position Monitor for a KAON Factory Ceramic Chamber

Yan Yin, Bill Rawnsley, George Mackenzie, Dave Pearce, John Worden
TRIUMF, 4004 Wesbrook Mall, Vancouver, B.C., V6T 2A3

Abstract

The rapid cycling synchrotron proposed for the TRIUMF KAON Factory uses ceramic beam pipe to suppress eddy currents. One design has metallic strips fixed onto the inner surface to carry the wall currents. A beam position monitor has been designed using these strips and tested successfully with the TRIUMF cyclotron beam.

I. Introduction

When beam goes through a beam pipe, an image current of the beam flows along the wall of the pipe. For an off axis beam the wall current distribution is asymmetric, the asymettry being a function of beam position. A conventional wall current monitor diverts the current through resistors bridging a ceramic spacer between metal beam pipes. Positional information is obtained by comparing the voltage across resistors grouped in quadrants. The beam pipe devised by SAIC carries the wall current in silver strips 4 mm wide, 1 mm apart painted along the inner surface of the pipe which is then fired at 850°. A gap of 5 mm is introduced in the middle third of the strips on each wall, Fig. 1. Each set of these strips is merged at the gap and the current brought through the wall on pin vacuum feedthrus. Resistors soldered to the pins bridge the gap.

The test WBPM was fabricated by M. Featherby[1] using a spare section of 1 cm wall pipe 15 cm long with inner dimensions 9.4 cm high and 5 cm wide, Fig.1. Metal transistion pieces matched this rectangular pipe to the 10 cm diameter circular TRIUMF beam pipe. The circulating current in the KAON Factory will be ~1 A and resistors < 1 ohm offer ample signal strength and low impedance [1] [4], however ~150 μA cw extracted from TRIUMF has low peak intensity (1.5 mA) and 10 ohm resistors were used. The vertical surface has adapters on which tooling balls were mounted during bench calibration for alignment purpose.

II. WBPM Transfer Function Measurement

The transfer function was measured before installation using an antenna mounted on an X-Y table [2]. A 20 MHz sinewave from an HP8753 network analyzer was used for calibration (the TRIUMF rf is 23 MHz). After amplification of 40 dB the signals were collected by the analyzer, and stored in a computer for calculation and plotting. The mapping was done within the square area from -10 to 10 mm in both x and y direction with steps of 5 mm. The equations

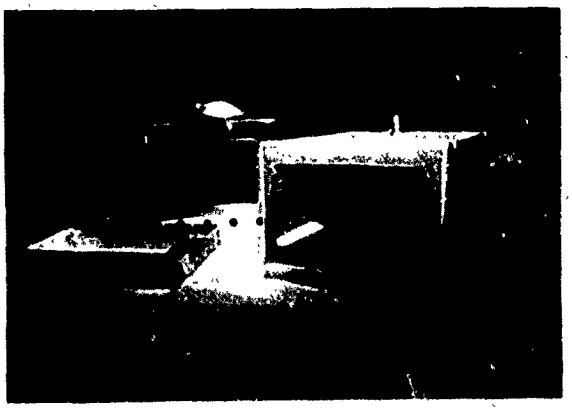


Figure 1: The ceramic chamber wall current monitor

$$U_I = (V_R - V_L)/(V_R + V_L) \tag{1}$$

$$V_I = (V_U - V_D)/(V_U + V_D) \tag{2}$$

are used to indicate the position. Because of the intrinsic non-linearity of the BPM, the polynomials

$$x_I = \sum_{i=0}^{N}\sum_{j=0}^{i} a_{i-j,j}(U_I - U_0)^{i-j}(V_I - V_0)^j \tag{3}$$

and similarily for y_I, are used to approximate the transfer function. U_0 and V_0 are the BPM readings when the antenna is at the center point. A least squares method is used to calulate the coefficients $a_{i-j,j}$, for the x and y directions separately. Using N=3, $a_{i-j,j}$ will have 10 numbers and the beam transfer function error will be less than 0.1 mm. The offsets between the electrical and mechanical center in the x and y directions can be also given.

A BPM transfer function was calculated for comparison with the measured one. J.H.Cupérus [3] expanded the beam charge in a Fourier series and obtained an approximate expression for the charge density induced on a surface at y=-b :

$$\sigma_{y=-b}(x,z) = -D_\lambda \cos\left[\frac{2\pi}{\lambda}(v_t + z_\lambda - z)\right] \times \sum_{m=1}^{\infty} \frac{\sinh[\alpha_m(b-y_0)]}{a\sinh(2b\alpha_m)} \sin\left[\frac{m\pi(x_0+a)}{2a}\right] \sin\left[\frac{m\pi(x+a)}{2a}\right] \tag{4}$$

[1] M.Featherby, SAIC, 10401 Roselle St. San Diego, CA 92121

0-7803-0135-8/91$01.00 ©IEEE

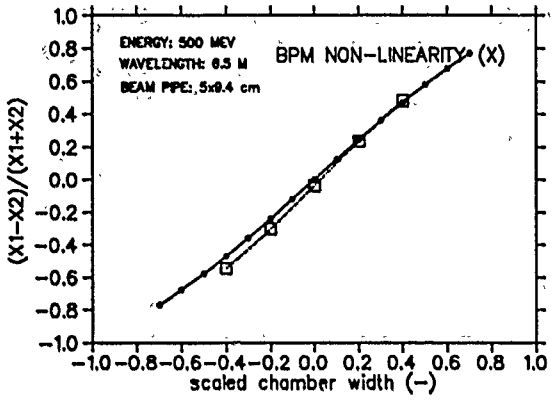


Figure 2: BPM Transfer Function (X)

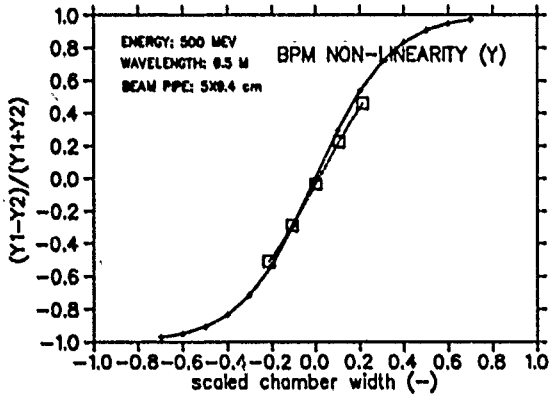


Figure 3: BPM Transfer Function (Y)

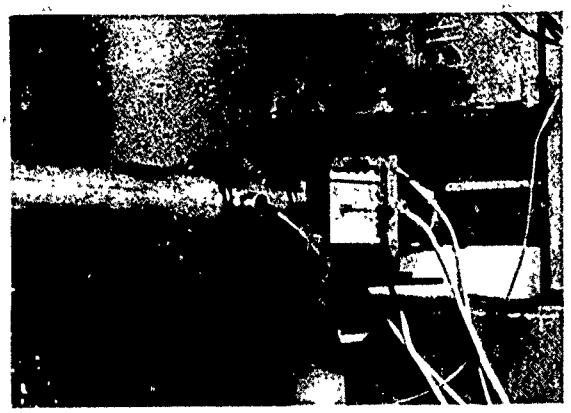


Figure 4: Experiment set up for the wall current BPM

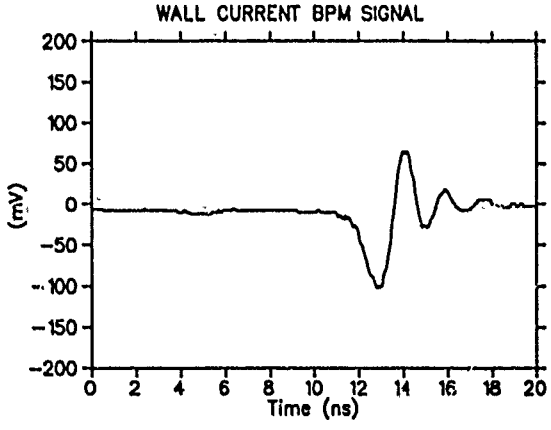


Figure 5: Beam signal picked up by the wall curren BPM

$$\alpha_m = \sqrt{\left(\frac{2\pi}{\gamma\lambda}\right)^2 + \left(\frac{m\pi}{2a}\right)^2}$$

In the formula, a is the half width of the chamber, b is the half height of the chamber, v_t is the speed of the particle, D_λ is the amplitude, λ is the wavelength of the Fourier component.

The transfer function calculated using eq. 4 is compared with that measured in Fig. 2 and 3. Fig.2 and 3 show the theoretical and measured non-linearity of the transfer function along the x and y axes. They are quite consistent.

III. Measurement With Cyclotron Beam

A. *Experimental proceedure*

The WBPM was installed in a drift section in the TRIUMF high current beam line 1A between a multiwire and a scanning wire monitor. These gave both the profile and position.

The beam could be steered completely across the WBPM by horizontal and vertical steering magnets located upstream. The relation between steering magnet setting and beam position at the WBPM was inferred from measurement at the up and downsteam monitors. WBPM signals amplified by 40 dB were recorded as a function of the magnet settings. The experiment compares the WBPM reading and the position reading determined by the steering magnets.

Two methods were used to process the data. One method stored and transfered the raw signals, digitized by Tektronix 2440 oscilloscope, into a computer via a HPIB interface, then analysed them later with FFT. The other used the AM/PM electronic circuits originally obtained from Fermilab [5] which are used for other TRIUMF position monitors. These give a voltage which is a function of to V_R/V_L or V_U/V_D. The beam current was 3 μA with a 3% microduty cycle, equivalent to 100 μA cw, and for most of the measurement with a 10% microduty cycle at 23.055 MHz; equivalent to a peak intensity of 1 mA. The AM/PM circuits operate at 46 MHz. This frequency was also chosen for digital processing to reject any 23 MHz background.

B. *Processing data with the FFT method*

The WBPM signals were first enlarged by a 40 dB amplifier, then collected by electronics or oscilloscope (Fig.5). The FFT method was used to single out the amplitude of the 46 MHz component , then to calculate the position of beam from formulas (1) and (2).

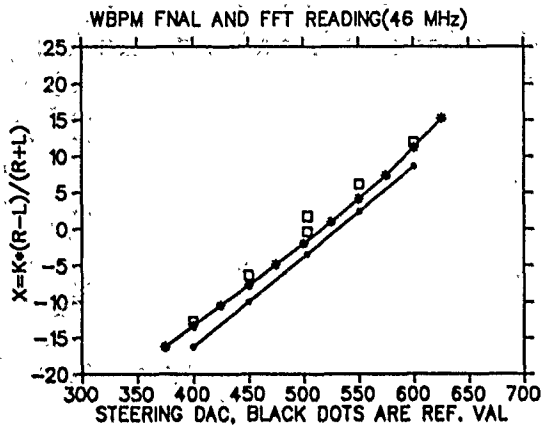


Figure 6: Beam reading via FFT and AM/PM circuit (X)

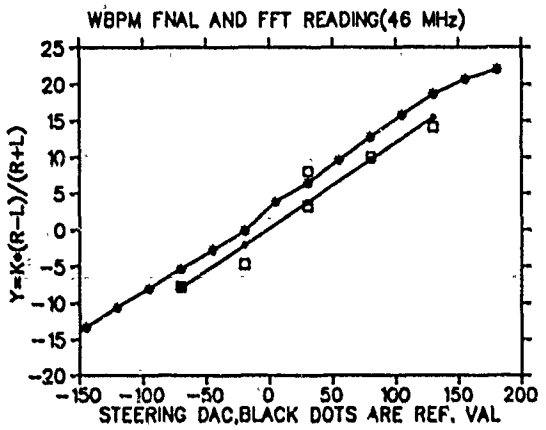


Figure 7: Beam reading via FFT and AM/PM circuit (Y)

Since only 2 cables were available for the experiment and horizontal and vertical data were taken separately the two dimenional equation (3) could not be used for analysis. The bench test data were re-analyzed in terms of separate planes, coefficients K_x and K_y determined for each plane and the measured data interpolated to determine the position. The position was also calculated from the Log ratio, 20Log(A/B), where A and B are the FFT 46 MHz component of opposite pairs of signals. The results agree with those from equation (1) and (2). The position sensitivity is $\approx$ 8 dB(voltage ratio) /cm.

C. *Processing Data With Fermi Lab Electronics*

The output of the Fermi Lab module [5] is a voltage

$$V = k[arctan(A/B) - \frac{\pi}{4}] \qquad (5)$$

where A and B are the signal strength of the 46 MHz component. Normally the input signals are sufficient to saturate internal amplifiers and k =3.5, however in this case insufficient preamplification was available and a value of 3.2 for x and 3.0 for y were determined experimentally.

IV. Results

Position

The position calculated from the off-line FFT analysis(□) and the AM/PM module output (*) compared with the position interpolated from adjacent beam line monitors in Fig 6 and 7. The slopes agree for small displacement. The AM/PM unit is less linear at large displacement. There appears to be an offset of 2 mm, which may be due to misalignment of the existing monitors; this is being re-checked during the current shutdown.

Amplitude

It was estimated [1] that the peak beam intensity will be about 1.5 mA and that about 10% of the wall current is shunted through each resistor to give peak voltages of 1.5 mV for a horizontally centred beam. The measured horizontal peak amplitude was 2/3 of this because the large resistance and capacitance bridging the gap reduce the high frequency response. Equipment is available to measure the longitudinal distribution but this was not used on this occasion.

Bandwidth

It was expected that reducing the resistor value from 10 ohms to 2 ohms would extend the high frequency response with reduced signal strength. Slits were used to reduce the beam bunch length below 2 ns however no change was seen with the amplitude. A reduced amplitude could be detected with a bunch length increased to 6 ns . The feedthru pins were actually 6.4 mm diameter rods, larger than specified, only less than one mm apart which increased their capacitance signifigantly.

V. Conclusion

The aim was to devise a BPM for the KAON Factory which could exploit the technology used to fabricate its vacuum chamber and thus reduce construction expense. The external dimensions are identical to the chamber and the device may be located at the end of, eg. a quadrupole, reducing demands on available lattice space. The KAON Factory beam will be ~1A, the resistors will be low, reducing impedance and extending the high frequency response to the 1.6 GHz measured in model tests [1].

VI. References

[1] Yan Yin:*A Wall Current BPM Built on a Ceramic Chamber*,TRI- DN-90-K144, July,1990.

[2] Yan Yin:*BPM Calibration and Its Test Station*,TRI-DN-90-143 July,1990.

[3] J.H.Cupérus:*Monitoring of Particle Beam at High Frequency*,CERN, 1977,NIM V145 p219.

[4] Yan Yin, Chris Oram, N.Ilinsky and P.Reinhardt-Nikulin: *Measurement of Longitudinal Impedance for a KAON Test Pipe Model with TSD-Calibration Method*, TRI-DN-90-142

[5] S.P.Jackim, R.C.Webber, R.E.Shafer, *An RF Beam Position Measurement Module for the Fermilab Energy Doubler*, IEEE NS-28,1981,P2323

Measurements and Performance of a Microstrip Beam Probe System

J. D. Gilpatrick, K. F. Johnson, S. Lloyd, D. Martinez, R. Meyer, G. Neuschaefer, J. Power, R. B. Shurter, and F. D. Wells
Los Alamos National Laboratory, Los Alamos, NM 87545

Abstract

Microstrip probes and associated processing electronics have been designed and used to measure charged-beam position, angle, intensity, output phase, and energy. As a bunched, charged beam periodically passes through a microstrip probe, a bipolar signal proportional to the beam's current and position is induced into each of the probe's four axial symmetric lobes. Processing electronics and computer algorithms transform two probe signals into beam intensity and into centroids of the six-dimensional, phase-space beam distributions. These beam centroids can then be plotted with cavity data so that output beam characteristics can be expressed as a function of cavity power and phase. This paper will describe the system, and discuss typical beam/cavity interaction data, measurement errors, and system performance.

I. THE MICROSTRIP SYSTEM

The microstrip systems consist of three components: the microstrip probe, the processing electronics, and the computer hardware and software that provide experimenters with beam information. This section will concentrate primarily on the first two items, and the measurement algorithms.

The microstrip probe is a short version of typical directional coupler probes [1]. These noninterceptive, electromagnetic beam probes consist of four symmetrically-placed lobes that sense the bunched-beam image currents. Stripline transmission lines are attached to the front and back of each microstrip transmission-line lobe. As the beam image currents pass through the probe, periodic bipolar signals are launched to both the downstream termination, via the stripline, and the processing electronics, via the upstream transmission line. Table I shows the key parameters of these probes as well as the expected signal power of the 425-MHz frequency component [2].

Table I. Installed Probe Geometries and Signal Powers

Probe Bore (mm)	Lobe Subtended Angle (Radians)	Lobe Length (mm)	Overall Probe Length (mm)	Signal Power 10mA, 5 MeV Beam (dBm)
45	$\pi/4$	2.25	12.7	-34
16	$\pi/4$	2.25	8.2	-33
10	$\pi/4$	6.13	11.3	-30

The electrical characterization of the probe must provide a measure of position sensitivity and offset, phase delay through the probe, and beam coupling for the bunched beam. The first two items are measured with an automated, movable-wire test fixture [3] that calculates the centered-beam-position sensitivity and offset. The phase delay and beam coupling are measured using a coaxial, transmission-line test fixture and network analyzer. Measured position sensitivities range from 4.5 dB/mm to 1.2 dB/mm and offsets are $< \pm 0.15$ mm. Coupling between the probe lobe and the center conductor of the test fixture is typically -37 to -40 dB, and probe phase delays are 12.8 radians at 425 MHz.

The processing electronics consist of three modules [4]. A down-converter module converts the bunched-beam 425-MHz radio-frequency (RF) signals from the microstrip probe, and an accelerating-cavity field-monitor signal, to intermediate frequency (IF) signals of 20 MHz. This conversion improves the accuracy of the IF processing electronics and decreases the component costs. After the signals are down-converted, they are appropriately divided, phase-matched, and fed to the other two modules: a position and intensity module, and an output-phase and time-of-flight (TOF) module.

The position and intensity module comprises a position circuit and an intensity circuit. The position circuit uses the amplitude-to-phase conversion technique [5] to transform the IF lobe signals to an output voltage that is a function of beam position. The intensity circuit synchronously detects the amplitude of the converted and summed four-lobe signals. The third module, output-phase and TOF circuitry, compares the phases of two sets of signals using two digital phase detectors. For the beam output phase, the converted cavity-field sample is compared with the converted and summed probe-lobe signals; the output signal is proportional to the phase between these signals. The TOF circuitry compares the summed and converted signals from two different probes having a known separation along the beamline. This output is proportional to the flight time of the last partial $\beta\lambda$ distance of a bunch traveling between the two probes.

For each of the output signals, algorithms transform, linearize, and calculate the final measured values. The horizontal- and vertical-position output-signal nonlinearities are corrected in the digitizing computer software. Equations 1 and 2 are the corrections for the nonlinearities in the microstrip probe and position-processing electronics, respectively.

$$\bar{x} = x_0 + S_x R_{\bar{x}} - 1.797\text{X}10^{-4} R_{\bar{x}}^2 - 1.412\text{X}10^{-4} R_{\bar{x}}^3 \qquad (1)$$

and

$$R_{\bar{x}} = 20 \log\left[\tan\left(\left(\frac{\pi}{1.5\text{A}V_{RF}}\right)V + \frac{\pi}{4}\right)\right], \qquad (2)$$

where $R_{\bar{x}}$ is the nonlinear correction of the position-processing electronics, $\bar{x}$ is the beam position, V is the signal from the microstrip processing electronics, A and V_{RF} are gain and circuit signal constants, and x_0 and S_x are the measured probe-position offset and sensitivity. The beam angle is also calculated if there is a drift between two probes.

*Work supported and funded by the US Department of Defense, Army Strategic Defense Command, under the auspices of the US Department of Energy.

0-7803-0135-8/91$01.00 ©IEEE

The intensity output signal is transformed from volts to milliamperes of beam current by a conversion factor of 10 to 20 mA per volt [2].

The TOF signal is transformed to flight time, normalized beam velocity, and finally, beam energy [6].

$$\overline{W} = M_0c^2\left[\left(1-\left(\frac{dw}{c\left(n_wT+\frac{T}{T_{IF}}\tau_{IF}\right)}\right)^2\right)^{-\frac{1}{2}}-1\right], \qquad (3)$$

where $\overline{W}$ is the mean beam energy, τ_{IF} is the flight time of the last partial $\beta\lambda$ distance of a bunch traveling a distance dw, n_w is the integer number of $\beta\lambda$s in distance dw, T and T_{IF} are the bunching and IF periods, and M_0c^2 is the beam's rest energy. The output beam phase with respect to an upstream cavity is calculated using the phase difference between the probe signal and a cavity-field monitor loop signal. The correction for beam phase changes due to beam energy changes during the drift is shown in Equation 4.

$$\overline{\phi} = \phi_s - \left(\frac{d_\phi}{\beta\lambda_0} - n_\phi\right)2\pi, \qquad (4)$$

where $\overline{\phi}$ is the average output phase of the beam, ϕ_s is the phase recorded by the processing electronics, λ_0 is the free-space bunching wavelength, and n_ϕ is the number of integer $\beta\lambda$s in d_ϕ (the distance between an RF cavity reference-plane and a microstrip probe).

II. Beam/Cavity Interaction Measurements

Because beam output phase and energy are measured as well as beam position and intensity, the interaction between the accelerating cavity and its output beam can be determined. The linac RF-field phase and amplitude can be determined by measuring the beam's energy, output phase, and transmission efficiency. These data are then compared with single-particle simulations as generated by particle and ray-tracing simulation codes (e.g., PARMILA, TRACE).

At Los Alamos, these graphical studies describing the output beam as a function of two independent variables are known as phase scans. Phase scans plot output beam current, intensity, phase, and energy as a function of the two independent variables, cavity (or input-beam) phase and cavity power (or gap voltage). A fourth plot, output beam energy as a function of output beam phase, is shown in Figure 1 for a 5-MeV, H^- linac. Each of the "pin wheel" loci corresponds to single-particle simulations for a particular cavity power level or gap voltage. The 206-kW data show that the linac gap voltage was 8% higher than the 1.00 x design gap voltage [7]. A semiautomated version of these scans has been implemented on the drift-tube linac, providing data acquisition and analysis within a few minutes.

Transmission scans are a specific subset of the general beam/cavity measurements used to determine the RF power set points for a Radio-Frequency Quadrupole (RFQ). Beamtransmission efficiency, output beam current, intensity, phase, and energy are calculated and displayed as a function of

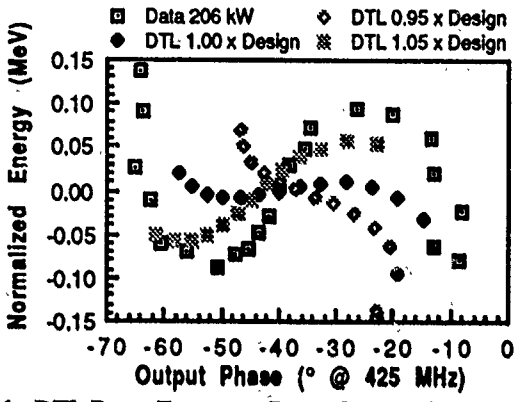


Figure 1. DTL Beam Energy vs Beam Output Phase.

power inside the cavity. To compare data with simulations (e.g., using PARMTEQ), transmission scans are expressed in terms of the RFQ vane voltage (Figure 2). The transmission is different from the theoretical design because the

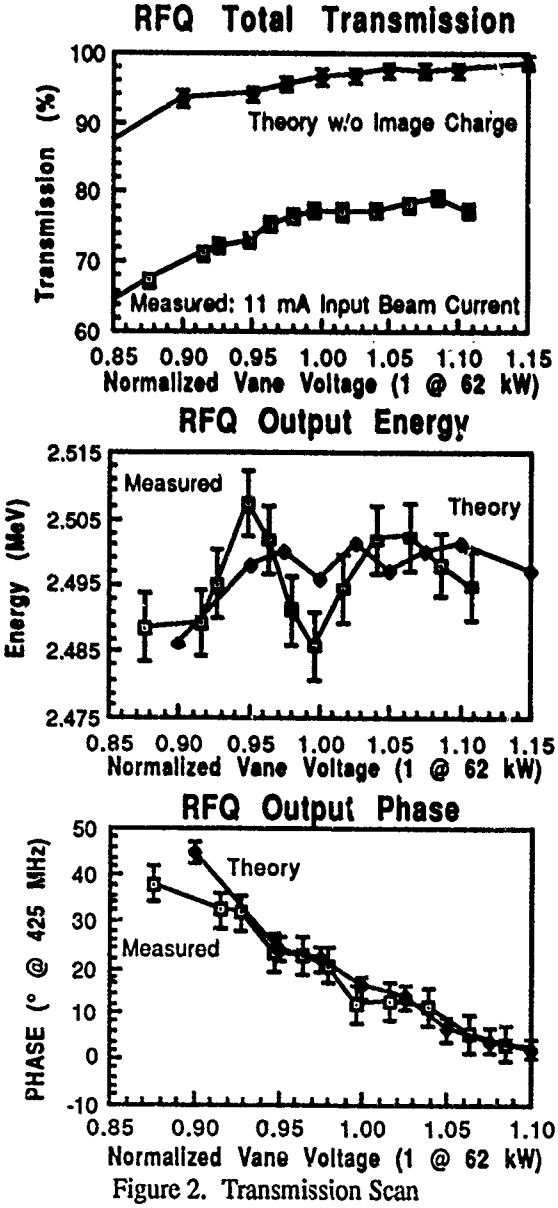


Figure 2. Transmission Scan

input beam was not properly positioned entering the RFQ, and image currents were not included in the simulations.

III. Measurement Errors

There are two types of measurement errors: fundamental and systematic. Fundamental errors are errors that cannot be reduced because of natural laws of physics; these limit both the measurement resolution and accuracy. Examples are thermal and shot noise. Systematic errors are errors that limit accuracies but do not limit resolution of the measurements. Examples are transverse probe-alignment errors with respect to the beamline (which affect the absolute beam position accuracy).

Table II. Measurement Errors and Uncertainties

Beam Variable	Error	Upper Limits (% Full Range)
Fundamental Errors (Accuracy & Resolution)		
Energy**/Phase	Thermal Noise*	± 0.002/± 0.02
	Electronic Noise	± 0.014/± 0.3
	RFI (-34 dBc)	± 0.03/± 0.6
Intensity	Thermal/Shot Noise*	± 0.004
	Probe/Beam Coupling	± 5
	Electronic Noise	± 0.14
	RFI (-34 dBc)	± 2
Position	Thermal Noise*	± 0.05
	Electronic Noise	± 0.3
	RFI (-34 dBc)	± 0.5
Systematic Errors (Accuracy)		
Energy**/Phase	Cable Delays	±0.08/± 2.3
	Probe Alignment	± 0.021/± 0.09
	Electronic Drift	± 0.024/± 0.3
	Probe/Elect. Match	± 0.19/± 2.2
Intensity	Cable Losses	± 1
	Electronic Drift	± 0.2
	Probe/Elect. Match	± 3.5
Position	Cable Losses & Delays	± 0.14
	Probe Alignment	± 1.0
	Electronic Drift	± 0.5
	Probe/Elect. Match	± 1.0

* Noise limits assume a 1-MHz bandwidth to the electronics and a 40-dB electronic signal-to-noise ratio.
** The energy measurement errors are based on a flight path length of 12 $\beta\lambda$ at nominal beam energy.

The time and flight path uncertainty relationship can be calculated by differentiating Equation 3. The measured beam-energy resolution or accuracy, ΔW, is expressed as

$$\Delta W = \frac{(\beta\gamma)^3 M_0 c^2 c \Delta\tau}{dw} , \qquad (5)$$

where β and γ are the relativistic beam factors, c is the speed of light, and $\Delta\tau$ is the TOF variation.

Although not listed in this fashion, the resolution is a component of the overall measurement accuracy. As Table II shows, the largest errors are usually linked to the operation and implementation of the measurement (such as electronics noise, alignment, and cable delay errors) and contribute to a majority of the measurement inaccuracies. Although not shown as a problem, radio-frequency interference (RFI) contributions can easily be far greater than those listed in the table. During the early stages of the beam measurement, the RFI noise was as high as -6dBc, which is 25 times greater than that listed in the table – and it effectively rendered most of the beam measurements useless.

III. Conclusions

Measurements done with the microstrip probe can provide more information than just the usual beam position and intensity. If two probes with a known, pure drift-distance between them are used, beam angle, energy, and output phase can also be directly measured. These added measurements provide information on the interaction between a beam and an upstream accelerating cavity. The 425-MHz microstrip system developed at Los Alamos initially suffered from RFI-induced errors, but these errors have now been reduced to the point that the measurements provide reliable transverse and longitudinal phase-space beam information.

IV. References

1. R. E. Shafer, "Characteristics of Directional Coupler Position Monitors," IEEE Transaction of Nuclear Science, 32, No. 5, pp. 1933-1937.
2. J. D. Gilpatrick, "Microstrip Probe Impedance Function," AT-3:TN:87-38, 1987.
3. R. B. Shurter, J. D. Gilpatrick, "Tuned Antenna Driver for Microstrip Probe Sensitivity Testing," Workshop on Accelerator Instrumentation, Fermi National Accelerator Lab., Batavia, IL Oct. 1-4, 1990.
4. J. D. Gilpatrick, J. F. Power, F. D. Wells, R. B. Shurter, and R. Meyer, "Overview of the Microstrip Beam Diagnostics," LA-CP-89-460, 1989.
5. J. D. Gilpatrick, J. Power, F. D. Wells, and R. B. Shurter, "Microstrip Probe Electronics," LA-CP-89-488, 1989.
6. J. D. Gilpatrick, R. E. Meyer, F. D. Wells, J. F. Power, and R. E. Shafer, "Synchronous Phase and Energy Measurement System for a 6.7 MeV H^- Beam," 1988 Linear Accelerator Conference, pp. 134-136.
7. K. F. Johnson, O. R. Sander, G. O. Bolme, J. D. Gilpatrick, F. W. Guy, J. H. Marquardt, K. Saadatmand, D. Sandoval, and V. Yuan, "The Single-Beam Funnel Demonstration: Experiment and Simulation," 1990 Linear Accelerator Conference, pp. 701-703.

LOG-RATIO CIRCUIT FOR BEAM POSITION MONITORING*

F. D. Wells, J. D. Gilpatrick, R. E. Shafer and R. B. Shurter
Los Alamos National Laboratory, MS: H808
Los Alamos, NM 87545

Abstract

The logarithmic ratio of the signal amplitudes from beam-position probe-electrodes provides a normalized real-time analog signal that is more linear in beam displacement than other signal-processing techniques for circular cross-section, beam-position monitors. This paper describes work being done to develop a log-ratio circuit using an inexpensive, commercially available, logarithmic-response, integrated-circuit rf-amplifier. The circuit uses two amplifiers in a log (A) – log (B) = log (A/B) configuration to provide the logarithmic ratio of the two rf input signals from the probe. The output is a real-time analog signal proportional to beam displacement.

I. SIGNAL-PROCESSING TECHNIQUES

Three commonly available methods for deriving normalized beam-position signals are amplitude-modulation-to-phase-modulation conversion (AM/PM), difference-over-sum, and log-ratio processing [1]. Figure 1 shows the amplitude response of the three processing techniques for 45° electrodes in a 60-mm circular beam pipe. Notice that log-ratio processing provides the most linear response across the probe aperture.

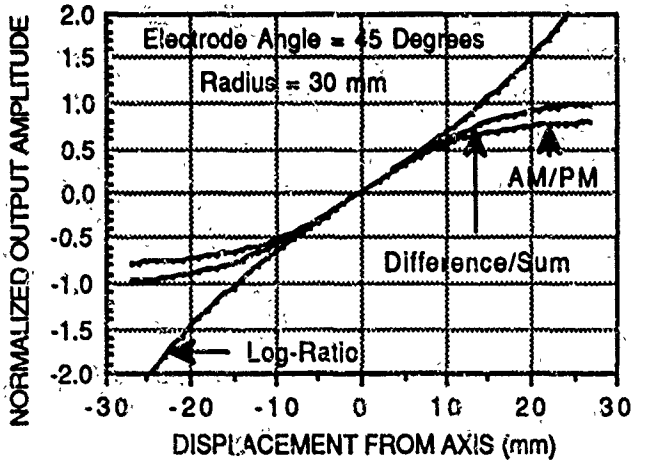


Figure 1. Response curves of the log-ratio, difference-over-sum, and AM/PM processing techniques.

Until recently, the log-ratio technique has not been a viable candidate because of amplifier cost and accuracy constraints. In 1989 Analog Devices Corporation announced the AD640 Logarithmic Amplifier, a monolithic device that provides a dynamic range of up to 50 dB for frequencies from dc to 120 MHz. Comprising the circuit are five cascaded, dc-coupled, amplifier/limiter stages, each having a small signal voltage gain of 10 dB with a –3-dB bandwidth of 350 MHz, and five full-wave detectors. These circuits implement a successive detection technique that approximates the logarithmic response characteristic. The five detected signals are summed to provide an output current proportional to the logarithm of the input voltage. The response is absolutely calibrated to within ±1 dB for dc or square-wave inputs. The linearity for sinusoidal inputs ranges from 0.75 to 1.5-dB [2]. Availability of this device was the impetus for an investigation of the log-ratio beam-position processing technique.

II. LOG-RATIO IMPLEMENTATION

For a pair of microstrip probe electrodes in a circular beam pipe, the ratio of the two currents produced by an rf-modulated beam current traveling in the z-direction past the electrodes can be expressed as [3]

$$\frac{I_A}{I_B} = \frac{1 + \frac{4}{\Phi_0}\sum_{n=1}^{\infty}\frac{1}{n}\left(\frac{r_0^n}{R^n}\right)\cos(n\theta_0)\sin\left(\frac{n\Phi_0}{2}\right)}{1 + \frac{4}{\Phi_0}\sum_{n=1}^{\infty}\frac{1}{n}\left(\frac{r_0^n}{R^n}\right)\cos(n\theta_0)\sin n\left(\pi + \frac{\Phi_0}{2}\right)} \qquad (1)$$

where Φ_0 is the angle in radians subtended by the probe electrodes,
R is the radius of the probe aperture,
r_0 and θ_0 are the coordinates of the beam bunch,
$r_0\cos\theta_0 = X$ is the beam displacement from the center.

By expanding and simplifying this equation, a solution for the beam displacement can be obtained as

$$X \equiv \frac{Ln10}{160}\left(\frac{R\Phi_0}{\sin(\Phi_0/2)}\right) 20\log\left(\frac{I_A}{I_B}\right) \qquad (2)$$

Thus, the displacement is expressed as a function of the logarithm of the ratio of the two currents.

Figure 2 shows a block diagram of the complete log-ratio circuit. Each logarithmic amplifier has two AD640 devices in cascade and an operational amplifier that sums and converts the currents to a voltage that is filtered to provide an envelope proportional in amplitude to the logarithm of the input signal. The filtered outputs are applied to a differencing amplifier to produce a beam-position signal proportional to log (A/B).

*Work supported by the US Department of Energy, Office of High Energy and Nuclear Physics.

0-7803-0135-8/91S01.00 ©IEEE

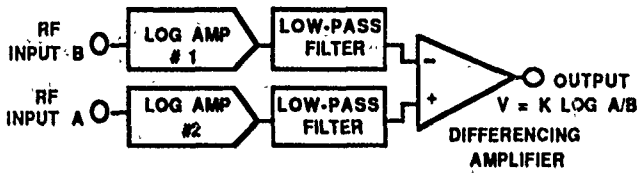


Figure 2. The log-ratio circuit block diagram.

In Figure 3 the transfer curve for one of the logarithmic amplifiers operating at 60 MHz is shown with an error plot giving the deviation from a straight line fit. Over the range from –50-dBm to –5-dBm the amplifier deviation is less than ±0.1-dB from the straight line fit. Amplifiers 1 and 2 have transfer slopes that differ by less than 1% and their zero crossing points are nearly identical.

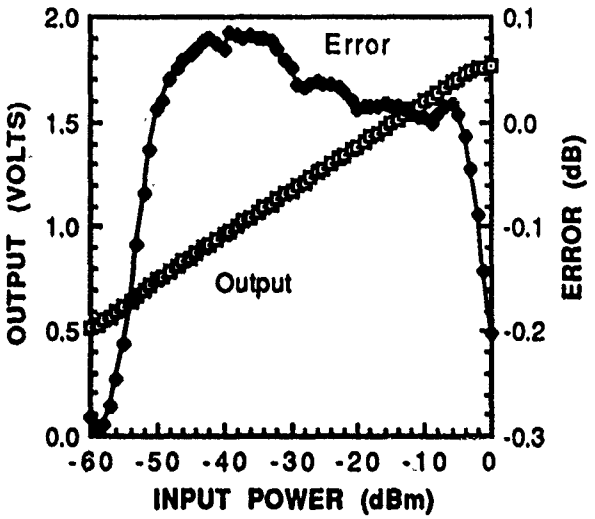


Figure 3. Transfer and error curves for a typical AD640 dual stage logarithmic amplifier.

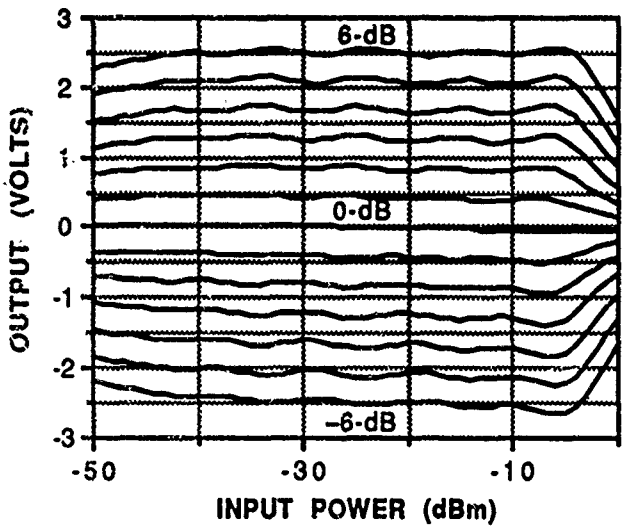


Figure 4. Log-ratio circuit transfer function curves for 60 MHz rf input signals.

The response of this circuit to 60-MHz rf input signals is shown in Figure 4. On the horizontal axis, the rf input power to the A and B channels is plotted, ranging from –50-dBm to 0-dBm. The family of curves represents 13 position values corresponding to signal input ratio changes from –6-dB to +6-dB in 1-dB steps. The center trace results when the two signals are equal (A=B). The upper traces correspond to A>B, whereas the lower traces result when A<B. Best operation occurs in the range of –45-dBm to –5-dBm, corresponding to a dynamic range of 100:1 in beam current. The transfer factor for the circuit is about 0.42 volts per dB.

III. Circuit Processing Errors

Ideally, the traces of Figure 4 should be straight horizontal lines. In reality the lines have non-zero slopes and they deviate from straight lines, indicating that the processed beam position output is a function of the rf-signal power level.

Some of the errors inherent in log-ratio processing are illustrated in Figures 5 and 6 where the 0-dB and 6-dB lines are normalized to the transfer factor. In each figure the lower curve is the output divided by the transfer factor, giving the normalized response in dB. The upper error curve is the same normalized curve with the straight line fit values subtracted. This curve shows the positional variation in the transfer function.

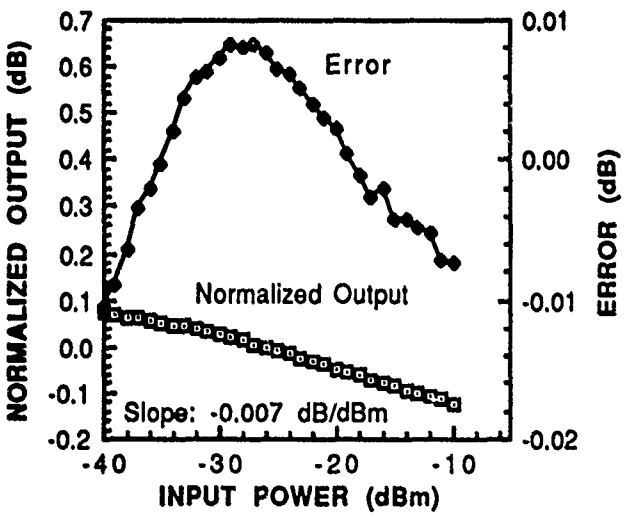


Figure 5. Error and normalized output curves for the 0-dB line of Figure 3.

For example, in Figure 6, the variation of ±0.14-dB compares to a variation of about ±0.05-dB for an AM/PM processor. If a typical 45-mm aperture microstrip probe having a sensitivity of 1.2 dB/mm is considered, the log-ratio positional error is ±0.12 mm. This compares to ±0.04 mm for the AM/PM processor, a factor of three smaller. The sinusoidal variation is a characteristic of the log-ratio circuit and is related to the successive approximation logarithmic amplification technique. It is described by the manufacturer's performance specifications.

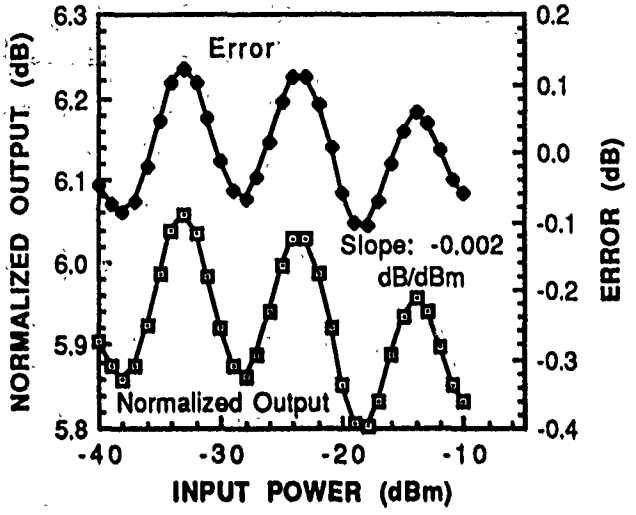


Figure 6. Error and normalized output curves for the 6-dB line of Figure 3.

IV. NOISE CONSIDERATIONS

Figure 7 compares the effective input noise of the log-ratio circuit operating at 60 MHz to that of an AM/PM circuit operating at 20 MHz and to the theoretical minimum noise. These plots are obtained by normalizing the measured RMS noise values at the circuit outputs by the transfer factor. The model for the theoretical noise plot assumes kTB noise at each back terminated probe electrode. A nominal bandwidth of 2 MHz for each plot is assumed. In the –40-dBm to –10-dBm input power range, the AM/PM circuit has a substantially lower noise level [4].

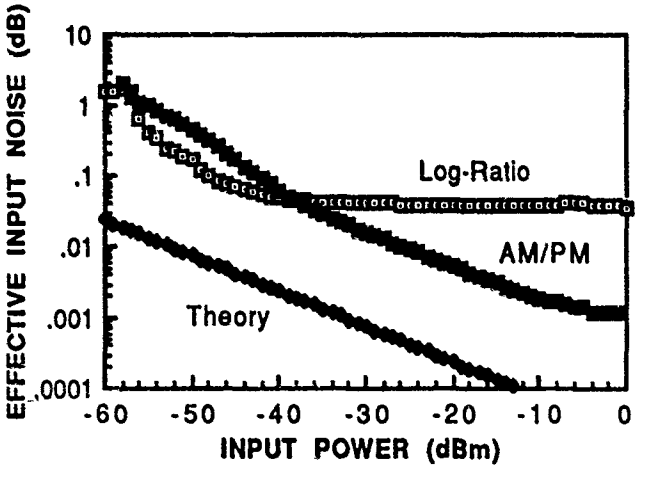


Figure 7. Noise comparisons of the log-ratio and AM/PM processors versus the theoretical minimum noise.

V. CONCLUSIONS

The log-ratio circuit technique gives a more linear response characteristic for circular cross-section beam-position probes than other types of processors. The output is a real-time normalized position signal with good bandwidth and the dynamic range is equivalent to that of the AM/PM processor. Potentially, the log-ratio processor will be less expensive to manufacture and its operating power will be lower. A major advantage over AM/PM processing is that cables connecting the pickup electrodes to the processor do not need to be closely phase matched because the log-ratio circuit responds to amplitude differences and is not sensitive to phase differences.

At this stage of development the positional error of the log-ratio circuit is substantially greater than that of the AM/PM processor. If a logarithmic-response, integrated-circuit rf-amplifier can be designed to be absolutely calibrated within ±0.1 dB, then the log-ratio circuit will become a more viable beam position processor.

VI. REFERENCES

[1] R. E. Shafer, "Beam Position Monitoring," AIP Conference Proceedings 212, Accelerator Instrumentation, p. 47, 1989.

[2] "Monolithic DC-to-120 MHz Log-Amp is Stable and Accurate," Analog Dialogue, Vol. 23, No. 3, p. 3, 1989, (Analog Devices, Inc., Norwood, MA 02062-9106).

[3] R. E. Shafer, "Characteristics of Directional Coupler Beam Position Monitors," IEEE Transactions on Nuclear Science, Vol. NS-32, No. 5, pp. 1933-1937, Oct. 1985.

[4] J. D. Gilpatrick, "Noise Measurements for Three Port Beam Position Circuits," AT-3:Technical Note, Los Alamos National Laboratory, 1991.

CAPACITIVE BEAM POSITION MONITORS AND AUTOMATIC BEAM CENTERING IN THE TRANSFER LINES OF GANIL

P. GUDEWICZ, E. PETIT

GANIL - B.P. 5027 - F-14021 Caen Cedex

Abstract

A non-interceptive beam position monitor, made of four capacitive electrodes, has been designed at GANIL in order to allow a permanent measurement of the ion beam position over a large intensity range (50 enA to 10 eμA). Signal processing is based on a 10 kHz heterodyne and on an amplitude to phase conversion in order to measure the beam position. The accelerator is equipped with ten of these probes, six of them on the first beam line. Seven other probes are planned. An immediate application of these monitors is the automatic beam centering. For this, two algorithms have been developed using the information on the center of gravity given by the beam position monitors which is then fed back to the steerers. The first is an iterative method based on an optimization algorithm (Pattern Search, Hooke and Jeeves). It consists in improving the criterion defined as the mean quadratic deviation of beam positions on the monitors. The second is a variational method which consists in determining for each steerers and each position monitor, the variation coefficient (mm/A) and solves a linear system. Both of these methods have been used on a section of beam line and have given similar and encouraging results. The next step is to center the beam on the completely equipped line.

I. INTRODUCTION

Up to now at GANIL, ion beam position in the beam lines was measured with profile monitors using wire grids. As they can not be used permanently to compute beam position in real time, a non interceptive beam position (BPM) has been designed. A first application of these probes was the development of software which should permit in a later stage the automatic centering of the beam in the different lines. The accelerator is equipped with ten probes, six of them on the first beam line. Seven other probes are planned.

II. TECHNICAL DESCRIPTION[3, 4]

1. *Expected technical specifications*

Technical specifications of this BPM were :
- beam intensity range : 10 enA to 10 eμA,
- beam structure frequency : 7 to 14 MHz,
- beam energy : 20 keV/u to 100 MeV/u,
- sensor aperture : 50 mm,
- accuracy of position measurement : < 10% ± 0.5 mm,
- resolution : < 0.2 mm,
- no tuning by the operators before measuring,
- automatic test procedure on request of the operators,
- mechanically compatible with profile sensors,
- linkable to the GANIL control system.

0-7803-0135-8/91$01.00 ©IEEE

2. *Sensor description*

a. Mechanical description

Probes are based on the electrostatic coupling, their geometry is a cylinder of 10 cm length cut into four equal parts. The ground electrode is machined in a copper block.

b. Sensitivity to beam position

The electrical charge Q_E deposited by the beam on an electrode is function of beam position P(x,y) and of beam current.

If Q is the total charge deposited on the four electrodes, the vertical position y is, for x = 0 :

$$y = R\,(Q_H - Q_B)/Q \qquad (1)$$

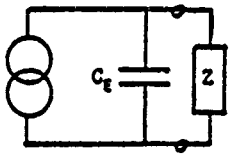
In practice, only the beam position at the center is important for us, so we detect

$$Py = (Q_H - Q_B) / (Q_H + Q_B) \qquad (2)$$

$$y = \frac{1}{2} R \times Py \qquad (3)$$

c. Sensitivity to beam current

The equivalent circuit of an electrode is :



Z is a 50Ω amplifier

$V_E(t) = 50\frac{dQ_E(t)}{dt}$ if $\frac{1}{C_E\omega} > 50\ \Omega$

As the electrode signal is very low, the second harmonic signal is extracted to avoid the RF parasitic noise.

$V_{E,2} = 50 \times 2\pi \times F \times Q_{E,2}$

$V_{E,2}$: rms value of the second harmonic of $V_E(t)$

For a quarter of cylinder

$$V_{E,2} = \pi\ 10^{-5} \times L \times F \frac{I}{\sqrt{W}} \qquad (4)$$

L : electrode length
F : beam structure frequency
I : beam intensity
W : beam energy in MeV/u

example : F = 10 MHz and L = 0,1 m

$V_{E,2} = 30\ I/\sqrt{W}$

that is 30 nV/enA for 1 MeV/u beam
3 nV/enA for 100 MeV/u beam

The theoritical resolution is limited by the electronic noise :

for a centered beam $y = \frac{V_{H,2}(t) - V_{B,2}(t)}{V_{H,2}(t) + V_{B,2}(t)}$

$V_{B,2}(t)$, $V_{H,2}(t)$ = 2nd harmonic electrode signals

with noise the measurement resolution is :

$$Ny = 3 \times 10^4 \times \frac{R \times N\sqrt{B}\sqrt{W}}{L \times F \times I} \quad (5)$$

N : amplifier noise
B : measurement bandwidth

for $N = 1\ nV/\sqrt{Hz}$, B = 10 Hz, F = 10 MHz, R = 30 mm and L = 0.1 m we get :

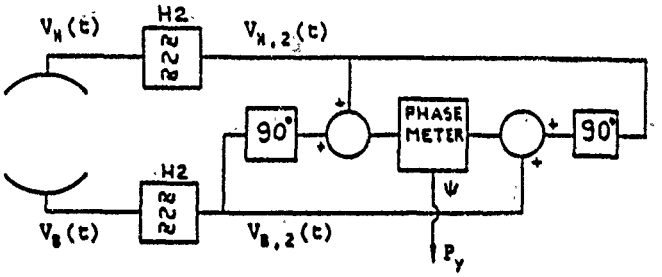
$$Ny = 3\sqrt{\frac{W}{I}} \text{ (in mm/enA)} \quad (6)$$

the expected resolution of 0.2 mm should be obtained with 1 enA if the energy beam is 1 MeV/u and 150 enA if the energy beam is 100 MeV/u.

3. *Processor*

a. Processor principle[1]

$V_{H,2}(t) = V_H \cos(\omega t + \phi)$ = 2nd harmonic of $V_H(t)$
$V_{B,2}(t) = V_B \cos(\omega t)$ = 2nd harmonic of $V_B(t)$



$C(t) = C\cos(\omega t + \psi c)$
$D(t) = D\cos(\omega t + \psi d)$

if $\phi = 0$ ($V_{H,2}(t)$ and $V_{B,2}(t)$ are in phase)

$C = D = \sqrt{V_H^2 + V_B^2}$

$$\tan \psi/2 = \tan(\psi d - \psi c)/2 = \frac{VH - VB}{VH + VB} = Py \quad (7)$$

if $Py \approx 0$ $\quad Py = \frac{\psi}{2}$

and $$y = \frac{R \times \psi}{4} \quad (8)$$

with R = 30 mm, the sensitivity to beam position is $\psi \approx 0.13$ rad/mm $\approx 7.5°$/mm

if $\phi \neq 0$

$y = 0 \rightarrow \psi = 0 \rightarrow Py = 0$
$y < 0.5\ R$

$$Py = \frac{\psi}{2} \cos \phi \quad (9)$$

The error is kept smaller than 10% when ϕ is not too large ($< \pi/3$)

b. Real processor system

Only the preamplification is made at the RF frequency to take advantage of the very low noise RF amplifier.

Then the 2nd harmonic of the electrode signals is detected by a 10 KHz heterodyne in order to realize the amplitude-phase conversion and the phase detection at 10 kHz.

The amplitude-phase conversion provides a phase noise $N\psi = \frac{4Ny}{R}$ [see (8)].

An analog memory allows to keep the position value when beam goes off. The beam position and the status of the processor are read by the accelerator control computer via the CAMAC.

III. AUTOMATIC BEAM CENTERING

Several steps to prove the faisability of automatic beam centering, using the information on the center of gravity given by the beam position monitor, have been initiated during the last two years, on a limited part of the first beam line (between the injector cyclotron and SSC1) and with only four position probes.

With this aim of view, two methods have been tested, using quite different research algorithms. The first of them is called iterative method and the second one variational method.

1. *Iterative method*[2]

This method is based on an optimization algorithm called Pattern Search of Hookes and Jeeves which has been adopted because it allows an iterative search with a low informatic cost. It is not necessary to solve complex numerical systems nor to know the analytical function of the criterion to optimize.

The general principle is : from a finite set of parameters which work on the criterion, the program finds a direction which improves the criterion starting from a local search around an initial point X_0 ($x_1, x_2, \ldots x_i$ with x_i value of the parameter i). In this direction, it arrives at the point x_1 for that the criterion is maximum, then it tries to find around X_1 another direction up to a point X_2 where the criterion is better, and so forth up to the optimUM. It may be possible to reduce the value of the optimization step of parameters such the field of variation.

The adjustment of this algorithm to the automatic beam centering is based on the following data :

- Criterion definition

As the purpose is to center the beam at the locations where its position is measured, the criterion is a global one, i.e. it is the mean quadratic deviation (m.q.d) of the beam positions on the four probes and it must be minimized.

$$\text{m.q.d.} = \sum_{i=1}^{4} ei^2/4 \text{ ; ei = beam position on the probe i}$$

- Constraint

It is only the variation limits of the steering equipments (for example ± 10 Amp for the steerers).

- Variation step

steerer : 0.5 Amp dipole : 0.2 Amp

For these values one step for one equipment gives a visible effect on the beam displacement. Other values seem to have no effect on the results but a sensitivity study must be done.

- Limitation of the criterion

With this algorithm and the criterion as defined it is necessary to give a limit to stop the search, otherwise programs could take too much time. Here, the limitation is

m.q.d. = 0.25, i.e. a beam deviation of ± 0.5 mm on each probe. When the program has finished one iteration, it is possible to stop it or to start another iteration with a smaller variation step.

2. *Variational method*

It is a numerical resolution method defined from experimental tuning considerations.

The principle is the following : the program searchs for each steering equipment and for each position probe the variation coefficient, in mm/Amp. From these coefficients, a linear equations system is deduced and it is solved as usually. The solution gives the current to apply to center the beam.

Initial hypothesises

- Linear effect of equipment on beam displacement.

It is assumed that the angle of deviation of the beam in a steerer is proportionnal with the current, inside the limits (± 10 Amp) and the angles are enough small to admit a linear displacement with the angle.

Then, with Y_i = beam position on the probe i,

X_j = current of the equipment j

$Y_i = a_{ij}.X_j + b_i$

with a_{ij} : variation coefficient of equipment on the probe i

b_j : beam position when $X_j = 0$

- The effect of an equipment is independent from another.

In the field of deviation angles the effect of a steerer on the beam is independent of the initial angle. Then, there is a non correlation between the deviation angles.

That gives :

$$Y_i = A_{ij}.X_1 + a_{i2}.X_2 + \ldots + a_{ij}.X_j + b_i = \sum_j a_{ij}.X_j + b_i$$

- The steering effects of other equipments are ignored.

The perturbating steering effects of other equipment (essentially the quadrupoles) are too complex to be described easily and become more and more weak that the beam is centered. The centering is made by convergence, i.e. using several times the algorithm.

The numerical system

Initial stage :

$$Y_{io} = \sum_j a_{ij} \cdot X_{jo} + b_i = B_i$$

For another set of currents :

$$X_i = X_{jo} + \Delta X_j$$

$$Y_i = \sum_j a_{ij} \cdot \Delta X_j + B_i$$

That gives the following equations sytem :

$$[Y]_i = [A]_{ij}\,[X]_j + [B]_j$$

with [Y] : beam position vectors

[A] : matrix of coefficients

[X] : current vector

[B] : initial conditions

The beam centering is given by [Y] = 0 and it is obtained by solving the system [A] . [X] + [B] = 0

The program organization

a. Statement of the initial state = acquisition of B_i

b. Determination of the matrix of coefficients

For each steering equipment and in order to take account of perturbating effects of other equipments, the coefficient is computed for six values of current, if possible (±2 Amp, ±5 Amp, ±7 Amp) by measuring the displacement on each probe. Thus, the matrix is made of mean variation coefficients.

c. Choice of linear system

It is necessary to have a square matrix, i.e. the same number of probes and steering equipments. For example, for the vertical plane, there are four probes and only three steerers. So, the linear system is made with the three probes with the most significant coefficients.

d. Calculation of the solution

The solution of the system is computed with the Gauss method with partial pivot.

e. Application of currents

Finally, the program applies the computed currents on the steering equipments. And, after checking the beam centering, it is possible to start the program at the point 1 again.

3. *Results*

position	Example 1		Example 2		Example 3	
(mm)	before	after	before	after	before	after
Probe 1	-6.8	+1.7	-2.2	+1.1	+3.7	+1.2
Probe 2	+3.5	+2.7	+5.7	+0.8	+6.6	-1.5
Probe 3	-2.5	+0.7	+0.7	+0.5	+1.7	-0.7
Probe 4	+7.7	+1.4	+12.2	+0.4	-4.4	0
Criterion	30.9	3.3	46.7	0.6	19.8	1.0
Plane	Horizontal		Vertical		Vertical	
Method	Iterative		Iterative		Variational	

The both methods have given encouraging results from the first tests. There is no great difference in the final centering. But the iterative method seems to be more interesting because it converges more quickly to a very correct centering with a lower informatic cost (less time consumed). Nevertheless, these programs which have been developed rapidly for these tests have to be improved to confirm their first results.

IV. CONCLUSION

As the first results of automatic centering seem to be correct, and as the running of these monitors are relaible it has been decided to equip the L1 beam line on totality. It is planned to adapt the programs to this new configuration and to test it on a whole beam line before using one to center automatically the beam in routine.

V. REFERENCES

[1] J. Bosser, L. Burn d, G. Ferioli "Beam position measurement by use of 90° hybrids" CERN int. report SPS/ABM/83-01/0058G, 1983

[2] R. Hooke, T.A. Jeeves, "Direct Search" : Solution at numerical and statistical problems, Journal of the association for computing machinery , vol 8 n° 2, 1961

[3] F. Loyer, "On line beam diagnostics at GANIL", 11th Int. Conf. on cycl. , Tokyo, 1986

[4] F. Loyer "Capacitive large range intensity beam position monitors at GANIL" A88-03

Operational Amplifier Based Stretcher for Stripline Beam Position Monitors

W. C. Sellyey and R. W. Kruse
Boeing Aerospace and Electronics Division
Boeing Defense and Space Group
PO Box 2499
Seattle, WA 98124, USA

I. CHARACTERISTICS AND DETAILED DESCRIPTION

The stretcher amp was designed to accommodate existing instrumentation at the Boeing Free-Electron Laser (FEL) facility. The beam format for this system consists of two macropulses per second. Each macropulse contains several hundred micropulses separated by 462ns. Thus, 462ns is the upper limit to which the pulse can be stretched. The corresponding filter bandwidth would be about 3 Mhz.

In the stripline data acquisition system, one of six striplines is switched to a single transient digitizer channel. Tektronix TSS46 microwave relay switches are used. The output of the TSS46 goes into stretcher amps described here. The resulting signals are digitized by Analytek 2004S or 2008S transient digitizers. The transient digitizer timing is such that it samples the negative peak of the stripline signal from each micropulse. It's analogue bandwidth is 300Mhz. For good temperature stability and linearity, the stretcher bandwidth should be much less than 300MHz, say 30Mhz. This defines a lower limit to the pulse width.

30Mhz was chosen for the filter bandwidth. Making the bandwidth smaller, would have required more gain in the output amplifier. This would have resulted in too much noise at the output. Additionally, temperature drift and nonlinearity would also increase.

Figure 1 is a block diagram of the stretcher amplifier. An overall gain of 10.5 is provided by the last two operational amplifiers. A single CLC401 could have been used to accomplish this, however, the resulting reduced bandwidth would have produced a larger temperature drift coefficient. The stretching filter is a linear-phase, low-pass filter with a 30Mhz 3db point. It has an approximate constant time delay and gaussian roll off up to 60Mhz.

The filter reflects significant amounts of power in the pass band. If the signal cable is connected directly to the filter, signal power will travel back to the stripline. Here it will be reflected and may combine with the signal from a later micropulse. This will result in erroneous signal voltages. The CLC400 before the 30 Mhz filter has about a 5K input impedance. The 50 ohm resistor provides the needed broad-band termination.

Adding the CLC400 causes the stretcher amplifier to be unacceptably nonlinear because a lot of incoming signal power is outside the 200Mhz bandwidth of this amplifier. A Mini Circuits PLP-100 filter is used to eliminate most of the signal above 100Mhz. This results in a return loss of over 20db for the amplifier up to 60 Mhz. Reflected power which combines with a later beam signal is additionally attenuated 7db by the cable. This results in a signal-voltage error of less than .1% in subsequent signal pulses.

The time delay and gain of the stretcher amp were measured. The gain drops by 3.2db at 30Mhz, and about 13db by 60Mhz. This is consistent with the intended gaussian behavior of the filter. The time delay fluctuates by less than .5ns around 26ns up to 60Mhz.

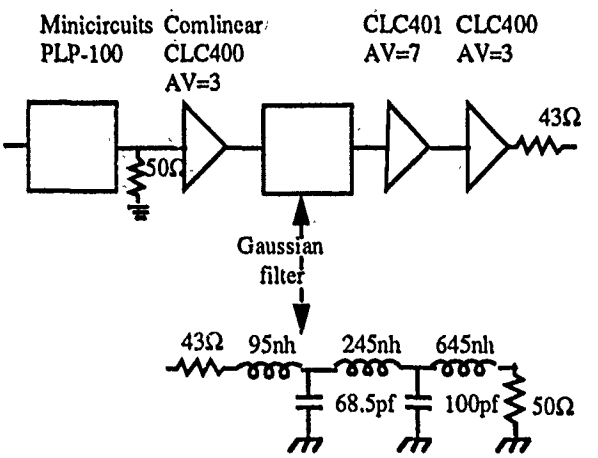


Figure 1. Stretcher amplifier.

The typical stretcher input signal consists of a negative leading lobe up to 900mv high and .9ns FWHM. This is followed by a 14ns positive tail with ringing and 1/10 the amplitude of the leading lobe. The output negative leading lobe is 9ns FWHM of about the same peak voltage as the input. The output positive trailing lobe has a peak value of about 3/4 the leading lobe, FWHM of about 10ns, and trails off in about 50ns.

II. NONLINEARITY MEASUREMENT

A Tektronix DSA 602 Digitizing Signal Analyzer was used to perform the linearity measurements. It was found that this oscilloscope had a nonlinear component to its response. Moreover, this nonlinearity depended on the signal shape being used. Thus, a direct input vs output measurement proved impractical. In the method described below, only output

0-7803-0135-8/91$01.00 ©IEEE

signals are observed by the oscilloscope. This assures that the signal shape is always the same. This also assures that frequencies involved in the measurement are kept an order of magnitude below the 1Ghz bandwidth imposed by the measurement setup.

Figure 2 shows the measurement setup. A pulser produces about 100v, 1ns FWHM, 10 pulses per second. This signal passes through the stripline test set. After a delay and attenuation, it serves as a trigger signal to the DSA 602. The stripline test set contains a standard stripline assembly of the type used in the Boeing FEL. One of the stripline outputs is connected to two variable attenuators in series. One of these attenuates in 1db step, the other in 10db steps. The signal then passes through 250 ft of RG-58. This is about the length of cable used with the FEL striplines to bring signals to the control room.

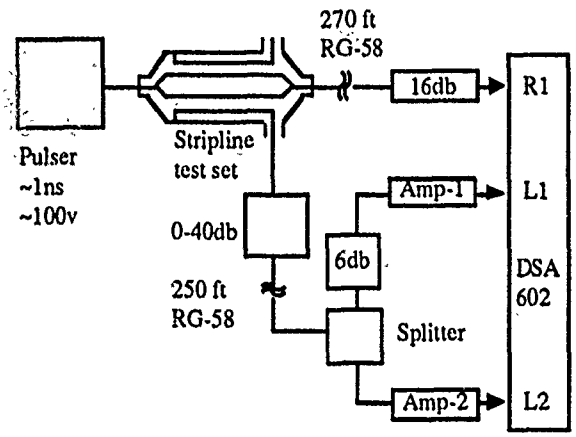


Figure 2. Nonlinearity measurement apparatus.

The signal is now split in two and fed into two amplifiers whose nonlinearity is to be measured. One stretcher amp gets about half the signal amplitude the other one does by introducing a 6db attenuator. If the two amplifier-plus-scope systems are linear, a plot of output 1 vs output 2 will be a straight line. If there is nonlinearity, the plot will no longer be a straight line. If the two channels are identical a fit to this data could be used to determine the n[illegible]v of the channels. If it is not assumed that the two channels are identical, an additional set of data is needed. This is done by moving the 6db attenuator from the amplifier 1 input to the amplifier 2 input.

Four sets of data were taken for four stretcher amplifiers. Their part numbers were SN001, SN002, SN003 and SN004. SN001 and SN002 were done as one pair. SN003 and SN004 were done as another pair. (All sets of data were taken with the same 11A72 plug-in module in the left slot of the DSA 602.)

A modification of the arrangement shown in figure 2 is used to measure the DSA602 nonlinearity. For this, everything is the same as for the amplifier measurements up to the end of the 250 ft. of RG-58. At this point, a stretcher amp is used to generate a wave form whose shape is the same as in the earlier measurements. A splitter and 6db attenuator are then used to generate signals for the L1 and L2 scope inputs. Two sets of data are taken with this arrangement, one for the 6db attenuator before L1, and one with the attenuator before L2.

As a first step in the data analysis, a linear fit is performed on the data (figure 3). All six sets of data display a complex nonlinearity. It consists of an oscillation around the straight-line fit. It is clearly due to the DSA602. The data involving the DSA602 only, are used to correct the data for the amplifiers. The result is then fitted with a linear-plus-quadratic function (figure 4).

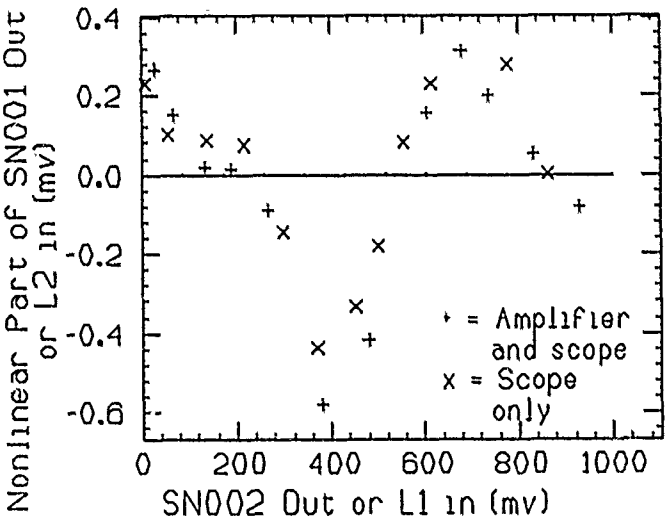


Figure 3. Example of nonlinear part of linear fit to the data. SN002 went to L1 and SN001 went to L2. The 6db attenuator was before SN001 or L2.

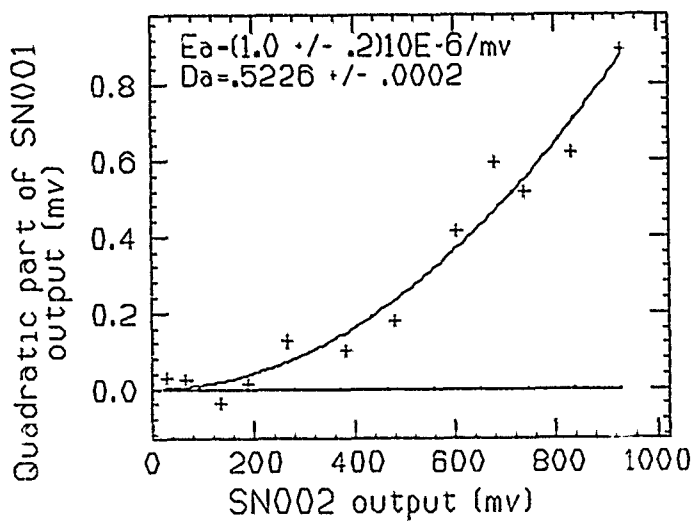


Figure 4. Example of corrected data. This shows the quadratic part of the fit of SN001 output ≈ .5 x SN002 output. The + are the data points and the solid curve is the quadratic part of the fit.

For the two amplifiers involved in a measurement, we write

$$v_{jo} = b_j v_{ji} + b^2_j C_j v^2_{ji} \quad (1)$$

Where j = 1 or 2, i and o refer to input and output. The fractional nonlinear part of the output is

$$\frac{b^2_j C_j v_{ji}}{v_{jo}} \approx C_j v_{ji} \quad (2)$$

Our objective now is to determine the C_j's

For the first of the two sets of data taken for each pair of amplifiers, $v_{2i} = f_a v_{1i}$. For the second set, $v_{1i} = f_b v_{2i}$. f_a and f_b are about .5, but are not exactly equal. Equation (1) can be inverted

$$v_{ji} = v_{jo}/b_j - C_j v^2_{jo}/b_j \quad (3)$$

Using this, one obtains

$$\begin{aligned} v_{2o} &= D_a v_{1o} + E_a v^2_{1o} \\ v_{1o} &= D_b v_{2o} + E_b v^2_{2o} \end{aligned} \quad (4)$$

The Ds and Es are expressed in terms of the Cs and fs. One can solve these to obtain

$$C_1 = \frac{D^2_a E_b + D_b E_a}{D_a D_b (D_a D_b - 1)} \qquad C_2 = \frac{D^2_b E_a + D_a E_b}{D_a D_b (D_a D_b - 1)} \quad (5)$$

The Ds and Es are determined in the fitting procedure described earlier. One thus obtains Table 1. 900mv is the maximum recommended output voltage for these amplifiers. As can be seen from the table, uncorrected nonlinearities will contribute less than 1/3% error. If corrected, the error will be reduced to .05%.

TABLE 1

	C(X1E-6/mv)	% nonlinearity at 900mv output	Worst case error (mm) a=1cm
SN001	-2.8±.5	.25±.05	.006
SN002	-3.4±.7	.31±.06	.008
SN003	-1.0±.6	.09±.05	.002
SN004	-1.7±.5	.15±.05	.004

A beamline stripline unit supplies four signals. We refer to these by v_n and v_s for the x-direction and v_t and v_o for the y direction. The error associated with the nonlinear part of the amplifiers is

$$\Delta \frac{x}{a} = \frac{C_s v^2_{os} - C_n v^2_{on}}{v_{on} + v_{os} + v_{ot} + v_{ob}} \quad (6)$$

C_n and C_s are the nonlinearity coefficients associated with the n and s amplifiers and a is the beam-tube radius. The measured Cs are all negative. If we assume that this is true for all amplifiers of this kind, the worst error will occur if one of C_s or C_n is zero. Taking all v = 900mv and using the Cs from Table 1, one gets the last column in Table 1. If the nonlinearity is corrected, the remaining uncertainty due to the measurement error in the Cs will be .002mm for a 1cm beam-tube radius.

III. Temperature Effects and Noise

The temperature dependence of gain and time delay are measured. The experimental setup is the same as in figure 6, except that no 6db attenuator is used and only one amplifier is used. The other amplifier is replaced by a direct connection from the splitter to the scope input. Thus, input and output waveforms are recorded simultaneously. The amplifier is placed in an oven and waveforms are recorded at 77.2 F and 117 F. The output voltage is at about 670mv. The ratio of the gain for the two temperatures is calculated. Also the change in time delay between the two temperatures was calculated. The average gain coefficient for the four amplifiers is -.0042%/C and the average time delay coefficient is 7.6ps/°C.

The amplifier noise is measured by putting the output of the amplifier into one of the scope channels, with no signal input to the amplifier. This is done with and without 250 ft of RG-58 connected to the amplifier input and with the amplifier input open, shorted and terminated in 50 ohms. The rms voltage feature of the DSA 602 in the measure mode is used to obtain the rms noise voltage. This is about 800 micro volts for all amplifiers under all conditions mentioned above. With the amplifier disconnected from the DSA 602, 200 micro volts of noise are observed, regardless of input termination. Thus, the amplifier output noise is taken as .8mv.

A BEAM POSITION MONITOR FOR AmPS

J.Noomen, J.Bijleveld, F.Kroes, T.Sluijk, H.Verkooijen,
NIKHEF-K
P.O.Box 41882, 1009 DB Amsterdam, The Netherlands.

Abstract

AmPS (Amsterdam Pulse Stretcher) is a 900 MeV electron storage and stretcher ring. Its construction started early 1991. A fast response, high resolution stripline type beam position monitor has been developed for the ring. The monitor has a quasi elliptic cross section. Its sensing strips have a length of $\lambda/4$; the operating frequency is 2856 MHz. The mechanical construction, the matching of the output ports and the on-line calibration system are described. The results of bench measurements as well as measurements with a 500 MeV beam are also presented.

Introduction

To obtain a duty factor of nearly 90%, the present accelerator facility will be extended with a stretcher ring [1],[2]. The horizontal tune of the ring is 8.30. For central orbit corrections 4 monitors per betatronwavelength are required adding up to 32 monitors in total. For measurement of tune, dynamic aperture and instabilities a fast response is required. Since the revolution time of the ring is 0.7 μs we decided the bandwidth of the monitors to be at least 15 MHz. The accuracy of position measurement must be 0.1 mm for beam currents down to 1 mA. Although for central orbit correction a fast response is not required, for reasons of uniformity we decided upon the fast response type for all monitors. The RF frequency of the ring has been chosen equal to the RF frequency of the accelerator (2856 MHz) [3]. Consequently we looked for monitors based upon this frequency. Stripline type position monitors have been chosen instead of buttons since the output power of a stripline electrode is roughly 20 db more than the output power of a button.

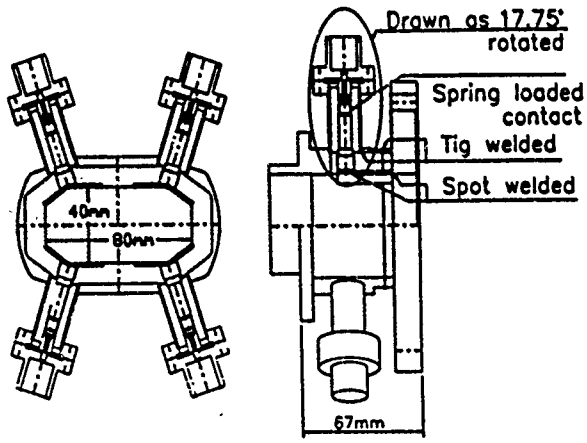


Fig.1. Electrode pick-up assembly.

Mechanical design

The fabrication of the various parts and the final assembly were ruled by the main condition that the electrical axis should not deviate more than 0.1mm from the mechanical axis. To reduce the costs we have chosen for TIG (Tungsten Inert Gas) welding instead of brazing, figure 1. The stripline electrodes are machined separately. At the short circuited side they are connected by spot welding to the stripline housing, see fig. 1. At the other side the inner conductor of the coaxial output port is connected to the electrode also by spot welding. Electrical contact with the output connector is provided by spring brushes. This avoids excessive stress in the ceramic of the vacuum tight output connector. Also the output connector can easily be replaced in case of vacuum leakage. To meet the 0.1 mm accuracy for the electrical axis all welding was caried out with special care using moulds if necessary.

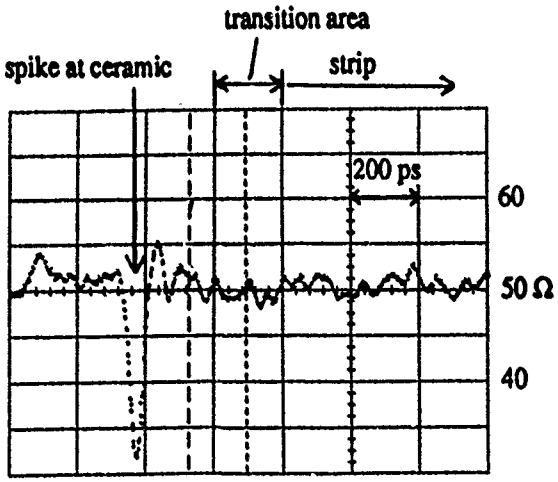


Fig.2. TDR plot of electrode impedance.

RF design electrode pick-up assembly

The available space in the ring is limited. To reduce required space and to lower the beam coupling impedance the lenght of the stripline has been chosen $\lambda/4$. The geometrical design was optimized to obtain equal sensitivities in x and y direction. The beam pipe has a quasi elliptical cross section with 8 and 4 cm as main dimensions (figure 1). All fundamental TM and TE modes that can disturb monitoring performance are below cut-off. For accurate position measurement and a low contribution to the overall longitudinal beam coupling impedance the strip assembly should be well matched to 50 Ω over a frequency range up to 20 GHz. Fine adjustment of the stripline characteristic impedance

0-7803-0135-8/91$01.00 ©IEEE

and matching the transition of the coaxial output port to the stripline has been carried out empirically. For this purpose a model has been constructed with 1.5 λ long, removable strips. In figure 2 a TDR plot of the final result is shown. The frequency ranged from DC to 20 GHz. We see that besides a spike located at the ceramic of the vacuum tight coaxial connector the impedance equals 50 Ω with an accuracy of +/- 2 Ω . For the transition area this could simply be achieved by small increments of the diameter of the central conductor of the output port and partial recess of the stripline length (figure 1).

Bench measurements

Bench measurements can be divided in measuring loss factor and measuring monitor response. In both cases the monitor is mounted between two pipes. Each pipe consists of 25 cm pipe with monitor cross section and a 25cm taper from monitor cross section to a coaxial connector. The coaxial connector is the same as used for the electrode pick-up assembly. For loss factor measurements the central conductor is a rod with the same diameter as the central conductor of the coaxial connector (7 mm). For monitor response measurements also a 0.3 mm wire is used as central conductor. For matching purposes this wire is connected to the inner conductor of the coaxial connector by means of a 190 Ω SMD. The measurements have been performed with a HP8720B network analyser. The bunch in the ring has a σ of 30 to 50 psec. Simulating a bunch width σ= 48 psec with the network analyser resulted in a loss factor of 0.04 V/pC. The monitor response measurements can be divided in calibration and position measurements. For calibration the rod is centered in the monitor with an accuracy of 0.03 mm. The output of the ports is measured with 0.02 dB accuracy. Since 1.2 dB corresponds with 1 mm displacement of the wire, the electrical axis can be calibrated with a total accuracy of 0.06 mm. For position response the wire is laterally displaced. The displacement can be more than 15 mm without exceeding the elasticity. Results of these measurements are combined with results of beam measurements shown in fig. 5.

Signal processing

The output power of each pick-up electrode is transmitted to a 90° hybrid through 2 m semi-rigid cable and an isolator (fig.3). Since the length of the stripline is λ / 4 only odd harmonics are coupled out. However the mixer attenuates the third harmonic already 50 dB with respect to the fundamental. Therefore filters in front of the hybrids are not required. Per diagonally positioned pair of electrodes AM is converted to PM in the hybrid. Behind the hybrid the frequency is converted by mixing to a 75 MHz IF frequency. The isolator is required since the stripline is shorted at the end. Reflections of the hybrid will be completely reflected by the stripline. Without isolator this will cause deterioration of the position measurement. For calibrating purposes the hybrid inputs are provided with 20 dB directional couplers. During the injection cycle (2.2 μs) RF power from the accelerator driveline can be fed into a calibration power line. Through this line RF power is distributed to the directional couplers of all monitors in

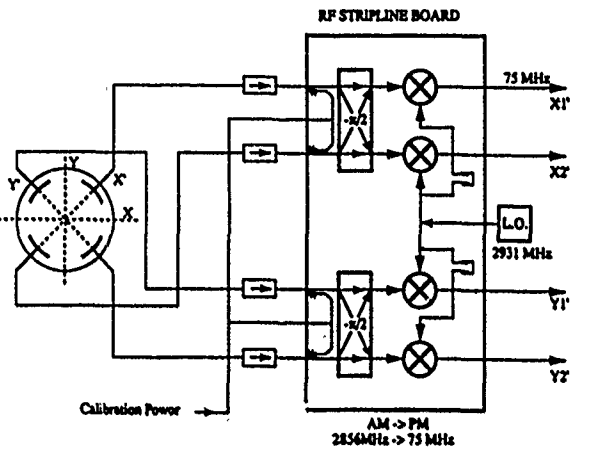


Fig.3. Block diagram of RF signal processing.

the ring. In this way a centered beam is simulated enabling to correct for thermal and (radiation) aging drifts of all components excluding those upstream of the couplers. However drifts in these upstream components (pick-up assembly, semi-rigid cable, isolator) are negligible. All components except isolators and oscillator are integrated in one stripline board. To compensate for different phase shifts of the mixers, adjustable phase shifters in the oscillator lines are incorporated on the stripline board. The 75 MHz output signal is transported outside the vault to the electronic unit shown in figure 4. The main specifications of the phase detector in this unit are,

bandwidth	15 MHz
phase range	-70 to +70°
phase linearity	0.2° for -40 to +40°
current dependent phase error	1° rms for 1 to 300 mA

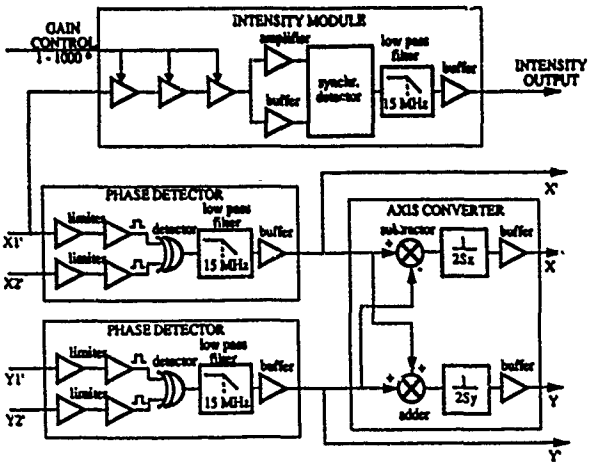


Fig.4. Block diagram of the electronic unit.

To measure amplitudes correlated with larger phase shifts than 70°, phase compression can be achieved by interconnecting the inputs X1',X2' and Y1',Y2' through resistors. The sensitivities Sx and Sy in figure 4 are defined by,

$$Sx = dX'/dx = -dY'/dx \quad \text{and} \quad Sy = dX'/dy = dY'/dy$$

Beam measurements

Tests have been done with a 6 mA peak current 380 MeV beam. The beam has been displaced in vertical and horizontal direction over +/- 3.5 mm. The response was linear. This is shown in figure 5 by the shaded area. The nonlinearity outside the shaded area was extrapolated from bench measurements. The sensitivities were ,

$$Sx = 3.0°/mm \quad \text{and} \quad Sy = 2.9°/mm$$

The resolution was 0.2 mA.mm. The measured sensitivities are about 30% below a theoretical estimate. We don't have an explanation yet for this deviation. Further measurements are going on.

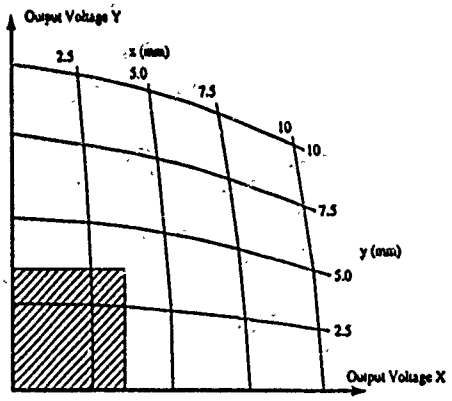


Fig.5. Monitor response, isoposition lines, shaded area shows beam measurements, outside shaded area shows extrapolations from bench measurements.

Acknowledgement

The work described in this paper is part of the research program of the National Institute for Nuclear Physics and High Energy physics (NIKHEF), made possible by financial support from the Foundation for Fundamental Research on Matter (FOM) and the Netherlands Foundation for Scientific Research (NWO).

References

[1] G. Luijckx e.a., The Amsterdam Pulse Stretcher project (AmPS), Proceedings of the 1989 IEEE Particle Accelerator Conference, Chicago, IL, pp. 46-48.

[2] G. Luijckx e.a., Status of the Amsterdam Pulse Stretcher project (AmPS), Proceedings of the European Particle Accelerator Conference, 1990, Nice, pp 589-591

[3] F. Kroes e.a., A fast amplitude and phase modulated RF source for AmPS, Proceedings of the 1991 IEEE Particle Accelerator Conference, San Francisco, May 6-9

The SSRL Injector Beam Position Monitoring Systems *

W. Lavender, S. Baird†, S. Brennan, M. Borland‡, R. Hettel, H.-D. Nuhn
R. Ortiz, J. Safranek, J. Sebek, C. Wermelskirchen§, J. Yang
Stanford Synchrotron Radiation Laboratory, P.O. Box 4349, Bin 69, Stanford, CA 94309-0210

Abstract

This article describes the software and processing electronics of the systems used to measure electron beam trajectories for the new SSRL injector for SPEAR.

I. Introduction

The beam position monitoring system of the SSRL injector forms a vital component of its operation.[1][2] Several different types of instrumentation are used to measure the position or intensity of the electron beam in the injector. These include current toroids, fluorescent screens, Faraday cups, the "Q" meter, a synchrotron light monitor, and electron beam position monitors. This paper will focus on the use of the electron beam position monitors to measure electron trajectories in the injector transport lines and the booster ring. The design of the beam position monitors themselves is described in another paper to be presented at this conference.[3]

There are three different beam position monitor systems in the injector. One system consists of a set of five BPMs located on the injection transport line from the linac to the booster (known as the LTB line). There is a second system of six BPMs located on the ejection transport line (known as the BTS line). Finally, there is an array of 40 BPMs installed on the main booster ring itself. We will consider first the booster BPMs.

II. Booster BPM System

Beam position monitors are located at 40 positions spaced equally around the ring. Of these, 21 are connected to the processing electronics. The connected BPMs are mostly those installed at odd numbered girders of the ring. Extra BPMs are connected at girders 14 and 16, just after the injection point. There is no BPM at girder 13, since its place is taken by a fluorescent screen.

Since the SSRL injector ramps from injection to ejection energy 10 times a second, one of the design criterion for the booster beam position monitor system is that it be able to measure a series of electron orbits during a particular 50 millisecond ramp up cycle. As it would be far too expensive to have dedicated processing electronics for each button of each BPM, the later stages of the processing electronics are shared by multiplexing the signals from the various BPMs down into one four-channel set of electronics with one channel for each button of a BPM.

The multiplexing occurs in two stages. The first stage is handled by a set of 12 ten-to-one multiplexer modules known as R10T modules which use a design[4] developed by SLAC for the SLAC Linear Collider project. The R10Ts are grouped into three banks of four R10Ts each with each R10T in a bank dedicated to a particular BPM button location. The four pickup buttons of each BPM are arranged in an orientation such that they pick up a signal to the upper left from the beam, to the upper right, to the lower left, and to the lower right from the beam. This gives sufficient information to calculate the x and y position of the beam at that BPM. The four cables from a given BPM are routed into separate R10Ts, so that all four buttons of a BPM may be measured simultaneously. Each R10T has one output, so there are 12 outputs to be fed to the next level of multiplexing.

The second level of multiplexing is handled by a device known as the "fast" multiplexer.[3] This is a four channel device which switches any one of four inputs to an output channel. Thus, there are 16 potential inputs and four output channels. Since we currently use only 12 R10Ts, only 12 of the inputs are used and the other four are left disconnected. Each of the output channels of the "fast" multiplexer corresponds to one of the four buttons on a BPM, namely, upper right, upper left, lower right, or lower left.

The electronics that processes the analog BPM signal is a combination of equipment designed and used by SLAC[4] and custom equipment of our own.[3] The typical input signal to our system is a mostly unipolar pulse, 2 ns wide, with an amplitude of 10 to 50 mV. The signal first passes through a 3 pole, 12 MHz high pass filter, which removes the large noise signals generated by the modulators, klystrons, and other noise sources in the accelerator. Then the SLAC RF BPM heads stretch and amplify the pulse. The pulses are still the same amplitude, but now 20 ns wide. The final analog stage is an integrating peak detector. Each pulse raises the output by one half the difference between the input pulse amplitude and the current output level. Negative pulses leave the output unchanged. Since the periods of our machine tunes are less than 5 microseconds and we sample each monitor for 25 microseconds, this system integrates out the amplitude modulation caused by the tunes. The voltage put out by the integrator is measured by a CAMAC-based Lecroy 6810 waveform recorder. After a complete series of orbits is recorded, the waveform recorder is read out by the control computer for display and later analysis.

Guard times of 5 microseconds before and 10 microseconds after the bank switching of the "fast" multiplexer are

*Work supported by the Department of Energy, Office of Basic Energy Sciences, Division of Material Sciences.

†visiting SSRL from CERN

‡Now at Argonne National Laboratory, Argonne, Illinois, U.S.A.

§Now at Gesellschaft für Mathematik und Datenverarbeitung (GMD), Bonn, Germany

0-7803-0135-8/91S01.00 ©IEEE

added to each BPM measurement for a total measurement time per BPM of 40 microseconds. This guard time is required since the "fast" multiplexer puts out a burst of electronic noise when it switches. The R10T modules also put out electronic noise when they switch, but the software arranges that they are only switched at times when the "fast" mux is looking at an R10T bank other than the one which is switching.

This processing system was chosen because of its accuracy and simplicity to implement. The final stage electronics are matched and linear over a dynamic range of 30 dB. This allows us to use the same electronics on all BPMs, regardless of the differences in signal attenuation from one BPM to another due to signal cable lengths. Our overall system allows us to measure beam positions to an accuracy of a few tenths of a millimeter over an order of magnitude of beam current in the accelerator.

Since the booster BPM system is configured to allow for 30 BPMs to be read during a ramp cycle, the total amount of time required to measure beam positions once from all the BPMs is 30 * 40 microseconds or 1200 microseconds. A dead time of 800 microseconds is appended to each measurement cycle in order to make the measurement interval come out to a round number, namely, 2 milliseconds. After the end of each measurement interval, the CAMAC hardware is programmed to immediately start another measurement cycle, for a total of 33 measurement cycles during a given ramp of the booster. Thus, the BPM system records measurements from 0 to 66 milliseconds into the ramp, which is well past the peak magnetic field point at 50 milliseconds. Reading out the information from the Lecroy waveform recorder, analyzing it, recording it in the control system database, and setting up for the next scan takes about one second. So, in practice, the BPM system measures orbits from a ramp cycle about once every two seconds. This has generally been found fast enough to give good feedback to operators of the machine.

During a ramp cycle, CAMAC instructions must be sent out at precise intervals in order for the measured orbits to accurately reflect the nominal measurement times. Since the main control computer is a multitasking system, it is not well suited to performing this function. Therefore, sequencing of instructions is offloaded onto a Kinetics Systems list sequence processor installed in the BPM CAMAC crate which functions as an auxiliary crate controller. Its function is to ensure that the CAMAC commands are sent out at a constant rate. The central control system computer's function in this case is to program the instruction list in the list sequence processor, enable the BPM system to receive an external trigger, and read out and process the BPM data at the end of the ramp cycle. Once the BPM system receives its external trigger, the list sequencer collects data asynchronously until it has recorded its 33 measurement cycles.

The external trigger for the booster is provided by a peaking strip. This is a device in the booster ring which consists of a magnetic material with a very narrow hysteresis curve and a steep magnetization curve. Thus, a change from a slightly negative magnetic field component in the booster dipole magnets to a slightly positive field causes the peaking strip to switch its magnetization from full magnetization in one direction to full magnetization in the opposite direction. This produces a pulse at the time that the ring magnet's magnetic field is at the field for injection, which is used as a timing trigger by many systems in the booster in addition to the booster BPMs.

The Lecroy waveform recorder in this system is programmed to digitize individual samples in each of its four channels in synchronization with an external clock signal. This clock signal is provided by a device known as the "slow" multiplexer. The "slow" multiplexer is intended for future expansion of the system to record other signals, but it is currently used only to provide the external clock for the Lecroy module. The command to the "slow" multiplexer to provide this signal forms part of the CAMAC list programmed into the list sequence processor. This mode of operation of the Lecroy module is not standard for it, since it normally expect the clock signal to always be present. But with some amount of work, it has proved possible to use the 6810 in this mode.

Once the BPM signals are read out of the Lecroy module, the control system takes sums and differences between the four signals, upper right, upper left, lower right, and lower left. These are used to calculate the x and y position of the electron beam at that BPM for that measurement cycle. This information is stored in the form of 33 complete orbit measurements in the control system database. The orbit measurement may be paused at any time to allow the orbits to be recorded to permanent storage. A program also exists that reads a given measured orbit from several ramp cycles and averages them to give better statistics for the orbit measurement.

A sliding buffer of 10 of these measurements is displayed on an operator menu, which allows the operator to see the electron orbit change as a function of time. An example of the appearance of one of these menus is shown in Figure 1, which demonstrates the "waterfall" effect used to achieve an illusion of depth.

III. Transport BPM System

The beam position monitor systems for the injection and ejection transport lines use the same kind of BPMs as the booster BPM system, differing in the processing electronics and the software interface. The transport line BPM system design faces a different kind of challenge from the booster BPM system. Instead of having to make many measurements over a period of tens of milliseconds, the transport BPM system must only make a measurement once every 0.1 seconds or more. However, it is important that the measurement be made at precisely the time the electron beam is passing.

The transport BPM systems also use R10Ts to multiplex signals from multiple BPMs, but since each transport line

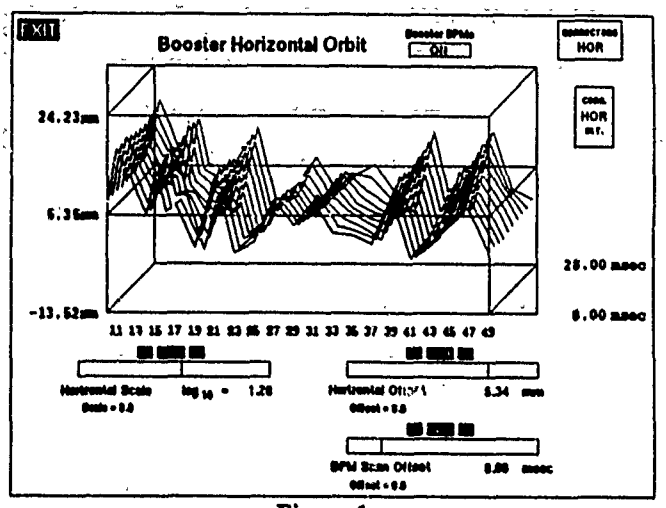


Figure 1
Injector control system horizontal orbit menu

has less than 10 BPMs, a second level of multiplexing is not necessary. Thus, the outputs from the R10T modules are fed into RF heads and then sent on to a pair of dual track and hold modules built by SLAC[4] which function as peak detectors. The transport BPM systems make use of a feature of the RF heads not used by the booster BPM system. This is the ability to sum the signals from each of its inputs to provide an output trigger signal which is used to reset the dual track and hold modules. Since the dual track and hold modules once triggered will simply store the largest signal they see, it is not necessary to synchronise the operation of the BPM system in any other way. In fact, the R10Ts are multiplexed asynchronously from any external trigger, with the only requirement being that they must dwell on a particular BPM for 0.12 seconds to ensure that the electron beam has passed through the BPM at least once. The control computer computes sums and differences of BPM button signals in a similar manner to the booster BPM system and displays the calculated x and y positions on a computer menu.

Some problems have been encountered in the operation of the transport BPM electronics while the injection and ejection kickers are on. The problem is that the kickers generate RF signals that propagate down the beam pipes to the locations of the BPMs and induce signals in their processing electronics. During normal ramping, this kicker "noise" is sufficient to trigger the dual track and hold well before the passage of the electron bunch, except for the first two BPMs in the injection line. This is not that much of a problem for steering the injection line, since one can turn off the injection kicker until the beam has been well steered. This solution is, of course, not possible for the ejection line, since if the ejection kicker is turned off, there is no beam in the ejection line. In actual operation, the normal practice has been to use the automatic measurement system for the injection line and steer through the ejection line by looking at the BPM signals directly on an oscilloscope.

The fact that the first two BPMs in the injection line are sufficiently far enough away from the injection kicker for its noise to not perturb them is quite fortunate. This is because position information from the second LTB BPM (the BPM after the first bending magnet) is used by the linac energy feedback system as a measure of the current acceleration energy of the linac. This feedback system is described further in another paper to be presented at this conference.[5]

IV. Conclusion

The injector beam position monitor systems have successfully been used to measure electron orbits and to diagnose configuration problems. The booster BPM system has proved capable of measuring orbits at intervals of 2 milliseconds during the ramp every two seconds. Further development is in progress to improve the system.

V. References

[1] H. Wiedemann, "3 GeV Injector Synchrotron for Spear." At this Conference.

[2] S. Baird et al, "Commissioning the SSRL Injector." At this Conference.

[3] J. Sebek et al, "Diagnostic Instrumentation for the SSRL 3 GeV Injector for SPEAR." At this Conference.

[4] SLAC Instrumetation and Control Division, "SLC Control System Hardware Manual, Release 3.0." SLAC internal document, 1988.

[5] L. Emery, "Energy Feedback system for the SSRL Injector Linac." At this Conference.

DELTA Beam Position Monitor

S. Brinker, R. Heisterhagen, K. Wille
Accelerator physics
University of Dortmund

Abstract

For the electron storage ring DELTA[1] (Dortmund ELectron Test Accelerator) a beam-position-monitor system based on button pickups has been designed. Two different concepts for the monitor electronics have been developed obtaining a long-term stability better than +/- 150 μm and a short-term resolution below +/- 10 μm. There are no hybrids integrated in the electronic circuits as all four button signals should be amplified and digitized to provide redundancy. First, a concept using four separated electronic branches, one for each button, was tested. Then a concept with a multiplexer in front followed by only one amplifier was designed.This concept, the electronic circuits and the measurements will be presented.

1 General elements of the BPM

The beam-position-monitor system of the DELTA synchrotron and storage ring is based on pickup monitors with four pickups[2] (fig 1.). The required short time resolution is about +/- 10 μm. The absolute accuracy has to be less than +/- 150 μm during some weeks [2][5].

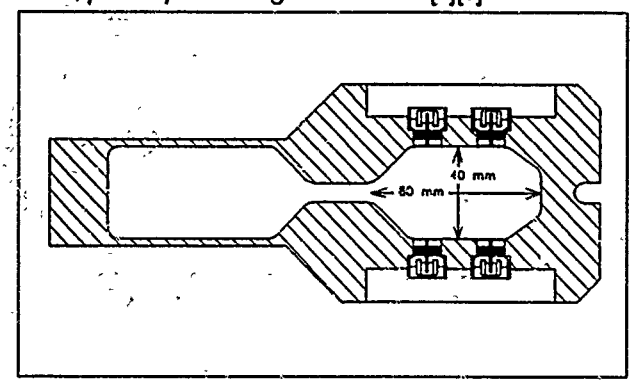


Figure 1: *Cross section of the DELTA beam position monitor.*

The dependence of the pickup signals on the beam position will be subject to further investigations, but in the central region of the monitor a linear approximation will be sufficient. In the vicinity of the orbit, the linear aproximation holds [1]

$$\Delta x = \alpha * \frac{s1 + s2 - s3 - s4}{s1 + s2 + s3 + s4} \quad (1)$$

$$\Delta z = \alpha * \frac{s2 + s3 - s1 - s4}{s1 + s2 + s3 + s4} \quad (2)$$

where α is the so called 'monitor constant' and s1...s4 are the signals received from the four pickups. α depends on the geometry of the monitor and is estimated to be less then 20 mm for the DELTA monitor. The following investigations refer to this value of α.

The monitor frequency is choosen to be 500MHz because it is the lowest frequency component in any mode of operation with different numbers of bunches [5].

The pickup signal is estimated to be [3]

$$U_{Pickup}[mV] = 0.5 * I_{beam}[mA] \quad (3)$$

with centered beam.

2 The BPM concept

It was decided to amplify each pickup signal separately as it is possible to calculate the beam position from only three of the four signals. The advantage is redundancy.

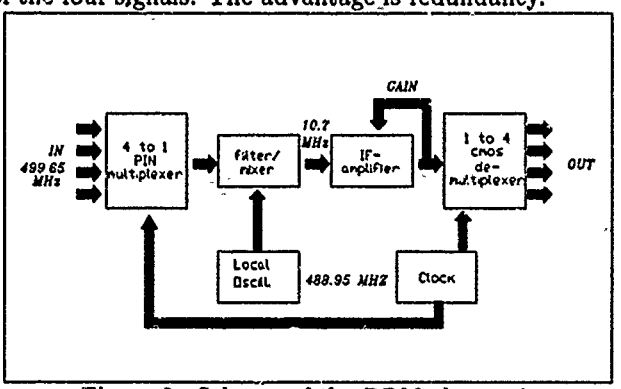


Figure 2: *Scheme of the BPM electronics*

A concept was developed with only one intermediate frequency (IF) amplifier and a four-to-one PIN switch multiplexer in front, which is subject to the following account. (fig. 2)

[1]Other contributions of DELTA to this conference
[2]The pickups were developed by the ESRF.

0-7803-0135-8/91$01.00 ©IEEE

3 The mixer circuit board

The pickups are connected to the filter/mixer unit by semi-rigide cables with SMA connectors. The filters are of the low-pass type of 5th order for protecting the following PIN switch from high frequency components of the pickup signal. The low passes are made in hybrid technique, combining printed inductivities and discrete chip capacitors (fig 3). Using discrete capacitors is necessary since the dimensions of printed capacitors are too large for mounting all four filters on one side of a standard circuit board, with sufficient distance. The subsequent multiplexing is performed by a PIN switch using a 100Hz clock signal. The output signal is mixed down to the intermediate frequency of 10.7MHz and then sent to the coaxial output channel.

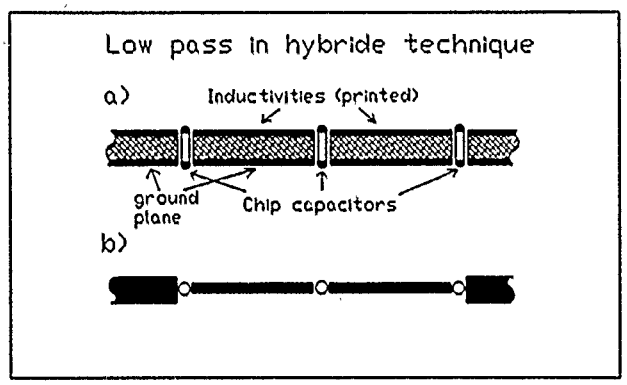


Figure 3: *Low-pass filter with chip capacitors and printed inductivities.*
a) Cross section of the circuit board
b) top view of the circuit board.

4 The IF amplifier board

The IF amplifier consists of two gain-controlled integrated circuit amplifiers followed by a fixed-gain amplifier and a fast rectifier (demodulator). The demodulated signal is distributed to two circuits: 1) One part of the signal is averaged over a long time and used for the gain control of the two leading amplifiers. Therefore, the output signal is independend of the beam current resp. the average of the four pickup signals. 2) The other part of the signal is demultiplexed to the four output channels, each averaged by a long-time-constant RC filter. This four 'DC' signals are sent to the output of the board.

5 The local oscillator board

The local oscillator is of the phase-locked-loop type, consisting of a crystal reference oscillator, a voltage controlled oscillator (VCO) of about 500MHz, a 1.256 divider and a phase comparator. The resonance frequency of the VCO is determined by a stripline resonator tuned with a voltage-variable capacitor, known as "varactor". The 500MHz signal is amplified by a Monolythic Microwave Integrated Circuit and distributed to four coaxial outputs by a power divider. One local oscillator provides four mixer boards because there will be four BPM electronics in one rack.

6 Measurements

The long-time frequency drift of the local oscillator is less then 10^{-6}, respectively 500Hz. Therefore there will be no problem with the narrow-band crystal filter (7kHz bandwidth) in the IF amplifier.

Fig. 4 shows the arrangement for testing the BPM electronics. The input signals are provided by a signal generator, a power divider and, if necessary, some attenuators. The analysis is done by a multi-channel millivolt meter conected to a personal computer.

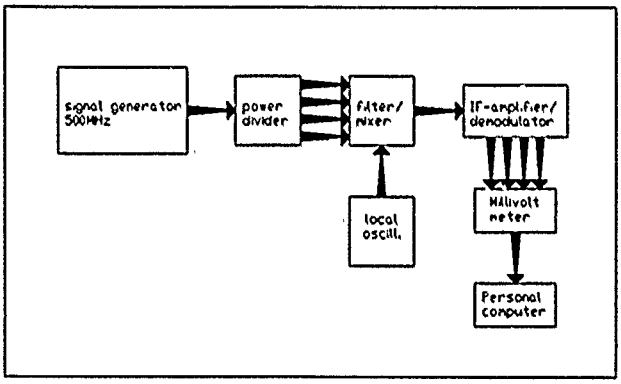


Figure 4: *Test arrangement for the BPM electronic.*

Fig. 5 exhibits the relative drift in μm during four days. The drift was less then +/- 15μm.

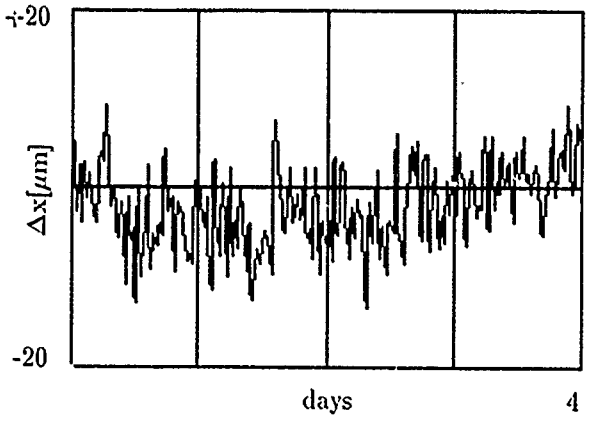


Figure 5: *Drift of the BPM electronics during four days.*

Fig. 6 shows the dynamic range of the BPM electronics. Figured is the evaluated position of the simulated beam versus the average pickup voltage. One can see that the linear range runs from 0.66mV to 118mV. This represents

a beam current varying from about 1.3mA to 240mA (see eq. 3) with an error of less than +/- 25μm.

Since the sensitivity of the IF amplifier can be choosen in a wide range, it is possible to shift the lineare range to higher beam currents, for example 500 mA. If necessary, this can be done after measuring the prototype of the DELTA monitor.

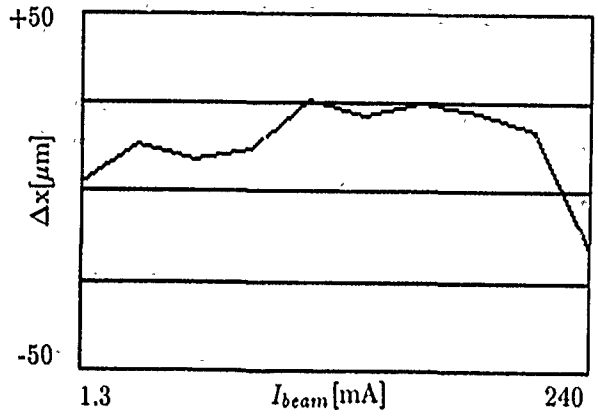


Figure 6: *Linearity of the BPM electronics in the range of beam currents from 1.3 mA to 240 mA.*

Fig. 7 is a plot of the distribution of 1000 measured values with constant signal input. It is a measure of the electronic noise. The standard deviation is less then 5μm.

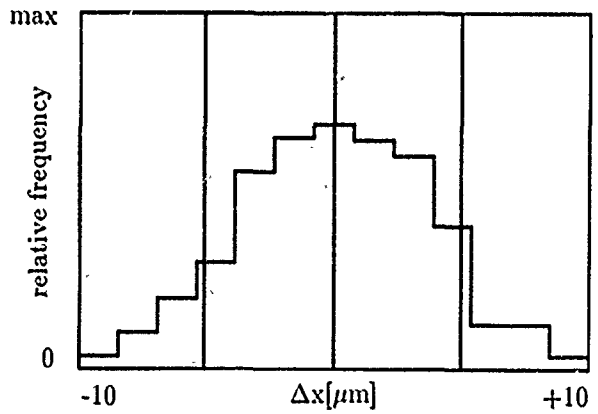


Figure 7: *Resolution of the BPM due to electronic noise.*

7 Conclusion

A prototype version of the BPM electronics was tested. For a fixed monitor constant α of 20 mm, a resolution of less then +/- 5μm is achived. Both, the deviation from linearity and the drift are less then +/- 25 μm. The overall deviation is less then +/- 50μm. Therefore the electronics fulfils the required demands.

8 Referenices

[1] J. Borer, C. Bovet: Computer response of four pick-up buttons in an elliptical vacuum chamber, LEP Note 461, 1983.

[2] DELTA Group, Status Report 1990.

[3] S. Brinkmann, R. Heisterhagen, K. Wille: Report on the Electronics for the BPM, DELTA Internal Report 1990.

[4] S.Brinker, Detailed Description of the BPM electronics, DELTA Internal Report 1991 (in preparation).

[5] S.Brinkmann, L. Falck, N. Marquardt, K.Wille: Design Study of the Beam Position Monitor for the ESRF, 1988.

Beam Position Measurement System for SRRC

G. J. Jan* and K. T. Hsu
Synchrotron Radiation Research Center
Hsinchu 30077, Taiwan, R. O. C.
* also Department of Electrical Engineering, National Taiwan University
Taipei 10764, Taiwan, R. O. C.

Abstract

The beam position monitors, processing electronics and VME crate based data acquisition system have been designed and implemented recently in SRRC. The beam position monitor is composed of four button-type electrodes mounted on skew position of vacuum chamber. The switched detector processing electronics and the high speed data acquisition system were chosen for fast beam position measurement due to the requirement of the global harmonic orbit correction and the local beam position feedback system. The beam position measurement system will be provided fast and accurate beam position information for the 1.3 GeV storage ring.

REQUIREMENT OF BEAM POSITION MONITORING SYSTEM

The beam position measurement system should be fulfilled the following goals:

* First turn beam trajectory measurement with accuracy ±1 mm to aid commissioning of the storage ring.
* Accurate beam position measurement for closed orbit correction.
* Provide fast beam position information for global harmonic feedback and local feedback purpose.
* High dynamic range, working form 0.2 mA to 200 mA of beam current with small current dependent accuracy.
* To aid lattice function measurement.

To meet above stringent requirements, all elements and modules in beam position measurement system should be carefully designed and implemented.

BEAM POSITION MONITOR

There are 47 sets of beam position monitor (BPM) to provide beam position information for the 1.3 GeV electron storage ring [1], each BPM is composed of four button type electrodes with SMA feedthrough connectors that are welded on the vacuum chamber directly as shown in Figure 1. The BPM will mount on the BPM fixture which is fixed on the magnet support near the quadrupole magnet via an aluminum frame block. The adjustment mechanism of BPM are used to adjust the position of BPM. The frame block fixes tightly with BPM and provides reference planes for BPM calibration before installation, and also provides reference plane for alignment with quadrupole bore after being installed. The setting error of BPM will be measured by dimensional measurement

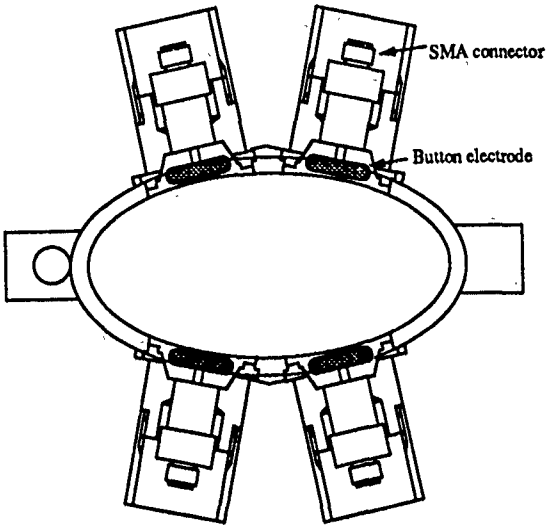


Figure 1. Beam position monitor.

equipment. The setting offset of each BPM will provide the correction information for beam position measurement.

The sensitivity of the BPM is about 7.5% and 6% change in signal strength near the center of the BPM in horizontal and vertical direction respectively. The calibration coefficient for nonlinearity correction are find out from the data of the BPM calibration measurement.

PROCESSING ELECTRONICS

The global harmonic feedback and the local beam position feedback plays an important role in the low emittance synchrotron light source. The high speed processing electronics for the beam position monitor are highly desirable.

Processing electronics is shown in Figure 2 which is slight modify from the design of NSLS [2]. There are several synchrotron radiation facilities [3,4,5] which are under construction will build the similar system. This approach uses solid state switch as RF multiplexer to select signal pickup by the button electrode. The selected signal is sent to the IF module by a 20-50 meter high quality coaxial cable. The IF module is a high dynamic range superheterodyne receiver turned at the 200th harmonic of the revolution frequency (500 MHz) to amplify and to detect the beam signal. The processing electronics are packaged in Eurocard bin. The signal from the BPM is connected to the front panel and the processed

0-7803-0135-8/91$01.00 ©IEEE

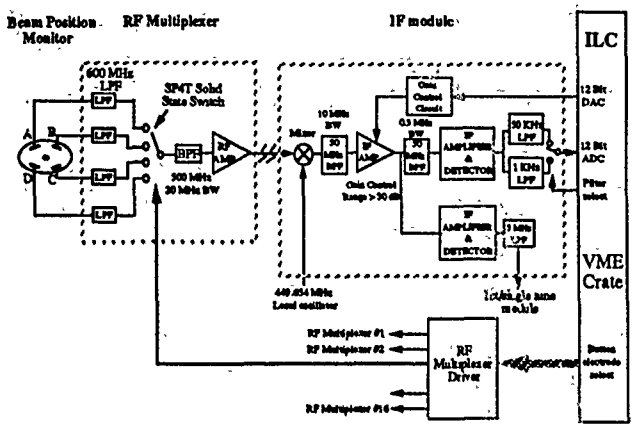


Figure 2. Functional block diagram of the processing electronics.

signal is send to VME crate based intelligent local controller (ILC) via backpanel DIN connector.

The beam signal from four button electrodes are read into ILC sequentially. The detected signal of processing electronics for four electrodes will be added, subtracted and normalized to obtain normalization horizontal and vertical signal by ILC. The beam position can be obtained by using suitable algorithm. The nonlinearity of BPM can be also linearized by appropriate linearization method.

The first turn trajectory measurement is helpful for the machine commissioning. Six special VME modules will be used to support the first turn and next 10^3 turns beam position measurement. This module have eight channels with 8 bits video analog-to-digital converter, each channel has 1 kbyte dual-port memory. The signal form each processing electronics are digitized and stored at memory for analysis. Since, the processing electronics is an multiplex system, only one signal is selected for each injection cycle. Hence, four injection cycle in needed to complete data acquisition sequence on the basis that cycle by cycle variation of injection condition is not change drastically. This special VME module with larger memory also will be used with the single turn position measurement electronics which will be installed conjunction with one or two BPM to provide a useful tool for machine study.

ORBIT ACQUISITION SYSTEM

The major role of orbit acquisition system is to collect electron beam position information. The measurement system of the electron orbit is composed of three set of electronic racks which are located at three locations at the inner area of the storage ring. Each BPM has its own processing electronics. Each set of electronic rack will handle the 16 BPMs of two superperiods as shown in Figure 3. The ILC are based on the Motorola MVME-147 CPU board with a 68030 microprocessor and a 68882 floating-point coprocessor, 4 Mbyte on board memory and etherne interface. The pSOS$^+$ real time kernel with network support pNA$^+$ was chosen for ILCs. The

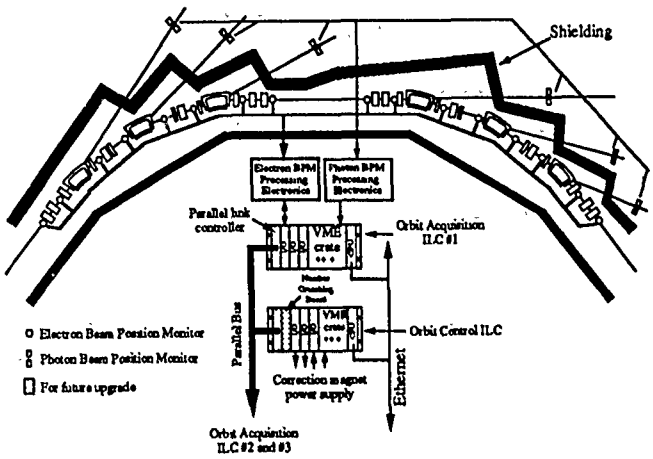


Figure 3. Beam position monitoring and beam position feedback system.

development environment is based on the Microtec cross development tools under VAX/VMS over a TCP/IP network. The software components at the ILCs for the beam position acquisition are composed network server, computation server, and I/O tasks.

The measurement system of the beam position performs as an orbit server. The high precision beam position information can be sent via ethernet to process computer or workstations for the use of the closed orbit correction or the other purpose. The nonlinearity of BPM is corrected by suitable algorithm [6,7], which is also done by the local orbit acquisition system. The orbit acquisition system also provide fast beam position information for real time beam position feedback system.

BEAM POSITION FEEDBACK SYSTEM

The global harmonic feedback and the local feedback will enhance the performance of the storage ring [8,9,10], provide a good stability for photon beam line, especially for the beam line of insertion devices.

Most of the existing global or local beam feedback systems were implemented by analog circuit, mainly because they were designed for operating machines and use small number of position monitor and corectors. It is difficult to implement analog global beam position feedback system at the third generation synchrotron radiation facility because these machine use a lot of BPMs and corectors to maintain its beam quality. All digital methods are more flexible and easy implement for a complex system than analog method.

The beam feedback system needs information of electron beam position and photon beam position. In order to damp fast beam motion due to unavoidable noise, beam position monitoring system should have fast response. The processing electronic of the BPM and the orbit acquisition ILCs can provide about 500 beam position reading per second.

At early operation stage of storage ring, position feedback is not necessary. In order to improve the performance of storage ring, the position feedback system will be implemented after machine commissioning. The beam position feedback system supports the global harmonic feedback mode or the local feedback mode as well as the combine of both approach.

Since speed is critical at the application of real time beam position feedback system, the beam position feedback will be done by a dedicated orbit control VME crate. The orbit control ILC is composed of CPU boards, number crunching boards and various input/output boards as shown in Figure 3. Since all equipments are installed at the inner side of the storage ring, the distance between three set orbit acquisition ILCs with orbit control ILC is within 100 m, commercially VMEbus multi-crate link with reflective memories will be adopted to transmit data between three BPM system's ILCs to orbit control ILC rather than develop a special module like fast interface module (FIM) [11] of ELETTRA due to limited time available for the project. The transfer rate requirement for fast beam feedback is about 1 Mbyte/sec (send 192 byte within 200 μsec) which is beyond the capacity of ethernet. When the CPU of orbit acquisition system write to the reflective memory, beam position information are transparently up-dated into the memory of orbit control ILC. This link will transfer the electron beam position and the photon beam position information to orbit control ILC. There are many choice about number crunching board on VMEbus system which is under evaluation, such as most advanced VMEbus based RISC processor board or digital signal processing board, all of these number crunching board support more than several tenth MFLOPS computing horsepower (such as Intel i860 can be provided 80 MFLOPS peak computing power, Motorola M96002 DSP chip can provide near 50 MFLOPS computing power, ...etc.). To speed up the system, orbit control ILC has analog output to control steering power supply directly to avoid additional delay through communication network. For a careful design, large than 50 Hz closed loop bandwidth of position feedback is easily achievable.

SUMMARY

The processing electronics and the VMEbus based fast orbit acquisition system for the beam position measurement system is under development. The system can be provided high accuracy beam position for the upper layer beam dynamic related applications. The orbit acquisition rate is about 500 orbit/sec, this rate satisfied the requirements of the fast beam position feedback system for the storage ring of SRRC which is also under intensive study.

ACKNOWLEDGEMENTS

The author is grateful to Prof. T. Katsura (KEK-PF), Dr. J. Hinkson (ALS), Dr. F. Loyer (ESRF) for their useful suggestion. The author also grateful to Dr. Y. Cheng and Dr. C. C. Kuo for the discussion about beam position feedback of the storage ring. The help from Prof. Y. C. Liu, Dr. J. R. Chen and Dr. K. K. Lin are also highly appreciate.

REFERENCES

[1] "SRRC Design Handbook", Synchrotron Radiation Research Center, April 1989.

[2] R. Biscardi and J. W. Bittner, "Switched detector for beam position monitor", Proceedings of the IEEE conference on Particle Accelerators, CH2669-0/89/0000-1516, 1989.

[3] J-C. Denard, A. Carniel, R. Aiello, T. Monaci, "Beam position monitoring system for ELETTRA", European Particle Accelerator Conference, Nice, June 1990.

[4] F. Loyer and K. Scheidt, "Beam position monitor: Proposed types of measurements", ESRF-BD-90-01 February 19, 1990.

[5] "Pohang Light Source - Conceptual design report", Pohang Institute of Science and Technology, January 1990, Pohang, Republic of Korea.

[6] H. Ishii, M. Tejima, T. Ieiri, J. Kishiro, Y. Mizumachi, K. Mori, A. Ogata and T. Shintake, "Beam position monitor system of TRISTAN main ring", The 6th Symp. on Accelerator Science and Technology, 1987, Tokyo, Japan.

[7] J. Borer, C. Bovet et D. Cocq, "Algorithmes de linearisation des pick-ups", LEP Note 582, 21 Mai 1987, Rev. Mai 1989.

[8] R. O. Hettel, "Beam steering at the Stanford synchrotron radiation laboratory", IEEE Trans. Nucl. Sci., Vol. NS-30, No. 4, 2278 (1983).

[9] R. J. Nawrocky et al., "Automatic beam steering in the NSLS storage ring using closed orbit feedback", Nucl. Instrum. and Meth. A266, 164 (1988).

[10] L. H. Yu, "Orbit stability and feedback control in synchrotron radiation storage rings", NSLS, 1989.

[11] D. Bulfone, "Real time orbit position feedback system for the ELETTRA storage ring". STM-89/19, Sincrotrone Trieste, Padriciano, 99, 34012 Trieste, Italy, April 1989.

THE LEP SYNCHROTRON LIGHT MONITORS

C.Bovet, G. Burtin, R.J. Colchester, B. Halvarsson, R. Jung, S. Levitt, J.M. Vouillot
European Organization for Nuclear Research (CERN)
CH-1211 Geneva 23, Switzerland.

Abstract

Four monitors are installed in LEP, two per particle type. Two of the monitors are at dispersion free locations which permit measurement of the transverse emittance, estimation of the energy spread and detection of various instabilities. The light has its origin in the main bending magnets. The source is imaged onto the detectors by means of catadioptric optics. Two detectors are used, one a CCD matrix and the other made up of a fast optoelectronic shutter and wavelength shifter coupled to a CCD matrix. Observations can either be made in the normal TV mode or in digital modes where one or more profiles (burst mode) are stored on the CCD and then digitized in 12 bit ADC's. In the burst mode, up to 18 profiles separated by 1 to 256 turns can be acquired. The results are either presented as data mixed with the TV picture or as two or three dimensional plots and projections on a workstation. Results and present performance are presented.

1. MONITOR LAYOUT

Four synchrotron light monitors are installed around intersection point 8. The light originates in the bending magnets at points close to defocusing quadrupoles in order to have maximum vertical beam dimensions. These quadrupoles are also equipped with position monitors. The first two telescopes on each side of the intersection observe a near dispersion free section, whereas the two others are located where the dispersion is large. This set-up permits the measurement of transverse emittances and an estimation of the energy dispersion.

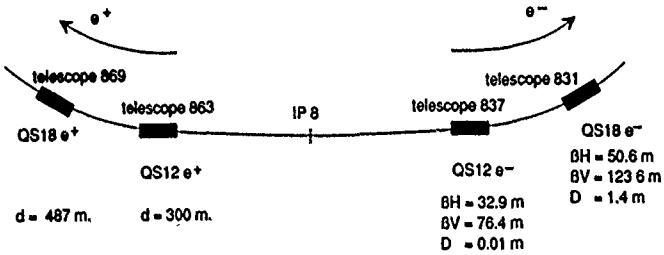


Fig. 1 : Synchrotron Light Monitors locations.

The four bunches in each beam are separated by 22 μs. The relevant beam optics parameters are given in Fig. 1. The nominal beam parameters for LEP phase 1 are a maximum beam energy of 50 GeV, a stored current of 3 mA per beam, nd at 46 GeV a horizontal emittance of 41.9 nm, a vertical emittance of 1.68 nm and an energy dispersion of 0.766 per mill.

2. PRINCIPLE OF OPERATION

A schematic view of a monitor is given in Fig.2. In order not to interfere with the circulating beams, the light extraction mirrors are located outside the nominal horizontal vacuum chamber acceptance of 131 mm. This leads to a light origin to mirror distance of 21.72 m, for a 20 mm wide mirror, which is slightly smaller than the length of a four bending magnet string (23.44 m). To make room for the synchrotron light, the vacuum chamber preceding the extraction mirror has been enlarged in the last bending magnet to a width of 159 mm. Calculations of the deformation due to thermal loading have imposed the use of a beryllium mirror in order to keep the surface irregularities within acceptable limits. With a 10 mm thick mirror, the original plane mirror is deformed into a spherical mirror of 700 m focal length with irregularities with respect to the sphere of 20 to 50 nm. The beryllium mirror is 23 mm high in order to fit into the available space. One of the main limitations of the monitors is the diffraction which increases with the light wavelength, therefore the shortest possible wavelength should be used for the profile measurements. The possibility of measuring profiles at various wavelengths for estimating the diffraction broadening is foreseen. The shortest wavelength is first limited by the extraction window separating the LEP vacuum from the outside. With a quartz window, this lower limit is fixed at 180 nm. The upper limit is determined by the detector and is equal to 1100 nm for the CCD detector used. This large domain led to the use of a catadioptric system which provides an achromatic focusing over the whole spectrum.

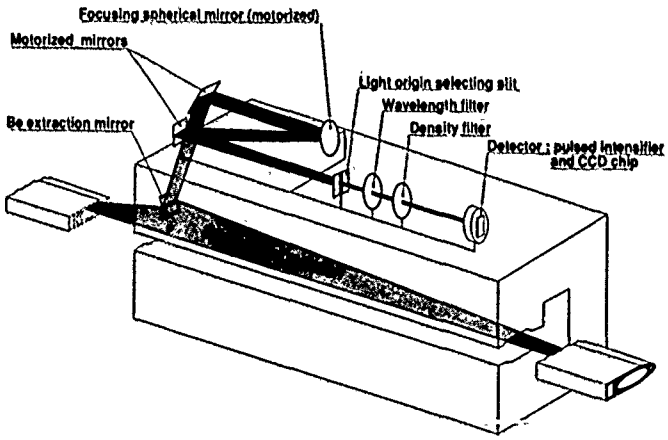


Fig. 2 : Schematic view of the LEP synchrotron light monitor.

Only the parallel polarization component of the light should be used for obtaining the best resolution. The vertical component is discarded by a combination of two metallic mirrors. The best combination fitting in the available space made use of the beryllium extraction mirror and a chromium coated mirror with incidence angles at the mirrors of 31° and 59°. This arrangement attenuates the power from the perpendicular polarization to about 5% of the total and brings the light back into the horizontal plane on top of the bending magnet. Next to diffraction, the longitudinal acceptance will limit the precision of the profile measurements through defocusing and, in the horizontal plane, orbit sagitta. These effects can be controlled by limiting the angular acceptance in the horizontal plane, which is best achieved by using a horizontal slit at the focal plane of the focusing mirror. This can be seen easily in the phase-space plot of Fig. 3. This phase-space has been described in [1], and the drawing is made at the nominal light origin. The horizontal axis is the horizontal beam position and the vertical axis is the horizontal angular deflection. The beam trajectory is a parabola, the extraction mirror is transformed in a skewed band and the slit in the focal plane is a horizontal acceptance band. As can be seen in the sketch, the longitudinal limits set by the slit are independent of orbit position changes, which would not be the case with a diaphragm located at any other position. This slit does not generate a vertical diffraction pattern which is a great advantage. The vertical diffraction will only result from the natural diffraction of the

0-7803-0135-8/91$01.00 ©IEEE

synchrotron light pattern and from the limitations in the vertical plane set by the extraction mirror.

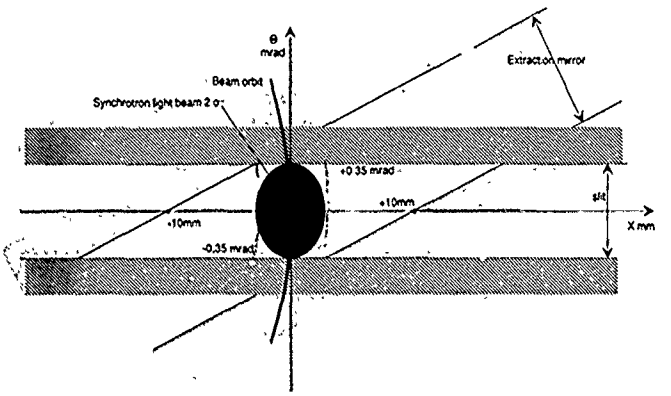


Fig. 3 : Horizontal phase-space plot of the synchrotron light monitor.

CCD frame transfer detectors are used. Their well defined geometry and control flexibility makes them very attractive for this application. Their main disadvantage is the lower cut-off wavelength of 450 nm which leads to the use of a wavelength shifter. The latter is included in a fast optoelectronic shutter enabling the separation of individual bunches and the choice of predetermined observation times.

3. SYSTEM DESCRIPTION

The enlarged vacuum chamber is connected to a small light extraction tank which takes the place of the hydroformed bellows used between adjacent chambers. The tank has a length of either 202 mm or 300 mm depending if it is at the QS 18 or QS 12 monitor. The tank is made of a machined and water-cooled copper piece to which a bellows is brazed to give some degree of freedom with respect to the adjacent chambers. Also brazed to it are the light extraction tube and the passage for the beryllium mirror. This tank will absorb most of the incoming synchrotron radiation power, i.e. 130 W in LEP phase 1. It provides as smooth a transition as possible between the two vacuum chamber sections. The light extraction tube, including the pieces up to the telescope, acts as a waveguide below cut-off for the electromagnetic fields induced by the beam. This keeps the RF losses of the set-up at a reasonable value. The beryllium mirror is tightly fixed onto a water cooled support and can be retracted from the light path if necessary. The mirror assembly is mounted on the telescope tube for maximum stability. A compensating bellows takes any stress from the telescope tube. The telescope itself is mounted in a stainless steel tube of 350 mm inner diameter and 3.44 m length. This tube is located above the bending magnet and rests on a stable support made of I shaped aluminium beams. The optical elements and the detectors are fixed on a 3.2 m long optical bench. As mentioned previously, the first folding mirror is chromium coated. The two other mirrors are aluminium coated for maximum reflectivity down to the UV domain. The incidence angle on the focusing mirror has been kept to less than 2 degrees to minimize the astigmatism. The focal length of this mirror is 4.04 m, which is a compromise between available length and magnification. The magnification of the telescope is G = 0.2. The first two mirrors can be rotated around the horizontal axis and the third mirror around the vertical axis to center the light spot on the detectors. Two sets of seven chromatic and seven density filters allow the choice of the wavelength used and adjustment of the light intensity to the dynamic range of the detectors. At present, filters centered around 480, 450, 253 nm are used for measuring the profiles, and filters centered around 622 and 800 nm are used to assess the contribution of the diffraction to the profile enlargements. Six density filters are available with transmissions from 100 to 1 %. The light origin selecting slit can be varied in aperture from 0 to 10 mm in 0.1 mm steps, adjusting the angular acceptance from 0 to +/- 1.25 mrad. Its center can be adjusted in the same way within +/- 5 mm. Two detectors are installed, either the light is focused directly on the entrance face of the wavelength shifter/fast shutter assembly, or it is deflected via a movable mirror/camera assembly [2] directly onto a CCD chip. All movements are made via stepping motors. The elements were first aligned in a surface laboratory and then again during the installation in the tunnel. The final tuning was made with the LEP beams.

The elements in the telescopes are remotely controlled via the LEP control system (Fig. 4). Two VME crates (ECA's) located in an underground cavern at about 500 m from the telescopes are used to control and read data from the four telescopes. The VME crates each house a 68010 CPU, communications and timing modules, stepping motor controllers, camera mode controllers and image acquisition cards. The software is written in Pascal and C using the RMS68K operating system. Image acquisition and processing is performed on request, at a user-defined frequency or on external events. Apollo workstations are used to display the results and images in the PCR (Prévessin Control Room). A menu-driven program for the PCA's gives complete test facilities, and can be used to display the two dimensional images and projections.

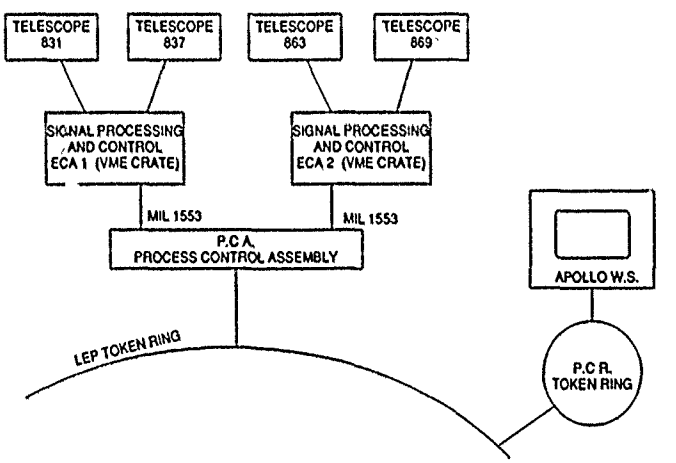


Fig. 4 : System control chain.

4. DETECTORS

The CCD chip [3] consists of 110'000 useful light sensitive pixels, each 23 µm square, arranged in 288 rows of 384 columns, the spectral response of the CCD extends from 450 to 1100 nm. The CCD is of the frame transfer type meaning that there are two active areas on the chip , one area (image zone) is used to acquire the new data whilst the second area (memory zone) is used to read out the previously acquired data. Transfer between the two zones occurs at the end of each integration period and takes 0.16 ms. The linear dynamic range of the CCD is greater than 1:700.

The CCD control electronics have been designed to give complete control of the integration and readout times of the chip. In the simplest mode of operation the CCD operates as a conventional TV camera with an integration time of 20 ms. In the normal digital operation mode the integration time can be varied from 100 µs to 65 ms and the pixels can be read out at a rate of 1 MHz, rate dictated by the ADC used. The start of the integration time can be synchronized to an external event. In these two modes of operation the complete image area of 288 rows is shifted to the memory zone for readout when the integration time has elapsed. The third and most complex operational mode of the detector is the "multi-image" or "burst" mode. In this mode, the image area is shifted to the memory zone in discrete blocks during the acquisition time, these blocks consist of a preselected number of rows (from 16 to 128). By using this block shifting technique, in conjunction with the external

fast electronic shutter, up to 18 images can be stored in the CCD during one acquisition period. The external shutter and the shifting of the pixel rows have to be synchronized to each other. There is a dead time between exposures of about 25 μs for 8 exposures. The readout of the memory zone is done in the same way as described previously.

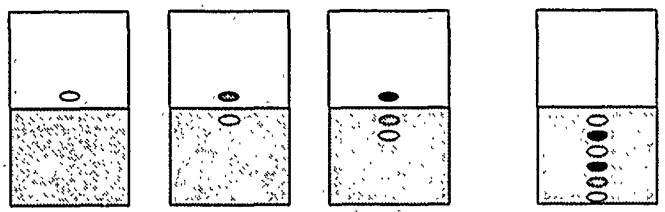


Fig. 5 : "Burst mode": The top zone is the image area on which the synchrotron light is imaged. The shaded zone is the memory area. Between successive light pulses, controlled by the fast shutter, the stored profiles are shifted down to the memory area. At the end of the process up to eighteen profiles (six illustrated) are stored in the memory area of the CCD.

The wavelength converter/shutter is a commercial product [4]. It consists of a two stage image intensifier with a magnification of 1/1/8. The input window is made of quartz and the photocathode is sensitive from below 180 nm up to 300 nm. The phosphor radiates at 520 nm and has a fast decay time of 100 ns to be compatible with the burst mode. The high voltage (5 to 10 kV) to the intensifier is pulsed so that the device behaves as an electronic shutter with a rise/fall time of a few microseconds and an open time of about 10 μs. The intensifier is directly coupled to the CCD chip via a fiberoptic bundle. The pulsing interval can be adjusted from 1 to 256 beam turns and can be locked onto any of the four circulating bunches.

5. DATA ACQUISITION AND PROCESSING

The CCD memory area is digitized with a 12 bit fast (1 MHz) ADC and the result is stored in an on-board buffer memory. Once the image has been acquired, an area of interest is found by scanning every fourth pixel on every fourth row to find the highest value, a rough measurement of the half height is used to define the dimensions of this area in both planes. Projections are then done within this area by summing every row to get the horizontal profile, and every column for the vertical profile. The profiles are corrected for thermal drift by subtracting the straight line between the endpoints of the area and a smoothing of the profiles is also done. The profiles are measured using a three pass calculation. Once the measurement is complete, the results, profiles and the sixty by sixty pixel portion of the image around the centre of charge are stored in a buffer, ready to be read by the PCA. The measured sigmas and their average and rms values over a predetermined number of measurements are superimposed on the TV picture via a commercial text generator and mixer card.

6. RESULTS WITH BEAM

As soon as sufficient current was circulating in LEP in July 1989, the synchrotron light monitors received their final tuning and were used in TV mode. They were very useful for real time observation of the beam size, coupling and various instabilities. This was mainly due to their good sensitivity as 1 μA beams were visible. Later in the year the images were digitized and the beam profile measuring algorithms tested. This information was then added to the TV picture. This is still the most used facility provided by the monitors. In 1990 software was written for the PCR workstations and the fast shutters were tested. The 3-D plots proved to be extremely useful for the fine tuning of the instruments. The precision of the monitor began to be evaluated over the five months of operation. The linearity of the monitors was checked and found good to 3% over two decades of intensity. The contribution of the slit width w_s was investigated and it was confirmed that for the measurement of the horizontal emittance there is an optimum slit opening around 3 mm where the combined contributions from the longitudinal acceptance and the diffraction are minimum. For the vertical emittance the best result is obtained with the smallest possible slit, a practical limit being around 0.5 mm. The variation of the beam rms values were measured as a function of the wavelength and the contribution of the diffraction evaluated. These various contributions can be considered as an rms broadening which will add quadratically to the beam size. The estimated values, given in μm, are:

$\sigma_{Dh} = 2\ \lambda / w_s$, for the horizontal diffraction,

$\sigma_{Dv} = 4\ \lambda^{2/3}$, for the vertical diffraction,

$\sigma_{LA} = 70\ w_s$, for the longitudinal acceptance,

λ being expressed in nm and w_s in mm.

No measurable difference could be observed between the horizontal and vertical broadenings due to the slit width. Further studies are needed to improve the precision of these estimations.

The fast shutter was operated in TV, digital full frame and digital burst modes. Below is the resulting 3-D plot of eight successive turns of the same bunch. The program gave also the plot of the centres of charge as well as various displays for the individual shots.

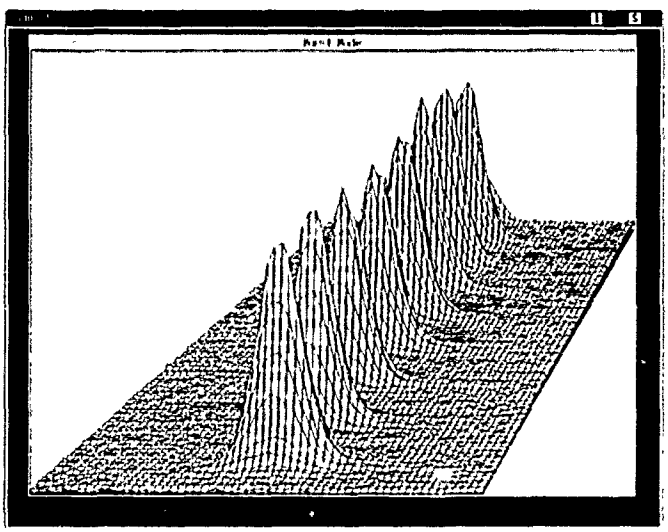


Fig. 6 : 3-D plot of eight successive turns of a selected bunch. The horizontal axis is the beam horizontal dimension, the other axis is the vertical beam axis within a time slot.

ACKNOWLEDGEMENTS

Acknowledgements are due to the many colleagues in the MT Design Office and Workshops, with a special mention to R. Perret, who have greatly contributed to the realization of these monitors.

REFERENCES

[1] A.P. Sabersky : The geometry and optics of synchrotron radiation, Particle Accelerators, 1973, Vol. 5, pp199-206.

[2] G. Burtin et al. : The Lep injection monitors : design and first results with beam, CERN/LEP-BI/89-06, March 1989, and Proc. of the 1989 IEEE Acc. Conf., Chicago.

[3] CCD chip TH7863, Thomson, France.

[4] Proxifier BV 2502 Cc X15 & BV 1811 KX, Proxitronic, Bensheim, Germany.

A CCD Camera Probe for a Superconducting Cyclotron

F. Marti, R. Blue, J. Kuchar, J.A. Nolen, B. Sherrill and J. Yurkon,
National Superconducting Cyclotron Laboratory,
Michigan State University,
East Lansing, Mi 48824

Abstract

The traditional internal beam probes in cyclotrons have consisted of a differential element, a wire or thin strip, and a main probe with several fingers to determine the vertical distribution of the beam. The resolution of these probes is limited, especially in the vertical direction. We have developed a probe for our K1200 superconducting cyclotron based on a CCD TV camera that works in a 6 T magnetic field. The camera looks at the beam spot on a scintillating screen. The TV image is processed by a frame grabber that digitizes and displays the image in pseudocolor in real time. This probe has much better resolution than traditional probes. We can see beams with total currents as low as 0.1 pA, with position resolution of about 0.05 mm.

Introduction

The standard beam probe for the K1200 cyclotron consists of a beam current measuring device that gives limited information on the vertical beam distribution. The probe head is made of three copper leaves separated by small insulating spacers in the vertical direction. The height of each leaf is approximately 6 mm. The probe thickness in the beam path direction is such that it stops completely most of the heavy ions in the energy range of our cyclotron, but not so for lighter ions. The only information that we obtain with this probe is the total current as a function of radius. This is probably enough to study vacuum loses and tune the beam through resonances by maximizing the transmitted beam current, but very little can be learned about beam dynamics. Several attempts have been made at other laboratories to obtain more information on the internal beam, but these techniques all have limitations [1, 2].

After our successful experience with the use of scintillators and a frame grabber to tune and study external beams [3] and similar experiments at other laboratories [4, 5, 6, 7], we decided to look into the possibility of building a beam probe physically compatible with the present current probe that could include a TV camera to look at a phosphor covered plate. This new kind of internal beam probe was then developed for the K1200 cyclotron. It consists of a small TV camera that looks at the image produced by the beam hitting a phosphor covered plate. The small size of the camera allows it to be placed close to the screen. The image gives a detailed view of the current density in r and z, with position resolution of about 0.05 mm. Total beam currents below one electrical pA are easily analyzed. This probe opens new possibilities for the study of internal beam dynamics and allows tuning very weak beams, below one pA.

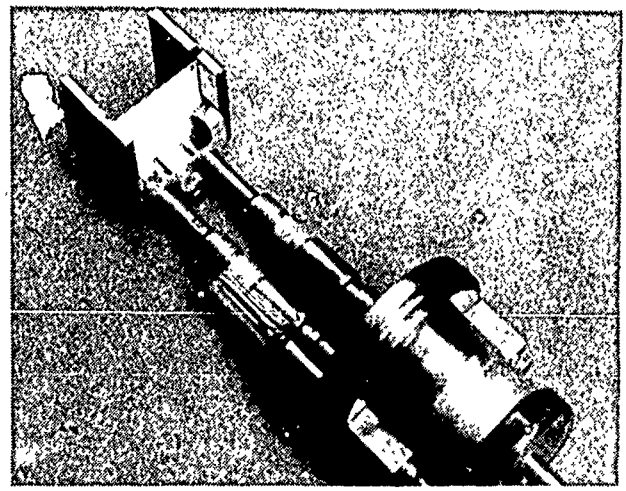


Figure 1: Close up view of the probe head before welding to the vacuum tube. The support for the scintillating plate is seen on the upper left. The plate is held in a groove by springs. The two supports are the electrical connection to the beam current monitors.

TV probe

The desire to make the new probe and the standard probe interchangeable, so as to use the same hardware for the drive presents severe restrictions on the physical dimensions. The space is limited to a tube of 1.25 inches diameter that is inserted in the median plane between the two sections of the superconducting coil.

Two major concerns were the possibility of radiation damage to the camera and the high magnetic field (6 T) in which the camera must work. The simplification offered by inserting the camera close to the plate, compared to

0-7803-0135-8/91$01.00 ©IEEE

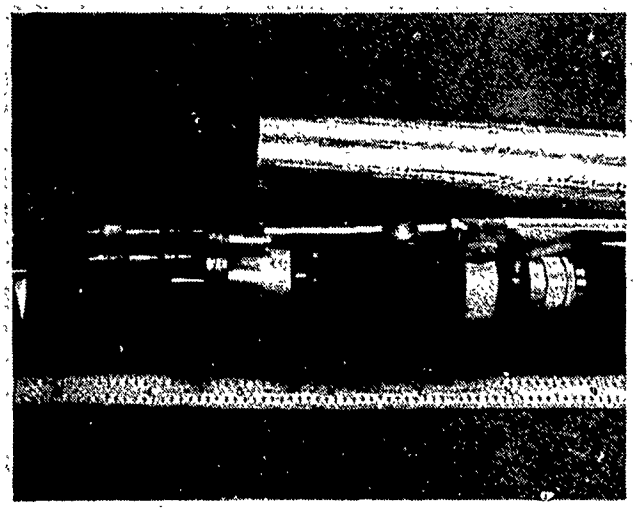


Figure 2: TV camera positioned behind the window as it would appear inside the stainless steel tube that is positioned above.

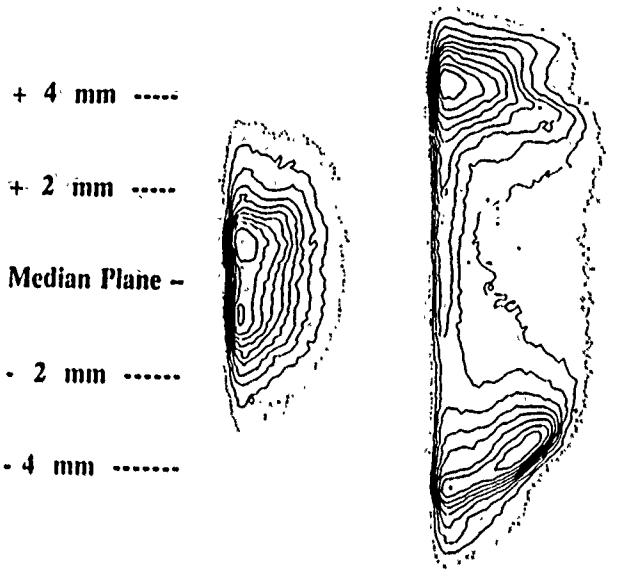


Figure 3: Contour plot of light intensity on the scintillator for a He beam of 40 MeV/u. The probe is at a fixed radius (0.83 m), just outside the $\nu_r = 2\nu_z$ coupling resonance. The plot on the left corresponds to a centered beam, while the one on the right is from an off-centered beam.

using an optical system with its associated loses, induced us to design and build the TV probe. We chose an ELMO 102BW camera after testing it in a magnetic field because of its small size and image quality.

Figure 1 shows a close up view of the probe head, while Figure 2 shows the TV camera placed behind the head next to the stainless tube that encloses the system. The ruler is marked in inches. The phosphor plate is removable, allowing an easy change of the phosphor if needed. The probe removal and reinsertion in the cyclotron can be done under vacuum in a period of 30 minutes. The screens are produced by spraying ZnS[8] phosphor with Krylon as a binding agent.

The two insulators that support the head are hollow, and a conducting rod traverses to carry the current signal to the beam current monitors (BCMs). We have had difficulties reading beam currents below 100 pA, but a beam current below 1 pA gives an easily viewable light output for the TV camera and produces no radiation damage to the CCD. We have noticed permanent radiation induced damage for currents above 1 nA. This threshold depends on the ion and its energy. But for the cases that we have tested this seems to happen at least 100 times above the currents that we would normally use for TV viewing. The tuning is normally performed with attenuators inserted in the injection beamline. These screens[9] which are available with different combination of transmissions, down to 10^{-7}, sample the beam over the complete phase space, rather than just collimating it. In the regime of negligible space charge, the small amount of current that is injected, is then representative of the total beam; the attenuator thus provides complete control of the beam intensity hitting the probe. Once the beam is tuned, the probe is retracted and the attenuator screens adjusted to match the experiment requirements. Working with low current allows the probe to run with no water cooling, which lowers the electrical noise. The ability to tune beams with very low intensities will allow us to accelerate to higher energies ions that are produced in limited quantities in the ion source. Modern 4π detector experiments require low intensities and can make use of these weak high energy beams.

The glass dome visible at the lower left in figure 1 is used to insert an illuminating optic fiber. The purpose is to inspect the condition of the screen in case there are doubts about its integrity.

The RS170 TV signal from the camera can be sent directly to a B&W monitor or to the frame grabber [3] which displays the intensity levels displayed in pseudocolor on a color monitor in real time. Figure 3 shows an example of the equicontours of the light intensity for two different centering coil values with the probe at a fixed radius. The beam probe was placed just beyond the region of the $\nu_r = 2\nu_z$ resonance. This coupling resonance transfers energy between the horizontal and vertical oscillation planes. Most of our beams have to cross this resonance, and severe losses can occur if the beam is not centered when crossing it. As the figure shows, the probe picture gives a dramatic visualization of the increase of the vertical oscillation between the centered beam (left picture) and an off-centered beam (right). These pictures were digitized from a video tape recording. Digitizing from a recorded image introduces some noise that is not present when capturing frames from a live image.

Figure 4 shows five intensity contour plots taken at approximately 2.5 mm increments apart in radius, with the innermost at a radius of 0.52 m. The $^4He^{2+}$ beam had an energy of approximately 10 Mev/u at this radius. The vertical oscillation of the beam about the median plane is clearly visible . Part of the beam hits the probe plate, and part continues for one more orbital revolution before hitting the plate. By then its vertical position has changed.

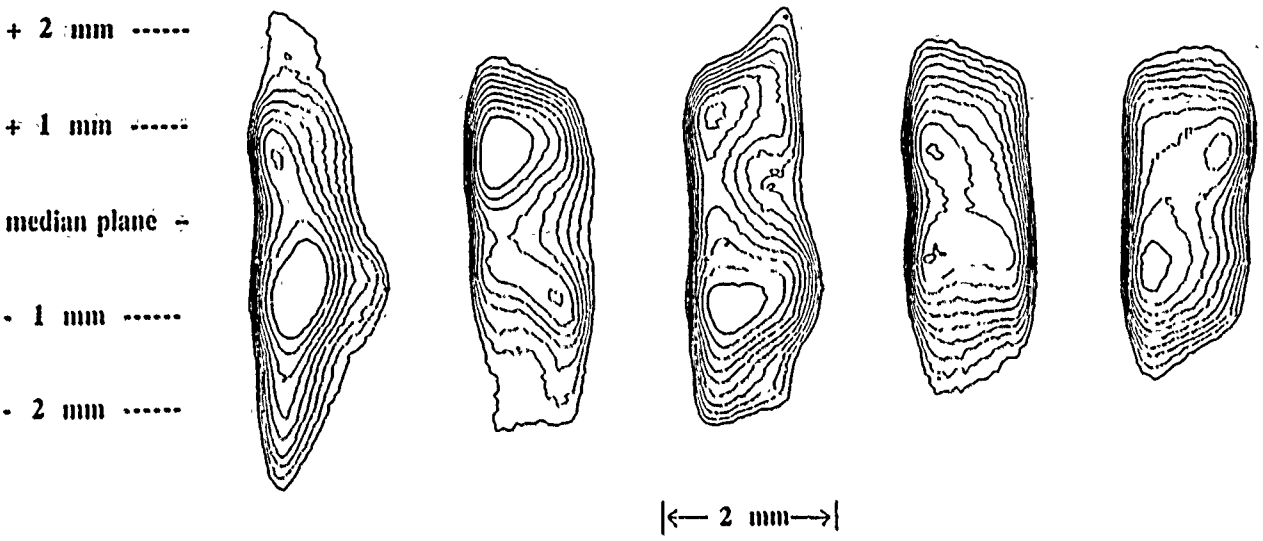


Figure 4: Contour plots at five radii showing the vertical oscillation of the beam around the magnetic median plane. See text for more details.

As the vertical focusing frequency $\nu_z \approx 0.4$ for this beam, it takes 2.5 orbital revolutions for one complete vertical oscillation.

The width of the beam trace in radius must be equal to the radius gain per turn for a centered beam. The calculated radius gain per turn is approximately 1.5 mm, in good agreement with the observed beam width. If there are fluctuations on the beam width when scanning the probe radially, that must be taken as an indication of off-centered beam. This is a very useful diagnostic in cyclotrons with closely separated turns, where it is difficult to detect the orbit precession from the turn pattern. It is possible to imagine a control program that analyzes the beam pattern and decides to change the centering coil and the dee voltages to center the beam automatically. The pictures observed during the probe motion remind us of the time exposure of a moving quartz plate shown by Kelly during the early operation of the LBL 88-inch cyclotron[10].

Conclusions

The detailed information that the new probe gives in the r and z planes with very low noise expands enormously the work that can be done in comparing with orbit tracking simulations. A rich new field opens to us with this new diagnostic tool.

This work was supported in part by NSF Grant PHY-8913815.

References

[1] U. Schryber. Upgrading the SIN facilities to higher intensities. In *Proc. of the 10th International Conference on Cyclotrons*, East Lansing, 1984.

[2] G. Minerbo. MENT: A maximum entropy algorithm for reconstructing a source from projection data. *Computer Graphics and Image Processing*, 10:48, 1979.

[3] F. Marti et al. Beam diagnostics developments at NSCL. In *Proc. of the 12th International Conference on Cyclotrons*, Berlin, 1989.

[4] M. C. Ross et al. Automated emittance measurements in the SLC. In *Proc. of the 1987 IEEE Particle Accelerator Conference*, pages 725–728.

[5] A.A. Hassan, C.L. Fink, and M.G. Rosing. A beam characterization of H^- particles. In *Proc. of the 1989 IEEE Particle Accelerator Conference*, pages 1504–1506.

[6] T.J. Yule et al. Beam characterization with video imaging systems at the ANL 50-MeV H^- beamline. In *Proc. of the 1989 IEEE Particle Accelerator Conference*, pages 1571–1573.

[7] D.P. Russell and K.T. McDonald. A beam-profile monitor for the BNL accelerator test facility (ATF). In *Proc. of the 1989 IEEE Particle Accelerator Conference*, pages 1510–1512.

[8] We are currently using ZnS Ag activated, GTE phosphor type 130.

[9] R.F. Burton, D.J. Clark, and C.M. Lyneis. Beam attenuator for the LBL 88 inch cyclotron. *Nucl. Instr. Meth.*, A270:198, 1988.

[10] E.L. Kelly. General description and operating characteristics of the Berkeley 88-inch cyclotron. In *Proc. of the International Conference on Sector-Focused Cyclotrons*, pages 33–40, 1962.

High-sensitive Remote Diagnostics of the Accelerated Particles' Beam Cross Section

P. Yu. Komissarov, V. G. Mikhailov, V. A. Rezvov,
A. A. Roschin, V. I. Sclyarenko, L. I. Judin
I. V. Kurchatov Atomic Energy Institute
Moscow 123182, USSR

Abstract

The gauge for remote monitoring of the density distribution of accelerated particles' beam over cross section is based on the analysis spatial distribution of residual gas ionization products. With the transverse homogeneous electric field the released charges are transported through narrow slot behind which they are analyzed over energy with the electric field. Then they are registered by the open electron-optical converter with micro-channel-plate amplifier. The image of the beam distribution over cross section from the electron-optical converter screen is read out by TV-camera for representation on monitor. The detector was tested on cyclotrons at IAE (Moscow), INP (Kiev) and INP (Prague). The threshold sensitivity on the proton beam with the energy 30 MeV 10^{-9} A.

I. INTRODUCTION

The accelerated beam dimension and position monitoring in beam transport tract (BTT) is significant when performing precise nuclear experiments, as well as irradiating various targets, e.g. production of isotopes. For example, beam profile detectors used wide which registrated residual gas ionisation products in BTT [1,2].

The device was proposed in [3-7] for unconnected measurements of the accelerated beam transverse distribution in cross section (fig.1).

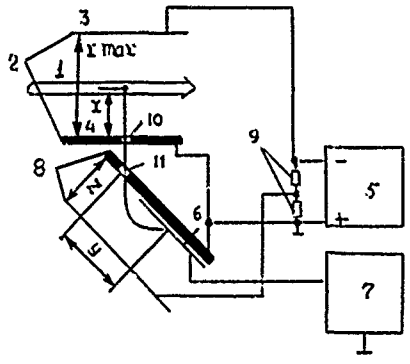


Fig.1. The circuit of the beam cross section unconnected detector.
1- investigated beam, 2-removing capacitor, 3,4-reflecting and removing electrodes, 5-permanent voltage course, 6-two-coordinate position sensitive detector, 7-registration circuit, 8-analysing capacitor, 9-resistive divider, 10-slot in removing electrode, 11-slot in the input plate of analysing capacitor.

The cross section detector includes removing and analyzing capacitors, current collector designed as electron-optical converter (EOC) with amplifier on microchannel plates (MCP) and corresponding power supplies. The guided beam ionizes BTT residual gas when passing the gap of removing capacitor. The ions released by the plane field are accelerated to the removing electrode with the shaping slot 1×50 mm in size and directed perpendicular to the BTT. Passing through the shaping slot the accelerated ions form the strip beam in which the spatial distribution of particles directed along the slot corresponds to the distribution of particles in the guided beam in this direction. Energy distribution of the removed ions corresponds to the investigated beam distribution over the other orthogonal coordinate. Electric field of analysing capacitor performs the analysis of this energy distribution. As a result, two-coordinate optical image of removed ions' distribution corresponding to the transverse cross section particle distribution in the guided accelerated particle beam, is formed on the EOC screen. Arrangement of analysing capacitor at an angle of 45° to the direction of removal and removing electrode plane provides linear correlation of the obtained image dimensions with the dimensions of the guided beam, and image dimension Y corresponding to the beam dimension X in the direction of removal are correlated by the dependence

$$Y = 2 \cdot (E_u / E_a) \cdot X ,$$

where E_u and E_a are intensities of removing and analysing fields, respectively. The detection of the optical image of the beam transverse cross section is performed with the industrial TV camera.

II. DEVICE CONSTRUCTION

At present, the standardized device for the accelerated beam dimension and shift monitoring was developed at IAE cyclotron. The elements of construction of the beam cross section unconnected detector are placed in a standard diagnostic section with overall dimensions 230×230×230 mm and hole diameter for a flange 186 mm. The supply voltage is introduced through

0-7803-0135-8/91$01.00 ©IEEE

the flange on which the removing electrode and analysing capacitor with EOC are fixed. The detection of optical image of the beam cross section is performed with TV camera on the side of a flange on which the reflecting electrode of removing capacitor is fixed. Thus, some electrodes of removing capacitor are designed in the form of a grid with high transparence. The observation of EOC screen is carried out at angle of 45°. FOR the current location of beam dimensions on both coordinates equation $E_a = \sqrt{2} \cdot E_u$ was chosen between the intensities of removing and analysing fields, and $Y = \sqrt{2} \cdot X$.

A remove drive which provides installation of luminescent screen into the removing capacitor gap is fixed on one of the sides of the diagnostic section. The center of the luminescent screen is brought into coincidence with the line joining the TV lens center and EOC screen center. This allows to perform initial tuning of the beam using traditional diagnostics with the increased sensitivity, also to carry out comparative measurements to estimate serviceability of unconnected detector. Fig. 2 shows pictures of the beam transverse cross section of current interception luminescent screen and EOC screen. It can be seen that the images are identical.

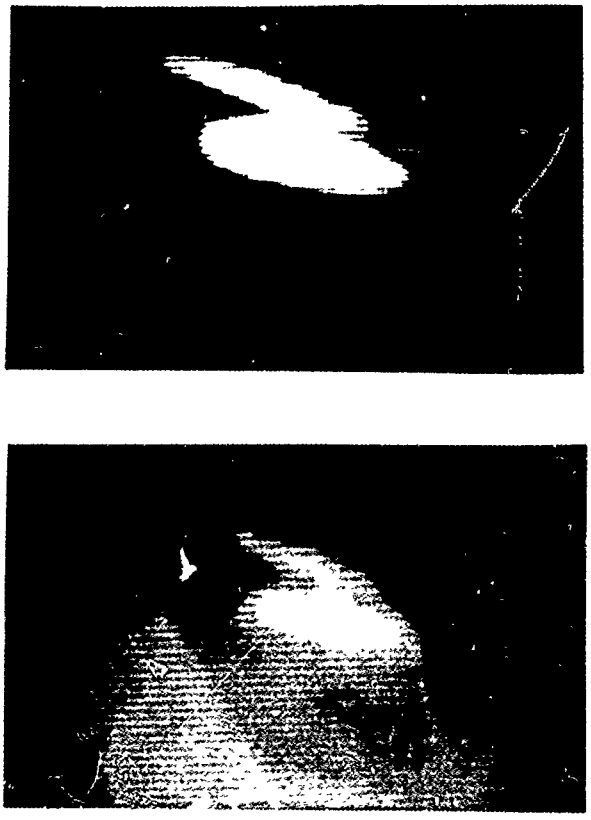


Fig. 2. Picture of the beam transverse cross section from the luminescent screen (a) and unconnected detector EOC screen (b).

Detector construction permits the beam intensity monitoring. It's enough to measure the screen EOC beam. But the sensitiveness of the device depends from the pressure in the BTT. For exclusing this dependence it is proposed to change MCP-multiplier amplification coefficient in accordance with pressure changing [5]. It may be reached as using some special functional converter for changing of MCP-amplification, as by the pressure changihg calculation when information is treated in computer.

The additional convenience for the user is produced by the unit of TV signal quasi-color presentation. The unit is based on rapidly stopped 8-stage ADC providing the upper step frequency up to 20 MHz. The 3 higher stages of ADC are used for modulation of 3 projectors of colored monitor. In this case the colored image of the beam cross section is formed on the monitor screen, and the shape of colored stripes of each color corresponds to the studied beam intensity distribution on the given comparison level. We also provided a device for separation of sync pulses from TV signal for current transmission of ADC codes into computer memory at digital processing of parameters of the guided beam cross section. An example of the computer data processing of the beam cross section is the beam diagnostics in a large scattering camera of IAE cyclotron. In this case by the signals from two separated beam cross section detectors we calculate position and angle of the current incidence on a physical target inaccessible for direct measurements (fig. 3). The section of the station for TV image digital processing was considered in [7].



FIG. 3. Example of determination of the beam position on an image target.

III. MAIN PARAMETERS

Let us give for conclusion the summary table of the principle parameters of the beam cross section unconnected detector.

Dimensions of the controlled area 40×40 mm

Aperture	80 mm
Spatial visual resolution	1×1 mm
Spatial resolution after computer processing	0.1×0.1 mm
Sensitivity on 30 MeV proton beam	10^{-8} A
Effective pressure range in BTT	3×10^{-5} torr
Power supply voltage	10 kV
Consumption current	10 μA
Multiplier amplification coefficient of MCP	10^{8}
Amplification inhomogeneity over area	20 %
Time of image shaping	100 ns
Number of ADC stages	8
Step frequency	5 MHz
Number of color intensity gradation on a colored monitor	8

One must note that in case of necessity the dimensions of the controlled area can be easily increased up to 80×80 mm. The further increase of these dimensions is limited by the sizes of produced MCP.

IV. CONCLUSION

An explotation such detector at the cyclotron and tandem in Kurchatov Atomic Energy Institute, (Moscow), in Institute of Nuclear Phisic (Kiev), in Institute of Nuclear Phisic (Prague-Rgage), an experiments in Zentralinstitute fur Kernforschung (Dresden-Rossendorf) show that our detectors are very usefull devices for unconnected beam diagnostic at difference accelerators. The production of such detectors is prepared now as for flances apperture 168 mm, so for flances apperture 160 mmand 100 mm in accordance with standard ISO/DIS 1609.

V. REFERENCES

[1] V. Agortsias, S. Batisti, K. D. Johnson, G. Shnider, "Metody izmereniya parametrov puchka uskorennyh chastits", in Trudy II Vsesoyuznogo soveschaniya po uskoritelyam zaryazhennyh chastits, t. 2, p. 8, Moscow, 1972.

[2] L. Rezzonico, "Beam diagnostic at SIN", in XI Intern. Conf. on Cycl. and their Appl., pp. 457-461, 1987, Jonics Publishing Comp., Tokyo.

[3] V. A. Rezvov, L. I. Yudin, "Sposob izmereniya poperechnogo raspredeleniya plotnosti puchka zaryazhennyh chastits". AS USSR N1392645, BOI N15, p. 32, 1988.

[4] V. G. Mikha'lov et al., "Ioniatsionnyi datchik raspredeleniya plotnosti puchka zaryazhennyh chastits po poperechnomu secheniyu". AS USSR N1462521, BOIN8, p. 294, 1989.

[5] A. N. Bryukhanov, V. A. Rezvov, L. I. Yudin, "Beskontaktnyi datchik parametrov uskorennogo puchka zaryazhennyh chastits". AS USSR N1009219, BOI N47, p. 211, 1984.

[6] P. Yu. Komissarov et al., "Beskontactnyi izmeritel secheniya puchka", in Trudy 11 Vsesoyuznogo soveschaniya po uskoritelyam zaryazhennyh chastits, DUBNA, 1989, t. 1, p. 87.

[7] P. Yu. Komissarov et al., "Operativniy kontrol vyvedennogo puchka cyklotrona", in Trudy 10 Vsesoyuznogo soveschaniya po uskoritelyam zaryazhennyh chastits, DUBNA, 1989, t. 1, p. 81.

Intensity Interferometry and Its Application to Beam Diagnostics

Efim Gluskin, Advanced Photon Source, APS/360,
Argonne National Laboratory, Argonne, IL 60439

Abstract

This paper presents an approach for the measurement of the particle beam size based on x-ray intensity interferometry. Two technically feasible schemes are proposed and analyzed. This type of interferometer will provide a resolution of a few tenths of a micron for a positron beam that emits undulator radiation. The minimum required time for the measurement is about 30 sec*.

I INTRODUCTION

Intensity interferometry as introduced and developed by H.Brown and R.Twiss [1,2] has widespread application now in different areas of physics [3,4], with one of the most successful application in laser physics due to high spectral power laser source [5]. The possibilities of intensity interferometry in the x-ray region are discussed elsewhere [6], but it appears useful to consider it again because of the creation of third-generation synchrotron radiation (SR) sources. The main goal of these sources is the utilization of the radiation from special insertions devices providing high spectral power in the x-ray wavelength region. Intensity interferometry could be an adequate tool for the particle beam diagnostics, as well as an instrument for the characterization of the coherent properties of x-ray radiation. Some possibilities for the use of intensity interferometry for synchrotron radiation sources have already been discussed [7,8]. However, it is essential to consider real technical schemes for applications in sources that exist now and are under costruction. This paper discusses an undulator at Advanced Photon Source as a source for intensity interferometry.

II. SR INTENSITY INTERFEROMETER

Fig.1 presents a simplified scheme for an intensity interferometer.

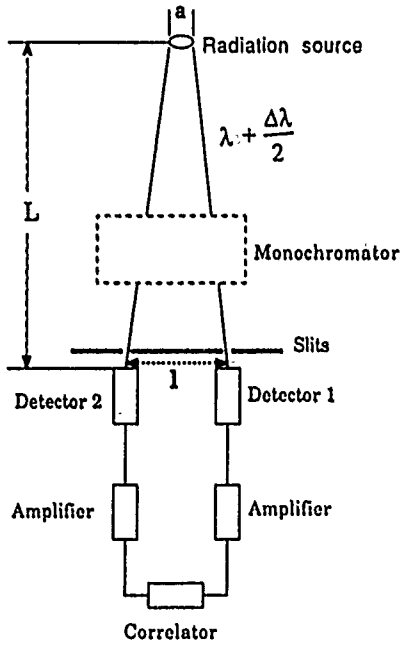


Fig. 1 Intensity interferometer scheme: a-source size,, L-distance source-detector, l-distance between slits, λ-wavelength, Δλ–wavelength bandwidth.

The signals from two "square law" detectors are amplified and multiplied together in the linear mixer. The average value of the product gives a measure of correlation in the fluctuations. The main result of the Brown-Twiss effect consists of the dependence of this product on the relative position of the slits in front of the detectors: the correlation is increased when slits are placed in the area coherently illuminated by the source.

Two of the main characteristics of the experimental scheme should be mentioned here: the coherent time of the source

* Work sponsored by U.S. Department of Energy, BES-Materials Sciences under Contract W-31-109-ENG-38
U.S. Government work not protected by U.S. Copyright.

$\tau_{coh} \sim \lambda^2/(\Delta\lambda c)$ and the resolving time τ_0 of the correlator which should be smaller than the reverse value of the amplifier bandpass. The relation between these parameters defines what kind of the experimental technique should be chosen for the signal detection. In the case $\tau_0 << \tau_{coh}$ the counting technique would be adequate, and if $\tau_{coh} << \tau_0$ the average current from the detector should be measured [9].

Before starting the comparison of these two different techniques we need to determine the optimum wavelength for the measurements, selecting as a source the Advanced Photon Source 7-Gev storage ring. The diffraction limit defines the relation between the source size a and the angular diveregence θ of the radiation:

$$\theta \cdot \Delta a \geq \lambda$$

But from other side:

$$\theta \equiv \frac{1}{\gamma\sqrt{N}}$$

where N is the number of undulator periods and γ is the relativistic factor. As a result:

$$\Delta a \sim \lambda\gamma\sqrt{N}$$

and for APS:

$$\gamma \sim 10^4, \sqrt{N} \sim 5, \Delta a \sim 10^{-4} \text{ cm}$$
$$\lambda \sim 1 \text{ Å}$$

The wavelength practically defines the type of the monochromator that can be used for the measurements. This is the crystal type monochromator. Recently a significant step in x-ray monochromatization was made by inventing of the nuclear-Bragg scheme [10,11]. As a result, a level of monochromatization of $\Delta\lambda/\lambda \sim 10^{-12}$ was achieved. Consequently, the feasible coherent time now is about 10^{-7} sec. This time is certainly larger than resolving time of the contemporary registration instrumentation and the counting technique is convenient. With the spectral flux from the APS undulator [12] of about 10^{21} p/s the detector counting rate N_d will be about 10^4 c/s and a coincidence rate $N_C \sim \tau_{coh} N_d^2$ of about 10 c/sec can be achieved. A beam size measurement time of about 20-60 sec seems realistic.

In the case of the crystal monocromator utilization the coherent time is equal 10^{-15} sec for the 1 Å wavelength radiation. This value is much smaller than typical resolving time for the amplifier, so the "current technique" should be chosen. The time measurement T can be estimated as follows:

$$T >> \frac{\tau_0}{\left(\frac{N_d \lambda^2}{c\,\Delta\lambda}\right)^2}$$

and is for the APS undulator radiation about 30-100 sec.

The spatial resolution of the beam size measurement does not depend what kind of registration technique is used and can expressed in the following form:

$$\Delta a = \frac{\Delta l\, a^2}{L\,\lambda}$$

It should be noted here that the approach considered in this paper is valid if

$$\theta \equiv \frac{1}{\gamma\sqrt{N}} > \theta_{coh} \sim \frac{\lambda}{a}$$

For the APS undulator this condition is satisfied.

III CONCLUSION

The feasibility of intensity interferometry for the APS undulator has been demonstrated. In addition, it has been shown that both an acceptable time scale for measurements and the spatial resolution are readily achievable.

Acknowledgement

The author is grateful to Dr. M. Zolotarev for fruitfull discussions.

V. REFERENCES

[1] R.H.Brown and R.Q.Twiss, Nature, v.177, n.4497, p.27, 1956.

[2] R.Q.Twiss, A.G.Little and R.H.Brown, Nature, v.180, n.4581, 1957.

[3] R.H.Brown, The intensity interferometer, Taylor and Francis, London, 1974.

[4] D.H.Boal, G.-K. Gelbke and B.Jennings, Review of Modern Physics, v.62, n.3, p.553, 1990.

[5] R.Loudon, The quantum theory of light, Clarendon Press, Oxford, 1973.

[6] M.L.Goldberger, H.W.Lewis and K.M.Watson, Physical Review, v.1412, n.1, p.25, 1966.

[7] E.V.Shuryak, Soviet Physics JETP, v40, n.1, p.30, 1975.

[8] M.Howells, private communication.

[9] J.W.Goodman, Statistical Optics, A Wiley-Iterscience Publication, New York, 1985.

[10] E.Gerdau, R.Ruffer, H.Winkler et. al., Phys.Rev.Lett. v.54, p.835, 1985.

[11] G.Faigel, D.P.Siddons, J.B.Hastings et.al.,Phys.Rev.Lett., v.61, p.2794, 1988.

[12] G.K.Shenoy, P.J.Viccaro and D.M.Mills, Characteristics of the 7-Gev Advanced Photon Source, ANL-88-9, Argonne, 1988.

H^- Beam Characterization using Laser-induced Neutralization*

V. W. Yuan, R. Garcia, K. F. Johnson, K. Saadatmand,†
O. R. Sander, D. Sandoval, M. Shinas
Los Alamos National Laboratory, Los Alamos, NM 87545

Abstract

The Laser-induced neutralization technique, LINDA, is important as a noninterceptive diagnostic for quantitatively measuring beam emittance values. It is also valuable for its capability to characterize, both quantitatively and qualitatively, the performance and match of linac components. In this paper we present LINDA experimental results that show how the output beam of a radio-frequency quadrupole (RFQ) and drift-tube linac (DTL) combination changes with the variation of RFQ-DTL relative phase and of DTL cavity power. We also present results showing the effect of a longitudinal buncher on beam emittance.

1 Introduction

The Laser-induced neutralization technique, LINDA, was developed primarily to quantitatively measure emittances of a high-intensity H^- beam. Because of its noninterceptive nature, the technique can be used continuously in a high-intensity beam without the survival problems that would accompany the use of an interceptive diagnostic. When used on the Los Alamos 5-MeV Accelerator Test Stand (ATS), LINDA has also proved to be an important diagnostic in characterizing the performance and match of various components of an accelerator structure. As an example, LINDA allowed the ATS experimental team to measure the longitudinal emittance at the exit of individual structures and provided information about the shape of the beam longitudinal phase space as a function of the operational settings of the accelerator elements. Because quantitative emittance values are discussed in another paper at this conference [1], this paper concentrates on how LINDA can be used to verify the optimum DTL field setting, the correct buncher setting, and finally, the optimum relative phase setting between the RFQ and the DTL.

*Work supported and funded by the US Department of Defense, Army Strategic Defense Command, under the auspices of the US Department of Energy.

†Grumman Corporate Research Center.

0-7803-0135-8/91$01.00 ©IEEE

2 Experimental Setup

A schematic of the LINDA setup for the ATS measurements is given in Yuan et al. [1]. The 1.064-μm fundamental from a pulsed, mode-locked YAG laser was amplified and frequency-doubled to produce intense pulses of 532 nm wavelength. The mode locking, in conjunction with pulse slicing, produced short, 5-Hz single pulses of 23 ps duration and 20-30 mJ average intensity. The laser beam intersected the ATS H^- beam at a location 6.3 cm downstream of the end of the DTL. The setup was basically the same one used in experiments to determine emittance growth and therefore a second laser intersection point was present 17.7 cm downstream of the end of the DTL. The neutralized portion of the beam was separated from the charged remainder with a bending magnet, and neutrals were detected with a secondary emission monitor (SEM) located 9.5 meters downstream of the laser intersection points. The time-of-flight (TOF) spectra of the arriving neutrals were digitized with a Tektronix AD7912 waveform digitizer, and the laser firing times were determined by a Nanofast 536-10B time-interval meter. TOF spectra and Nanofast times were recorded for analysis using a MicroVax II computer.

3 Characterization Results

Optimal transmission of the particle beam through both the RFQ and DTL sections of the accelerator depends on matching the settings of the two sections to the proper values. As the settings depart from the optimal values, transmission can suffer causing beam intensity to drop. However, with LINDA, we were able for the first time to see the actual change in shape of the longitudinal-emittance phase space that accompanies the reduction in transmission. Figure 1 shows a map of the observed longitudinal phase space as a function of the relative RFQ-DTL phase and of DTL cavity power. For each phase and amplitude setting at which a measurement was taken, one observes a pair of phase-space contours (reflecting the presence of the two laser intersection points, as mentioned above). The similarity of the two contours in each pair indicates that no major changes in emittance shape occur in the 11.4-cm

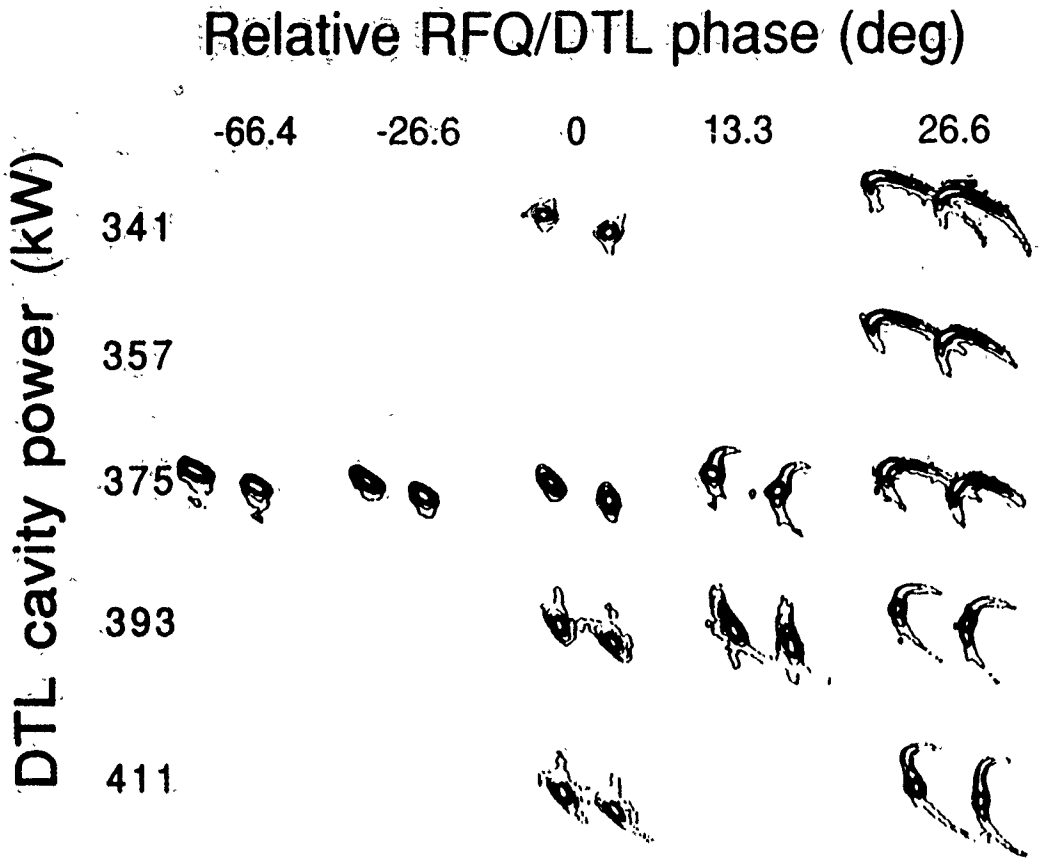


Figure 1: Map of longitudinal-emittance phase space plots measured for various DTL cavity power levels and for various RFQ/DTL relative phases.

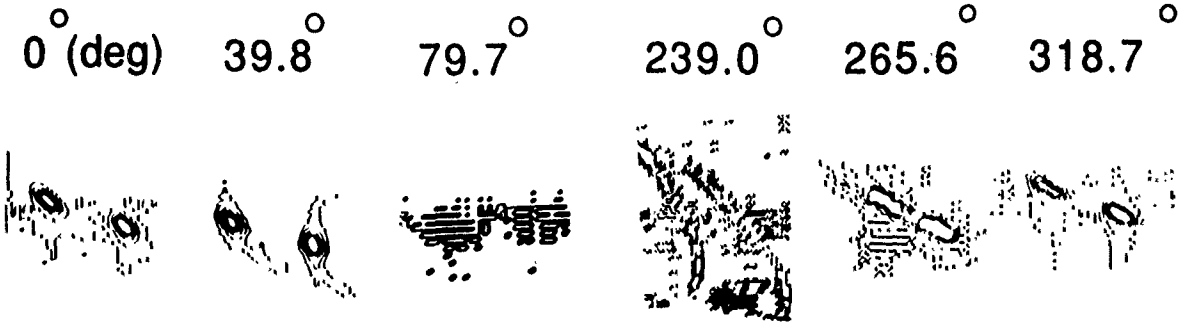


Figure 2: Succession of emittance plots depicting the change in longitudinal emittance as the relative RFQ/DTL phase undergoes a full 360 degree wraparound.

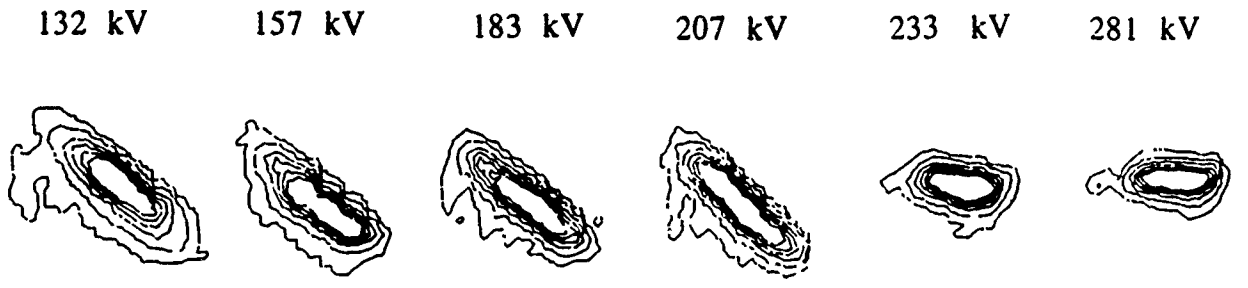


Figure 3: Plots of longitudinal emittance for different gap voltages of the "R1" buncher.

drift space between the laser intersection points.

Optimal transmission occurred at the relative phase setting of -26.6^o and a DTL power of 375 kW. One can see that the phase space remained elliptical for changes in relative phase of approximately 30^o to 40^o from this setting. At relative phase settings of 13.3^o and 26.6^o, the mismatch between RFQ and DTL resulted in the growth of long tails in the emittance phase space. The appearance of these tails is evidence that beam particles are beginning to fall out of the rf beam bucket. Figure 1 shows that with the relative phase held constant at 26.6^o, a variation in the DTL power resulted in a marked rotation of the orientation of the long phase-space tails. In repeating the measurements, we found that the phase setting for the onset of the rotations could change. This was later traced to a problem with the potentiometer on the trombone of the phase shifter. Hence, in addition to its value in determining emittance, LINDA allowed the experimental team to discover and correct an uncertainty in determining the overall relative phase.

A further variation of the relative RFQ-DTL phase can result in a large mismatch in which the entire beam falls out of the rf bucket and the transmission falls to zero. Figure 2 shows the longitudinal phase-space plots as the relative RFQ-DTL phase is wrapped around a full 360^o. One sees the progressive distortion of the phase-space ellipse, followed by the eventual disappearance of the beam. The beam reappears when the wraparound nears 360^o.

4 Buncher Modes

In a later stage of ATS development, a beam transport line [2] consisting of one arm of a beam funnel was installed immediately downstream of the DTL. After the first buncher of this funnel arm was installed, LINDA was used to characterize the buncher output beam. When a beam micropulse passes through the buncher, the phase of the power cycle that the buncher is in (buncher mode) determines the effect that the buncher will have on beam emittance. A micropulse passing through the buncher while the buncher field is changing most rapidly, will either be bunched or debunched, depending on whether the field is increasing or decreasing with time. In addition, since the average energies at the front of the bunch are altered relative to those at the rear of the bunch, the phase ellipse will be rotated after the beam has passed through the buncher. The bunch and debunch modes have the largest effect on beam phase space. If the beam enters the buncher field 90 degrees out of phase with the bunch or debunch modes, then the bunch is either accelerated or retarded (deaccelerated) as a whole without much change to the shape of the emittance ellipse. Figure 3 shows the effect of the buncher as a function of buncher gap voltage. One sees that there is no visible effect of the buncher until the gap voltage exceeds 200 kV. In Figure 4, the output emittance for each of four buncher modes is shown. For comparison,

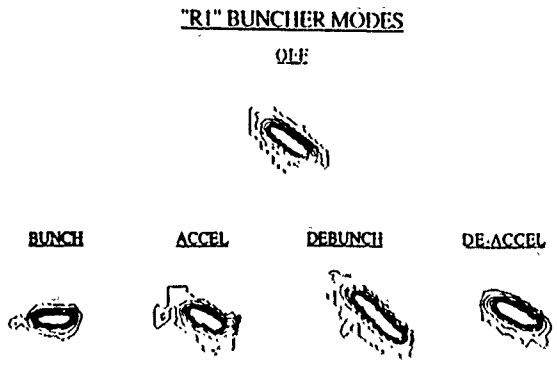


Figure 4: Measured longitudinal emittance for four different "R1" buncher settings and for buncher off.

the emittance is also shown for buncher off.

5 Summary

The capabilities of LINDA as a diagnostic go beyond its primary function of quantitatively determining emittance sizes. LINDA can also serve as a valuable check on whether set points for rf fields, buncher settings, and RFQ/DTL relative phases are optimal. When these set points are varied far enough from their optimal settings to affect the transmission of the beam, LINDA permits experimenters to graphically see the changes in longitudinal phase space that are causing the losses in transmission.

References

[1] V. W. Yuan, R. Garcia, K. F. Johnson, K. Saadatmand, O. R. Sander, D. Sandoval, and M. Shinas, *Measurement of Longitudinal Emittance Growth Using a Laser-induced Neutralization Method*, 1991 Particle Accelerator Conference, San Francisco, CA, May 1991.

[2] K. F. Johnson, O. R. Sander, G. O. Bolme, J. D. Gilpatrick, F. W. Guy, J. H. Marquardt, K. Saadatmand, D. Sandoval, and V. Yuan, "A Beam Funneling Demonstration: Experiment and Simulation," in *Proceedings of the International Symposium on Heavy ion Inertial Fusion*, Monterey, CA, Dec. 1990.

Upgrades to the Fermilab Flying Wire Systems

J. Zagel, A. A. Hahn, G. Jackson, T. Johnson, K. Martin, J. Misek, X.Q. Wang, W. Ye

Fermi National Accelerator Laboratory*
P.O. Box 500
Batavia, IL 60510

Abstract

Flying wire systems have been installed in the Fermilab Main Ring, Tevatron, Booster, and Accumulator to measure the transverse beam profiles. During the recent shut down many improvements were incorporated to increase the reliability of the hardware, software, and data obtained from their operation. These improvements include adding a double fork to the Tevatron systems, developing a new scintillator/photomultiplier tube combination, and a broken wire monitor. In addition an analysis of the motion control was performed to understand the frequent operational problems encountered.

I. INTRODUCTION

The Flying Wire systems have been operational in the Fermilab Main Ring and Tevatron for quite some time. The basic system has been described previously.[1] The installation of the new D0 colliding detector and electrostatic separator system has necessitated a move of most of the flying wire hardware. This presented an opportunity to upgrade the equipment and incorporate some system modifications.

Major problems existed in many areas. These areas include basic communications problems, mechanical variations of components, radiation damage to tunnel components, poor diagnostic capability, and equipment not meeting latest upgrade specifications.

In addition, a complete test system has been assembled incorporating a laser to simulate beam. This will allow us to test new ideas as well as provide a repair facility for failed components.

II. SYSTEM UPGRADES

A. Motion Control

The motion of the wire through the beam is controlled by a microprocessor chip set. This chip set implements a closed loop algorithm to maintain a fixed velocity vs position profile. Parameters must be set to control the feedback characteristics of this loop. The settings of most of these parameters appeared to vary widely from one installation to the others. An in-depth study was done to determine the best set of parameters for each wire. This resulted in finding the smoothest velocity profile with minimum drive current fluctuations while the wire is in motion, as well as minimum holding current with the wire at rest.

Analysis also indicated that a non-uniform tension in the neoprene/fiberglass timing belt was a major contributor to the unpredictable parameter settings. Mechanical adjustment to compensate for varying manufacturing tolerances of the belt was not originally provided. Thus when mechanical components need replacement no provision was made to allow retuning for optimum performance. By modifying the motor mount to allow a belt tensioning scheme we removed a potential non-linearity from the system.

B. Optical Encoder

The position feedback loop uses an optical encoder to provide relative position information. There are two quadrature position outputs and an index reference pulse output. The index is used during a reset of the system to determine a fixed reference point from which all angular measurements and linear projections are calculated.

These encoders are affected by radiation in two ways: 1) a false indication of index position is occasionally seen during high accelerator losses and 2) the index pulse totally disappears after only a few months of continuous use in the tunnel. The manufacturer has evaluated, and repaired, many units and reports the failure mode as a loss of the index track light emiting diode (LED) and receiver. These items are in plastic packages and apparently darken with exposure to radiation. The quadrature track LEDs and receivers have an automatic gain circuit and can accommodate some darkening; however we as yet do not know their approximate lifetime.

To eliminate both index related problems we have installed an inductive proximity detector in parallel with the encoder. A .075" dia. copper target was installed on the main drive gear and aligned to coincide with the optical index. Both devices work in parallel when the optical index is available with the proximity detector providing a gate window for the optical index. The system is switched to allow using either device independently or in the gated mode.

C. Loss Monitors

The primary detectors that have been used in the past were the so called "Elias Cans" and "Paint Cans". Both designs used a photomultiplier tube (PMT) immersed in a scintillator oil. The Elias Cans suffered from too high a conversion efficiency resulting in easily saturated tubes. Recent modifications to the Elias Cans included blinding the PMT

*Operated by Universities Research Association Inc., under contract with the U.S. Department of Energy.

0-7803-0135-8/91$01.00 ©IEEE

from the scintillator and extending the can to move it radially away from the loss shower. A major problem with both detectors has been the occurrence of leaks in the containers. All the scintillator oil detectors have since been removed from the system.

New PMT and plastic scintillator detectors have been installed at all of the flying wire locations. The new PMT uses a lower resistivity S-20 photocathode material. This results in a higher sustainable signal and yields good signal quality with the high voltage set at 750 volts. They should work well for higher intensity beam during collider operation.

Plastic paddles replace the mineral oil and leaky containers. The paddles are 1/2" thick and subtend a 180^{o} angle about the beam pipe to provide a uniform and smoother signal from losses created by the wire's motion through the beam. The PMT is mounted on the end of a 18" plexiglass extension to remove it from the primary shower.

D. Broken Wires

The key to obtaining reliable profile data is to have an intact wire. Two improvements have been incorporated into the Tevatron wire systems. A dual fork has been designed and installed that provides two wires 180^{o} apart within the can as shown in Figure 1. In the event a wire fails, the second wire can be rotated into position and used immediately. In order not to affect the motor's inertial loading, the new dual fork has a moment of inertia equivalent to the original single wire mount fork. This was achieved by fabricating the dual fork assembly from titanium. The original fork had been made from stainless steel.

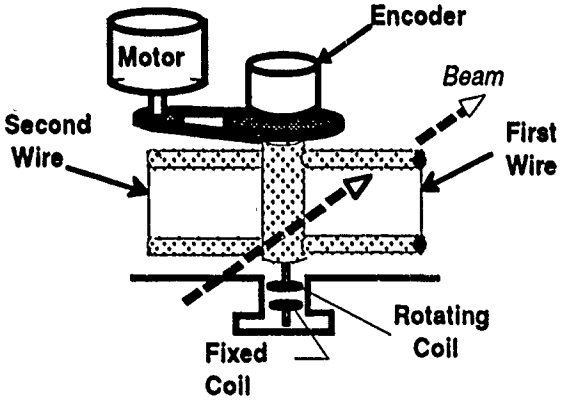


Figure 1. Tevatron Dual Fork Detail.

The second improvement is a broken wire monitor. A small switch is built into one end of the wire mounting printed circuit board. Normally the wire is in tension and the switch is open. If the wire breaks the switch closes completing a circuit that includes a 33 microfarad (first wire) or 47 microfarad (second wire) capacitor. The change of impedance is sensed through a set of coils wound on Teflon bobbins in the vacuum enclosure. The coil connecting the switches to capacitors rotates with the fork. The pickup coil is fixed and outputs through a vacuum feedthrough. Two status bits will be provided to the diagnostic application program to indicate the health of each wire.

E. Communications

Host communication is provided through a Fermilab-designed VME board designated the V080. This board contains a 68008 microprocessor. A problem has been identified in its arbitration scheme that allows conflicts to occur when this board is a participant in interrupt handling. The immediate fix was to eliminate interrupts in favor of a polling scheme. However there is a major disadvantage to this fix. The communication process moves large buffers of data after each measurement. The current scheme encounters many delays causing other programs to exhibit problems. Future work will be required to speed up data transfer.

III. Operation and Maintenance

A. Console Control

New control programs (diagnostic application pages) have been implemented that provide diagnostic information in an operator-friendly manner. The initial display shows the basic status of all the flying wire systems at a glance. Detailed displays of specific parameters for each wire are available on a subpage. These subpages allow the operator to modify motor drive parameters and settings of the mechanical aspects at each installation.

The procedure to reset a wire is now simplified by an interrupt field on the diagnostic application page. The software determines if the motor control board and position scalar board agree on the current wire position. If a difference is noted the wire is rotated one complete revolution and the new reference is noted. If the reference was not found on the first revolution a second revolution in the opposite direction is performed. The motor control chip set is then instructed to return to a parking position based on the new reference position.

Another new feature of the diagnostic application page allows the setting of the real time clock in each VME chassis. The real time clock is used to time stamp each fly's data for future evaluation. We now have a simple method to coordinate the time setting on each system.

A display of the boards present in the VME system chassis is now available using a subpage of the diagnostic application page. There are no longer two loss monitors per system for each of protons and antiprotons. Therefore some digitizer boards will be removed. The system now allows these boards to be removed and provides a mechanism to inform the operator that they are not installed. An additional benefit of this feature is that we now have an easy way to verify the addressing scheme within the chassis.

B. Test System

A complete collection of flying wire system parts has been assembled in our laboratory. We can now test the

mechanical and electrical components in a working environment.

We have incorporated a visible laser to simulate beam and look at scattering of the laser light into the standard PMT mounted directly on the end flange. The laser is a 670nm, 5mw lasing diode. It runs on 5 volts and is activated during a fly. Preliminary results are well correlated to the actual size of the laser beam.

The construction and use of this test system has led to the discovery of and solution to a few problems already. It will serve as a test bed for new ideas and software development.

C. Future

Six wire systems are installed and will be made operational in the Accumulator Ring of the Antiproton Source. Two of these wires were originally designated for experiment E760.[2] These two wires are operationally similar to the Main Ring and Tevatron wires except they rotate a full 360^0 for each fly. The remaining four wires will incorporate a secondary emission readout capability.

IV. ACKNOWLEDGMENTS

The authors would like to thank Warren Bowman, Bob Flora, Matt MacPherson, and Tom Groves for their expertise and hard work to accomplish these upgrades.

V. REFERENCES

[1] J. Gannon, et al., "Flying Wires at Fermilab," Proceedings of the 1989 IEEE Particle Accelerator Conference, pp. 68-70, March 20-23, 1989.

[2] X.Q. Wang, et al., "Design and Commissioning of Flying Wires in the Fermilab Accumulator", paper KR10 at this conference.

Results from a Prototype Beam Monitor in the Tevatron Using Synchrotron Light

A. A. Hahn, P. Hurh
Fermi National Accelerator Laboratory*
P.O. Box 500
Batavia, IL 60510

Abstract

A prototype synchrotron light monitor has been installed in the Tevatron at the downsteam edge of a superconducting dipole magnet. Synchrotron light produced at the upstream edge [1] of the magnet is sufficiently separated from the proton beam to be picked off by the monitor's mirror and diverted to its detector. The measured light intensity at different beam energies will be compared to the predicted values. The parameters of a beam profile monitor will be discussed.

I. INTRODUCTION

A charged particle accelerated transverse to its direction of motion will emit synchrotron radiation [2]. This radiation is sharply peaked in the forward direction, being almost completely contained within a cone of half angle $\Delta\theta = 1/\gamma = m/E$, where m is the mass of the particle and E its relativistic total energy. This radiation if imaged, can form a transverse profile of the beam itself. Synchrotron radiation profile monitors are quite common in electron machines due to the copious numbers of photons produced. Only relatively recently however [3] has such a device become available for routine use in a proton machine. The difficulty can be traced to two related factors. First the frequency of the typical synchrotron radiation is much too low to be easily detected. Secondly, the angular resolution of an imaging system which should be high to measure the profile of a narrow particle beam, will be limited by the extreme narrowness of the synchrotron radiation itself. This effect scales as $\lambda/\Delta\theta$. Since $\Delta\theta$ is set by the energy of the machine, the only way to improve resolution is to lower λ. As will be shown, the way to enrich the low wavelength region is to rely either upon short magnets (or an undulator which is a series of short magnets) or the sharp transition between the zero field region and the full field region of a dipole magnet.

Synchrotron Radiation - "Standard Theory"

The power emitted by a particle moving with velocity $c\boldsymbol{\beta}$ in a uniform magnetic field **B** can be estimated in the following way. Consider the particle in its own instantaneous rest frame. It is subjected to an effective electric field $\mathbf{E} = \gamma c\boldsymbol{\beta} \times \mathbf{B}$. The emitted power can be calculated by using Larmor's non-relativistic formula $P = (e^2/6\pi\varepsilon_o c^3)a^2$, a being the acceleration of the particle = F/m = eE/m. Assuming $\boldsymbol{\beta}$ and **B** are at 90°, $P = \frac{e^4\gamma^2\beta^2B^2}{6\pi\varepsilon_o m^2 c}$. In the rest frame this power is emitted symmetrically around the axis of acceleration in a toroidal shape. The power in the laboratory frame can be related to the rest frame by a Lorentz transformation. Recognizing that power = $\frac{\Delta\text{Energy}}{\Delta\text{time}}$, one needs to transform both the numerator and denominator. Due to the symmetry of the power around the acceleration axis, the average photon energy is just Lorentz boosted by a factor of γ, $\Delta E_{lab} = \gamma\Delta E_{rest}$. Since $\Delta t_{lab} = \gamma\Delta t_{crest}$, $P_{lab} = P_{rest}$. The power can be written in the more common form $P = \frac{e^2p^4}{6\pi\varepsilon_o m^4c^3R^2}$ where R and p are the radius of curvature and momentum of a charged particle in a magnetic field, ($R = \gamma mc\beta/eB = p/eB$).

The frequency spectrum of the radiation may be developed in a similar manner by considering the length of the radiation pulse at an observation point. Due to the directionality of the radiation this can be quite short. For a conventional synchrotron source, the beam arc length which can radiate in the direction of an observer is $R(2\Delta\theta) = 2R/\gamma$. Again from the perspective of the particle in its own series of instantaneous rest frames, this length is Lorentz contracted a factor of γ. Therefore the power radiated to reach the observer must occur in a time span of $2R/\gamma^2 c\beta$. A simple Fourier analysis says that the radiation will have frequency components (in the rest frame) proportional to $\frac{1}{2\pi\Delta t} = \frac{\gamma^2 c\beta}{4\pi R}$. In the lab frame these frequencies (or photons) will again be energy boosted another factor of γ as shown before. Putting a factor of 3 to reflect that Δt was actually the entire length of the pulse and also to end up with a familiar formula, one can define a critical frequency,

$\nu_{cr} = \frac{3\gamma^3 c\beta}{4\pi R}$. For a 900 GeV/c proton in a Fermilab Tevatron dipole magnet, R = 754 m, $\beta \approx 1$, $\gamma = 959$, and the critical wavelength is $\lambda_{cr} = c/\nu_{cr} = 3.5\ \mu m$, the far infrared region.

"Short" Magnet

A magnet is defined to be short if its length is much shorter than $R(2\Delta\theta)$ the arc length defined above. Effectively the deflection angle of the particle due to the magnet is smaller than the synchrotron radiation cone. The development for a

*Operated by Universities Research Association Inc., under contract with the U.S. Department of Energy.

0-7803-0135-8/91$01.00 ©IEEE

short magnet proceeds as above except for one detail. The path length is set by the magnet characteristic length L , not the arc length. Replacing $2R/\gamma$ by L the critical frequency becomes $\nu_{cr} = \frac{c\gamma^2}{2\pi L}$. For example a Gaussian magnet with $\sigma = 4.5$ cm length and a $\gamma = 959$ gives a critical wavelength of 307 nm, the ultraviolet region. Of course the total power emitted is less than in the standard case since the average field is less than the full magnet and the total path length is (in this case) roughly 10 times less. However in the short wavelength region around 300 nm, the standard case has a negligible intensity, down roughly $e^{-2(3500/300)}$ (using a rigorous formula) compared to the 3.5 μm region. Thus synchrotron radiation from a short magnet is much more intense in the short wavelength region.

The edge of a magnet behaves similarly to a short magnet in that a sharp transition from zero field to full field enriches the high frequency (low wavelength) portion of the synchrotron spectrum.

The rigorous derivation of the power spectrum for short magnets and the edge profiles of magnets can be found in Ref [1].

II. TEVATRON SYSTEM

Dipole field shape

The end field of a Tevatron superconducting dipole magnet was measured with a Hall probe. Figure 1 depicts the field intensity as the probe is inserted into the magnet. To facilitate calculations, several shapes were fit to the data. The best approximation was an error function with a characteristic width of 456 cm.

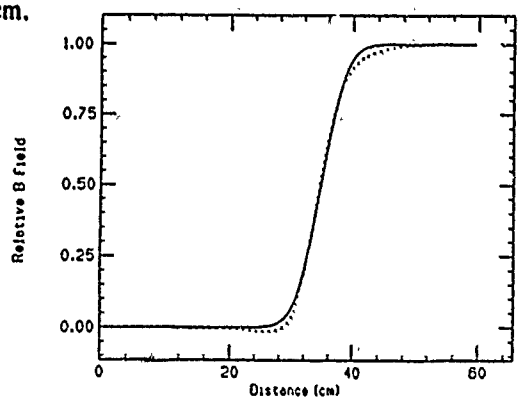


Figure 1: The relative magnetic field near the end of a Tevatron Superconducting Magnet. The dotted line represents the measured data. The solid line is an fit of the data to an Error Function.

Differential Power spectrum

With this function and width, the differential power spectrum [1] is

$$\frac{dW}{d\Omega d\lambda} = N\frac{C^2\gamma^6}{4\pi^2 c} f^2 B_o^2 \exp(-\pi^2 \frac{L\gamma}{2\gamma^2\lambda}),$$

with N the number of particles, $C^2 = 9.47*10^{-11} m(s/kg)^{0.5}$ (for protons), $f^2 = f^2_{\perp} + f^2_{\parallel} = y^{-6}[(1-(\gamma\theta)^2)^2 + 4(\gamma\theta\sin^2\phi)^2]$ representing the planes of polarization perpendicular and parallel to the motion , and $y = 1+(\gamma\theta)^2$. Figure 2 plots the power spectrum integrated over angles for several proton momenta.

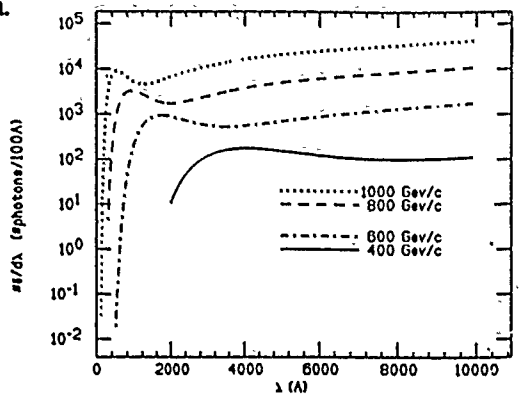


Figure 2: Photon Yield from the edge of a Tevatron dipole magnet vs wavelength for a $6* 10^{10}$ proton bunch of various momenta.

Detector

A port was installed on the Tevatron beam pipe at the C11 location. This location is a meter downstream of a 6.1 meter Tevatron Dipole magnet. The proton beam is bent a total angle of 8.12 mr from its original direction. Synchrotron light, produced tangentially at the far upstream edge, is separated horizontally 2.5 cm from the proton beam at the downstream end. Since the proton beam width is on the order of 1 mm, it is possible to reflect the synchrotron light by a suitably placed mirror without interfering with the proton beam. Figure 3 schematically shows the arrangement of the port. The mirror is an aluminized flat which can be remotely driven in and out of the beam pipe by a total distance of 3.8 cm. The window is 2mm thick Suprasil.

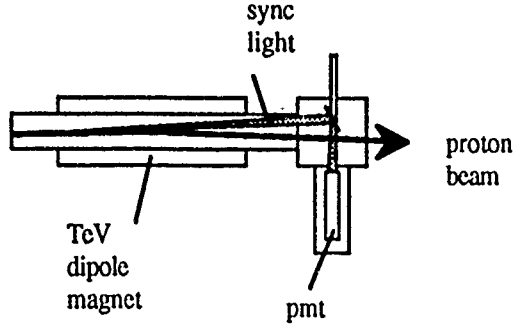


Figure3: Schematic view of prototype setup.

Prototype test

A Phillips 2" S20 photocathode photomultiplier tube (pmt) was installed adjacent to the Suprasil window. This tube was chosen since it was available and its quantum efficiency is similar to that of the eventual imaging detector. The pmt was calibrated with an LED with respect to gain so that using the

manufacturer's nominal quantum efficiency values, an estimate to the number of photons seen could be made. Figure 4 gives the predicted number of photons seen for both this pmt and a commercially available CCD.

In order to verify that we were indeed detecting synchrotron light instead of particle losses, the internal mirror was pushed into the beampipe in small steps. While in the full out position, no signal could be seen on the pmt. As the mirror was pushed into the beam pipe the signal could be seen to increase, eventually reaching a plateau.

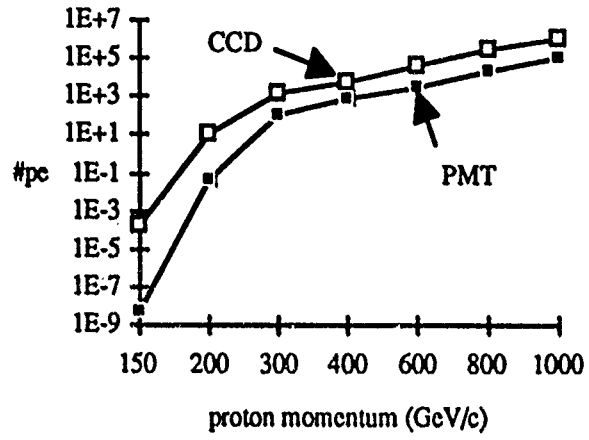


Figure 4: The photoelectron yield for a $6*10^{10}$ proton bunch from the edge of a Tevatron dipole magnet.

It is difficult to quantitatively compare the experimental intensity as a function of proton momenta since the beam pipe interferes with the synchrotron light beam at low momenta Qualitatively, the light is first seen at a proton momentum of about 500 GeV/c, and the intensity increases rapidly as the acceleration ramp progresses A comparison of the experimental yield at 800 GeV/c to the theoretical value gives twice the intensity expected. This is likely within the error of the known pmt response.

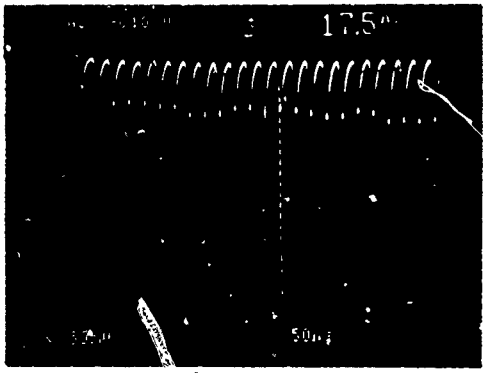


Figure 5: Oscilloscope photograph of response of pmt to a batch of 800 GeV/c protons. The individual buckets each contained approximately $0.6 * 10^{10}$ protons.

III. Future Imaging system

We are in the process of installing a complete imaging system. This system will use the same beam port as described above. In addition there will be two additional flat mirrors to fold the optical path, a spherical focusing mirror to make the image, and a intensified CCD camera.

Optics

The reflecting mirror is a 5 cm diameter spherical mirror with a focal length of 2 meters. Since the object distance is 7.5 meters away, the image is formed 2.7 meters from the mirror. The image height is 36% of the actual object (proton beam) size or approximately 360 μm. This configuration was chosen so that the area of the image plane (1.1×0.88 cm^2) would cover a large region of the beampipe at the object plane, thereby making it easier to find the beam image under startup conditions. The diffraction limit is 29 μm referred to the image plane. Note that 3.5 μm radiation diffraction limit would be 10 times worse. The depth of focus is ± 1 cm, well matched to the image length of 1.3 cm (for a 10 cm object length). Aberrations, dominated by astigmatism (due to a 1° off axis reflection on the primary mirror) are only 8μm, well below the diffraction limit and thus may be ignored.

Focal plane camera

Detection of the image will be done with a gateable microchannel-plate image-intensifier, optically coupled to a CCD camera. The gateable aspect (5ns time resolution) will allow single-bunch single-pass detection or single-bunch imultiple-pass integration. The CCD is a 483x378 pixel array with a fiber optic input window. Each pixel is spaced 30 μm horizontally, 18 μm vertically and is 12x18 μm^2 in size. Initial readout will be at video speeds.

We are exploring the possibility of including an optical scanning mirror. This device would be place near the camera so that the converging image could reflect off the mirror. In this manner it would be possible to record an multiple images of a single proton bunch on successive revolutions. Each image would be offset from the previous one due to the rotation of the scanner (a 10 element mirror rotating at 30000 rpm). At 10 images per line, and 10 lines a total of up to 100 images per video readout could be accomplished.

III. REFERENCES

[1] R.Coisson," Angular-spectral distribution and polarization of synchrotron radiation from a 'short' magnet", Phys Rev A 20 ,1979, pp. 524-28

[2] J.D.Jackson, *Classical Electrodynamics* ,John Wiley and Sons,(1962) ,Ch. 14

[3] J.Bosser et al., "Proton beam profile measurements with synchrotron light",preprint, CERN SPS/83-15, (1983)

Design and Commissioning of Flying Wires in the Fermilab Accumulator

X.Q.Wang, T.Groves, A.A.Hahn, G.Jackson, J.Marriner, K.Martin, and J.Misek
Fermi National Accelerator Laboratory*
P. O. Box 500
Batavia, IL 60510

Abstract

Six flying wire systems have been installed in the Fermilab Accumulator to measure the transverse beam profiles during antiproton stacking and extraction, and the beam momentum distribution during deceleration through transition. Each system measures a transverse beam profile by passing a 25 micron carbon filament through the beam transversely, and recording the flux of secondary particles which are produced from the collisions between the beam particles and the wire. The wire motion, data acquisition, and communication with the control system are managed by a 32-bit VME based microcomputer system. This paper summarises the hardware and software features of the Accumulator flying wire systems. The measured effect of wire passages on beam emittance is described.

1 Introduction

The Accumulator flying wire systems have been installed for measuring the transverse beam profiles during $\bar{p}$ stacking, extraction and the E760 deceleration operation [1]. Their design is very similar to that of the Main Ring and the Tevatron flying wire systems [2]. Each detector passes a 25 micron carbon fiber through the beam transversely at a constant velocity of 10 m/s. As the wire traverses the beam, collisions between the beam particles and the wire produce secondary particle cascades with the intensity proportional to the number of the beam particles at the wire position. These secondary particles are intercepted by a scintillator in which photons are then produced. A photomultiplier is used to measure the light intensity, and the wire position is determined by an optical encoder.

2 Wire Location

In the Accumulator, the two horizontal and two vertical flying wires to be used in normal stacking operation are located in the AP40 high dispersion section, covering the core orbit and the extraction orbit respectively. The two wires for E760 are both horisontal, one is located in the AP40 high dispersion region and covers the central orbit, the other in the AP30 low dispersion region. They are to be used to measure the momentum distribution of the beam. Figure 1 shows the covering range of the horisontal wires in the AP40 high dispersion region. The fork arm length of the E760 high dispersion wire is 7.02" and that of the other five wires is 5.02". The optical encoder provides an angular resolution of 0.022 degree (16384 steps per revolution).

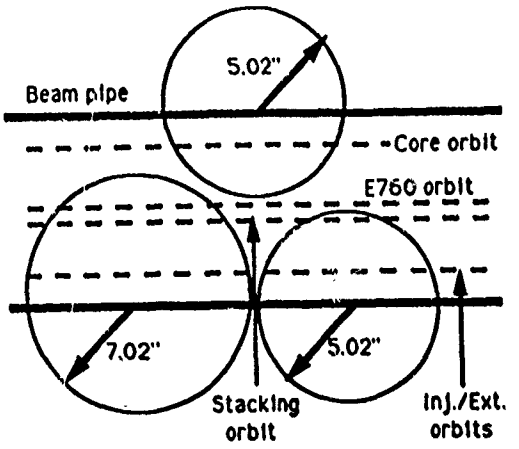


Figure 1: Location of the horisontal flying wires in the AP40 high dispersion region.

3 System Features

Since the Accumulator requires a higher vacuum than the other rings, commercially available bellows-sealed rotary motion feedthroughs (manufactured by Varian Vacuum Products, pt.#954-5151) are used for the Accumulator flying wire systems. These feedthroughs are capable of maintaining a vacuum of 10^{-11} Torr and are bakeable to a temperature of 300°C. Another major difference of the Accumulator wire systems from the existing Main Ring and

*Operated by the Universities Research Association Inc., under contract with the U. S. Department of Energy.

0-7803-0135-8/91S01.00 ©IEEE

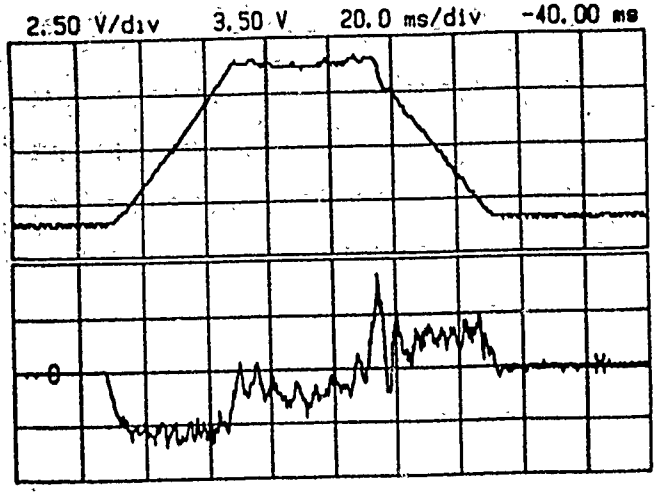


Figure 2: Top trace is the velocity profile of the wire in the AP30 low dispersion region. The bottom trace is the motor current.

Tevatron systems is that they also have an option to measure the beam profile by measuring the depletion current generated by the secondary emission of electrons. A *BeCu* spiral coiled torsion spring attached to each wire provides the path for the output signal. The wires, instead of being able to spin around, must stop within a single turn (2π) and reverse its direction for the next fly. Even though the wire motion is controlled via software, a limit switch is mounted on each flying wire to prevent further rotation which would damage the torsion spring.

The motion control and data acquisition of the Accumulator systems follow the design of the existing systems. The motion of the wire is controlled by a commercial 8-bit servo controller chip set (GL-2010 microprocessor chip and GL-100 interface chip manufactured by Galil Motion Control). The wire motion follows a preprogrammed trapezoidal velocity profile, and the maximum velocity is reached and maintained while the wire is passing through the beam aperture. In the process of the wire motion, the controller compares the actual position, measured by the optical encoder, with the programmed position. The error signal is filtered and sent to the power amplifier to drive the DC servomotor. In order for the closed-loop feedback system to have a fast and stable response, its bandwidth has been properly chosen. In the testing of the motion control, a resonance caused system trip. The resonance was removed by replacing the mechanical coupler between the optical encoder and the fork arm. Figure 2 shows the measured velocity profile of the wire in the A30 low dispersion region.

Data acquisition is initiated by an external triggering pulse. The amplitude signal from the phototube is processed with a gated integrator, digitised with a 12-bit high speed A/D convertor, and stored in a sixteen kilobyte FIFO memory. The position of the wire is also stored in another FIFO memory.

4 Wire Heating

In estimating the temperature rise of the wire in a single scan, we assume that only ionization loss of the incoming particles contributes to heating and that there is no cooling during wire traversal. Ignoring the relativistic effect, ionisation loss as a charged particle travels in a media can be expressed as [3]

$$\frac{dE}{dz} = \left.\frac{dE}{dz}\right|_{\min} \cdot \frac{1}{\beta^2}, \qquad (1)$$

where s is the direction of the particle's motion. If all this deposited energy is assumed to heat the wire, for a constant specific heat c_p the temperature rise of the wire in a single scan is

$$\Delta T = \frac{N_p k f_{\rm rev} \left.\frac{dE}{d(\rho x)}\right|_{\min}}{V_w c_p \beta^2} \sqrt{\frac{3\beta\gamma}{\epsilon_y \beta_y}}, \qquad (2)$$

where N_p is the total number of particles, k is the Boltzmann constant, ρ is the mass density of the wire, V_w is the sweeping speed of wire, $f_{\rm rev}$ is the revolution frequency of the beam particle, and ϵ_y and β_y are the beam emittance and the β-function respectively. Since carbon fiber has a specific heat which is a function of the temperature, eq. (2) should be modified for a correct result. The final temperature of the wire after one scan can be obtained from the equation below:

$$\int_{300}^{T_f} c_p(T)\, dT = \frac{N_p k f_{\rm rev} \left.\frac{dE}{d(\rho x)}\right|_{\min}}{V_w c_p \beta^2} \sqrt{\frac{3\beta\gamma}{\epsilon_y \beta_y}}. \qquad (3)$$

Since the beam size in the low dispersion region is much smaller than that in the high dispersion region, the temperature rise of the wire in the low dispersion region is expected to be much greater than that of the high dispersion wires. For a beam of 5×10^{11} particles and with a horisonal emittance of 1πmm-mrad, the temperature rise of AP30 low dispersion wire is estimated to be

$$\Delta T \approx 950\,^{\circ}C. \qquad (4)$$

The sweeping speed used in the calculation is 6 m/s. For a faster speed of 10 m/s, the temperature rise is lower. The result remains the same when taking into account the heat conduction along the wire.

According to this estimate, the temperature rise of the wire in a single scan is much lower than the melting point of the carbon wire, which is approximately $3550^{\circ}C$. In addition, study shows that only about 30% of the deposited energy heats the wire [4]. This fact will lead to a further reduction on the temperature rise of the wire. Therefore wire heating is not a problem.

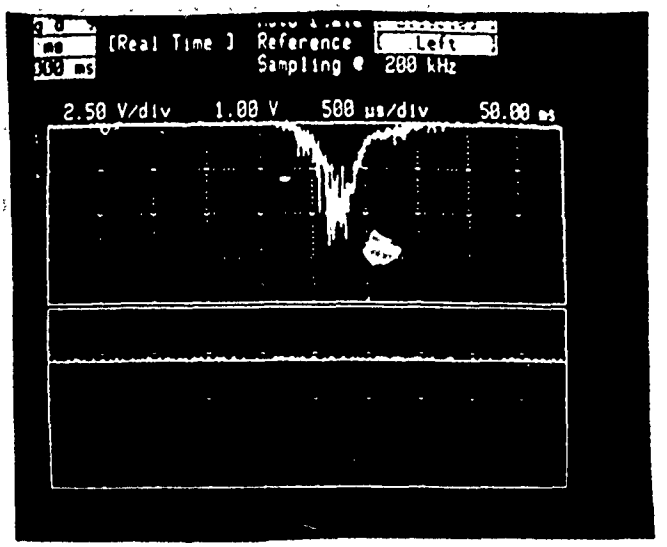


Figure 3: Photomultiplier output signal.

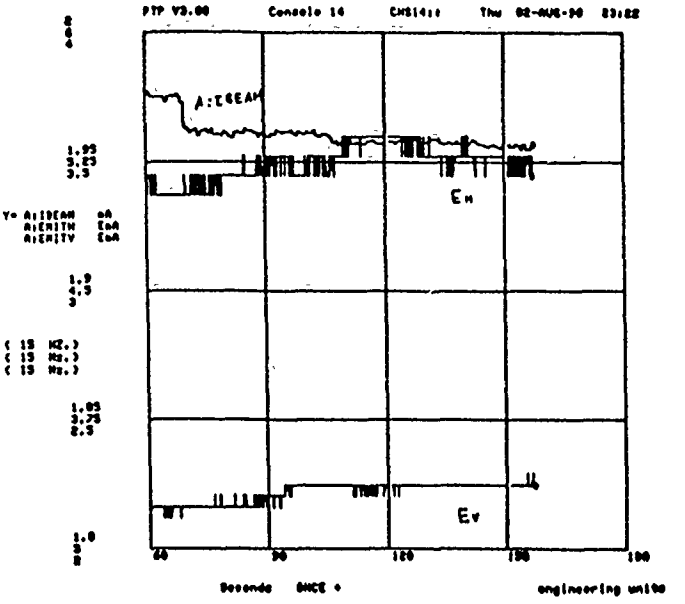


Figure 4: Beam current and transverse emittances.

5 Test Results

Figure 3 shows the output signal from the photomultiplier in a test fly of the E760 low dispersion wire. The trace represents the particle distribution of the beam in the horizontal direction. It was also found in a test fly that as the wire traversed the beam, it caused a beam intensity loss and emittance blow up. Figure 4 shows the measured beam intensity and transverse emittances in the test fly. For each sweep, the wire passed through the beam twice, and the beam loss was about 1%. The transverse emittance is obtained by measuring the total power of a betatron sideband. In figure 4, A:EMITH (A:EMITV) divided by the beam current A:IBEAM gives the horizontal (vertical) emittance, but the calibration is not accurate. Nonetheless, these measurements show emittance blow up in both transverse directions. The beam has an initial horizontal emittance of 2.6π mm-mrad and a vertical emittance of 1.1π mm-mrad. The increases of the horizontal and vertical emittances are roughly 0.1π mm-mrad and 0.05π mm-mrad respectively.

6 Future Work

In order to make the Accumulator flying wire systems fully operational, the data acquisition and reduction system must be calibrated so that the measured profile truly represents the beam particle distribution. This includes choosing the proper high voltage for each photomultiplier, and integrating time for obtaining the integrated light intensity. In addition, the depletion current readout capability will be completed in the upgrades of the Fermilab flying wire systems.

References

[1] V. Bharadwaj, *et al.*, "Operation of the Fermilab Accumulator for Medium Energy Proton-Antiproton Physics", Proceedings of the 2nd EUROPEAN PARTICLE ACCELERATOR CONFERENCE, June 12-16, 1990, pp.617-619.

[2] J. Gannon, *et al.*, "Flying Wires at Fermilab", Proceedings of the 1989 IEEE Particle Accelerator Conference, March 20-23, 1989, pp.68-70.

[3] D. H. Perkins, Introduction to High Energy Physics, Addison-Wesley Publishing Company, Inc., 1972, p.26.

[4] A. Burn, *et al.*, "Wire Scanner News from the CERN-SPS", Proceedings of the 1989 IEEE Particle Accelerator Conference, March 20-23, 1989, pp.1580-1582.

Beam Structure and Transverse Emittance Studies of High-Energy Ion Beams*

K. Saadatmand,† K. F. Johnson, J. D. Schneider
Los Alamos National Laboratory

Abstract

A visual diagnostic technique has been developed to monitor and study ion-beam structure, shape, and size along a transport line. In this technique, a commercially available fluorescent screen is used in conjunction with a video camera. The visual representation of the beam structure is digitized, enhanced through false-color coding, and displayed on a TV monitor for on-line viewing. The digitized information is stored for further off-line processing (e.g., extraction of beam profiles). An optional wire grid placed upstream of the fluor screen adds the capability of measuring transverse emittance (or angular spread). This technique allows real-time observation of the beam response to parameter changes (e.g., evolution of the beam structure, shifts in the beam intensity at various spatial locations within the beam perimeter, and shifts in the beam center and position).

I. INTRODUCTION

In order to demonstrate the effectiveness of this visual diagnostic technique, the system was placed at the output of the Accelerator Test Stand (ATS) funnel experiment [1,2,3]. The 425-MHz, 5-MeV H^- beam from the ATS drift-tube linac (DTL) was guided through four bunchers, two bends in the horizontal plane, an rf deflector, and a dipole sweep magnet. The diagnostic fluor was placed downstream of the rf deflector and the sweep magnet. Since the power density of the full 25-mA, 5-MeV H^- beam of was too high for direct observation, a laser pulse of 50- to 100-ns width was initially used to neutralize a segment of the beam upstream of the sweep magnet, while the remaining H^- beam was deflected into a Faraday cup. Thus, only the neutralized portion of the beam would reach the fluor for observation.

II. DESCRIPTION OF THE EXPERIMENT

We used a CCD Cohu camera (model # 4800) in conjunction with a 200-mm Nikkor lens to monitor the emitted light. The output of the video camera was digitized and stored in the computer for detailed analysis.

A laser pulse of 50-ns width was used to neutralize a segment of the beam upstream of the sweep magnet. However, since we could not trigger the camera externally, light was collected for the entire 50 μs of ATS beam pulse length. As a result, the laser-neutralized beam signal (50-ns duration) was completely washed out by the background neutrals. If these background neutrals originated in the localized drift region between the rf deflector and the bending magnet, one would expect them to carry the full signature of the output beam. This assumption is based on the fact that the ion beam (along with its associated neutrals) reaches the rf deflector at a steep angle, so that the neutrals strike the deflector housing and disperse while the ions are bent into the deflector by a quadrupole magnet at its entrance. For this reason, we decided to investigate the background neutrals that gave us a strong signal when integrated over the 50-μs ATS pulse duration.

Figure 1 shows the background neutral beam spot with the deflector off and with it on. The well-confined background neutral beam spot supports the assumption that these neutrals are created only in the last segment of the beam path, during the free drift from the deflector to the dipole magnet. Figure 1 also indicates a 2.7 ± 0.4-cm movement of the beam (the error comes from the uncertainty in locating the center of the beam spot). This movement is consistent with the data from the slit and collector that showed H^- beam deflection angle of 36 ± 2 mrad [2]. This deflection angle leads to a 2.9 ± 0.1-cm

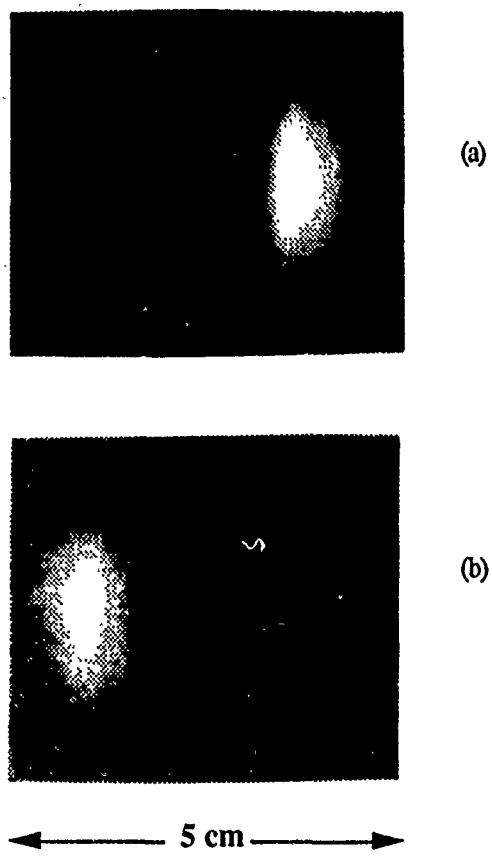


Figure 1. Horizontal beam spot movement with the deflector (a) off and (b) on

* Work supported by the Department of Defense, US Army Strategic Defense Command under the auspices of the US Department of Energy.

† Grumman Corporate Research Center.

0-7803-0135-8/91S01.00 ©IEEE

spatial movement of the beam after axial travel of 80 cm between the deflector and the fluor. The good agreement between these two independent measurements, confirms that the observed neutrals have originated in the drift region between the rf deflector and the fluor.

To continue our studies, we placed a wire grid 5 cm upstream of the fluor to measure the beam emittance [4]. Figure 2 shows the beam spot with the superimposed wire shadows. However, because of insufficient spatial resolution resulting from the wide camera field of view, these data could not be further analyzed to extract the emittance information. We continued the experiment by studying the effects of the rf phase of the deflector on the beam. Figure 3 is the optimized beam shape, which was achieved by varying the rf phase of the deflector by 53° with respect to the settings that resulted in the beam spot shown in figure 2. This simple test demonstrates how easily this visual technique can be used to optimize the parameter settings.

In another attempt to obtain emittance measurements, the camera optic was modified to reduce the field of view. The beam spot is shown in figures 4 with the deflector and all the bunchers on, and in figure 5 with them off. Notice the dramatic changes in the beam-spot size and shape. When the bunchers are off, the beam-spot size in the horizontal plane is increased due to beam debunching and dispersion in the bend plane of the funnel. Further analysis was hampered by poor spatial resolution, even though the resolution was significantly improved. Nevertheless, these data further

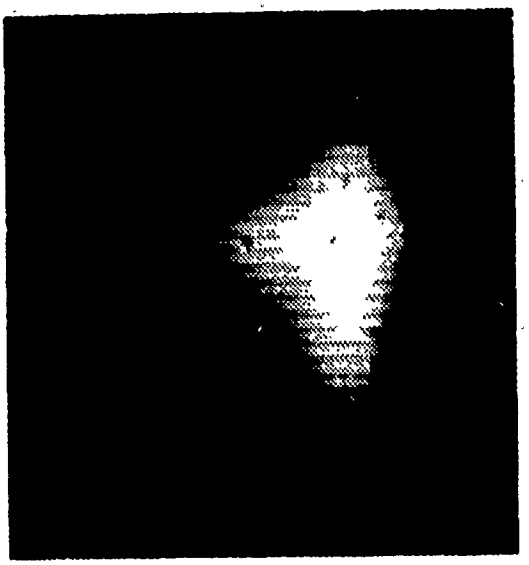


Figure 2. Beam spot and superimposed wire shadows.

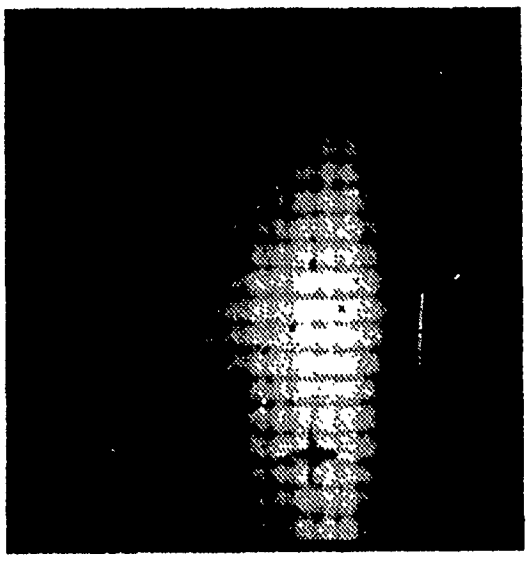


Figure 4. Beam spot with the deflector and all the bunchers on.

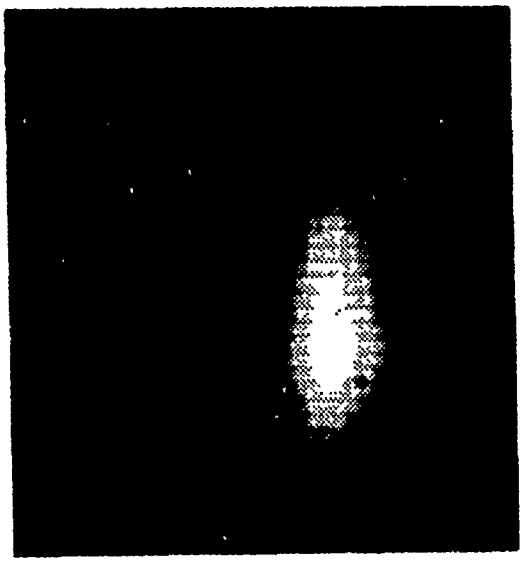


Figure 3. Beam spot at optimized rf phase of the deflector.

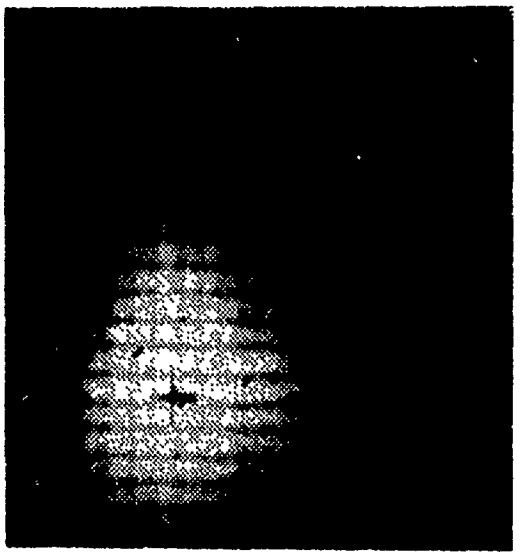


Figure 5. Beam spot with the deflector and all the bunchers off.

emphasize the effectiveness of this diagnostic in detecting the effects of accelerator parameter changes on the beam.

III. FUTURE WORK

We are tailoring our diagnostic technique to measure transverse emittance and beam profile at the output of the 2.5-MeV Ground Test Accelerator Radio-Frequency Quadrupole (GTA RFQ). Unlike the ATS funnel beamline, the GTA beamline is straight and the background neutrals cannot be used to determine H^- beam phase-space. However, the background gas pressure in GTA is at least an order of magnitude lower than that in the ATS and the background neutral signal is expected to be reduced accordingly. Thus, we can laser-neutralize the beam to enhance the signal in the lower-background environment of GTA.

To achieve this objective, we must utilize fast-gated cameras (having external triggering capability) that provide 50-ns beam viewing time (laser neutralization time). In addition, we want to improve the spatial resolution of the experiment. We hope to achieve both goals by acquiring a more sophisticated camera and optic system, that also allows remote control of both focus and aperture. This remote control capability is necessary to operate in the GTA environment.

IV. ACKNOWLEDGEMENT

We would like to thank N. Nerson, M.T. Smith, and D. Sandoval for their assistance in the experimental setup, and O. R. Sander for his technical contributions.

V. REFERENCES

[1] O. R. Sander et al., "Review of accelerator Test Stand Performance and Expectations," 1989 Neutral Particle Beam Technology Symposium, Monterey, CA, July 1989.

[2] K. F. Johnson et al., "The Single-Beam Funnel Demonstration: Experiment and Simulation," Proceedings of 1990 Linear Accelerator Conference, Albuquerque, NM, September 1990, p. 701.

[3] K. F. Johnson et al., "A Beam Funnelling Demonstration: Experiment and Simulation," Particle Accelerators (1991).

[4] K. Saadatmand et al., "A Fluor and Wire-Shadow Diagnostic for Low-Energy Ion Beams," Proceedings of 1990 Linear Accelerator Conference, Albuquerque, NM, September 1990,p. 462.

Wire Scanners at LEP

B. Bouchet, C. Bovet, A. Burns, J. Camas, G. Ferioli, C. Fischer, R. Jung,
Q. King, K.H. Kissler, J. Koopman, J. Mann, H. Michel, R. Schmidt, L. Vos
CERN-SL, GENEVA, Switzerland

Abstract Two sets of wire scanners, each for measuring the horizontal and vertical profile, are installed in LEP in a straight section where the dispersion in both planes is zero. A carbon fibre with a diameter of 36 μm moves through the beam with a speed of about 0.5 m/s. The Bremsstrahlung photons generated by the passage of the wire through the beam are detected in scintillators located 80 m downstream. These detectors are shielded against synchrotron radiation and allow a measurement of the beam profiles which is practically background free and has a resolution of better than 10 μm. We present the design, the results and discuss some limitations of the instrument. During the first months of LEP operation, the fibres were destructed occasionally. The various causes, tests and remedies are discussed. At injection energy a significant blow-up of the beam results from the wire scan and has to be taken into account for the estimation of the genuine emittance. A modellisation of this blow-up is proposed, wherein the effect is renormalized on the actual measured data. This provides an effective data treatment to obtain the unperturbed beam size.

1 Mechanics and Motor Control

The LEP wirescanner is based on a linear movement of a 36 μm carbon fibre through the beam at a speed of up to 1 m/s [2]. The mechanics of the wire scanner is shown in fig. 1 [1].

The carbon fibre is mounted on a fork with a gap of 55 mm. The fork holding the fibre is firstly accelerated, then kept at constant speed during the traversal of the fibre through the beam, and finally decelerated to the end of the 128 mm long stroke. The speed as a function of the position is programmable. An amplifier (with a maximum power of 1000 W) generates the signal for the motor. A feedback ensures that the scanner moves as requested (fig. 2).

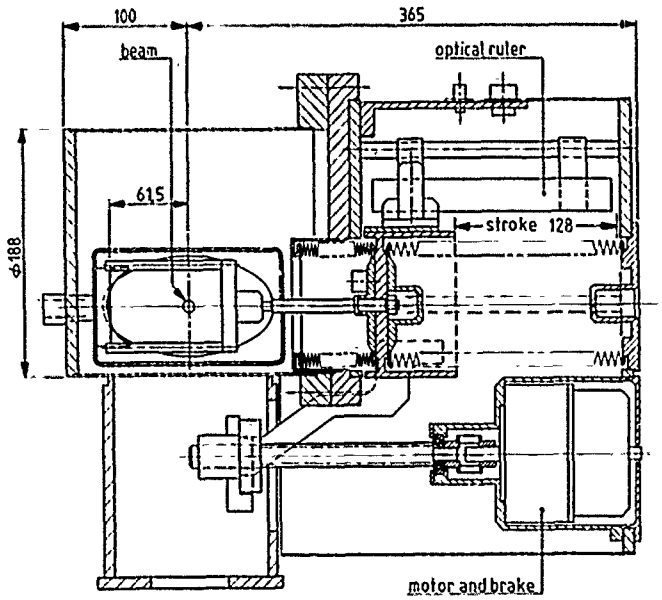


Figure 1: Wire Scanner Mechanics

The position of the fibre is measured with a high precision transducer [3]. A metal rod with reflecting rulings every 20 μm is scanned with the help of a light emitting diode and a light detector. As the rod moves the detector counts light pulses giving a measurement of the instantaneous position with a resolution of 4 μm. A reference mark is deposited onto the metal rod which allows the absolute spatial position to be determined. The ruler allows a maximum speed of 1 m/s. The wire mechanism is fixed to a vacuum tank designed for minimum beam induced wakefield losses.

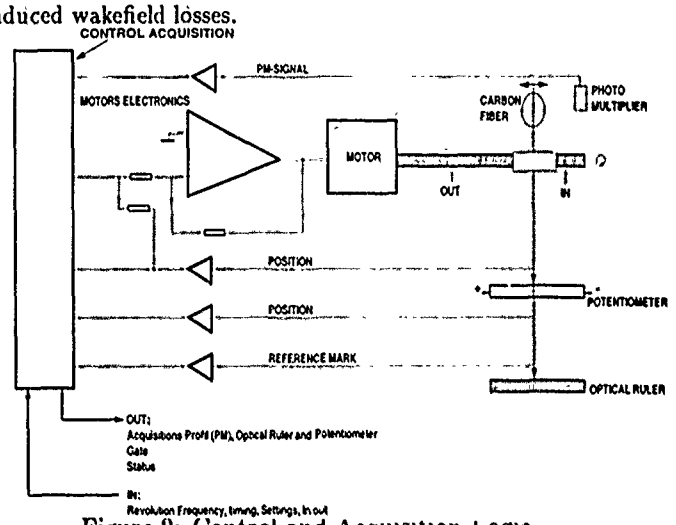


Figure 2: Control and Acquisition Logic

2 Detector and Acquisition System

The local density of the electrons traversing the fibre is detected by measuring the secondary particles produced by the interaction of the beam particles with the carbon fibre. For leptons the dominant interaction process is the emission of bremsstrahlung photons into a cone with an opening angle of about $1/\gamma$ with an energy spectrum up to the beam energy. The number of photons generated by one passage of the bunch through the fibre above an energy threshhold of 10 % of the beam energy is in the order of 10^5 to 10^6 [4] [5].

The scanners are installed in a straight section [6] (see fig. 3). For the detection of the photons the vacuum chamber and some of the magnets were modified: in the vacuum chamber a 50×20 mm^2, 2 mm thick aluminium window was foreseen and the magnets in that region have a gap to allow for the passage of the photons. The photon burst travels 80 m, traverses the window and is detected by a scintillator and a photomultiplier which measures the total energy of the photon burst. A lead shielding of 25 mm prohibits synchrotron radiation to enter the scintillator. The signals from the photomultiplier are practically noiseless (the noise is less than 10^{-3} of the signal). With this detector only bremsstrahlung photons generated by either electrons or positrons can be measured.

To measure with a single scan the emittances of both beams a second scintillator is installed close to the vacuum chamber

0-7803-0135-8/91$01.00 ©IEEE

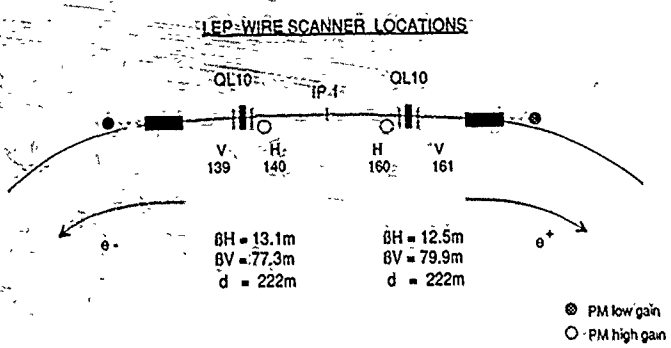


Figure 3: Wire Scanners Locations

towards the inside of the ring about 3 m downstream. The scintillator detects secondary particles with a much smaller signal and therefore high gain photomultipliers are used. The scintillator is sensitive to synchrotron radiation. The intensity of synchrotron radiation is independent of the fibre position and generates an offset in the profiles which becomes visible with LEP operating at high energy, e.g. 46 GeV.

The signals from the individual bunches are transmitted over a 300 m long cable and digitized in the electronics (fig. 2). After a scan the memory in the VME crate housing the electronics contains the digitized profiles from 4 electron and 4 positron bunches (LEP operates with 4 bunches per beam separated by 22 μs). In the local data preprocessing the software searches and finds the profiles within the memory, fits a Gaussian distribution and sends the results from the fit as well as the raw data to the operator consoles. The result of all scans are saved in a catalog and can be retrieved later.

3 Operation and Results

Since the start of LEP operation some thousand scans were done. The main use of the wire scanners is for the measurement and optimization of the vertical beam size, mainly at an energy of around 46 GeV (LEP was operating most of its time around this energy which corresponds to the enery of the Z_0).

Whereas the horizontal beam size is relatively independent on the fine tuning of the machine, the vertical emittance changes with parameters like betatron tune, closed orbit deviation etc. During luminosity operation the vertical emittance varies between about 2 and 20 nm, mainly due to the blow up of the beams caused by beam-beam effects. The blow-up depends on the tuning of the machine. In fig. 4 the vertical beam profile is shown. The beam energy was 46 GeV, the emittance 3 nm, and the rms beam size is 0.49 mm.

Always one IN scan is followed by one OUT scan. If the measured beam sizes from both scans do not agree within certain limits, it can be assumed that either the beam is not stable or the scanner is not working correctly. The results of a scan are displayed to the operator as shown in Table I.

The smallest emittance observed at 46 GeV beam energy was 0.7 nm after an orbit correction in the vertical plane down to an rms value of 0.65 mm and a careful coupling compensation. This corresponds to a betatron coupling between the horizontal and the vertical plane of about 2 %. The current per bunch was about 0.2 mA. Discrepancies with results from other emittance measurements were observed [7]. The cause of these discrepancies is still unknown. A similar scanner installed in the SPS using the same data acquisition system and the same software measures within the errors the same emittance as other instruments.

TABLE I: Bunch currents, beam sizes and emittances.

```
-------------------------------------------------------------------
LEP WS-Rul-Vertical OUT-45.50 GeV - 28/08/90 10.33.16
Energy:45.50 GeV    Beta:79.92 m   Velocity:-386mm/s
-------------------------------------------------------------------
## Len  mA   Amp  Mean /mm     Sigma /mm     Em /nm err%
p1 133 0.21 1179 0.026+-0.005 0.602+-0.004 4.532  1.4
p2 133 0.21 1204 0.024+-0.004 0.610+-0.004 4.657  1.2
p3 136 0.20 1158 0.025+-0.004 0.596+-0.004 4.440  1.1
p4 132 0.20 1209 0.019+-0.004 0.610+-0.004 4.650  1.2
e1 150 0.20  885 0.095+-0.000 0.618+-0.000 4.775  2.1
e2 153 0.18  906 0.132+-0.000 0.631+-0.000 4.986  2.6
e3 135 0.17  933 0.124+-0.000 0.561+-0.000 3.943  2.6
e4 148 0.18  900 0.103+-0.000 0.613+-0.000 4.701  2.0
-------------------------------------------------------------------
```

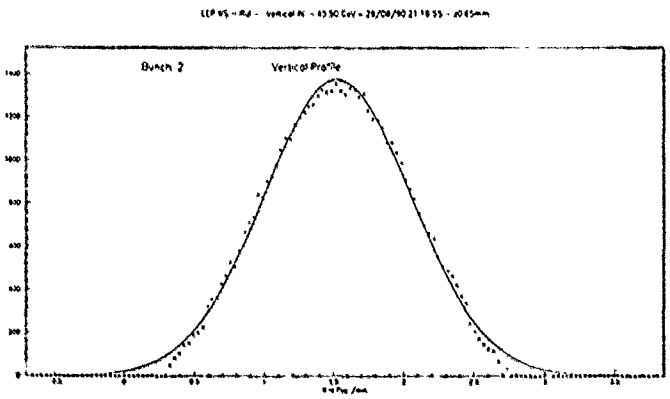


Figure 4: Scan in the vertical plane at 46 GeV beam energy

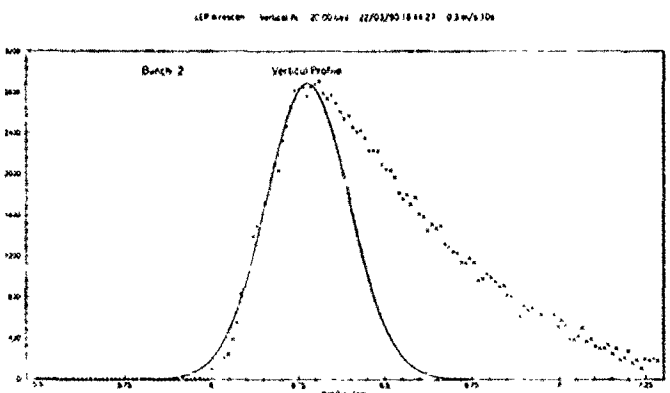


Figure 5: Scan in the vertical plane at 20 GeV beam energy

At high energy (46 GeV) most profiles have a regular shape and can be fitted by a Gaussian plus a constant offset. All the vertical scans done at a beam energy of 20 GeV show a large systematic asymmetry which can be explained by Coulomb scattering of the electrons at the Carbon atoms (see fig. 5). Due to scattering the emittance increases more and more as the fibre moves through the beam.

In the following we roughly estimate the emittance growth expected from a scan : the rms scatter angle is given by $\Theta = p_0/p \times \sqrt{(\frac{L}{L_r})}$ with $p_0 = 14$ MeV/c, p the beam momentum, L the effective thickness of the fibre and L_r the radiation length of the material, 0.275 m for carbon. The emittance increase for the Coulomb scattering becomes: $\Delta E = \beta\Theta^2/2$.

In Table II the estimated emittance increase for a scan at 20 GeV is compared with the design emittance and the measured emittance. Values of 2.5 % for the coupling and of 0.2 m/s for the speed of the fibre are assumed.

TABLE II: Blow-up by a scan at a beam energy of 20 GeV

Plane	β [m]	ΔE [nm]	E_m	E_t
H	12.4	0.31	15	6.7
V	78.4	2.0	1.5	0.27

β is the beta-function, E_m the measured emittance and E_t the theoretical emittance. At this fibre speed the emittance growth in the vertical plane is much larger than the emittance to be measured. As a consequence the speed of the fibre has been increased from initially 0.2 m/s to about 0.4 m/s which reduces the blow-up by a factor of two. To obtain a better estimation of the true emittance the measured profile is matched with a Gaussian fit at the less perturbed side in the data treatment. In general this method gives a too optimistic result and an improved data treatment is foreseen : It can be shown that only one parameter k is sufficient to fit the profiles in the case of blown up beams. This can be determined by the skewness $t = \mu_3/\mu_2^{3/2}$, where μ_i are the moments of the distribution. In Table 3 the different methods of fitting the profiles are compared.

TABLE III: Emittance estimation from three algorithms

Algorithm used in the analysis of vertical profile at 20 GeV	σ (μm	ϵ (nm)
$\sqrt{\mu_2}$	0.304	1.16
From Gaussian fit at one side	0.120	0.18
From skewness t	0.133	0.22

At 46 GeV beam energy no blow-up has been observed as expected : The emittance blow-up decreases with $1/\gamma^2$ and the emittance increases with γ (with γ the relativistic factor of the particles).

Some of the carbon fibres were destroyed during the 1990 LEP run. From previous experience with protons [2] it appeared unlikely that this was due to the beam energy deposition. Two of the four fibres were replaced by 50 μm beryllium fibres. After they were destroyed, the inspection showed clearly that the fibre was melted and not broken (see fig. 6). All fibres were not broken at the beam location. This indicated that electromagnetic heating of the whole fibre is probably the cause of the problem.

A resistance measurement for monitoring the temperature confirmed this hypothesis. A typical temperature evolution over a scan is shown in fig. 7. A the "OUT" position left, the temperature is about 400 degrees per mA circulating beam. As the fibre approaches to the beam, but before touching it, the temperature increases rapidly hinting to a coupling with the electromagnetic field of the bunch. The temperature increase is about 300 degrees for one mA beam current. After the beam traversal in the "IN" position, a new temperature level of 780 degrees is measured. The fibre is then brought back to its "OUT" position and the same phenomenon is observed. The two temperature peaks decrease with increasing fibre speed, whereas the steady levels stay unchanged. At a speed of 0.4 m/s no further fibre were broken.

One measure to reduce the temperature rise is to decrease the electromagnetic coupling. The parasitic loop enabling the current flow is suspected to be closed through ceramic pieces isolating the wire holders from the aluminium fork. These pieces were redone on two wire scanners to decrease the parasitic capacity. On the other two scanners the arms of the fork were entirely made of ceramics. Quantative measurements could only be made on the scanner with the modified isolation piece. They indicate a reduction of approximately 30 % of the temperature increase. The scanners with the complete ceramics arms seem to present a larger improvement. This has still to be confirmed.

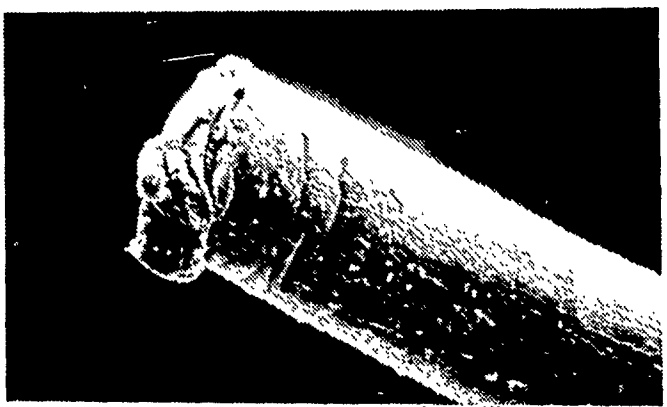


Figure 6: Destroyed Beryllium Fibre

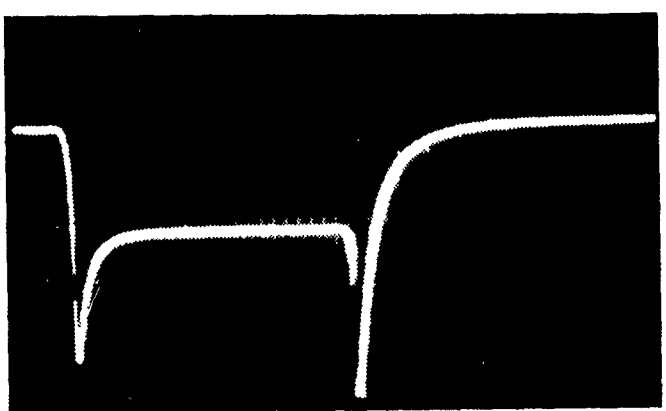


Figure 7: Fibre Temperature for IN-OUT Scan

References

[1] B.Bouchet: CERN-MT/Tech.Note, in preparation

[2] A.Burns et al.: Proc.Part.Acc.Conf. 1989, Chicago, March 20-23,1989

[3] Heidenhain: Numerische Positionsanzeigen, D-8225 Traunreut

[4] J.Bosser, R.Schmidt, CERN-SPS/ABM/Note/86-24

[5] C.Fischer: LEP-Note 563, 1986

[6] C.Fischer et al.: EPAC 1988, Rome June 7-11,p.1081

[7] Y.Funakoshi et al.: LEP Performance Note 34, 22.08.1990, CERN

DESIGN OF THE AGS BOOSTER IONIZATION PROFILE MONITOR*

A.N. Stillman, R.E. Thern, R.L. Witkover, W.H. Van Zwienen
AGS Department, Brookhaven National Laboratory
Upton, NY 11973

Abstract

The AGS Booster Ionization Profile Monitor (IPM) must operate in a vacuum of about 3×10^{-11} Torr. The ultra-high vacuum imposes certain requirements on detector gain and restrictions on construction techniques. Each detector is a two-stage microchannel plate with an integral substrate containing sixty-four printed anodes. Formed electrodes provide uniform collection fields without the use of resistors, which would be unacceptable in these vacuum conditions. An ultra-violet light calibrates the detector in its permanent mounting. An extra set of electrodes performs a first order correction to the perturbations imposed by the horizontal and vertical collection electrodes. This paper will present details of the design of the profile monitor.

INTRODUCTION

The AGS Booster is a synchrotron whose purpose is three fold. It will increase the AGS proton intensity by allowing the injection of four 1.5 GeV pulses rather than one 200 MeV pulse. It will accumulate twenty pulses of polarized protons to boost their intensity as well. Lastly, it will accelerate heavy ions to a momentum suitable for injection into the AGS and RHIC, the Relativistic Heavy Ion Collider. It is an intensifier for AGS beams and a necessary pre-accelerator for RHIC.

The profile monitor in the AGS Booster is a residual gas ionization monitor. The Booster beam ionizes gas molecules in the volume over two sets of collecting wires, one vertical, the other horizontal. The ions would naturally drift radially outward for the space charge of the beam, but electrical fields that are strong enough to redirect their natural radial motion send them to the wires. For strong enough collection fields, the ions travel in rather straight trajectories from their point of generation to the collection wires. The pattern on the wires is thus either a horizontal or vertical projection of the intensity of ion production, which is directly proportional to the beam intensity. Standard, high sensitivity integrating electronics and a real time computer interface acquire the signals, display them, and allow control of the collecting fields and other variables. Figure 1 is a block diagram of the profile monitor and its electronics.

* Work performed under the auspices of the U.S. Department of Energy.

0-7803-0135-8/91$01.00 ©IEEE

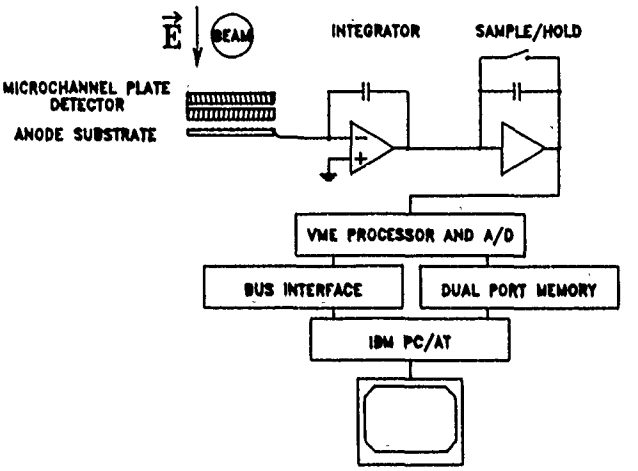


Fig. 1. A block diagram of the Ionization Profile Monitor and its readout electronics. AGS Booster timing signals control the integration and sampling times.

The most severe constraint on the ionization profile monitor design is the ultra-high vacuum of the AGS Booster, nominally 3×10^{-11} Torr. This pressure corresponds to a residual gas density of approximately 10^6 gas molecules per cm^3. At these rarefactions, the beam produces ionization signals on the order of picoamps. Furthermore, there is an extremely limited range of construction materials and techniques that one can use in vacuum of this quality. Resistors, for instance, cannot grade potentials in the vacuum since they outgas too much. Aluminum softens at the bake out temperatures in use, so metal parts must be of stainless steel. An appropriate choice of detector, therefore, is a microchannel plate. The microchannel plate has high gain, operates only in a vacuum, and can tolerate bake out temperatures of 300° C.

MCP DETECTOR

A typical microchannel plate has a gain of 10^4 electrons per input electron. Cascaded plates provide higher gain, though not strictly the product of the gains of the individual plates, since saturation effects in the last plate dominate very quickly. In the AGS Booster IPM, the detector is a dual microchannel plate[1] with a specified gain of 10^7 electron per electron. Ionic inputs to microchannel plates cause slightly different gains from the electron inputs. In fact, the gain of a typical plate can vary with ion species and energy.[2] In order to generate beam

intensity profiles that are not merely qualitative, the profile monitor design must make these gain variations insignificant. Careful shaping of the electrical collecting fields minimizes these gain effects.

The heart of the profile monitor is the dual microchannel plate detector, which comprises the microchannel plates and their associated anode array. A small distance from the exit end of the plates is a ceramic substrate with sixty-four linear anodes. Each anode is a collecting wire, and runs the length of the plate. The whole detector assembly attaches to four supporting posts on the vacuum side of a flange. Ceramic insulation covers the wires from the detector to two thirty-five pin instrumentation feedthroughs. Ceramic also insulates the wires that provide the bias voltage to the front and back sides of the plates. The unity of the detector/anode assembly allows the anode spacing to be at a rather fine pitch. In fact, the anodes are 1.1 mm wide and are 1.47 mm apart. The length of the anodes is 75 mm, the length of the detector active area.

The gain of the detector is set by the voltage across the input and output faces of the dual plate. There is no electrical separation between the two plates. Generally, the voltage is about 1 kV per plate for the specified gain of 10^7. However, the second plate can easily saturate in the presence of large input signals. This saturation is very deleterious, since microchannel plates have a finite life determined only by the charge extracted from them. Accordingly, the power supply that provides bias voltage also contains a protection circuit. This circuit reduces the bias voltage to half the full scale voltage, i.e. 500 V per plate. The circuit trips when the current flowing through the detector is 7% of the current that flows with no signal. This is the recommended value for the fraction of strip current at which to trip. This power supply circuit uses an optically isolated operational amplifier to compare the signal current to a set current. It also provides a small differential voltage between the exit side of the last microchannel plate and the collecting anodes.

FIELD SHAPING

The collecting fields in this profile monitor merit special consideration. There are constraints on them as well. The primary constraint is that they direct ions to the face of the detector in trajectories that accurately project the beam intensity distribution onto the anode wires. This voltage gradient, sufficient to overcome beam space charge effects, seems to be subject to a law of diminishing returns. There always seems to be a further reduction of beam profile width as the collection voltage increases.[3] However, the ability to generate large fields in confined vacuum chambers falls off rapidly at the higher voltages. The historical value of the voltage gradient at the AGS is somewhere in the range of 1 kV/cm.

A second constraint on the collecting field value, not often noted in devices like these, is that the microchannel plate is an energy analyzer for ions below about 20 keV. Thus, to form accurate profiles, the minimum ionic energy must be above this threshold. The ions of minimum energy form in the tail of the beam closest to the face of the detector, so the collecting field at this distance must accelerate these ions to 20 keV. With careful electrode design, it is possible to maintain a potential of -20 kV at this distance.

The ultra-high vacuum conditions also cause problems in generating graded potentials. Since resistors are forbidden and external resistors would require prohibitively many feedthroughs, shaping of the collection field electrodes is the best way to shape the field itself. Figure 2 shows the final shape of the electrodes and a plot of the equipotential lines. The size of the walls of the box-shaped electrodes should be one quarter the length of the electrode.[4] A close inspection of the equipotentials shows that they are certainly flat enough not to cause any distortion of the beam profile image. A four inch clear aperture being necessary for the beam, the electrodes must form part of the perimeter of an eight inch cube. They are of stainless steel, polished and with no sharp corners.

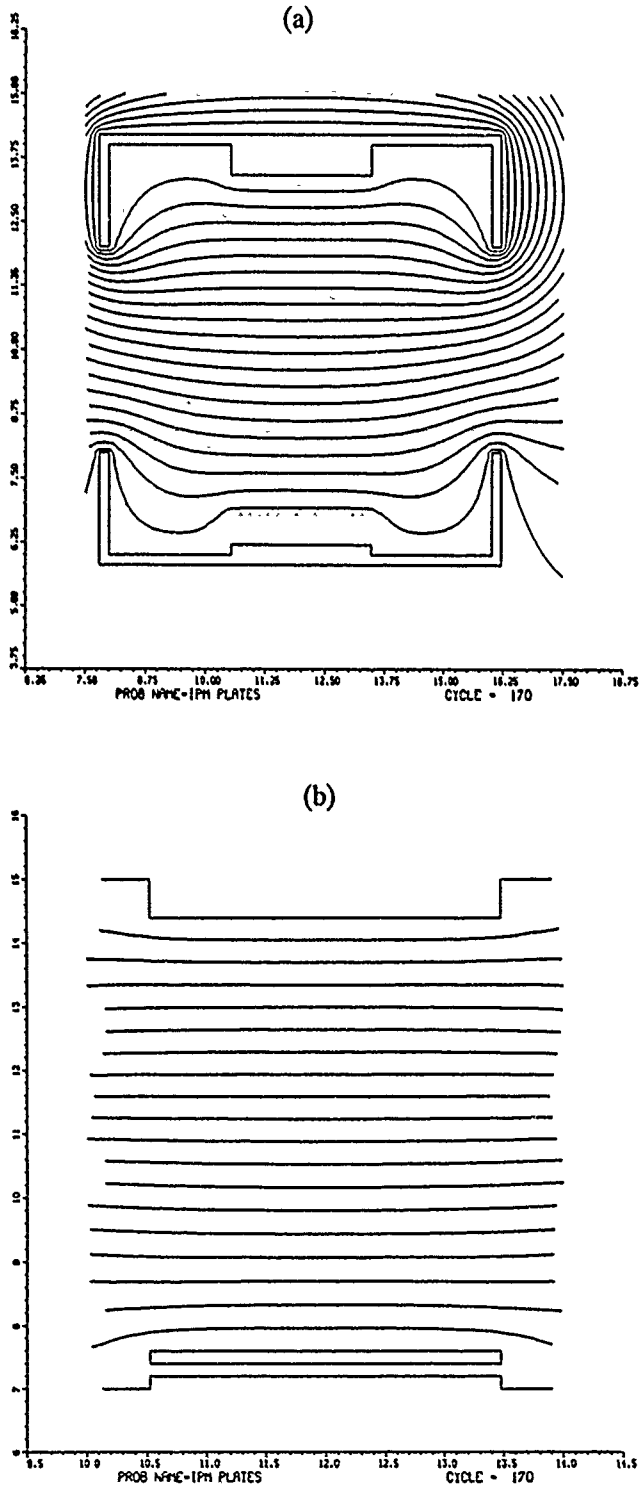
Each plane has a set of electrodes and the working voltage on each set is nominally 70 kV. To correct the kick on the beam from these fields, a third set of electrodes is between the two collection electrodes. These correction electrodes are at 45° to the horizontal and vertical collection electrodes. The corrector voltage, 99 kV, generates an electric field that cancels, to first order, the effect of the vector sum of the collector fields.

READOUT ELECTRONICS

Each detector plane has sixty-four channels. Each of these channels is input to a low leakage integrator. A commercial VME sample/hold multiplexer and A/D converter with an imbedded microprocessor stores the integrator outputs in a local memory. An IBM PC/AT then reads the memory locations via a commercial bus interface that connects the PC bus to the VME bus. The A/D can scan through all channels and load them into memory in about 1 msec. Timing for the data acquisition is by real time interrupts to the PC, which controls the scanner as if it were the VME host. The timing signals themselves are either standard AGS Booster time line codes or the Booster TO signal. Both are available for selection by the PC.

A simple calibration system is also available under PC control. An ultra-violet spectroscopy lamp of 180 nm wavelength illuminates the detector briefly in response to a

calibration pulse from the computer. The light shines on the detector face through a sapphire window in the vacuum chamber and then through the hole in the top of the collection electrode, since the lamp is physically outside the vacuum. The quantum efficiency of the micro-channel plates at this wavelength is about .5%. This calibration system can provide a roughly uniform input to the detector and will allow the monitoring of the inevitable decline of the detectors' gains.



SUMMARY

The AGS Booster Ionization Profile Monitor has the ability to generate beam profiles even in the tenuous residual gas of a 3 x 10^{-11} Torr vacuum. It uses a microchannel plate detector with an integral anode assembly to generate profiles with a 1.47 mm wire pitch. A computer based scanning ADC system allows for profile acquisition on AGS cycle time scales. Formed electrodes generate fields without the use of resistors and the high voltage design minimizes the distorting effects of beam space charge and differential detector response. A calibration system is integral to the design and may find use in generating quantitative information from the beam profiles as well as qualitative.

REFERENCES

1. Galileo Model 3810 with 64-element anode. Manufactured by Galileo Electro-Optics Corp., Galileo Park, P.O. Box 550, Sturbridge MA, 01566.

2. Hellsing, M., et al., "Performance of a Micro-channel Plate Ion Detector in the Energy Range 3-25 keV," J. Phys. E: Sci. Instrum., 18, 920 (1985).

3. Thern, R.E., "Space-Charge Distortion in the Brookhaven Ionization Profile Monitor," Proc. 1987 IEEE Particle Accelerator Conference, Washington, D.C.

4. Leal-Quiros, E., and Prelas, M.A., "New Tilted Poles Wien Filter with Enhanced Performance," Rev. Sci. Instr., 60, No. 3, 350 (1989).

Fig. 2. Poisson calculations of equipotential lines in the ionization profile monitor collection volume. These views are cross-sections of the collection volume and show the characteristic U-shape of the electrodes. Each electrode lip is one quarter the length of the electrode. In both views the -70 kV electrode is at the top and the ground electrode at the bottom; the voltage between potential lines is 3.5 kV. Scale is in cm. In (a), the input face of the microchannel plate detector is the upper dotted line. This face is held at -2 kV by the bias power supply. The characteristic dual plate capacitor potential lines have given way to flat potential lines due to the lips on the electrodes. In (b), a magnified view of the collecting volume shows that its electric field is essentially constant. Here the micro-channel plate detector is the rectangle above the lower electrode.

Beam Size Measurement at High Radiation Levels

Franz-Josef Decker

Stanford Linear Accelerator Center, Stanford, California 94309*

Abstract

At the end of the Stanford Linear Accelerator the high energy electron and positron beams are quite small. Beam sizes below 100 μm (σ) as well as the transverse distribution, especially tails, have to be determined. Fluorescent screens observed by TV cameras provide a quick two-dimensional picture, which can be analyzed by digitization. For running the SLAC Linear Collider (SLC) with low backgrounds at the interaction point, collimators are installed at the end of the linac. This causes a high radiation level so that the nearby cameras die within two weeks and so-called "radiation hard" cameras within two months. Therefore an optical system has been built, which guides a 5 mm wide picture with a resolution of about 30 μm over a distance of 12 m to an accessible region. The overall resolution is limited by the screen thickness, optical diffraction and the line resolution of the camera. Vibration, chromatic effects or air fluctuations play a much less important role. The pictures are colored to get fast information about the beam current, size and tails. Beside the emittance, more information about the tail size and betatron phase is obtained by using four screens. This will help to develop tail compensation schemes to decrease the emittance growth in the linac at high currents.

1 Introduction

The production rate for high energy physics events, called luminosity $\mathcal{L}$, of an accelerator is given by the simplified formula:

$$\mathcal{L} = \frac{N^2 f}{2\pi\sigma_\star^2}, \qquad (1)$$

where N is the number of particles in one of the colliding bunches, f the repetition frequency and $\sigma_\star$ the small spot size at the interaction point (IP). The size σ is given by

$$\sigma = \sqrt{\beta\varepsilon}, \qquad (2)$$

with β is the betatron function at that location and ε is the emittance of the beam, in principle a constant. Different conditions like beta-mismatch and filamentation, bad steering or alignment and transverse wakefield effects can cause a significant emittance blow-up. For a matched beam (beam-β is equal lattice-β) equation 2 shows that only the beam size has to be determined. For any case at least three sizes at different betatron phase Φ locations (or at different quadrupole settings) are necessary to calculate the beam parameters α, β, ε, where $\alpha = -1/2 \cdot \mathrm{d}\beta/\mathrm{d}\Phi$ [1]. Therefore the measurement of beam sizes is an important part of controlling emittance blow-up. The small beam sizes below 100 μm at the end of the SLAC-linac require a good resolution of the measuring system. This is investigated in the first sections. A high radiation level, which is produced by nearby collimators, forces the cameras to be moved to a remote location. A radiation hard system using only first surface mirrors in that area is shown next. At the end some first results are presented.

2 Resolution

The desired resolution is determined by the expected beam sizes and the allowable errors; while the achievable resolution depends on the screen thickness and granularity, the optical and the camera resolution.

2.1 Desired Resolution

The expected beam sizes at the end of the SLC linac are given by equation 2. With $\gamma\varepsilon = 3 \cdot 10^{-5}$ mrad, $\beta_{min(max)} = 25\,(50)$ m and a relativistic gamma-factor of $\gamma = 92\,000$ corresponding to 47 GeV, the beam sizes will be $\sigma = 90\,(130)\,\mu$m. So the resolution of the measurement should be below this. With about 50 μm resolution (see below) the measured beam size will be up to 15 % more ($\sigma_{meas} = \sqrt{90^2 + 50^2}/90 \cdot \sigma_0 = 1.15\,\sigma_0$) or the measured emittance 30 % more. By knowing the resolution to 20 % (50±10 μm) the measurement accuracy increases to about 7 % in size or 15 % in emittance at the low beta points. With half these values at the high beta points, this system provides besides the visual information a good absolute emittance value down to $0.2 \cdot 10^{-5}$ mrad.

2.2 Achievable Resolution

Different elements between the screen and the observer can degrade the resolution of a small beam size. The thickness and its granularity of the screen, the diffraction limit of the light path and the line resolution of the camera contribute to about $\sigma = 30\,\mu$m each [2]. In the following the resolution values are given as sigma (σ) of a gaussian corresponding to the beam size (magnification factor), sometimes calculated from the full-width half-maximum of a distribution by $\sigma \approx$ FWHM/2.35.

2.2.1 Screens

The screens are made out of Al_2O_3:Cr and emit light at 695 nm (Ruby). The self-supporting material is about

*Work supported by the Department of Energy contract DE-AC03-76SF00515.

0-7803-0135-8/91$01.00 ©IEEE

120 μm thick (t) and has a granularity of the order of 5–10 μm (up to 30 μm) in corn diameters.

Thickness The thickness ($t = 120\,\mu$m) contributes in two ways to the resolution. First, assume that the camera is looking straight at the beam (e.g. by a mirror with a hole) and is focused on the middle of the screen. A thin beam produces a line within the screen which is seen as a small disc with

$$\sigma_d = \frac{1}{2.35}\frac{t}{2F}. \tag{3}$$

With an F-number of the optical system of $F = 1.4$, the disc is as big as 18 μm. On the other hand for $F = 15$ and a resolution of 30 μm the focus can be ± 1 mm away from the screen.

Tilt Tilting a thin screen e.g. by 60° increases the resolution of the beam in one dimension and makes it easier to get access to the picture on the screen. A thick 60° tilted screen [3] gives the main contribution of the screen (44 μm):

$$\sigma_{sc} = \frac{\sqrt{3}\cdot t}{2\cdot 2.35}. \tag{4}$$

Granularity The different corn sizes around 10 μm of the screen material scatter the light and therefore contribute to the resolution. Not knowing the distribution of the corn sizes and the right mathematics (give me a hint) for calculating the effect, it has been measured in the lab. A resolution target has been imaged into the middle of the screen and the resolution measured to be 56 μm from the other side. The light produced by a beam traverses on average half the thickness, so the resolution due to granularity is $\sigma_g = 28\,\mu$m.

2.2.2 Optical System

The optical system should provide the imaging from the screen to the camera sitting in a low radiation environment without a significant degradation (see Fig. 1). Starting with a certain field of view (e.g. 3 × 4 mm), the desired resolution ($\approx 30\,\mu$m) and the distance to the camera ($\approx 12\,m$), the system can be designed.

Diffraction Limit Diffraction limits the principle resolution of an optical system. A lens of diameter D and a focal length f produces a spot diameter d (ring of the first diffraction minimum) of

$$d = 2.44\frac{f}{D}\lambda, \tag{5}$$

where λ is the wavelength of the light (695 nm). So an F-number of $F = f/D$ of 12–15 provides that $d =$ 20–25 μm. A non-obvious fact (reason: tails in distribution) should be mentioned: The resolution σ_o of the optical system is about d: $\sigma_o \approx d$, which can be checked by looking at MTFs (modulation transfer functions, e.g. [4]).

Light Path Distance The manageable distance over which light can be easily and inexpensively transported (no large diameter optics, no vacuum pipes) depends on the optical design, air fluctuation and the vibration levels.

Optical Design To keep the light diameter within the diameter D of a lens (e.g. 50 mm) the magnification can be $M = D/v = 10$, where $v = 5$ mm is the diameter of the field of view. With $F = 12$ or a corresponding focal length $f = 0.6$ m the picture would be $s = 6$ m away:

$$s = f \cdot M = D_1 F_1 \cdot D_2/v. \tag{6}$$

To achieve the necessary distance one bigger lens of $D_2 = 100$ mm is used at a distance of about 10 m, acting as a field lens, which concentrates the light of the nearby image to the camera 2 m away.

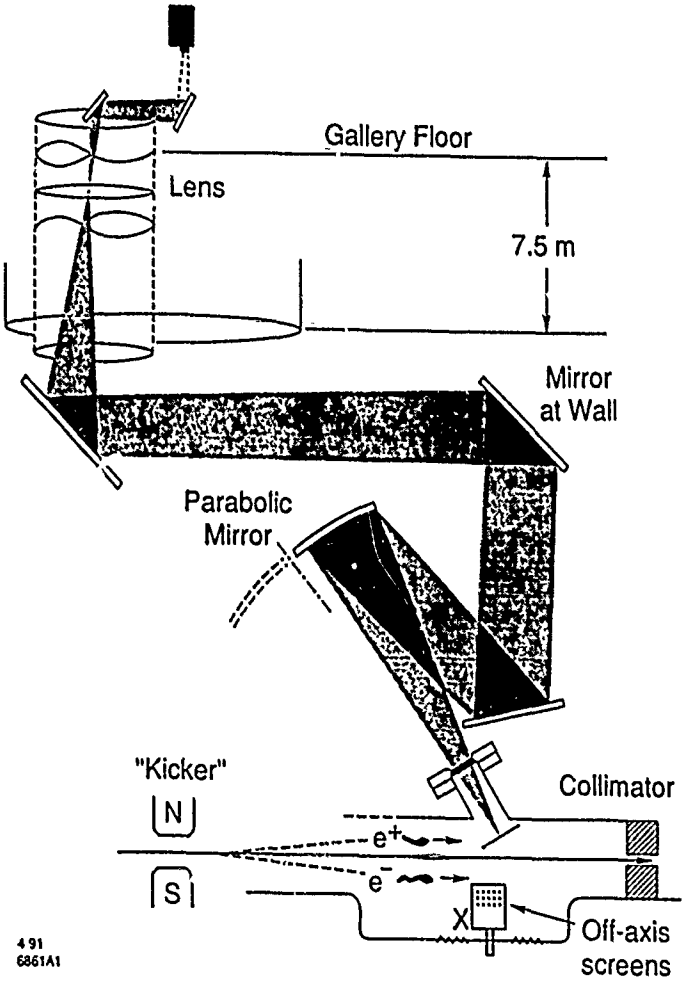


Figure 1: Light Path of the Off-Axis Screens.

Every two seconds the e^+ and e^--bunches are kicked onto the off-axis screens at the end of the SLC-linac. The radiation from the collimators near the screens forced the cameras to be moved to a low radiation area 12 m away. The first parabolic mirror provides a diffraction limited resolution below 30 μm and helps to achieve a small diameter of the light path and a low sensitivity to air fluctuations and vibration levels by enlarging the picture for the long distance.

It has turned out that this design has a lot of advantages: Beside smaller optical parts (not $D = s/F = 0.8$ m), the

quick (after 0.6 m) and big ($M \approx 16$) magnification provides less sensitivity to air motion. A motion of 200 μm over 12 m, observed by alignment crews, are decreased down to the 10 μm level. The one large lens, mounted near the top of a vertical penetration in a protection pipe, can be used for two light paths of two nearby screens (electrons and positrons).

A mirror flatness of about $\lambda/8$ and vibration levels of 0.1 μm over the diameter produce a disturbance or offsets of about $\Delta x = 40\,\mu$m in 10 m distance. Taking the magnification into account this is small compared to the diffraction limit (in design),

$$\Delta x \approx 2 \cdot \frac{f}{D}\frac{\lambda}{8} \ll d. \qquad (7)$$

On the other hand vibrations of up to 40 μm on the screen were observed in the first test setup, where one mirror was mounted on top of the water cooled accelerator. The resolution can be checked by looking at the smallest visible corn size over the whole imaging system. Shiny corns had two coma-like tails of about 25 μm, which decreased the resolution in the worst case to 50 μm (see below).

Abberations Geometric and chromatic abberations have been investigated. Achromatic and radiation hard lenses can be made in principle by a combination of silica (SiO_2) and MgF_2 (probably also CaF_2, LiF) lenses. Due to high costs and the lack of proof of real radiation hardness, lenses are avoided in the accelerator area and instead curved first surface mirrors are used.

Focusing parallel light, a spherical mirror has a geometric abberation of

$$\Delta x = \frac{1}{4}\frac{x^3}{(2f)^2}, \qquad (8)$$

where Δx is the minimum disc diameter and x the offset from the axis of the light (in this case the diameter $D = 2x$). In a one-to-one imaging situation with a tilted mirror astigmatism occurs:

$$\Delta x = \frac{D\,x^2}{(2f)^2}. \qquad (9)$$

An off-axis parabolic mirror avoids all of these above abberations and has been chosen for this reason. It has been observed, that these mirrors have to be aligned carefully to avoid coma:

$$\Delta x = \frac{2\,D^2\,x}{(2f)^2}. \qquad (10)$$

Here x is the offset of the focus point from the axis.

3 Experimental Results

The first experimental results with a beam on the screens have shown their usefulness in getting a visual colored picture of the beam. Fig. 2 shows, for instance, a beam with a huge wakefield tail. Steering the beam flat to the axis of the linac decreases the tail by a large amount. But at high currents, even with a well steered linac, tails are present. These can be decreased by introducing betatron oscillations with a certain phase and amplitude, so that no tails are visible on the screens.



Figure 2: Beam with a Wakefield Tail.

The (normally colored) picture gives a two-dimensional projection of the beam distribution. Contour lines help the black and white visibility.

4 Conclusion

A real radiation hard system has been achieved by moving the cameras far away and carefully designing the light path to get the desired resolution. The overall resolution is further limited by the screen thickness and the camera resolution to about 50 μm.

Acknowledgement

I would like to thank J.T. Seeman, R.K. Jobe and especially M.C. Ross for a lot of helpful discussions, the Mechanical and Controls Departments for their implementation and especially V. Brown for his quick and personal support and the reading the manuscript.

References

[1] E.D. Courant, H.S. Snyder, *Theory of the Alternating Gradient Synchrotron* , Annals of Physics: 3, 1–48 (1958).

[2] M. Ross, *Using Television Cameras to Measure Emittance*, SLAC-CN-280, Sept. 1984.

[3] C.D Johnson, *Limits to the Resolution of Beam Size Measurement from Fluorescent Screens due to the Thickness of the Phosphor* , SLAC-CN-366, July 1988.

[4] Melles Griot, *Optics Guide 5*, 1990.

BEAM EMITTANCE MEASUREMENT TECHNIQUE FOR PLS-IM-T LINAC*

Y. X. Luo†, W. Namkung , C. Ryu , I. S. Ko
Pohang Accelerator Laboratory/POSTECH
Pohang, Korea 790-600

Abstract

The PLS 60 MeV injector (PLS-IM-T) for the 2-GeV linac is expected to be commissioned by the end of 1991. A simple technique has been developed for the beam emittance measurement, which employs the bending magnet and the quardrupole magnets in the beam transport system. By varying the quadrupole strength, one can simultaneously determine the horisontal and vertical emittances, and the momentum spread of the beam.

I. Introduction

The PLS-IM-T, an injector of the PLS 2.0 Gev linac, will be commissioned by the end of 1991. In the PLS-IM-T, there will be no scintillation target in the beam line which can be used for emittance measurement. Thus, the measurement of the beam emittance will be performed at the beam energy analysing station, differently from the ordinary method . The layout is illustrated in Fig. 1.

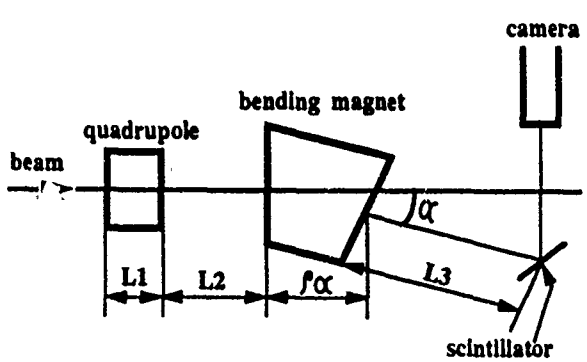


Fig.1 Layout of the beam analyzing station

*This project is supported by POSCO and MOST, KOREA.
†permanent address: IHEP, Beijing, PRC.

0-7803-0135-8/91$01.00 ©IEEE

II. Theory

It is taken that z is the direction of the beam transport, x and y are the horisontal and vertical coordinates respectively. It is also assumed that the quadruple is focusing in the x direction and defocusing in the y direction, and the bending magnet will bend the beam in the x direction. The beam matrix at the entrance of the quadruple is defined as σ_0, which is discribed by the super-ellipsoid equation as follows:

$$X^T \sigma_0^{-1} X = 1, \tag{1}$$

where

$$X = \begin{pmatrix} x \\ x' \\ y \\ y' \\ \delta \\ \frac{\Delta p}{p} \end{pmatrix}.$$

$x' = dx/dz$, $y' = dy/dz$, δ is the half width of the beam, and σ_0 is symmetric, *i.e.*

$$\sigma_{0ji}, \quad i,j = 1,2,\ldots,6.$$

Then, the beam matrix will satisfy the following fomula at the scintillator in the beam analysing station.

$$\sigma = R \sigma_0 R^T, \tag{2}$$

where R is the total transfer matrix from the quadruple to the scintillator.

Expression for R is:

$$R = \begin{pmatrix} R_{11} & R_{12} & R_{13} & R_{14} & R_{15} & R_{16} \\ R_{21} & R_{22} & R_{23} & R_{24} & R_{25} & R_{26} \\ R_{31} & R_{32} & R_{33} & R_{34} & R_{35} & R_{36} \\ R_{41} & R_{42} & R_{43} & R_{44} & R_{45} & R_{46} \\ R_{51} & R_{52} & R_{53} & R_{54} & R_{55} & R_{56} \\ R_{61} & R_{62} & R_{63} & R_{64} & R_{65} & R_{66} \end{pmatrix} \tag{3}$$

$$= \begin{pmatrix} 1 & L_3 & 0 & 0 & 0 & 0 \\ 0 & 1 & 0 & 0 & 0 & 0 \\ 0 & 0 & 1 & L_3 & 0 & 0 \\ 0 & 0 & 0 & 1 & 0 & 0 \\ 0 & 0 & 0 & 0 & 1 & \frac{L_3}{4w^2} \\ 0 & 0 & 0 & 0 & 0 & 1 \end{pmatrix} \cdot \begin{pmatrix} \cos\alpha & \rho\sin\alpha & 0 & 0 & 0 & \rho(1-\cos\alpha) \\ -\rho\sin\alpha & \cos\alpha & 0 & 0 & 0 & \sin\alpha \\ 0 & 0 & 1 & \rho\alpha & 0 & 0 \\ 0 & 0 & 0 & 1 & 0 & 0 \\ -\sin\alpha & -\rho(1-\cos\alpha) & 0 & 0 & 1 & \rho(\sin\alpha-\alpha) \\ 0 & 0 & 0 & 0 & 0 & 1 \end{pmatrix} \cdot$$

$$\begin{pmatrix} 1 & L_2 & 0 & 0 & 0 & 0 \\ 0 & 1 & 0 & 0 & 0 & 0 \\ 0 & 0 & 1 & L_2 & 0 & 0 \\ 0 & 0 & 0 & 1 & 0 & 0 \\ 0 & 0 & 0 & 0 & 1 & \frac{L_2}{4w^2} \\ 0 & 0 & 0 & 0 & 0 & 1 \end{pmatrix} \cdot \begin{pmatrix} \cos(kL_1) & \frac{1}{k}\sin(kL_1) & 0 & 0 & 0 & 0 \\ -k\sin(kL_1) & \cos(kL_1) & 0 & 0 & 1 & \rho(\sin\alpha-\alpha) \\ 0 & 0 & \cosh(kL_1) & \frac{1}{k}\sinh(kL_1) & 0 & 0 \\ 0 & 0 & k\sinh(kL_1) & \cosh(kL_1) & 0 & 0 \\ 0 & 0 & 0 & 0 & 1 & \frac{L_1}{4w^2} \\ 0 & 0 & 0 & 0 & 0 & 1 \end{pmatrix}.$$

At the scintillator, one can get a graph as shown in Fig. 2, from which it is easy to get the HWHM of the beam, Δx and Δy. As well known, the HWHM is related to the beam matrix by $\Delta x = \sqrt{\sigma_{11}}$ and $\Delta y = \sqrt{\sigma_{33}}$. If the quadruple strength is changed four times, one can get four graphs and therefore four different Δx and Δy.

From (2), it can be derived that

$$\sigma_{11} = R_{11}^2\sigma_{o11} + 2R_{11}R_{12}\sigma_{o12} + R_{12}^2\sigma_{o22} + R_{16}^2\sigma_{o66}, \tag{4}$$

$$\sigma_{33} = R_{33}^2\sigma_{o33} + 2R_{33}R_{34}\sigma_{o34} + R_{34}^2\sigma_{o44}, \tag{5}$$

$$\sigma_{66} = \sigma_{o66}. \tag{6}$$

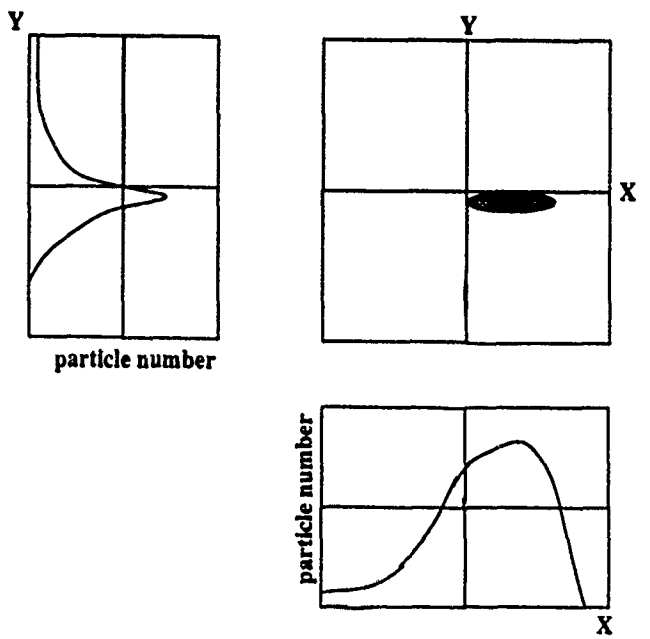


Fig.2 beam profile at the scintillator

From (3), one can get

$$R_{11} = \cos(kL_1)(\cos\alpha - \frac{L_3}{\rho}\sin\alpha) - k\sin(kL_1) \times \left[(L_2+L_3)\cos\alpha - \frac{L_2L_3}{\rho}\sin\alpha + \rho\sin\alpha\right], \tag{7}$$

$$R_{12} = \frac{1}{k}\cos(kL_1)(\cos\alpha - \frac{L_3}{\rho}\sin\alpha) + \cos(kL_1) \times \left[(L_2+L_3)\cos\alpha - \frac{L_2L_3}{\rho}\sin\alpha + \rho\sin\alpha\right], \tag{8}$$

$$R_{16} = \rho(1-\cos\alpha) + L_3\sin\alpha, \tag{9}$$

$$R_{33} = \cosh(kL_1) + k\sinh(kL_1)(L_2+L_3+\rho\alpha), \tag{10}$$

$$R_{34} = \frac{1}{k}\sinh(kL_1) + \cosh(kL_1)(L_2+L_3+\rho\alpha). \tag{11}$$

III. Beam emittance measuring method for PLS-IM-T

Values of Eqs. (7) through (11) will be changed as the quadruple strength varies. In the case of PLS-IM-T, $L_1 = 0.2m$, $L_2 = 1.14m$, $L_3 = 1.36m$, $\rho = 0.52m$ $\alpha = 0.418rad$, and $k = 24.245\sqrt{G/2w}$; $w = 60$ MeV, where G is the field gradient of the quadruple.

Substituting four Δx's into (4) and solving the equation set, one can get σ_{o11}, σ_{o12}, σ_{o22}, σ_{o66}, and thus the horizontal emittance

$$\varepsilon_x = \sqrt{\sigma_{o11}\sigma_{o22} - \sigma_{o12}^2} \quad (\pi m.rad), \tag{12}$$

and the beam momentum spread

$$\Delta p/p = \pm\sqrt{\sigma_{066}}. \qquad (13)$$

Using the same procedure for Eq. (5), it is possible to get the vertical emittance from the three Δy values.

Ordinarily, measuring the beam momentum spread by means of measuring Δx of the beam at the analysing station always includes the contribution of either the beam dimension or divergence at the focusing point. However, it is noticeable that the Eq. (13) has an expression of a pure beam momentum spread.

References

[1] K. L. Brown, et al., Transport. SLAC-91, Rev. 2, UC-28(1/A).

A CARBON JET BEAM PROFILE MONITOR FOR LEAR

R. Galiana, D. Manglunki and C. Mazeline
PS Division, CERN, CH-1211 Geneva 23

Abstract

CERN's Low Energy Antiproton Ring LEAR is now equipped with a non-destructive beam profile monitor. A pulsed carbon jet of 0.8 ms is used to minimize the disruption of the low energy beam. The jet is produced by a laser beam impinging on a solid carbon target. The atomic jet is collimated to form a thin curtain, which traverses the coasting antiproton beam. The electrons produced by the ionization of the jet are accelerated by electrodes before they hit a phosphorous screen. The image of the profile is acquired by a CCD camera and digitized for display on a workstation. This paper describes the techniques used, from generation of the carbon jet, to the analysis of the digitized image. Preliminary results and future improvements are discussed.

I. INTRODUCTION

The LEAR machine [1] needed a non-destructive beam profile monitor principally for measuring the evolution of the beam size in the presence of electron cooling [2] and for monitoring the size of the beam in its interaction with an internal gas jet target[3]. Operations required the device to be able to operate with a beam intensity ranging from 10^7 to 10^{11} particles having an energy in the range of 2 MeV to 1.3 GeV. It has been decided to adapt a gas curtain scheme already used in the Intersecting Storage Rings [4], where a continuous sodium curtain was used. Due to the small circumference of LEAR, and the low energy of its beams, a pulsed curtain was designed to avoid emittance blow-up induced by the device. A carbon jet of 0.8ms pulse length, produced by a LASER beam impinging on a solid carbon target is collimated to form a thin curtain inclined at 45° with the vertical. The carbon atoms are ionized by the coasting beam. The distribution of the electrons produced by the ionization provides a measurement of the beam distribution.

II. DESCRIPTION OF THE APPARATUS

A schematic can be found on Fig. 1.

A. Generation of the carbon jet.

We use a 1064nm YAG laser, delivering a 800 µs pulse of maximum energy 25J, with a maximum repetition rate of 0.5Hz to generate the carbon jet. The solid carbon target has the shape of the segment of a sphere. Stepping motors allow the target to be rotated about the centre of the sphere, thus letting the laser hit a different point. Each laser pulse drills a crater into the target. The latter is repositioned for the next shot, thus forming a honeycomb pattern. About 30% of the evaporated carbon (0.6mg) forms a 5000m/s atomic jet. This

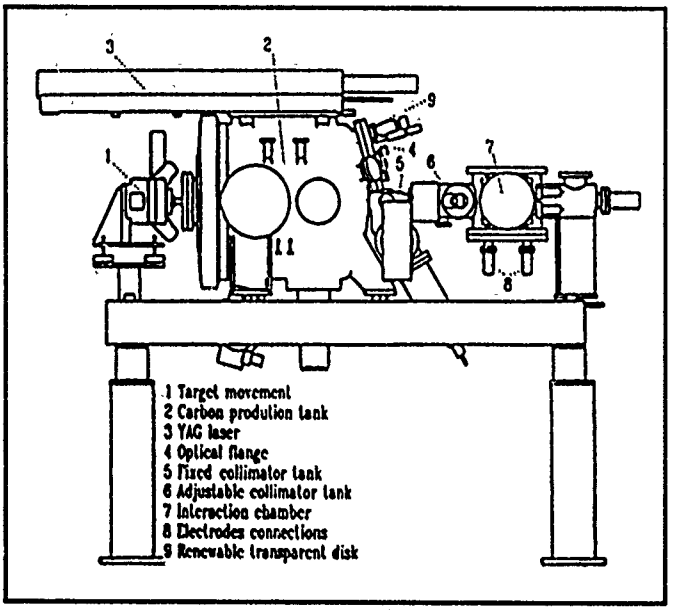


Fig. 1 : Schematic of the apparatus

jet then traverses a series of three (two fixed and one adjustable between 1 and 5 mm) collimators to form the thin curtain which is ionized by the antiproton beam in the interaction chamber.[5]

B. Accelerating electrodes

The electrons produced in the ionization of the jet by the antiproton beam are accelerated by two chemically polished titanium plates. The purity of the titanium (>98.5%) plays an important role to avoid cold emission phenomena. Each plate has its own high voltage power supply, thus allowing few flexibility in the configuration of the field. Typically, the field ranges from 1 to 2 kV/cm, over a distance of 15 cm, yielding 15-30 keV electrons.

C. Light collection and amplification

After traversing a 0.1 µm thick aluminium coating which serves as a grounded electrode, the electrons hit a phosphor (P20) coated fiber-optics window (90mm diameter). The emerging light is then guided through a fiber optics taper which reduces the image to a diameter of 25mm and feeds it into a light amplifier followed by a 625-line CCD camera which delivers a standard video signal (Fig. 2). For 10^9 antiprotons at 309MeV/c, 10^5 electrons are collected, yielding 2×10^8 photons in the phosphorous screen [6].

0-7803-0135-8/91$01.00 ©IEEE

D. Image acquisition

The video signal is digitized in a CAMAC digitizer module [7] which is triggered from the laser pulse and holds the image in a 312x512 pixels format. The digitizer contents are read using control system routines [8], and the information on the profiles are computed on-line in the LEAR consoles (VAX workstations). The profiles can also be analysed by observing the video signal on an oscilloscope: a fast sweep (100 µs) representing one raster line gives the horizontal profile, while a slow sweep (20ms) of the full image gives the vertical profile.

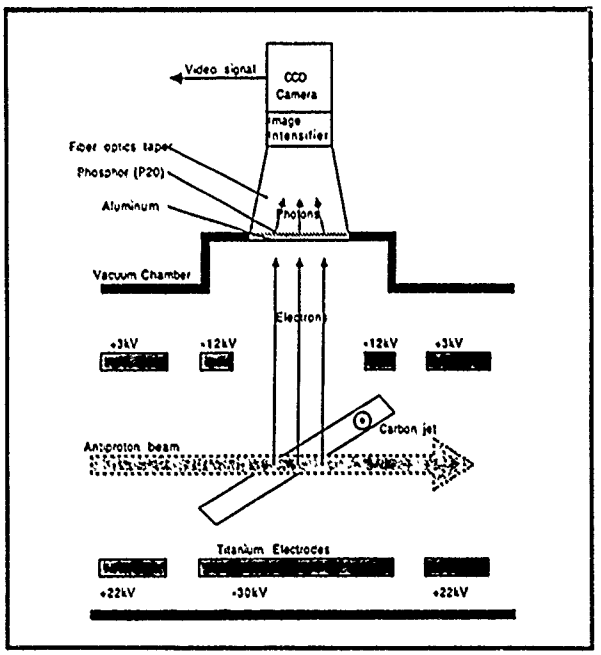


Fig. 2 : Profile production and acquisition

E. Controls

The local controls are entirely done in an HP6942A multiprogrammer crate, which communicates with an HP85 computer situated in the control room through a HPIB/RS232 link.

F. Operation mode

The laser pulse is synchronized with the video signal of the camera, and triggers the digitizer. In addition, to prevent carbon atoms polluting the optical window through which the laser beam enters the tank, the optical flange is in the region of a relatively high pressure ($4x10^{-4}$ Torr) during operation. As the vacuum conductance has to be kept very low by using a conical tube between the flange and the tank, a gas injection into the tank takes place at a rate of $3x10^{-5}$ Tl/s. It has to be compensated by a strong pumping scheme (described below).In these conditions, the optical window has to be renewed every 1000 impulsions. This is achieved by the rotation of a glass disc which allows 70 renewals in situ of the transparent surface [9].

G. Vacuum system

In order not to perturb the ultra-high vacuum (<10^{-11} Torr) of the LEAR machine, a differential pumping scheme has been implemented. The collimators act as conductance limitations between the different device volumes. Table 1 shows the vacuum parameters. [10]

Table 1 : Vacuum parameters

Volume	Pumping system	Design Pressure (Torr)
Optical flange	Gas injection ($3x10^{-5}$ T l/s)	$4x10^{-4}$
Carbon production tank	- Cryogenic (3000 l/s) - Turbomolecular (500 l/s) (in series with rotating primary)	10^{-8}
Fixed collimator tank	- Ti sublimator (800 l/s) - Ionic pump (50 l/s) - Non evaporable Getter (1000 l/s)	$2x10^{-10}$
Adjustable collimator tank	- Ti sublimator (1000 l/s) - Ionic pump (50 l/s)	10^{-11}
Interaction chamber	- Ionic pump (60 l/s) - Ti sublimator (1200 l/s)	10^{-12}

III. PERTURBATION ON THE BEAM

A. Vacuum effects

The 1ms carbon jet has a local pressure of 10^{-5} Torr over a distance of 1 to 5 mm. The design pressure of LEAR is 10^{-12} Torr (N_2 equivalent for scattering) and its circumference is 78m. Thus one gets an average increase of the residual gas pressure by 30%, assuming one measure per 2 seconds (the maximum rate at which the device can operate). Calculation shows that the emittance blow-up during a continuous measurement process is less than 10% of the one induced by scattering on the residual gas [11]. Indeed, no emittance blow-up could be detected on the Schottky scans during the first experiments.

B. Electrostatic effects

The vertical electric field used to accelerate the electrons gives a 2 mrad vertical kick on a 105MeV/c antiproton beam, which needs to be compensated. Compensation electrodes are therefore installed on both sides of the device, each with its own high voltage power supply. In addition to the dipolar perturbation of the accelerating plates, the finite width of the plates creates a quadrupolar effect which led to a detuning of the betatron frequencies in the early days of operations with the device. It has been shown to be proportional to the value of the electrical potential between the two main and the auxiliary plates [12], so it could be cured with an appropriate adjustment of the various potentials.

IV. RESULTS

A. *Problems encountered*

A parasitic spot has been observed, which shows up even in the absence of the antiproton beam. Though the direct cause has not been found, evidence shows it is due to self-ionization of the carbon jet in the electric field. The brightest part of this spurious image was moved out of the area of interest with a careful adjustment of the electrical potentials. The remaining halo is first acquired without antiproton beam for calibration, then substracted by software from the beam image. More investigations are taking place in order to understand - and hopefully eliminate - this phenomenon, which makes difficult the observation of very low density profiles.

B. *Profile measurements*

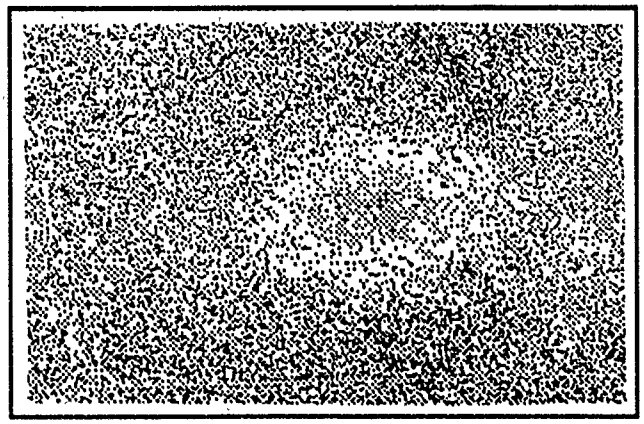


Fig. 3 : Digitized video signal

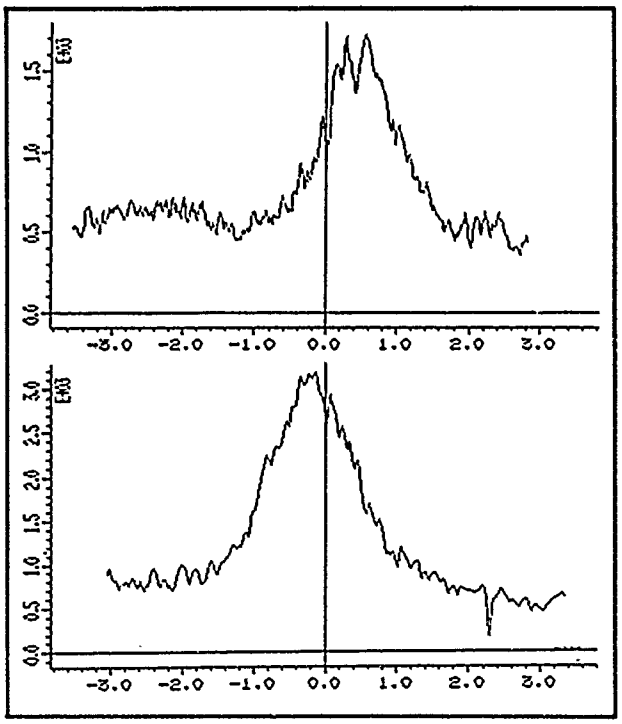


Fig. 4 : Horizontal and vertical beam profiles. The scales are expressed in centimeters.

Fig 3 shows a digitized picture of the image, as it is displayed on the workstations. Fig 4 shows the beam profiles extracted from this image.

V. PROPOSED IMPROVEMENTS

A. *Helmholtz coils*

In order to improve the sensitivity by better guidance of the electrons, Helmholtz coils have been designed. The sensitivity should increase from 2 mm to 0.7 mm with a field of 300 Gauss [13].

B. *Controls*

For the moment, the device is routinely operated using a stand-alone micro-computer.It is desirable to integrate it into the LEAR control system, and to convert the controls to operate from the VAX workstations.

C . *Software*

For full operationality, more sophisticated image processing is needed. Very good quality commercial software is available, which can be used to fulfill our needs for true image reconstruction, substraction, contour definition, etc.

VI CONCLUSION

LEAR's carbon jet beam profile monitor, which is now entering its operational stage, promises efficient emittance controls during normal runs and for machine developments, but more time is needed to improve and understand this complex but beautiful device.

VII REFERENCES

[1] P. Lefèvre. "LEAR, present status, future and developments", in *Proc. IVth LEAR Workshop*, Villars-sur-Ollon, 1987.

[2] J. Bosser, "Overview of Stochastic and Electron Cooling at LEAR", in *Proc LEAP'90*, Stockholm, July 1990.

[3] N. Hamann, "First antiproton interactions with the hydrogen-cluster jet target at LEAR", in.*Proc LEAP'90*, Stockholm, July 1990.

[4] B. Vosicki, K. Zankel, "The sodium curtain beam profile monitor of the ISR", . IEEE Transactions on Nuclear Science, Vol NS-28, nr 3, June 1981.

[5] R. Galiana, "Un jet moléculaire pulsé de Carbone", PS/CD/Note 81-1, unpublished.

[6] R. Galiana, "Luminosité de l'image du faisceau LEAR attendue du Carbon Jet BPM", 14/9/88, unpublished.

[7] R. Maccaferri, Private communication.

[8] T. Pettersson, "LEAR Control System Environment", PS/AR/Note 89-7, unpublished.

[9] R. Galiana, "Principes de réalisation du BPM autres que celui de la production du jet moléculaire", PS/CD/Note 81-6, unpublished.

[10] A. Alberici, "The Carbon Jet Target for the LEAR machine", March 15th, 1988, unpublished.

[11] P. Lefèvre, Private communication.

[12] D. Möhl, Private communication.

[13] C. Mazeline, Note to be published.

Wire Scanners for Beam Size and Emittance Measurements at the SLC

M. C. Ross, J. T. Seeman, E. Bong, L. Hendrickson, D. McCormick, L. Sanchez-Chopitea
Stanford Linear Accelerator Center, Stanford, Ca. 94309

ABSTRACT*

The SLC wire scanner beam profile monitors provide accurate beam size and emittance measurements for each bunch in the three bunch SLC beam. The beam size measurement error for typical 50GeV SLC linac beams (100μm $\sigma(x,y)$) is better than 5μm. Beam profile measurements can be performed throughout much of the SLC with no interruption to normal machine operation and no adverse impact on interaction region detector backgrounds. The linac input and output emittance is determined using sets of four scanners spaced by ~45° betatron phase advance. Each scanner contains three wires, x, y and u (45°), from which an estimate of the x - y coupling can be obtained. Advanced high level control software allows the use of wire scanner data in feedback and beam optimization procedures. Non-invasive scans are performed almost continually and the results are logged so that long term trends in emittance can be examined. In this paper we describe the design, construction, performance and uses of SLC wire scanners.

INTRODUCTION

Measurements of the beam size and associated optical parameters are key to SLC. In the past progress has been slowed by our inability to measure beam size accurately in a rapid, non-invasive manner.

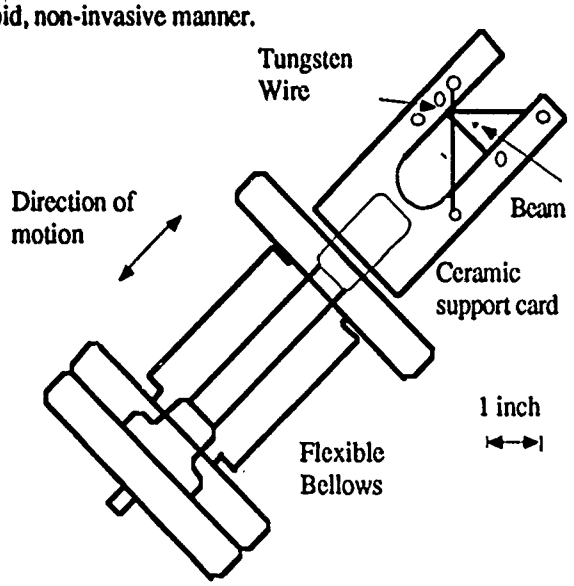


Figure 1: SLC wire scanner wire support card viewed in the beam direction. The translation stage and vacuum chamber are not shown.

In this paper we describe the design, construction, commissioning and ultimate uses of wire scanners in the SLC, focusing on the linac and upstream systems scanners. Of particular interest is the interaction between the wire and the scattered radiation from the wire with the extreme electric field of the beam. As this field reaches the level of several volts/angstrom, as it does easily at the SLC interaction point (and may in upstream parts of SLC), field emission from the wire may occur.

A key feature of SLC operation is the degree of high level active control required to keep it optimized. The high level of demand takes the instrument out of the category of a device primarily used for machine development or failure diagnosis purposes and elevates it to an online device.

Feedback requires a fast, non-invasive (or minimal impact) device which in turn means that the wire, not the beam, must be moved during the scan. The speed, range, vibration and other mechanical specifications can be generated from this requirement and from the expected beam sizes and rates. Table 1 shows the expected performance of the scanners.

MECHANICAL

The mechanical design effort addressed the following problems: 1) wire and wire retention, 2) vibration over the large speed range and 3) positioning errors and position transducers. A particular concern was radiation damage.

A schematic diagram of the scanner is shown in figure 1. Several labs have built scanners of a similar design [1,2,3]. The wire is strung around 1.5mm stainless steel studs set in a 3/16in thick alumina fork in such a way so that it can carry wires of three different orientations across the beam and provide x, y and u (45°) scans. The carriage motion is actuated by a stepping motor through a 2mm pitch ball screw, chosen because of the expected large number of cycles. Some difficulty was experienced obtaining the small pitch, high quality ball screw with no plastic parts. A 125μm thick stainless steel vacuum window opposite the wire allows low energy wide angle scattered radiation to emerge from the vacuum chamber.

Both the cantilever nature of the wire support and the stepping motor contribute to wire vibration. We have used a piezo- electric accelerometer to quantify the motor related system vibration.

The wire chosen for the scanner was gold plated tungsten with a diameter of 0.3 σ_{beam}. The wire has an effective 'σ' of radius/2 which, when added in quadrature to the beam size, causes a 3% apparent increase when $\sigma_{beam} \approx$ wire diameter. Under normal conditions the wire size can be subtracted in quadrature from the measured size.

At full SLC currents and rates, the beam can heat the wire substantially reaching a steady state temperature of 1000°C. In the fast scan mode, the wire is subjected to continuous beam for no more than a few seconds. However, the wire may be

* supported by DOE contract DE-AC03-76SF00515

0-7803-0135-8/91$01.00 ©IEEE

parked in the beam in error or for diagnostic purposes and must be able to withstand continuous beam. By measuring the increase in resistance of the wire assembly an estimate of the wire temperature rise can be made. Resistance tests show good agreement with a calculated rise of about 4° C/pulse.

Table 1: Wire scanner performance specifications.

Beam size resolution	<3% σ (≈ 3 - 10 μm)
Systematic error	<3% σ (≈ 3 - 10 μm)
Emittance (ε) error	10% (for $\gamma\varepsilon \approx 3 \times 10^{-5}$ m-rad)
Dynamic range	10^9 - 10^{11} particles/pulse
Vibration	Peak amplitude $< 0.2\sigma$
Relative positioning	20μm
Speed and acceleration	1cm/s max 0.3mm/s min; 0.2m/s^2 accel.
Multibunch operation	<5% signal contamination from nearby bunch (60ns)
Radiation resistant	10Mrad/year
Lifetime	100,000 cycles/year

As the wire is scanned through the beam its position is not encoded on each successive beam pulse, rather the current position of the wire is inferred from a check of the remaining step count. A position measurement using a radiation hard LVDT (linear differential transformer) is done at the limits of the scan to check that the expected position was reached.

CONTROLS

A scan consists of three steps: 1) move from PARK (near, but not in, any of the beams) to the start of scan at maximum speed, 2) scan at the speed corresponding to the desired inter-point spacing and beam rate and 3) return to PARK at full speed. Only brief pauses, to allow the device to come to a complete stop, occur during the scan sequence. During multiwire emittance or skew scans, the wire moves to the next appropriate PARK. An important feature of this scheme is the use of machine wide data acquisition codes which coordinate the readback of the scanner step count and the signals from the wire scanner detector and therefore allow a great deal of flexibility in the choice of detector including, for example, the use of detectors several miles away.

Because the scanners are to be used for feedback, the application software that controls them must have sophisticated exception handling, error logging and status reporting. The control system software built around these devices allows use of the wire scanner at several levels. The lowest is the single scan and associated single pulse detector signal readout. This information allows checking the fit quality, scan ranges and other details. At the next level higher, the fit results can be used in the SLC control system correlation plot utility[4]. This extremely powerful tool, allowing the acquisition of scan data with other beam diagnostic data and machine parameters, has been invaluable for commissioning the scanners. All aspects of the gaussian fit to the scan data are available and are automatically acquired as an upstream device setting is controlled in a programmed way. Most automated optimization procedures are built around this facility. The next level of software does multiple scans and accumulates these results in the correlation plot utility. This includes four wire emittance scan results and skew scan results. Finally, feedback can perform the scans as a background task and implement the desired corrections.

SIGNAL DETECTOR

The purpose of the wire signal detector is to indicate the amount of charge striking the wire. Secondary emission and forward scattering, used in many wire scanner systems, are often not practical at the SLC. The first because of problems discussed below and the second because of the very different beam line areas in which these devices have to operate. The most difficult region is just upstream of a high power collimator system. Radiation scattered by the wire in the forward direction is completely overwhelmed by the scattering from the collimator jaws thus making the use of small angle scattered radiation impossible.

When the SLC interaction point (IP) wire scanners[5] were first tested it was found that the secondary emission signal would increase dramatically when either the beam intensity exceeded about 5×10^9 or the $\sigma_{beam} < 10\mu m$. The onset of this dramatic increase is indicated by a very unstable signal. In the SLC linac, where the beam sizes are about 100μm, a beam intensity of about 2.5×10^{10} is required. This effect appears to be field emission induced by the field of the beam which peaks at about 20V/Å.

Because of these problems, tests were made to determine if a significant signal was present at 90° to the beam direction, directly opposite the wire support card. A strong, very low energy electron signal was seen in a bare photomultiplier (PMT) placed about 30cm from the wire. A thin window is required so that this scattered radiation is not absorbed by the vacuum chamber wall. Substantial shielding (±50 radiation lengths) is required in some locations to protect the PMT's from background generated by upstream beam losses. In regions where no collimators follow the scanners, small angle scattering monitors have been placed about 10m downstream to use for comparison with the PMT.

The detector linearity must be better than a few percent. A moderate gain, excellent linearity tube was chosen. In order to cross check PMT performance small fast ion chambers were built and installed downstream of some scanners[6]. The linearity of the ADC is also very important.

PERFORMANCE AND CONCLUSIONS

Performance tests have focused on understanding systematic errors. These tests fall into two broad categories: 1) tests made by varying beam size and / or intensity and 2) tests made with different detectors sensing scattered radiation from a single wire. Figure 3 shows the beam emittance measured using

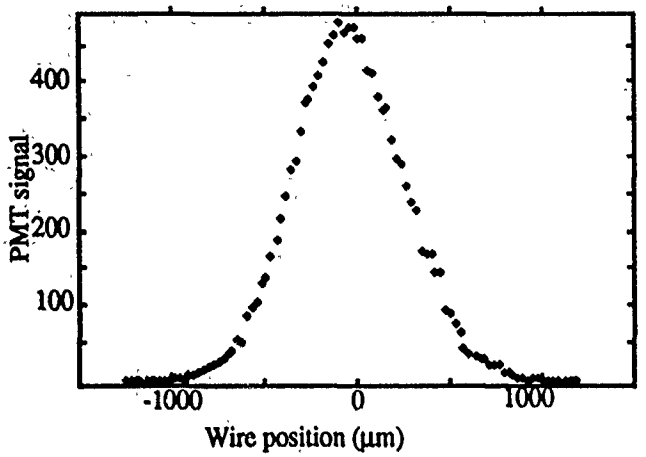


Figure 2: A typical single wire scan. The data are fit with a gaussian with an offset.

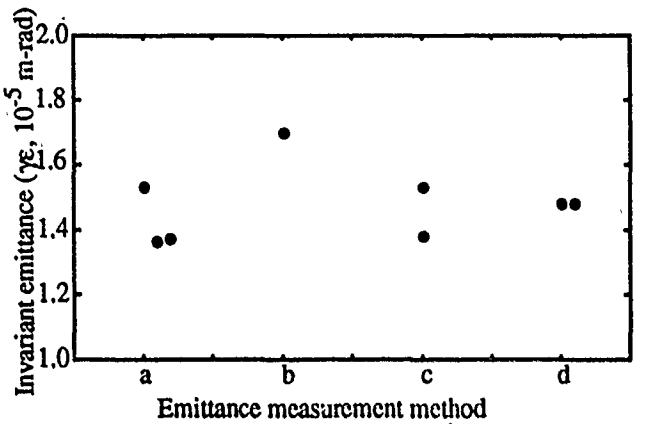


Figure 3: Comparison of emittance measurements made with: multi wire (*a*) and quadrupole scans (*b-d*) using different quadrupole magnet / wire scanner combinations. The results are in good agreement.

quadrupole scans[7] on three different scanners and multiwire scans at 1 GeV and 4.5 x 10^{10} e-/pulse, near the SLC nominal operating intensity. This is a good test of saturation effects since the beam sizes and signal strengths vary considerably over the scan range and from scanner to scanner. These tests were done using the downstream fast ion chamber.

The SLC wire scanners provide beam emittance data that is reliable enough to have already yielded new insights into the performance of the SLC. By late 1991, 32 scanners will be in use (figure 4). Future linear colliders will have a tighter emittance budget and will require improved resolution scanners. Piezo-electric motors, with their very small step size and ultra-high vacuum compatibility, may prove to be an appropriate technology for future wire scanners. Two such scanners are installed for use at the SLC IP.

ACKNOWLEDGEMENTS

We would like to acknowledge the efforts of the linac group for help in commissioning the scanners, the mechanical design and engineering group for mechanical design, A. Tilghman for controls, and C. Field, K. Bouldin and C. Young for PMT testing and data analysis.

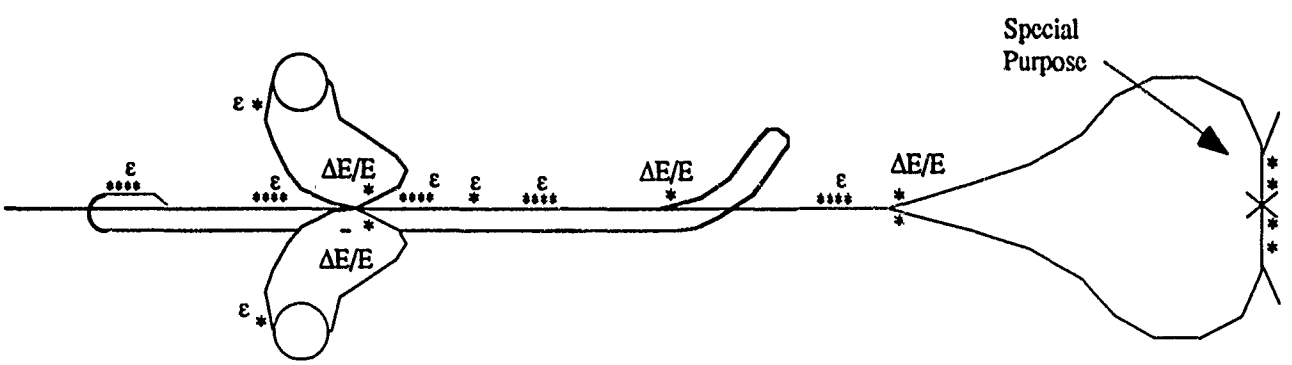


Figure 4: SLC schematic showing the locations of wire scanners. Wire scanners are used for emittance (ε), energy spread (ΔE/E) and special purpose functions in the final focus.

---

[1] R. Jung and R. J. Colchester, ' Development of Beam Profile and Fast Position Monitors for the LEP Injector Linacs', IEEE Trans. Nucl. Sci. NS32-5:1917, 1985.

[2] R.I. Cutler et. al., 'Performance of Wire Scanner Beam Profile Monitors to Determine the Emittance and Position of High Power CW Electron Beams of the NBS-Los Alamos Racetrack Microtron', Proceedings of the 1987 IEEE Particle Accelerator Conference, p. 625, 1987.

[3] K.D. Jacobs et.al., 'The Beam Profile Measurement System at the Bates Linac', Proceedings of the 1989 IEEE Particle Accelerator Conference, p. 1523, 1989.

[4] L. Sanchez-Chopitea et. al., 'Correlation Plot Facility in the SLC Control System', proceedings of this conference.

[5] R. Fulton et. al., ' A High Resolution Wire Scanner for Micron Size Profile Measurements at the SLC', Nucl. Instr. Meth. A274:37, 1989.

[6] D. McCormick, 'Fast Ion Chambers for SLC', proceedings of this conference.

[7] M. C. Ross et. al.,'Automated Emittance Measurements in the SLC', Proceedings of the 1987 IEEE Particle Accelerator Conference, p. 725, 1987.

Emittance Measurements of FEL Accelerators Using Optical Transition Radiation Methods

R.B. Fiorito and D.W. Rule
Naval Surface Warfare Center, MS R42
Silver Spring, MD. 20903

A.H. Lumpkin and R.L. Tokar
Los Alamos National Laboratory, P 15
Los Alamos, NM. 87545

D.H. Dowell, W.C. Sellyey and A.R. Lowrey
Boeing Physical Sciences
Seattle, WA. 98108

Abstract

Measurements of the emittance of the Boeing FEL accelerator operating at 107 Mev, were performed using optical transition radiation (OTR). The results of the three measurement methods: measurement of beam spot size as a function of magnetic quadrupole focusing strength, two screen beam spot measurements, and beam spot - divergence measurements using a OTR interferometer are compared and shown to be in excellent agreement.

I. Introduction

OTR techniques have proven to be very useful to diagnose electron beam spatial profiles, position, divergence, energy and emittance.[1-5] In early publications we have described the advantages of employing OTR techniques to characterise the properties of the Boeing 110 Mev accelerator, which is used to drive a visible free electron laser (FEL).[6] OTR has been shown to provide increased spatial and temporal resolution in the measurement of beam size, and position when compared to fused silica and phospor screens previously used to characterise the beam in the accelerator and in the wiggler. As a result, OTR foils have now replaced the fused silica and phosphor screens at both the Boeing and LANL HIBAF FEL accelerators.[4-6]

II. Experiments

The experimental setup for OTR measurements at both Boeing and LANL is shown in Figure 1. and discussed in ref.6. The The arrangement provides for an upstream station where a single foil maybe remotely placed in the electron beam path, and a downstream station housing a two position actuator to access either a single OTR foil, or a two foil OTR Wartski interferometer.[1] Using these two stations, which are separated by 2.2 meters, quadrupole scans, simultaneous beam spot measurements and beam spot-divergence measurements can be made. The apparatus is located is a straight section (A leg) of the Boeing accelerator.

Figure 1. shows the plane of incidence or horizontal plane, which contains the electron beam velocity vector (in the + z direction) and

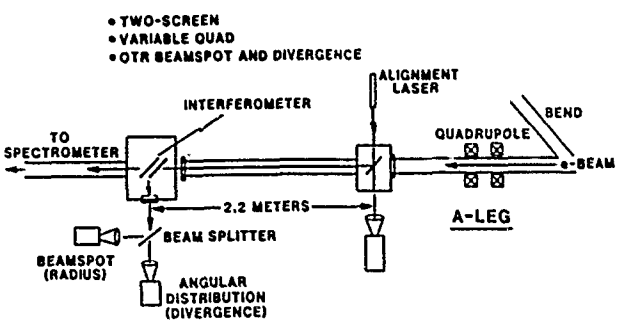


Figure 1. Experimental Arrangement

0-7803-0135-8/91$01.00 ©IEEE

the x direction which is perpendicular to z and parallel to the surface of the earth. The y direction is perpendicular to the plane of incidence. (y,z), then, refers to the vertical plane.

To make a quadrupole scan measurement, the beam is focused on the OTR foil at the upstream station. The field strength of magnetic quadrupole lenses upstream of this foil, which control focusing in either the x of y directions are then varied, and the OTR beam image at each field strength is captured and recorded.

In the two screen measurement, the beam spot images at the upstream and downstream single OTR foils are captured simultaneously. In this method the beam is focused with the quadrupole lenses to effect a minimum beam spot radius in either the x,z or y,z planes.

Finally the beamspot-divergence measurement is made at the downstream station. The single foil, which consists of a diamond machined Al mirror, is used to produce the beam spot image. The beam is focused here to achieve either an x or y minimum radius. The The divergence is measured using an OTR interferometer, which consists of two parallel foils: the mirror, and a thin (0.7 micron) Al foil separated by 2.5 cm. A detail of the interferometer is given in Figure 2. Standard optical polarizers and filters are used to obtain horizontally or vertically polarized OTR interferograms, from which either the x or y beam divergence can be obtained.[2-5]

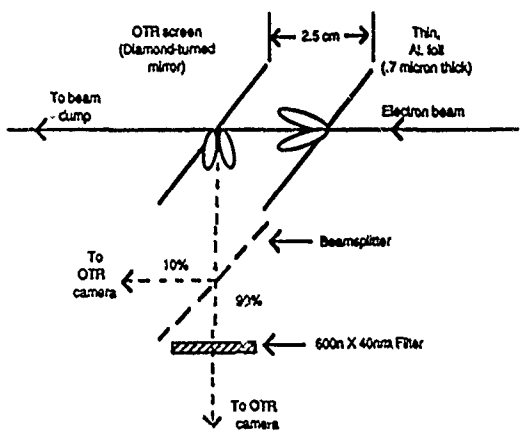


Figure 2. Detail of the OTR Interferometer

Intensified CID cameras with RS 170 ouputs are used at both stations to obtain beam images and interferograms.

III. Results and Discussion

In these experiments the accelerator was not tuned for optimum beam transport.

The horizontal plane emittance measured from the single foil quadrupole scan yields an x edge emittance value of 158±24 mm-mrad. The two foil method measurement produces an x emittance of 167 ±25 mm-mrad.

Figure 3 shows three line scans of horizontally polarized OTR interferograms obtained when the beam is focused to a minimum x diameter. The solid line represent the data, the dotted lines theory. The best overall fit is obtained using a beam energy of 106.8 Mev and an x divergence of 0.3 milliradians. The beam energy spread as determined by the PARMELA code is less than 5% and does not significantly affect the fringe visibility for this experiment, which is dominated by the effect of beam divergence. However, the Figure demonstrates that it is not possible to simultaneously fit all the data fringes by using a single divergence value. This is most likely caused by the fact that the beam is not precisely focused to a waist position at the site of the OTR interferometer. The resulting angular beam distribution cannot be represented by a single Gaussian function in x or y, which is the assumption of the theory.

The rms x,y emittances of the beam are obtained from the beam's rms radii and the rms divergences obtained from horizontally and vertically polarized interferograms respectively. At an x waist then,

$$\varepsilon_{x\,rms}=\beta\gamma x_{rms}\Theta_{x\,rms}\cong\varepsilon_{x\,edge}/4 \qquad (1)$$

where ε_{xrms} is the rms x emittance, x_{rms} is the rms x radius of the beam, Θ_{xrms} is the rms x divergence and $\varepsilon_{x\,edge}$ is the x edge emittance.

Table I. gives a comparison of the measured values using the three techniques as well as comparison with the predictions of the PARMELA simulation code. The results are all in good agreement.

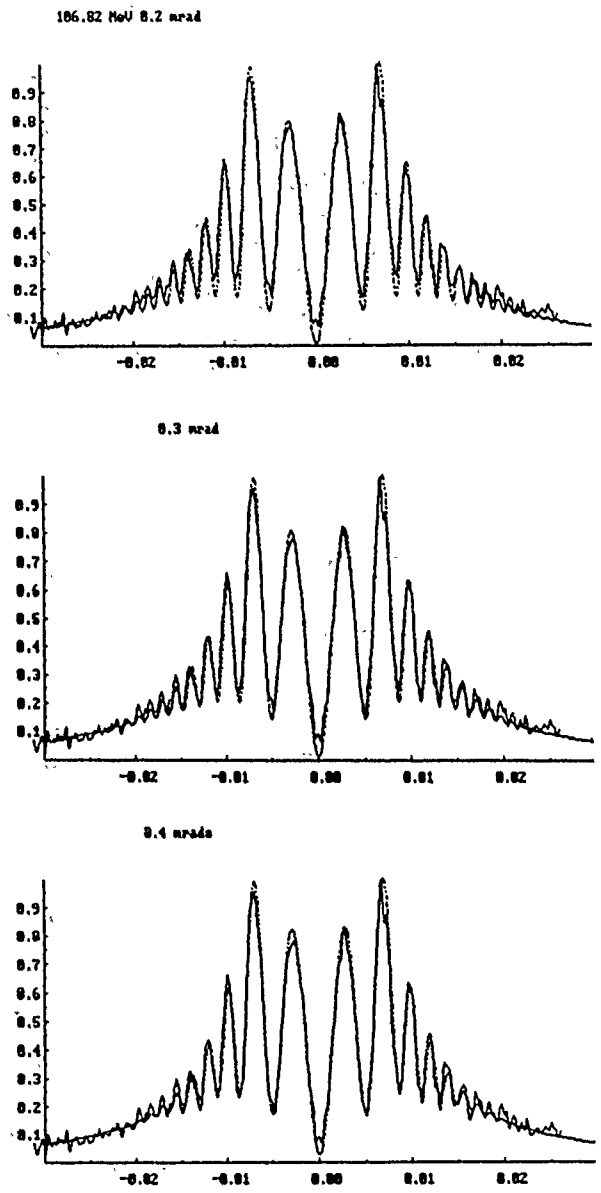


Figure 3. OTR Interferometer scans - relative intensity versus angle measured in radians for three values of x divergence; top: 0.2 mrad, middle: 0.3 mrad, bottom: 0.4 mrad.

Table I.

Comparison of measurements and simulation code results

Method	x edge emittance	x_{rms} (mm)	$\Theta_{x\ rms}$ (mrad)
Quad scan	158±24	------	------
Two foil	167±25	0.57	0.35
OTRI	144±25	0.57	0.3±.05
Parmela	143	0.81	0.21

IV. References

[1] L. Wartski, S. Roland , J. Lasalles, M. Bolore and G. Filippi, J. Appld. Phys. 46, 3644, 1975.

[2] R. B. Fiorito, et. al., Proc. 6th Intl. Conf. on High Power Beams, Kobe, Japan, 1986.

[3] D. W. Rule, Nucl. Instr. and Meth., B24/25, 90, 1987.

[4] D.W. Rule, R. B. Fiorito, A.H. Lumpkin, R.B. Feldman and B.E. Carlsten, Nucl. Inst.and Meth., A296, 739, 1990.

[5] X.K. Maruyama, R.B. Fiorito and D.W. Rule, Nuc. Inst. and Meth., A272, 237, 1988.

[6] A. H. Lumpkin, R. B. Fiorito, D.W. Rule, D.H. Dowell, W.C. Sellyey and A.R.Lowrey, Nuc. Inst. and Meth., A296, 150, 1990.

Beam Spot Size Measurement Using Beamstrahlung Signals at the SLC Interaction Point

E. Gero
University of Michigan, Ann Arbor, Michigan 48109

W. Kozanecki, P. Chen
Stanford Linear Accelerator Center, Stanford University, Stanford, California 94309

Abstract

We present a novel technique to measure separately the transverse sizes of e^+ and e^- beams in linear colliders, that is based on analyzing patterns of beamstrahlung energy recorded while the two beams are scanned across each other. After establishing the principle of the method, we compare our predicted radiated energy profiles to actual measurements, and verify the consistency of our results with an independent beam size determination based on coherent mutual electromagnetic deflection of the two beams.

I. Theory of Classical Beamstrahlung

Consider a micron-sized electron bunch, containing about 10^{10} particles, colliding with a positron bunch at the interaction point (IP) of the Stanford Linear Collider (SLC). The strong coherent electromagnetic field generated by the positron (resp. electron) bunch as a whole, slightly inflects the trajectory of each incoming electron (resp. positron), and causes the latter to emit synchrotron radiation, called "beamstrahlung", as already observed experimentally [1].

Field strengths at the SLC IP are sufficiently low that classical beamstrahlung theory [2] fully describes the properties of the emitted radiation. These depend on the intensities (N_1, N_2) of the two beams, their r.m.s. bunch lengths $(\sigma_{1z}, \sigma_{2z})$, their energy (E_b), their r.m.s transverse sizes $(\sigma_{1x}, \sigma_{1y}, \sigma_{2x}, \sigma_{2y})$, and finally on the beam orientation parameters (a, α, β) (subscript 1 indicates the beam whose emitted radiation is being calculated, while subscript 2 refers to the beam producing the electromagnetic field responsible for the synchrotron emission). The charge population within each bunch is assumed to be gaussian in all three dimensions. For each of the two bunches separately, we choose a coordinate system such that the z axis lies along the incoming beam direction, the x direction matches the major axis of the transverse beam profile (assumed elliptical), and the y-axis is aligned with its minor axis (the directions of the major and minor axis of the two beams need not coincide). a is the radial distance between the centers of the two beams, α is the angle between the major axis of bunch 2 and the line connecting the bunch centers, and β is the angle between the directions of the major axes of the two bunches.

The total number of photons radiated is given by [2]

$$N_{1\gamma} = \frac{5}{\sqrt{6\pi}} \left(\frac{N_1 N_2 \alpha_e r_e}{\sigma_{1x}} \right) B_x R_1 R_2 \times \int_{-\infty}^{\infty} \int_{-\infty}^{\infty} f(\mu, \nu, B_x, R_2) e^{-g(\mu,\nu,\alpha,\beta,\xi,R_1)} \, d\mu \, d\nu \quad (1)$$

where

$$f(\mu, \nu, B_x, R_2) = \frac{1}{\sqrt{R_2^2 - 1}} \left| w\left(\frac{B_x R_2 (\mu + i\nu)}{\sqrt{R_2^2 - 1}} \right) - e^{-B_x^2(\mu^2 + R_2^2 \nu^2)} w\left(\frac{B_x (\mu + i R_2^2 \nu)}{\sqrt{R_2^2 - 1}} \right) \right| \quad (2)$$

$$g(\mu, \nu, \alpha, \beta, \xi, R_1) = (\mu \cos\beta + \nu \sin\beta - \xi \cos(\beta - \alpha))^2 + R_1^2 (-\mu \sin\beta + \nu \cos\beta + \xi \sin(\beta - \alpha))^2 \quad (3)$$

Here, α_e is the fine structure constant and r_e is the classical radius of the electron; R_1 and R_2 are the aspect ratios of the bunches ($R_1 = \sigma_{1x}/\sigma_{1y}$, $R_2 = \sigma_{2x}/\sigma_{2y}$); and B_x and B_y are the beam size ratios ($B_x = \sigma_{1x}/\sigma_{2x}$, $B_y = \sigma_{1y}/\sigma_{2y}$). $w(z)$ is the complex error function: $w(z) = \exp(-z^2)\mathrm{erfc}(-iz)$. μ and ν equal $x/\sqrt{2}\sigma_{1x}$ and $y/\sqrt{2}\sigma_{1x}$, respectively, and ξ equals $a/\sqrt{2}\sigma_{1x}$.

The total energy emitted can be expressed as

$$U_1 = \frac{4}{3\sqrt{\pi}} \left(\frac{N_1 N_2^2 r_e^3 \gamma^2 mc^2}{\sigma_{1x}\sigma_{1y}\sigma_{2z}} \right) B_x^2 R_2^2 \times \int_{-\infty}^{\infty} \int_{-\infty}^{\infty} f^2(\mu, \nu, B_x, R_2) e^{-g(\mu,\nu,\alpha,\beta,\xi,R_1)} \, d\mu \, d\nu \quad (4)$$

where γ is the relativistic factor, m is the mass of the electron, and c is the speed of light.

The maximum critical energy is

$$(E_c)_{max} = 3 f_m(B_x, R_2) \left(\frac{N_2 r_e^2 \gamma^2 mc^2}{\alpha_e \sigma_{1x} \sigma_{2z}} \right) B_x R_2 \quad (5)$$

where $f_m(B_x, R_2)$ is the maximum magnitude of the electric field of bunch 2 in units of $(eN_2/\sigma_{2x}\sigma_{2z})$.

0-7803-0135-8/91$01.00 ©IEEE

Finally, the photon energy spectrum can be calculated :

$$\frac{dN_{1\gamma}}{dE_\gamma} = \frac{\sqrt{6}}{3\pi^2}\left(\frac{N_1\alpha^2\sigma_{2z}}{r_e\gamma^2 mc^2}\right) R_1 I(R_1, R_2, B_x, \alpha, \beta, \xi, \epsilon) \quad (6)$$

where

$$I(R_1, R_2, B_x, \alpha, \beta, \xi, \epsilon) = \int_{-\infty}^{\infty}\int_{-\infty}^{\infty}\int_{\epsilon h(\mu,\nu,B_x,R_2)}^{\infty} e^{-g(\mu,\nu,\alpha,\beta,\xi,R_1)} \times K_{5/3}(s)\sqrt{\ln\left(\frac{s}{\epsilon h(\mu,\nu,B_x,R_2)}\right)}\, ds\, d\mu\, d\nu \quad (7)$$

and

$$h(\mu,\nu,B_x,R_2) = \frac{f_m(B_x,R_2)}{f(\mu,\nu,B_x,R_2)} \qquad \epsilon = \frac{E_\gamma}{(E_c)_{max}} \quad (8)$$

II. Beamstrahlung radiation detector

Beamstrahlung photons emitted by electrons and positrons impinge on two detectors, located symmetrically on either side of the SLC IP, downstream of the first bending dipole encountered by the outgoing charged particle beams. In this section, we recall the principle and construction of these "beamstrahlung monitors", outlining as we proceed the physical processes that convert the beamstrahlung energy flux into a measurable electrical signal.

Each monitor [2,3] consists of a Čerenkov counter filled with ethylene gas at a pressure of 0.3 atmospheres. Beamstrahlung photons incident on the monitor first hit a converter plate, where about 3% of them (for $E_\gamma = 50$ MeV) convert into e^+e^- pairs. The Čerenkov light produced in the gas by the conversion products is then reflected by a field mirror onto a plane mirror, that guides it into a light channel, consisting in turn of a periscope with two 90° reflections. This light channel ends in five side-by-side vacuum windows of fused silica, held by a stainless steel jacket. Downstream of the windows, the light hits five Hamamatsu R580 photomultiplier tubes, whose output signals are integrated, digitized, and summed together.

The total charge collected from the phototubes, expressed in terms of ADC counts, is related to the total number of beamstrahlung photons radiated, by [2,4]

$$N_{ADC} = C\int_{E_{coff}}^{E_{cm}} \frac{dN_{1\gamma}}{dE_\gamma} N_c(E_\gamma) f_\gamma\, dE_\gamma \quad (9)$$

where C ($\approx 4.5 \times 10^{-5}$) is the number of ADC counts per Čerenkov photon detected, $dN_{1\gamma}/dE_\gamma$ is the number of beamstrahlung photons produced at energy E_γ, and $N_c(E_\gamma)$ is the average number of Čerenkov photons produced by a converted beamstrahlung photon of energy E_γ:

$$N_c(E_\gamma) = \frac{4\pi\alpha l\Delta\nu}{cE_\gamma}\left[\left(1-\frac{1}{n^2}\right)(E_\gamma - E_{coff}) + \frac{m^2c^4}{n^2}\left(\frac{1}{E_\gamma}-\frac{1}{E_{coff}}\right)\right] \quad (10)$$

Here l is the path length (21 cm) of a conversion electron or positron in the counter gas, n is the index of refraction of this gas (1.0002), $\Delta\nu$ is the frequency interval over which the phototubes are sensitive (8.57×10^{14} Hz), and E_{coff} is the Čerenkov threshold energy (approximately 26 MeV),

$$E_{coff} = \frac{nmc^2}{\sqrt{n^2-1}} \quad (11)$$

Finally, $f_\gamma(E_\gamma)$, the fraction of photons that pair produce, is given by

$$f_\gamma(E_\gamma) = \left(1 - e^{-N\sigma(E_\gamma)x}\right) \quad (12)$$

where N is the number of nuclei per unit volume, x is the thickness of the converter plate (0.79 mm), and $\sigma(E_\gamma)$ is the pair production total cross section per nucleus at energy E_γ, calculated using the Racah formula for pair production in the field of an unscreened point nucleus [2].

III. Spot size measurement technique

We can now predict and measure the total energy (convoluted with the acceptance, threshold and resolution functions of the beamstrahlung monitor) radiated by either beam. Our spot size measurement technique [2,5] fundamentally relies on the fact that the energy pattern radiated by one of the bunches depends, in different ways, both on its own charge distribution (i.e. on the spatial distribution of the radiating particles), and on that of the other beam (which determines the distribution of electromagnetic fields that induce the radiation process). By measuring the radiation patterns from both beams simultaneously as these are scanned across each other (thereby probing each other's charge distribution and field configuration), it is possible to unfold, in a global fit to these patterns, the parameters describing the transverse bunch shapes. As no attempt is made to measure the absolute magnitude of the beamstrahlung flux, variables such as bunch length or beam current, which greatly affect the energy and intensity of the photon flux, but not its spatial pattern, become largely irrelevant (except through their coupling with Čerenkov threshold effects).

In practice, the method consists in holding one of the beams fixed, and scanning the other beam transversely across it, first horizontally, and then vertically, using steering dipoles located on either side of the SLC IP. Each scan extends well beyond several beam radii, in order to probe the full spatial extent of the electromagnetic field of the bunch, and typically covers a range of $\pm 40\mu$m, in 2 μm steps [1,2]. At each scan point, the beamstrahlung flux (eq. 9) is recorded and averaged over 10 consecutive beam pulses; the beam is then moved to the next scan point, and the whole procedure is repeated. Such a "beamstrahlung scan" therefore results in a total of four beamstrahlung patterns, which can be adequately modelled by our beamstrahlung and detector simulation, as illustrated in fig. 1.

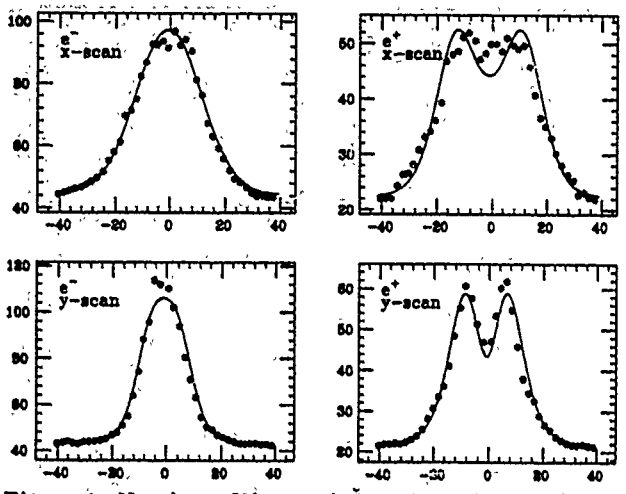


Figure 1: Number of detected Čerenkov photons (ADC counts) from radiating electrons (left) and positrons (right), vs. horizontal (top) or vertical (bottom) distance between the colliding bunches, for the data (points) and the simulation (curves).

One of the simplest shape parameters that characterizes such a beamstrahlung pattern is its 2-σ truncated r.m.s width W [2]. We can extract from the 4 radiation patterns above, 4 measured width parameters W_{1x}^m, W_{1y}^m, W_{2x}^m and W_{2y}^m. If both beams are upright, i.e. if their major and minor axes are all either horizontal or vertical, then 4 numbers suffice to describe the transverse profiles of the two beams, viz. the r.m.s beam sizes σ_{1x}, σ_{1y}, σ_{2x}, and σ_{2y}. It should therefore be possible to relate these 4 transverse beam sizes σ to the 4 width parameters W, and to thereby measure the beam sizes by matching the expected values of the width parameters W to their observed values.

To this effect, we first construct a "library" of beamstrahlung scans, by generating, according to the prescriptions of section II, several sets of simulated beamstrahlung patterns like the ones of fig. 1, that cover a sufficiently wide range of possible beam size combinations. For each of the generated combinations, the widths parameters are evaluated from the simulated beamstrahlung patterns and stored in a four-dimensional look-up table. This allows, given any combination of assumed values for σ_{1x}, σ_{1y}, σ_{2x}, and σ_{2y}, to calculate by interpolation, the expected values of the width parameters W_{1x}, W_{1y}, W_{2x}, and W_{2y}.

The four beam sizes σ_{1x}, σ_{1y}, σ_{2x} and σ_{2y} are then "measured" by finding the set of values of σ's that minimize the χ^2-like quantity

$$\chi^2 = \left(\frac{W_{1x}^m - W_{1x}}{W_{1x}^m}\right)^2 + \left(\frac{W_{1y}^m - W_{1y}}{W_{1y}^m}\right)^2 + \left(\frac{W_{2x}^m - W_{2x}}{W_{2x}^m}\right)^2 + \left(\frac{W_{2y}^m - W_{2y}}{W_{2y}^m}\right)^2 \qquad (13)$$

where W_{1x},...,W_{2y} are the expected values of the width parameters, corresponding to the assumed values of σ_{1x},...,σ_{2y}. Each W is a function of all four σs.

The validity of the method has been tested by measuring, simultaneously with the beamstrahlung patterns, the electromagnetic deflection induced by one beam on the other [6]. This technique directly measures the "interaction radii" $\Sigma_x = \sqrt{\sigma_{1x}^2 + \sigma_{2x}^2}$ and $\Sigma_y = \sqrt{\sigma_{1y}^2 + \sigma_{2y}^2}$, but is unable to separate the individual electron (σ_1) and positron (σ_2) contributions to Σ_x and Σ_y. We compare in fig. 2 the interaction radii as measured by the beam-beam deflections and by the beamstrahlung patterns, in a controlled experiment where all beam parameters are kept constant, except for the horizontal size of the electron beam which is varied using adjustable quadrupole magnets. As the longitudinal position of the horizontal electron waist is varied around the nominal (zero) position, Σ_y stays approximately constant (as it should), while Σ_x varies by the expected amount. Beamstrahlung and deflection measures of the spot sizes yield results consistent with each other, both qualitatively and quantitatively.

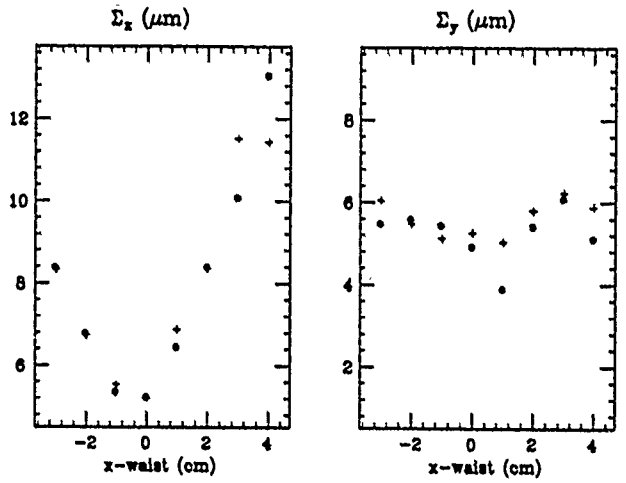


Figure 2: Σ_x and Σ_y vs. position of the horizontal e^- waist, as measured by beam-beam deflections ($*$) and by beamstrahlung patterns (+).

References

[1] G. Bonvicini et. al., "First Observation of Beamstrahlung," Phys. Rev. Lett., vol. 62, pp. 2381-2384, May 1989.

[2] E. Gero, "The Theory and Observation of Classical Beamstrahlung at the SLC," University of Michigan, Ann Arbor, Michigan, Ph.D. dissertation, 1991.

[3] G. Bonvicini et. al., "A Monitor for Gamma Radiation at at Zero Degrees from the SLC Collision Point," Nucl. Instr. and Meth. A, vol. 277, pp. 297-303, May 1989.

[4] P. Chen, "Can One Measure Beam Size with Beamstrahlung Monitor at SLC?" SLAC-AAS-40, Nov. 1988.

[5] E. Gero et. al., "Beamstrahlung as an Optics Tuning Tool at the SLAC IP," in *1989 IEEE Particle Accelerator Conference*, Chicago, Ill., Mar. 1989, pp. 1542-1543.

[6] W. Koska et. al., "Beam-beam Deflection as a Beam Tuning Tool at the SLAC Linear Collider." Nucl. Instr. and Meth. A, vol. 286, pp. 32-36, Jan. 1990.

Beam Diagnostic Systems in the IUCF Cooler and Cyclotron

Mark S. Ball, Timothy JP Ellison, Brett J Hamilton

The Indiana University Cyclotron Facility
2401 Milo Sampson Lane, Bloomington, IN 47405

Abstract

Beam diagnostics for the IUCF Cooler synchrotron which have been recently developed include a beam phase feedback system to damp synchrotron oscillations induced by the rf system and a transverse phase space tracking system to measure the betatron fractional tunes and to investigate non-linear beam dynamics. New cyclotron diagnostic systems include a new beam timing system which has been improved in sensitivity by over a factor of 10, a cyclotron beam turns counting system, and an electrostatic quadropole magnet modulator to vary beam intensity in synchronization with the beam switching magnet. The design, performance, and problems associated with these systems are discussed.

I. Cooler Beam Diagnostics

A. Beam phase feedback

The cooler low level rf system uses a DDS (Direct Digital Synthesizer) with 512 Hz resolution for acceleration. These fairly large discreet steps, corresponding to a $\Delta p/p$ of about 0.006% (to be compared with the Cooler momentum acceptance of ± 0.2%) occur at rates comparable to synchrotron oscillation frequency, typically 2 - 5 kHz. Consequently large synchrotron oscillations are induced during acceleration. Although the effect of these steps can be reduced by lowering the phase-locked-loop (PL^2) bandwidth, if the bandwidth is made too small the loop cannot track the ramp without losing lock; in addition, as the loop bandwidth is decreased, additional noise from the VCO, which also heats the beam, is introduced. As a result, with an optimized PL^2 bandwidth, we typically lost about 60% of the beam during acceleration.

To solve this problem we built a beam phase feedback (BPF) system. The BPF system compares the phase of a signal from the rf cavity with a beam signal from a wall gap monitor. Because the rf system operates at many different harmonics of the fundamental revolution frequency it was necessary to include an adjustable phase shifter with discreet settings for each harmonic number in series with the beam feedback signal in order to maintain a 90° phase difference between the beam and cavity monitor signals for the ECL discriminator which operates with an I.F. of 10.7 MHz. The discriminated phase signal, after being processed by a computer-controlled filter with adjustable cutoff frequency and gain, is fed into the PL^2 upstream of the loop filter. The performance of this system is demonstrated in Figure 1, which shows the damping of a deliberately induced synchrotron oscillation as a function of the system closed loop gain.

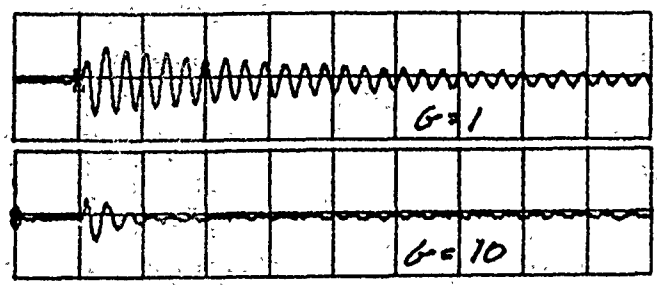


Figure 1. Beam phase with repect to the rf system as a function of time with the damping system in operation. Vertical: 45°/div; Horizontal: 1 ms/div. Top trace: BPF relative gain = 1; bottom trace: BPF relative gain = 10.

This system has increased transmission efficiencies during acceleration for about 30% to close 100%. The beam lifetime is also greatly improved. The system dynamic range is 50 dB (from 1 μA to 300 μA) limited on the high end by the saturation level of the beam pickup amplifier (easily correctable) and on the low end by poor signal to noise.

The rf low level system also uses an HP-3325A synthesizer when operating at stationary frequencies. In this operating mode the phase error signal is fed into a phase shifter with the same desirable effect.

B. Cooler beam phase space tracking system

1. System description

The extremely small emittance and momentum spread of the electron-cooled proton beams makes the Cooler an ideal laboratory for the study of nonlinear beam dynamics with unprecedented resolution. A data acquisition system is being developed to track the position of a single beam bunch in transverse phase space on a turn-by-turn basis in the Cooler. This system consists of four major subsystems: (1) the front-end electronics, (2) the level control with signal conditioning, (3) the sample and hold (S/H) module and (4) the digitizer.

The front-end electronics consists of two existing beam position monitor (BPM) electrodes separated by a betatron phase advance of close to 90°. The electrode amplifiers produce signals proportional to the beam intensity and the product of the beam position and intensity and have 55 dB gain.

0-7803-0135-8/91$01.00 ©IEEE

The automatic level control module increases the system dynamic range. The peak signal voltage is used in a feedback loop to adjust programmable step attenuators with 10 increments. After the attenuators, the short pulses (≈ 5 - 10 ns in length) are peak-detected by a passive circuit having a switch-selectable RC decay time which minimizes sampling errors due to jitter and drift in the sample and hold (S/H) timing signals.

The S/H module samples the peak-detected position and intensity levels with high speed sample and hold amplifiers having a 12 ns track-to-hold settling time. The output of two S/H modules are fed into a 2:1 analog multiplexer enabling a single digitizer to record both the position and intensity signals; the S/H electronics also reduce the required digitizer speed. Consequently, we have considerably reduced the system cost by minimizing the required speed and quantity of the digitizers. The trigger clock operates off the beam intensity signal and runs at the pulse repetition frequency divided by the rf harmonic number. The system can operate with beam fundamental revolution frequencies of up to 2.2 MHz.

We use a commercial transient recorder, DSP 2012, (TR) which has 12 bit resolution and an 8 k sample buffer as the digitizer. The TR is a CAMAC module which interfaces to the VAX network enabling the use of many existing software packages, consequently minimizing the amount of software overhead.

2. *System operation and performance*

The system is presently being developed for betatron fractional tune measurements and nonlinear beam dynamics studies. The beam is kicked using a horizontal kicker magnet. A fast fourier transform (FFT) of the beam position data after the kick yields the fractional tune as shown in Figure 2.

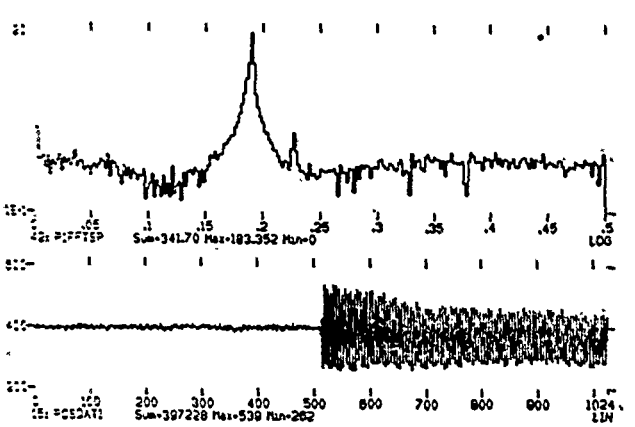


Figure 2. The bottom portion of the figure shows the beam position of a single beam bunch for 1024 turns. At turn 512 the injection kicker is fired producing a coherent betatron oscillation. The top portion is an FFT of the recorded beam postion; the peak corresponds to a betatron fractional tune of 0.189.

The system noise is determined by the input noise in the first amplifier (≈ 0.5 nV/√Hz) and the electrode sensitivity ($V/I_{peak}x_{mm}$) is about $0.2/\beta$ Ω/mm. Consequently, operating with peak currents (the product of current and bunching factor) of about 100 μA, a bandwidth of about 100 MHz, and a value for $\beta = v/c$ of 0.3, we expect rms noise of less than 0.1 mm. Although normalized beam position resolutions of 0.13 mm have been observed, more systematic testing is needed. The system has demonstrated a 1% amplitude linearity over the 10dB step attenuator range (Fig. 3).

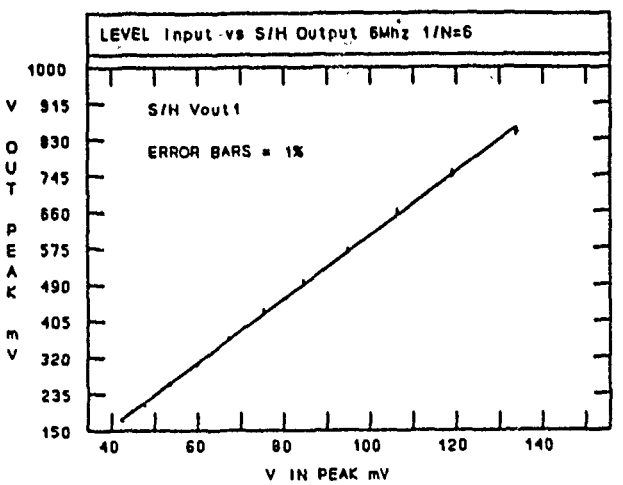


Figure 3. System linearity as a function of voltage in (x axis) vs voltage out (y axis). A simulated beam pulse input was increased in 1dB steps. The error bars are 1%.

Since the trigger circuitry operates directly off of the beam signals, no adjustments are required with varying beam velocity, harmonic number, bunching factor or intensity. This enables tune measurements to be made during the acceleration process, even where the beam velocity can change by over a factor of two.

Studies of the Poincar´e (x,x') map, mapping of resonance islands boundaries and dynamical aperture studies using this system for data acquisition will begin this summer.

III. CYCLOTRON BEAM DIAGNOSTICS

A. New beam timing system electronics[2]

The beam timing system provides an rf signal phase-locked (≈ ± 100 ps) to the beam from the cyclotron for experimentalists to use as a stop signal in energy measurements of reaction products using time of flight. Operation with the very low beam currents from the cyclotron (as low as a few nA) is very difficult and we have made many

improvements in our system in order to operate with currents of this level. Formerly, the lowest intensity beams we were able to operate reliably was ≈ 25 nA. There were two principle problems: wideband noise (causing an unacceptable amount of jitter in the timing signal) and rfi (causing changes in the phase of the timing signal with changes in the beam current).

The wideband noise problem was eliminated by replacing the HP 8405A vector voltmeter, which was used as the system phase detector, with a modified BPM system low bandwidth detector (LBWD). This reduced the amount of wideband noise by about an order of magnitude, to the level expected given the system bandwidth and pickup amplifier noise figure.

The maximum permissible amount of coherent rfi at the pickup for satisfactory operation with beam currents of 1 nA is about 2 nV at the second harmonic of the cyclotron rf frequency, typically 60 MHz. Despite all efforts at rfi shielding, such rfi levels could not be obtained. Consequently, we decided to operate the system at a frequency which is a harmonic of the beam pulse repetition frequency but not a harmonic of the rf frequency by using pulse-selected beams. The beam is pulse selected $1/n$ using a prebuncher operating at a frequency of f_{cycl}/n where f_{cycl} is the cyclotron rf frequency and n is an integer. In this situation, there is a beam signal at all frequencies given by mf_{cycl}/n where m is an integer, but rfi only when m/n is also an integer. The system operates with $m/n = 3/2$ for even n, and at $m/n = 5/3$ for values of n which are a multiple of 3. By changing the local oscillator frequency to 3/2 or 5/3 the cyclotron rf frequency (depending on the pulse selection of the beam) + 2.777 kHz, and adding an amplifier in the feedback at low gains, we have locked onto beams with intensities as low as 1 nA.

B. Beam turn counter

This system modulates the beam current at a frequency of about 100 kHz and measures and compares the phase of the beam current modulation detected at pickups immediatly before and after the cyclotron. An HP4195A Network Analyzer is used to monitor this phase difference, operating on a modulation sideband of a high harmonic of the pulse-selected beam repetition frequency which is not also a harmonic of the cyclotron rf system frequency.

In a test of this system we modulated the beam current by modulating the phase of the prebuncher rf systems. For a number of reasons, this is not a suitable system for modulating the beam intensity and we are installing a new beam intensity modulation system.(see Fig. 4)

C. Beam intensity modulation system

By first limiting the acceptance of the 600 keV beamline with two sets of 4-jaw slits, we can modulate the beam intensity by a factor of about 50 without altering the beam transmission efficiency through the following series of accelerators by modulating the voltage of an electrostatic quadrupole. The electrostatic quadrupole voltage will be modulated using a home-built triode vacuum tube which is being tested. Besides being useful for future beam diagnostic systems, this system will be essential for future beam splitting operations, where two simultaneous users require substantially different currents.

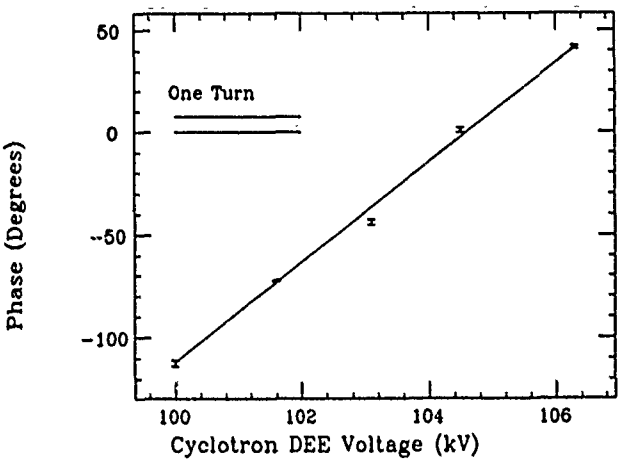


Figure 4. The cyclotron time space = n_{harm}/f_{cycl}. At the time of the test, f = 27.85 MHz, harmonic = 6, one turn = 215 ns and at 100 kHz modulation one turn = 7.75°. Because of the fractional tune, one of every 6 turns can be extracted.

IV. CONCLUSION

When a new beam diagnostic system is commissioned and used to make a systematic set of measurements, we invariably learn something new, if not exciting. Hopefully in the upcomming years we will have many interesting results to report on using these new systems.

V. ACKNOWLEDGEMENTS

We are grateful for the support of many staff members at IUCF especially Dave Caussyn, John Collins, Vladimir Derenchuk, Bill Jones, S. Y. Lee, and Terry Sloan.

IV. REFERENCES

[1] Timothy JP Ellison, C. Michael Fox, Steven W. Koch, Liu Rui, "Nondestructive diagnostics for measuring the phase, position, and intensity of 15 enA beams from the IUCF cyclotron", *Proc. 11th Int. conf. on Cyclotrons and their Applications*, edited by M. Sekiguchi, Y. Yano, K. Hatanaka (Ionics, Tokyo, Japan, 1986) 279-283; Timothy JP Ellison, C. Michael Fox, Steven W. Koch, *"Noninterceptive wideband pickups for measuring the properties of very low intensity beams"* Nucl. Inst. Meth., B24/25 (1987) 873-876.

[2] Mark Ball, Timothy JP Ellison, and C. Michael Fox, *"New nondestructive beam diagnostics for the IUCF Cylotron and Cooler" Proc. of the 12th Int. Conf. on Cyclotrons and their Applications*, (Berlin, 8-12 May, 1989)

THE COMMISSIONING OF THE LEP POLARIMETER

J. Badier, A. Blondel, M. Crozon
IN_2P_3, France
B. Dehning
Max Planck Institut, Munich
C. Bovet, P. Castro-Garcia, J. De Vries, G.P. Ferri, M. Glaser, C. Grunhagel,
R. Jung, L. Knudsen, F. Lemeilleur, J. Mann, M. Placidi, R. Schmidt, K. Unser
CERN, CH-1211 Geneva 23, Switzerland

Abstract A laser polarimeter has been installed in LEP to measure the transverse beam polarization. We describe the layout, the production and the control of the polarization of the laser light, the photon detector and the data acquisition philosophy. The commissioning experience in the first year of operation of the device is discussed together with recent results on the detection of transverse polarization.

1 Introduction

Studies on transverse polarization in LEP with simulation programs anticipated limitations from several effects like betatron coupling and residual vertical dispersion. A rather poor polarization level was then expected to be available by the end of the first year of LEP operation and a fast polarimeter [1] [2] capable of monitoring polarization changes of a few percent has been designed and installed as an essential tool to optimize orbit correction strategies required to improve the polarization level.

2 The Compton polarimeter

Suggested by Baier and Khoze [3] the laser polarimeter is based on spin-dependent Compton scattering of circularly polarized photons from polarized electrons or positrons.

In presence of transverse beam polarization the vertical angular distribution of the recoil high energy γ-rays shows an *up-down asymmetry* proportional to the lepton and photon polarization level, which flips sign under reversal of the handedness ξ_3 of the incident photons [4]:

$$A_T(y) = \frac{n_R - n_L}{n_R + n_L} = P_\perp \, \xi_3 \, \Pi_T(\theta', k'_o) \, \sin\phi', \qquad (1)$$

where $n_{R,L}(y)$ are the γ-rates at a vertical position y at the detector, Π_T is the transverse analyzing power while the kinematic notations are defined in [5].

The asymmetry (1) can be expressed in terms of the *mean shift* $\Delta\langle Y\rangle$ between the center-of-gravity of the two γ-distributions produced by the helicity states $\xi_3 = \pm 1$:

$$\Delta\langle Y\rangle = \kappa \, \xi_3 \, P_\perp , \qquad (2)$$

where the *mean-shift for full electron and photon polarization* κ simulated for our polarimeter is : $\kappa = 500 \pm 30\,\mu$m.

3 Layout

Quantitative considerations on background from gas bremsstrahlung and synchrotron radiation have been accounted for in [1] and guided the choice of the layout.

The 90 mJ light pulses from a 30 Hz Nd-YAG laser operated in the visible range ($\lambda_\phi = 532$ nm) and installed in an Optical Laboratory $\sim$ 15 m off the LEP tunnel are guided towards the Laser Interaction Region (LIR) over $\sim$ 115 m in a roughly evacuated beam pipe including three lenses and five multilayer dielectric mirrors. The final deflection onto the e^- beam under an angle of $2 \div 3$ mrad is provided by ($Ag + MgF_2$)-coated Cu mirrors [6]. Their position in the LIR vacuum chamber can be remotely adjusted to operate the polarimeter in parasitic mode during physics runs without affecting the beam life time nor the mirror reflectivity. Hundreds of high energy γ's per laser shot are backscattered in a 5-28 GeV range and reach the detector 247 m downstream the LIR through a 50×20 mm^2, 2 mm thick Al-window built in the modified vacuum chamber in the B1 main dipole about 225 m from the interaction point.

The upstream 10% weak dipole prevents the detector from being reached by the 56 keV critical energy synchrotron radiation from the LEP main dipoles. Proper shielding against the radiation emitted in the quadrupoles and the orbit correctors along the LSS1 straight section [1] has nevertheless to be provided.

Six TV cameras have been recently installed on the laser line for the alignment of the light beam on mirrors, windows and diaphragms.

4 The detector

Silicon calorimeters have been developed and successfully employed in 1990 [7] for the LEP luminosity monitors. Silicon strip planes behind a remotely-controlled variable-thickness lead absorber also constitute the active part of the polarimeter detector to measure the profiles of the recoil photons.

Some modifications to the calorimeter used in the 1990 runs have been performed during the '90/'91 shutdown and the new layout is shown in Fig. 1. Four strip detectors ($S_1 - S_4$) and five unsegmented pads ($F_1 - F_5$) are inserted between tungsten plates. The 40 mm $\times$ 40 mm

0-7803-0135-8/91$01.00 ©IEEE

"S" detectors have 16 horizontal strips with 2 mm pitch. The $S_{1,2,3}$ strip planes measure the vertical γ-profile and the S_4 the horizontal one. The first S_1 detector just behind 0.5 radiation lengths is intended to monitor the profile of the synchrotron radiation since any change of the mean value indicates a change of the beam position. The other detectors are installed after a 2 r.l. of tungsten.

The resolution of the polarimeter is proportional to the number of photons from Compton scattering which can vary in a wide range according to the luminosity of the laser-beam interaction. To cover this range strip detectors S_2 and S_3 are equipped with preamplifiers of different gain and they can be chosen according to the photon flux.

The five full plane "F" detectors are meant to monitor the deposited energy of the scattered photons. Three of them have preamplifier gains chosen to measure single photon energies while the other two measure the energy of multiphoton bursts.

A movable lead absorber is installed in front of the silicon calorimeter to shield the detector against the synchrotron radiation from LSS1. Absorber thicknesses of $0 \div 5$ r.l. can be selected according to the beam intensity.

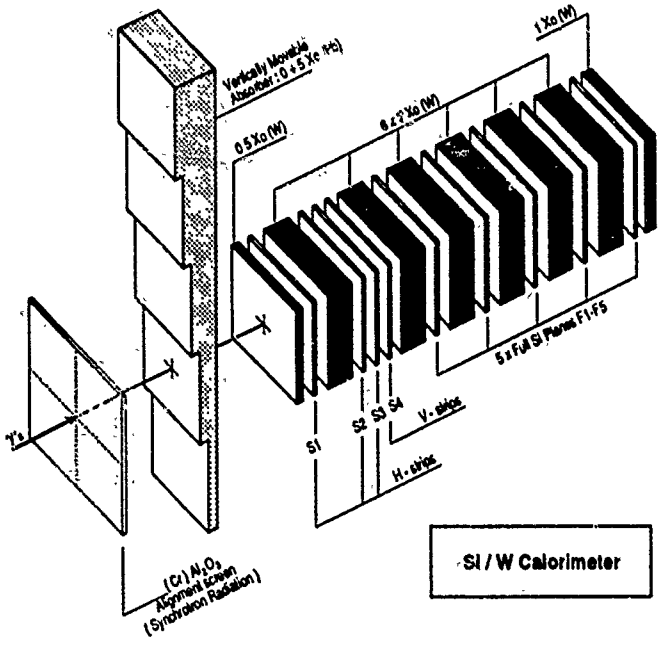


Figure 1: Schematic of the Si/W photon detector.

5 Data acquisition

The front end of the data acquisition system is based on a commercial VME board (CES8150) containing a Motorola DSP56001 Digital Signal Processor. Integrate-and-hold modules on a daughter board digitize the analog charges from the Si detectors by means of four ADC's. A 5 MHz sequencer on the DSP board controls the data flow from the daughter board to the DSP.

The data acquisition system has also been modified to improve speed and flexibility and data processing on each laser shot will be possible at a ~ 30 Hz rate.

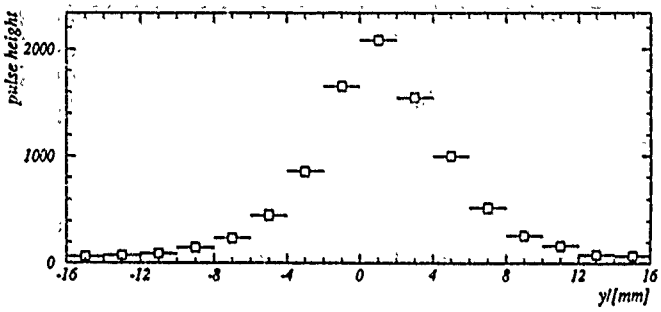


Figure 2 : Vertical profile of backscattered photons.

6 Commissioning results

Backscattered photons have been observed in the Si/W detector after e^- closed orbit correction at the LIR to steer the backscattered flux through the Al-window defining a $\pm 40\,\mu$rad vertical and a $\pm 110\,\mu$rad horizontal acceptance.

The optimum thickness of the lead absorber to reduce the synchrotron radiation flux was determined at a beam energy of 45.6 GeV.

The overlap at the LIR was optimized by varying the horizontal photon position and the synchronization between the laser pulse and the e^- bunch to the best signal at the detector. A typical vertical γ-profile at the $S1$ strip plane is shown in Fig. 2.

Special care has been devoted to the control of the polarization state of the laser photons. The *optical section* installed on a bench at the laser output was used to control the light polarization. A rotating $\lambda/2$ plate and a $\lambda/4$ plate can produce any elliptical light state, from linear to circular. Linear light has proved useful to the setting up of the polarimeter since in this case the Compton cross section does not depend on beam polarization (1). A "push-pull" $\lambda/2$ retarder introduces an additional π phase-shift, thus reversing once more the handedness. This provides a simple way to correlate the observed sign reversal in the measured mean-shift to the polarization signal.

The ellipticity of the light at the LIR was controlled in the optical section (Fig. 4) by timing the angular position of the rotating plate w.r.t. the laser pulse to compensate for depolarizing effects (reflections, birefringence etc.) from optical elements in the transport line which would spoil an initially perfect circular light.

The laser light is analyzed downstream the LIR by a combination of a $\lambda/4$ retardation plate and a dichroic polarizer. To evaluate the amount of circularly polarized light a two dimensional angle scan ($\theta_{\lambda/4}, \theta_{pol.}$) is used to determine the light minima and maxima. The measurement is done at the focus of a converging lens to avoid light intensity fluctuations from beam displacements. To be independent from shot by shot variations a non-polarizing prism splitter is used and the ratio of both light branches, with and without the plates, is considered for the calibration.

A new combined $\lambda/4$-polarizer analyzer for the laser optical section will be available for the '91 run period. A faster light polarization measuring system, where the intensity of the circularly polarized light measured after a rotating dichroic polarizer is independent of the rotation angle, will also be installed at the entrance of the LIR vacuum chamber.

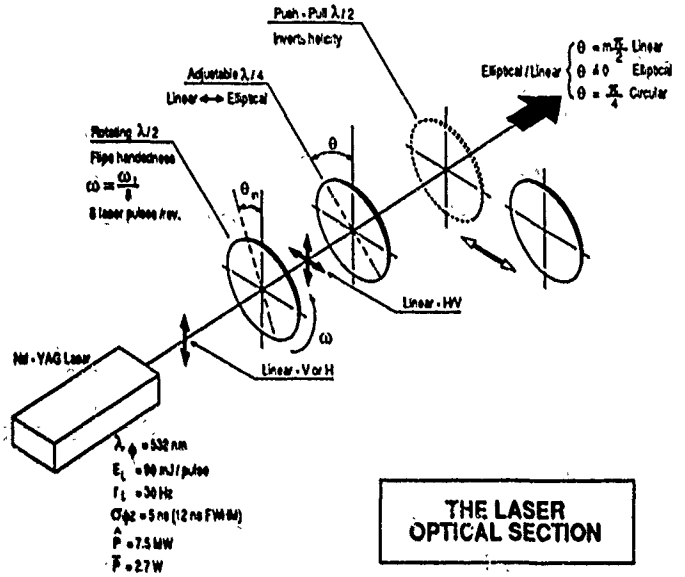


Figure 3: The optical section on the laser line.

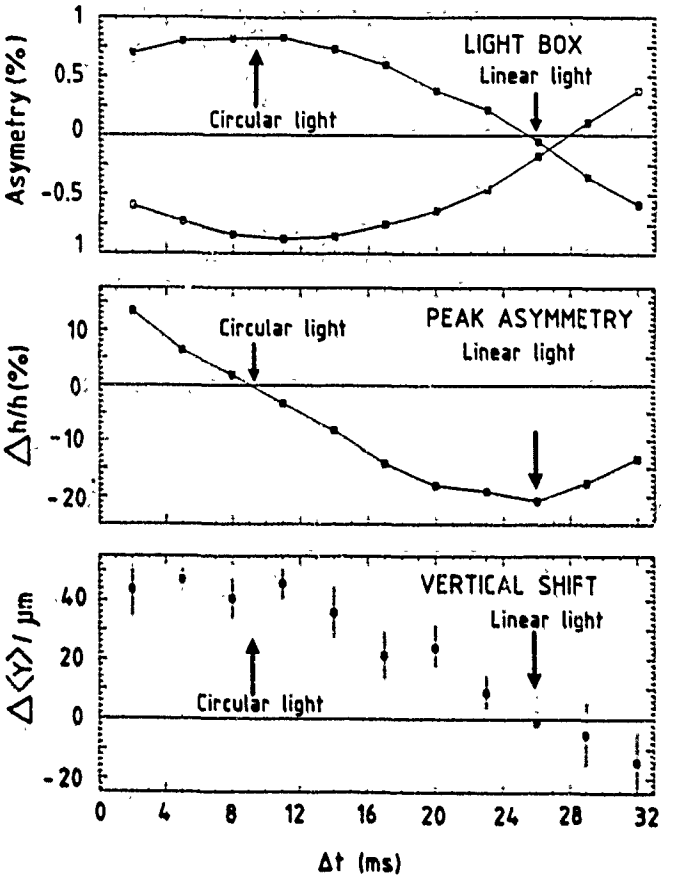


Figure 4: Degree of polarization of the laser photon states as a function of the arrival time Δt of the light pulses at the $\lambda/4$ plate.

7 Conclusions

The commissioning of the several components of the polarimeter has been carried on according to plans and with good results. Linear light proved extremely useful during the setting up of the polarimeter and the behavior of the instrument was found in agreement with the predicted performance.

The control and the optimization of the polarization states of the laser light was performed from the optical laboratory and the quality of the circular light was adequate to produce observable effects on the mean-shift of the vertical distributions.

Evidence of backscattered photons has been observed in the course of polarization-dedicated machine physics runs and first results on transverse polarization recorded [4].

8 Acknowledgments

The contribution and the skill of the many colleagues of the LEP Design office and of the LEP and ST workshops had a great impact in the realization of the polarimeter and we are indebted to them all.

References

[1] M. Placidi, R. Rossmanith, "e^+e^- Polarimetry at LEP", NIM A274 (1989) 79-94.

[2] M. Placidi *et al.*, "Design and First Performance of the LEP Laser Polarimeter", Proc. 2nd European Particle Acc. Conf., Nice, 1990.

[3] V.N. Baier, V.A. Khoze, Sov. J. Phys. 9 (1969) 238.

[4] J. Badier *et al.*, "Observation of transverse polarization in LEP", this Conference.

[5] M. Placidi, "CERN Academic Training, April 1991".

[6] The mirrors have been manufactured in the Frascati Laboratories. The fruitful collaboration with R. Habel, T. Letardi and D. Del Bugaro of the ENEA Department is gratefully acknowledged.

[7] G.P. Ferri *et al.*, "Silicon detectors used for beam diagnostics in the LEP collider", CERN/SL 90-110, October 1990.

AGS BOOSTER TUNE METER KICKERS[1]

W. Zhang, J. Bunicci, P.R. Cameron, A.V. Soukas, and W. van Asselt

AGS Department, Brookhaven National Laboratory, Upton, NY 11973

ABSTRACT

The AGS Booster tune meter kicker system consists of two identical kickers for horizontal and vertical tune measurements, and a control unit utilizing a programmable logic controller. The kicker modulators are line type pulsers. The pulse energy stored in the PFN is discharged through a set of matched cables to the load magnet and a matching terminating resistor. Some RC compensation networks are used to obtain the fast rising pulse waveforms. The Booster will be used to accelerate protons, as well as many species of heavy ion beams. Thus, it will cover a wide range of revolution frequencies. To cover this wide range, tunes will be measured by kicking the beams with two different pulse lengths. The short pulse duration is about 1 μs, and the long pulse duration is about 3 μs. A switch mode power supply with fast command tracking speed is used for PFN charging and enables the kickers to change pulse amplitudes on a pulse-by-pulse basis. The peak current is 1500 *amperes* at 20 kV. The pulse repetition rate can reach up to a maximum of 200 pulses per second (pps) at 20 kV and 2000 pps at 2.5 kV.

[1] Work performed under the auspices of the U.S. Department of Energy.

MODULATOR SYSTEM DESCRIPTION

The AGS Booster tune meter deflectors are located in the E3 section of the Booster ring, which deflect the passing beam by a pulsed magnetic field. There will be four Booster cycles per each AGS proton cycle. Each AGS FEB cycle is about 1.8 s, and 3.3 s in SEB mode. To track the beam energy during acceleration, it is desirable to have a tune measurement every 12 ms for protons, and every 60 ms for heavy ions. Thus the specifications calls for the tune measurement functions as shown in Figure 1 and Figure 2. Since the revolution time of proton varies from 729.2 ns to 1.19 μs, and it ranges from 772.3 ns to 14.08 μs in the heavy ion case, a selection of 1 μs or 3 μs pulse width kicks was specified prior to the modulator design. The acceleration duration for each proton cycle is only about 60 ms. To achieve multiple pulses with different amplitudes requires a fast charging, fast command tracking power source.



Figure 1. Tune measurement function for proton acceleration.

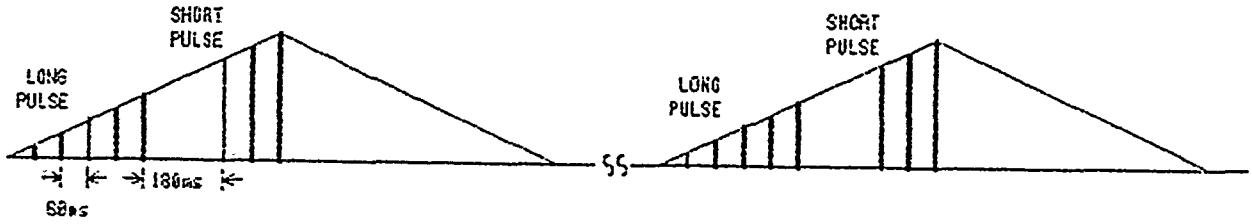


Figure 2. Tune measurement function for heavy ion acceleration.

0-7803-0135-8/91$01.00 ©IEEE

Taking advantage of the rapidly developing technology of switch-mode power supplies, the tune operation function can be achieved by adopting it as the modulator power source. A 3 *kWatts* switch mode power supply, ALE-302L, is used for this application. Its fast tracking, fast charging, and fast high voltage output inhibiting features are the main features for our application. Two identical modulators driving horizontal and vertical deflectors are line type pulsers as shown in Figure 3. Each modulator consists of two E-type pulse forming networks. The total capacitance is about $60nF$ for 1 μs PFN, and $220nF$ for 3 μs PFN. In proton operation, a high current discharge rate is required at peak energy. Therefore, we selected the EEV CX1572 thyratron as the discharging switch. The auxiliary grid supply of the thyratron is floating at the PFN high voltage level. A set of cables is used to deliver the current pulse to the magnet load and matching resistor inside the Booster tunnel. The maximum average power dissipation of each tune meter modulator for the above described operation function during the proton FEB mode or heavy ion mode is about 70 *watt*. Solid state diode stacks are used to protect power supply and cables.

At normal operation, the pulse forming network will be charged up right before discharge. To charge up the 1 μs PFN to 20 kV, the time is less than 3.5 ms. The charging time of 3 μs PFN up to peak voltage is less than 12 ms. At a fast pulse repetition rate, the charging supply will be used in a continuous operation mode. The high voltage power supply peak charging current is 500 mA. After each discharge, there is a hundred micro-second high voltage output interruption period, which is an internal function of the power supply. This gives sufficient time to allow thyratron recovery. A new command voltage level can be send to the high voltage power supply for the charging of next pulse, if desirable. During test, we have obtained a maximum pulse repetition rate up to 200 pulses per second (pps) at 20 kV, and 2000 pps at 2.5 kV. Shown in Figure 4 is the PFN charging waveforms at 2000 pps. This fast repetition rate will allow the further functional development of the tune meter kicker. It should be noticed that at this high repetition rate, average power dissipation can reach up to 4 *kWatt*, if used continuously. The system is designed for 70 *watt* average power dissipation. There are four 70 *watt* average power rated resistors used in parallel for the pulse termination, and will be cooled by forced air. Therefore, The high repetition rate operation can only be used periodically of short duration with average power dissipation not exceeding 70 *watt*.

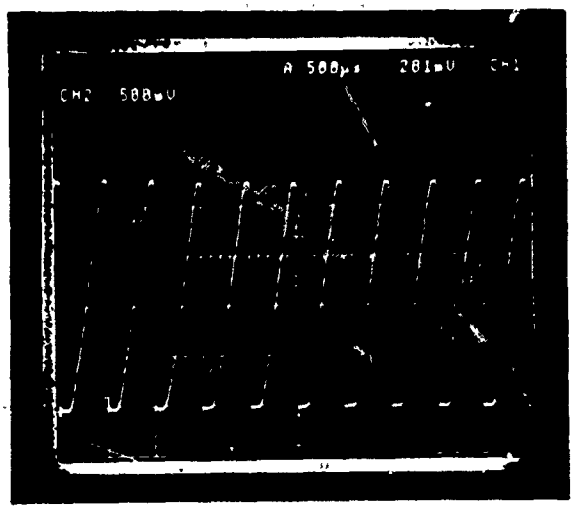


Figure 4. PFN charging wave form at 2.5 kV, 2000 pps rate.

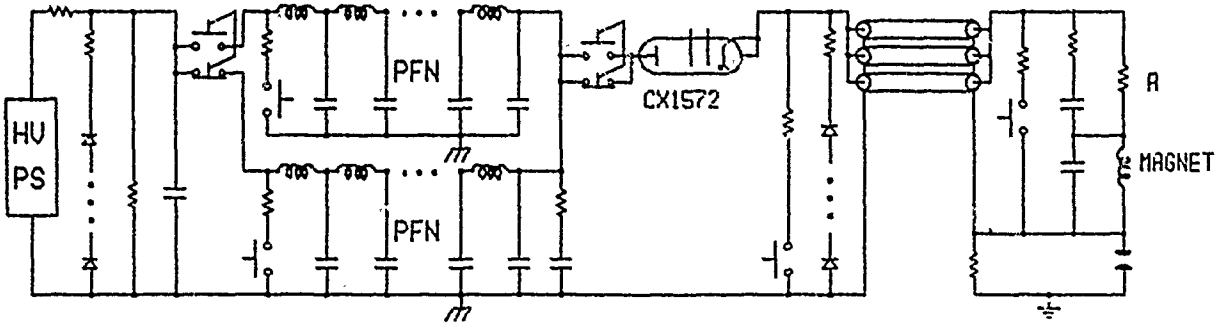


Figure 3. Tune meter modulator schematic diagram.

Two modulators can be synchronized or can be operated asynchronously. During asynchronous operation the pulse signal and noise isolation has to be controlled, to avoid false triggering. Shown in Figure 5 are the PFN charging waveforms of the horizontal and vertical modulators triggered 32 ms apart, at 20 kV in continuous charging mode.

The tune meter deflectors are the picture frame lumped ferrite magnets, located inside the same vacuum chamber. The inductance of the horizontal magnet is 1.8 μH, and the vertical magnet is 1.6 μH. Some R-C networks are used for pulse front compensation. The pulse rise time from 10% to 90% is about 140 ns for short pulse and 250 ns for long pulse. The pulse flat top at 90% lever is >600 ns for short pulse, and about 3 μs for long pulse.

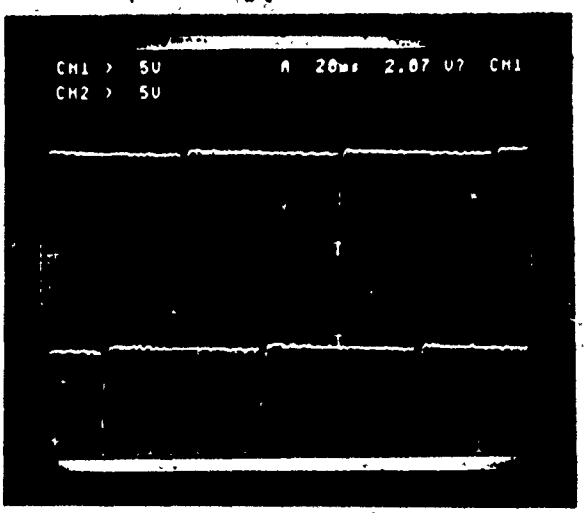


Figure 5. PFN charging waveforms at 20 kV, asynchronous operation mode.

A programmable logic controller controls both modulators, high voltage power supplies, interlock systems, and serves as a local remote station between main control and modulators. Based on the standardized AGS power supply control scheme, we use TTL input and output modules for remote control and readback; 10–60 V dc input and output modules for high voltage power supply, modulator, and interlock system control and readback; 115 V ac output module for fast 20 kV high voltage relay control. The different response times of low voltage and high voltage devices and possible pulsed noise problems have been put into consideration of the PLC software program design. The horizontal and vertical tune deflectors are usually pulsed at different times. However, the pulse interaction has not shown to be a problem for two synchronized/asynchronous high power modulators sharing the same PLC input/output modules.

The tune meter modulators have been tested with the Booster central control, and powered up to their maximum ratings with dummy coil loads. The installation and system testing are in progress.

REFERENCES

[1] "Booster Design Manual," AGS Booster Project, Brookhaven National Laboratory, 1988.

[2] A.V. Soukas, "AGS Booster Standardized Power Supply Control," AGS Booster tech. note #165, BNL, 1990.

MECHANICAL DESIGN OF THE BEAM CURRENT TRANSFORMERS FOR THE HERA PROTON RING

W Schütte - Deutsches Elektronen-Synchrotron DESY, Hamburg, Germany

Abstract

The warm sections of the HERA proton ring will be equipped with three DC and one combined fast and integrating current monitor. The toroids and associated electronics are of the Klaus Unser type [1]. Vacuum chambers with a DC gap, good RF properties and a maximum bakeout temperature of 300°C are designed. The toroids are completely passively cooled such that the toroid temperature will not exceed 70°C even for tunnel temperatures of 50°C. The DC monitor also has an extra 5-layer magnetic shield to allow high absolute accuracy in a varying magnetic environment.

I. INTRODUCTION

HERA is a complex of an 820 GeV proton accelerator and a 30 GeV electron accelerator with three common interaction regions [2]. Both rings share the 6.3 km long tunnel. The HERA proton ring itself consists of four "warm" straight sections operating at roughly tunnel temperature and the "cold" arcs with their superconducting magnets in a continuous cryostat. All current monitors are placed in the warm section and all are subject to vacuum bakeout of temperatures up to 300°C. The proton ring will contain a maximum of 210 bunches in 220 rf buckets. Each bunch consists of a few times 10^8 up to 10^{11} protons. The bunches will be between 0.3 m and 3 m long.

The current monitoring system has to supply the following information: bunch shape, fill status of the different buckets, total beam current and beam lifetime. The bunch shape is measured by two coaxial monitors with extremely wide bandwidth, the bucket fill status is measured by fast and integrating current transformers (FCT & ICT) and the last two properties are measured by up to three precision DC parametric current transformers (PCT). All three types of transformer monitors are based on toroids. The toroids with their associated electronics were developed at CERN [1] and built by Bergoz in Gex, France for us.

In the following the design of the beam current transformers shall be described. They consist of the vacuum pipe with its DC gap, two heating jackets, thermal insulation, a heat dissipating system, the toroid and in the case of the DC monitor of a good magnetic shielding.

II. THE VACUUM PIPE

It is important to choose a minimum pipe diameter to allow a simple thermal insulation. Also one needs at least one flange of moderate size to be able to mount and dismount the transformer without hazardous welding work. A 86 x 3 mm^2 pipe with a CA 100 conflat flange was chosen for the assembly side of the pipe. For the PETRA monitor a CDA 150 flange was necessary. Here the ring of the conflat flange had to be sawn into two pieces. The DC gap itself consists at the vacuum side of an alumina ring. The ceramic is brazed into the beampipe shock protected by a little bellow of two folds. The adjacent fold is made of a copper nickel alloy. It has a thermal expansion coefficient close to the ceramic one. Outside is a fold of stainless steel. Besides the added protection it allows to get the difficult and risky weld between steel and the copper alloy done early. The little, quite stiff bellow has to be relieved from all forces due to its adjacent beampipes. During bakeout the forces can be as high as 50 kp. The mechanical bypass is done by the space saving nut design shown in Fig. 1. It adds only very little to the pipe diameter. The DC gap is kept by a Vespel(r) ring. This material withstands routinely temperatures up to 260°C (shortterm up to 480°C) and has opposed to Teflon(r) an acceptable radiation resistance. The alternative Envex(r) was found to be quite brittle and the fragile ring for the DC gap is much more difficult and risky to machine precisely. The cavity between the nut and the ceramic bellow can be accessed from the outside with helium gas for leak searching by a thin steel pipe. A feature necessary for the routine operation of an accelerator.

Next we discuss the electrical properties of the beampipe. The DC gap forms with the nut design an electro magnetical cavity. The cavity was made as small as possible and the width of DC gaps were made thin to reduce the mode losses

0-7803-0135-8/91S01.00 ©IEEE

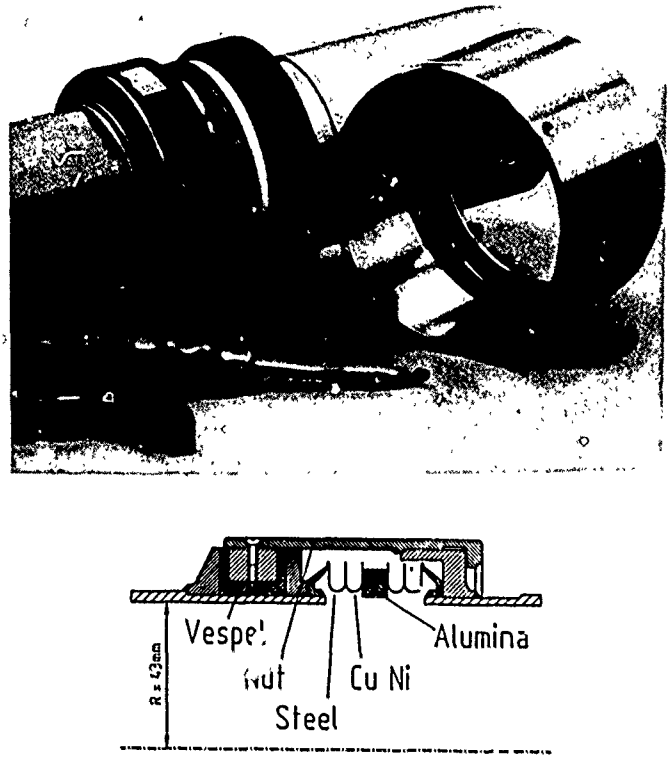


Fig. 1 Bakable DC Gap. The entire construction is secured by a stainless steel nut screwed into clamps isolated to the pipe by two thin half rings of Vespel (r). An extremely space saving design with good electrical properties.

of the beam optimally. Calculations with Urmel [4] show that gaps of up to 10 mm together with a cavity of the size of the entire toroid would still lead to acceptable impedances below 75 kΩ. At the low frequency end the resistance of the beampipe has to be less than 1 Ohm. This is done with copper braids connecting the flanges outside the pick up body. Obviously they need a good thermal isolation. Finally the pipe should not act as an RF transmitter. This is prevented by the thin long Vespel ring and the capacitance between the pipes of roughly 0.2 nF.

III. HEATING, THERMAL ISOLATION AND HEAT DISSIPATION

The current monitor station design allows beampipe bakeout at temperatures up to 300°C[1] in a 50°C warm tunnel. The temperature of the toroid will not exceed 70°C due to a totally passive and maintenance free isolation and cooling system. This is well below the maximum temperature allowed for the toroids of 80°C. Now the detailed description of the system (see Fig. 2): Each side of the beampipe is equiped with a separate heating sleave and a sensor to allow defined bakeout temperatures [5]. The necessary temperature gradient of more than 220°C requires excellent insulation over a very limited diameter range[2]. For our monitor between three and six layers of 3 mm Microtherm (r) panels were chosen leading to a 20-30 mm thick insulation. It has a heat conductivity of less than 0.03 W/Km in our temperature range. This is roughly a factor two smaller than still air.

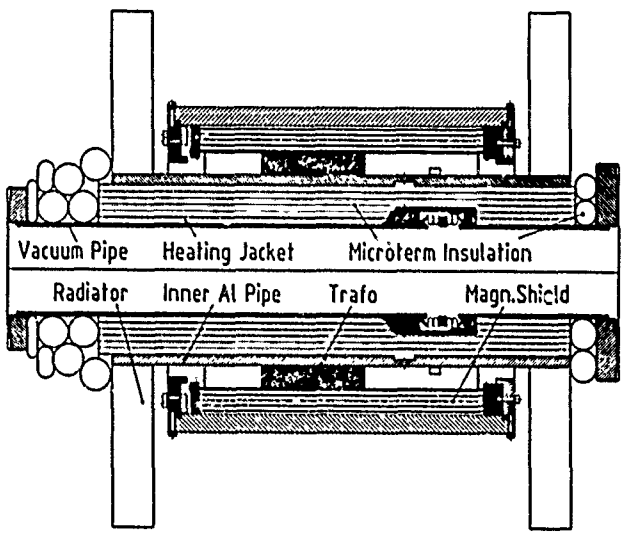


Fig. 2 Thermal design of the beampipe. The heating jackets around the pipe are isolated by microterm. The heat is conducted by the inner aluminium pipe away from the transformer to the two radiators and outer aluminium cylinder. Also the 5 layer magnetic shield of the CMPT is shown.

After getting the best insulation possible one has to dissipate the heat from the toroids efficiently. Therefore the insulation is surrounded by a 10 mm thick aluminium tube to allow the

[1]The vacuum group discusses currently to reduce the bakeout temperature to moderate 200°C.

[2]Although the more space would be helpful in our geometry the availability of considerably more space is of vanishing return in cylindrical insulation problems, since thicker insulation means higher diameter which in turn leads to a larger outer dissipation surface. Here only a material with a low heat conductivity helps.

heat to flow out of the well isolated toroidal area. The heat is then transmitted to the tunnel air by two large cooling radiators on both sides of the tube. We chose the same radiator type as used for medium sized electronic devices. Also the outer aluminium cover cylinder of the toroids constitutes an efficient radiator due to its good thermal connection to the inner aluminium tube. The entire layout requires for a 300°C hot beam pipe a tunnel temperature less than 20°C below the maximum toroid temperature. This should be even sufficient for the high tunnel temperature during bakeout after a long electron run at highest energies. As an added measure of safety there are two thermo relais in series which allow a maximum temperature of 67°C for the inner aluminium tube close to the toroids. A higher temperature will stop the heating of the monitor and the adjacent parts and an alarm will be sent to the vacuum controls.

IV. MAGNETIC SHIELDING

The DC stations need a good shielding against the varying magnetic fields of up to a few Gauß in its tunnel environment. It is basically done by five concentric Mu metal cylinders 297 mm long and 1 mm thick. Between adjacent cylinders there are air gaps of approximately 4 mm. The opening of the inner cylinder could only be closed a little because of the 10 mm aluminium tube for heat dissipation. The possible shielding of this setting is entirely limited to geometry and not to the quality of the shielding material anymore. It is for the important transversal magnetic fields up to 50 Hz better than a factor 100. The DC station for the PETRA II bypass with its extremly powerful current bars has added shielding with MU metal foils down to the beampipe. This was here and it is for the one in DESY III possible because their vacuum systems do not require a bakeout. In the design of the station we had to allow for tolerances of the cylinders higher than usual in mechanical engineering. They gave rise to quite a bit of touch up work and improvisations during the final assembly stage.

V. READOUT

The fast and integrating current monitor is located in HERA directly after the proton injection roughly 100 m inside the tunnel. It is connected to the control room West with two 7/8" coax cables for low losses over the long distance. The signals are fed into a 400 MHz digital scope, which can be accessed by the main control room via a GPIB bus. The scope screen is observed by a CCD camera and the video signal transmitted by optical cables to a screen in the main control room.

For the DC station the front end electronics is placed in a concrete shielded electronics tunnel within the storage ring tunnel next to the pick up station. Also quite some lead (15 - 30 mm) is required to keep the maximum radiation dose below the maximum allowed 1000 Rad. A long cable with many single shielded twisted pairs connects it then with the control room in the closest experimental hall. The first HERA DC station will be digitized by a precision voltmeter and read out via GPIB. The PETRA station signal is transmitted via V/f and f/V converters to the main control room. For DESY III a direct transmission via a line driver was for the beginning sufficient. Here one wishes for the future a computer readout to allow a display of the actual number of particles, since the current changes a factor of three just due to the acceleration of the modest energy protons. For both DESY III and PETRA II the DC monitors were found to be of vital importance.

VI. ACKNOWLEDGEMENTS

We are thankful to J. Bergoz, G. Dickel, R. Jung, K.-H. Meß, W. Radloff and K. Unser for helpful discussions, to G. Miat and H.P. Wedekind for help with the insulating ceramic, to T. Weiland and his old DESY group for running Urmel for us, to P. Duensing for many ideas and software support and finally to R. Hensler, F. Nowak, U. Ruesse, U. Rahtkens and S. Schollmeier for general support.

VII. REFERENCES

[1] K. Unser, "Measuring Bunch Intensity, Beam Loss and Bunch Lifetime in LEP", Proc. of the European Part. Accel. Conf., Nice 1990 p. 786 and CERN/SL/90-27(BI)

[2] B. H. Wiik, "HERA Status", Proc. of the Particle Accelerator Conference Chicago 1989 p. 431 and DESY HERA 89-11

[3] G. Lopez, "Broad Band Longitudinal Bunch Profile Monitors for the HERA Proton Storage Ring", Proc. of the Part. Accel. Conf., San Francisco 1991

[4] T. Weiland, "Urmel User Guide", DESY M-82-24, 1982

[5] J. Römer, Z. Sanok, D. Trines, A. Wyszogrodzki, "Dynamic in Situ Bakeout for the HERA Proton Ring", Vakuum 39(1989)835

BETATRON TUNE MEASUREMENT SYSTEM FOR THE HERA PROTON STORAGE RING

S.Herb
Deutsches Elektronen-Synchrotron DESY
2000 Hamburg 52 - Notkestrasse 85 - Germany

Abstract:

We describe the system of pickups, kickers, and controls which have been built for betatron tune measurements in the HERA proton ring. The Schottky-type resonant pickups should provide high sensitivity over the full range of beam currents to be used in HERA.

I. INTRODUCTION

The HERA superconducting magnet storage ring will accelerate protons from 40 to 820 GeV where they will be stored and collided against 30 GeV electrons; the design fill is 200 bunches of 10^{11} protons spaced 97 nsec apart. The tune measurement system must operate well in several very different regimes; for luminosity operation the system should be sensitive to very small oscillation amplitudes, so that emittance growth resulting from excitation of the bunches will be minimized. During setup of the machine very low beam currents will be used to avoid quenches of the superconducting magnets, but modest emittance growth will be acceptable, and strong excitation may compensate for the small currents. Another special consideration comes from the large field errors caused by superconducting persistent currents at and near injection energy, which will cause significant shifts in both the betatron tunes and the chromaticities.

II. PICKUP AND ELECTRONICS

Two pick-ups (horizontal and vertical) are mounted in the West straight section of HERA; the design (Fig. 1) is based on the Schottky monitors built for the CERN SPS proton collider [1]. Two 3 m long electrodes couple capacitively to the beam and form a resonant circuit with an external coil. A secondary loop couples the signal to a 50 Ω semi-rigid cable which ends at an electronics rack in the Halle West service building. The monitors have nominal resonant frequency 8.31 MHz and a loaded Q factor of about 180.
Fig. 2 shows an equivalent circuit. The inductor is in a closed can which also contains two variable capacitors driven by external stepping motors. One is used to tune the resonant frequency; a small coil permits injection of a test signal so that the resonant frequency can be measured. The other is a small split plate capacitor which effectively adjusts the electrical center of the monitor; it is hoped that this can be used to correct for the orbit offset of the beam in the monitor. One consequence of the resonant detector circuit is that the monitor output is an average over all bunches in the machine.

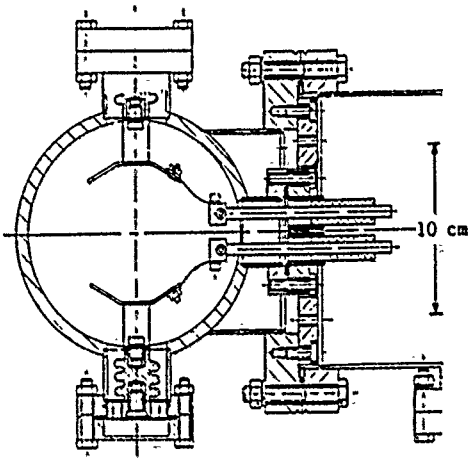


Fig. 1 Cross-section of the vertical monitor showing connection of the electrodes to feedthroughs leading to the inductor can.

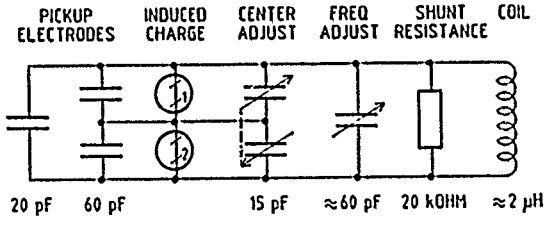


Fig. 2 Effective circuit for the monitor. The loading from the output loop is included in the shunt resistance.

Fig. 3 is a schematic of the electronics chain, which is based on a pair of 8 pole 20 kHz bandwidth elliptic quartz filters which attenuate the bunch revolution harmonic at 8.325 MHz while passing lower sidebands. The proton revolution frequency of 47.3 kHz changes by about 0.03% during acceleration, which moves the revolution harmonic by 2.3 kHz with respect to the passband.

0-7803-0135-8/91$01.00 ©IEEE

At 40 GeV this permits operation within 4.3 kHz of the revolution harmonic (dQ = 0.08) while giving 75 dB attenuation at 0 Hz offset and at 820 GeV 6.6 kHz (dQ = 0.14) and more than 100 dB attenuation. Because the system has no front end mixer or amplifier it is extremely insensitive to signals outside the passband. After amplification the signal is detected by mixing with an 8.33 MHz source generated from the 208 MHz HERA RF.

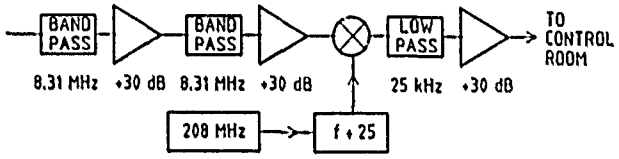


Fig. 3 Schematic of the electronics chain for the monitor

III. EXCITATION KICKER SYSTEM

The kicker system is a copy of that designed for transverse feedback on electrons in PETRA [2], and uses broadband 50 Ω ferrite magnets driven by 1 kW amplifiers to give an integrated field of 1 Gauss-m at peak power. The excitation signal is generated from a low frequency waveform which is mixed with an RF signal created from the 208 MHz HERA RF frequency, giving a single sideband output at 2.1 MHz, which is a multibunch alias of the 8.33 MHz monitor frequency. In the initial setup no time gating will be used, so that the kicker will excite all bunches in the machine; it is planned to use a sweep waveform (as for PETRA) or bandwidth-limited noise.

IV. CONTROL SYSTEM

The low frequency signals for the kicker and from the detector are connected to the HERA control room over about 500 m of RG-213 cable. Both generation of the waveform for the kicker and Fourier Transform processing of the detected signal are performed on processor cards which sit on the AT bus of the personal computer used for control and display. The computer system is very similar to that of PETRA [3], and could also be used for active control of the tunes if that becomes desirable.

V. MONITOR IMPEDANCE

A general concern for the HERA proton ring is that beam diagnostic devices may support high Q resonant modes which couple strongly to the beam, leading to instabilities or excessive heating when large beam currents are circulating, and a criterion was set that devices installed in HERA should not have any modes with longitudinal impedances larger than 100 kΩ [4]. MAFIA computer simulations were performed and laboratory measurements were made of Q and (using a bead-pull apparatus) of R/Q. The largest impedance measured was 22 kΩ for an antenna mode at 43 MHz, so the monitor satisfies the limit, but heating could be excessive if this or any of several other modes with impedances above 1 kΩ coincide with one of the multiples of the 10.3 MHz bunch spacing frequency which dominate the power spectrum for the 200 bunch filling of HERA. Since it is possible to measure these modes (and modify them by changing the coil inductance) after the monitors have been installed in HERA this should not be a severe problem.

VI. OPERATION

Boussard [5] gives a formula for sensitivity of the monitor which predicts about 7 Ω/mm (for optimal coupling of the signal). This must be compared to noise in the electronics chain; assuming 10 dB S/N degradation gives an effective input noise level at 50 Ω of 3 nv/√Hz. Thus in a 100 Hz frequency band a bunch with 10^{11} protons should yield a signal at the noise level for oscillation amplitude 8 nm, and sensitivity will increase in proportion to total beam current. If excitation at these levels is sufficient, emittance growth due to the kicker will not be an issue. The experience at the SPS collider and FERMILAB has been that when the machine is first turned on, many larger sources of excitation will be present and the monitor must be used first to diagnose and eliminate them [6].

A more relevant requirement for initial operation of HERA is that the system provide a signal 20 dB above background for a bunch with 2×10^8 protons, corresponding to amplitude 4 μm, or more if extra noise is present. This sets a scale for the excitation. The 1 Gauss-m maximum field integral of the kickers results, at 820 GeV, in an oscillation amplitude of about 1 μ at the monitors; thus a resonant excitation over 20-40 turns should easily provide an observable signal.

Because of the low fields in the superconducting magnets at injection energy, the complicated persistent current effects observed in such magnets make large contributions to the multipole field content. This results in tracking errors between the dipole and quadrupole fields during initial acceleration and in large magnet history dependent sextupole fields which must be cancelled using correction sextupole circuits. For tracking, the ability of the personal computer system to make disk recordings of the tune during the ramp should be useful. It is also planned that the PC will be able to insert small changes in the HERA RF frequency (± 400 Hz) so that measurement of the chromaticity can be automated.

A crucial point is correction of the tracking errors during acceleration; as for PETRA this must be supplied by circuits outside of the primary magnet control system. The philosophy used for the PETRA proton machine is that repeatable or predictable errors should be handled by programmed corrections rather than by feedback circuits so that successful operation of the machine does not depend on perfect operation of the tune measurement system. It is hoped that this approach will also be useful for HERA, however, the use of the personal computer should also permit a flexible mixture of programmed and feedback tune corrections if this is required.

VII. EARLY RESULTS

The first test of HERA with circulating protons has recently been concluded. Figures 4 and 5 show tune measurements taken for two different settings of a quadrupole bus, with one bunch of 10^9 protons. The beam excitation kicker is turned off, so the signals come from unknown excitation sources in the accelerator (with the exception of the low frequency noise below the 4 kHz cutoff of the filter passbands, which is pick-up of AC line harmonics). The peak amplitude of the horizontal signal at 6.9 kHz ($q_x = 0.14$) in Fig. 4 corresponds to an oscillation amplitude at the monitor of about 10 μm.

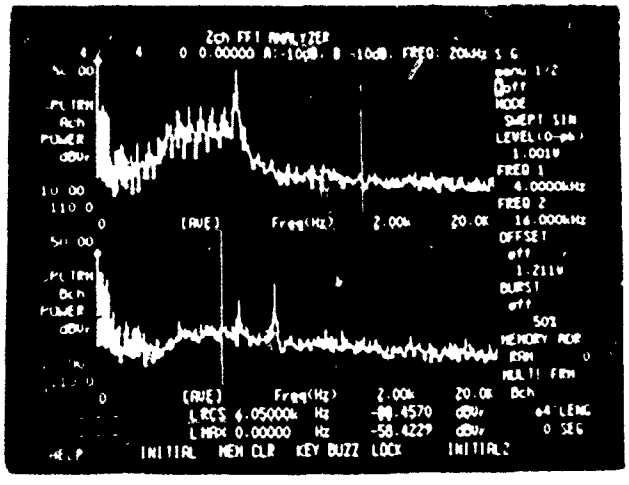


Fig. 4 Tune spectra from 0 to 20 kHz, without excitation kicker. The upper trace comes from the horizontal, and the lower from the vertical monitor. The tune values are $q_x = 0.14$ and $q_y = 0.18$.

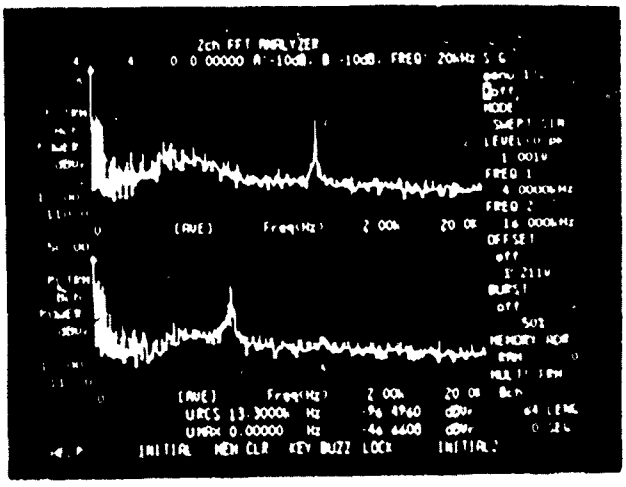


Fig. 5 Tune spectra without excitation kicker for $q_x = 0.24$ and $q_y = 0.14$.

VIII. ACKNOWLEDGEMENTS

I wish to thank D.Boussard and T.Linnecar at CERN for discussions and K.-H.Mess and D.Degele at DESY for encouragement and discussions. L.Becker contributed to the design of the electronics, and built it.

IX. REFERENCES

[1] T.Linnecar, W.Scandale, IEEE Trans.Nucl.Sci., Vol. NS-28, No.3
[2] J.Ruemmler, DESY, private communication
[3] S.Herb, submitted to this Conference
[4] T.Weiland and R.D.Kohaupt, DESY, private communication
[5] D.Boussard, CERN 87-03 (1987) 416
[6] D.Boussard, T.Linnecar, W.Scandale, IEEE Trans.Nucl.Sci., Vol. NS-32, No.5

Real Time Spectrum Analyzer

M. Bergher, E. Jules*, A. Louis-Joseph
Laboratoire pour l'Utilisation du Rayonnement Electromagnétique,
Bât. 209D, Université de Paris-Sud, 91405 Orsay Cedex, France

Abstract

A Real Time Spectrum Analyzer (RTSA) has been designed for the 50 MeV RF linac of the free electron laser named CLIO°. It displays in real time the beam distribution in 2 dimensions : energy and time with a resolution of 0.3 % and 64 sampled times respectively during the macropulse. RTSA is based on an optical transition radiation converter and linear diode array. It allows to measure the beam energy distribution along the macropulse with and without laser oscillation. RTSA includes in the same frame a 32 channels transient recorder and a digital oscilloscope with 8 bit amplitude resolution. It offers multiple presentation : 1 to 128 curves can be displayed simultaneously in montain view (3 D). Preliminary tests on a 20 MeV linac facility are reported. The results show the unique capabilities of our device to identify so as to correct the various instabilities that may appear on the operation of an RF linac. This is particulary useful for a FEL dedicated linac where the beam stability is crucial.

I. INTRODUCTION

In a RF linac dedicated to free electron laser (FEL), the laser oscillation gain depends on some electron beam parameters quality, as energy spread by the particles in the bunch. The optimum can be obtained if the operator, in control room, has opportunity to observe in a real-time display the consequences of the different parameter adjustement. The Real Time Spectrum Analyzer (RTSA) has been designed for this with good time efficiency. The RTSA has full time response, for both storage data and full graphical representations, in less than human reflex i.e. < 0.1 second.

II. DESCRIPTION

The first element of the RTSA [1] is the bending magnet which extracts the electron beam of the FEL optical cavity. It gives the horizontal spacial dispersion for the different energies particles in the beam.

The beam goes through an Optical Transition Radiator converter (OTR) made of a thin aluminum foil. This foil is stretched in a circular support, perpendicular horizontally to the nominal beam direction, vertically inclined at 45°.

The backward OTR at the specular angle is extracted through a sapphire window. The light is transmitted through a large aperture achromatic lens. The image of the dispersed beam is focused vertically by a cylindrical lens in a linear 32 photodiode array.

With a horizontal magnification of one, the energy resolution is 0.32 % and the total limit scale, 10 %.

Every photodiode has an adaptative amplifier with gain adjustment (that gives possibility to control the sensitivity of the 32 photodiodes) and a 50 Ω feed through coaxial cable bringing the signal to the control room.

All of the elements located in the radiative room are protected by appropriate shielding. 8 coaxials of successive photodiode signals are put together in 15 meters double shielded cable so as to suppress parasitic noise due to the E.M. induction synchronized with useful signal like klystron modulator pulse. 4 identical cables go through the shielded wall to the control room in a double Europe G64 crate which contains the hardware cards. The latters are managed by a 68000 microprocessor card supporting OS9 operating system. The software application has been developped in C language and based on default procedures as well as specialized keys. Overall view of the general architecture is shown on fig. 1.

A. *Specific cards*

A.1. <u>*Acquisition cards*</u> : Each card include 8 identical channels, they are designed in order to digitalise and memorise the analogic photodiode signals. A channel is made of :

- An adaptative amplifier which provides separation between the input and A/D converter.
- A sampling stage with a 8 bits flash A/D converter which operates at 6.4 MHz rate in a burst of 64 samples during the macropulse of the linac gun current.
- Then a storage memory is given with a depth of 8 K 8 bit RAM for 128 linac macropulses capability.
- Common adjustable flash A/D reference voltages are given by an annex card.

. In acquisition mode, data are loading in parrallel for the 32 channels.

. In reading and acquisition modes, data are controled via specific fast bus by synchro ; ldress card and transfered to the xzy card.

A.2. <u>*Synchroladdressing card*</u> : this double access card is programmable by the microprocessor on the G64 Bus. Synchronization, address and control signals are supplied to steer acquisition and display states by the specific fast bus.

A.3. <u>*XYZ card*</u> : Visualisation on a xyz general purpose monitor and transfer via a Fifo in RAM disc of the data are the two functions of this card. Data flow coming from the acquisition cards are treated to generate 1 to 128 curves made of 32-64 or 128 points each, according to the type of analysis wished (spectrum or temporal). Z axe is the video brightness. X and Y features axes are entirely programmable through the G64 Bus and we can act on the amplitude, the depth (for 3D presentation), the space and width of the curves. The software ensures a default configuration for each picture of

---

* Permanent address : Laboratoire de l'Accélérateur Linéaire, Bât. 200, Université Paris-Sud, 91405 Orsay Cedex, France.

° CLIO : Collaboration pour la réalisation d'un Laser Infrarouge à Orsay.

0-7803-0135-8/91S01.00 ©IEEE

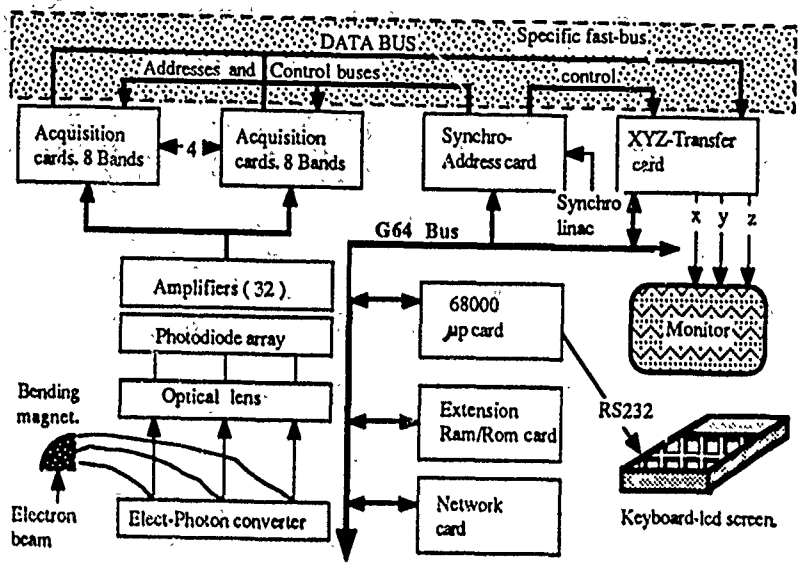


Figure 1 : Real Time Spectrum Analyzer architecture.

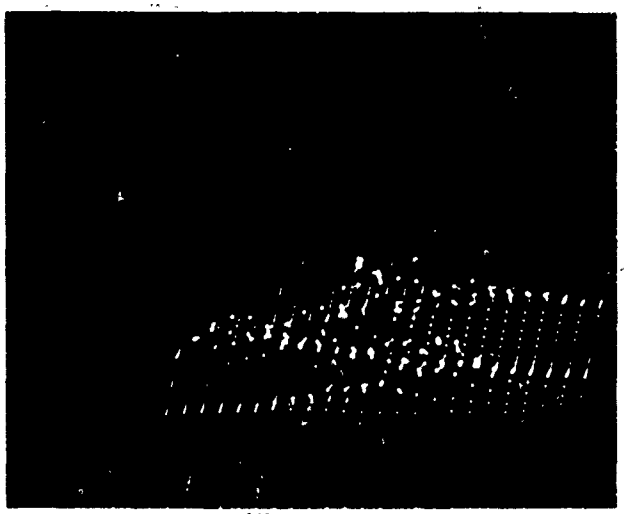
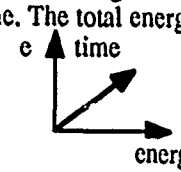


Figure 2 :
Expected energy profile during the macropulse every 156 ns sample time. The total energy scale is 3 %. .



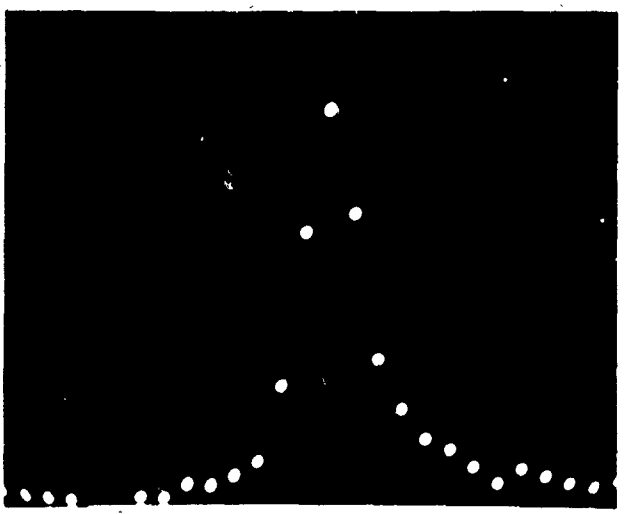


Figure 3 :
Energy spreading for particular sample time. Every dot corresponding at one photodiode signal and 0.1 % of energy dispersion.

points. X, and Z output amplitudes are settled to supply a 5 MHz bandwidth oscilloscope. Total view refreshed by recurrent read memory suppress unpleasant flicker and gives a good brightness.

B. Standard Cards

Standard microprocessor and extension Ram or Prom are needed to operate the system. Software application is in the extension Prom and Ram and are used for the safekeeping data. Exploitation of the whole may be done either through a terminal (VT100-200...) or a little keyboard with 8 rows of 40 characters.

C. Hardware and software design

Hardware and software are designed to support varied acquisition and display modes as well as transfer and optional functions. Users, choosing different "menus" realize the desired orders independantly of the running acquisition or display state. Three types of acquisition are allowed and all of them are released by a synchro pulse coming from the Linac machine.

a) Recurrent Mode

Each macropulse (10 µs lenght) is numerised and unfold the previous one. Spectrum or oscilloscopic display is offered in real time until the operator decide an another mode.

b) Single mode

Only one macropulse is acquired and displayed in a permanent way.

c) Multipulse mode

We numerise 128 macro-pulses (10 µs lenght -50 Hz repetition) while displaying each one then wire automatic stop and cyclic display (on the 128 macro-pulses) occurs.

Remembering that each macro-pulse is numerised in 64 samples on 32 energy bandwidths and this for 128 macropulses, 6 modes of visualisation are possible, offering 2 spectra or 4 temporal analysis ways. By default, spectrum display takes place. Some options make exploitation easier such as overbrightness x and/or y axes, to select curve for zooming or to access other viewes, curves number and extension, 3 dimension presentation, delayed acquisition and so on.

Remarks :

1) Analysis time can be extended by masking 2 to 127 synchro pulses of linac.

2) By a single 32 input relays commutator we can observe 32 different scaled signals given by pick-up along the linac like : intensity, xy positions, transverse sizes, direct and reflected RF power in the different accelerating structures, and so on.

We have tested [2] the RTSA on LAL 20 MeV linac facility(*). The sensitivity according to the prediction [3], [4] is less than a factor 2. (Results are affected by the lack of the definitive mechanical device).

The total noise is equivalent to 0,1 mA (CLIO nominal macropulse current is 200 mA RMS).

With the RTSA we have detected in the discret delay line of the modulator klystron, a bad adjustment of the sefs wich gives an oscillation in the beam energy particles during the macropulse (See fig. 2).

The best resolution obtained at one precise time during the macropulse is 0.2 % (See fig. 3).

III. CONCLUSION

The RTSA helps to obtain the optimum Linac adjustments and to observe different types of instability, i.e. temperature variations, magnitude and phase fluctuation of the RF power klystron, and so on. Its use on the CLIO machine will not miss to be effective as far as adjustment optimisation and pre-recorded treatment of the energy spread are concerned .

IV. REFERENCES

[1] A. Louis-Joseph, "Analyseur d'énergie du faisceau d'électrons pour le laser CLIO", Mémoire d'Ingénieur CNAM, Mai 1990.

[2] "Vérification du fonctionnement de l'analyseur de spectre de CLIO sur la station d'essais NEPAL, unpublished.

[3] "Rapport d'étude du projet de laser à électrons libres sur accélérateur linéaire HF 3 GHz : CLIO, LAL/IN2P3, LURE/CNRS/MEN/CEA.

[4] L. Wartski, "Etude du Rayonnement de Transition", Ph D Thesis, April 76, Université de Paris-Sud, p 31.

(*) NEPAL : Nouvelles expériences pour les Accélérateurs Linéaires.

A Frequency Tracking Synthesizer for Beam Diagnostic Systems

D. Peterson and J. Marriner
Fermi National Accelerator Laboratory *
P.O. Box 500
Batavia, Illinois 60510

Abstract

This paper describes a synthesizer scheme combining digital and analog synthesizer techniques to allow tracking of signals during acceleration. Virtually any ratio of synthesizer to beam revolution frequency may be generated by this scheme. Details of hardware and measurement results are presented.

I. INTRODUCTION

In low and medium energy synchrotrons the beam revolution frequency changes by a large factor during the acceleration process. High production rates require that these machines cycle rapidly. In attempting to diagnose instabilities which develop during the acceleration process it is useful to be able to select some frequency segment between revolution harmonics for viewing. Most types of test equipment operating in the frequency domain, such as spectrum analyzers and network analyzers, are not suited to making direct measurements on such rapidly sweeping signals. Ideally, one would want to set the frequency frame of reference to the spot in the accelerating revolution harmonic domain where the measurements are to be made. A scheme using a direct digital synthesizer (DDS) was developed to provide this moving reference frame.

II. THEORY OF OPERATION

The key to this tracking scheme is a DDS is used as an arbitrary ratio generator. Any type of frequency synthesizer and even digital divider circuits can be used to generate an output frequency which is proportional to the input frequency. For example, a phase locked loop (PLL) synthesizer generates an output which is related to the input clock frequency as

$$F_{out} = (F_{clock} * J) / K \qquad (1)$$

where J and K are integers, typically

$$1 \le J, K < 2^{15} .$$

Even though the frequency resolution of a PLL circuit would be sufficient for many applications, the main disadvantage for fine steps is the analog bandwidth of the loop filter must be proportionately narrow. This results in long settling times and frequency errors when attempting to lock to a rapidly sweeping clock frequency. The output phase noise of a PLL synthesizer increases if the loop is disturbed.

The DDS consists of digital adders, latches to hold the output of the adders, some type of sine conversion (a lookup table or algorithm), an output digital to analog convertor (DAC) connected to the most significant bits, and (usually) an analog low pass filter [1]. The system bandwidth is high and the total delay through the synthesizer is primarily due to the output filter. The close-in phase noise on the output of the DDS is equal to that of the input clock. The input digital word sets the phase accumulation per clock cycle and the rate at which the latch is clocked sets the phase update rate. Thus the output frequency is determined by the input digital word and the latch clock rate. The DDS output frequency can be expressed as

$$F_{out} = (F_{clock} * N) / 2^{M} \qquad (2)$$

where F_{clock} is the latch clock frequency and N is the digital input word value which can be any integer between 0 and $2^{M}-1$. M is 32 for most commercially available units. One can see that virtually any ratio of input to output frequencies can be created. The number of bits used in the output DAC determines the signal to spurious ratio (6 dB per bit). Low frequency DDS units typically use 12 bit DACs and high frequency units use 10 bit or 8 bit DACs. The primary limitation of the clock speed is the DAC. A practical limit to the output frequency of the DDS is roughly 0.4 times the clock rate. A low pass filter is required on the output to reduce clock harmonics and the upper image. This image frequency behaves as

$$F_{image} = F_{clock} - F_{out} \qquad (3)$$

Equ. 3 shows that as the input digital word value increases (causing an increase in output frequency for a given clock rate) the image frequency will decrease in frequency until the two signals eventually meet at half of the clock frequency. One could use this image frequency for driving test equipment if frequencies are needed above half the clock rate. Other methods

*Operated by Universities Research Association Inc., under contract with the U.S. Department of Energy.

0-7803-0135-8/91$01.00 ©IEEE

of obtaining higher output frequencies are to use frequency multipliers before or after the DDS unit. These will be discussed in the next section.

The net result of this is if the input clock frequency is a harmonic of the beam revolution frequency then the output frequency will also track proportionally. One can set the digital input word of the DDS to the desired value and clock the unit from the accelerator RF system and generate signals which will track with the accelerating frequency domain.

III. HARDWARE IMPLEMENTATION

The initial test unit used a Qualcomm 2334 DDS evaluation board [2]. The DDS chip used has a maximum recommended clock rate of 50 MHz (although our particular unit runs fine up to 54 MHz) and the input frequency word is entered from a standard computer terminal through an RS-232 port on the board. A 10 bit DAC provides better than 60 dB signal to spurious ratio at the output. The evaluation board was designed for 30 MHz operation and therefore has a 12 MHz low pass filter installed. Most preliminary tests were done below this frequency.

Eventually it was desirable to generate frequencies above 12 MHz and so two external tripler circuits were added for higher frequency tests. The triplers tended to be difficult to align and the output contained many harmonics and sub-harmonics so a PLL output multiplier was used on later circuits. It is perfectly acceptable to use a PLL at this point in the circuit because the DDS has taken care of the fine resolution requirements and provides the PLL with a reference frequency of a few MHz. The PLL filter can be fairly broadband and thus will track the changing clock frequency very accurately. There is some degradation of output signal to noise ratio but it is still within the requirements of the system.

The various components required for the tracking synthesizer are incorporated into a printed circuit board version which uses an STEL-1375A DDS unit and a Qualcomm Q3036 PLL as the main components [3], [4]. Input buffers allow for frequency programming either from a 32 bit parallel input or from a microprocessor bus configuration. The PLL multiplier value is set using on board DIP switches. The board configuration allows for outputs to be generated directly from the DDS unit or from the PLL voltage controlled oscillator (VCO). For most of our applications the Motorola MC1648 VCO chip is adequate for the desired frequency range. Other commercial VCO units could be substituted for higher frequency operation [5]. A simplified block diagram of the tracking synthesizer board is shown in Fig. 1. Table 1 lists the synthesizer parameters. The addition of a multiplier (before or) after the DDS increases the minimum step size by the multiplication factor. In most cases this is not a problem. For example, using a 53 MHz clock rate the minimum step size out of the DDS is 12.3 milliHz. A multiplication factor of 81 would still give 1 Hz resolution.

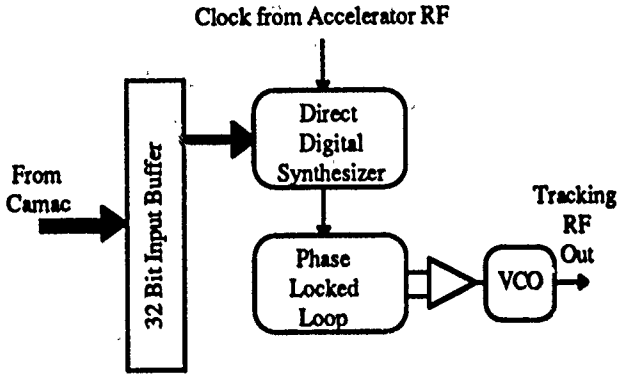


Fig. 1. Simplified block diagram of tracking synthesizer board.

Table 1
Tracking Synthesizer Parameters

Input frequency control	32 bit parallel or microprocessor bus
Maximum clock freq.	60 MHz
PLL multiplication	1 to 1295
Frequency resolution	1 part in 2^{32} / PLL factor
Output frequency range	DC to 24 MHz continuously, or octaves to 175 MHz (1.6 GHz with other VCOs)
Spurious outputs	< -55 dBc

An alternative to using a PLL or multiplier chain after the DDS unit would be to multiply the clock (by a factor of 20 or so) and use a much higher speed DDS unit. Commercial units are presently available with input clock rates up to 1 GHz [6], [7]. Advantages to this scheme are the need for only one multiplier design per accelerator and the ability to produce any desired output without changing circuit components. Disadvantages are the proportionally higher cost of the high speed DDS units and the limits to the DAC technology for output signal to noise ratio.

IV. APPLICATIONS

The tracking synthesizer scheme is used for studying coupled bunch modes in the Fermilab Booster [8]. In this installation the synthesizer provided the reference frequency for a network analyzer. Some pertinent Booster parameters are given in table 2.

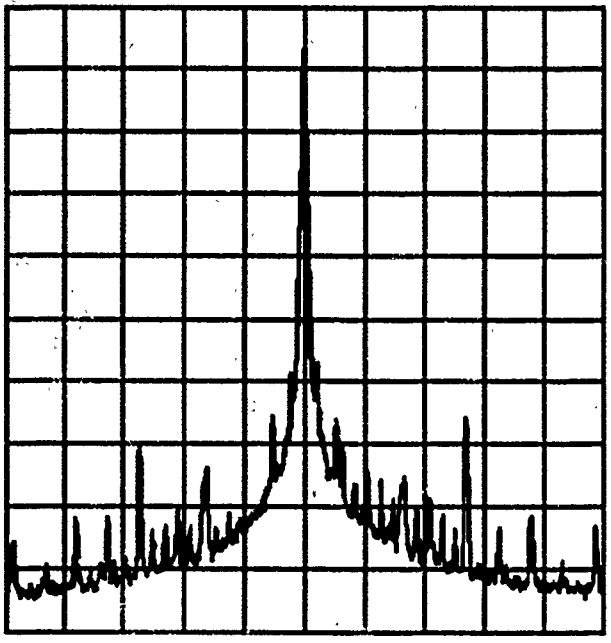
Since acceleration in the Fermilab Booster is dictated by the resonant characteristics of the magnets, the RF frequency is generated by a VCO which is in phase and radial position feedback loops.

Table 2
Fermilab Booster Parameters

Injection energy	200 MeV kinetic
Extraction energy	8.0 GeV kinetic
Circumference	474.2 meters
Cycle rate	15 Hz
RF frequency range	30.3 - 52.8 MHz
RF harmonic	84
Maximum frequency rate of change (@H=84)	5 GHz/sec

The magnetic field varies sinusoidally and therefore the RF frequency change is maximum near the beginning of the acceleration cycle. Also note that the frequency changes by a factor of 1.74 during the cycle. The tracking synthesizer works well for following such a rapidly changing signal.

Another installation which does not have nearly the slew rate requirements is the Tracking Emittance Monitor system in the Fermilab Antiproton source [9]. There the maximum frequency change is currently about 2.5% and occurs over a period of minutes for the E760 deceleration [10]. Fig. 2 shows the output spectrum from the tracking synthesizer for this installation.



Vertical = 10 dB/div. Horizontal = 100 kHz/div.
Center = 77.992 MHz.

Fig. 2. Output spectrum of tracking emittance monitor synthesizer board.

Future installations include general test oscillators and a longitudinal damper system for the Fermilab Booster [11].

V. Conclusion

A synthesizer scheme combining digital and analog synthesizer techniques to allow tracking of signals during acceleration is shown. This synthesizer makes use of the extremely fine frequency resolution of the DDS. It has been shown to track rapidly changing RF sources quite well and allowed measurements of various beam phenomena.

Acknowledgement

The authors wish to thank Pat Sheahan for his construction of the test units and the circuit boards. Thanks also to the members of the Fermilab Antiproton Source and Booster departments for their helpful suggestions and assistance in the testing of the synthesizers.

References

[1] D. A. Sunderland *et al.*, "CMOS/SOS Frequency Synthesizer LSI Circuit for Spread Spectrum Communications," IEEE Journal of Solid-State Circuits, Vol SC-19, No. 4, August 1984, pp. 497-505.

[2] "Direct Digital Synthesis, 21 Questions and Answers for RF Engineers" and Q2334 Direct Digital Synthesizer data sheet, Qualcomm Incorporated, San Diego, California.

[3] STEL-1375A 32-Bit Resolution Modulated Digital Direct Frequency Synthesizer Thick-film Hybrid data sheet, Stanford Telecommunications Inc., Santa Clara, California.

[4] Q3036 1.6 GHz PLL Frequency Synthesizer data sheet, Qualcomm Incorporated, San Diego, California.

[5] VCO Synthesizer Product Catalog, Z-Communications Inc., Fort Lauderdale, Florida.

[6] *The DDS Handbook*, Second ed., Stanford Telecommunications Inc., Santa Clara, California, July 1990.

[7] Frequency Synthesizers, Short Form Catalog, Sciteq Electronics Inc., San Diego, California.

[8] D.McGinnis, J. Marriner, V. Bharadwaj, "Network Analyzer Measurements of Accelerating Beam in the Fermilab Booster," *Proceedings of the 1991 Particle Accelerator Conference*, San Francisco, California, May 1991, session KRA42.

[9] D. Peterson, "Schottky Signal Monitoring at Fermilab," *Proceedings of the 1990 Instrumentation Workshop*, Fermilab, Batavia, Illinois, October 1990.

[10] V. Bharadwaj et al., "The Use of the Fermilab Antiproton Accumulator in Medium Energy Physics Experiments," Fermilab TM-1527, *Proceedings of the European Particle Accelerator Conference*, Rome, Italy, June 7-11, 1988.

[11] I. Haberman and I. Rypshtein, "Longitudinal Damping System for the Fermilab Booster," *Proceedings of the 1991 Particle Accelerator Conference*, San Francisco, California, May 1991, session KSC16.

THE AGS BOOSTER BEAM LOSS MONITOR SYSTEM*

E.R. Beadle, G.W. Bennett, and R.L. Witkover
AGS Department, Brookhaven National Laboratory
Upton, NY 11973

ABSTRACT

A beam loss monitor system has been developed for the Brookhaven National Laboratory Booster accelerator, and is designed for use with intensities of up to 1.5×10^{13} protons and carbon to gold ions at 50-3 x 10^{9} ions per pulse. This system is a significant advance over the present AGS system by improving the sensitivity, dynamic range, and data acquisition. In addition to the large dynamic range achievable, it is adaptively shifted when high losses are detected. The system uses up to 80 argon filled ion chambers as detectors, as well as newly designed electronics for processing and digitizing detector outputs. The hardware simultaneously integrates each detector output, interfaces to the beam interrupt systems, and digitizes all 80 channels to 12 bits at 170 KHz. This paper discusses the design, construction, and operation of the system.

ARCHITECTURE

The AGS Booster Radiation Loss Monitor (BRLM) system incorporates several features of the AGS radiation loss monitor system and provides new capabilities.[1][2] The most unique feature of the BRLM is the adaptive dynamic range limit, where the upper limit of the measurement range is increased with the lower limit and resolution fixed. Therefore, high loss levels that would otherwise saturate the processing electronics are tracked. This system also supports multiple users, each with multiple data windows per Booster cycle.

The hardware block diagram is shown in Figure 1. The detectors are biased at 200 VDC. The bias is developed using a dc/dc conversion circuit that directly couples the detector to the measurement electronics. The cables connecting the bias supplies to the detectors are triple-shielded coax (Belden 9054) and provide a shielding effectiveness of 110 db. The analog integrators accumulate the charge generated in the detector. The integrator circuit input resistance, in parallel with the signal cable capacitance, impacts the response time for the system. Therefore, the input resistance of channels in the injection and extraction locations has been selected to be compatible with use in the beam interlock functions. The integrators have two gain settings and the full-scale output at low gain measures a 10% localized beam loss at full energy without saturating the integrator.

Following the integrators is a commercial VME bus based data acquisition system (Datel, Inc.) consisting of several multiplexing S/H cards (Datel DVME 645) and an intelligent A/D board (Datel DVME 601). The system is configured for 80 channels and is expandable to 256 channels. The A/D card locally controls the entire acquisition process using preprogrammed firmware and the analog expansion bus. The channels are simultaneously held, sequentially digitized and written to the onboard dual port memory coded as bipolar 2's compliment. Additionally, the system accepts the circulating beam monitor which provides a measure of the beam intensity when the loss data is acquired.

A communications link (Bit 3 Corporation) transparently transfers the data between the Multibus instrument controller and the VME bus data acquisition hardware and provides the bus arbitration logic for the VME system. The translator presents the dual ported VME memory as local memory to the Multibus processor.

The comparator block provides threshold detection for the integrator outputs. The comparator outputs are used by the channel mask and interlocking functions. The threshold levels for each channel are individually adjustable. For transfer line channels, the thresholds will be set by operational requirements and other channels have their threshold nominally set at 80% of the ADC full-scale input.

The channel mask allows selected channels to be inhibited from requesting scan triggers. This is useful for disabling malfunctioning channels which may continually request the ADC to scan the system or to inhibit high loss channels from generating scan requests, allowing "zooming" to view low loss channels. Any or all of the channels can be disabled in software. The injection channels are not part of the mask because multiple ADC scans cannot be performed on the time scale of injection.

The beam interlock functions primarily include channels located in the transfer lines, although any other

*Work performed under the auspices of the U.S. Department of Energy.

0-7803-0135-8/91$01.00 ©IEEE

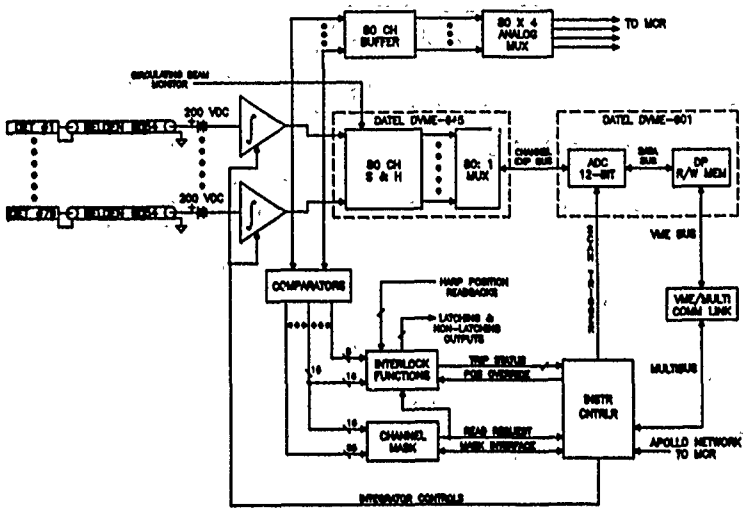


Figure 1. BRLM system block diagram.

channel may be "patched" into these systems. The interlocks are intended to prevent damage to the accelerator from a poorly steered or focused beam. There are two systems: the non-latching and latching beam interlock systems. The non-latching system causes the Linac injection pulse, 200 μs nominal, to be shut off at the ion source within 10 μs of detecting a high loss. The non-latching output is active only during injection and is formed by ORing the injection line detectors and the channel mask output. This system is automatically reset by the Booster timing system at the start of a new cycle. The latching system trips an external hardware latch, inhibiting injection into the Booster until a manual key switch is cleared. In this system, extraction line detectors are used, although provision for monitoring the ring channels via the channel mask output during extraction is included. There has also been provision made for sensing conditions when losses may be high such as those caused by beam invasive measurements. The BRLM system monitors the position of these devices and can selectively disable the interlocks until the measurement is complete.

ADAPTIVE DYNAMIC RANGE

The combination software and hardware generated read requests are used to implement an adaptive dynamic range. The system is adaptive in the sense that it responds to changing or unexpected loss patterns without losing data. If only software control was used, one or more channels might exceed the ADC full-scale limit between requests and some data would be lost. The comparators flag the condition that at least one channel is approaching the ADC full scale and the flag is processed by the channel mask to establish that it originates from a detector designated to generate read requests. If so, the flag is forwarded to the instrument controller as a read request. The controller then arbitrates, if necessary, between software and hardware sources before producing a scan trigger. In either case, the acquisition process is triggered, the integrators are reset to zero and continue to accumulate data. It is possible to have multiple hardware-generated triggers bracketed by software requests. The number will depend on the spatial and temporal loss character. However, the time required between scans is approximately 2 ms. This includes the ADC scan time and overhead in the controller. Each scan is stored as a table and sent to host. When the Booster cycle is complete, the host software assembles the individual scans into the time intervals requested by the users. Although the ADC limits the instantaneous dynamic range and resolution on each scan, the total dynamic range is bounded by the word size of the processor summing the individual scans. The dynamic range on each scan is the ratio of the data accumulated in the highest channel to one count. The single count represents the converter resolution. However, for channels with low count totals, the relative accuracy of the measurement decreases as the number of scans increases.

DETECTOR DESIGN AND MOUNTING

The detector is a coaxial ionization chamber made with an Andrews Corporation RG318 style Heliax cable pressurized with Argon to 10 psig. Most of the detectors are 5 meters long, although other lengths are also used. The detector is capped on one end with a standard bicycle valve as a pressure fitting. On the other end is a rexolite

UHF connector for the signal output and bias input. Rexolite is used because of its radiation resistance. The detectors are mounted close to the median plane on the inside tunnel wall cable tray approximately 30" radially inside the reference orbit. Median plane mounting maximizes the detector sensitivity and the cable tray provides constant geometry with respect to the central orbit while not blocking access to the magnets and beam pipe. In locations where the tunnel walls fall away from the beam pipe, special mounting stands are used to maintain the detector geometry. In the ring, there are 48 detectors, each spanning one half-cell with the ends of the chambers overlapping slightly at the middle of each dipole magnet reference location. In addition, there are 16 more detectors, 8 in each transfer line. These detectors are positioned below the beam line on the support girder, resulting in potentially less sensitivity than on the beam plane, but experience with similar devices shows the sensitivity is still adequate. There is also provision for mounting up to 15 auxiliary detectors to be located at arbitrary locations in the Booster and transfer lines as required.

CONTROLS INTERFACE AND SOFTWARE

The control for the system is provided by the instrument controller. It is a dual processor system, with one processor for I/O and the other for communications. The communication processor has a DMA channel between the controller and network station. The station connects to host computers using a token-ring LAN[4].

The software provides the user with control over the programmable scan times, display of data, channel mask, and overrides. Several graphical and numerical displays are available to the user, with the ability to overlay one cycle atop the other. The software also assembles the time sampled detector data for each user and schedules the programmed resets to avoid conflicts. There is also a standard user called the background logging task. This task runs continually to maintain a record of the machine operation. As an addition to this task, the ability to generate and display the mean and standard deviation for losses both spatially and in time are being considered. These parameters can be used to inhibit the machine when loss conditions deviate from acceptable limits. In addition, recent data is stored providing diagnostic aspects similar to an aircraft flight recorder. Several acceleration cycles of loss data will be buffered in a FIFO. At any time, the data can be "played back" to look for indicators of poor performance, or as diagnostic information for checking other systems.

COMMISSIONING

The BRLM hardware, detectors, and software were initially tested during Booster commissioning. The LTB detectors displayed a higher than expected sensitivity. As commissioning continues, the sensitivity will be quantified. Figure 2 shows the output of a single detector as monitored in the AGS Main Control Room. The detector is measuring a small loss at approximately 5% of the nominal Linac current. The loss correlates to the measured beam position errors. The non-latching interlock system was tested and functioned properly by promptly turning off the beam. The mask was successfully used to prevent hardware trips from triggering data acquisition. Hardware and software triggered ADC scans were observed in the same machine cycle. The software has allowed control of the functions to operate the system and has tabulated multiple scans correctly.

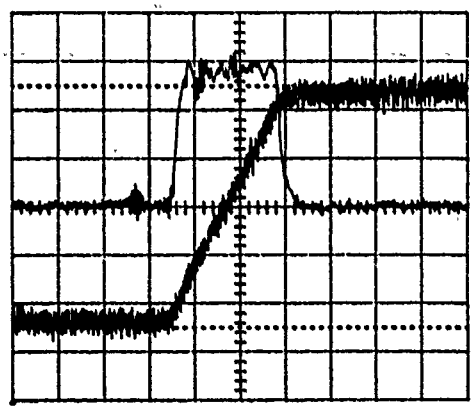


Figure 2. Detector output. Top: Linac output 0.5 mA/div. Bottom: Detector output 50 mV/div. Time scale: 10 μs/div.

REFERENCES

[1] R.L. Witkover, Microprocessor Based Beam Loss Monitor System for the AGS, IEEE Trans. Nucl. Sci., 3313-3315, June, 1979.

[2] E. Beadle and G. Bennett, The AGS Booster Radiation Loss Monitor System, Workshop on Accelerator Instrumentation, October 1-4, 1990.

[3] G. Bennett, E. Beadle, V. Castillo, R. Witkover, The Upgraded Ring Loss Radiation Monitoring System at the AGS, Proc. 1989 PAC, Chicago, IL, March, 1989.

[4] A. Stevens, T. Clifford, R. Frankel, Distribution of Computer Functionality for Accelerator Control at the Brookhaven AGS, IEEE Trans. Nucl. Sci., NS-32, 2023 (1985).

A WIDE BAND SLOT-COUPLED BEAM SENSING ELECTRODE FOR THE ADVANCED LIGHT SOURCE (ALS)*

J. Hinkson, K. Rex

Accelerator and Fusion Research Division
Lawrence Berkeley Laboratory
University of California
Berkeley, California 94720

Abstract

Stripline electrodes (traveling wave electrodes, directional couplers) are commonly used in particle accelerators as beam pickups and kickers. The longitudinally symmetric stripline has a constant beam coupling impedance as a function of length and has a characteristic magnitude sin(x) amplitude response in the frequency domain. An exponentially tapered stripline provides nearly constant coupling impedance vs. frequency and yields superior frequency-domain performance. In practice it is difficult to construct either of these devices for broad-band performance because of the transition from coaxial to stripline geometry. We report on the construction of an exponentially-tapered, slot-coupled "stripline" which was relatively easy to construct and has the desired frequency response.

I. INTRODUCTION

Part of the ALS booster synchrotron beam diagnostics system includes three stripline assemblies; a kicker and two pickups. The kicker will be used to excite the beam during fractional betatron tune measurements. The pickups will be used in the tune measurements and as general purpose, broad-band beam diagnostics. We wished to use exponentially tapered striplines in the pickups because of their superior frequency domain performance. With prototypes we had trouble holding mechanical dimensions which were important for impedance reasons. We also had difficulty with the transition from coaxial to stripline geometry. To overcome these problems we developed a slot-coupled "stripline".

II. THEORY

We show equations and calculations for ordinary striplines before discussing the slot-coupled stripline. Stripline pickups used in accelerators couple to the electromagnetic fields produced by the beam. Stripline kickers act reciprocally of course and produce fields that influence the beam. Figure 1 shows a typical stripline. The stripline electrode is held at the proper distance from the beam pipe wall by the center conductor of a coaxial vacuum feedthrough. In the case of stripline kickers feedthroughs are generally used on both ends. The down-stream feedthroughs in stripline pickups are often replaced with metal posts (shorts).

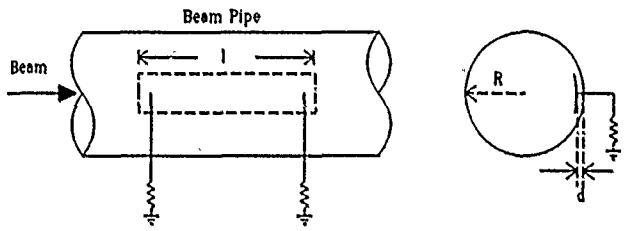


Fig. 1 Typical Stripline

The separation between the stripline and the wall is usually set at 1/5 the stripline width for 50 ohm self-impedance. In the following example the width is taken as 5 times the separation, d. The magnitude of the coupling impedance[1] of a longitudinally symmetric stripline to a relativistic beam in a round pipe (as a function of frequency) is:

$$Z_c = 60 \ln\frac{R}{R-d} \sin\frac{2\pi l}{\lambda} \qquad (1)$$

where R is beam pipe radius, d is stripline-to-wall distance, l is stripline length, and λ is wavelength.

The calculated frequency response of a typical stripline is shown as a sine curve in figure 2. Here the electrode length is 150mm, the spacing is 2.54mm, the beam pipe radius is 30mm, and the width is 12.7mm.

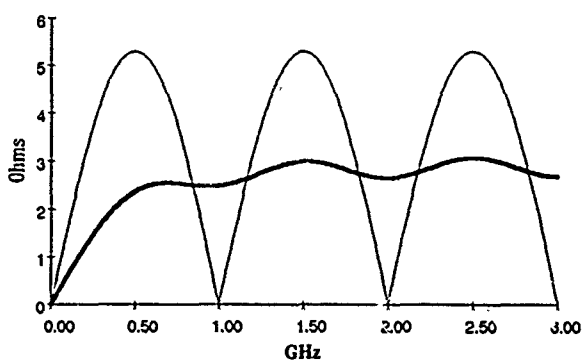


Fig. 2 Stripline Frequency Response: The dark line is the tapered stripline response. The lighter line is symmetrical (untapered) stripline response.

U.S. Government work not protected by U.S. Copyright.

Linnecar[2] reported on the superior frequency domain performance of tapered striplines. These striplines have no nulls in their response but do have some ripple. The ripple may be minimized with proper design.

The coupling impedance[2] of an exponentially tapered stripline in a round pipe (as a function of frequency) is:

$$Z_c = \frac{\frac{Kmax\ \omega\ l}{v}}{\sqrt{\alpha^2 + \frac{4\omega^2 l^2}{v^2}}} \sqrt{1 + \frac{1}{e^{2\alpha}} - \frac{2}{e^{\alpha}} \cos\frac{2\omega l}{v}} \qquad (2)$$

$$Kmax = 60 \ln \frac{r1}{r1-h1} \qquad (3)$$

$$Kmin = 60 \ln \frac{r2}{r2-h2} \qquad (4)$$

$$\alpha = \ln \frac{Kmax}{Kmin} \qquad (5)$$

where Kmax is stripline coupling at the wide end, Kmin is coupling at the narrow end, r1 is electrode radius at the wide end, r2 is electrode radius at the narrow end, h1 is electrode spacing at the wide end, h2 is electrode spacing at the narrow end, v is beam velocity, l is electrode length, ω is radian frequency, and α is the attenuation constant.

If the stripline is untapered (e.g., Kmin = Kmax, and $\alpha = 0$), equation (2) yields approximately the same results as equation (1). The difference in this case is that equation (1) calculates coupling impedance as a function of pipe radius, and equation (2) uses the electrode radius.

The calculated frequency response of an exponentially tapered stripline is shown in figure 2 as the heavier line. Here the electrode length is 150mm, the maximum width is 12.7mm, the minimum width is 1mm, the maximum spacing is 2.54mm, and the beam pipe radius is 30mm. The attenuation constant, α, is 2.668.

III. THE SLOT-COUPLED PICKUP

We explored slot coupling between two coaxial transmission lines in order to evaluate different slot shapes. The linear slot behaved similarly to the untapered stripline. An exponentially tapered slot gave a frequency response similar to the figure 2 darker curve. A linearly tapered slot with a 7 to 1 width ratio had more ripple and a steeper low frequency skirt. A gaussian taper gave an interesting time domain result. When driven by a very fast voltage step, the coupled line output was a Gaussian voltage pulse.

In order to simulate beam coupling through a slot we built a structure similar to figure 3 and modeled the beam with a 3mm wire centered in the beam pipe. Slots cut in a removable thin-wall cylinder having the same diameter as the beam pipe defined the coupling. An untapered slot behaved the same as an untapered stripline located at the beam pipe wall but with less coupling. The coupling of an untapered slot may be approximated by equation (2) (Kmax = Kmin) multiplied by a coupling constant k:

$$k = \frac{a}{2\pi} \frac{b}{2\pi} \qquad (6)$$

where angles a and b are defined by the aperture.

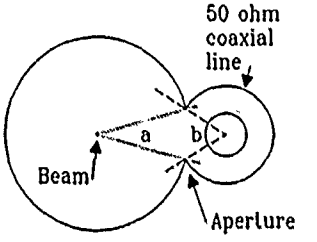


Fig. 3. Aperture Coupling

The coupling of a tapered slot is also approximated by equation (2) multiplied by the k factor. We calculate the performance of a tapered stripline at the wall and apply the k factor calculated for the widest aperture. The measured ripple is always less than equation (2) predicts.

IV. BEAM PICKUP MECHANICAL DETAILS

Figure 4 shows a cut-away view of the slot-line pickup. The body of the pickup is machined from a single piece of aluminum. The beam aperture, nominally 63mm in diameter is drilled through the center of the cylindrical aluminum block. Four holes 32mm in diameter are drilled through the block 44mm off the center of the beam axis and 90 degrees apart. The four holes intersect the beam pipe hole forming 16mm apertures the full length of the block. Aluminum rods inserted into the four holes form 50 ohm coaxial lines. The rods are supported by the center conductors of type-N constant-impedance vacuum feedthroughs welded into removable end-flanges. Beam field coupling to the rods is defined by exponentially tapered slots in a thin-wall brass tube with a diameter slightly less than the beam aperture. The slots are 15mm across on the widest end, 2.5mm on the narrow end, and 150mm long.

The ends of the rods are tapered down to the feedthrough center conductor diameter to maintain 50 ohm impedance.. On the vacuum side of the flanges where the feedthroughs are installed the flange is machined to form the impedance taper required to accommodate the tapered rod ends. The longitudinal position of the rods is important for impedance reasons. They are properly positioned by having a hole in one end of exact depth and a spring in the hole in the other end. With one end flange bolted to the body, the rods are fitted (spring loaded end first) onto the flange feedthrough center conductors. The other flange is then installed. The rod springs force them into proper longitudinal position. RF contact between the rods and the

feedthrough center-conductors is made with gold-plated RF "fingers" inside the holes.

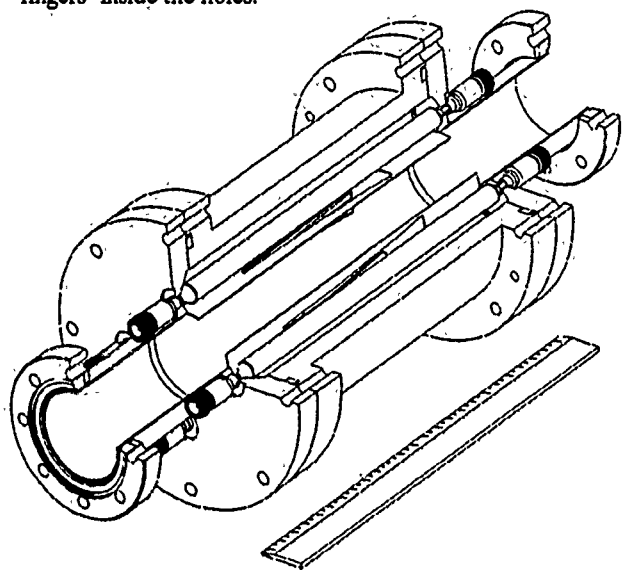


Fig. 4 Slot-coupled Pick Up

V. BEAM KICKER MECHANICAL DETAILS

Everything about the kicker is identical to the pickups except for the slots and the external cable connections. We use rectangular slots 15mm wide and 150mm long in the kicker.

VI. LABORATORY TESTS

We tested the pickups and kicker coaxial lines with a TDR to insure the internal connections were correct. Some impedance discontinuities were seen, the largest being a 40 ohm section in the feedthroughs. The influence of the tapered slot was seen as a 4 ohm increase in the line impedance at the slot location.

We tested the coupling characteristics of the pickups and kicker with a centered wire supported by tapered coaxial horns. The instruments we used were a 20GHz sampling scope, a 60ps gaussian pulser, a 300ps gaussian pulser, and a vector network analyzer. Figure 5 shows the frequency response of the four slotted couplers in one pickup. The nominal coupling is -44dB. The marker measurement in figure 5 indicates -47dB (-3dB down) at 500MHz. Figure 6 shows the response to a 60ps pulse. The coupled pulse amplitude corresponds to a coupling impedance of 0.6 ohm which agrees reasonably with equation (2) multiplied by the coupling factor. In figure 6 an echo pulse if any would occur 1ns after the prompt pulse. Unlike the symmetric stripline, the tapered coupler has no echo pulse.

We have no data on beam measurements to present here. The ALS injector is nearing completion, and we should have data soon.

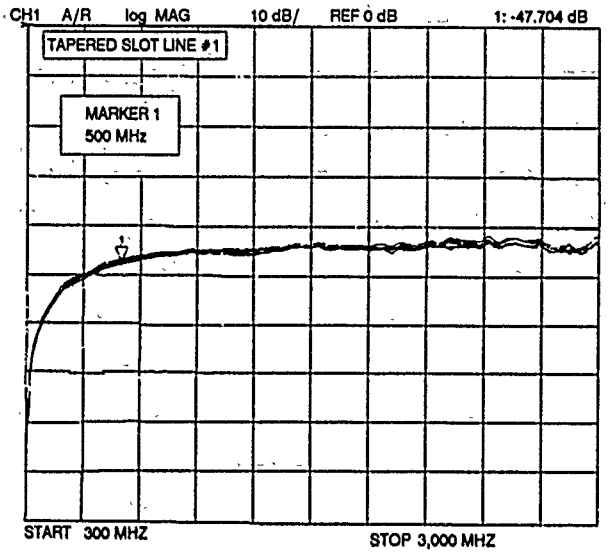


Fig. 5 Slot-Coupled Pickup Frequency Response

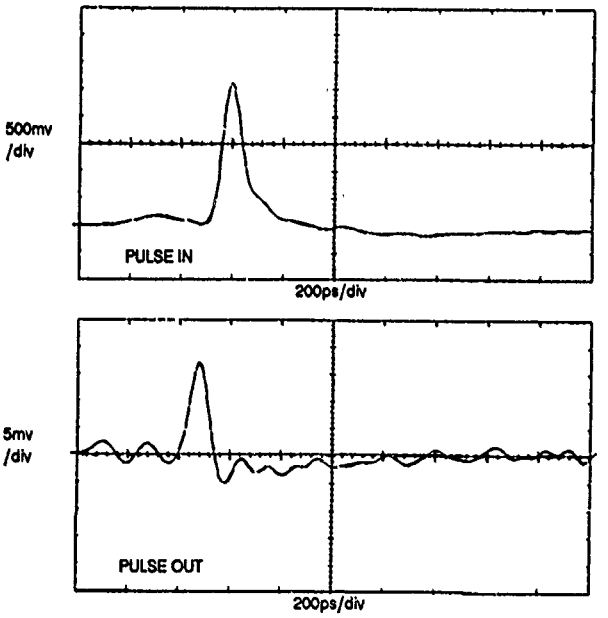


Fig. 6 Slot-Coupled Pickup Pulse Response

VII. ACKNOWLEDGEMENT

*This work was supported by the Director, Office of Energy Research, Office of Basic Energy Sciences, Materials Sciences Division of the U.S. Department of Energy, under Contract No. DE-AC03-76SF00098

VIII. REFERENCES

[1] R. Bossart and H. Rossi, "Test of Beam Position Monitors at Daresbury Nuclear Physics Laboratory", (1973)

[2] T. Linnecar, "The High Frequency Longitudinal and Transverse Pickup Used in the SPS"., European Organization for Nuclear Research, CERN-SPS/ARF/78-17, (1978)

A Real-Time Longitudinal Phase-Space Measurement Technique for H⁻ Beams

R. C. Connolly† and D. P. Sandoval
Los Alamos National Laboratory
Los Alamos, New Mexico 87545

Abstract

The longitudinal phase-space distribution of a bunched beam can be determined by selecting short-phase slices of the beam and measuring the energy distribution of each slice. This paper describes a system that should be capable of producing phase-space measurements of an H⁻ beam at a rate of 2 Hz. The phase is selected by photoneutralization with a mode-locked laser. A deflector magnet downstream of the neutralization point deflects the charged beam, and the neutral particles enter a spectrometer through a slit covered with a stripping foil. During the 20- to 40-μs laser burst, a ramp signal shifts the laser phase with respect to the beam phase. The same ramp signal controls electric deflection plates in the exit beamline of the spectrometer, which bend the beam perpendicular to the dispersion plane. If the spectrometer magnet bends the beam horizontally, then the beam-current distribution at the focal plane is analyzed horizontally in energy and vertically in phase.

I. Introduction

The Laser-Induced-Neutralization Diagnostic Approach (LINDA)[1], developed at Los Alamos National Laboratory, is a technique that uses light pulses from a laser to select portions of an H⁻ beam for analysis. Light pulses of the appropriate wavelength to neutralize H⁻ ions pass through the beam upstream of a deflection magnet. The neutralized beam passes through the magnet and into a detector.

Longitudinal phase-space distributions have been made measured using LINDA by firing single laser pulses through beams and measuring energy spread by time-of-flight. This technique requires several hundred laser pulses for each measurement and is applicable only to beams of less than about 10 MeV with rms bunch lengths of greater than about 30 ps.

This paper describes a system (see fig.1) that should be capable of producing longitudinal phase-space measurements of an H⁻ beam at a 2-Hz rate. It is applicable to high-brightness beams of energies greater than 100 MeV.

The phase is selected using light from a mode-locked laser whose frequency is locked to a subharmonic of the accelerator rf. A spectrometer is placed downstream of the deflector magnet for energy-spread analysis. During the laser firing, the rf phase of the laser is ramped at the same rate that the ion beam in the image line of the spectrometer is deflected perpendicular to the dispersion plane. The beam current on the spectrometer focal plane is analyzed in both phase and energy.

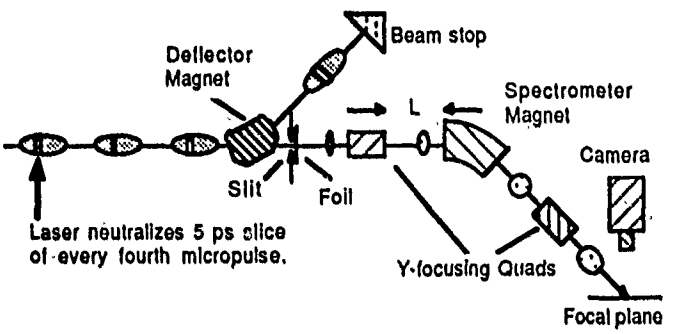


Figure 1. Schematic of measurement technique. The laser-firing frequency is one-fourth the accelerator rf.

II. Measurement System Requirements

The laser and spectrometer constitute a measurement system with a phase-space window having dimensions θ of rf phase and R of energy. The phase dimension of the window is equal to the time width provided by the laser pulses multiplied by $2\pi/T$ (where T is the rf period). The energy width is equal to the resolution of the spectrometer.

The detector resolution required to measure a particular beam is determined by calculating the effect the detector window size has on the measurement result. The following calculation is based on studies done by Gluckstern[2] and Connolly and Johnson[3].

If a beam of phase-space distribution $\rho(\phi,E)$ and true rms emittance E_t is measured using a detector having a window of dimensions θ of rf phase and R of energy, the measured distribution is $\rho_m(\phi,E)$ where

$$\rho_m(\phi_o,E_o) = \frac{1}{R\theta} \int_{\phi_o-\frac{\theta}{2}}^{\phi_o+\frac{\theta}{2}} \int_{E_o-\frac{R}{2}}^{E_o+\frac{R}{2}} \rho(\phi,E)\, d\phi\, dE. \qquad (1)$$

When $\rho(\phi,E)$ is expanded to second order around ϕ_o and E_o, the result of the integration is

Work supported and funded by the US Department of Defense, Army Strategic Command, under the auspices of the US Department of Energy.

† Industrial partner, Grumman Corporation

0-7803-0135-8/91S01.00 ©IEEE

$$\rho_m(\phi_o,E_o) = \rho(\phi_o,E_o) + \frac{\theta^2}{24}\left[\frac{\partial^2\rho(\phi,E)}{\partial\phi^2}\right]_{\phi o,Eo} + \frac{R^2}{24}\left[\frac{\partial^2\rho(\phi,E)}{\partial E^2}\right]_{\phi o,Eo}. \quad (2)$$

The rms emittance calculated from this measured beam distribution is

$$E_m = \pi\left[\frac{E_t^2}{\pi^2} + \frac{\theta^2}{12}\sigma_E^2 + \frac{R^2}{12}\sigma_\phi^2 + \frac{\theta^2R^2}{144}\right]^{1/2}. \quad (3)$$

where σ_ϕ and σ_E are the rms beam dimensions. Written in terms of the Twiss parameters β and γ, Eqn. 3 becomes

$$E_m = E_t\left[1 + \frac{\pi\gamma\theta^2}{12E_t} + \frac{\pi\beta R^2}{12E_t} + \left(\frac{\pi\theta R}{12E_t}\right)^2\right]^{1/2}. \quad (4)$$

An emittance measured by a detector whose window is small compared to the beam distribution is the true emittance of the beam. If the window size is comparable to the beam distribution, the measured emittance is larger than the true emittance.

Equation 4 shows that the effect of the detector on a measurement depends on the beam parameters. For the case of an upright ellipse, Fig. 2 shows how the ratio of E_m/E_t increases with detector window size. For this example, $\theta/\sigma_\phi = R/\sigma_E = A$. The ratio E_m/E_t is plotted as a function of A. This plot shows that a detector window with dimensions equal to the rms beam dimensions produces a measured emittance that is 1.08 times the true emittance. For most applications, the detector window should be no larger than σ_ϕ by σ_E.

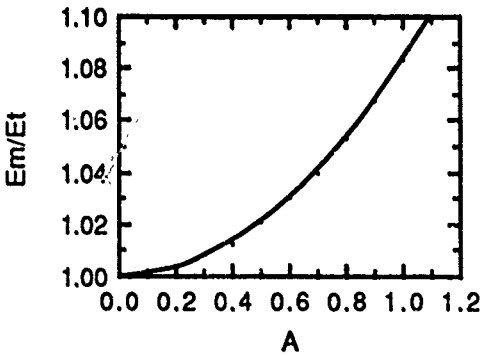


Figure 2. The ratio of measured emittance to true emittance as a function of detector window size for the case of an upright phase ellipse. The detector window dimensions are θ by R and $A = \theta/\sigma_\phi = R/\sigma_E$.

III. Measurement System

A. Mode-locked laser

The laser has to produce short pulses of an appropriate wavelength and photon flux to produce the required neutralization of the H^- beam. The required neutralization fraction depends on the beam current and the sensitivity of the spectrometer detector.

If the laser pulse duration is long compared to the flight time of the ions through the laser beam, the neutralization fraction is

$$P = 1 - \exp(-\sigma F t), \quad (5)$$

where σ is the neutralization cross section, F is the photon flux, and t is the time the ions spend in the photon field. The photon flux is given by

$$F = \frac{\mathcal{E}\lambda}{h c A \tau}, \quad (6)$$

where $\mathcal{E}$ is the laser-pulse energy, λ is the wavelength, h is Planck's constant, c is the speed of light, A is the laser beam cross-sectional area, and τ is the laser firing time.

The best laser for H^- beams is a CW mode-locked Nd:YLF laser tuned to a subharmonic of the accelerator frequency. This laser produces 50-ps pulses of 1062-nm light, giving a photoneutralization cross section of 3.6×10^{-17} cm^2[4]. These light pulses are chirped, amplified, and compressed to get pulses as short as 1 ps. The output energy of the pulses is controlled by the number of amplification stages. The amplifier rods limit the output bursts to 20-40 μs.

The laser beam is focused so its width along the ion beam is as narrow as possible. The detector phase window is the quadrature sum of the laser pulse length, the laser firing jitter, and the ion-beam transit time across the laser beam. If the laser-beam dimension is 0.1 mm in Z, a 5-MeV proton takes 3.2 ps to pass through it and a 20-MeV proton takes 1.6 ps. Detector windows of ~3 ps are possible with 20-MeV beams.

Neutralizing the smallest phase window possible requires that the laser beam intersect the H^- beam perpendicularly in the H^- rest frame. This is done by directing the laser beam through the H^- beam at a lab-frame angle of $\cos^{-1}(\beta)$ where β is the relativistic parameter v/c. For a 20-MeV H^- beam, the intersection angle is 78°.

An example of a laser system that can produce about 10% neutralization of a 20-MeV H^- beam is one being considered by Los Alamos[5]. It consists of a Quantronix[6], Series 4200 Nd:YLF CW mode-locked laser with an amplification and pulse-compression system from Continuum[7]. The laser is available with frequencies of 50 to 240 MHz. Firing jitter with respect to the rf source is reported to be ±1 ps.

B. Spectrometer

As with the laser, the spectrometer requirements depend on the specific application. A design that has been studied at Los Alamos[8] is shown in Fig. 1. It is a double-focusing transport line consisting of two y-focusing quads and a dipole with straight, perpendicular entrance and exit edges. One quad is in the middle of the image and object lines. These focus the beam through a waist in y in the center of the dipole [9].

The half length of each leg, L (see fig. 1), is approximately $1.5r/\sin(\alpha)$, where r is the bend radius and α is the bend angle. The momentum resolution is $\Delta P/P = s/6r$, where s is the entrance slit width in the dispersion plane. The spectrometer shown in Fig. 1 bends the beam 45° with r=1.5m and L=3.2m. With a 1-mm entrance slit, the energy resolution for a 20-MeV beam is about 4.5 keV.

The sensitivity of this design to magnet misalignments and vibrations has been studied with TRANSPORT[10]. The only strong sensitivities were found to be the roll angles of the quads and dipole. Errors in the roll angles produce mixing of the X and Y planes which is uncorrectable by focusing. The studies show that quad roll-angle has to be correct to ±5 mr and dipole roll correct to ±1 mr.

Focus sensitivity studies to quad settings and to harmonic contamination of the quad and dipole fields done to third order with GIOS[11] show this design to be extremely robust. The quad fields need to be within ±1% of the design value, and sextupole and octupole components of ±0.1% at the pole-tip radius have little effect on the focus. Similar harmonic components of the dipole field can be tolerated. The only critical field is that of the dipole, which needs to be stable to ±0.004%.

C. Integrated System

The complete measurement system is shown in fig. 4. A magnet, placed between the neutralization point and the entrance slit, deflects the charged beam into a beam stop. The analyzed beam is neutral, so a stripper foil is placed over the entrance slit. Angle scattering in the foil does not affect the analysis because the system produces a point-to-point focus.

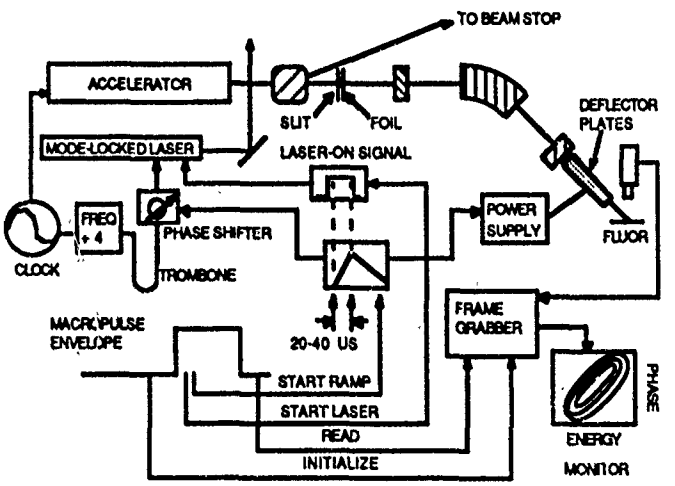


Figure 4. Block diagram of complete measurement system.

Electrostatic deflector plates in the image line deflect the proton beam perpendicular to the dispersion plane. During the overlap of the beam macropulse and the laser-firing time, both the phase of the laser and the deflection of the beam follow a common linear ramp. This produces an integrated current distribution on the image plane; the distribution's energy is analyzed in the dispersion plane and its phase in the perpendicular plane. One possible image-plane detector is a fluorescent screen and CCD camera. The image can be digitized for analysis and displayed on a monitor.

IV. Discussion

This system should be capable of producing complete longitudinal phase-space measurements of an H^- beam at a rate of 2 Hz. This is the firing rate of the laser amplifiers. Probably this technique can be used for other negative-ion beams, but it has been studied only for H^- beams.

This method is applicable to beams whose rms bunch lengths are as short as a few ps. The spectrometer described will work for beams with rms energy spreads of greater than $\sim 2 \times 10^{-4}$. For a 100-MeV beam the total length is ~12 m, so a more compact design probably is needed for higher-energy beams.

If the electrostatic deflector plate lengths are 0.75 times L and the maximum voltage between them is 20 kV, the total image deflection is 1.3 cm for all beam energies. This image width should probably correspond to 6σ, so the entrance slit height for this case should be ~2 mm.

V. Acknowledgement

We thank Hermann Wollnik for his valuable help in the spectrometer design.

VI. References

[1] W. B. Cottingame, G. P. Boicourt, J. H. Cortez, W. W. Higgins, O. R. Sander, and D. P. Sandoval, "Noninterceptive Techniques for the Measurement of Longitudinal Parameters for Intense H^- Beams," in "Proc. 1985 Part. Accel. Conf.", IEEE Trans. Nucl. Sci. 32 (5), 1871 (1985).

[2] R. L. Gluckstern, "Notes on Beam Dynamics in Linear Accelerators," Los Alamos National Laboratory report LA-8526-MS, pp. 48-52.

[3] R. C. Connolly and K. F. Johnson, "Longitudinal Emittance Measurements for GTA Experiments 1B and 1C,", Los Alamos National Laboratory report LA-CP-90-127 (1990).

[4] J. T. Broad and W. P. Reinhardt, Phys. Rev. A 14 (6), 2159 (1976).

[5] D. P. Sandoval, R. C. Connolly, V. Yuan, M. Shinas, and R. Garcia, "CW Mode-Locked Laser Design Report," , Los Alamos National Laboratory report LA-CP-91-158 (1991).

[6] Quantronix Corp., Smithtown, NY.

[7] Continuum, Santa Clara, CA.

[8] R. C. Connolly and A. J. Jason, "Spectrometer for 2D Longitudinal Emittance Measurements," Los Alamos National Laboratory report LA-CP-90-388 (1990).

[9] H. Wollnik, Optics of Charged Particles (San Diego: Academic Press, 1987), Chap. 9.

[10] K. L. Brown, K. C. Carey, Ch. Iselin, and F. Rothaker "TRANSPORT, A Computer Program for Designing Charged Particle Beam Transport Systems,", SLAC 91 (1973 rev.), NAL 91, and CERN 80-04.

[11] H. Wollnik, J. Heuser, T. Matsuo, E. Kasseckert, K. Becker, J. Brezina, C. Geisse, K. Lindemann, S. Meuser, J. Larson, and J. Trotscher, "Manual for Gios," Physikalisches Institut, Justus-Liebig-Universitat, Heinrich-Buff-Ring 16, 6300 Giessen, Germany.

Fast Ion Chambers For SLC

D. McCormick
Stanford Linear Accelerator Center

ABSTRACT*

Beam diagnostic ion chambers are used throughout the SLC to perform a variety of tasks including locating beam losses along the beam direction, determining localized losses from individual bunches in a multibunch beam, and detecting scattered particles from beam profile wire scanners where backgrounds are too high to use photomultiplier tubes. Construction and instrumentation of very fast ion chambers with pulse duration of less than 60ns are detailed. Long ion chambers referred to as PLIC (Panofsky's Long Ion Chamber) are the primary diagnostic used to locate losses in all the SLC transport lines. Accurately locating beam loss with the use of fiducial cables and coaxial switches will be discussed.

INTRODUCTION

Normal operation of the SLC requires two bunches of electrons and a single bunch of positrons to be present in the accelerator during each machine pulse. These bunches are approximately 1mm in length and about 60ns apart. In the past, beam losses detected by conventional ion chambers could not be attributed to a particular bunch. The pulse length of these ion chambers ranges from hundreds of nanoseconds to many milliseconds and hence their signals are the sum of the losses from all three bunches. In order to resolve losses from each bunch, fast ion chambers with a minimum pulse length of 35ns were constructed. Fast ion chambers have been installed at collimators or other aperture restrictions in the linac. Their signals are monitored on a real time basis and over long term running.

Wire scanner measurements of beam size are crucial to the successful operation of the SLC.[1] Fast ion chambers are used as wire scanner scattered particle detectors where backgrounds are too high for photomultiplier tubes. They are also used at all other wire scanner installations to provide a cross check on the photomultiplier tubes.

DESIGN

A cylindrical ion chamber design was optimized to: 1) produce pulses of less than 60ns, 2) provide reasonable sensitivity, 3) absorb high radiation without damage, and 4) allow ease of construction.

The body of the ion chamber is a brass tube 30cm in length with an inside diameter of 3.25 mm. For wire scanner applications where the pulse length must be as short as possible, the tube can be sleeved with another brass tube with an inside diameter of 2.35mm. Notching the tubes at either end allows the gas to flow freely when purging impurities. The end of an ion chamber tube is shown in fig. 1. The ends of the brass tube are fitted with insulating standoffs made from Vectra, a plastic which is radiation resistant to 5×10^8 rads.

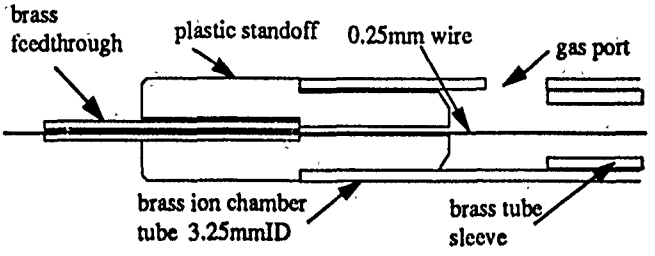


Fig. 1: Crossection of a fast ion chamber tube end

Gold-plated beryllium copper wire with a diameter of 0.250mm is used for the center conductor. The wire is soldered into a feedthrough made from small diameter brass tubing which fits into the outer hole in the standoff. It is then passed through the brass tube, the other standoff and another feedthrough. The standoffs are fitted into either end of the tube. The feedthroughs are seated in the standoffs, then the wire is tensioned and soldered to the second feedthrough. A short length of wire is left on one end to allow for connections. A number of these tubes are bundled together and connected electrically in parallel. The bundle is inserted into two polyethylene rings that act as supports and gas baffles. This assembly is placed inside a 2 inch diameter stainless steel can.

A positive voltage between 50 and 200 volts is applied to the center conductor through a current limiting resistor. The signal is obtained from the center conductor after being decoupled from the high voltage by a capacitor. Ten volt zener diodes are added to the low voltage side of the capacitor in case it breaks down. Originally the ends of the feedthroughs were left exposed at high voltage, and electrons collected over large distances produced tails on the pulse. These tails are eliminated by insulating the ends of the feedthroughs and then covering them with copper foil at ground potential.

The signals of the individual tubes are combined in parallel to increase the output of the fast ion chamber. The tubes have an impedance of about 150 ohms, and three tubes together provide the best match into 50 ohm cable. If more tubes are added, the impedance match becomes worse, and the pulse length increases due to signal reflections at the ion chamber cable boundary. Given the 60n unch spacing, 15 tubes is about the maximum number that can be combined and still produce the required pulse length. Ten tubes are used for wire scanner installations.

PULSE LENGTH

For a burst of radiation that is short compared to the electron collection time, the pulse length of a fast ion chamber is determined by the drift velocity of the electrons in the gas and by the distance between the electrodes.

0-7803-0135-8/91$01.00 ©IEEE

Initial tests were performed using a mixture of 95% Ar and 5% CO_2, which has a maximum electron drift velocity of about 4.5cm/μs. The pulse from the ion chamber using this mixture is shown in fig.2A. Although the pulse length is shorter than the SLC bunch spacing, a much cleaner separation is required for wire scanner beam size measurements.

Experimental results using pure CF_4 or CF_4 in mixtures with argon indicate an electron drift velocity of over 12cm/μs.[2] A fast ion chamber using a mixture of 80%Ar and 20% CF_4, produces the shorter pulse with increased amplitude seen in fig. 2B. This mixture was selected for use in fast ion chambers used as wire scanner particle detectors because of the short pulse length, and high amplitude signals it produced.

Another method of decreasing the pulse length is to effectively reduce the drift distance by using a mixture which contains an electronegative gas, such as Freon. Electrons liberated at large distances from the center conductor recombine with the Freon and do not contribute to the pulse length. The same fast ion chamber using a mixture of 95% Ar, 4.7% CO_2 and 0.3% Freon produced the pulse shown in fig. 2C. This mixture significantly reduces the signal amplitude but is ideal for fast ion chambers used at collimators where the radiation flux is very large.

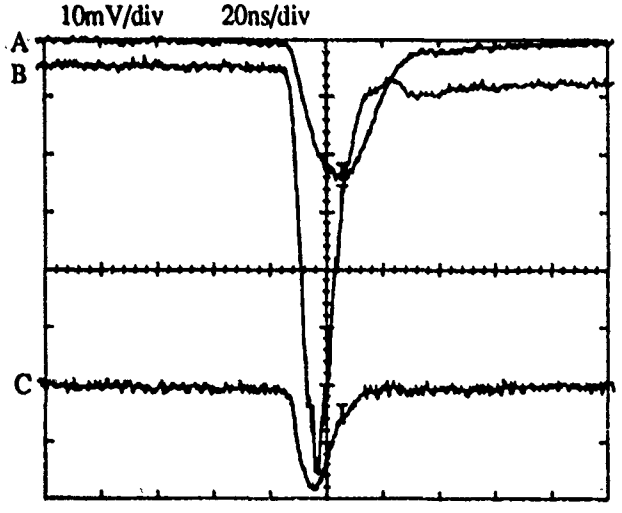


Fig. 2: Fast ion chamber signals with constant beam conditions, using: A) 95% Ar and 5% CO_2, B) 80% Ar, 20% CF_4, C) 95% Ar, 4.7% CO_2 and 0.3% Freon.

PERFORMANCE

The sensitivity of an ion chamber is proportional to the amount of gas between the electrodes. Because of the small volume of the tubes, signal levels of fast ion chambers used with wire scanners are only a few millivolts, and these levels depend heavily on the location of the ion chamber. Calculations indicate that multiple scattering of electrons off the wire scanner wire produce most of the signal.[3] Ray tracings on scale drawings have been helpful in selecting locations for these ion chambers. For a 1GeV beam, an ion chamber is installed about 7m downstream of its wire scanner. Locating fast ion chambers for primary beam collimators presents no problem. Because of the large amount of radiation, signals in the hundreds of millivolts are obtained by placing the ion chamber a few meters downstream of the device.

OPERATION

Signals from the fast ion chambers are monitored on real time displays (oscilloscopes) and/or fed into ADCs (Analog Digital Converter) to calculate beam sizes and monitor individual bunch losses over longer periods of time.

Fast ion chambers used with wire scanners typically have an output of 5mv and need to be amplified. The signal makes a single pass through a LeCroy 612 x10 amplifier before it is fed into an ADC. Fig. 3 shows a wire scanner fast ion chamber setup

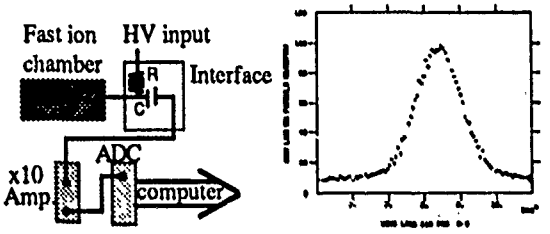


Fig. 3: Block diagram showing basic components of a wire scanner fast ion chamber

LONG ION CHAMBERS

Long ion chambers (PLIC) have been used to locate beam loss and protect the accelerator at SLAC since its beginning.[4] The system consists of a gas dielectric coaxial cable approximately 3500m in length installed on the ceiling of the accelerator housing. Time dispersed PLIC signals travel upstream to the start of the cable. They are reflected, and travel to the downstream end of the cable where they are observed. Because it is viewed from the downstream end of the cable the average PLIC pulse propagates over about 5300m of cable. The rise time of a PLIC signal is distorted by the cable, and this introduces an uncertainty of about 30ns in locating the leading edge of the PLIC pulse.[5]

During the construction of the SLC, PLIC cables were installed in all transport lines.[6] The SLC PLIC signal is viewed from the upstream end of the cable and on average, the signal propagates over only 300m. In this case, the leading edge can be determined to within 5ns.

When the beam path length and the length of the PLIC cable are equal, locating beam losses can be calculated by using an oscilloscope to measure the time from the start of the cable to the leading edge of a PLIC pulse. This interval is the sum of the time it takes the beam to travel from the start of the cable to where the loss occurs and the time for the pulse induced on the cable by the loss, to return to the start of the cable. The SLC PLIC cable has a propagation velocity of 0.914c so:

$$T_{scope} = T_{beam} + T_{beam}/0.914 \qquad (1)$$

where T_{scope} is the time between the start of the cable and the beam loss measured on the scope, and T_{beam} is beam time from the start of the cable to the beam loss.
The beam time between any two events is the time displayed on the scope divided by 2.09.

When there are obstacles and bends in the transport line, the cable length is no longer equal to the distance traveled by the beam, and equation 1 is no longer valid. This path length problem can be reduced by periodically referencing or fiducializing the PLIC signal to a particular beam line component, providing a local reference for beam loss calculations using equation 1. Two methods of fiducializing the PLIC signal, passive and active, have been devised.

A passive fiducial is produced by connecting a 50 or 100ns coil of solid polyethylene coax (which produces no PLIC signal when it is irradiated) between sections of PLIC cable. The notched pulse shown in fig. 4 is produced when sections of PLIC cable with this solid coax between them are irradiated. The thick line indicates the time of a 50ns fiducial cable. The leading edge of the second pulse (indicated by the second cursor) is produced by the end of the PLIC cable connected to the downstream end of the fiducial cable. From this known edge, the time or position of other losses can be measured.

Two discrete losses are unresolved when the time between the losses is less than the decay time of the PLIC signal from the first loss. The second loss can be resolved by inserting a fiducial cable in the PLIC cable just upstream of the second loss. The fiducial cable provides the extra time needed to allow the PLIC signal from the first loss to die away.

An active fiducial can be produced by installing a coaxial switch between sections of PLIC cable. When the switch is opened, pulses, created from earlier beam losses that propagate in the same direction as the beam, reflect off the open switch, producing an inflection in the PLIC signal at the switch's location. Because these pulses do not travel at the same speed as the beam, there must be beam loss at the switch's location in order for the spike to accurately indicate the position of the switch. This effect is shown in fig. 5.

CONCLUSION

Fast ion chambers provide beam loss information, both real time, and computer processed for each of the th[illegible] bunches. Accelerator operators monitor the real ti[illegible] to help them diagnose problems in machine performance. The processed information is used to determine beam sizes and emittances. This information is also stored so that individual bunch beam loss variations can checked for correlations with data from SLC subsystems to identify system failures.

Beam losses in SLC transport lines are located with greater accuracy when fiducials in the PLIC signal, produced by delay cables or coaxial switches, are used as references for beam loss calculations.

ACKNOWLEDGMENTS

I would like to thank C. Field for answering my many questions about radiation and ion chambers, and Y.Y. Sung, R. Stickley, R. Leonard and R. Baggs,who helped in the design and did the fabrication of the fast ion chambers.

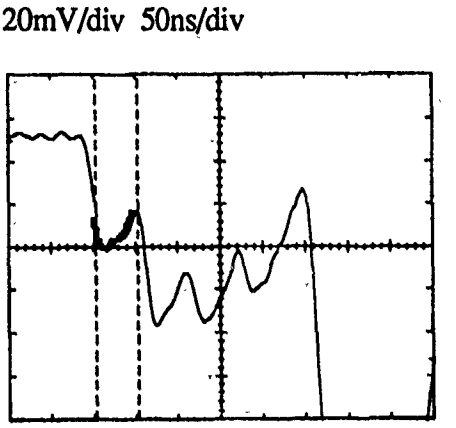


Fig. 4: SLC PLIC. Cursors indicate a notch in the PLIC signal produced by a 50 ns fiducial cable. The two notches to the right of the first are also produced by fiducial cables.

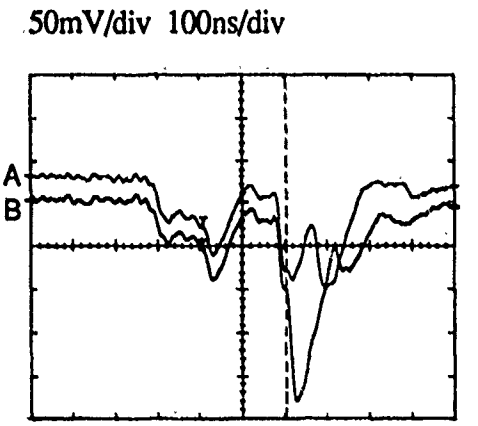


Fig. 5: SLC PLIC signals: Trace A, PLIC switch closed. Trace B, PLIC switch opened. The cursor indicates the position of the switch.

REFERENCES

* supported by DOE contract DE-AC03-76SF00515

[1] M.C. Ross et. al., proceedings of this conference.

[2] A. Peisert, F. Sauli, *Drift and Diffusion of Electrons In Gases: A compilation*, CERN 1984.

[3] Particle Data Group, "Review of Particle Properties," Physics Letters B, vol. 239, p.III.14, 1991.

[4] M. Fishman, D. Reagan, "The SLAC Long Ion Chamber For Machine Protection," IEEE *Transactions on Nuclear Science*, June 1967, vol. NS-14, pp. 1096-1098.

[5] Q. Kerns, F. Kirsten, C. Winningstad, "Pulse Response Of Coaxial Cables," Counting Note CC2-1B, Lawrence Radiation Laboratory, pp. 1-11, July 1966.

[6] J.Rolfe et. al., "Long Ion Chamber Systems For The SLC," Proceedings of the 1989 *IEEE Particle Accelerator Conference*, Vol.III, p. 1531.

Diagnostic Instrumentation for the SSRL 3 GeV Injector*

J. Sebek, M. Baltay, M. Borland‡ J. Cerino, L. Emery†, R. Hettel, H. Morales, D. Mostowfi, M. Rowen,
J. Safranek, J. Voss, J.N. Weaver, H. Wiedemann, Y. Yin‡ B. Youngman§
Stanford Synchrotron Radiation Laboratory, P.O. Box 4349, Bin 99, Stanford, CA 94309-0210
J.-L. Pellegrin, V. Smith
Stanford Linear Accelerator Center, Stanford University, Stanford, CA 94309-0210

Abstract

SSRL has built a 3 GeV injector to fill SPEAR. Many types of diagnostic instruments were built into the injector to facilitate and enable commissioning and operation. These instruments were designed to give accurate information for low beam currents seen in the early stages of commissioning [1] as well as for the higher currents in normal operation.

I. Introduction

SSRL has built and commissioned a 3.0 GeV electron accelerator as a dedicated, full energy, injector for its SPEAR storage ring [2]. The beginning of the injector is a 2856 MHz RF electron gun. This gun emits a peak current of 650 mA of 2 MeV electrons for 2.5 μsec. These electron bunches are compressed in an alpha magnet, and then pass through a pulsed chopper, which selects three of these s-band bunches. These bunches are then accelerated through three 2856 MHz linac sections to an energy of 130 MeV, transported and injected into the cycling booster. Here the bunches are compressed into one bunch at 358.54 MHz, the SPEAR frequency, and accelerated to 3 GeV. Finally, the bunch is ejected from the booster and injected into SPEAR. The injector cycles at a 10 Hz rate and currently delivers greater than 10^8 electrons per cycle to SPEAR.

The diagnostics required for the booster are dictated by the purpose and function of the machine. The low beam currents and single bunch character of the system reduce the need to be able to observe many high frequency phenomena associated with instabilities important at higher beam currents. The fact that the beam stays in the machine for only 50 msec also removes the need for diagnostics that looks for long term drifts in the beam. Also, since the SPEAR injection aperture is reasonably large, the knowledge of the position of the beam does not need to be more precise than a few hundred microns. The diagnostics and associated instrumentation will be discussed with these points in mind. The paper will describe the function of the various devices in three different situations:

- The initial commisioning of the machine when systems were being checked out with very low current.
- Machine physics on and characterization of the injector itself.
- The normal operation of the machine as a dedicated injector for SPEAR.

II. Faraday Cup

The injector has two Faraday cups for charge measurement. Both are used for machine characterization. The first, located at the entrance to the alpha magnet, is an insertable cup used to measure the charge emitted by the RF electron gun. Since the beam at this point has not yet been chopped, high currents require cooling of this cup. The cup is made of a water-cooled copper bar and serves a double purpose as the support for an insertable screen. Charge here is measured in μC/pulse. The second cup measures beam out of the linac. It is located at the end of a diagnostic beamline into which the linac current can be steered. Because of the higher energies of the beam here, this cup is made of lead. To prevent contamination of the injector vacuum, the lead is encased in stainless steel before it is placed in the vacuum system. This cup receives less than one nC/pulse.

The outputs of both of these cups were fed to general purpose, commercial devices for measurement. One of the most useful tools we have found in commissioning and running the accelerator has been a high bandwidth, fast digital sampling oscilloscope. This scope is used during operation to monitor the many diagnostic signals from the accelerator. During machine physics, these devices can sample signals, such as the current discharge from the Faraday cups, and perform a mathematical calculation, in this case integration, that gives the total charge.

III. Current Toroids

Measurement of beam current in many different parts of the injector is required. Current toroids make 8 of these measurements. Preliminary designs had toroids placed inside the vacuum system. Several early experiments showed, however, that toroids external to the beam pipes gave good results. This approach not only saved construction cost and time, but it also allowed toroids to be put in places where they would not have otherwise fit.

Toroid modules were constructed around a vacuum pipe with an inserted ceramic gap that prevented a DC path for the beam-induced wall current from travelling inside the toroid (Figure 1). The toroid itself was placed over this pipe before the end flanges were welded on. A tight fitting aluminum shroud was placed over the toroid assembly to provide a low impedance path for the wall current. Eight turns of wire on the toroid gave reasonable signal amplitudes for our beam currents. This wire was then brought out for detection through Twinax cable. A second, one turn, winding was also put on the toroid for calibration purposes. Although the toroid assemblies were made as compact as possible, the toroid does not have to be directly over the ceramic gap in order to work. As long as the toroid is within the shroud assembly, it functions properly. In one place where space was very tight, we even installed a toroid by first sawing it in two, grinding the faces to insure a smooth fit, and then mechanically joining the two halves around the ceramic gap.

Toroid electrical performance was also very good. Standard commercial magnetics are available with frequency response better than 500 MHz. Since our cables will not pass any greater frequency over the distance between the

*Work supported by the Department of Energy, Office of Basic Energy Sciences, Division of Material Sciences.

†Now at Argonne National Lab

‡Now at TRIUMF

§Now at SLAC

0-7803-0135-8/91$03.00 ©IEEE

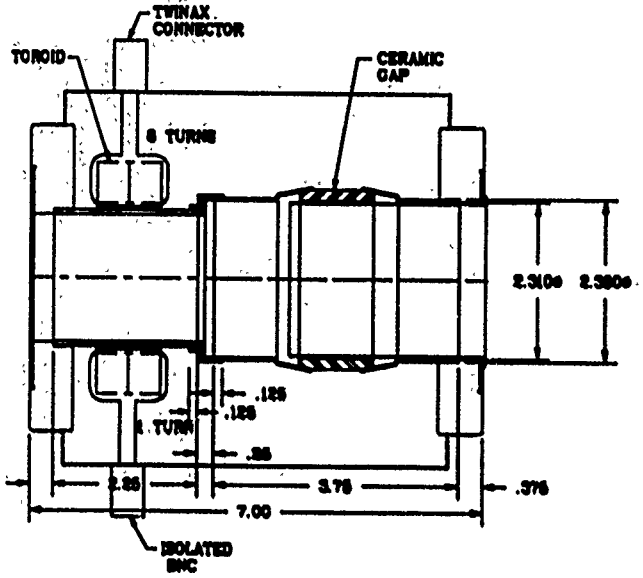


Figure 1
Booster toroid

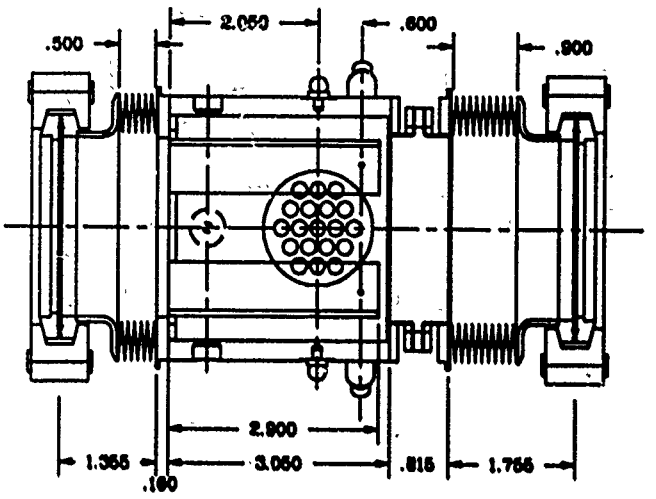


Figure 2
BPM

toroids and the measuring devices, these magnetics were acceptable. A toroid at the exit of the chopper enables us to see, to the resolution of our oscilloscopes, the number of bunches passing through the chopper. Because the toroids perform so well, we chose to use a toroid instead of developing a resistive wall current monitor in the linac. The basic instrument used for looking at these and other fast signals in the ring is a high bandwidth, image intensified oscilloscope, one that enables us to see these fast signals at a 10 Hz repetition rate.

IV. Insertable Screens

Insertable phosphor screens are used throughout the injector, providing valuable information on position and structure of the beam. All screens downstream of the chopper need no special cooling or construction since they see only very low beam currents. The screen which intercepts the largest current, that in the alpha magnet, is made of a more durable material so that it could be attached to a water cooled copper bar that also serves as a Faraday cup.

The screens are routinely used for position information during injection into SPEAR. Standard cameras are positioned outside viewports and bring the image spot back to the control center. Spot position aids beam steering; spot structure aids focusing. Spot intensity is a general machine diagnostic. Machine physics also uses these screens. Energy dispersion and beam emittance can be calculated from measured spot sizes. Quantitative measurements like these are made by analyzing the digitized outputs of an oscilloscope that outputs a standard video raster scan.

V. Beam Position Monitors (BPMs)

Our largest diagnostic system is the beam position measuring system. We greatly benefited from expert consultation from SLAC on the design of the BPMs. Forty modules in the booster ring and twelve in the transport lines provide position information everywhere in the accelerator. The original design called for button electrodes, but tests of prototype modules showed that a 20 dB improvement resulted from the use of shorted 50 Ω striplines in place of the buttons. Each BPM has four striplines 10 cm long, each subtending an azimuthal angle of $\pi/4$ (Figure 2). Even when we have only 10^8 electrons per bunch, the BPM signal is still about 15 mV after travelling through 100 m of RG223 signal cable. With our low normal current, this improvement is very important to maintaining a reasonable SNR for our beam position measuring system [3]. In fact, the BPMs are most valuable in the early stages of commissioning when the beam current is only a fraction of its final operating value. Without the added signal the striplines provide, the BPMs would have been useless during this time. The four striplines in each module allow us to measure both x and y position at each BPM. These modules are oriented azimuthally so that the striplines straddle the horizontal plane of the beam. This minimizes the synchrotron radiation received by any electrode. The BPM positional sensitivity has been measured to be about .6 dB/mm.

The fabrication of the modules was also crucial to their success. For cost reasons, the BPM is a welded assembly, not machined from a single piece of metal. The striplines are made from sectors of a machined tube with an inner diameter of 6 cm. Careful construction techniques and good quality control held the shape and position of the striplines to .1 mm after assembly. The center conductors of 50 Ω ceramic feedthroughs were welded to the striplines to insure a good electrical connection. Electrical center was tested on a fixture that was repeatable to .02 mm. A machined mounting bracket positions the BPMs to an accuracy of .1 mm with respect to the girder. After all tolerances are accounted for, the BPMs are aligned to within .5 mm of the neighboring quadrupoles.

The instrument module also serves as a vacuum pump out port to which a 20 l/sec ion pump may be attached. Good vacuum practice requires a large orifice for the port, while good electrical practice requires an electrically continuous wall for the image current. The compromise that was reached was a circular sieve-like hole pattern for the orifice. Bench tests showed no noticeable degradation of the electrical signal from these ports.

VI. Q Meter

The Q meter is a large, cylindrically symmetric capacitor that converts image current from the beam to a voltage that can be monitored (Figure 3). Because of its cylindrical

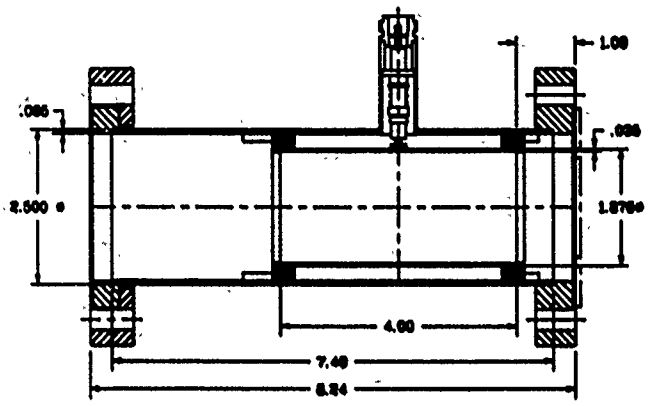


Figure 3
Q Meter

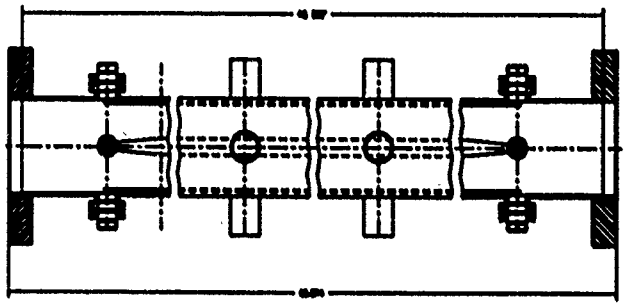


Figure 4
Stripline

symmetry, the Q Meter output is independent of beam position through first order. Its capacitance is about 40 pF, so its frequency response is more than adequate for our needs. The signal from the Q Meter gives the main diagnostic signal for the booster. Displayed on a high bandwidth, image intensified scope, this signal shows the instantaneous current in the booster. The quadrupole tracking supplies are adjusted so as to minimise the step losses from this signal. Since the magnitude of this signal, combined with the low loss cable that carries it to the control console, enables bunches of millions of electrons to be seen, the Q Meter was also very valuable in the early stages of commissioning.

VII. Stripline

One of the by-products of replacing the SLAC to SPEAR injection line was the acquisition of two, one meter striplines units (Figure 4). These units each have four 50 Ω striplines with connections on both ends of each line. We have currently installed one of these units in our booster. Although its signal is comparable to that of the Q Meter, its design gives it great value in allowing us to measure the tunes of the system. This unit is mounted so, like the BPMs, its striplines straddle the horizontal plane. By driving a pair of diagonally opposed striplines with a few watts of power near the tune frequencies, we can excite both the horizontal and vertical tunes of the beam. This is a much less invasive technique than exciting the tunes with large impulses from a kicker, for example. With this technique, one can observe the tunes without dramatically changing the stability or character of the beam. The unused striplines of this unit can then be used to observe the tunes. Coupling between striplines is less than 40 dB, so that the signal due to the beam can be clearly observed. Using a crude, homemade AM detector and a very nice spectrum analyzer that updates at audio rates, we were able to easily measure the tunes and use that information to set them at the design value. A future development project for the injector, using these striplines, is the implementation of a tune feedback system. This system will control the quadrupole supplies that control the tunes, keeping the tunes at the desired value. This system has already undergone preliminary tests at SPEAR.

VIII. Conclusion

The diagnostic instrumentation that was designed and installed at the SSRL injector has proved more than adequate to commission and run the machine. Careful testing of critical components to insure maximum signal output of these devices insured their usefulness and aided in the successful commissioning of the accelerator.

IX. References

[1] S. Baird et al, "Commissioning the SSRL Injector." At this Conference.
[2] H. Wiedemann, "3 GeV Injector Synchrotron for SPEAR." At this Conference.
[3] W. Lavender et al, "The SSRL Injector Beam Position Monitoring Systems." At this Conference.

Bunch Length Measurement using Beam Spectrum *

Z. Greenwald, D. L. Hartill, R. M. Littauer, S. B. Peck and D. H. Rice
Laboratory of Nuclear Studies, Cornell University, Ithaca, NY 14853

Abstract

A procedure for extracting the bunch length from the beam induced voltage spectrum is applied at CESR, for various bunch currents, to indicate whether the turbulent lengthening threshold is exceeded by short, high-current bunches. The approach is to monitor the signal spectrum from one of the detector buttons up to 8 GHz. The measuring system is calibrated by reference to a low-current bunch (1 mA), which is assumed to have a gaussian profile with the theoretically predicted length. In this experiment a single bunch was used with a natural length of 15 mm. No bunch lengthening was detected up to a current of 20 mA.

Introduction

Change of bunch length with current, indicating the turbulent lengthening threshold for short, high-current bunches was searched for in CESR. The approach, using readily available equipment, was to monitor the signal spectrum from one of the beam position detector buttons. To press the limit, the natural bunch length was reduced to $\sigma_l \cong 50\ ps$ by using a lattice with $Q_h \cong 13.2(\alpha_p = 0.0069)$. To calibrate the measuring system we assume that at low current (1 mA) the bunch had a gaussian profile with the theoretically predicted σ_l.

Characteristics of Observed Spectrum

In the absence of coherent beam oscillations, the signal spectrum from a pickup electrode consists entirely of harmonics of the revolution frequency. The envelope of this spectrum is determined by the bunch length. The spectrum is distorted by the transfer function, $F(\omega)$, of the pickup, cable, and any added filters. As indicated below, this distortion is a major effect. However, as long as $F(\omega)$ remains constant, *i.e.*, does not itself depend in any way on bunch current, any changes in the observed spectrum can be attributed to changes in the bunch length. The pickup electrode receives a signal induced by the electric field of the passing bunch. If the electrode has negligble length,

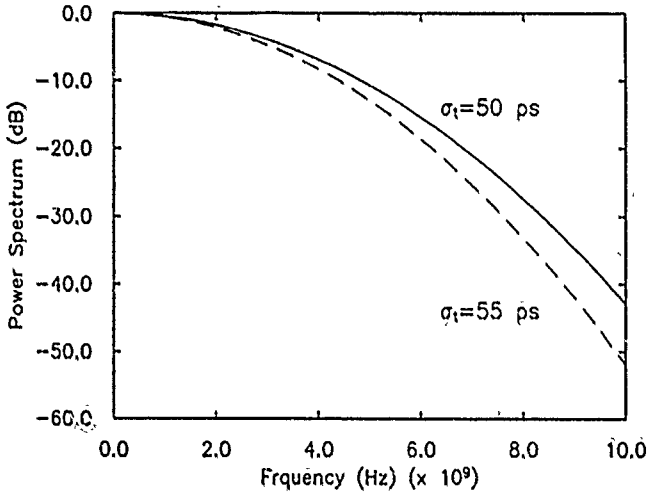


Figure 1: Normalized Gaussian Power Spectrum

the signal from a gaussian bunch, with charge profile characterized by $\sigma_t = \sigma_s/c$, has a gaussian spectrum envelope with $\sigma_\omega = 1/\sigma_t$:

$$V(\omega) = V_o e^{\frac{-\omega^2}{2\sigma_\omega^2}} = V_o e^{-2\pi^2\sigma_t^2 f^2} \qquad (1)$$

The corresponding power spectrum, expressed logarithmically, is

$$P(\omega) = 20\log_{10} V(\omega) = 20\log_{10} V_o - 171.4\sigma_t^2 f^2 [dB] \quad (2)$$

The normalized spectrum of equation 2 is plotted in Figure 1 for $\sigma_t = 50\ ps$ and, for comparison, also for 55 ps, which might be considered a significant fractional bunch lengthening.

As mentioned above, this spectrum is modified by the transfer function, $F(\omega)$ of the monitoring system. The spectrum envelope observed is quite different from that of Figure 1, for the following reasons:

a. If the length of the pickup button is not short compared to σ_s, the charge induced on it varies as the convolution of the button's geometry with the charge profile of the bunch.

b. If the RC time constant of the button is short compared to σ_t, the button signal is given by

*Work supported by the National Science Foundation

0-7803-0135-8/91$03.00 ©IEEE

the current, i.e., by the time derivative of the induced charge. This introduces a factor ω into $F(\omega)$, de-emphasizing the low-frequency components. In practice $RC \simeq 30\Omega \cdot 2pF = 60\ ps$, comparable to σ_t. Thus the actual shape of the low-frequency rolloff is more complicated.

c. The button structure is not properly matched, and the feedthrough insulator has frequency-dependent losses. The high frequency response is extremely uneven: it dips sharply above about 3 GHz, but fortunately shows some 'windows' of usable transmission around 7-8 GHz.

d. For convenience, the signal is brought all the way into the control room. A 26 m long cable has its own high frequency cutoff.

e. Because the signal at the end of the cable can be as large as 100 V peak, it must be attenuated. This was done with a 4 GHz high-pass filter.

Including the effect of the total transfer function $F(\omega)$ on the measured signal, the power spectrum is:

$$P(\omega) = 20\log_{10} F(\omega) + 20\log_{10} V_o - 171.4\sigma_I^2 f^2 [dB] \quad (3)$$

where σ_I is the bunch length at current I. (The bunch shape is assumed to remain gaussian.)

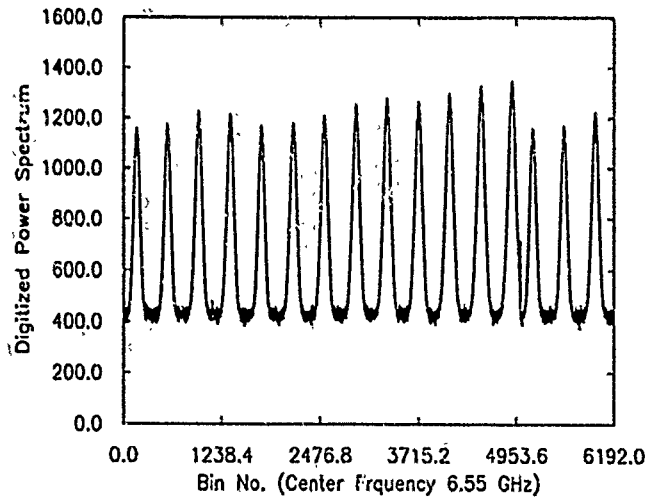


Figure 2: Digitized power spectrum at 12.6 mA in a window of 10 MHz around 6.55 GHz

Measurement Procedure

The measurement consists of recording parts of the spectrum with a low-current bunch, and then repeating the readings at the same frequencies with bunches of progressively larger current. It is clear from Figure 1 that bunch lengthening is most readily detected by covering the spectrum to the highest accessible frequency. The procedure, which eliminates the dependence of the signal on V_o, is to

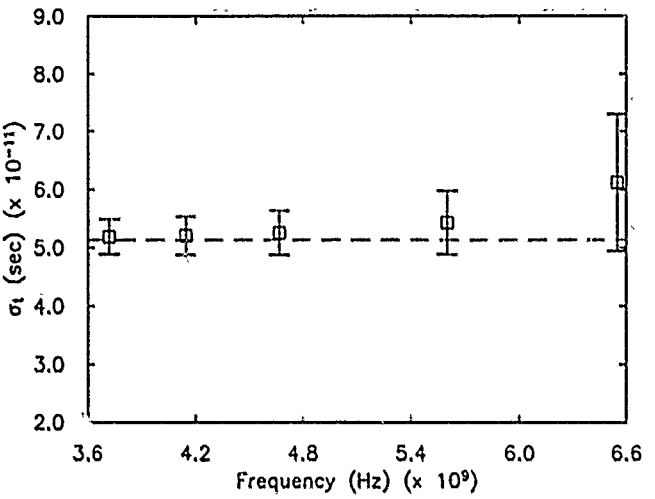


Figure 3: Values of σ_I at 12.7 ma obtained at the different frequencies of the power spectrum

monitor the ratio between the spectrum envelope at some selected frequency, f_n, and at a reference frequency, f_1. If P_n and P_1 are the power spectrum measured at frequencies f_n and f_1, then:

$$(P_n - P_1)_I = 20\log_{10} F_{n1} - 171.4(f_n^2 - f_1^2)\sigma_I^2 [dB] \quad (4)$$

where

$$F_{n1} = \frac{F(\omega_n)}{F(\omega_1)} \quad (5)$$

At low current, we assume that the bunch has the theoretical bunch length,

$$\sigma_o = \frac{\alpha_p \cdot \sigma_E}{\Omega_s \cdot E_o} \quad (6)$$

where $\alpha_p, \sigma_E, \Omega_s$ and E_o are the momentum compaction, energy spread, synchrotron frequency and electron energy, respectively. The low-current measurement then yields

$$20\log_{10} F_{n1} = (P_n - P_1)_o + 171.4(f_n^2 - f_1^2)\sigma_o^2 \quad (7)$$

and

$$\sigma_I = \left(\frac{(P_n - P_1)_o - (P_n - P_1)_I}{171.4\,(f_n^2 - f_1^2)} + \sigma_o^2 \right)^{1/2} \quad (8)$$

where the index '$_o$' is used to denote low current. The error in σ_I due to a measurement error in the spectrum is:

$$\Delta\sigma_I = \frac{\Delta\left[(P_n - P_1)_o - (P_n - P_1)_I\right]}{342.8\,(f_n^2 - f_1^2)\,\sigma_o} \quad (9)$$

Note that, the larger the distance between f_n and the reference frequency f_1, the smaller the error in σ_I.

At the time of the experiment, CESR was operating with a single RF cavity. The data were taken with a lattice of high horizontal tune, $Q_h = 13.2, \alpha_p = 0.0069, \sigma_o = 50psec$, with a single bunch of positrons. The output of the spectrum analyzer was connected to a digitizer and the

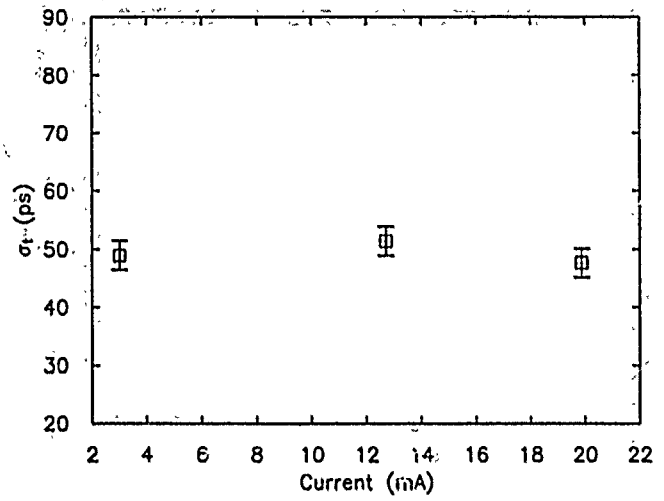


Figure 4: σ_t for different bunch current

data were recorded by a computer. A sample spectrum is shown in Figure 2.

The spectrum was measured at a few different frequencies f_n for each current. For each measurement the power spectrum peaks (see Figure 2) were averaged in a 10 MHz ($\simeq$25 revolution harmonics) window centered on f_n. The reference frequency f_1 was taken at 8 GHz. (For more details about the measurement, see reference [1]). Figure 3 shows values of σ_l at 12.7 mA calculated from equation 8 at the different f_n with the error calculated from equation 9 for $\Delta P = 1\ dB$. The straight line is a least-square fit to the data. Figure 4 shows the bunch length measured in CESR at three currents using the above procedure.

Conclusions

No significant bunch lengthening in CESR was observed up to a bunch current of 20 mA, as seen in Figure 4. This observation agrees with a previous result, obtained in 1983 by detecting the synchrotron light, before the installation of horizontal separators in CESR [2]. Both experiments assume that the bunch shape is gaussian and are thus unable to detect shape changes involving a particular mode [3].

Acknowledgement

Many people from the CESR operating staff helped with the measurements. In particular, thanks are due to R. H. Siemann, M. G. Billing and J. Byrd for suggestions and support.

References

[1] Z.Greenwald et al. CON 90-22

[2] E. B. Blum, R. H. Siemann, D. H. Auston, R. R. Freeman, P. Smith and D. M. Mills, "Bunch Length Measurements in CESR Using an X-ray Sensitive Photoconducting Detector," Nucl. Ins. & Methods, 207 (1983) p. 321

[3] P. B. Wilson, R. Servranckx, A. P. Sabersky, J. Gareyte, G. E. Fischer, A. W. Chao, "Bunch Lengthening and Related Effects in SPEAR II," IEEE Trans. Nucl. Sci., NS-24 (11977), p.1211.

Beam Diagnostics for the 400 MeV Fermilab Linac

Elliott S. McCrory, Fady Harfoush, G. Jackson, Glenn Lee and Dennis McConnell
Fermi National Accelerator Laboratory, Batavia, IL 60510*

Abstract

Prototype beam diagnostics for the 400 MeV linac are being designed and tested. These new diagnostics include: wire scanners, stripline beam position monitors which fit within the quadrupoles, Tevatron-style resistive wall-current-monitors and Feschenko-style bunch length detectors. Several of these devices have been tested with 116 MeV and 200 MeV H^- beam in the present 200 MeV linac.

I. Introduction

The last four 201 MHz Alverez tanks of the twenty-year-old, 200 MeV Fermilab Linac are being replaced by seven high-gradient (7 KV/m), high-frequency (805 MHz) side-coupled-cavity structures to produce a 400 MeV beam for injection into the Booster[1]. Good, reliable beam diagnostics are an important factor in the success of this project, particularly for the commissioning. The diagnostics are being designed with the following challenges in mind.

✓ The space available for diagnostics is limited. There is only the four-meter transition section and $3\beta\lambda/2$ drifts between each accelerating section for the diagnostics.

✓ Good steering is important because the beam takes up a greater percentage of the aperture in the new Linac. In the new Linac, the beam aperture is smaller (3 cm vs the old 4 cm) and β_{max} of the new beam is larger than in the old Linac.

✓ The longitudinal phase-space into which the beam is injected at the beginning of the new Linac is small. Therefore, measuring and understanding the longitudinal match between the two structures is important.

✓ Our old Linac, as reliable as it is, has yielded precious little information about the nature of its beam, especially in its middle where injection to the new linac is to occur. Thus, many plans and designs for the new Linac, the transition section in particular, rely on the existence of excellent diagnostics to identify and correct unexpected features of the beam revealed during commissioning.

✓ And, finally, we will need to commission the new Linac as quickly as possible, so it will be important to have reliable diagnostics as soon as commissioning begins.

We have mafe a design of each of the daignostics elements. Figure 1 shows the mechanical layout of the inter-section regions for the second accelerating module.

II. Diagnostics Systems

A. Beam Position Monitors and Steering Correction

A quadrupole-stripline, non-intercepting beam position monitor (BPM) has been designed and prototyped. The four plates each subtend 20°. The inside diameter of the monitor is 3.25 cm., and the outside diameter is 3.8 cm — just enough to fit inside the pole-tips of the new quadrupole magnets. The overall length is 9 cm. The SMA vacuum feedthrough connectors on the strips are easily accessible between the poles of the quad.

Compact, picture-frame iron dipole magnets of the type used currently are to be used in the new Linac. We have made two types of these magnets: Type 1 is 6.5 cm long and has a total $\int \mathbf{B} \cdot d\mathbf{l}$ equal to 3990 G-cm (at 5 A coil current); Type 2 is 9 cm long and has a total field of 5560 G-cm. The Type 1 magnets will go within modules 1 and 2, where space is most limited; the Type 2 magnets will go everywhere else, including the transition section [2]. With a Type 1 magnet at the beginning of module 1, a kick of 2.7 mrad is achieved.

There is to be a BPM within each quadrupole magnet, four per module, with instrumentation to read out four of the eight available signals from these monitors. This produces four position readings per 2π phase advance (79° per FODO cell),

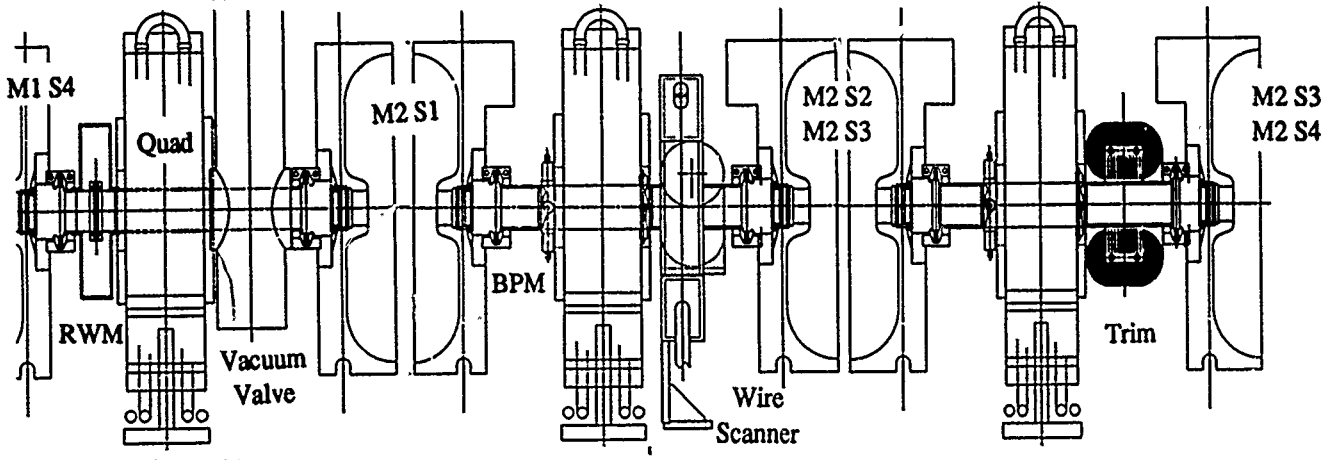


Figure 1, Mechanical layout of the diagnostics within Module 2 of the new Fermilab 805 MHz Linac. The final drift shown here is repeated between sections 3 and 4.

* Fermilab is operated by the Universities Research Association, Incorporated, under contract with the United States Department of Energy.

0-7803-0135-8/91$03.00 ©IEEE

enough readings to accurately measure the steering and the betatron amplitude.

The rf signals from opposite plates of a BPM are converted to dc voltages proportional to the beam position and to the rf intensity by an RF module/decoder similar to the one presently in use [3]. The old design has been modified to increase the bandwidth of the position signal to 25 MHz (from 0.8 MHz).

A Linac control system local control station [4] will run a local application program to actively correct the steering of the Linac on a pulse-by-pulse basis.

B. Wire Scanners

A new, compact two-plane wire scanner has been designed. This stepping-motor-driven device fits in only 4 cm of beam line. Two wire scanners will be installed within module 1, one at a waist in X and the other at a waist in Y. A single wire scanner will be placed in each of the other modules.

A prototype has been installed at the output of Tank 5 in the existing Linac, the injection point of the new side-coupled Linac. Using the penultimate quadrupole magnet in Tank 5, we have measured the beam Twiss parameters with this wire scanner. The technique is the standard one, where the quad gradient is varied and the width of the beam is measured. The resulting curve in gradient-versus-(width)^2-space traces out a parabola whose steepness is proportional to the beam emittance. The results are shown in Figure 2.

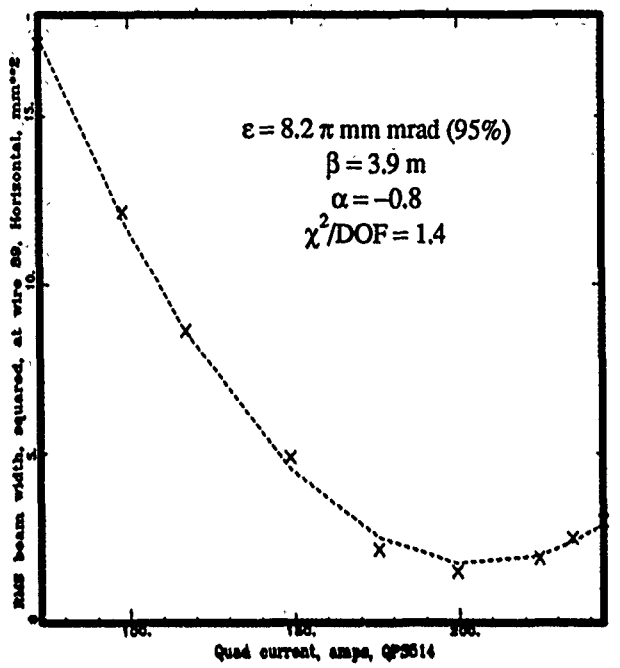


Figure 2, Emittrance results using a single scanning wire and a tuned quad at 116 MeV in the existing Fermilab Linac.

C. Bunch Length Detector (BLD)

A technique exists to accurately measure the phase extent (*a.k.a.* bunch length) and the phase density of a linac beam [5]. We have consulted with A. V. Feschenko and have built some prototypes. The details of the operation of this device can be found elsewhere.[6] Our goal is to obtain a resolution of approximately 1° at 805 MHz; Feschenko obtained a resolution of 0.8° at 198 MHz. Several small changes[6] in Feschenko's design are being implemented to obtain this increased resolution.

A rather high deflector gradient, around 2KV/cm, is required to achieve adequate resolution. A design for that deflector has been made using a pill-box cavity excited in a transverse mode. We will drive it with approximately 400 W of 805 MHz power with the same amplifier used for the driver stage of the klystrons.

We plan to install three BLD's in the transition section, two in the 400 MeV transfer line and one near the end of the linac, possibly within module 7.

D. Resistive Wall Monitors

Resistive Wall-current Monitors (RWM's) have been used with great success in the other accelerators at Fermilab.[7] A design has been made for the new Linac considering the smaller space (3 cm) and the smaller aperture (also 3 cm) of this accelerator. The RWM for Linac has a bandwidth of 6 GHz.

The RWM to be used in our new Linac will have triple duty. In addition to a rudimentary bunch length measurement (their main function in the other Fermilab accelerators), extra ferrite has been added to facilitate a low-frequency beam current measurement. To save space, we have opted not to include Pearson-type beam toroids in our Linac in favor of this readout.

The third function performed by the RWM's is to provide a fast, beam-induced rf signal which will be used in the Δt procedure as the beam-phase readout, see below.

A specially-modified Tevatron-style resistive wall monitor (aperture=8 cm, length=10 cm) has been installed at the output of Tank 5. The output of this detector has been analyzed. For a beam with velocity $\beta<1$, the electric fields from a single particle in the center of the beam pipe spread by an angle which is proportional to $1/\gamma$. Thus, a delta-function beam does not produce a delta-function signal on a wall-current detector. (This, by the way, is the motivation for constructing a bunch length detector as described in the previous section.) Nevertheless, some bunch length information can be obtained from this device. One can compensate for this effect through a deconvolution of the observed signal from the spreading function.[6] The photograph, Figure 3a, is from the new Linac RWM at the output of Tank 5. Using this technique, we infer that this signal was produced from a beam with a phase extent of approximately 30° (±10°), Figure 3b.

E. The Δt procedure

A procedure has been established at several laboratories, most notably LAMPF, to accurately set the phase and gradient of a series of linac accelerating modules. This procedure, referred to as the "Δt procedure," is described elsewhere at this conference [9]. As stated above, it uses the fast, beam-induced rf signal from the RWM at the input to each module for the approproiate time-of-flight/phase information.

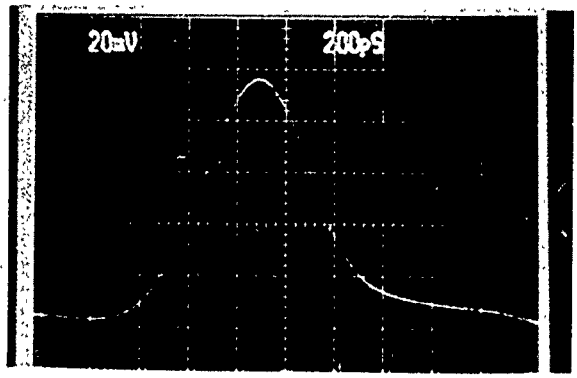


Figure 3a, Signal from RWM at 116.4 MeV (1 GHz scope), observed FWHM≈440 psec.

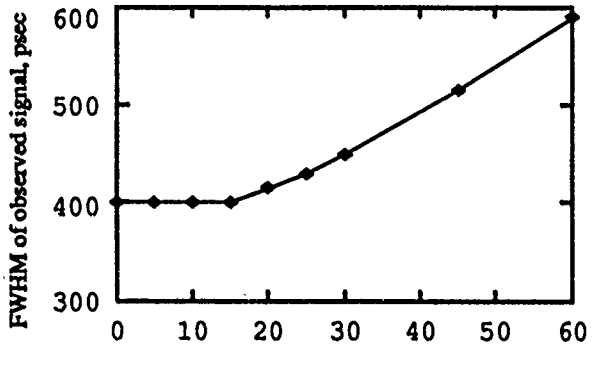


Figure 3b, Results of convoluting beam signal with RWM response function, r=4 cm, E=116.4 MeV

F. Beam Loss Monitors

We will also include beam loss monitors in the new Linac. These devices have not been designed yet.

III. Transition Section

The four-meter-long transition section matches the beam, transversely and longitudinally, from the 200 MHz drift-tube linac to the 805 MHz side-coupled cavity linac. Details on its design can be found elsewhere.[9] Since most of the transition section is drift spaces for longitudinal and transverse matching, there is plenty of space for diagnostics.

Wire scanners are be placed at the beginning, middle and the end of the transition section to facilitate emittance measurement. A simple way to measure emittance is to place the three wire scanners in a field-free region separated by drift spaces, as already implemented in the 200 MeV line. For a more general case, this method requires knowledge of the transfer matrices through the space containing the three wire scanners. For this, we have used TRACE3D [10] with the space charge effect included. (Including space charge makes the transfer matrix dependent on the beam profiles.) In particular, we studied the effects of measurement errors in the beam width, and of quadrupole reading errors on the resulting transverse emittance. For the transition section we have have found that the sensitivity of the calculated transverse emittance on the measured beam width around its nominal value is higher in the vertical plane than in the horizontal plane. The functional form of the sensitivity curve is very close to linear with respect to beam widths at the beginning and end wire scanners, and close to quadratic at the middle wire scanner. Changes in the sensitivity due to space-charge effects are small. Errors due to both quadrupole regulation during the measurement and to reading errors are not significant for the first and last quad, but a 1% error in the second quad makes a 2% error in the emittance.

We plan to include three bunch length detectors in the transition section to allow us to measure the longitudinal emittance of the beam. This method is essentially similar to the transverse emittance measurement just described. Because of the tight space between Tank 5 and the debuncher cavity, the latter had to be moved downward by 10 cm to accommodate a wire scanner, a steering coil and a bunch length detector. Calculations made with TRACE3D have shown that moving the debuncher in this manner without a significant change in its field gradient, still gives an acceptable longitudinal beam profile.

IV. Conclusions

In order to commission the new 805 MHz/400 MeV Fermilab Linac in the allotted time, extensive and accurate beam diagnostics are to be used. In addition to fairly standard beam position monitoring and correcting, we plan to include in the new Linac: wire scanners for emittance measurement, Δt pick-ups to aid in setting the phase and gradient of the high-power klystrons, and bunch length monitoring devices throughout the Linac.

IV. References

[1] Robert Noble, "The Fermilab Linac Upgrade," Proceedings of the 1990 Linear Accelerator Conference, pp 26-30.

[2] Terminology: sixteen side-coupled cavities are braised together to make a *section*, four sections are connected together to make a *module*, a module is powered by a klystron..

[3] R. Webber, *et al.*, "A Beam Position Monitoring System for the Fermilab Booster," Proceedings of the 1987 IEEE Particle Accelerator Conference, IEEE Catalog 87CH2387-9, pp 541-543.

[4] E. S. McCrory, R. W. Goodwin and M. S. Shea, "Upgrading the Controls for the Fermilab Linac," Proceedings of the 1990 Linear Accelerator Conference, pp 474-476.

[5] A. V. Feschenko and P. N. Ostroumov, "Bunch Shape Measuring Technique and its Application for an Ion Linac Tuning," 1986 Linac Conference Proceedings, pp 323-327.

[6] "Design Considerations for a Bunch Length Monitor for the Fermilab Linac" by E. McCrory; FNAL Linac Upgrade #161.

[7] C.D. Moore, *et al.*, "Single Bunch Intensity Monitoring System Using an Improved Wall Current Monitor," proceedings of the 1989 IEEE Particle Accelerator Conference, Vol 3, pp 1513-1515.

[8] T. Owens and E. McCrory, "The Delta-T Tuneup Procedure for the Fermilab Linac Upgrade," this conference, XRA-48.

[9] J. A. MacLachlan, F.E. Mills and L. W. Oleksiuk, "Transition Section Between a 200 MHz Drift Tube Linac and a High Gradient Coupled Cavity Linac for the Fermilab Upgrade," Proceedings of the 1988 Linear Accelerator Conference, pp 106-108.

[10] K. R. Crandall, "TRACE-3D," Los Alamos National Laboratory note LA-11054-MS, August, 1987.

TUNE TRACKERS FOR THE FERMILAB TEVATRON

J. Fitzgerald, R. Gonzalez
Fermi National Accelerator Laboratory*
P.O. Box 500, Batavia, Il. 60510

Abstract

A system for continuous real time measurement of betatron tune has been developed and installed for the Fermilab Tevatron and Accumulator ring. A phase-locked loop, using a considerable amount of input signal preconditioning, is used to lock to a betatron oscillation harmonic in the Schottky detector output signal. This system has demonstrated the capability of measuring the Tevatron fractional tune to an accuracy of $\pm$.002 at 100 Hz bandwidth. The desired tune spectrum line has a very low signal to noise ratio, undesired revolution frequency harmonics, frequency modulation with wide deviations, and amplitude modulation with levels to 100%. Shown are the techniques used to overcome some of these limitations, with examples of the systems accuracy and tracking performance.

Introduction

The tune number is described as the number of betatron oscillations around one revolution of the ring, which is normally in the range of 19.35 to 19.45 for the Tevatron. It is commonly referred to by the fractional part of the number, symbolized by ν. The signal originates from a Schottky detector as a 21 MHz signal, a harmonic of the Tevatron 47 KHz revolution frequency (Frev). This signal is down-converted in two stages by mixing with multiples of Frev leaving a difference frequency of ν(Frev) or nominally 19 KHz.[5] Measuring the frequency and scaling by a fixed value for Frev produces the desired fractional tune value. This method allows the use of a low frequency spectrum analyser to monitor the tune, however they are too slow for making fast time plots or for use in a possible feedback scheme. Another method is to use a phase-locked loop "tune tracker". Described in this report are the efforts to overcome some application problems and optimise the performance of a phase-locked loop (PLL) system.

Design Considerations

The Tevatron Signal:

1. The tune range of .35 to .45 for the Tevatron gives a tune signal range of 16.7 to 21.5 KHz.
2. The output amplitude level is nominally -20dBm, but ranges from -50 to 0 dBm depending on acceleration mode.
3. The signal is normally only 3 to 10 dB above the noise floor. The S/N ratio is calculated from the ratio of the power spectrums[2] and typically has a value less than one.
4. Revolution frequency and betatron oscillation harmonics and sidebands are present at every N(Frev). The largest of these is the tune signal image frequency at (1-ν)Frev (26-31 KHz), (Fig. 1) and is about equal to the desired signal.
5. The signal is frequency modulated (FM), with a gaussian distribution of frequency components of 0 to 1KHz.
6. The signal is also amplitude modulated (AM), (Fig. 2) with levels reaching 100%, and with frequency components to 1KHz BW.

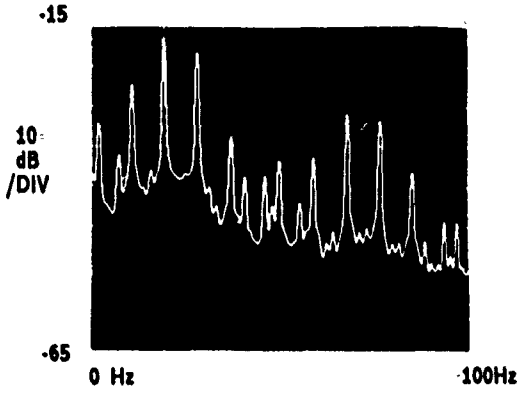


Fig. 1. Frequency spectrum of the tune signal, showing revolution frequency harmonics and sidebands present.

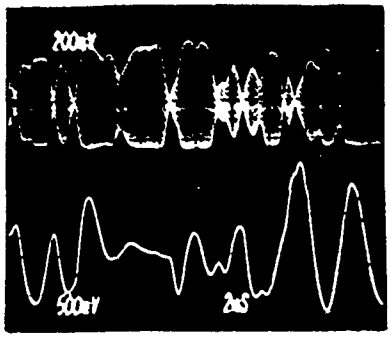


Fig. 2. Typical signal with 100% A.M. (top) and error signal of PLL trying to maintain lock to same signal.

For the Anti-Proton (AP) Accumulator ring a low frequency Schottky detector is used, with output at 245 KHz. A variation of the same PLL system is used, in this case without frequency conversion, but requiring a real time Frev measurement. The AP signal is similar to the Tevatron signal except that it has a better signal to noise ratio and the undesirable harmonics are farther away.

*Operated by Universities Research Association Inc. under contract with the U.S. Department of Energy.

0-7803-0135-8/91$03.00 ©IEEE

Performance Goals:

1. Use a PLL circuit to measure the fractional tune of the Tevatron in real time with resolution and accuracy to within .002 fractional tune.
2. The dynamic response characteristics of PLL, must enable tracking a tune signal containing FM of 500 Hz bandwidth (BW), at a 100 Hz Mod. rate, maintaining accuracy, and FM of 6 KHz BW maintaining lock.
3. The PLL must lock to and track the tune signal from an initial unlock condition, at turn on, or for any frequency step within the tune range.
4. Provide a noise free output to indicate a "locked" condition.

Circuit Design

A review of PLL design theory shows the relative merits of the various types of circuits. There are many types of phase-detectors, but all can be classified as either linear or digital. The PLL textbooks[1,2] strongly emphasize the use of a linear phase-detector for tracking filters, or for any application where the signal is buried in noise.

The digital detector, as its name implies, uses logic gates which are switched at threshold levels, zero crossings, or rising/falling edges. It is highly susceptible to any noise or jitter on the input signal at the threshold levels of the input comparator, while its internal logic functionally stores the resulting false triggers. The output uses logic levels with a varying duty cycle to indicate the phase error, again introducing uncorrelated digital noise.

The linear phase-detector is an analog device, usually a mixer or an integrated circuit multiplier, which actually multiplies the inputs together, giving an output product containing the phase error. Noise on the input signals has an effect on the output only in "linear" proportion to the relative noise power. Small glitches produce a corresponding small amount of phase noise, more readily reduced by the loop filter.

Several different types of phase-detectors were tried on the actual tune signals to check their performance. The above comments were verified, with the digital types able to maintain lock only about 75% of the time, compared to nearly 100% for the linear types. The linear detector however, is amplitude sensitive and since the input has a high level of AM and wide signal strength varation, additional conditioning circuitry is required. References[3,5] indicated that the best performance would be obtained by using a limiter, rather than an automatic gain control circuit.

Shown in Fig. 3 is a block diagram of the Tevatron circuit. The overall circuit includes a narrow bandpass filter, a high gain limiter, and a linear phase-detector. The BPF, an 8th order Chebyshev, attenuates most undesirable harmonics by 40 to 70 dB. The preamp, filter and the limiter combine to produce a dynamic range of about 80 dB, with the PLL section maintaining lock.

The PLL circuit (Fig. 4) used in this system is a second-order type using an active loop filter. The circuit is constructed using separate IC's for the major components, to allow flexibility in the loop filter, loop gain and the output scaling. The loop filter natural frequency is set as low as possible (about 2 Khz), consistent with a damping factor of .7 and gain that allows sufficient tracking and lock in range. The PLL error voltage passes through final filters (post PLL BW limiting), and buffers to provide the outputs.

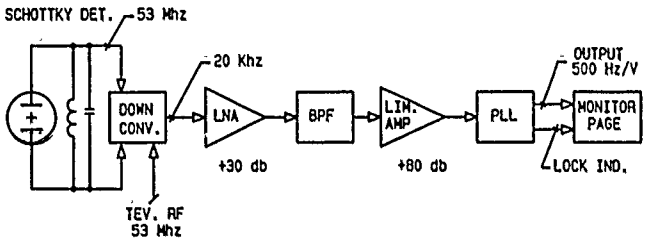


Fig.3. Block diagram of the Tevatron tune measurement system.

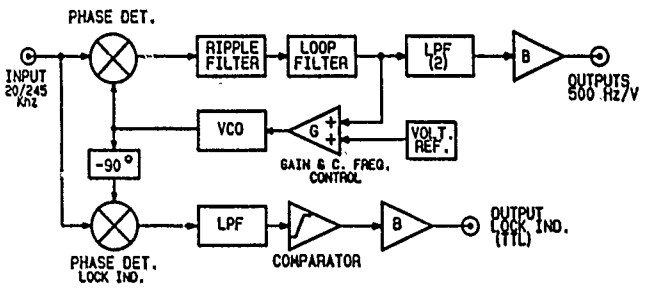


Fig.4. Block diagram of the phase-locked loop circuit.

Results

The performance was monitored during Collider operation and during a recent fixed target run where the "Tune" ranged from .45 at injection to .5 at extraction. Shown in Figs. 5 thru 7 are fast time plots of the PLL output, for complete Tevatron cycles, showing a continuous tune measurements. Comparisons with data from simultaneous measurements with a spectrum analyzer indicate that the system is capable of accuracy to $\pm$ .002 (of fractional tune). The Tevatron Tune distrubances caused by the Main Ring accelerator magnet ramping are quite apparent in Fig. 6. The quality of the signals has a wide variation, depending on the mode of accelerator operation, and is not always sufficient to give this accuracy, or even a locked condition. In this application, vertical signal feedthrough on the horizontal signal (and vice-versa) is too close to be completely filtered out, and tends to pull the PLL off frequency, producing a measurement error.

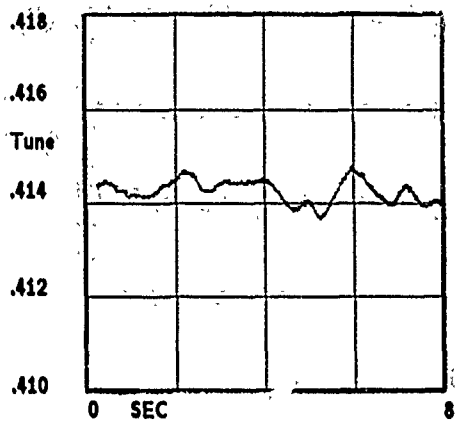


Fig.5 Plot of the Tevatron tune during collider operation.

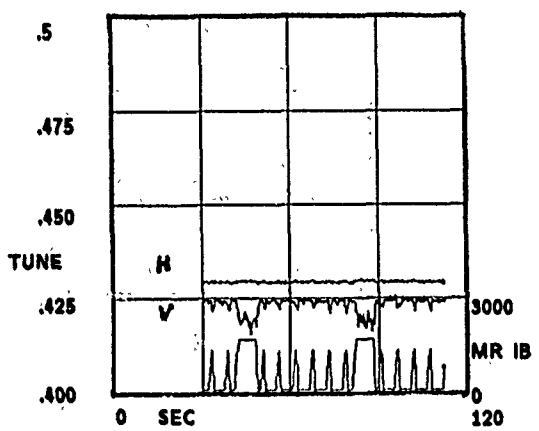


Fig. 6. Plot of the Tev. tune during fixed target run showing tune distrubances caused by the main ring bend current.

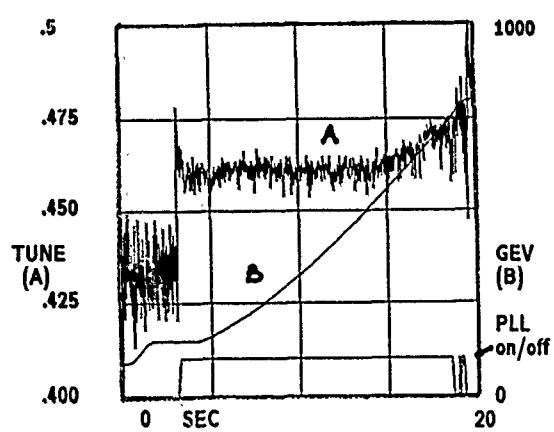


Fig. 7. Plot of the tune during fixed target run showing PLL locking and tracking during accereration.

Conclusions

Because of the complex nature of the input signal, the high noise level, and the various harmonics and modulation present, a study of performance is highly statistical in nature. A phase-locked loop, connected as a tracking filter, will "lock" or center its VCO on the average of the frequency spectrum of the input signal, not necessarily the peak harmonic. The PLL will respond to all harmonics or FM noise in its tracking range, in accordance with their relative power content, as modified by the roll-off characteristics of the loop filter.

The measurement accuracy is therefore somewhat dependent on the signal to noise ratio and the symmetry of the input spectrum. In general, the accuracy of $\pm$.002 tune requires a signal that is at least 5 dB above a relative flat noise floor. Although it is by no means perfect, and has not replaced the spectrum analyzer, this system has shown to be a useful tool for measuring the tune.

The system is under continuing development, in an effort to improve its performance when the signal quality is poor. Testing has shown that the input conditioning circuit is not yet optimised. Under consideration is a narrow-band tracking-filter (adaptive filter), that has shown considerable improvement in isolating the peak signal. Future developments will also include an expanded system, that will provide the capability of beam excitation[6] which greatly increases the detector signal strength when used.

References

[1] Gardner, Floyd M., "Phaselock Techniques", 2nd ed., John Wiley and Sons, New York, 1978

[2] Best, Roland E., "Phase-locked Loops", McGraw-Hill, Inc., New York, 1978

[3] Jaffe, R. and Rechtin E., "Design and Performance of Phase Lock Circuits Capable of Near Optimum Performance Over a Wide Range of Input Signal and Noise Levels", Reprinted by: Lindsey, William C. and Simon, Marvin K., "Phase-Locked Loops & their Application", IEEE Press, pp. 20, New York, 1978

[4] Johnson, David E. and Hilburn, John L., "Rapid Practical Designs of Active Filters", John Wiley & Sons, pp. 145, New York, 1978

[5] Martin, D. et al., "A Schottky Receiver for Non-Perturbative Tune Monitoring in the Tevatron", Proceedings of the 1989 IEEE Particle Accelerator Conference, Chicago, IL

[6] Linnecar, T. et al., "Continuous Tune Measurements Using the Schottky Detector", IEEE Transactions on Nuclear Science, Vol. NS-30, No. 4, pp. 2185, 1983

COUPLED BUNCH DIPOLE MODE MEASUREMENTS OF ACCELERATING BEAM IN THE FERMILAB BOOSTER

D. McGinnis, J. Marriner, V. Bharadwaj
Fermi National Accelerator Laboratory *

Abstract--The dipole oscillation of a coupled bunch mode is measured using a fast single shot digitizing oscilloscope. The phase centroid of the bunches is determined from the digitized waveform. The phase error of the bunches as a function of bunch number is then Fourier analyzed which provides the coupled bunch mode spectrum. The resulting spectrum is used to determine the evolution of coupled bunch mode instabilities in the Fermilab Booster. This method can determine the coupled bunch mode spectrum in a single turn in contrast to frequency domain methods which take at least a full synchrotron period to complete the measurement.

I. INTRODUCTION

The Fermilab Booster accelerates protons from 200 MeV to 8 GeV in 33.3 milliseconds. Coupled bunch oscillations occur when the intensity of the Booster reaches $1x10^{12}$ protons. While these oscillations are not a problem under the present operating conditions, the intensity in the Booster after the Fermilab Linac upgrade is completed is expected to be $5x10^{12}$ protons. With these intensities, the coherent motion of the bunches within the RF buckets causes a dilution of the longitudinal emittance. The dilution occurs primarily because of the unpredictable position of the bunches relative to the RF voltage when the beam is transfered from the Booster to the Main Ring. Presently, there is an effort to build longitudinal dampers that reduce the coupled bunch mode oscillations[1].

The Booster RF frequency swings from 30 MHz to 53 Mhz. The RF frequency slew rate has a maximum of 3 MHz/mS at the beginning of the acceleration cycle and is about 200 kHz/mS midway through the cycle. The synchrotron frequency ranges from 30 kHz at injection to 2 kHz at extraction. Bunch oscillations can be detected by examining the phase modulation (PM) sidebands around revolution lines of the longitudinal frequency spectrum [2]. The spacing between the PM sidebands is equal to the synchrotron frequency. Because of the large RF frequency slew rate, the 2 kHz resolution needed to resolve the PM sidebands is impossible to obtain with a conventional spectrum analyzer. With this lack of resolution in spectrum analyzer data, it is not possible to distinguish between unequal bunch population phenomena and coupled bunch modes.

This dilemma can be resolved by mixing the longitudinal signal with a harmonic of the revolution frequency which is derived from the RF. The mixed signal is then fed into a spectrum analyzer were the resolution can be increased so that the PM sidebands can be detected. The disadvantage to this approach is that a mixing circuit has to be built for each coupled bunch mode to detect all the coupled bunch modes with a single shot of beam. Also, because the signal is Fourier analyzed, the time at when a coupled bunch mode appeared in the acceleration cycle is uncertain to within the inverse of the resolution bandwidth of the spectrum analyzer.

II. THEORY OF MEASUREMENT

According to the theory of Sacherer [3], the distribution function for a single bunch in the presence of collective forces can be written as:

$$g(r,\theta) = g_0(r) + \sum_{m=1}^{\infty} g_m(r)\cos(m\theta) \qquad (1)$$

where g is the distribution including the instability and go is the unperturbed distribution. The variables r and θ are the radius and angle in the longitudinal phase space that have been normalized to make the unperturbed trajectories circular. The sum is taken over the unstable modes: m=1 for dipole, m=2 for quadrapole, etc. The distribution functions of the other bunches are identical to Eqn. 1 except that unstable modes a multiplied by a phase that advances by $2\pi n/K$ per bunch where K is the number of bunches. The complete distribution for the K bunches contains a double sum over m (mode type) and n (azimuthal mode number) with independent coefficients for each (m,n) pair:

$$g(r,\theta,k) = g_0(r) + \sum_{n=0}^{K-1}\sum_{m=1}^{\infty} B_n g_m(r)\, e^{j2\pi nk/K}\cos(m\theta) \qquad (2)$$

where k is the bunch index. If the left hand side of Eqn. 2 is measured, the dipole instability term can be isolated by multiplying both sides of the equation by $\phi = r\cos(\theta)$ and integrating over r and θ. The resulting equation:

$$\langle\phi_k\rangle = \pi\int r^2 g_1(r)\,dr \sum_{n=0}^{K-1} B_n e^{j2\pi nk/K} \qquad (3)$$

tells us that the average phase error is proportional to the strength of the dipole perturbation. While the isolation of the dipole term is exact within Sacher's formulation, the experimental technique is not sufficiently precise to guarantee that there is no admixture of higher modes. We have neglected changes the bucket area that occur during acceleration; these changes are relatively small during the portion of the cycle when the instability is observed.

* Operated by the Universities Research Association under contract with the United States Department of Energy.

0-7803-0135-8/91$03.00 ©IEEE

Given the average values $\langle\phi_k\rangle$ for the K bunches in the machine, one can use discrete Fourier analysis to determine the relative strengths B_n of the various azimuthal modes:

$$B_n = \frac{\sum_{k=0}^{K-1} \langle\phi_k\rangle e^{-j2\pi nk/K}}{K\pi \int r^2 g_1(r)\, dr} \qquad (4)$$

III. MEASUREMENT ALGORITHM

Step 1 The instantaneous beam current as a function of time is obtained for a single turn in the acceleration cycle. This is done by placing a detector (a resistive wall monitor) at a fixed location in the ring and digitizing the wall current as a function of time for one turn with an high speed oscilloscope. The oscilloscope used in this paper was the Tektronix DSA 602 which has a single shot digitizing rate of 2 gigasamples/second. Since the average length of a single turn in the Fermilab Booster is about 2 υS, a record length of 4096 points is needed (the DSA 602 has a maximum record length of 32,768.).

Step 2 The approximate location of the bunch centers is determined. This can be done by searching for the first bunch and then finding the rest of the centers aided with the knowledge of the RF frequency for the turn when the data was taken.

Step 3 For each bunch, the centroid is computed according to Eqn. 3. This is done by multiplying the bunch profile by time and integrating. The centroid is normalized by dividing by the total charge in the bunch. In this way variations due to unequal bunch populations are eliminated.

Step 4 The phase advance of the bunches due to the RF frequency and slew rate is found and removed from the data. The centroid spacing between adjacent bunches will be a combination of the coupled bunch mode oscillations and the phase due to the RF frequency. The phase differences due to the RF can be found by making a least squares fit to the the phase centroids according to the following form:

$$\langle\phi_k\rangle_{fit} = \phi_0 + \phi_1 k + \phi_2 k^2 \qquad (5)$$

The coefficient ϕ_0 is due to when the measurement was taken with respect to the RF. The coefficient ϕ_1 is due to the linear increase of phase due to a fixed RF frequency. The coefficient ϕ_2 is due to the slewing of the RF frequency with respect to time. Higher order corrections are small enough to be neglected. Once the coefficients ϕ_0, ϕ_1, ϕ_2 are obtained, they are subtracted from the actual phase centroid data to obtain the phase error due to the coupled bunch motion. The coupled bunch phase error for a typical turn in the Booster is shown in Fig. 1.

Step 5 Fourier analysis according to Eqn. 4 is performed to provide the coupled bunch mode coefficients B_n. From Eqn. 3 it can be shown that the number of phase oscillations for mode n is the same as the number of oscillations for mode K-n. The coupled bunch mode content of the wavefrom shown in Fig. 1 is displayed in Fig. 2.

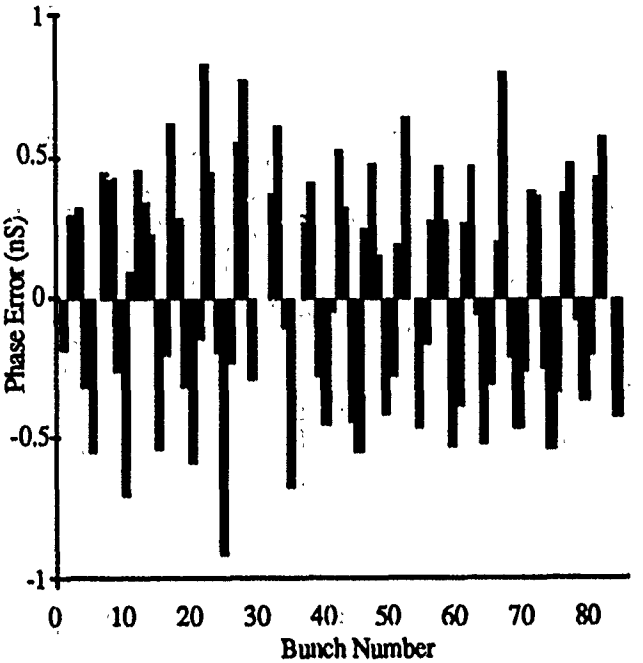


Fig. 1 Phase error of each bunch for 32 mS into the acceleration cycle. Intensity = $1x10^{12}$ protons.

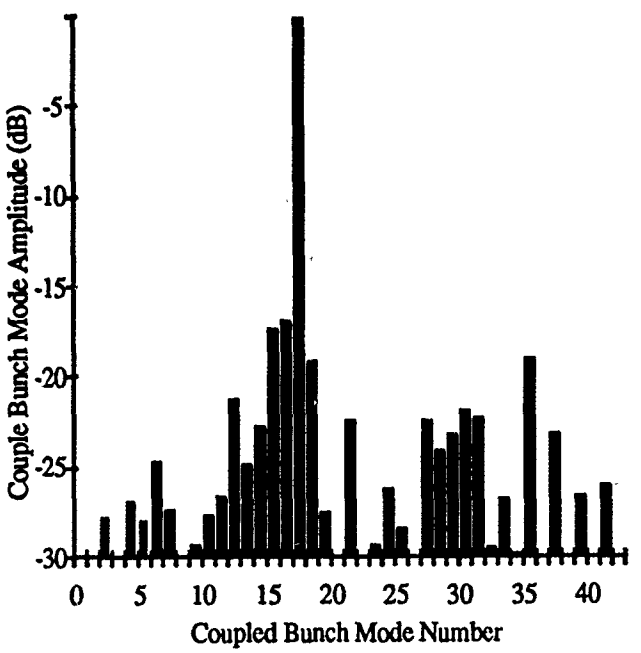


Fig. 2 The coupled bunch mode content of Fig. 1.

Step 6 The coupled bunch mode spectrum is obtained as a function of time in the cycle. This is done by repeating Steps 1-5 for different turns throughout the acceleration cycle. However, to record the entire acceleration cycle with a digital oscilloscope would require a record length of 66 million

points. Since such a record length is not possible, a new batch of beam can be injected for each measurement. This will yield satisfactory results if the operating conditions of the booster remains stable during the measurements. Experimentally this has been found to be the case. Figures 3 and 4 show the coupled bunch mode spectrum as a function of time for two different beam intensities.

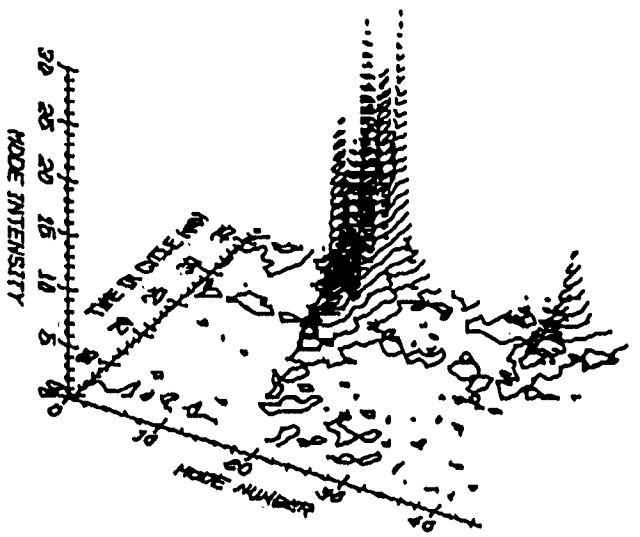


Fig. 3 Coupled bunch mode spectrum as a function of time for a beam intensity of $1.2x10^{12}$ protons. The mode intensity is units of nSx84

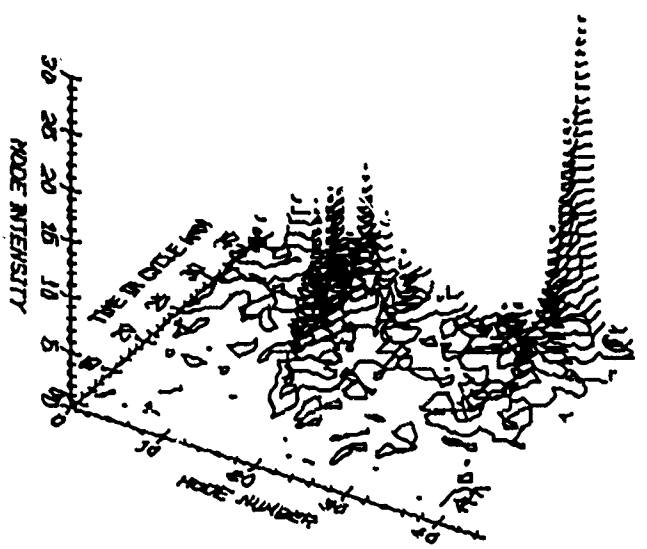


Fig. 4 Coupled bunch mode spectrum as a function of time for a beam intensity of $2.5x10^{12}$ protons. The mode intensity is units of nSx84

Once the mountain range display shown in Figs. 3 and 4 is obtained, the evolution of a particular mode as a function of time may be analyzed. Figure 5 shows the evolution of mode 17 for a beam intensity of $1.2x10^{12}$ protons. The data can be fitted to an e-folding rate of 5.5 mS. However, this number may not reflect the maximum growth rate due to nonlinearities during the growth process.

IV. SUMMARY

Using a fast single shot digitizing oscilloscope, one can determine the coupled bunch mode profile in a single turn. This has an advantage over frequency domain techniques which require at least a synchrotron period to determine the profile. However, one disadvantage to the time domain method is the higher order multipole contributions (quadrupole, sextapole,...) can not be completely resolved because of the limited digitizing rate of the oscilloscope.

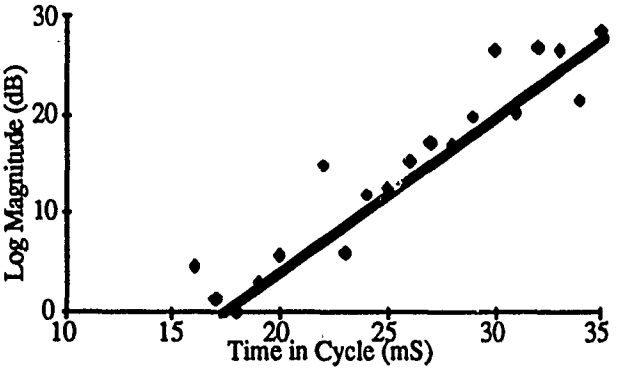


Fig. 5 Intensity of mode 17 versus time in the acceleration cycle for 1.2x1012 protons.

REFERENCES

[1] I. Haberman and I. Rypshtein, "Longitudinal Damping System For the Fermilab Booster," Presented at the IEEE 1991 Particle Accelerator Conference, San Francisco.

[2] F. Pederson and F. Sacherer, "Theory and Performance of the Longitudinal Active Damping System For the CERN PS Booster," Presented at the 7th National Particle Accelerator Conference, Chicago, March 1977.

[3] F. J. Sacherer, "A Longitudinal Stability Criterion for Bunched Beams," IEEE Transactions on Nuclear Science, Vol.NS-20, No. 3, pg 825, June 1973

BEAM TRANSFER FUNCTION MEASUREMENTS OF ACCELERATING BEAM IN THE FERMILAB BOOSTER

D. McGinnis, J. Marriner, V. Bharadwaj
Fermi National Accelerator Laboratory*

Abstract--Beam transfer function measurements were performed on accelerating beam in the Fermilab Booster with a network analyzer and a custom signal processing system. Since the Booster RF frequency slews from 30 to 53 MHz in 33 mS, an intermediate frequency processing circuit was built external to the reference and receive ports of the network analyzer. This circuit permitted resolution of 2.5 kHz synchrotron sidebands while the Booster RF frequency changed from 500 kHz in 15 mS.

I. INTRODUCTION

Presently, there is an effort at Fermilab to build longitudinal coupled bunch mode dampers for the Booster [1]. To determine the gain needed for the damper system, the transfer impedance of the pickup and kicker must be known. Also the delay and phase intercept of the damper system must match the beam response from pickup to kicker. These parameters can be measured using a network analyzer inserted in the damper system to measure the open loop gain as shown in Fig. 1.

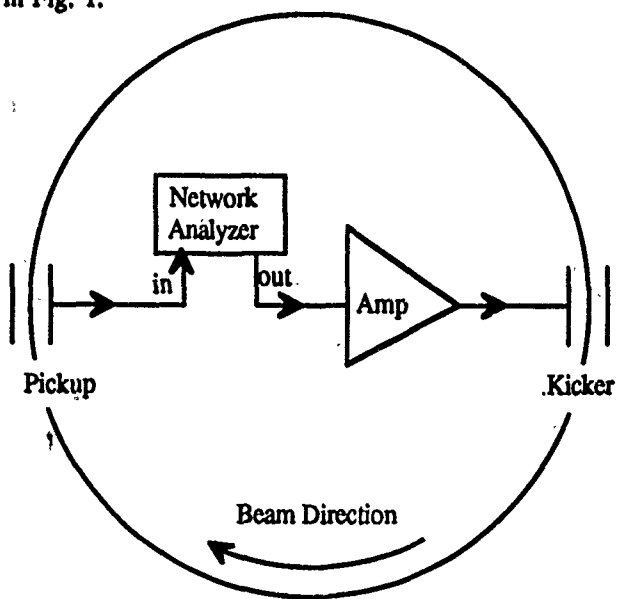


Fig. 1. Schematic of a network analyzer measurement for a circular accelerator.

The Booster accelerates protons from 200 MeV to 8 GeV in 33 mS. Since the machine circumference is 475 m, the revolution frequency must change from 360 kHz to 630 kHz in 33 mS. The revolution frequency for the last half of the acceleration cycle is shown in Fig. 2. A sketch of the beam transfer function at a given instant in the acceleration cycle is shown in Fig. 3. The spacing between the multipole lines is equal to the synchrotron frequency. After transition, which occurs about half way through the acceleration cycle, the synchrotron frequency is about 2.5 kHz and remains fairly constant until the end of the acceleration cycle.

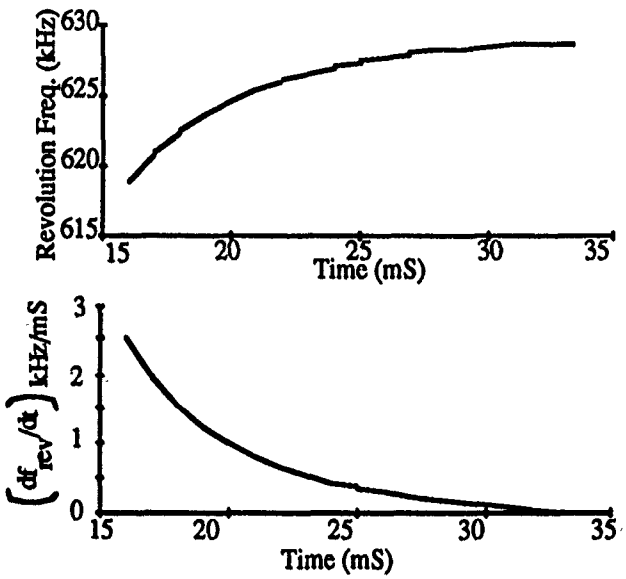


Fig. 2. Revolution frequency and rate of change of revolution frequency vs. time in the acceleration cycle for the last half of the cycle.

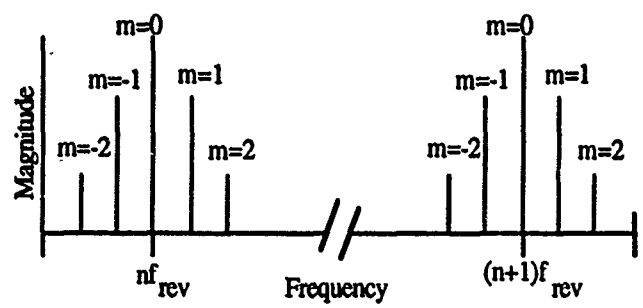


Fig. 3. A schematic representation of the magnitude of the beam transfer function for two neighboring revolution lines. m=0, ±1, ±2, ... indicate monopole, dipole, quadrupole, ... modes

The frequency scale of the beam transfer function shown in Fig. 3 will change during the acceleration cycle along a curve that is harmonically related to the frequency versus time curve of Fig. 2. The length of time that a network analyzer must dwell at a single frequency is inversely proportional to the resolution bandwidth of the network analyzer. Thus, if the resolution bandwidth is too low, the network analyzer will excite more than one multipole line for a given frequency. Expanding the frequency versus time curve in a Taylor series and keeping terms up to first order, it can be shown that in

* Operated by the Universities Research Association under contract from the United States Department of Energy.

0-7803-0135-8/91$03.00 ©IEEE

order for the network analyzer to excite only one multipole line, the following inequality must hold:

$$n\frac{df_r}{dt}\Big|_{t_0} < \frac{f_s f_{IF}}{2} \qquad (1)$$

where n is the harmonic number, f_r is the revolution frequency, t_0 is the time in the acceleration cycle when the measurement is taken, f_s is the synchrotron frequency, and f_{IF} is the resolution bandwidth of the network analyzer. For example, if n=84 (this is the harmonic number of the RF), f_s=2.5 Khz, f_{IF}=3 kHz, then the rate of change of the revolution frequency must be less than 44 Hz/mS. According to the second graph of Fig. 2, this condition does not occur until the last moment of the acceleration cycle.

II. Measurement Theory

To remedy the situation described by Eqn. 1, the frequency of the network analyzer reference should track a harmonic of the revolution frequency. A circuit that provides such a reference is shown in Fig. 4. In this circuit, a portion of the low level RF of the accelerator is fed into the clock of a direct digital synthesizer. The direct digital synthesizer (for more information on the DDS circuit, see Ref. [2]) is programmed by the computer to provide a frequency output that is a fraction of the clock signal. (for example if the RF harmonic number is 84 and the DDS fraction is 16/84, the output frequency of the DDS is equal to the sixteenth harmonic of the revolution frequency.)

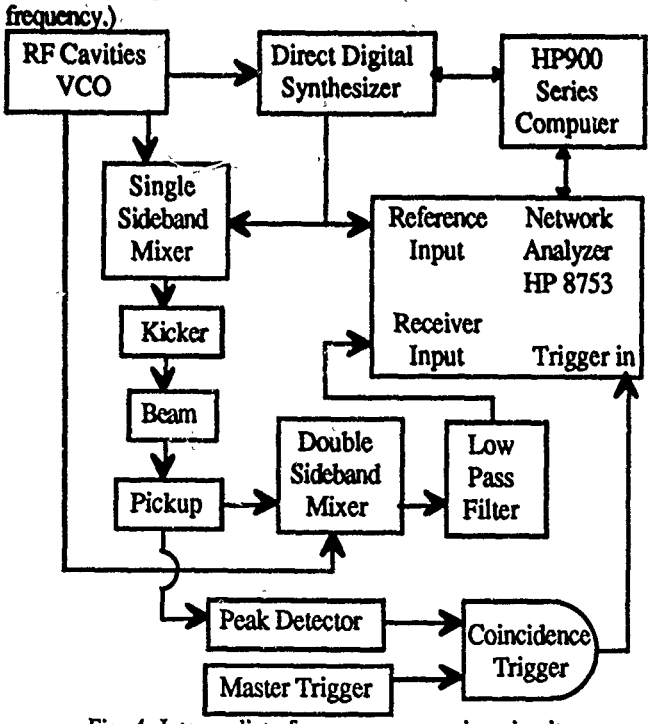


Fig. 4. Intermediate frequency processing circuit.

Because of the limited frequency range of the DDS circuit (The one used for this paper is the QUALCOMM Q0310 Evaluation Board which has a maximum frequency range of 25 MHz.), the DDS output is mixed in a single sideband mixer with the RF VCO output to provide a frequency that is (84 - $DDS_{fraction}$)*f_{rev}. A single sideband mixer is necessary so that only one RF harmonic is excited. To keep the frequency swing in the reference leg small so that the network analyzer will not lose phase lock, the DDS output is also used for reference leg of the network analyzer.

The mixed-up signal is then applied to the beam via the kicker and the response is detected by the pickup. To make the received signal frequency the same as the reference frequency, the pickup signal is mixed down with the low level RF signal where the high frequency component of the mixing product is eliminated by a low pass filter.

Since the reference frequency of the network analyzer is not constant during the measurement, the network analyzer is placed in the Continuous Wave (CW) mode and the amplitude and phase of the ratio of the pickup signal to the reference is displayed as a function of time throughout the accelerator cycle. To trigger the network analyzer at the proper time in the cycle and trigger only if there is beam in the machine, the pickup signal is peak detected and a coincidence gate is formed with the accelerator clock.

The measurement described above is performed for only one fractional revolution harmonic. To obtain the response as a function of the fractional revolution harmonic, the computer must increment the fraction, a new batch of beam must be injected into the accelerator, and the network analyzer must be re-triggered. This procedure will yield satisfactory results if the operating conditions of the Booster remains stable during the measurements. Experimentally, this has been found to be the case. However, for extra conditioning, the response for a given fractional revolution harmonic can be averaged for a number of beam batches before changing the fraction. This averaging also has the added benefit of reducing signals caused by beam instabilities the are not phase related to the kicker signal.

Since the DDS frequency will not track a multipole line exactly during the acceleration cycle, the width of a given multipole line must be large enough so that the crossing of the DDS frequency through the multipole line will take long enough to fill the IF filter of the network analyzer. By expanding the frequency versus time curve in a Taylor series and keeping terms up to first order, the requirement on the synchrotron line width can be written as:

$$\frac{\Delta f_s}{f_s} > \frac{2\left(\frac{1}{f_r}\frac{df_r}{dt} - \frac{1}{f_s}\frac{df_s}{dt}\right)}{f_{IF} + \frac{1}{f_s}\frac{df_s}{dt}} \qquad (2)$$

Near transition, which is at 18 mS in the Booster, the right hand side of Eqn. 2 will approach 100% because the synchrotron frequency goes to zero. However, after about 21 mSec into the cycle, the synchrotron frequency reaches 2.5 kHz and remains fairly constant for the rest of the cycle so that the right hand side of Eqn. 2 is well under 5%.

III. Results

Figs. 5-7 show the results of a network analyzer measurement performed on accelerating beam in the Booster during the last 15 mS of the acceleration cycle. The network analyzer was uncalibrated so the magnitude of the results is unnormalized. The beam intensity was $1x10^{12}$ protons. The number of points along the time axis is 26. The number of revolution fractions is 220. For this measurement, the number of averages at each revolution fraction was 10. With the Booster operating at a repetition rate of about 4 seconds, this measurement took about 2.5 hours to complete. The measurements were centered around the 74th revolution harmonic. (the DDS fractions were centered around 10/84.)

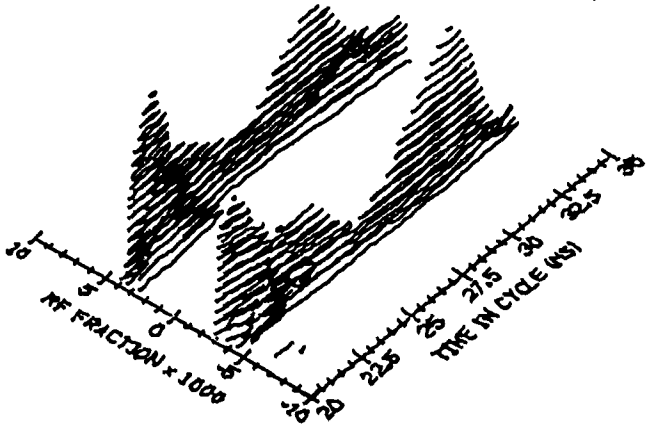


Fig. 5. The linear magnitude of a network analyzer measurement as a function of the DDS RF fraction and time in the acceleration cycle. The RF fraction axis is centered around the 74 revolution harmonic.

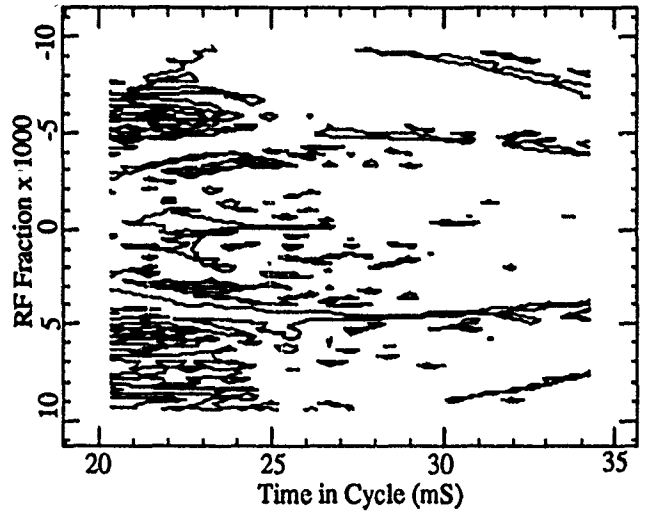


Fig. 6. The 90° phase contours of the network analyzer measurement shown in Fig. 5.

Figure 5 is a three dimensional contour plot of the beam transfer function versus time in the cycle and fractional revolution frequency. As seen in Fig. 5, the only part of the response that is greater than the noise floor is a set of dipole lines located near the revolution fraction = ±0.004. This revolution fraction coincides with a synchrotron frequency of 2.5 kHz. Figure 6 shows a phase contour of the response for 90°. Because the phase contour correlates well with the magnitude contours shown in Fig. 5, it is very likely the the signal received by the network analyzer is indeed due to the signal sent out by the network analyzer. Figures 7a-c are the response versus revolution fraction at a single instant in the acceleration cycle. These figures clearly show the dipole response of the beam. Also Figs. 6 and 7a show a slight hint of the quadrupole lines.

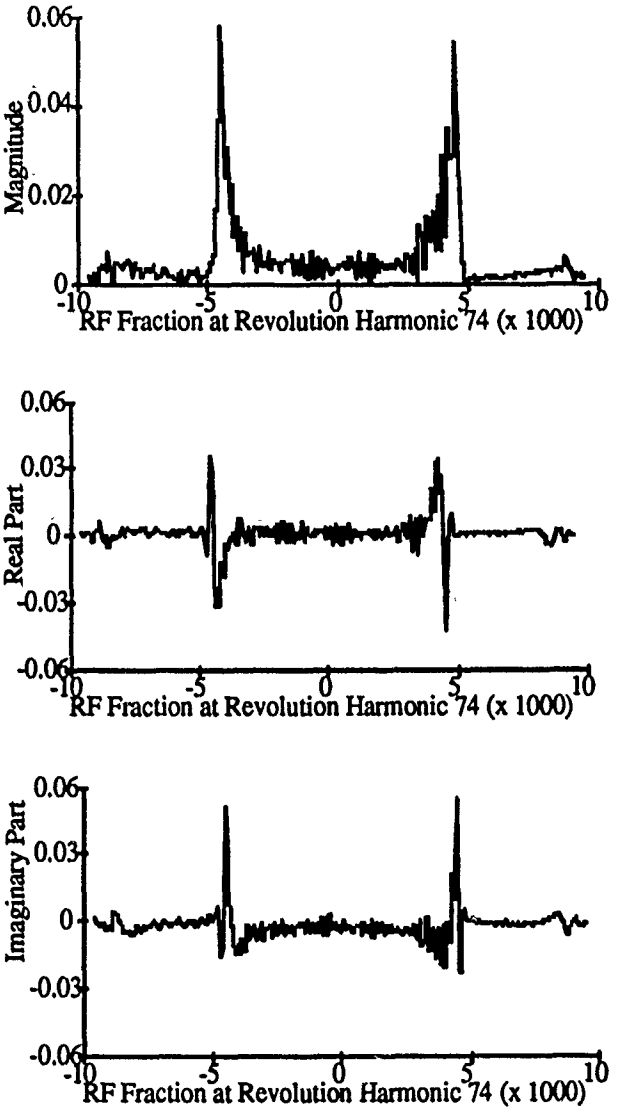


Fig. 7a-c. The magnitude, real, and imaginary response of the network analyzer measurement at a single instant in time centered around 31.5 mS into the acceleration cycle.

IV. ACKNOWLEDGEMENTS

The authors would like to thank J. Budlong and D. Peterson for their invaluable assistance.

REFERENECES

[1] I. Haberman and I. Rypshtein, "Longitudinal Damping System For the Fermilab Booster," Presented at the IEEE 1991 Particle Accelerator Conference, San Francisco.

[2] D. Peterson and J. Marriner, "A Frequency Tracking System for Beam Diagnostics," Presented at the IEEE 1991 Particle Accelerator Conference, San Francisco.

Diagnostics for the MLI Model 1.2-400 Synchrotron Light Source

Dan Y. Wang and Robert Legg
Maxwell Laboratories, Inc., Brobeck Division
4905 Central Avenue
Richmond, California 94804

Abstract

The MLI Model 1.2-400 Synchrotron Light Source is designed for operation at 1.2 GeV at a beam current of 400 mA. An integrated set of diagnostics that meets the needs of all stages of commissioning is required for this commercially produced storage ring. The design of each component will be discussed in light of its use during commissioning, with emphasis on the essential beam position monitoring electronic system.

I. Introduction

The ring consists of a Chasman-Green lattice with four-fold symmetry. The injector is a 200 MeV linac. The storage ring and linac are connected via a transport line useful for analyzing the linac beam. For a successful and rapid commissioning, it is necessary to have an integrated set of diagnostics which monitors relevant system performance parameters.

Section II contains a diagnostics plan relating key system performance parameters to specific beam measurements, and thence to the particular diagnostic element for performing this measurement. Sections III and IV describe the design specifications of individual diagnostics in the transport line and storage ring respectively and show how these designs are governed by the requirements established in section II. Proceeding from the diagnostic plan, these diagnostics are sufficient for commissioning with minimal frills. Section V is a detailed description of the beam button position monitor electronics system in the ring.

II. Diagnostics Plan

The system performance parameters of interest during commissioning, the corresponding beam property to be measured and the diagnostic to be used for this beam measurement are summarized in Table 1.

Table 1. Summary of Diagnostics

SYSTEM PERFORMANCE PARAMETER	BEAM PROPERTY/ MEASUREMENT	DIAGNOSTIC DEVICE
injection efficiency	linac beam intensity within specified energy spread	energy selective slit with current monitor, Faraday cup
transport line transmission efficiency	linac beam emittance	fluorescent screen assembly
	beam positions along transport line	fluorescent screen assemblies (8 total)

Table 1. Summary of Diagnostics, *continued*

SYSTEM PERFORMANCE PARAMETER	BEAM PROPERTY/ MEASUREMENT	DIAGNOSTIC DEVICE
ease of finding closed beam orbit	first turn beam position in ring	ring fluorescent screen assemblies (4 total); Sabersky finger
	multiple turn beam survival in ring	single buttons distributed in ring
ease of optimizing closed orbit	beam positions around ring	13 BPM stations distributed in ring
conformity of lattice with theoretical model:		
betatron tunes	beam oscillation frequencies	traveling wave electrodes (coupled to spectrum analyzer) (2 sets)
dispersion function	beam orbit at different rf frequencies	13 BPM stations
lattice Twiss functions	tune change with quadrupole perturbations	traveling wave electrodes
beam lifetime	beam current	dc current transformer (DCCT)
beam emittance	beam size within dipoles	optical monitoring station

III. Transport Line Diagnostics

The transport line diagnostics consist of two slit assemblies (with attached screens), three current monitors, a Faraday cup, and six fluorescent screen assemblies.

Slit assembly
- *slit jaw thickness:* 1 cm
- *jaw material:* heavy metal (tungsten-copper)
- *slit opening range:* 0-50 mm
- *resolution:* < 0.01 mm
- *alignment of beam:* fluorescent screen attached to front of jaws

Toroid current monitor
- *sensitivity:* 10 V/A
- *risetime:* < 2 ns

Faraday cup
- *range:* 0.2 nC to 20 nC (10 Hz rate) (with picoammeter)

0-7803-0135-8/91$03.00 ©IEEE

The linac beam has a nominal intensity of 25 mA (100 ns pulse average, 10 Hz cycle) within an energy spread of ± 0.25%. The slit assembly is placed after a 90 degree bend magnet, where the dispersion is 0.71 m and the intrinsic beam width is 0.22 mm (3σ). Thus by opening the slit width to 3.55 mm, the energy spread of the unscattered beam passing through will be ±0.25% with an uncertainty of ±0.03%. Its intensity is measured by the toroid monitor which is interfaced with an oscilloscope and calibrated against the Faraday cup.

fluorescent screen assembly

resolution: 0.25 – 0.4 mm (at 12.5 mA, 100 nsec pulse)
fluorescent screen material: chromox
camera: vidicon/ultricon

With a vacuum chamber aperture of 25–50 mm and beam sizes of a few millimeters, a resolution of 0.4 mm is more than adequate for measuring beam size and position along the transport line in general. However, a better resolution of 0.25 mm is needed for measuring the beam emittance of 0.31 π•mm•mrad.

IV. Ring Diagnostics

The ring diagnostics consist of a Sabersky finger, four fluorescent screens, 13 four-button beam position monitors, two traveling wave electrode stations, a dc current transformer (DCCT), and an optical monitoring station.

Sabersky finger (see figure 1)

width: 1.6 mm
material: heavy metal (tungsten-copper)
location: at injection point, placed to intercept part of injected beam from transport line
min. current sensitivity: 1.5 pA average (with picoammeter)

The stated minimum current sensitivity enables measuring the beam even if the transport line efficiency is only 25%.

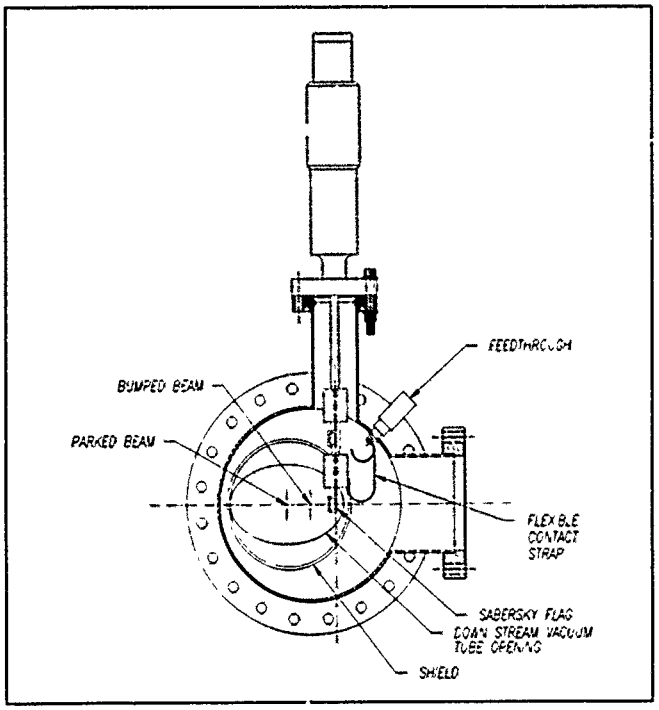


Figure 1. Sabersky finger assembly.

ring fluorescent screens

resolution: 0.7 mm (at 2.5 mA, 100 nsec pulse)
camera: ultricon

The resolution is adequate for viewing the beam on the first turn while it is performing betatron oscillations with a 20 mm amplitude. Use of an ultricon enables viewing a beam which is only 10% of the linac output.

button position monitors

button diameter: 1 cm
capacitance: 11 pF
mount: 4 to a flange assembly

The design specifications are more fully discussed in section IV, which also includes a figure showing the button assembly together with the electronics block diagram.

traveling wave electrodes

length of electrode: 15 cm
angular width of electrode (wide end): 32 deg
frequency response: >1.5 ohms from 0.2 to 1 GHz

The traveling wave electrode station is shown in figure 2. There are 4 electrodes per station. The length of 15 cm is chosen so that peaks in frequency response occur at odd multiples of 500 MHz, which is the ring rf frequency. By using a linear taper, the modulation in frequency response is reduced to less than about 6 db over the bandwidth of more than 1 GHz. These electrodes are coupled to a spectrum analyzer having a noise level of about -100 dbm for monitoring the betatron tunes even when the stored beam is 1 mA.

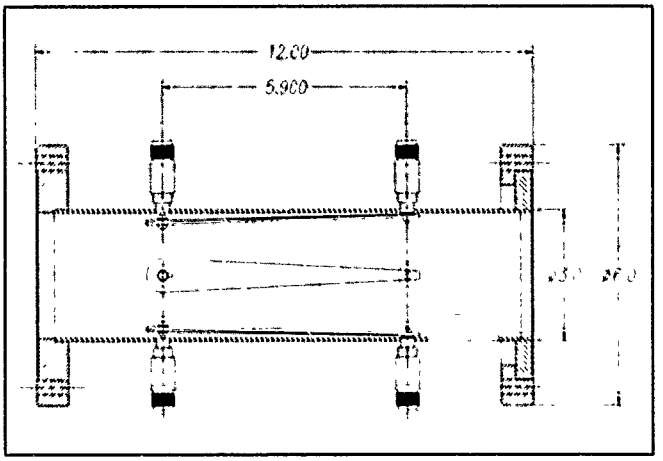


Figure 2. Traveling wave electrode station.

dc current transformer (DCCT)

current range: 0 - 600 mA
resolution: < ±0.016 mA (0.1 sec integration window)
< ±0.005 mA (1 sec integration window)

The DCCT assembly is shown in figure 3. The DCCT core and associated electronics were purchased from Bergoz. The device has an intrinsic di/dt output which can determine beam lifetimes as short as a minute, which is short compared to the expected lifetime of more than eight hours.

optical monitoring station

mirror material: copper with protective coating
system magnification: 1/3.8
resolution at source plane: 0.25 mm

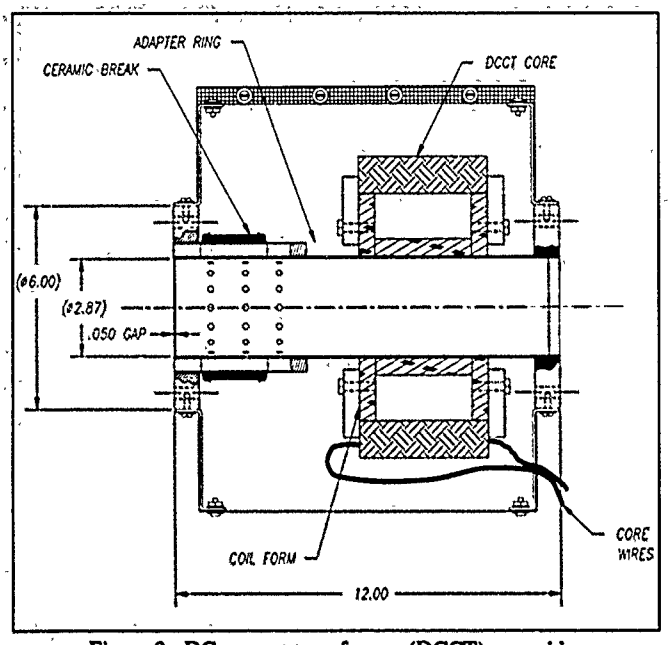


Figure 3. DC current transformer (DCCT) assembly.

camera: vidicon
optics: achromatic lens with a bandpass filter at 5500 angstroms

The optical monitor assembly is shown in figure 4. At 1.2 GeV, the storage ring beam emittance is 2×10^{-7} π•m•mrad, and the energy spread is 6×10^{-4}. For the position imaged, the rms beam sizes assuming 10% coupling are σ_x=0.64 mm and σ_y=0.39 mm. The resolution of 0.25 mm enables an accurate determination of the beam size for measuring the ring emittance.

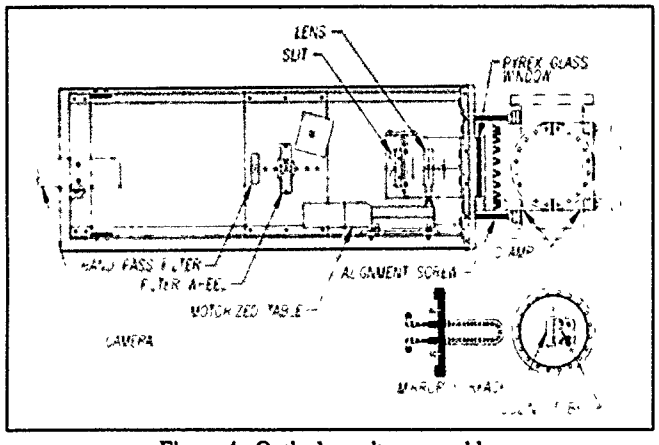


Figure 4. Optical monitor assembly.

V. BPM Electronics System

The beam position monitoring (BPM) electronics system monitors all 52 buttons of the 13 BPM stations, as shown in the block diagram (figure 5). The system consists of a multiplexer controlled by a line sequencer, followed by a signal processing stage that employs a bandpass filter, a gain stage controlled by the line sequencer, and then a diode detector and low-pass filter for signal averaging. The system uses a multiplexed analog switch system like NSLS and a diode detector like CEBAF. The multiplexed system is attractive because it minimizes the number of rf filter/amplifier/detector modules which are needed and thus obviates the need for cross calibration. The diode detector is attractive because its output conforms to a square law device over a 30 dB dynamic range. This reduces the number of steps needed in the gain stage. It also reduces the frequency with which the computer must look at the peak detector output to reset the gain setting. The diode detector is also very accurate. CEBAF is presently using a diode to make 100 ppm measurements with a 35 MHz bandwidth. This makes it possible to do direct measurements with the diode and a filtering system, eliminating the need for more complex signal averaging techniques.

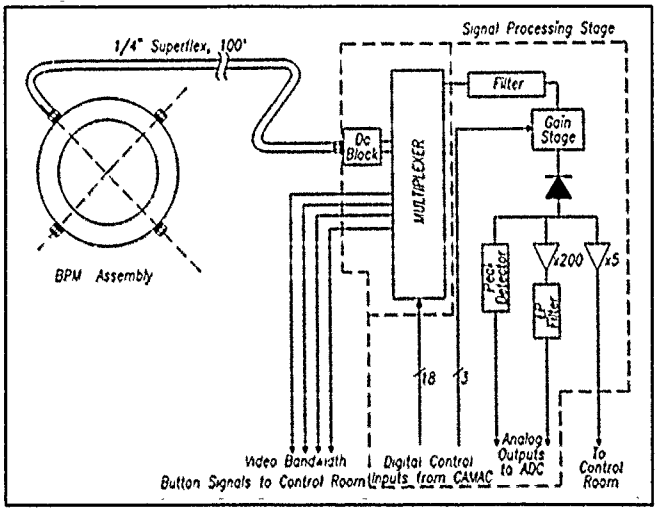


Figure 5. BPM button assembly and electronics block diagram.

When the sequencer is off, the raw signals from four specified buttons are continuously sent to the control room for observation on a fast oscilloscope. This enables monitoring of beam survival on a turn-by-turn basis.

For measuring the beam orbit, the CAMAC line sequencer is turned on so that 52 buttons are scanned. Four signal lines are further multiplexed down to one signal to be fed into the signal processing stage.

An analysis of the gain stage noise floor has been made since this is what ultimately determines the position resolution of the system. The most stringent requirement is to able to measure the beam position to within ±2 mm at a low current of 0.34 mA which corresponds to storing about 5% from one pulse of the linac. It is estimated that the input signal level for this condition is -81 dbm while the noise floor is -107 dbm, which is adequate. At a current of 400 mA, the system should be able to resolve beam positions down to ±0.1 mm.

VI. Conclusion

Testing of the diagnostics is now in progress. Tests on the button assembly are complete. Using a simulated current source, responses from individual buttons were measured with a network analyzer and found to be in good agreement with theory. The frequency response of the traveling wave electrodes has also been found to agree with calculations over 1 GHz. These results indicate that design specifications will be met.

THE DESIGN AND PACKAGING OF THE INSTRUMENTATION ELECTRONICS FOR THE AGS BOOSTER, A GENERIC APPROACH*

G.A. Smith, E. Beadle, V. Castillo, W. Sims, A. Stillman
T. Tallerico, R.L. Witkover, and E. Zitvogel

Brookhaven National Laboratory, Upton, New York 11973

Abstract

Instrumenting the new AGS Booster required the construction of a great deal of support electronics for many beam monitoring devices. Early in the project it was realized that it would be necessary to use a building block approach to the problem of providing the necessary equipment. Modules providing generic functions such as amplification, integration, sample and hold, etc., were designed and packaged so as to provide maximum flexibility in the implementation of typical instrumentation tasks. This paper describes these modules and includes some specific examples of how they have been combined to perform certain functions. Several unique features of the packaging will be described.

I. INTRODUCTION

The AGS Booster and its associated injection and extraction lines required, for the proper monitoring and control of the beam, a sizable collection of beam detectors to give accurate measurements of beam position, beam profile, beam intensity and beam loss during every phase of the acceleration cycle and for every species of particle (i.e. protons, polarized protons and heavy ions up to Au^{+33}).

Beam Instrumentation electronics is frequently designed to be detector specific. This is very often unavoidable given the requirements of sensitivity, timing and bandwidth imposed by special detection requirements and techniques.[1] However, while it is often the case that instrumentation must be tailored specifically to the special requirements found in accelerator environments, it is as well advantageous if it can be designed from a functionally modular point of view. The clear advantage of this is that a small group of identical building blocks can provide a wide variety of analog signal processing functions.

In order to provide the necessary support electronics for the Booster within rather severe constraints of time, money and manpower, several things were done. First as many common functions as possible were identified. Next, an appropriate packaging scheme was sought. Third, every attempt was made to exploit what was already part of our beam instrumentation design repertoire to reduce development time. Fourth, commercial vendors were sought at every stage, from the manufacture of small pieces to the construction of whole units.

II. PACKAGING

Except for one smaller project, almost all modular instrumentation electronics that was built by the accelerator instrumentation groups at BNL had been packaged in NIM[2] modules. NIM is an old established standard, the most vexing problem with the NIM packaging is the low density of pins in the standard rear connector and the necessity of coping with this by going to front panel connectors. Even with moderately dense input or output signal requirements front panel connections can cause an unwieldy mess. An alternative was needed.

It was decided to change to Eurocard packaging.[3] Since Eurocard is a mechanical standard for which hardware is becoming readily available, and since this standard has high density, mass terminated rear connector options, it seemed to offer many advantages that were needed.[4] Two standard modules, both 6U high by 220 mm deep, 7HP and 14HP wide have been adopted. This provides nearly the same physical board real estate and internal volume as the single and double width NIM modules.

One problem was finding a shielded enclosure for the modules similar to what NIM provides. In accelerator environments some electrical shielding is considered essential. No available options for enclosed Eurocard modules were completely suitable. A compromise was to use rails, side covers and front panel hardware from one manufacturer and to design our own back panels to fit these.

One important packaging issue is the crate design in this modular environment. For the particular module chosen many commercial choices for crates, or subracks as they are called, exist. These subracks usually include a selection of backplane construction techniques from simply mounting connectors on a rear frame to the use of a printed circuit backplane. To handle the interconnections, an aluminum enclosure (called a doghouse) was designed to fit over the rear of the crates. This metal enclosure provides additional shielding and a mounting point for connectors from external devices. It also serves as a protective enclosure for wires from these connectors to the module connectors.

III. THE MODULES

The modules developed for use in the Booster complex are described below in summary form. The descriptions are intended to point to their generic uses. All of the modules described here are packaged in 7HP by 6U by 220mm deep shielded Eurocard cassettes unless otherwise noted in the text.

Baseline Restorer

This module contains three channels, each is used to restore the proper baseline level to pulses that originate from capacitively or inductively coupled pickups or are AC coupled at some point in the front end of the system. It can also eliminate the effect of low frequency pickup on high speed pulses. A TTL input, at least 25 usec wide and at a rate commensurate with the expected baseline variations must be provided to sample the baseline at the appropriate time. The output then is the baseline at the sample time subtracted from the input. Bandwidth of each channel for inputs of a few volts is 1.5 MHz.

Beam Transformer Amplifier

*Work performed under the auspices of the U.S. Department of Energy.

0-7803-0135-8/91$03.00 ©IEEE

This module provides one channel with three current to voltage transfer ratios, 10mA/V with a 70 nsec rise time and 100uA/V or 10uA/V with a 1 usec rise time. It has a differential front end that is tuned to cancel common mode noise. A current boosted output stage provides cable drive capability. Selection of the gain can be done locally on the front panel and remotely on two rear connector pins.

Beam Current Integrator

This is a fast integrator that provides an output voltage proportional to the input charge of signals as narrow as 50 nsec occurring in a time window .5 to 1 μsec. Charge injection and offset voltage adjustments are provided and a peak hold circuit following the integrator stage allows the resultant integral to be retained for 10 msec with an accuracy of within 0.1%. The circuit provides a range of 10^5 in four gain ranges selected under external control.

Device Actuator

This module is a 14HP wide, two channel unit that is intended to provide drive to a detector positioner. Each channel accepts TTL commands and provides for 2 TTL status bits derived from limit switches. Thus the unit can be used to command the device to insert or retract and can provide bits to tell if the command suc-ceeded. All of the lines into or out to the device are optically isolated. Each channel can drive up to 24 VDC at 0.5 A. The unit may, in local mode, be used to drive the device from front panel switches. LED status indicators on the front panel show the status of the device and can indicate an "in process" or "hung" device. A bit is also provided to indicate to a remote computer if the module is in the local mode.

Digital Input/Output

The digital I/O module contains eight optically isolated, differential input and eight optically isolated output channels. Each input channel contains a TTL line receiver and each output a TTL line driver. High speed optical isolators separate the cable from the TTL receive and drive sections. In its standard application the module is used to transmit digital signals at one MHz over distances of 250 meters, and receive a corresponding "loopback" signal with high fidelity. However, the unit has also seen use as a sixteen channel, general purpose isolator.

Faraday Cup Amplifier

This module contains a single current to voltage amplifier channel which has four ranges selected from either the front panel (local mode) or by TTL inputs at the rear connector. Transfer ratios can be 1 or 10 nA/V (internal jumper selected) and 100 nA/volt with a 350 Hz bandwidth and 1 or 10 uA/V (again jumper selected) and 100 uA/volt with a 300 kHz bandwidth.

Faraday Cup Bias Supply

This high voltage bias supply generates -600 VDC using a DC to DC converter with a maximum output current of 3 mA. A comparator circuit monitors the output voltage and sets a bit (TTL level) at one of the rear connector pins if the output voltage varies from a window of -570V to -630V.

8-Channel Analog Receiver

This module has 8 individual, differential input receivers for signals transmitted from remote sources. The front end provides a resistor for cable termination and is tuned to cancel broadband common mode noise. A gain of two is provided to compensate for the attenuation due to the cable termination. The gain is variable by ± 10% to make up for cable losses. A final, back terminated, driving stage provides output cable drive capability.

8-Channel Individual Sample/Hold

The fast Sample and Hold module is an eight channel unit with a 1 μsec acquisition time to .1% and hold times of greater than 500 μsec. The circuit captures a sample of the input with a fast acquisition sample/hold, and transfers it to a second sample/hold which has very low droop. A TTL input pulse of at least 1 usec is required for sampling. Optional fast outputs from the first sample/hold appear on the upper (P1) Eurocard connector.

8-Channel Integrator

This module contains 8 independent charge integrators gated and reset by common TTL inputs. Any channel will provide a voltage proportional to the integral of the input current present during the gate interval. Outside the gate interval the resulting level is held to within a few percent for up to one second. Sensitivity is selected in two ranges and may be set from a maximum of 10^{10} Volts/Coulomb to 10^7 Volts/Coulomb. Input currents may go as high as 3 uA. Output dynamic range is ± 10 volts. Drift is less than 10pA equivalent input current. Output offset is less than 1 mvolt. Gating time must be greater than 10 μsec. Response time to input signals is 1 μsec. This module is now available commercially.

Low Level Multiplexer

This module contains one 32 pole double pole electronic switch that can be used to select either of two groups of 32 inputs. It is intended to be used to route signal arrays from multiple wire, low level analog devices to preamplifiers or other signal processing electronics. Group selection is accomplished either by front panel control or TTL level at the rear connector.

This unit features less than 100pa of leakage at any input, an input signal range of ± 10 volts, ± 2 mA, and 50 db of crosstalk and channel off isolation over a 1 Mhz bandwidth. The series resistance of any pole in the on state is less than 100 ohms.

Personality Module

This module can provide timing to the 8-Channel Integrator and the 64-Channel Analog Multiplexer. When operated remotely, it converts the computer timing signals to a form compatible with the Integrator and Multiplexer. In local mode, it provides adjustable timing from its built in clock. Locally, it can select a single channel of the Multiplexer instead of scanning. It is also designed for future expansion of the Multiplexer to as many as 256 channels.

16-Channel Comparator

This module provides 16 independent channels of adjustable threshold, analog voltage comparison for signals of ± 10 Volts at frequencies up to 100 kHz. Input impedance is 10 kohm. The threshold of each channel is set by internal potentiometers and is accurate to ± 20 mV with a hysteresis of 75 mV. The outputs are open collector TTL compatible. Each channel has an LED indicator on the front panel which is on when the trip point has been exceeded, and a test jack that can be used to measure the trip point setting.

16-Channel Sample and Hold

The sixteen channel sample/hold is a general

purpose sampler. It has an acquisition time of 20 μsec to .1% and a droop rate of 20 mV/sec. There are two blocks of eight channels, which allows some segmentation of input channels. Each block of channels requires its own sample signal, which can be either low or high true.

64-Channel Multiplexer

This module consists of two 32 to 1 analog multiplexers. Each multiplexer has an output current buffer with cable driving capability. Bandwidth is 70 kHz. Inverted outputs from either channel is an option. In addition the outputs of the two groups may be jumpered together to make a full 64-channel multiplexer. Channel selection is accomplished by TTL inputs that contain the binary channel number. Scanning is accomplished by combining this module with a Personality module.

32-Channel Amplifier

This module is a 32-channel general purpose preamplifier and signal buffer for low level currents. Two user determined gain ranges are allowed and are selected by changing the input resistance with TTL inputs on the rear connector or, in local mode, by a front panel switch. Circuit board pads are provided for the installation of feedback capacitors and output DC blocking capacitors or series resistors. The arrangement of the inputs and outputs allows the use of mass termination connectors in the Eurocard rack.

IV. A SAMPLE SYSTEM

A example of how the above module set might be used to assemble a system to perform an integrated task is typified by the HARP Crate shown in Fig. 1. This system is used to integrate the charge from a multiwire beam profile monitor and to produce a single output containing a time multiplexed version of the output of each integrator. Thus one can see on an oscilloscope an image of the beam profile.

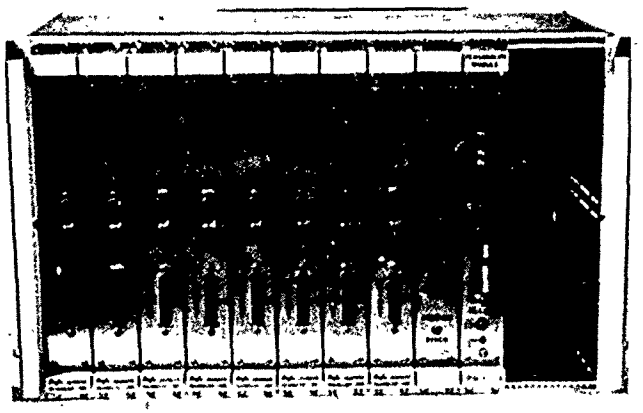


Figure 1 The HARP Crate

The HARP Crate is one of the more numerous that have been built at BNL. It contains eight, 8 Channel Integrator modules, one 64 channel Multiplexer module and one Personality module. Two 7HP slots are left open at the end of the crate with connectors installed and appropriately wired for power. These may be used for other modules as desired.

V. CONCLUSIONS

All in all the instrumentation effort has resulted in the construction of approximately 300 modules for 42 crates located in 20 racks around the Booster Complex. This large a construction project is beyond the normal manpower resources of the Beam Instrumentation group. To handle this, much of the work had to be done piecemeal through outside vendors. One of the most important aspects of this effort has been the struggle to involve commercial vendors in the design and construction of these modules and systems. Attempts to identify common building blocks is a key to the success of this.

It is hoped that future projects will see much more industry involvement, from the design stage through the production testing. Reports such as this are just a beginning attempt to disseminate information that might begin to attract some commercial interest. Beam instrumentation people from all the DOE laboratories have, at regular meetings, been discussing the prospects for establishing some commonalty in instrumentation on an intralaboratory scale.[5] In Addition, the new emphasis in USDOE on Technology Transfer is opening up some new possibilities for cooperation between DOE laboratories and industry.

VI. REFERENCES

1. D.J. Ciardullo, et al, "Design of the AGS Booster Beam Position Monitor Electronics", this conference.

2. U.S. NIM Committee, Standard NIM Instrumentation System, DOE/ER-0457T, May 1990.

3. Arnold Stillman, private communication.

4. DIN 41 494, DIN 41 612, IEC 297-1,2,3/3A and IEC 603-2 are some applicable standards.

5. Edward Beadle, et al, "Brookhaven Instrumentation Workshop Roundtable", AIP Conference Proceedings 212, Accelerator Instrumention, October 1989.

BEAM CURRENT MONITORING IN THE AGS BOOSTER AND ITS TRANSFER LINES*

R. L. Witkover, E. Zitvogel and V. Castillo
AGS Department
Brookhaven National Laboratory
Upton, NY 11973

ABSTRACT

The new AGS Booster is designed to accelerate low intensity polarized protons and heavy ions, and high intensity protons. The wide range of beam parameters and the vacuum, thermal and radiation environment, presented challenges in the instrumentation design. This paper describes the problems and solutions for the beam current monitors in the Booster and its transport lines. Where available, results of the initial operation will be presented.

INTRODUCTION

The AGS, with a long history as a proton machine, also accelerates polarized protons[1] and ions,[2] up to S^{+14}. The Booster, a multi-function machine with instrumentation to cover a wide range of beams, will enhance all of these operating modes. AGS proton intensity will be increased by injecting 4 pulses of 1.5 x 10^{13} protons at a 7.5 Hz rate. The 1.5 GeV proton energy will reduce space charge effects in the AGS at low momentum and allow it to accept ions up to Au^{+33} for delivery to RHIC. Polarized beam intensity will be increased by accumulating 20 Linac pulses at 2 x 10^{10} each. The Booster circumference is 201.8 meters, one-quarter that of the AGS. The rf duration for protons will be 60 msec, and 620 msec for heavy ions. Protons (H-minus) are injected in the Linac-to-Booster (LTB) line, while ions from the Tandem Van de Graaff are injected from the HITL-to-Booster (HTB) line. The Booster-to-AGS (BTA) line carries the beam to the AGS.

This flexibility causes many problems. The LTB beam current monitors require three orders of magnitude in range (10 μA to 25 mA) and at least two in resolution. The Linac beam can be as short as 300 nsec (one Booster bunch) or as long as 400 μsec. The HTB ion beams range from 10 μA to over 100 μA, with pulse widths from five to several hundred microseconds. DC beams used for tuning vary from 10 nA to over 100 nA. The BTA line will carry 2 x 10^{10} to 1.5 x 10^{13} charges in three bunches as narrow as 50 nsec. Booster current can vary from 10 μA for single turn polarized protons or heavy ions to 2.9 A at full intensity. Injection stacking requires a rise time of under 1 μsec, but polarized proton accumulation can last 3 seconds. The electronics for low intensity beams must be in the tunnel to maintain low noise wideband signals. Here they risk radiation damage from the high intensity beam which can be interleaved with low intensity. The vacuum will be 3 x 10^{-11} Torr in the ring and 10^{-10} in the transport lines. While most of the current monitors are external to the vacuum, they must tolerate bakeout at 150 to 300° C, depending on location. The various types of monitors employed will be described. Fast bunch intensity measurements made with the beam position monitors in the LTB line[3] and in the Booster Ring,[4] and the wall current monitors in the Ring will not be described here.

TRANSPORT LINE CURRENT TRANSFORMERS

The beam current transformers used in LTB and HTB are similar to those in the BTA line. They are improved versions of the HITL units,[5] which were derived from a LANL design.[6] The new transformers have 4-inch and 6-inch IDs and much faster rise times for the detectors and the electronics than earlier designs. The droop of the LTB and HTB signals had to be less than 1% for a 500 μsec beam. The time constant (L/R) of the winding inductance (L) and the input resistance (R) "passively" integrates the differentiated beam current. High permeability Supermalloy 2-mil tape cores[7] of 0.5 by 0.5 inch cross-section were used. A larger core would give a higher inductance but at much higher cost. Increasing the number of turns (N) causes L to go up as N^2 but the signal goes down and the rise time gets slower. The LTB and HTB units have a 200-turn winding which gives L = 0.5 H. The usable rise time was improved to 20 nsec by putting 1 kOhm resistors from every 20th turn to a copper foil around the core.[8] This damped the ringing of the turn-to-turn capacitance and the coil inductance, but about 25 % of the signal was lost. The BTA units had only 40 turns since the beam lasts < 1 μsec and a larger signal was needed. With fewer turns, it achieved the same rise time without damping resistors.

*Work performed under the auspices of the U.S. Department of Energy.

0-7803-0135-8/91$03.00 ©IEEE

Each core is mounted in a Mu-metal shield inside a 0.5 inch soft iron (1006) housing. This assembly sits on a three-point spring suspension isolating it from acoustic noise. The signals are carried differentially to the amplifier in the tunnel on RG-22 double shielded high frequency twinax cable. Units near the Booster have water cooling of the aluminum core casing to maintain it below 80° C during the 300° C bakeout.

Two separate amplifier chains are used to cover the three-decade intensity range, digitally selected by switches at the input and output of the board. Relays were chosen for their low contact resistance rather than FET analog switches which would have increased the droop rate. One amplifier chain was designed for high speed and low gain. Coupled to the standard 200-turn transformer it has a gain of 10 mA/V and a bandwidth of 5 MHz for a 70 nsec rise time. The slew rate of high speed AD848 op-amp is 225 V/μsec and not a factor in the rise time. Noise at the output is equivalent to 50 μA beam current. A differential input stage provides low frequency common mode rejection. The current boosted output stage has an output resistor for back-termination of long cables.

The other amplifier chain is designed for high gain with reduced bandwidth: 100 μA/V or 10 μA/V and a 1 μsec rise time when used with a 200-turn transformer. An OP37EZ was used for the first stages for its low noise and moderate speed. The final stage uses a high speed OP42EZ. A gain bit drives an FET analog switch to switch the gain of 10 stage in or out. The current equivalent noise for this amplifier chain is less than 1 μA for either gain. The input amplifier is differential with both high and low frequency common mode adjustments. Preceding the input is a "hum-bucker" transformer to further suppress high frequency common-mode noise. The final stage is current boosted and shares the output resistor with the faster amplifier.

A Base Line Restorer circuit located outside the tunnel is used to reduce the effect of 60 Hz pickup by the beam current transformer. The base line is sampled, using an AD582, just prior to beam time and subtracted from the pulse by a differential unity gain amplifier (OP27EZ), reducing the base line offset to 10 mV. An Elantec 2003 provides output drive capability.

The beam current monitors are calibrated by sending a current pulse to a single turn winding on the transformer core. The Calibrator Board provides a 50 mA, 500 μA, or 50 μA (± 0.1 %), 500 μsec (nominal) wide current pulse selected using the same bits that control the Beam Current Transformer Amplifier Board gain.

The BTA beam consists of three bunches as narrow as 50 nsec, extracted over 729 to 980 nsec, so total charge rather than current is of interest. To cover the range from 2×10^{10} to 1.5×10^{13} the circuit was designed with four gain states. The input signal is switched by an array of three rf relays (Aromat RF1E-DC5V) with 80 dB isolation at 250 MHz. This is critical to prevent coupling of the high intensity signal through the disconnected low intensity inputs. An amplifier stage (AD849) allows bunch viewing and optimization of the input resistance of the integrator stage (AD843). Charge injection and offset voltage adjustments are provided. A peak reader/hold circuit follows the fast bunch integral and retains the maximum, preventing the transformer backswing from causing a noticeable error. Drift is < 0.1 % in 10 msec. Tests indicate the area of simulated bunches to correct to within 0.1%.

FARADAY CUPS FOR THE HEAVY ION BEAMS

Beam current is monitored at eight locations in the HTB line using Faraday Cups mechanically identical to that in the HITL line.[9] Though destructive, they are necessary to monitor the DC beam used for tuning the line. The all stainless steel and ceramic design allows the units to be baked to 150° C. A -600 V bias suppresses secondary emission. The new amplifier design consists of separate relay selectable DC and pulse circuits each with two gain states. Mode selection (DC or pulse) and gain selection (X1 or X10) is available computer or locally. The DC circuit uses the stable OP97EZ to provide a gain of 1 or 10 nA/V (jumper selectable) in the high gain state and 100 nA/V in low gain. The bandwidth is kept to 350 Hz to limit noise. The pulse circuit uses an OP37EZ and an OP42EZ to provides a gain of 1 or 10 uA/V (jumper selectable) in the high gain state and 100 uA/V in the low gain. The bandwidth is 300 KHz. Both circuits use an Elantec 2003 as an output driver.

RING BEAM CURRENT TRANSFORMERS

The beam current measurement in the ring was specified to be from 10 μA to 10 A with a rise time of under 1 μsec and a droop time of at least 3000 sec. Two separate units, a fast injection beam monitor (BIBM) and a slower circulating beam monitor (BCBM) were installed to meet these requirements. The BIBM and the BCBM are mounted in a 0.5 inch thick, 1006 steel magnetic shield mounted on vibration isolators. A water cooled copper sheet between the transformers and the heater blanket keeps the temperature under 80° C during 300° C bakeout. A ceramic break in the beam pipe diverts the image current outside of the transformers. The electronics

are mounted near the floor with steel conduit shielding the cables to the transformers.

The BIBM uses a beam current toroid[10] which provides 0.1 V/A into 50 Ohms with a bandwidth of 0.5 Hz to 8 MHz. The core is enclosed in a 170 mm ID aluminum shield. The circuitry is similar to that in the LTB but with gains of 100 μA/V, 1 mA/V and 1 A/V. The rise time is 70 nsec for the high and 1 μsec for the low intensity range.

The BCBM uses magnetic modulation with synchronous second harmonic detection to measure current. This commercial unit[11] uses metal glass tape cores modulated at 6.928 kHz to obtain a DC to 15 kHz bandwidth. The Front End Electronics (FEE) must be within 3 meters of the detector while the Back End Electronics (BEE) can be 300 m away. With ranges of 1 A/V and 10 mA/V, it produced only 1 mV for a 10 μA beam, so a switchable amplifier (X 10) was put between the FEE and BEE.

The transformers were tested in the AGS. The BCBM showed RF sensitivity, both from pick-up and the beam, in the 3-4 MHz range. The circuits were modified by the vendor and are waiting to be tested with high intensity beam. An AGS dipole produced about 1 Gauss at the housing, causing pick up equal to 50 μA. Modulation noise equivalent to $\pm$ 150 μA was observed. See Figure 1. Since this was crystal generated, a filter with -40 dB notches at the fundamental and 3rd harmonic was able to reduce it to $\pm$ 10 μA of 5th harmonic. A 4th order 21 kHz low pass filter left only random noise of a similar level. Figure 2 shows a 50 μA test pulse measured with the BCBM. The BIBM reacts strongly to RF after 40 msec in the AGS cycle at highest gain. The high intensity range bandwidth overlaps that of the bunched beam. Rolling off the response at 1 MHz eliminated the problem while leaving enough bandwidth to observe stacking. Figure 3 shows a partial turn of 45 μA of O^{+8} spiraling in the AGS as seen with the BIBM. During LTB commissioning, the two beam transformers performed well and met the design requirements.

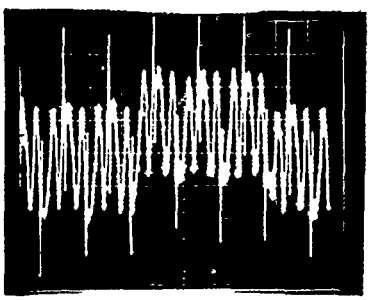


Fig. 1. Modulation noise of DCCT. 50 μA test pulse. 50 μA/div., 100 μsec/div.

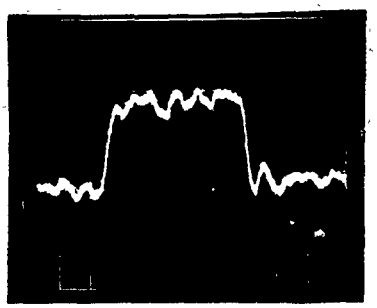


Fig. 2. 50 μA test pulse in DCCT after notch filter. 20 μA/div., 100 μsec/div.

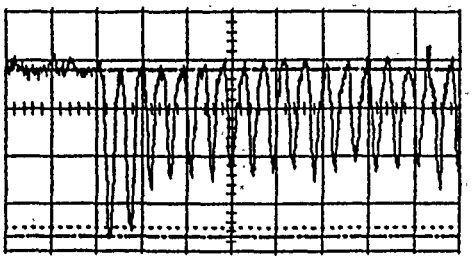


Fig. 3. Partial turn of 45 μA of O^{+8} in AGS viewed by BIBM. 50 μsec/div.

REFERENCES

[1] L.G. Ratner, et al., "Commissioning the Polarized Beam in the AGS", IEEE Trans. Nucl. Sci., NS-32, No. 5, 1656 (1985).

[2] R.K. Reece, et al., "Operational Experience with Light Ions at the AGS", IEEE Cat. No. 87CH2387-9, Washington, D.C., 1600 (1987).

[3] T.J. Shea, et al., "Beam Position Monitoring in the AGS Linac-to-Booster Transfer Line", this conference.

[4] D.J. Ciardullo, et al., "The AGS Booster Beam Position Monitor System", this conference.

[5] R.L. Witkover, et al., "Beam Instrumentation for the BNL Heavy Ion Transfer Line", IEEE Cat. No. 87CH2387-9, Washington, D.C., 567 (1987).

[6] F.R. Gallegos, et al., "The Development of a Current Monitor System for Measuring Pulsed-Beam Current Over a Wide Dynamic Range", IEEE Trans. Nucl. Sci., NS-32, No. 5, 1959 (1985).

[7] Arnold Engineering Company, Marengo, IL.

[8] M.J. Anderson, "Wide Frequency Range Current Transformers", Rev. Sci. Instrum. 42, No. 1, 915 (1971).

[9] Loc. Cit. Reference 5.

[10] Manufactured by Ion Physics Corp., 323 Andover St., Wilmington, MA 01887.

[11] Manufactured by BERGOZ, Crozet, 01170 GEX, France.

A Faraday Cup with High Frequency Response for a 200 MeV LINAC Proton Beam*

M. S. Zucker and J. W. Bittner
Brookhaven National Laboratory
Upton, NY 11973

Abstract

The purpose of this device, composed essentially of coaxial line elements, is monitoring, on a per micropulse basis, the beam intensity of a 200 MeV LINAC at the BNL Radiation Effects Facility. The center conductor of the coaxial line acts as a beam stop. The output pulses are suitable for fast timing.

I. MECHANICAL DESIGN AND CONSTRUCTION

Figure 1 shows the general mechanical configuration of the Faraday Cup.

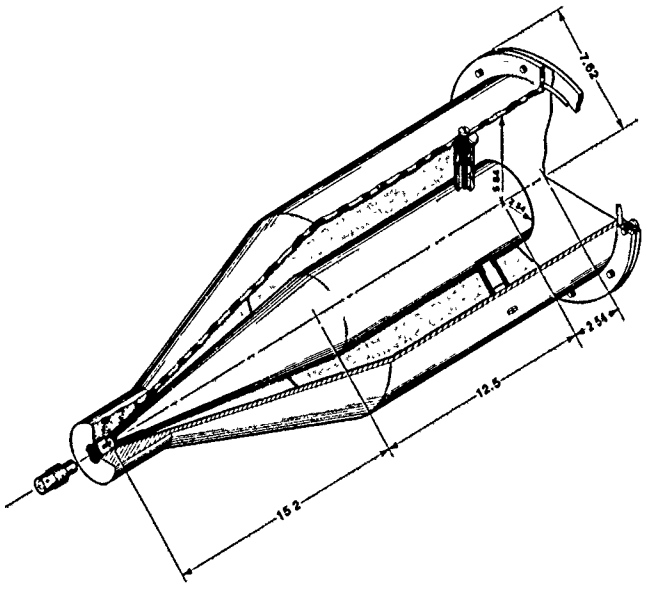


Figure 1.
Mechanical Configuration of the Faraday Cup

The front end of the center conductor, which acts as a beam stop, has to be range thick for 200 MeV protons, but as used in fast timing applications, requires only a modest lateral extent, since these beams are usually well-focused. A 5 cm diameter accommodates essentially all of a typical focused REF Gaussian beam profile (about 1 cm FWHM). The front of the beam stop is a right circular cylinder approximately range-thick in length, inside a cylindrical housing. The beam stop then tapers down, with a conical section forming the transition between the cylindrical portion of a 50 ohm cable connector which is fastened to the back end of the housing. This tapered section (half-angle 9.46 degrees) and the similarly tapered housing in that region (half-angle 21.57 degrees) form a section of a conical transmission line with 50 ohm impedance.

The beam stop is pure aluminum to minimize activation. The outer housing, normally struck only by stray or scattered beam, is hard aluminum for ease in machining and strength. The beam stop is mainly positioned relative to the outer housing by radial steatite insulators 120° apart. There is also some support by the center conductor of the coaxial connector which threads into the narrow end of the beam stop. The front is closed with Al foil (~.015 cm) held in place between a flange on the outer housing and a clamping ring, using an O-ring to make the seal. The intent is to use this Faraday Cup either evacuated to a forepump pressure or to have an atmosphere of argon or air; a side tube welded to the body of the outer housing allows for evacuation and filling.

II. ELECTRICAL DESIGN

A bias voltage can be applied to the beam stop through the side leg of a T introduced into the coaxial cable connected to the cup; the leg would have an isolation resistance in it to decouple the line from the bias source.

The high frequency design is based on two formulae for the characteristic impedance of, respectively, (circular cylindrical) coaxial, and bi-conical, transmission lines. The coaxial line impedance is given by $Z_0 = (1/2\pi)(\mu/\epsilon)^{1/2} ln(D/d)$ where ϵ and μ are the dielectric constant and permeability of the medium between the conductors, and D/d is the ratio of the outer to inner diameters of the concentric conductors. For Z_0 = 50 ohms, D/d = 2.303 . . . . The bi-conical line impedance is $Z_0 = (1/2\pi)(\mu/\epsilon)^{1/2} ln\{cot(\theta_1/2)/cot(\theta_2/2)\}$ where θ_1 and θ_2 are half-angles of the inner and outer cones, see Figure 2.[1,2]

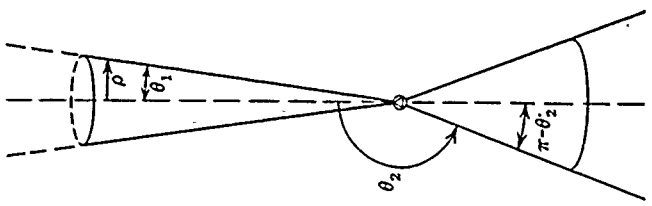


Figure 2
The Geometry of a Conical Transmission Line

0-7803-0135-8/91$03.00 ©IEEE

This latter formula applied to matching the diameter of the cylindrical portion of the beam stop to the coaxial cable connector led to the angular dimensions cited above. Each of these formulae strictly applies only to an infinite transmission line, however experience shows that if transitions are not "too abrupt", reflections from these places will not be significant. In the interest of simplifying the machine shop work, no special attempt was made to make the transition any more gradual than dictated by the purely mechanical constraints of joining the basic 50 ohm sections to one another. In fact, the only trouble in regard to impedance matching was experienced with a commercial hermetic seal BNC style connector that deviated grossly from 50 ohms. Replacing this with a modified type N unit gave the good results to be shown below.

III. TIME DOMAIN REFLECTOMETRY TESTS

The Faraday Cup was tested by putting a step function pulse into the BNC connector and looking for reflections. Figure 3 shows such a trace.

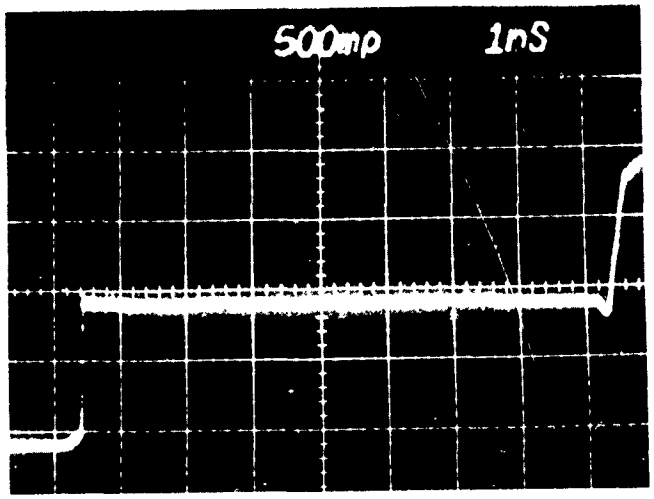


Figure 3
A Time Domain Reflectometry Test of the Faraday Cup

The vertical line on the left is the leading edge of the pulse put into a cable about 6 ns long connected to the Faraday Cup. The vertical line on the right represents the reflection from the end of the beam stop. The wiggles in the oscilloscope trace centered about 5 cm (6 ns) to the right of the leading edge is caused by poor matching in the vicinity of the coax connector. These deviations from the flatness that would signify perfect matching were worse by a factor of about 5 before replacing the connector with the N connector. The region between the wiggles at 6 cm and the vertical rise signifying the front end of the beam stop represents the matching behavior of the rest of the Faraday Cup.

IV. LINAC BEAM TESTS

The Faraday Cup output signal with REF facility LINAC beam entering the front end was examined with a 1 GHZ real time oscilloscope. Figure 4 shows the envelope of a macropulse about 480 microseconds long.

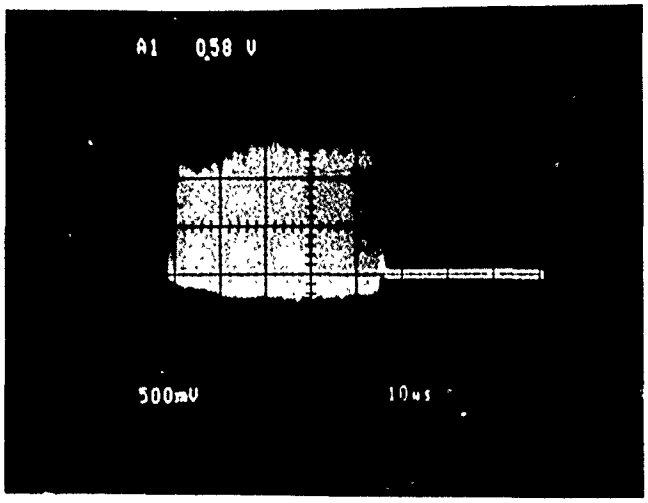


Figure 4
The Envelope of a (480 Microsecond) Macropulse

The envelope is greater than 1 V across 50 ohms, equivalent to 20 mA of beam current. This picture demonstrates the change of micropulse amplitude during the macropulse. Expanding the horizontal (time) axis to 2 ns per cm produced the trace in Figure 5, which shows some sections of the pulse train of individual micropulses superimposed on one another, since the oscilloscope beam made several sweeps during the film exposure. (This oscilloscope is capable of accurately displaying a Gaussian pulse shape with a FWHM equal to 0.5 ns.)

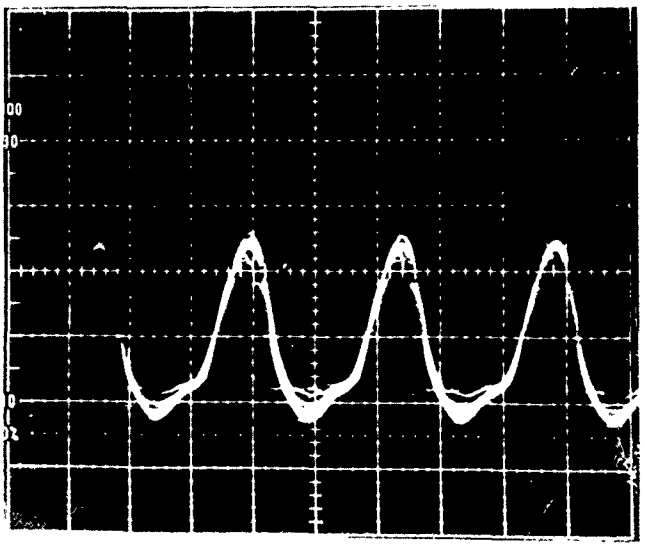


Figure 5
Individual Micropulses, Sweep Speed of 2 ns per cm

The results are disappointing in that a micropulse as measured by this device is somewhat wider (1.5 ns FWHM) than that measured by a wall gap monitor developed at the REF (about 1 ns FWHM). Another artifact that is not understood very well is the way the trace goes slightly negative. The only somewhat vague argument that can be mustered to explain this is that the assembly as a whole is acting as a cavity which is partially reacting to the shock excitation of the beam pulses by ringing a little.

V. EVALUATION AND FUTURE DEVELOPMENT

For the intended application, this Faraday Cup can be compared with a wall gap monitor. This device offers much the same facility as a wall gap monitor in that it sees the whole of the beam, and also has the frequency response to develop a pulse for each micropulse, and these pulses are as uniform in amplitude, presumably, as the envelope of the macropulse. The Faraday Cup is probably capable of a more accurate absolute beam current calibration than is the WGM, but must be placed after the target, which may lead in some cases to inaccuracy due to scattering of beam before the FC is reached. The wall gap monitor has to be installed in the beam pipe however, which require some effort every time the beam line is reconfigured to suite a particular experiment, while this device, being external to the vacuum system, is relatively easy to set up.

A possible course for future development would be to improve the matching at the cable-Faraday Cup interface, making larger diameter beam stops to accommodate less focused beams, and improving the vacuum capability.

VI. ACKNOWLEDGEMENTS

The support and interest of R. Lankshear were important in accomplishing this project. The machine shop work was by W. Eberl.

VII. REFERENCES

[1] W. R. Smythe, *Static and Dynamic Electricity,* 2nd edition, New York: McGraw-Hill Book Company, 1950, pp. 479-480.

[2] W. L. Weeks, *Electromagnetic Theory for Engineering Applications,* New York: John Wiley and Sons, 1964, pp. 530-533.

* This work was performed under the auspices of the U. S. Department of Energy under Contract No. DE-AC02-76CH00016.

THE TUNE METER SYSTEMS AT THE AGS COMPLEX*

W.K. van Asselt, L.A. Ahrens, P.R. Cameron,
S. Mandell, G.A. Smith, W. Zhang
AGS Department, Brookhaven National Laboratory
Upton, NY 11973

Abstract

A measurement system of the betatron tune is operational at the AGS and one for the AGS Booster is under development. Both systems use ferrite kicker magnets to excite coherent betatron oscillations. Difference signals are sampled at the revolution frequency and the tune is extracted from a Fast Fourier Transform. Details of the hardware of both systems will be described, as well as all the features of the application program through which the operator interacts with the hardware.

Introduction

To obtain the betatron tune, one generally kicks the beam in one of the transverse planes and analyzes the resulting coherent motion in that plane. The difference signal at a fixed position will contain all frequency components $(m-Q)f_0$, with Q the betatron tune, f_0 the revolution frequency and m the mode number. The modes which are closest to the tune have the strongest response [2]. All methods assume that the integer part of the tune is known and focus on determining the fractional part q. One way to extract q is to filter the position signal around one of the betatron sidebands and measure the frequency of the resulting signal with a fast electronic counter [1]. Fourier analysis is another way to obtain the fractional part of the tune. By sampling the position signal turn by turn, the Nyquist frequency of an FFT spectrum will equal $f_0/2$ and all the betatron sidebands will be folded back to the same frequency qf_0 or $(1-q)f_0$ for tunes below or above the half integer, respectively [3,4]. Both methods have been tested at the AGS. The second method has proven to be more robust and even provides tune values when the coherent signal lasts only for a very short time [5]. Also, more information is available in the frequency spectra than in an average frequency measurement; for example, when there is coupling between the horizontal and vertical plane. Therefore, this method has been selected for the tune meter systems at the AGS.

*Work performed under the auspices of the U.S. Department of Energy.

The AGS System

The kicker magnets used in the AGS are 90 cm long, full aperture window frame kickers made of stacked ferrite bricks with a single turn conductor. To prevent beam induced heating of the ferrite, shorted coils are mounted around the yoke in the longitudinal direction [6]. The power supplies are LC pulse-forming networks which are charged by 20 kV dc power supplies. These networks are located in the injection equipment building and connected to the magnets with 200 feet of coaxial cable. Thyratrons are used as switches for the discharge of the pulse forming networks. The current pulses have rise and fall times of roughly 0.5 μs, and a width which can be set to 2 or 4 μs. The maximum amplitudes of the current pulse is 1000 A for the horizontal and 2000 A for the vertical pulser. The charging time for the maximum pulse height is about 300 ms and therefore limits the kick repetition rate to effectively once per AGS cycle.

For each transverse plane, a position signal is fed into an eight-bit transient recorder. The revolution frequency is divided down from the rf frequency and is used as a clock for the transient recorders. For each transverse plane there is a master trigger, derived from either a real time clock or from the Gauss clock, which feeds variable delays to trigger the pulse forming networks to discharge and to stop the transient recorders.

All the different parameters can be controlled from an application program. The menu allows the operator to set the triggers and the kick amplitude, and to select the kick plane. Menu options include selection of multiple measurements, averaging of the spectra, and provisions to study coupling. When one or more measurements are done, the triggers are turned on and the transient recorders will generate an interrupt upon which a 10^4 point data record for the horizontal and/or vertical plane will be transferred into the application program. The FFT is calculated and the digitized data and the frequency spectra are displayed.

0-7803-0135-8/91$01.00 ©IEEE

Figure 1 shows an example of a measurement. The top trace shows the position signal in the vertical plane. The beam is kicked at roughly turn number 350. The maximum amplitude of the betatron oscillation is calculated to be 2 mm for this case. The fast beating of the signal is a result of undersampling of the position signal. The coherence is seen to decay in a few hundred turns due to the non-zero chromaticity. The lower trace shows the Fourier Transform. Figure 2 shows another example illustrating the sensitivity of the method. The kick amplitude for this case was reduced to 10% of the value in Figure 1. It is seen that, although the signal-to-noise ratio has become worse, the tune can still be obtained with the same precision. That the peak has the same height is because the program uses autoscaling routines when displaying frequency plots with linear vertical scales.

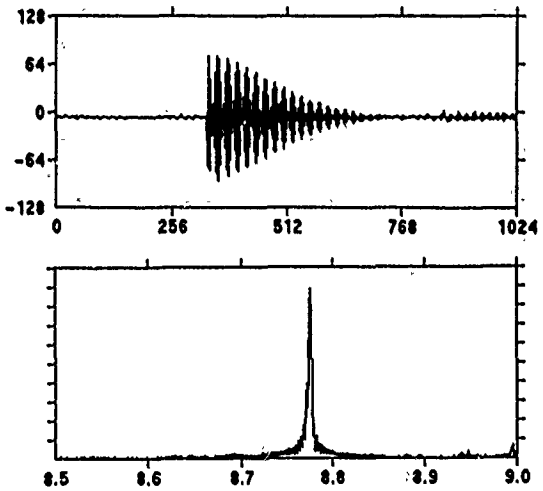


Fig. 1. Result of a tune measurement. At the top, the position signal is displayed versus the turn number. Bottom trace is the FFT spectrum assuming the tune is between 8.5 and 9.

A less ideal case, in which operator interaction is required to obtain a value for the tune, is shown in Figure 3. The beam has been kicked in the horizontal plane during an interval in the acceleration cycle of constant magnetic field, a large negative horizontal chromaticity, and small vertical chromaticity. The coherence in the horizontal plane is decays very rapidly, while some energy is coupled in the vertical plane. This motion is picked up and since it lats a very long time, it translates to the very well defined peak at 8.76 in the frequency display, as compared to the very broad peak around 8.68 for the horizontal tune. The very fast decay in the horizontal coherence

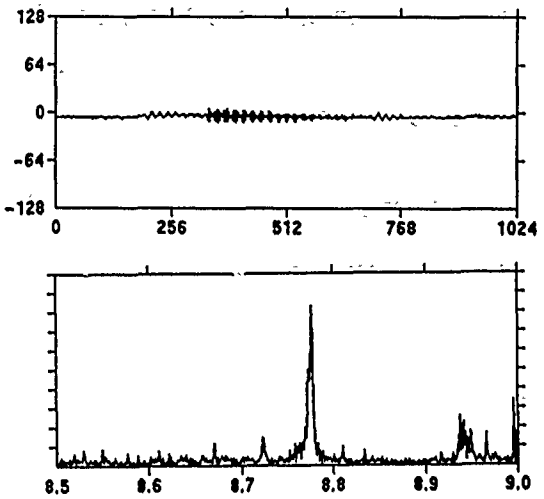


Fig. 2. Illustration of the sensitivity of the measurement. The kick amplitude has been reduced to 10% of the value of the kick used in Figure 1.

effectively acts as a window for the Fourier Transform and causes the fast beating in the horizontal peak. Identification of the tunes in these situations is facilitated by switching planes because when kicking in the vertical plane, the horizontal signal will be negligible compared to the strong vertical response.

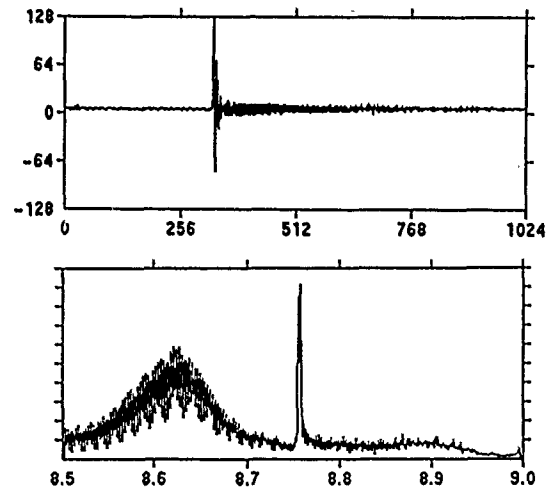


Fig. 3. Influence of betatron coupling and chromaticity on the frequency display.

The Booster System

The kicker magnets are full aperture window-frame ferrite magnets. Figure 4 shows a cross section of one for the horizontal plane. Copper sheets are inserted into the yoke to reduce coupling of the beam to the ferrite [7] and to maintain the magnetic properties of the ferrite [6]. These sheets are grounded to the vacuum chamber to provide a path for the image current. CMD 5005 ferrite was selected for its high rf permeability, low outgassing and high resistivity. Because the magnets have to operate in an ultra-high vacuum environment, all parts have been vacuum fired at 950° C except the ferrite, where the temperature was limited to 400° C to maintain its electrical characteristics [8,9].

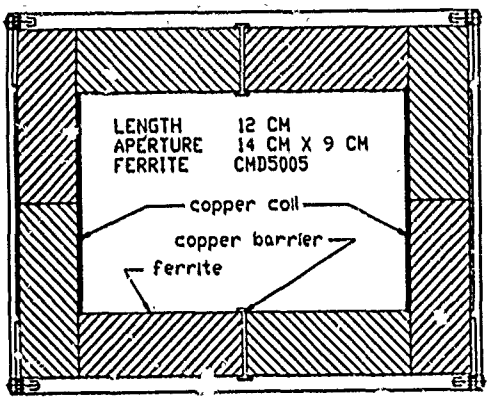


Fig. 4. Cross section of the horizontal kicker magnet.

The modulators for both the horizontal and vertical kicker are line-type pulsers with a maximum current of 1500 A at 20 kV. The pulse length can be selected to 1 μs or 3 μs. The principal difference from the AGS pulsers described above is the much faster charging time: 5 ms at 20 kV and a 1 μs pulse length. Details on the design and performance of the pulsers are described in a separate paper [10].

Position information is obtained from the Booster BPM system and transferred on an optical link to processing equipment, which is much more elaborate than that of the AGS system, because of the much larger range of revolution frequencies in the Booster. The revolution time in the Booster varies from roughly 0.7 to 15 μs and since a 1 μs or 3 μs pulse is available, it can happen that only a fraction of a turn will be kicked. The signals will be fed into high speed integrators. Baseline restoration circuitry will take care of the ac nature of the input signals. The revolution frequency will be used also as a clock for the transient recorders and with a small delay as reset for the fast integrators. All other timing signals for triggering the pulsers and to trigger the transient recorders are obtained from the central Booster timing system.

Another difference with the AGS system is the much higher repetition rate of the Booster (7 Hz). Four Booster pulses at this frequency will be needed to fill the AGS and comparative measurements in each of these cycles are highly desirable. The transient recorders are Camac modules which are connected to the station where the application code resides through a GPIB bus. The protocol for reading the transient recorders has been optimized such that data transfer from both planes is completed well within the time between interrupts. The selection of a particular cycle is therefore done in the application code and not at the system hardware level.

The application program will be very similar to the one for the AGS. The triggers which control the modulators and transient recorders will be derived from one single entry. The amplitude of the kick is the only other parameter, which has to be adjusted. Menu options will include selection of the result of a measurement in one or more cycles within a Booster group, averaging of spectra within a Booster group, and averaging cycles from consecutive Booster groups. Provisions will be made to acquire multiple measurements and transfer results to other application codes, for instance to the code which controls the tune correction power supplies.

All the system components are presently available and installation is in progress. First system tests are expected by the middle of May, 1991.

References

[1] E.C. Raka, private communication.
[2] H. Koziol, CERN MPS/Int. BR/74-14.
[3] K. Muto, et al., IEEE NS-24 (1977), 1818.
[4] R.E. Shafer, et al., Proc. XII Int. Conf. on High Energy Accelerators, Fermilab (1983), 609.
[5] W.K. van Asselt, private communication.
[6] W.K. van Asselt, Y.Y. Lee, these proceedings.
[7] F. Voelker, G. Lambertson, Proc. 1989 PAC, 851.
[8] H.C. Hseuh, et al., these proceedings.
[9] M. Goldman, J. Tuozzolo, private communication.
[10] W. Zhang, et al., these proceedings.

BETATRON TUNE MEASUREMENT AND CONTROL IN THE PETRA PROTON RING

S. Herb
Deutsches Elektronen-Synchrotron DESY
2000 Hamburg 52 - Notkestrasse 85 - Germany

Abstract

The PETRA storage ring, modified for use as an injector to the HERA proton ring, requires active control of betatron tunes during the proton acceleration cycle. A tune measurement system based on a personal computer equipped with commercial data acquisition and analysis cards is used for both measurement and control of the tunes.

I. INTRODUCTION

PETRA was designed as an electron storage ring for 7-20 GeV electron beam energy; it now serves both the HERA electron and proton rings as an intermediate energy booster. For the proton service, beam is injected at 7.5 GeV and accelerated at about .3 GeV/sec to 40 GeV; it is planned to accelerate a train of 50-70 bunches spaced 97 nanosec apart. There are significant betatron tune shifts during acceleration, at low energy from eddy currents in the aluminum vacuum chambers and at high energies from field saturation, especially in the bending magnets. We therefore decided to build a tune measurement system with relatively fast response to aid in understanding and correction of these effects; minimizing excitation of the proton bunches has at present second priority.

II. TUNE MEASUREMENT

A. Beam Pickup and Signal Processing

Fig. 1 shows a schematic of the measurement system. The signal source is a directional coupler pickup of the type designed for the HERA straight sections [1], mounted in the PETRA proton bypass. The electrodes are 40 cm long, which, together with the 2-3 m bunch length, results in a bipolar output pulse with signal energy concentrated between 50 and 150 MHz. The sensitivities are 50 mv pp/10^9 protons for a single electrode and 0.7 db/mm for the ratio of voltages from opposed electrodes.

Pulses from the monitor are transmitted about 100 m to a service hall, amplified in broadband chains with switchable gain, and stretched using Schottky diodes biassed to just below threshold, yielding about 30 dB dynamic range. The signals from opposing electrodes are subtracted, amplified, and subjected to 65 kHz low pass filters (the PETRA revolution frequency is about 130 kHz). There is no time gating of the pulse train, so the low frequency signal is a sum from all bunches in the machine, with high sensitivity to modes in which the bunches are moving almost in phase (multiples of 10.3 MHz for the 97 nsec bunch spacing in PETRA). The low frequency signals are brought on 1 km long RG-213 cables to the control room, where they are fed to anti-aliasing filters with a sharp cutoff above 65 kHz, and thence to A/D converters.

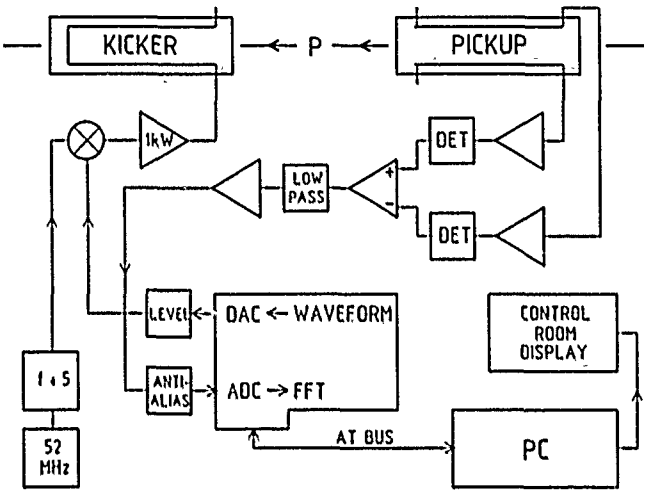


Fig. 1 Simplified schematic of one channel of the PETRA tune measurement system

A/D conversion is performed by special cards sitting on the AT bus of the personal computer used for control and display. The cards (Microstar DAP 2400/5) have also 80C186 CPU and 56001 DSP chips and are thus able to perform data processing, including fast Fourier transforms, before the data is transferred to the host PC. The 10 Hz rate is achieved with two cards (horizontal and vertical tunes) sampling at 160 kHz, performing 512 point real Fourier transforms, and transferring the 256 point power spectra to the host PC. Programming of the cards is done through high level commands which are easy to use but somewhat inflexible.

0-7803-0135-8/91$03.00 ©IEEE

The host is a 20 MHz 386-based passive bus PC with 12 AT bus slots in a 19" rack mount chassis. The keyboard and monitor use a commercially available extension system and are at the main PETRA console, about 30 m from the rack. The PC is used for control, display, and recording of tune spectra. It can record the spectra on disk at the full acquisition rate of 10 Hz per channel, and provides at several Hz updates of the spectra on a color monitor. In principle it could also perform intelligent peak finding; for the present the tunes are simply taken to be the highest points within settable windows. Fig. 2 shows a record of betatron tune frequency during a ramp from 7.5 to 40 GeV, with intermediate files at 30 and 35 GeV. One advantage of the PC system is

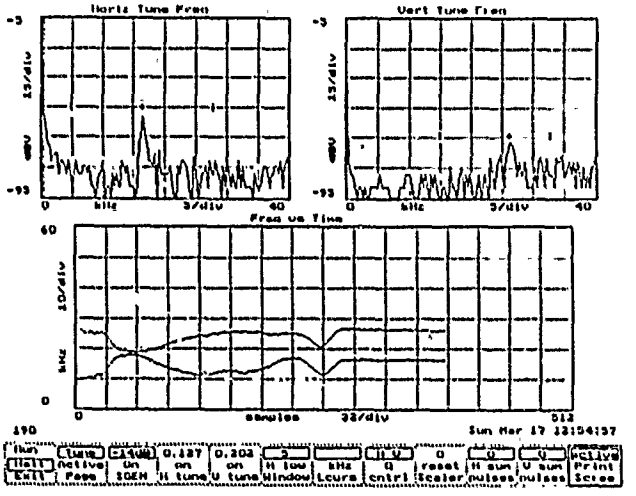


Fig. 2 Display from the tune control system. The horizontal scale is 12.8 sec per box and the vertical 10 kHz per box. Rate dependent tune shifts are compensated but various effects from non-linearities in the magnet excitation curves remain.

that it is easily reconfigured; a control menu permits, for example, switching back and forth between a program in which the data acquisition is triggered on injection, and a program in which the kicker excitation is used.

B. Beam Excitation

Beam excitation uses 50 Ω broadband ferrite loaded kickers driven by 1 kW RF amplifiers and capable of supplying about 1 G-m maximum field integral between 0.2-30 MHz. The kicker and amplifier are part of the transverse feedback system built for multibunch electron operation of PETRA [2], and are considerably stronger than necessary for excitation of tune signals. The RF waveform is created by mixing a low frequency (5-65 kHz) signal up to 10.3 MHz with a single side-band system. The 10.3 MHz comes from dividing the 52 MHz cavity RF frequency and thus tracks the RF frequency during acceleration. The low frequency signal is created by a D/A converter on the DAP card, which clocks out a pre-loaded signal as the ADC clocks in the data; the clocks are driven simultaneously by a 160 kHz pulse burst from a programmable timer card on the AT bus, with the excitation and acquisition lasting 512 samples/160 kHz or 3.2 msec. The level of the DAC cannot be quickly changed within the DAP card, so digital control lines are used to drive an external attenuator board, permitting for example control of the signal level during the accelerator cycle.

The waveform used at present is a frequency sweep moving between 5 and 45 kHz during the 3.2 msec, resulting in an excitation of the beam lasting for about 60 revolutions. Typical excitation voltage to the kicker is 2 volts, or about .01 Gauss-m maximum kick strength. As for the pickup, there is no time gating, so all bunches are excited.

Although not designed for minimum excitation, the system has several advantages in this respect. First, measurement duty factor is low (3 % for 512 pt transforms at 10 Hz), and second, the linear frequency sweep both excites and de-excites the betatron oscillation, providing that decoherence resulting from tune spread is small during the excitation. We have not yet made measurements which could indicate how well this is achieved in practice, but it is clear that at the start of acceleration eddy current induced multipoles result in tune spreads large compared to this criterion. Finally, the fact that both the excitation and the pickup work with all bunches in the machine means that as the number of bunches becomes large the excitation per bunch may be reduced.

III. TUNE CONTROL

The PETRA magnet ramp is driven by a clock with settable pulse frequency, with 512 Hz giving the design dE/dt of 0.3 GeV/sec. The ramp is performed as a series of file transfers in which all currents are stepped linearly between initial and final current values; non-linearities may be handled by increasing the number of intermediate magnet current files, but this requires stopping the

ramp, reloading step sizes, and restarting, which takes several seconds and may have consequences for the beam dynamics.

During tests of PETRA with protons in mid-1990 large tune shifts were observed during acceleration. The shifts at low energy are observed to be closely proportional to the ramp rate, as expected from field errors caused by eddy currents in the vacuum chamber, with a shift of about +10 kHz in the horizontal tune frequency ν̃ 128 Hz as shown in Fig. 3. The predicted shift of 40 kHz or dQ = 0.3 at the design ramp rate is not acceptable, so some additional control of the tunes during the ramp is necessary.

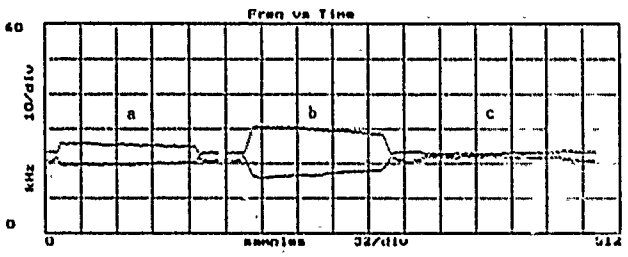


Fig. 3 Record of tune frequency vs time for three ramps from 7.5 to 9.5 GeV: a. 64 Hz magnet clock with 2.5 Hz sample rate b. 128 Hz magnet clock with 5 Hz sample rate, and c. 128 Hz magnet clock with rate dependent tune correction. The horizontal tune is initially the lower trace, and crosses above the vertical during the ramp for a. and b.

A tune control system based on a phase-locked loop already exists for PETRA electron operation; the beam is excited at fixed frequency and the loop is closed by incremental changes in the current in two specially modified quadrupole circuits [3]. For protons it was decided to build a control system not so dependent on excitation of the beam. In particular, to the extent that tune shifts are proportional to ramp rate (divided by beam energy) the quadrupole correction currents should be set proportional to the momentary ramp rate. To do this, while maintaining the possibility for other corrections, a third Microstar DAP processor on the AT bus is used, together with an input scaler receiving the clock pulses which drive the ramp. The entire correction procedure runs on the real-time multitasking operating system of the DAP, with only peripheral communication to the PC (Fig. 4).

The scaler count is read at 10 Hz by the DAP card, a smoothed second derivative is calculated, and numbers of up or down pulses proportional to the second derivative are sent to boxes which add these pulses to the clock pulse streams sent to the quadrupole current controllers.

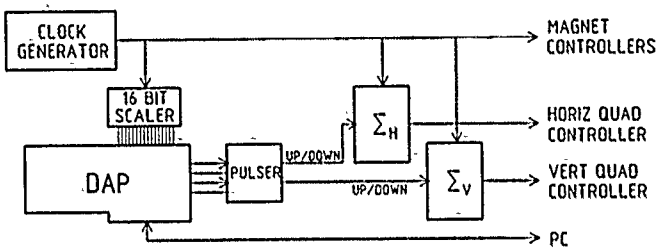


Fig. 4 Simplified schematic of the PETRA tune control system

This gives summed correction currents proportional to the clock frequency. The reaction time is limited by the maximum rate at which correction pulses can be accepted by the control system, which is about 500 Hz. At the 512 Hz clock rate 1000 correction pulses must be fed to the controller at ramp start (and again at ramp stop), so the clock frequency turn-on and turn-off times are set to 2 sec to ensure that the tunes remain constant. The correction system is effective (Fig. 3), showing that the tune shifts are indeed closely proportional to ramp rate.

It is also possible to add additional correction terms which are a function of the scaler count and could compensate magnet saturation effects. This is desirable (Fig. 2) but has not yet been tested with beam. Corrections based on the tune measurements from the PC are also possible.

IV. ACKNOWLEDGMENTS

We wish to thank at DESY K.-H. Mess for encourageme t, and L. Becker for construction of the equipment and for a large number of useful suggestions regarding the electronics and the computer system.

V. REFERENCES

[1] W. Schuette, pg. 21, DESY HERA Report 90-11

[2] J. Ruemmler, DESY, private communications

[3] S. Paetzold, DESY, private communications

PROMPT DIAGNOSTICS OF THE CYCLOTRON DEES SHIFT.

N. I. Karpov, Yu. M. Krasnikov, I. V. Naumov,
S. T. Latushkin, L. I. Judin.
I. V. Kurchatov Atomic Energy Institute.
Moscow 123182. USSR.

Abstract.

The device for prompt observation of the cyclotron dees shift in vertical and horizontal directions includes gas laser the light of which is reflected from concave spherical mirror fixed on the controlled duant and TV-monitoring system for con-trolling the light reflection shift. The tests on IAE cyclotron showed the sensitivity of the device up to tenth fractions of mm. The transmission of optical information over fibre optics line considerably simplifies the arrangement of construction elements.

I. INTRODUCTION.

Broad-band frequency change of coaxial oscillating lines in cyclotrons with the energy regulated by their heating and other reason can result to displacement of dees at the and this lines up to 2-3 mm. The same displacement of dees takes place and after some profilaction works. Such displacement changes the accelerating conditions and resonance frequency the ion shows work quality and may decrease the cyclotron beam intensity up to ten percents. Due to this reason the prompt monitoring of dees displacement is very useful.

II. OPTICAL MONITORING OF DEES SHIFT.

At Kurchatov IAE cyclotron there was proposed and realized the optical system for prompt and permanent observation dees shift [1]. The device (fig.1) used a gas laser the light of which comes trough collimators and glass window in vacuum chamber to a dee. It is reflected from copper concave spherical mirror fixed at the controlled dee and through the same window goes to a screen. TV-monitoring system is used for observation of the light displacement on the screen. The test of this system on IAE cyclotron showed the sensitivity of the device about 0,1 mm with the distance between the screen and dee about 8m.

The main defects of the present construction are a necessity to work with the straight light beam and along outer optical basis. So to test the medical cyclotron MPC-10 in Kurchatov IAE it was proposed another construction of optic transmitting and receiving tracts (fig.1).

In this construction the gas laser light is transported trough fiber optic line 50 mkm in vacuum chamber. It is focused by focus lens and spherical concave mirror placed at the dee at the enter surface of fiber optic regular line with dimensions 25×30 mm. This line transports the light from vacuum chamber. Outer ends of two such lines from both dees combined together before TV-camera and operator can see the displacement of two dees ON TV-monitor. Both optic lines - mono and regular - are mounted and have vacuum-tight at flange fixed at vacuum chamber. Such system does not need any additional alignment after its mounting.

The focal length of the lens is 25 mm, curvature radius of mirror is 100 mm, diameter 30mm, the distance between lens and mirror is 140mm.

III. CONCLUSION.

The testing of the model of this monitoring system shows that it is possible to fix dees vertical and horizontal displacement 0,5mm in the range 5mm.

The transmission of optical information through the fiber optic lines considerably simplifies the arrangement of construction elements and increases its reliability.

IV. REFERENCES.

[1] A. I. Belkov, V. V. Dushin, S. Yu. Garov et al. "Accelerating voltage oscillator of Kurchatov IAE cyclotron". Proceeding of 10 National conference on charget particles accelerators. Dubna USSR oct. 1986, vol. 1, pp. 263-268, Dubna 1987, D9-87-105.

[2] K. D. Burbesa, N. I. Venikov, P. Yu. Komissarov et al. "Status IAE mini cyclotron for PET". Proceeding of II International conference on cyclotrons and their application. Behine CSSR, may 1989, pp. 102-115, Dubna 1989, D9-89-108.

0-7803-0135-8/91$01.00 ©IEEE

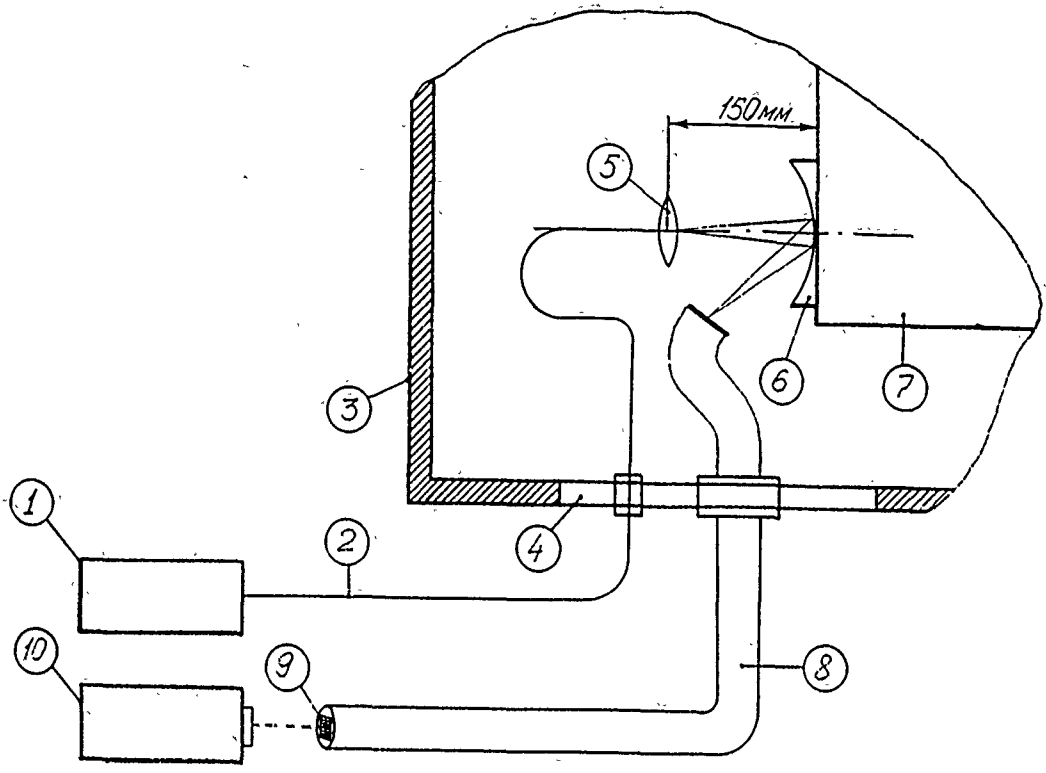


fig.1. Optical system for prompt and permanent observation dees shift.

1. Gas laser 1-2 mW, 2. Fiber optic line, 3. Cyclotron vacuum chamber, 4. Flange, 5. Lens, 6. Concave copper mirror, 7. Dee, 8. Many-vein regular optic line 25x30 mm, 9. Coordinate netwith image of laser ray, 10. TV-camera, 11. Vacuum tight.

Instrumentation for SSC Test Beams

Howard Fenker, Frank Stocker, and Ron Schailey
Superconducting Supercollider Laboratory*
2550 Beckleymeade Avenue
Dallas, Texas 75237

Abstract

Effective utilization of the SSC test beams for detector studies and calibration will require sophisticated beamline instrumentation. Current plans call for the Laboratory to develop an inventory of efficient and reliable intensity monitors, particle tracking systems, and particle identification systems which can cover the full range of particle energies and species expected to be demanded of the facility. Here we present some of those demands and the draft designs of the needed apparatus.

I. Introduction

Instrumentation for SSC test beams can be divided into two broad categories: that used for establishing and maintaining the desired flow of particles to the calibration hall, and that used in counting, tagging, or otherwise analyzing the beam to provide information to the experimenters making use of it. For the sake of this report, devices used in the former category will be referred to as "monitors", and those in the latter will be called "tagging" elements. Monitor systems are primarily the concern of the SSC Accelerator Systems Division, while tagging elements, since they are directly driven by the end-users, come under the jurisdiction of the Physics Research Division. This document is written from the Physics Research perspective, so it addresses only the tagging elements.

II. Instrumentation Specifications

Here we will analyze the requirements of the experiments which we anticipate will become parts of the experimental physics program. For the sake of this analysis we model this program as being composed of two colliding beam detectors: SDC [1] and L* [2], and one extracted beam experiment: SFT [3], which uses 20 TeV protons. We emphasize that this is only a model: while it is not inconsistent with any published plans of the Laboratory it also does not imply any intention on the part of the SSC Lab to carry out these particular experiments.

A. Demands of the Collider Experiments

Calorimeter Calibration

Taking the more demanding designs for calorimetry in the SDC experiment we find that the energy resolution will be $\Delta E/E = 40\%/\sqrt{E}\oplus 2\%$ for the hadronic section and $\Delta E/E = 15\%/\sqrt{E}\oplus 0.5\%$ in the electromagnetic compartment. (The symbol $\oplus$ indicates addition in quadrature. The energy "E" is measured in GeV.) In both scenarios the position resolution of the electromagnetic section of the calorimeters may be as fine as ± 2 mm.

The finest anticipated resolutions for calorimetry in L* are $\Delta E/E = 50\%/\sqrt{E}\oplus 2\%$ for the solid scintillator hadronic calorimeter which is used in combination with a barium fluoride electromagnetic calorimeter having $\Delta E/E = 1.3\%/\sqrt{E}\oplus 0.5\%$. The entire forward calorimeter structure in this experiment will use TMS as the sensitive medium. This provides $\Delta E/E = 17\%/\sqrt{E}\oplus 1\%$ electromagnetic resolution and $\Delta E/E = 54\%/\sqrt{E}\oplus 2\%$ hadronic resolution.

In order to effectively provide calibration and final testing of these calorimeters, the test beam energy and composition must be known better than the anticipated response of the detectors themselves. To probe a calorimeter having intrinsic resolution of $1.3\%/\sqrt{E}\oplus 2\%$ one must determine the incident particle energy to around 0.3 % absolute. Measuring the width of the calorimeter response requires that the relative energies of beam particles be known to a fraction of this, or about 0.05%.

Correct calorimeter calibration also requires knowledge of the type of the incident beam particle. This is needed because calorimeters respond differently to electrons and photons than they do to hadrons. This difference in response is used, in fact, to determine the particle species in the calorimeter. The calorimetry of both SDC and L* is designed to identify electrons with a rejection power of about 100:1. To test this in a beamline will require that the beam particles be identified somewhat better than this, or with a rejection power of order 1000 to 1.

Tracking Chamber Calibration and Testing

Both L* and SDC may use large-cell drift chambers in the outer regions of the detectors to track muons. At least some of these drift chambers will need to undergo final testing in a beam at the SSC site as late as reasonable before they are placed in their final positions in the experimental halls. The primary demand in these tests will be precision location of the beam particles. Since the drift chamber resolution will typically be about 150 μm (each wire taken alone), the beam track location must be known with slightly better precision.

Further demands on beam alignment accuracy will be made by the other tracking detector assemblies. Scintillating fiber trackers will have cell sizes of order 0.8 mm ($\sigma \approx 300\mu m$), and straw tube drift cells will achieve position measurement resolutions of around 100 μm. Both detector types may

*Operated by Universities Research Association under contract with the U.S. Department of Energy.

0-7803-0135-8/91$01.00 ©IEEE

require a tagged beam for establishment or validation of the engineered alignment because of inherent uncertainties in the positioning of their components. Plastic scintillating fibers are naturally flexible and imprecise, for example. All of the outer tracking chamber requirements can be met if the calibration beam position is known to about 50 μm.

More challenging will be the testing of the silicon inner trackers for the two detectors. Silicon strips and/or pixels are envisioned with sizes as small as 25 μm. Clearly, the only way to provide beam position information with a resolution meeting the survey needs of the silicon trackers will be to employ several layers of similar detectors in the beamline tracking system.

B. Extracted B-physics beam

The smaller SSC experiments have an advantage over the large, major ones in that they can postpone construction of detector elements, and therefore the final selection of technologies, to only a few years prior to turn-on. Because of this difference in scheduling the small experiments will be able to use the SSC test beams for developing and testing detector technologies as well as final calibration. This delayed schedule also allows the SSC scientific program planners to defer selection of experiments, so there is no "preferred" small physics experiment at present.

Tracking

The proposed "Super Fixed Target" (SFT) experiment would use a combination of silicon strips, silicon pixels, and proportional wire chambers as tracking detectors in a fixed-target arrangement. The pitch of the precision silicon strips would be less than or equal to 25 μm. The plans for the wire chambers call for wire spacing as small as 1 mm. Since all of these would be planar devices (typical for fixed-target experiments) the demand for survey using a test beam would likely be minimal or nonexistent. In any case, all but the 25 μm planes could be accurately probed using techniques similar to those already envisioned for the colliding beam detectors.

The muon system proposal consists of absorber with Resistive Plate Chambers (RPC's) interleaved. There is no difficulty meeting the position resolution requirements for testing these chambers (≥1 mm discharge size). It is expected that the test beam may be used for an extensive R&D program to develop them.

Particle Identification

For identifying charged particles SFT proposes a Ring Imaging Cerenkov counter (RICH). The device would be large (~750 m^3), and capable of differentiating among pions, kaons, and protons at momenta up to 300 GeV/c. The SFT Letter of Intent discusses design choices based on a misidentification rate of roughly 4.5% (20:1 rejection). Again, this is not a challenge for test beam instrumentation designed to accommodate the more demanding requirements of the collider detectors.

Calorimetry

The SFT proposal calls for an electromagnetic calorimeter with resolution $\sigma(E)/E \approx 9\%/\sqrt{E} \oplus 2\%$. This resolution is compatible with tagging systems required for the collider detectors.

C. Summary of Specifications

A summary of the test beam tagging system performance as described above is given in Table 1. The most demanding of the requirements in each category, i.e. those that drive the design of the test beam system, are indicated in boldface type.

Expermient	dX (mm)	dP/P Rel.	dP/P Abs	Part. ID Rejection
SDC				
Vertex	**0.01**			
Inner Tracker	0.01			
Fibers	0.30			
Straws	0.10			
E-Cal	2.00	2.4%	0.4%	**1000:1**
H-Cal		6.4%	1.1%	
Muon	**0.15**			
L*				
Inner Tracker	0.01			
Fibers	0.30			
Straws	0.10			
E-Cal		**0.3%**	**0.05%**	1000:1
H-Cal		8.0%	1.3%	
Muon	0.15			
SFT				
Silicon	0.01			
PWC's	0.30			
RICH				200:1
E-Cal		1.7%	0.3%	
Muon	1.00			

Table 1. Summary of Test Beam Tagging Requirements

III. INSTRUMENTATION PLANNED TO MEET THE SPECS

A. Momentum Tagging

As shown in Table 1, momentum tagging of the test beams is needed for calorimeter calibration and, to a lesser extent, for testing particle identification devices. The strictest requirement is for the L* BaF_2 electromagnetic calorimeter: $\Delta p/p \leq 0.3\%$ absolute, $\leq 0.05\%$ particle-to-particle.

Momentum tagging will be done by placing sets of tracking chambers in the beamline that measure the bend in the particle trajectories as they pass through a magnet. Thus four detectors are required: two before and two after the analyzing magnet. Using the present beamline optics design [4] we have an analyzing magnet which provides a 6 milliradian bend, and the maximum chamber separations are $L_{12} \leq 170$m, $L_{34} \leq 20$m. Thus conventional 1mm pitch proportional wire chambers at all four stations would provide absolute momentum resolution $\sigma_p/P \sim 0.34\%$. The magnetic field must be uniform and known to better than this precision, of course. Resolution of 0.05% will be provided for a subset of the full beam by placing 100 μm silicon strip detectors in locations near the two downstream wire chambers.

B. *Position Tagging*

Position tagging of the broad spray of muons can be achieved using relatively large wire chambers near the detector being tested. A 320mm x 320mm aperture drift chamber is being developed for this application. With a per-plane resolution of about 200μm, stacks of a few of these planes will provide beam position tagging adequate for all of the SSC detectors except the Vertex and Inner Tracking systems. These precision silicon strip or pixel detectors will require silicon strip tagging devices with smaller than 25 μm pitch for their calibration.

C. *Species Tagging: e/μ/h*

As indicated in Table 1, test beam tagging elements must be capable of positively identifying electrons and muons at the level of 1000:1 in the beam delivered to the calibration hall. Thus, for example, if the beam contains 10% unwanted particles the tagging system must work at the 100:1 level. Figure 1 shows the ranges of momenta over which two species of particles can be separated at this level or better by various techniques using the beamline tagging devices described below.

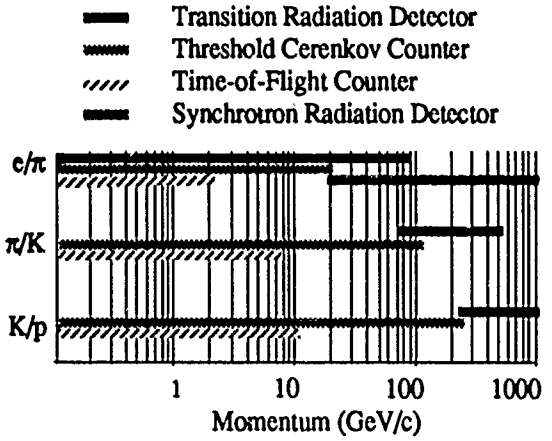


Figure 1. Useable momentum range of various particle identification techniques given limits on length (20m) and diameter (500mm) of detector.

To identify the electrons in the presence of heavier particles at energies above about 20 GeV one can employ a Synchrotron Radiation Detector (SRD). Installation of this type of device requires observation of the photons produced when the electrons pass through a bend in the beamline. As long as the size of the bend and the clear drift distance downstream of it allow placement of the photon detector outside of the beam halo this technique will work.

For simple discrimination between particles heavier or lighter than a chosen mass a long gas filled pipe with a single mirror and phototube at the downstream end is an economical choice. The design requires about 20m of parallel beam for each of two independent counters to achieve an efficiency of 90% or better for tagging the lighter particles.

The Transition Radiation Detector being considered for use in SSC test beams is based upon a device developed at Fermilab for a hadron beam fixed target experiment [5]. This is a modular device consisting of sets of radiator / detector assemblies. The discriminating power of the TRD can be adjusted, and the expense of the installation varied, by adding fewer or more modules to the system. The advantage of the TRD over Cerenkov counters or Synchrotron Radiation Detectors at those momenta where more than one technique applies is that it makes very few demands on the beam optics (beam does not need to be parallel, for example), and it requires relatively little real estate in the beamline.

IV. IMPLEMENTATION

Figure 2 shows a schematic diagram of the instrumentation in the secondary branch of a testbeam. The first magnet sweeps the spray of secondaries from the primary target across the momentum slit placed in front of the second magnet. Between the second and third bends are shown wire chambers, a Cerenkov counter, and a TRD. Following the last bend and before the final focus quadrupoles are a second Cerenkov, silicon strip detectors, and the SRD. In practice, of course, it may not be necessary to install all of these tagging elements in every beamline.

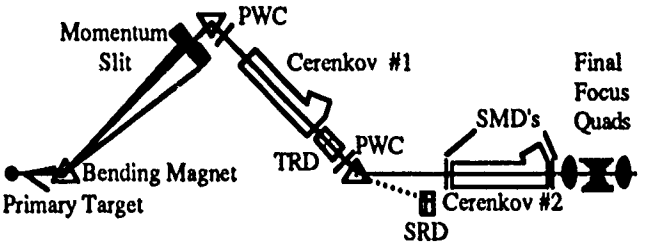


Figure 2. Beamline Instrumentation Schematic

V. REFERENCES

[1] G.H. Trilling, et al, SDC Letter of Intent to the SSCL, November 1990.

[2] S.C.C. Ting, et al, L* Letter of Intent to the SSCL, November 1990.

[3] B. Cox, et al, SFT Expression of Interest to the SSCL, May 1990.

[4] F. Stocker, et al, submitted to IEEE Particle Accelerator Conference, May 1991.

[5] D. Errede, et al, "The E769 TRD", submitted to Nucl. Inst. and Meth., March 1991.

Orbit Monitoring in the SLC

L. Sanchez-Chopitea P. Emma D. Van Olst
Stanford Linear Accelerator Center, Stanford University, Stanford, California 94309 *

Abstract

Beam orbits in the SLC are monitored in real time and the data is stored for future trend and correlation analysis. A background process acquires Beam Position Monitor (BPM) and Toroid data on a periodic basis and saves the general quantities such as orbit RMS and beam intensity in addition to the individual readings. Some of this data is archived by the SLC History Buffer facility and the rest is saved in files for later analysis. This has permitted the tracing of interaction point instabilities to specific devices as far away as the damping rings. In addition, the data is displayed for the operators both in summary and in full form. The different displays can be configured from the control consoles.

Introduction

During operation of the SLC, orbit stability is essential to maintaining low emittance beams and providing pulse to pulse reproducibility at the interaction point. In addition, long term histories of beam orbits have been useful in identifying device drifts and instabilities. Software has been developed that permits both realtime and offline continuous monitoring and analysis of the beam orbits in all parts of the machine. Several separate software modules used for logging and display have been incorporated into a unified orbit monitoring application[1].

Software Organization

The main program, BPM Sampler, is one of a set of batch processes which support updating summary displays in the SLC control room. The BPM Sampler generates orbit displays while other processes display summaries of general machine status, machine and personnel protection systems, and klystron population. History displays of beam intensity and luminosity are also available. All processes have the same skeleton which supports regularly scheduled monitoring and displays and responds to commands from the consoles or other SLC programs. These commands select which display will be presented on a particular monitor and specify the refresh time and other parameters. Any display may be selected on any of the ten monitors currently available in the control room. These are either RGB monitors driven from a Matrox board in the control console microcomputers, or DEC[1] VT1300 X Window terminals connected via Ethernet. Figure 1 shows the general data flow between these components.

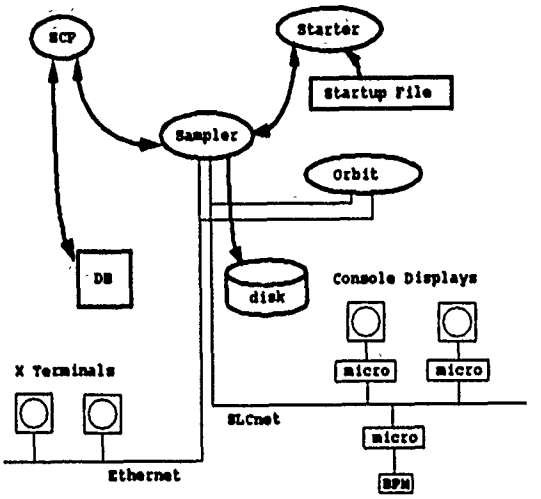


Figure 1: General Data Flow

In addition to the orbit displays, the BPM Sampler performs routine logging of beam orbits and intensities to the online SLC database or to disk files for later analysis. For specified regions of the machine, it also calculates and logs both the RMS of the absolute orbit and the RMS of the difference orbit with respect to a previously saved reference orbit. This reference or Gold orbit is usually an orbit which is known to minimize tails or transmission losses. The BPM Sampler also supports user requests for special purpose orbit acquisitions to disk file. These acquisitions are specified from the console and typically accumulate a few hundred orbits over a short duration.

Displays

The primary SLC orbit displays show the beam position and intensity as a function of location along the beam line. For the summary display monitors, the user may select to view any of the electron or positron bunches in predetermined ranges of the machine, as shown in Figure 2. The

*Work supported by the Department of Energy, contract DE-AC03-76SF00515
U.S. Government work not protected by U.S. Copyright.

[1] DEC is a registered trademark of Digital Equipment Corporation

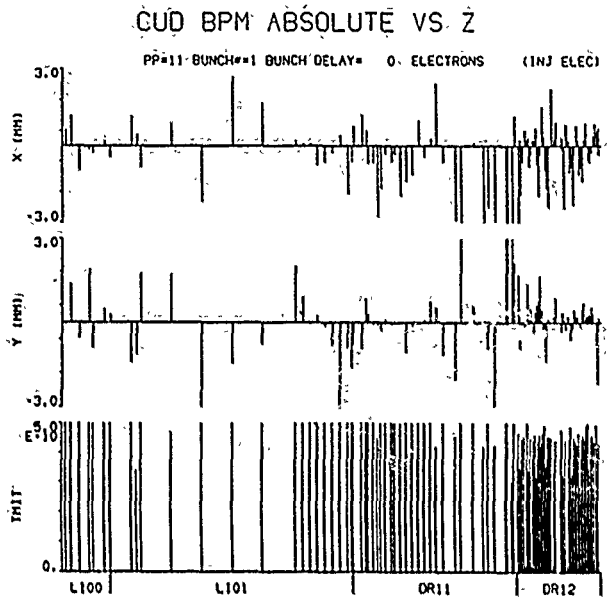


Figure 2: Typical BPM Sampler Display

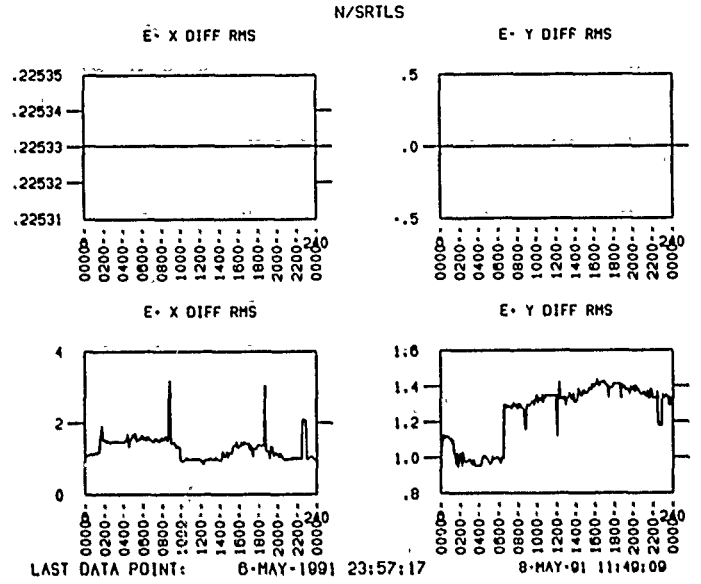


Figure 4: Orbit RMS History Buffer Display

positions may be displayed either as absolute orbits, or as differences with respect to the Gold reference orbit.

A separate display process, the SLC Orbit process, uses data calculated and logged by the BPM Sampler to present a summary of the whole machine, see Figure 3. The SLC Orbit Display summarizes the RMS values of the beam orbits calculated by the BPM Sampler. The RMS of the orbit with respect to the Gold reference orbit is displayed in numeric as well as bar graph format. The bar graph allows the operators to check at a glance whether the current orbit deviates significantly from the specified Gold orbit. At any particular time the SLC Orbit Display shows one particle beam's difference orbit RMS values for a section of the machine. At intervals of few seconds the display is updated with RMS information for a different beam and region.

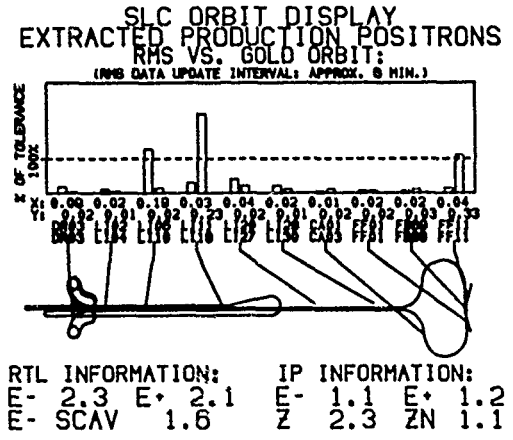


Figure 3: SLC Orbit Display

Data Logging

Data acquired by the BPM Sampler is logged by two different methods to support both offline analysis and online history buffers. When the amount of data is small, as for Toroid readings of beam intensity or diagnostic data from gated Analog to Digital Converters, it is stored directly in the online SLC database. The overall RMS of the orbit for sections of the machine is also calculated and logged to the database. This data is then periodically archived by the SLC History Buffer [2] software which provides both recent and long term data for display from the consoles, as in Figure 4.

For the larger quantities of data required for the actual orbits, the data is written out to disk files in raw format, and later converted to Matlab format so it can be analyzed offline.

Control

There are three separate paths used to control the acquisitions and displays of the BPM Sampler. The displays are controlled interactively from the SLC Control Program (SCP) through a general interface which supports all of the background display processes. The periodic data acquisition and logging is specified in control files. Special purpose user acquisitions are requested interactively from the console.

Display Control

The monitors of the Updating Display system are not dedicated to a single type of display, but rather are shared with the other related display processes. From the con-

sole, a user is provided with a common interface to select any of the displays for a particular monitor, or to modify the refresh rate or other parameters. When a display on a monitor is changed, the SCP is responsible for notifying all relevant processes via mailbox communication links. The online SLC database is shared by the consoles and display processes and contains the information necessary to define the monitors and displays. The display processes allow the same display to be selected on any number of monitors.

Acquisition and Logging Control

The periodic acquisition and logging of data is controlled via a text control file. This file specifies whether the orbit for a particular section of the machine should be logged to disk along with selected values from the SLC database. It also specifies whether beam intensities from toroids or other beam-related diagnostic devices should be logged to the database, and whether orbit RMS should be calculated and logged for sections of the machine. The file is parsed using the DEC Command Language Interface (CLI) utilities which provide a syntax familiar to users of the system. A separate initialization process reads the text file that describes the data and pertinent acquisition parameters and sends the information as mailbox requests to the BPM Sampler.

Special User Acquisition Control

Since the periodic acquisitions are scheduled to update rather infrequently, the BPM Sampler also supports user requests for special acquisitions at a high data rate for a limited period of time. This functionality was originally provided by a separate program which could not be controlled from the consoles. To aid in further analysis, auxiliary information from the SLC database may be collected synchronously with the orbit data and also logged. All of the resulting data files are formatted for later processing by Matlab.

Applications

The BPM Sampler together with the online SLC History Buffers provides the capability to correlate orbit and intensity fluctuations with data from other devices or diagnostics throughout the SLC. Using the data that has been logged to disk files, it is possible to track a single pulse (where BPM multiplexing permits) through most of the machine. This has been used successfully to trace instabilities at the IP to their origin at the Damping Ring kickers, as shown in Figure 5.

Conclusions

The updated and generalized BPM Sampler software has provided a variety of extremely useful tools for the analysis

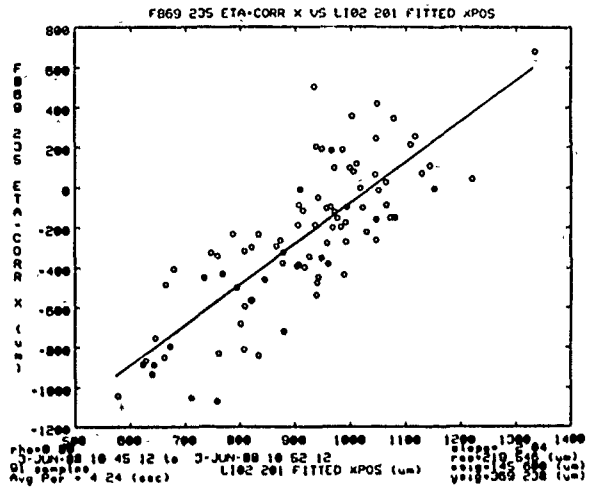


Figure 5: Correlation between kicker and IP

of the performance of the SLC. History buffers provide correlations of beam orbits and intensities with diurnal drifts or device variations. Synchronous orbit data has been analyzed to identify and correct sources of jitter throughout the machine. In addition, the current implementation has greatly improved the user interface for controlling acquisitions and facilitated the support of new summary displays to present the orbit information clearly and concisely to the operators of the SLC.

References

[1] M Flores III. CUD BPM Displays. Internal SLAC document, August 1987.

[2] Ralph Johnson. Stanford Linear Collider History Data Facility. In *Proceedings of the 1989 IEEE Particle Accelerator Conference*, 1989.

PROGRAM FOR AUTOMATIC CONTROL OF BEAM TRANSFER LINES

S.H. Ananian, R.H. Manukian
Yerevan Physics Institute, Armenia, U.S.S.R.

The traditional manual tuning of the beam transfor lines becomes inefficient with the increasing of both the beamlines length and the number of the magnets.That's why computer controlled beamlines are widely used now [1-3] .The set of programs is presented,which can be used for beamline automatic control.

1.Mathematical Formulation of the Problem

Let A_i be the transfer matrix between the monitors M_i and M_{i+1} and B_i be the influence of the correctors on the beam,which are located between these monitors.If X_i is the beam state vector on the i monitor,which is consisted of r and z coordinates and of their derivatives,then one will have

$$X_{i+1}=A_iX_i+B_iU_i, \quad i=0,1,\ldots,n, \qquad (1)$$

where U_i is the vector which includes the strength of the correctors and n is the number of the monitors.

Usually we get the coordinates r and z with some errors from the monitors.The observation vector on the i monitor will be

$$Z_i=H_iX_i+V_i, \quad i=0,1,\ldots,n, \qquad (2)$$

where H_i is the matrix for separation of the coordinates from the state vector,V_i is the measurement errors.

Let's discuss some versions of the mathematical formulation of the beamline optimal control versus the sequence of observation and control.

1. It is assumed that after sequential measurements of beam coordinates Z_i, i=0,1,...n we need to calculate the control vector U_k.If to take the result of minimizing

$$J=1/2||X_n||_S^2+1/2\sum_{k=0}^{n-1}(||X_k||_Q^2+||U_k||_R^2) \qquad (3)$$

with the constraints (1),(2) as a criterion of optimal U_k,we shall have a well known problem of optimal regulator [4], where S,Q and R are weighting matrices. Here $||U_k||_S^2=U_k^TRU_k$. Optimal control will be

$$U_k=-L_k\bar{X}_k, \qquad (4)$$

where the matrix L_k is a result of Ricatti equation solved backward in time

$$L_k=R^{-1}B_k^T(P_{k+1}+D_kR^{-1}B_k)^{-1}A_k, \qquad (5)$$

$$P_k=Q+A_k^T(P_{k+1}+B_kR^{-1}B_k^T)^{-1}A_k, \qquad (6)$$

where $P_n=S$ and k is changed from n-1 to 0. X_k is the estimate of the state vector formed by the Kalman filter [4]

$$\bar{X}_k^{j+1}=X_k+P_{j+1}A_jH_{j+1}^TR^{-1}(Z_{j+1}-H_{j+1}A_jX_k-H_{j+1}B_jU_j),$$

$$P_{j+1}=P_j-P_jA_jH_{j+1}^T(H_{j+1}A_jP_jA_jH_{j+1}^T+R)^{-1}H_{j+1}A_jP_j,$$

where $\bar{X}_k^0$ is the initial guess of X_k state vector and if more information is available it can be the mean value of X_k, R is the noise covariance matrix of $\bar{X}_k$, it shows the uncertainty of the initial guess and during the iteration procedure its diagonal components are decreasing, because the increase of available information reduces the parameter uncertainty.In this algorithm if the aprior information is not sufficient to get the Kalman estimation i.e. the matrices P_0,R and the mean value of X_k are not known, then one can use the sequential least square estimation or optimal estimation of maximal likelihood estimator ($\bar{X}_k^0=0$ and $P_0\to\infty$). It is important that the calculations structure is the same for all cases. These algorithms are attractive, because they are efficient in the case that there are unknown parameters in matrix A_j.

2.From the measurements of Z_i on the all monitors one can estimate state vector X_0 and after that calculate the optimal control U_i.

The estimation of $\bar{X}_0$ one can do with the Kalman filter and the control U_k can be

0-7803-0135-8/91$01.00 ©IEEE

calculated by the (4),where the sequence of

$$X_{i+1}=A_iX_i+B_iU_i, \qquad \bar{X}_0=X_0 \qquad (7)$$

can be used as X_k.

3.It is easy to get

$$\bar{X}=AX_0+BU, \qquad (8)$$

$$HX=HAX_0+HBU \qquad (9)$$

from (1),(2),where

$$X=[X_1,X_2,\ldots,X_n]^T,$$
$$U=[U_1,U_2,\ldots,U_n]^T,$$
$$Z=[Z_1,Z_2,\ldots,Z_n]^T,$$
$$H=[H_1,H_2,\ldots,H_n]^T,$$
$$V=[V_1,V_2,\ldots,V_n]^T.$$

The aim of optimal control is to have $||HX||^2 \to 0$.If $||HX|| \cong 0$,then

$$HAX_0=-HBU, \qquad Z=HAX_0+V,$$
$$Z=-HBU+V \qquad (10)$$

If we consider (10) as linear model of observation of Z_i measurements,the optimal estimation of U can be realized with the sequential Kalman estimator.

We consider,that the least approach of optimal control formation must be most efficient practically in spite of its heuristical form,because it is simple in calculation and the aprior information about B matrix can be easily improved experimentally by the simple calculation.

2.The Structure of the Program

A set of programs is written for the investigation of the estimation and control algorithms.The programs consist of several modules,each of them can be operated separately in real time scale.

The "TRANSPORT" [5] formalism is used here. The structure of the beamline is the input file of the program.It can include bending magnets, quadrupoles, synchroytron magnets, correctors. The tilts of the elements are given by the rotation matrix.The corrector is assumed to be an element which gives a kick in the middle.

It is possible to simulate the disturbances of the elements by vertical and horizontal kicks in the middle of each element.The program consists of following modules:

- the module of beam trajectory simulation;
- estimation of the beam parameters X, X´,Z ,Z´,ΔP/P;
- the control module.

This modules can operate separately using the structure file of the beamline.The control module is consisted subroutines of optimization based on the least square method (ordinary and sequential) and the subroutines for making local corrections.

3.The Results of Simulations

The efficiency of the algorithms are investigated on the electron beam transfer line from PETRA to HERA. The beam line is about 219 meter and is consisted of 19 bending magnets and 19 quadrupoles.The control system includes 20 monitors and 22 correctors: 12 vertical and 10 horizontal. Almost all the monitors and the correctors are attached to the quadrupoles.The tiltes of bending magnets and the quadrupoles cause the coupling of horizontal and vertical motion [6].

The process of measurement from the monitor is simulated with help of the beam trajectory simulation module and random number generation program.The normal distributed noise with 0 mean value and variance of 1mm is used (the accuracy of the monitors is of 0.5mm).

The beam initial parameters estimation quality and efficiency of control algorithms are investigated.

1.The beam parameters estimation.

The sequential maximal likelihood filter is used.The general results of the simulation are:

- the estimation convergence is not sensitive to the initial elements of covariance matrix P_0 if their are chosen to be 10^5 10^6 order of magnitude of the X_0 and the initial values of X_0 are 0;
- after 10 iterations estimated values are in the range of tolerable accuracy.

The typical process of parameters

X=2mm, X'=0.1mrad, Z=1mm, Z'=0.1mrad, ΔP/P=0.2% estimation versus the number of iteration are in fig.1-5.

2.The optimal control estimation.

The distorted trajectory is the result of not 0 initial X_0 values and/or disturbances of the beamline elements.The estimation is done by the algorithm 3 without X_0 estimation using sequential least square algorithm (maximal likelihood).

The results of the simulation show that after 5 iteration the corrected trajectory is in the range of tolerable accuracy.

The typical results of the control algorithm are shown in fig.6,7.Here the trajectories before and after correction are presented.

Roferences

[1] L.Dahl, F.Ehrich, "Computer Codes for Automatic Tuning of the Beam Transport Line at the Unilac" in Computing in Accelerator Design and Operation, Berlin, 1983.

[2] H.Pines, F.Selph, "Automatic tuning of the LBL Bevalac Transfer Line," LBL-11580, IEEE NS-28, 1983.

[3] M.Lee,S.Clearwater,E.Theil,V.Paxon, "Modern Approach to Accelerator Simulation and On-line Control," SLAC-PUB-4213, February, 1987.

[4] .A,P.Sage, "Optimum System Control," Printice-Hall Inc. Englewood Cliff, New Jersey, 07632, 1968.

[5] K.L.Brown, F.Rothacher, D.C.Carey, C H.Iselin, "Transport," SLAC-91, 1977.

[6] G.Jacobs (DESY) private communication.

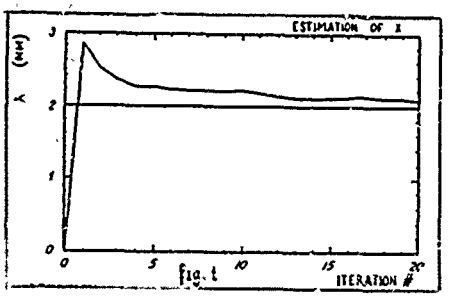


Fig.1

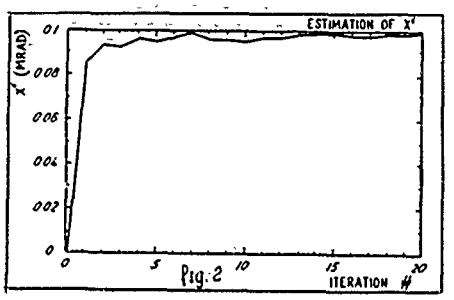


Fig.2

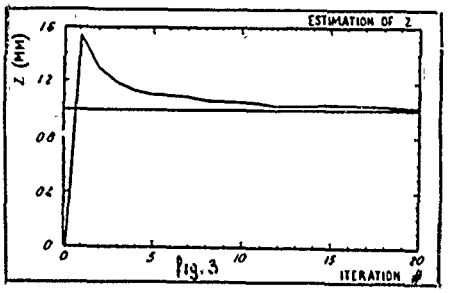


Fig.3

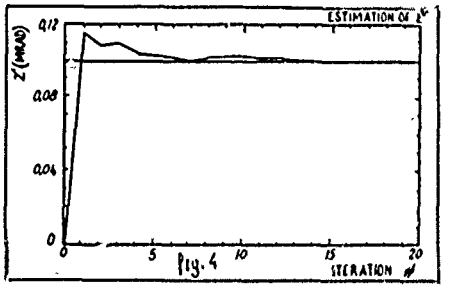


Fig.4

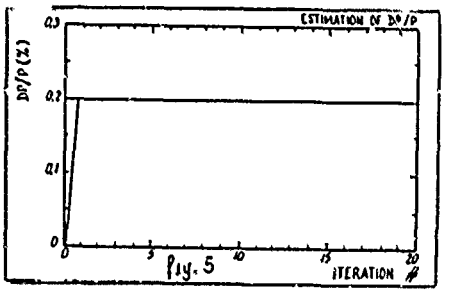


Fig.5

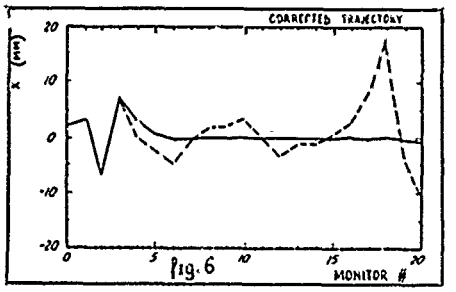


Fig.6

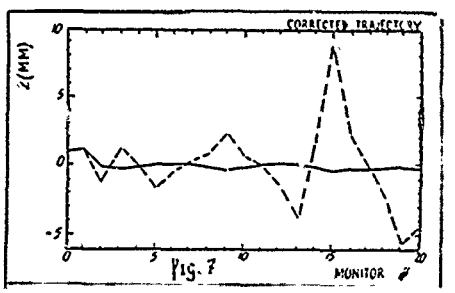


Fig.7

Embedded Software for the CEBAF RF Control Module*

G. Lahti, I. Ashkenazi, C. West, B. Morgan
Continuous Electron Beam Accelerator Facility
12000 Jefferson Avenue
Newport News, VA. 23606

ABSTRACT

The CEBAF accelerator control system employs a distributed computer strategy. As part of this strategy, the RF control sub-system uses 342 RF Control Modules, one for each of four warm section beam forming cavities (*i.e.*, choppers, buncher, capture) and 338 superconducting accelerating cavities. Each control module has its own microprocessor, which provides local intelligence to automatically control over 100 parameters, while keeping the user interface simple. The microprocessor controls analog and digital I/O, including the phase and gradient section, high power amplifier (HPA), and interlocks. Presently, the embedded code is used to commission the 14 RF control modules in the injector. This paper describes the operational experience of this complex real-time control system.

REQUIREMENTS

There are seven major requirements for the embedded software: (1) low power RF control, (2) high power RF control, (3) interlocks, (4) system calibration, (5) module hardware configuration, (6) manual and automatic control, and (7) diagnostics. These requirements are described as follows.

(1) Low Power RF Control

The low power RF control is handled by hardware internal to the RF control module. The phase and gradient loops are handled by this hardware, because of the speed needed. The embedded software's function is to set up the operating point of the hardware. This point can be determined manually (externally by the operator or high level control software) or automatically (internally), or a combination of both. A manually controlled parameter would be the gradient set point. An automatically controlled parameter would be the gradient clamp voltage, that varies with the gradient set point. Measured values are also monitored and sent to the higher level computer. The interface to this computer has been simplified. The transferred values are in convenient units, rather than base units or DAC/ADC bit patterns (*e.g.*, the RF module DACs and ADCs can be changed without changing the computer interface).

Some of the low power control signals are:

Phase	a. phase set point b. measured phase c. phase locking phase offset d. detector error e. amplifier gains and frequency response f. modulator bias g. reference oscillator power h. open/closed loop switch i. detuning angle of the cavity
Gradient	a. gradient set point b. measured gradient c. clamp modulator drive d. detector error e. amplifier gains and frequency f. offset drive g. quench detector h. open/closed loop switch
Output	a. RF attenuator b. output switch

(2) High Power RF Control

The high power RF is handled by both the HPA hardware and the RF module hardware. The filament and high voltage switches and some fault flags (bits) are handled by the HPA hardware and are set and measured by the upper level computer. The RF module handles the following HPA signals:

a. filament voltage set point
b. filament measured voltage
c. cathode current
d. body current (klystron)
e. mod anode voltage set point
f. mod anode measured voltage
g. forward and reflected power monitor
h. HV series relay to disable HV

(3) Interlocks

Interlocks are needed to keep the hardware in a safe condition. Some interlocks are handled in the hardware. The rest are handled by software, and are split into two groups: fast and slow response. Fast means within 150 μsec, and slow is measured in seconds. Detecting an interlock fault ranges from simply checking a hardware bit to checking a function of one or more analog signals. After an interlock fault is found, there can be various actions to take: (1) turn off RF, (2) turn off high voltage, (3) turn off filaments, or (4) a combination of these but wait at each stage to see if the fault goes away. In addition, some interlocks need the fast shutdown line pulled.

*Supported by D.O.E. contract #DE-AC05-84ER40150

0-7803-0135-8/91S01.00 ©IEEE

Some of the signals to check for interlock faults are:

a. excessive reflected power
b. excessive cathode current
c. excessive body current
d. arc detector trip
e. watch dog to verify computer activity

(4) Calibration Correction

There are two types of calibrations that affect the RF control module: (1) hardware variations internal to the module and (2) external hardware variations. The calibration coefficients are to be stored in the module's memory. This allows the internal coefficients to move with the module (*e.g.*, from warehouse to accelerator). When a module is moved to a new location in the accelerator, only the external coefficients need to be transferred to the module. Some coefficients are fixed, while others depend on temperature. The use of calibration correction implies the following: (1) a means to determine these coefficients, (2) a means to transfer these coefficients, and (3) a real-time method to use these coefficients efficiently.

External coefficients can be handled by typical measurement techniques (*e.g.*, measure the cable attenuation). For the internal coefficients, a test-stand is needed to exercise the RF module. This requires that the embedded software assist in this operation, which implies the following changes from the normal accelerator mode of operation. (1) Allow direct access to the DACs and ADCs (*e.g.*, phase set X & Y rather than simply the angle), (2) the interface values are voltages rather than usual units (*e.g.*, watts, amps, etc.), and (3) do not modify (*i.e.*, correct) these voltages.

These coefficients are transferred to the module via a download mechanism. This includes standard error checking. In addition, it would be helpful to have an upload feature to see if the downloaded values were loaded properly. As part of the total picture, other features are needed: (1) transfer coefficients from the test-stand to some database such as INGRES as a backup, (2) create download files from INGRES, and (3) create any version of download file (*e.g.*, present values or last month's).

To efficiently use these coefficients, the algorithms should do as much pre-computation as possible, so that the normal run time computations are as small as possible. This is especially important when the coefficients depend on very slow changing signals such as temperatures. When the temperature changes enough to make a difference, then a mechanism is needed to execute the pre-computation procedure during run time while affecting the normal operations as little as possible.

(5) Module Configuration

It is desirable to have only one version of the embedded software for all applications. There are six applications:

a. chopper section
b. buncher section
c. capture section
d. quarter cryo section
e. full cryo section
f. test stand

(6) Manual and Automatic Control

As mentioned above, in normal operation most signals are under automatic control. This is desired so as to simplify the interface to the upper computer (*i.e.*, distributed control strategy). However, during development or debug operation, a manual mode of operation is needed. This manual mode is not simply full manual mode for all signals; that would cause most debugging to be too complex. So, various levels of manual operation are needed (*i.e.*, allow varying percentages of signals to be under manual control, while the rest are automatic). The switch between automatic and manual modes must be "smooth" so that no glitches are introduced into the hardware.

(7) Diagnostics

There are two types of diagnostics: active all the time and active on command. The first type is basically a display of all important software control words (bit flags). The second type can be activated through normal data flow channels or via a secondary path (such as a RS232 port). As part of this second type, a specialized "peek & poke" could be used to access all major signals and control variables.

IMPLEMENTATION

The total RF control system consists of three supervisor computers (HP835s), one each for the injector, North Linac, and South Linac. These computers are used mainly for display purposes in the control room. However, they do contain some logic that is global to that one subsystem. Under these three computers are the locals, which reside in the service buildings. Next come the RF module microprocessors.

Injector: 1 supervisor, 5 locals (only 2 for RF), 22 microprocessors.
North Linac: 1 supervisor, 10 locals, 160 microprocessors
South Linac: 1 supervisor, 10 locals, 160 microprocessors

Supervisor to supervisor communication and supervisor to local communication is via LANs. The local to microprocessor communication is via CAMAC. The local can also communicate with other CAMAC devices, ranging from simple DACs/ADCs/switches to more complex devices (*e.g.*, cavity tuner motors).

The local to microprocessor path consists of 32 input channels and 32 output channels for normal communication and various other specialized CAMAC commands. Even with this number, the outputs from the RF module have to be multiplexed because more than 32 channels were needed. For critical signals, error detection is employed.

The software structure is based on a state machine. There are seven basic states: null, test-stand, download, idle, filament, high-voltage, and RF-on. Depending on the state, the various signal algorithms perform specific actions

particular to that state. The signal algorithms are also allowed to request a change to a lower state (*e.g.*, when an interlock fault condition is discovered). This allows more modular construction, since one signal can only affect a major change in another signal via a state change. For example, if the reflected RF power is too high, the state is changed from RF-on to HV; then the RF output switch is opened because the the RF-on state is no longer active. Minor changes are allowed by passing the output of one signal routine to the input of another routine. For example, the cable temperature sensor routine measures the temperature, and the other routines can use this as input to modify their calibration coefficients.

There is very little overlap of responsibilities between the local computer and the RF microprocessor. If the microprocessor has primary responsibility for a particular signal, it handles all aspects: reading the signal from hardware or CAMAC, calibration correction, fault and interlock detection, outputting the signal to CAMAC or hardware, and outputting the fault flag. The local computer will display the signal and fault flag, usually without secondary processing. In other words, the microprocessor will do as much as it can, from signal processing to fault detection.

OPERATIONAL EXPERIENCE

The RF module embedded software is written in the C language, except for the boot code which is in assembly language. The early development was done on one of the supervisor computers in a UNIX environment (HP835 computer). An in-house CAMAC interface emulation set of routines was used to join the local computer TACL (accelerator computer control system) logic with the RF module logic, while running both logics on the one HP835 computer. This allowed us to test both logics with very little (or no) change to either in this emulation environment. Two screens were used, one for the normal TACL display and the other for the RF module debug print statements. At this stage we were able to catch most logic errors.

The next stage was to port the embedded code to the target microprocessor (INTEL 80186). The INTEL development station was used to debug the hardware dependent features. There were not that many errors at this stage.

The final development stage was to transfer the code to the EPROMs and run the module with no development station emulator. This procedure went well. The C language code ported well. The following problems were noted, but they were generally minor.

a. HP and INTEL compilers have some minor differences. The INTEL compiler tended to be more strict in its checks, probably because it is one of the newer ANSI standard versions.
b. Some differences were also due to the different architectures of the processors. The INTEL 80186 uses a segmented memory.

For small changes to the code, we generally skip the UNIX emulation stage. But for new and complex features, we start development on the UNIX system.

The complexity of the software interface to the hardware is reduced by special hardware features. Instead of the software triggering an ADC and waiting for the value, the hardware contains a sequencer to trigger and read all ADCs and put the values into mapped memory. The software simply reads that memory when it needs it. The CAMAC input/output is also memory mapped. This ADC sequencer can also be set up to sample one particular signal at a software selected sampling rate and number of samples, and the hardware maps these sampled values to an array in memory. The software only needs to operate on this array (*e.g.*, digital signal processing).

The time to process one logic cycle in the RF module is about 33 msec (30 Hz). This time is for an RF module that uses the math coprocessor. With no coprocessor, the time increases to about 500 msec.

The time to process the major part of a fast shut d[illegible] interrupt ranges from 50 to 70 μsec.

CONCLUSION

The RF module software design followed object oriented design guidelines. However, the implementation used the standard C language. Code check out went quite well, and most new features have fitted well into the basic structure.

Our in-house UNIX emulation of the interface between the TACL computer and the RF module microprocessor aided greatly with early design and implementation. We could use the same UNIX tools that we used to develop the TACL system.

The INTEL development system (with microprocessor emulator) was a necessity when it came to finding and fixing hardware/software errors.

The RF module software performs well in reducing the computation burden of the local computers and in modularizing the RF control system.

THE TEVATRON ORBIT PROGRAM

B. Hendricks, R.P. Johnson, R. Joshel, E. Martensson and D. Siergiej
Fermi National Accelerator Laboratory*
P.O. Box 500
Batavia, Il. 60510

Abstract

The new application program which is used to control the closed orbit in the Tevatron is described. Unique features include the ability to acquire closed orbits at all energies on one ramp and provide dipole settings which smooth the orbit and are continuous as a function of energy. The program is also used to correct for the orbit distortions caused by the placement errors of the low β quadrupoles as the transition is made from the injection optics to the low β optics.

I. INTRODUCTION

The Tevatron upgrade program includes new features which require a more sophisticated program to control the closed orbit [1]. Electrostatic separators are used to provide separate orbits for the proton and antiproton beams and two new low beta insertions replace the single simple one. In addition, each of the new insertions has more quadrupoles which generate closed orbit distortions as the insertion is changed from the injection to the low beta optics. The two insertions may be energized individually or together, leading to a large number of possible intermediate steps and corresponding lattice solutions.

Past experience has also shown that the older programs[2] need to be made more flexible and able to do required manipulations with a minimum of dedicated control room activity. Experience has also shown that most problems with an orbit control program occur due to hardware problems. After a maintenance and development period, it is not uncommon to find beam position monitor polarities reversed due to cable interchanges. Other problems have included function generator and power supply failures. It has been convenient, even necessary, to include features in the Tevatron Orbit Program (TOP) to allow easy verification of the correction dipoles and the beam position monitor system.

At the same time, a new generation of control consoles has made more complex programs much easier to create [3]. The older method of generating lattice functions by using TEVLAT or SYNCH offline to provide many files of possible lattice configurations has been made obsolete.

II. OBTAINING A SMOOTHED ORBIT

TOP can calculate closed orbit corrections using either a standard three bump algorithm or a matrix inversion algorithm (χ^2 algorithm). Momentum corrections are optional in the calculation. One can smooth around the entire ring or do an individual three bump or four bump locally. The desired positions which TOP smooths to have three control bits per location which are used in the orbit correction algorithms. A position can be specified to be fixed, or a bad detector or corrector can be masked from the closed orbit smoothing. The energy levels and the tune values are also be specified by the user.

III. ONE RAMP SMOOTHING CAPABILITY

A main advantage of TOP is that it is capable of calculating a closed orbit at all energies from a single acceleration ramp and providing smoothed orbit corrections to the ramp tables of the magnetic correction elements for the next ramp. Orbit profile data for 108 beam position monitors, BPM's, located around the ring are read at nine energy levels up the ramp. A closed orbit correction is calculated at each energy level. A program display of an orbit in a Tevatron collider store is shown in Fig. 1. After calculating new settings for the correction Dipole Function Generators, DFG's, the predicted orbit after a TOP smoothing is shown in Fig. 2. The fact that these corrections can be applied simultaneously gives TOP the capability of placing continuity requirements on individual DFG settings as a function of energy. Discontinuities can cause tracking problems if steps between adjacent energy slots exceed the slew rate capabilities of the correctors. By maintaining continuity of the DFG settings during acceleration, orbit distortions due to large DFG current changes

0-7803-0135-8/91$01.00 ©IEEE

beyond the slew rate limitations of the power supplies are eliminated.

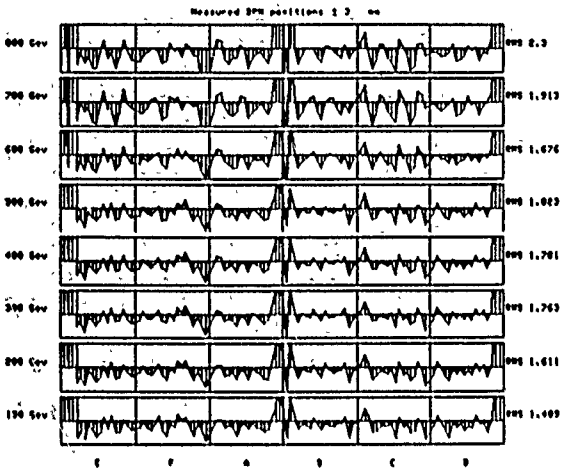


Fig. 1

Orbits in the horizontal plane for eight energy levels as the beam is accelerated in the Tevatron. The horizontal axis is the azimuthal position starting at E0. The rms position for the orbits is listed at the right. The scale of the plots is +/- 3mm.

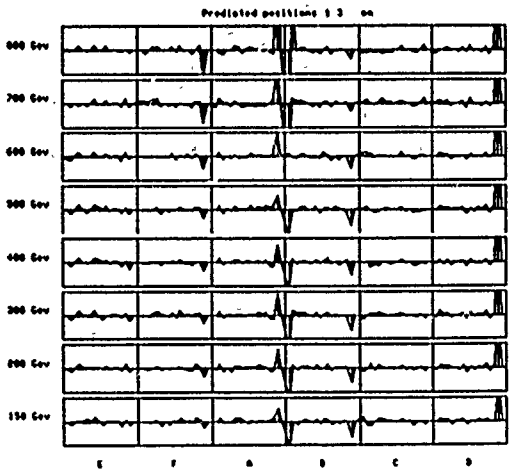


Fig. 2

The predicted positions after a smooth up the ramp of the orbits shown in Fig. 1. The horizontal axis is the azimuthal position starting at E0. The scale of the plots is +/- 3mm.

IV. Lattice Function Retrieval

The two low beta lattice insertions of the Tevatron present a problem to TOP in that it must be able to calculate closed orbits under multiple lattice configurations. The low beta squeeze, for example, occurs over seventeen steps, or seventeen different low beta quad lattice configurations. One may want to smooth the orbit at each of these steps during a low beta parsing session [5]. TOP is now capable of smoothing these orbits by obtaining lattice parameters in an interactive environment using a package, TEVCONFIG, which has recently been added to the Tevatron software library. TOP has the flexibility of obtaining any existing lattice configuration on a real-time basis or reading a stored lattice file using TEVCONFIG.

The ability to obtain various lattice configurations is especially useful for the orbit play capabilities of TOP. The orbit play option allows DFG settings, lattice parameters, orbit positions and tune values to be varied and the resultant changes displayed. Orbits which are on file or the present orbit can be used as input data. This feature allows one to view effects without affecting accelerator operation.

IV. Orbit Display Features

The user interface of TOP is made up of a set of hierarchical menus. A menu of options is displayed corresponding to the previous menu selection. This aids in maintaining a standard smoothing procedure which is very useful in a control room environment.

Predicted and measured values are displayed through a standardized graphics package. The compare capabilities of TOP allow differences in orbits, DFG settings or DFG corrections to be plotted. A single device feature allows one to look at DFG and BPM settings for all energy levels before and after a smooth at a specific location in the ring. A plot of a typical single device display is shown in Fig. 3. This allows the user to easily view the evolution of parameters through the accelerator cycle.

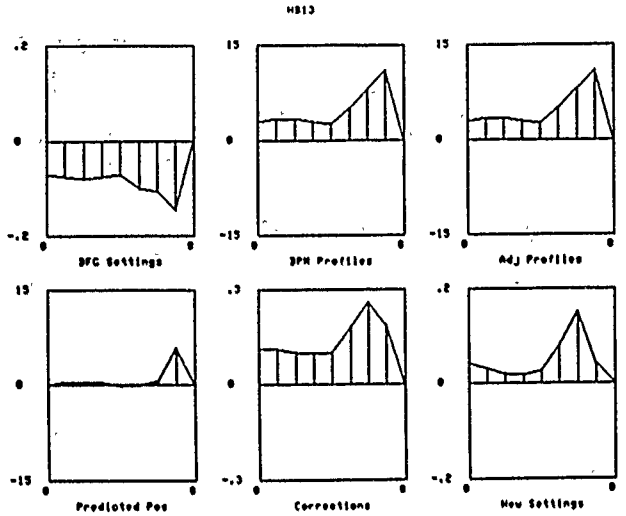


Fig. 3

A single device display feature of TOP. DFG settings, BPM profiles, adjusted BPM profiles, predicted positions, DFG corrections and new DFG settings, all shown at a specific location in the ring, can be plotted.

DIAGNOSTIC TESTS

One particularly useful test after a shutdown is to change the current in one dipole, causing an orbit distortion which can be compared to a predicted change. A BPM with incorrect polarity or an incorrect calibration can easily be seen. To check all BPMs in one plane, another DFG with 90 degrees betatron phase advance from the first must be varied. Thus it suffices to change four dipoles, one at a time, taking an orbit and comparing it to the predicted orbit to do a rather good check on all the BPMs. This along with a measurement of the dipole response without beam, setting all function generators to some preset value and comparing the measured currents in the correction dipole magnets, is necessary before using TOP to correct the orbit.

CONCLUSIONS

TOP is a powerful new program, consistent with the capabilities of a modern control system and required by the complexities of the Tevatron Collider. By making it easy for an operator to bring the orbit to the desired positions, TOP helps to make the Tevatron a reproducible and understandable machine.

ACKNOWLEDGMENTS

The authors would like to thank Glenn Goderre for his contributions to the Tevatron Orbit Program, most notably for the development of the interactive lattice program TEVCONFIG.

REFERENCES

*Operated by the Universities Research Assn. Inc., under contract with the U.S. Department of Energy.

[1] D. Herrup, et al., "Early Operating Experience with the New Tevatron Low-Beta Insertion", these proceedings.

[2] R. Raja, A. Russell and C. Ankenbrandt, "The Tevatron Orbit Program", Nucl. Instr. and Meth. A242 (1985), pg. 15.

[3] K. Cahill, J. Smedinghoff, "Converting the Fermilab Accelerator Control Consoles to x-Window Work Stations", Nucl. Instr. and Meth. A293 (1990), pg. 442.

[4] G. Goderre, B. Hendricks, D.E. Johnson, R.P. Johnson and R. Joshel, "An On-Line Model for Controlling the Tevatron", these proceedings.

[5] D.E. Johnson, G. Goderre, B. Hendricks, R.P. Johnson and R. Joshel, "Control of the Time and Energy Dependent Parameters of the Upgraded Tevatron Collider", these proceedings.

Control of the Time and Energy Dependent Parameters of the Upgraded Tevatron Collider

D. E. Johnson , G. Goderre, B. Hendricks, R. P. Johnson, and R. Joshel
*Fermi National Accelerator Laboratory**
P.O. Box 500
Batavia, Illinois 60510

Abstract

The upgraded Tevatron Collider has two new matched low beta insertions and operates with electrostatic separators to have different orbits for the proton and pbar beams. A general-purpose application program has been developed which allows the operator to control approximately 200 function generators and associated timers to commission, tune, and operate the machine. The program and relevant aspects of the Fermilab controls environment are discussed.

Introduction

With the replacement of the low beta insertion at B0, used during the first two Collider runs, and the addition of a second and identical insertion at D0 the number of quad circuits for controlling the lattice optics increased from 4 to 24. The addition of electrostatic separators and feed-down circuits to the already existing circuits used to control the proton tune, chromaticity, and coupling brings the number of circuits to be controlled to 78 excluding dipole circuits.[1] In addition to the increased number of circuits, many steps are required to bring protons and pbars into collision at the interaction regions and remain separated everywhere else.

With the prospect of the new VAXstation work stations as operator consoles[2] and the increased complexity of the Collider, an effort to design and implement the next generation Collider Software was initiated. The PDP-11 era software responsible for the Tevatron operation had been designed under the constraints of the PDP-11 consoles (i.e. Fortran source code and restrictive memory limitations required large programs to be heavily overlaid). Three independent programs coordinated by a fourth - the Colliding Beams Sequencer (CBS) [3] were required for the operation of the Tevatron during the last Collider run , helical orbit studies, and low beta studies. Much code was duplicated in the three programs and any hardware changes or reconfiguration required (sometimes extensive) code modifications. Since the VAXstations are virtual memory machines and C source code is being supported, a new user interface was written such that a single program, the Collider Ramp Generator (CRG), would be responsible for controlling the time and energy dependence of all circuits during all phases of Collider operation and studies. Many calculation algorithms [4] utilized in these programs are being converted to library routines.

A goal in the design for the operational control of Collider devices is to download all the necessary time and energy parameters (and timing events) in all circuits for the complete filling cycle at the end of the previous store during the "recover" process. Thus allowing clock events to initiate the transitions from injection to low beta with collisions. To facilitate this goal, a Fermilab designed microprocessor based programmable ramp generator (i.e. 465 series of CAMAC modules) [5] with digital and analog outputs is utilised. This module has 16 ramps (or interrupt levels) which are a function of time and/or energy. Each is triggered by the 'OR' of up to 8 clock events. It has a digital input for the Machine DATa link. One of the machine parameters transmitted on this link is the current (or energy) in the main Tevatron bus. This is used by the module to interpolate output values within its energy tables.

Collider Requirements

There are three "states" of the accelerator with respect to its energy: injection, acceleration, and flattop. Acceleration can be considered as a transition between injection and flattop where the energy of the accelerator changes. An energy ramp for the accelerator is defined as a collection of energy steps. Generally, all devices track the energy of the accelerator and have energy tables with values at each step. All of the beam manipulations at a constant energy (either injection or flattop) are carried out by time ramps. The values in the time ramps are considered deltas to the "base value" of the energy ramp at injection or flattop. Time ramps are generally triggered at the desired time by either the CRG or CBS programs. Figure 1 shows the currently defined ramps for the Collider operation along with the "clock events" used to trigger the ramps.

Program Organization

Generally speaking, a machine physicist or operator will want to control some set of devices (called PARAMETERS in the CRG) at a particular time in the cycle (i.e. injection, opening the helix, ramping, during the squeeze, etc.). Using the CRG, a user would specify a time in the cycle (called a RAMP) and a set of parameters (called a GROUP) to display parameters for adjustment.

There can be many GROUPS associated with each ramp. There are two types of ramps for the hardware module which are classified by their independent variable: energy ramps and time ramps. When the energy of the accelerator changes or a

*Operated by the Universities Research Association under contract with the U. S. Department of Energy

0-7803-0135-8/91$01.00 ©IEEE

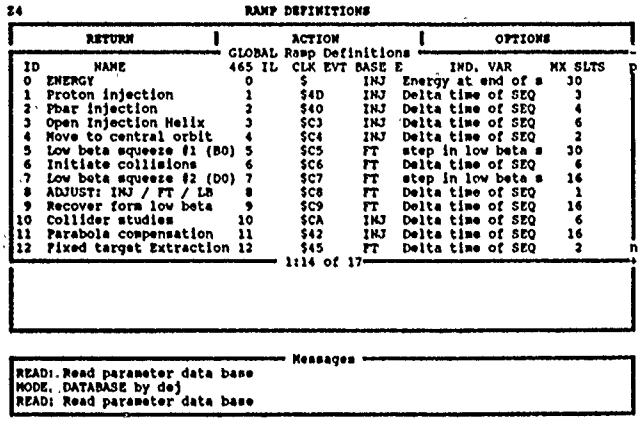


Figure 1: CRG Parameter database page image showing the currently defined ramps for use in Collider operation.

time RAMP is triggered, all devices in each of the GROUPS will synchronously generate their downloaded waveforms. A collection of RAMPS are stored in one of the USER FILES which then contains a complete set of information required to configure the accelerator for a specific operational mode (i.e. Collider operation with one or two insertions, fixed target mode, turn on mode, studies, etc.). To configure the accelerator for the desired operational mode the user would ACTIVATE a USER FILE. This will download all RAMPS defined in the file to the hardware ramp generators. This could take many minutes depending on the number of RAMPS in the file, the number of GROUPS in each ramp, and the number of PARAMETERS in each GROUP, and is only done when the mode of operation is changed.

CRG Parameter Database

One of the main goals of the program design was to accommodate the changing requirements of the accelerator without the need of software modifications. Therefore, a program database consisting of three classes of objects was designed to allow the on-line creation of parameters, groups, and ramp definitions. Interface routines to this database are provided to allow the input, modification, display, copying, and concatenation of each of the three classes.

From these interface routines, the user may specify how accelerator devices are related to each other (which set of PARAMETERS are assigned to a GROUP and which algorithm is used to calculate the output waveforms). The PARAMETERS are considered the low level or base class of objects and contain hardware and program control information. These may represent a desired physics quantity (such as tune, chromaticity) or a specific hardware device to be controlled or both. Currently there are two members to the parameter class: ramp cards and timers. All GROUPS have "input" PARAMETERS which are used to tag the input variables modified by the user and "output" PARAMETERS which are the current or table values to be loaded into the hardware ramp generators.

Program Calculations

The user is provided with the tools to input parameters in machine physics terms which requires a set of algorithms to relate input parameters to the required current waveforms destined for the hardware ramp generators. Many of the algorithms utilized are derived from mathematical models of the machine system while others are simple linear relationships. A library of all calculation algorithms required for Collider operation, is being built.

The constants used in the algorithms are derived from lattice calculations, magnet measurements, or empirically determined from machine data. Circuit configuration information is also included with the calculation constants to indicate which magnets, separator modules, etc. are powered and their polarity. A constants file, which contain all the constants for each unique group defined in a USER FILE, is maintained.

The algorithms and their constants may be viewed and modified during a session. Any modifications may be saved in a constants file associated with each USER FILE.

When the output waveform for a set of devices in the selected ramp is calculated, both the input parameters and output parameters may be plotted on a color graphics screen utilising a standardised plotting package.

Program Implementation

A crucial aspect in the development of the next generation Collider Software was the early development of a layered set of library routines optimised for the VAX console environment. These routines are built upon existing Console LIBrary routines to interface TV and graphics I/O, the accelerator database (for "static" data) and datapool (for "live" data), central filesharing facility, and network communications.These new libraries provide mid-level set of routines designed to create a richer programming environment and increase the ease and efficiency of writing application programs. In many cases, these routines substantially reduce the amount of code required by application programs for data and screen I/O. [6]

A new era at Fermilab for program control was entered upon the introduction of a new mode of program execution, called scripting.[6] A set of routines has been added to the library which allow the "tape recording" of console programs for later replay. A "script" is a record of the console interrupts and cursor movement while recording. These scripts may be accessible through a menu selection for replay or invoked by a remote task. The CRG utilizes these scripts to allow the user to automate an otherwise complicated or lengthy set of interrupts.

Interface to other Software

A set of library routines have been designed to aid in the communication between programs. These routines utilize VAX VMS mailbox, filesharing files and a routine for starting and passing data to remote tasks. The CRG is currently interfaced to three other software programs; the CBS, the Tevatron Orbit Program (TOP) [7], and the on-line lattice calculation program TEVCONFIG [8].

A communication path between the CBS and CRG provides an easy mechanism for adjustment of the common ma-

chine parameters (i.e. tune , chromaticity, and coupling) at injection, flattop, and low beta. The sequencer starts the CRG as a remote task and passes (via mailbox) the values to be adjusted. If the adjustments are successfully loaded in hardware, the CRG returns success and the new values are updated in sequencer files. Instead of passing parameter values, the sequencer can also start a CRG script. This is used for time dependent b2 adjustments, loading a specified ramp, or a file.

The communication between TEVCONFIG and the CRG primarily utilizes filesharing files. As the CRG loads the hardware tables it updates an "operational currents file" to reflect the currents in all Collider devices. Whenever any program requests lattice functions using operational currents, TEVCONFIG will recalculate the lattice functions if the "operational currents file" has been updated since its last calculation. An interactive mode will allow the user to update a "calculated currents file" and then request a lattice calculation. Communication between these programs allows the user to calculate the effect of the change before it is made. In addition, TEVCONFIG will provide the necessary coefficients for the independent pbar tune control algorithm.

The interface between the CRG and TOP also utilizes filesharing files. The primary interaction between these programs is during parsing the squeeze where TOP updates a file with the last sent angles to the dipole correctors. The CRG can read this file to maintain orbit corrections during the squeeze.

Parsing

A technique [9] to step forward or backward through any time ramp one (or more) sequences at a time, adjusting parameters at each step, is referred to as "parsing" a ramp. This technique has been used in building the final low beta squeeze tables for all Collider devices as beam measurements are made.

Continuity between the injection optics and the β^* of .25 meter low beta optics is achieved with a set of 17 "steps". Each of these steps is a solution to a lattice optimization program (i.e. SYNCH) which provide the approximate gradients for the insertion quads. To preserve beam intensity and emittance all parameters must be precisely controlled at each step of the transition to the final β^*. As the CRG loads the hardware to move to the next step, it sends the calculated currents for all devices to TEVCONFIG which will calculate new lattice functions corresponding to actual currents in the magnets. In order for the Tevatron Orbit Program TOP to calculate a correction to a measured orbit distortion at each step , it obtains lattice functions for the current step from TEVCONFIG based upon either the design gradients or the currents sent to the hardware. [Note: these lattice functions are available to any program via interface routines.] Once the desired orbit has been reached the correction angles are passed back to the CRG which saves them for the next execution of the low beta squeeze ramp. After the orbit has been smoothed, the coupling, tune, chromaticity, separators, and feeddown sextupoles may be optimized. When the operator is satisfied with the results, the ramp is parsed to the next step for beam measurements and adjustments.

User Interface

The console interface must be user friendly and provide the user with all possible information to allow intelligent operation. This implies the full usage of user prompts, program messages, error reporting, command logging, on-line program help, plotting functions, and utility routines. The interface is therefore menu driven in a windowed environment. Currently, there are five basic functional windows utilized in the program. They are: STATUS PAGE , DATABASE , RAMP CONTROL, CALCULATION DISPLAY, and PLOT CONTROL. To provide continuity, each window contains a menu bar at the top of the window indicating the possible choices the user may make. Each of the choices in the menu bar will either RETURN to the previous window, open another window, or display a "popup" menu for selection from an allowed set of menu options. Many of the menu bar items have a constant function through the program. Through the menu bar item labeled ACTION (see fig. 1), the user will find all the allowed "actions" that control program flow dependent on the program mode and active window. The OPTIONS menu bar item contains sets of switches or flags which allow the user to modify the default operation of the program in the following areas: plotting, sending to hardware, message display, and error logging.

Current Status

The first version of the CRG program was used during the commissioning of the new low beta insertion at B0. Upgrades to the program structure continue in a effort to produce a flexible, easy to use, menu driven software package for the coordinated control of the time and energy parameters of any accelerator.

References

[1] D. Herrup et. al. Early Operating Experience with the New Tevatron Low β Insertion, these proceedings.

[2] P. Lucas Modern Operators' Consoles for Accelerator Control at Fermilab, these proceedings

[3] D. E. Johnson and R. P. Johnson Proceedings of the 1989 IEEE Particle Accelerator Conference, March 20-23, 1989, Chicago. Illinois. p. 1657.

[4] R. W. Goodwin and R. P. Johnson Proceedings of the 12th Int. Conf. on High Energy Accelerators, Fermilab, Aug., 1983, p. 594

[5] A. Franck, J. Gomilar, B. Hendricks CAMAC Ramp Controller, Fermi internal memo.

[6] B. Hendricks and R. Joshel private communication.

[7] B. Hendricks et. al. The TEVATRON Orbit Control Program, these proceedings.

[8] G. Goderre private communication.

[9] D. E. Johnson Operations Bulletin 1148, Fermi internal memo.

Development and Application of General Purpose Data Acquisition Shell (GPDAS) at Advanced Photon Source*

Youngjoo Chung and Keeman Kim
Argonne National Laboratory
9700 S. Cass Avenue
Argonne, Illinois 60439

Abstract

An operating system shell GPDAS (General Purpose Data Acquisition Shell) on MS-DOS-based microcomputers has been developed to provide flexibility in data acquisition and device control for magnet measurements at the Advanced Photon Source. GPDAS is both a command interpreter and an integrated script-based programming environment. It also incorporates the MS-DOS shell to make use of the existing utility programs for file manipulation and data analysis. Features include: alias definition, virtual memory, windows, graphics, data and procedure backup, background operation, script programming language, and script level debugging. Data acquisition system devices can be controlled through IEEE488 board, multifunction I/O board, digital I/O board and Gespac crate via Euro G-64 bus. GPDAS is now being used for diagnostics R&D and accelerator physics studies as well as for magnet measurements. Their hardware configurations will also be discussed.

I. INTRODUCTION

GPDAS (General Purpose Data Acquisition Shell) has grown out of a concept of a command interpreter and a programming environment for streamlined data acquisition and analysis in a flexible laboratory measurement setting. Even though most operating systems on various platforms provide a command interpreter and certain levels of programmability, they are not specifically designed for laboratory environments for data acquisition, analysis and device control. These require command flow control, communication with external devices, storage and archival of the data. Conventionally, a dedicated stand-alone application would be developed for these purposes. The drawback of this approach, however, is that such applications are inflexible in their scope of capabilities and therefore cannot be easily modified to adapt to different laboratory environments or different configurations of devices, especially in the R&D phase which calls for frequent changes in the measurement procedures.

GPDAS was originally developed for the magnet measurement systems at the Advanced Photon Source. A standardized method using a rotating coil probe will be employed for multipole measurement. On the other hand, various schemes were being considered for dipole measurement. This flexible situation warranted the development of a data acquisition and analysis software that allowed for high-level user programming to simplify hardware debugging.

II. SYSTEM AND SOFTWARE

The current version of GPDAS runs on MS-DOS-based microcomputers. The computer system for magnet measurement at APS consists of a Compaq 386/20e computer equipped with 4 Mb RAM, a 40 Mb hard drive, a 44 Mb removable hard drive, a 5.25 inch 1.2 Mb floppy drive, a 3.5 inch 1.44 Mb floppy drive and a VGA monitor. The system is linked to other computers through Ethernet for data transfer and communication. Text and PostScript graphics files are downloaded to laser printers using AppleTalk connection.

The software package consists of a shell, utilities and script programs. Residing on top of the MS-DOS shell, it also incorporates the MS-DOS shell and takes advantage of existing utility programs for file manipulation and data analysis.

The shell can be directly interfaced with PC boards and control the data acquisition system devices. In conjunction with the magnet measurement system, software drivers for IEEE488, a digital I/O board and an ADC/DAC are built in the shell. The shell can be interfaced to other types of boards through source level modification. Developed with such possibilities in mind, the internal structure of the shell is highly modularized to facilitate such changes.

III. PROGRAMMING IN GPDAS

The shell can be programmed to perform desired tasks either interactively or non-interactively. In the interactive mode, commands are entered through the keyboard, while in the non-interactive mode the shell reads in commands from a script and serially executes them. The shell may also run in a mixed mode by embedding certain commands in the script.

The syntax of the commands must conform to DASL (Data Acquisition Shell Language), a high-level language developed for GPDAS. Commands that are not understood by the shell are passed to MS-DOS shell for further processing. Script programming is relatively easier than developing new

*Work supported by the U.S. Department of Energy, Office of Basic Energy Sciences, under Contract No. W-31-109-ENG-38.

U.S. Government work not protected by U.S. Copyright.

applications, therefore, debugging of hardware and testing of measurement procedures are simplified.

Design objectives of the shell include:

- Interactive mode for user command input
- Non-interactive mode for script execution
- Definition of command aliases
- History of commands
- Assignment of variables and arrays (integer, long, float, double, and string) in RAM and virtual memory
- Backup of aliases, history and variables in script format
- Mathematical, logical and text string operations
- Input and output
- Command flow control
- Device interface
- Windowing capability
- Graphics capability

Other utility applications have also been developed as integral parts of the software package. These include: PostScript graphics, graphical monitoring, file management, background printing and device control.

IV. APPLICATIONS

In this section, we will focus on the application of GPDAS to magnet measurement [1] at APS, which was the primary motivation for its development. Applications to the measurement of synchrotron BPM characteristic [2] and closed loop feedback for orbit stabilization [3] will also be discussed.

A. Harmonic Analysis of Quadrupole Magnet

National Instrument 16 bit digital I/O board for AT Bus is used as a communication bridge between the computer and a Gespac crate. Gespac devices include: encoder-motor controller, digital integrator, integrator trigger, time base trigger, power supply controller, ADC (current/voltage reader) and stepper motor controller. The encoder-motor controller is used to control the motion of the rotating search-coil and generates triggering signals for digital integrators. National Instrument 16 bit IEEE488 interface board for AT Bus is installed to control the devices equipped with IEEE488 interface.

The harmonic analysis of quadrupole magnets is accomplished with a GPDAS script and a few modularized utility programs which are called from the script. The entire process of data acquisition and analysis can thus be streamlined. This modular approach facilitates software debugging and helps overcome the 640 KB memory limitation imposed by MS-DOS.

Figure 1 shows the schematic of the quadrupole magnet measurement system. Both the radial and tangential winding type rotating coil probes have been tested. The script calls the data acquisition program to take raw data from integrators and then calls the harmonic analysis program to analyze the data. The results are then used to realign the magnet. The script saves the data and the analysis results in text, binary, and PostScript graphics files. Data base management and hard-copy printing are also done by the script. Figure 2 shows a sample PostScript graphics output from harmonic analysis of the quadrupole magnet using a radial winding coil.

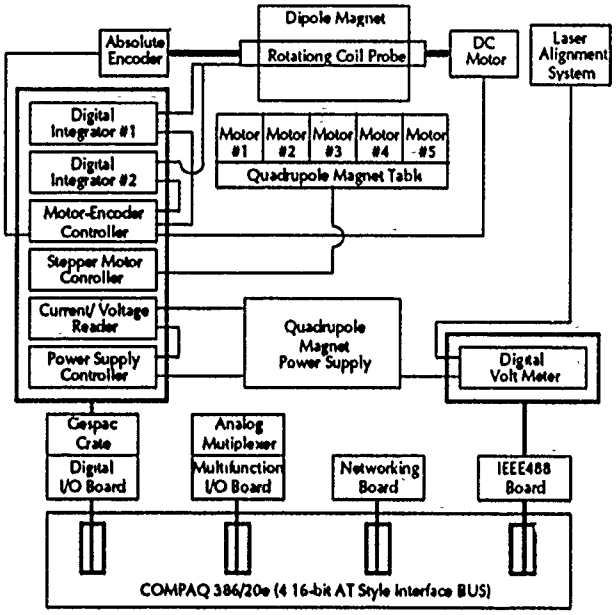


Figure 1. Schematic of quadrupole magnet measurement system.

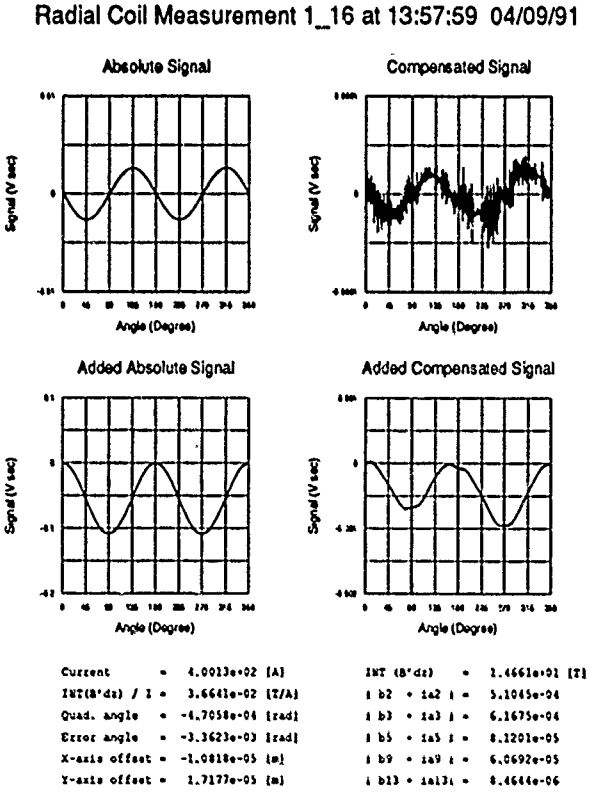


Figure 2. A sample PostScript graphics output from harmonic analysis measurement.

B. Mapping of Dipole Magnet

Two methods of mapping dipole magnets have been tested, one using a Hall probe and the other using a long coil. The schematic of these measurements is shown in Fig. 3. The 3-D mapping table is controlled by 3 stepper motors with encoders and an IEEE488-interfaced motor indexer. The Hall probe #1 is used for mapping and the Hall probe #2 and the NMR probe are used as reference. The digital output of the Hall probe #1 is transferred to the computer via IEEE488 interface and the analog output of the Hall probe #1 is connected to the digital voltmeter.

Two dimensional least square fitting of mapping data has been done for each mapping plane. Integral mapping using a long coil has been tested by moving the coil or ramping the current. Other measurements have been tried for coil manufacturing test, noise measurement, soldering effect, zero-Gauss chamber test and power supply fluctuation test. End field measurement using a short coil and a rotating coil probe will also be tested. At the final stage, integral mapping will be carried out by bucking the signals from the reference magnet and the magnet being measured.

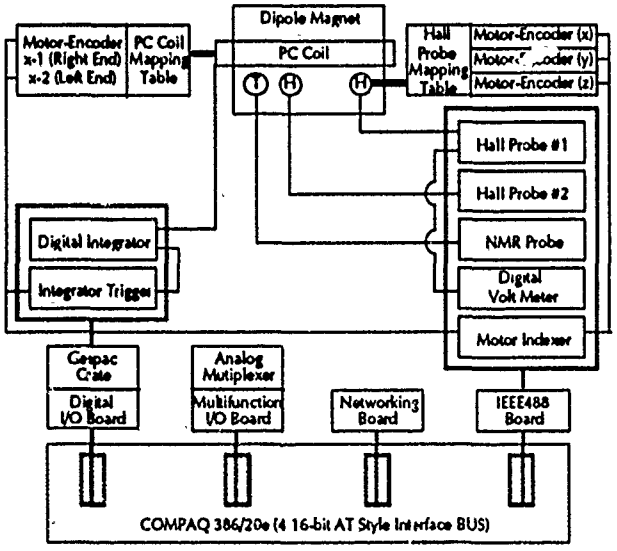


Figure 3. Schematic of dipole mapping system using Hall probes and a coil.

C. BPM Test Stand Measurement

GPDAS has been used to characterize the synchrotron beam position monitor (BPM) test stand. Four button-type pickups are mounted on a BPM unit made of stainless steel. A thin fixed wire of 0.012" diameter is suspended through the elliptic bore under tension in order to maintain straightness. The transverse position of the BPM unit relative to the wire is controlled by two stepper motors and a controller in a CAMAC crate. The buttons are multiplexed by a 4-throw-1-pull mechanical RF switch, and measurements are done using a network analyzer and a digital sampling scope.

The stepper motor controller, the switch driver, the network analyzer and the sampling scope are interfaced to the computer via IEEE488 bus. As in the case of the magnet measurement system, data acquisition and analysis are done by GPDAS scripts and accompanying utility programs. The scripts also format the measurement data and the analysis results for further processing on other computers.

D. Closed Loop Feedback Measurement

The APS will use a large number of correction magnets to create local bumps and to achieve global orbit stabilization. Efforts have been made to counter the effect due to the finite inductance of the magnet and the eddy current in the 1/2"-thick aluminum storage ring vacuum chamber. Significant amplitude attenuation and phase shift of the correction magnet field were anticipated. Measurements and compensation of this eddy current effect have been done using GPDAS.

The data acquisition was done primarily using an ADC, which registered the reference signal, the field inside the vacuum chamber and the control signal to the magnet power supply. Compensation was done by an analogue circuit, and data acquisition and analysis were done by a script and a few utility programs as discussed in previous cases.

V. CONCLUSION

GPDAS provides an integrated script-based environment for data acquisition and analysis. It has been successfully applied to the magnet measurement system, synchrotron BPM test stand and closed loop feedback measurement at the APS. It proved particularly useful for test measurements, such as equipment test, manufacturing technique development, and feasibility tests for measurement methods. Though it currently runs only on MS-DOS-based computers, it can be ported to other platforms, such as SUN or VAX workstations with modifications on the user command interface.

VI. REFERENCES

[1] S. H. Kim, K. H. Thompson, E. L. Black, and J. M. Jagger, "Fabrication and Tests of Prototype Quadrupole Magnets for the Storage Ring of the Advanced Photon Source," these proceedings

[2] G. Decker and Y. Chung, "Progress on the Development of APS Beam Position Monitoring System," these proceedings

[3] Y. Chung, J. Bridges, L. Emery, and G. Decker. "Open Loop Compensation for the Eddy Current Effect in the APS Storage Ring Vacuum Chamber," these proceedings

Unix Data Acquisition System

I. Kourbanis, S. Peggs, T. Satogata
*Fermi National Accelerator Laboratory,*P.O. Box 500 Batavia, Illinois 60510*
G. Tsironis
University of North Texas, Denton, TX 76203-5368
G. Bourianoff
SSCL†2550 Beckleymeade Ave., Dallas, TX 75237

Abstract

The Unix Data Acquisition System (UDAS) is a Fermilab-based prototype for on-line data acquisition and analysis. The system employs a shared memory approach for the storage and accessibility of the large set of data (approximately 0.5 Megasamples) it is capable of handling. It is currently used to analyze turn-by-turn data obtained through two beam position monitors of the Fermilab Main Ring. The data are digitized with a LeCroy 6810 fast waveform digitizer. Recently the system was used to obtain a continuous tune measurement in a single Main Ring cycle after applying a noise signal (white noise or a chirp signal) to the beam through the Main Ring slow dampers.

Introduction

The capture and analysis of turn by turn data, from beam position monitors and intensity monitors, was a central feature of the E778 nonlinear dynamics experiment at the Fermilab Tevatron. The UDAS data acquisition system represents a harden version of the "Mirabile" [1] instrumentation used for E778, with the intent to make it routinely available for diagnosis of Main Ring or Tevatron performance. Turn by turn instrumentation has been succesfully used at CERN to continuously monitor tunes through SPS [2] and LEP cycles [3]. So far the minimum goal for UDAS has been the reproduction in the Main Ring of the SPS's continuous tune measurement capability, although there is good reason to believe that other continuous measurements besides tunes will also be possible.

Hardware

A block diagram of the hardware configuration is shown in Figure 1. The beam is excited or "heated" by applying a noise signal to the Main Ring slow dampers. There are two noise gates, one for each plane, which are referenced to an arbitrary Main Ring event. Normal Main Ring beam position pickups are used to extract direct horizontal, vertical and intensity signals. The signals are digitized with a LeCroy 6810 5-Mhz, 12-bit transient digitizer, with 0.5 Megasamples of onboard memory. The "noise" signal used to heat the beam is digitized as well.

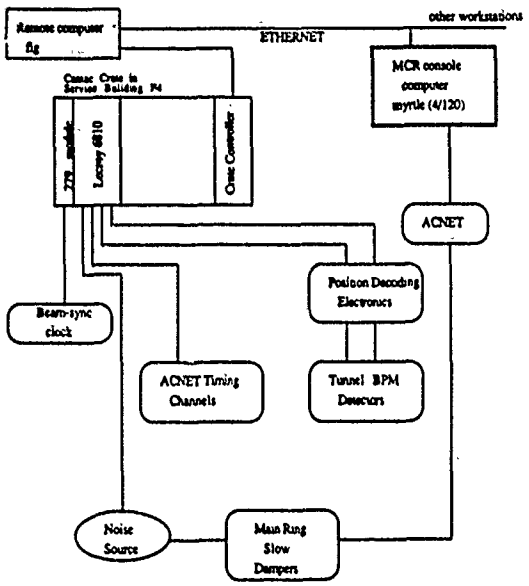


Figure 1: *Hardware configuration of the UNIX system for the Main Ring.*

The sampling clock for digitization is the Main Ring beam-synchronized revolution frequency clock. The 279 modules provide two separate timing pulses with a programmable delay from a Main Ring beam-synch clock. They are used for adjusting the timing of the gate inside which data is taken.

The digitizer, once armed, samples continuously until an external trigger signal, a standard Main Ring event; arrives. The number of samples stored in memory after a trigger event is controlled by the segment size (up to 0.5 Megasamples for 4 active channels), set in the module.

The camac-based LeCroy modules are controlled by a Sun 4 workstation(fig) via the Sun's VME backplane and a CES CBD/8210 camac branch driver. This is to be replaced with a Sparcstation 1E on a VME card in the future. The control and the data flow to the control room workstation is done through the Sun's ethernet link.

Software

The entire data acquisition system is based on the Integrated Scientific Tool Kit (ISTK) package developed at LBL

*Operated by the Universities Research Association under contract with the U. S. Department of Energy

†Operated by the Universities Research Association, Inc. for the U.S Dept. of Energy under contract DE-AC02-89ER40486

0-7803-0135-8/91$01.00 ©IEEE

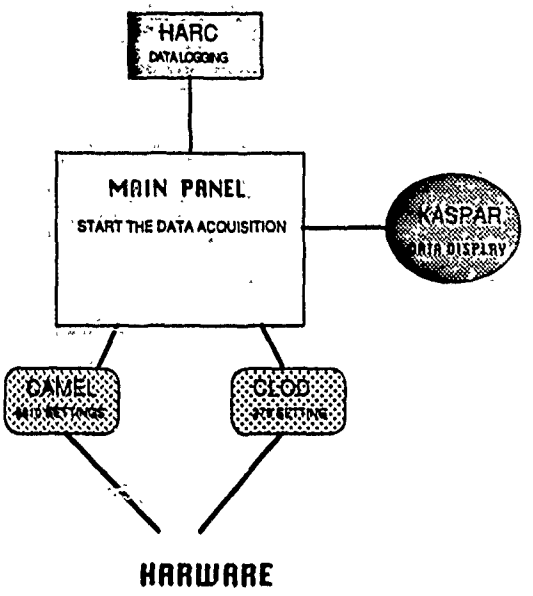


Figure 2: *Sofware configuration.*

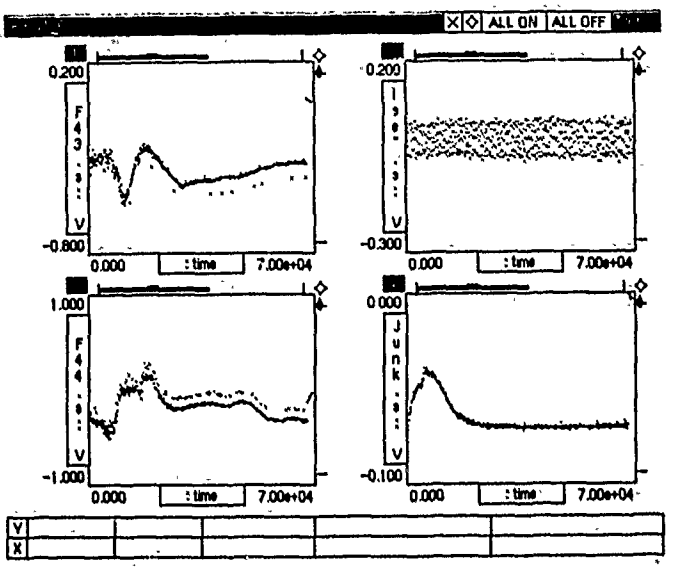


Figure 3: *Typical "kaspar" graphics picture of the digitized signals in UDAS. The vertical axes are in Volts and the horizontal axes are in number of beam revolutions.*

with funds from the SSC Accelerator Division. The ISTK package consists of a set of four tools:

a) "kaspar" graphics
b) "SDS" data management utilities
c) Relational database management system utilities
d) "glish" sequencer language.

Use of the ISTK package allows easy interface of control panels on screen with the actual control programs, written in C++.

There is a general acquisition control panel which controls the whole data taking operation. From this panel one can:

1. Control the data acquisition.

This part of the control panel initializes all the data-acquisition processes, starts the logging of the data to disk, and selects the data taking mode (single shot/auto shot). The logging of data is achieved by energizing another system called "harc" which looks at the shared memory of the remote computer and transfers the data to the disk of the computer at the control room.

2. Talk to individual camac modules.

From this part one makes changes to individual modules, both by turning them on and off and by calling subsidiary panels that make changes to the module settings. The 6810 is controlled by a panel called "camel" from which all the camac settings of the module can be set by toggling on pulldown menus. One has also the ability to save the entire set of module settings in a file for future reference. The 279 module is controlled by a panel called "clod" from which the adjustable delays to the beam-synch clock are set.

3. Control the documentation and display of the data.

From this part one can turn on the 'kaspar" graphics for the online display of the data and can also record whatever typed-in comments he wishes to accompany the data. Figure 2 shows a general picture of the software configuration used in UDAS.

Experimental Results

During the last study period of the Fermilab Accelerator the UNIX data aquisition system was tested in performing a continous tune measurement on a single MR cycle. The cycle chosen was a 29 cycle (pbar production), that had a total length of 1.4 sec and a flattop energy of 120 GeV. We used an HP 3582 Dynamic signal analyser as a noise source and applied the noise signal to the horizontal dampers over a gate extending from the beginning of the cycle to near the flattop energy. Two BPMs, one horizontal(F44) and one vertical(F43) were digitized along with the noise signal and the intensity signal provided by the F43 BPM. Figure 3 shows a "kaspar" graphics picture of the four signals for the whole Main Ring cycle chosen.

Two different types of noise source were used, a) periodic chirp and b) random noise. The frequency span of the noise source was varied from 3 – 34 kHz coresponding to different time records. The amplitude of the source was also varied, but remained constant during a particular cycle. We found that with white noise we could effectively excite the beam without any observable degradation. Horizontal tunes were observed by simply taking successive FFT's of the beam responce over the noise source time record. We did not have similar success in tune observations when we used a periodic chirp of a constant amplitude. In this case the beam was killed at an early stage for chirp amplitudes large enough to excite the beam at flattop energies.

In Figure 4 the "kaspar" plots of 16 successive FFT's taken over 4096 turns (0.086 sec) in one 29 cycle are shown. The horizontal tune lines are clear except around transition (13000-20000 turns) up to about 60000 turns or energy of 100 GeV.

By looking at the correlation between the beam response and the random noise signal we could identify the horizontal tune lines up to the flattop energy of 120 GeV, and could sometimes identify the vertical tunes lines due to coupling.

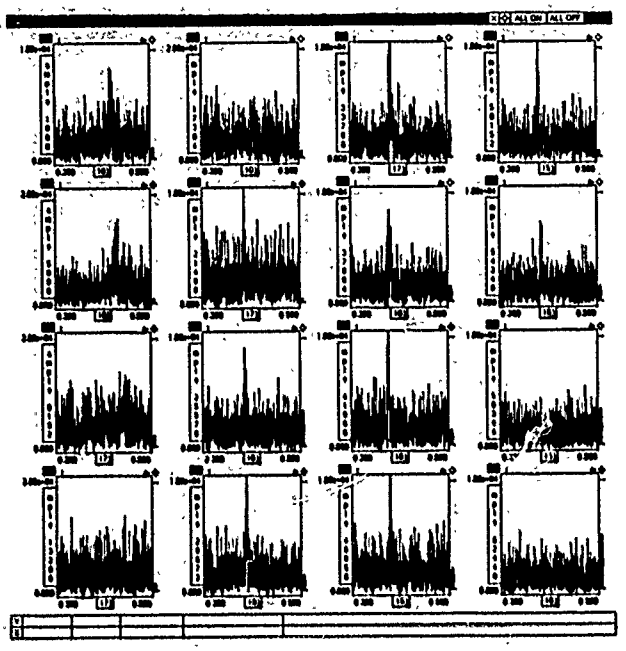


Figure 4: *Successive FFT's of the horizontal BPM signal through the Main Ring cycle for a random noise source drive signal.*

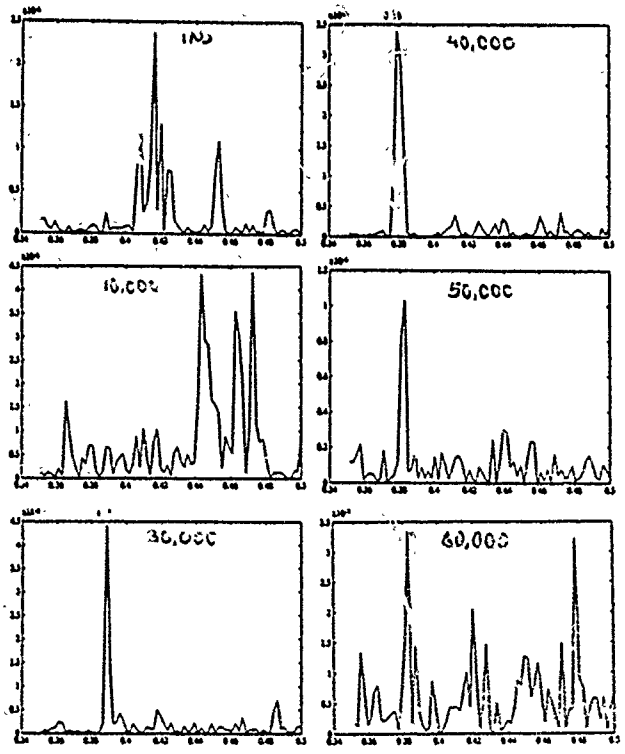


Figure 5: *Correlation function between the horizonal beam responce and the random noise signal at different points in the cycle. The plots correspond to injection, 10000, 30000,40000, 50000, and 60000 turns into the cycle.*

Conclusion

The UNIX data acquisition system was succesfuly tested in acquiring and analyzing turn by turn data to obtain horizontal tunes versus time in a single Main Ring cycle. More work needs to be done in determining the best way of extracting the tunes from the turn by turn data with the least possible beam disturbance and to incorporate this method into an automated procedure of a continuous tune measurement as performed in the CERN SPS.

Acknowledgment

Many thanks to C. Saltmarsh and M. Kane of SSCL and LBL for implemending most of our suggestions in the software, and for their overall support of the project. Thanks also to J. Crisp of Fermilab for his help in the implementation of the "noise" gates in the Main Ring dampers and for many useful discussions.

References

[1] S. Peggs, C. Saltmarch, and R. Talman *"Million Revolution Accelerator Beam Instrument for Logging and evaluation," SSC-169, March 1988.*

[2] R. Bossard et al, *"Tune Measurement and Control at the CERN-SPS," IEEE Trans. Nucl. Sci. NS-32, No. 5, October 1985.*

[3] K.D. Lohmann, M. Placidi, H. Schmickler *"Design and Functionality of the LEP Q-Meter," Proceedings of the 2nd European Particle Accelerator Conference, Nice, June 12-16, 1990, p. 774.*

Control System User Interface for Accelerator Commissioning and Operation

D. Dobrott, D. Keeley, G. Kolte and Z. Mikic
Science Applications International Corporation (SAIC)
2200 Powell Street, Suite 715
Emeryville, California 94608

M. Lee, J. Corbett, S. Howry and A. King
Stanford Linear Accelerator Center (SLAC)
Stanford, California 94305

Abstract*—An Interactive Accelerator Interface Module (AIM) has been developed in a workstation environment for the purposes of assisting in the commissioning and operation of any storage ring/collider system. The function of AIM is to integrate modeling and simulation codes into accelerator and beamline control systems for the purpose of rapid on-line data analysis and error-correction, resulting in significant time-saving. A system dependent module provides for the translation of specific control system data files to appropriate input format for application programs within AIM. Interactive screen graphics, including system function diagrams, menus, beamline element status and update information are standard in AIM. AIM is currently connected to the Stanford Linear Collider (SLC) control system, but is easily transportable to other facilities. This paper describes the development of AIM and its applications on SLC.

I. INTRODUCTION

There have been rapid advances in the analysis and the reduction of data from accelerators and beam storage systems in recent years. Analysis tools include model reference systems in a workstation environment. The Accelerator Interface Module (AIM) is an interactive graphics interface that functions in such an environment. The goal of AIM is rapid on-line data analysis and error correction for accelerators and storage rings. AIM follows many years of similar effort at the Stanford Linear Accelerator (SLAC) [1].

II. HISTORICAL BACKGROUND

Over the past few years, as the modeling codes for data analysis improved, the time it takes to find and correct errors in beam lines decreases from months to hours. For example, in 1983, a 3% power supply error prevented the SLC damping ring from storing the beam. This problem was resolved after approximately six man-months of effort using the code COMFORT [2]. In 1989, a similar problem which had caused a beam mismatch in a Storage Ring to LINAC subsection was resolved using COMFORT and a single-track analysis in ten man-days. As a result of the October 1989 Loma Prieta earthquake, SLAC Positron Electron Project (PEP) suffered misalignments. This problem was analyzed in two man-days using the beam trajectory simulation code RESOLVE [3].

In all cases, the man-time effort also included the time it took to develop error finding methods. Now with these analysis methods known, the time it takes to analyze similar problems is greatly reduced. AIM is a further development along this line but with automated control system data file translation to the format for the analysis codes. The resulting turn-around time from data recording, through analysis, to machine update may be reduced to as little as an hour. AIM currently is being used on the Stanford Linear Collider (SLC) to upgrade luminosity.

III. AIM STRUCTURE

In its operation mode, AIM performs some analysis functions on the measured BPM and screen/wire data, and prepares input for the spawned codes such as RESOLVE and COMFORT as needed. AIM may also be used in a design mode. Beamline and beam requirements developed by AIM may be used to suggest placement of various types of diagnostics and to study their sensitivity to errors. Additionally, AIM may be used as a simulator for the purpose of training operators off-line and for developing beam tuning procedures.

The current version of AIM functions with Digital's VMS system. The code has been developed by SAIC on a VAX-Workstation 3100 running VMS version 5.2 and VWS version 4.1 (UIS) eight plane color graphics. A four plane version is working at SLAC. There is also an earlier demo developed for Boeing that runs on a Micro VAX II GPX with VMS version 4.6 with eight plane graphics.

The interactive graphics code is mouse-and-menu driven. The menu system guides the user through different levels of the code in sequence. The user is automatically prevented from making selections out of sequence as required by a given beam tuning procedure. The user is also assisted by means of HELP menus.

AIM displays a beamline layout display of the accelerator/storage-ring/collider, Figure 1. After a subsection is selected, a beamline data file prepared by the translator from a database derived from the SLC control system is used to display graphically the components of the entire subsection in terms of mouse-active icons. The icons are set in a convenient

*Work supported by DOE Contract No. DE-AC03-76-SF00515.

0-7803-0135-8/91$01.00 ©IEEE

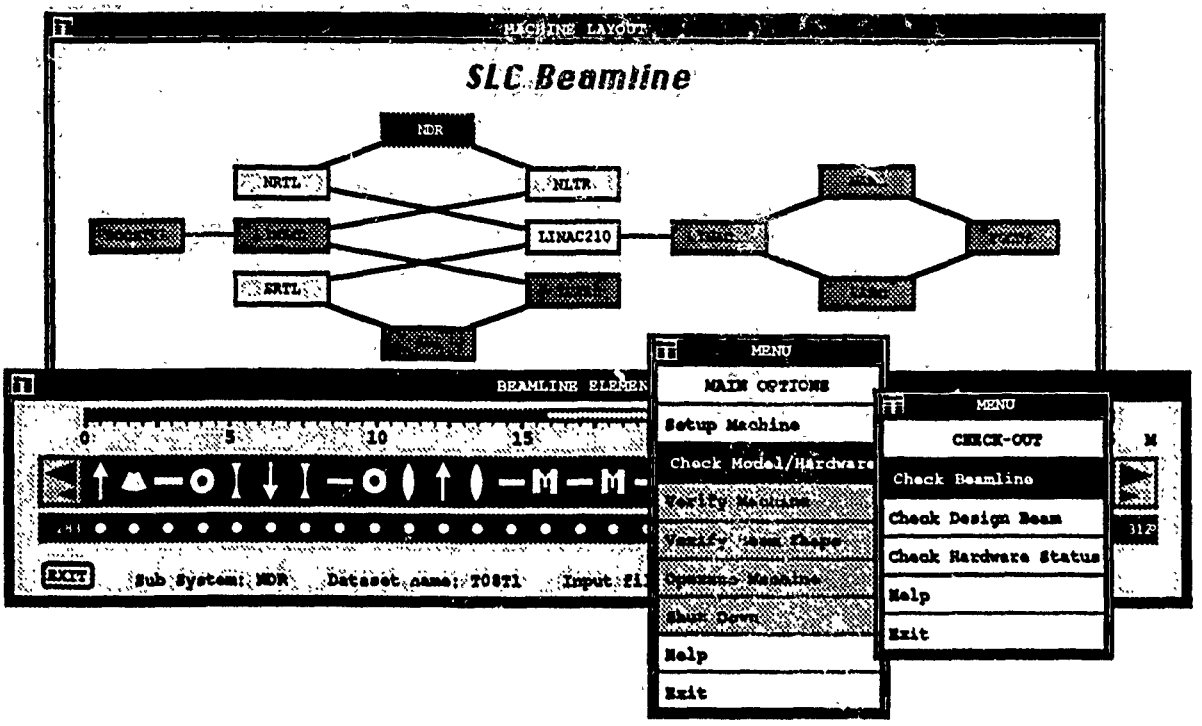


Figure 1. AIM Screen Layout

horizontal display that may be rapidly scrolled. Upon selection of a particular icon, technical data describing the element is displayed in a menu. In addition to the extensive analysis tools - all standard first order elements are available - within AIM, AIM can spawn codes such as COMFORT and RESOLVE and their associated graphics.

IV. APPLICATIONS

A. Analysis Functions in AIM

Beam launch errors, such as off-sets in position, pitch or energy may cause large trajectory deviations from the design orbit. An 'unknown' deviation in displacement and/or pitch is determined by sampling beam displacement at several BPMs interactively selected from the input data file. The values of x, x', y, y' estimated from the selected subset of the data are displayed in a window and then used to predict beam position downstream. This kind of analysis is used in the model-reference launch feedback system.

Additionally, the beam ellipse may be determined from using beam-intrusive screens/wires and by varying upstream quadrupoles. The illustration in Figure 2 shows the simulated result of recording the beam size at a downstream fluorescent screen while varying a single upstream quadrupole over a range of values. The beam size shows a minimum over variation in upstream quad strength. Size data are inverted to determine beam Twiss parameters [4]. The difference between the design and the experimentally determined phase ellipse are shown (along with the experimentally determined Twiss parameters).

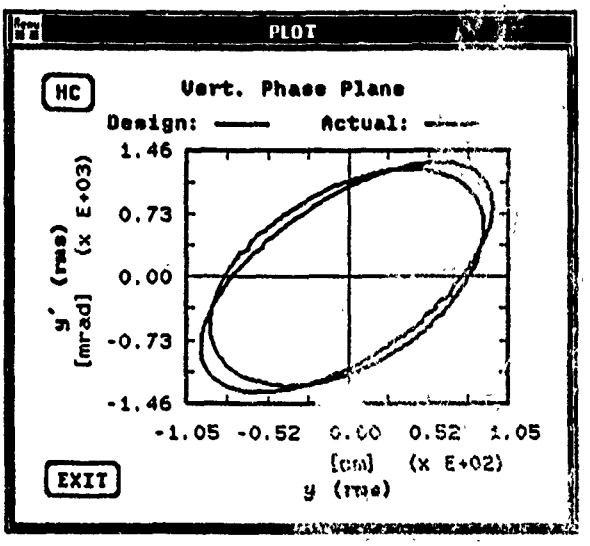


Figure 2. Shape Analysis Display.

B. Spawned Codes

Beam rematching is performed using the spawned code COMFORT. In this application, a comparison of the design beam with the unmatched simulated beam, and the design beam with the rematched beam may be displayed. Quadrupole changes required for the rematching can be determined by COMFORT.

RESOLVE is used primarily to identify errors and to recommend remedies. AIM (using RESOLVE) has been used to determine first order optical errors. The illustration in Figure 3 shows x and y displacements before and after the

location of a magnet field error and its adjustment. The fault analysis and recovery was performed using the spawned code RESOLVE. The beam was initially analyzed by finding the subsections of the beamline that agreed with design predictions, thus localizing the errors to segments between the "good" sections [5]. Then beamline model parameters - magnet field strength, BPM calibrations, and their alignments - in the "bad" sections are varied and the mean square error minimized to predict new parameter values which give the best fit to the measured orbit data. The analysis is then repeated with the new values. The effect of the located field error on the orbit is shown.

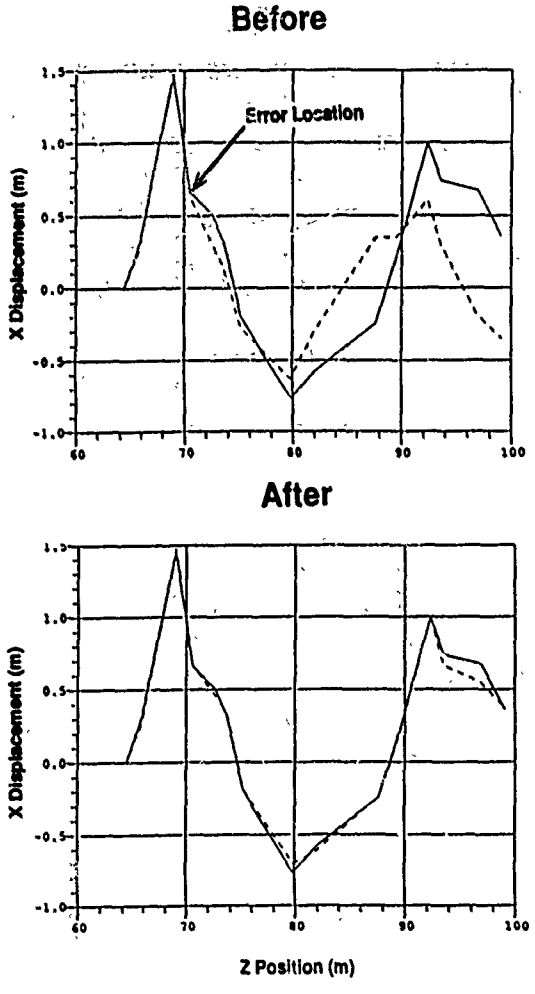


Figure 3. Field Error Analysis Displays.

RESOLVE may also be used to analyze higher order optical errors. The character of an error in the field of a septum magnet in the SLC electron damping ring is determined by using RESOLVE. The septum magnet was modified after design to add cooling channels. An electromagnetic kicker coil upstream of the septum magnet is varied and the centroid tracks downstream of the septum are studied. An 'equivalent' kicker at the septum location is deduced from the data. If the septum magnet were a pure dipole, there would be no inferred differential 'equivalent' kick. A linear differential kick would correspond to a quadrupole. The results illustrated in Figure 4 suggest higher-order, viz. more complicated field effects. This problem is still being investigated.

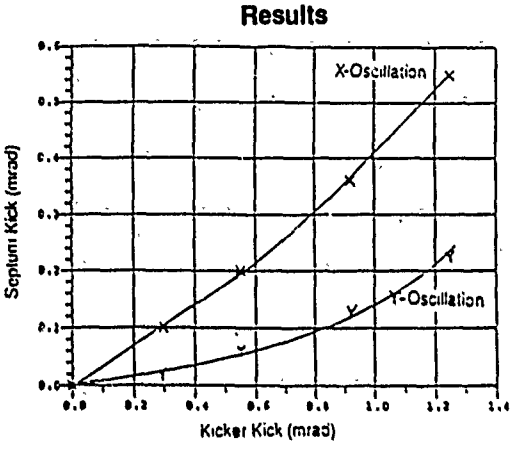


Figure 4. Field Analysis Result

V. Future Development

Long term objective of AIM is its software implementation in a complete on-line, model reference control system. The core of this control system software would be a real-time database RTDB, such as that developed for the PEP. Future AIM would provide the analysis, the graphics, displays, and the software interfaces for the RTDB, the system software between local nodes and the RTDB. "Look and adjust" analysis functions of AIM would be automated [6]. Other modeling and analysis capabilities will also be added. Future development is being extended to a UNIX-based Workstation and with X-WINDOWS graphics interface. For example, RESOLVE has already been extended to UNIX (with X-WINDOWS).

VII. References

[1] S. Kleban, M. Lee, Y. Zambre, "GENI: A Graphical Environment for Model-Based Control", Nuclear Instruments and Methods in Physics Research A293 (1990) 475-479.

[2] M. Woodley, M. Lee, J. Jager, A. King, "Controls of Machine Functions or Transport Systems", Proceeding of the Particle Accelerator Conference, Santa Fe, New Mexico, March 21-23, 1983.

[3] Cf. M. Lee, for information on RESOLVE.

[4] J. Sheppard, J. Clendenin, R. Helm, M. Lee, and R. Miller, "Emittance Calculations for the Stanford Linear Collider Injector", Proceeding of the Particle Accelerator Conference, Santa Fe, New Mexico, March 21-23, 1983.

[5] M. Lee, et al., "Analysis of the Orbit Errors in the CERN Accelerators Using Model Simulation", Proceeding of the Europhysics Conference on Control Systems for Experimental Physics, Villiars, Switzerland, September 28 - October 2, 1987.

[6] D. Nguyen, M. Lee, R. Sass, and H. Shoaee, "Accelerator and Feedback Control Simulation Using Neural Networks", Proceeding of this conference.

OVERVIEW OF REAL-TIME KERNELS AT THE SUPERCONDUCTING SUPER COLLIDER LABORATORY

K. Low, S. Acharya, M. Allen, E. Faught, D. Haenni, C. Kalbfleisch
SSC Laboratory *
2550 Beckleymeade Ave.
Dallas, Texas 75237

Abstract

The Superconducting Super Collider Laboratory (SSCL) will have many subsystems that will require real-time microprocessor control. Examples of such sub-systems requiring real-time controls are power supply ramp generators and quench protection monitors for the superconducting magnets. We plan on using a commercial multitasking real-time kernel in these systems. These kernels must perform in a consistent, reliable and efficient manner. Actual performance measurements have been conducted on four different kernels, all running on the same hardware platform. The measurements fall into two categories. Throughput measurements covering the "non-real-time" aspects of the kernel include process creation/termination times, interprocess communication facilities involving messages, semaphores and shared memory and memory allocation/deallocation. Measurements concentrating on real-time response are context switch times, interrupt latencies and interrupt task response.

I. INTRODUCTION

The process of evaluating real-time kernels from different vendors can be a confusing experience. One is faced with a plethora of performance numbers from the individual vendors' information packages, each displaying superiority and advantages over their competitors. Each vendor invariably measures performance numbers in different ways and on different hardware platforms thus making comparisons almost meaningless.

To compare and evaluate the different offerings, we performed our own tests in a controlled environment. Products from the four vendors that met our base requirements were tested on the same hardware platform. The platform on which all four vendors is supported is the MVME147S-1 [1]; a VME based, single board computer with a 25MHz 68030 from Motorola. The four kernels selected, listed in no particular order, were pSOS+ from Software Components Group [2], VRTX32 from Ready Systems [3], VxWorks (v4.02) from Wind River Systems [4] and LynxOS (v1.21) from Lynx Real-Time Systems [5].

It should be stressed that these tests only provide quantitative measurements of a particular system's performance. Qualitative aspects such as development environment, debug capabilities, connectivity, compliance with industry standards, technical support and host/target availability will be addressed at the end of this paper.

Each test was executed a number of times in order to compute the average time to complete a test. The entire measurement is then repeated several times to measure the variance of this average value in the form of maximum and minimum average values. Clock resolution, number of iterations and cache conditions were identical for all four kernels.

II. THROUGHPUT MEASUREMENTS

Throughput measurements are tabulated in Table 1 and what follows is a brief description of each test as it appears in the table. Idiosyncrasies of each kernel will also be noted. An asterisk means that a particular test could not be performed on that kernel.

1. Create/Delete Task This test measures the time it takes to create and delete a task. A task deletes itself as soon as it is created. The created task has a higher priority than the creator, so the time quoted actually includes a create, start, delete and two task context switches.

2. Ping Suspend/Resume Task A low priority task resumes a suspended high priority task. The high priority task immediately suspends itself. This measurement includes two task context switches and the time it takes to suspend and resume a task. There is no facility to suspend and resume a task on LynxOS apart from using signals. So this test was not performed under LynxOS.

3. Suspend/Resume Task This is identical to previous test except that a high priority task suspends and resumes a suspended lower priority task so that there is no context switching.

4. Ping Semaphore Two tasks of the same priority communicate with each other through semaphores. Task A creates a semaphore, gets the semaphore and then creates Task B which blocks when it attempts to get the semaphore. Task A then releases the semaphore which immediately unblocks Task B. Task A then attempts to get the semaphore which causes it to block until Task B releases it. The two tasks then alternate ownership of the semaphore thereby causing context switches. In our version of VxWorks, two separate semaphores are required because round-robin scheduling is not supported.

5. Getting/Releasing Semaphore The time reported includes the time it takes to get and immediately release a semaphore within the same task context.

6. Queue Fill, Drain, Fill Urgent We first time how long it takes to fill a queue with messages and then we time how

*Operated by the Universities Research Association, Inc., for the U.S. Department of Energy under Contract No. DE-AC02-89ER40486.

U.S. Government work not protected by U.S. Copyright.

Table 1: Throughput Measurements

Test Description	pSOS+ min/max/avg μsec	VRTX32 min/max/avg μsec	LynxOS min/max/avg μsec	VxWorks min/max/avg μsec
Create/Delete Task	540/600/591	370/380/371	*	1378/1446/1423
Ping Suspend/Resume Task	120/130/128	140/150/142	*	174/182/177
Suspend/Resume Task	80/90/83	80/90/87	*	68/74/69
Ping Semaphore	210/220/219	230/250/239	390/400/397	228/234/232
Getting/Releasing Semaphore	63/64/63	55/56/55	73/76/74	33/34/33
Queue Fill	40/50/46	20/30/26	136/146/140	19/21/20
Queue Drain	40/50/43	20/40/29	126/136/132	21/25/22
Queue Fill Urgent	40/50/47	20/30/27	166/175/170	70/76/72
Single Queue Fill/Drain	90/93/91	50/70/59	270/290/278	43/48/44
Alternate Queues Fill/Drain	230/240/238	250/260/252	860/900/867	366/376/371
Allocate Memory	40/40/40	20/30/27	34/79/57	67/71/68
Deallocate Memory	30/40/38	30/40/33	20/21/20	82/86/83

long it takes to drain the queue. Finally we repeat the two tests with priority messages i.e. messages are sent to the head of the queue. VxWorks 4.02 does not support message queues but ring buffers with semaphores gives the functionality of a message queue. LynxOS uses SysV message queues with priority messages handled differently.

7. Queue Fill/Drain A single task sends a message to a queue which the task immediately receives on the same queue. There is no task context switch nor is there any pending queue operations. The next test consists of two tasks with two queues. The two tasks alternate execution by sending to the queue that the other is blocked waiting to receive from. The total time now includes context switches, queue pends and sending plus receiving a message.

8. Allocating/Deallocating Memory We measure the time it takes to allocate a number of buffers from a memory partition and the time it takes to return those buffers to the partition.

III. REAL-TIME RESPONSE

The Motorola MVME147S-1 includes an auxiliary timer capable of generating interrupts. A driver for the timer was written for all four kernels. We quantify the real-time response of the kernels by measuring the interrupt service response and the interrupt task response. The interrupt service response is the time it takes to execute the first instruction of an interrupt service routine (ISR) from when the interrupt occurs. The task response is the time it takes for a user task to resume execution from when the interrupt occurs. These measurements were taken over a large number of times and the maximum, minimum and average times are reported over the span of the test. The LynxOS was the only kernel with a SCSI disk attached to it and all kernels had network attachments and a real-time clock as other sources of interrupts. The source of interrupts for the actual measurement was an auxiliary counter on the MVME147S-1 and the measurement task runs at the highest priority.

Typically, a user task is blocked waiting for a semaphore to be released by the ISR. The counter is programmed to start counting up from a preset value to a maximum value when it will generate an interrupt, resets itself to the preset value and begins counting up again. Each count corresponds to 6.25 μs. The ISR then immediately reads the counter, which gives the interrupt response time, and then releases the semaphore. When the kernel reschedules the user task after completion of the ISR, the user task becomes unblocked, reads the counter which then gives the task response time.

IV. OBSERVATIONS

pSOS+ is a robust real-time kernel. Code can be developed on a number of different host platforms and downloaded to the target with the final application stand-alone in ROM. Software Components Group (SCG) supports pSOS+ on many target systems and provides source to drivers making ports to specialized boards easier. The XRAY+ debugger, based on the popular XRAY debugger from Microtec [6] is capable of debugging target resident optimized C source code across ethernet or RS-232. There is also an X11 interface which offers increased versatility. In addition to task-level breakpoints, system-level breaks can also be set at the system-level; stopping all tasks. This allows access to the onboard monitor and the state of all pSOS+ objects. Optional components provide UNIX-compatible network facilities and an ANSI standard run-time library. Field support was excellent.

VRTX, from Ready Systems, provides a full complement of support software in addition to the VRTX/32 real-time kernel. These include packages for I/O file management, networking, multiprocessing and a run time library VRTX is supported on several commercially available target boards with supporting documentation for porting

Table 2: Real-Time Response

	pSOS+ min/max/avg μsec	VRTX32 min/max/avg μsec	LynxOS min/max/avg μsec	VxWorks min/max/avg μsec
Interrupt Service Response	6/6/6	6/6/6	13/88/13	6/56/6
Interrupt Task Response	100/169/163	169/343/169	163/262/175	119/319/125

VRTX to customized boards. Host support currently exists only for SUN3/SUN4 with Sun's own proprietary windowing environment. The source level debugger (RTsource) and the symbolic debugger (RTscope) can function across an ethernet/serial link between the host and target. Like pSOS+, breakpoints can be set at task as well as system level. Tasks may be stopped and information about kernel data structures displayed. A run-time shell with dynamic linking capability is available for quick prototyping of applications. Although somewhat daunting to the first-time user, VRTX is an extremely flexible and versatile system to the initiated.

VxWorks includes a proven real-time kernel and a UNIX cross-development package with extensive UNIX-compatible networking facilities. Version 4.02 supports only a preemptive priority scheduling kernel while V5.0 offers in addition round-robin scheduling. Version 5.0 also promises better performance with some compliance to Posix 1003.4 Real-Time Extensions. VxWorks currently is ported to a number of different target boards with the host support fully implemented only on the SUN3/SUN4 systems. The source-level debugger is a remote debugger based on the Free Software Foundation GDB [7]. The debugger can only debug single tasks and currently does not have an X11 interface. A symbolic debugger with some system status displays is also standard. Dynamic loading of objects over the network or from a disk together with an interactive C-interpreter interface can be useful during the development cycle.

LynxOS provides a complete Unix development environment. It can also be used for a cross-development system like the other three kernels. It offers good real-time performance with memory protection. LynxOS 1.21 currently offers compliance to Posix 1003.1, SVID 4.2 and BSD 4.3 with future releases complying with 1003.4 Draft 9 (Real-Time Extensions). It has been ported to four different computer architectures. It has a Unix System V.3 binary compatible interface built into the LynxOS kernel so that binaries work under LynxOS and the standard Unix for that architecture without modification. The debug environment consists of GDB as the source-level debugger. There is presently no kernel debugger.

V. CONCLUSIONS

It has been our experience that a compile-download-debug cycle common with all the embedded systems is not a major problem for us, Ethernet and NFS links make this a speedy process.

It has become apparent the importance of compliance with standards. Standards adherence makes code more portable. We had to effectively rewrite all the tests for all the kernels because of the interface differences.

Another conclusion is the importance of having a mature debugging environment, a source-level remote debugger with a X11 Windows interface that can debug optimized code is extremely useful. A good kernel debugger is also very important, allowing the user to halt all tasks and examine states of any individual task with relationship to other tasks.

After we factor in the hardware differences between our environment and the individual vendors' test bed, most of the timing results we obtain agrees surprisingly well with the respective vendors' published values.

Furthermore, we realize that differences in compilers can contribute to the overall performance of the kernels and will require further investigation.

Finally, the more hosts and targets that a given cross-development kernel supports, the more attractive it will be, especially in a vastly heterogeneous environment like the SSC.

References

[1] Motorola, Inc., Technical Systems Division, P.O. Box 2953, Phoenix AZ 85062

[2] Software Component Group, Inc., 1731 Technology Drive, San Jose, CA 95110, (408) 437-0700

[3] Ready Systems, Inc., 470 Potrero Ave., P.O. Box 60217, Sunnyvale, CA 94086

[4] Wind River Systems, Inc., 1010 Atlantic Ave., Alameda, CA 94501, (415) 748-4100

[5] Lynx Real-Time Systems, Inc., 16780 Lark Ave., Los Gatos, CA 95030, (408) 354-7770

[6] Microtec Research, Inc., 2350 Mission College Blvd., Santa Clara, CA 95054, (408) 980-1300

[7] Free Software Foundation, 675 Massachusetts Ave., Cambridge, MA 02139

A New Man-Machine-Interface at BESSY

R. Müller

Berliner Elektronenspeicherring-Gesellschaft für Synchrotronstrahlung m.b.H.
(BESSY), Lentzeallee 100, 1000 Berlin 33, FRG

H.-D. Doll, I. J. Donasch, H. Marxen*, H. Pause*

Gesellschaft für Oberflächenanalytik und Computertechnologie m.b.H.
(SPECS), Voltastraße 5, 1000 Berlin 65, FRG

Abstract

A UIMS (*user interface management system*) has been developed, that is completely based on non-proprietary software. Central part of our UIMS are processes (*mapper*) that act as universal X-clients for each specified X-server. Mapper (graphic server) and applications (graphic clients) exchange requests by an event driven interface. The communication protocol is free from any graphical information. The most powerful mapper client is a *form interpreter*, that can be programmed to act as an equipment access server. Mapper and form interpreter allow to compose control panels and synoptic views of the machine with statements in a simple and comprehensible UIDL (*user interface definition language*).

Introduction

The Berliner Elektronenspeicherring-Gesellschaft für Synchrotronstrahlung m.b.H. (BESSY) operates an 800 MeV storage ring dedicated to the generation of synchrotron light in the VUV and soft X-ray region [1].

Currently a new control system based on a distributed computing environment is developed and gradually installed at BESSY [2]. It replaces the aged control system [3] of the running light source BESSY and has to serve as the kernel for the control system of the planned 3rd generation light source BESSY II. Standards (IEEE 802.3, 802.4) or industry conventions (TCP/IP, X11.4, etc.) are used wherever possible. Large high resolution, bitmap oriented colour graphic screens with mouse and keyboard will become the standard operator console.

For a period of time old and new control system have to be operated in parallel to supply a reliable and unperturbed operation of the running light source. That imposes constraints and structural elements to the new system. Different aspects of the old system have their effect on a new user interface:

- The mental image (metaphor) must contain the existing control structure.
- Appearance characteristic (the look) has to be as similar to the familiar system as possible.
- Interaction sequencing (the feel) must take into account the experience and habits of trained and skilled operators.
- Well established driving and diagnostic programs will be ported to the new system with minimal effort. In a first stage they go into operation running in an ordinary terminal window.

Therefore our development is more in a danger to produce a replica of the existing system on a modern platform than to have any innovative impact on developments in other laboratories.

Nevertheless the basic concept of our new man machine interface system is of general interest:

- Associated with every X11 display station is a central graphics server program we call *mapper*, whose services have to be claimed by any application program. That program hides representational aspects completely from the applications.
- User interactions can assign code fragments in an action language to variables of a special application program we call *form interpreter*. Any access to the equipment can be specified and evaluated within this action language.
- Only non proprietary software has been used. We are not bothered by licence policies and independent of any company.

The Graphics Server

Characteristic for any UIMS (*user interface management system*) is the separation of code that implements the user interface to an application and the code of the application itself. The specification of the user interface is supported at a high level of abstraction.

The most common approach is to 'paint' the user interface representation with an interactive editor. Semantics and specification of the interface to the application is usually added in a special purpose language. Only at this stage modularity of software, separation of code for the graphical tasks and the code of the application itself is given. A user interface builder program binds the elements to the final application program.

*Now at Dr.Brunthaler, Industrielle Informationssysteme, Berlin

0-7803-0135-8/91$01.00 ©IEEE

Every application encorporates its own representational part. It has to be recompiled whenever a change becomes necessary.

In our system modularity with respect to representation and application functionality is especially emphasized. The representational aspects are encapsulated within a separate server program we call mapper. From the application programs point of view the running graphic server (mapper) is the frontend process that 'knows' how to present application variables on the associated display and that reports user interactions in an 'understandable' way.

An application programmer, who wants to offer variables to user interactions has to build up and maintain a connection (based on a socket link) to the mapper of the desired interaction display. The corresponding software interface is a complex object we call *application form interface* (Fig. 1). Routines and data structures necessary for the dialog have to by linked to the application program and are provided by a library.

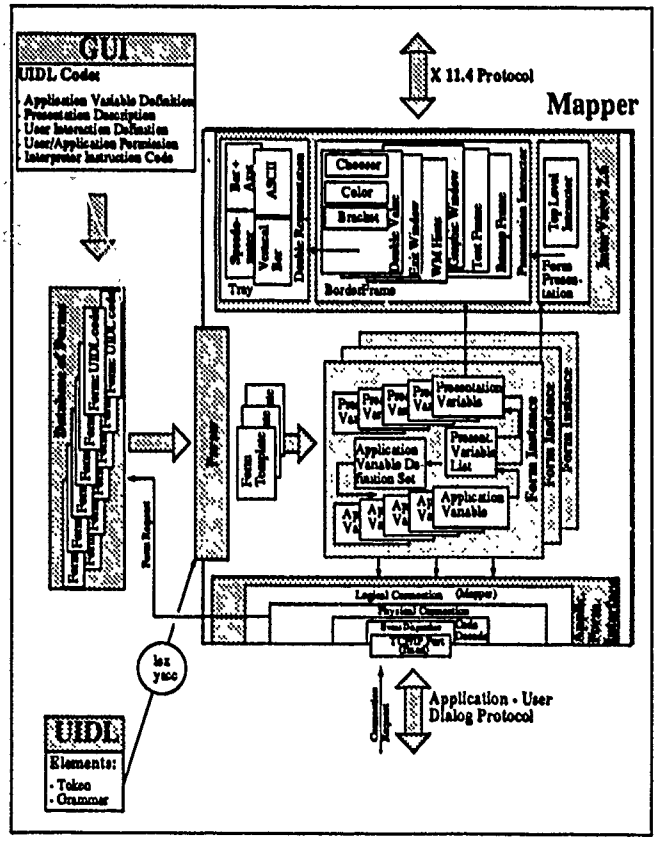


Figure 1: Details of the Graphic Server

Whenever an application that has no connection to a display requests access, the associated mapper reads specified configurational instructions, that are stored in a static (for the time of the applications life) database of files we call *forms* (Fig. 1). The forms specify assignments of graphical representations, user interactions and permissions to modify application variables. The syntax of the forms has been defined by *lex* and *yacc* source files.

A logical connection is build up between objects the mapper creates from the form template (the form instances) both within mapper and application (see Fig. 2 for a sample application program). The application specific data structures of the form instances and the eventdriven communication protocol form the interface between application and user interactions (mediated by the mapper process).

As long as the connection exists the mapper acts as a supervisor. Any event from application and user is reported to the mapper process. The mapper takes care of a consistent state of representational and applicational objects and variables. In the usual operation mode the mapper keeps the form templates in memory even after a connection has been cleared. After a phase of initialisation this type of 'down load' of the GUI improves response times drastically.

Presently the representational objects get their views and interaction feasibilities by means of the InterViews toolkit [4]. Slight modifications (pointer grabbing, polling) had to be introduced to the standard distribution to adopt the version 2.6 package to our needs.

Our first application program was a slider, that can be configured to control any analog device. Then no further individual application program has been written.

Generally application variables are used to notify to the application, that a specific action should be performed. On a next level of abstraction the code of the required action is no more part of the application, but it is assigned to the variable that should initiate the action. Evaluation and execution of the code is then done by an interpreter. The result of this abstraction is a programmable application we call *form interpreter*.

The Form Interpreter

Initially the form interpreter application was intended to supply a flexible tool, that allows to compose a variety of control panels and synoptic views of the machine by means of the static forms. Representation of the form is still provided by the mapper, the description of the semantic aspects is interpreted by the form interpreter. The available sets of application variables reflect the usable functionality.

- Forms are handled (e.g. freeze, unmap, position).
- Subforms are interpreted and handled, trees of forms are generated and managed.
- Actions specified in an action language are started, the context of the actions is specified.
- Periodic actions are scheduled, time instances are reported.
- Background processes are started and terminated.
- Forms are submitted to different displays.
- Gateways to networks on the field level are selected.

The elements of the interpreted action language are very similar to those of 'C'. Certain restrictions in the declaration

of variables have to be respected. Some statements like *switch* or *break* are not allowed, the use of labels needs some care. The syntax of the action language is very familiar to 'C' programmers. Built-in functions are some often used routines from the C library and utilities to change the operational mode or support the form handling of the form interpreter itself.

Communication with the equipment is enabled by the built-in library of equipment access calls. At BESSY this library is the standard interface between application programs and equipment. With the equipment access calls equipment can be checked and manipulated. Thus the composition of synoptic views and control panels becomes feasible.

In a client-server model the form interpreter is the equipment access server to abstract clients, namely the synoptic views and control panels specified in the database of forms.

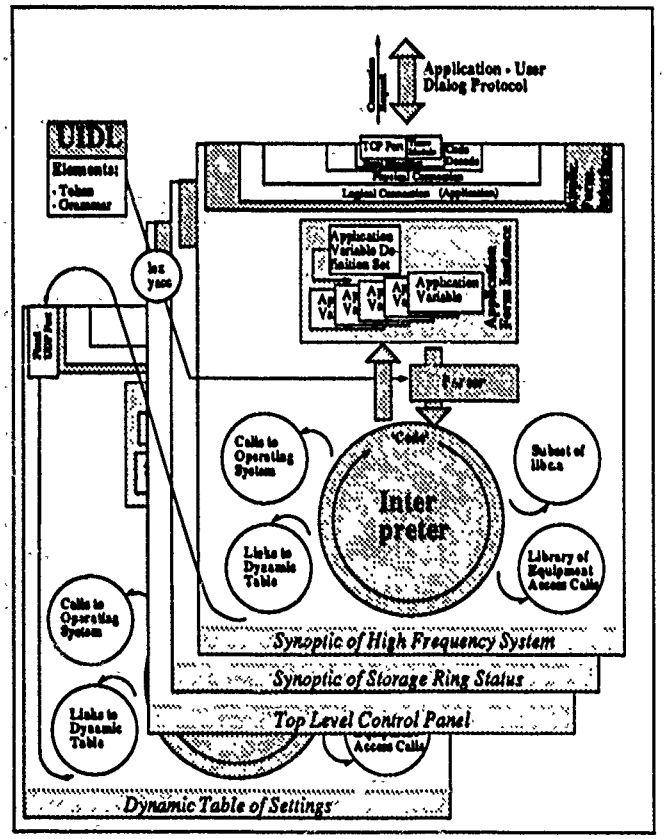


Figure 2: Copies of the Form Interpreter at Work

Another set of internal functions supports the interprocess communication needed for the dynamic configuration of equipment lists. These lists sets up the entries of a table managed by a specific form. That form displays (on demand or periodically) the settings of pieces of equipment, that have been entered to the list. The user can store and retrieve his favourite (once dynamically generated) equipment list as well as switch quickly between different lists.

In principle the slider control application could be realized simply by a form that programs the form interpreter to execute the desired actions. It will depend on the programs complexity and the programmers skills, whether it is advantageous to write a new application in a high level language to become a separate mapper client or in the interpreted action language within a new form.

The Graphical User Interface

A graphic editor that could be used to compose or modify synoptic views or panels is not provided for by our GUI system. The definition of our GUI is given in a textual form. Our own UIDL is especially appropriate to associate user interactions with actions that include equipment access. In our forms complex GUI objects are described in a comprehensible way. The tool, that is suited best to extend and maintain the GUI and that reflects the power and flexibility of our system is a plain text editor.

Based on two application programs, the form interpreter and the slider control, a GUI has been composed with about 5300 lines of statements in our UIDL, that provides all synoptic views and interaction tools to the operators, that are today available with the raster scan monitors, tracker balls, angle encoders and terminal screens of the old control system.

Summary

The concept of a graphics server and a form interpreter allows to shape the man machine interface in a descriptive way. Appropriate to the level of abstraction in our UIMS a specific UIDL had to be introduced like in other systems. This is a disadvantage because the usual programmer is not familiar with this language. But in contrast to commercial systems we are in a position to modify and extend language and functionality easily, since everything is present in source code.

The use of the object oriented toolkit InterViews for the realisation of graphical instances made programmers life easy. But to keep in step with current user interface developments it will become necessary to base the representations of our GUI on Xt and the OSF/Motif widget set. In principle this is no problem, but it means much work to compose the required graphical objects already offered by InterViews (e.g. *tray*, nonlinear deformation) within the usual Motif environment of Xlib calls, Xt elements and the OSF/Motif widget set.

References

[1] S. Bernstorff et. al., Physica Scripta, 36, 15 (1987)

[2] G. v. Egan-Krieger, R. Müller, Proceedings of the 2nd European Particle Accelerator Conference, Nice, pp. 872–874, 875–877 (1990)

[3] G. v. Egan-Krieger, W.-D. Klotz and R. Maier, IEEE Transactions on Nuclear Science, NS-30, 2273 (1983)

[4] M. A. Linton, J. M. Vlissides and P. R. Calder, *Composing User Interfaces with InterViews*, IEEE Computer, 8 (1989)

Alarm Handler for the Advanced Photon Source Control System*

Martin R. Kraimer, Ben-chin K. Cha, Mark Anderson
Argonne National Laboratory
Advanced Photon Source
9700 South Cass Avenue
Argonne, Illinois 60439

Abstract

The Advanced Photon Source (APS), now under construction at Argonne National Laboratory, will have a control system employing graphics workstations at the operator interface level and VME-based microprocessors operating with a distributed database at the field level. The alarm handler is an application utilizing X-Windows running on one or more operator interface workstations which monitors alarms generated by the VME-based microprocessors. Alarms can be grouped in a hierarchical manner. The operator can monitor, acknowledge, and mask alarms either individually or aggregately. Alarm changes of state and all operator modifications are logged. When alarms occur, display windows are automatically generated conveying system and subsystem relationships and severity. Menus are used to modify the alarm action configuration files and to obtain help. Since alarm groups are defined via an alarm configuration file, the alarm handler is a general purpose application which can be customized to monitor a single subsystem or configured to monitor the entire accelerator complex.

I. INTRODUCTION

The APS control system uses the Experimental Physics and Industrial Control System (EPICS) software. The original version of EPICS was developed by the Controls Group of the Accelerator Technology Division at Los Alamos National Laboratory (LANL). EPICS is currently being co-developed by the LANL group, and by the APS Controls Group.

EPICS is a distributed control system consisting of Operator Workstations and front end Input/Output Controllers (IOCs) all linked via a local area network. Each IOC contains a memory resident database composed of an arbitrary number of records. A software layer called Channel Access provides transparent network-wide access to the IOC databases. A record within a database is referenced via the field of "channel name". Each record contains alarm status and severity fields. Whenever a record is processed alarm conditions are checked. Software residing anywhere on the local network can request notification whenever alarm conditions change (value changes and archive changes can also be monitored). The Alarm Handler (ALH), which is an Operator Interface tool, uses this mechanism.

Because of the complexity of an advanced accelerator system, many hardware devices and thousands of IOC channels need to be monitored. The ALH allows the operator to quickly identify groups and channels entering an alarm state, acknowledge alarms, disable alarms, log alarms, etc. It provides a useful tool to help assure normal operation of the accelerator system.

This paper briefly describes how alarms are configured, what information is displayed, and how the operator interacts with the ALH.

II. ALARM CONFIGURATION

The ALH is a general purpose tool that can monitor alarms from subsystems as well as an entire facility. The ALH accepts as input an Alarm Configuration File, which determines the set of channels to be monitored. An alarm configuration file defines a set of alarm groups. Each group consists of a set of lower level groups and/or database channels. Each group is assigned a name. Figure 1 gives an example to demonstrate the hierarchy of an alarm configuration.

In this example, the system to be monitored is a Linac and only a subset of the Alarm Configuration groups are shown. The whole configuration is just a repetition of groups which are linked together to form a tree structure. Each group is composed of a list of subgroups and/or IOC channels. Each group, except the main group (Linac in Figure 1), has a parent group. The lowest "leaf" groups contain only channels. A complete branch of a link of subgroups always terminates at IOC channels (like the Coil1 in Figure 1).

III. GROUP DISPLAY WINDOW

Each group has an associated display window containing a line for each subgroup and each channel in the group. Each line (subgroup or channel) contains the following items: Acknowledgement button, Severity character, Name of subgroup or channel, and a mask. A subgroup line also shows how many channels in that group are at each alarm severity. A

*Work supported by U.S. Department of Energy, Office of Basic Energy Sciences under Contract No. W-31-109-ENG-38.

U.S. Government work not protected by U.S. Copyright.

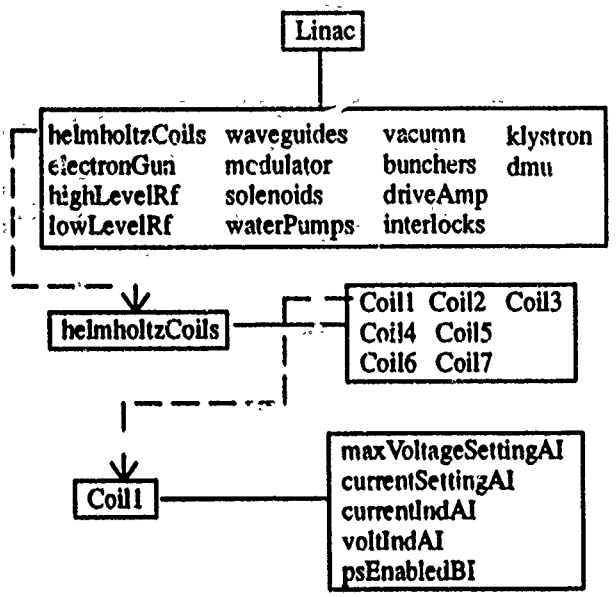


Figure 1. Example hierarchy of an alarm configuration.

channel line shows the current status and severity and the highest unacknowledged status and severity.

The acknowledgement button, which is color coded, is shown only if the group/line has gone into alarm state and has not been acknowledged by the operator. The alarm severity character, which is also color coded, shows the highest severity outstanding alarm for the group/channel.

The alarm mask, which is given defaults in the configuration file and can be dynamically changed by the operator, defines the following attributes: Add/Cancel, Enable/Disable, Ack/NoAck, Ack/NoAck transient, and Log/NoLog. If an alarm is canceled then the ALH is no longer notified by the IOC when a channel changes alarm state. If an alarm is disabled then it always appears to be in no alarm state. NoAck specifies that the operator is not required to acknowledge alarms for the group/channel. NoAck transient specifies that an automatic acknowledgment occurs if a group/channel goes into alarm and comes out before the operator has a chance to acknowledge. If NoLog is specified, changes of alarm state are not logged. Mask settings for a group apply to all channels in the group.

The ALH provides guidance information about each group and channel. The guidance information, which is specified in the configuration file, can help an operator quickly identify and correct the cause of an alarm.

IV. USER INTERFACE

The user interface is implemented via the OSF/Motif toolkit. Most ALH functions are invoked via the workstation mouse. The appropriate window display pops up according to the user specified actions. Selection menus are in the form of pulldown or popup menus. File selection is via file selection dialog. Help and dialog information is presented via menu and message dialogs.

Figure 2 gives the key ALH user interface components. They are represented by three windows: Icon, Setup, and Group/Subgroup. Each push button, i.e. active area, is enclosed in a rectangular box.

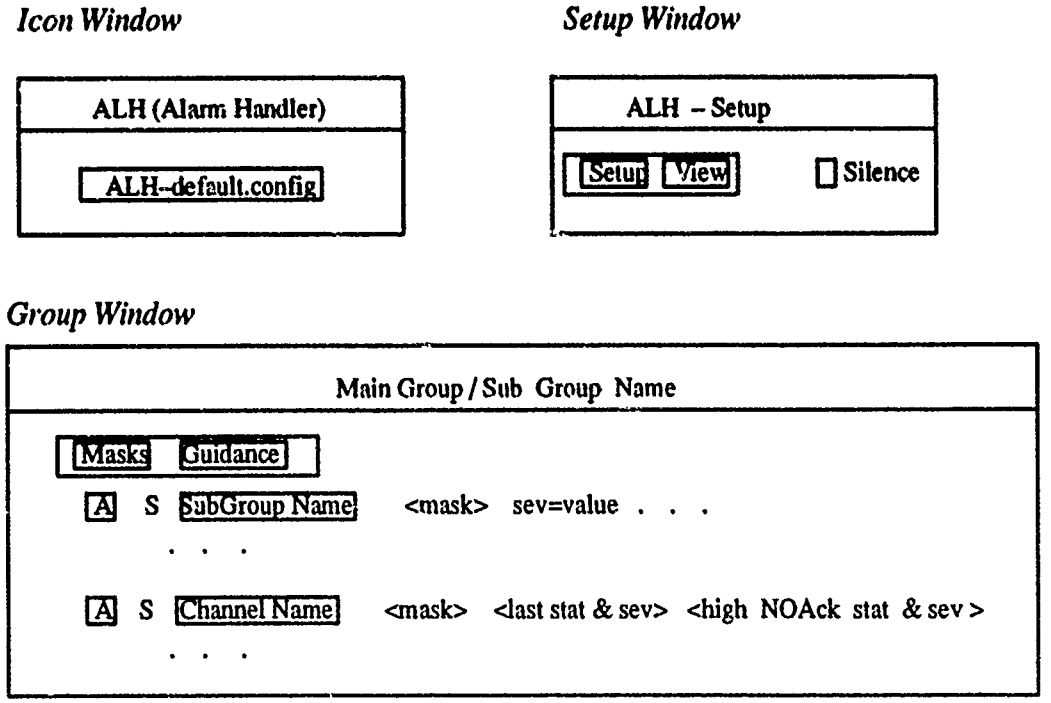


Figure 2. The key user interface components in the ALH.

A. Icon Window

The Icon window appears whenever the ALH is running. The Icon window contains a single control push button. This control button reflects the name of the configuration file. Pushing this control button pops up the setup window, the main group window, and possible lower level subgroup windows. Toggling this control button alternatively unmaps/remaps the lower level display windows. When any unacknowledged alarm is outstanding the control button starts blinking and beeping. It has a color reflecting the severity of the highest outstanding alarm.

B. Setup Window

The setup window contains three control buttons: Setup, View, and Silence. Setup allows the operator to specify the following: configuration file, alarm log file, operator modification log file It also allows the operator to save the current configuration, set a severity for beeping, or exit the ALH. View opens a text window which dynamically displays all information written to the log file. If unacknowledged alarms are outstanding, the silence button can be used to stop beeping.

C. Group Windows

Each group window shows the status of each subgroup and channel in the group. The window display strategy is to display an alarmed channel as quickly as possible. When a group window is displayed, if exactly one subgroup is in alarm state, that subgroup is also displayed, etc. The operator can, however, select any subgroup name. In this case, any lower level windows being displayed are removed and the selected subgroup is displayed.

The masks pulldown menu provides options for showing group masks, and changing group masks. The guidance pulldown menu provides options for showing group guidance and accessing online help information.

Pushing an acknowledgement button acknowledges the channel or subgroup, and updates the window display. Acknowledging a group is an implied acknowledgment for all subgroups and channels in the group. Pushing a subgroup name pops up the subgroup window. Pushing a channel name button, presents a menu providing options for displaying channel details, for changing channel masks, and for displaying channel guidance or help information.

V. REQUIREMENTS

The ALH was implemented on a SUN workstation using the X window system and the OSF/MOTIF toolkit. It requires a color monitor with X graphics capability.

The key to successful use of the ALH is the alarm configuration file. Alarm groups must be defined so that they properly model the system being monitored. A systematic group naming convention should be adopted so that operators can easily understand each display window.

VI. CONCLUSION

Preliminary testing of the ALH with a test IOC database has been performed. The test results show that the ALH can be a very useful alarm monitoring tool. It displays subsystem groups and channels according to easily defined configuration files. It brings alarms to the operator's attention, allows the operator to acknowledge alarms, logs alarms, records all operator modifications, and provides optional guidance information. The ALH is a general purpose tool which can monitor a single subsystem or a complete accelerator complex.

The ALH is installed and being used in the Los Alamos Ground Test Accelerator Facility. The performance of the ALH with a very large configuration file has not yet been tested but its design should provide good performance.

The alarm group configuration concept allows alarms to be filtered hierarchically. It allows the operator to see the summary of various alarmed groups. This automatically prevents the operator from being flooded with alarm messages when alarm storm occurs.

VII. ACKNOWLEDGEMENT

We are grateful to Ned Arnold for providing a test IOC database and alarm configuration file which simulates a Linac application. We are grateful to Bob Dalesio and many others of AT-8/GTA at Los Alamos National Laboratory for making release 2.0 of the control system available such that we could integrate the new channel access calling functions into the ALH.

VIII. REFERENCES

[1] OSF/Motif Programmer's Reference, Prentice Hall, Revision 1.0, 1990

[2] Bob Dalesio, Private communication, AT-8/GTA, Los Alamos National Laboratory.

Correlation Plot Facility in the SLC Control System

L. Hendrickson N. Phinney L. Sanchez-Chopitea
Stanford Linear Accelerator Center, Stanford University, Stanford, California 94309 *

Abstract

The Correlation Plot facility is a powerful interactive tool for data acquisition and analysis throughout the SLC. A generalized interface allows the user to perform a wide variety of machine physics experiments without the need for specialized software. It has been used extensively during SLC commissioning and operation.

The user may step one or two independent parameters such as magnet or feedback setpoints while measuring or calculating up to 160 others. Measured variables include all analog signals available to the control system as well as a variety of derived parameters such as beam size or emittance. Various fitting algorithms and display options are provided for data analysis.

A software-callable interface is also provided. Applications based on this facility are used to phase klystrons, measure emittance and dispersion, minimize beam size at the interaction point and maintain beam collisions.

Introduction

During the development of the SLC, the wide variety of machine experiments to be performed required software to allow the online acquisition, analysis, and display of a large number of different types of information. Rather than design and develop a different piece of code for each combination that might be of interest, the Correlation Plot facility was planned as a generic utility where many different types of information could be obtained from a large number of different devices. It was also designed to be easily extensible as new types of data were required. Due to the initial success in the implementation, a callable interface was provided so that other packages could take advantage of the plotting and fitting functions provided. This also provides a more consistent interface for other parts of the control system.

Organization

The main components of the Correlation Plot facility are:

- A general control package that can step the setpoints of magnets, klystrons, feedback loops, timing parameters and other devices.
- A general data acquisition package that can acquire information from a variety of sources, including high-level parameters derived from analysis of klystron fast time plots or wire scans.
- A variety of curve fitting algorithms, including average, linear, polynomial, gaussian, sinusoidal, and the specialized beam deflection curve.
- A general plotting package to display the acquired and fitted data. The sampled data may be plotted against the step variable, any of the sampled quantities or the step number.

For data acquisition, the user may select either manual or automatic mode. In automatic mode, the software runs the step variables through a range determined by the operator. In manual mode the operator requests a data point by pressing a button on the touch panel. At each of the steps, the acquisition may wait a specified settling time before all of the sampled data is acquired.

Interfaces

Touch panels

The Correlation Plot facility is an integral part of the SLC Control Program (SCP)[4]. The main user interface is by means of touch panels although the same functionality may be provided by a mouse, track ball or cursor keys, depending on the hardware. The main panel provides buttons for specifying the step and sample variables, selecting the range of the step variable, and setting other acquisition parameters. A generalized input parser interprets the input in a context sensitive manner where the meaning of each token depends on the valid tokens already accumulated. At any point a list of the valid responses may be requested to guide the user.

From the touch panel and keyboard, the user may initiate data acquisition, terminate acquisition or temporarily pause during an acquisition sequence. After data is acquired, display panels allow selection of fit and plotting options. The user may request displayed or printed plots as well as tabular displays. Capability is provided for users to manually exclude or include selected data points and recalculate fit parameters. An auxiliary output panel allows the user to save data to disk files in various formats for subsequent offline analysis. An option is also provided to reload previously stored data files for further analysis and

*Work supported by the Department of Energy, contract DE-AC03-76SF00515

U.S. Government work not protected by U.S. Copyright.

display. In the same manner, the set of control and sampled variables may be saved and reloaded.

A generic optimization feature is also available; users may set up a correlation plot to vary a step variable, obtain sampled data for each point, fit a parabola to the data and implement the value of the step variable which results in the fitted minimum.

Callable routines

All of the actions that are accessible via the operator interface are also available to software control. This makes it very easy to develop a layered application using well known building blocks. Callable functions support setting up variables and other data acquisition options and acquiring data. Applications may retrieve the data after it is acquired, or request data fitting and retrieve the fit parameters. Routines are also provided to select plots for display. Some applications acquire data through specialized protocols and then use the correlation plots for fitting and display functions.

Capabilities

Monitoring

Correlation plot support is provided to measure or calculate a wide variety of data. Up to 160 variables may be sampled within a single acquisition sequence and up to 100 data points are saved for each. Measured parameters include beam related data from position monitors or toroids, analog values from devices such as klystrons, magnets, thermocouples, vacuum pumps, etc. and the current time. For klystrons, in addition to simple analog values the user may sample values derived from an analysis of a 64 pulse Fast Time Plot such as phase and amplitude jitter, energy gain of the station or perveance. This makes it possible to quickly scan the energy gain as a function of klystron phase to find the optimum setting, or to map out buncher jitter as a function of phase shifter setting in the SLC injector.

Other calculated quantities available include energy, energy spread, particle yield and beam position or deflection angle at the IP. Residual dispersion at the collision point may be measured non-invasively by correlating position and angle at the IP with energy fluctuations. In addition, interfaces to other applications allow sampling of various derived quantities such as beam states calculated by feedback and beam sizes, emittance and skew parameters determined from wire scans, beam scans, or profile monitor digitizations. These quantities are used in a wide variety of beam optimization procedures Finally, a generic data acquisition capability allows user-provided ASCII command procedures to be used in data acquisition, this allows easy expansion to accommodate devices which are not standard for the SLC control system.

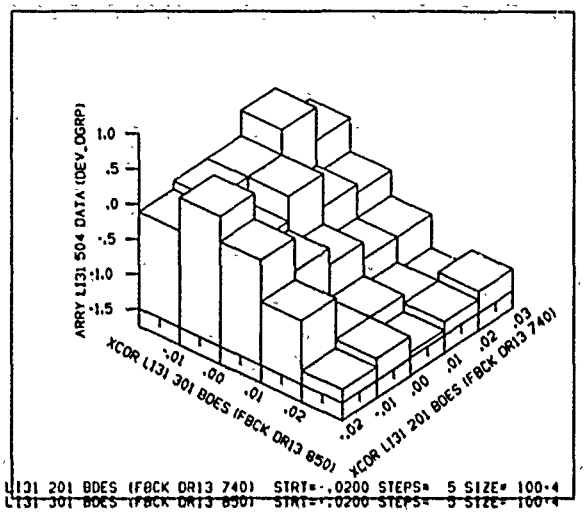


Figure 1: Results of 2 Variable Plot

Control

The user may select to use either one or two step variables. Most of the variables available to software control have been implemented. These include:

- Setpoints of magnets or other analog control devices
- Klystron setpoints, including amplitude, phase, and timing
- Timing delays for any triggered devices
- Combinations of devices through the Multiknob facility
- Setpoints of feedback loops stabilizing the beam [3][1]
- Time

For many experiments, the Time step variable provides a simple delay between samples in order to study the time structure of variations in normal running. Users can study correlations between sampled variables without modifying any control parameters. Most of the time only one step variable is used, so a third has not been considered necessary. When two step variables are used, they define a grid of values and the second is stepped through the whole range for each setting of the first. A display for two step variables is shown in Figure 1.

Data reduction

To aid in the analysis of the data, a variety of fitting routines may be used. These include average, linear, polynomial, sinusoidal, gaussian and beam deflection fits. The selection of fitting algorithms may be accomplished by user selection from the touch panel or by application software. Figure 2 shows the special beam-beam deflection fit which is used for optimizing collisions and estimating beam size.

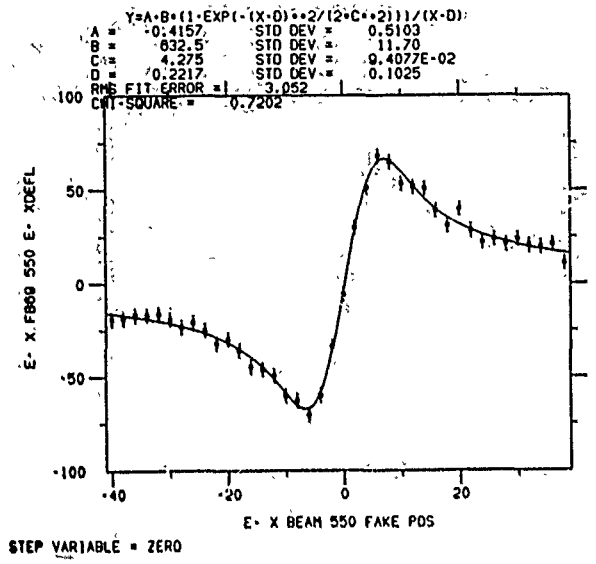


Figure 2: Fitting of Beam-Beam Deflection

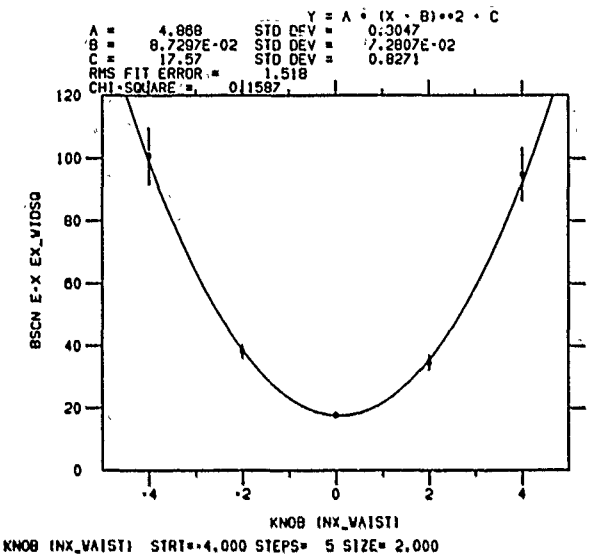


Figure 3: Beam Waist Optimization using Beam Scans

Applications

Various software applications used in the SLC have been built upon capabilities of the Correlation Plot facility. Automated wire and beam scan applications are used to optimize beam properties at the interaction point and minimize spot size. Auto beam collision software brings the beams into collision at the interaction point and provides calculations of beam sizes and luminosity. In several locations throughout the SLC, wire scan applications[2] provide measurements of emittance parameters and beam skewness. Another emittance package determines beam parameters by varying quadrupoles and measuring wire scan or digitized profile monitor data. A general package supports dispersion measurements throughout the machine. In the Linac, an automated application is used to determine optimal phases for the 240 klystrons.

Figure 3 is produced by an application which optimizes the interaction point waist position. For this plot, each point of the Y axis represents a beam width-squared as determined by a beam scan deflection fit. Each X axis point is a setting for a multiknob which adjusts the final quadrupoles to move the focal point along the beam line. The center of the parabola is the optimal waist position for the beam.

Conclusions

The Correlation Plot facility has proven to be an extremely powerful tool for the analysis of the new problems associated with the commissioning of the SLC and for building software applications. The flexibility provided by the different types of variables that may be controlled and monitored has allowed operators and machine physicists to rapidly design and execute a vast assortment of experiments without new software. In fact the Correlation Plots are used so extensively that most experimental data presented comes directly from the Correlation Plots and it is extremely rare that data needs to be plotted offline. Even for complicated experiments where further analysis is required, the Correlation Plots provide the data acquisition and online validation. The Correlation Plots facility has made an essential and invaluable contribution to SLC development.

Acknowledgements

The authors wish to thank Julian Kupiec, who wrote the original package, and Miguel Flores, who added many features.

References

[1] K Thompson et al. Feedback Systems in the SLC. In *Proceedings of the 12th Particle Accelerator Conference*, Washington, D.C., March 1987. SLAC-PUB-4217.

[2] M C Ross et al. Wire Scanners for Beam Size and Emittance Measurement at the SLC. In *These proceedings*, 1991.

[3] T Himel et al. General, Database Driven Fast Feedback System for the Stanford Linear Collider. In *These proceedings*, 1991.

[4] R E Melen. Centralized Digital Control of Accelerators. In *Proceedings of the Europhysics Conference*, September 1983. SLAC-PUB-3218.

INDIRECT PHASE LOCKING OF RF CLOCK TO THE BEAM FOR BNL BOOSTER BPM SYSTEM.*

T.Hayes, A.Zaltsman
AGS Department, Brookhaven National Laboratory
Upton, NY 11973

INTRODUCTION

The beam position monitoring (BPM) system for the BNL Booster consists of 48 main pick-up electrodes (PUE) symmetrically distributed around the ring and two special PUE's for the transverse dampers. The BPM system utilizes an integrator that is AC coupled to the PUE. In order to eliminate the cumulative error in the signal from the PUE introduced by the AC coupling, a base line restorer (BLR) is used to reestablish a reference value between the bunches. Three signals phase locked to the beam, 48 x f_{REV} and both quadrature components of f_{RF}, are needed to insure that the triggers to the BLR's occur between bunches. The triggers for the main PUE's require a clock at 48 times the revolution frequency as well as the RF frequency to time their occurrence. The quadrature components of RF frequency are used in a phase shifter to produce the triggers for the damper PUE's. By making use of direct digital synthesis technology, we were able to produce all three signals locked to the beam using only a single phase locked loop.

DDS OPERATION

The operation of our design relies upon the use of direct digital synthesis. A direct digital synthesizer (DDS) reproduces a sinusoid of a specific frequency from the digitally generated samples of that signal. As shown in the block diagram (Fig. 1) the heart of a DDS is a numerically controlled oscillator (NCO).The digital data loaded into the delta-phase register is the phase step that will be added to the phase accumulator on each clock pulse. The phase accumulator is used to address a look-up table which contains the amplitude of a sinusoid as a function of phase, accomplishing a phase to amplitude conversion. This digital value is then passed through a DAC to produce an analog signal. According to the sampling theorem, a sinusoid of the desired frequency can be extracted from this signal by filtering out all higher harmonics provided the sampling rate is greater than twice the frequency of the sinusoid. This translates to a maximum frequency output of half the clock frequency. Thus, the output frequency, f_o, depends on how often the phase accumulator is updated (f_{CLOCK}) and the size of each phase step (eq. 1).

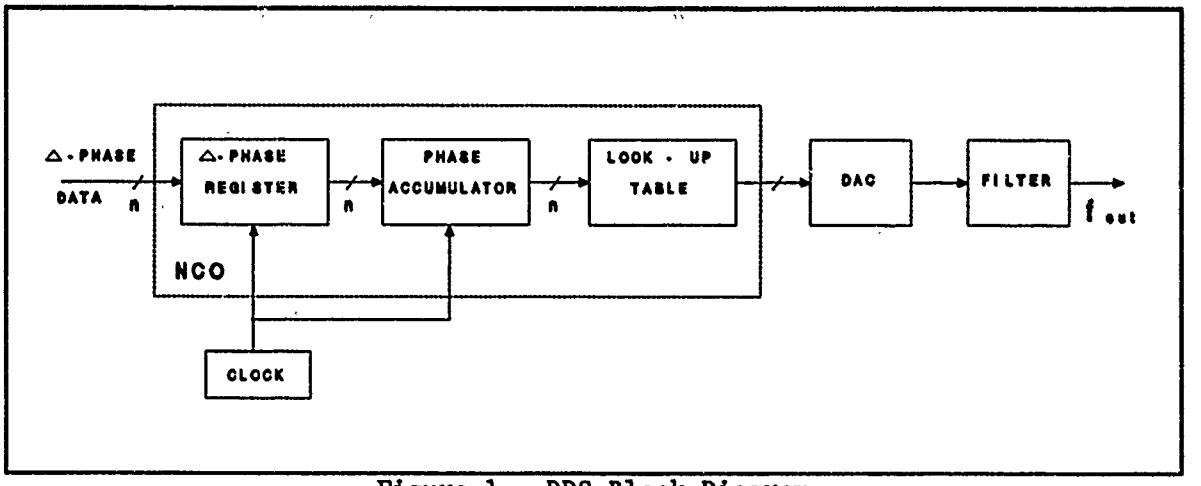


Figure 1. DDS Block Diagram

*Work performed under the auspices of the U.S. Dept. of Energy.

0-7803-0135-8/91$01.00 ©IEEE

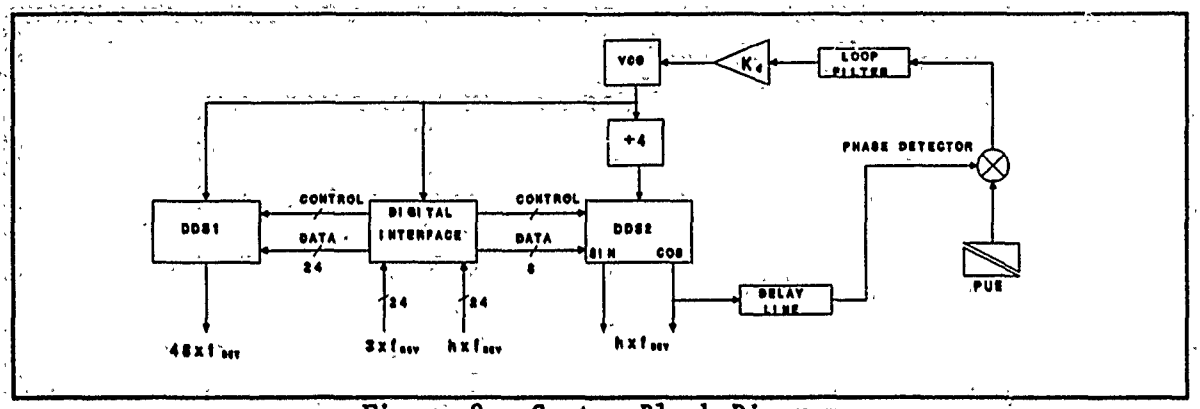


Figure 2. System Block Diagram

$$f_o = \frac{f_{CLOCK} \times \text{delta-phase}}{2^n} \quad (1)$$

Quadrature outputs can be obtained by using the phase accumulator to address two look-up tables, one with sinusoidal amplitude information and the other with cosinusoidal amplitude information. Each signal is then separately passed through a DAC and filtered.

SYSTEM DESCRIPTION

As shown on the block diagram of the system (Fig. 2) the VCO is used directly as the 200 MHz clock for DDS1 and is divided by four to provide the 50 MHz clock for DDS2. Therefore, for the same digital word (i.e. delta-phase step), the output frequency of the first synthesizer will be four times that of the second synthesizer. Also, as long as the digital words are exact multiples, the two outputs will remain phase locked.

The data for the two DDS's is received by the digital interface as two 24 bit words from an external frequency look-up table. The received data word for DDS1 is always 3 x f_{REV}. The received data word for DDS2 is h x f_{REV} (i.e, f_{RF}), where the harmonic number, h, is 3 when the machine is accelerating protons and switches from 12 to 3 during the acceleration of heavy ions. Thus, the two incoming digital words are identical for h = 3 and differ by exactly a factor of four for h = 12. A two bit shift to the left is introduced in the digital interface before the data is loaded into DDS1, so that the data now corresponds to 12 x f_{REV}. However, this frequency is based on the 50 MHz clock that DDS2 is running on. Since the clock for DDS1 is running at 200 MHz, the actual output frequency is the desired 48 x f_{REV}. Clearly, since the digital words are exact multiples and a common clock is used, the output of DDS1 and the quadrature outputs of DDS2 are phase locked regardless of variations in the VCO frequency.

In order to lock these signals to the beam, a phase locked loop is closed between one of the quadrature outputs of f_{RF} from DDS2 and the beam signal from a PUE. To simplify the design of the loop and to facilitate filtering the beam harmonics from the PUE signal, both signals are mixed up to an intermediate frequency of 10.7 MHz. Another design consideration for the loop was the need for a 1.5 μs delay line to compensate for the distance between the PUE and the DDS chassis, which effected the stability of the loop. In order to reduce the phase error accumulated over the RF frequency sweep, an active filter was chosen for the loop filter.

A unique feature of the phase loop is that the tracking range is not a constant but rather is a function of the frequency. In a standard phase locked loop:

$$\Delta f = k_d V_c$$

where k_d = gain of the VCO
V_c = VCO control voltage

However, in this loop, varying the VCO control voltage has the following effect on frequency:

$$\Delta f = \left(\frac{\text{delta-phase} \times f_{CLOCK}}{2^n}\right) \times V_c$$

Thus, the tracking range and the gain of the loop are directly proportional to the output frequency.

RESULTS

In order to test our system prior to Booster commissioning, we used an external source to simulate the beam signal. By introducing a frequency error into the external source, we were able to test the operation of our system. While sweeping over the Booster proton cycle from 2.4 - 4.2 MHz, a frequency error was introduced (Fig. 3). There was a maximum phase variation of less than 6° between sin f_{RF} and the "beam" signal (Fig. 4).

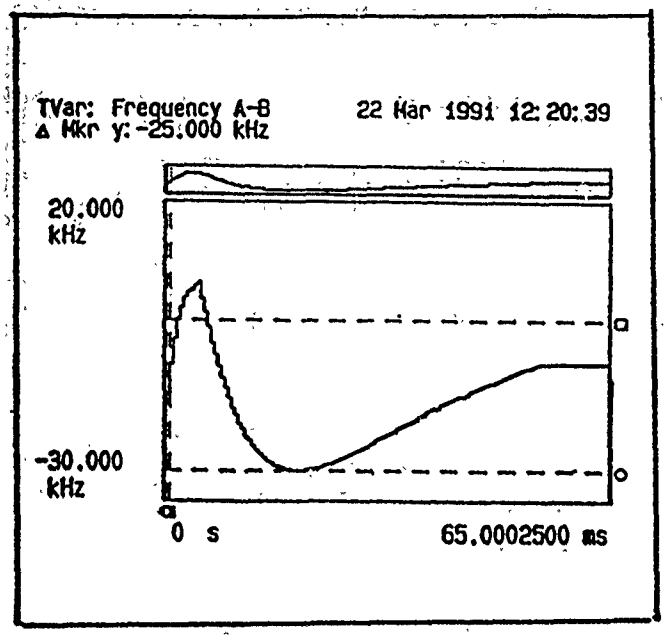


Figure 3. Open Loop Frequency Error

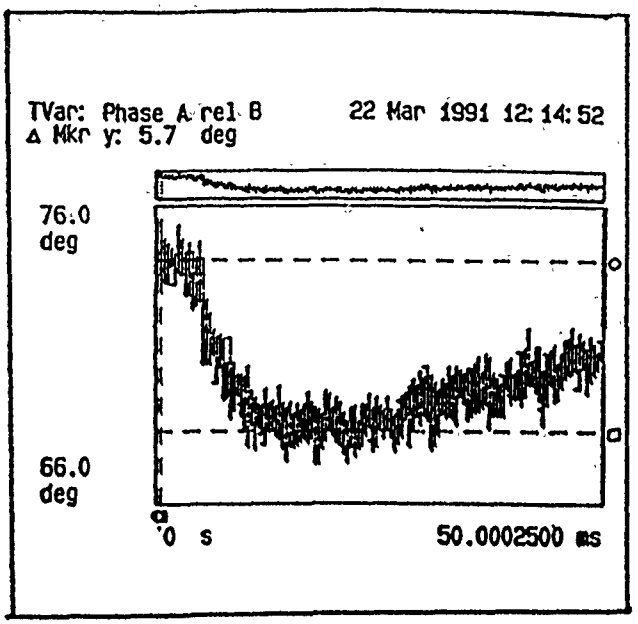


Figure 4. Phase of sin f_{RF} vs "beam"

CONCLUSION

By making use of DDS technology we successfully phase locked all 3 signals to the "beam", eliminating the need for three separate phase locked loops. Also, the use of direct digital synthesis provides quadrature outputs that are exactly 90° out of phase over the entire frequency range of the synthesizer. The only limitation of using this indirect phase-locking technique is the availability of high frequency DDS's.

ACKNOWLEDGEMENTS

We would like to express our thanks to J.M. Brennan for his help in the development of this system. We would also like to thank our technicians J. DeLong and D. Knoernschild for their efforts on this project.

REFERENCES

1. D. Ciardullo et.al, The AGS Booster Beam Position Monitoring System, these proceedings.

2. D. Ciardullo et.al, Design of the Booster Beam Position Monitoring Electronics, these proceedings.

3. The DDS Handbook, Stanford Telecom, 1990.

FEED FORWARD RF CONTROL SYSTEM OF THE ACCELERATOR TEST FACILITY

Ilan Ben-Zvi, Jialin Xie* and Renshan Zhang*
NSLS, Brookhaven National Laboratory, Upton, NY 11973

Abstract

We report a scheme to control the amplitude and phase of the rf accelerating field in a klystron driven electron linac. The amplitude and phase distribution within the rf pulse can be controlled to follow specified functions to reduce the energy spread of the electron beam being accelerated. The scheme employs fast beam energy and phase detectors and voltage-controlled electronic attenuator and phase shifter in the amplifier chain. The control voltages of these devices are generated by arbitrary function generators. The function generators' outputs are calculated numerically using an algorithm which takes into consideration the desired target function and the deviation (due to load variations or system parameter drift) from the target function. Results of preliminary tests on producing flat rf power and phase pulses from a high power klystron indicate that amplitude variation of ±0.2% and phase variation of ±1° can be readily achieved.

Introduction

In a TW linac, the energy gain of the electron bunch in the steady state depends on the amplitude and phase of the rf field with which the bunches are accelerated. To achieve a high degree of stability of the electron beam energy and small energy spread as required by FEL and other applications, a stable high power rf source with flat-top pulses is required. With high power klystrons as rf sources, the flatness of the output amplitude and phase is dominated mainly by the high voltage pulse from the modulator, which usually has a ripple due to parasitic resonances of the stray inductance and capacitance in the PFN and in the pulse transformer. With careful design and adjustment, the modulator voltage pulse fluctuation can be kept to a small fraction of a percent as the state of the art[1-2]. However, to achieve this level of performance, it is both expensive and time-consuming. Furthermore, even with rf pulses which are perfectly flat in power and phase, the beam loading transient and beam current fluctuations induce beam energy spread in a multi-bunch operation[3]. Therefore, it is necessary to explore some other way to reduce the linac's beam energy spread.

In the following we present a scheme, whereby the klystron's rf drive signal is modulated in amplitude and phase to produce the required low energy spread, thus eliminating the need for expensive PFN adjustments. This scheme will also remove beam loading effects and drifts in other system parameters.

The modulation of the drive signal in a given rf pulse is derived from the error signals acquired during previous pulses. The reason for this is that the ATF rf pulses are about 3 μs long, a time too short to make a feed-back control system work with the given delay times in the detection as well as the control system. Thus this control system is a feed-forward scheme. The prerequisite for the success of such a scheme is a reproducibility of the pulse-to-pulse waveforms on a time scale which is longer than the response time of the control system. The ultimate performance of this system is limited only by noise, reproducibility of the modulator pulses and the accuracy of the error measurement.

Preliminary tests of this system were made on both a klystron output pulse and the fields in the ATF RF gun cavity with very encouraging results.

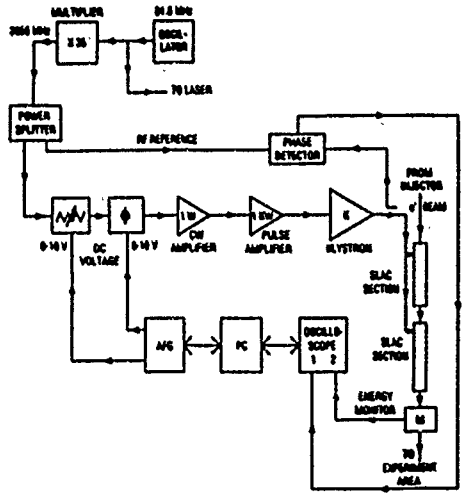


Figure 1: Schematic diagram of the feed-forward control system at ATF.

I. System Configuration

The schematic diagram of the present feed forward control system as used in the ATF is shown in Fig.1. [4] Voltage controlled fast electronic attenuator and phase shifter are installed in the drive chain of the XK-5 klystron to modulate its input. The output signal (for instance, the beam energy and rf phase) of the system are monitored with detectors read by a digital oscilloscope. The control waveforms to the attenuator and the phase-shifter are generated by the arbitrary function generators

*Permenant address: Institute of High Energy Physics, Academia Sinica, P.O. Box 918, Beijing, P.R. China.

0-7803-0135 8/91$01.00 ©IEEE

(AFG). The oscilloscope and the AFGs are controlled by a personal computer (PC).

The target curves are set in the computer according to system requirements. The system output signals shown on the oscilloscope are also accessible by the computer. The target function and the system output are compared in the PC. The difference signal is then used to calculate the control voltage data. The corresponding waveform corrections generated by the AFG are then applied to the attenuator and the phase-shifter.

II. Theoretical Description of the Control System

Consider a time invariant system with an input $x(t)$, and an output $y(\tau)$. Let us assume that the system is separable into a non-linear but instantaneous part represented by a function $f(x)$ and a linear part with an impulse response $g(t)$. Then one may express the output through a convolution

$$y(\tau) = \int_{-\infty}^{+\infty} f(x(t))\, g(t-\tau)\, dt \qquad (1)$$

If an increment function $\Delta x(t)$ is added to the input signal $x_0(t)$ (which may be considered as an operation level), the output of the system will be modified by the corresponding increment $\Delta y(\tau)$ around the normal operation output $y(\tau)$. If the function $f(x(t))$ is assumed to be differentiable, for a small enough $\Delta x(t)$, the relationship between the input and output increments can be expressed as:

$$\Delta y(\tau) = \int_{-\infty}^{+\infty} f^1(x_0(t))\, \Delta x(t)\, g(t-\tau)\, dt \qquad (2)$$

where $f^1(x_0)$ is the derivative of f with respect to x. By sampling the output increment $\Delta y(\tau)$ at times τ_i, eq.(2) can be written in a matrix form as follows:

$$\begin{pmatrix} \Delta y(\tau_1) \\ \Delta y(\tau_2) \\ \vdots \\ \Delta y(\tau_m) \end{pmatrix} = \begin{pmatrix} T_{11} & \dots & T_{1n} \\ T_{21} & \dots & T_{2n} \\ \vdots & \ddots & \vdots \\ T_{m1} & \dots & T_{mn} \end{pmatrix} \begin{pmatrix} \Delta x(t_1) \\ \Delta x(t_2) \\ \vdots \\ \Delta x(t_n) \end{pmatrix} \qquad (3)$$

where the subscripts m and n may have different values, τ_i may also be different from t_i, and $\Delta x(t_j)$ is the input increment value applied to the system at instant t_j. The matrix element T_{ij} is defined as:

$$T_{ij} = f^1(x_0(t_j))\, g(t_j - \tau_i)\Delta t \qquad (4)$$

where Δt is the sampling interval. As a result of causality, the matrix elements must satisfy the following equation.

$$T_{ij} = 0 \qquad for \quad \tau_i \le t_j \qquad (5)$$

As an approximation, the system can be assumed to be linear near $x_0(t)$. Then $f^1(x_0(t_j))$ is a constant, and we may also use causality (eq.(5)) and write eq.(3) in a very simple form:

$$\begin{pmatrix} \Delta y_1 \\ \Delta y_2 \\ \vdots \\ \Delta y_n \end{pmatrix} = \begin{pmatrix} T_1 & 0 & \dots & 0 \\ T_2 & T_1 & \dots & 0 \\ \vdots & \vdots & \vdots & \vdots \\ T_n & T_{n-1} & \dots & T_1 \end{pmatrix} \begin{pmatrix} \Delta x_1 \\ \Delta x_2 \\ \vdots \\ \Delta x_n \end{pmatrix} \qquad (6)$$

where the matrix elements T_i (i =1,2,...,n) are constant. The T matrix elements can be obtained by measurement. This is achieved by superimposing a step function, for instance, Δx_1, on the operation level $x_0(t)$, then measuring responses, Δy_i and solving eq.(6).

In the linac system we are discussing, the input variable $x(t)$ is the control voltage applied to the attenuator (V_a) or to the phase-shifter (V_p). The non-linear function $f(x)$ is the response of the rf system, $g(t)$ is the impulse response of the beam energy to the amplitude of the rf input to the linac cavity, and Δy_i is the beam energy error from the linac output to the system requirement (target curve). By inverting the matrix T, the control voltage needed to compensate the energy error will be:

$$\Delta V_j = \frac{1}{T_1}\left[\Delta U_j - \sum_{i=1}^{j-1} T_{j-i+1}\Delta V_i\right] \qquad (7)$$

where $\Delta U_j = U_j - U_{0j}$, and U_{0j} are the target beam energy values.

Thus we have a control procedure: First the matrix T is evaluated. Then the system response is compared with the target data to obtain ΔU_j. The voltage corrections are calculated by using eq.(7). Then the voltage corrections are applied to the attenuator to yield new values of system output U_j.

If the matrix T can represent the actual system precisely, the energy errors can be compensated by modifying the control voltage just once. With a T matrix which is a good approximation of the actual system and given an initial control voltage vector V_j which is close enough to the final value, the solution will converge fast. The required system output will be achieved after just a few applications of the correction process.

However there are a few technical problems. First, the linac system is usually nonlinear and the initial control vector V may be far from the exact solution. Furthermore, noise (both real and digital rounding error noise) results in errors in the evaluation of the matrix T. The first problem can be resolved by keeping the corrections ΔV_j small. When the accumulated correction (relative to the starting value of V_j) grows above a certain preset value, the T matrix will be re-evaluated. Thus this system will operate as an adaptive control system. The second problem can be reduced by averaging over several measurements with somewhat different applied control function deviations.

It should be pointed out that the same procedure can be applied to the rf phase control. However, for

controlling both the rf phase and the beam energy (or rf amplitude) simultaneously, some measures to decouple the rf amplitude and the rf phase are needed. We have been successful in decoupling the rf amplitude and phase in the cw part of the system and still have to address the decoupling in the pulsed amplifiers.

III. Preliminary Experimental Test Results.

The rf feed forward control system has been tested on the control of the rf output of a high power S-band klystron and on the control of the field in a cavity. For this purpose, the klystron is operated in an unsaturated power level. The controllable rf pulse width is about 3 μs for the ATF. Thus, about 300 samples points, 10 ns apart are used in the system.

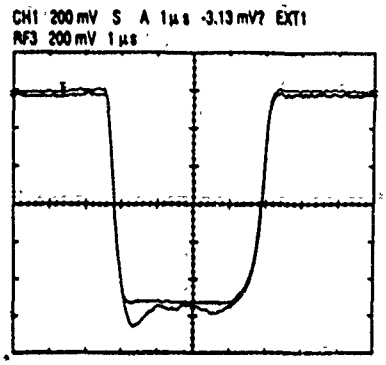


Figure 2: Comparision between uncompensated (lower curve) and compensated (upper curve) rf amplitude from the klystron output.

Fig. 2 shows the result of the klystron output control. The amplitude fluctuation before the control system is activated is about ±4% (lower curve). After four iterations of the control process, the power error is reduced to less than ±0.2% (upper curve). Fig. 3 shows the experimental results of controlling the field level of the ATF photocathode gun cavity. The amplitude variation after compensation is reduced from ±5% to less than ±1%. This result is not as good as the klystron regulation test since the available rf pickup electrode in the cavity provided a very small signal and the system suffered from noise. This is not an intrinsic problem of the control method and this result is by no means the ultimate performance of the system. The cavity control system is more interesting than the klystron control, because the filling time of the cavity (about 0.8 μs) results in many non vanishing matrix elements in T.

At the time being we have not used the full automated control system in which both rf amplitude and phase are controlled simultaneously. However we have demonstrated such a process by manual control of the AFG. In this test the phase error has been reduced from ±5° to about ±0.6° and the amplitude error from ±1.4% to ±0.3%. These experimental results, which are listed in Table I, demonstrate that amplitude fluctuation $< \pm 0.2\%$ and phase fluctuation $< 1°$ for a high power klystron output can be readily achieved.

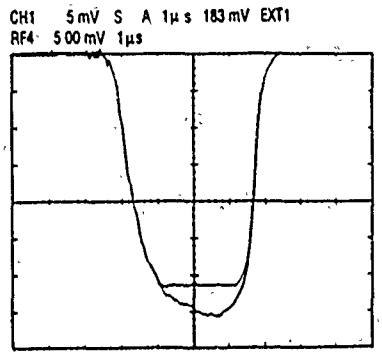


Figure 3: Comparision between uncompensated (lower curve) and compensated (upper curve) rf amplitude pulse from the rf gun cavity.

Table I. Summary of Preliminary Experiment Results.

ITEMS	No Control	With Control
Klystron Power $(\pm\frac{\Delta P}{P})$	4%	0.2%
RF Cavity Power $(\pm\frac{\Delta P}{P})$	5%	1.0%
Manual Control $(\pm\frac{\Delta P}{P})$	1.4%	0.3%
Klystron $(\pm\Delta\phi)$	5°	0.6°

Note: when the klystron is operated on saturated state, the rf power fluctuation is about ±0.6%.

In the future we would like to use this system to control the energy spread of the linac beam in ATF. For this purpose we shall use a fast-response strip-line beam position monitor in a suitable point at the post linac beam transport line, where the beam dispersion analysing power is high. The micro-pulse by micro-pulse energy of the beam will be read and this information will be used at the feed forward control system.

Acknowledgement

The authors wish to thank H. Schwartz of SLAC for providing the phase shifters and information about their application. Help from ATF members J. Sheehan and K. Batchelor has been extremely valuable. The technical support of L. De Santo and T. Monahan is also gratefully acknowledged.

Reference

1. A. R. Donaldson, The Second Generation Modulator, SLAC-PUB-3933 (1986).
2. T. Shidara, et.al, Nucl. Instr. and Meth. A279 (1989) 423.
3. J. Xie and R. Zhang, ATF Tech. Note #8, (1990).
4. J. Sheehan, private communication.

Progress on bunch lengthening at the NSLS VUV ring*

R. Biscardi, W.Broome, S. Buda, J. Keane, G. Ramirez, J. Wachtel, J. M. Wang

National Synchrotron Light Source
Brookhaven National Laboratory
Upton, New York 11973

Abstract- This paper describes the basic theory and experimental results on bunch lengthening at the NSLS VUV ring. Emphasis will be placed on results of experiments conducted since the last report. A fourth harmonic cavity is used to provide the necessary conditions for bunch lengthening. Recent experiments have included using the harmonic cavity in a beam excited mode as well as using an external generator to provide the desired conditions.

1. Introduction

In the NSLS VUV ring, high current operation is inhibited by Touschek lifetime. A fourth harmonic cavity has been installed in the VUV ring to operate as a bunch lengthening cavity. By lengthening the stored bunch of electrons, the density is decreased. This decrease in density will improve the Touschek lifetime and thereby allow higher usable currents in the VUV ring.

Experiments[1] have been conducted which prove the feasibility of using a harmonic cavity to lengthen the bunch. However, these experiments were limited by a stainless steel structure which was prone to thermal runaway. An all copper cavity has been installed since these experiments to provide better heat transfer.

The initial tests performed with the new copper cavity in a beam excited mode were quite favorable and the system became operational. Attention was then turned to methods of optimizing the system. This requires an external generator to drive the harmonic cavity. The entire system must be held to tight amplitude and phase requirements. The details for such a system have not been worked out as of this date. However, the beam excited mode has been enhanced by a simple feedforward system in which the resonant frequency of the harmonic cavity is made proportional to beam current.

2. Theory

The longitudinal profile of a bunched beam in an electron storage ring is determined by the shape of the restoring force (RF voltage), the type of excitation (quantum emission) and other machine parameters. The stationary profile is shown to be[2]

$$\rho(\phi) = K_1 e^{-K_2 U(\phi)}$$

where

$$U(\phi) = K_3 \int_0^{\phi} [eV(\phi) - U(0)]\, d\phi$$

K_1,K_2 and K_3 are dependent upon other machine parameters.

Under normal operating conditions (small energy deviations, small phase oscillations) the potential function is quadratic and the longitudinal distribution is gaussian. With the addition of a fourth harmonic cavity, the potential function can be made quartic, leading to a trapazoidal shaped bunch. The dual cavity system produces a less dense bunch and longer Touschek lifetime.

The desired conditions to produce a quartic potential bucket have been calculated[3]. They require that the first and second derivatives of the total accelerating voltage equal zero, while the total voltage itself is such that the particles receive an energy gain equal to the radiative energy loss per turn (fig. 1).

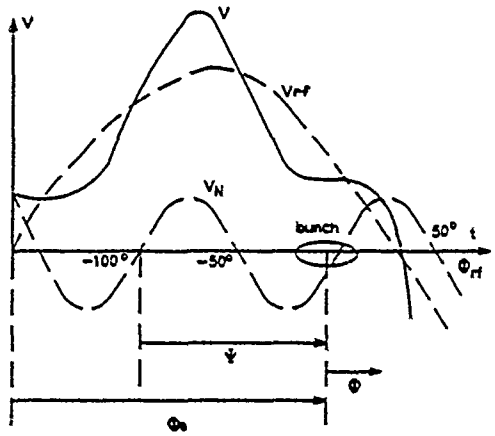


Fig. 1 Waveform with the double RF system.

*Work performed under the auspices of the U.S. Dept. of Energy

0-7803-0135-8/91$03.00 ©IEEE

To provide a true quartic potential for all beam currents, the harmonic cavity must be driven by an external generator. Tight tolerances on the required amplitude and phase must be maintained to produce an inflection point at the synchronous voltage. Using a passive system, these conditions may be approached by inductively detuning the harmonic cavity and allowing the beam alone to produce the harmonic cavity gap voltage. Although a true inflection point may never be reached, the bunch will be lengthened and lifetime improved.

3. Experimental results.

After the new cavity was installed, studies began using the harmonic cavity in the beam excited mode. The cavity was detuned inductively to 87 degrees. Bunch length was measured using a photodiode detector mounted at a synchrotron light port. After injecting to 900 mA, the harmonic cavity was brought closer to resonance.

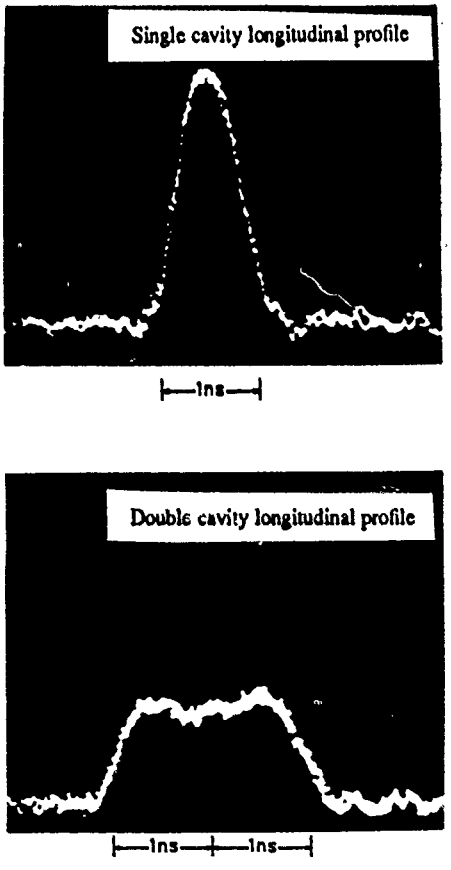


Fig. 2 Initial bunch length measurements.

As the cavity approached 84 degrees detuning the bunch began to lengthen. At 83 degrees detuning the bunch became trapazoidal in shape (Fig. 2). By this time the current had decayed to 700 mA, where the lifetime measured was improved by a factor of two over normal operating conditions. At this point there were no problems with instabilites, and the current was allowed to decay to 500 mA where the harmonic cavity was moved closer to resonance. The bunch changed shape accordingly. Going from trapazoidal to double peaked. At approximately 78 degrees detuning the beam dumped.

The results of the first studies were very encouraging. Using a passive cavity, a stored bunch of electrons was lengthened. Typical lifetime was improved from a factor of two at currents greater than 600 mA to a factor of 1.5 at currents greater than 400 mA. Typical current vs. time profiles are as shown in figure 3. Calculations of the induced voltage in the harmonic cavity at these detuning angles produced numbers around 20 KV. This is close to the voltage required for optimum bunch lengthening. The system went into operation with a fixed detuning angle of 83 degrees.

Two important observations were made during the studies. One being the irregular bunch profile of different bunches within a fill (fig. 4). The other being a jump in phase of the bunch just before beam dumped at 78 degrees detuning. Continuing studies were done to look for the causes of these observations.

The irregular bunch profile was attributed to either: 1) interaction with the longitudinal feedback system or 2) to a higher order mode other than the 211 MHZ cavity. Disconnecting the longitudinal feedback system during a fill showed no change in longitudinal profile, thus, removing it as a suspected cause.

The initial studies were done with an asymmetric fill (7 out of 9 bunches filled). When a symmetric three bunch fill was used, the profile of the 3 bunches were nearly identical. Therefore, it is believed that the cause of the irregular bunch profiles is a higher order mode which is driven by a rotation harmonic of the beam and is not an RF harmonic. A mode at an RF harmonic with high Q would act on each bunch in the same manner. Sweeps of the cavities showed a mode in the harmonic cavity at 270 MHz. This mode does lie on a rotation harmonic and is considered the probable cause of irregular bunch pattern. Plans are being made to damp this mode

Careful examination of the longitudinal profile of the bunch as the cavity was moved towards resonance showed the bunch jumping between two longitudinal phase locations. The rate at which the transition between the two states occured increased in frequency as the cavity was moved closer to resonance until beam dumped as mentioned above. The cause of this motion is not fully understood, and work is continuing to understand the mechanism for this motion.

4. Feedforward

A simple system to provide better operation of the passive system has been implemented. It involves changing the resonant frequency of the cavity proportional to beam current. A beam current signal is taken from a stripline pickup. This signal is filtered, detected, and scaled to drive a

temperature controller. By changing the temperature of the harmonic cavity, it's resonant frequency is changed. This system allows higher current to be stored in the ring while still providing lifetime improvement at lower currents. This is achieved by increasing the magnitude of the cavity impedance as the beam current decreases, keeping the magnitude of the gap voltage in the harmonic cavity relatively constant.

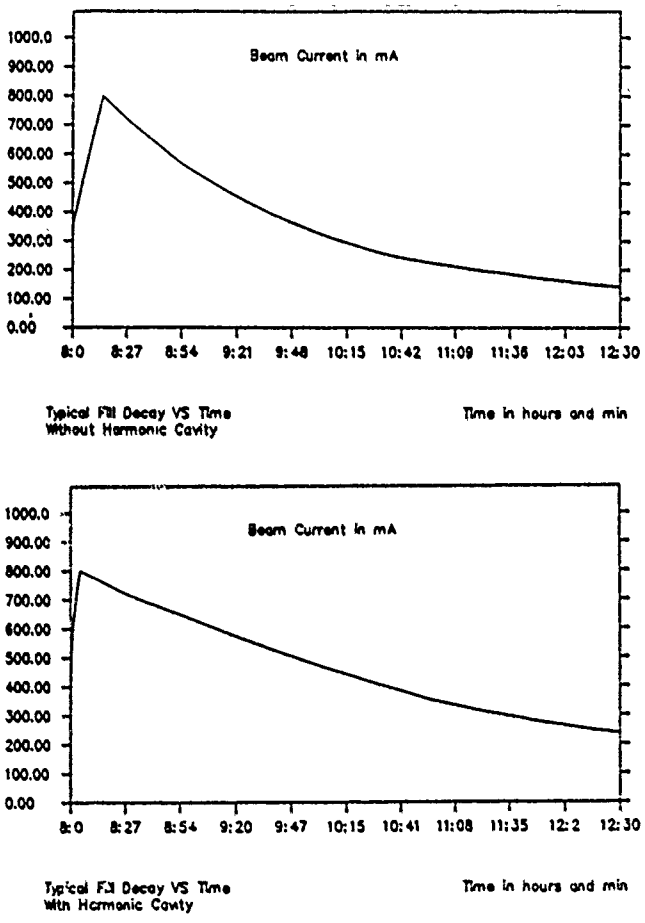


Fig. 3 Typical current decay

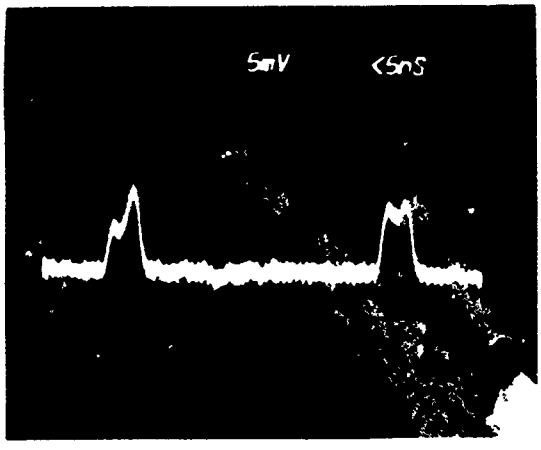


Fig. 4 Two bunches of a seven bunch fill

5. Summary

The bunch lengthening cavity is operational in the NSLS VUV ring in a passive mode. A feedfoward system is used to enhance it's operation. Lifetime improvements range from a factor of two at high currents to a factor of 1.5 at lower currents. Work is continuing on implementation of a generator system as well as on understanding observations made during studies.

6. Acknowledgements

The authors acknowledge the technical excellence of Jeffrey Aspenleiter during the fabrication and installation of the harmonic cavity.

7. References

[1] J. Keane, et al, "Bunch Lengthening Control using the Fourth Harmonic Cavity in the VUV Ring", *1989 IEEE Particle Accelerator Conference, pg 138.*

[2] J. Haissinski, *Nuovo Cimento, Vol. 18B, 72 (1973).*

[3] A. Hoffman and S. Meyers, *11TH Int. Conf. on High Energy Accelerators, 1980 ,Geneva, pg 610.*

Design Of A Multivariable RF Control System Using Gain-Shaping In The Frequency Domain*

Christopher D. Ziomek, Stephen P. Jachim, Eckard F. Natter
MS-H827, Los Alamos National Laboratory, Los Alamos, NM 87545

Abstract

Due to the time-varying nature of the radio-frequency (RF) accelerator, RF field amplitude and phase parameters must be precisely controlled in order to confine and accelerate the charged particle beam. Typically, a feedback control system regulates the RF field, rejects noise and disturbances, and maintains operational stability over changes in the electrical structure of the accelerator. This paper describes a multivariable control system that compensates the electrical structure of the accelerator by using gain-shaping in the frequency domain. The amplitude and phase quantities have been resolved into in-phase and quadrature (I&Q) variables. These orthogonal variables have simple mathematical relationships, and can be analyzed using linear transfer function matrices. The transfer matrix theory has been applied to the design of the multivariable control system that regulates the RF field in-phase and quadrature components. Frequency-domain controllers compensate these two signals to provide desired frequency response characteristics. A control predistorter performs an inverse coupling function, so that the I&Q components are effectively decoupled by the accelerator. Furthermore, computer interface circuitry allows the adaptive optimization of the mathematical transfer functions of the compensators.

I. Introduction

The radio-frequency (RF) accelerator uses a time-varying electromagnetic field to excite charged particles to high kinetic energies. Resonant structures support electromagnetic oscillations having a travelling wave component with a phase velocity of approximately the same velocity as that of the accelerated particles. Precision RF instrumentation is required to control and monitor the amplitude and phase of the time-varying RF field within the accelerating cavity. A two-input, two-output control system is needed to accurately maintain both the amplitude and the phase at a desired operating point. Since coupling between the two control loops can severely degrade the system performance, the control system must include a decoupling network to negate any interaction between the two control variables. The Los Alamos National Laboratory (LANL) has designed a multivariable feedback control system that regulates the in-phase and quadrature (I&Q) components of the RF field. Operating upon the orthogonal I&Q components reduces the complex dynamics of amplitude and phase control to a linear control problem. The LANL control system compensates the I&Q components of the RF field to provide the desired steady-state and transient performance characteristics. In addition, the control circuitry includes computer interface circuitry that allows direct supervisory control by a microprocessor [1]. This functionality can be extended to include the microprocessor-based adaptive optimization of the various parameters in the mathematical transfer functions of the control system.

*Work supported and funded by the United States Department of Defense, Army Strategic Defense Command, under the auspices of the United States Department of Energy.

0-7803-0135-8/91$03.00 ©IEEE

II. System Model

The dynamics of a single-mode accelerating cavity with drive and beam stimuli are well understood [2-4]. A mathematical model exists that accurately defines the effects of external stimuli upon the RF field within a resonant cavity. This model was derived from the various intrinsic cavity parameters. Using a mathematical representation of a sinusoidal signal, the amplitude and phase information can be resolved into I&Q components as

$$s(t) = i(t)\cos(\omega_0 t) - q(t)\sin(\omega_0 t). \qquad (1)$$

These I&Q components are orthogonal, creating a symmetry in the mathematical relationships of the high power amplifier and accelerating cavity, referred to as the plant. The time-domain analysis is simplified by using the complex-envelope isomorphism to eliminate the carrier frequency (ω_0) from the calculations[5]. This technique provides a mathematical tool to directly analyze the I&Q components of an RF signal independently of the carrier. Consequently, the system analysis within this paper examines the baseband I&Q components of the RF signals.

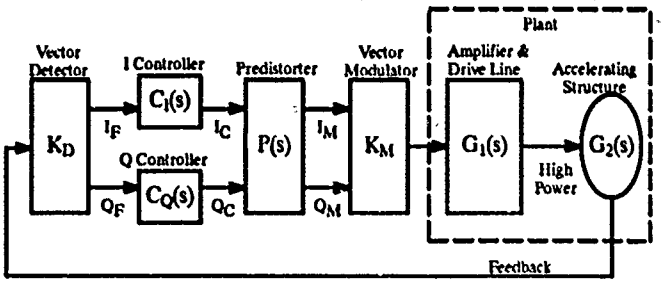


Figure 1. Simplified block diagram of I&Q control system

To accurately maintain the RF field in the accelerating cavity, a multivariable control system regulates both I&Q components of the field. Figure 1 depicts a simplified block diagram of the I&Q control system. Feedback and cascade compensation is used to adjust the dynamic behavior of the plant. The I&Q components of the cavity feedback RF signal are resolved by the vector detector into baseband analog signals that represent these quantities. Each baseband I&Q feedback signal is compared with a desired set point and the resulting error vector is compensated by the respective controller. The predistorter provides an inverse coupling function that negates any interaction between the two variables. The vector modulator uses these processed I&Q signals to modulate the

original RF carrier signal. The resulting modulated RF signal is subsequently used to drive the input of the plant.

The dynamics of the two-input, two-output plant in Figure 1 can be represented as a transfer function block diagram that relates the I&Q components of the drive signal to the I&Q components of the cavity field. Cross-coupling terms define the interactions between the two components. Coupling between the real and imaginary components of a sinusoidal signal is inherent to the dynamic behavior of the plant.

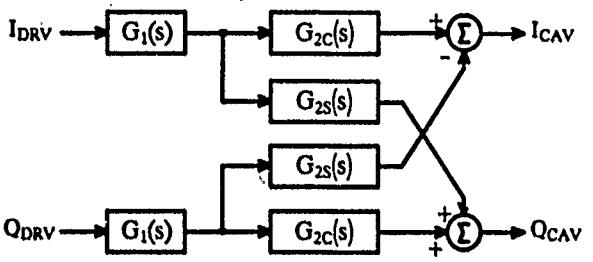


Figure 2. Diagram of cavity I&Q dynamics

Figure 2 depicts the transfer function network of a cascaded amplifier, transmission line, and accelerating cavity driven slightly off resonance. The transfer function of the cascaded RF amplifier and transmission line is

$$G_1(s) = \frac{K_A}{(s/\omega_A + 1)^n} e^{-sT_d} \quad . \tag{2}$$

$K_A \equiv$ RF amplifier gain
$\omega_A \equiv$ RF amplifier bunching cavity bandwidth
$n \equiv$ number of bunching cavities in RF amplifier
$T_d \equiv$ propagation delay within transmission line

Notice that the cross-coupling terms are assumed to be negligible for the RF amplifier and transmission line. The dynamics of a microwave junction and detuned cavity are described by the transfer function network terms:

$$G_{2C}(s) = \frac{2\left(Z_C(s)\left(Z_C(s) + Z_o\right) + Z_S^2(s)\right)}{\left(Z_C(s) + Z_o\right)^2 + Z_S^2(s)} \quad \text{; and}$$

$$G_{2S}(s) = \frac{2Z_o Z_S(s)}{\left(Z_C(s) + Z_o\right)^2 + Z_S^2(s)} \quad . \tag{3}$$

$Z_0 \equiv$ drive line characteristic impedance
$Z_C(s) \equiv$ cavity forward impedance function
$Z_S(s) \equiv$ cavity cross impedance function

The interaction between the I&Q components within this portion of the plant dominate the cross-coupling effects within the plant. The cross-coupling terms in the plant transfer function network describe the interaction between the I&Q components of the RF field.

III. Inverse Coupling

The cross-coupling within the plant causes interaction between the two feedback control loops that requires correction to accurately regulate the RF field. To separate the I&Q dynamics, a predistorter performs an inverse coupling function. The predistorter couples the I&Q components so that they are effectively decoupled by the plant. The function of the predistorter can be described using a transfer matrix approach. To reduce the complexity of the equations, two transfer functions are defined that describe the cascaded transfer matrix for the plant of figures 1 and 2.

$$\begin{aligned} A(s) &\equiv K_M \cdot G_1(s) \cdot G_{2C}(s) \\ B(s) &\equiv K_M \cdot G_1(s) \cdot G_{2S}(s) \end{aligned} \tag{4}$$

Figure 3 shows the linear transfer matrix equation that provides a design for the predistorter. To eliminate cross-coupling within the system, the off-diagonal terms of this combined system must be identically equal to zero. In addition, the dynamics of the forward terms should remain constant regardless of the cross-coupling terms. This is represented by the factor k_0 that scales the gain of the plant to that of one without cross-coupling.

$$\begin{bmatrix} A(s) & -B(s) \\ B(s) & A(s) \end{bmatrix} \begin{bmatrix} 1 & d(s) \\ -d(s) & 1 \end{bmatrix} \equiv \begin{bmatrix} k_o \cdot A(s) & 0 \\ 0 & k_o \cdot A(s) \end{bmatrix}$$

Figure 3. Transfer matrix representation of I&Q decoupling

Although the expressions for $A(s)$ and $B(s)$ are of fifth or higher order, the symmetry of the orthogonal I&Q variables reduces the ratio of the two functions to first order. This allows the predistorter to be realized as a first order, stable, lag compensator. Solving the linear matrix equation for the two unknowns results in

$$d(s) = \frac{B(s)}{A(s)} = \frac{1}{2Q_o}\left[\frac{s + 1/\tau + 2Q_0\Delta\omega}{s + 1/\tau - \Delta\omega/2Q_0 + R/\tau Z_o}\right]$$

$$k_o = \frac{A(0) + B(0)\cdot d(0)}{A(0)} = \frac{Z_C(0)\left(Z_C(0) + Z_o\right) + Z_S^2(0) - Z_o Z_S(0) d(0)}{Z_C(0)\left(Z_C(0) + Z_o\right) + Z_S^2(0)} \quad . \tag{5}$$

$Q_0 \equiv$ cavity unloaded quality factor
$\tau \equiv$ cavity damping time constant
$R \equiv$ cavity shunt resistance
$\Delta\omega \equiv$ cavity detuning frequency

A block diagram of the physical realization of the combined predistorter and plant is shown in Figure 4. This combined system will exhibit the uncoupled properties wherein an input I or Q control input will only affect the respective I or Q component of the cavity field. The decoupling of these two parameters has been analytically verified to better than 60dB correction using a complete RF system model.

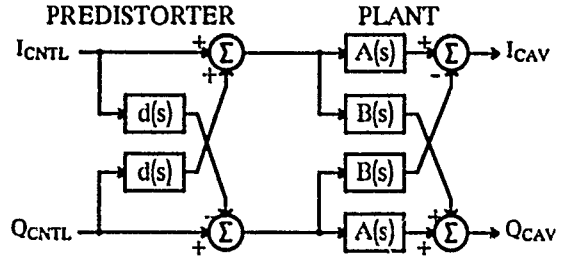


Figure 4. Block diagram representation of I&Q decoupling

The coefficients of the predistorter are adjusted remotely as the operating conditions of the plant vary. A local processor derives the coefficient values from measured sys

tem parameters, and automatically adjusts the hardware as necessary. In addition, an optimization algorithm can be used to correct any coefficient errors introduced by measurement uncertainties.

IV. Compensator Design

The predistorter reduces the dynamics of the coupled system into two single-input, single-output systems that can be treated independently. Consequently, I&Q controllers compensate the uncoupled components in parallel. Each feedback controller regulates its respective RF field component at a desired set point, rejects noise and disturbances, remains insensitive to variations in the electrical structure of the plant, and adjusts the closed-loop transient behavior.

The sensitivity of the closed-loop system to noise and disturbances or to variations in the plant parameters is inversely proportional to the loop transfer function of the cascaded compensator, plant, and feedback sensor. The loop transfer function for either of the decoupled systems can be expressed as

$$T(s) = C(s) \cdot K_M \cdot G_1(s) \cdot G_{2C}(s) \cdot k_o \cdot K_D \ , \qquad (6)$$

This expression provides a method to analyze the sensitivity functions versus frequency. High loop gains below the system bandwidth are desirable to provide disturbance rejection and insensitivity to parameter variations. Low loop gains are desirable at the sensor noise frequencies for immunity to these signals. The frequency response of the compensator is adjusted to shape the loop transfer function over frequency to meet the sensitivity criteria.

The transient response characteristics of the system can be adjusted within certain stability limitations using the same gain-shaping design techniques. The phase margin of the loop transfer function provides a method to predict the closed-loop transient behavior. The Nyquist stability criterion requires that

$$T(j\omega_C) = e^{j(180^\circ + \phi_m)} \qquad (7)$$

for a desired system bandwidth (ω_c) and phase margin (ϕ_m). This requirement specifies the exact phase of the loop transfer function at the cutoff frequency. For the accelerator RF application, the resonant cavity with a high quality factor will have the lowest frequency pole. In addition to the narrow cavity bandwidth, the plant may have nonlinear effects, such as saturation and phase droop within the RF amplifier, large propagation delays that add phase shifts, and a multitude of higher-order poles within the plant, actuators, and sensors. All of these factors affect the loop transfer function and influence the transient behavior of the system. The frequency response of the compensator is adjusted to shape the loop transfer function and create a desired transient response.

The I&Q controllers perform the gain-shaping functionality by using phase lag-lead compensation. Within each controller, a feedback signal, providing a measurement of a detected cavity field component, is compared to a desired set point. If the feedback signal deviates from the set point, an error signal is generated. A proportional, integral, derivative (PID) control algorithm is used to process the error signal and provide the required output drive signal. A phase lag compensator allows the low frequency gain to be increased (which means an improvement in steady-state behavior) without sacrificing the system bandwidth or stability margins. An integrator performs the lag compensation and essentially provides infinite gain at DC, creating zero steady-state error to a step input or step disturbance. The proportional gain stage provides instantaneous error correction for low-frequency disturbances. A phase lead compensator is used to increase the stability margin and bandwidth of the system. A differentiator performs the lead compensation to provide excess gain and phase margin at high frequencies and improve the transient behavior of the system. While the differentiator increases the high-frequency gains, its bandwidth is limited to decrease the susceptibility of the system to high-frequency noise.

The relative gains of each of the three PID terms determine the combined frequency response of the controller. This compensation allows the cascaded loop transfer function for a given plant to be shaped to provide the desired performance characteristics. In addition, the PID coefficients can be automatically adjusted by a local processor to accommodate various plant dynamic characteristics or to optimize the compensator for time-varying plant dynamics.

V. Conclusion

The LANL I&Q feedback control system provides an effective method for regulating the RF field within an accelerating cavity. The flexibility that has been designed into the predistorter and I&Q controllers allows the I&Q control system to be tailored to meet most accelerator applications. With some prior system analysis and modelling, the compensator can be adjusted to provide a desired closed-loop performance. In addition, the parameters of the control system can be empirically corrected by an autonomous optimization algorithm as the plant dynamics or operating conditions change.

VI. References

[1] C.D. Ziomek, "Interfacing RF control electronics to the VXIbus for the Ground Test Accelerator" *Proc. NPB Technical Interchange Symposium.* May, 1990.

[2] B. R. Cheo and S. P. Jachim, "Dynamic interactions between RF sources and LINAC cavities with beam loading," to be published, *IEEE Trans. Elec. Dev.*

[3] S.P. Jachim, "Some new methods of RF control," to be published, *Proc. Linear Accelerator Conference.* September, 1990.

[4] A. Young and S.P. Jachim, "A new approach in simulating RF linacs using a general, linear real-time signal processor," to be published, *Proc. Particle Accelerator Conference.* May, 1991.

[5] S. Haykin, *Communication Systems.* New York: John Wiley & Sons, 1983, pp. 80–108.

Synchronization of a Variable Frequency Source with a Fixed Frequency Source Using a Sliding-Mode Controller

L.K. Mestha
SSC Laboratory*, Dallas, Texas 75237

K.S. Yeung
University of Texas, Arlington, Texas 76019

Abstract

One way of synchronizing the SSC Low Energy Booster with the Medium Energy Booster is by matching the longitudinal phase of the designated RF buckets of two machines throughout acceleration to a pre-programmed trajectory. This makes the synchronization predictable in advance. The model associated with the phase-locking is time-varying and model parameters are subjected to disturbance due to errors in the bending magnetic field. Also the disturbance could be due to other feedback loops such as a B-field loop or a beam phase loop in the system. The measured phase error between the two reference waves may not be accurate. Hence in this paper we have shown the design of a Sliding-Mode controller for such an application. In the absence of measurement errors and parameter uncertainties and with no disturbance, the controller reduces to a classical gain feedback. Due to the general approach we have adopted in synthesizing the controller, the techniques can be applied to existing synchronization schemes.

I. INTRODUCTION

For extraction of beam from one accelerator to another, a synchronization loop of the type shown in Figure 1 can be used. This would involve synchronizing the beam frequency or the RF signal of the low-energy machine with an external reference source. The phase difference between the beam and the reference source is used to correct the input frequency of the low energy machine. The reference source could be a separate fixed frequency oscillator driving the high power RF system of the higher energy machine while the synchronization process is under way. Phase synchronization is obtained when the phase error between the reference source and the beam frequency is made equal to zero. A simple design of such a feedback system consists of a state feedback gain k, as shown in Figure 1. Apart from the synchronization loop, it is quite normal to have other feedback loops such as a beam phase loop or a B-field loop providing a small correction function to the variable frequency source. The B-field loop is not able to give full indication of the correction required because of measurement inaccuracy in the field. Hence the field error would act as disturbance to the system. Under those circumstances, the feedback controller, k, will not be able to drive the phase detector output to zero since the state feedback loop cannot handle external disturbance on the system. In this paper we show the synthesis of a sliding-mode controller using Lyapunov Stability Theory. This controller behaves very much like a state feedback controller when the gain associated with robustness is turned off. We also discuss the effects due to Q of the RF cavity when we implement this type of controller.

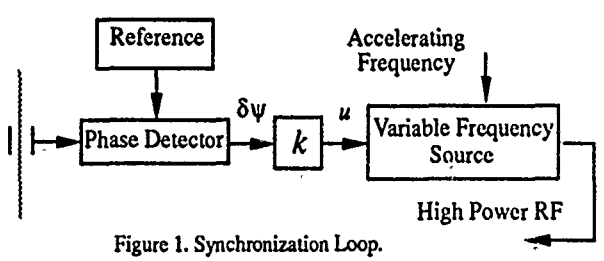


Figure 1. Synchronization Loop.

In our analysis we assume that the synchronization of the low energy machine can be done with the high energy machine throughout the acceleration. However, it can be switched on anytime during acceleration. Although the synchronization scheme in Reference 1 is different in its implementation from the conventional approach, in principle it is similar to Figure 1. Hence the feedback controller can be applied to the conventional phase-lock scheme.

II. FEEDBACK CONTROLLER

In the presence of B-field errors, the phase detector output, $\delta\psi$, can be represented[1] by the following equation with standard notations.

$$\frac{d\delta\psi(t)}{dt} = \frac{R\gamma_T^2}{\gamma_T^2-\gamma^2}\left(\frac{2\pi\delta f(t)}{h} - \frac{2\pi f}{h}\frac{1}{\gamma_T^2}\frac{\delta B(t)}{B(t)}\right) \quad (1)$$

This equation is derived by ignoring the non-linear terms. For the present analysis the terms associated with $\delta B(t)$ can be regarded as the disturbance to the system. Under no disturbance, a more general way to write the above equation is in state-space form with variables $\{A(t)\}$, $\{b(t)\}$, $\{C(t)\}$ as system matrices, $u(t)$ as the control signal, $y(t)$ the output signal, and $x(t)$ the state variable as follows:

$$\begin{aligned} \dot{x}(t) &= A(t)x(t) + b(t)u(t) \\ y(t) &= C(t)x(t) \end{aligned} \quad (2)$$

*Operated by Universities Research Association Inc., under Contract with U.S. Department of Energy, Contract No. DE-AC02-89ER40486.

U.S. Government work not protected by U.S. Copyright.

where

$$x(t) = \delta\psi(t)\ ,\quad A(t) = 0\ ,\quad b(t) = \frac{\gamma_T^2}{\gamma_T^2 - \gamma^2}R\ ,$$

$$C(t) = 1\ ;\ \text{and}\ u(t) = \frac{2\pi}{h}\delta f(t)\ .$$

The time variation of the parameters is represented by (t). For simplicity we do not write the script *(t)* in our discussion. With disturbance, i.e., $\delta B(t) \neq 0$, Equation 2 becomes equal to

$$\dot{x} = b\,(u + u_d)\ , \tag{3}$$

where u_d is regarded as the disturbance function and is equal to

$$u_d = -\frac{2\pi f}{h}\frac{1}{\gamma_T^2}\frac{\delta B}{B}\ . \tag{4}$$

Also, let us assume that the measured state, x_m has an error of x_d, then

$$x_m = x + x_d\ , \tag{5}$$

where x is the actual state as described by Equation 3. Now the sliding variable is defined with the measured state as follows.

$$S = x_m + \alpha\int_0^t x_m dt\ . \tag{6}$$

In this equation α is equal to the eigenvalue of the closed loop feedback system. Equation 5 is substituted in Equation 6, and resulting equation is differentiated with respect to time. The terms with $\dot{x}$ are replaced by Equation 3. After simplification, we get

$$b^{-1}\dot{S} = u + u_d + b^{-1}\dot{x}_d + b^{-1}\alpha x_m\ . \tag{7}$$

The justification for the choice of the stable feedback loop is based on the Lyapunov function candidate. There is however no unique Lyapunov function for this problem. A more suitable one could be as follows:

$$V = \frac{1}{2}b^{-1}S^2 \tag{8}$$

The above function is positive because the system parameter b is positive. Furthermore, from Lyapunov Stability Theory, a system of the type used in Equation 2 is stable when the time derivative of the positive definite Lyapunov function is negative. Hence we will differentiate Equation 8 with respect to time and substitute Equation 7 in place of $b^{-1}\dot{S}$. After simplification we get

$$\dot{V} = S\,[u + u_d + g\dot{x}_d + g\alpha\,(x + x_d) - hS]$$

where

$$g = b^{-1} \quad \text{and} \quad h = \frac{1}{2}\frac{\dot{b}}{b^2}\ . \tag{9}$$

Here we can assume that the disturbance signal u_d can be measured. Since the measurement will not be accurate, we can consider this term to have a nominal measurable term and an uncertainty function. When the measurements are not available, the nominal value will be zero. Similarly, parameter uncertainties can be assigned to g and h. Thus we can write:

$$\begin{aligned} u_d &= u_d^\circ + \Delta u_d \\ g &= g^\circ + \Delta g \\ h &= h^\circ + \Delta h \end{aligned} \tag{10}$$

where the terms u_d°, g° and h° are the nominal quantities, and Δu_d, Δg and Δh are uncertainties in the parameters u_d, g and h, respectively. Now, using Equation 10 into Equation 9, we obtain

$$\dot{V} = S\,[u + (u_d^\circ + \Delta u_d) + (g^\circ + \Delta g)\,\alpha x_m - (h^\circ + \Delta h)\,S + g\dot{x}_d\,] \tag{11}$$

The control law, u, is defined in such a way that Equation 11 is always negative. Let it consist of the continuous part u_c and a switching part u_s:

$$u = u_c + u_s$$

where $u_c = -u_d^\circ - g^\circ\alpha x_m + h^\circ S$ and

$$u_s = -(k_x|x_m| + k_s|S| + k_0)\ \mathrm{sgn}S\ . \tag{12}$$

The function $\mathrm{sgn}S$ in Equation 12 is a *signum* function which has a value of either +1 or -1 when $S \geq 0$ and $S < 0$, respectively. The constants k_x, k_s, and k_0 in Equation 12 are selected so as to make the time derivative of the Lyapunov function negative. With simple algebra we can arrive at the following condition.

$$\begin{aligned} k_x &> sup|\Delta g\alpha| \\ k_s &> sup|\Delta h| \\ k_0 &> sup|\Delta u_d + g\dot{x}_d|\ . \end{aligned} \tag{13}$$

In Equation 13, '*sup*' is pronounced as *supremum*, which is the maximum value of the function. The magnitude of the constants depends on the parameter uncertainties, but for stability they must satisfy Equation 13. The continuous part in the control law in Equation 12 holds the phase error zero, while at the same time the switching part introduces the robustness into the loop. Hence the switching part would take care of the disturbance rejection and parameter uncertainties. Equations 6 and 12 form the feedback controller, as shown in Figure 2.

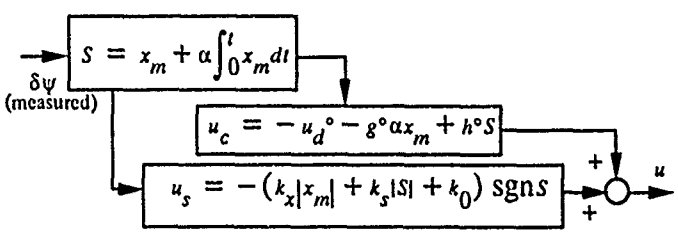


Figure 2. Sliding-mode controller.

Under the condition with no disturbance (u_d=0), no measurement error (x_d=0), and no parameter variation, the gains k_x=k_s=k_0=0. Also, h=0 for a time invariant system, since a state feedback design is applicable to only such systems. Hence the state equation of the closed loop feedback becomes equal to

$$\dot{x} = bu = -\alpha x\ , \tag{14}$$

where α/b is now equal to the gain, k, shown in Figure 1.

III. ANALYSIS OF THE LOOP PERFORMANCE

The performance of the feedback loop is analysed by considering the phase-locking between the Low Energy Booster and the Medium Energy Booster. The machine parameters shown in Reference 2 are used for the analysis. Figure 3(a) shows a plot of the decay of the phase detector output with respect to time, with the state feedback loop gain of k=2 and 5. The phase error converges to zero as expected. The profile of the phase error is, however, not important but it should be zero at the transfer time (ignoring all the fixed phase associated with the transfer line delays, etc). In an ideal situation, when there is no field error affecting the beam frequency, we would expect the synchronization to be good as shown in Figure 3. The loop performance deteriorates when a step magnitude of u_d=11.6 rad/sec (for $(\delta B)/B = 5 \times 10^{-4}$ for the Low Energy Booster) is introduced to the system and is held high until the extraction time. The time response of the phase error is shown in Figure 3(b) for this disturbance. It is clear from this figure that the system is not robust since the phase error is not held zero or at least to a tolerable value. It can be minimized by making the feedback gain excessively large which may lead to beam oscillations.

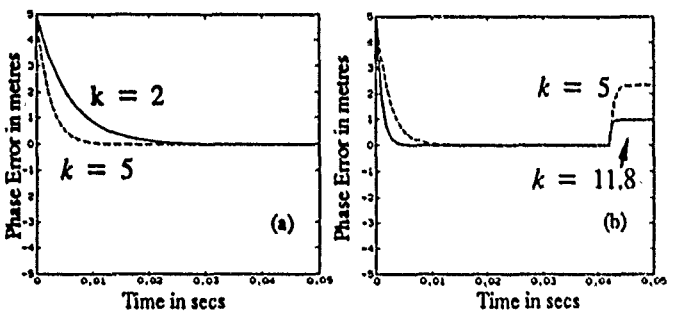


Figure 3. Time response of the phase error
(a) without disturbance; (b) with disturbance (step function at 42ms).

In Figure 4(a) the loop performance is shown with the disturbance function for the sliding-mode controller. In Figure 4(b) the time response of the sliding variable S (Equation 6) is displayed. From these figures it is clear that the product $S\dot{S}$ is always negative. Hence the loop is stable throughout the acceleration. Also, the loop performance is very good under field errors compared to the usual gain feedback. To overcome field errors the feedback controller generates the compensating frequency shift to the oscillator. Since the constant k_0 controls the magnitude of the disturbance rejection, it would be useful to have it set very high. Higher k_0 may result phase oscillations for digital implementation with low sampling rates. However, the

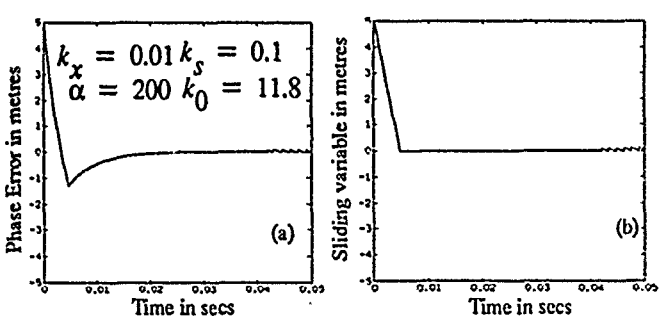


Figure 4. (a) Time response of the phase error (with disturbance);
(b) Time response of the sliding variable

analogue loops have no such problems. When there is no parameter variation ($\Delta g \cong 0$ and $\Delta h \cong 0$), the gains k_x and k_s can be negligible. Hence the switching part of the control input to the oscillator is mainly dominated by k_0. Thus it is dominated by the system uncertainties, whereas the continuous part acts on the initial phase error by the same principle by which the state feedback loop works. If the initial phase error is large, then a sudden frequency shift of few khz would introduce beam oscillations. Hence a good solution would be to use the time variation for appropriate gains including the eigenvalue, α. Implementation of such a gain sequence would be easier for a digital synchronization loop.

It is well known that the beam frequency does not change instantaneously when the oscillator is shifted by the control signal, u. The time constant is governed by the Q of the cavity and the amount of detuning caused by the beam current or a separate tuning loop. By assuming that the tuning error is well compensated, the equation between the beam frequency shift and the source frequency shift is given by

$$\dot{u} = -\frac{w_{cav}}{2Q}u + \frac{w_{cav}}{2Q}u_i \qquad (15)$$

where w_{cav} = resonant frequency of the cavity and $u_i = (2\pi\delta f_i)/h$, with δf_i as the oscillator frequency shift. A block diagram representing Equations 2 and 15 is shown in Figure 5. The time response of the phase error is not very differ

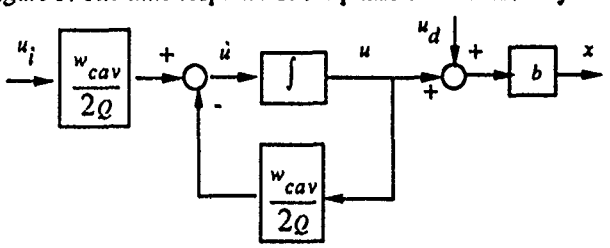


Figure 5.: System model with the Q of the RF cavity

ent from Figures 3 and 4 for the ratio $(2Q)/w_{cav}$ up to 1 millisecond.

IV. CONCLUSIONS

Analytical treatment of the synchronization feedback loop is shown in this paper. Although the gain feedback loop is easier to design and implement, the simulation results show that the controller properties are not useful to handle changes in the synchronization conditions with B-field errors. The sliding-mode controller shows robustness for such applications. For large disturbance rejection, the inherent oscillatory nature of the control signal can be overcome by introducing well-known saturation function.

V. REFERENCES

[1] L.K. Mestha, "Phase-Control Scheme for Synchronous Beam Transfer from the Low Energy Booster to the Medium Energy Booster", SSC Report, SSCL-340, 1990.

[2] Site-Specific Conceptual Design Report of the SSC, SSCL-SR-1056, July 1990.

PHASE AND AMPLITUDE STABILIZATION OF SHORT-PULSED, HIGH-POWER MICROWAVE AMPLIFIERS*

D. Hopkins and D. Yu
DULY Consultants, Rancho Palos Verdes, CA 90732
T. Orzechowski, G. Westenskow, and S. Yu
Lawrence Livermore National Laboratory, Livermore, CA 94550

Abstract

In recent years, much effort has gone into research on high-power, short-pulsed free-electron lasers (FELs) and relativistic klystrons (RKs) driven by linear induction accelerators (LIAs). These devices are potential power sources for future linear colliders several kilometers in length. The new high-power devices must meet certain practical requirements on such parameters as stability, efficiency and cost. In this paper, we address the problem of phase and amplitude stability of the rf pulse and present a technique for improving it in these devices to a level that is acceptable for accelerator applications. We summarize the results of bench tests and computer simulations, and discuss a proposed high-power klystron experiment aimed at establishing the feasibility of the overall concept and the workability of the stabilization circuits.

INTRODUCTION

The required amplitude and phase stability for future linear collider power sources, during the useful portion of the pulse flattop, is on the order of $< \pm 1\%$ and $< \pm 2°$, respectively[1]. A program underway at LLNL has reduced the beam energy variations in one LIA[2] to $< \pm 1\%$, a significant achievement. As LIA beam-driven high-power microwave amplifiers (HPMAs) are usually constructed and operated, however, beam energy and current variations during the pulse flattop can result in output rf amplitude fluctuations of 20% or more and phase variations of ±20 to 30 degrees. For such machines, it will be extremely difficult to achieve the level of stability necessary for powering particle accelerators without a method of compensating for the beam-caused fluctuations. Given such a method, on the other hand, the requirements for beam stability could be relaxed, resulting in important savings in the complexity and cost of the LIA driver.

In the operation of present-day RKs and FELs, it is observed that the fluctuations in the electron beam energy and current, and the resulting fluctuations in output rf phase and amplitude, are very repeatable from pulse to pulse. This is no doubt due to the systematic nature of the causes of beam variations. This repeatability is exploited in the stabilization technique described in detail below. It enables the rf output phase and amplitude error signals to be sampled on one pulse, held in memory circuits and suitably processed, then applied on the next pulse at the input of the HPMA in such a manner that errors on subsequent pulses are reduced. This feed-forward or delayed-feedback approach is especially suitable for repetitive, short-pulsed devices whose physical size causes excessive signal propagation delays that preclude the use of directly-closed feedback loop correction.

PHASE STABILIZATION SYSTEM

The 11.4-GHz RK phase stabilization system described below applies equally well to other HPMAs such as FELs, klystrons and cyclotron auto-resonance masers (CARMs). The RK is considered a worst-case example because of the retarding effect of its stored energy on response time.

Figure 1 shows a block diagram of the new phase-stabilizing system. A key component of the correction circuit is a fast varactor phase shifter, PS-1. The RK output phase signal is compared to the phase of the reference signal in the CC-1 circuits, generating a phase error signal which is processed and held in memory circuits. On the next machine pulse, this error-correction pulse is read out and sent to the varactor phase shifter. The device produces an offsetting phase shift in the RK input drive signal, compensating for the RK output phase error produced in the previous machine pulse by beam energy fluctuations.

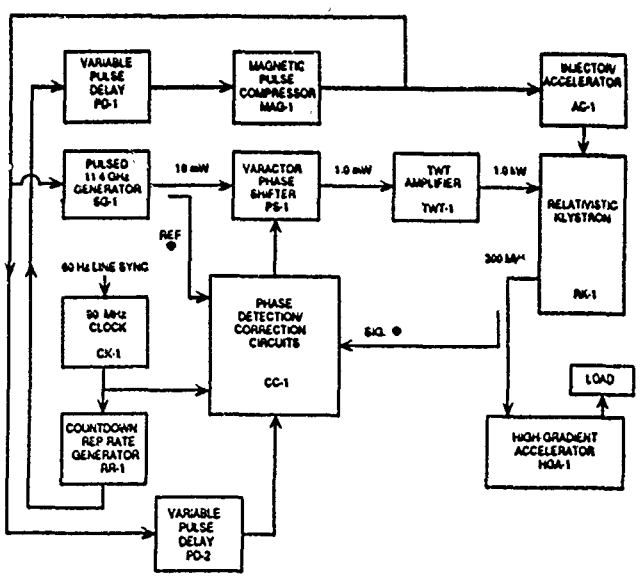


Fig 1 Block Diagram of a Phase Stabilization System

0-7803-0135-8/91$03.00 ©IEEE

Two techniques for implementing the CC-1 correction circuits have been considered in this paper. The first employs fast track-and-hold modules for sampling the phase error signal during ten sampling periods over the 40-50 ns pulse. On the next machine pulse, the signals are sequentially gated out of these ten memory units on a single line and, following appropriate amplifying, filtering and possibly inverting, sent to control the varactor phase shifter. This is likely to be the lower-cost approach and lends itself to miniaturized packaging. The second technique uses fast digitizers to sample the phase error signal and a microcomputer to process the correction samples and to program a fast waveform generator. On the next pulse, the generator is triggered and its output pulse commands the varactor phase shifter. A delayed feedback system using this technique was used to correct transverse position variations of a short electron pulse on an induction accelerator[3]. This approach has the advantages of flexibility and the use of existing instrumentation but its initial cost is higher. For both of these techniques, the error-correction process goes on continuously from pulse to pulse.

The question of the feasibility of such a system centers on overall response time, adequate circuit component performance and the general workability of the stabilization circuit. The response time required at SLAC to make a 180° phase change in the output of a high-power 8.56 GHz klystron was measured to be 20-30 ns[4]. A several-hundred megawatt, 11.4 GHz LLNL RK had an input buncher cavity with a Q ≈ 170. The typical 1.5-kW peak input power could produce a calculated phase-change rate of about 37 deg/ns in this cavity. Higher-power RKs could have lower Q-values and thus even faster response. We can conservatively take worst-case values of 20 deg/ns for the RK response rate and 20° for the maximum required phase correction from pulse to pulse. Making realistic estimates for the risetime contributions from the remainder of the stabilization circuit components, we calculate that the worst-case phase-change risetime for each correction step is ≤ 2.5 ns. If no further signal processing took place, during the correction pulse risetimes small error spikes of phase modulation would result. To minimize these, the CC-1 signal processing circuits can provide a smoothing, interpolating action during the risetime of each correction step.

To measure relevant risetimes and demonstrate phase-error correction, we assembled the test circuit shown in Figure 2. For the varactor phase-shifter, we purchased an 11.4 GHz, narrow-band, 0 to 100° unit custom-fabricated to our specifications and optimized for fast risetime. It has a nominal insertion loss of about 9 dB and operates with a 0 to -16V control pulse. It was also found to have an insertion loss that varied several dB over the control voltage range (see Amplitude Stabilization System, below). The circulator, fast PIN diode switch and short-circuit within the dotted enclosure (Figure 2) are used to produce a fast phase-change by changing the electrical path length traveled by the 11.4 GHz signal as it passes from port 1 to port 3 of the circulator. This phase-modified signal and the reference signal are the inputs to a phase detector consisting of a mixer and a back diode. The mixer IF bandwidth is specified as 3.0 GHz. The net response time, i.e. 10-90% step risetime, of the overall phase modulation and detection process was measured to be 0.8 ±0.1 ns (after subtracting the scope/plug-in contribution).

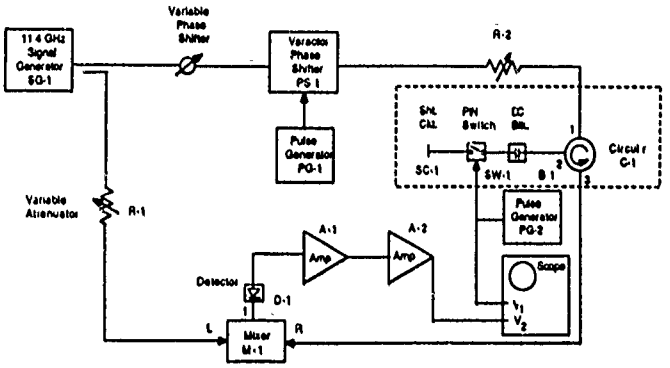


Fig 2 Test Circuit for Phase Error Correction

Once a phase-error signal is produced, detected and displayed on the scope, the PG-1 pulse generator can drive the PS-1 varactor phase shifter and demonstrate cancellation of the phase error. Being adjustable in amplitude and dc offset biasing, PG-1 permits the exploration of the PS-1 control parameter space. It simulates the output of the phase correction circuits in CC-1 of the full RK system. One can view the phase-error signal as a simulation of that being produced by an RK on one machine pulse, and the PG-1 output pulse as that simulating the phase-correction signal gated out of the CC-1 circuits on the following pulse. The scope can conveniently display the error signal before and after phase correction is performed. The lower trace of Figure 3a shows an uncorrected phase-error pulse simulated by the test circuit with the PG-1 pulser inactive. The upper trace is the waveform of the PIN switch driver pulse. Figure 3b shows a partial correction effected by adjusting the PG-1 pulser amplitude correctly (but whose pulse width is too short). Figure 3c shows correction that is complete except for some leading and trailing edge aberrations. This experiment thus demonstrates the basic feasibility of the correction technique and the adequacy of circuit components for achieving the desired response time.

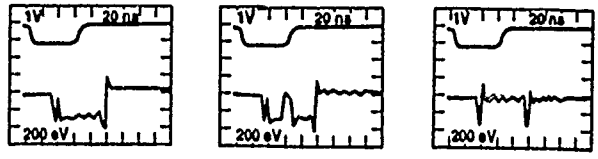


Fig 3 Phase Error and Correction Pulses

We further investigated the minimum resolvable phase correction that could be produced as limited by signal-to-noise considerations. By using a standard low-noise amplifier after the phase detector, it is clear that a stability (and minimum correction) of $\leq \pm 2^{\circ}$ can be achieved within the desired bandwidth of about 300 MHz. The minimum system dynamic range is then determined to be ± 2 to 50°, or 14 dB, with the existing varactor phase shifter.

A 1.6-MeV RK was realistically modeled along with the other elements of the phase stabilization system on Extend software. Simulated output phase errors were generated by simulating variations in the RK beam voltage. Figure 4a shows the open-loop (i.e. uncorrected) amplified and filtered phase-error signal resulting from a simulated $\pm 7.5\%$, 200 MHz square-wave modulation of the beam voltage. The $\pm 45\%$ phase error thus produced resulted in a ± 0.3 V error signal. Figure 4b shows the closed-loop error signal (note the vertical scale-change) settling to <1.0 mV in <1.5 ns. This corresponds to a phase stabilization level of 0.3%, or $\pm 0.15^{\circ}$, clearly demonstrating the workability of the circuit.

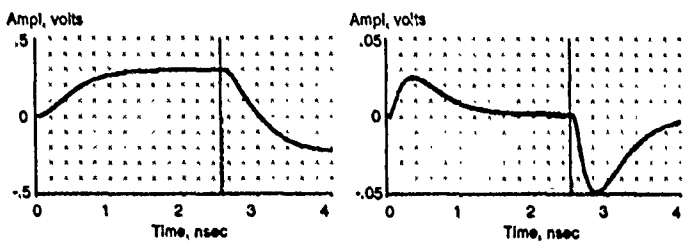


Fig 4 Open (a) & Closed (b) Loop Phase Correction Simulation

AMPLITUDE STABILIZATION SYSTEM

The amplitude stabilization system is similar to that shown in Figure 1 except that an amplitude comparator replaces the phase detector and a voltage-controllable attenuator replaces the varactor phase shifter. It may be difficult to achieve the desired bidirectional response time with PIN diode attenuators. A better solution is to make use of the fast amplitude modulating capability of the varactor phase shifter. This single unit can then become the dual-purpose controlling element in a combined phase and amplitude stabilization system. To avoid instabilities, the settling times, i.e. the poles of the response functions, of the two correction loops can be widely separated.

Bench tests of amplitude error cancellation were performed with results appearing nearly identical to those shown in Figure 3 for phase correction. We also showed that a minimum resolvable amplitude correction of $< \pm 1.5\%$ was achievable and that a maximum correction of $\geq \pm 20\%$ was easily achieved by the use of the varactor amplitude modulator. The results of Extend computer simulations of the stabilization circuit performance are shown in Figure 5 for a 500 MHz, $\pm 25\%$ square-wave modulation of the RK beam current. Figure 5a shows the open-loop behavior, e.g. the resultant 11.4- GHz amplitude fluctuations and the amplitude error signal settling to $\sim \pm 0.6$ V. Figure 5b shows the closed-loop results with the amplitude error settling to $< \pm 1.0$ mV in about 1.0 ns. This corresponds to a 0.17% amplitude stabilization level.

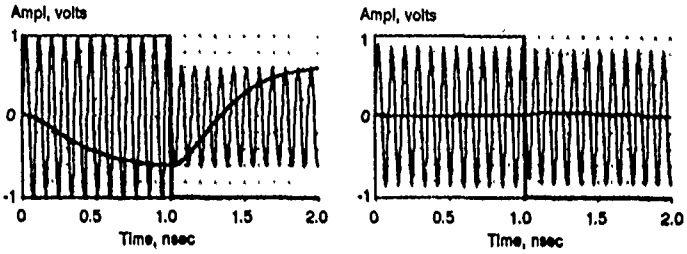


Fig 5 Open (a) & Closed (b) Loop Amplitude Simulation

HIGH-POWER KLYSTRON EXPERIMENT

We will be performing tests of a delayed feedback system to control the rf phase on the choppertron[5], an 11.4-GHz high power source now being studied at the Microwave Source Facility at Livermore. At modest currents the choppertron has so far produced 100-MW, 30-nsec rf pulses. Modifications should increase the amplitude of single output to several hundred megawatts without shortening the pulse width. Additional amplitude and phase variation in the rf output for testing the feedback system can be imposed by inducing a voltage variation during the pulse. The first experiments will determine how changes in the driver's phase will affect the phase of the rf output from the tube. The elements for a feedback control system using the second technique described above have been procured, and are undergoing bench test. In these tests the varactor phase shifter will be placed between the signal generator and the TWT. The rf pulse from the TWT is amplified to about 1 MW by a Thompson-CSF pulsed klystron before it is coupled to the drive cavity of the choppertron.

*Work supported by DOE SBIR grant no. DE-FG03-90ER80907 and DOE contract no. W-705-ENG-48 (LLNL) and DE-AC03-76SF00098 (LBL)

[1]R.D. Ruth, "Multibunch Energy Compensation", Proc. on Workshop on Physics of Linear Colliders, Capri, June 13-17 (1988) p. 291.

[2]W.C. Turner, "Control of Energy Sweep and Transverse Beam Motion in Induction Linacs," Proc. IEEE Part. Accel. Conf., San Francisco, Ca, May 6-9 (1991).

[3]F. Coffield, et al., "The Fast-Correction-Coil Feedback Control System," Nucl. Instr. & Meth., A293 (1990) pp 296-300.

[4]W.R. Fowkes, SLAC, private communication, December (1989).

[5]G. Westenskow, et al., "A Chopper Driven 11.4 GHz Traveling-Wave RF Generator", paper HRA4, this conference.

Measurement of Bunch Time-structure in KEK PF

M. Tobiyama, T. Kasuga, T. Obina, T. Takeo
Faculty of Science, Hiroshima University, Hiroshima 730, Japan
and
T. Katsura
National Laboratory for High Energy Physics, Tsukuba 305, Japan

Abstract

A photon counting system was installed in the Photon Factory storage ring at the KEK for precise measurement of the time-structure of bunches. Photons emitted in a bending section are detected with a microchannel-plate photomultiplier. The time interval between the output of the photomultiplier and the signal synchronized to the revolution frequency of the ring is converted to the pulse height. The distribution of the pulse height which corresponds to the time-structure of bunches in the ring is analyzed by a multichannel analyzer. In addition to the bunch length measurement, the single bunch impurity was also successfully measured since the system has an excellent dynamic range.

1 Introduction

The time-structure of bunches in an electron storage ring in the single-bunch-mode is interesting in two points of view. In the microscopic view, the length or the shape of bunch has great interest. The electromagnetic field induced in vacuum vessels of the ring by a bunch acts back to the bunch, changing its shape and length. By measuring bunch length as a function of the beam current, the coupling impedance of the vacuum chamber of the ring can be estimated.

In the macroscopic view, it is necessary to measure the single bunch impurity, which is the ratio of positrons in unwanted buckets to those in the main bucket, in order to improve the quality of time-resolved experiments[1].

There are several methods to measure the time-structure of bunches. We adopted a photon counting method. As the main error source of this method is the statistical one, an excellent resolution is obtainable when enough events are collected. This enables us to have much larger dynamic range compared with other methods such as a streak camera or photo-diode. The single bunch impurity cannot be measured quantitatively without the photon counting method[2].

We have installed a photon counting system in the beamline 21 in the Photon Factory of National Laboratory for High Energy Physics (KEK-PF) and measured the time and current dependence of the time-structure of bunches. The related parameters of the KEK-PF storage ring is listed in Table 1.

Table 1: Main Parameters of KEK-PF-Ring

Energy	E	2.5	GeV
Circumference	C	187.07	m
Betatron tune	ν_x	8.37	
	ν_y	3.39	
Revolution frequency	f_{rev}	1.6	MHz
Harmonic number	h	312	
Radio frequency	f_{rf}	500	MHz
Momentum compaction factor	α_p	0.0157	
Peak RF voltage	V	1.7	MV
Radiation damping time	τ_x	7.79	ms
	τ_y	7.82	ms
	τ_e	3.92	ms
Synchrotron frequency	f_s	36	kHz
Natural bunch length	σ_z	50	ps
Touschek lifetime (1A)	τ_T	2000	s

2 Experimental setup

Positrons circulating in the ring emit photons stochasticaly in a bending section. As the probability of the emission of photon is the same for all positrons in any RF-buckets, the time distribution of photons is proportional to that of the positrons.

The system is shown schematically in Fig. 1. Photons from the nearest bending section are led to a mirror chamber through a vacuum pipe. About 20% of the visible light are reflected by a mirror made of SiC. The mirror is cooled through a water-cooled Cu holder. The reflected light reaches a photomultiplier (PMT) through an ICF-70 view port, a Pb-acrylic glass of 22 mm thick, light reducing filters and a precise horizontal slit. The number of photons are reduced to the level of one photon detection per about hundred revolutions of a bunch. As it is necessary to use PMT with small transit time spread (TTS), we have chosen a microchannel-plate type PMT (Hamamatsu Photonics R2809U), TTS of which is about 55 ps.

0-7803-0135-8/91$03.00 ©IEEE

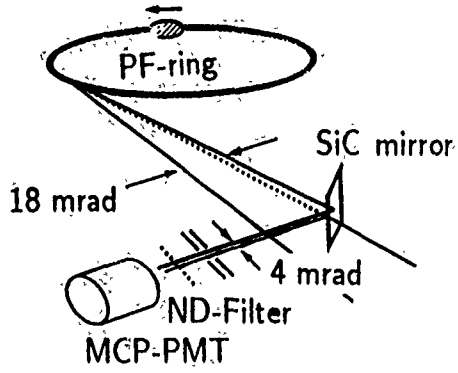


Figure 1: The photon counting system

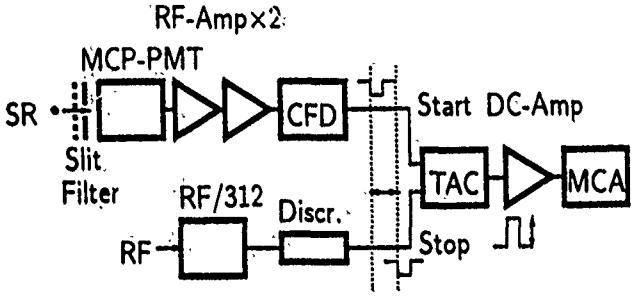


Figure 2: The block diagram of the electronics. MCP-PMT: Microchannel plate-type photomultiplier, CFD: Constant fraction discriminator, TAC: Time to amplitude converter, MCA: Mulitichannel analyzer, RF/312: Trigger signal synchronized to revolution frequency.

The block diagram of the electronics is shown in Fig. 2. Pulses from the PMT is amplified with a wideband amplifiers, the total gain and the bandwidth of which are 49 dB and $\sim$ 1 GHz respectively, and amplified signals are shaped with a constant fraction discriminator (CFD, Ortec 582). The RF from the acceleration system is divided by 312 that is the harmonic number of the PF ring in order to obtain the signal synchronized to the revolution of a bunch. A time to amplitude converter (TAC, Ortec 467) generates pulses the height of which is proportional to time interval between the shaped signal from the CFD and the synchronized signal. The outputs from the TAC are amplified by a DC-amplifier with a gain of $\sim$ 14 dB and the distribution of pulse heights are analyzed with a MCA (multichannel analyzer, EG&G 7800). The typical counting rate was about 20 kHz and the dead-time was about 30% at a beam current of 20 mA.

3 Results

Figure 3 shows an example of time-structure of the bunch in log scale at a circulating current of 10 mA. The abscissa shows the MCA channels correspond to time interval. In this figure, time flows from the right to the left, *i.e.*, the bunch on the left follows that on the right, and one channel corresponds to 5.05 ps. At least three bunches are clearly recognizable. The forth peak may be due to the internal reflection in the PMT. The ratio of positron number in the second bunch to that in the main bunch is about 1 %.

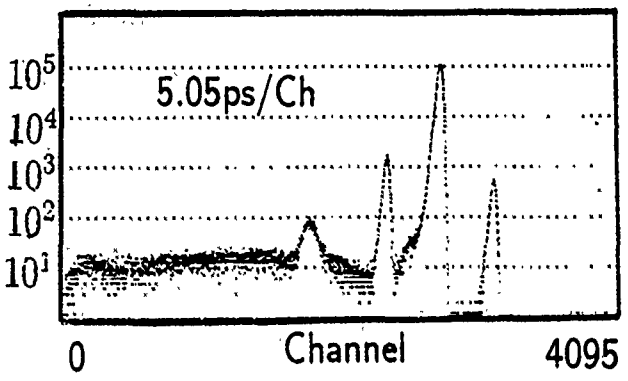


Figure 3: Time-structure of the bunch in log scale.

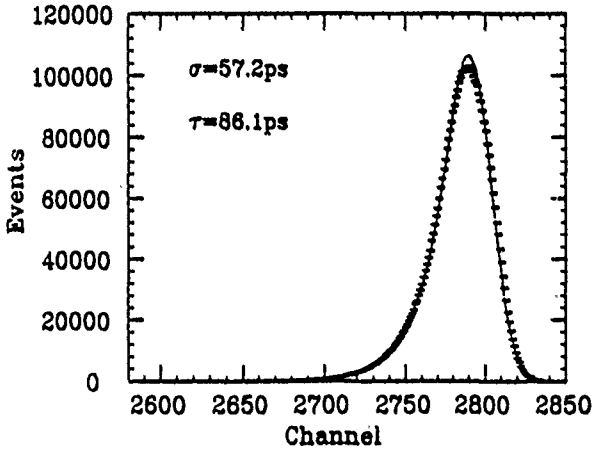


Figure 4: The shape of the main bunch in linear scale. The beam current was 10 mA.

Figure 4 shows the shape of the main bunch in linear scale at the beam current of 10 mA. The shape has an appreciable asymmetry. However, the current dependence of the asymmetry is not noticeable, as described in the next section. Therefore, the cause of the asymmetry seems not to be the wake field induced by the beam but to be the TTS in the PMT.

A preliminary result of the population versus time in the second bunch after injection is shown in Fig. 5. Though the systematic error due to analysis is uncertain, the increasing of population is clearly observed with this system. Detailed analysis is now under investigation.

4 Bunch Lengthening

We have tried to deconvolute the results by fitting them with the function

$$f(x) = \int_0^\infty \frac{a}{\tau\sqrt{2\pi}\sigma} \exp\left(-\frac{(x-h-\mu)^2}{2\sigma^2}\right) \exp\left(-\frac{h}{\tau}\right) dh$$

where the exponential and Gaussian functions show the TTS of the PMT and actual bunch shape respectively. The

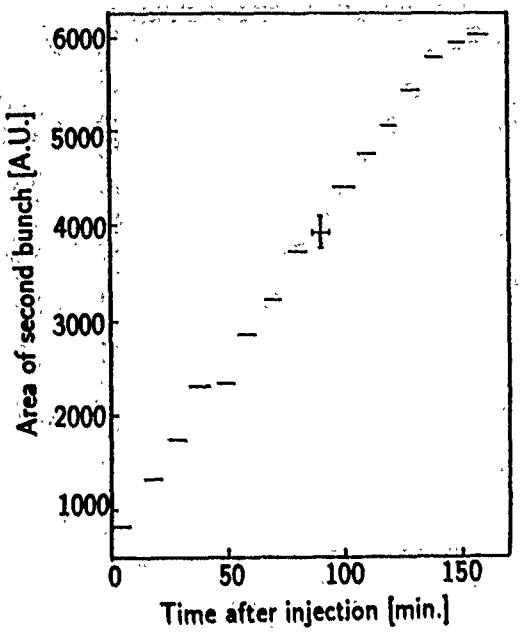


Figure 5: Increase in the population in the second bunch. The horizontal bars represent the time interval during each measurement.

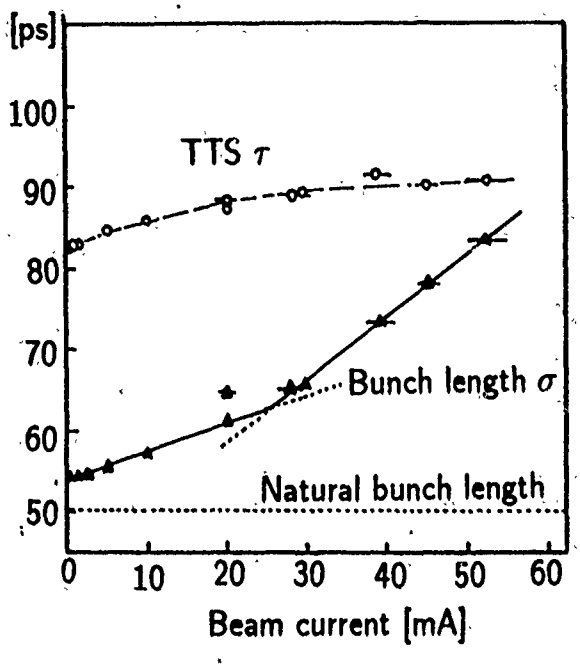


Figure 6: Current dependence of the bunch length σ (solid curve) and TTS τ (dashed curve). The natural bunch length is drawn in dotted line. The horizontal bars mean the current variation during each measurement.

code MINUIT was adopted assuming the statistical error of $\sqrt{N+1}$, where N is the event number. The fitted standard deviation (σ) and the "TTS" τ are plotted as a function of beam current in Fig. 6. The small change of τ shows this asymmetry does not come from the wake field. We have approximated the bunch lengthening data with two straight lines as shown in Fig. 6. The crossing point between two lines is near 25 mA and is consistent with other data independently obtained from a streak camera[3].

5 Summary

We have constructed a photon counting system at Beamline 21 in the KEK-PF. Though the background probably due to the multiple reflection in the photon beam pipe is not minimized enough, this system shows so large dynamic range as to measure the small change of the impurity quantitatively. With the method of deconvolution, the bunch lengthening is clearly obtained, which is consistent with the results from the streak camera.

We have a plan to use a focusing system to minimize the effect of the multiple reflection. The shape of TTS of the PMT will be measured by means of ultra-short-time laser.

The authors wish to express their sincere appreciation to Prof. H. Kobayakawa who kindly gave us an opportunity to make experiments in the PF ring. They wish to thank Prof. M. Kobayasi and the vacuum group of the PF-ring of their useful suggestions for the designing the vacuum system. They wish to thank Dr. N. Nakamura of his valuable information about the bunch lengthening data measured by the streak camera. They wish to acknowledge Dr. T. Mituhashi, Dr. S. Sakanaka and Dr. S. Kishimoto of their cooperation in the measurement of the single bunch impurity. They thank Dr. K. Haga and Mr. H. Nakamura of their help in the construction of the system. The mirror was provided by Mechatronics Products Development Department of Ishikawajima-Harima Heavy Industries Co., Ltd. The data analysis was mainly performed by using VAX computers of the Data Analysis Laboratory for High Energy Physics, Hiroshima University.

References

[1] T. Mituhashi: Pulsed synchrotron radiation in the single bunch operation and its application, Eds. Y. Hatano and K. Tanaka, KEK Proceedings (1991) to be published.

[2] T. Kasuga et. al. Jpn. J. Apl. Phys. 28 (1989) 541.

[3] N. Nakamura, S. Sakanaka, K. Haga, M. Izawa and T. Katsura: In this proceedings.

Conference Author Index

A

Abola, A. 1347
Acharya, S. 1308, 1365
Ackerman, G. D. 1955
Adams, F. P. 795, 3011
Adler, R. J. 3201
Adolphsen, C. E. 503, 905, 1499, 2064, 2949, 3207
Advani, R. 2104
Agababian, A. G. 1579
Aghamir, F. 2967
Ahrens, L. 52, 839
Ahrens, L. A. 1273
Aiello, G. R. 988
Aikens, B. 1455
Akai, K. 2405, 2408
Akemoto, M. 1008, 1031, 1034, 1037, 1040, 2014, 2061
Akimov, V. V. 1582
Akiyama, H. 2014
Aksel, B. 2200, 2209
Alessi, J. 839
Alessi, J. G. 896, 1913
Alexandrov, V. S. 195
Alferov, V. N. 1356
Allen, A. L. 3094
Allen, C. K. 1961
Allen, M. 819, 1308, 1365
Allen, S. L. 3085, 3103, 3106
Allison, L. 2958
Allison, P. 520, 2080, 2961
Allison, P. W. 3192
Allison, S. 1419
Almeida, B. 2325
Almeida, J. 979
Althoff, K. H. 1543
Alton, G. D. 1937, 2604
Amirmadhi, F. 1115
Anami, S. 1043
Ananian, S. H. 1287, 1446, 1579
Anderson, C. 2856
Anderson, D. 863
Anderson, D. R. 2757
Anderson, K. 1946
Anderson, M. 952, 1314
Anderson, M. D. 2526
Anderson, O. A. 1955
Anderson, R. 976
Ando, A. 875
Andreev, V. A. 2984, 3109
Andrews, W. D. 1115
Anerella, M. 2164, 2167
Angert, N. 2981, 3044
Ankenbrandt, C. 87, 90, 99, 434
Annala, G. 87, 1848
Antes, K. 1958, 2008
Anthouard, P. 3204
Antoine, C. 2393
Anton, F. 1341
Antropov, V. K. 195
Aoyagi, H. 2032
Aragona, A. 2970
Arai, F. 1118
Arai, S. 3035
Araki, A. 2709
Arbique, G. M. 842, 845
Archie, C. N. 1594
Arida, M. J. 2572
Arkhipov, O. V. 195
Arnold, N. D. 1496, 2526
Artiomov, A. S. 1573, 1576
Artru, X. 2101
Artusy, M. 3159
Arutunian, S. G. 198
Asami, A. 494, 497, 1043
Ash, W. W. 2152
Ashkenazi, I. 1290
Asseev, A. A. 189
Atkins, W. H. 1522
Auerbach, E. H. 1454
Aune, B. 2393
Autin, B. 1675
Averill, R. 926
Averill, R. J. 2348
Azuma, O. 2990

B

B., Phung Ngoc 2393
Baartman, R. 1606, 1731
Baba, T. 2032
Babaian, A. Z. 2146
Bacal, M. 2011
Badier, J. 147, 1213
Bagdasarian, G. B. 2146
Bagley, P. 467
Bahrdt, J. 266
Bailey, R. 848
Bailey, V. 3114, 3123
Bailey, V. L., Jr. 3120, 3195
Baiod, R. 2506
Baird, S. 769, 1151, 1476, 2688, 2748, 2865
Bajard, M. 2799
Baklakov, B. A. 3273
Baktash, C. 2604
Balandin, V. V. 2823
Balewski, K. 1791
Ball, M. 1770
Ball, M. S. 1210
Baltay, M. 769, 926, 976, 1243, 2328, 2688
Baltay, M. M. 2369
Band, H. 834, 2152
Bane, K. L. F. 506, 1800, 2064, 3207
Bangerter, R. O. 369
Barbagelata, L. 2760
Bardy, J. 3204
Baritchi, D. 2688
Baritchi, L. 2688
Barke, A. 1359
Barklow, T. 834, 2500
Barkov, L. M. 183
Barletta, W. 982, 2856, 2967, 2976
Barletta, W. A. 2289, 2307, 2310, 2751
Barnard, J. J. 260, 2592, 2595
Barnes, M. J. 699, 964, 967, 1531, 2883
Barnes, P. 664, 678, 786, 2411, 2414, 2420, 2423, 2426
Baron, E. 594
Barr, E. 207
Barry, A. 1443
Bartalucci, S. 2850
Barth, W. 3076
Bartlett, N. W. 2182
Barton, M. Q. 284
Bashmakov, Y. A. 1681, 1684
Bassetti, M. 2850
Batskich, G. I. 3067
Batskikh, G. I. 2601, 2823
Battistella, A. 2438
Baumann, S. 2880
Bavizhev, M. D. 177, 189
Bazarko, A. 834
Bazarko, A. O. 2152
Be, S. H. 2298
Beadle, E. 1264
Beadle, E. R. 1231, 1347, 1431, 1493
Becker, K. 1115
Beckert, K. 2880
Beetz, C. P. 1981
Begg, M. 2372
Bekefi, G. 751
Bekhtev, B. V. 2601
Belomestnykh, S. A. 183
Beloshitsky, P. F. 195
Belov, V. P. 2823
Benaroya, R. 29, 2275
Bender, S. C. 2754
Bengtsson, J. 1434
Benincasa, G. 1353
Bennett, G. W. 1231
Bennett, L. F. 3126
Bennett, M. J. 1401
Benson, E. 1028
Benvenuti, C. 1023
Ben-Zvi, I. 272, 550, 1323, 2444, 3038
Berg, J. S. 1654
Berger, G. 2610
Bergher, M. 1225
Berg-Sørensen, K. 1764
Bernard, P. 1023
Bernstein, D. 5
Bertuccio, T. 952
Berz, M. 354, 884, 3020
Bessler, U. 3044
Betz, D. 619
Betzold, H. 598
Bhandari, R. 572, 2993
Bhandari, R. K. 351
Bharadwaj, V. 1255, 1258, 1458
Bharadwaj, V. K. 1830
Bhat, C. M. 831, 1773, 1946
Bhatia, T. 572
Bhatia, T. S. 1884

Biagini, M. E. 2850
Bickley, M. H. 309
Bieth, C. 2802
Bijleveld, J. 1148, 2366
Billan, J. 2122
Billen, J. H. 1884
Billing, M. 467
Billing, M. G. 2923
Billing, R. 1371
Billquist, P. J. 2987
Birx, D. L. 754
Biryukov, V. M. 177
Biscardi, R. 804, 1107, 1326, 1794, 2542, 2790
Biscari, C. 2850
Bishop, D. 964, 1531
Bisoffi, G. 1934, 2438
Bisognano, J. J. 1054, 2073, 2745
Bittner, J. 1107, 2542
Bittner, J. W. 1270
Bizek, H. 210, 2778
Black, E. L. 2375
Blas, F. 1398
Bleadon, M. E. 2134, 2477
Bleser, E. 45, 839
Blind, B. 899
Blinov, V. E. 2342
Bloess, D. 1023
Blondel, A. 147, 1213
Bloom, E. 982
Blue, R. 1163
Blumberg, L. N. 1107, 2661, 2664
Blumberg, R. 2248
Bobbs, B. 2733, 2742
Bobyleva, L. V. 195
Boer Rookhuizen, H. 2366
Boers, J. E. 275, 278
Bogacz, A. 1660, 1749
Bogacz, S. A. 1657, 1815, 1848
Bogaty, J. M. 2987
Bogdanovich, B. Y. 1048
Bogert, D. 860
Boggasch, E. 2631
Bohl, T. 848
Bohn, C. L. 1809, 1812, 2441
Boicourt, G. P. 3017
Boiko, V. A. 2601
Bollinger, L. M. 2987
Bolme, G. O. 3017
Bomko, V. A. 2984
Bong, E. 1201
Bongardt, K. 1767
Boni, R. 961, 2850, 2970, 2973
Bonin, B. 2393
Bonneau, P. 2125
Borchardt, I. 857
Bordry, F. 848
Bork, R. 1443
Borland, M. 769, 976, 1151, 1243, 2688
Bosch, R. A. 1827
Boscolo, I. 2575
Bosland, P. 2393
Bosser, J. 2509, 2832
Bossert, R. 2173, 2176, 2179, 2215
Bossert, R. C. 2182, 2185
Bossi, M. 988
Bothe, W. 932
Botlo-Pilat, F. 3041
Bouchet, B. 1186
Boulais, K. A. 479
Bourat, C. 3180
Bourianoff, G. 204, 348, 363, 383, 1302
Boussard, D. 2447
Bovet, C. 1160, 1186, 1213
Bowden, G. 996
Bowen, B. 3114
Bowling, B. 446, 1443
Boyce, J. R. 3264
Boyce, R. 973, 2328, 2688
Boyd, J. 646
Boyd, J. K. 437
Bozoki, E. 272, 1107, 2313, 2703
Bracco, R. 2712
Bragin, S. 1014
Brand, H. 3079
Brand, H. R. 3082, 3094
Brandt, J. S. 2182
Brau, C. A. 1115
Brauer, D. 857
Braun, H. 141, 1845, 2098, 2964
Brefeld, W. 2793
Brennan, J. M. 839
Brennan, S. 926, 1151, 1383, 1476
Bres, M. 772
Bricault, P. 2802
Bridges, J. 1525, 1624
Bridges, J. F. 690, 693
Bridgman, C. 1522, 2459
Briegel, C. 2520
Briggs, D. 1404, 1407
Brinker, S. 1154
Brittner, P. 1425
Brodowski, J. 1428
Brodzik, D. 1952
Brook, V. L. 1356
Broome, W. 1326, 1794
Brossard, S. 1359
Browman, A. A. 893
Brown, B. C. 2128, 2134, 2230, 2233, 2477
Brown, I. G. 1943
Brown, J. 2733
Brown, K. 834, 2058, 2067
Brown, K. A. 825
Brown, M. J. 1464
Brown, R. 1922
Brück, H. 2149
Bruhwiler, D. L. 1648
Bubp, D. 766
Buchanan, E. 1758
Buchmann, L. 1925, 2607
Buda, S. 1326
Budlong, J. 1389, 1758
Budnick, J. 923
Buhler, S. 2393
Buller, T. 3029
Bulos, F. 982, 996, 2058, 3213, 3216
Bunch, P. 2322
Bundy, R. 2381
Bunicci, J. 999, 1216
Burchat, P. 628
Burke, D. 834, 2055, 2058, 2067, 3213, 3216
Burkhardt, H. 848
Burns, A. 1186
Burns, M. 2110, 2958, 2961
Burns, M. J. 520
Burtin, G. 1160
Burton, R. J. 3011
Butler, H. S. 281
Bylinsky, Y. V. 3062, 3067
Byrd, J. M. 1080, 1842

C

Cady, R. L. 670
Cahill, K. 2523
Cai, Y. 2218
Calame, J. 658
Calderon, M. 2310
Callahan, D. A. 263
Callin, R. S. 713, 798
Calvert, J. 742, 745
Calvo, O. 946, 1467
Camas, J. 1186
Cameron, P. 681, 739
Cameron, P. R. 1216, 1273
Campbell, B. M. 1020
Campisi, I. E. 2381
Cao, X. 2435
Capista, D. 1505
Caplan, M. 763, 766
Caporaso, G. 3079
Caporaso, G. J. 520, 3100
Cappi, R. 171
Carboni, V. 3114
Carey, D. C. 1618
Carlson, R. 2107
Carlson, R. L. 245, 3192
Carlsten, B. E. 649, 2754
Carnegie, D. W. 1091
Carrieri, J. 2739
Carroll, D. 1981
Carson, J. 2173, 2176, 2185
Carson, J. A. 2182, 2227, 2233, 2236
Carter, A. 1546
Carter, H. K. 2604
Carugno, G. 1934
Cary, J. R. 1648
Caryotakis, G. 798, 2928
Cassel, R. 996, 2331, 2334, 2955, 3138, 3147, 3156
Cassel, R. L. 3153, 3162, 3165, 3168
Castellano, M. 2970, 2973
Castillo, S. 1416, 1419
Castillo, V. 1264, 1267
Castro-Garcia, P. 1213
Catani, L. 1448, 2970
Caussyn, D. D. 1770
Cavallari, G. 1023
Cavallo, N. 2970
Cavedon, J. M. 2393
Cavenago, M. 1934, 2438
Celata, C. M. 1401
Centore, A. L., II 2757
Cerino, J. 973, 1028, 1243, 2328, 2369, 2688
Cervellera, F. 1934
Cevenini, F. 2970

Cha, B.-C. K. 1314, 2526
Chabert, A. 2802
Chae, Y.-c. 1603
Chambers, F. 3079, 3082
Chambers, F. W. 3085, 3094, 3097, 3103, 3106
Champion, M. 2996
Champion, M. S. 1511
Chan, C. F. 1955
Chanel, M. 2509, 2832
Chang, C. 572
Chang, C. R. 2993
Chang, H. P. 2667
Chang, S. S. 1368
Chao, A. W. 336, 345, 360
Chao, Y. 628, 1806
Chao, Y.-C. 2152, 3246
Chargin, A. 2856
Chavis, C. 769, 2688
Chehab, R. 2101
Chel, S. 2393
Chellis, K. 2110
Chen, C. 754, 786, 2423
Chen, C.-e. 2396, 2616
Chen, P. 222, 619, 1207, 1916, 1993, 3225, 3246, 3252, 3255
Chen, S. C. 751, 2026
Chen, T. 1642
Chen, Y.-J. 3094, 3100, 3106
Cheng, Y. 1704
Chermenin, S. 857
Chernin, D. P. 312, 613
Chesnokov, Y. A. 192
Chianelli, C. 2393
Chiaveri, E. 1023
Chida, K. 875
Chidley, B. G. 845, 3047
Chin, J. 2721
Chin, Y. H. 213
Ching, H. 1827
Cho, M. 575
Cho, Y. 1624
Choi, J. 2673
Choi, J. J. 1827
Choi, M. 29, 2301
Choi, M. S. 591
Chojnacki, E. 555, 2557, 3219
Chou, P. J. 1743, 1749
Chou, T. S. 2286, 2316
Chou, W. 126, 1710
Christensen, K. E. 2263, 2453
Christiansen, J. 2631
Chu, T. S. 772
Chugg, B. 3114
Chung, Y. 1121, 1299, 1525, 2545
Chupp, W. 1975
Church, M. 108
Chursin, A. G. 2823
Ciapala, E. 1490
Ciardullo, D. J. 1344, 1347, 1431
Ciarlette, D. 1624
Ciocci, F. 2760
Clark, D. J. 2796
Claus, J. 1422
Clausen, M. 2319
Clayton, C. E. 564, 2560
Clegg, T. B. 2083
Clendenin, J. E. 500, 2098, 2284
CLIC Study Group 2052
Clibald, J. R. 2622
Clifft, B. E. 2987
Cline, D. 619, 2856, 2967
Cline, D. B. 2751
Coacolo, M. 233, 236
Coffield, F. 3079, 3082
Coffield, F. E. 3094
Cohen, S. 929
Colchester, R. J. 1160
Cole, A. G. 520, 3100
Cole, B. 204, 348, 363
Colestock, P. 1749
Colestock, P. L. 1740, 1743, 1830
Collier, P. 848, 1490
Collins, J. 1770, 1922
Colombant, D. G. 637, 1609
Colton, E. 1896
Colvin, J. 2221
Connolly, R. C. 1237
Cook, D. L. 537
Cook, J. M. 693, 2182
Cooper, W. S. 1955
Coosemans, W. 2070
Corbett, J. 1305
Corbett, W. J. 905, 1797, 2868
Corcoran, P. 3114
Cork, C. 2739
Corker, V. 1443
Cornacchia, M. 1797, 2853, 2856
Cornelis, K. 153, 848
Corredoura, P. 1404, 1806
Cottingham, G. 2164
Cottingham, J. 2167, 2239
Cottingham, J. G. 42
Coulter, K. 2173, 2179
Coulter, K. J. 2191
Coupal, D. 834
Courant, E. D. 2506, 2829
Cowles, D. N. 1401
Craddock, M. K. 57
Craig, G. D. 3088
Crandall, K. R. 401, 2583
Crawford, C. 970
Crawford, K. 2381
Crenna, F. 2760
Crisp, J. 3189
Crist, C. E. 3129
Crook, K. 1028
Crosbie, E. 210, 902, 1624, 1692, 2778
Crozon, M. 147, 1213
Cucchetti, A. 251, 1884
Culver, J. 2008
Culwick, B. B. 1481
Cummings, U. 2278
Curry, R. 3123
Curtoni, A. 2393
Cutler R. 572

D

Dabrowski, J. 2790
Daems, G. 1353
Dahl, L. 2981
Dahlbacka, G. 2976
Daibo, H. 2298
Dainelli, A. 2820
Dalbacka, G. 2856
Dale, D. 1922
D'Alsace, R. 804, 1794
Daly, R. T. 1496, 2526
Damm, R. 52
Danilov, V. D. 2613
Danilov, V. V. 183, 186, 526
Danly, B. 2026
Danly, B. G. 754, 772
Danzglock, R. 1425
Daras, T. 2610
Darrow, C. B. 564
Datte, P. 736, 1958
D'Auria, G. 710, 1978
D'Auria, J. 2607
Davies, W. G. 303
Davis, J. 2967
Davis, J. G. 2751
Davis, T. J. 728
Dawson, J. M. 564
Dawson, R. 65
De Vries, J. 1213
DeFord, J. F. 3088
DeStaebler, H. 834
Deadrick, F. J. 3085, 3094, 3097, 3106
Debiak, T. 2023
Decker, C. B. 564
Decker, F.-J. 905, 1192, 1734, 2002, 2064, 2143, 2949, 3210
Decker, G. 1525, 2545, 2790
Degèle, D. 857
Dehen, J. 3053
Dehning, B. 147, 1213
Deitinghoff, H. 2981, 3041, 3044, 3053
de Jong, M. S. 795
de Lamare, J. 3138
Delayen, J. R. 1809, 1812, 2441
Delchamps, S. 2173, 2179, 2191
Delchamps, S. W. 2185
Dell, G. F. 288, 1627
Demmel, E. 757
Demos, P. T. 601, 716, 1791
Demroff, H. P. 725
Denney, P. M. 2946
Derbenev, Y. S. 1761, 2506
Derenchuk, V. 1770, 1922
de Rijk, G. 848
Derost, J. C. 1534
de Saint Simon, M. 3041
Desavouret, E. 2477
Desforges, B. 848
Desmond, E. 1107, 1374
Desmons, M. 2393
Despe, O. D. 1461
Destler, W. W. 2578
Detlefs, W. F. 1600
Devred, A. 2480
deVries, G. J. 1955
Devynck, P. 2011
Diamond, V. T. 979
Didenko, A. N. 1860, 2775, 3111
Dikansky, N. S. 183, 523
DiMarco, J. 2215, 2480
Di Massa, G. 789
Dinev, D. 1767
Ding, B. N. 1972, 2999
Di Pirro, G. 1448, 2970
DiVergilio, W. F. 1919

Diviacco, B. 2712
Dobeck, N. 935
Dobrott, D. 1305
Dodd, J. 2967
Dodd, J. W. 2751
Doering, D. 1981
Dohan, D. A. 1350
Dolique, J.-M. 233, 236
Doll, H.-D. 1311
Donald, M. H. R. 2841, 2868
Donaldson, A. 996, 2331, 2955, 3156, 3159
Donaldson, A. R. 3165, 3168
Donasch, I. J. 1311
Dortwegt, R. 2275
Dortwegt, R. J. 29
D'Ottavio, T. 896
Douglas, D. R. 309, 443, 446, 449
Douglas, S. R. 303
Dowell, D. H. 1204
Dowling, D. T. 2604
Drachenfels, W. v. 1543
Dragt, A. J. 1621, 1630
Drozhdin, A. I. 177
Drury, M. 2381
DuPlantis, D. 1770, 1922
Dubinsky, G. A. 2823
Dubrovin, A. N. 2835
Ducar, R. J. 1552
Dunaitsev, A. F. 1356
Dutt, S. K. 360
Dutto, G. 65
Duval, M. 2802
Dwersteg, B. 2429
Dwinell, R. 742
Dyling, O. H. 1026
Dylla, H. F. 2745
Dyson, A. 2560
Dzenus, M. 2390
Dziba, A. R. 177

E

Earley, L. 2958
Early, J. W. 2754
Early, R. A. 1964
Earsom, D. L. 129
East, G. 1770
Ecklund, S. D. 500, 2005, 2098
Edighoffer, J. 3117
Edighoffer, J. A. 3120
Egawa, K. 2257, 2462
Eickhoff, H. 2880
Eidelman, Y. 269
Einfeld, D. 887, 2372
Elian, V. V. 2601
Elias, L. R. 2575, 2757
Elleaume, P. 1083
Elliott, S. M. 725
Ellison, J. A. 216
Ellison, T. 1770, 1922
Ellison, T. J. P. 1210, 1612, 2506
Emery, L. 769, 976, 1243, 1413, 1525, 1633, 1713, 2688
Emig, H. 1943
Emma, P. 905, 1284, 1549, 2064, 2500
Emma, P. J. 503
Emura, K. 2655
Enchevich, I. B. 699, 2943
Enderlein, G. 2429, 2432
Endo, K. 2257, 2462
Enegren, T. A. 2943
Eng, W. 681, 739
Enge, H. A. 1695
Engeman, G. A. 1910
Eppley, K. 719
Eppley, K. R. 1964
Erdman, K. L. 65
Erickson, R. 2152
Ermakov, V. B. 1582
Esarey, E. 2563
Escherich, K. 857
Esin, S. K. 2823, 2984, 3067, 3109
Ewald, K. 2185
Eyharts, P. 3204
Eyl, P. 3204
Eylon, S. 1975, 3070, 3073

F

Fabbricatore, P. 2399, 2973
Fabris, A. 710
Faehl, R. 649
Fagot, J. 2393
Faillon, G. 772
Faini, S. 2970
Faltens, A. 616, 1952, 3070
Fant, K. S. 798
Farias, R. H. A. 2787
Farkas, Z. D. 652
Farkhondeh, M. 634, 990, 2125, 2348
Fathizadeh, M. 917
Fauchet, A. M. 1099, 2542
Faught, E. 1308, 1365
Faugier, A. 848
Fawley, W. 3070
Fawley, W. M. 3020
Fazio, M. V. 649
Featherby, M. 2272
Fedotov, A. P. 3067
Fedotov, Y. S. 177, 189
Feinberg, B. 1401
Feinstein, J. 719
Feldman, D. W. 2754
Feldman, R. B. 2754
Fellenz, B. 1743
Fenker, H. 890, 1281
Ferede, H. 348
Ferioli, G. 1186
Fermé, J. 2802
Fernandes, P. 366, 3026
Fernow, R. C. 2572
Ferrario, M. 2970, 2973
Ferrell, J. H. 661
Ferri, G. P. 1213
Ferry, R. 29
Ferry, R. J. 2304
Feschenko, A. V. 3062, 3067
Fessenden, T. J. 586, 3073
Fiander, D. 996
Fickett, R. A. 705
Fiebig, H. J. 857
Fieguth, T. H. 503
Figley, C. 869
Figley, C. B. 964
Filippov, A. N. 183, 186
Fink, C. L. 547
Finley, D. 81, 87, 90
Fiorito, R. B. 1204
Firjahn-Andersch, A. 3041
Fischer, C. 1186, 3231, 3234
Fischer, G. 2949
Fischer, H. 3156
Fisher, A. S. 976, 2748
Fitch, J. 1028
Fitzgerald, D. 228, 1893, 1896
Fitzgerald, J. 1252
Flannigan, J. 1528, 2790
Flanz, J. 1467
Flanz, J. B. 601, 716, 1791, 2125
Flynn, T. 21
Fockler, J. 3114
Foley, M. 1743
Fong, K. 810
Forest, E. 336, 1434, 1651
Forgas, R. 923
Fortgang, C. M. 3017
Fortuna, G. 1934
Fortunato, D. 2191
Fouaidy, M. 2393
Fowkes, W. R. 713, 798
Fowler, W. B. 854
Fox, J. D. 1404, 1407
Frammery, B. 1353
Franczak, B. 2880
Frank, K. 2631
Franzke, B. 2880
Fraser, J. S. 2607
Freeman, W. C. 3141
Frey, W. W. 999
Frias, R. 1401
Friedman, A. 263, 272, 2766
Friedrich, J. 2981, 3044, 3053
Friedrichs, C. 675
Friedrichs, C. C. 643, 1020
Friedrichs, P. 1410
Friesel, D. 1770, 1922
Fripp, M. 2073
Frost, C. A. 3059, 3129
Fugitt, J. 1470
Fujimura, S. 2694
Fujino, D. 834
Fujino, T. 2402
Fujita, Y. 2682
Fukuma, H. 2257
Fulton, H. 2185
Funk, L. 572
Funk, W. 62, 2993
Furman, M. A. 300, 386, 422
Furuya, T. 2032, 2405, 2408

G

Gabella, W. E. 1591
Gabusi, J. 2266
Gai, W. 555, 1984, 2554, 2557, 3219
Gaillard, M. J. 3053
Galayda, J. 1099, 1374, 2116
Galiana, R. 1198
Gall, D. 2149

Gallardo, J. 2724
Gallardo, J. C. 2748
Gallo, A. 2850, 2970, 2973
Galluccio, F. 1669, 1672
Galyaev, N. A. 192
Gammel, G. 2023
Ganetis, G. 2164, 2167, 2239
Gao, J. 2020
Garavaglia, T. 231
Garber, M. 2164, 2167, 2239
Garcia, R. 1171, 2529
Gardner, C. 1473
Garkusha, O. V. 1570
Garnett, R. 572
Garnett, R. W. 330
Garoby, R. 171, 1398
Garoutte, R. 1028
Garren, A. 62, 2844
Garren, A. A. 2829, 2841, 2868
Garrett, J. D. 2604
Garvey, J. D. 2477
Garvey, T. 1975, 3070, 3073
Garwin, E. L. 2029, 2284
Gass, V. G. 2613
Gass, V. P. 1949
Gastebois, J. 2393
Geisik, C. 2080
Gelfand, N. 87, 105, 114
Gelfand, N. M. 81, 102
Geller, J. 2266
Gemme, G. 2399
Genin, R. D. 769
Genre, R. 3053
Gentzlinger, R. C. 2263, 2456
Gerasimov, A. 1678
Gerig, R. 123
Gerlack, R. 678
Gero, E. 1207
Gevorkov, A. K. 1573
Ghosh, A. 2164, 2167, 2239
Gilgenbach, R. M. 1827
Gilpatrick, J. D. 1136, 1139, 3017
Gioumousis, A. 1404
Girault, P. 3005, 3180
Gjaja, I. 452
Gjaja, I. M. 1621
Glaser, M. 1213
Glaskov, A. A. 2613
Glass, H. D. 2134, 2477
Glatz, J. 2981
Glazov, A. A. 1017
Glosson, R. 2134
Gluckstern, R. L. 452, 1597, 1600
Glukhikh, V. A. 2823
Gluskin, E. 1169
Götz, T. 1383
Godechot, X. 1943
Goderre, G. 81, 87, 90, 1296
Goderre, G. P. 1848
Godin, A. 2393
Godlove, T. F. 2589
Godot, J.-C. 2964
Goeppner, G. A. 29
Goetz, T. 1543
Golceff, P. 976, 2278, 2688
Goldhar, J. 239
Goldman, M. 739
Goldman, M. A. 681
Goldman, T. 2569
Goloborodko, S. G. 1356
Golubeva, N. I. 1899, 2823
Gomei, Y. 828
Gomulka, S. 2137
Gonczy, J. D. 29, 2301, 2304
Gonichon, J. 1978
Gonzalez, R. 1252
Goodman, D. L. 754
Goodwin, J. E. 294, 2506
Goodwin, R. W. 1484
Goodzeit, C. 2164, 2167
Gorelov, D. V. 2984
Goren, Y. 813
Gormley, M. 2360
Gough, D. 2955, 3156
Gough, D. E. 3168
Gougnaud, F. 2393
Gourber, J. P. 2122
Gourcy, G. 2393
Gourlay, S. 2173, 2179
Gourlay, S. A. 2227, 2233, 2236
Gournay, J. F. 2393
Grabe, H. 857
Graber, J. 2411, 2417
Granatstein, V. L. 658, 731
Grattarola, M. 2760
Gray, E. R. 1046
Gray, R. 2152
Green, M. A. 1088, 2158
Green, M. I. 2161
Greene, A. 2164, 2167, 2239
Greenwald, S. 464, 1857
Greenwald, Z. 464, 1246, 1857
Grieggs, R. J. 2459
Grieser, M. 2817
Griffin, J. 1740
Griffin, J. E. 2826
Griffith, L. V. 3094
Grishanov, B. I. 183
Gromme, A. 5
Gromme, T. 1419, 3222
Gross, G. 2331, 2334, 2955
Grote, D. P. 263
Grote, H. 324
Groves, T. 1180
Grunberg, C. 594
Grundey, T. 2450
Grunhagel, C. 1213
Gürtler, P. 2793
Gualco, G. 2760
Gualco, G. C. 2399
Gudewicz, P. 1142
Guemas, F. 2393
Guharay, S. K. 1961
Guiducci, S. 2850
Guignard, G. 3231, 3234
Gundersen, M. 619
Gundersen, M. A. 591, 1990
Gunderson, G. R. 2526
Guo, Z. 1669, 1672, 2616
Gupta, R. 2164, 2167
Gupta, R. C. 42, 2239, 2242, 2245
Gurevitch, M. 2509
Gusarov, V. N. 1860
Guy, F. W. 578, 1884, 3032, 3056
Gyles, W. 65

H

Haber, I. 263
Haberman, I. 1386
Habiger, K. W. 2622
Habs, D. 2817
Hacker, H.-U. 1425
Hacker, U. 1362
Haddock, C. 2197, 2206, 2215
Hadinger, G. 3053
Haebel, E. 1023
Haenni, D. 1308
Haga, K. 440
Hagel, J. 488
Hahn, A. A. 1174, 1177, 1180
Hahn, H. 1627, 1707, 2239, 2242, 2245
Hahn, K. 3020, 3070, 3073
Hahn, R. v. 2817
Haimson, J. 646, 3183
Hairapetian, G. 2751, 2967
Halama, H. 1107, 2313, 2316
Halbach, K. 1797, 2718, 2721, 2856
Halbleib, J. A. 3135
Halemeyer, M. 2149
Hall, B. 1419
Halliwell, J. 943
Halvarsson, B. 1160
Hamilton, B. 1770
Hamilton, B. J. 1210
Hamm, M. E. 1377
Hamm, R. W. 1910, 2583
Han, H. S. 2345
Hanasaka, T. 2298
Hancock, S. 171, 174
Hand, L. 21
Hanft, R. 2227, 2230, 2233, 2480
Hanft, R. W. 2134
Hangst, J. 2360
Hangst, J. S. 1764
Hanna, B. 970
Hanna, S. M. 774
Hansen, T. A. 702
Hanus, X. 1534, 2393
Hara, M. 667, 2646
Harami, T. 707
Hardek, T. 1893, 1896
Hardek, T. W. 866, 872, 3150
Harding, D. J. 2134, 2477
Harfoush, F. 1249, 1660, 1743, 1749
Harfoush, F. A. 321, 2477, 2512
Harkay, K. 1743
Harkay, K. C. 1830
Harms, E. 1758
Harris, C. 926
Harris, K. 3159
Harris, S. 2328
Harrison, M. 96
Hartemann, F. 772
Hartill, D. L. 1246
Hartline, R. 1970, 2976
Hartman, S. 2967
Hartman, S. C. 2751
Hartung, W. 786, 2426
Harvey, A. 2331, 2955
Harwood, L. H. 446

Hassenzahl, W. V. 2721, 2736, 2739
Hatton, V. 848, 2952
Hattori, T. 875
Hauck, C. A. 1919
Hayano, H. 1008, 2061
Haydon, J. 2688
Hayes, T. 1320
Haynes, D. L. 2604
Hearty, C. 834
Heese, R. 993, 1107, 2248, 2652, 2658
Heifets, S. 458
Heine, E. 684
Heisterhagen, R. 1154
Helm, R. 219, 2058, 3213, 3216
Helm, R. H. 500, 2098
Hémery, J.-Y. 1564, 3041
Hendricks, B. 81, 87, 1293, 1296
Hendrickson, L. 1201, 1317, 1419, 1451
Henestroza, E. 1975, 3070, 3073
Henke, H. 380
Henn, K. 1362
Henrichsen, K. N. 2122
Henriot, C. 2393
Herb, S. 1222, 1276
Herr, W. 153, 1068
Herrera, J. 2164, 2167, 2239
Herrmannsfeldt, W. B. 1964
Herrup, D. 81, 1848
Herrup, D. A. 87
Hertzbach, S. 834
Hertzbach, S. S. 2152
Herzog, H. 2319
Hettel, R. 769, 926, 976, 1028, 1151, 1243, 1478, 2328, 2369, 2688
Hewett, D. W. 369, 1952, 2581, 2589
Heydari, H. 1687, 1940
Heymans, P. 1353
Hicks, J. 1922
Higo, T. 506, 1011
Hiller, M. 786, 2426
Hilleret, N. 1023
Himel, T. 1416, 1419, 1451
Himel, T. M. 1499
Hinderer, G. 2254
Hinkson, J. 1234
Hirabayashi, H. 2402
Hiramatsu, S. 165, 2625
Hirano, Y. 2298
Hirata, K. 482, 2847
Ho, C. 555
Ho, C.-H. 2554
Hodges, T. 2272
Hodgeson, J. 819
Hodgson, J. 2949
Hodgson, J. A. 1996
Hoffmann, C. R. 2337
Hofmann, I. 2492
Hogan, B. 658
Holmberg, S. P. 634, 2125
Holmes, S. D. 2477, 2896
Holz, J. 857
Honma, H. 1043
Hopkins, D. 1335
Hori, T. 2877
Horinaka, H. 2032
Horlitz, G. 2319
Horton, M. 926, 1028, 2328, 2688
Hoshi, Y. 2990
Hosseini, W. 1404, 1407
Hostetler, T. 973, 2688
Houck, T. 646, 766
Howard, D. 742, 745
Howell, J. 29, 2295, 2360
Howell, J. W. 690, 2301
Hower, N. 2278
Howry, S. 1305
Hoyer, E. 2721, 2736, 2739
Hoyt, E. W. 2284
Hoyt, M. W. 2284
Hseuh, H. C. 2266, 2292
Hsieh, H. 1107, 2119, 2248, 2316
Hsu, I. 905, 1464, 1734, 2064, 3210
Hsu, I. C. 1499
Hsu, K. T. 1157
Hsu, T.-Y. 1990
Hsue, C. S. 1704, 2667, 2670, 2697
Hsueh, S. Y. 81, 108
Hübner, K. 141, Ismann, P. 3023
Huang, Y. 374, 407, 509, 2017, 2020, 2649
Hubert, D. 857
Hughes, T. P. 245
Hui, M. 745
Hulbert, J. A. 2805
Humbert, J. C. 2477
Humphries, D. 2721
Humphries, S., Jr. 6
Hurd, J. W. 893, 2137
Hurh, P. 1177, 2360
Husmann, D. 1543
Huson, F. R. 736, 1958, 2008, 2221, 2649, 3050
Hutcheon, R. M. 795
Hutchinson, D. 2955
Hutchinson, D. P. 3168
Hutson, R. 228, 955, 1893
Hutton, A. 84

I

Ignatyev, A. P. 1048
Ikeda, M. 2402
Ikegami, K. 2694
Ikezawa, M. 1118
Iliev, A. I. 1899, 1904, 1907, 2823
Il'in, A. A. 2613
Ilinsky, N. 1014, 1722
Iljinov, A. S. 2984
Imanishi, A. 3035
In, S. R. 2298
Ingrassia, P. F. 1026
Inoue, K. 667
Ipe, N. 1028
Irwin, J. 219, 342, 1588, 2058, 3213, 3216
Isagawa, S. 757
Iselin, F. C. 327
Ishi, K. 1118
Issinsky, I. B. 2886
Itagaki, H. 2694
Itoga, K. 2032
Ivanchenkov, S. N. 2751
Ivanov, I. N. 1582
Ivanov, J. D. 2984
Ivanov, P. M. 183, 186, 523, 526
Ivanov, Y. D. 2823, 3067
Ivanov, Y. S. 2823
Ivers, J. D. 561, 2104
Iversen, K. 2390
Iwamoto, M. 2694
Iwata, H. 2990
Izawa, M. 440

J

Jablonka, J. 2393
Jablonka, M. 1534
Jablonski, E. 681
Jach, C. 816, 926, 2688
Jachim, S. P. 672, 1329
Jackson, A. 2637
Jackson, G. 1174, 1180, 1249, 1389, 1740, 1743, 1746, 1749, 1752, 1755, 1758, 2532
Jackson, R. 1359
Jacky, J. 1359
Jacobs, K. 716
Jacobs, K. D. 601, 1791
Jacobsen, R. 834, 2067
Jaeschke, E. 2817
Jaffery, T. 2215
Jaffery, T. S. 2173, 2179, 2191, 2227
Jagger, J. M. 2375, 2477
Jahnel, L. 2787
Jain, A. 2444, 3038
Jain, K. K. 1972
Jakobson, M. J. 893
Jan, G. J. 1157, 1380
Jaros, J. 834
Jayakumar, J. 2197
Jayakumar, R. 2206, 2215
Jayamanna, K. 1925
Jejcic, A. 2101
Jenkins, D. J. 702
Jenkins, T. 2310
Jenner, D. 1922
Jensen, C. 1740
Jensen, E. 3240
Jessen, P. S. 1764
Jiang, D. 2616
Jiang, H. B. 2757
Jiawen, X. 1878
Jin, S. 3264
Jöstlein, H. 2281
Jobe, R. K. 1464, 3210
Joh, K. 884
Johnson, C. D. 254
Johnson, D. E. 81, 87, 114, 120, 360, 1296, 2191
Johnson, G. 2688
Johnson, K. F. 578, 1136, 1171, 1183, 2529, 3017
Johnson, R. 1975
Johnson, R. G. 1540
Johnson, R. M. 1952
Johnson, R. P. 81, 87, 90, 93, 114, 1293, 1296

Johnson, S. 1505
Johnson, T. 1174
Johnson, W. J. D. 2754
Johnstone, C. 860
Joho, W. 141
Joly, J. M. 2393
Jones, B. 1770
Jones, C. M. 2604
Jones, F. W. 357
Jones, K. W. 893
Jong, R. A. 3103
Jordan, K. 2381
Joshel, R. 81, 87, 1293, 1296
Joshi, C. 564, 619, 2560, 2967
Joshi, C. J. 2751
Jostlein, H. 631, 2295
Joubert, A. 594, 2802
Joyce, G. 239, 242, 2563
Judin, L. I. 1166, 1279
Juillard, M. 2393
Jules, E. 1225
Jung, R. 1160, 1186, 1213
Junger, J. 2254
Junquera, T. 2393
Juras, R. C. 2604
Jurgens, T. G. 321, 2512, 2996

K

Kabe, A. 2257
Kahn, S. 2164, 2167, 2239
Kahn, S. A. 42, 2170, 2242, 2245
Kako, E. 2405, 2408
Kalbfleisch, C. 1308
Kalet, I. 1359
Kallas, N. 2197
Kalsi, S. 2119, 2248, 2652, 2658
Kaltchev, D. I. 195
Kamitsubo, H. 2646
Kamiya, Y. 2032, 2682, 2709
Kanazawa, K. 506
Kanazawa, M. 875
Kaneko, N. 2990
Kang, Y. G. 911
Kapchinskij, I. M. 3109
Karady, G. G. 949, 3132
Karantzoulis, E. 1782
Karpov, N. I. 1279
Karpov, V. A. 1681
Kasha, D. 681, 739
Kashinskij, D. A. 3109
Kasuga, T. 1338
Katayama, T. 76
Kato, R. 1118
Kato, T. 2032
Kats, J. M. 306
Katsouleas, T. 564, 619, 2967
Katsura, T. 440, 1338, 2682
Kauffmann, S. K. 339
Kauppila, T. 2107
Kauppila, T. J. 3192
Kawai, M. 828
Kawamoto, T. 1555
Kawashima, Y. 667
Kawazu, S. 707
Kazacha, V. I. 195
Kazakov, P. N. 1356
Kazarian, A. A. 1579
Kazarinov, N. Y. 195
Kazimi, R. 3050
Keane, J. 681, 774, 804, 1107, 1326, 1794
Keeley, D. 1305
Kehne, D. 248
Keil, E. 482
Keller, R. 2113
Kelley, J. P. 2381
Kellogg, N. 745
Kelly, E. 2164, 2167, 2239
Kennedy, P. 2733
Kennedy, W. L. 2441
Kerby, J. 2176, 2185
Kerns, Q. 1743
Kerslick, G. S. 561
Kettunen, L. 2140
Kewisch, J. 446, 1443, 3264
Kheifets, S. A. 3267
Khlebnikov, A. S. 2751
Khoetsian, M. Y. 1579
Kiaie, J. 1115
Kiefer, P. 2871
Kiehlmann, D. 2390
Killian, E. 2239
Kim, C. H. 2691
Kim, J. H. 1368
Kim, J. S. 1719
Kim, K. 1299
Kim, K.-J. 1088
Kim, M. S. 1368
Kim, S. H. 2375
Kim, T. 2316
Kimball, F. 2856
Kimel, I. 2757
Kimura, W. D. 558
Kincaid, B. 2721
King, A. 1305
King, Q. 1186
Kinney, W. 2173, 2179, 2191
Kipper, A. 3053
Kirchgessner, J. 21, 664, 678, 786, 2411, 2414, 2417, 2420, 2423, 2426
Kirk, H. G. 604, 2572
Kirkman-Amemiya, G. 591, 1990
Kissler, K. H. 1186
Kitamura, M. 2251
Klabunde, J. 2981, 3044
Klaisner, L. 1404, 1407
Kleffner, C. M. 2817
Klein, E. 2393
Klein, H. 2981, 3023, 3044
Klepper, O. 2880
Kloeppel, P. K. 3264
Kneisel, P. 2384, 2387
Knott, M. J. 2526
Knudsen, L. 147, 1213
Ko, I. S. 575, 1195, 2700
Ko, K. 719, 819
Kobayashi, T. 622
Kobayashi, Y. 2709
Kobliska, G. R. 2477
Kochkin, V. A. 1017
Kodera, I. 2694
Koechlin, F. 2393
Koepke, K. 81, 87, 2227
Kofler, R. R. 2152
Kogan, M. 3174
Kojima, Y. 16
Koljaskin, A. D. 1949, 2613
Kolomiets, A. A. 2984, 3109
Kolonko, J. 2751, 2856, 2967
Kolte, G. 1305
Komarov, V. V. 1356
Komissarov, P. Y. 1166
Konc, J. J. 2182
Kondo, Y. 1118
Konecny, R. 555, 3219
König, W. 2880
Konovalov, V. A. 2823
Koo, Y. M. 2345
Koop, I. A. 183, 186
Koopman, J. 1186
Körber, W. 2429, 2432
Korolev, O. S. 3067
Koscielniak, S. R. 377, 696, 1725, 1728
Koska, W. 2173, 2179, 2185, 2191
Kostas, C. 312, 613
Kotov, V. I. 192
Koul, R. K. 902
Kourbanis, I. 99, 111, 1302
Koutchouk, J.-P. 147, 2891
Kowalewicz, R. 2631
Kozanecki, W. 628, 1207, 3222
Kozawa, T. 622
Kozodaev, A. M. 3109
Kponou, A. 896, 1473
Krafft, G. A. 2073, 2745
Kraimer, M. R. 1314, 1496, 2526
Krall, J. 242, 1788, 2563
Kramer, S. 1107
Krasnikov, Y. M. 1279
Krasnykh, A. K. 195
Kratz, R. 2254
Krauter, K. 1419, 1487
Kravchuk, L. V. 2823, 3067
Krejcik, P. 2067, 2500, 3258
Krieger, C. 29
Krienen, F. 2474
Krinsky, S. 11, 1096, 2542, 2676
Krisch, A. D. 2506
Krishnagopal, S. 467, 1071
Krishnaswamy, J. 1107, 2119
Kristensen, M. 1764
Krivonosov, A. I. 2613
Kroc, T. 2378
Kroes, F. 1148
Kroes, F. B. 684
Kroll, N. 719, 819, 1716
Kroll, N. M. 801
Kruse, R. W. 1145
Krycuk, A. 1470
Krzywinski, J. 2149
Kubo, K. 1011, 1833, 2405, 2408
Kubo, T. 2257, 2462
Kuchar, J. 1163
Kuchnir, M. 93
Kuiper, B. 1356
Kukhtin, V. P. 2035
Kulikov, A. 1845, 3138
Kulikov, A. V. 500, 2005, 2098
Kulinski, S. 961, 2970
Kulke, B. 763, 766
Kumagai, K. 2465
Kumagai, N. 1698, 2465, 2646
Kung, P. 2688

Kunkel, W. B. 1916, 1919, 1955, 1993
Kuo, C. C. 2667, 2670, 2697
Kurakin, V. G. 2417
Kurihara, Y. 2032
Kuroda, S. 2257
Kurokawa, S. 2257
Kurokawa, S.-i. 138
Kurz, M. 3023
Kus, R. 857
Kushnick, P. 1508
Kustom, R. 1624
Kustom, R. L. 690, 693
Kuzmenko, G. A. 1860
Kuzminski, J. 2215, 2480
Kvasha, A. I. 3067
Kwan, J. W. 1955
Kwan, T. J. 649

L

Labedzki, J. 2254, 2450
Lachin, Y. Y. 2751
Lackey, J. 860, 1740
Laeger, H. 848
Lager, D. 3079
Lager, D. L. 3082, 3094
Lahti, G. 1290, 1443
Lambertson, G. 687, 819, 1404, 1407, 2537
Lamm, M. 2215
Lamm, M. J. 2173, 2179, 2191, 2227, 2233, 2236
Lamora, B. 935
Lampe, M. 242
Lampel, M. 2742, 3276
Lancaster, H. 807, 2721
Lane, S. N. 2604
Langdon, A. B. 263
Lange, R. 2319
Langstaff, R. 2272
Lankshear, R. 1695
Larkin, J. 935
Larson, D. J. 2575, 2581, 2757
Larson, J. D. 594
Larsson, A. 2008
Latham, P. E. 658, 731, 734
Latushkin, S. T. 1279
Latypov, T. A. 1582
Lau, Y. Y. 637, 1609
Laughton, C. 129
Lavender, W. 1151, 1383, 1476, 2688
Lavine, T. L. 652, 1964, 2284
Lawrence, G. P. 2598
Lawson, W. 658, 731, 734
Lax, J. 742
Laxdal, R. E. 810
LeDiberder, F. 628
Lebedev, P. K. 3273
Lebedev, V. A. 2342
Leboutet, H. 2763
Leconte, P. 2393
Lee, B. 725
Lee, E. P. 1737
Lee, G. 1249, 1758
Lee, G. C. 2182
Lee, I. Y. 2604
Lee, J. C. 2357, 2667, 2670
Lee, M. 1305, 1437
Lee, M. J. 1448
Lee, S. Y. 159, 162, 1059, 1627, 1636, 1639, 1770, 2506, 2679
Lee, T. 719, 2381, 2673
Lee, T. G. 798
Lee, T. N. 575
Lee, Y. Y. 881, 958
Lee-Whiting, G. E. 303
Leemann, C. W. 2745
Leemans, W. P. 2560
Leenen, M. 857
Legg, J. D. 725
Legg, R. 1261, 1371, 1970
Lehr, H. 2685
Lehrman, I. S. 2572
Leifete, G. 572
Leleux, G. 517
Lemeilleur, F. 1213
Lenkszus, F. R. 2526
Leonov, V. N. 2613
Leroy, J. 1534
Lessner, E. 210, 2778
Letellier, P. 3180
Leung, E. 2652
Leung, E. M. W. 2248
Leung, K. 2023, 2200
Leung, K. K. 2185
Leung, K. N. 1916, 1919, 1993, 2076
Levitt, S. 1160
Levy, C. D. P. 1925
Ley, R. 2832
Li, B. 2616
Li, C. Y. 1916, 1993
Li, K. 2616
Li, M. 371
Li, R. 452, 2616, 3264
Li, W. 2278, 2688
Li, Z. 281
Lidestri, J. 3123
Lidestri, J. P. 3120, 3195
Lienard, P. 1490
Lierl, H. 2319
Limar, V. V. 1573
Limberg, T. 1806, 2064
Lin, C. L. 2026
Lin, L. 2781, 2784, 2787
Lincoln, B. 1981
Lindner, A. 742, 745
Lindqvist, H. 425
Liou, R.-L. 1990
Lippmann, G. 598
Lipski, A. 2477
Liska, D. 2953
Liska, D. J. 2961
Littauer, R. 1130
Littauer, R. M. 1246
Liu, D. K. 1368
Liu, H. 2020, 2616
Liu, K. 2616
Liu, L. 1958
Liu, Y. 1624
Lloyd, S. 1136
Lloyd, S. C. 2456
Lo, C. C. 807
Lobanov, N. R. 2613
Loew, G. 982
Loew, G. A. 3219
Loiselet, M. 2610
Lombardi, A. 2444, 2820, 3038
Loomba, D. 2474
López, G. 392, 2203, 2212, 2224, 2468, 2471
Louie, W. 1107, 1374
Louis-Joseph, A. 1225
Low, K. 1308, 1365
Lowrey, A. R. 1204
Lu, X. 1740, 1749, 1752, 2616
Lubrano di Scampamorte, M. 2631
Lucas, P. 2523
Luccio, A. 839, 896, 1473
Luchini, K. 1371
Lucuta, P. 795
Ludewigt, B. 943
Ludgate, G. A. 1350
Ludmirsky, E. A. 189, 2146
Lueng, E. 2856
Luhmann, N., Jr. 2967
Luhmann, N. C., Jr. 766, 2751
Luijckx, G. 2366
Lujan, R. E. 2453
Lukyantsev, A. F. 1356
Lumpkin, A. H. 1204, 1967, 2754
Lundin, T. K. 129
Luo, Y. X. 575, 1195
Lyneis, C. M. 2796

M

Maas, R. 2366
MacKay, W. W. 736, 2221, 3050
MacLachlan, J. A. 1863, 2826
Macek, R. 228, 1893, 1896
Machida, S. 62, 383
Mackenzie, G. 1133
Mackenzie, G. H. 810
Madlung, J. 3053
Madura, D. 2856
Maggs, R. G. 1046
Mahale, N. K. 62, 383, 386, 389
Mahoney, K. 1470
Maier, R. 1425, 2808
Mailian, M. R. 198
Maillard, J. 2101
Main, W. 658, 731, 734
Maisheev, V. A. 189
Maki, N. 2251
Makowski, M. A. 2548
Malachov, N. A. 1582
Maldonado, J. R. 542
Malitskiy, N. D. 2823
Malyshev, O. B. 183
Malyshev, O. N. 2888
Mamaev, G. L. 1582
Mammosser, J. 2384
Mandell, S. 1273
Mane, S. R. 1585, 1690
Manfroi, T. 1978
Manglunki, D. 1198, 2509
Mann, J. 1186, 1213
Mansour, D. 1999, 2152
Mantsch, P. M. 2227, 2236
Manukian, R. H. 1287, 1446
Manz, C. 123

Mapes, M. 2292
Marc, M. R. 1115
Marchand, P. 780
Marchetti, C. 2970
Markovich, P. 2987
Marks, S. 2739
Marquardt, N. 2862
Marriner, J. 831, 1180, 1228, 1255, 1258, 1389, 1392, 1758, 1773, 1946
Marsh, K. 564
Marsh, K. A. 2560
Marshall, J. 2381
Martensson, E. 1293
Marti, F. 1163
Martin, B. 1374
Martin, D. J. 1124, 1127
Martin, J. 3053
Martin, K. 1174, 1180
Martin, P. S. 2477
Martin, S. 1767
Martinez, D. 1136
Martini, M. 171, 1890
Martinsen, G. 1365
Martirosian, Y. L. 257
Maruyama, A. 2694
Maruyama, T. 834, 2029
Marxen, H. 1311
Maschke, A. 389
Maslov, M. A. 625
Massarotti, A. 710, 3180
Massoletti, D. 2978
Masullo, M. R. 789, 2850
Masunov, E. S. 3177
Matevosian, A. P. 1446, 1579
Matheisen, A. 2429, 2432
Matrone, A. 2399, 2760
Matsuba, H. 2402
Matsuda, T. 2694
Matsuki, N. 2715
Matsumoto, H. 1008, 2061
Matsumoto, S. 908
Matthews, H. 731
Mattison, T. 982, 996, 2331, 2334, 2955, 3156, 3159
Mattison, T. S. 3162, 3165, 3168
Matveev, A. V. 2342
Matveev, V. A. 2823, 3067
Mauer, W. J. 3094
Maurer, W. J. 3082
Mavrogenes, G. 419
Maywald, H. 857
Mazarakis, M. G. 3059, 3126, 3129
Mazeline, C. 1198
Mazur, P. 2215
Mazur, P. O. 2128, 2134, 2477, 2480
McAtee, W. H. 3135
McConnell, D. 1249, 1743
McCormick, D. 1201, 1240
McCrory, E. S. 1249, 1484, 3064
McCullough, W. F. 2622
McCune, E. W. 705
McDermott, D. 2967
McDermott, D. B. 766
McDonald, D. 2023
McDonald, D. S. 1919
McDonald, M. 1925
McDowell, W. P. 1496, 2526
McGhee, D. G. 914
McGinnis, D. 1255, 1258, 1389, 1392, 1758
McGregor, J. E. 795
McInturff, A. D. 2227, 2233
McIntyre, P. M. 725
McKenna, C. M. 2088
McMichael, G. E. 845, 2093, 3047
McMurry, D. E. 2961
McNerney, A. 681
McNerney, A. J. 52, 739
Meade, A. 2164, 2239
Meadows, J. W. 547
Meads, P. F. 1767
Meaney, D. 1371, 3171
Mecklenburg, B. 646, 3183
Meddahi, M. 153
Mehta, N. 383
Meigs, M. J. 2604
Meinke, R. 2149
Meisner, K. 111
Meitzler, C. R. 1958, 2008
Mello, J. 2688
Mel'nikov, V. A. 1582
Mendelsohn, S. L. 395
Menegat, A. 652
Meng, W. 2474
Menge, P. R. 1827
Menninger, W. L. 754
Merminga, L. 2064
Merminga, N. 219, 461
Merrill, F. 2137
Merson, J. 3017
Meshcherov, R. A. 2823
Meshkov, I. N. 2888
Mestha, L. K. 783, 1332
Meth, M. 681, 739
Meuth, H. 1767
Meyer, F. 2215
Meyer, R. 1136
Meyrand, G. 3180
Miao, Y. 2221
Michailichenko, A. 458
Michailov, V. N. 3067
Michaut, C. 2011
Michel, H. 1186
Michel, W. L. 845
Michelato, P. 2973
Michelotti, L. 207, 1561, 1881
Mignardot, H. 777
Mikawa, M. 908
Mikhailov, V. A. 2886
Mikhailov, V. G. 1166
Mikheev, M. S. 1356
Mikic, Z. 1305
Milardi, C. 1448
Miles, J. 848
Miller, D. W. 532
Miller, E. 1464
Miller, H. W. 2996
Miller, J. D. 239, 3141
Miller, R. 982, 3276
Miller, R. B. 2622
Miller, R. H. 652, 769, 976, 1964, 2284
Millich, A. 3234
Mills, F. E. 2477
Mills, G. D. 2604
Milner, S. 2631
Milovanov, O. S. 2613
Milton, B. F. 65
Milton, S. 291
Milutinovic, J. 413
Minestrini, M. 2970, 2973
Minty, M. G. 1770, 2506
Mironov, V. I. 195
Mirzojan, A. N. 3067
Misek, J. 1174, 1180
Mishchenko, A. V. 2601
Mishiro, H. 1118
Mishukov, A. A. 2613
Mistry, N. B. 24
Mitchel, G. R. 979
Mitra, A. K. 938
Mitsuhashi, T. 1836
Mitsumoto, T. 2877
Mitsunobu, S. 2408
Mittig, W. 594
Miura, A. 1008
Miura, F. 2655
Miyahara, Y. 707
Mizuta, M. 2032
Mjae, E. A. 189
Mock, R. C. 3135
Mockler, C. 2110, 2958
Moffat, D. 21, 664, 678, 786, 2411, 2414, 2417, 2420, 2423, 2426
Möhl, D. 514, 2509, 2832
Moir, D. 2107
Moir, D. C. 245, 3192
Moiseev, V. A. 2984
Moisio, M. F. 1934
Mokhov, N. V. 625
Mokhtarani, A. 2227, 2230, 2233
Møller, S. P. 2811
Möller, W. D. 2429
Mølmer, K. 1764
Mondelaers, W. 2619
Mondelli, A. 312
Mondelli, A. A. 315, 613, 3261
Monteiro, S. 2307
Moore, C. 631
Morales, H. 769, 976, 1243, 2278, 2688
Moretti, A. 2996
Morgan, B. 1290
Morgan, G. 2164, 2239
Morgan, G. H. 42, 2167, 2170, 2242, 2245
Morgan, J. P. 851
Morgillo, A. 2167
Mori, W. B. 564
Mori, Y. 165
Morimoto, T. 3035
Morin, D. C. 2643
Morita, Y. 2257, 2462
Mortazavi, P. 804
Morton, P. 1407
Morton, P. L. 461, 1854, 2586
Moscatello, M. H. 2802
Moser, H. O. 3053
Moshammer, H. 905
Mosko, S. W. 2604
Mosnier, A. 2393
Mostowfi, D. 1243, 1478, 2688
Motonaga, S. 2465

Mourier, G. 772
Mouris, J. F. 2337
Mtingwa, S. 555
Mukoyama, S. 2402
Müller, G. 2417
Müller, R. 1311
Munson, F. H. 2987
Muratore, J. 2164, 2167, 2239
Murin, B. P. 2823, 2984
Murin, N. P. 3067
Murphy, J. 2248
Murphy, J. B. 1107, 1651, 2661, 2664, 2676
Musenich, F. 2973
Musenich, R. 2399
Muto, H. 875
Myakishev, D. G. 3002
Myznikov, K. P. 177

N

Nagafuchi, T. 707
Nagaitsev, S. S. 183
Nagaoka, R. 1074
Nah, Y. G. 2345
Naito, T. 1008, 2014, 2061
Nakagawa, T. 2694
Nakahara, K. 1558
Nakai, H. 2408
Nakajima, K. 622
Nakamura, N. 440
Nakamura, S. 2032, 2694
Nakamura, T. 667
Nakanishi, H. 622
Nakanishi, T. 2032, 2694
Nakano, M. 707
Nakao, K. 1043
Nakashizu, T. 2990
Nakata, S. 2694
Nakayama, H. 506
Nakazato, T. 1118
Nam, K. 2673
Namkung, W. 575, 1195, 1368
Nantista, C. 652
Napoly, O. 3228
Nassiri, A. 419
Nath, S. 485, 572
Nation, J. A. 561, 728, 2104
Natter, E. F. 1329
Naumov, I. V. 1279
Nawrocki, G. J. 1496
Nawrocky, R. 1107, 1528
Nawrocky, R. J. 2542, 2790
Nearing, J. C. 2188
Neckenig, M. 1543
Neil, G. R. 2745
Nelson, E. 719, 722
Nelson, G. 1028
Neri, F. 1597, 1630
Nesterenko, I. N. 183
Nesterov, V. 3138
Neuffer, D. 1893, 1896
Neuffer, D. V. 446, 1077
Neuschaefer, G. 485, 572, 1136, 1884
Newberger, B. S. 216
Newton, M. A. 2592, 2595
Nexsen, W. E. 3085, 3094, 3103
Nezhevenko, O. A. 2933, 3186
Ng, B. 1371, 1514, 3171
Ng, K. Y. 159, 162, 1743, 1749
Ng, K.-Y. 111, 1645
Nghiem, P. 517
Nguyen, D. 1437
Nguyen, K. T. 239, 3141
Nguyen, M. 2955, 3147
Nguyen, M. N. 3153
Nickogosian, V. T. 2146
Niczyporuk, B. 3264
Nielsen, J. S. 1764
Nielsen, R. W. 29
Niemann, R. C. 29, 2301, 2304
Niimura, N. 1118
Nikogossian, V. T. 1446
Ninomiya, S. 165
Nishida, Y. 622
Nishidono, T. 2298
Nishimoto, H. 3114
Nishimura, H. 1434
Nishinomiya, Y. 1031
Niven, W. A. 3097
Niwano, S. 1118
Noda, A. 875
Noda, K. 875
Noer, R. 21
Noguchi, S. 2405, 2408
Nolden, F. 2880
Nolen, J. A. 884, 1163
Nolker, K. 1443
Noomen, J. 1148
Norem, J. 555, 619, 1984
Novicov, A. P. 3177
Novikov, D. L. 1017
Nuhn, H.-D. 769, 973, 1151, 1410, 1476, 2688, 2748
Nuttall, J. A. 2284
Nyman, M. 943
Nyman, M. A. 1401

O

Obina, T. 1338
O'Connell, J. S. 404
O'Day, S. 2360
Odian, A. 3216
Odian, A. C. 2098
Oganessian, R. T. 2888
Oganessian, Y. T. 2888
Ogata, A. 622
Ogawa, Y. 494, 497
Ogitsu, T. 2480
Ohman, D. 5
Ohmi, K. 2847
Ohnishi, J. 2465
Ohno, H. 2715
Ohnuma, S. 371, 374, 407
Ohsaka, T. 1118
Ohsawa, Y. 2257, 2462
Ohshima, I. 1034
Ohuchi, N. 2257, 2462
Oide, K. 2058, 2488
Oikawa, Y. 2298
Okuda, S. 2694
Oleck, A. R. 2230
Ollis, C. W. 3097
Olsen, D. K. 2604
Olson, W. R. 3126
Omori, T. 2032
O'Neill, C. M. 2838
Onischenko, L. M. 195
Oram, C. 1722, 2272
Orlov, Y. 1839
Orlov, Y. F. 2838
Orrell, D. 2197
Orris, D. 2215, 2227, 2480
Orris, D. F. 2477
Ortiz, R. 1151, 1383, 1478, 2688
Orzechowski, T. 1335
Osberg, E. A. 1350
O'Shea, P. G. 2754
Ostiguy, J.-F. 2128, 2131, 2354, 2477
Ostreiko, G. N. 3186
Ostroumov, P. N. 2984, 3062, 3067, 3109
O'Sullivan, M. 935
Otake, Y. 1558
Otter, A. J. 2363
Ottonello, G. B. 2760
Owens, T. L. 3064
Oyamada, M. 1118
Ozaki, S. 2901
Ozaki, T. 2257, 2462
Ozelis, J. P. 2191

P

Pacak, V. 810
Pachnik, J. E. 2134, 2477
Padamsee, H. 21, 664, 678, 786, 2042, 2411, 2414, 2417, 2420, 2423, 2426
Padilla, R. 2996
Pagani, C. 2973
Palmer, R. B. 32
Palmieri, V. 1934
Palumbo, L. 2850
Pancella, P. V. 2506
Pang, Y. 725
Papavaritis, P. 772
Pappas, C. 863
Paramonov, V. V. 2823
Parazzoli, C. G. 2769
Pardo, R. C. 2987
Parfitt, C. P. 357
Park, E. S. 2345
Park, S. 2751, 2967
Parker, B. 1002
Parker, D. L. 725
Parkhomchuk, V. V. 529, 2888, 3273
Parodi, R. 366, 2399, 2973, 3026
Parsa, Z. 511, 1887
Parzen, G. 288, 1615, 1627, 1872, 1875
Pashenkov, A. S. 2823
Pasotti, C. 710
Pasquinelli, R. 1758
Pasquinelli, R. J. 1395
Patteri, P. 2970, 2973
Patterson, L. 2856
Paul, A. C. 3085, 3094, 3100, 3103, 3106
Paul, P. 2444, 3038

Paulson, C. C. 395
Pause, H. 1311
Paxson, V. 297
Payne, A. N. 3091, 3097
Pearce, D. 1133
Pearce, W. J. 822
Pearson, J. B. 810
Peck, S. 464
Peck, S. B. 1246
Pedersen, B. O. 2088
Pedersen, F. 2509, 2631
Peggs, S. 207, 318, 473, 476, 1302, 1458, 1657, 1660, 1848
Peggs, S. G. 2477
Pei, A. 1922
Pei, G. X. 2098
Peiniger, M. 2390
Pellegrin, J.-L. 1243, 1404, 1407
Pellegrini, C. 398, 2748, 2751, 2853, 2856, 2967, 2976
Pellico, W. 1749
Pendergast, K. D. 754
Pendleton, R. 819
Pennacchi, R. 2949
Penner, S. 351
Perelstein, E. A. 195
Perevedentsev, E. A. 183, 186, 526
Perkins, C. 2949
Perrier, J. C. 2832
Perriollat, F. 1353
Persov, B. Z. 3186
Pestrikov, D. V. 183, 523
Peters, O. 857
Peters, R. 2523
Petersen, B. 857
Peterson, D. 1228, 1758
Peterson, J. 62
Peterson, J. M. 1645
Peterson, T. 2227, 2230, 2480
Petillo, J. J. 312, 315, 613
Petit, E. 1142
Petri, H. 1922
Petronevich, S. A. 3067
Petrosian, M. L. 257
Pettersson, T. 1564
Pfister, U. 1425, 2808
Phelps, R. A. 2506
Phinney, N. 1317, 3222
Picard, M. 1383, 1543
Pieczora, K. 857
Piel, H. 2417
Pietryka, M. 2949
Pike, C. 1952
Pilat, F. 62, 204, 348, 363, 383
Pilyar, N. V. 1582
Pisent, A. 2964
Pishchulin, I. V. 1567, 1570
Pissanetzky, S. 2221
Pitthan, R. 500, 1845, 2098
Pivit, E. 774
Pjerov, S. 2248, 2316
Placidi, M. 147, 1213
Planner, C. 2272
Plate, D. 2721, 2739
Plotkin, M. 681
Plum, M. 1893, 1896
Poirier, P. 2070
Poirier, R. L. 699, 2943
Pokorny, P. 2888
Poll, D. 1389, 1758
Poloni, C. 2712
Ponomarev, O. 1890
Poole, J. 848
Popovic, M. 655, 725
Porcellato, A. M. 2438
Porter, T. 1999
Postiau, N. 2610
Potter, J. M. 1377, 1910, 2583
Potts, J. 2414
Potvin, L. 2628
Poukey, J. W. 3059, 3126, 3129
Poulsen, O. 1764
Pouryamout, J. 2417
Power, J. 1136
Powers, T. 1508, 2325
Prasuhn, D. 1425, 1767
Preble, J. 2381
Preger, M. 961
Preissner, H. 2149
Prelec, K. 1913
Prepost, R. 2029
Prestwich, K. R. 3126, 3129
Primdahl, K. 2281
Proch, D. 2414, 2429, 2432, 2435
Prodell, A. 2164, 2167, 2239
Promé, M. 2393
Pronin, A. N. 1949, 2613
Pruss, S. 87
Pruss, S. M. 294, 2128, 2340
Pugh, S. 1371, 1514
Puglisi, M. 681, 2634
Purser, K. H. 878
Pusch, G. D. 303
Putnam, S. D. 3120, 3195
Putris, F. 2351

Q

Qian, W. 2616
Qian, Y. 1692
Qian, Z. 2996
Qingwen, Q. 1878

R

Radusewicz, P. 2164, 2167
Rajagopalan, S. 222, 619
Raka, E. 1422
Rakowsky, G. 1096, 2733
Ramamoorthy, S. 2790
Ramirez, G. 1326
Ramirez, J. J. 3059
Rangarajan, G. 1621, 1630
Range, J. 2808
Rao, G. 2384
Raparia, D. 572, 2993
Rapidis, P. A. 108
Rashchikov, V. I. 3111
Raskopin, A. M. 3109
Rasmussen, N. 171
Ratner, L. G. 168, 2506
Ratti, A. 681, 739, 1803, 2820
Ratzinger, U. 567, 2981
Raubenheimer, T. O. 2503
Rawnsley, B. 1133
Read, M. E. 658
Reece, C. 1508, 2325
Reece, K. 1473
Reece, R. K. 839, 896
Rees, D. 640
Rees, D. E. 675
Reeve, P. A. 2363
Regan, A. H. 2946
Reginato, L. L. 2592, 2595, 2918, 3165
Rehak, M. 2164, 2167, 2239
Reinagel, D. J. 1537
Reinhardt, N. 591
Reinhardt-Nickulin, P. 1014, 1722
Reiniger, K. W. 920
Reiser, M. 248, 251, 658, 1818, 1821, 1961, 2497
Renbarger, V. L. 3085, 3097
Renieri, A. 2760
Renken, D. 2429
Rensfelt, K. G. 2814
Repnow, R. 2817
Reschke, D. 2417
Reusch, M. F. 1651, 2188, 2248, 2664
Reuter, E. 1999
Reuter, E. M. 1996, 2005
Revkov, A. A. 2613
Rex, K. 1234
Rezvov, V. A. 1166
Rhee, M. J. 479, 1972, 2999, 3141
Rice, D. 464
Rice, D. H. 1246, 1857
Richardson, J. R. 48
Richert, A. 1352
Richter, R. 742, 887
Richter-Sand, R. J. 3201
Rickel, D. G. 649
Riddiford, A. 2233
Riddiford, A. W. 2236
Ridgeway, W. 742, 745
Ridlon, R. 2107
Ridlon, R. N. 3192
Riege, H. 2631
Riemer, U. 857
Rimmer, R. 687, 801, 819
Rinckel, T. 2506
Ringrose, R. 786
Rinolfi, L. 2964
Ripouteau, F. 594, 2802
Risler, R. 1359
Risselada, T. 171, 1672
Ritson, D. M. 339
Riunaud, J. P. 171
Rivkin, L. 780
Rizawa, T. 707
Rizzo, S. 2399
Robb, J. 2381
Roberts, W. 1455
Robin, D. 398, 2853, 2856
Robinson, A. L. 2640
Rocha, R. 2221, 2649
Roche, C. T. 2441
Rodgers, J. 2578
Rogers, D. 646, 766
Rogers, J. D. 661
Rogers, R. P. 3267
Rohde, D. 1758
Rohrer, E. 2164, 2239

Rohrer, E. P. 2167
Romano, T. 1107, 2724
Romano, T. J. 993
Romashkin, O. B. 1567
Romashkin, O. V. 1570
Romea, R. D. 558
Roop, B. 29, 2304
Root, L. 810
Rosas, P. 2266
Rosatelli, F. 2399, 2760
Roschin, A. A. 1166
Rose, J. 804, 1794
Rose, R. 1107, 1374
Rosenzweig, J. 619, 2967
Rosenzweig, J. B. 1776, 1779, 1987, 2751, 3225
Roser, T. 2506
Rosing, M. 555
Ross, M. 2064
Ross, M. A. 2506
Ross, M. C. 1201, 1502, 2098
Rossi, C. 710
Rossmanith, R. 3264
Röth, R. W. 2417
Rothman, J. 1107, 2542, 2790
Rouse, F. 1416, 1419, 1451, 3222
Rowen, M. 1243
Roy, G. 2058, 3213, 3216
Royet, J. M. 2155
Rubbia, C. 3279
Rubin, D. 21, 467, 664, 678, 786, 1642, 2411, 2414, 2417, 2420, 2423, 2426
Rubin, D. L. 144, 470
Rubtsov, B. A. 3067
Rück, D. M. 1943
Rudd, H. 248
Rudolph, K. 1934
Ruegg, R. 1925
Ruggiero, A. G. 413, 1422, 1869, 2820
Ruggiero, F. 1666
Ruhe, J. 2958
Rule, D. W. 1204
Rummler, J. 2146
Rumrill, R. S. 1537
Rusnak, B. 1046
Russ, T. 946, 1467, 1546, 2125, 3174
Russell, A. 207
Rusthoi, D. P. 607
Ruth, R. 2058, 3216
Ruth, R. D. 219, 1591, 1854, 2037, 2503
Rutkowski, H. L. 1952
Ruvinsky, S. I. 3186
Ryckewaert, G. 2610
Rymer, J. P. 1910
Ryne, R. 646
Ryne, R. D. 760
Rypshtein, I. 1386
Ryu, C. 575, 1195, 1368

S

Saab, A. 3174
Saadatmand, K. 1171, 1183, 2529
Sabbi, G. 366
Safa, H. 2393
Safranek, J. 769, 1104, 1151, 1243, 2278, 2369, 2688, 2865
Sagalovsky, L. 2441
Sagan, D. 1080, 1839
Sage, J. 1365, 1443
Sagin, I. A. 3067
Saito, K. 2384, 2387
Saka, T. 2032
Sakai, I. 165
Sakanaka, S. 440, 1836
Sakano, M. 2402
Sakaue, H. A. 2298
Sakharov, V. P. 1356
Salomons, R. 1401
Saltmarsh, C. 1458
Samed, Y. 786, 2423
Sampayan, S. 3094, 3097
Sampayan, S. E. 3103
Sample, J. 65
Sampson, W. 2164, 2167, 2239
Sanchez, T. 2688
Sanchez-Chopitea, L. 1201, 1284, 1317
Sandburg, J. 2266
Sander, O. R. 578, 1171, 2529, 3017
Sanders, R. T. 681, 739
Sandoval, D. 1171, 2529
Sandoval, D. P. 1237, 3017
Sanelli, C. 2970
Sanford, T. W. L. 3135
Sanok, Z. 857
Sapp, W. W. 634, 2125, 2348
Saraniti, D. 786, 2426
Saritepe, S. 81, 87, 114, 207, 225, 318, 473, 1848
Sasaki, S. 2715, 2715
Sasaki, Y. 2877
Sass, B. 1416, 1419
Sass, R. 1437
Sato, H. 165, 908
Satogata, T. 476, 1302
Satoh, K. 138
Satoh, S. 707
Satti, J. 3189
Savoy, R. 1091, 2718, 2736
Sax, W. 1999
Scandale, W. 1669, 1672, 2260
Scanlan, R. M. 2155
Schaaf, U. 2880
Schachinger, L. 297, 1434
Schachrai, N. [illegible] 3109
Schachter, L. 561, 2104
Schaffer, G. 748
Schailey, R. 890, 985, 1281
Scharamentov, S. I. 3067
Scharlemann, E. T. 3097
Schauerte, W. 1543
Schegolev, L. M. 183
Schempp, A. 2981, 3023, 3041, 3044, 3053, 3076
Scherbakov, E. D. 1356
Schick, L. A. 144, 470
Schiffer, J. P. 1764
Schillo, M. 1543
Schindl, K. 171
Schirmer, D. 2859
Schittko, F. J. 1543
Schlachter, A. S. 2640
Schmeing, H. 979
Schmickler, H. 848
Schmidt, E. E. 2477
Schmidt, F. 1669, 1672
Schmidt, R. 147, 1186, 1213
Schmor, P. W. 65, 1925
Schmüser, P. 37, 857, 2149
Schneider, H. 2607
Schneider, H. R. 65
Schneider, J. D. 1183
Schneider, L. 863
Schneider, R. F. 239, 3141
Schneider, R. J. 878
Schneider, W. J. 2381
Schnell, W. 3237
Schnitzenbaumer, P. 2292
Schoessow, P. 555, 2557, 3219
Schofield, G. L. 3171
Schollmeier, S. 857
Schölz, F. 2432
Schönauer, H. 171
Schrage, D. L. 1046
Schuchman, J. 1107
Schuchman, J. C. 2316
Schulte, H. 2880, 2981
Schultz, D. C. 1964, 2084
Schulz, L. 2685
Schulze, M. E. 610
Schütte, W. 1219
Schütz, P. 2450
Schwandt, P. 1922
Schwarz, H. 819, 1410, 1806
Schwarz, W. 857
Schweppe, E.-G. 757
Sclyarenko, V. I. 1166
Sears, J. 21, 664, 786, 2411, 2414, 2417, 2420, 2423, 2426
Sebek, J. 769, 926, 976, 1028, 1151, 1243, 1478, 2688
Sedlyarov, I. K. 183
Seeman, J. T. 461, 905, 1201, 1499, 1734, 2064, 2949, 3207, 3210
Segall, K. 1981
Seifert, H. 757
Seifrid, P. 1758
Sekutowicz, J. 2429
Sellyey, W. C. 1145, 1204, 2769
Selph, F. 2978
Semunkin, Y. F. 2823
Sen, T. 336, 342, 345, 360
Senichev, Y. V. 1899, 1904, 2823
Senyukov, V. A. 1048
Seppi, E. 351
Serafini, L. 2973
Serdobintsev, G. V. 3186
Sereno, N. 3264
Serio, M. 2850, 2970
Serov, V. L. 3067
Serre, C. 1353
Servergin, Y. P. 2035
Servranckx, R. V. 287, 309
Sery, A. A. 529, 2888, 3273
Severgin, Y. P. 2823
Shafer, R. E. 1139
Shaimerdenov, E. N. 3186
Shapiro, A. H. 1046, 2961
Shaposhnikova, E. N. 2823

Sharma, S. 2248, 2661
Sharp, C. 935
Sharp, W. M. 260, 2592
Shatunov, Y. M. 183
Shay, H. D. 2592, 3088
Shcheulin, A. S. 1582
Shea, M. F. 1484
Shea, T. J. 1422, 1428, 1803
Sheffield, R. L. 1110, 2754
Sheikh, J. Y. 845
Shen, B. 2266, 2292
Shepard, K. W. 2987
Sherman, J. D. 2080
Sherrill, B. 1163
Sherrill, B. M. 884
Shi, J. 407
Shi, P. 1764
Shibasaki, Y. 1118
Shibata, H. 622
Shibata, Y. 1118
Shibuya, S. 3035
Shidara, T. 494, 497, 1034, 1040, 1043
Shiffler, D. 561
Shih, H.-J. 216
Shiho, M. 2625
Shiltsev, V. D. 529, 3273
Shimano, T. 2402
Shinas, M. 1171, 2529
Shintake, T. 757
Shintomi, T. 165
Shishido, T. 2405, 2408
Shoaee, H. 1416, 1419, 1437, 1451
Shokair, I. R. 3144
Shope, S. L. 3129
Shotzman, G. 2221
Shtirbu, S. 1484
Shu, Q. 21, 664, 2414
Shu, Q. S. 678, 786, 2411, 2417, 2420, 2423, 2426
Shukeilo, I. A. 2035, 2823
Shurter, R. B. 1136, 1139
Shurupov, P. B. 1949, 2613
Shutt, R. 2164, 2167, 2239
Si, H. 2616
Sibley, C. 946, 1546, 2125
Sicard, C.-H. 1353
Sidorov, V. P. 1573
Siemann, R. 467, 1071
Siemann, R. H. 2838
Siergiej, D. 81, 87, 90, 93, 1293
Sierra, S. 3180
Sievers, P. 3228
Sikora, J. P. 1130
Sikora, R. 2292
Silva, J. 2101
Sim, J. W. 2134, 2477
Simonov, E. A. 183, 523, 526
Simpson, J. 555, 2557, 3219
Simrock, S. 1470, 2515
Sims, R. 2173
Sims, W. 1264
Sinclair, C. K. 2745
Singer, H. 1425
Singh, O. V. 1528, 2542
Sissakian, A. N. 195
Skaritka, J. 2218
Skelly, J. 839, 896, 1473
Skrinsky, A. N. 183
Slater, J. M. 532
Slater, J. W. 532
Sledziewski, Z. 2011
Sleptsov, A. I. 3273
Slinker, S. 242
Sloan, T. 1770
Slobodrian, R. J. 2628
Sluijk, T. 1148
Sluijk, T. G. B. W. 684
Smedinghoff, J. 2523
Smirnov, Y. I. 195
Smith, B. H. 795
Smith, D. L. 547, 3126
Smith, G. A. 1264, 1273, 1347, 1431
Smith, H. 1028
Smith, H. V., Jr. 2080
Smith, J. 2790
Smith, J. R. 3144
Smith, J. S. 2029
Smith, L. 1064, 1737, 3070
Smith, S. A. 2206
Smith, V. 1243
Smolin, J. 2967
Smolin, J. A. 2751
Smythe, W. R. 643
Snead, C. L., Jr. 1695
Snitchler, G. 2197, 2209
Snowdon, S. C. 2477
So, T. 2790
Sobenin, N. P. 2613
Sobotta, K. 1362
Solomon, L. 1096, 2116
Solov'ev, N. G. 1567
Song, J. 2396
Song, J. J. 690
Song, J. J. H. 693
Soroka, L. 1955
Soukas, A. 839
Soukas, A. V. 940, 999, 1216
Soundranayagam, R. 625
Sowinski, J. 1922
Spädtke, P. 1943, 2880
Spalek, G. 652, 1046
Spataro, B. 961, 2850
Specht, V. 658
Spence, W. 1549, 2064
Spence, W. L. 461, 503, 905
Spencer, C. M. 1964, 2152
Spencer, J. E. 1440, 3270
Spencer, N. 5
Spencer, T. A. 1827
Sperisen, F. 2506
Spiess, W. 1425
Spigo, G. 2176, 2197
Spitz, R. 681, 739
Springer, R. W. 2754
Sredniawski, J. 2023
Sreenivas, A. 949
Stahl, S. 434, 1779
Staicu, F. 2316
Stampfer, M. 2817
Stampke, S. R. 2218
Stark, R. A. 3141
Stattel, P. 2266, 2292
Stecchi, A. 1448, 2970
Steck, M. 2817, 2880
Steele, W. F. 1955
Stefan, P. M. 1096
Stein, W. E. 2754
Steinhauer, L. C. 558
Stella, A. 3026
Stepantsov, S. V. 2888
Stephan, M. 1362
Stephenson, E. J. 2506
Stetter, M. 2631
Stever, R. 763
Stewart, M. D. 725
Stiening, R. 2149, 2480
Stillman, A. 1264
Stillman, A. N. 1189
Stitts, E. 2381
Stocker, F. 890, 1281
Stockhorst, H. 1425, 1767
Stolzenburg, C. 2149
Stover, G. 943
Stover, G. D. 1401
Stradtner, R. 943
Strait, J. 2173, 2176, 2179, 2185, 2191, 2215
Strickland, B. E. 3171
Striffler, C. D. 658, 731, 734, 2578
Stringfield, R. M. 649
Struckmeier, J. 2880
Struve, K. 3129
Struve, K. W. 3144
Studzinski, M. 713
Stuewe, R. 929
Stutzin, G. C. 1916
Su, J. J. 619
Sueno, T. 908
Sugahara, R. 2257, 2462
Sugitani, M. 2877
Sukiennicki, B. 982
Sullivan, M. 2844
Sullivan, T. 1749, 1848
Sun, D. 736
Sun, Y. 1410
Sundelin, R. 2384
Sundelin, R. M. 2381
Susta, J. 2325
Suyama, A. 1031
Suzuki, H. 707
Suzuki, T. 165
Svandrlik, M. 710
Swain, G. 3014
Swenson, C. A. 2649
Swenson, D. R. 1928, 1931
Swoboda, D. 1516
Swoyer, G. 2733
Sylvester, C. 2116
Symon, K. 1624
Syphers, M. J. 117, 129
Syresin, Y. A. 2888
Szumillo, A. 1999

T

Tajima, T. 2408
Takada, H. 2655
Takada, T. 2715
Takagi, A. 165
Takahashi, S. 2298
Takahashi, T. 2408
Takahashi, T. 1118

Takao, M. 494, 497, 506, 1011
Takasaki, E. 165
Takasaki, F. 138
Takata, K. 1011, 1034
Takayama, K. 2551, 2625
Takebe, H. 2465
Takeda, S. 1008, 1034, 1040, 2047, 2061
Takeo, T. 1338
Takeuchi, Y. 2032
Tallerico, P. 640
Tallerico, P. J. 649, 670
Tallerico, T. 1264
Talman, R. 204, 363, 383
Tanabe, Y. 707
Tanaka, H. 1698, 2694
Tanaka, M. 958
Tang, C.-M. 1788
Tang, J. 1443
Tang, J. Y. 443, 446
Tang, Z. 1946
Tantawi, S. 731
Taratin, A. M. 177
Tarovik, M. N. 2823
Tatchyn, R. 2748
Tatum, B. A. 1519, 2604
Tauchi, T. 834, 3252
Tavares, P. 2781, 2787
Taylor, B. 807
Taylor, T. 842, 2260, 3228
Tayursky, V. A. 2342
Tazzari, S. 2970, 2973
Tazzioli, F. 2970, 2973
Tecimer, M. 2757
Tekawa, M. M. 1401
Temkin, R. 2026
Temkin, R. J. 751, 754, 772
Teng, L. 210, 1524, 1692, 2679, 2778
Teng, L. C. 1603
Tepikian, S. 1627, 1636, 1639, 1707
Ter-Akopian, G. M. 2888
Teranishi, T. 1034
ter Avest, R. 2149
Terrien, J. 2967
Thern, R. 45
Thern, R. E. 1189
Thevenot, M. 3204
Thiagarajan, V. 2194
Thibault, C. 3041
Thiessen, H. 1893, 1896
Thiessen, H. A. 281, 866, 3132, 3198
Thomas, B. L. 3171
Thomas, M. 804, 1107, 2790
Thomas, R. 1344, 1347
Thompson, K. A. 431, 1404, 1407, 1854
Thompson, K. M. 2375
Thompson, P. 2164, 2167, 2239
Thompson, P. A. 2242, 2245
Thorndahl, L. 3243
Thrasher, M. H. 842
Tiefenback, M. 3123
Tiefenback, M. G. 3120, 3195
Tigner, M. 132, 786, 2423, 2910
Timakov, V. A. 2888
Tiunov, M. A. 3186
Tkatchenko, A. 517
Tkotz, R. 2631
Tlekhas, Y. I. 2613
Tobiyama, M. 1338
Toda, T. 908
Todd, A. M. M. 395
Tödten, G. 857
Toge, N. 628, 834, 2067, 2152
Tojyo, E. 3035
Tokar, R. L. 1204
Tokuda, N. 3035
Tomeoku, H. 2251
Tomimasu, T. 2655
Tomizawa, M. 875
Tomlin, R. 860
Tommassini, D. 2372
Tompkins, J. 2480
Tompkins, P. A. 1115
Tool, G. 2215
Tosi, L. 1074
Toth, K. S. 2604
Toumanian, A. R. 2146
Tourrette, T. 2393
Toyama, T. 165, 908
Trahern, C. G. 207
Tran, D. T. 3180
Tran-Ngoc, T. 3047
Tranquille, G. 2509, 2832
Trasatti, L. 1448, 2970
Trbojevic, D. 96, 99, 159, 162
Treado, T. A. 702
Trémeau, T. 772
Trimble, D. 766
Trines, D. 857
Trinks, U. 2254, 2450
Trofimov, N. N. 1356
Trombly-Freytag, K. 2134
Tronc, D. 3008, 3180
Truong, Q. V. 2802
Trzeciak, W. 1624
Trzeciak, W. S. 1088, 2643
Tsang, K. T. 312
Tsarik, S. V. 192
Tsironis, G. 1302
Tsoupas, N. 1695
Tsubata, M. 2032
Tsuchiya, K. 2257, 2462
Tsukishima, C. 2694
Tsumaki, K. 1698
Tsutaya, T. 1118
Tsutsui, Y. 2655
Tucker, H. 2958
Tucker, T. 2110
Tückmantel, J. 1023
Tumanian, A. R. 1446
Tupa, D. 1928, 1931
Turk, J. 834, 2152
Turkot, F. 2128, 2230
Turman, B. N. 3126, 3129
Turner, J. 2197, 2206
Turner, J. R. 2176
Turner, L. R. 2140
Turner, W. 3082
Turner, W. C. 581, 3085, 3094, 3097, 3100, 3103, 3106

U

Ueda, T. 622
Uher, J. 777
Uhm, H. S. 239, 455, 2566
Ungrin, J. 3011
Unser, K. 1213
Urakawa, J. 506, 1040, 1555, 2014
Urasawa, S. 1118
Uythoven, J. 1594

V

Vaganov, N. G. 1573
Valckx, F. P. G. 2011
Valdner, O. A. 1949
van Asselt, W. 839, 1216
van Asselt, W. K. 881, 1273
van de Klundert, L. J. M. 2149
Vandeplassche, D. 848, 2509
van der Linden, A. 2366
van Dyck, O. B. 1928, 1931
Vanecek, D. 1952
van Guilder, B. S. 2506
Van Maren, R. 2110
VanMaren, R. 766
Van Olst, D. 1284
van Steenbergen, A. 2724
van Zeijts, J. B. J. 1597
Van Zwienen, W. 1344, 1347
Van Zwienen, W. H. 1189
Varfolomeev, A. A. 2751
Vasas, M. 1981
Vasiliev, N. V. 1017
Vasserman, I. B. 183
Vaughn, G. D. 1522
Veith, R. 3044
Velasquez, G. 2110
Vengrov, R. M. 3109
Verdier, A. 156, 1669
Verkooijen, H. 1148
Vernon, W. 2351, 2871
Vescherevich, V. G. 183
Vescovi, M. 961, 2970
Vetrovec, J. 2730, 2742
Vetter, A. M. 1051
Veyssière, A. 2393
Viccaro, P. J. 1088, 1091
Vignola, G. 68, 961, 2850
Višnjic, V. 1701
Vjalov, G. N. 2984
Vlieks, A. E. 760, 798
Vobly, P. D. 183
Voelker, F. 687, 819
Voevodin, V. P. 1356
Volin, S. P. 1902, 2823
Volk, G. J. 2706
von Przewoski, B. 2506
von Reden, K. F. 878
Vormann, H. 3041
Vorobiev, S. A. 177
Vos, L. 1186
Voss, J. 769, 926, 1243, 2278, 2369, 2688
Vouillot, J. M. 1160
Voy, D. 1758
Vuaridel, B. 2506

Vylov, T. D. 195

W

Wachtel, J. 1326
Wadlinger, E. A. 607, 3017
Wagner, J. S. 3126
Wagner, R. 1767
Wagner, S. 834
Wait, G. D. 964, 967, 1531, 2883
Wake, D. 3120, 3123
Wake, M. 2173, 2179, 2185, 2191
Walbridge, D. G. 2134, 2477
Waldner, O. A. 2613
Walker, J. D. 2029
Walker, N. 2500
Walker, Q. 65
Walker, R. P. 2712
Wall, D. 1981
Walling, L. 1020, 2958, 2961
Walling, L. S. 643
Walther, S. R. 2088
Wanderer, P. 42, 2164, 2167, 2239
Wanderer, P. J. 2242, 2245
Wang, D. 769
Wang, D. F. 2688
Wang, D. X. 1818
Wang, D. Y. 1261, 2727
Wang, F. 985
Wang, G. 2396
Wang, H. 2444, 3038
Wang, J. 2706
Wang, J. G. 1818, 1821
Wang, J. M. 1107, 1326, 1794
Wang, J. W. 431, 3219
Wang, L. 2396
Wang, M. H. 2667, 2670, 2697
Wang, T. 1896
Wang, T.-S. 377, 1893
Wang, T.-S. F. 491
Wang, X. J. 604
Wang, X. Q. 1174, 1180, 1746, 1749
Wang, Y. 2020
Wangler, T. 251
Wangler, T. P. 330, 3056
Ward, T. E. 1695
Warkentien, R. 1347
Warnock, R. L. 1591, 1654, 1824
Wartski, L. 1534
Watanabe, K. 2298
Waters, G. 964, 1531
Watson, J. 572, 2993
Watson, J. A. 3097
Watson, J. M. 1993
Weaver, J. 996, 2688
Weaver, J. N. 769, 976, 1243
Wedekind, M. 1922
Wehrle, B. 2295
Wehrle, R. B. 29
Wei, J. 1866, 1869
Weichold, M. H. 725
Weidman, D. J. 239, 3141
Weihreter, E. 2685
Weinert, A. 1362
Weingarten, W. 1023
Weintraub, B. L. 2137
Weissenburger, D. W. 2188
Welch, D. 3129
Welch, J. 467
Welch, J. J. 792, 1851, 2838
Welch, K. M. 2269
Wells, F. D. 1136, 1139
Wells, J. 3126
Wells, R. P. 1955
Weng, W. T. 52, 839, 1585
Wenzel, J. 1543
Werkema, S. 108
Wermelskirchen, C. 1151, 1383, 1476, 2688
West, C. 1290
Westenskow, G. 646, 766, 1335
White, G. R. 1540
White, W. P. 3171
Whitehead, H. 2381
Whitney, R. 3264
Wiedemann, H. 769, 976, 1104 1243, 2278, 2369, 2688, 272
Wienands, U. 62, 357, 2829
Wiik, B. 2910
Wiik, B. H. 2905
Wildman, D. 410
Wilks, S. C. 564
Wille, K. 1154, 2859
Willeke, F. 135, 2483, 2910
Willen, E. 2164, 2167, 2239, 2242, 2245
Williams, D. J. 2832
Williams, R. 619
Williams, T. 1848
Wills, J. S. C. 842
Wilson, E. J. N. 171
Wilson, I. 2070, 3237
Wilson, M. 863
Wilson, M. A. D. 71
Wilson, N. 2322
Wilson, N. G. 2459
Wilson, P. 1806
Wilson, P. B. 652
Winick, H. 1410, 2748
Winn, D. R. 1981, 2874
Winters, M. 2173
Wirsbinski, J. 210, 2778
Wiseman, M. 2381
Witkover, R. 839, 1428
Witkover, R. L. 1189, 1231, 1264, 1267, 1347
Wolf, B. 2981
Wolf, B. H. 1943
Wolff, D. 93
Wolff, S. 857
Won, S. 575, 1368
Wong, R. 2310
Woodle, M. 2724
Woodley, M. 1845
Woodley, M. D. 2098
Woolfe, K. 745
Wootton, P. 1359
Worden, J. 1133
Wright, D. 2284
Wright, E. L. 798
Wright, P. 1046
Wrulich, A. 2634
Wu, G. 1458
Wu, X. 62
Wu, Y. 180, 2366
Wurtele, J. 1791
Wurtele, J. S. 2026
Wüstefeld, G. 266
Wyss, C. 150

X

Xi, X. 1878
Xiao, M. 2616
Xie, J. 1323, 2017, 2020
Xie, W. 1410
Xie, Z. 2796
Xiu, L. 2008
Xu, J. 1422
Xu, Z. X. 1851

Y

Yakimenko, V. 269
Yakovlev, V. P. 3002, 3186
Yamada, R. 2131
Yamada, T. 2694
Yamamoto, A. 2402
Yamamoto, H. 2251
Yamamoto, M. Y. 2990
Yamamoto, N. 2058, 3213, 3216
Yamamoto, S. 2694
Yan, S. 2616
Yan, Y. T. 333, 336, 339, 342, 345, 360, 1663
Yang, F. 2616
Yang, J. 1151, 1383, 1476, 2688
Yang, K. M. 2542
Yang, Z. 2616
Yao, R. L. 2578
Yarba, V. A. 2913
Yazunin, I. A. 177
Yazynin, I. A. 625
Ye, W. 1174
Yen, S. 1481
Yeremian, A. D. 1964
Yeung, K. S. 783, 1332
Yin, Y. 1133, 1243, 1722
Yokouchi, S. 2298
Yokoya, K. 506, 3252
Yoon, M. 428, 2673, 2700
York, R. 363
York, R. C. 62, 383, 443, 446
York, R. L. 1928, 1931
Yoshida, M. 757, 1034
Yoshida, Y. 622
Yoshii, M. 165
Yoshioka, M. 2032
Yoshiyuki, K. 707
Yoshizawa, J. 875
Yoshizawa, M. 875
Yotam, R. 1028, 1410, 2688
Young, A. 672
Young, A. T. 1916, 1993
Young, C. 1734
Young, L. 572
Young, L. M. 1884, 2754
Young, P. E. 2586
Younger, F. C. 2727
Youngman, B. 769, 976, 1243, 2688
Yu, D. 813, 1335, 1716, 1719
Yu, J. 2616

Yu, L. H. 2542
Yu, S. 1335
Yu, S. S. 260, 2592, 2595
Yu, W. 725
Yu, X. T. 1791
Yu, Y. 2480
Yuan, J. 2616
Yuan, V. 3017
Yuan, V. W. 1171, 2529
Yue, W. K. 725
Yugami, N. 622
Yu, V. 1961
Yunn, B. 2745
Yunn, B. C. 1785
Yurkon, J. 1163

Z

Zach, M. 810
Zacharian, A. G. 2146
Zagel, J. 1174
Zaharatos, R. M. 1026
Zaltsman, A. 1320
Zangrando, D. 2712
Zapalac, G. H. 2029
Zapasek, R. 2266
Zaplatin, E. N. 1017
Zapol'sky, V. N. 192
Zapryagaev, I. A. 3186
Zbasnik, J. 2206
Zeigler, J. 2221
Zeitlin, C. 834, 2152
Zelenskiki, A. N. 2984
Zelepoukin, S. A. 1356
Zeller, A. F. 884
Zhang, B. 2396, 2399
Zhang, P. 90, 93
Zhang, R. 1323, 2020, 2616
Zhang, S. Y. 940, 999, 1005
Zhang, W. 940, 999, 1216, 1273
Zhang, X. 2676
Zhang, Z. 2616
Zhao, Z. 2396
Zhefu, Z. 2757
Zheng, H. 2480
Zholents, A. A. 2342, 2835
Zhou, J. 207
Zhou, P. 1776, 1779
Zhou, X.-H. 2805
Zhou, Y. 1371
Ziemann, V. 201, 416, 2067, 2152, 3249
Zimmermann, F. 2483
Zinin, E. I. 183
Zinkann, G. P. 2987
Ziomek, C. D. 1329
Zisman, M. S. 1, 84
Zitvogel, E. 1264, 1267
Zolfaghari, A. 601, 716, 1791
Zotter, B. 488, 491, 3228
Zu, D. 2423
Zucker, M. 1695
Zucker, M. S. 1270
Zumbro, J. D. 634, 2125, 2348
Zuo, K. 2328, 2369, 2688
Zverev, B. V. 2613
Zyarylkapov, S. Z. 3067, 3067